CODEN: JASMAN

The Journal of the Acoustical Society of America

ISSN: 0001-4966

Vol. 123, No. 4 April 2008

(Continued)

CONTENTS—*Continued from preceding page*

(Continued)

CONTENTS—*Continued from preceding page*

(Continued)

CONTENTS—*Continued from preceding page*

(Continued)

Tissue mimicking materials for dental ultrasound

Rahul S. Singh, Martin O. Culjat, and Warren S. Grundfest
Center for Advanced Surgical and Interventional Technology (CASIT), University of California at Los Angeles, Los Angeles, California 90095
rst@ece.ucsb.edu, mculjat@mednet.ucla.edu, warrenbe@seas.ucla.edu

Elliott R. Brown
Department of Electrical and Computer Engineering, University of California at Santa Barbara, Santa Barbara, California 93106
erbrown@ece.ucsb.edu

Shane N. White
School of Dentistry, University of California at Los Angeles, Los Angeles, California 90095
snwhite@ucla.edu

Abstract: While acoustic tissue mimicking materials have been explored for a variety of soft and hard biological tissues, no dental hard tissue mimicking materials have been characterized. Tooth phantoms are necessary to better understand acoustic phenomenology within the tooth environment and to accelerate the advancement of dental ultrasound imaging systems. In this study, soda lime glass and dental composite were explored as surrogates for human enamel and dentin, respectively, in terms of compressional velocity, attenuation, and acoustic impedance. The results suggest that a tooth phantom consisting of glass and composite can effectively mimic the acoustic behavior of a natural human tooth.

© 2008 Acoustical Society of America
PACS numbers: 43.20.Hq, 43.35.Cg, 43.80.Ev [AN]
Date Received: October 12, 2007 **Date Accepted:** January 11, 2008

1. Introduction

Ultrasound is well suited for dental imaging due to its ability to penetrate hard tissues and metal restorations, its ability to provide depth information, its excellent range resolution, and its lack of ionizing radiation. Ultrasound has previously been investigated as a complement to dental radiography as a tool to detect caries, fractures, and debonded restorations.[1–4] However, progress in dental ultrasound has been limited by a number of factors. The high acoustic impedances of dental tissues result in surface losses that limit the use of commercially available medical transducers and acoustic scanning gels since these are not acoustically matched to teeth. Transducers used in nondestructive testing (NDT) are typically matched to low impedance liquids such as water or oil, and dry coupling is not feasible for rounded, jagged tooth surfaces.[5] In addition to coupling difficulties, acoustic scattering arises in teeth due to their complex microstructure and irregular macrostructure. High compressional velocities of hard dental tissues require short acoustic pulses and narrow acoustic radiation patterns. Finally, the small dimensions of teeth and limited space between teeth necessitate accurate transducer positioning and complicate imaging near proximal surfaces. Together, these challenges prohibit the use of commercial ultrasound transducers for clinical dental use, including medical transducers, NDT transducers, acoustic microscopes, and immersion hydrophones.

Customized ultrasound transducers and systems must be designed specifically for teeth if dental ultrasound is to advance to clinical use. A critical step toward realization of clinical ultrasound systems is the development of effective tooth phantoms. Tooth phantoms can enable ultrasound system testing and calibration on tooth-like targets with known acoustic properties, dimensions, surfaces geometries, and internal features. System performance, system limitations, and physical constraints related to dental imaging can then be studied experimentally. This also allows ultrasound systems to be developed incrementally on models of in-

creasing complexity, rather than on extracted teeth with high variability and unknown acoustical cross sections. Finally, phantoms can more easily be modeled in acoustic simulations of dental ultrasound systems, allowing accurate comparison between virtual and experimental data.

Physical models have previously been used to simulate soft tissues and bones for medical ultrasonography.[6,7] However, the acoustic properties of these models are not well suited for hard tissue dental ultrasonography. Hard dental tissues, enamel and dentin, differ greatly not only from soft tissues, but also from all other mammalian hard tissues. Dentin, the inner structural material of a tooth, is a complex composite consisting of a highly organized, mineralized collagenous matrix.[8] Unlike bone, dentin is organized around subparallel cellular extensions, or odontoblastic processes, that create tubules of micron-scale width and millimeter-scale length, and are organized in an oblique radial macropattern. Enamel, the hard outer tooth surface, is a very dense fibrous ceramic composite that forms a partly interrupted continuous matrix with nano-, micro-, and macroscale organizations.[9]

Initial studies suggested that among a variety of glasses, ceramics, and metals, soda lime glass might be the closest acoustic match to enamel.[10] Preliminary studies of a variety of dental cements, epoxies, and plastics for use as dentin surrogates found that cements and epoxies possessed high attenuation, and plastics were too low in acoustic impedance. Dental resin-based composites appeared to be reasonable candidates for dentin surrogates. An additional benefit to the use of dental composites is their ability to be molded into many shapes with various internal features that mimic those of dentin. In a previous study, a tooth phantom was fabricated using soda lime glass and dental composite to test the feasibility of crack detection with a custom dental ultrasound system.[2] However, the phantom materials were not thoroughly characterized or compared to their natural tissue counterparts. The purpose of this study was to compare the acoustic properties of soda lime glass and dental composite to natural enamel and dentin, respectively, in terms of compressional velocity, attenuation, and acoustic impedance.

2. Materials and methods

2.1 Tooth phantom material preparation

Twelve specimens of resin-based dental composite (Build-It™, Pentron Corp., Wallingford, CT) ranging in thickness from 1.00 to 3.05 mm were used to mimic dentin. Six soda lime glass samples (McMaster-Carr Supply Co., Santa Fe Springs, CA) ranging between 0.96 and 6.43 mm were used to physically model enamel. The resin-based composite was selected because it self-cures uniformly upon extrusion from its mixing gun. Unlike light-cured dental composites, its curing does not vary with depth or proximity to a light curing wand. Additionally, large tooth-sized monolithic specimens can be quickly and uniformly fabricated. The top and bottom surfaces were formed by closing a peripheral mold with glass microscope slides to ensure flat parallel surfaces. The thickness of each specimen was measured using calipers (Mitutoyo Corp., Kawasaki, Kanawaga, Japan) with an accuracy of ±0.01 mm.

2.2 Natural tooth types and preparation

Nineteen extracted teeth were sectioned into 22 different slices in cross-sectional and longitudinal planes. The teeth were kept moist in water at all times and disinfected using thymol. Six mesial, six buccal, and ten occlusal sections were used. Sections were taken from seven first molars, seven second molars, four premolars, and one canine. The extracted teeth were cut into paralleled specimens between 0.67 and 3.28 mm in thickness using a slow-speed saw with a narrow diamond impregnated blade. The thickness of each section was measured using the calipers. The teeth were routinely extracted due to preexisting pathology, discarded, stored in a solution of thymol, used for dental operative teaching purposes, again discarded, archived, and then used for this study. Because they were preexisting archived material, without any identifying links to the donors, they were exempt from Institutional Review Board approval.

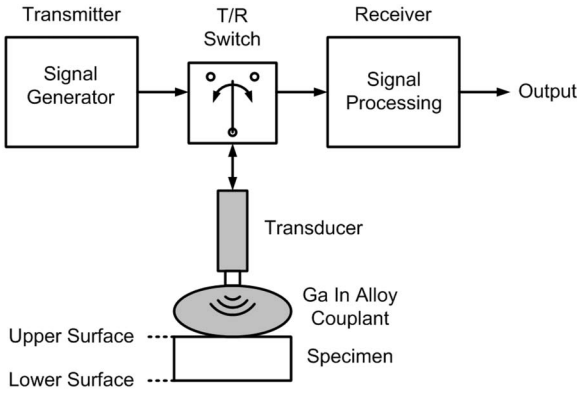

Fig. 1. Monostatic pulse-echo ultrasound setup with transducer coupled to specimen using gallium indium alloy.

2.3 Measurement of acoustic properties

A custom ultrasound imaging system, originally designed to detect cracks within teeth, was used to measure compressional velocity and attenuation (Fig. 1). This system features a PLZT (lanthanum-doped lead zirconate titanate) piezoelectric single-element thickness-mode transducer, a high-impedance gallium-indium alloy acoustic couplant, and custom signal processing and transmit/receive electronics.[2] The transducer had a 19 MHz center frequency, 6 MHz bandwidth, and 8° 3 dB full beam width. A Plexiglas™ jig was designed with a three-axis translation stage (±0.1 mm accuracy), a goniometer (±0.1° accuracy), and a two-axis tilt stage to allow the transducer to be precisely maneuvered relative to the dental hard tissue and phantom specimens. The specimens were mounted with wax on a stainless steel ring to provide an air backing, thereby maximizing reflected echo strength.

Monostatic pulse-echo time-of-flight measurements were taken on the specimens using pulsed-cw, 250 ns wide pulses centered at 19 MHz. An oscilloscope was used to measure the round-trip time Δt through a given thickness of a specimen, from which the velocity c through each specimen was then calculated. The pulse-echo scans were made at multiple points on the natural enamel and dentin specimens; 84 dentin and 53 enamel points were measured in total on 19 dentin and 11 enamel specimens. Points were arbitrarily selected on each natural specimen, but separated by at least 2 mm in distance to ensure measurement independence, since the acoustic spot size of the system is 210 μm at a range of 1.5 cm through the couplant. Because tooth structure is known to have considerable local variation in mechanical properties with respect to the measurement plane,[9] separate means and standard deviations were calculated for longitudinal and cross-sectional specimens. Due to the known microscale variability of tooth structure, data points on the natural enamel and dentin specimens were treated as being independent. A total of 30 arbitrarily selected measurements were made on the 12 composite specimens, and six arbitrarily selected measurements were made on three glass specimens. Only three glass specimens were measured due to the low observed variability.

The acoustic impedances of the specimens were calculated as the product of c and the density ρ; however, due to intrinsic density variations in dentin and enamel, it was not possible to measure ρ at each individual measurement point. Density was estimated from previous studies,[10] thus providing an approximation of the acoustic impedance for analytic purposes.

The attenuation coefficient A can be determined for liquids and low attenuation materials by through-transmission techniques.[6] However, through-transmission measurements are difficult at high frequencies in dense solids with moderate to high loss. Therefore A was estimated using a pulse-echo reflection method, by recording echo strength from the rear interface in specimens of dentin, composite, and glass of varying thickness. The reflected power from each sample was plotted as a function of sample thickness, and A was calculated from the slope

Table 1. Acoustic properties.

Material	Compressional velocity (m/s)		Number of measurements	Density (kg/m^3)	Acoustic impedance (MRa)	Attenuation (dB/cm)	Number of measurements
	Mean	s.d.					
Enamel	5219	597	53	2940	15.3	…	…
Longitudinal	5227	645	36	…	…	…	…
Cross-sectional	5202	499	17	…	…	…	…
Glass (soda lime)	5789	94	6	2240	13.0	6	10
Dentin	3647	434	84	2140	7.8	86	22
Longitudinal	3523	250	48	…	…	…	…
Cross-sectional	3813	560	36	…	…	…	…
Dental composite	3306	311	24	2090	6.9	108	10

of the linear fit. Loss by diffraction of the acoustic beam during propagation was assumed to be negligible due to the thin sample sizes in relation to the transducer aperture (1.275 mm), and reflective boundary losses were assumed to be constant for each material tested. Errors due to alignment were minimized due to careful alignment with the goniometer (±0.1° accuracy).

A total of 22 attenuation measurements were taken from eight dentin slices ranging in thickness between 0.67 and 3.28 mm, and 10 measurements were taken from four composite sections ranging in thickness from 1.00 to 3.05 mm. These specimens were selected due to their parallelism, minimizing errors in echo strength measurements. Both longitudinal and cross-sectional dentin slices were used. Ten attenuation measurements were taken from three glass samples ranging in thickness between 0.96 and 6.43 mm. The attenuation of human enamel could not be quantified accurately due to the difficulty in obtaining flat samples greater than 1 mm in thickness; human enamel is typically ~1 mm thick.

3. Results and discussion

The experimental results are summarized in Table 1. The mean compressional velocity of dental composite is within 2.3% of the mean compressional velocity of natural dentin. Soda lime glass had a higher mean velocity than natural enamel, but the mean enamel velocity was within 1 s.d. (assuming a Gaussian or normal distribution) of the mean glass velocity (Table 1). Soda lime glass and dental composite exhibited less overall variability than their natural analogues.

Substantial variation in compressional velocity was observed among and within individual specimens of dentin and enamel. This is consistent with prior studies, and is likely due to the variation in density and elastic modulus both within and among the samples.[1,8,11] A t-test revealed that there was a negligible statistical difference between longitudinal and cross-sectional samples of enamel ($P=0.44$); however, the difference between longitudinal and cross-sectional samples of dentin was significant ($P=0.003$). Others have reported dependence of velocity on occluso-apical depth in longitudinal specimens of dentin.[1,11] Possible explanations for the variations observed in the natural tooth specimens include variation in enamel rod and dentinal tubule orientation in each specimen, enamel irregularities including enamel lamellae and enamel tufts, localized differences in mineralization, and error in thickness measurement.

Variation among the dental composite specimens was less than that within natural dentin, but was considerably more than for soda lime glass. Although care was taken to produce consistent composite specimens, their curing may not have been identical. Variation within individual composite specimens was negligible.

The estimated average acoustic impedances for each material are provided in Table 1. Taking these values, the dentino-enamel junction of a tooth would have an average pressure reflection coefficient of $\Gamma=0.32$, and the composite–glass interface of a tissue mimicking phan-

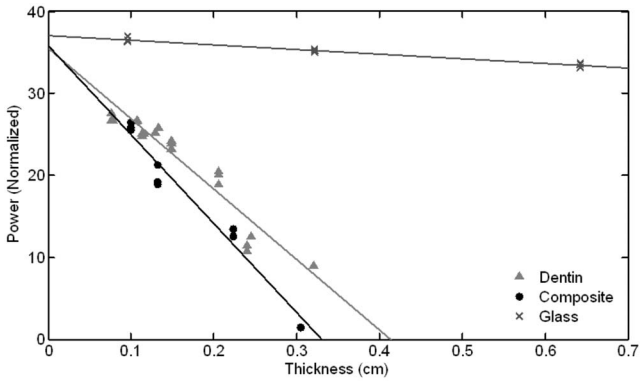

Fig. 2. Reflected acoustic power at 19 MHz through samples of dentin, composite, and glass. The attenuation coefficients of dentin, composite, and glass were 86, 108, and 6 dB/cm, respectively.

tom would have an average pressure reflection coefficient of $\Gamma = 0.31$. Therefore, the acoustic pressure transmitted through both interfaces, with similar geometries, would be expected to be nearly identical.

Attenuation is compared for dentin and composite by measuring echo power as a function of thickness (Fig. 2). Linear least-squares fitting of the data revealed that dentin had an attenuation coefficient of 86 dB/cm ($R^2 = 0.90$) and composite had an attenuation coefficient of 108 dB/cm ($R^2 = 0.96$) at 19 MHz. Dental composite contains a multitude of glassy filler particles within a resin matrix. These micron-scale filler particles are of varying size, of irregular shapes, and are randomly orientated. Their significant size in relation to the acoustic wavelength ($\lambda \approx 175\ \mu$m) increases scattering and results in a relatively high attenuation, comparable to that of mineralized dentin. Composite was assumed to be isotropic due to the random particle orientation; dentin has an organized tubular structure, but was considered isotropic in the attenuation measurements since longitudinal and cross-sectional measurements were averaged. The measured attenuation coefficient for dentin matches closely with a previously reported value of 80 dB/cm at 18 MHz.[12]

Soda lime glass had an attenuation of 6 dB/cm at 19 MHz, calculated from the slope of the linear least-squares fit ($R^2 = 0.98$). In these and prior studies, human enamel was observed to have low acoustic losses, comparable to those of glass. The attenuation of enamel was not measured quantitatively due to the difficulty in obtaining thick samples (>1 mm) and large resulting measurement errors. Enamel is expected to have a slightly higher attenuation than glass due to its fibrous microstructure and associated internal scattering. Acoustic losses were observed to be greater in dentin than in enamel; this is expected since enamel has a higher density and homogeneity. This is contrary to a previous study that reported the attenuation coefficient of enamel (120 dB/cm at 18 MHz) to be higher than that of dentin (80 dB/cm at 18 MHz) at 18 MHz;[12] however, the authors also conceded that their enamel measurement may have been off by an order of magnitude.

4. Conclusion

The measured compressional velocity was 3647 ± 434 m/s in dentin, 3306 ± 311 m/s in composite, 5219 ± 597 m/s in enamel, and 5789 ± 94 m/s in glass. Both glass and composite had lower velocity variation than enamel and dentin. Both composite (6.9 MRa) and dentin (7.8 MRa) and glass (13.0 MRa) and enamel (15.3 MRa) were closely matched in acoustic impedance. The attenuation coefficient of composite (108 dB/cm) was slightly higher than dentin (86 dB/cm) at 19 MHz, and the observed attenuation of both glass and enamel were low.

The results suggest that tooth phantoms consisting of soda lime glass and resin-based dental composite can effectively be used to mimic the acoustic behavior of natural human teeth.

Acknowledgments

The authors would like to thank Dr. Douglas Yoon for his early contributions to phantom and system development, Dr. Ratnakar Neurgaonkar for his piezoelectric materials expertise, and Dr. Jason Cho for his assistance in specimen preparation. The authors most gratefully appreciate partial funding provided for this work by the Telemedicine and Advanced Technology Research Center (TATRC)/Department of Defense under Award Nos. W81XWH-07–1–0672 and W81XWH-07–1–0668 and the National Institute of Health/National Institute for Dental and Craniofacial Research under Award No. DE14189.

References and links

[1]S. Lees and F. R. Rollins, "Anisotropy in hard dental tissues," J. Biomech. **5**, 557–566 (1972).
[2]M. O. Culjat, R. S. Singh, E. R. Brown, R. R. Neurgaonkar, D. C. Yoon, and S. N. White, "Ultrasonic crack detection in a simulated human tooth," Dentomaxillofac Radiol. **34**, 80–85 (2005).
[3]M. Culjat, M. R. S. Singh, D. C. Yoon, and E. R. Brown, "Imaging of human tooth enamel using ultrasound," IEEE Trans. Med. Imaging **22**, 526–529 (2003).
[4]R. S. Singh, M. O. Culjat, J. C. Cho, R. R. Neurgaonkar, D. C. Yoon, W. S. Grundfest, E. R. Brown, and S. N. White, "Penetration of radiopaque dental restorative materials using a novel ultrasound imaging system," Am. J. Dent. **20**, 221–226 (2007).
[5]J. Szilard, *Ultrasonic Testing: Non-Conventional Testing Techniques* (Wiley, Chinchester, UK, 1982).
[6]E. L. Madsen, J. A. Zagzebski, and G. R. Frank, "Oil-in-gelatin dispersions for use as ultrasonically tissue-mimicking materials," Ultrasound Med. Biol. **8**, 277–287 (1982).
[7]A. J. Clarke, J. A. Evans, J. G. Truscott, R. Milner, and M. A. Smith, "A phantom for quantitative ultrasound of trabecular bone," Phys. Med. Biol. **39**, 677–1687 (1994).
[8]J. H. Kinney, J. R. Gladden, G. W. Marshall, S. J. Marshall, J. H. So, and J. D. Maynard, "Resonant ultrasound spectroscopy measurements of the elastic constants of human dentin," J. Biomech. **37**, 437–441 (2004).
[9]S. N. White, W. Luo, M. L. Paine, H. Fong, M. Sarikaya, and M. L. Snead, "Biological organization of hydroxyapatite crystallites into a fibrous continuum toughens and controls anisotropy in human enamel," J. Dent. Res. **80**, 321–326 (2001).
[10]M. O. Culjat, "Development of an ultrasound imaging system for the detection of subsurface fractures and caries in human teeth," Ph.D. dissertation, University of California, Los Angeles, 2005.
[11]C. John, "The corono-apically varying ultrasonic velocity in human hard dental tissue," J. Acoust. Soc. Am. **116**, 545–556 (2004).
[12]G. Kossoff and C. J. Sharpe, "Examination of the contents of the pulp cavity in teeth," Ultrasonics **4**, 77–83 (1966).

The effect of stimulus range on two-interval frequency discrimination

William J. Matthews and Neil Stewart
Department of Psychology, University of Warwick, Coventry CV4 7AL, United Kingdom
w.j.matthews@warwick.ac.uk, neil.stewart@warwick.ac.uk

Abstract: It has traditionally been thought that performance in two-interval frequency discrimination tasks decreases as the range over which the standard tone varies is increased. Recent empirical evidence and a reexamination of previous results suggest that this may not be the case. The present experiment found that performance was significantly better when the standard roved over a wide range (1500 Hz) than a narrow range (30 Hz). This pattern cannot readily be accommodated by traditional models of frequency discrimination based on memory or attention, but may be explicable in terms of neural plasticity and the formation of perceptual anchors.

© 2008 Acoustical Society of America
PACS numbers: 43.66.Fe [QJF]
Date Received: November 30, 2007 **Date Accepted:** January 14, 2008

1. Introduction

In two-interval frequency discrimination experiments the participant is required to discriminate a temporally ordered pair of tones (e.g., a standard tone followed by a comparison tone) which differ only in frequency. It is well established that performance in such tasks is better with a fixed standard stimulus than when the standard roves over a range of frequencies from trial to trial (e.g., Harris, 1952). Note that here, and throughout this letter, we use "roving standard" to mean that on each trial a standard was selected from among a fixed number of unchanging frequencies, spread across a particular range. This is distinct from the use of a roving standard whose frequency is a random number sampled from a uniform distribution. As we discuss later, this distinction may be very important.

It is not clear how frequency discrimination is influenced by the range over which the standard roves (see Amitay *et al.*, 2005; Jesteadt and Bilger, 1974), although there are a number of reasons for expecting an increase in range to impair frequency discrimination. Studies of intensity perception have established that when the range over which the standard varies is increased, discrimination performance declines (Berliner and Durlach, 1973; Berliner *et al.*, 1977; Jesteadt and Bilger, 1974). It might reasonably be expected that frequency discrimination will follow the same pattern. Furthermore, several theoretical models of frequency discrimination, some emphasizing memory processes and others emphasizing auditory attention, predict that increases in stimulus range will reduce discrimination accuracy.

Perhaps the most well-known account of discrimination performance to emphasize the importance of memory processes is the theory of intensity perception developed by Durlach and Braida (1969). According to this model, performance depends on the use of two distinct memory modes. In the *sensory trace* mode, the participant attempts to maintain a trace of the standard tone and compares the comparison tone with this memory. In the *context coding* mode, the participant judges the comparison tone with respect to the general context of sounds in the experiment. The amount of noise in the trace mode depends upon the temporal interval between the standard and comparison tones; the noise in the context coding mode depends upon the range of stimuli presented. Thus, for a fixed temporal interval between standard and comparison tones, discrimination performance is predicted to be worse with a roving standard. Moreover, performance is predicted to decline as the range over which the standard varies is increased. Studies of two-interval intensity discrimination have provided support for this model (Berliner

and Durlach, 1973; Berliner *et al.*, 1977) and it has been argued that the model also applies to frequency discrimination (Jesteadt and Bilger, 1974).

Theories of frequency discrimination which emphasize auditory attention also predict that performance should be better when the standard roves over a narrower range of frequencies. When the participant is presented with the same standard on every trial, he or she can focus attention on a narrow frequency region. When the standard varies, the participant may either broaden his or her attentional band to cover a wider range of frequencies (e.g., Botte, 1995), or attempt to monitor more than one band, ignoring frequencies which fall in between (e.g., Macmillan and Schwartz, 1975). If the participant adopts the former strategy, performance will decrease as the range of frequencies increases because as the attentional band is broadened, resolution is diminished. If the participant instead elects to attend to two or more attentional bands simultaneously then the situation is more complicated and performance will depend on the precise placement and width of the bands, but will generally deteriorate as the number of bands and the distance between them increases.

Despite the prediction from both memory- and attention-oriented accounts of frequency perception that performance should be inversely related to stimulus range, there is relatively little evidence from two-interval discrimination tasks against which to test this prediction. In an assessment of the applicability of Durlach and Braida's (1969) theory of intensity perception to frequency discrimination, Jesteadt and Bilger (1974) examined the effect of stimulus range on frequency discrimination performance in two-interval forced choice and same–different tasks. In the fixed standard condition of their experiment, the same 1000 Hz tone was used as the standard on all trials; in the *jittered* condition, the standard varied over a relatively narrow range of frequencies (980, 990, 1000, 1010, 1020 Hz); in the *roving* condition, the range of standards was much wider (795, 890, 1000, 1120, and 1260 Hz). Jesteadt and Bilger reported that, as for intensity discrimination, frequency discrimination declined as the range over which the standards varied increased, and argued that Durlach and Braida's (1969) theory of intensity perception applies to frequency perception, too. Since Jesteadt and Bilger's work, it has generally been accepted that frequency discrimination is better when the standard roves over a narrow range than when it varies over a more disparate set of frequencies—perhaps partly because of the strong theoretical reasons for expecting this result. However, closer examination suggests that their data do not convincingly demonstrate worsening frequency discrimination when the range over which the standards varies is increased. Jesteadt and Bilger did not use inferential statistics to compare the performance in different conditions, and an examination of the qualitative pattern of their results reveals that, of their four participants, one showed uniformly poor performance while for the remaining three the ordering of performance in the jittered and roving conditions was not consistent between subjects within each task, or within subjects across tasks.

In a more recent study, Amitay *et al.* (2005) also examined the influence of stimulus range on two-interval frequency discrimination. They employed three conditions: fixed (1000 Hz) standard; *roving* standard, where standard frequencies ranged from 900 to 1100 Hz; and *wide roving* standard, where the standard varied from 570 to 2150 Hz. Amitay *et al.* examined the difference limen (or just noticeable difference) averaged across all stimuli in a condition. Difference limens were smallest for the fixed standard and, of interest here, difference limens were smaller (i.e., performance was better) for the wide roving standard than the (narrower) roving standard condition. Amitay *et al.* interpreted this result in terms of attentional bands by suggesting that in their wide-roving condition participants monitored several frequency bands and used the presentation of the standard tone as a cue to attend to the appropriate listening band, but that in their narrow-roving condition the frequencies may have been too close together to permit this strategy. Instead, the narrow-roving standard led participants to use a single, widened band with a subsequent loss of resolution. Amitay *et al.* further suggest that in Jesteadt and Bilger's (1974) study the jittered frequencies varied over a sufficiently narrow range (40 Hz) that the attentional band did not need to be broadened by much, whereas in their roving condition the range necessitated substantial broadening, resulting in poorer resolution.

The finding of Amitay *et al.* (2005) that discrimination was better when the standard roves over an intermediate range (200 Hz) than a wide range (1580 Hz) suggests that frequency discrimination is not always improved by widening the stimulus range. However, the attentional framework they adopt to explain this result predicts that using a narrow range of standards (i.e., a few tens of hertz) will lead to performance which is better than when a wide range (i.e., several hundred hertz) is used. Thus their attentional model, along with traditional attentional and memory models and the more general *prima facie* argument that frequency perception will be like intensity perception, predicts that frequency discrimination will be better when the stimulus range is narrow. If, on the other hand, the empirical result reported by Amitay *et al.* is indicative of a more general pattern of worsening discrimination as the stimulus range is reduced, performance will be better with wide-ranging standards, and alternative theoretical accounts will need to be developed. The current experiment directly addresses this issue.

2. Methods

On each trial, the participant heard a standard tone followed by a comparison tone which was either the same as the standard or fractionally lower, and made a same–different judgment. Each participant completed three conditions: a fixed standard condition, a narrow roving condition, in which the standard ranged over 30 Hz, and a wide roving condition, in which the standard ranged over 1500 Hz. In all three conditions, a 1000 Hz tone was used as the middle standard, allowing us to examine the effect of stimulus range on discrimination at a particular frequency. This approach seems preferable to averaging over the different standards used in each condition (Amitay *et al.*, 2005) because it separates the effect of stimulus range from the specific frequencies employed. This might be important if, for example, there were a departure from Weber's law so that sensitivity depended upon stimulus level (e.g., Berliner and Durlach, 1973).

2.1 Participants

Nine participants with experience of auditory psychophysical experiments took part; eight were paid £30 for participating, the other was author W.M.

2.2 Stimuli

All tones had a total duration of 1000 ms and were gated on and off with 50 ms cosinusoidal ramps at beginning and end. They were generated at a sampling rate of 44.1 kHz and played diotically over Sennheiser eH2270 and HD265 headphones at approximately 80 dB. In the single standard (SS) condition, the standard was a 1000 Hz tone. In the wide-roving condition (WR), three standards were used with frequencies of 500, 1000, and 2000 Hz (i.e., the frequency of each standard was a factor of 2.0 greater than the previous one so that they were evenly spaced on a logarithmic scale). In the narrow roving (NR) condition, the standard tones had frequencies of 985.2, 1000, and 1015 Hz (i.e., separated by a factor of 1.015). The difference between the standard and comparison tones, Δf, varied from 0.3% to 1.0% for different subjects; the difficulty was selected based upon their previous performance in frequency discrimination tasks and was intended to match approximate overall performance levels across participants.

2.3 Design and procedure

Each participant completed seven sessions, one in condition SS and three in WR and NR. Each session consisted of 4 blocks of 60 trials. The three NR sessions were grouped together, as were the three WR sessions, giving a total of six possible condition orders. Participants completed the sessions over the course of a few days, sometimes completing two or more sessions back to back with a short rest between. Trials from the first block of each session were treated as warm-up and excluded from the analyses. On each trial participants heard the standard tone. After a 1 s interval they heard the comparison tone and were asked to indicate whether it was the same as the standard or different, and were informed that, if different, the second tone would be slightly lower. They were provided with on-screen feedback about the accuracy of their re-

Table 1. Experimental results

Participant	Δf (%)	d'_{ss}	d'_{NR}	d'_{WR}
1	1.0	2.13	1.01	1.56
2	0.6	2.94	0.57	1.12
3	0.5	2.67	1.68	2.56
4	0.5	4.83	1.82	3.60
5	0.5	1.89	1.31	2.00
6	0.4	2.80	1.82	1.42
7	0.3	3.57	1.35	2.77
8	0.3	2.46	1.70	3.35
9	0.3	2.94	0.80	1.91
Mean		2.91	1.34	2.25
s.d.		0.87	0.46	0.87

sponse for 1 s and there was an additional 1 s interval before the start of the next trial. The timing of stimulus presentation and response collection was controlled by DMDX [a freely available program for presenting stimuli with millisecond accuracy, Forster and Forster (2003)].

3. Results

Trials on which the participant successfully detected a difference between standard and comparison tones were denoted hits; trials on which the participant correctly identified no difference between standard and comparison tones were denoted correct rejections. The proportion of hits and correct rejections for each level of the standard tone in each condition was used to calculate d' as a measure of frequency discrimination. The results are shown in Table 1.

To examine the effects of stimulus range on discrimination at a given frequency (e.g., Harris, 1952), we compared performance in the three conditions when the 1000 Hz tone was used as the standard. [An alternative approach is to measure performance in the NR and WR conditions by averaging the d' values for the different standard tones, and to compare there averages (e.g., Jesteadt and Bilger, 1974). This approach yielded exactly the same pattern of results.] Preliminary analyses established that neither block order nor difficulty (Δf) influenced the differences among the SS, NR, and WR conditions. A repeated measures analysis of variance (ANOVA) revealed a significant effect of condition, $F(2,16)=17.7$, $\eta_p^2=0.688$, $p<0.001$. Paired samples t-tests (Bonferroni corrected) indicated a significant difference in the d' values between the SS and NR conditions [$t(8)=5.46$, $p<0.001$] and between the NR and WR conditions, $t(8)=4.71$, $p=0.004$, but not between the WR and SS conditions [$t(8)=2.35$]. Inspection of the data from individual participants revealed that, for eight of the nine tested, frequency discrimination was worse when the standard roved over a narrow range than when it roved over a wide range. Finally, a repeated measures ANOVA was used to examine the effect of condition on response bias, c. The conditions did not differ ($F<1$).

4. Discussion

The present experiment demonstrates that frequency discrimination with a roving standard is better when the range of stimuli is wide (500–2000 Hz) than narrow (985–1015 Hz). This disagrees with Jesteadt and Bilger (1974), who claimed that performance with a standard which roved over a 40 Hz range was as good as that with a single standard. However, as noted earlier, Jesteadt and Bilger's data do not convincingly demonstrate a systematic effect of stimulus range on frequency discrimination. Given the highly significant and consistent finding in the current study that frequency discrimination is better when the standard roves over a wide range (1500 Hz) than a narrow range (30 Hz), and the finding by Amitay *et al.* (2005) of better performance when the standard ranges over a wide range (1580 Hz) than an intermediate range

(200 Hz), we suggest that, contrary to what has previously been thought, roving-standard frequency discrimination is not improved by decreasing the stimulus range. This result is unexpected and hard to reconcile with a number of existing theories of frequency discrimination. In what follows we briefly discuss possible explanations for this finding.

4.1 Memory

As noted in Sec. 1, it has been suggested that Durlach and Braida's (1969) highly influential model of intensity perception may be extended to describe frequency perception. This theory asserts that, with a fixed temporal interval between tones, performance should be a decreasing function of stimulus range. The results reported here, and those of Amitay *et al.* (2005), show the opposite pattern, and it is hard to see how the concept of context-coding memory noise could be modified to accommodate our findings.

Durlach and Braida's (1969) theory is not the only memory-based model to have been applied to frequency discrimination. Other workers (e.g., Massaro, 1970) have emphasized the importance of interference and trace decay to discrimination performance, but these similarly fail to account for the current results. Siegel (1972), for example, pointed out that as the number of tones in the stimulus set increases, the length of time and the number of trials intervening since the last presentation of the current tone also increase. While this implies that increasing the number of standard tones will reduce discrimination accuracy, it does not predict any effect of increasing the *range* of the standard tones. Similarly, it is unlikely that the current results can be explained in terms of proactive interference (where the retrieval of more recently presented stimuli is impaired by memories of earlier items); evidence from Ruusuvirta (2000) suggests that in same–different tasks like the one used here proactive interference will only influence response bias, not overall accuracy.

4.2 Attention

When the standard roves over a range of frequencies, participants may employ various attentional strategies but we would typically expect performance in the wide-roving condition to be, at best, the same as in the narrow-roving condition. The current results are therefore problematic for attentional theories. As noted earlier, Amitay *et al.* (2005) have tried to explain the finding that performance is better with a wide-roving standard by suggesting that participants use a mixed strategy: In the wide-roving condition, participants monitor several bands and use the standard as a cue to direct attention to the relevant band, whereas in the narrow-roving condition participants broaden a single band to encompass all of the relevant frequencies. In the narrow-roving condition of the current experiment, the standards only covered a 30 Hz range. As Amitay *et al.* note, it seems unlikely that there would need to be much broadening of the listening band to cover this range, or that such broadening would lead to performance that is so much worse than in the wide-roving condition. Furthermore, in the current experiment both standard and comparison tones were played for a full second, long enough that one might expect the participant fully to orient attention to the standard's frequency irrespective of whether he or she is monitoring a single broadened band or several separate channels. Although it is possible that participants use a strategy like that outlined by Amitay *et al.*, the present data necessitate the assumption that even slight widening of the attentional band leads to a dramatic loss of resolution. Thus, while it is undoubtedly the case that attention is an important determinant of frequency discrimination (e.g., Demany *et al.*, 2004), it is difficult to develop a convincing attention-based explanation for the current findings.

4.3 Perceptual anchors and plasticity

Conventional memory- and attention-based models struggle to accommodate the effects of stimulus range shown in the current experiment and in the experiment of Amitay *et al.* (2005). We therefore consider an alternative theoretical orientation which emphasizes learning about the standard tones over successive trials. As some researchers have pointed out (e.g., Ahissar *et al.*, 2006), when the same standard is used on every trial, participants can form a stable trace

of that tone across trials. That is, repeated presentation of the same tone allows formation of a perceptual anchor such that the comparison tones are judged against this anchor rather than against the single presentation of the standard tone on the current trial. In the multiple standards condition the presence of other standards, and the increased number of trials between successive presentations of each, will make it harder to form a perceptual anchor for the three different standards. [Note that we use the term perceptual anchor in the sense of a stable representation of each tone built up over successive trials, as in Ahissar *et al.* (2006). In a later development of their theory of intensity perception, Durlach and Braida (Braida *et al.*, 1984) use the same term to refer to the stimuli at the edge of the range; this modified theory can no more readily accommodate the present results than can the original theory.]

As it stands, this account is similar to the memory explanation of poor discrimination performance in one-interval paradigms developed by Siegel (1972) and makes no clear prediction regarding the effect of stimulus range. However, a consideration of the possible neural mechanisms underlying anchor formation does suggest an effect of stimulus range. Each neuron in the primary auditory cortex responds to a range of frequencies, with a peak response to a specific characteristic frequency. There is a growing appreciation that this tuning is somewhat plastic (see Weinberger, 2004, for a review). For example, in conditioning studies training produces systematic changes in the frequency receptive fields (RFs) of neurons in the primary auditory cortex, such that the RF tuning shifts away from the original characteristic frequency toward the frequency of the trained tone (e.g., Bakin and Weinberger, 1990). It seems plausible that a similar process subserves the formation of long-term representations (i.e., perceptual anchors) corresponding to the standard tones used in experiments like the one reported here. That is, we suggest that anchor formation involves retuning/recruiting neurons which normally respond maximally to nearby frequencies to the standard tone's frequency. When the standards are widely spaced, the anchor formation will involve distinct populations of neurons. However, as the standards are moved closer together, there will be an increasing overlap in the neural populations used to represent each one, and a resulting decrease in the fidelity of the anchor. That is, neurons with nearby characteristic frequencies cannot be recruited because they are already being used. As Ahissar *et al.* (2006) have noted, the failure to form a perceptual anchor may markedly impair discrimination performance. Thus, we suggest that when the standards occupy a narrow range of frequencies it is harder to form a long term trace of each because the representations involve extensively overlapping neural populations, and there is a resulting loss of frequency discrimination.

One advantage of this account is that it may provide an explanation for the difference between the current results and those for intensity discrimination, where increasing the stimulus range reduces accuracy. In intensity discrimination, for quiet and moderate level stimuli, the overall level of activity within a single population of neurons must be compared. Recruitment of neurons with nearby characteristic frequencies will increase the size of the population. Whether the intensity of the standard is kept fixed, varies over a narrow range of intensities, or varies over a wide range of intensities, the increased population size should benefit discrimination performance. So, to a first approximation, recruitment should not differentially affect performance in the different conditions. However, for louder stimuli, when all of the on-frequency neurons are saturated (i.e., firing maximally), loudness information is coded in the spread of activation to off-frequency neurons (Moore and Raab, 1974). If off-frequency neurons are recruited, the population of off-frequency neurons in which the spread of excitation is found will be reduced, and should reduce discrimination performance for louder stimuli. Because the wide-range condition includes more loud stimuli than the other conditions, the wide range condition will be most affected by recruitment.

Throughout this letter we have used the term roving standard to indicate a standard selected from a fixed set of unchanging frequencies, spread across a particular range (e.g., Amitay *et al.*, 2005). An alternative way to generate roving standards is by randomly selecting frequencies from a particular range; such a condition might be termed *truly roving*. The use of truly roving standards might provide a way to test the perceptual anchor explanation outlined earlier. When the standard on each trial is a randomly selected frequency, there will presumably be no

opportunity for neural recruitment and the formation of long-term representations of each stimulus. As such, a narrow roving condition will no longer be more difficult than a wide roving condition. Indeed, with a truly roving standard performance may well be better when the stimulus range is narrow, as a wider range will require greater shifts of attention from trial to trial. A future comparison of frequency discrimination in wide-range and narrow-range conditions of an experiment with a truly roving standard may therefore provide a useful way to test the generality of the result reported here, and of the model we propose to explain that result.

5. Conclusions

The key message of the present study is that two-interval frequency discrimination is worse when the standard roves over a narrow range than a wide range. Although we have argued that this pattern is difficult to reconcile with accounts based on memory noise or attention, it may be possible to modify these theories to accommodate the current result. Similarly, our suggestion that the result may be explicable in terms of learning and plasticity may prove incorrect. In either case, the present work, in conjunction with that of Amitay *et al.* (2005), provides an important empirical finding which demands explanation.

Acknowledgments

This work was supported by ESRC Grant No. RES-000-23-1372. We thank Sygal Amitay and Karolina Kluk for helpful discussion.

References and links

Ahissar, M., Lubin, Y., Putter-Katz, H., and Banai, K. (**2006**). "Dyslexia and the failure to form a perceptual anchor," Nat. Neurosci. **9**, 1558–1564.
Amitay, S., Hawkey, D. J. C., and Moore, D. R. (**2005**). "Auditory frequency discrimination learning is affected by stimulus variability," Percept. Psychophys. **67**, 691–698.
Bakin, J. S., and Weinberger, N. M. (**1990**). "Classical conditioning induces CS-specific receptive field plasticity in the auditory cortex of the guinea pig," Brain Res. **536**, 271–286.
Berliner, J. E., and Durlach, N. I. (**1973**). "Intensity perception. IV. Resolution in roving-level discrimination," J. Acoust. Soc. Am. **53**, 1270–1287.
Berliner, J. E., Durlach, N. I., and Braida, L. D. (**1977**). "Intensity perception. VII. Further data on roving-level discrimination and the resolution and bias edge effects," J. Acoust. Soc. Am. **61**, 1577–1585.
Botte, M.-C. (**1995**). "Auditory attentional bandwidth: Effect of level and frequency range," J. Acoust. Soc. Am. **98**, 2475–2485.
Braida, L. D., Lim, J. S., Berliner, J. E., Durlach, N. I., Rabinowitz, W. M., and Purks, S. R. (**1984**). "Intensity perception. XIII. Perceptual anchor model of context coding," J. Acoust. Soc. Am. **76**, 722–731.
Demany, L., Montandon, G., and Semal, C. (**2004**). "Pitch perception and retention: Two cumulative benefits of selective attention," Percept. Psychophys. **66**, 609–617.
Durlach, N. I., and Braida, L. D. (**1969**). "Intensity perception. I. Preliminary theory of intensity resolution," J. Acoust. Soc. Am. **46**, 372–383.
Forster, K. I., and Forster, J. C. (**2003**). "DMDX: A Windows display program with millisecond accuracy," Behav. Res. Methods Instrum. Comput. **35**, 116–124.
Harris, J. D. (**1952**). "The decline of pitch discrimination with time," J. Exp. Psychol. **43**, 96–99.
Jesteadt, W., and Bilger, R. C. (**1974**). "Intensity and frequency discrimination in one- and two-interval paradigms," J. Acoust. Soc. Am. **55**, 1266–1276.
Macmillan, N. A., and Schwartz, M. (**1975**). "A probe-signal investigation of uncertain-frequency detection," J. Acoust. Soc. Am. **58**, 1051–1058.
Massaro, D. W. (**1970**). "Forgetting: Interference or decay?," J. Exp. Psychol. **83**, 238–243.
Moore, B. C. J., and Raab, D. H. (**1974**). "Pure-tone intensity discrimination: Some experiments relating to the 'near-miss' to Weber's law," J. Acoust. Soc. Am. **55**, 1049–1054.
Ruusuvirta, T. (**2000**). "Proactive interference of a sequence of tones in a two-tone pitch comparison task," Psychol. Bull. Rev. **7**, 327–331.
Siegel, W. (**1972**). "Memory effects in the method of absolute judgment," J. Exp. Psychol. **94**, 121–131.
Weinberger, N. M. (**2004**). "Specific long-term memory traces in primary auditory cortex," Nat. Rev. Neurosci. **5**, 279–290.

Rollover effect of signal level on vowel formant discrimination[a)]

Chang Liu
Department of Communication Sciences and Disorders, 1 University Station A1100, The University of Texas at Austin, Austin, Taxes 78712
changliu@mail.utexas.edu

Abstract: The goal of this study was to measure the ability of normal-hearing listeners to discriminate formant frequency for vowels in isolation and sentences at three signal levels. Results showed significant elevation in formant thresholds as formant frequency and linguistic context increased. The signal level indicated a rollover effect, especially for F2, in which formant thresholds at 85 dB SPL were lower than thresholds at 70 or 100 dB SPL in both isolated vowels and sentences. This rollover level effect could be due to reduced frequency selectivity and forward/backward masking in sentence at high signal levels for normal-hearing listeners.

© 2008 Acoustical Society of America
PACS numbers: 43.71.Es, 43.66.Fe [JH]
Date Received: December 6, 2007 **Date Accepted:** January 23, 2008

1. Introduction

A number of studies have shown that vowel formants, referring to the spectral prominence of vowel sounds, play critical roles in vowel categorization and perception (Hillenbrand *et al.*, 1995; Nearey, 1989). Vowel formant discrimination measures the ability of human listeners to discriminate changes in formant frequency, especially F1 and F2. Thresholds of formant discrimination, ΔF, refer to the smallest changes in vowel formant frequency that can be detected. Kewley-Port and her colleagues have systematically examined the ability of human listeners to discriminate formant frequency under optimal and ordinary listening condition (Kewley-Port and Watson, 1994; Kewley-Port and Zheng, 1999; Kewley-Port, 2001; Liu and Kewley-Port, 2004a, b). Many factors have been shown to affect formant resolution, including the level of stimulus uncertainty (i.e., trial by trial variability in vowel stimuli), level of linguistic context (i.e., isolated vowel, syllable and sentence), listener training, and background noise. Increases in stimulus uncertainty or level of linguistic context (from isolated vowels to sentences) degraded vowel formant discrimination performance (Kewley-Port and Zheng, 1999; Liu and Kewley-Port, 2004a) as well as background noise (Liu and Kewley-Port, 2004b). However, all of these studies on vowel formant discrimination presented speech signals at 70 dB SPL, a conversational level, and by far there is no report on effects of signal level on formant discrimination for normal-hearing listeners. Liu and Kewley-Port (2007) found that thresholds of formant discrimination were higher at 95 dB SPL for hearing-impaired listeners than at 70 dB SPL, especially for vowels presented in sentence. Such a rollover effect of signal level was also found in other studies of speech perception. That is, a significant reduction in speech recognition occurred as speech level increased above moderate levels (Miranda and Pichora-Fuller, 2002; Molis and Summers, 2003; Studebaker *et al.*, 1999). Thus, the primary purpose of this study was to examine whether or not such a rollover effect was also present on vowel formant discrimination for normal-hearing listeners under optimal (i.e., isolated vowels) and ordinary listening conditions (i.e., sentence).

[a)]Portions of the data were presented at the Fourth Joint Meeting of the Acoustical Society of America and the Acoustic Society of Japan.

 © 2008 Acoustical Society of America

Table 1. Parameters of isolated vowels.

	ɪ	ɛ	æ	ʌ
F1 (Hz)	430	581	678	700
F2 (Hz)	1454	1960	2078	2132
Isolated vowel (ms)	107	125	198	123

Effects of speech levels on speech perception, especially at high presentation levels, are dependent on several factors such as listening conditions (e.g., in quiet or in noise), hearing status (e.g., normal hearing or hearing-impaired), speech spectral information (e.g., low- or high-frequency speech), and speech material (e.g., consonant, syllable, word, or sentence). For normal-hearing listeners in quiet listening conditions, the rollover effect of speech recognition was found for both high-pass- and low-pass-filtered speech from 75 to 105 dB SPL (Molis and Summers, 2003) as well as for temporally jittered speech at high levels (Miranda and Pichora-Fuller, 2002). In addition, Studebaker *et al.* (1999) reported that normal-hearing listeners showed a weak rollover effect ($<10\%$) of word recognition as the speech level increased from 64 to 99 dB SPL with the peak performance at 79 dB SPL. Therefore, it is important to assess how the level of speech sounds affects formant discrimination for normal-hearing listeners under different linguistic contexts. Three factors were manipulated to meet the purposes of the present study, signal level: 70, 85, and 100 dB SPL; formant frequency (eight vowel formants); level of linguistic context (isolated vowels and sentences).

2. Method

2.1 Stimuli

Four American English vowels /ɪ, ɛ, æ, ʌ/ were used as speech stimuli and they covered a wide range of formant frequencies from a low F1 to a high F2 over the English vowel space (see Table 1). Thresholds of formant discrimination for F1 and F2 of these four vowels were measured in two types of linguistic contexts: isolated vowel and sentence. The four original /bVd/ syllables recorded from a female talker were the same ones used in earlier studies (Liu and Kewley-Port, 2004a, 2007). Standard vowels without formant shifts and test vowels with formant changes were synthesized using a modified STRAIGHT procedure (Kawahara *et al.*, 1999). F1 and F2 for each standard syllable were shifted systematically by 24 steps using a linear scale. The range of formant frequency shifts was from 0.9% to 17% of the formant frequency for each F1 and F2. The procedure to shift target formant frequency is described briefly as follows: First, a matrix in Matlab representing the spectrogram (amplitude $\times$ time $\times$ frequency) of the standard syllable was obtained by the analysis in STRAIGHT. Second, to shift a formant peak, the temporal location of the formant across the syllable duration, including transitions, was visually identified. Third, in each time frame (i.e., one spectrum), the formant shift was manipulated for the portion between the valleys on either side of the formant peak. As shown in Fig. 1 for the standard /æ/ vowel and the /æ/ vowel with 10% shift of F2 frequency, amplitude in the low-frequency valley was adjusted to be a constant across the frequency range corresponding to the frequency shift, while the high-frequency valley was collapsed by replacing the original amplitude values with the shifted peak, such that the shift in the selected formant frequency resulted in no change in other formants. Thus, detail in the formant peaks was preserved in this procedure with the valleys only slightly changed. Finally, this modified two-dimensional matrix was reloaded into STRAIGHT and used with other unchanged acoustic parameters such as F0 and amplitude contours for resynthesis [for more details about formant shift synthesis, see Liu and Kewley-Port (2004a)]. Formant shifts included the steady-state portions as well as the onset and offset formant transitions in the /bVd/ syllables. The isolated vowels were subsequently edited by deleting the formant transition at the beginning and the end of the syllable such that only the steady-state vowel nucleus remained. Durations for the standard isolated vowels ranged from

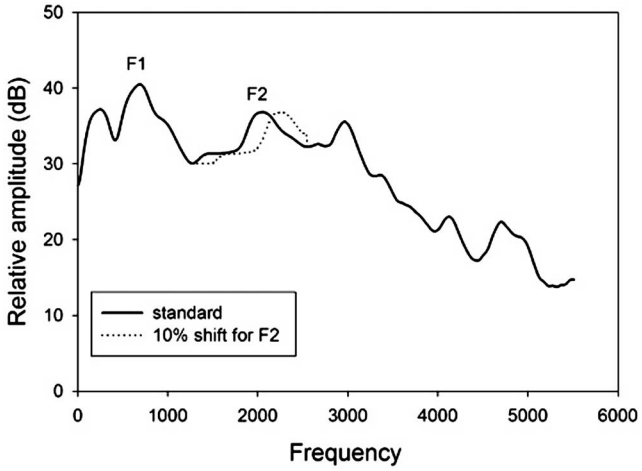

Fig. 1. STRAIGHT spectra from one middle analysis frame for the standard /æ/ is shown with the solid line. The dotted line indicates where the F2 peak was shifted for the 10% frequency increment.

107 to 198 ms (see Table 1). For the linguistic context of sentences, the target word /bVd/ was embedded in the middle of a carrier sentence: "The first word is /bVd/ on the page now." All the stimuli were presented at three levels, 70, 85, and 100 dB SPL.

Digital stimuli were sampled at 12 207 Hz by a two-channel, 20 bit D/A converter (TDT RP2.1), scaled to the appropriate presentation level by programmable attenuators (TDT PA5), routed to a headphone buffer (TDT HB7), and delivered to an insert earphone (Etymotic ER-2) inserted into the right ear of the listener who was seated in a sound attenuation chamber (IAC). Speech sound pressure levels were verified at the output of the insert earphones via G.R.A.S. IEC 126 2-cc coupler mated to the microphone of a Quest (Model 2700) sound level meter set to the linear weighting scale.

2.2 Listeners

Six American English native speakers, between 22 and 28 years old, participated in this study. All listeners had normal hearing with pure tone thresholds of 15 dB HL or better at octave intervals from 250 to 8000 Hz and were paid for their participation.

2.3 Procedures

Thresholds of vowel formant discrimination were measured for F1 and F2 of the four English vowels, using a three-interval (one reminder interval followed by two test intervals), forced-choice procedure with a two-down, one-up tracking algorithm, estimating 71% correct responses (Levitt, 1971). There were two levels of linguistic context: isolated vowel and sentence. For isolated vowel, the standard isolated vowel was presented in the reminder interval, followed by a standard and a test vowel randomly ordered in the two test intervals. The listener's task was to indicate which of the two test intervals contained the different vowel. For sentence, the standard syllable (/bVd/) was presented alone in the first interval followed by two test intervals, each containing one carrier sentence. The standard and test syllables were imbedded in the sentence, and listener's task was to detect which of the two intervals contained the comparison syllable. Presentation intervals were separated by a 400-ms silent period for each trial. Threshold for a given condition was taken as the average threshold based on three 60-trial blocks unless the standard deviation for the three blocks differed by more than 1% of the formant frequency, in which case a fourth block was completed and averaged with the first three. Listeners were tested with isolated vowel first followed by sentence, while the order of the other two experimental factors, vowel formant and signal level, were randomly selected for each listener. It took a total of about 18 h for each listener to complete the study with each session lasting 1–1.5 h.

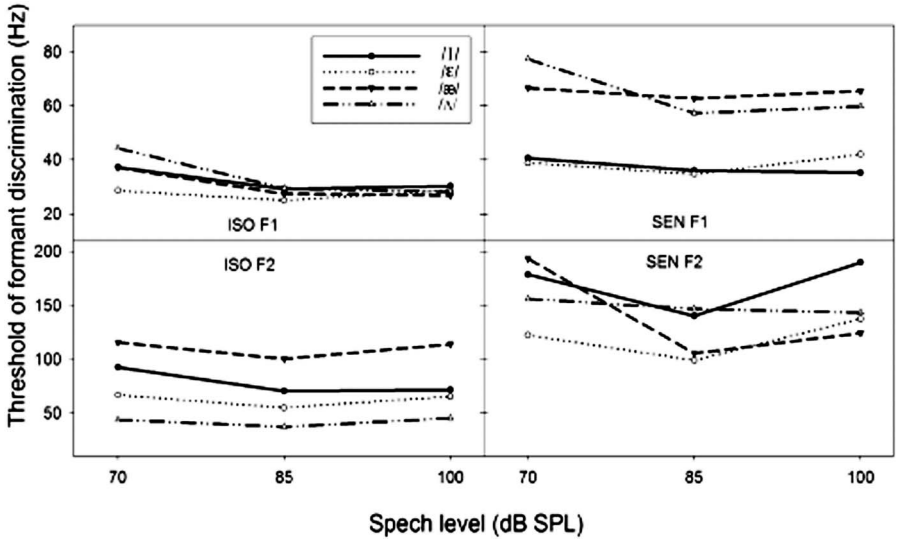

Fig. 2. Thresholds of formant discrimination in hertz as a function of speech level (70, 85, 100 dB SPL) for two linguistic contexts (isolated vowel and sentence) and four vowels (/ɪ, ɛ, æ, ʌ/): F1 in isolated vowel (top left), F1 in sentence (top right), F2 in isolated vowel (bottom left), and F2 in sentence (bottom right).

3. Results

As shown in Fig. 2, average thresholds across listeners are plotted as a function of speech level for the two linguistic contexts and eight vowel formants (F1 and F2 of four vowels). Overall, thresholds increased with complexity of the linguistic context (from isolated vowel to sentence) and the formant frequency, particularly in the F2 region, consistent with previous studies (Kewley-Port and Zheng, 1999; Liu and Kewley-Port, 2004a). The rollover effect of speech levels was obtained, i.e., thresholds at 85 dB SPL were lower than at 70 and 100 dB SPL. A three-factor (formant frequency × linguistic context × signal level) repeated-measures analysis of variance (ANOVA) with ΔF as the dependent variable showed that thresholds of formant discrimination were affected significantly by formant frequency [$F(7,35)=13.011$, $p<0.05$], linguistic context [$F(1,5)=13.238$, $p<0.05$], and signal level [$F(2,10)=6.934$, $p<0.05$]. None of the two-way and three-way interaction effects was significant ($p>0.1$) except the interaction effect of formant frequency and linguistic context [$F(7,35)=3.376$, $p<0.05$], suggesting that threshold-frequency functions showed similar patterns across signal level, but not linguistic context. Post hoc tests suggested that thresholds at 85 dB SPL were significantly better than at 70 dB SPL ($p<0.05$), but not than at 100 dB SPL ($p>0.05$) with no significant difference between 70 and 100 dB SPL ($p>0.05$).

In order to measure the simple main effect of signal level under linguistic context, two-way (formant frequency × signal level) ANOVAs were completed for isolated vowels and sentences, respectively. For isolated vowels, there was no significant effect of signal level [$F(2,10)=2.574$, $p>0.05$] on formant thresholds with the average thresholds increased by 25% for 70 dB SPL and 10% for 100 dB SPL compared to the average thresholds at 85 dB SPL. For sentences, speech level showed a significant effect on formant discrimination [$F(2,10)=4.328$, $p<0.05$] with the thresholds increased by 28% for 70 dB SPL and 17% for 100 dB SPL relative to the thresholds at 85 dB SPL. In addition, the present study showed that the effect of speech level is greater at the F2 region than at the F1 region, e.g., formant thresholds were increased by 23% at 70 dB SPL and 5% at 100 dB SPL for F1 relative to thresholds at 85 dB SPL while elevated by 28% at 70 dB SPL and 18% at 100 dB SPL for F2 compared to

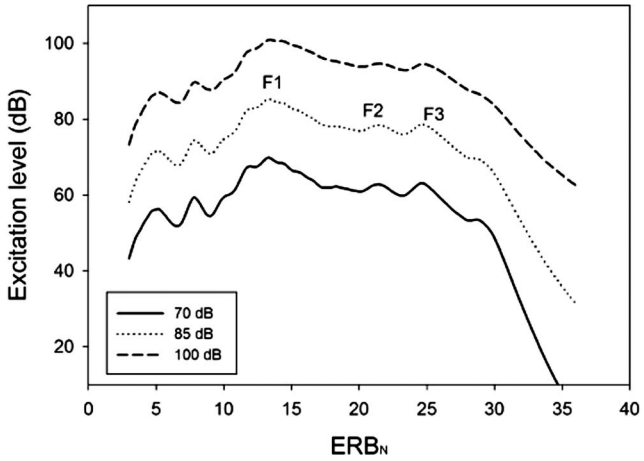

Fig. 3. Excitation patterns of the /æ/ vowel at three levels: 70 (solid line), 85 (dotted line), and 100 (dashed line) dB SPL. Note the changes in spectral contrasts for F1 and F2.

thresholds at 85 dB SPL. Thus, overall results indicate a greater effect of speech levels on formant discrimination for the longer linguistic context (sentence) than for the short linguistic context (isolated vowels) and a greater level effect on F2 than on F1 (see Fig. 2).

4. Discussion

The main purpose of this study was to assess the signal level effect on vowel formant discrimination. As shown in Fig. 2, a rollover effect of the signal level on vowel formant discrimination was observed for both isolated vowels and sentences. Such a rollover effect of speech levels was also found in other studies of speech perception for normal-hearing listeners (Meyer and Mishler, 1985; Miranda and Pichora-Fuller, 2002; Molis and Summers, 2003; Studebaker *et al.*, 1999). There are two possible interpretations of the rollover effect for vowel formant discrimination including level-dependent frequency selectivity and forward and backward masking on vowel formants in sentence context.

One mechanism accounting for the rollover effect is reduced frequency selectivity with increase of the signal level. Several psychophysical studies have suggested that the bandwidth of auditory filters becomes broader as the signal level increases (Moore and Glasberg, 1987) such that the internal representation of vowel spectrum is smoothed, resulting in lower peak-to-valley contrasts for F1 and F2. This is consistent with Javal's (1997) physiological findings on cats that an increase of stimulus level degraded the encoding of vowel formants, especially for higher formants, in terms of spectral response patterns in auditory neurons. Excitation patterns were calculated for the four vowels at 70, 85, and 100 dB SPL, using Moore and Glasberg's excitation model (1987). As shown in Fig. 3 (the /æ/ vowel), for normal-hearing listeners, the peak-to-valley contrasts of F1 were slightly reduced from 85 to 100 dB SPL by 0.5 dB on average across the four vowels, while the peak-to-valley contrasts of F2 in the excitation patterns for the four vowels were reduced by an average of 1.5 dB from 85 to 100 dB SPL. The reduction in the peak-to-valley contrasts of F1 and F2 at high levels may account for the rollover level effect of formant discrimination as well as the greater rollover effect on F2 than for F1. This is consistent with Molis and Summers' findings (2003) that there was a rollover effect of signal level on speech recognition for normal-hearing listeners and that the rollover effect was greater for high-frequency speech than for low-frequency speech. Altogether, such greater rollover effects of signal level on perception of high-frequency speech than on perception of low-frequency speech, found in both studies, were due to physiological and psychophysical facts that cochlear processing is more linear (i.e., more level independent) in low-frequency regions than in high-frequency regions (Rosen and Stock, 1992; Rosen *et al.*, 1998).

As noted in Sec. 3, the rollover level effect on formant discrimination was greater at the longer linguistic context (sentence) than the shorter linguistic context (isolated vowel), implying that there may be some mechanisms other than the one addressed earlier involved in the rollover level effect in sentence. One possibility may be that formant discrimination in sentences is affected by forward and backward masking resulting from the speech preceding and following the target vowel. Studies of intensity discrimination for pure tones under both forward and backward masking suggested a nonmonotonic function from 20 to 100 dB SPL for normal-hearing listeners (Zeng and Turner, 1992; Plack and Viemeister, 1992). For forward and backward masking, especially when the masking delay was short ($\leqslant$100 ms), the intensity discrimination function showed rollover in which thresholds for intensity discrimination were higher at middle levels than thresholds at either low or high signal levels. However, it should be noted that intensity discrimination was degraded with forward and backward masking at middle levels while formant discrimination became better at middle levels, indicating that effects of the forward and backward masking may be different between the two auditory tasks. Further research will be conducted to reveal how forward and backward masking affect formant discrimination.

Summarizing, two main mechanisms may interpret the rollover level effect on formant discrimination thresholds in the present study, depending on linguistic context. For vowel presented in isolation, the degradation of formant discrimination at the very high level is likely accounted for by the poorer representation of vowel formants. Moreover, at high levels, high-frequency formants are represented more poorly than low frequency due to greater nonlinearity at high frequencies. When the target vowel is embedded into a long linguistic context, the preceding and following speech, resulting in forward and backward masking, may additionally degrade formant discrimination at high levels.

Acknowledgments

The author is thankful to one anonymous reviewer and James Hillenbrand for their constructive comments on earlier versions of this manuscript.

References and links

Hillenbrand, J., Getty, L. J., Clark, M. J., and Weeler, K. (**1995**). "Acoustic characteristics of American English vowels," J. Acoust. Soc. Am. **97**, 3099–3111.
Javal, E. (**1997**). "Cochlear excitation patterns in sensorineural hearing loss," in *Modeling Sensorineural Hearing Loss*, edited by W. Jesteadt (Erlbaum, Mahwah, NJ), pp. 9–34.
Kawahara, H., Masuda-Kastuse, I., and Cheveigne, A. (**1999**). "Restructuring speech representations using a pitch-adaptive time-frequency smoothing and an instantaneous-frequency-based F0 extraction: Possible role of a repetitive structure in sounds," Speech Commun. **27**, 187–207.
Kewley-Port, D. (**2001**). "Vowel formant discrimination: Effects of stimulus uncertainty, consonantal context and training," J. Acoust. Soc. Am. **110**, 2141–2155.
Kewley-Port, D., and Watson, C. S. (**1994**). "Formant-frequency discrimination for isolated English vowels," J. Acoust. Soc. Am. **95**, 485–496.
Kewley-Port, D., and Zheng, Y. (**1999**). "Vowel formant discrimination: Towards more ordinary listening conditions," J. Acoust. Soc. Am. **106**, 2945–2958.
Levitt, H. (**1971**). "Transformed up-down methods in psychoacoustics," J. Acoust. Soc. Am. **49**, 467–477.
Liu, C., and Kewley-Port, D. (**2004a**). "Vowel formant discrimination for high-fidelity speech," J. Acoust. Soc. Am. **116**, 1224–1233.
Liu, C., and Kewley-Port, D. (**2004b**). "Formant discrimination in noise for isolated vowels," J. Acoust. Soc. Am. **116**, 3119–3129.
Liu, C., and Kewley-Port, D. (**2007**). "Factors affecting vowel formant discrimination by hearing-impaired listeners," J. Acoust. Soc. Am. **122**, 2855–2864.
Meyer, D., and Mishler, E. (**1985**). "Rollover measurements with auditec NU-6 word lists," J. Speech Hear Disord. **50**, 351–356.
Miranda, T., and Pichora-Fuller, M. (**2002**). "Temporally jittered speech produces performance intensity, phonetically balanced rollover in young normal-hearing listeners," J. Am. Acad. Audiol **13**, 50–58.
Molis, M., and Summers, V. (**2003**). "Effects of high presentation levels on recognitions of low- and high-frequency speech," ARLO **4**, 124–128.
Moore, B. C. J., and Glasberg, B. R. (**1987**). "Formulae describing frequency selectivity as a function of frequency and level and their use in calculating excitation pattern," Hear. Res. **28**, 209–225.
Nearey, T. M. (**1989**). "Static, dynamic, and relational properties in vowel perception," J. Acoust. Soc. Am. **85**,

2088–2113.
Plack, C. J., and Viemeister, N. F. (**1992**). "Intensity discrimination under backward masking," J. Acoust. Soc. Am. **92**, 3097–3101.
Rosen, S., Baker, R., and Darling, A. (**1998**). "Auditory filter nonlinearity at 2 kHz in normal-hearing listeners," J. Acoust. Soc. Am. **103**, 2359–2370.
Rosen, S., and Stock, B. (**1992**). "Auditory filter bandwidth as a function of level at low frequencies (125 Hz–1 kHz)," J. Acoust. Soc. Am. **92**, 773–781.
Studebaker, G., Sherbecoe, R., McDaniel, D., and Gwaltney, C. (**1999**). "Monosyllabic word recognition at higher-than-normal speech and noise levels," J. Acoust. Soc. Am. **105**, 2431–2444.
Zeng, F. -G., and Turner, C. W. (**1992**). "Intensity discrimination in forward masking," J. Acoust. Soc. Am. **92**, 782–787.

Effect of spectral resolution on the intelligibility of ideal binary masked speech

Ning Li and Philipos C. Loizou
Department of Electrical Engineering, University of Texas at Dallas, Richardson, Texas 75083-0688
nxl051000@utdallas.edu; loizou@utdallas.edu

Abstract: Most binary-mask studies assume a fine time–frequency representation of the signal that may not be available in some applications (e.g., cochlear implants). This study assesses the effect of spectral resolution on intelligibility of ideal-binary masked speech. In Experiment 1, speech corrupted in noise at −5 to 5 dB signal-to-noise ratio (SNR) was filtered into 6–32 channels and synthesized using the ideal binary mask. Results with normal-hearing listeners indicated substantial improvements in intelligibility with 24–32 channels, particularly in −5 dB SNR. Results from Experiment 2 indicated that having access to the ideal binary mask in the F1/F2 region is sufficient for good performance.

© 2008 Acoustical Society of America
PACS numbers: 43.72.Ar, 43.72.Ct [DO]
Date Received: December 18, 2007 **Date Accepted:** January 25, 2008

1. Introduction

The ideal binary mask (IdBM) has been set as a computational goal in computational auditory scene analysis algorithms (Wang, 2005) and has also been used extensively in "missing feature" speech recognition techniques (Cooke *et al.*, 2001). The ideal binary mask takes values of zero and one, and is constructed by comparing the local signal-to-noise ratio (SNR) in each time–frequency (T–F) bin against a preset threshold. The construction of the ideal binary mask requires knowledge of the signals (speech and interferer) prior to mixing. It is usually applied to the time–frequency representation of a mixture signal and eliminates portions of a signal (those assigned to a "zero" value) while preserving others (those assigned to a "one" value). A number of studies demonstrated high gains in speech intelligibility using the IdBM technique (Roman *et al.*, 2003; Brungart *et al.*, 2006; Li and Loizou, 2007, 2008). In the Brungart *et al.* (2006) study, for instance, performance was restored to the level attained in quiet when the IdBM technique was applied to a closed-set word test at −3 dB SNR (speech stimuli were corrupted by competing talkers).

The ideal binary mask was applied in the above-mentioned studies to the mixture signals assuming a fine time–frequency representation of the signal. The studies by Brungart *et al.* (2006) utilized a bank of 128 gammatone filters with auditory-like frequency resolution, while the study by Li and Loizou (2007) utilized a 512-point fast Fourier transform (256 channels). In applications such as hearing aids or cochlear implants, however, the time–frequency representation of the signal can be rather coarse (Loizou, 1998). In cochlear implants, for instance, speech is processed via a small number (12–22) of channels. Thus, it is not clear whether the ideal binary mask technique can bring substantial intelligibility gains, if any, when the T–F representation is poor as it is for instance in cochlear implants. Experiment 1 assesses the impact of spectral resolution on the intelligibility of IdBM speech. The spectral resolution was systematically varied by bandpass filtering speech into 6–32 channels and synthesizing it using a sinewave-excited vocoder. Since in practice algorithms that estimate the binary mask might not be accurate in all frequencies (channels), we assess in Experiment 2 the impact of frequency location of the ideal binary mask by restricting access to the ideal binary mask to a subset of channels.

2. Experiment 1: Effect of spectral resolution

2.1 Subjects and material

Fourteen normal-hearing listeners participated in this experiment. All subjects were native speakers of American English, and were paid for their participation. The speech material consisted of sentences taken from the IEEE database (IEEE, 1969). All sentences were produced by a male speaker. The sentences were recorded in a sound-proof booth (Acoustic Systems) in our lab at a 25 kHz sampling rate. Details about the recording setup and copies of the recordings are available in Loizou (2007). Two types of masker were used. The first was continuous (steady-state) noise, which had the same long-term spectrum as the test sentences in the IEEE corpus. The second masker was multitalker babble which was taken from the Auditec CD (St. Louis). The maskers were added to the target stimuli at −5, 0, and 5 dB SNR levels.

2.2 Signal processing

The stimuli were processed via an n-channel sinewave-excited vocoder (Loizou *et al.*, 1999) and synthesized with and without utilizing the ideal binary mask. In the baseline vocoder condition, signals were first processed through a preemphasis filter (2000 Hz cutoff), with a 3 dB/octave rulloff, and then bandpassed into n frequency bands ($n=6$, 12, 16, 24, and 32) using sixth-order Butterworth filters. Logarithmic filter spacing was used for $n \leqslant 16$ and mel filter spacing (linear up to 1 kHz and logarithmic thereafter) was used for higher number ($n > 16$) of channels. The envelope of the signal was extracted by full-wave rectification and low-pass filtering (second-order Butterworth) with a 400 Hz cutoff frequency. Sinusoids were generated with amplitudes equal to the rms energy of the envelopes (computed every 4 ms) and frequencies equal to the center frequencies of the bandpass filters. The sinusoids of each band were finally summed and the level of the synthesized speech segment was adjusted to have the same rms value as the original speech segment.

The stimuli were also processed and synthesized via the ideal binary mask as follows. The masker signal is first scaled (based on the rms energy of the target) to obtain the desired SNR level. The target and masker signals are then independently bandpass filtered as before into n channels (same frequency spacing), and envelopes are extracted by low-pass filtering (400 Hz cutoff) the rectified waveforms. The filtered target and masker signals are used to estimate the (true) instantaneous envelope SNR in each channel (the SNR is computed, every 4 ms, as the ratio of the rms energies of the target and masker envelope signals). If the SNR in a given channel is found to be greater than 0 dB, then the mixture envelope of that channel is retained (the 0 dB SNR threshold is adopted in this study as it is the threshold typically used for constructing ideal binary masks, Wang, 2005). If the SNR in a given channel is found to be less or equal to 0 dB, then the mixture envelope of that channel is discarded. Following the retention/discarding of the mixture envelopes in each channel, the signal is synthesized as a sum of m ($m \leqslant n$) sine waves with amplitudes set to the envelopes with positive SNR values and frequencies set to the center frequencies of the corresponding bandpass filters.

2.3 Procedure

The experiments were performed in a soundproof room (Acoustic Systems, Inc) using a PC connected to a Tucker-Davis system 3. Stimuli were played to the listeners monaurally through Sennheiser HD 250 Linear II circumaural headphones at a comfortable listening level. Prior to the test, each subject listened to vocoded speech to become familiar with the stimuli. The training session lasted for about 15–20 min. During the test, the subjects were asked to write down the words they heard. Subjects participated in a total of 60 conditions (=3 SNR levels $\times$ 2 algorithms $\times$ 2 maskers $\times$ 5 number of channels). Two different groups of subjects (seven in each group) were used due to the limited number of lists available in the IEEE corpus. The first group participated in the −5 and 0 dB conditions, and the second group participated in the 5 dB SNR conditions. Subjects were randomly assigned to the two groups. Two lists of sentences (i.e., 20 sentences) were used for each condition.[1] The sentence lists were counterbal-

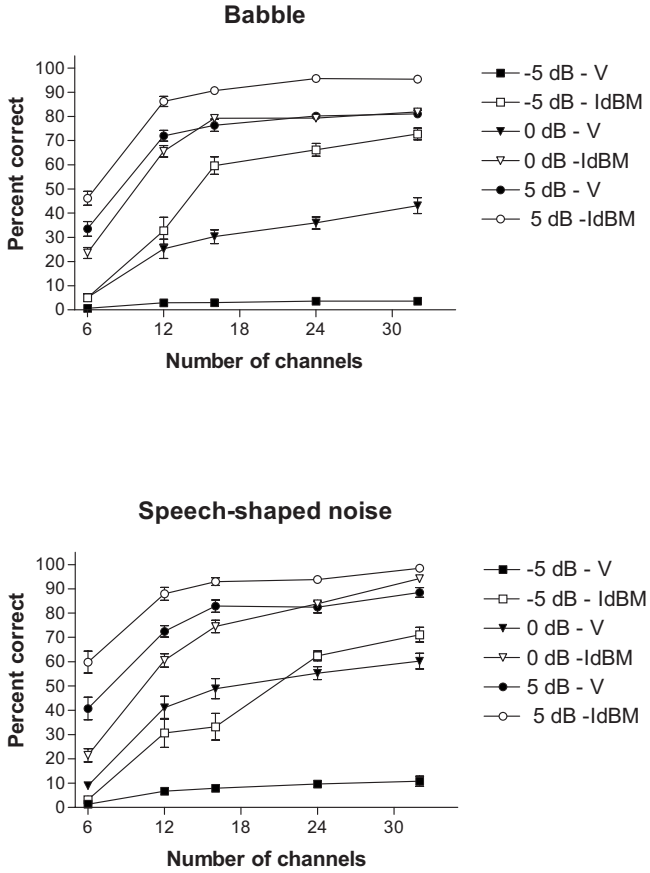

Fig. 1. Mean percent correct scores as a function of number of channels for the two types of maskers tested. The scores for the baseline vocoded stimuli (V) are shown in closed symbols and the scores for the IdBM-vocoded stimuli are shown in open symbols. Error bars indicate standard errors of the mean.

anced across subjects. Sentences were presented to the listeners in blocks, with 20 sentences/block for each condition. The different conditions were run in random order for each listener.

2.4 Results and discussion

The mean percent correct scores (all words were used in the scoring) are shown in Fig. 1 as a function of number of channels. The scores for the baseline vocoded stimuli are shown in closed symbols and the scores for the IdBM-vocoded stimuli are shown in open symbols. For the stimuli corrupted by multitalker babble, three-way analysis of variance (ANOVA) (with repeated measures) indicated significant effect [$F(4,24)=337.9, p<0.005$] of spectral resolution (number of channels), significant effect [$F(1,6)=476.0$, $p<0.005$] of processing (vocoding and IdBM vocoding), significant effect [$F(2,12)=720.5$, $p<0.005$] of SNR level (−5, 0, and 5 dB) and significant ($p<0.005$) interactions among all factors. Similar ANOVA was applied to the speech-shaped noise conditions. Analysis indicated significant effect [$F(4,24)=268.5$, $p<0.005$] of spectral resolution (number of channels), significant effect [$F(1,6)=248.8$, $p<0.005$] of processing (vocoding and IdBM vocoding), significant effect [$F(2,12)=359.4$, $p<0.005$] of SNR level (−5, 0, and 5 dB), and significant ($p<0.005$) interactions among all factors.

As expected, performance improved as the number of channels increased for both baseline and IdBM vocoded stimuli. Performance reached a plateau, however, in most conditions depending on the masker and SNR level used. Post-hoc tests (according to Scheffé) were run to find the number of channels needed to reach asymptotic performance. For the IdBM stimuli processed in babble, performance reached an asymptote with 16 channels of stimulation in the −5 and 0 dB SNR conditions. In the 5 dB SNR condition, performance obtained with 12 channels did not differ significantly ($p > 0.05$) from performance obtained with 16 channels. For the IdBM stimuli processed in speech-shaped noise, performance asymptoted at 24 channels of stimulation in −5 dB SNR, and at 12 channels of stimulation in 5 dB SNR. There was no asymptote in the 0 dB SNR condition.

The above-presented analysis clearly indicates that spectral resolution has a significant impact on the intelligibility of IdBM stimuli. The performance with the IdBM stimuli did not reach the same level (90%–100% correct) as attained by Brungart *et al.* (2006) with 128 channels in low (−3 dB) SNR conditions. Nevertheless, the improvement in performance obtained with the IdBM stimuli in the present study is quite substantial, particularly at low SNR levels (−5 and 0 dB). In the −5 dB SNR babble condition, for instance, performance improved by roughly 60 percentage points with 24–32 channels of stimulation.

3. Experiment 2: Effect of frequency location of binary mask

In the previous experiment we assumed that we had access to the ideal binary mask in all channels. In practice, the binary mask (or equivalently the envelope SNR) needs to be estimated from the noisy observations and the SNR estimation may not be accurate in all channels. Hence, in the present experiment we assess the impact of frequency location of the binary mask on speech intelligibility. This is done by assuming access to the ideal binary mask for only a subset of the channels and leaving the remaining channels unaltered.

3.1 Subjects and material

A different group of six normal-hearing listeners participated in this experiment. All subjects were native speakers of American English, and were paid for their participation. The same speech material from the IEEE database was used for the target stimuli, and the same types of maskers were used as in Experiment 1. The maskers were added to the target stimuli at −5, 0, and 5 dB SNR levels.

3.2 Signal processing

The stimuli were processed as before into 32 channels via the ideal binary mask technique, except for the following difference in implementation. Access to the ideal binary mask was restricted only to channels falling within a limited frequency region spanning 0–f Hz, where f=560, 1000, 1630, 2720, and 5500 Hz. Hence, channels falling within the 0–f Hz region were synthesized using the IdBM technique (same as in Experiment 1) and channels with upper cutoff frequencies greater than f Hz were synthesized via the baseline vocoding strategy. Note that the f=5500 Hz condition corresponds to the condition in which all channels had access to the ideal binary mask (same as in Experiment 1), and is included here for comparative purposes. The above-mentioned cutoff frequencies were chosen to assess the importance of having access to F1 information ($f < 1000$ Hz) alone or F1/F2 information ($f < 2720$ Hz) alone.

3.3 Procedure

The same experimental setup was used as in Experiment 1. Subjects participated in a total of 36 conditions (=3 SNR levels × 6 cutoff frequencies × 2 maskers) including the baseline vocoder and the IdBM-vocoded conditions. Two lists of sentences (i.e., 20 sentences) were used per condition, and none of the lists were repeated across conditions. The sentence lists were counterbalanced across subjects. Sentences were presented to the listeners in blocks, with 20 sentences/block in each condition. The different conditions were run in random order for each listener.

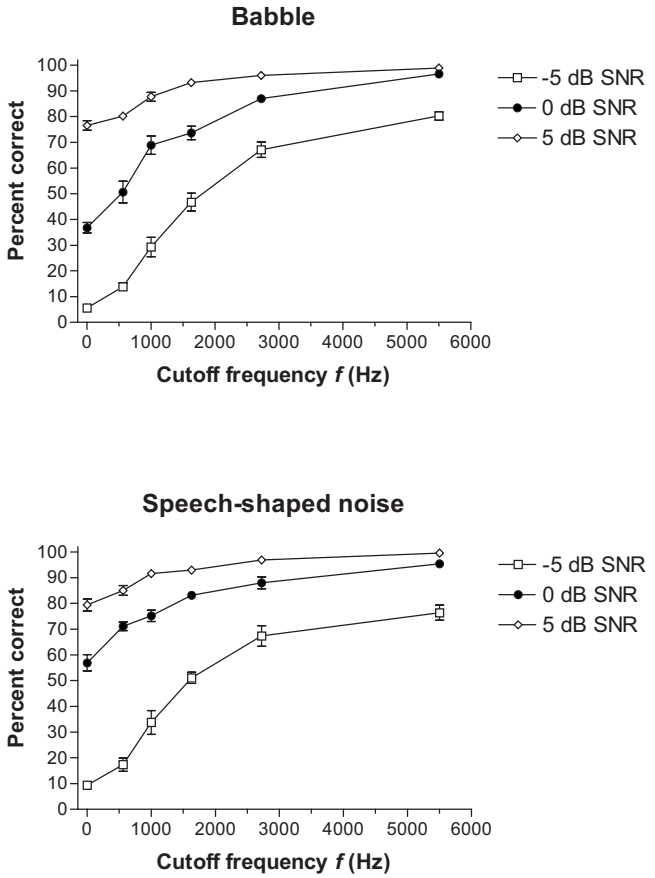

Fig. 2. Mean percent correct scores as a function of the cutoff frequency f (i.e., frequency location of the ideal binary mask) for the two types of maskers tested. The $f=0$ Hz condition corresponds to the baseline vocoded stimuli which made no use of the ideal binary mask. All stimuli were processed via 32 channels. Error bars indicate standard errors of the mean.

3.4 Results and discussion

The mean percent correct scores are shown in Fig. 2 as a function of the cutoff frequency f (Hz), i.e., the frequency location of the ideal binary mask. The $f=0$ Hz condition corresponds to the baseline vocoded stimuli (no access to the ideal binary mask) and the $f=5500$ Hz condition corresponds to the situation in which all 32 channels had access to the ideal binary mask (as in Experiment 1). For the stimuli corrupted by multitalker babble, two-way ANOVA (with repeated measures) indicated significant effect [$F(5,25)=269.5$, $p<0.005$] of the cutoff frequency, significant effect [$F(2,10)=862.3$, $p<0.005$] of SNR level, and significant interaction [$F(10,50)=35.7$, $p<0.005$]. For the stimuli corrupted by speech-shaped noise, two-way ANOVA (with repeated measures) indicated significant effect [$F(5,25)=266.3$, $p<0.005$] of the cutoff frequency, significant effect [$F(2,10)=492.4$, $p<0.005$] of SNR level, and significant interaction [$F(10,50)=32.9$, $p<0.005$].

As shown in Fig. 2, performance improved monotonically as the cutoff frequency f increased (i.e., more channels were included with access to the ideal binary mask). The above-presented statistical analysis yielded an interaction between SNR level and cutoff frequency, and that interaction stems from the fact that the rate of improvement in performance differed for the three SNR levels. A steep rate of improvement in intelligibility was observed for low SNR

levels (−5 dB) and a relatively shallow rate of improvement was observed for higher SNR levels (5 dB) as *f* increased (i.e., as more channels with ideal binary mask were added). Post-hoc tests, according to Scheffé, indicated that performance asymptoted at $f=2500$ Hz in the −5 and 0 dB SNR conditions for both maskers. Performance asymptoted at $f=1500$ Hz in the 5 dB SNR condition for both maskers.

The outcome from the present experiment suggests that it is important for algorithms that estimate the binary mask to be accurate in the low frequency region, and in particular the F1/F2 region. The intelligibility tests in Experiment 2 suggest that having access to the ideal binary mask in the low frequencies is sufficient for good performance. It is speculated that access to a better SNR in the low-frequency region makes it easier for listeners to segregate the target in complex listening situations via a glimpsing mechanism. Evidence of the advantage introduced by glimpsing the low-frequency region was provided in the study by Li and Loizou (2007) and Anzalone *et al.* (2006). Significant reductions in speech reception threshold were obtained in the study by Anzalone *et al.* (2006) by both normal-hearing and hearing-impaired listeners when the ideal speech detector was applied only to the lower frequencies (70–1500 Hz).

4. Conclusions

The present study extended previous findings on the intelligibility of ideal binary masked speech (Brungart *et al.*, 2006; Li and Loizou, 2008). The present results indicate that the use of ideal binary masks can bring substantial gains in speech intelligibility, particularly at low SNR levels (−5 and 0 dB), even when the spectral resolution is relatively low (16–24 channels). Access to the ideal binary mask in the low frequencies, particularly in the F1/F2 region, was found to be sufficient for good performance.

Acknowledgments

This research was supported by Grant No. R01 DC007527 from the National Institute of Deafness and other Communication Disorders, NIH.

References and links

[1]Due to the limited number of IEEE sentence lists, eight lists had to be reused in four conditions. These eight lists, however, were chosen from the −5dB SNR babble conditions, in which subjects performed very poorly (<5% correct). This was done to avoid learning effects.

Anzalone, M., Calandruccio, L., Doherty, K., and Carney, L. (**2006**). "Determination of the potential benefit of time-frequency gain manipulation." Ear Hear. **27**, 480–492.
Brungart, D., Chang, P., Simpson, B., and Wang, D. (**2006**). "Isolating the energetic component of speech-on-speech masking with ideal time-frequency segregation." J. Acoust. Soc. Am. **120**, 4007–4018.
Cooke, M. P., Green, P. D., Josifovski, L., and Vizinho, A. (**2001**). "Robust automatic speech recognition with missing and uncertain acoustic data." Speech Commun. **34**, 267–285.
IEEE (**1969**). "IEEE recommended practice for speech quality measurements." IEEE Trans. Audio Electroacoust. **17**, 225–246.
Li, N., and Loizou, P. (**2007**). "Factors influencing glimpsing of speech in noise." J. Acoust. Soc. Am. **122**, 1165–1172.
Li, N., and Loizou, P. (**2008**). "Factors influencing intelligibility of ideal binary-masked speech: Implications for noise reduction." J. Acoust. Soc. Am., **123**(3) (to be published).
Loizou, P. (**1998**). "Mimicking the human ear: An overview of signal processing techniques for converting sound to electrical signals in cochlear implants." IEEE Signal Process. Mag. **15**, 101–130.
Loizou, P. (**2007**). *Speech Enhancement: Theory and Practice*, (CRC Press, Boca Raton, FL).
Loizou, P., Dorman, M., and Tu, Z. (**1999**). "On the number of channels needed to understand speech." J. Acoust. Soc. Am. **106**, 2097–2103.
Roman, N., Wang, D., and Brown, G. (**2003**). "Speech segregation based on sound localization." J. Acoust. Soc. Am. **114**, 2236–2252.
Wang, D. (**2005**). "On ideal binary mask as the computational goal of auditory scene analysis," in *Speech Separation by Humans and Machines*, edited by P. Divenyi (Kluwer Academic, Dordrecht), pp. 181–197.

Interpretations on principal components analysis of head-related impulse responses in the median plane[a)]

Sungmok Hwang and Youngjin Park
Center for Noise and Vibration Control, Korea Advanced Institute of Science and Technology, Science Town, Daejeon, Republic of Korea
tjdahr78@kaist.ac.kr, yjpark@kaist.ac.kr

Abstract: A principal components analysis of the median-plane head-related impulse responses (HRIRs) in the CIPIC HRTF database reveals that the individual HRIRs can be reconstructed by a linear combination of 12 principal components (PCs) within 5% of error in the least-squares sense. The PCs include the intersubject and interelevation variations in the median-plane HRIRs. Each PC provides sound cues for the front–back discrimination and/or the vertical perception. There exist common systematic elevation dependencies in the weights of lower-numbered PCs which contribute to the pinna/head diffractions, whereas the elevation dependencies in the weights of higher-numbered PCs are different from subject to subject.

© 2008 Acoustical Society of America
PACS numbers: 43.66.Ba, 43.64.Bt, 43.66.Qp [BLM]
Date Received: November 4, 2007 **Date Accepted:** December 15, 2007

1. Introduction

The modeling of spatial dependence of head-related transfer functions (HRTFs) or head-related impulse responses (HRIRs) by a set of basis functions has been attempted by several authors. Martens (1987) applied the principal components analysis (PCA) to model HRTFs. He computed a set of basis functions from the critical-band-filtered HRTFs in the horizontal plane. Kistler and Wightman (1992) performed a PCA of the HRTFs data and they showed that the log magnitude of HRTFs can be adequately approximated by a linear combination of five basis spectral shapes, and they showed the systematic tendencies in the weights of the basis functions according to the source position. Middlebrooks (1999) demonstrated a systematic dependence of HRTFs on dimensions of 45 subjects. Chen *et al.* (1995) obtained the orthogonal basis functions from the Karhunen–Loève expansion of the complex valued (both magnitude and phase) HRTFs. However, these previous studies focused on HRTFs in the frequency domain only.

In the time domain, Wu *et al.* (1997) performed the Karhunen–Loève expansion of HRIRs. However, the basis functions cannot represent the intersubject variations because they included HRIRs of only single subject in the Karhunen–Loève expansion. More recently, Grantham *et al.* (2005) proposed a reduced order model of HRIRs in the time domain. They did not, however, deal with the intersubject and interelevation variations. Shin and Park (2008) performed a PCA of HRIRs of 45 subjects, and they proposed a HRTF customization technique based on subjective tuning of the pinna responses. They, however, performed a PCA at each source position, thus a set of basis functions is different at each source position and the basis functions cannot represent the interelevation variations. These previous studies carried out in the time domain did not show the systematic tendencies in the weights of the basis functions, whereas Kistler and Wightman (1992) showed those in the frequency domain.

[a)]Portions of this work were presented at the AES 31st International Conference in June 2007.

Table 1. Percentage variance (% var) and reconstruction error (% error) as a function of the number of PCs (k), and the kth largest eigenvalue (λ_k) of the covariance matrix.

k	% var	% error	λ_k	k	% var	% error	λ_k	k	% var	% error	λ_k
1	25.1	36.7	1.33$E-1$	7	76.9	11.3	2.63$E-2$	13	91.4	4.2	6.31$E-3$
2	42.4	28.2	9.21$E-2$	8	80.5	9.6	1.87$E-2$	14	92.4	3.7	5.31$E-3$
3	52.3	23.4	5.27$E-2$	9	83.9	7.9	1.82$E-2$	15	93.2	3.3	4.11$E-3$
4	59.8	19.7	3.96$E-2$	10	86.4	6.7	1.34$E-2$	16	93.9	3.0	3.66$E-3$
5	66.5	16.4	3.57$E-2$	11	88.7	5.5	1.25$E-2$	17	94.5	2.7	3.29$E-3$
6	72.0	13.8	2.92$E-2$	12	90.2	4.8	7.88$E-3$	18	95.1	2.4	3.03$E-3$

The purpose of the present letter is to show the systematic elevation-dependent tendencies in the weights of basis functions in the time domain and to clarify the contribution of each basis function to the vertical perception and the front–back discrimination.

2. PCA of HRIRs in the time domain

2.1 PCA of median-plane HRIRs

The general procedure of PCA of the median-plane HRIRs is briefly described. More specific details can be obtained from the authors' previous work (Hwang and Park, 2007).

In this letter, we present a set of basis functions obtained from PCA of the median-plane HRIRs in the CIPIC HRTF database (Algazi *et al.*, 2001). The number of median-plane HRIRs at each ear is 2205 (45 subjects $\times$ 49 elevations from $-45°$ to $225°$ at $5.625°$ intervals). Before PCA was performed, we carried out a preprocessing on the median-plane HRIRs to remove the initial time delay, defined as the time at which the pulse in HRIR first exceeds 12% of its maximum amplitude, and to extract the early response that lasts for 1.5 ms since the arrival of direct pulse. This early response over the 1.5 ms following the arrival of the direct pulse is the data on which PCA is performed, and this response includes the effects of pinna, head, shoulder, and torso (Brown and Duda, 1998). The basis functions (or basis vectors) can be obtained from the covariance matrix of the mean-subtracted data matrix, and the k dominant basis functions are the k eigenvectors of the covariance matrix corresponding to the k largest eigenvalues. These basis functions are called "principal components" (PCs), and the set of HRIRs can be reconstructed by a linear combination of the PCs. Reasonable measures to determine the number of PCs are the percentage variance and the percentage reconstruction error in the least-squares sense. The percentage variance in HRIRs reconstructed from the first k PCs is expressed as

$$\%\ \mathrm{var}(k) = \frac{\sum_{i=1}^{k} \lambda_i}{\sum_{i=1}^{N} \lambda_i} \times 100(\%) \quad (\lambda_1 \geqslant \cdots \geqslant \lambda_k \geqslant \cdots \geqslant \lambda_N), \tag{1}$$

where λ_i ($i=1,2,\ldots,N$) is the ith largest eigenvalue of the covariance matrix. The percentage reconstruction error of HRIRs is defined as

$$\%\ \mathrm{error}(k) = \frac{\|Y - \hat{Y}_k\|_F^2}{\|Y\|_F^2} \times 100\ (\%), \tag{2}$$

where Y and $\hat{Y}_k$ indicate the original data matrix, which is composed of the 2205 median-plane HRIRs and the reconstructed data matrix from the first k PCs, respectively. Subscript F indicates the matrix Frobenius norm. The variance excludes the empirical mean of HRIRs, whereas the reconstruction error includes it. The absolute values of the eigenvalues of the covariance

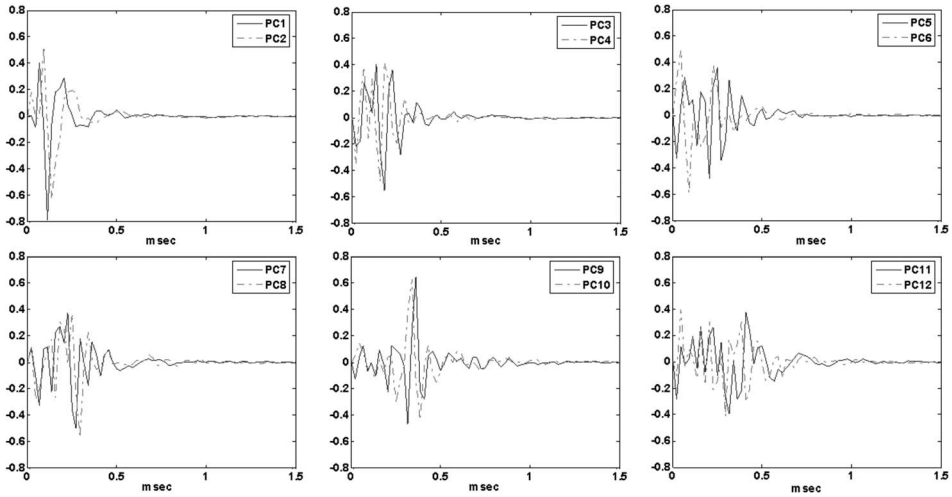

Fig. 1. Twelve PCs obtained from PCA of the left-ear HRIRs in the median plane.

matrix also may be a meaningful measure to determine the number of PCs. Table 1 summarizes the percentage variance and the percentage reconstruction error for the left-ear HRIRs as a function of the number of PCs (k) and the kth largest eigenvalue of the covariance matrix. As the number of PCs increases, the variance increases and the reconstruction error decreases exponentially. The more PCs are used to reconstruct HRIRs, the more exact reconstruction can be obtained. However, the nuisance PCs, which do not contribute significantly to the reconstruction, can be included. Previous studies determined the number of PCs to recover approximately 90% of the variance (Kistler and Wightman, 1992; Middlebrooks and Green, 1992). In this letter, we set the reconstruction error bound of 5%, which is comparable to 90% of the variance in HRIRs, yielding 12 PCs.

2.2 Interpretations on PCs and weight of PCs

Figure 1 shows the 12 PCs obtained from PCA of the left-ear HRIRs in the median plane. Because the initial time delay was removed before PCA was performed, 0 ms in the horizontal axis indicates the time at which the pulse in HRIR first exceeds 12% of its maximum amplitude. Note that PC1, PC2, PC3, and PC4 have high energy up to 0.2 ms, whereas PC9 and PC10 have high energy at around 0.4 ms. According to the previous study, the pinna mainly contributes to the early response up to 0.2 ms and the last responses are mainly due to the shoulder/torso reflections (Brown and Duda, 1998). Thus, it can be mentioned that PC1, PC2, PC3, and PC4 mainly contribute to the effect of pinna/head diffractions and that PC9 and PC10 mainly contribute to the effect of shoulder/torso reflections. Physical acoustics can support these interpretations. For example, 0.2 ms corresponds to the wave propagation distance of approximately 7 cm and this distance is comparable to the physical size of pinna.

The weight of PC (PCW) represents the contribution of each PC in the reconstructed HRIR. Figure 2 shows the distributions of PCWs for the left-ear HRIRs of the 45 subjects at each elevation in the median plane. Horizontal axis at each panel indicates the source elevation in degrees. At each elevation, the closed square (■) and vertical bar (|) indicate the mean value of PCWs (mPCW) and the ±1 s.d. of PCWs, respectively. The trace of mPCW according to elevation represents the common elevation dependency of PCW across all subjects, and the standard deviation represents how much the intersubject variation exists. Most energy in HRIRs is distributed to the responses of direct pulse and pinna/head diffractions and the lower-numbered PCs have high energy in that responses, thus the absolute values of lower-numbered mPCWs are generally larger than those of higher-numbered mPCWs.

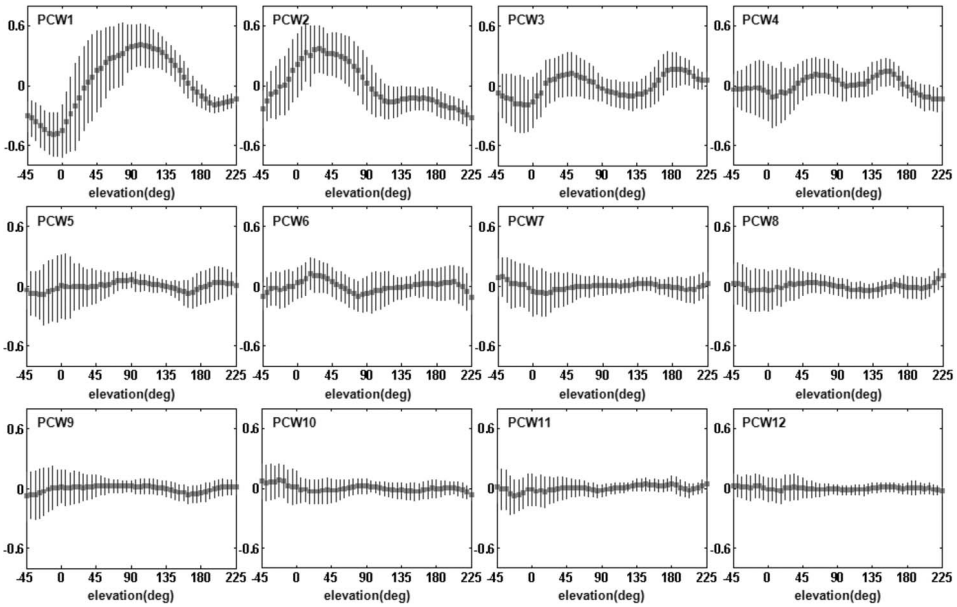

Fig. 2. Distributions of PCWs for the left-ear HRIRs of all subjects at each elevation (45 HRIRs) in the median plane. Horizontal axis at each panel indicates the source elevation in degrees. At each elevation, the closed square (■) and vertical bar (|) indicate the mean value and the ±1 s.d. of PCWs, respectively.

Figure 3 shows variations of mPCWs across all elevations and across all subjects. Open circles and squares indicate the maximum and minimum bounds of mPCWs across all elevations and across all subjects, respectively. Each error bar indicates the ±1 s.d. of mPCWs. All PCs contribute to both the interelevation variations and the intersubject variations; however, the degree of contribution to each of these variations is different from PC to PC. The information in Fig. 3 indicates whether each PC contributes more to the interelevation variations or to

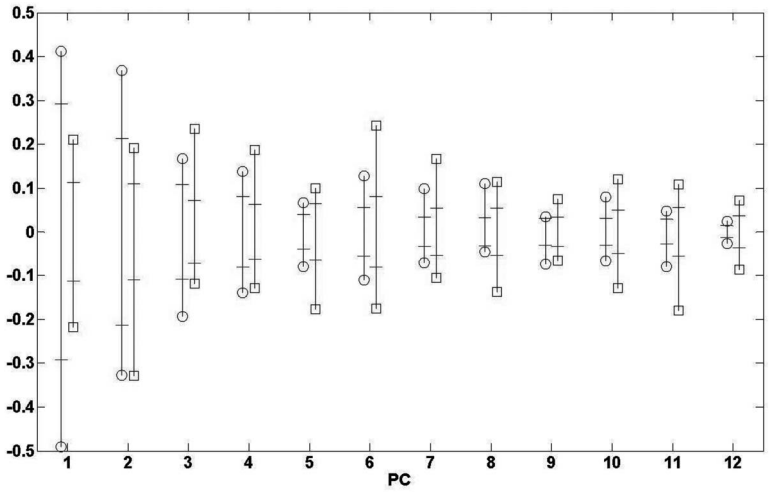

Fig. 3. Variations of mPCWs across elevations and across subjects. Open circles and squares indicate the maximum and minimum bounds of mPCWs across elevations and across subjects, respectively. Each error bar indicates the ±1 s.d. of mPCWs.

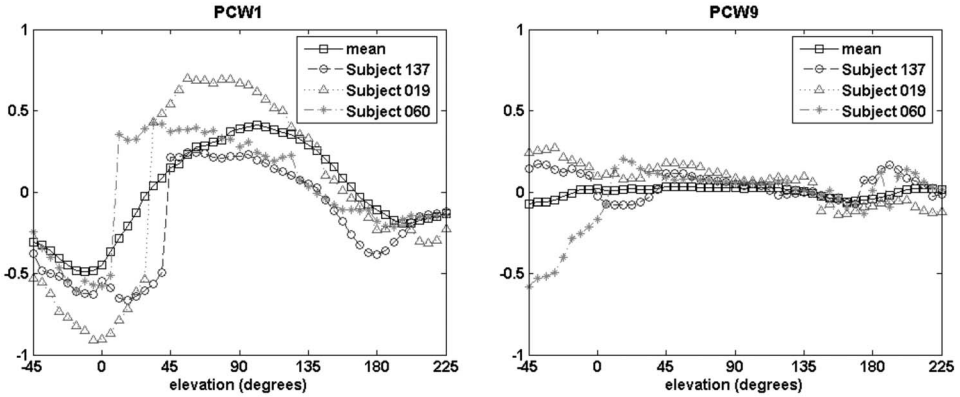

Fig. 4. PCW1 (left panel) and PCW9 (right panel) of representative subjects in the CIPIC HRTF database. Squares (⊟) indicate the mean values of PCWs for all 45 subjects.

the intersubject variations. PCs 1–4 have larger standard deviations of mPCWs across all elevations than those across all subjects, and PCs 5–12 show the opposite results. Thus, it can be mentioned that the interelevation variations in PCs 1–4 are larger than the intersubject variations, whereas the intersubject variations in PCs 5–12 are larger than the interelevation variations. PCWs 5–12 also show obvious elevation dependencies although the variations of mPCWs across all elevations are smaller than those across all subjects.

However, the elevation dependencies of PCWs 5–12 are different from subject to subject. In other words, common elevation dependencies of PCWs 5–12 across all subjects are relatively less obvious than those of the other PCWs. For example, Fig. 4 shows PCW1 and PCW9 of representative subjects according to the elevation. The weights of PC1 for all three subjects show the similar elevation dependency, and the dependency is comparable to that of mPCW1. The elevation where PCW1 rapidly increases is different from subject to subject; however, it is reflected in the variance of PCW1 in Fig. 2. On the other hand, the elevation dependency of PCW9 is different from subject to subject except around 90° of elevation. PCW9 for subject 060 increases rapidly from −45° to 20°, decreases gradually from 20° to 180°, and fluctuates at the other elevations, whereas with the increase of elevation the weights of PC9 for subject 019 and subject 137 decrease gradually and fluctuate, respectively. Therefore, it can be concluded that the elevation dependencies of the higher-numbered PCWs exist, but those are different from subject to subject and the intersubject differences are reflected in the variations of PCWs in Fig. 2.

Meaningful interpretations obtained from Figs. 2 to 4 are summarized as follows.

(a) PC1 has positive mPCW from about 30° to 150° and negative mPCW for other elevations, and mPCW increases monotonically from 0° to 90° and decreases monotonically from 90° to 180°. Therefore, it can be mentioned that there exists the common elevation dependency of PCW1 across all subjects and PC1 provides sound cue for the vertical perception. The intersubject variations are larger in the frontal region than in the rear region because the standard deviations of PCW1 across all subjects are larger in the frontal region.

(b) PC2 has positive mPCW in the frontal region except for low sources below −22.5° and has negative mPCW in the rear region, thus there exists the common elevation dependency of PCW1 across all subjects and PC2 provides sound cue for the front–back discrimination. The intersubject variation of PCW2 is large in the frontal region.

(c) mPCW of PC3 is almost asymmetric about 90°, and its sign changes at approximately 20°, 90°, and 160°. Therefore, the weights of PC3 for all subjects also show the common

elevation dependency, and PC3 provides sound cues for the front–back discrimination and the vertical perception. Similar to PC1 and PC2, PC3 shows larger intersubject variation in the frontal region than in the rear region.

(d) mPCW of PC4 is almost symmetric about 120°; however, it shows locally monotonic changes. Thus, the weights of PC4 for all subjects show the common elevation-dependent tendency and PC4 generally does not contribute to the front–back discrimination but to the vertical perception. PC4 shows larger intersubject variation for the frontal sources at around 0°.

(e) PC5 has almost zero mPCW for all elevated sources, thus there is no common elevation dependency of PCW5 across all subjects. However, the standard deviation of PCW5 is large for sources from −45° to 45° and for low sources in the rear region. Therefore, it can be inferred that the elevation dependency of PCW5 is different from subject to subject and PC5 mainly represents the intersubject variation for these sources.

(f) mPCW of PC6 is almost zero in the rear region except for low sources (above approximately 210°), whereas it is symmetric about 20° in the frontal region. Thus, PC6 generally contributes to the vertical perception in the frontal region. The standard deviation of PCW6 is almost the same for all sources in the median plane.

(g) mPCWs of PCs 7–12 are almost zeros except for low sources, and the standard deviations of these PCs are large for sources from −45° to 45° in the frontal region. Thus, it can be inferred that these PCs mainly represent the intersubject variations for elevated sources from −45° to 45° and the elevation dependencies of PCWs 7–12 are different from subject to subject for those elevated sources.

3. Discussion

PCAs of HRTFs in the frequency domain and PCAs of HRIRs in the time domain each have advantages and disadvantages. Previous studies based on PCA in the frequency domain (Kistler and Wightman, 1992; Middlebrooks and Green, 1992) deal with the log magnitude of HRTFs under the assumption of a minimum phase property of HRTFs, and this can reasonably represent human's sense of hearing because it is roughly logarithmic, whereas PCA in the time domain deals with the linear-scaled HRIRs. However, it is not clear which PCs in the frequency domain are due to the pinna or to the shoulder/torso only because the shoulder/torso response and pinna response are closely coupled. Moreover, the minimum phase assumption leads to HRIR approximation that is much shorter than the original HRIR and where the pinna and torso contributions are merged. On the other hand, PCs in the time domain can be classified into the effects of pinna or shoulder/torso because HRIR can be decomposed into a series of temporal sound events. Furthermore, to carry out PCA in the time domain, both the phase and magnitude information may be considered to obtain PCs.

The number of HRIRs included in our analysis is less than that of HRTFs included in the previous works performed in the frequency domain, but nevertheless the number of necessary PCs in this study is greater than that in the previous studies. Kistler and Wightman (1992) performed PCA using 5300 directional transfer functions (DTFs: mean-subtracted log magnitude of HRTFs) of 10 subjects and obtained 5 PCs to recover 90% of the variance in 5300 DTFs. Middlebrooks and Green (1992) also obtained 5 PCs to recover 89.5% of the variance in 5760 DTFs of 8 subjects. A reason why the number of PCs in our study is greater than that in the previous works is that the HRIRs of more subjects were included in the PCA. When the PCA was performed in the frequency domain using median-plane HRTFs of 45 subjects in the CIPIC HRTF database, the same number of PCs (12 PCs) were needed to recover 90% of the variance in 2205 DTFs (details are not included because PCA in the frequency domain is not within the scope of this letter). Thus, the requirement of a large number of PCs was not attributed to PCA in time domain but to large number of subjects.

One can obtain many sets of orthogonal basis functions by rotation of a specific set of basis functions, thus the set of 12 PCs presented in this letter is one of the sets of orthonormal

basis functions. Other sets of basis functions obtained by rotation may have some other meaningful property or be desirable in interpreting results although the rotation of a set of PCs is not included in this letter.

4. Conclusion

The present letter expands on the previous studies, which dealt with PCA of HRTFs or HRIRs. PCA of median-plane HRIRs in the CIPIC HRTF database was performed in the time domain. The individual HRIRs can be reconstructed by a linear combination of 12 PCs within 5% of error on average. These PCs are based on a larger population of subjects than that in the previous studies, and they include both the intersubject and interelevation variations in the HRIRs. Each PC contributes to effects of pinna/head or shoulder/torso and provides sound cues for the front–back discrimination and/or the vertical perception. There exist common systematic elevation-dependent tendencies of the weights of lower-numbered PCs which contribute to the pinna/head diffractions, whereas the elevation dependencies of the higher-numbered PCWs are different from subject to subject. The interelevation variations in the PCs 1–4 are larger than the intersubject variations, whereas the opposite results are shown in the other PCs.

Acknowledgments

This work was supported by the BK21 project and the Korea Science and Engineering Foundation (KOSEF) through the National Research Laboratory Program by the Ministry of Science and Technology (R0A-2005-000-10112-0).

References and links

Algazi, V. R., Duda, R. O., Thompson, D. M., and Avendano, C. (**2001**). "The CIPIC HRTF database," in *Proceedings of the 2001 IEEE ASSP Workshop on Applications of Signal Processing to Audio and Acoustics*, New Paltz, NY.

Brown, C. P., and Duda, R. O. (**1998**). "A structural model for binaural sound synthesis," IEEE Trans. Speech Audio Process. **6**, 476–488.

Chen, J., Van Veen, B. D., and Hecox, K. E. (**1995**). "A spatial feature extraction and regularization model for the head-related transfer function," J. Acoust. Soc. Am. **97**, 439–452.

Grantham, D. W., Willhite, J. A., Frampton, K. D., and Ashmead, D. H. (**2005**). "Reduced order modeling of head related impulse responses for virtual acoustic displays," J. Acoust. Soc. Am. **117**, 3116–3125.

Hwang, S., and Park, Y. (**2007**). "HRIR customization in the median plane via principal components analysis," in *Proceedings of the AES 31st International Conference*, London.

Kistler, D. J., and Wightman, F. L. (**1992**). "A model of head-related transfer functions based on principal components analysis and minimum-phase reconstruction," J. Acoust. Soc. Am. **91**, 1637–1647.

Martens, W. L. (**1987**). "Principal components analysis and resynthesis of spectral cues to perceived direction," in *Proceedings of International Computer Music Conference*, San Francisco, CA.

Middlebrooks, J. C. (**1999**). "Individual differences in external-ear transfer functions reduced by scaling in frequency," J. Acoust. Soc. Am. **106**, 1480–1492.

Middlebrooks, J. C., and Green, D. M. (**1992**). "Observations on a principal components analysis of head-related transfer functions," J. Acoust. Soc. Am. **92**, 597–599.

Shin, K., and Park, Y. (**2008**). "Enhanced vertical perception through head-related impulse response customization based on pinna response tuning in the median plane," IEICE Trans. Fundamentals **E91–A**, 345–356.

Wu, Z., Chan, F. H. Y., Lam, F. K., and Chan, J. C. K. (**1997**). "A time domain binaural model based on spatial feature extraction for the head-related transfer function," J. Acoust. Soc. Am. **102**, 2211–2218.

 [DOI: 10.1121/1.2884349] Published Online 17 March 2008

Tactile enhancement of auditory and visual speech perception in untrained perceivers

Bryan Gick
Department of Linguistics, University of British Columbia, Vancouver, British Columbia, V6T 1Z4 Canada
and Haskins Laboratories, New Haven, Connecticut 06511
gick@interchange.ubc.ca

Kristín M. Jóhannsdóttir
Department of Linguistics, University of British Columbia, Vancouver, British Columbia V6T 1Z4 Canada
stina@mail2skier.com

Diana Gibraiel
Center for Middle Eastern Studies, University of Chicago, Chicago, Illinois 60637
dgibraiel@uchicago.edu

Jeff Mühlbauer
Department of Linguistics, University of British Columbia, Vancouver, British Columbia V6T 1Z4 Canada
jefmuehl@interchange.ubc.ca

Abstract: A single pool of untrained subjects was tested for interactions across two bimodal perception conditions: audio-tactile, in which subjects heard and felt speech, and visual-tactile, in which subjects saw and felt speech. Identifications of English obstruent consonants were compared in bimodal and no-tactile baseline conditions. Results indicate that tactile information enhances speech perception by about 10 percent, regardless of which other mode (auditory or visual) is active. However, within-subject analysis indicates that individual subjects who benefit more from tactile information in one cross-modal condition tend to benefit less from tactile information in the other.

© 2008 Acoustical Society of America
PACS numbers: 43.71.Es [AL]
Date Received: October 2, 2007 **Date Accepted:** December 15, 2007

1. Introduction

It has long been known that both visual (McGurk and MacDonald, 1976) and tactile (Sparks *et al.*, 1978) information can influence auditory speech perception. Previous research on the effect of tactile information on speech perception has focused primarily on enhancing the communication abilities of deaf-blind individuals (Chomsky, 1986; Norton *et al.*, 1977; Reed *et al.*, 1989). Central to much of this research is the Tadoma method (Alcorn, 1932). Tadoma involves a perceiver placing his or her hand on a speaker's face in a specific position in order to gain tactile speech information. Typically, deaf-blind individuals require years of training in order to use Tadoma successfully. While a minority of previous studies have tested the use of the Tadoma method by individuals with normal hearing, speech, and visual systems (Blamey *et al.*, 1989, Reed *et al.*, 1978, 1982), the subjects of these studies were researchers who had extensively studied the Tadoma method, and who had additional training prior to undergoing the experiment.

In one of the few experiments demonstrating the influence of tactile information on speech perception in a completely untrained population, Fowler and Dekle (1991) showed that manual tactile contact with a speaker's face coupled with incongruous auditory input can elicit an audio-tactile (AT) McGurk-type illusion. However, the extent to which different modalities interact with one another in speech perception is not known. A relevant property of intermodal interaction is superadditivity, whereby a perceiver gains more benefit from information via one

 © 2008 Acoustical Society of America

modality when that information is coupled with information via another modality (e.g., McGrath and Summerfield, 1985). It is unknown, however, whether there exist complex relationships across modalities, such that a particular modality will receive greater enhancement when coupled with specific other modalities, or whether such interactions may vary across perceivers.

The present paper uses the Tadoma method to test interactions across two bimodal perception conditions for a single group of untrained perceivers. One condition involved audio-tactile (AT) speech perception in noise by perceivers unable to see the speaker, and one involved visual-tactile (VT) speech perception by perceivers when the speech was masked by noise.

2. Method

Twelve native speakers of North American English between the ages of 20 and 40 participated in the study—five male, and seven female. All subjects had normal speaking and hearing skills, and no training in linguistics, speech sciences, or any method of tactile speech perception.

Video and audio of all trials were recorded using a Sony DCR-TRV19 mini-DV camcorder. An experimenter (the third author, a female native speaker of English) read aloud from prepared lists of token utterances. All tokens on the list had the structure /aCá/, where the intervocalic consonant in each token was one of the 14 English obstruents: /b, p, t, d, k, g, f, v, θ, ð, s, z, ʃ, ʒ/. Five repetitions of each disyllable were included, for a total of 70 tokens per trial. For each subject, a different randomized list was used for each trial.

An audio-only pre-test was conducted prior to the main experiment to set subject-specific noise levels. Half of the subjects participated in the AT condition first, and half participated in the VT condition first, allowing for control of whether prior experience in one condition could affect performance in the other. A separate control trial was used to test participants' ability to perceive the relevant consonants based on audio-only or visual-only input (without tactile information). Thus, within AT and VT conditions, half of the subjects participated in the control trial first, while half participated in the test trial first.

(1) Pre-trial. Each subject wore isolating headphones playing white noise with a frequency band from 0 to 11 025 Hz at a sampling rate of 22 050 Hz, and was instructed to close his or her eyes. The subject sat at arm's length from the experimenter, who read from a randomized list of /aCá/ tokens prepared as described above. Simultaneously, a second experimenter adjusted the volume of the white noise in the headphones. Noise levels were set so that the subject could distinguish the correct segment with greater than chance frequency. During the pre-trial for the VT condition, each subject was instructed to raise a hand when he or she heard the experimenter speaking; noise levels were increased until the subject indicated (by a lowered hand) that the experimenter's voice was no longer audible at all. The final level was set slightly higher than this, and several additional utterances were used to confirm inaudibility.

(2) AT trial (With Tactile condition). Subjects wore isolating headphones playing white noise partially obscuring the acoustic speech signal as described above, and were instructed to keep their eyes closed for the duration of the trial (confirmed after the experiment based on the video record of each session). Each subject was seated at arm's length from the experimenter, with his or her right hand placed on the experimenter's face as per the Tadoma method: (a) the subject's index finger was placed horizontally just above the experimenter's mandibular ridge, (b) the other three fingers were fanned out beginning just below the mandibular ridge, across the experimenter's throat, (c) the palm was held over the experimenter's jaw and chin, and (d) the thumb was placed lightly on the experimenter's lips. Subjects received no instructions concerning how or whether to interpret the information conveyed through the hand-face contact. Once the subject was in place, the experimenter read aloud from a list of 70 token utterances prepared as described above. Despite many hours of training to ensure constant productions, the experimenter occasionally misspoke (as confirmed in the video and audio record of the experiment), with the result being that not all consonants in the stimuli lists were presented to each subject exactly five times. Subjects were instructed to listen to the experimenter, and to repeat each disyllable aloud in full to the best of his or her ability. A second experimenter recorded the subject's responses. This experimenter's record was later checked against the video and audio

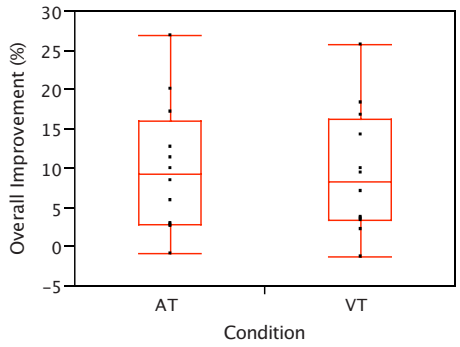

Fig. 1. (Color online) Overall percent improvement in correct segment identification due to tactile information in AT and VT conditions. Standard box plots show median, range and quartiles.

record by consensus among three phonetically trained experimenters. The audio record was also used to confirm that the experimenter spoke at a consistent amplitude across conditions.

(3) VT trial (With Tactile condition). Procedures were identical to the AT trial, except as follows: (a) the amplitude of the white noise was adjusted (as described above) to completely obscure the acoustic speech signal, (b) subjects kept their eyes open for the duration of the experiment, and (c) subjects were instructed to look at the primary experimenter throughout the trial.

(4) Control trials (Without Tactile conditions). Procedures were identical to the AT and VT trials, respectively, except that subjects had no physical contact with the experimenter during the trial.

3. Results

3.1 Overall results

Total percent improvement in consonant identification was compared across subjects and consonants for the Tactile conditions relative to the control conditions, i.e., auditory only or visual only, using paired t-tests (paired by subject). Results were highly significant, indicating a mean improvement of 9.96% (percentage points out of total possible correct, compared with a hypothesized difference of zero) for the AT condition [$t(11) = -4.2100$; $p = 0.0015$] and 9.42% for the VT condition [$t(11) = -4.0868$; $p = 0.0018$].

Total percentage improvement across VT and AT conditions was also compared using a paired t-test (paired by subject). Results indicate no difference between VT and AT conditions [$t(11) = 0.1483$; $p = 0.8848$]. Figure 1 plots improvements for all subjects with quartile box plots.

No significant effects of order of trial presentation were found, allowing all subjects to be included in all across-subject analyses.

3.2 Subject-by-subject results

Figure 2 shows percent accuracy results plotted by subject for AT and VT conditions. Although overall results were virtually identical across AT and VT conditions (Fig. 1), subject-specific results varied considerably. Figure 3 plots each subject's improvement in AT vs. VT conditions in a bivariate scatterplot. Linear regression indicates a significant negative correlation between improvement in AT vs. VT conditions ($r^2 = 0.4479$; $p = 0.0243$; Subject 7's values lay outside of a 95% confidence ellipse, and were therefore omitted from this analysis). No significant correlation was found between baseline accuracy in a modality and improvement due to adding tactile information.

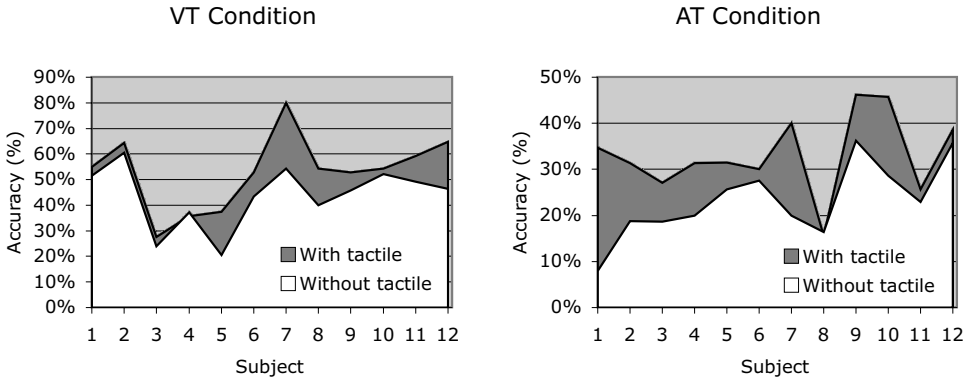

Fig. 2. Subject-by-subject improvement in correct segment identification in AT (left graph) and VT (right graph) conditions. The top line in each graph shows accuracy in With Tactile condition and the bottom line shows accuracy in Without Tactile condition. The gray region between the lines represents the improvement due to addition of tactile information.

4. Discussion

Across-subject results for the AT vs. VT conditions suggest that manual tactile information does enhance speech perception by about 10% in untrained perceivers. However, subject-specific results indicate that individual subjects vary substantially in how much improvement is gained from adding tactile information to each of the other perceptual modalities tested. Specifically, subjects who gain more from adding tactile information to the auditory modality tend to gain less from adding tactile information to the visual modality, and vice-versa. This supports the contention that modal additivity may differ for different cross-modal pairings across subjects.

5. Conclusion

The findings of this study support the notion that manual tactile information relevant to recovering speech gestures enhances speech perception in normal perceivers untrained in methods of tactile speech perception even for combinations of modalities where specific prior experience is unlikely (e.g., visual + tactile). Further, this enhancement occurs regardless of the other active modality—auditory or visual. However, the finding that subjects who gain more from tactile input coupled with an auditory baseline gain less from tactile input coupled with a visual baseline suggests that there is substantial individual variation in terms of which modality is favored for speech perception and how cross-modal information is combined.

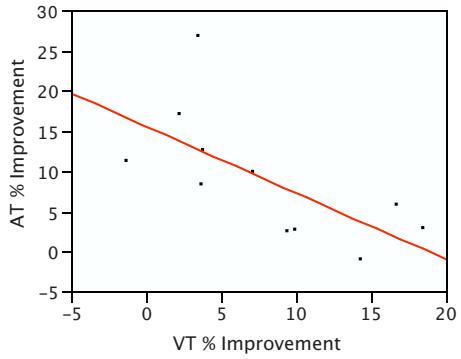

Fig. 3. (Color online) Relationship between percent improvement in correct segment identification due to adding tactile information. Linear fit shown indicates a significant negative correlation.

Acknowledgments

The authors thank Yoko Ikegami and Doug Whalen, and acknowledge support from an NSERC Discovery Grant to B.G. and NIH Grant No. DC-02717 to Haskins Laboratories.

References and links

Alcorn, S. (**1932**). "The Tadoma method," Volta Rev. **34**, 195–198.
Blamey, P. J., Cowan, R. S. C., Alcantara, J. I., Whitford, L. A., and Clark, G. M. (**1989**). "Speech perception using combinations of auditory, visual, and tactile information," J. Rehabil. Res. Dev. **26**(1), 15–24.
Chomsky, C. (**1986**). "Analytic study of the Tadoma method: Language abilities of three deaf-blind subjects," J. Speech Hear. Res. **29**, 332–347.
Fowler, C., and Dekle, D. (**1991**). "Listening with eye and hand: Crossmodal contributions to speech perception," J. Exp. Psychol. Hum. Percept. Perform. **17**, 816–828.
McGurk, H., and MacDonald, J. (**1976**). "Hearing lips and seeing voices," Nature (London) **264**, 746–748.
McGrath, M., and Summerfield, Q. (**1985**). "Intermodal timing relations and audio-visual speech recognition by normal hearing adults," J. Acoust. Soc. Am. **77**, 676–685.
Norton, S. J., Schultz, M. C., Reed, C. M., Braida, L. D., Durlach, N. I., Rabinowitz, W. M., and Chomsky, C. (**1977**). "Analytic study of the Tadoma method: Background and preliminary results," J. Speech Hear. Res. **20**, 574–595.
Reed, C. M., Rubin, S. I., Braida, L. D., and Durlach, N. I. (**1978**). "Analytic study of the Tadoma method: Discrimination ability of untrained observers," J. Speech Hear. Res. **21**, 625–637.
Reed, C. M., Doherty, M. J., Braida, L. D., and Durlach, N. I. (**1982**). "Analytic study of the Tadoma method: Further experiments with inexperienced observers," J. Speech Hear. Res. **25**, 216–223.
Reed, C. M., Durlach, N. I., Braida, L. D., and Schultz, M. C. (**1989**). "Analytic study of the Tadoma method: Effects of hand position on segmental speech perception," J. Speech Hear. Res. **32**, 921–929.
Sparks, D. W., Kuhl, P. K., Edmonds, A. E., and Gray, G. P. (**1978**). "Investigating the MESA (Multipoint Electrotactile Speech Aid): The transmission of segmental features of speech," J. Acoust. Soc. Am. **63**(1), 246–257.

Dial A440 for absolute pitch: Absolute pitch memory by non-absolute pitch possessors

Nicholas A. Smith
Boys Town National Research Hospital, 555 North 30th St., Omaha, Nebraska, 68144
smithn@boystown.org

Mark A. Schmuckler
Department of Psychology, University of Toronto Scarborough, 1265 Military Trail, Scarborough, Ontario, Canada, M1C 1A4
marksch@utsc.utoronto.ca

Abstract: Listeners without absolute (or "perfect") pitch have difficulty identifying or producing isolated musical pitches from memory. Instead, they process the relative pattern of pitches, which remains invariant across pitch transposition. Musically untrained non-absolute pitch possessors demonstrated absolute pitch memory for the telephone dial tone, a stimulus that is always heard at the same absolute frequency. Listeners accurately classified pitch-shifted versions of the dial tone as "normal," "higher than normal" or "lower than normal." However, the role of relative pitch processing was also evident, in that listeners' pitch judgments were also sensitive to the frequency range of stimuli.

© 2008 Acoustical Society of America
PACS numbers: 43.75.Cd, 43.66.Hg [DD]
Date Received: January 3, 2008 **Date Accepted:** February 6, 2008

1. Introduction

There is an apparent paradox in the way listeners process frequency information in music. Despite the transduction and encoding of sound on the basis of frequency, with tonotopic representations beginning in the cochlea, and continuing up through the auditory pathway to cortex (Merzenich and Reid, 1974; Wessinger *et al.*, 1997), in the context of music perception very few listeners are able to identify, remember, or produce musical sounds on the basis of absolute frequencies. Instead, most listeners process music in terms of relative pitch (RP); the relative differences, or intervals, between pitches.

However, this is not strictly true of all listeners. A minority of listeners, those who possess absolute pitch (AP; popularly known as "perfect pitch"), can explicitly produce or recognize an isolated tone, of say 277 Hz, as the musical pitch C#4. This ability is rare in North American culture with estimated incidences ranging from less than 0.1% in the general population (Profita and Bidder, 1988) to 15% among accomplished musicians (Baharloo *et al.*, 1998). However, cross culturally, the incidence is even higher (49%) among conservatory students who identify themselves as "Asian or Pacific Islander" (Gregersen *et al.*, 1999). This result has been confirmed using direct tests of AP ability in music conservatory students in China and the U.S. (Deutsch *et al.*, 2006).

The incidence of AP ability may be higher still if one considers more implicit forms that do not include a naming component. For example, musically trained listeners without absolute pitch can nevertheless identify whether familiar musical excerpts (Bach Preludes) were in the correct key (Terhardt and Seewann, 1983). Similarly, Schellenberg and Trehub (2003) found that listeners can discriminate original versions of familiar instrumental television theme songs from versions that were shifted in pitch by 1 or 2 semitones. Furthermore, production studies have found that even listeners without absolute pitch can sing or hum familiar songs from memory within a few semitones of the original recording (Halpern, 1989; Levitin, 1994).

In the related speech domain, Deutsch (2002) has observed that speakers of a tonal language (Vietnamese) show a high degree of pitch consistency (about 1 semitone or less) in their speech production across test sessions.

Despite the common view that absolute pitch is "special," relative pitch processing is actually quite sophisticated. For example, relative pitch processing allows listeners to correctly identify "Happy Birthday" when played on the piccolo or the cello, in the key of C or the key of G, when sung by a man or a 4-year-old girl, because the relative pitch pattern in the melody remains invariant even though the melody as a whole may be shifted up or down in frequency. In fact, most listeners may simply ignore the absolute pitch information encoded by the auditory system given that relative pitch patterns are of primary importance due to the considerable variance in absolute frequency across instruments, voices, and musical keys. In fact, theories of the psychological representation of melodic information (e.g., Deutsch and Feroe, 1981; Schmuckler, 1999) typically ignore absolute pitch information altogether.

If relative pitch processing allows listeners to perceive invariant structure amid the considerably variant absolute pitch information present in music, how do listeners process sounds for which there is little, if any, variance in frequency? There are few contexts in which this is the case. However, one, perhaps unique, example of such an "auditory standard" is the telephone dial tone, which was introduced in the 1960s. In North America, the dial tone consists of two simple tones with frequencies of 350 and 440 Hz (which incidentally happen to be related by the musical interval of a major third). Technical specifications call for tones within ±0.5% of these nominal frequencies (International Telecommunication Union, 1998). Our spectral analyses of multiple recording of dial tones produced by phones in Toronto and the surrounding area have confirmed that their frequencies are consistently within this range. For decades the dial tone has been ubiquitous, and listeners native to North America have had thousands of experiences with this particular sound. Although it hardly constitutes a sound with which musicians would choose to perform music, it does have a pitch quality for which listeners may have absolute pitch memory.

The fact that the dial tone is not musical actually makes it useful as a stimulus to test absolute pitch memory because people normally do not sing the dial tone. As a result, listeners have no motor memory associated with the production of this particular sound. This characteristic is important because previous studies have found that listeners' vocal productions for remembered music and speech in tonal languages are often quite consistent and/or accurate in their pitch content (Deutsch, 2002; Halpern, 1989; Levitin, 1994). Because it is not possible to entirely rule out memory for previous experiences of vocal tensions required to reproduce these pitches when singing along with one's favorite songs or speaking a tone language, such results may not exclusively reflect auditory memory for the music. In the likely absence of motor memory for the dial tone, however, one can be more confident that listeners' memory is auditory in nature.

The dial tone is also advantageous as a test stimulus because it is heard everywhere at the same frequency. Furthermore, because the pitch of the dial tone does not vary, it is not necessary to attach verbal labels to different pitches, as is done with musical notes (e.g., "do" or "F#"). The dial tone is simply "the dial tone," and even musically untrained listeners can say whether the dial tone sounds normal or not. This is, in fact, one of the limitations of traditional identification or production tests of absolute pitch: absolute pitch can only be tested in musically trained listeners because only they are able to use the verbal labels required for the task. Because the dial tone reflects a unique standard common to all listeners, absolute pitch memory for that standard can be tested in musically untrained listeners.

2. Experiment one

2.1 Method

Fifteen undergraduate students at the University of Toronto Scarborough participated in this experiment. They all reported normal hearing and an average 3.5 (SD=3.5) years of musical

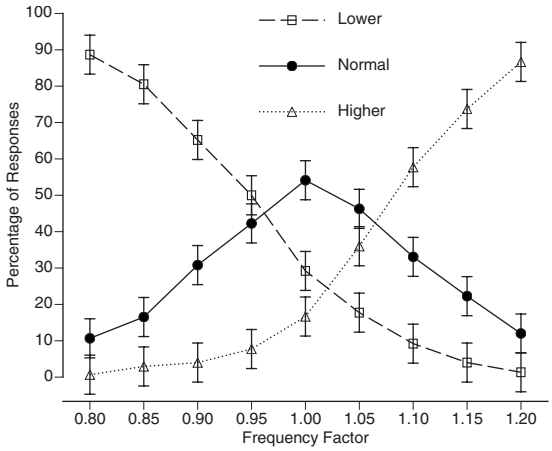

Fig. 1. The distribution of "normal," "higher than normal," and "lower than normal" responses as function of the frequency of the test dial tone from Experiment 1. The normal dial tone has a frequency factor of 1.00. Standard error bars are shown.

training, although there was no training requirement for participation. The nature of absolute pitch was defined and explained to all participants, and any listeners who believed that they possessed absolute pitch were excluded from this experiment.

Nine stimuli (i.e., test dial tones) were created by multiplying the component frequencies of the normal dial tone (350 and 440 Hz) by nine different scaling factors: 0.80, 0.85, 0.90, 0.95, 1.00, 1.05, 1.10, 1.15, and 1.20. Thus, the resulting components produced the normal dial tone when the factor was 1.00, and a higher or lower than normal dial tone when the factor was greater or lower than 1.00, respectively. The 0.5 increments represent a pitch shift of just under one semitone. Each 1-s-long auditory stimulus was generated by a PC and presented to listeners diotically through headphones, at a comfortable listening level.

On each trial listeners heard a randomly selected single test dial tone and were asked to judge whether it sounded "*normal*," "*higher than normal*," or "*lower than normal*." This experimental task was chosen because it did not require attaching a musical label to the stimulus. Because some listeners had no musical training, the experimenter ensured that each listener understood what was meant by "higher" or "lower" prior to the experiment, using a piano keyboard to demonstrate if necessary. Each listener judged each of the nine test dial tones 50 times in a random order. No feedback was given. The experimental session lasted approximately 30 min.

2.2 Results and discussion

For each listener the percentage of "*normal*," "*higher than normal*," and "*lower than normal*" responses for each of the test dial tones were calculated. Because these percentages are not independent (i.e., an increased proportion of "*normal*" responses must be accompanied by a decreased percentage of "*lower*" and/or "*higher than normal*" responses), they were treated as categorical data and analyzed using Pearson χ^2 tests. The rationale underlying this analysis is that if listeners have no absolute pitch memory for the dial tone, the distribution of these three types of responses should not significantly vary across stimuli. However, this null hypothesis was rejected as significant Pearson χ^2 scores were found for each individual listener, ranging from 168.2 to 421.5 ($M=336.20$, all $p's<0.0001$).

The percentage of each response for each test dial tone, averaged across the 15 listeners, is shown in Fig. 1. The percentage of "*normal*" responses significantly varied as a function of frequency, $F(8,112)=18.28$, $p<0.0001$), as did the percentage of "*higher than normal*" responses, $F(8,12)=165.15$, $p<0.0001$, and "*lower than normal*" responses, $F(8,12)$

$=160.00$, $p<0.0001$, although these latter effects are to be expected given the non-independence of these responses. As shown in Fig. 1, listeners were increasingly more likely to respond "*normal*" when test dial tones were normal, "*higher than normal*" when they were higher, and "*lower than normal*" when they were lower.

Altogether, these results demonstrate that listeners identified the normal dial tone amid pitch-shifted variants. Although the general shape and positions of these response functions demonstrate AP memory for the dial tone, listeners' accuracy falls well below that typically found in tests with AP possessors. For example, Takeuchi and Hulse (1993) review a number of studies in which AP possessors show identification accuracy well over 70% to comparisons within a semitone. In contrast, the present results reflect a more broadly tuned sensitivity to absolute pitch information (listeners accuracy only exceeded 70% for "higher/lower than normal" responses for stimuli at least three semitones away from normal). Regardless, the fact that non-AP possessors can make accurate pitch judgments based on their absolute pitch memory is noteworthy. Experiment 2 examines the potential role of relative pitch processing in this task.

3. Experiment two

In Experiment 1, listeners differentiated the normal dial tone from pitch-shifted variants. However, because the normal dial tone was always presented in the center of the range of all stimuli, it is uncertain whether listeners' responses reflect their long-term absolute memory for the dial tone, or relative judgments based on their short-term memory for the range of stimuli tested. In other words, after a number of trials, listeners might have acquired a sense of what the highest and lowest pitches in the stimulus set were and distributed their "higher," "lower," and "normal" responses according to this range. Listeners were tested in conditions in which the normal dial tone was either above or below the center of the pitch range of the test stimuli to examine both absolute and relative pitch processing.

3.1 Method

Thirty-two undergraduate students, none of whom had participated in Experiment 1, were recruited from the undergraduate subject pool at the University of Toronto Scarborough. They had an average 2.5 ($SD=3.2$) years of musical training, although there was no training requirement for participation. As in Experiment 1, AP was defined and explained to all participants, and any listeners who believed that they possessed AP were excluded.

The stimuli were generated in the same manner as Experiment 1, but with an expanded frequency range: 0.70–1.30. The "low range" test block tested stimuli with frequency factors of 0.70, 0.75, 0.80, 0.85, 0.90, 0.95, 1.00, 1.05, and 1.10. The "high range" test block tested stimuli with factors of 0.90, 0.95, 1.00, 1.05, 1.10, 1.15, 1.20, 1.25, and 1.30.

The procedure was identical to that of Experiment 1, with the exception that the testing session was split into two blocks of trials. The order of test blocks was counterbalanced across listeners. Listeners judged whether the stimulus presented was "*normal*," "*higher than normal*," or "*lower than normal*." Within each block listeners rated each stimulus 20 times in random order. The experimental session lasted approximately 30 min.

3.2 Results and discussion

For both the high and low range stimuli the proportion of "*normal*," "*higher than normal*," and "*lower than normal*" responses were calculated for each stimulus. As in Experiment 1, for each individual listener, and for both the high and low range stimuli, the distribution of these three responses significantly varied across test dial tones, with Pearson χ^2 scores ranging from 49.5 to 263.6 ($M=137.7$, all p's <0.0001).

The percentage of each response at each frequency for the high and low range stimuli, averaged across listeners, is shown in Fig. 2. The proportion of "normal" responses significantly varied as a function of frequency, for the low range, $F(8,248)=27.69$, $p<0.001$, and high range stimuli, $F(8,248)=13.17$, $p<0.001$. For the high range stimuli the proportion of "*normal*" responses peaked at 49% for the normal dialtone (1.00), and for the low range range stimuli the

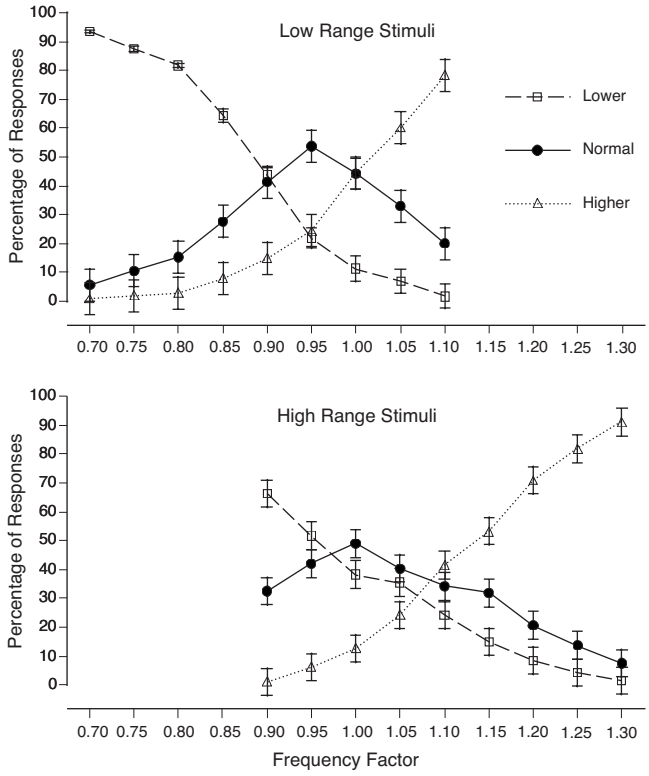

Fig. 2. The distribution of "normal," "higher than normal," and "lower than normal" responses as function of the frequency of the test dial tone for the low range (0.70–1.10) and high range (0.90–1.30) of Experiment 2. The normal dial tone has a frequency factor of 1.00. Standard error bars are shown.

peak was at 54% for the 0.95 dial tone. Thus, although the normal dial tone was shifted away from the center of the frequency range for each block, listeners were able to identify the normal dial tone to within one semitone.

The probability of responding "*higher than normal*" also significantly varied as a function of frequency, for both the high range, $F(8,248)=172.22$, $p<0.001$, and low range stimuli, $F(8,248)=146.47$, $p<0.001$. Finally, the probability of responding "*lower than normal*," varied as a function of dial tone frequency for both the high range, $F(8,248)=67.33$, $p<0.001$, and low range stimuli, $F(8,248)=248.89$, $p<0.001$. As shown in Fig. 2, listeners were increasingly more likely to respond "*higher than normal*" and "*lower than normal*" for test dial tones that were indeed higher and lower than normal, respectively.

Although listeners show fairly accurate discrimination of the normal dial tone from frequency shifted variants, listeners' responses demonstrate some sensitivity to the range properties of these stimuli. To test this statistically, difference scores were calculated by subtracting the percentage of lower responses from the percentage of higher response for each listener at each frequency level that was common across the two sets of stimuli (i.e., from 0.90 to 1.10). These difference scores (shown in Fig. 3) were submitted to a two-way repeated measures analysis of variance with the within-subjects factors of frequency (0.90–1.10) and range (low or high). As expected, a significant main effect of frequency was found, $F(4,124)=272.50$, $p<0.001$, which shows that as the test dial tones increase in frequency from 0.90 to 1.10 listeners shift from judging the test dial tones as "*lower than normal*" to judging them as "*higher than normal*."

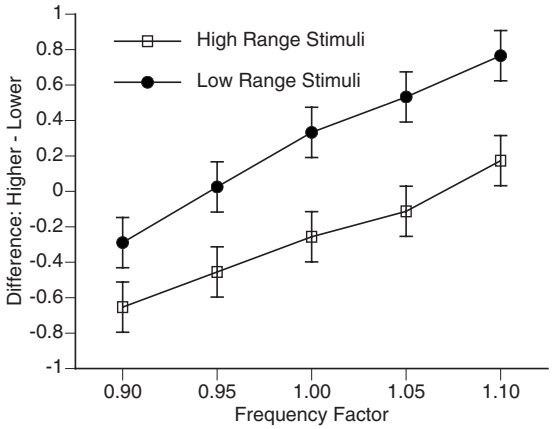

Fig. 3. Difference scores from Experiment 2, calculated by subtracting the percentage of "Lower than normal" responses from the percentage of "Higher than normal response" for the subset of stimuli common to both the high and low range stimuli. Standard error bars are shown.

A significant main effect of range was also found, $F(1,31)=112.63$, $p<0.001$, with mean difference scores of 0.27 and −0.26 for the low and high range stimuli, respectively. This difference illustrates an increased tendency to rate the same test dial tones as lower than normal when they were at the lower end of the range (i.e., the high range stimuli) than when they were at the upper end of the range (i.e., the low range stimuli), and as higher than normal when they were at the upper rather than lower end of the range tested.

The interaction between frequency and range was also significant, $F(4,124)=6.11$, $p<0.001$, and demonstrates that the general frequency range context (high versus low range) differentially influenced judgments, with the low range producing a wider range of responses across the various frequencies than the high range block. This interaction is at present difficult to interpret.

Overall, the results of Experiment 2 demonstrate both an absolute memory for the normal dial tone (as in Experiment 1), as illustrated by the broadly tuned distribution of "*normal*" responses centered to within a semitone of the true normal dial tone. Furthermore, the present results show that listeners' identification of the normal dial tone was not a simple artifact of this stimulus being presented at the center of the range of test dial tones, given that the response distributions show the appropriate skew when the normal dial tone was offset within the range of test stimuli. Finally, listeners' judgments were subtly influenced by changes in the range of the stimuli, suggesting a role for both absolute pitch memory for the dial tone in combination with relative pitch processing with respect to the range of other stimuli.

4. General discussion

The present study demonstrates that musically untrained listeners, who were not absolute pitch possessors, could nevertheless accurately identify the original telephone dial tone amid pitch-shifted variants. This finding demonstrates that over the course of everyday experience, listeners (1) have encoded the dial tone in long-term memory in a way that preserves the absolute frequency information contained in the sounds, and (2) can make accurate pitch judgments of new sounds relative to this internal standard. This ability is similar in some ways to what is typically considered absolute pitch, but also differs in some important respects.

As discussed above, the demonstration of implicit AP memory among listeners without AP is not entirely new (Deutsch, 2002; Halpern, 1989; Levitin, 1994; Schellenberg and Trehub, 2003; Terhardt and Seewan, 1983). The present study extends these results to a new context (i.e., the dial tone), one that is different is some important ways. Unlike other studies of AP, the dial tone stimulus is not musical, or even sing-able. Previous studies have employed

musical stimuli that were ultimately singable, and so the potential for motor memory remains. Thus the present results can more confidently be interpreted as reflecting auditory, not motor, memory.

Although the present study lends support to the idea that some form of absolute pitch memory may be present in listeners not possessing AP in the typical sense, there remain important reasons for constraining the implications of this finding. In particular, the absolute pitch memory demonstrated here may be different from that of "true" AP possessors in important ways.

First, listeners' identification was much less accurate than that typically found in tests of true AP possessors (reviewed in Takeuchi and Hulse, 1993). Furthermore, response functions in the present study were more broadly tuned than in other studies on AP, suggesting that the absolute pitch memory in true AP possessors may indeed be different in both degree and kind. Indeed it is possible that the processing of pitch in terms of musical labels may afford AP possessors greater accuracy.

Second, although listeners appear to be sensitive to absolute pitch information, their responses were also influenced by contextual or relative pitch information. Listeners engaged in both absolute and relative pitch processing in performing this task, which is presumably different from what true AP possessors do. It is interesting to consider what factors might influence the kind of processing listeners perform in different situations. In the present study, for instance, relative pitch information was minimal. Although listeners may have been able to estimate the range of stimuli, the fact that each trial contained only one dial tone, and that the dial tones were randomly selected, may have emphasized the use of absolute pitch information. In contrast, had the dial tones been combined into short melodic patterns, relative pitch processing might have been a more natural mode of processing, causing a loss of sensitivity to the absolute pitch information altogether.

Third, there is the issue of generalizability. The dial tone tested here (consisting of 350 and 400 Hz components) is standard to North America. However, dial tones vary from country to country (International Telecommunication Union, 2003). For example, most Europeans are familiar with a dial tone consisting of a single 425 or 440 Hz component. Accordingly, an important test of many of the processes discussed here would involve examining whether foreign listeners demonstrate a similar AP memory for their local dial tone. A European replication would be particularly interesting because it would also permit an examination of potential timbral influences on AP. Because the North American dial tone is made up of a combination of tones, it has a characteristic timbre that may also aid listeners' identification. Thus, a cross-cultural test of dial tone memory would provide a valuable extension of the current findings.

References and links

Baharloo, S., Johnston, P. A., Service, S. K., Gitschier, J., and Freimer, N. B. (**1998**). "Absolute pitch: An approach for identification of genetic and nongenetic components," Am. J. Hum. Genet. **62**, 224–231.

Deutsch, D. (**2002**). "The puzzle of absolute pitch," Curr. Dir. Psychol. Sci. **11**, 200–204.

Deutsch, D., and Feroe, J. (**1981**). "The internal representation of pitch sequences in tonal music," Psychol. Rev. **88**, 503–522.

Deutsch, D., Henthorn, T., Marvin, E., and Xu, H. (**2006**). "Absolute pitch among American and Chinese conservatory students: Prevalence differences, and evidence for a speech-related critical period," J. Acoust. Soc. Am. **119**, 719–722.

Gregersen, P. K., Kowalsky, E., Kohn, N., and Marvin, E. W. (**1999**). "Absolute pitch: Prevalence, ethnic variation, and estimation of the genetic component," Am. J. Hum. Genet. **65**, 911–913.

Halpern, A. R. (**1989**). "Memory for the absolute pitch of familiar songs," Mem. Cognit. **17**, 572–581.

International Telecommunication Union. (**1998**). "Technical characteristics of tones for the telephone service," ITU-T Rec., E.180/Q35.

International Telecommunication Union. (**2003**). "Various tones used in national networks (according to ITU-T recommendation E.180)," Ann. ITU. Op. Bull **781**, 1–31.

Levitin, D. J. (**1994**). "Absolute memory for musical pitch: Evidence from the production of learned melodies," Percept. Psychophys. **56**, 414–423.

Merzenich, M. M., and Reid, M. D. (**1974**). "Representations of the cochlea within the inferior colliculus of the cat," Brain Res. **77**, 397–415.

Profita, J., and Bidder, T. G. (**1988**). "Perfect pitch," Am. J. Med. Genet. **29**, 763–771.

Schellenberg, E. G., and Trehub, S. E. (**2003**). "Good pitch memory is widespread," Psychol. Sci. **14**, 262–266.

Schmuckler, M. A. (**1999**). "Testing models of melodic contour similarity," Music Percept. **16**, 295–326.
Takeuchi, A. H., and Hulse, S. H. (**1993**). "Absolute pitch," Psychol. Bull. **113**, 345–361.
Terhardt, E., and Seewann, M. (**1983**). "Aural key identification and its relationship to absolute pitch," Music Percept. **1**, 63–83.
Wessinger, C. M., Buonocore, M. H., Kussmaul, C. L., and Mangun, G. R. (**1997**). "Tonotopy in human auditory cortex examined with functional magnetic resonance imaging," Hum. Brain Mapp **5**, 18–25.

Simultaneous estimation of attenuation and structure parameters of aggregated red blood cells from backscatter measurements

Emilie Franceschini, François T. H. Yu, and Guy Cloutier
Laboratory of Biorheology and Medical Ultrasonics, University of Montreal Hospital Research Center, 2099 Alexandre de Sève (room Y-1619), Montréal, Québec, H2L 2W5, Canada
franceschiniemilie@yahoo.fr, francoisyu@videotron.ca, francoisyu@videotron.ca, guy.cloutier@umontreal.ca

Abstract: The analysis of the ultrasonic frequency-dependent backscatter coefficient of aggregating red blood cells reveals information about blood structural properties. The difficulty in applying this technique *in vivo* is due to the frequency-dependent attenuation caused by intervening tissue layers that distorts the spectral content of backscattering properties from blood microstructures. An optimization method is proposed to simultaneously estimate tissue attenuation and blood structure factor. With *in vitro* experiments, the method gave satisfactory estimates with relative errors below 22% for attenuations between 0.101 and 0.317 dB/cm/MHz, signal-to-noise ratios >28 dB and $kR<2.7$ (k being the wave number and R the aggregate radius).

© 2008 Acoustical Society of America
PACS numbers: 43.80.Qf, 43.80.Cs, 43.35.Bf, 43.35.Yb [CC]
Date Received: October 5, 2007 **Date Accepted:** January 15, 2008

1. Introduction

Ultrasonic (US) backscattered echoes from blood contain frequency-dependent information that can be used to obtain quantitative parameters reflecting the aggregation state of red blood cells (RBCs). Recently, two parameters describing RBC aggregation, the packing factor and mean fractal aggregate diameter, were extracted from the structure factor size estimator (SFSE).[1] The SFSE is a second-order data reduction model based on the structure factor and adapted to a dense medium such as blood. This approach is based on the analysis of the backscattered power spectrum that contains information about the size, spatial organization, concentration and mechanical properties of scatterers (i.e., RBCs). The difficulty in applying the SFSE *in vivo* is that the spectral content of backscattered echoes is also affected by attenuation caused by intervening tissue layers between the probe and the blood flow. More generally, ultrasound scatterer size estimation techniques for tissue characterization (such as liver, kidney, prostate or breast) are facing similar challenges.[2,3] To correctly evaluate microstructural parameters, it is thus of major interest to take into account tissue attenuation effects. A few groups[2,4,5] developed measurement techniques to evaluate the frequency-dependent attenuation in order to compensate *a posteriori* the backscattered power spectrum. The goal of this letter is to further develop this strategy for *in vivo* measures of RBC scatterer sizes. We propose to simultaneously determine blood structural parameters and total attenuation by using an optimization method, termed the structure factor size and attenuation estimator (SFSAE).

This method consists in fitting the spectrum of the backscattered radio-frequency (rf) echoes from blood to an estimated spectrum by a modified SFSE model. This approach is similar to that presented by Bigelow *et al.*,[3] who estimated the effective radius of tissue microstructure and total attenuation from simulated backscattered signals. Herein, *in vitro* experimental evaluation of the SFSAE is performed. Porcine RBCs were sheared in a Couette flow system, and ultrasonic rf echoes were obtained using a 25 MHz center-frequency transducer. Since skin is one of the most attenuating tissue layers during *in vivo* scanning, three skin-mimicking phantoms with different attenuation coefficients were successively introduced between the

transducer and the blood flow. This study shows the SFSAE ability to evaluate three parameters (the packing factor, mean fractal aggregate diameter, and total attenuation).

2. Structure factor size and attenuation estimator

Blood can be seen as a very dense suspension of red cells. These RBCs cannot be treated as independent scatterers since particle interactions (collision, attraction, deformation, flow dependent motions) are strong. The theoretical model of ultrasound backscattering by blood that we developed[1] is based on the particle approach,[6,7] which consists of summing contributions from individual RBCs and modeling the RBC interaction by a particle pair-correlation function. Assuming that the Born approximation is valid (weak scattering), the model proposed in Ref. 1 can be modified to predict the theoretical backscatter coefficient from blood

$$BSC_{\text{theor}}(k) = m\sigma_b(k)S(k)A(k), \tag{1}$$

where k is the wave vector, m is the number density of RBCs in blood estimated by measuring the hematocrit H by microcentrifugation ($m=H/V_s$, where V_s is the volume of a RBC), σ_b is the backscattering cross section of a single RBC, S is the structure factor describing the spatial organization of RBCs, and A is the frequency-dependent attenuation function. The backscattering cross section σ_b of a weak scattering particle small compared to the wavelength (Rayleigh scatterer) can be determined analytically as follows: $\sigma_b(k)=1/(4\pi^2)k^4V_s^2\gamma_z^2$, where γ_z is the variation of impedance between the RBC and its suspending medium (i.e., the plasma). The structure factor S is by definition the Fourier transform of the pair-correlation function[7] g and can be approximated by its second-order Taylor expansion[1] in k as

$$S(k) = 1 + m\int (g(r)-1)e^{-2jkr}dr \approx W - \frac{12}{5}(kR)^2. \tag{2}$$

In this expression, $g(r)$ represents the probability of finding two particles separated by a distance r. W is the low-frequency limit of the structure factor ($S(k)|_{k\to 0}$) called the packing factor.[7,8] R is the radius of three-dimensional (3D) RBC aggregates assumed to be isotropic. We introduce $D=R/a$ as the isotropic diameter of an aggregate (expressed in number of RBCs) with a the radius of one RBC sphere-shaped model of volume V_s. The attenuation function A is given by: $A(k)=e^{-4\alpha_0 f}$, where f is the frequency and α_0 is the attenuation coefficient (in dB/MHz) defined by: $\alpha_0=\Sigma_i\alpha_i e_i$, where α_i and e_i are, respectively, the intervening tissue layer attenuations (in dB/cm/MHz) and thicknesses. According to the above equation, we thus assume, as a first approximation, that the attenuation linearly increases with the frequency: $\alpha(f)=\alpha_0 f$.

The measured backscatter coefficient reported in this study was computed as

$$BSC_{\text{meas}}(k) = BSC_{\text{ref}}(k)\frac{\overline{P_{\text{meas}}(k)}}{\overline{P_{\text{ref}}(k)}}. \tag{3}$$

In Eq. (3), the mean backscattered power spectrum $\overline{P_{\text{means}}}$ was obtained by averaging the power spectra of 400 backscattered echoes from blood. The mean power spectrum $\overline{P_{\text{ref}}}$ was obtained from a reference sample of non-aggregated RBCs at a low hematocrit of 6% (i.e., Rayleigh scatterers).[9] In this case, 400 echoes were also averaged. The backscatter coefficient of this reference sample BSC_{ref} was estimated using the "Rayleigh estimation" approach used by Yu and Cloutier,[1] which theoretical value is given by Eq. (13) in Ref. 8 (three-dimensional Perkus Yevick packing factor for cylinders). This reference sample was used to compensate the backscattered power spectrum $\overline{P_{\text{meas}}}$ for the electromechanical system response, and the depth-dependent diffraction and focusing effects caused by the US beam.

The packing factor W, aggregate diameter D and total attenuation along the propagation path α_0 were determined by matching the measured BSC_{meas} given by Eq. (3) with the theoretical BSC_{theor} given by Eq. (1). For this purpose, we searched values of W, D, and α_0

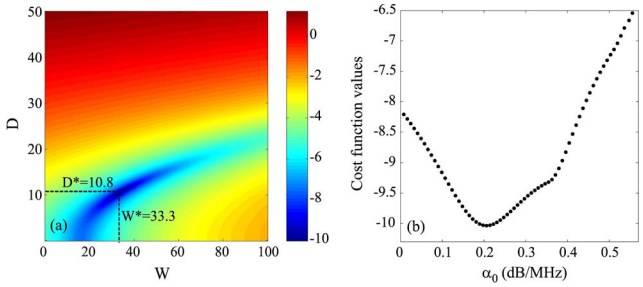

Fig. 1. (Color online) (a) Typical aspect of the logarithm of the cost function $F(W,D,\alpha_0)$ for a fixed value of α_0. The logarithm is shown here in order to enhance the visual contrast. This cost function has one minimum denoted (W^*,D^*) that depends on α_0. (b) Typical aspect of the function $\log(F(W^*,D^*,\alpha_0))$ for varying values of α_0 (W^* and D^* being calculated for each α_0). This cost function has a single minimum.

minimizing the cost function $F(W,D,\alpha_0)=\|BSC_{\text{meas}}-BSC_{\text{theor}}\|^2$. In all studied cases, the cost function seemed to have a unique global minimum, as was observed by plotting the cost function surface $F(W,D)$ with varying values of α_0. An example is given in Fig. 1.

3. Methods

3.1 Experimental setup

US measurements were performed in a Couette flow system to produce a linear blood velocity gradient at a given shear rate (see Fig. 1 in Ref. 10). The system consisted of a rotating inner cylinder with a diameter of 160 mm surrounded by a fixed concentric cylinder of diameter 164 mm. A 60 ml blood sample was sheared in the 2 mm annular space between the two coaxial cylinders. The US scanner (Vevo 770, Visualsonics, Toronto, Canada) equipped with the RMV 710 probe was used in M mode for this study. The single-element focused circular transducer had a center frequency of 25 MHz, a diameter of 7.1 mm and a focal depth of 15 mm. We operated at a sampling frequency of 250 MHz with 8 bits resolution (Gagescope, model 8500CS, Montreal, Canada). The probe was mounted in the sidewall of the fixed outer cylinder and was positioned to have its focal zone at the center of both cylinders. To ensure ultrasonic coupling, the hole within the outer stationary cylinder (containing the probe) was filled with a liquid agar gel based mixture. When solidified, this gel was cut to match the curvature of the cylinder to avoid any flow disturbance. The gel was a mixture of distilled water, 3% (w/w) agar powder (A9799, Sigma Chemical, Saint Louis, MO), 8% (w/w) glycerol, and a specific concentration of 50 μm cellulose scattering particles (S5504 Sigmacell, Sigma Chemical, Saint Louis, MO) that determined the attenuation coefficient. Four experiments were performed with four mixtures having Sigmacell (SC) concentrations varying from 0% to 0.75% (w/w). The 0% concentration constituted the nonattenuating gel and the three other mixtures mimicked skin attenuations.

3.2 Attenuation measurements

The attenuation coefficients of the reference (0%) and three skin-mimicking phantoms α_p were determined by using a standard substitution method. Two transducers with center frequencies of 25 MHz (Vevo 770, Visualsonics, Toronto, Canada) and 20 MHz (V317-SM Panametrics, Waltham, MA) were coaxially aligned facing each other for transmission measurements. Transmitted signals were recorded both with and without the agar gel sample in the acoustic path. The attenuation coefficient was then estimated using a log spectral difference technique.[11] For a given concentration of SC, measurements were obtained from two different sample thicknesses, and for each, four regions were scanned for averaging purpose. Values obtained were 0.007 ± 0.002, 0.101 ± 0.028, 0.208 ± 0.029, and 0.317 ± 0.039 dB/cm/MHz for SC concentrations of 0, 0.25, 0.50, and 0.75%, respectively. The thickness of the skin-mimicking phantoms

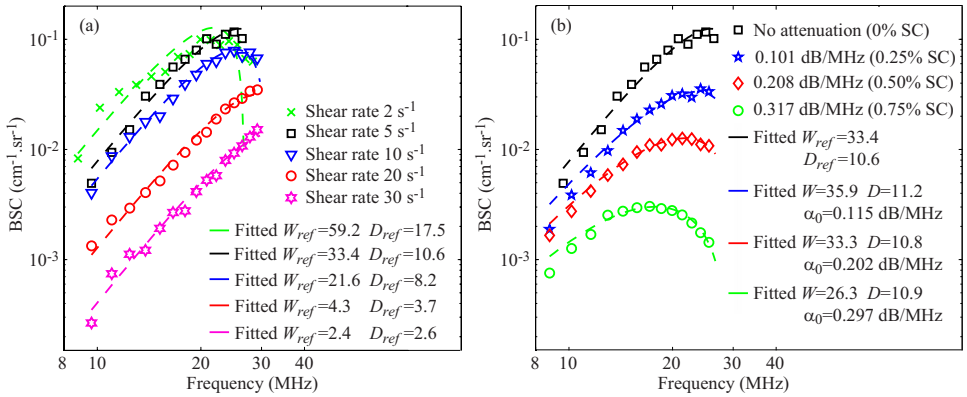

Fig. 2. (Color online) (a) Backscatter coefficients for blood sheared at different residual shear rates and measured with the 0% Sigmacell (SC) concentration phantom (no attenuation), and corresponding fitting with the classical SFSE with no compensation for attenuation. (b) Backscatter coefficients for blood sheared at 5 s^{-1} and measured with each of the four phantoms. The corresponding fitted models are the SFSE for the 0% SC phantom, and the SFSAE for the three other skin-mimicking phantoms (0.25, 0.5, and 0.75% SC).

e_p being fixed to 1 cm, their attenuation coefficients were thus in the same range as the human dermis (0.21 dB/MHz at 14–50 MHz considering a 1 mm dermis thickness[12]).

3.3 Blood preparation and measurement protocol

Fresh porcine whole blood was obtained from a local slaughterhouse, centrifuged and the plasma and buffy coat were removed. Two blood samples were then prepared: (i) a H6 reference sample, which was a 6% hematocrit non-aggregating RBCs resuspended in saline solution; and (ii) a 40% hematocrit T40 test sample, which consisted of RBCs resuspended in plasma to promote aggregation. The H6 sample was sheared at 50 s^{-1} and coupled with the 0% SC concentration agar gel. Echoes were selected with a rectangular window of length 0.8 mm at four depths every 0.2 mm (i.e., with 75% overlap between windows). For each depth, the power spectra of the backscattered echoes were averaged over 400 acquisitions to provide $\overline{P}_{\text{ref}}$. Then, the H6 sample was removed and the T40 blood was introduced in the Couette device. In the first 30 s, a shear rate of 500 s^{-1} was applied to disrupt RBC aggregates. The shear rate was then reduced to residual values of 2, 5, 10, 20, and 30 s^{-1} for 90 s. After that, for each shear rate, acquisitions of 400 rf lines were performed for 80 s. Echoes were windowed as for the H6 sample at the same depths and their power spectra were averaged to obtain $\overline{P}_{\text{meas}}$. This protocol was repeated four times with the four agar-based phantoms.

3.4 Reference measurements with the 0% SC concentration phantom

The experiment with the 0% SC phantom was realized in order to have reference results on packing factors W_{ref} and aggregate diameters D_{ref} obtained from the classical SFSE.[1] These parameters were assumed to be true values of packing factors and aggregate diameters for all shear rates, and will be compared in the next section with packing factors and diameters estimated by the SFSAE and by the SFSE when skin-mimicking phantoms are used.

It is important to emphasize the fact that the H6 reference sample was also measured with the 0% SC phantom. The phantom attenuation, although small with no SC, therefore affected equivalently both spectra $\overline{P}_{\text{meas}}$ and $\overline{P}_{\text{ref}}$ in Eq. (3). The resulting measured backscatter coefficient BSC_{ref} was thus not biased by attenuation. The terminology "no attenuation" was used for this experiment in the following.

4. Results and discussion

Figure 2(a) reports results on W_{ref} and D_{ref} for the SFSE in the case of no attenuation. Typical results of the SFSAE minimization procedure for the different agar phantoms at a shear rate of

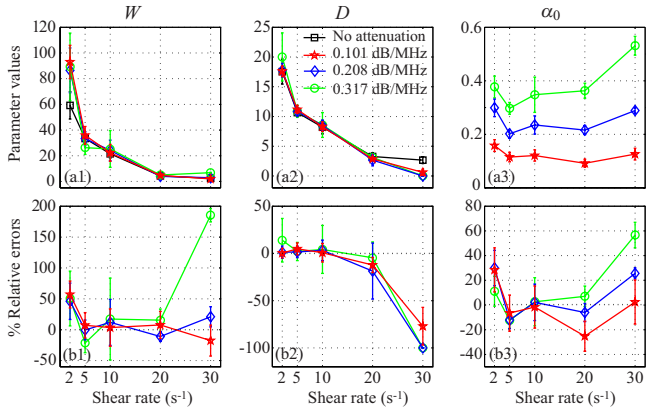

Fig. 3. (Color online) (a) Values of W, D, and α_0 (in dB/MHz) for different residual shear rates estimated by the classical SFSE for the 0% SC concentration and by the SFSAE for the three skin-mimicking phantoms. (b) Corresponding relative errors.

5 s^{-1} are given in Fig. 2(b). All results on W, D, and α_0 from the SFSAE are summarized in Fig. 3 for all residual shear rates. In this figure, the relative errors for each parameter correspond to: $(W-W_{\text{ref}})/W_{\text{ref}}$, $(D-D_{\text{ref}})/D_{\text{ref}}$, and $(\alpha_0-\alpha_{\text{ref}})/\alpha_{\text{ref}}$, with α_{ref} measured in transmissions. More specifically, α_{ref} corresponds to $\Sigma_i \alpha_i e_i = (\alpha_p e_p + \alpha_{\text{blood}} e_{\text{blood}})$, where $\alpha_p e_p$ is the skin-mimicking phantom attenuation estimated in transmission, and $\alpha_{\text{blood}} e_{\text{blood}}$ is the blood attenuation taken equal to 0.022 dB/MHz (Ref. 1) for all shear rates. To underline the necessity to take into account the attenuation, parameters W_{nocomp} and D_{nocomp} were evaluated with the SFSE without attenuation compensation when skin-mimicking phantoms were used. Because of the frequency-dependent distortion produced by the attenuating medium, large relative errors can be seen in Fig. 4(a) for both parameters. However, by compensating the backscatter coefficients

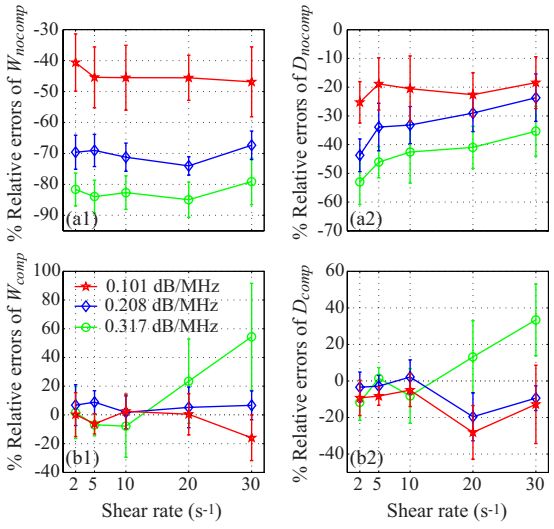

Fig. 4. (Color online) Relative errors of the packing factor and aggregate diameter for the three skin-mimicking phantoms obtained with the SFSE (a) with no compensation for attenuation (W_{nocomp} and D_{nocomp}), and (b) with attenuation compensation using the attenuation values estimated in transmission (W_{comp} and D_{comp}). Parameters W_{nocomp} and W_{comp} and similarly D_{nocomp} and D_{comp} are compared with W_{ref} and D_{ref}, respectively.

in the SFSE with the value measured in transmission (Sec. 3.2), relative errors in Fig. 4(b) are largely reduced to values comparable to those estimated with the SFSAE [see Fig. 3(b)].

The SFSAE (Fig. 3) gave quantitatively satisfactory estimates of W, D, and α_0 with relative errors below 22%, for shear rates between 5 and 20 s^{-1}. The SFSE with attenuation compensation [Fig. 4(b)] gave estimates of W_{comp} and D_{comp} with relative errors below 12% for shear rates between 2 and 10 s^{-1}, and below 28% for the shear rate of 20 s^{-1}. However, for the SFSAE, the average estimates for the shear rate of 2 s^{-1} were less accurate (relative errors below 57% for W and below 30% for α_0). The estimation of D was satisfactory at that shear rate (relative errors below 14%). The worse results of W, D, and α_0 were obtained at 30 s^{-1} for the highest attenuation.

The apparent limit of applicability of the SFSAE method for shear rates of 2 and 30 s^{-1} may be explained by considering the following. At 2 s^{-1}, for the frequency bandwidth considered (9–30 MHz), the SFSE and consequently the SFSAE seem to reach their limit of applicability for large aggregate sizes (typically $D_{ref}=17.5$ in Fig. 2(a), i.e., $kR=4.8$). This limit is illustrated by the bad fit of the SFSE model in Fig. 2(a) at 2 s^{-1}. The bad estimations of the SFSAE at 30 s^{-1} are explained by the fact that the aggregate diameters were estimated to zero and attenuations were overestimated. At this high shear rate, RBC aggregation is partially inhibited and the signal-to-noise ratio (SNR) of our measurements was reduced (≈ -4 dB between 20 and 30 s^{-1} for all phantoms). The accuracy of the estimates was thus degraded with increasing attenuations, as can be seen from the large relative errors at the highest attenuation with the SFSAE but also with the SFSE with attenuation compensation (W_{comp} and D_{comp}).

To conclude, the SFSAE performed well for $kR<2.7$ (i.e., $D=10$ at 5 s^{-1}) and under the condition that the SNR is sufficiently good (SNR >28 dB corresponding to the SNR at 30 s^{-1} for the 0.25% SC). Although the SFSAE gave less accurate estimates for 2 and 30 s^{-1}, the estimated parameter values presented in Fig. 3(a) show that the SFSAE gave qualitatively satisfactory estimates for the three SC skin-mimicking phantoms at all shear rates, since the estimates of W and D versus shear rates had the same behaviors as W_{ref} and D_{ref}.

5. Conclusions

The performance of the new SFSAE was assessed with experimental measurements on blood in a Couette flow device. The accuracy of the estimates obtained with the SFSAE was not as satisfactory as those obtained with the SFSE with attenuation compensation (i.e., when *a priori* are known about the attenuation). Nevertheless, the SFSAE has the major advantage to be easily applicable *in vivo* because of the simultaneous estimation of the blood structural properties and total attenuation (contrary to the SFSE attenuation-compensation method, needing the attenuation and thickness of the tissue intervening layers to be known). This work thus confirms the *in vivo* applicability of RBC aggregate size and structure estimations. Complementary studies are nevertheless required to determine the validity domain of the SFSAE according to kR and attenuation.

Acknowledgments

This work was supported by the Canadian Institutes of Health Research (Grant Nos. MOP-84358 and CMI-72323), by the Heart and Stroke Foundation of Canada (Grant No. PG-05-0313), and by the National Institutes of Health of USA (Grant No. RO1HL078655). Dr. Cloutier is recipient of a National Scientist award of the Fonds de la Recherche en Santé du Québec. The authors are also thankful to Dr. F. Destrempes for his helpful discussion on the optimization tool.

References

[1]F. T. H. Yu and G. Cloutier, "Experimental ultrasound characterization of red blood cell aggregation using the structure factor size estimator," J. Acoust. Soc. Am. **122**, 645–656 (2007).
[2]V. Roberjot, S. L. Bridal, P. Laugier, and G. Berger, "Absolute backscatter coefficient over a wide range of frequencies in a tissue-mimicking phantom containing two populations of scatterers," IEEE Trans. Ultrason. Ferroelectr. Freq. Control **43**, 970–978 (1996).
[3]T. A. Bigelow, M. L. Oelze, and W. D. O'Brien, "Estimation of total attenuation and scatterer size from

backscatter ultrasound waveforms," J. Acoust. Soc. Am. **117**, 1431–1439 (2005).
[4]P. He and J. F. Greenleaf, "Application of stochastic analysis to ultrasonic echoes—Estimation of attenuation and tissue heterogeneity from peaks of echo envelope," J. Acoust. Soc. Am. **79**, 526–534 (1986).
[5]B. J. Oosterveld, J. M. Thijssen, P. C. Hartman, R. L. Romijn, and G. J. E. Rosenbusch, "Ultrasound attenuation and texture analysis of diffuse liver disease: Methods and preliminary results," Phys. Med. Biol. **36**, 1039–1064 (1991).
[6]L. Y. L. Mo and R. S. C. Cobbold, "Theoretical models of ultrasonic scattering in blood," in *Ultrasonic Scattering in Biological Tissues*, edited by K. K. Shung and G. A. Thieme (CRC, Boca Raton, FL, 1993), Chap. 5, pp. 125–170.
[7]V. Twersky, "Low-frequency scattering by correlated distributions of randomly oriented particles," J. Acoust. Soc. Am. **81**, 1609–1618 (1987).
[8]K. K. Shung, "On the ultrasound scattering from blood as a function of hematocrit," IEEE Trans. Sonics Ultrason. **SU-29**, 327–331 (1982).
[9]S. H. Wang and K. K. Shung, "An approach for measuring ultrasonic backscattering from biological tissues with focused transducers," IEEE Trans. Biomed. Eng. **44**, 549–554 (1997).
[10]L.-C. Nguyen, F. Yu, and G. Cloutier, "*In vitro* study of frequency-dependent blood echogenicity under pulsatile flow," Proc.-IEEE Ultrason. Symp. 2007, 2507–2510.
[11]R. Kuc and M. Schwartz, "Estimating the acoustic attenuation coefficient slope for liver from reflected ultrasound signals," IEEE Trans. Sonics Ultrason. **SU-26**, 353–362 (1979).
[12]B. I. Raju and M. A. Srinivasan, "High-frequency ultrasonic attenuation and backscatter coefficients of *in vivo* normal human dermis and subcutaneous fat," Ultrasound Med. Biol. **27**, 1543–1556 (2001).

Illusory spectrotemporal ripples created with binaurally correlated noise

Reza Nassiri
Department of Biomedical Engineering, University of Connecticut, Storrs, Connecticut 06269-1157
rnassiri@gmail.com

Monty A. Escabí
Department of Biomedical Engineering and Department of Electrical and Computer Engineering, University of Connecticut, Storrs, Connecticut 06269-1157
escabi@engr.uconn.edu

Abstract: Binaural disparities are the primary acoustic cues employed in sound localization tasks. However, the degree of binaural correlation in a sound serves as a complementary cue for detecting competing sound sources [J. F. Culling, H. S. Colburn, and M. Spurchise, "Interaural correlation sensitivity," J. Acoust. Soc. Am. **110**(2), 1020–1029 (2001) and L. R. Bernstein and C. Trahiotis, "On the use of the normalized correlation as an index of interaural envelope correlation," J. Acoust. Soc. Am. **100**, 1754–1763 (1996)]. Here a *random chord stereogram* (RCS) sound is developed that produces a salient pop-out illusion of a slowly varying ripple sound [T. Chi *et al.*, "Spectro-temporal modulation transfer functions and speech intelligibility," J. Acoust. Soc. Am. **106**(5), 2719–2732 (1999)], even though the left and right ear sounds alone consist of noise-like random modulations. The quality and resolution of this percept is systematically controlled by adjusting the spectrotemporal correlation pattern between the left and right sounds. The prominence and limited time-frequency resolution for resolving the RCS suggests that envelope correlations are a dominant binaural cue for grouping acoustic objects.

© 2008 Acoustical Society of America
PACS numbers: 43.66.Lj, 43.66.Pn, 43.66.Rq [QJF]
Date Received: June 11, 2007 **Date Accepted:** August 29, 2007

1. Introduction

Interaural time difference (ITD) and interaural level difference (ILD) cues provide critical information about the spatial position of a sound source.[1] Although numerous studies have focused on the role of binaural *disparities* in sound localization phenomena, various studies have alternately emphasized the concept of *correlation* cues in binaural segregation and detection tasks.[2,3] In the *cocktail party problem*[4] for instance, one can attend to a single speaker since the left and right ear waveforms are highly correlated with each other but are uncorrelated with other competing signals. Indeed, subjects exhibit a "binaural advantage" in detection tasks over monaural conditions if two competing signals have independent binaural parameters.[5,6] Several studies have also investigated the ability to discriminate varying degrees of correlation.[2,3] However, only a few demonstrated that sound envelope correlations can enhance detection of a narrowband modulated signal in noise.[3]

One interesting demonstration of binaural grouping involves binaural beats and dichotic pitches where an illusory beating sound or a pitch is perceived when two distinct sounds are presented binaurally.[7,8] If two pure tones of different frequencies are presented dichotically, time-varying ITDs result at the difference frequency and give rise to a beating percept. In the case of Huggins pitch, a phase spectrum discontinuity in broadband noise produces a narrow spectral band with anticorrelated fine structure which gives rise to an internally computed "binaural spectrum".[7]

 © 2008 Acoustical Society of America

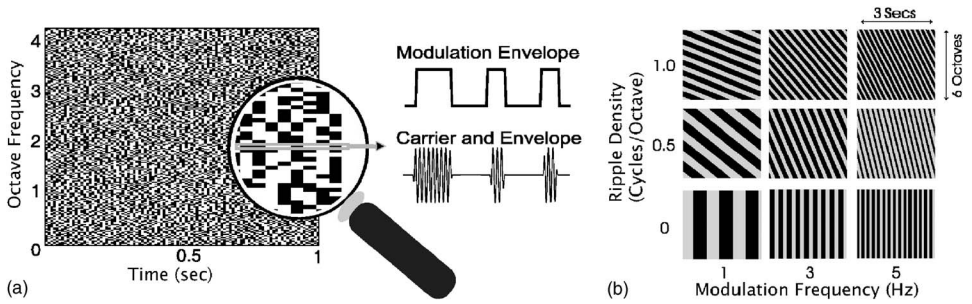

Fig. 1. (a) The right audio channel of the random chord stereogram is generated by modulating sinusoidal channels with a sequence of random spectrotemporal chords (a, left). The corresponding modulation envelope and fine structure (carrier) is shown for one frequency channel (magnifying glass inset) on the right. Black dots correspond to *on* tone-pips and *off* sounds are represented by white dots. (b) The left audio channel is generated by mapping the random chord pattern for the right sound in (a) with a binaural correlation map. The correlation coefficient value in this map determines the likelihood that the same tone-pip pattern is observed simultaneously in the left and right sound. Light bars designate a correlation coefficient of one so that left and right tone-pips at the corresponding time-frequency location occur simultaneously. Dark bars represent zero correlation between the left and right envelope implying that the left and right tone-pips at the specified time-frequency combination are independent. Nine distinct correlation patterns are shown at various spectral (ripple density, RD) and temporal resolutions (temporal modulation frequency, TMF). These binaural correlation map patterns are designed to resemble the spectrogram of a moving ripple sound (see text).

We developed a novel sound that we refer to as the *random chord stereogram* (RCS, samples available at http://www.engr.uconn.edu/~escabi/VRsounds.html) to demonstrate that binaural correlations in the spectrotemporal envelope of a sound can be fused binaurally to create a salient percept of an illusory moving ripple (MR) sound. MRs consist of a sinusoid spectrum noise ("ripples") in which the sound modulations vary with time to create a beating or frequency sweep percept. In contrast to dichotic pitch sounds, the proposed RCS targets binaural envelope correlations independently of interaural fine structure correlation and timing cues.

2. Methods

Experiments were performed in an acoustically shielded sound chamber (IAC, Bronx NY). Sounds were delivered via calibrated earphones (Senheiser HD 600) with a RME 9600 Hamerfall professional audio card and presented at 75 dB sound pressure level. Three-second-long acoustic signals were generated offline in MATLAB (Mathworks, Natick MA) programming environment at 44.1 kHz sampling rate. To generate a RCS sound a random tone-pip sequence (Fig. 1(a)) for the right audio channel was mapped to the left audio channel according to a correlation map (Fig. 1(b)). First, a noise sequence for the right audio channel $[x_R(t)]$ was generated as a sum of randomly chosen tone-pips:

$$x_R(t) = \sum_k \sum_l x_{k,l} \cdot w(t - T \cdot l) \cdot \sin(2\pi f_k t + \theta_k). \quad (1)$$

Here, $f_k = f_1 \cdot 2^{k \cdot \Delta X}$, is the octave frequency axis used for the component tone-pips (upper limit 20 kHz, $0 \le k \le 201$), $f_1 = 100$ Hz is the lowest frequency component, and $\Delta X = 0.0380$ octaves is the spectral separation between adjacent frequency carriers. A b-spline ramped window, $w(t)$ (10 ms duration, 2.5 ms rise time), was used to generate the envelope for each tone-pip with temporal spacing resolution of $T = 10$ ms ($0 \le l \le 300$). For each frequency the carrier phase, θ_k, was chosen from a uniform random distribution within the range $[0, 2\pi]$. Finally, $x_{k,l}$ is a Bernoulli number that randomly turns each tone-pip *on* (1) or *off* (0) at a given time-frequency location.

Once the right audio channel was generated, the left audio channel was constrained by the binaural correlation map (Fig. 1(b)). Correlation maps were generated so that the spectrotemporal correlation pattern between the left and right sounds resembled the spectrotemporal envelope of a moving ripple sound[9] using

$$r_{k,l} = round[0.5 + 0.5\sin(2\pi(\Omega X_k + F_m T_l))], \quad (2)$$

where $X_k = \log_2(f_k/f_1)$ is the octave frequency axis, $T_l = l \cdot T$ is the discrete time axis, Ω is the ripple density (RD, cycles/octave) and F_m is the temporal modulation frequency (TMF, Hz). A correlation of 1 indicates that a given tone-pip is present simultaneously on the left and right audio channels; 0 indicates that a given left and right audio tone-pip occur independently of each other (i.e., randomly; with 0.5 probability). Correlation maps with continuous correlation values (*round* operator removed) were also tested and produced similar results but are not reported here.

2.1 Subjects and procedures

All experiments were conducted with written approval of the University of Connecticut's Internal Review Board. Seven healthy adult subjects participated in various aspects of the study (five in Experiments 1 and 2; four in Experiment 3). Each subject was initially trained to recognize the virtual "beat" (ripple density=0) or "siren" (nonzero values) percepts that are associated with moving ripple sounds. Test sessions started with a "warm up" period and were carried for up to 2 h or until fatigued with 10 min of rest after a maximum of 25 min of testing. Every experiment contained the presentation of two consecutive 3-s-long sounds employing a two-alternative-forced-choice paradigm. A *single sample t-test* was employed to analyze the significance of results. Each subject was tested by fixing RD (0, 0.5, 1, or 1.5) and sequentially incrementing the TMF value. Tests were stopped when the null hypothesis of "subjects find the sound containing the percept at the rate of chance" could not be rejected for at least two consecutive TMF values. Sample sounds used in these experiments can be found at http://www.engr.uconn.edu/~escabi/VRsounds.html.

2.2 Experiment 1

This experiment was conducted to determine if interaural envelope correlations in the RCS produce an audible percept of a moving ripple sound. Since the intended moving ripple percept is not perceived monaurally and was only evident when spectrotemporal correlations are fused binaurally, we refer to this percept as the virtual ripple (VR). Only one of the two test sounds contained the VR effect with the order of presentation randomized. Control sounds consisted of RCS signals in which the binaural envelope correlations ($r_{k,l}$) were set to zero (random envelopes for left-right ears) or one (same sound to both ears). VRs were presented at varying TMF (Fig. 3(a)). The span of TMF was determined via initial trials to establish a relevant range. Each stimulus set was presented only ten times since all subjects had a perfect record of discriminating sound that contained the intended VR percept from the controls sounds (100% correct, *t*-test $p=0$).

2.3 Experiment 2

This experiment was designed to ascertain the resolution of the binaural system engaged in perception of the VR. Both sounds contained the VR effect with nonequal TMFs and the subjects were asked to identify the sound with a faster TMF by selecting the *first* or *second* sound. Each trial involved a set of stimuli with systematically increasing TMF value (Fig. 3(b)). Each set was presented a total of 30 times to each subject. The experiment was repeated with RD values of 0, 0.5, 1, and 1.5 cycles/octave, except for one subject who was tested only at 0 cycles/octave. All subjects were at chance for RD values 1.5 or greater when TMF was >1.

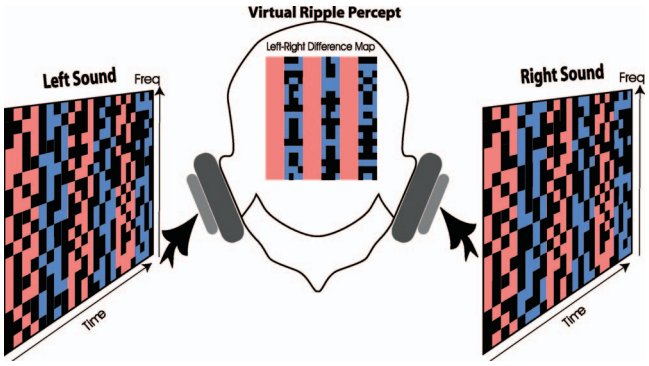

Fig. 2. The RCS paradigm is illustrated for a ripple correlation pattern of RD=0 cycles/octave and TMF=3 Hz. The random envelope modulations for the left and right sounds are individually shown with no evident structure. Superimposed on these patterns is the correlation map (blue: zero correlation, magenta: correlation of one). The absolute value of the difference between the left and right ear random chord patterns, (the difference map at the center) shows that the sounds are identical whenever the correlation map is one (magenta) and random whenever their correlation is zero (blue). Perceptual grouping of these structured correlations between the left and right audio channels produces the intended virtual ripple percept (Fig. 3).

2.4 Experiment 3

This test was conducted on four subjects to determine if binaural *carrier* correlations are required for the VR percept. Two RCS sounds were generated and tested at RD of 0 cycles/octave and TMF of 3 Hz because this combination produced a strong VR percept in experiment 2. The first sound consisted of a standard VR (as for experiments 1 and 2) in which the carrier phase, θ_k, was identical for the left and right ear. A second sound was designed where the carrier phases were uncorrelated for the left and right sounds. In both cases the left and right envelopes were identical (Fig. 1(b)). Subjects were asked to identify which of the two sounds contained the VR percept. Each subject was tested for ten trials, at which point the results were deemed statistically significant (100% correct for all subjects, t-test $p=0$).

3. Results

The proposed RCS sound may be viewed as an acoustic analog of the visual *random dot stereogram*.[10] It is generated by modulating frequency specific sinusoidal channels (carrier or fine structure) with a spectrotemporal envelope (Fig. 1(a)). The spectrotemporal envelope pattern consists of acoustic "chords" that are chosen randomly in time and frequency. The random chord pattern is devoid of any spectral or temporal structure (Fig. 1(a)) so that diotic presentation produces no distinct auditory percept.

We hypothesized that a desired illusory sound pattern could be produced by systematically incorporating binaural correlations to the random RCS sound envelope. To test this hypothesis, the binaural correlation pattern between the left and right sound was adjusted to resemble the spectrogram of a MR sound (Fig. 1(b); Fig. 2). MRs are analogous to visual sinusoid gratings and have been used to systematically characterize spectral and temporal acoustic preferences in humans[9] as well as map neuronal sensitivities in mammals.[11,12] Two key parameters determine the quality of a MR. The ripple density (RD) accounts for the number of spectral peaks and valleys existing over a one-octave frequency segment and is used to adjust the spectral resolution or a perceived timbre. The temporal modulation frequency (TMF) determines the number of onsets and offsets in the sound over time. Here, RD and TMF parameters are used to adjust the spectral and temporal resolution of the correlation map (Fig. 1(b)). Three tests were conducted to characterize whether subjects perceived the intended VR and the stimulus parameters contingent for this percept.

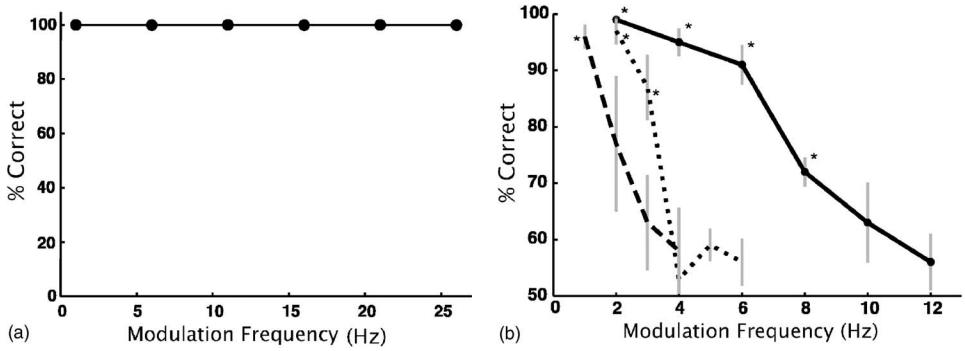

Fig. 3. RCS discrimination results showing the saliency of the virtual ripple percept. (a) RCS sounds with structured correlation are readily discriminated (100% correct, averaged over four subjects) from non-VR sounds. All sounds contained broadband spectral correlations (RD=0). (b) The subjects ability to identify the spectral and temporal quality of the sound was tested as a function of ripple density (RD, solid=0.0 cycles/octave; dotted=0.5 cycles/octave; dashed=1.0 cycles/octave) and temporal modulation frequency (Hz). Subjects accurately identified the spectrotemporal content of the VR percept for low ripple density and temporal modulation frequencies. Performance degrades with increasing spectral (ripple density) or temporal (temporal modulation frequency) resolution. Error bars represent standard error of the mean and * designate significant results at $p<0.01$.

3.1 Experiment 1

Subjects reported a strong VR percept whenever the RCS contained structured envelope correlations as in Fig. 2 (see Methods). Reference non-VR signals were generated either by constructing two uncorrelated (envelope correlation of zero) or two identical (envelope correlation of one) left and right ear random chord sounds. In all cases, subjects readily identified VR from non-VR signals (100% correct at all tested TMF and RD=0 cycles/octave; *t*-test $p=0$) (Fig. 3(a)). At zero ripple density (RD=0, broadband correlations) subjects reported a prominent "beating" sound against a noise background whose beat frequency was determined by the specific TMF value (Mm. 1 and Mm. 2). A nonzero RD produced a sequence of illusory frequency sweeps described as a "siren" in a noise background (Mm. 3).

Mm.1. Virtual ripple audio sample. RD=0 cycles/octave and TMF=3 Hz.

Mm.2. Virtual ripple audio sample. RD=0 cycles/octave and TMF=5 Hz.

Mm.3. Virtual ripple audio sample. RD=0.5 cycles/octave and Fm=1 Hz.

3.2 Experiment 2

VR sounds were easily discriminated at low TMF and zero RD values (Fig. 3(b)). Subjects performed a two alternative force choice task in which they were required to identify the VR sound with higher TMF (tested at RD=0, 0.5, 1, and 1.5 cycles/octave). Discrimination grew worse with increasing TMF [analysis of variance (ANOVA), $F_{1,8}=41$, $P<0.01$] or RD (ANOVA, $F_{1,2}=64$, $P<0.01$). Nonzero RDs gave rise to a notably fainter VR percept than sounds with RD=0. Subjects thus perceive the VR optimally at zero ripple density (broadband correlation) and slow (<8 Hz) temporal modulations.

3.3 Experiment 3

Are fine structure (carrier) correlations a prerequisite for the VR percept? Two RCS sounds were generated with identical envelope correlations to address this question. The fine structure correlations for these two sounds were independently adjusted as either one (identical carrier phase between left and right ear; as for Experiments 1 and 2 in Methods) or zero (independent

carrier phases). All subjects identified sounds with fine structure correlations of one as producing the VR percept and reported no audible percept when zero fine structure correlations were used (100% correct, t-test $p=0$).

4. Discussion

These results demonstrate a salient auditory illusion of a time-varying timbre that is generated by adjusting the pattern of left and right ear envelope correlations. Binaural envelope correlations are present in most listening conditions and likely enhance subjects' ability to group sound objects in the presence of directional head related cues (e.g., ITD and ILD) and background noise. Our results suggest that spectrotemporal correlations in the binaural envelope are an important cue for grouping sounds into a coherent acoustic object; in this case, the illusion of virtual ripples.

The observed grouping in the RCS potentially has some relevance for grouping sound objects in real environments and could contribute to the cocktail party effect.[4] Specifically, binaurally correlated spectrotemporal patterns in the RCS are grouped separately from its uncorrelated segments. These correlated and uncorrelated regions exhibit time-frequency continuity allowing them to be grouped and perceived as a VR. Similarly, when listening to two competing sound sources the spectrotemporal envelope of each sound will be highly correlated binaurally with itself but will be binaurally uncorrelated with the competing source. Thus similar to the RCS paradigm, the sound mixture contains correlated and uncorrelated binaural spectrotemporal components that can be separately grouped.

The perceptual limits underlying this binaural phenomenon differ significantly from monaural or diotic listening conditions in which ripple sounds are integrated and perceived at notably higher spectral and temporal resolutions.[9] Interestingly, the slow time constant for perception of the VR (<8 Hz) is consistent with previous work on binaural "sluggishness"[13] which has been described for moving sounds of varying ITD. Our paradigm differs from this scenario since our sounds have zero ITD with a correlation pattern that moves along the sensory epithelium (shifts from high to low frequency) and not in space. Our results also demonstrate that spectral resolution of the binaural system for grouping sound objects can be coarser than monaural integration. This degraded spectral resolution in the VR (upper limit of $\sim$0.5 cycle/octave) is significantly coarser than the upper limit on the spectral resolution for monaural/diotic ripples and speech (upper limit $\sim$10 cycles/octave).[14,15] Our results differ considerably from previously reported findings which indicate that spectral resolution for processing head related spectral cues for vertical plane localization lies within 0.5–2 cycles/octave.[16] In contrast, binaural critical band measurements suggest that spectral resolution can be equally high for monaural and binaural detection conditions.[17] Thus, while the auditory system is capable of analyzing fine details in the spectral content of a sound for both monaural and binaural tasks, grouping of auditory objects with binaural envelope correlations is restricted to coarse spectral resolutions ($<$0.5 cycles/octave). In theory, the desired correlation pattern in an RCS can be adjusted to any arbitrary spectrotemporal sound pattern. However, the perception of the VR exhibits a distinct trade-off in which high temporal and spectral resolution cannot be resolved concurrently (Fig. 3(b)).

Several mechanisms could contribute to the poor spectrotemporal resolution associated with the RCS. It is possible that these results reflect differences in anatomical convergence of the binaural circuitry or between monaural and binaural integration mechanisms. For instance, although the extraction of ITD information requires precise temporal integration in the brainstem,[18,19] the analysis of binaural envelope cues likely involves sluggish binaural spectrotemporal filters at the cortical level[20] that could potentially account for such distinctions.

Fine structure binaural correlations in the RCS sounds assumed a constant value of one and thus cannot account for the VR percept on their own. Instead, integration of binaural correlations in the sound envelope is consistent with the VR percept since these were designed to resemble the spectrotemporal pattern for MR sounds (Fig. 1(b)). The fact that the VR percept is evident exclusively when the fine structured correlations are one suggests that fine structure interaural correlations are analyzed first, prior to the structured interaural envelope correlations

that give rise to the VR percept. This result is consistent with the hierarchical architecture of the lemniscal auditory pathway where fine structure binaural information is analyzed early on in the auditory brainstem and envelope information is subsequently extracted in the auditory midbrain and cortex.[21] These results differ from previously described binaural phenomena such as Huggins pitch,[7,8] binaural masking release,[5,22] and binaural beats[23] which rely primarily on fine structure or ITD cues. RCS sounds are generated by manipulating the *envelope* correlation patterns while keeping the fine structure correlations constant. These results thus demonstrate that binaural envelope correlations can be grouped together to form a binaural illusory percept.

Acknowledgment

This work was supported by grants from the National Science Foundation (NSF-0139307) and the University of Connecticut research foundation. M.A.E. conceived and designed the RCS sounds. R.N. performed all experiments, data analysis and wrote the manuscript. The authors thank C. Trahiotis, C. E. Schreiner, and P. Crum for reviewing the manuscript and for comments on the interpretation of the results.

References and links

[1]J. C. Middlebrooks and D. M. Green, "Sound localization by human listeners," Annu. Rev. Psychol. **42**, 135–159 (1991).
[2]J. F. Culling, H. S. Colburn, and M. Spurchise, "Interaural correlation sensitivity," J. Acoust. Soc. Am. **110**(2), 1020–1029 (2001).
[3]L. R. Bernstein and C. Trahiotis, "On the use of the normalized correlation as an index of interaural envelope correlation," J. Acoust. Soc. Am. **100**(3), 1754–1763 (1996).
[4]P. Kuyper, "The cocktail party effect," Audiology **11**(5), 277–282 (1972).
[5]H. Levitt and L. R. Rabiner, "Predicting binaural gain in intelligibility and release from masking for speech," J. Acoust. Soc. Am. **42**(4), 820–829 (1967).
[6]M. L. Hawley, R. Y. Litovsky, and J. F. Culling, "The benefit of binaural hearing in a cocktail party: Effect of location and type of interferer," J. Acoust. Soc. Am. **115**(2), 833–843 (2004).
[7]F. A. Bilsen, "Pitch of noise signals: Evidence for a central spectrum," J. Acoust. Soc. Am. **61**(1), 150–161 (1976).
[8]E. M. Cramer and W. H. Huggins, "Creation of pitch through binaural interaction," J. Acoust. Soc. Am. **30**, 412–417 (1958).
[9]T. Chi, Y. Gao, M. C. Guyton, P. Ru, and S. Shamma, "Spectro-temporal modulation transfer functions and speech intelligibility," J. Acoust. Soc. Am. **106**(5), 2719–2732 (1999).
[10]B. Julesz, "Binocular depth perception of computer generated patterns," Bell Syst. Tech. J. **3**(9), 1125–1162 (1960).
[11]D. A. Depireux, J. Z. Simon, D. J. Klein, and S. A. Shamma, "Spectro-temporal response field characterization with dynamic ripples in ferret primary auditory cortex," J. Neurophysiol. **85**(3), 1220–1234 (2001).
[12]M. A. Escabí and C. E. Schreiner, "Nonlinear spectrotemporal sound analysis by neurons in the auditory midbrain," J. Neurosci. **22**(10), 4114–4131 (2002).
[13]D. W. Grantham and F. L. Wightman, "Detectability of varying interaural temporal differences," J. Acoust. Soc. Am. **63**(2), 511–523 (1978).
[14]A. Supin, V. V. Popov, O. N. Milekhina, and M. B. Tarakanov, "Ripple depth and density resolution of rippled noise," J. Acoust. Soc. Am. **106**(5), 2800–2804 (1999).
[15]T. M. van-Veen and T. Houtgast, "Spectral sharpness and vowel dissimilarity," J. Acoust. Soc. Am. **77**(2), 628–634 (1985).
[16]E. A. Macpherson and J. C. Middlebrooks, "Vertical-plane sound localization probed with ripple-spectrum noise," J. Acoust. Soc. Am. **114**(1), 430–445 (2003).
[17]M. van der Heijden and C. Trahiotis, "Binaural detection as a function of interaural correlation and bandwidth of masking noise: Implications for estimates of spectral resolution," J. Acoust. Soc. Am. **103**(3), 1609–1614 (1998).
[18]T. C. Yin and J. C. Chan, "Interaural time sensitivity in medial superior olive of cat," J. Neurophysiol. **64**(2), 465–488 (1990).
[19]R. Batra, S. Kuwada, and D. C. Fitzpatrick, "Sensitivity to interaural temporal disparities of low- and high-frequency neurons in the superior olivary complex. I. Heterogeneity of responses," J. Neurophysiol. **78**(3), 1222–1236 (1997).
[20]J. W. Schnupp, T. D. Mrsic-Flogel, and A. J. King, "Linear processing of spatial cues in primary auditory cortex," Nature (London) **414**(6860), 200–204 (2001).
[21]P. X. Joris, C. E. Schreiner, and A. Rees, "Neural processing of amplitude-modulated sounds," Physiol. Rev. **84**(2), 541–577 (2004).
[22]H. S. Colburn and N. I. Durlach, "Time-intensity relations in binaural unmasking," J. Acoust. Soc. Am. **38**, 93–103 (1965).
[23]J. F. Jarvis, "The binaural beat phenomenon," J. Laryngol. Otol. **69**(10), 685–686 (1955).

The low-frequency sound speed of fluid-like gas-bearing sediments

Preston S. Wilson
Applied Research Laboratories, The University of Texas at Austin, P.O.Box 8029, Austin, Texas 78713-8029 and Department of Mechanical Engineering, The University of Texas at Austin, 1 University Station C2200, Austin, Texas 78712-0292
pswilson@mail.utexas.edu

Allen H. Reed and Warren T. Wood
Marine GeoSciences Division, Naval Research Laboratory, Stennis Space Center, Mississippi 39529
allen.reed@nrlssc.navy.mil, warren.wood@nrlssc.navy.mil

Ronald A. Roy
Department of Aerospace and Mechanical Engineering, Boston University, Boston, Massachusetts 02215
ronroy@bu.edu

Abstract: The low-frequency sound speed in a fluid-like kaolinite sediment containing air bubbles was measured using an acoustic resonator technique and found to be 114 m/s with negligible dispersion between 100 and 400 Hz. The sediment's void fraction and bubble size distribution was determined from volumetric images obtained from x-ray computed tomography scans. A simplified version of Wood's effective medium model, which is dependent only upon the ambient pressure, the void fraction, the sediment's bulk mass density, and the assumption that all the bubbles are smaller than resonance size at the highest frequency of interest, described the measured sound speed.

© 2008 Acoustical Society of America
PACS numbers: 43.30.Ma [GD]
Date Received: December 7, 2007 **Date Accepted:** January 22, 2008

1. Introduction

The acoustic properties of gassy sediments are important in a diverse range of marine applications including sonar and mine hunting,[1] civil and petroleum engineering,[2] and the interpretation of seismic surveys,[3] among others. A number of studies have been performed regarding scattering from, and sound propagation and attenuation in, gas-bearing sediments. Examples are Refs. 4–7. Despite these and other similar studies, the various models for sound propagation in gassy sediments[8–10] have gone largely unverified. Wilkens and Richardson[11] investigated the gas-bearing sediments in Eckernförde Bay and observed resonant bubble acoustic effects consistent with their measured bubble size distribution and the predictions of the Anderson/Hampton model,[8] hereafter referred to as AH. Unfortunately, heterogeneous acoustic measurement techniques, and possibly heterogeneous gas distributions prevented an unambiguous characterization of the sediment acoustic properties. Recently, Best *et al.*[6] obtained wide band sound speed and attenuation measurements on a gassy sediment and enough environmental characterization data to compare the acoustic measurements to the predictions of AH. They found good agreement between measured and modeled acoustic attenuation (using a best fit bubble size distribution) but found poor agreement between measured and modeled sound speed. Again, heterogeneity of the bubble distribution, and deviation from spherical bubbles were cited.

In the present study, we sought to minimize the experimental complexity and uncertainty, and conducted a laboratory experiment with reconstituted kaolinite sediments that contained entrained air bubbles. Low-frequency (below 1 kHz) sound speed measurements were obtained with an acoustic resonator technique. A high-frequency (400 kHz), bistatic sound

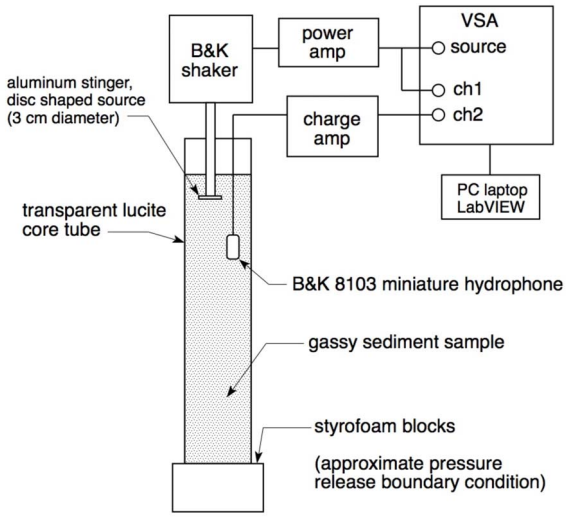

Fig. 1. (Color online) The acoustic resonator and associated apparatus used to obtain the low-frequency sound speed measurements.

speed measurement was attempted but failed due to excess attenuation. High-resolution x-ray computed tomography imagery was used to determine the bubble size distribution and overall void fraction. The fluid-like kaolinite sediment, which had bubbles of primarily spherical and spheroidal shape, exhibited a nondispersive sound speed that was accurately described by a simplified version of Wood's equation.[12] All measured sound speeds were at frequencies well below the lowest individual bubble resonance frequency (IBRF)

2. Description of the apparatus and measurement procedure

The sediment sample was prepared inside an acrylic core tube of circular cross section with 6.1 cm outer diameter, 1 mm wall thickness, and 0.463 m length. A latex rubber membrane (thickness=0.127 mm) was used to close the bottom of the tube. Dried kaolinite was mixed with de-ionized fresh water to a 65% water mass fraction. Air bubbles were entrained during the sample preparation. A measurement of the high frequency (400 kHz) sound speed was attempted using a pulse transmission technique and apparatus described in Refs. 11, 13, and 14, but it failed due to excess attenuation in the sediment. The low-frequency sound speed was determined using the acoustic resonator shown in Fig. 1. The sample-filled core tube was transferred to the acoustic apparatus and positioned as shown. The air–sediment interface at the top and a styrofoam block at the bottom provided pressure release acoustic boundary conditions to a high degree of approximation, as described in Ref. 15. Acoustic standing waves were generated with a 3-cm-diam aluminum piston that was attached to an electromechanical shaker via an aluminum stinger. Band-limited periodic chirps were produced by a vector signal analyzer (VSA) and directed to the shaker through a power amplifier. The source signal was also digitized by the VSA. The piston was positioned a few centimeters below the upper air–sediment interface. The acoustic pressure inside the sediment was received with a miniature hydrophone, positioned a few centimeters below the source. The received signals were bandpass filtered (10–10 kHz) and amplified with a charge amplifier, and digitized by the VSA. According to manufacturer specifications, the source velocity and receiver pressure responses were flat to within less than ±1 dB in the experimental frequency range.

Acoustic pressure spectra were then calculated onboard the VSA by way of a transfer function between the received acoustic pressure and the excitation signal using 20 spectral averages. This preserved the pressure magnitude and phase relative to the excitation signal and

Table 1. Physical properties used in the evaluation of the elastic waveguide model.

Longitudinal sound speed (m/s)	Transverse sound speed (m/s)	Wall material density (kg/m^3)	Inner wall radius (m)	Outer wall radius (m)
c_l=2664	c_t=1087	ρ_w=1185	b=0.0295	d=0.0305

yielded the coherence function. The number of averages and the amplitude of the excitation were chosen to achieve a near-unity coherence function at all frequencies of interest, which guaranteed a high signal-to-noise ratio and ensured linear bubble behavior.[16] Peak pressures inside the sediment were typically less than 160 dB re 1 μPa.

Immediately following the acoustic resonator measurements, the sediment sample was transferred to a Universal Systems HD-500 micro-computed x-ray tomography system.[17] Three-dimensional imaging scans (107 μm voxel size) were obtained over approximately 1/3 of the total sediment volume. A three-dimensional rendering of a portion of the scan is shown in Mm 1. The sediment contained relatively evenly dispersed gas bubbles of primarily spherical or spheroidal bubbles. Image analysis software was used to calculate total gas volume V_{gas} and bubble size distribution. Knowledge of the scanned sediment core tube volume V_{tot} was used to extrapolate global sediment void fraction $\chi = V_{\text{gas}}/V_{\text{tot}}$. The measured void fraction was $\chi = 0.0045$ and the void fraction measurement uncertainty was ± 0.001 due to the voxel size.

[Mm 1. Three-dimensional rendered views of subsets of the micro-CT scans are shown. The yellow-colored objects are gas bubbles. Neither the core tube walls nor the non-gas phases of the sediment are visible (2.9 Mb)]

The bulk mass density ρ_{sed} of gas-free sediment material was measured with a Quantachrome Penta pycnometer. Five samples taken from just below and five from 25 cm below the air–sediment interface were measured. No significant difference was found between the upper and lower locations. The mean density was 1581.4 kg/m^3 and the range of variation of the five samples was ± 5.6 kg/m^3. The density measurement uncertainty was 1 ppt (given in pycnometer's specifications).

3. Accounting for the elastic waveguide effect

In a gas-filled acoustic resonator, the walls are effectively rigid. In a liquid-filled resonator, there is significant coupling between the fill-liquid and the tube. The result is a reduced sound speed relative to that observed in an unconfined environment. This effect is hereafter referred to as the elastic waveguide effect. An exact analytic model[18] for sound propagation in a finite-thickness elastic-walled, fluid-filled cylindrical tube was used to relate the speeds observed in the resonator to the intrinsic sound speed the material would exhibit in an unconfined environment. This procedure (and its validity) is discussed in Ref. 15 and summarized here. Equation (A1) of Ref. 15 is the dispersion relation for the resonator waveguide. The intrinsic sound speed c_0 of the liquid that fills the resonator is an input parameter to Eq. (A1). The phase speed c_{ph} of the plane wave mode is an output. The resonator measurements described here yield the effective phase speed c_{eff} observed inside the waveguide. The intrinsic sound speed c_0 is then varied in Eq. (A1) until the model output c_{ph} matches the measured value c_{eff}. The value of c_0 that achieves the match is reported as the intrinsic sound speed of the sample. The physical parameters used in the elastic waveguide model [Eq. (Al), Ref 15] are given in Table 1. The sound speeds for the tube walls were initially taken from the literature, but the similar values that were ultimately used were obtained via resonator calibration with filtered degassed fresh water.

4. Model of sound propagation in fluid-like gas-bearing sediment

The sediment in this experiment was fluid-like. It flowed readily and its shape was not maintained when unsupported. Therefore, Wood's model[12] for the sound speed in a bubbly liquid was

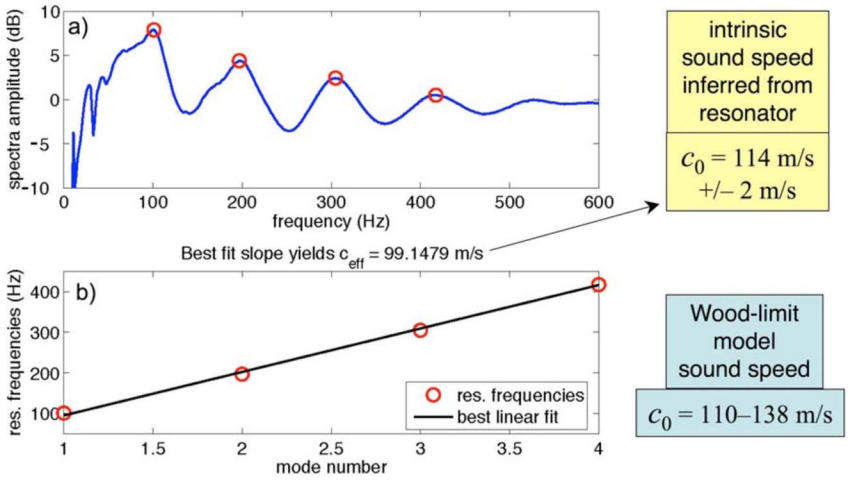

Fig. 2. (Color online) The resonator spectrum obtained for the kaolinite sediment. The four lowest resonance frequencies are identified with circles. (b) The effective sound speed c_{eff} inside the gassy kaolinite-filled waveguide is inferred from these frequencies, where a least-squares fit yields c_{eff}=99.1 m/s. After correcting for the elastic waveguide effect, the intrinsic sound speed inferred from the measurements was c_0=114 m/s ± 2 m/s, where the range is due to finite spectral resolution and the uncertainty in the resonator length L. The Wood limit model [Eq. (1)] predicted c_0=110–138 ms, where the range is due to the uncertainty of the void fraction.

used, which requires that the excitation frequency be well below the resonance frequency of the largest bubble. For $0.002 < \chi < 0.94$, and isothermal conditions (a good approximation for these bubble sizes) the model reduces to[19]

$$c_{\text{lfgs}} = \sqrt{\frac{P_{\text{atm}} + \rho_{\text{sed}} g(L/2)}{\chi(1-\chi)\rho_{\text{sed}}}}, \tag{1}$$

where c_{lfgs} is the low-frequency sound speed in the gassy sediment, P_{atm}=101.3 kPa is the atmospheric pressure, ρ_{sed} is the sediment mass density, g=9.81 m/s^2 is the acceleration of gravity, L is the length of the resonator, and χ is the void fraction. The terms in the numerator account for the mean dependence of the bubble compressibility on the local hydrostatic pressure. In this experiment, the largest bubble radius observed was 4.6 mm. The corresponding bubble resonance frequency is 4.91 kHz, determined by Eq. (1) of Ref. 8 using a conservatively low value for sediment shear modulus ($G=10^4$ Pa), also from Ref. 8. The highest frequency in these experiments was 0.8 kHz, which rendered the low-frequency approximation valid. Note that even if G was set to zero, the lowest bubble resonance frequency would still be about six times higher than the highest acoustic excitation frequency. The simplified form of Eq. (1) is used because it best illustrates the physical nature of sound propagation in near-surface gas-bearing fluid-like sediments.

5. Results

The measured resonator spectrum is shown in Fig. 2(a), where four resonance frequencies are identified. The effective sound speed c_{eff} is inferred from the slope of the curve in Fig. 2(b). The nth resonance frequency is given by $f_n=(c_{\text{eff}}/2L)n$ and L is the length of the resonator. After correction for the elastic waveguide effect (Sec. 3), the intrinsic gassy kaolinite sound speed was c_0=114 m/s±2 m/s. The measurement uncertainty was due to the finite spectral resolution and the uncertainty of L (±1.2 mm). For the length, void fraction and density reported in

Table 2. Measured and predicted sound speeds.

Sediment type	Frequency range of resonator measurements (Hz)	Low-frequency resonator sound speed (m/s)	Sound speed predicted by Eq. (1) (m/s)	400 kHz pulse transmission sound speed (m/s)
Gassy kaolinite	100–550	114 ± 2	110–138	n/a due to excess attenuation
Degassed filtered water (calibration)	200–1000	1494	n/a	1494

Sec. 2, the model [Eq. (1)] predicts a low-frequency gassy sediment sound speed between 110 and 138 m/s. The range of the prediction is due to the void fraction measurement uncertainty. Excellent agreement is observed between the measurement and the model. A summary of the measured and predicted sound speeds appear in Table 2.

6. Conclusions

The two major conclusions of this work are: (1) Resonator measurements of gassy sediments yield the sub-IBRF sound speed even where high-frequency pulse transmission measurements fail. (2) A simplified version of Wood's equation describes the sound speed in shallow gas-bearing fluid-like sediments in which the IBRF of the largest bubble is well above the frequency of the acoustic excitation, and the bubbles are evenly distributed throughout the sample. The gas phase dominates the compressibility. The sound speed is dependent only on the void fraction, the sediment mass density, and the local hydrostatic pressure. It does not depend at all on the material properties of the sediment grains and the fluid, other than through the bulk sediment density. This will cease to be true as the local hydrostatic pressure increases, which in turn decreases the compliance contrast between the gas phase and the longitudinal and shear compliances of the gas-free phase of the sediment. The range of applicability of this simple model is the subject of current work.

Acknowledgments

This work was supported by the University of Texas at Austin Cockrell School of Engineering, the Naval Research Laboratory-Stennis Space Center, Program Element No. 0601153N, and the Office of Naval Research Coastal Geosciences and Ocean Acoustics programs.

References and links

[1]D. R. Jackson and M. D. Richardson, *High-Frequency Seafloor Acoustics* (Springer, New York, 2007).
[2]A. M. Davis, "Shallow gas: An overview," Cont. Shelf Res. **12**, 1077–1079 (1992).
[3]S. N. Domenico, "Effect of brine-gas mixture on velocity in an unconsolidated sand reservoir," Geophysics **41**, 882–894 (1976).
[4]F. A. Boyle and N. P. Chotiros, "A model for high-frequency acoustic backscatter from gas bubbles in sandy sediments at shallow grazing angles," J. Acoust. Soc. Am. **98**, 531–541 (1995).
[5]A. P. Lyons, M. E. Duncan, A. L. Anderson, and J. A. Hawkins, "Predictions of the acoustic scattering response of free-methane bubbles in muddy sediments," J. Acoust. Soc. Am. **99**, 163–172 (1996).
[6]A. I. Best, M. D. J. Tuffin, J. K. Dix, and J. M. Bull, "Tidal height and frequency dependence of acoustic velocity and attenuation in shallow gassy marine sediments," J. Geophys. Res. **109**, B08101 (2004).
[7]T. Gardner, "Modeling signal loss in surficial marine sediments containing occluded gas," J. Acoust. Soc. Am. **113**, 1368–1378 (2003).
[8]A. L. Anderson and L. D. Hampton, "Acoustics of gas-bearing sedimets. II. Measurements and models," J. Acoust. Soc. Am. **67**, 1890–1903 (1980).
[9]A. Bedford and M. Stern, "A model for wave propagation in gassy sediments," J. Acoust. Soc. Am. **73**, 409–417 (1983).
[10]D. M. J. Smeulders and M. E. H. Van Dongen, "Wave propagation in porous media containing a dilute gas-liquid mixture: Theory and experiments," J. Fluid Mech. **343**, 351–373 (1997).
[11]R. H. Wilkens and M. D. Richardson, "The influence of gas bubbles on sediment acoustic properties: In situ, laboratory, and theoretical results from Eckernforde Bay, Baltic sea," Cont. Shelf Res. **18**, 1859–1892 (1998).
[12]A. B. Wood, *A Textbook of Sound*, 1st ed. (MacMillan, New York, 1930).

[13]M. D. Richardson and K. B. Briggs, "In situ and laboratory geoacoustic measurements in soft mud and hard-packed sand sediments: Implications for high-frequency acoustic propagation and scattering," Geo-Mar. Lett. **16**, 196–203 (1996).
[14]K. L. Williams, D. R. Jackson, E. I. Thorsos, D. Tang, and S. G. Schock, "Comparison of sound speed and attenuation measured in a sandy sediment to predictions based on the Biot theory of porous media," IEEE J. Ocean. Eng. **27**, 413–428 (2002).
[15]P. S. Wilson, A. H. Reed, J. C. Wilbur, and R. A. Roy, "Evidence of dispersion in an artificial water-saturated sand sediment," J. Acoust. Soc. Am. **121**, 824–832 (2007).
[16]J. S. Bendat and A. G. Piersol, *Engineering Applications of Correlation and Spectral Analysis*, 2nd ed. (Wiley, New York, 1993).
[17]http://www7430.nrlssc.navy.mil/facilities/CTScanner/hd500mct.htm (last viewed November 2007).
[18]V. A. Del Grosso, "Analysis of multimode acoustic propagation in liquid cylinders with realistic boundary conditions—Application to sound speed and absorption measurements," Acustica **24**, 299–311 (1971).
[19]L. van Wijngaarden, "On the equations of motion for mixtures of liquid and gas bubbles," J. Fluid Mech. **33**, 465–474 (1968).

Segmentation of verb forms in preverbal infants

Alexandra Marquis and Rushen Shi
Département de Psychologie, Université du Québec à Montréal, Montréal, Québec H3C 3P8, Canada
marquis.alexandra@courrier.uqam.ca, shi.rushen@uqam.ca

Abstract: It has been observed that children's early vocabulary is dominated by nouns, with verbs being much delayed. The current study investigated if this delay is related to infants' failure to segment verb forms. Using a preferential looking procedure, French-learning preverbal infants were tested on novel verbs segmentation. Infants at the onset of vocabulary learning (11-month-olds) succeeded in segmenting the targets: they listened longer to test sentences containing previously familiarized verbs versus those containing nonfamiliarized verbs, suggesting that the delay in verb learning is not due to segmentation difficulty. Semantic and syntactic complexities of verbs could be among the underlying factors.

© 2008 Acoustical Society of America
PACS numbers: 43.71.Ft, 43.71.Es [JH]
Date Received: October 18, 2007 **Date Accepted:** January 23, 2008

1. Introduction

Infants begin to develop a vocabulary around the age of one year. A prerequisite for word learning is the capacity to segment word forms from continuous speech. Unlike printed texts, words in utterances are not separated by obvious acoustic cues. Moreover, speech addressed to infants contains mostly multiword utterances rather than isolated words.[1] In addition to finding word boundaries, infants also face the variability problem. That is, the same word type is realized in variable forms due to factors such as phonetic contexts, intonation, speech rate, etc.

Most studies thus far have focused on English-learning infants' strategies and biases, showing that they can use prosodic cues,[2] phonotactic cues,[3] statistical cues,[4] and coarticulation cues[5] during word segmentation. Little work has examined infants learning other languages.[6–8] The existing evidence suggests that properties of the input language affect infants' strategies. English-learning infants use strong stress to determine word boundaries at an early age.[2] French-learning infants, on the other hand, segment nouns based on syllables: Infants around 12 months of age interpret a disyllabic word as two separate forms rather than one single word, and they only succeed in extracting disyllabic forms by 16 months of age.[8] The differential response patterns between the two languages reflect the fact that English is stress-timed and French is syllable-timed. Segmentation studies with infants learning distinct languages thus contribute to the understanding of the role of experience and infants' perceptual biases.

Most infant word segmentation studies that used natural language have focused on nouns. It is interesting to extend this work to other grammatical classes as this may reveal how infants learn linguistic structures. Different grammatical classes assume different roles in the grammar. Language acquisition literature indicates that certain grammatical categories emerge later than others in children's production.[9] For example, early speech typically lacks function words/morphemes. Is this because these items are semantically and syntactically complex and therefore harder to learn? Or is it because infants fail to segment functional items due to their weak, and perhaps less perceptually salient acoustic forms? Is it also possible that infants segment and store these items in memory but fail to produce them due to other constraints? Studies testing infants' initial segmentation of function words help narrow down these factors.

Recent work showed that preverbal infants already segment function words in English,[10,11] German,[12] and French,[13] even though function words are generally reduced in the input.[14] Furthermore, frequent function words assist infants in segmenting adjacent nouns by 8 months of age,[15,16] in syntactic categorization of content words after 1 year of age,[17,18] and in language comprehension at a later stage.[19,20] Therefore, the lack of functional elements in early

speech production does not imply an inability to segment and represent these words. On the contrary, these elements are an essential part of infants' early linguistic representations, and directly impact the acquisition of many aspects of the grammar.

The comparison of nouns and verbs represents another important issue. It is widely observed that children's early speech is dominated by nouns, with verbs much delayed.[21] The delay may be because verbs are conceptually more complex and difficult for word-meaning mapping.[22] But could this delay also be because infants fail to segment verb forms? Few studies on infants' verb segmentation exist.[23,24] It is known that nouns in English are largely trochaic in stress, and verbs tend to be iambic. Given that English-learning infants use strong syllables to find word onset,[2] nouns would be more favorable for segmentation. However, infants segment strong–weak verbs later than strong–weak nouns,[23] suggesting that more subtle acoustic/prosodic properties of verbs may be responsible for the delay. In fact, verbs are typically shorter than nouns in vowel duration in French[25] and English,[26] and therefore may be less perceptually salient. Interestingly, function words, which are segmented as early as initial segmentation of nouns (at the preverbal stage) as discussed earlier, are acoustically and prosodically weaker than nouns and verbs. It was shown that frequency was a dominant factor for infants' segmentation of function words.[15,16] The high frequency of function words seems to offset their less favorable acoustic/prosodic properties. Thus, multiple factors seem to be involved in word segmentation. There is a need in the field to determine how various factors interact in segmentation, what infants' perceptual biases are, and how the properties of the input language may affect segmentation strategies. Empirical data from different languages and across grammatical categories can give us valuable insight into these issues.

This study extends previous work on word segmentation to verbs in French. As in many languages, verbs in French emerge much later than nouns in early production.[27] It is unknown whether this delay is due to infants' difficulty handling semantic/conceptual complexity associated with verbs, or to an inability to segment verb forms. Hence, we aimed to determine if infants can segment some verb forms at the preverbal stage before word learning begins.

In Nazzi *et al.*,[23] disyllabic verbs were only segmented at 13 months of age by English-learning infants. Monosyllabic verbs were not examined, but are likely to be segmented earlier. In noun studies with French-learning infants, only monosyllabic forms appeared to be reliably segmented before 1 year of age: 8-month-old French learners segmented monosyllabic nouns.[16,28] With disyllabic nouns used as targets, infants listened longer to passages containing the targets.[7] These results were interpreted as suggesting that infants segmented the disyllabic forms. However, another interpretation is equally possible: Infants may have used a syllabic strategy and only segmented one of the two syllables of the targets. These possibilities were fully tested using disyllables and each of the two syllables of the disyllables as targets across experiments: Infants at 1-year of age interpreted disyllabic nouns as separate monosyllabic forms.[8] In light of these results, we decided to test 11- and 8-month-old infants and used monosyllabic verbs, to determine the initial verb segmentation ability.

2. Method

Monolingual French-learning infants (sixteen aged 11 months, and sixteen aged 8 months) completed the experiment. Sixteen additional infants were tested but their data were excluded due to parental interference (3), crying (7), experimenter error (1), and refusal to finish the task (5).

The verbs chosen for the task were /bif/ (to cross-out) and /tar/ (to weigh). They are rare in spoken French,[29] thus allowing us to assess infants' ability to segment novel verbs. The verbs belong to the most frequent conjugation group of French verbs. The CVC form is the variant of these verbs (infinitives: *biffer*, *tarer*) for the first/second/third person singular and the third person plural in the present tense, and the second person singular imperative. It is also the form used with the subject pronoun *on*, which is an indefinite pronoun that can refer to any person. In fact, *on* is nearly always used in informal speech. Based on our analysis of the speech of four mothers to their preverbal French-learning infants,[30] 62% of verb forms were monosyllabic, 53% present tense, and 16% imperatives. Thus, our target verbs correspond well with the

Table 1. Mean acoustic values and standard deviations (s.d.) of the vowels of the target words.

	Duration (ms)	Mean F0 (Hz)	Mean amplitude (dB)
/bif/ (6 citation tokens)	704.69 (116.40)	339.42 (91.07)	74.74 (2.69)
/tar/ (6 citation tokens)	575.98 (129.34)	324.17 (122.70)	70.9 (1.64)
/bif/ (7 tokens in sentences)[a]	382.14 (162.40)	335.76 (144.55)	77.77 (2.07)
/tar/ (7 tokens in sentences)[b]	495.08 (228.06)	182.11 (33.48)	73.69 (3.16)

[a]La jolie maman biffe les poèmes. Elle biffe les verbes. Évidemment on biffe la virgule. C'est le juron qu'il biffe. Le petit bébé biffe le graffiti. La syllabe je biffe. Biffes-tu le calembour? (The pretty mommy crosses the poems out. She crosses the verbs out. Obviously we cross the comma out. It's the curse that he crosses out. The little baby crosses the graffiti out. The syllable I cross out. Do you cross the pun out?)
[b]La nouvelle maman tare le magot. Il tare les grappes. Visiblement je tare la parcelle. C'est le lot qu'elle tare. Le gentil bébé tare les gondoles. Les rouets je tare. Tares-tu la coquille? (The new mommy weighs the pile. He weighs the clusters. Visibly I weigh the fragment. It's the share that she weighs. The nice baby weighs the gondola. The spinning wheels I weigh. Do you weigh the shell?)

general verb pattern in the input speech. Two passages were constructed, one with /bif/ and the other with /tar/ in sentences across various positions.

The stimuli were recorded by a native French female speaker, using an infant-directed register, in an IAC sound chamber. The final stimulus set (see Table 1) consisted of one version of the two passages, and six tokens of each verb in citation forms. The prosodic measures for the targets are in Table 1. The six isolated tokens of each verb were doubled and strung together in a random order to create a /bif/ file and a /tar/ file. The interstimulus interval was 435 ms, with minor adjustments to ensure that a length of 13.5 s was maintained for both target files. The duration of the two passage files were each 17.5 s. The sentences ranged from 1.66 to 2.67 s for the /bif/ passage, and from 1.40 to 2.90 s for the /tar/ passage, with an average of 250 ms of between-sentence interval. Two visual files were used, a picture of a black-and-white checkerboard and a video of a flashing light.

Infants were randomly assigned to one of the two familiarization groups, /bif/ or /tar/. One target file was presented repeatedly during the familiarization phase, until infants reached 30 s of total looking time. Infants were then tested with alternating trials of the /bif/ passage versus the /tar/ passage, for a total of 10 trials. The first test trial was either the /bif/ or /tar/ passage type, counterbalanced across infants. Boys and girls were assigned equally in all conditions.

In the testing room the infant sat on the caregiver's lap, facing a display monitor and a loudspeaker. The caregiver wore headphones hearing masking music. The researcher in the adjacent room, who was blind to the stimuli, controlled the experiment using a computer program, observed the infant's eye movements through a closed-circuit TV, and pressed down a computer key whenever the infant looked at the monitor. Each trial was initiated by the infant's look to the monitor, and continued until the end of the trial. When the infant accumulated 30 s of looking time during familiarization, the experiment moved automatically to the test phase. The software recorded all looks to the TV and calculated online the total looking time for each trial.

The checkerboard was displayed during each trial, accompanying the auditory stimuli. Between trials, the flashing light was presented to attract the infant's attention.

3. Results

Total looking times during the test phase were analyzed in a 2×2 mixed analysis of variance, with familiarity (passage containing the familiarized target verb versus the nonfamiliarized verb) as the within-subject factor, and age (8 versus 11 months) as the between-subject factor. Across all trials, there was a familiarity $\times$ age interaction [$F(1,30)=5.25$, $p=0.029$], but no main effect of familiarity [$F(1,30)=0.562$, $p=0.459$] or age [$F(1,30)=0.62$, $p=0.437$]. As is

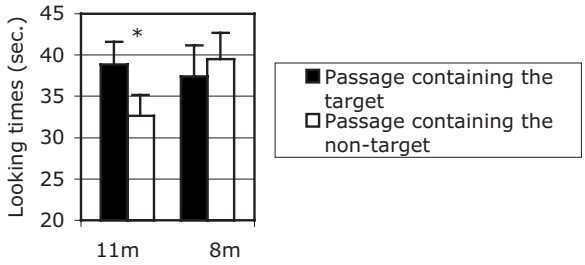

Fig. 1. French-learning infants' mean looking times (with SEs) during the test phase for the passage containing the target verb and the passage containing the nontarget verb.

standard with this procedure, another analysis was done with the first (often unstable) test trial of each type removed.[31] We obtained the same results: only a familiarity × age interaction [$F(1,30)=6.41$, $p=0.017$], indicating that the two age groups differ statistically. Follow-up analyses of each age were conducted. For the 11-month-olds, looking times across all trials tended to be longer for the passage containing the target [$t(15)=1.821$, $p=0.089$, two-tailed]. The analysis with the first trials removed yielded significantly longer looking times for the target trials [mean=38.88 s, SE=2.74 s] than for the nontarget trials [mean=32.66 s, SE =2.5 s; $t(15)=2.284$, $p=0.037$, two-tailed; see Fig. 1]. These results show that 11-month-olds recognized the targets.[32] For the 8-month-olds, total looking times during the two types of passage trials did not differ significantly [all trials, $t(15)=1.401$, $p=0.182$, two-tailed; excluding the first test trials, $t(15)=1.147$, $p=0.269$, two-tailed].

4. General discussion

This study shows that French-learning infants can segment verbs by 11 months of age, younger than the age shown in English-learning infants.[23] However, given that monosyllabic nouns are segmented earlier than disyllabic nouns,[33] the earlier segmentation in our study is reasonable since we used monosyllabic verbs, whereas Nazzi *et al.*[23] used disyllabic verbs.

Note that the 8-month-olds in our study failed to segment verbs. This contrasts with the results that infants of the same age segmented nouns in French.[7,16,28] Thus, verb segmentation seems somewhat delayed. It is possible that the less salient acoustic forms of verbs (e.g., shorter vowel duration[25,26]) contributed to the difficulty in segmenting verbs at 8 months.

Our target verbs in the passages often appeared adjacent to function words. Such contextual support may have contributed to the 11-month-olds' success in verb segmentation. But it was obviously not enough for the 8-month-olds. Previous work showed that frequent function words, but not infrequent ones, assist the segmentation of adjacent nouns in 8-month-olds.[15,16] The present study contained both high- and lower-frequency function words[29] adjacent to the target verbs. It is possible that if all contextual words are highly frequent, infants younger than 11 months may segment verbs. Future studies can test this effect by manipulating contextual words.

As discussed earlier, verbs appear much later than nouns in children's early speech. The present study shows that this delay is not related to an inability to segment verb forms. Although verb segmentation may occur somewhat later than noun segmentation due to their weaker forms than nouns, the ability is still present at 11 months, the age when speech production begins. The fact that infants in this study segmented rare verbs indicates that they are able to extract novel verb forms from the input. Note also that 62% of verb forms in parental speech in French are monosyllabic, while 46.4% of nouns are monosyllabic.[30] Given the syllabic based segmentation in French-learning infants shown in Nazzi *et al.*,[8] it is plausible that monosyllabic verb forms can be segmented at the preverbal stage and are available for learning meaning. The delay in the production of verbs must be due to other reasons, such as the difficulty in mapping verb concepts to word forms.[22,34] That is, the phonological forms of at least some verbs may be

segmented and represented in the system very early, but their semantic and syntactic representations require a much longer period of learning in comparison to the development of nouns.

In conclusion, this study extends the existing literature on word segmentation to the verb category. We demonstrated that French-learning infants can segment novel verb forms from continuous speech by 11 months of age (i.e., around the time when they begin to learn word meaning). This ability prepares them for the subsequent acquisition of syntactic and semantic properties associated with verb forms.

Acknowledgments

This research was funded by grants from NSERC, SSHRC, and CFI to the second author.

References and links

[1]J. van de Weijer, "Language input for word discovery," Ph.D. dissertation, Max Planck Institute for Psycholinguistics, Nijmegen, The Netherlands, 1998.
[2]P. W. Jusczyk, D. Houston, and M. Newsome, "The beginnings of word segmentation in English-learning infants," Cogn. Psychol. **39**, 159–207 (1999).
[3]L. Mattys and P. W. Jusczyk, "Phonotactic cues for segmentation of fluent speech by infants," Cognition **78**, 91–121 (2001).
[4]J. Saffran, R. Aslin, and E. Newport, "Statistical learning by 8-month-old children," Science **274**, 1926–1928 (1996).
[5]S. Curtin, T. H. Mintz, and D. Byrd, "Coarticulatory cues enhance infants' recognition of syllable sequences in speech," in *Proceedings of the 25th Annual Boston University Conference on Language Development*, edited by A. H. J. Do, L. Dominguez, and A. Johansen (Cascadilla, Somerville, 2001) Vol. **1**, pp. 190–201.
[6]V. Kooijman, P. Hagoort, and A. Cutler, "Electrophysiological evidence for prelinguistic infants' word recognition in continuous speech," Brain Res. Cognit. Brain Res. **24**, 109–116 (2005).
[7]L. Polka and M. Sundara, "Word segmentation in monolingual and bilingual infant learners of English and French," in *Proceedings of the 15th International Congress of Phonetic Sciences*, edited by M. J. Solé, D. Recasens, and J. Romero (UAB, Barcelona, Spain, 2003) pp. 1021–1024.
[8]T. Nazzi, G. Iakimova, J. Bertoncini, S. Frédonie, and C. Alcantara, "Early segmentation of fluent speech by infants acquiring French: Emerging evidence for cross-linguistic differences," J. Mem. Lang. **54**, 283–299 (2006).
[9]R. Brown, *A First Language* (Cambridge University Press, Cambridge, 1973).
[10]M. Shady, "Infants' sensitivity to function morphemes," Ph.D. dissertation, the State University of New York at Buffalo, Buffalo, NY, 1996.
[11]R. Shi, J. F. Werker, and A. Cutler, "Recognition and representation of function words in English-learning infants," Infancy **10**, 187–198 (2006).
[12]B. Höhle and J. Weissenborn, "German-learning infants' ability to detect unstressed closed class elements in continuous speech," Dev. Sci. **6**, 122–127 (2003).
[13]R. Shi, A. Marquis, and B. Gauthier, "Segmentation and representation of function words in preverbal French-learning infants," in *Proceedings of the 30th Annual Boston University Conference on Language Development*, edited by D. Bamman, T. Magnitskaia, and C. Zaller (Cascadilla, Somerville, 2006), pp. 549–560.
[14]R. Shi, J. L. Morgan, and P. Allopenna, "Phonological and acoustic bases for earliest grammatical category assignment: A cross-linguistic perspective," J. Child Lang. **25**, 169–201 (1998).
[15]R. Shi, A. Cutler, J. Werker, and M. Cruickshank, "Frequency and form as determinants of functor sensitivity in English-acquiring infants," J. Acoust. Soc. Am. **119**, EL61–EL66 (2006).
[16]R. Shi and M. Lepage, "The effect of functional morphemes on word segmentation in preverbal infants," Dev. Sci. (2008) in press.
[17]B. Höhle, J. Weissenborn, D. Kiefer, A. Schulz, and M. Schmitz, "Functional elements in infants' speech processing: The role of determiners in segmentation and categorization of lexical elements," Infancy **5**, 341–353 (2004).
[18]T. H. Mintz, "Finding the verbs: Distributional cues to categories available to young learners," in *Action Meets Word: How Children Learn Verbs*, edited by K. Hirsh-Pasek and R. M. Golinkoff (Oxford University Press, New York, 2006), pp. 31–63.
[19]S. Bernal, J. Lidz, S. Millotte, and A. Christophe, "Syntax constrains the acquisition of verb meaning," Lang. Learn. Dev. **3**, 325–341 (2007).
[20]L. A. Gerken, B. Landau, and R. Remez, "Function morphemes in young children's speech perception and production," Dev. Psychol. **27**, 204–216 (1990).
[21]S. Goldin-Meadow, M. Seligman, and R. Gelman, "Language in the two-year-old," Cognition **4**, 189–202 (1976).
[22]D. Gentner, "Why nouns are learned before before verbs: Linguistic relativity versus natural partitioning," in *Language, Thought and Culture*, Language Development Vol. 2, edited by S. A. Kuczaj II (Erlbaum, Hillsdale, NJ, 1982), pp. 301–334.
[23]T. Nazzi, L. C. Dilley, A. M. Jusczyk, S. Shattuck-Hufnagel, and P. W. Jusczyk, "English-learning infants' segmentation of verbs from fluent speech," Lang. Speech **48**, 279–298 (2005).

[24]T. H. Mintz, "Morphological segmentation in 15-month old infants," in *Proceedings of the 28th Annual Boston University Conference on Language Development*, edited by A. Brugos, L. Micciulla, and C. E. Smith (Cascadilla, Somerville, 2004), pp. 363–374.
[25]R. Shi and A. Moisan, "Prosodic cues to noun and verb categories in infant-directed speech," in *Proceedings of the 32nd Boston University Conference on Language Development* (2008) in press.
[26]J. M. Sorenson, W. E. Cooper, and J. M. Paccia, "Speech timing of grammatical categories," Cognition **6**, 135–153 (1978).
[27]D. Bassano, P. E. Eme, and C. Champaud, "A naturalistic study of early lexical development: General processes and inter-individual variations in French children," First Lang. **25**, 64–101 (2005).
[28]A. Gout, "Étapes précoces de l'acquisition du lexique," ("Early stages of lexicon acquisition"), Ph.D. dissertation, École des Hautes Études en Sciences Sociales, France, 2001.
[29]N. Beauchemin, P. Martel, and M. Théoret, *Dictionnaire de Fréquence des Mots du Francais parlé au Québec: Fréquence, Dispersion, Usage, Écart Réduit (Dictionary of Word Frequency in Québec Spoken French: Frequency, Scattering, Usage, Reduced Deviation)* (P. Lang, New York, 1992).
[30]M.-J. Cécyre and R. Shi, "Speech rate in maternal speech to French-learning infants," presented at the Canadian Society for Brain, Behaviour and Cognitive Science 15th Meeting, Montréal, 2005.
[31]R. Cooper and R. Aslin, "Developmental differences in infant attention to spectral properties of infant-directed speech," Child Dev. **65**, 1663–1677 (1994).
[32]Differential listening times to the target passage versus nontarget passage are standardly viewed in the field as evidence of word recognition (e.g., Refs. 2, 7, 8, 12, 23, 28, and 33). Indeed, previous work showed that infants only accept word forms during the test phase that are identical to the familiarized targets, and reject forms that are altered in one segment [e.g., P. W. Jusczyk and R. N. Aslin, "Infants' detection of the sound patterns of words in fluent speech," Cogn. Psychol. **29**, 1–23 (1995)], suggesting that segmentation occurs for the whole word forms in this type of task.
[33]H. Bortfeld, J. L. Morgan, R. Golinkoff, and K. Rathbun, "Mommy and me: Familiar names help launch babies into speech-stream segmentation," Psychol. Sci. **16**, 298–304 (2005).
[34]R. M. Golinkoff, R. C. Jacquet, K. Hirsh-Pasek, and R. Nandakumar, "Lexical principles may underlie the learning of verbs," Child Dev. **67**, 3101–3119 (1996).

ACOUSTICAL NEWS—USA

Elaine Moran
Acoustical Society of America, Suite 1NO1, 2 Huntington Quadrangle, Melville, NY 11747-4502

Editor's Note: *Readers of the journal are encouraged to submit new items on awards, appointments, and other activities about themselves or their colleagues. Deadline dates for news items and notices are 2 months prior to publication.*

New Fellow of the Acoustical Society of America

Larry E. Humes—For contributions to our understanding of the effects of aging and hearing loss on auditory perception.

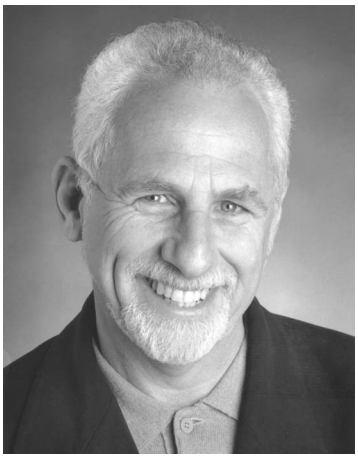

Anthony P. Nash—For contributions to the development of standards involving acoustical measurement protocols.

President's report on the 154th meeting of the Acoustical Society of America held in New Orleans, Louisiana

The 154th meeting of the Acoustical Society of America was held 27 November—1 December 2007 at the Sheraton New Orleans Hotel in New Orleans, Louisiana. This is the second time that the Society has met in this city, the previous meeting being held in 1992.

The meeting drew a total of 822 registrants, including 100 nonmembers, 184 students and 96 registrants from outside North America. There were 14 registrants from Japan; 11 from Korea; 10 from Germany; 9 each from France and the U.K.; 5 from Belgium; 4 each from Finland and Hong Kong; 3 each from Denmark, Netherlands, Portugal, People's Republic of China, Russia, and Sweden; 2 each from Israel, Italy, and Taiwan; and 1 each from Australia, Brazil, Norway, Slovenia, Spain, and Turkey. North American countries, Canada, Mexico and the United States, accounted for 26, 1 and 696, respectively.

A total of 600 papers, organized into 71 sessions, covered the areas of interest of all 13 Technical Committees. The meeting also included 19 meetings dealing with standards. The evening tutorial lecture series was continued by Alfred Bedard, National Oceanic and Atmospheric Administration. The tutorial titled "Weather and Acoustics" was presented to an audience of about 80.

The Society's thirteen Technical Committees held open meetings where they made plans for special sessions at upcoming ASA meetings, discussed topics of interest to the attendees and held informal socials after the end of the official business. These are working, collegial meetings and all people attending Society meetings are encouraged to attend and to participate in the discussions. More information about Technical Committees, including minutes of meetings, can be found on the ASA Website ⟨http://asa.aip.org/committees.html⟩ and in the Acoustical News USA section of JASA in the September, October and November issues.

An exhibit was held in conjunction with the meeting and included displays with materials and services for the acoustics and vibration community. It included exhibits of computer-based instrumentation, sound level meters, devices for noise control and sound prediction among others. The exhibit began with an opening reception on Tuesday evening and was open on Wednesday and Thursday.

The ASA Student Council hosted a Student Reception with over 100 people in attendance. This reception, which was supported by the National

FIG. 1. Gilles A. Daigle, President of the Acoustical Society of America, presides at the Plenary Session.

 0001-4966/2008/123(4)/1809/4/$23.00 © 2008 Acoustical Society of America

FIG. 2. Manell Zacharia, Cochair of Acoustics'08 Paris, invites ASA meeting participants to the Paris meeting.

FIG. 4. David Dowling (l), recipient of the 2007 Student Mentoring Award, is congratulated by ASA President Gilles Daigle.

Council of Acoustical Consultants, enabled students to meet with established members of the Acoustical Society of America. Also, the Student Council Mentoring Award was presented to David R. Dowling for excellence in a wide variety of mentoring arenas. The Student Council organized a Grant and Fellowship Workshop which was attended by representatives from the National Science Foundation, Office of Naval Research, National Institutes of Health, National Institute of Deafness and Other Communication Disorders, and the ASA Committee on Prizes and Special Fellowships. These representatives gave presentations on various aspects of applying for grants and fellowships. Several of the Technical Committees awarded Best Student Paper Awards or Young Presenter Awards to students and young professionals who presented papers at the meeting. The list of award recipients, as well as other information for students, can be found online at the ASA Student Zone website ⟨http://www.acosoc.org/student/⟩

The New Orleans meeting committee arranged a technical tour of the New Orleans levees which attracted over 50 participants. The tour, which was led by members of the Army Corps of Engineers, visited areas affected by Hurricane Katrina.

Social events included the two social hours held on Wednesday and Friday, an "icebreaker" and a reception for students, the Fellows Luncheon and the morning coffee breaks. A special program for students to meet one-on-one with members of the ASA over lunch, which is held at each meeting, was organized by the Committee on Education in Acoustics. These social events provided the settings for participants to meet in relaxed settings to encourage social exchange and informal discussions. The local committee arranged for special decorations for the socials in order to give the participants a sample of the exciting and fun atmosphere of the New Orleans scene. The Women in Acoustics Luncheon was held on Thursday afternoon and was attended by over 100 people.

Professor Shea Penland, University of New Orleans, was the speaker at the Fellows luncheon which was attended by about 100 people. The

FIG. 3. ASA President Gilles Daigle (l) congratulates Don Monroe, recipient of the 2006 Science Writing Award in Acoustics for Professionals.

FIG. 5. Preston Wilson (l), recipient of the 2007 A. B. Wood Medal and Prize, is congratulated by ASA President Gilles Daigle.

FIG. 6. ASA President Gilles Daigle (l) presents the 2007 Rossing Prize in Acoustics Education to David T. Blackstock.

subject of his talk was "Restoring coastal Louisiana: The challenge for tomorrow's geologists and engineers." The Fellows luncheon is open to all meeting attendees.

The New Orleans organizing committee also arranged for a program for Accompanying Persons which included daily presentations about New Orleans including its history, architecture, food and music. A special treat was the display of an elaborate gown worn at a Mardi Gras Ball.

The plenary session included a business meeting of the Society, announcements, acknowledgment of the members and other volunteers who organized the meeting and the presentation of awards and certificates to newly-elected Fellows.

ASA President Gilles Daigle presided over the Plenary Session and Awards Ceremony (see Fig. 1). Manell Zacharia, Cochair of Acoustics'08 Paris, addressed the audience and invited and encouraged them to attend the joint meeting of the Acoustical Society of America, the European Acoustics Association, and the French Acoustical Society to be held in Paris, 30 June to 4 July 2008 (see Fig. 2). Information about that meeting can be found online at ⟨http://www.acoustics08-paris.org/⟩.

The ASA awarded three Science Writing Awards. The 2006 Science Writing Award in Acoustics for Journalists was presented to Don Monroe for his article "Why the Inner Ear is Snail Shaped," published on the *Physical Revew Focus* website in May 2006 (see Fig. 3). A second 2006 Science Writing Award in Acoustics for Journalists was awarded to John Gierland for "The Sound of Silence," published in *WIRED* magazine in December 2006. The 2006 Science Writing Award for Professionals in Acoustics was awarded to Gary S. Settles for his article "High-speed imaging of shock waves, explosions, and gunshots," published in *American Scientist* magazine in the January/February 2006 issue.

The 2007 ASA Student Council Mentoring Award recipient, David Dowling of the University of Michigan, was introduced (see Fig. 4) as was Preston Wilson, recipient of the 2007 A. B. Wood Medal and Prize of the Institute of Acoustics (U.K.) (see Fig. 5).

The 2007 Rossing Prize in Acoustics Education was presented to David T. Blackstock, University of Texas at Austin. Dr. Blackstock presented the Acoustics Education Prize Lecture titled "Songs my students sang to me" earlier in the meeting (see Fig. 6).

FIG. 8. ASA President Gilles Daigle presents the Silver Medal in Engineering Acoustics to Allan J. Zuckerwar (l).

FIG. 7. ASA President Gilles Daigle (l) presents the Pioneers of Underwater Acoustics Medal to Willam M. Carey.

FIG. 9. ASA President Gilles Daigle (l) presents the Silver Medal in Speech Communication to Ingo R. Titze.

FIG. 10. New Fellows of the Acoustical Society with ASA President and Vice President: Top row: Brandon D. Tinianov, Ronald A. Wagstaff, Vladimir E. Ostashev, Anthony P. Lyons, R. Glynn Holt, Jean-Pierre Hermand, Sarah Hawkins. Bottom row: George V. Frisk (ASA Vice President), Steven I. Finette, William T. Ellison, Bruce E. Douglas, Dimitri M. Donskoy, Jeffrey E. Boisvert, William A. Ahroon, Gilles A. Daigle (ASA President).

The Pioneers of Underwater Acoustics Medal was presented to William M. Carey, Boston University, "for contributions to understanding ocean ambient noise and in defining the limits of acoustic array performance in the ocean" (see Fig. 7). The Silver Medal in Engineering Acoustics was presented to Allan J. Zuckerwar, NASA (retired), "for contributions to the theory and practical development of transducers and their use in fundamental measurements" (see Fig. 8). The Silver Medal in Speech Communication was presented to Ingo R. Titze, University of Iowa, "for contributions to fundamental understanding of the physics and biomechanics of vocal fold vibrations and for interdisciplinary work in voice studies" (see Fig. 9).

Election of sixteen members to Fellow grade was announced and fellowship certificates were presented. New fellows are: William A. Ahroon, Jeffrey E. Boisvert, Elizabeth A. Cohen, Dimitry M. Donskoy, Bruce E. Douglas, William T. Ellison, Steven I. Finette, Sarah Hawkins, Jean-Pierre Hermand, R. Glynn Holt, Anthony P. Lyons, Masayuki Morimoto, Vladimir E. Ostashev, Brandon D. Tinianov, and Ronald A. Wagstaff (see Fig. 10).

FIG. 11. Fred DeMetz, Chair of the New Orleans meeting.

ASA President Gilles Daigle expressed the Society's thanks to the Local Committee for the excellent execution of the meeting, which clearly evidenced meticulous planning. He introduced Fred DeMetz (see Fig. 11), Chair of the New Orleans meeting, who acknowledged the contributions of the members of his committee including: George E. Ioup and Juliette W. Ioup, Technical Program Cochairs; William Sanders/Dennis Lindwall, Audio-Visual; Sharon DeMetz/Jeanne Richardson, Food Service/Social Events/Accompanying Persons Program; Richard Keiffer/Josette Fabre, Signs; Michael D. Richardson/Kevin Briggs, Meeting Room Coordinators; Guy V. Norton, Posters; Becky Rotundo, Publicity. He also expressed thanks to the members of the Technical Program Organizing Committee: George E. Ioup and Juliette W. Ioup, Technical Program Cochairs; James F. Lynch, Acoustical Oceanography; Natalia A. Sidorovskaia, Animal Bioacoustics; David S. Woolworth, Angelo J. Campanella, Architectural Acoustics; Charles C. Church, Biomedical Ultrasound/ Bioresponse to Vibration; James M. Sabatier, Education in Acoustics; Daniel M. Warren, Engineering Acoustics; Scott D. McDermott, Musical Acoustics; Richard J. Peppin, Noise; James P. Chambers, James M. Sabatier, Physical Acoustics; Robert G. Turner, Psychological and Physiological Acoustics; Joe W. Posey, Signal Processing in Acoustics; Emily A. Tobey, Speech Communication; W. Steven Shepard, Structural Acoustics and Vibration; Guy V. Norton, William Sanders, Richard S. Keiffer, Underwater Acoustics.

The full technical program and award encomiums can be found in the printed meeting program or online for readers who wish to obtain further information about the New Orleans meeting (visit scitation.aip.org/jasa and select Volume 122, Issue 5, from the list of available volumes).

We hope that you will consider attending a future meeting of the Society to participate in the many interesting technical events and to meet with colleagues in both technical and social settings. Information about future meetings can be found in the *Journal* and on the ASA Home Page at ⟨http://asa.aip.org⟩.

GILLES A. DAIGLE
President 2007–2008

ACOUSTICAL NEWS—INTERNATIONAL

Walter G. Mayer
Physics Department, Georgetown University, Washington, DC 20057

International Meetings Calendar

Below are announcements of meetings and conferences to be held abroad. Entries preceded by an * are new or updated listings.

April 2008

8–11 **Oceans'08**, Kobe, Japan (Web: www.oceans08mtsieeekobe-technoocean08.org/index.cfm).

10–11 **Institute of Acoustics (UK) Spring Conference**, Reading, UK (Web: www.ioa.org.uk/viewupcoming.asp).

17–18 **Spring Meeting of the Swiss Acoustical Society**, Bellinzona (Tessin), Switzerland (Web. www.sga-ssa.ch).

May 2008

26–29 *__The Jubilee XXV Symposium on Hydroacoustics (7th EAA International Symposium on Hydroacoustics)__, Jastrzêbia Góra, Poland (Web: www.amw.gdynia.pl/sha2008).

June 2008

4–6 **5th International Styrian Noise, Vibration & Harshness Congress 2008**, Graz, Austria (Web: www.accgraz.com).

29–4 **Acoustics'08 Paris: 155th ASA Meeting + 5th Forum Acusticum (EAA) + 9th Congrès Français d'Acoustique (SFA)**, Paris, France (Web: www.acoustics08-paris.org).

July 2008

6–10 **15th International Congress on Sound and Vibration**, Daejeon, Korea (Web: www.icsvl5.org).

7–10 **l8th International Symposium on Nonlinear Acoustics (ISNA18)**, Stockholm, Sweden (Web: www.congrex.com/18th_isna).

27–31 **10th Mechanics of Hearing Workshop**, Keele University, UK (Web: www.mechanicsofhearing.com).

August 2008

25–28 **1st International Conference on Water Side Security**, Lyngby, Denmark (Web: www.wss2008.org).

25–29 **10th International Conference on Music Perception and Cognition (ICMPC 10)**, Sapporo, Japan (Web: icmpc10.typepad.jp).

September 2008

8–12 **International Symposium on Underwater Reverberation and Clutter**, Lerici, Italy (Web: isurc2008.org).

9–11 **6th International Symposium on Ultrasonic Doppler Methods for Fluid Mechanics and Fluid Engineering**, Prague, Czech Republic (Web: isud6.fsv.cvut.cz).

10–12 **Autumn Meeting of the Acoustical Society of Japan**, Fukuoka, Japan (Web: www.asj.gr.jp/index-en.html).

15–17 **International Conference on Noise and Vibration Engineering (ISMA2008)**, Leuven, Belgium (Web: www.isma-isaac.be).

22–26 **INTERSPEECH 2008 - 10th ICSLP**, Brisbane, Australia (Web: www.interspeech2008.org).

October 2008

6–8 *__Acoustics Week in Canada__, Vancouver, B.C., Canada (Web: www.caa-aca.ca/vancouver2008)

14–15 *__Underwater Noise Measurement__, Southampton, UK (Web: underwaternoise2008.lboro.ac.uk).

21–23 **International Conference on Low FrequencyNoise and Vibration**, Tokyo, Japan (Web. www.lowfrequency2008.org).

21–24 **acústica 2008**, Coimbra, Portugal (Web: www.spacustica.pt).

26–29 **inter-noise 2008**, Shanghai, China (Web: www.internoise2008.org).

November 2008

2–5 **IEEE International Ultrasonics Symposium**, Beijing, China (Web: ewh.ieee.org/conf/ius-2008).

5–7 **Iberamerican Acoustics Congress (FIA 2008)**, Buenos Aires, Argentina (Web: www.adaa.org.ar).

14–18 **20th Session of the Russian Acoustical Society**, Moscow, Russia (Web: www.akin.ru).

24–26 **Australian Acoustical Society National Conference**, Geelong, Vic., Australia (Web: www.acoustics.asn.au).

April 2009

5–9 **Noise and Vibration: Emerging Methods (NOVEM 2009)**, Oxford, UK (Web: www.isvr.soton.ac.uk/NOVEM2009)

13–17 **2nd International Conference on Shallow Water Acoustics**, Shanghai, China (Web [soon]: www.apl.washington.edu)

9–24 **International Conference on Acoustics, Speech, and Signal Processing**, Taipei. R.O.C. (Web: icassp09.com)

 0001-4966/2008/123(4)/1813/3/$23.00 © 2008 Acoustical Society of America

August 2009

23–28 **Inter-noise-2009**, Ottawa, Ont., Canada (Contact: TBA).

September 2009

6–10 **InterSpeech 2009**, Brighton, UK (Web: www.interspeech2009.org).

October 2009

26–28 **Euronoise 2009**, Edinburgh, UK (Web: www.euronoise2009.org.uk).

August 2010

23–27 **20th International Congress on Acoustics (ICA2010)**, Sydney, Australia (Web: www.ica2010sydney.org).

September 2010

26–30 **Interspeech 2010**, Makuhari, Japan (Web: www.interspeech2010.org).

Regional Chapter News

Madras Regional Chapter

The Madras Regional Chapter of the Acoustical Society of America (MIRC-ASA) held four meetings in 2007, on 16 June, 21 July, 4 December, and 5–7 December. The fourth meeting was held jointly with Acoustical Society of India (ASI).

On 16 December 2006, the second Stanley Ehrlich Distinguished Lecture was delivered by Baldev Raj, Distinguished Scientist and Director of India Gandhi Center for Atomic Energy, Govt. of India, Kalpakkam, T.N.

On 16 June 2007, V. Bhujanga Rao, President of ASI and Director of the Naval Science and Technology Lab., Govt. of India, Visakhapatnam, A.P., delivered the Distinguished Lecture on "Psychological and Physiological Aspects of Sound" and V. Rajendran, Vice President of ASI and Director, Research and Development and Center for Nanoscience and Technology, K. S. Rangasamy College of Technology, KSR Kalavi Nagar, Tiruchengode, T.N. delivered the invited lecture on "Prosperity of Ultrasonics in Science and Technology" at Tamil Nadu Science and Technology Centre (TNSTC), Chennai.

A core group of Chapter members including H.S. Paul, M. Kumaresan, J. Jayapandian, and Baldev Raj visited the International Research Institute for the Deaf (IRID), on July 18, 2007.

The MIRC-ASA and IRID Acoustics fair ceremony was conducted at TNSTC on 21 July 2007. The following 10 students under 17 years of age participated: B. K. Deepika, Sri S. Rajeswar, Sri C. Balajee, G. Brinda, M. Divya Bharathy, Sri A. Avinash, G. Srividya, Sri N. Viganesh from MIRC-ASA and K. Amrutha and K. Nivedidta from IRID. Since B.K. Deepika and K. Amrutha received equal scores, they were both named first place recipients by MIRC-ASA and IRID, respectively. H. S. Paul (Chapter Representative of MIRC-ASA and President of AFECT & IRID) and R. Dhilsha (Treasurer of MIRC-ASA) presented the awards (see Figs. 1 and 2).

On 4 and 5 December 2007, Allan D. Pierce, Editor-in-Chief of the Acoustical Society of America, delivered the Stanley Ehrlich Distinguished Lecture "Attenuation and Dispersion of Sound" at IIT Madras and KSRCT, Tiruchengode. Dipali Nag delivered an invited lecture on "Music Education as a Performing Art and its Cultural and Cognitive Impact" on 5 December 2007 at Tiruchengode.

Both A. D. Pierce and S. L. Ehrlich were elected Fellows of the Acoustical Foundation during their visit to the offices of MIRC-ASA and AFECT. A. Ramachandraiah (Vice President of MIRC-ASA and Trustee of AFECT) and S. Narayanan (First Technical Program Chair of MIRC-ASA and Past President of ASI) were also present (see Fig. 3). The photo shows Prof. Pierce writing in the minute book of MIRC-ASA.

The awards ceremony of MIRC-ASA and IRID (AFECT) was conducted during the joint meeting between MIRC-ASA and ASI held on 5–7 December 2007 at K. S. Rangasamy College of Technology, Tiruchengode, T.N. It was a memorable event for MIRC-ASA and AFECT to present the First Silver Medal to Stanley L. Ehrlich who not only received the First Gold Medal in 2001 but is also co-founder of MIRC-ASA and AFECT. The President and Vice President of ASI joined in the award ceremony as they are President of AFECT and Member-at-Large of MIRC-ASA, respectively.

FIG. 1. (Color online) (1 to r): H. S. Paul, B. K. Deepika, and R. Dhilsha.

All Silver and Gold Medals were presented in the presence of trustees of AFECT and the chapter's executive members, namely H. S. Paul (C.R. and Founder of AFECT and IRID), C. P. Vendhan (President of MIRC-ASA and Trustee of AFECT), V. Bhujanga Rao (President of ASI and AFECT) and V. Rajendran (Vice President of ASI and Member-at-Large of MIRC-ASA). The AFECT Silver Medal and citation were presented to Stanley L. Ehrlich (see Fig. 4) by C. P. Vendhan.

FIG. 2. (Color online) (1 to r): H. S. Paul, K. Amurutha, and R. Dhilsha.

FIG. 3. (Color online) (1 to r): H. S. Paul, C. P. Vendhan, A. D. Pierce, S. L. Ehrlich, S. Narayanan, and A. Ramachandraiah.

FIG. 4. (Color online) C. P. Vendhan presented the Silver Medal to S. L. Ehrlich (1 to r): H. S. Paul, V. B. Rao, S. L. Ehrhch, C. P. Vendhan, V. Rajendran.

FIG. 5. (Color online) S. L. Ehrlich (r) presents Stanley Ehrlich Gold Medal to Baldev Raj (1), (1 to r): V. Rajendran, H. S. Paul, V. B. Rao, Baldev Raj, S. L. Ehrlich, A. D. Pierce.

Two Stanley Ehrlich Gold Medals with citations were presented to Baldev Raj (see Fig. 5) and Allan D. Pierce (see Fig. 6), respectively, by Stanley L. Ehrlich (Adviser of AFECT and Past President of ASA) since the Gold Medal is a joint venture of AFECT and MIRC-ASA.

FIG. 6. (Color online) A. D. Pierce receives Stanley Ehrlich Gold Medal and citation from S. L. Ehrlich (1 to r): H. S. Paul, V. B. Rao, A. D. Pierce, S. L. Ehrlich, V. Rajendran.

FIG. 7. (Color online) (1 to r): C. P. Vendhan, Abhijit Sarkar, V. B. Rao, H. S. Paul, A. D. Pierce, R. Kalai Selvi, and S. P. A. Catherine.

The following students won the best paper award which was presented by Allan D. Pierce at the end of the meeting on 7 December 2007: Ms. R. Kalai Selvi, Ms. S. P. A. Catherine, Mr. S. Aravindran, Mr. Abhijit Sarkar, and Mr. D. M. Reddy. A group photo was taken with the students, trustees of AFECT and Chapter's officers at the end of meeting (see Fig. 7).

BOOK REVIEWS

P. L. Marston
Physics Department, Washington State University, Pullman, Washington 99164

These reviews of books and other forms of information express the opinions of the individual reviewers and are not necessarily endorsed by the Editorial Board of this Journal.

Riding the Waves—A Life in Sound, Science, and Industry

Leo Beranek

The MIT Press, Cambridge, MA, 2008, 256 pp. Price $24.95 (hardcover) ISBN: 978-0-262-02629-1

Fortune ("good luck") falls on those who are prepared. If you are not prepared, you may not even recognize the opportunity when it lands in your lap. When Leo Beranek was a college junior in Iowa, he helped a stranger with a flat tire. The conversation between them had an improbable twist: Just that morning Leo had been reading in the library about some radio work that the stranger had developed. Their instant friendship led to an invitation for Leo to apply to Harvard graduate school. It's an early example of "he was prepared" when the opportunity presented itself. Leo's drive and determination (and some other opportunities along the way) made other things happen, too. Now, 73 years after the flat tire incident, Leo can look back on a professional life filled with radio, electronics, acoustics, recording, research, engineering, teaching, consulting, writing, computers, communication, music, fund raising, television, administration, education, and diplomacy. Let's add family, travel, music appreciation, skiing, and philanthropy to that list. He puts it all together in his autobiography, "Riding the Waves—A Life in Sound, Science, and Industry."

Leo Beranek was born in 1914 in a little town in Iowa. There was both happiness and sadness in his early life. It was especially tough in the Depression years, but it is a revelation to learn of this farm boy's energy, drive, enthusiasm, and positive outlook as his family faced economic conditions in those times that we cannot believe possible now. After graduating from Cornell College in Iowa, Leo's good fortune from the earlier flat tire incident landed him in Harvard University, where, in his second year, he had an opportune interview with noted acoustician, Professor F. V. ("Ted") Hunt. They were a ready match, and Ted's job for him helped push Leo toward the field of acoustics. The two of them became lifelong friends and associates—and Cruft Lab at Harvard (an historic site itself) became home for much of Leo's early work. He was a student of such Harvard scientists and physicists as Leon Chaffee, G. W. Pierce, Harry Mimno, Roger Hickman, and John H. van Vleck. One of his early papers to the Journal of the Acoustical Society of America (JASA) attracted the attention of Professor Philip Morse at MIT and that led to another valuable association. A short time later, Professor Morse recommended Leo for a project that was being sponsored by the National Defense Research Committee (NDRC). This was the beginning of a noted run of important contributions to the war effort by the Electro-Acoustics Lab (EAL) that Leo directed at Harvard during WW II. It had a somewhat dubious start, however, when Leo was asked to offer a budget for what he first thought was involved. He proposed $4000. The Army Air Corps representative who came to the meeting was clearly underwhelmed. He authorized $80 000 for the first year. That was a lot of money in 1940 for this young Harvard doctorate, and it certainly raised the scope and emphasis of the work required. Leo even got a telephone for his office (unheard of at that time in Cruft Lab; they used a code of dots and dashes on a buzzer to call people to the phone).

Following EAL, Leo accepted a move to MIT, to become Associate Professor of Communication Engineering and Technical Director of MIT's Acoustics Laboratory, where Dick Bolt was already Administrative Director. This led to a challenging MIT teaching load plus a vital role in a variety of research undertakings at the growing Acoustics Lab. Those connections, in turn, led to other opportunities; one (for the Office of Naval Research—ONR) involved traveling to Europe to survey the acoustics activities of many of those countries. A short time later, as a result of having two class students from the Argentine Navy, Leo was invited to teach a summer course in electro-acoustics in Argentina. Most of his lectures were in English and were translated and handed out to the students. He gave one of his final lectures in Spanish, after being coached and well-practiced.

Even though they were on the MIT teaching staff, Leo and Dick Bolt had approval to take on limited consulting jobs, which they did. This led to the fairly early formation of their first consulting partnership, "Bolt and Beranek," in 1948 (Chapter 5). A variety of outside jobs kept them busy on their days off from teaching, and this justified their adding Sam Labate, Bill Lang (who later left to pursue his higher education elsewhere), Jordan Baruch, and Bob Newman (who had already worked with Leo in his Electro-Acoustics Lab and who had since taken an architectural degree at MIT). Two really big jobs soon came to this new group: one was to take on the architectural acoustics design work for several auditoriums of the United Nations Building, and the other was a horrendous noise problem in Cleveland when an early NACA jet engine facility was turned on one night. Both jobs were urgent and demanding, and both had some new and difficult concepts that had to be carefully solved. Those two jobs, however, were largely responsible for the early recognition of the growing company, then "Bolt Beranek & Newman Inc." (BBN). During the next few years, Leo was directly involved in several major acoustical and noise reduction problems for various well-known clients. He began to reduce his work load at MIT as the BBN work grew. One important decision and new development was the entrance of BBN into computer technology, assisted with a nudge from Jordan Baruch. Leo convinced J. C. R. ("Lick") Licklider that he had greater future opportunities at BBN than at MIT. It took a hard sell to bring it about, but Lick joined BBN and began an outstanding program of "man-machine symbiosis" that ultimately led to unbelievable advances in computer applications and communications. Have you heard of ARPAnet? How about the Internet?

Two pictures on the front cover of the book (at the left, the top one and third one down) show Leo at work on two BBN jobs. In the top photo, those straps over his shoulders were to a parachute; that was for a helicopter-quieting job. In the third photo, he was taking noise measurements in Seattle of one of the first Boeing 707's. With him on that field trip were Austin Tobin (Executive Director of the Port of New York Authority) and John Wiley (Director of Aviation for the Port Authority). At the meeting with Boeing personnel before the measurement flights, Mr. Tobin assured Boeing that their plane must not be noisier than the large four-engine propeller aircraft then in use in international flights from Idlewild Airport (now JFK). The whole unfolding story is told in Chapter 6, "Muffling the Jet Age." The dogged determination of Mr. Tobin, backed by the technical support of Leo Beranek and Karl Kryter, made a major impact on the aviation industry, leading to our present-day much-quieter commercial jet planes. Of course, a lot of people in the aviation industry made it possible, but it was largely Tobin and Beranek who applied the pressure at the right time and in the right way to force the issue.

The dramatic end of Chapter 6 tells of the beginning of international commercial jet travel, when, during the night of October 26-27, 1958, a Pan Am Boeing 707 flew with a passenger load from New York to London, and a BOAC de Havilland Comet 4 flew from London to New York. There are 14 pages of little-known aviation history in this chapter, and it's packed with dynamite!

Leo was deeply hurt by the critical assessments that some newspaper music critics gave him the morning after Philharmonic Hall (now Avery Fisher Hall) opened New York's Lincoln Center on September 23, 1962. The evening was so replete with famous personalities, the beautiful new building and its ambience and decorations, and the entrance of this new musical arrival in New York City, it is a wonder that anyone could concentrate on the music program that was presented. In his book, he faced that negative publicity headlong—right up there in front, in a four-page Prologue. Then, his Chapter 7, entitled "Music, Acoustics, and Architecture," summarizes this part of his life. It was during that period that Leo was President of the Acoustical Society of America and was a well-recognized acoustician internationally. In spite of that early unpleasant newspaper publicity, Leo received The Gold Medal Award of the Acoustical Society of America in 1975

 0001-4966/2008/123(4)/1817/2/$23.00 © 2008 Acoustical Society of America

and the National Medal of Science from President George W. Bush in 2003. Also, a Special Session was planned to celebrate Leo's 90th birthday at the 75th Anniversary Meeting of the Acoustical Society of America in New York City in 2004. It took eight men 20 minutes each to talk about a particular specialty of his life and accomplishments in acoustics. Leo completed the Session with a summary of his life under the title "My 65 Years in Acoustics," after which he received a long-lasting standing ovation for his life and for his many contributions. Those are much more valued endorsements than a few negative newspaper comments!

Chapter 8 is entitled "America's Best TV Station." That's a pretty big claim! Following a significant opening quotation from a January 1972 issue of the *Boston Globe*, Leo begins this chapter with a powerful summary, as follows:

"I took part in this dance (the analogy taken from the *Boston Globe* article), risking at one point all of my life savings. The stakes were high—financial independence or bankruptcy—yet even as I seemed to be losing like some compulsive gambler, I kept betting more chips. So did thirty of my colleagues. The story covers nearly a decade of legal dueling: four times to the Federal Communications Commission, four times to the U. S. Court of Appeals for the District of Columbia, and three times to the U. S. Supreme Court. There was much high drama along the way—personal conflicts, twists of fate and fortune, and the inevitable chance discoveries that, if not recognized and acted on promptly, could have sunk the whole endeavor."

Leo's serious interest in TV possibly began with a conversation that he had in October 1962 with Jordan Baruch. Things started moving quickly, and in about four months, while Leo and family were on a skiing vacation in Switzerland, he was elected President of the newly formed "BBI" (Boston Broadcasters Incorporated), which, indeed, had a distinguished group of early owners over a variety of professions. The immediate goal was to obtain FCC permission to start a TV station that would meet…

"the needs, problems and tastes of the community: One that brings the best of Boston's unique local resources…by infusing the whole schedule with more exciting and meaningful material."

It was a touch-and-go game lasting several years, that involved finances, personnel, equipment, building permits, construction, lots of legal back-and-forth wrangling, some unbelievably frequent and complicated delays that many times seemed to make the whole venture impossible, and enough bright spots to encourage them to keep going. One of his segments is entitled "Staying Calm with the Roof Falling In?," but that heading could have been used several other times as well. After one particular "Gut-Wrenching Day," they got the word, and Leo shouted out to anyone who was still in the building, "We're on the air!" Months later, the BBI Treasurer added up their accumulated costs to be around $7.8 million before a penny of revenue came in from the new station, WCVB-TV, Channel 5 in Boston. Leo tells us that *The New York Times* carried a full-page article in 1981, with the headline, "Some Say This is America's Best TV Station."

In 1982, Phyllis died, and this left Leo desolate. He always had excellent family relationships with their two sons, Jamie and Tom, who provided some much-needed consolation when their mother died. Friends and neighbors helped as much as they could. With Phyllis″ death and his earlier stepwise retirements from BBN and then BBI, Leo had to find other outlets for his restless energy. He already had committee connections with the Boston Symphony Orchestra and this grew into positions of stronger leadership as Chairman of the Board of Overseers, and later as Chairman of the Board of Trustees. Fund-raising was a major need, and Leo applied his available time and abilities to that pursuit. It was an ambitious program but they even went over their original goal for a One Hundredth Anniversary Fund. Other innovative fund raisers have placed the Boston Symphony Orchestra on fairly secure footing. Following retirement from the BSO job, Leo was chosen to become President of the American Academy of Arts and Sciences, where their financial considerations also became a major concern of his. In this general time frame, Leo came to know Gabriella Sohn, and they were married in 1985. Leo called it "one of the happiest times" in his life, and they have been actively involved in travel and other varied interests. Gabriella even got Leo into a new venture: sailing.

During the period 1989 to 2001, Leo's official title was "Acoustical Design Consultant" for most of the six buildings that he worked on in Japan. Chapter 10 gives considerable detail of his design work and his close collaboration with the architects and engineers on those jobs. In some situations, he had disagreements on certain architectural features that he believed would be deleterious to the acoustics of the space. With his usual calm, firm, technical, and gentle persistence, he was able to prevail (except in one situation which was not too serious anyway). He concludes this chapter with this statement: "My experience in Japan had been favorable overall, with many successful outcomes, and it was especially satisfying to call it quits on the high note reached with…" and then he named those Japanese halls in order of acoustical quality.

A few special anecdotes drop in on Leo's writings from time to time. About 68 years ago, Leo knew Arthur M. Schlesinger, Jr. (before Mr. Schlesinger became a noted historian) and even helped him tie his bow-tie before his wedding. One time, Leo had the job of recording the acclaimed violinist Jasha Heifetz playing on a "bad" violin Mrs. Heifetz said, "He can make any violin sound good." Twice, Leo had occasion to have lunch with Mrs. Eleanor Roosevelt. The first was quite by accident but the second was by invitation to the White House. In 1990, Dr. and Mrs. Beranek were invited by German Chancellor Helmut Kohl to attend meetings that he called to discuss European and German-American relations. Of course, there are detailed explanations of these situations in Leo's autobiography. For some of his work toward the end of WW II, Leo was dubbed "captain of the Navy warship *USS Beavertail*." That's a special story in itself—was he really a captain in the Navy?

Some of us had no idea that Leo was an accomplished skier. We just knew that he and Phyllis went off to Europe several winters, presumably on business, but he always carried skis. In 1957, he saw a sign, "Test your ski capabilities by means of the Swiss Ski Tests." He was considering the "Silver Badge Test" but his ski instructor said that he should try for the "Gold." Among several difficult maneuvers, there were two critical runs. At the end of the first, his examiner said, "There are not more than a dozen skiers in Switzerland who can handle deep snow better than you." At the end of the second run, the examiner said that he had passed. The "Gold Badge" asserts "It is the badge of a first-class skier." We should have expected it: Leo excels at anything he tries! He did have a problem one year, though, when he went to Moscow to collect the royalties gained from their printing and selling one of his books. He had trouble spending it all in Russia.

For just a moment, consider the concluding pages 231 through 233. With the title "Degrees, Awards, and Honors," Leo identifies two and one-half pages (41 items) of distinctions that he has received in his lifetime of accomplishment and public service in acoustics, education, national defense, music, engineering, and science. It is truly an impressive list for a very humble fellow.

Chapter 10 carries a meaningful heading: "Art+Physics=Beautiful Music." That was taken from an April 19, 2000, article in *The New York Times* that included photos in color of Leo and the architect, Yanagisawa, with this statement: "An unusually intense collaboration between architects and acousticians has put the science of acoustics to test, with two major successes in Tokyo." That heading also summarizes a lot of Leo's life. He has applied art and physics in a very careful, practical, quantitative, and realistic way, and has brought harmony to his life and ours. I especially value my contacts with him. I worked at BBN for 27 years, had many contacts with Leo during that time, and enjoyed working directly and closely with him on at least three major jobs, major for both of us. He has been a wonderful teacher: patient, thorough, kind, intensely honest, and a real motivator. There are so many things that I would like to add, but I've said enough. Nevertheless, it has been a distinct honor to be asked to review Leo's "Riding the Waves." He has taken us along for an enjoyable ride.

LAYMON N. MILLER, (Retired BBNer)
1504 Harbor Court
Fort Myers, FL 33908-1651
E-mail: laymnluce@aol.com

(Reviewer's personal comment: Leo Beranek is an icon in acoustics. I have known him for about 66 years and worked for him and with him at BBN for 27 of those years. I cannot keep some personal connections out of this review. Please forgive me. It's a wonderful book. How can I enthuse more than I have?)

REVIEWS OF ACOUSTICAL PATENTS

Sean A. Fulop
Dept. of Linguistics, California State University Fresno
5245 N. Backer Ave., Fresno, California 93740

Lloyd Rice
11222 Flatiron Drive, Lafayette, Colorado 80026

The purpose of these acoustical patent reviews is to provide enough information for a Journal reader to decide whether to seek more information from the patent itself. Any opinions expressed here are those of reviewers as individuals and are not legal opinions. Printed copies of United States Patents may be ordered at $3.00 each from the Commissioner of Patents and Trademarks, Washington, DC 20231. Patents are available via the internet at http://www.uspto.gov.

Reviewers for this issue:

ANGELO CAMPANELLA, *3201 Ridgewood Drive, Hilliard, Ohio 43026-2453*
DIMITRI DONSKOY, *Stevens Institute of Technology, Castle Point on the Hudson, Hoboken, New Jersey 07030*
GEOFFREY EDELMANN, *Naval Research Laboratory, Code 7145, 4555 Overlook Ave. SW, Washington, DC 20375*
DAVID PREVES, *Starkey Laboratories, 6600 Washington Ave. S., Eden Prairie, Minnesota 55344*
NEIL A. SHAW, *Menlo Scientific Acoustics, Inc., Post Office Box 1610, Topanga, California 90290*
KEVIN P. SHEPHERD, *Mail Stop 463, NASA Langley Research Center, Hampton, Virginia 23681*
ERIC E. UNGAR, *Acentech, Incorporated, 33 Moulton Street, Cambridge, Massachusetts 02138*
ROBERT C. WAAG, *Department of Electrical and Computer Engineering, University of Rochester, Rochester, New York 14627*

7,251,195

43.20.Ye APPARATUS FOR GENERATING AN ACOUSTIC SIGNAL

Christian G. Reiff *et al.*, assignors to United States of America as represented by the Secretary of the Army
31 July 2007 (Class 367/139); filed 23 October 2003

Electrodes **14–16**, which are rounded to prevent coronal discharge, are mounted to one side of a dielectric substrate **12**. A voltage is applied, via conductors **22** and **24**, from power supply **10**, that is just below that required for surface arc discharge. A connector strip **34** is placed on the other side of

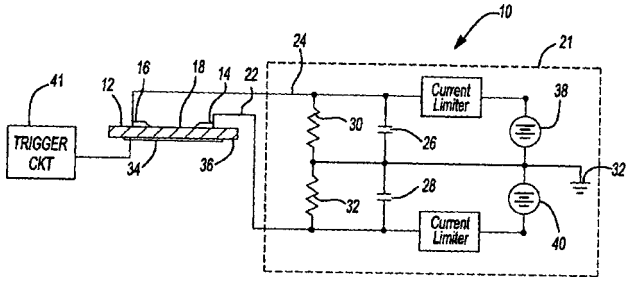

the dielectric. A trigger voltage is applied to strip **34** such that the electric field between the high voltage electrodes is exceeded, thus causing the air to ionize and create a surface arc. This arc produces an acoustic impulse.—NAS

7,280,433

43.30.Pc DEVICE AND METHOD FOR SONAR MEASUREMENT OF A SWIMMING POOL

Robert J. McEwen IV and Jeffrey D. McEwen, both of Charlotte, North Carolina
9 October 2007 (Class 367/96); filed 28 September 2005

Illustrated is a method of profiling a pool with sound prior to cutting a pool liner.—GFE

7,283,424

43.30.Wi HIGH SPEED UNDERWATER PROJECTILE TRACKING SYSTEM AND METHOD

Robert Kuklinski, assignor to The United States of America represented by the Secretary of the Navy
16 October 2007 (Class 367/118); filed 2 August 2006

A straightforward method of tracking underwater projectiles fired within a series of hoops is detailed.—GFE

7,260,229

43.38.Dv POSITION SENSOR FOR A LOUDSPEAKER

Stefan R. Hlibowicki, assignor to Audio Products International Corporation
21 August 2007 (Class 381/96); filed 16 October 2002

Tapered conductive element **28** induces a current in inductive coils **22–24** as it moves relative to voice coil **32**. The shape of element **28** is such that it generates a linear change in inductance as a function of displacement.

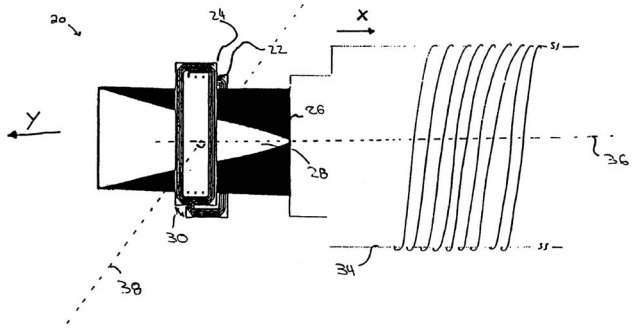

Coils **22–24** are connected to an electronic circuit that uses the inductance signal to compensate for some of the non-linearities in the voice coil (and loudspeaker) displacement.—NAS

 0001-4966/2008/123(4)/1819/12/$23.00 © 2008 Acoustical Society of America

7,292,227

43.38.Dv ELECTRONIC DEVICE, VIBRATION GENERATOR, VIBRATION-TYPE REPORTING METHOD, AND REPORT CONTROL METHOD

Masaaki Fukumoto and Toshiaki Sugimura, assignors to NTT DoCoMo, Incorporated
6 November 2007 (Class 345/173); filed in Japan 8 August 2000

Instead of acoustic (beeps) indication of a touch panel input the authors suggest the use of vibration. That is, if the touch panel input is received, the panel and/or the housing of the panel vibrates letting an operator know that his/her input is processed. This 86 page patent (including 85 figures and 82 claims) describes the operation of the reaction force shaker controlled by a magnetic brake.—DMD

7,289,919

43.40.Le CYCLIC TIME AVERAGING FOR MACHINE MONITORING

Johannes I. Boerhout, assignor to SKF Condition Monitoring Incorporated
30 October 2007 (Class 702/56); filed 30 July 2004

Monitoring of a machine for the early detection of potential faults is accomplished on the basis of signals obtained from accelerometers. The time signals from an accelerometer are averaged over several periods and each average is subjected to "cycle time averaging," which provides a circular diagram that relates the data to one period of the phenomenon under consideration. This permits determination of the energy contributions of various sources and thus the identification of potential problems.—EEU

7,250,832

43.38.Rh METHOD FOR REALIZING SURFACE ACOUSTIC WAVE FILTER ARRANGEMENTS AND FILTER ARRANGEMENT OBTAINED IN ACCORDANCE TO THIS METHOD

Serguei Kondratiev, assignor to TEMEX
31 July 2007 (Class 333/193); filed in the European Patent Office 21 December 2001

An improved surface acoustic wave (SAW) radio frequency band pass

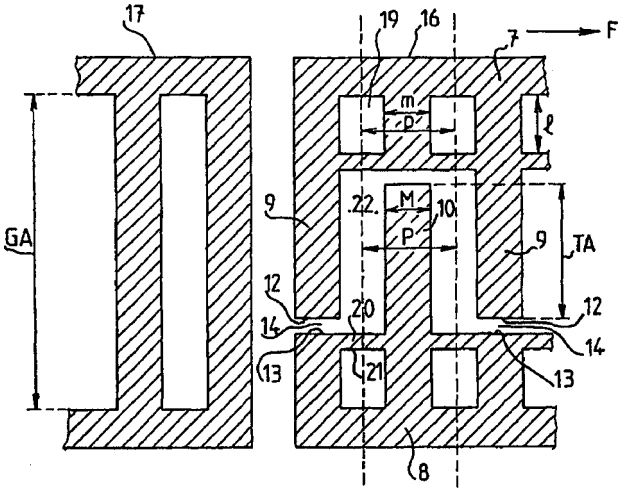

filter is claimed where parasitic elements of length 1 are added.—AJC

7,281,429

43.38.Zp OPTICAL HYDROPHONE FOR A SHOCK-WAVE FIELD WITH LONG SERVICE LIFE

Bernd Granz and Ralf Nanke, assignors to Siemens Aktiengesellschaft
16 October 2007 (Class 73/655); filed in Germany 29 November 2002

A fiber-optic hydrophone designed to measure the spatial distribution of an impinging shock wave is described by illuminating the boundary of an optically-transparent body and a sound-conducting medium.—GFE

7,249,442

43.40.Tm STORAGE RACK VIBRATION ISOLATORS AND RELATED STORAGE RACK SYSTEMS

John B. Pellegrino *et al.*, assignors to Ridg-U-Rak, Inc.
31 July 2007 (Class 52/167.8); filed 10 April 2006

A storage rack seismic isolator against horizontal seismic vibrations is claimed. Because of diagonal stiffeners **16**, such racks have more stiffness against cross-aisle motion **10** than for along-aisle motion **12**. Seismic (earthquake) events can cause stored objects in trays on **17** to slide off and fall

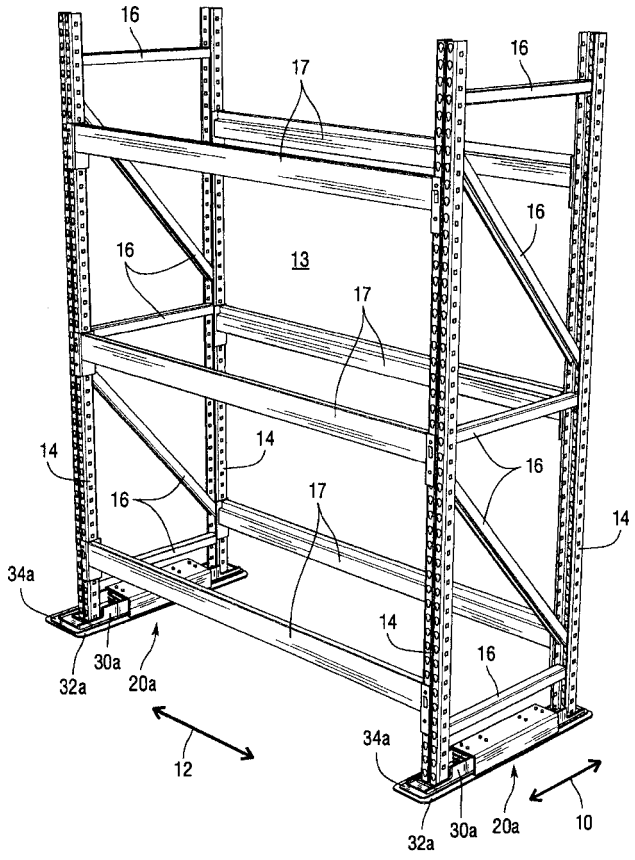

into aisles and onto personnel there. Movable supports **30a** are made free to slide in tracks **34a**. Horizontal restraint is direction **10** is provided by a spring or a stack of rubber pads fastened inside isolator housing **20a**, providing an isolator resonance frequency of from 0.5 to 1.6 Hz.—AJC

7,249,509

43.40.Tm ANGULAR VELOCITY DETECTOR

Kenji Hirano, assignor to DENSO Corporation
31 July 2007 (Class 73/504.12); filed in Japan 8 July 2004

Isolation **300** of angular velocity sensor **100** against vibration of package **S5** and its environment is claimed. Sensor **100** operates via coriolis force on an element vibrating at a high frequency within **100** resulting from angular velocity (rotation of) package **S5**. Environmental vibration of **S5** can

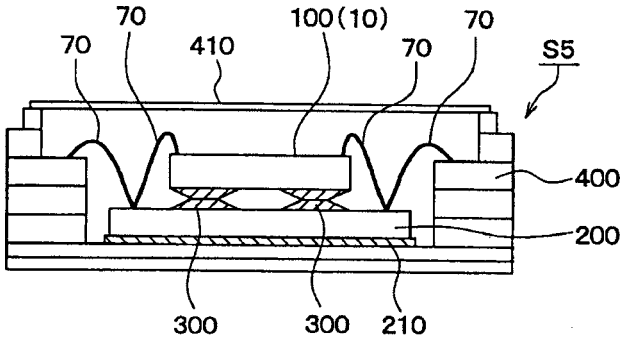

result in errors by the coriolis sensor **100**. Isolation against such environmental vibrations is provided by resilient buttons or strips **300** on each corner or side of sensor **100**.—AJC

7,255,529

43.40.Tm COOLING FAN MOUNTING ARRANGEMENT WITH VIBRATION ISOLATION MEMBER

Chin-Long Ku *et al.*, assignor to Fu Zhun Precision Industry (Shenzhen) Company, Limited
14 August 2007 (Class 415/119); filed 17 December 2004

An economical personal computer cooling fan vibration (noise) isolator **20** is claimed having locking protrusions **26** which pass through slotted

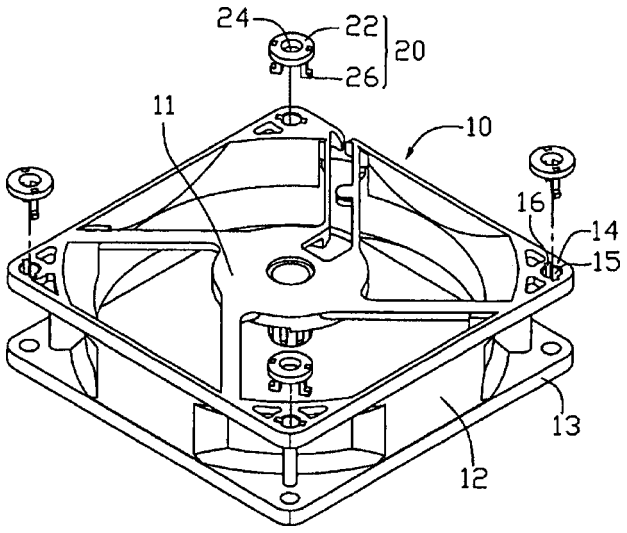

hole **15–16**. Isolator material **22, 26** is an elastomer. It was not made clear what sort of fastener is to be used to hold fan assembly **10** onto the computer framework.—AJC

7,284,527

43.40.Tm TUNED VIBRATION ABSORBER

Eric Herrera and Bilal A. Bazzi, assignors to Freudenberg-NOK General Partnership
23 October 2007 (Class 123/195 C); filed 6 April 2004

This dynamic absorber is intended to be used with a bolt, such as one that fastens a cover to an engine, and consists of a mass **26** that is attached to a supporting pedestal **22** via an elastic element **24**. The pedestal, which in essence is made of an upper ring that is connected to a lower ring by two rods, is fastened to the cover **30** by a bolt **28** that also holds the cover onto

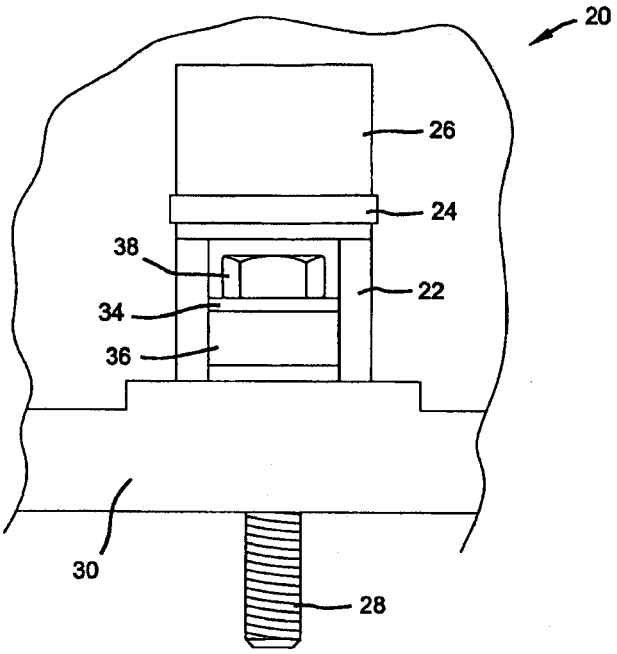

the engine via a washer **34** and grommet **36**. The mass **26** is in the form of a hollow cylinder and the element **24** is ring shaped to permit a tool to reach the bolt head. An absorber of this type may be added to each of several bolts on an engine cover.—EEU

7,290,374

43.40.Tm VIBRATION CONTROL APPARATUS USING WATER TANK LOCATED AT TOP FLOOR OF A TALL BUILDING

Sung Won Yoon *et al.*, assignors to Seoul National University of Technology
6 November 2007 (Class 52/167.1); filed in Republic of Korea 10 September 2003

Water in tanks atop tall buildings can serve as a dynamic absorber to protect the building from excessive lateral vibrations, such as those that may result from wind or seismic excitation. The water tanks are fitted with strategically located wire mesh screens to damp the water's sloshing motion. Rather than adding a water tank that only serves as a damper, it is desirable to use the building's water supply tank also to fulfill this function. The present patent describes constructions of such tanks that facilitate cleaning and replacement of the screens in these tanks.—EEU

7,290,644

43.40.Tm VIBRATION ABSORBER WITH DYNAMIC DAMPER

Kazuo Miyake, assignor to Kurashiki Kako Company, Limited
6 November 2007 (Class 188/379); filed in Japan 23 March 2005

This patent pertains to an engine mount in which an inner load-bearing element is isolated from an outer supporting shell via an elastomeric element. An outer toroidal rubber "stopper" is added to limit the relative motion between the two supporting elements in the event of an overload. One or more metal disks or spirals are embedded in the rubber stopper, so that this assembly also serves as a dynamic absorber.—EEU

7,286,919

43.40.Vn METHOD AND APPARATUS FOR CONTROLLING DAMPING OF A VEHICLE SUSPENSION

John Nordgren *et al.*, assignors to GM Global Technology Operations, Incorporated
23 October 2007 (Class 701/37); filed 18 May 2006

Semi-active control of the dampers of a vehicle suspension is achieved by an algorithm that limits heave, roll, and pitch of the vehicle body. The body movement is measured with accelerometers and vehicle-speed-dependent maximum and minimum limits to the damper control are applied. The rate of each damper is adjusted depending on its location on the vehicle, with the intent of always having a balanced setting of the four dampers.—EEU

7,250,087

43.40.Yq CLOGGED NOZZLE DETECTION

James Tyson, Pennsauken, New Jersey and Janez Makovsek, Maribor, Slovenia
31 July 2007 (Class 134/18); filed 16 May 2006

"…by monitoring the intensity of vibrations caused by the impingement of the spray jet, we can gauge the mass flow of the water producing the vibrations and consequently the performance of the jet nozzle itself." The patent claims use in cleaning the insides of tanks, and by mention, dishwashers, where multiple rotating nozzles are used for the cleaning process.—NAS

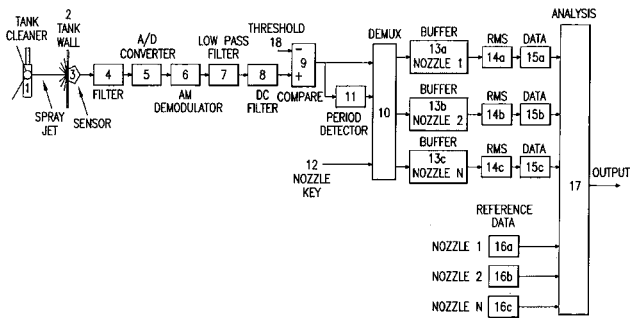

6,848,252

43.50.Gf EXHAUST ENHANCEMENT FOR AFTERMARKET MOTORCYCLE EXHAUST PIPES WITH A STRAIGHT PIPE TYPE DESIGN AND WITH INSIDE PIPE DIAMETER FROM 1.875″ AND LARGER

James Charles Maybeck, Charlotte, North Carolina
1 February 2005 (Class 60/312); filed 7 April 2003

As the title suggests, this patent is aimed at "enhancing" the noise and power of a motorcycle engine. The stock muffler baffles are removed and

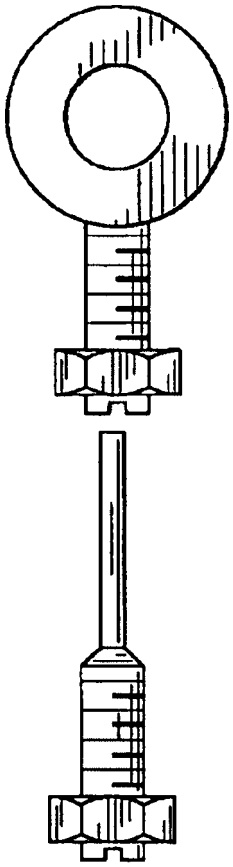

replaced by "thunderbolts," Fig. 4, and "thunderprobes," Fig. 5, which "create a vortex which allows the gases to exit more efficiently," thus providing improved throttle response and a deeper sound.—KPS

7,249,987

43.50.Gf AIR INTAKE DEVICE FOR WATERCRAFT

Yoshiaki Noda and Masatsugu Matsumoto, assignors to Honda Motor Company, Limited
31 July 2007 (Class 440/88 A); filed in Japan 29 March 2005

A personal watercraft engine air intake noise suppression method is claimed. Cool combustion air is drawn through an opening in the top front

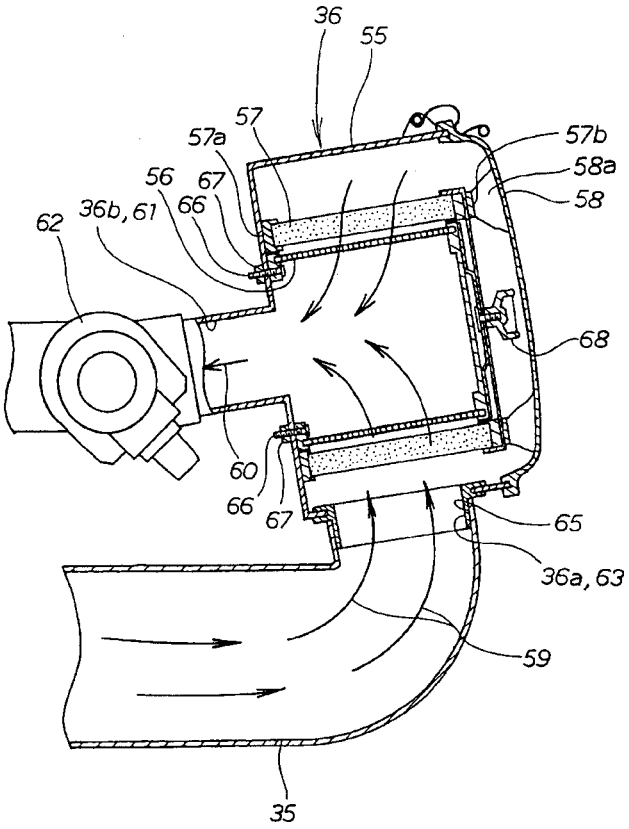

of the craft, through long duct **35**, air filter **57** and flame arrester **56** into throttle assembly **62**. The long length duct **35** promotes reduction of noise emission from the remote air inlet. Duct **35** also passes under air cleaner **36** so that the entire assembly can be narrower than, and placed behind, any in-line engine for a more compact craft assembly.—AJC

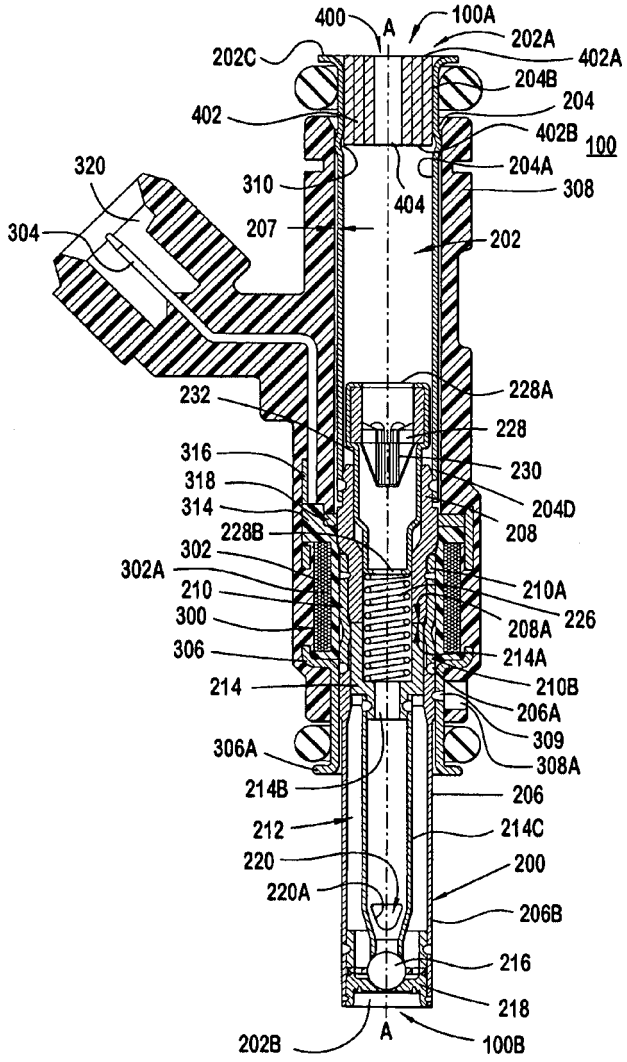

reduction of from 0.5 to 2.06 dBA, with an overall average noise reduction of 1.6 dBA.—AJC

7,258,287

43.50.Gf MODULAR FUEL INJECTOR WITH A SPIRAL DAMPER MEMBER AND METHOD OF REDUCING NOISE

Yong D. Cho and Zeki Alyanak, assignors to Siemens VDO Automotive Corporation
21 August 2007 (Class 239/585.1); filed 3 June 2004

This is an advancement over United States Patent 7,128,281 (reviewed in JASA **121**:2487). Engine fuel injector noise reduction is claimed where noise and vibration caused by armature **214** impacts is absorbed by damper **400**. Damper **400** is formed from 1-mm-thick sheet material of density 2.7 and greater, rolled into a cylinder and pressed into injector aperture **204A**. Acoustical tests of 23 treated injector samples indicated a noise emission

7,254,240

43.50.Ki ACTIVE NOISE CONTROL SYSTEM

Toshio Inoue *et al.*, assignor to Honda Giken Kogyo Kabushiki Kaisha
7 August 2007 (Class 381/71.4); filed in Japan 9 March 1999

This is an advancement over United States Patent No. 7,062,049 (reviewed JASA **120**:3448) which had error microphones under the driver's seat **31** and in the trunk **35** and under the roof center. Here, side microphones **43**, **44** by the front seat occupants' ears and **45** on the floor are added

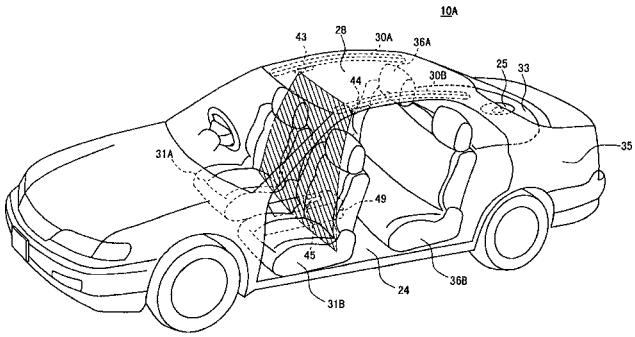

to update controller active noise control (ANC) coefficients to drive speaker **25**. Road noise frequency components to be suppressed are around 40 and 80 Hz.—AJC

6,848,410

43.50.Lj SOUND TRANSMISSION DEVICE FOR A MOTOR VEHICLE

Reinhard Hoffmann *et al.*, assignors to Mahle Filtersysteme GmbH
1 February 2005 (Class 123/184.57); filed in Germany 23 March 2001

A device to introduce engine sounds into the passenger cabin of an automobile is described in which sound transmission tubes connect between the air intake of the engine, **11**, and the bulkhead, **19**. Each transmission tube connects to resonators **13**, **15**, which in turn are connected to an exit throat

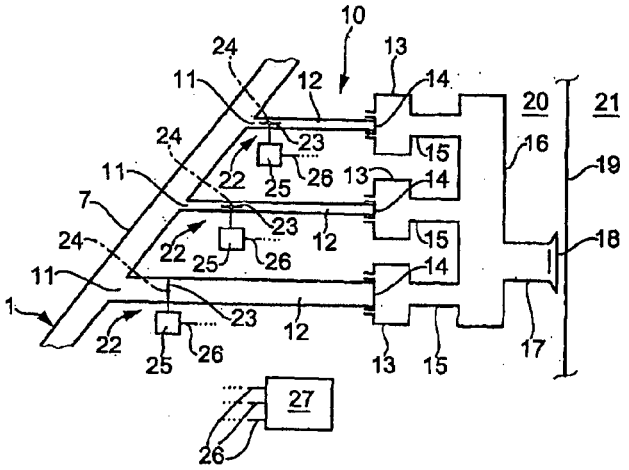

18. Each transmission tube may be tuned to a different resonant frequency by selection of the tube length and the resonator characteristics. Actuators **25**, and control flaps **23**, may be used to close off any of the transmission tubes, thus allowing control of the character of the noise reaching the vehicle occupants.—KPS

6,826,901

43.50.Nm CONVERGENT/DIVERGENT SEGMENTED EXHAUST NOZZLE

Leonard J. Hebert, assignor to The Boeing Company
7 December 2004 (Class 60/204); filed in 13 October 2003

Exhaust noise suppression in a high by-pass ratio turbofan engine can be achieved by means of segmentation of the nozzle exit, also known as chevrons (Fig. 1). These triangular chevrons are curved into the flow to promote mixing and hence noise reduction. The present invention aims to ameliorate the performance penalties associated with such designs. Figure 2 illustrates the inner, **12**, and outer, **14**, walls of the fan exhaust stream. The

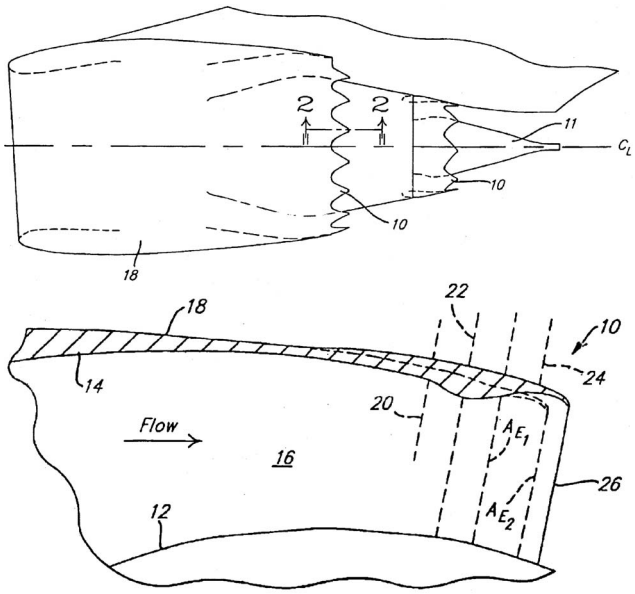

changes in cross section from **20** to **22** to **24** to **26** constitute a converging-diverging arrangement designed to minimize any performance penalties. Location **AE1** represents the exhaust area of a conventional nozzle, and **AE2** represents a typical chevron arrangement, absent the present invention.—KPS

7,257,230

43.55.Lb IMPULSE RESPONSE COLLECTING METHOD, SOUND EFFECT ADDING APPARATUS, AND RECORDING MEDIUM

Shigetaka Nagatani, assignor to Sony Corporation
14 August 2007 (Class 381/56); filed in Japan 24 September 1998

A fairly straightforward, but complex (there are at least 25 aspects of the invention disclosed just in the summary), means of simulating reverberation is presented. A digital signal, described as a time stretch pulse, is sent to

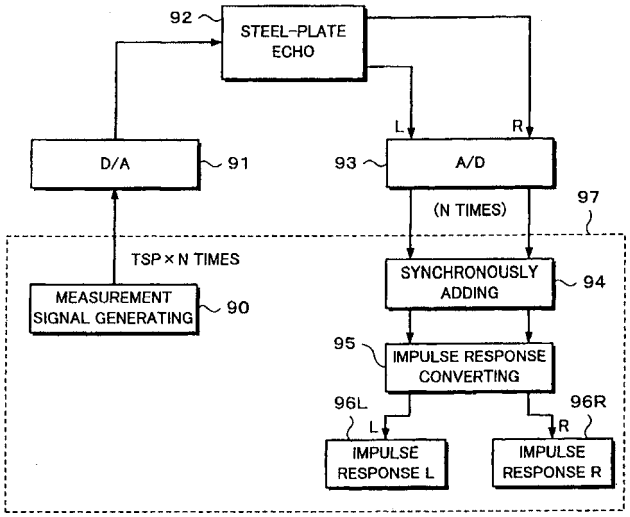

a device via D/A and A/D converter(s), which in the patent is a steel plate but could be almost any physical object including a concert hall. The digital signal thus obtained is synchronously averaged and the stereo impulse response is calculated.—NAS

7,249,654

43.55.Ti HEAT INSULATING ACOUSTICAL STRUCTURE AND CARBODY SHELL STRUCTURE USING THE SAME

Hidekazu Nakamoto *et al.*, assignor to Hitachi, Limited
31 July 2007 (Class 181/290); filed in Japan 9 February 2005

An improved and thinner railroad passenger car shell thermal and noise barrier assembly **10–20** is claimed. The rail car structural shell **10** is double skin aluminum with internal stiffener ribs **13** across a 40-mm-thick airspace. Vacuum insulating material **21** is 6 mm thick. Fibrous non-woven

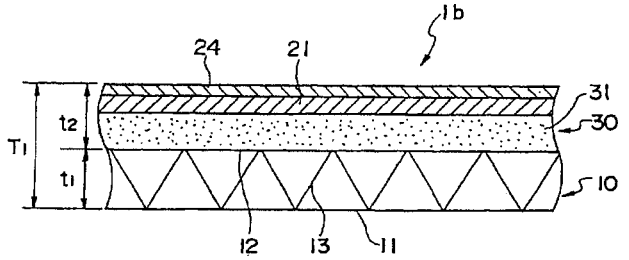

acoustical insulating material **30** is 16 mm thick. Interior panel finish material **24** is 2 mm thick plastic. Overall shell thickness is 64 mm. Compared with 90-mm-thick conventional construction, sound transmission loss at sound frequencies above 250 Hz is improved by 1–3 dB.—AJC

7,257,452

43.58.Ta GUI FOR DIGITAL AUDIO SIGNAL FILTERING MECHANISM

Philip R. Wiser *et al.*, assignor to Microsoft Corporation
14 August 2007 (Class 700/94); filed 29 June 2005

Digital distribution of audio files via computer networks, the internet, and other means is ubiquitous. The many different end user requirements and capabilities of the end user equipment means that the delivery format of the file may not be optimum. A comprehensive means of processing a source

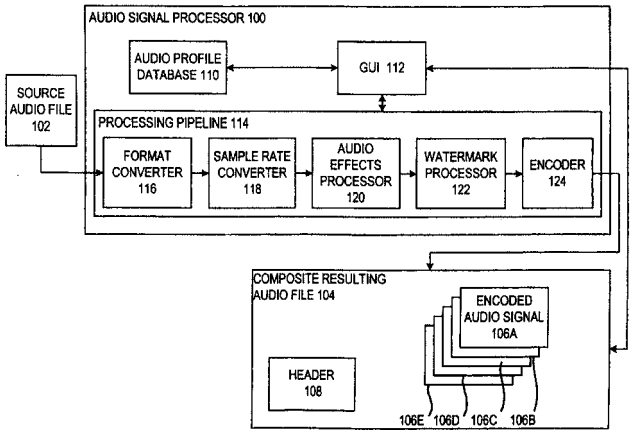

audio file or files for delivery in many encoded formats, for which a profile for each format is prepared, stored, and accessible, in which the end user requirements are considered, is disclosed.—NAS

7,273,105

43.60.Dh MONITORING OF A RESERVOIR

John A. Johansen and Morten Sivertsen, assignor to FMC Kongsberg Subsea AS
25 September 2007 (Class 166/336); filed in Norway 19 December 2001

Upon its completion, an underwater oil well is typically capped and temporarily ignored. A method to communicate with the completed wellhead via standard acoustic communications is described for the purpose of improving future well drilling in the area.—GFE

7,277,538

43.60.Dh DISTORTION COMPENSATION IN AN ACOUSTIC ECHO CANCELER

James H. Parry, assignor to Tandberg Telecom AS
2 October 2007 (Class 379/406.01); filed 4 October 2005

Another version of an adaptive equalizer to cancel echoes in telephony is described.—GFE

7,280,070

43.60.Fg ROBUST OPTIMAL SHADING SCHEME FOR ADAPTIVE BEAMFORMING WITH MISSING SENSOR ELEMENTS

Unnikrishna Sreedharan Pillai, Harrington Park, New Jersey
9 October 2007 (Class 342/195); filed 30 November 2004

A technique to automatically recalculate beam shading parameters when individual elements die is described.—GFE

7,277,116

43.60.Jn METHOD AND APPARATUS FOR AUTOMATICALLY CONTROLLING VIDEO CAMERAS USING MICROPHONES

Antonio Messina, 40126 Bologna, Italy
2 October 2007 (Class 348/14.08); filed in Italy 3 July 1998

Yet another time delay of arrival system is put forth, this one directing video cameras toward the direction of an acoustic source.—GFE

7,277,359

43.60.Jn NAVIGATION PROCESSOR, A SYSTEM COMPRISING SUCH A NAVIGATION PROCESSOR AND A METHOD OF CONTROLLING AN UNDERWATER SYSTEM BY SUCH A NAVIGATION PROCESSOR

Francois Bernard, assignor to Think! Global B.V.
2 October 2007 (Class 367/131); filed 28 December 2006

The obvious idea of using environmental measurements to improve acoustic propagation has been seized upon again. This time the improved acoustic estimations are used to more accurately position objects on the sea floor.—GFE

7,286,672

43.66.Ts BINAURAL HEARING DEVICE AND METHOD FOR CONTROLLING A HEARING DEVICE SYSTEM

Hans-Ueli Roeck, assignor to Phonak AG
23 October 2007 (Class 381/23.1); filed 7 March 2003

Beamforming is implemented in a monaural or binaural middle ear implantable hearing system, taking into account the acoustic signals present

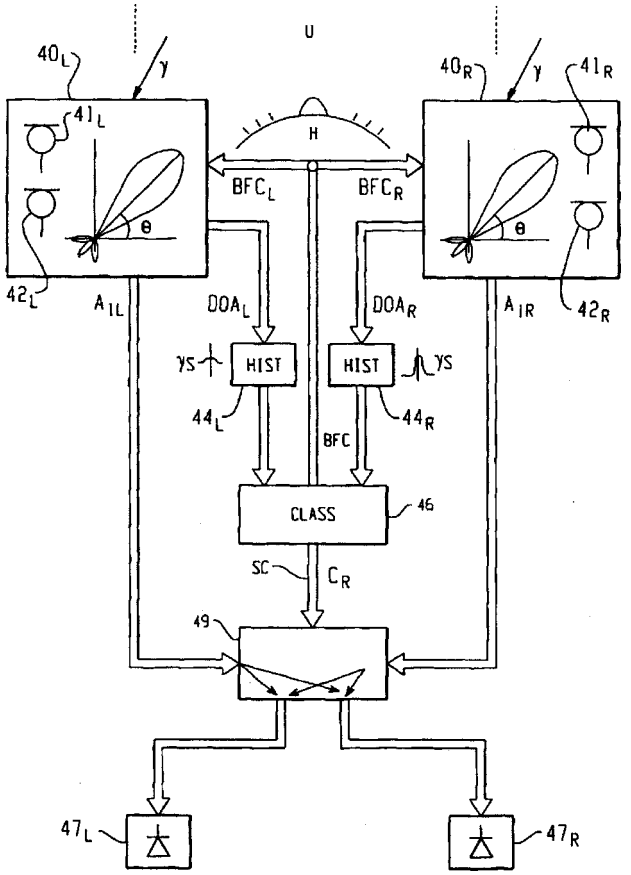

at the two ears of the wearer. A hard-wired, fiber optic or wireless communication link is established between the devices associated with each ear. One or more microphones may be utilized in each device, and Wiener filtering is performed before transmission to the other device. If two or more microphones are utilized in the device at each ear, their output signals are combined and pre-processed before transmission to the other device. Histograms keep track of acoustical source changes over time.—DAP

7,286,673

43.66.Ts EMBEDDED INTERNET FOR HEARING AIDS

Joerg Bindner and Wolfram Meyer, assignors to Siemens Audiologische Technik GmbH
23 October 2007 (Class 381/60); filed in Germany 15 January 2002

Diagnostic information such as status of the battery in a hearing aid is sent to a hearing aid specialist via the Internet or other wide-area network. The hearing aid has built in bi-directional communication, which may be

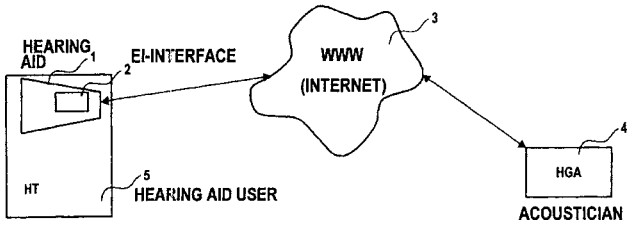

wireless, and Internet functionality. The goals are to determine if a battery was changed by the user at a time later than it should have been and training the user to change the battery at the appropriate time.—DAP

7,286,677

43.66.Ts DIRECTIONAL MICROPHONE ASSEMBLY

Mead C. Killion *et al.*, assignors to Etymotic Research, Incorporated
23 October 2007 (Class 381/313); filed 12 July 2004

To reduce size of an in-the-ear hearing aid directional microphone assembly, opposing side portions of a directional microphone cartridge extend partially into the opposing sound ducts of the opposing side walls of the directional microphone assembly. The result is that sound passage inlets for

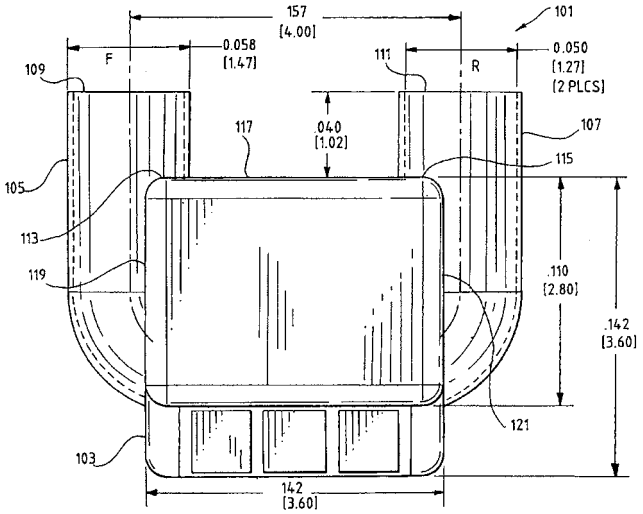

the directional microphones are spaced apart such that the shortest distance between them is less than or approximately equal to the length of the microphone cartridge.—DAP

7,286,678

43.66.Ts HEARING DEVICE WITH PERIPHERAL IDENTIFICATION UNITS

Herbert Bächler and Christian Berg, assignors to Phonak AG
23 October 2007 (Class 381/314); filed 6 July 2000

The hardware block configuration peripheral to the digital signal processing unit in a hearing aid is stored to facilitate a modular design and construction process with no manual writing required and self-identification of the system constellation during manufacturing and fitting. Components

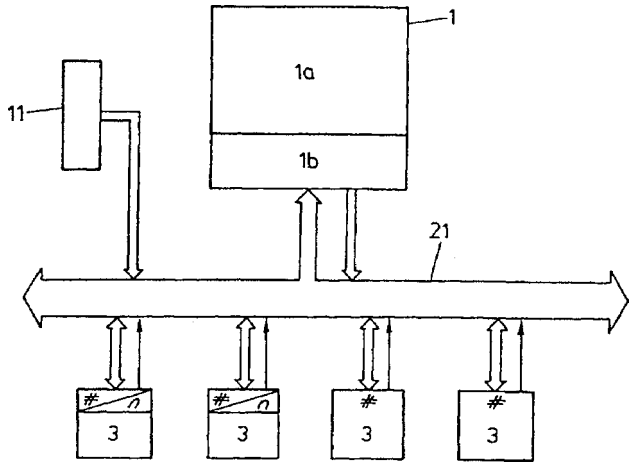

may be connected together on two buses. Included on the first bus are microphones, sensors, amplifiers, and receivers and on the second bus transceivers, memories and switches.—DAP

7,286,679

43.66.Ts AUTOMATIC BINAURAL SHELL MODELING FOR HEARING AIDS

Tong Fang *et al.*, assignors to Siemens Medical Solutions USA, Incorporated
23 October 2007 (Class 381/322); filed 18 December 2003

Data obtained from scanning the impressions of the first and second ears are used to automatically model and process relative position and

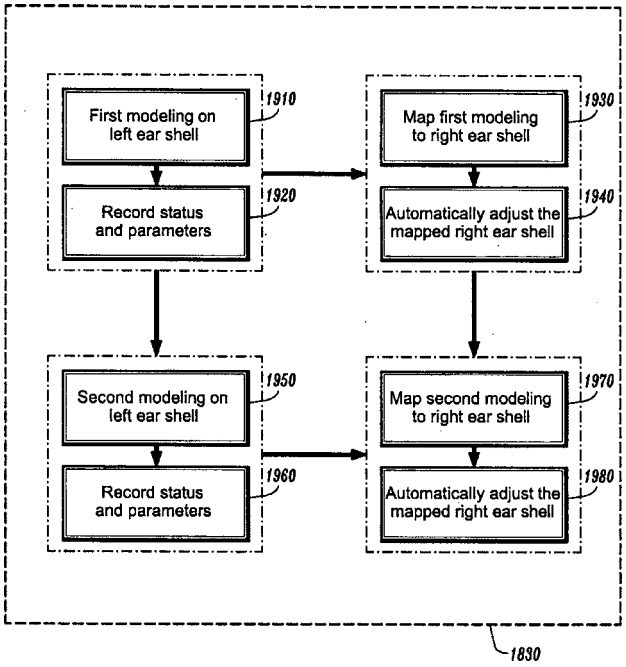

orientation information for the second custom earshell from the modeling results on the first earshell.—DAP

7,289,639

43.66.Ts HEARING IMPLANT

Eric Abel *et al.*, assignors to Sentient Medical Limited
30 October 2007 (Class 381/312); filed in United Kingdom 24 January 2002

An ear canal module houses a microphone and an LED or other light source converts incoming sounds to light energy such as infrared, which in turn is transmitted through the eardrum. A middle ear or inner ear implant includes a photoreceiver that detects the light signal, amplification circuitry

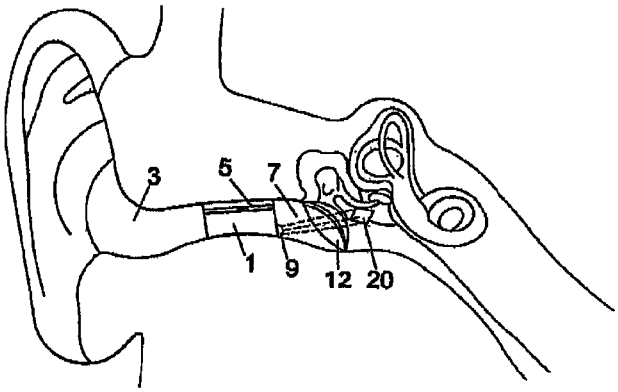

and a piezoelectric or other type of actuator that produces mechanical or electrical stimulation to the middle or inner ear. Also claimed is that a second light signal can be transmitted to charge a battery housed in the implantable portion of the device.—DAP

7,292,698

43.66.Ts DATA TRANSMISSION DEVICE FOR HEARING AIDS

Torsten Niederdränk *et al.*, assignors to Siemens Audiologische Technik GmbH
6 November 2007 (Class 381/315); filed in Germany 12 February 2003

To facilitate wireless communication in a hearing aid while minimizing extra space required, an inductor is used both as an antenna and as a coil in a modulatable LC resonant oscillator circuit. A current mirror and comparator actuation circuit monitors the polarity of oscillation and delivers an

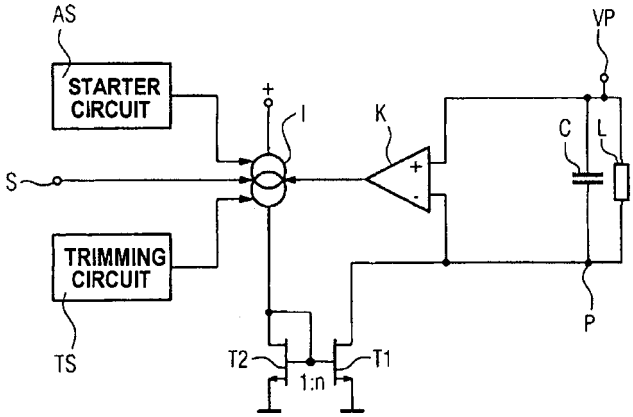

adjustable amount of energy into the oscillator circuit during a negative or positive half-cycle of oscillation. The current mirror can also be controlled externally to produce an amplitude modulation.—DAP

7,292,699

43.66.Ts BAND-LIMITED ADAPTIVE FEEDBACK CANCELLER FOR HEARING AIDS

Shawn X. Gao *et al.*, assignors to House Ear Institute
6 November 2007 (Class 381/318); filed 23 March 2005

To reduce adaptation time, signal distortion and signal processing complexity, acoustic feedback cancellation is performed only in a frequency band that encompasses unstable frequencies. An adaptive filter is formulated

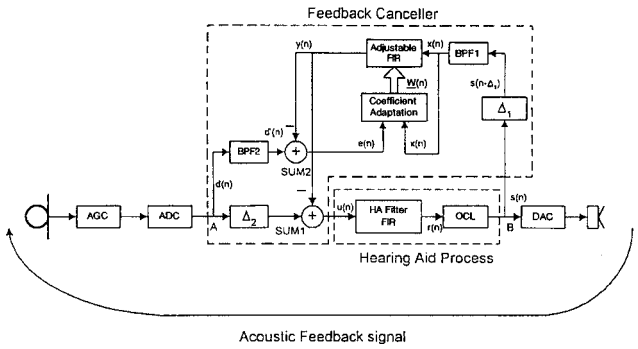

to approximate the external feedback path of the hearing aid in conjunction with first and second bandpass filters. Delays are shortened and optimized throughout the system to minimize phase distortion.—DAP

7,295,676

43.66.Ts HEARING AID AND METHOD OF ADAPTING A HEARING AID

Josef Chalupper, assignor to Siemens Audiologische Technik GmbH
13 November 2007 (Class 381/313); filed in Germany 5 November 2003

The goal is a system that focuses spatially on one desired sound source direction quickly using blind source separation, even during hearing aid wearer head movement. With the wearer's head position and the outputs of multiple microphones, the system can identify the direction of one acoustic signal. The position of the hearing aid wearer's head is determined with an accelerometer or a flux gate that detects the earth's magnetic field. The position of the head may be transmitted wirelessly from the first to the second hearing aid in a binaural fitting.—DAP

7,288,071

43.66.Yw SPEECH DISCRIMINATION IN AUTOMATED DIAGNOSTIC HEARING TEST

Jeffrey S. Harrison *et al.*, assignors to Tympany, Incorporated
30 October 2007 (Class 600/559); filed 16 May 2003

A patient uses a computer-based, multi-media device to perform speech discrimination and other audiometric tests automatically on his or her own hearing with minimal assistance from a hearing health professional

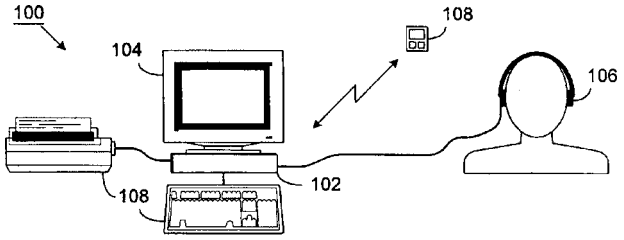

and without a sound isolation chamber. Optimal intensity and masking levels are calculated and presented during testing with word-picture groups.—DAP

7,292,971

43.70.Kv LANGUAGE PHONETIC SYSTEM AND METHOD THEREOF

Kuojui Su and Van Nuys, California
6 November 2007 (Class 704/5); filed in Taiwan 27 October 2003

This patent describes a new phonetic spelling system intended to ease the task for English speakers of learning to speak the Chinese language. Acknowledging the success of the now widely used Pinyin spelling system, a number of changes have been made to help sort out some of the confusions which can arise while using that system. For example, Pinyin uses the character combinations "zh," "ch," and "sh" to represent sounds which do not occur in English. The authors of this system argue that less confusion occurs through the use of nonoccurring combinations "tz," "td," and "s‴" to represent these sounds. Other similar innovations appear to reflect a good understanding of many of the issues involved in learning to speak a foreign language.—DLR

7,283,962

43.71.Bp METHODS AND SYSTEMS FOR DETECTING, MEASURING, AND MONITORING STRESS IN SPEECH

James L. Meyerhoff and John H. L. Hansen, assignors to United States of America as Represented by the Secretary of the Army
16 October 2007 (Class 704/270); filed 21 March 2003

This patent describes a method of speech analysis designed to detect stressful conditions affecting the speaker. While acknowledging that stress will often affect the speech pitch or pitch range, the method does not include a pitch analysis. Instead, the primary detector seems to be a peakiness detector, which looks for spikes in the energy across either time (analysis frames) or frequency (filter bands). The patent is a study in hedging one's bets. Ideally, the method would detect speaker stressful conditions, but another claim will also be satisfied if any of 42 other emotional states is detected. The error rate would ideally be 1% or less, but other claims are satisfied by error rates up to 4.7%. And so it goes.—DLR

7,292,901

43.72.Gy HYBRID MULTI-CHANNEL/CUE CODING/ DECODING OF AUDIO SIGNALS

Frank Baumgarte and Peter Kroon, assignors to Agere Systems Incorporated
6 November 2007 (Class 700/94); filed 18 September 2002

Conventional techniques of encoding the sum and the difference of left and right audio channels require a large amount of data and transmission bandwidth. With the binaural cue coding technique (BCC) recommended in this patent, the amount of data to be transmitted is reduced since the spectral

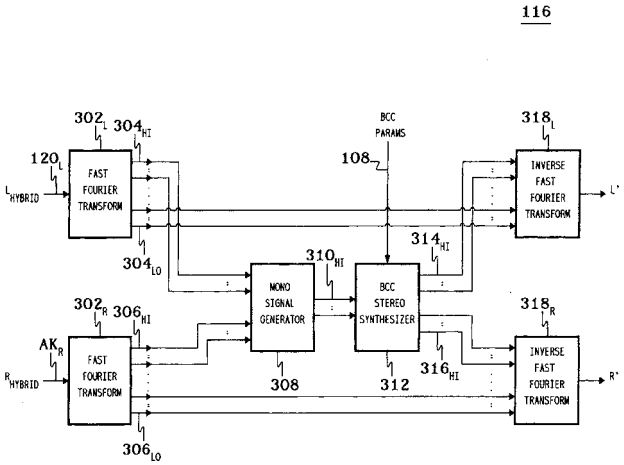

components for the input signals are downmixed into a single monaural signal which forms a hybrid signal with at least one spectral component for each input signal that was left unmixed. The result is encoded using conventional coding techniques.—DAP

7,286,987

43.72.Ne MULTI-PHONEME STREAMER AND KNOWLEDGE REPRESENTATION SPEECH RECOGNITION SYSTEM AND METHOD

Philippe Roy, assignor to Conceptual Speech LLC
23 October 2007 (Class 704/270); filed 30 June 2003

The speech recognizer presented here is said to perform better than others because of its front-to-back comprehensive set of domains and methods of analysis, including phoneme classification, word identification, part-of-speech analysis, syntactic parsability, and semantic appropriateness. Each

of these steps is described in considerable detail, resulting in a bulky patent of 71 pages and with 290 claims.—DLR

7,286,989

43.72.Ne SPEECH-PROCESSING SYSTEM AND METHOD

Gerhard Niedermair *et al.*, assignors to Siemens Aktiengesellschaft
23 October 2007 (Class 704/275); filed in Germany 3 September 1996

Selections from several different types of speech recognition modules and speech output modules are made depending on the specific type of input

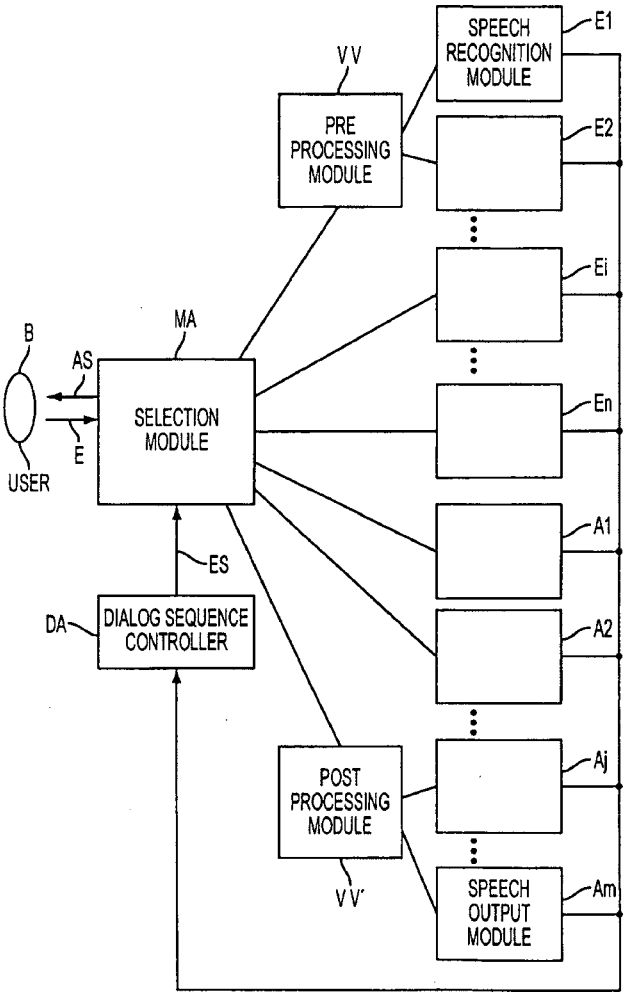

signal and application situation.—DAP

7,277,852

43.75.Xz METHOD, SYSTEM AND STORAGE MEDIUM FOR COMMERCIAL AND MUSICAL COMPOSITION RECOGNITION AND STORAGE

Miwako Iyoku and Tatsuhiro Kobayashi, assignors to NTT Communications Corporation
2 October 2007 (Class 704/236); filed in Japan 23 October 2000

Even though such tools already exist, a technique has been put forth to record music from the radio, extract features, and compare them to a known database, in order to automatically determine the singer and song title.—GFE

7,277,550

43.75.Zz ENHANCING AUDIO SIGNALS BY NONLINEAR SPECTRAL OPERATIONS

Carlos Avendano *et al.*, assignors to Creative Technology Limited
2 October 2007 (Class 381/94.2); filed 24 June 2003

A tool for sharpening or smoothing music is described using simple filters and the short-time Fourier transform.—GFE

7,285,092

43.80.Vj COMPUTERIZED ULTRASOUND RISK EVALUATION SYSTEM

Nebojsa Duric *et al.*, assignors to Barbara Ann Karmanos Cancer Institute
23 October 2007 (Class 600/443); filed 18 December 2002

Tissue is fixed in position and illuminated with acoustic waves. Reflected and transmitted waves are received. The received waves are

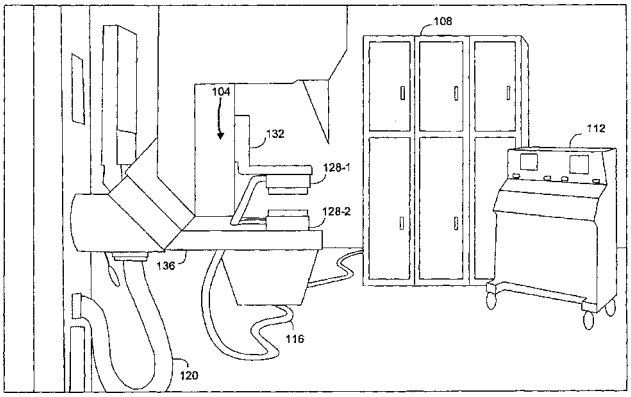

processed to derive a representation of the tissue.—RCW

7,285,093

43.80.Vj SYSTEMS FOR ULTRASONIC IMAGING OF A JAW, METHODS OF USE THEREOF AND COUPLING CUSHIONS SUITED FOR USE IN THE MOUTH

Victor Anisimov *et al.*, assignors to Imadent Limited
23 October 2007 (Class 600/443); filed 10 October 2003

The position of a specially configured ultrasonic probe that consists of one, two, or more transducer elements is used to image a portion of a jaw.—RCW

7,285,094

43.80.Vj 3D ULTRASONIC IMAGING APPARATUS AND METHOD

Timothy J. Nohara *et al.*, Fonthill, Ontario, Canada
23 October 2007 (Class 600/447); filed 28 January 2003

A two-dimensional array of transducer elements with a different pitch in each dimension is used to transmit and receive ultrasonic waves. Beamforming in an azimuth or elevation dimension or in both dimensions is used to scan a region. Data processing yields ultrasound echoes along a line, in a plane, or throughout a volume.—RCW

7,285,095

43.80.Vj METHOD OF ANALYZING AND DISPLAYING BLOOD VOLUME USING MYOCARDIAL BLOOD VOLUME MAP

Hiroshi Ito and Yasuhiro Nakajima, assignors to YD, Limited
23 October 2007 (Class 600/458); filed in Japan 27 December 2002

A contrast-echo image showing the myocardium and a cardiac chamber is used to determine the volume of blood within the myocardium. In the image, regions covering a portion of the myocardium and a corresponding portion of a cardiac chamber are identified. A difference in intensity between the myocardium region and chamber region is obtained and the myocardium region is colored using the difference.—RCW

7,289,842

43.80.Vj SYSTEM FOR MEDICAL EXAMINATION OR TREATMENT

Michael Maschke, assignor to Siemens Aktiengesellschaft
30 October 2007 (Class 600/478); filed in Germany 22 September 2003

This is a catheter-based system with a sensor for optical coherence tomography, a sensor for intravascular ultrasound imaging, and a processing unit to develop and display images derived from each sensor.—RCW

7,288,068

43.80.Vj AUTOMATIC OPTIMIZATION FOR ULTRASOUND MEDICAL IMAGING

Müge M. Bakircioglu *et al.*, assignors to Siemens Medical Solutions USA, Incorporated
30 October 2007 (Class 600/455); filed 15 December 2003

Blood flow velocity values are unwrapped to avoid aliasing artifacts. The unwrapped velocity information is used to optimize the pulse repetition rate and the frame rate. In the optimization, the pulse repetition rate is determined from a systolic time period of the heart cycle and the frame rate is determined by a correlation as a function of penetration depth. One or more thresholds for velocity or energy in a flow image or displacement in the imaging plane may be used in the process.—RCW

7,291,108

43.80.Vj ULTRASONIC TRANSMISSION/ RECEPTION APPARATUS FOR GENERATING AN IMAGE BASED ON ULTRASONIC ECHOES AND VIBRO-ACOUSTIC SOUNDS

Tomoo Satoh, assignor to FUJIFILM Corporation
6 November 2007 (Class 600/437); filed in Japan 19 September 2003

A small amount of tissue around a bone and also a small amount of tissue inside the bone are imaged with a high resolution by using a

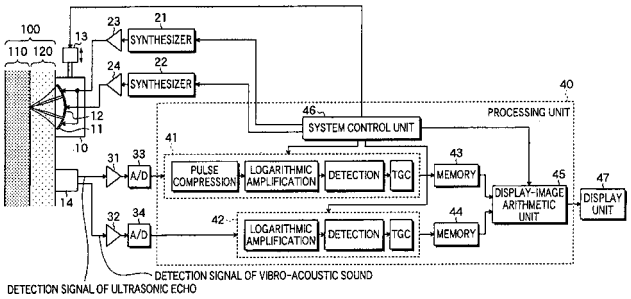

swept-frequency technique to excite a vibro-acoustic sensor from which signals are processed to obtain the image.—RCW

LETTERS TO THE EDITOR

This Letters section is for publishing (a) brief acoustical research or applied acoustical reports, (b) comments on articles or letters previously published in this Journal, and (c) a reply by the article author to criticism by the Letter author in (b). Extensive reports should be submitted as articles, not in a letter series. Letters are peer-reviewed on the same basis as articles, but usually require less review time before acceptance. Letters cannot exceed four printed pages (approximately 3000–4000 words) including figures, tables, references, and a required abstract of about 100 words.

Comment on "Silent research vessels are not quiet" [J. Acoust. Soc. Am. 121, EL145–EL150] (L)

Olav Sand[a)]
Department of Molecular Biosciences, University of Oslo, P.O. Box 1041 Blindern, NO-0316 Oslo, Norway

Hans Erik Karlsen
Department of Biology, University of Oslo, P.O. Box 1066 Blindern, NO-0316 Oslo, Norway

Frank R. Knudsen
Simrad, P.O. Box 111, NO-3191 Horten, Norway

(Received 13 November 2007; revised 4 January 2008; accepted 9 January 2008)

The recent paper by Ona *et al.* [J. Acoust. Soc. Am. **121**, EL145–EL150] compared avoidance reactions by herring (*Clupea harengus*) to a traditional and a "silent" research vessel. Surprisingly, the latter evoked the strongest avoidance, leading to the conclusion that "candidate stimuli for vessel avoidance remain obscure." In this Comment, it is emphasized that the otolith organs in fish are linear acceleration detectors with extreme sensitivity to infrasonic particle acceleration. Near-field particle motions generated by a moving hull are mainly in the infrasonic range, and infrasound is particularly potent in evoking directional avoidance responses in several species of fish. The stimuli initiating vessel avoidance may thus include infrasonic particle acceleration.
© *2008 Acoustical Society of America.* [DOI: 10.1121/1.2839134]

PACS number(s): 43.80.Nd, 43.30.Sf, 43.30.Nb, 43.80.Ev [RWG] Pages: 1831–1833

Several studies have demonstrated that fish may respond to an approaching vessel by diving and moving laterally away from the ship (for review, see Mitson and Knudsen, 2003). Vessel avoidance may bias estimates of fish abundance obtained by acoustic surveys (Olsen, 1979), and is thus a major concern in fisheries management. Assuming that vessel avoidance is mainly caused by propagating noise emitted from the ship, the International Council for the Exploration of the Sea (ICES) has formulated recommendations for maximum radiated underwater noise from research vessels (Mitson, 1995). The acceptable noise levels were defined approximately 30 dB above the hearing thresholds, expressed as sound pressure, for Atlantic cod (*Gadus morhua*) and herring (*Clupea harengus*). The herring is a hearing specialist with an upper frequency cut-off of about 3 kHz, whereas the cod is a hearing nonspecialist with its audible frequency range below about 500 Hz.

The recent paper by Ona *et al.* (2007) presents the first detailed comparison of the avoidance reactions by herring to a traditional research vessel and a vessel complying with the standards set by ICES for a silent survey vessel. Contrary to expectations, the avoidance reactions evoked by the "stealth" vessel were stronger and more prolonged than the responses initiated by the conventional vessel. The authors concluded that the "candidate stimuli for vessel avoidance remain obscure."

In this context, it is relevant to draw attention to previous reports demonstrating that fish are exceedingly sensitive to infrasonic particle motions, which dominate in the near field of a moving hull, and that such stimuli are particularly potent in evoking directional avoidance responses in several species of fish. In the following, these reports and some relevant facts about the hearing capabilities of fish are briefly reviewed.

Otolith organs in the inner ear of fish behave as nearly critically damped mass loaded accelerometers. They are thus inherently sensitive to the kinetic sound component (particle motion), and not to sound pressure (Chapman and Sand, 1974). However, the existence of a swim bladder may in addition make the fish sensitive to sound pressure, although the otolith organs remain sensitive to particle motion. When a volume of gas is exposed to oscillating pressure changes, it will display larger volume pulsations than a comparable volume of water. In a sound field, the radial motion amplitudes of the surface of a gas-filled bladder may therefore be larger than the water particle motions in the absence of the bladder. These amplified motions may be transmitted to the inner ear,

[a)]Electronic mail: olav.sand@imbv.uio.no

thus providing pressure sensitivity and auditory improvement. The pulsation amplitude of a gas-filled bladder exceeds the free field particle motion only above a certain frequency, and a gas-filled bladder therefore provides no auditory gain in the very low frequency range (Sand and Hawkins, 1973). It should be noted, however, that the acoustic behavior of a swim bladder is affected by the surrounding tissue. For instance, the resonance frequency may be higher than predicted due to added stiffness (Sand and Hawkins, 1973).

When auditory thresholds in fish are related to particle acceleration, which is the relevant stimulus parameter at very low frequencies even in species possessing a swim bladder, the audiogram displays no lower frequency cutoff and extends into the infrasound range. This was first demonstrated for the Atlantic cod by Sand and Karlsen (1986), who obtained a threshold value of about 10^{-5} ms^{-2} at 0.1 Hz. This represents a sensitivity to linear acceleration about 10 000 times higher than in humans. Similar high sensitivity to infrasound was later demonstrated in perch (*Perca fluviatilis*) (Karlsen, 1992a) and plaice (*Pleuronectes platessa*) (Karlsen, 1992b). The acute sensitivity to infrasound may provide fish with a wide range of information about the environment (for review, see Sand and Karlsen, 2000).

Acoustically, fish and other moving objects under water are best approximated by a dipole mainly producing sound with the major acceleration components in the infrasound range (Kalmijn, 1989). Infrasound sensitivity in fish may thus be important in, for instance, prey–predator interactions, and it is reasonable to suggest that avoidance reactions to infrasound may have evolved as protection against predators.

Juvenile Atlantic salmon (*Salmo salar*) display strong avoidance reactions to infrasound, while frequencies commonly assumed to be within the optimal hearing range (100–150 Hz) have hardly any deterring effect (Knudsen *et al.*, 1992). Pacific salmonids show similar avoidance reactions to infrasound (Knudsen *et al.*, 1997). Infrasonic acceleration and pressure are potent in eliciting directional fast start escape responses in roach (*Rutilus rutilus*) (Karlsen *et al.*, 2004). In field experiments, intense infrasound has been used to direct the movement of juvenile Atlantic salmon (Knudsen *et al.*, 1994), European silver eels (*Anguilla anguilla*) (Sand *et al.*, 2000), and various species of cyprinids (Sonny *et al.*, 2006).

It should be stressed, however, that the reports on responses of fish to infrasound are limited, both regarding species and the kinds of behavior elicited. For example, it is likely that predatory fish may be attracted to infrasound, as a cue signaling potential prey. It has been known for decades that predatory sharks are attracted to low frequency sound down to 20–60 Hz (Nelson and Gruber, 1963). It is thus possible that intense infrasound may evoke very different behaviors in for instance herring and adult cod. Obviously, more information is needed on the behavioral responses of various species of fish to infrasound in the field.

In the analyses of vessel noise, the focus has been on propagating sound rather than on the near-field particle motions generated by the moving hull, and only sound pressure measurements have been performed. It is not trivial to estimate particle motions within the acoustic near field based on single sound pressure measurements. Under such circumstances, and particularly for acoustic dipoles like a moving hull, it is preferable to measure the kinetic sound component directly in order to quantify the effective sound stimulus (particle acceleration).

The imaginary boundary between the near field and the far field, i.e., where the particle motions linked to the local flow and the propagating sound wave are equal, is wavelength (λ) dependent. For a dipole, the range of the nearfield is also dependent on the direction to the source. At the axis of movement, the boundary is at a distance of λ/π, compared to $\lambda/2\pi$ for a monopole, whereas the boundary recedes from the source at angles deviating from the dipole axis. At an angle of 90°, the boundary approaches infinity, as the far-field component vanishes (see Kalmijn, 1988 for a thorough discussion of this topic). For example, at 10 Hz the near field of the particle motions generated by a moving hull will extend to at least 50 m from the ship. Since the magnitude of the particle motions generated by a dipole is inversely related to the cube of the distance, it is likely that particle motions sufficiently large to evoke behavioral responses will mainly occur within the near field. However, it should be noted that clupeids, like herring, possess acute sound pressure sensitivity that extends into the infrasound range (Denton and Gray, 1980), in addition to detecting particle acceleration. Therefore, propagating (i.e., far reaching) infrasound may also be involved in avoidance responses to vessel noise in such species.

Experts studying vessel avoidance by fish should consider possible effects of near-field particle motions associated with the local flow field generated by the moving vessel. In particular, the directionality of such flow fields should be compared and correlated to the directionality of the avoidance responses. However, the recent paper by Ona *et al.* (2007) does not discuss the acute infrasound sensitivity in fish or the potency of infrasound to evoke directional avoidance responses in fish. It is tempting to suggest that the "obscure stimuli" for vessel avoidance may include infrasonic, near-field particle accelerations associated with the moving hull. This may also explain why the "stealth" vessel initiated more pronounced avoidance responses than the conventional vessel, because the displacement volume of the former was more than twice that of the latter (Ona *et al.*, 2007). The optimal stealth vessel for acoustic fish surveys should perhaps be constructed to generate minimum water displacement, like for instance hovercraft or foil type of vessels.

Chapman, C. J., and Sand, O. (**1974**). "Field studies of hearing in two species of flatfish *Pleuronectes platessa* (L.) and *Limanda limanda* (L.) (Family Pleuronectidae)," Comp. Biochem. Physiol. A **47A**, 371–385.

Denton, E. J., and Gray, J. A. B. (**1980**). "Receptor activity in the utriculus of the sprat," J. Mar. Biol. Assoc. U.K. **60**, 717–740.

Kalmijn, A. J. (**1988**). "Hydrodynamic and acoustic field detection," in *Sensory Biology of Aquatic Animals*, edited by A. Atema, R. R. Fay, A. N. Popper, and W. N. Tavolga (Springer, New York), pp. 83–130.

Kalmijn, A. J. (**1989**). "Functional evolution of lateral line and inner ear sensory systems," in *The Mechanosensory Lateral Line - Neurobiology and Evolution*, edited by S. Coombs, P. Görner, and M. Münz (Springer, Berlin), pp. 187–215.

Karlsen, H. E. (**1992a**). "The inner ear is responsible for detection of Infrasound in the perch (*Perca fluviatilis*)," J. Exp. Biol. **171**, 163–172.

Karlsen, H. E. (**1992b**). "Infrasound sensitivity in the plaice (*Pleuronectes platessa*)," J. Exp. Biol. **171**, 173–187.
Karlsen, H. E., Piddington, R. W., Enger, P. S., and Sand, O. (**2004**). "Infrasound initiates directional fast-start escape responses in juvenile roach *Rutilus rutilus*," J. Exp. Biol. **207**, 4185–4193.
Knudsen, F. R., Enger, P. S., and Sand, O. (**1992**). "Awareness reactions and avoidance responses to sound in juvenile Atlantic salmon, *Salmo salar* L," J. Fish Biol. **40**, 523–534.
Knudsen, F. R., Enger, P. S., and Sand, O. (**1994**). "Avoidance responses to low frequency sound in downstream migrating Atlantic salmon smolt, *Salmo salar* L," J. Fish Biol. **45**, 227–233.
Knudsen, F. R., Schreck, C. B., Knapp, S. M., Enger, P. S., and Sand, O. (**1997**). "Infrasound produces flight and avoidance responses in Pacific juvenile salmonids," J. Fish Biol. **51**, 824–829.
Mitson, R. B. (**1995**). "Underwater noise of research vessels: Review and recommendations," ICES Coop. Res. Rep. **209**, 1–61.
Mitson, R. B., and Knudsen, H. P. (**2003**). "Causes and effects of underwater noise on fish abundance estimation," Aquat. Liv. Res. **16**, 255–263.
Nelson, D. R., and Gruber, S. H. (**1963**). "Sharks: Attraction by low-frequency sounds," Science **142**, 975–977.
Olsen, K. (**1979**). "Observed avoidance behaviour in herring in relation to passage of an echo survey vessel," Copenhagen, ICES C.M.1979/B:18, 21 pp.
Ona, E., Godø, O. R., Handegard, N. O., Hjellvik, V., Patel, R., and Pedersen, G. (**2007**). "Silent vessels are not quiet," J. Acoust. Soc. Am. **121**, EL145–EL150.
Sand, O., Enger, P. S., Karlsen, H. E., Knudsen, F. R., and Kvernstuen, T. (**2000**). "Avoidance responses to infrasound in downstream migrating European silver eels, *Anguilla anguilla*," Environ. Biol. Fish. **57**, 327–336.
Sand, O., and Hawkins, A. D. (**1973**). "Acoustic properties of the cod swimbladder," J. Exp. Biol. **58**, 797–820.
Sand, O., and Karlsen, H. E. (**1986**). "Detection of infrasound by the Atlantic cod," J. Exp. Biol. **125**, 197–204.
Sand, O., and Karlsen, H. E. (**2000**). "Detection of infrasound and linear acceleration in fish," Philos. Trans. R. Soc. London, Ser. B **355**, 1295–1298.
Sonny, D., Knudsen, F. R., Enger, P. S., Kvernstuen, T., and Sand, O. (**2006**). "Reactions of cyprinids to infrasound in a lake and at the cooling water inlet of a nuclear power plant," J. Exp. Biol. **69**, 735–748.

Target detection and location with ambient noise (L)

Christopher H. Harrison[a)]
NATO Undersea Research Centre, Viale San Bartolomeo, 400, 19126 La Spezia, Italy

(Received 28 September 2007; revised 17 January 2008; accepted 17 January 2008)

By placing a vertical array in an ambient noise field and forming an upward and a downward beam one obtains two time series which can be cross correlated to reveal a subbottom profile of the seabed [Siderius *et al.*, J. Acoust. Soc. Am. **120**, 1315–1323 (2006)]. Here the cross-correlation approach is applied to the location in range and bearing of a point target. An experiment was designed using floats and weights mounted (and dismounted) on the same cable as the vertical array. Careful measurements were made of the location of all likely floats, ballast weights, array terminations, and so on. After suitable coherent averaging, peaks were seen at delays (correlation offsets) agreeing with the reflector positions and were shown to be absent when reflectors were removed. A trivial extension of the theory developed in Harrison and Siderius [J. Acoust. Soc. Am. **123**, 1282–1296 (2008)] is used to explain the rough amplitudes of the reflections. The approach differs from "acoustic daylight" principally in having a capability to determine a target range.
© *2008 Acoustical Society of America.* [DOI: 10.1121/1.2872516]

PACS number(s): 43.30.Pc, 43.30.Nb, 43.30.Gv, 43.30.Jx [RCG] Pages: 1834–1837

I. INTRODUCTION

The cross correlation of the time series received on a pair of hydrophones in a noise field is closely related to the impulse response that would be received on replacing one of them by a sound source. A relationship was established by Weaver and Lobkis (2004) and has since been developed in underwater acoustics by Roux and Kuperman (2004), Roux *et al.* (2005), Sabra *et al.* (2004), and Sabra *et al.* (2005). More recently it was demonstrated by Siderius *et al.* (2006) that the process could be used to survey subbottom layering with a moving vertical array. The correlation peak is caused by a small area of sea surface sources immediately above the array from which an almost identical wave form passes, first directly to the array, then to the seabed, and back to the array. The steered vertical beams cut out a large part of the ineffective, uncorrelated noise but retain contributions from this small area. By this reasoning one might also expect to see a reflection from a point scatterer (target) under, or at least, below the center line of the array. In fact, some circumstantial evidence for this has already been pointed out in Harrison and Siderius (2008) where correlation peaks at round-trip path lengths of about 20 m from the array were attributed to a reflection from a ballast weight mounted beneath the array. In principle, taking account of surface noise reflected from the seabed, both target and array are surrounded by sources, so targets above the array ought to be just as detectable. In practice, these would require much longer integration times to eliminate the competing direct and much louder surface noise. Laboratory passive imaging of objects has already been demonstrated using a single ultrasonic receiver and autocorrelation (Larose *et al.*, 2006). In principle, underwater subbottom profiling or target detection would also be possible with a single hydrophone (in effect, the hydrophone and its image in the seabed can be thought of as a pair), but integration times would be prohibitive.

In a recent experiment (CLUTTER 2007) the exact positions of the array elements, ballast, array termination, and so on were measured. In addition, on a separate occasion three hollow glass sphere floats were mounted between the array and the ballast weight. Thus all conceivable reflectors above and below the array were controlled. This letter reports the successful detection and ranging of these targets. To be precise there are correlation peaks where there are known scatterers below the array and no peaks where there are no scatterers. In addition, there are no peaks corresponding to the delays of the floats above the array, which agrees with expectations since the sound sources are predominantly at the surface.

Although this is not the first demonstration of target detection with noise, this approach is novel in resolving the target range, and it operates like a passive radar. In this respect it is quite distinct from acoustic daylight (Buckingham *et al.*, 1992; Potter, 1994; Epifanio *et al.*, 1999) which, being an analogue of daylight vision, resolves a two-dimensional angle. The passive radar range resolution is dependent on the bandwidth and is not particularly dependent on frequency. Its angle resolution just depends on the array size, and in principle, the cross-correlation process still functions with a single hydrophone, though with complete absence of angle resolution. Also, in principle, the weakest target can still be detected even though it sits in a noise field, provided it does not move and given long enough integration time.

II. THEORY

A recent paper (Harrison and Siderius, 2008) developed a formula for the correlation peak height given by a plane reflector and checked it against simulations and experimental results (BOUNDARY2003 and BOUNDARY2004) using a cross-correlation normalization that would result in a peak height of unity if the two arriving time series were identical.

[a)]Electronic mail: harrison@nurc.nato.int

 0001-4966/2008/123(4)/1834/4/$23.00 © 2008 Acoustical Society of America

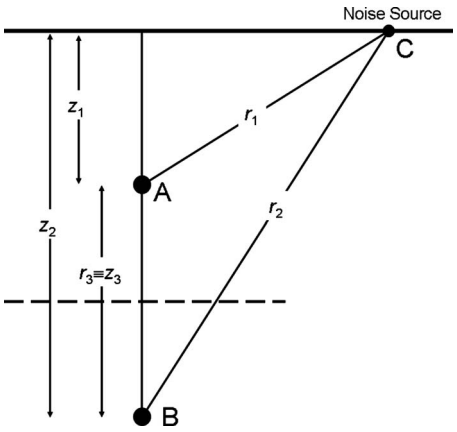

FIG. 1. Geometrical construction to convert existing horizontal plane reflection formulas for use with point targets. Ray paths associated with an arbitrary noise source *C* on the sea surface and the locations *A* and *B* are shown. *A* represents the receiving array, and the direct path has length r_1. In the reflection case, *B* is interpreted as the image of *A* in a horizontal plane reflector (dashed line), and the complete reflected path *CB* has length r_2. In the target scattering case, *B* is interpreted as a point target (in the absence of the plane reflector), and the complete scattered path *CBA* has length r_2+r_3.

With this normalization the result is independent of reflection coefficient magnitude since, with up and down beam time series denoted, respectively, by U, D, the cross-correlation numerator is $U*D$ and the denominator is the product of the standard deviations $(\langle U^2\rangle\langle D^2\rangle)^{1/2}$. Thus the magnitude of the reflection coefficient, which is contained only in D, cancels. One could just as easily have used a normalization where the denominator was $\langle U^2\rangle$ instead. Thus the magnitudes of the noise sources still cancel but the result does depend on the magnitude of the reflection coefficient. In the context of demonstrating a target detection it is desirable to avoid the first normalization because, although the peak height in the numerator would depend only on the target (through D), the standard deviation of D in the denominator would also depend on reflections from the seabed. With the second normalization the resulting peak height depends only on the target.

We avoid lengthy derivations here by modifying the formula for plane reflector peak height P derived by Harrison and Siderius (2008) with geometry as in Fig. 1, which was

$$P_{R1} = \frac{2L\ \mathrm{sign}(R)}{(z_2 - z_1)\gamma\beta}, \tag{1}$$

where L is the array length, γ is the ratio of sample frequency to design frequency for the array $\gamma = f_s/f_o$, β is a numerical constant, of order unity, that depends on the array's cross-spectral density matrix and shading, R is reflection coefficient, and z_1, z_2 are the respective depths of the array (center) and its image in the seabed.

With the second type of normalization the formula for a plane reflector converts to

$$P_{R2} = \frac{2LR}{(z_2 - z_1)\gamma\beta}. \tag{2}$$

First we note that the path of length r_1 from an arbitrary surface noise source to the array center is identical whether we consider plane reflectors or targets. Harrison and Siderius (2008) denoted the path from the same noise source to the image receiver (in the reflection surface) as r_2. To make use of the existing formula we remove the reflector and place the target where the image used to be. (This is a mathematical construct, and has nothing to do with the physical arrangement in the experiment. The point target and plane reflector geometries are both indicated in Fig. 1.)

The path from the noise source to the target is still r_2. The remaining path from target to array is a fixed length (denoted r_3), so from a cross-correlation point of view the geometry is the same for a target placed where the reflection image used to be except for a constant offset r_3. The original amplitude of the reflected arrival includes a spreading term R/r_2 (since r_2 is the complete path from source to image receiver), and this is now replaced for the target by $s/(r_2 r_3)$ [since the source to target range is r_2 and the target to receiver range is r_3, where target strength is $\mathrm{TS} = 20\log_{10}(s)$]. Thus for a point target at depth z_2 with the second normalization, noting that the depth difference $z_3 = z_2 - z_1$, we arrive at the formula

$$P_T = \frac{2Ls}{(z_2 - z_1)^2\gamma\beta}. \tag{3}$$

III. EXPERIMENTAL GEOMETRY

The experimental arrangement was a drifting 32-element vertical array with hydrophone separation 0.18 m connected by a length of cable to a radio buoy. The array was stabilized and isolated from wave motion by a 29 m length of buoyant hose forming a spar buoy. All potential targets of interest here are attached to the same cable as the array and so any vertical or horizontal motion of the array becomes unimportant. Beneath the array center there was always a solid metal termination of the array hose (approximately 0.10 m diameter) with top face at about 6.6 m, an Edgetech 8201 acoustic release between 16.3 and 17.5 m, and a ballast weight of 150 kg (a horizontal rectangular iron bar approximately $0.15 \times 0.15 \times 0.50$ m) with its top face at 19.45 m. Because the dominant noise sources are above the array one would expect targets only to be effective below the array since their reflections are the only ones to enter the downward beam. Nevertheless there were also objects above the array that are, in principle, capable of reflection and so to avoid postexperiment uncertainty because of sidelobes, etc., their distances from array center were set so as never to coincide. In fact, there is the upper array termination at 12.6 m above array center and a pair of buoyancy glass spheres at about 75 m above.

Rather than rely on these unchanging "targets of opportunity," in a separate experiment three Benthos 0.43-m-diam hollow glass spheres were attached to the cable (actually with their sides pressing against the taut cable) at center depths 9.64, 12.19, and 14.74 m. Their front (i.e., top) faces were therefore at depths 9.42, 11.97, and 14.52 m.

IV. TARGET STRENGTH ESTIMATES

As a check on the strength of the various target peaks we estimate their linear target strengths s. The design frequency

of the array is 4.167 kHz, and the processing passband is between 2 and 4 kHz. Thus all acoustic wavelengths considered are greater than 0.38 m, and the targets tend to be of the order of, or smaller than, the wavelength. We consider three types of target: A horizontal rectangular iron bar, the steel end cap at the bottom of the array hose, and a hollow glass sphere.

A. Horizontal rectangular iron bar

The iron bar has a rigid, flat, horizontal upper face whose area $a \times b$ is smaller than the Fresnel zone so that the scattering term $s=ab/\lambda$ (Urick, 1975), and for the highest frequency $s \approx 0.15 \times 0.5/0.38 = 0.20$ m.

B. Steel end cap

Treating the end cap as a rigid disc of radius $a = 0.045$ m we have $s=\pi a^2/\lambda$ (Urick, 1975) and $s \approx 0.017$.

C. Hollow glass sphere

The scattering term s for a rigid sphere depends on the wave-number-radius product ka (Urick, 1975) which in this case, with $a=0.215$ m, is between 1.8 and 3.6. Above $ka = 1$ the backscattering cross section is the same as the physical cross section, so s is given by $s=a/2 \approx 0.11$. However, the cavity and the wall thickness of 0.014 m result in Lamb waves which enhance s by a factor between 1 and 2. On the other hand, the glass sphere is housed in a protective plastic casing that is likely to spoil this enhancement. In addition, there is a spread in arrival time caused by the Lamb wave circumnavigating the sphere many times (Tesei *et al.*, 2002). The first and strongest of these arrives a couple of meters in path length behind the arrival from the front face.

Because the depth resolution with the cross-correlation technique and this bandwidth is about 0.5 m (i.e., 1 m in path length), the spheres are resolvable at their separations of 2.55 m, so (with the possible exception of weak Lamb wave multiples) one does not need to consider addition (coherent or incoherent) of the three spheres. Nevertheless, the spheres and the ballast weight are close enough to each other to be partially obscured by the upper spheres.

V. ACOUSTIC MEASUREMENTS AND PROCESSING

During the CLUTTER 2007 experiments in the area of the Mediterranean between Malta and Sicily several hours of ambient noise data were collected with and without the three spheres attached. The array center was at 115.6 m in the first experiment without spheres, and at 90.6 m in the second with spheres. Otherwise, cable lengths beneath the array were the same in both cases, and although the ballast weights were jettisoned, they were identical. The water depth was about 142 m depth in both cases and this ensured that competing bottom reflections were well separated in time from the desired target echoes. In fact subbottom layering, though not discussed here, has been extracted independently.

The ambient noise was sampled at 12.0 kHz and stored in files of length 131 072 samples (~11 s). Processing is the same as described in Harrison and Siderius (2008) for sub-

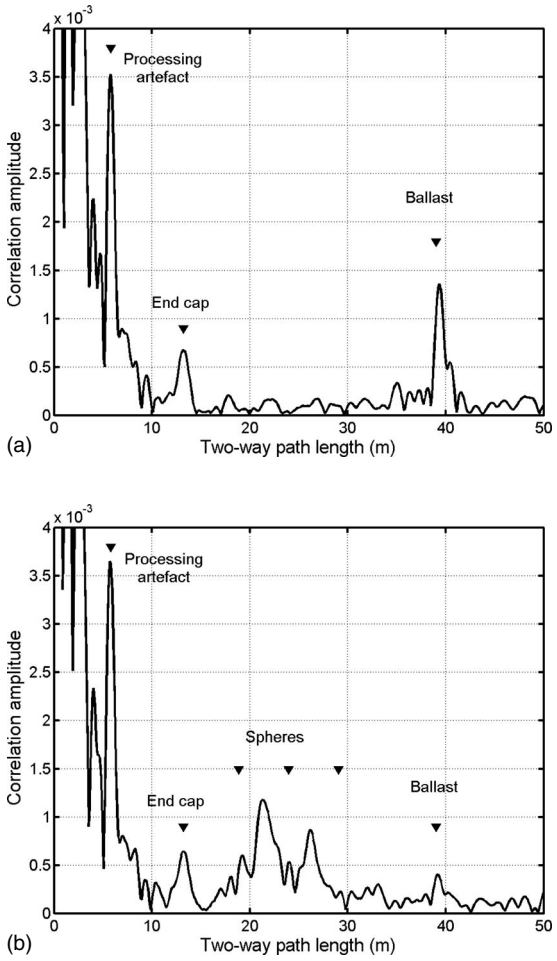

FIG. 2. Correlation amplitude, to be interpreted as an impulse response showing labeled returns (a) excluding the glass spheres and (b) including the glass spheres. Black triangles indicate measured two-way path lengths to the ballast weight, the array end cap, and the three spheres. The processing artifact corresponding to the array length is also indicated.

bottom layer extraction (namely, filter, beam form, cross correlate, differentiate). [Note that processing in Siderius *et al.* (2006) is the same except for omission of differentiation.] The processing is most efficient in the frequency domain since the filters, beam forming, cross correlation, and time differentiation can all be performed in the same operation. The only free parameter is the filter shape, and here a bandpass from half the design frequency up to the design frequency was used.

The time differentiated cross correlation of the upward and downward beam-formed time series is the impulse response, and the quantity plotted in the following graphs corresponds to the formula in Eq. (3) with $L=5.76$ m, $\gamma=2.88$, and $\beta=1.87$. The result in the first experiment with no spheres attached and coherently averaged over 600 files (approximately 100 min) is shown in Fig. 2(a). The abscissa is two-way path length assuming the measured sound speed in the vicinity of the array to be 1513 m/s. There are two clear peaks at two-way paths corresponding to the array hose termination (13.2 m) and the ballast weight (39.4 m). In between there are no significant peaks. The black triangles indicate the actual measured target positions (double their depths), and for comparison purposes, one should take the

actual acoustic peak position (rather than the leading edge) since time zero in this cross-correlation function corresponds to the central peak at zero meters. At shorter delays there is a peak corresponding to the length of the array (5.76 m), which is believed to be a processing artifact since it is enhanced by removing the beam-forming shading (Hamming) (see Gerstoft *et al.*, 2008). It is not surprising that there are large peaks at shorter delays still because the up and down beams are constructed from the same 32 hydrophones. Though not shown here, it is possible to investigate the stability of all these peaks and the reduction in the background level as the size of the average increases.

The peak height for the ballast weight is calculated using Eq. (3) with $z_2 - z_1 = 19.5$ m and values for L, s, γ, β specified earlier, as 0.0011. This is close to the actual peak height of 0.00135. Similarly, the expected peak height for the array end cap at 6.6 m away is calculated as 0.82×10^{-3}, and the actual peak is close at 0.67×10^{-3}.

With the spheres attached the result of a coherent sum over 600 files is shown in Fig. 2(b). First notice that the processing artifact at 5.76 m and the end cap return at 13.2 m are virtually identical to the earlier case. There are two additional broad peaks, each with a precursor, at two-way paths between 19 and 28 m. The position of the earliest arrival is close to that of the top face of the top sphere (shown by the left-most triangle), and the main peak is slightly later at about 21.3 m. This is believed to be the signature of a glass sphere that supports Lamb waves, possibly slightly suppressed by the plastic protective housing as discussed earlier. There is a similar but slightly weaker sequence corresponding to the second sphere starting at 23.5 m as indicated by the second black triangle. One cannot, however, see a clear return from the third sphere, but neither can one see a strong reflection from the ballast in this case. It is suspected that the first sphere has a slight screening effect. Substituting the estimated scattering term s in Eq. (3) the first sphere's peak height is calculated as 0.0027 and the second as 0.0016. The actual peaks are somewhat lower in both cases and a possible explanation is damping by the plastic cover.

VI. CONCLUSIONS

This paper has demonstrated the detection and ranging of targets suspended underneath a vertical array using only surface ambient noise sources. The targets always included the array's ballast weight and the array hose's end cap, and on a separate occasion three glass spheres were also attached. In the absence of the spheres there was a clear reflection from the ballast and from the end cap. When the spheres were added there was a strong reflection from the first sphere, a slightly weaker return from the second, and no evidence of the third. Also, the ballast weight return was weaker, suggesting that the lower targets were partially obscured by the upper ones. This is consistent with the effective source being located at the center of the array. In contrast, the peak height for the array end cap, which was obviously closer than the other targets, was identical in both cases. In all cases the strength of the peak values was well predicted by Eq. (3), which is adapted from an equivalent formula for plane reflectors. Equation (3) clearly shows that the strength depends only on separation of the array and target and not the positions of the noise sources.

It is important to note that this method differs from earlier acoustic daylight techniques in determining the range to the target and being more dependent on bandwidth than frequency. Its detection limits are set by the ability to discriminate one target from other target-like features rather than from noise, since the background of uncorrelated noise can be lowered without limit given enough integration time (and a stationary target and statistically stationary noise).

By coincidence in these experiments the targets were hanging under the vertical array, but there is no reason to doubt that the amplitude formula and detection should work just as well with the targets moved to one side of the vertical array axis. For practical integration times the target simply needs to be below the level of the array, so that one can draw a straight line *from* the target *through* the array *to* an area of noise sources on the sea surface. Range and intensity would be determined in exactly the same way as with a target on the vertical axis, and the normalization takes care of variation in noise source level. Angle would be resolved by the array's steered beams. By the same reasoning if angle resolution is sacrificed and there is unlimited integration time the array size can be reduced right down to a single hydrophone.

Buckingham, M. J., Berkhout, B. V., and Glegg, S. A. L. (**1992**). "Imaging the ocean with ambient noise," Nature (London) **356**, 327–329.

Epifanio, C. L., Potter, J. R., Deane, G. B., Readhead, M. L., and Buckingham, M. J. (**1999**). "Imaging in the ocean with ambient noise: The ORB experiments," J. Acoust. Soc. Am. **106**, 3211–3225.

Gerstoft, P., Hodgkiss, W. S., Siderius, M., Huang, C-F., and Harrison, C. H. (**2008**). "Passive fathometer processing," J. Acoust. Soc. Am. **123**, 1297–1305.

Harrison, C. H., and Siderius, M. (**2008**). "Bottom profiling by correlating beam-steered noise sequences," J. Acoust. Soc. Am. **123**, 1282–1296.

Larose, E., Montaldo, G., Derode, A., and Campillo, M. (**2006**). "Passive imaging of localized reflectors and interfaces in open media," Appl. Phys. Lett. **88**, 104103-1–104103-3.

Potter, J. R. (**1994**). "Acoustic imaging using ambient noise: Some theory and simulation results," J. Acoust. Soc. Am. **95**, 21–33.

Roux, P., and Kuperman, W. A. (**2004**). "Extracting coherent wave fronts from acoustic ambient noise in the ocean," J. Acoust. Soc. Am. **116**, 1995–2003.

Roux, P., Sabra, K. G., Kuperman, W. A., and Roux, A. (**2005**). "Ambient noise cross correlation in free space: Theoretical approach," J. Acoust. Soc. Am. **117**, 79–84.

Sabra, K. G., Roux, P., and Kuperman, W. A. (**2005**). "Emergence rate of the time-domain Green's function from the ambient noise cross-correlation function," J. Acoust. Soc. Am. **118**, 3524–3531.

Sabra, K. G., Roux, P., Kuperman, W. A., Hodgkiss, W. S., and D'Spain, G. L. (**2004**). "Using ocean ambient noise for array element localization," J. Acoust. Soc. Am. **115**, 2507 (Abstract).

Siderius, M., Harrison, C. H., and Porter, M. B. (**2006**). "A passive fathometer technique for imaging seabed layering using ambient noise," J. Acoust. Soc. Am. **120**, 1315–1323.

Tesei, A., Maguer, A., Fox, W. L. J., Lim, R., and Schmidt, H. (**2002**). "Measurements and modeling of acoustic scattering from partially and completely buried spherical shells," J. Acoust. Soc. Am. **112**, 1817–1830.

Urick, R. J. (**1975**). "Principles of underwater sound," 2nd Ed. Chap. 7, McGraw-Hill, New York.

Weaver, R. L., and Lobkis, O. I. (**2004**). "Diffuse fields in open systems and the emergence of the Green's function," J. Acoust. Soc. Am. **116**, 2731–2734.

The performance of active control of random noise in cars (L)

Janatul I. Mohammad[a] and Stephen J. Elliott
Institute of Sound and Vibration Research, University of Southampton, Southampton SO17 1BJ, United Kingdom

Andy Mackay
NVH Group, Lotus Engineering, Hethel, Norwich, NR14 8EZ, United Kingdom

(Received 20 November 2006; revised 6 November 2007; accepted 26 December 2007)

This letter investigates the effectiveness of various configurations of reference sensors for feedforward active control systems in vehicles using unconstrained frequency domain optimization. The results from a model problem are based on a fully coupled analysis between the vibration of a car panel and an enclosed acoustic field. These suggest that with correct locations, only a small number of microphones or accelerometers are needed to give good overall performance, despite many uncorrelated primary disturbances being present. Similar results are predicted from road test data. © *2008 Acoustical Society of America.* [DOI: 10.1121/1.2836745]

PACS number(s): 43.50.Ki, 43.55.Ka [KAC] Pages: 1838–1841

I. INTRODUCTION

Automotive manufacturers have recognized that reducing the interior noise of vehicles promises better quality in their products. The road noise inside vehicles arises from the irregularities in road profile, which generate the vibrations of tires and wheels. This random broadband noise is then transmitted into the car interior predominantly via structural paths at frequencies below about 300 Hz.[1]

The work presented here initially models the active control of sound transmission into a structural-acoustic system by considering a rectangular acoustic enclosure coupled with a flexible structural panel[2–4] driven by multiple random forces as the primary sources and with an acoustic monopole as the secondary sound source, as illustrated in Fig. 1. The use of alternative reference sensors in a feedforward controller are discussed, in order to achieve a more cost-effective method of active sound control. Measured road noise data are then analyzed to address the same issue, taken from a vehicle instrumented with 11 accelerometers (positioned at various locations on the suspension and body structure), 10 reference microphones (8 microphones were on the car floor and 2 were on the parcel shelf) with 4 error microphones (positioned at each headrests).

II. SIMULATIONS OF ACTIVE CONTROL IN A COUPLED STRUCTURAL-ACOUSTIC SYSTEM

In a fully coupled analysis, the kinetic energy of the panel not only depends on the primary force, excitation, but also from the backreaction of the pressure in the enclosure.[5] The potential energy of the stochastically excited loaded system, $\mathbf{E}_p$, can be calculated from[5–7]

$$\mathbf{E}_p = \mathrm{trace}[\mathbf{S}_{a_{c_t} a_{c_t}}] = \mathrm{trace}[E[\mathbf{a}_{c_t} \mathbf{a}_{c_t}^H]], \tag{1}$$

where E denotes expectation operator, $\mathbf{a}_{c_t}$ is the total complex amplitude of acoustic modal pressure vector, and all variables are implicitly functions of frequency. This can be written as

$$\mathbf{a}_{c_t} = \mathbf{a}_{c_p} + \mathbf{B}_c \mathbf{q}_s, \tag{2}$$

where

$$\mathbf{a}_{c_p} = \mathbf{Z}[\mathbf{I} + \mathbf{YZ}]^{-1} \mathbf{b}_u, \tag{3}$$

$$\mathbf{B}_c = [\mathbf{I} + \mathbf{ZY}]^{-1} \mathbf{B}_u, \tag{4}$$

and $\mathbf{a}_{c_p}$ is the coupled acoustic mode amplitude without active control, $\mathbf{B}_c$ is the matrix of structural-acoustic coupling coefficients, $\mathbf{Y}$ is the $M \times N$ structural modal mobility matrix of the panel, $\mathbf{Z}$ is the $N \times M$ acoustic modal impedance matrix of the enclosure, $\mathbf{b}_u$ is the uncoupled complex vibration velocity amplitude of the flexible panel in the absence of the enclosure, and $\mathbf{B}_u$ is the uncoupled coupling coefficient between the mth secondary actuator and the nth acoustic mode.[5]

In order to consider different reference signals as the input to the system, the secondary acoustic source can be assumed to be driven via a matrix of control filters, $\mathbf{W}$, by a general vector of K reference signals, $\mathbf{x}$, where

$$\mathbf{q}_s = \mathbf{W}\mathbf{x}. \tag{5}$$

Equation (2) can thus be written as

$$\mathbf{a}_{c_t} = \mathbf{a}_{c_p} + \mathbf{B}_c \mathbf{W}\mathbf{x}. \tag{6}$$

Expanding the outer vector product of Eq. (1), we then obtain

$$\mathbf{E}_p = \mathrm{trace}[\mathbf{B}_c \mathbf{W} \mathbf{S}_{xx} \mathbf{W}^H \mathbf{B}_c^H + \mathbf{B}_c \mathbf{W} \mathbf{S}_{x,a_{c_p}}^H + \mathbf{S}_{x,a_{c_p}} \mathbf{W}^H \mathbf{B}_c^H + \mathbf{S}_{a_{c_p} a_{c_p}}], \tag{7}$$

where

[a]Now at Faculty of Mechanical Engineering, Universiti Teknikal Malaysia Melaka, Melaka, Malaysia. Electronic mail: janatul@utem.edu.my

 0001-4966/2008/123(4)/1838/4/$23.00 © 2008 Acoustical Society of America

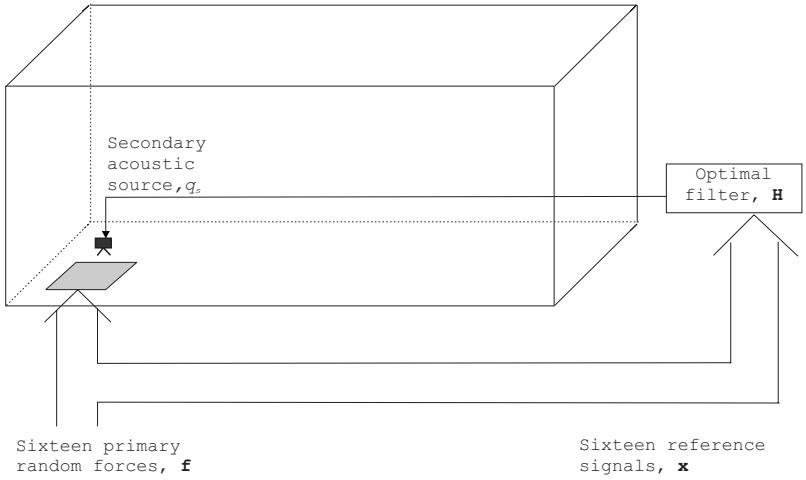

FIG. 1. Multiple random forces, which in this case also act as the reference signals, excite the flexible panel which is coupled to an acoustic enclosure controlled by a secondary acoustic source, $\mathbf{q}_s$.

$$\mathbf{S}_{xx} = E[\mathbf{x}\mathbf{x}^H], \quad K \times K \text{ matrix}, \tag{8}$$

$$\mathbf{S}_{x,a_{cp}} = E[\mathbf{a}_{cp}\mathbf{x}^H], \quad N \times K \text{ matrix}, \tag{9}$$

$$\mathbf{S}_{a_{cp}a_{cp}} = E[\mathbf{a}_{c_p}\mathbf{a}_{cp}^H], \quad N \times N \text{ matrix}, \tag{10}$$

are auto and cross-spectral density matrices between the reference signals and the primary mode amplitudes.

The optimal filter, $\mathbf{W}_{\text{opt}}$, which minimizes Eq. (1) is obtained by using least mean squares method, assuming that $\mathbf{B}_c^H\mathbf{B}_c$ and $\mathbf{S}_{xx}$ are nonsingular and can be written as[6]

$$\mathbf{W}_{\text{opt}} = -[\mathbf{B}_c^H\mathbf{B}_c]^{-1}\mathbf{B}_c^H\mathbf{S}_{x,a_{cp}}\mathbf{S}_{xx}^{-1}. \tag{11}$$

By substituting Eq. (11) into Eq. (7), the minimized acoustic potential energy can be written as[6]

$$\mathbf{E}_{p_{\min}} = \text{trace}[\mathbf{B}_c\mathbf{W}_{\text{opt}}\mathbf{S}_{xx}\mathbf{W}_{\text{opt}}^H\mathbf{B}_c^H + \mathbf{B}_c\mathbf{W}_{\text{opt}}\mathbf{S}_{x,a_{cp}}^H + \mathbf{S}_{x,a_{cp}}\mathbf{W}_{\text{opt}}^H\mathbf{B}_c^H + \mathbf{S}_{a_{cp}a_{cp}}]. \tag{12}$$

The reference signals could, in the simulation study, be assumed to be the primary forces driving the panel, as shown in Fig. 1. In general, however, the reference signals could be linearly derived from the acceleration of the panel or the pressure inside the enclosure, in which case the reference signals can be written as

$$\mathbf{x} = \mathbf{V}\mathbf{f}, \tag{13}$$

where $\mathbf{V}$ is a linear transformation matrix and $\mathbf{f}$ is the vector of primary random forces.

TABLE I. A list of dimension and material properties used in the model problem.

Descriptions	Properties
Size of acoustic enclosure	$(1.9\times1.1\times1.0)$ m
Size of structural panel	$(0.5\times0.2\times0.002)$ m
Position of panel	[0.1, 0.1, 0] from left front corner of enclosure
Young's modulus of panel	207×10^9 N/m^2
Density of panel	7870 kg/m^3
Density of air	1.21 kg/m^3
Speed of sound in air	343 m/s
Damping ratio of enclosure	0.1
Damping ratio of panel	0.05
Poisson's ratio	0.292

III. RESULTS OF THE SIMULATIONS WITH THE NUMERICAL MODEL

The structural-acoustic coupled model has the dimensions and material properties listed in Table I. The aim is to model a simplified automotive application in which a floor panel, with a first natural frequency of about 140 Hz, is coupled to an acoustic enclosure which has about the same dimensions as a small car and hence has a first longitudinal acoustic resonance at about 90 Hz.

For these simulations, it is assumed that 16 uncorrelated random forces are exciting the flexible panel simultaneously and up to 16 reference signals were used to determine the performance of a feedforward controller using Eq. (12). These reference signals could be obtained from direct observation of the primary forces, from accelerometers on the panel, or from microphones inside the enclosure adjacent to the panel. The results were not very sensitive to the positions of the random excitation forces or the reference sensors, but the details for this simulation are listed in Ref. 7. The result of these simulations is shown in Fig. 2, in which the overall acoustic potential energy within the enclosure, Eq. (1), is plotted as a function of frequency before control and after feedforward control with a single secondary loudspeaker, located in the middle of the panel with a distance 0.05 m above the panel, and either 4 accelerometers on the vibrating panel or 4 microphones next to the panel as reference sensors. Active control has clearly substantially reduced the energy in the enclosure at the resonances below about 170 Hz and slightly reduced the energy up to 500 Hz. If the acoustic potential energy is integrated up to 500 Hz, and the difference is taken between the level of the energy before and after control, a single value for the overall attenuation in energy level is derived. This is plotted in Fig. 3, not only for the 4 accelerometers and 4 microphone references, but also when using different numbers of these sensors as reference signals in the feedforward controller, together with the case when using different numbers of the primary forces as reference

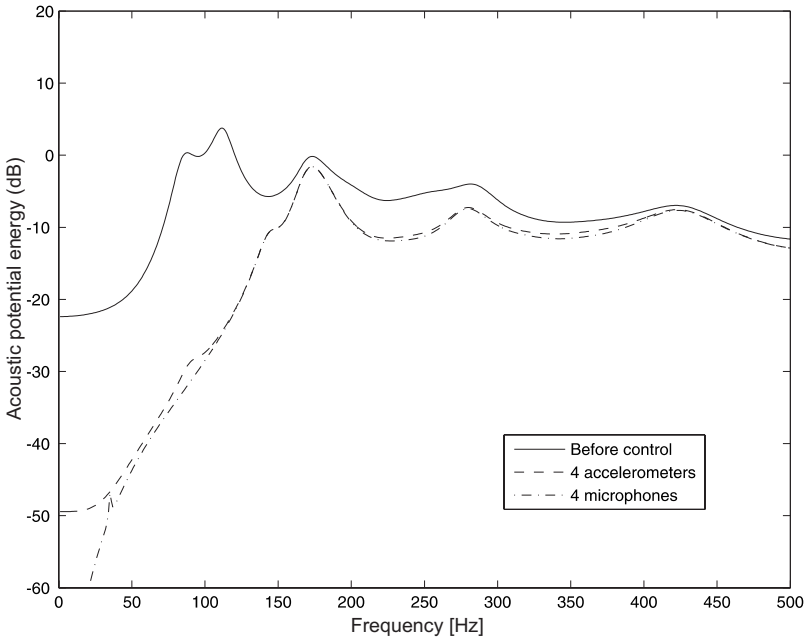

FIG. 2. The potential energy in the enclosure before control (—) and after control when 4 accelerometers (- - -) or 4 microphones (-··-) are used as the reference sensors.

sensors. In Fig. 3, we see that despite the fact that there are always 16 random forces acting as primary disturbances, as long as the accelerometers or microphones were carefully positioned on the panel, then only four reference sensors are needed to obtain near optimal attenuation in potential energy (about 4.3 dB), with the microphone having slightly better performance compared to using accelerometers.

Other simulations have been carried out with twice the number of primary disturbances as well as reference sensors in different sensor position configurations, and it was again found that only about four accelerometers or microphones are required for good control.

The required number of reference signals thus appears to depend on the number of modes that are significantly contributing to the energy in the enclosure, which appears to be about four in Fig. 2, rather than the number of uncorrelated sources exciting the system. As a consequence, the optimal attenuation of the potential energy is not reached in the configuration using only a limited number of primary forces as reference signals.

IV. ANALYSIS OF MEASURED ROAD NOISE DATA AS PRIMARY RANDOM DISTURBANCES

Road noise data were acquired by driving an Alfa Romeo 156 JTD saloon along a rough road surface at a constant speed of 70 mph. The signals from 10 accelerometers (positioned at various locations on the suspension and body structure), 10 reference microphones (8 microphones were on the car floor and 2 were on the parcel shelf), and 4 error microphones (positioned at each headrest) were recorded simultaneously using a 25-channel digital data acquisition

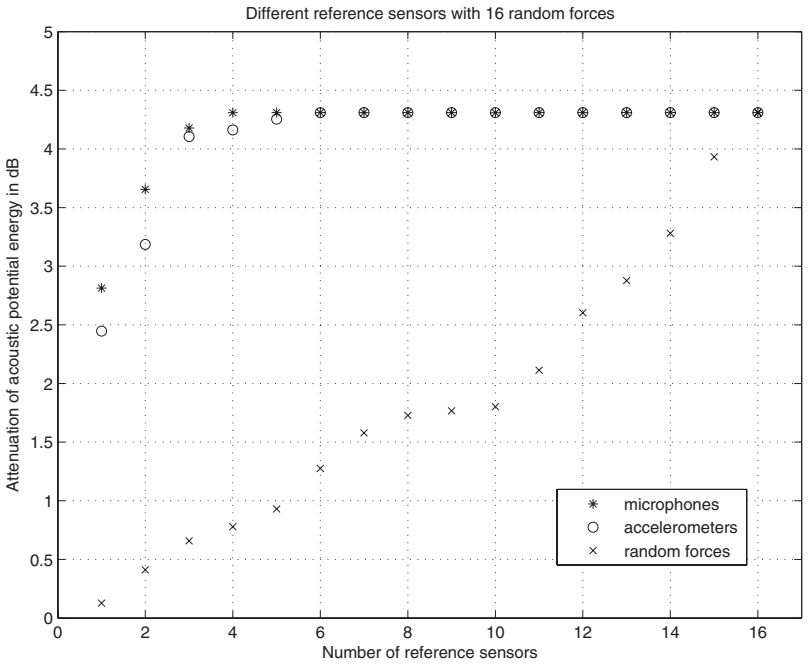

FIG. 3. The average attenuation in acoustic potential energy at all frequencies when 1–16 random forces were used as reference signals (×), or when selected accelerometers (○) or microphones (∗) are used as reference sensors.

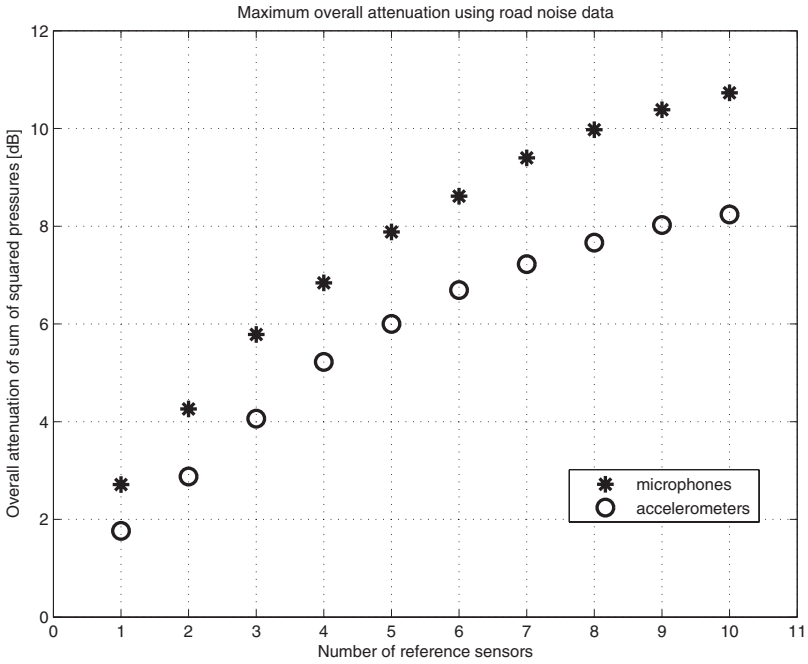

FIG. 4. The best overall attenuation with different numbers of reference microphones and accelerometers for the measured road noise data.

computer, with signal conditioning provided by two 16-channel filter boxes, which were all installed in the vehicle. The data were sampled at 1 kHz and stored directly into MATLAB. A feedforward controller was assumed with perfect internal cancellation of the feedback paths from the secondary loudspeakers to the reference sensors.[6] The optimum filter can be calculated from the power and cross-spectral density matrices of the measured reference and error signals in a similar way to that used in Sec. II.

The overall attenuation of the sum of squared error signals in decibels, averaged for all frequencies between 1 and 500 Hz, is shown in Fig. 4 for the best combinations of different numbers of reference signals selected either from both accelerometers and microphones.

The reference microphones have slightly better performance than the accelerometers, in this case, with 10 reference microphones, giving reductions of up to about 11 dB while 10 accelerometers give about 8 dB. It can also be observed in Fig. 4 that 4 reference microphones can give about the same maximum overall attenuation (approximately 7 dB) as using 6 accelerometers. These results are comparable with the theoretical result in Sec. III, since it is known that a very large number of partially coherent forces act on the car body to produce the internal noise, certainly greater than the maximum number of the available reference signals.[8]

V. CONCLUSIONS AND FURTHER WORK

The feedforward control of random sound transmission into a fully coupled structural-acoustic system has been considered when excited by many uncorrelated random forces. Less reference signals than excitation forces are required for good performance, using either microphones or accelerometers as reference sensors. The required number of reference sensors depends on the number of plate and enclosure modes significantly excited, rather than the details of the structural excitation. Minimizing the number of reference signals reduces the computational requirements of the controller and can hence help to control costs in a practical implementation. Similar results are observed from simulations on road test data taken in a vehicle, with slightly better performance being observed for microphone references.

Future work will investigate the effect of multiple random inputs with time domain optimization of the controller, in order to investigate the time advance available from the reference microphones and accelerometers. There are also possible robust stability problems that may arise due to variability in the feedback from the secondary sources to the reference microphones. Although these could, in principle, be completely canceled with an electrical model of these paths,[6] the responses of these paths will vary with temperature, the number of people in the vehicle, etc. Thus, if fixed feedback cancellation filters are used, residual feedback paths would still be present in practice. The effect on control performance of extraneous sounds in the car, such as speech and music, would also need to be investigated in a practical implementation.

[1]S. K. Jha, "Identification of road/tyre induced noise transmission paths in a vehicle," Int. J. Veh. Des. **5**, 143–158 (1984).
[2]J. Pan, C. H. Hansen, and D. A. Bies, "Active control of noise transmission through a panel into a cavity. I. Analytical study," J. Acoust. Soc. Am. **87**, 2098–2108 (1990).
[3]S. Koshigoe, J. T. Gillis, and E. T. Falangas, "A new approach for active control of sound transmission through an elastic plate backed by a rectangular cavity," J. Acoust. Soc. Am. **94**, 900–907 (1993).
[4]S. M. Kim and M. J. Brennan, "Active control of harmonic sound transmission into an acoustic enclosure using both structural and acoustic actuators," J. Acoust. Soc. Am. **107**, 2523–2534 (2000).
[5]J. I. Mohammad and S. J. Elliott, "Active control of fully-coupled structural-acoustic systems," InterNoise 2005 Conference, Rio de Janeiro, 2005.
[6]S. J. Elliott, *Signal Processing for Active Control* (Academic, New York, 2001).
[7]J. I. Mohammad, "The active control of random sound inside cars," Ph.D. thesis, University of Southampton, Southampton, UK, 2006.
[8]T. J. Sutton, S. J. Elliott, and A. M. McDonald, "Active control of road noise inside vehicles," Noise Control Eng. J. **42**, 137–147 (1994).

A comparison of statistically optimized near field acoustic holography using single layer pressure-velocity measurements and using double layer pressure measurements (L)[a]

Finn Jacobsen[b] and Xinyi Chen[c]
Acoustic Technology, Ørsted·DTU, Technical University of Denmark, Building 352, Ørsteds Plads, DK-2800 Kgs. Lyngby, Denmark

Virginie Jaud[d]
Laboratoire E3I2—EA3876, École Nationale Supérieure d'Ingénieurs des Études des Techniques d'Armement, 2 rue François Verny, F-29806 Brest Cedex 9, France

(Received 23 January 2008; accepted 24 January 2008)

Statistically optimized near field acoustic holography (SONAH) is usually based on the assumption that all sources are on one side of the measurement plane whereas the other side is source free. An extension of the SONAH procedure based on measurement with an array of pressure-velocity probes has recently been suggested. An alternative method uses a double layer array of pressure transducers. Both methods make it possible to distinguish between sources on the two sides of the array and thus suppress the influence of extraneous noise and reflections coming from the "wrong" side. This letter compares the two methods. © *2008 Acoustical Society of America.*
[DOI: 10.1121/1.2875308]

PACS number(s): 43.60.Sx, 43.60.Pt, 43.20.Rz [EJS] Pages: 1842–1845

I. INTRODUCTION

Near field acoustic holography (NAH) is used for experimental analysis of sound fields near sources.[1] Statistically optimized near field acoustic holography (SONAH) is a variant of NAH developed by Steiner and Hald in order to overcome the truncation errors associated with the spatial Fourier transform used in conventional NAH.[2,3]

NAH and SONAH are usually based on measurement of the sound pressure. However, it has recently been demonstrated that NAH based on measurement of both the pressure and the normal component of the particle velocity in general gives more accurate sound field reconstructions than NAH based exclusively on pressure measurements.[4] The performance of SONAH is also improved if it is based on measurements of both quantities.[5] An additional advantage of the pressure-velocity technique is that one can combine pressure- and velocity-based predictions, which makes it possible to distinguish between sound coming from the two sides of the measurement plane in the same way as one can do with a double layer array of pressure transducers.[6,7] This makes it possible to distinguish, e.g., between incident and reflected waves, which can be very useful when measurements take place under nonideal conditions. However, it is far more difficult to calibrate particle velocity transducers than condenser microphones.[8] Thus, the purpose of this letter is to compare SONAH based on pressure and velocity measurements in a single layer with SONAH based on pressure measurements in a double layer.

II. OUTLINE OF SONAH THEORY

The theory of SONAH has been presented, e.g., in Refs. 2 and 3; therefore the description given in what follows is very brief.

A. SONAH based on measurement of the sound pressure

The conventional SONAH procedure assumes that all sources are on one side of the measurement plane and expresses the pressures in the prediction plane as a weighted sum of pressures in the measurement plane,

$$\mathbf{p}^T(\mathbf{r}) = \mathbf{p}^T(\mathbf{r}_h)(\mathbf{A}^H\mathbf{A} + \theta^2\mathbf{I})^{-1}\mathbf{A}^H\boldsymbol{\alpha}(\mathbf{r}), \quad (1)$$

where $\mathbf{p}^T(\mathbf{r})$ is a transposed column vector with N pressures in the prediction plane, $\mathbf{p}^T(\mathbf{r}_h)$ is a similar vector with N pressures in the measurement plane, $\mathbf{A}^H\mathbf{A}$ is a matrix that depends on the N positions in the measurement plane, $\mathbf{A}^H\boldsymbol{\alpha}$ is a matrix that depends on the N positions in the prediction plane and the N positions in the measurement plane, $\mathbf{I}$ is the identity matrix, and θ is a regularization parameter.[3] All matrices are N by N. The transfer matrix represents the regularized optimal least-squares solution to the overdetermined problem posed by requiring that M propagating and evanescent elementary waves ($M > N$), all having a pressure amplitude of unity in the virtual source plane, satisfy Eq. (1). In the limit of $M \to \infty$ all matrix elements become integrals that can be evaluated partly analytically and partly numerically.[3]

[a] Portions of this work were presented in "Statistically optimized near field acoustic holography with pressure-velocity probes and with a double layer array," *Proceedings of Inter-Noise 2007*, Istanbul, Turkey, August 2007.
[b] Author to whom correspondence should be addressed. Electronic mail: fja@oersted.dtu.dk
[c] Electronic mail: xinyi.cc@gmail.com
[d] Electronic mail: virginie.jaud@ensieta.fr

 0001-4966/2008/123(4)/1842/4/$23.00 © 2008 Acoustical Society of America

The normal component of the particle velocity in the prediction plane is obtained from a similar transfer matrix where $\mathbf{A}^H\boldsymbol{\alpha}$ is replaced by

$$\mathbf{A}^H\boldsymbol{\beta}(\mathbf{r}) = \frac{-1}{j\omega\rho}\frac{\partial \mathbf{A}^H\boldsymbol{\alpha}(\mathbf{r})}{\partial z}. \tag{2}$$

B. SONAH based on measurement of the particle velocity

The normal component of the particle velocity in the prediction plane can also be determined from the normal component of the particle velocity in the measurement plane using the same transfer matrix as in Eq. (1).[5] The corresponding pressure can be determined from a similar transfer matrix where $\mathbf{A}^H\boldsymbol{\alpha}$ is replaced by

$$\mathbf{A}^H\boldsymbol{\gamma}(\mathbf{r}) = -j\omega\rho\int \mathbf{A}^H\boldsymbol{\alpha}(\mathbf{r})dz. \tag{3}$$

The two transfer matrices for particle velocity-based SONAH are determined from an infinite set of propagating and evanescent elementary waves with a *particle velocity* amplitude of unity in the virtual source plane, unlike the two transfer matrices for pressure-based SONAH. Surprisingly, the weighting of the elementary waves has been found to have almost no influence on the results.[9]

C. SONAH based on measurement of the pressure and the particle velocity

One cannot distinguish between wave components coming from the two sides of the measurement array from measurements of the pressure or from measurements of the particle velocity; hence, the assumption of the region opposite to the source side of the measurement plane being "source free." However, the fact that the particle velocity is a vector component, unlike the pressure, makes it possible to separate contributions from two sides of the measurement array from each other when both quantities are available.[5] Thus the sound pressure in the primary prediction plane generated by the primary source can be estimated as the average of a pressure- and a particle velocity-based estimate, and the sound pressure in the secondary prediction plane generated by a source on the other side of the measurement plane can be estimated as half the difference between a pressure- and a particle velocity-based estimate. The same holds for the particle velocity. In what follows this method of combining two estimates based on pressure and particle velocity measurements is referred to as "the *p-u* method."

Note that the prediction plane for estimates based on subtracting pressure- and particle velocity-based predictions, here referred to as the secondary prediction plane, is the symmetrically placed *image* of the prediction plane for estimates based on averaging pressure- and particle velocity-based predictions, here referred to as the primary prediction plane. The reason for this is that the elementary waves used in determining the transfer matrices appear to be coming from the image of the virtual source plane.

D. SONAH based on measurement of the pressure in two parallel planes

An alternative to the *p-u* method is based on measurement of the sound pressure in two parallel planes. The double layer technique, originally proposed by Tamura as an extension of NAH,[6] also works with SONAH.[7] The sound pressure in the prediction plane is expressed as a weighted sum of sound pressures measured in the two planes *a* and *b*, here assumed to be parallel,

$$\mathbf{p}^T(\mathbf{r}) = \begin{pmatrix}\mathbf{p}(\mathbf{r}_h^a)\\ \mathbf{p}(\mathbf{r}_h^b)\end{pmatrix}^T\left(\begin{pmatrix}\mathbf{G}_{aa} & \mathbf{G}_{ab}\\ \mathbf{G}_{ab}^H & \mathbf{G}_{aa}\end{pmatrix}^H\begin{pmatrix}\mathbf{G}_{aa} & \mathbf{G}_{ab}\\ \mathbf{G}_{ab}^H & \mathbf{G}_{aa}\end{pmatrix} + \theta^2\mathbf{I}\right)^{-1} \times\begin{pmatrix}\mathbf{h}_a(\mathbf{r})\\ \mathbf{h}_b(\mathbf{r})\end{pmatrix}, \tag{4}$$

where $\mathbf{p}(\mathbf{r}_h^a)$ and $\mathbf{p}(\mathbf{r}_h^b)$ are column vectors with N pressures in the two measurement planes, $\mathbf{G}_{aa}$ and $\mathbf{G}_{ab}$ are N by N matrices that depend on the N positions in measurement plane a and in both measurement planes, respectively, $\mathbf{I}$ is the identity matrix ($2N$ by $2N$), and $\mathbf{h}_a$ and $\mathbf{h}_b$ are N by N matrices that depend both on the N positions in the prediction plane and the N positions in measurement plane a and b, respectively. As noted earlier, the transfer matrix represents the regularized optimal least-squares solution to an overdetermined problem posed by requiring that a large number of propagating and evanescent elementary waves satisfy Eq. (4). However, now there are two virtual source planes placed symmetrically on either side of the two measurement planes, and two corresponding sets of elementary propagating and evanescent waves.

The normal component of the particle velocity can be determined from a similar transfer matrix where $\mathbf{h}_a$ and $\mathbf{h}_b$ are replaced by

$$\begin{pmatrix}\mathbf{h}_a^{(u)}(\mathbf{r})\\ \mathbf{h}_b^{(u)}(\mathbf{r})\end{pmatrix} = \frac{-1}{j\omega\rho}\frac{\partial}{\partial z}\begin{pmatrix}\mathbf{h}_a(\mathbf{r})\\ \mathbf{h}_b(\mathbf{r})\end{pmatrix}. \tag{5}$$

In what follows the method based on measurement of the pressure in a double layer is referred to as "the DLA method."

III. A SIMULATION STUDY

A study with simulated measurements has been carried out. The *p-u* method is compared with the DLA method for realistic, complicated sources. Regularization is done without human intervention using the generalized cross validation method.[10]

The measurement plane for the *p-u* method is placed midway between the two source regions at $z=0$, and the two measurement planes for the DLA method are placed symmetrically at $z=\pm 1.5$ cm. All measurement arrays have dimensions of 21×21 cm with 8×8 transducer positions. The prediction planes have the same dimensions. The two prediction planes of the *p-u* method are placed symmetrically at $z=\pm 4.5$ cm, and the same prediction planes have been chosen for the DLA method. The virtual source plane for the *p-u* method is at $z=-7.5$ cm, and the virtual source planes for the DLA method are at $z=\pm 7.5$ cm. In the primary prediction plane the sound field that would be generated by source re-

gion 1 in the absence of the disturbance from source region 2 is predicted; and in the secondary prediction plane on the other side of the double layer array the sound field that would be generated by source region 2 in the absence of the disturbance from source region 1 is predicted.

The test case consists of two baffled, simply supported, vibrating 5 mm steel panels, placed in the planes $z = \pm 7.5$ cm. Both panels have dimensions 1×1 m and a critical frequency of about 2.4 kHz, and both are driven by point forces of the same strength, but the driving points are not placed symmetrically. The two sources are modeled as modal sums, and the radiated sound field is calculated by a numerical approximation to Rayleigh's first integral.[1] Reflections from the panels and baffles have been ignored. Ignoring such reflections for this configuration is evidently not realistic. However, no method can take account of such reflections, and the purpose of this test case is not to model a realistic situation but to compare the performance of the two methods with a realistically complicated sound field. Note that the measurement arrays are much smaller than the sources; this is no problem for the SONAH method.[2,3,5,7]

Figure 1 shows a comparison of the "true" and predicted undisturbed pressure and particle velocity in a diagonal across the primary prediction plane when the two panels are driven at 1.5 kHz. It is apparent that both methods give acceptable results in spite of the strong disturbance. The *p-u* method predicts both the pressure and the particle velocity somewhat better than the DLA method.

Figure 2 shows the relative global errors of the predicted undisturbed pressure, particle velocity, and sound intensity for the same test case as functions of the frequency. The results are based on an ensemble of 20 pairs of vibrating panels with driving points at random positions. The relative global error is defined as the ratio of the Euclidian norm of the local deviations between predicted and true values to the Euclidean norm of the true quantity.[3] As can be seen the relative errors of all quantities are of the order of −17 dB (or 14%) in the medium frequency range. On the whole the DLA method predicts the sound pressure somewhat better than the *p-u* method, whereas the *p-u* method predicts the particle velocity and the sound intensity somewhat better than the DLA method.

Finally, Fig. 3 compares the results of the *p-u* and the DLA method with and without the disturbing sound field generated by a secondary source of the same strength as the primary source. Without the disturbing source the pressure is also predicted just from pressure measurements (in a single layer at $z=0$) and the particle velocity is predicted just from particle velocity measurements. It is clear that in the absence of disturbing sound from the other side of the measurement array the pressure is predicted better from the pressure in a single layer than with the *p-u* or the DLA method, and the particle velocity is predicted better from the the particle velocity than with the *p-u* or the DLA method. Under such circumstances the *p-u* and the DLA methods give similar results. With the disturbing sound field the DLA method predicts the pressure somewhat better than the *p-u* method, whereas the *p-u* method predicts the particle velocity slightly better than the DLA method.

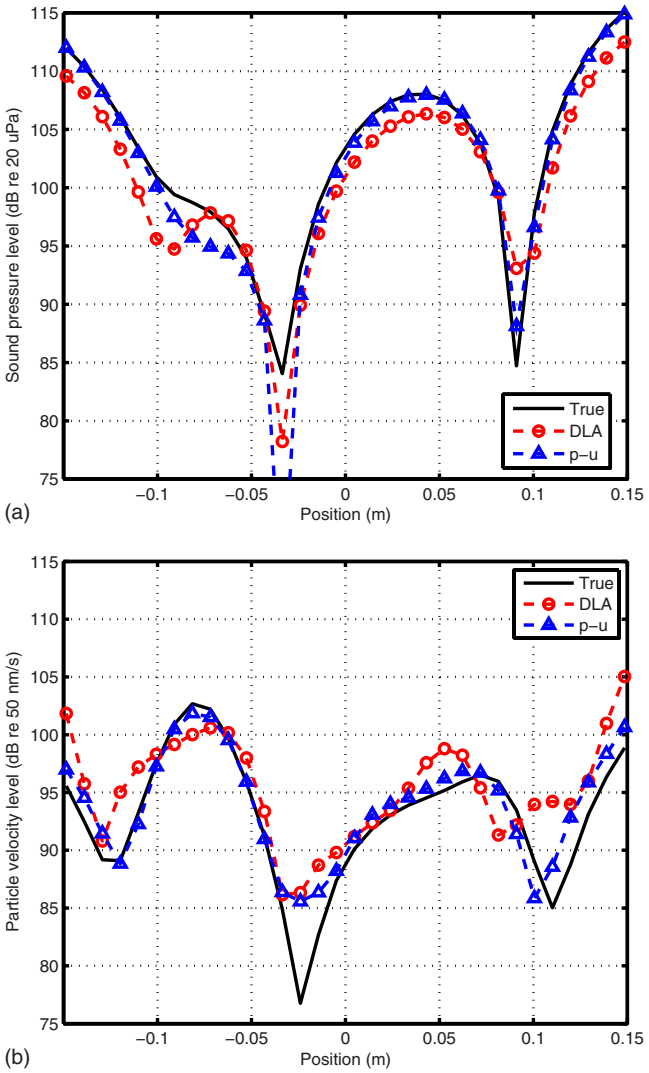

FIG. 1. (Color online) "True" and reconstructed undisturbed sound pressure (a) and particle velocity (b) in a diagonal across the primary prediction plane. Sources: Two baffled panels driven at 1.5 kHz by point forces of the same strength.

IV. DISCUSSION

In a previous investigation of SONAH it was concluded that prediction of the pressure from measurements of the pressure and prediction of the particle velocity from measurements of the particle velocity without disturbing sound from the other side of the measurement plane in general are better than predicting one quantity from the other.[5] Thus it is perhaps not surprising that the *p-u* method is no better than the DLA method in the absence of disturbing noise, and it is clear that these two methods should only be used when it is necessary to suppress noise coming from the other side of the measurement plane. In the presence of disturbing sound from the other side of the measurement plane, the *p-u* method relies on pressure- and particle velocity-based estimates of the same two quantities being identical; if this is not the case the disturbing sound will contaminate the prediction; this explains why the performance of the method is not significantly better than the performance of the DLA method.

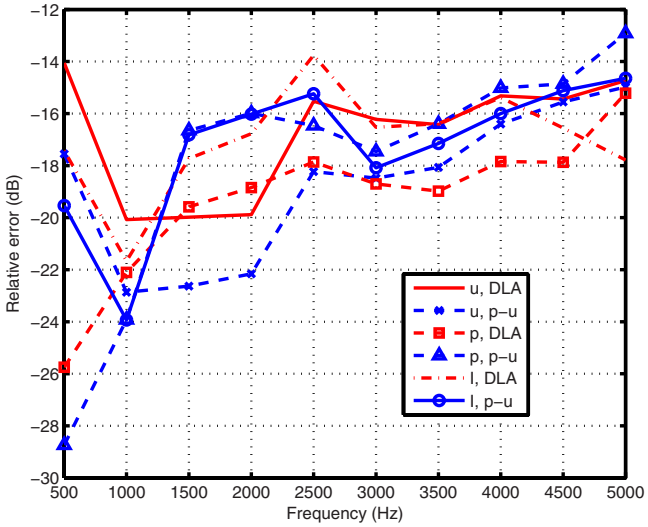

FIG. 2. (Color online) Relative global error of reconstructed undisturbed particle velocity, sound pressure, and sound intensity in the primary prediction plane as a function of the frequency. Sources: Two baffled panels driven by point forces of the same strength.

V. CONCLUSIONS

Statistically optimized near field acoustic holography can be based on measurements of the pressure in a plane, measurements of the normal component of the particle velocity in a plane, measurements of both quantities in the same plane, or measurements of the pressure in two parallel planes. Both the double layer method and the method based on measurements of pressure and particle velocity make it possible to distinguish between sound field components coming from the two sides of the measurement array and thus suppress even strong unwanted disturbing sound coming from the other side, and there is no significant difference between predictions determined with the two methods under such circumstances. However, in the absence of such disturbing sound field components then the most accurate prediction of the pressure near the source under test is obtained on the basis of pressure measurements in a single plane, and the most accurate prediction of the particle velocity is obtained from particle velocity measurements.

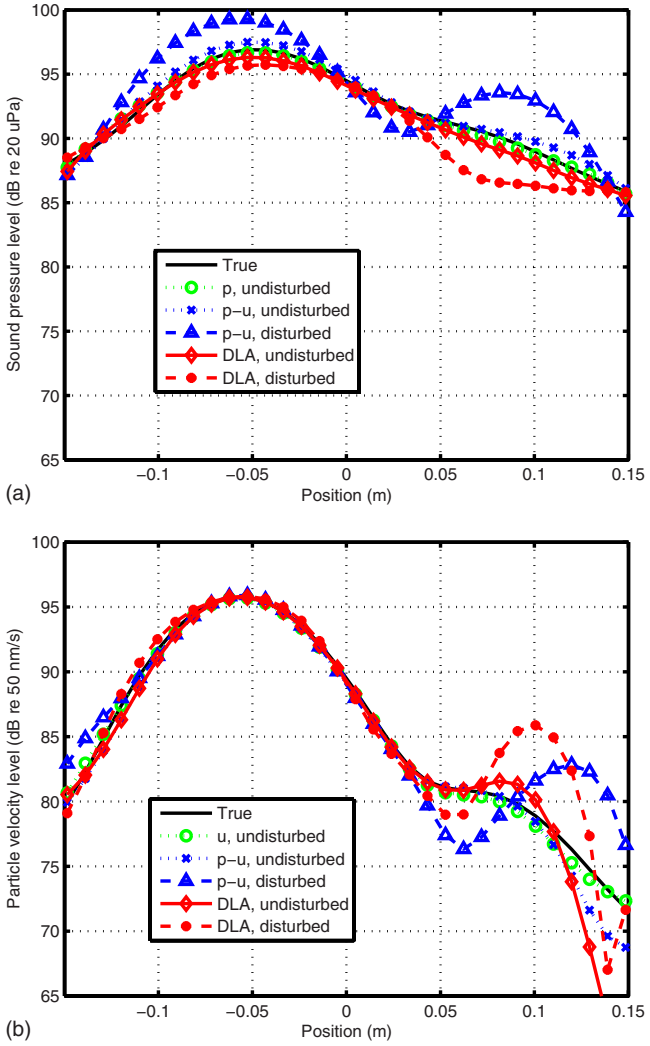

FIG. 3. (Color online) True and reconstructed undisturbed sound pressure (a) and particle velocity (b) in a diagonal across the primary prediction plane. Sources: Two baffled panels driven at 1.5 kHz by point forces of the same strength. Results predicted without the disturbing secondary source are also shown.

[1]E. G. Williams, *Fourier Acoustics—Sound Radiation and Nearfield Acoustical Holography* (Academic Press, San Diego, 1999).
[2]R. Steiner and J. Hald, "Near-field acoustical holography without the errors and limitations caused by the use of spatial DFT," Int. J. Acoust. Vib. **6**, 83–89 (2001).
[3]J. Hald, "Patch near-field acoustical holography using a new statistically optimal method," Proceedings of Inter-Noise 2003, Jeju Island, Korea, 2003, pp. 2203–2210.
[4]F. Jacobsen and Y. Liu, "Near field acoustic holography with particle velocity transducers," J. Acoust. Soc. Am. **118**, 3139–3144 (2005).
[5]F. Jacobsen and V. Jaud, "Statistically optimized near field acoustic holography using an array of pressure-velocity probes," J. Acoust. Soc. Am. **121**, 1550–1558 (2007).
[6]M. Tamura, "Spatial Fourier transform method of measuring transmission coefficients at oblique incidence. I. Theory and numerical examples," J. Acoust. Soc. Am. **88**, 2259–2264 (1990).
[7]J. Hald, "Patch holography using a two-layer handheld array with an extended SONAH algorithm," Proceedings of Euronoise, Tampere, Finland, 2006.
[8]F. Jacobsen and V. Jaud, "A note on the calibration of pressure-velocity sound intensity probes," J. Acoust. Soc. Am. **120**, 830–837 (2006).
[9]F. Jacobsen, X. Chen, and V. Jaud, "Weighted statistically optimised near field acoustic holography with pressure-velocity probes," Proceedings of 14th International Congress on Sound and Vibration, Cairns, Australia, 2007.
[10]P. C. Hansen, *Rank-Deficient and Discrete Ill-Posed Problems: Numerical Aspects of Linear Inversion* (SIAM, Philadelphia, 1997).

The decay of pitch memory during rehearsal (L)

Christian Kaernbach[a)]
Institut für Psychologie, Christian-Albrechts-Universität zu Kiel, Olshausenstrasse 62, 24098 Kiel, Germany

Kathrin Schlemmer
Institut für Musikwissenschaft, Martin-Luther-Universität Halle-Wittenberg, Kleine Marktstrasse 7, 06099 Halle, Germany

(Received 21 February 2007; revised 23 January 2008; accepted 24 January 2008)

The present study investigates the decay of pitch memory over time. In a delayed pitch comparison paradigm, participants had to memorize the pitch of a Shepard tone, with silent, overt, or without any rehearsal. During overt rehearsal, recordings of the rehearsing were effectuated. Performance was best for silent rehearsal and worst for overt rehearsal. The differences, although partially significant, were not marked. The voice pitch during overt rehearsal was compatible with a random walk model, providing a possible explanation of why rehearsal does not improve the retention of the pitch trace. © *2008 Acoustical Society of America.* [DOI: 10.1121/1.2875365]

PACS number(s): 43.66.Ba, 43.66.Hg, 43.66.Mk [AJO] Pages: 1846–1849

I. INTRODUCTION

Auditory sensory memory has been shown to share many characteristics with classical short-term memory, such as lifetime, capacity, and susceptibility to interference (Kaernbach, 2004). However, a major difference seems to be that rehearsal does not appear to be as effective with sensory information as with categorical information.

Keller *et al.* (1995) note that no measures are taken to prevent rehearsal in standard delayed pitch comparison tasks. However, this does not fully prevent the loss of auditory information over time. They found a slight decrease in performance in a pitch memory task, if a rehearsal-preventing distractor task is to be performed during the retention interval. They suggest that attention might help to maintain the trace in the condition without the distractor task.

In contrast to this, Demany *et al.* (2001, 2004) failed to demonstrate a beneficial influence of attention and/or covert rehearsal. They investigated the influence of a cue that directed the attention toward one out of three possible characteristics or components of a stimulus in a delayed matching experiment. If the cue fell in the retention interval, it made no difference whether it came early or late. If a rehearsal algorithm would have been effective, the early cue should have been more helpful.

The beneficial effects of rehearsal, if any, are small. Overt rehearsal has even been reported to be detrimental to the retention of a pitch trace (Massaro, 1970). This is in contrast to classical short-term memory for categorical information, where the lifetime of a trace can be lengthened, ad infinitum, by rehearsing the stored information. For a better understanding of this discrepancy it would be useful to study the temporal dynamics of the decay of the sensory trace. The voice pitch during overt rehearsal might be a tool to probe the actual state of the sensory trace during decay. Therefore, the present study compared overt, covert, and no rehearsal conditions. The recorded pitch data during overt rehearsal were compared to theoretical predictions of the time course of the sensory trace during the retention interval.

II. METHODS

Three individuals with an auditory-related profession (two female, one male, age range 29 to 30) participated in our experiment. All of them had been playing an instrument for 15 to 24 years. Two of them had had formal vocal training for 15 years. Participants had to compare two stimuli (S1 and S2) that were separated by a certain retention interval. The second stimulus would be slightly higher or slightly lower than the first stimulus, with equal probability. Participants had to indicate which of these two possibilities was the case.

In order to facilitate rehearsal, we employed Shepard tones (Shepard, 1964). These octave-complex tones elicit circular pitch percepts, with a well-defined chroma (pitch class, e.g., C vs C#), but an ambiguous pitch height (octave register, e.g., C4 vs C3). Shepard tones enable participants to rehearse the presented tone at whatever octave is most appropriate to their vocal range. The duration of the tones was 1 s, with 0.1 s ramps at the onset and the offset of the tones. We presented the tones at a level 60 dB above threshold. The chroma of the first stimulus was randomized uniformly on a logarithmic frequency scale over the range of one octave. After each single trial, we gave feedback in order to help the participants to improve their performance. The next trial started 1.2 s after the preceding trial.

Prior to the main experiment, we determined the just noticeable difference (JND) for these stimuli (interstimulus interval 0.5 s) for each participant. Using an unforced-choice adaptive procedure (Kaernbach, 2001), we estimated the point of the psychometric function where 75% of the judgments were correct. The JNDs for the three participants were close to 3, 4, and 5 cents. We rounded them off to these integer values. A JND of 4 cents corresponds to a frequency difference of 0.23%. This is compatible with what is known

a)Electronic mail: www.kaernbach.de.

 0001-4966/2008/123(4)/1846/4/$23.00 © 2008 Acoustical Society of America

about the JND for the pitch of complex tones (see, e.g., Hoekstra, 1979; Shackleton and Carlyon, 1994).

In the main experiment, we tested four different conditions. These conditions were tested blockwise in blocks of 20 trials of the same type. Participants performed several training blocks until they felt at ease with the different tasks. Then, they performed 20 blocks of each condition in rotating order.

In one condition, the duration of the retention interval was 0.5 s. In this condition, no specific rehearsal instruction was given. The second stimulus S2 differed from the first stimulus S1 by −1.67, −1, −0.33, +0.33, +1, or +1.67 JNDs. The actual difference was taken randomly from these six possibilities. This condition was tested 400 times per participant, i.e., approximately 400/6=67 times per difference.

In three other conditions, the duration of the retention interval was 6 s. The difference between S2 and S1 was taken randomly from −3, −1, +1, or +3 JNDs. Each difference was tested approximately 400/4=100 times per participant in each condition. The three different conditions differed only by the rehearsal instruction.

The first rehearsal instruction was "no rehearsal." It was symbolized by a mandala appearing on the computer screen, and the participants were told not to pay attention to the pitch of the first stimulus until the second stimulus appeared. The other two conditions were rehearsal conditions, with silent versus overt rehearsal. They were also symbolized by icons on the computer screen, but this time the participants had to direct their attention toward the pitch of S1. All participants stated that they were able to act differently in these conditions as compared to the no rehearsal condition, and that they believed that this would improve their performance. In the overt rehearsal condition, we recorded the voice during the retention interval.

III. PITCH DISCRIMINATION PERFORMANCE

The data analysis was performed by calculating maximum likelihood fits and likelihood ratios, in order to test the various hypotheses against each other.

The data of the three participants were similar if compared on a JND scale. A likelihood ratio test revealed that they could be pooled into a single data set. Figure 1 shows the pooled psychometric functions for all four conditions. The psychometric function for the 0.5 s retention condition is much steeper than the other three psychometric functions, illustrating that the precision of the trace is much higher after 0.5 s than after 6 s. The differences among the other three psychometric functions are not marked.

Cumulative normal distributions were fitted to the four psychometric functions. Table I shows the maximum likelihood estimates for the means and the standard deviations of the trace for these four conditions. The means are compatible with zero for the 0.5 s retention condition and for the 6 s silent rehearsal condition. For the other two conditions, the means are significantly different from zero ($p<0.05$). Note that the mean is lower than zero in the overt rehearsal condition, which would result from a decreasing voice pitch, as is often observed in singing.

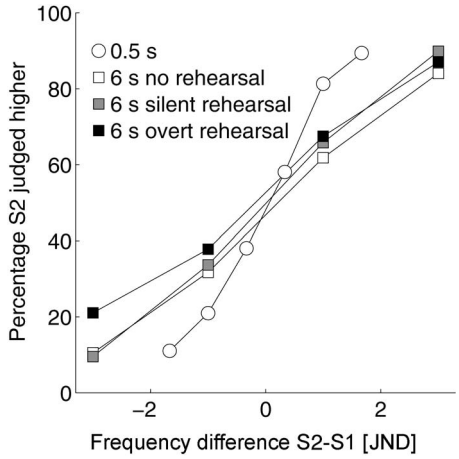

FIG. 1. Psychometric functions for the four experimental conditions.

The standard deviations for the three 6 s retention conditions differ slightly from each other, with the silent rehearsal condition resulting in the lowest spread of the trace, and the overt rehearsal condition resulting in the highest spread of the trace. The difference in the standard deviations between silent and overt rehearsal is significant ($p<0.05$), whereas the other two differences are not significant.

IV. VOICE PITCH ANALYSIS

In each single trial of the overt rehearsal condition, voice pitch during the retention interval was determined with the YIN algorithm (de Cheveigné and Kawahara, 2002) for eleven 1 s segments. These started with the interval $[0,1]$ s, going forward in steps of 0.5 s, and ending with the interval $[5,6]$ s. In total, there were 1200 trials of this condition, giving 13 200 1 s intervals. YIN could determine the voice pitch in 10 027 of these intervals. In the other 3173 intervals, the voice was either too soft or absent.

The voice pitch was then set into relation to the nearest octave component of the S1 stimulus. On average, it was 1.2 cents lower than this component. The standard deviation was 43 cents, i.e., nearly half of a semitone. In order to reduce the effect of outliers, voice pitches, which lay farther apart from the nearest component of S1 than 2 s.d., were excluded from further processing.

V. APPLYING A RANDOM-WALK MODEL OF SENSORY RETENTION

Kinchla and Smyzer (1967) have proposed and successfully tested a random walk model of sensory retention. Although this model was recently challenged by Gold *et al.*

TABLE I. Maximum likelihood estimates for the mean and the standard deviation of the trace expressed in just noticeable differences (3–5 cents). To obtain estimates in cents multiply by a factor of about 4.

	0.5 s	6 s no rehearsal	6 s silent rehearsal	6 s overt rehearsal
Mean	0.01	0.27	0.03	−0.34
Standard deviation	1.29	2.65	2.34	3.05

(2005) for visual information, and by Demany *et al.* (2005), concerning its dependence on the sensory noise, it should apply to the present data.

In this model, the stimulus S1 is encoded to trace S1′. The encoding process is affected by the encoding noise N_e with standard deviation S_e. During retention, the trace undergoes degradation and the standard deviation increases. The variance of the trace increases linearly with time with diffusion rate φ. Stimulus S2 is encoded to trace S2′ with the encoding noise having the same variance as for the encoding process for S1. The total variance of the comparison variable S2′−S1′ is hence:

$$\mathrm{Var}(S2' - S1') = S_e^2 + \varphi t + S_e^2. \quad (1)$$

In an unbiased model and for an infinite number of random walks, the mean across all random walks stays equal to the starting point. However, if the set of random walks to be averaged is selected depending on its end point (comparison with S2′), the subsets [S1′(end)>S2′ vs S1′(end)<S2′] will have drifting means. In this case, the mean of the subsets will drift linearly away from the starting point.

Overt rehearsal suffers from voicing noise, and the voice pitch feeds back on the trace S1′ and might possibly degrade it further. The standard deviation of the voice error (43 cents) is very large compared to the standard deviation derived from the judgments (5 cents after 0.5 s, about 12 cents after 6 s) and to the effect of the voice on the trace (difference between overt and silent rehearsal about 3 cents). This tells us two things: The audible feedback supplied by the voice can definitively not be helpful for the maintenance of the trace; on the other hand, it does not change much for the retention process.

While the voice is not helpful for the maintenance of S1′, it is a valuable probe into the state of S1′. It represents a noisy image of S1′, but this noise can be reduced by averaging across large numbers of recorded voice segments. It can thus help to understand what is going on during retention. By averaging across successful versus unsuccessful trials, we can test whether the voice data are compatible with the linearity predicted by the random walk model; and we can derive estimates for S_e and φ. Figure 2 shows the mean voice error during overt rehearsal as a function of time for successful and unsuccessful trials. The data of S2<S1 trials have been mirrored so that Fig. 2 can be interpreted in terms of S2>S1 trials. The direction of the voice error is correlated with the judgment of the participant: A large deviation of the voice in the direction of S2 (upwards in Fig. 2) is typical for an error of judgment.

The data show a clear tendency of increasing voice error over time. There is a contrary effect of large initial errors only for the first two time segments (center at 0.5 and 1 s); the smallest errors are found at 1.5 s. This initial error has certainly to do with the difficulties that the participants had in matching the internal trace S1′ with their voice. Once they achieved the match, the voice error increases due to the internal random walk process. Also plotted in Fig. 2 are the model predictions, with the two parameters of the model (S_e=1.3 JNDs, $\sqrt{}(\varphi \times 6\ \mathrm{s})$=2.0 JNDs) optimized, so as to minimize the χ^2 distance over all points of all curves, except

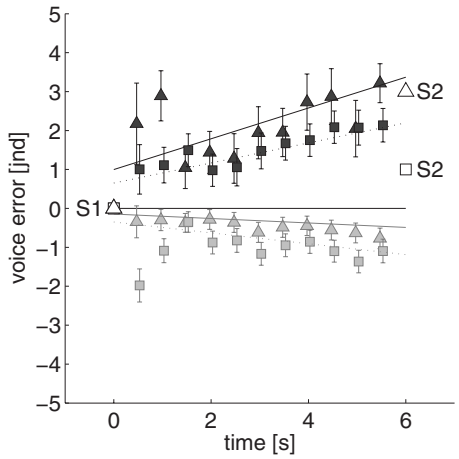

FIG. 2. Mean voice error during overt rehearsal for successful (light gray symbols) and unsuccessful (dark symbols) trials. Triangles are for trials with 3 JNDs difference, and squares are for trials with 1 JND difference between S2 and S1. Voice data of trials with S2<S1 have been mirrored at the nearest matching component of S1. Solid lines give the model prediction for a 3 JND difference, and dotted lines for a 1 JND difference.

the first two points. For these parameters, χ^2 is 3.18, indicating a very good fitting of the model. Note that the slopes and intercepts of all four straight lines in Fig. 2 (eight parameters) are not fitted individually but follow from only two parameters, S_e and φ.

The voice data allow the parameters of the random walk to be estimated. The estimates of these parameters give an estimate for the final judgment performance. Following the model, the decision of the participant should be determined by the total variance [see Eq. (1)], which, with the present data, yields a standard deviation of 2.72 JNDs, slightly better than the actual performance in the overt rehearsal condition (3.05 JNDs), and quite comparable to the performance in the no-rehearsal condition (2.65 JNDs).

VI. DISCUSSION

In our study, we have compared performance in a pitch memory task for three rehearsal conditions: no rehearsal, silent, and overt rehearsal. We found that the different rehearsal conditions had little effect on the performance in the memory task. This is quite in line with previous research, where rehearsal and/or attention effects on the retention of a sensory trace were either small or absent.

In our study, the different rehearsal conditions were created by instruction. There was no control of whether the participants did what they were instructed to do, except for the condition of overt rehearsal where we recorded the voice. It may be argued that this could be the cause of the similarity of the data. This "instruction only" approach may, on the other hand, be seen as an attempt to minimize other sources of variance, such as attention effects, or interfering noises produced by movements of the participants when performing the distractor tasks. To the best of our knowledge, our study is the first attempt to compare no rehearsal and silent rehearsal based on an instruction only approach. Given that the participants reported that they were able to follow the instructions, and that they were convinced that they would per-

form markedly better in the rehearsal conditions, the result may be seen as adding further evidence to the uselessness of rehearsal for the retention of a sensory trace.

The main focus of our study was, however, to compare overt and covert rehearsal and to test the explanatory power of voice recordings during overt rehearsal. The discrepancy between the large effect of rehearsal on categorical information and the small or absent effect of rehearsal on the retention of a sensory trace remains intriguing. The present study provides evidence in support of the random walk model of Kinchla and Smyzer (1967) for sensory retention. This model could offer an explanation: In this model of sensory retention, there is no place for rehearsal as a retention-supportive mechanism. The (overt or covert) rehearsal can, at best, mirror the actual state of the sensory trace as it undergoes the random walk. It is not at all helpful in maintaining this trace. For the rehearsal of categorical information (Baddeley and Hitch, 1974), however, the random walk model does not apply. It is assumed that the trace is perfectly reestablished at regular intervals.

In our study, the analysis of the voice recordings suggests that this view is plausible. The voice error was related to the judgment of the participants, which would not be true if the recorded voice had no relation to the sensory trace. The voice could hence be considered a mirror of the internal trace. At first view, the quality of this mirror is not excellent: The standard deviation of the voice was 43 cents, much larger than the quality of the sensory trace (about 12 cents). After averaging across many trials, however, the voice error reflected the linear drifts predicted for unsuccessful versus successful trials. Moreover, the judgment performance predicted from the voice errors (2.72 JNDs) was in the range of the actual judgment performance of the participants (3.05 JNDs). In other words, 80% $[(2.72/3.05)^2]$ of the internal variance leading to judgment errors is explained by analyzing averaged voice data. After all, voice data mirror the internal trace quite well.

The similarity of the performance in the overt and the covert rehearsal condition suggests that the results obtained for the dynamics of the internal trace, in the case of overt rehearsal, is also valid for the covert rehearsal condition. This would be different if the performance had been better for overt rehearsal than for covert rehearsal. In this case, one would have to assume that overt rehearsal involves retention algorithms different from those involved in covert rehearsal. As it is, however, the most parsimonious assumption is that both conditions involve very similar retention algorithms. If one accepts that participants did follow the instructions, this conclusion is also valid for the no rehearsal condition. The slight disadvantage for overt rehearsal is in line with previous findings (Massaro, 1970).

It is puzzling that the participants performed so well in the overt rehearsal condition (12 cents), given that the voice error (43 cents) was much larger than the judgment error in the silent rehearsal condition (9 cents). It is well known, from many experiments on pitch memory, that interfering tones during the retention interval degrade the performance in a pitch memory task (e.g., Deutsch, 1970). Why would it be that the sound of the participant's own voice, being sometimes nearly a semitone off, interferes less than sounds introduced by the experimenter? The sound of the participant's voice is surely different from the sound of the Shepard tones, however, experiments by Semal and Demany 1991, suggest that timbre differences do not explain this effect. We can only speculate that the fact that the participants produce these sounds themselves is crucial to this effect.

Voice data support the view that the sensory trace undergoes a random walk process during the retention interval. This would explain why rehearsal is of little help: It would at best reflect the increasingly distorted internal representation of the sensory trace. The present study has demonstrated that voice recordings can improve our understanding of the dynamics of sensory retention.

ACKNOWLEDGMENTS

We would like to thank Laurent Demany and an anonymous reviewer for helpful comments on the manuscript. Part of this work was presented at the ISH (International Symposium on Hearing) 2006 and will be published in a forthcoming book.

Baddeley, A. D., and Hitch, G. J. (**1974**). "Working memory," in *The Psychology of Learning and Motivation: Advances in Research and Theory*, edited by G. A. Bower (Academic, New York), Vol. **8**, pp. 47–89.

de Cheveigné, A., and Kawahara, H. (**2002**). "YIN, a fundamental frequency estimator for speech and music," J. Acoust. Soc. Am. **111**, 1917–1930.

Demany, L., Clément, S., and Semal, C. (**2001**). "Does auditory memory depend on attention?," in *Physiological and Psychophysical Bases of Auditory Function*, edited by D. J. Breebaart, A. J. M. Houtsma, A. Kohlrausch, V. F. Prijs, and R. Schoonhoven (Shaker, Maastricht), pp. 461–467.

Demany, L., Montandon, G., and Semal, C. (**2004**). "Pitch perception and retention: Two cumulative benefits of selective attention," Percept. Psychophys. **66**, 609–617.

Demany, L., Montandon, G., and Semal, C. (**2005**). "Internal noise and memory for pitch," in *Auditory Signal Processing: Physiology, Psychoacoustics, and Models*, edited by D. Pressnitzer, A. de Cheveigné, S. McAdams, and L. Collet (Springer, New York), pp. 136–142.

Deutsch, D. (**1970**). "Tones and Numbers: Specificity of interference in short-term memory," Science **168**, 1604–1605.

Gold, J. M., Murray, R. F., Sekuler, A. B., Bennett, P. J., and Sekuler, R. (**2005**). "Visual memory decay is deterministic." Psychol. Sci. **16**, 769–774.

Hoekstra, A. (**1979**). "Frequency discrimination and frequency analysis in hearing," Institute of Audiology, University Hospital, Groningen.

Kaernbach, C. (**2001**). "Adaptive threshold estimation with unforced-choice tasks," Percept. Psychophys. **63**, 1377–1388.

Kaernbach, C. (**2004**). "The memory of noise," J. Exp. Psychol. **51**, 240–248.

Keller, T. A., Cowan, N., and Saults, J. S. (**1995**). "Can auditory memory for tone pitch be rehearsed?," J. Exp. Psychol. Learn. Mem. Cogn., **21**, 635–645.

Kinchla, R. A., and Smyzer, F. (**1967**). "A diffusion model of perceptual memory," Percept. Psychophys. **2**, 219–229.

Massaro, D. W. (**1970**). "Retroactive interference in short-term recognition memory for pitch," J. Exp. Psychol. **83**, 32–39.

Semal, C., and Demany, L. (**1991**). "Dissociation of pitch from timbre in auditory short-term memory," J. Acoust. Soc. Am. **89**, 2404–2410.

Shackleton, T. M., and Carlyon, R. P. (**1994**). "The role of resolved and unresolved harmonics in pitch perception and frequency modulation discrimination," J. Acoust. Soc. Am. **95**, 3529–3540.

Shepard, R. N. (**1964**). "Circularity in judgments of relative pitch," J. Acoust. Soc. Am. **36**, 2346–2353.

Detection-theoretic analysis of the observer-based psychophysical procedure (L)

Raman Arora
Department of Electrical and Computer Engineering and Auditory Behavioral Research Lab, University of Wisconsin, Madison, Wisconsin 53706

Robert A. Lutfi[a)]
Department of Communicative Disorders and Auditory Behavioral Research Lab, University of Wisconsin, Madison, Wisconsin 53706

(Received 1 December 2006; revised 3 October 2007; accepted 25 October 2007)

The observer-based procedure, used in research applications to measure the hearing sensitivity of young infants, is analyzed within the framework of a two-stage (infant-judge) detection model involving a minimum number of assumptions. The model is taken to develop convergence theorems useful for estimating the number of judges and/or trials required to achieve a desired level of accuracy using the procedure. The model is also used to consider ways in which bias in estimates, known to be associated with the procedure, might be evaluated and reduced. Finally, a method is proposed by which the results of the analysis and different procedural variations designed to improve estimates can be evaluated empirically. © *2008 Acoustical Society of America.*
[DOI: 10.1121/1.2816559]

PACS number(s): 43.66.Yw, 43.66.Fe, 43.66.Ba [JHG] Pages: 1850–1853

I. INTRODUCTION

In the clinical evaluation of hearing, behavioral audiometry remains the gold standard. Yet, behavioral measures are not easily obtained from those who stand to benefit most from early diagnosis of a hearing loss: infants less than 5 months of age. Before 5 months of age the infant does not reliably turn their head in the direction of a sound; hence, hearing sensitivity is difficult to measure using standard visual reinforcement audiometry (cf. Moore and Wilson, 1978). Olsho *et al.* (1987) have proposed an alternative behavioral procedure for evaluating the hearing sensitivity of infants at this young age. In the observer-based procedure the sensitivity of the infant is estimated from a judge's ability to detect the presence or absence of the signal based exclusively on the infant's gross behavior. The procedure is essentially an adaptation to hearing of the forced-choice, preferential-looking procedure, developed some years earlier by Teller (1979) to measure visual acuity in infants. Though the procedure has been used primarily in research applications, it has a significant advantage of providing an objective means of evaluating the hearing sensitivity of infants. Specifically, there is a standard (the presence or absence of the signal) by which the judge's decision on each trial can be scored as correct or incorrect (see Olsho *et al.*, 1987 for a discussion of other advantages of the procedure). In this paper, we examine the observer-based procedure within the context of a simple two-stage (infant-judge) detection model to arrive at a few analytical results that might prove useful in evaluating and/or improving the accuracy of the procedure and its variants.

[a)]Author to whom correspondence should be addressed. Electronic mail: ralutfi@wisc.edu

II. TWO-STAGE DETECTION MODEL

Our analysis is undertaken within the framework of the general two-stage detection model shown in Fig. 1. The first-stage detector is the child whose sensitivity to sound we are interested in measuring; the second stage detector is the judge who must decide on each trial whether or not a signal was presented based exclusively on the various aspects $r_1, r_2 \ldots r_N$ of the child's observable behavior. The signal in this case is represented by the binary variable $s \in \{0,1\}$ indicating simple presence or absence; although s could just as easily represent two different sound waveforms or classes of waveforms that are to be discriminated by the child. All factors that would limit the child's ability to detect or discriminate s (neural noise, imperfections in auditory transduction and the like) are incorporated in the stochastic function f. Based on the outcome of $f(s)$ on each trial the child comes to a binary decision $x \in \{0,1\}$ regarding the presence or absence of the signal. The sensitivity of the child is, therefore, completely described by the hit and false alarm probabilities

$$\beta_C = P(x=1|s=1), \tag{1}$$

$$\alpha_C = P(x=1|s=0). \tag{2}$$

Now we wish to measure β_C and α_C, but cannot do so directly because we do not have direct access to child's decision, x. Instead, in the observer-based procedure, we take as an estimate of β_C and α_C the hit and false alarm rate of the child-judge duo. The estimate of the hit and false alarm rate of the child is

$$\hat{\beta}_C = \beta_{JC} = P(z=1|s=1). \tag{3}$$

$$\hat{\alpha}_C = \alpha_{JC} = P(z=1|s=0), \tag{4}$$

where, β_{JC} and α_{JC} are taken to denote the hit and false alarm rate of the child-judge duo. These estimates, of course,

 0001-4966/2008/123(4)/1850/4/$23.00 © 2008 Acoustical Society of America

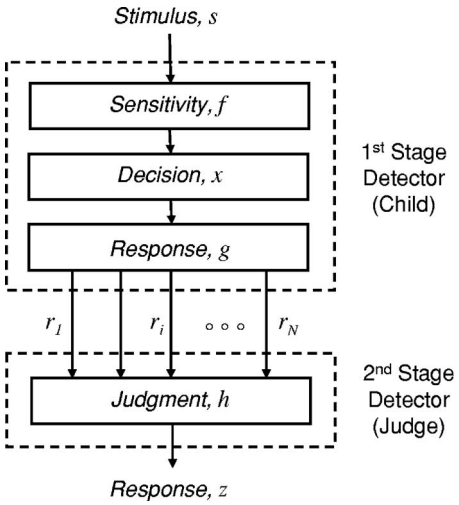

FIG. 1. Model of two-stage detection representing observer-based method for estimating child hearing sensitivity (see text for specific details).

are not perfect because the child does not generally convey their decision unambiguously through their behavior. Random movements of the child may be mistaken for a response to the sound, or no obvious response may be elicited even though the sound is clearly audible to the child, as might be the case, for example, when the child is not attending.[1] Here we represent the ambiguous relation between the child's decision and their behavior by the probabilistic function g. Other inaccuracies in the estimates of β_C and α_C result from the judge's perception of the child's response. For example, certain reliable indicators of the child's decision (possibly head movements) may go unnoticed by the judge, even while others (possibly facial expressions) are given much greater attention than they deserve. We represent all such imperfections in the judge's perception by the probabilistic function h. Taken together g and h represent all factors that limit the accuracy and reliability of the estimates of the child's sensitivity in the two-stage detector model. By allowing these functions to be quite general we encompass a wide variety of models of the possible relation between the child's decision and the judge's response.

The hit rate of the child-judge duo can now be expanded from the general expression of the two-stage detector model. Conditioning the probability β_{JC} on the child's decision x and using the law of total probability, we get

$$\beta_{JC} = P(z=1|s=1) = P(z=1|s=1,x=1)P(x=1|s=1) + P(z=1|s=1,x=0)P(x=0|s=1). \quad (5)$$

Now since $s \to x \to z$ forms a Markov chain, z is conditionally independent of s, given x. This means that $P(z=1|s=1,x=1)=P(z=1|x=1)$, which is the hit rate of second stage detector alone (i.e., the hit rate of the judge for the child's decision). Similarly, $P(z=1|s=1,x=0)=P(z=1|x=0)$ is the false alarm rate of the judge for the child's decision. Denoting these probabilities respectively as β_J and α_J, the hit rate of the child-judge duo from Eq. (5) is

$$\beta_{JC} = \beta_J\beta_C + \alpha_J\alpha_C. \quad (6)$$

The false alarm rate of the child-judge duo is obtained in similar fashion,

$$\alpha_{JC} = P(z=1|s=0) = P(z=1|s=0,x=1)P(x=1|s=0) + P(z=1|s=0,x=0)P(x=0|s=0) = \beta_J\alpha_C + \alpha_J(1-\alpha_C). \quad (7)$$

Now, Eqs. (6) and (7) lend themselves to mathematical analysis of various conditions in which the particular experiment or similar tests using the observer-based procedure may be performed. We consider three such conditions intended to improve estimates of the hit and false alarm rates of the child.

III. MULTIPLE JUDGES

Let us suppose that instead of a single judge, we have n judges, each of whom makes a binary decision $\{z_i\}_{i=1}^n$ regarding the presence or absence of the signal. The overall decision is taken to be some function of all the z_i. Here we give sufficient conditions on the statistical characterization of the judges to attain optimal detection performance. At the same time we develop expressions for the rate at which the estimation error decays with number of judges. This will give us the trade-off between the cost and accuracy of using multiple judges.

Consider then the following conditions for the second-stage detector: (1) The judges form independent decisions regarding s. (2) The statistical performance of individual judges differs, but for each judge the hit rate is at least slightly greater than the false alarm rate; i.e., $P(z_i=1|s=1) > P(z_i=1|s=0)$ for all $i=1\ldots n$. (3) The individual decisions from all judges are simply averaged to arrive at a group decision. Denoting $z^{(n)}=\Sigma z_i/n$ as the average, the group decision is

$$z = \begin{cases} 1, & z^{(n)} \geqslant \eta^{(n)} \\ 0, & z^{(n)} < \eta^{(n)}, \end{cases} \quad (8)$$

where $\eta^{(n)}$ is an arbitrary judgment criterion. Note here that we do not claim the simple averaging of the judges' responses to be optimal in any sense. We use the average as a means to derive the expressions for convergence which is mathematically tractable. Later we consider how more efficient combination rules may be implied by the results of experiments designed specifically to test the derived analytic expressions. Note too that condition (2) might otherwise be stated that the hit rate of a judge is *more likely* to be greater than their false alarm rate; the statement as given is simply more tractable mathematically.

Now, let $\beta_{JC}^{(n)}$ and $\alpha_{JC}^{(n)}$ denote the group hit and false alarm rates of judges, comparable to β_{JC} and α_{JC} for a single judge. We use a special case of the Hoeffding concentration inequality (Hoeffding, 1963) to show that $\beta_{JC}^{(n)}$ converges rapidly with n to β_C, while $\alpha_{JC}^{(n)}$ converges rapidly to α_C.

That is, for any $\varepsilon > 0$

$$P(z^{(n)} - E[z^{(n)}] \geqslant \varepsilon) \leqslant \exp(-2n\varepsilon^2). \quad (9)$$

where $z_i \in \{0,1\}$ and $S_n = nz^{(n)}$. Now, consider the false alarm rate of the second-stage detector alone; that is, the probability that the judges' decide a signal is present $(z=1)$ when the child, in fact, decides it is not $(x=0)$. We can express this probability as

$$\alpha_J^{(n)} = P(z^{(n)} \geq \eta^{(n)} | x=0)$$
$$= P(z^{(n)} - E_0[z^{(n)}] \geq \eta^{(n)} - E_0[z^{(n)}]), \quad (10)$$

where E_0 is used here to denote the expected value conditioned on $x=0$. The expression for convergence of $\alpha_J^{(n)}$ follows from Eq. (9) by conditioning on $x=0$ and by setting $\varepsilon = \eta^{(n)} - E_0[z^{(n)}] > 0$ according to condition (2),

$$\alpha_J^{(n)} \leq \exp[-2n\varepsilon^2]. \quad (11)$$

This shows that $\alpha_J^{(n)}$ converges to 0 exponentially as n becomes large. The convergence of the hit rate of the second-stage $\beta_J^{(n)} = P(z^{(n)} \geq \eta^{(n)} | x=1)$ is obtained in a similar fashion from the miss rate

$$1 - \beta_J^{(n)} = P(z^{(n)} - E_1[z^{(n)}] \geq E_1[z^{(n)}] - \eta^{(n)}). \quad (12)$$

Setting $\varepsilon = E_1[z^{(n)}] - \eta^{(n)} > 0$,

$$1 - \beta_J^{(n)} \leq \exp[-2n\varepsilon^2]. \quad (13)$$

This further shows that $\beta_J^{(n)}$ converges exponentially to 1 as n becomes large. Finally, from Eqs. (6) and (7) we determine that as $\alpha_J^{(n)} \to 0$ and $\beta_J^{(n)} \to 1$, $\beta_{JC}^{(n)}$ converges exponentially to β_C, while $\alpha_{JC}^{(n)}$ converges exponentially to α_C.

Equations (11) and (13) are useful for estimating the number of judges required to achieve a desired level of accuracy in the estimate of the child's hearing sensitivity. For example, if we wish to limit the false alarm rate of the second stage detector to a value α (Neyman-Pearson criterion) then the number of judges should be at least

$$n \geq \frac{1}{2\varepsilon^2} \ln\left(\frac{1}{\alpha}\right). \quad (14)$$

To get an idea of the rate of convergence implied by this inequality consider the following hypothetical case: The experimenter chooses an arbitrary criterion of $\eta^{(n)} = 0.7$ for determining whether the response of the judges as a group is positive or negative. They wish the false alarm rate for the child's response ($x=0$) to be no greater than $\alpha = 0.2$. Moreover, they estimate the average of judges' decisions when $x=0$ to be $E_0[z^{(n)}] = 0.3$ (yielding a value of $\varepsilon = \eta^{(n)} - E_0[z^{(n)}] = 0.4$). For these conditions the inequality above indicates that the clinician will require $n \geq 5$ judges. Furthermore, by adding two more judges the experimenter can cut this false alarm rate in half (for $\alpha = 0.1$, $n \geq 7$). The exponential rate of approximation is encouraging. It suggests that accurate measures of child sensitivity can be obtained in many fewer trials than when a single judge is used. Note in this regard that the conclusions derived here for multiple judges apply as well to multiple trials assuming that the decisions across trials are independent, as they were assumed for the individual judges.

IV. JUDGE'S TASK

Despite its many positives, the observer-based procedure is known to have at least one notable disadvantage: it generally underestimates the sensitivity of the child. The bias occurs because the expected performance of the judge can at best equal, but never exceed that of the child. In the context of the two-stage detector model, detection is limited by the second stage as an added noisy channel. Here we consider a change in the judge's task intended to reduce the bias in estimate.

Consider first that there is no bias when the second stage detector is transparent ($y=x$). Clearly, the sensitivity of the judge must equal that of the child when the judge's decisions exactly mimic those of the child. In theory, then, β_{JC} and α_{JC} are equivalently estimates of β_C and α_C when the judge is instructed to report the decision of the child, x, rather than the presence or absence of the signal. This, parenthetically, is the instruction given to the judge in what is known as behavioral observation audiometry (Thompson and Thompson, 1972). The advantage of this approach is that the judge may be given prior knowledge of the signal on each trial to both improve their performance and to provide an equal opportunity to overestimate as well as underestimate the sensitivity of the child.

Consider then that second stage detector conditions its decision on knowledge of the random variable s on each trial. The hit rate of the two-stage detector in this case is given by Eq. (5) as before. However, $s \to x \to z$ now no longer forms a Markov chain; z is now conditioned on s. Reflecting this dependency, the hit rate of the second-stage detector with prior signal knowledge is denoted $\tilde{\beta}_J = P(z=1 | s=1, x=1)$. The probability $\tilde{\beta}_J$ can be expressed as

$$\tilde{\beta}_J = P(z=1|x=1) \cdot \frac{P(z=1|s=1,x=1)}{P(z=1|x=1)} = \beta_J \cdot b, \quad (15)$$

where $\beta_J = P(z=1|x=1)$, as in the previous section, denotes the hit rate of the second-stage detector *without* prior knowledge of the signal. In a similar fashion, the false alarm rate of the second-stage detector with prior knowledge is given by

$$\tilde{\alpha}_J = P(z=1|x=0) \cdot \frac{P(z=1|s=0,x=0)}{P(z=1|x=0)} = \alpha_J \cdot a. \quad (16)$$

Now, knowing that the signal was present, the judge can improve their performance by more often reporting that the child responded positively. That is, for $P(z=1|s=1,x=1) > P(z=1|x=1)$, $b>1$ so that $\tilde{\beta}_J > \beta_J$. Similarly, knowing that the signal was not present, the judge can improve their performance by more often reporting that the child did not respond; in this case, $a<1$ so that $\tilde{\alpha}_J < \alpha_J$.

Of course, whether or not judges will make appropriate use of the signal knowledge is ultimately an empirical question. Too much or too little reliance on the signal will either result in an overestimate or underestimate of the sensitivity of the child. However, by allowing the outcome to go in either direction, the average is expected to be a less biased estimator than when all judges underestimate sensitivity, as they can only do not knowing the signal.

Finally, it is important to note here that, while asking the judge to report the child's decision may reduce the problem of the bias in estimate, the cost is a loss of objectivity in the estimate. One can determine with certainty how accurately judges report the presence or absence of a signal, but not the decision of the child. What is needed is a cross check on the judge's performance against some other type of empirical estimate of accuracy. One such measure, which can be applied with or without signal knowledge, is proposed in the next section.

V. HIGH SIGNAL STRENGTH

We consider next a means by which the analytic results of the previous two sections might be put to an empirical test. The method involves presenting the signal at a high level so that, except in the case of a profound hearing loss, one can be reasonably sure that the signal is audible to the child. In this case we expect the hit rate of the child to be near one and the false alarm rate to be near zero. (Note here we take the position, consistent with other authors, that inattention would affect how the child responds to the signal, g in the model, not what they hear, f in the model; cf. Bargones *et al.*, 1995; Werner and Boike, 2001). Using an asterisk to denote the high signal level condition, we have $\beta_C^* \approx 1$ and $\alpha_C^* \approx 0$. The judge is not given information about the level of the signal; hence, it seems reasonable to assume that neither g nor h is changed by presenting the signal at a high level. If so, then β_C^* and α_C^* can be substituted for β_C and α_C in Eqs. (6) and (7) to yield $\beta_J \approx \beta_{JC}^*$ and $\alpha_J \approx \alpha_{JC}^*$. In other words, the observed hit and false alarm rates of the child-judge duo for the high signal level condition can be used to estimate the hit and false alarm rates of the judge alone. Substituting these empirically obtained values into Eqs. (6) and (7) and solving for β_C and α_C then gives an estimate of the hit and false alarm rate of the child when the signal is presented at a lower level. Specifically,

$$\beta_C \approx \frac{\beta_{JC} - \alpha_{JC}^* \alpha_C}{\beta_{JC}^*}, \tag{17}$$

$$\alpha_C \approx \frac{\alpha_{JC} - \alpha_{JC}^*}{\beta_{JC}^* - \alpha_{JC}^*}, \tag{18}$$

where, β_{JC} and α_{JC} denote, as before, the hit and false alarm rate of the child-judge duo obtained at the lower-level signal.

Note here that β_{JC}^* and α_{JC}^* represent the empirical equivalent of the asymptotic performance of judges as the number of judges increases. Given that the child detects the high-level signal with perfect accuracy, β_{JC}^* and α_{JC}^* are only limited by the random component of the child's response and the perception of the judge. This leads to two outcomes. First, it allows the analytic results of Secs. III and IV to be tested empirically. This can be done by measuring the rate at which β_{JC} and α_{JC} converge to β_{JC}^* and α_{JC}^* for various conditions of feedback and multiple judges, and then comparing the obtained rate in these cases to that predicted by the analytic expressions of Secs. III and IV. Second, it means that the high-level signal method can be used to improve procedures for estimating the child's response. This can be done, for example, by selecting only the best judges to participate in the observation; those previously found to produce the highest values of β_{JC}^* and the lowest values of α_{JC}^*. Or, it can be done by differentially weighting judges' responses based on these values for each judge. It can also be done by informing an appropriate selection of criterion $\eta^{(n)}$ for deciding the group or individual response of judges. Note, in this regard, that having obtained estimates of hit and false alarm rates of the child using the high-level signal method, we also have an estimate of the child's response bias. One may then use this information in subsequent observations to improve estimates by selecting a judgment criterion $\eta^{(n)}$ that more closely matches that of the child. The benefit could be great as a mismatch of judgment criteria for the two-stage detector model has been shown to have a significantly adverse effect on estimates of sensitivity (Sorkin *et al.*, 2001). The authors know of two cases in the literature where results from high signal level conditions have been used to calibrate judge's performance in a fashion similar to that proposed here (Bargones *et al.*, 1995; Werner and Boike, 2001). However, we know of no attempts so far to use such information to specifically select or give differential weighting to judges.

VI. CONCLUSIONS

The observer-based procedure offers an objective behavioral assessment of the hearing sensitivity of young infants who are otherwise incapable of performing visual reinforcement audiometry or other standard behavioral tests. In the present paper, we offer a theoretical analysis of the procedure within the context of a two-stage detection model to derive some analytic results that might be used improve estimates of the hearing sensitivity of infants. Clearly it remains for future studies to determine whether the analytic results presented here will survive empirical tests, and whether they can be used to any advantage in clinical and/or research settings.

ACKNOWLEDGMENTS

The authors wish to thank Dr. Lynne Werner and an anonymous reviewer for helpful comments on an early version of this manuscript. The work was supported by NIDCD Grant No. R01 DC01262-15.

[1]Here we assume a model of attention, consistent with the tenets of detection theory, in which inattention is a source of noise that serves to weaken (more or less) the relation between signal and infant response on different trials. An alternative model is to assume that there is absolutely no information in the child's response when they are not attending (i.e., an all-or-none model of attention). While the later has been used as a convenient vehicle for analyzing the effects of inattention, it has not been suggested in this work as a realistic model of attention (Viemeister and Schlauch, 1992). Notwithstanding, the analytic development given here would not apply if the all-or-none model is correct.

Bargones, J. Y., Werner, L. A., and Marean, G. C. (**1995**). "Infant psychometric functions for detection: Mechanisms of immature sensitivity," J. Acoust. Soc. Am. **98**, 99–111.

Hoeffding, W. (**1963**). "Probability inequalities for sums of bounded random variables," J. Am. Stat. Assoc. **58**, 13–30.

Moore, J. M., and Wilson, W. (**1978**). "Visual reinforcement audiometry (VRA) with infants." In *Early Diagnosis of Hearing Loss*, edited by S. E. Gerber and G. T. Mencher (Grune and Stratton, New York), pp. 177–213.

Olsho, L., Koch, E., Halpin, C., and Carter, E. (**1987**). "An observer-based psychoacoustic procedure for use with young infants," Dev. Psychol. **23**, 627–640.

Sorkin, R. D., Hays, C. J., and West, R. (**2001**). "Signal detection analysis of group decision making," Psychol. Rev. **108**, 183–203.

Teller, D. Y. (**1979**). "The forced-choice preferential looking procedure: A psychophysical technique for use with human infants," Infant Behav. Dev. **2**, 135–153.

Thompson, M., and Thompson, G. (**1972**). "Responses of infants and young children as a function of auditory stimuli and test methods," J. Speech Hear Disord. **15**, 699–707.

Viemeister, N. F., and Schlauch, R. S. (**1992**). "Issues in infant psychoacoustics," in *Developmental Psychoacoustics*, edited by L. A. Werner and E. W. Rubel (APA, Washington, DC), pp. 191–209.

Werner, L. A., and Boike, K. (**2001**). "Infant's sensitivity to broadband noise," J. Acoust. Soc. Am. **109**, 2103–2111.

A simulation tool for brassiness studies (L)

Joël Gilbert[a] and Ludovic Menguy
Laboratoire d'Acoustique de l'Université du Maine, UMR CNRS 6613, Le Mans, France

Murray Campbell
University of Edinburgh, Edinburgh EH9 3JZ, United Kingdom

(Received 18 July 2007; revised 17 January 2008; accepted 17 January 2008)

A frequency-domain numerical model of brass instrument sound production is proposed as a tool to predict their brassiness, defined as the rate of spectral enrichment with increasing dynamic level. It is based on generalized Burger's equations dedicated to weakly nonlinear wave propagation in nonuniform ducts, and is an extension of previous work by Menguy and Gilbert [Acta Acustica **86**, 798–810 (2000)], initially limited to short cylindrical tubes. The relevance of the present tool is evaluated by carrying out simulations over distances longer than typical shock formation distances, and by doing preliminary simulations of periodic regimes in a typical brass trombone bore geometry. © *2008 Acoustical Society of America.* [DOI: 10.1121/1.2872342]

PACS number(s): 43.75.Fg, 43.25.Gf [NFH] Pages: 1854–1857

I. INTRODUCTION

At high dynamic levels, brass instruments generate sounds having strong high frequency components; these sounds are called "brassy" or "cuivrés." They are due to the essential nonlinearity of the wave propagation in the pipe (Hirschberg *et al.*, 1996). The brassiness of the instruments defined as the rate of spectral enrichment with increasing dynamic level, can be very different due to the variety of their bore geometry. For example, a conical bore implies a faster decay of the wave than a cylindrical bore, which reduces the nonlinear wave steepening. Recently, Gilbert (2006), Myers *et al.* (2007), and Gilbert *et al.* (2007) have suggested classifying brass instruments from the brassiness point of view. A numerical model would be a useful tool to investigate the brassiness behavior of brass instruments characterized by their bore geometry. Numerical models have been developed in the time domain (Msallam *et al.*, 2000; Vergez and Rodet, 2000), or in the frequency domain (Thompson and Strong, 2001) by making some restrictive assumptions like modeling the wave steepening only on a part of the bore or ignoring backward nonlinear wave propagation.

In this letter we present a simulation tool in the frequency domain extending the work of Menguy and Gilbert (2000), which was limited to short cylindrical tubes. Brass instruments are characterized by nonuniform ducts which can be significantly longer than typical shock formation distances. It is shown (Sec. II) that the tool is relevant, first by exploring the weakly nonlinear wave propagation at long distances, and second, by doing preliminary simulations of periodic regimes in a typical brass trombone bore geometry (Sec. III).

[a]Electronic mail: joel.gilbert@univ-lemans.fr

II. WEAKLY NONLINEAR ACOUSTIC SIMULATIONS IN DUCTS

A. Theoretical background

The study of weakly nonlinear propagation in a dissipative viscothermal homogeneous fluid assuming a one-dimensional flow in a nonuniform duct leads to first-order nonlinear differential twin equations using the dimensionless variables σ (a slow geometric scale equal to $(\gamma+1)/2Mx$, where γ is the specific heat ratio, M a Mach number, x a dimensionless geometric scale), θ_+ and θ_- (dimensionless delayed time scales), and q_+ and q_- (forward and backward variables). They are the "generalized Burgers equation" for the forward-traveling wave [Eq. (1)], and for the backward-traveling wave [Eq. (2)],

$$\frac{\partial q_+}{\partial \sigma} - q_+ \frac{\partial q_+}{\partial \theta_+} + q_+ \frac{\partial \ln(D(\sigma)/D(0))}{\partial \sigma} = +\frac{1}{\Gamma}\frac{\partial^2 q_+}{\partial \theta_+^2} - \frac{T}{\epsilon}\frac{\partial^{1/2} q_+}{\partial \theta_+^{1/2}}, \tag{1}$$

$$\frac{\partial q_-}{\partial \sigma} + q_- \frac{\partial q_-}{\partial \theta_-} - q_- \frac{\partial \ln(D(\sigma)/D(0))}{\partial \sigma} = -\frac{1}{\Gamma}\frac{\partial^2 q_-}{\partial \theta_-^2} + \frac{T}{\epsilon}\frac{\partial^{1/2} q_-}{\partial \theta_-^{1/2}}, \tag{2}$$

where Γ, the Gold'berg number, is a measure of the importance of effects of volume dissipation compared to those of nonlinearity. A plane wave that propagates in a duct with rigid walls experiences dispersion and attenuation as a result of the viscothermal boundary layer along the walls. As a consequence, the right-hand side of Eqs. (1) and (2) contains a second term controlled by the dimensionless number T/ε (Menguy and Gilbert, 2000), which is a measure of the strength of nonlinearity relative to that of wall dissipation. If the volume viscothermal effects—controlled by Γ—are frequency squared dependent, the classical dependence of the viscothermal boundary-layer losses—controlled by T/ε—is on the square root of the frequency. The left-hand side of

 0001-4966/2008/123(4)/1854/4/$23.00 © 2008 Acoustical Society of America

Eqs. (1) and (2) exhibits a term which is function of the interior diameter $D(x)$ of the nonuniform duct, characterizing its slowly varying cross section. This term is linear in q. It is assumed that the duct diameter D is small enough ($kD<1$, k being the wave number), and that the area varies sufficiently slowly on the scale of a wavelength, $(1/kD).(dD/dx)\ll 1$, to justify a one-dimensional propagation model.

The two waves are assumed to propagate in opposite directions, independently in the linear limit. They are nonintegrable, and there is almost no chance of general analytical progress (Hamilton and Blackstock, 1998). That is why numerical methods such as the one described in the following section should be used.

B. Simulations in uniform and nonuniform ducts

Generalized Burger's equations (1) and (2) have no known analytical solutions. Numerical solutions are performed in the frequency domain, the method described in Menguy and Gilbert (2000) is summarized hereafter.

The following simple wave $q_+(\sigma,\theta)$ is considered:

$$q_+(\sigma,\theta)=\sum_{n=1}^{\infty}[a_n(\sigma)\sin n\theta+b_n(\sigma)\cos n\theta]. \tag{3}$$

Equalizing each term of the Fourier series coming from Eq. (1) leads, for each harmonic component n, to

$$\frac{\partial a_n}{\partial\sigma}=n\left(\sum_{p=1}^{n-1}\left(\frac{a_pa_{n-p}}{2}-\frac{b_pb_{n-p}}{2}\right)-\sum_{p=n+1}^{+\infty}(a_{p-n}a_p+b_pb_{p-n})\right)+\frac{1}{\Gamma}n^2a_n-a_n\left(\frac{\partial\ln(D(\sigma)/D(0))}{\partial\sigma}\right)-\frac{T}{\epsilon}\frac{D(0)}{D(\sigma)}\sqrt{\frac{n}{2}}(a_n-b_n),$$

$$\frac{\partial b_n}{\partial\sigma}=n\left(\sum_{p=1}^{n-1}\left(\frac{a_pb_{n-p}}{2}+\frac{b_pa_{n-p}}{2}\right)+\sum_{p=n+1}^{+\infty}(b_{p-n}a_p-b_pa_{p-n})\right)+\frac{1}{\Gamma}n^2b_n-b_n\left(\frac{\partial\ln(D(\sigma)/D(0))}{\partial\sigma}\right)-\frac{T}{\epsilon}\frac{D(0)}{D(\sigma)}\sqrt{\frac{n}{2}}(a_n+b_n). \tag{4}$$

Equation (4) is solved numerically using a spatial finite difference method, with the boundary condition $q_+(0,\theta)$, which is a time periodic function. At first order, the classical Euler method is used, and correction is performed using the Adams Moulton second-order method.

Although the simulation method has been verified for small propagation distances in Menguy and Gilbert (2000), it has to be tested for distances greater than the shock formation distance σ_c, in order to be used in brass instrument simulations. Tests have therefore been carried out for weakly dissipative fluids without any viscothermal wall effects ($T/\varepsilon=0$) for which weakly nonlinear propagation can be described by the Burgers equation. One of them, defined by a Gold'berg number Γ equal to 100 ($\Gamma\gg 1$), is discussed now.

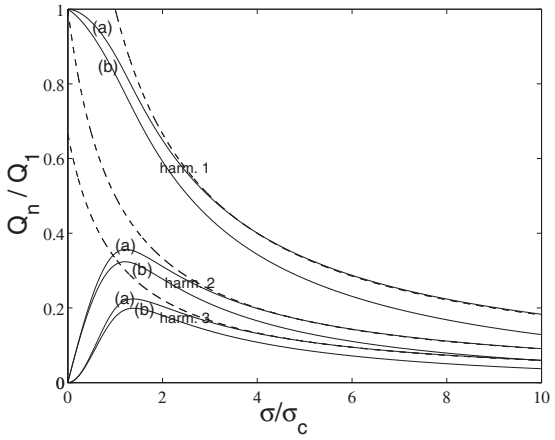

FIG. 1. First three Fourier coefficients Q_n (harmonics 1 to 3) vs the dimensionless propagation distance σ/σ_c for a weakly dissipative fluid ($\Gamma=100$) in uniform duct, according to two cases: (a) $T/\varepsilon=0$ and (b) $T/\varepsilon=10$. The fluid is excited at $\sigma=0$ by a monofrequency source. There are two calculations: Results simulated from Eq. (1) (solid lines) and Fay–Blackstock approximation, Eq. (5) (dashed lines).

The harmonic components, $P_n=\sqrt{a_n^2+b_n^2}$, as a function of σ/σ_c varying from 0 to 10 for a wave generated by a monofrequency source are displayed in Fig. 1. The behavior of the harmonic components simulated from Eq. (4) is close to the so-called Fay–Blackstock solutions available for $\sigma>3$. These analytic Fourier coefficients Q_n are written as follows:

$$q_+(\sigma,\theta)=\sum_{n=1}^{\infty}\sin(n\theta)Q_n(\sigma)=\frac{2}{\Gamma}\sum_{n=1}^{\infty}\frac{\sin(n\theta)}{\sinh[n(1+\sigma)/\Gamma]}. \tag{5}$$

Moreover, simulations of a plane wave propagating in a uniform duct, defined by $T/\varepsilon=10$, are carried out from Eq. (4). The harmonic components as a function of σ varying from 0 to 10 for a wave generated by a monofrequency source are displayed in Fig. 1. The wave deformation along the propagation, from sine wave to a decreasing amplitude sawtooth wave, is obtained. The wave forms are typical of those reported in literature for high intensity sound in ducts (Hamilton and Blackstock, 1998): The boundary-layer losses are predominant, their dispersion effects are visible on the wave forms, and the Fay–Blackstock solutions are not a good approximation anymore. The spectral enrichment can be globally estimated from the following dimensionless parameter, called the spectral centroid SC:

$$\mathrm{SC}=\frac{\Sigma_n nQ_n}{\Sigma_n Q_n}. \tag{6}$$

Figure 2 shows the rapidly increasing and then slowly decreasing evolution of SC, respectively, before one and after three shock formation distance values corresponding to the results displayed in Fig. 1, the shock formation distance σ_c being still defined from the cylindrical tube.

Simulations of a plane wave propagating in a nonuniform duct, a cone, are also carried out from Eq. (1). The expanding bore of the cone implies a faster decay of the wave which reduces the nonlinear wave steepening; the

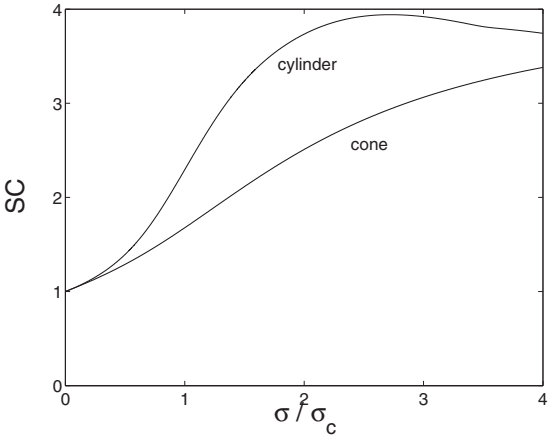

FIG. 2. Spectral centroid SC vs the dimensionless propagation distance σ/σ_c for a cylindrical tube, and a cone having the same input radius as the cylindrical tube.

spectral enrichment SC increases more slowly than in a cylindrical tube having the same input radius (see Fig. 2).

III. BRASSINESS SIMULATIONS

A. Numerical method summary

The brassiness of the sound, in other words its spectral enrichment, generated by brass instruments at high dynamic level is mainly due to the essential nonlinearity of wave propagation in the pipe, resulting in wave steepening and generation of shock waves (Hirschberg *et al.*, 1996). The spectral enrichment can be evaluated from the radiated pressure SC estimation during a crescendo. In expanding bores, a faster decay of the wave amplitude reduces the nonlinear steepening effect: This provides a hypothesis to explain the fact that "conical" instruments are not as brassy as "cylindrical" instruments. More precisely, the brassiness of two brass instruments, or of two fingerings or positions of a given instrument, can be compared from their spectral centroid values for a given crescendo (Gilbert, 2006). The comparison can also be made by simulation, the input data being the internal geometry of the instrument, its bore, and typical acoustical pressures at the input end of the instrument.

The frequency model simulation method is based on the previous publications of Menguy and Gilbert (2000) and Gilbert *et al.* (2005) dedicated to uniform ducts and clarinet-like instruments, and here adapted to nonuniform ducts and brass instruments. The simulation can be summarized as follows: Postulating the pressure spectrum P_{in} at the input end, a radiated impedance boundary condition at the output end [radiation impedance formula from Caussé *et al.* (1984), extended by the iterative impedance when kR is greater than 4.84], and the bore geometry of the instrument, the pressure, and velocity acoustic field are first calculated everywhere inside the bore using the weakly nonlinear approximation. Indeed the simple waves propagating in each direction are supposed not to interact in the body of the fluid as in the linear approximation, and they are solutions of the nonlinear differential equations (1) and (2). The numerical solving of Eq. (4) and its twin has been presented in the previous section, details of the numerical method and a harmonic balance convergence method is detailed in Menguy and Gilbert (2000). The volume velocity spectrum Q_{out} at the output end of the instrument is estimated by multiplying the output area by the output acoustic velocity spectrum. By using the low-frequency approximation for a monopole having a volume strength equal to Q_{out}, a radiated pressure spectrum P_{rad} and its spectral centroid SC_{rad} are estimated at a distance d from the open end of the pipe from

$$P_{rad} = \frac{\varrho}{4\pi d} j\omega Q_{out}. \tag{7}$$

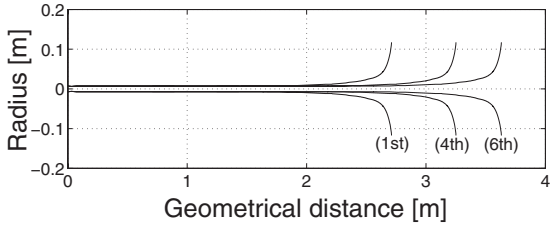

FIG. 3. The bore profiles corresponding to the three slide positions (first), (fourth), and (sixth) of a bass trombone vs the geometric position from the input end of the instrument without its mouthpiece.

B. Testing the model

Simulations were done using the bore geometries of a bass trombone corresponding to three slide positions in which F4 can be played: first, fourth, and sixth positions (see Fig. 3). From the first to the fourth (sixth), there is an added cylindrical tube of 2×0.27 m (2×0.46 m). Pressures spectra P_{in} at the input end have been measured to provide input data for simulations. They come from experimental data collected in the side of the mouthpiece backbore during playing performance of a F4 using the bass trombone. One corresponding to loud playing having a SC_{in} value equal to 1.6 is displayed in Fig. 4. The simulated radiated pressure is displayed, too.

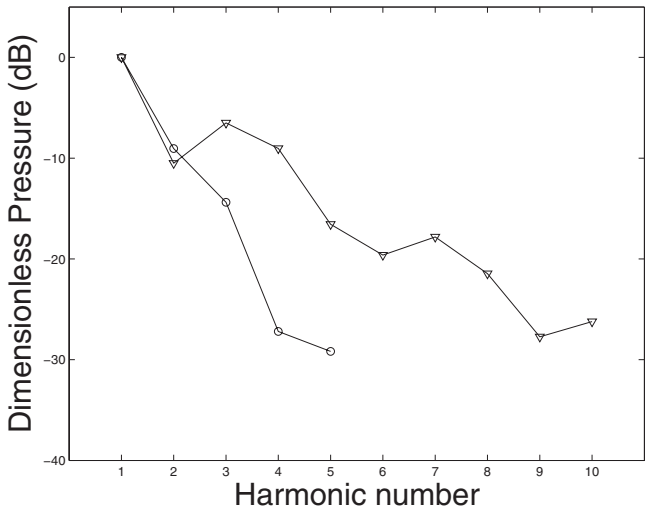

FIG. 4. Dimensionless pressure spectra P_{in} (circle) at the input end, and P_{rad} (triangle) radiated, corresponding to a loudly played F4 at the first position.

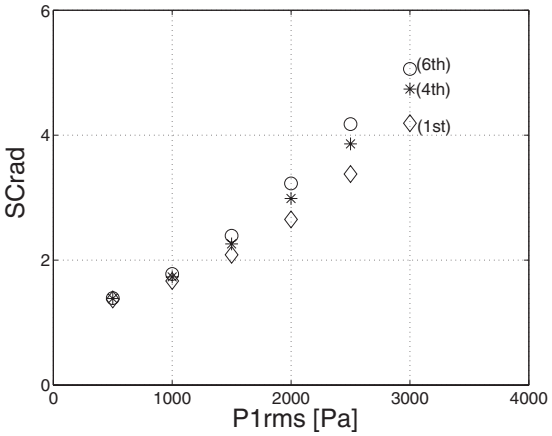

FIG. 5. Spectrum centroid SC_{rad} vs rms pressure of P_{in} having an increasing value of SC_{in} from 1.22 to 1.62, simulations corresponding to the first (diamond), fourth (asterisk), and sixth (circle) positions.

Several tests were performed to determine the reliability of the simulation method. Two kinds of crescendo have been chosen for simulations. One is created by the input pressure P_{in} being a sine wave (spectral centroid SC_{in} constant equal to 1), and having an increasing rms value from 500 to 3000 Pa. The second is created by the input pressure P_{in} increasing with a rms value from 500 to 3000 Pa, its spectral centroid varying linearly from 1.22 to 1.62 (see Fig. 5). The fundamental frequency is 350 Hz in both cases and the wave forms are defined by their first ten harmonics. The two simulated crescendos have been carried out using the three bore profiles displayed in Fig. 3. The resulting values of the spectral centroid SC_{rad} of the radiated sound are displayed in Fig. 5. All the simulated spectral centroid values are increasing with the rms pressure P_{in} at the entrance of the instruments, showing the spectral enrichment of the radiated sound. As expected the spectral enrichment is greater and greater from the first to the sixth slide position because of the increasing length of the cylindrical part of the instrument. These predictions are qualitatively comparable with experimental results shown in Gilbert (2006). Note that the values of SC_{rad} are depending on the input data P_{in}: Results obtained using a variable SC_{in} are greater than the one obtained from SC_{in} constant equal to one.

IV. CONCLUDING REMARKS

A frequency domain simulation tool has been developed to predict the brassiness behavior of brass instruments. It is based on the generalized Burger's equations (1) and (2) applied to weakly nonlinear acoustic propagation in nonuniform ducts. First, numerical simulations of traveling waves in uniform ducts have been carried out over large distances to check their reliability far from the shock formation distance. The results have been successfully compared with known theoretical predictions. Second, in the weakly nonlinear propagation approximation, waves in ducts of finite length propagate in both directions, independently as in the linear limit, except for coupling at the ends. Then the internal sound field can be described by the superposition of two simple waves propagating in opposite directions which do not interact in the body of the fluid. This is the major hypothesis of the simulation tool already described in Menguy and Gilbert (2000), applied to cylindrical tubes of short length. In the present paper it has been extended to nonuniform ducts, having lengths greater than realistic shock formation distances, and has been used with a bass trombone bore. The spectral enrichment of the radiated sound during crescendos has been simulated, and the results are comparable with experimental results already presented in conference (Gilbert, 2006; Gilbert *et al.*, 2007).

While the numerical tool presented in the present paper is promising, it must be borne in mind that many simulations have to be carried out and compared with experimental results, in order to establish the reliability of the tool as a predictor of the brassiness of brass instruments defined by their bore (Myers *et al.*, 2007).

Caussé, R., Kergomard, J., and Lurton, X. (**1984**). "Input impedance of brass instruments—Comparison between experiment and numerical models," J. Acoust. Soc. Am. **75**, 241–254.
Gilbert, J. (**2006**). "Differences between cylindrical and conical brass instruments, the nonlinear propagation point of view from experiments and simulations," J. Acoust. Soc. Am., Honolulu.
Gilbert, J., Campbell, D. M., Myers, A., and Pyle, R. W. (**2007**). "Difference between brass instruments arising from variations in brassiness due to non-linear propagation," Proceedings of International Symposium of Musical Acoustics, Barcelona.
Gilbert, J., Dalmont, J. P., and Guimezanes, T. (**2005**). "Nonlinear propagation in woodwinds," Proceedings of the Forum Acusticum, Budapest.
Hamilton, M. F. and Blackstock, D. T., editors (**1998**). *Nonlinear Acoustics* (Academic, New York).
Hirschberg, A., Gilbert, J., Msallam, R., and Wijnands, A. P. J. (**1996**). "Shock waves in trombones," J. Acoust. Soc. Am. **99**, 1754–1758.
Menguy, L. and Gilbert, J. (**2000**). "Weakly non-linear gas oscillations in air-filled tubes; solutions and experiments," Acta Acust. **86**, 798–810.
Msallam, R., Dequidt, S., Caussé, R., and Tassart, S. (**2000**). "Physical model of the trombone including nonlinear effects, application to the sound synthesis of loud tones," Acta Acust. **86**, 725–736.
Myers, A., Gilbert, J., Pyle, R. W., and Campbell, D. M. (**2007**). "Non-linear propagation characteristics in the evolution of brass musical instrument design," Proceedings of the International Congress on Acoustics, Madrid.
Thompson, M. W. and Strong, W. J. (**2001**). "Inclusion of wave steepening in a frequency-domain model of trombone sound production," J. Acoust. Soc. Am. **110**, 556–562.
Vergez, C. and Rodet, X. (**2000**). "New algorithm for nonlinear propagation of a sound wave, application to a physical model of a trumpet," J. Signal Process. **4**, 79–87.

Behavioral avoidance threshold level of a harbor porpoise (*Phocoena phocoena*) for a continuous 50 kHz pure tone (L)

Ronald A. Kastelein[a)]
Sea Mammal Research Company (SEAMARCO), Julianalaan 46, 3843 CC Harderwijk, The Netherlands

Willem C. Verboom
Department of Underwater Technology, TNO Observation Systems, P.O. Box 96864, 2509 JG Den Haag, The Netherlands

Nancy Jennings
Dotmoth, 1 Mendip Villas, Crabtree Lane, Dundry, Bristol BS41 8LN, United Kingdom

Dick de Haan
Institute for Marine Research and Ecosystem Studies (IMARES), P.O. Box 68, 1970 AB IJmuiden, The Netherlands

(Received 10 September 2007; revised 30 December 2007; accepted 18 January 2008)

The use of ultrasonic sounds in alarms for gillnets may be advantageous, but the deterring effects of ultrasound on porpoises are not well understood. Therefore a harbor porpoise in a large floating pen was subjected to a continuous 50 kHz pure tone with a source level of 122 ± 3 dB (re 1 μPa, rms). When the test signal was switched on during test periods, the animal moved away from the sound source. Its respiration rate was similar to that during baseline periods, when the sound was switched off. The behavior of the porpoise was related to the sound pressure level distribution in the pen. The sound level at the animal's average swimming location during the test periods was approximately 107 ± 3 dB (re 1 μPa, rms). The avoidance threshold sound pressure level for a continuous 50 kHz pure tone for this porpoise, in the context of this study, is estimated to be 108 ± 3 dB (re 1 μPa, rms). This study demonstrates that porpoises may be deterred from an area by high frequency sounds that are not typically audible to fish and pinnipeds and would be less likely masked by ambient noise. © *2008 Acoustical Society of America.* [DOI: 10.1121/1.2874557]

PACS number(s): 43.80.Nd, 43.80.Ev, 43.80.Jz, 43.80.Lb [WWA] Pages: 1858–1861

I. INTRODUCTION

At present, most acoustic alarms used in fisheries to reduce harbor porpoise (*Phocoena phocoena*) bycatch have a fundamental frequency of 11 kHz and harmonics to above 100 kHz (Kastelein *et al.*, 2007). The fundamental frequency and some of the harmonics can be heard by pinnipeds, and possibly by certain fish species. Since odontocetes are the target taxa, it may be advantageous to choose a fundamental frequency outside the range of fish and pinniped hearing, so above ~50 kHz. Higher frequencies suffer more attenuation than lower frequencies, but background noise levels above 40 kHz (from sea and shipping noise) are relatively low intensity, so that the alarms' source levels (SLs) in this frequency range could be relatively low, and their energy consumption could be reduced. Kastelein *et al.* (1997) quantified the effects of 70 kHz sweeps and pure tone pulses on porpoises, and found that sweeps had a stronger deterring effect than tones. Teilmann *et al.* (2006) tested three 200 ms signals between 100 and 140 kHz, produced every 4 s, and noticed displacement of the porpoises, but the animals' reaction decreased over time.

Most alarms produce pulsed sounds to reduce energy consumption. However, continuous sounds may be better deterrents. It is therefore important to know the effect of duty cycle on the deterring effect of a sound signal, so that any trade-off between effect and energy consumption can be optimized. It is also of applied interest to quantify the acoustic avoidance threshold level (the boundary between the areas that animals generally occupy during the transmission of sounds and areas that they generally do not enter during transmission). Knowing the avoidance threshold level can aid in determining the effectiveness of alarms and the necessary spacing between them on the net. The aim of the present study is to determine if a continuous 50 kHz pure tone (duty cycle 100%) can deter porpoises, and if so, to determine the avoidance threshold level.

II. MATERIALS AND METHODS

The study animal was a rehabilitated male harbor porpoise (PpSH048), which stranded in 1998. At the time of the study the animal was around 2 years old, healthy, weighed around 23 kg and was about 118 cm long. It was fed six times a day. The hearing of the study animal was not investigated; the animal was not trained for a psychoacoustic hearing study because it was due to be released after the current

[a)]Author to whom correspondence should be addressed. Electronic mail: researchteam@zonnet.nl

 0001-4966/2008/123(4)/1858/4/$23.00 © 2008 Acoustical Society of America

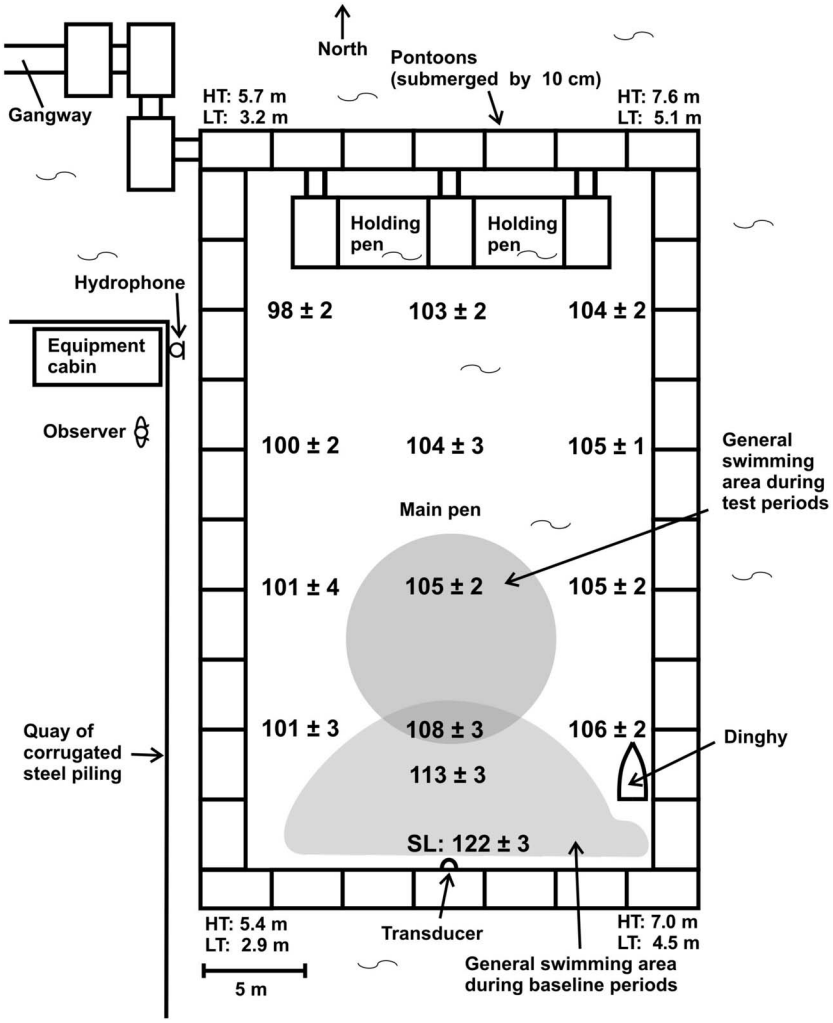

FIG. 1. Top view of the study area, showing locations of the transducer, equipment cabin, monitoring hydrophone, and observer. The water depths at the corners of the pen at high tides (HT) and low tides (LT) are given. The numbers in the pen indicate mean and standard deviation SPLs ($n=8$ measurements per location) of the 50 kHz continuous pure tone produced by the transducer at the southern end of the pen (SL was 122 ± 3 dB re 1 μPa at 1 m, rms). The grey areas indicate the porpoise's general swimming areas during the 66 baseline and 66 test periods (each grey area is based on approximately 3500 surfacing locations).

study. However, the animal showed normal behavior (compared to other rehabilitated porpoises) during the 7 months that it was in the study area.

The porpoise was housed alone in a floating pen (34 $\times$20 m; 3.5 m deep at the sides and 4–6 m deep in the center depending on the tide; Fig. 1). Details of the study area are described in Kastelein *et al.* (2006). The mean water temperature was 18 ± 0.7 °C ($n=21$), and the mean underwater visibility (determined with a Secchi disc) was 3.7 ± 0.9 m ($n=21$).

The equipment used to measure the sound pressure level (SPL) distribution of the sound stimulus and the equipment used to measure the background noise were the same as described in Kastelein *et al.* (2006). Background noise levels in the pen were determined several times in the range 250 Hz–80 kHz and were converted to "spectrum level" (dB re 1 μPa/$\sqrt{}$Hz; Fig. 2).

When this study was designed, only the porpoise audiogram by Andersen (1970) had been published. Andersen's hearing curve suggests that porpoise hearing starts to decline gradually above 32 kHz. As we aimed to test the deterrent effect of ultrasound, we selected an ultrasound frequency that would still be easily audible. The stimulus was a continuous sinusoidal 50 kHz signal, produced by a wave generator (Tektronix, model FG501), an amplifier (Toellner, model 7607), and a transducer (EDO Western Corporation, model 6166). The transducer was lowered to a depth of 1.6 m at the center of the southern end of the floating pen (Fig. 1). During each session the voltage output of the amplifier was checked with an oscilloscope (Tektronix, model 464) and the frequency was checked with a counter (Hewlett Packard, model 5302 A).

Before the actual experiment started, a pilot study was conducted in which the SL of the 50 kHz sound was increased until the study animal reacted to it by swimming away from the sound source. A SL of 122 ± 3 dB (re 1 μPa at 1 m, rms) was found to be the approximate threshold SL at which the animal reacted, so during the experiment this SL was used. The SL was calculated from the SPL measured 2 m north of the sound source (Fig. 1).

The SPL distribution in the floating pen was measured at 13 locations (with the 50 kHz tone produced at the SL of

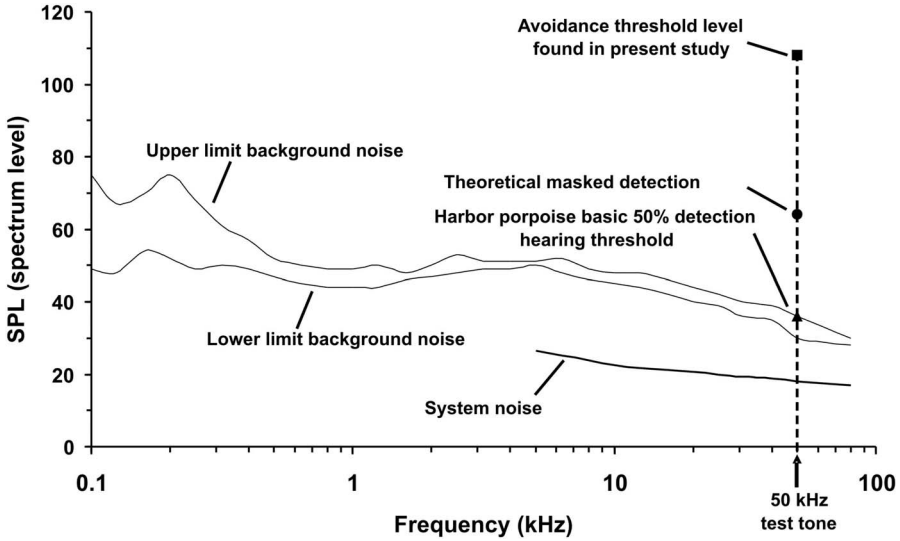

FIG. 2. Background noise level range in the floating pen (in dB re 1 μPa, spectrum level). Also shown are the harbor porpoise basic audiogram 50% detection threshold level for 50 kHz tonal signals (Kastelein *et al.*, 2002), the theoretical masked detection threshold level caused by the background noise level in the floating pen (for calculation see the Discussion), and the avoidance threshold level for a 50 kHz continuous pure tone found in the present study.

122 ± 3 dB re 1 μPa at 1 m, rms). The hydrophone was lowered to a depth of 1.6 m from the surface for all locations (Fig. 1). The analysis of the SPL distribution in the pen was carried out in eight samples per location of 0.3 s (bandwidth 20 Hz–400 kHz, window type uniform, block size 240 000, $\delta f = 3.3$ Hz), covering a total time period of 2.4 s. There was a SPL gradient, but the average SPLs on the shallower western side were lower than SPLs on the deeper eastern side of the floating pen due to sound propagation effects in the shallow water (Fig. 1).

At 0830 h the transducer was placed in the water (Fig. 1). Each session consisted of a 15 min baseline period (only background noise), immediately followed by a 15 min test period (50 kHz continuous tone transmitted). Usually three, but sometimes four, sessions were conducted per day between 1030 and 1100, 1200 and 1230, 1330 and 1400, and 1700 and 1730 h. During the sessions, no people were allowed on the pontoons, and the sound was switched on from the equipment cabin. In total, 66 sessions were conducted between 11 July and 3 August 1998. Sessions were carried out under various tidal conditions, but not in rain or when the wind speed was above Beaufort 4.

The underwater listening system, used to monitor the audible part of the background noise during the sessions, consisted of a hydrophone (Labforce 1 BV, model 90.02.01), a charge amplifier (Brüel & Kjaer, model 2635), and a portable radio. The hydrophone was placed 1 m below the water surface near the western side of the pen (Fig. 1).

During the baseline and test periods the locations where the animal surfaced were plotted on a map of the pen by an observer (Fig. 1). It was assumed that the surfacings indicated the animal's general swimming area (this was the case when water clarity was good, and the animal could be seen even when submerged). The following response variables were derived from the maps: (1) the mean distance of surfacings from the transducer during baseline and test periods, and (2) the number of respirations during baseline and test periods.

Statistical analysis was carried out on MINITAB version 14 for Windows (Ryan and Joiner, 1994). The relationships between the response variables and the environmental parameters were investigated in initial data screening by correlation analysis, and were negligible, so the environmental parameters were not taken into account in further analysis. A separate analysis of covariance (ANCOVA) was carried out on each of the response variables (mean distance from transducer to porpoise, and number of respirations during each session). The factor was the period (baseline or test). The session number was included as a covariate, in order to investigate the possible habituation effect throughout the experiment. The distances and log transformed (log 10+1) numbers of respirations conformed well to the assumptions of analysis of variance (Zar, 1984). A significance level of 5% was used.

III. RESULTS

In the 66 sessions, the porpoise was on average significantly further from the transducer during test periods than during baseline periods (ANCOVA results for factor "period," DOF (degrees of freedom)=1, $F=13.5$, $P<0.001$, for covariate "session number," DOF=1, $F=1.35$, not significant). During baseline periods, the porpoise swam in a relatively small, oval area at the southern end of the pen, close to the location of the transducer, but it moved northward when the test signal was switched on (Fig. 1). No habituation (expressed as changes in distance to the active transducer related to the covariate session number) was observed during the 3 week study period.

The average number of respirations in baseline periods was similar to that in test periods (ANCOVA results for factor period, DOF=1, $F=0.87$, not significant, for covariate session number, DOF=1, $F=15.2$, $P-0.0001$).

The 50 kHz signal had a deterring effect on the harbor porpoise. When the test signal was switched on, the SPL in the usual small swimming area of the porpoise during the

baseline periods was estimated to be around 113 ± 3 dB (re 1 μPa, rms). In the general area where the animal swam during test periods, the SPL was estimated to be around 107 ± 3 dB (re 1 μPa, rms). Thus, a received level of around 107 dB (re 1 μPa, rms) was acceptable to this harbor porpoise. An acoustic avoidance threshold SPL is defined as the boundary SPL between areas that animals generally occupy during sound emission and areas that they generally do not enter during sound emission. Based on the SPL distribution in the pen (Fig. 1), the avoidance threshold SPL for the 50 kHz signal (in the context of the present study, and for this particular harbor porpoise) is thus estimated to be around 108 ± 3 dB (re 1 μPa, rms).

IV. DISCUSSION AND CONCLUSIONS

Only one frequency was tested because of time constraints: The animal had to be released at sea at the end of the floating pen's operational season. The pen was primarily built for rehabilitation of stranded porpoises. However, this study demonstrated that an ultrasonic tone can deter a harbor porpoise from an area. It may be possible to use such an acoustic deterrent to displace porpoises from fishing nets. A harbor porpoise audiogram obtained after the present study shows that porpoise hearing is more sensitive for 50 kHz signals than for lower frequency signals (Kastelein *et al.*, 2002).

During both baseline and test periods, the porpoise used only a small portion of the available space in the floating pen. All porpoises kept in the floating pen had favorite swimming locations, which varied during the season and sometimes depended on the time of day. In general, the animals stayed away from the small pens, perhaps because most human activities took place there.

It was unexpected that the animal did not habituate to the 50 kHz sound, even after being exposed to it 66 times. Maybe the short duration of the test sessions (15 min followed by at least 1 h without the test sound) prevented habituation.

To check if the porpoise could detect the 50 kHz signal, the theoretical masked detection threshold was calculated, using the following formula: MDT=ABN+CR−DI, in which MDT=theoretical masked detection threshold for pure tone signals (dB re 1 μPa), ABN=average background noise (spectrum level: 35 dB re 1 μPa/$\sqrt{}$Hz), CR=estimated porpoise critical ratio at 50 kHz (35.8 dB), DI=porpoise directivity index at 50 kHz (7.1 dB; from Kastelein *et al.*, 2005b). The theoretical masked detection threshold for 50 kHz pure tone signals under the background noise conditions during the study is approximately 64 dB (re 1 μPa, line level). This is well below the 107 dB (re 1 μPa, rms) received level of the harbor porpoise in the area it occupied during the test periods (Fig. 2). Consequently, the 50 kHz tone was not masked by background noise during the study, and the tone was audible to the porpoise in the entire pen.

The porpoise swam northward, away from the transducer, when the 50 kHz tone was presented in test periods. At the SL offered, this sound therefore had a deterring effect on the harbor porpoise. The lack of an effect of the continuous 50 kHz tone on the respiration rate suggests that the porpoise, by swimming away, was able to go to a location in which the SPL of the signal was comfortable (around 107 dB re 1 μPa). The avoidance threshold SPL found in this study is for a 50 kHz continuous pure tone, for this particular harbor porpoise in this particular context. Since only one animal was available, it may be risky to extrapolate the findings of the present study to all members of the species. The animal's hearing sensitivity was not investigated. In addition, age, sex, location, experience and many other factors may influence the behavior of individuals (Kastelein *et al.*, 2005a). Therefore this study should be repeated in the future when more porpoises become available for research, to investigate whether the responses of the animal in the present study were representative of those of its species.

ACKNOWLEDGMENTS

The authors thank Nicole Schooneman and Lydia de Boer for collecting the data, Carolien Staal for part of the data analysis, and Wim Zoetebier for technical assistance. Rob Triesscheijn made the figures. This project was funded by SEAMARCO, Harderwijk, The Netherlands, and the North Sea Directorate-General of the Netherlands Ministry of Transport, Public Works and Water Management (via Christoph Reuther). The research was conducted under authorization of the Netherlands Ministry of Agriculture, Nature Management and Fisheries, Department of Nature Management. Endangered Species Permit FEF27 06/2/98/0184.

Andersen, S. (**1970**). "Auditory sensitivity of the harbour porpoise, *Phocoena phocoena*," in *Investigations on Cetacea*, edited by G. Pilleri (Institute for Brain Research, Bern), Vol. 2, pp. 255–259.

Kastelein, R. A., Bunskoek, P., Hagedoorn, M., Au, W. W. L., and de Haan, D. (**2002**). "Audiogram of a harbor porpoise (*Phocoena phocoena*) measured with narrow-band frequency-modulated signals," J. Acoust. Soc. Am. **112**, 334–344.

Kastelein, R. A., de Haan, D., Goodson, A. D., Staal, C., and Vaughan, N. (**1997**). "The effects of various sounds on a harbour porpoise (*Phocoena phocoena*)," in *The Biology of the Harbour Porpoise*, edited by A. J. Read, P. R. Wiepkema, and P. E. Nachtigall (De Spil, Woerden, The Netherlands), pp. 367–383.

Kastelein, R. A., Janssen, M., Verboom, W. C., and de Haan, D. (**2005b**). "Receiving beam patterns in the horizontal plane of a harbor porpoise (*Phocoena phocoena*)," J. Acoust. Soc. Am. **118**, 1172–1179.

Kastelein, R. A., Jennings, N., Verboom, W. C., de Haan, D., and Schooneman, N. M. (**2006**). "Differences in the response of a striped dolphin (*Stenella coeruleoalba*) and a harbour porpoise (*Phocoena phocoena*) to an acoustic alarm," Mar. Environ. Res. **61**, 363–378.

Kastelein, R. A., van der Heul, S., van der Veen, J., Verboom, W. C., Jennings, N., and Reijnders P. (**2007**). "Effects of acoustic alarms, designed to reduce small cetacean bycatch, on the behaviour of North Sea fish species in a large tank," Mar. Environ. Res. **64**, 160–180.

Kastelein, R. A., Verboom, W. C., Muijsers, M., Jennings, N. V., and van der Heul, S. (**2005a**). "The influence of acoustic emissions for underwater data transmission on the behaviour of harbour porpoises (*Phocoena phocoena*) in a floating pen," Mar. Environ. Res. **59**, 287–307.

Ryan, B. F., and Joiner, B. L. (**1994**). *Minitab Handbook*, 3rd ed. (Wadsworth, Belmont, CA).

Teilmann, J., Tougaard, J., Miller, L. A., Kirketerp, T., Hansen, K., and Brando, S., (**2006**). "Reactions of captive harbor porpoises, (*Phocoena phocoena*), to pinger-like sounds," Marine Mammal Sci. **22**, 240–260.

Zar, J. H. (**1984**). *Biostatistical Analysis*, 2nd ed. (Prentice Hall, Englewood Cliffs, NJ), pp. 718.

Modeling the acoustic radiation force in microfluidic chambers (L)

Karl A. Fisher[a] and Robin Miles[b]
Lawrence Livermore National Laboratory, L-333, 7000 E. Avenue, Livermore, California, 94566

(Received 20 August 2007; revised 8 January 2008; accepted 9 January 2008)

A procedure is demonstrated to quantitatively evaluate the acoustic radiation forces in microfluidic particle manipulation chambers. Typical estimates of the acoustic pressure and the acoustic radiation force are based on an analytical solution for a simple one-dimensional standing wave pattern. The complexities of a typical microfluidic channel limit the usefulness of this approach. By leveraging finite elements, and a generalized equation for the acoustic radiation force, channel designs can be investigated in two and three dimensions. Calculations and experimental observations in this report and the literature, confirm these claims. © *2008 Acoustical Society of America.*
[DOI: 10.1121/1.2839140]

PACS number(s): 43.25.Gf, 43.20.Ks, 43.25.Qp [EJS] Pages: 1862–1865

I. INTRODUCTION

The motivation for this letter is to report on a modeling approach to evaluate the acoustic radiation force field in microfluidic acoustic separation devices.[1] Typical solutions begin with a one-dimensional approximation of the standing wave pattern based on the wave equation and incorporate piezoelectric effects.[2,3] However, microfluidic particle separation and sample preparation devices usually do not have geometries that can be easily idealized as one-dimensional systems.[4–7] Thus the accuracy of these modeling estimates has been limited. In addition, the size and fluidic requirements of these systems tend to favor characteristic lengths of the fluidic channels that are on the order of the structural wavelengths of the operation frequency. Therefore, modeling approaches that address the significant two- and three-dimensional effects are necessary.

Modeling the complexity of fluid-structure-piezoelectric systems in microfluidic settings necessitates the use of multiphysics finite element codes. Commercial codes are readily available to address the modeling requirements. However, the resulting solution is typically the pressure field in the fluid and displacement field in the elastic and piezoelectric structure.[8] For complicated two- and three-dimensional sound fields, simply locating the pressure node and antinodes can lead to inaccurate predictions where microparticles will migrate. Also, a useful figure of merit for evaluating design performance is the time averaged energy density of the fluid region, which requires estimates for the pressure and velocity fields in the fluid.[9] A generalized formulation for the energy density and the radiation force fields in two- and three-dimensional geometries is developed.

II. THEORETICAL FORMULATION

The solution method approaches the problem by constructing a finite-difference approximation of the *generalized* equation for the radiation force on a small particle ($ka \ll 1$), in a standing wave field,[2,10]

$$F = \tfrac{4}{3}\pi a^3\{B(\nabla\langle \mathrm{KE}_a\rangle) - (1-\gamma)(\nabla\langle \mathrm{PE}_a\rangle)\}. \tag{1}$$

The force, F, is a combination of the gradients of the time-averaged kinetic energy, $\langle \mathrm{KE}_a\rangle$, and time-averaged potential energy, $\langle \mathrm{PE}_a\rangle$, with, $B=3(\rho-\rho_0)/(2\rho+\rho_0)$ and $\lambda=\beta/\beta_0$. Here, the density the fluid and particle are ρ_0 and ρ_0, respectively, and the bulk compressibility of the fluid and particle are β_0 and β, respectively. If we expand the time-averaged energy terms as a functions of pressure, and realizing that, $\boldsymbol{\nu}(t)=1/\rho\int_{-\infty}^{t}\nabla p(\tau)d\tau$, then without any loss of generality, the time-averaged kinetic energy is

$$\langle \mathrm{KE}_a\rangle = \lim_{T\to\infty}\frac{1}{T}\int_0^T \frac{\rho}{2}\left\{\int_{-\infty}^{t}\frac{1}{\rho}(\nabla p(\tau))d\tau\right\}^2 dt, \tag{2}$$

and the time averaged potential energy is

$$\langle \mathrm{PE}_a\rangle = \lim_{T\to\infty}\frac{1}{T}\int_0^T \frac{1}{2\rho c^2}p^2(t)dt. \tag{3}$$

Application of Parseval's theorem in conjunction with second-order approximations for the spatial and temporal derivatives in Eq. (2) results in a discrete approximation for the time-averaged kinetic energy,[11,12]

$$\langle \mathrm{KE}_a\rangle_{i,j,k} \approx \frac{1}{2\omega\rho}\left[\left|\frac{\hat{P}_{i+1,j,k}-\hat{P}_{i-1,j,k}}{2\Delta x}\right|^2 + \left|\frac{\hat{P}_{i,j+1,k}-\hat{P}_{i,j-1,k}}{2\Delta y}\right|^2 + \left|\frac{\hat{P}_{i,j,k+1}-\hat{P}_{i,j,k-1}}{2\Delta z}\right|^2\right]. \tag{4}$$

Similarly, the discrete time-averaged potential energy is

$$\langle \mathrm{PE}_a\rangle_{i,j,k} \approx \frac{1}{2\rho c^2}|\hat{P}_{i,j,k}|^2. \tag{5}$$

[a]Electronic mail: fisher34@llnl.gov
[b]Electronic mail: miles7@llnl.gov

 0001-4966/2008/123(4)/1862/4/$23.00 © 2008 Acoustical Society of America

The spatial indices i,j and k correspond to x, y, and z directions and $\hat{P}_{i,j,k}$ is the complex pressure amplitude. For clarity the index for each frequency component corresponding to each ω as not been shown. Equations (4) and (5) are combined into Eq. (1) resulting in

$$F_{i,j,k} = \frac{4\pi a^3}{3}\left\{ B\left\{ \left(\frac{\langle \mathrm{KE}_a\rangle_{i+1,j,k} - \langle \mathrm{KE}_a\rangle_{i-1,j,k}}{2\Delta x} \right) + \left(\frac{\langle \mathrm{KE}_a\rangle_{i,j+1,k} - \langle \mathrm{KE}_a\rangle_{i,j-1,k}}{2\Delta y} \right) + \left(\frac{\langle \mathrm{KE}_a\rangle_{i,j,k+1} - \langle \mathrm{KE}_a\rangle_{i,j,k-1}}{2\Delta z} \right) \right\} + (1-\lambda)\left\{ \left(\frac{\langle \mathrm{PE}_a\rangle_{i+1,j,k} - \langle \mathrm{PE}_a\rangle_{i-1,j,k}}{2\Delta x} \right) + \left(\frac{\langle \mathrm{PE}_a\rangle_{i,j+1,k} - \langle \mathrm{PE}_a\rangle_{i,j-1,k}}{2\Delta y} \right) + \left(\frac{\langle \mathrm{PE}_a\rangle_{i,j,k+1} - \langle \mathrm{PE}_a\rangle_{i,j,k-1}}{2\Delta z} \right) \right\} \right\}. \quad (6)$$

Equation (6) relates the pressure field in the fluid to a vector representing the acoustic radiation force at the location (i,j,k). Thus given any pressure field $\hat{P}_{i,j,k}$, defined on a known computational grid, the corresponding radiation force field can be determined. Of particular use in determining the performance of a particular geometry is the resultant time-averaged and spatially averaged energy density

$$\langle E_D\rangle = \sum_i \sum_j \sum_k \{\langle \mathrm{KE}_a\rangle + \langle \mathrm{PE}_a\rangle\}_{i,j,k}. \quad (7)$$

Equation (7) is a figure of merit, for quickly analyzing the maximum amount of available energy that can be utilized by the acoustic force field on small particles.

III. MODELING AND EXPERIMENTAL SETUP

A two-dimensional numerical simulation was performed to generate the pressure field as a function of position and frequency, $\hat{P}_{i,j,k}(\omega)$ in the fluid channel. The simulation results were obtained using ATILA, a multiphysics finite element package.[8] The code can simulate coupled fluid, elastic, and piezoelectric effects in either one, two, or three dimensions. The required elastic input parameters are based on the bulk modulus, Poisson ratio, and density. The piezoelectric materials require the appropriate piezoelastic coefficients, defining a poling direction and electrical boundary conditions. Figure 1 depicts a two-dimensional model of a microfluidic acoustic separation device currently under investigation. The design is similar to a previously published device.[1] Here, a thin layer of thickness poled PZT is bonded to the lower surface of a silicon wafer. Fluid channels are etched into the upper surface of the silicon layer and a glass layer is bonded to the upper surface. The resulting encapsulated volume is where the acoustic force will interact on the flow. The computational mesh is shown for completeness. The resulting pressure field $P_{i,j}$ is calculated at a series of discrete frequencies between 0.5 and 4.5 MHz. A 1 V drive voltage

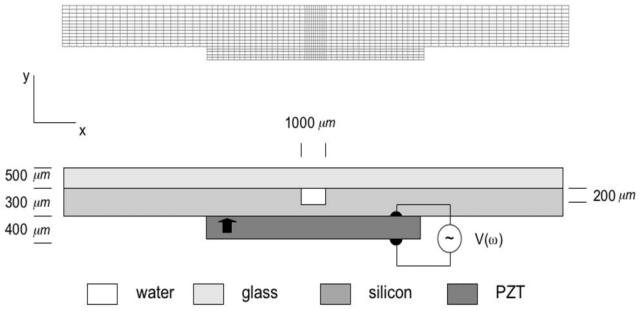

FIG. 1. Two-dimensional computational region for the ATILA finite element code. The planar structure is comprised of an upper glass layer, and a silicon wafer in the middle with a fluidic channel etched into the upper surface. The structure is acoustically driven into resonance by a thin thickness poled PZT layer, bonded to the bottom of the silicon wafer. The fluid flow is perpendicular into the modeled plane. Dynamic flow behavior of the fluid is not taken into account in this approximation.

was used in the finite element computation. The calculated pressure field is then input into Eqs. (4)–(7) to calculate the channel energy density and determine the corresponding acoustic radiation force field as functions of position and frequency. The sign on the force is determined in part by the material properties of the particles and the fluid. For this analysis we are assuming soft solid particles in a "stiff" liquid where $(\rho > \rho_0)$ and $(\beta < \beta_0)$ (e.g., latex spheres in water). Thus conventional wisdom suggests that the direction of the force vectors will tend to migrate particles toward pressure minimums.[7]

An experimental platform of the microfluidic system was fabricated similar to published designs.[1] Top and bottom views of the device are shown in Fig. 2. The device has the same in-plane dimensions and construction as described in Fig. 1, the working length of the channel is ~31 mm. The PZT chip is glued to the silicon layer and driven by a *single* sinusoidal voltage $V(\omega_\iota)$ where the frequency, ω_ι, is chosen from peak values of the calculated energy density. The amplitude of the experimental drive voltage was 5 $V_{\text{pk-pk}}$. Water with latex microspheres (5 μm in diameter and concentrations $\sim 10^5$ ppml) are injected into the microchannel at the inlet ports. A syringe pump is used to obtain a consistent

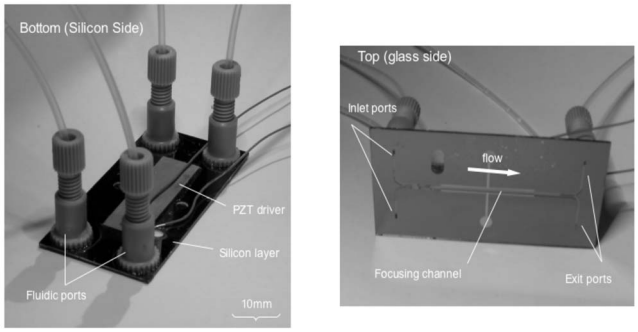

FIG. 2. The experimental micro fluidic chip (H-bridge) test package, owing to similar designs found in the literature. (Ref. 1). Here, the PZT is bonded to the silicon layer and plastic surface mounted fluidic ports are used to couple the fluid and beads from a syringe pump into the focusing channel. The channel splits at the ends resulting in two inlet and two exit ports. A wide variety of separation, mixing, and fractionation schemes can be realized with this design.

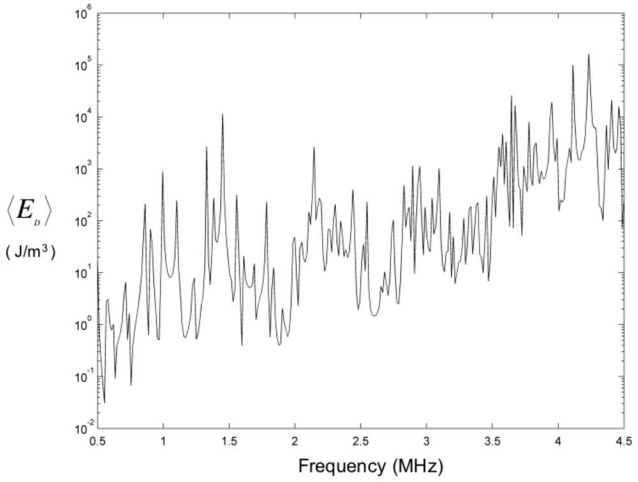

FIG. 3. Theoretical energy density in the water as a function of frequency for the two-dimensional channel described in Fig. 1. The amplitude of the drive voltage is 1 V. Several frequencies show energy densities in excess of 5×10^3 J/m^3. Large energy densities indicate potentially useful operating force fields for manipulation of particles. Conversely, useful force field distributions may have small energy densities ($<1\times10^3$ J/m^3), thus exhibiting weak performance and little utility.

volumetric flow rate of 0.03 ml/min through the device. As the mixture of latex spheres and water flows through the microchamber, the force field generated by the standing wave pattern in the fluid concentrates the particles into regions where the force vectors converge. Focused streams of particles continue through the device and flow out the exit ports.

IV. RESULTS

The time and spatially averaged energy density $\langle E_D\rangle$ for the two-dimensional fluid region is plotted as a function of drive frequency $f_i=2\pi\omega_i$, in Fig. 3. Several frequencies show energy densities in excess of 5×10^3 J/m^3. Large energy densities indicate potentially useful operating conditions for manipulation of particles. However, this is not always the case. The energy density may be quite large for a given frequency, but the corresponding force field in the microchannel is not focused. Conversely, there are regions where there is very little energy in the fluid (implying that all of the energy is in the elastic structure) and useful focusing fields, but the lack of available energy precludes the efficient control of particles.

Using Fig. 3 as a guide, two representative operating frequencies are chosen at 1.405 and 2.9398 MHz and presented in Fig. 4. The upper image is a microscope view of the channel through the glass substrate as the fluid and latex spheres flow from the inlet to the exit through the standing wave pattern in the channel. The dashed white lines correspond to the channel boundaries (the right wall of the channel is obscured by a misaligned electrode on the glass). The particles (seen here as white cloudy regions) are focused into zones parallel with the flow direction. The bright spherical areas, consistent in each image, are spurious reflections from the upper surface of the glass. The lower image is the two-dimensional numerical estimate of the pressure field, orthogonal to the flow direction. The acoustic radiation force (quiver plot) is superimposed onto the pressure field to show the relation between the focusing regions and the pressure field.

The dark regions in the numerical results represent regions of minimal pressure (nodes) in the sound field and the light regions are pressure maximums (antinodes). The orientation of the particles in the channel corresponds to half wavelength $n(\lambda/2)$ ($n=2$ and 4) distributions across the width of the channel. At 1.454 MHz, the pressure field and the corresponding force field [Eq. (6)] drive the latex spheres to the pressure *minimums* (nodes) of the channel, which is consistent with observations stated in the open literature.[1,3,4,7] When the channel is driven at 2.939 MHz, the nodal pattern of the pressure field and the force plots are the

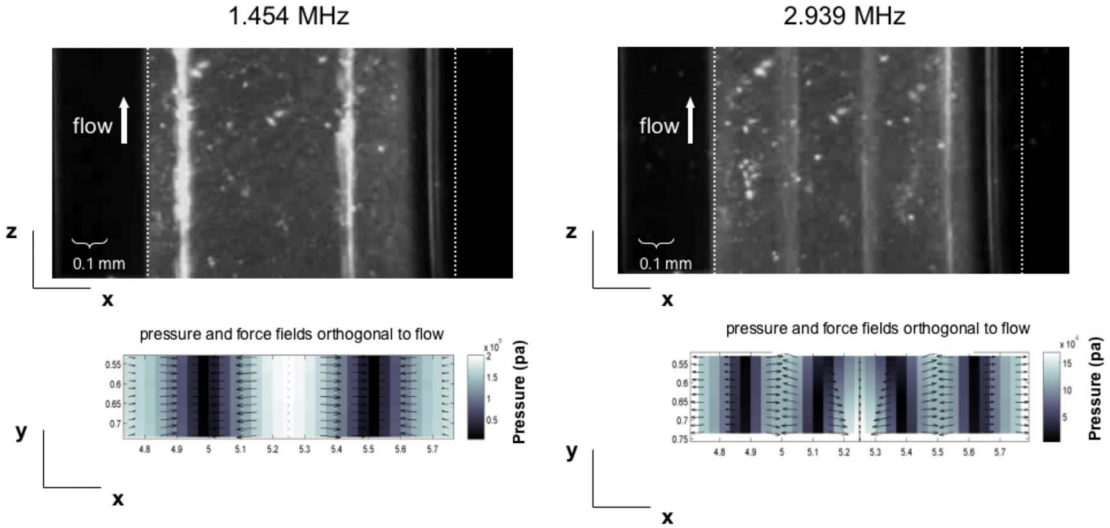

FIG. 4. (Color online) Two representative operating conditions of the microfluidic channel $f=1.454$ and 2.939 MHz. The upper images are a microscope view of the channel through the glass substrate as the fluid and latex spheres flow from the inlet to the exit through the standing wave pattern in the channel. The focused particles are the long white cloudy regions parallel to the flow. The dashed white lines indicate the actual channel walls. The lower images are the two-dimensional numerical estimate of the pressure field from ATILA and a vector plot corresponding to the direction of the acoustic force fields calculated from Eq. (6). Here the dark regions represent nodes in the sound field and the light regions are antinodes.

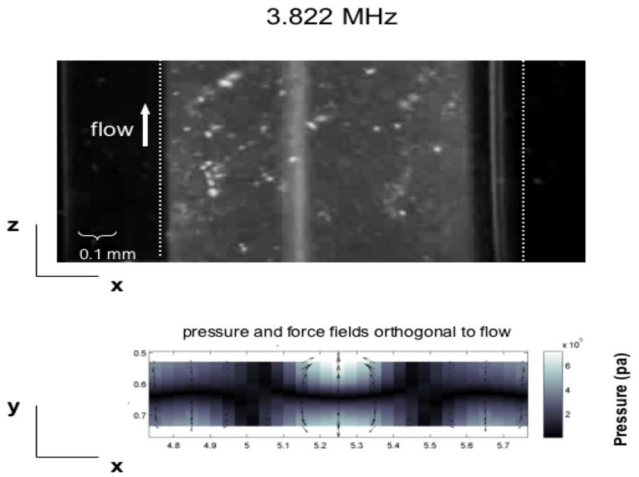

FIG. 5. (Color online) A single node in the channel at 3.822 MHz. The upper image is a microscope view of the channel through the glass substrate as the fluid and latex spheres (white cloudy region) flow along the channel under the influence of the acoustic force field. The lower image is the pressure and force vector calculations from ATILA and Eq. (6).

inverse of the conventional predictions. Here the force vectors are directing the latex spheres to three regions in the fluid channel which are pressure *maximums* (antinodes). Figure 5 shows another example where the net forcing effect on the particles is not obvious. Here, the channel is operating at 3.822 MHz and a single line of latex beads focused at the center of the channel. The pressure and force plot shows that once again the particles are being concentrated by the force field yet, contrary to convention, at that location is a strong pressure antinode. Clearly, the pressure field alone is not an accurate indicator for the functionality at a given frequency. The contribution of the velocity field, through the gradient of the kinetic energy, improves the prediction where the particles will concentrate.

Interestingly, the one-dimensional theory predicts a single half wavelength mode at approximately 0.75 MHz, which has been reported as ill suited for focusing due to the weak strength of the available radiation force.[1] Inspection of Fig. 3 reveals a sharp drop in the energy density below 1 MHz for this design, which supports this observation. The calculated half-wavelength solution based on the finite element approximation is at 0.861 MHz, with an available energy density of approximately 200 J/m^3, which is still far below typical useful energy densities.

V. CONCLUSIONS

A method to assess the performance and focusing capabilities of microfluidic particle separation devices has been presented. Simple analytical approximations are not sufficient to approximate the higher order modes, which may have useful operational functionality. Modeling and experiments of a typical device illustrate the complexity of the sound field and the corresponding force fields. Two-dimensional estimates for the pressure field and corresponding force field compare well with experiments. The approach can easily be expanded into three dimensions when characteristic lengths dictate. Future work will entail calibration and actual force estimates based on particle size and drive voltage.

ACKNOWLEDGMENTS

The author would like to thank his 8-year-old daughter, Rose Fisher, for the extended use of her usb-microscope to capture channel images and Klint Rose, Kevin Ness, Ray Mariella, and Kerry Bettencourt for technical assistance. This work was performed under the auspices of the U.S. Department of Energy, by Lawrence Livermore National Laboratory Security, LLC, under Contract No. DE-AC52-07NA27344.

[1] A. Nilsson, F. Petersson, H. Jonsson, and T. Laurell, "Acoustic control of suspended particles in micro fluidic chips," Lab Chip **4**, 131–135 (2004).
[2] L. P. Gor'kov, "On the forces acting on a small particle in an acoustical field in an ideal flow," Sov. Phys. Dokl. **6**, 773–775 (1962).
[3] T. Kozuka, T. Tuziuti, and H. Mitome, "One-dimensional transportation of particles using an ultrasonic standing wave," *Proceedings of the Sixth International IEEE Symposium on Micro Machine and Human Science*, Nagoya Municipal Industrial Research Institute, Japan, Oct. 4–6, 1995, pp. 179–189.
[4] K. Yasuda, S. S. Haupt, and S. Umemura, "Using acoustic radiation as a concentration method for erythrocytes," J. Acoust. Soc. Am. **102**, 642–645 (1997).
[5] C. J. Schram, "Manipulation of particles in an acoustic field," *Advances in Sonochemistry* (JAI, London, England, 1991), Vol. **2**, pp. 293–323.
[6] K. Yasuda and S. Umemura, "Particle separation using acoustic radiation force and electrostatic force," J. Acoust. Soc. Am. **99**, 1965–1970 (1996).
[7] K. Yasuda, S. Umemura, and K. Takedam, "Concentration and fractionation of small particles in liquid by ultrasound," Jpn. J. Appl. Phys., Part 1 **44**, 1965–1970 (1995).
[8] ATILA 6.0.2 Piezoelectric Analysis for Piezoelectric Structures, *Users Manual* (Institut Supérieur d'Electronique du Nord, Lille Cedex, France, 2003).
[9] J. Ghan, B. S. Cazzilato, and S. D. Snyder, "Expression for the estimation of time-averaged acoustic energy density using the two-microphone method," J. Acoust. Soc. Am. **113**, 2404–2407 (2003).
[10] W. L. Nyborg, "Radiation pressure on a small rigid sphere," J. Acoust. Soc. Am. **42**, 947–952 (1967).
[11] A. Pierce, *Acoustics, An Introduction to Its Physical Principles and Applications* (AIP Press, Woodbury, NY, 1989), pp. 78,79.
[12] L. Lapidus and G. F. Pinder, *Numerical Solution of Partial Differential Equations in Science and Engineering* (Wiley, New York, 1982).

Low-frequency sound transmission through a gas–liquid interface

Oleg A. Godin[a)]
CIRES, University of Colorado and NOAA/Earth System Research Laboratory, Boulder, Colorado 80305

(Received 20 September 2007; revised 3 January 2008; accepted 18 January 2008)

Typically, sound speed in gases is smaller and mass density is much smaller than in liquids, resulting in a very strong acoustic impedance contrast at a gas–liquid interface. Sound transmission through a boundary with a strong impedance contrast is normally very weak. This paper studies the power output of localized sound sources and acoustic power fluxes through a plane gas–liquid interface in a layered medium. It is shown that, for low-frequency sound, a phenomenon of anomalous transparency can occur where most of the acoustic power generated by a source in a liquid half-space can be radiated into a gas half-space. The main physical mechanism responsible for anomalous transparency is found to be an acoustic power transfer by inhomogeneous (evanescent) waves in the plane-wave decomposition of the acoustic field in the liquid. The effects of a liquid's stratification and of guided sound propagation in the liquid on the anomalous transparency of the gas–liquid interface are considered. Geophysical and biological implications of anomalous transparency of water–air interface to infrasound are indicated.
© *2008 Acoustical Society of America.* [DOI: 10.1121/1.2874631]

PACS number(s): 43.20.El, 43.20.Bi, 43.28.Dm, 43.30.Jx [RMW] Pages: 1866–1879

I. INTRODUCTION

The absolute value of the plane-wave reflection coefficient at a plane interface of two homogeneous media tends to unity and the interface becomes a perfect reflector, when the ratio of impedances of the two media tends to zero or infinity. In acoustics, the ratio of impedances is especially large at a gas–liquid interface as long as sound speeds in gases are usually several times smaller, while the mass density of gases is typically several orders of magnitude smaller than in liquids. For instance, in the geophysically important special case of air–water interface, under normal conditions the ratio of the sound speed in water to that in air $n \approx 4.5$, while the ratio of the mass density of air to that of water $m \approx 0.0013$. When considering the acoustic field due to a source in a liquid or a gas, the gas–liquid interface is usually replaced by a perfectly reflecting (respectively, pressure release or rigid) boundary (Ref. 1, p. 134; Ref. 2, p. 90).

Transmission of sound through an interface into a homogeneous half-space can be characterized by the ratio of acoustic power radiated by the transmitted sound wave to the source output, i.e., the total acoustic power emitted by the source. The ratio is referred to as acoustic transparency, T, of the interface; $0 \leqslant T \leqslant 1$. For a plane wave incident on the interface from the liquid, T decreases steadily from $T = 4mn(m+n)^{-2}$ at normal incidence to $T=0$ at a zero grazing angle (Ref. 3, p. 24). Calculations of acoustic power transmission through gas–liquid interfaces, which rely on ray-theoretical concepts, predict transmission of a small fraction of the incident power, with the transparency of the interface being of the order of the impedance ratio (Ref. 1, p. 143; Ref. 4; Ref. 5, p. 134). For a source with a directivity pattern, which is symmetric with respect to the horizontal plane but is otherwise arbitrary, the ray theory predicts that T does not exceed $2m/n$, or 0.06% for the air–water interface.

Recently, Godin[6] established theoretically that acoustic power transmission through a plane interface of gas and liquid homogeneous half-spaces increases dramatically, when a point sound source is located in the liquid at a distance from the interface that is small compared to the acoustic wavelength. Rather counterintuitively, most of the acoustic power, which is emitted by a shallow, low-frequency source, can be radiated into the gas.[6] This phenomenon of anomalous transparency has been shown to be robust with respect to the roughness of the gas–liquid interface, provided the roughness height is small compared to the acoustic wavelength in the gas and the source separation from the interface.[7] A portion of the results reported in Ref. 6 has been rederived in a recent paper.[8]

Earlier work on sound transmission through the gas–liquid interface is briefly reviewed in Chap. 1 of Ref. 9 and in Ref. 10. Theoretical[10–25] and experimental[18,22–24,26–29] studies focused primarily on sound transmission under water from a source in air due to the existence of powerful airborne noise sources (such as helicopters,[28] propeller-driven aircraft,[10,23] and supersonic transport, including the sonic booms it generates[22,24,25,29]). The studies were motivated, in part, by the use of airplane-generated sound for acoustic remote sensing of the ocean[10,23] and concerns about possible effects of the airborne sources on marine life.[22,28] Deep insights into sound transmission of a spherical wave through an interface with a strong density contrast were obtained by Brekhovskikh.[30,31] He considered transmitted waves at large (compared to wavelength) lateral separations between a point source and a receiver and showed, in particular, that when a point source is located in a liquid close to a gas–liquid interface, the geometrical (ray) component of the field in the gas

[a)]Electronic mail: oleg.godin@noaa.gov

 0001-4966/2008/123(4)/1866/14/$23.00 © 2008 Acoustical Society of America

is small compared to diffraction corrections associated with evanescent plane waves emitted by the source (Ref. 30; Ref. 31, p. 302). The evanescent waves also play a key role in the occurrence of an anomalous transparency, but the power flux through the interface, which is responsible for the phenomenon, takes place at small distances of the order of acoustic wavelength or less from the source.[6]

With the gas–liquid interface being acoustically transparent at low frequencies, rather than an almost perfect mirror as previously believed, the feasibility of acoustic communication through such an interface as well as possible manifestations of natural underwater sound sources in the acoustic field in the atmosphere need to be reevaluated. However, the anomalous transparency has been demonstrated[6] only for a highly idealized model of two homogeneous half-spaces in contact. In both laboratory and geophysical settings the extent of the liquid in the direction normal to the interface is limited by a reflective boundary (bottom). In this paper, we investigate the influence of liquid stratification and a reflective bottom on sound transmission through a gas–liquid interface. To elucidate conditions of and physical mechanisms responsible for the anomalous transparency, sound transmission from a liquid into a gas is compared with transmission in the opposite direction for various source types.

The remainder of this paper is organized as follows. The role of inhomogeneous plane waves in sound radiation by a point source in a homogeneous layer and in acoustic power fluxes through the layer's boundaries is considered in Sec. II. The particular case of the interface of homogeneous liquid and gas half-spaces is analyzed in Sec. III. The effects of guided propagation are studied, and the results of Sec. II are extended to an arbitrary stratified liquid and a liquid with a solid bottom in Sec. IV. Section V summarizes our findings.

II. ACOUSTIC POWER TRANSMISSION AND SOURCE OUTPUT

Here we introduce Cartesian coordinate system $\mathbf{R}=(x,y,z)$. The parameters of the medium are functions of the coordinate z, which will be called the vertical coordinate and is assumed to be increasing downwards. All interfaces are parallel to the horizontal plane xy. Half-space $z<0$ is occupied by a light fluid (gas) with sound speed c_1 and mass density ρ_1 (Fig. 1). Half-space $z>H$ can be either a fluid or an isotropic solid. Sound speed and mass density in the homogeneous dense fluid (liquid) layer $0<z<H$ are $c_2=nc_1$, $\rho_2=\rho_1/m$, respectively. We are interested in a case in which the refraction index $n>1$ and the gas–liquid mass density ratio $m\ll 1$, but first we will derive results applicable in a general layered (i.e., one-dimensionally inhomogeneous) medium.

Let a point source be situated at a point $\mathbf{R}_0=(0,0,z_0)$, $0<z_0<H$ in the homogeneous layer. Acoustic pressure p_1 due to the source in the absence of interfaces $z=0$ and $z=H$ and actual acoustic pressure p_2 within the layer are given by integrals over plane waves:

$$p_j(\mathbf{R})=(2\pi)^{-1}i\int d^2\mathbf{q}e^{i\mathbf{q}\cdot\mathbf{R}}\nu_2^{-1}Q_j(\mathbf{q}), \tag{1}$$

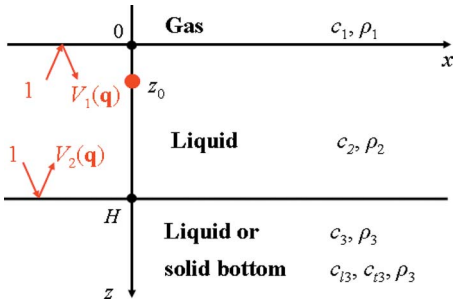

FIG. 1. (Color online) Geometry of the problem. Sound source is located at a point $(0,0,z_0)$ in a liquid layer between a gas half-space $z<0$ and a liquid or solid half-space $z>H$. Plane-wave reflection coefficients at the boundaries $z=0$ and $z=H$ of the layer are V_1 and V_2.

$$Q_1=S_g(\mathbf{q})e^{i\nu_2|z-z_0|},\quad g=0.5[3-(z-z_0)/|z-z_0|], \tag{2}$$

$$\begin{aligned}Q_2=&[1-V_1(\mathbf{q})V_2(\mathbf{q})e^{2i\nu_2H}]^{-1}\\&\times[S_g(\mathbf{q})e^{i\nu_2|z-z_0|}+S_1(\mathbf{q})V_2(\mathbf{q})e^{i\nu_2(2H-z-z_0)}\\&+S_2(\mathbf{q})V_1(\mathbf{q})e^{i\nu_2(z+z_0)}+S_{3-g}(\mathbf{q})V_1(\mathbf{q})V_2(\mathbf{q})\\&\times e^{i\nu_2(2H-|z-z_0|)}],\end{aligned} \tag{3}$$

where components of the two-dimensional vector $\mathbf{q}=(q_1,q_2,0)$ take all real values, $q\equiv|\mathbf{q}|$; $\nu_s=(k_s^2-q^2)^{1/2}$, $\mathrm{Im}\,\nu_s\geqslant 0$; $k_s=\omega/c_s$, $s=1,2$; ω is sound frequency, and $V_1(\mathbf{q})$ and $V_2(\mathbf{q})$ are reflection coefficients of incident plane waves with the wave vectors $(q_1,q_2,-\nu_2)$ and (q_1,q_2,ν_2) from half-spaces $z<0$ and $z>H$, respectively. Plane-wave spectra $S_1(\mathbf{q})$ and $S_2(\mathbf{q})$ define the point sound source and describe the directivity of sound radiated by the source into the lower and upper hemispheres. Time dependence $\exp(-i\omega t)$ of cw is assumed and suppressed. Being defined in Eq. (2), the subscript g takes values 1 or 2 in Eqs. (2) and (3) depending on the observation point location relative to the sound source. The integral representation (1) includes homogeneous plane waves $(q\leqslant k_2, \mathrm{Im}\,\nu_2=0)$ as well as inhomogeneous (evanescent) plane waves $(q>k_2, \mathrm{Re}\,\nu_2=0)$, the amplitude of which varies exponentially with z.

As will become clear later, source directivity, including relative weight of homogeneous and inhomogeneous plane waves in the spectra $S_1(\mathbf{q})$ and $S_2(\mathbf{q})$, plays a major role in sound transmission through a gas–liquid interface. For a monopole sound source of unit magnitude with $p_1=p_0$, $p_0=R_0^{-1}\exp(ik_2R_0)$, $R_0=[x^2+y^2+(z-z_0)^2]^{1/2}$, we have $S_1=S_2=1$ (Ref. 9, p. 3). When $S_1=-S_2=i\nu_2/k_2$, we have a vertically oriented dipole source with $p_1=k_2^{-1}\partial p_0/\partial z$. The spectra $S_1=S_2=iq_1/k_2$ correspond to a horizontal dipole source with $p_1=k_2^{-1}\partial p_0/\partial x$. If the half-spaces $z<0$ are homogeneous, V_1 is the Fresnel reflection coefficient (Ref. 3, p. 21):

$$V_1=(m\nu_2-\nu_1)/(m\nu_2+\nu_1). \tag{4}$$

The integral representations (1) and (3) for the acoustic field p_2 in a layer with reflective boundaries is obtained from the integral representations (1) and (2) of p_1 by summing contributions of plane waves with a different number of reflections from the boundaries, as in Ref. 3 (p. 29), and of plane waves originally emitted into the upper and lower

hemispheres. For a monopole (i.e., omnidirectional) source, Eqs. (1) and (3) reduce to a previously known result (Ref. 9, p. 393).

We will characterize sound transmission through the interface $z=0$ by time-averaged acoustic power flux J_{21} from the layer into the half-space $z<0$ and by acoustic transparency, defined as the ratio of J_{21} to the source output J_t, i.e., the total acoustic power emitted by the source. In a monochromatic sound field, acoustic power flux density averaged over wave period is (Ref. 9, p. 387)

$$\mathbf{j} = (2\omega\rho)^{-1}\,\mathrm{Im}(p^*\nabla p). \tag{5}$$

Here, the asterisk denotes complex conjugation. Integrating the vertical component of $\mathbf{j}$ over the plane $z=+0$, from Eqs. (1) and (3) we obtain

$$J_{21} = \frac{J_0}{4\pi k_2}\int d^2\mathbf{q}\left|\frac{S_2(\mathbf{q}) + S_1(\mathbf{q})V_2(\mathbf{q})e^{2i\nu_2(H-z_0)}}{1 - V_1(\mathbf{q})V_2(\mathbf{q})e^{2i\nu_2 H}}\right|^2 \times \mathrm{Re}\left(\frac{1-|V_1|^2+2i\,\mathrm{Im}\,V_1}{\nu_2}\right)e^{-2z_0\,\mathrm{Im}\,\nu_2}, \tag{6}$$

where $J_0=2\pi/\rho_2 c_2$ is the acoustic power radiated by the monopole source of unit magnitude in the absence of the interfaces $z=0$ and $z=H$. Similarly, the acoustic power flux into half-space $z>H$ is

$$J_{23} = \frac{J_0}{4\pi k_2}\int d^2\mathbf{q}\left|\frac{S_1(\mathbf{q}) + S_2(\mathbf{q})V_1(\mathbf{q})e^{2i\nu_2 z_0}}{1 - V_1(\mathbf{q})V_2(\mathbf{q})e^{2i\nu_2 H}}\right|^2 \times \mathrm{Re}\left(\frac{1-|V_2|^2+2i\,\mathrm{Im}\,V_2}{\nu_2}\right)e^{-2(H-z_0)\mathrm{Im}\,\nu_2}. \tag{7}$$

Acoustic pressure decreases as r^{-1}, where $r=(x^2+y^2)^{1/2}$, at $r\to\infty$ (Ref. 9, p. 151), there is no power flux to infinity within the layer $0<z<H$, and

$$J_t = J_{21} + J_{23}, \tag{8}$$

unless propagating normal modes or surface waves are supported by the layered medium. In the latter case, the power flux carried out to infinity within the layer $0<z<H$ by guided waves (normal modes and surface waves) should be added to $J_{21}+J_{23}$ to obtain J_t. We will assume that, because of energy leakage to $|z|\to\infty$ or sound absorption at $z>H$, the amplitudes of the guided waves, if any, decrease exponentially with r. Then, Eq. (8) is valid regardless of the existence of guided waves. Moreover, integrands in Eqs. (1) for p_2, (6) and (7) considered as a function of q have no poles at real q. Note that, according to Eq. (8), the output of a given sound source depends on the reflection coefficients $V_{1,2}$ because reflected waves affect acoustic pressure at the source location, against which the source performs its work. In other words, the radiation impedances of homogeneous and inhomogeneous environments differ (see Ref. 9, p. 396).

Equations (6)–(8) show that power fluxes are additive in plane waves with different values of the horizontal wave vector $\mathbf{q}$, but not necessarily for plane waves with the same $\mathbf{q}$ and opposite vertical components of the wave vector. In the case of a homogeneous medium $V_1=V_2=0$, and from Eqs. (6) and (7), one obtains

$$J_{21} = \frac{J_0}{4\pi k_2}\int_{q<k_2} d^2\mathbf{q}|S_2(\mathbf{q})|^2/\nu_2,$$
$$J_{23} = \frac{J_0}{4\pi k_2}\int_{q<k_2} d^2\mathbf{q}|S_1(\mathbf{q})|^2/\nu_2. \tag{9}$$

Hence, only homogeneous plane waves contribute to time-averaged power fluxes; evanescent waves do not contribute to the source output. This is not necessarily the case in an inhomogeneous medium. Although the vertical component of the power flux is zero in a monochromatic inhomogeneous wave with the wave vector $(q_1,q_2,\pm i|\nu_2|)$, superposition of such inhomogeneous plane waves with opposite signs of the vertical component of the wave vector results in a nonzero power flux in the vertical direction, provided $\mathrm{Im}\,V_{1,2}\neq 0$, i.e., there is a phase shift between an incident and reflected evanescent wave.

III. TWO HOMOGENEOUS FLUIDS WITH A STRONG DENSITY CONTRAST

A. Sound transmission from liquid to gas

Consider sound transmission through a plane interface of two homogeneous fluids with sharply distinct mass densities: $m\ll 1$, and with sound speed being greater in the denser fluid: $n>1$. The source output and acoustic power fluxes in this problem are obtained from general equations of Sec. II by letting $V_2=0$ and using Fresnel Eq. (4) for the reflection coefficient V_1. Equations (6) and (7) give

$$J_{21} = J_{21}^{(h)} + J_{21}^{(e)},$$
$$J_{23} = \frac{J_0}{4\pi k_2}\int_{q<k_2}\frac{d^2\mathbf{q}}{\nu_2}\left|S_1(\mathbf{q})e^{-2i\nu_2 z_0} - S_2(\mathbf{q})\left(1-\frac{2m\nu_2}{m\nu_2+\nu_1}\right)\right|^2, \tag{10}$$

$$J_{21}^{(h)} = \frac{mJ_0}{\pi k_2}\int_{q<k_2} d^2\mathbf{q}\frac{\nu_1|S_2(\mathbf{q})|^2}{(m\nu_2+\nu_1)^2},$$
$$J_{21}^{(e)} = \frac{mJ_0}{\pi k_2}\int_{k_2<q<k_1} d^2\mathbf{q}\frac{\nu_1|S_2(\mathbf{q})|^2}{m^2|\nu_2|^2+\nu_1^2}e^{-2z_0|\nu_2|}. \tag{11}$$

The integrals in Eqs. (10) and (11) are taken over finite domains and are absolutely convergent. Their numerical evaluation presents no difficulty. Theoretical analysis of Eqs. (10) and (11) is simplified by the fact that all integrands are nonnegative. Only homogeneous plane waves contribute to the power flux J_{23}, which is radiated to infinity within the dense (liquid) half-space $z>0$. J_{23} is affected by interference of direct and reflected waves, which enters through the factor $\exp(-2i\nu_2 z_0)$ in the integrand in Eq. (10); J_{23} is close to its value in the limit $m\to 0$, where the interface $z=0$ becomes a pressure-release boundary with the reflection coefficient $V_1=-1$. Note that, because of the destructive interference of direct and reflected waves, J_{23} becomes very small compared to its value in a homogeneous medium for sources with a

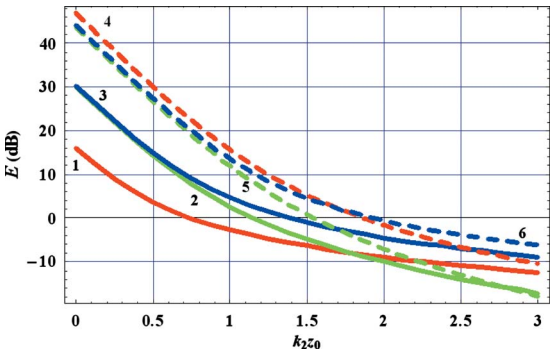

FIG. 2. (Color online) Relative contribution of inhomogeneous waves into sound transmission through a liquid–gas interface. Ratio E of acoustic power fluxes into a uniform gas half-space from a uniform liquid half-space due to inhomogeneous (evanescent) and homogeneous incident plane waves is shown as a function of nondimensional source depth k_2z_0 for various source types: (1) monopole, (2) vertical dipole, (3) horizontal dipole, (4) vertical–horizontal quadrupole, (5) vertical–vertical quadrupole, and (6) horizontal–horizontal quadrupole. Mass density ratio $m=0.0013$ and refraction index $n=4.5$.

directivity pattern symmetric with respect to the horizontal plane $[S_1(\mathbf{q})=S_2(\mathbf{q})]$, when $z_0\to+0$; $J_{23}=O(m^2)$ in this limit. In the opposite case, when $z_0\to\infty$, $\exp(-2i\nu_2z_0)$ becomes a rapidly oscillating factor, and one can replace $|S_1e^{-2i\nu_2z_0}-S_2[1-2m\nu_2/(m\nu_2+\nu_1)]|^2$ by $|S_1|^2+|S_2|^2[1-2m\nu_2/(m\nu_2+\nu_1)]^2$ in the integrand in Eq. (10). It follows then from Eqs. (9)–(11) that the source output at large z_0 reduces to the output of the same source in a homogeneous fluid.

Acoustic power flux J_{21} into the rarified (gas) half-space $z<0$ contains contributions due to homogeneous, $J_{21}^{(h)}$, and inhomogeneous, $J_{21}^{(e)}$, waves. Both contributions $J_{21}^{(h)}, J_{21}^{(e)}=O(m)$ and are small compared to J_0, when $m\ll1$. In the high-frequency limit $\omega\to\infty$, one obtains $J_{21}=J_{21}^{(h)}$, when $z_0\neq0$. The same result for J_{21} can be obtained by solving the problem in the geometrical acoustics (ray) approximation (Ref. 9, p. 18). In this approximation, J_{21} is independent of source position and decreases with n. According to Snell's law (Ref. 3, p. 20), the interval $k_2<q<k_1$ of wave numbers in Eq. (11) corresponds to incident plane waves, which are evanescent in the liquid half-space $z>0$ and become homogeneous (propagating) plane waves in the gas half-space $z<0$ upon refraction. Incident homogeneous plane waves upon refraction carry acoustic power in directions making angles $0\leqslant\theta_1\leqslant\delta$ with the normal to the interface, where $\delta=\arcsin n^{-1}$, while incident evanescent waves are responsible for energy flux in the directions $\delta<\theta_1\leqslant\pi/2$. Ratio $E=J_{21}^{(e)}/J_{21}^{(h)}$ of the contributions of the evanescent waves and homogeneous plane waves depends on source directivity, nondimensional distance k_2z_0 from the source to the interface, and the refraction index n. It is insensitive to the density ratio m as long as $m\ll1$. The contribution $J_{21}^{(e)}$ of the evanescent waves decreases monotonically with k_2z_0; $J_{21}^{(e)}\propto1/k_2z_0$ at $k_2z_0\gg1$.

When n^2 is large, the domain of integration in Eq. (11) is much larger for $J_{21}^{(e)}$ than for $J_{21}^{(h)}$, and, if the dimensionless source distance from the interface $k_2z_0<1$, the inhomogeneous plane waves provide a dominant contribution to the energy flux into the rarified (gas) half-space (Fig. 2). For point multipole sources, the ratio $E(z_0)$ of power fluxes through the interface due to inhomogeneous and homogeneous waves increases with the order of the multipole because plane-wave spectra of multipoles are obtained from the spectrum of the monopole by multiplying by integer powers of respective wave-vector components, and the relative weight of inhomogeneous waves compared to homogeneous ones increases with the multipole order. In particular, for monopole and dipole sound sources we find from Eq. (11) that $E=2n^2[1+O(m+n^{-2})]$ and $E=(8n^4/3)[1+O(m+n^{-2})]$ in the limit $z_0\to+0$.[32] Consider vertical–vertical (vv), horizontal–horizontal (hh), and vertical–horizontal (vh) quadrupole point sound sources, which generate acoustic pressure fields $p=k_2^{-2}\partial^2p_0/\partial z^2$, $p=k_2^{-2}\partial^2p_0/\partial x^2$, and $p=k_2^{-2}\partial^2p_0/\partial x\partial z$, respectively, in an unbounded liquid. For vv and hh quadrupoles $E=(16n^6/5)[1+O(m+n^{-2})]$, while for the vh quadrupole $E=(32n^6/5)[1+O(m+n^{-2})]$, according to Eq. (11). In the important special case of air–water interface, where $n=4.5, m=1.3\times10^{-3}$ under normal conditions, the contributions of inhomogeneous waves into the acoustic power flux into air exceed those of homogeneous waves by more than 16, 30, and 47 dB for sufficiently shallow monopole, dipole, and vh quadrupole sources in water (Fig. 2).

The acoustic power flux into the gas half-space, $[1+E(z_0)]J_{21}^{(h)}$, approaches its ray-theoretical value at $k_2z_0\gg1$ and steadily increases with decreasing sound frequency or the distance z_0. When $n^2\gg1$ and $m\ll1$, energy flux in inhomogeneous waves results in a dramatic increase in sound transmission through the interface, when the nondimensional source distance from the interface, k_2z_0, decreases and becomes less than unity. This phenomenon is referred to as anomalous transparency.[6]

B. Sound transmission from gas to liquid

To better understand the anomalous transparency, it is instructive to examine the variation of the acoustic field, when a sound source approaches and then crosses the interface. To be specific, consider a monochromatic source of volume velocity (also known as volume-infusion source). It can be visualized, for instance, as a pulsating sphere. In quiescent fluids the point source of volume velocity is a monopole, with the pressure field in a homogeneous fluid proportional to the product of the amplitude of the volume velocity oscillations and the mass density (Ref. 9, p. 136). We further assume that the magnitude and frequency of the monochromatic volume velocity created by the source are independent of its position. (For a pulsating sphere, it means that the mean radius of the sphere as well as the magnitude and frequency of the radius oscillations are kept constant.) A source, which generates an incident wave with acoustic pressure $p_0=R_0^{-1}\exp(ik_2R_0)$, when located in the liquid half-space (i.e., at $z_0>0$), will generate an incident wave with pressure $mR_0^{-1}\exp(ik_1R_0)$, when located in the gas half-space (i.e., at $z_0<0$). Total acoustic power radiated by the source located in an unbounded gas is mnJ_0.

When the source is located on the gas side of the gas–

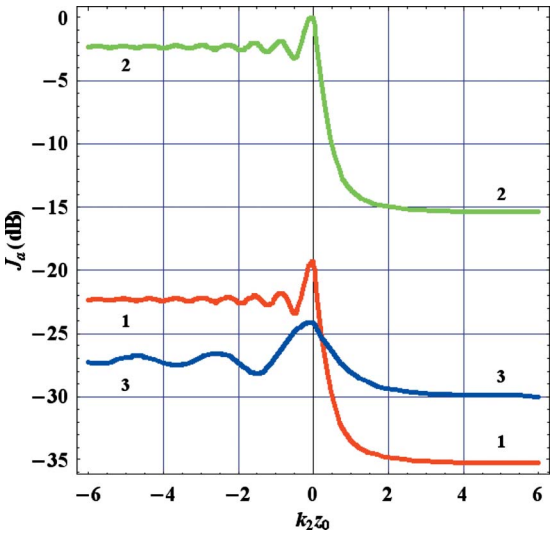

FIG. 3. (Color online) Radiation of sound into a gas by a monochromatic source of volume velocity located near a gas–liquid interface. Acoustic power radiated to infinity within the gas half-space is shown as a function of nondimensional source separation k_2z_0 from the interface for various media parameters: (1) $n=4.5$, $m=1.3\times10^{-3}$, (2) $n=4.5$, $m=0.13$, and (3) $n=1.5$, $m=1.3\times10^{-3}$. The source is located either in gas ($z_0<0$) or in liquid ($z_0>0$). Acoustic power is normalized by the power output J_0 of the source in an infinite liquid.

liquid interface, similar to a derivation in Sec. II, we find power fluxes J_{12} into the liquid and J_{11}, which is radiated to infinity within the gas half-space:

$$J_{11}=\frac{mJ_0}{2k_2}\int_0^{k_1}\left|e^{2i\nu_1 z_0}+\frac{\nu_1-m\nu_2}{\nu_1+m\nu_2}\right|^2\frac{qdq}{\nu_1},$$

$$J_{12}=\frac{2m^2J_0}{k_2}\int_0^{k_2}\frac{\nu_2 qdq}{(\nu_1+m\nu_2)^2}. \tag{12}$$

Integration in Eq. (12) for J_{11} is over those q values, which correspond to homogeneous plane waves in the gas. Integration for J_{12} is over a smaller range of q values, which correspond to homogeneous plane waves in the liquid. With a sound source located in a medium with lower sound speed, unlike the case $z_0>0$ considered earlier, inhomogeneous waves do not contribute to the time-averaged power fluxes. The power flux into the liquid $J_{12}=2m^2J_0[1-(n^2-1)^{1/2}\arctan(n^2-1)^{-1/2}]=O(m^2/n^2)$ and is independent of the source position. The power flux $J_{11}=O(mn)$, is much larger than J_{12}, oscillates with z_0 variation due to the interference of incident and reflected waves, and is close to its value $J_{11}=mnJ_0[1+(2k_1z_0)^{-1}\sin 2k_1z_0]$ in the limiting case of a rigid boundary at $z=0$. The source output $J_{11}+J_{12}=J_{11}[1+O(m/n)]\approx J_{11}$.

Comparison of Eqs. (10) and (11) (with $S_1=S_2=1$) to Eq. (12) shows that $J_{21}(z_0=+0)=J_{11}(z_0=-0)$, $J_{23}(z_0=+0)=J_{12}(z_0=-0)$ (Fig. 3). The continuity of the power fluxes, which are radiated to infinity within the liquid and gas half-spaces, when the monopole source crosses the gas–liquid interface, is a manifestation of a more general property of continuity of the acoustic field as a function of the position of a source of volume velocity, which is discussed in Sec. IV.

Note that, for the monopole source in liquid far from the interface, acoustic power flux $J_{21}\approx J_{21}^{(h)}=2mJ_0/(1+\sqrt{n^2-1})\ll J_{11}(z_0=-0)$. Thus, the strong increase of J_{21}, when $k_2z_0>0$ decreases and $n^2\gg1$, can be understood as a consequence of the continuity with respect to z_0 of the energy flux radiated to infinity within the gas half-space. Radiation into gas from a very shallow monopole source in liquid is the same as from the source on the interface, which is not attenuated (and in fact is enhanced) by the interface. According to Eq. (11), the relative increase in the power flux into the gas half-space, when k_2z_0 goes from positive infinity to zero, is, unlike the magnitude of the power flux, insensitive to the mass density ratio, as long as $m\ll1$, and is determined by the refraction index n (Fig. 3).

C. Acoustic transparency of the interface

Transparency of the interface $T(z_0)=J_{21}/(J_{21}+J_{23})$, when $k_2z_0>0$, and $T(z_0)=J_{12}/(J_{11}+J_{12})$, when $k_2z_0<0$. By definition, $0\leqslant T\leqslant1$ and is generally discontinuous at $z_0=0$. When a monopole source is located in the gas, transparency changes with z_0 only because of J_{11} variations, is small compared to unity, and admits an estimate $T=O(m/n^3)$. When a monopole source is located in liquid and $k_2z_0\gg1$, $T=O(m/n)$ and, when $n^2\gg1$, significantly exceeds transparency of the interface for sound incident from gas [Fig. 4(a)]. The transparency further increases when the source approaches the interface from the liquid side, and, according to Eq. (10), differs from unity by a small quantity $O(m/n^3)$ in the limit $k_2z_0\to+0$. At $0<k_2z_0\ll1$, the transparency of the gas–liquid interface exceeds that of an imaginary interface, where there is no change in medium parameters ($m=n=1$) and therefore $T=\frac{1}{2}$. The dramatic increase in transparency at small, positive k_2z_0 is due to an increasing contribution of inhomogeneous plane waves into J_{21}, discussed earlier, and a simultaneous decrease in J_{23}. When the source approaches the interface, incident and reflected waves interfere destructively, and acoustic pressure in the liquid becomes small away from the interface: $p_2=O(m/n)$ according to Eqs. (1)–(4). The acoustic power flux radiated to infinity within the liquid $J_{23}(z_0\to+0)=O(m^2/n^2)$, see Eq. (10) where $S_1=S_2$. For the monopole source approaching the interface from the liquid side, the increase in the power flux into the gas is given by a factor $O(n^2)$, while the decrease in the source output is given by a factor $O(mn)$ and typically accounts for the larger part of the transparency increase.

Dependence of the interface transparency on source position is qualitatively similar for other source types, as illustrated in Figs. 4(b) and 4(c) for horizontal and vertical dipoles. The dipole sources are understood as point sources of external force (Ref. 9, p. 136). The amplitude and frequency of the oscillating external force applied to the medium are supposed to be independent of the source position. The sources of horizontal and vertical external forces, which generate incident waves $p=k_2^{-1}(\partial/\partial x)R_0^{-1}\exp(ik_2R_0)$ and $p=k_2^{-1}(\partial/\partial z)R_0^{-1}\exp(ik_2R_0)$, when located in liquid, will generate incident waves $p=k_2^{-1}(\partial/\partial x)R_0^{-1}\exp(ik_1R_0)$ and $p=k_2^{-1}(\partial/\partial z)R_0^{-1}\exp(ik_1R_0)$, respectively, when located in gas (Ref. 9, p. 136). The source output of the dipole sources is

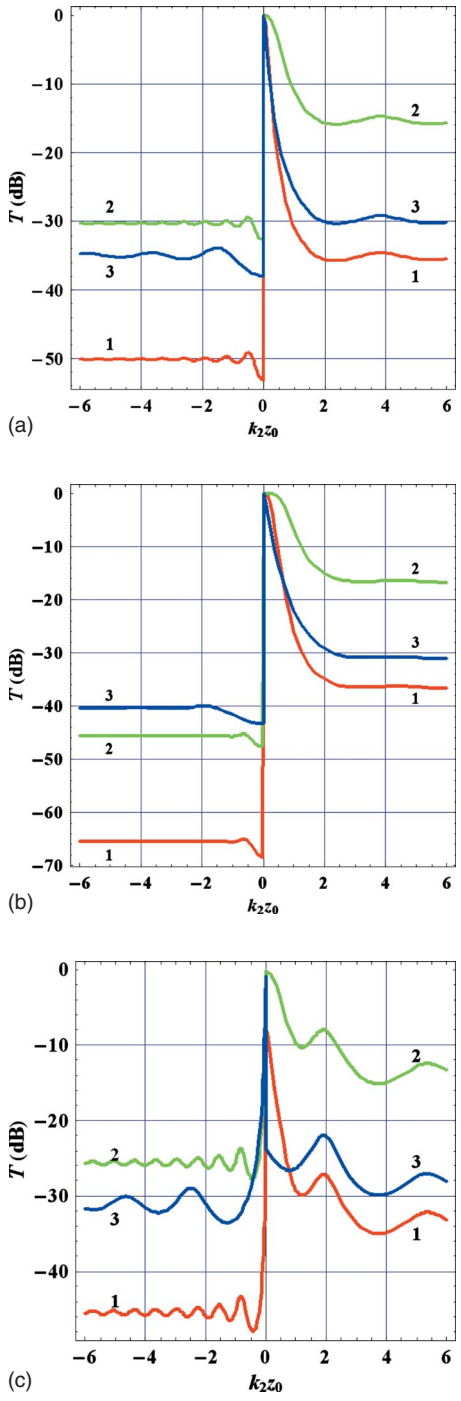

FIG. 4. (Color online) Acoustic transparency of a liquid–gas interface for monochromatic sound sources of volume velocity (a) and horizontal (b) and vertical (c) external force. The source is located either in gas ($z_0<0$) or in liquid ($z_0>0$). Transparency is shown as a function of nondimensional source separation k_2z_0 from the interface for various media parameters: (1) $n=4.5$, $m=1.3\times10^{-3}$, (2) $n=4.5$, $m=0.13$, and (3) $n=1.5$, $m=1.3\times10^{-3}$.

$J_0/3$, when located in an unbounded liquid, and $J_0/3m$, when located in an unbounded gas. For the source of the vertical external force, acoustic power fluxes to infinity within the liquid and gas half-spaces prove continuous with respect to the source position. Acoustic field and power fluxes due to the point source of the horizontal external force experience a jump when the source crosses the interface.

For the horizontal dipole, as for the monopole and any source with horizontally symmetric plane-wave spectra ($S_1=S_2$), an increase in transparency at decreasing $k_2z_0>0$ is due to a combination of an increase in J_{21} (because of the power flux in inhomogeneous plane waves) and decrease in J_t (because of the destructive interference of incident and reflected waves). When $k_2z_0\to+0$, transparency closely approaches unity: $1-T=O(m/n^5)$. For the vertical dipole (and any source with antisymmetric plane-wave spectra, where $S_1=-S_2$), incident and reflected waves interfere constructively, when $0<k_2z_0\ll1$. Because of variation in the power flux in inhomogeneous waves, transparency steadily increases from a value $O(m/n)$ at $k_2z_0\gg1$ to a value $O(mn^3)$ at $k_2z_0\to+0$, but remains small compared to unity when $m\ll n^{-3}\ll1$. As for the monopole source, interface transparency is very asymmetric, when $n^2\gg1$ (Fig. 4). The interface is significantly more transparent for waves incident from the liquid than for waves incident from the gas. This is because inhomogeneous plane waves contribute only to acoustic power transmission in the direction of decreasing sound speed.

The asymmetry of sound transmission through the gas–liquid interface, when the acoustic field is generated by a spatially localized source, is in contrast to the well-known reciprocity of plane-wave transmission coefficients. The energy transmission coefficient of a plane wave (i.e., the ratio of normal to the interface components of the power fluxes in incident and refracted waves) at a plane interface of homogeneous fluid half-spaces is the same for waves with the same value of the horizontal wave vector **q**, which are incident from the different half-spaces, even when an arbitrary stratified layer is enclosed between the half-spaces (Ref. 33; Ref. 3, p. 128). It seems that, being valid for every plane wave in a spectral decomposition of a field due to a localized source, the symmetry of transmitted power fluxes should extend to arbitrary acoustic fields. The apparent contradiction is resolved by noting that, first, the reciprocity of the transmission coefficients applies only to those plane waves that are homogeneous in both half-spaces, and second, plane waves with the same value of the horizontal wave vector **q** have different spectral densities in plane-wave decompositions of incident waves, when a localized source is placed in different fluids.

Actual liquid–gas interface is typically a time-dependent rough surface rather than a plane. For low-frequency sound, roughness elevation h is small compared to other relevant spatial scales. Assuming $k_2h\ll1$, $h/z_0\ll1$, it can be shown[7] that the effect of surface roughness on sound transmission and sound source output is negligible.

IV. SOUND SOURCE IN A WAVEGUIDE

Some of the properties of sound transmission through a plane liquid–gas interface, discussed in Sec. III assuming homogeneous liquid, remain valid for an arbitrarily stratified liquid. Consider an acoustic field generated by a monochromatic point source of volume velocity and/or external force in a vertically stratified fluid. The source is located at point $(0,0,z_0)$. Acoustic pressure is given by an integral (Ref. 9, p. 144; Ref. 34)

$$p(\mathbf{R}) = (2\pi)^{-2}\left[i\omega A + \frac{1}{\rho(z_0)}\left(F_1\frac{\partial}{\partial x} + F_2\frac{\partial}{\partial y} - F_3\frac{\partial}{\partial z_0}\right)\right] \times \int d^2\mathbf{q} e^{i\mathbf{q}\cdot\mathbf{R}}\frac{f_1(q,z_<)f_2(q,z_>)}{w(q)}, \quad (13)$$

over quasiplane waves, i.e., waves with harmonic dependence $\exp(i\mathbf{q}\cdot\mathbf{R})$ on horizontal coordinates. Here A and $\mathbf{F}$ are complex amplitude of the volume velocity and external force exerted by the sound source, $z_< = \min(z,z_0)$, $z_> = \max(z,z_0)$, $f_{1,2}$ are solutions of one-dimensional reduced wave equation:

$$\frac{\partial}{\partial z}\left(\frac{1}{\rho}\frac{\partial f(q,z)}{\partial z}\right) + \frac{\omega^2 c^{-2} - q^2}{\rho} f(q,z) = 0, \quad (14)$$

which satisfy conditions at $z \to -\infty$ and at $z \to +\infty$ (or at the lower boundary in the case of semi-infinite fluid), respectively. Sound speed c and mass density ρ of the fluid are piecewise smooth functions of z. At internal interfaces $z = h_j$, where fluid parameters are discontinuous, the solutions of the one-dimensional reduced wave equation satisfy the following boundary conditions:

$$f(q,z)\big|_{z=h_j-0}^{z=h_j+0} = 0, \qquad \frac{1}{\rho(z)}\frac{\partial f(q,z)}{\partial z}\bigg|_{z=h_j-0}^{z=h_j+0} = 0. \quad (15)$$

The conditions express continuity of acoustic pressure and the vertical component of particle velocity at the interfaces. The function w in Eq. (13) is defined as

$$w = \frac{1}{\rho(z)}\left[f_1(q,z)\frac{\partial}{\partial z}f_2(q,z) - f_2(q,z)\frac{\partial}{\partial z}f_1(q,z)\right]$$

and, according to Eqs. (14) and (15), is independent of z (Ref. 9, p. 143).

If A and $\mathbf{F}$ are constant (or variable but continuous when the source crosses an interface), it immediately follows from the integral representation (13) and the boundary conditions (15) that acoustic pressure is a continuous function of a source position for sources of volume velocity (monopoles) and vertical force (vertical dipoles). Continuity of acoustic pressure implies continuity of particle velocity and, consequently, of acoustic power flux density with respect to source position. The continuity does not take place for all sound sources. For instance, it follows from the integral representation (13) and the first of the two boundary conditions (15) that acoustic pressure at a given point $\mathbf{r}$ changes discontinuously when a point source of horizontal force crosses an interface where the mass density $\rho(z)$ experiences a jump. Ultimately, this is because tangential components of particle velocity, unlike the normal component, are discontinuous at an interface where the density of inviscid fluid is discontinuous.

A. Anomalous transparency of a gas-stratified liquid interface

Consider a point source of volume velocity located in a homogeneous gas half-space above a gas–liquid interface $z = 0$. Because of the strong mass density contrast between the gas and the liquid, the plane-wave reflection coefficient for sound incident on the interface from gas is close to unity for all $\mathbf{q}$, except for small grazing angles, where $\nu_1 \to 0$, whether the liquid is homogeneous or inhomogeneous. Therefore, the acoustic field at $z < 0$ and, in particular, the acoustic power flux radiated to infinity within the gas are insensitive to medium stratification at $z > 0$. Continuity of the acoustic field with respect to source position indicates, then, that the acoustic power flux into gas from a shallow monopole source in stratified liquid is essentially the same as in the case of a homogeneous liquid half-space, which is considered in Sec. III.[35]

In particular, it is shown in Sec. III that for monopole sound sources located in a homogeneous liquid half-space close to its boundary with a homogeneous gas half-space, transparency of the interface differs from unity by a small quantity $O(m)$. We show now that this result remains valid for an interface of a homogeneous gas half-space with an arbitrarily stratified dense medium. The parameter m is now understood as the ratio of the mass density of the gas to the value that the mass density of the liquid takes close to the interface: $m = \rho_1/\rho(z = +0)$.

Acoustic pressure in the liquid near the interface can be calculated with Eq. (13). For the function f_1 in Eq. (13) one finds from Eq. (14) that $f_1(q,z) = \text{const}\cdot\exp(-i\nu_1(q)z)$ at $z < 0$. From the boundary conditions (15) we have

$$f_j(q, z = 0) = \frac{im}{\nu_1(q)}\frac{\partial f_j}{\partial z}(q, z = +0), \quad j = 1,2. \quad (16)$$

When $m = 0$, i.e., in the case of the free boundary of a liquid, $f_1(q,z=0) = 0$, $\partial f_1(q,z=+0)/\partial z \equiv b(q) \neq 0$, and generally $f_2(q,z=0) \neq 0$. When $0 < m \ll 1$, calculating $f_1(q,z=0)$ from Eq. (16), we find that

$$f_1(q,z) = b(q)[z + im\nu_1^{-1}(q)] + O(z^2) + O(m^2) \quad (17)$$

for small, non-negative z. According to Eq. (17), the acoustic effect of gas loading of a boundary of an inhomogeneous liquid is, to first order, equivalent to the shift of the free boundary by a wave-number-dependent quantity $\delta z = -im\nu_1^{-1}(q)$. In the special case where there is a homogeneous liquid layer near the surface $z = 0$, the same result can be obtained from different considerations, which are similar to Weston's derivation[36] of an effective depth of an underwater waveguide with a penetrable bottom. Indeed, the plane-wave reflection coefficient (4) from the surface for sound in a liquid can be written as $V_1 = -\exp(-2m\nu_1^{-1}\nu_2) + O(m^2)$ and coincides, to first order in m, with the reflection coefficient $V = -\exp(-2i\nu_2\delta z)$ from a virtual pressure-release surface located at $z = \delta z$.

It follows from Eqs. (13) and (17) that, for sufficiently small $z_0 > 0$, $f_j(q,z_0) = O(m^{2-j})$ and $p = O(m)$ in both the liquid and the gas. Because of the density contrast between the two media, the acoustic power fluxes in the gas and the liquid are $J_0 O(m)$ and $J_0 O(m^2)$, respectively. Hence, transparency of the interface between a gas and an inhomogeneous liquid $T = 1 + O(m)$. The result and its derivation also hold when a finite liquid layer $0 < z < H$ overlays a solid half-space $z > H$.

B. Normal mode attenuation and sound radiation into gas

When a sound source is located in a liquid waveguide and is not too close to the gas–liquid interface, sound transmission into the gas can be profoundly different from the case of a homogeneous liquid half-space. Let a liquid layer $0<z<H$ be bounded at $z=H$ by a perfectly reflecting surface: $|V_2(q)|\equiv 1$. In the absence of absorption, all acoustic power emitted by the source is radiated into the gas. When the geometry of the problem is fixed, energy flux into the gas remains finite in the limit $m\to+0$ unlike the case of the interface of homogeneous gas and liquid half-spaces (Sec. III), where the power flux J_{21} into the gas as given by Eqs. (10) and (11) is $O(m)$. The cause of the difference can be easily understood in terms of the number of reflections from the interface $z=0$. At each reflection of a homogeneous plane wave from the interface, a small, $O(m)$ fraction of the power flux in the incident wave is transmitted from the liquid into the gas. In the case of an interface of homogeneous half-spaces, reflected waves never return to the interface. In a waveguide, which is infinite in x and y directions and has a perfectly reflecting boundary at $z=H$, reflected waves return to the liquid–gas interface an infinite number of times until all acoustic power is radiated into the gas.

In reality, acoustic radiation into a gas from a source in a liquid waveguide is limited by finite lateral dimensions of the waveguide, sound absorption in the liquid, and acoustic power leakage through the lower boundary. Let the liquid in the layer $0<z<H$ have sound speed $c_2(z)$ and density $\rho_2(z)$, and the half-space $z>H$ be occupied by a homogeneous liquid with sound speed c_3 and mass density ρ_3. When $m=0$ and $c_3>\min c_2(z)$, the medium can support propagating normal modes (Ref. 9, Chap. 4). Designate mode shape functions and wave numbers $\psi_n(z)$ and ξ_n; $n=1,2,\ldots$, $\xi_n>\omega/c_3$, $\mathrm{Im}\,\psi_n(z)=0$ (Ref. 9, Chap. 4). At horizontal distances $r\gg\xi_n^{-1}$ from the source located at the point $(0,0,z_0)$, acoustic pressure in the nth normal mode is

$$p=B_n r^{-1/2}\psi_n(z)\exp(i\xi_n r), \tag{18}$$

where complex amplitude B_n is determined by the type and strength of the source. When $m\neq 0$, the acoustic power flux into the gas causes attenuation of acoustic modes in the liquid. Let $\tilde{\psi}_n(z)$ and $\tilde{\xi}_n$ be complex shape functions and wave numbers of modes at $m\neq 0$. Both $\psi_n(z)$ and $\tilde{\psi}_n(z)$ tend to zero at $z\to+\infty$ and satisfy at $z>0$ the wave equation (14) (with $q=\xi_n$ and $q=\tilde{\xi}_n$, respectively). At $z=0$, $\tilde{\psi}_n(z)$ satisfies the boundary condition (16) (with $q=\tilde{\xi}_n$), while $\psi_n(0)=0$. To determine mode attenuation, we multiply the reduced wave equation for ψ_n by $\tilde{\psi}_n$, subtract the product of ψ_n and the reduced wave equation for $\tilde{\psi}_n$, and integrate the result over z to obtain:

$$(\xi_n^2-\tilde{\xi}_n^2)\int_0^{+\infty}\rho^{-1}\psi_n\tilde{\psi}_n dz = \rho^{-1}(\psi_n\partial\tilde{\psi}_n/\partial z-\tilde{\psi}_n\partial\psi_n/\partial z)|_{z=+0}. \tag{19}$$

Using the boundary conditions at $z=0$, for the wave-number perturbation $\delta\xi_n^{(1)}\equiv\tilde{\xi}_n-\xi_n$ from Eq. (19) we find that

$$\delta\xi_n^{(1)}=\frac{im}{2\xi_n\nu_1(\xi_n)\rho_2(0)}\left(\frac{\partial\psi_n}{\partial z}\right)_{z=+0}^2\times\left(\int_0^{+\infty}\psi_n^2\frac{dz}{\rho}\right)^{-1}+O(m^2). \tag{20}$$

Note that the wave-number correction is purely imaginary when the sound speed in the gas is smaller than in the liquid. In the special case when the layer $0<z<H$ is homogeneous, Eq. (20) reduces to the results obtained by Tindle *et al.*[37] and Chapman and Ward[17] from other considerations.

Absorption of sound in a liquid can be described approximately by multiplying the sound speed by the factor $[1+i\alpha(z)]^{-1}$, $\alpha\geqslant 0$ in the reduced wave equation. A correction to the modal wave number due to sound absorption is (Ref. 9, p. 172)

$$\delta\xi_n^{(2)}=\frac{i\omega^2}{\xi_n}\left(\int_0^{+\infty}\psi_n^2\frac{dz}{\rho}\right)^{-1}\int_0^{+\infty}\alpha\psi_n^2\frac{dz}{\rho c^2}+O(\alpha^2). \tag{21}$$

It is purely imaginary. To first order in m and α, contributions Eq. (20) and Eq. (21) to the imaginary part of the wave number of a mode are additive.

Contributions of individual normal modes into the acoustic power radiated by a source are additive (Ref. 9, p. 434). Integrating the power flux density (5) over the surface of an infinite cylinder $r=\mathrm{const}\ll 1/\mathrm{Im}\,\tilde{\xi}_n$, for the power flux carried from a sound source by the nth mode (18) one finds that

$$J^{(n)}=\frac{\pi}{\omega}|B_n^2|\mathrm{Re}\,\tilde{\xi}_n\int_0^{+\infty}\psi_n^2\frac{dz}{\rho}. \tag{22}$$

Here, mode attenuation is assumed to be weak: $0\leqslant\mathrm{Im}\,\tilde{\xi}_n\ll\mathrm{Re}\,\tilde{\xi}_n$ and corrections to the mode shape function ψ_n due to attenuation are neglected. A portion $J_{21}^{(n)}$ of the power flux $J^{(n)}$, which is radiated into the gas, is obtained by integrating the vertical component of the power flux density (5) in liquid over the plane $z=+0$. Using the boundary condition (16) for ψ_n, we find that

$$J_{21}^{(n)}=\frac{\pi m}{2\omega\rho_2(0)\nu_1(\xi_n)\mathrm{Im}\,\tilde{\xi}_n}|B_n^2|\left(\frac{\partial\psi_n}{\partial z}\right)_{z=+0}^2. \tag{23}$$

With the range dependence of the vertical component of the power flux density (5) given by the factor $r^{-1}\exp(-2r\times\mathrm{Im}\,\tilde{\xi}_n)$, the main contribution to $J_{21}^{(n)}$ comes from points at horizontal separation $r\sim 1/\mathrm{Im}\,\tilde{\xi}_n\gg 1/\mathrm{Re}\,\tilde{\xi}_n$ from the source. From Eqs. (20)–(23) it follows that the ratio of the power radiated by a normal mode into the gas to the total power carried by the mode from a sound source is independent of the source type and location and equals the relative contribution of radiation losses $\delta\xi_n^{(1)}$ to the total value of the mode attenuation $\mathrm{Im}\,\tilde{\xi}_n$:

$$J_{21}^{(n)}/J^{(n)}=\delta\xi_n^{(1)}/[\delta\xi_n^{(1)}+\delta\xi_n^{(2)}]. \tag{24}$$

The relation (24) between sound radiation into the gas and different contributions to mode attenuation becomes par-

ticularly clear in the special case when liquid in the layer $0<z<H$ is either homogeneous or slowly varying with the vertical coordinate z, so that the correspondence between normal modes and acoustic rays (see, e.g., Ref. 9, p. 205) can be utilized. Let absorption within the layer $0<z<H$ be negligible. Reflection coefficients from the layer boundaries $z=0$ and $z=H$ are $V_1(q)$ and $V_2(q)$, respectively. We assume for definiteness that normal modes do not have turning points (Ref. 9, p. 205) within the layer. For a normal mode to propagate without attenuation, rays corresponding to the mode should be totally reflected: $|V_1(\xi_n)|=|V_2(\xi_n)|=1$. When reflection is not total, the rays experience relative power loss $1-|V_j(\xi_n)|^2$, $j=1,2$, which is assumed small, at each reflection from respective boundaries. These power losses result in contributions $[1-|V_j(\xi_n)|^2]/2L(\xi_n)$ to the mode attenuation $\mathrm{Im}\,\tilde{\xi}_n$, where $L(\xi_n)$ is the skip distance (i.e., the spatial period) of a ray corresponding to the normal mode. As acoustic power carried by the mode eventually dissipates and on each cycle the ray experiences one reflection from each boundary, the fraction of the power radiated into the gas is

$$J_{21}^{(n)}/J^{(n)}=N[1-|V_1(\xi_n)|^2],$$
$$N=[2-|V_1(\xi_n)|^2-|V_2(\xi_n)|^2]^{-1} \tag{25}$$

in agreement with Eq. (24). The quantity N in Eq. (25) can be viewed as an effective number of reflections from the gas–liquid interface before the mode is extinguished. For the nth normal mode, the bulk of sound radiation into the gas occurs at horizontal separations $r=L(\xi_n)O(N)\gg L(\xi_n)$ from the source. The above-presented reasoning does not depend on the nature of the reflecting boundary at $z=H$ and remains unchanged if the half-space $z>H$ is occupied by a stratified solid rather than by a liquid.

According to Eqs. (17), (24), and (25), the contribution of the discrete spectrum of the acoustic field in a liquid waveguide into sound transmission into the gas strongly depends on mode attenuation and the source depth, which determines the excitation coefficients of the normal modes. In the important case of natural underwater acoustic waveguides, absorption of sound in water is negligible at frequencies below a few hundred hertz; attenuation of bottom-interacting normal modes is dominated by energy losses in the bottom (Ref. 2, p. 36). For normal modes with a turning point above the bottom, the shape functions of which are exponentially small between the turning point in water and the bottom, mode attenuation is primarily due to volume scattering in the water column and/or scattering on the ocean surface, and the contribution to the mode attenuation due to radiation losses into air remains negligible.[17,37] Under these conditions, the acoustic power flux into air due to the discrete spectrum of the field in the waveguide is a small fraction (24) of the underwater power flux in the normal modes. For sufficiently deep sources (or sufficiently high frequencies), the acoustic power flux into air due to the discrete spectrum may still be large compared to the power flux into air due to the continuous spectrum of the field, including evanescent plane waves generated by the source. However, the acoustic power flux into air due to normal modes is spread over an area on the ocean surface with a large linear scale compared to the ray cycle length $L(\xi_n)$, which is in turn large compared to the water depth and the linear scale of the region, where the bulk of the energy is radiated into air by inhomogeneous plane waves and steep rays emanating from the source.

C. Three-layer waveguide

We analyze in more detail the particular case of a point sound source in a homogeneous liquid layer $0<z<H$ overlying a homogeneous half-space $z>H$, which is either liquid or solid. Acoustic pressure in the liquid layer and power fluxes from the layer through planes $z=0$ and $z=H$ are given by Eqs. (1), (3), (4), (6), and (7). Reflection coefficients $V_{1,2}$ in these expressions are independent of the angle φ which determines the direction of the horizontal wave vector $\mathbf{q}=q(\cos\varphi,\sin\varphi,0)$. The power flux (6) into the gas from a source in a homogeneous liquid layer differs from the power flux (10) and (11) from the same source in a liquid half-space by a factor $\beta_1=|1+S_1S_2^{-1}V_2e^{2i\nu_2(H-z_0)}|^2$ in the integrand in Eq. (6), which describes interference of plane waves radiated upwards with plane waves reflected once from the lower boundary $z=H$, and a factor $\beta_2=|1-V_1V_2e^{2i\nu_2H}|^{-2}$, which describes the effects of multiple reflections from the boundaries. The factor β_2 is independent of the source and receiver positions and becomes infinite at q such that

$$1-V_1V_2e^{2i\nu_2H}=0. \tag{26}$$

Equation (26) is the dispersion equation of the waveguide, and its roots give wave numbers ξ_n of the normal modes (Ref. 3, p. 225; Ref. 31, p. 349). It is easy to check that, for the waveguide we consider, Eq. (26) is equivalent to $w(q)=0$ in Eq. (13).

When $m=0$ and H is sufficiently large, Eq. (26) has roots at such real $q=\xi_n<\omega/c_2$ that $|V_2(\xi_n)|=1$. Total reflection from a fluid half-space with sound speed $c_3>c_2$ occurs when there is no dissipation and requires $\xi_n>\omega/c_3$. In the case of a solid half-space with the same mass density and speeds $c_{l3}>c_{t3}$ of longitudinal and transverse waves, $|V_2|=1$ at $\xi_n>\omega/c_{t3}$ provided that $c_{t3}>c_2$. These ξ_n values correspond to homogeneous plane waves in the layer $0<z<H$.[38] When $m>0$ and there exists weak attenuation in the half-space, the poles $q=\xi_n$ of the integral representation (13) shift from the real axis into the complex q plane. The factor β_2 and integrand in Eq. (6) are then finite but have strong peaks in vicinities of $q=\mathrm{Re}\,\xi_n$, $n=1,2,\ldots$. Because of the location of the peaks, the waveguide parameters (wave speeds, mass density, and wave attenuation in the half-space and the layer thickness H), which determine the position and height of the peaks, have a stronger effect on the contributions of the homogeneous plane waves in the liquid layer into the power flux into the gas than on contributions due to the inhomogeneous plane waves (cf. Figs. 5–8).

For very shallow sources with a symmetric directivity pattern, we have $\beta_1\beta_2=1$ to leading order in the small parameter m, when $k_2z_0\ll 1$ and $S_1(\mathbf{q})=S_2(\mathbf{q})$. From Eq. (6), it follows then that, to leading order in m, radiation into the gas from the waveguide is the same as from a homogeneous

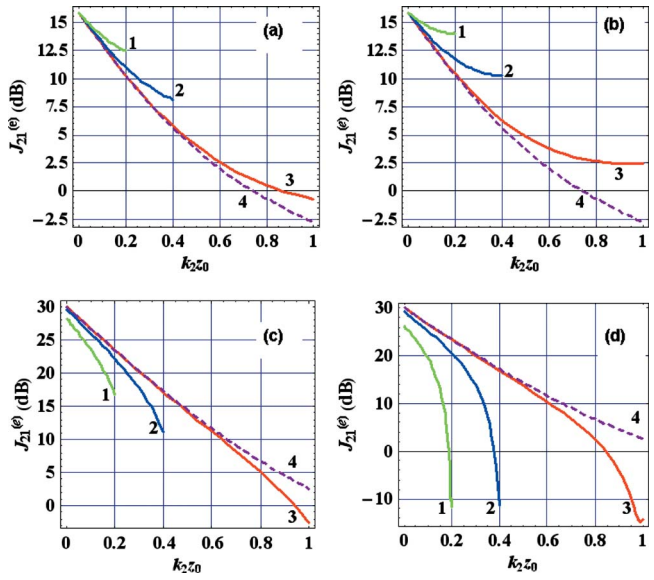

FIG. 5. (Color online) Acoustic power flux into gas due to inhomogeneous plane waves generated within a liquid layer by either a monopole [(a), (b)] or a vertical dipole [(c), (d)] sound source. The liquid layer overlays an homogeneous liquid [(a), (c)] or solid [(b), (d)] half-space with the following parameters: $\rho_3/\rho_2=3$, $c_2/c_3=0.5$, $\alpha=0.02$, $c_2/c_{l3}=0.33$, $\alpha_l=0.01$, $c_2/c_{t3}=0.7$, $\alpha_t=0.02$. Refraction index and the mass density ratio at the gas–liquid interface are $n=c_2/c_1=4.5$ and $m=\rho_1/\rho_2=1.3\times10^{-3}$. The nondimensional liquid layer thickness is $k_2H=0.2$ (1), 0.4 (2), 1.0 (3), and 100 (4). Acoustic power is normalized by the power flux into the gas from the same source located away from the gas–liquid interface in an homogeneous liquid half-space with parameters of the layer.

liquid half-space [see Figs. 5(a), 5(b), 6(a), 7, and 8]. This property has been established earlier for a monopole sound source from different considerations and is now extended to arbitrary sources with a symmetric directivity pattern with respect to the horizontal plane.

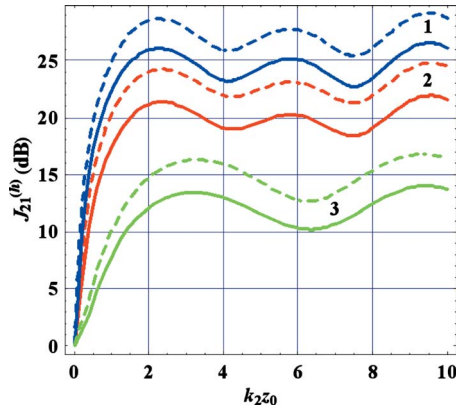

FIG. 7. (Color online) Acoustic power flux into gas due to homogeneous plane waves generated by a monopole sound source within a liquid layer overlying a liquid half-space. Parameters of the liquid half-space are: $c_2/c_3=0.33$ (1), 0.5 (2), and 0.75 (3); $\alpha=0.02$ (solid lines) and 0.01 (dashed lines); $\rho_3/\rho_2=3$. The nondimensional liquid layer thickness $k_2H=10$. Parameters of the liquid layer and the gas half-space as well as normalization of the power flux are the same as in Fig. 5.

Figures 5–8, which are obtained using Eqs. (4) and (6), illustrate the effects of the boundary $z=H$ on sound radiation into the gas. The parameters of the liquid layer and gas, liquid, and solid half-spaces assumed in Figs. 5–8, including wave attenuation, are chosen to represent typical values encountered in problems of low-frequency sound propagation in the ocean. When the half-space $z>H$ is liquid, reflection coefficient V_2 is given by the Fresnel equation $V_2=(\rho_3\nu_2-\rho_2\nu_3)/(\rho_3\nu_2+\rho_2\nu_3)$, $\nu_3=(\omega^2c_3^{-2}-q^2)^{1/2}$, Im $\nu_3\geqslant0$, which is similar to Eq. (4). When the half-space $z>H$ is solid,

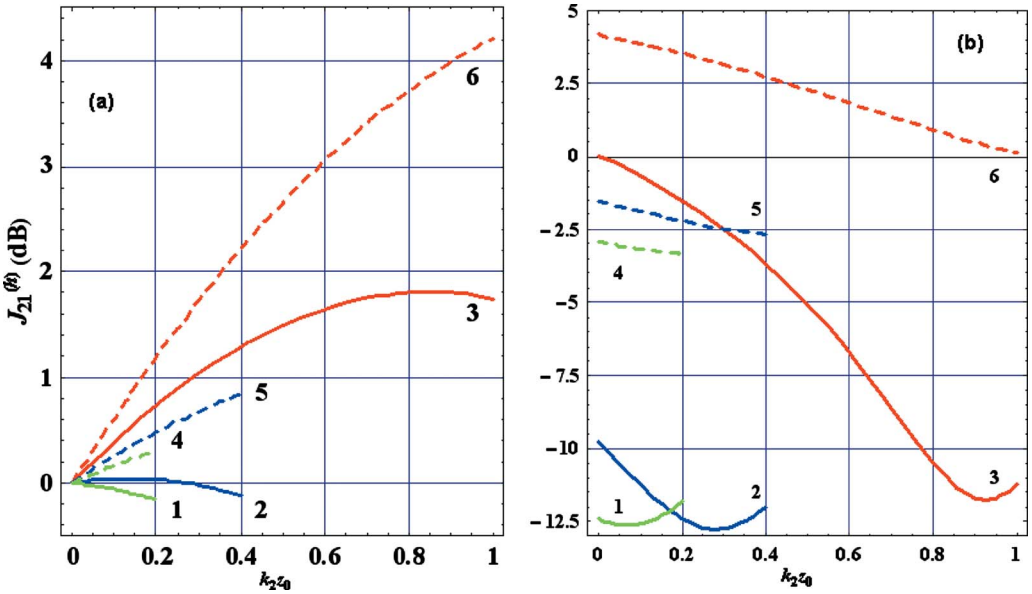

FIG. 6. (Color online) Acoustic power flux into gas due to homogeneous plane waves generated within a thin liquid layer by either a monopole (a) or a vertical dipole (b) sound source. Solid (dashed) lines correspond to the half-space $z>H$ being liquid (solid). The nondimensional liquid layer thickness is $k_2H=0.2$ (lines 1 and 4), 0.4 (2 and 5), or 1.0 (3 and 6). Normalization of the power flux and physical parameters of the liquid layer and gas, liquid, and solid half-spaces are the same as in Fig. 5.

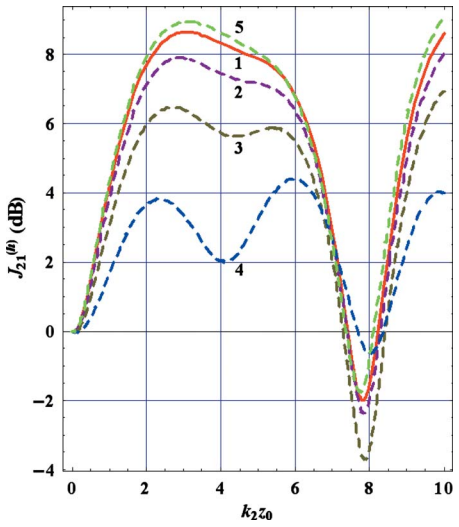

FIG. 8. (Color online) Acoustic power flux into gas due to homogeneous plane waves generated by a monopole sound source within a liquid layer overlying a solid half-space. Speeds and attenuation of compressional and shear waves in the solid half-space: $c_2/c_{l3}=0.33$, $\alpha_l=0.01$, $c_2/c_{t3}=0.7$, $\alpha_t=0.02$ (1); $c_2/c_{l3}=0.33$, $\alpha_l=0.04$, $c_2/c_{t3}=0.7$, $\alpha_t=0.02$ (2); $c_2/c_{l3}=0.33$, $\alpha_l=0.01$, $c_2/c_{t3}=0.7$, $\alpha_t=0.04$ (3); $c_2/c_{l3}=0.33$, $\alpha_l=0.01$, $c_2/c_{t3}=0.9$, $\alpha_t=0.02$ (4); $c_2/c_{l3}=0.25$, $\alpha_l=0.01$, $c_2/c_{t3}=0.7$, $\alpha_t=0.02$ (5); mass density ratio $\rho_3/\rho_2=3$. The nondimensional liquid layer thickness $k_2H=10$. Parameters of the liquid layer and the gas half-space as well as normalization of the power flux are the same as in Fig. 5.

$$V_2=\frac{4u\sqrt{n_t^2-u}+(2u-n_t^2)^2/\sqrt{n_l^2-u}-\rho_2 n_t^4/\rho_3\sqrt{1-u}}{4u\sqrt{n_t^2-u}+(2u-n_t^2)^2/\sqrt{n_l^2-u}+\rho_2 n_t^4/\rho_3\sqrt{1-u}}, \tag{27}$$

where $u=q^2/k_2^2$, $n_l=(1+i\alpha_l)c_2/c_{l3}$, $n_t=(1+i\alpha_t)c_2/c_{t3}$, $\alpha_l\geqslant 0$ and $\alpha_t\geqslant 0$ describe attenuation of compressional and shear waves, and the imaginary part of all square roots is nonnegative (Ref. 3, p. 94).

When absorption of sound is negligible at $z<H$, it is convenient to distinguish contributions $J_{21}^{(h)}$ and $J_{21}^{(e)}$ of homogeneous and inhomogeneous plane waves in the layer into the acoustic power flux into the gas. $J_{21}^{(h)}$ and $J_{21}^{(e)}$ are obtained by limiting the domain of integration in Eq. (6) for J_{21} to $0\leqslant q\leqslant k_2$ and $k_2<q\leqslant k_1$, respectively. As in the case of an interface of homogeneous gas and liquid half-spaces [see Eqs. (10) and (11)], plane waves with $q>k_1$ do not contribute to sound radiation into the gas. Dependencies of $J_{21}^{(e)}$ on layer thickness, distance from a point sound source to the gas–liquid interface, type of the reflecting boundary at $z=H$, and source directivity are illustrated in Fig. 5. For $J_{21}^{(h)}$, similar dependencies are illustrated in Figs. 6–8.

For the monopole sound source in a thin liquid layer ($k_2H\leqslant 1$), the effects of the reflecting boundary at $z=H$ are negligible at $k_2z_0\ll 1$, as expected, and reach several decibels as the source moves further from the gas–liquid interface and approaches the interface $z=H$ [Figs. 5(a), 5(b), and 6(a)]. Reflection coefficients V_2 from liquid and solid half-spaces have a small imaginary part and $\mathrm{Re}\,V_2>0$ for inhomogeneous plane waves with $q=k_2$ $O(n)$, which make the main contribution to $J_{21}^{(e)}$. Hence, the factor $\beta_1>1$ and increases with z_0. Therefore, reflection from the interface $z=H$ increases the power flux into the gas due to inhomogeneous plane waves, the effect being the largest for the deepest sources [Figs. 5(a) and 5(b)]. For the vertical dipole source, the effect is the opposite [Figs. 5(c) and 5(d)] because of the opposite sign of the ratio S_1/S_2 [see Eq. (6)]. When sound frequency and z_0 are fixed, the effect of the interface $z=H$ on $J_{21}^{(e)}$ rapidly decreases with H increasing [Figs. 5(a)–5(d)] because of the attenuation of inhomogeneous waves propagating from the source to the interface $z=H$ and back to the gas–liquid interface.

For thin layers, reflection from the boundary $z=H$ may increase or decrease sound transmission into the gas due to homogeneous plane waves in the liquid, depending on conditions of interference at $z=+0$ of the direct wave from the source and a wave reflected once from the boundary $z=H$ (Fig. 6). Inhomogeneous plane waves in the liquid dominate sound transmission into the gas from a source in a thin liquid layer; $J_{21}^{(e)}\gg J_{21}^{(h)}$, as in the case of an interface of homogeneous gas and liquid half-spaces.

An increase in the nondimensional layer thickness k_2H allows for larger values of k_2z_0 and has a different effect on $J_{21}^{(h)}$ than on $J_{21}^{(e)}$. For a monopole source, $J_{21}^{(h)}$ increases, when the source moves away from the gas–liquid interface, and exceeds $J_{21}^{(e)}$. When $k_2H>1$, the total acoustic power radiated into the gas, $J_{21}^{(h)}+J_{21}^{(e)}$, can be much larger for a deep source than for a shallow one [see Figs. 5(a) and 7], unlike the case of an interface of homogeneous gas and liquid half-spaces. Comparison of Figs. 6–8 with Fig. 5 illustrates higher sensitivity of the power flux due to homogeneous plane waves, $J_{21}^{(h)}$, to physical properties of the half-space $z>H$, compared to the sensitivity of the power flux $J_{21}^{(e)}$ due to inhomogeneous plane waves. When the half-space $z>H$ is liquid, in agreement with Eqs. (24) and (25), $J_{21}^{(h)}$ is larger, when sound speed is larger and attenuation is smaller in the liquid half-space (Fig. 7), which makes reflection from the interface $z=H$ stronger and the mode attenuation due to losses in the half-space weaker. Similarly, when the half-space $z>H$ is solid, the contribution $J_{21}^{(h)}$ of the homogeneous plane waves in the liquid layer increases, when speeds $\mathrm{Re}\,c_{l3}$ and $\mathrm{Re}\,c_{t3}$ of the compressional and shear waves in the solid increase and their attenuations α_l and α_t decrease (Fig. 8). Figure 8 shows that when the shear waves are faster than sound in the liquid layer, $J_{21}^{(h)}$ is much more sensitive to variations in shear rather than compressional wave parameters. This can be traced back to the higher sensitivity of the plane wave reflection coefficient (27) and mode attenuation to c_{t3} and α_t compared to c_{l3} and α_l, respectively.

Note a sharp decrease in $J_{21}^{(h)}$, the contribution of homogeneous plane waves in liquid into the acoustic power flux into gas, around $k_2z_0\approx 8$ in Fig. 8. In the case at hand, the liquid layer supports two normal modes, attenuation of the first mode being much smaller than that of the fundamental mode. In the limit of attenuation tending to zero, the first and the fundamental modes have one and zero nodes within the liquid layer, respectively. The dip in $J_{21}^{(h)}$ occurs when the sound source is located close to the node of the first mode. Put differently, as a function of z_0, $J_{21}^{(h)}$ has a deep minimum when the factor $\beta_1(\mathbf{q},z_0)=0$, i.e., plane waves radiated up-

wards interfere destructively with plane waves reflected once from the boundary $z=H$, at such $\mathbf{q}$ that the factor $\beta_2(\mathbf{q})$ is at maximum.

V. SUMMARY AND DISCUSSION

Sound transmission through the interface of a light fluid with a small sound speed and a dense fluid with a large sound speed, which we refer to as gas and liquid, respectively, is usually weak because of the strong contrast of the acoustic parameters of the two media. An exception to this general rule occurs when the acoustic field is generated by a localized, low-frequency sound source in the liquid. When a source with small linear dimensions compared to the acoustic wavelength approaches a plane interface of homogeneous gas and liquid half-spaces from the liquid side, and its distance from the interface decreases from a large value compared to the wavelength to a small value compared to the wavelength, the acoustic power flux transmitted into the gas increases dramatically. The relative increase is insensitive to the mass densities ratio m of the gas and the liquid and is controlled by the refraction index n and the source type. For point multipole sound sources of order 2^{l-1}, the relative increase in the power flux into gas is proportional to n^{2l}, provided m is sufficiently small, e.g., for a point monopole, a dipole, and a quadrupole source with vertical and horizontal axes in water, the power flux into air, when $n \approx 4.5$, increases with decreasing source depth by factors of about 40, 10^3, and 5×10^4, respectively.

Representation of monochromatic acoustic fields as a superposition of quasiplane waves [i.e., waves with harmonic dependence $\exp(i\mathbf{q} \cdot \mathbf{R})$ on horizontal coordinates] provides a convenient way to calculate and interpret sound transmission through horizontal interfaces. For a plane horizontal interface, power fluxes through the interface are additive for quasiplane waves with different projections of their wave vectors on the horizontal plane. The increase in the acoustic power flux into the gas is found to be due to those source-generated inhomogeneous (evanescent) plane waves in liquid, which become homogeneous plane waves in gas upon refraction at the interface. The contribution of the inhomogeneous plane waves into the transmitted power flux is negligible, when the source is far from the interface, but increases with decreasing source depth and, when $n^2 \gg 1$, overshadows the contribution of homogeneous plane waves for sufficiently shallow sources. The dependence of the relative increase in the sound transmission into the gas, when the nondimensional depth of a point source decreases, on the order of a multipole source mirrors the relative weight of the evanescent waves in the plane-wave spectra of the multipole sources.

Transmission of acoustic energy from a compact source through a fluid–fluid interface is found to be nonreciprocal. Unlike the case of a single incident plane wave, for point sources there is no symmetry between the power fluxes transmitted from a gas into a liquid and from a liquid into a gas. When a monochromatic source of a volume velocity, an external force, or a force couple is located in a gas and the source strength (i.e., the amplitude of the volume velocity, force, or force-moment oscillations exerted by the source) is kept constant, the power flux transmitted through the interface is independent of the source position. In other words, the gas–liquid interface becomes anomalously transparent at low frequencies for sound generated by compact sources in the liquid, but not for sound generated by sources in the gas. Ultimately, this is because inhomogeneous plane waves contribute to acoustic power transmission through an interface only in the direction of decreasing sound speed.

When a sound source is located in a liquid, which is stratified and/or bounded by a reflective boundary, sound transmission through a gas–liquid interface can be profoundly different than in the case of a homogeneous liquid half-space. However, certain aspects of the sound transmission process have been shown to be universal and independent from the liquid stratification. In particular, a power flux radiated into the gas is a continuous function of the position of a source of volume velocity or vertical force. When the nondimensional depth of a source of volume velocity in liquid is sufficiently small, the gas–liquid interface becomes anomalously transparent, and the ratio of acoustic power radiated into the gas to the total power output of the source differs from unity by a small quantity $O(m)$. The phenomenon occurs in an arbitrarily stratified liquid, is a direct consequence of the mass density ratio m being small compared to unity, and is caused by the destructive interference of direct waves and waves reflected from the gas–liquid interface. Thus, for a monopole source at a fixed depth in liquid, almost all emitted energy is radiated into the gas rather than into the liquid, as long as the sound frequency is sufficiently low.

The magnitude of the power flux into the gas from a given source in the liquid away from the gas–liquid interface depends on variations of sound speed and mass density within the liquid. The contribution of homogeneous waves in liquid into the power flux is found to be more sensitive than the contribution of source-generated evanescent waves to the liquid stratification, the thickness of a liquid layer between the gas–liquid interface and lower reflective boundary (bottom) and the bottom properties, especially when the thickness is of the order of the acoustic wavelength in the liquid or greater. In the case of guided sound propagation, homogeneous waves can experience multiple reflections from the gas–liquid interface. The effective number of the reflections is determined by energy losses due to absorption and at reflection from the waveguide boundaries. While the bulk of the power flux into the gas due to the evanescent waves occurs at distances from the source of the order of the acoustic wavelength or the source depth, the power flux due to homogeneous waves is distributed over a large surface area with a linear dimension much larger than the wavelength and the waveguide thickness. When the losses due to absorption and at bottom reflection are small compared to radiation losses at reflection from the gas–liquid interface, the acoustic power flux into the gas is no longer proportional to the small parameter m and is much larger than in the case of a homogeneous liquid half-space.

A different regime is typical for natural waveguides. While the normal modes of an underwater acoustic wave-

guide are weakly attenuated at low frequencies, bottom losses and/or surface and volume scattering in the water column give a much larger contribution to the mode attenuation than sound radiation into the air (Ref. 2, p. 36; Refs. 17 and 37). In terms of acoustic rays, losses from reflection from the ocean bottom and/or attenuation in the water column over the ray cycle length exceed by far the losses due to sound transmission into air. Then the power flux into air due to homogeneous waves in water is again distributed over the surface area with large linear dimensions compared to ocean depth and acoustic wavelength, but only a small fraction of the power carried from the source by the homogeneous waves is transmitted into air. In all cases, for sufficiently low frequencies, the acoustic power flux into gas from a compact source in liquid is dominated by the contribution of source-generated evanescent waves in the vicinity of the source.

Our results indicate that in contrast with high-frequency fields, low-frequency acoustic fields on opposite sides of a gas–liquid interface are much more closely connected than previously believed possible. Likely practical applications are related to the air–water interface, which occupies about two-thirds of the Earth's surface. The anomalous transparency of the interface at low frequencies calls for reevaluation of the possibility of acoustic communication through the water–air interface and acoustic monitoring of physical processes occurring under water. For instance, the transparency of the interface at infrasonic and low acoustic frequencies completely changes the outlook on the possible role of hearing in marine birds in location of their underwater prey. Contributions of underwater acoustic sources, such as collapsing bubbles, into low-frequency acoustic noise in the troposphere and heating of the upper atmosphere due to absorption of infrasound should be compared to contributions of sources at the ocean surface. At infrasonic frequencies of a few tenths of a hertz, underwater explosions are located at a fraction of the wavelength from the ocean surface and, consequently, should radiate infrasound mainly into the atmosphere. Combined with the ambient noise level in the atmosphere being several orders of magnitude lower than in the ocean,[39] such a distribution of the radiated energy between water and air suggests that infrasonic observations in air may be better suited for acoustic detection of powerful underwater explosions for the purposes of the Comprehensive Nuclear-Test-Ban Treaty than observations with underwater receivers.

An experimental verification of the theoretically predicted anomalous transparency of the gas–liquid interface for low-frequency sound would appear to be highly desirable.

ACKNOWLEDGMENTS

Fruitful discussions with M. Charnotskii, I. M. Fuks, C. May, S. F. Clifford, and S. Harrison are gratefully acknowledged. This work was supported, in part, by the Office of Naval Research.

[1]A. D. Pierce, *Acoustics. An Introduction to Its Physical Principles and Applications* (AIP, New York, 1994).
[2]F. B. Jensen, W. A. Kuperman, M. B. Porter, and H. Schmidt, *Computational Ocean Acoustics* (Springer, New York, 2000).
[3]L. M. Brekhovskikh and O. A. Godin, *Acoustics of Layered Media 1: Plane and Quasi-Plane Waves*, 2nd ed. (Springer, Berlin, 1998).
[4]R. W. Young, "Sound pressure in water from a source in air and vice versa," J. Acoust. Soc. Am. **53**, 1708–1716 (1973).
[5]M. A. Isakovich, *General Acoustics* (Nauka, Moscow, 1973) (In Russian).
[6]O. A. Godin, "Anomalous transparency of water-air interface for low-frequency sound," Phys. Rev. Lett. **97**, 164301 (2006).
[7]O. A. Godin, "Transmission of low-frequency sound through the water-to-air interface," Acoust. Phys. **53**, 305–312 (2007).
[8]B. E. McDonald and D. C. Calvo, "Enhanced sound transmission from water to air at low frequencies," J. Acoust. Soc. Am. **122**, 3159–3161 (2007).
[9]L. M. Brekhovskikh and O. A. Godin, *Acoustics of Layered Media. 2: Point Sources and Bounded Beams*, 2nd ed. (Springer, Berlin, 1999).
[10]M. J. Buckingham and E. M. Giddens, "Theory of sound propagation from a moving source in a three-layer Pekeris waveguide," J. Acoust. Soc. Am. **120**, 1825–1841 (2006).
[11]E. Gerjuoy, "Refraction of waves from a point source into a medium of a higher velocity," Phys. Rev. **73**, 1442–1449 (1948).
[12]A. A. Hudimac, "Ray theory solution for the sound intensity in water due to a point source above it," J. Acoust. Soc. Am. **29**, 916–917 (1957).
[13]M. S. Weinstein and A. G. Henney, "Wave solution for air-to-water sound transmission," J. Acoust. Soc. Am. **37**, 899–901 (1965).
[14]Yu. K. Alekhin and I. A. Urusovskii, "Sound transmission through an uneven air-water interface," Proc. Acoust. Institute **5**, 252–271 (1969) (In Russian).
[15]Yu. K. Alekhin, "On sound transmission through an uneven air-water interface," Proc. Acoust. Institute **13**, 72–76 (1970) (In Russian).
[16]A. V. Razin, "Peculiarities of the penetration of sound into water from air," Izv., Acad. Sci., USSR, Atmos. Oceanic Phys. **20**, 156–158 (1984).
[17]D. M. F. Chapman and P. D. Ward, "The normal-mode theory of air-to-water sound transmission in the ocean," J. Acoust. Soc. Am. **87**, 601–618 (1990).
[18]G. Saracco, G. Corsain, J. Leandre, and C. Gazanhes, "Propagation d'ondes sphériques monochromatiques travers l'interface fluide/fluide: Applications numériques et expérimentales au dioptre plan air/eau," (Propagation of monochromatic and spherical waves through a plane interface fluid/fluid: Numerical and experimental results for the air/water interface) Acustica **73**, 21–32 (1991).
[19]V. S. Buldyrev and N. S. Grigor'eva, "Sound field generated in a water layer of variable depth by a source moving in the atmosphere. I. Time-dependent normal modes," Acoust. Phys. **39**, 413–418 (1993).
[20]V. S. Buldyrev and N. S. Grigor'eva, "Sound field generated in a water layer of variable depth by a source moving in the atmosphere. 2. Time-variation of the normal-mode characteristics," Acoust. Phys. **39**, 537–542 (1993).
[21]L. Kazandjian and L. Leviandier, "A normal mode theory of air-to-water sound transmission by a moving source," J. Acoust. Soc. Am. **96**, 1732–1740 (1994).
[22]V. W. Sparrow, "Review and status of sonic boom penetration into the ocean," J. Acoust. Soc. Am. **111**, 537–543 (2002).
[23]M. J. Buckingham, E. M. Giddens, F. Simonet, and T. R. Hahn, "Propeller noise from a light aircraft for low-frequency measurements of the speed of sound in a marine sediment," J. Comput. Acoust. **10**, 445–464 (2002).
[24]H. K. Cheng and C. J. Lee, "Sonic-boom noise penetration under a wavy ocean: theory," J. Fluid Mech. **514**, 281–312 (2004).
[25]D. M. F. Chapman and O. A. Godin, "Sonic booms in shallow water: The influence of the seabed," in *Proceedings of the Seventh European Conference on Underwater Acoustics*, Delft University of Technology, Delft, The Netherlands, 2004, Vol. **1**, pp. 187–192.
[26]R. J. Urick, "Noise signature of an aircraft in level flight over a hydrophone in the sea," J. Acoust. Soc. Am. **52**, 993–999 (1972).
[27]B. G. Ferguson, "Doppler effect for sound emitted by a moving airborne source and received by acoustic sensors located above and below the sea surface," J. Acoust. Soc. Am. **94**, 3244–3247 (1993).
[28]W. J. Richardson, C. R. Greene, Jr., C. I. Malme, and D. H. Thomson, *Marine Mammals and Noise* (Academic, New York, 1995).
[29]R. A. Sohn, F. Vernon, J. A. Hildebrand, and S. C. Webb, "Field measurements of sonic boom penetration into the ocean," J. Acoust. Soc. Am. **107**, 3073–3083 (2000).
[30]L. M. Brekhovskikh, "Reflection and refraction of spherical waves," Usp. Fiz. Nauk **38**, 1–41 (1949) (In Russian).
[31]L. M. Brekhovskikh, *Waves in Layered Media* (Academic, New York, 1960).

[32]In deriving this equation, we took into account that acoustic power flux $J_d(\chi,\psi)$ through any horizontal plane in an acoustic field due to an arbitrary oriented point dipole source of unit strength, which generates acoustic pressure $k_2^{-1}\mathbf{d}\cdot\nabla p_0$, where $\mathbf{d}=(\cos\chi\cos\psi,\cos\chi\sin\psi,\sin\chi)$, in unbounded liquid, is related to power fluxes $J_d^{(v)}$ and $J_d^{(h)}$ through the same plane in acoustic fields due to vertical and horizontal dipoles defined in Sec. II as follows: $J_d(\chi,\psi)=J_d^{(h)}\cos^2\chi+J_d^{(v)}\sin^2\chi$.
[33]K. P. Scharnhorst, "Properties of acoustic and electromagnetic transmission coefficients and transfer matrices of multilayered plates," J. Acoust. Soc. Am. **74**, 1883–1886 (1983).
[34]O. A. Godin, "Calculation of amplitudes of acoustic normal modes from the reciprocity principle," J. Acoust. Soc. Am. **119**, 2096–2100 (2006).
[35]Unlike the source of volume velocity, this reasoning does not apply to a point source of vertical force, for which acoustic pressure is also a continuous function of the source position. For a vertical dipole source in gas, destructive interference of a direct wave in the gas and a wave reflected from the gas–liquid interface leads to a rapid variation of the field as a function of z_0 at $0<-k_1z_0\ll 1$. The spatial scale of this variation is $|z_0|=k_1^{-1}O(m)$. Amplitudes of plane-wave components of the field due to a vertical dipole source in the gas near the gas–liquid interface are proportional to small, $O(m)$ deviations of the reflection coefficient from unity, which are sensitive to the medium stratification at $z>0$. In the particular case of a homogeneous liquid layer $0<z<H$ with a reflective boundary at $z=H$, this reasoning is illustrated by Eq. (6) (with $S_1=-S_2$) and Figs. 5(c), 5(d), and 6(b).
[36]D. E. Weston, "A Moiré fringe analog of sound propagation in shallow water," J. Acoust. Soc. Am. **32**, 647–654 (1960).
[37]C. T. Tindle, A. P. Stamp, and K. M. Guthrie, "Virtual modes and the surface boundary condition in underwater acoustics," J. Sound Vib. **49**, 231–240 (1976).
[38]In the case of a solid half-space $z>H$ with $c_{t3}>c_2$, the dispersion equation (26) has an additional solution such that $\omega/c_2<\xi_n<\omega/c_{t3}$. Unlike the other normal modes, this fundamental mode can exist at arbitrarily small k_2H; in the limit $\rho_2/\rho_3\to 0$ the fundamental mode reduces to the Rayleigh surface wave (Ref. 3, p. 106).
[39]R. Waxler and K. E. Gilbert, "The radiation of atmospheric microbaroms by ocean waves," J. Acoust. Soc. Am. **119**, 2651–2664 (2006).

On the sound field of a resilient disk in free space

Tim Mellow[a)]
Nokia UK Ltd., Nokia House, Summit Avenue, Farnborough, Hants GU14 0NG, England

(Received 20 May 2007; revised 18 December 2007; accepted 11 January 2008)

Radiation characteristics are calculated for a circular planar sound source in free space with a uniform surface pressure distribution, which can be regarded as a freely suspended membrane with zero mass and stiffness. This idealized dipole source is shown to have closed form solutions for its far-field pressure response and radiation admittance. The latter is found to have a simple mathematical relationship with the radiation impedance of a rigid piston in an infinite baffle. Also, a single expansion is derived for the near-field pressure field, which degenerates to a closed form solution on the axis of symmetry. From the normal gradient of the surface pressure, the surface velocity is calculated. The near-field expression is then generalized to an arbitrary surface pressure distribution. It is shown how this can be used as a simplified solution for a rigid disk in free space or a more realistic sound source such as pre-tensioned membrane in free space with non-zero mass and a clamped rim. © *2008 Acoustical Society of America.* [DOI: 10.1121/1.2839891]

PACS number(s): 43.20.Rz, 43.20.Tb, 43.40.Dx, 43.38.Bs [JGM] Pages: 1880–1891

I. INTRODUCTION

The resilient disk in free space is the dipole complement of the rigid disk in an infinite baffle. Together with a few variants,[1] these are the only axisymmetric planar sources that yield compact closed-form solutions for their axial and far-field pressure responses and radiation impedances. Interchanging the boundary conditions leads to another complementary pair of axisymmetric planar sources, namely the resilient disk in an infinite baffle and rigid disk in free space. These are slightly more complicated, but the solutions are also applicable to diffraction problems using Babinet's principle,[2] as modified by Bouwkamp.[3] The reason for the extra complexity is the mixture of velocity and pressure boundary conditions in the plane of the disk. In a baffle, the resilient disk has a uniform driving pressure across its surface and zero velocity beyond its rim. Early solutions to this problem involved iterative methods based upon oblate spheroidal wave functions.[3,4] An alternative approach[5] is to use the King integral, which is similar to the Rayleigh[6] integral except that the Green's function in cylindrical coordinates (which has been termed the Lamb–Sommerfeld integral) is used, as opposed to the rotationally symmetric spherical Green's function. The disk velocity distribution can be represented by a trial function which itself is based upon the solution to the free space wave equation in oblate spheroidal coordinates.

The rigid disk in free space, conversely, has uniform velocity across its surface and zero pressure beyond its rim, so that a similar approach[7] can be applied, but using a trial function for the disk pressure distribution instead. Sets of simultaneous equations are then developed and solved numerically for the unknown trial function coefficients. A similar approach can also be applied to fluid-structure coupled problems,[8–12] where neither the disk velocity nor pressure distributions are uniform, and so the coupled disk and free space wave equations have to be solved simultaneously.

The simplest monopole planar source is the rigid disk (or piston) in an infinite baffle, which has a velocity boundary condition on both its face and the surrounding baffle. Remarkably, this was first derived by Rayleigh[6] before the direct radiator loudspeaker had even been invented,[13] yet it has been widely accepted as a model for such when mounted in a box near a wall or, even better, mounted directly in a wall as commonly found in recording studios. The model is useful in the frequency range up to the first diaphragm breakup mode.

Unfortunately, the Rayleigh integral is not particularly amenable to numerical calculation of the near-field pressure, especially at high frequencies. The integrand is oscillatory and the Green's function is singular at the source. Hence there has been a strong motivation to find alternative methods, especially those using fast converging expansions. A useful review of previous literature relating to the baffled planar piston was provided by Harris,[14] which includes some early movable origin schemes, whereby the origin of the coordinate system was moved to the same radial distance as the observation point when projected onto the plane of the radiator. Later, Hasagawa *et al.*[15] moved the origin axially in front of the radiator in order to achieve convergence in the immediate near field. Recently, Mast and Yu[16] have supplied an elegant single-expansion solution in a similar manner, but locking the origin in the same plane as the observation point. It is shown in this paper how a similar expansion can be obtained for the resilient disk. Also, apodized radiators have been studied by Kelly and McGough.[17]

The resilient disk in free space is the simplest dipole planar source, having a uniform driving pressure across its face and zero pressure extending beyond its rim. It can be used as an approximate model for unbaffled loudspeakers of the electrostatic or planar magnetic type, in which it is assumed that a perfectly uniform driving pressure is applied to a very light flexible membrane diaphragm in free space.

[a)]Electronic mail: tim.mellow@nokia.com

 0001-4966/2008/123(4)/1880/12/$23.00 © 2008 Acoustical Society of America

Walker[18] pointed out that such a source is acoustically transparent, in that it does not disturb the field around it, and used this idealized model to derive the far-field on-axis pressure response of an electrostatic loudspeaker, which provides a useful approximation over the loudspeaker's working range. However, it should be noted that the model assumes a freely suspended membrane, whereas in reality it is usually clamped at the rim, which effectively removes the singularity from the rim of the idealized model.

Bouwkamp[3] solved the real radiation admittance (or conductance, aka transmission coefficient), but the imaginary radiation admittance (or susceptance) has remained hitherto unsolved. An alternative derivation to that of Bouwkamp for the conductance is provided here, which is based upon the dipole version of the King[19] integral. Although this approach has previously been used by Morse and Ingard,[20] they did not solve the equations for the conductance or susceptance, but presented approximate solutions based upon an oscillating rigid sphere, together with the correct far-field expression. Here, a formal derivation is presented, using known identities, which shows a simple relationship between the admittance of a resilient disk and the impedance of a rigid disk.

In Sec. II of this paper, the boundary conditions of the problem are set out, after which a solution to the free space wave equation using the dipole King integral is presented in Sec. III, following the approach of Morse *et al.* In Sec. IV the radiation conductance and susceptance are rigorously derived and it is shown how these relate to the resistance and reactance of a rigid disk in an infinite baffle. Some remarks on an earlier attempt by the author to solve the susceptance integral by symbolic computation are also included.

In Sec. V, a solution to the free space equation using the dipole Rayleigh integral is derived, where the Green's function is expanded using the Gegenbauer addition theorem (or multipole expansion). This leads to a single-expansion expression for the pressure field when the distance from the center of the disk to the observation point is greater than the disk's radius. A solution for a planar axisymmetric source with an arbitrary surface pressure distribution is also included. In Sec. VI, the paraxial pressure field is derived, which converges in the immediate near field and is again a single expansion, reducing to a single term, or closed-form solution, on the axis of symmetry. From the paraxial solution, the expression for the surface-velocity distribution, given in Sec. VII, is fairly straightforward to derive due to the fact that the paraxial solution is in cylindrical coordinates. This makes it fairly easy to take the normal derivative of the pressure with respect to the axial ordinate at the surface of the disk. Finally, in Sec. VII, the expression for the far-field pressure is presented. Although this expression is nothing new, it is interesting to compare the beam pattern with that of a rigid disk and it is shown that, in the case of an electrostatic loudspeaker, this gives the same on-axis pressure as Walker's equation.

The general aim of this paper is to provide a full set of radiation characteristics of the resilient disk in free space and to show that they generally have simple relationships with those of a rigid disk in an infinite baffle.

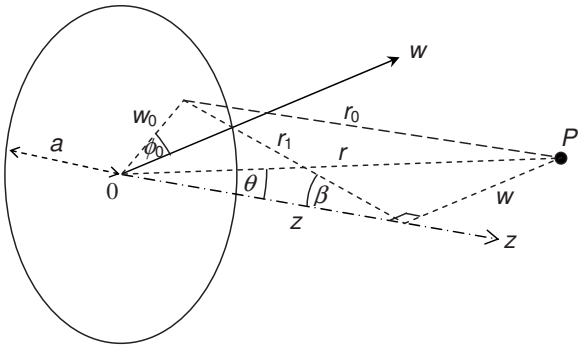

FIG. 1. Geometry of the disk.

II. BOUNDARY CONDITIONS

The infinitesimally thin resilient disk shown in Fig. 1 has a radius a and lies in the w plane with its center at the origin. Due to axial symmetry, the tangential ordinate ϕ of the coordinate system for the observation point P can be ignored. Hence it is simply defined, in spherical coordinates, by the radial and azimuthal ordinates r and θ, respectively or, in cylindrical coordinates, by the radial and axial ordinates w and z, respectively. The infinitesimally thin membrane-like resilient disk is assumed to be perfectly flexible, has zero mass, and is free at its perimeter. It is driven by a uniformly distributed harmonically varying pressure $\tilde{p}_0$ and thus radiates sound from both sides into a homogeneous loss-free acoustic medium. In fact, there need not be a disk present at all and instead the driving pressure could be acting upon the air particles directly. However, for expedience, the area over which this driving pressure is applied shall be referred to as a disk from here onwards. The pressure field on one side of the xy plane is the symmetrical "negative" of that on the other, so that

$$\tilde{p}(w,z) = -\tilde{p}(w,-z). \tag{1}$$

Consequently, there is a Dirichlet boundary condition in the plane of the disk where these equal and opposite fields meet

$$\tilde{p}(w,0) = 0, \quad a < w \leqslant \infty. \tag{2}$$

On the front and rear surfaces of the disk, the pressures are $\tilde{p}_+$ and $\tilde{p}_-$, respectively, which are given by

$$\tilde{p}_+(w_0) = -\tilde{p}_-(w_0) = \tilde{p}_0/2, \quad 0 \leqslant w_0 \leqslant a \tag{3}$$

and k is the wave number given by $k=\omega/c=2\pi/\lambda$, where ω is the angular frequency of excitation, ρ is the density of the surrounding medium, c is the speed of sound in that medium, and λ is the wavelength. The annotation ~denotes a harmonically time-varying quantity.

III. SOLUTION OF THE FREE-SPACE WAVE EQUATION

Using the dipole King integral,[19] the pressure distribution is defined by

$$\tilde{p}(w,z) = \int_0^{2\pi}\int_0^a (\tilde{p}_+(w_0) - \tilde{p}_-(w_0)) \times \frac{\partial}{\partial z_0} g(w,z|w_0,z_0)\big|_{z_0=0+} w_0 dw_0 d\phi_0, \quad (4)$$

where the Green's function[20] is defined, in cylindrical coordinates, by

$$g(w,z|w_0,z_0) = \frac{i}{4\pi}\int_0^\infty J_0(\mu w)J_0(\mu w_0)\frac{\mu}{\sigma}e^{-i\sigma|z-z_0|}d\mu, \quad (5)$$

where

$$\sigma = \begin{cases} \sqrt{k^2-\mu^2}, & 0 \leqslant \mu < k \\ -i\sqrt{\mu^2-k^2}, & \mu > k \end{cases} \quad (6)$$

and J_n is the Bessel function of the first kind. Substituting Eqs. (3), (5), and (6) in Eq. (4) and integrating over the surface of the disk yields

$$\tilde{p}(w,z) = \frac{a\tilde{p}_0}{2}\int_0^\infty J_1(\mu a)J_0(\mu w)e^{-i\sigma z}d\mu, \quad (7)$$

where the following identity[22] has been used

$$\int_0^a J_0(\mu w_0)w_0 dw_0 = \frac{a}{\mu}J_1(a\mu). \quad (8)$$

IV. RADIATION ADMITTANCE

A. Admittance as an integral expression

The disk velocity $\tilde{u}_0(w)$ can be derived using the following relationship for the normal pressure gradient:

$$\tilde{u}_0(w) = \frac{i}{k\rho c}\frac{\partial}{\partial z}\tilde{p}(w,z)\bigg|_{z=0+} = \frac{a\tilde{p}_0}{2k\rho c}\int_0^\infty J_1(\mu a)J_0(\mu w)\sigma d\mu. \quad (9)$$

For small k, this reduces to the Weber–Schafheitlin integral[21,22]

$$\begin{aligned}\tilde{u}_0(w)|_{k\to 0} &= \frac{ia\tilde{p}_0}{2k\rho c}\int_0^\infty J_1(\mu a)J_0(\mu w)\mu d\mu \\ &= \frac{i\tilde{p}_0}{2ka\rho c}{}_2F_1\left(\frac{3}{2},\frac{1}{2};1;\frac{w^2}{a^2}\right) \\ &= \frac{i\tilde{p}_0 \boldsymbol{E}(w^2/a^2)}{\pi ka\rho c}\left(1-\frac{w^2}{a^2}\right)^{-1} \\ &\approx \frac{i\tilde{p}_0}{2ka\rho c}\left\{1-\left(1-\frac{2}{\pi}\right)\frac{w^3}{a^3}\right\}\left(1-\frac{w^2}{a^2}\right)^{-1},\end{aligned} \quad (10)$$

where $\boldsymbol{E}$ is the complete elliptic integral of the second kind. Hence there is a singularity at the rim. Integrating the velocity from Eq. (9) over the area of the disk provides the total volume velocity $\tilde{U}_0$ as follows:

$$\tilde{U}_0 = \int_0^{2\pi}\int_0^a \tilde{u}_0(w)w dw d\phi = \frac{\pi a^2\tilde{p}_0}{k\rho c}\int_0^\infty J_1^2(\mu a)\frac{\sigma}{\mu}d\mu, \quad (11)$$

where Eq. (8) has again been used. The acoustic radiation admittance is then given by

$$y_{ar} = \frac{\tilde{U}_0}{\tilde{p}_0} = \frac{S\tilde{u}_0}{\tilde{p}_0} = \frac{S}{2\rho c}(G_R(k) - iB_R(k)), \quad (12)$$

where G_R is the normalized *conductance* given by

$$G_R(k) = \frac{2}{k}\int_0^k \frac{\sqrt{k^2-\mu^2}}{\mu}J_1^2(\mu a)d\mu, \quad (13)$$

B_R is the normalized *susceptance* given by

$$B_R(k) = \frac{2}{k}\int_k^\infty \frac{\sqrt{\mu^2-k^2}}{\mu}J_1^2(\mu a)d\mu, \quad (14)$$

and $S=\pi a^2$ is the surface area of the disk.

B. Solution of the real integral

Substituting $\mu = k\sin\theta$ and $\zeta = ka$ in Eq. (13) yields

$$G_R(\zeta) = 2\int_0^{\pi/2}\frac{\cos^2\theta}{\sin\theta}J_1^2(\zeta\sin\theta)d\theta, \quad (15)$$

which, after differentiating with respect to ζ, gives

$$\frac{d}{d\zeta}G_R(\zeta) = 2\int_0^{\pi/2} J_1(\zeta\sin\theta) \times (J_0(\zeta\sin\theta) - J_2(\zeta\sin\theta))\cos^2\theta d\theta. \quad (16)$$

Using the following identities[23]

$$J_1(\zeta\sin\theta)J_0(\zeta\sin\theta) = \frac{2}{\pi}\int_0^{\pi/2}\cos\phi J_1(2\zeta\sin\theta\cos\phi)d\phi \quad (17)$$

and

$$J_1(\zeta\sin\theta)J_2(\zeta\sin\theta) = -\frac{2}{\pi}\int_0^{\pi/2}\cos 3\phi J_1(2\zeta\sin\theta\cos\phi)d\phi \quad (18)$$

together with[22]

$$\cos\phi + \cos 3\phi = 2\cos\phi\cos 2\phi, \quad (19)$$

Eq. (16) becomes

$$\frac{d}{d\zeta}G_R(\zeta) = \frac{8}{\pi}\int_0^{\pi/2}\cos\phi\cos 2\phi \times \int_0^{\pi/2} J_1(2\zeta\cos\phi\sin\theta)\cos^2\theta d\theta d\phi. \quad (20)$$

The integral over θ is split into two using $\cos^2\theta = 1-\sin^2\theta$ and then solved with the help of the following identities:[22]

$$\int_0^{\pi/2} J_1(\psi \sin\theta)d\theta = \sqrt{\frac{\pi}{2\psi}}\mathbf{H}_{1/2}(\psi) = \frac{1-\cos\psi}{\psi}, \quad (21)$$

$$\int_0^{\pi/2} J_1(\psi \sin\theta)\sin^2\theta d\theta = \sqrt{\frac{\pi}{2\psi}}J_{3/2}(\psi) = \frac{\sin\psi}{\psi^2} - \frac{\cos\psi}{\psi}, \quad (22)$$

where $\mathbf{H}_n$ is the Struve function and $\psi=2\zeta\cos\phi$, so that

$$\frac{d}{d\zeta}G_R(\zeta) = \frac{8}{\pi}\int_0^{\pi/2} \cos\phi\cos 2\phi\left(\frac{1}{\psi} - \frac{\sin\psi}{\psi^2}\right)d\phi. \quad (23)$$

The integral of the first term in the bracket vanishes and using the identity $\cos 2\phi=2\cos^2\phi-1$, gives

$$\frac{d}{d\zeta}G_R(\zeta) = \frac{2}{\pi\zeta^2}\int_0^{\pi/2}\frac{\sin(2\zeta\cos\phi)}{\cos\phi}d\phi - \frac{4}{\pi\zeta^2}\int_0^{\pi/2}\sin(2\zeta\cos\phi)\cos\phi d\phi. \quad (24)$$

The first integral in Eq. (24) is differentiated to give[22]

$$\frac{d}{d\zeta}\int_0^{\pi/2}\frac{\sin(2\zeta\cos\phi)}{\cos\phi}d\phi = 2\int_0^{\pi/2}\cos(2\zeta\cos\phi)d\phi = \pi J_0(2\zeta). \quad (25)$$

The second is solved using the identity[22]

$$\int_0^{\pi/2}\sin(2\zeta\cos\phi)\cos\phi d\phi = \frac{\pi}{2}J_1(2\zeta). \quad (26)$$

Hence

$$\frac{d}{d\zeta}G_R(\zeta) = \frac{2}{\zeta^2}\left(\int J_0(2\zeta)d\zeta - J_1(2\zeta)\right), \quad (27)$$

or using the product rule

$$\zeta\frac{d}{d\zeta}G_R(\zeta) = \frac{2}{\zeta}\left(\int J_0(2\zeta)d\zeta - J_1(2\zeta)\right) = \frac{d}{d\zeta}\zeta G_R(\zeta) - G_R(\zeta). \quad (28)$$

Let the solution be

$$G_R(\zeta) = 1 - \frac{J_1(2\zeta)}{\zeta} - \frac{2}{\zeta}\left(\int J_0(2\zeta)d\zeta - J_1(2\zeta)\right) = 1 + \frac{J_1(2\zeta)}{\zeta} - \frac{2}{\zeta}\int J_0(2\zeta)d\zeta. \quad (29)$$

Then[22]

$$\frac{d}{d\zeta}\zeta G_R(\zeta) = 1 + J_0(2\zeta) - J_2(2\zeta) - 2J_0(2\zeta) = 1 - \frac{J_1(2\zeta)}{\zeta}, \quad (30)$$

which is the radiation resistance of a rigid disk in an infinite baffle.[7,19] It can easily be seen that Eqs. (29) and (30) satisfy Eq. (28). With help from the following identity:[24]

$$\int J_0(2\zeta)d\zeta = \int_0^{\zeta} J_0(2\zeta)d\zeta = \zeta J_0(2\zeta) + \pi\zeta \times \frac{J_1(2\zeta)\mathbf{H}_0(2\zeta) - J_0(2\zeta)\mathbf{H}_1(2\zeta)}{2}, \quad (31)$$

the final solution is then given by

$$G_R(ka) = 1 + \frac{J_1(2ka)}{ka} - 2J_0(2ka) - \pi(J_1(2ka)\mathbf{H}_0(2ka) - J_0(2ka)\mathbf{H}_1(2ka)) \approx \frac{k^2a^2}{6}, \quad ka < 0.5. \quad (32)$$

C. Solution of the imaginary integral

Substituting $\mu=k\sin\theta$ and $\zeta=ka$ in Eq. (14) yields

$$B_R(\zeta) = 2i\int_{(\pi/2)+i0}^{(\pi/2)+i\infty}\frac{\cos^2\theta}{\sin\theta}J_1^2(\zeta\sin\theta)d\theta, \quad (33)$$

which, after differentiating with respect to ζ, gives

$$\frac{d}{d\zeta}B_R(\zeta) = 2i\int_{(\pi/2)+i0}^{(\pi/2)+i\infty}J_1(\zeta\sin\theta) \times (J_0(\zeta\sin\theta) - J_2(\zeta\sin\theta))\cos^2\theta d\theta. \quad (34)$$

Using the identities of Eqs. (17)–(19), Eq. (34) becomes

$$\frac{d}{d\zeta}B_R(\zeta) = \frac{8i}{\pi}\int_0^{\pi/2}\cos\phi\cos 2\phi \times \int_{(\pi/2)+i0}^{(\pi/2)+i\infty}J_1(2\zeta\cos\phi\sin\theta)\cos^2\theta d\theta d\phi \quad (35)$$

and let $t=\sin\theta$ so that

$$\frac{d}{d\zeta}B_R(\zeta) = -\frac{8}{\pi}\int_0^{\pi/2}\cos\phi\cos 2\phi \times \int_1^{\infty}J_1(2\zeta\cos\phi t)\sqrt{t^2-1}dtd\phi. \quad (36)$$

The integral over t is then solved with the help of the following identity:[22]

$$\int_1^{\infty}J_1(\psi t)\sqrt{t^2-1}dt = \frac{\cos\psi}{\psi^2}, \quad (37)$$

where $\psi=2\zeta\cos\phi$, so that

$$\frac{d}{d\zeta}B_R(\zeta) = -\frac{2}{\pi\zeta^2}\int_0^{\pi/2}\frac{\cos 2\phi\cos\psi}{\cos\phi}d\phi. \quad (38)$$

Using the identity $\cos 2\phi=2\cos^2\phi-1$, gives

$$\frac{d}{d\zeta}B_R(\zeta) = \frac{2}{\pi\zeta^2}\int_0^{\pi/2}\frac{\cos(\psi)}{\cos\phi}d\phi - \frac{4}{\pi\zeta^2}\int_0^{\pi/2}\cos(\psi)\cos\phi d\phi. \tag{39}$$

The first integral in Eq. (39) is differentiated to give[22]

$$\frac{d}{d\zeta}\int_0^{\pi/2}\frac{\cos(2\zeta\cos\phi)}{\cos\phi}d\phi = -2\int_0^{\pi/2}\sin(2\zeta\cos\phi)d\phi = -\pi\mathbf{H}_0(2z). \tag{40}$$

The second is solved using the identity[22]

$$\int_0^{\pi/2}\cos(\psi)\cos\phi d\phi = \frac{d}{d\zeta}\int_0^{\pi/2}\int\cos(2\zeta\cos\phi)\cos\phi d\zeta d\phi = \frac{d}{d\zeta}\int_0^{\pi/2}\frac{\sin(2\zeta\cos\phi)}{2}d\phi = \frac{d}{d\zeta}\frac{\pi\mathbf{H}_0(2\zeta)}{4} = \frac{\pi\mathbf{H}_{-1}(2\zeta)}{2}. \tag{41}$$

Hence

$$\frac{d}{d\zeta}B_R(\zeta) = -\frac{2}{\zeta^2}\left(\int\mathbf{H}_0(2\zeta)d\zeta + \mathbf{H}_{-1}(2\zeta)\right), \tag{42}$$

or using the product rule

$$\zeta\frac{d}{d\zeta}B_R(\zeta) = -\frac{2}{\zeta}\left(\int\mathbf{H}_0(2\zeta)d\zeta + \mathbf{H}_{-1}(2\zeta)\right) = \frac{d}{d\zeta}\zeta B_R(\zeta) - B_R(\zeta). \tag{43}$$

Let the solution be

$$B_R(\zeta) = \frac{\mathbf{H}_1(2\zeta)}{\zeta} + \frac{2}{\zeta}\left(\int\mathbf{H}_0(2\zeta)d\zeta + \mathbf{H}_{-1}(2\zeta)\right) = \frac{4}{\pi\zeta} - \frac{\mathbf{H}_1(2\zeta)}{\zeta} + \frac{2}{\zeta}\int\mathbf{H}_0(2\zeta)d\zeta. \tag{44}$$

Then[22]

$$\frac{d}{d\zeta}\zeta B_R(\zeta) = \mathbf{H}_0(2\zeta) + \mathbf{H}_2(2\zeta) - \frac{4\zeta}{3\pi} = \frac{\mathbf{H}_1(2\zeta)}{\zeta}, \tag{45}$$

which is the radiation reactance of a rigid disk in an infinite baffle.[7,19] It can easily be seen that Eqs. (44) and (45) satisfy Eq. (43). With help from the following identity[22] (after substituting $\zeta=bx^{1/2}$, $\nu=0$, and $\mu=\lambda=0$):

$$\int_0^b\mathbf{H}_0\left(\frac{a\zeta}{b}\right)d\zeta = \frac{ab}{\pi}{}_2F_3\left(1,1;\frac{3}{2},\frac{3}{2},2;-\frac{a^2}{4}\right), \tag{46}$$

where ${}_pF_q$ is the hypergeometric function. Then, letting $a=2\zeta$ and $b=\zeta$, leads to

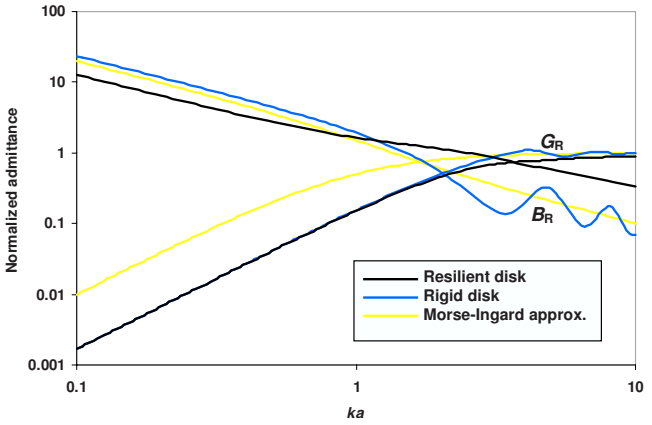

FIG. 2. (Color online) Normalized radiation admittances of the resilient and rigid disks in free space.

$$\int\mathbf{H}_0(2\zeta)d\zeta = \int_0^{\zeta}\mathbf{H}_0(2\zeta)d\zeta = \frac{2\zeta^2}{\pi}{}_2F_3\left(1,1;\frac{3}{2},\frac{3}{2},2;-\zeta^2\right), \tag{47}$$

so that the final solution is then given by

$$B_R(ka) = \frac{4}{\pi ka} - \frac{\mathbf{H}_1(2ka)}{ka} + \frac{4ka}{\pi}{}_2F_3\left(1,1;\frac{3}{2},\frac{3}{2},2;-k^2a^2\right) \approx \frac{4}{\pi ka}, \quad ka<0.5. \tag{48}$$

The conductance G_R and reactance B_R are plotted in Fig. 2, along with the conductance and reactance of a rigid disk in free space for comparison. A third pair of curves shows the conductance and reactance of an oscillating sphere, used as approximations by Morse and Ingard,[20] whereby $G_R(ka)=k^2a^2/(1+k^2a^2)$ and $B_R(ka)=(2+k^2a^2)/(ka+k^3a^3)$. The same results are shown as impedances in Fig. 3.

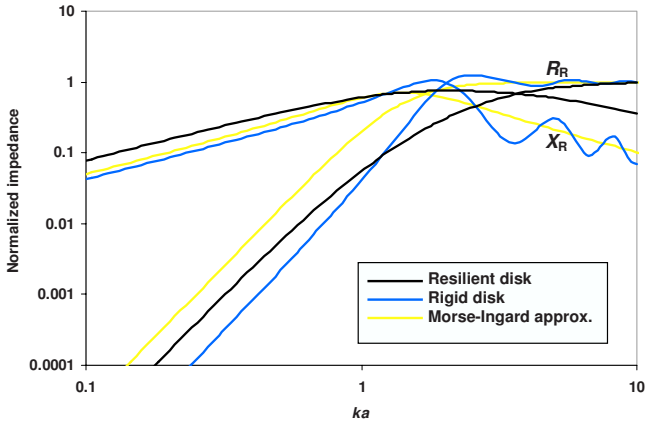

FIG. 3. (Color online) Normalized radiation impedances of the resilient and rigid disks in free space.

D. Relationship between a resilient disk in free space and a rigid disk in an infinite baffle

Suppose that the radiation resistance and reactance of a rigid disk in an infinite baffle are denoted by $R_R(ka)$ and X_R, respectively, then

$$\frac{d}{d(ka)}kaG_R(ka) = R_R(ka) = 1 - \frac{J_1(2ka)}{ka}, \tag{49}$$

or

$$G_R(ka) = \frac{1}{ka}\int R_R(ka)d(ka) \tag{50}$$

and

$$\frac{d}{d(ka)}kaB_R(ka) = X_R(ka) = \frac{\mathbf{H}_1(2ka)}{ka}, \tag{51}$$

or

$$B_R(ka) = \frac{1}{ka}\left(\int X_R(ka)d(ka) + \frac{4}{\pi}\right), \tag{52}$$

where G_R and B_R are the radiation conductance and susceptance, respectively, of a resilient disk in free space as defined in Eqs. (32) and (48). The constant of integration $4/\pi$ in Eq. (52) comes from Eq. (44). The low-frequency asymptotic values of disks in general are related by

$$R_R(\text{baffled resilient}) = R_R(\text{baffled rigid}) = k^2a^2/2, \tag{53}$$

$$X_R(\text{baffled resilient}) = X_R(\text{unbaffled resilient}) = \pi ka/4, \tag{54}$$

$$G_R(\text{unbaffled rigid}) = G_R(\text{unbaffled resilient}) = k^2a^2/6, \tag{55}$$

$$B_R(\text{unbaffled rigid}) = 2B_R(\text{baffled rigid}) = 3\pi/(4ka). \tag{56}$$

E. Some remarks on the solution by symbolic computation

This section reports an earlier attempt that had been made to solve the susceptance integral by symbolic computation,[21] but the result contained some erroneous terms and, without prior knowledge of the correct solution, it was impossible to tell which terms were correct and which were not. After substituting $\mu=kt$ in Eq. (14), the result of the symbolic computation[21] (after gathering a few terms) is

$$\begin{aligned} B_R(ka) &= 2\int_1^\infty \frac{\sqrt{t^2-1}}{t}J_1^2(kat)dt \\ &= 2\frac{2-\log(8ka)-\gamma}{\pi ka} \\ &\quad + \frac{4ka}{3\pi}{}_2F_3\left(1,1;\frac{3}{2},2,\frac{5}{2};-k^2a^2\right), \end{aligned} \tag{57}$$

which contains two erroneous negative terms. However, the correct form can be obtained from Eq. (52), which, after symbolic computation, gives

$$B_R(ka) = \frac{4}{\pi ka} + \frac{4ka}{3\pi}{}_2F_3\left(1,1;\frac{3}{2},2,\frac{5}{2};-k^2a^2\right). \tag{58}$$

Admittedly this is a particularly difficult integral to compute due to the oscillatory and slowly converging nature of the integrand. These days, symbolic computation is fairly reliable, but it is always worth checking the results numerically where possible, although in this case that is not so easy to do. Similarly, symbolic computation[21] of the integral in Eq. (50) gives

$$G_R(ka) = 1 - {}_1F_2\left(\frac{1}{2};\frac{3}{2},2;-k^2a^2\right). \tag{59}$$

V. NEAR-FIELD PRESSURE WHEN THE DISTANCE FROM THE CENTER OF THE DISK TO THE OBSERVATION POINT IS GREATER THAN THE DISK'S RADIUS

A. Uniform pressure distribution

Using the dipole Rayleigh integral, the sound pressure at the observation point P can be written as

$$\begin{aligned} \tilde{p}(r,\theta) = &\int_{-\pi}^{\pi}\int_0^a (\tilde{p}_+(w_0) - \tilde{p}_-(w_0)) \\ &\times g'(r,\theta|w_0,\phi_0)w_0dw_0d\phi_0, \end{aligned} \tag{60}$$

where g' is the normal gradient of the Green's function, as the surface of integration shrinks back to the disk, defined by

$$g'(r,\theta|w_0,\phi_0) = \frac{\partial}{\partial z_0}g(r,\theta|w_0,\phi_0,z_0)|_{z=0+}, \tag{61}$$

and $g(r,\theta|w_0,\phi_0,z_0)$ is the Green's function in cylindrical-spherical coordinates defined by $g(r,\theta|w_0,\phi_0,z_0) = e^{-ikr_1}/(4\pi r_1)$, where $r_1^2 = r^2 + w_0^2 + z_0^2 - 2r(w_0\cos\phi_0\sin\theta + z_0\cos\theta)$. The normal gradient of the Green's function is then given by

$$g'(r,\theta|w_0,\phi_0) = r\cos\theta\frac{1+ikr_0}{r_0^2}g(r,\theta|w_0,\phi_0), \tag{62}$$

where

$$g(r,\theta|w_0,\phi_0) = \frac{e^{-ikr_0}}{4\pi r_0} \tag{63}$$

and $r_0^2 = r^2 + w_0^2 - 2rw_0\cos\phi_0\sin\theta$. In order to expand g', it is first necessary to reduce it to a simpler function of g by eliminating some of the r_0 terms. This can be achieved by integrating g' with respect to θ as follows:

$$\int g'(r,\theta|w_0,\phi_0)d\theta = -\frac{g(r,\theta|w_0,\phi_0)}{w_0\cos\phi_0} \tag{64}$$

so that

$$g'(r,\theta|w_0,\phi_0) = -\frac{1}{w_0\cos\phi_0}\frac{d}{d\theta}g(r,\theta|w_0,\phi_0). \tag{65}$$

The Green's function of Eq. (63) can be expanded using the following formula, which is a special case of Gegenbauer's addition theorem:[22]

$$g(r,\theta|w_0,\phi_0) = -\frac{ik}{4\pi}\sum_{p=0}^{\infty}(2p+1)h_p^{(2)}(kr) \times j_p(kw_0)P_p(\cos\phi_0\sin\theta), \tag{66}$$

where j_p is the spherical Bessel function of the first kind and $h_p^{(2)}$ is the spherical Hankel function.[24] The Legendre function P_p can be expanded using the following addition theorem[22] (after setting one of the three angles in the original formula to $\pi/2$):

$$P_p(\cos\phi_0\sin\theta) = P_p(0)P_p(\cos\theta) + 2\sum_{q=1}^{\infty}(-1)^q P_p^{-q}(0)P_p^q(\cos\theta)\cos q\phi_0. \tag{67}$$

Inserting Eqs. (65)–(67) in Eq. (60) while noting that

$$\int_{-\pi}^{\pi}\frac{\cos q\phi_0}{\cos\phi_0}d\phi_0 = 2\pi\sin\frac{q\pi}{2}, \tag{68}$$

and applying the boundary condition of Eq. (3) leads to

$$\tilde{p}(r,\theta) = ik\tilde{p}_0\sum_{p=0}^{\infty}(2p+1)h_p^{(2)}(kr)\int_0^a j_p(kw_0)dw_0 \times\sum_{q=1}^{\infty}(-1)^q P_p^{-q}(0)\frac{d}{d\theta}P_p^q(\cos\theta)\sin\frac{q\pi}{2}. \tag{69}$$

It is noted that $P_p^{-q}(x)|_{p>q}=0$, so that the infinite limit of the summation in q can be replaced with p. Also, the even terms in p and q disappear so that

$$\tilde{p}(r,\theta) = ik\tilde{p}_0\sum_{p=0}^{\infty}(4p+3)h_{2p+1}^{(2)} \times(kr)\int_0^a j_{2p+1}(kw_0)dw_0\xi_{2p+1}(\cos\theta), \tag{70}$$

where

$$\xi_{2p+1}(\cos\theta) = \sum_{q=0}^{p}(-1)^q P_{2p+1}^{-2q-1}(0)\frac{d}{d\theta}P_{2p+1}^{2q+1}(\cos\theta). \tag{71}$$

Defining a new function

$$\chi_{2p+1}(\cos\theta) = \frac{\sqrt{\pi}(-1)^p p!}{\Gamma(p+(3/2))}\xi_{2p+1}(\cos\theta) \tag{72}$$

gives $\chi_1(\cos\theta)=\cos\theta$, $\chi_3(\cos\theta)=(5\cos^3\theta-3\cos\theta)/2$, $\chi_5(\cos\theta)=(63\cos^5\theta-70\cos^3\theta+15\cos\theta)/8$, and $\chi_7(\cos\theta)=(429\cos^7\theta-693\cos^5\theta+315\cos^3\theta-35\cos\theta)/16$. Hence it can be shown that[22]

$$\chi_{2p+1}(\cos\theta) = \frac{1}{2^{2p+1}}\sum_{q=0}^{p}\frac{(-1)^q\Gamma(4p-2q+3)(\cos\theta)^{2p-2q+1}}{q!\,\Gamma(2p-q+2)\Gamma(2p-2q+2)} = P_{2p+1}(\cos\theta), \tag{73}$$

which, after inserting Eqs. (72) and (73) in Eq. (70), gives

$$\tilde{p}(r,\theta) = \frac{ik\tilde{p}_0}{\sqrt{\pi}}\sum_{p=0}^{\infty}(-1)^p(4p+3)\frac{\Gamma(p+(3/2))}{p!} \times\int_0^a j_{2p+1}(kw_0)dw_0h_{2p+1}^{(2)}(kr)P_{2p+1}(\cos\theta). \tag{74}$$

This is equivalent to an expression previously presented by Bouwkamp,[3] although no derivation was provided. A simpler solution[25] than Bouwkamp's to the integral over w_0 can be written as

$$\int_0^a j_{2p+1}(kw_0)dw_0 = \frac{\sqrt{\pi}}{2k}\left(\frac{ka}{2}\right)^{2p+2}\frac{{}_1F_2(p+1;p+2,2p+(5/2);-k^2a^2/4)}{(p+1)\Gamma(2p+(5/2))}, \tag{75}$$

so that, after truncating the summation limit to P, the final expression for the pressure field becomes

$$\tilde{p}(r,\theta) = -i\tilde{p}_0\sum_{p=0}^{P}\frac{(-1)^p\Gamma(p+(3/2))}{\Gamma(p+2)\Gamma(2p+(3/2))}\left(\frac{ka}{2}\right)^{2p+2} \times{}_1F_2\left(p+1;p+2,2p+\frac{5}{2};-\frac{k^2a^2}{4}\right) \times h_{2p+1}^{(2)}(kr)P_{2p+1}(\cos\theta). \tag{76}$$

This expansion converges providing $r\geqslant a$, and was used for the region $w\geqslant a$. It is similar in form to the "outer" solution obtained by Mast and Yu[16] for the piston in an infinite baffle, except that the current solution is an expansion of the odd terms of the spherical Hankel and Legendre functions as opposed to even ones. These odd eigenfunctions are a result of the odd boundary condition given by Eq. (1). Let an error function be defined by

$$\varepsilon(r,\theta) = \frac{|\tilde{p}(r,\theta)-\tilde{p}_{ref}(r,\theta)|}{|\tilde{p}(r,\theta)|}, \tag{77}$$

where the reference pressure is that obtained using the original dipole Rayleigh integral or Eq. (60) with the unexpanded Green's function normal gradient of Eq. (62). The calculations were performed using 30 digit precision with $P\approx 4ka$, whereby P was rounded down to the nearest integer value. This produced values of ε typically less than 0.00001, but rising to around 0.1 in the immediate vicinity of the rim ($r=a$ and $\theta=\pi/2$) where convergence was slowest. At $ka=6\pi$, the expansion calculated four times faster than numerical integration. Furthermore, the calculation time for the expansion roughly doubles for every doubling of ka, whereas for numerical integration it nearly quadruples for every doubling of ka.

B. Generalization to an arbitrary surface pressure distribution

Let the arbitrary surface pressure distribution be defined by the power series

$$\tilde{p}_+(w_0) = -\tilde{p}_-(w_0) = \sum_{m=0}^{M} \tilde{A}_m \left(1 - \frac{w_0^2}{a^2}\right)^{m+1/2}, \quad 0 \leqslant w_0 \leqslant a, \tag{78}$$

where, in the case of a rigid disk in free space,[7] the unknown series coefficients $\tilde{A}_m$ are related to normalized coefficients $\tilde{\tau}_m$ by $\tilde{A}_m = \tilde{\tau}_m (m+(3/2))ka\rho c\tilde{u}_0$, or, in the case of a membrane in free space,[11] by $\tilde{A}_m = \tilde{\tau}_m (m+(3/2))\tilde{p}_I/2$. Inserting the above expressions in Eq. (60) and using the identity[21]

$$\int_0^a \left(1 - \frac{w_0^2}{a^2}\right)^{m+1/2} j_{2p+1}(kw_0)dw_0 = \frac{\sqrt{\pi}}{2k} \frac{\Gamma(m+(3/2))p!}{\Gamma(p+m+(5/2))\Gamma(2p+(5/2))} \left(\frac{ka}{2}\right)^{2p+2} \times {}_1F_2\left(p+1; p+m+\frac{5}{2}, 2p+\frac{5}{2}; -\frac{k^2a^2}{4}\right), \tag{79}$$

leads to the final expression for the pressure field which is given by

$$\tilde{p}(r,\theta) = 2i \sum_{m=0}^{M} \tau_m \sum_{p=0}^{P} \frac{(-1)^p \Gamma(p+(3/2)) h_{2p+1}^{(2)}(kr) P_{2p+1}(\cos\theta)}{\Gamma(2p+(3/2))(m+(5/2))_p} \times \left(\frac{ka}{2}\right)^{2p+2} {}_1F_2\left(p+1; p+m+\frac{5}{2}, 2p+\frac{5}{2}; -\frac{k^2a^2}{4}\right) \times \begin{cases} ka\rho c\tilde{u}_0, & \text{Rigid disk} \\ \tilde{p}_I/2, & \text{Membrane} \end{cases}. \tag{80}$$

where $\tilde{u}_0$ is the disk velocity and $\tilde{p}_I$ is the membrane driving pressure.

VI. NEAR-FIELD PRESSURE PARAXIAL SOLUTION

In order to find a solution which converges up to the face of the disk, a trick previously used by Mast and Yu[16] is to move the center of the coordinate system from the center of the disk out to the same axial distance as the observation point. Referring to Fig. 1 the distance r_0 from a point source on the disk to the observation point is $r_0^2 = r_1^2 + w^2 - 2r_1 w \cos\phi_0 \sin\beta$, where $w = r\sin\theta$, $r_1 = \sqrt{z^2 + w_0^2}$, and $z = r\cos\theta$. The angle β is defined by $\cos\beta = z/r_1$ and $\sin\beta = w_0/r_1$. Putting these new parameters in Eq. (74) gives

$$\tilde{p}(w,z) = \frac{ik\tilde{p}_0}{\sqrt{\pi}} \sum_{p=0}^{\infty} (-1)^p (4p+3) \frac{\Gamma(p+(3/2))}{\Gamma(p+1)} \times \frac{j_{2p+1}(kw)}{w} \int_z^{r_a} h_{2p+1}^{(2)}(kr_1) P_{2p+1}(\cos\beta) r_1 dr_1, \tag{81}$$

where $r_a = \sqrt{z^2 + a^2}$. Let

$$\tilde{p}(w,z) = \frac{i\tilde{p}_0}{\sqrt{\pi}kw} \sum_{p=0}^{P} (-1)^p (4p+3) \times \frac{\Gamma(p+(3/2))}{\Gamma(p+1)} j_{2p+1}(kw) f_{2p+1}, \tag{82}$$

where, after substituting $\zeta = kr_1$,

$$f_{2p+1} = \int_{kz}^{kr_a} h_{2p+1}^{(2)}(\zeta) P_{2p+1}\left(\frac{kz}{\zeta}\right) \zeta d\zeta. \tag{83}$$

Then the following indefinite integral g_{2p+1} is denoted by

$$g_{2p+1}(\zeta) = \int h_{2p+1}^{(2)}(\zeta) P_{2p+1}\left(\frac{kz}{\zeta}\right) \zeta d\zeta, \tag{84}$$

so that $f_{2p+1} = g_{2p+1}(kr_a) - g_{2p+1}(kz)$. When $p=0$, the first term is given by

$$g_1(\zeta) = \int h_1^{(2)}(\zeta) P_1\left(\frac{kz}{\zeta}\right) \zeta d\zeta = i\frac{kz}{\zeta} e^{-i\zeta}, \tag{85}$$

so that

$$f_1 = i\left(\frac{z}{r_a} e^{-ikr_a} - e^{-ikz}\right). \tag{86}$$

According to Hasagawa *et al.*,[15] the remaining terms can be determined from the following recursion formulas:

$$g_{2p+1}(\zeta) + g_{2p-1}(\zeta) = \zeta h_{2p}^{(2)}(\zeta)\left(P_{2p+1}\left(\frac{kz}{\zeta}\right) - P_{2p-1}\left(\frac{kz}{\zeta}\right)\right), \tag{87}$$

$$g_{2p+1}(kz) + g_{2p-1}(kz) = 0. \tag{88}$$

Hence

$$f_{2p+1} = -f_{2p-1} + kr_a h_{2p}^{(2)}(kr_a)\left(P_{2p+1}\left(\frac{z}{r_a}\right) - P_{2p-1}\left(\frac{z}{r_a}\right)\right). \tag{89}$$

Thus the solution is given by the combination of Eqs. (82), (86), and (89), which converges for $w^2 < a^2 + z^2$. Again, this is essentially an odd term version of the "paraxial" expansion obtained by Mast and Yu[16] for the piston in an infinite baffle. Toward the axis of symmetry, convergence is achieved with fewer terms until only the first term of the expansion remains, which is the closed-form axial solution. This can also be derived directly by setting $\theta=0$ in Eq. (63) before integrating over the surface to give

$$\tilde{p}(r,0) = \frac{\tilde{p}_0}{2}\left(e^{-ikr} - \frac{r}{\sqrt{r^2+a^2}} e^{-ik\sqrt{r^2+a^2}}\right). \tag{90}$$

For comparison, the Backhaus and Trendelenburg axial solution[26] for a piston in an infinite baffle is

$$\tilde{p}(r,0) = \rho c\tilde{u}_0 (e^{-ikr} - e^{-ik\sqrt{r^2+a^2}}). \tag{91}$$

The calculations for Eqs. (82), (86), and (89) were performed using 30 digit precision for the region $w < a$ with $P \approx 4kw$, whereby P was rounded down to the nearest integer value.

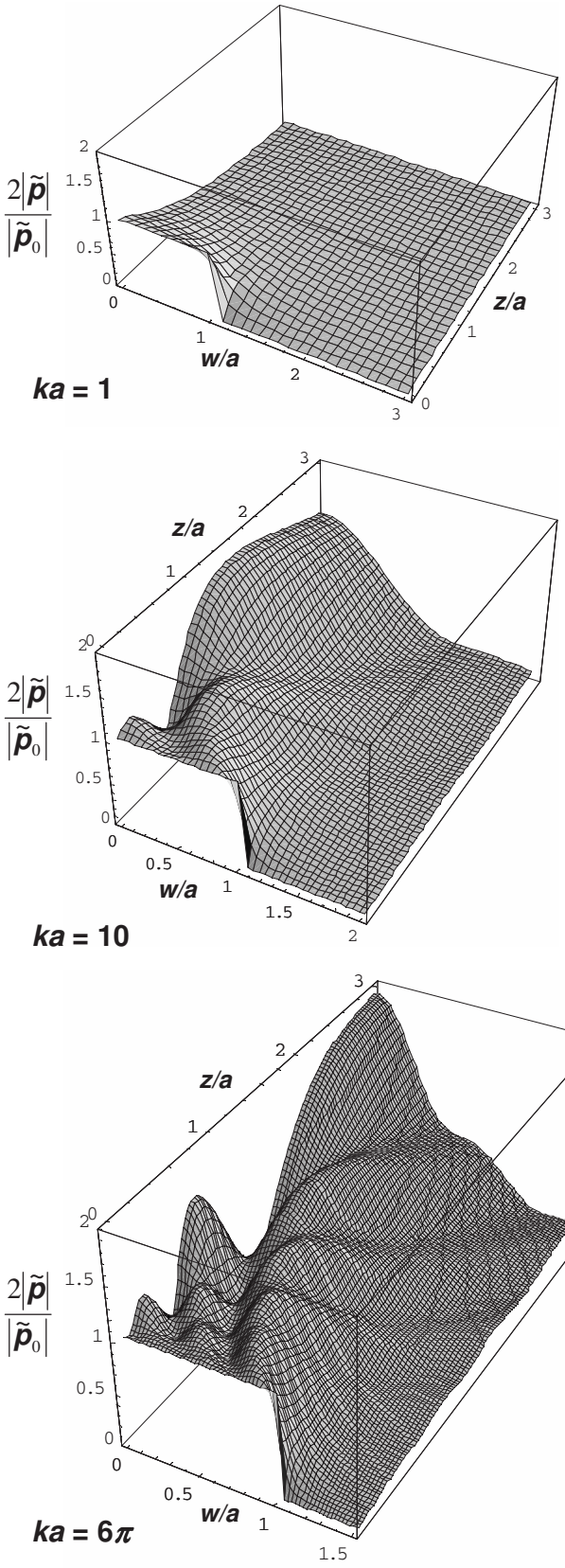

FIG. 4. Near-field pressure of the resilient disk in free space for $ka=1$, 10, and 6π.

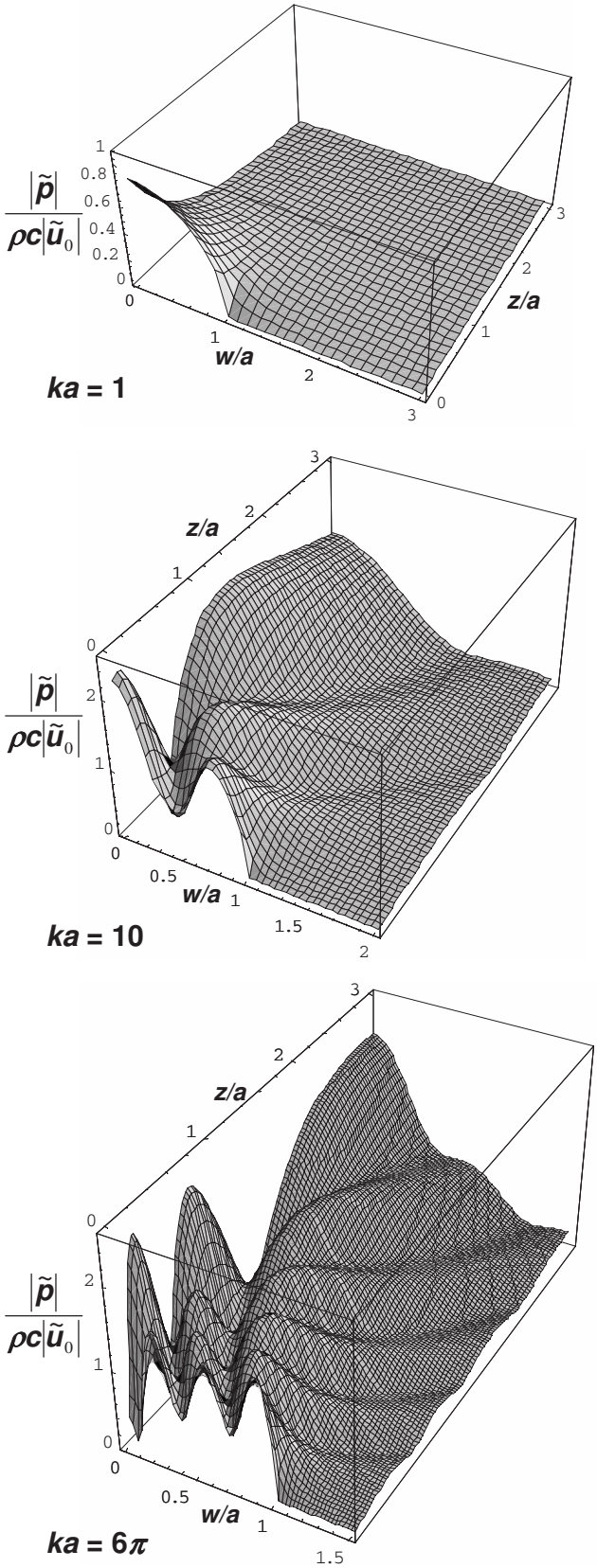

FIG. 5. Near-field pressure of the rigid disk in free space for $ka=1$, 10, and 6π.

Again, this produced values of ε typically of the order of 0.00001, but rising to around 0.1 in the immediate vicinity of the rim. For various values of ka, pressure fields are shown in Fig. 4 for a resilient disk in free space and in Fig. 5 for a rigid disk in free space. The latter were calculated using Eq. (80) for $r \geqslant a$ and, in the case of $r < a$, using similar formulation to that previously derived for a membrane in free space.[11]

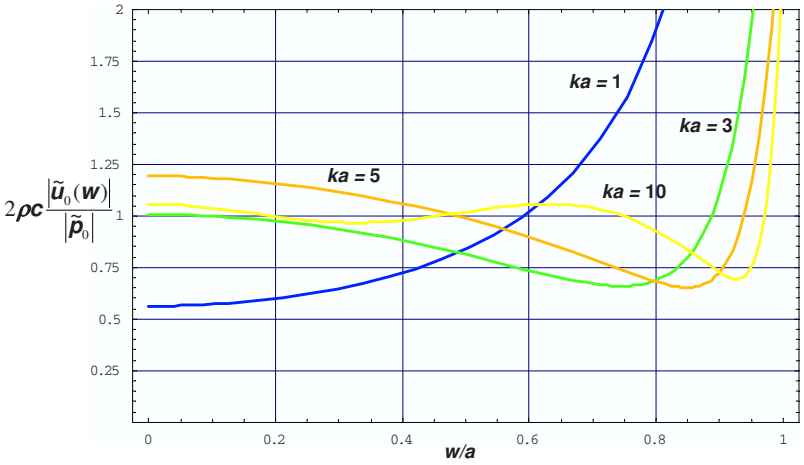

FIG. 6. (Color online) Normalized surface velocity magnitude of the resilient disk in free space.

VII. SURFACE VELOCITY

Using the solutions for the near-field pressure from Eqs. (82), (86), and (89), the surface velocity is given by

$$\tilde{u}_0(w) = \frac{i}{k\rho c}\frac{d}{dz}\tilde{p}(w,z)\bigg|_{z=0+}$$
$$= -\frac{\tilde{p}_0}{\rho c\sqrt{\pi}}\sum_{p=0}^{\infty}(-1)^p(4p+3)$$
$$\times\frac{\Gamma(p+(3/2))}{\Gamma(p+1)}f'_{2p}\frac{j_{2p+1}(kw)}{kw}, \tag{92}$$

where

$$f'_0 = 1 - i\frac{e^{-ika}}{ka}, \tag{93}$$

$$f'_{2p} = -f'_{2p-2} - h^{(2)}_{2p}(ka)$$
$$\times((2p+1)P_{2p}(0) - (2p-1)P_{2p-2}(0)). \tag{94}$$

The magnitude and phase of the normalized velocity are shown in Figs. 6 and 7, respectively, for various values of ka. For small k, it can be shown to agree well with asymptotic expression given by Eq. (10).

VIII. FAR-FIELD PRESSURE

A far-field expression can be derived using the usual procedure,[7,20] which involves an asymptotic version of Eq. (62) for large r, giving

$$\tilde{p}(r,\theta) = -\frac{ia\tilde{p}_0}{4r}e^{-ikr}D(\theta), \tag{95}$$

where $D(\theta)$ is the directivity function, which is given by

$$D(\theta) = \frac{2J_1(ka\sin\theta)}{\sin\theta}\cos\theta \tag{96}$$

and plotted in Fig. 8 for various values of ka. The directivity function of a rigid disk in free space is plotted in Fig. 9 for comparison. Since $D(0)=ka$, the on-axis response is simply

$$\tilde{p}(r,0) = -\frac{ika^2\tilde{p}_0}{4r}e^{-ikr}, \tag{97}$$

which just gives a constant 6 dB/octave rising slope at all frequencies. In the case of an electrostatic loudspeaker

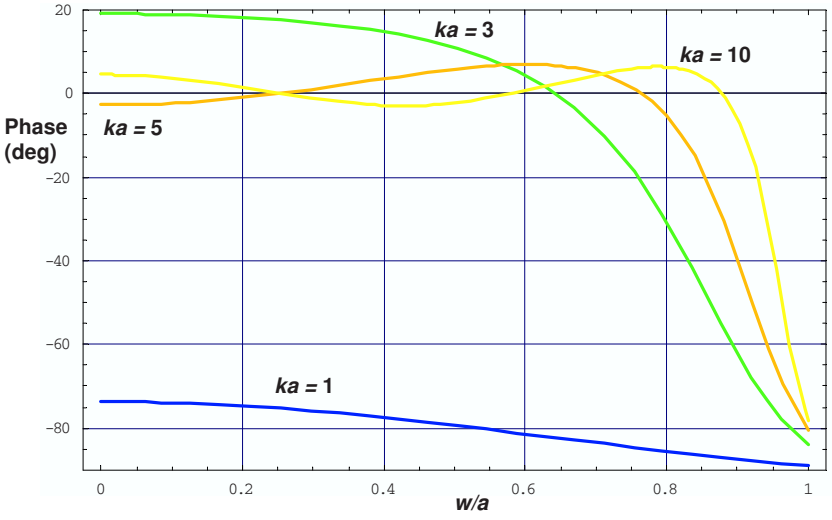

FIG. 7. (Color online) Surface velocity phase of the resilient disk in free space.

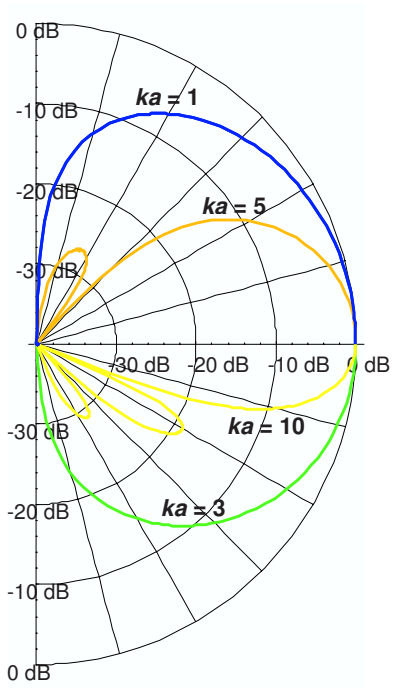

FIG. 8. (Color online) Normalized far-field directivity function of the resilient disk in free space.

$$\tilde{p}_0 = \frac{E_P}{d} \cdot \frac{2\tilde{I}_{in}}{i\omega\pi a^2}, \tag{98}$$

where E_P is the polarizing voltage, d is the membrane-electrode separation, and $\tilde{I}_{in}$ is the input static current, assuming that the motional current is negligible in comparison. Substituting this in Eq. (97) yields

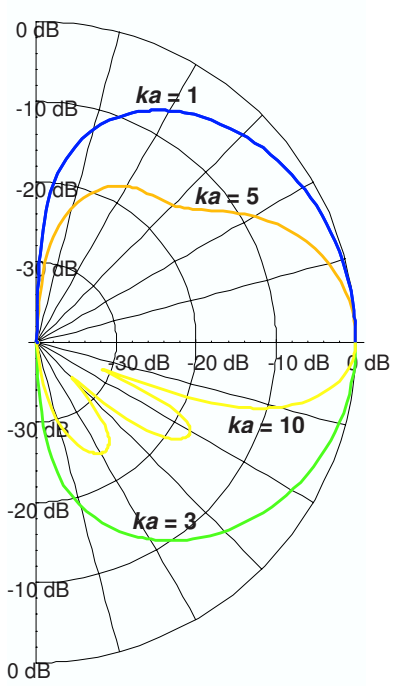

FIG. 9. (Color online) Normalized far-field directivity function of the rigid disk in free space.

$$\tilde{p}(r,0) = -\frac{E_P}{d} \cdot \frac{\tilde{I}_{in}}{2\pi rc} e^{-ikr}, \tag{99}$$

which is Walker's equation,[18] albeit obtained by a slightly different method.

IX. DISCUSSION

The results presented here are intended to provide a full set of radiation characteristics for a fundamental axisymmetric planar dipole source. Starting with the radiation admittance and impedance, it can be seen from Figs. 2 and 3 that in the case of unbaffled radiators, the rigid disk has ripples in both the real and imaginary parts, whereas those of the resilient disk are smooth almost monotonic functions, as are also those of the oscillating rigid sphere (or Morse Ingard approximation). These are entirely consistent with the results previously found for baffled radiators.[5] The solution presented for the susceptance integral contradicts a previous statement[7] made by the author that it could not be solved. At least, that is how it seemed when trying to tackle it numerically. The integrand is strongly oscillatory and converges more slowly than just about any other integral in fundamental sound radiation theory, due to the combination of the singularity and acoustic short circuit at the rim. Also, an attempt to solve it by symbolic computation gave somewhat unexpected results as discussed in Sec. IV E.

At medium to high frequencies, the pressure field can be divided into two regions: the Fresnel diffraction region in the near field and the Fraunhofer diffraction region in the far field. It is well understood that the Fresnel region is characterized by complex non-propagating interference patterns, whereas the Fraunhofer region is characterized by spherically propagating waves in a beam pattern with a strong central lobe (Airy disk) accompanied by smaller side lobes (Airy pattern). At higher frequencies, a third "shadow region" begins to form at the surface of the radiator which is characterized by plane waves in a straight beam with the same cross section as the radiator, like a virtual transmission line in space. It appears from Figs. 4 and 5 that this shadow region forms more readily at lower frequencies in the case of the resilient disk, no doubt aided by the constant pressure distribution at the surface of the disk. At $ka=6\pi$, the pressure field fluctuations in the vicinity of the rigid disk are considerably greater than for the resilient disk. Furthermore, the axial pressure response of a rigid disk given by Eq. (91) has nulls, whereas the resilient disk axial response given by Eq. (90) is oscilliatory but with decreasing magnitude towards the face of the disk.

In Figs. 6 and 7, the velocity magnitude and phase distributions are generally similar in shape to those of the resilient disk in an infinite baffle, except that the magnitude rises more rapidly towards the rim due to the acoustic short circuit there in the absence of a baffle. This is also accompanied by increased phase shift.

Previously, the author has stated that at high frequencies the directivity function of the resilient disk in free space does not converge towards that of a rigid disk in an infinite baffle.[6] This is not strictly true. They must converge eventu-

ally because the only difference between them is a factor of $\cos\theta$, which produces the classic figure-of-eight dipole pattern at low frequencies. As the directivity pattern becomes narrower, this factor has less of an effect. However, the convergence is rather slow. At $ka=10$, the beam pattern of an unbaffled rigid disk, shown in Fig. 9, is rather similar to that of a baffled one, except that the latter has nulls due to the *velocity* boundary conditions on both the disk and surrounding baffle. This can also be derived by taking the Hankel transform of the velocity distribution in the plane of the disk, which is a rotationally symmetric step function. By contrast, the side lobes of the unbaffled resilient disk, shown in Fig. 8, are somewhat smaller. This pattern also has nulls due to the *pressure* boundary conditions on both the disk and surrounding plane.

X. CONCLUSIONS

Closed-form expressions have been derived for the radiation admittance of a resilient disk in free space and these have been shown to have a simple relationship with the radiation impedance of a rigid piston in an infinite baffle. Also, rapidly converging single expansions have been derived for the near-field pressure and surface velocity. Furthermore, the near-field pressure has been generalized to an arbitrary surface pressure distribution, yielding a double expansion, whereas a triple expansion was previously derived by the author for a membrane in free space.[11] Hence the solution is now similar in form to that of the membrane in an infinite baffle.[11]

ACKNOWLEDGMENTS

The author would like to express his gratitude to N. Lobo for his invaluable advice in numerical matters and also to L. M. Kärkkäinen for his many useful suggestions.

[1]M. Greenspan, "Piston radiator: Some extensions of the theory," J. Acoust. Soc. Am. **65**(3), 608–621 (1979).
[2]J. Babinet, "Mémoires d'optique météorologique (Memoirs on meteorological optics)," C. R. Hebd. Seances Acad. Sci. **4**, 638 (1837).
[3]C. J. Bouwkamp, "Theoretical and numerical treatment of diffraction through a circular aperture," IEEE Trans. Antennas Propag. **AP18-2**, 152–176 (1970).
[4]R. D. Spence, "The diffraction of sound by circular disks and apertures," J. Acoust. Soc. Am. **20**(4), 380–386 (1948).
[5]T. J. Mellow, "On the sound field of a resilient disk in an infinite baffle," J. Acoust. Soc. Am. **120**(1), 90–101 (2006).
[6]J. W. S. Rayleigh, *The Theory of Sound* (Dover, New York, 1945), Vol. **II**, pp. 107 and 162.
[7]T. J. Mellow and L. M. Kärkkäinen, "On the sound field of an oscillating disk in an open and closed circular baffle," J. Acoust. Soc. Am. **118**(3), 1311–1325 (2005).
[8]H. Suzuki and J. Tichy, "Sound radiation from an elastically supported circular plate," J. Acoust. Soc. Am. **65**(1), 106–111 (1979).
[9]J. H. Streng, "Calculation of the surface pressure on a vibrating circular stretched membrane in free space," J. Acoust. Soc. Am. **82**(2), 679–686 (1987).
[10]J. H. Streng, "Sound radiation from a circular stretched membrane in free space," J. Audio Eng. Soc. **37**(3), 107–118 (1989).
[11]T. J. Mellow and L. M. Kärkkäinen, "On the sound field of a membrane in free space and an infinite baffle," J. Acoust. Soc. Am. **120**(5), 2460–2477 (2006).
[12]T. J. Mellow and L. M. Kärkkäinen, "On the sound field of a shallow spherical shell in an infinite baffle," J. Acoust. Soc. Am. **121**(6), 3527–3541 (2007).
[13]C. W. Rice and E. W. Kellogg, "Notes on the development of a new type of hornless loudspeaker," Trans. Am. Inst. Electr. Eng. **44**, 461–475 (1925). Reprinted JAES, **30**(7/8), 512–521 (1982).
[14]G. R. Harris, "Review of transient theory for a baffled planar piston," J. Acoust. Soc. Am. **70**(1), 10–20 (1981).
[15]T. Hasegawa, N. Inoue, and K. Matsuzawa, "A new rigorous expansion for the velocity potential of a circular piston source," J. Acoust. Soc. Am. **74**(3), 1044–1047 (1983).
[16]T. D. Mast and F. Yu, "Simplified expansions for radiation from a baffled circular piston," J. Acoust. Soc. Am. **118**(6), 3457–3464 (2005).
[17]J. F. Kelly and R. J. McGough, "An annular superposition integral for axisymmetric radiators," J. Acoust. Soc. Am. **121**(2), 759–765 (2006).
[18]P. J. Walker, "New developments in electrostatic loudspeakers," J. Audio Eng. Soc. **28**(11), 795–799 (1980).
[19]L. V. King, "On the acoustic radiation field of the piezoelectric oscillator and the effect of viscosity on the transmission," Can. J. Res. **11**, 135–146 (1934).
[20]P. M. Morse and K. U. Ingard, *Theoretical Acoustics* (McGraw–Hill, New York, 1968), p. 321, pp. 364–366, pp. 389–390.
[21]I. S. Gradshteyn and I. M. Ryzhik, *Table of Integrals, Series, and Products*, 6th ed., edited by A. Jeffrey (Academic, New York, 2000), p. 668, Eq. (6.561.5), p. 675, Eq. (6.574.1), p. 31, Eqs. (1.323.1) and (1.323.2), p. 718, Eq. (6.683.5), p. 933, Eq. (8.552.6), p. 717, Eq. (6.682.1), p. 914, Eq. (8.464.3), p. 414, Eq. (3.715.14), p. 902, Eq. (8.411.4), p. 916, Eqs. (8.471.1) and (8.471.2), p. 673, Eq. (6.567.17), p. 932, Eq. (8.551.1), p. 933, Eq. (8.553.2), p. 933, Eqs. (8.553.4) and (8.553.5), p.747, Eq. (6.815.2), p. 899, Eq. (8.384.1), p. 930, Eq. (8.533.2), p. 963, Eq. (8.794.1), p. 974, Eqs. (8.912.1)–(8.912.8), p. 974, Eq. (8.911.1).
[22]S. Wolfram, *The MATHEMATICA BOOK*, 5th ed. (Wolfram Media, Champaign, IL, 2003). Symbolic computation by MATHEMATICA.
[23]G. N. Watson, *A Treatise on the Theory of Bessel Functions*, 2nd ed. (Cambridge University Press, London, 1944), pp. 150, Sec. 5.43, Eqs. (1) and (2).
[24]M. Abramowitz and I. A. Stegun, *Handbook of Mathematical Functions* (Dover, New York, 1964), p. 480, Eq. (8.411.4), p. 437, Eq. (10.1.1).
[25]A. P. Prudnikov, Yu A. Brychkov, and O. I. Marichev, *Integrals and Series, Volume 2: Special Functions* (Gordon and Breach, New York, 1986), p. 37.
[26]H. Backhaus and F. Trendelenburg, "Über die Richtwirkung von Kolbenmembranen (On the directivity of piston membranes)," Z. Tech. Phys. (Leipzig) **7**, 630 (1927).

An acoustic intensity-based method for reconstruction of radiated fields

Chao Yu
Department of Mechanical Engineering, Michigan State University, East Lansing, Michigan 48824

Zhengfang Zhou
Department of Mathematics, Michigan State University, East Lansing, Michigan 48824

Mei Zhuang[a)]
Department of Mechanical Engineering, Michigan State University, East Lansing, Michigan 48824

(Received 27 February 2007; revised 21 January 2008; accepted 23 January 2008)

An acoustic intensity-based method is proposed for the reconstruction of acoustic radiation pressure. Unlike the traditional inverse acoustic methods, the proposed method includes the acoustic pressure gradient as an input in addition to its simultaneous, co-located acoustic pressure in a radiated field. As a result, the reconstruction of acoustic radiation pressure from the input acoustic data over a portion of a surface enclosing all the acoustic sources, i.e., an open surface, becomes unique due to the unique continuation theory of elliptic equations. Hence the method is more stable and the reconstructed acoustic pressure is less dependable on the locations of the input acoustic data. Furthermore, the proposed method can be applied for both inverse and forward problems up to the minimum sphere enclosing the sources of interest. The effectiveness of the method is demonstrated by the results of several acoustic radiation examples with single or multi-frequency source in a two-dimensional configuration. The results from the method also show a measurable improvement in accuracy and consistency of reconstructed acoustic radiation pressure, in particular when the effect of the signal-to-noise ratio is included. © *2008 Acoustical Society of America.*
[DOI: 10.1121/1.2875046]

PACS number(s): 43.20.Rz, 43.50.Yw, 43.50.Rq [SFW] Pages: 1892–1901

I. INTRODUCTION

Several prominent inverse acoustic methods have been developed for the near-field acoustic holograph (NAH).[1–10] These methods can be classified into three categories: (1) Fourier acoustics, (2) the inverse boundary element methods (IBEMs), and (3) the Helmholtz equation least squares (HELS) method. Among these traditional inverse methods, the acoustic pressure measurement by itself is considered as the input of the inverse methods. The solution of these inverse methods, therefore, is not unique unless the input acoustic pressure is provided over a surface enclosing all the acoustic sources, i.e., a closed surface.[11–13] As a result, the effectiveness of these methods weakens when the input acoustic pressure is only available over a portion of a closed surface (i.e., open surface). In many engineering applications, however, the acoustic pressure measurement over a closed surface is often infeasible or impossible, in particular for the far-field measurement. Therefore, there is a need to improve the accuracy and consistency of the inverse methods especially in the case where the input acoustic data are only available over an open surface.

Recently, with the advent of new signal processing techniques and the advances in transducer technology, acoustic intensity measurement devices have been improved to make them more reliable, accurate, and compact.[14] Using these devices, the acoustic intensity as well as simultaneous, co-located acoustic pressure can be evaluated. The acoustic pressure gradient can thus be derived along a given axis, e.g., the axis of a microphone pair.

Motivated by the advances in acoustic measurement technology and the NAH methods, especially the HELS method, an acoustic intensity-based method (AIBM) is proposed for the accurate reconstruction of the acoustic radiation pressure in both the near and far fields. The method uses the acoustic pressure gradient and its simultaneous pressure as the input acoustic data for the calculations.

Because of the addition of the acoustic pressure gradient in the input acoustic data, the solution of the AIBM becomes unique with the input given over an open surface. However, the solution is not stable since it is a Cauchy problem for Helmholz equation. Mathematically, this instability comes from the highly oscillatory modes. By carefully removing these modes, the AIBM, compared with the traditional inverse methods, could provide a measurable improvement in terms of accuracy and consistency of the reconstructed acoustic pressure. The objectives of the current study are twofold (1) developing, numerically implementing and verifying the AIBM and (2) demonstrating the advantages, effectiveness and potential of the AIBM for engineering applications.

The paper is organized as follows. The mathematical and numerical formulations of the AIBM are discussed in Sec. II. The exact mathematical solution of the Helmholz

[a)]Author to whom correspondence should be addressed. Electronic mail: zhuangm@egr.msu.edu

 0001-4966/2008/123(4)/1892/10/$23.00 © 2008 Acoustical Society of America

equation is approximated by finite linear combinations of basis functions. The numerical formulation and implementation are developed to effectively determine the coefficients of these basis functions by the method with an input of acoustic pressure and its derivative of a given direction. In Sec. III, three numerical examples of acoustic radiations from either single or multi-frequency acoustic source are presented and verified. The advantages of the AIBM over a traditional inverse method are demonstrated. Furthermore, the sensitivity of the AIBM to random noises with various signal-to-noise ratios (SNRs) in the input acoustic data is examined and analyzed. The concluding remarks are drawn in Sec. IV.

II. MATHEMATICAL AND NUMERICAL FORMULATIONS

A. Mathematical formulation

The acoustic pressure field P in the frequency domain is governed by the Helmholtz equation

$$\nabla^2 P + k^2 P = 0, \quad \text{in } \Omega = R^2 \setminus \Omega_{in}, \tag{1}$$

where Ω_{in} is a bounded domain in R^2 containing all acoustic sources, $k=\omega/c$ is the wave number with the angular frequency ω and the speed of sound c. If the standard polar coordinates are used in a two-dimensional (2D) configuration, Eq. (1) can be written as

$$\frac{\partial^2 P}{\partial r^2} + \frac{1}{r}\frac{\partial P}{\partial r} + \frac{1}{r^2}\frac{\partial^2 P}{\partial \theta^2} + k^2 P = 0, \quad \text{in } \Omega = R^2 \setminus \Omega_{in}. \tag{2}$$

With the Sommerfeld radiation condition

$$\lim_{r\to\infty} r^{1/2}[\partial_r P(r,\theta) - ikP(r,\theta) = 0],$$

the solution of Equation (2) can be written as[15,16]

$$P(r,\theta) = \sum_{n=0}^{\infty} (a_n \cos n\theta + b_n \sin n\theta) H_n(kr), \tag{3}$$

where H_n is the nth-order Hankel function of the second kind. In order to obtain a solution from Eq. (3), it is necessary to determine the coefficients a_n and b_n. These coefficients are determined by matching the assumed form of the solution to the input acoustic pressure in the HELS method.[8] Strictly speaking the solution is unique only if the input acoustic pressure is made on a boundary Γ which encloses all the acoustic sources in the domain Ω. The acoustic pressure measurement on the boundary Γ is usually impractical or infeasible for engineering applications. In practice, the input acoustic pressure is only available on a number of segments of the boundary, Γ_1 (an open surface, see Fig. 1).

Although the AIBM could be implemented in various inverse acoustic methods, it is formulated here similar to that of the HELS.[8] It will be demonstrated later that when the input acoustic data are given over an open surface the AIBM strengthens the HELS method, and improves its mathematical well posedness and practical applicability.

In the AIBM, both the acoustic pressure and its co-located derivative (normal to Γ_1) on the boundary Γ_1 are considered as the input acoustic data for the reconstruction of acoustic radiation pressure in the domain Ω. With the pressure derivative boundary condition as an additional input, the uniqueness of the reconstructed acoustic pressure solution is guaranteed from the unique continuation theory of elliptic equations.[11–13] In the AIBM, the partial boundary value problem for acoustic radiation pressure is defined as

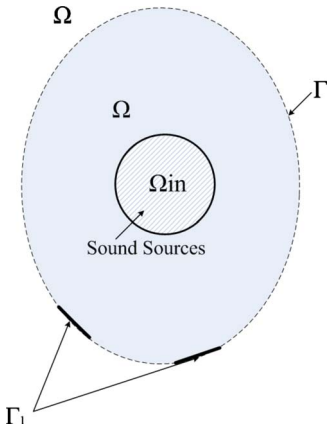

FIG. 1. Acoustic radiation field with input acoustic data locations.

$$\begin{cases} \nabla^2 P + k^2 P = 0, & \text{in } \Omega = R^2 \setminus \Omega_{in}, \\ P\big|_{\Gamma_1} = g_1, \partial_\nu P\big|_{\Gamma_1} = g_2, & \lim\limits_{r\to\infty} r^{1/2}[\partial_r P(r,\theta) - ikP(r,\theta)] = 0, \end{cases} \tag{4}$$

where ν is the outward normal to the boundary Γ_1, g_1 is the acoustic pressure and g_2 is the acoustic pressure derivative normal to Γ_1. The solution can then be expressed as Eq. (3) on and outside the minimum sphere, which encloses all the acoustic sources under consideration. It is worth mentioning that the boundary Γ_1 where the input acoustic data are provided needs to be outside of the minimum sphere.

Although this partial boundary value problem is unique, it is not stable. Small variations in g_1 and g_2 may lead to large differences in the solution P. In the following section, the numerical techniques and schemes are described for solving this partial boundary value problem. The stability conditions and other restrictions of the numerical formulation and implementation are discussed in details.

B. Numerical formulation

In the current study, the numerical solution of Eq. (4) is being sought by the following three steps.

(a) Instead of using the infinite summation in Eq. (3), the exact solution of Eq. (4) is approximated by a finite summation, i.e.,

$$P(r,\theta) \sim a_0 H_0(kr) + \sum_{n=1}^{N} (a_n \cos n\theta + b_n \sin n\theta) H_n(kr), \tag{5}$$

where N is a suitable integer. The choice for N will be discussed later in the section. In the AIBM, the solution P is achieved by obtaining the coefficients a_n and b_n. The coefficients are numerically determined by matching the assumed

form of the solution to the input acoustic data, g_1 and g_2 over the boundary Γ_1. One obvious restriction of N is that the number of coefficients $(2N+1)$ to be determined must be less than the number of the input data over Γ_1.

(b) In order to determine the coefficients a_n and b_n numerically, an accurate and efficient method must be developed to evaluate each H_n. When kr is relatively large, the first Q terms in the asymptotic expansion of $H_0(kr)$[15] are used in the current numerical calculation

$$H_0(kr) \sim H_{0,Q}(kr) = \sqrt{\frac{2}{\pi kr}} e^{-i\left(kr-\frac{\pi}{4}\right)} \times \left[1 + \sum_{q=1}^{Q-1} (-1)^q \frac{(1/2)_q (1/2)_q}{q\,!\,(2ikr)^q} \right], \quad kr \to \infty, \tag{6}$$

where $(1/2)_q = 1/2(1+1/2)\ldots(q-1+1/2)$. It can be shown that the order of accuracy established in the above approximation is of order $O(Q!/(2kr)^Q)$. It is also noted that the error generated by the approximation would become unacceptable when Q is much larger than $2kr$. Since the accuracy of the method depends on a good approximation of the Hankel functions, the restriction of $Q \leqslant 1.5kr$ is used. For the approximation of other H_n, the recurrence relation for H_n is employed. Because of the initial error of $O(1/r^Q)$, N has to be restricted to prevent the propagation of the errors for H_n. From a careful analysis, N should be less than $2kr$ to ensure that the error for H_n is also in the order of $O(1/r^Q)$. In addition, since the partial boundary value problem, Eq. (4), is not stable due to the presence of functions for large index n in Eq. (5), a proper limit on the upper bound of n is needed to control the solution instability.

When kr is relatively small, one can use the expansion of $H_0(kr)$ for $r \to 0$, or a higher order numerical integration method to evaluate $H_0(kr)$. Other H_n can be obtained again by the recurrence relation.

In the current numerical calculation, a relatively large kr (e.g., $kr=6$) is considered and the above asymptotic expansion formulation is used. Thus, the definition of the minimum sphere in terms of the numerical solution of P needs to be extended beyond enclosing all the acoustic sources. For a given wave number k, the radius of the minimum sphere, r_m, is given by, e.g., $r_m \geqslant 6/k$. The numerical solution is valid on and outside the minimum sphere.

(c) After the evaluation of the Hankel functions, a suitable optimization method is used to determine the coefficients a_n and b_n in Eq. (5) for the partial boundary value problem [Eq. (4)]. The simplest method is the least squares technique. Because of the underlying partial differential equation and the particular basis functions used in this calculation, some numerical techniques are introduced to improve the condition numbers of the numerical schemes.

C. Numerical implementation

If the input acoustic data, g_1 (acoustic pressure) and g_2 (acoustic pressure derivative normal to Γ_1), are known at M discrete points $(r_1,\theta_1),\ldots,(r_M,\theta_M)$ over the boundary Γ_1, the linear system for the coefficients a_n and b_n is given by the following $2M$ equations:

$$a_0 H_{0,Q}(kr_j) + \sum_{n=1}^{N} (a_n \cos n\theta_j + b_n \sin n\theta_j) H_{n,Q}(kr_j) = g_1(r_j,\theta_j), \quad j = 1,\ldots,M \tag{7}$$

$$a_0 \partial_\nu H_{0,Q}(kr_j) + \sum_{n=1}^{N} \partial_\nu [(a_n \cos n\theta + b_n \sin n\theta) H_{n,Q}(kr)]_{r_j,\theta_j} = g_2(r_j,\theta_j), \quad j = 1,\ldots,M. \tag{8}$$

The above system can be expressed in a matrix form as $Ax = B$, where

$$x = [a_0,\ldots,a_N,b_1,\ldots,b_N]^T, \tag{9}$$

$$B = [g_1(r_1,\theta_1),\ldots,g_1(r_M,\theta_M),g_2(r_1,\theta_1),\ldots,g_2(r_M,\theta_M)]^T \tag{10}$$

and $A=(A_1,A_2)^T$, A_1 corresponds to g_1 and A_2 corresponds to g_2. The vector coefficients x can be determined by minimizing $\|Ax-B\|$ directly for a choice of norm $\|\cdot\|$. However, when $r_1=r_2=\ldots=r_m$, i.e., the input acoustic data is prescribed on a circular segment, it is well known that $\partial_\nu H_{n,Q}(kr) = \partial_r H_{n,Q}(kr) = ikH_{n,Q}(kr) + Q(1/(kr))$ and therefore the matrix $A_2 \sim ikA_1$ for a large r. In many cases, this will result in a large condition number for the system $Ax=B$, and more importantly, this proportionality between A_2 and A_1 will not allow us to take the full advantage of the additional input acoustic data g_2.

To overcome this difficulty, the original system is first modified as follows:

$$\begin{pmatrix} A_1 \\ kr(A_2 - ikA_1) \end{pmatrix} x = \begin{pmatrix} g_1 \\ kr(g_2 - ikg_1) \end{pmatrix}. \tag{11}$$

Then, to further improve the condition number for the linear system, the coefficients vector x is replaced by the vector y defined as

$$y = (a_0 H_0, a_1 H_1, \ldots, a_N H_N, b_1 H_1, \ldots, b_N H_N)^T. \tag{12}$$

The new linear system for the vector y has much simpler matrix forms

$$\begin{pmatrix} D_1 \\ D_2 \end{pmatrix} y = \begin{pmatrix} g_1 \\ kr(g_2 - ikg_1) \end{pmatrix}, \tag{13}$$

where

$$D_1 = \begin{pmatrix} 1 & \cos\theta_1 & \dots & \cos N\theta_1 & \sin\theta_1 & \dots & \sin N\theta_1 \\ 1 & \cos\theta_2 & \dots & \cos N\theta_2 & \sin\theta_2 & \dots & \sin N\theta_2 \\ \vdots & \vdots & \vdots & \vdots & \vdots & \vdots & \vdots \\ 1 & \cos\theta_M & \dots & \cos N\theta_M & \sin\theta_M & \dots & \sin N\theta_M \end{pmatrix}, \tag{14}$$

$$D_2 = \begin{pmatrix} E_0 & E_1\cos\theta_1 & \dots & E_N\cos N\theta_1 & E_1\sin\theta_1 & \dots & E_N\sin N\theta_1 \\ E_0 & E_1\cos\theta_2 & \dots & E_N\cos N\theta_2 & E_1\sin\theta_2 & \dots & E_N\sin N\theta_2 \\ \vdots & \vdots & \vdots & \vdots & \vdots & \vdots & \vdots \\ E_0 & E_1\cos\theta_M & \dots & E_N\cos N\theta_M & E_1\sin\theta_M & \dots & E_N\sin N\theta_M \end{pmatrix} kr \tag{15}$$

and $E_j = [H_j'(kr)/H_j(kr)] - ik$, E_j can be obtained easily from a recurrence relation.[15]

The least squares method that minimizes the standard L^2 norm $\|Dy - B\|$ is used to determine the vector y, which in turn gives values of the coefficients a_n and b_n. In the current numerical study, it is observed that, although some regularization methods may be needed to improve the stability of the system for large N, they are not necessary for relatively small N. Based on the analysis given in Sec. II B ($N \leqslant 2kr$), N is initialized within a given range of 2–12. The reconstructed solutions of acoustic radiation pressure for various N are compared with the input acoustic data given on the boundary Γ_1. The total error at all the input points is then computed for each N. The optimum N within the given range is determined from the minimum overall error. The reconstruction of the acoustic field is then carried out using the optimum N.

It should be pointed out that without the addition of the pressure gradient to the input acoustic data the reconstructed acoustic pressure could not be unique if only $P|_{\Gamma_1}$ is specified. For example, let Ω_{in} be the unit disk centered at the origin and all the acoustic sources are enclosed by the unit circle, the acoustic pressure should then satisfy the following equation:

$$a_0 H_0(k) + \sum_{n=1}^{\infty} (a_n \cos n\theta + b_n \sin n\theta) H_n(k) = g(\theta), \quad \theta \in [0, \pi] \tag{16}$$

if the upper half boundary of the unit circle ($0 \leqslant \theta \leqslant \pi$) is considered as the boundary Γ_1. It is well known that a_n and b_n are not unique from the Fourier analysis. Especially $g(\theta)$ has always a cosine expansion for $\theta \in [0, \pi]$, i.e., $b_1 = b_2 = \dots = 0$. It is therefore impossible to predict solutions for $\theta \in (\pi, 2\pi)$.

III. NUMERICAL RESULTS AND DISCUSSIONS

Numerical examples are considered in this section for the purposes of: (1) verifying the AIBM and indicating the advantages of the method, (2) discussing the effects of the signal-to-noise ratio, and (3) demonstrating the potential of using the AIBM to reconstruct the acoustic radiation field for engineering applications.

TABLE I. The strength and distribution of the acoustic sources.

	A_0(W/m^2)	x (m)	y (m)
Quadrupole I	1.00	0.30	0.60
	−1.00	−0.10	0.60
	1.00	−0.10	0.20
	−1.00	0.30	0.20
Quadrupole II	−1.20	0.49	−0.12
	1.20	0.20	−0.20
	−1.20	0.28	−0.49
	1.20	0.57	−0.41
Dipole	−0.80	−0.54	−0.16
	0.80	−0.78	−0.45
Monopole	0.90	−0.58	0.58

A. Verification and advantages of AIBM

The example used here is formulated by the acoustic radiation from a combination of one monopole, one dipole, and two quadrupoles in a two-dimensional domain. The acoustic pressure generated by a dipole and quadrupole source can be expressed as a summation of the pressure generated by a monopole, i.e., $P(r, \theta) = \Sigma_{i=1}^{L} (A_0)_i H_0(kR_i)$, where A_0 is the strength of the monopole and R is the distance between a field point and the monopole source. A dipole ($L = 2$) consists of two monopole sources separated by a small distance compared with the wavelength of acoustic radiation. In the frequency domain the strengths of these two monopoles are of equal amplitude but opposite sign. A quadrupole ($L = 4$) is made of two opposite dipoles. The strengths and locations of these acoustic sources used in this example are given in Table I. The acoustic sources are enclosed in the circle of radius $r = 1$ m. The wavenumber of the sources is considered as $k = 2$ m^{-1} and the minimum sphere is then chosen as the circle of radius $r_m = 3$ m (see discussions on the size of the minimum sphere in Sec. II). The label $P(r, \theta)$ used in the figures of the paper denotes the real part of the acoustic pressure in the frequency domain. The units used for r and θ are the meter and the radian, respectively. The reconstruction of acoustic radiation pressure is carried out on and outside the minimum sphere. The input acoustic data are given at two circular (or straight line) segments. The schematic diagram of the acoustic sources and each input segment's location is given in Fig. 2. The starting and ending point coordinates of the two segments are chosen as

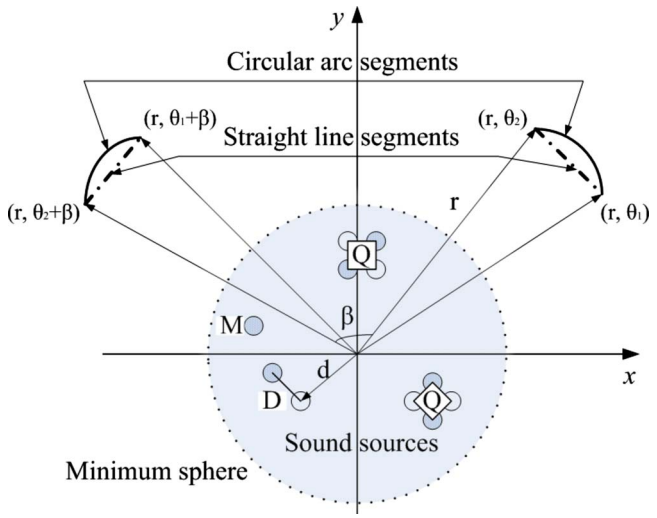

FIG. 2. Schematic diagram of acoustic sources and each input segment's location.

$(6\ \mathrm{m}, 63\pi/128)$, $(6\ \mathrm{m}, 65\pi/128)$ and $(6\ \mathrm{m}, 63\pi/128+\beta)$, $(6\ \mathrm{m}, 65\pi/128+\beta)$ in the polar coordinates. It is noted that the input data are given over an open surface and the circular arc length of each segment is only 1/128 of the circumference of the circle. Each segment is then discretized uniformly into ten grid points where the analytical acoustic pressure and its derivative normal to the segments are given as the input acoustic data. The angle β shown in Fig. 2 is a measure of the dimensionless distance between the two segments of the input, with $\beta=\pi$ being the farthest, i.e., the segments are at the opposite sides of the minimum sphere. Different values of β are considered to examine the sensitivity of the reconstructed acoustic radiation pressure against various input locations of an open surface.

In order to determine if the addition of the pressure gradient in the input acoustic data would improve the accuracy and consistency of the inverse method, two sets of the input acoustic data are considered. The first set of the input consists of the analytical acoustic pressure and its normal derivative, i.e., the AIBM, and the second set of the input consists of only the analytical acoustic pressure, which is referred to as the AIBM_without. Since in this study both the AIBM and AIBM_without are implemented using the least squares method, it allows us to examine the sole effect of the addition of the pressure derivative in the input acoustic data.

The reconstructed acoustic radiation pressure at $r=50$ m is compared with the analytical solution for four different values of β in Fig. 3. Since the reconstructed pressure calculated using the input acoustic data from the two straight line segments is identical to that using the input from the two circular segments, only the results based on the input from the circular segments are shown in Fig. 3. It can be seen clearly that the reconstructed acoustic pressure obtained from the AIBM_without deteriorates in some regions as β deviates from π. On the other hand, the reconstructed acoustic pressure from the AIBM agrees reasonably well with the analytical solution for $\beta=0.8\pi$ and 0.6π. The results demonstrate that the reconstructed acoustic pressure using the AIBM is less dependable on the input location of the acoustic data. The AIBM gives more consistent, reliable and accurate reconstruction of acoustic radiation pressure when the input acoustic data are available over an open surface. However, for the case of $\beta=0.4\pi$, the solution of the AIBM starts to deviate from the analytical solution. As β decreases further, the effectiveness of the AIBM becomes hindered. As a general rule, the more complete the input around an acoustic source, the more accurate the reconstructed acoustic pressure solution. If the input is given on a single segment over an open surface, a considerable extent of the segment is needed in order to achieve acoustic pressure reconstructions with acceptable accuracy. If the input is available on multiple segments over an open surface around an acoustic source, then a better accuracy of the reconstructed solution will be obtained when the segments are on the opposite sides of the minimum sphere, although the exact location of the acoustic source may not be known.

It is also worth mentioning that for an input given over a closed surface, the reconstructed acoustic pressure solution is unique without the addition of the pressure gradient to the input acoustic data. The advantage of the AIBM over the AIBM_without diminishes. The formulation used for the AIBM_without is identical to that of the HELS.[8] Therefore, by including the pressure gradient in the input of the HELS, the mathematical well posedness of the HELS will be improved and the method will be enhanced.

B. Effect of signal-to-noise ratio (SNR)

Until now the analytical solution has been used as the input acoustic data for the calculation. In practice, however, the input data are usually experimentally measured. The acoustic measurements are unfortunately prone to random errors. It is therefore desirable to have the reconstructed acoustic radiation pressure less sensitive to random noises. In the following, the effect of the signal-to-noise-ratio (SNR) is investigated in a two-dimensional configuration using an acoustic source similar to a monopole but with an amplitude proportional to a sine function. To be precise, we use $P(x,y)=\sin\alpha H_1(k\sqrt{(x-0.8)^2+(y-0.6)^2})$, where α is the shifted angle and is given by $\tan\alpha=(x-0.8)/(y-0.6)$. Like the previous example, the acoustic source is enclosed in the circle of $r=1$ m. The wavenumber and the radius of the minimum sphere are given as $k=2\ \mathrm{m}^{-1}$ and $r_m=3$ m, respectively. The input acoustic data consist of the analytical acoustic pressure solution with an added random noise of a given SNR. The location of the input is chosen as the upper half circle of radius $r=6$ m (an open surface). The SNR is defined as $\mathrm{SNR}=\sqrt{\Sigma_{j=1}^{200}|P(6,\theta_j)|^2/\Sigma_{j=1}^{200}|RN(6,\theta_j)|^2}$, where $RN(6,\theta_j)$ is the random noise at the point $(6,\theta_j)$ in the polar coordinates, j represents uniformly distributed 200 grid points over the upper half circle, and the random noise has zero mean and the identity covariance matrix. The reconstructed acoustic radiation pressure from the AIBM and AIBM_without is compared with the analytical solution in Fig. 4 for different SNRs. The results demonstrate that the accuracy of the reconstructed acoustic pressure with the SNR up to 10 is overall acceptable for the AIBM. However, without the addition of the acoustic pressure gradient in the input acoustic data,

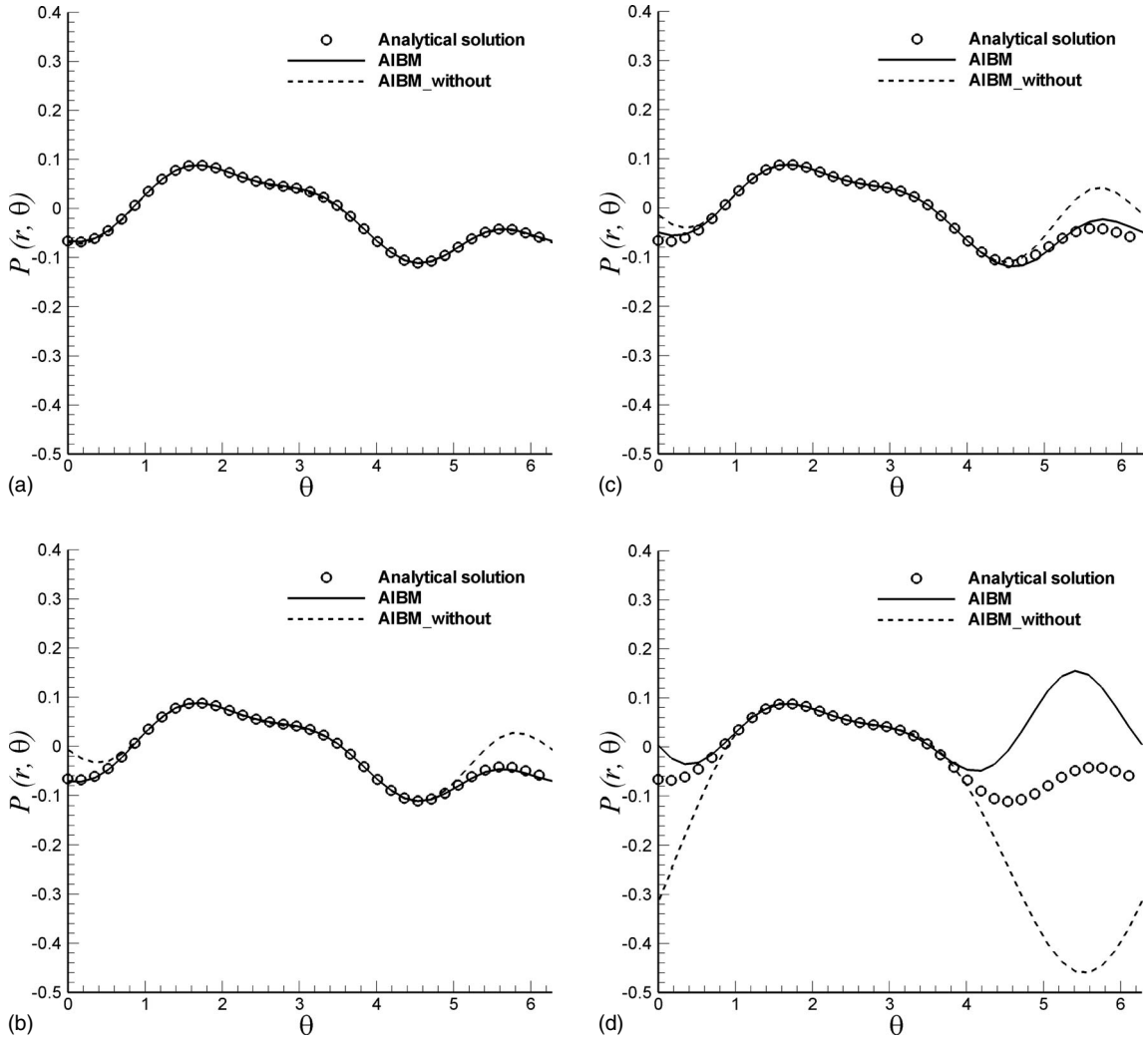

FIG. 3. Comparisons of reconstructed acoustic radiation pressure with analytical solution at $r=50$ m for different β. (a) $\beta=1.0\pi$; (b) $\beta=0.8\pi$; (c) $\beta=0.6\pi$; (d) $\beta=0.4\pi$.

the reconstructed acoustic pressure from the AIBM_without is unacceptable even for the SNR as large as 100. In order to have an overview of the reconstructed acoustic radiation field, the acoustic pressure contours of the analytical solution and the reconstructed solutions from the two inverse methods are given in Fig. 5. Since the input acoustic data are given over the upper half circle, as expected the reconstructed acoustic pressure for the upper half domain is very accurate using both inverse methods. The contour plots also show that the reconstructed pressure contours in the lower half domain of the AIBM_without are completely different from the analytical solution even with SNR=100. On the other hand, the accuracy of the reconstructed acoustic pressure in the lower half domain of the AIBM is very good for the same SNR. The results indicate that by including the pressure gradient in the input acoustic data, the AIBM can handle random noises much more effectively. As is shown in Fig. 4, with up to 10% random noises (SNR=10), the reconstructed acoustic radiation pressure using the AIBM agrees with the analytical solution reasonably well.

C. Application to multi-frequency acoustic radiation problem

The acoustic radiation from 2D vortex filament moving around the edge of a semi-infinite plane is a simplified model for the radiation of flow-airfoil interaction problem in relation to the air frame noise study. Ffowcs Williams and Hall[17] initially developed the general theory of the scattering of aerodynamic noise by flow-surface interaction. Shortly after, Crighton[18] developed the simplified 2D vortex model and derived the analytical acoustic solution in the form of the potential function using the singular perturbation method. Since then, the model has been used[19] to verify the effectiveness of the numerical methods of solving the Ffowcs Williams and Hawkings integral equation.

In the current study, the vortex model is used to show the capability and potential of applying the AIBM for multi-frequency acoustic radiation problems in general.

A schematic diagram of a 2D vortex moving around a semi-infinite half plane is shown in Fig. 6. The origin of the polar (or Cartesian) coordinates is located at the edge of the semi-infinite plane. Based on the analysis given by

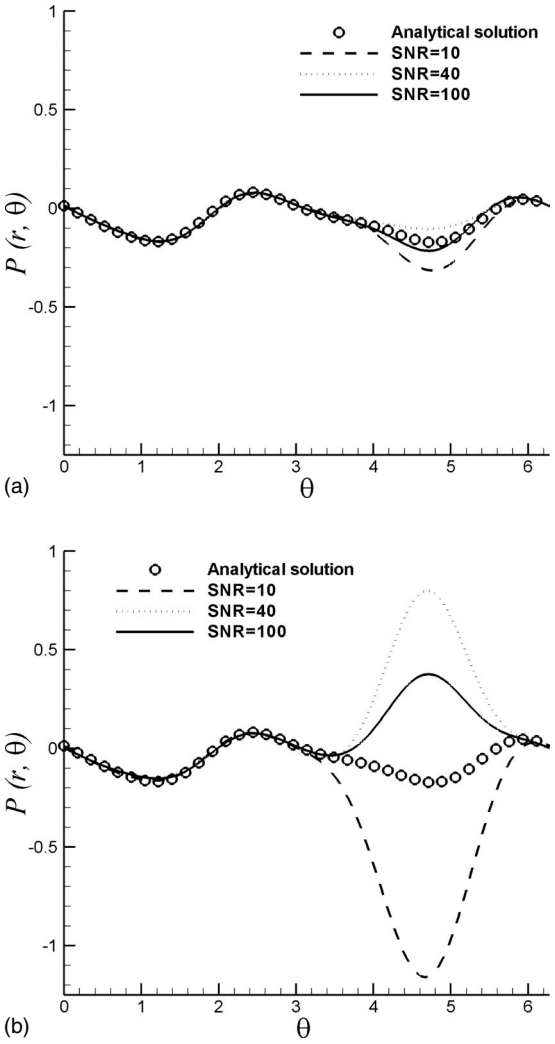

FIG. 4. Effect of SNRs on reconstructed acoustic radiation pressure at $r=10$ m. (a) AIBM; (b) AIBM_without.

Crighton,[18] the first term in the asymptotic expansion of the analytical potential function as $U \to 0$ is given by

$$\phi(r,\theta,t) = \frac{4^{3/4} U d^2}{[M_a^2 (r - tc)^2 + 4]^{1/4}} \frac{\sin \frac{1}{2}\theta}{r^{1/2}}, \quad \theta \in (-\pi, \pi), \qquad (17)$$

where c is the speed of sound, d is the shortest distance between the vortex and the edge (see Fig. 6), U is the maximum speed of vortex motion, and the Mach number M_a is denned as $M_a - U/c$. These variables are considered as $c = 344$ m/s, $d = 1$ m and $M_a = 0.01$ in the current numerical investigation. It can be easily shown that the acoustic pressure derived from the above potential function satisfies the wave equation and the solid wall boundary condition, $\partial p / \partial y = 0$ at the top and bottom surfaces of the plane. Since the acoustic radiation of the vortex model problem is not in a free space, the general approximated solution [Eq. (5)] for the Helmholtz equation needs to be modified to satisfy the solid wall boundary condition and can be written as

$$P(r,\theta) = \sum_{n=0}^{N} \left[a_n \cos n\theta H_n(kr) + b_n \sin\left(n + \frac{1}{2}\right)\theta H_{n+\frac{1}{2}}(kr) \right]. \qquad (18)$$

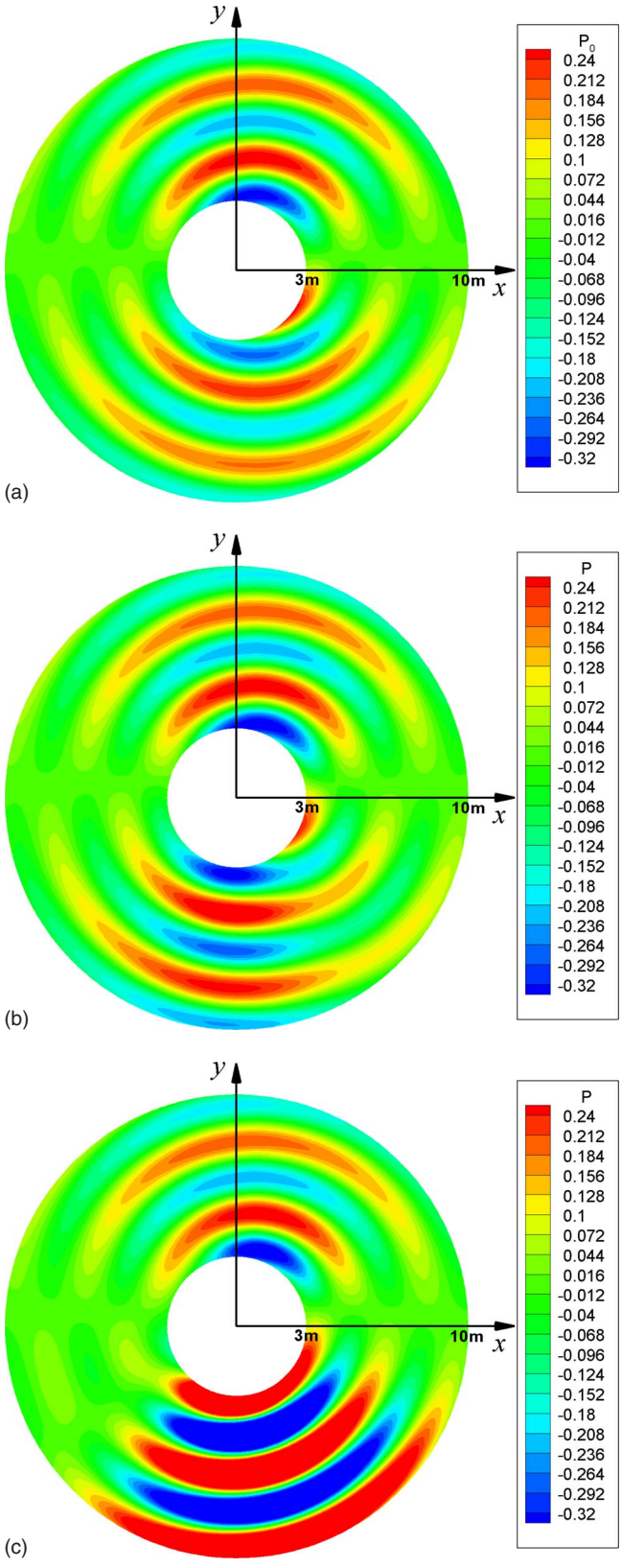

FIG. 5. Comparisons of reconstructed acoustic radiation pressure $P(r,\theta)$ contours for SNR=100 with analytical solution. (a) Analytical solution; (b) AIBM; (c) AIBM_without.

As can be seen from Eq. (17), the acoustic radiation of the vortex model problem is not a single frequency problem. The fast Fourier transform (FFT) of the acoustic pressure time history at a field point with the polar coordinates

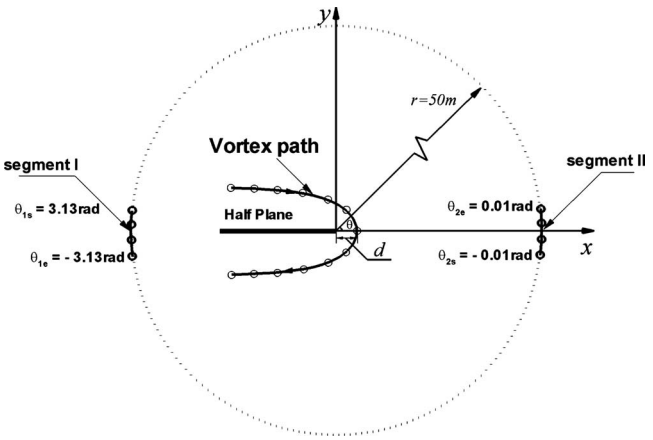

FIG. 6. Schematic diagram of 2D vortex filament moving around the edge of a semi-infinite plane with input acoustic data points on specified segments.

$(75\ \mathrm{m}, \pi/4)$ is shown in Fig. 7. The continuum spectrum demonstrates the multi-frequency nature of the acoustic radiation. It can also be shown mathematically that the pressure time history of any given point in the field has the same

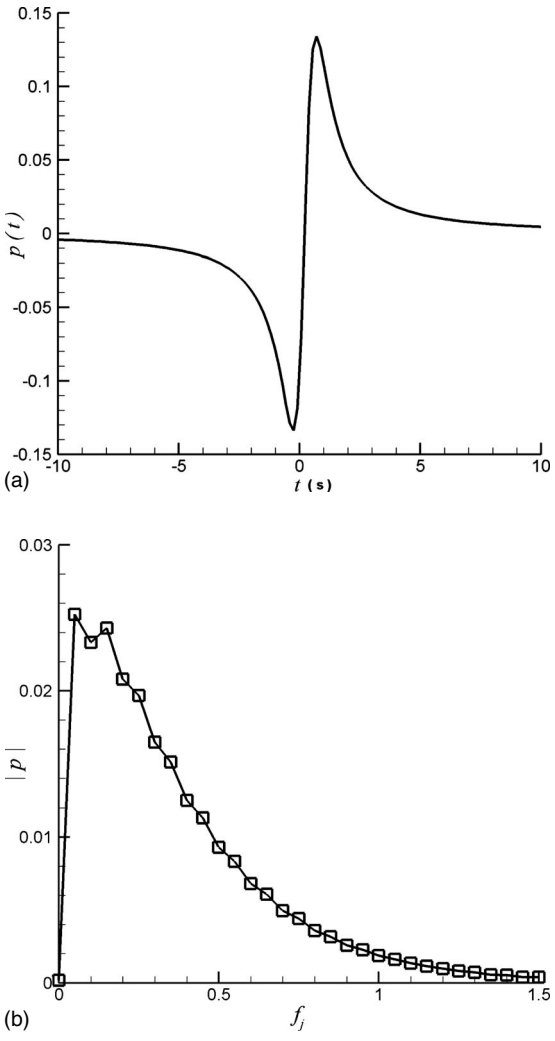

FIG. 7. Spectrum of acoustic radiation pressure time history of 2D vortex model at $r=75$ m, $\theta=\pi/4$, $M_a=0.01$ and $d=1$ m. (a) Acoustic pressure time history; (b) frequency spectrum.

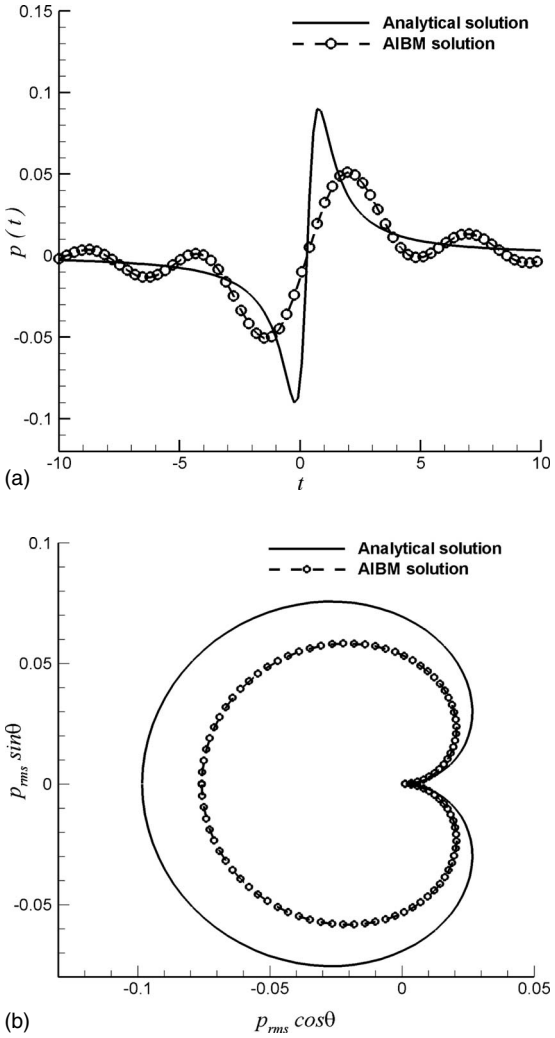

FIG. 8. Acoustic radiation pressure and directivity calculated from the input data with frequency range of 0.05–0.2 Hz. (a) Acoustic pressure time history $(r=100\ \mathrm{m}, \theta=\pi/5)$; (b) directivity $(r=100\ \mathrm{m})$.

frequency spectrum although the amplitude may vary. Since the AIBM is a frequency domain method, the reconstructed acoustic pressure field for each frequency component needs to be calculated. A superposition of the contribution from each frequency gives the total acoustic pressure field in the frequency domain. The reconstructed acoustic pressure field in the time domain can then be obtained by an inverse FFT. In order to accurately reconstruct the acoustic pressure, all the dominant frequency components need to be included in the calculation. The input acoustic data for the AIBM consists of the analytical acoustic pressure at four uniformly distributed points on each of the two circular segments ($r=50$ m) as shown in Fig. 6.

The reconstructed acoustic pressure time history at a field point with the polar coordinates $(100\ \mathrm{m}, \pi/5)$ and the directivity pattern at the radius of $r=100$ m are calculated by the AIBM and compared to the respective analytical solutions in Figs. 8–10 for three selected ranges of the frequency components. The poor agreement between the analytical and

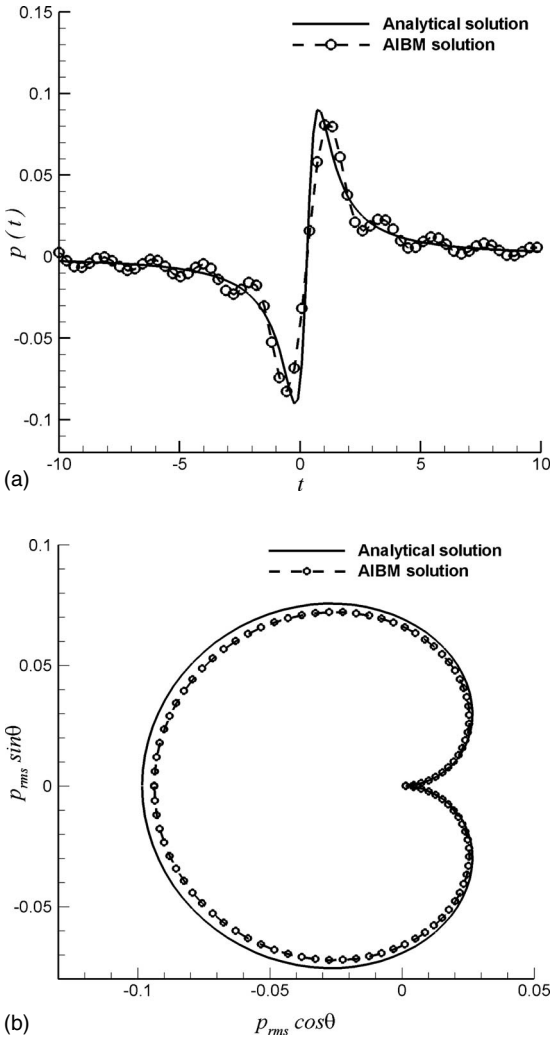

FIG. 9. Acoustic radiation pressure and directivity calculated from the input data with frequency range of 0.05–0.45 Hz. (a) Acoustic pressure time history ($r=100$ m, $\theta=\pi/5$); (b) directivity ($r=100$ m).

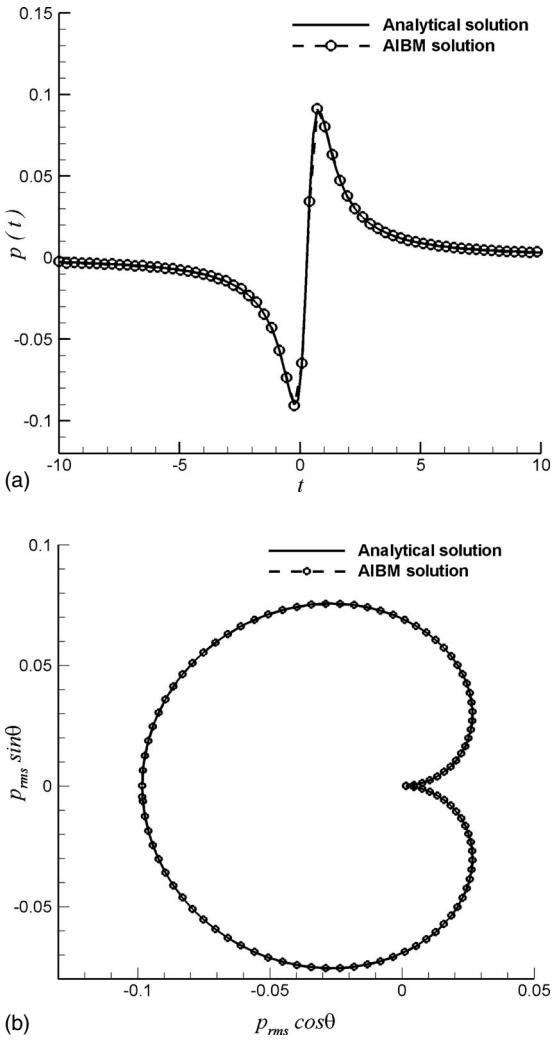

FIG. 10. Acoustic radiation pressure and directivity calculated from the input data with frequency range of 0.05–1.45 Hz. (a) Acoustic pressure time history ($r=100$ m, $\theta=\pi/5$); (b) directivity ($r=100$ m).

the reconstructed acoustic pressure shown in Fig. 8 is expected since the input acoustic data include only a small portion (0.05–0.2 Hz) of the dominant frequency components. As the frequency range widens to include more dominant frequency components (0.05–0.45 Hz), the accuracy of the reconstructed acoustic solutions using the AIBM improves significantly (see Fig. 9). Finally, an excellent agreement is achieved between the analytical and the AIBM solutions if the frequency range widens further to include all frequency components from 0.05 to 1.45 Hz in the input acoustic data (see Fig. 10).

After the verification of the AIBM for the reconstruction of acoustic radiation pressure generated by the multi-frequency model problem, it is important to examine the sensitivity of the reconstructed acoustic pressure to the SNR to ensure the potential of the AIBM for engineering applications. Since the acoustic radiation of the vortex model problem involves multi-frequency components, a random noise is added to the input acoustic data in the time domain. For a given set of the input acoustic data, the SNR is defined as

$$\mathrm{SNR} = \left[\frac{\sum_{i=1}^{M} \sum_{j=1}^{N} p^2(t_j, \mathbf{x}_i)}{M \cdot N \cdot \sigma} \right]^{1/2}, \tag{19}$$

where M and N are the numbers of the input locations (points) and the time discretization over a period of measurement time (or data collection time), σ is the variance of the random noise. The mean of the random noise is zero. It is noted from Eq. (19) that the SNR is defined based on the average of the input acoustic data in the time domain. Since the magnitude of the input data varies, the SNR could be larger or smaller than defined for an input at a specific location.

Using the input locations shown in Fig. 6, the effect of the SNR on the acoustic radiation pressure time history at a given point in the field is shown in Fig. 11 for different SNRs. As it is shown, a very good agreement between the reconstructed solution and the analytical solution is obtained for the case of SNR=10. As the SNR decreases to 5, the error of the reconstructed acoustic pressure increases as expected, particularly in the region where the amplitude of the

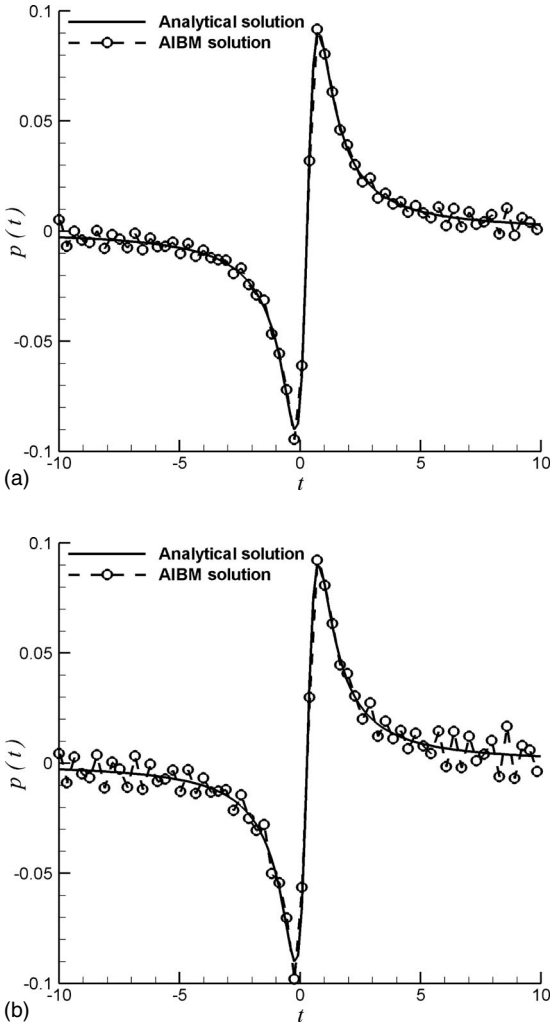

FIG. 11. Acoustic radiation pressure time history ($r=100$ m, $\theta=\pi/5$). (a) SNR=10; (b) SNR=5.

analytical pressure is small as expected. Nevertheless, the results demonstrate that the AIBM can effectively handle the input acoustic data with up to 20% random noise.

IV. CONCLUSIONS

An acoustic intensity-based method (AIBM) is proposed and verified in a two-dimensional configuration. The proposed method includes the acoustic pressure gradient as an input in addition to its simultaneous, co-located acoustic pressure. Compared to the traditional inverse methods, when the input acoustic data are only provided over an open surface, the AIBM improves the accuracy, reliability and consistency of reconstructed acoustic radiation pressure. The improvement, however, becomes less significant when the input segments are clustered. The AIBM is especially effective when random noises are added in the input acoustic data. The results indicate that without the addition of the pressure gradient to the input acoustic data, the reconstructed acoustic radiation pressure starts to deteriorate even with 1% of random noise in the input from an open surface. The AIBM, on the other hand, can give reasonably accurate reconstructed acoustic pressure from the input acoustic data with up to 20% random noise. Furthermore, the accuracy and efficiency of the AIBM are demonstrated through a multi-frequency acoustic radiation model problem. The overall effectiveness of the method indicates that the AIBM has the capability and potential for the reconstruction of acoustic radiations encountered in engineering applications.

ACKNOWLEDGMENT

We would like to acknowledge the partial financial support from the National Science Foundation under Grant No. NSF-ITR-0325760.

[1]E. G. Williams and J. D. Maynard, "Holographic imaging without the wavelength resolution limit," Phys. Rev. Lett. **45**, 554–557 (1980).
[2]J. D. Maynard, E. G. Williams, and Y. Lee, "Nearfield acoustic holography: I. Theory of generalized holography and the development of NAH," J. Acoust. Soc. Am. **78**, 1395–1413 (1985).
[3]B. K. Gardner and R. J. Bernhard, "A noise source identification technique using an inverse Helmholtz integral equation method," Trans. ASME, J. Vib., Acoust., Stress, Reliab. Des. **110**, 84–90 (1988).
[4]M. R. Bai, "Application of BEM (boundary element method)-based acoustic holography to radiation analysis of sound sources with arbitrarily shaped geometries," J. Acoust. Soc. Am. **92**, 533–549 (1992).
[5]B. K. Kim and J. G. Ih, "On the reconstruction of the vibro-acoustic field over the surface enclosing an interior space using the boundary element method," J. Acoust. Soc. Am. **100**, 3003–3016 (1996).
[6]E. G. Williams, B. H. Houston, P. C. Herdic, S. T. Raveendra, and B. Gardner, "Interior near-field acoustical holography in flight," J. Acoust. Soc. Am. **108**, 1451–1463 (2000).
[7]Z. Zhang, N. Vlahopoulos, S. T. Raveendra, T. Allen, and K. Y. Zhang, "A computational acoustic field reconstruction process based on an indirect boundary element formulation," J. Acoust. Soc. Am. **108**, 2167–2178 (2000).
[8]Z. Wang and S. F. Wu, "Helmholtz equation least-squares (HELS) method for reconstructing the acoustic pressure field," J. Acoust. Soc. Am. **102**, 2020–2032 (1997).
[9]S. F. Wu, "On reconstruction of acoustic pressure fields by using HELS method," J. Acoust. Soc. Am. **107**, 2511–2522 (2000).
[10]V. Isakov and S. F. Wu, "On theory and application of the Helmholtz equation least squares method in inverse acoustics," Inverse Probl. **18**, 1147–1159 (2002).
[11]D. Jerison and C. E. Kenig, "Unique continuitation and absence of positive eigenvalue for Schrödinger operators," J. Anal. Math. **121**, 463–494 (1985).
[12]L. Hormander, "Uniqueness theorems for second order elliptic differential equations," Commun. Partial Differ. Equ. **8**(1), 21–64 (1983).
[13]M. Schechter and B. Simon, "Unique continuation for Schrödinger operators with unbounded potential," J. Math. Anal. Appl. **77**, 482–492 (1980).
[14]F. Jacobsen and H. E. de Bree, "A comparison of two different sound intensity measurement principles," J. Acoust. Soc. Am. **118**, 1510–1517 (2005).
[15]F. Bowman, *Introduction to Bessel functions* (Dover, New York, 1958).
[16]C. Muller, *SphericaI Harmonics, Lectures Notes in Mathematics, No. 17* (Springer-Verlag, Berlin, 1996).
[17]J. E. Ffowcs Williams and L. H. Hall, "Aerodynamic sound generation by turbulent flow in the vicinity of a scattering half plane," J. Fluid Mech. **40**(2), 657–670 (1970).
[18]D. G. Crighton, "Radiation form vortex filament motion near a half plane," J. Fluid Mech. **51**(2), 357–362 (1972).
[19]D. P. Lockard, "An efficient, two-dimensional implementation of the Ffowcs Williams and Hawkings equation," J. Sound Vib. **229**(4), 897–911 (2000).

Nonlinear source–filter coupling in phonation: Vocal exercises

Ingo Titze[a)]
National Center for Voice and Speech, The Denver Center for the Performing Arts, Denver, Colorado and Department of Speech Pathology and Audiology, The University of Iowa, Iowa City, Iowa 52242

Tobias Riede
National Center for Voice and Speech, The Denver Center for the Performing Arts, Denver, Colorado and Department of Biology, University of Colorado at Denver, Denver, Colorado 80204

Peter Popolo
National Center for Voice and Speech, The Denver Center for the Performing Arts, Denver, Colorado and Department of Speech Pathology and Audiology, The University of Iowa, Iowa City, Iowa 52242

(Received 3 August 2007; revised 10 December 2007; accepted 14 December 2007)

Nonlinear source–filter coupling has been demonstrated in computer simulations, in excised larynx experiments, and in physical models, but not in a consistent and unequivocal way in natural human phonations. Eighteen subjects (nine adult males and nine adult females) performed three vocal exercises that represented a combination of various fundamental frequency and formant glides. The goal of this study was to pinpoint the proportion of source instabilities that are due to nonlinear source–tract coupling. It was hypothesized that vocal fold vibration is maximally destabilized when F_0 crosses F_1, where the acoustic load changes dramatically. A companion paper provides the theoretical underpinnings. Expected manifestations of a source–filter interaction were sudden frequency jumps, subharmonic generation, or chaotic vocal fold vibrations that coincide with F_0-F_1 crossovers. Results indicated that the bifurcations occur more often in phonations with F_0-F_1 crossovers, suggesting that nonlinear source–filter coupling is partly responsible for source instabilities. Furthermore it was observed that male subjects show more bifurcations in phonations with F_0-F_1 crossovers, presumably because in normal speech they are less likely to encounter these crossovers as much as females and hence have less practice in suppressing unwanted instabilities.
© *2008 Acoustical Society of America.* [DOI: 10.1121/1.2832339]

PACS number(s): 43.25.Ts, 43.70.Aj, 43.70.Gr, 43.80.Ka [BHS] Pages: 1902–1915

I. INTRODUCTION

A hypothesis is being pursued that humans can engage their sound source in the larynx and their vocal tract airways (the filter) in two fundamentally different ways. The first is linear source–filter coupling, where the source frequencies are produced independently of the acoustic pressures in the airways. The glottal airflow in the larynx is produced aerodynamically, with a quasisteady transglottal pressure and a flow pulse that mirrors the time-varying glottal area. The second is nonlinear coupling, where the acoustic airway pressures contribute to the production of frequencies at the source. In the nonlinear case, the transglottal pressure includes a strong acoustic component, much like in woodwind instruments where the airflow through the reed is driven by acoustic pressures of the instrument bore, or in brass instrument playing, where the lip flow is driven by the acoustic pressures in the brass tube (Fletcher, 1979). The major parameter in nonlinear coupling for voiced speech appears to be related to the diameter of the epilaryngeal tube (also known as laryngeal vestibule), which serves to either match or mismatch the output impedance of the glottis to the input impedance of the vocal tract. Weak coupling is obtained when the glottal impedance is high and the epilarynx tube input impedance is low, whereas strong coupling (nonlinear interaction) is obtained when the impedances are comparable.

Some evidence of nonlinear source–filter coupling comes from earlier voice source analysis (Rothenberg, 1981; Fant, 1986), excised larynx experiments (Alipour *et al.*, 2001), and physical model experiments (Chan and Titze, 2006; Zhang *et al.*, 2006). A more extensive discussion and bibliography is given in the companion paper (Titze, 2008). The investigations demonstrated that the addition of a vocal tract filter to the isolated larynx or a vocal fold model lowers phonation threshold pressure and thereby eases the onset of phonation. Analytical calculations and computational simulations are a second source of evidence (Ishizaka and Flanagan, 1972; Titze, 1988; Titze and Story, 1995; Titze, 2004; Chan and Titze, 2006; Zañartu *et al.*, 2007). Those simulations showed that an acoustically inertive supraglottal tract facilitates vocal fold vibration and lowers F_0. By contrast, an acoustically compliant supraglottal tract hinders vocal fold oscillation (sometimes squelching it entirely) and raises F_0 (Titze, 2006a, Chap. 7). A third source of evidence is experiments in which human subjects phonate into tubes, artificially elongating the vocal tract (e.g., Story *et al.*, 2000; Hatzikirou *et al.*, 2006). In those experiments it was shown that instabilities are more likely to occur when F_0 and F_1 cross. What is currently missing is an investigation with a

a)Electronic mail: ingo-titze@uiowa.edu

sufficient sample of real human voice production on a variety of vowels. In this current investigation we demonstrate that F_0–F_1 crossovers can occur naturally in the human voice and that instabilities are more likely to occur near such crossovers.

But why this duality of source–filter coupling? The advantage of linear coupling appears to be greater source stability when vowel and F_0 need perceptual clarity. Modes of vibration of the vocal fold tissues are not disturbed by articulatory adjustments, an obvious advantage for speech. Self-sustained oscillation is then based on a mucosal wave that propagates on the vocal fold surface and aerodynamic pressures in the glottis that are in synchrony with the tissue velocity of the vocal folds (Titze, 1988). The vocalist needs only to control the laryngeal configuration and lung pressure to produce the sound (Sundberg *et al.*, 1993; Sundberg and Hogset, 2001; Henrich *et al.*, 2005). Articulation is then merely a modulation of the source harmonic amplitudes. This has been the fundamental assumption in the linear source–filter theory of vowel and voiced consonant production (e.g., Fant, 1960; Stevens, 1998; Schutte and Miller, 1993).

The advantage of nonlinear coupling may be that more output power can be produced because stored energy in the vocal tract is fed back to the source to increase the glottal flow energy. But this may be at the expense of less stability at the source. In some forms of vocal communication, this may not matter. Lower stability leads to a greater variety of source qualities, including cultivated frequency jumps as in a yodel, subharmonics, low frequency modulations at the source, and chaotic vibration. Some of these instabilities may be advantageous in an artistic context (Neubauer *et al.*, 2004), or for survival as in an infant cry (Mende *et al.*, 1990), but they may be considered pathological in a speech context (Hirano, 1981). Source instability due to nonlinear source–filter coupling may be greatly exaggerated when there is a vocal pathology. Asymmetry in the larynx, nodules and polyps, paralysis, and other voice disorders affect the normal modes of vibration of the tissue, which can easily be desynchronized by additional nonlinear coupling to the vocal tract.

Historically, clinicians have used a battery of test utterances for assessment of voice disorders that progress from vowels to isolated syllables or words and then to complete sentences or paragraphs. Test utterances are also useful for monitoring the effectiveness of vocal training. Almost everyone agrees that the tasks must reveal control of fundamental frequency, loudness, and some aspect of vocal quality. But, the interactions among respiratory, phonatory, and articulatory components of speech have not been specifically targeted as important components of assessment. Although a collection of vowels and voiced consonants may be part of the test material, there is generally no hypothesis about whether the voice disorder is more affected by one vowel shape versus another.

It is generally thought that steady vowels alone are insufficient to provide a diagnostic "treadmill" for vocalization. They test the stability (or steadiness) of a vocal and articulatory posture, but allow little to be said about interactivity. Such interactivity becomes evident when either source or filter is dynamically changing. Dynamic testing has been proposed by Kent *et al.* (1987) for speech articulation and by Freund and Büdingen (1978) and Schmidt and Lee (1989) for limb movement, but little has been implemented for voice diagnostics.

To maximize the diagnostic value of test utterances for vocal control, it is suggested here that source–filter interaction exercises may become part of a diagnostic battery. A variety of voice disorders may manifest themselves in the lack of voice control when source harmonics and formant frequencies are forced to interfere with each other. In particular, sudden frequency jumps occur when specific formants and harmonics cross (see the companion paper for theoretical explanation). Often, bifurcations in the vibratory patterns of the vocal folds occur involuntarily at these locations.

The purpose of this study was to test three F_0–F_1 crossover exercises, (1) a fundamental frequency glide at a constant vowel, (2) a vowel glide at a constant fundamental frequency, and (3) a combination fundamental frequency–vowel glide. Fundamental frequency and vowels were chosen such that maximum interaction would likely take place.

II. METHODS

A. Subjects

Eighteen volunteers participated in the study, nine females (ranging in age from 25 to 50 with an average of 31) and nine males (ranging in age from 25 to 44 with an average of 31.6). All subjects reported no vocal pathologies. Several claimed that they sing as amateurs, but none had extensive vocal training. Two certified speech-language pathologists assessed their voices as normal, not containing any dysphonia. Experiments were in compliance with guidelines of the NIH and were reviewed and approved by the institutional review boards.

B. Three vocal exercises

As a first exercise, subjects were asked to produce fundamental frequency (F_0) glides. The pattern was high to low, then low to high, with an intermediate vocal fry. This exercise was produced on four vowels (/α/, /æ/, /i/, /u/), with two different starting fundamental frequencies per vowel and two different vocal efforts (soft and loud). Table I lists all three exercises and Fig. 1 shows the F_0 glides in musical notation. The vocal fry utterance was elicited between the fundamental frequency glides to estimate the formant frequencies and bandwidths of the vowels, since both measures are most reliably extracted from low F_0 phonations.

Females phonated the two higher fundamental frequency glides and males the two lower fundamental frequency glides, such that the middle glide was common to both genders. Subjects were prompted with computer simulated signals that had no source–filter coupling (see the companion paper, Titze, 2008, for the computer model). A spectrogram of the prompts is shown in Fig. 2, with Fig. 2(A) representing the prompt for the first exercise. The first formant frequency location is represented by the gray dots in Fig. 2 and the sloping lines are the harmonics.

TABLE I. Three vocal exercises.

Exercise 1. Pitch glides and reversals (at least two octaves with vocal fry included)
1. C5 to F3, vocal fry, F3 to C5 with steady vowels /i/, /u/, /ɑ/, and /æ/, soft and loud, males and females
2. Repeat with C6 to F4 for females, C4 to F2 for males, all else the same
Exercise 2. Vowel glides and reversals
1. C5, /i/-/æ/-/i/ and /u/-/ɑ/-/u/, soft and loud, males and females
2. Repeat with C6 for females, C4 for males, all else the same
Exercise 3. Simultaneous vowel and pitch glides
1. C5 to F3, vocal fry, F3 to C5 while vowels change in the sequence /i/-/æ/-/i/ and /u/-/ɑ/-/u/, soft and loud, males and females
2. Repeat with C6 to F4 for females, C4 to F2 for males, all else the same

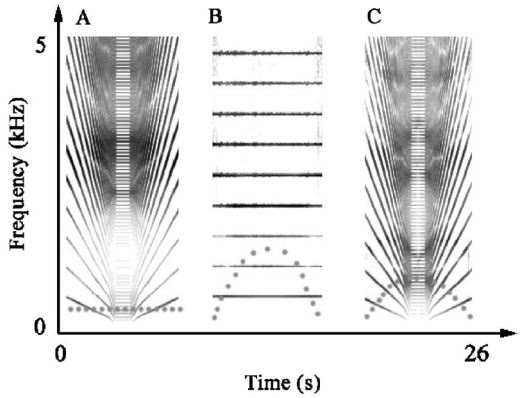

FIG. 2. Spectrograms of computer generated stimuli that were used to prompt the subjects. (A) Exercise 1, (B) Exercise 2, and (C) Exercise 3. First formant (F_1) is indicated by gray dots.

The second exercise consisted of two vowel glides and their returns (from /i/ to /æ/ and back to /i/; and from /u/ to /ɑ/ and back to /u/). These vowel glides were phonated in succession on two constant fundamental frequencies (C5 and C6 for females and C5 and C4 for males). Returning to the musical notation of Fig. 1, this would be one sustained note (e.g., C5, second note from the top) while vowel formant frequencies are changing upward as shown on the right side of the graph. Two vocal efforts were used (soft and loud) for all exercises. Figure 2(B) illustrates a spectrographic version of a computer simulation that served to prompt a subject. Note that the harmonics remain constant while F_1 follows a low-high-low trajectory.

The third exercise consisted of simultaneous vowel and fundamental frequency changes. In Fig. 1, the fundamental frequency glides (glissandi) were again used, but this time with the simultaneous vowel changes as shown to the right. The spectrographic version of the prompt is shown in Fig. 2(C). F_0 and F_1 were moved in opposite directions and were forced to cross. Subjects were instructed to start with an /i/ vowel ($F_1 \approx 300$ Hz) and change to an /æ/ vowel ($F_1 \approx 800$ Hz) while gliding fundamental frequency downward, as in Exercise 1, then change back to an /i/ vowel while gliding fundamental frequency upward. Intermediate vocal fry was also elicited. Starting fundamental frequencies were C5 (523 Hz) and C6 (1047 Hz) for females and C5 (523 Hz) and C4 (262 Hz) for males. This exercise was repeated for the /u/-/ɑ/-/u/ vowel transition. Each phonation was produced at two different vocal efforts (soft and loud).

For each of the exercises described, subjects were asked to produce three tokens for statistical power; however, some subjects were only able to produce one or two tokens. Actual sample size is given in Table II.

C. Recordings

Recordings were conducted in a single-wall IAC sound isolation booth. Subjects wore a head-mounted microphone (Countryman Associates omnidirectional B3 Lavalier; CSL Model 4400 pre-amp) mounted on a wire boom attached to a plastic frame, worn like a pair of eyeglasses. The microphone element was about 5 cm from the mouth and slightly to the side, out of the airstream.

The microphone signal was recorded with CUBASE SE software (version 3.0.3) on a PC. The recording level was adjusted to achieve the maximum signal strength and to avoid clipping. All phonations were digitized at a 44.1 kHz sampling rate and 16 bit quantization.

A Brüel & Kjaer 2238 sound level meter, set to linear frequency weighting, was positioned at the distance of 30 cm from the mouth. The sound level meter was used to visually obtain a sound pressure level reading at the outset of the recording session, while the subject phonated on /ɑ/ at a high and low fundamental frequency and loud and soft intensity, for the purpose of calibrating the microphone signal to SPL at 30 cm. (SPL levels are not discussed in this paper, however.)

The modeled vocalizations (Fig. 2) were generated with the SPEAK program (Titze, 2006a, Chap. 5) and were played back over a loudspeaker in the booth prior to the subjects

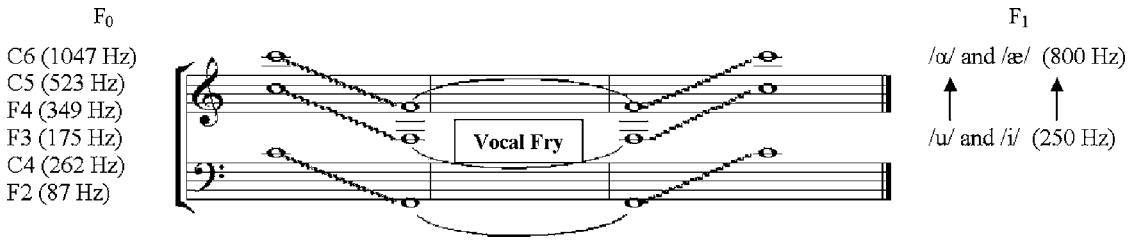

FIG. 1. Musical notation of F_0 glides used in Exercises 1 and 3, and vowel changes (far right) drawn at an approximate height so that F_1 corresponds to fundamental frequency on the left.

TABLE II. Information and sample sizes for each subject for Exercises E1, E2, E3.

Subject	Sex	E1	E2	E3
1	M	48	24	24
2	M	47	24	24
3	M	32	15	17
4	F	36	14	16
5	F	27	13	17
6	F	32	16	18
7	M	48	24	24
8	F	31	16	16
9	F	32	24	24
10	F	48	24	24
11	M	48	24	24
12	F	48	24	24
13	F	48	24	24
14	M	48	24	24
15	M	47	24	24
16	F	48	24	24
17	M	48	24	24
18	M	34	16	18

performing each task, as a first auditory cue for the desired smoothness of fundamental and formant frequency change. In addition, the investigator was present in the sound booth during the vocal tasks to help the subject find the proper vowels and starting and ending fundamental frequency, if necessary. The vowels /i/, /æ/, /ɑ/, and /u/ were announced (speech-like) by the investigator prior to each task. An electronic keyboard (Casio® Casiotone MT-35) was used to give the starting fundamental frequency as often as necessary for repeat tokens. The actual starting fundamental frequency did vary within and between subjects for particular exercises. No subject was specifically forced to phonate at the instructed starting fundamental frequency. The instructions were given only before the start of each token of the exercises. No corrections were attempted during the exercise.

D. Data analysis

Three bifurcations of vocal fold vibration were considered in this work, namely frequency jumps, subharmonics, and deterministic chaos (Fig. 3 shows stylistic sketches for two harmonics in a spectrogram). Biphonation, a fourth nonlinear phenomenon, was not found in any phonations. Each phonation was examined for the occurrence of those phenomena through visual inspection of narrow-band spectrograms (512-point Hanning window) and associated Fourier frequency spectra. Frequency jumps are sudden F_0 changes in which vibration rate moves up or down abruptly and discontinuously, and is qualitatively different from continuous, smooth F_0 change (Fig. 3, example I). Subharmonics are additional spectral components that can suddenly appear at integer fractional values of an identifiable F_0 (e.g., $F_0/2$, $F_0/3$, and so on) and as harmonics of these values. The result is that energy can appear at evenly spaced intervals below F_0 and between adjacent harmonics throughout the frequency spectrum (Fig. 3, example II). While the vibration pattern of the vocal folds is still regular in these cases, it is characterized by periods that are multiples of the F_0 period.

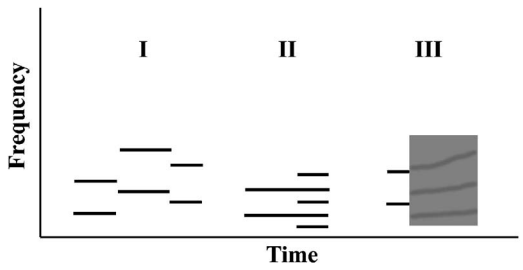

FIG. 3. Sketches of narrow-band spectrogram of the three bifurcations considered in this study. In each example two harmonics (F_0 and $2F_0$) are indicated. I: Two subsequent frequency jumps. II: Subharmonics. III: Deterministic chaos.

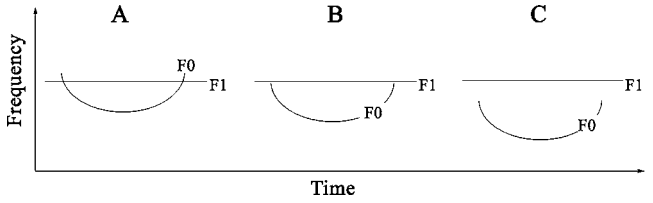

FIG. 4. Schematics of fundamental frequency contours around a steady formant. Three relationships between F_0 and F_1 were found in phonations of Exercise 1. (A) F_0 and F_1 crossed, (B) F_0 and F_1 came within 100 Hz of each other at some point during the phonation, (C) F_0 and F_1 were never less than 101 Hz apart at any point during the phonation. Only (A) and (B) counted as "crossover present."

Deterministic chaos refers to episodes of nonrandom noise. This chaotic noise is technically distinguishable from random noise by the number of dimensions needed to describe it (Tokuda *et al.*, 2002). An alternative to decide whether a noisy segment can be considered deterministic chaos is to evaluate characteristics visible in narrow-band spectrograms (Herzel, 1998), including sudden on- and offset, preceding or following subharmonics and harmonic "windows" occurring in otherwise noisy segments (Fig. 3, example III).

The following parameters were measured in each phonation: maximum and minimum fundamental frequency at the beginning, the middle, and end of the phonation; first and second formant frequency. The measurement of those parameters allowed the decision whether or not there was a F_0–F_1 crossover present (Fig. 4). Formant bandwidth was measured in the middle of the phonations of Exercise 1 (the vocal fry portion). Because energy loss to the subglottal system is minimum for vocal fry (a long glottal closure), we expected the measured formant bandwidths to be underestimated for the glides.

Additionally, we measured the higher and lower fundamental frequencies of a frequency jump; the fundamental frequency before the onset of a subharmonic; the onset of a chaotic segment; and we noted the type of subharmonic event ($F_0/2$, $F_0/3$, and so on).

All measurements were performed using sound analysis software PRAAT (Boersma & Weenick, 2007). Linear predictive coding (autocorrelation procedure) was used to track formants. Formant bandwidth is the difference in frequency between the points on either side of the peak (frequency with

peak amplitude) which have amplitude $A/(\sqrt{2})$ (corresponding to 3 dB down from the peak).

E. Statistics

Source instabilities during a fundamental frequency or vowel glide can occur either as a result of mode of vibration changes in the sound source (e.g., a register change induced by changes in muscle activation), or as a result of nonlinear source–tract coupling. In a nonlinear source–filter system, source instabilities are expected when F_0 and F_1 cross, and therefore source instabilities can serve as indicators of nonlinear source–tract coupling. To sort out the instabilities that result from nonlinear source–tract coupling, we statistically compared the occurrences of instabilities in phonations without F_0-F_1 crossovers to those with F_0-F_1 crossovers. If instabilities were to result only from a source-specific mode change, we would expect no differences between the two samples. However if instabilities do result from a nonlinear source–filter interaction, we would expect more source instabilities in phonations with F_0-F_1 crossovers. Nonparametric tests were used for comparison of averages of matched (Wilcoxon test) or unmatched (Mann–Whitney test) samples.

III. RESULTS

A. Exercise 1: Fundamental frequency glide on steady vowels

Frequency jumps were the most commonly observed bifurcation type. They were found in 21% of all phonations across all individuals (s.d.=14%; range: 0–42%; $N=18$ subjects). The majority of frequency jumps were downward on the descending F_0 glide and upward on the ascending F_0 glide (161 cases out of 167). Examples are seen in Figs. 5(A) and 5(C) at the first and third arrows. Frequency jumps from all 18 subjects showed a mean frequency change of 31 Hz (s.d.=20 Hz; range: 0–79 Hz), or about 2 semitones, for the descending fundamental frequency. Subharmonics were found in 14% of all phonations across individuals (s.d. =9%; range: 2%–35%; $N=18$ subjects). Examples are seen at the second arrow in Fig. 5(A) and at the second arrow in Fig. 5(B). Chaotic segments were found in 3% of all phonations across individuals (s.d.=5%; range: 0–15%; $N=18$ subjects).

Crossovers occurred predominantly with /i/ and /u/ vowels because they had lower F_1 and were more likely to be in the path of the gliding F_0. The proportion of crossovers for all vowels in $N=9$ women were: /ɑ/: $11.0\pm2.5\%$; /æ/: $9.6\pm5.6\%$; /i/: $24.7\pm1\%$; /u/: $24.9\pm1\%$. For $N=9$ men they were: /ɑ/: $1.7\pm2.9\%$, /æ/: $2.0\pm4.2\%$; /i/: $20.0\pm3\%$; /u/: $18.3\pm4\%$; mean ±s.d.). The smaller percentage of crossovers in men comes from the fact that men started half of the F_0 glides an octave lower (C4; 262 Hz) while females started half of the glides an octave higher (C5; 523 Hz). All glides ended in vocal fry, which is below all formants. Hence, there was a greater likelihood that females always crossed F_1, while many males did not have fundamental frequencies above or near F_1 for the high-F_1 vowels /ɑ/ and /æ/. In women, F_0-F_1 crossovers occurred in 70% of all phonations (s.d.=7%; range: 58%–78%; $N=9$). In men, F_0-F_1 crossovers occurred in only 42% of all phonations (s.d.=10%; range: 31%–66%; $N=9$).

Independent of loudness, the overall mean proportion of instabilities in phonations with F_0-F_1 crossover was 54% across male subjects (s.d.=17; range: 23%–78%; $N=9$), whereas without F_0-F_1 crossover it was 35% (s.d.=15; range: 7%–59%; $N=9$). This difference was statistically significant (Wilcoxon; $Z=2.19$; $P<0.05$; $N=9$). Across females, on the other hand, the overall mean proportion of source instabilities in phonations with F_0-F_1 crossover was 27% (s.d.=14; range: 11%–52%; $N=9$), whereas without F_0-F_1 crossover it was 24% (s.d.=30; range: 0%–90%; $N=9$). This difference is not significant (Wilcoxon; $Z=0.59$; $P=0.55$; $N=9$). The male–female difference in instabilities with F_0-F_1 crossover (54% vs 27%) was significant (Mann–Whitney; $U=9$; $P<0.01$; N_F, $N_M=9$).

1. Effect of loudness

A sufficient sample ($N=75$) of crossover and noncrossover phonations within the two categories "loud" and "soft" was available in male high glide and female low glide phonations. The overall mean proportion of source instabilities in *loud* phonations with F_0-F_1 crossover was 77% in males (s.d.=28; range: 25%–100%; $N=9$), whereas without F_0-F_1 crossover it was 65% (s.d.=41; range: 0%–100%; $N=9$). This difference was not statistically significant (Wilcoxon; $Z=1.12$; $P=0.13$; $N=9$). The overall mean proportion of source instabilities in *soft* phonations with F_0-F_1 crossover was 64% (s.d.=23; range: 37%–100%; $N=9$), whereas without F_0-F_1 crossover it was 38% (s.d.=36; range: 0%–100%; $N=9$). This difference in males for soft phonation was significant (Wilcoxon; $Z=1.84$; $P<0.05$; $N=9$).

For females, the overall mean proportion of source instabilities in *loud* phonations with F_0-F_1 crossover was 35% (s.d.=29; range: 0%–100%; $N=9$), whereas without F_0-F_1 crossover it was 23% (s.d.=25; range: 0%–75%; $N=9$). This difference was not significant (Wilcoxon; $Z=0.59$ $P=0.23$; $N=9$). The overall mean proportion of instabilities in *soft* phonations with F_0-F_1 crossover was 29% (s.d.=28; range: 0%–80%; $N=9$), whereas without F_0-F_1 crossover it was 20% (s.d.=33; range: 0%–100%; $N=9$), again not significantly different (Wilcoxon; $Z=1.19$ $P=0.11$; $N=9$). Results did not change when considering frequency jumps only, instead of summarizing all three observed instabilities (frequency jumps, subharmonics, and deterministic chaos).

2. F_0-F_1 vicinity

In 31 of 167 cases of frequency jumps (18%), the first formant frequency was in a 50 Hz vicinity of the fundamental frequency. In 21 additional cases, F_1 was in a 100 Hz vicinity of F_0. In 23 additional cases, F_1 was in a 200 Hz vicinity of F_0. In the remaining 92 cases, F_1 was more than 200 Hz away from F_0. For an average formant bandwidth of about 100 Hz in vocal fry (which is likely to be an underestimate for the glide phonations) it appears that at least 30% of instabilities occurred inside a formant bandwidth. But even if they occurred outside the bandwidth, the inertive re-

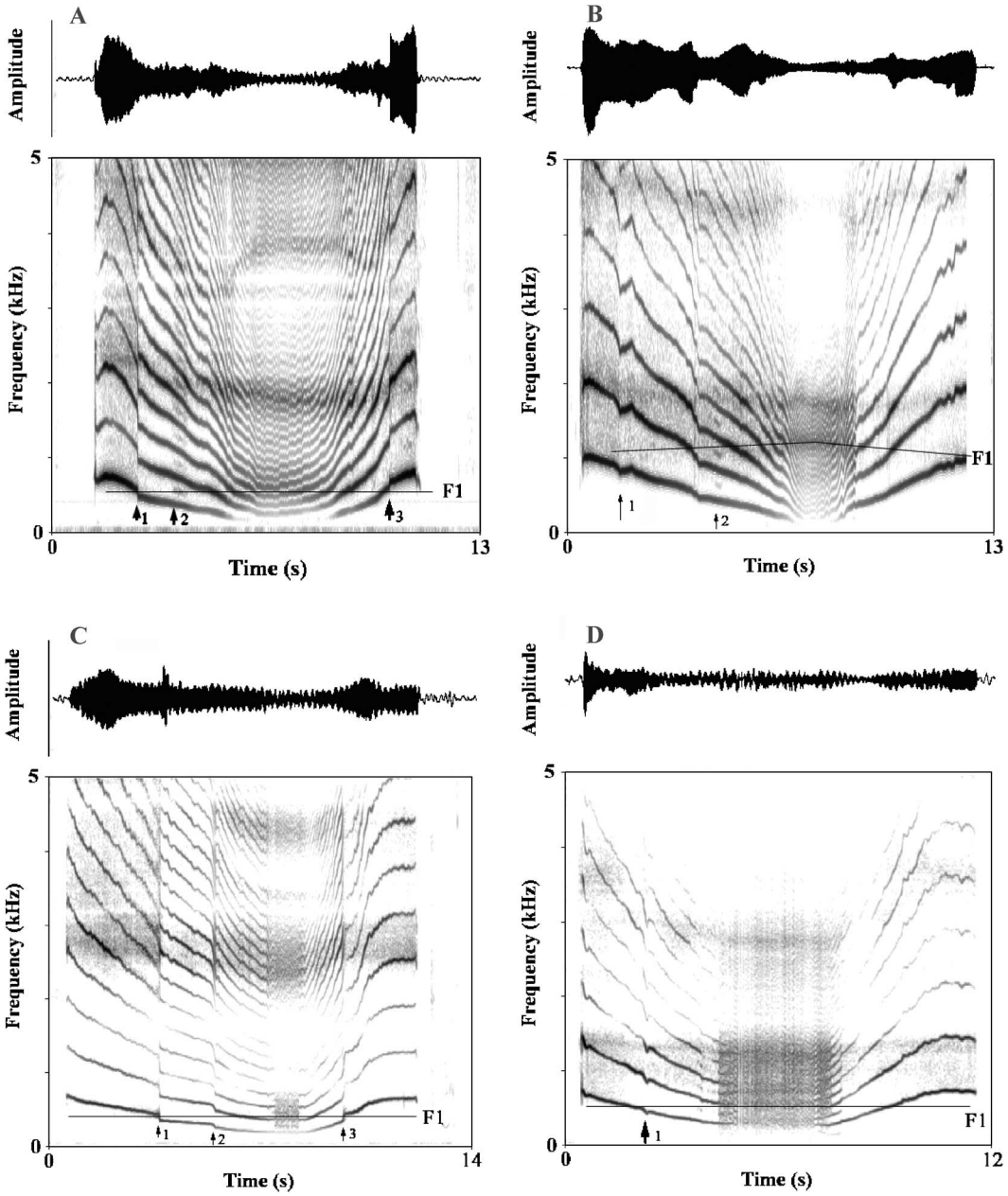

FIG. 5. Examples of bifurcations in Exercise 1. Time axes are slightly variable. Location of the first formant (F_1) is indicated by a horizontal line overlaid on the spectrograms. (A) Phonation of a male subject. Two frequency jumps are noted (arrows 1 and 3). A short subharmonic regime starts at arrow 2. (B) Phonation of an additional male subject. Source instabilities are not frequency jumps but only a slight perturbation of the descending F_0 trajectory (arrow). (C), (D) Phonations of two female subjects. Instabilities are indicated by arrows.

actance of the vocal tract may still have been large enough to trigger an F_0 change (see the companion paper, Titze, 2008).

B. Discussion of Exercise 1

Exercise 1 delivered at least three new findings. First, source instabilities occur more often in phonations in which F_0–F_1 crossovers are present. This is significant for male phonations. Second, instabilities occur more often in soft voice than loud voice, again primarily among males. Third, when F_0 jumps occur, they are mostly downward on a downgliding F_0 and upward on an upgliding F_0.

Consider the following explanations. When an instability in F_0 occurs near F_1, we expect the proximity of F_0 and F_1 to be on the order of the formant bandwidth, because most of the vocal tract acoustic reactance change occurs in this frequency interval. Figure 6 shows an impedance calculation for a vocal tract in the shape of the vowel /u/. The top panel shows an outline of the vocal tract radius across length, and the bottom panel shows the supraglottal impedance curves in the vicinity of formants F_1 and F_2. (For a detailed discussion of the impedance curves, see the companion paper.) The thick solid curve is the supraglottal reactance, the thin solid line is the resistance, and the dashed curve is the magnitude of the impedance. The formant frequency is where the resistance has its maximum. This is where the reactance is midway between its positive and its negative peak, which is above the zero line because the laryngeal vestibule (epilarynx tube) adds a linear component with a positive slope to

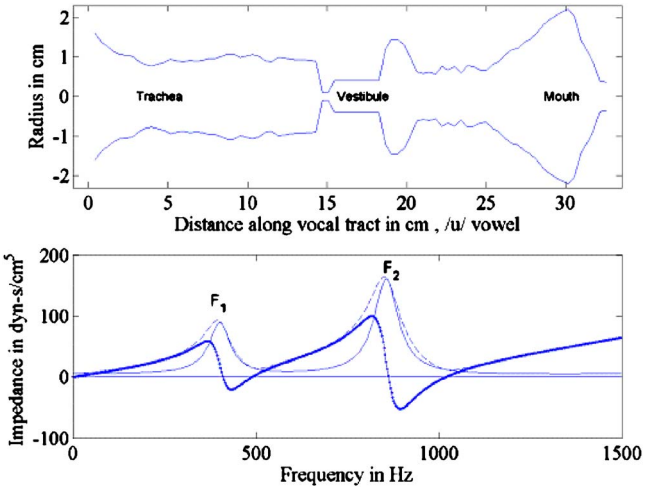

FIG. 6. (Color online) Calculation of reactance, resistance, and impedance magnitude (bottom) for a vocal tract shape resembling a /u/ vowel (top).

the reactance. Reactance above zero is inertive and reactance below zero is compliant. Only the 400–500 and 800–1000 Hz regions have compliant reactance.

The bandwidth of the formant is roughly the frequency distance between the peak and the trough in the reactance curve. But note that reactance can still be high (both positive and negative) a considerable distance outside the bandwidth. In our first data set, 31% of the frequency jumps we found occurred when F_0 was in the 100 Hz vicinity of F_1. Estimates of bandwidth values for vowels from this study, and two other studies, are given in Table III. The wide range in bandwidths across these studies stems from the differences in the methods by which they were obtained. The Fujimura and Lindqvist-Gauffin (1971) values were obtained from a vocal tract transfer function measured with a sweep tone from a transducer applied to the surface of the neck, with the glottis tightly closed, which leads to less energy loss to the subglottic system and thus would account for the lower bandwidth values. The Childers and Wu (1991) values were obtained from a weighted recursive least-squares computation of the vocal tract filter function from the acoustic speech signal, similar to the method of linear prediction coefficients, which could include glottal leakage. Our measurements lie between the values from these two other studies because they were obtained during the vocal fry portion of the phonation. Vocal fry has a relative long closed phase, but the glottis is not completely closed. On the F_0 glides, bandwidths are expected to be higher because less glottal closure occurs at high F_0, where the phonation register is often falsetto-like. Thus, the assumption of an average 100–200 Hz bandwidth for both males and females at a wide range of F_0 is reasonable. This means that most of the frequency jumps were likely to be triggered by reactance changes.

Further evidence for this assertion comes from the directions of the frequency change. Inertive reactance lowers F_0 because it effectively adds mass to the oscillating system (vocal folds plus a moving air column). The companion paper, Titze, 2008, gives calculations of this F_0 drop of about 50 Hz. Compliant reactance raises F_0 because it effectively adds stiffness to the oscillating system. As F_0 moves through the formant in a downward glide, one might first see a small increase in F_0 (due to a small amount of compliant reactance) followed by a sudden much larger decrease in F_0 because there is a dominance of inertive reactance.

As a second point of discussion, males experience more source instabilities than females in Exercise 1. Anatomically, the most important difference in the vocal system of males is a 60% greater vibrating vocal fold length, but only a 10%–20% greater vocal tract length. This leads to an overall greater difference between fundamental frequencies and lower formant frequencies in male phonations. Hence F_0–F_1 crossovers are generally less likely to occur in male normal speech. We hypothesize that this lower probability in male phonation may have led to fewer adaptive mechanisms to the destabilizing effects of F_0–F_1 crossovers.

A second factor is registration. Males phonate predominantly in modal register, whereas females have cultivated a more mixed register phonation. The second harmonic is of primary importance in modal register (male phonation) but less so in mixed register. It characterizes the closed portion of the glottal flow waveform (Titze, 2000, Chap. 5, Fig. 5.4), which is more important in male phonation than female phonation. Disturbance of the second harmonic by an additional

TABLE III. First formant frequencies (F1) and bandwidths (B1) from phonations of Exercise 1 of our study and from three other studies (PB: Peterson and Barney, 1952; CW: Childers and Wu, 1991; FL: Fujimura and Lindqvist-Gauffin, 1971).

	Average F1 (Hz)			Average B1 (Hz)		
Vowel	Measured	PB	CW	Measured	FL	CW
α—female	839	850	838	138	50	272
α—male	657	730	673	96	41	154
æ—female	840	860	842	128	50	221
æ—male	688	660	645	81	40	145
i—female	407	310	379	79	76	144
i—male	343	270	303	66	59	134
u—female	428	370	410	77	64	132
u—male	374	300	342	91	54	134

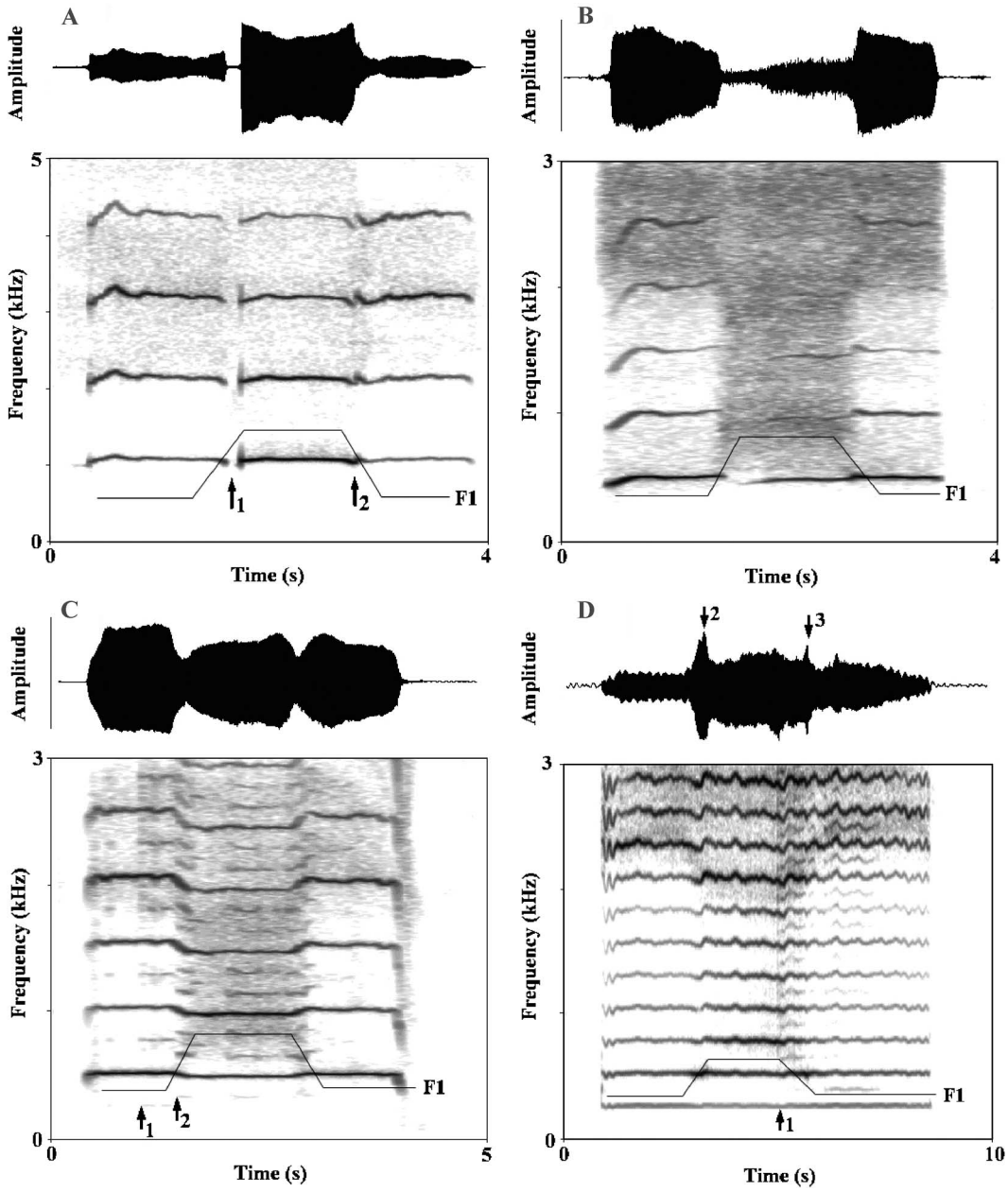

FIG. 7. Waveform and spectrogram examples of source instabilities in Exercise 2. Time and frequency axes are slightly variable across the four spectrograms. Trajectory of the first formant (F_1) is indicated by a thin solid line overlaid on the spectrograms. (A) Phonation of a female subject. Near the upgliding formant transition there is a short break (arrow 1) and a frequency perturbation (arrow 2). (B) Phonations of a female subject. There is a break near the upgliding formant transition and a frequency jump near the downgliding formant transition. Note that the harmonics become more faint, in the background of some chaotic noise in the high formant vowel. (C) Phonation of a male subject. $F_0/2$ subharmonics start at arrow 1 and $F_0/3$ subharmonics start at arrow 2. (D) Phonation of a male subject. A short subharmonic regime starts at arrow 1. This location is the same as the downgliding formant transition. Arrows 2 and 3 in the waveform envelope above point to sudden amplitude increase near the formant transition, a pattern common in many subjects.

loading effect (for instance during F_1-2F_0 crossovers) is more likely in males than in females because of the lower F_0. This can lead to larger source instabilities in males.

C. Exercise 2: Vowel transition on steady fundamental frequency

In this exercise, frequency jumps were found in 15% of all phonations across all subjects (s.d.=13%; range: 0%–41%; N=18). Six individuals showed no frequency jumps. Frequency jumps showed a mean frequency change of 20 Hz (s.d.=9.9 Hz; range: 10–42 Hz, N=12), which amounts to 1–2 semitones. Subharmonics were found in 21% of all phonations across 18 subjects (s.d.=15%; range: 0%–53%; N=18). Chaotic segments were found in 5% of all phonations across all subjects (s.d.=7%; range: 0%–25%; N=18). F_0-F_1 crossovers occurred in 89% of all phonations across all subjects (s.d.=16%; range 50%–100%; N=18).

Figures 7(A)–7(C) are examples of F_0-F_1 crossovers. In Fig. 7(A) there is an aphonic segment, in Fig. 7(B) a lowering of F_0 in the middle vowel portion combined with a chaotic segment, and in Fig. 7(C) an F_0 lowering combined with a period 2 and a period 3 subharmonic segment. In Fig. 7(D), F_1 crossed the second harmonic ($2F_0$), which revealed a

small period 2 subharmonic segment near the end of the return crossover. $2F_0-F_1$ crossovers represented 11% of the cases.

Independent of loudness, the overall mean proportion of source instabilities in phonations with F_0-F_1 crossover was 54% across male subjects (s.d.=28; range: 3%–89%; $N=9$). Five male subjects had five or more phonations without crossover that served for comparison. Without F_0-F_1 crossovers, the overall mean proportion of source instabilities in phonations was 23% (s.d.=23; range: 0%–43%; $N=5$). The difference was statistically significant (Wilcoxon; $Z=2.02$; $P<0.05$; $N=5$). For females, the overall mean proportion of source instabilities in phonations with F_0-F_1 crossover was 34% (s.d.=18; range: 8%–61%; $N=9$). Unfortunately, the female subject did not produce enough phonations without crossover for statistical comparison. Nevertheless, the result is that the proportion of source instabilities in phonations with F_0-F_1 crossover is significantly less in women (34%) than in men (54%) (Mann–Whitney; $U=21.5$; $P<0.05$; N_F, $N_M=9$).

1. Effect of loudness

A sufficient sample of noncrossover phonations within the two categories "loud" and "soft" was not available. When F_0-F_1 crossover occurred, however, the overall mean proportion of source instabilities in *loud* phonations was 59% in all males (s.d.=25; range: 9%–100%; $N=9$), whereas in *soft* phonations with F_0-F_1 crossover it was 65% (s.d.=22; range: 33%–100%; $N=9$). This difference was statistically not significant (Wilcoxon; $Z=0.77$; $P=0.77$; $N=9$). In females, the overall mean proportion of source instabilities in *loud* phonations with F_0-F_1 crossover was 23% across all subjects (s.d.=15; range: 11%–73%; $N=9$), whereas in *soft* phonations with F_0-F_1 crossover it was 43% (s.d.=25; range: 0%–100%; $N=9$). This difference was statistically significant (Wilcoxon; $Z=-2.01$; $P<0.05$; $N=9$), indicating that soft phonations are more prone to instability than loud phonations.

The location of the instability relative to the position of the crossover was investigated. Exercise 2 was designed to provoke two points of crossovers at the transitions from the first vowel to the second vowel, and back to the first vowels. Figure 8 indicates that instabilities were much more common near the two F_0-F_1 crossovers ("near" means within a 500 ms vicinity from the midpoint of the F_0-F_1 crossover) than in the steady portions of the exercise.

2. F_0 Symmetry at the F_0-F_1 crossover

Near the F_0-F_1 crossovers we often observed F_0 perturbations that were not sudden fundamental frequency jumps or voice breaks, but rather a dip with a recovery (Fig. 9). A similar phenomenon was part of an earlier figure for Exercise 1, Figs. 5(B) and 5(D) at arrow 1. These dips and recoveries often showed either symmetric or antisymmetric patterns at the two formant transition of Exercise 2. For example, note the zoomed-in contours in the lowest panels of Fig. 9(A). The two arrows indicate symmetric or antisymmetric fundamental frequency perturbations. Figure 9(B) shows upward

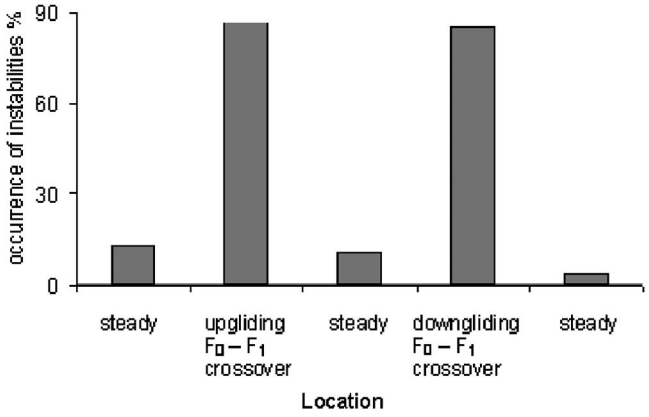

FIG. 8. Relative occurrences of frequency jumps at five locations in Exercise 2 across 18 individuals. We tested if the instability occurred either in the steady segments or in a 500 ms vicinity of the gliding formant transitions.

(symmetric) perturbations at the transitions, opposite to what was seen in Fig. 9(A). In addition, F_0 lowered in the middle portion as reactance changed [Figs. 9(A), 9(B), and 9(D)]. Figure 9(C) shows a reduction in vibrato at the vowel transitions. Figure 9(D) shows a general fundamental frequency lowering in the middle vowel, with a period 2 subharmonic.

D. Discussion of Exercise 2

Exercise 2 delivered at least three findings, which confirmed findings from Exercise 1. First, source instabilities occur more often in phonations in which F_0-F_1 crossovers are present. Second, source instabilities occur more often in male phonations than in female phonations when there are F_0-F_1 crossovers. Third, there are more source instabilities in soft phonations than in loud phonations when there are F_0-F_1 crossovers. The effect of loudness is not clear. In Exercise 1 males phonating softly were troubled profoundly by F_0-F_1 crossovers, but in Exercise 2 females produced more irregularities in soft utterances with F_0-F_1 crossovers.

Although the exercise was designed to keep fundamental frequency constant, many subjects failed to do so. In F_0-F_1 crossover utterances, F_0 often decreased by up to 50 Hz, when F_0 was on the reactive side of F_1, suggesting a direct effect on F_0 during strong nonlinear coupling.

We have little explanation to offer for the sometimes opposite behavior of F_0 perturbation in the middle part (during onset and offset of the second vowel) between subjects [Figs. 9(A) and 9(B)], except that possibly there exists individual-specific patterns in the correction pattern in reaction to the disturbance when F_0 and F_1 cross. Whether such individual specificity relates to vocal fold morphology or motor pattern of intrinsic laryngeal muscles remains speculation at this stage.

E. Exercise 3: Simultaneous vowel and fundamental frequency transitions

Frequency jumps were found in 15% of all phonations of Exercise 3 across 18 subjects (s.d.=15%; range: 0%–46%; $N=18$). Examples are shown in Figs. 10(A) and 10(D). By contrast, Fig. 10(B) shows an example of no frequency jumps when F_0 crosses F_1. Three individuals showed no fre-

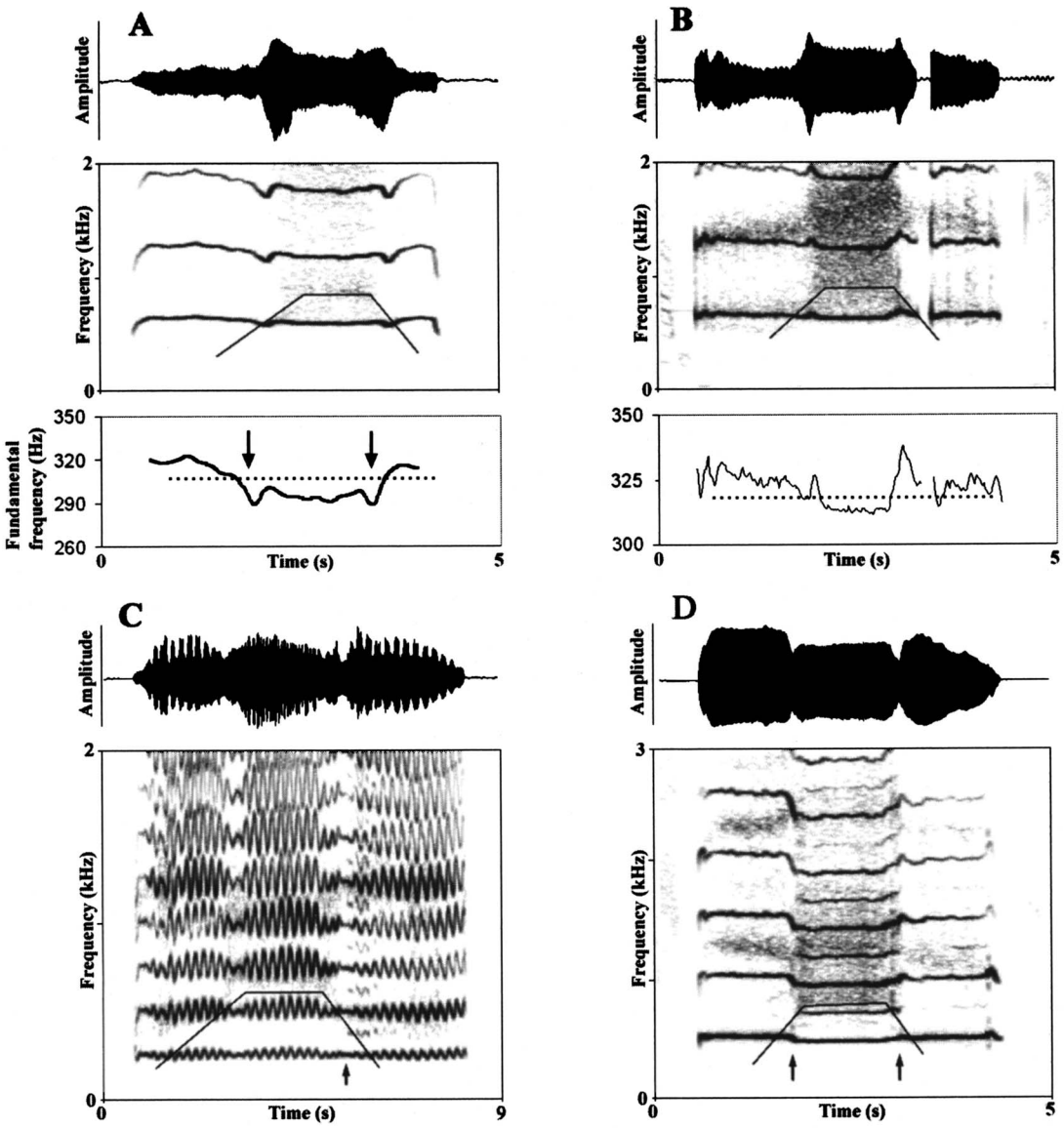

FIG. 9. Waveforms, spectrograms, and F_0 contours for Exercise 2. Trajectory of the first formant (F_1) is indicated by a thin solid line overlaid on the spectrograms. (A) Phonation of a male. Note that F_0 contours show a symmetry and an antisymmetry pattern near the formant transitions (arrows). (B) Female phonation. Note the increase of F_0 near both vowel transitions, with a phonation break near the second vowel transition. The F_0 increase near both vowel transitions is associated with sudden and short amplitude increases (see wave envelope above spectrum). However, both sustained vowels are similar in amplitude. (C) Male phonation. Note the strong vibrato during sustained vowel phonation, its offset during the vowel transition, as well as the onset of subharmonics at the second vowel transition (arrow). (D) Male phonation. Note the subharmonic onset and offset near the formant transitions (arrows) and the overall F_0 drop throughout the high F_1 (/æ/) vowel (between the two arrows).

quency jumps, or only a F_0 perturbation without bifurcation, as in Fig. 10(C). Frequency jumps from 15 subjects show a mean frequency change of 61 Hz (s.d.=38 Hz; range: 11–127 Hz, N=15), which amounts to about 2–3 semitones. Subharmonics were found in 20% of all phonations across 18 subjects (s.d.=15%; range: 0%–53%; N=18). Chaotic segments were found in 5% of all phonations across 18 subjects (s.d.=7%; range: 0%–25%; N=18). F_0–F_1 crossovers occurred in 89% of all phonations (s.d.=16%; range: 50%–100%, N=18 subjects), in women more often (99%) than in men (78%) (Mann–Whitney; U=5.5; $P<0.01$; N_F, N_M=9), for reasons given earlier.

Independent of loudness, the overall mean proportion of source instabilities in phonations with F_0–F_1 crossover was 62% across the male subjects (s.d.=20; range: 26%–89%; N=9). Five male subjects had five or more phonations without crossover that served for comparison. Without F_0–F_1 crossover, the overall mean proportion of source instabilities was 21% across individuals (s.d.=24; range: 0%–50%; N=5). The difference in the proportion of source instabilities in phonations with and without F_0–F_1 crossovers was statistically significant (Wilcoxon; Z=2.02; $P<0.05$; N=5). For females, the overall mean proportion of source instabilities in phonations with F_0–F_1 crossover was 30% (s.d.=16; range: 8%–59%; N=9). Female subjects did not produce enough phonations without crossover to make a statistical comparison. The proportion of source instabilities in phonations with F_0–F_1 crossover was significantly less in women (30%) than men (62%) (Mann–Whitney; U=8.5; $P<0.01$; N_F, N_M=9).

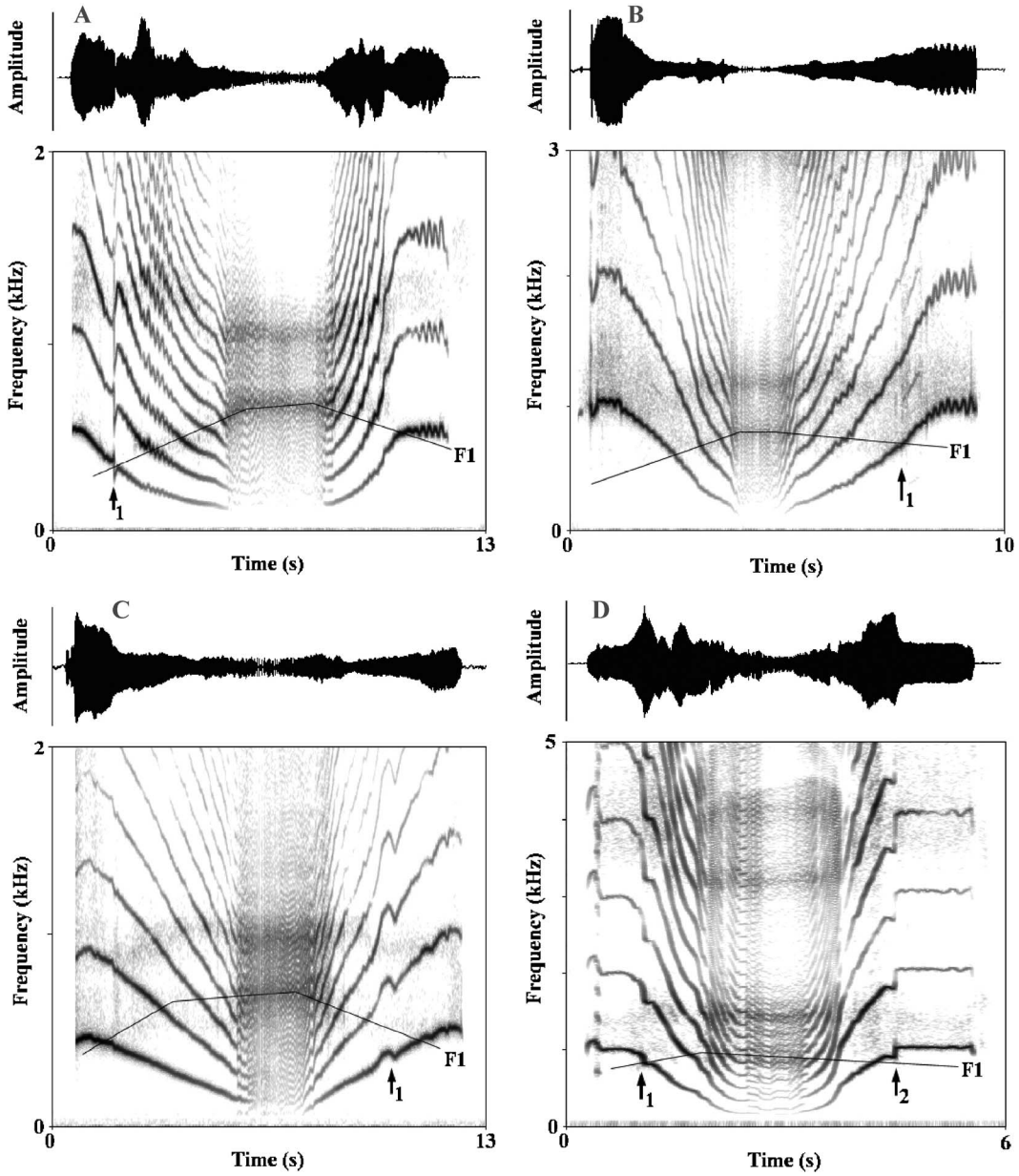

FIG. 10. Waveforms and spectrogram examples of source instabilities in Exercise 3. Trajectory of the first formant (F_1) is indicated by a horizontal line overlaid on the spectrograms. Time and frequency axes are scaled variably. (A) Phonation of a male subject. A frequency jump is indicated at arrow 1. (B) Phonation of a female subject. In the upgliding F_0 and downgliding formant transition, a subharmonic segment starts when F_1 and F_0 cross. (C) Phonations of a male subject. There is fundamental frequency perturbation without a jump or a break (arrow 1). (D) Phonation of a female subject. Frequency jumps are present at arrow 1 and arrow 2.

1. Effect of loudness

A sufficient sample of noncrossover phonations within the two categories "loud" and "soft" was not available. For crossovers, males showed an overall mean proportion of source instabilities in *loud* phonations of 59% (s.d.=25; range: 9%–100%; $N=9$), whereas in *soft* phonations it was 63% (s.d.=21; range: 33%–100%; $N=9$). The difference was statistically not significant (Wilcoxon; $Z=-0.47$; $P=0.63$; $N=9$). For females the overall mean proportion of source instabilities in *loud* phonations with F_0–F_1 crossover was 23% (s.d.=16; range: 0%–50%; $N=9$), whereas in *soft* phonations it was 45% (s.d.=27; range: 0%–77%; $N=9$). This difference was statistically significant (Wilcoxon; $Z=2.25$; $P<0.05$; $N=9$).

F. Discussion of Exercise 3, and comparative data

The design of the exercise did not allow the comparison between crossover and noncrossover phonations. However, results of Exercise 3 suggest that males seem more susceptible to produce source instabilities in crossover phonation, confirming findings from Exercises 1 and 2. Exercise 3 also confirmed that soft phonations are more susceptible to instabilities than loud phonations when F_0 and F_1 cross.

Frequency jumps, which were the most frequent instability, were larger in Exercise 3 than in either Exercise 1 or Exercise 2. Specifically, the frequency jumps of 2–3 semitones were more than twice as large as those of Exercise 2, where vowel changes alone were targeted. Exercise 2 was presumably produced with constant laryngeal muscle activa-

tions to keep F_0 constant, thereby resisting F_0 changes. The larger frequency jumps in Exercise 3 may be attributable to two motor patterns (intrinsic laryngeal muscles and vocal tract configuration) changing simultaneously. At the F_0–F_1 crossing, the intrinsic laryngeal muscles are programmed to continuously change F_0, but the vocal tract impedance is disturbing the normal vocal fold vibrations. Somato-sensory feedback in the vocal fold muscles has not been consistently found (Loucks *et al.*, 2005). Whether or not a feedback mechanism is responsible for differences in the size of frequency jumps (via mucosal mechanoreceptors), as opposed to a passive biomechanical mechanism, remains to be investigated.

G. General discussion

The exercises were designed to control for either vocal tract changes (Exercise 1) or for source changes (Exercise 2), or both (Exercise 3). With human subjects, however, the source and vocal tract changes never occur completely in isolation because supraglottal tissues and laryngeal tissues are connected and often influence one another, even if the attempt is to keep one or the other unchanged. For example, fundamental frequency changes can be associated with tongue-hyoid movement or with larynx height (Shipp *et al.*, 1984; Maurer *et al.*, 1991). Articulations (vowel transitions) are associated with F_0 changes (Whalen and Levitt, 1995; Whalen *et al.*, 1998). These interdependencies must be taken into account because they may contribute to a higher incidence of F_0 instabilities. Biomechanical changes associated with articulation may cause less control over vocal fold adduction and thereby predispose the vocal folds vibration patterns to bifurcate. Nevertheless, the higher incidence of source instabilities with F_0–F_1 crossover supports the hypothesis that nonlinear source filter coupling is at work, independent of whether or not the vibrating source is predisposed to instabilities for additional reasons. In the companion paper (Titze, 2008), where a purely theoretical analysis was performed with single parameter variations, similar bifurcations were observed by contrasting nonlinear versus linear coupling.

By way of an unexpected and untargeted result, we observed sudden dramatic amplitude increases near the F_0–F_1 crossovers (Fig. 11). Across individuals, the amplitude surges could be up to 15 dB [for example, Fig. 11(D)]. This phenomenon was mostly observed in Exercise 2 but did also occur in Exercises 1 and 3, although to a much lesser amount. These sudden and very short-term amplitude increases were synchronized with F_0–F_1 crossovers and never occurred in phonations without crossovers.

The sudden amplitude surges could be explained by linear source-filter theory in terms of rapid vocal tract, pressure changes in a dynamically changing vocal tract especially when vocal tract constrictions are suddenly made or released. Alternatively, nonlinear source–tract coupling could cause a sudden change in the vocal fold vibration amplitude that results in an increase of the power output of the source signal. Glottal source power output varies with open quotient and maximum flow declination rate (Titze, 2006b; companion paper, Titze 2008). There is the distinct possibility that when F_0 first traverses the compliant reactance range of F_1 and then suddenly enters the inertive reactance range (or vice versa), the maximum flow declination rate can fluctuate greatly.

In future studies, Exercises 2 and 3 might be individual specific in design so that more noncrossover phonations are produced, for comparative purposes. A subject's first formant range for /ɑ/ and /æ/ vowels might determine the starting F_0 and the range of /i/ and /u/ might decide the ending F_0 for the respective exercise. Although Exercise 3 shows the most dramatic effects, it may not be ideal for diagnostic purposes because of the difficulty of pinpointing the crossover point. Measurement of F_0 and F_1 is more difficult and contains a number of possible errors (more than for Exercises 1 and 2). Keeping either source frequency (F_0) or vocal tract frequency (F_1) constant allows a relatively reliable measurement, even in high F_0 phonations (if they are combined with vocal fry phonation).

There may be an exercise-specific bias for certain nonlinear phenomena. For instance, the greatest number of frequency jumps occurred in Exercise 1. One might test the generality of this in future studies with computational models.

There is also an individual-specific pattern of nonlinear phenomena occurring in crossover phonations. In our data set, two males and one female subject showed dramatic differences in the ratio of source instabilities between phonations with and without F_0–F_1 crossover (100% in phonations with and 0% in phonations without crossovers). Some subjects seem to show a bias in their productions toward one or another nonlinear phenomenon. An account for an individual-specific patterning of nonlinear phenomena has been given in several nonhumans (Riede *et al.*, 1997, 2000, 2007). This brings us back to the original hypothesis that humans (and perhaps other species) have some flexibility in operating their source–filter combination with either linear or nonlinear coupling. With human subject experiments, the nonlinear coupling parameter (the diameter of the epilarynx tube) was not controlled. Greater detail, with specific parameters identified and controlled for this nonlinear coupling, is given in the companion paper.

It is perhaps a little premature to make specific recommendations for clinical or pedagogical use of the exercises investigated here. Voice disorders resulting from lesions (nodules or polyps) create mode-of-vibration instabilities. Bilateral asymmetries cause difficulties with synchronization between left and right vocal fold movement. A rapidly changing acoustic load, as proposed in these exercises, may exacerbate these instabilities, thereby lowering the threshold for detection of a disorder. It is our belief that in the near future the traditional reliance on comfortable fundamental frequency and loudness vowel utterances will be replaced with exercises that are a bit more out of the comfort zone. These exercises designed here were not easy for some subjects. Much like running and jumping may be more telling about problems with locomotion than easy walking, vocal fold disorders may be more detectable when the vibrations are destabilized with more challenging acoustic loads. Sing-

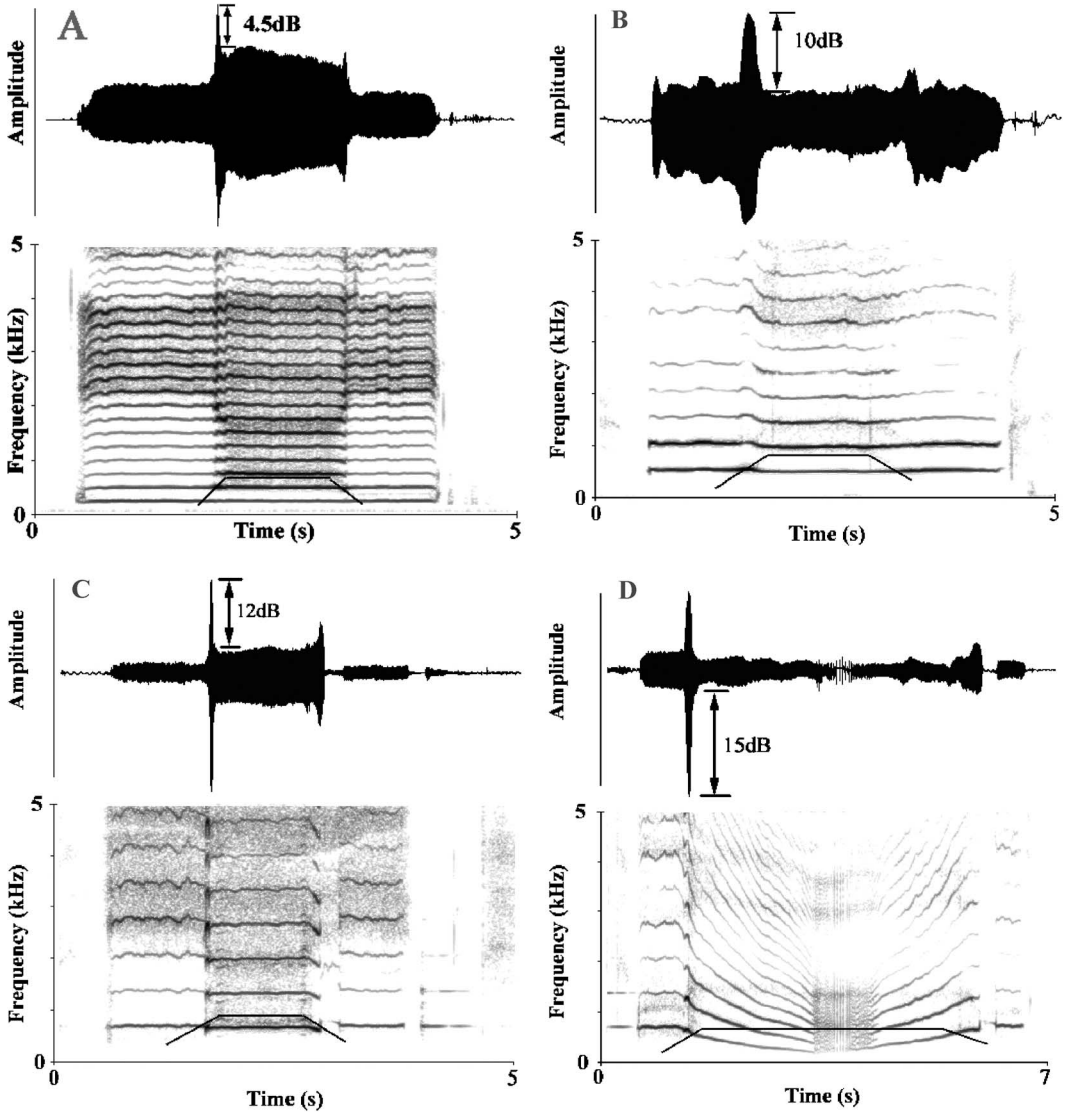

FIG. 11. Waveforms and spectrograms of phonations showing sudden amplitude bursts near the F_0-F_1 crossover. Trajectory of the first formant (F_1) is indicated by a thin solid line overlaid on the spectrograms. (A) Male phonation. Amplitude increase of 4.5 dB. (B) Female phonation. Amplitude burst of 10 dB. (C) Female phonation. Amplitude burst of 12 dB. (D) Same female as in (C) but on Exercise 3. Amplitude burst of 15 dB. In none of the phonations there is a strong bifurcation.

ers who want to avoid these instabilities could possibly benefit from structured practice in the instability region, with the intent of developing muscle patterns that counteract the instabilities.

ACKNOWLEDGMENTS

This work was supported by the National Institutes of Health Grant No. 5R01 DC004224-08 from the National Institute on Deafness and Other Communication Disorders. T.R. was supported by a fellowship of the "Deutsche Akademie der Naturforscher, Leopoldina" (BMBF-LPD 9901/8-127).

Alipour, F., Montequin, D., and Tayama, N. (**2001**). "Aerodynamic profiles of a hemilarynx with a vocal tract," Ann. Otol. Rhinol. Laryngol. **110**, 550–555.

Boersma & Weenick (**2007**). "Praat: Doing phonetics by computer," retrieved from www.praat.org 29 October and 4 December.

Chan, R. W., and Titze, I. R. (**2006**). "Dependence of phonation threshold pressure on vocal tract acoustics and vocal fold tissue mechanics," J. Acoust. Soc. Am. **119**, 2351–2362.

Childers, D., and Wu, K. (**1991**). "Gender recognition from speech. II. Fine analysis," J. Acoust. Soc. Am. **4**, 1841–1856.

Fant, G. (**1960**). *Acoustic Theory of Speech Production*, 2nd ed. (Mouton, The Hague, The Netherlands).

Fant, G. (**1986**). "Glottal flow: Models and interaction," J. Phonetics **14**, 393–399.

Fletcher, N. H. (**1979**). "Excitation mechanisms in woodwind and brass instruments," Acustica **43**, 63–72.

Freund, H. J., and Büdingen, H. J. (**1978**). "The relationship between speed and amplitude of the fastest voluntary contractions of human arm muscles," Exp. Brain Res. **31**, 1–12.

Fujimura, O., and Lindqvist-Gauffin, J. (**1971**). "Sweep-tone measurements of vocal tract characteristics," J. Acoust. Soc. Am. **49**, 541–558.

Hatzikirou, H., Fitch, W. T., and Herzel, H. (**2006**). "Voice instabilities due to source-tract interactions," Acta. Acust. Acust. **92**, 468–475.

Henrich, N., d'Alessandro, C., Castellengo, M., and Doval, B. (**2005**). "Glottal open quotient in singing: Measurements and correlation with laryngeal mechanisms, vocal intensity, and fundamental frequency," J. Acoust. Soc. Am. **117**, 1417–1430.

Herzel, H. P. (**1998**). "Nonlinear dynamics of the voice: Time series analysis, modeling and experiments," Curr. Top. Acoust. Res. **2**, 17–30.

Hirano, M. (**1981**). *Clinical Examination of Voice* (Springer, Vienna).

Ishizaka, K., and Flanagan, J. L. (**1972**). "Synthesis of voiced source sounds

from a two-mass model of the vocal cords," Bell Syst. Tech. J. **51**, 1233–1268.
Kent, R., Kent, J., and Rosenbek, J. (**1987**). "Maximum performance tests of speech production," J. Speech Hear Disord. **52**, 367–387.
Loucks, T. M. J., Poletto, C. J., Saxon, K. G., and Ludlow, C. L. (**2005**). "Laryngeal muscle responses to mechanical displacement of the thyroid cartilage in humans," J. Appl. Physiol. **99**, 922–930.
Maurer, D., Landis, T., and d'Heureuse, C. (**1991**). "Formant movement and formant number alteration with rising F0 in real vocalizations of the German vowels [u], [o] and [a]," Int. J. Neurosci. **57**, 25–38.
Mende, W., Herzel, H., and Wermeke, K. (**1990**). "Bifurcations and chaos in newborn infant cries," Phys. Lett. A **145**, 418–424.
Neubauer, J., Edgerton, M., and Herzel, H. (**2004**). "Nonlinear phenomena in contemporary vocal music," J. Voice **18**, 1–12.
Peterson, G. E., and Barney, H. L. (**1952**). "Control methods used in a study of the vowels," J. Acoust. Soc. Am. **24**, 175–184.
Riede, T., Arcadi, A. C., and Owren, M. J. (**2007**). "Nonlinear acoustics in pant hoots of common chimpanzees (*Pan troglodytes*): Vocalizing at the edge." J. Acoust. Soc. Am. **121**, 1758–1767.
Riede, T., Herzel, H., Mehwald, D., Seidner, W., Trumler, E., Böhme, G., and Tembrock, G. (**2000**). "Nonlinear phenomena and their anatomical basis in the natural howling of a female dog-wolf breed," J. Acoust. Soc. Am. **108**, 1435–1442.
Riede, T., Wilden, I., and Tembrock, G. (**1997**). "Subharmonics, biphonations, and frequency jumps–Common components of mammalian vocalization or indicators for disorders?," Z. Säugetierkunde **62**, 198–203.
Rothenberg, M. (**1981**). "Acoustic interaction between the glottal source and the vocal tract," in *Vocal Fold Physiology*, edited by K. N. Stevens and M. Hirano (University of Tokyo Press, Tokyo), pp. 305–328.
Schmidt, R. A., and Lee, T. D. (**1989**). *Motor Control and Learning: A Behavioral Emphasis*, 3rd ed. (Human Kinetics, Champaign, IL).
Schutte, H. K., and Miller, D. G. (**1993**). "Belting and pop, nonclassical approaches to the female middle voice: Some preliminary considerations," J. Voice **7**, 142–150.
Shipp, T. (**1984**). "Effects of vocal frequency and effort on vertical laryngeal position," Journal of Research in Singing **7**, 1–5.
Stevens, K. (**1998**). *Acoustic Phonetics (Current Studies in Linguistics)* (MIT, Cambridge, MA).
Story, B. H., Laukkanen, A. M., and Titze, I. R. (**2000**). "Acoustic impedance of an artificially lengthened and constricted vocal tract," J. Voice **14**, 455–469.
Sundberg, J., Gramming, P., and Lovetri, J. (**1993**). "Comparisons of pharynx, source, formant, and pressure characteristics in operatic and musical theatre singing," J. Voice **7**, 301–310.
Sundberg, J., and Hogset, C. (**2001**). "Voice source differences between falsetto and modal registers in counter tenors, tenors and baritones," Logoped. Phoniatr. Vocol. **26**, 26–36.
Titze, I. R. (**1988**). "The physics of small-amplitude oscillation of the vocal folds," J. Acoust. Soc. Am. **83**, 1536–1552.
Titze, I. R. (**2000**). *Principles of Voice Production*, 2nd ed. (National Center for Voice and Speech, Denver, CO).
Titze, I. R. (**2004**). "Theory of glottal airflow and source-filter interaction in speaking and singing," Acta. Acust. Acust. **90**, 641–648.
Titze, I. R. (**2006a**). *The Myoelastic-Aerodynamic Theory of Phonation* (National Center for Voice and Speech, Denver, CO).
Titze, I. R. (**2006b**). "Theory of maximum flow declination rate vs. maximum area declination rate in phonation." J. Speech Lang. Hear. Res. **49**, 439–447.
Titze, I. R. (**2008**). "Nonlinear source-filter coupling in phonation: Theory," J. Acoust. Soc. Am. **123**(3), XXX-XXX
Titze, I. R., and Story, B. H. (**1995**). "Acoustic interaction of the voice source with the lower vocal tract," J. Acoust. Soc. Am. **101**, 2234–2243.
Tokuda, I., Riede, T., Neubauer, J., Owren, M. J., and Herzel, H. (**2002**). "Nonlinear analysis of irregular animal vocalizations," J. Acoust. Soc. Am. **111**, 2908–2919.
Whalen, D. H., Gick, B., Kumada, M., and Honda, K. (**1998**). "Cricothyroid activity in high and low vowels: Exploring the automaticity of intrinsic F0," J. Phonetics **27**, 125–142.
Whalen, D. H., and Levitt, A. G. (**1995**). "The universality of intrinsic F0 of vowels," J. Phonetics **23**, 249–366.
Zañartu, M., Mongeau, L., and Wodlicka, G. R. (**2007**). "Influence of acoustic loading on an effective single mass model of the vocal folds," J. Acoust. Soc. Am. **121**, 1119–1129.
Zhang, Z., Neubauer, J., and Berry, D. A. (**2006**). "The influence of subglottal acoustics on laboratory models of phonation," J. Acoust. Soc. Am. **120**, 1558–1569.

Optimized translation of microbubbles driven by acoustic fields

Jean O. Toilliez and Andrew J. Szeri[a)]
Department of Mechanical Engineering, University of California at Berkeley, Berkeley, California 94720

(Received 23 October 2007; revised 1 February 2008; accepted 4 February 2008)

The problem of a single acoustically driven bubble translating unsteadily in a fluid is considered. The investigation of the translation equation identifies the inverse Reynolds number as a small perturbation parameter. The objective is to obtain a closed-form, leading order solution for the translation of the bubble, assuming nonlinear radial oscillations and a pressure field as the forcing term. In a second part, the periodic attractor of the Rayleigh–Plesset equation serves as basis for an optimal acoustic forcing designed to achieve maximized bubble translation over one dimensionless period. At near-resonant or super-resonant driving frequencies, it seems one cannot improve much on sinusoidal forcing. However at moderate acoustic intensity and sub-resonant frequencies, acoustic wave forms that enhance bubble collapse lead to displacement many times larger than the case of purely sinusoidal forcing. The survey covers a wide spectrum of driving ratios and bubble diameters including those relevant to biomedical applications. Shape stability issues are considered. Together, these results suggest new ways to predict some of the direct and indirect effects of the acoustic radiation force in applications such as targeted drug delivery, selective bubble driving, and accumulation. © *2008 Acoustical Society of America.* [DOI: 10.1121/1.2887413]

PACS number(s): 43.25.Yw, 43.25.Ts [CCC] Pages: 1916–1930

I. INTRODUCTION

The present analysis deals with translating bubbles in a viscous fluid. Under the action of an acoustic pressure wave (either traveling or standing), the bubble undergoes volume oscillations. The pressure gradient creates a "Bjerknes force" that induces a net translation that allows the bubble to move along the direction of the wave,[1] as it undergoes shape oscillations that affect the overall translation.[2,3] The coupled equations that govern the radial and translational oscillations cannot be solved analytically in a straightforward fashion. Among other methods, that of decoupling and averaging the two motions has proved successful at providing an estimate of the *steady* translation velocity.[4–6] The radial oscillations are assumed sinusoidal and the perturbations around the equilibrium radius, small. In other words, this method requires the acoustic forcing and bubble volume oscillations to be weak.

The first part of the present work is an extension of the theory to handle transients in the translation dynamics and fully nonlinear radial oscillations. It is based on a previous analysis, originally applied to the dissolution of spherically oscillating bubbles, by Fyrillas and Szeri.[7,8] The goal is to provide a good approximation for the bubble displacement, so as to understand a bubble under the action of an external acoustic driving. This work represents a preliminary step toward understanding bubble translation in more complex settings, such as in computationally demanding[9] bubble cloud[10,11] simulations, for instance. Because the translation equation used here does not contain the secondary Bjerknes force, the approximation is only valid within disperse clouds, where the attracting or repelling force between two neighboring bubbles is negligible and the acoustic scattering is low enough to not significantly distort the incident acoustic forcing. First, the equations of motion are presented in their dimensionless form. Then, a preliminary numerical investigation provides insight into the bubble behavior in response to a traveling acoustic wave. A formal study based on the method of *splitting* is performed upon the translation equation.[2,4,10,12,13] This is motivated by the oscillatory nature of the velocity history. The method consists in recasting the bubble velocity as the sum of two components. An appropriate time-averaging scheme in conjunction with the method of multiple scales allows one to develop an approximation of the two components of the velocity, which are finally added and compared to the actual numerical solution. The outcome of the analysis is a better understanding of bubble displacement, which serves as basis for an optimization problem.

The second part focuses on optimizing bubble displacement. This study proceeds along similar lines to prior work on enhanced acoustic scattering.[14,15] Such a theoretical investigation is potentially of interest for a better understanding of bubble management in microgravity using an acoustic wave, or in various medical applications. A number of authors have described the ability of sound fields to displace micron-sized bubbles—or more recently, liquispheres—sometimes over significant distances and velocities, up to half a meter per second.[16,17] For instance, gas-filled liquispheres pushed by an external acoustic field are being actively investigated as potential drug delivery vehicles;[18] when used as contrast agents, the controlled displacement—under the action of the Bjerknes force—of ligand-coated, micron-sized spheres can facilitate ultrasonic imaging[19–21] by way of enhanced binding to the targeted sites. For specific examples we choose bubble radii and frequencies that are relevant to experiments, such as enhanced targeted delivery of contrast microbubbles.[22]

[a)]Author to whom correspondence should be addressed. Electronic mail: aszeri@me.berkeley.edu

 0001-4966/2008/123(4)/1916/15/$23.00 © 2008 Acoustical Society of America

This work presents an indirect way to solve for an optimum displacement. We show that by promoting a stronger collapse, the bubble should experience a more significant lurch forward, eventually accompanied by a larger net displacement. This technique is implemented using subresonant frequencies, where bubble has a longer time to grow in response to the rarefaction—leading to a stronger collapse. A combination of small bubbles and high frequencies is studied in order to fit within the biomedical context of greatest interest. First, we lay out the theoretical background necessary to establish the optimization strategy. Then, the Euler–Lagrange equations are solved using a successive continuation method. Numerical results follow, later expanded upon so as to study the influence of the forcing depending on the intensity of the signal, bubble size, and driving frequencies.

II. EQUATIONS OF MOTION

In the following section we set up the theoretical background used to solve for the leading order bubble velocity and, in a second part, to optimize bubble translation.

A. Bubble motion

Under the action of an acoustic wave, a microbubble undergoes motion. This motion is governed, in the present situation, by the translation equation, which appears in a number of publications[2,4,10,12,13] and reads:

$$\frac{2\pi}{3}\rho\frac{d}{dt}[R^3(\dot{X}-U_a)] = -12\pi\mu R(\dot{X}-U_a) - \frac{4\pi}{3}R^3\nabla P_\infty. \tag{1}$$

R is the bubble radius, U_a is the velocity of the surrounding liquid, moving under the action of the external pressure gradient ∇P_∞, while X and $\dot{X}$ refer to the bubble translation displacement and velocity, respectively. There are a number of ways to accommodate the translation equation to additional physical constraints, e.g., wall effects, shell behavior, etc. For example, Dayton *et al.*[16] use a translation equation relying on experimental data to calculate lipid-membrane microspheres under the action of an ultrasonic inducer. For simplicity, we shall use Eq. (1). Using a Lagrangian formalism applied to a single bubble subject to an external pressure field allows for retrieving the same equation, along with an gradient term proportional to $\nabla|\dot{X}-U_a|$, as described by Ilinskii *et al.*[23]

The translation equation is made dimensionless. To that end, the following characteristic scales and dimensionless parameters are used: $X=R_0x$, $U_a=f_dR_0u_a$, $t=\tau/f_d$, $P_\infty=P_0p_\infty$, and $R=R_0r$. X is the bubble translation with respect to a fixed frame, f_d is the driving frequency, and R_0 is the equilibrium radius of the bubble. p_∞ represents the dimensionless acoustic wave originating from the transducer. Here, for illustrative purposes, the form of the acoustic wave is considered as traveling:

$$p_\infty = 1 + P_a\sin(2\pi R_0/\Lambda x - 2\pi\tau). \tag{2}$$

In order to decouple the equation for radial oscillations from the translation equation, it is assumed that the bubble translation per period is negligible compared to the wavelength Λ of the pressure wave, that is, the pressure gradient is simply a function of time. Alternatively, one can argue that the wave pressure is passing by relatively quickly, with the consequence that the minute bubble translation per period does not introduce any significant phase lag, thereby reducing to a simpler form for use in Eq. (6):

$$p_\infty = 1 - P_a\sin(2\pi\tau). \tag{3}$$

This is a useful step that allows one to solve for the radial oscillations, independent of the velocity. By use of these variables, the dimensionless form of the translation equation reads

$$\frac{d}{d\tau}[r^3(\dot{x}-u_a)] = -\frac{18}{\mathrm{Re}}r(\dot{x}-u_a) - C_pr^3\frac{dp_\infty}{dx}. \tag{4}$$

Dimensionless coefficients C_p and Re are defined in detail in Appendix D. This is a first-order, variable coefficient ordinary differential equation in $\dot{x}=u$, provided that all other parameters are known. From the application of a balance of linear momentum in the acoustic limit, it is found that, instantaneously,

$$\rho\dot{U}_a = -\nabla P_\infty, \tag{5}$$

Integrating Eq. (5) allows for obtaining a closed-form expression for $U_a(\tau)$, under the action of the external forcing $P_\infty(\tau)$, as derived for example in Reddy and Szeri.[13]

B. Bubble dynamics

Whereas the study of translation transients does not rely directly on the Rayleigh–Plesset equation (RPE), the optimization problem explicitly requires its use in the set of Euler–Lagrange equations. RPE governs the evolution of the bubble radius $R(t)$ subject to some external forcing P_∞ and is recalled in its simplified form:[1]

$$R\ddot{R} + \frac{3}{2}\dot{R}^2 = \frac{1}{\rho}[P_l - P_\infty]. \tag{6}$$

The exact form of Eq. (6) can be chosen to accommodate a large array of situations including, for instance, pulse driving at large amplitudes,[13,14,24] viscous damping effects,[25] compressibility terms, among others. In this particular case, we have not included the term proportional to $\dot{X}^2$ discussed by Doinikov:[10] It is most important for higher-intensity driving of translating bubbles, where the acoustic coefficient P_a is well over 1.0 times the ambient pressure. The dimensionless pressure at the bubble wall $p_l=P_l/P_0$, where $P_0=1.01325\times10^5$ N m^{-2} is the static pressure, reads

$$p_l = p_g + p_v^* - \frac{1}{\mathrm{We}\,r} - \frac{4\dot{r}}{\mathrm{Re}\,\mathrm{Eu}\,r}. \tag{7}$$

All dimensionless groups, including the Reynolds (Re), Euler (Eu), and Weber (We) numbers are given in Appendix D. The gas pressure p_g depends on the dimensionless, normalized internal gas pressure $p_{g0}^*=1-p_v^*+\sigma/(P_0R_0)$ and is given by

$$p_g = p_{g0}^* r^{-3k} \tag{8}$$

and k stands for the polytropic exponent. Therefore, we rely on the method laid out in Leighton[1] to determine an appropriate value for the polytropic exponent (see Appendix D for details). Additionally, the RPE often includes terms taking into account compressibility effects. Here we simply neglect compressibility effects as is suitable for mild or moderate forcing within the RPE. Therefore, recast in its well-known[1,26,27] dimensionless form, it becomes

$$r\ddot{r} + \frac{3\dot{r}^2}{2} = \mathrm{Eu}[p_l - p_\infty]. \tag{9}$$

In the present context it is proposed to optimize bubble translation based on the periodic attractor of its radial oscillations: We thus restrict the problem to continuous forcing of small bubbles and periodic radial oscillations.

III. APPROXIMATION FOR THE SMOOTH BUBBLE VELOCITY

A. Motivation for splitting

1. Overall objective and method

The analysis starts with the Rayleigh–Plesset equation, as recast in its decoupled form [obtained by combining Eqs. (6) and (3)], which does not depend on the bubble position $x(t)$. Therefore, obtaining $r(t)$ over a given time interval is straightforward. Then, the translation equation (1) is integrated so as to obtain the velocity of the bubble, subject to the pressure field and using the known function $r(t)$.

Numerical investigations suggest that the translation may be understood as being the sum of two distinct components, namely a *smooth* part and an *oscillatory* part: These features are particularly striking when one examines the velocity of the bubble. The form of the oscillatory problem suggests an appropriate time-averaging scheme that serves to define the splitting method.

The scheme relies on the stable periodic radial attractor to build the velocity approximation. The transient radial dynamics do not significantly alter the slowly evolving, *smooth* bubble velocity.

2. Slow time scale

Using a pressure field in the form of a traveling wave, several numerical tests are performed; here we focus on $\mathrm{Re}_1=280$ and $\mathrm{Re}_2=28$. Then the velocity $u(t)$ is plotted against a stretched time axis. A common time scale for the slow transient is then deduced from this analysis, proportional to the inverse of the Reynolds number. Hence,

$$\xi = \frac{1}{\mathrm{Re}}\tau = \epsilon\tau, \tag{10}$$

where τ now refers to the fast time. Figure 1 summarizes these results.

3. Splitting method

A close look at the translation equation justifies the idea to view the velocity as possessing two components. One would be purely oscillatory, that is, with no net contribution on the translation over time in a periodic acoustic field, after the decay of transients in the radial dynamics. This component is driven by the oscillating part of the pressure forcing and also by the oscillating liquid itself moving under the influence of the pressure field. The other part, referred to as the "smooth" part, is, on the contrary, responsible for the bubble's net displacement per period. Because bubble translation is the result of a balance between the drag force and the Bjerknes force, and because the drag force is on the order of ϵ, as seen earlier, it is expected that the smooth solution will show a slow transient before a more uniform behavior (in a plane wave). This is a well-known consequence of a small-order damping term that eventually affects the leading-order solution of a driven oscillator. These observations suggest the following splitting:

$$u = u^{\mathrm{sm}} + u^{\mathrm{osc}} \tag{11}$$

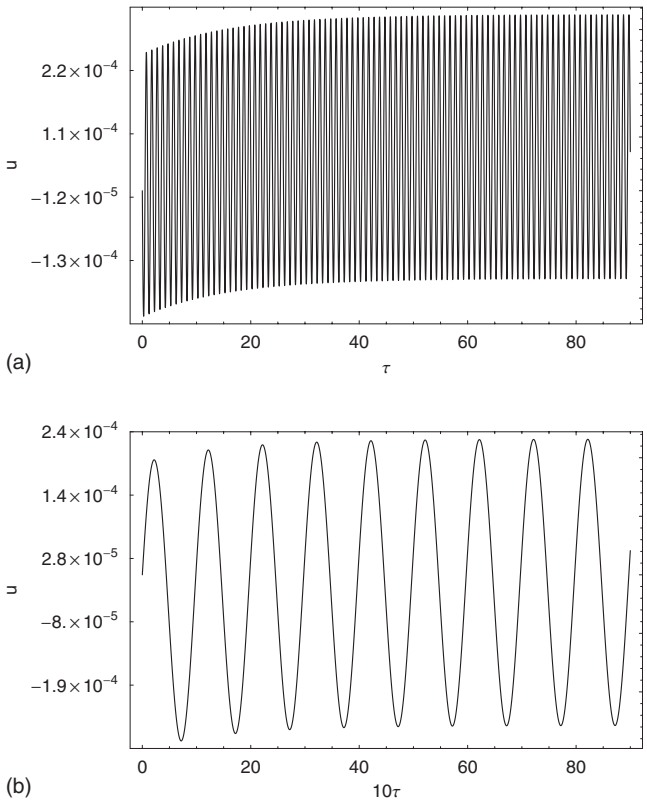

FIG. 1. An illustrative comparison of bubble translation velocity vs rescaled time at different Re: (a) $u(\tau)$ plotted against τ for $\mathrm{Re}=280$ and (b) $u(\tau)$ against 10τ and $\mathrm{Re}=28$. The slow transients appear to expire around the same dimensionless time $\tau_0 \sim 60-70$, which suggests $\xi \sim \epsilon\tau$ where $\epsilon = 1/\mathrm{Re}$.

B. Application of splitting

We begin by introducing a new, nonuniformly evolving time

$$\hat{\tau}(\tau) = \int_0^\tau \frac{d\theta}{r^3}. \tag{12}$$

Alternatives for the nonlinear time such as $\hat{\tau}(\tau)=\int_0^\tau d\theta r^{-2}$ are possible. Nonetheless, that of Eq. (12) is a particularly con-

venient choice: The derivative on the left-hand side of Eq. (4) is much simplified in the transformed ordinary differential equation (ODE). Indeed, by use of the chain rule, Eq. (4) is recast as

$$\frac{d}{d\hat{\tau}}(\hat{u}-\hat{u}_a)+18\epsilon r(\hat{u}-\hat{u}_a)=-C_p r^6\frac{dp_\infty}{dx}, \tag{13}$$

where it is understood that

$$r^3u_a=r^3\frac{d}{d\tau}x_a=x_{a\hat{\tau}},$$

$$r^3u=\cdots=x_{\hat{\tau}}, \tag{14}$$

and that, by convention, the terms $x_{\hat{\tau}\hat{\tau}}=\hat{u}_{\hat{\tau}}$ and $x_{\hat{\tau}}=\hat{u}$. The liquid displacement with respect to a fixed frame $x_a(\tau)$ is found by integrating $u_a(\tau)$ with respect to τ. Finally, the following nonlinear time average is defined:

$$\langle f(\hat{\tau})\rangle_{\hat{\tau}}\equiv\frac{1}{\int_0^T d\hat{\tau}}\int_0^{\hat{\tau}(T)}f(\hat{\tau})d\hat{\tau}. \tag{15}$$

Here T is the period of the acoustic field and bubble radial oscillation. Note that

$$\langle(\cdot)\rangle_{\hat{\tau}}=\frac{\langle r^{-3}(\cdot)\rangle_\tau}{\langle r^{-3}\rangle_\tau}, \tag{16}$$

where

$$\langle(\cdot)\rangle_\tau\equiv\frac{1}{T}\int_0^T(\cdot)d\tau. \tag{17}$$

1. Application of the decomposition

First, we note that $u=u_a$ is obviously a solution of the following inhomogeneous ODE:

$$\frac{d}{d\hat{\tau}}(\hat{u}-\hat{u}_a)+18\epsilon r(\hat{u}-\hat{u}_a)=0, \tag{18}$$

therefore, the term u_a will be conveniently removed from the problem and replaced at the end.

Substitution of Eqs. (11) and (12) in Eq. (13) yields

$$\frac{d}{d\hat{\tau}}(\hat{u}^{\mathrm{sm}}+\hat{u}^{\mathrm{osc}})+18\epsilon r(\hat{u}^{\mathrm{sm}}+\hat{u}^{\mathrm{osc}})=-f(\tau). \tag{19}$$

The function $f(\tau)$ represents the pressure forcing. The forcing is itself split into two parts using the time average, so that

$$\frac{d}{d\hat{\tau}}\hat{u}^{\mathrm{osc}}+18\epsilon r\hat{u}^{\mathrm{osc}}=-\tilde{f}(\tau), \tag{20}$$

where

$$\tilde{f}(\tau)\equiv f(\tau)-\langle f(\tau)\rangle_{\hat{\tau}}, \tag{21}$$

the solution of the oscillatory problem is set not to grow without bound over time. Conversely, the smooth problem should be excited by an appropriate forcing, so as to guarantee that the split problem is identical to its original form:

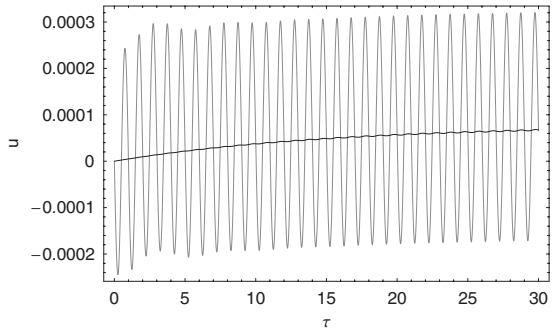

FIG. 2. The grey line represents the bubble velocity as obtained by integrating (4) and using the periodic attractor for $r(t)$. The "net" velocity component, represented by the continuous black line, u^{sm} has been calculated from the smooth problem (22). In this case the average forcing and averaged solutions are very close.

$$\frac{d}{d\hat{\tau}}\hat{u}^{\mathrm{sm}}+18\epsilon r\hat{u}^{\mathrm{sm}}=-\langle f\rangle_{\hat{\tau}}. \tag{22}$$

Importantly, Eqs. (20) and (22) are such that their linear combination yields the original problem to solve. Prior to proceeding to perturbation approximation, the two components of the velocity are solved for numerically, as shown in Fig. 2.

2. Perturbation solution of the smooth problem

As argued earlier, it is expected that the smooth solution $\hat{u}^{\mathrm{sm}}$ is primarily a function of a slow time scale. That is, the small viscous drag manages to influence the motion to leading order. Thus, the method of multiple scales in time is employed, so that

$$\hat{u}^{\mathrm{sm}}(\hat{\tau};\epsilon)=\hat{u}_0^{\mathrm{sm}}+\epsilon\hat{u}_1^{\mathrm{sm}}+\epsilon^2\hat{u}_2^{\mathrm{sm}}+\cdots, \tag{23}$$

where $\hat{u}_i^{\mathrm{sm}}=\hat{u}_i^{\mathrm{sm}}(\hat{\tau},\hat{\xi})|_{i=0,1,2}$ and $\hat{\xi}=\epsilon\hat{\tau}$ is used as a slow time scale to capture explicitly the slow drifting behavior. Thus Eq. (22) becomes

$$\frac{d}{d\hat{\tau}}(\hat{u}_0^{\mathrm{sm}}+\epsilon\hat{u}_1^{\mathrm{sm}}+\cdots)+\epsilon\frac{d}{d\hat{\xi}}(\hat{u}_0^{\mathrm{sm}}+\epsilon\hat{u}_1^{\mathrm{sm}}+\cdots)$$
$$+18\epsilon r(\hat{u}_0^{\mathrm{sm}}+\epsilon\hat{u}_1^{\mathrm{sm}}+\cdots)=-\langle f\rangle_{\hat{\tau}}. \tag{24}$$

The forcing itself is assumed to be on the order of ϵ. Indeed, physically, the drag force and the pressure forcing—coupled with radial oscillations—should be balanced. Now, if the forcing is assumed to be on the order of ϵ^0, then the smooth solution would grow without bound, which is not physical. Therefore it is proposed to rewrite $\langle f\rangle_{\hat{\tau}}$ so as to extract a new pressure coefficient, such that

$$-\langle f\rangle_{\hat{\tau}}=-C_p\left\langle r^6\frac{dp_\infty}{dx}\right\rangle_{\hat{\tau}}=-\mathcal{J}\epsilon\left\langle r^6\frac{dp_\infty}{dx}\right\rangle_{\hat{\tau}}, \tag{25}$$

where $\mathcal{J}$ represents a new scaling for the pressure forcing. Explicitly,

$$\mathcal{J} = C_p \,\mathrm{Re} = \frac{2P_0}{f_d \mu}, \tag{26}$$

which, for the weak pressure driving case, is such that $\mathcal{J} = \mathcal{O}(10^2)$. Furthermore, based on physical reasoning, it is assumed that

$$\mathcal{J}\left\langle r^6 \frac{dp_\infty}{dx} \right\rangle_{\hat{\tau}} \sim \mathcal{O}(1), \tag{27}$$

i.e., the averaged forcing excites the first component of $\hat{u}^{\mathrm{sm}}$ on the slow time scale. Therefore it is expected that the forcing term is on the same order as the drag force, directly proportional to ϵ. Hence, to leading order, from Eq. (22)

$$\hat{u}^{\mathrm{sm}}_{0,\hat{\tau}} = 0 \Leftrightarrow \hat{u}^{\mathrm{sm}}_0 = C(\hat{\xi}). \tag{28}$$

To solve for the constant $C(\hat{\xi})$, a second equation is sought from the ϵ^1 terms in Eq. (24):

$$\hat{u}^{\mathrm{sm}}_{1,\hat{\tau}} = -\hat{u}^{\mathrm{sm}}_{0,\hat{\xi}} - 18 r \hat{u}^{\mathrm{sm}}_0 - \mathcal{J}\left\langle r^6 \frac{dp_\infty}{dx} \right\rangle_{\hat{\tau}}. \tag{29}$$

The right-hand side must be constrained so as to prevent the asymptotic expansion (23) from behaving in a secular manner. Therefore, an additional condition on $C(\hat{\xi})$ is established, so that

$$\langle \mathrm{RHS}(29) \rangle_{\hat{\tau}} = 0. \tag{30}$$

Now, combining the fact that the leading order approximation of $\hat{u}^{\mathrm{sm}}$ is not a function of the fast time scale, but only dependent on $\hat{\xi}$ and that the forcing term is a constant, Eq. (30) is recast as

$$C' + 18\langle r \rangle_{\hat{\tau}} C(\hat{\xi}) = -\mathcal{J}\left\langle r^6 \frac{dp_\infty}{dx} \right\rangle_{\hat{\tau}}. \tag{31}$$

Along with $\hat{u}^{\mathrm{sm}}_0(0) = C(0) = 0$, to leading order, the smooth component of the bubble velocity reads

$$\hat{u}^{\mathrm{sm}}_0 = \mathcal{J}\frac{\left\langle r^6 \frac{dp_\infty}{dx} \right\rangle_{\hat{\tau}}}{18\langle r \rangle_{\hat{\tau}}} \{\exp[-18\langle r \rangle_{\hat{\tau}} \hat{\xi}] - 1\}. \tag{32}$$

The next higher order term is computed in the Appendix. It employs the same strategy, that is, a method combining multiple scales with the same appropriate averaging.

3. The oscillatory problem

The issue is to solve the following ODE:

$$\hat{u}^{\mathrm{osc}}_{\hat{\tau}} + 18\epsilon r \hat{u}^{\mathrm{osc}} = -C_p \left\{ \frac{r^6 dp_\infty}{dx} - \left\langle r^6 \frac{dp_\infty}{dx} \right\rangle_{\hat{\tau}} \right\}. \tag{33}$$

Obviously, the oscillatory term is expected to evolve with the fast time scale. Importantly, the right-hand side of Eq. (33) has no net average when computed over a nonlinear period. Physically, the oscillatory part of the pressure term $r^3 dp_\infty / dx$ forces the bubble to oscillate back and forth in a rapid fashion, without being significantly affected by the viscous term. Mathematically, we can write

$$C_p \left\{ \frac{r^6 dp_\infty}{dx} - \left\langle r^6 \frac{dp_\infty}{dx} \right\rangle \right\} \sim \mathcal{O}(\epsilon^0), \tag{34}$$

i.e., the oscillatory component of the pressure field excites the zeroth-order term of u^{osc}, recast as a regular perturbation expansion, such that

$$\hat{u}^{\mathrm{osc}}(\hat{\tau}) = \hat{u}^{\mathrm{osc}}_0 + \epsilon \hat{u}^{\mathrm{osc}}_1 + \epsilon^2 \hat{u}^{\mathrm{osc}}_2 + \cdots. \tag{35}$$

The leading order terms of Eq. (20) provide

$$\hat{u}^{\mathrm{osc}}_{0,\hat{\tau}} = -C_p \left\{ \frac{r^6 dp_\infty}{dx} - \left\langle r^6 \frac{dp_\infty}{dx} \right\rangle \right\}, \tag{36}$$

which, given the initial condition $\hat{u}^{\mathrm{osc}}_0(0) = 0$, yields

$$\hat{u}^{\mathrm{osc}}_0 = -C_p \left[\int_0^{\hat{\tau}} \frac{r^6 dp_\infty}{dx} d\theta - \left\langle r^6 \frac{dp_\infty}{dx} \right\rangle \hat{\tau} \right]. \tag{37}$$

A comment is in order. It is clear that the arguments we have advanced for the splitting—which lead to Eqs. (32) and (37)—are still valid even in the case where the time averages are slowly evolving (on the time scale $\hat{\xi}$). This occurs, for example, when the amplitude or wave form are spatially inhomogeneous and the bubble slowly translates through different areas.

4. Composite leading-order approximation

Thus far a solution has been derived using the nonuniform time, $\hat{\tau}$. Conversion of the solution to a function of the "true" time is straightforward. The steps described in Eq. (14) are taken in a reverse order, thereby obtaining for the smooth problem

$$u^{\mathrm{sm}}_0 = \frac{C_p \,\mathrm{Re}}{18 r^3} \frac{\left\langle r^3 \frac{dp_\infty}{dx} \right\rangle_\tau}{\langle r^{-2} \rangle_\tau} \times \left\{ \exp\left[-\frac{18\langle r^{-2} \rangle_\tau}{\mathrm{Re}\langle r^{-3} \rangle_\tau} \int_0^\tau \frac{d\theta}{r^3} \right] - 1 \right\}. \tag{38}$$

As shown in Fig. 3(a) the leading order solution rapidly and uniformly converges toward the numerical result. The solution for the bubble velocity of Eq. (38) obtained by the method of splitting provides a better rendering of the transients and a more faithful approximation for the net velocity than a simpler average-equation solution. Time averaging Eq. (4) allows for deriving the constant, asymptotic velocity

$$\langle u \rangle^{\mathrm{Classical}}_{\tau \to \infty} = -\frac{C_p \,\mathrm{Re}}{18} \frac{\left\langle r^3 \frac{dp_\infty}{dx} \right\rangle_\tau}{\langle r \rangle_\tau}, \tag{39}$$

which contrasts sharply with the time-dependent $u^{\mathrm{sm}}_0(\tau)$.

Likewise, the leading order oscillatory component is transformed and is augmented by the liquid velocity u_a, so as to read

$$u^{\mathrm{osc}}_0 \equiv u_a - \frac{C_p}{r^3} \tilde{u}^{\mathrm{osc}}_0, \tag{40}$$

where

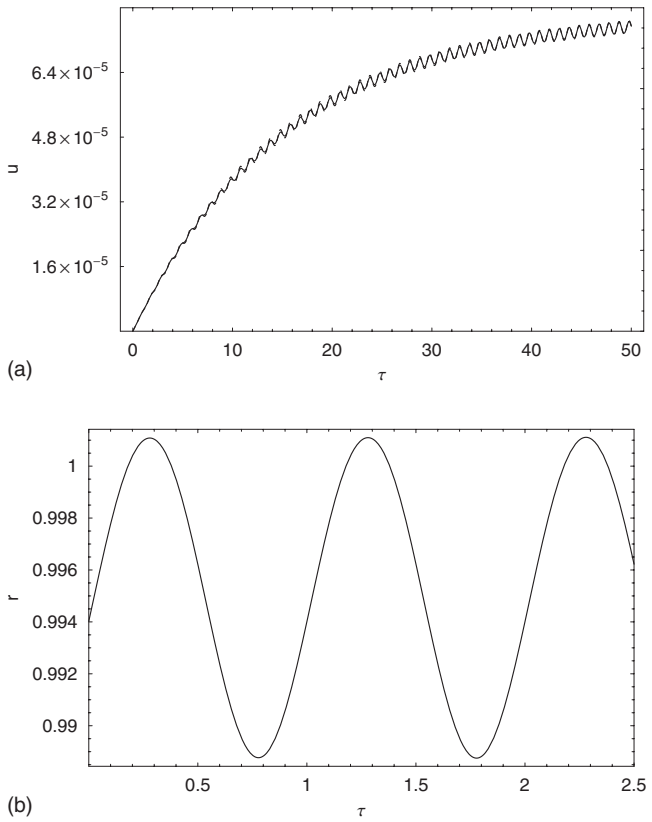

FIG. 3. (a) The leading-order, smooth approximation (38) (solid curve) successfully renders the transients and rapidly converges to its asymptotic solution, very close to the numerical solution of (22) (dashed curve; obscured by solid curve). (b) The bubble undergoes small perturbations around its equilibrium radius. These curves were obtained using the following parameters: $Pa=0.01$, $R_0=1.0\times10^{-5}$ m, $\mu=1.0\times10^{-4}$ N s m^{-2}, and $f_d=28\times10^4$ Hz. Re=280.

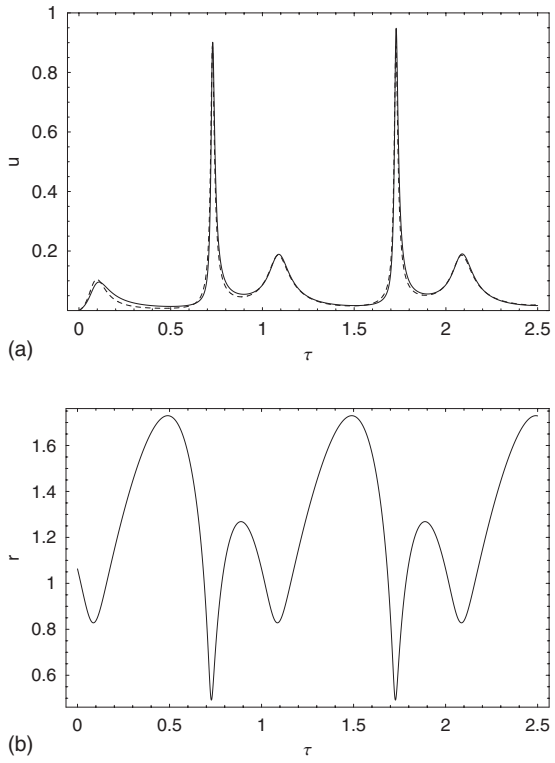

FIG. 4. (a) Same as Fig. 3 but for stronger collapses and Re=3.2. The smooth velocity is dominated by some sizable excursions due to the violent radial collapses experienced by the bubble, as illustrated in (b). Nevertheless, it is properly regarded as being responsible for such net translation as occurs over the period. These solutions were obtained using using stronger driving amplitude, $Pa=1.0$, $R_0=2.0\times10^{-6}$ m, $\mu=1.0\times10^{-3}$ N s m^{-2}, and $f_d=80\times10^4$ Hz. Due to the lower Reynolds number, the transients expire. Thus, after two periods only a close match is achieved between the approximate solution (38) and its numerical counterpart obtained by integration of (22).

$$\tilde{u}_0^{\mathrm{osc}}=\int_0^\tau r^3\frac{dp_\infty}{dx}d\theta-\frac{\left\langle r^3\dfrac{dp_\infty}{dx}\right\rangle_\tau}{\langle r^{-3}\rangle_\tau}\int_0^\tau\frac{d\theta}{r^3}. \tag{41}$$

When combined together, these two expressions make a good approximation of the numerical solution. It should be noted that proceeding similarly with the ϵ^1 terms for the smooth and oscillating components provides a very slight improvement in the composite solution: We have chosen not to report them in this work.

The argument used in Eq. (27) might be seen as an inherent limitation of the proposed method. It is necessary to test the validity of the model for stronger collapses, such as those featured in Fig. 4(b). For that case, the bubble velocity features rapid accelerations each time the radius collapses: Every time this happens, the bubble lurches forward, for reasons explained in Reddy and Szeri.[13] In this case, it is more subtle to interpret the velocity in terms of *smooth* and *oscillating* terms, as plotted in Fig. 4(a). Once again the approximate smooth solution (32) is checked against the numerical solution of Eq. (22), obtained by using $r(\tau)$ in the translation equation. It captures the *mean* behavior well. Because the value of the *smooth* velocity significantly departs from the average over a period of the bubble translation velocity—as is the case in Fig. 3(a)—Fig. 4(a) illustrates the fact that the velocity resulting from the averaged forcing is not the averaged velocity, as is the case for weaker acoustic forcing: This observation confirms the conclusions obtained from previous studies.[4,13] Indeed, for small radial oscillations, the average of the velocity is approximately the same as the velocity that one would obtain from the average of the forcing.[4] However, for stronger forcing, it is not true. For example, this error can be quantified by the root mean square of the difference between the averaged-forcing solution of Eq. (22), u^{sm}, and the averaged numerical solution of Eq. (4), $\bar{u}^{\mathrm{num}}$:

$$\nu^2=\left[\int_{0+d}^{1+d}(u^{\mathrm{sm}}-\bar{u}^{\mathrm{num}})^2d\tau\right]\times\left[\int_{0+d}^{1+d}(u^{\mathrm{sm}})^2d\tau\right]^{-1}, \tag{42}$$

where $d>0$. Both solutions are taken when the translation has reached its asymptotic form. In the case of the example in Fig. 2, $\nu=2.887\,74\times10^{-2}$. For stronger cases such as that of Fig. 4(a), $\nu=80.1154\times10^{-2}$.

C. Displacement predictions and shape stability issues

We may now obtain a simple solution for the distance traveled by a bubble subject to a uniform, acoustic pressure field. To do so, the asymptotic value for the leading-order

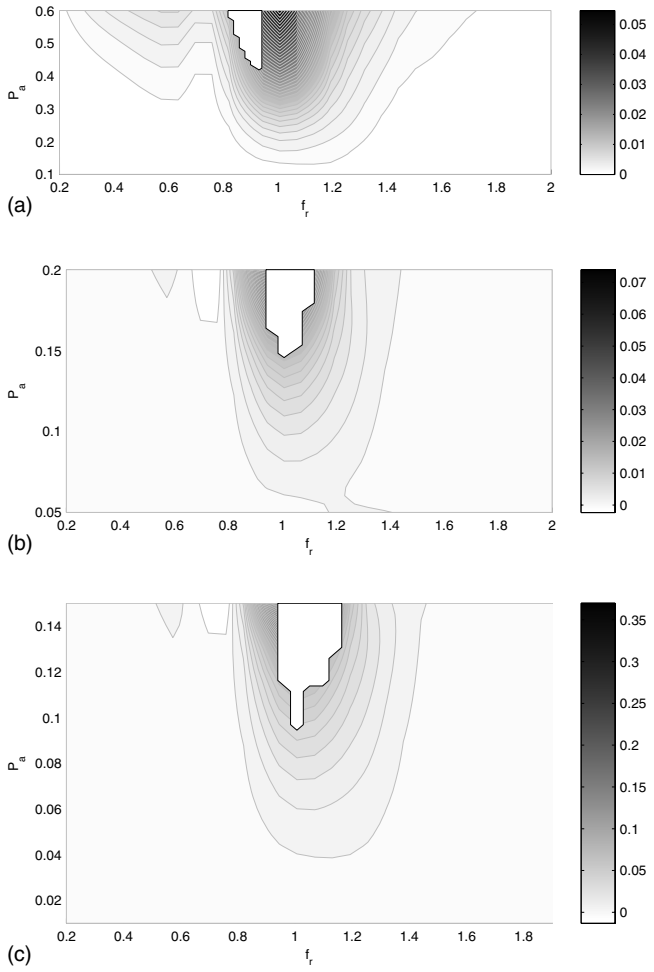

FIG. 5. Contour plots showing the smooth, leading-order, dimensionless, steady displacement of a bubble of equilibrium radius R_0, over one period of driving. The white patches atop the contour plots indicate the regions of shape instability. Displacement predictions were computed for three bubble sizes: (a) $R_0=2\times10^{-6}$ m, (b) $R_0=10\times10^{-6}$ m, and (c) $R_0=100\times10^{-6}$ m. The horizontal axis corresponds to to the driving ratio $f_r=f_d/f_n$, where f_d is the driving frequency and f_n the natural frequency, indicated for each equilibrium radius.

approximation for the smooth bubble velocity is integrated over one period of driving, so as to yield the asymptotic, one-period, leading-order, dimensionless, smooth bubble displacement, referred to as $\Delta x_{0,\infty}^{\mathrm{sm}}$. We can also assess any stability issues arising from the unsteadily translating, spherically oscillating bubble. To do so, the numerical procedure of Reddy and Szeri[24] is employed and overlaid onto the displacement predictions, as illustrated in Fig. 5.

Subsequently, it is possible to estimate the efficiency of the driving, as a function of some mechanical parameters, namely the acoustic wave pressure coefficient P_a and the driving frequency ratio, $f_r=f_d/f_n$, where f_n is the natural frequency of the bubble of nominal radius R_0. A series of experiments is run with $R_0=\{2,10,100\}\times10^{-6}$ m. The results are presented in the form of contour plots. The dark regions represent areas of greater displacement, whereas whiter regions show less bubble travel per period. For these tests, the parameter range has been restricted in order to focus on a more stable region.

A bubble tends to reach its maximum net displacement per period when the driving frequency reaches the natural frequency of the oscillator. For smaller bubbles—$R_0\sim2\times10^{-6}$ m—instabilities arise above a threshold for overpressure coefficients of $P_a=0.4$ and above. However, for larger bubbles, shape instabilities arise at lower amplitudes, as seen in Fig. 5(b). These results can be further extended to an even broader range of pressure coefficients and frequencies, allowing for a comprehensive mapping of bubble displacement in various applications of ultrasonic driving.

D. Summary of the perturbation approach

The method of splitting has been successfully applied to approximate the rapid and slow transients in the velocity of an acoustically driven bubble. A scaling was first performed to identify the slow transient time scale, after which two components were distinguished and determined. This method relies on the fact that the radial oscillations—and pressure field—are asymptotically periodic in time. There is no additional requirement on the nature of the radial dynamics: As such, the method is reliable even in the case of stronger collapses. The main contribution of this technique is its ability to combine usefulness and simplicity. It is useful because it explicitly captures the slow drifting motion. It is simple to implement numerically because it only requires knowledge of radial periodic attractor. More generally, we have developed a technique to approximate the response of a periodically driven, linear oscillator with nonconstant coefficients. Finally, because the bubble displacement can be written down as a simple, closed-form expression, with only a limited set of parameters, it opens the way for new investigations such as optimizing bubble travel by using an appropriate forcing. It is the subject of Sec. IV.

IV. OPTIMAL FORCING PROBLEM

A. Acoustic forcing

Regardless of the method chosen to reach a larger displacement, the objective is to design an optimal acoustic forcing, F, in the form of a traveling wave, of period 1. To evaluate the performance of the optimized forcing, an additional reference forcing is defined. It has the form of pure, ideal sine wave of identical fundamental frequency. Thus:

$$p_\infty^{\mathrm{Conv}} = 1 + P_a \sin\left(2\pi\frac{xR_0}{\Lambda} - 2\pi\tau\right) \approx 1 - P_a \sin(2\pi\tau), \tag{43}$$

$$p_\infty^{\mathrm{Opt}} = 1 + F\left(2\pi\frac{xR_0}{\Lambda} - 2\pi\tau\right) \approx 1 + \hat{F}(\tau). \tag{44}$$

The dimensionless time $\tau=t/T$; the period $T=1/f_d$. $M_L=R_0/(c_lT)=R_0/\Lambda$ is the local Mach number. It is taken as infinity inside the argument of F, which remains valid as long as the quantity $R_0/\Lambda\ll1$, as is the case here, which allows for a useful simplification, turning $F(x,\tau)$ into $\hat{F}(\tau)$ only. However, it is assumed finite when taken as a multiplicative factor, because the net force on the bubble is due to the spatial variation of the pressure field. Thus, spatial and time derivatives are related:

$$\frac{dp_\infty^{\mathrm{Opt}}}{dx} = -\frac{R_0 f_d}{c_L}\frac{d\hat{F}}{d\tau} = -M_L\frac{d\hat{F}}{d\tau}. \tag{45}$$

The pressure gradient of p_∞^{Conv} is computed in a similar way. Periodic conditions are enforced in the boundary problem. Here, for purposes of comparison, we want to synchronize the optimized wave form to that of an ideal sine wave of dimensionless period of unity, as is the case in Eq. (43). In what follows, the *conventional* forcing of Eq. (43) will be used to compare the performance of the *optimal* forcing of (44). The acoustic coefficient P_a will be adjusted to achieve equal acoustic energy, computed from the L_2 norm of the forcing. To that end, an adjusted coefficient P_a^e is computed, such that:

$$\int_0^1 [P_a^e \sin 2\pi\tau]^2 d\tau = \int_0^1 \hat{F}^2 d\tau \Leftrightarrow P_a^e = \left[2\int_0^1 \hat{F}^2 d\tau\right]^{1/2}. \tag{46}$$

The focus of this work is on continuous wave driving. Pulse driving was the subject of another recent paper.[15] Though not dealing with translation, an optimal acoustic forcing was calculated to maximize the processed signal emitted by a bubble. We note that bubble translation in response to pulse driving can be tackled using the approximation of Sec. III for the oscillating component of the velocity. Assuming that the acoustic wave being pulsed is fast enough, its contribution on the slow time scale is essentially zero. Therefore, the dynamics of the bubble are limited to that of the fast time scale. However, this is beyond the scope of this paper. Here we focus on net bubble displacement asymptotically due to continuous forcing.

B. Optimal problem

In what follows, a cost function is constructed with a goal to maximize bubble displacement over a dimensionless period, while three constraints complete the problem.

1. Objective, rationale, and strategy

The most straightforward method to try to maximize bubble displacement is to maximize the following integral:

$$\mathcal{Z} = \int_0^1 u_0^{\mathrm{sm}} d\tau, \tag{47}$$

which serves as basis for an optimization problem. Two cases are conveniently distinguished, namely, superresonant ($f_r \geqslant 1.0$) and subresonant forcing ($f_r < 1.0$).

At superresonant frequencies, this particular method yields slight improvement to the bubble displacement compared to sinusoidal forcing of the same frequency. The solution for the optimal problem is thus very similar to a sine wave, adjusted in phase. In turn, the averaged Bjerknes force,

$$\int_0^1 r^3 \frac{dp_\infty}{dx} d\tau, \tag{48}$$

is maximized. Consequently, u_0^{sm} becomes larger: In the specific case of a 15 μm bubble forced at 1.25 times its natural frequency, a 6% increase in the overall smooth velocity is experienced for optimized relative to sinusoidal forcing. Recall that at superresonant frequencies, the bubble can only undergo smaller oscillations. As the superresonant case is straightforward we shall not go into further detail here.

Still, the above-mentioned cost function is unsuccessful within the subresonant frequency domain: The solution for the optimized displacement appears to be trapped in a local minimum. Such a displacement-minimizing solution serves a purpose, however. By computing the radial variance σ^2, it appears that larger displacements (using a regular sine wave) correspond to smaller values of σ^2. While it remains necessary to seek another way to achieve larger displacement for these specific subresonant frequencies, this observation brings new light on the problem. In what follows, an alternative cost function, based on minimized radial variance, allows one to maximize displacement indirectly by enhancing bubble contraction.

Recall that bubble behavior at subresonant forcing is very much different than that observed at superresonant frequencies. For instance, the very nonlinear sonoluminescence phenomenon might be obtained using very low frequencies ($f_r = 0.035$, $R_0 = 4.5$ μm) and high intensities ($P_a = 1.25$). Under these conditions, a bubble sees its radius expand up to ten times its nominal size, before collapsing violently. At this time the rising temperature due primarily to compression heating ionizes the gas inside the bubble, forming a plasma; the recombination of ions and electrons eventually produces light emission.[28,29]

While replicating these extreme conditions and phenomena is not the subject of this work, it is of interest to favor these nonlinearities to induce a larger displacement. As shown by Reddy and Szeri,[13] at subresonant frequencies, displacement mostly occurs when the bubble undergoes a collapse: Conservation of linear momentum allows the bubble to lurch forward when its volume reaches its smallest value.

This physical reasoning concurs with the numerical observations mentioned earlier regarding radial variance. It supports the idea that, at low subresonant frequencies, a larger displacement can be achieved when the radial variance is minimized. Small radial variance means that the bubble has more time to grow to a large radius and features a sharp and short contraction, itself accompanied by a significant lurch forward. Because subresonant forcing favors such radial contractions, computations are carried out at driving frequencies that are well below unity, on the order of $f_d = 0.2 f_n$. Therefore, the new cost function provides an indirect way of achieving larger displacement, compared to that obtained in the case of a pure, sine wave with equal intensity and driving frequency. Admittedly, this particular cost function remains only one possibility among other potentially successful ones. Their existence is beyond the scope of this study.

2. Cost function and constraints in the subresonant case

The new cost function is

$$\mathcal{Z} = \int_0^1 (r - \bar{r})^2 d\tau. \tag{49}$$

$\bar{r}$ is the time average of the radius over a dimensionless period. Its value is not necessarily close to unity, though it might be the case at low-intensity forcing. The first *differential* constraint is in the form of RPE multiplied by a time-dependent Lagrange multiplier $\lambda(\tau)$:

$$\int_0^1 \lambda(\tau)(\mathrm{RPE}) d\tau. \tag{50}$$

The second (integral) constraint is straightforward: It is required that the L_2 norm of $\hat{F}$ be limited to a constant, referred to as c. Recall that the dimensional power E of an incoming acoustic wave is proportional to its square divided by ρc_L. From a technical point of view, constraining this sets a reasonable level of driving intensity. Mathematically, introducing a power threshold allows for restricting the problem to shape-stable bubble behavior. Therefore, it is imposed that, for the dimensionless acoustic wave of Eq. (44),

$$\int_0^1 \hat{F}^2(\tau) d\tau = c. \tag{51}$$

The third (integral) constraint enforces that the acoustic forcing has no average, lest the problem involve a net displacement of the surrounding fluid over one dimensionless period. Indeed, the pressure gradient and the velocity U_a are related through the balance of linear momentum in the acoustic limit by

$$\rho \dot{U}_a = -\frac{dP_\infty}{dx} \Leftrightarrow \rho \dot{U}_a = -M_L \hat{F}'. \tag{52}$$

The complete dimensionless expression for u_a is given in Eq. (C2), and is shown to depend directly on the forcing $\hat{F}$. Therefore, integrating Eq. (52) once with respect to time, while holding the bubble displacement $X(t)$ to some constant X_0—a valid assumption given the pressure driving amplitude and size of the bubble—and imposing no net displacement of the surrounding liquid translates to

$$\int_0^1 \hat{F}(\tau) d\tau = 0. \tag{53}$$

Because the constraints on the norm and average of the continuous forcing are integral—as opposed to the differential constraint of Eq. (50)—and not a function of τ, the two Lagrange multipliers associated with these are scalars. Combining Eqs. (49)–(53) allows for writing the final cost function, incorporating the constraints:

$$\mathcal{Z} = \int_0^1 (r - \bar{r})^2 d\tau + \int_0^1 \{\phi(\hat{F}^2(\tau) - c) + \lambda(\tau)(\mathrm{RPE}) + \eta \hat{F}(\tau)\} d\tau. \tag{54}$$

The derivation of the Euler–Lagrange equations associated with minimization of the cost function are relegated to Appendix A.

C. Results

Here we report the displacement gain realized by minimizing the radial variance at subresonant frequencies. Results focus on three bubble sizes, R_0=5, 15, and 25 μm. One particular set of driving frequency f_r=0.2 and radius R_0 =15 μm is examined to illustrate the close relation existing between minimized radial variance and larger displacement. Some plots focus on the resulting bubble radial response and smooth velocity, when driven by the optimized acoustic forcing. Additional figures emphasize the correlation between minimized variance and larger displacement under various forcing frequency and bubble radius conditions. Figure 11 summarizes these results by providing an overview of optimal acoustic forcing depending on the bubble size and driving frequency.

1. Solution of the optimization problem

Equations (6) and (A5), (A3) and (A4), (51) and (53) define the optimal subresonant forcing problem, i.e., the solution of these equations will minimize variance, which in turn we show will increase overall displacement of the bubble when f_r is less than 1. The software AUTO is chosen to handle these calculations.[30–32] It uses the pseudoarclength continuation method to continue a branch of solution to a given system, given one so-called free parameter and a set of initial solutions on the branch. We use it to enforce successively the various integral constraints and periodic conditions. For simplicity, the mathematical details of the problem, including the implementation steps of the successive continuation method, have been relegated to Appendix B.

The average dimensionless bubble displacement over one dimensionless cycle, A_{Lim}, is the result of the integration of the asymptotic value for the velocity approximation over one dimensionless period:

$$\int_0^1 u_0^{\mathrm{sm}} d\tau = \mathrm{A_{Lim}} = \mathcal{J} M_L \frac{\langle r^3 \hat{F}' \rangle_\tau \langle r^{-3} \rangle_\tau}{18 \langle r^{-2} \rangle_\tau}. \tag{55}$$

Thus, to recover a dimensional displacement over one second, A_{Lim} should be multiplied by $R_0 f_d$.

2. Optimal and sinusoidal forcing

The solution to the system of Euler–Lagrange equations provides a particular acoustic forcing $\hat{F}$: one that minimizes variance at subresonant frequencies. A smaller variance (49) is achieved in conjunction with a larger displacement (55) when employing the optimized forcing. The results reported here were obtained by letting f_r=0.2, c=0.01, and R_0=5, 15, and 25 μm. For each bubble size, the optimized forcing $\hat{F}_{R_0}$

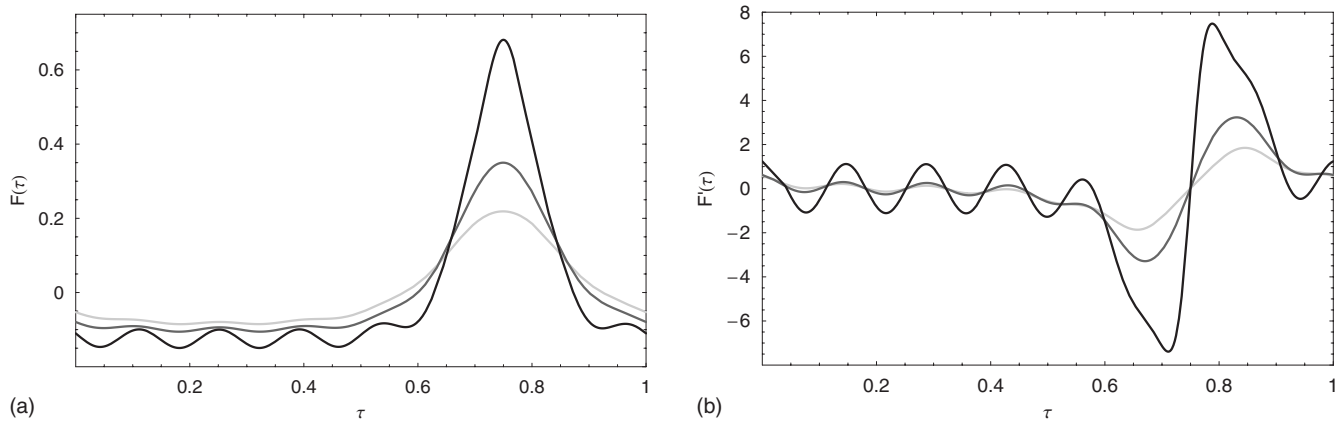

FIG. 6. (a) Three levels of acoustic energy (color coded from light gray to black), where $c=[0.01,0.02,0.05]$, affect the shape of the optimal forcing $F(\tau)$ designed to minimize radial variance of 15 μm bubble with $f_d=0.2f_r$. At larger intensities some wiggles appear. (b) The Bjerknes force is proportional to $dF/d\tau$, plotted for the three same values of c.

is used to compute the corresponding displacement and radial variance. Regardless of the size, a smaller variance strongly correlates with a larger displacement at this subresonant frequency. These results are shown later in Fig. 9.

An illustrative example is intended to show the effect of minimized variance upon radial collapse and subsequent lurching for a 15 μm bubble forced at $f_d=0.2f_n$. This combination {15 μm, 0.2} is highly representative of the method employed in the present work. For completeness, an additional continuation step was performed so as to compute an optimal forcing for three levels of intensity $c=0.01,0.02,0.05$.[33] At each level, the optimized forcing features a sharp compression after a longer period of rarefaction. With increasing intensity come wiggles due to the stronger nonlinear behavior of the bubble (Fig. 6). The resulting larger velocity and radial oscillations are shown in Fig. 7. When compared to the case of an ideal, pure sine wave of identical frequency and intensity, the bubble undergoes stronger collapse around $\tau=0.75$. In turn, the smooth velocity shows large spikes: This is an expected consequence from the analysis of the driving term in Eq. (38). In this particular example, the dimensionless radial variance has been reduced by 9%, resulting in a translation velocity that is 71% larger than the case employing a pure, ideal sine wave. To ensure the shape stability of the solution, $c=0.01$. Because the methodology itself is not significantly affected by the intensity level (this issue is discussed in a later section), we shall focus our attention on this particular value for c. Moreover, the method implemented to check the stability of the periodic attractor is discussed in Sec. IV D.

A third continuation step, using R_0 as a free parameter, is performed to calculate a series of optimal solutions $\hat{F}_{R_0}$. Each of these solutions minimizes the radial variance of a given bubble radius, R_0, at $f_r=0.2$. Figure 8 shows how these solutions evolve with bubble size. As the bubble grows larger, the solution for the optimal wave forcing does not evolve any further. The existence of this aggregate solution for the optimal acoustic suggests the following question: By how much is the bubble displacement affected when driven by that particular solution? A numerical test is conducted. Each bubble $R_0=5$, 15, and 25 μm is acoustically driven three times using $\hat{F}_{5\ \mu\mathrm{m}}$, $\hat{F}_{15\ \mu\mathrm{m}}$, and $\hat{F}_{25\ \mu\mathrm{m}}$ using an intensity level of $c=0.01$. The latter optimal forcing ($\hat{F}_{25\ \mu\mathrm{m}}$) we refer to as the optimal limit forcing (OLF). It turns out that $\hat{F}_{25\ \mu\mathrm{m}}$ is the forcing that provides the best displacement possible

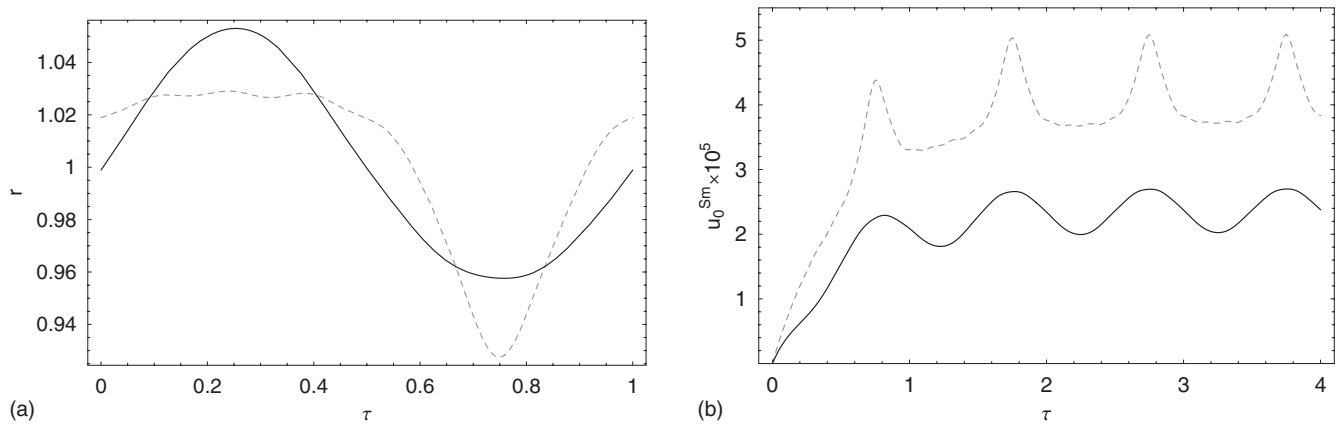

FIG. 7. (a) The radial oscillation is shown for $c=0.01$. The dotted curve represents the optimized dynamics. The radial response to a sinusoidal wave with $P_a=\sqrt{2c}$ (continuous curve) features a collapse around $\tau=0.75$; this is intensified with optimal forcing. (b) The bubble velocity as approximated by (38) is larger when subject to the optimal forcing. On average, the velocity is in this case 71% larger.

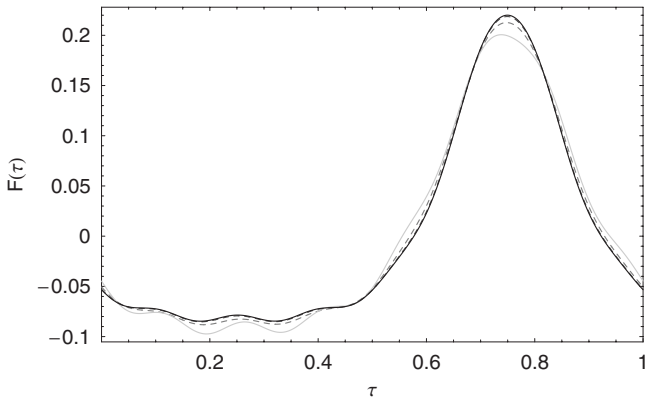

FIG. 8. Evolution of the optimal acoustic forcing for bubble radii of $R_0=[2,5,15,25]$ μm, all driven at $f_r=0.2$, color-coded solid gray, dotted gray, dotted black, solid black, respectively, while $c=0.01$. For larger radius sizes, there is no significant change in the optimal forcing shape. The black curve corresponds to the OLF.

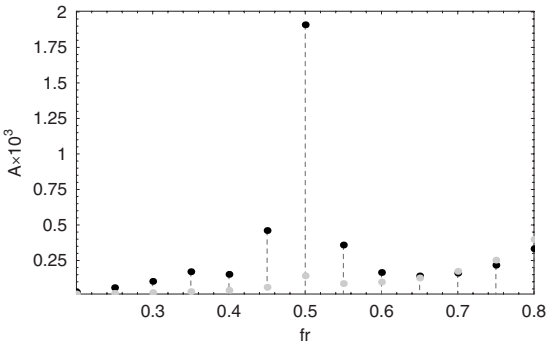

FIG. 10. For $f_r<0.665$, bubble displacement A is consistently larger when driven by the OLF (black dots) than when using a pure sine wave (gray dots). For $f_r\geqslant 0.665$, the situation is reversed. $R_0=2\times10^{-6}$ m, $c=0.01$, and $\mu=1.0\times10^{-3}$ N s m^{-2}.

over this range of bubble sizes, given this particular method. While it does not yield the smallest radial variance at 5 and 15 μm, it still outperforms the pure sine wave which features a larger radial variance and a smaller displacement (see Fig. 9). From here on, at subresonant frequencies we shall use this OLF scaled appropriately, regardless of bubble sizes, for reasons explained in the following.

We now proceed to the practical identification of the area of parameter space where it is more favorable to force bubbles with the OLF. The results are shown in Fig. 11. For a fixed radius, as the driving ratio is increased from low values (Fig. 10), the displacement in response to OLF remains larger than the case of purely sinusoidal forcing for $f_r<f_r^*=0.665$. For $f_r\geqslant f_r^*$, the situation is fully reversed. As an illustration of displacement gains, Fig. 10 shows how the optimized dimensionless displacement experienced by a 2 μm bubble can be up to 12 times larger with the OLF at $f_r=0.5$.

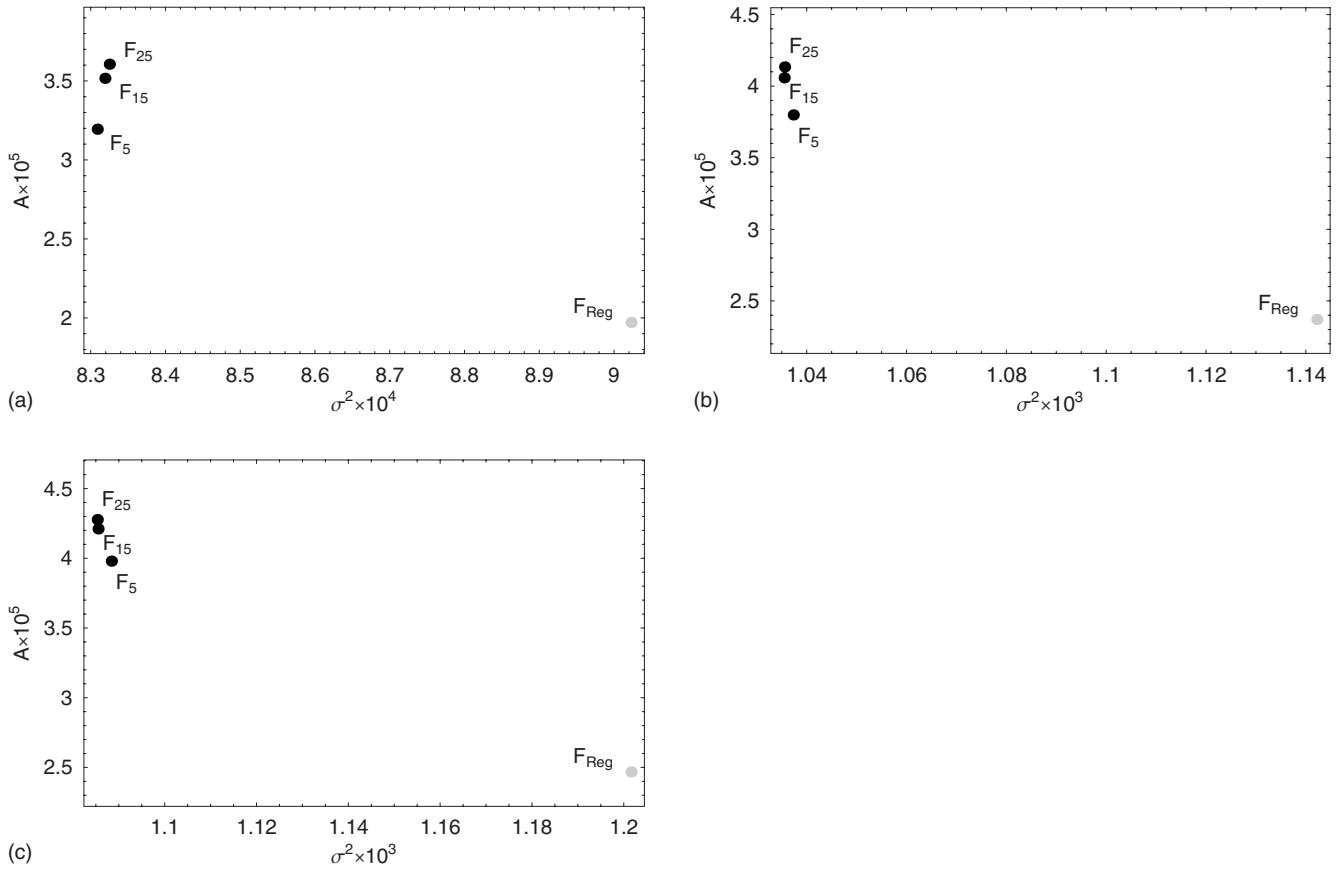

FIG. 9. (a) The top figure shows the asymptotic smooth displacement A over one dimensionless period vs the dimensionless radial variance σ^2 of a 5 μm bubble forced at $f_r=0.2$ using optimized forcing corresponding to specific bubble sizes of 5, 15, and 25, labeled $F_{5\ \mu m}$, $F_{15\ \mu m}$, and $F_{25\ \mu m}$, respectively. (b) The middle figure corresponds to the same experiment conducted with a 15 μm while (c) the bottom figure uses a 25 μm bubble.

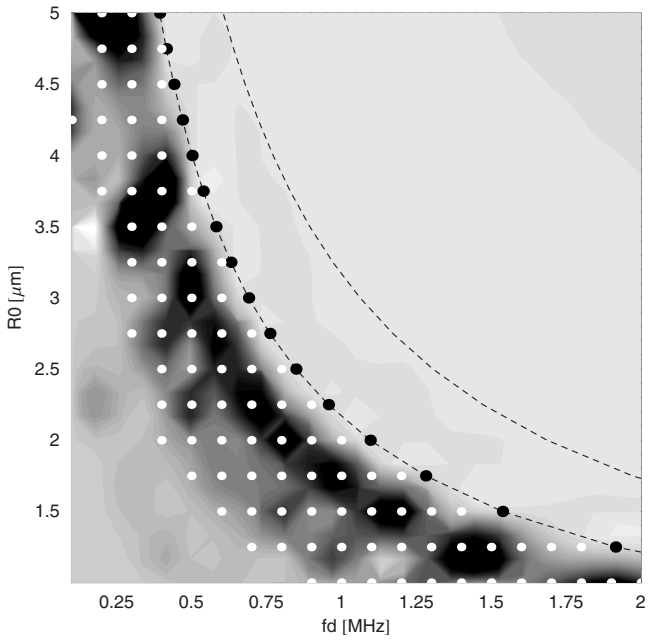

FIG. 11. The darker shades of the contour plot represent the regions where $A_{\mathrm{Lim}}^{\mathrm{OLF}}/A_{\mathrm{Lim}}^{\mathrm{Sine}}>1$. Additional information is overlaid as follows. Below the limit depicted by the black dots (representing $f_d=0.665f_n$), the optimal forcing provides larger displacement than the case of a conventional sine wave. Small white dots reveal the region where an optimally forced bubble yields larger radial variance than for a sinusoidal wave, yet undergoes a larger translational velocity. For driving ratio of $f_r=0.665$ and above (limit represented by the black dots), a larger displacement is obtained using a pure sine wave for subresonant frequencies. Above the natural frequency limit (dashed grey curve), the superresonant results apply. The driving intensity $c=0.01$.

In other words at any driving frequency ratio above 0.665, a pure sine wave is preferable to the OLF for overall translation. In fact, close to resonance, forcing the bubble at its natural frequency promotes a more significant response than that experienced when subject to a blend of frequencies. Thus optimizing the variance to achieve larger displacement does not work at subresonant frequencies where $f_r \geqslant 0.665$.

These data are assembled in Fig. 11 which is intended to be a design diagram, whose purpose is to choose at-a-glance an appropriate forcing that maximizes displacement, given a driving frequency and a bubble rest radius. Note that a similar diagram can be constructed for higher intensities.

D. Discussion

Because the solution to the problem $\delta\mathcal{Z}=0$ is obtained using a continuation method, one must ensure that the solution for RPE is realizable. First, it has to be stable and second, it has to be reachable from the particular initial condition $r(0)=1.0$ and $\dot{r}(0)=0$ (quiescent bubble). To guarantee these criteria, all the solutions for the volume oscillations are integrated through the transients, and convergence is observed for all the cases investigated. We therefore conclude that all optimal solutions deriving from the method presented here are stable. Besides, the use of results such as those plotted in Fig. 5 allow us to predict the intensity levels ($c=P_a^2/2$) that are likely to create shape instability. Note that for the bubble sizes we have studied so far ($R_0 \sim 10$ μm), $c=0.01125$ is a limit value ($P_a=0.15$), which, for frequencies next to resonance, is likely to induce shape instabilities.

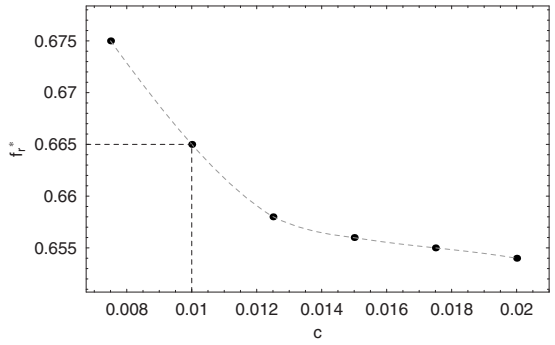

FIG. 12. The cutoff frequency ratio f_r^* depends on the intensity of the incoming acoustic wave. As c increases, the frequency range where the OLF provides a larger displacement than a pure sine wave is reduced. The set $\{c=0.01, f_r^*=0.665\}$ used in the text is highlighted for convenience. Note that $c=0.02$ corresponds to $P_a^e=0.2$.

For completion we have repeated the numerical tests for a range of acoustic intensities $c=\{0.0075, 0.0125, 0.015, 0.0175, 0.02\}$ in addition to the $c=0.01$ results. Of significant interest is the fact that the form for the OLF is very similar in its overall shape as c increases. Also, we have identified a slight dependence between the cutoff frequency f_r^* and c, which is plotted in Fig. 12.

E. Summary of the optimization problem

In this work we have set up a method to optimize acoustic forcing in order to induce a larger bubble displacement within the subresonant and superresonant frequency range. At superresonant frequencies, one can directly optimize the distance traveled over a period to find the optimal wave form is quite similar to a sinusoidal wave form. Near resonance, a sinusoidal wave form is the best. For subresonant frequencies, the method used to maximize displacement is indirect, i.e., to minimize radial variance and thus promote stronger collapse. The correlation between minimized variance and larger displacement is limited to a particular frequency band. To develop a practical result, a single, OLF has been computed. This forcing is able, in terms of bubble displacement, to outperform a regular sine wave for all subresonant frequencies up to a cutoff frequency ratio $f_r^*=0.665$, for the case $c=0.01$.

To conclude, if the bubble is driven at a superresonant frequency, a direct method, as explained earlier, is successful. However, the improvement is rather modest. Near resonance, sinusoidal forcing is best. For $f_r<0.665$ the OLF is a straightforward way to deliver larger overall displacements than a pure sine wave. In some cases, the latter improvement is spectacular.

ACKNOWLEDGMENTS

This work was funded by a grant from the NASA Microgravity Fluid Physics program. The authors thank an anonymous referee for providing some pertinent suggestions.

J.O.T. thanks Anil Reddy for his code to calculate bubble shape stability and Ben Gallup for useful conversations about the optimization problem.

APPENDIX A: DERIVATION OF THE EULER–LAGRANGE EQUATIONS

Here, we develop the differential equations and integral constraints that are equivalent to the statement of the optimization problem. To do so, it is assumed that an optimal solution exists, and we perturb away from it. The change in the cost function $\mathcal{Z}$ should be zero, to first order in the departure from the optimal solution. To this end, each variable is recast as the sum of the optimal solution—denoted by an asterisk—in addition to some small variation $\epsilon\delta f_i$, where f_i refers to any of the system variables. Hence $r(\tau)=r^*(\tau)+\epsilon\delta r(\tau)$, etc. The cost function $\mathcal{Z}$ becomes $\mathcal{Z}^*+\varepsilon\delta\mathcal{Z}$, where we have used integration by parts to simplify the equation in the usual manner:

$$\delta\mathcal{Z}=\left[\delta r\left(\frac{2\lambda}{9\,\mathrm{Re}\,r}+2\lambda\dot{r}-r\dot{\lambda}\right)\right]_0^1+[\delta\dot{r}r\lambda]_0^1+\delta\phi\int_0^1\{F^2-c\}d\tau+\delta\eta\int_0^1 F d\tau+\int_0^1\delta F\{\eta+2\phi F+\mathrm{Eu}\,\lambda\}d\tau+\int_0^1\delta r\left\{2(r-\bar{r})-\frac{4\dot{\lambda}}{\mathrm{Re}\,r}-\dot{r}\dot{\lambda}+r\ddot{\lambda}+\lambda\left(\frac{3\,\mathrm{Eu}\,P_{g0}^*k}{r^{1+3k}}-\frac{\mathrm{Eu}}{\mathrm{We}\,r^2}-\ddot{r}\right)\right\}+\int_0^1\delta\lambda\{\mathrm{RPE}\}d\tau. \tag{A1}$$

The RPE (6) is forced by an external pressure wave form p_∞ now featuring the function to optimized F and an additional "homotopic part," forcing we use for convenience; its use is discussed in Appendix B:

$$p_\infty=1+F+\alpha\sin(2\pi\tau). \tag{A2}$$

The objective is to solve for the forcing $F(\tau)$ so that $\delta\mathcal{Z}$ of Eq. (A1) is zero.

Because we focus our attention on asymptotic dynamics subject to periodic forcing, the radial boundary conditions are straightforward:

$$r(0)=r(1),\quad \dot{r}(0)=\dot{r}(1). \tag{A3}$$

The inspection of Eq. (A1) combined with these boundary conditions suggests a convenient choice of similar conditions for the time-dependent Lagrange multiplier and the acoustic forcing F:

$$F(0)=F(1),\quad \lambda(0)=\lambda(1),\quad \dot{\lambda}(0)=\dot{\lambda}(1). \tag{A4}$$

These results simplify the variation of the cost function in Eq. (A1). Recalling the fact that the variations δr and $\delta\lambda$ are arbitrary and independent for all τ, we require that the integrands associated with these variations be zero at all times. Hence, in addition to the forced RPE, the differential equation for the Lagrange multiplier is

$$\ddot{\lambda}=-2-3\frac{\mathrm{Eu}\,kP_{g0}^*}{r^{2+3k}}\lambda+\frac{\mathrm{Eu}\,\lambda}{\mathrm{We}\,r^3}+\frac{4\dot{\lambda}}{\mathrm{Re}\,r^2}+\left(2\bar{r}+\frac{d\lambda\dot{r}}{d\tau}\right)r^{-1}. \tag{A5}$$

A similar argument yields a new condition for the δF factor in the integrand, hence

$$\eta+2\phi F+\mathrm{Eu}\,\lambda=0. \tag{A6}$$

On the other hand, because ϕ and η are scalar, the two integral conditions remain. However, the zero-average constraint is easily enforced by adjustment of η, tuned in such a way that

$$\eta=-\int_0^1\mathrm{Eu}\,\lambda d\tau. \tag{A7}$$

Therefore, a closed form for the forcing F is obtained by combining Eqs. (A6) and (A7), so as to read

$$F=-\frac{\mathrm{Eu}\,\lambda+\eta}{2\phi}. \tag{A8}$$

The final set of Euler–Lagrange now consists of the two differential equations (6) and (A5) along with boundary conditions (A3) and (A4) and the integral condition (51). The forcing F and the constant η are then fully determined from the other components of the solution.

APPENDIX B: DETAILS OF SOLUTION USING AUTO

To explore the optimal forcing we use the pseudoarclength continuation software AUTO. In what follows, the objective is the following: obtain the optimal solution for the acoustic forcing so as to maximize bubble translation over a period, while enforcing the integral constraint (51). The process is realized in several steps, based on the continuation strategy of Doedel [31,32].

In the first continuation the solution of the system starts at a quiescent solution, i.e., $r(t)=1.0$, $\lambda(t)=0$, and $r_0=1.0$. All the other variables are set to zero while ϕ is set to an arbitrary value. α, c, and η are free to float. The homotopic forcing amplitude α is increased from zero to a finite value. Because Eq. (51) is relaxed, F becomes nonzero due to the Lagrange multiplier, itself forced through Eqs. (6) and (A5). Note that allowing η to float is necessary so as to enforce automatically the integral constraint (53). For the second continuation run, c is held at some finite value, thus enforcing integral constraint (51). Physically, this prevents F from going to zero as the homotopic forcing is slowly turned down. The homotopic amplitude is then turned off completely, while ϕ and η are allowed to float. This yields the first optimal solution for the forcing F, with some finite energy c. The third continuation run involves varying the c parameter, so as to explore a broader spectrum of intensities for the acoustic forcing. Again, the two scalar Lagrange multipliers ϕ and η are free to float. In the fourth continuation, starting from a given energy level, the radius serves as free parameter while the driving frequency is adjusted to a fixed

ratio of the corresponding natural frequency. Similarly, the two scalar Lagrange multipliers ϕ and η are free to float so as to yield optimal solutions.

APPENDIX C: LIQUID VELOCITY

Let the external dimensional pressure field $P_\infty = P_0(1 + P_a F(2\pi X/\lambda - 2\pi f_d t))$ where X and t are dimensional. In the acoustic limit [24] the balance of linear momentum reads, in dimensional terms:

$$\rho \dot{U}_a = -\frac{dP_\infty}{dX}. \tag{C1}$$

With an appropriate set of dimensionless variables ($U_a = R_0 f_d u_a$, $P_\infty = P_0 p_\infty$, $X = R_0 x$, and $t = \tau/f_d$) and holding the bubble displacement x constant, one obtains the expression of the dimensionless liquid velocity under the action of the external pressure field as

$$u_a \approx \frac{P_0}{\lambda f_d^2 \rho R_0} \hat{F}(\tau). \tag{C2}$$

APPENDIX D: DIMENSIONLESS COEFFICIENTS AND PARAMETER VALUES

The Mach number M_l in the fluid surrounding the bubble $M_l = R_0/c_L T$, where R_0 is the equilibrium radius of the bubble, c_L is the sound velocity in water—set to 1484.70 m s^{-1} in this context—and T is the time scale equal to the inverse of the driving frequency f_d. The Reynolds number Re is defined from the translation equation (1) as

$$\mathrm{Re} = \frac{\rho R_0^2}{\mu T}, \tag{D1}$$

where $\rho = 998.0$ kg m^{-2} is the fluid density and $\mu = 1.0 \times 10^{-3}$ N s m^{-2} its dynamic viscosity. The Euler number Eu scales the atmospheric pressure $P_0 = 1.013\,25 \times 10^5$ by some characteristic kinetic energy, so as to read

$$\mathrm{Eu} = \frac{P_0 T^2}{\rho R_0^2}. \tag{D2}$$

The Weber number We relates surface tension $\sigma = 0.0728$ N m^{-1} to the pressure at equilibrium, so that

$$\mathrm{We} = \frac{P_0 R_0}{2\sigma}. \tag{D3}$$

The equilibrium gas pressure P_{g0}^* is defined as

$$P_{g0}^* = 1 + \frac{2\sigma}{P_0 R_0} - P_v^*, \tag{D4}$$

where P_v^* stands for the ratio of the vapor pressure and static pressure P_0. The pressure coefficients C_p and $\mathcal{J}$ are calculated from the translation equation:

$$C_p = \frac{P_0}{1/2\rho(f_d R_0)^2}, \tag{D5}$$

From the product of C_p and Re, the dimensionless number $\mathcal{J}$ was defined earlier as

$$\mathcal{J} = \mathrm{Re}\, C_p. \tag{D6}$$

The equilibrium radius $R_0 = 2.0 \times 10^{-6}$ m corresponds to a natural frequency (f_n) of 1.69 MHz; $R_0 = 4.5 \times 10^{-6}$ m implies $f_n = 0.68$ MHz. The natural frequency is calculated by recasting RPE in a linear form, letting $r(\tau) = r_0 + \epsilon \tilde{r}(\tau)$. It is then straightforward to show that, for the Rayleigh-Plesset equation as stated in Eq. (6),

$$f_n = \frac{1}{2\pi\rho R_0^2} \sqrt{|4\mu^2 - \rho R_0 (3P_0 R_0 + 4\sigma)|}. \tag{D7}$$

In this document, the driving frequency is referred to as a fraction of f_n, thereby defining the frequency ratio $f_r = f_d/f_n$. Finally the choice of the polytropic exponent is calculated from Leighton[1] and Prosperetti[34] using the ratio of the bubble radius to the thermal penetration depth and the ratio of the conduction layer thickness to the acoustic wavelength in the gas. Since the first ratio

$$G_2 = \frac{f_d R_0^2}{D_g} \sim 10^{-1} \tag{D8}$$

at a 100 kHz range, micron-sized bubbles with a thermal diffusivity of $D_g \sim 10^{-4}$, the polytropic exponent is thus set to unity (isothermal model).

[1] T. G. Leighton, *The Acoustic Bubble* (Academic, New York, 1994).
[2] A. A. Doinikov, "Translational motion of a bubble undergoing shape oscillations," J. Fluid Mech. **501**, 1–24 (2004).
[3] S. J. Shaw, "Translation and oscillation of a bubble under axisymmetric deformation," Phys. Fluids **18**, 72104–72119 (2006).
[4] D. Krefting, J. O. Toilliez, A. J. Szeri, R. Mettin, and W. Lauterborn, "Translation of bubbles subject to weak acoustic forcing and error in decoupling from volume oscillations," J. Acoust. Soc. Am. **120**, 670–675 (2006).
[5] L. Crum and A. Eller, "Motion of bubbles in a stationary sound field," J. Acoust. Soc. Am. **48**, 181–189 (1970).
[6] S. Popinet and S. Zaleski, "Coupling of radial and translational motion in small viscous bubbles," *Proceedings of FEDSM99, 3rd ASME/JSME Joint Fluids Engineering Conference* (ASME, New York, NY, 1999).
[7] M. M. Fyrillas and A. J. Szeri, "Dissolution or growth of soluble spherical oscillating bubbles," J. Fluid Mech. **277**, 381–407 (1994).
[8] M. M. Fyrillas and A. J. Szeri, "Dissolution or growth of soluble spherical oscillating bubbles: The effect of surfactants," J. Fluid Mech. **289**, 295–314 (1995).
[9] U. Parlitz, R. Mettin, S. Luther, I. Akhatov, M. Voss, and W. Lauterborn, "Spatio-temporal dynamics of acoustic cavitation bubble clouds," Philos. Trans. R. Soc. London, Ser. A **357**, 313–334 (1999).
[10] A. A. Doinikov, "Mathematical model for collective bubble dynamics in strong ultrasound fields," J. Acoust. Soc. Am. **116**, 821–827 (2004).
[11] A. A. Doinikov, "Time delays in coupled multibubble systems. I," J. Acoust. Soc. Am. **117**, 47–50 (2005).
[12] J. Magnaudet and D. Legendre, "The viscous drag force on a spherical bubble with a time-dependent radius," Phys. Fluids **10**, 550–554 (1998).
[13] A. J. Reddy and A. J. Szeri, "Coupled dynamics of translation and collapse of acoustically driven microbubbles," J. Acoust. Soc. Am. **112**, 1346–1352 (2002).
[14] M. Wyczalkowski and A. J. Szeri, "Optimization of acoustic scattering from dual-frequency driven microbubbles at the difference frequency," J. Acoust. Soc. Am. **113**, 3373–3379 (2003).
[15] A. J. Reddy and A. J. Szeri, "Optimal pulse-inversion imaging for microsphere contrast agents," Ultrasound Med. Biol. **28**, 483–494 (2002).
[16] P. A. Dayton, J. S. Allen, and K. W. Ferrara, "The magnitude of radiation force on ultrasound contrast agents," J. Acoust. Soc. Am. **112**, 2183–2193 (2002).
[17] P. A. Dayton, K. E. Morgan, A. L. Klibanov, K. R. Nightingale, G. Brandenburger, and K. W. Ferrara, "A preliminary evaluation of the effects of primary and secondary radiation forces on acoustic contrast agents," IEEE Trans. Ultrason. Ferroelectr. Freq. Control **44**, 1264–1277 (1997).

[18]M. J. Shortencarier, P. A. Dayton, S. H. Bloch, P. A. Schumann, T. O. Matsunaga, and K. W. Ferrara, "A method for radiation-force localized drug delivery using gas-filled lipospheres," IEEE Trans. Ultrason. Ferroelectr. Freq. Control **51**, 822–831 (2004).
[19]S. Zhao, M. Borden, S. H. Bloch, D. Kruse, K. W. Ferrara, and P. A. Dayton, "Radiation-force assisted targeting facilitates ultrasonic molecular imaging," Mol. Imaging **3**, 135–148 (2004).
[20]P. Dayton, A. Klibanov, G. Brandenburger, and K. Ferrara, "Acoustic radiation force in vivo: A mechanism to assist targeting of microbubbles," Ultrasound Med. Biol. **25**, 1195–1201 (1999).
[21]A. L. Klibanov, "Microbubble contrast agents: Targeted ultrasound imaging and ultrasound-assisted drug-delivery applications," Invest. Radiol. **41**, 421–433 (2006).
[22]J. J. Rychak, A. L. Klibanov, and J. A. Hossack, "Acoustic radiation force enhances targeted delivery of ultrasound contrast microbubbles: In vitro verification," IEEE Trans. Ultrason. Ferroelectr. Freq. Control **52**, 421–433 (2005).
[23]Y. A. Ilinskii, M. F. Hamilton, and E. A. Zabolotskaya, "Bubble interaction dynamics in Lagrangian and Hamiltonian Mechanics," J. Acoust. Soc. Am. **121**, 786-795 (2007).
[24]A. J. Reddy and A. J. Szeri, "Shape stability of unsteadily translating bubbles," Phys. Fluids **14**, 2216–2224 (2002).
[25]C. Moss, J. L. Levatin, and A. J. Szeri, "A new damping mechanism in strongly collapsing bubbles," Proc. R. Soc. London, Ser. A **456**, 2983–2994 (2000).
[26]M. S. Plesset and A. Prosperetti, "Bubble dynamics and cavitation," Annu. Rev. Fluid Mech. **9**, 145–185 (1977).
[27]L. G. Leal, *Laminar Flow and Convective Transport Processes* (Butterworth-Heinemann, London, 1992).
[28]K. S. Suslick, Y. Didenko, M. M. Fang, T. Hyeon, K. J. Kolbeck, W. B. McNamara III, M. M. Mdeleni, and M. Wong, "Acoustic cavitation and its chemical consequences," Philos. Trans. R. Soc. London, Ser. A **357**, 335–353 (1999).
[29]M. P. Brenner, S. Hilgenfeldt, and D. Lohse, "Single-bubble sonoluminescence," Rev. Mod. Phys. **74**, 425–484 (2002).
[30]E. J. Doedel, R. C. Paffenroth, A. R. Champneys, T. F. Farigrieve, Y. A. Kuznetsov, B. E. Oldeman, B. Sandstede, and X. Wang, "AUTO 2000: Continuation and Bifurcation Software for Ordinary Differential Equations (with HomCont)," Montreal, Canada, 2002.
[31]H. B. Keller, E. A. Doedel, and J. P. Kernevez, "Numerical analysis and control of bifurcation problems. I: Bifurcation in finite dimensions," Int. J. Bifurcation Chaos Appl. Sci. Eng. **1**, 493–520 (1991).
[32]H. B. Keller, E. A. Doedel, and J. P. Kernevez, "Numerical analysis and control of bifurcation problems. II: Bifurcation in infinite dimensions," Int. J. Bifurcation Chaos Appl. Sci. Eng. **1**, 745–772 (1991).
[33]The $c=0.05$, theoretical level of forcing, however, corresponds to $P_a \sim 0.30$, which is likely to induce shape instabilities for bubble radii $R_0 \geqslant 10^{-6}$ μm.
[34]A. Prosperetti, "Thermal effects and damping mechanisms in the forced radial oscillations of gas bubbles in liquids," J. Acoust. Soc. Am. **61**, 17–27 (1977).

Sound velocity and attenuation in bubbly gels measured by transmission experiments

Valentin Leroy,[a] Anatoliy Strybulevych, and John H. Page
Department of Physics and Astronomy, University of Manitoba, Winnipeg, Manitoba R3T 2N2, Canada

Martin G. Scanlon
Department of Food Science, University of Manitoba, Winnipeg, Manitoba R3T 2N2, Canada

(Received 9 August 2007; revised 25 January 2008; accepted 25 January 2008)

Measurements of the phase velocity and attenuation of sound in concentrated samples of bubbly gels are presented. Hair gel was used as a matrix material to obtain well characterized distributions of bubbles. Ultrasonic measurements were conducted over a large range of frequencies, including the resonance frequencies of the bubbles. Surprisingly good agreement with Foldy's prediction was found, even for monodisperse samples at resonance frequencies, up to volume fraction of 1%. Beyond this concentration, the effects of high-order multiple scattering were observed. These results support the feasability of ultrasonic techniques to investigate the size distribution of bubbles in a weak gel or liquid. © *2008 Acoustical Society of America.* [DOI: 10.1121/1.2875420]

PACS number(s): 43.30.Es, 43.35.Bf [TDM] Pages: 1931–1940

I. INTRODUCTION

It is well known that the presence of bubbles in a liquid has a tremendous impact on its acoustic properties. For example, the injection of air in water with a volume fraction of $\Phi=0.4\%$ is enough to reduce the velocity of sound at low frequencies to roughly 0.2 mm/μs, a value which is even lower than the velocity of sound in the air that comprises the bubbles. This property, strange as it may seem, is well established[1] and has been thoroughly checked experimentally.[2–4] On the other hand, the behavior of ultrasonic velocity and attenuation at higher frequencies is still not fully understood. According to Foldy's model,[5] the effective wave vector k for a monodisperse population of bubbles is given by

$$k^2=\left(\frac{\omega}{v}+\mathrm{i}\frac{\alpha}{2}\right)^2=\frac{\omega^2}{v_0^2}+4\pi n f(\omega,r), \tag{1}$$

where v_0 is the velocity of sound in the pure medium, n the number of bubbles per unit volume, and $f(\omega,r)$ the scattering function at angular frequency ω for a bubble of radius r. Figure 1 shows the attenuation α and phase velocity v in water for a 0.4% volume fraction of 100 μm radius bubbles, as calculated by Eq. (1). As the frequency gets close to the resonance frequency of the bubbles ($\simeq$30 kHz in this case), the dispersion and the attenuation dramatically increase. Few experiments have been done to check the validity of Foldy's expression around the resonances of bubbles. In 1957, Silberman[6] acquired data by measuring standing waves in pipes filled with bubbly water. Unfortunately, the method was not very accurate for high attenuation regimes, because the requisite standing waves could not develop. Only a rough estimation of the attenuation was possible and results exhibited a strong discrepancy with the model in the presence of resonant effects, *even at volume fractions as low as a few hundredths of* 1%, as pointed out by Commander and Prosperetti.[7] More recently, Wilson *et al.* reported significant progress[4] by developing an impedance tube specifically designed for exploring the high attenuation regime in bubbly liquids. [8] They found good agreement with Foldy's model, but their bubbly liquids were very dilute (0.054% at most) and the exact distribution of the bubble radii was not known.

In contrast to the lack of experimental investigations on this subject, the number of theoretical discussions of Foldy's model is striking.[9–13] In 1961, Waterman and Truell[9] published a criterion for the validity of Foldy's equation, demonstrating that an improvement of the model was needed when resonant effects were to be considered. The failure of Foldy's model is usually attributed to its inability to take into account the coupling between bubbles. Indeed, in Eq. (1), the scattering function f is that of an individual bubble. When the response of the bubbles to the acoustic energy input is so strong that interactions between them cannot be neglected, f should be replaced by a "collective" scattering function F. Several authors, using different approaches to the problem, proposed expressions for this new scattering function.[10–13] But none of these corrections[14] to Foldy's model has been able to fit Silberman's historical data better than Foldy's original model.

The aim of the present paper is to fill the gap in reliable experimental data on the propagation of sound in a bubbly medium at frequencies close to the resonance frequency of the bubbles. Wilson's work[4] represented a significant advance on Silberman's experiments, but results for higher concentrations of bubbles ($\Phi>0.1\%$) and for accurately known size distributions are critically needed. In Sec. II, we present the experimental setup we developed to produce well-characterized bubbly media, and to investigate their acoustic properties. Section III briefly introduces Foldy's model, and the correction proposed by Henyey.[12] Section IV is devoted to the results for four different samples, with volume fractions of bubbles ranging from 0.15% to 5%. These

[a]Electronic mail: valeroy77@yahoo.fr

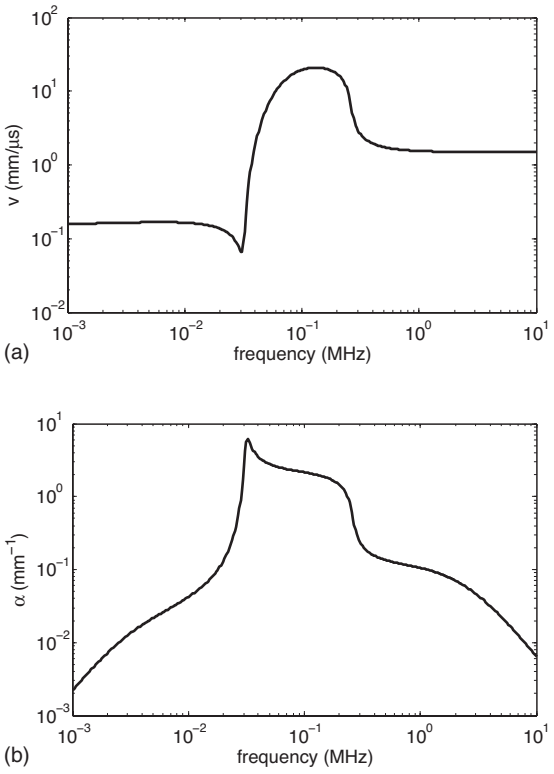

FIG. 1. Prediction of Foldy's model for the phase velocity and attenuation of sound in water with a 0.4% volume fraction of 100-μm radius bubbles.

new results will be compared with Foldy's prediction, as well as with Henyey's model. Finally, Sec. V examines the conclusions that can be drawn from our analysis of these experiments.

It is worth noting that this question of knowing how sound propagates in a bubbly liquid when resonant effects are strong is not only of academic interest. From a practical point of view, acoustic methods are a very promising tool for investigating the size distribution of bubbles in a medium.[15,16] Since such methods rely precisely on the resonances of bubbles, a reliable model, valid for resonance frequencies, is necessary.

II. EXPERIMENTAL SETUP

To bring something new to the subject matter, experiments on propagation of sound in bubbly liquids have to satisfy three criteria: (1) Media with a range of bubble concentrations, going from very dilute to volume fractions of several percent, should be investigated; (2) the population of bubbles should be well characterized; and (3) the range of frequencies should include the resonance frequencies of the bubbles. With these stipulations, several experimental difficulties are apparent.

Standard techniques to measure the acoustic properties of a material involve propagating an acoustic pulse of short duration through a sample of the material. The time taken for each monochromatic wave component of the pulse to traverse the sample gives the phase velocity of sound in the material $v(\omega)$ [more precisely, $v(\omega)$ is the speed at which a surface of constant phase propagates at each frequency], and the change in the wave amplitude gives the attenuation. In practice, a precise analysis with Fourier transforms is used, and comparison with propagation in a reference medium (usually water) is necessary. Such an experiment gives accurate measurements provided that the wavelength of the acoustic wave is small compared with two length scales: the lateral dimension of the sample, and the distance between the sample and the sound source. If this condition is not respected, diffraction and multiple reflections jeopardize the success of the technique. For bubbly liquids, this restriction has been a major impediment to experimental success. Indeed, the resonance of a bubble occurs at a very low frequency. As a rule of the thumb, a 1-mm-radius air bubble resonates in water at 3 kHz, which corresponds to a wavelength of 50 cm. Wilson *et al.* by-passed this difficulty by using the confined geometry of an impedance tube.[8] This solution necessitated the use of very thick stiff walls for the tube, so that the waves propagating in the tube were well approximated as plane waves. But the approximation is correct only for a narrow range of frequencies (specially designed to include the resonances of the bubbles in Wilson's case), and the use of thick walls makes *in situ* imaging of bubbles impossible. We used a different approach. As the resonance frequency of a bubble is inversely proportional to its radius, smaller bubbles make the experiment easier. In our samples, the bubble radius was typically 80 μm. The resonance frequency for bubbles of such a radius is 50 kHz, decreasing the wavelength to the more manageable scale of 3 cm.

A second experimental difficulty comes from the huge attenuation of sound in bubbly liquids. The consequence is that, in a transmission experiment, signals are of very small amplitude. A potential solution is to use a reflection configuration instead of a transmission one. But when the wavelength is large, so that it is not totally negligible compared with the dimensions of the setup, many complications arise in a reflection setup. Wilson *et al.* took advantage of their confined geometry to solve this problem. In our case, we used very thin samples, to ensure a sufficiently large signal in transmission despite the huge attenuation.

Finally, the question of obtaining a well-characterized medium is not a trivial one. Standard techniques of injection of gas in water, with needles and a pump or with an electrolysis device, are known to be capricious.[4,17] The production of bubbles is usually not repeatable from one experiment to the next or even during a single experiment. Moreover, the experimental sample cell is more difficult to design because a bubble generator has to be included. Our solution to this problem was to build stable samples of bubbly media by trapping bubbles in a gel whose yield stress was large enough to compensate for the buoyancy of the bubbles. This approach allowed us to work with samples whose bubble content was precisely known.

A. Sample preparation

A commercial hair gel,[18] diluted with water and degassed, was used as the liquid in which bubbles were injected. The benefit of hair gel for this experiment is that it

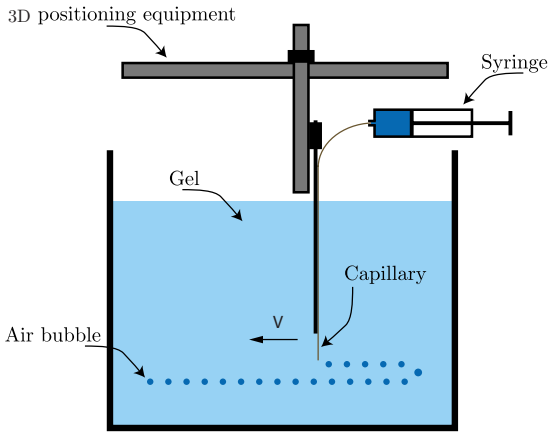

FIG. 2. (Color online) Injection of bubbles: A capillary is moved in a preprogrammed pattern of positions within the gel, delivering rows of equally sized bubbles. Capillary speed V and pressure in the syringe P are the two parameters governing the bubble size and the distance between bubbles.

flows only if the applied stress is larger than a threshold value (the yield stress). Hence if bubbles are sufficiently small, they remain trapped in the gel, at the exact place that they have been injected. In addition, from the acoustic point of view, the hair gel is very similar to water, at least for the frequencies considered in these experiments.

The samples were produced by a method developed in our laboratory and depicted in Fig. 2. A thin capillary (inner diameter of 20 μm), connected to a syringe with air at pressure P, is moved at constant speed V in the gel. With a well-controlled flow of gas through the capillary, as set by the pressure P, the movement generated an array of equally spaced bubbles of the same size. Although a discussion of the exact mechanisms involved in this process is outside the scope of this paper, we note that by varying the two parameters P and V, different bubble radii and distances between bubbles could be obtained. For our samples, we used a typical speed of $V=1$ cm/s and a pressure of $P=1.7$ bar, generating 80 μm bubbles separated by 500 μm. Thanks to a three-dimensional displacement stage, the vertical and lateral distance between successive rows of bubbles could be preprogrammed, depending on the desired total concentration. Once enough bubbles had been created, a sample of the bubbly medium was extracted with a syringe and injected into the cell designed for the ultrasonic device. Note that this last stage destroyed the ordered state of the bubbly medium. Future work is underway to investigate the acoustic properties of these crystals of bubbles. However, in the framework of an experimental test of Foldy's model, random collections of bubbles were needed. An important issue is the stability of the sample: If the degassed gel was undersaturated with air, bubbles dissolved in a matter of minutes. To prevent this, an interval of several days was required between the degassing of the gel and the injection, so that the hair gel was saturated.

Once the cell was filled with the bubbly gel and sealed, it was placed on a light box and images of the bubbles were taken with a digital camera connected to a microscope (2× magnification). Figure 3 shows examples of images taken for samples 2 and 3. The quality and contrast of the images were excellent, allowing an estimation of the diameter of the

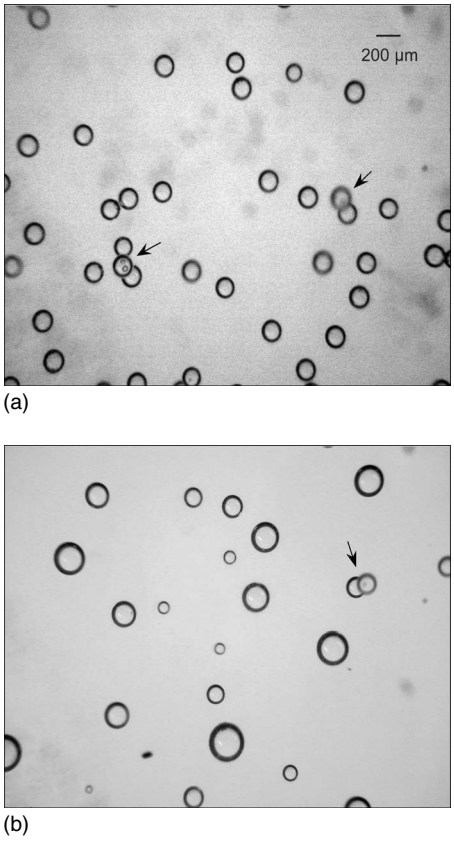

FIG. 3. Images of Sample 2 (monodisperse with a median radius of 86 μm) and Sample 3 (polydisperse). Arrows indicate clusters of bubbles ignored for the image analysis of the samples. The scale is the same on both images. Note that the dark spots in the background are not bubbles but dust on the back wall of the cell.

bubbles, with a resolution better than 2 pixels, by measuring the outer diameter of the dark ring appearing in the bubbles. Given the resolution of the images (438 pixels/mm), the uncertainty in the radii measurements was thus 2 μm. A dozen images, acquired at different positions within the samples, were analyzed with the "analyze particle" function of NIH IMAGEJ.[19] Furthermore, to check that the size of the bubbles remained stable during the experiment, images were taken both before and after the ultrasonic measurements. No significant evolution was noted. To avoid biased measurements of big bubbles, overlayed bubbles (such as the one marked with arrows in Fig. 3) were excluded from the size analysis. However, those bubbles were counted for the determination of the void fraction. Because the depth of field (>3 mm) was larger than the thickness of the cell (1.01 mm), the volume of one image was known and the number of bubbles per unit volume could be precisely determined (note that the darker grey marks in the background of the left image in Fig. 3 are not bubbles but are likely dust or dirt on the back wall of the cell). The resulting distributions $n(r)$ of radii r, as shown in Fig. 4, were well fitted by a lognormal distribution:

$$n(r) = \frac{n_{\text{tot}}}{\sqrt{2\pi}\epsilon r} \exp\left[-\frac{(\ln r/r_0)^2}{2\epsilon^2} \right], \tag{2}$$

with a median radius r_0, a logarithmic standard deviation ϵ, and a total number of bubbles per unit volume of n_{tot}. Un-

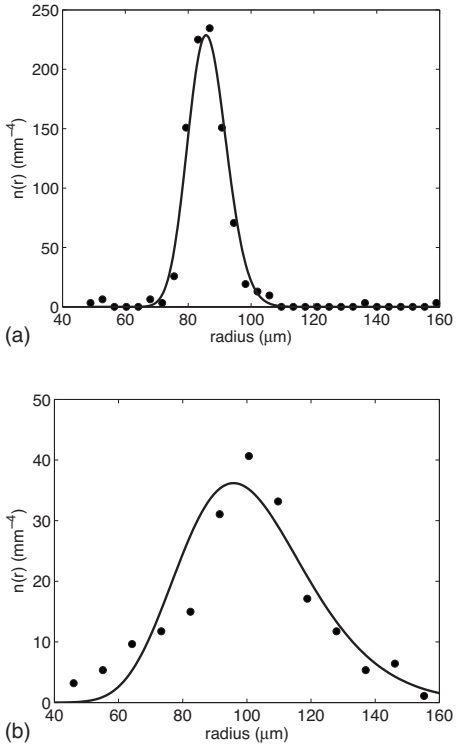

FIG. 4. Measured radius distributions for Samples 2 (top) and 3 (bottom) and best-fitted lognormal distributions.

certainty in volume fraction was estimated from the uncertainty in the radius measurement and uncertainty in the thickness of the cell.

The results of the image analysis procedure for the four samples we are presenting in this paper are given in Table I. The main parameter we varied was the volume fraction Φ, which ranged from 0.15% to almost 5%. Samples 1, 2, and 4 were very monodisperse. Sample 3 was obtained by letting Sample 2 evolve for 24 h. On this long time scale, there is a clear evolution of the size distribution: Larger bubbles grew at the expense of the smaller ones due to their different Laplace pressures, a process called Ostwald ripening.[20] The distribution of bubbles became polydisperse, as is evident from Fig. 3. Interestingly, the total volume fraction of air remained almost constant, indicating that the main mechanism of radius evolution was indeed ripening. Note that testing Foldy's model on a polydisperse sample is crucial for the goal of developing an acoustic bubble counting and sizing technique.

B. Ultrasonic measurements

The acoustic properties of the samples were measured with the setup of Fig. 5. In a large tank ($60\times60\times120$ cm^3) filled with reverse osmosis water, a piezoelectric transducer generated a pulse that propagated through water, traversed the sample, and reached the hydrophone. The amplitude of the acoustic signal was small enough ($\sim10^3$ Pa) to prevent nonlinear response of the bubbles. Because the attenuation in the sample was large, and because the divergence of the beam was not negligible (especially at low frequencies), the use of a screen (a plastic ring wrapped with Teflon™ tape) was essential for reducing spurious signals. The aperture, D, of the screen had to be larger than the wavelength of the pulse, to limit diffraction effects, but smaller than the diameter of the cell. In our experiments, D was 6 cm, the cell diameter was 7 cm, and the maximum wavelength was 5 cm (for the lowest frequency of 30 kHz).

TABLE I. Measured parameters of the bubble size distributions for each sample. The number N of bubbles counted for the size analysis is indicated.

Sample	N	Φ	r_0	ϵ
1	50	$0.15\pm0.01\%$	81 ± 2 μm	0.05 ± 0.01
2	288	$0.94\pm0.06\%$	86 ± 2 μm	0.07 ± 0.01
3	186	$0.91\pm0.05\%$	100 ± 2 μm	0.2 ± 0.02
4	141	$4.9\pm0.3\%$	80 ± 2 μm	0.08 ± 0.01

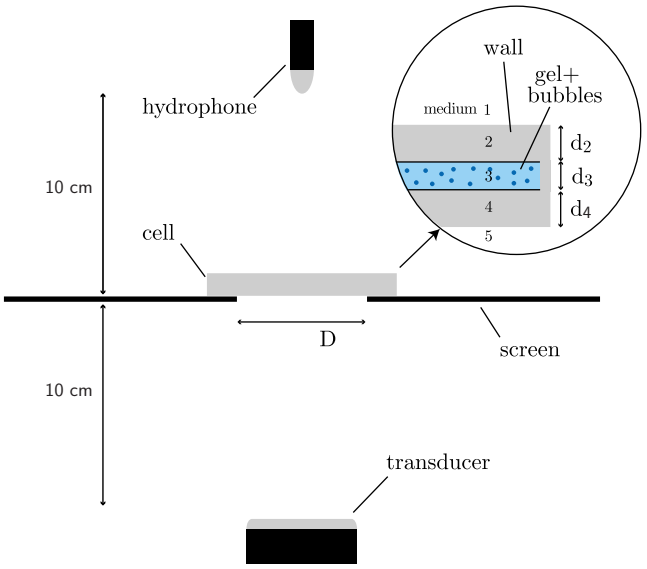

FIG. 5. (Color online) Sketch of the setup for ultrasonic measurements. A piezoelectric transducer emits an acoustic pulse that traverses the cell containing the bubbly medium.

Gaussian pulses, with central frequencies ranging from 30 to 400 kHz, were generated by an Arbitrary Wave Generator, and two different transducers, having central frequencies of 100 and 250 kHz, were used to cover the range of frequencies. The pulses were recorded, with a hydrophone, in two different cases: when the cell was mounted on the screen $[s_1(t)]$, and when the cell was absent $[s_2(t)]$. The signals were averaged over 100 acquisitions when the attenuation was low (for reference measurements, for example), and up to 5000 acquisitions for highly attenuated signals. Signals $s_1(t)$ and $s_2(t)$ were then Fourier transformed into $S_1(\omega)$ and $S_1(\omega)$, respectively, and $x(\omega)$, the ratio of the transmission with and without the cell in the path of the acoustic beam at a given angular frequency, was calculated.

The data processing was complicated by the multilayer aspect of the cell. Indeed, the pulse did not propagate only through the bubbly medium but through five media (see Fig. 5): water (1), plastic (2), sample (3), plastic (4), and water again (5). Following Brekhovskikh,[21] when a plane monochromatic wave $\exp(ikx-i\omega t)$ propagates through the multilayered cell, it results in a transmitted plane wave $T\exp(ikx-i\omega t)$, where the complex transmission T is given by

TABLE II. Characteristics of the cell containing the bubbly medium. The walls were made of clear polycarbonate: Our measured values for density and phase velocity of sound are in agreement with values in the literature (Ref. 22).

$d=d_3=1.01\pm0.05$ mm
$d_2=d_4=1.63\pm0.01$ mm
Velocity in walls: 2.28 ± 0.01 mm/μs
Density of walls: 1.19 ± 0.05g/cm^3

$$T = T_{54}T_{43}T_{32}T_{21} = \frac{Z_4^{\text{in}}+Z_4}{Z_4^{\text{in}}+Z_5}e^{ik_4d_4}\frac{Z_3^{\text{in}}+Z_3}{Z_3^{\text{in}}+Z_4}e^{ik_3d_3}\frac{Z_2^{\text{in}}+Z_2}{Z_2^{\text{in}}+Z_3}e^{ik_2d_2}\frac{2Z_1}{Z_1+Z_2}, \quad (3)$$

where d_i is the thickness of layer i, $Z_i=\rho_i\omega/k_i$, k_i stands for the impedance and the wave vector in medium i respectively, and Z_i^{in} is the input impedance, which is given by

$$Z_i^{\text{in}} = \frac{Z_{i-1}^{\text{in}} - iZ_i\tan(k_id_i)}{Z_i - iZ_{i-1}^{\text{in}}\tan(k_id_i)}Z_i \quad \text{for } i>1. \quad (4)$$

The unknown quantity in Eq. (3) is k_3. In the following, index 3 will be omitted: $d=d_3$, $k=k_3$. The ratio $x(\omega)$ is related to T by

$$x = T(k)e^{-ik_5(d_4+d+d_2)}. \quad (5)$$

As $T(k)$ is a complicated function, inversion of Eq. (5) to extract k is not analytically possible. Note that the complication not only arises from the multiple reflections existing within the system, but also from the huge attenuation of sound in the bubbly medium. Indeed, as α and v are large, the wave vector in the sample $k=\omega/v+i\alpha/2$ has a nonnegligible imaginary part. It follows that the phase shift of the pulse traversing the sample is not only due to propagation (as in standard cases) but also to the crossing of the interfaces 4-3 and 3-2. In other words, one cannot consider that the phase of the pulse is only dictated by the velocity in the sample, and that the amplitude of the pulse is only related to attenuation, which is a good approximation only when the term $\exp(ikd)$ dominates in Eq. (3). To address this issue, an iterative method can be set up. Let us define $\tilde{T}$ such that $T=\tilde{T}e^{ikd}$. Equation (5) can then be expressed as

$$e^{ikd} = xe^{ik_5(d_4+d+d_2)}/\tilde{T}(k), \quad (6)$$

and with Eq. (6) we can define the iteration:

$$k^{[j+1]} = -\frac{i}{d}\ln(xe^{ik_5(d_4+d+d_2)}/\tilde{T}(k^{[j]})). \quad (7)$$

The iteration can be initialized with $k^{[0]}=\omega/v_0$. It was tested with other initial values of $k^{[0]}$ and found to converge to the same final values of k even when the starting values were quite far from the final ones, indicating the robustness of the iteration procedure. Parameters of the cell are given in Table II. The uncertainty of the calculated wave vector k was evaluated by taking into account the uncertainty in the parameters (see Table II). It is worth noting that our experimental setup is adapted only for measurements in hugely attenuating materials. Filling the cell with water to measure the velocity of sound in water, for example, does not yield very accurate results (namely, the precision is 0.5 mm/μs). The reason for this is that fully developed multiple reflections, as they exist when the cell is thin compared with the wavelength, make the inversion technique very sensitive to the exact parameters of the walls (density, velocity of sound, thickness). But when attenuation is large, the influence of multiple reflection within the cell is less pronounced, and reliable results can be obtained using a sufficiently thin sample that the transmitted pulse is of measurable amplitude.

III. THEORY

In this section we give a brief description of the two models that are compared with our experimental results. Equation (1) of Foldy's original model needs to be generalized to the polydisperse case:

$$k^2 = \frac{\omega^2}{v_0^2} + \int 4\pi n(r)dr f(\omega,r). \quad (8)$$

The scattering function at angular frequency ω for a bubble of radius r is given by

$$f(\omega,r) = \frac{r}{(\omega_0/\omega)^2 - 1 + i(\delta^{\text{the}}+\delta^{\text{vis}}+\delta^{\text{rad}})}, \quad (9)$$

where ω_0 is the resonance frequency of the bubbles and the three δ terms are the damping constants due to thermal, viscous, and radiative losses, respectively. A detailed model of the thermodynamic behavior of the oscillating bubble is due to Prosperetti.[23] A complex polytropic index can be defined as a function of the radius and the frequency:

$$\kappa(\omega,r) = \frac{\gamma}{1-3(\gamma-1)i\dfrac{D_{\text{th}}}{\omega r^2}\mathcal{B}}, \quad (10a)$$

with

$$\mathcal{B} = 1 - \sqrt{-i}r\sqrt{\frac{\omega}{D_{\text{th}}}}\coth\left(\sqrt{-i}r\sqrt{\frac{\omega}{D_{\text{th}}}}\right), \quad (10b)$$

where γ is the ratio of specific heat capacities for air, D_{th} the thermal diffusivity of air, and where $\sqrt{-i}$ stands for $e^{i(3\pi/4)}$. Moreover, because our bubbles are in a gel, we also include the effect of the shear modulus, following Alekseev and Rybak.[24] The resonance angular frequency and the damping constants are then:

$$\omega_0^2 = \frac{3\,\text{Re}(\kappa)(P_0+2A/r)+4\mu'}{\rho r^2} - \frac{2A}{\rho r^3}, \quad (10c)$$

$$\delta^{\text{rad}} = rk_0, \quad \delta^{\text{the}} = \frac{3\,\text{Im}(\kappa)P_0}{\rho r^2\omega^2}, \quad \delta^{\text{vis}} = \frac{4\mu''}{\rho r^2\omega^2}, \quad (10d)$$

where $k_0=\omega/v_0$ is the wave vector in the gel, $\mu=\mu'+i\mu''$ the shear modulus of the gel, A its surface tension, ρ its density, and P_0 the ambient pressure. Values of the physical parameters we used for evaluating the equations are given in Table III. For the surface tension of the gel, we assumed it to be the same value as for water, which is probably an overestimation. In any case, surface tension effects are almost negligible for the bubble size considered in our experiments. Es-

TABLE III. Values of the physical parameters used for the model. The phase velocity of sound in the gel was measured by propagating an acoustic pulse through a known thickness of gel. Shear moduli were obtained by standard rheological techniques. Density was measured with a specific gravity bottle.

$v_0=1.49$ mm/μs	$D_{th}=2\times10^{-5}$ m^2/s
$\gamma=1.4$	$P_0=10^5$ Pa
$A=70$ mJ/m^2	$\rho=1$ g/cm^3
$\mu'=60$ Pa$(\omega/2\pi\text{Hz})^{0.1}$	
$\mu''=13$ Pa$(\omega/2\pi\text{Hz})^{0.5}$	

timation of the shear modulus was obtained via standard measurements with a rheometer, which gave the frequency dependence of μ up to 100 Hz. Extrapolation of this frequency dependence to 400 kHz is certainly a crude approximation. However, as μ' remains small compared with atmospheric pressure, its influence on the resonance frequencies of bubbles is weak [see Eq. (10c)], a fact that we experimentally checked by measuring the resonance frequency of individual bubbles in gel. Moreover, because thermal and radiative losses dominate, the effect of μ'' is not crucial: It changes, by 20% at most, the maximum of the attenuation of sound in the bubbly medium. As a result, the acoustic behavior of the bubbly gel is expected to be almost identical to what it would be for bubbly water.

In 1999, Henyey proposed a diagrammatic approach for the problem of propagation in a bubbly medium.[12] His result has a simple interpretation: It amounts to considering that the bubble does not radiate in the pure liquid, but in the effective medium. As a consequence, the radiative damping term in Eq. (10d) has to be modified, namely, k_0 in the formula of δ^{rad} has to be substituted by the effective wave vector k. We calculated Henyey's predictions by an iterative process, with 20 iterations. Note that Kargl, in 2002, obtained the same expression as Henyey, but with a different approach to the problem.[13]

IV. EXPERIMENTAL RESULTS

We present the experimental measurements of the attenuation and the phase velocity in four different samples of bubbly gels, with the parameters that characterize the bubble size distributions being given in Table I. For each sample, a comparison with Foldy's and Henyey's predictions is performed.

A. Low volume fraction

The first sample we investigated had a volume fraction of 0.15% with a monodisperse distribution of bubbles. Figure 6 compares an example of the pulse transmitted through the sample with the reference pulse through water, for a Gaussian pulse centered at 50 kHz. To measure the phase velocity and attenuation as a function of frequency, the Fourier transforms of the signals were computed. Figure 7 shows the magnitude of the Fourier transforms (top plot) and the difference between the phase of the reference signal and the phase of the sample signal (bottom plot), as functions of frequency. The dispersive character of the bubbly medium is clearly visible: Both the magnitude and the phase changed

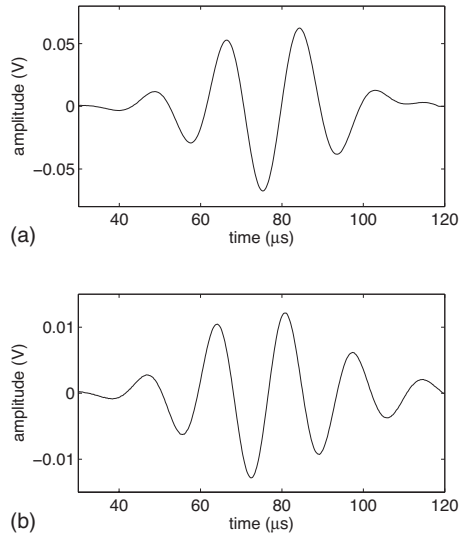

FIG. 6. Top: The reference pulse for a central frequency of 0.05 MHz. Bottom: The corresponding pulse transmitted through Sample 1.

significantly with frequency, particularly around 40 kHz, which is the resonance frequency of the bubbles.

From these calculations, the ratio x defined in Sec. II B was calculated and the attenuation and phase velocity were then determined using the procedure that was also described in this section (Sec. II B). Figure 8 displays the attenuation and velocity as a function of frequency for Sample 1. It is worth emphasizing that the entire regime of high attenuation is covered. For comparison, Wilson *et al.*[4] measured only the first part of the peak, and this was done for samples with a smaller concentration of bubbles. The error bars in the plots were calculated from the uncertainties in the different param-

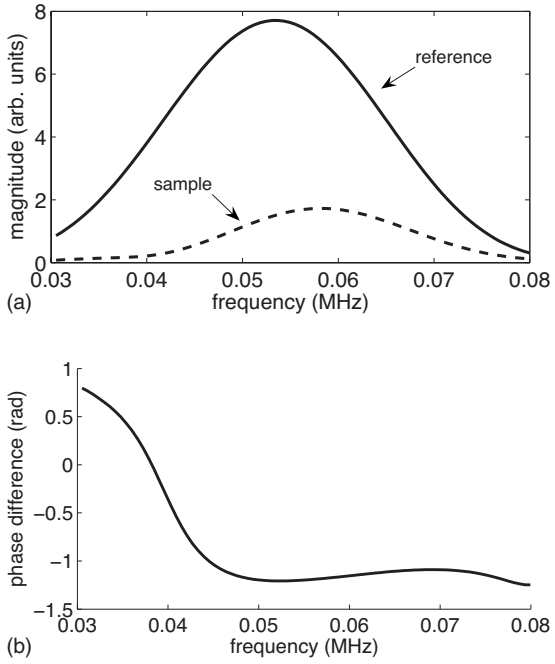

FIG. 7. Top: Magnitude of the Fourier transform of the reference signal of Fig. 6 (solid line) and of the sample signal of Fig. 6 (dashed line). Bottom: The phase of the Fourier transform of the reference signal minus the phase of the Fourier transform of the sample signal.

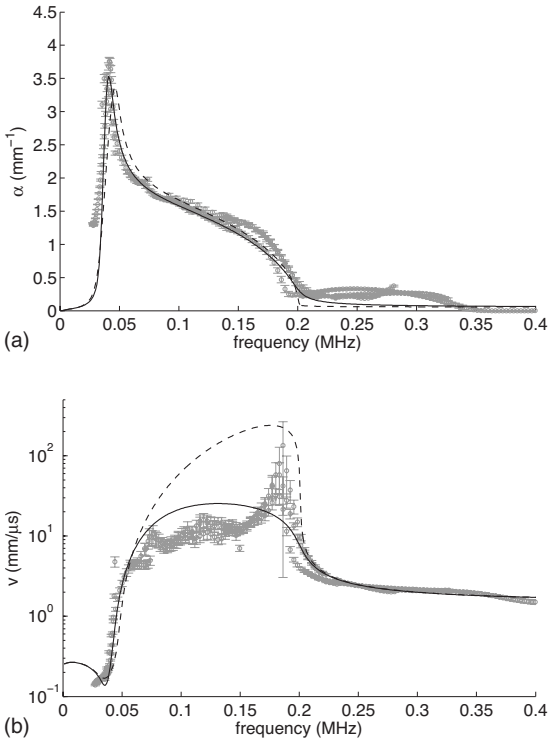

FIG. 8. Attenuation and velocity measured in Sample 1 (Φ=0.15%, r_0 =81 μm, ϵ=0.05). Predictions from the Foldy (continuous lines) and Henyey (dashed lines) models are shown.

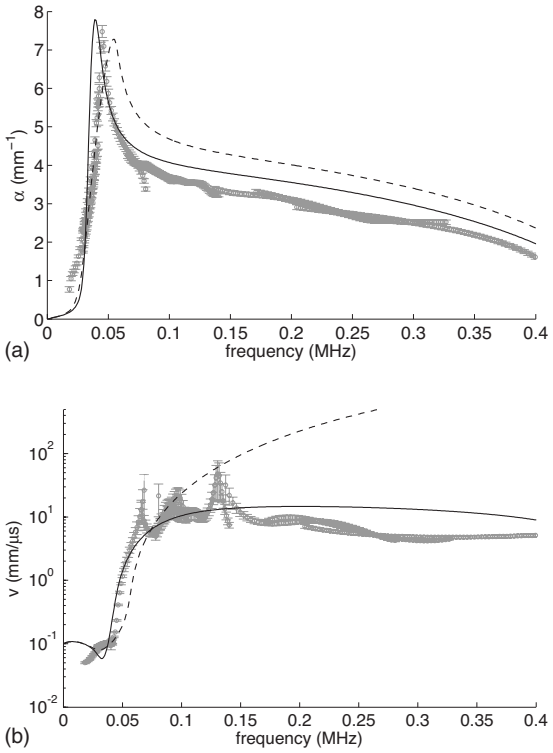

FIG. 9. Attenuation and velocity measured in Sample 2 (Φ=0.94%, r_0 =86 μm, ϵ=0.07). Predictions from the Foldy (continuous lines) and Henyey (dashed lines) models are shown.

eters needed for the inversion procedure (see Table II). Error bars are bigger when the phase velocity is large, because high values of velocity required measurement of small phase shifts. Note that the overlap in frequency between the different runs of data (with different Gaussian pulses) is satisfactory: One obtains more or less smooth curves. When differences are visible, they give indications about the uncertainty of the measurement.

Figure 8 also gives the predictions of Foldy's and Henyey's models for the bubble size distribution that was *measured in the sample*. In other words, there are no adjustable parameters in this treatment. For attenuation, there is good agreement with Foldy's model. A huge sharp peak of attenuation, due to resonance of the bubbles, is followed by a high attenuation regime (up to 200 kHz). The Henyey result (in dashed line) is not very different from Foldy's predictions for this sample, in which the concentration of bubbles is low. Nevertheless, the position of the attenuation peak is distinct from one model to the other, and Foldy's peak position is in better agreement with the measurements. Measurements of the velocity are more difficult to interpret. If only the rising and the decrease of the peak of velocity are examined, the agreement between Foldy's prediction and the experimental values is excellent. On the other hand, measurements from 100 to 200kHz display a large discrepancy with Foldy's model (note the logarithmic scale).

This discrepancy in the velocity may be a consequence of performing the experiments on well-characterized samples with fixed distributions of bubbles. Indeed, because our bubbles are trapped in the gel matrix—allowing us to take good and reliable images of them—our measurements are made with a particular realization, whereas the models calculate the properties of an average medium. In practice, it means that the signal acquired after passage through Sample 1 might be different from that measured through another sample with the same concentration of bubbles of the same size, but with bubbles in different positions. The signal obtained by averaging over the different configurations of the sample is usually called the coherent signal. The other part, which is related to a particular configuration, is called the incoherent signal. In our experiments, the incoherent part is expected to be very small, because the acoustic wavelength is so large compared with the typical distance between bubbles. It is therefore usually considered that the exact positions of the scatterers are not of crucial importance. However, a slight difference can exist and become non-negligible when one has to measure high values of α and v. Indeed, the relative magnitude of the incoherent part will increase as the coherent part is attenuated.[25] Furthermore, high velocities necessitate the measurement of small phase shifts, which may become blurred by the incoherent signal. This effect may explain the discrepancy between the models and our measurements of velocities larger than 10 mm/μs.

B. Intermediate volume fraction

The volume fraction of bubbles in Sample 2 was almost 1%. As displayed in Fig. 9, the measured attenuation shows a similar frequency dependence to that of Sample 1. The sharp peak of large attenuation is still at the same position (as expected, since the bubbles had the same radius), but of significantly larger magnitude. It is also apparent that the re-

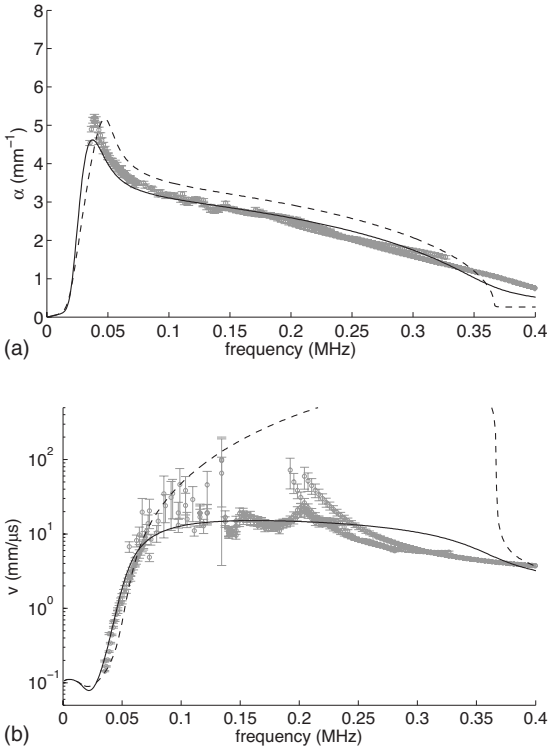

FIG. 10. Attenuation and velocity measured in Sample 3 (Φ=0.91%, r_0 =100 μm, ϵ=0.2). Predictions from the Foldy (continuous lines) and Henyey (dashed lines) models are shown.

gime of large attenuation is broader: α is still larger than 2 mm^{-1} at 0.4 MHz. The comparison with Foldy's prediction is not as good as for Sample 1. Although the magnitude of the sharp peak is well depicted, its position is not perfect. Furthermore, Foldy predicts an attenuation on the plateau which is 10% higher than what is measured. Henyey's model is in even worse agreement with the measurements. As for the velocity, its initial low frequency rise is well depicted by Foldy's model. On the other hand, above 100 kHz, agreement deteriorates, and Foldy's model predicts a larger velocity of sound than is found in the experiment. Velocity predictions from Henyey's model are in worse agreement.

C. Effect of polydispersity

Sample 3 had almost the same concentration of bubbles as Sample 2, but with a much more polydisperse distribution (see Fig. 4). Such well-defined samples provide a good opportunity to test the accuracy of ultrasonic measurements for obtaining details about the size distribution of bubbles in a sample. Comparison of Figs. 9 and 10 shows that a polydisperse sample can clearly be distinguished from a monodisperse one: The sharp peak in attenuation is shifted to a lower frequency and the general level of attenuation is substantially lower. The effect on velocity is less dramatic, the only clear difference being a less pronounced slope around bubble resonance for the polydisperse sample. All these features are well depicted by Foldy's model, which is again in better agreement with the experimental data than Henyey's model.

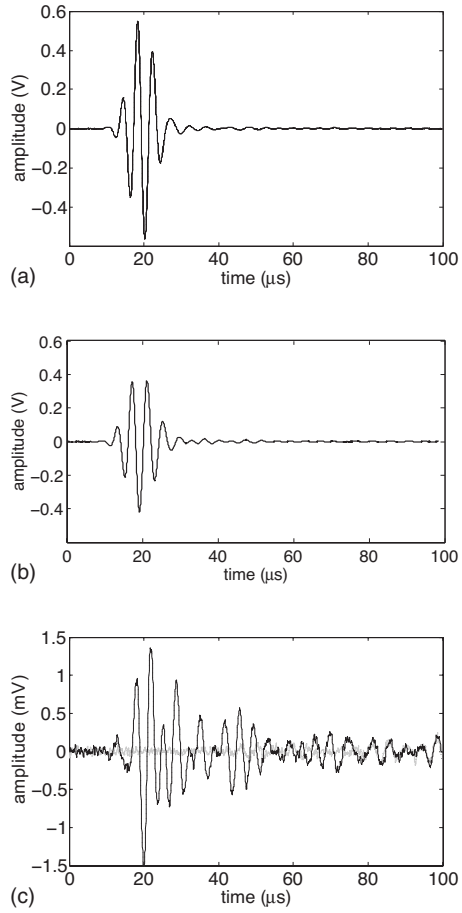

FIG. 11. Top: The reference pulse for a central frequency of 0.25 MHz. Middle: The corresponding pulse traversing Sample 1 (Φ=0.15%, r_0 =81 μm, ϵ=0.05). Bottom: The corresponding pulse traversing Sample 4 (Φ=4.9%, r_0=80 μm, ϵ=0.08). Note factor of 10^3 reduction in amplitude. Data in light grey correspond to the signal acquired when the aperture of the screen is closed.

D. High concentration

With the high concentration (almost 5%) of monodisperse bubbles in Sample 4, we observed high-order multiple scattering. Figure 11 gives an example of the signal transmitted through Sample 4 (bottom plot) for a pulse of central frequency 0.25 MHz. For comparison, the pulses at the same frequency propagating through only water, as well as through Sample 1, are presented in Fig. 11 (top plot, and middle plot, respectively). It is clear from the top and bottom pulses in Fig. 11 that Sample 4 highly attenuates sound (by a factor 500), and also gives rise to high-order multiple scattering that is manifest as a tail of oscillations that follow the initial arrival of the signal.[25] By contrast, the pulses through the other samples, which have lower bubble concentrations, show no measurable signs of high-order multiple scattering (e.g., see the middle plot in Fig. 11). To check that this multiply scattered signal is due to the bubbly sample—and not to reflections in the water tank or around the screen—we also measured the transmitted signal when the aperture of the screen was closed (grey curve in Fig. 11). The pulse that has traveled through the bubbly medium is clearly much larger than this background signal, confirming the presence of high-

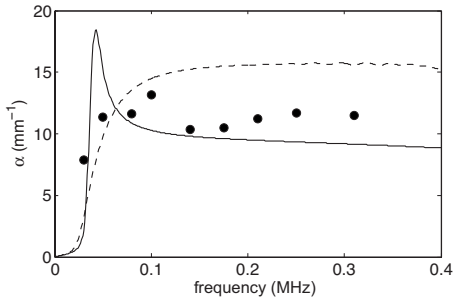

FIG. 12. Approximate measurements of the attenuation in Sample 4, and comparison with the Foldy (solid line) and Henyey (dashed line) models.

order multiple scattering and revealing that incoherent scattering is competing with the coherent field at this high concentration of bubbles.

For low frequencies, the presence of high-order multiple scattering was much less clear. Indeed, because the screen is less opaque to low frequency ultrasound, and because Sample 4 strongly attenuates the incident pulse, only the very first part of the acquired signal was different when the pulse was going through the sample or through the screen. We found that 0.15 MHz was the lowest frequency at which the existence of high-order multiple scattering could be clearly seen.

With a signal such as the one of Fig. 11, the analysis described in Sec. II B cannot be used because the coherent pulse cannot be clearly distinguished from the total measured field. However, a crude estimation of the attenuation can be performed by taking only the three first cycles of the signal, which likely consist mostly of the coherent component of the field, and by considering that the loss in transmission in Eq. (3) is dominated by $\exp(-\alpha d/2)$. The result of such a procedure is given in Fig. 12. The order of magnitude of the result is comparable to that of the theoretical models. But, due to the crudeness of the measurements, it is not possible to discern which model is better at predicting experimental results for samples with such high concentrations of bubbles.

V. CONCLUSIONS

We have measured the phase velocity and the attenuation in monodisperse bubbly media over a large range of frequencies that include the resonance frequency of the bubbles. For concentrations of 0.15% and 1%, we find that Foldy's model gives an imperfect but satisfactory description of the attenuation and phase velocity in our samples. In particular, the attenuation is well predicted by Foldy's model, but the phase velocity is overestimated for frequencies corresponding to the higher frequency part of the large attenuation regime. It is important to note that this range of frequencies over which the agreement between theory and experiment deteriorates *did not include the resonant frequencies of the bubbles.* This is a surprising result, as there is a general consensus in the literature about the inability of Foldy's model to describe the propagation of sound in a bubbly liquid *in the presence of resonant effects.* In that sense, our results confirm what Wilson *et al.*[4] obtained, but with better characterized samples that contain higher concentrations of bubbles.

However, the question of knowing whether Foldy's model needs corrections or not, and what this correction should be, is still open. Indeed, our measurements with a small number of quenched samples did not allow us to unambiguously separate the coherent part of the signal from the incoherent scattering, even though each sample contained a large number of bubbles; thus, for this range of bubble concentrations, a definitive comparison of experimental data with theories for ensemble average properties, such as Foldy's or Henyey's models, must await additional experiments with a larger number of well-characterized samples. Also, our samples were thin, and, even though the samples were sufficiently dilute that significant short range correlations in the positions of the bubbles due the sample boundaries are unlikely, most of the bubbles were still near a boundary, and therefore may not have experienced the same effective field as in the idealized infinite sample assumed in the models. In future work, this question will be addressed through measurements on samples of different thickness, as has been done for other strongly scattering media, where the ability of effective medium theories to accurately describe velocity and attenuation data in thin samples has been demonstrated.[26,27] Despite the limited number of samples investigated in the current experiments, it is still interesting to note that better agreement with the data was found with Foldy's model than with Henyey's model.

Nevertheless, from a practical point of view, the results reported in this paper are encouraging for achieving the objective of measuring the bubble size distribution in a medium using ultrasonic techniques. In many such applications, the bubble sizes in a particular sample are needed. For concentrations of bubbles up to 1%, measuring the position, height, and shape of the peak of attenuation should give enough information to determine the distribution of bubble radii using Foldy's model. A demonstration of the feasibility of this approach was made with Samples 2 and 3, whose different polydispersity could be differentiated using attenuation measurements. Note that for higher volume fractions, when high-order multiple scattering is directly observable, it becomes more difficult to measure the velocity and attenuation; however, in this regime, useful information can still be obtained with techniques based on diffusing acoustic wave spectroscopy,[28,29] which can be applied to investigate the dynamics of the bubbles (e.g., Ostwald ripening) with excellent sensitivity.

ACKNOWLEDGMENT

Support from the Natural Sciences and Engineering Research Council of Canada is gratefully acknowledged.

[1]A. B. Wood, *A Textbook of Sound* (Bell, London, 1932).
[2]F. S. Crawford, "The hot chocolate effect," Am. J. Phys. **50**, 398–404 (1982).
[3]M. Nicholas, R. A. Roy, L. A. Crum, H. Oguz, and A. Prosperetti, "Sound emissions by a laboratory bubble cloud," J. Acoust. Soc. Am. **95**, 3171–3182 (1994).
[4]P. S. Wilson, R. A. Roy, and W. M. Carey, "Phase speed and attenuation in bubbly liquids inferred from impedance measurements near individual

bubble resonance frequency," J. Acoust. Soc. Am. **117**, 1895–1910 (2005).
[5]L. L. Foldy, "The multiple scattering of waves," Phys. Rev. **67**, 107–119 (1945).
[6]E. Silberman, "Sound velocity and attenuation in bubbly mixture measured in standing wave tubes," J. Acoust. Soc. Am. **29**, 925–933 (1957).
[7]K. W. Commander and A. Prosperetti, "Linear pressure waves in bubbly liquids: Comparison between theory and experiments," J. Acoust. Soc. Am. **85**, 732–746 (1989).
[8]P. S. Wilson, R. A. Roy, and W. M. Carey, "An improved water-filled impedance tube," J. Acoust. Soc. Am. **113**, 3245–3252 (2003).
[9]P. C. Waterman and R. Truell, "Multiple scattering of waves," J. Math. Phys. **2**, 512–537 (1961).
[10]C. Feuillade, "The attenuation and dispersion of sound in water containing multiply interacting bubbles," J. Acoust. Soc. Am. **99**, 3412–3430 (1996).
[11]Z. Ye and L. Ding, "Acoustic dispersion and attenuation relations in bubbly mixture," J. Acoust. Soc. Am. **98**, 1629–1635 (1995).
[12]F. S. Henyey, "Corrections to Foldy's effective medium theory for propagation in bubble clouds and other collections of very small scatterers," J. Acoust. Soc. Am. **105**, 2149–2154 (1999).
[13]S. G. Kargl, "Effective medium approach to linear acoustics in bubbly liquids," J. Acoust. Soc. Am. **111**, 168–173 (2002).
[14]Feuillade's model gives good agreement with experimental results, but it introduces an *ad hoc* adjustable parameter without a clear justification.
[15]R. Duraiswami and S. Prabhukumar, "Bubble counting using an inverse acoustic scattering method," J. Acoust. Soc. Am. **104**, 2699–2717 (1998).
[16]V. Leroy, Y. Fan, A. L. Strybulevych, G. G. Bellido, J. H. Page, and M. G. Scanlon, "Investigating the bubble size distribution in dough using ultrasound," in *Bubbles in Food 2: Novelty, Health and Luxury*, edited by G. M. Campbell, M. G. Scanlon, and D. L. Pyle (Eagan, St. Paul, MN, 2008).
[17]F. van der Biest, "Diffusion multiple et renversement du temps ultrasonore dans des milieux périodiques et désordonnés (multiple scattering and time reversal of acoustic waves in periodic and disordered media)," Ph. D. thesis, Université Paris 7, 2005.
[18]Dep, sport endurance gel, made in USA by Henkel corporation.
[19]M. D. Abramoff, P. J. Magelhaes, and S. J. Ram, "Image processing with image," Biophotonics Int. **11**, 36–42 (2004).
[20]R. Ettelaie, E. Dickinson, Z. Du, and B. S. Murray, "Disproportionation of clustered protein-stabilized bubbles at planar air-water interfaces," J. Colloid Interface Sci. **263**, 47–58 (2003).
[21]L. M. Brekhovskikh, *Waves in Layered Media* (Academic, New York, 1960).
[22]A. R. Selfridge, "Approximate material properties in isotropic materials," IEEE Trans. Sonics Ultrason. **SU-32**, 381–394 (1985).
[23]A. Prosperetti, "Thermal effects and damping mechanisms in the forced radial oscillations of gas bubbles in liquids," J. Acoust. Soc. Am. **61**, 17–27 (1977).
[24]V. N. Alekseev and S. A. Rybak, "Gas bubble oscillations in elastic media," Acoust. Phys. **45**, 535–540 (1999).
[25]Z. Q. Zhang, I. P. Jones, H. P. Schriemer, J. H. Page, D. Weitz, and P. Sheng, "Wave transport in random media: The ballistic to diffusive transition," Phys. Rev. E **60**, 4843–4850 (1999).
[26]J. H. Page, P. Sheng, H. P. Schriemer, I. Jones, X. Jing, and D. A. Weitz, "Group velocity in strongly scattering media," Science **271**, 634–637 (1996).
[27]M. L. Cowan, K. Beaty, J. H. Page, Z. Liu, and P. Sheng, "Group velocity of acoustic waves in strongly scattering media: Dependence on the volume fraction of scatterers," Phys. Rev. E **58**, 6626–6636 (1998).
[28]M. L. Cowan, J. H. Page, and D. A. Weitz, "Velocity fluctuations in fluidized suspensions probed by ultrasonic correlation spectroscopy," Phys. Rev. Lett. **85**, 453–456 (2000).
[29]M. L. Cowan, I. P. Jones, J. H. Page, and D. A. Weitz, "Diffusing acoustic wave spectroscopy," Phys. Rev. E **65**, 066605 (2002).

Acoustics of marine sediment under compaction: Binary grain-size model and viscoelastic extension of Biot's theory

Klaus C. Leurer[a] and Colin Brown
Department of Earth and Ocean Sciences, National University of Ireland, Galway, University Road, Galway, Ireland

(Received 4 July 2007; revised 16 January 2008; accepted 16 January 2008)

This paper presents a model of acoustic wave propagation in unconsolidated marine sediment, including compaction, using a concept of a simplified sediment structure, modeled as a binary grain-size sphere pack. Compressional- and shear-wave velocities and attenuation follow from a combination of Biot's model, used as the general framework, and two viscoelastic extensions resulting in complex grain and frame moduli, respectively. An effective-grain model accounts for the viscoelasticity arising from local fluid flow in expandable clay minerals in clay-bearing sediments. A viscoelastic-contact model describes local fluid flow at the grain contacts. Porosity, density, and the structural Biot parameters (permeability, pore size, structure factor) as a function of pressure follow from the binary model, so that the remaining input parameters to the acoustic model consist solely of the mass fractions and the known mechanical properties of each constituent (e.g., carbonates, sand, clay, and expandable clay) of the sediment, effective pressure, or depth, and the environmental parameters (water depth, salinity, temperature). Velocity and attenuation as a function of pressure from the model are in good agreement with data on coarse- and fine-grained unconsolidated marine sediments. © *2008 Acoustical Society of America.*
[DOI: 10.1121/1.2871839]

PACS number(s): 43.30.Ma [RCG] Pages: 1941–1951

I. INTRODUCTION

The characterization of marine sediments with acoustic methods is more reliable the better one understands, quantitatively, the nature of unconsolidated water-saturated granular aggregates in terms of their physical properties, and how these influence the velocity and attenuation of compressional and shear waves. The most comprehensive theory that provides a relationship between physical and acoustic properties was formulated by Biot[1] for a porous solid saturated with viscous compressible fluid. The stress-induced viscous flow of the pore fluid relative to the frame is responsible for wave-energy dissipation, which peaks at a characteristic frequency determined by the viscosity of the fluid and the spatial distribution of the pore network, the corresponding attenuation coefficient being proportional to f^2 (f=frequency) and $f^{1/2}$ toward lower and higher frequencies, respectively. Buckingham[2] took a principally different approach by adding an intergranular friction term to the wave equation leading to a variation of the attenuation coefficient close to the first power of frequency, corresponding to nearly constant specific dissipation $1/Q$ and to low velocity dispersion, arguing that the viscosity of the pore fluid is not involved in wave attenuation in marine sediments. (To explain discrepancies between this approach and, e.g., SAX99[3] data, Buckingham[4] has recently introduced a viscoelastic modification to his original approach by modeling the acoustic response ascribed to molecular surface-water layers by a phenomenological spring/dashpot model.)

Several investigations[5–7] appear to confirm Biot's theory, in particular the experimental detection[8] of the predicted second, or slow, dilatational wave. Although the occurrence of the slow wave has not yet been reported for unconsolidated granular material, there is no physical reason for its nonexistence other than a lack in the necessary sensitivity in the experimental equipment to detect strongly attenuated signals. Although Biot generalized[9] his theory to accommodate a number of additional stress-induced relaxation mechanisms including local fluid flow from cracks in the solid and in the immediate vicinity of grain contacts, Stoll and Bryan[10] were the first to systematically adapt Biot's theory to marine sediments. They postulated global grain-to-grain friction as a significant mechanism for acoustic-wave attenuation and introduced a phenomenological model described by constant complex frame bulk and shear moduli that replace the elastic ones in Biot's original formulation, the combined model known since as the Biot–Stoll model (BSM). Constant complex frame moduli cause a linear dependence on frequency of the attenuation coefficient, a pattern suggested by a large collection of compressional-wave attenuation data.[11] Subsets from individual sediments, however, do not necessarily confirm this simple pattern, and more recent field and experimental results[12] are in favor of the BSM approach, in which the frame moduli can be empirically adjusted so that the combined attenuation due to frame loss and Biot attenuation mechanism matches the data in coarse-grained marine sediments. To accommodate the fine-grained sediments, Stoll[13]

[a]Electronic mail: klaus.leurer@nuigalway.ie

introduced a phenomenological model of the Cole–Cole type[14] for the frame moduli to account for additional viscoelastic losses in the skeletal frame, adding a frequency-dependent component to the constant complex frame moduli. It has been argued[15] that such a model cannot account for the losses observed in near-surface clay-rich sediments, because the comparatively low frame moduli known for these do not sufficiently contribute to the overall attenuation.

The concept of a linear dependence on frequency of the attenuation coefficient has been characterized as physically problematic[16] and so is that of an inelastic frame, because with the postulate of grain-to-grain friction—an irreversible, nonlinear process—attenuation becomes strain dependent.[17] Despite this objection, the BSM is a comprehensive formalism for modeling unconsolidated marine sediments and has been widely used for this purpose[18,19] or serves as the basis for extensions and refinements[20,21] to remove some of its phenomenological aspects. Although most of these efforts consider sands or sandy sediments, the model proposed here is intended to cover a wider spectrum of marine sediment and, therefore, has to take into account the varying amounts of smaller grains such as silt and clay particles that strongly influence the mechanical response.[22] As it is impossible to specify quantitatively the actual structure of any earth material, a geometrical abstraction of the sediment as a binary grain-size sphere pack is introduced as an attempt to account for the intricate interrelation among the sediment structural parameters. Similar binary grain-size approaches[22,23] lack the explicit particulate formulation of the grain-contact mechanics and their consequences for the propagation of acoustic waves and do not provide a quantitative relationship between porosity and effective pressure for highly compactable sediments.

The model presented here further attempts to eliminate the disadvantage in Biot's theory and the BSM not to provide an explicitly formulated relation between bulk and shear moduli of the grain material on one hand and those of the sediment frame on the other. Yet the mechanical properties of the frame strongly depend on the grain-contact stiffness, which is affected by the grain material. Further, none of the previous Biot-derived models include an explicit quantitative consideration of a dependence on pressure or, equivalently, depth below the ocean bottom of any Biot parameter. In unconsolidated sediments, however, all of the structural parameters are highly sensitive to compaction.

The proposed model describes the acoustic response in unconsolidated marine sediment as a function of frequency as well as of—purely mechanical—compaction. Rather than modifying the BSM, the original Biot formulation is used as the general framework. Two viscoelastic models are included that consist of extended formulations of (1) an effective-grain model[15] (EGM) and (2) a viscoelastic-contact model[24] (VCM). Nevertheless, it can still be argued that the model presented here, apart from the EGM, represents a refinement of the BSM, because it was the original idea of introducing an energy-dissipating skeletal frame that made Biot's theory applicable to unconsolidated marine sediment.

II. SEDIMENT MODEL CONCEPTION

The reader is referred to Stoll[25] for the recapitulation of Biot's theory in its application to marine sediment. In summary, the theory considers the stress-induced global fluid flow in the pore network as the sole relaxation mechanism and allows the calculation of velocity and attenuation of compressional and shear waves of a fluid-filled porous solid from a set of sediment physical parameters, viz., density, ρ_r, and bulk modulus, K_r, of the solid phase; density, ρ_f, bulk modulus, K_f, and viscosity η of the fluid phase; bulk modulus, K_b, and shear modulus, G_b, of the solid frame; permeability, κ, pore size, s_p, and tortuosity, ξ.

The structural input parameters to Biot's theory are intricately dependent on one another and on the degree of compaction or, equivalently, effective pressure. The main purpose of considering a simplified model of the sediment structure is to ensure a quantitative access to the interrelation of the structural input parameters as a function of both composition and depth below the ocean bottom. This, in effect, reduces the comparatively large set of input parameters to the previous Biot-derived models.

A. Sediment structure model: Binary grain-size sphere pack

The structural model presented here considers spherical grains of two sizes in a macroscopically homogeneous and isotropic distribution and is assumed to represent the grain-size distribution in marine sediment. In particular, the smaller spheres are to represent the clay fraction and the finer range of the silt fraction. The finer grains are assumed to be two orders of magnitude smaller than the coarse grains to guarantee that the individual large- and small-sphere packings do not significantly influence each other in the rearrangement during compaction.

1. Pressure-dependent porosity of the binary grain-size model

Starting at the high-porosity limit assumed for the loosest small-sphere pack, the entire porosity range in uncompacted, surficial seafloor sediments can be visualized by adding increasing amounts large spheres to the binary mixture. The replacement of high-porosity domains by large spheres gradually reduces the overall porosity. The loosest random pack of the large spheres, filled with the loosest-possible (highest-porosity) small-grain pack, defines the coarse-grain end member in the present binary model.

Mechanical compaction is associated with a rearrangement of the sediment particles leading to a gradually closer packing. At the depth of maximum compaction, the lowest possible effective porosity in a binary mixture is reached when the interstices of the densest large-sphere pack are occupied by the densest small-sphere pack. This critical stage is very important as it separates two distinct domains. Toward higher or lower small-sphere volume fractions, respectively, the small spheres or the large ones, respectively, exist in densest packing, whereas the packing density of the respective other decreases.

The effective porosity of an uncompacted binary sphere pack as a function of the small-sphere volume fraction c_s can be written as

$$\phi_0(c_s) = \frac{\phi_{\max} c_s}{1 - \phi_{\max}(1 - c_s)} \quad \text{for } c_s \geq 1 - \phi_{\max}, \tag{1}$$

where $\phi_{\max}$ is the high-porosity limit of the small-sphere pack. At the depth of maximum compaction, minimum effective porosity is given by

$$\phi_{\min} = \phi_{\mathrm{RD}}^2, \tag{2}$$

where ϕ_{RD} is the porosity of the random dense pack of identical spheres. This minimum porosity is reached when the small-sphere volume content c_s within the solid phase assumes the critical value

$$c_{s,\mathrm{crit}} = \frac{\phi_{\mathrm{RD}}}{1 + \phi_{\mathrm{RD}}}. \tag{3}$$

For lower small-sphere fractions than $c_{s,\mathrm{crit}}$, the lowest effective porosity ϕ_1 is given by

$$\phi_1(c_s) = \frac{\phi_{\mathrm{RD}} - c_s}{1 - c_s}, \quad 1 - \phi_{\max} \leq c_s < c_{s,\mathrm{crit}}, \tag{4}$$

whereas for higher small-sphere fractions

$$\phi_1(c_s) = \frac{\phi_{\mathrm{RD}} c_s}{1 - \phi_{\mathrm{RD}}(1 - c_s)}, \quad c_s > c_{s,\mathrm{crit}}. \tag{5}$$

The porosity/depth function presented in the following is a phenomenological derivation using porosity versus depth data from the near-surface environment and porosity versus effective pressure data from large-scale compaction, both of which suggest a logarithmic variation of porosity with depth from a few centimeters downwards to depths corresponding to effective pressures of about 20 MPa (Fig. 1). The porosity of any given binary mixture can be expressed as a function of fine-grained content and depth according to

$$\phi(c_s, z) = \phi_0(c_s) - [\phi_0(c_s) - \phi_1(c_s)] \frac{\ln(z/z_0)}{\ln(z_1/z_0)}, \tag{6}$$

where z is depth, z_0 and z_1 are the depth values that correspond to the end members of effective porosity, and where the appropriate porosity limit $\phi_1(c_s)$ from Eqs. (4) and (5) has to be substituted. The variation of porosity ϕ_s with depth in the small-sphere pack can be calculated from

$$\phi_s(c_s, z) = \phi_{\max} - \left[\phi_{\max} - \frac{\phi_1(c_s)}{\phi_{\mathrm{RD}}} \right] \frac{\ln(z/z_0)}{\ln(z_1/z_0)}, \quad 1 - \phi_{\max} < c_s < c_{s,\mathrm{crit}}, \tag{7}$$

and

$$\phi_s(z) = \phi_{\max} - [\phi_{\max} - \phi_{\mathrm{RD}}] \frac{\ln(z/z_0)}{\ln(z_1/z_0)}, \quad c_s \geq c_{s,\mathrm{crit}}. \tag{8}$$

The individual porosity ϕ_l of the large-sphere pack—throughout the whole range of volume content c_s and of depth z—is given by

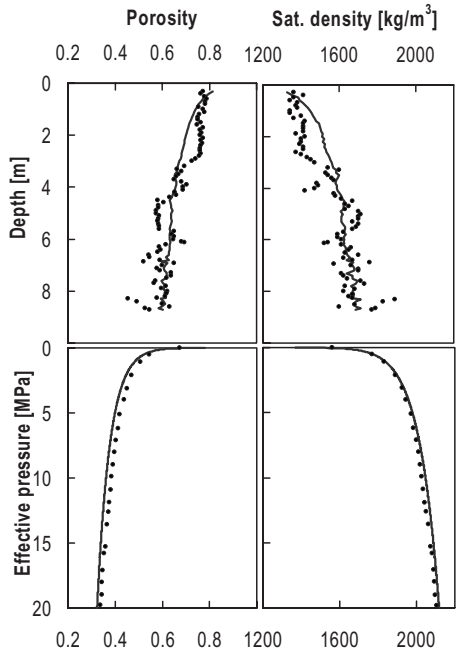

FIG. 1. Comparison of predicted and measured porosity (left) and saturated density (right) as a function of depth in sample SC (top) and as a function of effective pressure in sample LC (bottom). Symbols: data and curves: predictions.

$$\phi_l = \frac{\phi}{\phi_s}, \tag{9}$$

where the appropriate expression for ϕ_s the sand domain, Eq. (7), or clay domain, Eq. (8), respectively, has to be substituted.

Considering the subsurface sediment structure as a stack of sediment layers, the average effective pressure p_e in the nth sediment layer at depth z can be calculated recursively according to

$$p_{e,n} = g(\rho - \rho_f) z + p_{e,n-1}, \tag{10}$$

where g is the gravitational acceleration, $p_{e,n-1}$ is the effective pressure of the layer package above the layer under consideration and $\rho = \phi \rho_f + (1 - \phi)\rho_g$ is the saturated-sediment density, ρ_g being grain density which is calculated according to the partial fractions of the constituents present.

2. Permeability, pore-size parameter, and tortuosity

Although porosity and density of the binary sphere pack can be calculated in a straightforward way from the composition, permeability requires an assumption of absolute geometrical dimensions of grains and pores. Generalizing the Kozeny–Carman equation for a binary sphere pack of effective grain size D yields[26]

$$\kappa = B \frac{\phi^3}{(1 - \phi)^2} D^2, \quad \frac{1}{D} = \frac{(1 - c_s)}{d_l} + \frac{c_s}{d_s}, \tag{11}$$

in which a constant $B = 0.007$ is used, as reported for spherical grams.[27] The pore size parameter δ is estimated assuming that the ratio $h = \kappa / s_p^2$ is constant, and that the pore size in a dense pack of spheres is approximately 1/6 of the grain size.[28] The constant h is then determined using the perme-

TABLE I. Sediment compositions and mineral properties of sample LC and model silty clay, sample MFG, corresponding binary grain-size distribution, and environmental parameters. The mass fractions denote percentages of carbonates, percentages of sand, silt, and clay in the silicates, percentage of montmorillonite in the clay, and percentages of interlayer water in the montmorillonite.[a]

	Mass fraction (%)					
Constituent	MFG	LC	Bulk modulus (GPa)	Shear modulus (GPa)	Density (kg/m^3)	Viscosity (Pa s)
Carbonates	···	14	70	30	2800	···
Sand	5	5	36	44	2650	···
Silt	45	28	36	44	2650	···
Clay	50	67	60	40	2700	···
Montmorillonite.	0–25	35	60	40	2700	···
Interlayer water	25	25	2	···	975	0.005
Binary grain-size distribution						
Large	20	20				
Small	80	80				
Water parameters						
Depth (m)	1	1				
Temperature (°C)	4	18				
Salinity (ppt)	35	0.03				

Carbonates and clay mineral moduli and densities are averages from Ref. 26, p. 307; interlayer-water properties from Ref. 15. The water parameters are used to calculate (Ref. 46) its density, bulk modulus. and viscosity. Biot structural parameters follow from the considerations in Sec. II A.

ability [Eq. (11)] of a given binary mixture with the porosity of its densest pack, given by Eq. (4) or (5), respectively, and using that value to calculate the pore size for/at lower compaction/depths from $s_p(z)=\sqrt{\kappa(z)/h}$. Tortuosity ξ is estimated using the relation obtained by Berryman[7] for spheres, $\xi=1/2(1+1/\phi)$.

3. Predicted versus measured porosity, saturated density, and permeability

Assuming a porosity of $\phi_{\max}=0.92$ at depth $z_0=0.1$ m in the pure small-sphere pack and minimum porosity for both the individual large- and the small-sphere dense packings at the maximum depth of $z_1=2000$ m considered here of $\phi_{\mathrm{RD}}=0.35$, model predictions for porosity and saturated density are compared to the respective measured values in a near-surface sediment column[29] (SC) and in an individual sample under large-scale compaction[30] (LC); the composition of the latter is listed in Table I. Permeability measurements exist for LC only. The continuous grain-size distributions of the respective sediment materials were converted in such a way that 84% of the combined clay and silt fraction was considered the small-grain fraction of the binary sphere pack. The results are shown in Fig. 1. The comparison for SC shows that the binary model reflects the general trend in porosity and density decrease with depth in the near-surface domain. For LC, calculated porosity and density values fit excellently the measured ones from the compaction experiment. In both near-surface and large-scale compaction, porosity and saturated density as the physical parameters most significantly influencing sound propagation in unconsolidated sediment, can each be reproduced to a satisfactory degree of accuracy by the binary model.

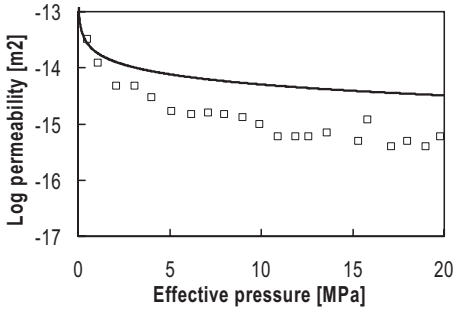

FIG. 2. Comparison of model predicted permeability (curve) and measured permeability (symbols) as a function of effective pressure for sample LC.

For permeability, the most significant difference between the predicted and observed values is the somewhat narrower range of variation. Assuming in the model grain diameters of 0.2 and 0.002 mm for the large and small spheres, respectively, the model permeabilities span 5 orders of magnitude beginning at $\kappa\approx 10^{-11}$ m^2 for a binary mixture with lowest small-sphere fraction ($c_s=0.08$). Although this high-permeability limit largely corresponds to typical values in loose unconsolidated sand,[31] permeability values of the order of 10^{-18} m^2 or less, as often observed in compacted clay, cannot be explained by the binary sphere-pack model. Figure 2 clearly shows permeability values increasingly overpredicted with pressure as compared to the measured values from the compaction experiment.

B. Acoustic model for the binary grain-size model

Biot's theory is used as the general framework into which the viscoelastic extensions EGM and VCM are introduced. The EGM is introduced to accommodate the fine-grained range of the spectrum of marine sediments, where the mechanical properties of clay influence the acoustic response. The VCM is introduced to account for the unconsolidated granular nature of marine sediment. EGM and VCM replace the elastic moduli of the grain material and the sediment frame, respectively, by complex frequency-dependent ones. In the following, a representative model for a fine-grained sediment (MFG), whose composition is listed in Table I, is considered to demonstrate the general acoustic response of the EGM, the VCM and the overall Biot–EGM–VCM formalism. In the following, all effective moduli of composite materials are calculated as Voight–Reuss–Hill averages.[26]

1. Biot-theory extension I—effective-grain model

The EGM is based on the postulate that the description of the grain material by elastic moduli is not adequate if the sediment has a significant clay fraction and expandable clay minerals, represented mainly by montmorillonites, are present, the latter being the case in virtually all clay-bearing marine sediments. The EGM is applied to the small-sphere

pack only, as part of this fraction represents the clay fraction of a given sediment. The large-sphere fraction is treated as elastic.

In the EGM, the intracrystalline water layers in the montmorillonite are considered as oblate ellipsoidal inclusions homogeneously and isotropically distributed throughout the elastic mineral phase. The relaxation mechanism thereby introduced is a stress wave-induced flow of intracrystalline water from these low-aspect ratio inclusions into the free pore space of aspect ratio near unity and its delayed reentry, thus constituting a "squirt-flow" process.[32] Instead of choosing an average inclusion of a single size, a distribution of aspect ratios for the intracrystalline water layers is considered in an attempt to reflect the grain-size distribution of the montmorillonite. Each size class of aspect ratios ϵ_m contains its respective volume fraction $c(\epsilon_m)$ of the intracrystalline water.[15] The corresponding relaxation process is described by complex frequency-dependent bulk and shear moduli, $\hat{K}_g$ and $\hat{G}_g$, respectively, of the two-phase grain material given by[33]

$$\frac{\hat{K}_g - K_r}{3\hat{K}_g + 4G_r} = \frac{1}{3}\frac{\hat{K}_{\text{ads}} - K_r}{3K_r + 4G_r}\sum_m c(\epsilon_m)T_{iijj}(\epsilon_m), \tag{12}$$

for the bulk modulus and

$$\frac{\hat{G}_g - G_r}{6\hat{G}_g(K_r + 2G_r) + G_r(9K_r + 8G_r)} = \frac{\hat{G}_{\text{ads}} - G_r}{25G_r(3K_r + 4G_r)}\sum_m c(\epsilon_m)\left[T_{ijij}(\epsilon_m) - \frac{1}{3}T_{iijj}(\epsilon_m)\right] \tag{13}$$

for the shear modulus, where K_r and G_r are the bulk and shear moduli of the mineral phase and where the bulk modulus $\hat{K}_{\text{ads}}$ of the intracrystalline water in the montmorillonite and its response to shear loading, $\hat{G}_{\text{ads}}$, follow as a result from applying the correspondence principle as

$$\hat{K}_{\text{ads}}(\omega) = \Re(\hat{K}_{\text{ads}}) + i\omega\gamma, \tag{14}$$

with

$$\gamma = \tau K_r = \frac{3\eta_{\text{ads}}}{2\epsilon^2\Re(\hat{K}_{\text{ads}})}K_r, \tag{15}$$

where τ is the relaxation time of the attenuation mechanism, and

$$\hat{G}_{\text{ads}}(\omega) = i\omega\eta_{\text{ads}}, \tag{16}$$

where η_{ads} is the viscosity of the interlayer water. The scalar quantities T_{iijj} and T_{ijij} in Eqs. (12) and (13) are elements of a tensor that relates a uniform strain field at infinity to the strain field at an ellipsoidal inclusion.[34]

The pressure-induced expulsion of intracrystalline is accounted for by considering the relationship between swelling pressure and water content in the montmorillonite. The swelling pressure counteracts the effective pressure and therefore determines the amount of water retained in the interlayers. Solving the relationship[35] $p_s = 403\exp(-0.178w)$ between swelling pressure, p_s, and interlayer-water content, w, for the interlayer-water content and equating p_s with p_e yields

$$w = 0.47 - 0.056\ln\left(\frac{p_e}{p_0}\right). \tag{17}$$

Assuming that the grain dimensions of the mineral phase of the clay particles remain constant with pressure, the expulsion of interlayer water is equivalent to a decrease of the inclusions's aspect ratios, following from the pressure-induced change of the first aspect ratio class ϵ_1 of the distribution, whereas the distribution itself retains its shape. Assuming a clay-particle equivalent diameter of 0.002 mm and an initial interlayer thickness of 10 Å, the thinning with increasing effective pressure of the aspect ratios has been found to follow the heuristic relationship[36]

$$\epsilon_1 = 10^{-4}\left(9.3 - 1.1\ln\left(\frac{p_e}{p_0}\right)\right). \tag{18}$$

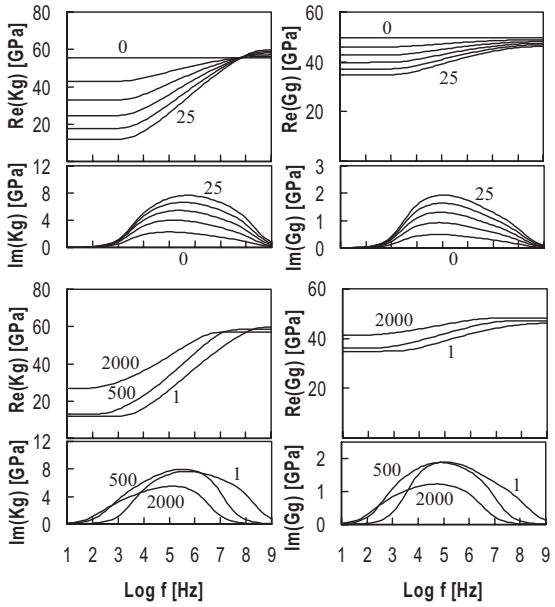

FIG. 3. Real and imaginary parts of bulk (left) and shear (right) moduli of the effective grain for sample MFG (Table I) as a function of frequency at a water depth of 1 m and montmorillonite contents of {0,5,10,15,20,25}% of the clay fraction (top); and at subbottom depths of {1;500;2000} m and montmorillonite content of 25% of the clay fraction (bottom).

The mechanical response of the effective grain material at low effective pressure is shown in Fig. 3 (top) in terms of its bulk and shear moduli as a function of frequency for sample MFG. Increasing the montmorillonite content—equivalently, the volume concentration of the inclusions—leads to an increased modulus defect, given by $\Delta M = (M_\infty - M_0)/\sqrt{M_\infty/M_0}$, where subscripts refer to frequency. The use of a distribution of aspect ratios of the inclusions is considered rather than a single one; the frequency-dependent response is a combined effect of the contributions from each of the individual inclusion classes. The transition from the relaxed to the unrelaxed state occurs over several frequency

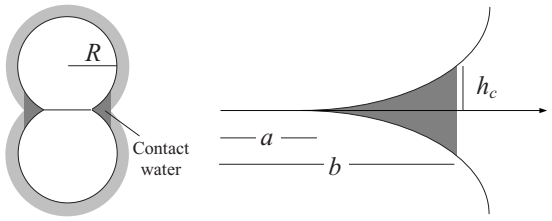

FIG. 4. Schematic (contact geometry exaggerated) of a combination of two identical elastic spheres of radius R with contact water distributed in a pendular ring of outer radius b and outer thickness d around the direct sphere-to-sphere contact of radius a.

decades; accordingly, the relaxation peak is widened to a plateau-like shape. Figure 3 (bottom) shows the decrease with pressure in efficiency of the relaxation mechanism in the EGM, corresponding to a decreasing modulus defect. In addition, the thinning of the inclusions, i.e., the decrease of their aspect ratios, leads to longer relaxation times and, therefore, the transition zone from relaxed to unrelaxed modulus is shifted to lower frequencies.

2. Biot-theory extension II—viscoelastic-contact model

The original conception of this model[24] assumes the granular material to consist of identical elastic spheres. Here, this approach is modified to accommodate the binary sphere pack and to include the effective-grain model. Interactions between large and small spheres are not considered at present.

The traditional Hertz–Mindlin approach to obtain the bulk and shear moduli of a pack of spheres consists in finding the normal and tangential contact stiffnesses S_n and S_t, respectively, of a single two-sphere combination, where stiffness is defined as the ratio of an applied normal or tangential force to the respective resulting displacement of the spheres' centers with respect to the contact plane. The normal and tangential contact stiffnesses S_n and S_t, respectively, are[37]

$$S_n = \frac{4aG}{1-\nu}, \quad S_t = \frac{8aG}{2-\nu}, \tag{19}$$

wherein G and ν are the shear modulus and Poisson's ratio of the sphere material, respectively, and a is the radius of the circular contact plane forming between the compressed spheres of radius R,[38]

$$a = \sqrt[3]{\frac{3F_H R(1-\nu)}{8G}}, \tag{20}$$

where F_H is the Hertzian normal contact force that can be calculated from the effective pressure p_e acting on a random pack of identical spheres,

$$F_H = \frac{4\pi R^2 p_e}{N(1-\phi)}, \tag{21}$$

where N is the coordination number.

It has been shown[24] that small amounts, viz., a few volume percent of the pore space, of viscous fluid at the grain contacts (Fig. 4) may significantly increase the contact stiffness of a two-sphere combination. Upon oscillatory loading, in a certain frequency range that is determined by the contact geometry and the mechanical properties of the contact fluid, local (squirt-) flow develops in a pendular ring around the direct sphere-to-sphere contact. This frequency range represents the transition from the low-frequency relaxed state, in which pressure equilibrium prevails, to the high-frequency unrelaxed state in which the fluid essentially acts as an elastic solid and significantly stiffens the grain contact. The magnitude of the stiffness-frequency dispersion is determined by the amount and the mechanical properties of the contact fluid. The tangential contact stiffness is affected mechanically to a negligible degree by the presence of the contact fluid. An accurate approximation of the Cole–Cole[14] form can be used instead of the rigorous numerical solution for the complex normal contact stiffness S_n whose real and imaginary parts can be written as

$$\frac{\Re(S_n)}{2\pi R K_w} = S_0 + (S_0 - S_\infty)\frac{1 + (\omega\tau)^\psi \cos(\psi\pi/2)}{1 + 2(\omega\tau)^\psi \cos(\psi\pi/2) + (\omega\tau)^{2\psi}},$$

$$\frac{\Im(S_n)}{2\pi R K_w} = (S_\infty - S_0)\frac{(\omega\tau)^\psi \sin(\psi\pi/2)}{1 + 2(\omega\tau)^\psi \cos(\psi\pi/2) + (\omega\tau)^{2\psi}}, \tag{22}$$

where K_w is the bulk modulus of the contact fluid. The relaxation time τ and the distribution parameter ψ are

$$\tau = [2.7 - 0.33\ln(p_e - p_0)]\frac{\eta}{K_w \delta^2},$$

$$\psi = 0.12\ln(s_c) + 0.92, \tag{23}$$

wherein p_e and p_0 are effective and atmospheric pressure, respectively, η is the viscosity of the contact water, and δ is the ratio of outer thickness h_c to outer radius b of the space occupied by the contact water (Fig. 4). The relaxed and unrelaxed normal stiffnesses S_0 and S_∞, respectively, with a being the dry direct sphere-to-sphere radius, are given by

$$S_0 = \frac{S_n}{2\pi R K_w}, \quad S_\infty = S_0 + \tilde{A}\frac{b-a}{R}, \tag{24}$$

with S_n from Eq. (19) and

$$\tilde{A} = \tilde{B}\ln(K_w(1-\nu)/G) + \tilde{C},$$

$$\tilde{B} = 0.11\ln(p_e/p_0) - 2.1,$$

$$\tilde{C} = 0.050\ln(p_e/p_0) - 1.5. \tag{25}$$

The outer radius b is related to the thickness h_c of the contact-water layer by[24]

$$h_c(b) = \frac{a^2}{\pi R}\left[\left(\frac{b^2}{a^2} - 2\right)\arctan\sqrt{\frac{b^2}{a^2} - 1} + \sqrt{\frac{b^2}{a^2} - 1}\right], \tag{26}$$

and the amount s_c of the water present in the sediment in terms of its volume fraction of the total pore space is given by

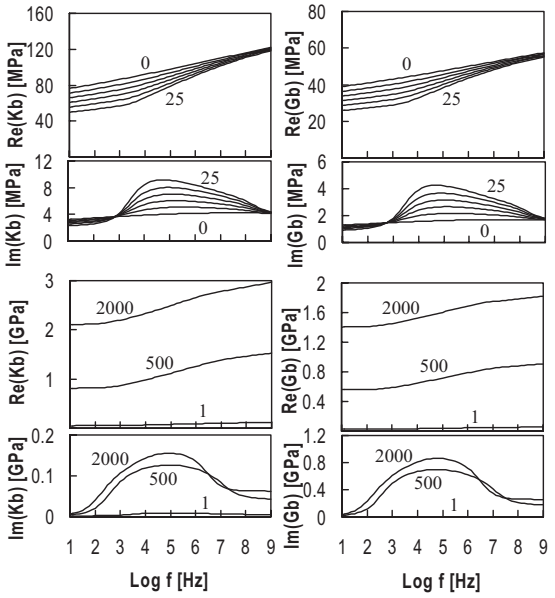

FIG. 5. Real and imaginary parts of bulk (left) and shear (right) moduli of the sediment frame in sample MFG as a function of frequency at water depth of 1 m and montmorillonite contents of {0,5,10,15,20,25}% of the clay fraction (top); and at subbottom depths of {1;500;2000} m and montmorillonite content of 25% of the clay fraction (bottom).

$$s_c = \frac{N\pi(a+b)}{R^3}\frac{1-\phi}{\phi}\int_a^b h_c(r)dr. \tag{27}$$

The frame bulk and shear moduli of the binary sphere pack are calculated using the contact stiffnesses, S_n from Eq. (22) and S_t from Eq. (19), from Walton's[39] expressions, which are modified here by introducing a heuristic correction term, L, to overcome the discrepancy[24] between the (overpredicted) theoretical and measured shear-wave velocities,

$$K_b = \frac{1}{L}\frac{N(1-\phi)}{12\pi R}S_n, \quad G_b = \frac{N(1-\phi)}{20\pi R}\left(S_n + L^2\frac{3}{2}S_t\right). \tag{28}$$

Figure 5 shows the frame bulk and shear moduli as a function of frequency and effective pressure, respectively, for sample MFG, with $L=2/3$. For the calculation, the fraction of the pore water s_c, that is considered as the contact water, is determined from Eq. (27) assuming a maximum half-thickness $h_c=0.01R$ of the contact-water layer at radius b in Eq. (26). The coordination number is estimated for the respective porosity according to the relationship $N \approx 24.1\exp(-2.68\phi)$ that follows from Murphy's[40] investigations. The curves for the frame moduli in the low-pressure range in the case of purely elastic grains—corresponding to zero montmorillonite content—exhibit an extremely wide relaxation maximum visible in the imaginary parts, associated with a nearly linear transition zone between relaxed and unrelaxed moduli over the entire frequency range of interest for sediment acoustics. This is a result of the dependence of the distribution parameter ψ on the geometry of the contact water layer Eq. (23). An increase of the concentration of montmorillonite in the clay fraction results in a corresponding increase of the modulus defect. This is a combined effect of the relaxation mechanism in the EGM and, to a lesser extent, the associated increased—and complex—compliance of the small grains affecting the VCM. The strong overall increase of the real parts of the frame moduli with pressure is caused by increasing frame stiffness and a decrease in the compliance of the effective grain material. At the same time, the modulus defect decreases with increasing pressure. The complex and frequency-dependent frame moduli following from the VCM replace the corresponding elastic ones in the original Biot formulation.

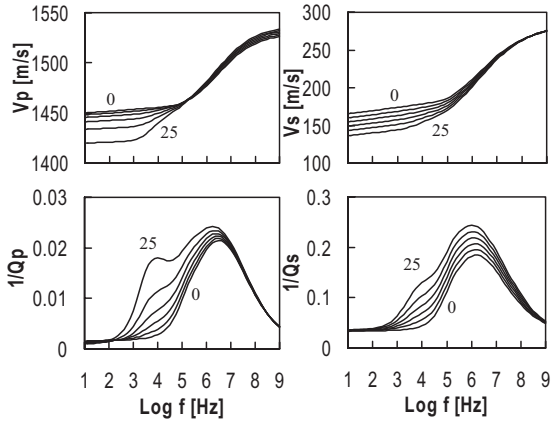

FIG. 6. Velocity (top) and specific dissipation $1/Q$ (bottom) of compressional (left) and shear waves (right) in sample MFG as a function of frequency at water depth 1 m for montmorillonite contents of {0,5,10,15,20,25}% of the clay fraction.

3. Combined Biot–EGM–VCM: attenuation and velocities

The EGM and the VCM consider two viscoelastic attenuation mechanisms with their respective dependences on frequency in addition to the attenuation mechanism in Biot theory. The resultant attenuation—in terms of the specific dissipation $1/Q$—and the velocities of the compressional and shear waves are shown as a function of frequency for the case of the silty clay in Fig. 6 for the low-pressure range ($z=1$ m) with varying montmorillonite content. Apart from the substantial attenuation peak caused by (Biot-) global fluid flow at higher frequencies (Fig. 6), the local fluid flow in the EGM represents a significant contribution at medium frequencies if montmorillonite is present. The effect of the local fluid flow in the VCM causes a background attenuation of relatively small magnitude over the entire frequency range considered, corresponding to the slight increase in velocity in the lower frequency range. Figure 7 demonstrates the influence of increasing effective pressure on the attenuation mechanisms of EGM and VCM at constant montmorillonite content. An interesting result is that, over a wide frequency range, $1/Q_P$ is greater at 500 m depth than it is at both 1 m and at 2000 m depth. At shallow depths, the strong increase of the grain fraction is associated with an increase of $1/Q_P$ with depth. In the depth range of a few hundred meters, corresponding to about 4 MPa effective pressure, $1/Q_P$ assumes a maximum value, $1/Q_S$ to a much lesser degree. This is a consequence of the EGM, wherein the strong decrease in porosity with depth in the shallower depth range leads to an

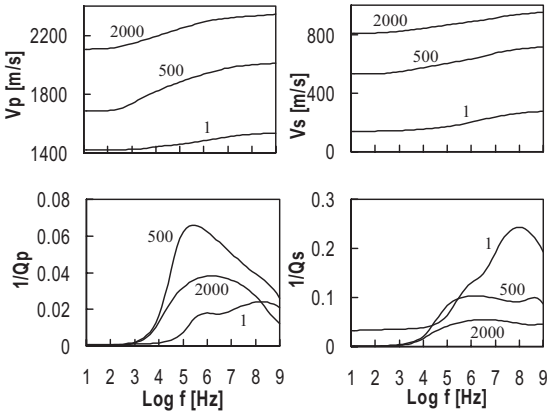

FIG. 7. Velocity (top) and specific dissipation $1/Q$ (bottom) of compressional (left) and shear waves (right) in sample MFG as a function of frequency at subbottom depths {1;500;2000} m for montmorillonite content of 25% of the clay fraction.

increase of the concentration of inclusions in the grain materialdown to the depth range where expulsion of intracrystalline water becomes possible and the EGM attenuation mechanism gradually loses significance towards greater depths. The occurrence of a depth-dependent maximum in compressional-wave attenuation as a possibly general phenomenon in fine-grained marine sediment has first been addressed by Hamilton.[41] In a preview of the comparison of results from the model with measured data, Fig. 8 shows a collection of data and attenuation/depth trends[41] in fine- and coarse-grained sediments, together with curves of the model at a frequency of 3.5 kHz. The comparison is only approximate, because of Hamilton's assumption of a linear frequency dependence of the attenuation coefficient, but it can be seen that the model reproduces the distinctly different trends in the observed variation with depth of the attenuation data.

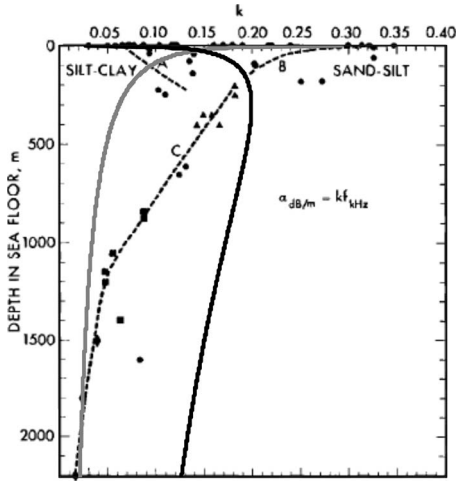

FIG. 8. Attenuation [expressed as k in α (dB/m)=kf(kHz)] of compressional waves as a function of depth in the sea floor, taken from Ref. 41, with model curves for 3.5 kHz; gray: sandy sediment (20% carbonates, 80% of silicates, of which 92% sand, 8% clay, all grains elastic); black: clayey sediment (20% carbonates, 80% of silicates, of which 5% sand, 60% silt, 35% clay, of which 10% montmorillonite).

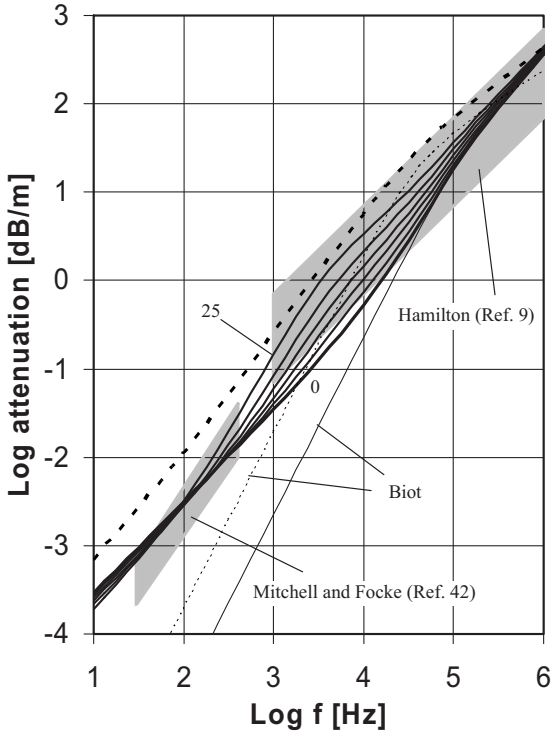

FIG. 9. Compressional-wave attenuation coefficient from Biot–EGM–VCM as a function of frequency in the near-surface regime for sample MFG. Thin solid line: Biot theory for silty-clay with (corrected) Hertz–Mindlin elastic contact; thin dashed line: Biot theory for sand with (corrected) Hertz–Mindlin elastic contact; thick solid line: combined Biot–VCM binary grain-size model, elastic grains only; medium solid lines: Biot-EGM-VCM with montmorillonite contents of 0%, 5%, 10%, 15%, 20%, and 25% of the clay fraction; dashed line: Biot–EGM–VCM for lowest small-sphere content of 8%, all grains elastic; large gray area: all grain sizes (Ref. 11); small gray area: deep ocean sediments (Ref. 42).

III. COMPARISON OF MODEL RESPONSE WITH DATA

A. Compressional- and shear-wave attenuation in near-surface sediments

Figure 9 shows predictions from the model for the attenuation coefficient in the near-surface regime of the compressional waves in sample MFG with varying montmorillonite content (solid lines) and in sandy sediment with 8% of clay (heavy dashed line) as a function of frequency, together with data ranges from the literature.[11,42] and, illucidating the significance of the model extensions presented here, the corresponding curves resulting from the original Biot theory. In the lower frequency range, it can be clearly seen that the significance of the VCM consists of creating a background attenuation proportional close to the first power of frequency. This is achieved without introducing irreversible, i.e., nonlinear mechanical processes like grain-to-grain friction. The heavy dashed line, representing coarse-grained sediments, clearly runs along the upper edge of the Hamilton band (>1 kHz), which is defined by attenuation data from sands, whereas the deep-ocean data band (<1 kHz) "with essentially no sand component" (Mitchell and Focke)[42] is matched by the curves representing fine-grained sediments resulting from the model proposed here. For the coarse-grained range of sediments, Fig. 10 shows an excellent fit between our

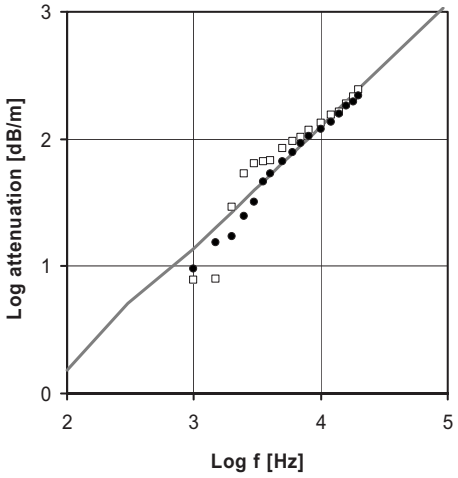

FIG. 10. Shear-wave attenuation from Biot–EGM–VCM (gray curve) as a function of frequency in coarse-grained model sediment in the near-surface regime in comparison with data from Brunson (Ref. 43); squares: sorted sand and filled circles: sorted glass beads.

model prediction and experimental data on shear-wave attenuation as a function of frequency in unconsolidated sorted sand and sorted glass beads from Brunson.[43]

B. Velocity and specific dissipation versus effective pressure

The data shown in Figs. 11 and 12 were obtained from pulse transmission experiments at about 50 kHz (P wave) and 100 kHz (S wave) on saturated samples of unconsolidated sediments. Examples for coarse- and fine-grained sediment are shown to demonstrate the ability of the proposed model to describe a wide range of the possible grain-size spectrum of marine sediments. The two coarse-grained samples[44] represent the grain fractions of diameter $0.60<d<0.71$ mm and $d<0.355$ mm, respectively, of a well-rounded sand (quartz content >95%). The fine-grained sample is sample LC (Table I).

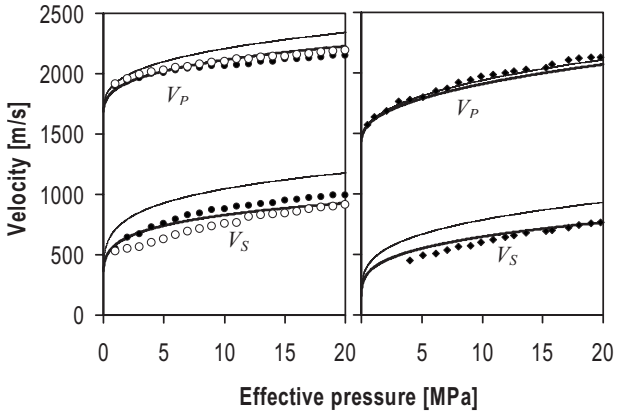

FIG. 11. Velocities of compressional-waves at 50 kHz and shear waves at 100 kHz as a function of effective pressure from Biot–EGM–VCM (curves) in coarse-grained sediment together with data from Ref. 44 (left) and for fine-grained sample LC from Ref. 30 (right). Filled circles: sand ($0.60<d<0.71$ mm); open circles: sand ($d<0.355$ mm); and filled diamonds: sample LC. Solid lines: model predictions for binary sphere pack with lowest small-grain fraction of 8%, all elastic grains (left); and for sample LC with parameters from Table I; thin lines: model predictions using original Hertz–Mindlin/Walton formulation without correction, corresponding to $L=1$ in Eq. (28).

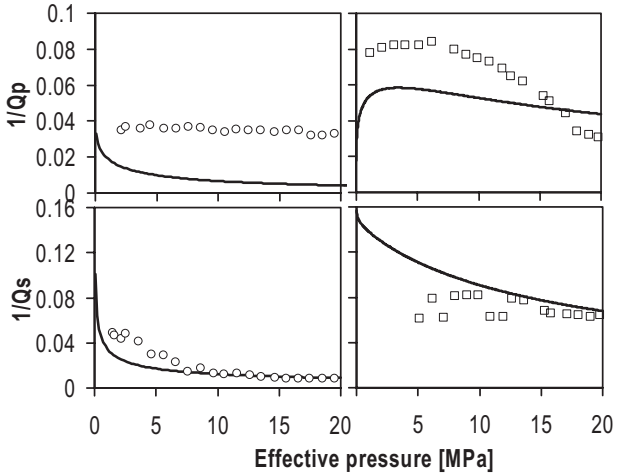

FIG. 12. Specific dissipation of compressional-waves (top) at 50 kHz and shear waves (bottom) at 100 kHz as a function of effective pressure from Biot–EGM–VCM (curves) in coarse-grained sediment together with data from Ref. 44 (left) on and for fine-grained sample LC from Ref. 30 (right). Circles: sand (0.55 mm mean diameter) and squares: sample LC. Solid lines: model predictions for binary sphere pack with lowest small-grain fraction of 8%, all elastic grains (left); and for sample LC with parameters from Table I; thin lines: model predictions using original Hertz–Mmdlm/Walton formulation without correction, corresponding to $L=1$ in Eq. (28).

Compressional- and shear-wave velocities in the two coarse-grained sediment samples and in sample LC are shown in Fig. 11. The predictions from the binary sediment model fit satisfactorily with the experimental data. This fit is achieved with a correction term $L=2/3$ in Eq. (28). For a comparison, the uncorrected compressional- and shear-wave velocities are shown in Fig. 11 as well, exhibiting the significant overestimation of the shear-wave velocity. For the fine-grained sample LC the model appears to slightly underpredict the compressional-wave velocity in the higher-pressure range and slightly overpredict the shear-wave velocity in the lower pressure range, however, theoretical and experimental data show overall satisfactory fits.

The specific dissipation $1/Q_P$ of the compressional waves in coarse-grained sediments, though following the trend in the data, is underestimated for the sand[45] shown in Fig. 12, whereas $1/Q_S$ exhibits a good fit in the lower pressure range and an excellent fit in the higher range from about 8 to 20 MPa. In the case of fine-grained sediments (Fig. 12), the same excellent fit in $1/Q_S$ at medium to high effective pressure is observed. There is a better fit in $1/Q_P$ than in the coarse-grained case, although there is still a discrepancy. The most important characteristic, however, is that the model predicts the pressure-dependent maximum in the specific dissipation of the compressional waves. This observation is in agreement with Hamilton's[41] collection of data shown in Fig. 8 and corroborates his conjecture that this maximum could be a characteristic property of fine-grained marine sediment. This attenuation maximum as a function of depth is a consequence of the EGM. A reason for the lack of fit in absolute values for $1/Q_P$ as compared to $1/Q_S$ might be that the nor-

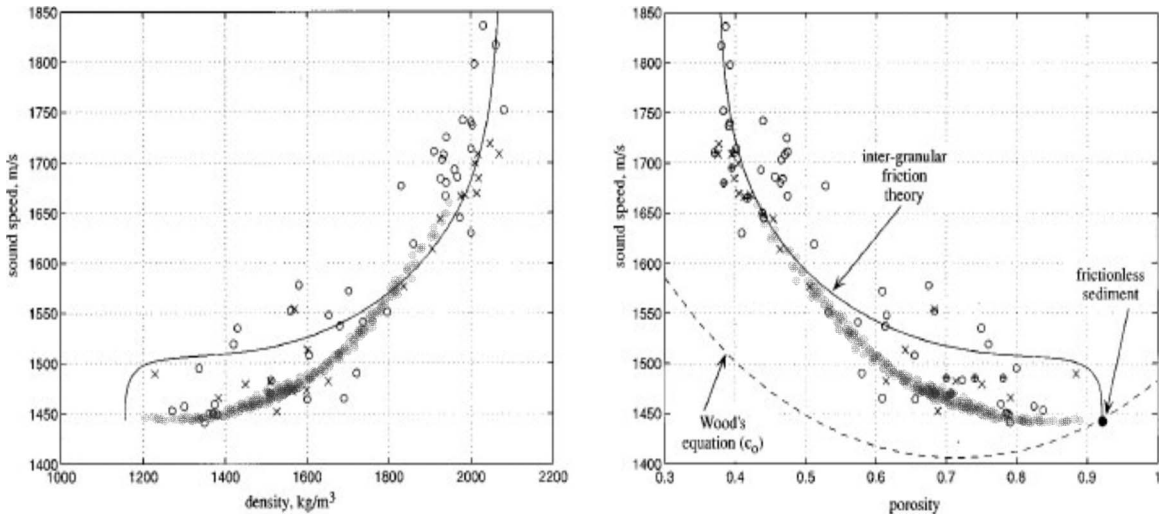

FIG. 13. Compressional-wave velocity versus density (left) and versus porosity (right) in marine unconsolidated sediment. Black curve and symbols: Buckingham's (Ref. 2) grain-shear model together with data from the literature (figure reproduced from Ref. 2). Gray symbols: 500 randomly generated realizations of the binary grain-size Biot–EGM–VCM model with varying sand content, 10%–90%; clay content, 8%–50% of grains smaller than sand; montmorillonite content, 0%–25% of clay fraction; at depths between 0.1 and 2.5 m below the sea floor.

mal contact stiffness is more sensitive to deviations from the exact shape and smoothness of the spherical grains than the tangential one.

C. Compressional-wave velocity versus density and porosity

For a comparison of theoretical and measured sound speed as a function of density and porosity, respectively, Fig. 13 shows, along with data and model curves from Buckingham,[2] predictions from the proposed model for 500 realizations of binary grain-size model sediments randomly generated with varying sand content, 10–90 mass % of the silicate fraction, clay content, 5–50 mass % of grains smaller than sand, and montmorillonite content, 0–25 mass % of the clay fraction for a depth range between 0.1 and 2.5 m below the sea floor. The model predictions of sound speed as plotted against saturated density as well as against porosity are distributed over a thin curved band that coincides with the regions in which the respective data points show the highest concentration.

IV. CONCLUSIONS

The introduction of EGM and VCM into Biot theory constitutes a comprehensive model of acoustic wave propagation for a wide spectrum of unconsolidated marine sediment structurally simplified as a binary grain-size sphere pack. The combined model determines sediment physical parameters from its constituents and from depth and derives the sediment-frame mechanical properties explicitly from those of the grains and from effective pressure. The model matches satisfactorily close laboratory data on compressional- and shear-wave velocities of as different sediment types as sand and silty clay. The model response shows that the apparent linear dependence of the attenuation coefficient, corresponding to constant specific dissipation, can be explained by the superposition of the three considered attenuation mechanisms. The most important conclusion from the results is that the proposed model can reproduce the significantly different variation of compressional-wave attenuation observed between coarse-grained as and fine-grained marine sediment, i.e., a monotonic decrease with depth in the former and an increase to a maximum value and a subsequent decrease in the latter, as a function of effective pressure, thus quantitatively corroborating Hamilton's supposition of a combined effect of porosity decrease and pressure increase for this phenomenon.

Natural sediments exhibit strong variations in, e.g., grain-size distribution, roundness, sphericity, and sorting. A binary grain-size sphere pack might therefore appear as oversimplified to retain important mechanical properties that influence the propagation of compressional- and shear waves. Despite the limited set of experimental data, the comparison between predicted and measured mechanical properties indicates, however, that the model may be further developed to serve as a basis for a standardized characterization of seabed sediments.

ACKNOWLEDGMENT

This study was supported by the Higher Education Authority of Ireland under their Programme for Research in Third-Level Institutions, Cycle 3.

[1]M. A. Biot, "Theory of propagation of elastic waves in a fluid-saturated porous medium, I. lower frequency range," J. Acoust. Soc. Am. **28**, 168–178 (1956); "Theory of propagation of elastic waves in a fluid-saturated porous medium, II. higher frequency range," J. Acoust. Soc. Am. **28**, 179–191 (1956).
[2]M. J. Buckingham, "Theory of acoustic attenuation, dispersion, and pulse propagation in unconsolidated granular materials including marine sediments," J. Acoust. Soc. Am. **102**, 2579–2596 (1997).
[3]K. L. Williams, D. R. Jackson, E. I. Thorsos, D. Tang, and S. G. Schock, "Comparison of sound speed and attenuation measured in a sandy sediment to predictions based on the Biot theory of porous media," IEEE J. Ocean. Eng. **27**, 413–428 (2002).
[4]M. J. Buckingham, "On pore-fluid viscosity and the wave properties of

saturated granular materials including marine sediments," J. Acoust. Soc. Am. **122**, 1486–1501 (2007).
[5]J. Geertsma and D. C. Smit, "Some aspects of elastic wave propagation in fluid-saturated porous solids," Geophysics **26**, 169–181 (1961).
[6]J. G. Berryman, "Confirmation of Biot's theory," Appl. Phys. Lett. **37**, 382–384 (1980).
[7]J. G. Berryman, "Elastic wave propagation in fluid-saturated porous media," J. Acoust. Soc. Am. **69**, 416–424 (1981).
[8]T. J. Plona, "Observation of a second bulk compressional wave in a porous medium at ultrasonic frequencies," Appl. Phys. Lett. **36**, 259–261 (1980).
[9]M. A. Biot, "Generalized theory of acoustic propagation in porous dissipative media," J. Acoust. Soc. Am. **34**, 1254–1264 (1962).
[10]R. D. Stoll and G. M. Bryan, "Wave attenuation in saturated sediments," J. Acoust. Soc. Am. **47**, 1440–1447 (1970).
[11]E. L. Hamilton, "Compressional-wave attenuation in marine sediments," Geophysics **37**, 620–646 (1972).
[12]R. D. Stoll, "Marine sediment acoustics," J. Acoust. Soc. Am. **77**, 1789–1799 (1985).
[13]R. D. Stoll, *Sediment Acoustics* (Springer, Berlin, 1989), p. 96.
[14]K. S. Cole and R. H. Cole, "Dispersion and absorption in dielectrics," J. Chem. Phys. **9**, 341–351 (1941).
[15]K. C. Leurer, "Attenuation in fine-grained marine sediments: Extension of the Biot-Stoll model by the "effective grain model" (EGM)," Geophysics **62**, 1465–1479 (1997).
[16]A. B. Wood and D. E. Weston, "The propagation of sound in mud," Acustica **14**, 156–162 (1964).
[17]K. W. Winkler, A. Nur, and M. Gladwin, "Friction and seismic attenuation in rocks," Nature (London) **277**, 528–531 (1979).
[18]C. W. Holland and B. A. Brunson, "The Biot–Stoll sediment model: An experimental assessment," J. Acoust. Soc. Am. **84**, 1437–1443 (1988).
[19]A. Turgut and T. Yamamoto, "Measurements of acoustic wave velocities and attenuation in marine sediments," J. Acoust. Soc. Am. **87**, 2376–2383 (1990).
[20]A. Turgut, "Approximate expressions for viscous attenuation in marine sediments: relating Biot's 'critical' and 'peak' frequencies," J. Acoust. Soc. Am. **108**, 513–518 (2000).
[21]N. P. Chotiros and M. J. Isakson, "A broadband model of sandy ocean sediments: Biot-Stoll with contact squirt flow and shear drag," J. Acoust. Soc. Am. **116**, 2011–2022 (2004).
[22]A. Nur, D. Marion, and H. Yin, "Wave velocities in sediments," in *Shear Waves in Marine Sediments*, edited by J. M. Hovem, M. D. Richardson, R. D. Stoll (Kluwer, Dordrecht, 1991), pp. 131–140.
[23]J. Dvorkin and M. A. Gutierrez, "Textural sorting effect on elastic velocities, part II: Elasticity of a bimodal grain mixture," 71st SEG Annual Meeting, San Antonio, TX, Expanded Abstracts, 2001, pp. 1764–1767.
[24]K. C. Leurer and J. Dvorkin, "Viscoelasticity of unconsolidated sand with viscous cement," Geophysics **71**, T31–T40 (2006).
[25]R. D. Stoll, "Acoustic waves in ocean sediments," Geophysics **42**, 715–725 (1977).
[26]G. Mavko, T. Mukerji, and J. Dvorkin, *The Rock Physics Handbook* (Cambridge University Press, Cambridge, 1998), pp. 261 and pp. 263.
[27]J. M. Hovem and G. D. Ingram, "Viscous attenuation of sound in saturated sand," J. Acoust. Soc. Am. **66**, 1807–1812 (1979).
[28]R. D. Stoll, *Sediment Acoustics* (Springer, Berlin, 1989), p. 83.
[29]P. Holler and H. Kassens, "Sedimentphysikalische Eigenschaften aus dem Europäischen Nordmeer" (Sediment physical properties from the European Nordic Seas), Berichte aus dem Sonderforschungsbereich 313, **15** 28–30 (1989).
[30]K. C. Leurer, "Compressional- and shear-wave velocities and attenuation in deep-sea sediment during laboratory compaction," J. Acoust. Soc. Am. **116**, 2023–2030 (2004).
[31]G. V. Chilingarian, K. H. Wolf, and D. R. Allen, *Introduction to: Developments in sedimentology*, Vol. **18A**, Compaction of coarse-grained sediments, I, edited by G. V. Chilingarian and K. H. Wolf (Elsevier, Amsterdam, 1975), p. 34.
[32]G. Mavko and A. Nur, "Melt squirt in the asthenosphere," Geophysics **34**, 882–892 (1975).
[33]D. H. Johnston, M. N. Toksöz, and A. Timur, "Attenuation of seismic waves in dry and saturated rocks: II. Mechanisms," Geophysics **44**, 691–711 (1979).
[34]T. T. Wu, "The effect of inclusion shape on the elastic moduli of a two-phase material," Int. J. Solids Struct. **2**, 1–8 (1966).
[35]G. Kahr, F. Kraehenbuehl, H. F. Stoeckli, and M. Mueller-Vonmoos, "Study of the water-bentonite system by vapour adsorption, immersion calorimetry, and x-ray techniques: II. Heats of immersion, swelling pressures and thermodynamic properties," Clay Miner. **25**, 499–506 (1990).
[36]K. C. Leurer, "Geschwindigkeit und Absorption von Kompressions- und Scherwellen in gesättigten unkonsolidierten feinkörnigen marinen Sedimenten…" (Velocity and absorption of compressional- and shear waves in saturated unconsolidated fine-grained marine sediments…), Ph.D. thesis, Christian Albrechts Universität zu Kiel, Kiel, Germany, 1994.
[37]R. D. Mindlin, "Compliance of elastic bodies in contact," J. Appl. Mech. **16**, 259–268 (1949).
[38]H. R. Hertz, "Über die Berührung fester elastischer Körper" (On the contact of solid elastic bodies), Z. Reine Angew. Math. **92**, 156–171 (1882).
[39]K. Walton, "The effective elastic moduli of a random pack of spheres," J. Mech. Phys. Solids **35**, 213–216 (1987).
[40]W. F. Murphy III, "Effects of microstructure and pore fluids on the acoustic properties of granular sedimentary materials," Ph.D. thesis, Stanford University, Standford, California, 1982.
[41]E. L. Hamilton, "Sound attenuation as a function of depth in the sea floor," J. Acoust. Soc. Am. **59**, 528–535 (1976).
[42]S. K. Mitchell and K. C. Focke, "New measurements of compressional wave attenuation in deep ocean sediments," J. Acoust. Soc. Am. **67**, 1582–1589 (1980).
[43]B. A. Brunson, "Shear wave attenuation in unconsolidated laboratory sediments," in *Shear Waves in Marine Sediments*, edited by J. M. Hovem, M. D. Richardson, and R. D. Stoll (Kluwer, Dordrecht, 1991), pp. 141–147.
[44]R. Muckelmann, "Theoretische und experimental Untersuchungen von P- und S- Wellen in Sanden unter besonderer Berücksichtigung ihrer Dämpfungseigenschaften" (Theoretical and experimental investigations on P- and S- waves in sands with special consideration of their attenuation properties), Ph.D. thesis, Christian Albrechts Universität zu Kiel, Kiel, Germany, 1985.
[45]M. Prasad, "Acoustic measurements in unconsolidated sands at low effective pressure and overpressure detection," Geophysics **67**, 405–412 (2002).
[46]G. Dietrich, K. Kalle, W. Krauss, and G. Siedler, *Allgemeine Meereskunde*, 2nd ed., (Bornträger, Berlin, 1975).

Spatial averaging of oceanic rainfall variability using underwater sound: Ionian sea rainfall experiment 2004

Jeffrey A. Nystuen[a)]
Applied Physics Laboratory, University of Washington, 1013 NE 40th Street, Seattle, Washington 98105-6698

Eyal Amitai
Center for Earth Observing and Space Research, George Mason University, Fairfax, Virginia 22030 and NASA Goddard Space Flight Center, Code 613.1, Greenbelt, Maryland 20771

Emmanuel N. Anagnostou and Marios N. Anagnostou
Department of Civil and Environmental Engineering, University of Connecticut, 261 Glennbrook Rd., Storrs, CT 06269

(Received 2 July 2007; revised 9 January 2008; accepted 15 January 2008)

An experiment to evaluate the inherent spatial averaging of the underwater acoustic signal from rainfall was conducted in the winter of 2004 in the Ionian Sea southwest of Greece. A mooring with four passive aquatic listeners (PALs) at 60, 200, 1000, and 2000 m was deployed at 36.85°N, 21.52°E, 17 km west of a dual-polarization X-band coastal radar at Methoni, Greece. The acoustic signal is classified into wind, rain, shipping, and whale categories. It is similar at all depths and rainfall is detected at all depths. A signal that is consistent with the clicking of deep-diving beaked whales is present 2% of the time, although there was no visual confirmation of whale presence. Co-detection of rainfall with the radar verifies that the acoustic detection of rainfall is excellent. Once detection is made, the correlation between acoustic and radar rainfall rates is high. Spatial averaging of the radar rainfall rates in concentric circles over the mooring verifies the larger inherent spatial averaging of the rainfall signal with recording depth. For the PAL at 2000 m, the maximum correlation was at 3–4 km, suggesting a listening area for the acoustic rainfall measurement of roughly 30–50 km^2. © *2008 Acoustical Society of America.* [DOI: 10.1121/1.2871485]

PACS number(s): 43.30.Pc, 43.30.Nb, 43.30.Sf [JAC] Pages: 1952–1962

I. INTRODUCTION

The ambient sound field in the ocean contains information about the physical, biological, and anthropogenic processes in the ocean. Interpretation of the ambient sound field can be used to quantify these processes. In particular, rainfall on the sea surface generates a loud and distinctive sound underwater that can be used to detect and quantitatively measure rain at sea (Ma and Nystuen, 2005). Further, different raindrop sizes produce distinctive sound underwater, allowing for the inversion of the sound to measurement drop size distribution within the rain (Nystuen, 2001; 2005). This allows the potential for rainfall classification at sea using sound (Nystuen and Amitai, 2003). One interesting feature of the acoustical measurement is that the listening area for a hydrophone, its effective "catchment basin," is proportional to its depth, and yet the signal should be independent of depth if the sound source is uniformly distributed on the sea surface. Thus, the acoustical measurement of rainfall has an inherent spatial averaging that can be compared to the beam filling assumption of radar or satellite measurements of rainfall. By making sound measurements at different depths (60, 200, 1000, and 2000 m) and comparing those measurements to simultaneous high resolution radar observations, the spatial averaging of the acoustic signal can be explored.

[a)]Electronic mail: nystuen@apl.washington.edu

II. EXPERIMENTAL SETUP

In the winter of 2004, an experiment was carried out in the Ionian Sea off the southwestern coast of Greece (Fig. 1). This location offers deep water (over 3 km deep) within the coverage area of a coastal radar. The mooring configuration is shown in Fig. 2. Four acoustic sensors were deployed at 60, 200, 1000, and 2000 m depths on a single mooring. The coastal radar was a mobile high-resolution dual-polarization X-band radar (XPOL). The radar was located at Methoni (Fig. 1), 17 km east of the mooring. A dense rain gauge network and a two-dimensional video distrometer were deployed at Finikounda, 10 km east of the radar, but in the opposite direction from the mooring. The acoustical measurements and rain gauge network measurements were continuous from mid-January to mid-April, however the radar needed to have an operator present and so its temporal coverage was not continuous. Six precipitation events were captured by all three systems. Table I lists the rainfall events that were detected and recorded during the experiment. It also gives the rainfall accumulation totals for each system.

Ocean currents will bend the mooring, causing horizontal displacement of the acoustic sensors. In order to determine this potential displacement, a pressure sensor was placed on the mooring 2 m below the shallowest acoustic recorder. During most of the experiment the mooring line can be assumed to be vertical, but there are a few episodes

 0001-4966/2008/123(4)/1952/11/$23.00 © 2008 Acoustical Society of America

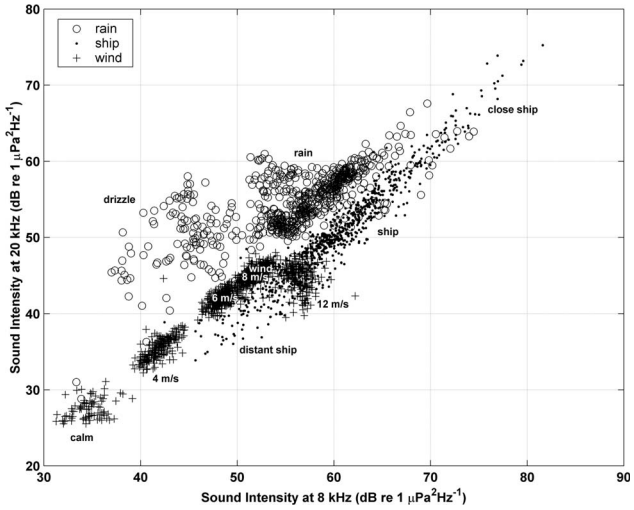

FIG. 1. Overview of the experimental site near Methoni, Greece. The X-Pol radar is at Methoni. Concentric circles at 5 km intervals are shown for the radar. The mooring location is 17 km west of Methoni. The shaded concentric circles over the mooring show the nominal listening areas for the four passive aquatic listeners (PALs) (M, N, O, and P). The dense rain gauge network is at Finikounda, 10 km east of Methoni.

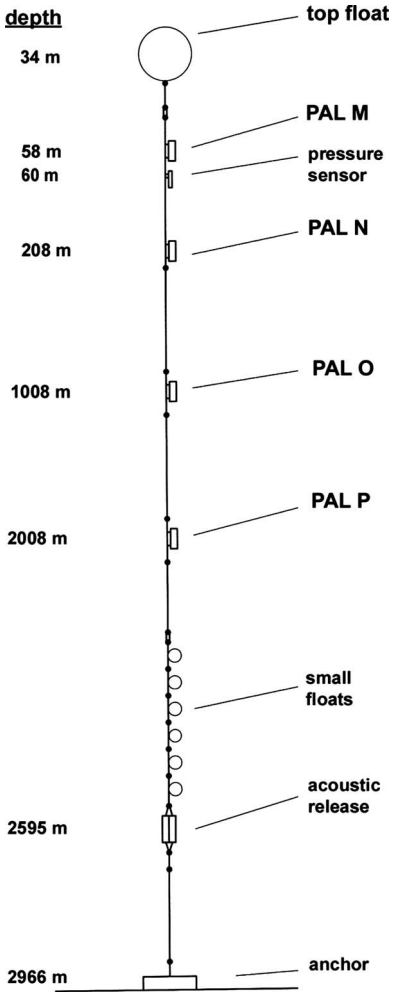

FIG. 2. Mooring configuration. Four PALs are deployed at 58, 208, 1008, and 2008 m, respectively (PALs M, N, O, and P).

when the top of the mooring dips and horizontal displacement is assumed to be present. The maximum vertical excursion is 5 m on 5 February, giving the maximum horizontal displacement of the shallowest acoustic recorder as 170 m. The displacements of the deeper recorders will be less. The spatial resolution of the radar (single pixel) is 150 m at the range of the mooring (17 km) and so the mooring can be assumed to be within a single radar range cell throughout the experiment.

The temperature and salinity structure of the ocean affect the sound speed profile, which in turn, will cause a refraction of sound. The temperature, salinity and sound speed structure of the upper 500 m at the mooring site were measured during the deployment (14 January) and recovery (14 April) of the mooring. The water is well mixed to 50 m. There is a layer of warmer and slightly fresher water that is about 130 m thick in January and about 50 m thick in April. This produces a weak sound channel centered at about 150 m deep in January and at about 70 m in April. The sound speed variations associated with these temperatures and salinity structures are potentially important for low frequency (<2 kHz) sound traveling at near horizontal grazing angles, but for higher frequency (>5 kHz) sound produced at the sea surface (vertical dipole) the refraction of the sound is small and spherical spreading will be assumed.

A sound source at a free surface is an acoustic dipole. Thus the sound intensity recorded at an omnidirectional hydrophone is given by

TABLE I. Rain events during the deployment. Accumulations are given in millimeters.

Date	PALs				XPOL	Rain gauges	Methoni station
	M	N	O	P			
21/22 January	68.5	67.5	61.1	52.4	No	No	96.8 mm
12 February	13.7	14.6	14.5	11.0	12.1	22.5	20.1
3 March	9.9	9.1	9.7	10.3	2.8[a]	1.0	1.4
4 March	4.2	4.2	4.7	3.9	3.6	13.4	13.0
8 March	7.0	8.9	12.8	13.4	4.0	11.9	7.9
9 March	12.7	11.8	10.7	9.4	13.0	14.1	8.3
12 March	29.9	31.2	30.1	23.1	18.1	5.1	5.8
1 April	34.0	36.3	31.1	20.1	No	23.5	25.5

[a]On 3 March the XPOL was only operational during part of the rain event.

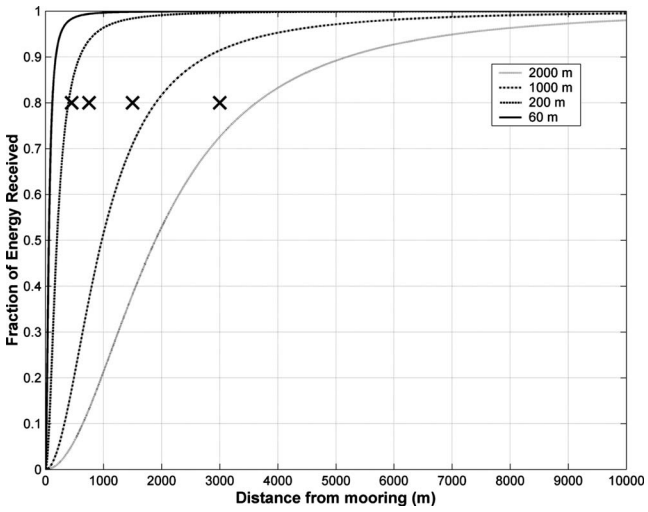

FIG. 3. Listening radius for the 4 PALs (M at 58 m; N at 208 m; O at 1008 m; and P at 2008 m) at 5 kHz. The listening radius is reduced at higher frequency by higher absorption of sound. Also shown are the observed length scales for maximum correlation between the PAL rainfall rates and averaged XPOL rainfall rates for the event on 8 March (to be discussed in Sec. VI).

$$I = \int I_0 \cos^2 \theta \, \mathrm{atten}(p) dA, \tag{1}$$

where I is the sound intensity measured at the hydrophone, I_0 is the sound intensity at the surface, $\cos^2 \theta$ is the directional radiation pattern for a surface source (vertically oriented dipole), and atten(p) is the attenuation along the acoustic path p. The integral is taken over the surface area A. The attenuation is due to geometric spreading, scattering, and absorption. Scattering is assumed to be negligible. Geometric spreading is affected by the sound speed profile of the ocean. Thus, the attenuation from a surface source to an acoustic recorder is given by

$$\mathrm{atten}(p) = \frac{\exp(-\alpha p)}{r^2 + h^2}, \tag{2}$$

where $p^2 = r^2 + h^2$, r is the horizontal range to the sound source, h is the depth of the recorder, and $\alpha = \alpha(f, S, T)$ is the absorption of sound in seawater and is a function of frequency, salinity, and temperature (Medwin and Clay, 1998, p. 109). If one makes the assumption that I_0 is uniform over the sea surface, then Eq. (1) can be used to estimate the effective listening area for each sensor.

Figure 3 shows the fraction of the total energy received at 5 kHz for sensors at 60, 200, 1000, and 2000 m depths. If the listening radius for a sensor is defined as the area receiving 90% of the sound, then the listening radii for the sensors at 5 kHz are 170, 610, 2735, and 4800 m, respectively, roughly three times the depth of the sensor. At lower frequencies these numbers are higher and at higher frequencies they are lower. The principal rainfall signal is at 5 kHz. Figure 3 also shows the weighting function of the listening radius for a uniform surface source. Within the defined listening area most of the energy is arriving from a much smaller area centered over the mooring. For example, at 5 kHz, 50% of the energy is arriving from the surface area with radii 58, 200, 970, and 1860 m, respectively, which is roughly the depth of the sensor. Also shown in Fig. 3 are comparison results from the spatial averaging analysis to be discussed in Sec. VI.

III. DATA COLLECTED

A. Acoustic data

The acoustic data were collected on four passive aquatic listeners (PALs). PALs consist of a low-noise wideband hydrophone, signal preamplifiers and a recording computer. The nominal sensitivity of these instruments is −160 dB relative to 1 V/μPa with an instrument noise equal to an equivalent oceanic background noise level of about 28 dB relative to 1 $\mu\mathrm{Pa}^2\,\mathrm{Hz}^{-1}$. Band-pass filters are present to reduce saturation from low frequency sound (high pass at 300 Hz) and aliasing from above 50 kHz (low pass at 40 kHz). The hydrophone sensitivity also rolls off above its resonance frequency, about 40 kHz. A further sensitivity correction due to the depth of deployment is also present.

A data collection sequence takes about 15 s and consists of four 10.24 ms time series each separated by 5 s. Each of these time series is fast Fourier transformed to obtain a 512-point (0–50 kHz) power spectrum. These four spectra are spectrally compressed to 64 frequency bins, with frequency resolution of 200 Hz from 100 to 3000 Hz and 1 kHz from 3 to 50 kHz. Geophysically generated sounds from rain, drizzle, or wind are generally stationary over a 15 s time interval, whereas banging from ships or moorings, or chirps, whistles, or clicks from biological sources are sound signals that usually are nonstationary over a 15 s time interval. Thus, a preliminary evaluation of the sound source is performed by comparing the four spectra from a single data collection sequence. A nonstationary signal is rejected as noise, and another data collection sequence is collected. Otherwise, the four spectra are averaged into a single spectrum that is stored to memory for later analysis. This average spectrum is evaluated to determine the acoustic source (rain, wind, or drizzle) and the source identification is used to set the time interval to the next data collection sequence. For example, if rain is detected, the time interval to the next data collection sequence is set to 30 s, whereas if "wind" is detected, the time interval to the next data collection sequence is set to 5 min. This allows the PAL to conserve energy between data collection sequences, but maximizes the sampling interval during periods of rainfall.

There is a residual frequency dependent instrument sensitivity that needs to be removed from the data. This is accomplished by assuming that the signal from wind generated wave breaking is a signal with a uniform spectral slope from 1 to 40 kHz (Ma and Nystuen, 2005). At low wind speeds the recorded signal includes a component from the ambient background and from instrument noise. At high wind speeds, there is a change to the spectral shape of the wind signal due to attenuation of the signal from ambient bubbles in the water. But at moderate wind speeds (4–8 m/s), the sound signal is well above the background noise and has a uniform spectral slope between 1 and 40 kHz. The difference between the observed spectral shape and a uniform spectral

slope is assumed to be the frequency dependent sensitivity correction for the PAL. This procedure might remove a real small scale feature of the wind generated sound signal, but such a feature should not be present in the sound signal from a different sound source, such as rain, drizzle or ships. Thus, the correction procedure is confirmed by examining the data from other sound sources, such as rain, drizzle or ships, and observing that the spectral features of the sensitivity correction (usually smaller than 1 dB) have been removed.

An unexpected depth dependent sensitivity change was observed, and confirmed by postexperiment testing. Again assuming a uniform sound source at the surface, Eq. (1) predicts a uniform signal with depth, except for the influence of absorption. The absorption of sound in the ocean is known (Medwin and Clay, 1998, p. 109) and can be calculated as a function of frequency and depth. Again choosing a sound condition when the signal to ratio is high and a uniform surface sound source is expected, e.g., when the wind speed is 8 m/s, this depth dependent sensitivity change can be detected. After adjusting for absorption, a depth dependent offset remains. Between 2 and 10 kHz, this offset is 0.5, 3, and 6 dB for the PALs at 200, 1000, and 2000 m depth, respectively (Amitai *et al.*, 2007). There are two consequences for these offsets. Quantitative acoustic measurements of wind speed and rainfall rate depend on the absolute sound intensity at 8 kHz (Vagle *et al.*, 1990) and at 5 kHz (Ma and Nystuen, 2005), respectively. Second, the automatic triggering algorithm for a higher sampling rate was dependent on the absolute sound level, and thus did not trigger as often for the two deeper PALs. Thus, the time step of the acoustic sampling for the two deeper PALs often remains at 5 min (the default), rather than switching to 30 s (the maximum). Fortunately, the signal to noise ratio during rainfall is very high and all instruments usually switched into the high sampling rate during part of each event.

B. Radar data

The radar data were collected from the National Observatory of Athens high-resolution mobile Doppler XPOL radar. It is a low power [~25 kW root mean square power] radar with selectable pulse and simultaneous transmission of signal at horizontal and vertical polarization. The antenna is mounted on the back of a truck with 8 ft radius and has a 0.95° (3 dB) beamwidth. During each storm event the radar was in the planar position indicator scan mode at low elevation (~2°) above the horizon. The pulse repetition frequency was 1000 Hz with 150 m gate length (range resolution) and 400 gates to give a total range of 60 km. Thus, the nominal backscattering volume at the range of the mooring is 150 m range by 300 m azimuth at an elevation of roughly 500 m above the ocean surface. The scanning rate was less than 1 min. The radar was manually operated during storm events, and does not provide continuous temporal coverage. Parts of storm events were missed, but several storms had long periods (several hours) of continuous coverage.

These data were used to provide an overview of the spatial structure of the rain events, and then to provide quantitative estimates of rainfall rates at each radar backscattering cell using radar reflectivity/rainfall algorithms. The radar rainfall maps were then averaged in concentric circles centered at the mooring location to provide an averaged rainfall for each concentric circles. These averaged rainfall measurements are compared to the rainfall measurements from the PALs.

C. Ground validation network

XPOL validation is based on the dense network of rain gauges (typical tipping bucket) and a 2D-Video (2DVD) disdrometer deployed within a 1 km^2 area and roughly 10 km away from XPOL (see Fig. 1). The gauge network consists of six dual-gauge clusters and a site consisting of three gauges and the 2DVD. Summary of the measured events is presented in Table I. These data are used to correct the radar rainfall rate estimate for bias during each rain event.

D. Methoni weather station

There is a weather station at Methoni that reports wind speed and direction hourly, and rainfall amounts. These data are available during local working hours (0500–1800 local time). This location is 17 km east of the mooring site. There was a bias associated with wind direction when compared to the acoustic wind speed measurements at the mooring. When the winds were from the east, the Methoni wind speeds were consistently lower than the acoustic wind speed measurements at the mooring location (17 km west). When the winds were from the west or northwest, the Methoni wind measurements were closer to the acoustic wind speed measurements. Acoustic wind speed measurements are typically ±0.5 m/s when compared to colocated surface-mounted anemometers (Vagle *et al.*, 1990; Nystuen *et al.*, 2000), and thus this discrepancy is likely to have an orographic explanation.

IV. ACOUSTIC DATA ANALYSIS

Ambient sound in the ocean is a combination of natural and manmade sounds. Various physical processes including wind, rain, and drizzle are primary sound sources in the frequency range from a few hundred hertz to 50 kHz. These are sound sources at the sea surface. The microphysics of the sound generation are resonating bubbles created during the splashing of wind waves or raindrop splashes (Medwin and Beaky, 1988; Medwin *et al.*, 1992; Nystuen, 2001). These bubbles are very near the free surface of the ocean, and consequently are assumed to behave as vertically oriented acoustic dipole sources. Human generated sounds include ships and sonars, and different marine animals, especially cetaceans, produce sound underwater in this same frequency band. These human and biological sources should be considered point sources, which may or may not be near the ocean surface depending on frequency, and thus the acoustic directivity of source should not be assumed. An underwater acoustic recorder will hear all of these sounds. Acoustic monitoring requires that the sound be recorded, the source identified and then quantified.

Different sound sources are identified by their spectral characteristics. Features of sound source spectra that can be used to identify the source include spectral levels at various

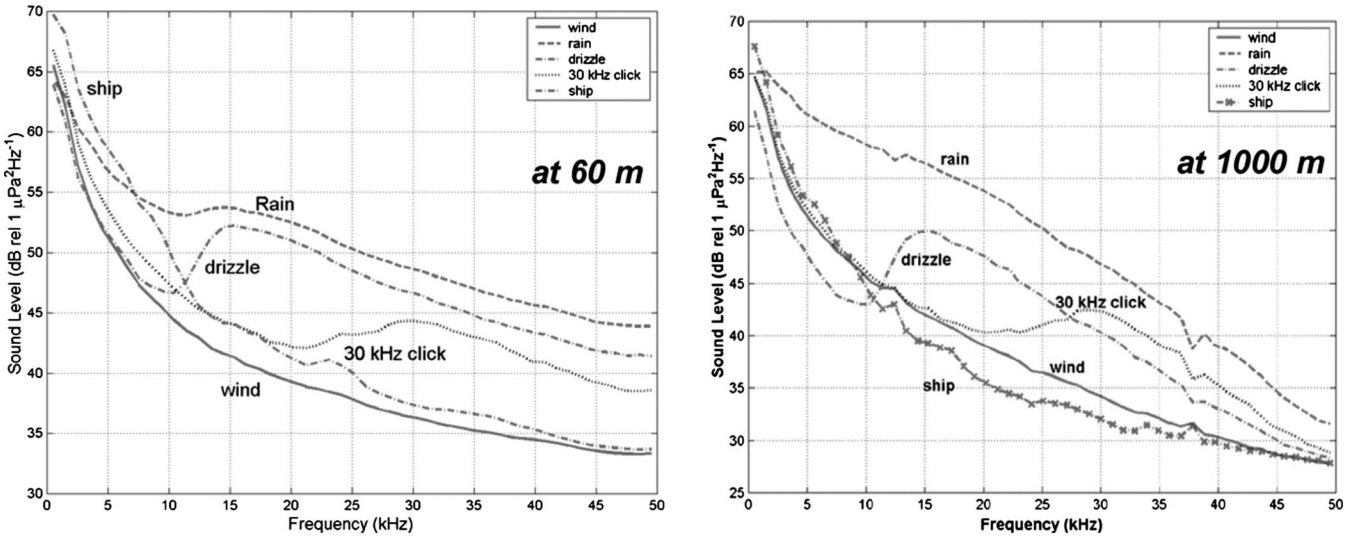

FIG. 4. Spectral signatures of five distinctive sound sources: wind, rain, drizzle, ships, and 30-kHz clicking recorded at the Ionian Sea mooring at (left) 60 m and at (right) 1000 m.

frequencies, ratios of these levels, spectral slopes and the temporal persistence of the sound source. The data were examined to find times when the sound source could be confidently assumed. Long periods (hours) of steady uniform sound were assumed to be periods of constant wind. Short loud events consistent with typical ship spectra (very loud at low frequency) during nonrainy periods were assumed to be ships. Distinctive rain and drizzle spectra were identified and confirmed with radar. These typical sound sources are shown in Fig. 4 and were used to build an acoustic classification algorithm that can be used to objectively identify the sound source in remaining data. The goal is to reliably detect the sound source so that subsequent analysis is not contaminated by sound generated by other source. Figure 5 shows the relationship between 8 and 20 kHz for these test case sound sources. This comparison of sound levels at two frequencies is particularly illustrative for demonstrating the ability to use

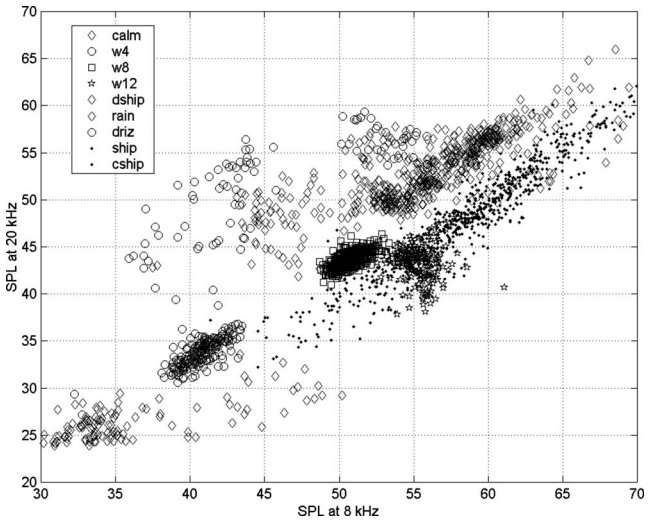

FIG. 5. Scatter diagram showing the ratio of sound levels at 8 and 20 kHz for the PAL at 200 m depth. Different loci of points are associated with different sound sources. Five different wind speeds are shown: calm, 4 m/s, 6 m/s, 8 m/s and 12 m/s.

ambient sound to identify the sound sources. In fact, multiple measures are actually used. For example, there is an ambiguity for the sound source "wind=12 m/s" and "ships." Other features of the sound field are needed to separate these two sources. For this situation, periods of high wind are usually of long durations (hours), whereas ships pass the mooring in minutes. And there may be other spectral measures that are diagnostic. Other useful measures are the sound levels at 2 kHz, the ratio of sound levels from 1 to 2 kHz, the slope of the spectrum from 2 to 8 kHz, the slope of the spectrum from 8 to 15 kHz and the sound level at 20 kHz.

These relationships change as function of depth because of absorption. As the relationships are used to identify the sound sources, a correction for absorption needs to be applied. For uniform surface sound sources, such as wind, Eq. (1) can be used to adjust for absorption. However, for nonuniform sound sources, such as a ship, Eq. (1) is inappropriate and so the relative position of the sound source on the diagram changes. In particular, loud ships at depth show an increased ratio of sound intensity at higher frequency (20 kHz) to lower frequency (8 kHz). This makes the classification of loud ships at depth is more difficult as their spectra begin to sound like heavy rainfall.

A sound budget for a location describes the sound levels, sound sources, which sound source is dominant, and the relative loudness of the sources. Different distinctive sound sources are objectively detected based on the spectral and temporal characteristics for that sound source. Exact identity of all sounds in the ocean will never be achieved, however several categories of sounds can be identified. In the Ionian Sea objective analysis for five distinctive sounds were attempted: wind, rain, drizzle, shipping and a 30 kHz clicking that is consistent with the echo location click of cetaceans. The median sound spectrum for each of these sound categories are shown in Fig. 4 for two different listening depths. Note that the signal from shipping is relatively weaker at 1000 m than at 60 m. This is because a point source (ship) occupies a smaller and smaller part of the listening area as

TABLE II. Percentage of time that a specific sound source is detected. The deployment is broken into four time periods (Days 20–40, 40–60, 60–80 and 80–100).

Days 20–40	Wind	Rain	Ships	30 kHz click
M—60 m	81.5	5.8	11.1	0.9
N—200 m	82.5	7.1	9.1	1.3
O—1000 m	83.1	4.5	11.8	0.7
P—2000 m	84.0	2.6	13.4	0.07
Days 40–60	Wind	Rain	Ships	30 kHz click
M—60 m	75.1	2.9	19.6	1.3
N—200 m	78.1	4.3	15.4	2.1
O—1000 m	80.4	2.3	16.3	1.0
P—2000 m	83.2	1.0	15.7	0.1
Days 60–80	Wind	Rain	Ships	30 kHz click
M—60 m	67.2	3.1	28.7	0.9
N—200 m	73.5	3.9	21.0	1.6
O—1000 m	73.2	3.9	22.3	0.7
P—2000 m	78.3	2.5	19.1	0.1
Days 80–100	Wind	Rain	Ships	30 kHz click
M—60 m	58.4	3.0	37.9	0.7
N—200 m	71.0	4.3	23.6	1.1
O—1000 m	70.0	3.7	26.1	0.3
P—2000 m	76.2	2.2	21.5	0.05

the depth of the hydrophone increases. The 30 kHz click signal is actually of similar strength at each depth, suggesting that this source is local, e.g., a whale echo locating at depth near the PAL. After applying an objective classification code to the data from each listening depth, the sound source can be identified. Once the sound source is identified, different statistics relating to each sound source can be quantified. Table II quantifies the percentage of time that each sound source is dominant for four 20 day periods during the deployment. Rainfall is present roughly 6% of the time during the first 20 day period and then is detected 4% of the time during the rest of the experiment. There are also some depth dependent trends. The highest rate for rainfall detection is from the PAL at 200 m, and the lowest is at 2000 m. This may be due to the threshold triggering problem encountered at the deep PALs or because the high frequency component of the rainfall signal has been attenuated by absorption.

A trend of increasing shipping is evident: from roughly 11% in late January/early February (days 20–40) to nearly 30% of the time in late March/early April (days 80–100). The shallowest PAL has the highest rate of shipping detection. The shipping signal is dominant at low frequency and distant propagation in the weak sound channel near the surface may allow the shallow PAL to detect "distant shipping" more often than the deep hydrophones. The distant shipping detection often occurs during very calm ocean surface conditions. These conditions increased in duration as the experiment progressed and thus the trend of increasing shipping may reflect an increase in calm ocean conditions as winter changes to summer.

An interesting signal that is present in the data are 30 kHz clicks. The spectral shape of the clicks is shown in Fig. 4 and is consistent with the clicking from beaked whales (Johnson *et al.*, 2004). Beaked whales are a type of cetacean that are difficult to observe visually as they are pelagic and spend a majority of time underwater. It is also a whale type that is sensitive to human noise (Cox *et al.*, 2006). Different cetaceans also echo-locate, but generally at different frequencies, allowing potential identification of the whale type based on the character of the click. Another clue that these clicks may be from beaked whales is the time and depth pattern of the clicking. The depth with the greatest number of clicks detected was 200 m. In Johnson *et al.* (2004) tagged beaked whales began clicking at 200 m depth and dove to a maximum depth of 1267 m. In this situation, clicks are detected at 1000 m regularly, and occasionally at 2000 m. The signal strength is independent of depth, suggesting that the whale is at depth. But clicks are detected at 60 m, which is above the 200 m depth documented by Johnson *et al.* (2004). However, the PALs are listening for a signal; they are not physically on the whale.

V. VALIDATION OF RAINFALL DETECTION

Validation of acoustic rainfall detection using the radar was available for six rain events: 12 February, 3, 4, 8, 9, and 12 March. The radar was not operating on 21/22 January and 1 April. The 12 February event was a complicated frontal weather system within imbedded rain cells and lulls, periods of low winds, high winds and a few ship passages. 3 and 4 March were widespread light rain events with low winds (<5 m/s). 8 March was a day with high winds (~ 10 m/s) and included an isolated squall line. 9 and 12 March were both relatively long, continuous rain events in moderate (5–10 m/s) wind conditions. Radar coverage was not complete on 12 February and 3 or 8 March.

A. Case study—12 February 2004

On 12 February 2004 a frontal system passed over the mooring. This was a complicated system consisting of several rain cells and lulls. The acoustic record of the day contains a wide variety of signals, including distant shipping, a close ship passage, some loud noises and the sound of high wind conditions. An acoustic overview of the day is shown in Fig. 6, with the periods when different acoustic signals were recorded labeled and described in Table III. The XPOL radar data are also shown in Fig. 6 with three different thresholds: over 1 mm/h, over 2 mm/h, and over 5 mm/h. The radar was not turned on until Min 240, missing the initial rain events (periods B and D). Period E shows the strongest radar rainfall, with light rain detected in period H. Period I is apparently a strong, but brief rain cell. The radar was turned off at Min 1080, after the passage of the weather front.

Sound spectra for each time period are shown in Fig. 7 with a corresponding classification diagram shown in Fig. 8. The start of the day (period A) shows the typical spectra of the sound category distant shipping. In this situation propagation conditions are excellent and distant low-frequency (under 2 kHz) sound is detected, but the sound levels at high frequency (over 20 kHz) are very low suggesting that the high frequency sound from the distant source has been absorbed. The ocean surface is very flat (no wind waves), allowing good reflectivity for order decimeter wavelength

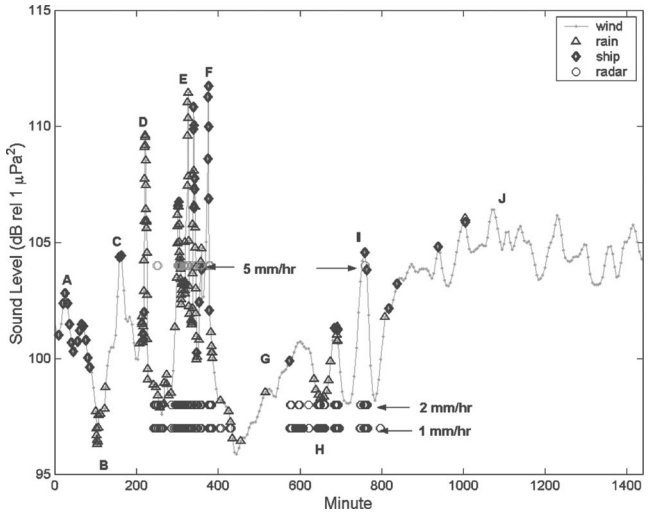

FIG. 6. The time series of sound level from PAL N at 200 m depth during 12 February 2004. Distinctive periods of the day are labeled A-J. Rainfall and shipping detections are shown. The XPOL radar rainfall detection is shown at 3 different thresholds: 1 mm/hr, 2 mm/hr and 5 mm/hr.

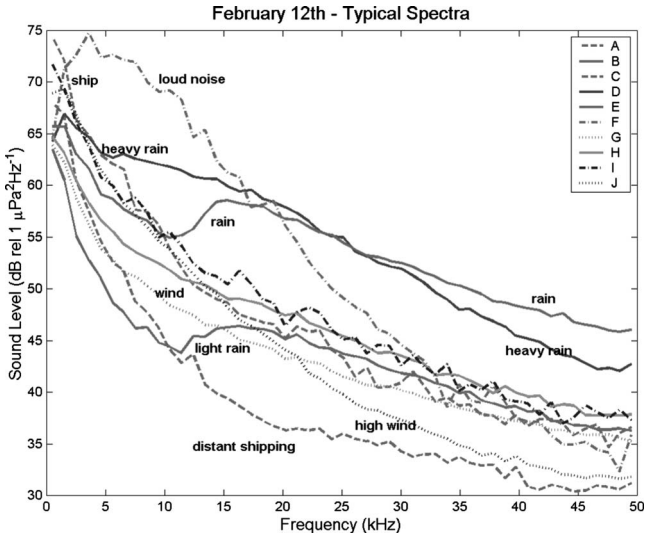

FIG. 7. Typical sound spectra for different periods of the day on 12 February 2004 from PAL N at 200 m depth.

(5–10 kHz) sound waves from the surface. This signal ends as the first light rainfall occurs (period B), likely ruffling the surface and reducing long range propagation of the lower frequency sound (5–10 kHz). Note that the sound levels below 10 kHz actually drop between periods A and B, although there is likely more local sound being generated in period B. At high frequency, the sound levels in period B are elevated by bubbles from small raindrop splashes. A ship passes at Min 180 (event C), producing a "typical" ship spectrum with very high sound levels below 2 kHz, and a consequently relatively steep spectral slope between 5 and 15 kHz. In contrast, rainfall produces a relatively flat spectral slope between 5 and 15 kHz.

The first strong rain cell occurs in period D. This cell is detected by all four PALs and has high sound levels at all frequencies, but especially between 2 and 20 kHz, where larger raindrops produce sound from their splashes. This signal often obscures the 13–25 kHz signal from small raindrops, as is apparently the case in this example. In contrast, period E is a longer, more continuous rain, with a few stronger rain cells imbedded in a nonhomogeneous rain field. The XPOL weather radar was turned on at Min 240, was offline from 265 to 285 and then on again after Min 285, verifying rainfall over the mooring. Period E will be described in more detail in the following. Within period E, a loud sound was detected at Min 373 (marked F). This spectrum is shown in Fig. 7 and the classification points in Fig. 8 put it into the category of "a close ship passage," however the peak in this spectrum at 4 kHz is not a typical ship signature. Sometimes ship engines "howl," and this may be the case here. There is no strong radar echo at Min 373, and so it is not rainfall.

Period G is an interlude between rain events. The winds are low, under 5 m/s, and rise gradually during this period. A typical wind spectrum is recorded by all four PALs, and no rain conditions are verified by the radar. The radar reports light rainfall during period H. During this time period there is partial acoustic detection of rainfall (see Fig. 8) with relatively high sound levels at lower frequencies, indicating that

TABLE III. Time periods with acoustic interpretations for 12 February 2004.

Period	Acoustic interpretation	Radar
A	Distant shipping	Off
B	Light drizzle	Off
C	Ship passage	Off
D	Rain cell	Off
E	Steady rain	Rain
F	Loud noise	No rain
G	Wind	No rain
H	Light rain	Light rain
I	Uncertain	Rain cell
J	High wind	No rain

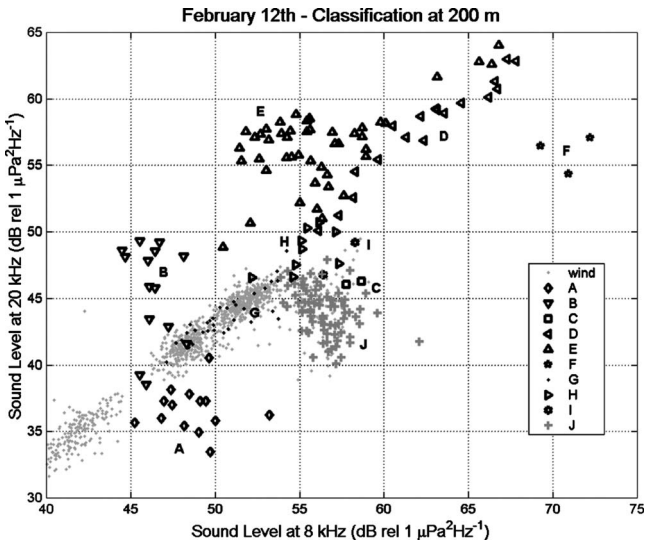

FIG. 8. Classification diagram for PAL N at 200 m on 12 February 2004. The "wind" points are a background reference for the entire deployment for "wind only" conditions. Deviations from these points are "other" sound sources including rain, drizzle, and shipping.

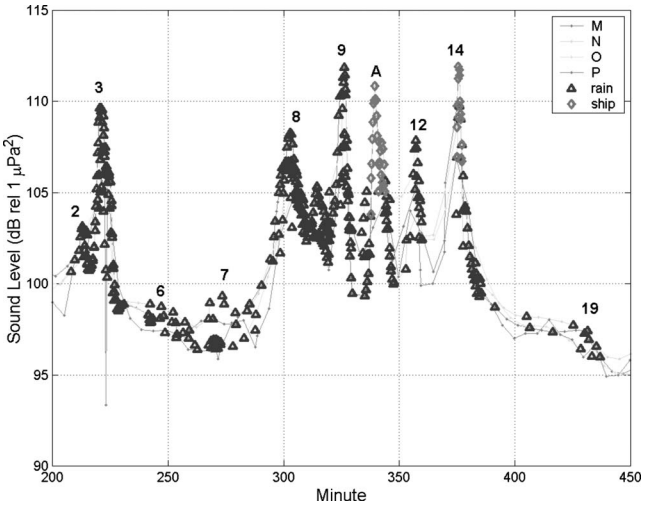

FIG. 9. Time series of sound levels for all four PALs during the main rain event on 12 February 2004. The four time series overlay one another. Classification as rain and ships are shown. Selected labels refer to the time periods given in Table IV.

TABLE IV. Time periods with acoustic and radar interpretations for the major rain event on 12 February 2004. Note that event A, a ship passage, occurs between periods 10 and 11.

Period	Time	Interpretation	Radar
1	200–210	Lull	Off
2	215–220	Rain	Off
3	220–223	Downpour	Off
4	225	Rain	Off
5	230	Lull	Off
6	240–265	Light rain	Light rain
7	265–285	Light rain	Off
8	285–320	Rain	Rain
9	325–327	Downpour	Rain cell
10	345	Rain	Rain
11	350	Rain	Rain
12	355–360	Downpour	Heavy rain
13	360–370	Lull	Lull
14	373	Very loud noise	Lull
15	375–380	Rain	Rain
16	390	Lull	Lull
17	405	Lull	Light rain
18	415	Lull	Lull
19	430	Light rain	Light rain
20	440	Lull	Lull
A	339–341	Ship	Lull

the wind speed is relatively high (~8–10 m/s). At Min 800, the wind speed increases to over 10 m/s and becomes steady for many hours. The Methoni weather station reported sustained winds over 15 m/s. The sound levels above 20 kHz actually drop, and are relatively lower than the sound levels when the wind speed is less (period G). This is due to ambient bubble clouds below the ocean surface from breaking waves. These small bubbles are absorbing the high frequency sound being produced at the ocean surface by newly breaking waves, and thus distort the spectral sound signature of those waves. [Wind speed is measured using the sound level at 8 kHz (Vagle *et al.*, 1990) to avoid this distortion of the signal from absorption. Bubbles that absorb sound at 8 kHz are large enough that they rise to the surface quickly.]

The longest sustained rain event (period E) is examined in more detail in Fig. 9. Figure 9 shows the time series of the sound levels for all four PALs, at depths 60, 200, 1000, and 2000 m, respectively, with the classifications of rain and shipping shown. The acoustic rainfall signals are overlain on one another to show that the rainfall signal is similar at all depths. Distinct periods during this period are again labeled, plus there is a ship detection that will be referred to as event A. Table IV presents the acoustic and radar interpretation for each identified period. The strongest radar reflectivities are at periods 9 and 12. Light rain is detected by the radar at periods 6, 17, and 19. The mean spectrum for the lulls (periods 1, 5, 13, 16, 17, and 18) is the typical spectrum for 6 m/s wind conditions, suggesting that the background wind is about 6 m/s. The Methoni weather station reports 4 m/s during this part of the day. The acoustic wind measurement is 4 m/s after the event (Min 450). The two ship detections are verified by the absence of radar rainfall detection at Min 343 (A) and at Min 373 (period 14). There was rain detected at Min 375–380, however the acoustic signal at Min 373 (signal F in Fig. 7) is very loud and would require a rainfall rate over 100 mm/h if it were classified as rain. Note that the ship at Min 343 is not well detected at depth. In fact, it is not detected by the deepest PAL. The signal from a ship is a point source, in contrast to a wide-spread surface source from rain, and is relatively weaker at depth. The ship detection at Min 343 may be a more distant ship, with sound propagating near the surface. The loud sound at Min 373–375 (signal F in Figs. 6–8; period 14 in Fig. 9) is detected by all of the PALs and is presumably a ship passing very close to the mooring.

Once classification is established, a comparison of rainfall rates is possible. Figure 10 shows the comparison of the shallow PALs, at 60 and 200 m, respectively with the XPOL radar rainfall rates averaged over a 2.25 km (15 cells) radius circle above the mooring location. The strong rain cell

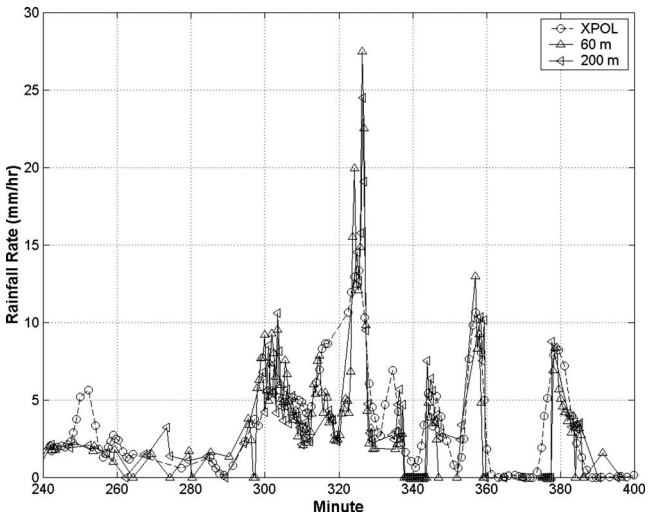

FIG. 10. Rainfall rate comparison between the shallow PALs at 60 and 200 m, and the XPOL rainfall rate averaged over a 2.25 km radius circle centered above the mooring on 12 February.

(PALs) at Min 325 is period 9 in Fig. 9 and the strong rain cell at Min 355 is period 12. The correlation coefficients when the radar is operating and the acoustic data are good (no ship contamination present) are roughly 0.8 depending on the averaging area for the radar data and the hydrophone depth and will be discussed further in Sec. VI.

B. Case studies: Light rain in light wind conditions—3 and 4 March

Light wind conditions are ideal for the sound production mechanism for small raindrops (1 mm diameter) (Nystuen, 2001) and the sound is surprisingly loud. This drop size is present in most light rain (<1 mm/h) and consequently drizzle is easily detected acoustically during light wind conditions. The codetection of light rainfall on 3 and 4 March was high, even during intermittent periods of light rain. The radar rainfall rates were low, and yet all of the times that the radar reported rain are confirmed by acoustic detection.

C. Case studies: Moderate rain in moderate wind conditions—9 and 12 March

Both of these events had long periods of rainfall with codetection by both the radar and the PALs. On 9 March, shipping contamination is detected is by the shallow PALs during the later part of the event and these data are discarded from further analysis. This shipping contamination was not well detected at depth (the PALs at 1000 and 2000 m) suggesting that the noise source had been averaged out when heard at depth. This suggests an isolated point source distant from the mooring, with a shallow acoustic propagation path to the upper PALs.

On 12 March, the wind speed is relatively high, with acoustic wind speed measurements of ~10 m/s before the start of the event and 8 m/s at the Methoni weather station (17 km to the east). Methoni reports a drop in the wind speed to 6 m/s during the rain; no acoustic wind speed estimates are available during the rain because the sound from the rain dominates during the rain. The comparison of PAL and XPOL radar rainfall rates is shown in Fig. 11. The rainfall starts as a relatively strong rain (6 mm/h) and then tapers off after Min 910. Codetection of rainfall remains excellent and the comparison of rainfall rates from the radar and the PALs remains highly correlated with correlation coefficients of order 0.9.

D. Case study: Squall line on 8 March

Perhaps the most serendipitous rain event was an isolated squall line that passed over the mooring on 8 March. The radar scan for this event is shown in Fig. 12 shortly before the passage of the squall line at the mooring location. Based on the echo-location position of the squall from consecutive radar scans, the local wind speed is 8 m/s (Amitai *et al.*, 2007). The acoustic wind measurement at the beginning of the squall is 9 m/s, in agreement with the wind measurement at the Methoni weather station. A comparison of rainfall rates is shown in Fig. 13. One comparison of rainfall rates is from the shallow PALs (60 and 200 m) and the XPOL ZdR rainfall rate at the mooring (single cell). This

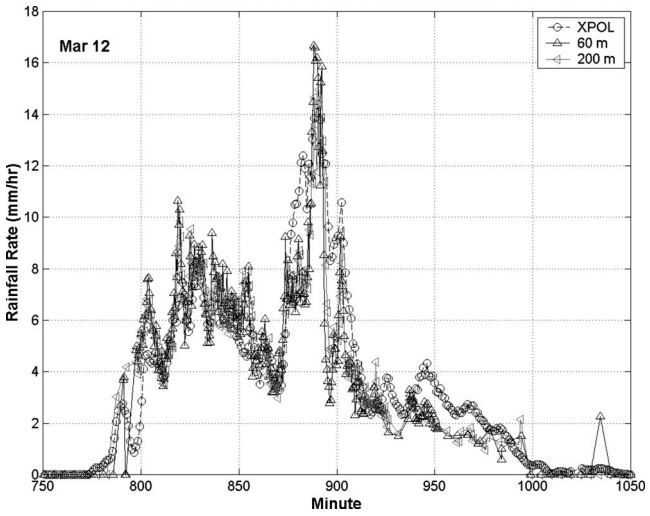

FIG. 11. Comparison of XPOL radar rainfall rates and PAL rainfall rates on 12 March. The radar data have been averaged over a 2.25 km (15 cells) radius circle above the mooring. The PALs shown here are at 60 and 200 m (the shallow PALs).

shows that the rain cell is brief (2–3 min) and intense (60–90 mm/h). The second comparison is from the deeper PALs (1000 and 2000 m) and the XPOL ZdR rainfall rate averaged over 4.5 km radius circle (30 cells) over the mooring. The rain cell detection is longer, of order 10 min, and less intense (15–40 mm/h). This is consistent with spatial averaging of an intense small rain cell over a larger area and is evidence of a larger listening area for the deeper hydrophones.

A curious feature of this rain event is a "moment of silence" at Min 909. This is indicated by a drop in rainfall rate at Min 909 in Fig. 13. All four PALs recorded a sharp and very brief (about 1 min) drop in sound levels at this minute. The PALs are totally independent of one another, and

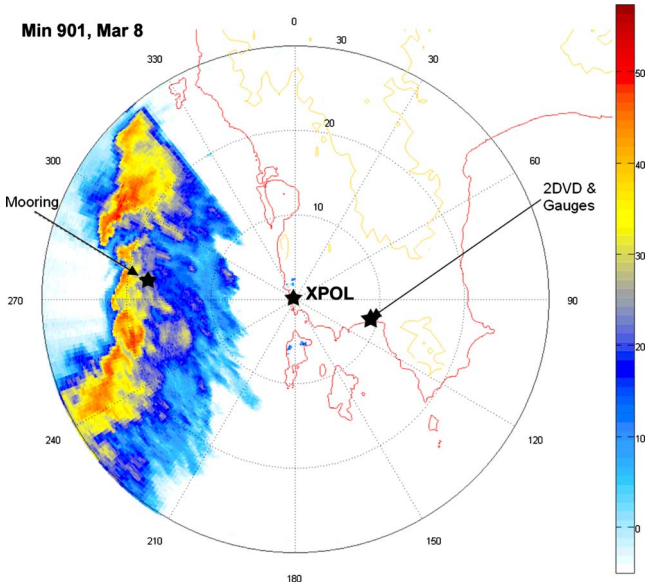

FIG. 12. (Color online) Radar PPI scan at Min 901 (15:01 GMT) on 8 March. The squall line passed over the mooring from Min 900 to 905. There was a moment of silence at Min 909. Based on echo-location motion the wind speed is 7 m/s.

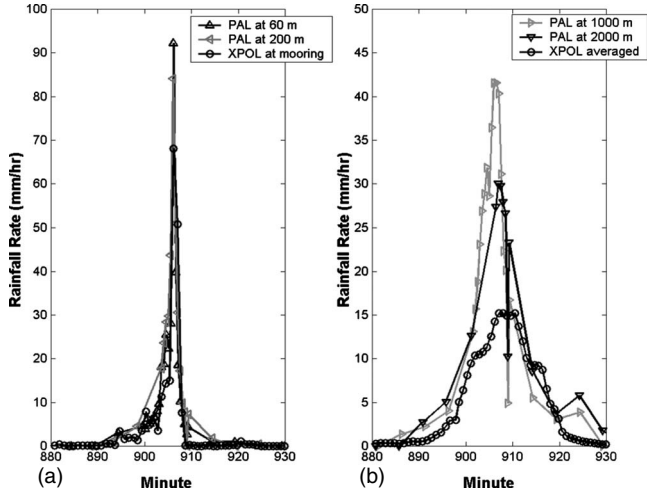

FIG. 13. Comparison of rainfall rates during the squall line on 8 March. (a) Comparison between the shallow PALs (at 60 and 200 m) and the radar rainfall rates at the cell (single cell) over the mooring. (b) Comparison between the deep PALs (at 1000 and 2000 m) and the radar rainfall rates averaged over a circle of radius 4.5 km (30 cells) centered over the mooring.

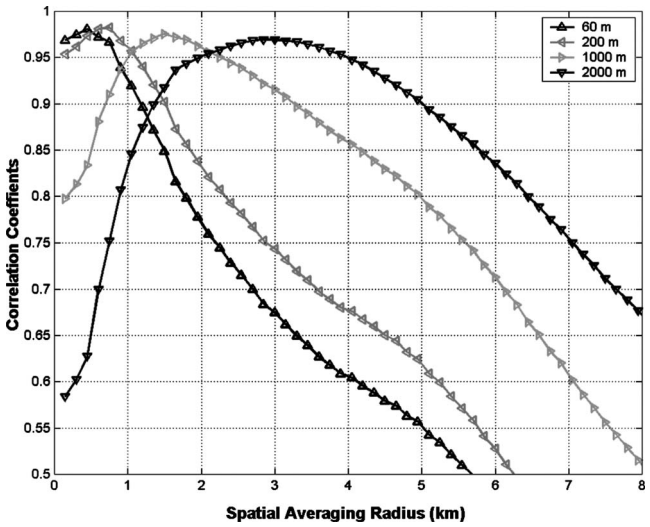

FIG. 14. Correlation coefficients between the acoustic rainfall measurements at 60, 200, 1000, and 2000 m depth compared to the averaged radar rainfall rates averaged over a circle of different radii centered over the mooring. The radar cell size is 150 m.

so this is a real feature. The sound level at 200 m is actually quieter than the sound levels before or after the squall line. This suggests that the sound production mechanism for wind (breaking waves) has been disrupted by the intense rain. It is widely reported, but undocumented, that "rain calms the seas." This is acoustical evidence that this is true. The radar reports no echo return at Min 909 [Fig. 13(a)] in the cell directly over the mooring, and the radar scan at Min 901 (Fig. 12) show an abrupt end to the rear side of the squall. Note however, that severe attenuation of the radar signal through the rain cell may also cause no echo return from the radar. The acoustical evidence suggests that this is not the case here and that there really is no rain on the rear side of the squall line.

VI. SPATIAL AVERAGING OF THE RAINFALL SIGNAL

Three examples of coincident observations of relatively continuous rainfall are used to investigate the spatial averaging of the acoustic rainfall signal (12 February, 8 and 12 March). The rainfall rates from the PALs are compared to averaged rainfall rates from the radar for different averaging radii in a circle centered over the mooring location. The results for 8 March are shown in Fig. 14. This event had a much smaller spatial and temporal scale than the other two examples. The averaging radii producing the highest correlation between the radar and the PALs increases from 450, 750, and 1500 to 3000 m for the measurements at 60, 200, 1000, and 2000 m, respectively. These results are shown in Fig. 3 (arbitrarily at fraction value 0.8) where the prediction assuming an uniform weighting of the acoustic signal within the listening area from Fig. 3 is 170, 610, 2735, and 4800 m, respectively. Thus, the signal from the shallowest hydrophone is most highly correlated to the radar rainfall measurement averaged over a larger listening area than expected, and the deeper hydrophones to smaller areas than expected. It was noted that the weighting of the acoustic signal is not uniform, but is weighted toward the center of the listening area, thus reducing the expected listening area for the hydrophones. When the other two examples (12 February and 12 March) are considered, the averaging radii producing the highest correlation for the PAL at 2000 m remains between 3 and 4 km. This suggests an effective listening area of about $\pi r^2 = 30-50$ km^2. In contrast, the averaging radii producing the highest correlation for the PAL at 60 m goes from 450 m for the squall line on 8 March to 1 and 2 km, respectively, for the rain events on 12 February and 12 March. These events were more widespread with longer spatial and temporal time scales, suggesting that physical scale of the rain itself may be responsible for this result. Nevertheless, the trend is as expected. The deeper acoustic measurements have higher correlations to the radar rainfall averaged over larger apparent listening areas. The intermediate PALs at 200 and 1000 m show intermediate results.

VII. CONCLUSIONS

High frequency (1–50 kHz) acoustic measurements of the marine environment at four depths (60, 200, 1000, and 2000 m) are used to describe the physical, biological, and anthropogenic processes present at a deep water mooring site near Methoni, Greece from mid-January to mid-April in 2004. The acoustic signal is classified into five categories: wind, rain, drizzle, shipping, and a 30 kHz clicking that is consistent with deep-diving beaked whales. The background acoustic signal is from breaking wind waves, and is nearly identical at all listening depths. This signal is clean, that is, not contaminated by other sound sources, 70%–80% of the time and can be used to quantitatively measure wind speed (Vagle *et al.* 1990). The accuracy of this measurement is often ± 0.5 m/s (Nystuen *et al.*, 2000; Ma and Nystuen, 2005), however, comparisons with the Methoni weather station 17 km to the east show a systematic bias when the winds are from the east or southeast during this experiment.

The mooring location is near an ocean shipping lane and consequently frequent close passages of ships were detected acoustically. These events are usually loud at all frequencies

(1–50 kHz) and brief (a few minutes) with relatively high low frequency sound levels allowing their detection and classification at all hydrophone depths. Another category of shipping noise is distant shipping. Very calm ocean surface conditions allow the propagation of distant shipping sound near the ocean surface, especially at lower frequencies (<2 kHz) where the shipping signal is often relatively loud and sound absorption by seawater is relatively low. In contrast, higher frequency sound (>10 kHz) is absorbed and does not propagate long distances (tens of kilometers). These conditions were more prevalent in the later periods of the experiment and the level of shipping acoustically detected increased significantly from 12% of the time in the first part of the experiment to over 25% of the time at the end (Table II). This increase was most pronounced at the shallowest hydrophone at 60 m depth. This depth was within a weak surface sound channel that might be enhanced during very calm ocean surface conditions.

Another distinctive sound that was detected is a 30 kHz spectral peak that is consistent with the echo-location click of beaked whales (Johnson *et al.* 2004). This type of whale is pelagic (found only in deep water locations) and is difficult to detect visually as they spend most of the time diving underwater. This signal was present 1%–2% of the time and was most often detected by the hydrophone at 200 m depth. This is the depth that Johnson *et al.* report that beaked whales begin clicking during deep dives. These whales are known to dive to depths below 1000 m and thus detections of this signal at 1000 m, and even occasionally at 2000 m, are consistent with beaked whales. There were no visual observations of whales during the experiment.

The main focus of the experiment was the detection of precipitation in deep water at different depths. In order to validate these detections, a dual-polarization, high resolution, X-band, coastal weather radar (XPOL radar) was located at Methoni, 17 km to the east of the mooring. Eight significant rain events were acoustically detected during the experiment (Table I). Six of these events had partial or full radar coverage. All were confirmed by the weather station at Methoni, and all rain events recorded at Methoni during the experiment were detected acoustically. The radar data were used to verify the acoustic classification of rainfall, and the acoustic detection of imbedded shipping noise within a rain event (e.g., Fig. 10). Three simultaneous records of radar and acoustic rainfall measurements were compared to investigate averaging of the acoustic rainfall signal as a function of listening depth. These comparisons show an increase in effective listening area with increasing listening depth. The averaging radius for the radar data that resulted in the highest correlation with the rainfall measurement for the shallowest hydrophone (at 60 m) was between 450 m and 2 km, suggesting a listening area for the shallowest hydrophone between 1 and 12 km^2. This is larger than expected (Fig. 3). In contrast, the averaging radius for the deepest hydrophone (at 2000 m) was between 3 and 4 km, suggesting a listening area between 30 and 50 km^2, less than expected (Fig. 3). This result was clearest for the rain event on 8 March when an intense isolated squall line passed over the mooring very rapidly (2–3 min with rainfall rates over 50 mm/h). An interesting acoustical feature of this event was a moment of silence just after the passage of the squall. All of the hydrophones recorded a brief drop in sound level, including a drop to a level below the prevailing background sound before or after the squall at 200 m. This suggests that the background sound production mechanism (breaking waves from wind) had been suppressed by the intense rain, acoustical evidence of rain calms the seas. There was no radar echo return at the moment of silence.

ACKNOWLEDGMENTS

E. Boget designed and deployed the deepwater mooring. The National Observatory of Athens (NOA) made the XPOL radar available to the experiment. G. Chronos at Hellanic Center for Marine Research (HCMR) arranged for the R/V Philia, captained by M. Kokos, to deploy and recover the mooring. T. Paganis and A. Gomta, at the Methoni weather station provided their handwritten data to help interpret the acoustic data. E. Anassontzis, University of Athens, provided logistical support via the NESTOR Institute for Deep Sea Research in Pylos, Greece. The citizens of Finikounda allowed rain gauges to be set up in their yards during the experiment. Funding was provided by the National Science Foundation, Physical Oceanography Division, Grant No. 0241245.

Amitai, E., Nystuen, J. A., Anagnostou, E. N., and Anagnostou, M. N. (**2007**). "Comparison of deep underwater measurements and radar observations of rainfall," IEEE Trans. Geosci. Remote Sens. **4**, 406–410.

Johnson, M., Madsen, P. T., Zimmer, W. M. X., Aguilar de Soto, N., and Tyack, P. L. (**2004**). "Beaked whales echolocate on prey," Proc. R. Soc. London, Ser. B **271**, 5383–5386.

Ma, B. B., and Nystuen, J. A. (**2005**). "Passive acoustic detection and measurement of rainfall at sea," J. Atmos. Ocean. Technol. **22**, 1225–1248.

Medwin, H., and Beaky, M. M. (**1988**). "Bubble sources of the Knudsen sea noise spectra," J. Acoust. Soc. Am. **86**, 1124–1130.

Medwin, H., and Clay, C. S. (**1998**). *Fundamentals of Acoustical Oceanography* (Academic, New York).

Medwin, H., Nystuen, J. A., Jacobus, P. W., Ostwald, L. H., and Synder, D. E. (**1992**). "The anatomy of underwater rain noise," J. Acoust. Soc. Am. **92**, 1613–1623.

Nystuen, J. A. (**2001**). "Listening to raindrops from underwater, An acoustic disdrometer," J. Atmos. Ocean. Technol. **18**, 1640–1657.

Nystuen, J. A. (**2005**). "Using underwater sound to determine drop size distribution," in *Sounds in the Seas, Introduction to Acoustical Oceanography*, edited by H. Medwin, (Cambridge Unversity Press, Cambridge, MA).

Nystuen, J. A., and Amitai, E. (**2003**). "High temporal resolution of extreme rainfall rate variability and the acoustic classification of rainfall," J. Geophys. Res., [Atmos.] **108**(D8), 8378–8388.

Nystuen, J. A., McPhaden, M. J., and Freitag, H. P. (**2000**). "Surface measurements of precipitation from an ocean mooring: The underwater acoustic log from the South China Sea," J. Appl. Meteorol. **39**, 2182–2197.

Vagle, S., Large, W. G., and Farmer, D. M. (**1990**). "An evaluation of the WOTAN technique for inferring oceanic wind from underwater sound," J. Atmos. Ocean. Technol. **7**, 576–595.

Cox, T. M., Ragen, T. J., Read, A. J., Vos, E., Baird, R. W., Balcomb, K., Barlow, J., Caldwel, J., Cranford, T., Crum, L., D'Amico, A., D'Spain, G., Fernández, A., Finneran, J., Gentry, R., Gerth, W., Gulland, F., Hildebrand, J., Houser, D., Hullar, T., Jepson, P. D., Ketten, D., MacLeod, C. D., Miller, P., Moore, S., Mountain, D. C., Palka, D., Ponganis, P., S., Rommel, Rowles, T., Taylor, B., Tyack, P., Wartzok, D., Gisiner, R., Mead, J., and Benner, L. (**2006**). "Understanding the impacts of anthropogenic sound on beaked whales," J. Cetacean Res. Manage. **7**, 177–187.

Finite element simulation of the generation and detection by air-coupled transducers of guided waves in viscoelastic and anisotropic materials

Bernard Hosten[a] and Christine Biateau
Laboratoire de Mécanique Physique, Bordeaux 1 University, UMR C.N.R.S. 5469, 351 cours de la Libération, 33405 Talence Cedex, France

(Received 22 September 2007; revised 29 January 2008; accepted 31 January 2008)

The measured characteristics (efficiency and sensitivity) of two air-coupled transducers allow for the prediction of the absolute values of the pressure of the bulk waves generated in air and for the measurement of the pressure of the field radiated in air by guided waves propagating in a structure. With finite element software, the pressure field generated by an air-coupled transducer is simulated by introducing a right-hand side member in the Helmholtz equation, which is used for computing the propagation from the transducer to a plate. The simulated source is rotated in order to impose an angle of incidence with respect to the normal of the plate and generate the corresponding guided mode. Inside the plate, the propagation is simulated with the dynamic equations of equilibrium and a complex stiffness tensor to take into account the viscoelastic anisotropy of the material. For modeling the three-dimensional fields of the guided modes propagating in a two-dimensional non-symmetry plane, a 2.5 dimensional model is introduced. The model computes the value of the pressure field radiated in air by the plates for any guided modes and can predict the detectability of the system for a known defect in a structure. A test bed incorporating two air-coupled transducers is used to generate and receive various guided modes. Two plates made of Perspex and carbon-epoxy composite are tested. The pressure measured by the receiver at various positions is compared to the results of the model to validate it. © *2008 Acoustical Society of America.*
[DOI: 10.1121/1.2885742]

PACS number(s): 43.35.Cg, 43.20.El, 43.35.Yb, 43.20.Fn [YHB] Pages: 1963–1971

I. INTRODUCTION

The use of air-coupled transducers is a promising technique for generating and detecting guided waves in structures. In the last decade, it was shown that their use was feasible for generating and detecting guided waves in metal or composite materials.[1–6] The main advantages of this single sided technique are the absence of contact and the possibility of generating guided modes with low phase velocities (A_0, for instance). However, the main drawback is the very high impedance mismatch between the air and solid.

There are two main limitations of the use of air-coupled transducers: the dynamic range and the bandwidth of the system are limited by the efficiency and the sensitivity of the transducers and the attenuation of the guided waves. Therefore, if the receiver or the defects are too far from the emitter, the amplitude of the corresponding signals can be smaller than the measurable amplitude.

In consequence, before using this technique for specified structures and transducers, it is highly valuable to predict the intensity of the stress fields in air and in the structure, the response of the receiver, the detectability of the corresponding signals, and their variations due to the presence of defects.

In the past, some investigations were done for predicting the air-coupled system response from the transmission coefficient[1,2] or from a finite element (FE) model in non-absorbing plates.[3] It is the purpose of this paper to present a finite element model that includes the simulation of the bulk mode propagation in air, the guided modes propagation in a viscoelastic anisotropic plate, and the coupling between these modes at the interfaces. The starting point is the measurement of the efficiency of the air-coupled transducer that is entered into the model to predict the plate response in terms of absolute values of stresses, displacements, and particle velocities.

The previous approach[1,2] based on analytical computations and reflection/transmission coefficients of a plate is fast and can be used in inverse problems, such that the identification of the plate characteristics.[4] However, they are not available for complex curved structures including stiffeners, lap joints, rivets, screws, etc.

The main advantage of the finite elements approach is its capability to simulate the propagation in complex structures, with or without defects and for various shapes of a transducer like, for instance, focused air-coupled transducers or phased arrays. In this perspective, a first step is presented in this paper for verifying the model from experimental data.

In the first part of the paper, the reader is reminded of the procedure for characterizing the air-coupled transducer emitter in terms of efficiency, which means the amplitude of the pressure as a function of the excitation amplitude. The

[a]Author to whom correspondence should be addressed. Electronic mail: b.hosten@lmp.u-bordeaux1.fr

knowledge of this efficiency permits one to measure the sensitivity of the air-coupled transducer receiver. Then the absolute value of the amplitude of the pressure can be introduced in the FE model.

The bulk mode generation and propagation in air is simulated by the inhomogeneous Helmholtz equation and the guided waves in a plate by the equation of motion in a solid. The simulation of the generation is initially tested by comparison with the measurements of the normal displacement of the guided waves propagating along an absorbing Perspex plate. Then, the generation of bulk waves in air with an air-coupled transducer, the propagation of guided waves in a carbon epoxy plate, and the reception with a second air-coupled transducer are predicted with the FE model and compared to the measurements.

II. TRANSDUCERS CHARACTERIZATION

For predicting the real field produced by an air-coupled transducer in a plate and the potentiality of producing guided waves with sufficient energy to be detected, the first step is to measure the efficiency of the transducer emitter.

A. Efficiency

The efficiency is defined as the pressure produced in air, measured in Pascals per volt applied to the transducer. A procedure was described to measure this efficiency.[7] It is based on the measurement, done with a Laser velocimeter, of the particle velocity V_m of a very thin membrane placed in the acoustic field. The membrane is maintained perpendicular to the beam axis, without stress. Its lateral dimension must be larger than the transducer beam width. It is made of Polyethylene Terephtalate (PET) and the thickness is 5 μm. Its acoustic impedance is $Z=1.82\ 10^6\ \mathrm{kgm^{-2}\ s^{-1}}$ and the air impedance is $Z_a=420\ \mathrm{kgm^{-2}\ s^{-1}}$. The computed transmission coefficient of the membrane, T_m, permits one to compute the acoustic pressure P_a produced by the transducer when the membrane is withdrawn,[7] according the formula

$$P_a = \frac{Z_a}{T_m} V_m. \tag{1}$$

In this paper, the results are given for a commercial available transducer (ULTRAN NCT-102 241710). Its active diameter is 25 mm and all the measurements are done at 200 mm from the transducer. The results of the measurements, given in Fig. 1(a), show the efficiency of this transducer as a function of the frequency.

In the experiments described later, the transducer emitter is fed with two long bursts at 0.25 and 0.20 MHz. The tension of the excitation voltage is adjusted for obtaining 100 Pa along the normal of the front face, at 200 mm from the transducer.

B. Sensitivity and detectability

For measuring the sensitivity of the air-coupled receiver transducer (ULTRAN NCT102X 242307), it is placed in front of the emitter. Since the pressure is known, it is straightforward to deduce its sensitivity. In fact, this characteristic is strongly dependent on the amplifier that is connected to the receiver. Here it is the amplifier section of a PANAMETRIC 5058 PR device. The sensitivity in Volts per Pascal, is given at Fig. 1(b). Knowing that, the measurements furnished by the receiver are converted to Pascals in the following for easy comparison with the results of the model.

Another important characteristic is the minimum amplitude of the pressure that the receiver/amplifier combination is able to detect, called in the following detectability. Of course, this notion depends on the way the signals are processed. Here, the simplest definition is chosen: it is the signal

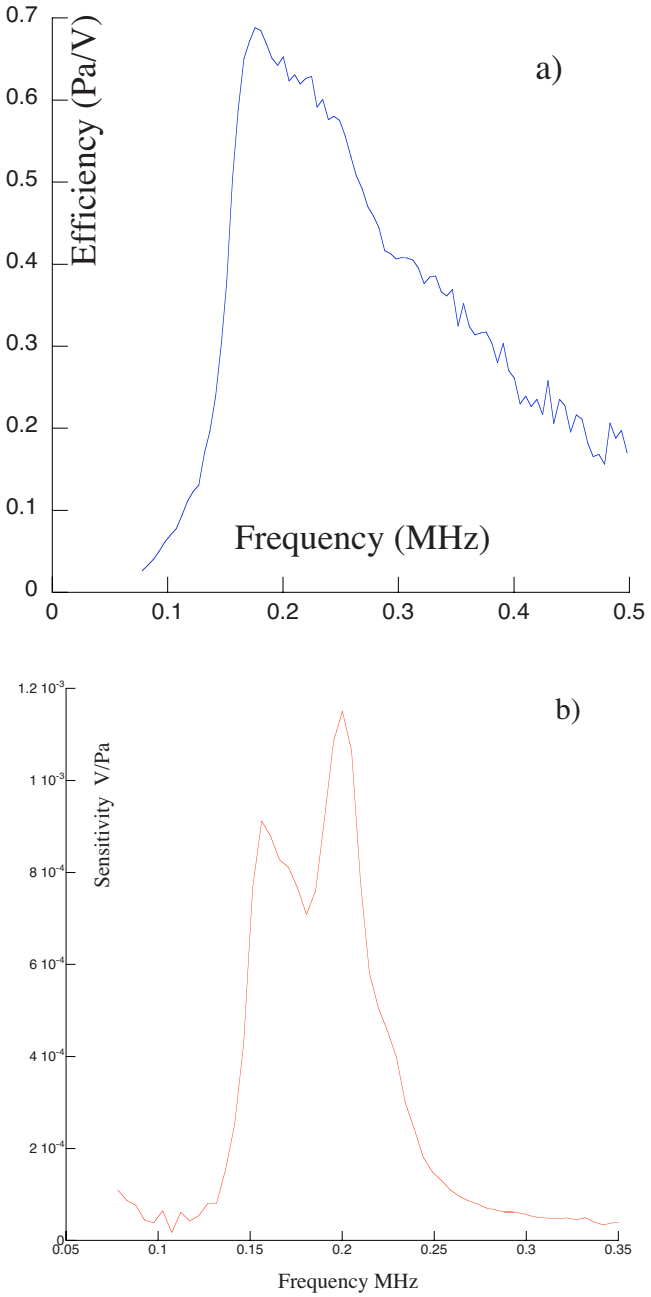

FIG. 1. (Color online) (a) Efficiency of the air-coupled emitter (Ultran NCT102X 241710) and the sensitivity (V/Pa) of the transducer receiver (Ultran NCT102X 242307) as a function of frequency.

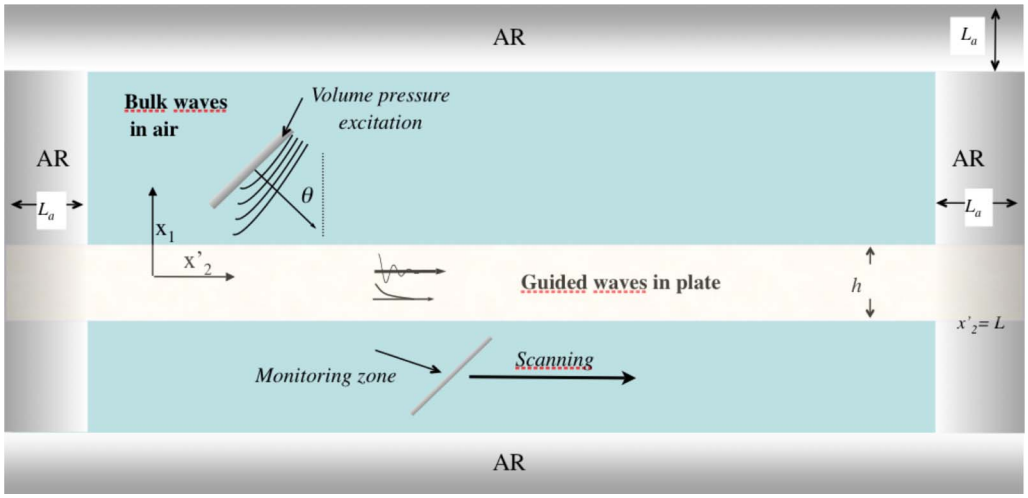

FIG. 2. (Color online) Schematic of the FE model to simulate the generation of the incident bulk wave propagating in air and its conversion to a guided wave propagating inside the plate.

amplitude that is equal to the noise amplitude, without averaging. Then, any amplitude or any variation of the pressure under 0.01 Pa is considered as not detectable.

Subsequently, for any guided modes, any materials for which the properties are known and for any defect for which the geometry is defined, the model must be able to predict the detectability of this defect.

III. SOLID PROPAGATION FE MODEL

In a previous reference,[8] it was verified that the use of the FE method for solving the equation of dynamic equilibrium in the frequency domain permits one to simulate properly the propagation of attenuated guided waves in viscoelastic plates, with the plane of propagation being a plane of symmetry. The propagation of guided waves in symmetry and non-symmetry planes for a plate made of an orthotropic viscoelastic material, is considered in this paper. Since a three-dimensional (3D) model is time consuming, the simulation is limited to a two-dimensional (2D) problem, along the direction x_1 (perpendicular to the plate) and the direction x_2' (which is the direction of the propagation of the guided waves inside the plate) (Fig. 2). As a consequence, the derivatives of the displacements and stress fields along the direction three are null. When propagating in a non-symmetry plane, the displacement field must be represented by three components. In the following, the Fourier transform of these components is represented by u_1, u_2, u_3. This intermediate situation between a 2D and 3D model is called 2.5D.

The azimuthal angle φ is defined by the rotation around the axis x_1, of the axes of symmetry x_2 to the axis x_2' and x_3 to the axis x_3'. For an orthotropic material and in the rotated axes $[x_1, x_2', x_3']$, the Hooke's law that links the displacements to the stresses is given by:

$$\begin{bmatrix} \sigma_1 \\ \sigma_2 \\ \sigma_3 \\ \sigma_4 \\ \sigma_5 \\ \sigma_6 \end{bmatrix} = \begin{pmatrix} C'_{11} & C'_{12} & C'_{13} & C'_{14} & 0 & 0 \\ C'_{12} & C'_{22} & C'_{23} & C'_{24} & 0 & 0 \\ C'_{13} & C'_{23} & C'_{33} & C'_{34} & 0 & 0 \\ C'_{14} & C'_{24} & C'_{34} & C'_{44} & 0 & 0 \\ 0 & 0 & 0 & 0 & C'_{55} & C'_{56} \\ 0 & 0 & 0 & 0 & C'_{56} & C'_{66} \end{pmatrix} \times \begin{bmatrix} u_{1,1} \\ u_{2,2} \\ 0 \\ u_{3,2} \\ u_{3,1} \\ u_{1,2} + u_{2,1} \end{bmatrix}, \tag{2}$$

where the notation j is the partial derivative along the direction j.

The C'_{ij} are obtained by rotation of the azimuthal angle φ from the nine complex moduli, $C_{11}, C_{22}, C_{12}, C_{66}, C_{33}, C_{13}, C_{55}, C_{23}, C_{44}$,[9] defined in the axes of symmetry. The values of these moduli can be measured with ultrasonic techniques in immersion.[10]

In the equations of propagation:

$$\begin{aligned} &\partial_1(C'_{11}u_{1,1} + C'_{12}u_{2,2} + C'_{14}u_{3,2}) + \partial_2(C'_{56}u_{3,1} + C'_{66}(u_{1,2} + u_{2,1})) + \rho\omega^2 u_1 = 0 \\ &\partial_2(C'_{12}u_{1,1} + C'_{22}u_{2,2} + C'_{24}u_{3,2}) + \partial_1(C'_{56}u_{3,1} + C'_{66}(u_{1,2} + u_{2,1})) + \rho\omega^2 u_2 = 0, \\ &\partial_2(C'_{14}u_{1,1} + C'_{24}u_{2,2} + C'_{44}u_{3,2}) + \partial_1(C'_{55}u_{3,1} + C'_{56}(u_{1,2} + u_{2,1})) + \rho\omega^2 u_3 = 0 \end{aligned} \tag{3}$$

where ρ is the mass density, ω is the pulsation, and the rotated moduli C'_{ij} are computed with these relations:

$$C'_{11} = C_{11}$$

$$C'_{22} = C_{22}c^4 + C_{33}s^4 + 2C_{23}c^2s^2 + 4C_{44}c^2s^2$$

$$C'_{44} = (c^2 - s^2)^2 C_{44} + c^2s^2(C_{33} + C_{22} - 2C_{23})$$

$$C'_{55} = c^2C_{55} + s^2C_{66} \quad C'_{66} = s^2C_{55} + c^2C_{66} \quad C'_{12} = c^2C_{12} + s^2C_{13}$$

$$C'_{14} = cs(C_{13} - C_{12}) \quad C'_{56} = cs(C_{55} - C_{66})$$

$$C'_{24} = cs(C_{23}(c^2 - s^2) - C_{22}c^2 + C_{33}s^2 + 2(c^2 - s^2)C_{44}), \tag{4}$$

where c and s are: $c=\cos(\varphi)$, $s=\sin(\varphi)$.

The above differential equations must be written in the following FE-code form:[11]

$$\nabla \cdot (\mathbf{C}_s \nabla \mathbf{U}) - a\mathbf{U} = 0, \tag{5}$$

where $\mathbf{C}_s$ is a (3×3) matrix composed of 6 (2×2) sub matrices and a (3×3) matrix. Some tedious but simple computations give the content of these matrices:

$$\mathbf{C}_s = \begin{bmatrix} \begin{pmatrix} C'_{11} & 0 \\ 0 & C'_{66} \end{pmatrix} & \begin{pmatrix} 0 & C'_{12} \\ C'_{66} & 0 \end{pmatrix} & \begin{pmatrix} 0 & C'_{14} \\ C'_{56} & 0 \end{pmatrix} \\ \begin{pmatrix} 0 & C'_{66} \\ C'_{12} & 0 \end{pmatrix} & \begin{pmatrix} C'_{66} & 0 \\ 0 & C'_{22} \end{pmatrix} & \begin{pmatrix} C'_{56} & 0 \\ 0 & C'_{24} \end{pmatrix} \\ \begin{pmatrix} 0 & C'_{56} \\ C'_{14} & 0 \end{pmatrix} & \begin{pmatrix} C'_{56} & 0 \\ 0 & C'_{24} \end{pmatrix} & \begin{pmatrix} C'_{55} & 0 \\ 0 & C'_{44} \end{pmatrix} \end{bmatrix} a$$

$$= \begin{pmatrix} -\rho\omega^2 & 0 & 0 \\ 0 & -\rho\omega^2 & 0 \\ 0 & 0 & -\rho\omega^2 \end{pmatrix}. \tag{6}$$

IV. GENERATION AND PROPAGATION IN AIR

In air, the propagation of the pressure field p is given by the inhomogeneous Helmholtz equation

$$-\nabla C_a \nabla p - \rho_a\omega^2 p = f(x_1, x'_2). \tag{7}$$

In this equation, p is the Fourier transform of the pressure. The stiffness $C_a=\rho_a^* c_a^2=0.00014(1+i0.0002)$ GPa is the product of the mass density $\rho_a=0.001225$ gr/cm^3 and the square of the speed of sound $c_a=0.34$ mm/μs in air. The imaginary part represents a realistic attenuation in air.[12] To simulate the action of the transducer, the right-hand side member of the Eq. (7) is set equal to

$$f(x_1, x'_2) = A\rho_a\omega^2 p_0 \exp(-ik_a m)\,\delta(x_1, x'_2), \tag{8}$$

where p_0 is equal to the pressure measured at the position of the measuring thin membrane. In the following, all the results will be given for an incident pressure of 100 Pa. The space-limited $\delta(x_1, x'_2)$ function defines an excitation line inclined with an incident angle θ, the length of which corresponds to the diameter of the transducer; $k_a=\omega/\lambda_a$ is the wave number in air and m is the width of the excitation line. Then, a bulk wave in air is generated in the desired direction.

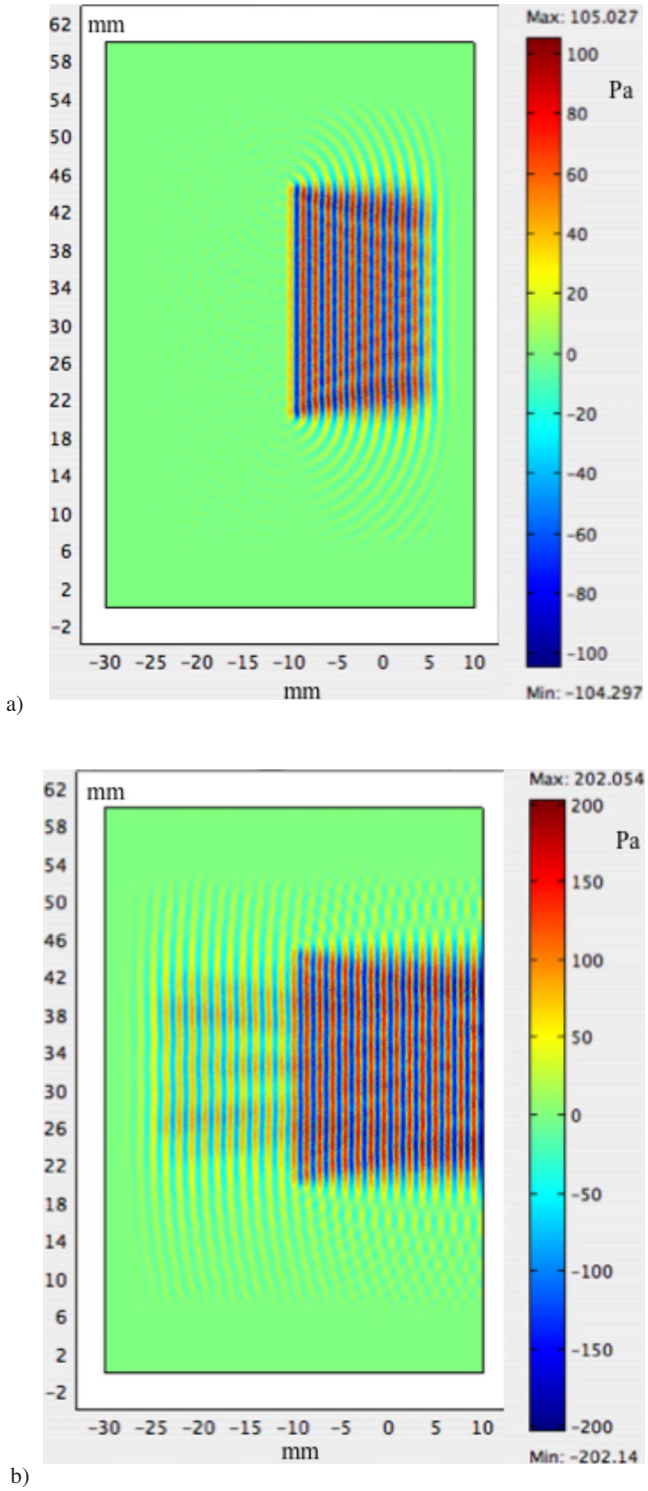

FIG. 3. (Color online) Generation of the incident bulk wave propagating in air: (a) in an infinite medium, (b): with a reflective surface.

The term $\rho_a\omega^2 p_0$ is a way to approach the required pressure value for simulating the real field. In fact, the result depends on the geometry of the excitation zone and on the frequency. It is straightforward to compute the field with $A=1$ and to run again the computation by adjusting the value of A to obtain the correct value of the incident pressure field.

Figure 3(a) shows the generation of the bulk wave at $f=0.25$ MHz in an infinite medium simulated with absorbing regions (defined in the next paragraph). For $m=0.5\lambda_a$ and

$A=0.27$ the peak value of the pressure is 105 Pa. In that case ($\theta=0$), the wave propagates only in the right direction. Figure 3(b) shows the same generation in the presence of a free reflective surface (reflection coefficient=−1). The peak value of the pressure is now 202 Pa in the zone were the incident and the reflected waves interfere. The reflected wave goes through the excitation zone without being perturbed.

V. ABSORBING REGIONS AND BOUNDARY CONDITIONS

In the frequency domain for simulating the propagation in a semi-infinite air medium and an infinite plate, it is mandatory to eliminate the reflection at the edges. An absorbing region is simulated with a fictitious material for which the viscoelastic moduli C_{ij}^{*AR} are increased progressively in order to absorb any waves entering this region.[13] In the plate, the imaginary parts of the stiffness moduli are regularly increased at the right and the left edges. In air, two absorbing regions are also introduced at the top and bottom sides (Fig. 2). For instance, the imaginary part of the viscoelastic moduli for defining the right absorbing region is:

$$x_2 > L - L_a \quad C_{ij}''^{AR} = C_{ij}'' + A(x_2 - (L - L_a)/L_a)^3 C_{ij}', \qquad (9)$$

where L is the length of the plate. The length of the absorber L_a and the factor A are adjusted to minimize the reflections at the edges of the plate.

Since the relation between the pressure and the displacement field in air is given by $\mathbf{grad}(p)=\rho_a\omega^2\mathbf{U}$, at the interface air/solid, the stress is given by the Neumann conditions:

$$\text{Air side: } \mathbf{n}\,.\,C_a\nabla p = -C_a\rho_a\omega^2 u_1, \quad \text{Solid side: } \mathbf{n}\,.\,\cdot(\mathbf{C}_a\nabla\mathbf{U}) = -p \qquad (10)$$

where u_1 is the normal displacement in the solid at the interface and $\mathbf{x}_1\cdot(\mathbf{C}_s\nabla\mathbf{U})$ is the stress at the surface of the plate. At the solid/air interface, the conditions are the same as the conditions in Eq. (10), except the signs are changed. At the other interfaces, the Dirichlet conditions ($p=0$) are imposed in air and the Neumann ($\mathbf{n}\cdot(\mathbf{C}_s\nabla\mathbf{U})=0$) conditions in solid.

VI. VALIDATION OF THE NUMERICAL MODEL FOR AIR-COUPLED GENERATION

The model is tested in two steps. The purpose of the first step is the validation of the model for the generation of the bulk mode in air and its conversion to a guided mode in the plate.

A. Equipment for measuring the particle velocity at the surface of the plate

A Doppler velocimeter (Polytec OFV-353-3001, sensitivity 0.005 ms^{-1}/V for a frequency limit of 0.25 MHz) is used as a reference to measure the particle velocity at the surface of the plate. The plate is placed between the air-coupled transducer and the laser probe (Fig. 4(a)). The laser beam is fixed and focused on a very small piece of a retro-reflective tape. It was verified that the measured displacement by the laser probe was the same with or without the tape. The tape is useful only to adjust the perpendicularity between the laser beam and the plate and to reduce the signal to noise ratio. The transducer is mounted on a goniometer that imposed the incident angle and moved by a translation table that permits a precise scan parallel to the plate. It is positioned at around 200 mm from the plate for applying the pressure of 100 Pa (similar to the FE model).

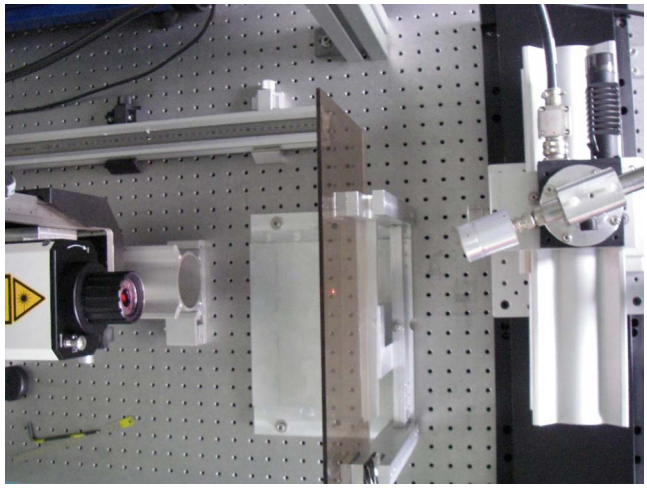
(a)

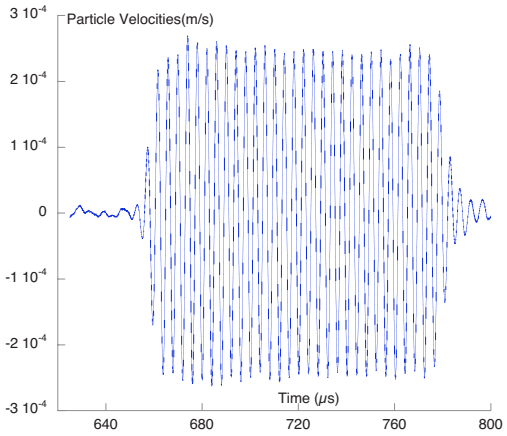

(b)

FIG. 4. (Color online) (a) Picture of the setup to measure the particle velocity at the surface of the plate. (b) Waveform measured by the laser probe when the transducer is excited at 0.250 MHz (angle of 17°, *A*0 mode).

B. Comparison between FE results and measurements

In this first preliminary test, the plate is isotropic and made of Perspex. Its characteristics, given in Table I, were measured with a classical immersion technique.[10] Figure 4(b) shows a typical waveform measured by the laser probe when the transducer is excited with a long burst at 0.250 MHz and a tension of 165 V, which produces an acoustic pressure of 100 Pa near the plate with an angle of incidence of 17° for

TABLE I. Measured complex viscoelasticity moduli (in GPa) of the Perspex plate.

Thickness (mm) 3.90		Density ρ (g/cm^3) 1.19	
C_{11}^*	$8.5(1+i0.03)$	C_{66}^*	$2.3(1+i0.03)$
C_{22}^*	C_{11}^*	C_{12}^*	$C_{11}^*-2C_{66}^*$

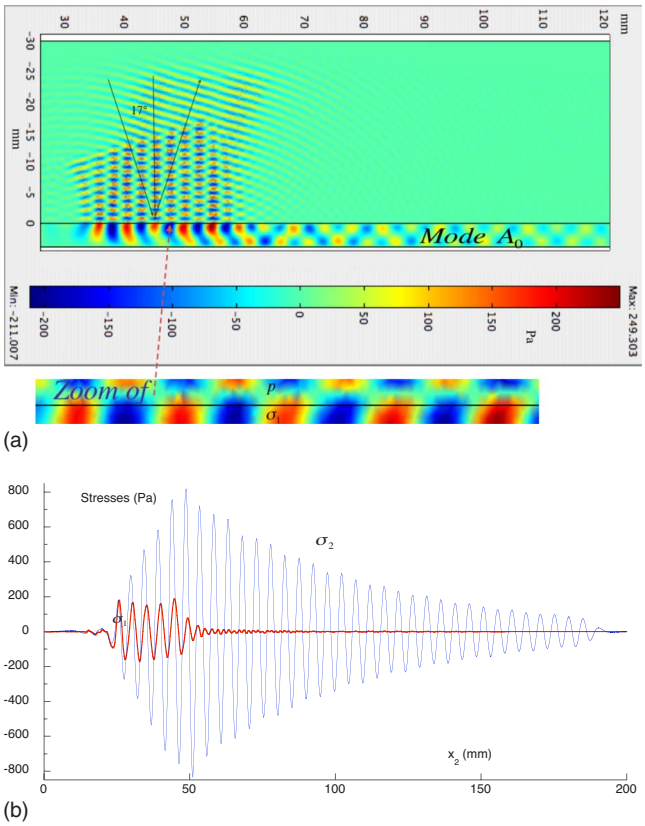

FIG. 5. (Color online) (a) Image of the real part of the pressure p in air and the stress σ_1 in the plate (in Pa) for the mode A_0 simulated by the FE model. (b) Comparison between the stress normal to the interface σ_1 and the stress σ_2 along the interface at the interface.

the A_0 mode generation. Figure 5(a) presents the image of the real part of the pressure p in air and of the stress normal to the interface σ_1 in the plate (in Pa) for the mode A_0 simulated by the FE model. It is clearly visible that there is a first portion along the propagation where the mode is progressively established. The zoom of the model results at the interface shows the good continuity between p and σ_1. Also, Fig. 5(b) presents the real part of the stress normal to the interface σ_1 at the interface and shows the tail after the excitation zone due to the transducer edge diffraction. In the same figure, the shape of the real part of the stress σ_2 along the interface at the interface shows the quality of the absorbing area.

The particle velocity, at the surface of the plate, obtained from this model is also presented in Fig. 6(a). In the same figure, the laser measurements of the particle velocity are plotted for comparison. The correspondence with the FE computation is fairly good, although the model is bidimensional. Probably, this can be explained by the fact that the major contribution of the diffraction effect caused by the size limited transducer is due to the rotation around the vertical axis, and this is taken into account in the model. This should be confirmed with a 3D model.

At this frequency-thickness product ($\approx$1 mm MHz), three guided modes can exist (A_0, S_0 and A_1) and one can expect to generate mainly A_0 by choosing the corresponding angle, but a small quantity of S_0 and A_1 can also be generated, depending on the aperture of the transducer. An advantage of the FE model is that it is able to predict this effect. Figure 6(b) presents the spatial Fourier transform of the particle velocity shown in Fig. 6(a), on a monitoring zone of length 100 mm. The purity of the generated mode defined as the ratio in % between the amplitudes of the larger unwanted mode (here S_0) and the desired mode (here A_0) is 12% for the computation and 9% in the experiment.

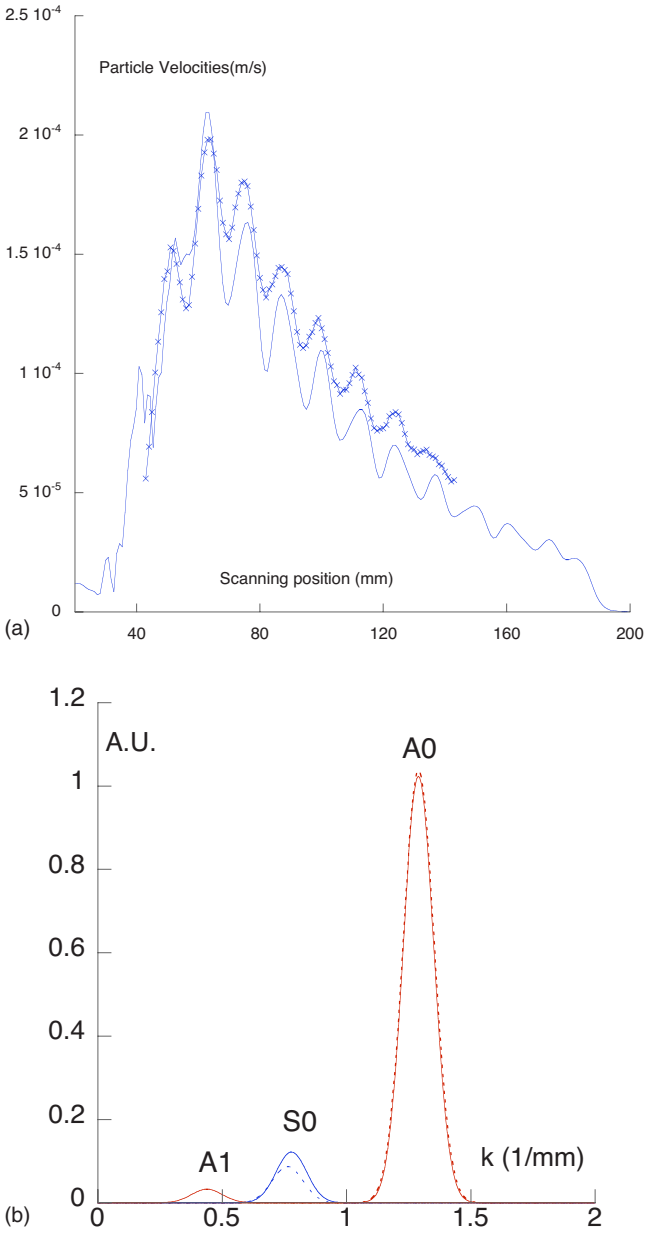

FIG. 6. (Color online) (a) Particle velocities for the A_0 mode computed (—) and measured (×–×–) as a function of a scanning position at the surface of the plate. (b) Amplitude of the spatial Fourier transform of the particle velocity measured (…..) and computed (—).

The same computation and experiment were made with the angle of incidence, the value of which is imposed to 9.8°, corresponding to the coincidence angle for the S_0 mode. Figure 7 shows that for this mode, the comparison model experiment is not as good as for the A_0 mode. However, the amplitude of the particle velocities is of the same order, showing that the prediction is valuable enough.

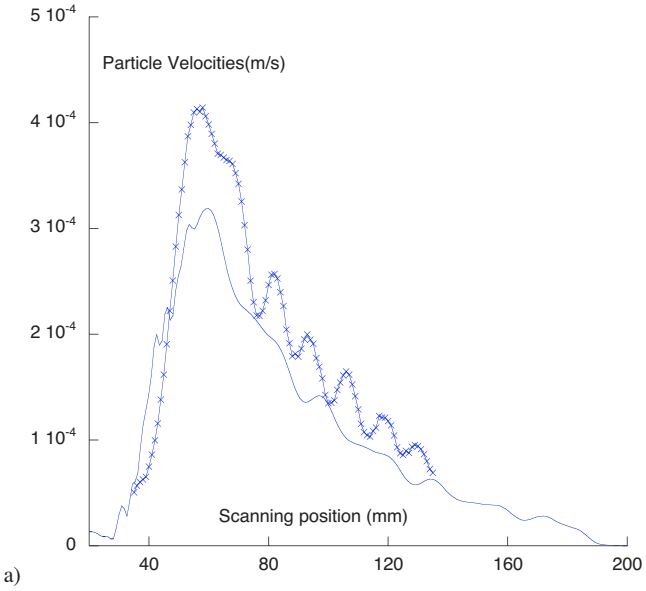

a)

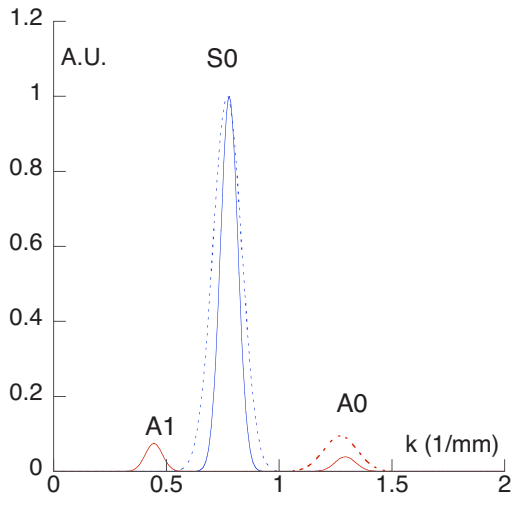

b)

FIG. 7. (Color online) (a) Particle velocities for the S_0 mode simulated (—) by the FE model and measured (×–×–) as a function of a scanning position at the surface of the plate. (b) Amplitude of the spatial Fourier transform of the particle velocity measured (…..) and computed (—).

VII. VALIDATION OF THE FE MODEL FOR AIR-COUPLED GENERATION AND RECEPTION OF GUIDED WAVES IN ANISOTROPIC MATERIALS

The purpose of this second step is the complete validation of the model of the guided waves in viscoelastic anisotropic materials for the generation and the reception with air-coupled transducers. The laser velocimeter is now replaced by another air-coupled transducer (Fig. 8) and the plate is made of a carbon-epoxy composite material, with unidirectional fibers oriented along the x_3 axis. The properties of this viscoelastic anisotropic material, measured with the classical immersion method,[10] are given in Table II. Both transducers are mounted on a goniometer that imposes the same angle of incidence. Since the receiver sensitivity at 0.25 MHz is very low (Fig. 1(b)), the frequency used in this step is decreased to 0.20 MHz (for which the sensitivity is maximum −0.115 mV/Pa). The dispersion curves for the carbon-epoxy composite plate permits one to compute the angles for generating the corresponding modes. There are many methods for computing these curves. Here they are computed with the surface impedance matrices method.[14] Figure 9 shows only the modes A_0 and S_0 that can be generated at this frequency. The SH modes in the symmetry planes $P_{\varphi=0^\circ}$ and $P_{\varphi=90^\circ}$ are not coupled to the incident bulk wave and the coupling of the SH mode in the non-symmetry plane $P_{\varphi=45^\circ}$ is very weak.

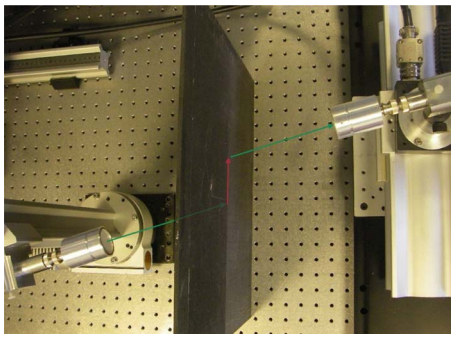

FIG. 8. (Color online) Picture of the setup to generate and receive guided modes with air-coupled transducers.

These angles are successively imposed in the model and in the experiment. A transducer is scanned along a line parallel to the plate and the amplitude of each signal is converted into Pascals and plotted in Fig. 10. With the FE model, the stress field in the plate and the pressure in each semi-infinite air medium are computed. With air-coupled transducers generating guided modes, it is convenient to place the transducers in the same side of the structure. The guided waves are faster than the direct bulk waves transmitted through air and it is easy to separate them in the temporal domain. Working in the frequency domain, it is also possible to place a screen. However, this screen must be surrounded by absorbing areas and it is simpler to place the transducers in both sides of the plate for validating the model.

To compare with the experimental results, the value of the pressure field is monitored along a line inclined with the corresponding angle (Fig. 2). The length of this monitoring zone corresponds to the diameter of the transducer. The values along the line are added for providing a value that rep-

TABLE II. Measured complex viscoelasticity moduli (in GPa) of the carbon/epoxy plate.

Thickness (mm)		4.1	Density ρ (g/cm^3)	1.53	
C^*_{11}	15(1+i0.03)	C^*_{44}	5.4(1+i0.08)	C^*_{23}	6.3(1+i0.12)
C^*_{22}	13(1+i0.07)	C^*_{66}	3.4(1+i0.02)	C^*_{12}	7.0(1+i0.05)
C^*_{33}	139(1+i0.09)	C^*_{55}	6.1(1+i0.08)	C^*_{13}	7.6(1+i0.12)

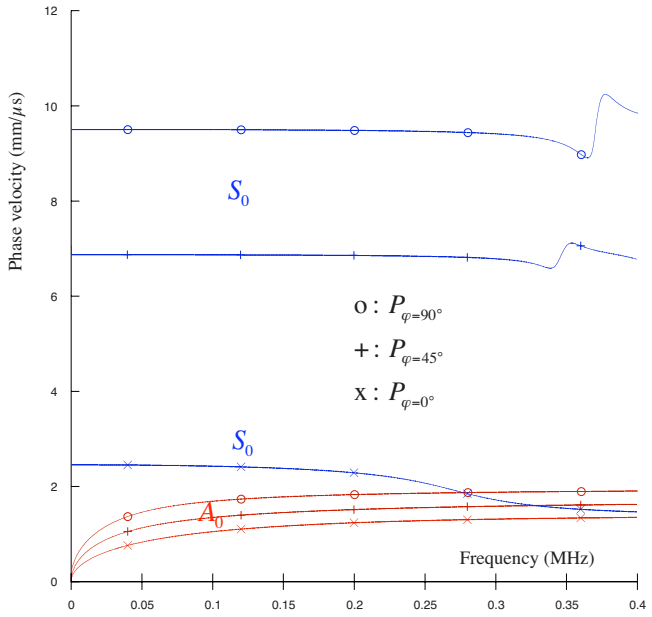

FIG. 9. (Color online) Dispersion curves for the carbon/epoxy plate.

resents the receiver amplitude in Pascals. This line is scanned in the results of the model and the values of this scanning are also plotted in Fig. 10.

Despite many uncertainties associated with the measurements of the transducers' characteristics (efficiency and sensitivity) and of the materials' properties, it is noticeable than the absolute intensities of the pressures measured and computed are very similar. The main error is the decrease of the amplitude of the A_0 guided mode propagating in the direction of the fibers ($P_{\varphi=90°}$). This is probably due to the uncertainties of the imaginary part of the moduli in that plane. In the future, this could be adjusted to get better precision on these quantities. It is difficult to estimate the uncertainties, however an approach is to consider the detectability threshold as the uncertainty for each measurement. With this assumption, the experimental and computed curves overlap in Fig. 10.

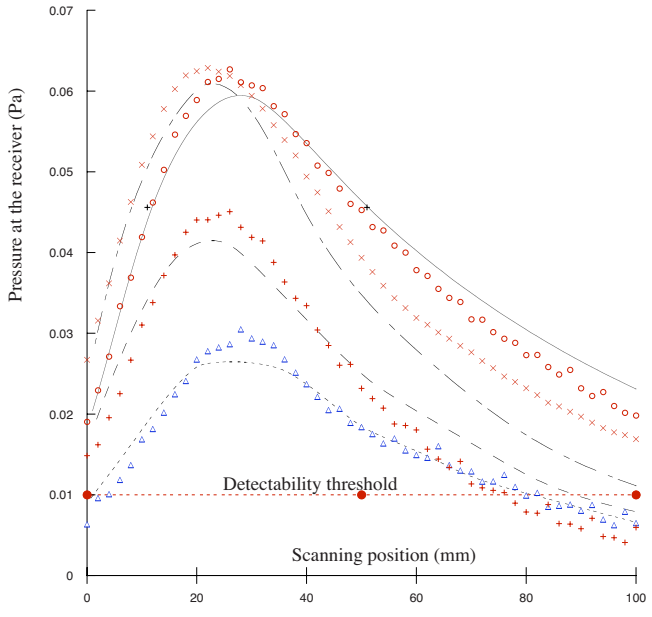

FIG. 10. (Color online) Amplitude of the signal given by the transducer receiver converted to Pascals as a function of the scanning position. Frequency: 200 KHz. Experimental results: Mode A_0 ○: *in* $P_{\varphi=0°}$, ×: $P_{\varphi=90°}$, +: *in* $P_{\varphi=45°}$ Mode S_0 △: *in* $P_{\varphi=0°}$ Computed results: Mode A_0 —: *in* $P_{\varphi=0°}$:, –––: *in* $P_{\varphi=90°}$. ----: *in* $P_{\varphi=45°}$ Mode S_0 …..: *in* $P_{\varphi=0°}$

The S_0 mode was measurable only in the plane perpendicular to the fiber ($P_{\varphi=0°}$). The S_0 mode has a noticeable normal displacement only after the frequency area of the dispersion curve that starts to have a negative slope (Fig. 9). That is not true in the two other planes at the frequency 0.2 MHz; then, S_0 is not well coupled to the air bulk mode. As expected, the amplitudes of the air bulk modes radiated from the S_0 guided mode propagating in the plane $P_{\varphi=45°}$ and $P_{\varphi=90°}$, were predicted, by the model, to be much less than the detectability threshold.

VIII. CONCLUSIONS

A finite element model has been tested for computing, in absolute values, the generation of the bulk wave in air and its interaction with a plate for generating guided waves. The 2D FE model associated with the measurements of the efficiency of the air-coupled transducer leads to a good representation, in absolute values, of the stress and displacement fields inside the plate.

Hence, if one knows *a priori* the viscoelastic properties of the material constituting a structure, he can predict the possibility for testing the structure with an air-coupled system. For that, the sensitivity and the detectability of the air-coupled transducer receiver must be measured to simulate the complete air-coupled system. The complete model was checked by comparison with the measurements of the amplitudes of the bulk mode in air, due to the leakage of the guided waves propagating in symmetry and non-symmetry planes of an anisotropic carbon-epoxy plate.

With this model, many systematic studies can be considered like, for instance, parametric computations with various dimensions of a defect—notches, delaminations—and their various positions in the thickness of multilayered composite materials in order to predict the detectability of the defect.

[1]A. Safaeinili, O. I. Lobkis, and D. E. Chimenti, "Quantitative materials characterization using air-coupled leaky Lamb waves," Ultrasonics **34**, 393–396 (1996).
[2]O. Lobkis and D. Chimenti, "3-D voltage model for detection of sound radiated from anisotropic materials," Ultrasonics **38**, 237–241 (2000).
[3]M. Castaings and P. Cawley, "The generation, propagation, and detection of Lamb waves in plates using air-coupled ultrasonic transducers," J. Acoust. Soc. Am. **100**(5), 3070–3077 (1996).
[4]O. I. Lobkis, D. E. Chimenti, and Han Zhang, "In-plane elastic property characterization in composite plates," J. Acoust. Soc. Am. **107**(4), 1852–1858 (2000).
[5]M. Castaings and B. Hosten, "Lamb and SH waves generated and detected by air-coupled ultrasonic transducers in composite material plates," NDT & E Int. **34**, 249–258 (2001).
[6]S. Holland, S. Teles, and D. Chimenti, "Air-coupled, focused ultrasonic dispersion spectrum reconstruction in plates," J. Acoust. Soc. Am. **115**(6), 2866–2872 (2004).
[7]C. Biateau, B. Hosten, and D. Roziere, "Measurement of air-coupled transducer characteristics for ultrasonic non-destructive evaluation," QNDE **21A**, 921–928 (2002).
[8]M. Castaings, C. Bacon, B. Hosten, and M. V. Predoi, "Finite element predictions for the dynamic response of thermo-viscoelastic material

structures," J. Acoust. Soc. Am. **115**(3), 1125–1133 (2004).
[9]B. A. Auld, *Acoustic Fields and Waves in Solids* (Krieger, Malabar, FL, 1990).
[10]M. Castaings, B. Hosten, and T. Kundu, "Inversion of ultrasonic, plane-wave transmission data in composite plates to infer viscoelastic material properties," NDT & E Int. **33**(6), 377–392 (2000).
[11]COMSOL Multiphysics User's Guide, Version 3.3 by—http://www.comsol.com/ (last viewed December, 2007).
[12]H. E. Bass and F. Douglas Shields, "Absorption of sound in air: High-frequency measurements," J. Acoust. Soc. Am. **62**(3), 571–576 (1977).
[13]G. R. Liu and J. D. Achenbach, "A strip element method for stress analysis of anisotropic linearly elastic solids," J. Appl. Mech. **61**, 270–277 (1994).
[14]B. Hosten and M. Castaings, "Surface impedance matrices to model the propagation in multilayered media," Ultrasonics **41**, 501–507 (2003).

Piezoacoustic wave spectra using improved surface impedance matrix: Application to high impedance-contrast layered plates

Victor Y. Zhang[a)]
Institut d'Electronique, de Microélectronique, et de Nanotechnologie, UMR 8520, Laboratoire Central de l'Institut, Avenue Poincaré - BP 6009, 59652 Villeneuve d'Ascq Cedex, France

Bertrand Dubus[b)]
Institut Supérieur d'Electronique et Numérique, 41 Boulevard Vauban, 59046 Lille Cedex, France

Bernard Collet[c)] and Michel Destrade[d)]
Institut Jean Le Rond d'Alembert, UMR 7190, Case 162, CNRS/Université Pierre et Marie Curie, 4 Place Jussieu, 75252 Paris Cedex 05, France

(Received 19 December 2006; revised 12 November 2007; accepted 27 December 2007)

Starting from the general modal solutions for a homogeneous layer of arbitrary material and crystalline symmetry, a matrix formalism is developed to establish the semianalytical expressions of the surface impedance matrices (SIM) for a single piezoelectric layer. By applying the electrical boundary conditions, the layer impedance matrix is reduced to a unified elastic form whether the material is piezoelectric or not. The characteristic equation for the dispersion curves is derived in both forms of a three-dimensional acoustic SIM and of an electrical scalar function. The same approach is extended to multilayered structures such as a piezoelectric layer sandwiched in between two metallic electrodes, a Bragg coupler, and a semi-infinite substrate as well. The effectiveness of the approach is numerically demonstrated by its ability to determine the full spectra of guided modes, even at extremely high frequencies, in layered plates comprising up to four layers and three materials. Negative slope in $f-k$ curve for some modes, asymptotic behavior at short wavelength regime, as well as wave confinement phenomena made evident by the numerical results are analyzed and interpreted in terms of the surface acoustic waves and of the interfacial waves in connection with the bulk waves in massive materials.
© *2008 Acoustical Society of America.* [DOI: 10.1121/1.2836756]

PACS number(s): 43.35.Pt, 43.35.Cg, 43.40.Le [PEB] Pages: 1972–1982

I. INTRODUCTION

Engineering applications in surface acoustic wave (SAW) devices, composite material characterization, and smart structures, require the analysis of acoustic wave interaction with anisotropic and/or piezoelectric multilayers. Recently, the analysis of *bulk acoustic waves* (BAW) in multilayered structures composed of stacked piezoelectric, dielectric, and metallic materials has once again attracted the attention of engineers and researchers working on radio frequency components such as stacked crystals filter, coupled resonator filter, and multiplexers built on *solidly mounted resonators* (SMR) and thin film bulk acoustic resonators. The development of efficient simulation tools is needed to characterize accurately the electromechanical behavior of complex stratified structures accounting for realistic electrical and mechanical interface and *boundary conditions* (BC).

Many methods have been developed for studying the acoustic waves spectra in layered media, and a majority of them are based on the matrix formalism. The most commonly known is without any doubt the *transfer matrix method* (TMM),[1] which in its simplest form is conceptually intuitive but intrinsically suffers from numerical instability at high frequencies. Following many efforts to improve the TMM,[2–4] a genuine advance in breaking through the numerical limitation of the classical TMM was the approach using the *surface impedance matrix* (SIM).[5–18] Although the concept of the acoustical (or mechanical) impedance is an old one for all physicists and engineers, the SIM expressed in its initial form[13] did not guarantee numerical stability at high frequencies because the exponential dichotomy factors generating instability were not arranged in a convenient way. By means of a reformulated form of the SIM[9,11,12,14,16,17] and its equivalent variants—reflection matrix,[19] scattering matrix,[20,21] or compliance/stiffness matrix,[22,23] for individual layers and with the help of a recursive algorithm for the overall multilayers.[9,11,12,16,17,19–23] correct transitions of the state vector across layer interfaces can be achieved. This in turn allows numerically stable and robust algorithms to be elaborated without increasing the basic matrix size.

The SIM approach consists in first, expressing the state vector values at the two surfaces of a piezoelectric layer by means of an eight-dimensional layer impedance matrix; then, calculating the global surface impedance matrix of a

[a)]Electronic mail: victor.zhang@iemn.univ-lillel.fr
[b)]Electronic mail: bertrand.dubus@isen.fr
[c)]Electronic mail: bc@ccr.jussieu.fr
[d)]Electronic mail: destrade@lmm.jusssieu.fr

multilayer with the help of a recursive algorithm from the impedance matrix of the individual layers along with the imposed/known BC; and finally, formulating the characteristic equations of guided waves by canceling the determinant of the final impedance matrix formulated for a selected interface where the acoustic energy is concentrated. The key point in calculating the layer impedance matrix, which guarantees the numerical stability, is the appropriate arrangement of the eight partial modes resulting from the constitutive relations and the equilibrium equations. Common to various possible forms, it is essential to avoid exponential dichotomy by absorbing the exponentially large terms through the negligibly small amplitudes,[17] both of which are associated with the same partial modes. The advantages of the SIM approach over the well-known TMM approach are analyzed in some detail in many published works. The approach, based on the decomposition of incident and reflected partial waves at the different interfaces, acts on the amplitudes of partial modes of each layer rather than on the physical quantities themselves. Thus as a result of energy conservation, such an approach is guaranteed to be stable.[19] The loss of precision in the SIM is delineated in terms of upward-bounded and downward-bounded waves. The resultant expressions and algorithm are terse so that their implementation is more convenient and efficient than the TMM. This alternative formulation is stable, efficient, and illuminating,[21] while being as fast as the TMM.[16] The matrix form is concise, thus simple to program and implement.[22] The two concise recursive algorithms, based on combining Stroh formalism and a SIM approach, are more stable than the standard matrix method and are faster than the global matrix method. They also appear to be extremely straightforward and efficient at least from the computational point of view.[17] The SIM approach also has the advantage of being conceptually simple and numerically flexible. Namely, a SIM can be defined for any interface as well as for an external surface when the structure is a multilayer. This flexibility allows one to numerically determine the dispersion curves and field distributions with more accuracy by selecting the appropriate interface in the neighborhood of which the electromechanical energy flux is localized, and to obtain the full set of solutions, even under extreme conditions, by repeatedly formulating the SIM at different locations. The modeling of Lowe[1,24] for ultrasonic waves in multilayered media is also restricted to isotropic and purely elastic materials. Stewart and Yong[25] performed an analysis of the acoustic propagation in multilayered piezoelectric plates using the TMM. Both simple thickness modes and general dispersion behaviors for propagating straight-crested waves in zinc oxide on silicon thin film resonators were studied. However, only the mass and no stiffness effects of the electrodes on the resonators were considered in their model. Acoustical spectra become very complex in multilayered plates composed of layers having significantly different material properties, especially when the constituent layers have high velocity and/or impedance contrast. With a slight variation of the pair $\omega-k$ value in the spectral domain, where ω is the frequency and k the wave number, the nature of the guided modes can be radically different, from Lamb-like to SAW-like.

In this paper, we develop a detailed formalism enabling the full spectra of guided waves in layered plates to be calculated even with a high impedance contrast and at extremely high frequencies. The exemplified structure consists of a piezoelectric AlN layer, a high-impedance metallic tungsten (W) layer, and a low-impedance dielectric SiO_2. This study was motivated by the SMR design employing AlN as active resonator and the stacked cells made of bilayer W/SiO_2 as Bragg coupler, to isolate the resonator from the substrate. We develop a semianalytical model to calculate the dispersion curves for various multilayer configurations. Starting from an adaptation of the general Stroh formalism[26,27] to the special case of homogeneous materials for every layer[7,10,11,28,29] we recall briefly in Sec. II the main results and formulas necessary for further developments. SIM expressions and dispersion relations in terms of the SIM elements are derived in Sec. III first for a single piezoelectric layer and then extended to include two surrounding metallic electrodes and a semi-infinite supporting substrate via a Bragg coupler. Section IV is devoted to numerical investigations considering only a piezoelectric AlN layer combined with a few W/SiO_2 cells in order to facilitate the analysis of the rather complicated spectra of guided acoustic modes. Some conclusions and discussions are given in Sec. V.

II. BASIC STROH FORMALISM AND MAIN RESULTS

To simplify the formulation, we choose the reference coordinate system such that the x_1 axis is the propagation direction in the layering plane, the x_2 axis is parallel to the layering thickness, and the layering plane is assumed to be unbounded. The vibration state of a structure can be described by means of a state vector (τ) whose components are composed of physical variables that are continuous across the interfaces.[27–29]

The state vector we chose is defined by $\tau=[T_{21}T_{22}T_{23}D_2v_1v_2v_3\psi]^T$, where v_i are the components of particle velocity vector v, T_{2i} are the components of stress tensor in x_2 plane; $\psi\equiv j\omega\phi$; $j^2\equiv-1$, ϕ is the electric potential, ω is the angular frequency, and D_2 is the normal electric displacement. The superscript T means transpose, and the subscript $i(=1,2,3)$, corresponds to the space variable x_i. This choice of the state vector is identical to the choice in Ref. 28, but different from that adopted in Refs. 9–11 where the displacement was employed instead of the velocity and where the components of $\boldsymbol{\tau}$ were not arranged in the same order. According to results established in Refs.28, 29, and 13, the state vector $\boldsymbol{\tau}$ obeys the following system of ordinary differential equation of first order in the harmonic regime:

$$\frac{d\boldsymbol{\tau}}{dx_2}=j\omega\mathbf{A}\boldsymbol{\tau}. \tag{1}$$

The system matrix $\mathbf{A}$, also named the state matrix or Stroh matrix, is given by

$$\mathbf{A}=\begin{bmatrix}\boldsymbol{\Gamma}_{12}\boldsymbol{\Gamma}_{22}^{-1}s_1 & (\boldsymbol{\Gamma}_{12}\boldsymbol{\Gamma}_{22}^{-1}\boldsymbol{\Gamma}_{21}-\boldsymbol{\Gamma}_{11})S_1^2+\boldsymbol{\rho}_0\\ \boldsymbol{\Gamma}_{22}^{-1} & \boldsymbol{\Gamma}_{22}^{-1}\boldsymbol{\Gamma}_{21}s_1\end{bmatrix}$$

with

$$\mathbf{\Gamma}_{ab} = \begin{bmatrix} c_{1a1b} & c_{1a2b} & c_{1a3b} & e_{b1a} \\ c_{2a1b} & c_{2a2b} & c_{2a3b} & e_{ba} \\ c_{3a1b} & c_{3a2b} & c_{3a3b} & e_{b3a} \\ e_{a1b} & e_{a2b} & e_{a3b} & -\varepsilon_{ab} \end{bmatrix} \times (a,b = 1,2,3),$$

where $\boldsymbol{\rho}_0$ is ρ times a four-dimensional identity matrix with a fourth element equal to zero, and c, e, ε, and ρ denote material constants. It is worthwhile recalling that the material constants appearing in the matrices $\mathbf{\Gamma}_{ab}$ are those evaluated in the working reference system. The matrix $\mathbf{A}$ has a frequency-independent form. It depends, apart from the material constants, on a unique variable s_1, with $s_i = k_i/\omega$, k_i being the component along x_i of the wave number, and s_i the slowness component. It is from the $\mathbf{A}$ matrix that result the proper modes, also called partial waves, susceptible of propagating in a homogeneous unbounded medium. According to the linear system theory, the general solution of $\boldsymbol{\tau}$ can be constructed by a linear combination of modal solutions weighted with modal amplitude ($\mathbf{y}$). This yields the general form for the state vector

$$\boldsymbol{\tau}(x_1,x_2,t) = \mathbf{Q}\mathbf{E}(x_2)\mathbf{y}e^{j\omega(t-s_1x_1)}, \tag{2}$$

where

$$\mathbf{E}(x_2) = e^{-j\omega s_2 x_2} \tag{3}$$

is the transition matrix, also called the "propagator matrix," and $\mathbf{s}_2$ is the diagonal spectral matrix of Eq. (1), $\mathbf{Q}$ is the associated modal matrix, and $\mathbf{y}$ is the amplitude vector. The components $s_2^{(r)}$ of $\mathbf{s}_2$ and $\mathbf{Q}^{(r)}$ of $\mathbf{Q}$ $(r=1,\ldots,8)$, are eigenvalues and eigenvectors determined from the following homogeneous system:

$$[\mathbf{A} + s_2^{(r)}\mathbf{I}]\mathbf{Q}^{(r)} = \mathbf{0}, \quad r = 1,\ldots,8, \tag{4}$$

where $\mathbf{I}$ is a eight-dimensional identity matrix. In what follows, we assume that the partial modes are arranged in such a manner that the matrices $\mathbf{s}_2$ and $\mathbf{Q}$ can be put into the form:

$$\mathbf{s}_1 = \begin{bmatrix} \mathbf{s}_D & \mathbf{0} \\ \mathbf{0} & \mathbf{s}_I \end{bmatrix}, \quad \mathbf{Q} = \begin{bmatrix} \mathbf{t}_D & \mathbf{t}_I \\ \mathbf{v}_D & \mathbf{v}_I \end{bmatrix}, \tag{5}$$

where all submatrices are four-dimensional.

Hereafter, the subscripts D and I stand for *direct* and *inverse* partial waves, respectively, see Ref. 29 for their definition. Note that in Ref. 29 the words "diffracted" and "incident" were used in the place of "direct" and "inverse," respectively, in the context on surface wave problems. We point out that the real s_2's represent the upward- and downward-propagating oblique plane waves in the layers (propagating in x_1 and standing in x_2), and that their interaction is the origin of the resultant guided modes pertaining to the layered plate. We recall that all eight partial modes are required for a finite thickness layer, whereas only the four D or I modes are needed for a semi-infinite substrate according to the Sommerfeld radiation condition. In this paper, the case $s_1=0$, which corresponds to normal propagation, will not be considered, and the rare degenerated cases where the eigenvalue (or Christoffel equation's root) s_2 is double valued for certain isolated special values of s_1 are also excluded, so that

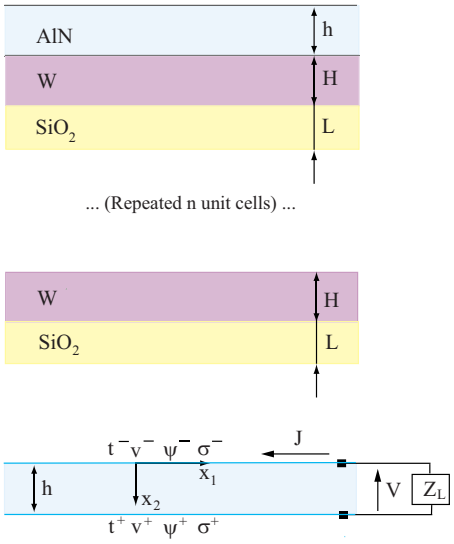

FIG. 1. (Color online) A layered plate composed of a piezoelectric AlN layer with N identical cells of bilayer W/SiO_2. Also shown are the coordinates system and the relevant physical quantities at the surface of a layer. Electric variables are not involved for nonpiezoelectric layers.

Eq. (2) is used as the valid solution throughout the paper.

III. MATRIX FORMALISM FOR GUIDED WAVES IN LAYERED STRUCTURES

We first consider a plate composed of three materials, namely a piezoelectric {c}-oriented AlN layer, a metallic W layer, and a purely dielectric SiO_2 layer, as illustrated by Fig. 1. In order to apply the results of Sec. II and to develop the matrix formalism for the purpose of deriving the characteristic equation leading to the dispersion relation of acoustic waves in this structure, we introduce some specific quantities for the values of the relevant physical variables at the layer surfaces. In Fig. 1 the superscript that is a negative sign refers to the upper surface and the superscript that is a positive sign to the bottom surface, $\sigma^{\pm}$ stands for surface charge density, V is the voltage across the piezoelectric layer, and J is the current entering into the piezoelectric layer when an external load impedance Z_L is connected between two surface electrodes. The latter are assumed for the moment to be perfectly conducting and negligibly thin so that they have no mechanical effects on the piezoelectric resonator. The effects of actual metallic electrodes of finite thickness are discussed in Sec. III D.

A. Single piezoelectric layer

We first look for expressions of the characteristic impedance matrices in terms of the modal ($\mathbf{Q}$) and spectral ($\boldsymbol{s}_2$) matrices for a piezoelectric layer. For this purpose, we introduce a *generalized mixed matrix* $\mathbf{G}$ defined by

$$\begin{bmatrix} \mathbf{T}^- \\ \mathbf{T}^+ \end{bmatrix} \equiv [\mathbf{G}] \begin{bmatrix} \mathbf{V}^- \\ \mathbf{V}^+ \end{bmatrix}, \tag{6}$$

with $\mathbf{T}^{\pm} \equiv [\mathbf{t}^{\pm} \quad D_2^{\pm}]^T$, $\mathbf{V}^{\pm} \equiv [\mathbf{v}^{\pm} \quad \psi^{\pm}]^T$, $\mathbf{t} \equiv [t_{21}\ t_{22}\ t_{23}]^T$, $\mathbf{v} \equiv [v_1\ v_2\ v_3]^T$. After Eqs. (2), (3), and (5), we derive an expression of the $\mathbf{G}$ matrix as follows:

$$\mathbf{G} = \begin{bmatrix} \mathbf{t}_D & \mathbf{t}_I(\mathbf{E}_I^0)^{-1} \\ \mathbf{t}_D\mathbf{E}_D^0 & \mathbf{t}_I \end{bmatrix} \begin{bmatrix} \mathbf{v}_D & \mathbf{v}_I(\mathbf{E}_I^0)^{-1} \\ \mathbf{v}_D\mathbf{E}_D^0 & \mathbf{v}_I \end{bmatrix}^{-1}, \quad (7)$$

where $\mathbf{E}_{D,I}^0 = e^{-j\omega s_{D,I}h}$ is the submatrix of the transition matrix $\mathbf{E}^0 \equiv \mathbf{E}(x_2 = h)$. We point out that other forms of $\mathbf{G}$ matrix exist.[17,23] Each of the four submatrices $\mathbf{G}_{ij}$, $i, j = 1, 2$, of $\mathbf{G}$ is four dimensional and contains elements of different physical signification. Take $\mathbf{G}_{11}$ for example and rewrite it in the form

$$\mathbf{G}_{11} = \begin{bmatrix} \mathbf{Z}_{11}^p & \mathbf{K}_{11} \\ \mathbf{X}_{11} & \mathbf{Y}_{11} \end{bmatrix} \equiv \begin{bmatrix} \mathbf{Z}_m & \mathbf{K} \\ \mathbf{X} & Y_e \end{bmatrix}. \quad (8)$$

In Eq. (8), $\mathbf{Z}_m$ is a 3-by-3 matrix representing a mechanical impedance, Y_e is a scalar proportional to an electrical admittance, while $\mathbf{K}$ and $\mathbf{X}$ have the dimension of a piezoelectric coefficient. $\mathbf{X} = \mathbf{K}^T$ provided an appropriate normalization is operated for the state vector. We emphasize that $\mathbf{Z}_m$ itself already includes a part originated from piezoelectricity. $\mathbf{G}_{11}$ is the counterpart to the *generalized surface impedance* matrix involved in the SAW problem.[29] When the layer material is nonpiezoelectric (dielectric or metallic, say), $\mathbf{K} = \mathbf{0}$ holds and $\mathbf{G}_{11}$ is decoupled into two independent parts, namely $\mathbf{Z}_m$ for the acoustic part and Y_e for the electric part. This means that the electrical and mechanical variables can be dealt with independently. This happens equally to a piezoinactive acoustical mode in piezoelectric materials. The same is true for the other submatrices of $\mathbf{G}$ which have analogous properties. Some interesting relations exist linking these submatrices. For a metallic layer, we take into account the mechanical effects by assuming it to be perfectly conductive. We conclude by saying that Eq. (7) naturally applies for a nonpiezoelectric layer.

In order to keep the matrix dimension compatibility and to facilitate the transition at interfaces within a heterostructure, we find it more useful to define the *acoustic impedance* ($\mathbf{Z}$) matrix as follows:

$$\begin{bmatrix} \mathbf{t}^- \\ \mathbf{t}^+ \end{bmatrix} \equiv [\mathbf{Z}] \begin{bmatrix} \mathbf{v}^- \\ \mathbf{v}^+ \end{bmatrix}. \quad (9)$$

$\mathbf{Z}$ is six dimensional and appears in a purely elastic form. However, it implicitly includes the dielectric and piezoelectric effects when the layer is piezoelectric. This new definition applies whether the layer is piezoelectric or not.

B. Electrical BC and characteristic equations

We now express the $\mathbf{Z}$ matrix defined in Eq. (9) in terms of the elements of the matrix $\mathbf{G}$ by eliminating the electrical variables upon applying the known electrical BC. The surface charge is written as $\sigma^- = D_2^- - D_0^-$ and $\sigma^+ = D_0^- - D_2^+$ at the upper and bottom surfaces, respectively. Relations between the electric potential and displacement $D_0^\pm$ in the vacuum side are established, after having resolved the Laplace equation, as $D_0^+ = g\psi^-$ and $D_0^- = -g\psi^+$ with $g \equiv j|s_1|\varepsilon_0$. We deduce from them that

$$\sigma^- = D_2^- - g\psi^- \quad (10a)$$

and that

$$\sigma^+ = -[D_2^+ + g\psi^+]. \quad (10b)$$

The charge conservation reads $\sigma^- + \sigma^+ = 0$, which gives

$$\sigma^- = -\sigma^+ \equiv \sigma. \quad (11)$$

Two types of electrical BC are to be distinguished for a piezoelectric layer:

(1) The surface is metallized and short-circuited (SC), in which case $Z_L = 0$, leading to

$$j\omega V \equiv \psi^- - \psi^+ = 0. \quad (12)$$

(2) The surface is nonmetallized and open-circuited (OC), in which case $Z_L = \infty$, leading to

$$\sigma = 0 \quad \text{with } \psi^- \neq \psi^+ \text{ in general.} \quad (13)$$

In order to make the subsequent development easier, and especially in order to facilitate the introduction of the BC, we rewrite the relation (6) defining the $\mathbf{G}$ matrix more explicitly and in a slightly different form:

$$\begin{bmatrix} \mathbf{t}^- \\ \mathbf{t}^+ \\ \sigma \\ \sigma \end{bmatrix} \equiv \begin{bmatrix} \mathbf{Z}_{11}^p & \mathbf{Z}_{12}^p & \mathbf{K}_{11} & \mathbf{K}_{12} \\ \mathbf{Z}_{21}^p & \mathbf{Z}_{22}^p & \mathbf{K}_{21} & \mathbf{K}_{22} \\ \mathbf{X}_{11} & \mathbf{X}_{12} & Y_{11} - g & Y_{12} \\ \mathbf{X}_{21} & \mathbf{X}_{22} & Y_{21} & Y_{22} + g \end{bmatrix} \begin{bmatrix} \mathbf{v}^- \\ \mathbf{v}^+ \\ \psi^- \\ \psi^+ \end{bmatrix}. \quad (14)$$

Equations (10a), (10b), and (11) have been taken into account in arriving at Eq. (14). The upper-left sub-block in Eq. (14) is a mechanical impedance, the lower-right sub-block is an electrical admittance with the term g coming from the vacuum contribution. The antidiagonal sub-blocks represent the piezoelectric terms.

Since the AlN layer in a resonator configuration is usually sandwiched between two metallic electrodes, we consider mainly the case where both surfaces are SC and we determine the characteristic equations corresponding to this condition. Electric SC condition implies $V = 0$, i.e., $\psi^- = \psi^+$. Since the value of the potential is relative to a certain reference arbitrarily chosen, it is usual to set them both equal to zero. Use of $\psi^- = \psi^+ = 0$ in Eq. (14) yields, according to Eq. (9), the $\mathbf{Z}$ matrix for a SC piezoelectric layer:

$$\begin{bmatrix} \mathbf{t}^- \\ \mathbf{t}^+ \end{bmatrix} = [\mathbf{Z}^{\mathrm{SC}}] \begin{bmatrix} \mathbf{v}^- \\ \mathbf{v}^+ \end{bmatrix} \quad \text{with } \mathbf{Z}^{\mathrm{SC}} \equiv \begin{bmatrix} \mathbf{Z}_{11}^p & \mathbf{Z}_{12}^p \\ \mathbf{Z}_{21}^p & \mathbf{Z}_{22}^p \end{bmatrix}. \quad (15)$$

$\mathbf{Z}^{\mathrm{SC}}$ is the layer mechanical impedance matrix when its surfaces are both short-circuited (superscript SC). By further applying the stress-free mechanical BC, say $\mathbf{t}^- = \mathbf{0}$ at the upper surface, we finally arrive at the so-called *surface impedance matrix* (SIM) $\mathbf{Z}^+$ defined for the bottom surface as

$$\mathbf{t}^+ \equiv \mathbf{Z}^+\mathbf{v}^+, \quad \text{with } \mathbf{Z}^+ = \mathbf{Z}_{22}^{\mathrm{SC}} - \mathbf{Z}_{21}^{\mathrm{SC}}(\mathbf{Z}_{11}^{\mathrm{SC}})^{-1}\mathbf{Z}_{12}^{\mathrm{SC}}. \quad (16a)$$

In the same way, we can define the SIM $\mathbf{Z}^-$ for the top surface by applying SC and stress-free BC at the bottom surface. The result is, after interchanging the matrix indices 1 and 2 in Eq. (16a),

$$\mathbf{t}^- \equiv \mathbf{Z}^-\mathbf{v}^- \quad \text{with } \mathbf{Z}^- = \mathbf{Z}_{11}^{SC} - \mathbf{Z}_{12}^{SC}(\mathbf{Z}_{22}^{SC})^{-1}\mathbf{Z}_{21}^{SC}. \tag{16b}$$

Here, $\mathbf{Z}_{ij}^{SC}$ refer to the submatrices of $\mathbf{Z}^{SC}$. The SIM $\mathbf{Z}^{\pm}$ defined in Eq. (16) are the acoustic impedances looking outward from one surface toward and accounting for the mechanical BC imposed upon the other surface along with the electrical BC applied at both surfaces. The solutions of plate modes in general, and of the Lamb and SH modes in particular, in a piezoelectric layer with SC and stress-free at both surfaces are then obtained by simply canceling the $\mathbf{Z}^{\pm}$ determinant:

$$[\mathbf{Z}^{\pm}]\mathbf{v}^{\pm} = \mathbf{0}:\mathbf{v}^{\pm} \neq 0$$

and

$$\Delta^{SC}(\omega,k_1) \equiv \det[\mathbf{Z}^{\pm}] = 0 \rightarrow k_{SC}(\omega). \tag{17}$$

Any one of the couple sign $(\pm)$ can be used and it results, in principle, in identical solutions. However, the functional behavior of $\det[\mathbf{Z}^{\pm}(\omega,k_1)]$ is different in the case of a multilayer and especially at high frequencies. This has practical consequences in numerical resolution.

Once the values of k_1 are found for a given ω (usually by means of an iterative algorithm), the corresponding modes polarization can be determined from Eq. (17). The form of the characteristic equation in Eq. (17) has the advantage of easily separating the sagittal plane (SP) modes $(|\mathbf{Z}^{\pm}(1:2,1:2)|=0)$ from the shear horizontal (SH) modes $[\mathbf{Z}^{\pm}(3,3)=0]$ when they are uncoupled. Such is the case for acoustic modes in the layered structure depictured by Fig. 1. The dispersion relation of plate modes is a plot of ω versus k_1 over a certain range with like modes following regular curves, which gives a graphical picture of the solutions of the wave equation for a (specific layered) plate. There is an infinite number of ω values which can satisfy Eq. (17) for a given k_1. But there will be in general a finite number of real k_{SC} that can be found for a given ω, and that number increases with ω. Of course, the situation becomes complicated if the solutions are not restricted to within the real domain. At a given real frequency, besides the propagating modes, which are associated with the real solutions of k_1, there are a finite number of nonpropagating modes having purely imaginary wave numbers and an infinite number of inhomogeneous modes having complex wave numbers.[30] In this paper, we limit our investigation to the propagating plate modes. Most of the solutions exist only for a frequency larger than a critical threshold (cutoff). The cutoff frequencies of the propagating plate modes in the limit of $k_1 \rightarrow 0$ represent nothing but the resonant frequencies of thickness modes, which are the main waves for BAW devices.

The $\mathbf{Z}$ matrix associated to the OC condition can be determined by simply canceling out the electrical charge in Eq. (14). With $\sigma=0$, we obtain the counterpart to Eq. (15) as

$$\begin{bmatrix} \mathbf{t}^- \\ \mathbf{t}^+ \end{bmatrix} \equiv [\mathbf{Z}^{OC}] \begin{bmatrix} \mathbf{v}^- \\ \mathbf{v}^+ \end{bmatrix} \quad \text{with } \mathbf{Z}^{OC} = \mathbf{Z}^{SC} - \mathbf{K}\mathbf{Y}^{-1}\mathbf{X}. \tag{18a}$$

The matrices $\mathbf{K}$, $\mathbf{X}$, and $\mathbf{Y}$ involved in the $\mathbf{Z}^{OC}$ expression are defined by

$$\mathbf{K} \equiv \begin{bmatrix} \mathbf{K}_{11} & \mathbf{K}_{12} \\ \mathbf{K}_{21} & \mathbf{K}_{22} \end{bmatrix}, \quad \mathbf{X} \equiv \begin{bmatrix} \mathbf{X}_{11} & \mathbf{X}_{12} \\ \mathbf{X}_{21} & \mathbf{X}_{22} \end{bmatrix},$$

$$\mathbf{Y} \equiv \begin{bmatrix} Y_{11} - g & Y_{12} \\ Y_{21} & Y_{22} + g \end{bmatrix}. \tag{18b}$$

Use of $\mathbf{Z}^{OC}$ in the place of $\mathbf{Z}^{SC}$ in Eqs. (16) and (17) results in solutions (pairs $k_{OC}-\omega$ and modes polarization) of the plate modes in the piezoelectric layer with OC and stress-free surfaces.

Another alternative form of the characteristic equations consists in using exclusively the electrical variables. Applying $\mathbf{t}^{\pm}=\mathbf{0}$ to eliminate $\mathbf{v}^{\pm}$ in Eq. (14) leads to an electrical system

$$\begin{bmatrix} \sigma \\ \sigma \end{bmatrix} \equiv [\mathbf{E}] \begin{bmatrix} \psi^- \\ \psi^+ \end{bmatrix} \quad \text{with } \mathbf{E} = \mathbf{Y} - \mathbf{X}(\mathbf{Z}^{SC})^{-1}\mathbf{K}. \tag{19a}$$

Elimination of ψ^+ from Eq. (19a) leads to a relation between σ and ψ^- via a scalar function, the so-called effective surface permittivity ε_{eff} defined for the top surface by

$$\varepsilon_{eff}(\omega,k_1) \equiv \frac{\sigma}{-j|s_1|\psi^-} = \frac{E_{11}E_{22} - E_{12}E_{21}}{j|s_1|(E_{12} - E_{22})}. \tag{19b}$$

Here E_{ij} are the elements of the $\mathbf{E}$ matrix. ε_{eff} defined in Eq. (19b) is similar to the real part of the effective surface permittivity function of SAW problems[29] for all real $s_1 \equiv k_1/\omega$ values except that it tends to infinity with $s_1 \rightarrow 0$ for all finite frequencies. Compared with the $\mathbf{Z}$ determinant, the ε_{eff} function has the advantage of being sensitive only to the piezoactive modes. However, a pole and a zero of ε_{eff}, which are associated with the proper mode for respectively a SC and OC top surface, could be situated in extremely close proximity when the electromechanical coupling of the mode is poor.

C. Multilayered plates

So far we have shown that guided waves in a piezoelectric layer can be obtained by first formulating the acoustic impedances and then reducing them to a SIM or an effective surface permittivity for one surface. The $\mathbf{Z}$ matrix for a single layer can be calculated directly from its definition (9) in terms of the associated spectral and modal matrices. But for a multilayer consisting of a finite number of different layers, writing out the overall $\mathbf{Z}$ matrix, which requires having recourse to a recursive procedure[9,16,17,19,21,22] is longer than writing out the overall transfer $\mathbf{P}$ matrix, which needs simple cascading (series multiplication) of the individual layers' $\mathbf{P}$ matrix. An alternative way consists in expressing the overall $\mathbf{Z}$ matrix in terms of the easy-processed overall $\mathbf{P}$ matrix using the following relations, which apply to a layered plate as well as to a single layer:

$$\mathbf{Z}_{11} = -\mathbf{P}_{21}^{-1}\mathbf{P}_{22}, \quad \mathbf{Z}_{12} = \mathbf{P}_{21}^{-1},$$

$$\mathbf{Z}_{21} = \mathbf{P}_{12} - \mathbf{P}_{11}\mathbf{P}_{21}^{-1}\mathbf{P}_{22}, \quad \mathbf{Z}_{22} = \mathbf{P}_{11}\mathbf{P}_{21}^{-1}, \tag{20a}$$

$$\mathbf{P}_{22} = -\mathbf{Z}_{12}^{-1}\mathbf{Z}_{11}, \quad \mathbf{P}_{21} = \mathbf{Z}_{12}^{-1},$$

$$\mathbf{P}_{12} = \mathbf{Z}_{21} - \mathbf{Z}_{22}\mathbf{Z}_{12}^{-1}\mathbf{Z}_{11}, \quad \mathbf{P}_{11} = \mathbf{Z}_{22}\mathbf{Z}_{12}^{-1}. \tag{20b}$$

Calculating the overall **Z** matrix from the overall **P** matrix after Eq. (20a) is viable and simpler than using the recursive algorithm as long as the numerical instability is absent. Otherwise, the recursive algorithm[17,22] has to be used to calculate the overall **Z** matrix. We shall not further deal with this aspect of the problem by assuming that the right SIM results we need are numerically available.

Now we return to the consideration of a unit cell in the Bragg coupler, which comprises two layers of nonpiezoelectric materials with high impedance contrast. The mechanical contact at any interface is assumed to be perfect throughout this paper. We define the **Z** matrix for a unit cell in the same way as for a single layer, see Eq. (9), with at present $\mathbf{t}^{\pm}$ and $\mathbf{v}^{\pm}$ denoting the state vector evaluated at the top surface of the SiO_2-layer (−) and at the bottom surface of the W-layer (+). The same procedure applies to a periodic coupler consisting of m unit cells, or to an arbitrarily multilayered plate, when $\mathbf{t}^{\pm}$ and $\mathbf{v}^{\pm}$ refer to the state vector evaluated at the top (−) and bottom (+) surfaces of the whole structure. To stay general, we assume the coupler to be terminated with a known impedance $\mathbf{Z}_s$, which means that the relation $\mathbf{t}^+ = \mathbf{Z}_s\mathbf{v}^+$ holds. Applying this relation to Eq. (9) leads to the expression of the SIM ($\mathbf{Z}_M$) defined for the coupler top surface:

$$\mathbf{t}^- \equiv \mathbf{Z}_M\mathbf{v}^- \quad \text{with } \mathbf{Z}_M = \mathbf{Z}_{11} - \mathbf{Z}_{12}(\mathbf{Z}_{22} - \mathbf{Z}_s)^{-1}\mathbf{Z}_{21}. \tag{21}$$

In Eq. (21), $\mathbf{Z}_{ij}$ are the submatrices of the overall matrix **Z** referring to the whole coupler.

To determine the solutions proper to an AlN-Bragg plate with an electrically SC and stress-free surface, we apply the continuity condition at the AlN–coupler interface, expressed by $\mathbf{t}_c^- = \mathbf{t}_p^+$, and $\mathbf{v}_c^- = \mathbf{v}_p^+$. Here $\mathbf{t}_c^-$ and $\mathbf{t}_p^+$ (respectively, $\mathbf{v}_c^-$ and $\mathbf{v}_p^+$) are the normal surface stress (respectively, velocity) at the coupler and AlN side, respectively, of the interface. It yields

$$\mathbf{Z}_1\mathbf{v} = 0 \quad \text{with } \mathbf{Z}_1(\omega, k_1) = \mathbf{Z}_M - \mathbf{Z}^+. \tag{22}$$

In Eq. (22), **v** denotes the interface vibration velocity and $\mathbf{Z}^+$ is the SIM as determined in Eq. (16a) for an isolated AlN layer. When the coupler bottom surface is stress free, $\mathbf{Z}_s = \mathbf{0}$ in the $\mathbf{Z}_M$ expression. Using $\mathbf{Z}_M = \mathbf{Z}_{11} - \mathbf{Z}_{12}\mathbf{Z}_{22}^{-1}\mathbf{Z}_{21}$ in the $\mathbf{Z}_1$ expression and then locating the $\mathbf{Z}_1$-determinant zeros, we can obtain the guided wave solutions (pairs $k_{SC} - \omega$) for a multilayer without substrate. A systematic computation yields the dispersion curves. The OC modes naturally result from replacing $\mathbf{Z}^{SC}$ with $\mathbf{Z}^{OC}$ in the matrix $\mathbf{Z}^{\pm}$, cf. Eqs. 16–18.

D. Effects of the resonator's electrodes and bottom substrate

Now we show briefly how to include electrodes of finite thickness and a bottom substrate in the matrix formalism when dealing with a complete and more realistic SMR structure. Including the mechanical effects of finite thickness electrodes in the analysis complicates the formulation only to a small extent. For the inner electrode, a simple way is to incorporate its transfer matrix $\mathbf{P}_e$ into the coupler's one, and then to use the resultant matrix $\mathbf{P}'_m = \mathbf{P}_m\mathbf{P}_e$ instead of $\mathbf{P}_m$ everywhere. Another way of including the inner electrode, when making use of the recursive algorithm, consists in writing out first the submatrices of the inner electrode's **Z** matrix, say $\mathbf{Z}'_{ij}$, and then looking for the SIM $\mathbf{Z}'_M$ defined for its top surface with a known SIM $\mathbf{Z}_M$ exterior to its bottom surface. In this way, we easily obtain the expression of $\mathbf{Z}'_M$ as

$$\mathbf{t}_e^- \equiv \mathbf{Z}'_M\mathbf{v}_e^- \quad \text{with } \mathbf{Z}'_M = \mathbf{Z}'_{11} - \mathbf{Z}'_{12}(\mathbf{Z}'_{22} - \mathbf{Z}_M)^{-1}\mathbf{Z}'_{21}. \tag{23}$$

In Eq. (23), $\mathbf{Z}_M$ is the same as given in Eq. (21) referring to the coupler upper surface and including the substrate ($\mathbf{Z}_s$) when it is present, and $\mathbf{t}_e^-$, $\mathbf{v}_e^-$ refer to the state vector values calculated at the upper surface of the inner electrode. Comparison of Eqs. (23) and (21) gives a hint at how the general SIM recursive relation looks. Namely, the contribution of an additional bottom part to the considered plate is expressed by subtracting the SIM ($\mathbf{Z}_s, \mathbf{Z}_M$) defined for the upper surface of the bottom part from the submatrix ($\mathbf{Z}_{22}, \mathbf{Z}'_{22}$) to be inversed of the plate under consideration. As to the top electrode, let $\mathbf{Z}_e^+$ be the SIM defined for its bottom surface obtained by accounting for the zero stress at its upper surface. Instead of using $\mathbf{t}^- = \mathbf{0}$ in Eq. (15), we substitute the AlN-layer's upper surface stress $\mathbf{t}^-$ by $\mathbf{Z}_e^+\mathbf{v}^-$. As a result, Eq. (16a) becomes

$$\mathbf{t}^+ \equiv \mathbf{Z}^+\mathbf{v}^+ \quad \text{with } \mathbf{Z}^+ = \mathbf{Z}_{22}^{SC} - \mathbf{Z}_{21}^{SC}(\mathbf{Z}_{11}^{SC} - \mathbf{Z}_e^+)^{-1}\mathbf{Z}_{12}^{SC}. \tag{24}$$

Then, substituting $\mathbf{Z}^+$ in Eq. (22) with $\mathbf{Z}^+$ given by Eq. (24) allows the guided modes to be determined accounting for the top electrode.

As to substrate, $\mathbf{Z}_s = \mathbf{0}$ holds if the bottom substrate is the vacuum, and $\mathbf{Z}_s = \mathbf{Z}_{11}^p$, see Eq. (8), if it is a nonpiezoelectric semi-infinite solid or a piezoelectric one with a SC surface. For the OC piezoelectric substrate, $\mathbf{Z}_s = \mathbf{Z}_{11}^{OC}$, see Eq. (18). In addition, the factor g appearing in the expression of σ^+ in Eq. (10b) must be replaced with the element Y_{11} calculated according to Eq. (8) for the substrate.

IV. NUMERICAL RESULTS OF GUIDED MODES IN LAYERED PLATES

We numerically investigated structures consisting of a piezoelectric c-axis oriented AlN layer and a Bragg coupler having different numbers of layers W/SiO_2. Because of the coupler materials being isotropic and because of the special orientation of the AlN layer, the SH partial waves are decoupled from the SP ones and are piezo-inactive. In what follows, we focus only on the SP vibrations which are coupled with the electrical field. In our numerical examples, the thickness h of AlN layer was taken as 1 μm. For W (SiO_2), the thickness $H(L)$ was chosen as $H = 238.79$ nm ($L = 278.81$ nm), which corresponds to $\lambda/4$ when the wavelength λ of the longitudinal thickness mode in AlN is $\lambda = 2h$. First, we calculated the characteristic wave speeds for the three materials involved in our study. Table I lists the values we obtained with the physical constants we used in simulations. It shows that AlN is the fastest material and that W is the slowest one.

Then the acoustic spectra of Lamb waves in each individual layer were calculated. Though not reproduced here, they confirm that the Lamb and SH modes are uncoupled. We verified that the spectra of Lamb waves comprise both

TABLE I. Characteristic wave speeds of the three materials used in the multilayers.

	V_L (m/s)	Y-polar-V_s (m/s)	Second V_s (m/s)	V_{SAW} (m/s)
c-axis AlN: SC/OC	10 605/10 939	5796	5796	5394/5402
X propagation	9911 (nonpiezo)	5597	5796/5867	5417/5437
W (high impedance)	5224	2887		2669
SiO_2 (low impedance)	6099	3655		3342

symmetric and antisymmetric modes, and that as the frequency increases, all of them tend to the vertically polarized shear bulk wave speed (V_S), except for the two lowest ones which tend to the SAW velocity (V_{SAW}) on the free surface of a half-space, which will be termed massive material in the subsequent text.

Second, we calculated the dispersion curves, as plotted in Fig. 2, for two different bilayer plates, AlN/W and A1N/SiO_2. The former represents a high wave speed-contrast combination, and the latter is for the purpose of comparison with more complicated configurations. The electrical BC of the AlN layer was assumed to be SC in all numerical calculations. In addition to the form $f-k$, frequency as a function of wave number (here named k instead of k_1), we also plotted the same curves in the form V_p-f, phase velocity versus frequency. All variables are in a normalized form ($f_n=f/f_0, f_0=V_0/2h$), and $V_0=5882$ m/s is an arbitrarily chosen reference wave speed) for the purpose of more easily observing the asymptotic behavior of curves featured in plateau form. Two modes exist for all frequencies. The other modes (named higher order) do not appear below a corresponding threshold value f_c (cut-off). None of modes is rigorously symmetric or antisymmetric because the bilayer plates themselves do not exhibit any structural symmetry. Near the cut-off ($k\approx 0^+$), a few modes have a negative slope in the dispersion curve of $f-k$ plot, a phenomenon similar to what happens to the so-called "anomalous Lamb modes."[31,32] The slope is usually considered as the group velocity (V_g) though some researchers consider that the original definition of V_g is not applicable in this special k range because the mode is amplitude modulated in time.[32] As a general rule, the phase velocity V_p of higher-order guided modes decreases with increasing frequency, with a limit corresponding to the speed V_S of the vertically polarized shear bulk wave. With increasing frequency, the lowest branch goes up and then down after passing by a peak value of V_p, and finally tends to the SAW speed of the slower material (W or SiO_2). The next lowest branch goes directly down to the shear bulk speed of W for the AlN/W bilayer. For the A1N/SiO_2 bilayer, it first approaches the SAW speed of AlN ($V_p/V_0\cong 0.9$) where it stays awhile between $f_n=2-3$ near a horizontal line, termed plateau, before joining the shear bulk speed of massive SiO_2. Here we observe the mode repulsion phenomenon, i.e., the same branch of dispersion curves "shifts" above and below the plateau, as illustrated in Fig. 2 by the numbers 2 and 3. The wave patterns in this region resemble those of the nondispersive SAW in massive AlN. The asymptotical lines for longitudinal BAW are not yet observable in the shown frequency range. For any mode exhibiting cutoff, the group velocity V_g defined by the slope in

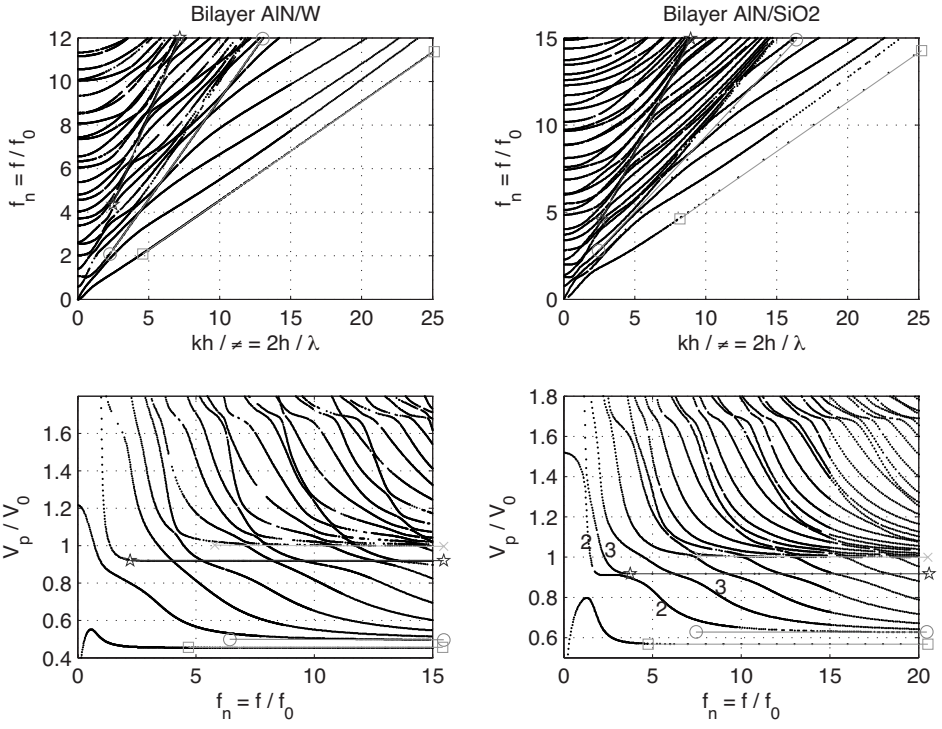

FIG. 2. Dispersion curves of guided waves in two bilayer plates, AlN/W (left) and A1N/SiO_2 (right). The top panes are the overall views of frequency against wave number, both normalized, and the bottom panes are enlarged views of the phase velocity vs frequency to show the cluster and plateau behavior of guided modes in some dispersion regions. Star-marked lines: SAW in massive AlN; square-marked lines: SAW in the other material; circle-marked lines: Shear BAW in the slower material; cross-marked lines: Shear BAW in AlN.

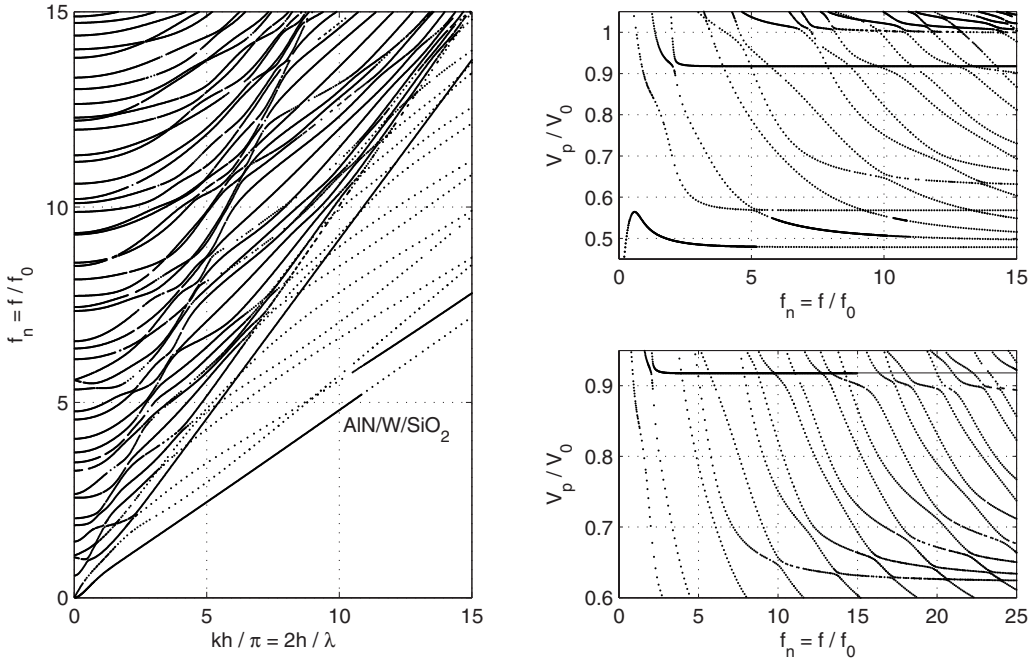

FIG. 3. Dispersion curves of guided waves in a three-layer A1N/W/SiO_2 plate: On the left is the normalized frequency f_n vs the wave number k in a limited range, on the right are two enlarged views of the phase velocity V_p as a function of the frequency f_n, within a restricted V_p range and an extended f_n range. The curve branch with the slowest speed ($V_p/V_0 \cong 0.479$) is the interface mode existing near the interface of W and SiO_2 layers and having essentially the same properties as the one that would exist and propagate at the interface between these two materials when they are massive half-spaces (Stoneley waves).

$f-k$ curve is zero at $f=f_c$. The interpretation is that a wave transversely resonant and sanding along x_1 ($k=0$) transfers no energy in the x_1 direction.

Figure 3 presents the acoustic modes spectra calculated for a three-layer A1N/W/SiO_2 plate, a sandwich with the slowest layer embedded in between two relatively faster ones. As in bilayer plates, two branches exist for all frequencies, and higher order branches appear for $f \geq f_c$, with a few of them exhibiting negative slope in the $f-k$ plot of the dispersion curves near cutoff f_c. No mode in the full spectra is symmetric or antisymmetric. In the enlarged views of the dispersion curves V_p-f plot, in a restricted velocity range but in more extended frequency range (up to $f_n=25$), we can easily observe some plateaus where the wave speed seems to reach an asymptotic limit (horizontal line). An analysis of the origin of these peculiar behaviors enables one to get deeper physical insight of the wave motion in the layered structure. A plateau appears clearly in the V_p-f plot as soon as $f_n \geq 2$, which is the speed of SAW in massive AlN. Two other plateaus exist, one above $V_p/V_0=0.5$ and one below $V_p/V_0=0.5$. The higher one is due to the SAW speed of massive SiO_2; however, the lower one is not due to the SAW in massive W. Contrary to what is expected, the lowest branch in this structure approaches a wave speed that is not the SAW velocity, neither in any of the two external materials SiO_2 and AlN, nor in the middle W. A careful analysis reveals that it tends to the wave speed of the interfacial (Stoneley) mode which would exist and propagate near the interface of W and SiO_2 when both fill up half-spaces. In addition, we observe another asymptotic limit at $V_p/V_0 \cong 0.5$ for $f_n > 10$, which is the shear bulk wave in massive W. At higher frequencies ($f_n > 15$), some branches reach a plateau-like zone just below $V_p/V_0=0.9$ over a finite frequency range, which is due to the longitudinal bulk wave of massive W; the branches then undergo a sharp decrease in phase velocity, after which they first approach the asymptotic limit of shear bulk speed of massive SiO_2 ($V_p/V_0 \approx 0.63$) and then the shear bulk speed of massive W ($V_p/V_0 \approx 0.5$). These results clearly show the acoustic confinement in the slow layer (W) of the guided modes at very short wavelength regime. In addition to one interface and two surface modes, two families of guided modes can be distinguished, one for those tending to the shear bulk speed of W ($V_p/V_0 \approx 0.5$) and the other for those approaching the shear bulk speed of SiO_2($V_p/V_0 \approx 0.63$).

To go further, we have also calculated the dispersion curves for a four-layer A1N/W/SiO_2/W plate, as shown in Fig. 4. The characteristics of higher modes cutoff, no symmetry, and negative slope are similar to the previously presented two- and three-layer plates, except that here the number of modes is larger (58 against 47 in Fig. 3, and 36 for both A1N/SiO_2 and AlN/W configurations in Fig. 2) within the same frequency range ($f_n \leq 15$). The lowest branch tends to the SAW speed of massive W because W is now one of the outside layers. The next lowest branch approaches rapidly (at $f_n \geq 2$) the speed of the interfacial mode. Another branch also tends to the interface mode speed, but at a much higher frequency, $f_n \geq 8$. This phenomenon is logically explained by the presence of two W/SiO_2 interfaces in the current configuration-piezoelectric AlN combined with a three-layer coupler W/SiO_2/W. The branch that reaches the interfacial wave speed first is essentially at the interface of SiO_2 with the outside W layer, while the other one is mainly at the interface of SiO_2 with the embedded W layer. No mode tends to the SAW speed of massive SiO_2 because this layer has no stress-free surface. The plateau above $V_p/V_0=0.9$ is attrib-

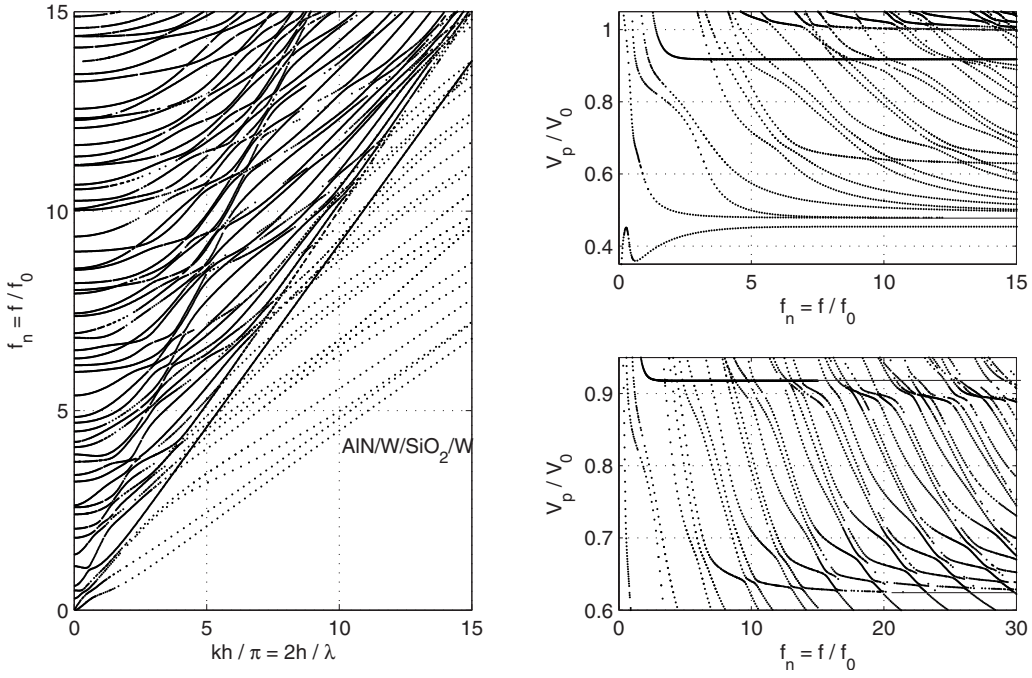

FIG. 4. Dispersion curves of guided waves in a four-layer A1N/W/SiO_2/W plate: On the left is the normalized frequency f_n vs the wave number k in a limited range, on the right are two enlarged views of phase velocity V_p plotted as a function of frequency f_n within a restricted V_p range and an extended f_n range. The curve branch with the slowest speed ($V_p/V_o \cong 0.454$) is the SAW existing near the exterior W-layer surface. Two branches tend to the same wave speed of the interface mode because there are two interfaces of W–SiO_2.

uted to the SAW in massive AlN material as in Fig. 3. To observe the guided modes near the bulk wave speeds in massive materials, it is necessary to go further in frequencies.

Figure 5 presents the dispersion curves for f_n up to 50 along with all asymptotic lines associated with a characteristic wave speed. In sufficiently short wavelength regime, the guided modes can be classified into two families according to their asymptotic behavior. The family with lower speeds reaches by pair the shear bulk speed ($V_p/V_0 \approx 0.5$) of massive W, a phenomenon due to the presence of two separate layers of W in the structure. The family with higher speeds goes singly to the shear bulk speed ($V_p/V_0 \approx 0.63$) of massive SiO_2, as expected when only one layer is made of SiO_2 material in the whole structure. We also observe a double-mode plateau around $V_p/V_0 \approx 0.9$, the speed of longitudinal bulk wave in massive W, which can be interpreted as an intermediate wave confinement in either W layer. The guided modes near these plateaus have almost the same properties as the classical shear or longitudinal bulk waves in unbounded W material. The longitudinal BAW speed in SiO_2 is a little higher than the line 7, and the longitudinal BAW in AlN is too high to be shown in this graph.

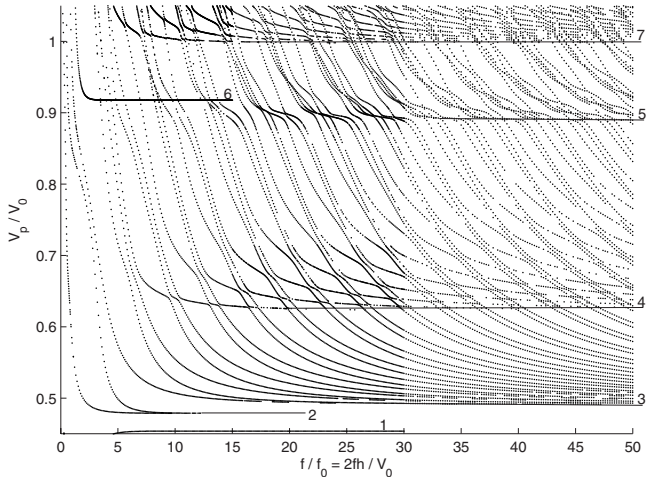

FIG. 5. Dispersion curves of the same plate as in Fig. 4, showing the phase velocity V_p vs the frequency f for a more extended f range, to show their asymptotic limits. The line numbered 1 is for SAW in massive W; line 2 is for interface waves (two branches merging into one); line 3 is for shear BAW in massive W (a group of two modes, one in the inner W and the other in the outer W layer); line 4 is for shear BAW in massive SiO_2; line 5 is longitudinal wave in massive W; and lines 6 and 7 are for SAW and BAW in massive AlN, respectively.

Numerical instabilities were appearing for f_n higher than 10 around $V_p/V_0=1$ during computations using the transfer matrix. No instability was observed when using the impedance matrix formalism although some modes could not be determined (missing data) using the SIM defined for one specific surface. However, thanks to the SIM approach, which is unconditionally stable irrespective of the total number of layers and individual layer thickness, in contrast to the well-known TMM, it suffices to repeatedly apply the SIM at different locations within the layered structure for the complete wave spectra of all guided modes to be determined, even in extremely short wavelength regime. This mainly concerns regions where guided modes tend to SAW or bulk wave speeds of a component material. Relatively straightforward and efficient from the computational point of view, the approach is also flexible because the characteristic equation, always in a form of $|Z_l^m - Z_u^{m+1}| = 0$, can be written for an arbitrary interface as well as for an external surface. This

flexibility allows the numerical results to be obtained for the dispersion curves and field distributions by selecting the only interface in the neighbourhood of which mode confinement occurs or the electromechanical energy flux is concentered when the full set of solutions is not required.

V. CONCLUSIONS AND FURTHER DISCUSSION

Calculations of guided waves in layered plates mixing piezoelectric, dielectric, and metallic layers have been developed using the Stroh formalism and matrix presentation. The characteristic equations for the dispersion curves are derived in two forms: an acoustic SIM and an electrical scalar function. The SIM is expressed in a unified elastic form for both piezo and nonpiezo-materials, which makes easy the application of the field continuity at the interfaces of heterostructures. By repeatedly applying the unconditionally stable SIM formalism at different interface locations, we have been able to obtain the full set of solutions, even for frequencies up to several tenths of the fundamental thickness mode resonant frequency. Numerical investigations for plates having up to four layers and three materials show an extreme complexity of the acoustic spectra. They include (1) the slope of $f-k$ curves near the cut-off, for a given mode, can be negative or positive depending on the specific stack configuration, and more than one mode exhibits this feature. This suggests that the sign of the dispersion curve slope of certain modes can be controlled by layers' stack order and/or relative thickness ratio; (2) interfacial waves exist at short wavelength regime between the W and SiO_2 layers, but they do not appear at the interface between AIN and W or between AlN and SiO_2 layers. As a general rule, this depends on the velocity ratio; (3) the energy of all guided acoustic waves is confined in the slow W layer when the wavelength is short enough, though intermediate confinement occurs in the SiO_2 layer when it is embedded. The asymptotic behavior of the dispersion curves is physically originated from the proper modes of BAW and SAW in massive materials of the constituent materials. The mode clustering and forbidden regions are not yet observed because the number of layers is still low and the structural periodicity is insignificant. With an increase in the number of unit cells, say for $N \geq 3$, one can expect the appearance of pseudo band gaps in the wave spectra due to Bragg effects.

Investigation of Lamb modes in SMR including two metal electrodes and a Si substrate are underway. The effects of the semi-infinite substrate and thick electrodes, already included in the general expressions derived in Sec. III D, are to be accounted for in future numerical simulations. An extension of the analysis to the purely imaginary domain as well as to the complex domain of the wave number is needed in order to have a complete knowledge of the full Lamb wave spectra, which becomes indispensable for modeling the lateral propagation phenomena[33,34] and for understanding the spurious signals observed in SMR-based filter responses. Knowledge of the energy trapping properties and wave motion patterns, if desired, can be gained by examining the through-thickness distribution of electroacoustic fields for any specific mode defined by the pair value of $\omega-k_1$. The most direct effects of the electrodes (of material Mo) are a considerable lowering of the proper resonant frequencies of the piezoelectric AlN resonator. The presence of a bottom substrate ($\mathbf{Z}_s \neq \mathbf{0}$) leads to solutions of guided surface modes which are multiple and dispersive, similar to the conventional Rayleigh SAW, provided that the substrate is a faster material and the wavelength is comparable to the overall thickness of AlN layer added to the coupler. In the considered configuration (Fig. 1), this type of solution only exists for very low frequencies. In normal resonator operation, most of the solutions are of leaky SAW type which pertain more or less to bulk radiation into the substrate depending on the coupler parameters and frequency. As a consequence, the wave number of any mode having a phase speed faster than the SV-polarized BAW in the substrate is necessarily complex, leading to an attenuation as they propagate along the surface (in x_1). At short wavelength regime ($\lambda < h/5$) and for a given $\omega-k_1$ pair, the wave pattern in each layer tends to be independent one from the other. As a result, one cannot talk about the mode type (SAW- or Lamb-like) for the overall structure, which no longer has a precise signification. The exact wave pattern in a heterostructure is easy to access in all cases by examining the field profiles as a function of the thickness position (for a fixed $\omega-k_1$ pair).

[1]For a complete bibliography on matrix methods, see for example the references cited in: M. J. S. Lowe, "Matrix technique for modeling ultrasonic waves in multilayered media," IEEE Trans. Ultrason. Ferroelectr. Freq. Control **42**, 525–542 (1995).

[2]D. Leveque and L. Piche, "A robust transfer matrix formulation for the ultrasonic response of multilayered absorbing media," J. Acoust. Soc. Am. **92**, 452–467 (1992).

[3]B. Hosten and M. Castaings, "Delta operator technique to improve the Thomson-Haskell-method stability for propagation in multilayered anisotropic absorbing plates," J. Acoust. Soc. Am. **95**, 1931–1941 (1994).

[4]A. K. Mal, "Wave propagation in multilayered composite laminates under periodic surface loads," Wave Motion **9**, 231–238 (1988).

[5]K. A. Ingebrigtsen and A. Tonning, "Elastic surface waves in crystals," Phys. Rev. **184**, 942–951 (1969).

[6]J. Lothe and D. M. Barnett, "Integral formalism for surface waves in piezoelectric crystals, existence considerations," J. Appl. Phys. **47**, 1799–1807 (1976).

[7]D. M. Barnett and J. Lothe, "Free surface (Rayleigh) waves in anisotropic elastic half-spaces: The surface impedance method," Proc. R. Soc. London, Ser. A **A402**, 135–152 (1985).

[8]S. V. Birykov, "Impedance method in the theory of elastic surface waves," Sov. Phys. Acoust. **31**, 350–345 (1985).

[9]B. Honein, A. M. B. Braga, P. Barbone, and G. Herrmann, "Wave propagation in piezoelectric layered media with some applications," J. Intell. Mater. Syst. Struct. **2**, 542–557 (1991).

[10]S. V. Birykov, Yu. V. Gulyaev, V. V. Krylov, and V. P. Plessky, *Surface Acoustic Waves in Inhomogeneous Media* (Springer, Berlin, 1995).

[11]J. M. Orellana and B. Collet "Propagation of guided in stratified piezoelectric structures," *in Proceedings of the Symposium on the Mechanics of Electromagnetic Materials and Structures of the ASME Mechanics and Materials Conference*, edited by J. Yang and G. A. Maugin (IOS Press, Amsterdam, 2000), pp. 124–137.

[12]J. M. Orellana and B. Collet, "Ultrasonic Lamb waves in layered piezoelectric plates," *in Proceedings of the IUTAM Symposium on Mechanical Waves for Composites Structures Characterization*, edited by D. A. Sotiropoulos (Kluwer, Dordrecht, 2001), pp. 125–140.

[13]V. Y. Zhang, T. Gryba, J. M. Orellana, and B. Collet, "Surface impedance matrix for the study of acoustical propagation in multilayered structures," J. Austral. Math. Soc **88**, 218–230 (2002).

[14]T. T. Wu and Y. Y. Chen, "Exact analysis of dispersive SAW devices on ZnO/Diamond/Si layered structures," IEEE Trans. Ultrason. Ferroelectr. Freq. Control **49**, 142–149 (2002).

[15]A. L. Shuvalov and A. G. Every, "Some properties of surface acoustic waves in anisotropic-coated solids, studied by the impedance method,"

Wave Motion **36**, 257–273 (2002).
[16]B. Hosten and M. Castaings, "Surface impedance matrices to model the propagation in multilayered media," Ultrasonics, **41**, 501–507 (2003).
[17]B. Collet, "Recursive surface impedance matrix methods for ultrasonic wave propagation in piezoelectric multilayers," Ultrasonics **42**, 189–197 (2004).
[18]E. Le Clezio and A. L. Shuvalov, "Transmission of acoustic waves through piezoelectric plates: Modeling and experiment," Proceedings of 2004 IEEE Ultrasonics Symposium, edited by Marjone Passini Yuhao, Montreal, Canada, 23–27 Aug. 2004, pp. 553–556.
[19]T. Pastureaud, V. Laude, and S. Ballandras, "Stable scattering-matrix method for surface acoustic waves in piezoelectric multilayers," Appl. Phys. Lett. **80**, 2544–2546 (2002).
[20]A. Reinhardt, Th. Pastureaud, S. Ballandras, and V. Laude, "Scattering-matrix method for modelling acoustic waves in piezoelectric, fluid, and metallic multilayers," J. Appl. Phys. **94**, 6923–6931 (2003).
[21]E. N. Tan, "A concise and efficient scattering formalism for stable analysis of elastic wave in multilayered anisotropic solids," Ultrasonics **41**, 229–236 (2003).
[22]S. I. Rokhlin and L. Wang, "Stable recursive algorithm for the elastic propagation in layered anisotropic media: Stiffness matrix method," J. Acoust. Soc. Am. **112**, 822–834 (2002).
[23]L. Wang and S. I. Rokhlin, "A compliance/stiffness matrix formulation of general Green's function and effective permittivity for piezoelectric multilayers," IEEE Trans. Ultrason. Ferroelectr. Freq. Control **51**, 453–463 (2004).
[24]N. Ryden and M. J. S. Lowe, "Guided wave propagation in three-layer pavement structures," J. Acoust. Soc. Am. **116**, 2902–2913 (2004).
[25]J. T. Stewart and Y. K. Yong, "Exact analysis of the propagation of acoustic waves in multilayered anisotropic piezoelectric plates," IEEE Trans. Ultrason. Ferroelectr. Freq. Control **41**, 375–390 (1994).
[26]A. N. Stroh, "Steady state problems in anisotropic elasticity," J. Math. Phys. **41**, 77–103 (1962).
[27]A. M. B. Braga and G. Herrmann, "Floquet waves in anisotropic periodically layered composites," J. Acoust. Soc. Am. **91**, 1211–1227 (1992).
[28]E. L. Adler, "Matrix methods applied to acoustic waves in multilayers," IEEE Trans. Ultrason. Ferroelectr. Freq. Control **37**, 485–490 (1990).
[29]V. Y. Zhang, J. E. Lefebvre, and T. Gryba, "A unified formalism using effective surface permittivity to study acoustic waves in various anisotropy and piezoelectric multilayers," IEEE Trans. Ultrason. Ferroelectr. Freq. Control **48**, 1449–1461 (2001).
[30]M. Castaings, E. Le Clezio, and B. Hosten, "Modal decomposition method for modeling the interaction of Lamb waves with cracks," J. Acoust. Soc. Am. **112**, 2567–2582 (2002).
[31]P. L. Marston, "Negative group velocity Lamb waves on plates and applications to the scattering of sound by shells," J. Acoust. Soc. Am. **113**, 2659–2662 (2003).
[32]M. F. Werby and H. Uberall, "The analysis and interpretation of some special properties of higher order symmetric Lamb waves: The case for plates," J. Acoust. Soc. Am. **111**, 2686–2691 (2002).
[33]E. Le Clezio, M. V. Predoi, M. Castaings, B. Hosten, and M. Rousseau, "Numerical prediction and experiments on the free-plate edge mode," J. Acoust. Soc. Am. **112**, 2567–2582 (2002).
[34]O. Diligent and M. J. S. Lowe, "Prediction and measurement of non propagating Lamb modes at the free end of a plate when the fundamental anti-symmetric mode A_0 is incident," J. Acoust. Soc. Am. **113**, 3032–3042 (2003).

Acoustic energy harvesting using an electromechanical Helmholtz resonator[a)]

Fei Liu
Department of Mechanical and Aerospace Engineering, University of Florida, Gainesville, Florida 32611-6250, USA

Alex Phipps
Department of Electrical and Computer Engineering, University of Florida, Gainesville, Florida 32611-6130, USA

Stephen Horowitz
Department of Mechanical and Aerospace Engineering, University of Florida, Gainesville, Florida 32611-6250, USA

Khai Ngo[b)]
Department of Electrical and Computer Engineering, University of Florida, Gainesville, Florida 32611-6130, USA

Louis Cattafesta
Department of Mechanical and Aerospace Engineering, University of Florida, Gainesville, Florida 32611-6250, USA

Toshikazu Nishida
Department of Electrical and Computer Engineering, University of Florida, Gainesville, Florida 32611-6130, USA

Mark Sheplak[c)]
Department of Mechanical and Aerospace Engineering, University of Florida, Gainesville, Florida 32611-6250, USA

(Received 3 August 2007; revised 3 January 2008; accepted 4 January 2008)

This paper presents the development of an acoustic energy harvester using an electromechanical Helmholtz resonator (EMHR). The EMHR consists of an orifice, cavity, and a piezoelectric diaphragm. Acoustic energy is converted to mechanical energy when sound incident on the orifice generates an oscillatory pressure in the cavity, which in turns causes the vibration of the diaphragm. The conversion of acoustic energy to electrical energy is achieved via piezoelectric transduction in the diaphragm of the EMHR. Moreover, the diaphragm is coupled with energy reclamation circuitry to increase the efficiency of the energy conversion. Lumped element modeling of the EMHR is used to provide physical insight into the coupled energy domain dynamics governing the energy reclamation process. The feasibility of acoustic energy reclamation using an EMHR is demonstrated in a plane wave tube for two power converter topologies. The first is comprised of only a rectifier, and the second uses a rectifier connected to a flyback converter to improve load matching. Experimental results indicate that approximately 30 mW of output power is harvested for an incident sound pressure level of 160 dB with a flyback converter. Such power level is sufficient to power a variety of low power electronic devices. © *2008 Acoustical Society of America.*
[DOI: 10.1121/1.2839000]

PACS number(s): 43.38.Fx, 43.50.Gf, 43.50.Ki [AJZ] Pages: 1983–1990

I. INTRODUCTION

Acoustic liners are used to attenuate propulsion noise within turbofan engines. The liners provide complex impedance boundary conditions for the noise propagation along the engine duct and can be passive or active.[1] A passive acoustic liner has a structure similar to a conventional Helmholtz resonator. The primary advantage of a passive liner is its simplicity; however, a passive liner is only effective over a narrow frequency range (e.g., one octave for single degree freedom passive liner).[1] Active liner technologies have attracted attention from researchers due to their potential to attenuate engine noise under different operating conditions by changing the liner geometry or by using steady bias

[a)]Preliminary portions of this work were presented in "Technology Development for Electromechanical Acoustic Liners," Paper A04-093, at Active 04, Williamsburg, VA, September 2004.
[b)]Current address: Department of Electrical and Computer Engineering, Virginia Tech, Blacksburg, Virginia 24061
[c)]Author to whom correspondence should be addressed. Electronic mail: sheplak@ufl.edu.

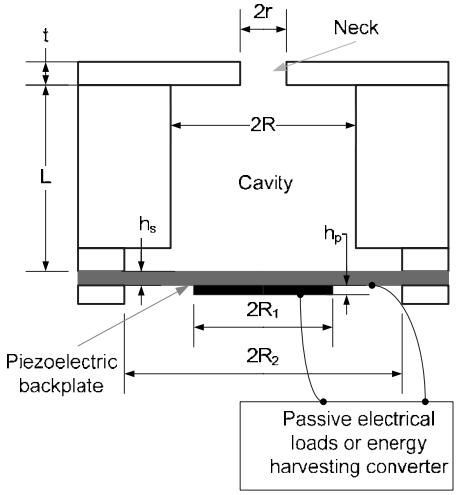

FIG. 1. Schematic of an EMHR.

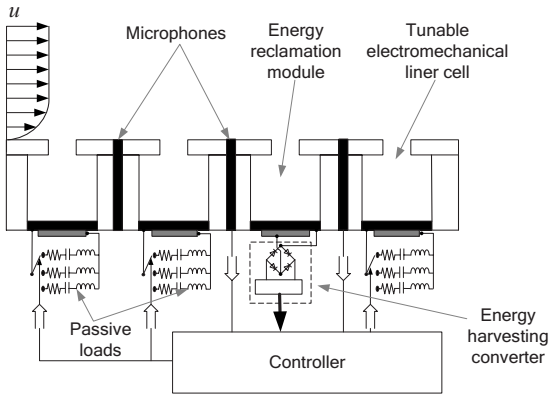

FIG. 2. Schematic of a self-powered active liner system.

flow.[2–4] Although active liners possess a wider operation bandwidth, they are generally more complex and require a power supply and external circuitry to power actuators, sensors, and a controller. Some of these issues may be alleviated by using a conventional battery as the power supply. However, once the battery is exhausted, replacement can be time consuming and costly.

An alternative approach is to harvest energy from available sources surrounding the system and convert it into electrical energy to power the liner system. Possible energy sources include ambient mechanical vibrations, which can be reclaimed using piezoelectric materials. Piezoelectric materials can convert mechanical energy into electrical energy via the direct piezoelectric effect and vice versa through the inverse piezoelectric effect.[5] While harvesting mechanical energy from the environment using piezoelectric materials has been investigated by many researchers,[6–17] reclaiming ambient acoustic energy has received less attention.

This paper presents the development of an energy harvester to capture energy from an acoustic field by using an electromechanical Helmholtz resonator (EMHR). The EMHR consists of a narrow neck, backing cavity, and a compliant piezoelectric diaphragm, as shown in Fig. 1.[18,19] The piezoelectric composite diaphragm of the EMHR provides coupling between the acoustic and electric energy domains. We have previously reported that the acoustic impedance of the EMHR can be adjusted by modifying the shunt loads across the piezoelectric composite diaphragm.[18,19] When employed for energy reclamation purposes, the shunt load of the EMHR is replaced by a power conversion circuit. The EMHR can then gather energy from the high intensity acoustic field present in the engine nacelle which can reach levels up to 160 dB (Ref. 20 μPa).[20] One possible active acoustic liner system using the EMHR as the primary element is illustrated in Fig. 2. The liner system consists of a group of energy harvesting EMHRs to supply power, an array of tunable EMHRs to suppress the noise, a set of low-power microphones for sensing, and circuitry for feedback control. Another possible implementation consists of replacing the feedback system with a wireless communication transceiver and switching circuitry with adjustable settings operating in an open-loop mode to set the desired impedance conditions.[21] For such a system, typical power requirements range from 0.01 mW for a low power analog switch and a microcontroller in standby mode to 10 mW for a low power wireless transceiver during transmit mode.[21]

The outline of this paper is as follows. Section II briefly reviews the lumped element model (LEM) of the EMHR that captures the relevant multi-energy domain physics. In Sec. III, two energy reclamation circuitries are presented. Sections IV and V discuss the experimental setup and results, respectively. Finally, conclusions are provided in Sec. VI.

II. LUMPED ELEMENT MODEL OF THE EMHR

At the low acoustic frequencies investigated in this paper, the dimensions of the EMHR, as listed in Table I, are smaller than the acoustic wavelength. As such, the dynamic behavior of the EMHR can be lumped into idealized discrete circuit elements.[22] We have previously presented a detailed discussion of the LEM of the EMHR including analytical expressions for all elements, and will only briefly review the basics here for completeness.[19] In the notation below, the first subscript denotes the energy domain (e.g., "*a*" for acoustic), while the second subscript describes the element (e.g., "*N*" for the neck and "*C*" for the cavity). An EMHR is essentially a conventional solid-walled Helmholtz resonator

TABLE I. Dimensions of the EMHRs (Unit: mm, resolution 0.01 mm).

Properties	Values
Orifice	
Radius r	2.42
Length t	3.16
Cavity	
Radius R	6.34
Depth L	16.4
Piezoelectric backplate	
Radius of the piezoelectric layer R_1	10.1
Thickness of the piezoelectric layer h_p	0.11
Radius of the shim R_2	12.4
Thickness of the shim h_s	0.18

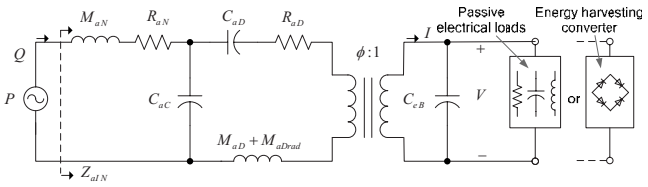

FIG. 3. Multi-energy domain equivalent circuit representation for an EMHR connected to passive loads or an energy harvesting converter.

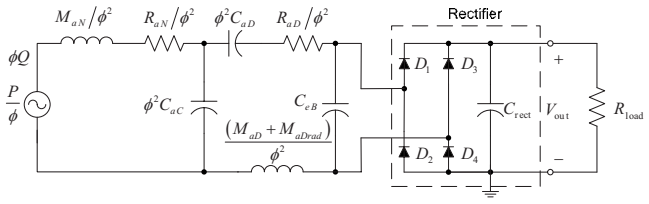

FIG. 4. Equivalent circuit representation in the electrical domain for an EMHR connected to a direct charging circuitry (Ref. 29). Used with permission.

possessing a piezoelectric composite diaphragm as illustrated in Fig. 1. Figure 3 shows the equivalent circuit representation for the EMHR, where P and Q represent the input pressure at the entrance of the EMHR and volumetric flow rates, respectively, while V and I represent the output voltage and current, respectively. The orifice of the EMHR possesses both dissipative (R_{aN}) and inertial (M_{aN}) components, which share the same volume velocity and are thus connected in series. The compact cavity is modeled by an acoustic compliance (C_{aC}) which is loaded by the diaphragm pressure. The piezoelectric-composite diaphragm is represented by an acoustic mass (M_{aD}), radiation acoustic mass (M_{aDrad}), damping loss (R_{aD}), and compliance (C_{aD}). Electroacoustic transduction is modeled by an ideal transformer representing the effective piezoelectric transduction ratio (ϕ) and the electrical blocked capacitance of the piezoelectric diaphragm (C_{eB}). All parameters in the LEM can be calculated via analytical expressions.[19,23,24] However, experimental measurements can improve the accuracy of some LEM parameters such as R_{aD} and ϕ. The damping loss R_{aD} of the piezoelectric diaphragm may arise from radiation loss, thermo-elastic dissipation, compliant boundaries, and other intrinsic loss mechanisms that are difficult to evaluate. The damping loss can be estimated by

$$R_{aD} = 2\xi\sqrt{\frac{M_{aD} + M_{aDrad}}{C_{aD}}}, \tag{1}$$

where ξ is an experimentally determined damping factor that can be determined using the logarithmic decrement method.[25] The transduction ratio ϕ is determined by

$$\phi = \frac{-d_a}{C_{aD}} = \frac{-\int_0^{R_2} 2\pi r w(r) dr \Big/ V\Big|_{P=0}}{C_{aD}}, \tag{2}$$

where $w(r)$ is the transverse displacement of the piezoelectric backplate, in this instance due to the application of a voltage V with zero pressure loading, and d_a is the effective acoustic piezoelectric coefficient.[24] In general, the analytical prediction for d_a differs from the experimentally determined value because an ideal clamped boundary is difficult to achieve in practice. Any compliance in the boundaries or in-plane compressive stress due to mounting may result in an enhanced d_a. For more details on the estimation of other parameters, please refer to Liu *et al.*[19]

III. ENERGY HARVESTING CIRCUITRY

As mentioned in Sec. I, the acoustic energy harvester using an EMHR is comprised of two components, the EMHR and the power converter. The EMHR transforms incident acoustic energy into electrical energy across the high-impedance piezoelectric composite diaphragm. The voltage output from the piezoelectric diaphragm is time varying and is not a feasible power source for most electronics. It is therefore necessary to utilize a power converter (i.e., energy harvesting circuitry) to condition the energy generated by the EMHR and to ensure that maximum power is delivered to the load.[9,26] Two power converters, a direct charging circuit and a flyback converter, are considered.

The direct charging circuit, shown in Fig. 4, is the simplest energy harvesting configuration. The direct charging circuit consists of a full-bridge rectifier, large filter capacitor C_{rect}, and a resistive load R_{load}, representing the circuit to be powered. Specifically, the diode bridge rectifies the ac voltage, and the filter capacitor smoothes the output to generate a constant dc voltage for the load. The voltage across R_{load} is comprised of an average component, $\langle V_{\text{out}}\rangle$, and a ripple component, V'_{out} (i.e., $V_{\text{out}}=\langle V_{\text{out}}\rangle+V'_{\text{out}}$). If the filter capacitor is large enough such that the time constant $R_{\text{load}}C_{\text{rect}}$ is much larger than the oscillation period of the EMHR, V'_{out} is negligible and $\langle V_{\text{out}}\rangle$ is independent of C_{rect}.[27] Such is the case in this work.

For the direct charging circuit connected to a resistive load, the power delivered to the load is defined as the product of the current through the resistor, I_{load}, and the voltage across it. The amount of power delivered to the load is a function of the load resistance and is governed by Ohm's Law, $V_{\text{out}}=I_{\text{load}}R_{\text{load}}$. As R_{load} approaches a short circuit ($R_{\text{load}}\to 0$), then $V_{\text{out}}\to 0$, as does the output power. Similarly, as the resistance is increased and approaches an open circuit ($R_{\text{load}}\to\infty$), $I_{\text{load}}\to 0$ and, again, there is no power transfer. Between these two extreme cases, the voltage and current are nonzero, and some power is delivered to the load. There exists an optimal resistance, R_{opt}, where the product of the voltage and current is maximized. Typically, R_{load} changes for different electronic devices, such as sensors, transceivers, and microprocessors. The direct charging circuit efficiency decreases when R_{load} deviates from R_{opt}.

Another common configuration for energy harvesting applications is realized by replacing the load resistance in Fig. 4 with a battery. This implementation is useful when it is desirable to store the harvested energy for extended periods. A battery cannot be modeled by a simple resistor, so the concept of R_{opt} is not tractable. A better model for a simple battery is a dc voltage source. The load condition for maximum power transfer then becomes an optimal voltage condition, V_{opt}. The two optimal conditions, R_{opt} and V_{opt}, are

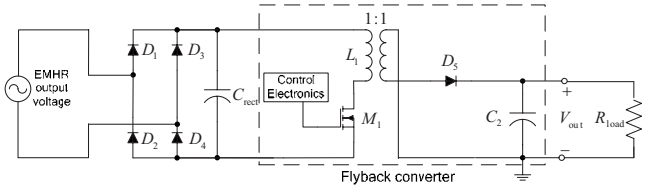

FIG. 5. Equivalent circuit representation for an EMHR connected to a flyback converter after the rectifier (Ref. 29). Used with permission.

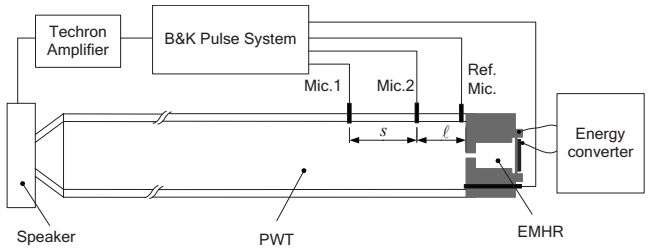

FIG. 6. Schematic of the experimental setup.

consistent for the resistive load case. With the exception of the short and open circuit loads, for each value of R_{load}, a real, nonzero voltage, V_{out}, occurs across the load. When R_{load} equals R_{opt}, the power transfer will be maximized, and the corresponding value of V_{out} will equal V_{opt}. For direct charging using a resistive load, R_{opt} and V_{opt} refer to the same load condition and can be used interchangeably. When using a battery load, however, the optimal condition will be constrained to V_{opt}. As in the resistive case, when the battery voltage does not equal V_{opt}, a load mismatch will limit the transfer of power.

The mismatch problem associated with the direct charging circuitry is alleviated by using a flyback converter between the rectifier and the load, as shown in Fig. 5. The flyback converter introduces an intermediate circuit which decouples the direct charging circuit from the actual load. When the flyback converter operates in discontinuous conduction mode (DCM), the input impedance of the flyback converter is resistive and independent of R_{load}.[28] Thus by tuning the input impedance of the flyback converter to R_{opt}, the optimal load condition is achieved. Since the input impedance of the flyback converter is independent of the output load, the optimal load condition will be maintained even if the actual load changes.

As shown in Fig. 5, the flyback circuit consists of a switching metal-oxide-semiconductor field-effect transistor (MOSFET) M_1 with associated pulse-width-modulation (PWM) control electronics, diode D_5, coupled inductor L_1, and large filter capacitor C_2.[29] Operation of the flyback converter in DCM can be divided into three stages. During the first stage, the control electronics close the MOSFET switch and current flows through the primary side of the transformer. This stage continues for a time $d \times T_s$, where d is the duty cycle of the PWM signal, and T_s is the switching period of the converter. Due to the polarity of the transformer, diode D_5 prevents current from flowing out of the secondary side of the transformer, and the EMHR energy is stored as current on the transformer. The second and third stages comprise the remainder of the switching period, $(1-d) \times T_s$. During the second stage, the MOSFET switch opens, and current now flows out of the secondary side of the transformer and into R_{load}. Since the flyback is operating in DCM, the energy stored on the inductor will be completely discharged by the end of the second stage. The third stage is marked by the absence of current in either side of the transformer. A detailed analysis of the flyback converter operating in DCM is provided by Chen and Ngo.[28] The average input impedance of the flyback converter operating in DCM is purely resistive and electronically controllable via d, T_s, and L_1. The input impedance of the flyback converter, R_{inF}, is given as[28]

$$R_{inF} = \frac{2L_1}{T_s d^2}. \tag{3}$$

In general, T_s and L_1 are fixed for a specific flyback converter. Thus, by adjusting d of the PWM control signal, R_{inF} can be tuned to R_{opt}, and the condition for maximum power transfer can be achieved.

IV. EXPERIMENTAL SETUP

The experimental setup of the energy harvester using an EMHR is shown in Fig. 6. The dimensions of the EMHR and the material properties of the piezoelectric backplate are listed in Tables I and II, respectively. The experimental setup is similar to the acoustic impedance measurements of a tunable EMHR with two exceptions.[19] First, the EMHR is connected to a power converter instead of a passive load. Second, a single tone (i.e., a sine wave) is used to excite the EMHR. The frequency of the single tone coincides with one of the resonant frequencies of the EMHR.

TABLE II. Materials parameters for the piezoelectric backplate.

Piezoceramic (APC 850)	
Young's modulus (N/m^2) E_p	6.3E10
Poisson's ratio ν_p	0.31
Density (kg/m^3) ρ_p	7700
Relative dielectric constant ε_r	1750
Piezoelectric strain constant (pC/N)d_{31}	−175
Shim (260 half hard brass)	
Young's modulus (N/m^2) E_s	11.0E10
Poisson's ratio ν_s	0.38
Density (kg/m^3) ρ_s	8530

Four sets of experiments were performed. First, the resonant frequencies of the open-circuit EMHR were determined. A pseudo random signal was bandpass filtered from 300 Hz to 6.7 kHz (Δf=2 Hz) to excite the EMHR. Meanwhile, the acoustic input pressure, P, at the entrance of and the electrical output voltage across the EMHR were recorded using the Brüel and Kjær (B&K) PULSE Multi-Analyzer System Type 3560. Note that the acoustic input pressure was the summation of the incident and reflected acoustic pressure at the entrance of the EMHR. A fast Fourier transform (frequency span 3.2 kHz, center frequency 1.9 kHz, 1600 lines, and 3000 ensemble averages) was performed on each signal. The frequency response function (FRF) between the output voltage and the total acoustic input pressure was calculated. The FRF curve exhibited two peaks which coincided with the two resonant frequencies of the open-circuit EMHR.

Once the resonant frequencies of the open-circuit EMHR were determined, a sinusoidal signal was used to excite the EMHR connected to the energy converter. In this work, the frequency of the sinusoidal signal was set to the second resonant frequency of the open-circuit EMHR.[19] The second resonant frequency of the EMHR is associated with the resonant frequency of the piezoelectric diaphragm. Three power levels were then measured as a function of the sound pressure level (SPL) of the acoustic input wave at the entrance of the EMHR: (1) the power dissipated in purely resistive loads via the direct charging circuitry; (2) the power delivered to a rechargeable battery via the direct charging circuitry; and (3) the power delivered to the battery via the rectifier-flyback converter. In the first case, for a given incident SPL, R_{opt} was determined as the load resistance at which the dissipated power was maximized. The power dissipated in the resistor is

$$W_{\text{out}} = \frac{\langle V_{\text{out}} \rangle^2}{R_{\text{load}}} \tag{4}$$

since the ripple component of the output voltage, V'_{out}, was negligible. When using a rechargeable battery to store the harvested energy, the power delivered to the battery (W_{out}) was measured as the product of the dc battery voltage and the dc current flowing into the battery. For the rectifier-flyback converter, the input impedance of the flyback converter was tuned to R_{opt} by adjusting d.

Additionally, the standard two-microphone method was used to determine the acoustic input impedance of the EMHR, Z_{aIN}.[30,31] Once the acoustic impedance of the EMHR is known, the incident acoustic power of the incident plane wave in the PWT is then calculated as

$$W_{\text{In}} = \frac{|P|^2}{2|Z_{aIN}|[1 - |(Z_{aIN} - \rho_0 c_0/A_D)/(Z_{aIN} + \rho_0 c_0/A_D)|^2]} \times \cos\theta, \tag{5}$$

where θ is the phase angle of Z_{aIN}, $\rho_0 c_0$ is the characteristic impedance of air, and A_D is the cross-sectional area of the plane wave tube (PWT). Note that the net power into the EMHR was less than the incident acoustic power calculated via Eq. (5) since a portion of the incident acoustic power was reflected by the EMHR. The overall power harvesting efficiency, $\eta_{overall}$, is the ratio of the output power to the incident acoustic power,

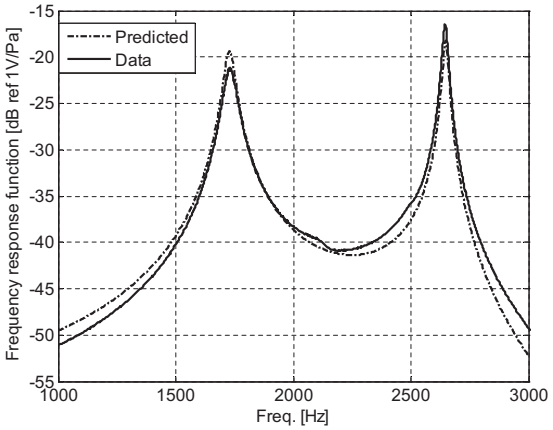

FIG. 7. The frequency response function (FRF) between the output voltage and total acoustic input pressure for the open-circuit EMHR.

$$\eta_{\text{overall}} = \frac{W_{\text{out}}}{W_{\text{In}}}. \tag{6}$$

Some intermediate system efficiencies were determined as well. For instance, the acoustic transmission efficiency, η_{acoustic}, is the ratio of the acoustic power flowing into the EMHR to the total incident acoustic power

$$\eta_{\text{acoustic}} = 1 - \left| \frac{Z_{aIN} - \rho_0 c_0/A_D}{Z_{aIN} + \rho_0 c_0/A_D} \right|^2. \tag{7}$$

The EMHR conversion efficiency, η_{EMHR}, is defined as the ratio of the electrical output power from the EMHR to the acoustic input power into the EMHR,

$$\eta_{\text{EMHR}} = \frac{W_{\text{EMHR}}}{W_{\text{In}}\eta_{\text{acoustic}}}, \tag{8}$$

where W_{EMHR} is the electric output power measured across the EMHR output terminals. The power conversion efficiency of the flyback connected to the rectifier, $\eta_{\text{rectifier+flyback}}$, is

$$\eta_{\text{rectifier+flyback}} = \frac{W_{\text{out}}}{W_{\text{EMHR}}}. \tag{9}$$

Clearly, from Eqs. (6)–(9), the overall power harvesting efficiency is given by the product of the intermediate efficiencies

$$\eta_{\text{overall}} = \eta_{\text{acoustic}}\eta_{\text{EMHR}}\eta_{\text{rectifier+flyback}}. \tag{10}$$

V. RESULTS AND DISCUSSION

Prior to demonstrating acoustic energy harvesting using the EMHR, the resonant frequencies of the open-circuit EMHR were determined. Figure 7 shows the measured frequency response function (FRF) between the output voltage and the input acoustic pressure signal for the open-circuit EMHR and the predicted result using the LEM of the EMHR. The theoretical values were calculated using the experimentally extracted d_a and ζ (i.e., d_a=71.4e−12 m^3/V

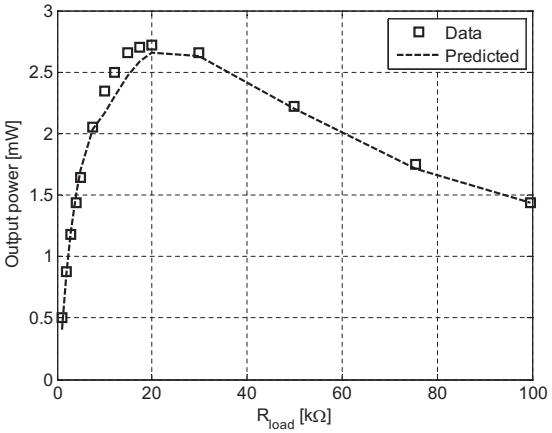

FIG. 8. The output electric power delivered to resistive loads connected to the EMHR through the rectifier for an incident SPL of 140 dB.

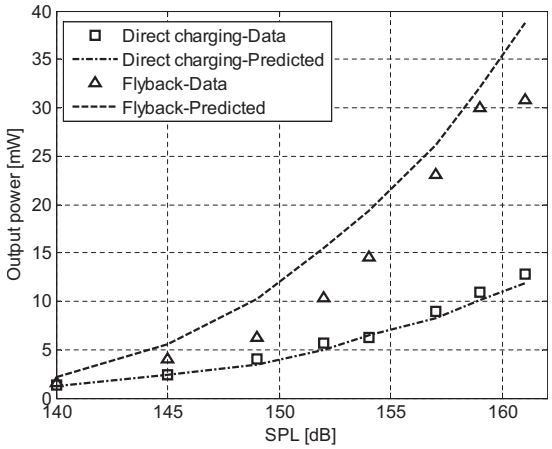

FIG. 9. Measured output power vs incident pressure for the flyback converter and direct charging method.

and $\zeta=0.01$ in this study). The FRF curve shows two peaks. Due to the weak coupling between the piezoelectric diaphragm and the Helmholtz resonator,[19] the first peak is associated with the solid-walled Helmholtz resonator and occurs around 1732 Hz. The second peak is associated with the resonant frequency of the piezoelectric backplate of the EMHR and occurs at 2646 Hz.

A single tone sine wave at 2646 Hz was used to excite the EMHR, which was connected to a variety of resistive loads as shown in Fig. 4. Figure 8 shows the measured output power delivered to varying resistive loads for a 140 dB SPL input wave and the theoretical power calculated from an equivalent circuit simulation using SABER.[32] Good agreement is obtained between the measurement and the EMHR/power converter model. The resistance, R_{opt}, for maximum output power was found to be 20 kΩ.

In subsequent experiments designed to investigate energy harvesting to a battery load in a controlled manner without the uncertainty due to changing battery voltage levels, a dc voltage supply was used instead of a resistive load. The dc voltage is set to 2 V and kept constant during the experiment. The EMHR was connected to a flyback converter through the diode rectifier as shown in Fig. 5. Based on the results of the previous experiment, the input impedance of the flyback circuit was set to 20 kΩ. The specific component values used for the power converter are shown in Table III. The input acoustic wave was steadily increased in amplitude from 140 to 161 dB. The output current into the dc voltage supply was measured. The power delivered to the dc voltage supply load was then calculated as the product of the dc voltage and current, as shown in Fig. 9. The figure also shows the electric output power delivered to the same load using the direct charging method for comparison. The output power curves predicted using SABER circuit simulations for both methods are also included in Fig. 9. The higher output power levels predicted for the rectifier-flyback configuration are most likely due to unmodeled parasitic losses of the flyback. Uncertainty in the LEM parameters due to device nonlinearity also introduces some error. At 161 dB, the measured output power saturated, which is most likely associated with the magnetic core saturation of the flyback transformer. The results indicate that the flyback converter achieves greater output power delivered to the load than the direct charging method, which is due to the impedance matching inherent in the flyback circuit topology. Specifically, in comparison with the direct charging method, at an incident SPL of 161 dB, the flyback reclaims 260% more power.

Figure 10 shows the overall power harvesting efficiency, $\eta_{overall}$, of the EMHR connected to the flyback converter after the diode rectifier as a function of acoustic input pressure. Figure 10 also includes intermediate efficiencies of the system. The data show that the overall efficiency varied from 6% to 1.5% for acoustic input pressures between 145 and 161 dB. Some factors that contribute to the low efficiency include the acoustic impedance mismatch of the EMHR with the acoustic PWT and energy losses in the system, such as the acoustic damping loss at the orifice of the EMHR, the electrical energy dissipated by the diodes, and the electrical energy required by the PWM controller of the flyback con-

TABLE III. Circuit parameters and component values for the flyback converter.

Parameter/Component	Symbol	Value	Manufacturer
Duty cycle	d	6.0%	—
Switching frequency	f_s	5.2 kHz	—
Inductor	L_1	6.8 mH	Coilcraft
Input resistance	R_{inF}	12 kΩ	—
MOSFET	M_1	BSS138	Fairchild
Diode	D_5	BAT54	Fairchild
Output capacitor	C_2	220 μF	Panasonic

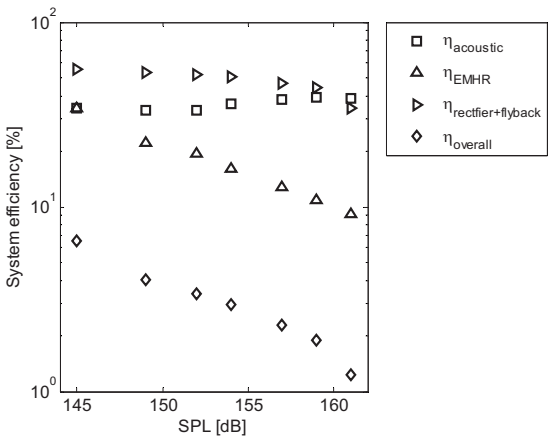

FIG. 10. System efficiencies vs total acoustic pressure for the EMHR connected to the flyback converter after the rectifier.

verter. The decrease in EMHR efficiency at high SPL is mainly attributed to the nonlinearity of the orifice resistance of the EMHR which increases when the SPL increases. The drop in the efficiency of the flyback converter at high SPL is caused by increased conduction losses. At low SPL, the currents flowing through the flyback are reduced, and energy dissipated through Joule heating is low. However, as the SPL approaches 160 dB, the current increases and the parasitic resistances in the MOSFET and inductor dissipate more energy as heat.

VI. CONCLUSIONS

The feasibility of acoustic energy reclamation using an electromechanical Helmholtz resonator has been demonstrated. Experimental investigation shows that the EMHR connected via the flyback converter is more effective in reclaiming energy than the direct charging method due to the impedance matching inherent in the flyback circuit topology. The harvested energy using the flyback converter increases by as much as 260% compared to the direct charging circuit when the same incident acoustic SPL of 161 dB is applied. The electrical output power harvested at 161dB SPL is approximately 30 mW. This continuous power level is sufficient for many low power electronics and sensors, including low power rf transceivers (20 mW for transmit and 0.2 mW for receive) operating at intermediate frequencies (300–1000 MHz) and low power analog switches (less than 10 μW) which are key components necessary for wireless self-powered acoustic liners.[21]

ACKNOWLEDGMENTS

Financial support for this project is provided by NASA Langley Research Center (Grant No. 1 NAG-1-2261), monitored by Michael G. Jones. The authors gratefully acknowledge the helpful suggestions of Robert Taylor and Shu Jiang regarding energy reclamation circuitry.

[1]R. E. Motsinger and R. E. Kraft, "Design and performance of duct acoustic treatment," in *Aeroacoustics of Flight Vehicles: Theory and Practice Volume 2: Noise Control*, edited by H. H. Hubbard (Acoustical Society of America, New York, 1995), Chap. 14, pp. 165–206.

[2]J. M. De Bedout, M. A. Franchek, R. J. Bernhard, and L. Mongeau, "Adaptive-passive noise control with self-tuning Helmholtz resonators," J. Sound Vib. **202**, 109–123 (1997).

[3]X. D. Jing and X. F. Sun, "Experimental investigations of perforated liner with bias flow," J. Acoust. Soc. Am. **106**, 2436–2441 (1999).

[4]M. A. Galland, B. Mazeaud, and N. Sellen, "Hybrid passive/active absorbers for flow ducts," Appl. Acoust. **66**, 691–708 (2005).

[5]D. Royer and E. Dieulesaint, *Elastic Waves in Solids* (Springer, Germany, 2000), Vol. **1**, pp. 147–152.

[6]E. Hausler and E. Stein, "Implantable physiological power supply with PVDF film," Ferroelectrics **60**, 277–282 (1984).

[7]M. Umeda, K. Nakamura, and S. Ueha, "Energy storage characteristics of a piezo-generator using impact induced vibrations," Jpn. J. Appl. Phys., Part 1 **36**, 3146–3151 (1997).

[8]J. Kymissis, D. Kendall, J. Paradiso, and N. Gershenfeld, "Parasitic power harvesting in shoes," *Proceedings of the Second IEEE International Symposium on Wearable Computers*, October 19–20, 132–139 (1998).

[9]N. S. Shenck and J. A. Paradiso, "Energy scavenging with shoe-mounted piezoelectrics," IEEE Micro. **21**(3), 30–42 (2001).

[10]M. J. Ramsay and W. W. Clark, "Piezoelectric energy harvesting for bio MEMS applications," in *Proceedings of Smart Structures and Materials 2001: Industrial and Commercial Applications of Smart Structures Technologies*. Newport Beach, CA (2001).

[11]P. Glynne-Jones, S. P. Beeby, and N. M. White, "Towards a piezoelectric vibration powered microgenerator," IEEE Proc. Sci. Meas. Technol. **148**, 68–72 (2001).

[12]A. Kasyap, J. Lim, D. Johnson, S. B. Horowitz, T. Nishida, K. Ngo, M. Sheplak, and L. Cattafesta, "Energy reclamation from a vibrating piezoceramic composite beam," Paper No. 271, *Proceedings of 9th International Congress on Sound and Vibration*, Orlando, FL (2002).

[13]S. Roundy, P. K. Wright, and J. Rabaey, "A study of low level vibrations as a power source for wireless sensor nodes," Comput. Commun. **26**, 1131–1144 (2003).

[14]A. Bayrashev, W. P. Robbins, and B. Ziaie, "Low frequency wireless powering of microsystems using piezoelectric-magnetostrictive laminate composites," Sens. Actuators, A **114**, 244–249 (2004).

[15]S. Kim, W. W. Clark, and Q.-M. Wang, "Piezoelectric energy harvesting with a clamped circular plate: Experimental study," J. Intell. Mater. Syst. Struct. **16**(10), 855–863 (2005).

[16]Y. B. Jeon, R. Sood, J.-h. Jeong, and S. G. Kim, "MEMS power generator with transverse mode thin film PZT," Sens. Actuators, A **122**, 16–22 (2005).

[17]S. B. Horowitz, M. Sheplak, L. Cattafesta, and T. Nishida, "A MEMS acoustic energy harvester," J. Micromech. Microeng. **16**, S174-S181 (2006).

[18]M. Sheplak, L. Cattafesta, T. Nishida, and S. B. Horowitz, "Electromechanical acoustic liner," U.S. Patent No. 6,782,109 (2004).

[19]F. Liu, S. B. Horowitz, T. Nishida, L. Cattafesta, and M. Sheplak, "A multiple degree of freedom electromechanical Helmholtz resonator," J. Acoust. Soc. Am. **122**, 291–301 (2007).

[20]R. A. Manglarotty, "Acoustic-lining concepts and materials for engine ducts," J. Acoust. Soc. Am. **48**, 783–794 (1973).

[21]S. Kadirvel, F. Liu, S. B. Horowitz, T. Nishida, L. Cattafesta, and M. Sheplak, "A self-powered wireless active acoustic liner," AIAA Paper No. 2006–2400, in *12th AIAA/CEAS Aeroacoustics Conference*, Cambridge, MA (2006).

[22]M. Rossi, *Acoustics and Electroacoustics* (Artech, Norwood, MA, 1988), pp. 245–373.

[23]S. B. Horowitz, T. Nishida, L. Cattafesta, and M. Sheplak, "Characterization of a compliant-backplate Helmholtz resonator for an electromechanical acoustic liner," Int. J. Aeroacoust. **1**, 183–205 (2002).

[24]S. Prasad, Q. Gallas, S. Horowitz, B. Homeijer, B. Sankar, L. Cattafesta, and M. Sheplak, "An analytical electroacoustic model of a piezoelectric composite circular plate," AIAA J. **44**(10), 2311–2318 (2006).

[25]L. Meirovitch, *Fundamentals of Vibrations* (McGraw-Hill, New York, 2001), pp. 94–98.

[26]G. K. Ottman, H. F. Hofmann, and G. A. Lesieutre, "Optimized piezoelectric energy harvesting circuit using step-down converter in discontinuous conduction mode," IEEE Trans. Power Electron. **18**(2), 696–703 (2003).

[27]Y. C. Shu and I. C. Lien, "Analysis of power output for piezoelectric energy harvesting systems," Smart Mater. Struct. **15**(6), 1499–1512 (2006).

[28]J. Chen and K. D. T. Ngo, "Alternate forms of the PWM switch model in

discontinuous conduction mode," IEEE Trans. Aerosp. Electron. Syst. **37**(2), 754–758 (2001).
[29]R. Taylor, F. Liu, S. B. Horowitz, K. Ngo, T. Nishida, L. Cattafesta, and M. Sheplak, "Technology development for electromechanical acoustic liners," Paper A04–093, in Active 04. Williamsburg, VA, 2004.
[30]ASTM-E1050-98, "Impedance and absorption of acoustical materials using a tube, two microphones, and a digital frequency analysis system," ASTM International.
[31]T. Schultz, M. Sheplak, and L. Cattafesta, "Uncertainty analysis of the two-microphone method," J. Sound Vib. **304**, 91–109 (2007).
[32]Synopsys, Inc., *Syber Sketch User Guide* (Synopsys, Mountain View, CA, 2005).

Adaptive wave field synthesis for active sound field reproduction: Experimental results

Philippe-Aubert Gauthier[a] and Alain Berry
Groupe d'Acoustique de l'Université de Sherbrooke, Université de Sherbrooke, 2500 boul. de l'Université, Sherbrooke, Québec J1K 2R1, Canada

(Received 31 May 2007; revised 28 January 2008; accepted 28 January 2008)

Sound field reproduction has applications in music reproduction, spatial audio, sound environment reproduction, and experimental acoustics. Sound field reproduction can be used to artificially reproduce the spatial character of natural hearing. The objective is then to reproduce a sound field in a real reproduction environment. Wave field synthesis (WFS) is a known open-loop technology which assumes that the reproduction environment is anechoic. The room response thus reduces the quality of the physical sound field reproduction by WFS. In recent research papers, adaptive wave field synthesis (AWFS) was defined as a potential solution to compensate for these quality reductions from which WFS objective performance suffers. In this paper, AWFS is experimentally investigated as an active sound field reproduction system with a limited number of reproduction error sensors to compensate for the response of the listening environment. Two digital signal processing algorithms for AWFS are used for comparison purposes, one of which is based on independent radiation mode control. AWFS performed propagating sound field reproduction better than WFS in three tested reproduction spaces (hemianechoic chamber, standard laboratory space, and reverberation chamber). © *2008 Acoustical Society of America.* [DOI: 10.1121/1.2875844]

PACS number(s): 43.38.Md, 43.60.Tj, 43.50.Ki [AJZ] Pages: 1991–2002

I. INTRODUCTION

With the constantly evolving digital signal processing and the relatively recent advent of multichannel audio, spatial audio has gained more attention in the past decades from researchers and practitioners for applications such as high-fidelity sound reproduction, music reproduction, virtual reality display, interactive multisensory environments, auralization, and sound installations (Camurri and Ferrentino, 1999; Epain *et al.*, 2004; AES Staff Writer, 2005; Woszczyk *et al.*, 2005; Keller *et al.*, 2006; Blesser and Salter, 2007). The interest in immersion and convincing multisensory environments is not new (Grau, 2003) and various techniques for spatial audio have been introduced in the past (Kendall, 1995; Verheijen, 1997; Poletti, 2000; Rumsey, 2001; Davis, 2003).

Within spatial sound, sound field reproduction methods attempt to reproduce physical stimulus (wave field), thereby avoiding any perceptual considerations in the implementation. Sound field reproduction was investigated by researchers in the past decades (Berkhout *et al.*, 1993; Nelson *et al.*, 1997; Verheijen, 1997; Poletti, 2000; Choi and Kim, 2004; Epain *et al.*, 2004; Takane and Sone, 2004; Keller *et al.*, 2006). One of the most active and recent related matters is room compensation (Spors *et al.*, 2003; Gauthier *et al.*, 2005a; Betlehem and Abhayapala, 2005; Spors *et al.*, 2005; Fuster *et al.*, 2005; Gauthier and Berry, 2006), which is essential for sound field reproduction in a real reproduction space on the basis of objective, physically measurable, performances. This is especially true when acoustical treatment of the reproduction space is not possible, like for sound field reproduction in vehicle mock-ups where the visual reproduction of the original space is important.

This paper deals with the problem of sound pressure field reproduction using adaptive digital signal processing applied to adaptive wave field synthesis (AWFS) [originally introduced by Gauthier *et al.* (2005b)]. More specifically it validates by experiments the AWFS concept.

The concepts and results shown in this paper are not limited to audio applications. Indeed, sound field reproduction may also be applied to experimental acoustics (Veit and Sander, 1987; Bravo and Elliott, 2004), psychoacoustics (Epain *et al.*, 2004; Keller *et al.*, 2006), and sound environment reproduction or even used as a vibroacoustics design tool. These are promising applications of sound field reproduction.

This paper is divided in four parts. In Sec. I, sound field reproduction, WFS, and AWFS are described. The complete experimental procedures and setups are described in Sec. II. Results of experiments with AWFS are then reported in Sec. III for three different reproduction spaces. Section IV discusses the results and exposes our conclusions.

A. Sound field reproduction

The main objective of sound field reproduction can be generally stated as the aim to recreate a given acoustical property of the sound field, such as sound pressure, sound intensity (Choi and Kim, 2004; Merimaa and Pulkki, 2005), spatial diffuseness (Merimaa and Pulkki, 2005), etc., over an extended region of space. This can be achieved using a reproduction system including electroacoustical sources and receivers, signal processing, and the desired physical target

[a]Electronic mail: philippe_aubert_gauthier@hotmail.com

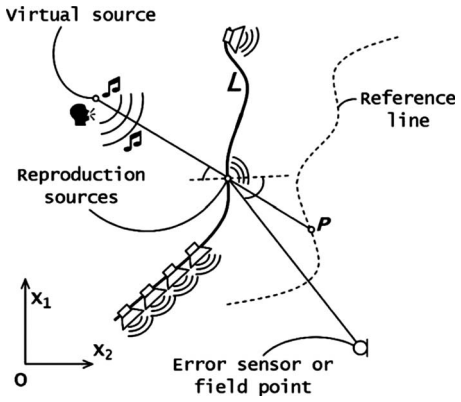

FIG. 1. Term convention for WFS definition. The virtual source is located in $\mathbf{x}_0$. L is the reproduction source line, the virtual source is on the left of the source line and the reproduction space is on the right of the source line. All sources and sensors are located in the x_1–x_2 plane.

description. In several of these cases, use of adaptive filtering implies the minimization of a cost function which is representative of this reproduction objective (Gauthier *et al.*, 2005a; Gauthier and Berry, 2006). Adaptive signal processing for spatial sound reproduction has been considered in various forms by researchers (Asano and Swanson, 1995; Takane *et al.*, 1999; Radlović *et al.*, 2000; Santillań, 2001; Epain *et al.*, 2004; Choi and Kim, 2004; Gauthier *et al.*, 2005b; Spors *et al.*, 2005; Gauthier and Berry, 2006).

B. Wave field synthesis

WFS research started with the theoretical propositions by Berkhout (Berkhout *et al.*, 1993; Verheijen, 1997; Start *et al.*, 1999). From the simple source formulation of the Kirchhoff–Helmholtz integral theorem (Williams, 1999), WFS operators are designed to "link" a given simple virtual source (typically creating spherical or plane wave in an horizontal plane, the listening plane), fed by a monophonic signal, to a loudspeaker array which reproduces the acoustic field of the virtual source (that is the target, or virtual, sound field). A schematic and simplified representation of the problem is shown in Fig. 1. The problem is usually limited to reproduction in the horizontal plane with a finite number of discrete reproduction sources using appropriate simplifications of the integral formulation (Verheijen, 1997). WFS studies have investigated: spatial aliasing (de Vries *et al.*, 1994; Start *et al.*, 1995; Spors and Rabenstein, 2006; Corteel, 2006a), objective performance, room effect, (Klehs and Sporer, 2003; Sporer and Klehs, 2004), acoustic room compensation (Spors *et al.*, 2003, 2005; Fuster *et al.*, 2005), WFS equalization (Corteel, 2006b), and more.

On one hand, the benefit of current WFS prototypes is their effectiveness in transmitting a spatial impression (in terms of sound localization) over a broad area surrounded by loudspeakers. On the other hand, WFS drawbacks are related to the definition of the synthesis operators: The reproduction room response or electroacoustical system limits (Corteel, 2006b) are not considered in the definition of WFS. The typical WFS system is consequently based on an open-loop architecture assuming a free field as the reproduction space. Active room compensation or system equalization for WFS is an active research topic for objective sound field reproduction in real room (Elliott and Nelson, 1989; Asano and Swanson, 1995; Bouchard and Quednau, 2000; Santillań 2001; Spors *et al.*, 2003; Gauthier *et al.*, 2005b; Spors *et al.*, 2005; Fuster *et al.*, 2005; Corteel, 2006b).

To lighten the present paper, which focuses on experimental results, the readers are referred to Verheijen (1997) for a more detailed review of WFS. A complete description of WFS adapted to the specific problem of AWFS was published by Gauthier and Berry (2006).

C. Adaptive wave field synthesis and independent radiation mode control

In a recent paper (Gauthier and Berry, 2006), AWFS was suggested as a practical compromise between WFS and active room compensation that usually requires a large amount of sensors. AWFS is based on a cost function to be minimized. Although implemented here in a specific configuration, the AWFS concept described by this cost function can readily be applied to any configuration. The cost function is a quadratic function of: (1) the reproduction errors and (2) the adaptive filters departure from the WFS solution [expressed as a set of finite impulse response (FIR) filter coefficients]. The penalization of the departure from the WFS filters is what makes AWFS original in comparison with other research done on sound field reproduction using active noise control techniques. The interest of such an approach stems from a simple observation: The direct sound field reproduced by WFS approaches the virtual sound field (Gauthier and Berry, 2007) and then allows for proper sound localization [on the basis of precedence effect (Blauert, 1999)]. Accordingly, WFS can be taken as a starting point or an *a priori* solution for the adaptive algorithm which will minimize the reproduction errors caused by the room response. Moreover, the weighted penalization of any departure from the WFS solution may prevent the degradation of sound localization since it limits the contribution of the secondary sources which are normally not activated by the WFS solution, given the fact that the WFS solution already contains spatial information that cannot be completely measured using a limited number of error microphones. For example, when using more reproduction sources than error sensors, the WFS solution contributes to the proper reconstruction of the direct sound field outside the control region defined by the error sensor locations (Gauthier and Berry, 2006). Finally, this penalization, which is controlled by a set of penalization parameters, can be used to control the balance between a purely WFS solution and a "closed-loop realization of Ambisonics sound field reproduction" (Gauthier and Berry, 2006).

This specific definition of a cost function for a multichannel adaptive system leads to a simple modification of the leaky filtered-reference least-mean-square (FXLMS) algorithm (Elliott, 2001). The modification is the inclusion of the WFS solution in the adaptation rule. Here, we will refer to modified FXLMS for AWFS when this algorithm is used.

Via the singular value decomposition (SVD) of the plant matrix [frequency response functions (FRFs) between repro-

duction sources and error sensors] involved in AWFS, it was shown that the underlying AWFS mechanism is the independent control of radiation modes (Gauthier and Berry, 2006) using plant decoupling. It is also related to the Principal-Components LMS (PC-LMS) algorithm (Cabell and Fuller, 1999). This suggested a practical implementation of AWFS signal processing which had already been textually described by Gauthier and Berry (2006). [This reference on signal processing for AWFS should suffice for the purpose of this paper, see also Gauthier and Berry (2008)]. In the case of AWFS based on independent radiation mode control, a set of analysis filters is used to transform the sound pressure in the SVD basis and a set of synthesis filters is used to create the loudspeaker signals from the SVD basis. In this transformed domain a set of single-channel independent adaptive filters operate to control each radiation mode individually. This reduces the computational burden and allows for a fine tuning of the convergence properties of the algorithm (i.e., independent fine tuning of the radiation modes convergence properties). Adaptive sound reproduction using plant decoupling via SVD was already proposed by Bai and Elliott (2004) via simulations for cross-talk cancellation. The main differences between Bai's work and the present paper are (1) the experimental application to sound field reproduction, (2) further considerations for the proper construction of the synthesis and analysis filters from a signal processing perspective, and (3) the inclusion of an *a priori* solution (the WFS solution). The inclusion of the WFS solution in the cost function (Gauthier and Berry, 2006) significantly changes the algorithm since the WFS solution must be projected on the SVD basis (radiation mode synthesis filters and nullspace synthesis filters). The proper construction of the synthesis and analysis filters is also what make this paper on AWFS original. Moreover, this construction of the synthesis and analysis filters had proven to be of critical importance for the efficient projection of the WFS solution on the SVD basis. However, such detailed considerations for signal processing are beyond the scope of this paper.

In this paper, the performance of AWFS based on modified FXLMS and independent radiation mode control algorithms is derived from experiments with a real AWFS system in three different acoustical situations. This paper therefore validates the AWFS concepts, previously investigated in theory (Gauthier and Berry, 2006). See Elliott (2001) for a general review on adaptive filtering for active noise control and sound field reproduction.

II. EXPERIMENTAL PROTOCOL

A. Experimental setups

The tested system includes 24 reproduction sources and 4 reproduction error sensors. The complete system is shown in Fig. 2. The reproduction sources create a 2-m-diam circular array in the horizontal plane. Sources are separated by 26 cm, thus giving an approximate minimal spatial aliasing frequency of 634 Hz ($\lambda/2=26$ cm, where λ is the acoustical wavelength) (Spors and Rabenstein, 2006). This minimal spatial aliasing frequency gives the frequency range of focus for the experiments. Above the spatial aliasing frequency, the

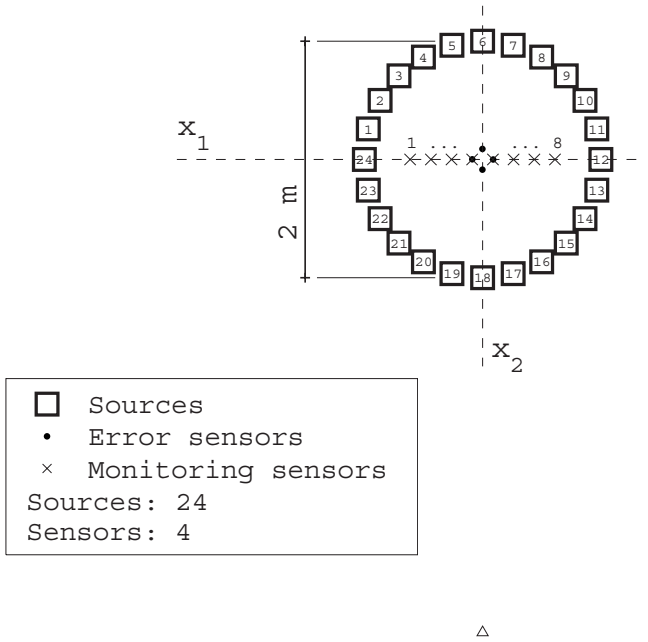

FIG. 2. Schematic AWFS setup made of 24 reproduction sources, 4 reproduction error sensors, and 8 monitoring sensors. (△) Typical virtual source position.

sound field reconstruction is impossible over the reproduction region. The error microphones form a cross, in the same horizontal plane as the reproduction sources, and their separation distance along x_1 and x_2 axes is 17.5 cm. Sources and sensors stand 1.22 m above the floor.

The loudspeakers are studio monitors (amplified two-way cabinets). The error sensors are 1/4 in. electret microphones. For the off-line broadband AWFS implementation, the loudspeakers and the microphones are connected to a signal conditioner and a computer using a sound card (24 analog inputs and 24 analog outputs). In this setup, the AWFS signal processing operates off-line. The setup is schematically shown in Fig. 3(a). For the second setup involving harmonic target wave fields, the loudspeakers and microphones are connected to reconstruction and antialiasing filters (440 Hz low-pass, eighth order, Butterworth), respectively, before being connected to a digital signal processing station used for on-line harmonic AWFS. The station is built around a Texas Instrument TMS320C40 floating point digital

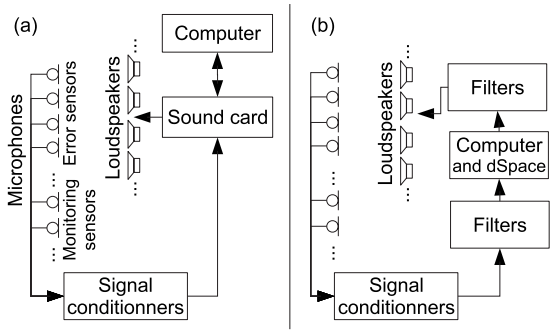

FIG. 3. Schematic representation of the AWFS instrumentations, (a) Broadband and (b) harmonic.

FIG. 4. Experimental AWFS setup in the hemianechoic chamber.

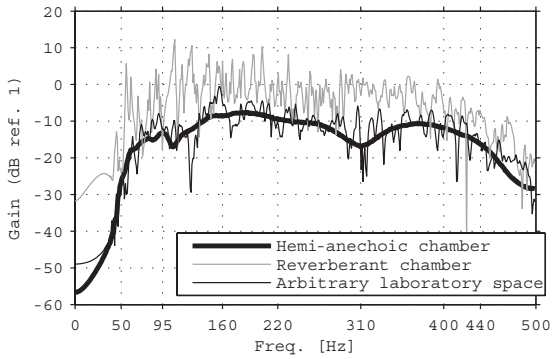

FIG. 5. Typical identified FRFs (from a reproduction source to an error microphone) in the hemianechoic chamber, standard laboratory space, and reverberation chamber.

signal processor. The setup is shown in Fig. 3(b). The experimental methods differ for these two setups. The system is pictured in Fig. 4.

B. Methods of experiments

Two types of reproduction methods and experiments are reported. As for the first type, the AWFS algorithms operate off-line. In this case, the experimental procedure is: (1) identification of the plant impulse responses (from all reproduction sources to all error sensors). Sweep-sine identification was used to cover from 0 to 600 Hz. The number of coefficients varies according to the reproduction environment. (2) Off-line running, by simulation, of the AWFS algorithms textually described by Gauthier and Berry (2006). (3) Rendering, with the real electroacoustical system, of the AWFS solution after convergence of the control filters. (4) Measurement of the reproduced sound fields. The reproduced sound field measurements are based on reproduced impulse responses [from the reference signal to the eight monitor microphones (see Fig. 2)]. Broadband AWFS results shown in Sec. III include measurements of the reproduced sound fields using swept sines.

As for the second type of reproduction methods and experiments, the objective is to evaluate the performance of AWFS with an on-line adaptation system. To reach this goal, several practical trade-offs are included to reduce the computational burden so that on-line adaptation can be performed using the available hardware. In the case of harmonic sound field reproduction, all the AWFS filters (including adaptive filters, target operators, synthesis, and analysis filters) are implemented using two-coefficient FIR filters. The algorithm then approaches the PC-LMS algorithm (Cabell and Fuller, 1999) with a supplementary penalization term and an *a priori* solution. In this very specific situation, the computational load is drastically reduced and on-line adaptation is possible using the algorithms as textually described by Gauthier and Berry (2006).

For both types of AWFS realization, the convergence coefficients used in the adaptive algorithms are set near the maximum values, which guaranteed stability and convergence of the adaptation.

III. AWFS EXPERIMENTS

A. Acoustical characteristics of the reproduction rooms

The three reproduction environments were selected to cover a large spectrum of reverberation properties. These environments are: (1) a hemianechoic chamber, (2) a standard laboratory space, and (3) a reverberation chamber.

The hemianechoic chamber (Fig. 4) has a volume of 125 m^3 ($6.55 \times 6.25 \times 3.05$ m) with a floor surface of 41 m^2. A typical frequency response function (FRF) (transfer function between a reproduction source and an error microphone) is shown in Fig. 5. In this situation, the FRFs are smooth and the dip around 310 Hz is created by the destructive interference with the floor reflection at this frequency. In the hemianechoic chamber, the error sensor signals are mostly dominated by the direct sound field of the reproduction sources.

The volume of the standard laboratory space is 469 m^3 ($8.23 \times 14.02 \times 4.06$ m) with a floor surface of 115 m^2. The typical FRF shown in Fig. 5 is more complex and shows various dips. The reverberation radius (the distance from the source at which the sound pressure level of the direct sound field is equal to the sound pressure level of the diffuse sound field) was estimated to be more than 1.4 m with broadband noise (audio bandwidth). The approximation of the reverberation radius is derived from the spatial sound pressure level decay curve from an omnidirectional loudspeaker array. The mean curve was estimated from four measurement lines in the horizontal plane (1.22 m above the floor) randomly selected in the room. From the mean curve, the sound source power level is computed from the measured direct sound field using a curve fitting with a theoretical free-field decay curve. The homogeneous reverberation level is evaluated from the last part of the decay curve. The approximation of the reverberation radius is then derived from the crossing of this homogeneous level and the theoretical free-field decay curve for the approximated sound source power level. Given a reverberation radius of more than 1.4 m in this laboratory space, the error sensors (at 1 m of the reproduction sources) are exposed to the direct sound field of the reproduction source and the field reflected by the room walls with a well-balanced proportion (in comparison with the hemianechoic space).

The volume of the reverberation chamber is 142 m^3 with a floor surface of 46.5 m^2 ($7.5 \times 6.2 \times 3.05$ m). Several sheets of damping material were placed in corners of the room to reduce the excessively long reverberation time. The typical FRF shown in Fig. 5 has gains that vary strongly with frequency and the transitions from frequency to frequency are very sharp. The reverberation radius was estimated to be between 0.45 and 0.51 m for broadband signal. Therefore, in this highly reverberant space, the error sensors are mostly exposed to the diffuse sound field of the reproduction sources. This is an hostile environment both for WFS and AWFS.

B. Hemianechoic space

1. Broadband AWFS

The broadband off-line demonstration of AWFS is interesting because it validates the complete AWFS concept, as described in previous papers (Gauthier and Berry, 2006). The broadband nature of the off-line system places a general point of view on the results.

In a preliminary stage, the system FRFs are identified using swept sines with an average over 200 realizations. The resulting impulse responses include 256 coefficients. The sampling rate is 1200 Hz for all the broadband experiments. Using the identified plant, the modified FXLMS algorithm can readily be applied (Elliott, 2001; Gauthier and Berry, 2006).

The independent radiation mode control implementation requires an additional initialization step. Singular value decomposition of the system plant in the frequency domain is achieved as textually described by Gauthier and Berry (2006) for each frequency. This gives the radiation modes (source modes, singular values, and pressure modes) at each frequency. Radiation mode reordering and phase optimization algorithms are then applied in the frequency domain to smooth the source and pressure mode phase responses. This creates a novelty in comparison with Bai's work with broadband plant decoupling (Bai and Elliott, 2004). Inverse discrete-time Fourier transform is then applied to obtain the synthesis filters and analysis filters (to move to and from the SVD basis) in the time domain for AWFS based on independent radiation mode control. Note that using such synthesis and analysis filters, the plant is uncoupled but not whitened. The synthesis filters (Gauthier and Berry, 2006) for the first four source modes are shown in Fig. 6. Each group of synthesis filters (there are 4 groups of 24 filters) produces one of the source modes at the reproduction source array. The analysis filters for the four pressure modes are shown in Fig. 7. Each group of analysis filters (there are 4 groups of 4 filters) transforms the physical acoustical pressures in the pressure mode basis (SVD basis). Interestingly, the synthesis and analysis filters show a sharp concentrated time response: Time leakage is reduced in comparison with SVD filters presented by Bai and Elliott (2004), thanks to the radiation modes reordering and to the phase optimization algorithms.

Figure 8 shows the reproduced impulse responses (from the virtual source to the monitoring sensor array shown in Fig. 2) for WFS. The transfer function units are 1/m [sound pressure (Pa) divided by virtual monopole amplitude (Pa m)]. The virtual source is a spherical source located at $\mathbf{x}_o=[0,4,0]$ m. Clearly, the direct field of the reproduced impulse responses approaches the target impulse responses. After the direct wave front passage, the reflection from the floor appears and instants later the low frequency echo of the

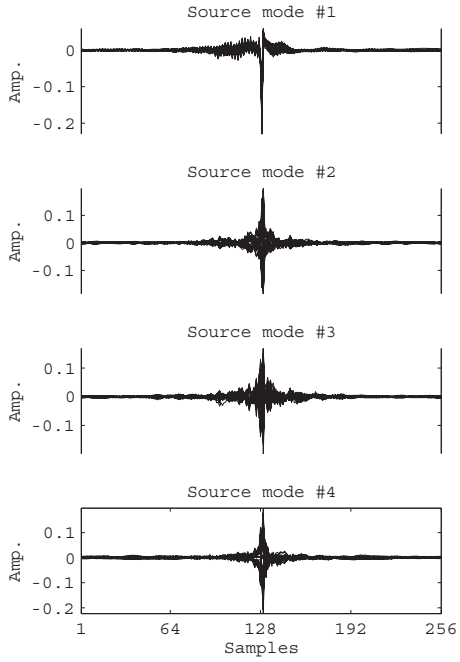

FIG. 6. First synthesis filters (Gauthier and Berry, 2006) in the time domain for source modes 1–4 in the hemianechoic chamber. Each plot includes 24 synthesis filters to create the given source mode with 24 reproduction sources. Each filter includes 256 coefficients.

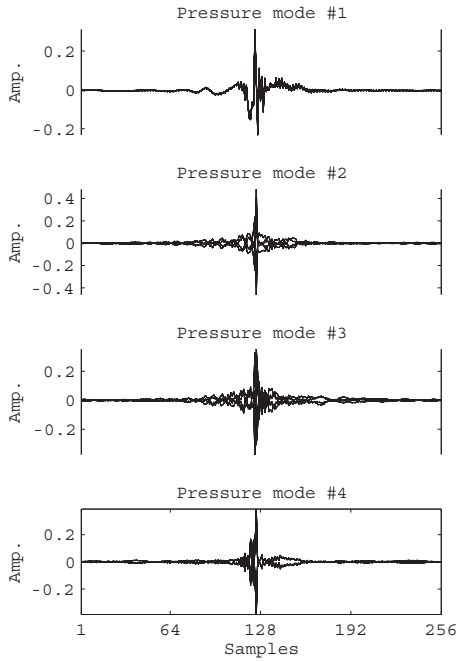

FIG. 7. Analysis filters (Gauthier and Berry, 2006) in the time domain for pressure modes 1–4 in the hemianechoic chamber. Each plot includes 4 analysis filters to catch the pressure mode with 4 pressure sensors. Each filter includes 256 coefficients.

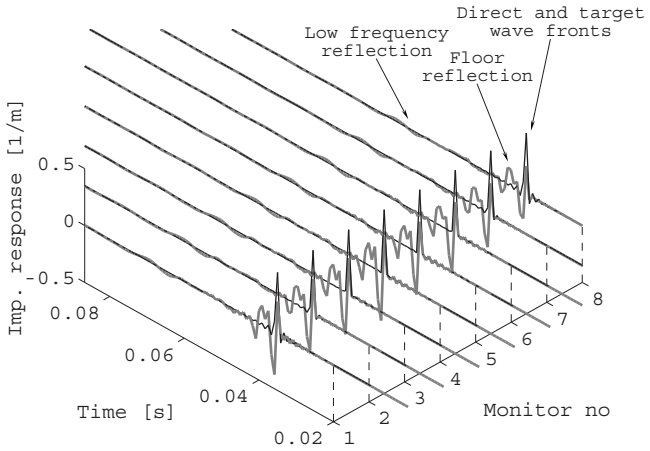

FIG. 8. Reproduced (thick gray lines) and virtual (thin black lines) impulse responses at the monitoring sensor array (shown in Fig. 2) for WFS with the system in the hemianechoic chamber.

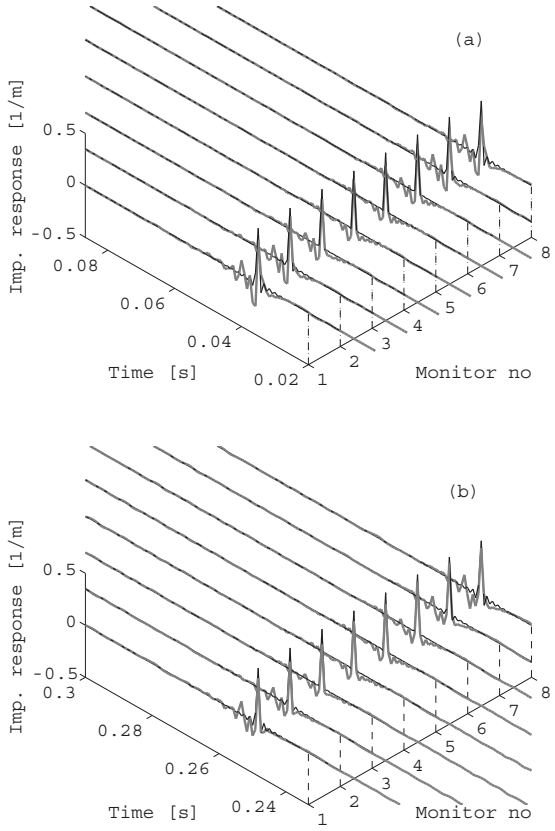

FIG. 9. Reproduced (thick gray lines) and virtual (thin black lines) impulse responses at the monitoring sensor array (shown in Fig. 2) for AWFS [(a) FXLMS algorithm with a penalization parameter set to 20 and (b) independent radiation mode control] with the system in the hemianechoic chamber.

hemianechoic chamber impinges the monitoring array. This echo is caused by the chamber which is hemianechoic only above 150 Hz. Moreover, another physical imperfection of the WFS reproduced sound field appears: The direct wave front has an undesirable coloration (the impulse is spread over two or three samples, passing from positive to negative values), possibly caused by the loudspeaker response or the WFS approximations.

The convergence coefficient was set to 0.00001 for the modified FXLMS algorithm. The convergence coefficient (α_m), for the independent radiation mode control algorithm, were set to $\alpha_1=0.0001$, $\alpha_2=\alpha_3=0.0004$, and $\alpha_4=0.002$ for the four radiation modes, where the subscript indicates the radiation mode number. The penalization parameter for the FXLMS algorithm was set to $\lambda=20$ (Gauthier and Berry, 2006). The penalization parameters for the AWFS based on independent radiation mode control were $\lambda_1=2$, $\lambda_2=\lambda_3=0.2$ and $\lambda_4=0.1$.

The impulse responses reproduced by AWFS are shown in Fig. 9(a) by FXLMS and Fig. 9(b) by independent radiation mode control. Clearly, the imperfections of WFS shown in Fig. 8 are partly corrected by AWFS even outside the error sensor array [note that the two central monitors (see Fig. 2) correspond to two of the error sensors]. Both the modified FXLMS and independent radiation mode control algorithms reduce these imperfections. The floor reflection is attenuated and the low frequency echo disappears from the sound field reproduced by AWFS. Moreover, the direct sound field reproduced by AWFS is closer to the target wave field than the sound field reproduced by WFS. Therefore, AWFS compensates for the room effects, for the loudspeaker colorations, and for some classical WFS approximations which introduce supplementary physical errors in the reproduced sound field.

According to Fig. 9, the independent radiation mode control algorithm [Fig. 9(b)] achieves a better sound field reproduction than the FXLMS algorithm [Fig. 9(a)] at the farther monitoring sensors. This is visible for the direct sound field reproduced by independent radiation mode control, in which case the negative sign excursion of the impulse responses one or two samples after the direct wave front passage is drastically reduced for nearly all monitoring sensors. This is due to the ability to fine tune each of the radiation modes with the independent radiation mode controller realization of AWFS. In the FXLMS case, the higher-order radiation modes are often far too penalized and their possible beneficial contribution in the sound field reproduction process is greatly diminished. Further explanations are presented in Sec. III D.

A different representation of the results allows for a general comparison between WFS and the two AWFS algorithms in terms of the reproduction error reduction as a function of space. Figure 10 shows the normalized energies of the reproduction errors at each of the monitoring microphones. They are computed from the differences between the virtual and reproduced impulse responses (IRs) shown in Figs. 8 and 9 and from others IRs measured for different virtual source positions. The normalized energies are computed as the sums of the quadratic error signals (differences between virtual IRs and reproduced IRs in the time domain) over the length of the IRs normalized by the total quadratic sum of the virtual IR, divided by the number of monitoring microphones. The normalization is thus achieved through division by the mean virtual IR energy at the monitoring microphones. According to the results shown in Fig. 10, the AWFS algorithms reduce on average the reproduction errors in comparison with WFS by controlling the reproduction errors at the four error sensors (two of which are monitors 4 and 5).

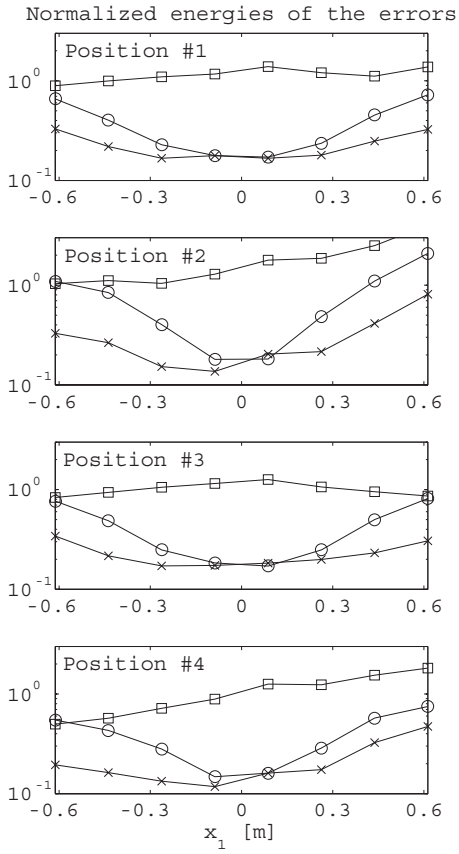

FIG. 10. Normalized energies of the error signals at each monitoring microphone for four virtual source positions in the hemianechoic chamber. Position 1: $\mathbf{x}_o=[0,4,0]$ m, position 2: $\mathbf{x}_o=[-4,0,0]$ m, position 3: $\mathbf{x}_0=[0,1.5,0]$ m, and position 4: $\mathbf{x}_0=[-1.19,-0.91,0]$ m. (□) WFS errors; (○) errors of AWFS by FXLMS; and (×) errors of AWFS by independent radiation mode control.

AWFS based on independent radiation mode control effectively provides a larger reproduction region since the higher-order modes are included in the controller in that case. Note that the size of the effective control region is also blurred by this type of representation which includes all the frequencies. AWFS by modified FXLMS provides a significant reproduction error reduction at the two central monitoring microphones, but the reproduction errors are not more important for the other monitoring microphones. AWFS performs better than WFS for all the reported virtual source positions.

2. Harmonic AWFS and radiation modes at 220 Hz

Harmonic AWFS results in the hemianechoic space, not reported in this paper for the sake of brevity, were in agreement with the broadband results described in Sec. III B.2. To support previous propositions (Gauthier and Berry, 2006) concerning the shapes of the radiation modes, Fig. 11 presents the four pressure modes at the error sensor array. Clearly, these pressure modes correspond to finite approximations of pressure, pressure gradients, and crossed second-order spatial derivative. Accordingly, the interpretation of AWFS based on independent radiation mode control (or independent control of pressure, pressure gradients, and crossed second-order spatial derivative) originally presented by Gauthier and Berry (2006) is supported by this experiment. This also explains why, in the broadband experiments, the size of the control region is larger for the AWFS algorithm based on independent radiation mode control which allows the higher-order radiation modes to converge. More detailed harmonic AWFS experiments are reported in Sec. III C.

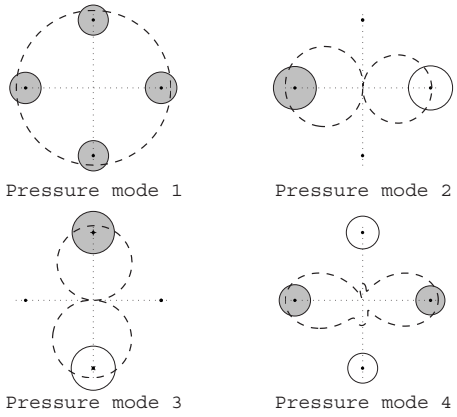

FIG. 11. Measured pressure modes at 220 Hz in the hemianechoic chamber. (…) Sensor position; (○) positive real part; (●) negative real part; (+) positive imaginary part; and (×) negative imaginary part. Symbol diameter illustrates the magnitude of the corresponding value. (---): Corresponding computed free-field directivity.

C. Laboratory space and reverberation chamber

The following summarizes the results obtained for the laboratory space and the reverberation chamber. As these two reproduction environments enhance the room effect on WFS, only parts of the results are shown to support the effectiveness of AWFS to compensate for the room effect.

1. Broadband AWFS

Since the rooms' IRs were longer than for the hemianechoic space, the identified IRs and control filters were selected to have 512 coefficients for the laboratory space and 1024 for the reverberation chamber with an average over 200 realizations. The resulting synthesis and analysis filters are shown in Figs. 12 and 13 for the laboratory space. Once again, a phase optimization algorithm is applied in the frequency domain to smooth the source and pressure modes' phase responses before inverse discrete-time Fourier transform. Moreover, a bandpass filter (fourth-order Butterworth, 60–540 Hz) is applied to all synthesis and analysis filters to reduce DC components that tend to appear in long SVD filters. Clearly the responses of the synthesis and analysis filters are longer than for the hemianechoic room. These filters are again concentrated impulses and show a reduced time leakage, thanks to the phase optimization and radiation modes' reordering algorithms which avoid any abrupt phase or gain transitions in the frequency domain before inverse discrete-time Fourier transform.

Measured impulse responses reproduced by classical WFS are shown in Fig. 14 for the laboratory space and in Fig. 15 for the reverberation chamber. The difference be-

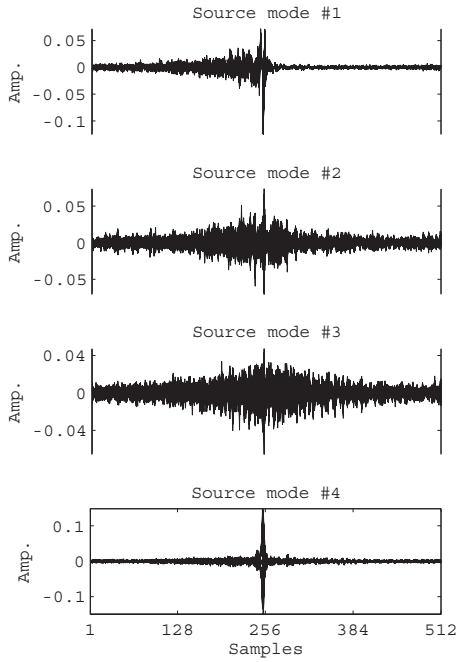

FIG. 12. First synthesis filters (Gauthier and Berry, 2006) in the time domain for source modes 1–4 in the laboratory space. Each plot includes 24 synthesis filters to create the given source mode with 24 reproduction sources. Each filter includes 512 coefficients.

tween the WFS reproduced sound field and the virtual sound field at the monitor sensor array is increased when compared with WFS in the hemianechoic room.

AWFS was tested to reduce the reproduction errors at the four error microphones. The convergence coefficient was set to 0.000002, and the penalization parameter was set to 30

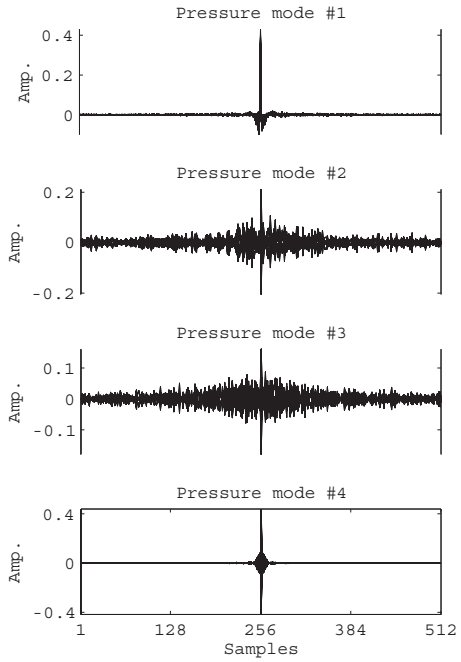

FIG. 13. Analysis filters (Gauthier and Berry, 2006) in the time domain for pressure modes 1–4 in the laboratory space. Each plot includes 4 analysis filters to catch the pressure mode with 4 pressure sensors. Each filter includes 512 coefficients.

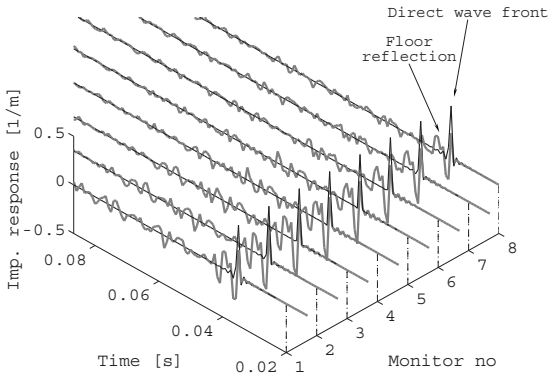

FIG. 14. Reproduced (thick gray lines) and virtual (thin black lines) impulse responses at the monitoring sensor array (shown in Fig. 2) for WFS with the system in the laboratory space.

for AWFS by FXLMS in laboratory space. The individual convergence coefficients were set to $\alpha_1=0.0000075$, $\alpha_2=\alpha_3=0.00003$, and $\alpha_4=0.00015$, and the penalization parameters were set to $\lambda_1=2$, $\lambda_2=\lambda_3=0.2$, and $\lambda_4=0.1$ for AWFS by independent radiation mode control in the laboratory. The convergence coefficient was set to 0.0000005, and the penalization parameter was set to 0 for AWFS by FXLMS in the reverberation chamber. The individual convergence coefficients were $\alpha_1=0.0000125$, $\alpha_2=\alpha_3=0.00005$, and $\alpha_4=0.00025$, and the penalization parameters were set to $\lambda_m=0$ for AWFS by independent radiation mode control in the reverberation chamber. Although the penalization parameters are set to zero in the reverberation chamber, the WFS solution still contributes to the AWFS solution because the adaptive filters are initialized with the WFS solution. The convergence coefficients are smaller than for the hemianechoic case because the size of the control filters is increased.

The reproduced impulse responses by AWFS are shown in Figs. 16 and 17 [Figs. 16(a) and 17(a) for AWFS by FXLMS and Figs. 16(b) and 17(b) for AWFS by independent radiation mode control]. The imperfections of WFS shown in Figs. 14 and 15 are partly corrected by AWFS even outside the error sensor array. Both the modified FXLMS and independent radiation mode control algorithms reduce these imperfections for the two reproduction spaces. Remarkably, the

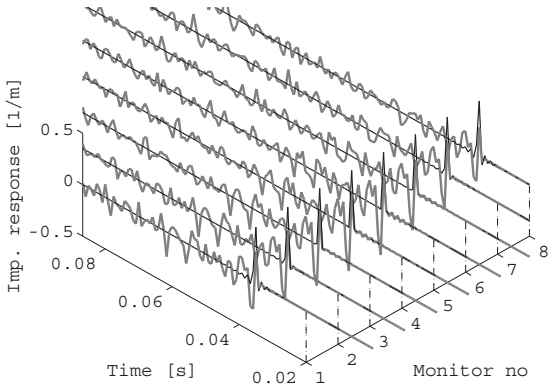

FIG. 15. Reproduced (thick gray lines) and virtual (thin black lines) impulse responses at the monitoring sensor array (shown in Fig. 2) for WFS with the system in the reverberation chamber.

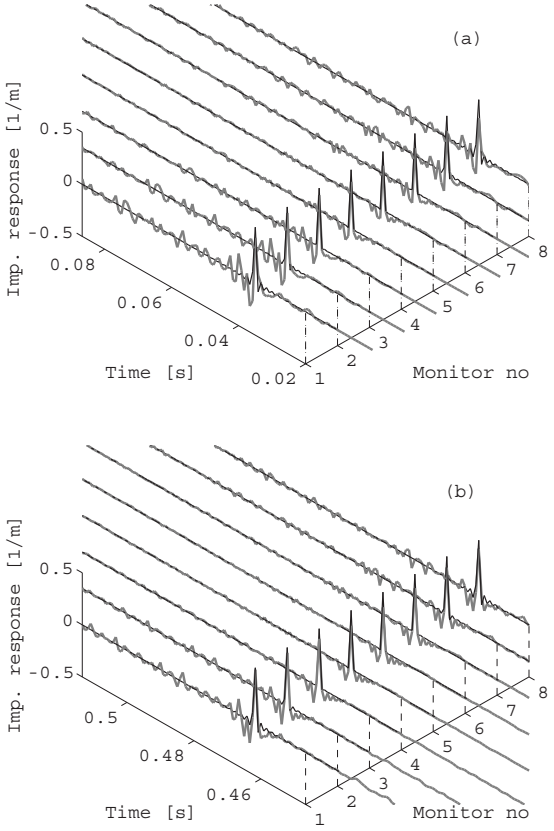

FIG. 16. Reproduced (thick gray lines) and virtual (thin black lines) impulse responses at the monitoring sensor array (shown in Fig. 2) for AWFS [(a) FXLMS algorithm with a penalization parameter set to 20 and (b) independent radiation mode control] with the system in the laboratory space.

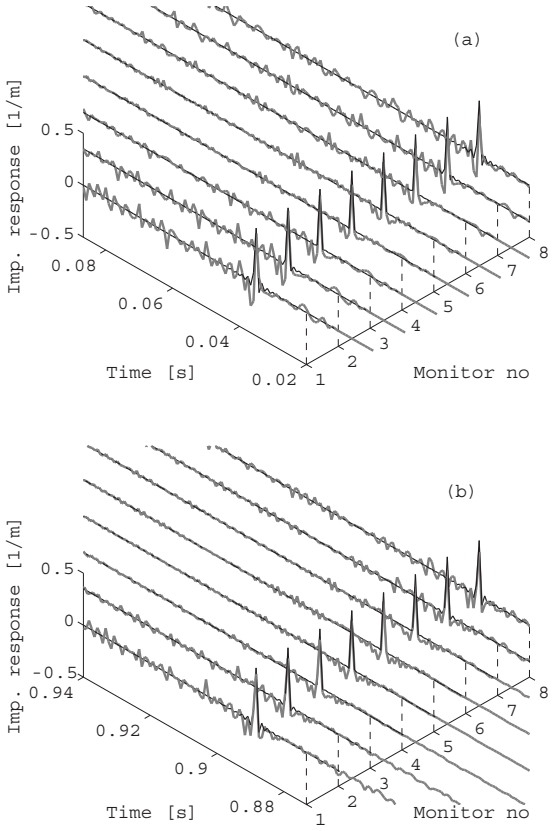

FIG. 17. Reproduced (thick gray lines) and virtual (thin black lines) impulse responses at the monitoring sensor array (shown in Fig. 2) for AWFS [(a) FXLMS algorithm with $\lambda=0$ and (b) independent radiation mode control with $\lambda_m=0$] with the system in the reverberation chamber.

room compensation is achieved over a wide time range. Again, more than simply reducing the undesirable room effect in the reproduced sound field, AWFS more closely reproduces the direct sound field than WFS.

The normalized energies of the errors at each of the monitor microphones are shown in Fig. 18 for the laboratory space. The AWFS algorithms reduce on average the reproduction errors in comparison with WFS by controlling the reproduction errors at the four error sensors. AWFS based on independent radiation mode control gives a larger reproduction region as the higher-order radiation modes (typically corresponding to higher-order spatial derivatives) are included in the controller in that case. This again highlights the benefits of AWFS based on independent radiation mode control. AWFS performs better than WFS for all the reported virtual source positions. Similar results were obtained for the reverberation chamber with different virtual source positions.

2. Harmonic AWFS

The harmonic AWFS results are only reported for the laboratory space. Consistent results were obtained for the reverberation chamber. According to the typical FRF shown in Fig. 5, the following frequencies were selected for on-line AWFS: 133, 160, 220, 280, 340, and 400 Hz.

Examples of pressure modes are shown for 220 Hz in Fig. 19. Again the radiation modes approach simple multipole directivity patterns: monopole, two orthogonal dipoles, and tesseral quadrupole at the sensor array.

The convergence coefficient was set to 0.01 for all frequencies while the penalization parameter was fixed to 1 (except at 133 and 160 Hz where they were set to 0.0005 and 0.005, respectively) for AWFS by the modified FXLMS algorithm. The convergence coefficients and penalization parameters for the AWFS algorithm based on independent radiation mode control were then adjusted to reach a roughly similar residual error level (at the error sensors) than for the FXLMS algorithm. However, each higher-order radiation modes were less penalized than for the FXLMS algorithm (when possible) to increase the performance outside the error sensor location (Gauthier and Berry, 2006). This was achieved using either $\lambda_m=\lambda$ or $\lambda_{m+1}<\lambda_m$. The coefficients are shown in Table I.

The results are summarized in Fig. 20, for a virtual source in $\mathbf{x}_o=[0,4,0]$ m, where the color axis represents the E_{LS} normalized criterion at each of the monitor positions along x_1. The criterion E_{LS} is the moving average of the quadratic sum of the reproduction errors normalized by the quadratic sum of the target signals at the monitor sensors. As one can note, the WFS performance is reduced in comparison with the other algorithms. As for the hemianechoic results, using the FXLMS algorithm, the error is effectively reduced near the error sensors. However, as frequency in-

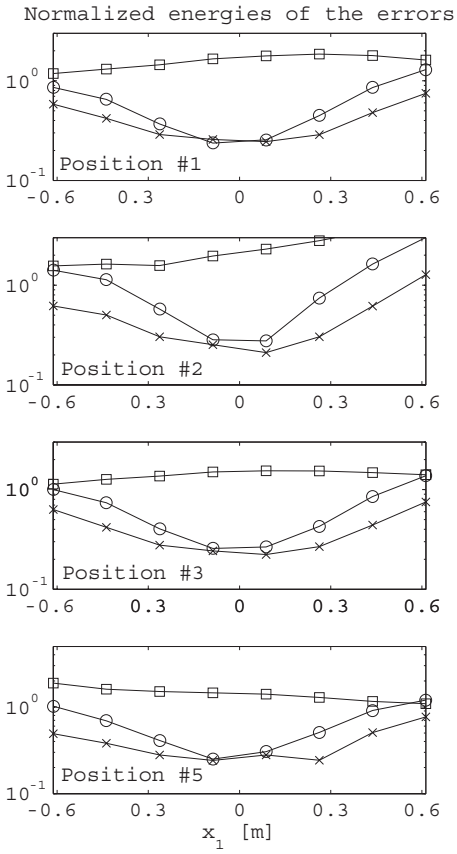

FIG. 18. Normalized energies of the error signals at each monitoring microphone for four virtual source positions in the laboratory space. Position 1: $\mathbf{x}_o=[0,4,0]$ m, position 2: $\mathbf{x}_o=[-4,0,0]$ m, position 3: $\mathbf{x}_o=[0,1.5,0]$ m, and position 5: $\mathbf{x}_o=[2.8289,-2.8234,0]$ m. (□) WFS errors; (○) errors of AWFS by FXLMS; and (×) errors of AWFS by independent radiation mode control.

creases, this control region is spatially reduced. This is in accordance with typical active noise control results. AWFS based on independent radiation mode control advantageously produces, as shown in Fig. 20, a larger control region since

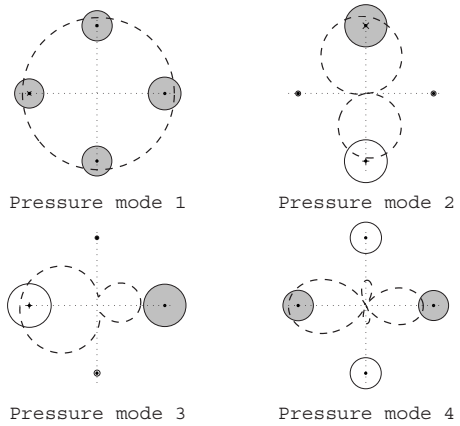

FIG. 19. Measured pressure modes at 220 Hz in the laboratory. (…) Sensor position; (○) positive real part; (●), negative real part; (+) positive imaginary part; and (×) negative imaginary part. Symbol diameter illustrates the magnitude of the corresponding value. (---) Corresponding computed free-field directivity.

TABLE I. Convergence coefficients (α_m) and regularization parameters (λ_m) for harmonic AWFS based on independent radiation mode control in laboratory space.

Freq. (Hz)	α_m	λ_m
133	0.01, 0.1, 0.1, 0.5	0.1, 0.01, 0.01, 0.001
160	0.02, 0.1, 0.1, 0.5	0.1, 0.01, 0.01, 0.001
220	0.02, 0.2, 0.2, 0.5	0.1, 0.01, 0.01, 0.001
280	0.02, 0.1, 0.1, 0.5	0.1, 0.01, 0.01, 0.0005
340	0.02, 0.1, 0.1, 0.5	0.1, 0.01, 0.01, 0.001
400	0.02, 0.1, 0.1, 0.5	0.1, 0.01, 0.01, 0.001

the higher-order radiation modes [which typically imply higher-order spatial derivatives at the error sensor array (see Fig. 19)] are allowed to converge.

D. Importance of the higher-order radiation modes

The importance of the higher-order radiation modes is highlighted by a specific set of experiments. The size of the active sound field reproduction effective region is shown in Fig. 21 in relation to the acoustic wavelength. In Fig. 21, several harmonic AWFS results with the WFS solution forced to zero are presented for a harmonic wave field at 400 Hz in the laboratory space. The WFS solution is forced to zero to illustrate only the effects of the individual radiation modes. Clearly, when AWFS based on independent radiation mode control includes only one radiation mode, the results correspond to AWFS by FXLMS. When the number of

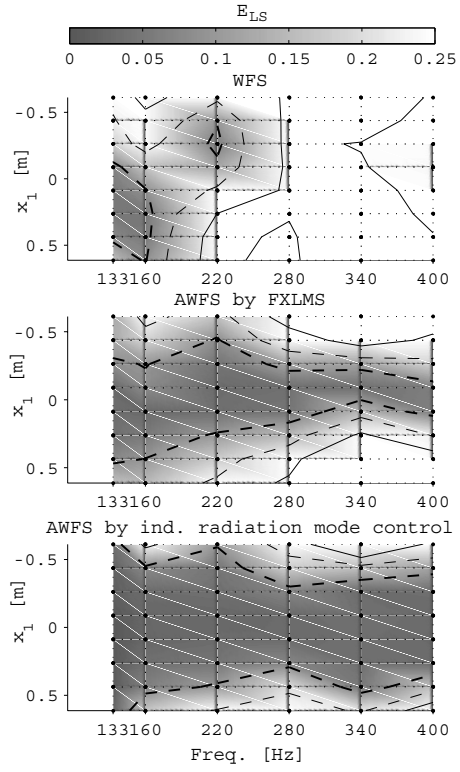

FIG. 20. Normalized E_{LS} criterion at the monitoring sensors for various frequencies and harmonic algorithms after convergence in the laboratory. From top to bottom: WFS, AWFS based on FXLMS and AWFS based on independent radiation mode control. (.) Measurement points. (———) The 0.1 contour lines; (---) the 0.25 contour lines; and (—) the 0.5 contour lines.

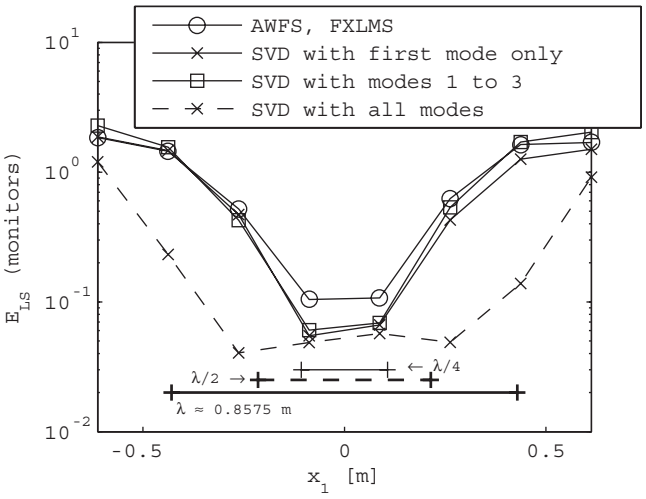

FIG. 21. Normalized E_{LS} criterion at the monitoring sensors for harmonic algorithms at 400 Hz after convergence in the laboratory space using AWFS with the WFS solution forced to zero. The wavelength and some corresponding fractions are included.

higher-order modes included in AWFS based on independent radiation mode control increases, the size of the effective control region increases from a quarter wavelength to half the wavelength. This supports the previous observation on the importance of the higher-order radiation modes to enlarge the effective active sound field reproduction region. The adaptation coefficients and penalization parameters are shown in Table I.

IV. CONCLUSION AND PERSPECTIVES

This paper investigated the objective performances of AWFS to compensate for the room effects (or any sound field reproduction errors) on WFS in experimental situations. The basic idea of AWFS is a simple combination of active noise control principles and classic WFS. Such a combination is entirely contained in the AWFS general cost function (Gauthier and Berry, 2006), which consists of minimization of the reproduction errors [typically caused by the room response (Klehs and Sporer, 2003; Sporer and Klehs, 2004) or the system limitation (Corteel, 2006b)] at several points in space, along with a regularization that penalizes the adaptive solution departure from the classic WFS solution. This penalizing is what makes AWFS original in comparison with other sound field reproduction techniques based on active sound control and adaptive filtering.

The results presented in this paper show that the AWFS system successfully achieves active sound field reproduction in more or less reflective spaces: hemianechoic chamber, laboratory space, and reverberation chamber. These experiments validate the AWFS concept and demonstrate the physical possibility of progressive sound field reproduction in reflective rooms. For the three rooms, it was shown that AWFS reduces the reproduction errors with respect to WFS reproduction errors in the reproduction region. AWFS based on independent control provides an extended effective area of sound field reproduction since each radiation mode convergence is independently adjusted so that higher-order modes converge in the allowed time. Since these higher-order modes are of great importance to enlarge the effective reproduction region, the possibility to control them independently is a major advantage of AWFS based on independent radiation mode control in comparison with modified FXLMS, which does not allow such independent control of each radiation mode convergence.

One of the original contributions of these results is that they establish, for the first time to the authors' knowledge, the validity of the AWFS concept based on independent radiation mode control (including SVD broadband filters) for broadband impulse reproduction by the way of controlled experiments. Bai and Elliott (2004) already considered SVD plant decoupling for cross-talk cancellation, but their paper was limited to theoretical investigations. Moreover, at the heart of the AWFS concept, is the definition of an *a priori* solution (WFS) which, to the authors' knowledge, was never used or experimentally tested within an adaptive signal processing or active noise control architecture. This paper on experimental AWFS supports the practical interest of AWFS.

The reported experiments were performed with a specific reproduction source and error sensor configuration. However, AWFS is not limited to a specific configuration. These experiments with AWFS were performed to evaluate the method. AWFS could be tested with different configurations or for different practical problems: sound environment reproduction, mock-up with sound field simulation system, etc. A typical AWFS extension would, for example, include more loudspeakers and more error sensors. Indeed, we expect that a larger effective reproduction region is achievable with a compact sensor array which would include more sensors, like a dense circular microphone array. Three-dimensional configurations of either loudspeaker or microphone arrays could also be implemented within the AWFS framework.

The tested AWFS system and implementation should be regarded as proto-AWFS. Indeed, before AWFS can be used for a practical application, several modifications should be done. For example, to reduce the obstruction of the error sensors in the listening area, the control filters can be calculated off-line for the virtual source positions and saved, after which the error sensors can be removed. An example of effective bank of compensation filters for WFS direct-sound-field equalization has been reported by Corteel (2006b). Moreover, several adaptive algorithms could be applied to AWFS, such as frequency-domain adaptation, sparse adaptation, etc. (Elliott, 2001) to improve the convergence properties of the algorithm or to reduce the computational burden.

Future research on AWFS should be conducted within a specific practical application such as sound environment reproduction or sound reproduction in a dedicated listening room to evaluate the potential of the method in real situations, possibly using more reproduction sources and more error sensors. AWFS and the corresponding algorithms should also be tested and evaluated on the basis of subjective performance.

ACKNOWLEDGMENTS

This work was supported by NSERC (Natural Sciences and Engineering Research Council of Canada), NATEQ (Fond Québecois de la Recherche sur la Nature et les Technologies), VRQ (Valorisation Recherche Québec), and Université de Sherbrooke. This research was conducted in collaboration with CIRMMT (Center for Interdisciplinary Research in Music Media and Technology, McGill University). The authors acknowledge the contribution of Emmanuel Corratgé, who contributed to the construction of the harmonic AWFS system and harmonic experiments.

AES Staff Writer (**2005**). "Multichannel audio systems and techniques," J. Audio Eng. Soc. **53**, 329–335.

Asano, F., and Swanson, D. C. (**1995**). "Sound equalization in enclosures using modal reconstruction," J. Acoust. Soc. Am. **98**, 2062–2069.

Bai, M. R., and Elliott, S. J. (**2004**). "Preconditioning multichannel adaptive filtering algorithms using EVD- and SVD-based signal prewhitening and system and decoupling," J. Sound Vib. **270**, 639–655.

Berkhout, A. J., de Vries, D., and Vogel, P. (**1993**). "Acoustic control by wave field synthesis," J. Acoust. Soc. Am. **93**, 2764–2778.

Betlehem, T., and Abhayapala, T. D. (**2005**). "Theory and design of sound field reproduction in reverberant rooms," J. Acoust. Soc. Am. **117**, 2100–2111.

Blauert, J. (**1999**). *Spatial Hearing, The Psychophysics of Human Sound Localization* (MIT, Cambridge).

Blesser, B., and Salter, L.-R. (**2007**). *Spaces Speak, Are You Listening? Experiencing Aural Architecture* (MIT, Cambridge).

Bouchard, M., and Quednau, S. (**2000**). "Multichannel recursive-least-squares algorithms and fast-transversal-filter algorithms for active noise control and sound reproduction systems," IEEE Trans. Speech Audio Process. **8**, 606–618.

Bravo, T., and Elliott, S. J. (**2004**). "Variability of low frequency sound transmission measurements," J. Acoust. Soc. Am. **115**, 2986–2997.

Cabell, R. H., and Fuller, C. R. (**1999**). "A principal component algorithm for feedforward active noise and vibration control," J. Sound Vib. **227**, 159–181.

Camurri, A., and Ferrentino, P. (**1999**). "Interactive environments for music and multimedia," Multimedia Syst. **7**, 32–47.

Choi, J.-W., and Kim, Y.-H. (**2004**). "Manipulation of sound intensity within a selected region using multiple sources," J. Acoust. Soc. Am. **116**, 843–852.

Corteel, E. (**2006a**). "On the use of irregurlarly spaced loudspeaker arrays for wave field synthesis, potential impact on spatial aliasing frequency," Proceedings of the Ninth International Conference on Digital Audio Effects (DAFX), Montreal, Canada, Sept. 18–20, 2006.

Corteel, E. (**2006b**). "Equalization in an extended area using multichannel inversion and wave field synthesis," J. Audio Eng. Soc. **54**, 1140–1161.

Davis, M. F. (**2003**). "History of spatial coding," J. Audio Eng. Soc. **51**, 554–569.

de Vries, D., Start, E. W., and Valstar, V. G. (**1994**). "The wave field synthesis concept applied to sound reinforcement: Restrictions and solutions," AES 96th Convention, Convention Paper 3812, Amsterdam, Feb. **1994**.

Elliott, S. (**2001**). *Signal Processing for Active Control* (Academic, London).

Elliott, S. J., and Nelson, P. A. (**1989**). "Multiple-point equalization in room using adaptive digital filters," J. Audio Eng. Soc. **37**, 899–907.

Epain, N., Friot, E., and Rabau, G. (**2004**). "Indoor sonic boom reproduction using ANC," Proceedings of Active 2004, Williamsburg, USA, Sept. 20–22, 2004.

Fuster, L., López, J. J., González, A., and Zuccarello, P. D. (**2005**). "Room compensation using multichannel inverse filters for wavefield synthesis systems," AES 118th Convention, Convention Paper 6401, Barcelona, Spain, May 28-31, **2005**.

Gauthier, P.-A., and Berry, A. (**2006**). "Adaptive wave field synthesis with independent radiation mode control for active sound field reproduction: Theory," J. Acoust. Soc. Am. **119**, 2721–2737.

Gauthier, P.-A., and Berry, A. (**2007**). "Objective evaluation of room effects on wave field synthesis," Acta. Acust. Acust. **93**, 824–836.

Gaunthier, P.-A., and Berry, A. (**2008**). "Adaptive wave field synthesis for broadband active sound field reproduction: Signal processing," J. Acoust. Soc. Am. **123**, 2003–2016.

Gauthier, P.-A., Berry, A., and Woszczyk, W. (**2005a**). "Sound-field reproduction in-room using optimal control techniques: Simulations in the frequency domain," J. Acoust. Soc. Am. **117**, 662–678.

Gauthier, P.-A., Berry, A., and Woszczyk, W. (**2005b**). "Wave field synthesis, adaptive wave field synthesis and ambisonics using decentralized transformed control: Potential applications to sound field reproduction and active noise control," J. Acoust. Soc. Am. **118**, 1967.

Grau, O. (**2003**). *Virtual Art—From Illusion to Immersion* (MIT, Cambridge).

Keller, M., Roure, A., and Marrot, F. (**2006**). "Acoustic field reproduction for psychoacoustic experiments: Application to aircraft interior noise," Proceedings of Active 2006, Adelaide, Australia, Sept. 18–20, 2006.

Kendall, G. S. (**1995**). "A 3-D sound primer: Directional hearing and stereo reproduction," Comput. Music J. **19**, 23–46.

Klehs, B., and Sporer, T. (**2003**). "Wave field synthesis in the real world. 1. In the living room," AES 114th Convention, Convention Paper 5727, Amsterdam, March 22–25, 2005.

Merimaa, J., and Pulkki, V. (**2005**). "Spatial impulse response rendering. I. Analysis and synthesis," J. Audio Eng. Soc. **12**, 1115–1127.

Nelson, P. S., Kirkeby, O., and Takeuchi, T. (**1997**). "Sound fields for the production of virtual acoustic images," J. Sound Vib. **204**, 386–396.

Poletti, M. A. (**2000**). "A unified theory of horizontal holographic sound systems," J. Audio Eng. Soc. **48**, 1155–1182.

Radlović, B. D., Williamson, R. C., and Kennedy, R. A. (**2000**). "Equalization in an acoustic reveberant environment: Robustness results," IEEE Trans. Speech Audio Process. **8**, 311–319.

Rumsey, F. (**2001**). *Spatial Audio* (Focal, Oxford).

Santillań, A. O. (**2001**). "Spatially extended sound equalization in rectangular rooms," J. Acoust. Soc. Am. **110**, 1989–1997.

Sporer, T., and Klehs, B. (**2004**). "Wave field synthesis in the real world. 2. In the movie theatre," AES 116th Convention, Convention Paper 6055, Berlin, Germany, May 8–11, 2004.

Spors, S., Kuntz, A., and Rabenstein, R. (**2003**). "An approach to listening room compensation with wave field synthesis," Proceedings of the AES 24th International Conference, Canada, June 26–28, 2003, pp. 70–82.

Spors, S., Renk, M., and Rabenstein, R. (**2005**). "Limiting effects of active room compensation using wave field synthesis," AES 118th Convention, Convention Paper 6400, Barcelona, Spain, May 28–31, 2005.

Spors, S., and Rabenstein, R. (**2006**). "Spatial aliasing artifacts produced by linear and circular-loudspeaker arrays used for wave field synthesis," AES 120th Convention, Convention Paper.

Start, E. W., de Vries, D., and Berkhout, A. J. (**1999**). "Wave field synthesis operators for bent line arrays in 3D space," Acust. Acta Acust. **85**, 883–892.

Start, E. W., Valstar, V. G., and de Vries, D. (**1995**). "Application of spatial bandwidth reduction in wave field synthesis," AES 98th Convention, Convention Paper 3972.

Takane, S., and Sone, T. (**2004**). "A new theory for active suppression of reflected sound waves from the walls based on Kirchhoff-Helmholtz boundary integral equation," Acoust. Sci. & Tech. **25**, 37–44.

Takane, S., Suzuki, Y., and Sone, T. (**1999**). "A new method for global sound field reproduction based on Kirchhoff's integral equation," Acust. Acta Acust. **85**, 250–257.

Veit, I., and Sander, H. (**1987**). "Production of spatially limited ⟨⟨diffuse⟩⟩ sound field in an anechoic room," J. Audio Eng. Soc. **35**, 138–143.

Verheijen, E. N. G. (**1997**). "Sound reproduction by wave field synthesis," Ph.D. thesis, Delft University of Technology, Delft, The Netherlands.

Williams, E. G. (**1999**). *Fourier Acoustics—Sound Radiation and Nearfield Acoustical Holography* (Academic, London).

Woszczyk, W., Cooperstock, J., Roston, J., and Martens, W. (**2005**). "Shake, rattle, and roll: Getting immersed in multisensory, interactive music via broadband networks," J. Audio Eng. Soc. **53**, 336–344.

Adaptive wave field synthesis for broadband active sound field reproduction: Signal processing[a)]

Philippe-Aubert Gauthier[b)] and Alain Berry
Groupe d'Acoustique de l'Université de Sherbrooke, Université de Sherbrooke, 2500 boul. de l'Université, Sherbrooke, Québec, Canada, J1K 2R1

(Received 26 April 2007; revised 23 January 2008; accepted 24 January 2008)

Sound field reproduction is a physical approach to the reproduction of the natural spatial character of hearing. It is also useful in experimental acoustics and psychoacoustics. Wave field synthesis (WFS) is a known open-loop technology which assumes that the reproduction environment is anechoic. A real reflective reproduction space thus reduces the objective accuracy of WFS. Recently, adaptive wave field synthesis (AWFS) was defined as a combination of WFS and active compensation. AWFS is based on the minimization of reproduction errors and on the penalization of departure from the WFS solution. This paper focuses on signal processing for AWFS. A classical adaptive algorithm is modified for AWFS: filtered-reference least-mean-square. This modified algorithm and the classical equivalent leaky algorithm have similar convergence properties except that the WFS solution influences the adaptation rule of the modified algorithm. The paper also introduces signal processing for independent radiation mode control of AWFS on the basis of plant decoupling. Simulation results for AWFS are introduced for free-field and reflective spaces. The two algorithms effectively reproduce the sound field and compensate for the reproduction errors at the error sensors. The independent radiation mode control allows a more flexible tuning of the algorithm. © *2008 Acoustical Society of America.* [DOI: 10.1121/1.2875269]

PACS number(s): 43.38.Md, 43.60.Tj, 43.50.Ki [NX] Pages: 2003–2016

I. INTRODUCTION

Following in the footsteps of the constantly evolving digital signal processing and the relatively recent advent of multichannel audio, spatial audio has gained more attention in the past few decades from researchers and practitioners for applications such as high-fidelity sound reproduction, music reproduction, virtual reality display, interactive multisensory environments, and spatial sound (Camurri and Ferrentino, 1999; Wilson, 2001; AES Staff Writer, 2005; Woszczyk *et al.*, 2005). The interest for immersion and convincing multisensory environments is not new and various techniques for spatial audio have been introduced in the past (Kleiner *et al.*, 1993; Kendall, 1995; Verheijen, 1997; Poletti, 2000; Rumsey, 2001; Davis, 2003).

Sound field simulation (as a spatial sound technique) attempts to reproduce the physical stimulus (wave field) of spatial hearing. Sound field reproduction was investigated by researchers in the past few decades (Berkhout *et al.*, 1993; Nelson *et al.*, 1997; Verheijen, 1997; Poletti, 2000; Choi and Kim, 2004; Takane and Sone, 2004). Recently one of the most active and related matters is room compensation (Spors *et al.*, 2003; Gauthier *et al.*, 2005a; Betlehem and Abhayapala, 2005; Fuster *et al.*, 2005; Gauthier and Berry, 2006), which is essential for sound field reproduction in a real reproduction space.

This paper deals with the problem of sound pressure field reproduction using adaptive digital signal processing applied to adaptive wave field synthesis (AWFS) initially introduced by Gauthier *et al.* (2005b) (see also Gauthier and Berry, 2006). The paper focuses on digital signal processing realization for AWFS.

Within this introductory section, the problem of sound pressure field reproduction and a review of corresponding technologies are presented. Section II A introduces WFS. Section II B presents the filtered-reference least-mean-square (FXLMS) realization of AWFS. Section II C presents AWFS on the basis of independent radiation mode control including the plant singular value decomposition (SVD) (Gauthier *et al.*, 2005b; Gauthier and Berry, 2006). Appendices A–C detail some aspects of AWFS based on independent radiation mode control. Digital signal processing simulation results are reported in Sec. III for AWFS using the proposed algorithms. Section IV discusses the results.

A. Sound field reproduction

In sound field simulation, the main objective can be generally stated as the aim to recreate a given physical quantity, such as sound pressure, sound intensity (Choi and Kim, 2004), spatial diffuseness (Merimaa and Pulkki, 2005), etc., over a certain space. This can be achieved using a reproduction system including electroacoustical sources and receivers, signal processing, and the desired physical output description. In several cases, use of adaptive filtering implies the minimization of a cost function which is representative of the reproduction objective (Gauthier and Berry, 2006). Adaptive signal processing for spatial sound reproduction has

[a)]Portions of this work were presented in "Wave field synthesis, adaptive wave field synthesis and ambisonics using decentralized transformed control: Potential applications to sound field reproduction and active noise control," 150th ASA meeting, Minneapolis, MN, October 2005.

[b)]Author to whom correspondence should be addressed. Electronic mail: philippe_aubert_gauthier@hotmail.com.

 0001-4966/2008/123(4)/2003/14/$23.00 © 2008 Acoustical Society of America

been studied in various forms by researchers (examples are: Nelson, 1994; Asano and Swanson, 1995; Ise, 1999; Takane *et al.*, 1999; Radlović *et al.*, 2000; Santillàn, 2001; Choi and Kim, 2004; Gauthier *et al.*, 2005a: Gauthier and Berry, 2006).

B. Wave field synthesis (WFS)

Work on WFS originates from the theoretical investigations by Berkhout (Berkhout *et al.*, 1993; Verheijen, 1997). It is assumed that the reproduction space is a free field. From the simple source formulation of the Kirchhoff–Helmholtz integral theorem (Williams, 1999), WFS operators are defined to "link" a given simple virtual source (typically creating spherical or plane waves in a planar listening area), fed by a monophonic signal, to a loudspeaker array which reproduces the virtual source's acoustic field (also called the target sound field). The problem usually concerns reproduction in the horizontal plane with a finite number of discrete sources using appropriate simplifications of the integral formulation (Verheijen, 1997). Some WFS studies have investigated spatial aliasing (Spors and Rabenstein, 2006; Corteel, 2006), objective performance in-room situation (Klehs and Sporer, 2003; Sporer and Klehs, 2004; Gauthier and Berry, 2007) and compensation of listening room acoustics (Spors *et al.*, 2003; Fuster *et al.*, 2005).

The benefit of current WFS prototypes is their effectiveness in creating a rich spatial impression over a broad area surrounded by loudspeakers. One of the WFS drawbacks is related to synthesis operators which rely on an important assumption: the reproduction room's response is not considered in the process (except in specific WFS research (Spors *et al.*, 2003). This typically introduces reproduction errors that AWFS can possibly reduce (Gauthier and Berry, 2007). Active room compensation for WFS is an active research topic for objective sound field reproduction (Elliott and Nelson, 1989; Asano and Swanson, 1995; Bouchard and Quednau, 2000; Santillàn, 2001; Spors *et al.*, 2003; Gauthier *et al.*, 2005b; Fuster *et al.*, 2005).

C. Adaptive wave field synthesis (AWFS)

In a recent paper (Gauthier and Berry, 2006), AWFS was defined as a possible practical compromise between WFS and active room compensation. AWFS is based on a cost function to be minimized by the reproduction sources. The cost function is defined from measurements of the reproduced sound field using error sensors at a number of discrete locations, and it is a quadratic function of: (1) the reproduction errors and (2) the adaptive filters departure from the WFS filters. Using a singular value decomposition (SVD) of the plant matrix (frequency response functions between reproduction sources and error sensors) (Gauthier and Berry, 2006), it was shown that the underlying AWFS mechanism is the independent control of radiation modes. The radiation modes correspond to the left and right singular vectors (Lancaster and Tismenetsky, 1985) from the plant SVD. This suggested a decoupled implementation of AWFS which is practically developed in this paper from a signal processing perspective.

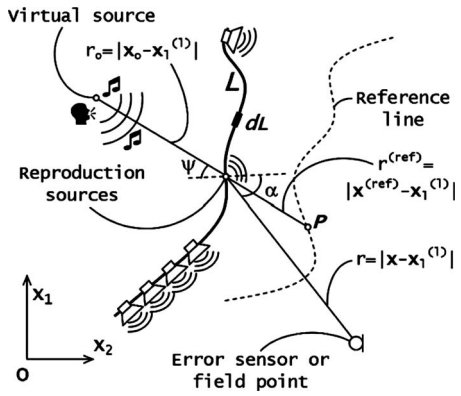

FIG. 1. Symbol convention for the WFS operators and filters definition. The virtual source is located in $\mathbf{x}_o$. The reproduction source l is located in $\mathbf{x}_l^{(l)}$; $\mathbf{x}^{(ref)}$ describes points which belong to the reference line; $\mathbf{x}$ describes any field point and $\mathbf{x}_m^{(m)}$ is the mth sensor position. L is the reproduction source line, the virtual source is on the left of the source line and the reproduction space is on the right of the source line. All sources and sensors are located in the x_1-x_2 plane.

II. SIGNAL PROCESSING FOR ADAPTIVE WAVE FIELD SYNTHESIS

For a target sound field produced by a virtual monopole with amplitude A [Pa m], $\mathbf{a}(z)$ is defined as the z transform of discrete-time sequences having the frequency response functions

$$\mathbf{a}(e^{j\omega}) = A[e^{-j\omega\Delta_1}/r_1\ e^{-j\omega\Delta_2}/r_2 \ldots e^{-j\omega\Delta_m}/r_m \ldots e^{-j\omega\Delta_M}/r_M]^T, \quad (1)$$

where Δ_m is the time delay which corresponds to r_m/c. The time convention is $e^{j\omega t}$, c [m/s] is the sound phase velocity and $r_m=|\mathbf{x}_m^{(m)}-\mathbf{x}_o|$ represents the distance between the virtual source in $\mathbf{x}_o$ and the mth error sensor in the reproduction space (Fig. 1), $\mathbf{x}_l^{(l)}$ is the reproduction source l position in three-dimensional space $(\mathbf{x}_1^{(l)},\mathbf{x}_2^{(l)},\ldots,\mathbf{x}_L^{(l)})$, $\mathbf{x}$ is the position of an arbitrary point in the reproduced wave field, and $\mathbf{x}_m^{(m)}$ is the position of the mth error sensor $(\mathbf{x}_1^{(m)},\mathbf{x}_2^{(m)},\ldots,\mathbf{x}_M^{(m)})$.

A. Review of WFS operators for AWFS

According to Verheijen (1997), the following general WFS operators are obtained in the frequency domain:

$$Q(\mathbf{x}_l^{(l)},e^{j\omega}) = \sqrt{\frac{jk}{2\pi}}A\cos(\Psi)\frac{e^{-j(kr_o)}e^{-j(\omega T_s\Delta)}}{\sqrt{r_o}}\sqrt{\frac{r^{(ref)}}{(r^{(ref)}+r_o)}} \quad (2)$$

and the reproduced sound field in free space is

$$p(\mathbf{x},e^{j\omega}) = \int_{-\infty}^{\infty} Q(\mathbf{x}_l^{(l)},e^{j\omega})\frac{e^{-jkr}}{r}dL, \quad (3)$$

where A is the target pressure field amplitude (virtual source monopole amplitude), $Q(\mathbf{x}_l^{(l)},e^{j\omega})$ is the driving function (expressed as a monopole amplitude density) for the reproduction sources along the line L, $k=\omega/c$ is the wavenumber and e^{-jkr}/r (with $r=|\mathbf{x}_l^{(l)}-\mathbf{x}|$) is the complex sound pressure pro-

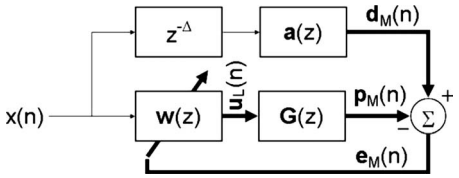

FIG. 2. Generalized sound field reproduction using adaptive filtering. Capitalized subscripts denote signal dimensions.

duced at $\mathbf{x}$ by a unitary amplitude monopole source in $\mathbf{x}_l^{(l)}$. The exponent $-j(\omega T_s \Delta)$ has been artificially added in Eq. (2) to add a modeling delay of Δ samples. The sampling period is T_s [s]. It is assumed that the virtual source and the reproduction sources are both in the horizontal plane (x_1, x_2). All other variables are shown in Fig. 1.

The reference line is chosen as a circle centered at the virtual source and passing through the center of the reproduction source array (Verheijen, 1997; Gauthier and Berry, 2006).

Practical WFS implementation using discrete reproduction sources on a finite line replaces Eq. (3) by

$$p(\mathbf{x}, e^{j\omega}) = \sum_{l=1}^{L} \Delta_s Q(\mathbf{x}_l^{(l)}, e^{j\omega}) \frac{e^{-jkr}}{r}, \tag{4}$$

where Δ_s is the reproduction source separation distance [m].

For WFS, a reproduction source is active (i.e. $Q(\mathbf{x}_l^{(l)}, e^{j\omega}) \neq 0$) if $|\Psi| < 90°$ where Ψ is shown in Fig. 1. Truncation effects are reduced using a spatial weighting window which reduces the amplitude of the reproduction sources at the end of the activated set. In this paper, half-Hanning window (with a half length of 1 m) is applied to the driving function (Eq. (2) at the ends of the active set of reproduction sources) (Gauthier and Berry, 2006).

B. FXLMS for AWFS

The classical FXLMS algorithm (Elliott, 2001) is adapted for the implementation of AWFS in a discrete-time domain.

Figure 2 presents the generalized sound field reproduction system for M reproduction points (Nelson, 1994; Nelson *et al.*, 1997). In this case, the problem is to reproduce a set of signals (the desired signals $\mathbf{d}_M(n)$, n is a sample index) at a set of M positions in the reproduction space using L reproduction sources. The term $\mathbf{w}(z)$ is the adaptive control filter vector and $\mathbf{G}(z)$ the acoustical plant responses z transform (between reproduction sources and error sensors). Here, $x(n)$ is the reference signal that is used to define a given simple source field prescribed in space and time domains through the target vector $\mathbf{a}(z)$ and $\mathbf{d}_M(n)$ ($\mathbf{d}_M(z) = \mathbf{a}(z) z^{-\Delta} x(z)$ is the target wave field at the M error sensors), and Δ is the modeling delay.

The system is characterized by one reference signal and L FIR (finite impulse response) control filters each including I coefficients (w_{li}). The multichannel reproduction system can thus be described by the reproduction error vector (capitalized subscript pairs denote matrix dimensions)

$$\mathbf{e}(n)_{M\times 1} = \mathbf{d}(n)_{M\times 1} - \mathbf{R}(n)_{M\times LI} \mathbf{w}(n)_{LI\times 1}, \tag{5}$$

with the error vector structured as

$$\mathbf{e}(n) = [e_1(n) \ldots e_M(n)]^T. \tag{6}$$

The desired signals are

$$\mathbf{d}(n) = [d_1(n) \ldots d_M(n)]^T. \tag{7}$$

The control filter vector is defined by

$$\mathbf{w}(n) = [\mathbf{w}_0^T(n) \ldots \mathbf{w}_{I-1}^T(n)]^T, \tag{8}$$

$$\mathbf{w}_i(n) = [w_{1i}(n) \ldots w_{Li}(n)]^T \tag{9}$$

and the matrix of filtered reference is

$$\mathbf{R}(n) = \begin{bmatrix} \mathbf{r}_1^T(n) & \mathbf{r}_1^T(n-1) & \ldots & \mathbf{r}_1^T(n-I+1) \\ \mathbf{r}_2^T(n) & \mathbf{r}_2^T(n-1) & \ldots & \mathbf{r}_2^T(n-I+1) \\ \vdots & \vdots & & \vdots \\ \mathbf{r}_M^T(n) & \mathbf{r}_M^T(n-1) & \ldots & \mathbf{r}_M^T(n-I+1) \end{bmatrix}, \tag{10}$$

where a filtered reference vector was introduced as

$$\mathbf{r}_m(n) = [\mathrm{r}_{1m}(n) \ldots \mathrm{r}_{Lm}(n)]^T. \tag{11}$$

The filtered reference $r_{lm}(n)$ corresponds to the reference signal convolved with the plant impulse response from reproduction source l to error sensor m

$$r_{lm}(n) = \sum_{j=0}^{J-1} G_{lmj} x(n-j), \tag{12}$$

where the J-coefficient plant impulse responses are stocked $\mathbf{G}_{L\times M\times J}$.

The general cost function for multichannel AWFS is (Gauthier and Berry, 2006)

$$J_{AWFS} = E[\mathbf{e}^T(n)\mathbf{e}(n)] + \gamma \mathbf{w}^T(n)\mathbf{w}(n) + \lambda(\mathbf{w}(n) - \mathbf{w}_{WFS})^T(\mathbf{w}(n) - \mathbf{w}_{WFS}), \tag{13}$$

where the first term represents the summation of the quadratic reproduction errors, the second term represents a control effort penalty (Elliott, 2001), the third term corresponds to a quadratic penalty for the coefficients $\mathbf{w}(n)$ deviation from $\mathbf{w}_{WFS}$ (the time-domain WFS operators). The mathematical expectation is denoted $E[\cdot]$. The time-domain WFS operators are obtained from inverse discrete-time Fourier transform of the WFS operator $Q(\mathbf{x}_1^{(l)}, e^{j\omega})$ defined in Eq. (2). In Eq. (13) the WFS operators $\mathbf{w}_{WFS}$ have been arranged similarly to the control filter coefficient vector in Eq. (8).

The stochastic gradient, using instantaneous values of the gradient of Eq. (13) is

$$\frac{\partial J_{AWFS}}{\partial \mathbf{w}} = 2[\mathbf{R}^T(n)\mathbf{R}(n) + (\gamma + \lambda)\mathbf{I}]\mathbf{w}(n) - 2\mathbf{R}^T(n)\mathbf{d}(n) - 2\lambda \mathbf{w}_{WFS}. \tag{14}$$

Using a classical gradient algorithm (Elliott, 2001) ($\mathbf{w}(n+1) = \mathbf{w}(n) - \mu \partial J_{AWFS}/\partial \mathbf{w}$), a multichannel recursive algorithm is obtained

$$\mathbf{w}(n+1) = (1 - \alpha(\gamma+\lambda))\mathbf{w}(n) + \alpha\lambda\mathbf{w}_{WFS} + \alpha\hat{\mathbf{R}}^T(n)\mathbf{e}(n), \tag{15}$$

which corresponds to a modified version of the multichannel leaky LMS algorithm (Elliott, 2001) where α, $(1-\alpha(\gamma+\lambda))$, $\alpha\lambda\mathbf{w}_{WFS}$, and $\hat{\mathbf{R}}^T(n)\mathbf{e}(n)$ are, respectively, the convergence coefficient ($\alpha=2\mu$), the leakage term, the *WFS* operators coefficients ($\mathbf{w}_{WFS}$) re-injection in the solution and the adaptive filter update according to the instantaneous errors. The WFS departure term in Eq. (13) introduces a leakage term in the filter update (Eq. (15)) plus a bias which is proportional to $\mathbf{w}_{WFS}$ ($\alpha\lambda\mathbf{w}_{WFS}$). In Eq. (15), the matrix $\mathbf{R}^T(n)$ has been replaced by $\hat{\mathbf{R}}^T(n)$ which uses a plant model to compute the estimated filtered reference.

Analysis of convergence of FXLMS applied to AWFS is detailed in the remainder of this section. Using these results, one may evaluate the convergence behavior of the multichannel AWFS in comparison with standard FXLMS or leaky FXLMS.

Equation (15) is rewritten using the error vector definition of Eq. (5)

$$\mathbf{w}(n+1) = \mathbf{w}(n) + \alpha\lambda\mathbf{w}_{WFS} + \alpha\hat{\mathbf{R}}(n)\mathbf{d}(n) - \alpha[(\hat{\mathbf{R}}^T(n)\mathbf{R}(n) + (\gamma+\lambda)\mathbf{I})]\mathbf{w}(n), \tag{16}$$

which allows the derivation of the asymptotic filter coefficients $\mathbf{w}_\infty = \lim_{n\to\infty} E[\mathbf{w}(n)]$

$$\mathbf{w}_\infty = \frac{E[\hat{\mathbf{R}}^T(n)\mathbf{d}(n)] + \lambda\mathbf{w}_{WFS}}{E[\hat{\mathbf{R}}^T(n)\mathbf{R}(n)] + (\gamma+\lambda)\mathbf{I}}, \tag{17}$$

where it is assumed that $E[\mathbf{w}_\infty]=\mathbf{w}_\infty$ and $E[\mathbf{w}_{WFS}]=\mathbf{w}_{WFS}$ since $\mathbf{w}_{WFS}$ is constant for a fixed virtual source position. Equation (17) shows that the reproduction filters after convergence of the adaptation algorithm are partly defined by the WFS operators to an extent determined by λ and partly by the leaky LMS error attenuation.

Using Eq. (17), and Eq. (15),

$$E[\mathbf{w}(n+1) - \mathbf{w}_\infty] = [\mathbf{I} - \alpha E[\hat{\mathbf{R}}^T(n)\mathbf{R}(n) + (\gamma+\lambda)\mathbf{I}]]E[\mathbf{w}(n) - \mathbf{w}_\infty]. \tag{18}$$

The eigenvalue decomposition of the matrix $E[\hat{\mathbf{R}}^T(n)\mathbf{R}(n)+(\gamma+\lambda)\mathbf{I}]$ is introduced

$$E[\hat{\mathbf{R}}^T(n)\mathbf{R}(n) + (\gamma+\lambda)\mathbf{I}] = \mathbf{Q}\mathbf{T}\mathbf{Q}^{-1}, \tag{19}$$

where $\mathbf{T}$ is a diagonal matrix of eigenvalues and $\mathbf{Q}$ is the matrix of the eigenvectors. The transformed adaptive filter is

$$\mathbf{t}(n) = \mathbf{Q}^{-1}E[\mathbf{w}(n) - \mathbf{w}_\infty]. \tag{20}$$

One can rewrite Eq. (18) as a set of uncoupled update equations for the various convergence modes since $\mathbf{T}$ is diagonal

$$\mathbf{t}(n+1) = [\mathbf{I} - \alpha\mathbf{T}]\mathbf{t}(n). \tag{21}$$

Each convergence mode will converge provided that $0<|1-\alpha T_i|<1$ with T_i being the ith eigenvalue of the decomposition introduced in Eq. (19). This allows the following criterion for the convergence factor which would provide stable convergence (Morgan, 1980; Elliott, 2001)

$$0 < \alpha < 2\frac{\Re[T_i]}{|T_i|^2}, \tag{22}$$

where $\Re[\cdot]$ indicates the real part of the argument. This is a typical FXLMS result for which convergence properties in relation with plant responses are known (Elliott, 2001), thus supporting that modified FXLMS for AWFS has the same convergence properties as classical FXLMS. Since the penalization terms $[(\gamma+\lambda)\mathbf{I}]$ in Eq. (19) form a diagonal matrix, they have the effect of stabilizing standard FXLMS algorithm by compensating for potentially small or negative eigenvalues T_i' (Elliott, 2001), where T_i' is the ith eigenvalue of $E[\hat{\mathbf{R}}^T(n)\mathbf{R}(n)]$. This effect can be shown by rewriting Eq. (22) using the eigenvalue decomposition of $E[\hat{\mathbf{R}}^T(n)\mathbf{R}(n)]$ as $\mathbf{Q}'\mathbf{T}'\mathbf{Q}'^{-1}$

$$0 < \alpha < 2\frac{\Re[T_i'] + (\gamma+\lambda)}{|T_i' + (\gamma+\lambda)|^2}. \tag{23}$$

Both the control effort penalization (γ) and the WFS penalization λ have the same effect in terms of convergence condition and may both equally stabilize a system by compensating for small negative eigenvalues T_i'.

Although sound field reproduction using AWFS as defined by the adaptation algorithm of Eq. (15) is readily applicable, some well-known disadvantages of multichannel FXLMS also apply to AWFS. These are related to the slow FXLMS convergence properties and computational load associated with an increasing number of filter coefficients I and reproduction sources L. Most of the slow convergence properties of the multichannel FXLMS are related to the cross-coupling paths and the non-flat frequency responses of the electroacoustical multichannel plant between the sources and the sensors (Elliott, 2001; Bai and Elliott, 2004). Since a sound field reproduction system like a AWFS system implies many reproduction sources, this might limit the application of FXLMS for AWFS. With this in mind, it would be interesting to transform the multichannel problem in a set of independent single-channel systems. This is possible on the basis of independent radiation mode control (Gauthier and Berry, 2006) and is related to the principal-component LMS (PC-LMS) algorithm (Cabell and Fuller, 1999; Elliott, 2000; Bai and Elliott, 2004).

C. AWFS with independent radiation mode control

This section presents the system preconditioning for independent radiation mode control using parallel single-channel adaptive systems (as already suggested in a previous paper (Gauthier and Berry, 2006)). Independent radiation mode control is based on singular value decomposition (SVD) of the plant matrix $\mathbf{G}(e^{j\omega})$. Further details are provided in Appendix A.

The control architecture is shown in Fig. 3. The upper branch is the target wave field definition. The second branch represents the fixed WFS contribution, obtained by the WFS operators projection on the null space of $\mathbf{G}(e^{j\omega})$. This part is

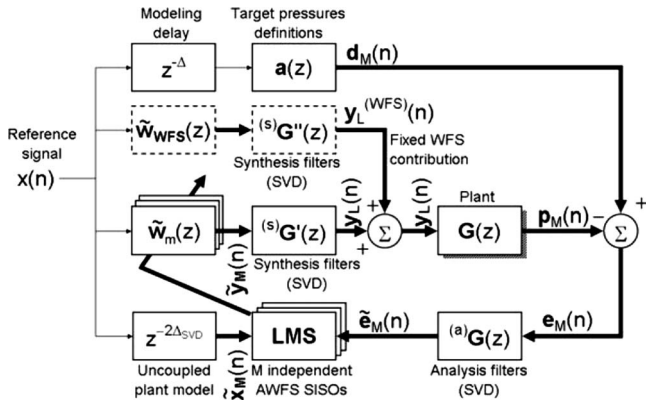

FIG. 3. Block diagram of the AWFS least-mean-square adaptive digital processing implementation based on independent radiation mode control. Subscripts denotes signal dimensions.

non-adaptive. Note that the corresponding two dashed blocks in this figure are combined in a single operation with an additional delay of Δ_{SVD} samples (see Appendix B). The third branch includes the independent adaptive controllers $\tilde{\mathbf{w}}_m$, the first synthesis filter matrix $^{(s)}\mathbf{G}'(z)$, the reproduction source signals $\mathbf{y}_L(n)$, and the plant response $\mathbf{G}(z)$ to produce the reproduced sound pressures $\mathbf{p}_M(n)$. The bottom branch includes the uncoupled plant model $z^{-2\Delta_{SVD}}$, the independent single-channel LMS gradient algorithms and the analysis filter matrix $^{(a)}\mathbf{G}(z)$ (to transform the reproduction errors into the pressure mode basis). Details about the synthesis and analysis filters are given in Appendices A–C.

The independent LMS algorithms operate on the decoupled plant. This means that each single-channel independent LMS algorithm controls a single radiation mode obtained from the SVD of $\mathbf{G}(e^{j\omega})$.

Several preconditioning methods have been published for feedforward control (Cabell and Fuller, 1999; Cabell *et al.*, 2001; Elliott, 2001, 2000; Bai and Elliott, 2004). Preconditioning using plant decoupling has been treated using principal component LMS (PC-LMS) algorithm, based on SVD, for tonal disturbances (Cabell and Fuller, 1999) or, equivalently, SVD controller for tonal disturbances (Elliott, 2000). SVD decoupling has been recently extended for broadband signals using a decoupling filter formulation in the frequency domain and inverse transformation towards the time domain for two-channel cross-talk cancelation (Bai and Elliott, 2004). This paper includes considerations for the null space of the plant response (which has proven to be of importance for AWFS (Gauthier and Berry, 2006) and for the realization of singular vectors reordering and modification (to reduce the time-domain leakage in the decoupling filters (synthesis and analysis filters)). Moreover, the AWFS approach implies the projection of the WFS operators on the source mode basis. This differs from Bai's work which was also devoted to a different application. All these special considerations are described in the Appendices to lighten the main content of the paper.

For the sake of brevity, the following developments are presented for system uncoupling and whitening. Minor modifications are needed when the system is only decoupled. Since the control system shown in Fig. 3 can be considered as a set of independent single-channel radiation-mode controllers, for the mth independent radiation mode controller the instantaneous reproduction error is

$$\tilde{e}_m(n) = \tilde{d}_m(n) - \tilde{p}_m(n), \tag{24}$$

where $\tilde{d}_m(n)$ is the mth element of $\mathbf{d}(n)$ passed through the analysis filter matrix $^{(a)}\mathbf{G}(z)$ and $\tilde{p}_m(n)$ is the mth element of $\mathbf{p}(n)$ passed through the analysis filter matrix. This equation can be rewritten as follows:

$$\tilde{e}_m(n) = \tilde{d}_m(n) - \tilde{\mathbf{w}}_m^T(n)\mathbf{x}(n - 2\Delta_{SVD}), \tag{25}$$

where $\tilde{\mathbf{w}}_m(n)$ is the I-coefficient vector associated with the control filter for the mth radiation mode and the reference signal vector is $\mathbf{x}(n)=[x(n)x(n-1)\ldots\ x(n-I-1)]^T$. In this case the cost function associated with the mth radiation mode is expressed as

$$\tilde{J}_m = E[\tilde{e}_m^2(n)] + \lambda_m[\tilde{\mathbf{w}}_m(n) - \tilde{\mathbf{w}}_{WFS_m}]^T[\tilde{\mathbf{w}}_m(n) - \tilde{\mathbf{w}}_{WFS_m}], \tag{26}$$

where $\tilde{\mathbf{w}}_{WFS_m}$ is the I-coefficient vector of the WFS operators projected on the mth first synthesis filter (see Appendix C). The gradient of this cost function is

$$\frac{\partial \tilde{J}_m}{\partial \tilde{\mathbf{w}}_m} = -2\mathbf{r}_{x\tilde{d}_m}(2\Delta_{SVD}) + 2\mathbf{R}_{xx}(0)\tilde{\mathbf{w}}_m(n) + 2\lambda_m\tilde{\mathbf{w}}_m(n) - 2\lambda_m\tilde{\mathbf{w}}_{WFS_m} \tag{27}$$

with $\mathbf{r}_{x\tilde{d}_m}(t)=E[\tilde{d}_m(n+t)\mathbf{x}(n)]$ and $\mathbf{R}_{xx}(t)=E[\mathbf{x}(n+t)\mathbf{x}^T(n)]$. Using Eq. (25), the instantaneous value of the gradient becomes

$$\frac{\partial \tilde{J}_m}{\partial \tilde{\mathbf{w}}_m} = -2\tilde{e}_m(n + 2\Delta_{SVD})\mathbf{x}(n) + 2\lambda_m\tilde{\mathbf{w}}_m(n) - 2\lambda_m\tilde{\mathbf{w}}_{WFS_m}. \tag{28}$$

A single-channel LMS algorithm $(\tilde{\mathbf{w}}_m(n+1)=\tilde{\mathbf{w}}_m(n) - (\alpha_m/2)\,\partial\tilde{J}_m/\partial\tilde{\mathbf{w}}_m)$ with a convergence coefficient α_m for the mth controller gives

$$\tilde{\mathbf{w}}_m(n+1) = (1 - \alpha_m\lambda_m)\tilde{\mathbf{w}}_m(n) + \alpha_m\tilde{e}_m(n + 2\Delta_{SVD})\mathbf{x}(n) + \alpha_m\lambda_m\tilde{\mathbf{w}}_{WFS_m}. \tag{29}$$

The adaptation rule is, however, based on future values of the reproduction error $\tilde{e}_m(n+2\Delta_{SVD})$ so that a modification of this algorithm is introduced

$$\tilde{\mathbf{w}}_m(n+1) = (1 - \alpha_m\lambda_m)\tilde{\mathbf{w}}_m(n) + \alpha_m\tilde{e}_m(n)\mathbf{x}(n - 2\Delta_{SVD}) + \alpha_m\lambda_m\tilde{\mathbf{w}}_{WFS_m}, \tag{30}$$

where $\mathbf{x}(n-2\Delta_{SVD})$ represents the filtered reference in the SVD-transformed domain which includes decoupling and whitening. This last equation can be implemented for each radiation mode controller for practical applications of AWFS based on plant decoupling. If plant whitening is excluded, it is still possible to use the last equation as an adaptation algorithm since $\mathbf{x}(n-2\Delta_{SVD})$ would then correspond to a de-

layed version of the reference signals. (This implementation is related to the DXLMS (delayed-reference LMS) algorithm (Ahn and Voltz, 1996). More than simplifying the computation by replacing a multichannel implementation by a set of independent controllers, the amount of operation is also reduced since the filtered reference is now replaced by a simple delay operation ($\mathbf{x}(n-2\Delta_{SVD})$) in Eq. (30). In the FXLMS algorithm (Eq. (15)), the computation of the filtered reference ($\hat{\mathbf{R}}^T(n)$) involved a multichannel convolution. This is an advantage of AWFS based on independent radiation mode control.

Denoting $\tilde{\mathbf{w}}_{m_\infty}=\lim_{n\to\infty}E[\tilde{\mathbf{w}}_m(n)]$ and finding the mathematical expectation of Eq. (30), one finds

$$\tilde{\mathbf{w}}_{m_\infty}=\frac{\mathbf{r}_{x\tilde{d}_m}(2\Delta_{SVD})+\lambda_m\mathbf{w}_{WFS_m}}{\mathbf{R}_{xx}(0)+\lambda_m\mathbf{I}}$$

$$=\frac{E[\tilde{d}_m(n)\mathbf{x}(n-2\Delta_{SVD})]+\lambda_m\tilde{\mathbf{w}}_{WFS_m}}{E[\mathbf{x}(n-2\Delta_{SVD})\mathbf{x}^T(n-2\Delta_{SVD})]+\lambda_m\mathbf{I}}. \quad (31)$$

The structure of Eq. (31) is very similar to the one obtained for the multichannel FXLMS case (Eq. (17)), except that it applies independently to each radiation mode. Such implementation therefore allows for the independent tuning of the convergence properties of each radiation mode. This is the second advantage of AWFS based on independent radiation mode control.

III. SIMULATIONS RESULTS

In order to demonstrate the feasibility of an AWFS system based on the adaptive signal processing described in this paper, numerical simulations were performed.

A. Free field

The system shown in Fig. 4 was simulated using a simple free-field model: The reproduction sources were represented by monopoles with a radiated sound pressure field e^{-jkr}/r where $r[m]$ is the distance from the reproduction source and k the wavenumber. There are four error sensors and 24 reproduction sources. The four error sensors are separated by 0.175 m along x_1 and x_2. The source array has a diameter of 2 m and the source separation is 0.2611 m. The impulse responses from the reproduction sources to the error sensors were then computed using an inverse fast Fourier transform (IFFT) of the frequency-domain response functions. Since the function e^{-jkr}/r generally involves fractional time delays (Laakso *et al.*, 1996), Hanning windows were applied in the time domain (centered on the main impulsion of the response) to reduce time aliasing. For the free-field simulations, the circular group of monitor sensors shown in Fig. 4 is used. The sampling frequency is 1200 Hz.

Results of time-domain AWFS simulations for this case are shown in Figs. 5–7. (Appendix B presents the synthesis and analysis filters.) The results, shown in Fig. 5, are described in terms of the E_{LS} performance criterion defined by

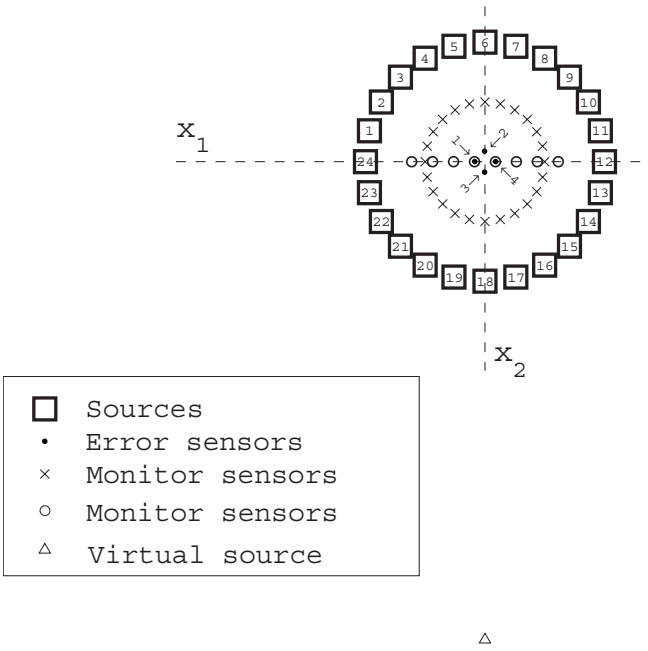

FIG. 4. Configuration of the reproduction source, error sensor and monitor sensor arrays. The error sensors' numbers are identified with arrows. Two different groups of monitor sensors are used: a linear array of eight monitors or a circular array of 24 monitors. Δ: virtual source in $\mathbf{x}_o=[0,4,0]$ m.

$$E_{LS}(n)=\mathbf{e}(n)^T\mathbf{e}(n) \quad (32)$$

and corresponds to the sum of the squared reproduction errors either at the error microphones (top of Fig. 5) or at the monitoring microphones (bottom of Fig. 5). In Fig. 5, E_{LS} is also smoothed with a moving-average filter to enhance the figure readability.

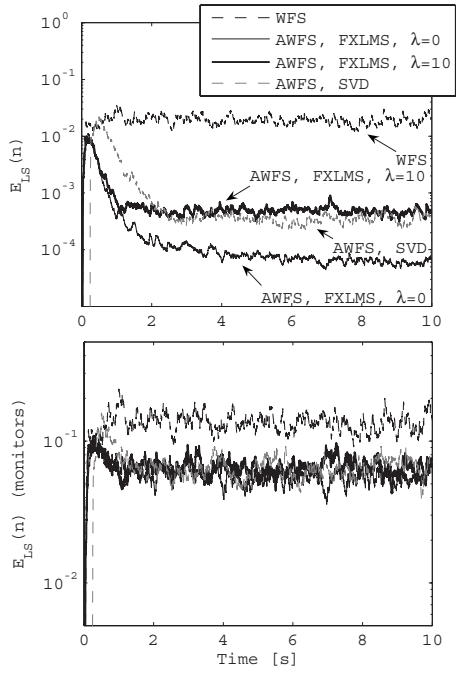

FIG. 5. Learning curves for reproduction errors at the error sensors and at the monitor sensors using FXLMS and independent radiation mode control algorithms in free field.

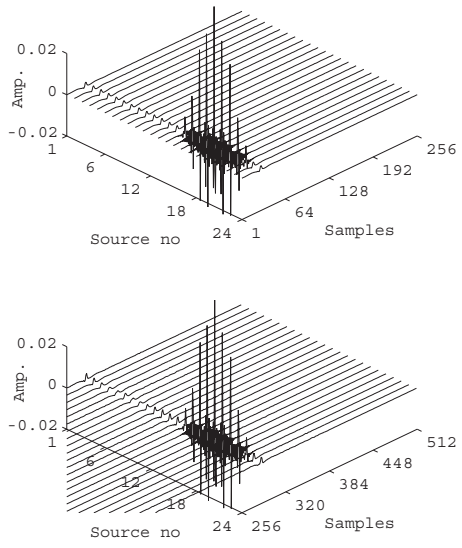

FIG. 6. Examples of the L resulting control filters for AWFS by FXLMS (top) and by independent radiation mode control (bottom) in free field.

The fixed WFS solution is obtained by setting the convergence coefficient $\alpha=0$ and the penalization parameter $\lambda=0$ in Eq. (15). Since $\alpha=0$, the control filters then coincide with the WFS solution which is used as the initial value for the control filters. We used $\alpha=0.00004$ and $\lambda=0$ for the first FXLMS case while $\alpha=0.00004$ and $\lambda=10$ were used for the second FXLMS case. As for the AWFS algorithm based on independent radiation mode control, each radiation mode is associated with its own values of the convergence coefficients $\alpha_1=0.0002$, $\alpha_2=\alpha_3=0.001$, $\alpha_4=0.004$ and penalization parameters $\lambda_1=\lambda_2=\lambda_3=\lambda_4=1$. In all cases, the size of the control filters was set to 256 and γ was set to 0. The convergence coefficients were chosen to approach the maximum value for stable convergence. A modeling delay of 16 samples, $\Delta=16$, was used in these simulations. The SVD delay was set to 128, $\Delta_{SVD}=128$. The first and second synthesis filters and the analysis filters all include 256 coefficients.

Figure 5 shows that the different algorithms effectively reduce the reproduction error in comparison with WFS. The independent radiation mode control implementation implies a delayed adaptation caused by the supplementary delay in the synthesis and analysis filters (a total of $2\Delta_{SVD}$ samples delay). Although the FXLMS algorithm can reach a similar residual criterion as the AWFS algorithm based on independent radiation mode control, the independent implementation allows for fine tuning of the convergence properties of each

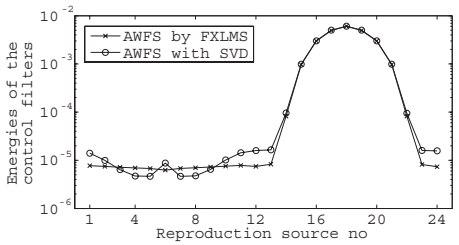

FIG. 7. Total energies of the L control filters shown in Fig. 6.

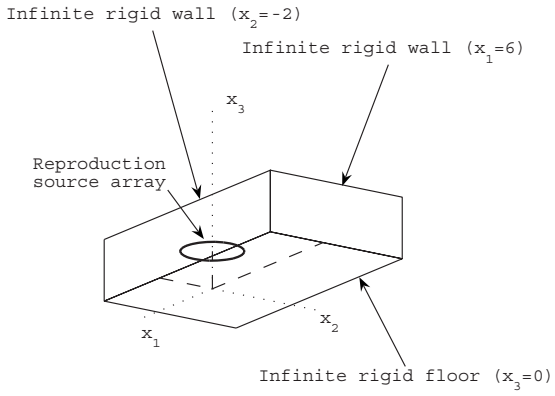

FIG. 8. Circular reproduction source array in three-dimensional semi-infinite space.

mode, which is not possible with the FXLMS algorithm. This is highlighted in Fig. 6, which shows the 24 control filters after convergence for the FXLMS and SVD-based algorithms. Note that for the SVD-based algorithm, these control filters correspond to the multiplication of the adaptive filter matrix ($M\times256$, with $M=4$) with the first synthesis filter matrix ${}^{(s)}\mathbf{G}'(z)(L\times M\times256)$ along with the addition of the null space synthesis filters matrix ${}^{(s)}\mathbf{G}''(z)(L\times256)$. Clearly, both algorithms result in a similar set of control filters. However, for the SVD-based algorithm, the presence of the higher-order SVD radiation modes is visible from sources 1–12 where the spatial variation of the control filters with reproduction source number is more pronounced (Gauthier and Berry, 2006). This is also shown in Fig. 7 where the total energies (quadratic sums of all the coefficients) of the control filters are shown for each reproduction source. This more pronounced variation for the reproduction sources 1–12 is due to the faster convergence of higher-order radiation modes in independent radiation mode control, because it is based on modal convergence coefficients α_m and penalization λ_m. (With the FXLMS algorithm, these radiation modes are not allowed to converge in the given adaptation time.) Indeed, see Appendix B, the higher-order radiation modes correspond to more pronounced spatial variations of the corresponding first synthesis filters.

B. Semi-infinite space delimited by a rigid floor and two hard walls

To investigate the effectiveness of the AWFS algorithms for active sound field reproduction in non-anechoic environments, other simulations were performed where the acoustical responses included three rigid surfaces. The sources and the sensors are 1.22 m above a rigid floor. Two perpendicular walls are also included as planes located at $x_2=-2$ m and $x_1=-6$ m. The configuration is shown in Fig. 8. For the simulation results presented here, the linear array of monitoring sensors shown in Fig. 4 is used.

Although this reproduction space is simpler than a real listening room, it provides enough departures with respect to the free field situation to investigate AWFS in a reflective reproduction space.

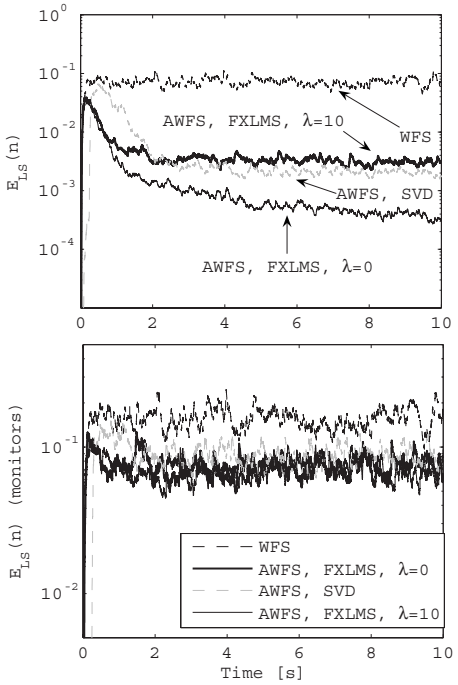

FIG. 9. Learning curves for reproduction errors at the error sensors and at the monitor sensors using FXLMS and independent radiation mode control algorithms using the system with a rigid floor and two hard walls.

Appendix B presents the first synthesis filters ${}^{(s)}\mathbf{G}'(z)$ and analysis filters ${}^{(a)}\mathbf{G}(z)$ each of which includes 256 coefficients. A modeling delay of 16 samples, $\Delta=16$, was used in these simulations.

A comparison of WFS and AWFS is reported in Fig. 9 in terms of the learning curves for the various algorithms. The following values were used: $\alpha=0$ and $\lambda=0$ for WFS. We used $\alpha=0.00004$ and $\lambda=0$ for the first FXLMS case while $\alpha=0.00004$ and $\lambda=10$ were used for the second FXLMS case. As for the AWFS algorithm based on independent radiation mode control, the convergence and penalization parameters were adjusted for each individual radiation mode: $\alpha_1=0.00015$, $\alpha_2=\alpha_3=0.0004$, $\alpha_4=0.003$ and $\lambda_1=1$, $\lambda_2=\lambda_3=0.1$, $\lambda_4=0.01$. The adaptation coefficients were chosen to approach the maximum value for stable convergence. It is possible to reduce the corresponding penalization parameter so that the convergence of the higher-order modes is not blocked by excessively large penalization parameters. In all cases, the size of the control filters was 256 and γ was set to 0. According to the learning curves of Fig. 9, it is clear that AWFS provides a reduction of the reproduction error both at the error and monitor sensors when compared to WFS.

The effects of the reflective surfaces on sound field reproduction in space are shown in Figs. 10–12, which present the reproduced impulse responses (instantaneous sound pressure) at the monitoring sensors for the linear monitor array shown in Fig. 4. For the WFS solution, one can clearly distinguish the undesirable reflections reaching the monitor array in Fig. 10. The FXLMS case, Fig. 11, is obtained for a penalization parameter $\lambda=10$. In this figure, one can note the reduction of the reflections. This reduction of room effects is most notable for the floor and late reflections. The attenuation of the room effects is noticeable at the central monitoring sensors (this region corresponds to the control region (error sensors position), that is monitor sensors Nos. 4 and 5). The comparison between Figs. 11 and 12 shows how the AWFS algorithm based on independent control effectively reduces the undesirable reflections at the monitoring sensors.

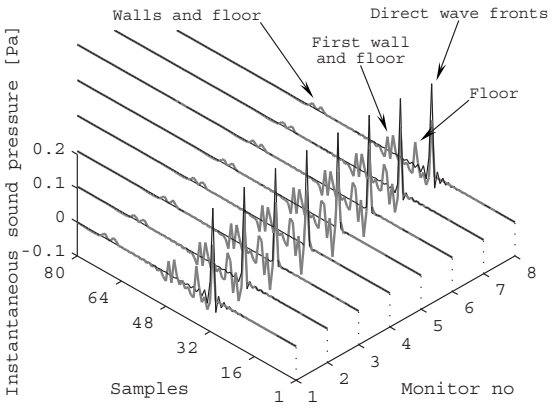

FIG. 10. Reproduced (thin lines) and virtual (thick dashed lines) impulse responses at the monitor sensor array (linear array shown in Fig. 4) for WFS using the system with a rigid floor and two hard walls.

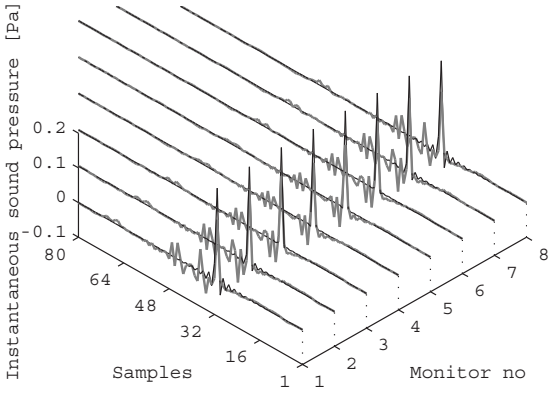

FIG. 11. Reproduced (thin lines) and virtual (thick dashed lines) impulse responses at the monitor sensor array (linear array shown in Fig. 4) for AWFS by FXLMS using the system with a rigid floor and two hard walls.

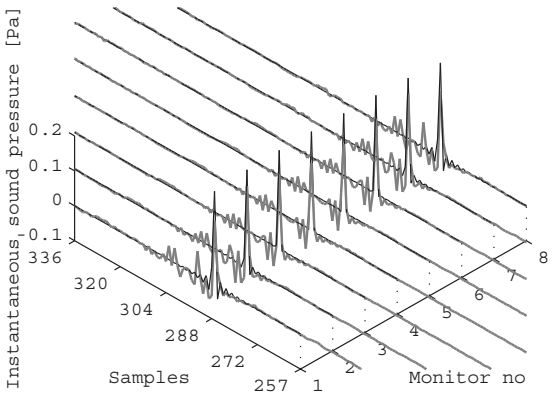

FIG. 12. Reproduced (thin lines) and virtual (thick dashed lines) impulse responses at the monitor sensor array (linear array shown in Fig. 4) for AWFS based on independent radiation mode control using the system with a rigid floor and two hard walls.

IV. CONCLUSION AND PERSPECTIVES

Adaptive wave field synthesis, as introduced by the authors (Gauthier and Berry, 2006), was originally proposed as a solution for active sound field reproduction and active room compensation for WFS. AWFS is based on minimization of the reproduction errors with a departure penalty from the WFS solution. Such penalization is what makes the AWFS original. This paper furthered the understanding and definition of AWFS by analyzing broadband signal processing and implementation on the basis of two algorithms: modified FXLMS and independent radiation mode control based on plant decoupling by singular value decomposition.

It was shown theoretically that the application of classical adaptive algorithm for active noise control such as FXLMS provides a practical implementation frame for AWFS. The convergence properties of the modified FXLMS algorithm are very similar to the properties of the classical leaky FXLMS algorithm. The main difference between this classical algorithm and its modified counterpart for AWFS is the constant reintroduction of a scaled part of the WFS solution at each sample in the adaptation rule. Plant SVD and AWFS based on independent radiation mode control were then introduced. The corresponding adaptation equation showed that it is possible to control independently the convergence properties of each of the radiation modes. This is a major advantage of plant decoupling for AWFS along with reduction of the computational burden (partly caused by the simplification of the adaptation rules and of the computation of the filtered reference signals). In comparison with other published results on plant preconditioning by SVD (Bai and Elliott, 2004), further practical considerations for first synthesis and analysis filters were presented in the Appendices. It was shown that either a reordering algorithm or a sign change tracking algorithm (both working in the frequency domain) are needed before any tractable time-domain implementation of AWFS can be achieved. Moreover, special attention was given to the practical null space definition which is of great importance for AWFS.

Simulations results for free field and in a semi-infinite space bounded by three rigid surfaces were presented. The first case was introduced to validate the AWFS algorithms in a simple situation. It proved the workability of the algorithms. The second case was introduced as a demonstration of the interest of AWFS: active sound field reproduction and active room compensation. A simple semi-infinite space was chosen as an example where identifiable discrete reflected wave fronts impinge on the sound field reproduction system. In this example, it was demonstrated that in-plane AWFS can effectively be used to compensate for undesirable room effects such as discrete reflections in the vicinity of the error sensors. These included reflections from vertical and horizontal surfaces. It is therefore possible to compensate for reflections coming from horizontal surfaces with a planar horizontal system using AWFS and the presented configuration. Recent experiments with AWFS support these observations.

From all these remarks and from the detailed results presented in Sec. III, we conclude that AWFS can be used for active sound field reproduction and active room compensation according to the original AWFS definition (Gauthier and Berry, 2006). An experimental AWFS system using the configuration depicted in Fig. 4 was recently evaluated in several environments: hemi-anechoic chamber, laboratory space, and reverberation chamber. Experimental evaluations of physical AWFS performance for active sound field reproduction is thus a topic of current research.

As for most recent WFS systems, the configuration retained here was a two-dimensional distribution of reproduction sources. Simplicity and lower cost are the usual reasons behind this choice. Such a configuration was selected for illustration purposes and because it corresponds to our experimental system (not presented in this paper). In all cases, the presented algorithms and AWFS concepts are not limited to a given specific configuration. As an example, use of compact sensor arrays can easily be extended to three dimensions. Another example is a three-dimensional reproduction source array.

Recent experiments with AWFS in real reproduction spaces also confirmed the importance of the higher-order radiation modes for the enlargement of the effective control region. This is only possible with the independent radiation mode control algorithm. Experiments also showed an even better performance of AWFS in several reproduction environments.

Other issues related to AWFS are open questions:evaluation of system size on performance, possible use of several compact error sensor arrays in a larger distributed reproduction region, effects of modeling delay, supplementary considerations for causality, modification of other classical adaptive algorithms (frequency domain implementation, sparse adaptation and others (Garas, 1999; Elliott, 2000), or various types of penalization) for AWFS and both subjective and objective evaluations of AWFS performance in several reproduction rooms.

ACKNOWLEDGMENTS

This work has been supported by NSERC (Natural Sciences and Engineering Research Council of Canada), NATEQ (Fond Québecois de la Recherche sur la Nature et les Technologies), VRQ (Valorisation Recherche Québec) and Université de Sherbrooke. This research has been conducted in collaboration with CIRMMT (Centre for Interdisciplinary Research in Music Media and Technology, McGill University).

APPENDIX A: SYSTEM DECOUPLING AND WHITENING USING SINGULAR VALUE DECOMPOSITION (SVD) IN THE FREQUENCY DOMAIN

The electroacoustical plant $\mathbf{G}(z)$ is represented in the frequency domain by $\mathbf{G}(e^{j\omega})=\mathbf{G}(z)|_{z=e^{j\omega}}$ where $j=\sqrt{-1}$. Using the SVD, the plant matrix can be expressed as

$$\mathbf{G}(e^{j\omega})_{M\times L}=\mathbf{U}(e^{j\omega})_{M\times M}\mathbf{\Sigma}(e^{j\omega})_{M\times L}\mathbf{V}^{H}(e^{j\omega})_{L\times L} \quad \text{(A1)}$$

with

$$\mathbf{\Sigma}(e^{j\omega}) = \begin{bmatrix} \sigma_1(e^{j\omega}) & \cdots & 0 & \\ \vdots & \ddots & \vdots & [\mathbf{0}]_{M\times(L-M)} \\ 0 & \cdots & \sigma_M(e^{j\omega}) & \end{bmatrix}_{M\times L}, \tag{A2}$$

where $\mathbf{U}$ is the column matrix of the left singular vectors, $\mathbf{V}$ is the column matrix of the right singular vectors, $\mathbf{\Sigma}(e^{j\omega})$ is a pseudo-diagonal matrix of the real singular values $\sigma_i(e^{j\omega})$ (ordered on the main diagonal by decreasing amplitude). The left singular vectors are defined as pressure modes (i.e., radiation modes evaluated at the error sensor array) and the right singular vectors are defined as source modes (i.e., radiation modes evaluated at the reproduction source array). Superscript ^{H} denotes Hermitian transposition. In Eq. (A2), the plant matrix rank r was assumed to be M for notation convenience and we assume $L>M$.

The first radiation mode synthesis filter $L\times M$ matrix ${}^{(s)}\mathbf{G}'(e^{j\omega})$ is defined by

$${}^{(s)}\mathbf{G}'(e^{j\omega})_{L\times M} = \mathbf{V}(e^{j\omega})_{L\times L}[\mathbf{\Sigma}(e^{j\omega})]^{+}_{L\times M}, \tag{A3}$$

where the pseudo inversion $[\cdot]^+$ of the pseudo-diagonal matrix $\mathbf{\Sigma}$ is defined as follows:

$$\mathbf{\Sigma}^{+}(e^{j\omega}) = \begin{bmatrix} 1/\sigma_1(e^{j\omega}) & \cdots & 0 & \\ \vdots & \ddots & \vdots & [\mathbf{0}]_{M\times(M-L)} \\ 0 & \cdots & 1/\sigma_M(e^{j\omega}) & \end{bmatrix}^T. \tag{A4}$$

The first synthesis filters ${}^{(s)}\mathbf{G}'(e^{j\omega})$ are used to define reproduction source inputs in the frequency domain that corresponds to the source modes (not belonging to the null space). Each column of ${}^{(s)}\mathbf{G}'(e^{j\omega})$ is a set of L synthesis filters that creates one of the source modes. According to this definition, one notes that: (1) the ${}^{(s)}\mathbf{G}'(e^{j\omega})$ columns cover the range of the matrix $\mathbf{G}(e^{j\omega})$ by its multiplication with the plant FRF matrix $\mathbf{G}(e^{j\omega})$ and (2) the first radiation mode synthesis filter matrix ${}^{(s)}\mathbf{G}'(e^{j\omega})$ removes from $\mathbf{V}(e^{j\omega})$ the null space of $\mathbf{G}(e^{j\omega})$ by post-multiplication by $\mathbf{\Sigma}^{+}(e^{j\omega})$ in Eq. (A3). Alternatively, the $1/\sigma_i$ can be replaced by 1 on the main diagonal of Eq. (A4) so that the plant is decoupled but not whitened. In this specific case, the same terminology and notation, for the synthesis filters, are used. For the simulations reported in this paper, the plant is only decoupled, but not whitened.

An analysis filter matrix ${}^{(a)}\mathbf{G}(e^{j\omega})_{M\times M}$ is defined from the SVD

$${}^{(a)}\mathbf{G}(e^{j\omega})_{M\times M} = \mathbf{U}^H(e^{j\omega})_{M\times M}, \tag{A5}$$

The analysis filter matrix transforms the physical sound pressures ($\mathbf{p}_M(n)$ or $\mathbf{e}_M(n)$) in pressure mode basis (giving $\tilde{\mathbf{p}}_M(n)$ or $\tilde{\mathbf{e}}_M(n)$). Each column of ${}^{(a)}\mathbf{G}(e^{j\omega})$ is a set of M analysis filters that create a pressure mode. The first step of plant decoupling is the multiplication of the plant matrix by the first synthesis filter matrix

$$\begin{aligned}\mathbf{G}(e^{j\omega}){}^{(s)}\mathbf{G}'(e^{j\omega}) &= \mathbf{U}(e^{j\omega})\mathbf{\Sigma}(e^{j\omega})\mathbf{V}^H(e^{j\omega})\mathbf{V}(e^{j\omega})\mathbf{\Sigma}^{+}(e^{j\omega}) \\ &= \mathbf{U}(e^{j\omega}).\end{aligned} \tag{A6}$$

The second step is the pre-multiplication of Eq. (A6) by the analysis filter matrix

$${}^{(a)}\mathbf{G}(e^{j\omega})\mathbf{G}(e^{j\omega}){}^{(s)}\mathbf{G}'(e^{j\omega}) = \mathbf{I}(e^{j\omega}), \tag{A7}$$

since $\mathbf{V}(e^{j\omega})$ and $\mathbf{U}(e^{j\omega})$ are unitary matrices. $\mathbf{I}$ is the identity matrix. Equation (A7) allows plant decoupling and prewhitening by pre- and post-multiplication with synthesis and analysis filters. This property is of fundamental importance for practical implementation of AWFS based on independent radiation mode control (Gauthier and Berry, 2006). If, as noted earlier, the plant is only decoupled, one has: ${}^{(a)}\mathbf{G}(e^{j\omega})\mathbf{G}(e^{j\omega}){}^{(s)}\mathbf{G}'(e^{j\omega}) = \mathbf{\Sigma}'(e^{j\omega})$, where $\mathbf{\Sigma}'(e^{j\omega})$ is the first $M\times M$ submatrix of $\mathbf{\Sigma}(e^{j\omega})$.

The second radiation mode synthesis filter matrix ${}^{(s)}\mathbf{G}''(e^{j\omega})$ (producing the null space of $\mathbf{G}(e^{j\omega})$) is

$${}^{(s)}\mathbf{G}''(e^{j\omega})_{L\times 1} = \mathbf{V}(e^{j\omega})_{L\times L}\mathbf{i}_{L\times 1}, \tag{A8}$$

where $\mathbf{i}$ is a block vector defined by $\mathbf{i}_{L\times 1} = [[\mathbf{0}]_{1\times M}[\mathbf{0}]_{1\times(L-M)}]^T$. This filter matrix produces all the radiation modes which belong to the null space of the plant matrix $\mathbf{G}(e^{j\omega})$ so that, according to the null space definition (Lancaster and Tismenetsky, 1985), $\mathbf{G}(e^{j\omega}){}^{(s)}\mathbf{G}''(e^{j\omega}) = \mathbf{0}_{M\times 1}$.

APPENDIX B: TIME-DOMAIN FILTERS FROM SVD IN THE FREQUENCY DOMAIN

The procedure used to generate time-domain decoupling filters from the frequency response matrices ${}^{(s)}\mathbf{G}'(e^{j\omega})$ and ${}^{(a)}\mathbf{G}(e^{j\omega})$ has been described by Bai and Elliott (2004). For AWFS, a similar procedure must also be applied to ${}^{(s)}\mathbf{G}''(e^{j\omega})$. Other procedures such as WFS projection on the SVD basis and radiation mode reordering are also original aspects.

The frequency response matrices, temporarily denoted $\mathbf{F}(e^{j\omega})$, are calculated (for simulations) or measured (for practical implementations). Using inverse discrete-time Fourier transform (DTFT), a discrete-time sequence matrix $\mathbf{F}(n)$ is obtained: $\mathbf{F}(e^{j\omega})|_{\omega=(2\pi/N)k} \leftrightarrow \mathbf{F}(n)$, where k represents a frequency index and N the number of samples in the frequency domain. A time delay of Δ_{SVD} samples is then added for causality purposes. $\mathbf{F}(n)$ is then transformed to produce the filter coefficient matrix $\mathbf{F}(z)$.

Although this procedure is readily applicable to derive the synthesis and analysis filters, the SVD decoupling being independently computed at each frequency, the complex frequency response functions may not be directly passed into inverse DTFT to create time-domain filters without risk. The limitation comes from the SVD definition that involves a singular value matrix $\mathbf{\Sigma}(e^{j\omega})$ in which the singular values are ranked in decreasing order of magnitude. Left and right singular vectors are accordingly ranked in the matrices $\mathbf{U}(e^{j\omega})$ and $\mathbf{V}(e^{j\omega})$. Some singular values may thus coincide or cross over a frequency range so that singular vector ordering arbitrarily switches between the two singular values. At this point, the SVD calculation with classical numerical algorithms will introduce a switch in the radiation mode ordering

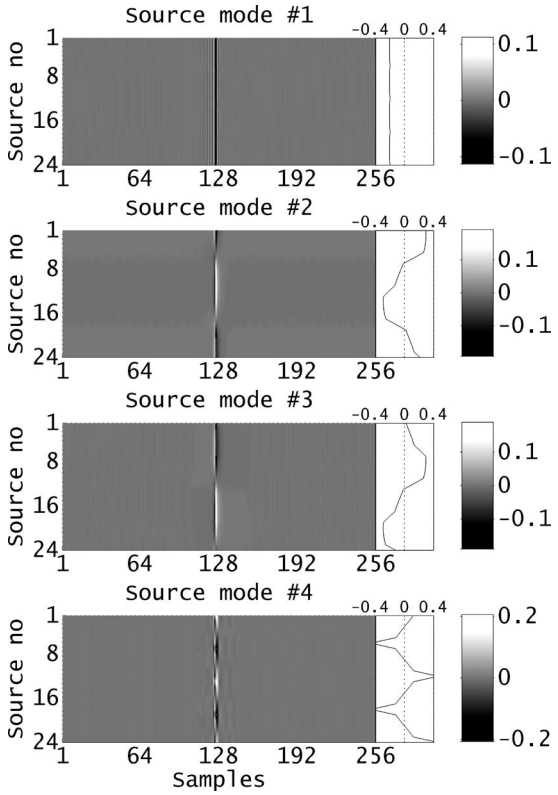

FIG. 13. Free-field theoretical synthesis filters in the time domain for the source modes 1–4. Each plot includes 24 synthesis filters to create the given source mode with 24 reproduction sources. Each filter includes 256 coefficients. The small plots on the right display the algebraic sum of the filters response along the 256 coefficients.

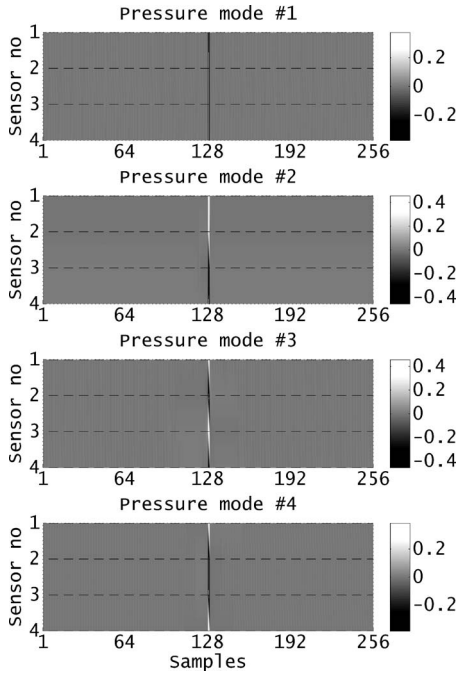

FIG. 14. Free-field theoretical analysis filters in the time domain for the pressure modes 1–4. Each plot includes four analysis filters to construct the pressure mode from four pressure sensors. Each filter includes 256 coefficients.

so that the frequency responses ${}^{(s)}\mathbf{G}'(e^{j\omega})$, ${}^{(s)}\mathbf{G}''(e^{j\omega})$, ${}^{(a)}\mathbf{G}(e^{j\omega})$ and their components go through abrupt transitions over the frequency range of interest. Such discontinuities (amplitude and phase) as function of frequency produce longer impulse responses when inverse DTFT is applied. Applying a simple smoothing algorithm to the SVD matrices in the frequency domain (that is radiation mode reordering so that they smoothly change shape over the reproduction source array as function frequency) before taking the inverse DTFT proved to greatly decrease the length of the impulse responses of the filters. This constitutes an originality of the present work in comparison with Bai and Elliott (2004).

Note that to increase the robustness of the reordering algorithm for the simulations reported in this paper, an artifact has been introduced for a practical SVD decoupling demonstration. A random variation (normal distribution with zero mean and 1 mm variance) of the source and sensor positions (in the horizontal plane) proved, along with standard SVD algorithm and smoothing process, to enhance the decoupling results. Placing of such random artifact in the theoretical configuration is somewhat more representative of a real situation than the otherwise geometrically perfect configuration.

1. Examples

To illustrate these ideas, an example of plant decoupling based on SVD and smoothing process is introduced for the free-field condition in Figs. 13–16 for the configuration shown in Fig. 4. Note that this example does not include plant whitening. In Fig. 13, the 24 synthesis filter impulse responses for each source mode (corresponding to the first synthesis filters matrix) are shown with 256 points in the time domain with a sampling frequency of 1200 Hz (a conservative approximation of the minimal spatial aliasing frequency for the given reproduction source separation distance is 634 Hz, at least two reproduction sources per wavelength, so that a sampling frequency of 1200 Hz covers the frequency range of interest). These impulse responses have been delayed by 128 samples ($\Delta_{SVD}=128$). Each of the sub-

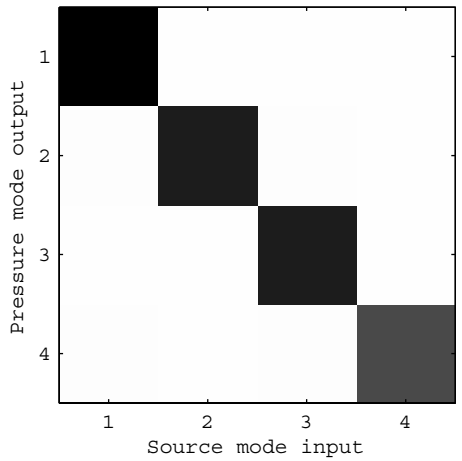

FIG. 15. Plant decoupling: $10\log_{10}$ of the total energies of the impulse responses of individual components of the 4×4 matrix ${}^{(a)}\mathbf{G}(e^{j\omega}){}^{(s)}\mathbf{G}'(e^{j\omega})$ using the synthesis and analysis filters shown in Figs. 13 and 14.

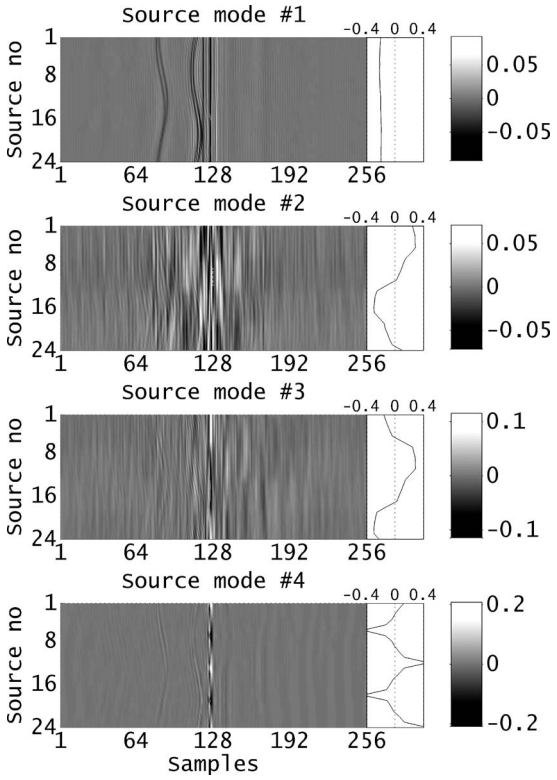

FIG. 16. Synthesis filters in the time domain for the source modes 1–4 for the system with a rigid floor and two hard walls. Each plot includes 24 synthesis filters to create the given source mode with 24 reproduction sources. Each filter includes 256 coefficients. The small plots on the right display the algebraic sum of the filter's response along the 256 coefficients.

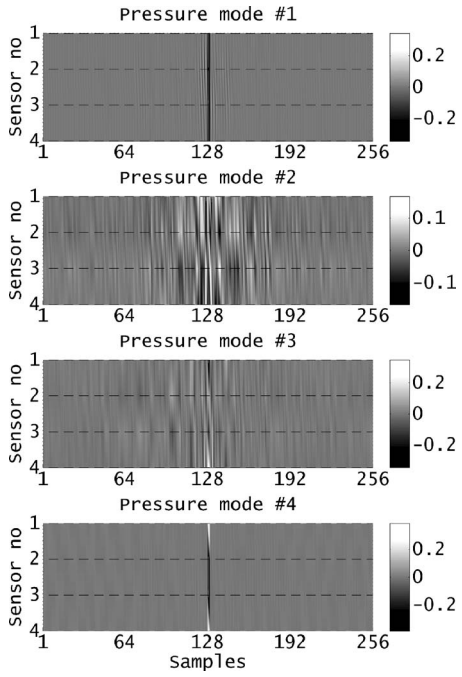

FIG. 17. Analysis filters in the time domain for the pressure modes 1–4 for the system with a rigid floor and two hard walls. Each plot includes four analysis filters to construct the pressure mode with four pressure sensors. Each filter includes 256 coefficients.

plots represents the 24 impulse responses of a column of the first synthesis filter matrix ${}^{(s)}\mathbf{G}'(z)_{L\times M}$ to produce $\mathbf{y}_L(n)$ from $\tilde{\mathbf{y}}_M(n)$ (see Fig. 3). Without the smoothing algorithm before inverse DTFT, the time leakage of these filters had proven to be much more important. Figure 14 shows the four analysis filters (for each pressure mode) in the time domain using $\Delta_{SVD}=128$ samples delay. Each of the subplots represents the four impulse responses of a column of the analysis filter matrix ${}^{(a)}\mathbf{G}(z)_{M\times M}$to transform the reproduction errors $\mathbf{e}_M(n)$ into $\tilde{\mathbf{e}}_M(n)$. To illustrate the fact the higher-order source modes imply more spatial variations than lower-order radiation modes, a set of small subplots are included in Fig. 13. They show the algebraic sums of the filter coefficients over the 256 coefficients. Clearly, the first source mode involves an in-phase radiation from all the reproduction sources on the average. The other modes involve more source-to-source variations, but they show simple spatial distributions. As an example, it is clear that the fourth source mode appears in AWFS based on independent radiation mode control shown in Fig. 7. In contrast, for AWFS based on FXLMS algorithm, the first radiation dominates more in Fig. 7. Another point should be noted: both the synthesis and analysis filters approach simple multipolar patterns. The first radiation mode implies an in-phase radiation from the reproduction sources and in-phase capture from the error sensors. The higher-order radiation modes imply an alternation of in-phase and out-of-phase average over the reproduction source and error sensors arrays; these are then approaching simple multipolar patterns (Gauthier and Berry, 2006).

To test the validity of the SVD decoupling using these filters, the plant decoupling has been simulated using the synthesis and analysis filters described above. The total energies of the impulse responses in individual components of the 4×4 matrix ${}^{(a)}\mathbf{G}(e^{j\omega}){\mathbf{G}}(e^{j\omega}){}^{(s)}\mathbf{G}'(e^{j\omega})$ are shown in Fig. 15. Clearly, this matrix is diagonal. This proves that broadband plant decoupling using SVD as described herein is effective.

For the simulated case with three rigid surfaces, the synthesis and analysis filters impulse responses are shown in Figs. 16 and 17. The same small subplots on the right of Fig. 16 show the algebraic sums of the filter coefficients along the 256 coefficients. These filters show a more complex response than those of the free-field case (see Figs. 13 and 14), but they have a mean spatial distribution approaching the filters for the free-field case. The synthesis filters of the first source mode clearly show an in-phase response from all the reproduction sources this; is in agreement with our previous theoretical results (Gauthier and Berry, 2006). Again both the synthesis and analysis filters approach simple multipolar patterns. The first radiation mode implies an in-phase radiation from the reproduction sources and in-phase sensing at the error sensors. The higher-order radiation modes imply an alternance of in phase and out of phase over the reproduction source and error sensors arrays, they then approach simple multipolar patterns. Note that, the synthesis and analysis filters only include plant decoupling. The SVD delay was set to 128, $\Delta_{SVD}=128$.

APPENDIX C: PROJECTION OF THE WFS OPERATORS ON THE SOURCE MODES AND PRACTICAL SYNTHESIS OF THE NULL SPACE OF $G(e^{j\omega})$

The AWFS algorithm based on SVD decoupling requires the projection of the WFS operators on the synthesis filters (Gauthier and Berry, 2006).

Once the first radiation modes are reordered, it is possible to write the column-reordered matrix $\mathbf{V}(e^{j\omega})$ as a block matrix: $\mathbf{V}(e^{j\omega})_{L\times L}=[\mathbf{V}'(e^{j\omega})_{L\times M}\mathbf{V}''(e^{j\omega})_{L\times(L-M)}]$ where $\mathbf{V}'$ was used to create the first synthesis filter according to the method described in Appendix B while $\mathbf{V}''$ is used for the second synthesis filters. In a similar manner, $\mathbf{\Sigma}(e^{j\omega})$ is made of two blocks: $\mathbf{\Sigma}_{M\times L}=[\mathbf{\Sigma}'_{M\times M}\mathbf{0}_{M\times(L-M)}]$. The projection of the WFS operators on the first radiation modes is a vector of dimension M defined by $\tilde{\mathbf{q}}_{WFS}(e^{j\omega})=\mathbf{\Sigma}'(e^{j\omega})\mathbf{V}'^{H}(e^{j\omega})\mathbf{q}_{WFS}(e^{j\omega})$. Each component of $\tilde{\mathbf{q}}_{WFS}$ represents a projection of the WFS operators on the given source mode multiplied by the corresponding singular value. The multiplication by the singular value is needed since the first synthesis filters are made from $\mathbf{V}'(e^{j\omega})\mathbf{\Sigma}'^{-1}(e^{j\omega})$ according to the method described in Appendix B. If the system is only decoupled, the projection of the WFS operators becomes $\tilde{\mathbf{q}}_{WFS}(e^{j\omega})=\mathbf{V}'^{H}(e^{jm})\mathbf{q}_{WFS}(e^{j\omega})$. Taking the inverse discrete-time Fourier transform (DTFT) of a component of $\tilde{\mathbf{q}}_{WFS}$ gives the impulse response $\tilde{\mathbf{w}}_{WFS_m}$ for the mth source mode (see Eq. (29)), that is the projection of the WFS filters on the source mode m. This impulse response is non-causal and an additional delay of Δ_{SVD} is added to make it causal. The importance of the resulting filter (projection of the WFS operators on the first synthesis filters) is clear in light of the algorithm described in Sec. II C.

For the null space basis, any smoothing or reordering operation on the corresponding source modes is by far more complicated and less effective than for the first synthesis filters. For the projection of the WFS operators on the null space, a different approach is used. Rather than directly projecting the WFS operators on the null space (with $\mathbf{V}''^{H}(e^{j\omega})\mathbf{q}_{WFS}(e^{j\omega})$), a simple approach is to substract the first radiation mode contributions from the WFS operators so that $\mathbf{q}_{WFS_{null}}(e^{j\omega})=[\mathbf{I}_{L\times L}-\mathbf{V}'(e^{j\omega})_{L\times M}\mathbf{V}'^{H}(e^{j\omega})_{M\times L}]\mathbf{q}_{WFS}(e^{j\omega})$ where both $\mathbf{q}_{WFS_{null}}(e^{j\omega})$ and $\mathbf{q}_{WFS}(e^{j\omega})$ are $L\times 1$ vectors. The vector $\mathbf{q}_{WFS_{null}}(e^{j\omega})$ is the portion of $\mathbf{q}_{WFS}(e^{j\omega})$ which belongs to the null space. This was defined without using the projection of the WFS operators on the null space basis. Since the impulse responses corresponding to $\mathbf{q}_{WFS_{null}}(e^{j\omega})$ are non-causal, an additional delay of Δ_{SVD} is included in the impulse responses for the synthesis of the WFS operators projected on the null space basis.

AES Staff Writer (**2005**). "Multichannel audio systems and techniques," J. Audio Eng. Soc. **53**, 329–335.

Ahn, S.-S., and Voltz, P. J. (**1996**). "Convergence of the delayed normalized LMS algorithm with decreasing step size," IEEE Trans. Signal Process. **44**, 3008–3016.

Asano, F., and Swanson, D. C. (**1995**). "Sound equalization in enclosures using modal reconstruction," J. Acoust. Soc. Am. **98**, 2062–2069.

Bai, M. R., and Elliott, S. J. (**2004**). "Preconditioning multichannel adaptive filtering algorithms using EVD- and SVD-based signal prewhitening and system decoupling," J. Sound Vib. **270**, 639–655.

Berkhout, A. J., de Vries, D., and Vogel, P. (**1993**). "Acoustic control by wave field synthesis," J. Acoust. Soc. Am. **93**, 2764–2778.

Betlehem, T., and Abhayapala, T. D. (**2005**). "Theory and design of sound field reproduction in reverberant rooms," J. Acoust. Soc. Am. **117**, 2100–2111.

Bouchard, M., and Quednau, S. (**2000**). "Multichannel recursive-least-squares algorithms, and fast-transversal-filter algorithms for active noise control and sound reproduction systems," IEEE Trans. Speech Audio Process. **8**, 606–618.

Cabell, R. H., and Fuller, C. R. (**1999**). "A principal component algorithm for feedforward active noise and vibration control," J. Sound Vib. **227**, 159–181.

Cabell, R. H., Palumbo, D., and Vipperman, J. (**2001**). "A principal component feedforward algorithm for active noise control: Flight test results," IEEE Trans. Control Syst. Technol. **9**, 76–83.

Camurri, A., and Ferrentino, P. (**1999**). "Interactive environments for music and multimedia," Multimedia Syst. **7**, 32–47.

Choi, J.-W., and Kim, Y.-H. (**2004**). "Manipulation of sound intensity within a selected region using multiple sources," J. Acoust. Soc. Am. **116**, 843–852.

Corteel (**2006**). "On the use of irregurlarly spaced loudspeaker arrays for wave field synthesis, potential impact on spatial aliasing frequency," *Proceedings of the 9th International Conference on Digital Audio Effects (DAFX)*, Montreal, Canada, September 18–20, 2006.

Davis, M. F. (**2003**). "History of spatial coding," J. Audio Eng. Soc. **51**, 554–569.

Elliott, S. J., and Nelson, P. A. (**1989**). "Multiple-point equalization in room using adaptive digital filters," J. Audio Eng. Soc. **37**, 899–907.

Elliott, S. J. (**2000**). "Optimal controllers and adaptive controllers for multichannel feed-forward control of stochastic disturbances," IEEE Trans. Signal Process. **48**, 1053–1060.

Elliott, S. (**2001**). *Signal Processing for Active Control* (Academic, London).

Fuster, L., López, J. J., González, A., and Zuccarello, P. D. (**2005**). "Room compensation using multichannel inverse filters for wavefield synthesis systems," convention paper No. 6401, *AES 118th Convention*, Barcelona, Spain, May 28–31.

Gauthier, P.-A., Berry, A., and Woszczyk, W. (**2005a**). "Sound-field reproduction in-room using optimal control techniques: Simulations in the frequency domain," J. Acoust. Soc. Am. **117**, 662–678.

Gauthier, P.-A., Berry, A., and Woszczyk, W. (**2005b**). "Wave field synthesis, adaptive wave field synthesis and ambisonics using decentralized transformed control: Potential applications to sound field reproduction and active noise control," J. Acoust. Soc. Am. **118**, 1967.

Gauthier, P.-A., and Berry, A. (**2006**). "Adaptive wave field synthesis with independent radiation mode control for active sound field reproduction: Theory," J. Acoust. Soc. Am. **119**, 2721–2737.

Gauthier, P.-A., and Berry, A. (**2007**). "Objective evaluation of room effects on wave field synthesis," Acta. Acust. Acust. **93**, 824–836.

Garas, J. (**1999**). *Adaptive 3D Sound Systems* (Technische Universiteit Eindhoven, Eindhoven).

Ise, S. (**1999**). "A principle of sound field control based on the Kirchhoff-Helmholtz integral equation and the theory of inverse system," Acust. Acta Acust. **85**, 78–87.

Kendall, G. S. (**1995**). "A 3-D sound prime: Directional hearing and stereo reproduction," Comput. Music J. **19**, 23–46.

Klehs, B., and Sporer, T. (**2003**). "Wave field synthesis in the real world: Part 1 - In the living room," convention paper No. 5727, *AES 114th convention*, Amsterdam, The Netherlands, March 22–25, 2003.

Kleiner, M., Dalenbäck, B.-I., and Svensson, P. (**1993**). "Auralizarion-An overview," J. Audio Eng. Soc. **41**, 861–875.

Laakso, T. I., Välimäki, V., Karjalainen, M., and Laine, U. K. (**1996**). "Splitting the unit delay," IEEE Signal Process. Mag. **13**, 30–60.

Lancaster, P., and Tismenetsky, M. (**1985**). *The Theory of Matrices* (Academic, Orlando, FL).

Merimaa, J., and Pulkki, V. (**2005**). "Spatial impulse response rendering I: Analysis and synthesis," J. Audio Eng. Soc. **12**, 1115–1127.

Morgan, D. R. (**1980**). "An analysis of multiple correlation cancellation loops with a filter in the auxiliary path," IEEE Trans. Acoust., Speech, Signal Process. **28**, 454–467.

Nelson, P. A. (**1994**). "Active control of acoustic fields and the reproduction of sound," J. Sound Vib. **177**, 447–477.

Nelson, P. S., Kirkeby, O., and Takeuchi, T. (**1997**). "Sound fields for the production of virtual acoustic images," J. Sound Vib. **204**, 386–396.

Poletti, M. A. (**2000**). "A unified theory of horizontal holographic sound

systems," J. Audio Eng. Soc. **48**, 1155–1182.
Radlović, B. D., Williamson, R. C., and Kennedy, R. A. (**2000**). "Equalization in an acoustic reveberant environment: Robustness results," IEEE Trans. Speech Audio Process. **8**, 311–319.
Rumsey, F. (**2001**). *Spatial Audio* (Focal, Oxford).
Santillàn, A. O. (**2001**). "Spatially extended sound equalization in rectangular rooms," J. Acoust. Soc. Am. **110**, 1989–1997.
Sporer, T., and Klehs, B. (**2004**). "Wave field synthesis in the real world: Part 2 - In the movie theatre," convention paper No. 6055, *AES 116th Convention*, Berlin, Germany, May 8–11, 2004.
Spors, S., Kuntz, A., and Rabenstein, R. (**2003**). "An approach to listening room compensation with wave field synthesis," *Proceedings of the AES 24th International Conference*, Banff, Canada, June 26–28, 70–82.
Spors, S., and Rabenstein, R. (**2006**). "Spatial aliasing artifacts produced by linear and circular loudspeaker arrays used for wave field synthesis," convention paper, *AES 120th Convention*, Paris, France, May 20–23, 2006.
Takane, S., Suzuki, Y., and Sone, T. (**1999**). "A new method for global sound field reproduction based on Kirchhoff's integral equation," Acust. Acta Acust. **85**, 250–257.
Takane, S., and Sone, T. (**2004**). "A new theory for active suppression of reflected sound waves from the walls based on Kirchhoff–Helmholtz boundary integral equation," Acoust. Sci. & Tech. **25**, 37–44.
Verheijen, E. N. G. (**1997**). Sound Reproduction by Wave Field Synthesis, Ph.D. thesis (Delft University of Technology, Delft).
Williams, E. G. (**1999**). *Fourier Acoustics - Sound Radiation and Nearfield Acoustical Holography* (Academic, London).
Wilson, S. (**2001**). *Information Arts: Intersection of Art, Science, and Technology* (MIT Press, Cambridge).
Woszczyk, W., Cooperstock, J., Roston, J., and Martens, W. (**2005**). "Shake, rattle, and roll: Getting immersed in multisensory, interactive music via broadband networks," J. Audio Eng. Soc. **53**, 336–344.

Effect of damping on the propensity of squeal instability: An experimental investigation

Francesco Massi[a)]
LaMCoS, INSA-Lyon CNRS UMR5259, F69621, France

Oliviero Giannini
Department of Mechanics and Aeronautics, University of Rome "La Sapienza," via Eudossiana 18, 00184 Rome, Italy

(Received 23 May 2007; revised 9 December 2007; accepted 27 January 2008)

Friction induced vibrations in automotive brakes is recognized as a major problem in industry. Squeal is a difficult subject because of its unpredictability caused by a not completely understood sensitivity to variation of the system parameters. In the literature several analytical and numerical studies deal with the relationship between damping and system propensity to have instability. These studies highlight the existence of a nonintuitive effect of damping distribution on modal coupling that gives rise to the unstable vibrations. The complexity of commercial brakes and the difficulties to identify the values of modal damping in brake assemblies lead to the necessity to rely on experimental analysis using simplified test rigs. This paper presents an experimental investigation of the relationship between the distribution of modal damping and the propensity to develop squeal in a beam-on-disk setup, which reliably reproduces squeal events with easy control and measurement of the damping of the disk and the beam, respectively. The experiments highlight the key role played by the modal damping distribution on squeal: A nonuniform repartition of the modal damping causes an increase of the squeal propensity. © *2008 Acoustical Society of America.*
[DOI: 10.1121/1.2875628]

PACS number(s): 43.40.At, 43.50.Lj, 43.20.Ks [JGM] Pages: 2017–2023

I. INTRODUCTION

Brake squeal is an example of noise caused by vibrations induced by friction forces that can induce a dynamic instability.[1] Analytical and numerical[2,3] approaches have been proposed to explain the self-excited vibrations of the brake apparatus which cause the squeal sound emission. Mills[4] and Fosberry and Holubecki[5,6] tried to correlate the occurrence of squeal with a negative slope of the friction coefficient-relative velocity curve, while Spurr[7] proposed his sprag-slip theory, followed later by Earles *et al.*[8,9] and Jarvis and Mills.[10] In 1972, North,[11,12] published the first experimental work on a real brake apparatus. Akay *et al.*,[13] Tucinda *et al.*,[14,15] Allgaier *et al.*,[16,17] and Tarter[18] conducted extensive analyses on the beam-on-disk setup. Nowadays, the modal coupling[11–13] (mode lock-in) between two system modes, one of which becomes unstable, is one of the most accepted theories.

The squeal unpredictability is due both to the sensitivity to the system parameters and to the still unknown effect of some system characteristics such as the structural damping. In brake design several modifications are applied to suppress the instability, nevertheless no effective solution for a "squeal-free" design has been reached.

Recent works investigate the role of damping on the squeal occurrence. Douffor[19] included the damping effect into an analytical analysis of instabilities between bodies in sliding contact, with a particular addressing to brake squeal. This work highlights the importance of the damping distribution between the coupling modes.

The complex eigenvalue analysis is a popular numerical tool for squeal instability prediction.[20–22] Hoffmann *et al.*[23] conducted numerical studies on the effect of damping on the mode lock-in on a two degrees of freedom system. Sinou,[24] and Fritz *et al.*[25] performed an extensive numerical analysis by a finite element model to investigate the effect of damping on squeal prediction. As in the other cases, their analysis highlighted the increase of the squeal propensity with the ratio between the modal damping of the two coalescing modes.

Nevertheless, either because of the complexity of a commercial brake system or because the difficulty to retrieve the modal damping experimentally, only analytical or numerical analyses have been developed in the literature.

To overcome the above-mentioned difficulties, here the authors present an experimental analysis developed on a simplified brake apparatus, the beam-on-disk setup that allows a reduction of the parameter uncertainties, a consistent reproducibility of the squeal events and, above all, an easy measurement and variation of the modal damping of the coalescing modes.

The obtained experimental results agree and confirm the analytical and numerical findings existing in literature and mentioned earlier.

II. EXPERIMENTAL SETUP

The beam-on-disk is an extension of the pin-on-disk proposed by Earles and Soar[8,9] in the 1960s. It was proposed

a)Electronic mail: francesco.massi@insa-lyon.fr

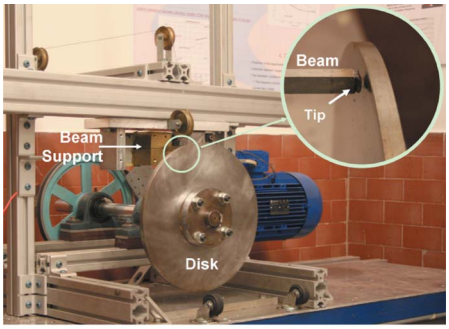

(a)

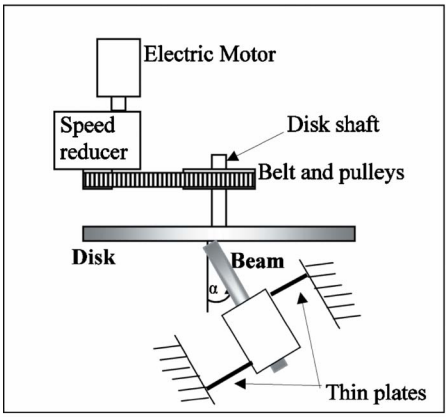

(b)

FIG. 1. (Color online) (a) Experimental setup and (b) schema of the experimental rig.

by Akay *et al.*,[13] and later used, with the same basic geometry, by Tuchinda *et al.*[14,15] and Allgaier *et al.*[16,17] For the analysis presented in this paper the setup is redesigned for the specific aim of investigating the effect of modal damping.

The analyzed beam-on-disk consists of a cantilever beam (representing the brake pad) and a rotating disk (the disk brake rotor) pressed against each other using a dead weight. Figure 1 shows a photograph and a schema of the setup: The disk and the cantilever beam are both made of steel. The disk has a diameter of 600 mm and thickness of 10 mm. The beam cross section is $10\times10=100$ mm^2. The angle of incidence of the beam and its length are adjustable. The cantilever beam is mounted on a massive block which is held by two thin plates. This design allows the cantilever beam to be preloaded against the disk with a specified normal load by using weights and a system of pulleys. The thin plates let the beam follow the misalignments of the rotating disk so to ensure constant boundary conditions. In fact, the normal force is one of the several parameters characterizing the system. By changing the normal force, the contact stiffness and the boundary conditions at the beam constraints change. Therefore, the squeal conditions can be varied by varying the normal force. This is the reason to perform this analysis mantaining the normal force constant (as all the other parameters). A small tip is attached to the edge of the beam in contact with the disk and is made by machining a commercial brake pad. The tip is 1 mm large and is applied to increase the friction coefficient (up to 0.3) and to avoid the wear of the disk and beam surfaces.

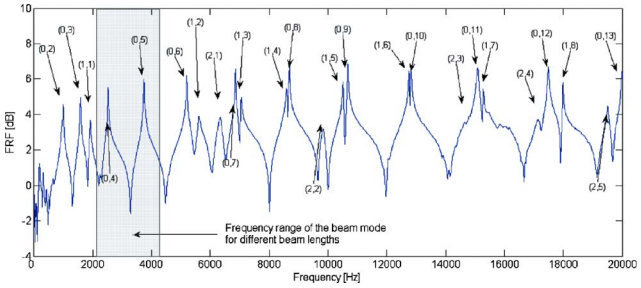

FIG. 2. (Color online) FRF of the setup measured on the disk periphery and frequency range covered by the second bending mode of the beam.

This setup, even if it is a reduced order form of a real brake, is able to capture features of the interaction between the disk and the brake pad for the purpose of analyzing the squeal mechanism. In particular, the beam-on-disk setup is suitable to reproduce and study the mode lock-in phenomenon that is widely considered to be the cause of the squeal instabilities in brakes.

Figure 2 shows the Frequency Response Function (FRF) measured on the disk. The FRF is obtained by a multi-impulse excitation with an instrumented hammer. Several impulses in random sequence are applied while the bending acceleration of the disc at the drive point is measured by an accelerometer. The signals are treated as random, and the FRF is estimated by the H1 function. Because of the large frequency range covered by squeal (1–20 kHz), this method is used to introduce enough energy at high frequency, where the pass band of a single hammer impulse is lower than 7 kHz. The grey band is the range of frequency covered by the natural frequency of the second bending mode of the beam, when the beam length is ranged between 90 and 130 mm. As shown in Fig. 2, the natural frequency of the bending mode of the beam crosses the natural frequencies of the (0,4)[26] and (0,5) bending modes of the disk, respectively, at 2521 Hz (length of the beam 130 mm) and 3729 Hz (103 mm).

The coalescence between the mode of the beam [Fig. 3(b)] and the (0,4) mode of the disk [Fig. 3(a)] is chosen for the presented analysis, in order to have a larger surface of the beam where to place the damping material. Nevertheless, the same qualitative results have been obtained by selecting the coalescence between the mode of the third beam and the (0,5) mode of the disk. The coupling conditions between these couples of modes have been selected because they provide the more suitable conditions to have robust and reproducible squeal. Damping is in fact a really highly sensitive parameter and squeal is a highly fugitive phenomenon.

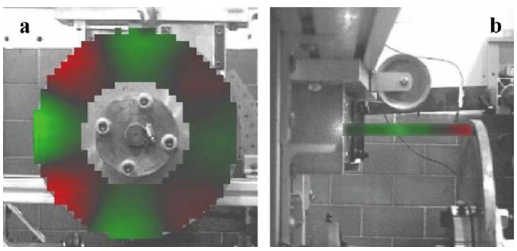

FIG. 3. (Color online) Operative deflection shape for the: (a) (0,4) mode of the disk and (b) second mode of the beam.

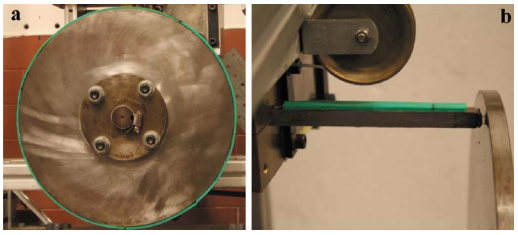

FIG. 4. (Color online) Addition of layers of damping material: (a) On the disk and (b) on the beam.

III. DAMPING AND SQUEAL PROPENSITY

The aim of this paper is to retrieve the propensity of the squeal instability in function of the modal damping of the two coalescing modes. The simple dynamics of the setup allows having a reliable measurement of the modal damping. Moreover, the addition of damping material along the external circumference of the disk [Fig. 4(a)] or along the surface of the beam [Fig. 4(b)] allows one to modify separately the value of the structural damping related to the two substructures, and thus the damping values of the two coalescing modes.

Five cases are studied and presented hereafter:

(A) Naturally damped system: no damping layer is used.
(B) Parallel distribution of added damping: one damping layer attached to both the disk and the beam.
(C) Unequal distribution of added damping: one damping layer added to the beam.
(D) Unequal distribution of added damping: two damping layers added to the beam.
(E) Unequal distribution of added damping: one damping layer added to the disk.

The modal damping of both the disk mode[26] and the beam mode changes consistently depending on the contact condition, i.e., when the two subparts of the system are in sliding contact a larger value of the modal damping is measured. Table I shows the values of the respective modal damping with and without contact. The modal damping of the substructures not in contact are evaluated from the measured FRFs by the software ICATS for modal analysis using the half-power points and the circle-fitting method.

To obtain the actual modal damping when the two subsystems are in contact, during the disk rotation, each subsystem is excited with an hammer impact, the response to the impulse is filtered and the logarithmic decrement is measured.

In order to have a representative value (not affected by any uncertainty related to the variation of the contact conditions) of the modal damping of each mode of the substructures, the values presented throughout the paper are calculated when the disk and the beam are not in contact. Nevertheless, the obtained results can be as well referred to the values obtained with the contact.

TABLE I. Modal damping of the beam and disk with and without contact.

Setup configuration	Modal damping (%)
Disk without contact	0.48
Disk with contact	0.7
Beam without contact	2.5
Beam with contact	3.5

TABLE II. Modal damping of the beam and disk mode for different configurations.

Disk configuration	Modal damping of the disk mode (%)
Disk without damping layer	0.48
Disk with damping layer	1.45
Beam configuration	Modal damping of the beam mode (%)
Beam without damping layer	2.5
Beam with one damping layer	3.7
Beam with two damping layers	5.7

Table II shows the modal damping of the disk and beam modes calculated for different configurations of the setup. The application of the damping layers to the substructures increases sensibly the modal damping of the respective mode, as shown by the FRFs of the beam calculated for the different configurations (Fig. 5).

The propensity of the system to be unstable is referred to here as the range of variation of the system parameters that brings the instability. The wider the range of the parameters that bring the instability the larger the squeal propensity.

The following procedure is performed in order to retrieve experimentally (see Figs. 6–10) the lock-in curves that can be obtained numerically by the complex eigenvalue analysis:[21]

(1) The length of the beam is previously fixed in order to have the natural frequency of the beam slightly higher than the natural frequency of the disk.
(2) A lumped mass is then added at a point of the beam to decrease its natural frequency. Different values of the mass are added and for each value a brake phase is performed.

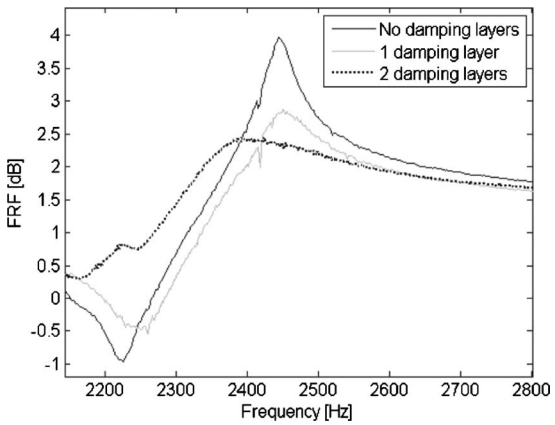

FIG. 5. FRFs of the beam for, respectively, no damping layer (black line); one damping layer (grey line); and two damping layers (dashed line).

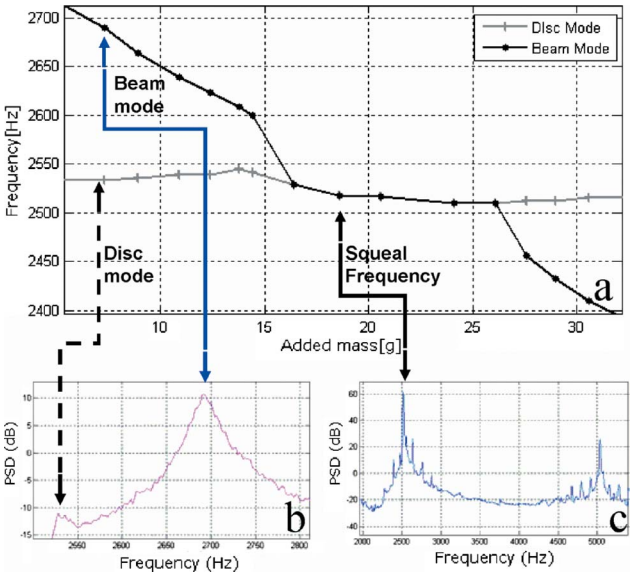

FIG. 6. (Color online) Experimental evaluation of the lock-in plot.

(3) For each value of the mass, the natural frequency of the beam and of the disk are measured during the braking.
(4) During the tests, for a well-defined value of the added mass, the natural frequency of the beam reaches the natural frequency of the disk and squeal vibration occurs: This coalescing point is labeled as the lock-in point.[13]
(5) The mass is increased in steps (about 2 g); for each step, a braking phase with squeal is obtained and the squeal frequency is measured.
(6) For a well-defined value of the added mass the lock-out point is obtained: The two natural frequencies split at two different frequencies, and the squeal noise disappears.
(7) The mass is still increased: The beam natural frequency decreases moving away from the disk natural frequency.

The squeal conditions are identified by the harmonic sound emission that can reach 100 dB, and by the power spectral density (PSD) of the system acceleration that during

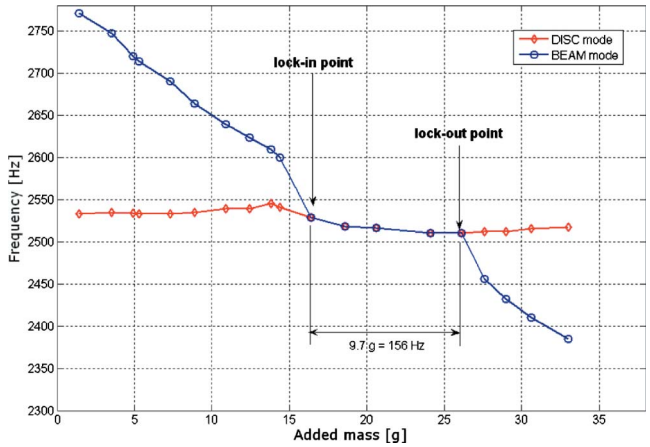

FIG. 7. (Color online) Plot of the system instability (lock-in graphic) for system without damping layers. The unstable range of the system parameter (added mass) and the corresponding frequency range (beam dynamics).

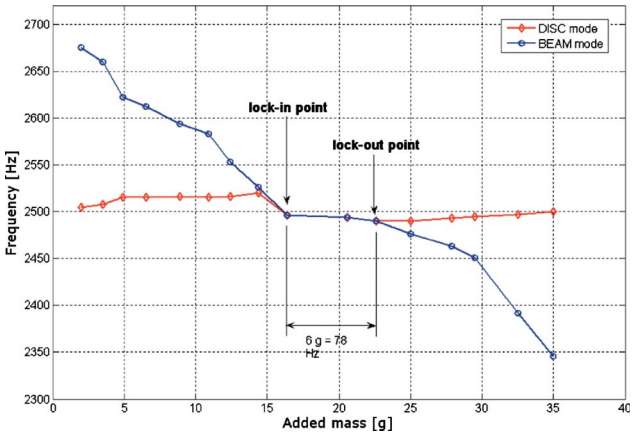

FIG. 8. (Color online) Plot of the system instability (lock-in graphic) when one damping layer is applied on both the disk and the beam.

squeal conditions presents a pick in frequency that is 40–100 dB above the whole frequency spectrum. In stable conditions the frequency spectrum is characterized by a low quasirandom spectrum characteristic of the "friction noise."[1] Before and after "lock-in" no squeal is recognized.

The measurement of the natural frequencies of the coupled system has to be performed in the effective operating conditions, i.e., when the beam is in contact with the disk

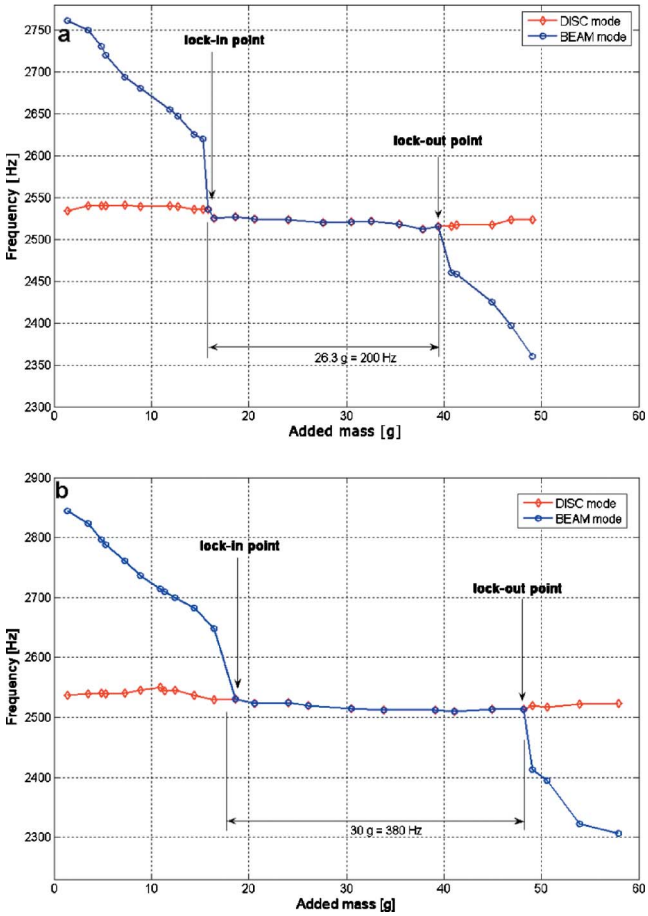

FIG. 9. (Color online) Plot of the system instability (lock-in graphic) when one (a) and two (b) damping layers are applied to the beam; no damping layers are applied to the disk.

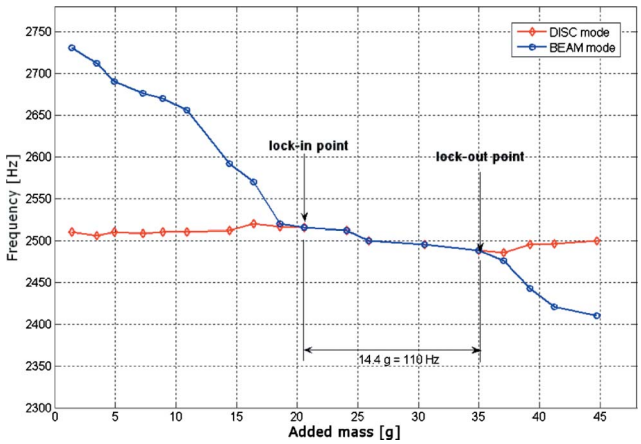

FIG. 10. (Color online) Plot of the system instability (lock-in graphic) when one damping layer is applied to the disk; no damping layers are applied to the beam.

and the disk rotates. In fact, contact conditions have a strong effect on the dynamics of the setup and, if neglected, produce nonrepresentative results.

Figure 6 shows how the lock-in plots are obtained. Before the lock-in point and after the lock-out point the system is stable. In these conditions the PSD of the signal coming from the accelerometer placed on the tip of the beam contains picks corresponding to the natural frequencies of the two components [Fig. 6(b)]. An external excitation of the system is, in these conditions, useful to increase the modal response.

In the unstable range, between the lock-in and the lock-out points, the signal is characterized by only one main harmonic, corresponding with the squeal frequency [Fig. 6(c)]. The frequency of this main harmonic is reported in the lock-in plot.

Moreover, for each step of the added mass, a measurement of the natural frequencies of the beam, when not in contact with the disk is also measured.

In the presented particular case, the dynamics of one component of the system (i.e., the beam) is varied by modifying the added mass. An increase of the mass corresponds to a decrease of the natural frequencies of the beam.

Because a commercial brake apparatus is extremely more complicated than the beam-on-disk, several parameters can be varied to modify the system dynamics.

In order to generalize the obtained results, the ranges of the substructure dynamics that bring the unstable behavior (for different values of the damping distribution) are compared by comparing the values of the natural frequencies of the beam (when not in contact with the disk) at the lock-in and lock-out point (see Table III). The wider the range of the natural frequencies that bring the unstable coalescence, the more probable it is to have squeal. Comparing the natural frequencies of the beam allows one to compare directly the range of the subsystem dynamics that leads to the instability.

A. Naturally damped system (case A)

The first set of tests is performed on the beam-on-disk without the addition of damping materials. The damping coefficient of the second mode of the beam is 2.5%, while the damping of the (0,4) mode of the disk is 0.48%. The large damping of the beam mode is due to the contact damping at the connection between the beam and the massive block. The relative motion between the beam sides and the block surfaces introduces the damping due to the friction between these surfaces. The lumped mass is added at 25 mm from the constraint. Such point is chosen to have the best compromise between the range of frequency covered by the application of the mass (to range the system dynamics from the lock-in to the lock-out points), and an acceptable sensitivity (about 20 Hz/g) to the mass increment, so that an accurate measure of the coalescing zone can be obtained. Figure 7 shows the behavior of the system natural frequencies, calculated during the braking phase) in function of the value of the added mass. In this case the mass ranges between 0 and 33 g to shift the natural frequency of the beam from 2800 to 2370 Hz. When 17 g are attached the mode of the beam coalesces with the (0,4) mode of the disk and squeal vibration and noise (over 100 dB) appear. This point is labeled as lock-in point.

By increasing the attached mass, squeal occurs at every braking test at the coalescing frequency, which remains almost constant. Once the lock-out point is reached, the mode of the beam shifts at a frequency lower than the mode of the disk and the squeal disappears.

The graphic in figure 6 is the experimental equivalent of the lock-in plots, often obtained numerically in the literature by the complex eigenvalue analysis.[21,22]

The difference of added mass between the lock-in and

TABLE III. Modal damping distribution and unstable frequency range for different configurations.

	Setup configuration	Damping of disk mode (%)	Damping of beam mode (%)	Damping ratio	Lock-in frequency range (Hz)
A	No damping layers	0.48	2.5	5.2	150
B	Damping layer on both the disk and the beam	1.45	3.7	2.6	80
C	One damping layer on the beam	0.48	3.7	7.7	200
D	Two damping layers on the beam	0.48	5.7	11.8	380
E	Damping layer on the disk	1.45	2.5	1.7	110

lock-out points is in this case 9.7 g. As mentioned earlier, to generalize the problem to whatever change in the parameters of a brake system, the dynamics of the substructures giving instability is accounted for. The natural frequency of the beam (not in contact with the disk) is calculated for the mass values corresponding to the lock-in (2450 Hz) and lock-out point (2606 Hz). The frequency range corresponding to the unstable interval is then 156 Hz.

It can be asserted that whatever configuration of the parameters influencing the dynamics of the beam, which maintains the natural frequency of the second mode of the beam in such frequency range, leads to the unstable coalescence.[27]

B. Parallel distribution of added damping (case B)

Figure 8 shows the lock-in graphic when a layer of the material damping is added to both the beam and the disk. In this case the damping of the beam mode is 3.7% and the damping of the disk mode is 1.45%. Two different effects are obtained by the simultaneous addition of the damping layers to the beam and the disk: (i) a general increase of the system damping with a reduction of the system vibrations, and (ii) an homogenization of the two modal damping values from a ratio[28] of 5 (no damping layers) to a ratio of 2.5 (with damping layers). In such a condition the vibrational response of the subsystems is reduced. The coalescence of the two modes is obtained for an addition of mass of 17 g, and the lock-out is obtained at 23 g. The unstable range of the mass is of 6 g, equivalent to an unstable frequency range of the natural frequency of the beam equal to 78 Hz (lock-in at 2563 Hz, lock-out at 2485 Hz).

C. Unequal distribution of added damping (cases C, D, and E)

Figure 9(a) (case C) and Fig. 9(b) (case D) show the lock-in plots when one and two damping layers are attached to the beam, respectively. No damping material is attached to the disk. In these cases only the modal damping of the beam mode is increased. Therefore, other than to increase the damping of a substructure, the difference between the modal damping of the coalescing modes is increased. The ratio between the damping of the beam and disk mode is, respectively, 7.7 for one damping layer and 11.9 for two damping layers. The unstable ranges become, respectively; 23.6 g for one damping layer (equivalent to 200 Hz) and 30 g for the two damping layers (equivalent to 380 Hz).

A secondary effect of the increase of the range where the unstable coalescence happens is the increase of the vertical frequency jump of the natural frequency of the beam shown in the graphics. In fact, at the lock-in point the measured frequency drops to the squeal frequency that is close to the natural frequency of the less damped mode (the disk mode in this case). The authors showed[29] that the range of frequency in which a mode can coalesce ("tuning-in" frequency range) with another one depends on its modal damping. This effect is caused by the smoother frequency phase shift of such a mode due to the larger damping, so that the larger the damping the wider the tuning-in frequency range. The coalescence happens, indeed, when the tuning-in frequency range of the beam mode overlay with the tuning-in frequency range of the disk mode. The disk mode has a tuning-in frequency range extremely smaller than the one of the beam mode. Therefore, the squeal frequency is closer to the disk natural frequency.

The last tested case is presented in Fig. 10 (case E): The damping layer is attached to the disk, and not to the beam. In this case the ratio between the two modal damping values is decreased to 1.7. The unstable range of the added mass is 14.4 g (equivalent to 110 Hz of the natural frequency of the beam).

The squeal frequency is no more coincident with the disk natural frequency, but rather lies in between the disk and the beam natural frequencies. This is due to the fact that the tuning-in range of the disk mode is increased with the increase of the modal damping.

IV. RESULT DISCUSSION

The tests reported in this paper are aimed to reproduce the behavior of the unstable coalescence between two appropriate modes of the system at the variation of a system parameter that allows modifying appropriately the system dynamics. The tests are performed for different distributions of the modal damping, and the mode lock-in plots are measured. The propensity of the system to be unstable is valued by the comparison of the ranges of the parameter that leads to the instability. To generalize the results, the range of the parameter (the added mass in the proposed set of experiments) is also measured as the frequency range covered by the natural frequency of the coalescing mode that is influenced by the variation of the parameter. The natural frequency of the beam is measured at the lock-in and the lock-out points; the difference gives an index of the range of the beam dynamics able to couple with the disk.

Table III shows the damping distribution, the ratio between the damping values and frequency range of the beam mode that leads to squeal. From the comparison between case A and case B it can be asserted that a homogeneous increasing of the modal damping of the two coalescing modes stabilizes the system by decreasing the unstable frequency range.

Comparing case A with cases C and D it is evident that increasing the damping of the beam mode increases the difference between the damping of the two coalescing modes (larger damping ratio); the effect is a large increase of the unstable range of the system dynamics, from 150 up to 380 Hz. On the contrary, passing from case A to case E only the disk damping is increased, the damping ratio decreases and, consequently, the unstable range decreases.

In conclusion, the results of the analysis indicate two different, almost opposite, effects due to the addition of damping material:

(1) An homogeneous increase of the structural damping of the system leads to a simultaneous increase of the modal damping of the coalescing modes, by lowering the system response and the propensity of the system to generate squeal.
(2) A nonhomogeneous increase of the system damping that increases the difference between the damping of the coalescing modes, leads to an increase of the propensity of the system to squeal.

This analysis confirms the numerical results obtained in literature,[19,23–25] highlighting the importance of the distribution of the structural damping in a brake apparatus. Moreover, by analyzing the different graphics it is clear that the smaller the modal damping, the closer the squeal frequency to the natural frequency of one mode of the coupled system (usually a disk mode). In fact, a large modal damping increases the tuning-in frequency range, by increasing the frequency range where the excited mode responds with a sufficient phase shift.[29]

V. CONCLUSIONS

Notwithstanding decades of research on squeal and the considerable effort by the brake industries, an effective solution to obtain "squeal-free" brakes is not yet reached. Several solutions adopted in brake design are based on increasing system damping. Several recent studies[19,23–25] numerically investigate the behavior of system stability as a function of modal damping distribution. Due to the complexity of commercial brake systems it is not possible to have a clear experimental measurement of the modal damping distribution or to perform controlled modifications in the modal damping. Thus, an experimental analysis on commercial brakes, correlating the damping distribution and the squeal propensity, has not yet been performed. This paper reports measurements conducted on a simplified brake system, the beam-on-disk, aimed at investigating the influence of damping on the squeal propensity. The simple dynamics of the system and the robustness and reproducibility of the squeal events allow for consistent results.

The key role of the ratio between the modal damping values of the two coalescing modes is highlighted: The larger the ratio between the modal damping, the larger the propensity of the system to squeal.

Therefore, when increasing the modal damping of one of the two coalescing modes different effects can develop as a function of the damping ratio: By increasing the damping of the lower-damped mode a decrease of the squeal propensity is obtained (the damping ratio decreases); by increasing the damping of the larger damped mode an increase of the squeal propensity is obtained (the damping ratio increases). These results agree with the analytical[19] and numerical[23–26] analyses reported in literature. Moreover, a homogeneous increase of the system damping decreases the squeal propensity of the system.

These results also explain the difficulties in designing squeal-free brakes since such systems are characterized by large modal density with several localized sources of damping due to parts in contact (including the sliding contact between pads and disk). Thus, several pairs of modes that are characterized by large damping ratios can coalesce and lead to the squeal.

[1]A. Akay, "Acoustic of friction," J. Acoust. Soc. Am. **111**, 1525–1548 (2002).

[2]N. M. Kinkaid, O. M. O'Reilly, and P. Papadopoulos, "Automotive disk brake squeal," J. Sound Vib. **267**, 105–166 (2003).

[3]H. Ouyang, W. Nack, Y. Yuan, and F. Chen, "Numerical analysis of automotive disk brake squeal: A review," Int. J. Vehicle Noise Vibr. **1**, 207–231 (2005).

[4]H. R. Mills, "Brake squeak," Technical Report No. 9000 B, Institution of Automobile Engineers, London, UK, 1938.

[5]R. A. C. Fosberry and Z. Holubecki, "Interim report on disk brake squeal," Technical Report No. 1959/4, Motor Industry Research Association, Warwickshire, UK, 1959.

[6]R. A. C. Fosberry and Z. Holubecki, "Disk brake squeal: Its mechanism and suppression," Technical Report No. 1961/1, Motor Industry Research Association, Warwickshire, UK, 1961.

[7]R. T. Spurr, "A theory of brake squeal," in Proceedings of the Automobile Division, Institution of Mechanical Engineers, London, UK, 1961–1962, pp. 33–52.

[8]S. W. E. Earles and G. B. Soar, "Squeal noise in disk brakes," Vibration and Noise in Motor Vehicles, Institution of Mechanical Engineers, London, 1971, pp. 61–69.

[9]S. W. E. Earles, "A mechanism of disk-brake squeal," Technical Report No. 770181, SAE, Warrendale, PA, 1977.

[10]R. P. Jarvis and B. Mills, "Vibrations induced by friction," Proc. Inst. Mech. Eng. **178**, 847–857 (1963).

[11]M. R. North, "Disk brake squeal, a theoretical model," Technical Report No. 1972/5, Motor Industry Research Association, Warwickshire, UK, 1972.

[12]M. R. North, "Disk brake squeal," in *Braking of Road Vehicles* (Automobile Division of the Institution of Mechanical Engineers, Mechanical Engineering Publications Limited, London, 1976), pp. 169–176.

[13]A. Akay, J. Wickert, and Z. Xu, "Investigation of mode lock-in and friction interface," Final Report, Department of Mechanical Engineering, Carnegie Mellon University, Pittsburgh, PA, 2000.

[14]A. Tuchinda, N. P. Hoffmann, D. J. Ewins, and W. Keiper, "Effect of pin finite width on instability of pin-on-disk systems," Proceedings of the International Modal Analysis Conference—IMAC, 2002, Vol. 1, pp. 552–557.

[15]A. Tuchinda, N. P. Hoffmann, D. J. Ewins, and W. Keiper, "Mode lock-in characteristics and instability study of the pin-on-disk system," Proceedings of the International Modal Analysis Conference—IMAC, Kissimmee, FL, 2001, Vol. **1**, pp. 71–77.

[16]R. Allgaier, L. Gaul, W. Keiper, K. Willnery, and N. Hoffmann, "A study on brake squeal using a Beam-on-Disk," Proceedings of the International Modal Analysis Conference—IMAC, 2002, Vol. 1, pp. 528–534.

[17]R. Allgaier, "Experimentelle und numerische untersuchungen zum bremsenquietschen" (Experimental and numerical examinations on the brake-squeaks), Ph.D. thesis, University of Stuttgart, Stuttgart, Germany.

[18]J. F. Tarter, "Instabilities in a beam-disk system due to friction," Ph.D. thesis, Carnagie Mellon University, Pittsburgh, PA, 2004.

[19]P. Duffour and J. Woodhouse, "Instability of systems with a frictional point contact. 1 Basic modelling," J. Sound Vib. **271**, 365–390 (2004).

[20]Q. Cao, H. Ouyang, M. I. Friswell, and J. E Mottershead, "Linear eigenvalue analysis of the disk-brake squeal problem," Int. J. Numer. Methods Eng. **61**, 1546–1563 (2004).

[21]F. Massi, L. Baillet, O. Giannini, and A. Sestieri, "Brake squeal: Linear and nonlinear numerical approaches," Mech. Syst. Signal Process. **21**, 2374–2393 (2007).

[22]O. Giannini and A. Sestieri, "Predictive model of squeal noise occurring on a laboratory brake," J. Sound Vib. **296**, 583–601 (2006).

[23]N. Hoffmann and L. Gaul, "Effect of damping on mode-coupling instability in friction induced oscillations," Z. Angew. Math. Mech. **83**, 524–534 (2003).

[24]J. J. Sinou and L. Jèzèquel, "Mode coupling instability in friction-induced vibrations and its dependency on system parameters including damping," Eur. J. Mech. A/Solids **26**, 106–122 (2007).

[25]G. Fritz, J. J. Sinou, J. M. Dufal, and L. Jèzèquel, "Effects of damping on brake squeal coalescence patterns—application on a finite element model," Mech. Res. Commun. **34**, 181–190 (2007).

[26]The disk modes are labeled (n,m) modes n and m being the numbers of nodal circumferences and diameters, respectively. Into the text the modes of the assembled system are still labeled as beam and disk modes, because, due to the low coupling between the two substructures, the vibration energy is concentrated in one of them.

[27]The use of the frequency range of one mode of the system that leads to the squeal behavior as an index of squeal propensity is proposed by Giannini and Sestieri (Ref. 22).

[28]Ratio between the modal damping of the beam mode and the disc mode.

[29]F. Massi, O. Giannini, and L. Baillet, "Brake squeal as dynamic instability: An experimental investigation," J. Acoust. Soc. Am. **120**, 1388–1399 (2006).

A model for sonar interrogation of complex bottom and surface targets in shallow-water waveguides

Thomas E. Giddings[a] and Joseph J. Shirron
Metron, Inc., 11911 Freedom Drive, Suite 800, Reston, Virginia 20190-5602, USA

(Received 23 August 2007; revised 2 January 2008; accepted 7 January 2008)

Many problems of current interest in underwater acoustics involve low-frequency broadband sonar interrogation of objects near the sea surface or sea floor of a shallow-water environment. When the target is situated near the upper or lower boundary of the water column the acoustic interactions with the target objects are complicated by interactions with the nearby free surface or fluid-sediment interface, respectively. A practical numerical method to address such situations is presented. The model provides high levels of accuracy with the flexibility to handle complex, three-dimensional targets in range-independent environments. The model is demonstrated using several bottom target scenarios, with and without locally undulating seabeds. The impact of interface and boundary interactions is considered with an eye toward using the sonar return signal as the basis for acoustic imaging or spectral classification. © *2008 Acoustical Society of America.*
[DOI: 10.1121/1.2839002]

PACS number(s): 43.40.Fz, 43.20.Tb, 43.30.Bp, 43.20.Fn [DSB] Pages: 2024–2034

I. INTRODUCTION

Sonar detection, classification, and identification systems often involve broadband acoustic interrogation of complex targets in shallow-water environments. Sonar imaging systems rely on a return signal that is a nearly undistorted replica of the emitted pulse, whereas structural acoustics-based classifiers exploit the spectral features imprinted by the target on the return signal. Imaging resolves the spatial features of the external target geometry, while spectral classification techniques also probe the internal structure and material composition of the target. For either approach, system design and analysis require a great deal of data involving a wide variety of target structures and environmental situations. Numerical simulations provide a cost-effective means for developing these computer-aided detection and classification technologies and for assessing their performance characteristics without relying only on expensive field data.

Many practical problems of current interest involve low- to mid-frequency acoustic interrogation of complex bottom objects in shallow-water ocean environments. Typical ranges run from tens to hundreds of meters and targets can be proud, partially buried or fully buried in the seabed sediment layer. As illustrated in Fig. 1, the sonar simulation problem involves the propagation of an acoustic pulse from a projector to the target, acoustic wave scattering from the elastic target, and the propagation of the scattered waves back to a hydrophone. This problem can be modeled with a single, unified approach such as finite difference, finite element, or boundary element methods, but for most practical situations the computational burden would be prohibitive. This is especially true when considering broadband signals in the low- to mid-frequency range where a dense sampling in frequency is required to resolve spectral details in the scattered wave field.

Alternatively, by coupling a waveguide propagation code with a near-field structural acoustics solver a more efficient hybrid model can be achieved. With a hybrid approach, a waveguide propagation code transmits the signal from the source to the target and back to the receiver, a structural acoustics solver accounts for the complex interactions of the acoustic waves with the elastic target in its local environment, and coupling mechanisms link the two models. Several propagation models exist to handle the signal transfer between the sensor and the target, but these models and the coupling mechanisms joining them to the structural acoustics problem may engender important modeling limitations. The structural acoustics problem has proven to be a significant challenge for complex targets at the ocean surface or at the sea floor. The main difficulty here is in approximating the radiation condition while using a small truncated computational domain when the exterior acoustic medium contains contact surfaces and/or other strong inhomogeneities.

The formulation presented in the following sections is conceptually similar to the wave-field superposition method, introduced by Kravtsov *et al.*[1] and developed more fully by Ingenito,[2] which couples the target free-field, plane-wave scattering function to a local plane-wave decomposition of the normal mode representation of the waveguide pressure field. This approach is also used by Norton and Werby[3] and Sarkissian.[4,5] Due to the plane-wave decomposition of the normal modes at the target depth and the far-field approximations used, this methodology is restricted to longer-range problems where the scatterer is a significant distance away from the waveguide boundaries. Makris *et al.*[6,7] reformulated the approach using wave number integration techniques for waveguide propagation and extended the approach to three dimensional (3D), thereby making it suitable for short-range

[a]Author to whom correspondence should be addressed. Electronic mail: giddings@metsci.com.

 0001-4966/2008/123(4)/2024/11/$23.00 © 2008 Acoustical Society of America

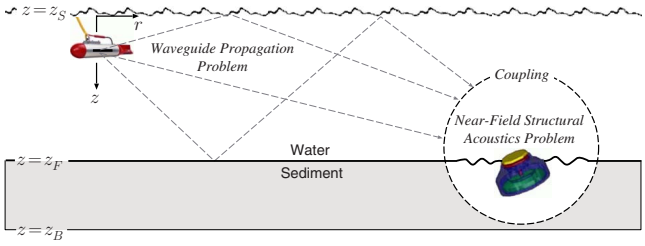

FIG. 1. (Color online) Sonar simulation as a waveguide propagation model coupled to a structural acoustics model.

problems. The virtual source formulation of Schmidt *et al.*[8,9] also uses wave number integration and has been applied to problems with scatterers at the seabed interface.

Other approaches, like those based on the T-matrix method,[10–12] boundary integral equation,[13,14] invariant embedding,[15] or parabolic equations,[16] neither meet our objectives nor are they closely related to the present approach. Furthermore, none of the aforementioned articles explicitly treat the problem of a structurally complex scatterer near or penetrating a boundary or material interface of the waveguide. In Sec. II A we employ a 3D normal mode propagation model, and retain all physically relevant modes, to resolve the near-field acoustic behavior in a stratified, finite-depth waveguide. Model coupling occurs in close proximity to the target using a projection technique, as described in Sec. II C. The accurate simulation of near-field scattering physics for complex elastic objects located at the air-water or water-sediment interface has been the main impediment to realistic sonar simulations involving surface or bottom targets, and this is our primary focus.

Near-field acoustic scattering from underwater targets located at the waveguide boundaries cannot be accurately treated with free-field scattering formulations. Furthermore, neither Absorbing Boundary Conditions[17–21] nor Infinite Element Methods[22–24] are directly applicable when the medium that surrounds the targets contains contact surfaces or other strong inhomogeneities. The Dirichlet-to-Neumann map[25] may be applicable but would likely be less efficient than the approach offered here. The T-Matrix[26,27] approach has been successfully applied to the two-fluid problem by Lim *et al.*[28,29] but it is limited to relatively simple target geometries. In Sec. II B we detail a finite element model for structural acoustics in unbounded, inhomogeneous domains, which is an extension of prior work.[30,31] The approach uses a Perfectly Matched Layer (PML) at the truncation boundary,[32–34] which has been successfully applied to several exterior structural acoustics problems.[30,35,36] In the present development targets may be structurally complex with variable internal elastic material composition, and can be arbitrarily close to, or penetrating, flat or locally undulating waveguide boundaries or material interfaces. Example computations are provided in Sec. III.

II. NUMERICAL APPROACH

We outline the computational procedure for resolving the ensonification of, and scattering from, an elastic target in a range-independent waveguide with depth-varying density and speed of sound. Physically, the waveguide represents a stratified fluid layer overlaying a stratified fluid-saturated sediment layer. This scenario will serve to illustrate the coupling of the waveguide propagation and near-field structural acoustics models, and to demonstrate the importance of accounting for the interface between external media when computing the scattered field of a nearby target. A 3D normal mode approach is used for the channel propagation problem, and a finite element formulation is used for the near-field structural acoustics problem, as introduced in a recent paper.[37]

A. Waveguide propagation model

Consider a time-harmonic pressure field of frequency f, or circular frequency $\omega=2\pi f$, with spatial variation p in an acoustic waveguide with depth-dependent density ρ_0 and sound speed c_0. The density is real and positive, $\rho_0>0$, and the sound speed is generally complex with positive real part, $\Re(c_0)>0$, and negative imaginary part, $\Im(c_0)\leqslant 0$. We may take the origin of the coordinate system to be at the water surface, where the positive z direction is pointing downward, as shown in Fig. 1, so that $z=z_S$ corresponds to the water surface, $z=z_F$ corresponds to the sea floor, and $z=z_B\geqslant z_F$ is the top of the ocean basement, which is the lower boundary of the computational domain.

1. Review of 3D normal mode expansion

We consider the spatial variation of the acoustic pressure field $p(\mathbf{x})=p(r,\theta,z)$, which is governed by the Helmholtz equation. Applying the Helmholtz operator $\mathcal{L}$ in cylindrical coordinates to the pressure field leads to the linear differential expression

$$\mathcal{L}p=\frac{1}{r}\frac{\partial}{\partial r}\left(r\frac{\partial p}{\partial r}\right)+\rho_0\frac{\partial}{\partial z}\left(\frac{1}{\rho_0}\frac{\partial p}{\partial z}\right)+\frac{1}{r^2}\frac{\partial^2}{\partial\theta^2}+\frac{\omega^2}{c_0^2}p, \tag{1}$$

where separated boundary conditions are prescribed at the upper and lower waveguide boundaries. The pressure field must also satisfy the radiation condition in the radial direction. We can construct the solution to such problems using the normal mode expansion method.[38,39]

The solution for the above problem can be obtained by constructing a spectral representation of the Helmholtz operator. Using the separation of variables technique, solutions of the following form are proposed:

$$p(r,\theta,z)=\phi(r)\chi(\theta)\psi(z), \tag{2}$$

where the complete solution for a given problem is a linear superposition of individual modes, each taking the form in Eq. (2). Substituting the above representation into the homogeneous form of the Helmholtz equation,

$$\mathcal{L}p=0, \tag{3}$$

we obtain three ordinary differential equations linked by separation constants. The equation governing the depth-dependent term is

$$\frac{d}{dz}\left(\frac{1}{\rho_0}\frac{d\psi}{dz}\right)+\left[\frac{\omega^2}{\rho_0 c_0^2}-\frac{\lambda^2}{\rho_0}\right]\psi=0, \tag{4}$$

where λ^2 is the separation constant. At the water surface we prescribe a pressure-release boundary condition,

$$\psi(z_S)=0. \tag{5}$$

We impose a Neumann boundary condition at the lower computational boundary of the domain,

$$\left.\frac{d\psi}{dz}\right|_{z_B}=0, \tag{6}$$

to approximate the rigid basement layer.

Equation (4) together with boundary conditions (5) and (6) constitute an eigenvalue problem. Since we restrict attention to finite depths, this problem admits a countably infinite number of solutions ψ_n, at discrete eigenvalues λ_n, indexed by n. These eigenfunctions ψ_n form a complete orthonormal basis with respect to the weighted inner product,

$$\int_{z_S}^{z_B}\frac{1}{\rho_0(z)}\psi_m(z)\psi_n(z)dz=\begin{cases}1, & m=n\\ 0, & m\neq n\end{cases}. \tag{7}$$

A procedure for computing the eigenvalues λ_n and eigenfunctions ψ_n is outlined in the next subsection.

Since $\{\psi_n|n=0,1,2,\ldots\}$ constitutes a complete basis on the interval (z_S,z_B), we propose an expansion for the pressure field,

$$p(r,\theta,z)=\sum_{m,n}\phi_{mn}(r)\chi_m(\theta)\psi_n(z).$$

Substituting this expansion into Eq. (3), simplifying according to Eq. (4), multiplying through by ψ_n/ρ_0, and integrating over $z\in(z_S,z_B)$, we obtain the equation

$$\frac{r}{\phi_{mn}}\frac{\partial}{\partial r}\left(r\frac{\partial\phi_{mn}}{\partial r}\right)+\frac{1}{\chi_m}\frac{\partial^2\chi_m}{\partial\theta^2}+r^2\lambda_n^2=0, \tag{8}$$

where λ_n is the eigenvalue corresponding to ψ_n.

The eigenvalue problem for the angle-dependent term is given by

$$\frac{d^2\chi_m}{d\theta^2}+\mu_m^2\chi_m=0,$$

with periodic boundary condition $\chi_m(0)=\chi_m(2\pi)$. Solutions exist for discrete μ_m and are given by

$$\chi_m(\theta)=\frac{e^{im\theta}}{\sqrt{2\pi}}, \tag{9}$$

where the separation constant $\mu_m=m$, for $m=0,1,2,\ldots$. The set $\{\chi_m|m=0,1,2,\ldots\}$ constitutes a complete orthonormal basis on the interval $\theta\in[0,2\pi]$ with respect to the unweighted inner product.

The equation governing the range-dependent term is then

$$r\frac{d}{dr}\left(r\frac{d\phi_{mn}}{dr}\right)+(\lambda_n^2r^2-m^2)\phi_{mn}=0.$$

The relevant solutions to this equation, which satisfy the radiation condition, are

$$\phi_{mn}(r)=H_m^{(1)}(\lambda_n r), \tag{10}$$

where $H_m^{(1)}$ is the Hankel function of the first kind of order m.

The complete three-dimensional eigenfunction expansion of the pressure field then takes the form

$$p(r,\theta,z)=\sum_{m,n}a_{mn}H_m^{(1)}(\lambda_n r)e^{im\theta}\psi_n(z), \tag{11}$$

where all multiplicative factors have been absorbed into the coefficients a_{mn}. Solutions of the above form satisfy all physical boundary conditions by construction, where each $H_m^{(1)}(\lambda_n r)e^{im\theta}\psi_n(z)$ constitutes a *normal mode* of the waveguide propagation problem. The coefficients a_{mn} are determined by the applied forces and/or prescribed boundary values.

2. Calculation of the depth modes

The eigenvalue problem we need to solve is specified by Eq. (4), with the pressure-release boundary condition (5) at the water surface and a sound hard condition (6) at the lower boundary. When the properties are uniform in the fluid and sediment layers the depth problem can be reduced to a root-finding problem using the end point method.[39] Then the complex roots can be found using what has come to be called the Lehmer–Schur algorithm. In general, however, the eigenvalues and eigenfunctions of the depth problem can be found using finite difference or finite element techniques. We opt for the latter approach because of its potential accuracy and flexibility. The eigenvalues and corresponding eigenfunctions are found by solving a (Rayleigh–Ritz) variational problem using the (Galerkin) finite element method.[37]

The eigenvalue problem has a purely discrete spectrum. Multiplying Eq. (4) by a suitable test function φ and integrating over the interval (z_S,z_B) we obtain

$$A(\varphi,\psi)-\lambda^2B(\varphi,\psi)=0, \tag{12}$$

where the bilinear forms are

$$A(\varphi,\psi)=\int_{z_S}^{z_B}\left[-\frac{1}{\rho_0}\frac{d\varphi}{dz}\frac{d\psi}{dz}+\frac{\omega^2}{\rho_0 c_0^2}\varphi\psi\right]dz$$

and

$$B(\varphi,\psi)=\int_{z_S}^{z_B}\frac{1}{\rho_0}\varphi\psi dz.$$

We note that $\varphi(z_S)=0$ and $\psi'(z_B)=0$.

Expanding φ and ψ in terms of a piecewise polynomial finite element basis, substituting these expansions into Eq. (12), and specifying that the resulting relation holds for any φ results in a generalized eigenvalue problem,

$$\mathbf{Ax}-\lambda^2\mathbf{Bx}=0. \tag{13}$$

The matrices $\mathbf{A}$ and $\mathbf{B}$ are tridiagonal in the case of linear elements and are banded, with a narrow bandwidth, for

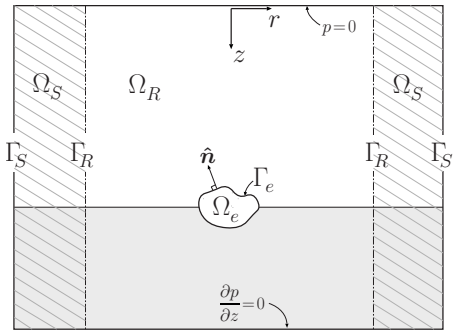

FIG. 2. Computational domain for the structural acoustics problem with a flat seabed.

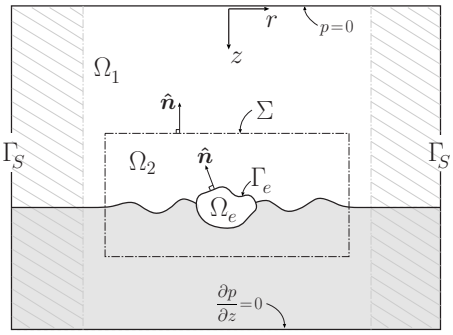

FIG. 3. Computational domain for the structural acoustics problem with locally undulating seabed.

higher-order elements. The matrices are real symmetric when c is real, but $\mathbf{A}$ is complex symmetric (non-Hermitian) when c is complex. $\mathbf{B}$ is positive definite.

The standard eigenvalue problem (13) can be solved with the Implicitly Restarted Arnoldi Method,[40] using the routines available in ARPACK.[41] The routines compute λ^2 and one must take $\pm\sqrt{\lambda^2}$ as appropriate, i.e., the root with non-negative real and imaginary parts. Thus we obtain numerical approximations of the eigenfunctions in terms of the piecewise polynomial finite element basis functions. These eigenfunctions should be normalized according to Eq. (7). The normal mode propagation model has been verified against full finite element solutions for very short ranges (i.e., 1 m) out to tens of meters, which encompasses the most challenging modeling regime, and excellent agreement was observed throughout.

B. Structural acoustics model

The structural acoustics model consists of a finite element formulation for target scattering near a fluid-fluid interface or pressure release surface in a domain that is unbounded in at least one direction.[30,31] Since the acoustic waveguide is infinite in the radial direction we truncate the physical domain at some finite radial distance from the scatterer to obtain a bounded computational domain. The finite element formulation uses a Perfectly Matched Layer (PML) in the radial direction to approximate a nonreflecting boundary where the computational domain has been truncated.[32–34] The PML approach has been successfully applied to various exterior structural acoustics problems,[30,35,36] and is more readily adaptable to the present situation than the boundary truncation techniques mentioned in the introduction.[17,19–23,25] In the following, we consider two possible scattering scenarios: (1) an elastic target occupying the open domain Ω_e with wet surface Γ_e, where the water-sediment interface is flat, as in Fig. 2; and, (2) a target near a locally undulating water-sediment interface, as in Fig. 3.

Referring to Fig. 2, we consider a problem domain that extends from the surface of the water column ($z=z_S$) to some depth $z_B \geqslant z_F$ within the sediment layer, which matches the upper and lower boundaries of the waveguide propagation problem. The domain Ω_R, which is the open annular region between Γ_e and Γ_R, is the physically relevant portion of the fluid, where the properties are the same as those specified in the waveguide. We truncate the computational domain at a radial distance $r=S>R$, and let Γ_S denote the surface of this outer cylindrical boundary. The thin cylindrical annulus Ω_S between Γ_R and Γ_S is the fluid PML. The PML is a numerical contrivance used to prevent the reflection of outgoing waves, so that the eventual solution within Ω_S has no physical meaning. The entire computational fluid domain is $\Omega_f = \Omega_R \cup \Omega_S \cup \Gamma_R$. We aim to calculate the scattered acoustic pressure field on a cylindrical surface Γ_R at some radial distance $r=R$ from the center of the scatterer.

1. PML treatment of the truncation boundary

Consider the scattered acoustic pressure field p_s arising from the forcing due to sources outside the computational domain. The acoustic pressure field satisfies the Helmholtz equation for inhomogeneous media in the physically relevant portion of the fluid domain,

$$\nabla \cdot \left(\frac{1}{\rho} \nabla p_s \right) + \frac{\omega^2}{\rho c^2} p_s = 0 \quad \text{in } \Omega_R, \tag{14}$$

where we specify a pressure release surface and sound hard bottom,

$$p_s(z_S) = 0 \quad \text{and} \quad \left. \frac{\partial p_s}{\partial z} \right|_{z_B} = 0. \tag{15}$$

For the depth-dependent waveguide properties, ρ_0 and c_0, the differential equation in Eq. (14) is equivalent to Eq. (1), but here we develop the more general case where the density ρ and speed of sound c can be fairly arbitrary [i.e., $\rho, c \in L_2(\Omega_f)$].

We extend consideration to the PML region Ω_S by applying a transformation $\mathcal{T}$ to the physical coordinates $\mathbf{x} = (x_1, x_2, x_3)$ to obtain[42–46]

$$\tilde{\mathbf{x}} = \mathcal{T}(\mathbf{x}) = (\tilde{x}_1, \tilde{x}_2, \tilde{x}_3). \tag{16}$$

As a function of the transformed coordinates, the pressure field satisfies the modified Helmholtz equation

$$\tilde{\nabla} \cdot \left(\frac{1}{\rho} \tilde{\nabla} p_s \right) + \frac{\omega^2}{\rho c^2} p_s = 0 \quad \text{in } \tilde{\Omega}_f, \tag{17}$$

where $\tilde{\nabla}$ is the gradient operator with respect to $\tilde{\mathbf{x}}$, and $\tilde{\Omega}_f = \{\mathcal{T}(\mathbf{x}) : \mathbf{x} \in \Omega_f\}$ is the image of Ω_f under the transformation $\mathcal{T}$. The transformation will be constructed so that $\tilde{\mathbf{x}} = \mathbf{x}$ inside

Γ_R such that Eq. (17) reduces to the usual Helmholtz Eq. (14) in Ω_R. Consequently, the solution in Ω_R is physically meaningful and all boundary conditions internal to Γ_R are unmodified in the PML formulation.

The radial distance R is chosen to be just large enough so that the domain Ω_R encloses the scatterer Ω_e and any undulations of the fluid-fluid interface, but otherwise it is as small as possible to minimize computational cost. The choice of boundary condition on the artificial truncation boundary Γ_S is somewhat arbitrary as it does not have an appreciable affect on the solution within Ω_R.[47,48] For simplicity we impose the boundary condition

$$\hat{\mathbf{n}} \cdot \tilde{\nabla} p_s = 0 \quad \text{on } \tilde{\Gamma}_S, \tag{18}$$

where $\tilde{\Gamma}_S = \{\mathcal{T}(\mathbf{x}) : \mathbf{x} \in \Gamma_S\}$ is the image of Γ_S under the transformation $\mathcal{T}$.

We formally derive a weak form of Eq. (17) by multiplying this equation by a test function q, integrating over the closure of the fluid domain, applying the divergence theorem, and imposing the truncation boundary condition (18), to yield

$$\int_{\tilde{\Omega}_f} \frac{1}{\rho}\left[\tilde{\nabla} q \cdot \tilde{\nabla} p_s - \frac{w^2}{c^2} q p_s\right] d\tilde{\Omega}_f + \int_{\Gamma_e} \frac{1}{\rho} q \hat{\mathbf{n}} \cdot \nabla p_s d\Gamma_e = 0.$$

The boundary integral term will couple the acoustic pressure field in the fluid to the response of the scatterer under the prescribed loading through the appropriate boundary condition, which will be addressed in the next subsection.

From the chain rule for differentiation

$$\frac{\partial}{\partial x_j} = \sum_{k=1}^{3} \frac{\partial \tilde{x}_k}{\partial x_j} \frac{\partial}{\partial \tilde{x}_k} \quad \text{or} \quad \nabla = \mathbf{J} \tilde{\nabla},$$

where the matrix $\mathbf{J}$ has components $J_{jk} = \partial \tilde{x}_k / \partial x_j$. Letting

$$\mathbf{M} = \mathbf{J}^{-1} \quad \text{and} \quad W = \det(\mathbf{J}),$$

we arrive at the weak form of the scattering problem in the physical coordinates $\mathbf{x}$: Find $p \in H^1(\Omega_f)$ such that

$$\int_{\Omega_f} \frac{1}{\rho}\left[(\mathbf{M} \nabla q) \cdot (\mathbf{M} \nabla p_s) - \frac{\omega^2}{c^2} q p_s\right] W d\Omega_f + \int_{\Gamma_e} \frac{1}{\rho} q \hat{\mathbf{n}} \cdot \nabla p_s d\Gamma_e = 0, \tag{19}$$

for all $q \in H^1(\Omega_f)$. Within the subdomain Ω_R we have $\mathbf{M} = \mathbf{I}$ (the identity matrix) and $W = 1$, so that Eq. (19) reduces to the usual weak form of the Helmholtz equation on that part of the computational domain.

We now provide an explicit form of the transformation $\mathcal{T}$. Let (r, θ, z) be cylindrical coordinates, and let $\sigma_r \geqslant 0$ be a monotonically increasing function satisfying $\sigma_r(r) = 0$ for $0 \leqslant r \leqslant R$. For example, we use

$$\sigma_r = \xi(e^{\gamma \xi} - 1) \quad \text{for } R \leqslant r \leqslant S$$

and zero otherwise, where $\xi(r) = (r - R)/(S - R)$ and γ is a real, positive parameter that determines the amount of wave attenuation. We construct the complex change of variables $\tilde{r} = \alpha_r(r) r$, where

$$\alpha_r(r) = 1 + \frac{(1+i)}{r} \int_0^{\xi(r)} \sigma_r(\xi') d\xi' \quad \text{for } R \leqslant r \leqslant S$$

and $\alpha_r(r) = 1$ for $r < R$. The gradient in cylindrical coordinates is given by

$$\nabla = \left(\frac{\partial}{\partial r}, \frac{1}{r}\frac{\partial}{\partial \theta}, \frac{\partial}{\partial z}\right).$$

It is straightforward to derive

$$\mathbf{M}(r) = \operatorname{diag}\left(\frac{1}{\beta_r(r)}, \frac{1}{\alpha_r(r)}, 1\right)$$

and

$$W(r) = \alpha(r) \beta_r(r),$$

where

$$\beta_r(r) = \frac{\partial \tilde{r}}{\partial r} = 1 + (1+i)\sigma_r(r).$$

This treatment ensures that there are no significant wave reflections at the truncation boundary so that waves propagate only away from their source, and it is suitable for both propagating and evanescent waves.

2. Elastic target near a flat interface

Apart from the treatment of the truncation boundary, the finite element formulation for this case follows standard *hp*-finite element procedure for structural acoustics.[49,50] The target structure supports an elastic displacement field $\mathbf{u} = (u_1, u_2, u_3)$ in Cartesian coordinates, which is governed by the equations of linear elasticity

$$\sigma_{ij,j}(\mathbf{u}) + \rho_e \omega^2 u_i = 0 \quad \text{in } \Omega_e, \tag{20}$$

where ρ_e is the density of the elastic material. The stress tensor σ_{ij} is related to the strain tensor ϵ_{ij} through the generalized Hooke's Law

$$\sigma_{ij}(\mathbf{u}) = C_{ijkl} \epsilon_{kl}(\mathbf{u}), \tag{21}$$

where C_{ijkl} is a fourth-order tensor of material constants, and the strain tensor has components

$$\epsilon_{ij}(\mathbf{u}) = \frac{1}{2}\left(\frac{\partial u_i}{\partial x_j} + \frac{\partial u_j}{\partial x_i}\right).$$

The boundary conditions on the wet surface are

$$\left.\begin{aligned} \sigma_{ij}(\mathbf{u}) n_j &= -p n_i \\ \frac{1}{\rho} \hat{\mathbf{n}} \cdot \nabla p &= \omega^2 \mathbf{u} \cdot \hat{\mathbf{n}} \end{aligned}\right\} \quad \text{on } \Gamma_e, \tag{22}$$

where $\hat{n} = (n_1, n_2, n_3)$ is a unit vector normal to the surface of the scatterer and directed into the surrounding fluid. The re-

lations in Eq. (22) provide for the balance of force and normal velocity on the wet surface of the elastic target.

A weak form of the elasto-dynamics equation can be developed by integrating the scalar product of Eq. (20) with a test function $\mathbf{v} \in H^1(\Omega_e)^3$ over the domain Ω_e and applying the divergence theorem to obtain

$$\int_{\Omega_e} [\epsilon_{ij}(\mathbf{v})\sigma_{ij}(\mathbf{u}) - \rho\omega^2 \mathbf{v}\cdot\mathbf{u}]d\Omega_e - \int_{\Gamma_e} v_i \sigma_{ij}(\mathbf{u}) n_j d\Gamma_e = 0, \tag{23}$$

where $\mathbf{v}=(v_1,v_2,v_3)$. The surface integrals of Eqs. (19) and (23) couple the elastic response to the pressure loading through the boundary conditions (22).

The total pressure in the fluid is written as $p=p_0+p_s$, where p_0 is the incident pressure field due to acoustic sources in the waveguide in the absence of a scatterer and p_s is the scattered pressure field. The total pressure must satisfy Eq. (14). The incident pressure p_0 satisfies Eq. (1), and since the properties in Ω_f are the same as those throughout the waveguide, i.e.,

$$\rho = \rho_0 \text{ and } c = c_0 \text{ in } \Omega_f, \tag{24}$$

Eq. (14) is the same as (1). Linearity then implies that p_s also satisfies Eq. (14) so that Eq. (19) is the appropriate weak form for p_s in the entire fluid domain.

The weak formulation for the coupled problem is then to find $p_s \in H^1(\Omega_f)$ and $\mathbf{u} \in H^1(\Omega_e)^3$ such that

$$\mathcal{A}(p_s,q) + \omega^2 \mathcal{C}(q,\mathbf{u}) = \mathcal{D}(p_0,q) \tag{25}$$

and

$$\mathcal{B}(\mathbf{u},\mathbf{v}) + \mathcal{C}(p_s,\mathbf{v}) = -\mathcal{C}(p_0,\mathbf{v}) \tag{26}$$

for all $q \in H^1(\Omega_f)$ and $\mathbf{v} \in H^1(\Omega_e)^3$. In the above, we have made use of the weak forms (19) and (23), and boundary conditions (15) and (22). To simplify notation, we have defined the bilinear forms

$$\mathcal{A}(p,q) = \int_{\Omega_f} \frac{1}{\rho}\left[(\mathbf{M}\nabla q)\cdot(\mathbf{M}\nabla p) - \frac{\omega^2}{c^2} qp \right] W d\Omega_f \tag{27}$$

$$\mathcal{B}(\mathbf{u},\mathbf{v}) = \int_{\Omega_e} [\epsilon_{ij}(\mathbf{v})\sigma_{ij}(\mathbf{u}) - \rho\omega^2 \mathbf{v}\cdot\mathbf{u}]d\Omega_e \tag{28}$$

$$\mathcal{C}(p,\mathbf{u}) = \int_{\Gamma_e} p\mathbf{u}\cdot\hat{\mathbf{n}} d\Gamma_e \tag{29}$$

$$\mathcal{D}(p,q) = \int_{\Gamma_e} \frac{1}{\rho} q\hat{\mathbf{n}}\cdot\nabla p d\Gamma_e. \tag{30}$$

3. Scattering volume around an undulating interface

Here we introduce a boundary Σ that completely encloses an *inner fluid* domain Ω_2, or scattering volume, which is the annular region bounded by Γ_e and Σ in which the fluid properties may vary arbitrarily in space (see Fig. 3). The *outer fluid* domain Ω_1 is the annular region exterior to Σ where the fluid properties vary only with depth and are the same as those throughout the waveguide. Note that Ω_2 is inside Ω_R so that the Helmholtz equation and all boundary conditions on and interior to Σ are unmodified by the PML formulation.

We formally write the total pressure $p=p_0+p_s$ as the sum of the incident pressure p_0 and the scattered pressure p_s. The incident pressure field satisfies Eq. (1) throughout the waveguide, and we can rewrite this equation as

$$\nabla\cdot\left(\frac{1}{\rho_0}\nabla p_0\right) + \frac{\omega^2}{\rho_0 c_0^2} p_0 = 0, \tag{31}$$

where the density ρ_0 and speed of sound c_0 are those specified for the waveguide propagation problem.

The density and speed of sound in the outer fluid domain are the same as those throughout the waveguide,

$$\rho = \rho_0 \text{ and } c = c_0 \text{ in } \Omega_1, \tag{32}$$

so that the incident pressure p_0 and scattered pressure p_s satisfy the Helmholtz equation individually in Ω_1. In particular,

$$\tilde{\nabla}\cdot\left(\frac{1}{\rho}\tilde{\nabla} p_s\right) + \frac{\omega^2}{\rho c^2} p_s = 0 \text{ in } \Omega_1, \tag{33}$$

where we have extended consideration to the PML region.

Within the inner fluid domain Ω_2 the fluid properties may vary in all directions, but the total pressure $p=p_0+p_s$ must satisfy the Helmholtz equation, so that

$$\nabla\cdot\left(\frac{1}{\rho}\nabla p_s\right) + \frac{\omega^2}{\rho c^2} p_s = -\nabla\cdot\left[\left(\frac{1}{\rho} - \frac{1}{\rho_0}\right)\nabla p_0\right] - \omega^2\left(\frac{1}{\rho c^2} - \frac{1}{\rho_0 c_0^2}\right) p_0 \text{ in } \Omega_2, \tag{34}$$

where we have made use of Eq. (31). Note that within Ω_2 the definition of $p=p_0+p_s$ is merely a convenience, and not a physically meaningful decomposition.

We label the total pressure field

$$p = \begin{cases} p_1 & \text{in } \Omega_1 \\ p_2 & \text{in } \Omega_2 \end{cases},$$

so that the subscripts "1" and "2" indicate the fluid properties in the outer and inner fluids, respectively. We then have the fluid-fluid interface boundary condition

$$\left.\begin{aligned} p_1 &= p_2 \\ \frac{1}{\rho_1}\hat{\mathbf{n}}\cdot\nabla p_1 &= \frac{1}{\rho_2}\hat{\mathbf{n}}\cdot\nabla p_2 \end{aligned}\right\} \text{ on } \Sigma. \tag{35}$$

We note that $\rho_1=\rho_0$ by construction, and p_0 is continuous across the interface Σ.

We note that the entire fluid domain $\Omega_f=\Omega_1\cup\Omega_2\cup\Sigma$. Combining the weak forms for Eqs. (33) and (34) with Eq. (23), and using the boundary conditions (15), (18), (22), and (35), the weak formulation for the structural acoustics problem is then to find $p_s \in H^1(\Omega_f)$ and $\mathbf{u} \in H^1(\Omega_e)^3$ such that

$$\mathcal{A}(p_s,q) + \omega^2 \mathcal{C}(q,\mathbf{u}) = \mathcal{D}(p_0,q) - \mathcal{A}_2(p_0,q) - \mathcal{D}_2(p_0,q) \tag{36}$$

and

$$\mathcal{B}(\mathbf{u},\mathbf{v}) + \mathcal{C}(p_s,\mathbf{v}) = -\mathcal{C}(p_0,\mathbf{v}) \tag{37}$$

for all $q \in H^1(\Omega_f)$ and $\mathbf{v} \in H^1(\Omega_e)^3$, where $\mathcal{A}(p,q)$, $\mathcal{B}(\mathbf{u},\mathbf{v})$, $\mathcal{C}(p,\mathbf{u})$, and $\mathcal{D}(p,q)$ are defined as before in Eqs. (27)–(30). The new terms arising in the formulation are:

$$\mathcal{A}_2(p,q) = \int_{\Omega_2} \left[\left(\frac{1}{\rho} - \frac{1}{\rho_0} \right) \nabla q \cdot \nabla p - \omega^2 \left(\frac{1}{\rho c^2} - \frac{1}{\rho_0 c_0^2} \right) qp \right] d\Omega_2, \tag{38}$$

which is the contribution from the scattering volume, and

$$\mathcal{D}_2(p,q) = \int_{\Gamma_e} \left(\frac{1}{\rho} - \frac{1}{\rho_0} \right) q \hat{\mathbf{n}} \cdot \nabla p d\Gamma_e. \tag{39}$$

It is clear that when the density and sound speed in Ω_2 are the same as those throughout the waveguide, i.e.,

$$\rho = \rho_0 \text{ and } c = c_0 \text{ in } \Omega_2,$$

then $\mathcal{A}_2(p,q)=0$ and $\mathcal{D}_2(p,q)=0$, and we revert to the formulation for the flat interface given in the previous subsection. Note that p_s is not really the scattered field in Ω_2 because p_0 is not really the incident field there. We are only interested in the solution at radius R, however, where p_s is indeed the scattered field.

C. Coupling waveguide and structural acoustics models

We will consider the response of a complex scatterer to a point source at depth z_0 in the water column (i.e., $z_S < z_0 < z_F$). We first determine the pressure field incident on the scatterer. The pressure field in the channel due to an omnidirectional point source situated at (r_0, θ_0, z_0) is

$$p_0(r,\theta,z) = \frac{i}{4\rho(z_0)} \sum_{m,n} H_m^{(1)}(\lambda_n r_>) \psi_n(z_0) \psi_n(z) \times J_m(\lambda_n r_<) e^{im(\theta-\theta_0)}, \tag{40}$$

where $r_> = \max(r, r_0)$ and $r_< = \min(r, r_0)$.[51] With Eq. (40) we can evaluate the loading of the incident pressure field on the surface of the scatterer.

The structural acoustics problem involving the target is solved using the finite element formulation described in the previous subsection, which is an extension of prior work.[30,31] The computational domain for the structural acoustics problem is a cylindrical "plug" that extends from the water surface, $z=z_S$, to the bottom of the computational domain used for the waveguide problem, $z=z_B$, as depicted in Fig. 4. The radius of the plug $r=S$ is large enough to contain the target and a thin radial PML layer. The solution to the structural acoustics problem yields the pressure due to the scattered wave field on the (level) surface of the cylinder Γ_R, i.e., $p_s(R,\theta,z)$.

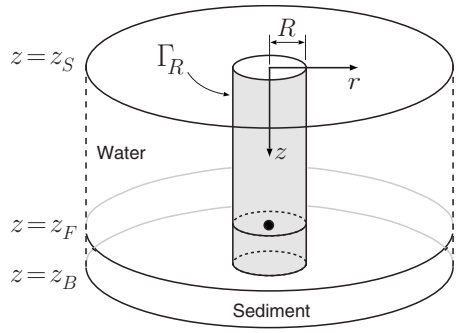

FIG. 4. Schematic illustrating the coupling of the waveguide propagation and structural acoustics models.

In order to propagate the scattered waves back to a receiver some distance away (i.e., radius $r > R$) we propose a normal mode expansion, as given in Eq. (11), for the field outside Γ_R. On the surface Γ_R we have the matching condition

$$\sum_{m,n} a_{mn} H_m^{(1)}(\lambda_n R) e^{im\theta} \psi_n(z) = p_s(R,\theta,z), \tag{41}$$

where $p_s(R,\theta,z)$ is the solution to the structural acoustics problem on Γ_R. The coefficients are, therefore,

$$a_{mn} = \frac{1}{C} \int_0^{2\pi} e^{-im\theta} \int_{z_S}^{z_B} \psi_n(z) p_s(R,\theta,z) \frac{d\theta dz}{\rho(z)}, \tag{42}$$

where $C = \sqrt{2\pi} H_m^{(1)}(\lambda_n R)$. Using the resulting expansion we can evaluate the scattered pressure field anywhere in the channel away from the target. Note that the scattered acoustic pressure field is generally three-dimensional, even for axisymmetric target geometries, so that higher azimuthal harmonics ($m > 0$) must be included. Typically, ten azimuthal harmonics are required to resolve the scattered field for $f \leq 5$ kHz.

III. RESULTS

To demonstrate the capabilities of the formulation we consider two scenarios: (1) scattering from an evacuated sphere at the seafloor; and, (2) scattering from a more complex elastic target near a locally undulating seafloor. The examples illustrate the resolution of the relevant physics and also provide an opportunity to make some observations concerning the computational costs. The normal mode problem was solved using the ARPACK suite of eigensolvers,[41] and for the structural acoustics problem we modified the SONAX *hp*-finite element implementation for axially symmetric target geometries developed by Shirron.[24]

First, we consider an evacuated spherical shell near the bottom of a water column that is bounded below by a water-saturated sediment layer as illustrated in Fig. 5. Both the water column and the sediment layer are treated acoustically as fluids. The water column is 20 m deep with constant density of 1000 kg/m^3 and sound speed of 1500 m/s. The sediment layer is 10 m thick with constant density of

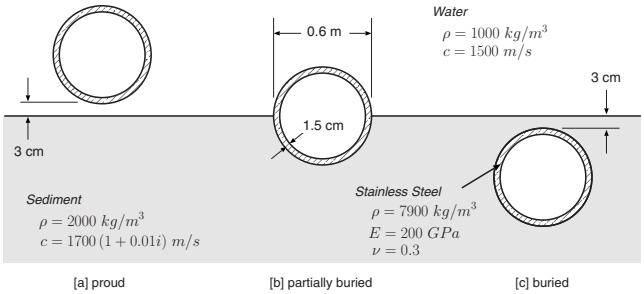

FIG. 5. Positions, properties, and dimensions used in evacuated sphere example problems.

2000 kg/m^3 and complex sound speed of 1700(1 $-0.01i$)m/s. The bottom boundary of the sediment layer is taken to be sound hard, which models the rigid interface of the ocean basement rock layer.

The outer diameter of the evacuated spherical shell is 0.6 m and the wall thickness is 1.5 cm. The elastic shell is made of stainless steel with density of 7900 kg/m^3, Young's modulus E=200 GPa, and a Poisson ratio of ν=0.3. We provide results for proud, partially buried, and fully buried shells, as illustrated in Fig. 5. For the proud and fully buried cases the shell is three centimeters away from the flat fluid-sediment interface at its closest point. In the partially buried case the center of the shell is at the depth of the interface $z=z_F$, so that the shell is half buried. In all cases the inner compartment of the shell is evacuated (p=0).

For the results shown in Figs. 6–8 the omnidirectional source is located at a depth of z_0=10 m in the water column. The source is at a range of r_0=10 m from the spherical target and is to the right of the targets in the figures (θ_0=0). A thin horizontal line marks the water-sediment interface. The figures show the amplitude of the scattered pressure field at 1 kHz out to a range of 15 m on either side of the shell (θ =0,180°). Results for the three cases differ perceptibly due to the position of the shell relative to the interface. Run times for these cases were about 15 s per harmonic per frequency on a 1.4 GHz PC system where cubic finite elements, with an average element size of about 0.1 m, were used. Results in Figs. 6–8 were verified against full finite element solutions and were in near-perfect agreement.

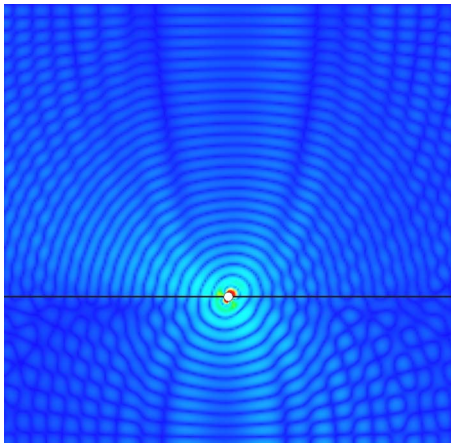

FIG. 7. (Color online) Amplitude of the scattered pressure field at 1 kHz for a half-buried spherical shell.

In Fig. 9 we compare the target strength for the previously described spherical shell in the free field (exterior fluid with properties of water), half buried in semi-infinite fluid/fluid medium (water/sediment), and half buried in 30 m channel (20 m water overlying 10 m sediment). In each case the source is 9 m above the shell center and at a range of 9 m. The scattered pressure is evaluated 10 m above the shell and at a range of 10 m from the shell. There are corresponding resonances in the free-field and water/sediment results, shifted due the different sound speed in the sediment layer. These resonances are also present in the waveguide results but are obscured by the multipath channel distortion and the reflections off the basement layer. These channel effects are mitigated when the sediment layer is more dissipative or when the bottom boundary ($z=z_B$) is moved further below the water/sediment interface.

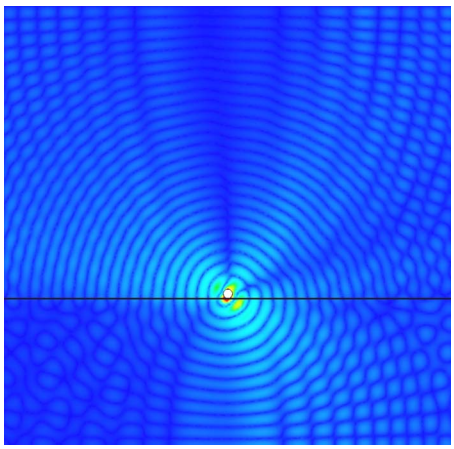

FIG. 6. (Color online) Amplitude of the scattered pressure field at 1 kHz for a proud spherical shell.

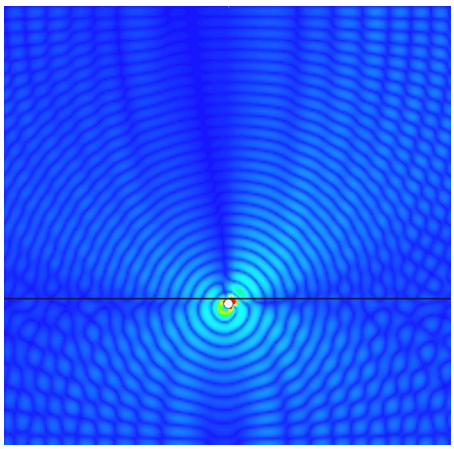

FIG. 8. (Color online) Amplitude of the scattered pressure field at 1 kHz for a buried spherical shell.

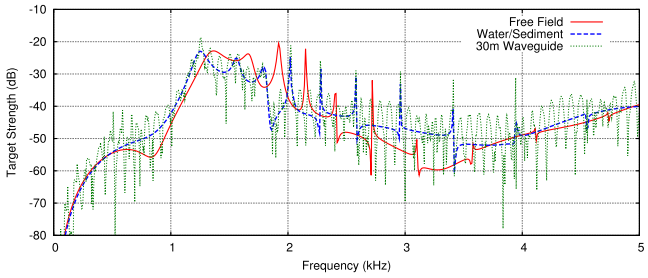

FIG. 9. (Color online) Comparison of the spectra from half-buried, evacuated spherical shell.

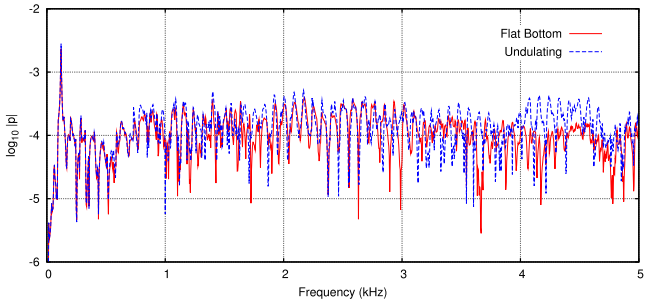

FIG. 11. (Color online) Received spectra for a half-buried target with flat and undulating seabed interfaces.

We next consider the case illustrated in Fig. 10, where the axisymmetric target is more complicated and the seabed is locally undulating. This situation is intended to model a more realistic bottom object with scouring. The outer elastic target frame is made of stainless steel and is 1.0 cm thick. The upper and lower compartments are separated by 2.0 cm of stainless steel welded to the outer shell. The outer geometry is roughly that of a truncated cone 50 cm high with a lower radius of 65 cm and upper radius of 32.5 cm. The target has two compartments, where the upper compartment is evacuated and the lower compartment is filled with concrete (with properties listed in Fig. 10). For the structural acoustics problem, the "plug" is 30 m deep and 3 m in radius (including 1 m of radial PML) and is discretized using 166 cubic elastic elements for the target and 26,628 quadratic fluid elements for a total of 82,000 DOFs (axisymmetric). Run time was approximately 17 s per harmonic per frequency.

The water column is again 20 m deep, overlying a 10-m-thick sediment layer with a sound hard lower boundary. The water and sediment properties are the same as those used in the previous example. A single omnidirectional point source is positioned $r_0 = 10$ m away from the target and $z_0 = 10$ m below the water surface. The scattered pressure is computed at the location of the source. Figure 11 compares the spectra of the received signal for flat and undulating bottoms. The spectra are in good agreement at low frequencies but their differences are readily apparent at the higher frequencies. This indicates that the local shape of the water/sediment interface near the target may have a significant influence on the received signal even in the low- to mid-frequency range.

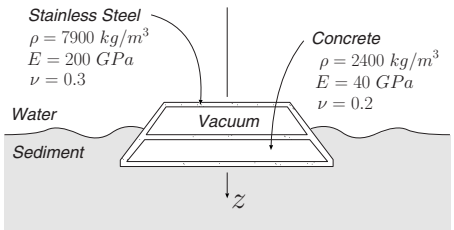

FIG. 10. Schematic of a structurally complex bottom target, partially buried with scouring.

IV. CONCLUSIONS

We are concerned with the acoustic response of an object that is located at a locally wavy sea surface or seabed within a shallow-water waveguide. The numerical formulation detailed here treats realistic, structurally complex objects, with irregular external geometry, internal structures and compartments, and varying material composition. The coupling of a 3D normal-mode waveguide propagation model and a 3D *hp*-finite element formulation for structural acoustics provides an efficient, flexible and accurate methodology for the simulation of low- to mid-frequency acoustic scattering from surface, volume, and bottom objects in shallow-water environments. The coupling is accomplished so that targets can be at any depth in the waveguide, even penetrating the upper or lower boundary, without violating model assumptions.

The present formulation considers a finite-depth waveguide and resolves all acoustic interactions, including multiple scattering between the target, the sea surface, the seabed, and the basement boundaries. This all-inclusive approach carries with it some limitations. Formally, the restriction to finite depth precludes consideration of waveguides with bottoms that are modeled as fluid half spaces, such as a Pekeris waveguide; however, the physics for such situations can be very closely approximated by including a thin PML layer at the lower computational boundary. This fictitious bottom layer effectively absorbs outgoing acoustic waves, approximating the effect of a fluid half space.

Inclusion of multiple scattering from the upper and lower waveguide boundaries is a technical advantage of the present approach that introduces a numerical disadvantage. To resolve these interactions we consider a structural acoustics problem on a domain that runs the full vertical extent of the waveguide. As the waveguide depth increases so too does the compuational cost of the structural acoustics problem. Still, the present approach provides a practical method for shallow-water waveguides and can be used to validate other numerical approaches, which may involve simplifying assumptions related to the upper and lower boundary interactions.

The approach presented here provides a new capability and is applicable to the study of several problems of current interest. With high-fidelity simulations one can ascertain when lower-frequency signals become too distorted upon in-

teraction with prospective targets to permit detailed sonar imagery. Another area of potential investigation is related to object classification based on the spectral characteristics of the scattered wave field. Classification can be based on single returns,[52–54] or sequences of returns that take advantage of the aspect dependence.[55–60] The present simulation model can inform feature selection and help characterize performance for these structural acoustics-based classification systems.[61]

[1]Y. A. Kravtsov, V. M. Kuz'kin, and V. G. Petnikov, "Wave diffraction by regular scatterers in multimode waveguides," Sov. Phys. Acoust. **30**, 199–202 (1984).
[2]F. Ingenito, "Scattering from an object in a stratified medium," J. Acoust. Soc. Am. **82**, 2051–2059 (1987).
[3]G. V. Norton and M. F. Werby, "A numerical technique to describe acoustical scattering and propagation from an object in a waveguide," J. Appl. Phys. **70**, 4101–4112 (1991).
[4]A. Sarkissian, "Multiple scattering effects when scattering from a target in a bounded medium," J. Acoust. Soc. Am. **95**, 3137–3144 (1994).
[5]A. Sarkissian, "Extraction of a target scattering response from measurements made over long ranges in shallow water," J. Acoust. Soc. Am. **102**, 825–832 (1997).
[6]N. C. Makris, F. Ingenito, and W. A. Kuperman, "Detection of a submerged object insonified by surface noise in an ocean waveguide," J. Acoust. Soc. Am. **96**, 1703–1724 (1994).
[7]N. C. Makris, "A spectral approach to 3-D object scattering in layered media applied to scattering from submerged spheres," J. Acoust. Soc. Am. **104**, 2105–2113 (1998).
[8]H. Schmidt and J. Lee, "Physics of 3-D scattering from rippled seabeds and buried targets in shallow water," J. Acoust. Soc. Am. **105**, 1605–1617 (1999).
[9]H. Schmidt, "Virtual source approach to scattering from partially buried elastic targets," in *High Frequency Ocean Acoustics Conf. Proc.*, edited by M. B. Porter, M. Siderius, and W. A. Kuperman, **728**, 456–463 (American Institute of Physics, New York, 2004).
[10]A. Boström, "Transmission and reflection of acoustic waves by an obstacle in a waveguide," Wave Motion **2**, 167–184 (1980).
[11]R. H. Hackman and G. S. Sammelmann, "Acoustic scattering in an inhomogeneous waveguide: Theory," J. Acoust. Soc. Am. **80**, 1447–1458 (1986).
[12]R. H. Hackman and G. S. Sammelmann, "Multiple-scattering analysis for a target in an oceanic waveguide," J. Acoust. Soc. Am. **84**, 1813–1825 (1988).
[13]P. Gerstoft and H. Schmidt, "A boundary element approach to siesmo-acoustic facet reverberation," J. Acoust. Soc. Am. **89**, 1629–1642 (1991).
[14]J. A. Fawcett, "Modeling of scattering by partially buried elastic cylinders," J. Acoust. Soc. Am. **105**, 2628–2633 (1999).
[15]J. A. Fawcett, "A plane-wave decomposition method for modeling scattering from objects and bathymetry in a waveguide," J. Acoust. Soc. Am. **100**, 183–192 (1996).
[16]M. D. Collins and M. F. Werby, "A parabolic equation model for scattering in the ocean," J. Acoust. Soc. Am. **85**, 1895–1902 (1989).
[17]B. Engquist and A. Majda, "Absorbing boundary conditions for the numerical simulation of waves," Math. Comput. **31**, 629–651 (1977).
[18]B. Engquist and A. Majda, "Radiation boundary conditions for acoustic and elastic wave calculations," Commun. Pure Appl. Math. **32**, 313–357 (1979).
[19]A. Bayliss and E. Turkel, "Radiation boundary conditions for wave-like equations," Commun. Pure Appl. Math. **33**, 707–725 (1980).
[20]A. Bayliss and E. Turkel, "Far-field boundary conditions for compressible flows," J. Comput. Phys. **48**, 182–199 (1982).
[21]A. Bayliss, M. Gunzburger, and E. Turkel, "Boundary conditions for the numerical solution of elliptic equations in exterior regions," SIAM J. Appl. Math. **42**, 430–451 (1982).
[22]D. S. Burnett, "A three-dimensional acoustic infinite element based on a prolate spheroidal multipole expansion," J. Acoust. Soc. Am. **96**, 2798–2816 (1994).
[23]J. J. Shirron and S. Dey, "Acoustic infinite elements for non-separable geometries," Comput. Methods Appl. Mech. Eng. **191**, 4123–3149 (2002).
[24]J. J. Shirron, "Solution of exterior Helmholtz problems using finite and infinite elements," Ph.D. thesis, University of Maryland, College Park, MD (1995).
[25]J. B. Keller and D. Givoli, "Exact non-reflecting boundary condition," J. Comput. Phys. **82**, 172–192 (1989).
[26]P. C. Waterman, "New formulation of acoustic scattering," J. Acoust. Soc. Am. **45**, 1417–1429 (1969).
[27]P. C. Waterman, "Matrix formulation of electromagnetic scattering," Proc. IEEE **53**, 805–812 (1965).
[28]R. Lim, "Acoustical scattering by a partially buried three-dimensional elastic obstacle," J. Acoust. Soc. Am. **104**, 769–782 (1998).
[29]R. Lim, K. L. Williams, and E. I. Thorsos, "Acoustic scattering by a three-dimensional elastic object near a rough surface," J. Acoust. Soc. Am. **107**, 1246–1462 (2000).
[30]J. J. Shirron and T. E. Giddings, "A finite element model for acoustic scattering from objects near a fluid-fluid Interface," Comput. Methods Appl. Mech. Eng. **196**, 279–288 (2006).
[31]J. J. Shirron and T. E. Giddings, "A finite element model for acoustic scattering from objects near the ocean bottom," in *MTS/IEEE Oceans 2005 Conference Proceedings*, **2**, 1644–1651 (2005).
[32]J.-P. Bérenger, "A perfectly matched layer for the absorption of electromagnetic waves," J. Comput. Phys. **114**, 185–200 (1994).
[33]J.-P. Bérenger, "Three-dimensional perfectly matched layer for the absorption of electromagnetic waves," J. Comput. Phys. **127**, 363–379 (1996).
[34]J.-P. Bérenger, "Perfectly matched layer for the FDTD solution of wave-structure interaction problems," IEEE Trans. Antennas Propag. **44**, 100–117 (1996).
[35]I. Harari, M. Slavutin, and E. Turkel, "Analytical and numerical studies of a finite element PML for the Helmholtz equation," J. Comput. Acoust. **8**, 121–137 (2000).
[36]M. Zampolli, A. Tesei, F. B. Jensen, N. Malm, and J. B. Blottman III, "A computationally efficient finite element model with perfectly matched layers applied to scattering from axially symmetric objects," J. Acoust. Soc. Am. **122**, 1472–1485 (2007).
[37]T. E. Giddings and J. J. Shirron, "High-fidelity model for sonar interrogation of bottom and surface targets in shallow water," in *MTS/IEEE Oceans 2006 Conference Proceedings* (Boston, MA) (2006).
[38]F. B. Jensen, W. A. Kuperman, M. B. Porter, and H. Schmidt, *Computational Ocean Acoustics* (Springer-Verlag, New York, 2000).
[39]G. V. Frisk, *Ocean and Seabed Acoustics* (P T R Prentice–Hall, Englewood Cliffs, NJ, 1994).
[40]D. C. Sorensen, "Implicit application of polynomial filters in a k-step Arnoldi method," SIAM J. Matrix Anal. Appl. **13**, 357–385 (1992).
[41]R. B. Lehoucq, D. C. Sorensen, and C. Yang, *ARPACK Users' Guide* (SIAM, Philadelphia, PA, 1998).
[42]F. Collino and P. Monk, "The perfectly matched layer in curvilinear coordinates," SIAM J. Sci. Comput. (USA) **19**, 2061–2090 (1998).
[43]W. C. Chew and W. H. Weedon, "A 3-D perfectly matched medium from modified Maxwell's equations with stretched coordinates," Microwave Opt. Technol. Lett. **15**, 363–369 (1997).
[44]W. C. Chew, J. Jin, and E. Michielssen, "Complex coordinate stretching as a generalized absorbing boundary condition," Microwave Opt. Technol. Lett. **7**, 599–604 (1994).
[45]J. De Moerloose and M. A. Stuchly, "Behavior of Berenger's ABC for evanescent waves," IEEE Microw. Guid. Wave Lett. **5**, 344–346 (1995).
[46]T. K. Katsibas and C. S. Antonopoulos, "A general form of perfectly matched layers for three-dimensional problems of acoustic scattering in lossless and lossy fluid media," IEEE Trans. Ultrason. Ferroelectr. Freq. Control **51**, 964–972 (2004).
[47]P. G. Petropoulos, "On the termination of the perfectly matched layer with local absorbing boundary conditions," J. Comput. Phys. **143**, 665–673 (1998).
[48]F. Collino and P. Monk, "Optimizing the perfectly matched layer," Comput. Methods Appl. Mech. Eng. **164**, 157–171 (1998).
[49]F. Ihlenburg, *Finite Element Analysis of Acoustic Scattering* (Springer-Verlag, New York, 1998).
[50]R. Ohayon and C. Soize, *Structural Acoustics and Vibration* (Academic, New York, 1998).
[51]P. M. Morse and K. Uno Ingard, *Theoretical Acoustics* (McGraw-Hill, New York 1968), (reprinted by Princeton University Press, 1986).
[52]R. P. Gorman and T. J. Sejnowski, "Learned classification of sonar targets using a massively parallel network," IEEE Trans. Acoust., Speech, Signal Process. **36**, 1135–1140 (1988).
[53]R. P. Gorman and T. J. Sejnowski, "Analysis of hidden units in a layered network trained to classify sonar targets," Neural Networks **1**, 75–89 (1988).

[54]H. L. Roitblat, W. W. L. Au, P. E. Nachtigall, R. Shizumura, and G. Moons, "Sonar recognition of targets embedded in sediment," Neural Networks **8**, 1263–1273 (1995).
[55]P. R. Runkle, P. K. Bharadwaj, L. Couchman, and L. Carin, "Hidden Markov models for multiaspect target classification," IEEE Trans. Signal Process. **47**, 2035–2040 (1999).
[56]P. Runkle, L. Carin, L. Couchman, J. A. Bucaro, and T. Yoder, "Multi-aspect identification of submerged elastic targets via wave-based matching pursuits and hidden Markov models," J. Acoust. Soc. Am. **106**, 605-616 (1999).
[57]P. K. Bharadwaj, P. R. Runkle, and L. Carin, "Target identification with wave-based matching pursuits and hidden Markov models," IEEE Trans. Antennas Propag. **47**, 1543–1554 (1999).
[58]J. Salazar, M. Robinson, and M. R. Azimi-Sadjadi, "Multi-aspect discrimination of underwater mine-like objects using hidden Markov models," *MTS/IEEE Oceans 2002 Conf. Proc.* **1**, 46–53 (2002).
[59]H. Liu, P. Runkle, L. Carin, T. Yoder, T. Giddings, L. Couchman, and J. Bucaro, "Classification of distant targets situated near channel bottoms," J. Acoust. Soc. Am. **115**, 1185–1197 (2004).
[60]M. Robinson, M. R. Azimi-Sadjadi, and J. Salazar, "Multi-Aspect Target Discrimination Using Hidden Markov Models and Neural Networks," IEEE Trans. Neural Netw. **16**, 447–459 (2005).
[61]B. H. Houston, J. A. Bucaro, T. Yoder, L. Kraus, J. Tressler, J. Fernandez, T. Montgomery, and T. Howarth, "Broadband low frequency sonar for non-imaging based identification," in *MTS/IEEE Oceans 2002 Conf. Proc.* **1**, 383–387 (Biloxi, MS) (2002).

Lüke and power residue sequence diffusers[a)]

Konstantinos Dadiotis,[b)] Jamie A. S. Angus, and Trevor J. Cox
Acoustics Research Centre, University of Salford, Salford M5 4WT, United Kingdom

(Received 21 September 2007; revised 22 January 2008; accepted 4 February 2008)

Conventional Schroeder diffusers have been successfully used for many years. However, their frequency range is limited by the flat plate effect that occurs when all the wells radiate in phase. This occurs at harmonics of p times the design frequency f_0, where p is the small prime that is used to generate the structure. A typical diffuser, using $p=7$ and $f_0=500$ Hz, has an upper frequency limit of only 3.5 kHz. Achieving a first flat plate frequency above 20 kHz requires a prime equal to at least 41 and results in diffusers that are too big to be practical in most applications. This paper suggests an alternative approach using number theoretic sequences that, although short in length, are based on large integers. Two new sequences, Type-II Lüke and power residue, have this desired characteristic. They are investigated using both simple models and the more exact boundary element method. The results show the flat plate effect is moved to much higher frequencies as expected. For Lüke sequences at certain frequencies, redirection rather than dispersion is achieved. Modulation techniques can be used to mitigate these problems. Power residue sequences perform the best, providing good diffusion and a flat plate frequency outside the audible range.
© *2008 Acoustical Society of America.* [DOI: 10.1121/1.2885761]

PACS number(s): 43.55.Br [NX] Pages: 2035–2042

I. INTRODUCTION

In the 1970s, Schroeder introduced the concept of using maximum length sequences in diffuser design to improve sound diffusion in concert halls and reverberation chambers.[1] Since then, a variety of diffusers has been developed.[2] A well known and widely applied class of diffusers is one that consists of wells with the depths being determined by an integer-based pseudorandom sequence. The most common examples are quadratic residue diffusers (QRDs) or primitive root diffusers (PRDs).[2,3] A cross-section through such a device is shown in Fig. 1(a).

When sound is incident on this surface, the wave has to travel different distances before it is reflected back out of each well. Thus the reflected waves display different phases as they exit the wells. By choosing well depths which result in appropriate radiated phases, scattering via interference between these reflected waves is achieved.

The depth of the nth well d_n in the diffuser is set using a pseudorandom sequence:[2]

$$d_n = \frac{s_n \lambda_0}{2P}, \tag{1}$$

where s_n is the nth term of the pseudorandom sequence, λ_0 is the design wavelength, and P is the integer the sequence has generated using, e.g., the prime p for QRDs.

Unfortunately, at certain specific frequencies, the wells of these diffusers radiate in phase and the whole structure will reflect sound as though it is a flat surface. This flat plate effect arises because there is a simple integer relationship between the different well depths. To illustrate this, consider a $N=7$ QRD which is based on the sequence [0,1,4,2,2,4,1]. Because of this construction, there will be a frequency for which the wells corresponding to 1 in the sequence will equal half a wavelength. At this frequency, all the reflected waves radiated from the diffuser wells will be in phase, due to their integer relationship. The lowest frequency that this flat plate effect is noticed is usually Pf_0, where f_0 is the design frequency.[2] The flat plate effect is also seen at harmonics of this lowest frequency. Unfortunately, for both the QRD and PRD, the prime number is directly linked with the period of the sequence and therefore the number of wells in the diffuser N. For the QRD $P=N$ while for the PRD $P=N+1$. One solution is to move the first flat plate frequency to a high enough frequency so that it is not of concern. For QRDs and PRDs, however, in order to move the flat plate effect to higher frequencies, one is forced to use much longer sequences, which results in wider diffusers. The experience of the last 30 years shows that short period diffusers are used much more often than wide diffusers, not least because such surfaces are cheaper to make and install.

Angus suggested the use of non-integer based sequences to remove this problem,[4] but the physical realization of the diffusers suggested is problematic. Angus also suggested ways of mitigating the problem using orthogonal modulation schemes.[5] Another solution to this problem is to use numerical optimization where a computer searches for the best well depths.[6] Because the computer no longer uses depths that are integer based, then the flat plate effect is not a problem. However, the optimization process is a rather brute-force design method, and consequently, a more elegant solution based on number theory was sought.

It is suggested that by utilizing integer-based sequences that have small periods, but are generated using larger inte-

[a)]Portions of this work were presented in "Lüke and Power Residue Sequence Diffusers," Proceedings of International Conference of Acoustics, Madrid, Spain, September 2007.

[b)]Author to whom correspondence should be addressed. Electronic mail: k.dadiotis@pgr.salford.ac.uk.

gers, the flat plate effect can be avoided. Two possible sequences are investigated: Type-II Lüke and power residue. The paper begins by outlining the Fourier prediction model used as it enables the underlying principles to be more easily understood. Then the general principles behind the sequences are given and their performance considered using this model. Finally, a boundary element model (BEM) is used to gain more accurate predictions.

II. THEORY

Consider a structure with a distribution of reflection coefficients R_n across its surface. The structure is considered to be extruded in one direction, so that significant diffraction only occurs in one plane. This simplifies the prediction and interpretation of the results. For normal incidence sound, the far field reflected pressure, p, can be found using[2]

$$p(\theta) = \sum_{n=0}^{N-1} R_n e^{-inkd_n \sin(\theta)}, \tag{2}$$

where θ is the angle of reflection, n is the well number, R_n is the reflection coefficient of the nth well, k the wavenumber and N the number of wells. Note that this is a discrete Fourier transform using $kd\ sin(\theta)$, and for this reason the prediction model is often referred to as a Fourier model.

III. SEQUENCES

The goal of a diffuser design is usually a uniform scattered pressure distribution, and therefore a structure that has reflection coefficients whose Fourier transform has a uniform magnitude should diffuse well. The Wiener–Khinchin theorem states that the square of the magnitude of the sequence's Fourier transform is equal to the Fourier transform of its autocovariance (or autocorrelation) function. As a result a sequence of reflection coefficients, whose autocorrelation function is a Kronecker delta function, will display good diffusion properties. Consequently, pseudo-random number sequences should be a good choice, because they display this ideal property, and many have been devised for use in other areas of engineering and science.

The reflection coefficients of the wells are given by

$$R_n(f) = \exp\left[i2\pi \frac{s_n}{P} \frac{f}{f_0} \right], \tag{3}$$

where f is the frequency and f_0 is the design frequency of the diffuser.

For some frequencies, all the phases of the reflection coefficients will become multiples of 2π, and so all the reflection coefficients will be 1. This occurs when the fraction $f/(Pf_0)$ is an integer. These flat plate frequencies, as shown in Fig. 1(b), are given by

$$f_m = mPf_0, \quad \text{where } m = 1,2,3\ldots \tag{4}$$

While in theory every structure displays an infinite number of flat plate frequencies, in reality it is rare for there to be more than one of these frequencies in the bandwidth of concern. Therefore, it is common to refer to the first of them as "the" flat plate frequency.

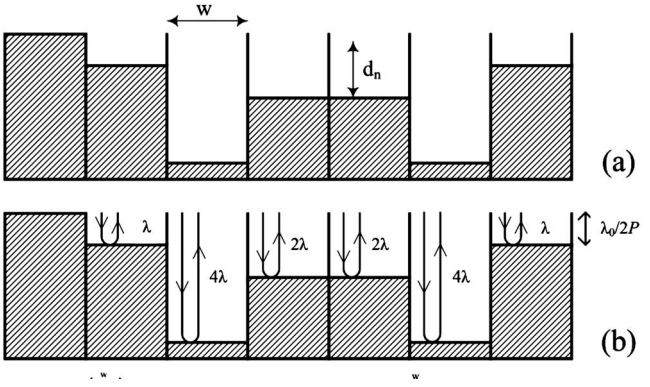

FIG. 1. (a) One period of a quadratic residue diffuser (QRD) of well width w and depth of the nth well, d_n. (b) The flat plate effect occurs when a multiple of $\lambda/2$ exactly fits in all the wells.

Of interest in this paper are power residue and Type-II Lüke sequences, which are both manipulations of primitive root sequences.

A. Type-II Lüke sequences

Type-II Lüke sequences are generated in families which have $p-1$ members, each of which could be used to make a diffuser. For any given prime p the nth terms of the sequences are given by[7,8]

$$s_n^{(r)} = (\alpha^n(p-1) + rnp) \bmod p(p-1), \tag{5}$$

where α is the primitive root of the prime p, r denotes the family member and mod indicates the least non-negative remainder. The sequences are generated via the integer $P = p(p-1)$ and have a period length of $N = p-1$. A necessary condition is $0 \leqslant n, r \leqslant p-2$.

The reflection coefficients of Type-II Lüke sequences have the following, two valued, autocorrelation magnitudes:

$$|G_{r,r}(\tau)| = \begin{cases} p-1, & \tau = 0 \\ 1, & -\dfrac{p-1}{2} \leqslant \tau \leqslant \dfrac{p-1}{2} \quad \tau \neq 0, \end{cases} \tag{6}$$

where G is the autocorrelation and τ is the autocorrelation delay variable. This autocorrelation function is the same as that of a PRD of the same period. Note that it is the autocorrelation magnitude that is constant for $|\tau| > 0$, which is unusual for sequences used in diffuser design. Table I shows the properties for an example sequence based $p = 7$.

TABLE I. Characteristics of the autocorrelation function for some cases of Type-II Lüke and power residue sequences.

Sequence	p	M	N	$\lvert G\rvert$ $(\tau=0)$	$\lvert G\rvert$ $(\tau\neq 0)$
Quadratic residue	7	n/a	7	7	0
Primitive root	7	n/a	6	6	1
Type-II luke	7	n/a	6	6	1
Power residue	19	2	9	9	2.236
Power residue	37	4	9	9	2.646
Power residue	73	8	9	9	2.828

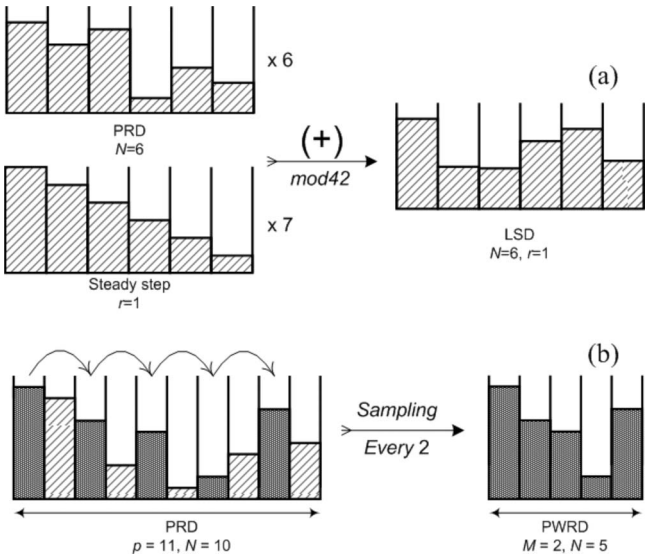

FIG. 2. Schematic showing the generation of (a) Lüke $(p=7,r=1)$ and (b) power residue $(p=11,M=2,r=0)$ sequences.

Essentially the Type-II Lüke sequences are formed by superposing the primitive root sequence q of prime p:

$$q_n = a^n \bmod p \tag{7}$$

and a steady step sequence t of the same period:

$$t_n = rn \bmod p - 1 \tag{8}$$

with r giving the step size, as shown in Fig. 2.

This is possible because a linear ramp can be added to any number sequence, provided the period is correct, without changing the autocorrelation properties.[8]

For the above reason, every primitive root sequence can be considered to be the first sequence $(r=0)$ of each Type-II Lüke sequence family. From any primitive root sequence a set of $p-2$ new Type-II Lüke sequences can be generated, each one with a different step size.

To give an example for $p=7$, $\alpha=3$ and $r=0$ the primitive root sequence is $q=[1,3,2,6,4,5]$. The phases of the reflection coefficients of this sequence, at the design frequency f_0, are $2\pi/7$ $2\pi 3/7$, $2\pi 2/7$, etc. The flat plate effect will occur when all phases are multiples of 2π; this can be accomplished by multiplying all the arguments by a factor of 7, which happens when the incident wave is of frequency $f=7f_0$ as previously discussed.

On the other hand for $p=7$, $\alpha=3$ and $r=1$ the Type-II Lüke sequence is given by $s=[6,25,26,15,10,23]$. The phases of the reflection coefficients in this case, at the design frequency f_0, are $2\pi 6/42$, $2\pi 25/42$, etc. For all the phases in this case to become multiples of 2π they need to be multiplied by a factor 42 which happens when the incident wave is of frequency $f=42f_0$. Therefore, by using Type-II Lüke sequences it is possible to increase the frequency at which all the wells radiate in phase by a factor of 6.

B. Power residue sequence

For a prime number p that can be expressed in the form:

$$p = MN + 1, \tag{9}$$

where M and N are integers, M power residue sequences of period N can be generated using the equation[8]

$$s_n^{(r)} = (\alpha^r \beta^n) \bmod p, \tag{10}$$

where $0 \leqslant r < M$, $0 \leqslant n < N$, α is a primitive root of p and β is α raised to the power of M $(\beta=\alpha^M)$.

In the case that a set of N integers $D=[d_1,d_2,\ldots d_N]$ are modulo an integer p they are said to form an integer difference set if every integer $h \neq 0$ can be expressed in exactly λ ways in the form:

$$d_i - d_j \equiv h \bmod p \tag{11}$$

The properties of the difference set are usually represented using the nomenclature (p,N,λ).

If, and only if, the power residue sequence forms a cyclic difference set (p,N,λ), then the reflection coefficients that it generates displays two level autocorrelation magnitudes:[8]

$$|G_{r,r}(\tau)| = \begin{cases} N, & \tau = 0 \\ \sqrt{N - \dfrac{N}{M} + \dfrac{1}{M}}, & \dfrac{N-1}{2} \leqslant \tau \leqslant \dfrac{N-1}{2} \end{cases}, \quad (\tau \neq 0), \tag{12}$$

where Table I gives a few examples, and demonstrates that power residue sequences display worse autocorrelation properties than QRD, PRD and Type-II Lüke sequences, as the out-of-phase magnitude is always greater than 1 and becomes greater as M increases.

Essentially, power residue sequences are under-sampled primitive root sequences, with a sample taken every Mth coefficient, with a different starting point, as shown in Fig. 2(b).

The starting point is set by r. For instance, for $p=11$, the primitive root is 2, and the primitive root sequence is $q=[1,2,4,8,5,10,9,7,3,6]$. For $M=2$, and $r=0$ every other coefficient is taken to form the power residue sequence starting from the first $s^{(0)}=[1,4,5,9,3]$ while for $r=1$ the starting point is the second $s^{(1)}=[2,8,10,7,6]$. Note that the one sequence is the inverse of the other. If the coefficients of $s^{(1)}$ are cyclically shifted back 2 positions, it becomes [10,7,6,2,8]. So in this case, the two power residue sequences are connected via the equation

$$s^{(0)} = p - s^{(1)}. \tag{13}$$

This connection between the two sequences results in pairs of diffusers in a family that performs similarly, because pairs have reflection coefficients with opposite phases.

To postpone the flat plate effect to a higher frequency, sequences with larger p are needed. There are three cases that form cyclic difference sets and need to be considered:[8]

$M = 2$ and N odd

$M = 4$ and $N = j^2$ where j is odd

$M = 8$ and $p = 8j^2 + 1 = 62m^2 + 9$

where j and m are odd (14)

Since the goal is to push the flat plate effect to higher frequencies, the most promising case is the last as it combines higher primes p with the shortest sequences possible. The first case that falls under this category is

$M = 8, \quad n = 3, \quad m = 1 \Rightarrow p = 73.$

This generates a short sequence typical of the length used in practical Schroeder diffusers (period $N=9$) but with a prime number generator of 73. One such a sequence is $s^{(1)}=[5,10,20,40,7,14,28,56,39]$, which is the second of the family ($r=1$). The higher prime number gives a first flat plate frequency of 73 times the design frequency.

IV. SCHROEDER DIFFUSERS

In order to evaluate the performances of the two new sequences, diffusers were simulated and predictions of their scattered pressure distribution were made. From these their diffusion coefficient[2] was calculated and comparisons with other integer based diffusers such as the standard QRD and PRD were made.

As the main reason for choosing these new sequences was the fact that they are both based on large prime number generators and display two level autocorrelation properties, according to a Fourier model, this model will initially be used to estimate their relative performance.

A. Type-II Lüke diffusers

Type-II Lüke sequences are formed by the addition of a step sequence to a primitive root sequence. Consequently, diffusers that are generated with steady step sequences of opposing inclinations can be paired as they perform similarly. This leaves one sequence that cannot be paired, the middle one which is generated for $r=M/2$.

The case of Type-II Lüke sequence diffusers (LSD) generated by the integer $P=42$ is considered. These are diffusers of period $N=6$ and well width approximately 4.2 cm. Their design frequency is $f_0=500$ Hz. Eight periods of the diffuser are used. This gives a structure with an overall width of 2 m.

The diffusion coefficient will be used initially to estimate the overall performance of the diffusers. This coefficient has values from 0 to 1, where 0 represents perfect specular reflection (no diffusion) and 1 represents uniform scattered distribution into all angles of reflection[9] (complete diffusion).

Figure 3 displays the diffusion coefficients of some diffusers of this family of LSDs along with the equivalent PRD of the same characteristics. Since the design frequency used is 500 Hz the PRD is expected to display a flat plate effect at 7500 Hz=3.5 kHz while the LSDs are expected to display their first flat plate effect at 42×500 Hz=21 kHz.

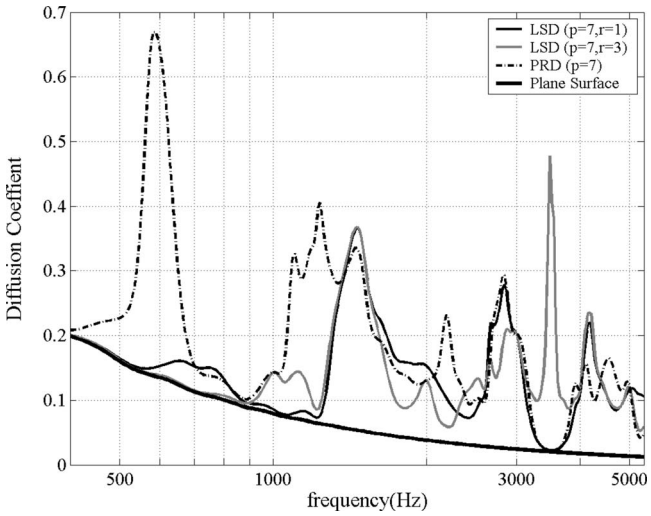

FIG. 3. Autocorrelation diffusion coefficient, as predicted using the Fourier model, of different types of periodic Lüke and primitive root diffusers of the same total width.

Unfortunately the LSD with $r=1$ displays a dip in the diffusion coefficient similar to the PRD's flat plate effect at 3.5 kHz. This is because the $r=1$ LSD causes redirection rather than diffusion at this frequency. The reflection coefficients at 3.5 kHz have phases of 0, $\pi/3$, $2\pi/3$, π, $4\pi/3$, $5\pi/3$ which have equal phase shift increment of $\pi/3$ from one well to the next. This constant phase increment of the reflection coefficients is why the main reflected lobe is redirected into another direction; it is identical to the phase shifts used to beam steer loudspeaker arrays. This behavior is inherent in Lüke sequence diffusers because they are formed by adding a PRD to a linear stepped ramp. At the frequency in question, all the reflection coefficients of the base PRD are equal to 1 with a phase shift of 0, leaving only the linear stepped ramp. Essentially the PRD disappears and the diffuser acts like a tilted flat plate.

This can be seen in Fig. 4 where the scattered intensity distribution from one period of this LSD with $r=1$ is compared to that from a plane surface of the same size and shows that the diffuser is redirecting instead of scattering the incident wave.

All the LSDs of the family display this behavior with the exception of the middle one (in this case $r=3$) (Fig. 3) which appears to be dispersing the incident wave uniformly. How-

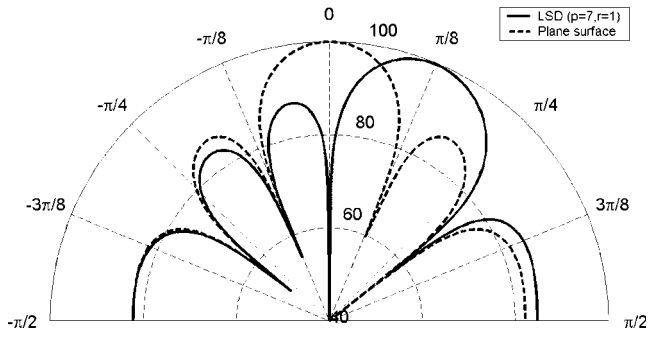

FIG. 4. Scattered intensity distribution (dB) at the tilted flat plate frequency of a Lüke diffuser.

ever, a closer inspection reveals that the reflection coefficients at this frequency are simply +1 and −1 one after the other (representing a steady phase shift of π). Based on the Fourier model, cancellation in the specular reflection direction occurs. However, mutual interactions between adjacent wells will tend to "smooth out" the surface pressure distribution and reduce the cancellation in real surfaces.

All sequences of the same family perform almost identically when considered in a 1/3rd octave band. They vary in their performance at specific frequencies and in the overall variation of their diffusion coefficient with frequency. The diffusers that have $r=2$ and $r=4$ display more variation of diffusion with frequency and have many dips in the diffusion coefficient. For this reason they are considered to perform worse than $r=1$, $r=3$, and $r=5$. However, it remains to be verified whether the $r=3$ LSD will perform as well as predicted by the Fourier model.

Another aspect worth taking into consideration is the maximum depth of the diffusers because of the space it removes from the room. For this family of LSDs $r=1$ displays the smallest maximum depth of 21.3 cm which is considerably smaller than that of the equivalent PRD which is 29.5 cm, for the given design frequency. However, although LSD ($r=1$) appears to be the most promising of its family it does not seem to perform any better than the equivalent PRD.

The dips that are evident in the diffusion coefficients of all three structures around 1.2 and 2.4 kHz are due to the periodicity caused by the repetition of the base diffuser 8 time. Because of this, the structures can be considered as 8 point sources spaced 25 cm apart which will generate additional minima due to the grating lobes generated by that periodicity.

B. Power residue diffusers

Power residue diffusers (PWRDs) of the same family can be separated into pairs that diffuse similarly as well. Each diffuser is paired with its inverse, which is found in the same family $M/2$ sequences away ($|r_1-r_2|=M/2$).

The cases of PWRD of period $N=9$ are taken into consideration. They can be generated by the following cases:

$$M=2, N=9 \Rightarrow p=19$$

$$M=4, N=9 \Rightarrow p=37$$

$$M=5, N=9 \Rightarrow p=73$$

Their well width was set to approximately 4.4 cm so that a structure of 5 periods was 2 m long and their design frequency was also set to 500 Hz. This allows direct comparison of their diffusion performance with the Lüke sequence diffusers. Given their design frequency and their prime number generator their flat plate frequencies are expected to be 8.5, 18.5 and 37.5 kHz, respectively.

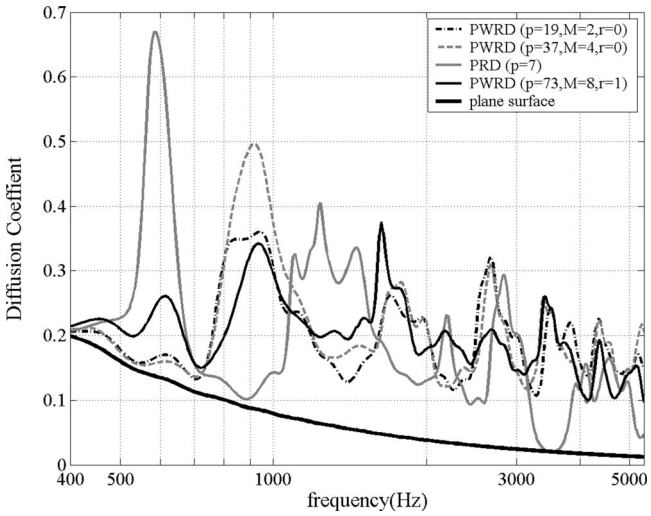

FIG. 5. Autocorrelation diffusion coefficient, as predicted using the Fourier model, of different types of periodic power residue and primitive root diffusers of the same total width.

Figure 5 shows the performance of one case of each PWRD family compared to 8 periods of a PRD ($p=7$). Their flat plate frequency is, as expected, far beyond the frequency range of the PRD, and that of the graph. However, they seem to perform worse than the PRD at some frequencies. However, they display a more uniform performance over the whole frequency range. Again the diffusers all display poor performance at just over 700 Hz due to the repetition of a single diffuser.

These three diffusers were chosen over others of their family because they performed better. Both PWRD ($p=19$) performed identically on their own, as one is the inverse of the other. The other two PWRDs were chosen because they appeared to perform better, or as well as, the rest of the diffusers in their family. Overall, the most promising are the diffusers of larger integer number ($p=37$ and $p=73$) as they display more uniform diffusion over the bandwidth. Furthermore, the fact that there are more than two diffusers in these families allows more design options. The shallowest diffuser is the PWRD based on the prime $p=73$ which displays a maximum depth of 26.4 cm. The other cases have maximum depths around 30 cm.

C. Boundary element method (BEM)

Having predicted the performance of the diffusers using the Fourier method, and established their overall behavior, a more detailed and exact BEM[10] simulation was used for prediction as it has been shown to give accurate results for Schroeder diffusers.[11] The design frequency and dimensions of the diffusers are the same as given previously and the results are displayed in Figs. 6 and 7. The diffusion coefficients display a broadly similar pattern to those of the Fourier model but they seem to have more variation with frequency.

Figure 6 displays the performance of LSDs in comparison with the PRD of the same size. It is evident from this

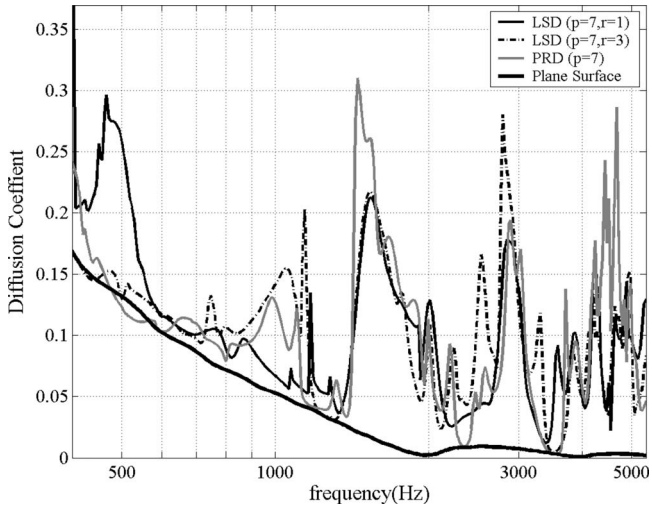

FIG. 6. Autocorrelation diffusion coefficient, as predicted using the boundary element model, of different types of periodic Lüke and primitive root diffusers of the same total width.

graph that the middle diffuser of the family ($r=3$) performs almost identically to the PRD at the flat plate frequency of the latter. This contradicts the earlier prediction of good diffusion from the Fourier model (Fig. 3). On the other hand, the initial prediction of the behavior of the other LSD ($r=1$) is quite accurate. It is also evident that none of the LSDs perform any better than the PRD.

Figure 7 shows the behavior of PWRD of period $N=9$ with the same characteristics that were used for the Fourier model in comparison with the PRD of period $N=6$ in 1/3rd octave bands. Once again, the results display a similar pattern to that of the Fourier model. Unlike the LSDs the PWRDs have no problematic frequencies within this bandwidth in particular $p=73$ has; better diffusion than all the other ones.

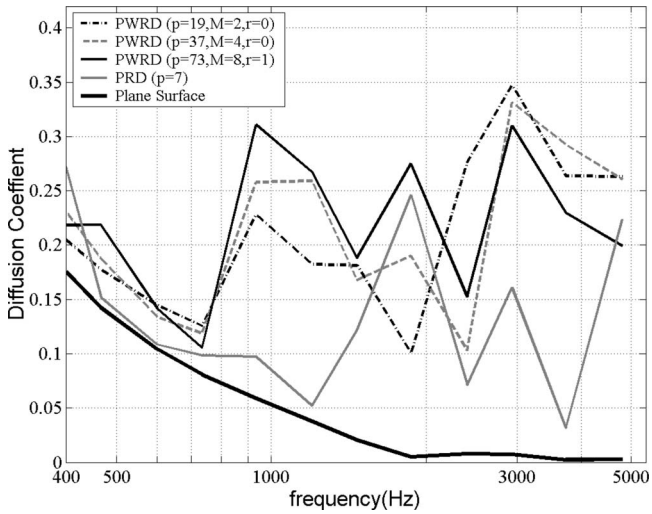

FIG. 7. One-third octave band autocorrelation diffusion coefficient, as predicted using the boundary element model, of different types of periodic power residue and primitive root diffusers of the same total width.

V. MODULATION AND PERIODICITY

To cover large surface areas more than one period of a diffuser structure is commonly used. The repetition of the sequences introduces the problem of periodicity. Periodicity causes harmonics to be created in the autocorrelation function this; creates sharper grating lobes and as a result a less uniform scattering distribution.[5,12]

One method of dealing with the effects of periodicity is to modulate the base sequence with another.[5,12] In order to modulate two sequences a binary pseudorandom sequence is required. The binary sequence defines the order in which the sequences will be placed with 1 corresponding to the first sequence and 0 to the second.

There are three major ways of choosing the second sequence to be used in the modulation. These are as follows:

(1) **Using the inverse of the base sequence**: An inverse sequence is created by subtracting the original sequence from the integer that it was generated from. So, for example, the sequence that will generate the inverse diffuser of the LSD with $P=42$ and $r=1$ [6,25,26,15,10,23] is calculated by subtracting this sequence's coefficients from its integer number generator, 42 in this case, to give [36,17,16,27,32,19] as the inverse.
(2) **Using the base sequence in reverse order**: Another technique for modulation is to use the same sequence but in reverse order. In practice this is easily achieved by rotating the diffuser in its plane such that its left becomes its right.[13] The modulation is essentially a diffuser and its mirror image. For example, for LSD with $P=42$ and $r=1$ [6,25,26,15,10,23] the mirror diffuser is simply [23,10,15,26,25,6]. This method has the added advantage of the overall structure having the same depth as the base diffuser; in addition it only requires one base diffuser. However, it only works if there is a degree of asymmetry in the base diffuser.
(3) **Using a different sequence to that of the base diffuser**: In principle any alternate sequence may be used, but it is usual to use one that is performing better than the base sequence at the frequencies where it is performing badly. For example, for the base sequence above, a suitable sequence would be $P=42$ and $r=5$ [6,11,40,15,38,37 because it complements the base sequence in performance.

A. Type-II Lüke diffusers

As shown above, at some frequencies the LSDs simply redirect the sound because they act like beam steerers. In general, diffusers should be dispersing sound and not simply redirecting it. An effective solution is to modulate the diffuser with another that, at the problematic frequencies, redirects sounds into another angle. Such a diffuser could be the inverse or the mirror image of the first diffuser or an LSD from the same family constructed from a step sequence of opposing inclination. Figure 8 displays the scattered distribution from such composite structures at this frequency. The main lobe of the periodic diffuser has been substituted by

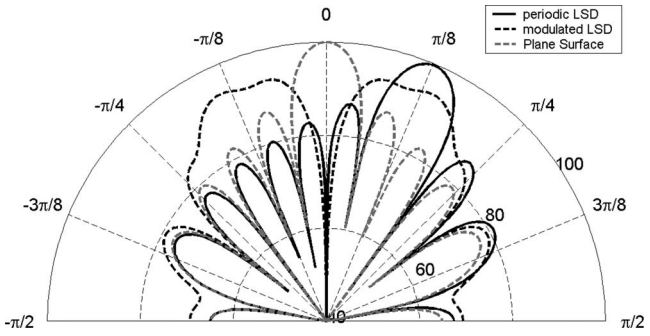

FIG. 8. Scattered intensity distribution (dB) at the flat plate frequency for two periods of LSD ($p=7, r=1$) periodic and modulated with its inverse in comparison with a plane surface of the same width.

two wider lobes of less energy. Thus the incident wave is scattered more uniformly in comparison to the periodic diffuser.

The binary sequence [1,0,0,1,1,0,1,0] was used to modulate the base diffuser, LSD ($r=1$, $P=42$), in the three different ways discussed earlier. Modulation in all three ways improves the overall performance of the diffuser, as shown in Fig. 9, because the diffusion coefficient is higher for all frequencies compared to the periodic case.

It is important to note that for the periodic case and the modulation with the mirror diffuser the maximum depth is 21.3 cm while for the inverse it is 29.5 cm and for the LSD of opposing inclination ($r=5$) it is 32.7 cm. From these three modulations the one with the inverse diffuser and the other with the LSD ($r=5$) seem to disperse best. However, if the maximum depth is taken into account, the fact that the modulated with the mirror diffuser will take up less space from the volume of the room could make it more desirable for some applications. If the lost volume is of no concern, it is important to note that the modulation with the other LSD manages to treat the notable dip of the diffusion coefficient that is evident in the other cases around 2.4 kHz.

The phenomenon of periodicity could be used to treat the problem of beam steering occurring with the LSD. Consider a structure that is composed of the periodic repetition of LSDs. If the maximum reflection lobe could be set on the angle that a minimum of the periodicity pattern occurs, it could be cancelled out. Unfortunately, in order for that to be accomplished a large number of periods must be considered while the wells must be thinned down to unrealistic values. Even in the cases that uniform diffusion in achieved at the flat plate frequencies, the performance of the diffuser is worse than poor for the frequencies up to that.

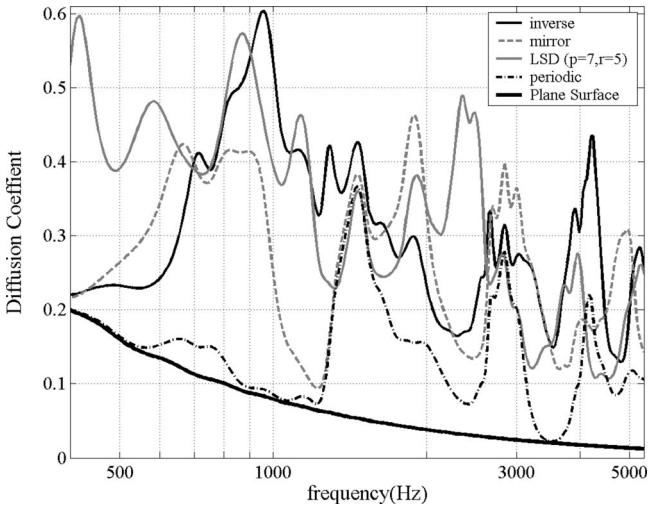

FIG. 9. Autocorrelation diffusion coefficient, as predicted using the Fourier model, of different modulations of Lüke diffusers of the same total width.

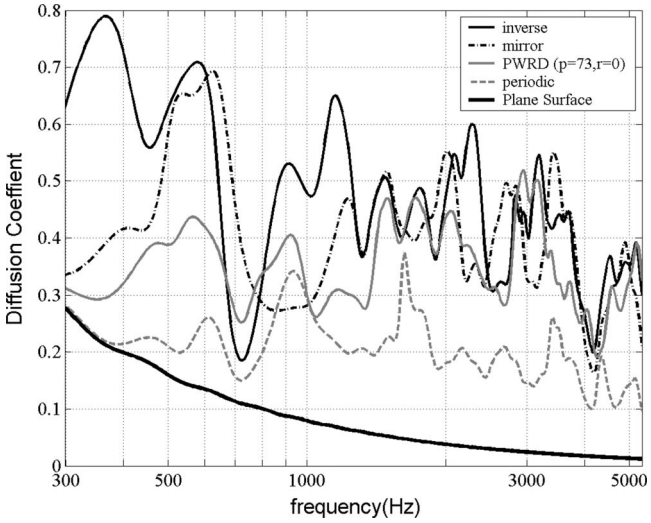

FIG. 10. Autocorrelation diffusion coefficient, as predicted using the Fourier model, of different modulations of power residue diffusers of the same total width.

B. Power residue diffusers

PWRDs do not present any notable problems until their flat plate frequency. So the only problem that needs dealing with is periodicity. The widely used modulation with the diffusers inverse can be applied in this case. The modulations with the mirror diffuser and another diffuser of the same family can be used as well. The binary sequence [1,0,1,1,0] has been used for the modulation.

Figure 10 shows the diffusion coefficient of a PWRD of period $N=9$, prime number generator $p=73$ and $r=1$. All modulations diffuse much better than the periodic case, in addition modulation with the inverse diffuser performs more uniformly compared to the others.

VI. DISCUSSION

This paper has presented two new types of diffusers, estimated their performance, and showed improved performance compared to a standard PRD. But which is the best sequence, Type-II Lüke or power residue?

The PWRDs seem to be the best. As Fig. 11 shows, both PWRDs in their modulated version have better diffusion coefficients than the other diffusers. They have no problematic frequencies, where they are unable to scatter the incident wave, and they have a more uniform diffusion coefficient over this bandwidth. The PWRD generated when $p=73$ could be preferable as it displays steadier diffusion with frequency.

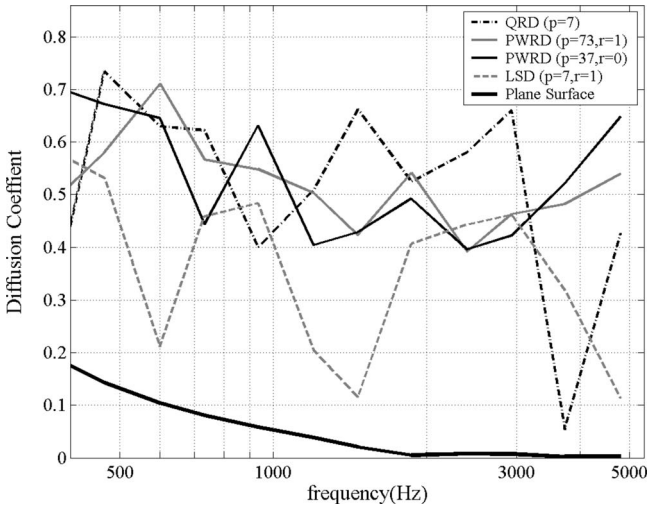

FIG. 11. One-third octave band autocorrelation diffusion coefficient, as predicted using the BEM, of different types of modulated diffusers of the same total width.

The LSD, shown in the above figure, is more ambiguous. It is evident that they do not diffuse as well as the QRD and the PRD except at their flat plate frequencies (3.5 kHz). The periodic version of the LSDs has a tilted flat plate at that frequency, but when modulated manages to avoid the problem. Modulated the LSD is preferred to a PRD or QRD because it is well behaved until the flat plate frequency at 21 kHz.

VII. CONCLUSIONS

This paper has proposed the use of Type-II Lüke and power residue sequences for the design of number theoretic diffusers with a small numbers of wells per period. The logical and mathematical background has been presented and their performance has been predicted with both the Fourier and the boundary element methods. Classic Schroeder diffusers based on quadratic residue and primitive root sequences suffer from flat plate frequencies where no scattering is achieved. Type-II Lüke and power residue sequences use larger numbers to generate the sequence, and consequently their flat plate frequencies are at much higher frequencies, often outside the audible range for practical diffusers.

The results show that Type-II Lüke sequences act like beam steerers at some frequencies, and consequently at these frequencies diffusion is poor. Modulation techniques have been presented to mitigate this problem. However, the performance of Power Residue sequences has been found to meet the initial demands for more-uniform diffusion and very high flat plate frequency and with the addition of modulation their performance is greatly improved.

Finally both types of diffuser are shown to display better diffusion characteristics when modulated than standard modulated quadratic and power residue diffusers.

[1]M. R. Schroeder, "Diffuse sound reflection by maximum-length sequences," J. Acoust. Soc. Am. **57**, 149–150 (1975).
[2]T. J. Cox and P. D'Antonio, *Acoustic Absorbers and Diffusers: Theory, Design and Application* (Spon, 2004).
[3]T. J. Cox and P. D'Antonio, "Acoustic phase grating for reduced specular reflection," Appl. Acoust. **60**, 167–186 (2000).
[4]J. A. S. Angus, "Non-integer-based diffusers," Audio Engineering Society 107th Convention (1999).
[5]J. A. S. Angus and C. I. McManmon, "Orthogonal sequence modulated phase reflection grating for wideband diffusion," J. Audio Eng. Soc. **46**, 1109–1118 (1998).
[6]T. J. Cox, "The optimization of profiled diffusers," J. Acoust. Soc. Am. **97**, 2928–2936 (1995).
[7]H. D. Lüke, "Families of polyphase sequences with near-optimal two-valued auto- and crosscorrelation functions," Electron. Lett. **28**, 1–2 (1992).
[8]P. Fan and M. Darnell, *Sequence Design for Communications Applications* (Wiley, New York, 1996).
[9]AES-4id-2001, "AES information document for room acoustics and sound reinforcement systems-characterization and measurment of surface scattering uniformity," J. Acoust. Soc. Am. **49**, 149–165 (2001).
[10]T. Terai, "On the calculation of the fields around three-dimensional objects by integral equation methods," J. Acoust. Soc. Am. **68**, 71–100 (1980).
[11]T. J. Cox, "Predicting the scattering from reflectors and diffusers using two-dimensional boundary element methods," J. Acoust. Soc. Am. **96**, 874–877 (1994).
[12]J. A. S. Angus, "Using grating modulation to achieve wideband large area diffusers," Appl. Acoust. **60**, 143–165 (1999).
[13]P. D'Antonio and T. J. Cox, "Aperiodic tiling of diffusers using a single asymmetric base shape," *18th ICA* Kyoto, Japan (2004).

Acoustic model for robustness analysis of optimal multipoint room equalization

Lae-Hoon Kim[a] and Mark Hasegawa-Johnson[b]
Department of Electrical and Computer Engineering, University of Illinois at Urbana-Champaign, Urbana, Illinois 61801

Jun-Seok Lim[c]
Department of Electronics Engineering, Sejong University, Seoul, Republic of Korea

Koeng-Mo Sung[d]
School of Electrical Engineering and INMC, Seoul National University, Seoul, Republic of Korea

(Received 29 March 2007; revised 3 January 2008; accepted 3 January 2008)

In this paper, an acoustic model for the robustness analysis of optimal multipoint room equalization is proposed. The optimal multipoint equalization aims to have the optimal performance in a least-squares sense for all measured points. The model can be used for theoretical robustness estimation depending on the critical design parameters such as the number of measurement points, the distance between measurements, or the frequency before applying real equalization system. The analysis results show that it is important to set the appropriate number of measurement points and the distances between measurement points to ensure the enlarged equalization region at a specific frequency. © *2008 Acoustical Society of America.* [DOI: 10.1121/1.2837285]

PACS number(s): 43.55.Br, 43.60.Cg, 43.60.Pt [NX] Pages: 2043–2053

I. INTRODUCTION

Room equalization has been one of the essential issues in various application areas including car audio, home theatre, wave field synthesis (WFS), three-dimensional audio using loudspeakers, acoustic echo cancellation, speech enhancement, and speech recognition. Especially, robustness to the perturbations due to movement of the sound source or receiver is one of the most important aspects for room equalization to be used in those applications. In this paper, we propose an acoustic model for the robustness analysis of multipoint optimal equalization based on measured room impulse responses (RIRs) around the target receiving point. Since the equalization is based on the multipoint RIRs, it can be easily expected to be more robust to changes in listener position compared to the case using only one RIR.[1] However, the robustness tends to vary depending on design parameters such as the distance between measurement points, the number of the measurement points, and the frequency. Therefore, it is necessary to have an acoustic model for the robustness analysis and it can be used for the theoretical robustness estimation before implementing the real equalization system.

There has been previous research to propose robustness analysis in different circumstances. Radlovic *et al.* proposed an acoustic model for the robustness analysis of the room equalization[1] for the first time, but their model is restricted to the case of using only one measured RIR from the source to the measurement point. The robustness analysis of the single point shall be generalized by the proposed multipoint model later. Talantzis and Ward proposed a multichannel version of the acoustic model, under the assumption that postprocessing equalization filters are applied to all channels after the room response.[2] This postprocessing is not applicable for the scenario of human listening. We are focusing on the case when we use a fixed prefiltering for the room equalization. Therefore, their robustness analysis cannot be applied in this situation, although they developed a robustness model for one form of optimal multipoint equalization method. Bharitkar *et al.* proposed the robustness analysis of a spatial average equalization,[3] in which several room responses are averaged in order to create a representative response, which is then inverted using a reciprocal fast Fourier transform (FFT). The general purpose of the optimal multipoint equalization is to guarantee the similar equalization performance at all measured points in the sense of minimizing mean-squared error,[4–7] but the equalization of the spatial average of the room responses does not always meet this optimality criterion. This approach also does not explicitly produce robustness analysis depending on the critical design parameters such as the distance between measurement points, the number of the measurement points.

All of these approaches measure the robustness of an equalizer in terms of the expected squared error of the equalized room response, where the expectation is computed using the theoretical model of Cook *et al.* of the spatial coherence of the reverberant field.[8] Some researchers,[4–7] possibly inspired by these methods, proposed designing an equalization filter specifically for the purpose of minimizing the mean squared equalization error, with mean computed by summing squared error over a "receiver multipoint," that is to say, a vector of room responses measured at several points in the vicinity of the expected listener location. It is reasonable to

[a]Electronic mail: lkim9@uiuc.edu
[b]Electronic mail: jhasegaw@uiuc.edu
[c]Electronic mail: jslim@sejong.ac.kr
[d]Electronic mail: kmsung@snu.ac.kr

speculate that this approach should be more robust than most previous equalizer design methods, in the sense of the expected squared error defined by Radlovic *et al.* because of the similarity between the expected-squared-error and mean-squared-error criteria. Although the criteria are similar, they are not identical: The expected-squared error criterion is computed using a theoretical approximation to the sound field coherence, while the multipoint design criterion is computed using a finite number of measured samples of the room response. The goal of this paper is to analyze the spatial robustness of an optimal multipoint equalizer in the minimum mean squared error sense. Results will show that the multipoint equalizer is, as predicted, more robust than any single-point equalizer, but that the robustness of the equalizer depends in important ways upon frequency, and upon the number and spatial distribution of the measurement points used to design the equalizer.

This paper is organized as follows. In Sec. II, we review optimal equalization using multipoint RIRs. In Sec. III, we propose an acoustic model for the robustness analysis of the optimal multipoint equalization. In Sec. IV the proposed acoustic model is validated using 102 simulated room impulse response sets with randomly chosen position of the source and primary receiver. Also, we compare the robustness of the existing multipoint equalization methods. Finally, we address how the design parameters affect the robustness, and why we should take the low frequency response more into account in terms of the robustness. Section V concludes our paper.

II. OPTIMAL EQUALIZATION USING MULTIPOINT ROOM IMPULSE RESPONSES

In this section, we review optimal least-squares equalization using multipoint RIRs. For easy comprehension, we first consider the simplest multipoint, only two measurement points. Let H_1, H_2 be RIR convolution matrixes as shown in Eq. (1) for the two RIRs respectively, let $\underline{\hat{x}}$ be the equalization filter, and let $\underline{b}$ represent the target impulse response (usually a Dirac delta).

$$H_i = \begin{bmatrix} h_i(0) & 0 & \cdots & 0 \\ h_i(1) & h_i(0) & \ddots & \vdots \\ \vdots & h_i(1) & \ddots & 0 \\ h_i(l_h-1) & \vdots & \ddots & h_i(0) \\ 0 & h_i(l_h-1) & \vdots & h_i(1) \\ \vdots & \ddots & \ddots & \vdots \\ 0 & \cdots & 0 & h_i(l_h-1) \end{bmatrix}, \quad i = 1,2, \tag{1}$$

where $[h_i(0)h_i(1)\cdots h_i(l_h-1)]^T$ is ith room impulse response, l_h is the length of it, and the superscript T means transpose. The general purpose of the optimal multipoint equalization is to guarantee the similar equalization performance at all measured points as shown in the following:

$$\begin{aligned} \underline{\hat{x}} &= \text{argmin}_{\underline{x}} \|H_1\underline{x} - \underline{b}\|^2 + \|H_2\underline{x} - \underline{b}\|^2 \\ &= \text{argmin}_{\underline{x}} \left\| \begin{bmatrix} H_1 \\ H_2 \end{bmatrix} \underline{x} - \begin{bmatrix} \underline{b} \\ \underline{b} \end{bmatrix} \right\|^2 \\ &= \left(\begin{bmatrix} H_1 \\ H_2 \end{bmatrix}^T \begin{bmatrix} H_1 \\ H_2 \end{bmatrix} \right)^{-1} \begin{bmatrix} H_1 \\ H_2 \end{bmatrix}^T \begin{bmatrix} \underline{b} \\ \underline{b} \end{bmatrix}. \end{aligned} \tag{2}$$

Equation (2) can be reformulated in frequency domain as shown in Eq. (4) after transforming the convolution matrixes in Eq. (1) into the circulant matrixes in the following:

$$H_i' = \begin{bmatrix} h_i'(0) & h_i'(N-1) & h_i'(N-2) & \cdots & h_i'(1) \\ h_i'(1) & h_i'(0) & h_i'(N-1) & \cdots & h_i'(2) \\ h_i'(2) & h_i'(1) & h_i'(0) & \cdots & h_i'(3) \\ \vdots & \vdots & \vdots & \ddots & \vdots \\ h_i'(N-1) & h_i'(N-2) & h_i'(N-3) & \ldots & h_i'(0) \end{bmatrix}, \quad i = 1,2, \tag{3}$$

where $[h_i'(0)h_i'(1)\cdots h_i'(l_h-1)]^T$ is ith modified room impulse response to have circular representation and N is the length of it,

$$\underline{\hat{X}}_f = \text{argmin}_{\underline{X}_f} \left\| \begin{bmatrix} \Lambda_1 \\ \Lambda_2 \end{bmatrix} \underline{X}_f - \begin{bmatrix} \underline{B}_f \\ \underline{B}_f \end{bmatrix} \right\|^2, \tag{4}$$

where if F^H and F are discrete Fourier transform (DFT) and inverse DFT matrixes, respectively, $\Lambda_1 = F^H H_1' F$, $\Lambda_2 = F^H H_2' F$ are diagonal matrixes, whose diagonal entries, σ_{1f} and σ_{2f}, are frequency samples of the room response computed by applying DFT to the RIRs, and $\underline{X}_f = F^H x$, $\underline{B}_f = F^H b$. If we simply set $\underline{B}_f = 1$, then the solution $\underline{\hat{X}}_f$ is given by

$$\underline{\hat{X}}_f = \frac{\Lambda_1^H + \Lambda_2^H}{|\Lambda_1|^2 + |\Lambda_2|^2}. \tag{5}$$

In the limiting case when multipoint inversion is performed using only one measured room response, then Λ_1 and Λ_2 are the same as a single measured Λ_f, $\underline{\hat{X}}_f = \Lambda_f^{-1}$. Equation (5) can be expanded into the case of the optimal N-point RIR equalization as

$$\underline{\hat{X}}_f = \frac{\Lambda_1^H + \Lambda_2^H \cdots \Lambda_N^H}{|\Lambda_1|^2 + |\Lambda_2|^2 \cdots |\Lambda_N|^2}. \tag{6}$$

III. ROBUSTNESS ANALYSIS OF OPTIMAL MULTIPOINT EQUALIZATION

Here, we propose an acoustic model for the robustness analysis of the optimal multipoint equalization and show that the equalization error coming from the mismatch between measurement and target points can be predicted through this acoustic model. Basic assumption is given by statistical wave acoustics, which is that above "Schroeder's frequency" we can consider the steady state room responses as statistical quantities.[9] The low frequency response below Schroeder frequency should be dealt with in a deterministic way, in other words, it is really dependent on the specific acoustic space, the position of source and receiver. Schroeder fre-

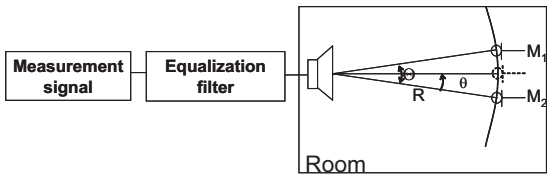

FIG. 1. Conceptual diagram for the robustness analysis of the two-point optimal equalization: M1, M2 are measurement positions, dotted microphone is the target position. Error is simulated by changing the target position.

quency specifies the frequency above which the average spacing of the resonance frequencies is smaller than one-third of their bandwidth:[9,10]

$$f_s = c\sqrt{\frac{6}{A}} \approx 2000\sqrt{\frac{T}{V}}, \tag{7}$$

where c is the speed of the sound, A is the absorbtion area of the room (m^2), Sabine's reverberation time $T=0.163V/A$, (s) and $V(m^3)$ is the volume of the space.

A. Two-point case

We consider a very simple two-point case first as shown in Fig. 1 and will expand it into N-point case later. The distances between the source and two measurement points are both R. Mean squared error at specific frequency f is

$$E_f = E\{|\tilde{H}_f\hat{X}_f - 1|^2\} \tag{8}$$

where $\tilde{H}_f$ is the frequency response of the source to target position at the specific frequency f and we define it to have the value σ_f hereafter, $\hat{X}_f$ is the equalization filter response at the same frequency, designed using RIRs from the source to measurement points. Note that Λ_i, $i=1,2$ or $i=1,2,\ldots,N$, respectively, from Eqs. (5) and (6) are diagonal matrixes, therefore we can proceed with the frequency bin by bin approach as in Eq. (8). As is the case in Sec. II, we assume that $\hat{X}_f$ has been designed using RIRs measured at two points. Therefore the equalization filter is

$$\hat{X}_f = \frac{\sigma_{f,1}^* + \sigma_{f,2}^*}{|\sigma_{f,1}|^2 + |\sigma_{f,2}|^2},$$

which is the solution of Eq. (5) at frequency f. If we define $\hat{H}_f = 1/\hat{X}_f$, Eq. (8) is reformulated as shown in the following:

In order to simplify Taylor series expansion, we define the error term at specified measurement point to be

$$g(\tilde{H}_f\tilde{H}_f^*, \hat{H}_f\hat{H}_f^*, \tilde{H}_f\hat{H}_f^*, \tilde{H}_f^*\hat{H}_f) = \frac{\tilde{H}_f\tilde{H}_f^*}{\hat{H}_f\hat{H}_f^*} - \frac{\tilde{H}_f\hat{H}_f^*}{\hat{H}_f\hat{H}_f^*} - \frac{\tilde{H}_f^*\hat{H}_f}{\hat{H}_f^*\hat{H}_f} + 1. \tag{10}$$

Radlovic *et al.*[1] define the zeroth-order Taylor series expansion of Eq. (10) as

$$g(\tilde{H}_f\tilde{H}_f^*, \hat{H}_f\hat{H}_f^*, \tilde{H}_f\hat{H}_f^*, \tilde{H}_f^*\hat{H}_f) \cong g(E\{\tilde{H}_f\tilde{H}_f^*\}, E\{\hat{H}_f\hat{H}_f^*\}, E\{\tilde{H}_f\hat{H}_f^*\}, E\{\tilde{H}_f^*\hat{H}_f\}) \tag{11}$$

which can be further approximated as

$$E_f \cong \frac{E\{\tilde{H}_f\tilde{H}_f^*\}}{E\{\hat{H}_f\hat{H}_f^*\}} - \frac{E\{\tilde{H}_f\hat{H}_f^*\}}{E\{\hat{H}_f\hat{H}_f^*\}} - \frac{E\{\tilde{H}_f^*\hat{H}_f\}}{E\{\hat{H}_f^*\hat{H}_f\}} + 1. \tag{12}$$

Because we can assume that the direct path is uncorrelated with reverberation part, $\tilde{H}_f$ and $\hat{H}_f$ can be divided into two parts as in the following:

$$\tilde{H}_f = \tilde{H}_{f,\mathrm{dir}} + \tilde{H}_{f,\mathrm{rev}},$$

$$\hat{H}_f = \hat{H}_{f,\mathrm{dir}} + \hat{H}_{f,\mathrm{rev}}. \tag{13}$$

Equation (12) can be rewritten using Eq. (13) as in the following:

$$E_f \cong \frac{\tilde{H}_{f,\mathrm{dir}}\tilde{H}_{f,\mathrm{dir}}^* + E\{\tilde{H}_{f,\mathrm{rev}}\tilde{H}_{f,\mathrm{rev}}^*\}}{\hat{H}_{f,\mathrm{dir}}\hat{H}_{f,\mathrm{dir}}^* + E\{\hat{H}_{f,\mathrm{rev}}\hat{H}_{f,\mathrm{rev}}^*\}} - \frac{\tilde{H}_{f,\mathrm{dir}}\hat{H}_{f,\mathrm{dir}}^* + E\{\tilde{H}_{f,\mathrm{rev}}\hat{H}_{f,\mathrm{rev}}^*\}}{\hat{H}_{f,\mathrm{dir}}\hat{H}_{f,\mathrm{dir}}^* + E\{\hat{H}_{f,\mathrm{rev}}\hat{H}_{f,\mathrm{rev}}^*\}} - \frac{\tilde{H}_{f,\mathrm{dir}}^*\hat{H}_{f,\mathrm{dir}} + E\{\tilde{H}_{f,\mathrm{rev}}^*\hat{H}_{f,\mathrm{rev}}\}}{\hat{H}_{f,\mathrm{dir}}^*\hat{H}_{f,\mathrm{dir}} + E\{\hat{H}_{f,\mathrm{rev}}^*\hat{H}_{f,\mathrm{rev}}\}} + 1. \tag{14}$$

The derivations presented above have been used in the acoustic model of Radlovic *et al.*[1] We will now extend the above-described model to analyze multipoint least-squares equalization. As shown in Fig. 1, the distance between source and measurement positions are both R, therefore the response of the direct path from the source to the two measurement points and the target point are all the same as shown in the following:

$$\tilde{H}_{f,\mathrm{dir}} = \sigma_{f,\mathrm{dir}} = \sigma_{f,\mathrm{dir},1} = \sigma_{f,\mathrm{dir},2} = -jk\rho cS_f\frac{1}{4\pi R}e^{jkR}, \tag{15}$$

where k is the wave number, ρ is the air density, c is the speed of sound, and S_f is the source strength at frequency f. Therefore,

$$\tilde{H}_{f,\mathrm{dir}}\tilde{H}^*_{f,\mathrm{dir}} = \sigma_{f,\mathrm{dir}}\sigma^*_{f,\mathrm{dir}} = 4\rho c\pi\left(\frac{1}{4\pi R}\right)^2\left((4\pi R)^2\left(\rho c\left(\frac{1}{2\lambda R}\right)^2|S_f|^2\right)\right) = \frac{\rho c\Pi}{4\pi R^2}, \tag{16}$$

where Π is the power of the acoustic source.[11] Similarly,

$$\hat{H}_{f,\mathrm{dir}} = \frac{\sigma_{f,\mathrm{dir},1}\sigma^*_{f,\mathrm{dir},1} + \sigma_{f,\mathrm{dir},2}\sigma^*_{f,\mathrm{dir},2}}{\sigma^*_{f,\mathrm{dir},1} + \sigma^*_{f,\mathrm{dir},2}} = \frac{\sigma_{f,\mathrm{dir}}\sigma^*_{f,\mathrm{dir}} + \sigma_{f,\mathrm{dir}}\sigma^*_{f,\mathrm{dir}}}{\sigma^*_{f,\mathrm{dir}} + \sigma^*_{f,\mathrm{dir}}} = \sigma_{f,\mathrm{dir}}, \tag{17}$$

$$\hat{H}_{f,\mathrm{dir}}\hat{H}^*_{f,\mathrm{dir}} = \sigma_{f,\mathrm{dir}}\sigma^*_{f,\mathrm{dir}} = \frac{\rho c\Pi}{4\pi R^2}, \tag{18}$$

$$\tilde{H}_{f,\mathrm{dir}}\hat{H}^*_{f,\mathrm{dir}} = \frac{\rho c\Pi}{4\pi R^2}. \tag{19}$$

Hence, as shown in Eqs. (16), (18), and (19), $\tilde{H}_{f,\mathrm{dir}}\tilde{H}^*_{f,\mathrm{dir}} = \hat{H}_{f,\mathrm{dir}}\hat{H}^*_{f,\mathrm{dir}} = \tilde{H}_{f,\mathrm{dir}}\hat{H}^*_{f,\mathrm{dir}} = \rho c\Pi/4\pi R^2$. Next we consider the reverberation part in Eq. (14). First, the mean squared response of the reverberation part is defined as in the following:

$$E\{\tilde{H}_{f,\mathrm{rev}}\tilde{H}^*_{f,\mathrm{rev}}\} = E\{\sigma_{f,\mathrm{rev}}\sigma^*_{f,\mathrm{rev}}\} = E\{\sigma_{f,\mathrm{rev},1}\sigma^*_{f,\mathrm{rev},1}\} = E\{\sigma_{f,\mathrm{rev},2}\sigma^*_{f,\mathrm{rev},2}\} = \frac{4\rho c\Pi(1-\bar{\alpha})}{S\bar{\alpha}}, \tag{20}$$

where S is the wall area of the room and $\bar{\alpha}$ is the averaged absorption coefficient. Next, the mean squared reverberant tail of the inverse equalization filter is

$$E\{\hat{H}_{f,\mathrm{rev}}\hat{H}^*_{f,\mathrm{rev}}\} = E\left\{\frac{(\sigma_{f,\mathrm{rev},1}\sigma^*_{f,\mathrm{rev},1} + \sigma_{f,\mathrm{rev},2}\sigma^*_{f,\mathrm{rev},2})^2}{\sigma_{f,\mathrm{rev},1}\sigma^*_{f,\mathrm{rev},1} + \sigma_{f,\mathrm{rev},2}\sigma^*_{f,\mathrm{rev},2} + \sigma_{f,\mathrm{rev},1}\sigma^*_{f,\mathrm{rev},2} + \sigma_{f,\mathrm{rev},2}\sigma^*_{f,\mathrm{rev},1}}\right\}. \tag{21}$$

As in Eq. (20) we note that $E\{\sigma_{f,\mathrm{rev},1}\sigma^*_{f,\mathrm{rev},1}\} = E\{\sigma_{f,\mathrm{rev},2}\sigma^*_{f,\mathrm{rev},2}\} = 4\rho c\Pi(1-\bar{\alpha})/S\bar{\alpha}$, therefore we can greatly simplify Eq. (21) by dividing both denominator and numerator using $\sigma_{f,\mathrm{rev},1}\sigma^*_{f,\mathrm{rev},1} + \sigma_{f,\mathrm{rev},2}\sigma^*_{f,\mathrm{rev},2}$.

Cook *et al.*[8] demonstrated that the normalized spatial coherence function of an isotropic noise field has the form $\mathrm{sinc}(kd)$, where k is the wave number, and d is the distance between any two measurement points. If we assume, as in the approach of Radlovic *et al.*,[1] that the reverberant field is approximately isotropic, then we may make the following approximations: We also note that the normalized cross correlation has the form of the sinc function as shown in the following:

$$\frac{E\{\sigma_{f,\mathrm{rev},1}\sigma^*_{f,\mathrm{rev},2}\}}{E\{\sigma_{f,\mathrm{rev},1}\sigma^*_{f,\mathrm{rev},1}\}} = \frac{E\{\sigma_{f,\mathrm{rev},2}\sigma^*_{f,\mathrm{rev},1}\}}{E\{\sigma_{f,\mathrm{rev},2}\sigma^*_{f,\mathrm{rev},2}\}} \cong \frac{\sin(kd)}{kd} = \mathrm{sinc}(kd) \tag{22}$$

or

$$\frac{E\{\sigma_{f,\mathrm{rev},1}\sigma^*_{f,\mathrm{rev},2}\}}{E\{\sigma_{f,\mathrm{rev},2}\sigma^*_{f,\mathrm{rev},2}\}} = \frac{E\{\sigma_{f,\mathrm{rev},2}\sigma^*_{f,\mathrm{rev},1}\}}{E\{\sigma_{f,\mathrm{rev},1}\sigma^*_{f,\mathrm{rev},1}\}} \cong \mathrm{sinc}(kd), \tag{23}$$

where d is the distance between the two measurement points used to compute the multipoint equalizer. Therefore Eq. (21) can be reformulated as

$$\begin{aligned} E\{\hat{H}_{f,\mathrm{rev}}\hat{H}^*_{f,\mathrm{rev}}\} &= E\left\{\frac{\sigma_{f,\mathrm{rev},1}\sigma^*_{f,\mathrm{rev},1} + \sigma_{f,\mathrm{rev},2}\sigma^*_{f,\mathrm{rev},2}}{1 + \dfrac{\sigma_{f,\mathrm{rev},1}\sigma^*_{f,\mathrm{rev},2} + \sigma_{f,\mathrm{rev},2}\sigma^*_{f,\mathrm{rev},1}}{\sigma_{f,\mathrm{rev},1}\sigma^*_{f,\mathrm{rev},1} + \sigma_{f,\mathrm{rev},2}\sigma^*_{f,\mathrm{rev},2}}}\right\} \\ &\cong \frac{E\{\sigma_{f,\mathrm{rev},1}\sigma^*_{f,\mathrm{rev},1}\} + E\{\sigma_{f,\mathrm{rev},2}\sigma^*_{f,\mathrm{rev},2}\}}{1 + \dfrac{1}{2}\dfrac{E\{\sigma_{f,\mathrm{rev},1}\sigma^*_{f,\mathrm{rev},2}\}}{E\{\sigma_{f,\mathrm{rev},1}\sigma^*_{f,\mathrm{rev},1}\}} + \dfrac{1}{2}\dfrac{E\{\sigma_{f,\mathrm{rev},2}\sigma^*_{f,\mathrm{rev},1}\}}{E\{\sigma_{f,\mathrm{rev},2}\sigma^*_{f,\mathrm{rev},2}\}}} \\ &\cong \frac{2\dfrac{4\rho c\Pi(1-\bar{\alpha})}{S\bar{\alpha}}}{1 + \mathrm{sinc}(kd)}. \end{aligned} \tag{24}$$

Using similar approximations,

$$E\{\tilde{H}_{f,\mathrm{rev}}\hat{H}^*_{f,\mathrm{rev}}\} = E\left\{\sigma_{f,\mathrm{rev}}\frac{\sigma_{f,\mathrm{rev},1}\sigma^*_{f,\mathrm{rev},1} + \sigma_{f,\mathrm{rev},2}\sigma^*_{f,\mathrm{rev},2}}{\sigma_{f,\mathrm{rev},1} + \sigma_{f,\mathrm{rev},2}}\right\} \cong \frac{E\{\sigma_{f,\mathrm{rev}}\sigma^*_{f,\mathrm{rev},1}\}}{E\left\{\dfrac{\sigma_{f,\mathrm{rev},1} + \sigma_{f,\mathrm{rev},2}}{\sigma_{f,\mathrm{rev},1}}\right\}} + \frac{E\{\sigma_{f,\mathrm{rev}}\sigma^*_{f,\mathrm{rev},2}\}}{E\left\{\dfrac{\sigma_{f,\mathrm{rev},1} + \sigma_{f,\mathrm{rev},2}}{\sigma_{f,\mathrm{rev},2}}\right\}}$$

$$\cong \frac{E\{\sigma_{f,\mathrm{rev}}\sigma^*_{f,\mathrm{rev},1}\}}{1+\dfrac{E\{\sigma_{f,\mathrm{rev},2}\sigma^*_{f,\mathrm{rev},1}\}}{E\{\sigma_{f,\mathrm{rev},1}\sigma^*_{f,\mathrm{rev},1}\}}} + \frac{E\{\sigma_{f,\mathrm{rev}}\sigma^*_{f,\mathrm{rev},2}\}}{1+\dfrac{E\{\sigma_{f,\mathrm{rev},1}\sigma^*_{f,\mathrm{rev},2}\}}{E\{\sigma_{f,\mathrm{rev},2}\sigma^*_{f,\mathrm{rev},2}\}}}$$

$$\cong \frac{E\{\sigma_{f,\mathrm{rev}}\sigma^*_{f,\mathrm{rev},1}\}+E\{\sigma_{f,\mathrm{rev}}\sigma^*_{f,\mathrm{rev},2}\}}{1+\mathrm{sinc}(kd)}. \quad (25)$$

If we define the ratio of the energy of the direct path and the reverberant part to be

$$\gamma \equiv \frac{E_d}{E_r} = \frac{\dfrac{\rho c \Pi}{4\pi R^2}}{\dfrac{4\rho c \Pi(1-\bar{\alpha})}{S\bar{\alpha}}} = \frac{S\bar{\alpha}}{16\pi R^2(1-\bar{\alpha})} \quad (26)$$

and if we denote the distances between target point and each measurement point as r_1, r_2, then

$$\frac{E\{\sigma_{f,\mathrm{rev}}\sigma^*_{f,\mathrm{rev},1}\}}{E\{\sigma_{f,\mathrm{rev}}\sigma^*_{f,\mathrm{rev}}\}} \cong \mathrm{sinc}(kr_1), \quad (27)$$

$$\frac{E\{\sigma_{f,\mathrm{rev}}\sigma^*_{f,\mathrm{rev},2}\}}{E\{\sigma_{f,\mathrm{rev}}\sigma^*_{f,\mathrm{rev}}\}} \cong \mathrm{sinc}(kr_2) \quad (28)$$

and the final acoustic model for error analysis, based on Eqs. (14), (16), (18)–(20), and (24)–(26) is

$$E_f \cong \frac{\gamma+1}{\gamma+\dfrac{2}{1+\mathrm{sinc}(kd)}} - 2\frac{\gamma+\dfrac{\mathrm{sinc}(kr_1)+\mathrm{sinc}(kr_2)}{1+\mathrm{sinc}(kd)}}{\gamma+\dfrac{2}{1+\mathrm{sinc}(kd)}} + 1. \quad (29)$$

We should note that the error due to the variation of the target point is mainly dependent on the distances between the target point and the measurement points, r_1 and r_2. As shown in Fig. 1, if we shift the target point by an angle θ along a circle of radius R centered at the source, then

$$r_1 = 2R\sin\frac{|\theta|}{2}, \quad (30)$$

$$r_2 = 2R\sin\frac{|\Theta-\theta|}{2}, \quad (31)$$

where $\Theta = 2\sin^{-1}(d/2R)$. If $\Theta=0$, in other words, if the two measured RIRs are both measured at the same specific position, Eq. (29) reduces to the one-point robustness formula similar to the formula of Radlovic *et al.*:[1]

$$E_f \cong \frac{2-2\dfrac{\sin(kr_1)}{kr_1}}{\gamma+1}. \quad (32)$$

B. *N*-point case

Now, let us formally consider the N-point measurement case. Equation (14) still holds. Equation (17) can be expanded as shown in Eq. (33), therefore, $E\{\tilde{H}_{f,\mathrm{dir}}\tilde{H}^*_{f,\mathrm{dir}}\} = E\{\hat{H}_{f,\mathrm{dir}}\hat{H}^*_{f,\mathrm{dir}}\} = E\{\tilde{H}_{f,\mathrm{dir}}\hat{H}^*_{f,\mathrm{dir}}\} = \rho c\Pi/4\pi R^2$,

$$\hat{H}_{f,\mathrm{dir}} = \frac{(\sigma_{f,\mathrm{dir},1}\sigma^*_{f,\mathrm{dir},1}+\sigma_{f,\mathrm{dir},2}\sigma^*_{f,\mathrm{dir},2}+\cdots+\sigma_{f,\mathrm{dir},N}\sigma^*_{f,\mathrm{dir},N})}{\sigma^*_{f,\mathrm{dir},1}+\sigma^*_{f,\mathrm{dir},2}+\cdots+\sigma^*_{f,\mathrm{dir},N}} = \frac{(N\sigma_{f,\mathrm{dir}}\sigma^*_{f,\mathrm{dir}})}{N\sigma^*_{f,\mathrm{dir}}} = \sigma_{f,\mathrm{dir}}. \quad (33)$$

Equations (24) and (25) can be expanded as in the following:

$$E\{\hat{H}_{f,\mathrm{rev}}\hat{H}^*_{f,\mathrm{rev}}\} \cong \frac{N\dfrac{4\rho c\Pi(1-\bar{\alpha})}{S\bar{\alpha}}}{1+\dfrac{2}{N}\left(\sum_{n=1}^{N-1}\mathrm{sinc}(kd_{n,n+1})+\sum_{n=1}^{N-2}\mathrm{sinc}(kd_{n,n+2})+\sum_{n=1}^{N-(N-1)}\mathrm{sinc}(kd_{n,n+N-1})\right)} = \frac{N\dfrac{4\rho c\Pi(1-\bar{\alpha})}{S\bar{\alpha}}}{1+\dfrac{2}{N}\sum_{i<j}\mathrm{sinc}(kd_{i,j})}, \quad (34)$$

where d_{ij}, $i,j=1,2,\ldots,N$ is the distance between measurement points i, j,

$$E\{\tilde{H}_{f,\mathrm{rev}}\hat{H}^*_{f,\mathrm{rev}}\} = E\left\{\sigma_{f,\mathrm{rev}}\frac{\sigma_{f,\mathrm{rev},1}\sigma^*_{f,\mathrm{rev},1}+\sigma_{f,\mathrm{rev},2}\sigma^*_{f,\mathrm{rev},2}+\cdots+\sigma_{f,\mathrm{rev},N}\sigma^*_{f,\mathrm{rev},N}}{\sigma_{f,\mathrm{rev},1}+\sigma_{f,\mathrm{rev},2}+\cdots+\sigma_{f,\mathrm{rev},N}}\right\}$$
$$\cong \frac{E\{\sigma_{f,\mathrm{rev}}\sigma^*_{f,\mathrm{rev},1}\}}{E\left\{\frac{\sigma_{f,\mathrm{rev},1}+\sigma_{f,\mathrm{rev},2}+\cdots+\sigma_{f,\mathrm{rev},N}}{\sigma_{f,\mathrm{rev},1}}\right\}} + \frac{E\{\sigma_{f,\mathrm{rev}}\sigma^*_{f,\mathrm{rev},2}\}}{E\left\{\frac{\sigma_{f,\mathrm{rev},1}+\sigma_{f,\mathrm{rev},2}+\cdots+\sigma_{f,\mathrm{rev},N}}{\sigma_{f,\mathrm{rev},2}}\right\}} + \cdots$$
$$+ \frac{E\{\sigma_{f,\mathrm{rev}}\sigma^*_{f,\mathrm{rev},1}\}}{E\left\{\frac{\sigma_{f,\mathrm{rev},1}+\sigma_{f,\mathrm{rev},2}+\cdots+\sigma_{f,\mathrm{rev},N}}{\sigma_{f,\mathrm{rev},1}}\right\}}$$
$$\cong \sum_{m=1}^{N}\frac{E\{\sigma_{f,\mathrm{rev}}\sigma^*_{f,\mathrm{rev},n}\}}{1+\sum_{n=1,\neq m}^{N}\mathrm{sinc}(kd_{m,n})}. \tag{35}$$

If r_n, $n=1,2,\ldots,N$, is the distance between the target point and the nth measurement point, then

$$\frac{E\{\sigma_{f,\mathrm{rev}}\sigma^*_{f,\mathrm{rev},n}\}}{E\{\sigma_{f,\mathrm{rev}}\sigma^*_{f,\mathrm{rev}}\}} = \mathrm{sinc}(kr_n), \quad n=1,2,\ldots,N \tag{36}$$

and therefore the complete acoustic model for robustness analysis of a multipoint equalizer is

$$E_f \cong \frac{\gamma+1}{\gamma+\dfrac{N}{1+\dfrac{2}{N}\sum_{i<j}\mathrm{sinc}(kd_{i,j})}} - 2\frac{\gamma+\sum_{m=1}^{N}\dfrac{\mathrm{sinc}(kr_m)}{1+\sum_{n=1,\neq m}^{N}\mathrm{sinc}(kd_{m,n})}}{\gamma+\dfrac{N}{1+\dfrac{2}{N}\sum_{i<j}\mathrm{sinc}(kd_{i,j})}}+1. \tag{37}$$

IV. VERIFICATION, COMPARISON, AND ANALYSIS

Here, we first verify the model using total $102\times41=4182$ simulated RIRs, and compare the robustness of the existing multipoint equalization methods with the proposed acoustic model. Finally, the robustness results depending on design parameters are presented and discussed.

A. Verification of the acoustic model

To verify the proposed acoustic model for robustness analysis, 102 room impulse response sets are simulated with randomly chosen position of the source and primary receiver using conventionaly used room simulation method "image-method."[12,13] One set includes 41 RIRs measured at aligned 41 different positions, the distance between the measurement positions for each RIR is set to 0.01 m. To avoid the situation that source is too close to the receivers, we set the 1 m distance between them at least. A shoebox type of acoustic space has been used, the dimension of which is 6.25 m $\times$ 3.75 m $\times$ 2.5 m and volume of which is 58.59 m^3. The speed of sound, the average absorption coefficient, and the reverberation time are set to 343 m/s, 0.45, and 0.25, respectively. To simulate Eq. (8), the sample mean has been used:

$$\hat{E}_f = \frac{1}{N}\sum_{i=1}^{N}\|\hat{H}_f\hat{X}_f-1\|^2. \tag{38}$$

Figure 2 compares mean squared error between theoretical result (solid line) and simulation result (dotted line) at different octave frequencies (250, 500 Hz, 1, 2, 4, 16 kHz), distance between measurement points is 0.1 m, and the number of the measurement points is 2. We could confirm similar result when the number of measurement points is 3. As we expected from theoretical model, at each frequency, we can see that it fits the trend of the simulated result.

B. Comparison

As we see in the verification result, robust region to the perturbation due to the movement of source or receiver position tends to be much wider in lower frequency region. Above around 2 kHz, we may not be able to expect reasonable robustness regardless of the number of the measurement points to get the equalization filter. Therefore, we should pay more attention to the lower frequency range rather than to the entire frequency range equally. Note that the model is derived under the assumption that reciprocal of FFT can be used as an inverse filter, which is known to be accomplished by introducing modeling delay.[14] However, previously proposed multipoint equalization algorithms approximate the inverse filter with smaller number of taps.[4–7]

Figure 3 shows the robustness analysis result using Eq. (2) with short filter length (around one quarter of original RIR length) and modeling delay (half of the filter length), which can be considered as the result of the approach of

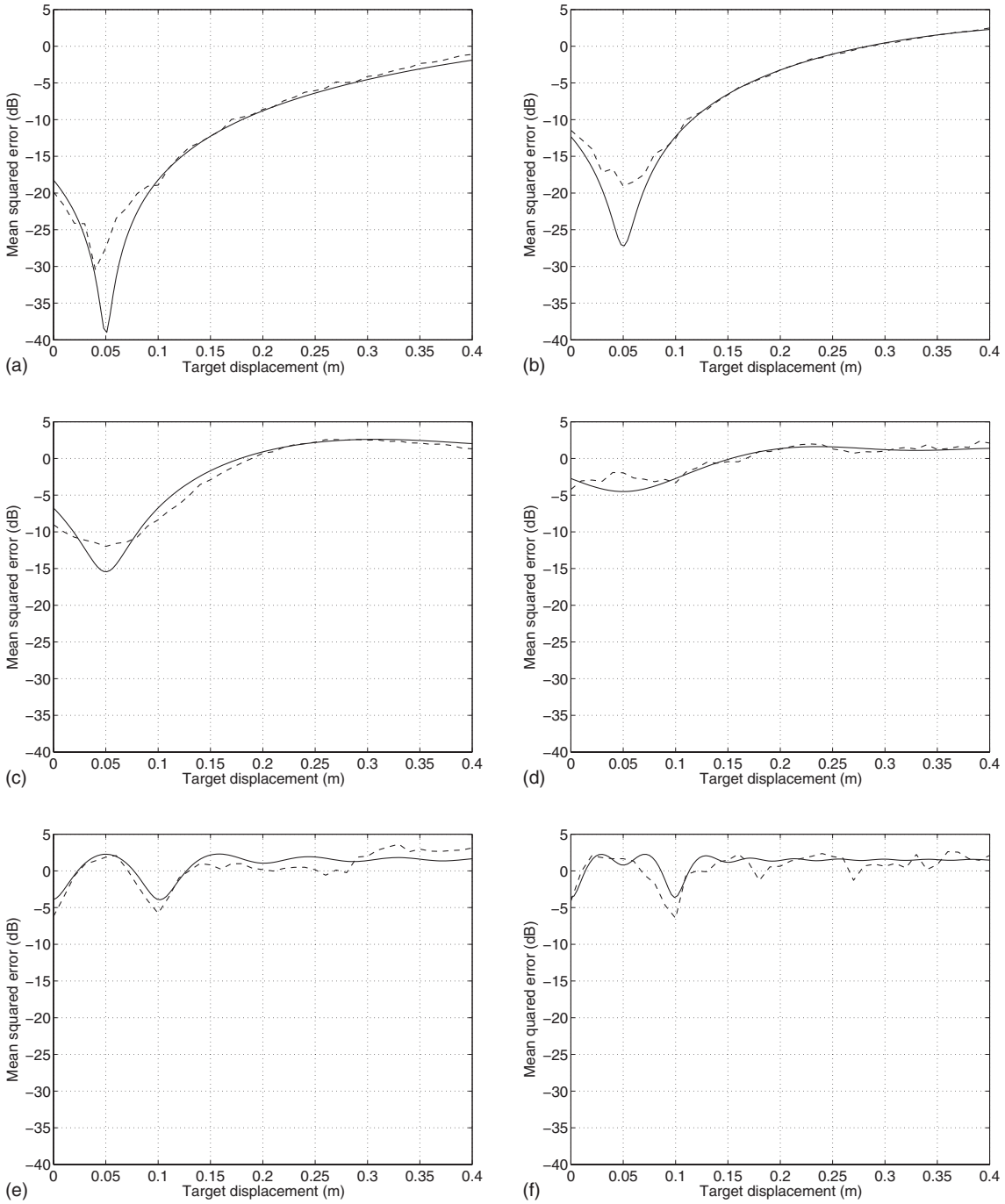

FIG. 2. Verification of the proposed acoustic model by comparing mean squared error between theoretical result (solid line) and simulation result (dashed line) at different octave frequencies, measurement positions are located at 0 and 0.1 m, distance between receiving points d=0.1 m, and number of measurement points is N=2: (a) 250 Hz, (b) 500 Hz, (c) 1 kHz, (d) 2 kHz, (e) 4 kHz, and (f) 8 kHz.

Elliott *et al.*[4,5] As expected, the robustness result becomes worse, because we cannot model the similar part across the room responses accurately enough using shorter filter length. However, we can confirm that the theoretical estimation gives maximally achievable performance limit. Figure 4 shows the robustness analysis of the approach of Haneda *et al.* and the approach of Kim *et al.* To deal with the all-pole modeling approach cases,[6,7] we modified Eq. (38) as minimum-phase version of it, because by all-pole modeling we cannot compensate the nonminimum phase part:

$$\hat{E}_f^{\mathrm{MP}} = \frac{1}{N}\sum_{i=1}^{N} \|\tilde{H}_f^{\mathrm{MP}}\hat{X}_f^{\mathrm{MP}} - 1\|^2, \tag{39}$$

where $\hat{X}_f^{\mathrm{MP}}$ and $\tilde{H}_f^{\mathrm{MP}}$ are minimum phase portion of $\hat{X}_f$ and $\tilde{H}_f$, respectively. If we simply use Eq. (38), then error related to residual after minimum-phase inversion always shows up. However, because the all-pole modeling approaches rather have an objective that is to maximally flatten the magnitude response except sharp nulls,[7] Eq. (39) makes more sense if it gives similar result when we use Eq. (39) compared with the

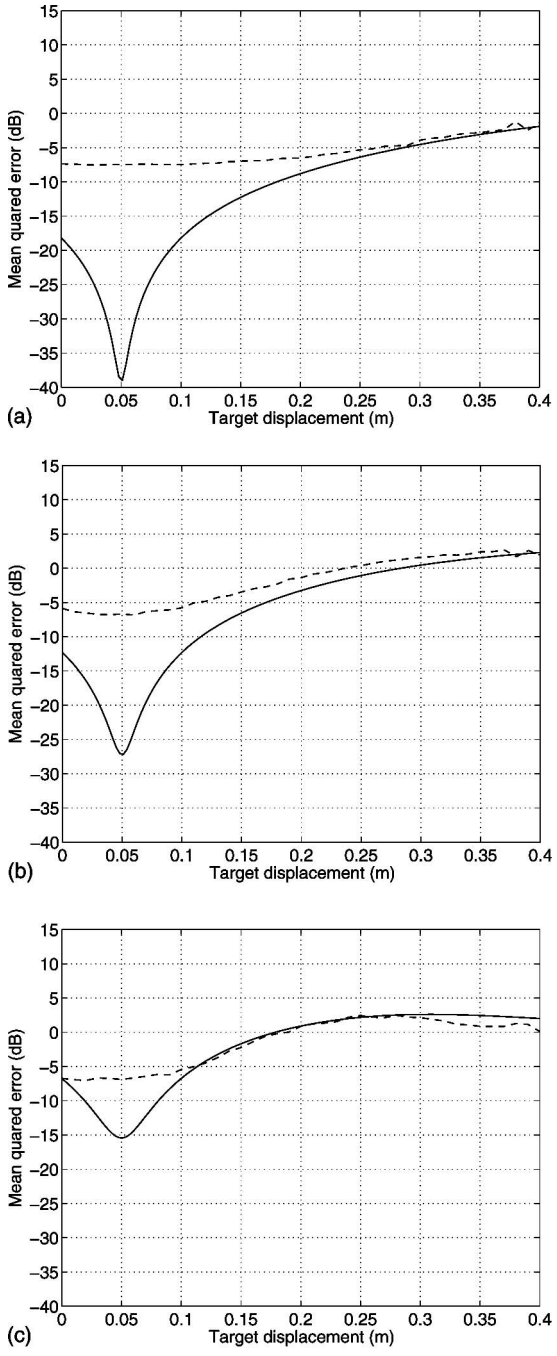

FIG. 3. Comparison of mean squared error between theoretical result (solid line) and simulation result with shorter filter length (dashed line) at different octave frequencies, measurement positions are located at 0 and 0.1 m, distance between receiving points $d=0.1$ m, and number of measurement points is $N=2$: (a) 250 Hz, (b) 500 Hz, and (c) 1 kHz.

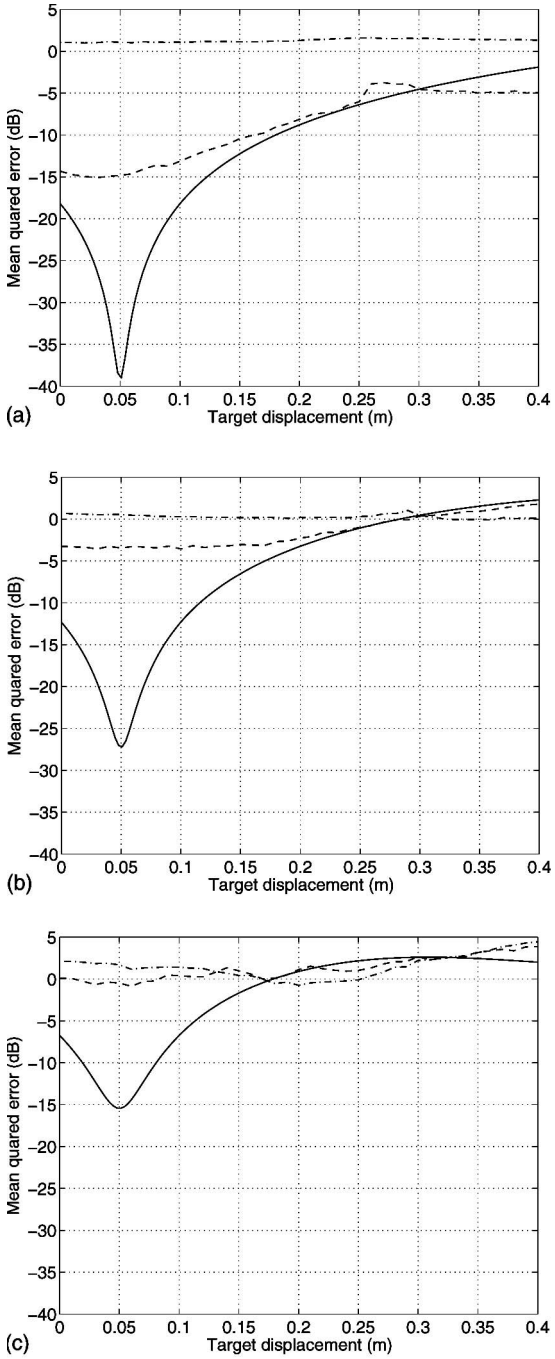

FIG. 4. Comparison of mean squared error, theoretical result (solid line), the model of Haneda *et al.* (dash-dotted line)—Ref. 6—and the model of Kim *et al.* (dashed line)—Ref. 7—at different octave frequencies, measurement positions are located at 0 and 0.1 m, distance between receiving points $d=0.1$ m, and number of measurement points is $N=2$: (a) 250 Hz, (b) 500 Hz, and (c) 1 kHz.

theoretical estimation of Eq. (8). Interestingly enough, even with this modification, we could confirm that Eq. (39) still fit the trend reasonably well with theoretical model. Figure 5 shows the robustness result of Eq. (39) with the theoretic estimation given by Eq. (8). For each all-pole approximation modeling,[6,7] the $\hat{X}_f^{\mathrm{MP}}$ of Eq. (39) is replaced by the inverse filter of each method. From the result shown in Fig. 4, we might be able to say that the approach of Kim *et al.* is better in terms of the robustness than the approach of Haneda *et al.*, because the former gives better robustness result in the low frequency range with same number of filter taps, one-twentieth of the RIR length. Actually, the robustness result of the approach of Haneda *et al.* is nearly similar to the result of RIRs themselves without equalization, because with this amount of taps ordinary all-pole system cannot accurately model the room response even in the low frequency region where the RIRs show similar pattern. However, in the case of the approach of Kim *et al.*, due to the warping property, it is

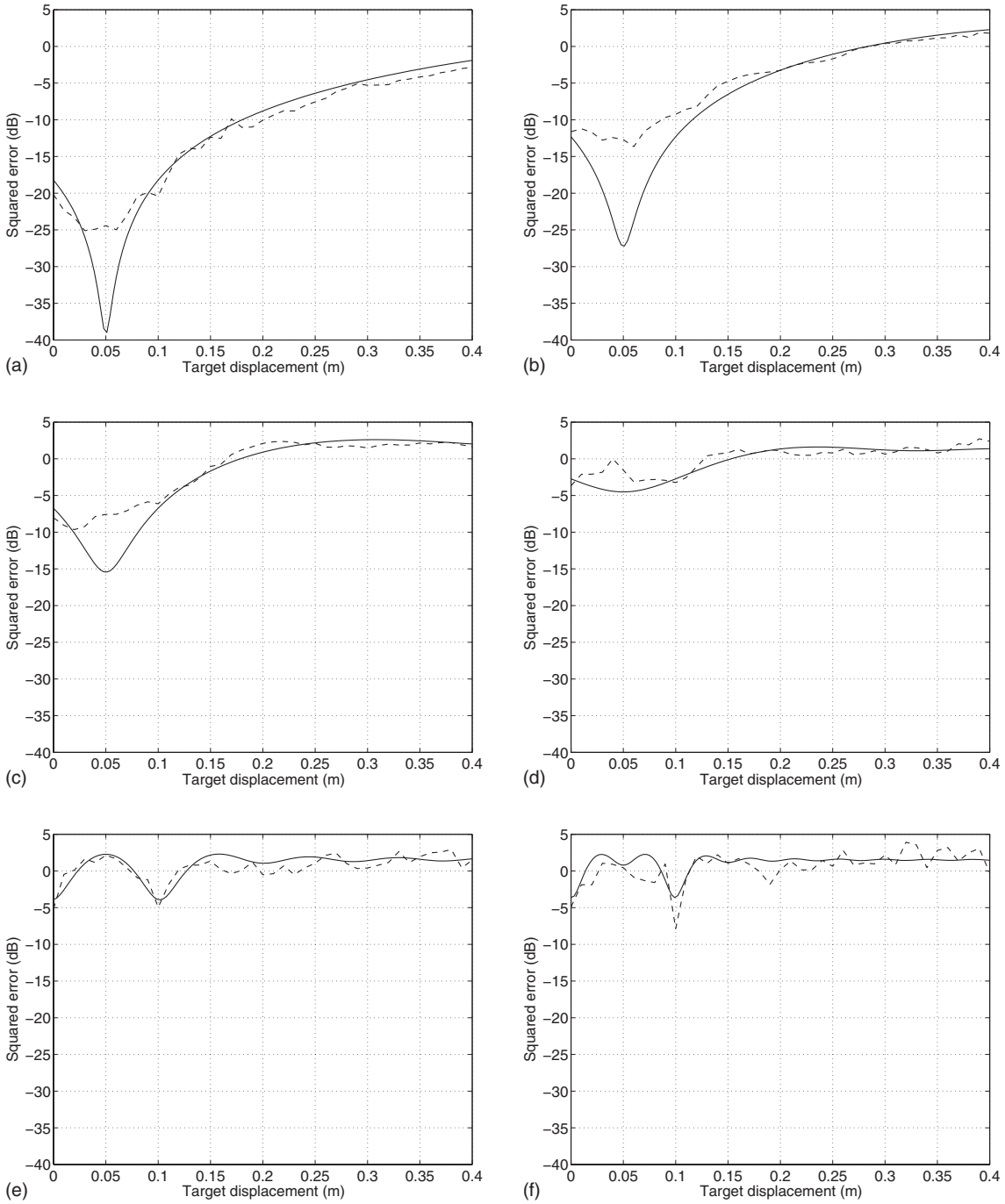

FIG. 5. Verification of the proposed acoustic model by comparing mean squared error between theoretical result (solid line) and simulation result using minimum-phase responses only (dashed line) at different octave frequencies, measurement positions are located at 0 and 0.1 m, distance between receiving points $d=0.1$ m, and number of measurement points is $N=2$: (a) 250 Hz, (b) 500 Hz, (c) 1 kHz, (d) 2 kHz, (e) 4 kHz, and (f) 8 kHz.

possible to model lower frequency much more accurately such that it can produce better robustness result in the low frequency range.

Because previously proposed multipoint methods try to perform equalization with short filter length, it produces worse robustness result than theoretical estimation. However, it is possible to evaluate each method by comparing with the theoretical estimation, because we know that it is the theoretical upper bound of the robustness performance when we do not have any restriction with the filter length.

C. Analysis

Figure 6 is the simulation result of the error analysis at 1 kHz as we change the distance between two measurement points from 0.05 to 0.15 m with 0.05 m interval. As shown in Fig. 6, increasing the distance between measurement points increases the width of the equalization region, but also increases the mean squared error. Therefore, the distance between measurement points can be determined based on the simulation result at a specific frequency while considering

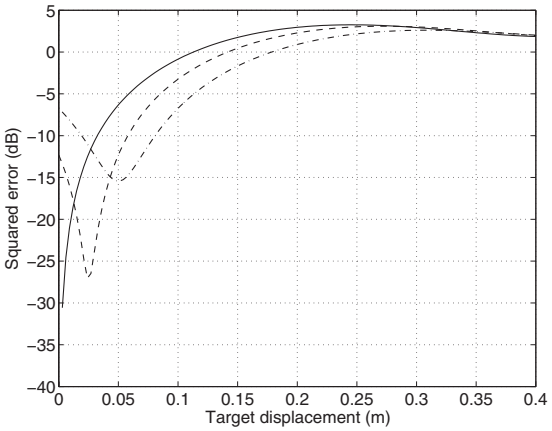

FIG. 6. Squared error (dB) at 1 kHz as a function of the displacement from the position of one of two receiving positions to the direction toward the other receiving position. Parameter is the distance between measurement points: $d=0.05$ m (solid line), 0.1 m (dashed line), and 0.15 m (dash-dotted line).

the mean squared errors and the width of the equalization region at the same time. In this simulation, the target point is constrained to lie on the circle of radius R centered at the source, as shown in Fig. 1. However, this simplified mismatch trajectory gives an acceptable simulation result if we assume that the distance between the source and the target point is much larger than the distance between the target point and the measurement points so that the response of the direct path is almost the same regardless of the target point. Under this typical far-field assumption, Eq. (29) holds not only in the simplified trajectory given in Fig. 1, but also for any target point if we just set the distances between the target and measurement points, r_1 and r_2, correctly. Adding a third measurement point will enhance the robustness in the direction of the added point: The error curve along a horizontal line connecting any two of the three measurement points will be similar to that shown in Fig. 6. Figures 7 and 8 are the results of the simulation at frequencies 1, 8 kHz as we increase the number of measurement points from one to three with an interpoint spacing of 0.05 m. Note that the normalized distance kd is equal to $200\pi/c$ in Fig. 7, and $1600\pi/c$ in Fig. 8. The same plots apply to any other combination of distance and frequency resulting in the same values of kd. We can see that equalization region is restricted more in the vicinity of the measurement points in Fig. 8 than in Fig. 7, with a concomitant increase in the mean-squared error within the equalization region, because the distance between measurement points is quite far compared with the wavelength. Therefore, to ensure the equalization performance, we should set an appropriate distance between the measurement points depending on the frequency range over which equalization should be effective. We can see the width of equalization region is directly related to the number of measurement points. In other words, we can see that equalization based on careful selection of the measurement number and distance among the measurement points may allow enlarged equalization region with an acceptably low level of mean-squared error.

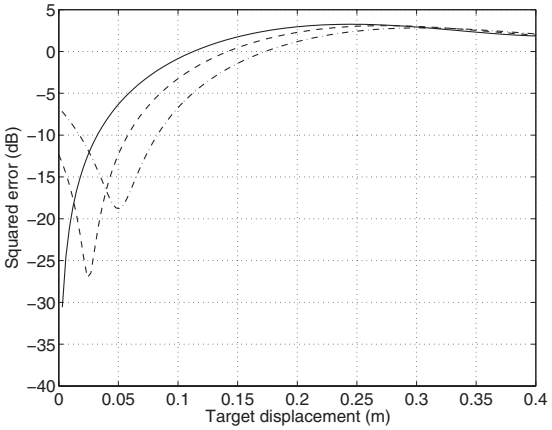

FIG. 7. Squared error (dB) at 1 kHz, the distance between receiving positions $d=0.05$ m: The number of the receiving position $N=1$ (solid line), $N=2$ (dashed line), $N=3$ (dash-dotted line).

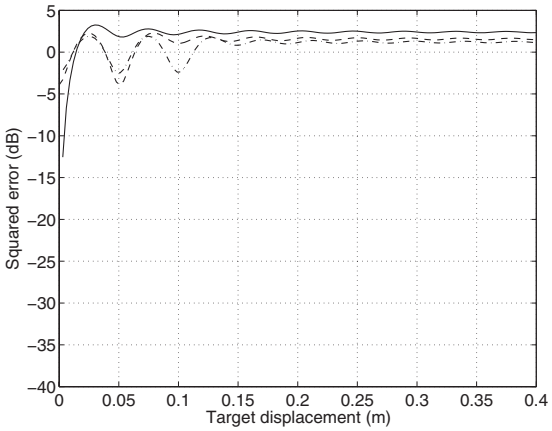

FIG. 8. Squared error (dB) at 8 kHz, the distance between receiving positions $d=0.05$ m: The number of the receiving position $N=1$ (solid line), $N=2$ (dashed line), $N=3$ (dash-dotted line).

V. CONCLUSION

In this paper, we propose an acoustic model which can be used for estimating the theoretical error of the optimal multipoint equalization algorithm before implementing an equalization system, this model can be used for simulating the robustness of the designed equalizer, as a function of the number of measurement points, the distance between the measurement points, and the frequency.

[1]B. D. Radlovic, R. C. Williamson, and R. A. Kennedy, "Equalization in acoustic reverberant environment: Robustness results," IEEE Trans. Speech Audio Process. **8**, 311–319 (2000).
[2]T. Talantzis and D. B. Ward, "Robustness of multichannel equalization in an acoustic reverberant environment," J. Acoust. Soc. Am. **114**, 833–841 (2003).
[3]S. Bharitkar, P. Hilmes, and C. Kyriakakis, "Robustness of spatial average equalization: A statistical reverberation model approach," J. Acoust. Soc. Am. **116**, 3491–3497 (2004).
[4]S. J. Elliott and P. A. Nelson, "Multiple-point equalization in a room using adaptive digital filters," J. Audio Eng. Soc. **37**, 899–907 (1989).
[5]S. J. Elliott, L. P. Bhatia, F. S. Deghan, A. H. Fu, N. S. Stewart, and D. W. Wilson, "Practical implementation of low-frequency equalization using adaptive digital filters," J. Audio Eng. Soc. **42**, 988–998 (1994).
[6]Y. Haneda, S. Makino, and Y. Kaneda, "Multi-point equalization of room transfer functions by using common acoustical poles," IEEE Trans. Speech Audio Process. **5**, 325–333 (1997).

[7]L. Kim, M. Hasegawa-Johnson, J. Lim, and K. Sung, "Room equalization based on acoustic and human perceptual features," in *Proceedings of the 122nd Audio Engineering Society Convention*, Vienna, May 5–8, 2007.
[8]R. K. Cook, R. V. Waterhouse, R. D. Berendt, S. Edelman, and J. M. C. Thompson, "Measurement of correlation coefficients in reverberant sound fields," J. Acoust. Soc. Am. **27**, 1072–1077 (1955).
[9]M. R. Schroeder, "Frequency-correlation functions of frequency responses in rooms," J. Acoust. Soc. Am. **34**, 1819–1823 (1962).
[10]H. Kuttruff, *Room Acoustics*, 4th ed. (Spon, New York, 2000).
[11]P. M. Morse and K. U. Ingard, *Theoretical Acoustics* (McGraw-Hill, London, 1968).
[12]J. B. Allen and D. A. Berkley, "Image method for efficiently simulating small-room acoustics," J. Acoust. Soc. Am. **65**, 943–950 (1979).
[13]D. R. Campbell, K. J. Palomaki, and G. J. Brown, "Roomsim, a matlab simulation of shoebox room acoustics for use in teaching and research," in http://media.paisley.ac.uk/campbell/Roomsim/(last visited on 3 January 2008).
[14]J. N. Mourjopoulos, "Digital equalization of room acoustics," J. Audio Eng. Soc. **42**, 884–900 (1994).

Expressions of dissipated powers and stored energies in poroelastic media modeled by {u,U} and {u,*P*} formulations

Olivier Dazel[a)]
Laboratoire d'Acoustique de l'Université du Maine — UMR CNRS 6613, Avenue Olivier Messiaen, F-72 085 Le Mans Cedex, France

Franck Sgard and François-Xavier Becot
Département Génie Civil et Bâtiment-URA CNRS 1652, Ecole Nationale des Travaux Publics de l'Etat, F-69518 Vaulx-en-Velin Cedex, France

Noureddine Atalla
Groupe Acoustique de l'Université de Sherbrooke, 2500 Boulevard de l'Université, Sherbroke, Quebec J1K2R1, Canada

(Received 3 October 2006; revised 10 January 2008; accepted 18 January 2008)

This paper is devoted to the rigorous obtention of the energy balance in porous materials. The wave propagation in the porous media is described by Biot-Allard's {**u**,**U**} and {**u**,*P*} formulations. The paper derives the expressions for stored kinetic and strain energies together with dissipated energies. It is shown that, in the case of mixed formulations, these expressions do not correspond to the real and imaginary parts of the variational formulations. A quantitative convergence analysis of finite element scheme is then undertaken with the help of these indicators. It is shown that the order of convergence of these indicators for linear finite-element is one and that they are then well fitted to check the validity of finite-element models.
© *2008 Acoustical Society of America.* [DOI: 10.1121/1.2874520]

PACS number(s): 43.55.Ev, 43.20.Bi [KA] Pages: 2054–2063

I. INTRODUCTION

Porous materials are commonly used in noise control issues as passive devices for reducing both structure and airborne sound. Today, most of the vibroacoustic prediction tools are able to account for the coupling of structures with a porous medium. These tools are mainly based on Biot–Allard's[1,2] model. In noise control analysis, it is often desirable to understand how energy is stored and how power flows from one system component to the other. Two sets of poroelastic formulations can be distinguished: The first one deals with displacement formulations[1,2] and the second one is concerned with mixed formulations.[3–5] The finite-element modeling of porous material by the way of {**u**,**U**}[6,7] techniques or {**u**,*P*}[4,5] techniques. {**u**,*P*} finite-element methods have shown their efficiency compared to displacement formulation[4,5] and a key point to improve them is to study their convergence and their physical interpretation. Due to the biphasic nature of porous materials and also to the fact that in mixed pressure-displacement formulations the fields are of different nature, the derivation of the expressions of energies and powers in these media is not obvious; in particular they cannot be obtained through separating the real and imaginary parts of the variational formulations. In the past, only equations related to the dissipated powers have been presented in the case of Biot–Allard's {**u**,*P*} formulations.[8–10] The first objective of this paper is to rigorously derive the expressions of both stored and dissipated energies in poroelastic materials based on the theorem of kinetic energy in the framework of {**u**,**U**} and {**u**,*P*} formulations of Biot–Allard's poroelasticity equations. The second objective of this paper is to propose a quantitative convergence analysis of finite element scheme with the help of these indicators. This analysis shows that these indicators are of order one and can advantageously be used to check the validity of finite-element schemes.

In the following, the considered porous medium are usual sound absorbing materials like fibrous aggregates and foams. As acoustical applications are considered, the porous skeleton is assumed to be fully saturated by air. According to Biot's theory, the porous medium is considered as a superposition of a solid phase and fluid phase described by homogenized fields. K (respectively, W) denotes the total kinetic (respectively, strain) energy of the porous media. The separation of these two quantities into a solid part and a fluid part must be handled with particular care since one deals with homogenized quantities. In the porous material, three dissipation mechanisms associated with viscous and thermal effects together with structural damping occur. Unlike stored energies, the derivation of the dissipated powers into a solid and fluid part is more tractable since the physical phenomenon is intrinsically linked to a particular phase (solid phase for structural damping and fluid phase for viscous and thermal effects).

In this paper, a temporal dependency $e^{j\omega t}$ is chosen. For a given quantity X, an index 0 will represent its complex amplitude so that $X=X_0e^{j\omega t}$. $\mathcal{R}(\,)$ and $\mathcal{I}(\,)$ denote the real part and imaginary part functions of complex numbers, the star exponent is associated with the complex conjugation.

a)Electronic mail: olivier.dazel@univ-lemans.fr

 0001-4966/2008/123(4)/2054/10/$23.00 © 2008 Acoustical Society of America

Moreover, for all inertial and constitutive coefficients appearing in the model, a $\tilde{(\ )}$ above a coefficient indicates that it is complex-valued and frequency-dependent. Y_r and Y_i refer to the real part and imaginary part of $\tilde{Y}$, respectively.

The classical techniques, dealing with the real and imaginary parts of variational formulations, must be handled with care in the case of poroelastic problems. Hence, the methodology of our derivation is to express in the time domain the kinetic energy theorem and the thermodynamics first principle. Both of these theorems are expressed in the case of the $\{\mathbf{u},\mathbf{U}\}$ formulation as this one is fitted for a clear explanation and separation of the different physical mechanisms. This first step is, by itself, not original and has been applied in previous works for geomaterials.[1,11] Nevertheless, it has never been applied to acoustical materials involving frequency-dependent parameters and the link with the poroelastic $\{\mathbf{u},\mathbf{U}\}$ variational formulations has never been established. This first step is also interesting as the different notations and mechanisms can be defined. Once the temporal expressions of stored energies and dissipated powers are written, their mean value over a vibrating cycle can easily be obtained. The expressions of these indicators in the case of the $\{\mathbf{u},P\}$ formulation are directly derived from the one of the displacement formulation through a variable change. Hence, no energetic demonstration is done in the case of the mixed formulation, but the expressions are derived from the displacement ones.

This paper is organized as follows. First, the equations of motion and stress–strain relationships for a saturated poroelastic material are recalled (Sec. II). Then the expressions of stored and dissipated energies are derived in the case of $\{\mathbf{u},\mathbf{U}\}$ formulation (Sec. III). These expressions are then provided in the case of the $\{\mathbf{u},P\}$ formulation (Sec. IV). A simple example is then presented in order to illustrate and a quantitative and original convergence investigation of a finite-element scheme, based on the proposed indicators, is finally described in Sec. V.

II. OVERVIEW OF BIOT'S EQUATIONS

For sake of clarity, Biot–Allard's poroelasticity equations are first recalled in order to identify the different terms appearing in the expressions of the energies given in the following.

A. Equations of motion

The equations of motion of $\{\mathbf{u},\mathbf{U}\}$ formulation are[1]

$$-\omega^2\rho_1\mathbf{u} = \boldsymbol{\nabla}\cdot\boldsymbol{\sigma}^s(\mathbf{u},\mathbf{U}) + \omega^2\rho_{12}(\mathbf{U}-\mathbf{u}) + j\omega\tilde{b}(\mathbf{u}-\mathbf{U}), \tag{1a}$$

$$-\omega^2\rho_2\mathbf{U} = \boldsymbol{\nabla}\cdot\boldsymbol{\sigma}^f(\mathbf{u},\mathbf{U}) + \omega^2\rho_{12}(\mathbf{u}-\mathbf{U}) - j\omega\tilde{b}(\mathbf{u}-\mathbf{U}). \tag{1b}$$

$\boldsymbol{\sigma}^s(\mathbf{u},\mathbf{U})$ [respectively, $\boldsymbol{\sigma}^f(\mathbf{u},\mathbf{U})$] denotes the partial stress tensor of the solid (respectively, fluid) phase. ρ_1, ρ_2, and ρ_{12} represent homogenized densities. They are given by

$$\rho_1 = (1-\phi)\rho_s, \quad \rho_2 = \phi\rho_f, \quad \rho_{12} = -\phi\rho_f(\alpha_\infty - 1). \tag{2}$$

ϕ is the porosity, ρ_s is the skeleton material density, ρ_f is the interstitial fluid density, and α_∞ refers to geometric tortuosity. ρ_{12} accounts for the interaction between the inertia forces of the solid and fluid phase. $(j\omega)\tilde{b}(\mathbf{u}-\mathbf{U})$ represents the contribution of viscous forces. It is worth noting that the real part b_r and imaginary part b_i of $\tilde{b}$ are respectively associated with the dissipative part of viscous forces and with the modification of tortuosity due to the added mass effect associated with the viscous behavior of the fluid in the pores. In order to simplify Eqs. (1a) and (1b) an apparent inertial mass can be introduced,

$$\tilde{\rho}_{12} = \rho_{12} - \frac{\tilde{b}}{j\omega} = \underbrace{\left(\rho_{12} - \frac{b_i}{\omega}\right)}_{\rho'_{12}} + j\frac{b_r}{\omega},$$

hence the last two terms on the right-hand side of Eq. (1) can be grouped; this new coefficient provides a more compact writing but hides the two different phenomena (geometry and viscosity) in the real part (denoted by ρ'_{12}).

B. Constitutive relations

In order to identify all the macroscopical coefficients, stress–strain relations must be considered. They read:[1,12]

$$\boldsymbol{\sigma}^s(\mathbf{u},\mathbf{U}) = \tilde{A}\,\boldsymbol{\nabla}\cdot\mathbf{u}\mathbb{I} + 2\hat{N}\boldsymbol{\varepsilon}^s(\mathbf{u}) + \tilde{Q}\,\boldsymbol{\nabla}\cdot\mathbf{U}\mathbb{I}, \tag{3a}$$

$$\boldsymbol{\sigma}^f(\mathbf{u},\mathbf{U}) = \tilde{R}\,\boldsymbol{\nabla}\cdot\mathbf{U}\mathbb{I} + \tilde{Q}\,\boldsymbol{\nabla}\cdot\mathbf{u}\mathbb{I}. \tag{3b}$$

$\boldsymbol{\varepsilon}^s(\mathbf{u})$ is the strain tensor of the fluid phase and $\mathbb{I}$ is the identity tensor of rank 3. All the constitutive coefficients but $\hat{N}$ are also complex and frequency dependent and their expression can be found in Biot and Willis's work.[12] Their complex and frequency-dependent nature is due to thermal effects; the real part corresponds to conservative effects (stress) and the imaginary part to thermal dissipative effects. It is important to note that $\tilde{A}$ is frequency dependent but can be split into two terms as

$$\tilde{A} = \hat{A} + \frac{\tilde{Q}^2}{\tilde{R}}, \tag{4}$$

where $\hat{A}$ is linked to the property of the solid *in vacuo* and $\tilde{Q}^2/\tilde{R}$ can be related to a restoring elastic force induced by the fluid phase on the solid phase. One can then introduce the *in vacuo* solid stress tensor:

$$\hat{\boldsymbol{\sigma}}(\mathbf{u}) = \hat{A}\,\boldsymbol{\nabla}\cdot\mathbf{u}\mathbb{I} + 2\hat{N}\boldsymbol{\varepsilon}(\mathbf{u}). \tag{5}$$

Unlike the partial stress tensor of the solid part, $\hat{\boldsymbol{\sigma}}(\mathbf{u})$ is independent of the motion of the fluid phase; in addition its constitutive coefficients do not depend on frequency since the contribution of the fluid phase has been withdrawn. This tensor plays an important role in the mixed formulation. Another interesting property is that in all cases, the ratio $\tilde{Q}/\tilde{R}$ is real so that a useful nondimensional real parameter can be defined

$$\xi = \frac{\tilde{Q}}{\tilde{R}} = \frac{Q_r}{R_r} = \frac{Q_i}{R_i} \in \mathbb{R}. \tag{6}$$

In order to take into account dissipation in the porous skeleton a hysteretic model is often used and it is then assumed that

$$\hat{A} = A_r + jA_i = A(1 + j\eta_s), \quad \hat{N} = N_r + jN_i = N(1 + j\eta_s), \tag{7}$$

where η_s is the skeleton structural damping coefficient. Note that other damping models can be substituted. In order to make a distinction between conservative and dissipative effects let $\hat{\boldsymbol{\sigma}}_r^s(\mathbf{u})$ [respectively, $\hat{\boldsymbol{\sigma}}_i^s(\mathbf{u})$] be the *in vacuo* tensor associated to the real (respectively, imaginary) part of coefficients.

III. EXPRESSIONS OF ENERGIES AND POWERS IN THE CASE OF {U,U} FORMALISM

A. Theorem of kinetic energy

The theorem of kinetic energy should be first expressed for Biot's equations. The methodology is inspired from the one presented in Ref. 11 and is based on the mechanics and thermodynamics of open continuous media. This paper extends Coussy's purpose to the case of acoustic materials and gives explicit expressions of all the terms of both $\{\mathbf{u},\mathbf{U}\}$ and $\{\mathbf{u},P\}$ formulations which are not given in detail in the previous references.

The theorem of kinetic energy is a particular case of the theorem of virtual powers. This theorem stipulates that for any material subdomain and for any velocity field whether actual or virtual, the sum of the powers of external, inertia, and internal forces is zero; the kinetic energy corresponds to the case of the actual velocity field. In order to obtain the expression of theorem of virtual powers, the temporal point of view must be considered; hence, by introducing $\mathbf{v}$ (respectively, $\mathbf{V}$), the complex velocity field of the solid (respectively, fluid) phase, Eq. (1) is rewritten in the time domain as

$$\rho_1 \frac{d\mathcal{R}(\mathbf{v})}{dt} + \rho_{12}' \frac{d}{dt}\mathcal{R}(\mathbf{V}-\mathbf{v}) = \mathcal{R}(\boldsymbol{\nabla}\cdot\boldsymbol{\sigma}^s(\mathbf{u},\mathbf{U})) - b_r\mathcal{R}(\mathbf{v}-\mathbf{V}), \tag{8a}$$

and

$$\rho_2 \frac{d\mathcal{R}(\mathbf{V})}{dt} + \rho_{12}' \frac{d}{dt}\mathcal{R}(\mathbf{v}-\mathbf{V}) = \mathcal{R}(\boldsymbol{\nabla}\cdot\boldsymbol{\sigma}^f(\mathbf{u},\mathbf{U})) - b_r\mathcal{R}(\mathbf{V}-\mathbf{v}). \tag{8b}$$

In order to obtain the kinetic energy theorem, Eq. (8a) [respectively, (8b)] is multiplied by $\mathcal{R}(\mathbf{v})$ [respectively, $\mathcal{R}(\mathbf{V})$], both equations are integrated on the porous domain Ω and the sum of the two obtained equations is performed. The resulting term corresponding to the left-hand side of Eqs. (8a) and (8b) can be interpreted as the total derivative of the total kinetic energy K defined by

$$K = \frac{1}{2}\int_\Omega \rho_1\mathcal{R}^2(\mathbf{v}) + \rho_2\mathcal{R}^2(\mathbf{V}) - \rho_{12}'\mathcal{R}^2(\mathbf{V}-\mathbf{v})d\Omega. \tag{9}$$

In order to distinguish the powers of external and internal forces, Green's second formula is used and the term corresponding to the right-hand side of Eqs. (8a) and (8b) then reads:

$$P_{\text{ext}} = \oint_{\partial\Omega} \mathcal{R}(\boldsymbol{\sigma}^s(\mathbf{u},\mathbf{U}))\cdot\mathcal{R}(\mathbf{v})\cdot\mathbf{n}d\Gamma + \oint_{\partial\Omega} \mathcal{R}(\boldsymbol{\sigma}^f(\mathbf{u},\mathbf{U}))\cdot\mathcal{R}(\mathbf{V})\cdot\mathbf{n}d\Gamma, \tag{10}$$

$$P_{\text{int}} = \int_\Omega \mathcal{R}(\boldsymbol{\sigma}^s(\mathbf{u},\mathbf{U})):\mathcal{R}(\mathbf{d}^s) + \mathcal{R}(\boldsymbol{\sigma}^f(\mathbf{u},\mathbf{U})):\mathcal{R}(\mathbf{d}^f) - b_r\mathcal{R}(\mathbf{v}-\mathbf{V})^2 d\Omega, \tag{11}$$

where $\mathbf{d}^s$ and $\mathbf{d}^f$ are the time derivatives of strain tensors associated with the solid phase and fluid phase, respectively. The kinetic energy theorem is then in its classical form:

$$\mathcal{P}_{\text{ext}} = \mathcal{P}_{\text{int}} + \frac{DK}{Dt}. \tag{12}$$

B. Expression of the first law

For dissipative media, the only use of the kinetic energy theorem is not sufficient to detail and separate the different aspects of energy stored and exchanged by the porous media. It is necessary to use the first law of thermodynamics, which expresses the conservation of energy in all its forms. This principle states that at any time, the material derivative of the total energy $\mathcal{E}$ is equal to the sum of the work rate $\mathcal{P}_{\text{ext}}$ of the external forces acting upon the porous material and of the rate $\mathcal{Q}^0$ of external heat supply. The total energy is in fact the sum of the kinetic energy K defined in the following and of the internal energy E associated with both the deformation of the media and the random, disordered motion of molecules at atomic scale:

$$\frac{D\mathcal{E}}{Dt} = \mathcal{P}_{\text{ext}} + \mathcal{Q}^0. \tag{13}$$

In the classical models used in acoustics of porous media, it is always assumed that this internal energy is only due to deformation effects without modification of the temperature of the matter. This is due to the high ratio of thermal conductivity to thermal capacity in both media which causes all the heat produced by dissipation mechanisms to go outside of the porous medium without warming it up.

By combining Eqs. (12) and (13), one obtains

$$\frac{DE}{Dt} = \mathcal{Q}^0 + \mathcal{P}_{\text{int}}. \tag{14}$$

Hence, the integration over a cycle of equations (12) and (13) leads to

$$\int_T \mathcal{P}_{\text{ext}} dt = \int_T \mathcal{P}_{\text{int}} dt = -\int_T \mathcal{Q}^0 dt. \tag{15}$$

The interpretation is as follows: If over a cycle, mechanical energy is algebraically provided to the system, an equal amount of heat is released by the porous medium; in other words, no energy is stored in the porous media. The transformation of nature of energy is due to the dissipation phenomena inside the porous medium which is more easily understandable by detailing $\mathcal{P}_{\text{int}}$. The latter is the sum of four terms:

$$\mathcal{P}_{\text{int}} = dW_{\text{def}} - \mathcal{P}_{\text{vis}} - \mathcal{P}_{\text{str}} - \mathcal{P}_{\text{th}} \tag{16}$$

dW_{def} corresponds to the conservative elastic effects defined by

$$dW_{\text{def}} = \int_\Omega \hat{\boldsymbol{\sigma}}_r^s(\mathcal{R}(\mathbf{u})) : \mathcal{R}(\mathbf{d}^s) + R_r \boldsymbol{\nabla} \cdot \mathcal{R}(\xi \mathbf{u} + \mathbf{U}) \boldsymbol{\nabla} \cdot \mathcal{R}(\xi \mathbf{v} + \mathbf{V}) d\Omega. \tag{17}$$

dW_{def} is the material derivative of the strain energy W_{def} defined by

$$W_{\text{def}} = \frac{1}{2}\int_\Omega \hat{\boldsymbol{\sigma}}_r^s(\mathcal{R}(\mathbf{u})) : \mathcal{R}(\boldsymbol{\varepsilon}^s) + R_r(\boldsymbol{\nabla} \cdot \mathcal{R}(\xi \mathbf{u} + \mathbf{U}))^2 d\Omega. \tag{18}$$

P_{vis}, P_{str}, P_{th} are the powers dissipated by viscous effects, structural damping, and thermal effects. They read:

$$P_{\text{vis}} = \int_\Omega b_r \mathcal{R}^2(\mathbf{v} - \mathbf{V}) d\Omega, \tag{19a}$$

$$\mathcal{P}_{\text{str}} = \int_\Omega \hat{\boldsymbol{\sigma}}_i^s(\mathcal{I}(\mathbf{u})) : \mathcal{R}(\mathbf{d}^s) d\Omega, \tag{19b}$$

$$\mathcal{P}_{\text{th}} = \int_\Omega R_i \boldsymbol{\nabla} \cdot \mathcal{I}(\xi \mathbf{u} + \mathbf{U}) \boldsymbol{\nabla} \cdot \mathcal{R}(\xi \mathbf{v} + \mathbf{V}) d\Omega. \tag{19c}$$

C. Separation of energies stored in the solid and fluid part

The distinction between the solid and fluid is now undertaken to separate the contribution of each phase to K and W_{def}.

The definition (9) of the kinetic energy K comprises three terms. The first one can be interpreted as the kinetic energy of the solid phase K_s:

$$K_s = \frac{1}{2}\int_\Omega \rho_1 \mathcal{R}^2(\mathbf{v}) d\Omega. \tag{20}$$

The last two terms represent the kinetic energy of the fluid phase K_f:

$$K_f = \frac{1}{2}\int_\Omega \rho_2 \mathcal{R}^2(\mathbf{V}) - \rho_{12}' \mathcal{R}^2(\mathbf{V} - \mathbf{v}) d\Omega. \tag{21}$$

Let us now consider the strain energy. In Eq. (18), two terms appear. The first term (referred to in the following as $\hat{W}_{\text{def}}^s$) can easily be defined as the strain energy of the *in vacuo* solid phase. To interpret the second part, the stress–strain relation of the fluid phase must be considered. Since

$$-\phi \frac{P}{\tilde{R}} = \xi \boldsymbol{\nabla} \cdot \mathbf{u} + \boldsymbol{\nabla} \cdot \mathbf{U}, \tag{22}$$

the second term can be expressed and defined as

$$\hat{W}_{\text{def}}^f = \frac{1}{2}\phi^2 R_r \int_\Omega \mathcal{R}^2\left(\frac{P}{\tilde{R}}\right) d\Omega, \tag{23}$$

which can be interpreted as the strain energy of a closed fluid media. Nevertheless neither the solid is *in vacuo*, nor the media is closed. The best way to separate the solid and fluid phase is to go back to the partial stress tensor. Hence:

$$\begin{aligned} W_{\text{def}}^s &= \frac{1}{2}\int_\Omega \mathcal{R}(\boldsymbol{\sigma}^s(\mathbf{u},\mathbf{U})) : \mathcal{R}(\boldsymbol{\varepsilon}^s(u)) d\Omega \\ &= \frac{1}{2}\int_\Omega \hat{\boldsymbol{\sigma}}_r^s(\mathcal{R}(\mathbf{u})) : \mathcal{R}(\boldsymbol{\varepsilon}^s) \\ &\quad + Q_r(\boldsymbol{\nabla} \cdot \mathcal{R}(\xi \mathbf{u} + \mathbf{U})) \boldsymbol{\nabla} \cdot \mathcal{R}(\mathbf{u}) d\Omega \end{aligned}$$

is defined as the strain energy of the solid phase. The strain energy of the fluid phase reads:

$$\begin{aligned} W_{\text{def}}^f &= \frac{1}{2}\int_\Omega \mathcal{R}(\boldsymbol{\sigma}^f(\mathbf{u},\mathbf{U})) : \mathcal{R}(\boldsymbol{\varepsilon}^s(u)) d\Omega \\ &= \frac{1}{2}\int_\Omega R_r(\boldsymbol{\nabla} \cdot \mathcal{R}(\xi \mathbf{u} + \mathbf{U})) \boldsymbol{\nabla} \cdot \mathcal{R}(\mathbf{U}) d\Omega. \end{aligned}$$

Concerning the dissipated powers, there is no need to separate them into solid and fluid phases.

D. Time-averaged expressions

All the expressions given in the following are instantaneous values. As harmonic excitations are considered, it is more common to present time-averaged values. Table I summarizes the time-averaged expressions of kinetic and strain energies together with energies dissipated over a cycle through the considered mechanism. This energy is defined by $\mathcal{W}$ with the index corresponding to the considered mechanism. $\langle . \rangle$ is the time-average operator. For this formulation it is straightforward to check that these time-averaged expressions of the stored energies and dissipated powers are the ones that can be obtained with the help of the real and imaginary part of the variational formulations.

IV. EXPRESSIONS OF ENERGIES AND POWERS IN THE CASE OF $\{\mathbf{u}, P\}$ FORMULATION

In order to transpose the previous results obtained in the case of $\{\mathbf{u},\mathbf{U}\}$ formulation to the $\{\mathbf{u};P\}$ formulation,[4] a change of variable is performed. It is based on a combination of both the constitutive relation and the equation of motion of the fluid phase. Hence:

TABLE I. Summary of the energy expressions in the case of $\{\mathbf{u},\mathbf{U}\}$ formulation.

$\langle K_s\rangle$	$\frac{\omega^2}{4}\int_\Omega \rho_1 \lvert\mathbf{u}_0\rvert^2 d\Omega$
$\langle K_f\rangle$	$\frac{\omega^2}{4}\int_\Omega \rho_2 \lvert\mathbf{U}_0\rvert^2 - \rho'_{12}\lvert\mathbf{u}_0-\mathbf{U}_0\rvert^2 d\Omega$
$\langle W_{\text{def}}\rangle$	$\frac{1}{4}\int_\Omega \hat{\boldsymbol{\sigma}}_r^s(\mathbf{u}_0):\boldsymbol{\varepsilon}^s(\mathbf{u}_0^*)+R_r\lvert\xi\boldsymbol{\nabla}\cdot\mathbf{u}_0+\boldsymbol{\nabla}\cdot\mathbf{U}_0\rvert^2 d\Omega$
$\langle \hat{W}^s_{\text{def}}\rangle$	$\frac{1}{4}\int_\Omega \hat{\boldsymbol{\sigma}}_r^s(\mathbf{u}_0):\boldsymbol{\varepsilon}(\mathbf{u}_0^*) d\Omega$
$\langle \hat{W}^f_{\text{def}}\rangle$	$\frac{R_r}{4}\int_\Omega \lvert\xi\boldsymbol{\nabla}\cdot\mathbf{u}_0+\boldsymbol{\nabla}\cdot\mathbf{U}_0\rvert^2 d\Omega$
$\langle W^s_{\text{def}}\rangle$	$\frac{1}{4}\int_\Omega \hat{\boldsymbol{\sigma}}_r^s(\mathbf{u}_0):\boldsymbol{\varepsilon}(\mathbf{u}_0^*)+Q_r\xi\lvert\boldsymbol{\nabla}\cdot\mathbf{u}_0\rvert^2+Q_r\mathcal{R}(\boldsymbol{\nabla}\cdot\mathbf{U}_0\boldsymbol{\nabla}\cdot\mathbf{u}_0^*) d\Omega$
$\langle W^f_{\text{def}}\rangle$	$\frac{R_r}{4}\int_\Omega \xi\mathcal{R}(\boldsymbol{\nabla}\cdot\mathbf{u}_0\boldsymbol{\nabla}\cdot\mathbf{U}_0^*)+\lvert\boldsymbol{\nabla}\cdot\mathbf{U}_0\rvert^2 d\Omega$
$\mathcal{W}_{\text{vis}}$	$b_r\pi\omega\int_\Omega \lvert\mathbf{u}_0-\mathbf{U}_0\rvert^2 dS$
$\mathcal{W}_{\text{struct}}$	$\pi\int_\Omega \hat{\boldsymbol{\sigma}}_i^s(\mathbf{u}_0):\boldsymbol{\varepsilon}(\mathbf{u}_0^*) d\Omega$
$\mathcal{W}_{\text{th}}$	$R_i\pi\int_\Omega \lvert\xi\boldsymbol{\nabla}\cdot\mathbf{u}_0+\boldsymbol{\nabla}\cdot\mathbf{U}_0\rvert^2 d\Omega$

$$\mathbf{U}=\frac{\phi}{\tilde{\rho}_{22}\omega^2}\boldsymbol{\nabla}P-\frac{\tilde{\rho}_{12}}{\tilde{\rho}_{22}}\mathbf{u}\Leftrightarrow\mathbf{U}_0=\frac{\phi}{\tilde{\rho}_{22}\omega^2}\boldsymbol{\nabla}P_0-\frac{\tilde{\rho}_{12}}{\tilde{\rho}_{22}}\mathbf{u}_0. \tag{24}$$

Recall that the apparent Biot densities are defined by

$$\tilde{\rho}_{11}=\rho_1-\tilde{\rho}_{12};\quad \tilde{\rho}_{22}=\rho_2-\tilde{\rho}_{12}. \tag{25}$$

In order to obtain the expressions of the strain energies and thermal and structural dissipated powers, it is necessary to calculate $\boldsymbol{\nabla}\cdot\mathbf{U}_0$. It is directly given by the constitutive relation of the fluid phase:

$$\boldsymbol{\nabla}\cdot\mathbf{U}=-\frac{\phi}{\tilde{R}}P-\xi\boldsymbol{\nabla}\cdot\mathbf{u}\Leftrightarrow\boldsymbol{\nabla}\cdot\mathbf{U}_0=-\frac{\phi}{\tilde{R}}P_0-\xi\boldsymbol{\nabla}\cdot\mathbf{u}_0. \tag{26}$$

A. Kinetic energies and viscous dissipated power

It is possible to obtain directly both kinetic energies and viscous dissipated energies by considering the following complex quantity $X=(4/\omega^2)\langle K^s\rangle+(4/\omega^2)\langle K^f\rangle-j(1/\pi\omega^2)\mathcal{W}_{\text{vis}}$. Hence, X can be written as a function of the displacement amplitude:

$$X=\int_\Omega(\tilde{\rho}_{11}\lvert\mathbf{u}_0\rvert^2+\tilde{\rho}_{12}\mathbf{u}_0^*\mathbf{U}_0+\tilde{\rho}_{12}\mathbf{U}_0^*\mathbf{u}_0+\tilde{\rho}_{22}\lvert\mathbf{U}_0\rvert^2)d\Omega. \tag{27}$$

By using Eq. (24), one obtains

$$X=\int_\Omega\tilde{\rho}\lvert\mathbf{u}_0\rvert^2+\frac{\phi^2}{\tilde{\rho}_{22}^*\omega^4}\lvert\boldsymbol{\nabla}P_0\rvert^2+\frac{2j\phi}{\omega^2}\mathcal{I}\left(\frac{\tilde{\rho}_{12}}{\tilde{\rho}_{22}}\right)\mathbf{u}_0^*\boldsymbol{\nabla}P_0 d\Omega. \tag{28}$$

$\tilde{\rho}$ has been introduced by Atalla *et al.*[4] and is defined by

$$\tilde{\rho}=\tilde{\rho}_{11}-\frac{\tilde{\rho}_{12}^2}{\tilde{\rho}_{22}}. \tag{29}$$

In order to use the modified $\{\mathbf{u},P\}$ formulation[5] it is necessary to recall the definition of the dynamic tortuosity[2] $\tilde{\alpha}$ and its consequence:

$$\tilde{\alpha}=\frac{\tilde{\rho}_{22}}{\rho_2}.\ \Rightarrow\mathcal{I}\left(\frac{\widetilde{\rho_{12}}}{\widetilde{\rho_{22}}}\right)=\mathcal{I}\left(\frac{1}{\tilde{\alpha}}\right). \tag{30}$$

Hence,

$$X=\omega^2\int_\Omega\tilde{\rho}\lvert\mathbf{u}_0\rvert^2+\frac{\phi^2}{\widetilde{\rho_{22}}^*\omega^4}\lvert\boldsymbol{\nabla}P_0\rvert^2+\frac{2j}{\omega^2}\mathcal{I}\left(\frac{\phi}{\tilde{\alpha}}\right)\mathbf{u}_0^*\boldsymbol{\nabla}P_0 d\Omega \tag{31}$$

$$\frac{\phi}{\tilde{\alpha}}=\tilde{\gamma}+h\left(1+\frac{\tilde{Q}}{\tilde{R}}\right)\Rightarrow\mathcal{I}\left(\frac{\phi}{\tilde{\alpha}}\right)=\mathcal{I}(\tilde{\gamma}). \tag{32}$$

By identifying real and imaginary parts of X, it is possible to separate kinetic energies and viscous dissipated powers:

$$\langle K\rangle=\frac{\omega^2}{4}\int_\Omega\mathcal{R}(\tilde{\rho})\lvert\mathbf{u}_0\rvert^2+\mathcal{R}\left(\frac{\phi^2}{\widetilde{\rho_{22}}^*\omega^4}\right)\lvert\boldsymbol{\nabla}P_0\rvert^2-\frac{2}{\omega^2}\mathcal{I}\left(\frac{\phi}{\tilde{\alpha}}\right)\mathcal{I}(\mathbf{u}_0^*\boldsymbol{\nabla}P_0)d\Omega. \tag{33}$$

The last expression can be separated into solid and fluid parts,

$$\langle K_s\rangle=\frac{\omega^2}{4}\int_\Omega\rho_1\lvert\mathbf{u}_0\rvert^2 d\Omega, \tag{34}$$

$$\langle K_f\rangle=\frac{\omega^2}{4}\int_\Omega\mathcal{R}(\tilde{\rho}-\rho_1)\lvert\mathbf{u}_0\rvert^2+\mathcal{R}\left(\frac{\phi^2}{\widetilde{\rho_{22}}^*\omega^4}\right)\lvert\boldsymbol{\nabla}P_0\rvert^2-\frac{2}{\omega^2}\mathcal{I}\left(\frac{\phi}{\tilde{\alpha}}\right)\mathcal{I}(\mathbf{u}_0^*\boldsymbol{\nabla}P_0)d\Omega. \tag{35}$$

It is possible to define $\tilde{\rho}_f=\tilde{\rho}-\rho_1$ in order to condense the former expression.

The imaginary part of X allows for the obtention of the viscous dissipated energy:

$$\mathcal{W}_{\text{vis}}=-\pi\omega^2\int_\Omega\mathcal{I}(\tilde{\rho})\lvert\mathbf{u}_0\rvert^2-\mathcal{I}\left(\frac{\phi^2}{\widetilde{\rho_{22}\omega^4}}\right)\lvert\boldsymbol{\nabla}P_0\rvert^2+\frac{2}{\omega^2}\mathcal{I}\left(\frac{\phi}{\tilde{\alpha}}\right)\mathcal{R}(\mathbf{u}_0^*\boldsymbol{\nabla}P_0)d\Omega. \tag{36}$$

This last expression agree with the ones given by Sgard *et al.*[8]

B. Strain energy and thermal dissipation

Let us now consider the expressions of strain energies together with thermal and structural dissipated powers. First,

$\langle \hat{W}^s_{\text{def}} \rangle$ and $\mathcal{W}_{\text{struct}}$ remain unchanged as they depend only on the solid displacement. A second set of expressions can easily be expressed by using Eq. (26),

$$\langle W_{\text{def}} \rangle = \frac{1}{4}\int_\Omega \hat{\boldsymbol{\sigma}}^s_r(\mathbf{u}_0):\boldsymbol{\varepsilon}^s(\mathbf{u}_0^*) + \frac{\phi^2 R_r}{|\tilde{R}|^2}|P_0|^2 d\Omega, \tag{37a}$$

$$\langle \hat{W}^f_{\text{def}} \rangle = \frac{\phi^2 R_r}{4|\tilde{R}|^2}\int_\Omega |P_0|^2 d\Omega, \tag{37b}$$

$$\mathcal{W}_{\text{th}} = \frac{\phi^2 \pi R_i}{|\tilde{R}|^2}\int_\Omega |P_0|^2 d\Omega. \tag{37c}$$

In order to obtain Eqs. (37b) and (37c), two intermediate results are given:

$$\int_\Omega |\boldsymbol{\nabla}\cdot\mathbf{U}_0|^2 d\Omega = \int_\Omega \left(\frac{-\phi}{\tilde{R}^*}P_0^* - \xi\boldsymbol{\nabla}\cdot\mathbf{u}_0^*\right) \times \left(\frac{-\phi}{\tilde{R}}P_0 - \xi\boldsymbol{\nabla}\cdot\mathbf{u}_0\right) d\Omega$$
$$= \int_\Omega \frac{\phi^2}{|\tilde{R}|^2}|P_0|^2 + 2\phi\xi\mathcal{R}\left(\frac{\boldsymbol{\nabla}\cdot\mathbf{u}_0^* P_0}{\tilde{R}}\right) + \xi^2|\boldsymbol{\nabla}\cdot\mathbf{u}_0|^2 d\Omega,$$

$$\int_\Omega \mathcal{R}(\boldsymbol{\nabla}\cdot\mathbf{u}_0\,\boldsymbol{\nabla}\cdot\mathbf{U}_0^*)d\Omega = -\int_\Omega \mathcal{R}\left(\frac{\phi}{\tilde{R}^*}\boldsymbol{\nabla}\cdot\mathbf{u}_0 P_0^*\right) + \xi|\boldsymbol{\nabla}\cdot\mathbf{u}_0|^2 d\Omega.$$

Therefore,

$$\langle W^s_{\text{def}} \rangle = \frac{1}{4}\int_\Omega \hat{\boldsymbol{\sigma}}^s_r(\mathbf{u}_0):\boldsymbol{\varepsilon}(\mathbf{u}_0^*) - Q_r\mathcal{R}\left(\frac{\phi^2}{\tilde{R}^*}\boldsymbol{\nabla}\cdot\mathbf{u}_0 P_0^*\right)d\Omega, \tag{38}$$

$$\langle W^f_{\text{def}} \rangle = \frac{R_r}{4}\int_\Omega \xi\phi\mathcal{R}\left(\frac{\boldsymbol{\nabla}\cdot\mathbf{u}_0\,.\,P_0^*}{\tilde{R}^*}\right) + \frac{\phi^2}{|\tilde{R}|^2}|P_0|^2 d\Omega. \tag{39}$$

All the results for the modified $\{\mathbf{u},P\}$ formulation are summarized in Table II.

TABLE II. Summary of the energy expressions in the case of modified $\{\mathbf{u},P\}$ formulation.

$\langle K_s \rangle$	$\frac{\omega^2}{4}\int_\Omega \rho_1 \lvert\mathbf{u}_0\rvert^2 d\Omega$
$\langle K_f \rangle$	$\frac{\omega^2}{4}\int_\Omega \mathcal{R}(\tilde{\rho}_f)\lvert\mathbf{u}_0\rvert^2 + \mathcal{R}\left(\frac{\phi^2}{\tilde{\rho}_{22}{}^*\omega^4}\right)\lvert\boldsymbol{\nabla}P_0\rvert^2 - \frac{2}{\omega^2}\mathcal{I}\left(\frac{\phi}{\tilde{\alpha}}\right)\mathcal{I}(\mathbf{u}_0^*\boldsymbol{\nabla}P_0)d\Omega$
$\langle W_{\text{def}} \rangle$	$\frac{1}{4}\int_\Omega \hat{\boldsymbol{\sigma}}^s_r(\mathbf{u}_0):\boldsymbol{\varepsilon}^s(\mathbf{u}_0^*) + \frac{\phi^2 R_r}{\lvert\tilde{R}\rvert^2}\lvert P_0\rvert^2 d\Omega$
$\langle \hat{W}^s_{\text{def}} \rangle$	$\frac{1}{4}\int_\Omega \hat{\boldsymbol{\sigma}}^s_r(\mathbf{u}_0):\boldsymbol{\varepsilon}(\mathbf{u}_0^*)d\Omega$
$\langle \hat{W}^f_{\text{def}} \rangle$	$\frac{\phi R_r}{4\lvert\tilde{R}\rvert^2}\int_\Omega \lvert P_0\rvert^2 d\Omega$
$\langle W^s_{\text{def}} \rangle$	$\frac{1}{4}\int_\Omega \hat{\boldsymbol{\sigma}}^s_r(\mathbf{u}_0):\boldsymbol{\varepsilon}(\mathbf{u}_0^*) - Q_r\mathcal{R}\left(\frac{\phi}{\tilde{R}^*}\boldsymbol{\nabla}\cdot\mathbf{u}_0 P_0^*\right)d\Omega$
$\langle W^f_{\text{def}} \rangle$	$\frac{R_r}{4}\int_\Omega \xi\phi\mathcal{R}\left(\frac{\boldsymbol{\nabla}\cdot\mathbf{u}_0\cdot P_0^*}{\tilde{R}^*}\right) + \frac{\phi^2}{\lvert\tilde{R}\rvert^2}\lvert P_0\rvert^2 d\Omega$
$\mathcal{W}_{\text{vis}}$	$-\pi\omega^2\int_\Omega \mathcal{I}(\tilde{\rho})\lvert\mathbf{u}_0\rvert^2 - \mathcal{I}\left(\frac{\phi^2}{\tilde{\rho}_{22}\omega^4}\right)\lvert\boldsymbol{\nabla}P_0\rvert^2 + \frac{2}{\omega^2}\mathcal{I}\left(\frac{\phi}{\tilde{\alpha}}\right)\mathcal{R}(\mathbf{u}_0^*\boldsymbol{\nabla}P_0)d\Omega$
$\mathcal{W}_{\text{struct}}$	$\pi\int_\Omega \hat{\boldsymbol{\sigma}}^s_i(\mathbf{u}_0):\boldsymbol{\varepsilon}(\mathbf{u}_0^*)d\Omega$
$\mathcal{W}_{\text{th}}$	$\frac{\phi^2\pi R_i}{\lvert\tilde{R}\rvert^2}\int_\Omega \lvert P_0\rvert^2 d\Omega$

C. Discussion

It is necessary to underline that the $\{\mathbf{u},P\}$ expressions of the stored energies proposed in Sec. IV B are not the ones which can be obtained by taking the real part of the classically called mixed poroelastic variational formulations.[4] This identification, well known as a classical vibration problem [as well as the $\{\mathbf{u},\mathbf{U}\}$ formulation], is not valid in this case. The reason for this difference lies in the derivation of the mixed formulation,[4] which is not obtained from the differentiation of a Lagrangian density dealing with the whole porous material (solid and fluid phase). The methodology is in fact in two steps; the first one is the obtention of motion equations in terms of $\{\mathbf{u},P\}$ fields for each phase. The second step of the method of Attala *et al.* is to multiply by an admissible field each one of these two motion equations. Hence, two bilinear formulations are then obtained. The global mixed formulation is obtained by adding equations of the solid and fluid phase. It is interesting to note that every combination of these two equations could have been used. Several differences occur while comparing this sum to the expressions given in Sec. IV B.[4,5,8]

Despite the remarks of this section, it is fundamental to indicate that the numerical results obtained through the finite-element discretization of the mixed formulations based on Ref. 4 are correct even if the energetic interpretation of these formulations must be handled with care. This is confirmed in Sec. V.

V. APPLICATION TO A MULTILAYERED PROBLEM

A. Presentation of the problem

The following is devoted to the adaptation of the analytical energetic indicators proposed in the preceding sections to a discretized problem. The convergence of finite element schemes is often made through global indicators, it is then interesting to use the proposed ones. They are complementary to the mathematical $\mathcal{L}^2$ ones (mean square pressure or velocity, for example) which do not have physical significance. It is then necessary to investigate in which way they are able to check the validity of a finite-element discretization.

The configuration of interest is a monodimensional two layer problem depicted in Fig. 1. The second layer is bonded on a rigid wall and the first one is excited by a normalized pressure plane wave. The properties of the two porous media are given in Table III and the Appendix presents the expres-

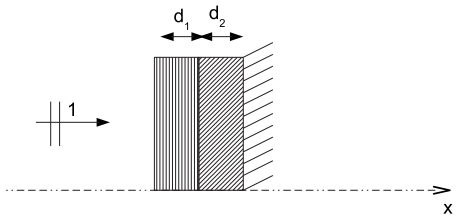

FIG. 1. Configuration of the problem.

sions of the coefficients of the Biot–Allard[2] model. This problem is numerically interesting as the acoustical behavior of these two porous materials is more complex than the case for a single porous structure. The second advantage is that an exact analytical solution can be obtained. Hence, the accuracy of the discretization scheme can be estimated by a comparison to the exact analytical solution of the problem considered as reference. It is not the case of the convergence analysis of poroelastic finite element models of the literature for which the reference solution is a numerical overmeshed discretized result.

B. Physical considerations

This simple problem can be solved analytically and the methodology is as follows. The shear waves are not excited by the normal incident plane wave and only the two compressional waves are involved. The solid and fluid displacements and the pressure can be written as a function of the amplitude of these waves (similar to Allard's[2] methodology). Nine unknowns are then involved (eight amplitude unknowns and the reflection coefficient R at the air–porous interface). The problem can be solved by way of the nine following relations. At the rigid backing interface, one has two relations: cancellation of the solid and total displacement[13] [defined by $\mathbf{u}^t=(1-\phi)\mathbf{u}+\phi\mathbf{U}$]. At the two porous substructure interface, four continuity relations are involved (solid and total displacement, *in vacuo* stress tensor[13] and pressure). At the air–porous interface there are three relations: the air displacement is equal to the porous structure total displacement, the *in vacuo* stress is null, and the pressure is continuous. It is then possible to solve analytically this nine linear equation system with Cramer's determinant, to find the amplitudes of the eight waves and then to deduce the analytical expressions of the solid displacement and the pressure. The energetic indicator of Tables I and II can be deduced through a formal spatial integration.

TABLE III. Material properties.

		Material 1	Material 2
ϕ	(1)	0.952	0.937
σ	($N\,s\,m^{-4}$)	21300	50485
α_∞	(1)	1.9	2.57
Λ	(μm)	100	57.41
Λ'	(μm)	300	61.62
ρ_1	($kg\,m^{-3}$)	38.4	95.66
E	(kPa)	30	66
η_s	(1)	0.04	0.105
d	(cm)	5	5

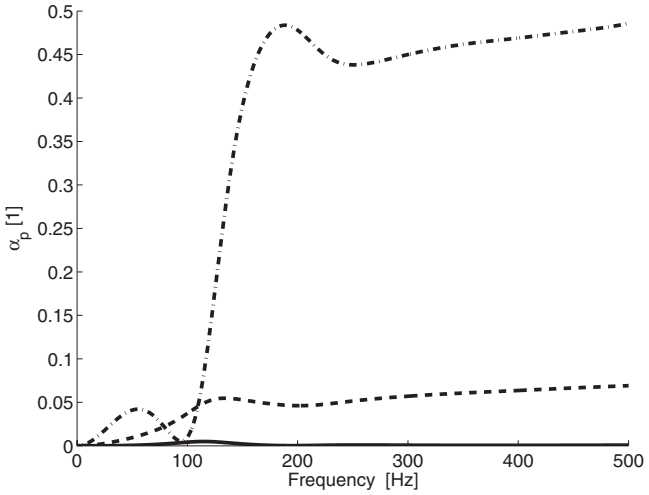

FIG. 2. Partial absorption coefficient of the first layer. Solid line: Structural dissipation; dashed line: Thermal effects; and dash-dot line: Viscous effects.

It is interesting to first analyze the physics of the problem in order to point out the interest of energetic indicators. All the results presented in this section correspond to the analytical ones. Figures 2 and 3, respectively, present the partial absorption of the left and the right layer in the $[1;500]$ Hz frequency band. (1) means nondimensional parameter. The classical absorption coefficient is defined as the ratio of the absorbed power over the incident one. Each one of these six partial absorption coefficients involves the restriction of this ratio to a particular mechanism for a considered layer. For example, the dash-dotted curve of Fig. 2 represents the dissipation by viscous effects in the first layer:

$$\alpha^l_{\text{vis}} = \frac{W^l_{\text{vis}}}{W^l_{\text{vis}} + W^l_{\text{struct}} + W^l_{\text{th}} + W^r_{\text{vis}} + W^r_{\text{struct}} + W^r_{\text{th}}}(1-|R|^2). \tag{40}$$

The l and r exponents are related to the left and right layer, respectively. These figures clearly show that viscous effects

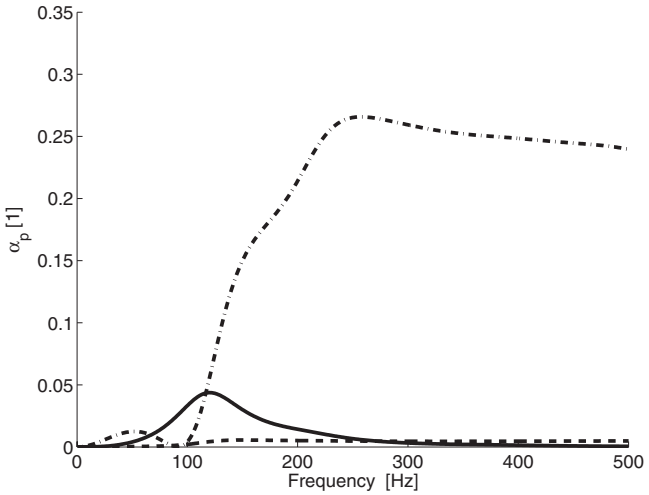

FIG. 3. Partial absorption coefficient of the second layer. Solid line: Structural dissipation; dashed line: Thermal effects; and dash-dot line: Viscous effects.

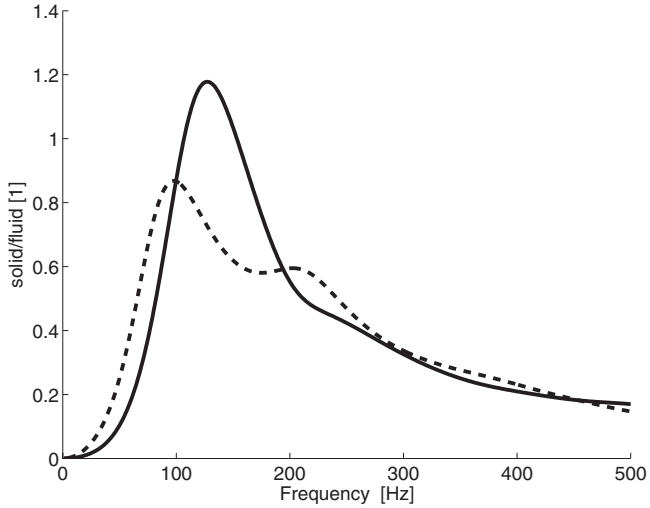

FIG. 4. Ratio of the mean total energy in the solid phase over the fluid one. Solid line: first layer and dashed line: Second layer.

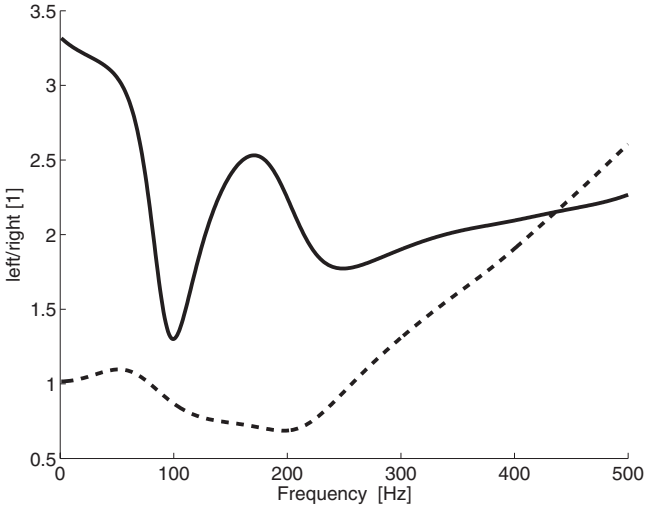

FIG. 5. Ratio of the left layer over the right one. Solid line: Total dissipated power and dashed line: Mean total energy.

correspond to the major dissipation mechanism. It is a general comment which is well known for sound-absorbing materials. In particular, it is interesting to notice that, at the resonance frequency of the solid wave (around 90 Hz), the viscous effects vanish thereby reducing the global absorption of the system. In addition, the resonance of the fluid wave (around 200 Hz) corresponds to a maximum of absorption of the material induced by a strong contribution of viscous effects. In addition, the relative influence of thermal and structural effects mainly depends on the properties of the materials: In the left layer, structural effects are predominant and in the right layer, thermal effects are predominant. This difference is of course explained by the comparison of structural coefficients η_s and acoustical parameters of both materials.

Figure 4 presents the ratio of the mean total energy in the solid phase over the one of the fluid phase. It is of interest to obtain the resonance of the solid-borne waves corresponding to a maximum of this function. The maximum in the first and second layers do not perfectly coincide as the properties of the Biot waves are different, but they are close due to the boundary conditions between the structures inducing a strong coupling of the solid phases of both materials. It can also be noticed that for higher frequencies, the energy is mainly in the fluid phase as suggested by Zwikker and Kosten[14] and Biot.[1,2]

Figure 5 presents both the ratio of total mean energy and dissipated power of the first layer over the second one. Energy is of course mainly in the first layer than in the second one. It can be easily explained by pointing out that the acoustical wave enters by the left layer and that the second structure is bonded then vanishing the solid and fluid displacements at the end of the material. A noticeable difference between the conservative curve and the dissipative one can be observed. There is no physical reason for an agreement of these indicators and it can be checked that the one corresponding to dissipated powers is most influenced by the resonance of the solid and fluid waves.

C. Convergence analysis

Several convergence studies of poroelastic finite-element schemes were published in the past.[15–17] The methods proposed in these works could be considered as qualitative in the sense that the convergence was shown and analyzed but not compared to a model. In this paper, an alternative method is proposed on a simple multilayer case. The main objective of this section is to study the convergence of the finite element method with the energetic indicators and to obtain quantitative estimation of the validity of the discretization by a comparison to a theoretical convergence model. A finite-element scheme is of order d if

$$\|X - X_h\|_I \approx C(I,\omega)h^d, \tag{41}$$

where X and X_h are the exact and discretized solution, $\|\cdot\|_I$ is the norm associated with indicator I. h is the spatial discretization step. $C(I,\omega)$ is a quantitative parameter of the convergence and d corresponds to the order of the interpolation set. Relation (41) is more tractable in logarithm representation:

$$\log(\|X - X_h\|_I) \approx \log[C(I,\omega)] + d\log(h). \tag{42}$$

Hence the logarithm of the relative error is an affine function of the logarithm of the discretization step whose slope (respectively, y intercept) is d (respectively, $\log[C(I,\omega)]$). The problem is discretized with both $\{\mathbf{u},\mathbf{U}\}$ and $\{\mathbf{u},P\}$ linear elements with a regular spatial mesh. The numerical simulations have been done in a frequency range from 100 to 3500 Hz with a 25 Hz step. For each frequency the substructures are meshed with the same number of nodes. This number of nodes goes from 5 to 300. Hence, more than 80 000 numerical simulations $(137\times296\times2)$ were performed. Three-hundred nodes for each layer are of course not necessary to obtain an adequate solution in terms of industrial classical approximation. It is nevertheless interesting from a numerical point of view as it confirms for very refined meshes the results obtained for standard ones.[18]

Figure 6 (respectively, Fig. 7) presents the convergence of the mean total energy (respectively, mean total dissipated

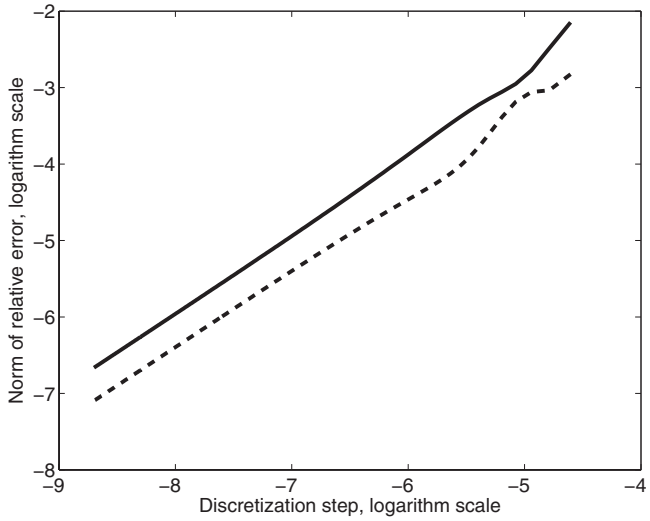

FIG. 6. Convergence of the mean total stored energy. Solid line: $\{\mathbf{u},\mathbf{U}\}$ formulation and dashed line: $\{\mathbf{u},P\}$ formulation.

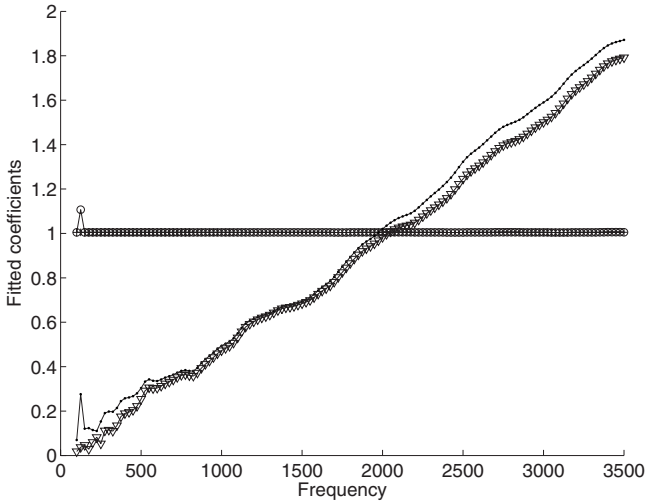

FIG. 8. Evolution of the fitted coefficients for K_f, second substructure. (○) $\{\mathbf{u},\mathbf{U}\}$ formulation d; (+) $\{\mathbf{u},P\}$ formulation d; (···) $\{\mathbf{u},\mathbf{U}\}$ formulation $\log(C(I,\omega))/60$; (▽) $\{\mathbf{u},P\}$ formulation $\log(C(I,\omega))/60$.

energy) of the whole structure at 1 kHz in a log–log representation. The error is plotted as a function of the discretization step. In the considered case, both material layers have the same discretization step to simplify the graphical representation, nevertheless additional numerical investigation not shown here for sake of conciseness allows one to generalize these results even when the discretization steps of the two layers are different.

It can be noticed that both relative errors tend to zero with the discretization step. This means that both $\{\mathbf{u},\mathbf{U}\}$ and $\{\mathbf{u},P\}$ discretization converge toward the exact analytical value. Hence, even if there is an energetic ambiguity with the mixed formulation, the authors want to underline once more that there is no doubt about the results of the finite-element discretization. In addition, it is also interesting to add a comment on the order of the convergence. The two proposed results (Figs. 6 and 7) are representative of the whole set of simulations and one can identify an affine function of slope around 1. This result means that the order d of the convergence of linear finite element for these two energetic indicators is equal to unity. Figures 6 and 7 enable one to identify the value of the convergence parameters $C(I,\omega)$ as the exponential of the y intercept of the linear interpolation line. This value is a function of ω as the physical parameters of the model are themselves functions of the pulsation.

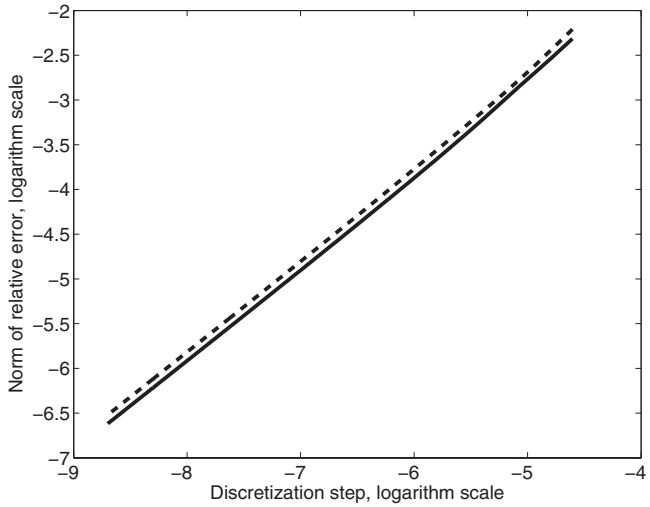

FIG. 7. Convergence of the mean total dissipated power. Solid line: $\{\mathbf{u},\mathbf{U}\}$ formulation and dashed line: $\{\mathbf{u},P\}$ formulation.

A fitting process has been done on the whole set of simulations. It is as follows: For each frequency, relations (42) are fitted and d and $C(I,\omega)$ are obtained. Figure 8 shows the evolution of these two parameters $C(I,\omega)$ and d versus the frequency for the kinetic energy of the fluid phase of the second substructure. The value of $C(I,\omega)$ is divided by 60 in order to plot the two evolutions on the same graph. It can be noticed that for both formulations the order d is really close to one for each frequency thereby validating that the energetic convergence of the finite-element scheme for linear poroelastic elements is unity. This has been observed for all the other indicators. In addition, function $C(I,\omega)$ is always a crossing function of ω. The spatial step must be shortened with increasing frequencies. It can also be noticed that the frequency evolution of $C(I,\omega)$ can be fitted through a linear interpolation in this case. It is unfortunately not possible to obtain a general interpolation for $C(I,\omega)$ law available for all indicators.

This numerical study proposed a methodology to obtain the quantitative parameters of the convergence of linear finite elements for the proposed indicators. This result shows that the proposed energetic indicators may be used to evaluate the convergence of finite element schemes and that the order of convergence is equal to one for all of them. Even if this result could seem natural, it has never been checked. Further investigations must be undertaken in order to model the evolution of $C(I,\omega)$ and it is a perspective of this paper.

VI. CONCLUSION

This paper was devoted to the rigorous obtention of stored energies (kinetic and strain) and dissipated ones for porous materials described by the Biot–Allard model ex-

pressed in $\{\mathbf{u},\mathbf{U}\}$ and $\{\mathbf{u},P\}$ formulations. It has been shown that the classical techniques dealing with the real and imaginary parts of the variational formulations are not valid and must be handled with care. The methodology was based on the mechanics and thermodynamics of open porous continua.[11] Both kinetic and strain mean energies have been given and separated into solid and fluid parts. The expressions of energies dissipated over a cycle were also provided for the three dissipation mechanisms. These expressions could be very useful to identify the contributions of the different dissipation mechanisms to the sound absorption or the damping induced by a sound package.

A numerical example has been considered to illustrate the theoretical results. First, the validity of the analytical expressions given in the preceding sections has been demonstrated. Second, the convergence of the finite element method has been shown to be of order one for the considered energetic indicators. A methodology to obtain the quantitative parameters of the convergence has also been applied to a simplified case and must be furthered. It seems then interesting to use these indicators to evaluate the convergence of finite element methods.

APPENDIX: TOPICS ON BIOT–ALLARD MODEL

This Appendix provides the expressions of the inertial and constitutive parameters of the Biot–Allard model All these expressions can be found in Allard.[2] This model allows one to find the expressions of the coefficient used in the manuscript as a function of the material properties of Table III. These expressions are given for a circular frequency ω.

The viscous effects are modeled through $\tilde{b}$ coefficient whose expression is

$$\tilde{b} = j\omega\phi\rho_0(\tilde{\alpha} - \alpha_\infty), \tag{A1}$$

where α_∞ is the geometric tortuosity, ϕ is the porosity, and ρ_0 is the density of the air. $\tilde{\alpha}$ is the dynamic tortuosity defined by

$$\tilde{\alpha} = 1 - \frac{j\phi\sigma}{\alpha_\infty\rho_0\omega}\sqrt{1 - \frac{4j\alpha_\infty^2\eta_a\rho_0\omega}{(\sigma\Lambda\phi)^2}}, \tag{A2}$$

σ is the flow resistivity, η_a is the dynamic viscosity of air, and Λ is the viscous characteristic length. The thermal properties are given by the dynamic compressibility $\tilde{K}_{\mathrm{eq}}$:

$$\tilde{K}_{\mathrm{eq}} = \frac{\gamma P_0}{\gamma - (\gamma-1)\left[1 + \frac{8\eta_a}{j\Lambda'\mathrm{Pr}\omega\rho_0}\sqrt{1 + \frac{j\rho_0\omega\mathrm{Pr}\Lambda'^2}{16\eta_a}}\right]}, \tag{A3}$$

where Λ' is the thermal characteristic length, Pr is the Prandtl number, P_0 is the ambient pressure, and γ is the ratio of specific heats of air. For sound-absorbing materials, one has

$$\tilde{Q} = \phi(1-\phi)\tilde{K}_{\mathrm{eq}}, \quad \tilde{R} = \phi^2\tilde{K}_{\mathrm{eq}}. \tag{A4}$$

The structural mechanical parameters N and $\hat{A}$ are given by

$$N = \frac{E(1+j\eta_s)}{2(1+\nu)}, \quad \hat{A} = \frac{2N\nu}{1-2\nu}. \tag{A5}$$

[1] M. A. Biot, "Theory of propagation of elastic waves in a fluid-saturated porous solid. I. Low frequency range," J. Acoust. Soc. Am. **28**, 168–178 (1956).

[2] J. Allard, *Propagation of Sound in Porous Media, Modelling Sound Absorbing Materials* (Elsevier Application Science, Amsterdam, 1993).

[3] B. R. Simon, J. S. S. Wu, O. C. Zienkiewicz, and D. K. Paul, "Evaluation of u-w and u-π finite element formulation for the dynamic response of saturated porous media using one-dimensional models," Int. J. Numer. Analyt. Meth. Geomech. **10**, 461–482 (1986).

[4] N. Atalla, R. Panneton, and P. Debergue, "A mixed displacement-pressure formulation for poroelastic materials," J. Acoust. Soc. Am. **104**, 1444–1452 (1998).

[5] N. Atalla, M. A. Hamdi, and R. Panneton, "Enhanced weak integral formulation for the mixed {u,P} poroelastic equations," J. Acoust. Soc. Am. **109**, 3065–3068 (2001).

[6] R. Panneton and N. Atalla, "An efficient finite element scheme for solving the three-dimensional poroelasticity problem in acoustics," J. Acoust. Soc. Am. **101**, 3287–3298 (1997).

[7] P. Göransson, "A 3d, symmetric finite element formulation of the Biot equations with application to acoustic wave propagation through an elastic porous medium," Int. J. Numer. Methods Eng. **41**, 167–192 (1998).

[8] F. C. Sgard, N. Atalla, and J. Nicolas, "A numerical model for the low frequency diffuse field sound transmission loss of double-wall sound barriers with elastic porous linings," J. Acoust. Soc. Am. **108**, 2865–2872 (2000).

[9] O. Dazel, F. Sgard, C.-H. Lamarque, and N. Atalla, "An extension of complex modes for the resolution of finite-element poroelastic problems," J. Sound Vib. **253**, 421–445 (2001).

[10] O. Dazel, F. Sgard, and C.-H. Lamarque, "Application of generalized complex modes for the calculation of the forced response of three dimensionnal porous structures," J. Sound Vib. **268**, 555–580 (2003).

[11] O. Coussy, *Mechanics of Porous Continua* (Wiley, New York, 1995).

[12] M. A. Biot and D. G. Willis, "The elastic coefficients of the theory of consolidation," J. Appl. Mech. **24**, 179–191 (1957).

[13] O. Dazel, B. Brouard, C. Depollier, and S. Griffiths, "An alternative Biot's displacement formulation for porous materials," J. Acoust. Soc. Am. **121**, 3509–3516 (2007).

[14] C. Zwikker and C. Kosten, *Sound Absorbing Materials* (Elsevier, New York, 1949).

[15] N. Dauchez, S. Sahraoui, and N. Atalla, "Convergence of poroelastic finite elements based on Biot displacement formulation," J. Acoust. Soc. Am. **109**, 33–40 (2001).

[16] N.-E. Hörlin, M. Nordström, and P. Göransson, "A 3D hierarchical FE formulation of Biot's equations for elasto-acoustic modelling of porous media," J. Sound Vib. **245**, 633–652 (2001).

[17] S. Rigobert, N. Atalla, and F. C. Sgard, "Investigation of the convergence of the mixed displacement-pressure formulation for three-dimensional poroelastic materials using hierarchical elements," J. Acoust. Soc. Am. **114**, 2607–2617 (2003).

[18] O. Dazel, "Component mode synthesis for porous media," Ph.D., Insa de Lyon 2003 (In French).

Evaluation of acoustical conditions for speech communication in working elementary school classrooms

Hiroshi Sato[a)]
Institute for Human Science & Biomedical Engineering, National Institute of Advanced Industrial Science and Technology, 1-1-1 Higashi, Tsukuba, Ibaraki 305-8566, Japan

John S. Bradley
*Institute for Research in Construction, National Research Council, Ottawa K1A 0R6, Canada*I

(Received 12 July 2007; revised 9 November 2007; accepted 9 January 2008)

Detailed acoustical measurements were made in 41 working elementary school classrooms near Ottawa, Canada to obtain more representative and more accurate indications of the acoustical quality of conditions for speech communication during actual teaching activities. This paper describes the room acoustics characteristics and noise environment of 27 traditional rectangular classrooms from the 41 measured rooms. The purpose of the work was to better understand how to improve speech communication between teachers and students. The study found, that on average, the students experienced: teacher speech levels of 60.4 dB A, noise levels of 49.1 dB A, and a mean speech-to-noise ratio of 11 dB A during teaching activities. The mean reverberation time in the occupied classrooms was 0.41 s, which was 10% less than in the unoccupied rooms. The reverberation time measurements were used to determine the average absorption added by each student. Detailed analyses of early and late-arriving speech sounds showed these sound levels could be predicted quite accurately and suggest improved approaches to room acoustics design. © *2008 Acoustical Society of America.* [DOI: 10.1121/1.2839283]

PACS number(s): 43.55.Gx, 43.55.Hy [NX] Pages: 2064–2077

I. INTRODUCTION

There have been many published studies of acoustical conditions in classrooms and a recent review[1] summarized the trends from many of these. Measurements of classroom noise levels were found to be highest for classes of the youngest children varying from means of about 60 dB A for kindergarten (5 year olds) to approximately 50 dB A for grade 12 classrooms (17 year olds). Fewer measurements of teachers' voice levels, as heard by the students, were found and these varied from about 50 to 65 dB A, tending to decrease with increasing age of the students. Reported measurements of classroom reverberation times were mostly in the range between 0.4 and 1.2 s.

In an earlier study, Houtgast[2] determined from classroom measurements that a signal-to-noise ratio of 15 dB was desirable for good communication in classrooms. This was confirmed by acoustical measurements and related speech intelligibility tests in 10 classrooms by Bradley.[3] The mean measured reverberation time in the 10 classrooms was 0.7 s (at 1 kHz) and ambient noise levels (in occupied classrooms without student activity) varied from 38 to 45 dB A. He also reported values of various room acoustics parameters and related intelligibility scores to combinations of reverberation time and signal-to-noise ratios as well as to useful-to-detrimental sound ratios.

More recently Iannace *et al.*[4] published results for schools exposed to high outdoor noise levels with indoor background levels of 51–61 dB A and early decay times of 1.2–1.5 s. Another study of Italian schools[5] found similar quite reverberant conditions. More adverse conditions were also reported by Losso *et al.*[6] in Brazilian classrooms. They reported ambient noise levels varying from 51 to 70 dB A and reverberation times ranging from 1.1 to 1.7 s. Results from Japanese schools indicated shorter reverberation times of 0.2–1.0 s[7,8] and ambient noise levels between 22 and 59 dB A.[8] Ueno *et al.*[9] reported 30 s L_{eq} values for various activities in Japanese schools varying from 45 dB A for "moral education" to over 80 dB A for musical activities. A recent United States study[10] also reported less extreme results with ambient noise levels varying between 38 and 55 dB A (unoccupied) and reverberation times from 0.3 to 1.1 s (occupied).

While the published results represent a very wide range of conditions, few provide information on the acoustical conditions in occupied classrooms. Almost all reported ambient noise levels exceed current recommendations such as those in the ANSI S12.60 classroom acoustics standard.[11] There was an obvious lack of information on what really matters, that is, the conditions in active classrooms, and there were strong indications that most classrooms have serious acoustical problems (usually in the form of excessive background noise levels). There was a clear need for better information on acoustical conditions in classrooms when they are occupied and in operation. It is only by studying occupied classrooms with teaching activities that we can optimally refine our estimates of the required acoustical criteria for classrooms and learn how best to achieve these criteria.

[a)]Electronic mail: sato.hiro@aist.go.jp.

 0001-4966/2008/123(4)/2064/14/$23.00 © 2008 Acoustical Society of America

TABLE I. Mean dimensions of the 30 classrooms and the number of children present.

	Width (m)	Depth (m)	Height (m)	Floor area (m^2)	Surface area (m^2)	Volume (m^3)	Number of students
Average	9.3	7.7	2.8	71	236	198	20.6
s.d.	0.9	0.7	0.2	7.3	21.6	28.0	4.5
Max	10.6	9.6	3.4	97	314	293	30
Min	7.0	6.6	2.3	50	176	136	13

II. ROOM ACOUSTICS MEASUREMENTS IN CLASSROOMS

A. Measured classrooms

In this project, 41 classrooms were investigated including 16 grade 1 classrooms, 12 grade 3 classrooms, and 13 grade 6 classrooms. The grade 1 students were 6 to 7 year olds, the grade 3 students 8 to 9 year olds, and the grade 6 students were 11 to 12 year olds. Of the classrooms, 30 were conventional rectangular shaped classrooms, which were measured to determine room acoustics properties and noise levels in unoccupied conditions. Of the 30 classrooms, 27 were also successfully evaluated when occupied to determine teachers' voice levels as well as occupied noise levels and room acoustics properties. Table I presents the mean dimensions of the 30 classrooms and the mean number of children present during the measurements.

B. Room acoustics measurement procedure

Room acoustics quantities were obtained from impulse response measurements in occupied and unoccupied classrooms. A sine sweep signal (covering the 6 octave bands from 125 Hz to 4 kHz) was used to obtain the impulse responses and was radiated into the classroom from a small loudspeaker with directional properties similar to a human talker. The loudspeaker was set 1.5 m above the floor at the front of the room where the teacher would frequently stand. Sound level meters, with digital wireless transmitters, were located 1.2 m above the floor at four locations evenly distributed among the seated students in each classroom. The outputs of the digital receivers were fed to an eight channel sound card (Echo Layla 24/96) and processed on a laptop PC. The validity of the new measurement software was determined by comparison with our previously validated RAMSOFT-3 room acoustics measurement software.[12]

C. Results of room acoustics measurements

1. Reverberation time, early decay time, and clarity in occupied and unoccupied classrooms

It is important to know room acoustics properties for both occupied and unoccupied classrooms to be able to determine the effects of students including the sound absorption that they add to the room. Table II shows reverberation times (T_{60}), early decay times (EDT), which were obtained from the first 10 dB of decay,[13] and early-to-late energy ratios (C_{50}) for both occupied and unoccupied classrooms. Reverberation times were calculated by backward integration of the octave band filtered impulse responses and using the −5 to −35 dB range of the decay as recommended in ISO3382.[13] More than a 45 dB difference between the initial level and noise floor was found for all measured impulse responses and all octave bands. Results are given for the octave bands from 125 Hz to 4 kHz and also for a double-octave band representing midfrequency results and including the 500 Hz and 1 kHz bands. Because the loudspeaker used had direc-

TABLE II. Reverberation times (T_{60}), early decay time (EDT), and early-to-late energy ratios (C_{50}) for both occupied and unoccupied classrooms.

Octave band center frequency (Hz)	125	250	500	1000	2000	4000	0.5–1000, 2 octave band
Occupied							
Mean reverberation time (s)	0.57	0.49	0.43	0.37	0.36	0.38	0.41
s.d.	0.14	0.08	0.09	0.10	0.09	0.08	0.09
Mean early decay time (s)	0.47	0.46	0.41	0.35	0.32	0.33	0.37
s.d.	0.17	0.13	0.12	0.11	0.11	0.11	0.10
Mean C_{50} (dB)	5.84	6.94	8.59	10.65	12.01	12.18	9.51
s.d.	3.51	2.71	2.34	2.66	2.81	2.64	2.26
Unoccupied							
Mean reverberation time (s)	0.59	0.51	0.46	0.42	0.41	0.42	0.45
s.d.	0.16	0.09	0.10	0.12	0.12	0.12	0.11
Mean early decay timer (s)	0.48	0.48	0.44	0.41	0.38	0.39	0.42
s.d.	0.18	0.14	0.13	0.13	0.13	0.12	0.12
Mean C_{50} (dB)	5.74	6.47	7.83	9.06	10.35	10.46	8.42
s.d.	3.69	2.52	2.30	2.77	2.96	2.67	2.38

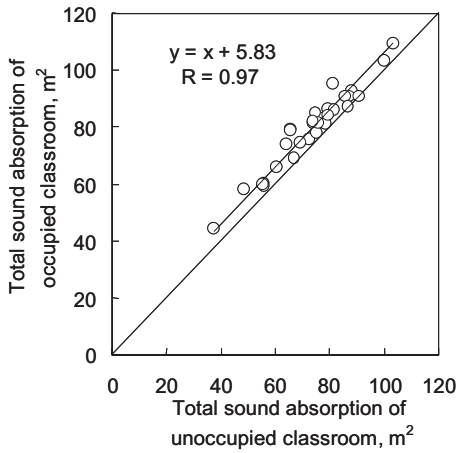

FIG. 1. The relationship between the sound absorption of the occupied classrooms and that of the unoccupied rooms in the 500 Hz and 1000 Hz double-octave band.

tional characteristics similar to a human talker, these measured values should be representative of conditions in the classrooms when the teacher is talking.

For the unoccupied classrooms, midfrequency reverberation times varied from 0.3 to 0.7 s with a mean of 0.45 s. When the classrooms were occupied, reverberation times were decreased by approximately 10%. Early decay times also indicated similar results, but early decay times sometimes exceeded reverberation times due to strong flutter echoes observed in some classrooms. Furthermore, C_{50} values increased on average by 1.34 dB A when the rooms were occupied compared to the unoccupied conditions. This improvement consisted of a 0.49 dB A (s.d.=0.54) decrease of early reflection energy (including the direct sound) and a 1.84 dB A (s.d.=0.79) decrease of late-arriving energy.

2. Sound absorption of students in classrooms

The sound absorption of the students was determined from the measured occupied and unoccupied reverberation times. For each condition, the total sound absorption was calculated using the Sabine equation,

$$A = 0.16\ V/T_{60}, \tag{1}$$

where A is total sound absorption (m^2), V is the room volume (m^3), and T_{60} is the reverberation time (s).

Figure 1 shows the relationship between sound absorption at midfrequencies (i.e., in the double-octave band of 500 Hz and 1 kHz) for the occupied and unoccupied classrooms. These values were obtained from the measured reverberation times, room volumes, and by using Eq. (1). Each point is the room average of the four measurement points in one classroom. The regression line shows that occupied rooms have on average 5.83 m^2 more sound absorption than the unoccupied rooms. The mean number of children in each classroom during the room acoustics measurements was 20.6 and hence the absorption per child was 0.28 m^2 for the 500 Hz and 1 kHz double-octave band. Table III also presents the sound absorption of the children in each of the 6 octave bands.

Because the sound source had directional characteristics similar to a human talker and classrooms may not have completely diffuse sound fields, these data should realistically represent the added absorption of children in real classrooms. As Table III shows, sound absorption per student is lowest in the lowest two octave bands and highest in the 1 kHz band. The standard deviations are large because of variations among the rooms and differences in the distribution of children in the rooms relative to the positions of the measurement microphones. These estimates of the added absorption per student, obtained from the differences of the mean sound absorption values in each octave band, should give values representative of the acoustical effect of children in this type of elementary school classroom.

3. Measured values of strength (G) and their calibration

The sound strength, G, can be measured using a calibrated sound source, as the logarithmic ratio of the sound energy (integrated sound pressure squared) of the measured impulse response to that of the response to the same source measured at a distance of 10 m in a free field.[13] Strength is an important parameter that indicates how much the reflected sounds in the room enhance the direct sound from a source and increase the speech levels heard by listeners in classrooms. Here results for the midfrequency range, obtained from the double-octave band including the 500 Hz and 1 kHz octaves, are assumed to be important for speech. In addition to G values obtained from the complete impulse responses, G_{50} values for the initial 50 ms of the impulse responses and G_{late} values for the remaining part of the impulse responses were also determined (as described in Ref. 14). Finally, the G value for the direct sound component, G_{direct}, was also determined to help in the calibration of the

TABLE III. Mean measured sound absorption (m^2) for occupied and unoccupied classrooms and the mean absorption per student from these measured values in the 30 classrooms.

Octave band center frequency (Hz)	125	250	500	1000	2000	4000	500–1000, 2 octave band
Occupied							
Mean sound absorption (m^2)	57.5	65.8	75.4	89.6	90.8	86.1	79.5
Unoccupied							
Mean sound absorption (m^2)	55.8	63.8	70.6	80.0	82.4	79.7	73.7
Difference of sound absorption (occupied-unoccupied) (m^2)	1.67	2.06	4.81	9.50	8.43	6.35	5.83
Sound absorption per child from mean sound absorption (m^2/person)	0.08	0.10	0.23	0.46	0.41	0.31	0.28

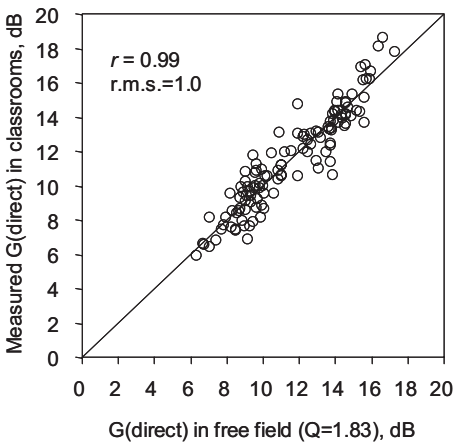

FIG. 2. The relationship between predicted G_{direct} values for free field conditions with $Q=1.83$ and measured G_{direct} values in the classrooms. The least-squares best fit regression line was given by $y=x$ ($r=0.99$, rms=1.0).

sound source. These are indicative of the relative levels of the direct sound (G_{direct}), direct and early arriving sound (G_{50}), and late-arriving sound (G_{late}). The boundary between early reflections and late-arriving sound was 50 ms after the arrival of the direct sound.

Calculation of the G values requires knowledge of the output sound power level of the source. Because the output sound power level of the source was not determined before measurements in the classrooms, a more complex source calibration procedure was required. This calibration of the source sound power levels is described in the Appendix.

Figure 2 presents the relationship between estimated G_{direct}, calculated for free field conditions with $Q=1.83$ (equivalent to assuming an average angle for the directivity index of 38.7° from on-axis) and measured G_{direct}. Equations (2) and (3) give the procedure for calculating G_{direct}. The relative energy of the direct sound dr is proportional to the directivity index (Q) and inversely proportional to the distance squared. That is,

$$\text{dr} = 100Q/d^2, \tag{2}$$

$$G_{\text{direct}} = 10\log(\text{dr})\ (\text{dB}), \tag{3}$$

where d is the source-receiver distance (m) from the sound source to the receiver.

The value of $Q=1.83$ was obtained by a least-squares regression analysis of the differences between the G_{direct} values, measured in the classrooms, and those predicted for free field conditions, as a function of Q values. This was done because the exact angles from the source to each receiver in the classrooms were not known and only approximate average angles for front and rear microphones could be estimated. The value of $Q=1.83$ is used throughout all further analyses of the classroom data in this paper. The scatter in Fig. 2 would include the effect of individual differences between the actual Q values and the average best-fit value of $Q=1.83$.

4. Modification of Barron's revised theory for classroom acoustics

Barron and Lee[15] developed their revised theory for sound levels in concert spaces by calculating energy sums for the early (direct plus first 50 ms) and late parts of the sound reflections in impulse responses. Marshall applied the theory to predict C_{50} values for speech intelligibility.[16] In this section, energy sums of the early and late parts of the sound reflections in the impulse responses measured in the classrooms are compared with those predicted using Barron's revised theory.

As Barron and Lee proposed, three components of the relative sound energy are estimated: the direct sound (dr), the early reflected sound (up to 50 ms after the direct sound arrival er), and late reflected sound (more than 50 ms after the direct sound arrival, l). They produced the following equations to predict er and l values:

$$\text{er} = (31\,200T_{60}/V)e^{-0.04d/T_{60}}(1 - e^{(-0.05)13.82/T_{60}}), \tag{4}$$

$$l = (31\,200T_{60}/V)e^{-0.04d/T_{60}}e^{(-0.05)13.82/T_{60}}, \tag{5}$$

where d is the source–receiver distance (m), T_{60} the reverberation time (s), and V the room volume (m^3).

The mean values of V and T_{60} of the measured classrooms ($V=198\ \text{m}^3, T_{60}=0.41$ s) were used to calculate G values according to Barron's revised theory.

The strength of each component of G is as follows:

$$G_{\text{er}} = 10\log(\text{er})(\text{dB}), \tag{6}$$

where G_{er} is the G value for the early reflected sound,

$$G_{50} = 10\log(\text{dr} + \text{er})(\text{dB}), \tag{7}$$

$$G_{\text{late}} = 10\log(l)(\text{dB}), \tag{8}$$

$$G_{\text{total}} = 10\log(\text{dr} + \text{er} + l)(\text{dB}). \tag{9}$$

Because measured and predicted G_{direct} values are well related and both G_{50} and G_{total} are the result of summation of the reflected sound and the direct sound, G_{er} and G_{late} are selected to compare measured and predicted values from Barron's revised theory. Figure 3 presents G_{er} and G_{late} values as a function of distance and compares measured and predicted values of each.

In the revised theory, both G_{er} and G_{late} have the same slope with distance as Eqs. (4) and (5) show. Because G_{er} values are less scattered than G_{late} values, and because G_{late} depends on G_{er}, the matching of the prediction line and the regression line for G_{er} values was examined.

The equation for the regression line for G_{er} versus distance in Fig. 3 is

$$G_{\text{er}} = -0.84d + 18.6 \quad (r = 0.62,\ \ p < 0.001). \tag{10}$$

The following regression equation fits the predicted values from Barron's revised theory for mean V and T_{60}, with distance d varied from 1 to 10 m in 0.5 m intervals,

$$G_{\text{er}} = -0.42d + 17.2\ \ (r = 1.0,\ \ p < 0.001). \tag{11}$$

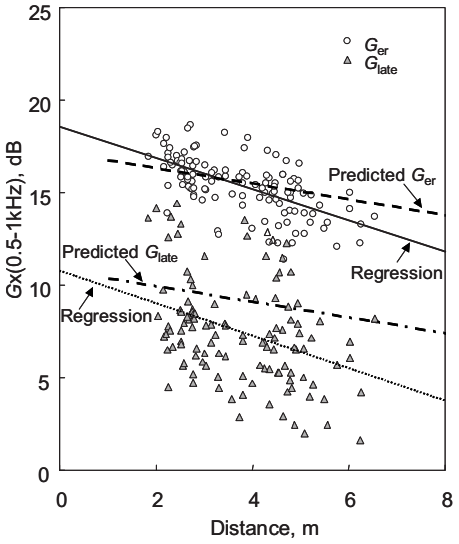

FIG. 3. G_{er} (open circles) and G_{late} (closed triangles) as a function of source–receiver distance. Solid lines represent the least-squares regression lines (r=0.62 for G_{er} and r=0.36 for G_{late}). The dashed lines are the predictions of Barron's revised theory.

Comparing these two equations, the slope of the regression line for the measured data in Eq. (10) is twice that of the revised theory (i.e., −0.84 compared to −0.42). If the slope of the early reflection energy term in Barron's revised theory is modified by a factor of 2, the average difference in measured and predicted values is 1.34 dB for G_{er} values and nothing for G_{late} values. Doubling the slope of the early reflected energy and adding a constant of 1.34 dB results in the following modified versions of Eqs. (4) and (5),

$$\mathrm{er}' = (31\,200T_{60}/V)e^{(-0.04d)2/T_{60}}(1 - e^{(-0.05)13.82/T_{60}}) \times 10^{1.34/10}, \quad (4')$$

$$l' = (31\,200T_{60}/V)e^{(-0.04d)2/T_{60}}e^{(-0.05)13.82/T_{60}}. \quad (5')$$

The result of these modifications adjusts both of the prediction lines in Fig. 3 to be almost the same as the regression lines for the measured G_{er} and G_{late} values. The modifications indicate that the early reflection energy decreases twice as rapidly with distance as the revised theory predicts. Barron and Lee noted that the slope is steeper in large auditoria with more highly diffusing ceilings.[15] Such ceilings may tend to scatter sound back toward the source and cause reflected sound levels to decrease more rapidly with distance from the source. More recently, Chiles and Barron demonstrated that the revised theory predicts reflected sound levels well in large rooms with highly diffused sound fields using measurements in scale models.[16] The classrooms are different in that they are much smaller than the rooms considered by Chiles and Barron and the classrooms are relatively full of objects such as desks and other furniture. In the measured classrooms, floors were usually covered with chairs, desks, and other furniture. The walls were usually covered with posters, cabinets, and bookshelves. These objects would tend to scatter sound back toward the sound source much as occurs in some industrial spaces that are filled with various fittings.[17] It seems likely that the modifications to the revised theory are required to account for the effects of the scattering of sound by these many objects in the classrooms that are smaller than the rooms originally considered in developing the revised theory. To further explain these differences would require further detailed study, which is beyond the scope of this paper that aims to describe the general trend of acoustical conditions in the measured classrooms.

Because the early and late parts of the reflected sound energy are well estimated by the modified revised theory, G_{50} and G_{total} predictions are also in good agreement with measurements when the modification is applied to the revised theory.

Using the various values measured in the classrooms in conjunction with Eqs. (4′) and (5′) makes it possible to predict G_{er}, G_{50}, G_{late}, and G_{total} quite accurately. That is, values of er′ and l' are used instead of er and l. Figure 4 shows measured versus predicted values of each of these four G values and hence validates the success of the modification to Barr0n's revised theory. All of the parts of Fig. 4 show a diagonal line given by $y=x$ and all of the measured values are highly significantly correlated with the predicted values ($p<0.001$). The correlation coefficients "r" in Fig. 4 are calculated from regressions forced to go through origin and are different from the "r" obtained from ordinary least-squares regression.[18] The rms error of the estimates in each part of Fig. 4 are all about 1 dB. It is clear that the modified version of Barron's revised theory can be used to accurately predict conditions in these classrooms.

Figure 5 shows predictions of various sound strength components (G values) using the modified version of the revised theory as a function of source–receiver distance (d). For the predictions, mean values of V and $T_{60}(V$

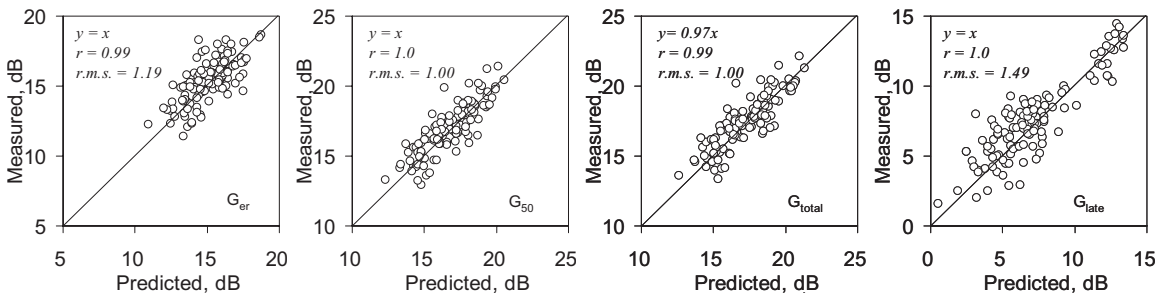

FIG. 4. Comparison of measured and predicted sound strength components, G_{er}, G_{50}, G_{late}, and G_{total} using a modified version of Barron's revised theory. The correlation coefficients r and rms errors of the estimates are included in each panel. The total number of points for each figure is 120.

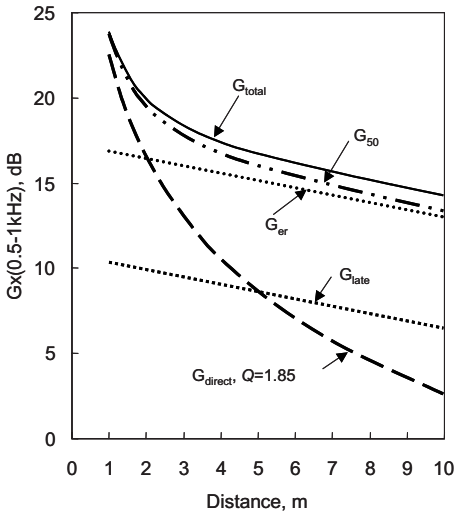

FIG. 5. Predictions of various components of sound strength, G_{er}, G_{50}, G_{late}, and G_{total} using the modified version of Barron's revised theory presented as a function of source–receiver distance (d). $V=198$ m^3, $T_{60}=0.41$ s were used as the mean values for the measured classrooms.

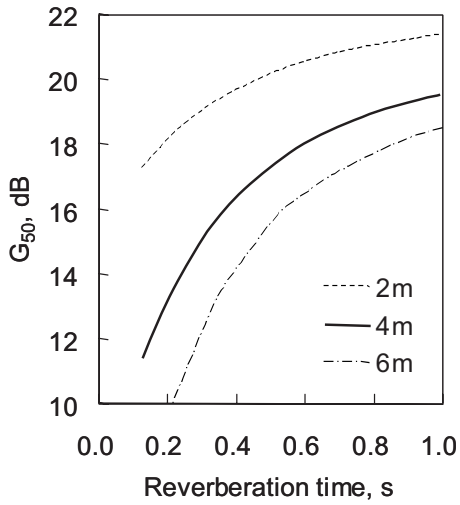

FIG. 6. Relationship between reverberation time and G_{50} for $d=2$, 4, and 6 m.

$=198$ m^3, $T_{60}=0.41$ s) for measured classrooms were used. For distances greater than about 5 m, the direct sound is lower than the late-arriving sound (G_{late}) and G_{50} and G_{late} values tend to decrease in parallel as distance increases further. It is at these more distant listening positions that the useful speech sound (as measured by G_{50}) is closest to the detrimental late-arriving speech sound (as measured by G_{late}). The most important room acoustics improvements to conditions for speech in the classroom could be achieved by reducing the late-arriving sound levels to extend better conditions to a larger portion of the classroom.

5. The relationship between early arriving sound and reverberation time

In the previous section, the modified version of Barron's revised theory was shown to predict well both early and late-arriving components of the measured impulse responses from reverberation time, source–receiver distance, and room volume as shown in Fig. 4. Figure 5 shows the general trends of the variation of the sound strength components with source–receiver distance using the mean room volume and reverberation time. Because optimum reverberation time is a key issue for classroom acoustics, the effects of reverberation time on each of the sound strength components were examined by using the modified version of Barron's revised theory. For these investigations, three distances ($d=2$, 4, and 6 m), $Q=1.83$, and $V=198$ m^3, were used.

a. The effect of reverberation time on early sound components It is well known[19] that early arriving reflections of speech sounds reaching the listener within 50 ms after the arrival of the direct sound are useful because they can help to increase the effective signal-to-noise ratio and hence the intelligibility of the speech.

G_{50} measures the relative energy of the direct sound and useful early arriving reflections. As Fig. 5 shows, G_{50} is strongly related to the distance (d). Figure 6 plots calculated G_{50} values versus reverberation time for $r=2$, 4, and 6 m. G_{50} changes dramatically when reverberation time increases from 0.2 to 0.6 s and especially at the 6 m distance. This means that a room with shorter reverberation time will be lacking in early reflection energy (i.e., lower G_{50}) at positions farther from the teacher where the early reflection energy would be most helpful to add to the weaker direct speech sound.

The authors have previously demonstrated the importance of early reflections and used the early reflection benefit (ERB) to assess their effectiveness.[20] ERB is given by the following:

$$\mathrm{ERB} = G_{50} - G_{\mathrm{direct}}. \tag{12}$$

ERB is the relative increase in early arriving sound caused by the early reflection energy arriving within 50 ms after the direct sound arrival and expressed relative to the direct sound strength. Barron referred to this same concept as an early reflection ratio.[21] Figure 7 shows how ERB values increase with increasing distance and that this trend is the same as in the authors' previous study.[20] Very steep changes in ERB values are found at very short reverberation times and especially for $r=6$ m. This means that early reflections

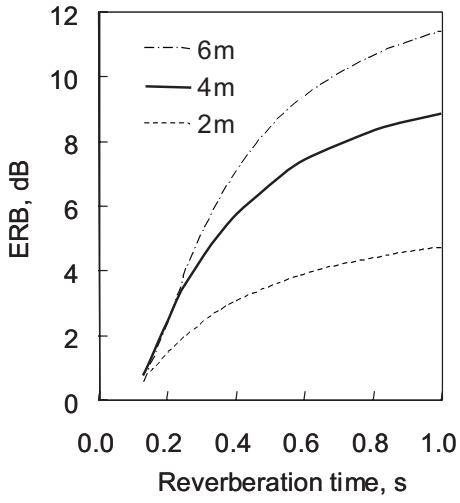

FIG. 7. Relationship between reverberation time and ERB for $d=2$, 4, and 6 m.

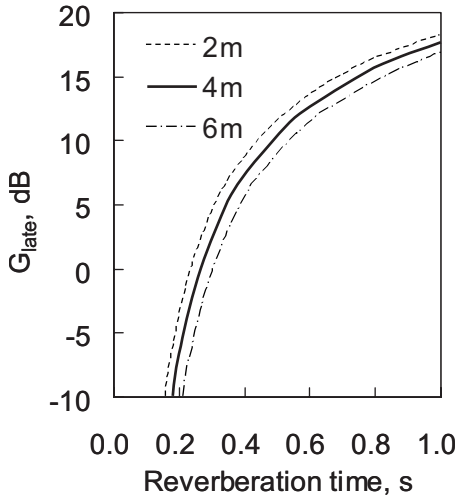

FIG. 8. The relationship between reverberation time and G_{late} values.

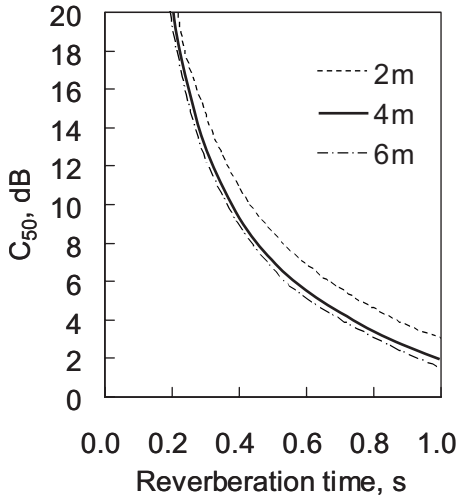

FIG. 9. The relationship between reverberation time and C_{50} values.

can be most helpful for enhancing teachers voice levels at positions further from the teacher. For the mean measured reverberation time of 0.41 s, ERB values of up to 7 dB are expected according to Fig. 7. In other words, the voice level of the teacher at a position 6 m from the teacher would be enhanced 7 dB by the expected early arriving reflection energy. Increasing the classroom reverberation time from 0.2 to 0.4 s, for the same 6 m distance, would increase effective voice levels by about 4 dB. These predictions, based on the measurements in the 30 classrooms analyzed here, make it clear that very short reverberation times should be avoided so that the room can usefully enhance teacher voice levels and help to reduce voice strain for teachers.

b. The effect of reverberation time on late-arriving reflections The late-arriving sound energy may be more affected by reflections and scattering from the many objects that filled the classrooms (such as desks), than is the early arriving sound. Consequently, G_{late} values do not correlate well with distance as seen in Fig. 3. However, G_{late} values are expected to correlate well with reverberation times. The relationship between reverberation times and G_{late} values is presented in Fig. 8 for three source–receiver distances. Figure 8 shows that G_{late} values vary little with distance and vary more with reverberation time. Because G_{late} values have a steeper rate of change when plotted versus reverberation time than the early components (Fig. 6), shorter reverberation times lead to higher early-to-late arriving sound ratios. This is confirmed in Fig. 9, which shows how C_{50} values decrease with increasing reverberation time. Figure 9 indicates that C_{50} values will have their highest value for $T_{60}=0$ s, which may lead to suggestions that $T_{60}=0$ s is the optimum reverberation time. This is incorrect because one must also consider how these room acoustic effects combine with speech and noise levels to determine speech intelligibility scores. This is discussed later in this paper.

III. SPEECH AND NOISE LEVEL MEASUREMENT DURING ACTIVE CLASSES

It is very important to know the levels of teachers' voices and classroom noises during actual teaching activities. It is the resulting signal-to-noise ratios that will determine how intelligible the teacher's speech will be to the students. To obtain the basic information, background noise levels were first measured in each octave band during impulse response measurements in occupied and unoccupied classrooms under conditions without any student activity. Table IV presents the means measured octave band noise levels. Even these average noise levels in the unoccupied classrooms were more than the 35 dB A recommended by ANSI S12.60.[11] Two of the classrooms had slightly lower average ambient levels for unoccupied conditions with averages of 34.8 and 33.0 dB A. In all others, ambient noise levels exceeded 35 dB A.

The sources of noises in the unoccupied classrooms were: ventilation noises, and noise from adjacent spaces including other classrooms and outdoors. As the schools were in relatively quiet rural areas there was no significant outdoor road traffic noise.

TABLE IV. Mean background noise levels in occupied classrooms without student activity and in unoccupied classrooms in each octave band along with the overall *A*-weighted noise levels for each condition.

Frequency (Hz)	125	250	500	1000	2000	4000	*A*-weighted
Occupied							
Mean	48.0	44.1	41.4	38.0	35.2	31.8	44.4
s.d.	5.9	4.1	3.7	3.6	3.3	3.2	3.5
Unoccupied							
Mean	47.1	42.2	39.7	36.0	31.7	27.0	42.2
s.d.	5.3	4.6	4.9	5.0	4.7	3.8	4.4

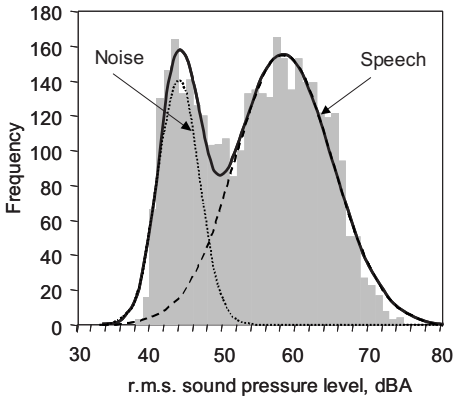

FIG. 10. Example frequency distribution of rms sound pressure levels of the recorded 200 ms segments and the fitting of two normal distributions to the data. The left part of the distribution includes the predominantly noise segments (mean 43.6 dB A, s.d. 2.8) and the right part the predominantly speech segments (mean 58.0 dB A, s.d. 6.7). Summation of both normal distributions is shown by the solid line and is seen to approximate the measured data.

A. Speech and noise level measurements in active classrooms

Recordings of speech and noise levels in active classrooms were successfully completed in 27 rectangular shaped classrooms. The instruments used for the recording were the same as for the sound receiving part of the impulse response measurement system. Sound recording software (COOL EDIT PRO Ver. 1.5) was used for the PC-based recordings using 16 bit integers and a sampling rate of 44.1 kHz. Typically 15–20 min of a teaching activity in which the teacher talked quite frequently to the children were recorded.

The processing of the recorded speech and noise levels first calculated *A*-weighted sound levels for each 200 ms interval of the recorded classroom sounds. Distributions of these levels were used to estimate separate speech and noise levels as suggested by Hodgson.[22] Two normal distributions were fitted to each histogram of the combined *A*-weighted levels. One distribution identified the noise and the other the teachers' voice levels. In some cases, Hodgson describes using three distributions (to identify speech, ventilation noise, and student activity noise) for university classroom measurements, but only two distributions were used in the present study because the main purpose was to measure teachers' voice levels relative to all other sounds. In addition, the activity noises of children in elementary schools have a wide range of levels and are difficult to differentiate from other noise sources with this technique. Figure 10 describes the fitting of two normal distributions to the recorded combined speech and noise levels.

It is interesting to note that this technique could not be applied to data from eight open-plan classrooms that were measured in this project. Because of poor isolation between adjacent classrooms, wanted and unwanted speech sounds could not be separated using this technique. That is, frequently the voice level of the teacher in the next classroom was of a similar level to the voice of the teacher in the classroom being measured. However, these analyses were completed for 27 of the enclosed rectangular classrooms.

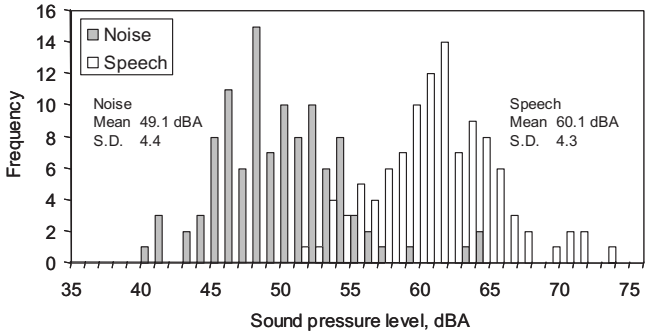

FIG. 11. Frequency distributions of the speech and noise levels of 108 points in 27 active classrooms.

B. Results

1. Noise levels and teachers' voice levels in active classrooms

Figure 11 presents distributions of the measured speech and noise levels for 108 cases (4 microphone positions ×27 rooms). For these data the mean speech level was 60.1 dB A (see Fig. 11) (s.d.=4.4 dB A) and the mean ambient noise level 49.1 dB A (s.d.=4.3 dB A).

2. Speech-to-noise ratios in active classrooms

The distribution of mean speech-to-noise ratios (SNR) in the 27 classrooms is shown in Fig. 12. These results ignore some variations with time within each recording. Figure 12 shows that in these results only 6.25% of the active class situations satisfy the SNR≥15 dB A requirement for 12 to 13 year old children to get near perfect word recognition scores.[3] The standard deviation of speech-to-noise ratios is smaller than for the noise and speech levels. This suggests that teachers' voice levels tend to increase with increasing noise levels as would be predicted by the Lombard effect.[23]

IV. DISCUSSION

A. Estimation of voice levels 1 m from the teacher's mouth and evidence of the Lombard effect

The corresponding free field speech level 1 m from the talker was estimated from the impulse responses and the distance from the measurement loudspeaker to each microphone. The effect of sound reflections was estimated by subtracting the direct sound energy from total energy of the

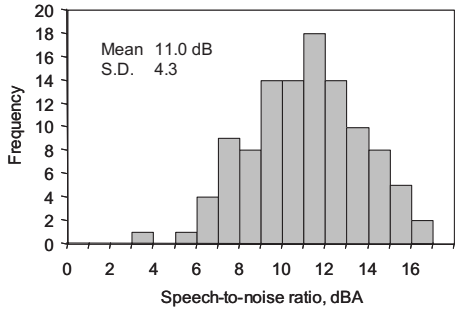

FIG. 12. Frequency distribution of mean speech-to-noise ratios for the 108 points in the 27 active classrooms.

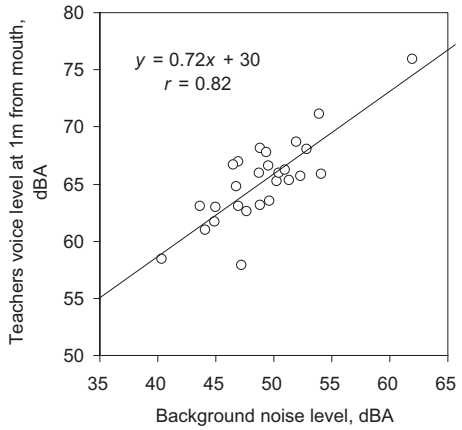

FIG. 13. Relationship between room average teachers' voice levels and noise levels during an active class. Each point is from the average of the measurements at the four microphone positions in each classroom.

impulse response. The direct sound energy was calculated as described in the Appendix. This process assumes that the teacher always talked from the same position as the location of the measurement loudspeaker. These calculations were carried out for the results of the *A*-weighted speech levels.

The mean voice level of the 27 teachers was estimated to be 65.3 dB A for a position 1 m from the mouth of the teacher in a free field and the standard deviation of these voice levels was 3.69 dB A. The average difference between the highest and the lowest voice levels, from the four measurement positions in each classroom, was 2.8 dB A, varying from a maximum of a difference of 12.5 dB A to a minimum of 0.6 dB A.

The average voice level of 65.3 dB corresponds to being between Pearsons' categories[24] for "Raised" and "Loud" speech for female talkers. (Most but not all teachers were female.) Pearsons also reported that teachers' voice levels were 62–66 dB A at positions near the front of classrooms (at a 2 m distance). If one adjusts our result to an increased distance of 2 m (−6 dB) and adds on the expected increase due to room reflections (+2.89 dB) our mean voice level would approximate 62.1 dB A at 2 m in a classroom, which is in the range reported by Pearsons *et al.*.

Figure 13 shows the relation between room-average speech and noise levels. They are well correlated (correlation coefficient, $r=0.82$, $p<0.001$). These speech levels, obtained by the distribution technique, were the average of measurements from the four individual measurement points in each classroom. The increasing teacher voice levels with increasing noise levels shown here are an example of the Lombard effect. Lane and Tranel found a 0.5 dB increase of speech level per 1 dB increase of noise level[23] and Pearson's found a 1 dB increase of speech levels per 1 dB increase of noise level.[24] Figure 13 shows a 0.75 dB increase of speech level per 1 dB increase of noise level.

B. Variations of speech-to-noise ratios in active classes among grade levels

Table V presents speech levels, noise levels, and speech-to-noise ratios averaged over the results for each grade level and obtained from recordings of teaching activities. There are not large differences between the results for the three different grades. The speech level and SNR of the grade 3 group is a couple of decibels higher than the other grades because there was one especially loud-voiced teacher in this group. The s.d. of SNR of grade 1 classes is smallest even though both the speech levels and noise levels for the grade ones have the largest standard deviations. This suggests that teachers of the grade 1 classes better controlled their voice level relative to the ambient noise level than the other teachers. As Fig. 13 demonstrated, speech and noise levels are correlated due to the Lombard effect. Grade 1 children may be distracted by noise more easily than older students and this may be evidence that teachers of the grade 1 students try harder to keep their attention by adjusting their voice levels to the ambient noise level.

TABLE V. Average speech levels, noise levels, and speech-to-noise ratios for each grade measured in an active class.

Grade	1	3	6
Mean speech level (dB A)	59.9	61.7	58.8
s.d.	5.2	3.3	3.3
Mean noise level (dB A)	49.5	49.5	48.2
s.d.	5.9	2.8	3.1
Mean speech-to-noise ratio (dB A)	10.5	12.2	10.7
s.d.	2.0	2.7	2.9

C. Comparison of background noise levels in active classrooms with those in inactive classrooms

Figure 14 shows the relation between noise levels in active classrooms and those in the same classrooms for quiet but occupied conditions. In quiet condition, noise from heating and ventilation systems and noise from adjacent rooms were found during measurements. There was little traffic noise observed near the measured classrooms. On average, in the active classrooms, the noise generated by children increases the noise level by 5 dB A and the increases vary up to a maximum of 10 dB A relative to the occupied levels in the same classrooms without student activity.

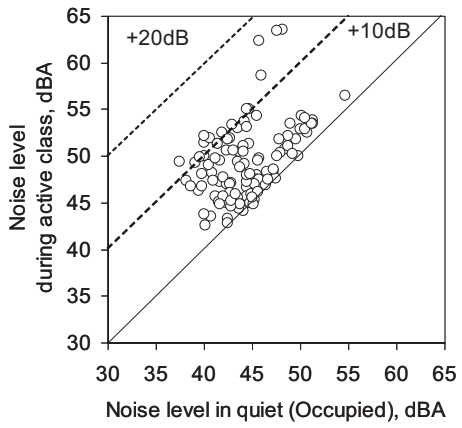

FIG. 14. The relationship between noise levels in active classrooms and those in quiet but occupied conditions.

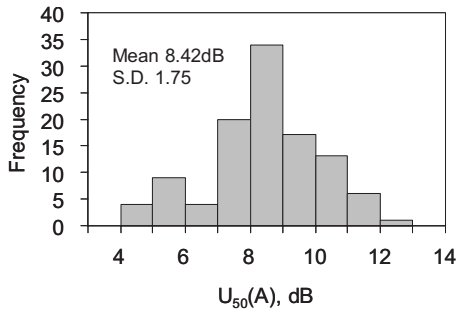

FIG. 15. Frequency distribution of $U_{50}(A)$ values from the 108 measurement points in 27 active classrooms.

There is an obvious trend in Fig. 14 for the student activity noise levels to increase with increasing ambient noise levels in the rooms without any student activity. This is another example of the Lombard effect. Most of the student activity noise was low level talking among the students. The level of this chatter increases with the general level of ambient noise in the room. That is, the children talk loud enough to be heard over the ambient noise from other sources such as heating and ventilating equipment or sounds from adjacent spaces. Thus reducing the ambient noise levels as measured in the unoccupied conditions is expected to also reduce the levels measured in active classrooms.

Student activity noise can also be reduced by controlling the student activities generating the noise. It is very important that teachers appreciate the importance of controlling student activity noise when important information is to be orally communicated. Since most of the noise from the students will arrive as direct sound or early reflections, adding sound absorbing material in the classrooms is not likely to be particularly effective for reducing student activity noise.

D. The combined effect of room acoustics and background noise

Useful-to-detrimental sounds ratio $[U_{50}(A)]$ values depend on both the speech-to-noise ratios and measured C_{50} values. Figure 15 shows the distribution of A-weighted useful-to-detrimental sound ratios, $U_{50}(A)$ calculated from A-weighted C_{50} and A-weighted speech-to-noise ratios obtained during the recorded teaching activities. [The relation between C_{50}(mid) and $C_{50}(A)$ is $C_{50}(A)=0.98C_{50}(\text{mid})+1.9$, $r=0.92$, $p<0.001$.]

Figure 16 shows the relationship between $U_{50}(A)$ values and SNR values. The scatter in the plot is due to room acoustics effects that are reflected in $U_{50}(A)$ values but not in SNR (A) values. The grey triangles in Fig. 16 were measured in rooms in which T_{60} was greater than 0.55 s. These rooms had painted concrete ceilings and walls. Such relatively longer reverberation times cause the obvious reduction in $U_{50}(A)$ values by about 2 dB relative to other rooms with similar SNR values. Because the results in the current analyses include only A-weighted SNR values obtained from the distribution technique, further work is required to obtain signal-to-noise ratios in octave bands and other measures combining signal-to-noise ratios and room acoustics factors, such as the Speech Transmission Index.[25]

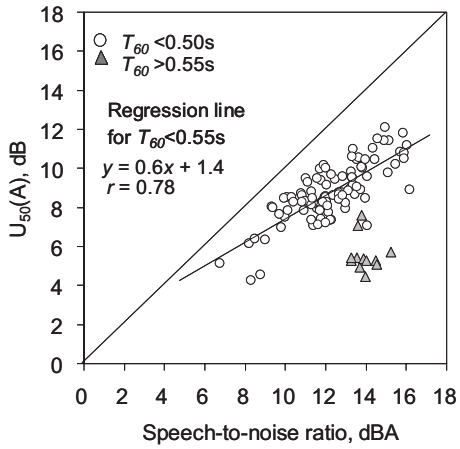

FIG. 16. Open circles are measured points with T_{60} less than 0.5 s. Closed-triangles are for conditions with $T_{60}<0.55$ s.

The mean $U_{50}(A)$ value in these classrooms is expected to correspond to a 97% speech intelligibility score and a 24% listening difficulty rating measured using a rhyme test with young adult subjects.[26] Of course lower scores are expected for the young children in the current study and intelligibility scores will be presented in a second paper. Mean SNR (A) and mean $U_{50}(A)$ are 11 and 8.4 dB, respectively.

E. Relationships among room acoustics factors, speech, and noise levels

The measured speech levels of teachers in the active classes did not correlate significantly with ERB values ($r=-0.085$, n.s.). Speech levels were only weakly related to C_{50} values ($r=-0.34, p<0.01$) and reverberation times ($r=0.48, p<0.01$) because of the effect of reverberation time on late-arriving speech energy. These weak relationships are of course largely due to the limited range of acoustical conditions found in the measured classrooms. Similarly, noise levels were not related to ERB values and were weakly correlated with C_{50} values ($r=-0.24, p<0.05$) and reverberation times ($r=0.33, p<0.01$). The measured noise levels can be predicted as 15.7 times the reverberation time plus 42.7 dB. However, the rms error for the prediction of noise levels from reverberation times is ± 4.11 dB and the correlation coefficient is small. This estimation is not practically useful.

Even though very short reverberation times are sometimes recommended[27] to control noise levels, the new results in this study suggest that values between 0.3 and 0.6 s had no practically useful effects on noise levels. That is, adding absorption would not be expected to systematically reduce these noise levels. This indicates that noise levels are mostly due to the direct sound and early reflections from the noise sources rather than the late arriving reverberant sound. Of course in the occupied classrooms, the children were usually the dominant source of the noise and were located quite close to the microphones.

This is illustrated by Fig. 5, which indicates that for a noise source, the direct sound and early reflections of the noise source would be dominant. Hence, adding absorption,

which will mostly reduce the later-arriving sound, will have little effect on the total noise levels. In the classrooms, the late-arriving reflections of noise sources, as indicated by the quite low G_{late} values, are a not so important component of the total noise levels, even though G_{late} values are related to measured reverberation times. Noise control should be focused on the sources of the noise.

Figure 5 shows how the early part of the sound energy (G_{50}) decreases rapidly with increasing distance and how G_{late} values are more gradually reduced with increasing distance. It is therefore at larger distances that the detrimental late arriving speech sounds will most interfere with the useful direct and early-reflected speech sounds. The result is seen in the rapidly decreasing C_{50} values with increasing distance shown in Fig. 9.

Determining an optimum reverberation time for a classroom must include consideration of a number of factors. Increased reverberation times will have a negative effect on speech intelligibility because of the related decreases in C_{50} values. At the same time, increased reverberation times will lead to increased speech intelligibility because of the increasing levels of early arriving speech sounds (Fig. 6). In general, such increases in reverberation times will have little effect on the ambient noise levels largely produced by the students and so the effective speech-to-noise ratios will increase with increasing reverberation times. However, at some point increasing reverberation times will lead to large increases in late arriving speech sounds and much larger G_{late} values. The combination of these effects is best understood by calculating the related useful-to-detrimental sound ratios [e.g., $U_{50}(A)$] that combine all of the important parameters influencing the expected speech intelligibility into a single measure. This is discussed in the following.

F. Optimum reverberation time for classrooms

Classrooms are often designed to meet an optimum reverberation time goal. However, the calculated results in Fig. 5 illustrate that ideal room acoustics for speech might be more directly achieved by designing to ensure that G_{50} values are sufficiently larger than G_{late} values at more distant listening positions in classrooms. The intelligibility of speech is degraded when the late-arriving speech sound begins to mask the direct and early arriving speech sounds. Sound absorption treatments should be designed to reduce late-arriving sound levels sufficiently at locations where students will be located. Although late-arriving sound levels are related to reverberation times, they are also related to room volume and source–receiver distance.

Figure 5 also shows that when students move closer to the teacher, the negative effects of reverberant sound are minimized. Moving closer does not reduce the reverberation time; it reduces the relative importance of the late-arriving speech sounds that are detrimental to speech intelligibility. Practical application of this solution was found in the classrooms for the grade 1 students who frequently sat in a circle close to the teacher while the teacher talked to them.

Figure 17 illustrates an approach to the acoustical design of classrooms that would aim to optimize conditions at a 6 m distance from the teacher. A 6 m distance is assumed to represent the more distant listening locations in a typical elementary school classroom. Figure 17 shows how the early and late-arriving components of the speech level will vary with reverberation time for an average classroom. The calculations used the mean measured speech source level in classrooms (65.3 dB A), the mean level of background noise (49.1 dB A), the mean room volume (V=198 m^3), and the modified revised theory. Figure 17 also shows A-weighted useful-to-detrimental energy ratios [$U_{50}(A)$]. It was confirmed that the calculated A-weighted G_{total} was very similar to the mean measured G_{total} at midfrequencies from the data presented in Fig. 4.

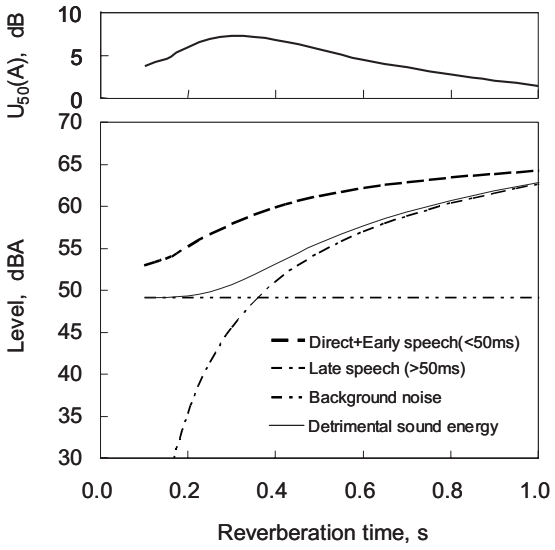

FIG. 17. Relationship between reverberation time and direct+early speech level, late speech level, background noise level, detrimental sound energy level, and U_{50}. Detrimental sound energy is the summation of the late speech level and the background noise level.

The proposed design approach is to use information in the form of Fig. 17 to select the optimum reverberation time as the one that maximizes $U_{50}(A)$ values. $U_{50}(A)$ values are used because they combine the detrimental effects of late-arriving speech and ambient noise relative to the useful direct and early reflected speech sounds. For the case of the average of the measured conditions, Fig. 17 suggests an optimum reverberation time of about 0.3 s for occupied classrooms. However, reducing the reverberation time to 0.2 s or increasing it to about 0.5 s only reduces $U_{50}(A)$ values by slightly over 1 dB and hence near ideal conditions can be achieved over quite a broad range of reverberation time values. Of course this analysis ignores the benefit of early reflections to listeners who are not directly in front of the talker and for whom the direct sound would be diminished. For listeners located where the direct sound is reduced, more early reflected sound energy and hence somewhat increased reverberation times would be better. In no situation would T_{60}=0 s be the optimum reverberation time and very short reverberation times should be avoided.

The reverberation time, which leads to the maximum useful-to-detrimental ratio, varies when speech and noise levels are changed. Lower background noise levels allow

shorter reverberation times because adequate speech-to-noise ratios can be achieved with the help of less early reflection energy. The optimum useful-to-detrimental ratio will also vary with varied voice level. The mean voice level measured in this study was 65.3 dB A. A lower speech level would shift the optimum $U_{50}(A)$ value to a longer reverberation time to increase the early sound component.

Although the concept illustrated in Fig. 17 may be clear, there are a number of details that need further investigation. The simple $U_{50}(A)$ measure used here assumes a particular combination of room acoustics and SNR values is best correlated with speech intelligibility scores. Other combinations might be more successful. Although one previous study concluded that a simple abrupt boundary at 50 ms for early speech energy was appropriate,[3] Lochner and Burger[28] originally proposed a more complex procedure for weighting the importance of early reflections to speech intelligibility. The time window used to define "early arriving" sound needs further investigation. These initial analyses have been in terms of *A*-weighted speech and noise levels and *A*-weighted useful-to-detrimental sound ratios. Many studies have shown that using frequency weightings more appropriate for speech intelligibility than *A*-weightings leads to better relationships with speech intelligibility scores. Finally, Kobayashi *et al.* have suggested that a 55 dB A speech level can minimize listening difficulty ratings[29] and might indicate a preference for lower speech levels from teachers in classrooms if noise levels can also be lowered to maintain optimum SNR values.

V. CONCLUSIONS

In the measured classrooms, excessive noise levels were a much more significant problem than poor room acoustics. Even in unoccupied classrooms measured ambient noise levels were almost always greater than the 35 dB A recommend in ANSI S12.60. In working classrooms (i.e., while the teacher was teaching) the average measured noise level was 49.1 dB. Excessive noise levels make it impossible to achieve ideal signal-to-noise ratios and near ideal speech communication conditions. From various previous studies in classrooms (see the review in Sec. I) this is generally true for most classrooms.

Student activity is the dominant noise source in active classrooms even when the children are quite well behaved. Student activity increases noise levels by an average of 5 dB A and as much as 10 dB A in some classrooms. The noise levels measured in active classrooms are related to those in classrooms without student activities. That is, because of the Lombard effect, the student noise, which is mostly due to talking, increases with the general level of ambient noise from other sources. Therefore, it is very important for unoccupied noise levels in classrooms to be very low. In addition, there is no evidence that added absorption would decrease these noise levels. The measured noise levels in occupied classrooms are largely due to the direct and early reflected sound from nearby student activity and can only be controlled at the source. It is therefore important that teachers appreciate the need to control student noise when important information is to be orally communicated.

Teachers' voice levels were similar to those previously reported by Pearsons and the average measured teacher voice level would correspond to being between Pearsons' categories for Raised and Loud speech for female talkers. Students experienced an average speech level of 60.4 dB A from teachers and there is clear evidence that teachers increase their voice level to overcome ambient noise as predicted by the Lombard effect. In these classrooms, effective speech levels are enhanced by early reflection energy. The new results give a better understanding of the interrelationships of various room acoustic parameters in classrooms.

The measurements found an average midfrequency reverberation time of 0.41 s and the reverberation times were about 10% greater in the unoccupied condition. By combining the occupied and unoccupied reverberation times it was possible to determine the average absorption per student in each octave band.

Detailed analyses of early and late-arriving sound levels showed that these could be quite accurately predicted by a modified version of Barron's revised theory for sound levels in concert halls. The modifications are thought to adapt the theory to the acoustical conditions typical of the elementary school classrooms that were measured in this work.

Analyses of early and late-arriving sound levels also suggest that the room acoustics design of classrooms should aim to reduce late-arriving sound levels at more distant listening positions to acceptable values that are well below the levels of the useful direct and early reflections of the speech sound. This would more directly ensure optimum conditions for speech communication than designing for an optimum reverberation time.

ACKNOWLEDGMENTS

This work was supported by a grant from the Canadian Language and Literacy Research Network. The very helpful cooperation of the teachers and administration of the Upper Canada District School Board made this work possible.

APPENDIX: CALIBRATION OF THE SOUND POWER LEVEL OF THE SOUND SOURCE USED IN CLASSROOM MEASUREMENTS

The sound power level of the sound source for the measurements was not successfully measured before the classroom measurements and the following process was used to later calibrate the output of the source. First, the directivity pattern of sound source was measured in 5° intervals in three dimensions. Second, typical relationships between the locations of the sound source and the microphones in the classrooms were estimated by the following steps: (1) Use the mean floor dimensions of classrooms (9.3 m width and 7.7 m depth). (2) Microphones were typically set in the middle of each quarter of the seating area of the classroom and the sound source was located on the center line and 0.5 m away from front wall of the classroom. (3) From the floor dimensions, the mean angle from the central axis of the source to the two front microphones was estimated to be $\pm 50°$ and $\pm 22°$ for the two rear microphones. (4) The height of the microphones were always 1.2 m and that of sound

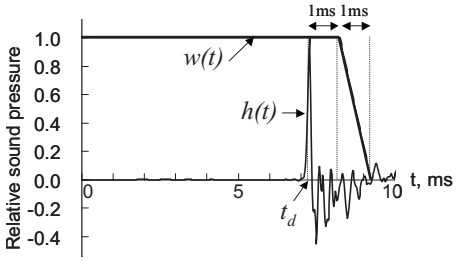

FIG. 18. Initial part of measured impulse response [$h(t)$] and the time window [$w(t)$] used to obtain the energy of direct sound.

source 1.5 m and this height difference gives a mean vertical angle of 5.7° with a s.d. of 1.6°. This variation of the vertical angle would only lead to variations of the direct sound level within a 0.2 dB range. (5) The direct sound was selected from the measured impulse responses using a 1 ms (44 points at the 44.1 kHz sampling rate) time window from the peak of direct sound (t_d in Fig. 18), followed by a linear fade out for the next 1 ms (44 points). The direct sound energy was calculated from this windowed segment of the impulse response and including the initial part of the impulse response before the arrival of the direct sound. That is, the initial part of the impulse response and a further 88 points starting from the peak of the direct sound arrival were included. Measurements in an anechoic room confirmed that this time window did not decrease direct sound energy in the 500 Hz and 1 kHz double-octave band. Figure 18 illustrates the initial part of the measured impulse response and illustrates the method used to obtain the energy of direct sound.

Since the same equipment and the same output sound levels were used in all classrooms, the sound power of the test signal was the same for all measurements. Microphones were calibrated at the beginning of measurements in each classroom.

The sound power level of the sound source was estimated by the following procedure: (1) The measured impulse responses were divided into two groups, those from the two closer microphones nearer the front of the classrooms and those from the two microphones nearer the rear of the classrooms. (2) Next, relative values (i.e., uncalibrated) for G_{direct} were determined for all impulse responses. (3) Then the free field sound pressure levels (direct sound) were calculated for all measurement positions: for the front microphones (horizontal angle, $\pm 50°$), and for the rear microphones (horizontal angle $\pm 22°$), and in all cases the vertical angles were calculated as a function of distance. (4) Determine the sound power level that minimizes the difference between the free field calculated levels and the measured direct sound levels. The least-squares error fitting included all front and rear microphones at the same time. (5) The sound power level of the measurement source was estimated as 38 dB in the 500 Hz and 1 kHz double-octave band.

This procedure was confirmed by new measurements with the same equipment in a meeting room with size and acoustical characteristics similar to the classrooms. For the meeting room measurements, the sound power level of the sound source was measured (in a reverberation chamber) and the above-described calculation was again performed. In the meeting room the horizontal angle of the six microphone positions relative to the central axis of the sound source were measured and varied between 16° and 26°. Both the horizontal and vertical measured angles were used for the estimation. The mean estimated sound power level was 0.73 dB more than the sound power level measured in the reverberation chamber. Both estimated (y) and measured (x) sound pressure levels at the six measuring positions in the meeting room were well correlated ($y=x-0.73$) with $r=1.0$, $p<0.001$.

[1]M. Picard and J. S. Bradley, "Revisiting speech interference and remedial solutions in classrooms," Audiology **40**, 221–244 (2001).
[2]T. Houtgast, "The effect of ambient noise on speech intelligibility in classrooms," Appl. Acoust. **14**, 15–25 (1981).
[3]J. S. Bradley, "Speech intelligibility studies in classrooms," J. Acoust. Soc. Am. **80**, 846–854 (1986).
[4]G. Iannace, L. Maffei, C. Ianniello, and R. Romano, "Noise problems inside schools in densely built and temperate climate urban area," *Proceedings of Inter-Noise*, Dearborn, Vol. 451, 2002.
[5]A. Astolfi and V. Corrado, "Acoustical quality assessment of Italian school classrooms," *Proceedings of Inter-Noise*, Dearborn, Vol. 392, 2002.
[6]M. Losso, E. Viveiros, and T. Figueiredo, "An overview of acoustical features in Brazilian school buildings," *Proceedings of Inter-Noise*, Prague, Czech Republic, Vol. 666, 2004.
[7]H. Tachibana, K. Ueno, and A. Aoki, "Study of acoustical conditions in elementary schools of open-plan type in Japan. 1. Plan features and acoustic properties of schoolrooms," *Proceedings of Inter-Noise*, Dearborn, Vol. 323, 2002.
[8]K. Nishizawa, J. Munakata, and T. Sakuma, "Survey on acoustic environments for hearing impaired students at schools in Japan," *Proceedings of the 18th International Congress on Acoustics*, Kyoto, 2004, Paper Tu2.B1.5.
[9]K. Ueno, H. Tachibana, and A. Aoki, "Study of acoustical conditions in elementary schools of open-plan type in Japan. 1. Observation of classworks and inquiring survey," *Proceedings of Inter-Noise*, Dearborn, Vol. 324, 2002.
[10]E. E. Bowden, L. M. Wang, and D. Bradley, "Classroom acoustics in Omaha, Nebraska: Measurements and outreach," *Proceedings of the First Pan-American/Iberian Meeting on Acoustics*, Cancún, 2004.
[11]American National Standards Institute, "Acoustical performance criteria, design requirements, and guidelines for schools," ANSI S12.60, New York, 2004.
[12]J. S. Bradley, "An international comparison of room acoustics measurements systems," IRC Internal Report No. 714, National Research Council, Ottawa, 1996.
[13]International Organization for Standardization, "Acoustics—Measurement of the reverberation time of rooms with reference to other acoustical parameters," ISO 3382, Geneva, Switzerland, 1998.
[14]J. S. Bradley, "Using ISO3382 measures, and their extensions, to evaluate acoustical conditions in concert halls," Acoust. Sci. & Tech. **26**, 170–178 (2005).
[15]M. Barron and L.-J. Lee, "Energy relations in concert auditoriums. I," J. Acoust. Soc. Am. **84**, 618–628 (1988).
[16]S. Chiles and M. Barron, "Sound level distribution and scatter in proportionate spaces," J. Acoust. Soc. Am. **116**, 1585–1595 (2004).
[17]I. L. Ver and L. L. Beranek, *Noise and Vibration Control Engineering*, 2nd ed. (Wiley, New York, 2006), p. 197.
[18]J. G. Eisenhauer, "Regression through the origin," Teach. Stat. **25**, 76–80 (2003).
[19]L. G. Marshall, "Speech intelligibility prediction from calculated C50 values," J. Acoust. Soc. Am. **98**, 2845–2847 (1995).
[20]J. S. Bradley, Hi. Sato, and M. Picard, "On the importance of early reflections for speech in rooms," J. Acoust. Soc. Am. **113**, 3233–3244 (2003).
[21]M. Barron, *Auditorium Acoustics and Architectural Design* (Spon, London, 1993).
[22]M. R. Hodgson, R. Rempel, and S. Kennedy, "Measurement and prediction of typical speech and background-noise levels in university classrooms during lectures," J. Acoust. Soc. Am. **105**, 226–233 (1999).
[23]H. L. Lane and B. Tranel, "The Lombard sign and the role of hearing in speech," J. Speech Hear. Res. **14**, 677–709 (1971).

[24]K. S. Pearsons, R. L. Bennett, and S. Fidell, "Speech levels in various noise environments," Report No. EPA-600/1-77-025, EPA, Washington, DC, 1977. Summarised in W. O. Olsen, "Average speech levels and spectra in various speaking/listening conditions: A summary of the Pearsons, Bennett, and Fidell (1977) Report," J. of Audiol. **7**, 1–5 (1998).
[25]H. J. M. Steeneken and T. Houtgast, "Mutual dependence of the octave-band weights in predicting speech intelligibility," Speech Commun. **28**, 109–123 (1999).
[26]Hi. Sato, J. S. Bradley, and M. Morimoto, "Using listening difficulty ratings of conditions for speech communication in rooms," J. Acoust. Soc. Am. **117**, 1157–1167 (2005).
[27]M. R. Hodgson and E. M. Nosal, "Effect of noise and occupancy on optimal reverberation times for speech intelligibility in classrooms," J. Acoust. Soc. Am. **111**, 931–939 (1999).
[28]J. P. A. Lochner and J. F. Burger, "The influence of reflections on auditorium acoustics," J. Sound Vib. **1**, 426–454 (1964).
[29]M. Kobayashi, M. Morimoto, Hi. Sato, and Ha. Sato, "Optimum speech level to minimize listening difficulty in public spaces," J. Acoust. Soc. Am. **121**, 251–256 (2007).

The intelligibility of speech in elementary school classrooms

J. S. Bradley[a)]
National Research Council, Montreal Road, Ottawa, K1A 0R6, Canada

H. Sato
*Institute for Human Science & Biomedical Engineering, National Institute of Advanced Industrial Science and Technology (AIST), 1-1-1 Higashi, Tsukuba, Ibaraki 305-8566, Japan*II

(Received 16 July 2007; revised 11 November 2007; accepted 8 January 2008)

This is the second of two papers describing the results of acoustical measurements and speech intelligibility tests in elementary school classrooms. The intelligibility tests were performed in 41 classrooms in 12 different schools evenly divided among grades 1, 3, and 6 students (nominally 6, 8, and 11 year olds). Speech intelligibility tests were carried out on classes of students seated at their own desks in their regular classrooms. Mean intelligibility scores were significantly related to signal-to-noise ratios and to the grade of the students. While the results are different than those from some previous laboratory studies that included less realistic conditions, they agree with previous in-classroom experiments. The results indicate that +15 dB signal-to-noise ratio is not adequate for the youngest children. By combining the speech intelligibility test results with measurements of speech and noise levels during actual teaching situations, estimates of the fraction of students experiencing near-ideal acoustical conditions were made. The results are used as a basis for estimating ideal acoustical criteria for elementary school classrooms. [DOI: 10.1121/1.2839285]

PACS number(s): 43.55.Hy, 43.71.Gv [RYL] Pages: 2078–2086

I. INTRODUCTION

There has recently been renewed interest in achieving improved acoustical conditions in classrooms. Although there is a general consensus as to acoustical criteria for good classrooms,[1] the supporting evidence from studies in actual classrooms is limited. The renewed interest in classroom acoustics is related to our growing understanding of the negative effects of ambient noise and poor room acoustics on children's ability to learn in schools (see also Anderson[2] for an extensive review).

There is evidence that increased levels of noise affect memory[3] and are associated with decreased reading scores.[4–6] It is reasonable to assume that a mechanism to explain the association of decreased educational progress, such as the effect of noise on reading scores, is simply that noise interferes with verbal communication (especially that between teachers and students), which is the predominant mechanism for learning in elementary schools.

It is well known that younger children have greater difficulty understanding speech in even modest levels of ambient noise.[7–9] In fact several authors have reported results showing that the ability to recognize speech in noise improves systematically with age.[7,10,11] Although it is clear that children need quieter conditions and corresponding larger signal-to-noise ratios than adults to achieve high speech recognition scores,[8] and that the younger the children, the quieter the conditions should be, the results of the various previous studies reveal large differences and do not agree well with previous results of tests carried out in actual classrooms.[12]

Figure 1 compares results from Marshal[11] and Elliott[7] with previous classroom measurements of speech intelligibility scores versus *A*-weighted speech–noise level differences, S/N(*A*). Marshal and Elliott's results are both based on simple word recognition tasks and both indicate large variations in intelligibility scores with the age of the listener. However, when examined in detail, these two sets of results show quite different effects of age and show some much lower intelligibility scores than the previous classroom results for 12 year olds. The previous classroom results were from a 1986 study that included ten classes of 12 year old students[12] and used a rhyme test in which subjects identified the correct response of several possible rhyming words. The subjects were seated in their regular seats in their own classrooms and listened to the recorded speech material from a small loudspeaker with directionality similar to a human talker.

The differences in Fig. 1 are thought to be due to the laboratory studies using monaural headphone presentation of speech and noise signals, which increases the negative effects of noise and reverberation. Listening naturally with two ears leads to a "binaural advantage" that can make it easier to understand speech in noise. MacKeith and Coles[13] measured binaural advantages equivalent to as much as an 18 dB improvement in signal-to-noise ratio for extreme cases in free field conditions. Neuman and Hochberg[9] tested 5 to 13 year old children, finding small binaural advantages for all ages in reverberant conditions. They pointed out that the binaural advantages would probably be much larger in lower signal-to-noise situations. Nábělek and Robinson[14] tested subjects with ages from 10 to 72 years and found an average binaural advantage corresponding to a 5% increase in intelligibility scores in reverberant conditions but without significant masking noise. They did not include the effects of lower

[a)]Electronic mail: john.bradley@nrc-cnrc.gc.ca

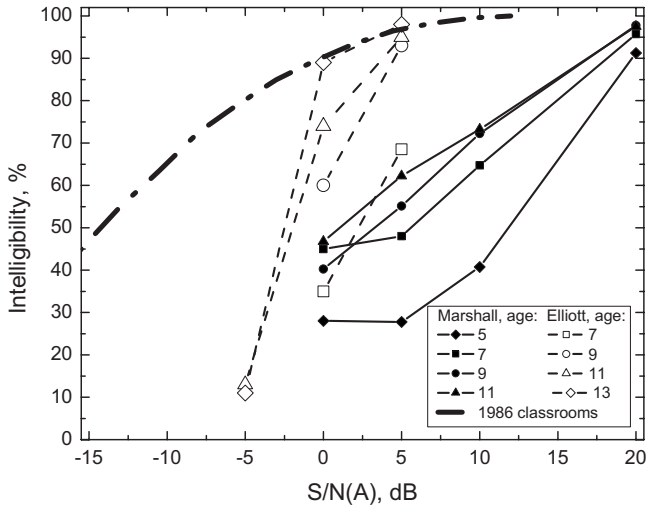

FIG. 1. Laboratory word intelligibility test results from Marshall—Ref. 11 (5, 7, 9, and 11 year olds) and Elliott—Ref. 7 (7, 9, 11, and 13 year olds) showing the effect of listener age on intelligibility scores vs *A*-weighted speech–noise level differences, S/N(*A*), and compared with previous in-classroom intelligibility test results from 12 year olds (Ref. 12).

signal-to-noise ratios where larger effects would be expected. It is clear that the older laboratory based speech intelligibility studies in which monaural headphone presentation was used would exaggerate the negative effects of noise on speech recognition but the magnitude of these effects cannot be accurately estimated.

Similarly there are previous studies indicating that younger children's ability to understand speech is more adversely affected by room reverberation.[9,14,15] Some early studies used monaural headphone presentation of the test signals,[10] which would exaggerate the negative effects of reverberation on speech recognition scores.[16] Because shorter reverberation times led to improved speech recognition scores in these tests, they have led some to recommend very short reverberation times for classrooms. Of course, excessive absorptive treatments may control reverberation but will also decrease effective speech levels and exaggerate the more common problem of inadequate signal-to-noise ratios in classrooms.

The limitations of the various previous studies carried out in laboratory settings can be avoided by testing children in their classrooms where the children listen in realistic conditions with both ears. The work reported in this paper and in a companion paper[17] was intended to provide a more complete basis for deriving acoustical criteria for classrooms from speech intelligibility tests of students in their own classrooms and acoustical measurements in the same classrooms. More specifically it was intended to show younger children's ability to understand speech in real classroom conditions as a function of signal-to-noise ratios, varied room acoustics, and the age of the children. At the same time it was planned to determine speech and noise levels in classrooms during actual teaching situations in order to understand the actual signal-to-noise ratios experienced in active classrooms. By combining these two types of information, this paper estimates ideal acoustical conditions in classrooms for children of various ages. At the same time the data are used to estimate the fraction of students in the measured classrooms who would experience these ideal conditions. That is, a new basis for classroom acoustics criteria as well as estimates of the negative impact of common existing conditions were produced.

II. MEASUREMENT PROCEDURES

The measurements included speech recognition tests of complete classes of grades 1, 3, and 6 students (nominally 6, 8, and 11 year olds) in their own classrooms. The signal-to-noise ratios experienced by the students were varied over a wide range by varying the speech playback level. Room acoustics conditions were varied by testing in a number of different classrooms. Speech and noise levels were measured during the speech tests as well as during normal teaching activities. Room acoustics measurements were made with the classroom occupied and also unoccupied.

A. Speech recognition tests

The speech intelligibility scores were obtained using the Word Identification by Picture Identification (WIPI) test[11,18,19] that includes four lists of 25 phonetically balanced simple nouns. This was selected as an easy test that 6 year olds and older students could quickly learn and respond to individually in a classroom situation. It consists of simple test words said to be familiar to 5 year olds and these were presented in the carrier phrase, "Please mark the ____ now." While sitting at their desks in their regular classroom, the students responded by placing a sticker on one of six pictures to indicate the correct word. Each sentence was approximately 3 s long and the next sentence was played to the students when all were ready to proceed.

The tests were carried out in 41 classrooms evenly distributed among grade 1, grade 3, and grade 6 students in 12 different schools. The schools were in relatively quiet rural areas and small towns in Eastern Ontario, Canada. A total of 840 students were evaluated in 41 classrooms. Grade 1 students were each tested at two different signal-to-noise values and the other students at three different signal-to-noise values. A total of 2285 individual speech recognition tests were obtained.

All students in each class with parental permission participated in the tests. The parental permission form asked whether the student had any known hearing problems. Almost all students with known hearing impairment did not receive parental permission and did not participate. As a result the test results of the few students with reported hearing problems were not included in these analyses because of the very small numbers of these students.

The speech source was a small loudspeaker with similar directionality to that of a human talker. Digital recordings of the WIPI test material were made in an anechoic room so that they were reflection free and with negligible noise. A female talker was used and the recordings were edited to use exactly the same version of the carrier phrase for all test words and to have the same sound levels for all test words. Varied S/N(*A*) values were obtained by changing the playback level of the speech material relative to the existing

natural ambient noise in the classroom. This included some tests with 20–30 dB S/N(A) values to determine intelligibility scores in truly ideal conditions for these students. This made it possible to obtain speech recognition scores for a very wide range of signal-to-noise ratios with natural ambient noises. Room acoustics conditions were varied by carrying out the tests in a number of different classrooms. It was not possible to artificially modify room acoustics conditions as part of the experiments.

B. Acoustical measurements

Speech and noise levels were recorded during the speech recognition tests at four positions in the fully occupied classrooms. There were on average 20.4 students in each classroom (s.d. ± 3.96) and hence there were about five students near each measuring microphone. These recordings were used to determine speech and noise levels during the tests by statistical analysis of the distributions of recorded sound levels.[17]

Speech and noise levels were also recorded at the same four microphone positions during a normal teaching activity in each classroom. Recordings were made during a period when the teacher planned to be mostly talking to the class of students as a complete group. Finally, ambient noise levels were also recorded at these same four positions when the classroom was unoccupied.

Room acoustics parameters were also measured from impulse responses obtained at the same microphone locations for both occupied and unoccupied conditions. These included decay times and energy ratios as described in the companion paper[17] along with the various speech and noise level measurements. All sounds were digitally recorded on a portable computer. To avoid running cables through the classrooms, the signals from the four microphones were connected to a central computer via 16 bit digital transmitters and receivers.

III. MEAN TRENDS OF SPEECH RECOGNITION TEST RESULTS

A. Speech recognition scores as a function of S/N(A)

Speech recognition scores were first examined as a function of S/N(A) as this was the key independent variable that was varied in these experiments. The speech recognition scores were averaged over the scores of the approximately five students located close to each microphone in each classroom. These average scores are plotted versus the measured signal-to-noise ratios [S/N(A)] in Fig. 2. They are plotted versus S/N(A) separately for the results of the grades 1, 3, and 6 students. An analysis of variance of the scores showed that there were highly significant main effects of age and S/N(A) ($p<0.001$) as well as a highly significant interaction effect of these two independent variables, age and S/N(A) ($p<0.001$). That is, although there is significant scatter in the results, there are highly significant effects related to S/N(A) and the age of the listeners. The younger children need significantly higher S/N(A) values to obtain the same intelligibility scores as the older children in these classrooms.

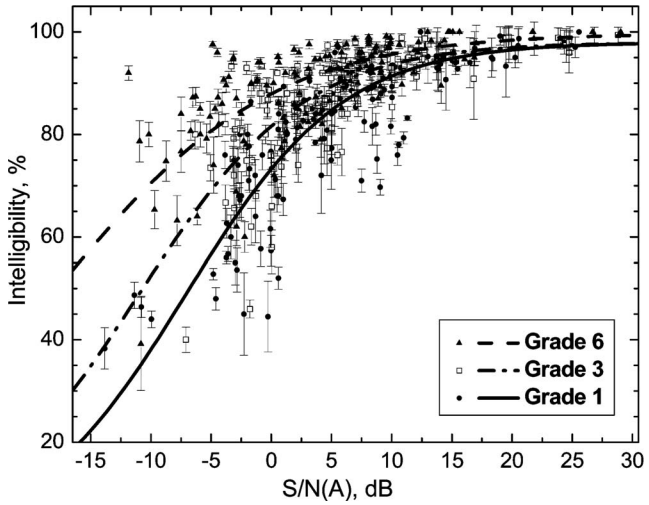

FIG. 2. Mean intelligibility scores of groups of approximately five students vs A-weighted speech–noise level difference, S/N(A). The error bars indicate the standard deviations of the scores of each group of students.

There is also a large amount of scatter about the mean trends that tends to increase with decreasing S/N(A) values. The scatter is partly due to the approximately five students near each microphone being slightly different distances from the microphone. The larger scatter at lower S/N(A) values may be indicative of how students react to more difficult listening conditions. At lower S/N(A), some students can still do quite well, but others may more or less give up and get much lower scores.

The best-fit regression lines to the data in Fig. 2 are repeated in Fig. 3 and are compared with the previous speech intelligibility scores from 12 year olds in classrooms. The previous results[12] used a rhyme test with simple rhyming words presented in a carrier phrase. Given the amount of scatter in both sets of data, and possible larger inaccuracies in the older results, there is remarkable agreement between the old results for 12 year olds and the results for 11 year olds (i.e., the grade 6 students). This agreement suggests that

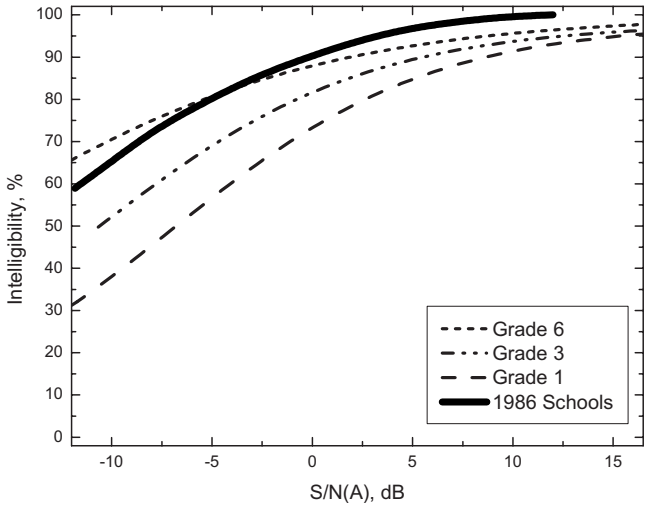

FIG. 3. Comparison of the best-fit regression lines from Fig. 2 with the mean trend of previous speech intelligibility scores for 12 year olds in classrooms (Ref. 12).

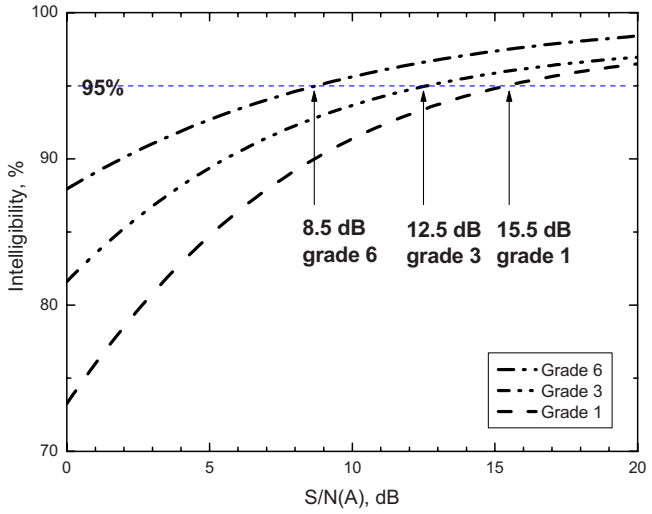

FIG. 4. (Color online) Expanded view of the mean trends from Fig. 2 showing the point at which each regression line reaches a 95% speech intelligibility score.

the results are a more representative indication of children's ability to understand speech as a function of S/N(A) in real classroom conditions than some previous laboratory speech tests.

Figure 4 shows an expanded view of the best-fit regression lines from Fig. 2. The performance of the three age groups can be compared by considering the required S/N(A) for each group to achieve near-ideal conditions for speech communication. For the results of simple word intelligibility tests such as the WIPI test, a speech intelligibility score of 95% correct is used to indicate near-ideal conditions, because 95% correct scores are readily achievable in high S/N(A) conditions. For example, Fig. 2 shows that for very high S/N(A) (+23 to +30 dB), the grade 1 and 3 students scored ~98% correct and the grade 6 students scored ~99.5% correct. That is, although the younger children might be expected to find the test a little more difficult, all three age groups are capable of getting higher scores than 95% in very high S/N(A) conditions.

The mean trends in Fig. 4 show that the grade 6 students could, on average, achieve 95% correct scores for a S/N(A) of +8.5 dB. However, the grade 3 students required +12.5 dB S/N(A) and the grade 1 students required +15.5 dB S/N(A) to obtain a mean score of 95% correct. In this case there is a 7 dB difference between the average needs of grade 1 and grade 6 students. That is, the grade 1 students would need a 7 dB greater S/N(A) value, or a corresponding 7 dB quieter ambient noise level, to obtain the same intelligibility scores as the grade 6 students. Further, it is likely that the grade 6 students would have somewhat lower speech intelligibility scores than would young adult listeners in the same situations.[9]

B. Effects of room acoustics on speech recognition scores

Table I lists the mean values of key room-acoustics parameters[20] along with the standard deviations of these parameters for each grade level group. These included mid-frequency values of early-to-late arriving sound ratios (C_{50}), early decay times (EDT), reverberation times (T_{60}), and A-weighted signal-to-noise ratios [S/N(A)]. The acquisition of these data are described in the companion paper.[17] It was hoped that there would be sufficient variation of room acoustics conditions among the classrooms to determine the additional effects of room acoustics on speech intelligibility scores. In practice, Table I indicates relatively small variations about the mean conditions that were close to ideal.

TABLE I. Summary of mean values and standard deviations (σ) of key room-acoustics parameters for occupied conditions. C_{50}, EDT, and T_{60} are midfrequency results for the combined 500 and 1000 Hz octave bands. S/N(A) is the signal-to-noise ratio in terms of A-weighted speech–noise level differences.

	C_{50}(500–1000)	EDT(500–1000)	T_{60}(500–1000)	S/N(A)
Grade 1				
Mean	8.9	0.40	0.43	6.5
σ	2.19	0.10	0.09	7.30
Grade 3				
Mean	8.6	0.42	0.44	3.8
σ	2.41	0.12	0.11	5.2
Grade 6				
Mean	8.8	0.37	0.40	3.4
σ	2.94	0.13	0.10	9.0

To investigate possible additional effects of room acoustics on intelligibility scores, multiple regression analyses were performed regressing speech intelligibility scores on values of S/N(A), S/N(A)^2, and one of the room acoustics parameters. Table II summarizes the results in terms of the resulting R^2 (coefficient of determination) values. The R^2 values for the combination of the S/N(A) and S/N(A)^2 are first given for each grade level of students. If there are significant additional effects of room acoustics, then when values of one of the room acoustics parameters were added to the regression analysis, the R^2 value would be expected to increase. For the grade 1 results none of the room acoustics parameters added significantly to the prediction and the R^2 values did not increase. For the grade 3 and 6 results, adding one of the room acoustics parameters to the prediction did result in modest but significant increases in the prediction accuracy of the intelligibility scores. Of the three room acoustics parameters considered, C_{50} values tended to be slightly more effective in increasing the R^2 values.

Figure 5 illustrates the resulting multiple regression equations for combinations of S/N(A), S/N(A)^2, and C_{50}

TABLE II. R^2 values from multiple regression analyses of intelligibility scores on the predictors shown at the top of each column. The subscript ns, indicates that the room acoustics predictor variable (C_{50}, EDT, or T_{60}) did not add significantly to the prediction ($p<0.05$).

	N	S/N(A) S/N(A)^2	S/N(A) S/N(A)^2 C_{50}	S/N(A) S/N(A)^2 EDT	S/N(A) S/N(A)^2 T_{60}
Grade 1	136	0.707	0.710_{ns}	0.707_{ns}	0.707_{ns}
Grade 3	96	0.625	0.660	0.655	0.663
Grade 6	156	0.355	0.508	0.475	0.474

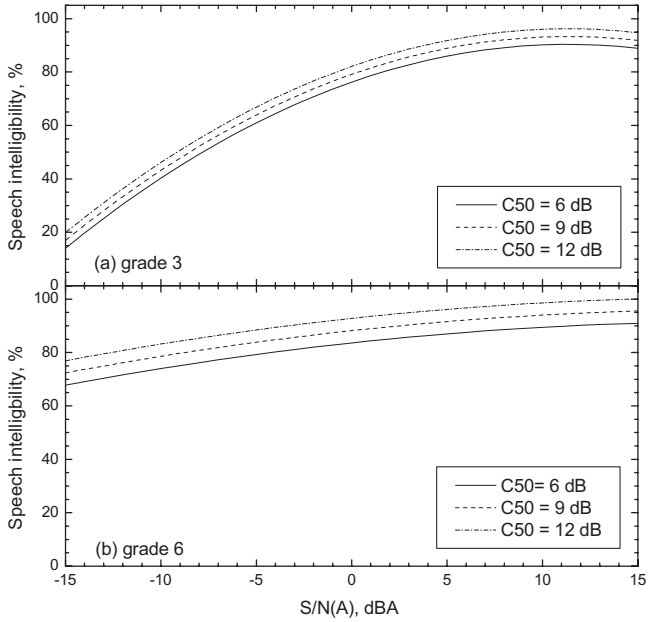

FIG. 5. Multiple regression results for prediction of speech intelligibility scores from S/N(A), S/N(A)^2, and C_{50} values for (a) grade 3 results and (b) grade 6 results. Results are given for C_{50} values of 6, 9, and 12 dB roughly corresponding to the range of frequently found conditions in the measured classrooms.

values for the grade 3 and grade 6 results. The regression equations in Fig. 5 are given by the following:

$$\text{Grade 3,} \quad \text{SI} = 2.495\ \text{S/N}(A) - 0.110\ \text{S/N}(A)^2 + 0.98C_{50} + 70.37,$$

$$\text{Grade 6,} \quad \text{SI} = 0.772\ \text{S/N}(A) - 0.0189\ \text{S/N}(A)^2 + 1.53C_{50} + 74.46.$$

The above-mentioned grade 3 results suggest that a 1 dB change in C_{50} values would result in about a 1.0% change in intelligibility scores. However, the grade 6 results indicate a 1.53% change in intelligibility scores would result for a 1 dB change in C_{50} values. If most of the data are within ± 1 s.d. of the mean, most C_{50} values would be within a range of about 6–12 dB depending on the grade. The largest effect would be for the grade six results where changes in C_{50} values are likely to result in changes to intelligibility scores of up to about 9% (obtained by multiplying the standard deviation value in Table I for C_{50} values in grade 6 classrooms by the coefficient of C_{50} in the equation for the above-presented grade 6 results, and doubling the result to include positive and negative deviations about the mean). Of course, this is much smaller than the effect of S/N(A) values illustrated in Fig. 2.

These data do not show large effects of room acoustics parameters because there were not large variations in room acoustics conditions among the various classrooms. This is illustrated in Fig. 5 that plots the regression equations for the case when C_{50} was used as the added room acoustics parameter. Similar results were obtained using EDT and T_{60} values as the added room acoustics parameter. Since these classrooms are assumed to be "typical" of many classrooms in Canadian schools, these results suggest that room acoustics in these elementary school classrooms tend to be homogeneously reasonably acceptable.

TABLE III. Average intelligibility scores for each grade and overall average standard deviations (σ) for all grades determined for each S/N(A) interval.

S/N(A) (dB)	Avg. grade 1(%)	Avg. grade 3(%)	Avg. grade 6(%)	σ(%)
−10	38.0	···	70.5	16.50
−5	56.5	69.0	80.5	12.30
0	73.2	81.5	87.9	9.00
5	84.7	89.3	92.6	5.68
10	91.3	93.6	95.0	3.50
15	94.8	95.9	97.3	2.20
20	96.4	97.0	98.3	1.29
25	97.3	···	···	0.70

IV. DISTRIBUTION OF INTELLIGIBILITY SCORES ABOUT THE MEAN TRENDS

While Sec. II discusses the mean trends of speech intelligibility scores, it is clear that many individual student results deviate significantly from the mean trends. That is, while the average student may for some condition be able to understand reasonably well, many cannot. It is therefore important to also examine the distribution of intelligibility scores about the mean trend. The ultimate goal is to determine the fraction of the students that can understand speech well at each S/N(A) value and the required conditions to enable most children to understand speech well.

The distribution of the intelligibility scores about the mean trends seen in Fig. 2 was analyzed by dividing the results into 5 dB wide S/N(A) intervals for the data from the students of each grade. It was then possible to examine the distribution of scores within each of these S/N(A) segments. Although in most cases there were approximately normal distributions of scores in each segment, in some cases there were not adequate numbers of data points to provide regular distributions. A procedure was required to approximate the distributions in all segments of the data. To do this, the mean scores and the standard deviations of the scores about the mean values were calculated for each S/N(A) segment. These values were then plotted versus the mean S/N(A) values for each interval. The mean values are listed in Table III and are different for each grade and follow trends almost identical to those in Fig. 2.

The standard deviations of the scores in each S/N(A) interval were similarly plotted versus the mean S/N(A) value for each interval. As illustrated in Fig. 6, the results for all three grades follow an approximately similar trend but with some considerable uncertainty in the lowest S/N(A) interval. The mean trend in Fig. 6 gives a good estimate of the variation in the standard deviation of scores over a wide range of S/N(A) values and is quite adequate for the purposes of these analyses in which the focus is on very good conditions for speech communication. Therefore this mean trend is used as an estimate of the standard deviations for all grades. [There is some uncertainty in the mean trend at the lowest S/N(A) category where the mean S/N(A) is −10 dB. This is

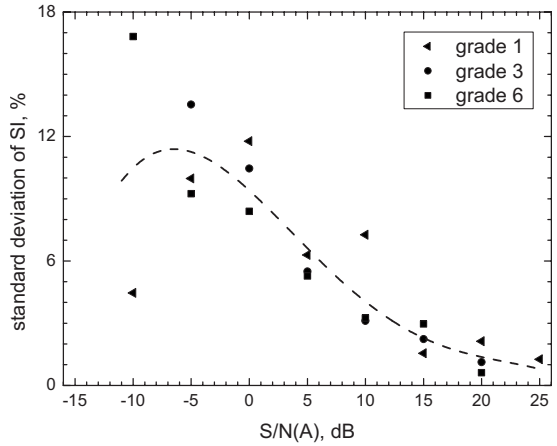

FIG. 6. Mean trend of standard deviations of speech intelligibility scores for all three grades as a function of the S/N(*A*) values.

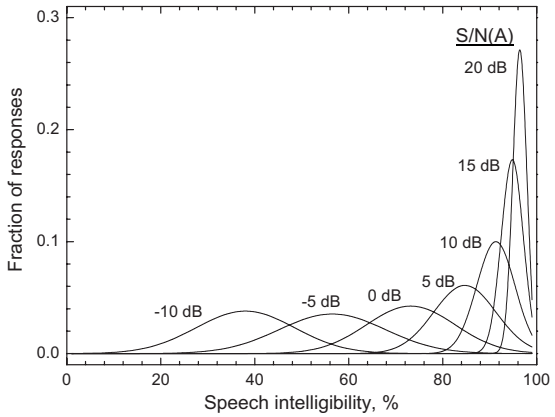

FIG. 7. Distribution of the speech intelligibility scores in S/N(*A*) intervals from −10 to +20 dB for the grade 1 results.

to be expected as conditions get more difficult and at extremely low S/N(*A*) values intelligibility scores must eventually all approach 0% with a standard deviation of zero.] The mean trend standard deviations from Fig. 6 are included in Table III.

Assuming a normal distribution is a reasonable approximation to the distribution of scores in each S/N(*A*) interval, one can estimate the distributions of scores for each interval from the mean and standard deviation of the scores in each interval. That is, the number of speech intelligibility scores in each S/N(*A*) interval can be estimated from the following expression for a normal distribution:[21]

$$y = N/\{\sigma\sqrt{2\pi}\}e^{-(x-\mu)^2/2\sigma^2}, \quad (1)$$

where N is the total number of intelligibility scores in the distribution for one S/N(*A*) interval, y is the number of scores at intelligibility x, x is the speech intelligibility score, σ is the standard deviation of the intelligibility scores in each S/N(*A*) interval, and μ is the mean speech intelligibility score in each S/N(*A*) interval.

With the mean scores and standard deviations for each S/N(*A*) interval given in Table III, one can construct a simple mathematical model of the speech intelligibility scores for the responses of students in each grade. This model can describe the distribution of scores as well as the mean trend of the scores for each age of student. Figure 7 shows the resulting speech intelligibility distributions in each S/N(*A*) interval for the grade 1 results.

One can more easily describe the fraction of students experiencing some high level of speech intelligibility by replotting the information as cumulative probability plots. This is done in Fig. 8 for the data from all three grade levels. The goal is to determine the required S/N(*A*) at each grade level for students to experience near-ideal conditions. Near-ideal is again defined as corresponding to speech intelligibility scores of 95% or better.

Figure 8 can be used to determine the fraction of students at each S/N(*A*) category that would experience near-ideal conditions with intelligibility scores of 95% or better. For the example of the grade 6 students at a 20 dB S/N(*A*), essentially all would experience 95% intelligibility or better. At a S/N(*A*) of +15 dB only 25.4% of the grade 6 students would not experience 95% or better speech intelligibility. One might therefore argue that the common recommendation for a +15 dB S/N(*A*) value[12,22] is satisfactory for the grade 6 students because at this S/N(*A*), 74.6% of the students would experience near-ideal conditions.

For the grade 3 students at a +15 dB S/N(*A*) value, only 54.5% would experience 95% or better speech intelligibility and for the grade 1 students, only 36.6% would experience this near-ideal speech intelligibility for conditions of +15 dB S/N(*A*). However, for a +20 dB S/N(*A*), 74.8% of the grade 1 students would experience 95% or better speech intelligibility. It is therefore important to note that a +15 dB S/N(*A*) does not provide near-ideal conditions for most of the grade 1 students.

V. COMPARISON OF ACTUAL S/N(*A*) VALUES WITH IDEAL REQUIREMENTS

A. Ideal S/N(*A*) goals

The data in Fig. 8 can be replotted as the percentage of students who would experience 95% speech intelligibility or

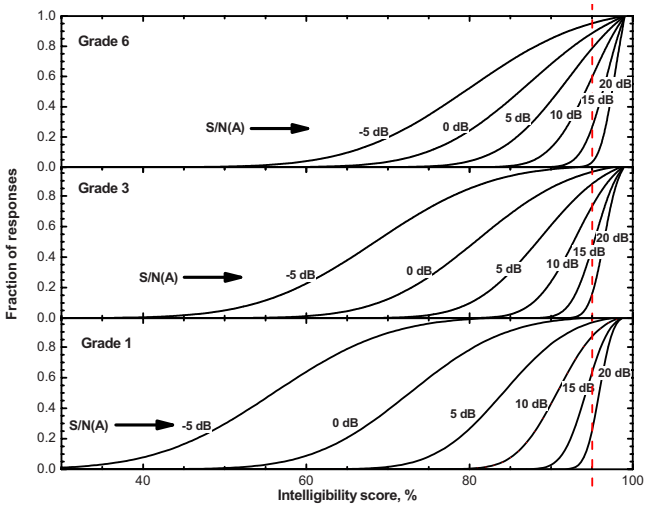

FIG. 8. (Color online) Cumulative probability distributions of intelligibility scores by S/N(*A*) category and student grade level. Vertical dashed line indicates 95% speech intelligibility.

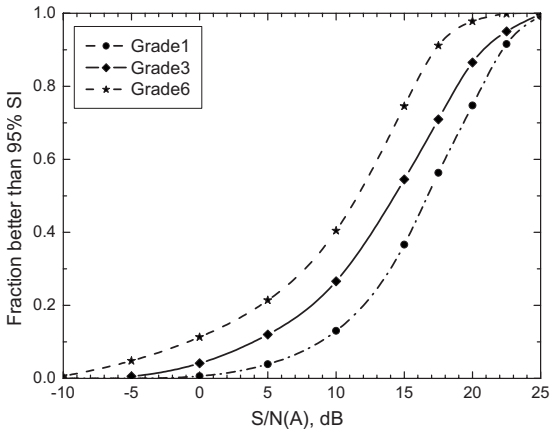

FIG. 9. Percentage of students who would experience 95% speech intelligibility or higher as a function of the S/N(*A*) value.

better as a function of the existing S/N(*A*) value, as illustrated in Fig. 9. This again assumes that 95% speech intelligibility on a simple word intelligibility test represents near-ideal conditions for speech communication. In this format one can directly determine the S/N(*A*) required for a certain percentage of the students to experience 95% speech intelligibility or better. That is, one could choose a desired S/N(*A*) goal so that some large percentage of the students would experience these near-ideal conditions for speech communication. For example, one might aim for acoustical conditions in which at least 80% of the students would experience 95% speech intelligibility or better. Figure 9 shows that for the grade 6 results a S/N(*A*) value of just above +15 dB is required. The grade 3 results indicate a minimum S/N(*A*) of +18.5 dB would be required and the grade 1 results indicate a minimum required S/N(*A*) of close to +20.5 dB.

One could require that a larger or smaller percentage of the students should experience such near-ideal conditions. For example, requiring that 90% of the students should experience such near-ideal conditions rather than 80% would increase the minimum S/N(*A*) values needed by about 2 dB. One might also include a small safety factor to be sure that the desired S/N(*A*) value is actually achieved in real classrooms. Some differences in approach are possible, but Fig. 9 can serve as the basis for setting acceptable S/N(*A*) criteria for elementary school students. One could readily interpolate for intermediate grade results and perhaps even assume that grade 7 and 8 results would yield a curve only slightly to the left of the grade 6 results in Fig. 9.

To accommodate the needs of younger children and/or to include even a modest safety factor leads to required S/N(*A*) values greater than the common recommendation for an ideal S/N(*A*) of +15 dB.

B. Conditions in active classrooms

As part of this work, speech and noise levels were recorded in active classrooms and separate speech and noise levels were determined using a statistical procedure.[17] ("Active" indicates the classrooms were fully occupied with students active in educational activities with their teacher.) The mean teacher speech level at the microphone locations near the students was 59.5 dBA with a standard deviation of ±5.5 dB. The distribution of measured S/N(*A*) values in active classrooms is shown in Fig. 12 of Ref. 17. The mean S/N(*A*) was approximately +11 dB. Although a S/N(*A*) of +11 dB is often said to correspond to somewhat acceptable conditions for speech communication, Sec. V A demonstrated that much higher S/N(*A*) values are required for good speech communication for younger children. In the actual teaching situations shown in Fig. 12 of Ref. 17, S/N(*A*) values of +15 dB or more only occurred in 6.25% of the measured cases. The S/N(*A*) conditions during the measurements of actual teaching sessions were considerably inferior to the S/N(*A*) values required for near-ideal conditions in Sec. IV.

Knowing children's ability to understand speech at various S/N(*A*) values and knowing the distribution of S/N(*A*) values found in active elementary school classrooms, one can now estimate the proportion of the students in the measured classrooms who would experience near-ideal conditions for speech communication. First, the distribution of measured S/N(*A*) values in the active classrooms was recalculated with the same 5 dB intervals as were used in Table III and Figs. 7 and 8. These values are listed in the left-hand 3 columns of Table IV and show that most of the measured conditions (61.6%) had S/N(*A*) values in the category with a mean S/N(*A*) of +10 dB.

The middle three columns in Table IV show the percentage of students who would experience 95% speech intelligi-

TABLE IV. Calculation of the percentage of students at each grade level who would experience near-ideal acoustical conditions for speech communication in the measured active classrooms. Columns 1–3, distribution of S/N(*A*) values while teachers were talking. Columns 4–6, percentages of students who would experience 95% speech intelligibility or better in each S/N(*A*) category. Columns 7–9, total percentages of students who would experience near-ideal conditions in the measured active classrooms.

Mean S/N(*A*) (dB)	*N* cases	% cases	Percent scoring >95% SI			%cases × %students		
			Grade 1	Grade 3	Grade 6	Grade 1	Grade 3	Grade 6
0	0	0.0						
5	9	8.0	3.9	12.0	21.4	0.31	0.96	1.72
10	69	61.6	13.0	26.6	40.5	8.03	16.39	24.93
15	34	30.4	36.6	54.5	74.6	11.12	16.55	22.63
20	0	0.0						
Total	**112**	**100.0**				**19.5**	**33.9**	**49.3**

TABLE V. Calculation example to determine maximum acceptable ambient noise levels.

59.5 dB A	Mean classroom speech level from teachers
−5.5 dB A	Standard deviation of measured speech levels
−20 dB A	Required S/N(A) for grade 1 students
34 dB A	Required maximum ambient noise level
35 dB A	ANSI S12.60 maximum ambient noise level criteria

bility or better in each of these same S/N(A) categories and these were obtained from Fig. 8. By multiplying the percentage of cases in each S/N(A) category by the corresponding percentage of students who would experience 95% speech intelligibility or better in that category, the total percentage of all students who would experience near-ideal conditions is obtained in the three right-hand columns for each age group. These final percentages are summed over all three S/N(A) categories at the lower right-hand side of Table IV.

The quite surprising result is that only 19.5% of the grade 1 students would experience near-ideal conditions during the measured teaching activities. This rises to 33.9% of the grade 3 students and 49.3% of the grade 6 students. This is in spite of the fact that room acoustics parameters were near-ideal and the rooms seemed to have only minimal acoustical problems to the (adult) experimenters carrying out these tests.

C. Maximum ambient noise level criteria

By combining the various results from this study, one can estimate maximum acceptable ambient noise levels that would provide near-ideal speech communication for students of various ages. Table V illustrates the process for grade 1 students for whom a minimum S/N(A) of 20 dB was found to be necessary in the previous sections of this paper. This estimate results in a recommended maximum ambient noise level that is almost identical to that recommended in the ANSI S12.60 classroom acoustics standard. This is strong confirmation of the validity of the recommendation in ANSI S12.60.

Similar estimates could be made for grade 3 and 6 students. If these estimates included a small safety factor of 2–4 dB to account for various uncertainties, the results would again be close to the recommendations of ANSI S12.60. It is therefore justifiable and practical to recommend a maximum ambient noise level in all elementary school classrooms of no more than 35 dBA. It is important to realize too, that although occupied noise levels may be higher than 35 dBA, lower unoccupied levels lead to lower occupied levels[17] and hence it is particularly important to make unoccupied ambient noise levels as low as possible.

Unfortunately the current data are not adequate to estimate ideal room acoustics criteria for classrooms. There was simply very little variation in room acoustics conditions. This means that the conclusions with respect to desirable S/N(A) and ambient noise levels are directly applicable to classrooms with room acoustics conditions similar to those in these classrooms. However, the room acoustics measurement results in Table I show that conditions in these classrooms were close to most recommended values for classrooms. Thus, the recommended S/N(A) values can be said to be an important component of an ideal classroom.

VI. DISCUSSION AND CONCLUSIONS

This study has provided data that better describe the abilities of elementary school children to understand speech in noise in real classrooms of schools near Ottawa, Canada. The results are better because they are from a large sample of children and are based on natural binaural listening in actual classrooms with realistic ambient noises. These results also realistically include the other distractions that are expected to occur in actual classrooms such as those from other students both in the classroom and in adjacent spaces.

The form of the relationships between intelligibility scores and S/N(A) values is similar to previous in-classroom speech intelligibility tests but different than earlier laboratory studies using monaural headphone playback of the speech material.

The mean trends of the results indicate that grade 1 students (6 year olds) require 7 dB higher S/N(A) values to achieve the same speech intelligibility scores as would grade 6 students (11 year olds). Although no adult data were obtained, it is likely that young adult listeners would get somewhat higher speech intelligibility scores than the grade 6 students at the same S/N(A) conditions.[9]

There is also much scatter in the speech intelligibility scores about the mean trends indicating that many students would often have more difficulty understanding speech than indicated by the mean trends. The distribution of speech intelligibility scores about the mean trends was therefore also examined and a mathematical model of the means and distributions of scores was developed to more completely define children's abilities to understand speech in noise.

From this model estimates of the S/N(A) values required for grade 1, grade 3, and grade 6 students to experience near-ideal conditions for speech communication were made. Near-ideal conditions were defined as 95% speech intelligibility scores on simple word intelligibility tests and all ages of student could do better than this in very high S/N(A) conditions. For 80% of the students to experience such near-ideal conditions, S/N(A) values of +20, +18, and +15 dB would be required for grade 1, grade 3, and grade 6 students, respectively.

Measurements during actual teaching activities showed an average S/N(A) of 11 dB and in only 6.25% of the cases were the S/N(A) +15 dB or higher. In the actual teaching situations only 19.5% of the grade 1, 33.9% of the grade 2, and 49.3% of the grade 6 students would experience near-ideal conditions for speech communication. That is, in the measured classrooms that appeared to have acceptable acoustical conditions to the adult experimenters, less than half of the students would experience near-ideal speech communication.

The inability of younger children to understand many of the words that a teacher is saying must make it more difficult for the children to learn new concepts. There is a growing literature of results indicating that increased noise levels are

associated with a number of educational factors such as delayed reading ability, effects on memory, and student behavior.[2]

Further calculations based on the new measurements led to estimates of maximum acceptable ambient noise levels that were very close to the 35 dBA recommendation in ANSI S12.60.

The range of room acoustics conditions measured in the classrooms was quite small and close to values thought to be optimum. Although there were significant effects of room acoustics parameters, the limited range of the data made it impossible to produce new estimates of ideal room acoustics conditions for speech communication in classrooms as a function of student age. Further research is required to consider the question of optimum room acoustics criteria to maximize intelligibility and the quality of speech communication.

ACKNOWLEDGMENTS

This work was supported by a grant from the Canadian Language and Literacy Research Network. The very helpful cooperation of the teachers and administration of the Upper Canada District School Board made this work possible.

[1]American National Standards Institute, "Acoustical performance criteria, design requirements, and guidelines for schools," ANSI S12.60, New York, 2002.
[2]K. Anderson, "The problem of classroom acoustics: The typical classroom soundscape is a barrier to learning," Semin. Hear. **25**, 117–129 (2004).
[3]S. Hygge, "Classroom experiments on the effects of different noise sources and sound levels on long-term recall and recognition in children," Appl. Cognit. Psychol. **17**, 895–914 (2003).
[4]A. L. Bronzaft and D. P. McCarthy, "The effect of elevated train noise on reading ability," Environ. Behav. **7**, 517–528 (1975).
[5]A. L. Bronzaft, "The effect of a noise abatement program on reading ability," J. Environ. Psychol. **1**, 215–222 (1981).
[6]G. W. Evans and L. Maxwell, "Chronic noise exposure and reading deficits," Environ. Behav. **29**, 638–656 (1997).
[7]L. L. Elliott, S. Connors, E. Kille, S. Levin, K. Bell, and D. Katz, "Children's understanding of monosyllabic nouns in quiet and in noise," J. Acoust. Soc. Am. **66**, 12–21 (1979).
[8]L. L. Elliott, "Performance of children aged 9 to 17 years on a test of speech intelligibility in noise using sentence material—With controlled word predictability," J. Acoust. Soc. Am. **66**, 651–653 (1979).
[9]A. Neuman and I. Hochberg, "Children's perception of speech in reverberation," J. Acoust. Soc. Am. **73**, 2145–2149 (1983).
[10]T. Finitzo-Hieber and T. W. Tillman, "Room acoustics effects on monosyllabic word discrimination ability for normal and hearing-impaired children," J. Speech Hear. Res. **21**, 440–458 (1978).
[11]N. B. Marshall, "The effects of different signal-to-noise ratios on the speech recognition scores of children," Ph.D. thesis, University of Alabama, Tuscaloosa, AL, 1987.
[12]J. S. Bradley, "Speech intelligibility studies in classrooms," J. Acoust. Soc. Am. **80**, 846–854 (1986).
[13]N. W. MacKeith and R. R. A. Coles, "Binaural advantages in hearing of speech," J. Laryngol. Otol. **85**, 213–232 (1971).
[14]A. K. Nábělek and P. K. Robinson, "Monaural and binaural speech perception in reverberation for listeners of various ages," J. Acoust. Soc. Am. **71**, 1242–1248 (1982).
[15]A. K. Nábělek and J. M. Pickett, "Reception of consonants in a classroom as affected by monaural and binaural listening, noise, reverberation and hearing aids," J. Acoust. Soc. Am. **56**, 628–639 (1974).
[16]J. P. Moncur and D. Dirks, "Binaural and monaural speech intelligibility in reverberation," J. Speech Hear. Res. **10**, 186–195 (1967).
[17]H. Sato and J. S. Bradley, "Evaluation of acoustical conditions for speech communication in active elementary school classrooms," J. Acoust. Soc. Am. **123**, 2064–2077 (2008).
[18]M. Ross and J. Lerman, "A picture identification test for hearing impaired children," J. Speech Hear. Res. **13**, 44–53 (1970).
[19]M. Ross and J. Lerman, *Word Intelligibility by Picture Identification* (Stanwix House, Pittsburgh, 1971).
[20]International Organisation for Standardisation, "Acoustics—Measurement of the reverberation time of rooms with reference to other acoustical parameters," ISO3382, Geneva, Switzerland.
[21]G. F. Ferguson and Y. Takane, *Statistical Analysis in Psychology and Education*, 6th ed. (McGraw Hill, New York, 1989).
[22]T. Houtgast, "The effect if ambient noise on speech intelligibility in classrooms," Appl. Acoust. **14**, 15–25 (1981).

Relationship between listening difficulty and acoustical objective measures in reverberant sound fields

Hayato Sato[a] and Masayuki Morimoto
Environmental Acoustics Laboratory, Graduate School of Engineering, Kobe University, Rokko, Nada, Kobe 657-8501, Japan

Hiroshi Sato
Institute for Human Science & Biomedical Engineering, National Institute of Advanced Industrial Science and Technology, Tsukuba Central, Tsukuba, Ibaraki 305-8568, Japan

Megumi Wada
Environmental Acoustics Laboratory, Graduate School of Engineering, Kobe University, Rokko, Nada, Kobe 657-8501, Japan

(Received 6 August 2007; revised 29 January 2008; accepted 3 February 2008)

The previous work [Morimoto *et al.*, J. Acoust. Soc. Am. **116**, 1607–1613] showed that listening difficulty ratings can be used to evaluate speech transmission performance more exactly and sensitively than intelligibility. Meanwhile, speech transmission performance is usually evaluated using acoustical objective measures, which are directly associated with physical parameters of room acoustic design. However, the relationship between listening difficulty ratings and acoustical objective measures was not minutely investigated. In the present study, a total of 96 impulse responses were used to investigate the relationship between listening difficulty ratings and several objective measures in unidirectional sound fields. The result of the listening test showed that (1) the correlation between listening difficulty ratings and speech transmission index (STI) is the strongest of all tested objective measures, and (2) A-weighted D_{50}, C_{50}, and center time, which are obtained from the impulse responses passed through an A-weighted filter, also strongly correlate with listening difficulty ratings, and their correlations with listening difficulty ratings are not statistically different from the correlation between listening difficulty ratings and STI.
© *2008 Acoustical Society of America.* [DOI: 10.1121/1.2885750]

PACS number(s): 43.55.Hy, 43.71.Gv [NX] Pages: 2087–2093

I. INTRODUCTION

Evaluation of speech transmission performance is essential for designing rooms for speech communication. Ideally, speech transmission performance should be subjectively evaluated by listeners, because the performance indicates how accurately and comfortably speech information is transmitted to listeners. Morimoto *et al.*[1] suggested listening difficulty ratings as a subjective measure to evaluate the speech transmission performance of rooms. Listening difficulty ratings are the percentage of responses that indicate some level of difficulty in listening to the most familiar words. Sato *et al.*[2] reported that listening difficulty is a more appropriate evaluation tool than word intelligibility tests for conditions with speech-to-noise ratios between 0 and 15 dBA that are commonly found in everyday life. Therefore, it is advisable that the design and evaluation of rooms for speech communication be carried out on the basis of listening difficulty ratings.

However, objective measures are usually used to evaluate speech transmission performance, because they are directly associated with the physical parameters of room acoustic design, and it takes much time to obtain subjective measures. Therefore, the relationship between subjective and objective measures needs to be clarified in advance to convert objective measure to subjective measure, and vice versa.

Background noise and reverberant sounds are critical factors in determining speech transmission performance in rooms. Useful-to-detrimental ratio proposed by Lochner and Burger,[3] and speech transmission index (STI) proposed by Houtgast and Steeneken[4] can estimate the combined effects of the two critical factors on speech intelligibility. The two objective measures have different concepts in estimating the effect of reverberation sounds on speech intelligibility. The concept of useful-to-detrimental ratio is that the energy of the direct sound and reflected sounds can be divided into useful energy and detrimental energy for speech intelligibility according to the interval from the direct sound. Meanwhile, the concept of STI is based on the reduction of the modulation transfer function (MTF) due to reverberant sounds. Although the concept of STI is different from that of useful-to-detrimental ratio, Bradley[5] reported that the correlation coefficients between speech intelligibility and the two objective measures are essentially equivalent.

The relationship between listening difficulty ratings and objective measures was investigated in the previous studies.[1,2,6] Morimoto *et al.*[1] and Kobayashi *et al.*[6] reported that listening difficulty ratings increased with increasing reverberation time and decreasing speech-to-noise ratio. Sato

[a]Author to whom correspondence should be addressed. Electronic mail: hayato@kobe-u.ac.jp.

et al.[2] reported that a logistic curve could be used to explain the relationship between listening difficulty ratings and $U_{50(A)}$, that is, A-weighted useful-to-detrimental ratio with 50 ms early time interval. However, reverberant sounds used in the previous studies[1,2,6] were artificial and simple ones, while reverberant sounds in real rooms have complex properties and vary widely. In addition, the number of reverberant sound fields used in the previous studies was not enough to investigate the relationship between listening difficulty ratings and objective measures.

In the present study, the relationship between listening difficulty ratings and objective measures is investigated focusing on the effect of time sequences of sound reflections. A total of 96 reverberant sound fields that cover a wide variety of acoustic conditions were tested. These sound fields were unidirectional, and were simulated by convolving test signals with monaural impulse responses measured in real rooms.

II. METHOD

A. Test words and sound fields

A hundred Japanese words were used as test words. Test words were selected from the word lists proposed by Sakamoto *et al.*[7] to be most familiar to young adults. Each test word has four syllables. Test words were spoken by a female speaker, and recorded in an anechoic room.

A total of 96 impulse responses were used as test sound fields. Seventy-one of them were selected from the impulse response database compiled by the Speech Communication Research Working Group of the Architectural Institute of Japan.[8] The database included 966 digitized impulse responses measured at various types of rooms in Japan, for example, a meeting room, an auditorium, a concert hall, a film theater, and a sports area. The impulse responses, which had been measured using a one-point omni-directional microphone, were used in the present study. The impulse responses were selected to have a wide variety of acoustic conditions.

The other 25 impulse responses were artificially created to cover less and much reverberant sound fields that are lacking in number in the database. Artificial impulse responses were created by reverberating or trimming monaural impulse responses in the database[8] using software (SEKD Samplitude) on a personal computer. Figure 1 represents the numbers of real and artificial impulse responses used in the listening test as a function of STI. Open and closed bars respectively represent the numbers of real and artificial impulse responses. The STIs of artificial impulse responses were controlled in order to flatten the distribution of the number of impulse responses as a function of STI.

B. Participant

Fifty-five young adults (male: 27, female: 28) participated in the listening test. They were university students in their twenties. The results of pure-tone audiometry show that all participants had normal hearing sensitivity. All participants had the experience of participating in listening tests on evaluating speech transmission performance.

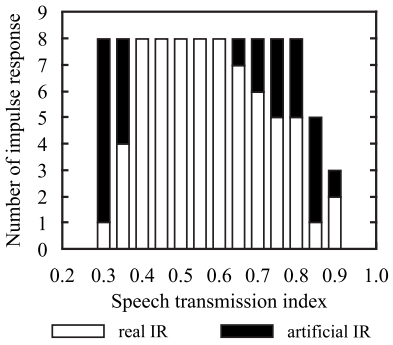

FIG. 1. Numbers of real and artificial impulse responses (IR) used in the listening test as a function of STI in steps of 0.05. Open and closed bars respectively represent frequencies of real and artificial impulse responses.

C. Procedure

Each of the test words was preliminarily convolved with each of the test impulse responses on a personal computer. Thus, a total of 9600 test signals (100 words $\times$ 96 impulse responses) were prepared. The test signals were divided into 100 different sets consisting of 96 test signals.

Moreover, four reverberation-free words were added to each set. Sato *et al.*[9] reported that the reproducibility of listening difficulty ratings improved when a reverberation-free and quiet sound field and an extremely reverberant and noisy sound field were included in the test sound fields as reference signals. The four reverberation-free words were expected to work as the highest-quality reference signals, and the lowest-quality reference signals, that is, extremely reverberant sound fields, were already included in the test sound fields in the present study. Therefore, each set consisted of 96 test signals and four highest-quality reference signals. Each set contained all test words and impulse responses, and combinations of the test words and the test impulse responses were different in different sets.

Each participant listened to four different sets of test signals. A total of 220 sets of test signals (55 participants $\times$ 4 sets) were presented throughout the listening test. Each set was used twice or thrice. The listening test was divided into eight sessions each of which allows participants to listen to 50 test signals. Test signals were presented in random order, except that the first signal in each session was always the highest-quality reference signal. The interval for the presentation of each signal was 10 s. It took about 7 min. to complete each session.

The test signals were unidirectionally presented from a loudspeaker (Fujitsu Ten, TD512) at a distance of 1.5 m in front of the participant in an anechoic room. The frequency characteristics of the loudspeaker were flat within ± 5 dB in the range from 100 Hz to 10 kHz. The sound pressure level of each test signal was measured at the position of the center of the subject's head using a sound level meter, which was set at A-weighted and slow response. The differences among the peak levels of the test signals were within ± 1.5 dBA, and the level averaged over all test signals was set at 65 dBA. No additional noise was added to the test signals.

TABLE I. Categories of listening difficulty (see Ref. 1).

1	Not	difficult
2	A little	difficult
3	Fairly	difficult
4	Extremely	difficult

Each participant was asked to take dictation of each test signal as they listened using katakana characters (Japanese phonograms) and to simultaneously rate the listening difficulty into one of the four categories shown in Table I. Before the listening test, each participant listened to ten signals as an exercise. The signals for exercises were made by convolving ten words that were not included in the 100 test words with ten different impulse responses used in the listening test so that the signals for exercises contained the widest range of the test sound fields.

D. Acoustical objective measures

A total of six types of acoustical objective measures were tested in the present study. The tested objective measures were speech transmission index (STI),[4] Deutlichkeit (D_{50}),[10] an early-to-late ratio with the fixed boundary at 50 ms from the direct sound (C_{50}),[11] center time (t_s),[12] reverberation time (RT), and early decay time (EDT). STI was obtained from the impulse responses according to the original method documented in a review by Houtgast and Steeneken.[13] The objective measures except STI were obtained from the impulse responses passed though 1/1 octave band filters with center frequencies from 125 Hz to 8 kHz. In addition, a two-octave-band filter that covers octave bands of 500 Hz and 1 kHz, and an A-weighted filter were used for a trial, because these filters are often used to evaluate acoustical environments. Furthermore, the frequency weighting sum of D_{50} and that of C_{50} were also obtained using the weighting factors for STI[13] and speech intelligibility index[14] (1/1 octave band method, female) as a trial. The slope of bandpass filters was −48 dB/oct. RT and EDT were, respectively, obtained from the slopes of the reverberation energy decay curve from −5 to −35 dB and from −5 to −15 dB using Shoreder's method.[15]

III. RESULTS AND DISCUSSION

A. Relationship between word intelligibility scores and listening difficulty ratings

Word intelligibility scores and listening difficulty ratings for each impulse response were obtained from the collective results of the listening test for all participants. This means that the number of samples for each impulse response was 220. The word intelligibility score is the percentage of the test signals written down correctly. The listening difficulty rating is the percentage of the sum of listening difficulty ratings evaluated from "2" to "4" in Table I. Note that listening difficulty ratings decrease when speech transmission performance improves, in contrast to word intelligibility scores.

The listening difficulty rating for the reverberant-free reference signal was 1.3%, and the maximum listening difficulty rating was 98%. These results indicated that the sound fields used in the present study included both high-end and low-end reference signals, and that the listening difficulty ratings obtained in the present study will have high reproducibility.

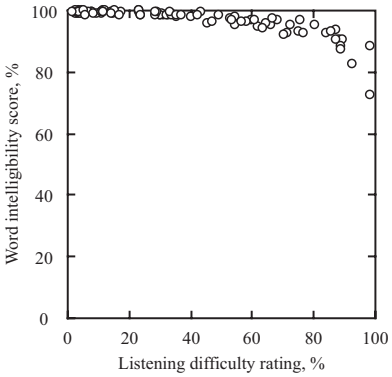

FIG. 2. Relationship between word intelligibility scores and listening difficulty ratings.

Figure 2 represents the relationship between word intelligibility scores and listening difficulty ratings. Word intelligibility scores decreased with increasing listening difficulty ratings. However, word intelligibility scores varied over a range of only 27% (i.e., from 73 to 100%), while listening difficulty ratings varied over almost the full range (from 2 to 98%). This behavior corresponds to those observed in the previous studies.[1,2,6]

B. Relationship between listening difficulty ratings and objective measures

Generally speaking, the relationship between a subjective value and an objective value is nonlinear, and a cumulative normal distribution function or a logistic curve is often used to approximate a subjective-objective function. As reported by Sato *et al.*,[2] this relationship seems to be similar to the case of the relationship between listening difficulty ratings and objective measures. In the present study, a cumulative normal distribution function was used to approximate listening difficulty ratings as a function of each objective measure. Listening difficulty ratings were converted into standard scores (z scores)[16] to simplify the approximation using a linear regression analysis. The z scores of −1, 0, and 1, respectively, correspond to the listening difficulty ratings of 16, 50, and 84%.

Linear regression analyses between z scores of listening difficulty ratings and each objective measure were performed. The listening difficulty ratings that were less than 5% ($z<-1.64$) and more than 95% ($z>1.64$) were omitted to prevent their excessive effect on linear regression analyses. A total of 16 test sound fields were omitted in the following analyses.

TABLE II. Correlation coefficients between the z scores of listening difficulty ratings and each of the objective measures. The objective measures except STI were calculated using the impulse responses passed though 1/1 octave bandpass filters for each center frequency, a two-octave bandpass filter that covers octave bands of 500 Hz and 1 kHz, and an A-weighted filter. The frequency weighting sum of D_{50} and that of C_{50} were obtained using the weighting factors for STI (see Ref. 13) and speech intelligibility index (Ref. 14). (SII).

Frequency weighting		STI	D_{50}	C_{50}	t_s	EDT	RT
1/1 oct. bandpass	125 Hz	···	−0.74*	−0.75*	0.81*	0.76*	0.67*
	250 Hz	···	−0.86*	−0.85*	0.92*	0.77*	0.72*
	500 Hz	···	−0.88*	−0.88*	0.92*	0.80*	0.81*
	1 kHz	···	−0.94*	−0.93*	0.94	0.81*	0.83*
	2 kHz	···	−0.93*	−0.92*	0.95	0.82*	0.83*
	4 kHz	···	−0.92*	−0.93*	0.96	0.80*	0.85*
	8 kHz	···	−0.88*	−0.88*	0.92*	0.72*	0.82*
Two-oct. bandpass	500-1 kHz	···	−0.93*	−0.93*	0.94	0.81*	0.82*
A-weighted		···	−0.94	−0.94	0.95	0.82*	0.84*
Frequency weighting sum	STI	−0.97	−0.94	−0.94	···	···	···
	SII	···	−0.94	−0.94	···	···	···

*Statistically different from STI ($p<0.05$)

1. Correlation coefficient

Table II represents correlation coefficients between z scores of listening difficulty ratings and each of the objective measures. The correlation between z scores of listening difficulty ratings and STI was the strongest of all objective measures ($r=-0.97$). The differences between the absolute value of correlation coefficient for STI and the other absolute values of correlation coefficients were statistically tested using Fisher's z transformation.[16] The lower limit of the absolute value of correlation coefficient that is not statistically different from that for STI is calculated to be 0.937 ($p<0.05$). This means that the correlation coefficients between −0.937 and 0.937 are statistically weaker than that for STI. Asterisks on the right-hand side of the correlation coefficients in Table II denote that the correlation is statistically weaker than that for STI. The correlations for RT and EDT were statistically weaker than that for STI for all cases. It was common to observe for D_{50}, C_{50}, and t_s that the correlations for the A-weighted filter were not statistically weaker than that for STI. The correlations for 1–4 kHz were instead stronger than those for 250 Hz, 500 Hz, and 8 kHz regardless of the objective measures. These results indicate that listening difficulty is more strongly affected by reverberant sounds within octave bands from 1 to 4 kHz than other octave bands. The A-weighted function relatively increases sound energy within octave bands from 1 to 4 kHz, and decreases other frequency sounds that are not very important for listening difficulty ratings. Therefore, A-weighted objective measures seem to strongly correlate with listening difficulty ratings. The mid-two-octave band (500 Hz–1 kHz) objective measures, the frequency weighting sum of D_{50}, and that of C_{50} also showed strong correlations, which were almost the same as those for A-weighted objective measures.

2. Scatter diagram, linear regression line and prediction interval

Figure 3 represents scatter diagrams for STI and A-weighted objective measures. A linear regression line and 95% prediction intervals are also shown in each panel. Linear regression equations for other frequencies are shown in the Appendix. The prediction intervals for EDT(A) and RT(A) were around $\pm 0.9\sigma$ at the z score of listening difficulty ratings of zero. Meanwhile, the prediction intervals for other objective measures were around half as small as those for EDT(A) and RT(A). The prediction intervals at the z score of listening difficulty ratings of zero are $\pm 0.43\sigma$ for STI, $\pm 0.57\sigma$ for D_{50}(A), $\pm 0.56\sigma$ for C_{50}(A) and $\pm 0.51\sigma$ for t_s(A). The differences between the prediction interval for STI and that for other objective measures ranged from 0.08 to 0.14σ. This also indicates that the estimation accuracies of D_{50}(A), C_{50}(A) and t_s(A) are not inferior to that of STI. The relationship between z scores of listening difficulty ratings and t_s(A) showed a logarithmic function rather than a linear function. However, the correlation coefficient between z scores of listening difficulty ratings and the base-10 logarithm of t_s(A) ($r=-0.96$) was not significantly increased from that for t_s(A).

Note that the test sound fields used in the present study were unidirectional sound fields. It is unclear whether the results of the present study are applicable in real sound fields or not at this time. Further studies will clarify this problem. Considering a masking level difference[17] due to spatial aspects of reverberant sounds, listening difficulty ratings in real sound fields might improve relative to those estimated from monaural objective measures. Even if that were true, the estimation error would be at least on the safe side.

C. Evaluation of speech transmission performance using listening difficulty and objective measures

Figure 2 clearly demonstrates that listening difficulty ratings can present the difference between speech transmission performances that word intelligibility scores cannot. Moreover, Fig. 3 shows that z scores of listening difficulty ratings were linearly proportional to STI in the range of STI from 0.3 to 0.9. This demonstrates that listening difficulty

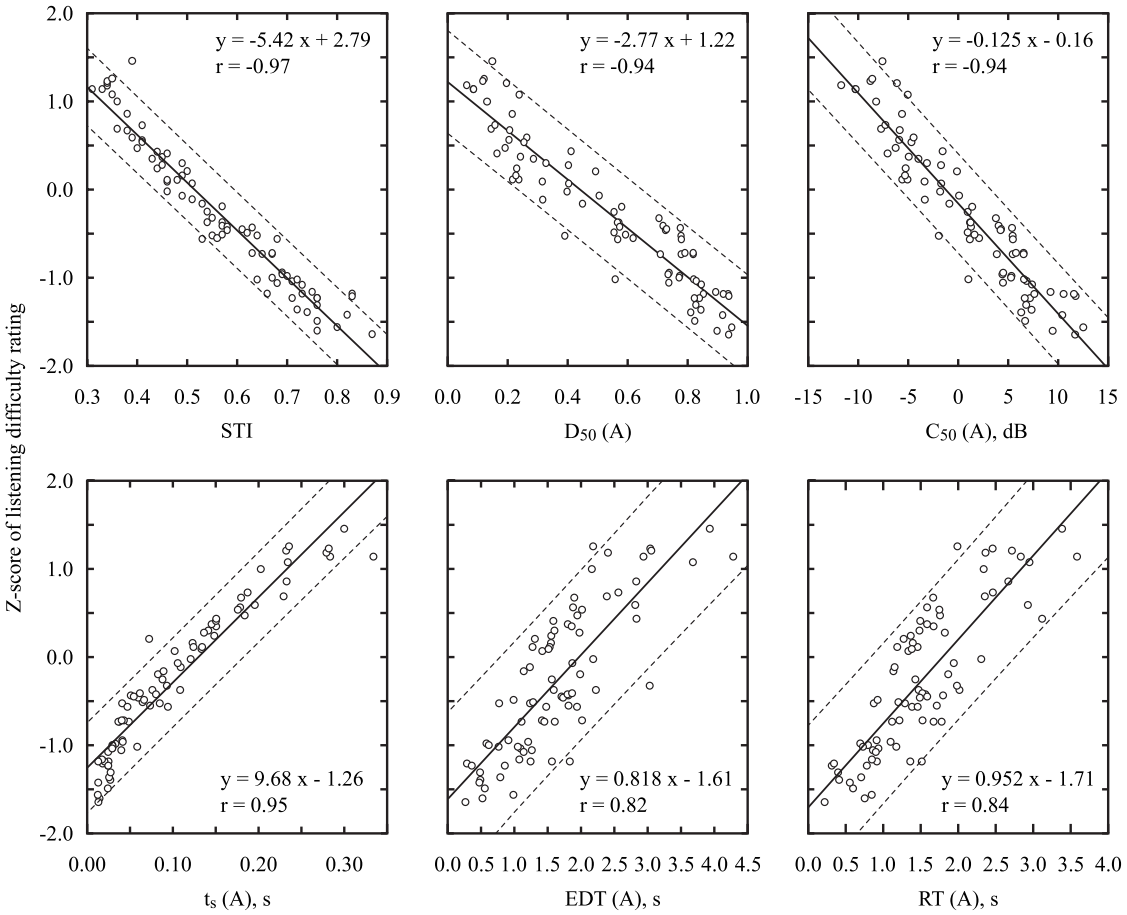

FIG. 3. *Z* score of listening difficulty rating as a function of each of the objective measures. A solid line and dashed lines in each panel respectively represent a linear regression line and 95% prediction intervals.

ratings can present the difference between most speech transmission performances of room acoustics that appear in real situations.

Objective measures are used to evaluate the speech transmission performance of rooms in various stages of acoustic design. Before construction of rooms, estimation of RT from volume and sound absorbing power is usually performed on the assumption of a diffuse sound field. However, the correlation between listening difficulty and reverberation time is significantly weaker than in the case of other objective measures. Therefore, it is better to consider RT as a simple but rough predictor of listening difficulty. Meanwhile, impulse responses are needed to obtain objective measures other than RT. Bistafa and Bradley[18] suggested the formulation of D_{50} and C_{50} in a diffuse sound field by introducing an ideal impulse response consisting of the direct sound and exponential decay that start at the same time. Houtgast and Steeneken[13] also suggested the formulation of MTF in a diffuse sound field based on the same ideal impulse response. Barron's revised theory[19] also enables us to obtain D_{50} and C_{50} from RT and source-receiver distance. These would be more accurate predictors of listening difficulty than RT at sound receiving points where the direct sound is dominant.

Impulse responses can be obtained from measurements in scale model or computer simulations before constructing rooms. These methods are useful for optimizing speech transmission performance by arranging reflective or absorptive materials on room surfaces. In this manipulation, information on whether each reflected sound is useful or detrimental for speech perception is directly related to the arrangement of room surfaces. The concept of an early-to-late ratio more clearly provides this information than that of STI. Considering that A-weighted D_{50} and C_{50} strongly correlate with listening difficulty ratings and that the correlations are not statistically different from the correlation for STI, A-weighted D_{50} and C_{50} are more useful than STI from the viewpoint of the acoustical design of rooms.

After construction of rooms, impulse responses can be measured in the constructed rooms. STI can estimate listening difficulty most accurately from impulse responses of rooms. Therefore, it is better to use STI to conclusively determine listening difficulty in the constructed rooms. A-weighted D_{50}, C_{50}, and t_s are simple alternatives for such use. Figure 4 represents the relationship between listening difficulty ratings and other measures to evaluate speech transmission performance on the basis of the linear regres-

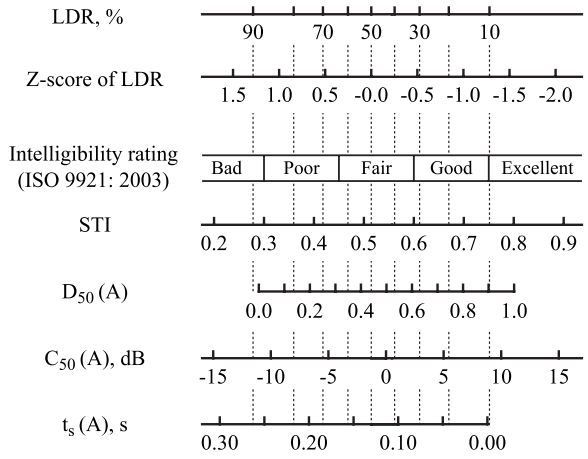

FIG. 4. Chart for converting listening difficulty ratings to other measures: intelligibility rating, STI, D_{50}(A), C_{50}(A), and t_s(A).

sion equations presented in Fig. 3. This chart enables us to convert listening difficulty ratings to intelligibility rating,[20] STI, A-weighted D_{50}, C_{50}, and t_s, and vice versa. For example, a listening difficulty rating of 50% roughly corresponds to an STI of 0.5, and the boundary between intelligibility ratings of "Fair" and "Good" corresponds to a listening difficulty rating of around 30%.

IV. CONCLUSION

The relationship between listening difficulty ratings and acoustical objective measures was investigated using the monaural impulse responses measured at various types of rooms in Japan, focusing on the effect of time sequences of sound reflections. The results of listening tests and analyses clarified that (1) the correlation between listening difficulty ratings and STI is the strongest of all tested objective measures, and (2) A-weighted D_{50}, C_{50}, and t_s, which are calculated from the impulse responses passed through an A-weighted filter, also strongly correlated with listening difficulty ratings, and their correlations with listening difficulty ratings are not statistically different from the correlation between listening difficulty ratings and STI.

Note that the results of the present study were obtained in quiet sound fields. The effect of background noise needs to be investigated to determine the best objective measure for estimating listening difficulty ratings in noisy sound fields, such as public spaces.

ACKNOWLEDGMENTS

This research project was partially supported by the research and development grant of the Japan Institute of Construction and Engineering, 03011, 2004, and by the Japan Society for the Promotion of Science, Grant-in-Aid for Scientific Research (B), 16360292, 2004–2006.

APPENDIX: LINEAR REGRESSION EQUATIONS BETWEEN *Z* SCORES OF LISTENING DIFFICULTY RATINGS AND ACOUSTICAL OBJECTIVE MEASURES

TABLE A1. Linear regression equations and correlation coefficients between z scores of listening difficulty ratings (y) and objective measures (x) for octave bands of 500 Hz, 1 kHz, and 2 kHz, and for two-octave bands of 500 Hz and 1 kHz.

Objective measure (x)	Linear regression equation	Correlation coefficient
D_{50}(500)	$y=-2.93x+1.08$	−0.88
D_{50}(1k)	$y=-3.01x+1.27$	−0.94
D_{50}(2k)	$y=-2.84x+1.14$	−0.93
D_{50}(500-1k)	$y=-3.03x+1.25$	−0.93
C_{50}(500)	$y=-0.134x-0.38$	−0.88
C_{50}(1k)	$y=-0.137x-0.24$	−0.93
C_{50}(2k)	$y=-0.126x-1.27$	−0.92
C_{50}(500-1k)	$y=-0.140x-0.27$	−0.93
t_s(500)	$y=9.49x-1.39$	0.92
t_s(1k)	$y=9.56x-1.32$	0.94
t_s(2k)	$y=9.36x-1.34$	0.95
t_s(500-k)	$y=9.77x-1.36$	0.94
EDT(500)	$y=0.793x-1.56$	0.80
EDT(1k)	$y=0.773x-1.59$	0.81
EDT(2k)	$y=0.804x-1.62$	0.82
EDT(500-1k)	$y=0.780x-1.58$	0.81
RT(500)	$y=0.902x-1.62$	0.81
RT(1k)	$y=0.889x-1.65$	0.83
RT(2k)	$y=0.957x-1.73$	0.83
RT(500-1k)	$y=0.900x-1.65$	0.82

[1]M. Morimoto, Hi. Sato, and M. Kobayashi, "Listening difficulty as a subjective measure for evaluation of speech transmission performance in public spaces," J. Acoust. Soc. Am. **116**, 1607–1613 (2004).
[2]Hi. Sato, J. Bradley, and M. Morimoto, "Using listening difficulty ratings of conditions for speech communication in rooms," J. Acoust. Soc. Am. **117**, 1157–1167 (2005).
[3]J. P. A. Lochner and J. F. Burger, "The influence of reflections on auditorium acoustics," J. Sound Vib. **1**, 426–454 (1964).
[4]T. Houtgast and H. J. M. Steeneken, "The modulation transfer function in room acoustics as a predictor of speech intelligibility," Acustica **28**, 66–73 (1973).
[5]J. S. Bradley, "Relationships among measures of speech intelligibility in rooms," J. Audio Eng. Soc. **46**, 396–405 (1998).
[6]M. Kobayashi, M. Morimoto, Hi. Sato, and Ha. Sato, "Optimum speech level to minimize listening difficulty in public spaces," J. Acoust. Soc. Am. **121**, 251–256 (2007).
[7]S. Sakamoto, Y. Suzuki, S. Amano, K. Ozawa, T. Kondo, and T. Sone, "New lists for word intelligibility test based on word familiarity and phonetic balance," J. Acoust. Soc. Jpn. **54**, 842–849 (1998). (in Japanese)
[8]Y. Nishikawa, Hi. Sato, S. Inoue, and Y. Kobayashi, "Evaluation of speech transmission performance with impulse response in rooms," J. Environ. Eng. **605**, 9–14 (2006). (in Japanese).
[9]Ha. Sato, M. Morimoto, A. Hakamada, M. Kobayashi, and Hi. Sato, "Learning effect and reduction of context effect on listening difficulty for words," Memoirs of Graduate School of Science and Technology, Kobe University, **22**, 47–57 (2004). (in Japanese).
[10]R. Thiele, "Richtungsverteilung und Zeitfolge der Schallrückwürfe in Räumen," Acustica **3**, 291–302 (1953). (Title in English: "Directional distribution and time sequence of sound reflections in rooms.")
[11]J. S. Bradley, "Predictors of speech intelligibility in rooms," J. Acoust. Soc. Am. **80**, 837–845 (1986).
[12]R. Kürer, "Zur Gewinnung von Einzahlkriterien bei Impulsmessungen in der Raumakustik," Acustica **21**, 370–372 (1969). (Title in English: "Extraction of single-number criteria from impulse measurements of room acoustics.")

[13]T. Houtgast and H. J. M. Steeneken, "A review of the MTF concept in room acoustics and its use for estimating speech intelligibility in auditoria," J. Acoust. Soc. Am. **77**, 1069–1077 (1985).
[14]ANSI S3.5-1997, *Methods for the Calculation of the Speech Intelligibility Index* (American National Standards Institute, New York, 1997).
[15]M. R. Schroeder, "New method of measuring reverberation time," J. Acoust. Soc. Am. **38**, 409–412 (1965).
[16]B. S. Everitt, *The Cambridge Dictionary of Statistics* (Cambridge University Press, Cambridge, 1998).
[17]B. C. J. Moore, *An Introduction to the Psychology of Hearing* (Academic, London, 1982), pp. 168–171.
[18]S. R. Bistafa and J. S. Bradley, "Reverberation time and maximum background-noise level for classrooms from a comparative study of speech intelligibility metrics," J. Acoust. Soc. Am. **107**, 861–875 (2000).
[19]M. Barron, *Auditorium Acoustics and Architectural Design* (E & FN Spon, London, 1993), pp. 418–419.
[20]ISO 19921: 2003, *Ergonomics—Assessment of Speech Communication in Rooms* (International Organization of Standardization, Geneva, 2003).

Two-dimensional poroelastic acoustical foam shape design for absorption coefficient maximization by topology optimization method

Joong Seok Lee and Yoon Young Kim[a)]
National Creative Research Initiatives Multiscale Design Center, School of Mechanical and Aerospace Engineering, Seoul National University, Shinlim-Dong San 56-1, Kwanak-Gu, Seoul 151-742, Korea

Jung Soo Kim and Yeon June Kang
Advanced Automotive Research Center, School of Mechanical and Aerospace Engineering, Seoul National University, Shinlim-Dong San 56-1, Kwanak-Gu, Seoul 151-742, Korea

(Received 6 September 2007; revised 10 December 2007; accepted 7 January 2008)

Optimal shape design of a two-dimensional poroelastic acoustical foam is formulated as a topology optimization problem. For a poroelastic acoustical system consisting of an air region and a poroelastic foam region, two different physical regions are continuously changed in an iterative design process. To automatically account for the moving interfaces between two regions, we propose a new unified model to analyze the whole poroelastic acoustical foam system with one set of governing equations; Biot's equations are modified with a material property interpolation from a topology optimization method. With the unified analysis model, we carry out two-dimensional optimal shape design of a poroelastic acoustical foam by a gradient-based topology optimization setting. The specific objective is the maximization of the absorption coefficient in low and middle ranges of frequencies with different amounts of a poroelastic material. The performances of the obtained shapes are compared with those of well-known wedge shapes, and the improvement of absorption is physically interpreted. © *2008 Acoustical Society of America.*
[DOI: 10.1121/1.2839001]

PACS number(s): 43.55.Pe, 43.20.Gp, 43.50.Gf, 43.20.Mv [NX] Pages: 2094–2106

I. INTRODUCTION

In anechoic chambers, many kinds of shaped foams, not flat foams, are installed on the wall for sound absorption. For the shaped foams, their cross-sectional shape is the principal factor that determines the sound absorption performance. In most of the anechoic rooms, wedge shapes of acoustical treatments are generally used since they show better performance at relatively lower frequencies than the flat ones do. However, for improvement of absorption ability of the wedge foam in low and middle ranges of frequencies, it is known that longer and sharper foam shape should be installed in the room. This type of shape requires more absorbing material and larger space. In this situation, we intend to design an optimal shape (i.e., cross-sectional shape) of a poroelastic acoustical foam for maximization of the absorption coefficient at ranges of low and middle of frequencies. To carry out our objective, we set a poroelastic acoustical foam shape design as a two-dimensional topology optimization problem in this work.

Much research related to shape treatment for improvement of its absorbing performance has been reported. Beranek and Sleeper[1] carried out various experiments over five different types of structures including the exponentially taped pyramidal and wedge structures for use in an anechoic chamber. Koidan *et al.*[2] described a hybrid wedge design composed of different weight materials and air space for anechoic room through parametric studies. For numerical analysis of a wedge foam, Easwaran and Munjal[3] proposed a finite element model based on the bulk reaction concept. In their work, the effects of geometric parameters of wedge as well as material properties were widely considered. Kang and Bolton[4] studied optimal wedge shape with wedge angle as a design parameter. They found an optimal wedge angle under constant wedge volume through various numerical calculations with their finite element model on a poroelastic acoustical foam.[5] Later, Chen *et al.*[6] carried out numerical and experimental studies about the effects of surface shapes of an acoustical absorber: triangular, semicircular and convex rectangular surface shapes were compared in their absorption coefficients. Simón *et al.*[7] proposed an analytical approximation for the calculation of the absorption on porous corrugated surfaces. As well as the wedge shape itself, research related to inner structures of an absorbing foam was also reported. Lee and Chen[8] studied the effect of inner structures on the sound absorption of multilayered absorbers. And Sgard *et al.*[9] used the concept of double porosity to improve the absorption of porous materials.

Although the previous works have contributed to foam shape design for improvement of absorption performance, most of the works were based on a given configuration of absorbing materials. Therefore, their shape designs were conducted by slight changes of the configuration or by comparisons of acoustical performance for some kinds of typical shapes with repeated analyses or experiments. No complete

[a)]Author to whom correspondence should be addressed. Electronic mail: yykim@snu.ac.kr

 0001-4966/2008/123(4)/2094/13/$23.00 © 2008 Acoustical Society of America

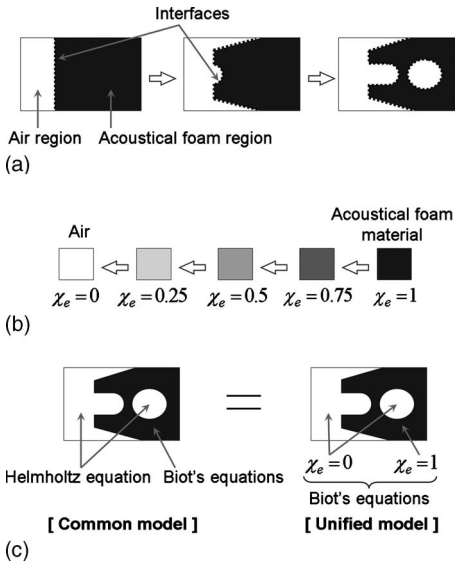

FIG. 1. Schematic descriptions of an iterative design process for an optimal poroelastic acoustical foam shape. (a) Changing interfaces between air region and poroelastic acoustical foam region during optimization process, (b) a conceptual material property interpolation between the states of air and a poroelastic material with respect to the real-valued material state variables χ_e, and (c) a common analysis model and the proposed unified analysis model.

and systematic work has been done on the design of an optimal foam shape. Especially, any design method of an optimal foam shape for low and middle ranges of frequencies without any given configuration has not been reported.

The difficulties in the shape design of acoustical foams are due to the absence of a systematic design method based on an iterative optimization process. The air region and acoustical foam region are continuously changed in an iterative design process as shown in Fig. 1(a). The moving interfaces between two regions should be reflected in the analysis at each iteration. In a common analysis model, different governing equations represent different physical regions (e.g., the scalar Helmholtz equation for an air region and Biot's equations for a poroelastic acoustical foam region, respectively), and couplings between them at interfaces are considered [refer to the left figure in Fig. 1(c)]. Since any common analysis model has to repeat reconstruction of the two regions and modification of the coupling between them manually at every iterative step, it is very time consuming to reflect continuously moving interfaces using common analysis model automatically. Therefore, a general analysis model is not proper to implement a foam shape design to a systematic design process.

To cope with the difficulties, we propose a new unified model to apply the foam shape design in a systematic iterative optimization process. The unified analysis model is based on Biot's theory.[10] In addition, a material property interpolation concept from a topology optimization method[11] modifies Biot's equations to express an air region as well as a poroelastic acoustical foam region. The material properties of an element are formulated as functions of real-valued material state variables (χ_e), which are imposed on elements. The real-valued material state variables interpolate the states of an element between a poroelastic material and air. For example, the value of 1 for the real-valued material state variables corresponds to the state of a poroelastic material and the value of 0, for the state of air as shown in Fig. 1(b). Therefore, two different physical regions are expressed with the same governing equation by controlling the value of the real-valued material state variables between 1 and 0 as shown in the right figure in Fig. 1(c). Consequently, changing interfaces in an iterative design process between an air region and a poroelastic acoustical foam region are automatically constructed using the proposed unified analysis model.

The advantage of the automatic construction of moving interfaces between an air region and a poroelastic acoustical foam region in any iteration step is appropriate in the formulation of an optimal foam shape design problem in a topology optimization setting. In this work, a topology optimization formulation is implemented with a general finite element method to design a two-dimensional poroelastic acoustical foam shape. Although existing wedge shapes yield good performance of sound absorption in high frequency range, their absorption performance in low and middle ranges of frequencies is not as good as that in high frequency range. Our optimal design of a poroelastic acoustical foam shape is, therefore, focused on the low and middle ranges of frequencies. In this investigation, the specific objective of the design process is to find an optimal shape of a poroelastic acoustical foam for maximizing the absorption coefficient in the range of frequencies from 100 to 1500 Hz. The design processes are conducted with different limits of the allowable amount of a poroelastic material: 50, 55, 60, and 65% within a design domain. Absorption performances of the obtained optimal shapes are compared with those of well-known wedge shapes having the same amount of a poroelastic material in the frequency range of interest.

II. MATHEMATICAL DESCRIPTION

In the first part of this section, two different forms of Biot's equations are overviewed. The two forms are mathematically the same, but they are different in their implementation in numerical analysis. A material property interpolation concept from a topology optimization method is then introduced to accomplish a unified model for expressing an air region and a poroelastic acoustical foam region.

A. The poroelastic material theory

The poroelastic material theory of Bolton *et al.*[12] (itself based on Biot's theory[10]) presents two coupled, vectorial differential equations that govern the wave propagation in poroelastic media. For harmonic motion, they are expressed as the following equations:

$$\text{div } \underline{\boldsymbol{\sigma}}^s + \omega^2(\rho_{11}\mathbf{u} + \rho_{12}\mathbf{U}) - j\omega b(\mathbf{u} - \mathbf{U}) = 0, \tag{1a}$$

$$\text{div } \underline{\boldsymbol{\sigma}}^f + \omega^2(\rho_{12}\mathbf{u} + \rho_{22}\mathbf{U}) + j\omega b(\mathbf{u} - \mathbf{U}) = 0, \tag{1b}$$

where $\mathbf{u}$ is the vector-field solid displacement and $\mathbf{U}$ is the vector-field fluid displacement in poroelastic media. The symbols ρ_{11}, ρ_{12}, and ρ_{22} denote mass coefficients that account for the effects of nonuniform relative fluid flow

through pores between the solid and the fluid phases. The parameter b represents the effect of viscous coupling. The symbols $\underline{\boldsymbol{\sigma}}^s$ and $\underline{\boldsymbol{\sigma}}^f$ denote the partial stress tensors associated with the solid and the fluid phases in a poroelastic material, respectively. The symbol "div" represents the divergence operator and the symbol ω is the angular frequency. The symbol j denotes $\sqrt{-1}$.

In Eq. (1), the mass coefficients ρ_{11}, ρ_{12}, and ρ_{22} are expressed as follows:

$$\rho_{11} = \rho_1 + \rho_a, \tag{2a}$$

$$\rho_{12} = -\rho_a, \tag{2b}$$

$$\rho_{22} = \rho_2 + \rho_a, \tag{2c}$$

where

$$\rho_1 = (1-h)\rho_m, \tag{2d}$$

$$\rho_2 = h\rho_{air}, \tag{2e}$$

$$\rho_a = \rho_2(\varepsilon' - 1). \tag{2f}$$

Here, the symbols ρ_1 and ρ_2 denote mass of the solid and mass of the fluid per unit volume of a poroelastic material, respectively. And mass coupling parameter is denoted by ρ_a. The mass densities of corresponding materials of the solid and the fluid phases are denoted by ρ_m and ρ_{air}, respectively. The symbol h is the porosity of a poroelastic material and the symbol ε' is the geometrical structure factor associated with tortuosity.

According to the stress-strain relations in Biot's theory, the stress tensors in Eq. (1) are expressed as

$$\underline{\boldsymbol{\sigma}}^s = A\ \text{div}\ \mathbf{u}\underline{\mathbf{1}} + 2N\underline{\boldsymbol{\varepsilon}}^s + Q\ \text{div}\ \mathbf{U}\underline{\mathbf{1}}, \tag{3a}$$

$$\underline{\boldsymbol{\sigma}}^f = -hp\underline{\mathbf{1}} = Q\ \text{div}\ \mathbf{u}\underline{\mathbf{1}} + R\ \text{div}\ \mathbf{U}\underline{\mathbf{1}}, \tag{3b}$$

where the elastic shear modulus is denoted by N and the first Lamé constant, by A.

The coefficients Q and R represent the coupling phenomena between the volume change of the solid phase of a poroelastic material and that of the interstitial fluid. The symbol p denotes the interstitial pressure in pores. The symbols $\underline{\boldsymbol{\varepsilon}}^s$ and $\underline{\mathbf{1}}$ denote the stain tensor in the solid phase and the identity tensor, respectively. The coefficients N, A, Q, and R in Eq. (3) depend on several intrinsic parameters such as the modulus of elasticity:[10,12,13]

$$N = \frac{E_1}{2(1+\nu)}, \tag{4a}$$

$$A = \frac{\nu E_1}{(1+\nu)(1-2\nu)}, \tag{4b}$$

$$Q = (1-h)E_2, \tag{4c}$$

$$R = hE_2. \tag{4d}$$

In Eqs. (4a) and (4b), E_1 and ν are the modulus of elasticity and Poisson's ratio of the solid phase. Because of $E_1 = E_m(1+j\eta)$ (E_m: real-valued Young's modulus, η: loss factor), E_1 is complex valued. The symbol E_2 denotes the bulk modulus of the fluid phase in pores of a poroelastic material. More details of the materials presented in this section may be found in Refs. 10, 12, and 13.

Atalla *et al.*[14,15] reformulated Eq. (1) using the solid phase displacement vector $\mathbf{u}$ and the interstitial pressure p as primary variables

$$\text{div}\ \hat{\underline{\boldsymbol{\sigma}}}^s + \omega^2\rho\mathbf{u} + \gamma\nabla p = 0, \tag{5a}$$

$$\text{div}\ \nabla p + \omega^2\frac{\rho_{22}^*}{R}p - \omega^2\frac{\rho_{22}^*}{h^2}\gamma\,\text{div}\,\mathbf{u} = 0, \tag{5b}$$

where the symbols ρ and γ denote the effective density and the coupling coefficient,

$$\rho = \rho_{11}^* - \frac{(\rho_{12}^*)^2}{\rho_{22}^*}, \tag{6a}$$

$$\gamma = h\left(\frac{\rho_{12}^*}{\rho_{22}^*} - \frac{Q}{R}\right), \tag{6b}$$

and

$$\rho_{11}^* = \rho_{11} + \frac{b}{j\omega}, \tag{6c}$$

$$\rho_{12}^* = \rho_{12} - \frac{b}{j\omega}, \tag{6d}$$

$$\rho_{22}^* = \rho_{22} + \frac{b}{j\omega}. \tag{6e}$$

In Eq. (5a), the symbol $\hat{\underline{\boldsymbol{\sigma}}}^s$ denotes the stress tensor of a poroelastic material *in vacuo*. Therefore, $\hat{\underline{\boldsymbol{\sigma}}}^s$ depends simply on the solid phase displacement $\mathbf{u}$, differently from $\underline{\boldsymbol{\sigma}}^s = \underline{\boldsymbol{\sigma}}^s(\mathbf{u},\mathbf{U})$ in Eqs. (1a) and (3a), i.e.,

$$\hat{\underline{\boldsymbol{\sigma}}}^s = \left(A - \frac{Q^2}{R}\right)\text{div}\,\mathbf{u}\underline{\mathbf{1}} + 2N\underline{\boldsymbol{\varepsilon}}^s. \tag{7}$$

More mathematical details in the reformulation may be found in Ref. 15.

Although Eqs. (1) and (5) are exactly the same in mathematical point of view, there are some differences in finite element implementation. When two different kinds of poroelastic materials are adjacent to each other, continuity conditions for a normal volume velocity and total stresses should be ensured at interfaces between them.[5,12–15] The continuity conditions cannot be guaranteed by the connectivity of the interfacial nodes in the finite elements implementation of Eq. (1). Therefore, additional treatments are needed in the finite element analysis to ensure these boundary conditions. However, in Eq. (5), the connectivity at the nodes guarantees both the continuity of the solid phase displacement vector and the pressure in pores ($\mathbf{u}$ and p). And the continuity conditions at the interfaces can be expressed with the solid phase displacement vector, the pressure in pores, and the porosity ($\mathbf{u}$, p, and h). According to Ref. 15, for the majority of poroelastic materials used in acoustics, the consideration of kinematical relations [i.e., the solid phase displacement vector and the

pressure in pores (**u** and p)] are enough to impose the continuity conditions at interfaces of two different kinds of poroelastic materials. Moreover, this approximation is also applied to the case of interface between an air region and a poroelastic material region. Therefore, Eq. (5) is used to represent the acoustic behavior of a poroelastic material in the present work.

B. Unified modeling using material state variables

Based on Eq. (5), we adopt a material property interpolation concept from a topology optimization method[11] to build a unified model for both an air region and a poroelastic acoustical foam region. Figure 1(b) shows the material property interpolation schematically. In a poroelastic acoustical foam region, the foam is discretized into finite elements. The real-valued material state variables (χ_e), which have a value of 1 or 0, are imposed on each element. Then, poroelastic material properties of the foam can be expressed as functions of the material state variables. If the material state variable is 1, the state of an element is the original poroelastic material [black in Fig. 1(b)]. When the value of the material state variable of the element changes, the corresponding poroelastic material properties of the element also change [grays in Fig. 1(b)]. Finally, when the value of the material state variable reaches zero there is no poroelastic material in the element. The element having zero value of the material state variable is filled with air [white in Fig. 1(b)]. Thus, an air element can, whenever needed, be expressed with a poroelastic material element simply by controlling the value of the material state variables between 1 and 0 in the material property interpolation.

The material property interpolation may be conducted in two ways. One way is the interpolation of intrinsic material parameters such as porosity (h), flow resistivity (σ), *in vacuo* bulk modulus (E_m), bulk density (ρ_m), loss factor (η), bulk Poisson's ratio (ν), and structure factor (ε') of a poroelastic material. The other is the interpolation of macro coefficients which are shown in the governing equation of Eq. (5) such as effective density (ρ), coupling coefficient (γ), etc.

In this work, the macro coefficient interpolation scheme is employed since sensitivity analysis required for topology optimization is easier with the macro coefficients than the intrinsic parameters. If the intrinsic material parameters were interpolated, complicated processes for analytic sensitivity analysis should be done because the intrinsic material parameters build the macro coefficients with complex functional form. The sensitivity analysis will be handled in Sec. IV.

In the macro coefficient interpolation scheme, we make the following six groups as functions of the real-valued material state variables directly from Eqs. (5)–(7). Equation (5b) is just divided by $\omega^2\rho_{22}^*/h^2$, so that a weak form of Eq. (5) is symmetrically coupled. For the discretized eth element having the real-valued material state variable χ_e, they may be written as

$$\left(A-\frac{Q^2}{R}\right)_e=\left\{\left(A-\frac{Q^2}{R}\right)_{\text{foam}}-\left(A-\frac{Q^2}{R}\right)_{\text{air}}\right\}(\chi_e)^p+\left(A-\frac{Q^2}{R}\right)_{\text{air}}, \tag{8a}$$

$$(N)_e=\{(N)_{\text{foam}}-(N)_{\text{air}}\}(\chi_e)^q+(N)_{\text{air}}, \tag{8b}$$

$$(\rho)_e=\{(\rho)_{\text{foam}}-(\rho)_{\text{air}}\}(\chi_e)^r+(\rho)_{\text{air}}, \tag{8c}$$

$$(\gamma)_e=\{(\gamma)_{\text{foam}}-(\gamma)_{\text{air}}\}(\chi_e)^s+(\gamma)_{\text{air}}, \tag{8d}$$

$$\left(\frac{h^2}{\rho_{22}^*}\right)_e=\left\{\left(\frac{h^2}{\rho_{22}^*}\right)_{\text{foam}}-\left(\frac{h^2}{\rho_{22}^*}\right)_{\text{air}}\right\}(\chi_e)^l+\left(\frac{h^2}{\rho_{22}^*}\right)_{\text{air}}, \tag{8e}$$

$$\left(\frac{h^2}{R}\right)_e=\left\{\left(\frac{h^2}{R}\right)_{\text{foam}}-\left(\frac{h^2}{R}\right)_{\text{air}}\right\}(\chi_e)^m+\left(\frac{h^2}{R}\right)_{\text{air}}, \tag{8f}$$

where the symbols p, q, r, s, l, and m denote the exponents of the material property interpolation functions. Note that when the value of the material state variables is 1, the macro coefficients in Eq. (8) have values of a poroelastic material (the subscript, foam), and that the macro coefficients correspond to those of air state for zero material state variables (the subscript, air). When an element is filled with air only, we can estimate the limit values of the macro coefficients based on the physical definition of material parameters (e.g., $h=1$, $E_m=0$, $\rho_m=0$, etc. when an element is represented as air state.)

$$\left(A-\frac{Q^2}{R}\right)_{\text{air}}=0, \tag{9a}$$

$$(N)_{\text{air}}=0, \tag{9b}$$

$$(\rho)_{\text{air}}=0, \tag{9c}$$

$$(\gamma)_{\text{air}}=0, \tag{9d}$$

$$\left(\frac{h^2}{\rho_{22}^*}\right)_{\text{air}}=\frac{1}{\rho_{\text{air}}}, \tag{9e}$$

$$\left(\frac{h^2}{R}\right)_{\text{air}}=\frac{1}{E_{\text{air}}}. \tag{9f}$$

If the limit values in Eq. (9) corresponding to the air state are substituted into Eq. (5), the equation for acoustic wave propagation in air can be recovered; Eq. (5b) is degenerated to the scalar Helmholtz equation while Eq. (5a) is nullified to express a solid-empty state. Though this degeneration is evident from an analytical viewpoint, some care must be taken when the degeneration from Eq. (5) is numerically done within a finite element model. If the limit values in Eq. (9) are substituted into the finite element model used to solve Eq. (5), the system matrix for the finite element model will become singular because the matrix components corresponding to the degrees of the freedom of the solid state vanish. The singularity can be avoided by some numerical treatments such as elimination of the degrees and rearrange-

ment of the system matrix, but these processes become cumbersome and undesirable for computational efficiency. For this reason, nonzero small values, instead of the limit values, are used to express the air state if it is necessary. Then, Eq. (5) cannot be degenerated exactly, however the difference between the exact scalar Helmholtz equation and the derived equation from Eq. (5) can be insignificant when Eq. (8) with a very small value of the material state variable χ_e is used. (As shall be demonstrated later, the value of $\chi_{e,\min}=0.001$ gives satisfactory results.)

Based on Eq. (5), the material property interpolation proposed in Eq. (8) builds a unified model that can represent air and poroelastic acoustical foam regions with one set of governing equations. The proposed unified model is very useful for analyzing the poroelastic acoustical foam system having complicated interfaces between the air region and the poroelastic acoustical foam region. In the next section, the proposed unified analysis model will be verified for its accuracy against various foam shapes in references.

III. VERIFICATION OF THE UNIFIED MODEL

In this section, the calculations of poroelastic acoustical foam systems with the proposed unified analysis model are compared with previously reported results.[4,5] The previous results were obtained by a common analysis model; the Helmholtz equation was used for analysis of an air region, Biot's theory was used to handle a poroelastic acoustical foam region, and couplings at interfaces between two regions were considered. On the other hand, the present calculations by the unified model are performed with just one set of governing equations to analyze the whole poroelastic acoustical foam system; the air region and the poroelastic acoustical foam region are differentiated by the value of the material state variables which are imposed on the regions.

A. Cases of rectangular foam

For the configuration of the unfaced foam layer as shown in Fig. 2(a), the proposed unified analysis model is verified by varying the depth of the foam layer.[5] In the model, the foam is assumed to be open at the incident surface and fully constrained at its upper and lower edges ($y=0$ and d). The rigid wall boundary condition is imposed on the right-hand side of the foam, and a uniform plane wave is generated from the left-hand side of the system ($x=0$). While nine-noded quadratic elements were used in Ref. 5, four-noded quadratic elements were used in implementing the proposed unified model with the finite element method. Therefore, the size of an element was set to be smaller than that of Ref. 5: elements of 0.675 cm $\times$ 0.675 cm ($x \times y$) were used here.

To analyze the acoustical foam system with the proposed unified model, first both the air and poroelastic acoustical foam regions were formulated with a weak form of Eq. (5). The value of the material state variables of the elements in the air region was then set to be very close to zero in Eq. (8). To escape from numerical instability, we selected a minimum value of the material state variables as 0.001 ($\chi_{e,\min}=0.001$), not zero. The value of the material state variables of

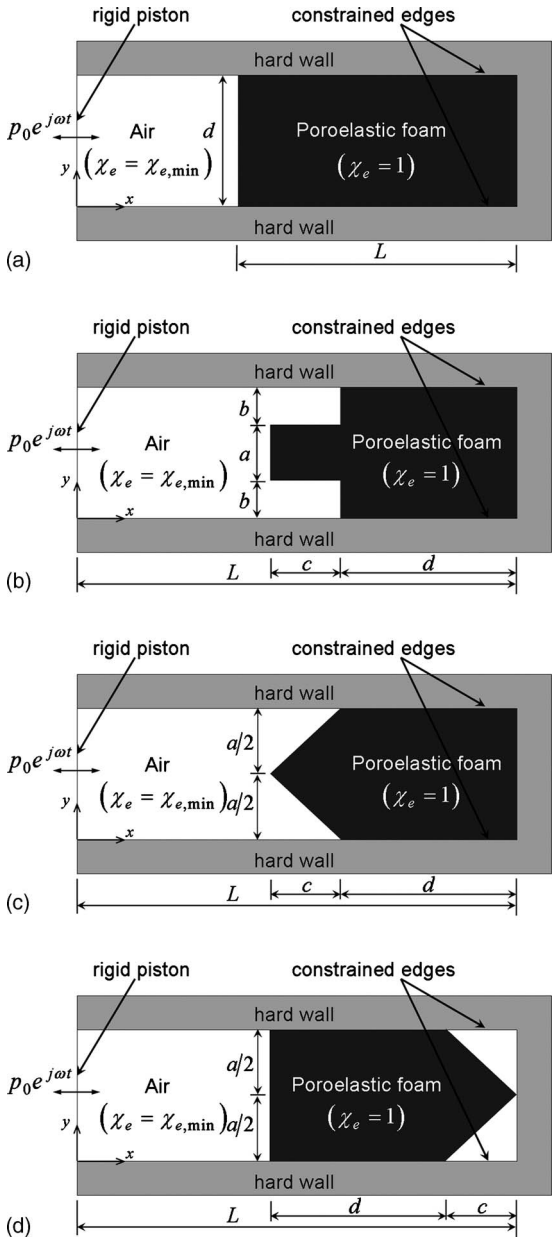

FIG. 2. Illustrations of poroelastic acoustical foam systems having various foam shapes. (a) Rectangular foam shapes, (b) corrugated foam shapes, (c) wedge foam shapes, and (d) inverse wedge foam shapes.

the remaining elements in the poroelastic acoustical foam region was set to 1 in Eq. (8). To meet boundary conditions surrounding the poroelastic acoustical foam system, we imposed $u_x=0$, $u_y=0$ at both horizontal edges ($y=0$ and d) and at the right-hand side of the foam. Reticulated polyurethane foam parameters used in all of the numerical case studies in this paper are identical with those of Ref. 5 and listed in Table I.

The plane wave reflection coefficient R_n, thus the absorption coefficient $\alpha_n=1-|R_n|^2$ [see Eq. (11)], was calculated by the proposed unified model for different depths of poroelastic acoustical foams. Figure 3(a) shows the plane wave absorption coefficient α_n with different depths (L) of poroelastic acoustical foams (the width was fixed as $d=5.4$ cm). In comparison with the previous results[5] shown in

TABLE I. Parameters of the poroelastic material used in the present investigation.

Material parameter	Value
Solid density (ρ_m)	300 kg/m^3
In *vacuo* bulk Young's modulus (E_m)	8×10^5 Pa
In *vacuo* loss factor (η)	0.265
Bulk Poisson's ratio (ν)	0.4
Flow resistivity (σ)	25×10^3 MKS Rayls/m
Porosity (h)	0.9
Structure factor (ε')	7.8

Fig. 3(a), the results calculated by the proposed unified model are almost the same with those by the common analysis model.

B. Cases of shaped foam

We considered a poroelastic acoustical foam system having a 27-cm-long and 5.4-cm-wide waveguide[4] shown in Figs. 2(b)–2(d). Figure 2(b) shows a poroelastic acoustical foam having a rectangular corrugation in its front surface. Figures 2(c) and 2(d) depict poroelastic acoustical foams having a wedge at either their front or rear surfaces, respectively. In Ref. 4, both the air region and the poroelastic acoustical foam region were discretized by using three-noded linear triangular elements, which were smaller than 0.6 cm $\times$0.6 cm. In this work, uniformly meshed four-noded quadratic elements were used for the proposed unified model. Dimensions of the poroelastic acoustical foam shown in Figs. 2(b)–2(d) are listed in Tables II and III. The indicators "W" and "IW" in Table III mean wedge and inverse wedge corresponding to Figs. 2(c) and 2(d), respectively. All of the boundary conditions were the same as those of the previous case studies in this section.

For the foams with a rectangular corrugation in their front surfaces shown in Fig. 2(b) and Table II, the plane wave absorption coefficients calculated by the proposed unified model are shown in Fig. 3(b). The reference results[4] are also shown in Fig. 3(b). The present results are almost the same as the reference results within the frequency range considered here.

For the wedge-shaped poroelastic acoustical foams

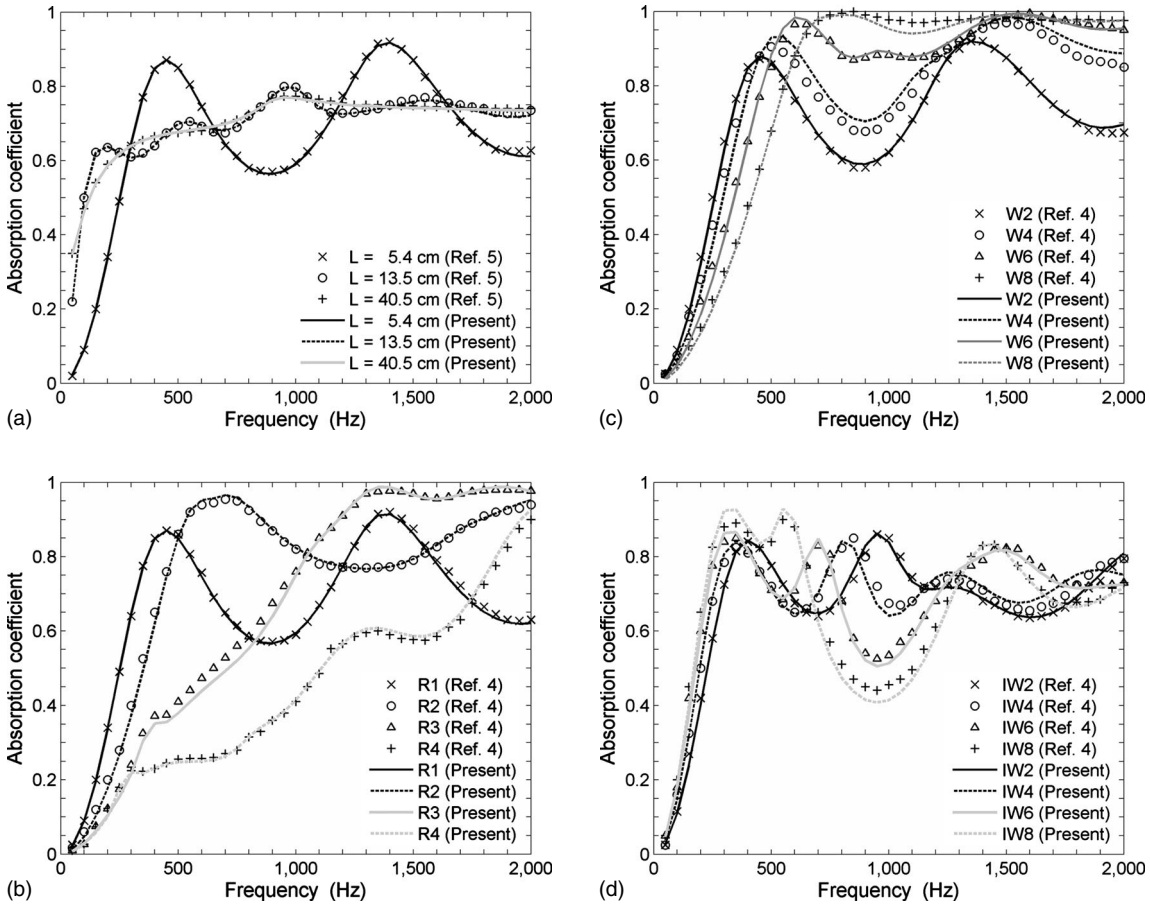

FIG. 3. Comparison of the absorption coefficients by the proposed unified analysis model (lines) and by a common analysis model (marks) (a) for rectangular foam shapes, (b) for corrugated foam shapes, (c) for wedge foam shapes, and (d) for inverse wedge foam shapes.

TABLE II. Dimensions of the corrugated foams shown in Fig. 2(b).

Case	a (cm)	b (cm)	c (cm)	d (cm)
R1	5.40	0.00	0.00	5.40
R2	1.80	1.80	5.40	3.60
R3	1.80	1.80	10.80	1.80
R4	1.80	1.80	16.20	0.00

shown in Fig. 2(c) and Table III, the plane wave absorption coefficients obtained by the proposed unified analysis model are shown in Fig. 3(c). Figure 3(c) shows that the present results agree well with the reference results.[4] For the inverse wedge-shaped poroelastic acoustical foams shown in Fig. 2(d) and Table III, the plane wave absorption coefficients calculated by the present unified model are shown in Fig. 3(d). There are some differences between the calculated absorption coefficients and the marked reference values[4] as shown in Fig. 3(d). However, the calculated absorption coefficients have the same tendency as the reference results in the considered frequency ranges. The differences were caused by the use of the four-noded quadratic elements in analysis of the tapered shape, not from the incorrectness of the proposed unified analysis model. We did not use the triangular elements because the quadratic elements are generally used in a topology optimization method to obtain stable configurations in the optimization process.

In this section, we carried out the calculations of the plane wave absorption coefficient for various foam shapes to compare the results by the proposed unified model with the reference results. As shown in Fig. 3, the proposed unified analysis model has good agreement with the conventional model. Though some differences between the present results and the previous ones were observed for the inverse wedge shapes, the present calculations showed consistency with the reference results within the concerned frequency range. Therefore, the calculations in this section showed the validity of the proposed unified model for the analysis of the entire poroelastic acoustical foam system. With this evaluation, we conduct an optimal shape design of a poroelastic acoustical foam to maximize the absorption coefficient in the next section.

IV. OPTIMAL FOAM SHAPE DESIGN BY TOPOLOGY OPTIMIZATION METHOD

This section presents the main development of the topology optimization formulation for the optimal shape design of a poroelastic acoustical foam. After the problem definition in the topology optimization setting is given, the sensitivity analyses to update design variables are studied. Absorption performances of the designed optimal foam shapes are compared with those of well-known wedge shapes.

TABLE III. Dimensions of the wedge and inverse wedge foams shown in Figs. 2(c) and 2(d).

Case	θ (degree)	a (cm)	c (cm)	d (cm)
W2, IW2	132	5.40	1.20	4.80
W4, IW4	74	5.40	3.60	3.60
W6, IW6	48	5.40	6.00	2.40
W8, IW8	36	5.40	8.40	1.20

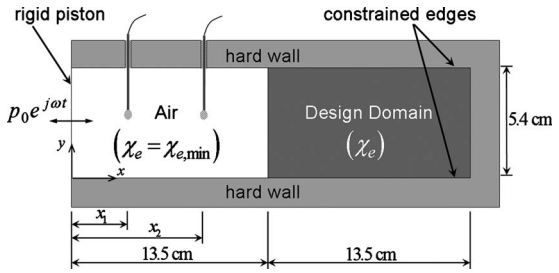

FIG. 4. Configuration of a design domain to find an optimal shape of a poroelastic acoustical foam by a topology optimization formulation.

A. Topology optimization formulation

In many structural design problems, topology optimization has been very successful. (see, e.g., Refs. 11 and 16). Recently, Lee *et al.*[17] developed a topology optimization formulation for optimal layer sequencing in a one-dimensional multilayered poroelastic acoustical foam system. In their work, the transfer matrix method was used for the efficient calculation of the sound transmission loss of a multilayered foam system. Although a foam shape design was not involved in their work, they introduced a topology optimization setting for a poroelastic acoustical system. In this work, we intend to design an optimal shape of a two-dimensional poroelastic acoustical foam to maximize the plane wave absorption coefficient (α_n) in the ranges of low and middle frequencies.

For the calculation of the plane wave absorption coefficient of a two-dimensional system, the proposed unified model which was introduced in the previous section was implemented in the general finite element method. The design problem can be expressed by the following conceptual equation:

$$\max \sum_{f=f_l}^{f_u} \alpha_n(f). \tag{10}$$

In Eq. (10), the design problem allows the use of a constrained amount of a poroelastic material. When a range of frequencies between the lower frequency f_l and the upper frequency f_u is considered, a simple discrete combination of $\alpha_n(f)$ at some selected frequencies is used.

Figure 4 shows a poroelastic acoustical foam system that was used to conduct the optimal shape design in this section. A design domain is where an optimal shape of a poroelastic acoustical foam will be found as the result of the topology optimization. The air region in Fig. 4 is a nondesign domain in which the incident and reflected plane waves travel. The fixed value of $\chi_{e,\min}$(=0.001) is imposed on the elements in the air region using Eq. (8). The plane wave reflection coefficient R_n and corresponding plane wave absorption coefficient α_n can be calculated with pressures at the two points shown in Fig. 4[18,19]

$$R_n(\chi_e;f) = \frac{-P_2 \cdot \exp(-jkx_1) + P_1 \cdot \exp(-jkx_2)}{P_2 \cdot \exp(jkx_1) - P_1 \cdot \exp(jkx_2)}, \quad (11a)$$

$$\alpha_n(\chi_e;f) = 1 - |R_n(\chi_e;f)|^2, \quad (11b)$$

where the symbols x_1 and x_2 denote the distances to the measurement points from $x=0$. The symbols P_1 and P_2 denote pressure amplitudes at the two points. To emphasize the dependence of related values on design variables χ_e and frequency f, $R_n(\chi_e;f)$ and $\alpha_n(\chi_e;f)$ are used in Eq. (11). And the symbol k represents the wave number in an air region, which is a function of excitation frequency and sound speed.

To carry out the design problem of Eq. (10), the topology optimization formulation for the optimal shape design of a poroelastic acoustical foam in a range of frequencies can be stated as

$$\min_{\chi_e} F(\chi_e;f_l,f_u) = \min_{\chi_e}\left[w \cdot \left\{ \sum_{f=f_l}^{f_u} \alpha_n(\chi_e;f) \right\}^{-1} + (1-w) \cdot \sum_{e=1}^{N_e} \chi_e(1-\chi_e) \right], \quad (12a)$$

subject to a mass constraint

$$C(\chi_e): \frac{1}{N_e}\sum_{e=1}^{N_e} \chi_e - V_0 \leqslant 0. \quad (12b)$$

In Eq. (12a), F denotes an objective function expressed in terms of design variables χ_e ($1 \leqslant e \leqslant N_e$; N_e: number of discretized elements in a design domain). The symbol w denotes a weight factor, which controls the relative contribution between two functions in the right-hand side of the objective function. The design variables χ_e that are assigned to each element of the discretized design domain in Fig. 4 can vary from 0 to 1 continuously. The function $\Sigma_{e=1}^{N_e}\chi_e(1-\chi_e)$ in Eq. (12a) is used to help solution convergence to distinct air-poroelastic material states; that enforces design variables to converge to either 1 or 0 in optimization process. The poroelastic material properties will be interpolated as functions of χ_e such that the states of air and a poroelastic material correspond to $\chi_e=0$ and $\chi_e=1$, respectively, as given by Eq. (8). (As mentioned, $\chi_{e,\min}=0.001$, not zero, was used to prevent numerical instability.) In Eq. (12b), C denotes a constraint equation in the formulation. The constraint equation implies that the maximum volume usage of a poroelastic material is limited by V_0 in the design domain shown in Fig. 4.

To solve the minimization problem of Eq. (12a) and (12b) by a gradient-based optimizer, the sensitivities of the objective function and the constraint equation with respect to the design variables must be computed. In Eq. (11), the sensitivities of the plane wave absorption coefficient and the reflection coefficient with respect to the design variables (χ_e) can be analytically obtained by the following equations:

$$\frac{\partial \alpha_n(\chi_e;f)}{\partial \chi_e} = -2|R_n(\chi_e;f)| \cdot \frac{\partial |R_n(\chi_e;f)|}{\partial \chi_e}, \quad (13a)$$

$$\frac{\partial R_n(\chi_e;f)}{\partial \chi_e} = \frac{\left\{ -\frac{\partial P_2}{\partial \chi_e} \cdot \exp(-jkx_1) + \frac{\partial P_1}{\partial \chi_e} \cdot \exp(-jkx_2) \right\} \{P_2 \cdot \exp(jkx_1) - P_1 \cdot \exp(jkx_2)\}}{\{P_2 \cdot \exp(jkx_1) - P_1 \cdot \exp(jkx_2)\}^2} - \frac{\{-P_2 \cdot \exp(-jkx_1) + P_1 \cdot \exp(-jkx_2)\} \left\{ \frac{\partial P_2}{\partial \chi_e} \cdot \exp(jkx_1) - \frac{\partial P_1}{\partial \chi_e} \cdot \exp(jkx_2) \right\}}{\{P_2 \cdot \exp(jkx_1) - P_1 \cdot \exp(jkx_2)\}^2}. \quad (13b)$$

In Eq. (13b), the values of $\partial P_{1,2}/\partial \chi_e$ are calculated from the following matrix equation of the weak form (i.e., the discretized form) of Eq. (5):

$$[\mathbf{K}] \cdot \begin{Bmatrix} \mathbf{u} \\ P \end{Bmatrix} = \begin{Bmatrix} \mathbf{F_u} \\ \mathbf{F}_P \end{Bmatrix}, \quad (14a)$$

$$\frac{\partial P}{\partial \chi_e} = [\mathbf{K}]^{-1} \cdot \left[-\frac{\partial \mathbf{K}}{\partial \chi_e} \right] \cdot \{P\}, \quad (14b)$$

where the symbol $[\mathbf{K}]$ denotes a system matrix of a poroelastic acoustical foam system. The symbols $\mathbf{F_u}$ and $\mathbf{F}_P$ are the external force vectors imposed at each node. The matrix $[\partial \mathbf{K}/\partial \chi_e]$, a gradient of the system matrix by the design variables, can be calculated in the discretized form of Eq. (5) with consideration of the material property interpolation given by Eq. (8).

The exponents in Eq. (8) were basically set to 1 for all problems in this investigation. Because a connected foam should be designed after an optimization process, it is important to choose proper values of the exponents. In typical structural topology optimization, exponent values between 2 and 3 are widely used to penalize the state of an element. The implicit penalization enforces physical convergence of design variables to a value of either 1 or 0. However, in this investigation, the use of the values between 2 and 3 did not yield satisfactory results; segmented foams that did not form single foams were obtained. The difficulties in interpolating material properties of a poroelastic material foam are due to

its composition of two phases and its frequency dependency of acoustical response. Moreover, a long range of frequencies was considered in the topology optimization formulation in this work. Consequently, the acoustical response (i.e., absorption coefficient) was very sensitive to the variation of the design variables. The difficulties become worsened by the use of the values between 2 and 3 in the material property interpolation in this investigation. Therefore, instead of penalizing the macro coefficients with the exponents of 2 or 3, we interpolated the macro coefficients with the exponents of 1 in Eq. (8) and used an explicit condition to enforce design variables to converge to either 1 or 0 with the function of $\Sigma_{e=1}^{N_e}\chi_e(1-\chi_e)$ in Eq. (12a).

Finally, the analytical expression for the sensitivities of the objective function and the constraint equation with respect to the design variables is expressed as

$$\frac{\partial F(\chi_e;f_l,f_u)}{\partial \chi_e} = -w \cdot \left\{ \sum_{f=f_l}^{f_u} \alpha_n(\chi_e;f) \right\}^{-2} \cdot \sum_{f=f_l}^{f_u} \frac{\partial \alpha_n(\chi_e;f)}{\partial \chi_e} + (1-w)\cdot(1-2\chi_e), \tag{15a}$$

$$\frac{\partial C(\chi_e)}{\partial \chi_e} = \frac{1}{N_e}. \tag{15b}$$

The calculated values of the objective function and the constraint equation in Eq. (12a) and (12b) with the gradients of them in Eq. (15) at an iterative optimization step determine a new set of design variables for the next iteration. This updating process has been continued until the topology optimization problem in Eq. (12a) and (12b) is converged. The method of moving asymptotes[20] was used as an optimizer for all problems considered in this investigation.

B. Numerical case studies

To design an optimal shape of a poroelastic acoustical foam for maximizing the plane wave absorption coefficient, the target frequency range was set to be from 100 to 1500 Hz. Different allowable amounts of a poroelastic material were considered in the design process, i.e., the same or a lower amount of a poroelastic material with 50, 55, 60, and 65% in a design domain was allowed. As shown in Fig. 4, the dimensions of the air region and the design domain were the same as 13.5 cm $\times$ 5.4 cm, respectively. Each region was discretized with 50×40 four-noded quadratic elements. The plane wave absorption coefficient α_n was calculated at every 100 Hz in the frequency range of interest, and then summed to the objective function. On the elements in the air region, the minimum value of the material state variables ($\chi_{e,\min}=0.001$) was imposed. The initial value of the design variables in the design domain was set to be the same as the mass constraint V_0 in Eq. (12b) ($V_0=0.50$, 0.55, 0.60, and 0.65).

Figures 5(a) and 5(b) show a topology optimization process with iteration numbers and absorption coefficients at each corresponding iteration, respectively. The allowable amount of a poroelastic acoustical foam was 50% of the design domain in this case [i.e., $V_0=0.50$ in Eq. (12b)]. The exponents of the macro coefficients interpolation functions were set to 1 in Eq. (8). The finally converged shape shown in Fig. 5(a) is considerably different from well-known wedge shapes. As shown in Fig. 5(a), a thick air layer was designed in the back of the optimized foam. A bowl-like foam is located in the front part and connected to the main wedge-like foam in the middle part of the design domain. The absorption performances of the optimized foam shape and conventional wedge shape having the same amount of a poroelastic material are shown in Fig. 5(c). As may be seen in Fig. 5(c), the optimal foam shape made a big improvement in absorption in low and middle frequency ranges by lowering the frequency of the first peak in absorption coefficient to 350 Hz. However, the absorption coefficient of the optimal shape above 1200 Hz becomes smaller than that of the wedge shape. It is because the target frequency range was set to the low and middle of frequencies in this investigation.

For the topology optimization using more amounts of a poroelastic acoustical foam in the design domain, the optimal foam shapes are shown in Fig. 6. In the figures, each case was designed under 55, 60, and 65% of mass constraint, respectively. The frequency considered in the topology optimization ranged from 100 to 1500 Hz, and the exponents in Eq. (8) were set to 1. In Fig. 7, the absorption coefficients of the optimal foam shapes are compared with those of conventional wedge shapes having the same amount of a poroelastic material for each case.

Note that in all cases of mass constraints, 50–65%, a thick, backing air layer was designed in the rear part of the design domain. That air layer created the first resonance of the acoustical foam system, which resulted in improvement of the absorption performance at low frequencies. The air layer also made antiresonance in the absorption coefficient. The antiresonance reduced the absorption coefficient after the first peak.[21] As may be seen in Figs. 5(c) and 7, for the cases of $V_0=0.50$, $V_0=0.55$, and $V_0=0.60$, the antiresonant frequency appears near 450 Hz, respectively, and near 400 Hz for the case of $V_0=0.65$. Except for the case of $V_0=0.65$, the unique front and connecting parts of the optimal foam shapes were found to affect the plane wave absorption coefficient in middle frequency range. When the front and connecting parts were eliminated from the optimal foam shape, the remaining main foam part did not have enough length to absorb sound waves having middle frequencies. For the shortened foam, the absorption coefficient fluctuates between the ups and downs along with frequencies. Therefore, it may be said that the designed front and connecting parts of the optimal foam shapes reduce the fluctuation and contribute to the improvement of the absorption ability in the middle frequency range. This observation was checked by numerical simulations with the obtained foam shapes.

As the allowable amount of a poroelastic material in a design domain increased, the bowl-like foam part disappeared in the optimal foam shape. On the other hand, a thin and flat poroelastic material layer was designed at the front part of the design domain as shown in Figs. 6(b) and 6(c). Furthermore, the front and connecting parts of the optimized foams were designed to become similar to the wedge shape such as Fig. 6(c). Thus, as shown in Figs. 5(c) and 7, the differences in the absorption coefficient between the optimal

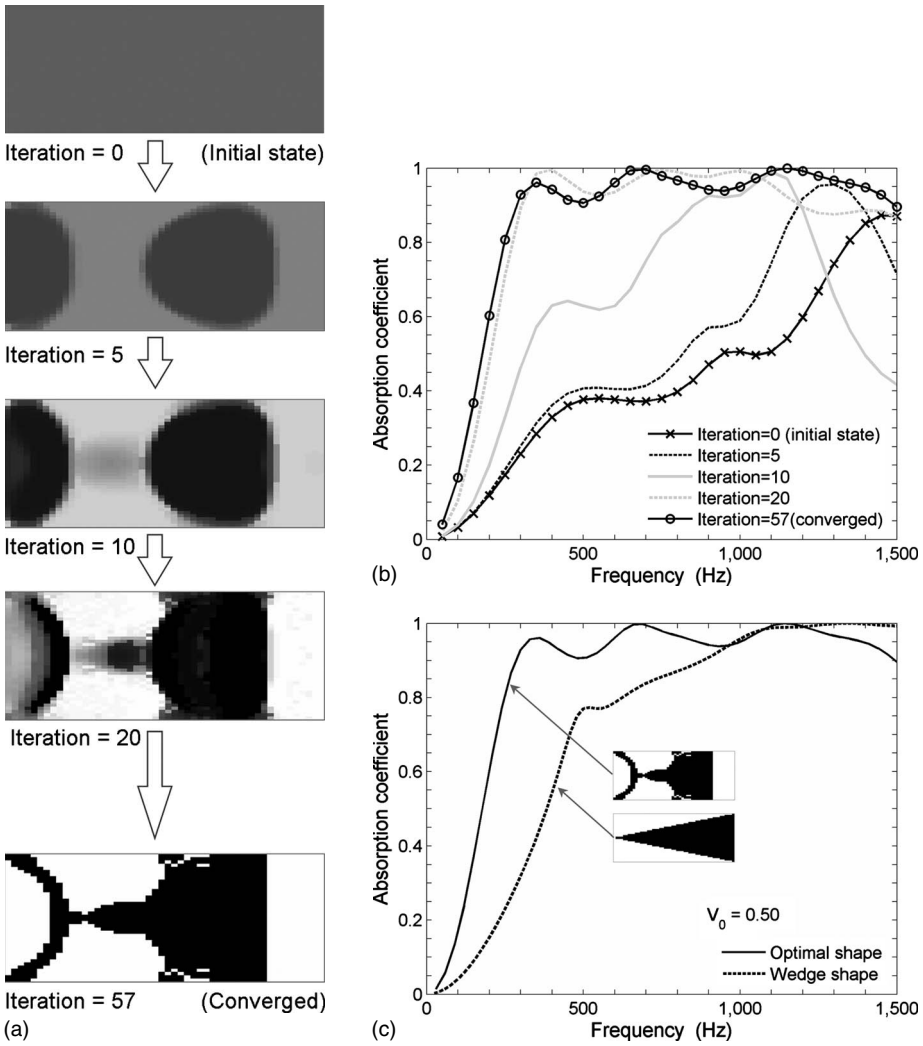

FIG. 5. Result of the topology optimization to find an optimal foam shape. (a) A topology optimization process and the obtained foam shape for V_0=0.50, (b) changes of the plane wave absorption coefficients with iterations and (c) the plane wave absorption coefficient of the optimal foam shape compared with that of the well-known wedge shape having the same allowable amount of a poroelastic material (V_0=0.50).

foam shape and the well-known conventional wedge shape were also reduced in the low and middle of frequencies as the amount of a poroelastic material in the design domain increased.

It will be also interesting to compare the absorption performance of the optimized foam shape and those of other foam shapes such as those in Refs. 1–4 and 6. The selected foam shapes from the references are an optimally angled wedge shape,[4] a semicircular shape[6] and a rectangular shape. The dimensions and other data of the selected foams are slightly changed for the comparison. Optimally angled wedge shapes having different length of a backing air layer are also considered for the comparison. They are shown in Fig. 8.

Figure 9(a) compares the absorption coefficient of the optimized foam shape shown in Fig. 5(a) and those of the foam shapes shown in Figs. 8(a)–8(c). In comparison with the optimally angled wedge shapes, the present optimal foam shape has a lower first resonant frequency. Therefore, it has a better absorption capability in a lower frequency range. The

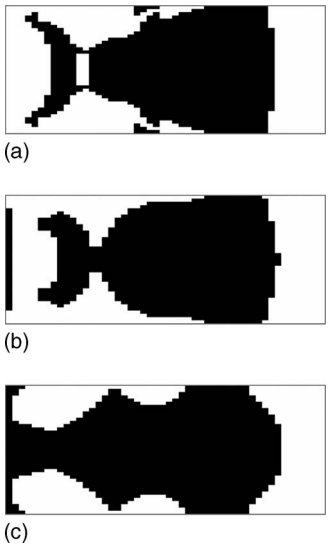

FIG. 6. Optimal foam shapes under different allowable amounts of a poroelastic material in a design domain. (a) V_0=0.55, (b) V_0=0.60, and (c) V_0=0.65.

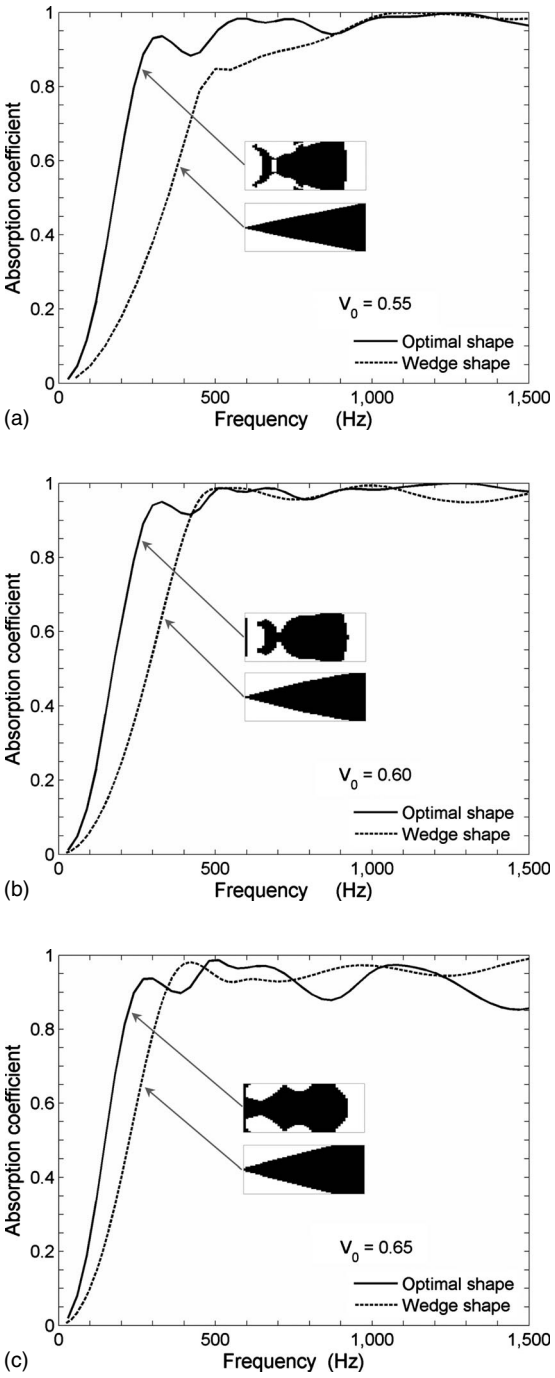

FIG. 7. The plane wave absorption coefficients corresponding to the optimal foam shapes shown in Fig. 6. Absorption performance of each foam shape is compared with that of the well-known wedge shape having the same amount of a poroelastic material. (a) V_0=0.55, (b) V_0=0.60, and (c) V_0=0.65.

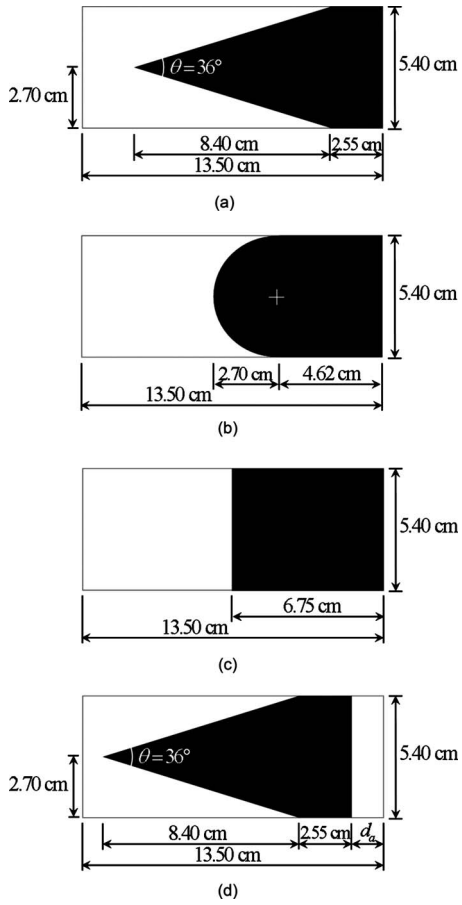

FIG. 8. Various foam shapes and their dimensions for comparison of the absorption performance with the optimized foam shape. Dimensions of each shape are determined by restriction of the same amount of a poroelastic material with the optimized foam shape (V_0=0.50). (a) An optimally angled wedge shape (θ=36°, Ref. 4), (b) a semicircular shape, (c) a rectangular shape, and (d) an optimally angled wedge shape having a backing air layer. (Allowable maximum length of a backing air layer is determined by the length of the design domain and that of an optimally angled wedge shape.)

absorption capabilities of the semicircular and rectangular shapes are far inferior to that of the present optimal foam shape.

Figure 9(b) compares the absorption coefficient of the present optimal foam shape and those of an optimally angled wedge shape with different length of a backing air layer. The addition of a backing air layer to the wedge lowers the first resonant frequency, but the presence of a backing air layer results in the fluctuation of the absorption coefficient. The amplitude of the first resonant peak of the wedge foam is also reduced by a backing air layer. Thus, one can confirm that the present optimal foam shape outperforms wedges having backing air layers. A reason for the better performance of the present foam shape is that the front and connecting parts reduce the frequency fluctuation and improve the absorption performance in a middle frequency range. Also, the combined effects of several parts of the optimized foam shape keep the first peak amplitude higher and enhance the absorption performance in the whole frequency range of interest. These observations may be also evident from Fig. 9(c).

In the present investigation, the aspect of the manufacturing of a poroelastic acoustical foam was not explicitly considered in the design process. The optimized foam shapes shown in Figs. 5(a) and 6 could be changed for actual fabrication. Also, different shapes could be designed for different poroelastic materials. For actual fabrication, the minimum length scale may be controlled within the topology optimization setting because it may be difficult to fabricate some part of the optimized foam such as the thin connecting part

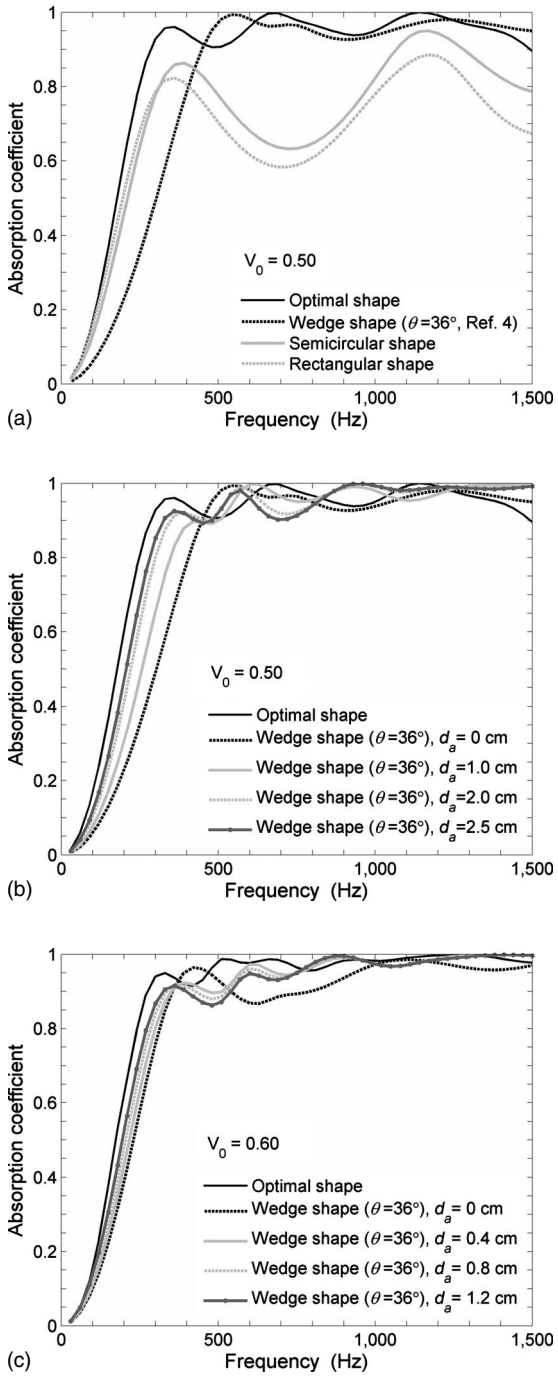

FIG. 9. The plane wave absorption coefficients of the optimal foam shapes and other foam shapes. (a) Comparison with an optimally angled wedge shape, a semicircular shape, and a rectangular shape (V_0=0.50), (b) comparison with an optimally angled wedge shape having different length of a backing air layer (V_0=0.50), and (c) comparison with an optimally angled wedge shape having different length of a backing air layer (V_0=0.60).

shown in Fig. 5(a). However, the minimum scale controlling technique is not pursued here because the physical interpretation of the optimized shape is a main concern of this investigation.

V. CONCLUDING REMARKS

Two-dimensional optimal shapes of a poroelastic acoustical foam having maximized plane wave absorption coefficient were designed in the low and middle ranges of frequencies by a topology optimization method. In the design process, the use of a poroelastic material was limited not to exceed 50, 55, 60, and 65% of a design domain. For each case, the optimal shape had an improvement in sound absorption compared with the conventional wedge shape having the same amount of a poroelastic material in the target frequency range: from 100 to 1500 Hz. A thick air layer-filled back space of the optimal foam shape lowered the first resonant frequency of the acoustical foam system, which improved the absorption performance at the low frequencies. And the front and connecting parts of the optimal foam shape reduced the fluctuation of the absorption coefficient in the middle frequencies. Proper material property interpolation in the topology optimization formulation was important for obtaining a connected optimal foam shape. Unlike in typical structural topology optimization, the exponent value of 1 was used to interpolate the states of an element between air and a poroelastic material. The topology optimization formulation was based on a newly proposed unified analysis model. The unified model expressed both an air region and a poroelastic acoustical foam region by using the same governing equation with the material property interpolation, and consequently, the moving interfaces between two regions were automatically constructed in the iterative optimization process. The accuracy of the unified model was verified for several foam shapes against a conventional analysis method.

ACKNOWLEDGMENT

This research was supported by the National Creative Research Initiatives Program (Korea Science and Technology Foundation Grant No. 2007-019) contracted through the Institute of Advanced Machinery and Design at Seoul National University.

[1]L. L. Beranek and H. P. Sleeper, Jr., "The design and construction of anechoic sound chambers," J. Acoust. Soc. Am. **18**, 140–150 (1946).
[2]W. Koidan, G. R. Hruska, and M. A. Pickett, "Wedge design for national bureau of standards anechoic chamber," J. Acoust. Soc. Am. **52**(4), 1071–1076 (1972).
[3]V. Easwaran and M. L. Munjal, "Finite element analysis of wedges used in anechoic chambers," J. Sound Vib. **160**(2), 333–350 (1993).
[4]Y. J. Kang and J. S. Bolton, "Optimal design of acoustical foam treatments," ASME J. Vibr. Acoust. **118**, 498–504 (1996).
[5]Y. J. Kang and J. S. Bolton, "Finite element modeling of isotropic elastic porous materials coupled with acoustical finite elements," J. Acoust. Soc. Am. **98**(1), 635–643 (1995).
[6]W. H. Chen, F. C. Lee, and D. M. Chiang, "On the acoustic absorption of porous materials with different surface shapes and perforated plates," J. Sound Vib. **237**(2), 337–355 (2000).
[7]F. Simón, R. M. Rodríguez, and J. Pfretzschner, "On the absorption coefficient of porous corrugated surfaces," ASME J. Vibr. Acoust. **124**, 329–333 (2002).
[8]F. C. Lee and W. H. Chen, "On the acoustic absorption of multilayer absorbers with different inner structures," J. Sound Vib. **259**(4), 761–777 (2003).
[9]F. C. Sgard, X. Olny, N. Atalla, and F. Castel, "On the use of perforations to improve the sound absorption of porous materials," Appl. Acoust. **66**, 625–651 (2005).
[10]M. A. Biot, "Theory of propagation of elastic waves in a fluid-saturated porous solid," J. Acoust. Soc. Am. **28**, 168–191 (1956).
[11]M. P. Bendsøe and O. Sigmund, *Topology Optimization: Theory, Methods and Applications* (Springer, Germany, 2003).
[12]J. S. Bolton, N.-M. Shiau, and Y. J. Kang, "Sound transmission through multi-panel structures lined with elastic porous materials," J. Sound Vib.

191(3), 317–347 (1996).
[13]J. F. Allard, *Propagation of Sound in Porous Media: Modeling Sound Absorbing Materials* (Elsevier Science, New York, 1993).
[14]N. Atalla and R. Panneton, "The effects of multilayer sound-absorbing treatments on the noise field inside a plate backed cavity," Noise Control Eng. J. **44**, 235–243 (1996).
[15]N. Atalla, R. Panneton, and P. Debergue, "A mixed displacement-pressure formulation for poroelastic materials," J. Acoust. Soc. Am. **104**(3), 1444–1452 (1998).
[16]M. P. Bendsøe and N. Kikuchi, "Generating optimal topologies in structural design using a homogenization method," Comput. Methods Appl. Mech. Eng. **71**(2), 197–224 (1988).
[17]J. S. Lee, E. I. Kim, Y. Y. Kim, J. S. Kim, and Y. J. Kang, "Optimal poroelastic layer sequencing for sound transmission loss maximization by topology optimization method," J. Acoust. Soc. Am. **122**(4), 2097–2106 (2007).
[18]ASTM E1050–98(2006) Standard Test Method for Impedance and Absorption of Acoustical Materials Using A Tube, Two Microphones and A Digital Frequency Analysis System.
[19]ISO 10534–2:1998 Acoustics—Determination of sound absorption coefficient and impedance in impedance tubes—Part 2: Transfer-function method (International Organization for Standardization, Geneva, 1998).
[20]K. Svanberg, "The method of moving asymptotes: A new model for structural optimization," Int. J. Numer. Methods Eng. **24**, 359–373 (1987).
[21]F. Fahy, *Foundations of Engineering Acoustics* (Academic, London, 2001), Chap. 7, pp. 167–170.

Causal impulse response for circular sources in viscous media

James F. Kelly[a] and Robert J. McGough
Department of Electrical and Computer Engineering, Michigan State University, East Lansing, Michigan 48824

(Received 6 March 2007; revised 29 January 2008; accepted 30 January 2008)

The causal impulse response of the velocity potential for the Stokes wave equation is derived for calculations of transient velocity potential fields generated by circular pistons in viscous media. The causal Green's function is numerically verified using the material impulse response function approach. The causal, lossy impulse response for a baffled circular piston is then calculated within the near field and the far field regions using expressions previously derived for the fast near field method. Transient velocity potential fields in viscous media are computed with the causal, lossy impulse response and compared to results obtained with the lossless impulse response. The numerical error in the computed velocity potential field is quantitatively analyzed for a range of viscous relaxation times and piston radii. Results show that the largest errors are generated in locations near the piston face and for large relaxation times, and errors are relatively small otherwise. Unlike previous frequency-domain methods that require numerical inverse Fourier transforms for the evaluation of the lossy impulse response, the present approach calculates the lossy impulse response directly in the time domain. The results indicate that this causal impulse response is ideal for time-domain calculations that simultaneously account for diffraction and quadratic frequency-dependent attenuation in viscous media.
© *2008 Acoustical Society of America.* [DOI: 10.1121/1.2885737]

PACS number(s): 43.58.Bh, 43.20.Px, 43.20.Hq, 43.35.Bf [TDM] Pages: 2107–2116

I. INTRODUCTION

Several applications, including medical ultrasound, SONAR, and seismology, utilize broadband, three-dimensional (3D) sound beams in dissipative media, where attenuation is often modeled via a power-law relation.[1–3] Since no closed-form Green's functions for arbitrary power-law media have been reported in the literature, loss is often approximated via viscous relaxation. As discussed elsewhere,[4,5] the transient solutions in a viscous medium in 1D may be approximated in terms of Gaussian functions, thus avoiding the mathematical complexity encountered in the general power-law case. Since viscous media is a special case of power-law media, insight into general dissipative media is gained by studying the approximations available in viscous media.

The underlying physics of viscous diffusion are well documented,[6] yet time-domain studies of wave propagation in viscous and other lossy media have been primarily limited to one-dimensional (1D) plane wave propagation. For example, the classic study by Blackstock[4] approximated the viscous term in the Stokes wave equation by a third derivative, leading to a non-causal solution. The Stokes equation has also been approximated by the telegrapher's equation,[7] leading to causal solutions with sharp wavefronts similar to electromagnetic propagation in conductive media. Recent studies derived causal Green's function solutions in the form of contour integrals,[8] infinite series,[9] and closed-form approximations.[5] Although the combined effects of diffraction and loss have been thoroughly studied in the frequency domain both analytically[10] and numerically,[11] most time-domain studies have been analytical. For example, the combined effects of diffraction, dissipation, and nonlinearity were studied numerically in Ref. 12 under the parabolic approximation. In Ref. 13, a general approach combining linear with frequency loss[14] and time-domain diffraction was proposed. A general 3D numerical model incorporating power-law loss and finite apertures was developed in Ref. 15.

In order to understand the interplay between diffraction and frequency-dependent attenuation, time-domain impulse response expressions for simple piston geometries are needed. Although impulse response expressions exist for lossless, homogeneous media for circular[16,17] and rectangular[18] apertures, no analytical expressions for the transient field radiated by finite planar apertures in a viscous medium have been published. An analytical expression for the on-axis velocity potential produced by a focused spherical shell was recently derived in Ref. 19, although field points off axis were not considered. In particular, the effect of viscous loss on the impulse response of a baffled circular piston has not been addressed.

The goal of this work is to derive the causal impulse response of the velocity potential for circular sources in viscous media satisfying the Stokes wave equation. In Sec. II, a method for computing solutions to the Stokes wave equation is developed. By decomposing a causal, approximate Green's function into diffraction and loss components, an analytical relationship between the lossless and lossy impulse response is determined. In Sec. III, this method is applied to the transient fast near field method[20] to compute the lossy impulse

[a]Author to whom correspondence should be addressed. Electronic mail: kellyja8@msu.edu.

responses for the uniform circular piston. In Secs. IV and V, the lossy impulse responses are numerically evaluated and physically interpreted.

II. THEORY

In this section, an approximate causal Green's function solution to the Stokes wave equation is analyzed. The lossy impulse response in a viscous medium is then related to the corresponding impulse response in a lossless medium. The medium is assumed to be linear, isotropic, and homogeneous and bounded by an infinite, rigid baffle in the $z=0$ plane. Moreover, the transient Green's function $g(R,t)$ is assumed to satisfy the viscous wave equation, or Stokes equation:[5]

$$\nabla^2 g - \frac{1}{c_0^2}\frac{\partial^2 g}{\partial t^2} + \gamma\frac{\partial}{\partial t}\nabla^2 g = -\delta(t)\delta(\mathbf{R}), \tag{1}$$

where c_0 is the thermodynamic speed of sound and γ is the relaxation time of the medium. The relaxation time, which is proportional to the coefficient of shear viscosity μ, measures the time necessary to restore equilibrium to the translational degrees of freedom in the fluid following a small thermodynamic disturbance. If $\gamma=0$, equilibrium is restored immediately and Eq. (1) reduces to the lossless wave equation. The viscous term in Eq. (1) is a singular perturbation which transforms the lossless, second-order hyperbolic wave equation into a third-order parabolic equation. The dispersion relation between wavenumber k and angular frequency ω are computed via a space-time Fourier transform applied to Eq. (1), which are summarized by Eqs. (58) and (59) in Ref. 9:

$$k(\omega) = \frac{\omega}{c_0\sqrt{1+(\omega\gamma)^2}}\sqrt{1-i\omega\gamma} \tag{2}$$

yielding an attenuation coefficient that is approximately proportional to ω^2 for $\omega\gamma \ll 1$.

A. Green's function decomposition

Unfortunately, no closed-form analytical Green's function is known to exist for the Stokes waves equation. However, an asymptotic causal Green's function for the 3D problem has been found.[21] Alternatively, the 3D Green's function is derived in Appendix A with the methodology developed in Ref. 21, yielding

$$g(R,t) \approx \frac{u(t)}{4\pi R\sqrt{2\pi t\gamma}}\exp\left(-\frac{(t-R/c_0)^2}{2t\gamma}\right), \tag{3}$$

where $R=|\mathbf{r}-\mathbf{r}'|$ is the distance between observer $\mathbf{r}$ and source $\mathbf{r}'$ and $u(t)$ is the Heaviside unit step function. Equation (3), which is valid for small viscosity ($\gamma\to 0$) and large times ($t\to\infty$), supports infinite propagation speed, yet is strictly causal due to the Heaviside function $u(t)$. As shown in Sec. IV, Eq. (3) is an excellent, causal approximation except in the extreme near field or highly viscous media.

Equation (3) is recognized as the composition of (a) the Green's function for the 3D wave equation and (b) the Green's function for the (1D) diffusion equation. This observation motivates decomposing Eq. (3) into individual diffraction and loss factors via

$$g(R,t) = \int_{-\infty}^{\infty}\left[\frac{\delta(t-t'-R/c_0)}{4\pi R}\right] \times\left[u(t)\frac{1}{\sqrt{2\pi t\gamma}}\exp\left(-\frac{t'^2}{2t\gamma}\right)\right]dt', \tag{4}$$

where the sifting property of the Dirac delta function applied to Eq. (4) yields Eq. (3). Identifying the first bracketed expression as a diffraction component and the second bracketed expression as a loss component via

$$g_D(R,t) = \frac{\delta(t-R/c_0)}{4\pi R}, \tag{5a}$$

$$g_L(t,t') = u(t)\frac{1}{\sqrt{2\pi t\gamma}}\exp\left(-\frac{t'^2}{2t\gamma}\right), \tag{5b}$$

allows Eq. (4) to be expressed as

$$g(R,t) = g_L(t,t') \otimes g_D(R,t) \equiv \int_{-\infty}^{\infty} g_D(R,t-t')g_L(t,t')dt', \tag{6}$$

where the convolution denoted by $\otimes$ is performed with respect to the t' variable. In Eq. (6), the subscript "D" refers to diffraction, whereas the subscript "L" refers to loss. Equation (5a) is responsible for diffraction and the directivity of the radiating aperture. Equation (5b) is a Gaussian function centered at $t'=0$ having width, or standard deviation, $\sqrt{t\gamma}$. The t' variable is interpreted as "propagation time" (fast), whereas t is interpreted as the "diffusion time" (slow). In fact, Eq. (5b) is the causal Green's function for the 1D diffusion equation[22]

$$\left(\frac{\partial}{\partial t} - \frac{\gamma}{2}\frac{\partial^2}{\partial t'^2}\right)g_L(t,t') = \delta(t)\delta(t'), \tag{7}$$

where $c_0 t'$ plays the role of the spatial variable. Thus, Eq. (6) is interpreted as the non-stationary convolution of the 1D Green's function for the diffusion equation with the Green's function with the 3D wave equation. As shown below, the decomposition embodied in Eq. (6) facilitates the generalization of the impulse response for circular apertures to viscous media.

B. Lossy impulse response function

The impulse response function $h_L(\mathbf{r},t)$ in the half space is obtained by integrating Eq. (3) over the surface of the radiating aperture and multiplying by two to account for the infinite, planar baffle in the $z=0$ plane. Analytically, Eq. (6) allows the lossy impulse response to be evaluated for a circular piston. Integrating the decomposed Green's function over the aperture S and multiplying by two yields

$$h_L(\mathbf{r},t) = g_L(t,t') \otimes \int_S \frac{\delta(t-R/c_0)}{2\pi R}d^2\mathbf{r}'. \tag{8}$$

The second factor in Eq. (8) is identical to the standard impulse response for a uniform aperture, which has been calculated previously for a circular source. Therefore, the lossy impulse response function is expressed as a non-stationary convolution of the standard impulse response with a loss

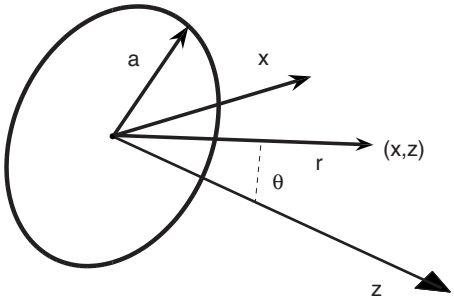

FIG. 1. Piston and coordinate geometry. The piston, centered at the origin and surrounded by an infinite rigid baffle in the $z=0$ plane, has a radius a. The radial and axial observation coordinates are denoted by x and z, respectively. The distance between origin and observer is given by r and the angle between the radial and axial coordinates is θ.

function, where the convolution is taken over t':

$$h_L(\mathbf{r},t) = g_L(t,t') \otimes h(\mathbf{r},t). \tag{9}$$

Equation (9) maps solutions of the hyperbolic wave equation to solutions of the parabolic Stokes equation, similar to the Q transform.[23] Since the loss function $g_L(t,t')$ is independent of R, the integration in Eq. (9) is independent of the geometry associated with the aperture S, allowing the lossy impulse response to be calculated from a known lossless impulse response.

III. CIRCULAR PISTON

Figure 1 displays the geometry and coordinate systems used in the following derivations. The lossy impulse response is determined for a uniform piston at all observation points in both the near and far fields. Equation (9) is evaluated analytically, yielding either closed-form or single-integral expressions which are then evaluated numerically. The transient velocity potential is then recovered via fast Fourier transform (FFT)-based convolutions.

A. Near field

1. Lossless impulse response

The near field solution to the transient, lossless, baffled circular piston problem may be expressed piecewise in terms of the rect function and the inverse cosine function.[16,18] The non-stationary convolution is difficult to compute with these piecewise expressions; therefore, a single-integral expression that is valid for all observation points is instead utilized. In Ref. 20, a single integral expression for the pulsed pressure was derived. Assuming a Dirac delta excitation $v(t)=\delta(t)$ in Eq. 12 in Ref. 20 and utilizing the expression $h(x,z,t) = \int_{-\infty}^{t} p(x,z,t')dt'/\rho_0$ yields the time-domain impulse response

$$h(x,z,t) = \frac{c_0 a}{\pi}\int_0^{\pi} \frac{x\cos\psi - a}{x^2 + a^2 - 2ax\cos\psi} \times [u(t-\tau_1) - u(t-\tau_2)]d\psi, \tag{10}$$

where the delays τ_i are specified by

$$\tau_1 = \sqrt{x^2 + z^2 + a^2 - 2ax\cos\psi}/c_0 \text{ and} \tag{11a}$$

$$\tau_2 = z/c_0. \tag{11b}$$

In Eqs. (10) and (11), x is the radial coordinate and z is the axial coordinate. The integration over ψ can be evaluated in closed form, yielding the piecewise-defined lossless impulse response given in Ref. 18. However, the integral representation given by Eq. (10) leads directly to the lossy impulse response that follows.

2. Lossy impulse response

The lossless near field solution given by Eq. (10) solves the transient wave equation assuming a uniform piston in an infinite rigid baffle. The lossy impulse response is computed by inserting Eq. (10) into Eq. (9) and evaluating the unit step functions in Eq. (10). The integration over t' is evaluated in terms of the error function[24] $\mathrm{erf}(z)$, yielding

$$h_L(x,z,t) = \frac{c_0 a}{2\pi}u(t)\int_0^{\pi} \frac{x\cos\psi - a}{x^2 + a^2 - 2ax\cos\psi} \times \left[\mathrm{erf}\left(\frac{t-\tau_1}{\sqrt{2t\gamma}}\right) - \mathrm{erf}\left(\frac{t-\tau_2}{\sqrt{2t\gamma}}\right)\right]d\psi, \tag{12}$$

with τ_1 and τ_2 defined in Eq. (11). On axis ($x=0$), the lossy impulse response reduces to

$$h_L(0,z,t) = \frac{c_0 u(t)}{2}\left[\mathrm{erf}\left(\frac{t - z/c_0}{\sqrt{2t\gamma}}\right) - \mathrm{erf}\left(\frac{t - \sqrt{z^2 + a^2}/c_0}{\sqrt{2t\gamma}}\right)\right]. \tag{13}$$

As in the lossless case, the first and second delays in Eq. (13) correspond to the closest point and the furthest point on the radiating piston, respectively. In Eqs. (12) and (13), The "slow" time scale is embodied in the denominator of the erf functions $\sqrt{2t\gamma}$, whereas the "fast" time scale is embodied in the numerator. The lossy impulse response described by Eqs. (12) and (13) possesses an infinitely long tail that decays like a Gaussian.

B. Far field

1. Lossless impulse response

Although Eq. (12) is valid for all field points, a simpler expression exists in the far field, where the effects of attenuation are more pronounced. Here, the definition of the far field is the same as that utilized by Morse and Ingard,[25] where the observation distance is much larger than the radius of the aperture ($r \gg a$). This definition of the far field is distinguished from the traditional far field distance $r > a^2/\lambda$, which is only valid over a finite frequency band. As shown in Appendix B, the lossless impulse response in the far field is represented by the single-integral expression

$$h(r,\theta,t) = \frac{c_0 a}{\pi r \sin\theta}\int_0^{\pi} \cos\psi u(t - r/c_0 + a\sin\theta\cos\psi/c_0)d\psi, \tag{14}$$

which is valid for $r \gg a$ and $\theta > 0$. Note that Eq. (14) has support on the time interval $[r/c_0 - a\sin\theta/c_0,\ r/c_0$

$+a \sin\theta/c_0]$, which follows from the fact that $\int_0^\pi \cos\psi d\psi = 0$. On axis ($\theta=0$), the impulse response reduces to

$$h(z,0,t) = \frac{a^2}{2z}\delta(t - z/c_0), \tag{15}$$

which is the limiting case of Eq. (10) as $z \to \infty$.

2. Lossy impulse response

The far field viscous lossy impulse response is now computed from Eqs. (14) and (15). For the off-axis case, Eq. (14) is substituted into Eq. (9). Interchanging the order of integration and evaluating the unit-step function in the integrand yields

$$h_L(r,\theta,t) = \frac{c_0}{\pi r \sin\theta}\frac{u(t)}{\sqrt{2\pi t\gamma}}\int_0^\pi \int_{-\infty}^{\tau'(\psi)} \exp\left(-\frac{t'^2}{2t\gamma}\right) \times \cos\psi dt' d\psi, \tag{16}$$

where

$$\tau'(\psi) = t - r/c_0 + a \sin\theta \cos\psi/c_0. \tag{17}$$

The integration over t' is evaluated using $2/\sqrt{\pi}\int_{-\infty}^{x} e^{-z^2} dz = 1 + \mathrm{erf}(x)$. Due to the $\cos\psi$ term in Eq. (16), the constant term vanishes, yielding a single integral expression

$$h_L(r,\theta,t) = \frac{c_0 a u(t)}{2\pi r \sin\theta}\int_0^\pi \mathrm{erf}\left(\frac{t - r/c_0 + a \sin\theta\cos\psi/c_0}{\sqrt{2t\gamma}}\right) \times \cos\psi d\psi. \tag{18}$$

The on-axis case is computed by inserting Eq. (15) into Eq. (9) and utilizing the sifting property of the Dirac delta function, yielding

$$h_L(r,0,t) = u(t)\frac{a^2}{2r}\frac{\exp(-(t - r/c_0)^2/2t\gamma)}{\sqrt{2\pi t\gamma}}, \tag{19}$$

which can also be derived by letting $z \to \infty$ in Eq. (13). Unlike the lossless case, the lossy impulse response does not have compact support in time. Since both the Gaussian and error functions have infinite support, the lossy impulse responses defined by Eqs. (18) and (19) are also non-zero for all positive time values. In physical terms, this semi-infinite region of support implies wave components traveling with phase speeds varying from zero to infinity, but the infinite phase speeds are infinitely attenuated,[5] so the result is causal.

IV. NUMERICAL RESULTS

A. Green's function evaluation

A reference solution to the Stokes wave equation is evaluated using the material impulse response function (MIRF) approach outlined in Ref. 3, and the result is compared to Eq. (3). The wavenumber $k(\omega)$ is calculated via the reference dispersion relation given by Eq. (2), allowing the material transfer function to be calculated in the frequency domain. As specified by Eq. (10) in Ref. 3, the reference Green's function, or MIRF, is then recovered by inverse Fourier transforming the material transfer function (MTF), or frequency-domain Green's function, via the inverse fast Fourier transform (FFT), where

$$g(R,t) = \mathcal{F}^{-1}\left(\frac{e^{ik(\omega)R}}{4\pi R}\right) \tag{20}$$

Since $g(R,t)$ is necessarily real, conjugate symmetry of the MTF is enforced in the frequency domain. The relative L^2 error, defined via

$$\text{error} = \frac{\sqrt{\int_{-\infty}^{\infty}|\phi(t) - \phi_{ref}(t)|^2 dt}}{\sqrt{\int_{-\infty}^{\infty}|\phi_{ref}(t)|^2 dt}} \tag{21}$$

is calculated with the MIRF approach used as the reference.

Figure 2 summarizes the results of this comparison for various combinations of observation distance R and viscous relaxation time γ. Panel (a), which shows the numerical reference and approximate Green's functions using $R=1$ mm and $\gamma=0.01$ μs, displays a significant disparity between the reference and asymptotic Green's functions when γ is relatively large and R is relatively small. Panel (b), which is evaluated with $R=1$ mm and $\gamma=0.01$ μs, shows a much smaller variation between the asymptotic and reference Green's functions. Panels (c) and (d) show the Green's functions for $R=1$ mm and $\gamma=0.01$ μs and $\gamma=0.001$ μs, respectively; these panels show very close agreement between the reference and asymptotic Green's functions. The asymptotic and reference Green's functions are virtually identical in panel (d) of Fig. 2, implying that Eq. (3) is an excellent approximation for $R>1$ mm and $\gamma<0.001$ μs.

The root mean square (RMS) error is a function of the dimensionless parameter $R/(\gamma c_0)$. A quantitative error analysis comparing the asymptotic Green's function to the MIRF result is displayed in Fig. 3 in terms of $R/(\gamma c_0)$ on a log-log plot. From the slope of the curve in Fig. 3, the RMS error is approximately proportional to $\sqrt{\gamma c_0/R}$. As expected, the error increases as R increases and decreases as R increases. For a 1% error threshold, $R/(\gamma c_0) \geqslant 3.3\times 10^3$, yielding the relation $\gamma \leqslant 3\times 10^{-4} R/c_0$. By fixing γ and letting R vary, the minimum acceptable distance is determined by $R \geqslant 5\times 10^3 c_0\gamma$.

B. Circular piston evaluation

Since the lossy impulse response solutions utilize an approximate transient Green's function to the Stokes wave equation, a numerical comparison is made to a reference frequency-domain solution. The numerical reference is computed by computing the Fourier transform of the velocity potential $\hat{\Phi}(\mathbf{r},\omega) = \hat{v}(\omega)\hat{h}(\mathbf{r},k(\omega))$ using the dispersion relations $k(\omega)$ given by Eq. (2). This product is computed over the effective bandwidth of $\hat{v}(\omega)$ and then numerically inverse Fourier transformed using an inverse FFT. For a uniform circular piston of radius a, the on-axis ($r=0$) transfer function $\hat{h}(0,z;\omega)$ exists in closed form, thereby obviating the need for numerical integration.

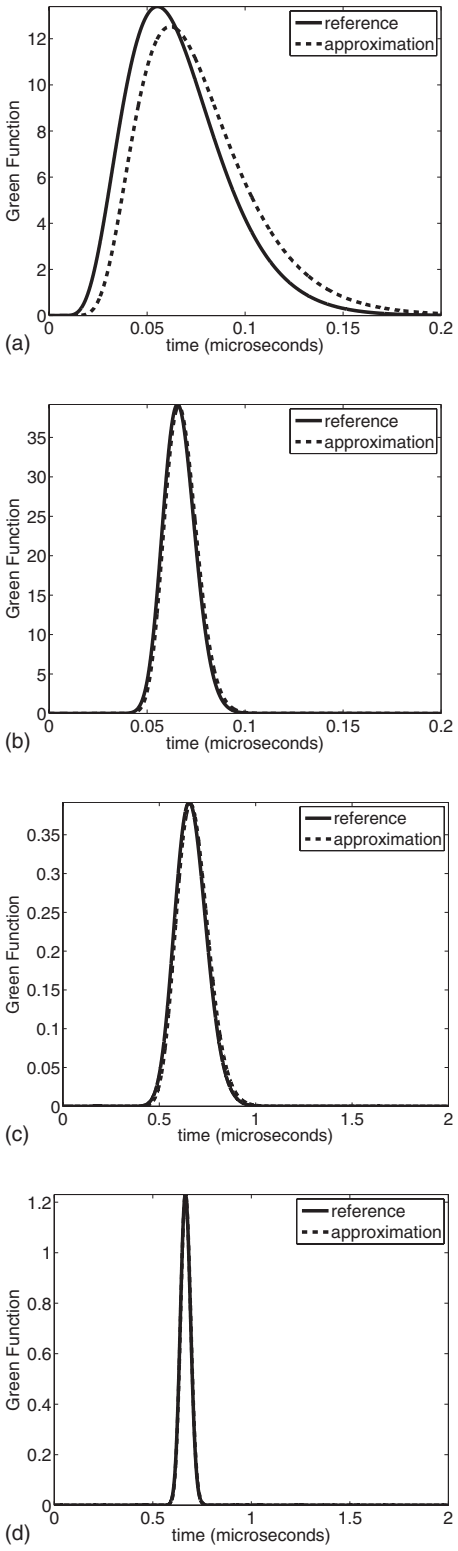

FIG. 2. Comparison of the asymptotic form of the Green's function for the Stokes wave equation (Eq. (3)) and the reference Green's function computed numerically via the MIRF approach. The Green's function is shown for (a) $R=0.1$ mm and $\gamma=0.01$ μs, (b) $R=0.1$ mm and $\gamma=0.001$ μs, $R=1.0$ mm and $\gamma=0.01$ μs and (d) $R=1.0$ mm and $\gamma=0.001$ μs.

Figure 4 displays the on-axis velocity potential for a circular piston of radius $a=10$ mm in a viscous medium for the same combinations of z and γ utilized in Fig. 2. A Hanning-weighted toneburst

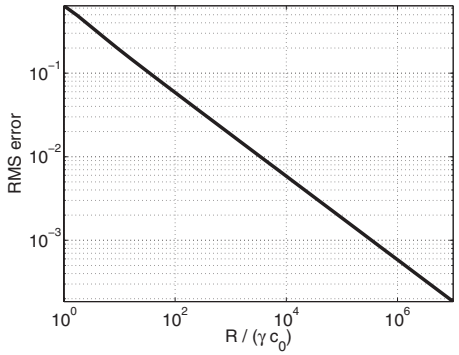

FIG. 3. The RMS error for the asymptotic Green's function relative to the reference MIRF result. The RMS error is displayed on a log-log plot relative to the dimensionless parameter $R/(\gamma c_0)$. The slope on the log-log plot is approximately 0.5, indicating that RMS error is proportional to $\sqrt{\gamma c_0/R}$.

$$v(t) = \frac{1}{2}(1-\cos(2\pi t/W))\mathrm{rect}\left(\frac{t}{W}\right)\sin(2\pi f_0 t) \tag{22}$$

with center frequency $f_0=6.0$ MHz and duration $W=0.5$ μs is applied, where $\mathrm{rect}(t)=u(t)-u(t-1)$. The velocity potential is obtained for (a) $z=0.1$ mm and $\gamma=0.01$ μs, (b) $z=0.1$ mm and $\gamma=0.001$ μs, (c) $z=1$ mm and $\gamma=0.01$ μs, and (d) $z=1$ mm and $\gamma=0.001$ μs. The error is computed between the lossy impulse response and the MIRF method using Eq. (21), using the MIRF field as reference. The resulting errors for the four cases are (a) 26.7%, (b) 3.26%, (c) 6.89%, and (d) 2.71%, respectively. Thus, larger errors are observed for points closer to the piston and large relaxation times due to the approximation in the Green's function given by Eq. (3). For $z>10$ mm and $\gamma\leqslant 0.001$ μs, the relative L^2 error is less than or equal to 1%. Since the effects of viscous dissipation are negligible in the extreme near field, the lossy impulse response yields an accurate solution that captures the combined effects of diffraction and viscous dissipation. Finally, Eq. (9) accounts for the small differences in the arrival time of each attenuated spherical wave emitted by the radiating aperture via the non-stationary convolution. Hence, no additional error is introduced in the calculation of the lossy impulse response.

Figure 5 plots the RMS error versus axial distance in terms of the normalized distance z/a for the on-axis lossy impulse response relative to the reference MIRF result. Error is shown for four representative viscous relaxation times γ. For $\gamma=0.0001$ μs, 0.0003 μs, and 0.001 μs, the RMS error decreases as a function of normalized distance. For $\gamma=0.003$ μs, the minimum RMS error occurs at $z/a\approx 2$, however. Unlike the Green's function error shown in Fig. 2, the error here is not controlled by a single parameter. Rather, error decreases slowly as a function of z/a, eventually reaching an error floor that depends on the viscous relaxation time.

C. Evaluation of the lossy impulse response

In this section, the lossy impulse response expressions derived in Secs. II and III are numerically evaluated. The velocity potential $\Psi(\mathbf{r},t)$ resulting from the temporal convolution of a transient excitation with the lossy impulse response is also computed and discussed. All single-integral

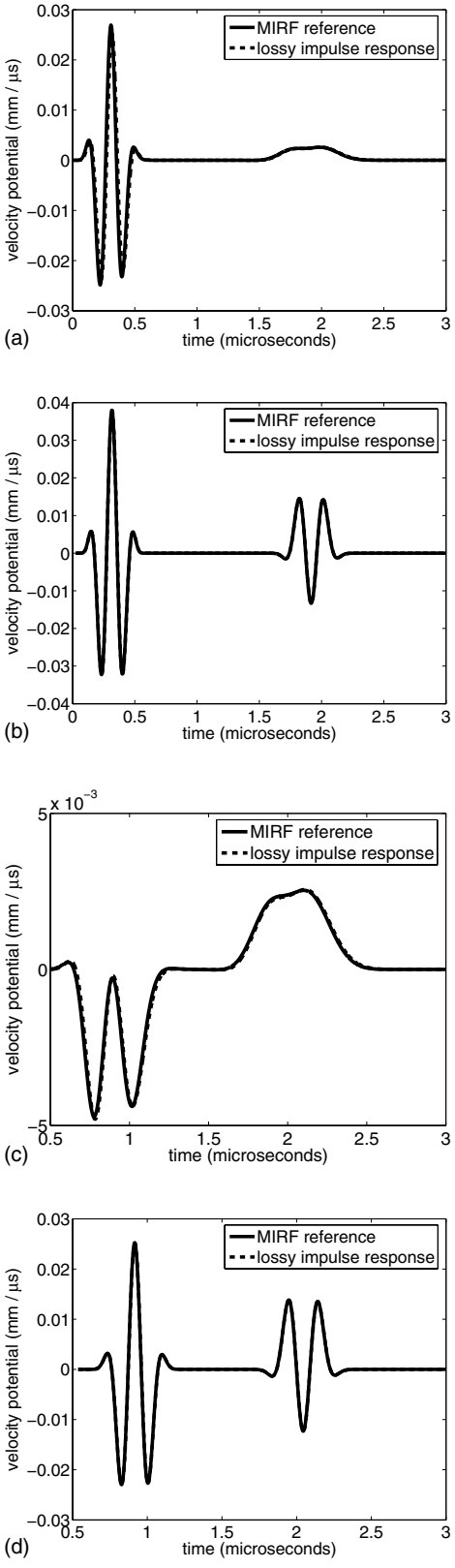

FIG. 4. On-axis ($x=0$ mm) velocity potential for a circular piston of radius $a=10$ mm in a viscous medium. The piston is excited by a Hanning-weighted toneburst with center frequency $f_0=6.0$ MHz and pulse length $W=0.5$ μs for four combinations of axial distance z and relaxation time γ: (a) $z=0.1$ mm and $\gamma=0.01$ μs, (b) $z=0.1$ mm and $\gamma=0.001$ μs, (c) $z=1$ mm and $\gamma=0.01$ μs, (d) $z=1$ mm and $\gamma=0.001$ μs. The velocity potential for each combination of z and γ is computed via both the lossy impulse response approach and a frequency-synthesis approach for verification.

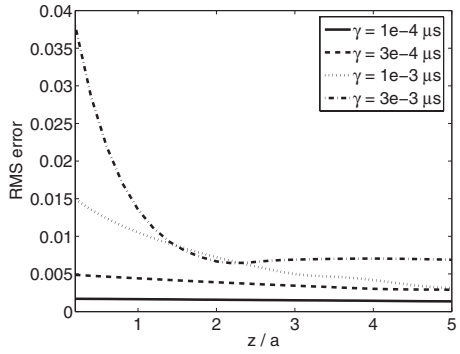

FIG. 5. The RMS error for the on-axis lossy impulse response relative to the reference MIRF result for a piston with radius $a=10$ mm. The RMS error is plotted versus the normalized axial distance z/a.

expressions are numerically integrated using Gauss–Legendre quadrature.[26] In the following velocity potential computations, the Hanning-weighted toneburst given by Eq. (22) is utilized.

Figures 6 and 7 display the near field impulse response for a circular piston with radius $a=10$ mm for lossless media and viscous media, respectively. Figure 6 shows two snapshots of the lossless impulse response ($\gamma=0$) on a two-dimensional computational grid extending from $x=-40$ mm to $x=40$ mm in the lateral direction and $z=20$ to $z=60$ mm in the axial direction. Snapshots of the impulse response are shown at two instances in time: $t=22$ μs and $t=34$ μs. As shown in Fig. 6, the field within the paraxial region ($|x|\leq 10$ mm) in the lossless case is unattenu-

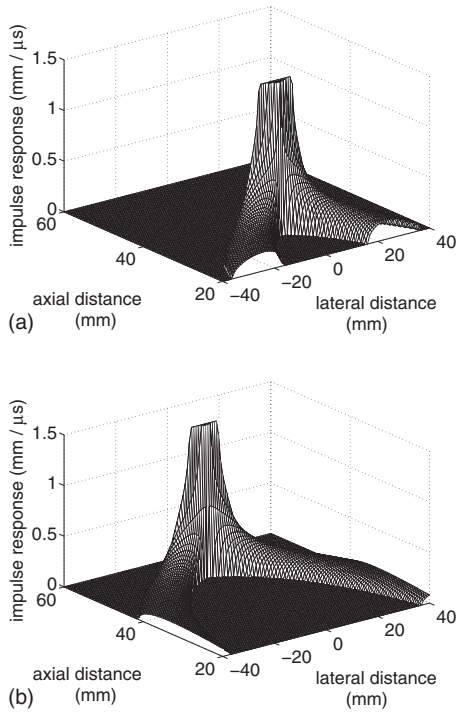

FIG. 6. Snapshots of the lossless impulse response generated by a circular piston with radius $a=10$ mm at $t=22$ μs and $t=34$ μs are displayed in panels (a) and (b). The constant amplitude component within the paraxial region $|x|<a$ represents the direct wave. The remaining component represents the edge wave generated by the discontinuity in particle velocity at $x=a$.

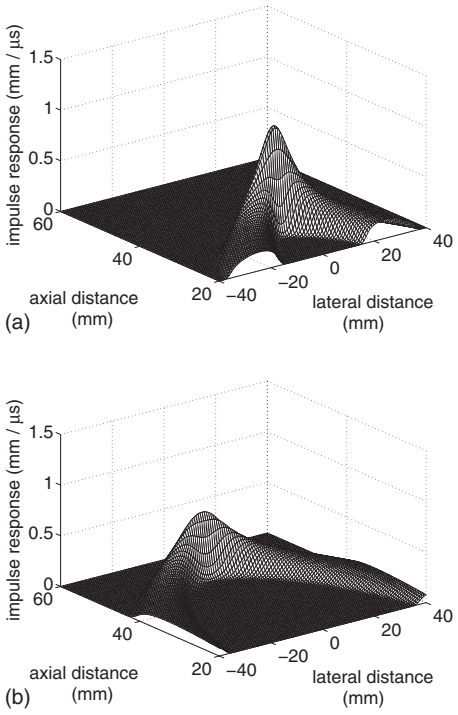

FIG. 7. Snapshots of the lossy impulse response generated by a circular piston with radius $a=10$ mm with $\gamma=0.01$ μs for $t=22$ μs and $t=34$ μs are displayed in panels (a) and (b). Unlike the lossless impulse response depicted in Fig. 6, the direct wave is attenuated due to viscous diffusion. The edge wave also experiences additional attenuation relative to Fig. 6.

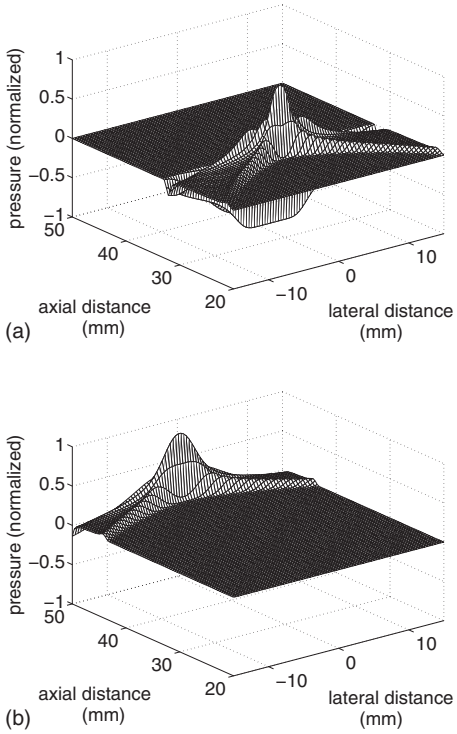

FIG. 8. Normalized velocity potential field produced by a circular piston of radius $a=10$ mm excited by a Hanning-weighted toneburst in a viscous medium with relaxation time $\gamma=0.001$ μs. Snapshots of the normalized velocity potential for $t=22$ μs and $t=34$ μs are displayed in panels (a) and (b).

ated, while the corresponding region in Fig. 7 experiences attenuation and stretching due to viscous diffusion. For increasing relaxation times, the field becomes progressively closer to that generated by an omni-directional source as the directivity of the aperture is weakened far from the source.

The near field velocity potential field generated by a piston with radius $a=10$ mm within a viscous medium with relaxation time $\gamma=0.001$ μs is displayed in Fig. 8 at two successive snapshots in time. At $t=22$ μs, distinct direct and edge waves are evident, with little apparent viscous spreading. As time increases, the edge and direct waves becomes less distinct, while spreading and attenuation due to viscous loss become more pronounced. Unlike the lossless case, the direct wave in Fig. 8 experiences a significant decrease in amplitude.

Figure 9 displays both the near field and far field lossy impulse responses for a circular piston ($a=5$ mm). Panel (a) evaluates the lossy impulse response at $r=50$ mm both on axis ($\theta=0$) and off axis ($\theta=\pi/12$ and $\phi=0$). In this region, the far field approximation differs significantly from the near field solution. Panel (b) evaluates the impulse response at $r=200$ mm both on axis ($\theta=0$) and off axis ($\theta=\pi/12$ and $\phi=0$). In this region, the far field approximation agrees with the near field solution, indicating that the simplified far field expressions accurately represent the lossy impulse response at distances far from the source.

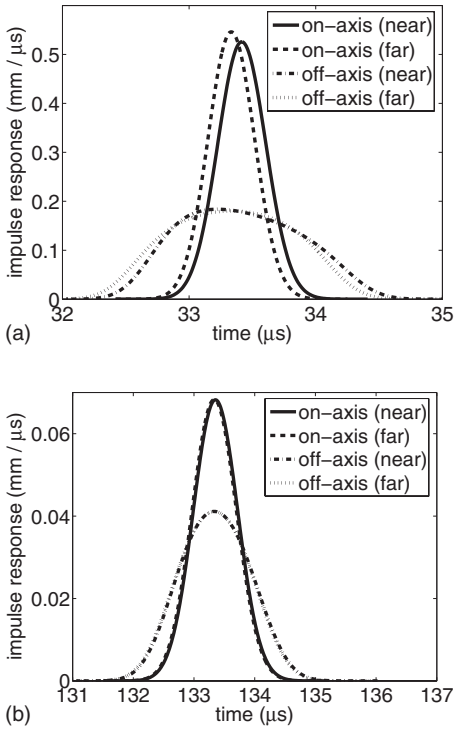

FIG. 9. Lossy impulse response for a circular piston ($a=5$ mm) and $\tau_s=0.001$ μs. In panel (a), the near field impulse response and the far field impulse response were evaluated at $r=50$ mm both on axis ($\theta=0$) and off axis ($\theta=\pi/12$ and $\phi=0$). Panel (b) shows the near field and far field impulse responses evaluated at $r=200$ mm on axis ($\theta=0$) and off axis ($\theta=\pi/12$ and $\phi=0$).

V. DISCUSSION

A. Physical interpretation

The physical interpretation of the uniformly excited circular piston discussed in Ref. 27 is also applicable to transient propagation in viscous media. Physically, the first term in Eq. (12) corresponds to the *edge wave* generated by the discontinuity at the edge of the piston, whereas the second term corresponds to the *direct wave* due to the bulk motion of the piston. In the lossless case given by Eq. (10), the direct wave contribution localized within the paraxial region of the radiator maintains a constant amplitude; however, for the lossy wave, the direct wave decays as z increases. As Fig. 6 shows, the direct and edge waves are clearly discernible in the lossless case, while Fig. 7 shows the smooth transition between edge and direct waves in the presence of loss.

Numerical evaluations of the lossy impulse response show distinct behavior within the near field, the transition region, and the far field. For the values of γ evaluated in Fig. 9, the diffraction component dominates in the near field, with only a small amount of smoothing in the vicinity of the head and tail of the response. For observation points in the transition region between the near and far fields, the effects of diffraction and loss are both apparent. In this transition region, the impulse response is both smooth and asymmetric. Finally, in the far field, the effects of viscous loss predominate, yielding increasingly symmetric and broad responses with a reduced directivity.

Large values of γ were chosen to determine the range of values for which the approximation holds. The viscous relaxation time is related to the attenuation coefficient α at a fixed frequency f via the relation[28] $\gamma=c_0\alpha/(2\pi^2 f^2)$. For instance, soft tissue at $f=3$ MHz with an attenuation coefficient of $\alpha=0.345$ cm^{-1} and sound speed $c_0=1.5$ mm/μs corresponds to $\gamma=3\times10^{-4}$ μs. Applying the error analysis developed in the Results section, R must be chosen larger than 1.5 mm to maintain less than 1% error for these parameters.

B. Implementation issues

Unlike the MIRF method and other schemes that synthesize fields in the frequency domain, the lossy impulse response solution presented here is computed directly in the time domain without inverse FFTs. Numerical inverse FFTs pose several difficulties, including (1) additional computational burden and (2) incursion of numerical error due to undersampling in the frequency domain. Since the bandwidth of the MIRF is a function of distance from the source, the Nyquist sampling frequency is a function of distance. Therefore, an efficient MIRF implementation requires multirate sampling. The lossy impulse response method eliminates these problems by replacing numerical inverse Fourier transforms that utilize a compact time-domain expression with a constant sampling rate for all observation points. In addition, computing snapshots of the impulse response at one particular point in time is particularly straightforward with the lossy impulse response method presented in Eq. (12).

C. Numerical evaluation and aliasing

As discussed in Ref. 29, evaluation of the lossless impulse response requires artificially high sampling rates in order to accommodate the discontinuities in the derivative of the impulse response, which result in large bandwidths. These discontinuities are magnified on axis and in the far field, where the lossless impulse response is represented by a short-duration rect function in the near field and a scaled delta function in the far field. However, these numerical difficulties are caused, in part, by an inaccurate physical model which assumes zero loss and viscous spreading. In reality, some loss is always present, effectively acting as a low-pass filter and removing the high-frequency components of the impulse response. This filtering effect is reflected in the lossy impulse response expressions, which are infinitely smooth, implying a Fourier transform that decays faster than $1/f^n$ for any $n>1$ where f represents the frequency.[30] In contrast, the Fourier transform of the lossless impulse response, due to discontinuities on axis, decays as $1/f$. Due to this rapid decay in the frequency domain, the lossy impulse response is bandlimited, whereas the lossless response is band unlimited. The numerical difficulties arising from the band unlimited lossless impulse response are thus eliminated by the inclusion of a loss mechanism, which effectively band limits the impulse response. Since both the the diffraction and loss components are evaluated simultaneously in the present formulation [cf. Eq. (6)], sampling errors are reduced with the lossless impulse response.

D. Other dispersive media

Since the Stokes wave equation serves as a first approximation for loss in biological tissue, more accurate models, such as power-law media,[2,15,31,32] also demand consideration. In power-law media, phase velocity is an increasing function of frequency, resulting in an asymmetric loss function function g_L. In a future effort, loss functions for power-law media will be derived, allowing the lossy impulse responses generated by various piston sources to be computed in tissue-like media. The general power-law case will utilize the same machinery as the viscous case with an altered loss function. Therefore, the main benefits of the lossy impulse response approach (no inverse FFTs, lack of aliasing, etc.) should apply in the more general power-law setting. Since all calculations are directly in the time domain, the lossy impulse response approach should provide a more intuitive solution to transient, dispersive problems. Unlike the frequency-squared case, the general loss function for power-law media cannot be approximated via a simple expression such as a Gaussian. Thus, the derivation of the impulse response for finite aperture radiators in power-law media becomes more complicated, necessitating more advanced mathematics. Nevertheless, these analytical models will facilitate validation of numerical scattering studies in linear dissipative media.[33]

VI. CONCLUSION

The lossy impulse response for a circular piston is derived by decomposing an asymptotic Green's function into diffraction and loss operators. This decomposed Green's

function relates the solutions to the Stokes wave solution and the lossless wave equation via Eq. (9), facilitating the derivation of the lossy impulse response in Eq. (12). The resulting expressions are strongly causal and straightforward to implement numerically. Equation (12) also eliminates the aliasing problems associated with the lossless impulse response. The error incurred via the approximate Green's function given by Eq. (3) is analyzed as function of relaxation time γ and distance from the source R, yielding the simple relation between γ and R for a 1% error threshold. Velocity potential computations display a significant attenuation of the direct wave within the paraxial region of the piston due to viscous diffusion. The validity of the far field expression given by Eq. (18) is also studied as a function of distance. Both the physical and numerical properties of the resulting lossy impulse responses are analyzed, revealing the critical role of dissipation in the far field.

ACKNOWLEDGMENTS

Insightful discussions with Liyong Wu, GE Medical Systems, and Thomas L. Szabo, University of Boston, are acknowledged with pleasure. This work was funded in part by NIH Grant Nos. 1R01 CA093669 and 1R21 CA121235.

APPENDIX A: DERIVATION OF THE ASYMPTOTIC GREEN'S FUNCTION

Fourier transforming Eq. (1) from the space-time domain $(\mathbf{R},t)$ to the spectral-frequency domain $(\mathbf{p},\omega)$ via the convention utilized in Ref. 5 produces

$$\left(-p^2+\frac{\omega^2}{c_0^2}-\gamma i p^2\omega\right)g_{\omega p}=-1, \tag{A1}$$

where $p=|\mathbf{p}|$ is the magnitude of the spatial frequency vector $\mathbf{p}$. Solving for $g_{\omega p}$ and performing an inverse Fourier transform over ω gives

$$g_p=\frac{1}{2\pi}\int_{-\infty}^{\infty} g_{\omega p}\exp(i\omega t)d\omega \tag{A2}$$

$$=-\frac{c_0^2}{2\pi}\int_{-\infty}^{\infty}\frac{\exp(i\omega t)}{(\omega-\omega_+)(\omega-\omega_-)}d\omega, \tag{A3}$$

where $\omega_\pm=i\gamma c_0^2p^2/2\pm c_0p\chi$ and $\chi=\sqrt{1-\gamma^2c_0^2p^2/4}$. Evaluating Eq. (A3) via contour integration yields

$$g_p(t)=\frac{c_0u(t)}{\chi p}\exp\left(-\frac{\gamma c_0^2p^2t}{2}\right)\sin(c_0p\chi t). \tag{A4}$$

The 3D Green's function is recovered via a threefold inverse Fourier transform expressed in spherical coordinates (p,θ_p,ϕ_p), giving

$$g(R,t)=\frac{1}{8\pi^3}\int_0^\infty\int_0^\pi\int_0^{2\pi} g_p(t)\exp(ipR\cos\theta_p)\times\sin\theta_p p^2d\phi_pd\theta_pdp. \tag{A5}$$

The ϕ_p integral and the θ_p integral are evaluated, yielding

$$g(R,t)=\frac{1}{2\pi^2R}\int_0^\infty p\sin(pR)g_p(t)dp. \tag{A6}$$

Inserting Eq. (A4) into Eq. (A6) and exploiting the evenness of the integrand produces

$$g(R,t)=\frac{c_0u(t)}{4\pi^2R}\int_{-\infty}^{\infty}\frac{\sin(pR)\exp\left(-\frac{\gamma c_0^2p^2t}{2}\right)\sin(c_0p\chi t)}{\chi}dp. \tag{A7}$$

Note that Eq. (A7) is an exact Fourier integral representation of the 3D Green's function. Unfortunately, this integral cannot be evaluated in closed form. However, approximating $\chi=1$ yields

$$g(R,t)=\frac{c_0u(t)}{4\pi^2R}\int_{-\infty}^{\infty}\sin(pR)\exp\left(-\frac{\gamma c_0^2p^2t}{2}\right)\sin(c_0pt)dp. \tag{A8}$$

By exploiting the cosine addition formula, the following identity is obtained:

$$\frac{1}{\pi}\int_{-\infty}^{\infty}\exp(-ap^2)\sin(Rp)\sin(bp)dp$$

$$=\frac{1}{\sqrt{4\pi a}}[\exp(-(R-b)^2/4a)-\exp(-(R+b)^2/4a)]. \tag{A9}$$

Evaluating the inverse transform of Eq. (A8) by taking $a=\gamma c_0^2t/2$ and $b=c_0t$ yields

$$g(R,t)\approx\frac{u(t)}{4\pi R\sqrt{2\pi\gamma t}}\left[\exp\left(-\frac{(t-R/c_0)^2}{2\gamma t}\right)-\exp\left(-\frac{(t+R/c_0)^2}{2\gamma t}\right)\right]. \tag{A10}$$

Physically, the first term in Eq. (A10) represents an outgoing wave, while the second term represents an incoming wave. For large times $\gamma t\gg 1$, the incoming wave is negligible, yielding Eq. (3).

APPENDIX B: DERIVATION OF LOSSLESS FAR FIELD EXPRESSION

The single-integral representation of the far field lossless impulse response function utilized in Sec. III is derived from their well-known frequency-domain counterparts. In the far field region, the impulse response is expressed via an inverse Fourier transform

$$h(r,\theta,t)=\mathcal{F}^{-1}[\hat{h}(r,\theta,\omega)]=\frac{1}{2\pi}\int_{-\infty}^{\infty}\frac{e^{ikr}}{2\pi r}D(\theta;\omega)e^{-i\omega t}d\omega, \tag{B1}$$

where $D(\theta;\omega)$ is the far-field pattern and $k=\omega/c_0$ is the (lossless) wavenumber. Equation (14) is computed via inverse Fourier transforming the classical frequency-domain result. The far field pattern is given by

$$D(\theta;\omega) = \pi a^2 \frac{2J_1(ka\sin\theta)}{ka\sin\theta}, \tag{B2}$$

where $J_1(z)$ is the Bessel function of the first kind of order 1. To invert the Bessel function in Eq. (B1), an integral representation is utilized:

$$J_n(z) = \frac{(i)^n}{\pi}\int_0^\pi \cos n\psi e^{-iz\cos\psi} d\psi. \tag{B3}$$

Inserting Eqs. (B3) with $n=1$ and (B2) into Eq. (B1) yields

$$h(r,\theta,t) = \frac{c_0 a}{\pi r\sin\theta}\mathcal{F}^{-1}\left[\frac{e^{iwr/c_0}}{-iw}\int_0^\pi \cos\psi e^{-ika\sin\theta\cos\psi} d\psi\right]. \tag{B4}$$

Noting the spectral integration and applying the shifting properties of the Fourier transform yields Eq. (14).

[1]P. He, "Simulation of ultrasound pulse propagation in lossy media obeyng a frequency power law," IEEE Trans. Ultrason. Ferroelectr. Freq. Control **45**, 114–125 (1998).
[2]R. S. C. Cobbold, N. V. Sushilov, and A. C. Weathermon, "Transient propagation in media with classical or power-law loss," J. Acoust. Soc. Am. **116**, 3294–3303 (2004).
[3]T. L. Szabo, "The material impulse response for broadband pulses in lossy media," *Proceedings of the IEEE Ultrasonics Symposium*, Honolulu, HI (2003), pp. 748–751.
[4]D. T. Blackstock, "Transient solution for sound radiated into a viscous fluid," J. Acoust. Soc. Am. **41**, 1312–1319 (1967).
[5]M. J. Buckingham, "Causality, Stokes' wave equation, and acoustic pulse propagation in a viscous fluid," Phys. Rev. E **72**, 026610 (2005).
[6]P. M. Morse and K. U. Ingard, *Theoretical Acoustics* (Princeton University Press, Princeton, NJ, 1968), pp. 270–300.
[7]P. M. Jordan, M. R. Meyer, and A. Puri, "Causal implications of viscous damping in compressible fluid flows," Phys. Rev. E **62**, 7918 (2000).
[8]R. Ludwig and P. L. Levin, "Analytical and numerical treatment of pulsed wave propagation into a viscous fluid," IEEE Trans. Ultrason. Ferroelectr. Freq. Control **42**, 789–792 (1995).
[9]G. C. Gaunaurd and G. C. Everstine, "Viscosity effects on the propagation of acoustic transients," J. Vibr. Acoust. **124**, 19–25 (2002).
[10]G.-P. J. Too, "New phenomena on King integral with dissipation," J. Acoust. Soc. Am. **101**, 119–124 (1997).
[11]P. T. Christopher and K. J. Parker, "New approaches to linear propagation of acoustic fields," J. Acoust. Soc. Am. **90**, 507–521 (1991).
[12]Y.-S. Lee and M. F. Hamilton, "Time-domain modeling of pulsed finite-amplitude sound beams," J. Acoust. Soc. Am. **97**, 906–917 (1995).
[13]J. A. Jensen, D. Gandhi, and W. D. O'Brien, "Ultrasound fields in an attenuating medium," *Proceedings of the IEEE Ultrasonics Symposium*, Baltimore, MD (1993), pp. 943–946.
[14]K. V. Gurumurthy and R. M. Arthur, "A dispersive model for the propagation of ultrasound in soft-tissue," Ultrason. Imaging **4**, 355–377 (1982).
[15]M. G. Wismer and R. Ludwig, "An explicit numerical time domain formulation to simulate pulsed pressure waves in viscous fluids exhibiting arbitrary frequency power law attenuation," IEEE Trans. Ultrason. Ferroelectr. Freq. Control **42**, 1040–1049 (1995).
[16]F. Oberhettinger, "On transient solutions of the baffled piston problem," J. Res. Natl. Bur. Stand., Sect. B **65B**, 1–6 (1961).
[17]G. R. Harris, "Review of transient field theory for a baffled planar piston," J. Acoust. Soc. Am. **70**, 10–20 (1981).
[18]J. C. Lockwood and J. G. Willette, "High-speed method for computing the exact solution for the pressure variations in the nearfield of a baffled piston," J. Acoust. Soc. Am. **53**, 735–741 (1973).
[19]J. Djelouah, N. Bouaoua, A. Alia, H. Khelladi, and D. Belgrounde, "Theoretical and experimental study of the diffraction of focused ultrasonic waves in viscous fluids," *2003 World Congress on Ultrasonics*, Paris 1347–1350 (2003).
[20]J. F. Kelly and R. J. McGough, "A time-space decomposition method for calculating the nearfield pressure generated by a pulsed circular piston," IEEE Trans. Ultrason. Ferroelectr. Freq. Control **53**, 1150–1159 (2006).
[21]D. G. Crighton, *Modern Methods in Analytical Acoustics: Lecture Notes* (Springer-Verlag, London, 1996).
[22]I. Stakgold, *Green's Functions and Boundary Value Problems*, 2nd ed. (Wiley, New York, 1998), p. 198.
[23]K. H. Lee and G. Xie, "A new approach to imaging with low frequency electromagnetic fields," Geophysics **58**, 780–796 (1993).
[24]M. Abramowitz and I. A. Stegun, *Handbook of Mathematical Functions, with Formulas, Graphs, and Mathematical Tables* (Dover, New York, 1972), pp. 295–309.
[25]P. M. Morse and K. U. Ingard, *Theoretical Acoustics* (McGraw–Hill, New York, 1968), p. 388.
[26]P. J. Davis and P. Rabinowitz, *Numerical Integration* (Academic, New York, 1975), pp. 138–140.
[27]G. E. Tupholme, "Generation of acoustic pulses by baffled plane pistons," Mathematika **16**, 209–224 (1969).
[28]L. E. Kinsler, A. R. Frey, A. B. Coppens, and J. V. Sanders, *Fundamentals of Acoustics*, 4th ed. (Wiley, New York, 2000), p. 213.
[29]D. P. Orofino and P. C. Pedersen, "Multirate digital signal-processing algorithm to calculate complex acoustic pressure fields," J. Acoust. Soc. Am. **92**, 563–582 (1992).
[30]R. N. Bracewell, *The Fourier Transform and Its Applications* (McGraw–Hill, New York, 1978), p. 144.
[31]T. L. Szabo, "Time-domain wave equations for lossy media obeying a frequency power-law," J. Acoust. Soc. Am. **96**, 491–500 (1994).
[32]N. V. Sushilov and R. S. Cobbold, "Frequency-domain wave equation and its time-domain solutions in attenuating media," J. Acoust. Soc. Am. **115**, 1431–1436 (2004).
[33]M. G. Wismer, "Finite element analysis of broadband acoustic pulses through inhomogeneous media with power law attenuation," J. Acoust. Soc. Am. **120**, 3493–3502 (2006).

An acoustical array combining microphones and piezoelectric devices

Mitsuharu Matsumoto[a] and Shuji Hashimoto[b]
Department of Applied Physics, Waseda University, 55N-4F-10A, 3-4-1 Okubo, Shinjuku-ku, Tokyo 169-8555 Japan

(Received 29 October 2007; revised 15 January 2008; accepted 15 January 2008)

This paper describes an acoustical array combining microphones and piezoelectric devices. Conventional microphone arrays have been widely utilized to realize noise reduction, sound separation and direction of arrival estimation system. However, when a conventional microphone array is mounted on a real system, such as a machine, vehicle or robot, the microphones are set extremely close to the system's actual body. In such cases, the noise from the system itself, such as motors, gears, and engines, namely *internal noise*, often becomes a troublesome problem. It is difficult to reduce internal noise utilizing a conventional microphone array because internal noise sources are extremely close to the microphones. As internal noise is not always stationary, statistically independent or sparse, most useful blind source separation approaches, such as independent component analysis and the sparseness approach, cannot be employed. Our aim is to reduce internal noise utilizing microphones and piezoelectric devices attached to the internal noise source. In this paper, a general description of the acoustical array is formulated and the characteristic features of microphones and piezoelectric devices in an acoustical array are given. An acoustical array combining microphones and piezoelectric devices is also described with some experimental results. © *2008 Acoustical Society of America.* [DOI: 10.1121/1.2871764]

PACS number(s): 43.60.Fg, 43.60.Vx, 43.60.Ac [EJS] Pages: 2117–2125

I. INTRODUCTION

The microphone array plays an important role in acoustical signal processing.[1–5] It is applicable to hearing aids,[6] speech enhancement,[7] car navigation,[8,9] robot audition,[10–12] and so on. A conventional microphone array realizes the delay-sum type microphone array,[13] the adaptive microphone array[14–16] and direction of arrival estimation such as high resolution algorithms,[17–20] by utilizing the phase difference or power difference of each microphone. However, when a conventional microphone array is mounted on a real system such as a machine, vehicle, or robot, the noise from the system itself often becomes a problem. In those cases, the noise source is extremely close to the microphones. The number of noises is not always known. Moreover, the noise is also often larger than the sound sources, because the main sound propagation path is not the air but the solid frame of the machine. For these reasons, it is difficult to reduce internal noise, such as motor noise and gear noise, from systems using only a conventional microphone array. Independent component analysis (ICA) is a blind source separation (BSS) algorithm that utilizes the statistical independence of received sounds. ICA is based on the unitary diagonalization of the whitened data covariance matrix.[21–23] There also exist some BSS algorithms that utilize higher order statistics.[24] However, as the internal noise is not always stationary or statistically independent, it is difficult to employ ICA to reduce the internal noise. ICA can also not be employed when the number of noise sources is larger than the number of the microphones. Some approaches utilize sparseness to solve the BSS problem.[25–27] Sparseness means that most of the frequency components of a signal are zero, so the sources rarely overlap in the frequency domain. Under this assumption, it is possible to extract each signal using time-frequency binary masks. However, internal noise is not always disjoint, and it is difficult to employ the sparseness approach to reduce internal noise.

To solve these problems, we look to piezoelectric devices. A piezoelectric device is a passive device that transforms the force on the device to the voltage, and vice versa, based on piezoelectric effect. In mechatronics, there has been a lot of research into controlling vibration with piezoelectric devices as actuators.[28–30] However, there is little research into applying piezoelectric devices to a microphone array to reduce internal noise. Our aim is to reduce internal noise by combining microphones and piezoelectric devices that have been attached to an internal noise source. In Sec. II, we describe a general formulation of an acoustical array in three-dimensional space and give the characteristic features of a conventional microphone array and piezoelectric devices. We give a description of the implementation based on an acoustical array combining microphones and piezoelectric devices to reduce the internal noise in Sec. III. The experimental results are demonstrated to confirm the performance of the proposed method in Sec. IV. The conclusions follow in Sec. V.

II. PROBLEM FORMULATION

A. General description

Let us consider a three-dimensional space where the coordinate is represented as (r, θ, ϕ) by a spherical polar coor-

[a]Electronic mail: matsu@shalab.phys.waseda.ac.jp
[b]Electronic mail: shuji@waseda.jp

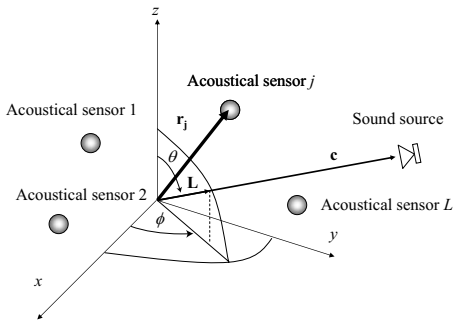

FIG. 1. General description of an acoustical array system.

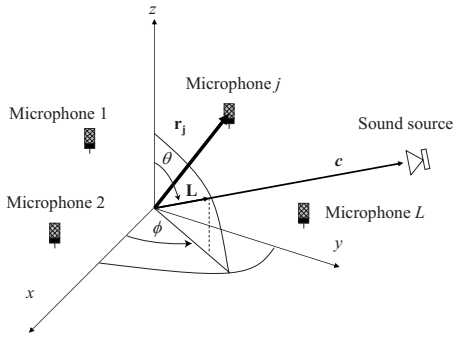

FIG. 2. A general model of a conventional microphone array.

dinate system as illustrated in Fig. 1. Let us consider a sound $s(t)$ generated at the position $\mathbf{c}=(r,\theta,\phi)$ at time t. The unit vector $\mathbf{L}(\theta,\phi)$ is described as follows:

$$\mathbf{L}(\theta,\phi)=[\sin\theta\cos\phi,\sin\theta\sin\phi,\cos\theta]^T, \tag{1}$$

where $[\cdot]^T$ represents the transpose. Let us also consider L acoustical sensors. O represents the origin. $\mathbf{r}_i=(r_i,\theta_i,\phi_i)$ represents the coordinate of the ith acoustical sensor position. According to the survey by O'Grady *et al.*, signal mixtures of an acoustical array are categorized as the instantaneous, anechoic and echoic mixings.[31] In this paper, we discuss an echoic mixing. In this case, the signal $x_i(t)$ obtained by the ith acoustical sensor can be described as follows:

$$x_i(t)=a_i(\mathbf{c})*s(t), \tag{2}$$

where the $a_i(\mathbf{c})$ represents the acoustic impulse responses from the sound source at the position $\mathbf{c}$ to the ith acoustical sensor. The asterisk represents the convolution. In frequency domain, we can describe the signal $X_i(\tau,\omega)$ obtained by the ith microphone as follows:

$$X_i(\tau,\omega)=A_i(\omega,\mathbf{c})S(\tau,\omega), \tag{3}$$

where τ and ω represent the time frame and angular frequency, respectively. $S(\tau,\omega)$ represents the signal in the frequency domain. $A_i(\omega,\mathbf{c})$ represents the transfer function from the position $\mathbf{c}$ to the ith acoustical sensor at angular frequency ω. The vector of the received sound $\mathbf{X}(\tau,\omega)$ can be expressed as follows:

$$\mathbf{X}(\tau,\omega)=\begin{bmatrix}X_1(\tau,\omega)\\X_2(\tau,\omega)\\\vdots\\X_L(\tau,\omega)\end{bmatrix} \tag{4}$$

$$=\mathbf{A}(\omega,\mathbf{c})S(\tau,\omega), \tag{5}$$

where $\mathbf{A}(\omega,\mathbf{c})$ represents the directional vector described as follows:

$$\mathbf{A}(\omega,\mathbf{c})=\begin{bmatrix}A_1(\omega,\mathbf{c})\\A_2(\omega,\mathbf{c})\\\vdots\\A_L(\omega,\mathbf{c})\end{bmatrix}. \tag{6}$$

The linear combination of the array output can be described as follows:

$$Y(\tau,\omega)=\sum_{i=1}^{L}W_i^*(\omega)X_i(\tau,\omega) \tag{7}$$

$$=\sum_{i=1}^{L}W_i^*(\omega)A_i(\omega,\mathbf{c})S(\tau,\omega) \tag{8}$$

$$=\mathbf{A}^T(\omega,\mathbf{c})\mathbf{W}^*(\omega)S(\tau,\omega), \tag{9}$$

where $[\cdot]^*$ represents the conjugate. $\mathbf{W}(\omega)$ is described as follows:

$$\mathbf{W}(\omega)=\begin{bmatrix}W_1(\omega)\\W_2(\omega)\\\vdots\\W_L(\omega)\end{bmatrix}. \tag{10}$$

Let us consider the directional distribution $D(\omega,\mathbf{c})$, which is the directivity for all the coordinates created by the optimal weight $\mathbf{W}_{\text{opt}}(\omega)$ depending on the constraint condition. $D(\omega,\mathbf{c})$ can be expressed as follows:

$$D(\omega,\mathbf{c})=\mathbf{A}^T(\omega,\mathbf{c})\mathbf{W}_{\text{opt}}^*(\omega). \tag{11}$$

The directional distribution is determined by the function $\mathbf{A}(\omega,\mathbf{c})$ and the optimal weight $\mathbf{W}_{\text{opt}}(\omega)$. As is well known, we cannot constrain all points by utilizing L acoustical sensors. We can only steer, at most, $L-1$ null points by setting the various constraints, such as sound direction, noise direction, and noise power.[13–15] In other words, the function $\mathbf{A}(\omega,\mathbf{c})$ determines the characteristic of the directional distribution and the limitation of an acoustical array.

B. Characteristic features of a conventional microphone array

Figure 2 illustrates a general model of a conventional microphone array with L microphones placed in a three-dimensional space. The following conditions are usually assumed in a conventional microphone array system:

(1) Position differences: All microphones are located at different positions.
(2) Omnidirectional microphones: The directivity of microphones is identical for all angles.

Under the previous constraints, the directional vector is usually described as follows:

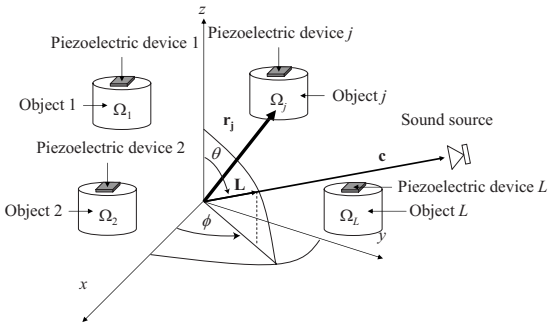

FIG. 3. A general model of piezoelectric devices.

$$A_i(\omega,\mathbf{c}) = A_i^M(\omega,\mathbf{c}) = \exp(j\Phi_i(\omega,\theta,\phi)), \tag{12}$$

where $\Phi_i(\omega,\theta,\phi)$ is described as follows:

$$\Phi_i(\omega,\theta,\phi) = \frac{\omega}{v}\mathbf{r}_i^T\mathbf{L}(\theta,\phi), \tag{13}$$

where v represents the sound velocity. As $\Phi_i(\omega,\theta,\phi)$ includes only θ and ϕ as geometric parameters, the conventional microphone array can steer the null not for the noise point but for the noise direction.

C. Characteristic features of piezoelectric devices

Figure 3 illustrates a general model of L piezoelectric devices placed in three-dimensional space. When we utilize piezoelectric devices, we attach the device to the corresponding object to directly detect object vibration. Let us consider L objects that generate sound due to their vibrations. Ω_i represents the region of the ith object. The following conditions can be assumed when piezoelectric devices are utilized:

(1) Direct detection of object vibration: The piezoelectric device directly detects the mechanical vibration of the attached object.
(2) Independence of other noise sources: The piezoelectric device does not detect object noise where it is not attached.

Under the previous constraints, the directional vector can be described as follows:

$$A_i(\omega,\mathbf{c}) = A_i^P(\omega,\mathbf{c}) = \begin{cases} \neq 0 & (\mathbf{c} \in \Omega_i) \\ =0 & (\mathbf{c} \in \neg\Omega_i), \end{cases} \tag{14}$$

where $-\Omega_i$ represents the complement of Ω_i. Due to the features of Eq. (14), we can steer the null for the noise point utilizing piezoelectric devices if we combine them with microphones. Based on the features of microphones and piezoelectric devices, we aim to enlarge the application range of the acoustical array by combining microphones and piezoelectric devices.

III. AN ACOUSTICAL ARRAY COMBINING MICROPHONES AND PIEZOELECTRIC DEVICES

When we consider noises in practical systems such as vehicles, machines, and robots, they may be categorized into two groups. One is *external noise* from the environment and the other is *internal noise*, the noise from internal systems such as engines, gears, and robot motors. Although external noise can usually be regarded as the point source of sound, it is difficult to know the number and location of noises in advance. External noise sources also often move in living space. On the other hand, although the number and location of internal noises can often be known in advance, the noise source is not always regarded as the point source of sound. Paying attention to the features of these two kinds of noise, we aim to directly reduce internal noise by using not only microphones but also piezoelectric devices. Figures 4 and 5 illustrate the basic concepts of a conventional microphone array and an acoustical array combining microphones and piezoelectric devices, respectively. As described in the previous section, we can control the null of the external noise direction by steering the null utilizing a conventional microphone array. However, we cannot control the null of an internal noise point, as illustrated in Fig. 4. To solve the problem, we aim to control the null, not only for the external noise direction by utilizing microphones, but also for the internal noise point by utilizing piezoelectric devices. The process of the algorithm is as follows:

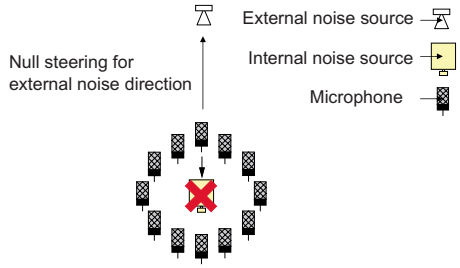

FIG. 4. (Color online) Basic concept of a conventional microphone array.

In our methods, we directly set piezoelectric devices onto noise source objects like motors and engines. Let us consider a sound, K kinds of internal noise, N kinds of external noise, and L microphones. Let us consider K objects which generate sound due to their vibrations. Ω_i represents the region of the ith object. To reduce internal noise, we also prepare K piezoelectric devices corresponding to each internal noise. We attached the piezoelectric devices to the noise sources. We modify the notation in the previous section to clarify the difference between microphones and piezoelectric devices. $s(t)$ represents the sound at the position $\mathbf{c}$. $n_j^I(t)$ and

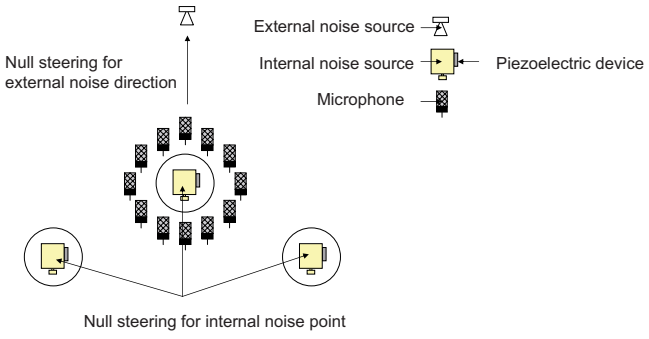

FIG. 5. (Color online) Basic concept of an acoustical array combining microphones and piezoelectric devices.

$n_k^E(t)$ represent the jth internal noise at the position $\mathbf{c}_j^I = (r_j^I, \theta_j^I, \phi_j^I)$ and the kth external noise at the position $\mathbf{c}_k^E = (r_k^E, \theta_k^E, \phi_k^E)$, respectively. The signal obtained by the ith microphone $x_i^M(t)$ can be described as follows:

$$x_i^M(t) = m_i(\mathbf{c}) * s(t) + \sum_j m_{ij}^I(\mathbf{c}_j^I) * n_j^I(t) + \sum_k m_{ik}^E(\mathbf{c}_k^E) * n_k^E(t), \tag{15}$$

where $m_i(\mathbf{c})$ is an acoustic impulse response from the signal source to the ith microphone. The $m_{ij}^I(\mathbf{c}_j^I)$ represents the acoustic impulse responses from the jth internal noise source to the ith microphone. The $m_{ik}^E(\mathbf{c}_k^E)$ is the acoustic impulse responses from the kth external noise source to the ith microphone. The signal obtained by the ith piezoelectric device $x_i^P(t)$ can also be described as follows:

$$x_i^P(t) = \sum_j p_{ij}^I(\mathbf{c}_j^I) * n_j^I(t), \tag{16}$$

where $p_{ij}^I(\mathbf{c}_j^I)$ is the acoustic impulse responses from the jth internal noise source to the ith piezoelectric device. Terms for the signal and the external noise can be omitted because of the features of piezoelectric devices. Our aim is to detect noise characteristics from the output of the piezoelectric devices. Here, we consider the problem in the frequency domain. Let us define the output vector of the microphones and piezoelectric devices $\mathbf{X}^M(\tau,\omega)$ and $\mathbf{X}^P(\tau,\omega)$ as follows:

$$\mathbf{X}^M(\tau,\omega) = [X_1^M(\tau,\omega), X_2^M(\tau,\omega), \ldots, X_L^M(\tau,\omega)]^T, \tag{17}$$

$$\mathbf{X}^P(\tau,\omega) = [X_1^P(\tau,\omega), X_2^P(\tau,\omega), \ldots, X_K^P(\tau,\omega)]^T, \tag{18}$$

where $X_i^M(\tau,\omega)$ and $X_j^P(\tau,\omega)$ represent the output signal from the ith microphone and jth piezoelectric device in the angular frequency ω at time frame τ, respectively. Also, we can express the noise vector of the internal noise and external noise $\mathbf{N}^I(\tau,\omega)$ and $\mathbf{N}^E(\tau,\omega)$ as follows:

$$\mathbf{N}^I(\omega) = [N_1^I(\tau,\omega), N_2^I(\tau,\omega), \ldots, N_K^I(\tau,\omega)]^T, \tag{19}$$

$$\mathbf{N}^E(\omega) = [N_1^E(\tau,\omega), N_2^E(\tau,\omega), \ldots, N_N^E(\tau,\omega)]^T, \tag{20}$$

where $N_i^I(\tau,\omega)$ and $N_j^E(\tau,\omega)$ represent the ith internal noise and jth external noise, respectively. The mixing vector for the signal of the microphones $\mathbf{M}(\omega)$ is defined as follows:

$$\mathbf{M}(\omega) = [M_1(\omega), M_2(\omega), \ldots, M_L(\omega)]^T \tag{21}$$

where $M_i(\omega)$ represents the transfer function from the sound to the ith microphone and is described as follows:

$$M_i(\omega) = A_i^M(\omega, \mathbf{c}) \tag{22}$$

The mixing matrices for both the internal noise and the external noise of the microphones $\mathbf{M}^I(\omega)$ and $\mathbf{M}^E(\omega)$ are defined as follows:

$$\mathbf{M}^I(\omega) = \begin{bmatrix} M_{11}^I(\omega) & \cdots & M_{1K}^I(\omega) \\ M_{21}^I(\omega) & \cdots & M_{2K}^I(\omega) \\ \vdots & & \vdots \\ M_{L1}^I(\omega) & \cdots & M_{LK}^I(\omega) \end{bmatrix}, \tag{23}$$

$$\mathbf{M}^E(\omega) = \begin{bmatrix} M_{11}^E(\omega) & \cdots & M_{1N}^E(\omega) \\ M_{21}^E(\omega) & \cdots & M_{2N}^E(\omega) \\ \vdots & & \vdots \\ M_{L1}^E(\omega) & \cdots & M_{LN}^E(\omega) \end{bmatrix}, \tag{24}$$

where $M_{ij}^I(\omega)$ and $M_{ik}^E(\omega)$ represent the transfer function from the jth internal noise source to the ith microphone and the transfer function from the kth external noise source to the ith microphone, respectively. $M_{ij}^I(\omega)$ and $M_{ik}^E(\omega)$ are described as follows:

$$M_{ij}^I(\omega) = A_i^M(\omega, \mathbf{c}_j^I), \tag{25}$$

$$M_{ik}^E(\omega) = A_i^M(\omega, \mathbf{c}_k^E). \tag{26}$$

In the same way, the mixing matrices of the internal noise $\mathbf{P}^I(\omega)$ are expressed as follows:

$$\mathbf{P}^I(\omega) = \begin{bmatrix} P_{11}^I(\omega) & \cdots & P_{1K}^I(\omega) \\ P_{21}^I(\omega) & \cdots & P_{2K}^I(\omega) \\ \vdots & & \vdots \\ P_{K1}^I(\omega) & \cdots & P_{KK}^I(\omega) \end{bmatrix}, \tag{27}$$

where $P_{ij}^I(\omega)$ represents the transfer function from the jth internal noise source to the ith piezoelectric device and is described as follows:

$$P_{ij}^I(\omega) = A_i^I(\omega, \mathbf{c}_j^I)\delta_{ij}, \tag{28}$$

where δ_{ij} represents Kronecker delta. When piezoelectric devices are utilized, the transfer function from the sound source to the piezoelectric devices and the transfer function from the external noise to the piezoelectric devices are ideally zero due to the characteristics described in Eq. (14). In the frequency domain, we can express the $K+L$ mixtures of microphones and piezoelectric devices as follows:

$$\mathbf{X}(\tau,\omega) = \mathbf{H}(\omega)\mathbf{S}(\tau,\omega), \tag{29}$$

where

$$\mathbf{X}(\tau,\omega) = \begin{bmatrix} \mathbf{X}^M(\tau,\omega) \\ \mathbf{X}^P(\tau,\omega) \end{bmatrix}, \tag{30}$$

$$\mathbf{H}(\omega) = \begin{bmatrix} \mathbf{M}(\omega) & \mathbf{M}^E(\omega) & \mathbf{M}^I(\omega) \\ \mathbf{0} & \mathbf{0} & \mathbf{P}^I(\omega) \end{bmatrix}, \tag{31}$$

$$\mathbf{S}(\tau,\omega) = \begin{bmatrix} S(\tau,\omega) \\ \mathbf{N}^E(\tau,\omega) \\ \mathbf{N}^I(\tau,\omega) \end{bmatrix}, \tag{32}$$

where $M_i(\omega)$ and $M_{ij}^E(\omega)$ vary because the positional relationship of the external noise, the microphones and the piezoelectric devices often changes in real systems. Conversely, $M_{ij}^I(\omega)$ and $P_{ij}^I(\omega)$ do not very because the positional relations among internal noise, microphones and piezoelectric devices are fixed. Therefore, $M_{ij}^I(\omega)$ and $P_{ij}^I(\omega)$ can be measured in advance, whereas $M_i(\tau,\omega)$ and $M_{ij}^E(\tau,\omega)$ cannot be measured in advance. Paying attention to the features, we define $\mathbf{W}^E(\omega)$ and $\mathbf{W}^I(\omega)$ as the weight matrices of linear transformation for reducing the external noise and the inter-

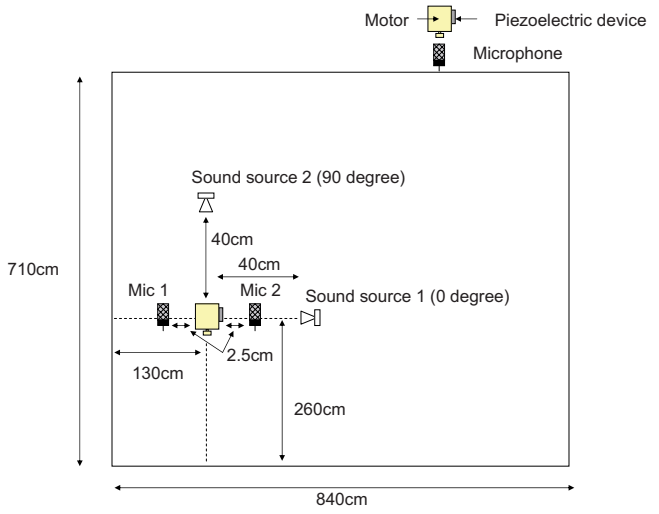

FIG. 6. (Color online) Experimental setup when we utilized two microphones and one piezoelectric device.

nal noise, respectively. The sizes of $\mathbf{W}^E(\omega)$ and $\mathbf{W}^I(\omega)$ are $(K+L)\times(K+L)$. The output vector $\mathbf{Y}(\tau,\omega)$ is described to steer the null for the internal noise point as follows:

$$\mathbf{Y}(\tau,\omega)=\mathbf{W}^E(\omega)\mathbf{W}^I(\omega)\mathbf{X}(\tau,\omega). \tag{33}$$

Hence, we first find the matrix $\mathbf{W}^I(\omega)$ as follows:

$$\mathbf{H}'(\omega)=\mathbf{W}^I(\omega)\mathbf{H}(\omega)=\begin{bmatrix}\mathbf{M}(\omega) & \mathbf{M}^E(\omega) & \mathbf{0}\\ \mathbf{0} & \mathbf{0} & \mathbf{0}\end{bmatrix}. \tag{34}$$

In other words, we set $\mathbf{W}^I(\omega)$ as

$$\mathbf{W}^I(\omega)=\begin{bmatrix}\mathbf{1} & \mathbf{0}\\ \mathbf{1} & \mathbf{0}\\ \mathbf{1} & -\mathbf{R}\end{bmatrix}, \tag{35}$$

where $\mathbf{R}=[M^I_{ij}(\omega)/P^I_{ii}(\omega)]$ and $\mathbf{1}$ represents the unit matrix. As both $M^I_{ij}(\omega)$ and $P^I_{ij}(\omega)$ are measured in advance, we can easily set $\mathbf{W}^I(\omega)$. We then optimize $\mathbf{W}^E(\omega)$ by employing various kinds of methods based on the microphone array, such as beam-forming and adaptive microphone array, ICA and sparseness approaches.

IV. EXPERIMENT

A. Experiment to confirm the robustness on the position of the microphones

We first conducted experiments to confirm whether we can reduce the noise of the microphones regardless of their position. The experimental setup is illustrated in Fig. 6. We attached a piezoelectric device (BGT-2000, Belcat) to the motor. Two microphones (RP-VC200, Panasonic) were set 2.5 cm apart from the motor. Two sound sources were set 40 cm apart from the motor in the 0° and 90° directions. The recording room was not a special room such as an anechoic room but an ordinary room in our laboratory because we aim to apply the proposed method to robots in a practical environment. The reverberation time was 207 ms. The transfer function from the motor to the piezoelectric device and to the microphones was measured using the cross-spectrum method. The transfer functions from sounds to the piezoelectric device and the microphones are unknown. As sound sources, we selected five male voices and five female voices from "Japanese Newspaper Article Sentences," edited by the Acoustical Society of Japan. We utilized the amplitude transfer characteristics in the experiments. We calculate the signal-to-noise ratio (SNR) as follows:

$$\mathrm{SNR}=10\log_{10}\frac{\Sigma_{t=0}^{T}s^2(t)}{\Sigma_{t=0}^{T}n^2(t)}, \tag{36}$$

where T represents the time length. To calculate SNR, we separately sampled $s(t)$ and $n(t)$ in the room. Noise reduction ratio (NRR) is defined as follows:

$$\mathrm{NRR}=\mathrm{SNR}_{\mathrm{after}}\text{-}\mathrm{SNR}_{\mathrm{before}}, \tag{37}$$

where $\mathrm{SNR}_{\mathrm{before}}$ and $\mathrm{SNR}_{\mathrm{after}}$ is the SNR before and after noise reduction, respectively. Tables I and II show the results of $\mathrm{SNR}_{\mathrm{before}}$, $\mathrm{SNR}_{\mathrm{after}}$, and NRR from microphones 1 and 2 when the sound was generated from 0°. Tables III and IV show the results of $\mathrm{SNR}_{\mathrm{before}}$, $\mathrm{SNR}_{\mathrm{after}}$, and NRR for microphones 1 and 2 when the sound was generated from 90 degrees. As shown in Tables I–IV, the proposed method could reduce noise by about 5 dB throughout all the experiments although the $\mathrm{SNR}_{\mathrm{before}}$ was various and the noise was sometimes extremely large.

TABLE I. NRR results regarding microphone 1 when the sound was generated from 0° in the first experiment. The noise source is a motor.

Gender	Sound	$\mathrm{SNR}_{\mathrm{before}}$ (dB)	$\mathrm{SNR}_{\mathrm{after}}$ (dB)	NRR (dB)
Male	1	6.422	11.5829	5.1609
	2	0.1751	5.2455	5.0704
	3	2.9197	8.1913	5.2716
	4	2.5161	7.4856	4.9695
	5	0.5704	5.608	5.0376
Female	6	8.7747	14.5856	5.8109
	7	6.9936	12.6984	5.7048
	8	11.7249	17.4616	5.7367
	9	6.9946	12.5627	5.5681
	10	7.154	12.8517	5.6977

TABLE II. NRR results regarding microphone 2 when the sound was generated from 0° in the first experiment. The noise source is a motor.

Gender	Sound	$\mathrm{SNR}_{\mathrm{before}}$ (dB)	$\mathrm{SNR}_{\mathrm{after}}$ (dB)	NRR (dB)
Male	1	0.1022	4.9226	4.8204
	2	−8.6535	−4.5085	4.145
	3	−5.1196	−0.3294	4.7902
	4	−4.9436	−0.3695	4.5742
	5	−7.626	−3.5132	4.1128
Female	6	1.3515	6.8181	5.4666
	7	−0.5715	5.1886	5.7601
	8	4.8225	10.5394	5.7168
	9	−0.121	5.3227	5.4437
	10	−0.3939	5.0632	5.457

TABLE III. NRR results regarding microphone 1 when the sound was generated from 90° in the first experiment. The noise source is a motor.

Gender	Sound	SNR_{before} (dB)	SNR_{after} (dB)	NRR (dB)
Male	1	8.2144	13.5877	5.3733
	2	1.6894	7.1683	5.4789
	3	4.3527	9.5377	5.185
	4	4.3316	9.2532	4.9216
	5	1.527	6.5957	5.0687
Female	6	8.3054	13.7754	5.4701
	7	2.9744	8.5008	5.5264
	8	10.0962	15.898	5.8018
	9	5.213	10.7174	5.5045
	10	9.5528	15.3111	5.7583

TABLE V. NRR results regarding microphone when the sound was generated from 0° in the second experiment. The noise source is the motor 1.

Gender	Sound	SNR_{before} (dB)	SNR_{after} (dB)	NRR (dB)
Male	1	−2.9199	0.9377	3.8576
	2	−3.1989	0.8252	4.0241
	3	−1.5203	2.5275	4.0478
	4	2.9811	7.2725	4.2915
	5	−0.5829	3.346	3.9289
Female	6	−1.1008	3.075	4.1759
	7	−0.8804	3.1668	4.0472
	8	−0.0286	4.0016	4.0302
	9	−1.5111	2.5274	4.0385
	10	1.1979	5.2324	4.0346

B. Experiment to confirm the robustness of the noise source

Next, we conducted experiments to confirm whether we could reduce the noise of the microphones regardless of the noise source. The experimental setup is illustrated in Fig. 7. We attached two piezoelectric devices (BGT-2000, Belcat) to two motors. A microphone (RP-VC200, Panasonic) was set at the center of the motors. Motor 1 was 5.0 cm apart from motor 2. Two sound sources were set 40 cm apart from the microphone in the 0° and 90° directions. The recording room was the same as the previous experiment. As sound sources, we also selected five male voices and five female voices, the same as the previous experiment. Tables V and VI show the results of SNR_{before}, SNR_{after}, and NRR regarding the microphone on noise sources 1 and 2 when the sound was generated from the 0° direction, respectively. Tables VII and VIII show the results of SNR_{before}, SNR_{after}, and NRR regarding the microphone on noise sources 1 and 2 when the sound was generated from the 90° direction. As shown in Tables V–VIII, the proposed method could also reduce noise by about 4 dB in both cases.

TABLE IV. NRR results regarding microphone 2 when the sound was generated from 90° in the first experiment. The noise source is a motor.

Gender	Sound	SNR_{before} (dB)	SNR_{after} (dB)	NRR (dB)
Male	1	11.6401	17.3126	5.6725
	2	5.2921	11.2572	5.9651
	3	5.5724	11.0729	5.5005
	4	6.8612	12.0353	5.1741
	5	3.0761	8.5696	5.4935
Female	6	11.2589	17.1217	5.8628
	7	5.8103	11.6529	5.8425
	8	13.0188	18.9333	5.9145
	9	9.9648	15.771	5.8062
	10	12.9875	18.8438	5.8563

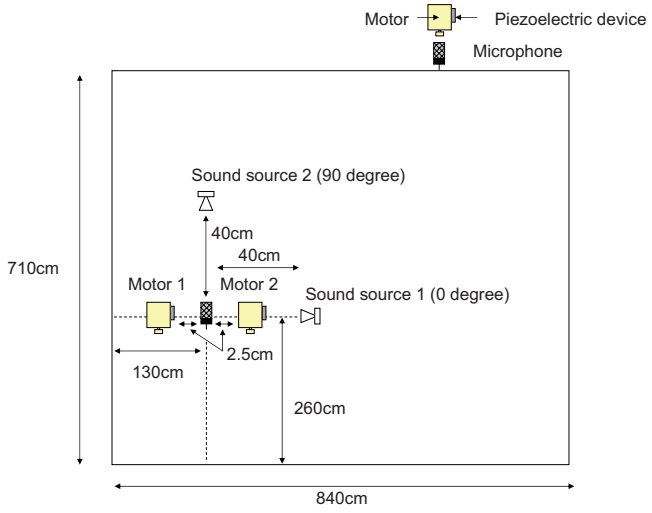

FIG. 7. (Color online) Experimental setup when we utilized one microphone and two piezoelectric devices.

TABLE VI. NRR results regarding microphone when the sound was generated from 0° in the second experiment. The noise source is the motor 2.

Gender	Sound	SNR_{before} (dB)	SNR_{after} (dB)	NRR (dB)
Male	1	−2.5248	1.2619	3.7866
	2	−2.8037	1.0958	3.8995
	3	−1.1252	2.9515	4.0766
	4	3.3762	7.7938	4.4206
	5	−0.2083	3.7511	3.9594
Female	6	−0.7057	3.5066	4.2123
	7	−0.5198	3.5795	4.0992
	8	−0.3349	4.4253	4.0904
	9	−1.116	2.9457	4.0617
	10	1.593	5.7232	4.1302

TABLE VII. NRR results regarding microphone when the sound was generated from 90° in the second experiment. The noise source is the motor 1.

Gender	Sound	SNR_{before} (dB)	SNR_{after} (dB)	NRR (dB)
Male	1	−1.4386	2.4447	3.8833
	2	−0.9323	3.0617	3.994
	3	−1.5203	3.0617	3.994
	4	3.2124	7.402	4.1896
	5	2.7256	6.7428	4.0172
Female	6	2.2119	6.3779	4.1659
	7	3.0098	7.0333	4.0234
	8	2.6385	6.6423	4.0038
	9	2.5825	6.6387	4.0562
	10	3.1966	7.2447	4.0481

TABLE VIII. NRR results regarding microphone when the sound was generated from 90° in the second experiment. The noise source is the motor 2.

Gender	Sound	SNR_{before} (dB)	SNR_{after} (dB)	NRR (dB)
Male	1	−1.2321	2.5471	3.7792
	2	−0.5788	3.6049	4.1837
	3	0.3565	4.4494	4.093
	4	3.6075	7.9494	4.3419
	5	3.0751	7.2096	4.1346
Female	6	2.5232	6.7732	4.25
	7	3.3508	7.4453	4.0945
	8	2.99	7.0795	4.0895
	9	2.9777	7.1791	4.2014
	10	3.5917	7.7957	4.204

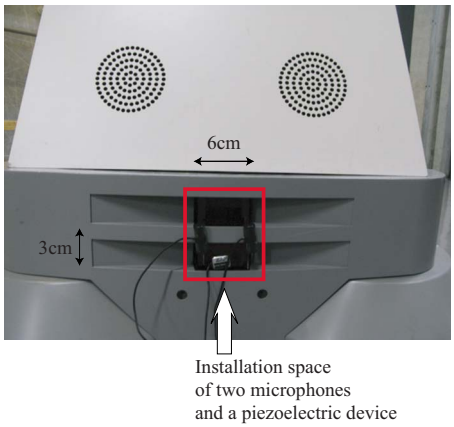

FIG. 9. (Color online) Layout of two microphones and a piezoelectric device.

C. Experiment to reduce the noise of an autonomous robot

We next conducted experiments to apply the proposed method to an actual robot. For the experiments, we utilized an autonomous mobile robot called UBIRO, which was developed in our laboratory. Figure 8 depicts UBIRO's appearance. Table IX shows UBIRO's specifications. As shown in Fig. 8, we set two microphones and a piezoelectric device on the front side of UBIRO. Figure 9 depicts the physical layout of the two microphones and the piezoelectric device on UBIRO. The piezoelectric device (BGT-2000, Belcat) was set on a photoelectronic sensor that had a motor for scanning. Two microphones (RP-VC200, Panasonic) were set 3 cm apart from the sensor. The experimental setup is illustrated in Fig. 10. The sound sources were set 40 cm apart from the motor. Sound was generated from 0° and 90°. The recording room was not a special room but an ordinary conference room. Reverberation time was 387 ms. As sound sources, we selected the same five male and five female voices that were used in the previous experiment. Tables X and XI show the results of SNR_{before} and NRR from microphones 1 and 2 when the sound was generated from 0°, respectively. Tables XII and XIII show the results of SNR_{before} and NRR for microphones 1 and 2 when sound was generated from 90°, respectively. As shown in Tables X–XIII, the proposed method could also reduce the noise about 5 dB throughout all the experiments even if we applied the proposed method to a real robot.

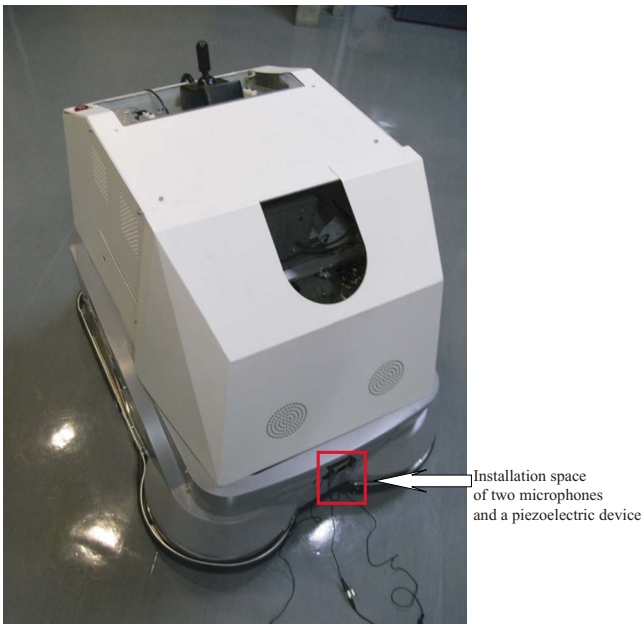

FIG. 8. (Color online) Autonomous mobile robot: UBIRO.

TABLE IX. Specification of UBIRO.

Feature	Description
Size	800 mm × 900 mm × 900 mm
Weight	90 kg
Speed	Max 6.0 km/h
Operating system	Windows XP (Pentium III 850 MHz)
Communications	Wireless LAN and RS-232C
Batteries	Two 12 V 35 Ah

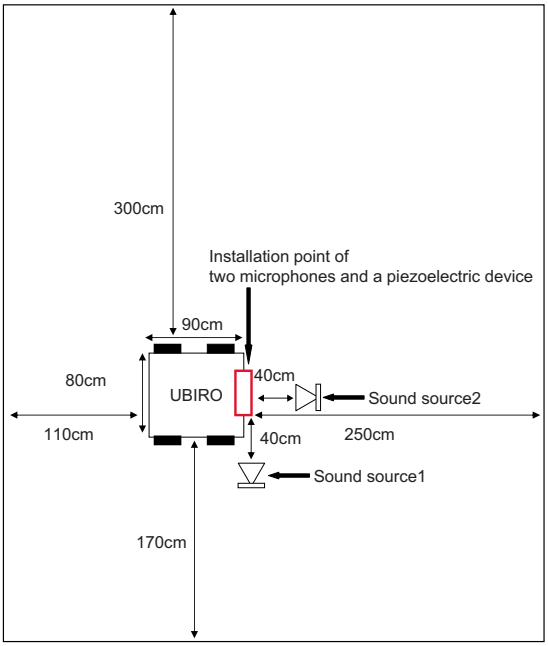

FIG. 10. (Color online) Experimental setup when we utilized two microphones and a piezoelectric device on UBIRO.

TABLE X. NRR results regarding microphone 1 when the sound was generated from 0° in the third experiment. The noise source is a photoelectronic sensor, which has a motor for scanning on UBIRO.

Gender	Sound	SNR_{before} (dB)	SNR_{after} (dB)	NRR (dB)
Male	1	−4.4724	−0.3703	4.1021
	2	−5.7224	−0.1061	5.6163
	3	−5.8685	−2.0413	3.8272
	4	−5.5692	−1.2318	4.3375
	5	−5.9978	−1.4189	4.579
Female	6	−4.9375	−0.4163	4.5212
	7	−5.1763	−0.496	4.6803
	8	−3.6958	1.391	5.0867
	9	−5.0352	−0.4156	4.6197
	10	−4.3316	0.0204	4.352

V. CONCLUSION

In this paper, we proposed an acoustical array combining microphones and piezoelectric devices. The proposed method can reduce internal noise even when the number of noises is larger than the number of microphones and piezoelectric devices. The proposed method does not conflict with conventional techniques for noise reduction. The proposed method as preprocessing of the conventional microphone array will be able to be utilized. For future works, we aim to develop a method combining the proposed method and conventional blind source separation algorithms such as ICA and sparseness approaches. The proposed method to a real robot audition and speech recognition system would also like to be applied. Noise reduction combining the proposed method and vibration control based on piezoelectric devices will also be developed. If one can measure the transfer functions accurately and they are fixed in the true sense of the term, one may be able to reduce internal noise more drastically. However, practically, the transfer functions may change a bit. The piezoelectric devices may also include some noise other than the attached noise source. To solve this problem, one needs to estimate the desired features of the piezoelectric devices and the optimal setting for microphones and piezoelectric devices.

TABLE XI. NRR results regarding microphone 2 when the sound was generated from 0° in the third experiment. The noise source is a photoelectronic sensor, which has a motor for scanning on UBIRO.

Gender	Sound	SNR_{before} (dB)	SNR_{after} (dB)	NRR (dB)
Male	1	1.1813	5.6605	4.4791
	2	−3.1725	3.3889	6.5614
	3	−3.1974	2.9294	6.1268
	4	−1.4359	4.0753	5.5112
	5	−3.9473	2.5925	6.5398
Female	6	0.146	5.4858	5.3399
	7	0.1696	5.4952	5.3256
	8	4.5977	9.3495	4.7518
	9	−0.2988	5.0759	5.3747
	10	2.685	7.5834	4.8984

TABLE XII. NRR results regarding microphone 1 when the sound was generated from 90° in the third experiment. The noise source is a photoelectronic sensor, which has a motor for scanning on UBIRO.

Gender	Sound	SNR_{before} (dB)	SNR_{after} (dB)	NRR (dB)
Male	1	−4.941	0.4962	5.4372
	2	−6.1817	−0.3721	5.8097
	3	−6.4055	−1.3825	5.023
	4	−6.286	−1.2904	4.9957
	5	−6.3836	−1.3085	5.0751
Female	6	−5.6583	−0.6783	4.98
	7	−4.4033	0.4234	4.8268
	8	−4.4996	0.2953	4.7949
	9	−5.5381	−0.5223	5.0158
	10	−4.7867	0.0847	4.8713

TABLE XIII. NRR results regarding microphone 2 when the sound was generated from 90° in the third experiment. The noise source is a photoelectronic sensor, which has a motor for scanning on UBIRO.

Gender	Sound	SNR_{before} (dB)	SNR_{after} (dB)	NRR (dB)
Male	1	−0.1355	4.7043	4.8397
	2	−4.7157	1.9586	6.6743
	3	−6.9259	1.1487	8.0746
	4	−3.0849	2.8499	5.9348
	5	−5.9942	1.2139	7.2082
Female	6	−2.9079	3.197	6.1049
	7	0.197	5.3797	5.1827
	8	0.5035	5.549	5.0455
	9	−2.2429	3.5104	5.7533
	10	−1.0728	4.411	5.4838

ACKNOWLEDGMENTS

This research was supported (in part) by a Grant-in-Aid for the WABOT-HOUSE Project from Gifu Prefecture and the 21st Century Center of Excellence Program, "Innovative research on symbiosis technologies for human and robots in an elderly dominated society," Waseda University. This research was also supported by the CREST project "Foundation of technology supporting the creation of digital media contents" of JST and a Waseda University Grant for Special Research Projects (2007B-168). This research was also supported by the research grant of Support Center for Advanced Telecommunications Technology Research (SCAT), and Project for Strategic Development of Advanced Robotics Elemental Technologies (NEDO: 06002090).

[1]K. Sasaki and K. Hirata, "3D-localization of a stationary random acoustic source in near-field by using three point-detectors," Trans. SICE **34**, 1329–1337 (1998).

[2]Y. Yamasaki and T. Itow, "Measurement of spatial information in sound fields by the closely located four point microphone method," J. Acoust. Soc. Jpn. **10–2**, 101–110 (1990).

[3]J. Huang, N. Ohnishi, and N. Sugie, "Spatial localization of sound sources: azimuth and elevation estimation," *Proceedings of the IEEE Instrumentation and Measurement Technology Conference*, 1998, pp. 330–333.

[4]H. F. Silverman, "An algorithm for determining talker location using a linear microphone array and optical hyperbolic fit," *Proceedings of the Speech and Natural Language Workshop*, 1990, pp. 151–156.

[5]S. Azuma, S. Uchikoshi, and K. Kido, "Studies on the spatial distribution of sensitivity in an arc-arrayed microphone system," J. Acoust. Soc. Jpn. **40–10**, 677–683 (1985).

[6]A. Wang, K. Yao, R. E. Hudson, D. Korompis, and F. Lorenzelli, "Microphone array for hearing aid and speech enhancement applications," *International Conference on Application-Specific Systems, Architectures, and*

Processors, 1996, pp. 231–239.
[7]H. Luts, J. Maj, W. Soede, and J. Wouters, "Better speech perception in noise with an assistive multi-microphone array for hearing aids," Ear Hear. **25**, 411–420 (2004).
[8]J. Cho and A. Krishnamurthy, "Speech enhancement using microphone array in moving vehicle environment," *Proceedings of the IEEE Intelligent Vehicles Symposium*, 2003, pp. 366–371.
[9]W. Li, C. Miyajima, T. Nishino, K. Itou, K. Takeda, and F. Itakura, "Adaptive nonlinear regression using multiple distributed microphones for in-car speech recognition," IEICE Trans. Fundamentals **E88-A**, 1716–1723 (2005).
[10]T. Nishiura, M. Nakamura, A. Lee, H. Saruwatari, and K. Shikano, "Talker tracking display on autonomous mobile robot with a moving microphone array," *Proceedings of the International Conference on Auditory Display*, 2002, pp. 244–247.
[11]J.-M. Valin, J. Rouat, and F. Michaud, "Enhanced robot audition based on microphone array source separation with post-filter," *Proceedings of the IEEE/RSJ International Conference on Robots and Intelligent Systems*, 2004, pp. 2123–2128.
[12]J. M. Valin, F. Michaud, B. Hadjou, and J. Rouat, "Localization of simultaneous moving sound sources for mobile robot using a frequency-domain steered beamformer approach," *IEEE International Conference on Robotics and Automation*, 2004, pp. 1033–1038.
[13]K. Kiyohara, Y. Kaneda, S. Takahashi, H. Nomura, and J. Kojima, "A microphone array system for speech recognition," *Proceedings of the IEEE International Conference on Acoustics, Speech, and Signal Processing*, 1997, pp. 215–218.
[14]Y. Kaneda and J. Ohga, "Adaptive microphone array system for noise reduction," IEEE Trans. Acoust., Speech, Signal Process. ASSP- **34**, 1391–1400 (1986).
[15]K. Takao, M. Fujita, and T. Nishi, "An adaptive antenna array under directional constraint," IEEE Trans. Antennas Propag. **24**, 662–669 (1976).
[16]M. Matsumoto and S. Hashimoto, "A miniaturized adaptive microphone array under directional constraint utilizing aggregated microphones," J. Acoust. Soc. Am. **119**, 352–359 (2006).
[17]J. Capon, "High resolution frequency-wavenumber spectrum analysis," Proc. IEEE **57**, 2408–2418 (1969).
[18]S. S. Reddi, "Multiple source location: A digital approach," IEEE Trans. Aerosp. Electron. Syst. **AES-15**, 95–105 (1979).
[19]R. O. Schmidt, "Multiple emitter location and signal parameter estimation," IEEE Trans. Antennas Propag. **AP-34**, 276–280 (1986).
[20]M. Matsumoto and S. Hashimoto, "Multiple signal classification by aggregated microphones," IEICE Trans. Fundamentals **E88-A**, 1701–1707 (2005).
[21]A. Belouchrani, K. Abed Maraim, J. F. Cardoso, and E. Moulines, "A blind source separation technique based on second order statistics," IEEE Trans. Signal Process. **45**, 434–444 (1997).
[22]D. Nuzillard and J. M. Nuzillard, "Second order blind source separation on the Fourier space of data," Signal Process. **83**, 627–631 (2003).
[23]K. I. Diamantaras, A. P. Petropulu, and B. Chen, "Blind two-input-two-output FIR channel identification based on frequency domain second-order statistics," IEEE Trans. Signal Process. **48**, 534–542 (2000).
[24]B. Chen and A. P. Petropulu, "Frequency domain blind MIMO system identification based on second- and higher-order statistics," IEEE Trans. Signal Process. **49**, 1677–1688 (2001).
[25]T. Ihara, M. Handa, T. Nagai, and A. Kurematsu, "Multi-channel speech separation and localization by frequency assignment," IEICE Trans. Fundamentals **J86-A**, 998–1009 (2003).
[26]S. Rickard and O. Yilmaz, "On the approximate w-disjoint orthogonality of speech," *Proceedings of the IEEE International Conference on Acoustics, Speech, and Signal Processing*, 2002, pp. 529–532.
[27]O. Yilmaz and S. Rickard, "Blind separation of speech mixtures via time-frequency masking," IEEE Trans. Signal Process. **52**, 1830–1847 (2004).
[28]T. S. Ho, H. Matsuhisa, and Y. Honda, "Passive vibration suppression of beams by piezoelectric elements," Trans. Jpn. Soc. Mech. Eng., Ser. C **66**, 737–743 (2000).
[29]K. Yamada, H. Matsuhisa, and H. Utsuno, "Hybrid vibration suppression of multiple vibrational modes of flexible structures using piezoelectric elements," Trans. Jpn. Soc. Mech. Eng., Ser. C **73**, 461–469 (2007).
[30]K. Takagi, K. Nagase, K. Oshima, Y. Hayakawa, and H. Ichikawa, "Optimization of passive piezoelectric shunt damping based on the robust performance index," Trans. Jpn. Soc. Mech. Eng., Ser. C **69**, 3183–3190 (2003).
[31]P. D. O'Grady, B. A. Pearlmutter, and S. T. Rickard, "Survey of sparse and non-sparse methods in source separation," Int. J. Imaging Syst. Technol. **15**, 18–33 (2005).

Bending wavelet for flexural impulse response

Richard Büssow[a)]
Einsteinufer 25, 10587 Berlin, Germany

(Received 5 October 2007; revised 30 January 2008; accepted 31 January 2008)

The work addresses the definition of a wavelet that is adapted to analyze a flexural impulse response of a beam or plate that can be modeled with the Euler–Bernoulli bending theory. The wavelet gives the opportunity to directly analyze the dispersion characteristics of a pulse. The aim is to localize a source or to measure material parameters. An overview of the mathematical properties of the wavelet is presented. An algorithm for the optimal extraction of the dispersion characteristics with the use of genetic algorithms is outlined. The application of the wavelet is shown in an example and experiment. © *2008 Acoustical Society of America.* [DOI: 10.1121/1.2885746]

PACS number(s): 43.60.Hj, 43.60.Jn [EJS] Pages: 2126–2135

I. INTRODUCTION

The Morlet wavelet transform is a method for time-frequency analysis. Its application for acoustic signals can be found in several publications. These publications deal, for example, with the analysis of dispersive waves,[1,2] source or damage localization,[3–7] investigation of system parameters[8,9] or active control.[10] A comparison of the short time Fourier transform and the Morlet wavelet transform is done by Kim and Kim.[11] It is found that the continuous wavelet transform (CWT) of acoustic signals is a promising method to obtain the time-frequency energy distribution of a signal. These applications are based on the evaluation of the frequency dependent arrival time of a pulse in a dispersive media.

An adjacent application is the construction of contact sensitive devices[12,13] with the dispersive signal technology.

The underlying concept of this method will be briefly explained for a one-dimensional structure (e.g., a beam). Nevertheless, the method was also sucessfully applied by the author to a plate. The additional step is that the two-dimensional source position has to be calculated from at least two observer positions and the two distances that were obtained in the same way as explained here.

A fundamental difference between most waveforms in structures and fluids is the dispersion. A pulse propagating in a structure with the frequency dependent group velocity c_g changes its shape. Due to this dispersion the pulse is not recognizable with correlation techniques that can be useful for locating airborne sound sources.[14]

The wavelet transform is very useful to extract exactly the arrival time t_a of a pulse in a dispersive media

$$t_a = x/c_g, \tag{1}$$

where x is the distance. The continuous wavelet transform W_ψ^y of a function y is

$$W_\psi^y(a,b) = \frac{1}{\sqrt{c_\psi |a|}} \int_{-\infty}^{\infty} y(t)\psi^*\left(\frac{t-b}{a}\right)dt, \tag{2}$$

where $(.)^*$ denotes the complex conjugate. A useful wavelet in this context is the Morlet wavelet, that is defined as

$$\psi(t) = e^{-\beta t^2/2} e^{j\omega_0 t} \tag{3}$$

and $c_\psi = \sqrt{\pi/\beta}$. The analog to the spectrogram or power density is the scalogram or energy density defined as

$$|W_\psi^y(a,b)|^2. \tag{4}$$

It can be shown that for a fixed scaling parameter a the arrival time t_a is the point in time where the maximum of the scalogram occurs

$$max(|W_\psi^y(a,b)|^2) = |W_\psi^y(a,b=t_a)|^2. \tag{5}$$

To locate a source one needs

1. the point in time the pulse occurred, the group velocity and a sensor, or
2. two sensors, or
3. one sensor measuring two distinguishable wave types.[15]

If the position of the source is known, it is possible to extract material parameters.[8,9]

To improve this method, dispersion based transforms have been proposed,[16,17] which is based on a method called Chirplet transform.[18,19] These transforms improved the analysis. Nevertheless, the bending wavelet that is presented is a new approach.

Here a different wavelet suitable for bending waves which can be modeled with the Euler beam theory is presented.

The underlying concept is not to measure the arrival time but to extract directly the so-called dispersion factor of the pulse. The dispersion of the pulse depends on the distance between source and receiver and the material properties. If it is possible to extract exactly the spreading of the pulse one has directly the distance or the material properties, depending on which is known. To define a wavelet that extracts the dispersion characteristics it is necessary to know the impulse response function in the time domain. For plates

[a)]Author to whom correspondence should be addressed. Present address: Institute of Fluid Mechanics and Engineering Acoustics, Berlin University of Technology; Electronic mail: richard.buessow@tu-berlin.de.

 0001-4966/2008/123(4)/2126/10/$23.00 © 2008 Acoustical Society of America

which can be modeled with the Euler beam theory this function is derived first by Boussinesq[20] and can be found in textbooks.[21] For beams it is treated in the Appendix since only the Green's functions for a initial deflection and velocity are found in the literature.[22,23]

The velocity $v(r,t)$ resulting from the bending wave propagation on a infinite plate of a force impulse $F_a(t) = F_0\delta(t)$ at $r=0$ is

$$v(r,t) = \frac{F_0}{4\pi t\sqrt{B'm''}} \sin\left(\frac{r^2}{4\zeta t}\right), \tag{6}$$

where r is the distance from the source, $\zeta = \sqrt{B'/m''}$, bending stiffness $B' = Eh^3/(12(1-\nu^2))$, E the elastic or Young's modulus, h the plate thickness, ν the Poisson's ratio and m'' the mass per unit area.

The bending wave velocity $v(x,t)$ on an infinite beam, resulting in a force impulse $F_a(t) = F_0\delta(t)$ at $x=0$ is given by

$$v(x,t) = \frac{F_0}{m'}\sqrt{\frac{2}{\pi\zeta t}} \cos\left(\frac{x^2}{4\zeta t}\right), \tag{7}$$

therein x is the distance from the source, $\zeta = \sqrt{B/m'}$, where B is the bending stiffness of the beam and m' mass per unit length.

The term

$$d_i = \frac{x^2}{4\zeta} \tag{8}$$

is the factor that controls this spreading and is called the dispersion factor. Whereas the dispersion factor is a time value the non-dimensional term

$$Di = \frac{x^2 f_{max}}{4\zeta}, \tag{9}$$

is called the dispersion number. The applicability of the following method depends on the dispersion number. Higher dispersion numbers result in a longer useful time period and this case is better to analyze. An exact quantification is given in the following, Eq. (30). A high dispersion number is the reason for choosing a thin plate and a slender beam.

In the following a new adapted wavelet will be derived to extract the dispersion factor from the measured pulse. Usually a wavelet is designed to localize a certain frequency. On the contrary, the proposed wavelet localizes a frequency range that is distributed over the wavelet length just like Eqs. (6) or (7). Such a choice follows the paradigm of signal processing, that "the analysing function should look like the signal."

One may interpret the continuous wavelet transform as a cross correlation of y and ψ. Hence, the idea is to find the function which is highly correlated with the impulse response. The difference is the role of the scaling parameter a. It is vital to produce the presented results to use the scaling parameter as it is defined in Eq. (2).

The dispersion factor is determined by the scaling factor with the highest value of the scalogram. In principle this can be done with a fine grid of (a,b) values. A more efficient way is to use an optimization scheme. Gradient based optimization is not reliable in finding a global optimum. A second problem is the localization of several overlapping pulses. A well known method that is able to fulfill these requirements is the use of genetic algorithms.

II. BENDING WAVELET

Several different definitions based on the Morlet wavelet and the Chirplet transform[18,19] have been investigated. Please note that the Chirplet transform cannot be used directly since the functions[18,19] describe a linear chirp, whereas the flexural impulse response is a $1/t^2$ chirp, as will be explained in Sec. II D. For brevity an extensive discussion about the different efforts is omitted, but can be found in the author's Ph.D. thesis.[24] The details of the mathematical background of the wavelet transform can be found in the literature.[25,26] The section begins with the definition of a wavelet with compact support and zero mean. It follows a comment on the amplitude and frequency distribution and ends with possible optional definitions.

A. Definition

The mother wavelet

$$\psi_s(t) = \begin{cases} \dfrac{\sin(1/t)}{t} & \text{for } t_{min} < t < t_{max} \\ 0 & \text{otherwise} \end{cases} \tag{10}$$

is called bending wavelet.

A wavelet ψ must fulfill the admissibility condition

$$0 < c_\psi = \int_{-\infty}^{\infty} \frac{|\hat{\psi}(\omega)|^2}{|\omega|} d\omega < \infty, \tag{11}$$

where $\hat{\psi}(\omega)$ is the Fourier transform of the wavelet. The proposed wavelet (10) has a compact support (t_{min}, t_{max}), which means that the admissibility condition is fulfilled if

$$\int_{t_{min}}^{t_{max}} \psi(t)dt = 0 \tag{12}$$

holds. To fulfill the admissibility condition t_{min} and t_{max} are defined so that Eq. (12) holds. With the integral-sine function $\mathrm{Si}(x) = \int_0^x \sin(t)/t dt$ one finds that

$$\int_{t_{min}}^{t_{max}} \frac{\sin(1/t)}{t} dt = \mathrm{Si}\left(\frac{1}{t_{max}}\right) - \mathrm{Si}\left(\frac{1}{t_{min}}\right). \tag{13}$$

Since $\lim_{t\to 0} \mathrm{Si}(1/t) = \pi/2$ and that the Si function for $t < 2/\pi$ oscillates around $\pi/2$, one is able to choose t_{min} and t_{max} so that

$$\mathrm{Si}(1/t_{min}) = \mathrm{Si}(1/t_{max}) = \pi/2. \tag{14}$$

This is a very easy option to define a wavelet and it will be used later to define similar wavelets. Equation (14) can only be solved numerically so a good approximation should be used that leads to a simple expression for c_ψ. The support of the wavelet is defined by

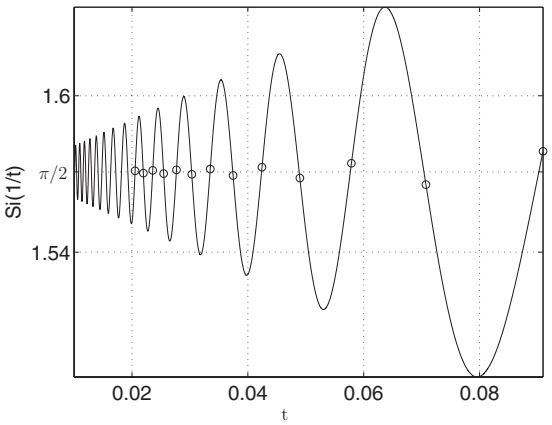

FIG. 1. Si$(1/t)$ and circles at possible values of t_{min} and t_{max}.

$$\frac{1}{t_{min}} = \frac{(2n_{max}-1)\pi}{2}, \quad \frac{1}{t_{max}} = \frac{(2n_{min}-1)\pi}{2}. \tag{15}$$

The function Si$(1/t)$ and proposed possible values of t_{min} or t_{max} are plotted in Fig. 1. In the worst case for $t_{max}=2/\pi$ and $t_{min}\to\infty$ the difference in Eq. (12) is around 0.2, but for higher values of n_{min} the magnitude is in the order of other inaccuracies (like the effect of the sampling), so that it should be negligible. Like the Morlet wavelet, which fulfills the admissibility condition in an asymptotic sense the bending wavelet fulfills the admissibility for $\lim t\to 0$. The value of the constant is calculated c_ψ with the norm in the Lebesgue space L^2 of square integrable functions

$$\|\psi(t)\|_2 = \left(\int_{-\infty}^{\infty} \psi(t)^2 dt\right)^{1/2}. \tag{16}$$

The integral in Eq. (16) is

$$\int_{t_{min}}^{t_{max}} \sin(1/t)^2/t^2 dt = \frac{1}{4}\left(\frac{2}{t_{min}} - \frac{2}{t_{max}} - \sin\left(\frac{2}{t_{min}}\right) + \sin\left(\frac{2}{t_{max}}\right)\right). \tag{17}$$

With the proposed choice of t_{min} and t_{max}, the sine vanishes and a normalized $\|\psi(t)\|_2=1$ wavelet is obtained if c_ψ is chosen to be

$$c_\psi = \frac{1}{2}\left(\frac{1}{t_{min}} - \frac{1}{t_{max}}\right) = \frac{\pi}{2}(n_{max}-n_{min}). \tag{18}$$

B. Complex bending wavelet

Wavelets that are defined by real functions have the property that the scalogram depends on the phase of the analyzed function. Wavelets that are complex functions as e.g., the Morlet wavelet, are called displacement invariant. A wavelet

$$\psi = \psi_c + i\psi_s \tag{19}$$

that consists of a sine, ψ_s Eq. (10), and a cosine wavelet which is

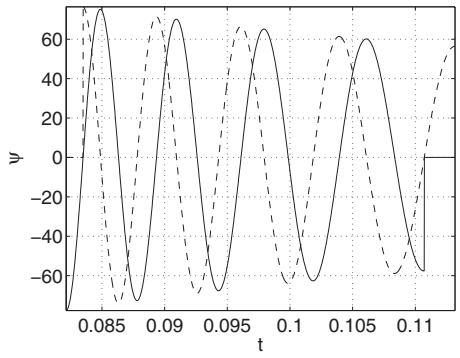

FIG. 2. Real (solid) and imaginary part (dashed) of the complex bending wavelet equation (19) with $a=8$, $n_{min}=23$, $n_{max}=31$.

$$\psi_c(t) = \begin{cases} \dfrac{\cos(1/t)}{t} & \text{for } t_{min} < t < t_{max} \\ 0 & \text{otherwise} \end{cases}. \tag{20}$$

can be beneficial. With the integral-cosine function $\mathrm{Ci}(x) = \int_0^x \cos(t)/t dt$ one finds that

$$\int_{t_{min}}^{t_{max}} \frac{\cos(1/t)}{t} dt = \mathrm{Ci}\left(\frac{1}{t_{max}}\right) - \mathrm{Ci}\left(\frac{1}{t_{min}}\right). \tag{21}$$

The analogous definition of the value $\pi/2$ for the Ci function is

$$\mathrm{Ci}(1/t_{min}) = \mathrm{Ci}(1/t_{max}) = 0. \tag{22}$$

The approximation is given by

$$\frac{1}{t_{min/max}} = n_{max/min}\pi. \tag{23}$$

The integral in Eq. (16) is for the cosine wavelet

$$\int_{t_{min}}^{t_{max}} \cos(1/t)^2/t^2 dt = \frac{1}{4}\left(\frac{2}{t_{min}} - \frac{2}{t_{max}} - \sin\left(\frac{2}{t_{max}}\right) + \sin\left(\frac{2}{t_{min}}\right)\right). \tag{24}$$

With the proposed choice of t_{min} and t_{max}, the same value of c_ψ as in Eq. (18) is obtained.

The effect is that the real and the imaginary part of the resulting wavelet do not share the same support. This is an awkward definition of a mother wavelet but the difference between the two supports is rather small if the same value for $n_{max/min}$ is used, as in Fig. 2. To keep things simple only the real valued sine wavelet is used in following.

C. Orthogonality of the bending wavelet

The trigonometric functions that are used for the Fourier transform establish an orthogonal base. Hence, the Fourier transform has the convenient characteristic that only one value represents one frequency in the analyzed signal. Every deviation of this is due to the windowing function that is analyzed with the signal. Already the short time Fourier transform is not orthogonal, if the different windows overlap each other. Because of this overlap the continuous wavelet

transform cannot be orthogonal. The proposed wavelet should still be investigated since it is instructive for the interpretation of the results.

The condition for an orthogonal basis in Lebesgue space L^2 of square integrable functions is

$$(\psi_j, \psi_k) = \int_{-\infty}^{\infty} \psi_j \psi_k = \delta_{jk}. \tag{25}$$

Two different wavelets ψ_j and ψ_k can be obtained by using different scaling parameters a and/or different displacement parameters b. Here the effect of two scaling parameters is investigated, so the following integral is to be solved:

$$\int \frac{a_j a_k}{t^2} \sin\left(\frac{a_j}{t}\right) \sin\left(\frac{a_k}{t}\right) dt = \frac{a_j a_k}{a_k^2 - a_j^2} \left[a_j \cos\left(\frac{a_j}{t}\right) \sin\left(\frac{a_k}{t}\right) - a_k \cos\left(\frac{a_k}{t}\right) \sin\left(\frac{a_j}{t}\right) \right]. \tag{26}$$

One finds with Eqs. (26) and (10) that

$$\int_{-\infty}^{\infty} \psi_s\left(\frac{t}{a_j}\right) \psi_s\left(\frac{t}{a_k}\right) dt = \frac{a_j a_k}{a_k^2 - a_j^2} \left[a_j \cos\left(\frac{a_j}{t}\right) \sin\left(\frac{a_k}{t}\right) - a_k \cos\left(\frac{a_k}{t}\right) \sin\left(\frac{a_j}{t}\right) \right] \Bigg|_{t_{min}}^{t_{max}}. \tag{27}$$

The sine term in Eq. (27) vanishes since $t_{min/max}$, also scale with a, but actually there are two different values of a and so not all four sine terms vanish. With this result one expects a rather broad area in (a,b) with high values of the scalogram. To illustrate the integral, two different versions of the wavelet are plotted in Fig. 3.

D. Time amplitude/frequency distribution

The time-frequency distribution of the wavelet for a certain scaling factor a is determined by the argument of the sine function. The instantaneous frequency $\omega(t)$ can theoretically be obtained with a relationship for almost periodic functions, see Bochner.[27] The actual frequency of the wavelet is given by

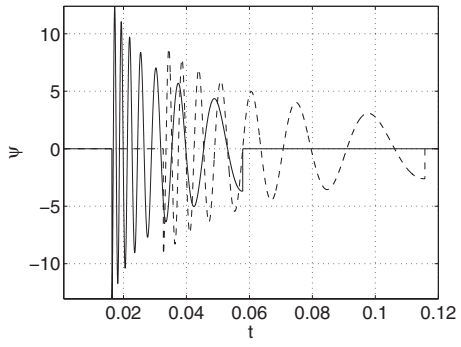

FIG. 3. Bending wavelet (10) for $a_1=1$ (solid) and $a_2=2$ (dashed), $n_{min}=6$ and $n_{max}=20$.

$$\sin(\varphi(t)) \rightarrow \omega(t) = \varphi'(t) = \frac{a}{t^2}. \tag{28}$$

With this result one finds that the highest and lowest frequency of the wavelet is given by

$$f_{max} = \frac{a}{2\pi t_{min}^2}, \quad f_{min} = \frac{a}{2\pi t_{max}^2}. \tag{29}$$

The $1/t$ leading term affects the amplitude of the wavelet. Usually it is desired that the whole signal contributes linearly to the transform. To achieve this it is useful to have an amplitude distribution over time of the wavelet that is reciprocal to the amplitude distribution of the analyzed signal. Since the bending wavelet has the same amplitude distribution as Eq. (6) this may lead to stronger weighting of the early high frequency components of the impulse response.

A force impulse that compensates the amplitude distribution of the impulse response follows a $\sim 1/\omega^2$ dependence.

III. CONTINUOUS WAVELET TRANSFORM WITH THE BENDING WAVELET

The application in the given context is to extract precisely the scaling factor with the highest value. How this is achieved will be discussed in the next section. Here the realization of a transform with a set of scaling factors is presented since it is illustrative.

The algorithm implementing the continuous wavelet transform with the bending wavelet can not be the same as the algorithm implementing a transform with any continuous wavelet, like the Morlet wavelet. The bending wavelet has a compact support, which must be defined prior to the transform. This can be done with an estimation of the frequency range and the dispersion number. With the Eqs. (15) and (29) it holds that $n \approx \sqrt{2 f d_i/\pi} + 1/2$ and so a choice of the support that always excludes f_{min} and f_{max} and guarantees that $n_{max} > n_{min}$ is

$$n_{max} = \text{floor}\left(\sqrt{\frac{2 d_i f_{max}}{\pi}} + \frac{1}{2} \right)$$

$$n_{min} = \text{ceil}\left(\sqrt{\frac{2 d_i f_{min}}{\pi}} + \frac{1}{2} \right), \tag{30}$$

where floor(·) rounds down towards the nearest integer and ceil(·) rounds up. Please note that the definition of $n_{max/min}$ gives the support of the wavelet. In principle the support is abitrary, but to obtain useful results it should match as well as possible the user defined values of $f_{min/max}$.

The knowledge of a useful frequency range should not provide any problems. But to have to know beforehand which dispersion number will dominate the result is rather unsatisfactory. A more practical solution is to calculate the corresponding n value within the algorithm, which is an easy task since $a=d_i$. The problem with this possibility is that the support of the wavelet changes within the transform. Since the support is part of the wavelet this means that strictly one compares the results of two different wavelets. Since the wavelet is normalized the effect is rather small, but nevertheless it should be interpreted with care.

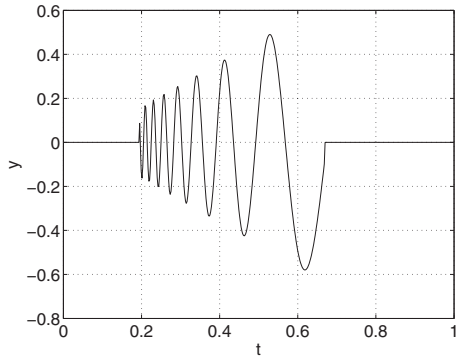

FIG. 4. Analyzed example function (31).

Example

To illustrate the use of the proposed wavelet the following function is transformed:

$$y(t) = \begin{cases} t\sin(a/t), & \text{for } t_{min} < t < t_{max} \\ 0 & \text{otherwise,} \end{cases} \tag{31}$$

with $a=10$. The sampling frequency is $f_s=1/\Delta t=2^9$, t_{min} and t_{max} are defined by the corresponding values of $f_{max}=f_s/8$ and $f_{min}=4$, for convenience the point $t=t_{min}$ is shifted to $100\Delta t$. The example function in Eq. (31) is plotted in Fig. 4.

The example function is transformed with the algorithm that calculates n_{min} and n_{max} with the corresponding value of f_{max}, f_{min} and a. The choice of the frequency range is critical. If it is too small, information will be lost and if it is too big the parts that overlap the pulse may distort the result. Here the same frequency range as the analyzed function is used.

The resulting scalogram is not plotted directly against the factor b, but shifted with the value of t_{min}. This means that the maximum value is at $100\Delta t$ (Fig. 5), which is the value of t where f_{max} is located. The maximum value is shifted when $f_{max}=f_s/12$ is used, as can be seen in Fig. 6.

One may recognize that there are very high values if the wavelet is shifted and scaled along the curve a/t. This is expected theoretically, as discussed in Sec. II C and can be

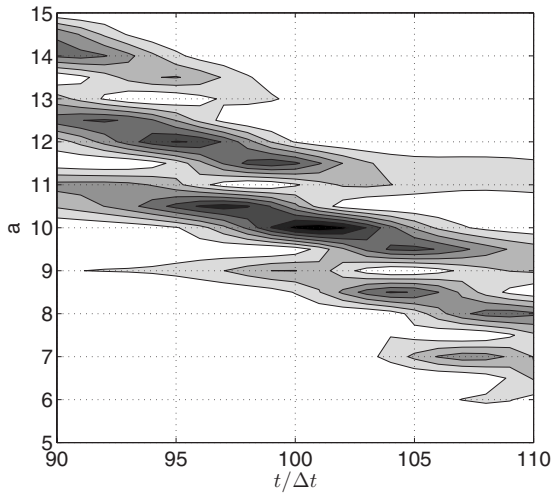

FIG. 5. Contour plot of the scalogram build with the bending wavelet transform of equation (31) with $f_{max}=f_s/8$ and $f_{min}=4$.

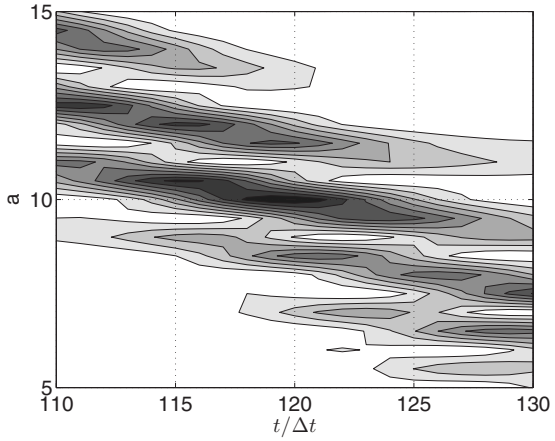

FIG. 6. Contour plot of the scalogram build with the bending wavelet transform of equation (31) with $f_{max}=f_s/12$ and $f_{min}=4$.

interpreted descriptive since the wavelet does not localize one frequency, but has a wide frequency range that spreads over time. It can be quantified with Eq. (25). Evaluating this integral numerically for the values of $a_1=10$, $a_2=11.75$ and $b_2=7\Delta t$ results in value of 0.68, which means that the peak at $a_2=11.75$ has 68% of the peak at $a_1=10$.

This problem of non-orthogonality is addressed by the following algorithm. The pulse is extracted from the signal by first locating the position t_{start} in the signal, where f_{max} has its maximum. This is done by a Morlet wavelet transform with which one may find the value of t_{start} that has the highest value of f_{max}. Now the transformation with the bending wavelet is only done in the vicinity of t_{start}. Technically the displacement parameters b are defined with t_{start}.

IV. LOCALIZATION WITH A GENETIC ALGORITHM

Genetic algorithms (GAs) form a particular class of evolutionary algorithms that use techniques inspired by evolutionary biology such as inheritance, mutation, selection, and crossover. Genetic algorithms are categorized as global search heuristics. Details of the method can be found in the extensive literature, e.g., Ref. 28.

The genetic algorithm is chosen, since it is usually very reliable in finding a global optimum and its ability to find Pareto optimums to locate several pulses. However, the drawback is the slow convergence, that can be improved with a local search method. Recent publications on this topic are shown in Refs. 29 and 30.

The implementation is done with functions provided by the open source MATLAB toolbox,[31] if not stated otherwise. Principally possible but not used in the example is the localization of two pulses that are overlapping. For the sake of brevity a discussion on how this can be achieved will be omitted. The algorithm works with two variables, the displacement parameter and the scaling factor of the bending wavelet.

The displacement parameter is defined by $t_{start}\pm\lambda/2$, with $\lambda=1/f_{max}$, or smaller values. This depends on the size of the Morlet wavelet. For discrete functions it is an integer value but nevertheless implemented as a floating point number, because of lacking support for such a combination in the

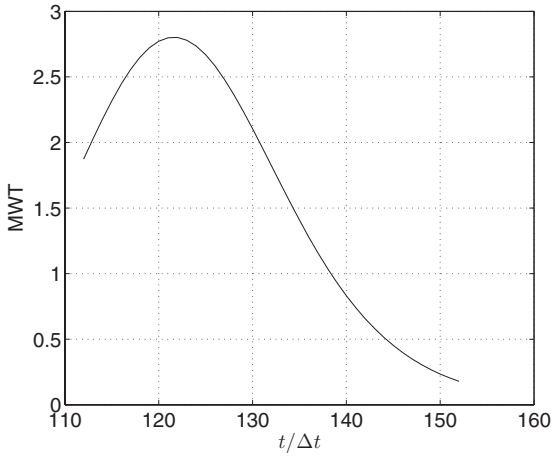

FIG. 7. Morlet wavelet transform of equation (31) with $f=f_s/12$.

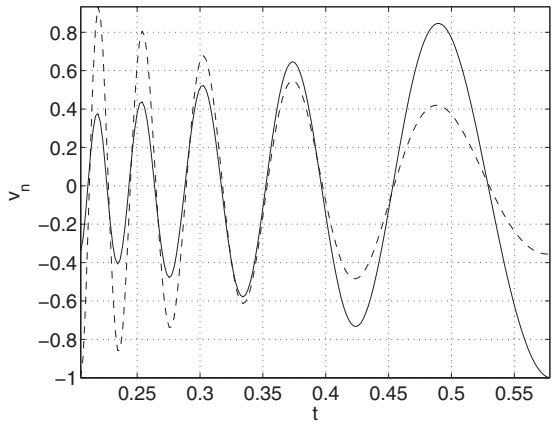

FIG. 8. Bending wavelet at $a=9.99$ and the example function.

toolbox. This fact is taken into account when calculating the wavelet transform. A pseudo code that describes the genetic algorithm can be found in Appendix B.

In the end only the fittest individual is extracted. The algorithm is usually quite reliable. Since it is a stochastic method, it can be beneficial to restart the whole process or to work with several sub populations.

Example

As an example, the already transformed Eq. (31) is investigated. The frequency range is the same as the example plotted in Fig. 6. As a first step the value t_{start} is calculated with a Morlet wavelet transform at $f_s/12$. The result is plotted in Fig. 7, where the maximum is at $t_i=122$. From Fig. 6 one may conclude that the correct value is 120. This slight deviation is due to the fact that the Morlet wavelet has a rather broad frequency resolution and the amplitude of the signal is increasing with time. If the signal $\sin(a/t)/t$ is used, the maximum is located at 118. The number of individuals is chosen to 100 and the number of generations to 400.

The initial chromosome has a time index range of (106, 138) which is $3/4\lambda$ and the range of the scaling factor is (5, 15). The obtained scaling factor is $a=9.99$. The frequency range of the bending wavelet (4.756, 37.7) follows with Eq. (29). The range is shorter than the given values $f_{min}=4$ and $f_{max}=f_s/12=42.7$, this due to Eq. (30). The wavelet with the best scaling factor and the example function on the support of the wavelet are plotted together in Fig. 8. One may recognize that the frequency-time distributions of both functions match. As discussed in Sec. II D the different amplitude distributions have only a minor effect.

V. TRANSFORMATION WITH THE COMPLEX BENDING WAVELET

In the previous examples the sine bending wavelet was used. The transform with the complex bending wavelet is similar. The support of the cosine wavelet is given with Eq. (23) and the integer values of

$$n_{min/max} \approx \sqrt{\frac{2d_i f_{min/max}}{\pi}}. \tag{32}$$

In practice this is achieved by using the same value for the cosine and the sine term by applying

$$n_{max} = \text{round}\left(\sqrt{\frac{2d_i f_{max}}{\pi}}\right)$$

$$n_{min} = \text{ceil}\left(\sqrt{\frac{2d_i f_{min}}{\pi}}\right), \tag{33}$$

where round $(\cdot)$ gives the next integer value, whereas the definition of n_{max} is equal to Eq. (30). The value of n_{min} can be lower, but Eq. (30) could result in quite high differences.

To visualize the complex wavelet the value W_ψ^y is divided in amplitude and phase

$$\mathcal{W}_\psi^y = |\mathcal{W}_\psi^y| e^{i\alpha}. \tag{34}$$

The wavelet is plotted using

$$v(t) = \frac{1}{t}\cos\left(\frac{d_i}{t} - \alpha\right). \tag{35}$$

VI. EXPERIMENTAL RESULTS

Measurements are carried out on a slender aluminum beam for different distances and configurations. The results show the same tendency. For the sake of brevity just one typical measurement of the beam is presented and discussed.

The dimensions of the round beam are a diameter of $d=6$ mm, a length of $l=3$ m and a density of $\rho=2830$ kg/m^3. The material parameters for aluminium are tested with resonance frequencies of the beam and a elastic modulus $E=68{,}0$ GPa is obtained.

The beam is clamped at one end and freely hanging on a twine at the other. The acceleration is measured with an accelerometer with a sampling frequency of 50 kHz placed at 1.68 m from the free end. The beam is excited by means of an impacting hammer equipped with a force transducer at the free end. The theoretical dispersion index is according to Eq. (8) $d_i=0.096$.

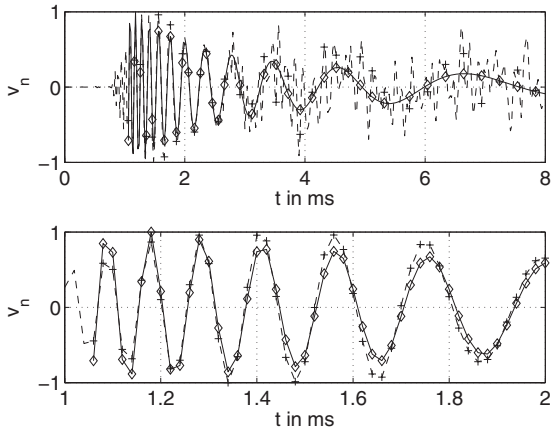

FIG. 9. Impulse response of a beam on different time windows, normalized velocity $v(x=1.64m,t)/|v(x=1.64m,t)|_{\max}$: measured (plus/dashed), complex bending wavelet with equation (35) (diamond/solid).

Since the real beam is not infinite, only the first passage of the pulse is considered. The beam acceleration is plotted in Fig. 9. The time axis is started at the maximum of the force signal. One may recognize that after around 2.8 ms the reflections from the clamped end are visible.

For the transform a range of the scaling factor from $0.5d_i$ to $10d_i$ and the complex bending wavelet is chosen. The analysis is quite insensitive to the range of the scaling factor. More problematic is the choice of a valid frequency range. Here the biggest range chosen was sensible and stable results were found.

The maximum of the transform is found at a scaling factor of $a=0.0955$. The analysis is done approximately from 1 to 8 ms, that corresponds with the given scaling factor a to a frequency range from 200 Hz to 12 kHz. Using the sine bending wavelet and the same frequency range results in a value of $a=0.0936$.

The curves are normalized with their maximum value, since in this context the distribution of amplitude and frequency over time is of interest, but not the absolute value.

The first reflection can be analyzed by using a time value that has the highest energy value at the maximum frequency and is not in the vicinity of the time value of the first pulse.

For this analysis it helps to reduce the frequency range. A frequency range from 400 to 8 kHz was chosen. The obtained values for the first pulse are quite stable $a=0.0959$ for the complex bending wavelet and $a=0.0938$ for the sine. The second pulse (first reflection) was located at $a=0.605$ in both cases. This value means that the second pulse travels a distance of 4.218 m which matches with the distance of the reflected pulse astonishingly well (through the hole beam until the clamp (width 5 cm) is reached and back to the accelerometer 4.22 m). The reflected pulse can be found in the contour diagram of the energy density in Fig. 10 (dashed curve).

Comparison with the arrival time method

The Morlet wavelet scalogram (4) is calculated with an adapted algorithm[32] and shown together with the arrival time curve

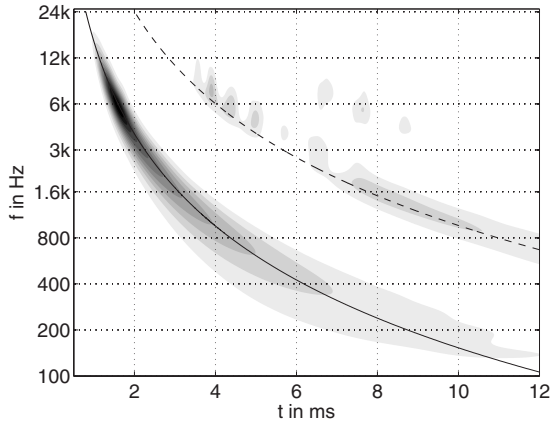

FIG. 10. Contour diagram: Morlet scalogram of the free-clamped beam, line: arrival time curve equation (36) with $d_i=0.0955$ (solid) and $d_i=0.605$ (dashed).

$$t_{bw} = \sqrt{\frac{d_i}{\omega}} \tag{36}$$

of the direct and reflected curve in Fig. 10. The difference between the arrival time that is found with Eq. (5) and the arrival time curve Eq. (36) is shown in Fig. 11. The curve in Fig. 11 shows the effect that the gradient of the energy density influences the localization that is already discussed in Sec. IV A. Since the energy density increases towards the maximum at around 6 kHz the maximum of the energy density deviates towards higher frequencies that are earlier and vice versa.

The deviations for the frequencies below 300 Hz are found also in numerical examples and can be explained by the fact that the almost periodic condition[27] is violated for very low frequencies.

VII. CONCLUDING REMARKS

A definition of a new adapted wavelet, the bending wavelet, is given. The mathematical properties of the bending wavelet are discussed. It is shown in examples and in experiment that the transform is useful to analyze a flexural impulse response.

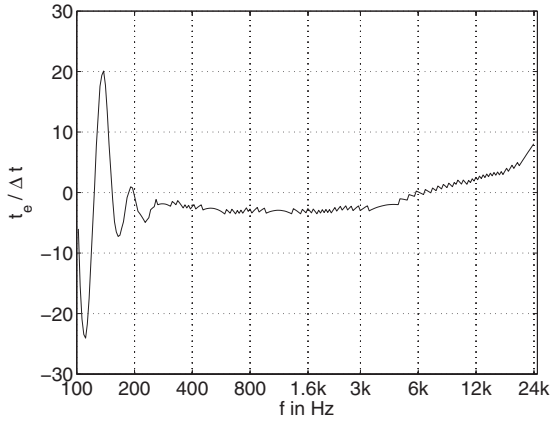

FIG. 11. Difference $t_e=t_a-t_{bw}$ of the direct pulse ($d_i=0.0955$) normalized with the time step $\Delta t=1/f_s$.

Besides source localization a possible application is the measurement of material properties in a built-in situation of finite structures, since the method does not depend on the boundary conditions.

The drawback of the proposed method is that it is only applicable to bending waves that can be modeled with the simple Euler beam theory or any wave that has a dispersion relation that follows a $\sim 1/\sqrt{\omega}$ dependence. Another precondition is the rather high dispersion number and the choice of a useful frequency range can be problematic. Nevertheless, bending waves are dominant in structure borne sound problems and for thin structures the simplifications of the Euler bending theory are usually valid.

The method is accurate, fast and easy to implement. In the experiments a source could be localized with a deviation lower than 10%. One can build real time applications for source detection. The method has also principle advantages. It is possible to:

1. Obtain the distance of an impulse or the material properties with only one measurement,
2. analyze two overlapping pulses, which is not possible with the maximum of the Morlet wavelet transform, where for each frequency, one maximum value is extracted.

APPENDIX A: IMPULSE RESPONSE FUNCTION FOR BEAMS

Consider a theoretical setup of a semi-infinite ($x \in [0,\infty]$) or infinite beam, which is excited at $x=0$ with an arbitrarily short force pulse F_a. The pulse is modeled by the Dirac δ-function $F_a(t)=F_0\delta(t)$ whose Fourier transform is given by

$$\hat{F}_a(\omega) = \lim_{T\to\infty} \int_{-\infty}^{T} F_a(t) e^{-j\omega t} dt = F_0 H(T), \tag{A1}$$

where $H(T)$ is the Heaviside Function. To find the response function to the impulse one may proceed with the boundary conditions for this elementary problem. The governing equation for the velocity $v(x,t)$ of a beam is

$$B\frac{\partial^4 v}{\partial x^4} + m'\frac{\partial^2 v}{\partial t^2} = 0, \tag{A2}$$

where x is the distance from the source, $\zeta=\sqrt{B/m'}$, where B is the flexural rigidity and m' mass per unit length.

The equations for the angular velocity w, bending moment M, shear force F_y and velocity v of a beam which can be modeled with the Euler beam theory, Eq. (A2) are

$$\hat{w} = \frac{\partial \hat{v}}{\partial x}, \quad \hat{M} = -\frac{B}{j\omega}\frac{\partial \hat{w}}{\partial x}, \quad \hat{F}_y = -\frac{\partial \hat{M}}{\partial x},$$

$$j\omega m' \hat{v} = -\frac{\partial \hat{F}_y}{\partial x}. \tag{A3}$$

Further is the bending wave number $k_b=\omega/c_b$, the bending wave velocity $c_b=\sqrt[4]{\omega^2 B/m'}$, the flexural rigidity $B=EI_y$, E the elastic or Young's modulus, I_y the second moment of area. For more details see another publication by the author.[33]

For a semi-infinite beam the waves propagate away from the excitation point which leads with $v=\mathrm{Re}\{\hat{v}e^{j\omega t}\}$ to

$$\hat{v} = \hat{v}_+ e^{-jk_b x} + \hat{v}_{+j} e^{-k_b x}. \tag{A4}$$

Herein the term $\hat{v}_+$ is the amplitude of the far-field wave and $\hat{v}_{+j}$ that of the near-field wave. At the free end the bending moment and shear force must be equal to the excitation $F(x=0)=F_a$ and the moment must vanish $M(x=0)=0$. It follows with $1+j=\sqrt{2j}$ that

$$\hat{v}(x,\omega) = \frac{2\hat{F}_a(\omega)}{\sqrt{2jm'c_b}}(e^{-jk_b x} + e^{-k_b x}). \tag{A5}$$

To obtain the response function $v(x,t)$ one may use the real part of the inverse Fourier transform of Eq. (A5)

$$v(x,t) = \mathrm{Re}\left\{\frac{1}{2\pi}\int_{-\infty}^{\infty} \hat{v}(x,\omega) e^{j\omega t} d\omega\right\}, \tag{A6}$$

which with $\omega/\sqrt[4]{\omega^2}=\omega/|\omega|\sqrt{|\omega|}$ ensures that the waves always propagate away from the excitation point. Upon substitution the expression for the semi-infinite beam reads

$$v(x,t) = \frac{F_0 H(t)}{\pi m'\sqrt{\zeta}} \times \mathrm{Re}\left\{\int_{-\infty}^{\infty} \frac{e^{-j\frac{\omega}{|\omega|\sqrt{\zeta}}\sqrt{|\omega|}x} + e^{-\frac{\omega}{|\omega|\sqrt{\zeta}}\sqrt{|\omega|}x}}{\sqrt{2j|\omega|}} e^{j\omega t} d\omega\right\}, \tag{A7}$$

where $\zeta=\sqrt{B/m'}$. This integral is solved with Mathematica's Integrate [ ] command with use of the hyper-geometric function ${}_pF_q$ for $t>0$. The hyper-geometric functions were found by Pochhammer.[34] Surprisingly he also solved the problem of bending waves in a circular beam without assuming that the radial movements can be neglected.[35,36]

He gives also an exact expression for the bending wave velocity in this general case.[37] An overview of Pochhammer's work and its application towards transient response can be found in Miklowitz.[38]

In the case of $t<0$ the integral vanishes due to the Heaviside function. One thus finds that

$$\int_{-\infty}^{\infty} \frac{e^{-j\frac{\omega}{|\omega|\sqrt{\zeta}}\sqrt{|\omega|}x} + e^{-\frac{\omega}{|\omega|\sqrt{\zeta}}\sqrt{|\omega|}x}}{\sqrt{2j\omega}} e^{j\omega t} d\omega = \sqrt{\frac{2\pi}{t}}\cos\frac{x^2}{4\zeta t} - j\left(\frac{j2x}{\sqrt{\zeta t}}{}_1\mathrm{F}_2\left(1, \frac{3}{4}\frac{5}{4}, -\frac{x^4}{64\zeta^2 t^2}\right) - \sqrt{\frac{2\pi}{t}}\cos\frac{x^2}{4\zeta t}\right), \tag{A8}$$

where ${}_1\mathrm{F}_2$ is the hyper-geometric function with $p=1$ and $q=2$. The impulse response function for semi-infinite beams is with the real part of Eq. (A8) given by

$$\boxed{v(x,t) = \frac{F_0 H(t)}{m'}\sqrt{\frac{2}{\pi\zeta t}}\cos\frac{x^2}{4\zeta t}}. \tag{A9}$$

It should be mentioned that to produce this result it is vital to

use the near- and far-field terms in Eq. (A7). For the origin at $x=0$, it follows that

$$v(x=0,t)=\frac{F_0H(t)}{m'}\sqrt{\frac{2}{\pi\zeta t}}. \tag{A10}$$

The dependence $v\sim 1/\sqrt{t}$ can be found approximately in[21] for the example of a sticking mass.

The antiderivative of Eq. (A9) gives the deflection

$$\xi(x,t)=\frac{2F_0H(t)}{m'}\left(\sqrt{\frac{2t}{\pi\zeta}}\cos\frac{x^2}{4\zeta t}+\frac{x}{\zeta}S\left(\frac{x}{2\pi ct}\right)\right), \tag{A11}$$

where $S(x)=\int_0^x \sin(\pi t^2/2)dt$ is the Fresnel-Sine-Integral.

The Fourier transform $\hat{\Psi}(\omega)$ of a function $\psi(t)=\gamma(t)\times\phi(t)$ is

$$\hat{\Psi}(\omega)=\frac{1}{2\pi}\hat{\Gamma}(\omega)*\hat{\Phi}(\omega), \tag{A12}$$

where $*$ denotes the convolution. In case of an inverted Fourier transform there is no factor $1/(2\pi)$ and it follows that

$$v(x,t)=F_a(t)*\frac{1}{m'}\sqrt{\frac{2}{\pi\zeta t}}\cos\frac{x^2}{4\zeta t}. \tag{A13}$$

For an arbitrary force $F_a(t)$, $\mathrm{Im}\{\hat{F}_a(\omega)\}=0$ does not hold. But $F_a(t)$ is always real and $v(x,t)$ is real such that only the real part of Eq. (A8) needs to be taken into account. It is a straightforward test to use the Dirac δ function as the force and to obtain (A9).

In case of an infinite beam symmetry implies that

$$\hat{v}=\hat{v}_+e^{-jk|x|}+\hat{v}_{+j}e^{-k|x|}. \tag{A14}$$

At $x=0$ the angular velocity is $w(x=0)=0$ and $F_a/2=F_y(x=0)$, therefore

$$\hat{v}(x,\omega)=\frac{\hat{F_a}(\omega)}{2m'c_b\sqrt{2j}}(e^{-jk_b|x|}-je^{-k_b|x|}). \tag{A15}$$

This is the same result at the origin $x=0$ as in Eq. (A5), except for the factor $1/4$. The difference between Eqs. (A5) and (A15) for the propagation $x>0$ is a phase change.

The impulse response function for infinite beams is given by

$$v(x,t)=\frac{F_0H(t)}{m'}\sqrt{\frac{2}{\pi\zeta t}}\sin\frac{x^2}{4\zeta t}. \tag{A16}$$

The inverse Fourier transform is similar to the case of semi-infinite beams so only the result is stated.

APPENDIX B: GENETIC ALGORITHM

1 Linear distributed
  initial chromosome of t and a.
2 Bending wavelet transform with
  the initial chromosome.
3 Assignment to the
  current population.
  Repeat
4 Self-written rank based
  fitness assignment (current pop.).
5 Selection with
  stochastic universal sampling.
6 Recombination with the
  extended intermediate function.
7 Real-value mutation with
  reeder genetic algorithm.
8 Bending wavelet transform with the
  selected chromosome.
9 Self-written fitness based insertion
  with 70% new individuals.

Until max number of generations

[1] T. Önsay and A. G. Haddow, "Wavelet transform analysis of transient wave propagation in a dispersive medium," J. Acoust. Soc. Am. **95**, 1441–1449 (1994).
[2] K. Kishimoto, M. H. H. Inoue, and T. Shibuya, "Time frequency analysis of dispersive waves by means of wavelet transform," J. Appl. Mech. **62**, 841–46 (1995).
[3] H. Yamada, Y. Mizutani, H. Nishino, M. Takemoto, and K. Ono, "Lamb wave source location of impact on anisotropic plates," J. Acoust. Emiss. **18**, 51–60 (2000).
[4] L. Gaul and S. Hurlebaus, "Identification of the impact location on a plate using wavelets," Mech. Syst. Signal Process. **12**(6), 783–795 (1998).
[5] C. Junsheng, Y. Dejie, and Y. Yu, "Application of an impulse response wavelet to fault diagnosis of rolling bearings," Mech. Syst. Signal Process. **21**, 920–929 (2005).
[6] F. L. di Scalea and J. McNamara, "Measuring high-frequency wave propagation in railroad tracks by joint time-frequency analysis," J. Sound Vib. **273**(3), 637–651 (2004).
[7] A. Messina, "Detecting damage in beams through digital differentiator filters and continuous wavelet transforms," J. Sound Vib. **272**(1), 385–412 (2004).
[8] Y. Hayashi, S. Ogawa, H. Cho, and M. Takemoto, "Non-contact estimation of thickness and elastic properties of metallic foils by the wavelet transform of laser-generated Lamb waves," NDT & E Int. **32**(1), 21–27 (1998).
[9] M.-N. Ta and J. Lardies, "Identification of weak nonlinearities on damping and stiffness by the continuous wavelet transform," J. Sound Vib. **293**(1), 16–37 (2006).
[10] P. Masson, A. Berry, and P. Micheau, "A wavelet approach for the active structural acoustic control," J. Acoust. Soc. Am. **104**(3), 1453–1466 (1998).
[11] Y. Kim and E. Kim, "Effectiveness of the continuous wavelet transform in the analysis of some dispersive elastic waves," J. Acoust. Soc. Am. **110**(1), 86–94 (2001).
[12] N. P. R. Hill, "Contact sensitive device," New Transducers Limited U.S. Patent No. 7,157,649 (2000).
[13] D. M. Sullivan, "Contact sensitive device," New Transducers Limited U.S. Patent No. 6,922,642 (2004).
[14] M. Brandstein and D. Ward, *Microphone Arrays Signal Processing Techniques and Applications* (Springer, New York, 2001).
[15] J. Jiao, C. He, B. Wu, and R. Fei, "Application of wavelet transform on modal acoustic emission source location in thin plates with one sensor," Int. J. Pressure Vessels Piping **81**, 427–431 (2004).
[16] J. C. Hong, K. H. Sun, and Y. Y. Kim, "Dispersion-based short-time Fourier transform applied to dispersive waves," J. Acoust. Soc. Am. **117**(5), 2949–2960 (2005).
[17] B. Liu, "Adaptive harmonic wavelet transform with applications in vibration analysis," J. Sound Vib. **262**(1), 45–64 (2003).
[18] S. Mann and S. Haykin, "The chirplet transform: A generalization of Gabor's logon transform," *Vision Interface '91*, 205–212 (1991).
[19] S. Mann and S. Haykin, "The chirplet transform: Physical considerations," IEEE Trans. Signal Process. **43**, 2745–2761 (1995).
[20] J. Boussinesq, *Application des Potentials a l'Etude de l'Equilibre et du Mouvement des Solides Elastiques* (Gauthier-Villars, Paris, 1885), (Applications of the Potential to the Research of the Equilibrium and Movement of Elastic Solids).
[21] L. Cremer, M. Heckl, and B. Petersson, *Structure-Borne Sound* (Springer-Verlag, Berlin, 2005).
[22] W. Nowacki, *Dynamics of Elastic Systems* (Chapman and Hall, London,

1963).
[23]L. Meirovitch, *Analytical Methods in Vibrations* (Collier-Macmillan, 1967).
[24]R. Büssow, "Wavelet transformation of structure borne sound signals for dispersion characterization and source localization," Ph.D. thesis, Berlin University of Technology (2008).
[25]S. Mallat, *A Wavelet Tour of Signal Processing* (Academic Press, New York, 1998).
[26]A. Louis, P. Maaß, and A. Rieder, *Wavelets* (Teubner, Leipzig, 1994).
[27]S. Bochner, "Beiträge zur Theorie der fastperiodischen Funktionen," Ann. Math. **96**(1), 119–147 (1927), (Contributions to the theory of almost periodic functions).
[28]H. Pohlheim, *Evolutionäre Algorithmen* (Springer, New York, 2000), (Evolutionary algorithms).
[29]C. Park, W. Seong, and P. Gerstoft, "Geoacoustic inversion in time domain using ship of opportunity noise recorded on a horizontal towed array," J. Acoust. Soc. Am. **117**(4), 1933–1941 (2005).
[30]L. Carin, H. Liu, T. Yoder, L. Couchman, B. Houston, and J. Bucaro, "Wideband time-reversal imaging of an elastic target in an acoustic waveguide," J. Acoust. Soc. Am. **115**(1), 259–268 (2004).
[31]A. Chipperfield, P. Fleming, H. Pohlheim, and C. Fonseca, *The Genetic Algorithm Toolbox for MATLAB*, Department of Automatic Control and Systems Engineering of The University of Sheffield, Sheffield, United Kingdom.
[32]R. Büssow, "An algorithm for the continuous morlet wavelet transform," Mech. Syst. Signal Process. **21**(8), 2970–2979 (2007).
[33]R. Büssow, "Applications of the flexural impulse response functions in the time domain," Acta. Acust. Acust. **94**(2), 207–214 (2008).
[34]L. Pochhammer, "Über hypergeometrische Funktionen *n*ter Ordnung," J. Reine Angew. Math. **71**, 316–352 (1869), (on hypergeometric functions of *n*th order).
[35]S. P. Timoshenko, *History of Strength of Materials* (McGraw–Hill, New York, 1953).
[36]L. Pochhammer, "Beitrag zur Theorie der Biegung des Kreiszylinder," J. Reine Angew. Math. **81**, 33–61 (1876), (Contributions to the theory of bending of a cylinder).
[37]L. Pochhammer, "Über die Fortpflanzungsgeschwindigkeiten kleiner Schwingungen in einem unbegrenzten isotropen Kreiszylinder," J. Reine Angew. Math. **81**, 324–336 (1876), (On the propagation velocity of small vibrations in an infinite isotropis cylinder).
[38]J. Miklowitz, *The Theory of Elastic Waves and Waveguides* (North-Holland, Amsterdam, 1978).

Localization of multiple acoustic sources with small arrays using a coherence test

Satish Mohan,[a] Michael E. Lockwood,[b] Michael L. Kramer,[c] and Douglas L. Jones[d]
Beckman Institute, Department of Electrical and Computer Engineering, University of Illinois at Urbana-Champaign, 405 N. Mathews Avenue, Urbana, Illinois 61801

(Received 17 December 2006; revised 14 January 2008; accepted 15 January 2008)

Direction finding of more sources than sensors is appealing in situations with small sensor arrays. Potential applications include surveillance, teleconferencing, and auditory scene analysis for hearing aids. A new technique for time-frequency-sparse sources, such as speech and vehicle sounds, uses a coherence test to identify low-rank time-frequency bins. These low-rank bins are processed in one of two ways: (1) narrowband spatial spectrum estimation at each bin followed by summation of directional spectra across time and frequency or (2) clustering low-rank covariance matrices, averaging covariance matrices within clusters, and narrowband spatial spectrum estimation of each cluster. Experimental results with omnidirectional microphones and colocated directional microphones demonstrate the algorithm's ability to localize 3–5 simultaneous speech sources over 4 s with 2–3 microphones to less than 1 degree of error, and the ability to localize simultaneously two moving military vehicles and small arms gunfire. © *2008 Acoustical Society of America.*
[DOI: 10.1121/1.2871597]

PACS number(s): 43.60.Jn, 43.60.Fg [DOS] Pages: 2136–2147

I. INTRODUCTION

Acoustic localization or direction finding with arrays of only a few microphones finds applications in areas such as surveillance, auditory scene analysis for hearing aids, and many other applications. For instance, localization of the source of a gunshot in a crowded battlefield environment may be useful in military applications. Similarly, localization of multiple talkers in a crowded restaurant or social event might be useful for a hearing aid. In many applications such as hearing aids, only a small array is practical. In many situations with such arrays, the number of sources often exceeds the number of sensors, and most localization algorithms cannot deal with this case. In general, with stationary Gaussian sources, only fewer sources than the number of sensors can be localized (Schmidt, 1986). However, if there are fewer sources than sensors in disjoint frequency bands, then by localizing in each band, overall localization of more sources than sensors is possible. Taking advantage of such sparseness is crucial to localize more sources than sensors.

Previous methods for localizing more sources than sensors implicitly assume such sparse time-frequency structures. Pham and Sadler (1996) use an incoherent wideband MUSIC (Schmidt, 1986) approach where they assume that "a single frequency bin is occupied by a single source only" and sum the individual MUSIC spectra across all time-frequency bins. However, their method makes no provision for cases when this is not the case, and thus can be expected to fail for multiple sources that are similar or are not extremely sparse, e.g., a cocktail-party scene with multiple human speakers. The method presented in this paper overcomes this limitation. Using the same assumption, Rickard and Dietrich (2000) estimate the source locations at each time-frequency (TF) bin using a ratio-based technique followed by a histogram-like clustering of all the estimates across time and frequency. Two other methods use parametric models for the sources' temporal behavior. Su and Morf (1983) model the sources as rational processes. Assuming that the number of sources sharing a pole is less than the number of sensors, they apply MUSIC to the data at the estimated poles and combine the directional spectra across poles. The TF-MUSIC method of Zhang *et al.* (2001) uses a quadratic TF representation. Assuming frequency-modulated sources, they are able to identify time-frequency bins that correspond to a certain source and average the covariance matrices from those bins. The averaged covariance matrix has a higher signal-to-noise ratio (SNR) and thus leads to a better directional spectrum.

The previous methods exploit the nonstationarity of the sources through prior knowledge of the source's time-frequency structure or through assumptions on the reduced-rank nature of the data. When dealing with mixtures of more nonstationary sources than sensors, such as four speech signals and two microphones, an approach requiring no knowledge of the source's spectra to identify time-frequency bins where the data is low rank or contains fewer active sources than the number of sensors would be attractive. Conventional methods of spectral estimation can be applied to low-rank data. But as different low-rank data are available across time and frequency, the issue of coherently combining or incoherently combining the data is investigated. Specifically, creating directional spectra at each low-rank bin and incoherently combining those or coherently combining the low-rank data in some manner and then creating a directional spectrum is compared.

[a]Electronic mail: smohan@uiuc.edu
[b]Electronic mail: melockwo@uiuc.edu
[c]Currently affiliated with Phonak Hearing Systems. Electronic mail: kramtek@gmail.com
[d]Electronic mail: dl-jones@uiuc.edu

 0001-4966/2008/123(4)/2136/12/$23.00 © 2008 Acoustical Society of America

Although the time-frequency sparsity of the sources is key to localizing more sources than sensors, the response of the array itself plays an important role. Most direction-finding techniques use an array of spaced omnidirectional sensors, each with an isotropic spatial response. These techniques exploit the time delays between the sensors that vary as a function of direction (Johnson and Dudgeon, 1993). Directional sensors have a spatial response that is preferential to certain directions. Gradient, cardioid, and hypercardioid microphones are examples of different spatial responses. An array of two or three colocated directional sensors that are oriented in orthogonal directions form a vector sensor, providing an *amplitude difference* between the sensors that varies as a function of direction. Single-source localization with a vector sensor using the minimum variance or Capon spectrum has been described by Nehorai and Paldi (1994) and Hawkes and Nehorai (1998). Multisource localization with a vector sensor using an ESPRIT-based method was presented by Wong and Zoltowski (1997) and Tichavsky *et al.* (2001). In these methods, the authors assume the sources are sinusoidal and disjoint in the frequency domain, noting that "it is necessary that no two sources have the same frequency" as only one source can be localized in each frequency bin (Tichavsky *et al.*, 2001). They also mention that their algorithm could be "adapted to handle frequency-hopped signals of unknown hop sequences" (Tichavsky *et al.*, 2001). To deal with signals with time-varying overlapping frequency content, identifying low-rank time-frequency bins is a key element of our algorithm. Last, an important practical advantage of a vector-sensor is that it can be designed to occupy a very small space or volume (Miles *et al.*, 2001).

In the following sections, an algorithm is presented that can localize more acoustic sources than the number of microphones employed for common types of nonstationary wideband sources. The algorithm's ability to localize (1) simultaneous speech sources and (2) gunshot sounds simultaneous with military vehicles using different microphone arrays of omnidirectional and gradient microphones is demonstrated. To our knowledge, this is the first time that high-resolution multisource localization has been practically demonstrated with aeroacoustic gradient microphones.

II. SIGNAL MODEL

We briefly establish the signal model and notation here before describing the localization algorithm.

(1) All text in bold denotes vector quantities or vector operations.
(2) $(\cdot)^H$ denotes Hermitian transpose.
(3) $(\cdot)^*$ denotes the complex conjugate.
(4) Let $\{s_i(t)\}_{i=1}^L$ be the temporal waveforms of the sources, where L is the number of sources. We assume that the sources are bandlimited to B Hz.
(5) Let $s_i(n)$ be samples at times $t=nT$ of the ith source signal, where the sampling interval $T \leqslant 1/2B$ satisfies the Nyquist requirement.
(6) We assume that the sources are independent and block stationary; i.e., the $\{s_i(n)\}_{i=1}^L$ are essentially stationary over several adjacent N-sample intervals and $E[s_i(n)s_j^*(n-l)]=0\ \forall_i \neq j, |l-n| < N$.
(7) Let M be the number of sensors in the array.
(8) Let $\mathbf{x}(n)$ be the discrete-time signal at the array output after sampling at or above the Nyquist frequency of $2B$ Hz. We assume that the system is linear and time invariant so that the received signal is a convolutive mixture of the sources:

$$\mathbf{x}(n) = \sum_{i=1}^{L} s_i(n) \star \mathbf{h}(n, \theta_i). \tag{1}$$

(9) $\mathbf{h}(n, \theta_i)$ is an $M \times 1$ impulse response vector that is a function of θ_i, the direction-of-arrival (DOA) of the ith source.
(10) $\star$ denotes discrete-time convolution.

Section III explains the localization algorithm. Section IV describes the results of testing the algorithm on microphone arrays with acoustic sources. Section V contains the conclusions.

III. MULTISOURCE LOCALIZATION ALGORITHM

The algorithm uses four main steps to localize simultaneous nonstationary wideband sources when the number of sources may be greater than the number of sensors. First, the discrete-time data from the microphone array is transformed into an overlapped short-time Fourier transform (STFT) representation. Second, a coherence test is used to find time-frequency bins with fewer active sources than the number of sensors. After that step, there are two variants of the algorithm. In variant 1, a directional spectrum is computed from the covariance matrix at each low-rank bin. The directional spectra from all low-rank bins are summed to yield a final directional spectrum, which is used to estimate the DOAs of the sources. In variant 2, the covariance matrices from low-rank bins are clustered across time into groups based on Frobenius norm. The goal is for each cluster to contain low-rank data corresponding to a particular source. As the steering vector is frequency dependent, a separate clustering must be performed (across time) at each frequency bin. Next, the low-rank covariance matrices within each cluster are averaged and the averaged matrix is used to compute a directional spectrum. The directional spectra from all clusters are summed to yield a final directional spectrum, which is used to estimate the directions of arrival of the sources. Figure 1 contains a block diagram of the localization algorithm.

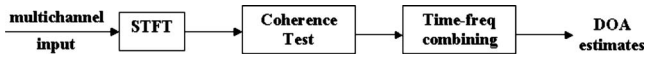

FIG. 1. Block diagram of the localization algorithm with variants 1 and 2.

A. Transformation to time-frequency

The first step in the algorithm is to transform the time-domain data into an overlapped STFT representation (Hlawatsch and Boudreaux-Bartels, 1992). The STFT of a signal $s(n)$ is defined as

$$\mathbf{S}(m,\omega_k)=\sum_{n=0}^{N-1} w(n)s(n+mF)e^{-j\omega_k n}, \tag{2}$$

where $w(n)$ is an N-point window, F is the offset between successive time blocks in samples, m is the time-block index, and ω_k is the frequency-bin index ($\omega_k=2\pi k/N, k=0,\ldots,N-1$). $\mathbf{X}(m,\omega_k)$ is the STFT of the $\mathbf{x}(n)$ and is a linear combination of the source STFTs:

$$\mathbf{X}(m,\omega_k)=\sum_{i=1}^{L} S_i(m,\omega_k)\mathbf{h}(\omega_k,\theta_i), \tag{3}$$

where $\mathbf{h}(\omega_k,\theta)$ is the $M\times 1$ frequency-domain steering vector (i.e., location-to-microphones channel response) that is parametrized by a source's location.

B. Coherence test

Next, time-frequency bins with low-rank data are identified by applying a coherence test to the estimated covariance (or power spectral density) matrix at each time-frequency bin. The true (unknown) $M\times M$ time-varying frequency-domain covariance matrix is $\mathbf{R}(m,\omega_k)$, a linear combination of rank-1 outer products of the source steering vectors weighted by the source powers:

$$\mathbf{R}(m,\omega_k)=E[\mathbf{X}(m,\omega_k)\mathbf{X}^{\mathbf{H}}(m,\omega_k)] \tag{4}$$

$$=\sum_{i=1}^{L}\sigma_i^2(m,\omega_k)\mathbf{h}(\omega_k,\theta_i)\mathbf{h}(\omega_k,\theta_i)^{\mathbf{H}}, \tag{5}$$

where $\sigma_i^2(m,\omega_k)$ is the power (and variance) of the ith source over the (m,ω_k)th time-frequency bin. A causal sample covariance matrix is used to estimate the covariance matrix at time-frequency bin (m,ω_k):

$$\hat{\mathbf{R}}(m,\omega_k)=\frac{1}{C}\sum_{l=m-C+1}^{m}\mathbf{X}(l,\omega_k)\mathbf{X}(l,\omega_k)^{\mathbf{H}}, \tag{6}$$

where C is the number of time-blocks averaged to obtain the short-time estimate. Due to the time-frequency uncertainty principle (Hlawatsch and Boudreaux-Bartels, 1992), a specific short-time Fourier transform value represents signal content over a region of time and frequency (loosely referred to as a "time-frequency bin") around that frequency and time. As the estimation of a covariance matrix requires averaging, the averaging across time blocks in Eq. (6) increases the temporal spread of this bin accordingly above the minimum required by the time-frequency uncertainty principle.

At any time-frequency bin, for many common nonstationary wideband sources such as speech and transient sounds like gunfire and passing vehicles, some source powers will be large, whereas other source powers will be negligible. A source that contributes a significant fraction of power (e.g., more than 10%) to the covariance matrix is an *active source* at that time-frequency bin. Equation (5) shows that time-frequency bins with the number of active sources greater than or equal to the number of sensors will have effective full rank, whereas time-frequency bins with fewer active sources than the number of sensors will have low effective rank or be poorly conditioned.

Identification of a low-rank bin is usually done by performing an eigendecomposition of the covariance matrix and examining its eigenvalues (Schmidt, 1986). The following algorithm can be applied to all *low-rank time-frequency bins*, defined as any time-frequency interval with a short-time-frequency correlation matrix with a maximum-to-minimum eigenvalue ratio greater than a selected threshold. However, a particularly simple statistical test arises if the search for low-rank bins is restricted to finding rank-1 bins, or time-frequency bins with only one active source.

A simple test for a rank-1 time-frequency bin involves the pairwise magnitude-squared coherences or the elements of the covariance matrix. Let $T_{\mathrm{coh}}^{(i,j)}(m,\omega_k)$ be the MSC between sensors i and j (Carter, 1987):

$$T_{\mathrm{coh}}^{(i,j)}(m,\omega_k)=\frac{|[\mathbf{R}(m,\omega_k)]_{ij}|^2}{[\mathbf{R}(m,\omega_k)]_{ii}[\mathbf{R}(m,\omega_k)]_{jj}}. \tag{7}$$

Theorem 1: Necessary and sufficient conditions for an $M\times M$ covariance matrix to be rank-1 are that the $M(M-1)/2$ pairwise MSCs are equal to 1, and that for $M>2$, the phases of the off-diagonal components of the matrix satisfy $\angle(R_{ij})-\angle(R_{ik})+\angle(R_{jk})=0\ \forall i<j<k$, where $\angle(R_{ij})$ is the phase of the ijth element of the covariance matrix. *Proof*: See the Appendix.

Thus, the coherence test for identifying a rank-1 time-frequency bin involves computing the MSCs at that bin, checking if they are above a threshold (such as 0.90) and checking if the phases of the covariance matrix satisfy certain constraints.

If we were dealing with stationary sources, estimating the covariance matrix at different times would provide no new information. With nonstationary sources, the covariance matrix at each frequency bin is time varying, providing "new looks" at the statistics of different sources as time evolves. The coherence test (and any test aimed at finding low-rank bins) implicitly exploits the sparse time-frequency structure of the sources to find low-rank bins.

C. Time-frequency clustering and/or combining

At this point, all rank-1 time-frequency bins have been identified, but the number and location of sources, and which source is associated with each rank-1 bin, remains to be determined. In variant 1 of the algorithm, a narrowband spectral estimator is computed at each low-rank time-frequency bin. The directional spectra are then combined incoherently across time and frequency, yielding a final directional spectrum. The peaks of this final spectrum are used to estimate the source DOAs (Mohan *et al.*, 2003a,b). This approach is similar to the incoherent combining of Pham and Sadler (1996), but through the coherence test avoids the degradation they report by discarding low-SNR or higher-rank bins containing corrupt spatial-spectral estimates. Whereas Pham and Sadler require most time-frequency bins to be sparse for good performance, this method requires only a few nonoverlapped bins from each source to produce accurate, high-resolution localization of all sources.

In variant 2 of the algorithm, the normalized rank-1 covariance matrices at each frequency-bin are clustered across time into groups. The goal is to create groups containing rank-1 covariance matrices corresponding to the same active source. Thus, after the clustering, each frequency-bin ω_k contains Q groups, each corresponding to one of the Q distinct sources detected, such as $\{\mathbf{R}(m_{1,1},\omega_k),\ldots,\mathbf{R}(m_{1,P_1},\omega_k)\},\ldots,\{\mathbf{R}(m_{Q,1},\omega_k),\ldots,\mathbf{R}(m_{Q,P_Q},\omega_k)\},\ldots$, where P_i is the number of rank-1 time-frequency bins at that frequency associated with the ith source. The covariance matrices in a group cluster together because they have the same structure (up to a scaling which is removed by the normalization); i.e., $\mathbf{R}(m_1,\omega_k)=\sigma(m_1,\omega_k)^2\mathbf{h}(\omega_k,\theta_1)\mathbf{h}(\omega_k,\theta_1)^{\mathbf{H}}$, $\mathbf{R}(m_P,\omega_k)=\sigma(m_P,\omega_k)^2\mathbf{h}(\omega_k,\theta_1)\mathbf{h}(\omega_k,\theta_1)^{\mathbf{H}}$. As the steering vector $\mathbf{h}(\omega_\mathbf{k},\theta)$ varies as a function of ω_k, a separate clustering must be performed at each frequency bin. Next, the covariance matrices within each group are averaged and a directional spectrum is computed from each averaged matrix. The directional spectra from each frequency bin are summed across frequency to yield a final spectrum from which the source DOAs are estimated.

MATLAB's `clusterdata` command was used to cluster low-rank matrices by pairwise distance; the matrices were normalized to unit Frobenius norm prior to clustering. This algorithm forms a hierarchical tree linking the elements by pairwise distance and then prunes this tree to automatically determine the optimal number of distinct clusters (and hence sources) as well as the cluster assignments. After clustering, the normalization was removed before averaging matrices within a group because a covariance matrix with a higher norm usually indicates a higher instantaneous SNR for that active source; the averaging of unnormalized covariance matrices can reduce the effects of low-rank bins with bad SNR.

Variant 2 of the algorithm aims to exploit the assumption of spatial stationarity of the sources (which implies that their steering vectors are not changing as a function of time and can therefore be clustered) to improve the accuracy of the localization. Variant 1 of the algorithm would likely be more useful for tracking moving sources.

D. Directional spectrum estimation

The well-known MUSIC spectral estimator was used to compute a directional spectrum. The MUSIC estimator requires $\mathbf{R}(m,\omega_k)$ to have low rank so that a basis, $\mathbf{U}_N(m,\omega_k)$, for the noise-subspace exists (Schmidt, 1986). The MUSIC estimator is then defined as

$$f_{\mathrm{MUSIC}}(m,\theta,\omega_k)=[\|\mathbf{U}_N(m,\omega_k)^{\mathbf{H}}\mathbf{h}(\omega_k,\theta)\|^2]^{-1}. \quad (8)$$

What separates variants 1 and 2 of the algorithm is the covariance matrix that is used to implement the above spectral estimators. Variant 1 can be described as incoherent combining of directional information as in Pham and Sadler (1996) (but only of coherent bins) because the data at each time-frequency bin is first transformed nonlinearly to a directional representation before combining across time and frequency. Variant 2 first combines the data at a low level by averaging covariance matrices within clusters and can be described as coherent combining of correlation data prior to nonlinear transformation to a directional representation.

Having described all the aspects of the localization algorithm in detail, in the next section, we test our algorithm with speech sources and microphone arrays.

IV. EXPERIMENTAL RESULTS

An experimental study of the localization algorithm was performed using a microphone array intended for hearing-aid research. The Hearing-Aid-6 (HA6) microphone array contains three omnidirectional microphones and three gradient microphones mounted on a single behind-the-ear hearing-aid shell. The three gradient microphones are orthogonally oriented. One or two HA6 arrays were mounted on the ears of a Knowles Electronic Mannekin for Acoustical Research (KEMAR). This array was chosen both because of interest in hearing-aid applications and because it represents an extreme test case including a small number of microphones, very small aperture requiring super-resolution, and HRTF distortions. Free-field experiments with this array yielded even better performance, so are not reported here.

The HA6 array allows for various choices of microphone processing. The five different array configurations tested were:

1. OO_m: two omnidirectional microphones of the same HA6 array on the right ear of a KEMAR, 8 mm separation between microphones;
2. OOO_m: three omnidirectional microphones of the same HA6 array on the right ear of a KEMAR, 8 mm separation between microphones;
3. GG_m: two colocated gradient microphones of the same HA6 array on the right ear of a KEMAR;
4. OO_b: two omnidirectional microphones, one each from an HA6 array on the right and left ears of a KEMAR, 15 cm separation between microphones; and
5. OOO_b: three omnidirectional microphones, two from an HA6 array on the right ear of a KEMAR with 8 mm separation and one from an HA6 array on the left ear of a KEMAR, separated 15 cm from the other two microphones.

The subscripts m and b refer to monaural and binaural. Using the OO_m, OOO_m, and GG_m arrays leads to monaural processing because the microphones are all on one side of the head, whereas use of the OO_b and OOO_b arrays leads to binaural processing because microphones are located on both sides of the head.

Comparisons between the OO_m and OOO_m evaluate the benefit of three microphones versus two microphones with the same microphone spacing. Arrays OO_m and GG_m compare using two omnidirectional microphones versus two gradient microphones. Differences between arrays OO_m and OO_b reflect the effect of aperture (specifically, 8 mm versus 15 cm). Array OOO_b tests the addition of both an extra microphone and more aperture with respect to array OO_m.

A second test of the localization algorithm was performed using two elements of a four-microphone free-field acoustic-vector-sensor array, the *XYZO* array, with acoustic

data recorded at the DARPA Spesutie Island Field Trials at the Aberdeen Proving Ground in August 2003. The *XYZO* array consists of three gradient microphones and one omnidirectional microphone. The gradient microphones are mutually orthogonally oriented, creating a vector sensor. Only two of the gradient microphones were used to localize military vehicles and gunfire in azimuth. This test was intended to demonstrate the algorithm's ability to localize acoustic sources other than speech sources and to localize in a free-field situation rather than in a room environment.

Vector gradient arrays of hydrophones have been used in the past for underwater direction-finding by Nickles *et al.* (1992) and Tichavsky *et al.* (2001). However, the successful application of aeroacoustic vector gradient arrays for high-resolution direction-finding has not been reported to our knowledge, except in our initial studies (Mohan *et al.*, 2003a,b).

A. Steering vector of the microphone arrays

In array signal processing, the steering vector $\mathbf{h}(\omega_k, \theta)$ describes the response of an array as a function of frequency and DOA. Arrays of spaced omnidirectional sensors have been well studied; These arrays are characterized by a time delay between the microphones that varies with the DOA of a source (Johnson and Dudgeon, 1993). For an array of two omnidirectional microphones in a free-field anechoic environment, the steering vector of a source with a DOA of θ degrees azimuth is

$$\mathbf{h}(\omega_k, \theta) = [e^{j\omega_k d \sin(\theta)/2c} \; e^{j\omega_k d \sin(-\theta)/2c}]^T, \tag{9}$$

where ω_k=frequency bin, d=spacing between the microphones, and c=speed of sound.

Arrays of directional microphones, especially colocated arrays, have been studied to a lesser extent. Directional microphones respond preferentially to certain directions. Various types of directional responses such as gradient, cardioid and hypercardioid can be constructed (McConnell, 2003). The HA6 and *XYZO* arrays contain colocated gradient microphones that are oriented in mutually orthogonal directions, causing an *amplitude-difference* to exist between the microphones that varies with the DOA of a source (Nehorai and Paldi, 1994). The steering vector of two colocated orthogonally oriented microphones for a source with a DOA of θ degrees azimuth is

$$\mathbf{h}(\omega_k, \theta) = [\cos(\theta) \; \sin(\theta)]^{\mathbf{T}} \tag{10}$$

Although the steering vector described previously is ideally frequency independent, real gradient microphones possess a low-frequency rolloff due to the large wavelength at lower frequencies.

When omnidirectional or gradient microphones are placed on the head of a KEMAR, the steering vectors (the responses of the array as a function of the source DOAs) are distorted by the head shadow of the KEMAR (Gardner and Martin, 1995). The head-shadow effect reduces the amplitude of a microphone's response to directions from the side of the head opposite to where the microphone is placed.

B. Steering vector estimation and calibration

Impulse responses are often used in acoustical studies to capture the response of a microphone array in a room; these methods can also be applied to measurements from a free-field environment. The steering vectors for arrays on or near objects, such as the hearing-aid arrays in the experiments reported later in this section, are strongly altered and must be measured as a function of direction before the algorithm can be applied. The frequency-domain steering vector is obtained from the Fourier transforms of the impulse responses. One method for calculating an impulse response involves maximum-length sequences (MLS) (Gardner and Martin, 1995). Impulse responses were measured as a function of azimuth (with 15° resolution) around each microphone array by playing MLS from loudspeakers and recording the response from the microphones. As the frequency response of the MLS signal is known, the frequency-domain steering vector was calculated by frequency-domain deconvolution. The inverse discrete Fourier transform of the steering vector is the vector of room impulse responses. These impulse responses and their corresponding Fourier transforms are referred to as the measured impulse responses and the measured steering vector. More details on this method of calculating impulse responses are described by Lockwood *et al.* (1999, 2004). For the first experimental study, recordings were performed using the HA6 array and a KEMAR in a modestly sound-treated room ($T_{60} \approx 0.25$ sec reverberation time) in the Beckman Institute; further physical and acoustical details of the room were described by Lockwood *et al.* (1999, 2004). Similar recordings were conducted using the *XYZO* array at the Aberdeen Proving Ground.

In order to increase the azimuthal resolution of the steering vector, the measured steering vector was interpolated from 15° resolution to 1° resolution using a Fourier-series technique. The coefficients of the Fourier-series expansion that best fit the data were found by least-squares solution to an overdetermined system of equations where the knowns consisted of the frequency-domain steering vector at 24 measured angles (15° azimuthal resolution) and the coefficients of the system were complex exponentials in azimuth evaluated at the 24 measured angles.

For an *nth*-order Fourier series fit for microphone i of an array, the least squares solution to the following equation is found:

$$\mathbf{Ac}(\omega_k) = \mathbf{h}(\omega_k), \tag{11}$$

$$\mathbf{h}(\omega_k) = [h_i(\omega_k, 0^\circ) \; h_i(\omega_k, 15^\circ) \; \cdots \; h_i(\omega_k, 345^\circ)]^T, \tag{12}$$

$$\mathbf{A} = \begin{pmatrix} 1 & e^{j0\cdot 1} & e^{-j0\cdot 1} & \cdots & e^{j0\cdot n} & e^{-j0\cdot n} \\ 1 & e^{j\pi/24\cdot 1} & e^{-j\pi/24\cdot 1} & \cdots & e^{j\pi/24\cdot n} & e^{-j\pi/24\cdot n} \\ \vdots & \vdots & \vdots & & & \\ 1 & e^{j23\pi/24\cdot 1} & e^{-j23\pi/24\cdot 1} & \cdots & e^{j23\pi/24\cdot n} & e^{-j23\pi/24\cdot n} \end{pmatrix}, \tag{13}$$

$$\mathbf{c}(\omega_k) = [c_0(\omega_k) \; c_1(\omega_k) \; c_{-1}(\omega_k) \; \cdots \; c_n(\omega_k) c_{-n}(\omega_k)]^T. \tag{14}$$

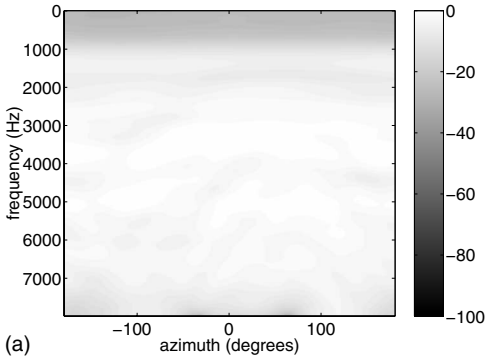

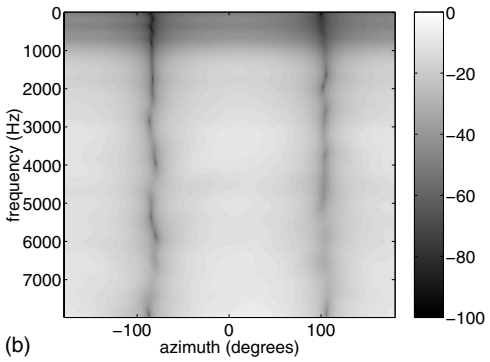

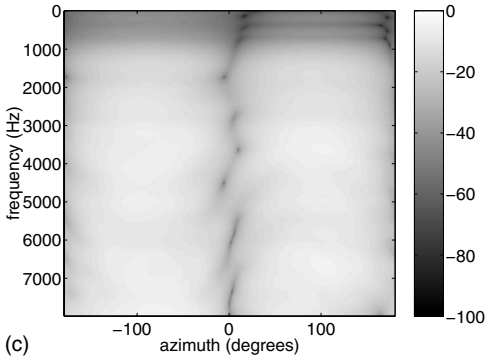

FIG. 2. Decibel magnitudes of the responses from the HA6 array in free-field (a) omnidirectional microphone and (b) and (c) two orthogonal gradient microphones.

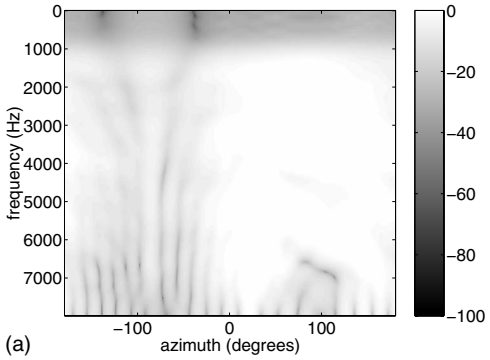

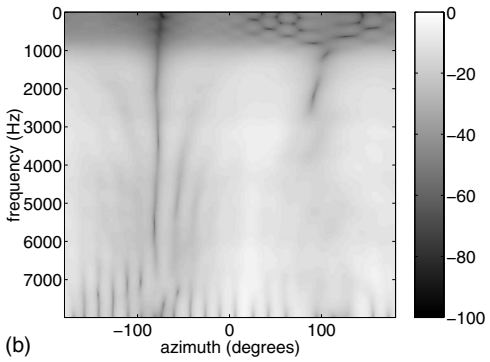

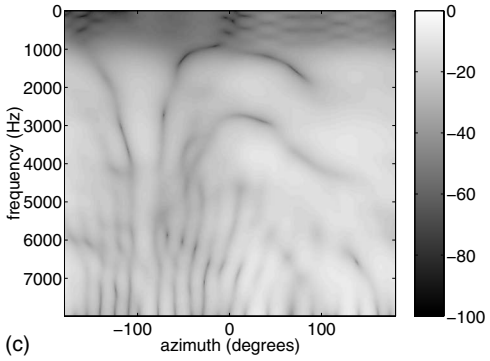

FIG. 3. Decibel magnitudes of the responses from the HA6 array on the left ear of a KEMAR (a) omnidirectional microphone and (b) and (c) two orthogonal gradient microphones.

After solving for $\mathbf{c}(\omega_k)$, the coefficients of the Fourier expansion, the expansion was computed at 1° resolution in azimuth to produce the interpolated steering vector. A twelfth-order (full-order) Fourier-series fit was used for most of the localization tests. One localization test used a fourth-order fit to determine if similar localization results could be obtained with a lower-order interpolation. A separate fit was computed for each microphone in an array. Figures 2 and 3 show the magnitudes (in decibels) of the interpolated microphone responses using a full-order fit as a function of frequency and azimuth for one of the omni microphones and two of the orthogonally oriented gradient microphones from the HA6 array both in free-field and on the left ear of KEMAR. The nulls of the gradient microphones, the dark lines in Figs. 2(b) and 2(c), are clearly seen in the free-field situation. Distortion of the nulls caused by the head shadow of KEMAR is seen in Fig. 3.

C. Results

The localization algorithm was implemented in MATLAB and tested with the microphone subsets of the HA6 array described in the five arrays OO_m, OOO_m, GG_m, OO_b, and OOO_b. Acoustic scenes were created by convolving 4 s of speech signals sampled at 16 kHz from the TIMIT database with the measured impulse responses corresponding to each source's DOA (Garofolo *et al.*, 1993). The power of each speech signal was equalized by scaling the signal appropriately. The number of sources was varied from 3 to 5. For each number of sources, 50 acoustic scenes were constructed by choosing the speech signals randomly from the TIMIT database. The short-time processing parameters used by both variants 1 and 2 of the localization algorithm were 16 ms rectangular windows with 4 ms overlap, 256-pt fast Fourier transform and 120 ms (30 adjacent frames) averaging for each covariance matrix estimate. In variant 2 of the algo-

TABLE I. Bias of the DOA estimates using the MUSIC spectrum.

	Variant 1					Variant 2				
True DOA (deg)	OO_m (deg)	OOO_m (deg)	GG_m (deg)	OO_b (deg)	OOO_b (deg)	OO_m (deg)	OOO_m (deg)	GG_m (deg)	OO_b (deg)	OOO_b (deg)
Three talkers										
0	0	0	0.02	0	0	0.02	0	0.22	0	0
30	0	0.02	0.3	0	0	−0.02	0.08	0.45	0	0
45	0	0	−0.04	0	0	0	0	−0.2	0	0
Four talkers										
−60	0.17	0.08	0.16	0.06	0	0.48	0	0	0	0
0	0	0.22	0.17	0.02	0.02	0.06	0.02	0	0	0
30	0.23	0.02	0.22	0.04	0.27	0.18	−0.04	−0.16	0	0
45	0.15	−0.3	−0.29	0.15	−0.04	0.19	0.04	−0.10	0	0.15
Five talkers										
−75	0.05	0	0.03	0.05	0	0.29	0.04	0.32	0.42	0
−60	0	0	0	0	0	−0.02	0	−0.02	0.17	0.02
0	0.1	0.06	0	0.1	0.06	0.04	0	−0.08	0	0
30	−0.1	0.03	1.0	−0.1	0.03	0.04	0.02	0	0	0
45	0.08	−0.08	0.3	0.08	−0.08	0.11	−0.08	0.33	0	0.04

rithm, the clustering described in Sec. III C was performed using MATLAB's `clusterdata` command. The covariance matrices were normalized to unit norm prior to clustering. The number and location of sources is determined automatically by finding all local maxima in the composite directional spectrum and counting all above an empirically determined threshhold.

Tables I and II show the bias and standard deviation of the DOA estimates from the 50 trials, respectively. Tables III and IV, respectively, show the average number of sources localized per trial and the number of trials that did not localize all sources. Some entries in Tables I and II are exactly zero, indicating no error or bias. This is an artifact of the processing; direction was discretized to one-degree increments in these experiments, so zero standard deviation and bias actually indicates that in all 50 trials, the error never exceeded half a degree, which merely indicates that the biases and standard deviations are a great deal less than half a degree under these conditions.

Tables I and II show that when a source is localized, it is localized very accurately or near its true DOA. The binaural arrays performed better than the monaural arrays, indicating that the addition of aperture improves the performance more than the addition of an extra microphone at smaller aperture. Also, the gradient microphones performed worse than the omnidirectionals both in terms of accuracy and the average number of sources localized. In all the arrays, the localization of more speech sources than microphones seemed to break down at five speech sources; on average, only two to three out of the five total sources were localized. This occurs because the speech sources have overlapping time-frequency spectra, and the undetected sources overlap others in all or

TABLE II. Standard deviation of the DOA estimates using the MUSIC spectrum.

	Variant 1					Variant 2				
True DOA (deg)	OO_m (deg)	OOO_m (deg)	GG_m (deg)	OO_b (deg)	OOO_b (deg)	OO_m (deg)	OOO_m (deg)	GG_m (deg)	OO_b (deg)	OOO_b (deg)
Three talkers										
0	0	0	0.14	0	0	0.15	0	0.42	0	0
30	0	0.14	0.61	0	0	0.26	0.34	0.5	0	0
45	0	0	0.20	0	0	0	0	.64	0	0
Four talkers										
−60	0.38	0.28	0.37	0.24	0	0.51	0	0	0	0
0	0	0.42	0.38	0.15	0.14	0.24	0.14	0	0	0
30	0.79	0.25	0.88	0.51	0.41	0.39	0.20	0.44	0	0
45	0.66	0.58	0.75	0.35	0.29	0.38	0.28	0.66	0	0.02
Five talkers										
−75	0.21	0	0.16	0.21	0	0.73	0.3	0.54	0.08	0
−60	0	0	0.35	0	0	0.40	0	0.35	−0.03	0.15
0	0.31	0.25	0.45	0.31	0.25	0.20	0	0.49	0	0
30	0.33	0.16	0	0.33	0.16	0.55	0.15	0	0	0
45	0.28	0.35	0.58	0.28	0.35	0.52	0.35	0.58	0	0.2

TABLE III. Average number sources localized per trial using the MUSIC spectrum.

	Variant 1					Variant 2				
Number of talkers	OO_m	OOO_m	GG_m	OO_b	OOO_b	OO_m	OOO_m	GG_m	OO_b	OOO_b
3	3	3	3	3	3	2.9	2.98	2.98	2.95	3
4	3.98	4	3.50	3.28	4	3.7	3.95	3.6	3.83	3.71
5	2.7	4.3	2.1	2.7	4.32	2.9	4.4	2.2	4.0	3.8

almost all time-frequency bins over the test interval. This gives some indication of the fundamental effective sparseness of active speech; sparser types of sources would allow more sources to be localized, as would real conversations in which speakers sometimes stop talking. However, it does appear that the three-microphone arrays on average localize somewhat more sources than the two-element arrays, so there is some dependence on the number of microphones as well. With more microphones the energy from multiple weaker sources of noise is likely spread across more small eigenvalues, thus increasing the probability of a successful rank-1 coherence result and providing more bins with which to localize. When the power of some sources is weaker than others, the probability of detecting these sources decreases, but the directional accuracy when detected is similar.

The accuracy of variant 2 of the algorithm was similar to variant 1, but in most of the arrays, variant 2 did not localize as many sources on average as variant 1. The results seem to show that variant 2 is susceptible to errors in clustering, which can account for fewer sources being localized. If a source exhibits only a few low-rank covariance matrices which are improperly clustered at a particular frequency-bin, the contribution of these matrices vanishes in the averaging within a cluster. This is a weakness of variant 2. Similarly, a weakness of variant 1 is that a source with fewer low-rank data contributes fewer spectra peaked at that source's DOA; sources with more low-rank data can dominate the final directional spectrum. One goal of the experiment was to study the tradeoffs in the two approaches, and variant 1 seems to be better at capturing more sources.

Table V shows the performance of the algorithm (variant 1) with a two-element free-field 15 cm array with three speech sources at directions −45°, −10°, and 20° with additional additive white Gaussian noise on each channel at SNRs ranging from 15 to 30 dB. In all cases, the biases and standard deviations are all well less than a degree, demonstrating that the method offers considerable robustness to additive noise. The method performs well with substantial additive noise both because the coherence test rejects low-SNR bins rather than allowing them to degrade the directional estimates and because the errors introduced are uncorrelated from bin to bin and tend to average away in either the clustering or the averaging that produces the composite directional spectrum. Excessive additive noise eventually causes the coherence test to reject most bins, however, so the technique will eventually fail at very low SNRs. A thorough study of the performance in reverberant conditions is beyond the scope of this work, but preliminary simulations show tolerance to reflections of the order expected in typical rooms.

Figures 4(a) and 4(b) are the composite MUSIC spatial spectra at each frequency taken from an acoustic scene with the OO_b array and four speech sources, using steering vectors estimated from HRTF measurements on the KEMAR head as in Sec. IV B. Darker areas in the plots indicate higher values in the MUSIC spectra. The dashed lines in Figs. 4(a) and 4(b) indicate the true DOAs of the sources. Figures 4(a) and 4(b) demonstrate that multiple sources are being localized at many frequency bins. In this example, with variant 1, three sources at −60°, 30°, and 45° are localized at 1 kHz while two sources at 0° and 30° are localized at 1.5 kHz. Figures 4(c) and 4(d) show the final MUSIC spectra after summing across frequency.

As more than 4 s of data are accumulated, if more low-rank time-frequency bins are available, then the localization performance may improve. However, an inherent property of the algorithm is better localization of sources that exhibit more low-rank time-frequency bins. Thus, peaks due to other sources may disappear when summing across time and frequency. An alternate approach is to observe how the algorithm tracks different sources' DOAs as a function of time for longer time periods. Figures 5(a) and 5(b) show the MUSIC spectra computed every 100 and 500 ms with the short-time-frequency covariance matrix estimates averaged over the corresponding intervals, respectively, as a function of time and azimuth for an acoustic scene with the OO_b array on the KEMAR and 10 s of four simultaneous speech sources. The sources' sparseness in the time domain is clearly observed; peaks for the four sources appear and disappear depending on the availability of low-rank time-frequency bins.

TABLE IV. Percent of trials that did not localize all sources using the MUSIC spectrum.

	Variant 1					Variant 2				
Number of talkers	OO_m	OOO_m	GG_m	OO_b	OOO_b	OO_m	OOO_m	GG_m	OO_b	OOO_b
3	0	0	0	0	0	10	2	2	4	0
4	2	0	42	56	0	80	2	26	14	22
5	98	56	100	98	56	84	40	84	61	66

TABLE V. Mean locations and standard deviations of location estimates with uncorrelated additive noise.

SNR (dB)	Mean locations (deg)			Standard deviations (deg)		
15	−44.72,	−9.65,	20.08	0.13,	0.61,	0.14
20	−44.54,	−9.94,	20.13	0.09,	0.26,	0.09
25	−44.50,	−9.83,	20.10	0.06,	0.13,	0.07
30	−44.54,	−9.63,	19.95	0.05,	0.07,	0.06

In recordings from the Spesutie Island field trials, military vehicles moved around a track, and the microphone array was located 27 meters away from the edge of the track. A composite recording was constructed containing a moving M60 tank, a moving HEMET vehicle, and small arms fire about 30–40 m away from the *XYZO* array. Figure 6 shows the MUSIC spectrum as a function of time and azimuth, in which the two vehicles were localized in azimuth to within their physical spans and the small arms fire was sharply localized in azimuth. Three gunshots were localized, occurring at 10, 11.5, and 13 s, at azimuths of 90°, 98°, and 105°. The azimuths were obtained by looking at the first onset of the peak in the MUSIC spectrum, which is at 90° for the first shot (not readily apparent in the plot, but visible with some magnification). These shots were recorded as the shooter fired his weapon at three locations on the track, separated by approximately 4 m. As the distance to the track was 27 m, an expected change in angle was calculated to be approximately 8.4° between shots, which correlates very well with the localization results.

V. CONCLUSION

The successful localization of multiple speech sources was experimentally demonstrated using different subsets of omnidirectional and gradient microphones from the HA6 array located on a KEMAR dummy. Localization of military vehicles and gunfire in a free-field environment using gradient microphones from an acoustic-vector-sensor array was also experimentally demonstrated. To our knowledge, this study contains the first demonstration of high-resolution localization using an aeroacoustic vector sensor.

The two variants of the algorithm localize more speech sources than sensors by exploiting the sparse time-frequency structure and spatial stationarity of the speech sources. First, the coherence test provides a simple means to identify low-rank time-frequency bins, specifically those containing one

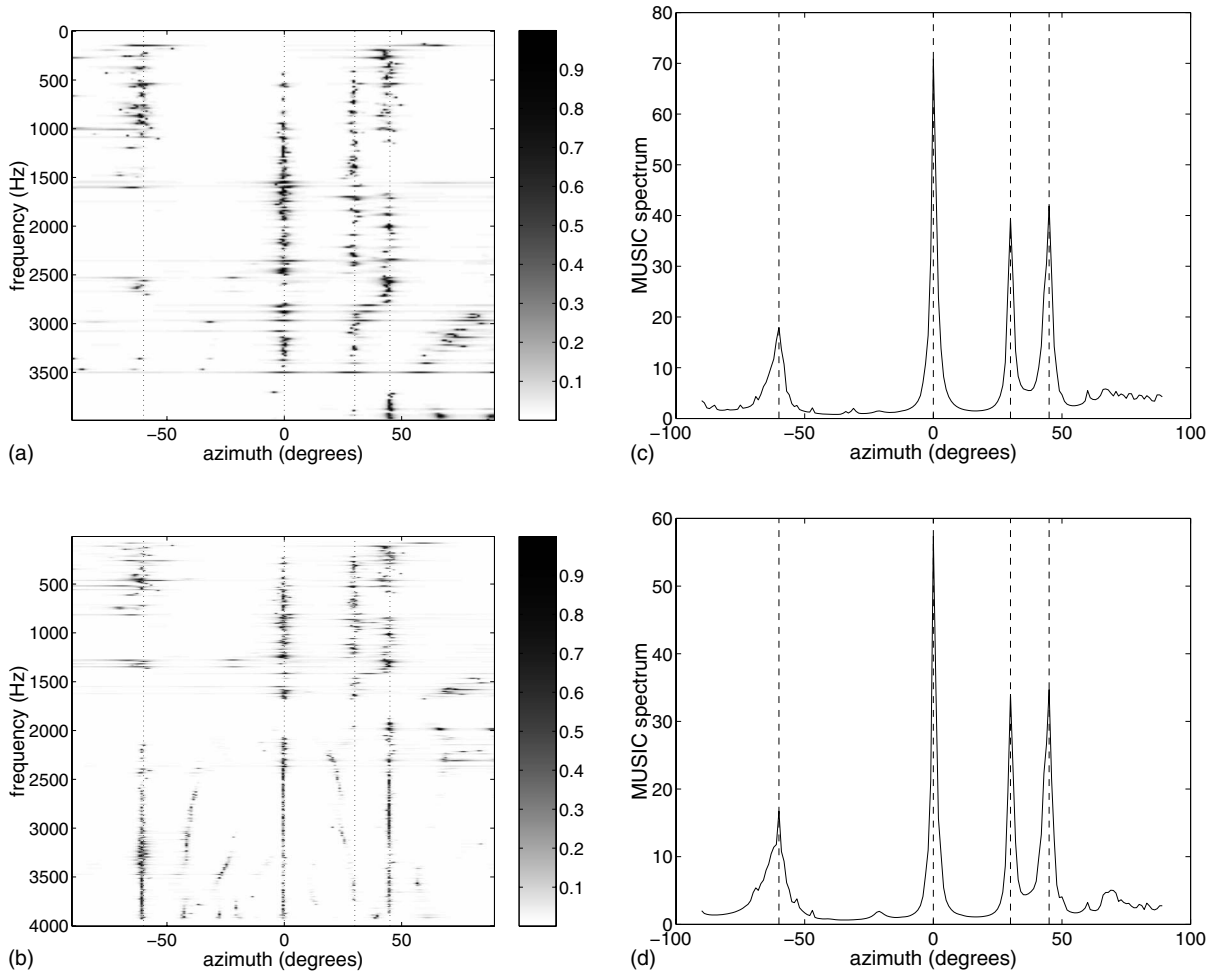

FIG. 4. MUSIC spectra from 4 s of four simultaneous speech sources using the measured responses of the OO_b array on the KEMAR head. Dashed lines show the sources' true DOAs (−60°, 0°, 30°, and 45°). (a) and (b) MUSIC spectra as a function of frequency and azimuth using variants 1 and 2 and (c) and (d) final MUSIC spectra using variants 1 and 2.

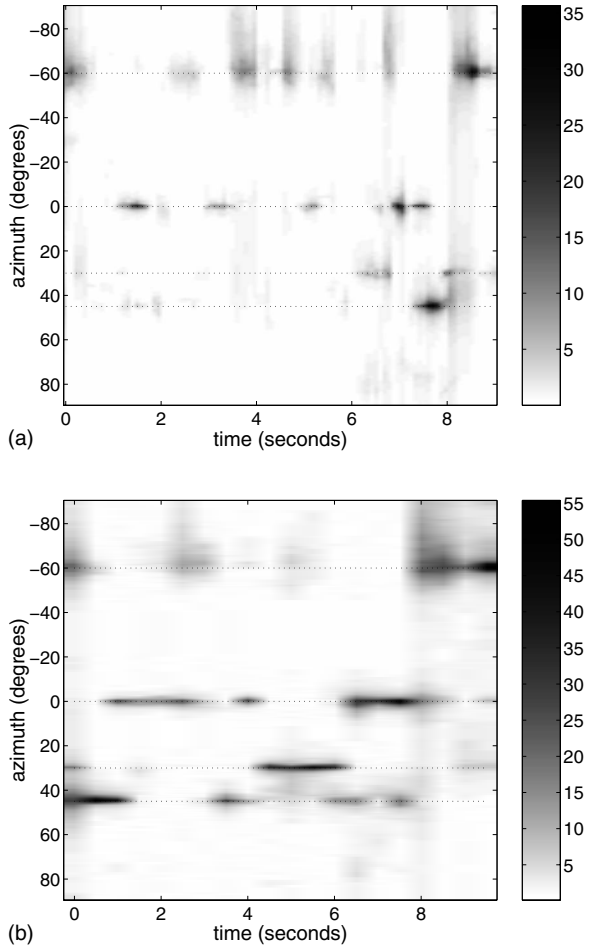

FIG. 5. MUSIC spectra as a function of time and azimuth for 10 s of four simultaneous speech sources using the measured responses of the OO_b array on a KEMAR. MUSIC spectra were computed every, (a) 100 and (b) 500 ms. Dashed lines show the sources' true DOAs (−60°, 0°, 30°, and 45°).

active source. The data at these low-rank bins can be used in two ways: Variant 1 of the algorithm can be used to perform incoherent combining of directional information across time and frequency, or variant 2 can be used to perform coherent combining of data (by clustering low-rank covariance matrices and averaging within each cluster) followed by transformation to a directional representation. The source direction of arrivals are estimated from the composite directional spectrum regardless of which variant of the algorithm was used.

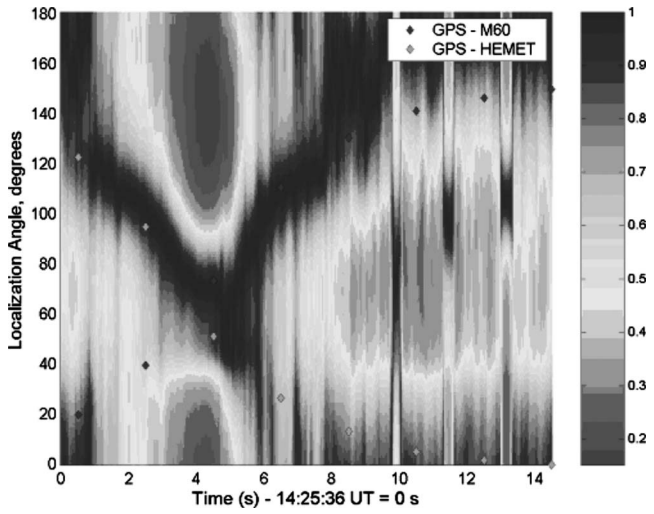

FIG. 6. MUSIC spectrum as a function of time for an acoustic scene consisting of an M60, a HEMET, and small arms fire.

When speech sources were localized, they were localized accurately, since the bias and standard deviation of the DOA estimates were both less than 1° among all various arrays tested. The average number of sources localized dropped significantly across all microphone arrays tested with 4 s of speech when changing from four speech sources to five speech sources. The upper limit appears largely to be a function of the inherent time-frequency sparsity of the sources, and can be expected to be higher or lower depending on the source sparseness characteristics. Both variants of the algorithm performed similarly in bias and standard deviation, whereas variant 1 typically localized more sources on average than variant 2. The performance of the binaural arrays was also usually better than the monaural arrays, probably due to the increase in aperture, which leads to a greater diversity in the steering vectors as a function of azimuth.

The algorithm complexity is of the same order but generally less than that of Pham and Sadler (1996), with the primary complexity in the computation of the individual bin-by-bin MUSIC directional spectra. By restricting the computation only to rank-1 bins, the coherence test becomes simple and inexpensive, and the degradation in performance observed by Pham and Sadler with some source overlap is avoided. In addition, the number of relatively expensive MUSIC directional spectra computations are reduced. The complexity depends on the required resolution, but it should be possible to implement at least variant 1 in real time on a modern DSP microprocessor.

ACKNOWLEDGMENTS

This work was supported by U.S. Army Research Laboratory Contract No. DAAD17-00-0149, National Institute on Deafness and Other Communication Disorders R01 DC005762-02, and NSF CCR 03-12432 ITR. Portions of this work were reported in Mohan *et al.* (2003a,b).

APPENDIX: COHERENCE TEST

1. TWO-SENSOR COHERENCE TEST

Claim: A necessary and sufficient condition for a 2×2 covariance matrix $\mathbf{R}$ to be rank 1 is that the pairwise MSC is equal to 1.

Proof: Let the 2×2 covariance matrix be

$$\mathbf{R}=\begin{pmatrix} R_{11} & R_{12} \\ R_{21} & R_{22} \end{pmatrix}. \tag{A1}$$

Now, let $\mathbf{R}$ be rank 1; then

$$\mathbf{R}=\sigma^2\mathbf{h}\mathbf{h}^{\mathbf{H}}, \tag{A2}$$

where $\mathbf{h}=[a\ b]^{\mathbf{T}}$ for some $a,b\in\mathbb{C}$.

Then, the covariance matrix is

$$\mathbf{R} = \sigma^2 \begin{pmatrix} aa^* & ab^* \\ ba^* & bb^* \end{pmatrix}. \tag{A3}$$

The pairwise MSC is

$$T_{\text{coh}}^{(1,2)} = \frac{ab^* ba^*}{aa^* bb^*} = \frac{|ab|^2}{|a|^2|b|^2} = 1. \tag{A4}$$

Now, assume that the pairwise MSC is equal to 1 and show that **R** is rank-1. As the pairwise MSC is equal to 1, then

$$\frac{|R_{12}|^2}{R_{11}R_{22}} = 1, \tag{A5}$$

$$|R_{12}| = \sqrt{R_{11}R_{22}}, \tag{A6}$$

$$R_{12} = \sqrt{R_{11}R_{22}} e^{j\phi_{12}} \quad \text{for some } \phi_{12} \in \mathbb{R}. \tag{A7}$$

So, we can express the covariance matrix as

$$\mathbf{R} = \begin{pmatrix} R_{11} & \sqrt{R_{11}R_{22}} e^{j\phi_{12}} \\ \sqrt{R_{11}R_{22}} e^{-j\phi_{12}} & R_{22} \end{pmatrix} \tag{A8}$$

and we see that

$$(\text{column 1 of } \mathbf{R}) \sqrt{\frac{R_{22}}{R_{11}}} e^{j\phi_{12}} = (\text{column 2 of } \mathbf{R}). \tag{A9}$$

So, **R** is rank-1 (regardless of the phase ϕ_{12}).

2. M-SENSOR COHERENCE TEST

Claim: A necessary and sufficient condition for an $M \times M$ covariance matrix to be rank 1 is that its $\binom{M}{2}$ pairwise MSCs are equal to 1 and the phases of the its off-diagonal components satisfy $\angle(R_{ij}) - \angle(R_{ik}) + \angle(R_{jk}) = 0 \ \forall i < j < k$ where $\angle(R_{ij})$ is the phase of the ijth element of the covariance matrix.

Proof: Let **R** be rank 1.

$$\mathbf{R} = \sigma^2 \mathbf{h}\mathbf{h}^{\mathbf{H}}, \tag{A10}$$

$$\mathbf{h} = [h_1 \ \dots \ h_M]^{\mathbf{T}} h_i \in \mathbb{C}, \quad i = 1 \dots M. \tag{A11}$$

Then, the ijth component of **R** is

$$R_{ij} = \begin{cases} |h_i|^2 & \text{if } i = j \\ h_i h_j^* = |h_i||h_j| e^{j(\angle h_i - \angle h_j)} & \text{if } i \neq j. \end{cases} \tag{A12}$$

The pairwise MSCs are all equal to 1.

$$T_{\text{coh},ij} = \frac{h_i h_j^* h_j h_i^*}{h_i h_i^* h_j h_j^*} = \frac{|h_i h_j|^2}{|h_i|^2 |h_j|^2} = 1 \ \ \forall j > i. \tag{A13}$$

The phase constraint, $\angle(R_{ij}) - \angle(R_{ik}) + \angle(R_{jk}) = 0 \ \forall i < j < k$, is also satisfied.

$$\angle(R_{ij}) - \angle(R_{ik}) + \angle(R_{jk}) = \tag{A14}$$

$$= (\angle h_i - \angle h_j) - (\angle h_i - \angle h_k) + (\angle h_j - \angle h_k) \tag{A15}$$

$$= \angle h_i - \angle h_i + \angle h_j - \angle h_j + \angle h_k + - \angle h_k \tag{A16}$$

$$= 0. \tag{A17}$$

Now, assume that the $\binom{M}{2}$ pairwise MSCs are equal to 1 and the phase constraint is satisfied. We can then show that **R** is rank-1.

$$R_{ij} = \begin{cases} R_{ii} & \text{if } i = j \\ \sqrt{R_{ii}R_{jj}} e^{j\phi_{ij}} & \text{if } i < j \\ \sqrt{R_{ii}R_{jj}} e^{-j\phi_{ij}} & \text{if } i > j. \end{cases} \tag{A18}$$

We obtain the following relationships between the columns of the covariance matrix.

$$(\text{column } i \text{ of } \mathbf{R}) \sqrt{\frac{R_{kk}}{R_{ii}}} e^{-j\phi_{ik}} = \text{column } k \text{ of } \mathbf{R} \ \ \forall i \neq k, \tag{A19}$$

$$\phi_{ij} - \phi_{ik} + \phi_{jk} = 0 \ \ \forall i < j < k. \tag{A20}$$

Thus, only a single linearly independent column exists in **R**, or **R** is rank-1.

Carter, G.C. (**1987**). "Coherence and time delay estimation," Proc. IEEE **75**, 236–255.

Gardner, W., and Martin, K. (**1995**). "HRTF measurements of a KEMAR," J. Acoust. Soc. Am. **97**, 3907–3908.

Garofolo, J. S., Lamel, L. F., Fisher, W. M., Fiscus, J. G., Pallett, D. S., and Dahlgren, N. L. (**1993**). "DARPA TIMIT acoustic-phonetic continuous speech corpus," US National Institute of Standards and Technology, *CD-ROM*.

Hawkes, M., and Nehorai, A. (**1998**). "Acoustic vector-sensor beamforming and Capon direction estimation," IEEE Trans. Signal Process. **46**, 2291–2304.

Hlawatsch, F., and Boudreaux-Bartels, G. F. (**1992**). "Linear and quadratic time-frequency signal representations," IEEE Signal Process. Mag. **9**, 21–67.

Johnson, D., and Dudgeon, D. (**1993**). *Array Signal Processing: Concepts and Techniques* (Prentice Hall, Englewood Cliffs, NJ).

Lockwood, M., Jones, D., Bilger, R., Lansing, C., O'Brien, W., Wheeler, B., and Feng, A. (**2004**). "Performance of time- and frequency-domain binaural beamformers based on recorded signals from real rooms," J. Acoust. Soc. Am. **115**, 379–391.

Lockwood, M., Jones, D., Elledge, M., Bilger, R., Goueygou, M., Lansing, C., Liu, C., O'Brien, W., and Wheeler, B. (**1999**). "A minimum variance frequency-domain algorithm for binaural hearing aid processing," J. Acoust. Soc. Am. **106**, 2278 (Abstract).

McConnell, J. (**2003**). "Highly directional receivers using various combina-

tions of scalar, vector, and dyadic sensors," J. Acoust. Soc. Am. **114**, 2427 (Abstract).
Miles, R., Gibbons, C., Gao, J., Yoo, K., Su, Q., and Cui, W. (**2001**). "A silicon nitride microphone diaphragm inspired by the ears of the parasitoid fly Ormia ochracea," J. Acoust. Soc. Am. **110**, 2645 (Abstract).
Mohan, S., Kramer, M., Wheeler, B., and Jones, D. (**2003a**). "Localization of nonstationary sources using a coherence test," 2003 IEEE Workshop on Statistical Signal Processing, pp. 470–473.
Mohan, S., Lockwood, M., Jones, D., Su, Q., and Miles, R. (**2003b**). "Sound source localization with a gradient array using a coherence test," J. Acoust. Soc. Am. **114**, 2451 (Abstract).
Nehorai, A., and Paldi, E. (**1994**). "Acoustic vector-sensor array processing," IEEE Trans. Signal Process. **42**, 2481–2491.
Nickles, J. C., Edmonds, G., Harriss, R., Fisher, F., Hodgkiss, W.S., Giles, J., and D'Spain, G. (**1992**). "A vertical array of directional acoustic sensors," IEEE Oceans Conference **1**, 340–345.
Pham, T., and Sadler, B. (**1996**). "Adaptive wideband aeroacoustic array processing," in 8th IEEE Signal Processing Workshop on Statistical Signal and Array Processing, pp. 295–298.
Rickard, S., and Dietrich, F. (**2000**). "DOA estimation of many W-disjoint orthogonal sources from two mixtures using DUET," *Proceedings of the Tenth IEEE Workshop on Statistical Signal and Array Processing*, pp. 311–314.
Schmidt, R. (**1986**). "Multiple emitter location and signal parameter estimation," IEEE Trans. Antennas Propag. **AP-34**, 276–280.
Su, G., and Morf, M. (**1983**). "The signal subspace approach for multiple wide-band emitter location," IEEE Trans. Acoust., Speech, Signal Process. **ASSP-31**, 1502–1522.
Tichavsky, P., Wong, K., and Zoltowski, M. (**2001**). "Near-field/far-field azimuth and elevation angle estimation using a single vector hydrophone," IEEE Trans. Signal Process. **49**, 2498–2510.
Wong, K., and Zoltowski, M. (**1997**). "Uni-vector-sensor ESPRIT for multisource azimuth, elevation, and polarization estimation," IEEE Trans. Antennas Propag. **45**, 1467–1474.
Zhang, Y., Mu, W., and Amin, M. (**2001**). "Subspace analysis of spatial time-frequency distribution matrices," IEEE Trans. Signal Process. **49**, 747–759.

Angle-dependent ultrasonic detection and imaging of brachytherapy seeds using singular spectrum analysis

Jonathan Mamou,[a] Sarayu Ramachandran, and Ernest J. Feleppa
Frederic L. Lizzi Center for Biomedical Engineering, Riverside Research Institute, 156 William Street, 9th Floor, New York, New York 10038, USA

(Received 24 October 2007; revised 21 January 2008; accepted 27 January 2008)

Transrectal-ultrasound-guided brachytherapy uses small titanium-shelled radioactive seeds to locally treat prostate cancer. During the implantation procedure, needles inserted transperitoneally cause gland movement resulting in seed misplacement and suboptimal dosimetry. In a previous study, an algorithm based on singular spectrum analysis (SSA) applied to envelope-detected ultrasound signals was proposed to determine seed locations [J. Mamou and E. J. Feleppa, J. Acoust. Soc. Am. **121**, 1790–1801 (2007)]. Successful implementation of the SSA algorithm could allow correcting dosimetry errors during the implantation procedure. The algorithm demonstrated promise when the seed orientation was parallel to the needle and normal to the ultrasound beam. In this present study, the algorithm was tested when the seed orientation deviated up to 22° from normality. Experimental data from a seed in an ideal environment and in beef were collected with a single-element, spherically focused, 5 MHz transducer. Simulations were designed and evaluated with the algorithm. Finally, objective quantitative scoring metrics were developed to evaluate the algorithm performance and for comparison with *B*-mode images. The results quantitatively established that the SSA algorithm always outperformed *B*-mode images and that seeds could be detected accurately up to a deviation of approximately 10°. © *2008 Acoustical Society of America.* [DOI: 10.1121/1.2875740]

PACS number(s): 43.80.Vj, 43.60.Lq, 43.35.Yb [FD] Pages: 2148–2159

I. INTRODUCTION

Brachytherapy is a cancer-treatment procedure that is becoming widely accepted for treating prostate cancer. This procedure consists of the permanent implantation of small radioactive seeds (containing iodine or palladium) within the prostate gland.[1,2] Most types of prostate-brachytherapy seeds consist of a thin, rigid, smooth, cylindrical, titanium shell, and are 4.5 mm long by 0.8 mm in diameter. Currently, transrectal ultrasound (TRUS) is the standard imaging modality for treatment-planning dosimetry, guiding, and monitoring seed implantation.[3,4]

Seeds are inserted transperitoneally through a needle guided by a fixture that is linked to the TRUS probe. After insertion, the seeds ideally are oriented normally to the ultrasonic beam and parallel to the needle. However, movement of the prostate during seed insertion often leads to the seeds being inserted away from their optimal location and with an orientation that deviates from being normal to the transducer beam. Sometimes seeds even are placed outside of the prostate, for example, in the bladder, the urethra, or the circulatory system[5,6] leading to potentially harmful bioeffects from radioactivity. An imaging method that enables visualization of seeds during the implantation procedure would be valuable for taking immediate corrective action by implanting seeds in underdosed regions. Unfortunately, existing TRUS imaging systems used to plan and guide seed implantation do not reliably image implanted seeds. The predominant causes for the difficulty in ultrasonically imaging implanted seeds are seed specularity, shadowing, and clutter from other highly reflecting entities (e.g., calcifications or hemorrhage) in the gland.

Currently, seed location and orientation typically are determined from postimplant x-ray computed tomography (CT) or magnetic resonance imaging (MRI) performed 3 h to 2 weeks after the implantation procedure.[7–9] If, based on imaging results, the radiation oncologist decides that the current dosage is not sufficient to successfully treat the cancer, patients must undergo additional, multiweek, external-beam radiation therapy for dose correction. Therefore, radiation oncologists would find a real-time TRUS-based imaging method that is capable of providing accurate, postinsertion, seed-location and seed-orientation information to be very valuable. Such a modality would enable timely feedback for intraoperatively correcting deficiencies in the radiation dose delivered to the gland and would eliminate the need for CT or MRI imaging and follow-up radiation therapy.

To date, only modest investigations have been conducted to establish the expected distribution of seed angles after insertion in the prostate gland. Follow-up CT or MRI images cannot reliably establish the location and orientation information of each seed.[10] A recent study by Corbet *et al.* looking at quantifying the effect of seed orientation on dose derived an angle probability distribution function based on postimplant radiographs of 10 patients.[11] Their distribution model had a mean angle of 0° between the seed axis and the ultrasound beam, but the distribution had long tails: Only 58% of seeds were predicted to have an angle smaller than 20° from normal to the beam. The actual immediate postim-

[a]Electronic mail: mamou@rrinyc.org.

 0001-4966/2008/123(4)/2148/12/$23.00 © 2008 Acoustical Society of America

plant angle distribution might have a smaller variance around 0°, because in this study the radiographs were taken a month after seed implantation.

In a previous publication, we described a novel ultrasonic method for detecting and imaging brachytherapy seeds.[12] The method seeks to exploit the "tail" of repeating echoes that typically appears beyond the seed, distal to the transducer. It uses the envelope-detected signals derived from the (rf) echo signals produced by an ultrasound probe as the input and forms a color-coded image termed a *P*-mode image. A *P*-mode image consists of the conventional *B*-mode image augmented by color-coded information indicative of the likelihood of seed presence. The strength of the method is the envelope-detected signals used as algorithm inputs are available readily in the operating room because these signals are the video signals used to generate the clinical image. The algorithm is based on a signal-processing framework called singular spectrum analysis (SSA)[13–15] and the color-coded information displayed on the *P*-mode image is obtained by detecting and quantifying the strength of the seed tail signal using the SSA framework.

Our first publication described the SSA algorithm as a viable method to detect and image seeds.[12] However, because the emphasis was on the development and validation of the SSA algorithm, the experiments and simulations were limited to the case where a single seed was oriented orthogonally to the transducer axis. In the present paper, the SSA-algorithm performance is evaluated when the seed orientation with respect to the transducer is varied. Ultrasound experiments were conducted in an ideal environment (i.e., acoustically transparent gelpad) and in a tissue-like (i.e., degassed *ex vivo* beef) environment. Simulations also were developed based on empirical data acquired from the ideal-environment experiments. To quantify performance, we developed two score metrics. The first metric quantifies how well the seed location is determined by the SSA algorithm (i.e., the true-positives produced by the algorithm) and the second metric evaluates whether the SSA algorithm produces false-positives. The paper is organized as follows: Section II presents the methods used to acquire data, to simulate data, to compute the score metrics, and briefly reviews *P*-mode image formation; Sec. III presents the results of the simulations and experiments; and Sec. IV presents the discussion and conclusions of the study.

II. MATERIAL AND METHODS

A. Seeds

The seeds used in this study were nonradioactive versions of commonly used palladium (Pd^{103}) seeds. The seeds were described in Ref. 12 and are an increasingly popular seed for brachytherapy treatment of prostate cancer.

B. Data collection and experiments

All the data were acquired using a 5 MHz, single-element transducer (S/N 25653, Panametrics Inc., Waltham, MA). The transducer has a focal length of 51 mm and a diameter of 14 mm (i.e., an F-number=3.7). The transducer was excited with a Panametrics 5900 pulser/receiver unit.

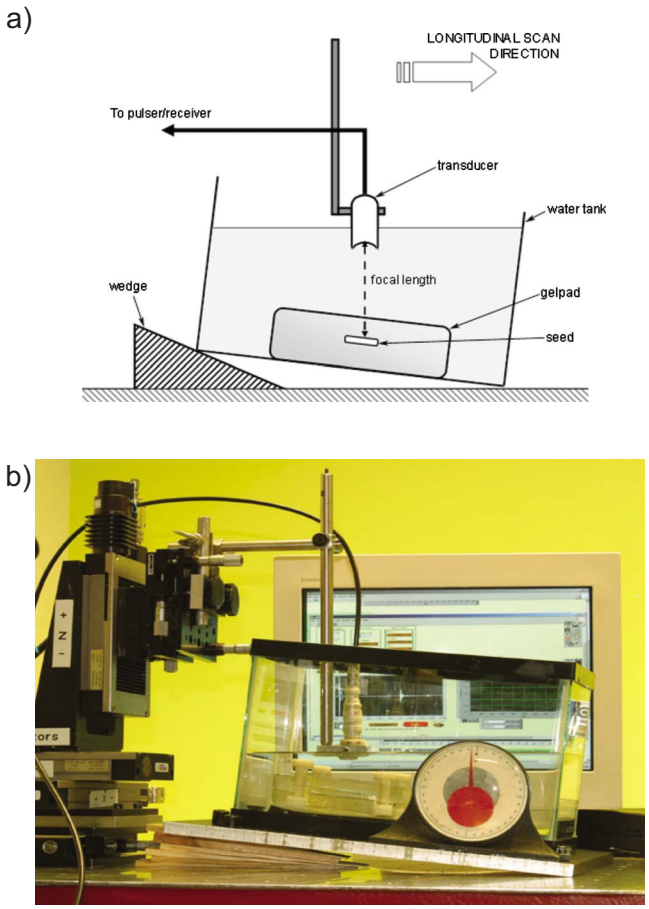

FIG. 1. (Color online) Laboratory setup for gel-pad experiments. (a) Schematic of the experimental setup showing the seed inserted into an acoustically transparent gel pad in a water tank. The angle of the seed is changed by using different wedges. (b) Actual experimental setup with a protractor measuring the tilt angle. The monitor in the background displays the GUI for the data-acquisition software.

The rf echo signals were digitized using an Acqiris DB-110 A/D board (Acqiris, Monroe, NY) at a sampling rate of 50 MS/s. The spacing between adjacent *A* lines was 100 μm. Following digitization, the rf data were saved, envelope-detected, and processed offline using the SSA algorithm.

In the first set of experiments, a seed was inserted into an acoustically transparent gelpad (Aquaflex, Parker Laboratories, Fairfield, NJ) that was placed in a water bath for scanning. The angle between the seed and the acoustic-beam axis was varied by tilting the bath while the transducer remained vertical [Fig. 1(a)]. This setup allowed us to change the angle of the seed with respect to the ultrasound beam by increasing or decreasing the tilt angle of the tank. The initial angle of the seed was determined by scanning along the long axis of the seed. This longitudinal *B*-mode scan indicated whether the seed was inserted into the gelpad at an angle. If the seed appeared slanted in the longitudinal scan, the angle of the tank was adjusted to remove the incline. Once the seed was horizontal (i.e., at 0°), it was scanned in two directions: along the long axis of the seed (a longitudinal scan) and across the cross section of the seed (a transverse scan). Care was taken to ensure that the seed was centered simulta-

neously in the transverse and longitudinal scan planes. The seed also was maintained in the focal region of the transducer. To vary the angle of the seed, angled wedges were placed under the water tank. The tilt angle was measured with a protractor attached to the base of the tank [Fig. 1(b)]. The angle was varied from 0° (i.e., horizontal) to 22° from the horizontal in steps of 1°, with centered transverse and longitudinal scans performed at each angle. Figure 1(b) shows the experimental laboratory setup. The monitor in the background displays a single *A* line using the custom LABVIEW (National Instruments, Austin, TX) software that acquired the rf data.

In the second set of experiments, a similar assembly was used to acquire data from a seed inserted in a piece of beef. The beef was degassed prior to seed insertion and had a thickness of 2 cm. The tank was filled with phosphate-buffered saline, and echo data were collected at 1° increments from 0° to 21° employing the method that was used in the gelpad experiments (Fig. 1).

C. Angle-dependent simulations

Simulations of seed rf echo signals from 0° to 11° were performed in order to evaluate the performance of the SSA algorithm under controlled conditions. The simulations were based on the empirical data obtained from the gelpad experiments and designed so that a complete *B*-mode image could be formed. The rf data corresponding to each *A* line was simulated at a sampling rate of 50 MS/s, and the spacing between two adjacent *A* lines was 100 μm for consistency with acquired experimental data.

Figure 2 displays rf echo signals (i.e., one *A* line) from experimental longitudinal scans (seed in gelpad) in the left column, and the corresponding simulated rf echo signals in the right column. The rf echo signal from the center of the seed at an angle of 0° (in longitudinal and transverse directions) was modeled as four pulses, 0.8 μs apart, with center frequencies of 5 MHz. Figures 2(a) and 2(b) show the central *A* line (i.e., echo from the center of the seed) at 0° with the four pulses (i.e., a1, a2, a3, and a4). Pulses a1 and a3 were modeled as Hanning-windowed, three-cycle tone bursts. Pulses a2 and a4 were modeled as having five and four cycles, respectively. Similar *A* lines were simulated on either side of the central *A* line to obtain a complete *B*-mode image. The off-center *A* lines were deduced from the center *A* line by weighting the central *A* line so that the maximum amplitude of the seed echoes gradually decreased on moving away from the center of the seed (as observed experimentally). Figures 2(c) and 2(d) show the experimental and simulated *A* lines 2 mm away from the center of the seed. The peak amplitudes of these off-center *A* lines are 34% (i.e., 9.3 dB) lower than those of Figs. 2(a) and 2(b).

In the transverse and longitudinal simulations, as the angle of the seed increased, the peak amplitude values of the modeling pulses were lowered to match the corresponding experimental values. In the simulated longitudinal scans only, the seed itself had to appear tilted in the *B*-mode image. Simulating the tilt of the seed was achieved by delaying the off-center *A* lines to simulate one end of the seed being farther from the transducer than the other. The delays were computed based on the angle being modeled. Figures 2(e) and 2(f) display off-center *A* lines from experiments and simulated echo signals at an angle of 6°. The dotted plots represent the central *A* lines at 0°. Figures 2(e) and 2(f) illustrate the added delay for tilting and the change in peak amplitude of the echo data as the angle of the seed with the ultrasound beam is varied.

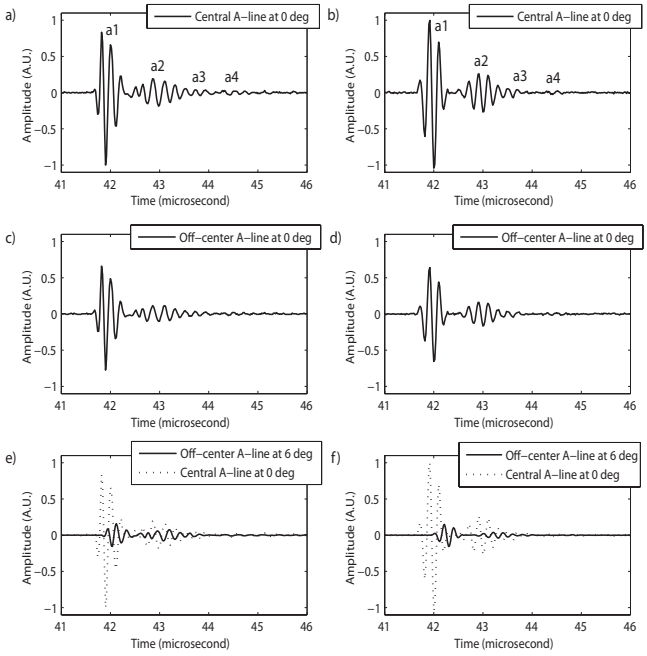

FIG. 2. Comparison of experimental and simulated rf *A* lines for longitudinal scans. Left column displays *A* lines from gel pad experiments. Right column displays the corresponding simulated *A* lines. (a) and (b) *A* lines from the center of a seed at 0°. (c) and (d) Off-center *A* lines from a seed at 0°, showing lower peak amplitudes. (e) and (f) Off-center *A* lines from a seed at 6°, showing the delays introduced to model tilting of the seed. Central *A* lines from a seed at 0° are shown for reference.

For all simulations, white Gaussian noise was added to the simulated rf signals to match the same signal-to-noise ratio (SNR) as in the experimental data. Finally, the simulated rf signals were envelope-detected to form simulated *B*-mode images and to provide the signals needed as input for the SSA algorithm.

D. Performance-evaluation metrics

Two types of scoring metrics were developed to evaluate the ability of the SSA algorithm to detect and image seeds at various angles. The first type of metric was used for the gelpad experiments and the corresponding simulations. This metric termed Score was chosen to equal the maximum *P*-mode value in a region-of-interest (ROI) containing the actual and known location of the seed. In the case of the gelpad experiments and simulations, this metric captures the complete performance of the algorithm because false-positives never occurred (i.e., the SSA algorithm never interpreted the envelope-detected white Gaussian noise as being a seed).

However, for the beef experiments, a second type of metric needed to be created to account for possible false-

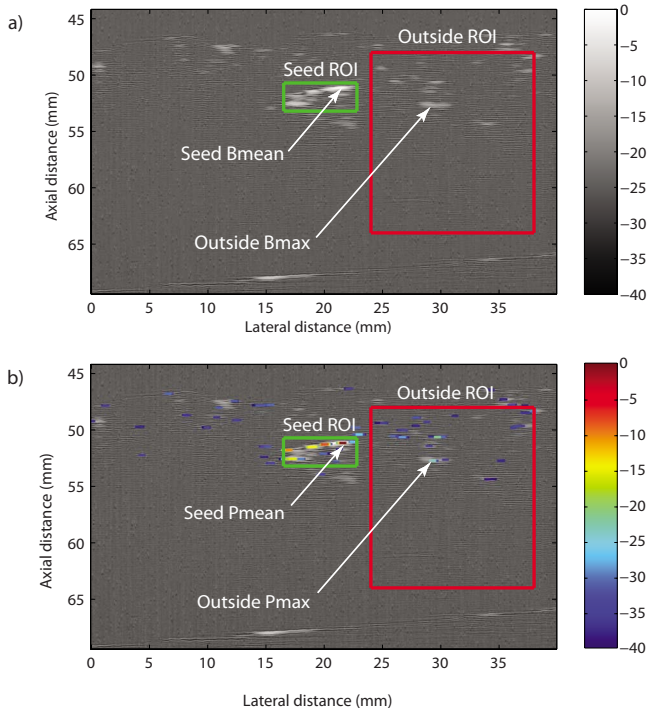

FIG. 3. (Color online) Illustration of the seed and outside ROIs used to evaluate algorithm performance (i.e., SS and WFP). (a) Longitudinal *B*-mode scan of a seed at 6°. (b) *P*-mode values superimposed on the *B*-mode image. The same seed ROI and outside ROI are used to compute *B*-mode and *P*-mode scores.

positives as well as false-negatives. Two measures of the second type were computed from the generated *P*-mode values by applying the SSA algorithm to the envelope-detected rf echo signals. The first measure of the second type was termed the Seed Score (SS) and the second was the Worst False Positive (WFP). The metrics were designed so that the SS indicates how well the seed is detected and imaged by the algorithm and WFP provides information regarding the possible false-positives.

To illustrate how SS and WFP were computed, Figure 3(a) shows a longitudinal *B*-mode image of a seed at an angle of 6° marked with two ROIs: one termed "seed" ROI includes the seed and the other termed "outside" ROI includes highly echogenic structures but not the seed. Figure 3(b) shows the corresponding *P*-mode image. SS was estimated using

$$\mathrm{SS}_{\mathbf{P}} = \mathrm{Seed}_{\mathbf{P}_{\mathrm{Mean}}} - \mathrm{Outside}_{\mathbf{P}_{\mathrm{rms}}}, \tag{1}$$

where $\mathrm{Seed}_{\mathbf{P}_{\mathrm{Mean}}}$ is the mean of the three maximum *P*-mode values within the seed ROI, and $\mathrm{Outside}_{\mathbf{P}_{\mathrm{rms}}}$ is the root-mean-square of all *P*-mode values within the outside ROI.

To compute WFP, a matched filter was used to compute the two-dimensional (2D) correlation between the *P*-mode values in the outside ROI and a rectangular mask of size 0.19 mm × 0.5 mm. From an image-processing standpoint this operation is a 2D moving-average filter (i.e., a low-pass operation). This 2D filtering allows selecting areas where large *P* values are adjacent to each other (i.e., form a connected component having large *P* values, like a possible seed) and discarding large *P* values that are isolated (i.e., probably noise and not a seed). Thus, the rationale is that the peak of the 2D correlation indicates where in the outside ROI a connected component of large *P* values looks the most like a seed. The quantity $\mathrm{Outside}_{\mathbf{P}_{\mathrm{Max}}}$ was defined as the *P*-mode value at the location of the maximum of the 2D correlation and WFP was defined by

$$\mathrm{WFP}_{\mathbf{P}} = \mathrm{Outside}_{\mathbf{P}_{\mathrm{max}}} - \mathrm{Outside}_{\mathbf{P}_{\mathrm{rms}}}. \tag{2}$$

Arrows in Fig. 3(b) indicate the positions of the $\mathrm{Seed}_{\mathbf{P}_{\mathrm{Mean}}}$ and $\mathrm{Outside}_{\mathbf{P}_{\mathrm{Max}}}$.

In Eqs. (1) and (2), the subscript **P** indicates that $\mathrm{SS}_{\mathbf{P}}$ and $\mathrm{WFP}_{\mathbf{P}}$ were computed from the *P*-mode values. For comparison, the same scores were computed from the *B*-mode data. Equations (3) and (4) define the seed Score and WFP for the *B*-mode image:

$$\mathrm{SS}_{\mathbf{B}} = \mathrm{Seed}_{\mathbf{B}_{\mathrm{Mean}}} - \mathrm{Outside}_{\mathbf{B}_{\mathrm{rms}}}, \tag{3}$$

and

$$\mathrm{WFP}_{\mathbf{B}} = \mathrm{Outside}_{\mathbf{B}_{\mathrm{max}}} - \mathrm{Outside}_{\mathbf{B}_{\mathrm{rms}}}. \tag{4}$$

Arrows in Fig. 3(a) indicate the positions of $\mathrm{Seed}_{\mathbf{B}_{\mathrm{Mean}}}$ and $\mathrm{Outside}_{\mathbf{B}_{\mathrm{Max}}}$. (The subscript **B** indicates that $\mathrm{SS}_{\mathbf{B}}$ and the $\mathrm{WFP}_{\mathbf{B}}$ were computed from the *B*-mode values.)

Comparing the scores obtained with the *P*-mode data with those obtained with the *B*-mode data determines whether the SSA algorithm improves the quality of the detection and imaging of seeds over visual assessment of conventional (i.e., *B*-mode) ultrasound images.

E. Singular spectrum analysis algorithm

The current SSA algorithm is identical to the algorithm presented in great detail in a previous publication[12] except for the introduction of *soft thresholds* in the eigenvalue-pair selection process. In the previous version of the algorithm, eigenvalue pairs of the auto-correlation matrix of the envelope-detected signals were selected when the following three inequalities were true:

1) $i < k_{90}$ and $j < k_{90}$, where $k_{90} = \mathrm{Min}\ \{l,$ such that $\Sigma_{i=1}^{l}\lambda_i / \Sigma_{i=1}^{M}\lambda_i > 0.9\}$.
2) $|1 - \lambda_i/\lambda_j| < 0.04$.
3) The frequencies, f_i and f_j, at which the spectra (i.e., the magnitude of the Fourier transforms) of eigenvectors E^i and E^j reach their maxima, respectively, are such that $|1 - f_i/f_j| < 0.03$.

In these inequalities, the eigenvalues of the autocorrelation matrix are ordered from the largest to the smallest, $(\lambda_1 > \cdots > \lambda_M)$, and $E^1, \cdots, E^M$ are the corresponding eigenvectors. The set of selected eigenvalues is denoted by Γ. Following eigenvalue selection, a new time signal, s_r, is constructed from the selected pairs by (see Ref. 12 for notations):

$$s_r(i+j) = \sum_{k \in \Gamma} a_i^k E_j^k, \tag{5}$$

A *P* value indicative of the likelihood of a seed presence is derived from s_r. The last step of the algorithm consists of

forming the color-coded P-mode image that indicates where the algorithm believes each seed is located.[12]

Soft thresholds. Simulations of signals having eigenvalue pairs near the thresholds of the three inequalities led to results with large standard deviations depending on whether for a particular realization the eigenvalues satisfied the inequalities. The hard thresholds used in the previous version of the algorithm essentially made the P-mode image a noncontinuous function of the rf data, but continuity translates into greater algorithm robustness. The soft-threshold approach presented below makes the SSA algorithm continuous.

To implement the soft threshold, we kept the first inequality the same (i.e., item 1 in Sec. II E) and defined:

$$\delta(i,j) = \frac{\left|1 - \frac{\lambda_i}{\lambda_j}\right|}{0.04}, \tag{6}$$

$$\delta'(i,j) = \frac{\left|1 - \frac{f_i}{f_j}\right|}{0.03}, \tag{7}$$

$$\Delta(k) = \min\{\delta(k-1,k), \delta(k,k+1)\}, \tag{8}$$

$$\Delta'(k) = \min\{\delta'(k-1,k), \delta'(k,k+1)\}, \tag{9}$$

Equation (5) then was rewritten as

$$s_r(i+j) = \sum_{k<k_{90}} \gamma_k a_i^k E_j^k, \tag{10}$$

where

$$\gamma_k = \Gamma(\Delta(k))\Gamma(\Delta'(k)), \tag{11}$$

and

$$\Gamma(x) = \frac{1}{2} - \frac{\tanh[\alpha(x-1)]}{2}, \tag{12}$$

where the parameter α can be adjusted to select how "soft" the thresholds should be. The criteria for choosing α are discussed in the following.

Equation (10) essentially says that the sum is extended to all eigenvalues up to the 90% total variance of the signal (i.e., index k_{90}) but weighted by a coefficient, γ_k, that is now continuous. Note that Eq. (11) reduces to Eq. (5) if γ_k is defined to be equal to 1 when $\Delta(k)<1$ and $\Delta'(k)<1$ and equal to 0 otherwise.

Figure 4 displays the function $\Gamma(x)$ for three different values of α. Figure 4 shows that as the numerical value of α increases, the function $\Gamma(x)$ converges to a discontinuous function (see curve for $\alpha=100$) and Eq. (11) reduces to Eq. (5). The smaller the value of α the "softer" the thresholds become (e.g., $\alpha=3$). The solid curve is the one used in this study, and the value of α was chosen such that $\Gamma(0.8)=1-\Gamma(1.2)=0.99$. Essentially, if $\Delta(k)<0.8$ and $\Delta'(k)<0.8$ or if $\Delta(k)>1.2$ and $\Delta'(k)>1.2$, then the eigenvalues are summed or dismissed, respectively, just as in the hard threshold case. Between these values, the algorithm behaves continuously; the eigenvalues are added, but are weighted by a coefficient that depends on how "certain" the algorithm is that the considered eigenvalue is part of a pair. This behavior is the reason that the thresholds are termed soft, and because $\Gamma(x)$ is continuous (actually infinitely differentiable), the algorithm is continuous.

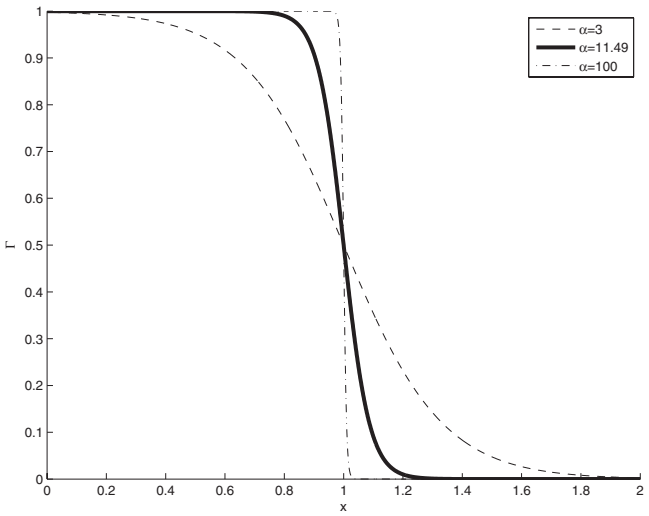

FIG. 4. Soft-threshold $\Gamma(x)$ function for three different values of parameter α.

III. RESULTS

A. Gel-pad experiments and single-seed simulations

The longitudinal and transverse scans of a seed in a gel pad were analyzed with the SSA algorithm. The simulations of seed echoes based on the acquired experimental data also were employed to generate P-mode images. To evaluate simulation performance, each angle (from 0° to 11° incremented in 1° steps) in each direction was simulated ten times with different realizations of white Gaussian noise.

Figure 5 displays the longitudinal P-mode images of experimental data (first, third, and fifth rows) and of one realization of the simulated data (second and fourth rows). The SNRs of the experimental data varied from 44 dB at 0° to 39 dB at 22°. The SNRs of the simulated data were matched to those of the experimental data at each seed angle. The P-mode images are displayed with a 40 dB dynamic range.

For the experiments and the simulations, Fig. 5 shows that the seed was perfectly detected (as shown by the red area on the P-mode images) by the SSA algorithm when the angle of the seed was below 6°. The P values at these low angles were well-localized at the first echo from the seed. As the angle of the seed increased above 6°, the shape of the seed in the longitudinal B-mode images changed: Echo amplitudes at the center of the seed became noticeably lower than those at the ends of the seed (third and fifth rows of Fig. 5). Overall, the P-mode images at angles greater than 6° were of lower quality than those obtained at smaller angles, but the seed could always be detected. For example, at angles between 12° and 22° (fifth row in Fig. 5), large P values were still visible at the first echo from the seed, but other regions of the P-mode image also lit up. The undesired

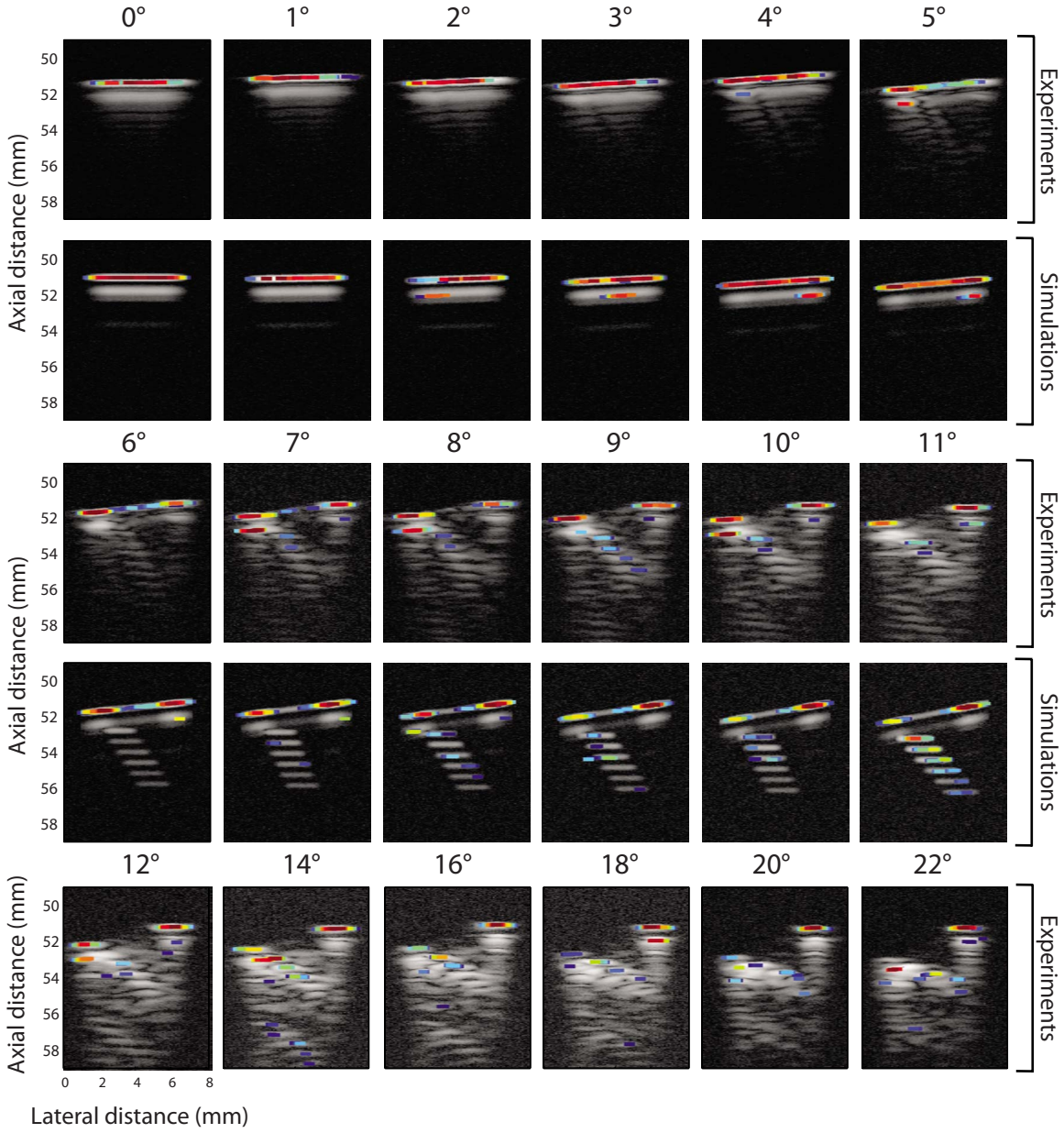

FIG. 5. (Color online) Longitudinal *P*-mode images of a seed in a gel pad at different angles with corresponding simulations. The first, third, and fifth rows display experimental data from 0° to 22° of seed tilt. Second and fourth rows show simulated *B*-mode images from 0° to 11° of seed tilt. All scans are 8 mm across, and the *P* values have a dynamic range of 40 dB.

P values centered over multiple reflections at the back of the seed (i.e., the side of the seed farthest from the transducer) weakened the specificity of the algorithm at higher angles. Overall, the performance of the algorithm in the longitudinal case was very good. The seed always was found and displayed by the algorithm and only a few possible false-positives occurred.

Figure 6 displays the *P*-mode images for the transverse data in the same format as Fig. 5. The results demonstrate that the algorithm performed perfectly up to an angle of 6°. At angles greater than 6°, the seed also was detected, but the corresponding *P* values appeared slightly below the actual seed location (e.g., 2 mm below for the 11° and 22° cases). Such a difference is not of great importance for dosimetry, but we are currently investigating ways of modifying the algorithm to correctly recover depth. Just as in the longitudinal case, weak but undesired *P* values occurred away from the actual seed location at angles greater than 8° (e.g., the 10° or 20° cases). These weak, spurious *P* values would most likely not be falsely interpreted as seeds in a clinical setting. Overall, the performance of the SSA algorithm was perfect up to 6°, and satisfactory up to 22°. The seed always was detected but sometimes was imaged at an apparent location that was deeper than the actual location.

Figures 5 and 6 also demonstrate that our simulation method produced *P*-mode images that were visually similar to those of the experiments for both seed orientations and for angles up to 11°. At lower angles, the seed is perfectly recovered (e.g., in the 4° case for both orientations), but when the angle increased, the performance of the algorithm worsened in simulations just as it did in experiments.

To quantify the above-noted observations, Score values

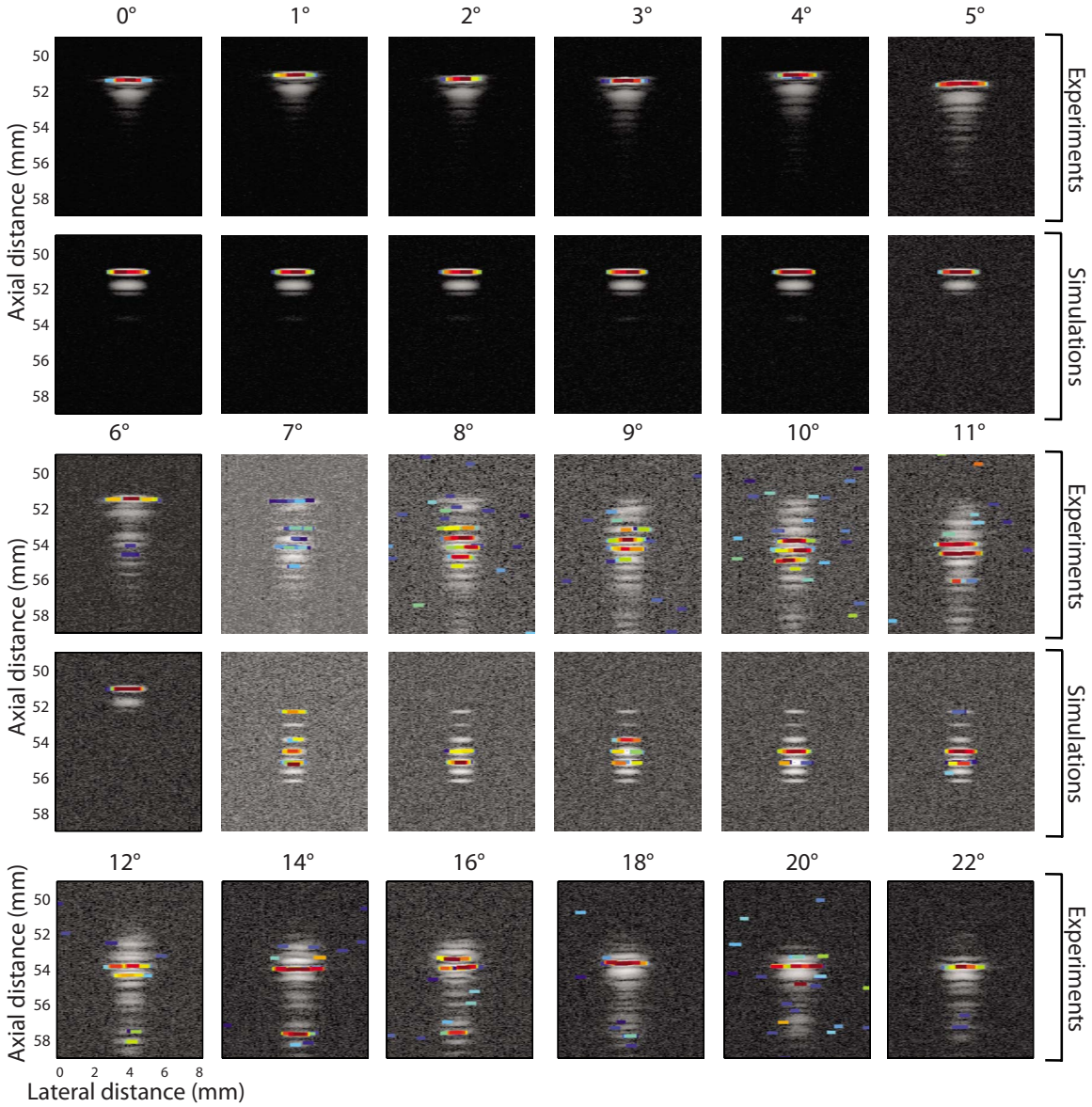

FIG. 6. (Color online) Transverse *P*-mode images of a seed in a gel pad at different angles, with corresponding simulations. The first, third, and fifth rows display experimental data from 0° to 22° of seed tilt. The second and fourth rows show simulated *B*-mode images from 0° to 11° of seed tilt. All scans are 8 mm across, and the *P* values have a dynamic range of 40 dB.

were computed for the longitudinal and transverse scans and displayed in Figs. 7(a) and 7(b), respectively. For the simulations, each data point is the mean of ten realizations and is displayed with error bars symbolizing standard deviations. The experimental results of Fig. 7(a) are fairly constant in demonstrating that the algorithm detects the seed at every angle the same way. The simulation results are slightly more angle dependent; results are better at lower angles (up to 20 dB better) before stabilizing at about 5 dB below the experimental curve.

The trend of the Score value is different for the transverse seed orientation [Fig. 7(b)]. The experimental and simulated curves are very similar and follow the same trend. The Score value decreased very quickly from about 140 dB at 0° to about 75 dB at 7°. Beyond 7°, both curves remained fairly low (i.e., below 100 dB) except for an odd high experimental value of 120 dB for 21°. Figure 7(b) demonstrates that, as is qualitatively apparent in Fig. 6, the SSA algorithm performance drops quickly with increasing angles in the transverse direction.

B. Multiple-seed simulations

Figure 8 shows a clinically more-realistic application of our seed-simulation methods. In Figs. 5 and 6, only a single seed was modeled. In this section, we describe a multiseed simulation study.

Figure 8 displays a simulated conventional *B*-mode image containing three seeds. Two of the seeds (T2 and T11) are simulated in the transverse direction with angles of 2° and 11°, respectively, and the third seed (L6) is simulated in the longitudinal direction with an angle of 6°. Figure 8(a) was obtained by adding white Gaussian noise to the simulated seeds to simulate a gel-pad experiment. Figure 8(b) was

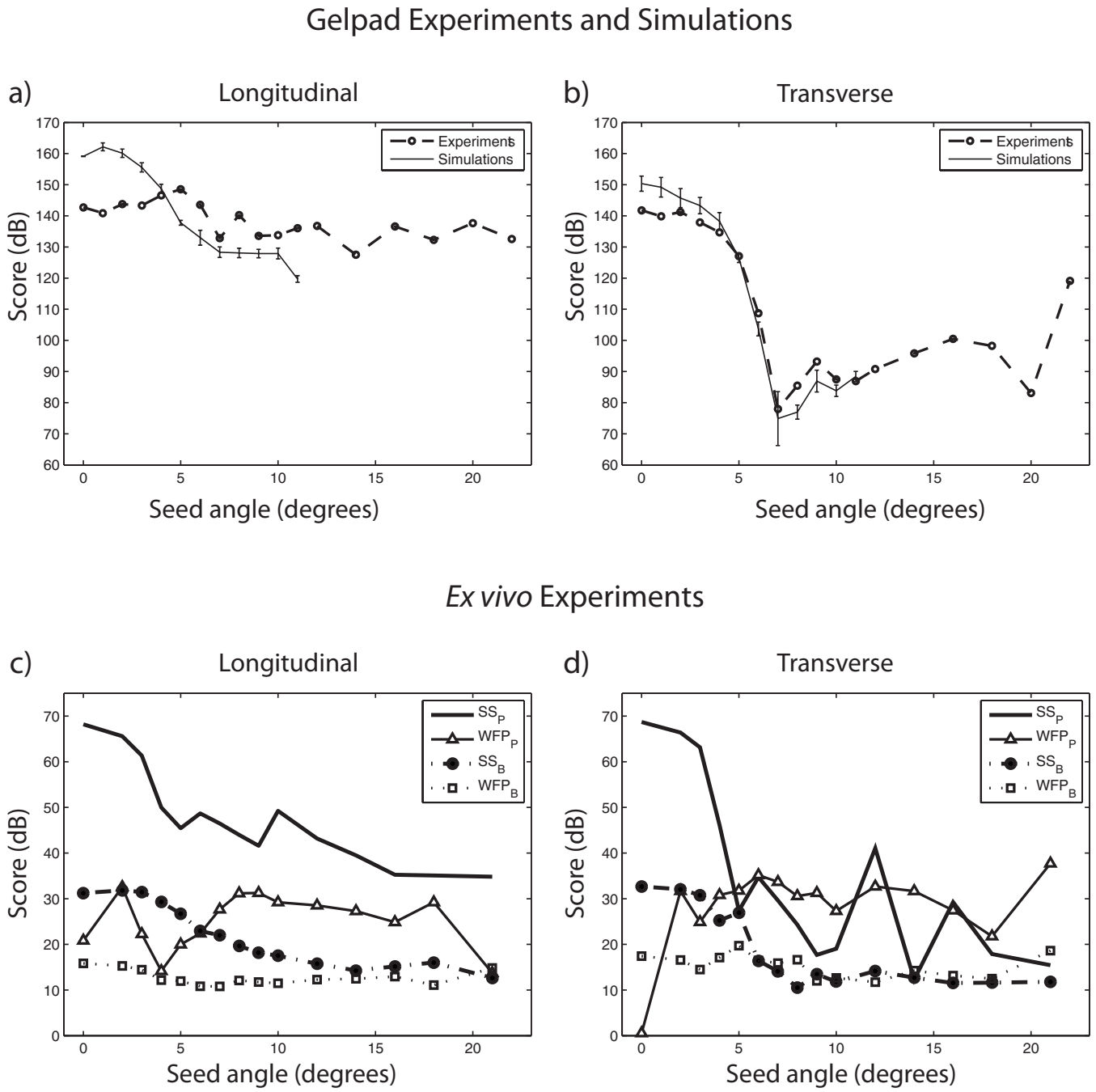

FIG. 7. Evaluation of the performance of the SSA algorithm in simulations and using experimental data. Scores for a seed in a gel pad (a) from longitudinal scans and simulations and (b) from transverse scans and simulations. Seed Scores (SS) and Worst False Positive (WFP) measures from *P*-mode and *B*-mode data of a seed in beef for (c) longitudinal and (d) transverse scan directions.

obtained by adding echoes from beef tissue to the simulated seed to simulate a seed in clutter-containing beef experiments. For both cases, the SNR was set to 40 dB.

Figures 8(c) and 8(d) display the resulting *P*-mode images with 40 dB dynamic range. T2 and L6 are easily identified by the algorithm in both images. However, noise and the weaker echo magnitude did not allow identification of L11.

Figures 8(e) and 8(f) display the same *P*-mode images as Figs. 8(c) and 8(d), but with a 60 dB dynamic range to evaluate whether an extended dynamic range would allow detecting and imaging T11. The resulting images demonstrate that the algorithm simply did not detect T11 even with the extended dynamic range; the seed is not visible either in Fig. 8(e) or in Fig. 8(f)

This multiseed simulation demonstrates that our seed-simulation method can be used for objective evaluation of all the native versions of the SSA algorithm or of other algorithms without the immediate need for experimental data. Future versions of the SSA algorithm will be tested first on multiseed simulations and then, if encouraging results are obtained, on experimental data.

C. *Ex vivo* experiments

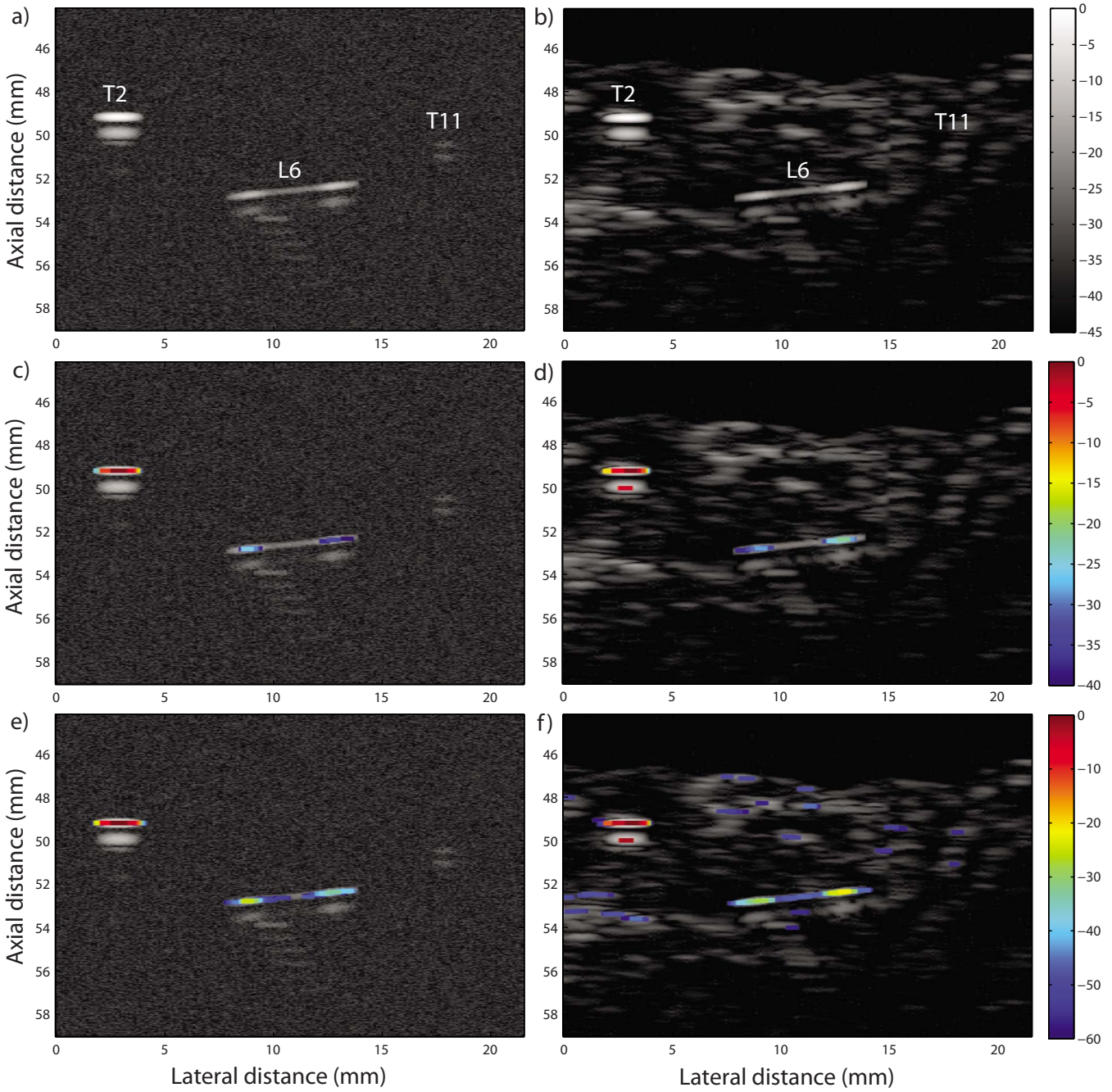

FIG. 8. (Color online) Simulated data with Gaussian noise background in the left column and beef tissue background in the right column. Three simulated seeds are shown in each image: two seeds scanned in the transverse direction, one at 2° (T2) and the other at 11° (T11), and a seed at 6° scanned in the longitudinal direction (L6). (a), (b) The simulated *B*-mode images. (c), (d) The corresponding *P* mode with a 40 dB dynamic range. (e), (f) The corresponding *P* mode with a 60 dB dynamic range.

A set of *ex vivo* experiments tested the performance of the SSA algorithm in an environment that more realistically resembles the prostate. In these *ex vivo* experiments, a single seed was inserted into a piece of degassed beef and scanned in longitudinal and transverse directions at angles ranging from 0° to 21° using the same apparatus as for the gel pad experiments (Fig. 1). Some of the resulting *P*-mode images are displayed in Fig. 9. The dynamic range of the *P* values was maintained at 40 dB for all the images.

Increasing the angle of the normal to the seed with respect to the transducer beam reduced the SNR of the *B*-mode images because the echo signal amplitude reflected by the seed decreased. Thus, detection of the seed in the conventional *B*-mode image was more difficult at larger seed-tilt angles. Detection of the seed from *P*-mode images was possible over a much larger angle range (i.e., up to 20°) than was possible using the *B*-mode images. However, as in the gel-pad experiments, the best identification of the seed by the algorithm occurred at smaller angles (i.e., between 0° and 6° with respect to the normal). As the tilt angle of the seed increased, more possible false positives appeared in the surrounding tissue. In most cases, the *P* values of the possible false-positives were 20 to 30 dB lower than the *P* value at the seed location. These spurious *P* values increased the un-

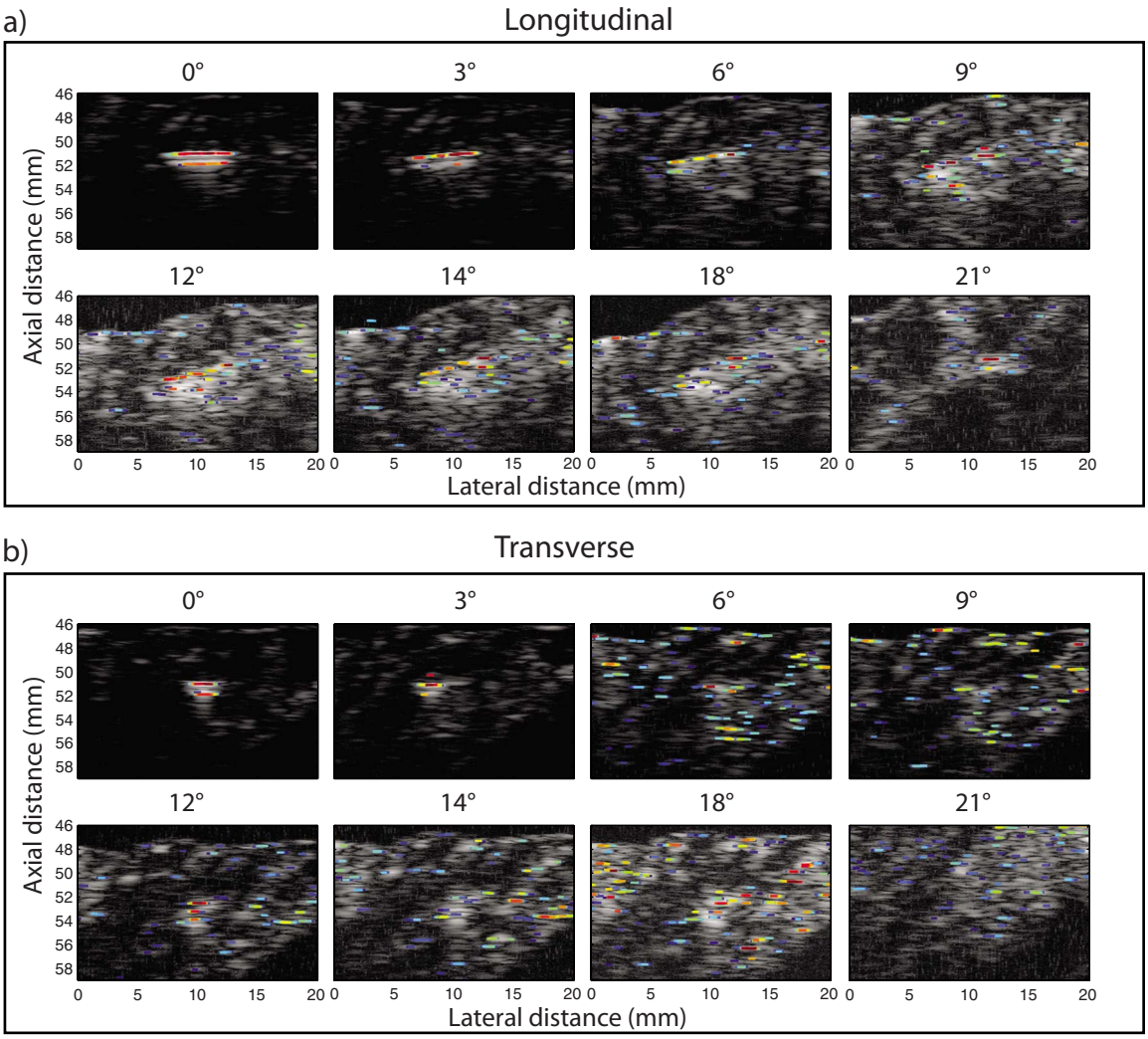

FIG. 9. (Color online) *Ex vivo* experiments: *B*-mode scans of a seed inserted into a piece of fresh, degassed, beef overlaid with *P*-mode data. (a) Longitudinal scans of the seed at various angles. (b) Transverse scans of the seed at the same angles. The *P* values have a dynamic range of 40 dB.

certainty in seed localization. In order to quantity these observations, SS_P, SS_B, WFP_P, and WFP_B were evaluated at each angle and for each seed orientation.

For the longitudinal cases [Fig. 7(c)], the SS_P curve indicates that, as expected, the performance of the algorithm degrades with increasing angle. However, because SS_P is greater than WFP_P at every angle; the actual seed always has the highest *P*-mode value, so that it would always be detected as a seed before anything else in the image is falsely identified as a seed. This fact tends to confirm that the seed always is detected, but that as the angle increases, more *P*-mode structures mimic seeds. WFP_P does not vary substantially with angle; it is nearly constant at 30 dB. This uniformity is expected because WFP_P measures an intrinsic property of the beef tissue that should be independent of angle. The SS_B curve has the same trend as the SS_P, but is about 40 dB lower, which means that *P* mode has about 40 dB better seed contrast than the *B*-mode image does. Moreover, the difference between the SS_P and the WFP_P is much more than that between SS_B and the WFP_B. This means that the likelihood of producing a false positive is greater using the *B*-mode image than using the *P*-mode image. This is particularly true at angles greater than 11° when the SS_B and WFP_B curves meet (i.e., on the *B*-mode image the seed looks exactly like the background). The longitudinal study demonstrates that at any angle, the *P*-mode image dramatically outperforms the *B*-mode image. The actual seed always would be detected on the *P*-mode image, while in the *B*-mode image it merges into the background at angles greater than 11°. Although both methods would find the seed at smaller angles, the *P*-mode image provides about 40 dB more contrast between the seed and the background than the *B*-mode image provides.

For the transverse results [Fig. 7(c)], the SS_P curve shows that the ability of the algorithm to detect a seed decreases quickly with increasing angle. Beyond 6°, SS_P essentially oscillates at low values near 25 dB. Except for the anomalous value at 0°, WFP_P is fairly constant at the same value as in the longitudinal case (i.e., 30 dB). Thus, the SS_P is not always greater than WFP_P, which means that in certain cases (e.g., the 11° case), false-positives will be produced preferentially to the actual seed because they have larger *P* values. At a tilt angle less than 5°, SS_B is about 40 dB below SS_P, meaning that the *P*-mode image has better seed contrast

than the *B*-mode image. At angles beyond 5°, $SS_B \approx WFP_B$, which means that on the *B*-mode image, the seed looks just like the background. The transverse study shows that at low angles, the *P*-mode image dramatically outperforms the *B*-mode image in terms of seed contrast and detection. However, beyond 6°, the two methods perform approximately equally.

These *ex vivo* experiments clearly demonstrate the superiority of the SSA algorithm over the visual assessment of a conventional *B*-mode image for detecting and locating seeds. However, the results also indicate that in a realistic, clutter-containing environment, the SSA method works best at modest angles.

IV. DISCUSSION

The proposed SSA algorithm appears to be an attractive choice for real-time clinical detection and imaging of seeds inserted into the prostate (or other treated organ). The only inputs required by the algorithm are the envelope-detected signals that readily are available on clinical scanners, i.e., the envelope-detected signals that are used to form the conventional *B*-mode implantation planning and guidance images. Furthermore, because the SSA method exploits the existence of the seed-signal repetitions,[12] the algorithm should be able to perform independently of the transducer technology, time-gain compensation methods, or beamforming techniques that are used.

In this study, one of the weaknesses of the previously described SSA algorithm[12] was mitigated by introducing the soft-threshold approach. From our experience, the standard deviations of some specific simulation cases were reduced using the new approach. This standard-deviation reduction suggests that the robustness of the algorithm was improved. From a theoretical standpoint, the use of soft thresholds made the *P*-mode image a continuous function of the envelope-detected data. However, with our chosen value for α, we did not experience major changes in the results of the actual experiments. This suggests that in most experimental cases, eigenvalue pairs are well inside the chosen tolerance values. We currently are investigating how lowering the tolerance values and increasing α (i.e., applying a softer threshold) will influence the algorithm performance. We anticipate that we may be able to optimize these parameters to increase the sensitivity of the SSA algorithm.

SSA algorithm performance was evaluated for its dependence on seed orientation. The cylindrical geometry and highly specular reflective symmetry of the seed make the efficacy of the algorithm depend upon the angle between the seed and the ultrasound beam axis. The findings of this study suggest that while the SSA algorithm performs well at modest angles, it performs far better than conventional *B*-mode imaging over a wide range of angles. The far superior contrast obtained in the *P*-mode image compared to the *B*-mode image was demonstrated quantitatively as illustrated in Fig. 7. Certainly, finding a way to improve the algorithm to perform at larger angles would be of great value, but considering the modest echo strength of the seed at angles greater than 10°, the algorithm would need to be made robust in low SNRs and high-clutter environments. Our hope is that the SSA algorithm performs well in real-time during the implantation procedure so that it can be used even if its most-reliable performance occurs at angles below 10°.

At this stage of development, making the SSA algorithm real-time is not yet a priority. Nevertheless, by simple optimization of our Matlab (Mathworks Inc., Natick, MA) programs along with improvements in computer technologies, we have been able to reduce the processing time necessary to generate a *P*-mode image by about 60% to less than 1 min. While this is still far from real-time, we are confident that the SSA algorithm can be implemented in a more-rapid manner (e.g., using C++ language) and we anticipate that using graphics processing units can reduce the necessary processing time sufficiently to allow for clinically practical, real-time computation of *P*-mode images.

Our scoring system offers a quantitative and systematic means of evaluating the performance of any seed-imaging algorithm whose output is a spatial "likelihood" map. In this study, we compared *B* mode and *P* mode, but other investigators may develop other imaging approaches, and their performances could be compared objectively using our score metrics.

Also, new TRUS probes that are currently becoming available will allow for obtaining real-time three-dimensional (3D) *B*-mode images of the prostate either through mechanical scanning or through beam-forming algorithms. For example, the probe of the TargetScan system (Envisioneering Medical Technologies, St. Louis, MO) contains a single-element transducer that is mechanically scanned inside the probe to obtain a series of adjacent sector scans leading to a complete 3D data set.[16] A slightly different approach is used in the probe of the Sonablate-500 system (Focus Surgery Inc., Indianapolis, IN) which contains two transducers: one for high-intensity focused ultrasound treatment and one for imaging. Both transducers can be mechanically scanned within the probe to image or treat the prostate in a 3D fashion.[17] We hypothesize that the SSA algorithm used in conjunction with advanced TRUS probes may become an extremely valuable tool because each seed within the gland would be insonified at a modest angle (e.g., $<10°$) with respect to one of the insonification axes employed (or simulated) by such TRUS probes.

Another thrust of our investigation is to understand the physical origin of the repetition signals backscattered from a seed. To date, we have not yet determined conclusively what the origin of these signals is. Our hope is that if we fully can comprehend how the repetition signals originate, then the SSA algorithm can be optimized to be more specific to seed repetitions than to actual tissue structures that might be about 1 μs apart (i.e., ~0.75 mm). This certainly would decrease the incidence of false-positives that result from randomly occurring periodic arrangements of scatterers in the prostate gland. We also will seek to determine whether we can predict how the repetition changes as a function of seed orientation. The SSA algorithm then could be used not only to detect and images seeds, but also to recover orientation information.

Finally, we are initiating a clinical study with the current version of the SSA algorithm. The algorithm will be tested

over a large number of patients to obtain receiver operator characteristic curves that will provide an objective assessment of algorithm performance under actual clinical conditions.

ACKNOWLEDGMENT

This research is supported in part by NIH Grant No. CA098465.

[1]H. H. Holm, N. Juul, J. F. Pedersen, H. Hansen, and I. Stroyer, "Transperineal ^{125}iodine seed implantation in prostatic cancer guided by transrectal ultrasonography," J. Urol. (Baltimore) **130**, 283–286 (1983).

[2]J. C. Blasko, H. Ragde, and D. Schumacher, "Transperineal percutaneous iodine-125 implantation for prostatic carcinoma using transrectal ultrasound and template guidance," Endocurie/Hyperthermal Oncol. **3**, 131–139 (1987).

[3]J. Crook, M. McLean, C. Catton, I. Yeung, J. Tsihlias, and M. Pintilie, "Factors influencing risk of acute urinary retention after trus-guided permanent prostate seed implantation," Int. J. Radiat. Oncol., Biol., Phys. **52**, 453–460 (2002).

[4]Z. Wei, M. Ding, D. Downey, and A. Fenster, "3D TRUS guided robot assisted prostate brachytherapy," Med. Image Comput. Comput. Assist. Interv. **8**, 17–24 (2005).

[5]H. Sommerkamp, M. Rupprecht, and M. Wannemacher, "Seed loss in interstitial radiotherapy or prostatic carcinoma with I-125," Int. J. Radiat. Oncol., Biol., Phys. **14**, 389–392 (1988).

[6]G. S. Merrick, W. M. Butler, A. T. Dorsey, J. H. Lief, and M. L. Benson, "Seed fixity in the prostate/perprostatic region following brachytherapy," Int. J. Radiat. Oncol., Biol., Phys. **46**, 215–220 (2000).

[7]D. H. Brinkmann and R. W. Kline, "Automated seed localization from ct data sets of the prostate," Med. Phys. **25**, 1667–1672 (1998).

[8]H. Liu, G. Cheng, Y. Yu, R. Brasacchio, D. Rubens, J. Strang, L. Liao, and E. Messing, "Automatic localization of implanted seeds from post-implant ct images," Phys. Med. Biol. **48**, 1191–1203 (2003).

[9]M. E. Miquel, K. S. Rhode, P. L. Acher, N. D. Macdougall, J. Blackall, R. P. Gaston, S. Hegde, S. L. Morris, R. Beaney, C. Deehan, R. Popert, and S. F. Keevil, "Using combined x-ray and mr imaging for prostate i-125 postimplant dosimetry: Phantom validation and preliminary patient work," Phys. Med. Biol. **51**, 1129–1137 (2006).

[10]B. N. Bloch, R. E. Lenkinski, T. H. Helbich, L. Ngo, R. Oismueller, S. Jaromi, K. Kubin, R. Hawliczek, I. D. Kaplan, and N. M. Rofsky, "Prostate postbrachytherapy seed distribution: Comparison of high-resolution, contrast-enhanced, T1- and T2-weighted endorectal magnetic resonance imaging versus computed tomography: Initial experience," Int. J. Radiat. Oncol., Biol., Phys. **69**, 70–78 (2007).

[11]J. F. Corbett, J. J. Jezioranski, J. Crook, T. Tran, and I. W. Yeung, "The effect of seed orientation deviations on the quality of ^{125}I prostate implants," Phys. Med. Biol. **46**, 2785–2800 (2001).

[12]J. Mamou and E. J. Feleppa, "Singular spectrum analysis applied to ultrasonic detection and imaging of brachytherapy seeds," J. Acoust. Soc. Am. **121**, 1790–1801 (2007).

[13]R. Vautard and M. Ghil, "Singular spectrum analysis in nonlinear dynamics, with applications to paleoclimatic time series," Physica D **35**, 395–424 (1989).

[14]R. Vautard, P. Yiou, and M. Ghil, "Singular-spectrum analysis: A toolkit for short, noisy chaotic signals," Physica D **58**, 95–126 (1992).

[15]D. Broomhead and G. King, "Extracting qualitative dynamics from experimental data," Physica D **20D**, 217–236 (1986).

[16]E. J. Traxel, J. S. Belani, D. G. Bostwick, P. A. Humphrey, and G. L. Andriole, "Evaluation of target scan device in prostate cancer detection," J. Endourol **19**, 918–919 (2005).

[17]R. Illing and M. Emberton, "Sonablate-500: Transrectal high-intensity focused ultrasound for the treatment of prostate cancer," Expert Rev. Med. Devices **3**, 717–729 (2006).

Orthotropic material properties of the gerbil basilar membrane

Shuangqin Liu and Robert D. White[a)]
Mechanical Engineering Department, Tufts University, 200 College Avenue, Medford, Massachusetts 02155

(Received 2 July 2007; revised 15 January 2008; accepted 16 January 2008)

In this paper, two sets of experimental results to extract the two effective elastic moduli, the effective shear modulus, and the effective Poisson's ratio for the gerbil cochlear partition are analyzed. In order to accomplish this, a geometrically nonlinear composite orthotropic plate model is employed. The model is used to predict both out-of-plane and in-plane motion of the partition under a static finite area distributed load. This loading condition models the small, but finite size, probe tips used in experiments. Both in-plane and out-of-plane motion are needed for comparison with recent experimental results. It is shown that the spatial decay rate (the space constant) for the in-plane deflection is different than for the out-of-plane deflection, which has a significant effect on the derived partition properties. The size of the probe tip is shown to have little influence on the results. Results are presented for two types of boundary conditions. Orthotropy ratios determined from the experimental data are found to vary with longitudinal position and choice of boundary conditions. Orthotropy ratios (the ratio of the two elastic moduli) are in the range of 65 close to the base to 10 in the upper middle turn of the cochlea. © *2008 Acoustical Society of America.*
[DOI: 10.1121/1.2871682]

PACS number(s): 43.64.Bt, 43.64.Kc [BLM] Pages: 2160–2171

I. INTRODUCTION

The accuracy of mechanical models of traveling fluid-structure waves in the cochlea depend on accurate structural models for the cochlear partition. The cochlear partition has variously been modeled as a locally reacting impedance (Lynch *et al.*, 1982; Neely and Kim, 1986; Ramamoorthy *et al.*, 2007) a one dimensional beam (Allaire *et al.*, 1974; Miller, 1985), a two-dimensional orthotropic plate (Steele and Taber, 1979), or a two-dimensional orthotropic pretensioned plate (Naidu and Mountain, 2007). The parameters required for each of these models can be determined from a knowledge of the geometry and the pointwise effective material properties of the cochlear partition. Geometry can be determined from physiological studies (Schweitzer *et al.*, 1996; Edge *et al.*, 1998). Pointwise effective material properties must be determined indirectly by observing the response of the structure *in vivo* to carefully conducted experiments.

This paper focuses on determination of effective pointwise material properties using point load experiments published by Naidu and Mountain (1998; 2001) and Emadi *et al.* (2004). A particular aim of this work is to quantify the orthotropic properties of the cochlear partition. It is well known that the cochlear partition is orthotropic, based on physiology (Iurato, 1962; Miller, 1985), qualitative observations of static partition deflection (Voldrich, 1978), and quantitative dynamic measurements (Richter *et al.*, 1998). However, most prior quantitative static experimental work gave only point stiffness measurements (Gummer *et al.*, 1981; Miller, 1985; Olson and Mountain, 1991; Naidu and Mountain, 1998), from which it is not possible to determine orthotropic properties.

In 2001, quantitative measurements of the *shape* of the deflected region during point load experiments were made by Naidu and Mountain (2001). These experiments allow quantitative determination of the level of orthotropy. In Naidu and Mountain (2001), the BM was deflected from 1 to 15 μm in a 1 μm increment. In addition to the point stiffness, the shape of the *lateral* deflection region was measured quantitatively for each case. The normalized shape of the lateral deflection profile exhibited exponential decay away from the center; the exponent characterizing this decay was expressed as a "space constant." Two sets of space constants were reported in their paper. One was with the organ of Corti present and the other is with the organ of Corti removed. The space constant used in this paper was the one with the organ of Corti present. In Emadi *et al.* (2004), the point stiffness of the cochlear partition in a hemicochlea preparation was measured as a function of distance from the cut edge. The variation of stiffness as a function of distance from the cut edge is related to longitudinal coupling in the cochlear partition, albeit in a different way than the lateral deflection results of Naidu and Mountain.

In this paper, we use these two sets of experimental results to extract the two effective elastic moduli, the effective shear modulus, and the effective Poisson's ratio for the cochlear partition. In order to accomplish this, we employ a geometrically nonlinear composite orthotropic plate model. Despite the small deflections, a nonlinear geometric model must be used in order to determine *lateral deflections*, which are not present in a linear plate model. The *lateral deflections* are the quantities measured by Naidu and Mountain. We show that the shape of the lateral deflection is not the same as the shape of the vertical deflection; thus it is not correct to assume that the shape constant for the vertical deflection is the same as the shape constant for the lateral deflection.

[a)]Electronic mail: r.white@tufts.edu

 0001-4966/2008/123(4)/2160/12/$23.00 © 2008 Acoustical Society of America

Two boundary conditions for the model were investigated. The first is all four edges of the plate simply supported (SS). The second is one edge clamped and others simply supported (CS). Based on the stiffness and space constant reported in Naidu and Mountain with the organ of Corti present, we determine the following: using SS boundary conditions, the radial elastic modulus decreases from 15 to 1 MPa from base to the upper middle turn of gerbil cochlea; longitudinal modulus decreases from 0.2 to 0.05 MPa. Using CS boundary conditions, radial elastic modulus decreases from 6.6 to 0.5 MPa from base to the upper middle turn of gerbil cochlea; longitudinal modulus decreases from 0.4 to 0.05 MPa. The orthotropy varies along the length of the cochlear partition from a maximum of 65 close to the base to a minimum of 10 in the upper middle turn. We also investigate the effect of changing probe contact area for the point measurements, showing that for probes of radius from 2 to 12.5 μm, the probe diameter has little effect on the shape of the deflected region.

The material properties computed based on the experimental data in Emadi *et al.*, which was measured approximately two-thirds of the way from base to apex, suggest considerably less orthotropy than Naidu and Mountain's data. Using the SS boundary condition, Emadi *et al.*'s data suggest a transverse modulus of 0.048 MPa and a longitudinal modulus of 0.026 MPa. Using the CS boundary condition, the transverse modulus is 0.025 MPa and the longitudinal modulus is 0.023 MPa.

The physiology of the cochlea partition is more complicated than the model we used. For instance, the stiffness measurements can easily be affected by factors including the organ of Corti (Naidu and Mountain, 1998), and the tectorial membrane (Emadi *et al.*, 2004). The stiffness is not uniform in arcuate zone or pectinate zone (Naidu and Mountain, 1998). Radial pretension may also be present (Naidu and Mountain, 2007). If all the complexities are embedded in the model, there would be too many free parameters to be determined. By simplifying the model, and thus reducing the number of the free parameters, we can use currently available experiment data to compute the effective material properties. Thus, pretension, radial variation and the tectorial membrane are not included in our current model, as they are not needed to explain the observed longitudinally varying space constants and point stiffness.

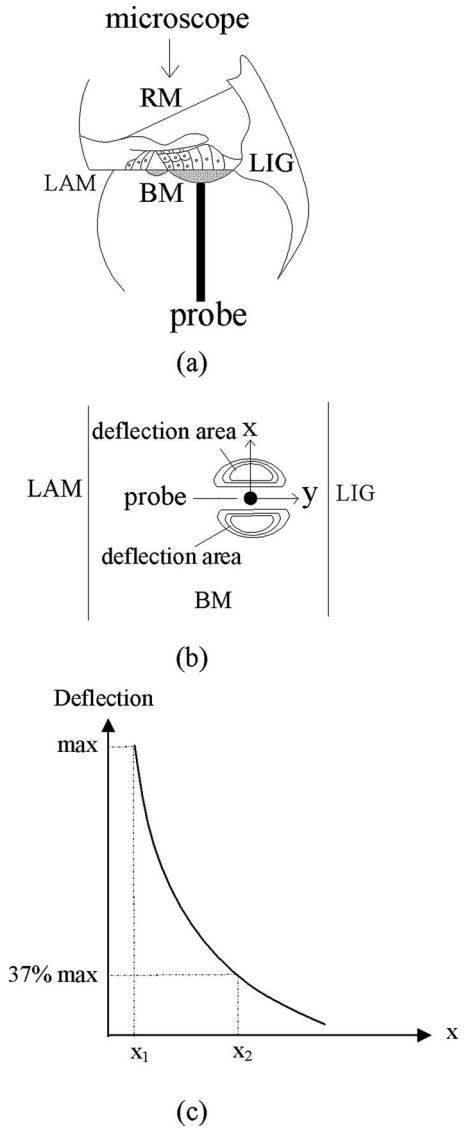

FIG. 1. Schematic of BM stiffness measurement procedure from Naidu and Mountain (1998, 2001): (a) A circular probe is pushed into the cochlear partition, and the force vs deflection curve is measured; (b) a top-down view of BM; the contours show the shape of the lateral (x direction) deflections (c) deflection space constant is described as the distance x_2-x_1 along the x direction where the deflection decreases exponentially from its maximum value to 37% of maximum value. In this drawing, BM is the basilar membrane, LAM is the spiral lamina, and LIG is the spiral ligament.

II. MATHEMATICAL MODEL

The structural model used herein is best understood by considering the experiments it is used to analyze, shown schematically in Fig. 1. This experimental work (Naidu and Mountain, 1998, 2001), provides two pieces of information: (1) point stiffness, which is measured by pushing a probe into the partition and reporting the deflection versus restoring force, and (2) the space constant, which is the distance from the location of the probe that the *lateral* deflection of a mark on the cochlear partition reduces to 37% of its maximum level.

We emphasize again that in the cited experimental work, the space constant was determined by observing *lateral* deflections of the cochlear partition using microscopy (Naidu and Mountain, 2001). A linear plate model has no lateral deflections. However, a geometrically nonlinear plate model (for deflection amplitudes as applied in the experiment) does experience observable lateral deflections. It was assumed by Naidu and Mountain that the out-of-plane deflections were proportional to these observed lateral deflections. The major motivation for the use of a geometrically nonlinear plate model in this work is to explore the validity of the assumed proportionality between out of plane and lateral deflections, and potential effects on predictions of the small-deflection material properties.

The orthotropic composite plate model used here requires four independent material properties: elastic moduli in both longitudinal and transverse directions (E_x, E_y), shear

modulus (G_{xy}), and Poisson's ratio (ν_{xy}). These properties must be determined to match the point stiffness and space constants that have been reported. Since there are four quantities to determine, but only two available measurements, some additional assumptions must be made based on composite plate theory. These are explained in detail in the following.

The overall procedure is as follows. First, an Euler–Bernoulli beam model with a single material property, E_y, is used to match point stiffness data (Naidu and Mountain, 1998; Emadi *et al.*, 2004). This gives an initial estimate of the transverse plate modulus, E_y. An orthotropy ratio, E_y/E_x, is then arbitrarily chosen. E_y/E_x is always in the range 1–1000. With E_y/E_x chosen, it is possible to compute G_{xy} and ν_{xy} by making use of a composite plate material model, as explained in the following. With all four plate constants in hand, a linear analytic plate model or a nonlinear finite element scheme is then used to compute the shape of the deflected region produced by a finite area static probe load. The point stiffness and space constant are determined from the result, and compared to that reported in the experimental data. The values of E_y and E_x are then adjusted, G_{xy} and ν_{xy} recomputed, and the procedure repeated until a match with experiment is obtained.

Two sets of boundary conditions have been employed by previous authors modeling the cochlear partition. In some works, one edge is taken to be simply supported and the other clamped. This is motivated by Iurato's anatomical studies of the rat cochlea, in which he observed that the main supporting bundles of the spiral lamina continue directly into the fibers of the basilar membrane (Iurato, 1962), suggesting a clamped end condition. The fibers on the other side of the Basilar Membrane (BM) continue directly into the spiral ligament but suddenly become thinner prior to joining the spiral ligament, which suggests a simply supported boundary condition. However, the movements at the boundaries of the BM are difficult to observe, thus leaving open the possibility for other boundary conditions. For this reason, and perhaps for simplicity, other authors have chosen to use simply supported boundary conditions along both edges (Naidu and Mountain, 2007). In order to explore the effect of changing boundary conditions on the material properties, we have carried out computations using both sets of boundary conditions: (SS) simply supported at both ends and (CS) clamped at the spiral lamina but simply supported at the spiral ligament.

III. BEAM MODEL

The first step in our procedure is to make use of a beam model to produce an initial estimate of the local elastic modulus E_y. The width of the beam is taken to be the probe's diameter: 10 μm in Naidu and Mountain (1998), 25 μm in Emadi *et al.* (2004). This is the same as assuming that the cochlear partition is perfectly orthotropic.

Figure 2 is a schematic of the beam model under probe load (with CS boundary conditions).

The elastic modulus calculated from the beam model (Budynas, 1999) for CS boundary condition is

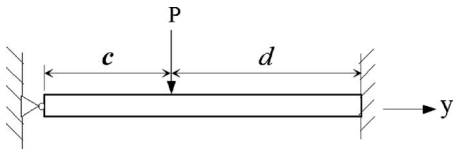

FIG. 2. Schematic of a beam model under load with one end simply supported and the other clamped.

$$E = \frac{-dc^2[3L(d^2 - L^2) + c(3L^2 - d^2)]}{12IL^3}k \tag{1}$$

and for SS boundary condition is

$$E = \frac{-dc(2c^2 - 2cL)}{6IL}k, \tag{2}$$

where k is the point stiffness of the beam, $L=c+d$ is the length of the beam, $I=wh^3/12$ is the area moment of inertia of the beam, w is the beam width, taken to be the probe diameter, and h is the beam thickness. Both the thickness and length of the beam, h and L, are taken from BM thickness and width as measured by Schweitzer *et al.* (1996). Note that these are dehydrated properties. These properties are used throughout this paper; we use Schweitzer *et al.*'s measurements because they also include information on fiber band thickness, which is important for our composite model, as explained in the following.

According to Naidu and Mountain (1998, Fig. 5 Panel D), the stiffness decreases along the longitudinal direction from base to apex as

$$k(x) = \frac{5.755}{e^{0.31x}}\frac{N}{m}. \tag{3}$$

According to Emadi *et al.* (2004, Fig. 3 Panel A) stiffness decreases as

$$k(x) = \frac{3.25}{e^{0.5x}}\frac{N}{m}. \tag{4}$$

For both equations, x has dimension millimeter.

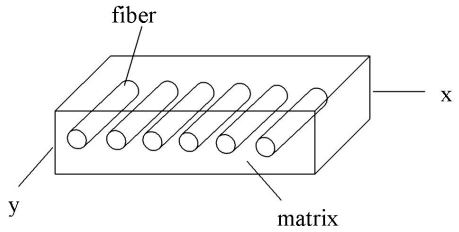

FIG. 3. Composite material with fibers and matrix.

TABLE I. Initial estimate of radial elastic modulus as determined from measured stiffness using a beam model.

Location from base (mm)	Beam length L (μm)	Thickness h (μm)	Position of applied load c (μm)	stiffness (N/m)	Boundary conditions	E_y (kPa)
1.14[a]	150	15.8	60	4.04	SS	79 700
					CS	40 600
3.99[a]	194	17.3	78	1.67	SS	54 300
					CS	27 700
6.612[a]	232	23.7	87	0.741	SS	15 300
					CS	8 060
7.3[a]	242	25.3	91	0.599	SS	11 500
					CS	6 080
7.3[b]	242	25.3	91	0.08	SS	601
					CS	317

[a]Naidu and Mountain (1998, 2001).
[b]Emadi *et al.* (2004).

Material properties were computed at three locations along the BM according to the experimental data from Naidu and Mountain (1998). These three locations are chosen because of the availability of experimental data for the dimensions of BM width and thickness for those locations in Schweitzer *et al.* (1996).

The first location is 1.14 mm from the base, the second is 3.99 mm from the base, and the last one is 6.612 mm from the base. An additional location 7.3 mm from the base is picked because it is the location at which the longitudinal coupling was measured by Emadi *et al.* (2004). Although the dimensions of the BM at this location are not given explicitly in Schweitzer *et al.* (1996), width and thickness of the BM can be estimated from Panels A and B in Fig. 5. Table I shows the stiffness and radial elastic modulus computed using this procedure at the different locations.

IV. PLATE MODEL

A. Composite material model

With an initial estimate of transverse elastic modulus in hand, we now move on to an orthotropic composite plate model. There are four independent material properties for the plate, but only two measurements at each location, requiring that additional assumptions be introduced. We use a composite plate model which allows us to reduce the number of unknowns. In particular, shear modulus, G_{xy}, and Poisson's ratio, ν_{xy} are estimated using the volume fraction method (Dowling, 1999).

TABLE II. Volume fractions at different locations taken from Schweitzer *et al.* (1996).

Location from base (mm)	1.14	3.99	6.612	7.3
V_r	0.192	0.089	0.05	0.041
V_m	0.808	0.911	0.95	0.959

In this method, the cochlear partition is treated as a fiber-reinforced composite. The fibers are considered as an isotropic linear elastic material with elastic constants E_r and υ_r, and the matrix another isotropic linear elastic material, with material properties E_m and υ_m. The composite has volume fractions occupied by the fibers and matrix, V_r, which is the ratio of fiber area to the total area and V_m, which is the ratio of matrix area to the total area, respectively. The composite plate model is shown in Fig. 3.

The relationships between the elastic moduli of the component materials and the effective elastic moduli of the composite plate are (Dowling, 1999)

$$E_x = \frac{E_r E_m}{V_r E_m + V_m E_r}$$

$$E_y = V_r E_r + V_m E_m \tag{5}$$

The lower and upper fiber band thicknesses can be estimated from Schweitzer *et al.* (1996), Panels B and C in Fig. 7. We make the simplifying assumption that the fiber bands are fully dense. The fibers are then treated as uniformly distributed throughout the thickness, maintaining these volume fractions. From the information from Schweitzer *et al.* (1996), the cross-sectional areas of the fibers and matrix are estimated, leading to the volume fractions V_r and V_m, listed in Table II.

We have an estimate of E_y based on the beam model, and have arbitrarily chosen E_x (recall for our procedure we chose an E_x,compute a space constant, and iterate to match experiment). We can therefore compute the required values of E_r and E_m as follows:

$$E_r = \frac{E_x V_r^2 - E_x V_m^2 + E_y}{2V_r} \pm \frac{\sqrt{E_x^2 V_r^4 - 2E_x^2 V_r^2 V_m^2 - 2E_x E_y V_r^2 + E_x^2 V_m^4 - 2E_x E_y V_m^2 + E_y^2}}{2V_r}, \tag{6}$$

$$E_m = \frac{-E_x V_r^2 + E_x V_m^2 + E_y}{2V_m} \mp \frac{\sqrt{E_x^2 V_r^4 - 2E_x^2 V_r^2 V_m^2 - 2E_x E_y V_r^2 + E_x^2 V_m^4 - 2E_x E_y V_m^2 + E_y^2}}{2V_m}. \tag{7}$$

The shear moduli of the component materials are then directly computed from (Dowling, 1999),

$$G_r = \frac{E_r}{2(1+\nu_r)},$$

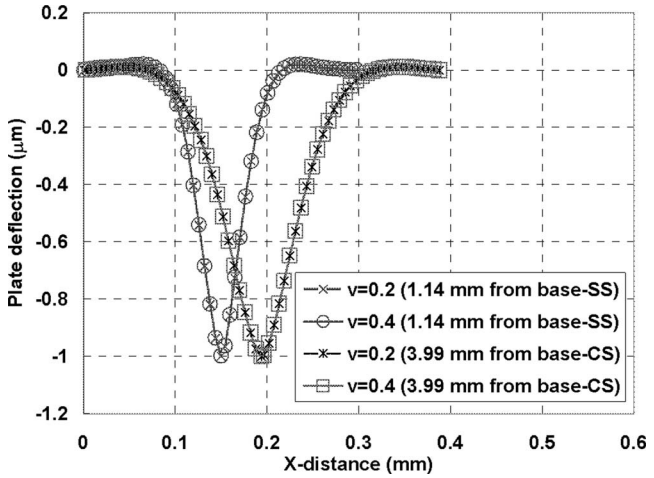

FIG. 4. Comparison of vertical displacement computed with different fiber Poisson's ratios for two different locations and boundary conditions. The Poisson ratio of the fiber has little impact on the result.

$$G_m = \frac{E_m}{2(1+\nu_m)}. \tag{8}$$

So we have the shear modulus of the composite (Dowling, 1999),

$$G_{xy} = \frac{G_r G_m}{V_r G_m + V_m G_r}. \tag{9}$$

We still need to compute the Poisson ratio of the composite plate. The Poisson's ratio of tissue ranges widely. Two different sets of Poisson's ratios ν_r=0.2 (Jurvelin *et al.*, 1997), which is estimated from bovine humeral articular cartilage, and ν_r=0.4 (Lai-Fook *et al.*, 1976), which is estimated from dog lung tissue, are investigated. Figure 4 shows that the choice of this parameter does not have a major impact on our results. The ground substance behaves as a layer of incompressible fluid (Miller, 1985), so we take ν_m=0.5. From these two component Poisson ratios and the volume fractions, we can compute the two Poisson ratios for the composite orthotropic plate (Dowling, 1999),

$$\nu_{yx} = V_r \nu_r + V_m \nu_m$$

$$\nu_{xy} = \frac{E_x}{E_y}\nu_{yx} \tag{10}$$

B. Analytic linear plate model

At this point, all four plate properties are defined. It is now possible to proceed to an orthotropic linear plate solution and compared computed and measured stiffness and space constant. The governing equation for a linear orthotropic Kirchhoff plate under a distributed load is Timoshenko, 1959

$$D_x \frac{\partial^4 w}{\partial^4 x} + 2D_{xy}\frac{\partial^4 w}{\partial^2 x \partial^2 y} + D_y \frac{\partial^4 w}{\partial^4 y} = q(x,y), \tag{11}$$

where

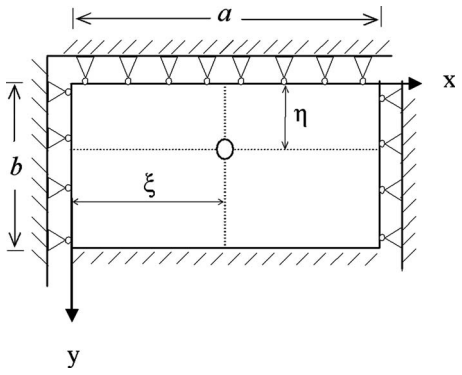

FIG. 5. Schematic of plate boundary conditions and load area.

$$D_x = \frac{E_x h^3}{12(1-\nu_{xy}\nu_{yx})} \tag{12}$$

is the flexural rigidity of the plate in x direction,

$$D_y = \frac{E_y h^3}{12(1-\nu_{xy}\nu_{yx})} \tag{13}$$

is the flexural rigidity of the plate in y direction,

$$D_{xy} = \frac{E_x h^3 \nu_{yx}}{12(1-\nu_{xy}\nu_{yx})} + \frac{G_{xy} h^3}{6} \tag{14}$$

is the tensional rigidity of the plate, and $q(x,y)$ is the normal load per unit area applied on the plate. The quantity h is the plate thickness, and E_x, E_y, G_{xy}, ν_{xy}, and ν_{yx} are the orthotropic plate material properties as described previously.

In the experiments, the load is applied on the middle of the pectinate zone. The load contact area is taken to be a circle whose diameter is the same as that of the probe. $q(x,y)$ is taken to be a uniform pressure over that contact area. Figure 5 is a schematic for one of the two choices of boundary conditions (CS).

The analytic displacement solutions for a circular region of distributed load with rectilinear boundary conditions have been derived based on plate theory (Szilard, 2004; Whitney, 1987; Ugural, 1999). The solution for the simply supported plate under circular load can be written as

$$w = \sum_{m=1}^{\infty}\sum_{n=1}^{\infty}\left[\frac{\dfrac{4P}{ab\pi^4}\displaystyle\int_0^{2\pi}\int_0^{c}\sin(\alpha)\sin(\beta)\rho\, d\rho\, d\theta}{D_x\dfrac{m^4}{a^4} + 2D_{xy}\dfrac{m^2 n^2}{a^2 b^2} + D_y\dfrac{n^4}{b^4}} \times \sin\left(\frac{m\pi x}{a}\right)\sin\left(\frac{n\pi y}{b}\right)\right], \tag{15}$$

where

$$\alpha = \left(\frac{m\pi(\xi+\rho\cos(\theta))}{a}\right),$$

$$\beta = \left(\frac{n\pi(\eta + \rho \sin(\theta))}{a} \right), \tag{16}$$

where a is the length of the plate, b is the width of the plate, c is the radius of the circle of load, P is the total load, ξ is the load location in the x direction, η is the load location in the y direction.

The solution for the one edge clamped and three edges simply supported with a circular load can be written as

$$w = \sum_{m=1}^{\infty} \sum_{n=1}^{\infty} \left[A \sin\left(\frac{m\pi\lambda_2 y}{a} \right) \cosh\left(\frac{m\pi\lambda_1 y}{a} \right) + B \cos\left(\frac{m\pi\lambda_2 y}{a} \right) \sinh\left(\frac{m\pi\lambda_1 y}{a} \right) + C \sin\left(\frac{n\pi y}{b} \right) \right] \sin\left(\frac{m\pi x}{b} \right), \tag{17}$$

where

$$C = \sum_{m=1}^{\infty} \sum_{n=1}^{\infty} \frac{\frac{4P}{ab\pi^4} \int_0^{2\pi} \int_0^c \sin(\alpha)\sin(\beta)\rho \, d\rho \, d\theta}{D_x \frac{m^4}{a^4} + 2D_{xy} \frac{m^2 n^2}{a^2 b^2} + D_y \frac{n^4}{b^4}}, \tag{18}$$

where α and β are defined in Eq. (16)

$$B = \frac{-Cna \cos(n\pi) \sin\left(\frac{m\pi\lambda_2 b}{a} \right) \cosh\left(\frac{m\pi\lambda_1 b}{a} \right)}{mb(-D + E - F)}, \tag{19}$$

where

$$D = -\lambda_2 \sinh\left(\frac{m\pi\lambda_1 b}{a} \right) \cosh\left(\frac{m\pi\lambda_1 b}{a} \right),$$

$$E = \lambda_1 \cos\left(\frac{m\pi\lambda_2 b}{a} \right) \sin\left(\frac{m\pi\lambda_2 b}{a} \right) \left[\cosh\left(\frac{m\pi\lambda_1 b}{a} \right) \right]^2,$$

$$F = \lambda_1 \sin\left(\frac{m\pi\lambda_2 b}{a} \right) \cos\left(\frac{m\pi\lambda_2 b}{a} \right) \left[\sinh\left(\frac{m\pi\lambda_1 b}{a} \right) \right]^2, \tag{20}$$

$$A = \frac{-C \sinh\left(\frac{m\pi\lambda_1 b}{a} \right) \cos\left(\frac{m\pi\lambda_2 b}{a} \right)}{\sin\left(\frac{m\pi\lambda_2 b}{a} \right) \cosh\left(\frac{m\pi\lambda_1 b}{a} \right)}, \tag{21}$$

and λ_1 and λ_2 are two constants

$$\lambda_1 = \mathrm{Re}\left\{ \sqrt{\frac{D_{xy} \pm \sqrt{D_{xy}^2 - D_x D_y}}{D_y}} \right\},$$

$$\lambda_2 = \mathrm{Im}\left\{ \sqrt{\frac{D_{xy} \pm \sqrt{D_{xy}^2 - D_x D_y}}{D_y}} \right\}. \tag{22}$$

Figure 6 shows the results for an analytic model after iteration of the values of E_y and E_x to produce a match to the point stiffness and space constant reported in Naidu and Mountain (1998, 2001) at $x=3.99$ mm from the base. Identical iterative procedures were applied at the other locations to produce the material properties shown in Table III. We emphasize again that these are based on a *linear* composite analytic plate model. Note that the linear plate only deflects normal to its surface. Thus, in matching the space constant, it is necessary to use the assumption of Naidu and Mountain that the observed *lateral* deflections of the plate are proportional to *out of plane* deflections. It is to explore the validity of this assumption that we move on to the geometrically nonlinear plate model.

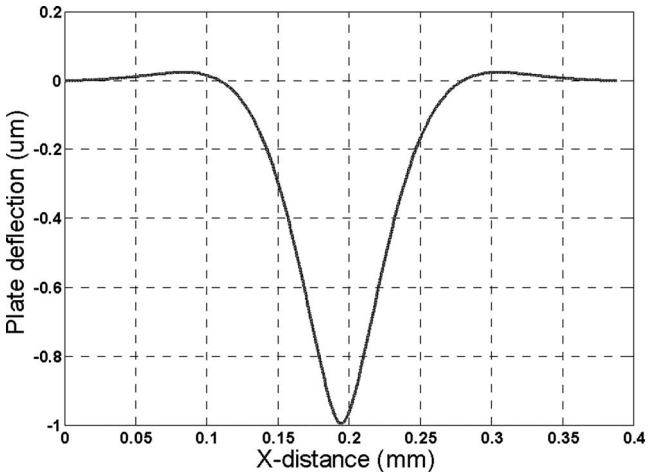

FIG. 6. Deflection profile using linear model.

C. Nonlinear finite element plate model

In Naidu and Mountain (1998, Fig. 2) the stiffness stays constant when the BM deflection remains in the 1–3 μm range. In addition, the displacements in this range (1–3 μm) are small compared to the plate thickness (16–25 μm). Thus, the use of a linear structural model for deflections of up to 3 μm appears to be justified. However, the space constant in Naidu and Mountain (2001) is based on the *lateral* displacement. A linear plate model gives no lateral displacements. On the other hand, a finite element analysis (FEA) solution using linear elastic material constitutive laws, but including *geometric nonlinearities*, will give nonzero lateral displacements. Such a solution was implemented in the finite element software package ABAQUS™.

Figure 7 shows the mesh that was used at location 1.14 mm from the base. The element used is S4R: a four-node doubly curved thin or thick shell element with reduced integration and hourglass control for finite membrane strains. A half-plate model is used as the plate model is symmetric about $x=0$. In order to reduce model size, the mesh is truncated in the x direction in a way that makes the symmetric model square. A rectangular plate model whose length is twice its width was also tested to verify that the truncation does not affect the model results. Convergence was tested by increasing the number of elements. A mesh with characteristic element length 0.6 μm is sufficient to produce a converged solution.

TABLE III. Material properties computed using the analytical linear model to match experimental point stiffness and space constant reported by Naidu and Mountain (1998, 2001). These results are based on the assumption of Naidu and Mountain, that the observed transverse displacements are linearly proportional to the out-of-plane displacements, an assumption we question in Sec. V.A.

							Composite plate properties determined by matching experiment			
Distance from base[a] (mm)	Space constant (μm)	b (μm)	η (μm)	Thickness (μm)	Stiffness (N/m)	Boundary conditions	E_x (kPa)	E_y (kPa)	G_{xy} (kPa)	ν_{xy}
1.14	13.2	150	60	15.8	4.042	SS	106	21500	35.5	0.0022
	13.2					CS	82.7	13100	27.6	0.0028
3.99	23.8	194	77.6	17.3	1.671	SS	150	8100	50.0	0.0088
	23.8					CS	148	4430	49.0	0.016
6.612	33.5	232	87	23.7	0.741	SS	36.0	1920	12.0	0.0091
	33.5					CS	42.0	1000	14.0	0.021
7.3	36.0	242	91	25.3	0.599	SS	26.0	1400	8.60	0.009
	36.0					CS	30.0	735	10.0	0.02

[a]Naidu and Mountain (1998, 2001).

V. DISCUSSIONS

A. Linearity versus nonlinearity

The geometrically nonlinear orthotropic plate model was first used to duplicate the previously conducted linear analytic analyses for both boundary conditions (using the material properties and geometry shown in Table III). A contour plot of the out-of-plane and lateral deflections computed with the nonlinear model are shown below in Fig. 9. An example of a comparison of the result with the analytical solution is shown in Fig. 8. The out-of-plane deflections are almost identical to the linear model results, verifying the FEA solution and demonstrating that the out-of-plane deflections are well captured by a linear model.

The lateral deflections, computed due to nonlinear geometric effects, are also shown. A cross section of the lateral deflection and out-of-plane deflection curves in the longitudinal direction through the centroid of the load region are shown in Fig. 10. The lateral deflections exhibit a different space constant than the out-of-plane deflections. It is the lateral deflection space constant that was measured by Naidu and Mountain.

The value of E_x and E_y in the geometrically nonlinear finite element model were iterated, starting from the linear results. The point stiffness and space constants reported by Naidu and Mountain were matched at each location along the BM. The space constant is now determined based on the *lateral* deflections. The shear modulus and Poisson ratio are determined using the volume fraction method described earlier. Table IV shows the parameters used and the resulting effective plate properties. Figure 11 shows how the results of material properties in Table IV vary along the longitudinal direction. The flexural rigidities of the plate are calculated using effective plate properties and presented in Table VI.

B. Comparison with hemicochlea experiment

In Emadi *et al.* (2004), the plateau stiffness at increasing distances from the upper middle turn (7.3 mm from the base)

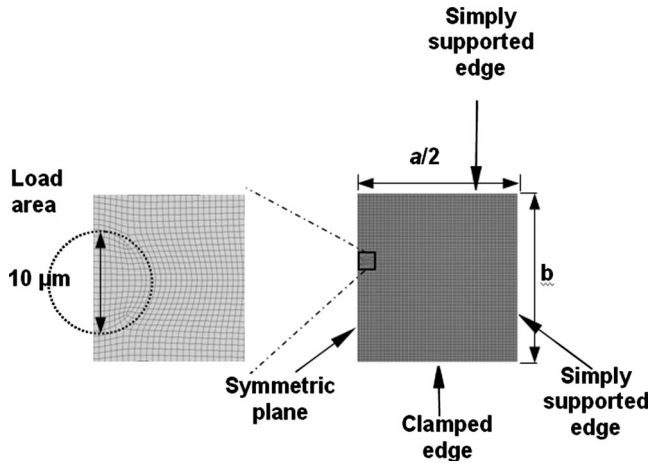

FIG. 7. One particular case (at a position of 1.14 mm from the base) of a meshed symmetric plate model in ABAQUS. 62 158 elements are used for this model, and the model is truncated to produce a square model.

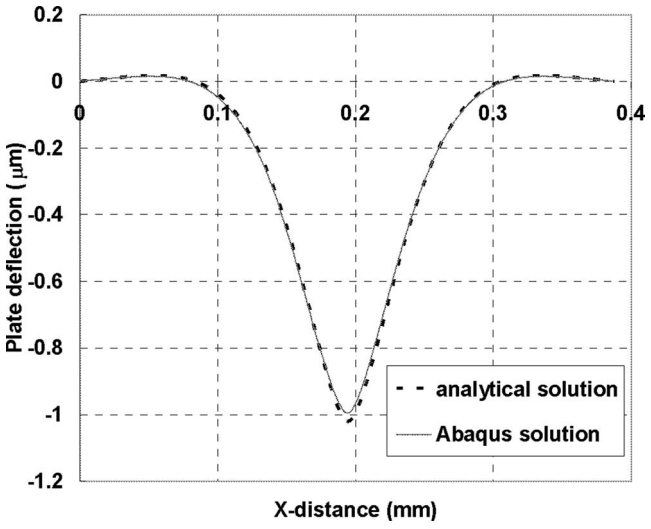

FIG. 8. Comparison of analytical solution with ABAQUS solution for SS boundary conditions at a position 3.99 mm from the base of the BM.

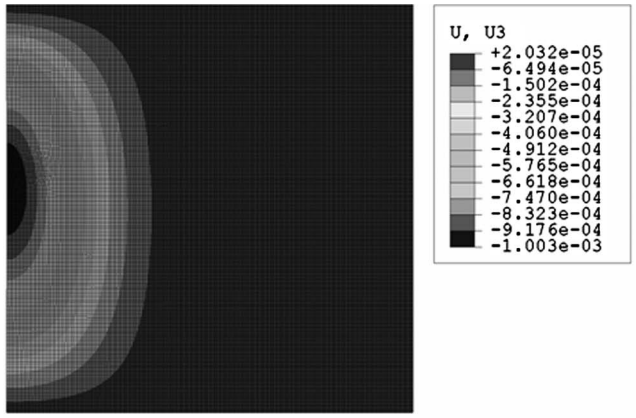

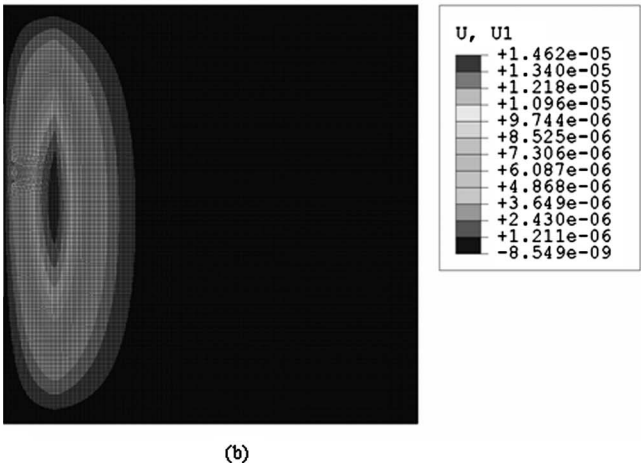

FIG. 9. Contour plot shows plate deflection at 1.14 mm from base. This is for an applied load of 4 μN distributed uniformly over the 5 μm radius contact region. (a) Out-of-plane deflection (mm) and (b) in-plane deflection (mm).

cut edge of a hemicochlea are measured. They used the change of stiffness very close to the cut edge to quantify the longitudinal coupling within the basilar membrane. They computed the space constant by fitting the plateau stiffness

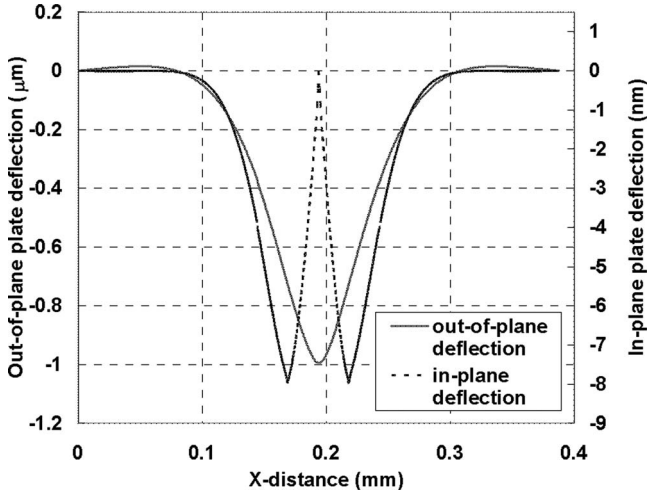

FIG. 10. Comparison of out-of-plane deflection and in-plane deflection for SS boundary conditions at a position 3.99 mm from the base of the BM. Out-of-plane deflection uses left vertical axis and in-plane deflection uses right vertical axis. Note that the space constant for the out-of-plane deflection and in-plane deflection are different.

with an exponential rise to an asymptote. The space constant they computed is 21 μm, which is smaller than a 40 μm space constant reported by Naidu and Mountain (2001), who pushed on the basilar membrane with a rigid probe and optically measured deflections of nearby structures. Thus, they stated there is relatively little longitudinal coupling within the pectinate zone of the basilar membrane in contrast to the intermediate levels of longitudinal coupling measured by Naidu and Mountain (2001).

As Emadi *et al.* and Naidu and Mountain used different methods to measure the space constant, and, indeed, different definitions for what the space constant is, it is difficult to compare their interpretation. We employ our orthotropic finite element plate model with a cut (free) edge to obtain the plateau stiffness profile in Emadi, *et al.* [2004, in Fig. 4(B)]. From this, we extract material properties from Emadi *et al.*'s experimental data. Figure 12 shows the stiffness profiles from Emadi *et al.*'s hemicochlea experiment and ABAQUS

TABLE IV. Results for material properties to match stiffness and *lateral* space constant. These are computed using the geometrically nonlinear orthotropic plate FEA model.

								Composite plate properties determined by matching experiment			
Distance from base[a] (mm)	Space constant (μm)	b (μm)	η (μm)	Thickness (μm)	Applied pressure load (kPa)	Stiffness (N/m)	Boundary conditions	E_x (kPa)	E_y (kPa)	G_{xy} (kPa)	ν_{xy}
1.14	13.2	150	60	15.8	51.5	4.042	SS	236	15300	78.6	0.0068
							CS	415	6640	138	0.028
3.99	23.8	194	77.6	17.3	21.27	1.671	SS	260	6240	86.7	0.020
							CS	326	2930	109	0.053
6.612	33.5	232	87	23.7	9.436	0.741	SS	76	1360	25.2	0.027
							CS	88.5	664	30.0	0.065
7.3	36.0	242	91	25.3	7.623	0.599	SS	47.7	1050	16.0	0.022
							CS	55.2	525	18.4	0.051

[a]Naidu and Mountain (1998, 2001).

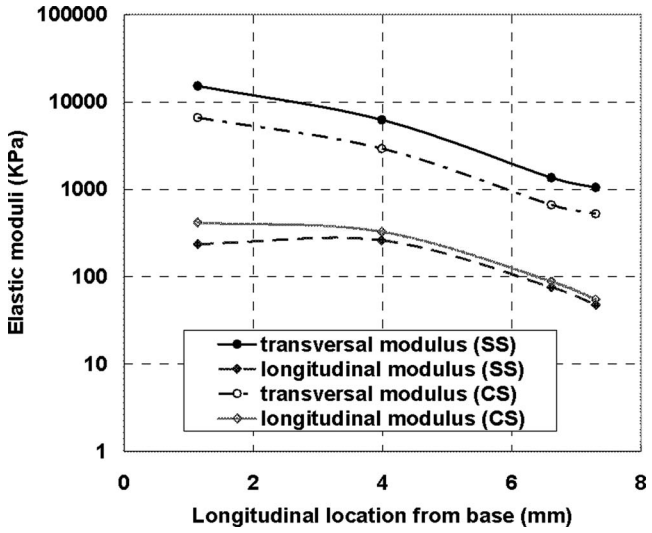

FIG. 11. Material property variations along the longitudinal direction for SS boundary condition.

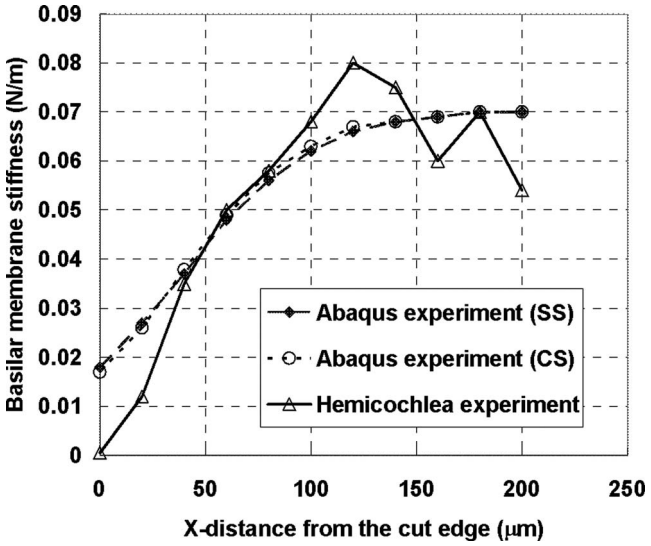

FIG. 12. Comparison of stiffness profile in hemicochlea experiment and ABAQUS experiments for different boundary conditions.

simulations for both types of boundary conditions. Stiffness measured by Emadi *et al.* at the cut edge is approximately an order of magnitude below the noise floor and so is treated in their work as effectively as zero. However, from a mechanics point of view, the stiffness at the edge cannot be truly zero; thus the model results, which include no noise, will always show a nonzero stiffness at the edge. The asymptotic stiffness is 0.07 N/m in Emadi *et al.* (2004), which we match. The variation of stiffness with distance from the cut edge is matched as closely as possible, giving a stiffness that gradually increases at distance increments up to the asymptotic stiffness, as shown in Fig. 12.

Attempts had been made to use ABAQUS data to fit the hemicochlea data for the points close to the cut edge before we came to the final fit curve. When the cut edge and the measured point closest to the cut edge are matched well with the hemicochlea data, the stiffness reduces and does not reach the stiffness far from the edge. We believe it is important to match the stiffness far from the edge. The discrepancy close to the cut edge can be explained by the possibility that the edge was damaged, whereas the cochlea was cut in half. In addition, the probe is 25 μm in diameter, which is relative large compared to the distance from the edge for the closest point. As the cut edge cannot support much force, it is also possible that the probe might slip.

The material properties determined to produce this matched result for the hemicochlea experiment are shown in Table V. Using these material properties, we are then able to compute a Naidu and Mountain space constant from Emadi *et al.*'s experimental data. This space constant is 185 μm for SS boundary conditions and 126 μm for CS boundary conditions. These space constants demonstrate considerable longitudinal coupling is present in Emadi *et al.*'s results. Indeed, their results seem to suggest a greater degree of coupling than is present in the data of Naidu and Mountain, where the space constant at this location was 36 μm.

TABLE V. Material properties obtained to match hemicochlea stiffness experiment.[a]

Boundary condition	E_x (kPa)	E_y (kPa)	G_{xy} (kPa)	ν_{xy}
SS	26	48	8.69	0.2645
CS	23	25	7.7	0.4436

[a]Emadi *et al.* (2004).

C. Probe area

In an experiment the contact area of the probe with the BM may not be precisely known. The maximum contact area is the total size of the probe, a 5 μm radius for the experiments of Naidu and Mountain, a 12.5 μm radius for Emadi *et al.* In order to investigate the sensitivity of the results to probe contact area, four different load areas, with radii 2, 5, 8, and 12.5 μm were investigated in both analytical and finite element solutions. In all cases, the results indicate that the probes with radius from 2 to 12.5 μm have little effect on the shape of the deflected region. An example result is shown below in Fig. 13.

Gueta *et al.* (2006) indicated that two different research groups obtained similar indentation shape on the tectorial membrane when both used nanoscale indenters but there was no agreement between the results when microscale indenters were used. They used a microscale indenter with radius 1 μm, whereas the other group used 5 μm. The 5 μm radius indenter is about half of the width of the tectorial membrane, which caused significant difference from the results measured by a 1 μm radius indenter, which is only 1/10 of the width of the tectorial membrane. The basilar membrane is much wider, 150–250 μm wide, and does not show much variation in our computations for radii of 2–12.5 μm. We suggest that the probe size has little effect on the deflection shape when it is small compared with the dimensions of the object being measured, but still larger than the embedded fibers.

TABLE VI. Composite plate flexural rigidity computed using plate material properties.

Distance from base (mm)	b (μm)	Thickness (μm)	Boundary conditions	Composite plate flexural rigidity computed using plate material properties: D_x (N m)	D_y (N m)	D_{xy} (N m)
1.14[a] (Naidu & Mountain)	150	15.8	SS	7.78×10^{-11}	5.044×10^{-9}	8.597×10^{-11}
			CS	1.38×10^{-10}	2.21×10^{-9}	1.526×10^{-10}
3.99[a] (Naidu & Mountain)	194	17.3	SS	1.133×10^{-10}	2.72×10^{-9}	1.29×10^{-10}
			CS	1.443×10^{-10}	1.297×10^{-9}	1.628×10^{-10}
6.612[a] (Naidu & Mountain)	232	23.7	SS	8.54×10^{-11}	1.53×10^{-9}	9.72×10^{-11}
			CS	1.014×10^{-10}	7.61×10^{-10}	1.16×10^{-10}
7.3[a] (Naidu & Mountain)	242	25.3	SS	6.51×10^{-11}	1.43×10^{-9}	7.47×10^{-11}
			CS	7.64×10^{-11}	7.265×10^{-10}	8.67×10^{-11}
7.3[b] (Emadi *et al.*)	242	25.3	SS	4.03×10^{-11}	7.44×10^{-11}	4.313×10^{-11}
			CS	3.95×10^{-11}	4.29×10^{-11}	3.98×10^{-11}

[a]Naidu and Mountain (1998, 2001).
[b]Emadi *et al.* (2004).

D. Stiffness linearity

In Fig. 2 in Naidu and Mountain (1998), the stiffness measured in the 1–3 μm deflection range is approximately constant. That is to say, the deflection versus applied force curve is linear. The stiffness linearity of the geometrically nonlinear FEA plate model was examined by applying double and triple the test load. Figure 14 below shows the FEA results for center point deflection for both boundary conditions. The geometric nonlinearity contributes approximately 10% nonlinear stiffening at a displacement of 3 μm. This appears to be within the experimental error seen in Naidu and Mountain (1998, Fig. 2).

E. Basilar membrane dimensions

The basilar membrane dimensions used in the models were reported by Schweitzer *et al.* (1996), which were derived from fixed tissue. The fixation process results in a decrease in the thickness of the basilar membrane. The reason we used the dimension data of Schweitzer *et al.* for the basilar membrane is that they also reported the fiber band dimensions, which are essential for the volume fraction method. In addition, the basilar membrane does not have a uniform thickness along radial direction, but the curvature of the membrane is not known. To simplify the problem, we used a uniform thickness and a flat plate. The maximum thickness value for a given longitudinal position in Schweitzer *et al.* is used as the uniform thickness of our plate. When applying the material properties calculated in this paper to model the BM as a plate, the reader should use the same thickness that we use for the computations. Alternatively, the reader can use the plate properties from Table VI.

VI. CONCLUSION

The effective material properties of the gerbil BM were determined from experimental data using a geometric nonlinear orthotropic plate model implement using a finite ele-

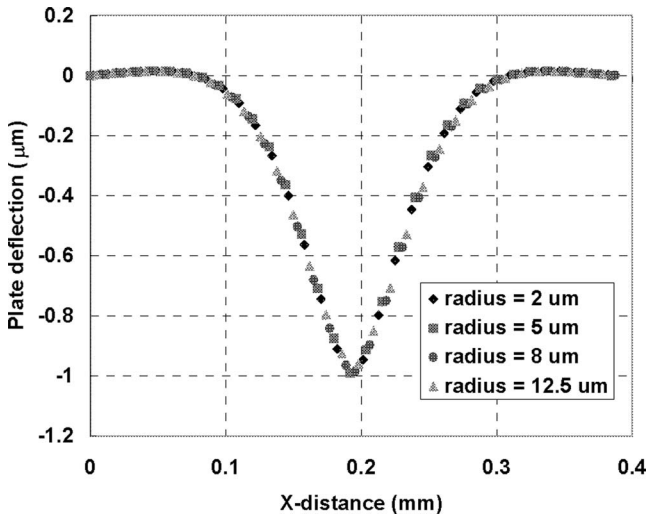

FIG. 13. Comparison of contact area effect for ABAQUS solution.

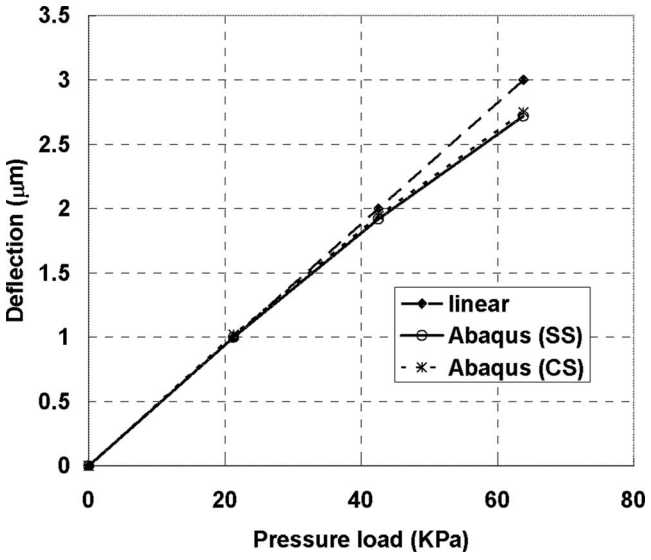

FIG. 14. Plate model linearity in the constant stiffness range at 3.99 mm from base.

ment framework. It is important to recognize that an orthotropic plate model cannot capture the full complexity of the cochlea physiology. However, using a simple model reduces the number of free parameters, allowing them to be determined from available data. It is important that the reader understands that material properties are effective properties, which should be used only for a flat orthotropic plate of the same uniform thickness used to derive the properties. Alternatively, models can use the plate properties shown in Table VI.

The resulting model is useful as an effective plate, representing a combination of effects coming from the complex physiology. Some examples of the complexities that are subsumed into the plate model include: the effect of organ of Corti (Naidu and Mountain, 1998; 2001), the effect of tectorial membrane (Emadi *et al.*, 2004), and the effect of radial variations. A variety of computations were conducted to explore different possibilities related to *in vivo* experiments as detailed in the following.

Different probe sizes were investigated in the simulations and it was shown that the exact contact area between probe and BM does not affect the results for probes of radius 2–12.5 μm. Under the same total load, by choosing a contact area radius of 2–12.5 μm, the plate deformed similarly.

The space constant for the out-of-plane deflection, computed by both linear and geometrically nonlinear models, is very different than the space constant for in-plane deflections. Computation of the in-plane deflection requires a geometrically nonlinear model. The results from the geometric nonlinear model demonstrate that such a model is necessary to interpret the experimental data of Naidu and Mountain, and thus produce an improved estimate of material properties for the BM. The assumption that *lateral* deflection is proportional to *vertical* deflection is inaccurate, and a purely linear model will produce imprecise estimates of material properties even for small deflections.

Using the point stiffness and space constant data from Naidu and Mountain (1998, 2001) and Emadi *et al.* (2004), a complete set of orthotropic plate properties was determined using a geometrically nonlinear model and two possible boundary conditions. For both simple supported (SS) and clamped-simply supported (CS) boundary conditions, a decrease of radial modulus is observed from base to apex. For SS (CS) boundary conditions, the radial modulus varies from 15 MPa (6.6 MPa) to 1 MPa (0.5 MPa) from the base to the upper middle turn of gerbil cochlea; in the same region the longitudinal modulus decreases from 0.2 MPa (0.4 MPa) to 0.05 MPa (0.05 MPa). From these results, it can be seen that the orthotropy varies along the length of the cochlear partition from a maximum of 65 close to the base to a minimum of 10 in the upper middle turn. This can be explained by the longitudinal decrease in thickness of fiber bands (Schweitzer *et al.*, 1996), which mainly contribute to the material properties in the transverse direction. For SS boundary conditions, both moduli are larger than for CS boundary conditions, as expected. The orthotropy ratio is similar for either choice of boundary conditions.

Naidu and Mountain observed that the BM of the gerbil is nearly isotropic at the apex and calculated an orthotropy ratio of 2 at the apex (Naidu and Mountain, 2007). Our orthotropy ratio is about 20 for SS boundary conditions and 10 for CS conditions at the upper middle turn (two thirds of the distance to the apex), which is a similar result. Skrodzka used a longitudinal elastic modulus 200 kPa and a transverse elastic modulus 250 kPa for human basilar membrane (Skrodzka, 2005), indicating a constant orthotropic ratio of 2.5 along the basilar membrane, which is close to our orthotropy ratio toward the apex. Gross properties of chinchilla basilar membrane used in a three-dimensional nonlinear active cochlear model by Lim and Steele were taken as 1.0 GPa for transverse modulus and 0.01 GPa for longitudinal modulus along the entire length of the BM (Lim and Steele, 2002). This 100 orthotropy ratio is close to our orthotropy ratio at the base of gerbil cochlea.

The different methods for measuring space constant by Emadi *et al.* and Naidu and Mountain were reconciled through the plate model presented in this paper. Material properties were retrieved through matching a stiffness profile in Emadi *et al.* (2004) and then used in the same model as that of Naidu and Mountain. The material properties determined from the experiment of Emadi *et al.* were used to simulate a Naidu and Mountain space constant. For the experimental data of Emadi *et al.*, this resulted in a space constant of 185 μm for SS boundary conditions, and 126 μm for CS boundary conditions. Both of these results are considerably higher than the 36 μm space constant measured by Naidu and Mountain at this location, demonstrating that the data of Emadi *et al.* also shows considerably longitudinal coupling.

Stiffness measured by Naidu and Mountain differ significantly from that by Emadi *et al.* The material properties estimated using these two sets of data thus also differ. The major difference is in the radial elastic modulus. This suggests something fundamentally different between the different experimental setups used by these two research group. Naidu and Mountain used isolated turn preparation for the cochlea experiments, in which the turn of interest was isolated while the adjacent turns were removed. The resulting preparation consisted of an entire cochlea turn with the OC and its attachments to the spiral lamina and spiral ligament intact. Emadi *et al.* cut the cochlea from apex to base along the modiolar plane. The cut effectively removed one half of the cochlea and left behind a hemicochlea. We suggest that these differences in preparation may be the cause of the different observed material properties. As stated earlier, the difference is not caused by the different probe sizes used by the two groups. Both experimental data sets do show considerable longitudinal coupling, but they do not result in identical material properties as derived by the methods of this paper.

These results all indicate that longitudinal coupling in the gerbil BM is significant, with orthotropy ratios on the order of 1–100, increasing from apex to base. Dynamic models of traveling wave motion in the passive cochlea demonstrate that low orthotropy ratios result in a more spatially distributed BM response, which would lead to less frequency discrimination. The next step in this work is to implement a

dynamic model using these material properties. The details of how this will affect the modeled dynamic response remain to be seen.

Allaire, P., Raynor, S., and Billone, M. (**1974**). "Cochlear partition stiffness-composite beam model," J. Acoust. Soc. Am. **55**, 1252–1258.

Budynas, R. G. (**1999**). *Advanced Strength and Applied Stress Analysis* (McGraw-Hill, New York).

Dowling, N. E. (**1999**). *Mechanical Behavior of Materials* (Prentice-Hall, Englewood Cliffs, NJ).

Edge, R. M., Evans, B. N., Pearce, M., Richter, C. P., Hu, X., and Dallos, P., (**1998**). "Morphology of the unfixed cochlea," Hear. Res. **124**, 1–16.

Emadi, G., Richter, C. P. Dallos, and P. (**2004**). "Stiffness of the gerbil basilar membrane: Radial and longitudinal variations," J. Neurophysiol. **91**, 474–488.

Gueta, R., Barlam, D. Shneck, R. Z., and Rousso, I. (**2006**). "Measurement of the mechanical properties of isolated tectorial membrane using atomic force microscopy," Proc. Natl. Acad. Sci. U.S.A. **103**, 14790–14795.

Gummer, A. W., Johnstone, B. M., and Arstrong, N. J. (**1981**). "Direct measurement of basilar-membrane stiffness in the guinea-pig," J. Acoust. Soc. Am. **70**, 1298–1309.

Iurato, S. (**1962**). "Functional implications of the nature and submicroscopic structure of the tectorial and basilar membranes," J. Acoust. Soc. Am. **34**, 1386–1395.

Jurvelin, J. S., Buschmann, M. D., and Hunziker, E. B. (**1997**). "Optical and mechanical determination of Poisson's ratio of adult bovine humeral articular cartilage," J. Biomech. **30**, 235–241.

Lai-Fook, S. J., Wilson, T. A., Hyatt, R. E., and Rodarte, J. R. (**1976**). "Elastic constants of inflated lobes of dog lungs," J. Appl. Physiol. **40**, 508–513.

Lim, K. M., and Steele, C. R. (**2002**). "A three-dimensional nonlinear active cochlear model analyzed by the WKB-numeric method." Hear. Res. **170**, 190–205.

Lynch, T. J., Nedzelnitsky, V., and Peake, W. T. (**1982**). "Input impedance of the cochlea in cat," J. Acoust. Soc. Am. **72**, 108–130.

Miller, C. E. (**1985**). "Structural implications of basilar-membrane compliance measurements," J. Acoust. Soc. Am. **77**, 1465–1474.

Naidu, R. C., and Mountain, D. C. (**1998**). "Measurements of the stiffness map challenge a basic tenet of cochlear theories," Hear. Res. **124**, 124–131.

Naidu, R. C., and Mountain, D. C. (**2001**). "Longitudinal coupling in the basilar membrane," J. Assoc. Res. Otolaryngol. **2**, 257–267.

Naidu, R. C., and Mountain, D. C. (**2007**). "Basilar membrane tension calculations for the gerbil cochlea," J. Acoust. Soc. Am. **121**, 994–1002.

Neely, S. T., and Kim, D. O. (**1986**). "A model for active elements in cochlear biomechanics," J. Acoust. Soc. Am. **79**, 1472–1480.

Olson, E. S., and Mountain, D. C. (**1991**). "In vivo measurement of basilar membrane stiffness." J. Acoust. Soc. Am. **89**, 1262–1275.

Ramamoorthy, S., Deo, N. V., and Grosh, K. (**2007**). "A mechano-electro-acoustical model for the cochlea: Response to acoustic stimuli," J. Acoust. Soc. Am. **121**, 2758–2773.

Richter, C. P., Evans, B. N., Edge, R., and Dallos, P.(**1998**). "Basilar membrane vibration in the gerbil hemicochlea," J. Neurophysiol. **79**, 2255–2264.

Schweitzer, L., Lutz, C., Hobbs, M., and Weaver, S. (**1996**). "Anatomical correlates of the passive properties underlying the developmental shift in the frequency map of the mammalian cochlea," Hear. Res. **97**, 84–94.

Skrodzka, E. B. (**2005**). "Mechanical passive and active models of the human basilar membrane," Appl. Acoust. **66**, 1321–1338.

Steele, C. R., and Taber, L. A. (**1979**). "Comparison of WKB calculations and experimental results for 3-dimensional cochlear models," J. Acoust. Soc. Am. **65**, 1007–1018.

Szilard, R. (**2004**). *Theories and Applications of Plate Analysis* (Wiley, New York)

Timoshenko, S., and Woinowsky-Krieger, S. (**1959**). *Theory of Plates and Shells* (McGraw-Hill, NY).

Ugural, A. C. (**1999**). *Stress in Plates and Shells* (McGraw-Hill, New York)

Voldrich, L. (**1978**). "Mechanical-properties of basilar-membrane," Acta Oto-Laryngol. **86**, 331–335.

Whitney, J. M. (**1987**). *Structural Analysis of Laminated Anisotropic Plates* (Technomic Publ. Co., Inc., Lancaster, PA).

Low-frequency and high-frequency distortion product otoacoustic emission suppression in humans

Michael P. Gorga,[a] Stephen T. Neely, Darcia M. Dierking, Judy Kopun, Kristin Jolkowski, Kristin Groenenboom, Hongyang Tan, and Bettina Stiegemann
Boys Town National Research Hospital, 555 North 30th Street, Omaha, Nebraska 68131

(Received 23 October 2007; revised 9 January 2008; accepted 9 January 2008)

Distortion product otoacoustic emission suppression (quantified as decrements) was measured for f_2=500 and 4000 Hz, for a range of primary levels (L_2), suppressor frequencies (f_3), and suppressor levels (L_3) in 19 normal-hearing subjects. Slopes of decrement-versus-L_3 functions were similar at both f_2 frequencies, and decreased as f_3 increased. Suppression tuning curves, constructed from decrement functions, were used to estimate (1) suppression for on- and low-frequency suppressors, (2) tip-to-tail differences, (3) Q_{ERB}, and (4) best frequency. Compression, estimated from the slope of functions relating suppression "threshold" to L_2 for off-frequency suppressors, was similar for 500 and 4000 Hz. Tip-to-tail differences, Q_{ERB}, and best frequency decreased as L_2 increased for both frequencies. However, tip-to-tail difference (an estimate of cochlear-amplifier gain) was 20 dB greater at 4000 Hz, compared to 500 Hz. Q_{ERB} decreased to a greater extent with L_2 when f_2 =4000 Hz, but, on an octave scale, best frequency shifted more with level when f_2=500 Hz. These data indicate that, at both frequencies, cochlear processing is nonlinear. Response growth and compression are similar at the two frequencies, but gain is greater at 4000 Hz and spread of excitation is greater at 500 Hz. © *2008 Acoustical Society of America.* [DOI: 10.1121/1.2839138]

PACS number(s): 43.64.Jb, 43.64.Kc [BLM] Pages: 2172–2190

I. INTRODUCTION

The purpose of this study was to compare low- and high-frequency cochlear processing in humans, using distortion product otoacoustic emission (DPOAE) measurements. Specifically, we were interested in evaluating response growth, compression, cochlear-amplifier gain, tuning and spread of excitation, based on measurements of DPOAE suppression, to determine if the human cochlea processes low- and high-frequency sounds differently.

DPOAEs typically are measured in response to two primary tones of slightly different frequency, with f_2 representing the higher frequency in the primary-frequency pair and f_1 representing the lower frequency in the pair. It is generally assumed that DPOAEs (at least initially) are generated at a location in the cochlea near the best place for f_2, even though the response is typically measured at the $2f_1$–f_2 frequency, which is about $\frac{1}{2}$ octave lower in frequency than f_2. This fact has implications for DPOAE measurements as a function of frequency because noise in DPOAE measurements increases as frequency decreases. It is this interaction between frequency and noise level that is probably the most important factor contributing to the poorer test performance of DPOAE measurements in determining auditory status at lower frequencies in humans (e.g., Gorga *et al.*, 1993, 1997). However, the difference in noise levels as a function of frequency potentially could have an impact on every OAE measurement in which low- and high-frequency cochlear processing are compared.

In a recent paper, low- and high-frequency cochlear nonlinearity was examined by measuring DPOAE input/output (I/O) functions for f_2 frequencies of 500 and 4000 Hz (Gorga *et al.*, 2007). Long averaging times were used in efforts to reduce the noise levels when f_2=500 Hz. Behavioral thresholds were measured at both f_2 frequencies for each subject, allowing us to set L_2 (the level of f_2) in sensation level (SL) relative to each subject's threshold. To a first approximation, this approach provided a way to equate the representation of stimuli in the cochlea, both across frequency and subjects, and helped to account for differences in forward middle-ear transmission between 500 and 4000 Hz. For each subject, techniques were followed that allowed us to select the optimal L_1 for each L_2 for each subject individually (Neely *et al.*, 2005; Gorga *et al.*, 2007). Finally, the slopes of I/O functions were evaluated as a way of comparing cochlear responses across frequency on the assumption that slope should be independent of reverse middle-ear transmission. While previous work has shown that reverse middle-ear transmission would be expected to affect the relative position of the DPOAE I/O function along the y axis (Keefe, 2002), it would not be expected to influence the slope of that function. In total, these stimulus conditions and response measurements were selected in an effort to reduce noise to similar, low levels at both frequencies, account for forward middle-ear transmission, set optimal stimulus-level conditions individually, and provide a metric that was independent of reverse middle-ear transmission.

DPOAE I/O functions at 500 and 4000 Hz differed at low levels of stimulation, with a maximum low-level slope of about 1 achieved at lower levels when f_2=4000 Hz (Gorga *et al.*, 2007). In contrast, the minimum slope in the I/O functions was observed at similar stimulus levels of 40–50 dB SL for the two frequencies. When combined, these two observations provide support for the view that

[a]Electronic mail: gorga@boystown.org

 0001-4966/2008/123(4)/2172/19/$23.00 © 2008 Acoustical Society of America

there was a wider dynamic range when f_2=4000 Hz. These results also suggest that there may be greater cochlear-amplifier gain at 4000 Hz, compared to 500 Hz, to the extent that the observation of responses at lower levels reflects greater gain.

An important limitation of the previous study, however, was the differences in noise floor between 500 and 4000 Hz. Despite using long averaging times (as much as 210 s), residual noise floors were higher when f_2=500 Hz. The influence of this difference in noise floor was greatest for low-level stimulus conditions, where differences in response properties at the two frequencies were observed. While the signal-to-noise ratio (SNR) was such that the responses at both frequencies exceeded the noise floor for the conditions in which the maximum slope was achieved, we were cautious in our interpretation of these data because we could not completely rule out the influence of differences in noise floor on the slope of the DPOAE I/O functions at low levels of stimulation.

Our previous work, described earlier, was motivated by several observations, based on physiological and behavioral data, in which differences in cochlear processing for high and low frequencies have been evaluated. For example, frequency-threshold curves (FTCs) differ for auditory-nerve fibers innervating more basal, high-frequency cochlear regions, compared to fibers innervating lower frequency, apical regions (e.g., Kiang *et al.*, 1965; Kiang and Maxon, 1974). In their normal state, fibers innervating the cochlear base are characterized by low thresholds and sharp tuning around their characteristic frequency (CF, the frequency to which the fiber has the lowest threshold), decreased sensitivity (higher thresholds) as frequency moves away from CF, and a low-frequency tail on which thresholds either increase slowly or remain relatively constant. In contrast, low-CF fibers have FTCs that are more symmetrical around their CF, and often lack the low-frequency, relatively constant-threshold tail that is evident in the responses of high-CF fibers.

Sewell (1984) provided data in which furosemide treatment resulted in greater changes in thresholds around the CF of high-frequency fibers, compared to fibers with low CFs. It has been argued that the low thresholds around fiber CF are a reflection of cochlear-amplifier gain at that frequency, and that the motile behavior of outer hair cells (OHC) is the source of this gain (Dallos *et al.*, 1997; Hudspeth, 1997; Neely and Kim, 1983). Support for this view comes from lesion studies in which OHC damage resulted in threshold elevations near CF, with little or no change in thresholds on the low-frequency tail of the FTC (e.g., Dallos and Harris, 1978; Liberman and Dodds, 1984). The fact that thresholds change more for high-CF fibers following furosemide treatment may be interpreted to mean that there is more gain (that was affected by the treatment) for high-CF fibers. It is impossible to examine the responses of individual auditory neurons in humans; however, OAE responses are related to OHC function, and these responses can be measured in humans. For this reason, our efforts to compare low- and high-frequency cochlear responses in humans have focused on DPOAE I/O measurements. We hope to exploit these features in further efforts, described in the following, to better understand cochlear function at high and low frequencies in humans.

The majority of data based on direct measurements of basilar-membrane responses comes from observations at the basal, high-frequency end of the cochlea of lower animals. Apparently, this is the case because access to the cochlear apex, even in experimental animals, is difficult, and the risk exists that the procedures that are used to gain access may cause damage to the cochlea. The OHCs are among the most vulnerable structures in the cochlea, and one would expect that their response properties would be altered if damage were to occur during the preparation. When OHC damage occurs, less nonlinearity is observed, regardless of frequency, because OHCs are the source of the nonlinear response. Thus, the experimental difficulty in obtaining access without causing damage has resulted in a situation in which fewer data are available that describe normal cochlear responses at the apex. There are, however, several studies that have directly assessed nonlinearity at the apical end of the cochlea (Cooper and Rhode, 1995, 1997, 1998; Rhode and Cooper, 1996). These studies suggest that nonlinearity is evident in both apical- and basal-region cochlear responses. However, differences were noted, in that the nonlinearity at the apical end of the cochlea exists for a wider range of frequencies and may be less in magnitude, compared to response properties at the cochlear base. In contrast to these findings, Zinn *et al.* (2000) did not observe compression at low and moderate stimulus levels for apical cochlear regions. Furthermore, they concluded that there was cochlear-amplifier gain at the base, but not at the apex. The apparent discrepancies may be due to factors associated with the relative inaccessibility of the cochlear apex.

With the exception of our recent paper (Gorga *et al.*, 2007), the data related to this issue in humans comes mainly from studies in which behavioral-measurement techniques were used. Interestingly, early work on combination-tone generation indicated that nonlinear distortion was present in the human cochlea over a range of frequencies from below 500 to as high as 8000 Hz with no apparent trend in distortion level as a function of frequency (e.g., Plomp, 1965; Goldstein, 1967). More recently, Hicks and Bacon (1999) and Plack and Oxenham (1998) reported psychoacoustical data that suggest greater nonlinearity for high frequencies, whereas Plack and Drga (2003), Plack and O'Hanlon (2003), Lopez-Poveda *et al.* (2003), and Schairer *et al.* (private communication) observed no differences in nonlinearity between high and low frequencies in humans. The differences in results from the two groups of studies may be due, in part, to differences in measurement technique. In some of these studies, conclusions about cochlear nonlinearity were based on comparisons between response properties for on-frequency versus low-frequency stimuli (relative to the frequency of interest). In other studies, conclusions were based on measurements in which such on-frequency/low-frequency comparisons were not used. The argument against the case in which on-frequency and low-frequency responses were compared is based on the view that the low-frequency stimulus (relative to the frequency of interest) may not have been

sufficiently low enough to result in a linear response at the place where the frequency of interest is represented. Some support for this view is perhaps provided in the differences in FTCs for low-CF and high-CF fibers. Additional support may be provided by the work of Cooper and Rhode (1995), in which they noted that the nonlinearity at the apical end of the cochlea extends over a wider range of frequencies, compared to the extent of the nonlinear region at the cochlear base.

Sufficient uncertainty exists that further effort would be useful in evaluating cochlear nonlinearity in humans for high versus low frequencies. Our initial efforts suggested that differences do exist, based on an analysis of DPOAE I/O functions. While evidence existed in those data for nonlinearity in response to both high- and low-frequency stimuli, the results would be consistent with the view that there is greater cochlear-amplifier gain for higher frequencies. Those data, however, were interpreted cautiously because the influence of differences in noise floor between low- and high-frequency measurements could not be completely controlled. The present study was designed to further explore cochlear nonlinearity in humans, using measurements of DPOAE suppression. These measurements were made for f_2 frequencies of 500 and 4000 Hz, using a wide range of suppressor frequencies and levels for each f_2. In addition, these measurements were made for a range of stimulus (probe) levels (L_2). An advantage of the suppression measurements over I/O functions is that they may be less affected by the noise floor. At both 500 and 4000 Hz, the response that was suppressed was above the noise during control conditions (the condition in which no suppressor was presented). Thus, the influence of noise is expected to be less in the present measurements.

II. METHODS

A. Subjects

Nineteen subjects participated in this study. These subjects were drawn from a larger sample of 103 subjects who participated in our previous studies in which DPOAE I/O functions were measured (Gorga *et al.*, 2007). In addition to inclusion criteria related to hearing sensitivity, which will be described in the following, these subjects were selected for two reasons. First, they indicated that they would be able to devote the amount of time that was required in order to complete data collection (about 40 h/subject). An additional three subjects were enrolled in the study, but withdrew after several sessions because of difficulties meeting the time commitment. The data reported in the following came only from the 19 subjects who completed the study. In addition to the time-commitment inclusion criterion, subjects were selected because they produced DPOAEs above the noise floor for both 500 and 4000 Hz for a wide range of L_2 levels. This determination was based on data that were obtained from the larger sample of subjects who participated in the I/O study. Using the previous data to help in subject selection made it possible to describe suppression effects for both high- and low-level probes, which is important because previous data suggest that cochlear-amplifier gain is level dependent (Rhode, 1971; Ruggero and Rich, 1991), an effect that has been observed in data similar to those collected as part of this study (e.g., Gorga *et al.*, 2002a, b, 2003).

Subjects ranged in age from 17 to 42 years, with a mean age of 24.8 years (s.d.=6.2). Each subject had audiometric thresholds of 15 dB HL or better (re: ANSI, 1996) for standard octave and interoctave audiometric frequencies from 250 to 8000 Hz. Additionally, subjects were required to have audiometric thresholds of 10 dB HL or better at 250, 500, 2000, 3000, and 4000 Hz, which included the primary (f_2) frequencies (500 and 4000 Hz) that were the focus of the present measurements. These behavioral-threshold subject-inclusion data were collected using routine clinical procedures, to be contrasted with the procedures that were used later to determine the behavioral thresholds in order to set stimulus levels during DPOAE measurements (see the following). Each subject had a normal 226-Hz tympanogram on each day on which DPOAE measurements were made. Only one ear of each subject was tested, and was chosen as the ear with the lowest audiometric thresholds at 500 and 4000 Hz, in the hope that such a choice would result in the widest dynamic range of DPOAE measurements for individual subjects (e.g., Dorn *et al.*, 1998). If the audiometric thresholds did not differ between ears, then the test ear was chosen at random.

B. Stimuli

DPOAEs were elicited in response to a pair of primary frequencies (f_1 and f_2), with f_2=500 or 4000 Hz. These two frequencies were chosen because they represent distant locations in the cochlea, one closer to the base and the other closer to the apex. However, cochlear maps for humans suggest that these two frequencies are not represented at "extreme ends" of the cochlea, being approximately 71% and 33% from the base for 500 and 4000 Hz, respectively (Greenwood, 1990). Still, 500 Hz represents a lower practical limit for reliable DPOAE measurements. With an f_2 of 500 Hz, the $2f_1$-f_2 distortion product frequency (the frequency at which responses were measured) occurs at 320 Hz. At this measurement frequency, noise levels are high, making it difficult to measure responses. Reliable measurements are possible with an f_2 of 500 Hz only if long averaging times are used. However, it would be even more difficult to obtain measurements for $f_2 < 500$ Hz, because the further increase in noise with decreasing $2f_1$–f_2 would require impracticably long averaging times. In a similar fashion, f_2=4000 Hz was viewed as a practical high-frequency limit, but for different reasons. With the limitations of our current calibration approach (see the following), it was possible to avoid standing-wave problems for this frequency and its associated suppressor frequencies, something that would not have been possible if measurements included higher frequencies. In addition, the hardware used in the present study produced less output for higher frequencies, and would have reduced the range of primary and suppressor levels for which measurements could be made. The adequacy of these frequency limits is supported by recent data suggesting that cochleae in humans function differently for frequencies above 1000 Hz, compared to lower frequencies (Shera *et al.*,

2007). Thus, the f_2 frequencies used in the present study may provide insights from cochlear regions having different response properties. For both f_2 frequencies, the ratio of f_2 to f_1 was constant at about 1.22. A larger ratio might have reduced the contributions from the DP place (the reflection source), although this is not always the case (Dhar *et al.*, 2005). Even so, this would also have had the effect of reducing the overall level (and SNR) of the DPOAE (e.g., Dhar *et al.*, 2005; Gaskill and Brown, 1990). Our interest in measuring suppression at low stimulus levels, where cochlear-amplifier gain is greatest, made the use of larger f_2/f_1 undesirable.

The level of the higher frequency in the primary-frequency pair (L_2) was set in dB sensation level (SL) relative to each subject's behavioral threshold at f_2. L_2 varied from 20 to 50 dB SL when f_2=500 Hz, and from 10 to 50 dB SL when f_2=4000 Hz. These conditions were chosen because they resulted in at least a 10-dB SNR for conditions in which no suppressor was presented in the majority of subjects. The inclusion of the 10-dB SL condition at 4000 Hz reflects the fact that it was possible to achieve a positive SNR at lower L_2 levels at 4000 Hz, compared to 500 Hz. The greater SNR at 4000 Hz is a consequence of the lower noise levels that are routinely observed at this frequency. Stimuli at 500 and 4000 Hz were presented relative to behavioral threshold in an effort to equate the "effective" representation of the two stimuli in the cochlea. In part, this approach should (to a first approximation) take into account differences in forward transmission through the middle ear at the two test frequencies. The "optimal" level of L_1 (the level of f_1, the lower frequency in the primary-frequency pair) was selected individually for each L_2 and for each f_2. By optimal level, we mean the L_1 at each L_2 for which the DPOAE level was largest in individual subjects. Different procedures were used to select these optimal conditions at 500 and 4000 Hz. At 4000 Hz, a procedure was used in which both L_1 and L_2 varied continuously (Neely *et al.*, 2005), whereas the higher noise levels at 500 Hz required longer averaging times, which, in turn, required measurements at discrete combinations of L_1 and L_2 (Gorga *et al.*, 2007). The procedures with which these levels were selected were described in detail previously (Neely *et al.*, 2005; Gorga *et al.*, 2007), and will not be repeated here. Although the procedures differed for each f_2, in both cases, a range of L_1 levels were tested for each L_2 so that the L_1 resulting in the largest DPOAE was identified and used in the main experiment. We elected to use this general approach because it took into account both subject and frequency differences in optimal-level conditions. While previous studies suggest that the decibel difference between L_1 and L_2 should increase as L_2 decreases, the results from those studies are not entirely in agreement in the exact form of the primary-level relationship. For example, Kummer *et al.* (1998, 2000) presented data showing that a single equation (referred to as the scissor paradigm) is appropriate for setting optimal stimulus-level ratios independent of f_2. In contrast, Neely *et al.* (2005) and Johnson *et al.* (2006) reported data in which the optimal level ratio varied across subjects and also depended on f_2. The approach taken in the present study, which follows the procedures used by Neely *et al.*, Johnson *et al.*, and Gorga *et al.*, makes no assumptions about the generalizability of the relationship between L_1 and L_2, either across subjects or across frequency. It results in optimal levels for each f_2 and for each subject, thus assuring that stimulus conditions producing the largest DPOAE are used in every case.

Nine suppressor frequencies (f_3) were used during suppression measurements when f_2=500 Hz. They ranged from 129 to 750 Hz. When f_2=4000 Hz, 14 f_3 frequencies were used, ranging from 2064 to 5667 Hz. During DPOAE suppression measurements, it is not possible to select a suppressor whose frequency is identical to f_2. A frequency slightly different from f_2 must be used as the "on-frequency" condition. When f_2=500 Hz, 515 Hz was used as the on-frequency suppressor, whereas when f_2=4000 Hz, 4100 Hz served as the on-frequency suppressor. Suppressor level (L_3) ranged from −20 to 85 dB SPL in 5-dB steps.

C. Procedures

Following obtaining informed consent, subjects were screened according to the above- described inclusion criteria. Once it was determined that the subject met inclusion criteria, behavioral thresholds were obtained with a more precise psychophysical procedure, compared to the routine clinical techniques that were used during the screening procedures associated with the inclusion criteria. Thresholds were measured with a two-interval, forced-choice, transformed up-down procedure that estimated the 71% correct point on the psychometric function (Levitt, 1971), using the same hardware that was used during DPOAE measurements. Averaged across subjects, the mean behavioral thresholds from these measurements were 11.9 dB SPL at 500 Hz (s.d.=3.2 dB) and 4.4 dB SPL at 4000 Hz (s.d.=4.8 dB). The individual thresholds for each subject were then used to set L_2 in dB SL during the suppression measurements, which are the main focus of the study.

For all DPOAE measurements, approximately 1 s recorded waveforms were stored in alternating response buffers. The contents of the buffers were summed and the resulting level in the $2f_1$-f_2 frequency bin was used to estimate DPOAE level. The contents of the two buffers were subtracted and the level in the $2f_1$-f_2 frequency bin and the level in five frequency bins above and below $2f_1$-f_2 were averaged to provide an estimate of noise level. During suppression measurements, L_2 was set at one of four values (f_2 =500 Hz) or one of five values (f_2=4000 Hz). This two-tone "probe" stimulus was presented as a control condition, in which there was no suppressor, and then presented with one of the suppressor frequencies, whose level was varied. Following the presentation of the highest L_3, another control condition was included. This process was repeated for all of the suppressor frequencies, all L_2 levels and both f_2 frequencies for each subject.

Measurement-based stopping rules were used throughout data collection, but the rules differed for the two f_2 frequencies. When f_2=4000 Hz, measurements continued until the noise floor was $\leq$−25 dB SPL, the SNR $\geq$20 dB, or until 210 s of artifact-free averaging had taken place, whichever

occurred first. In essentially every condition for this frequency, averaging stopped on the noise level and SNR rules, which were often met simultaneously. A compromise was needed, however, when f_2=500 Hz, because the noise levels were higher at this frequency. At 500 Hz, averaging stopped when the noise floor was $\leqslant$−25 dB SPL, the SNR was $\geqslant$12 dB, or 210 s of artifact-free averaging had been completed. The only difference between this rule and the one used when f_2=4000 Hz is the SNR stopping criterion. With this "compromise," we were able to achieve reliable estimates of DPOAE level for a range of L_2 conditions when f_2=500 Hz (on the assumption that a SNR $\geqslant$12 dB would result in a reliable estimate of DPOAE level), without averaging for the prohibitively long times that would be necessary to achieve the same low noise levels as were achieved routinely when f_2=4000 Hz. For any conditions in which the presence of the suppressor reduced the SNR to less than 12 dB (by reducing DPOAE level), the effective stopping rules were the same at 500 and 4000 Hz. In general (depending on L_2 and the extent to which the response was suppressed), measurements stopped either on the SNR criterion or the averaging-time criterion when f_2=500 Hz, but almost never stopped on the noise-floor criterion. Differences in the conditions under which measurements stopped (and, therefore, the noise floor associated with measurements) was not considered a significant problem because the responses in the control conditions had positive SNRs at both f_2 frequencies. Furthermore, a suppression threshold of 3 dB was used during the construction of DPOAE suppression tuning curves (STCs), from which main observations from the present study were made. This means that the SNR for the points on the STCs were positive. Even with differences in stopping rules designed to increase data-collection efficiency, each subject participated in about 40 h of data collection in order to complete measurements for all stimulus conditions. As expected from the previous description of stopping rules, the majority of the time was spent collecting data when f_2 =500 Hz.

Stimuli were produced by a 24 bit sound card (Digital Audio Labs, Card Deluxe) that drove a probe-microphone system (Etymotic, ER-10C). The "receiver equalization" of the ER-10C was bypassed to allow up to 20 dB higher level stimuli to be produced. Even so, there were conditions for which the maximum level produced by the hardware was insufficient to produce complete suppression. This occurred for f_3 frequencies at the high- and low-frequency ends of the range of suppressors and for the higher L_2 levels. Psychophysical thresholds were measured using custom-designed software that implemented the 2IFC procedure. Only one channel of the sound card and probe-microphone system were used for behavioral-threshold estimates. DPOAE data were collected with the same hardware that was used for the behavioral-threshold measurements, and were collected with custom-designed software (EMAV, Neely and Liu, 1994). Both channels of the sound card and probe-microphone system were used during DPOAE measurements, with f_2 presented on one channel and f_1 presented on the other. When a suppressor was included, it was presented on the same channel as f_2. For both behavioral-threshold and DPOAE measurements, in-the-ear SPL calibration was used to determine stimulus levels. There are concerns regarding standing waves when this calibration approach is followed (e.g., Siegel and Hirohata, 1994; Siegel, 2007). In efforts to avoid these problems, the probe was repositioned more deeply whenever a notch in the calibration spectrum was observed in the vicinity of 4000 Hz. In this way, the notch (and presumably, the standing-wave problems producing it) was shifted toward higher frequencies outside the range of interest for the present study.

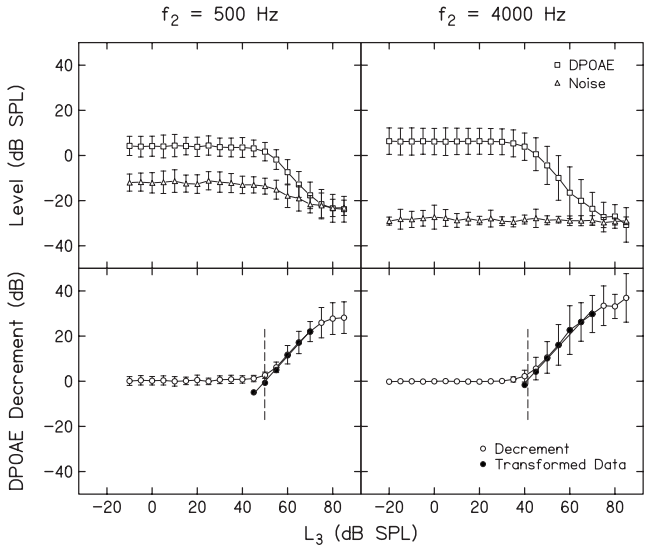

FIG. 1. Top row: Mean DPOAE (squares) and noise (triangles) levels in dB SPL as a function of suppressor level, L_3, in dB SPL. Bottom row: Mean DPOAE decrements (circles) in dB as a function of L_3. Left column shows data when f_2=500 Hz; right column shows data when f_2=4000 Hz. In both cases, L_2=40 dB SL, and an on-frequency suppressor (f_3) was used (f_3 =515 and 4100 Hz for f_2=500 and 4000 Hz, respectively). Closed symbols represent the transformed data points and the line represents a linear regression fit to the closed symbols. In all cases, error bars represent ±1 s.d. The short vertical dashed lines in the bottom row of panels are drawn at a decrement of 3 dB, which was used as suppression threshold for the construction of STCs.

Figure 1 illustrates features of the procedures used in the present experiment. It provides examples of data that were collected during the suppression measurements, the conversion of these suppression data into decrements as a result of the presence of the suppressor, transformation of the data, and finally linear fits that were applied to the transformed data. The left column presents data when f_2=500 Hz, while the right column shows data when f_2=4000 Hz. For both f_2 frequencies, L_2 was presented at 40 dB SL. Results are shown for the on-frequency suppressor condition (f_3 =515 Hz for f_2=500 Hz and f_3=4100 Hz when f_2 =4000 Hz). Individual data points represent the means (±1 s.d.) based on data from all 19 subjects. In the top row, DPOAE and noise levels are plotted as a function of L_3. An estimate of the DPOAE level for the control condition (when no suppressor was presented) is provided by the levels during the flat portion of the DPOAE level functions (i.e., when $L_3<$ about 40 dB SPL). The SNR can be estimated by comparing these values to the corresponding noise levels shown in Fig. 1. The differences in the results for 500 and 4000 Hz are due mainly to differences in noise floors, with smaller

differences in DPOAE level. This is to be expected given the differences in noise for these two f_2 frequencies, and occurred despite the measurement-based stopping rules and the long averaging times associated with them when f_2 =500 Hz. Still, suppressive effects were reliably measured for a range of L_3 levels at both f_2 frequencies. The data shown in the top row of Fig. 1 show that the suppressor had little or no effect on DPOAE level until L_3 was about 40 dB SPL. As L_3 increased above this level, DPOAE level was systematically reduced until it eventually equaled the noise floor, which occurred when $L_3 \approx 75$ dB SPL at both f_2 frequencies.

The influence of differences in the stopping rules for the two frequencies also is evident in Fig. 1. Note that for all L_3 levels, the mean noise floor at 4000 Hz is $\leqslant -25$ dB SPL because this noise level was always achieved. In contrast, the noise floor is higher when $f_2=500$ Hz for L_3 levels <40 dB SPL, which represent conditions in which the SNR stopping rule (12 dB) at this frequency caused measurements to stop. For higher L_3 levels, the mean noise floor for $f_2=500$ Hz was lower because the DPOAE was reduced by suppression and the SNR criterion was not met, resulting in longer averaging times. However, even after the full 210 s of artifact-free averaging time, the noise floor was still higher at 500 Hz than it was at 4000 Hz.

Once the data were collected for both f_2 frequencies, all L_2 levels, and all f_3 frequencies and L_3 levels, the DPOAE levels in the presence of suppressors were converted into decrements. We have used decrements in DPOAE level in the past to represent the response to the suppressor for several reasons (Gorga *et al.*, 2002a, b; 2003; Johnson *et al.*, 2004). First, decrements describe the amount of suppression as a result of the presentation of the suppressor, which is the measure of interest. They also partially account for individual variability across subjects in DPOAE levels for control conditions. To convert the DPOAE data (as shown in the top row of Fig. 1) into decrements (as shown in the bottom row), the DPOAE levels for the control conditions at the beginning and the end of the L_3 series for each f_3 were averaged. To calculate the decrement, the DPOAE level in the presence of the suppressor was subtracted from the average level during the control conditions associated with each f_3. The open circles in the bottom row of Fig. 1 show decrements (± 1 s.d.) that were derived from the data shown in the top row of panels. A comparison of the error bars for DPOAE level in the top panel to the error bars for the decrements in the lower panel demonstrates the expected outcome in which the variability across subjects is reduced for some stimulus conditions by the conversion to decrements. In this representation, decrements of 0 dB indicate conditions for which there was no suppression. Conditions in which the response was suppressed into the noise floor are represented on the right-hand side of these functions, where an asymptotic maximum decrement was approximated. For these latter conditions, the SNR is approximately zero, as they correspond to the conditions in the top row of panels when DPOAE and noise levels were the same, meaning that the response was completely suppressed.

We were interested in linearizing the responsive portions of the decrement-versus-L_3 functions because decrement curves typically have a shallower slope for small decrements. To meet this goal, the following rules were used before fitting the decrement functions: (1) only data points for which the SNR $\geqslant 3$ dB were included, (2) decrement-versus-L_3 functions were fit only if at least one decrement was observed in the range from 3 to 15 dB, and (3) data points were included in the fits so long as the decrements increased monotonically with L_3. The first inclusion criterion placed emphasis on data points for which the SNR was high, including those for which only a small amount of suppression (as little as 1 dB) was observed. The second criterion assured that only decrement-versus-L_3 functions showing some suppression were fit. The third criterion was needed to assure that data points for which the reliability was low (i.e., those for which the SNR approached or equaled zero) were excluded; it also excluded those points for which no suppression was observed. The data points meeting the above-noted criteria on each decrement-versus-L_3 function were transformed by

$$D = 10 \log_{10}(10^{\text{decr}/10} - 1). \quad (1)$$

The points shown as closed circles in the bottom row of panels of Fig. 1 represent the transformed data for those conditions that met the inclusion criteria. The application of the transformation resulted in a linearization of the decrement-versus-L_3 functions, in which the decrement is 3 dB when $D=0$. The solid line drawn in each panel represents the best linear fit to the decrement data, but only included those points shown as closed circles. The equations describing these fits for each combination of f_2, L_2, and f_3 were used to estimate the slope of these functions (growth of suppression) and to determine the decrement "threshold" for construction of DPOAE STC. The short vertical dashed lines in Fig. 1 represent conditions for which the decrement=3 dB [$D=0$ in Eq. (1)], which was used as suppression threshold for the purpose of constructing STCs.

III. RESULTS

A. Control conditions

Recall that measurements for every f_3 were preceded and followed by a control condition in which no suppressor was presented. With 9 (500 Hz) or 14 (4000 Hz) f_3 frequencies, there were either 18 ($f_2=500$ Hz) or 28 ($f_2=4000$ Hz) measurements of the control condition for each f_2, L_2 combination, which were averaged separately for every subject. Table I presents the means and standard deviations of these control conditions for each subject when $f_2=500$ Hz, while similar data when $f_2=4000$ Hz are provided in Table II. Tables I and II also provide grand means and standard deviations (averaged across subjects) of the individual mean DPOAE levels and individual standard deviations. Notably, for 2 of the 19 subjects at 20 dB SL when $f_2=500$ Hz and for 1 of 19 subjects at 10 dB SL when $f_2=4000$ Hz, the SNR was too low to permit reliable measurements of suppression. For all other conditions, reliable suppression measurements were possible because every subject produced responses that were above the noise floor for the control condition.

TABLE I. Means and standard deviations for the control condition in each of the 19 subjects at each of the four L_2 levels when f_2=500 Hz. Grand means and standard deviations are provided in the bottom two rows.

	L_2=20 SL		L_2=30 SL		L_2=40 SL		L_2=50 SL	
Subject	Mean	s.d.	Mean	s.d.	Mean	s.d.	Mean	s.d.
01	−7.544	2.785	−0.362	1.931	5.813	1.761	8.039	1.355
02	−1.887	1.909	0.985	2.474	3.857	2.675	7.114	1.703
03	−7.266	2.920	−0.484	3.359	6.836	2.035	6.958	2.268
05	−0.099	2.159	7.001	1.322	8.838	1.555	9.976	1.594
06	−7.065	3.509	0.643	2.123	2.571	1.900	2.294	1.889
07			−1.990	2.287	4.844	1.909	7.904	2.222
08			−9.527	2.713	−7.854	2.070	−2.401	2.158
09	−7.958	3.606	−3.509	2.128	−0.952	1.442	1.402	1.683
10	−8.043	4.419	1.558	2.230	6.427	2.312	9.447	2.304
11	−7.077	2.984	0.339	2.405	5.503	1.633	7.235	1.879
12	−9.031	3.747	−1.047	1.861	5.727	1.820	6.071	1.462
15	−2.414	3.860	3.333	2.094	6.070	2.706	7.756	2.653
16	−0.318	1.582	4.507	2.133	7.670	1.154	8.673	1.429
17	−1.481	2.535	5.941	1.432	7.179	2.093	4.990	1.450
18	−6.453	2.135	−1.001	1.488	2.351	2.376	1.090	2.867
19	−7.396	1.631	−1.164	2.310	4.859	2.424	8.509	2.648
20	−6.037	2.185	0.494	2.466	4.730	3.307	5.726	5.022
21	−9.774	2.415	−2.056	1.847	1.979	1.890	5.102	1.459
22	−15.044	2.817	−5.969	2.069	−0.441	2.545	2.092	3.449
Mean	−6.171	2.776	−0.121	2.141	4.000	2.085	5.683	2.184
s.d.	3.861	0.826	3.875	0.470	3.868	0.513	3.337	0.896

As expected, mean DPOAE levels varied across subjects. For example, the mean level varied from a low of −9.5 dB SPL in one subject (S#08) to a high of 7.0 dB SPL in another subject (S#05) when f_2=500 Hz and L_2=30 dB SPL. However, variability in the absolute DPOAE level across subjects is perhaps less important than the within-subject variability in the level produced for the control conditions. Within each subject, the level in the control condition had relatively small standard deviations, meaning that DPOAE level in the control condition was repeatable. In the

TABLE II. Means and standard deviations for the control condition in each of the 19 subjects at each of the five L_2 levels when f_2=4000 Hz. Grand means and standard deviations are provided in the bottom two rows.

	L_2=10 SL		L_2=20 SL		L_2=30 SL		L_2=40 SL		L_2=50 SL	
Subject	Mean	s.d.	Mean	s.d.	Mean	s.d.	Mean	s.d.	Mean	s.d.
01	−15.609	3.379	−5.626	1.350	−1.263	1.789	4.853	1.172	8.733	1.529
02	−3.733	2.473	2.483	3.057	7.419	2.484	11.247	2.556	13.500	2.792
03	−2.394	1.423	0.425	2.546	2.695	2.562	2.648	3.615	6.148	2.538
05	−8.408	1.424	−2.240	1.070	1.974	0.695	6.268	0.830	8.565	1.764
06	−3.299	2.779	4.655	1.577	10.679	0.964	14.080	0.875	16.571	1.012
07	−16.459	1.926	−14.510	3.722	−8.206	4.655	−5.113	4.588	0.444	4.237
08			−16.455	2.089	−11.472	3.572	−5.444	3.171	−1.295	2.410
09	−14.122	1.564	−6.770	1.427	−3.153	0.927	1.192	1.672	6.566	1.700
10	−0.130	2.177	1.011	2.238	2.593	3.043	7.847	1.385	11.911	0.951
11	−2.104	1.786	1.847	1.366	4.842	1.301	8.267	1.120	10.312	2.321
12	−6.853	2.900	−2.063	2.116	1.059	1.406	4.813	1.041	7.637	0.853
15	−7.970	1.230	−5.003	1.759	0.021	1.821	4.164	2.228	7.958	1.086
16	−11.720	3.076	−3.560	2.376	2.051	3.591	8.264	3.051	11.399	4.277
17	−7.731	1.265	−1.651	2.733	5.422	1.082	10.508	0.678	13.702	0.345
18	−2.412	3.847	4.516	1.263	7.065	1.258	8.623	1.597	10.561	1.494
19	2.269	1.314	5.551	0.910	9.004	1.424	13.324	1.389	16.224	1.020
20	−11.011	2.654	−0.641	1.612	5.505	0.921	9.644	0.697	12.507	0.614
21	−8.916	1.126	−4.524	0.839	1.112	0.802	4.992	0.534	8.688	0.447
22	−4.387	2.944	1.128	1.894	4.805	1.747	7.660	2.206	9.817	2.402
Mean	−6.944	2.183	−2.181	1.892	2.218	1.897	6.202	1.811	9.471	1.779
s.d.	5.371	0.845	5.888	0.761	5.516	1.124	5.263	1.134	4.568	1.142

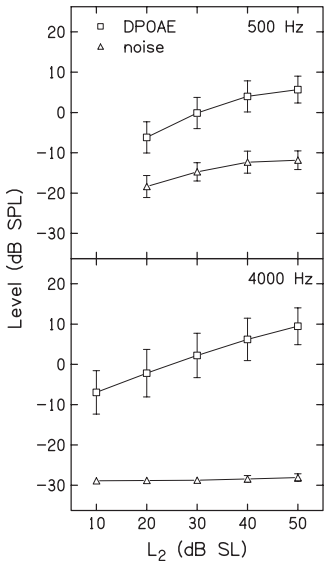

FIG. 2. DPOAE and noise levels for the control conditions, in which there was no suppressor. Top: Mean DPOAE (squares) and noise (triangles) levels in dB SPL as a function of L_2 in dB SL when f_2=500 Hz. Bottom: Mean DPOAE (squares) and noise (triangles) levels in dB SPL as a function of L_2 in dB SL when f_2=4000 Hz. In both panels, error bars represent ±1 s.d.

two above-mentioned cases, the standard deviations for the control conditions were 2.7 and 1.3 dB, respectively, despite the large differences in mean absolute DPOAE level. The between-subject variability in DPOAE level always exceeded the within-subject variability, based on comparisons of the standard deviations for the control conditions. Averaged across all subjects and all f_2, L_2 combinations, the mean standard deviation for the control conditions was about 2.1 dB. Within-subject variability for the control conditions was only slightly greater at 500 Hz, compared to 4000 Hz. Thus, the control conditions were relatively stable within a subject at both f_2 frequencies, despite the fact that subjects differed in the DPOAE level they produced for the same stimulus conditions.

Figure 2 plots mean DPOAE and noise levels as a function of L_2 at 500 Hz and 4000 Hz in top and bottom panels, respectively. These data were averaged across the 19 subjects, and provide a graphic representation of the mean DPOAE levels for the control conditions listed in Tables I and II, along with the corresponding mean noise levels, which were not provided in the tables. Error bars represent ±1 s.d. As expected, the SNR was always less at 500 Hz, compared to 4000 Hz, as seen in the differences between DPOAE and noise levels within each panel. The influence of the stopping-rule differences also is evident in Fig. 2. First, the noise floor was more variable at 500 Hz, compared to 4000 Hz. This occurred because measurements almost always stopped on the noise floor criterion when f_2 =4000 Hz, resulting in the same noise floor across subjects for all stimulus conditions, including the control conditions, for which data are shown in Fig. 2. In contrast, measurements stopped either on the SNR or test-time criterion (but almost never on the noise-floor rule), resulting in more variable noise levels across subjects and conditions. Also note that when f_2=500 Hz, the noise floor increased as L_2 increased. This is a consequence of including the 12 dB SNR stopping rule at this frequency. For higher L_2 levels, the response was larger, causing the averaging to stop when the noise levels were higher, compared to the case for lower L_2 levels. Even so, there was at least a 12-dB SNR in the mean control conditions, even when L_2=20 dB SL and f_2 =500 Hz. In contrast, the mean noise floor always was less than −28 dB SPL and did not vary with L_2 when f_2 =4000 Hz. Both of these observations reflect the fact that, at this frequency, averaging stopped when the noise-floor criterion was met. Despite the remaining differences in SNR between frequencies, even after allowing averaging to continue for up to 210 s of artifact-free averaging time, the mean differences between DPOAE and noise levels were large enough to permit reliable measurements for a wide range of L_2 levels at both 500 and 4000 Hz.

B. Decrement-versus-suppressor level functions

Figure 3 provides a family of decrement-versus-L_3 functions when f_2=500 Hz and L_2=30 dB SL. Open symbols represent the decrement data, while closed symbols represent the transformed conditions meeting the inclusion criteria described earlier. The line in each panel represents the linear fit to the closed symbols. Mean decrements across all 19 subjects (±1 s.d.) are plotted. Data are shown for the nine f_3 frequencies used when f_2=500 Hz, and is indicated within each panel. An f_3 of 515 Hz represents the on-frequency condition, in which $f_3 \approx f_2$. Several observations can be made based on an examination of these decrement functions. First, suppression is observed at the lowest L_3 when $f_3 \approx f_2$. In this example, suppression is initially observed when L_3 =40 dB SPL, with the amount of suppression (decrement) increasing as L_3 increases above this level until the response is completely suppressed, which occurs when L_3=60 dB SPL. As one moves toward higher f_3 frequencies, the L_3 at which suppression first appears is similar to or slightly higher, compared to the case when $f_3 \approx f_2$. As one moves further away from f_2 on the low-frequency side, the L_3 at which suppression is first observed increases. For lower-frequency suppressors, complete suppression is observed, so long as sufficiently high suppressor levels can be presented. For $f_3 > f_2$, complete suppression is not observed, even at the highest L_3 of 85 dB SPL. This observation relates to an interaction between the L_3 at which suppression first emerges, the way the decrement (suppression) grows with L_3 for high f_3 frequencies, and output limitations of our hardware. The slopes of the decrement-versus-L_3 functions are frequency dependent, with a slope of approximately 1 for the on-frequency condition. As f_3 decreases, the slope increases, with the steepest slope observed for suppressors 1 to 2 octaves below f_2=500 Hz. In contrast, the slope decreases as f_3 increases above the on-frequency condition, with the highest f_3 (750 Hz) showing the shallowest slope. The combination of higher suppression thresholds and shallower slopes, when coupled with output limitations, makes it difficult to observe complete suppression when $f_3 > f_2$, regardless of L_2. The advantages of the transformation are particularly evident when f_3=750 Hz. Despite the fact that decrement grows slowly

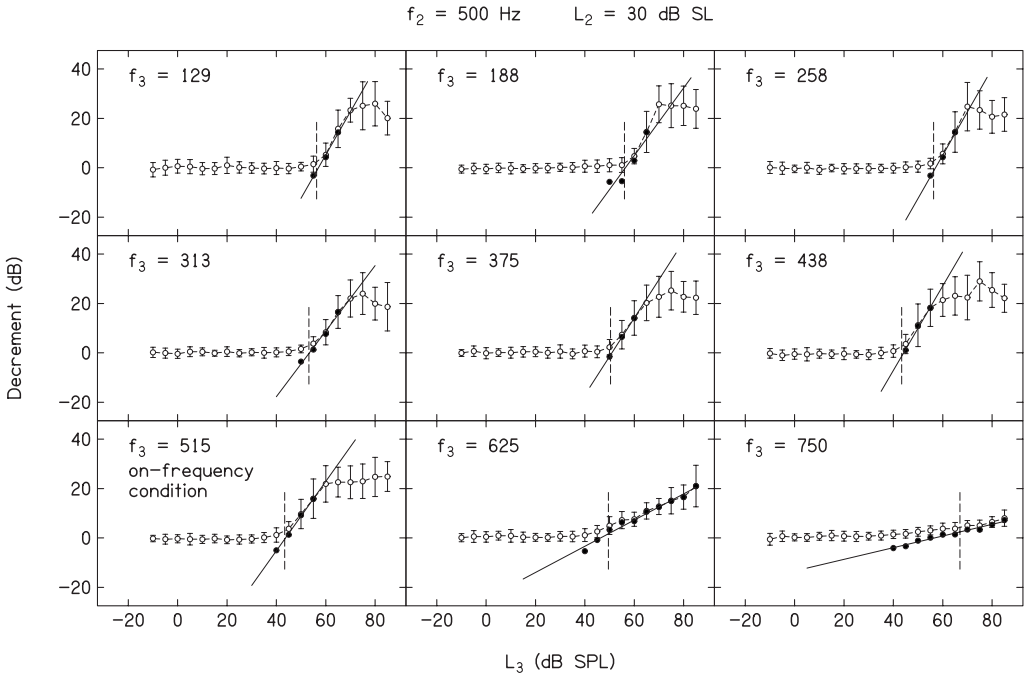

FIG. 3. Mean DPOAE decrements in dB as a function of L_3 in dB SPL when f_2=500 Hz and L_2=30 dB SL. Error bars represent ±1 s.d. Suppressor frequency is indicated within each panel. Closed symbols represent the transformed data to which a linear regression, represented by the solid line, was fit. The short vertical dashed lines in each panel are drawn at a decrement of 3 dB, which was used as suppression threshold for the construction of STCs.

with L_3, the linearization of the function that resulted from the transformation allowed us to fit these data with a regression line that enabled us to estimate slope. The short vertical dashed lines in Fig. 3 (and in Fig. 4) are drawn at the same L_3 levels as in Fig. 1, namely the L_3 resulting in a decrement of 3 dB. These "thresholds" were used to construct STCs.

Figure 4 presents decrement-versus-L_3 functions when f_2=4000 Hz and L_2=30 dB SL, following the conventions

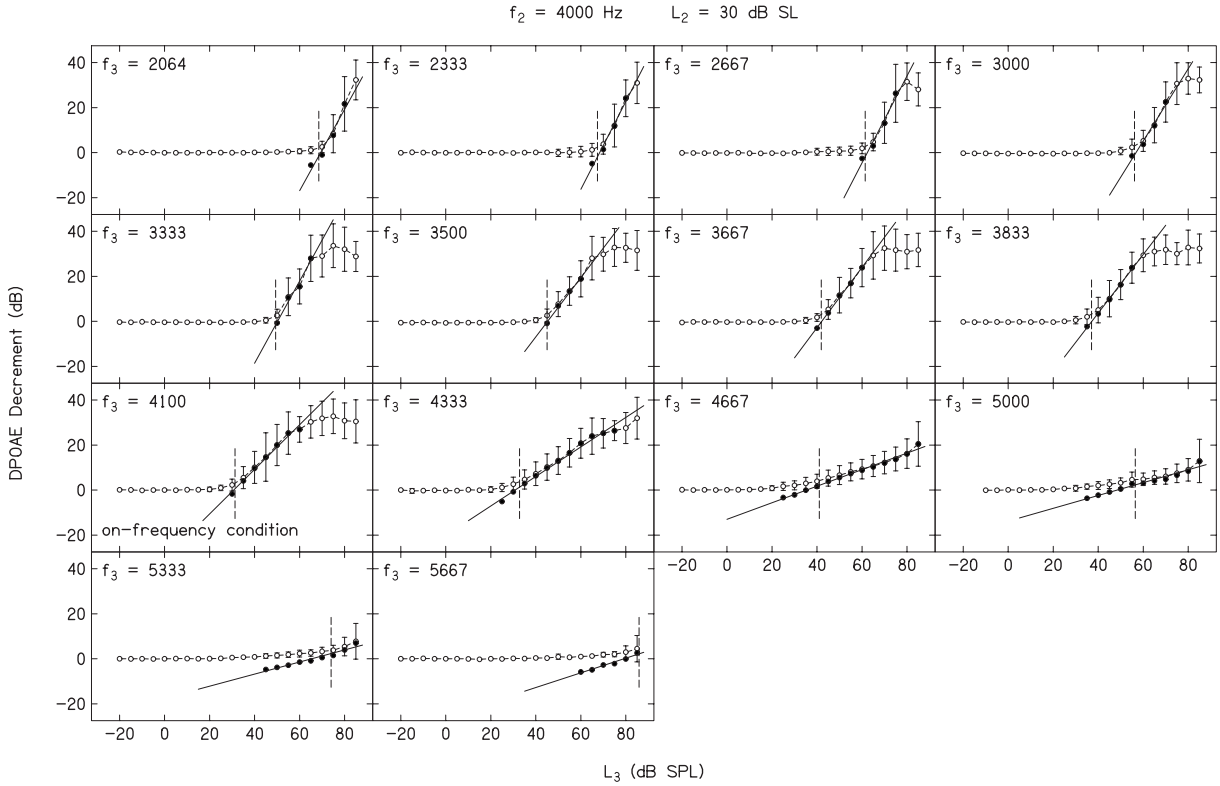

FIG. 4. Mean DPOAE decrements in dB as a function of L_3 in dB SPL when f_2=4000 Hz and L_2=30 dB SL. Error bars represent ±1 s.d. Suppressor frequency is indicated within each panel. Closed symbols represent the transformed data to which a linear regression, represented by the solid line, was fit. The short vertical dashed lines in each panel are drawn at a decrement of 3 dB, which was used as suppression threshold for the construction of STCs.

that were used in Fig. 3. Data are shown for the 14 f_3 frequencies that were used at 4000 Hz. As was the case when f_2=500 Hz, suppression was observed at the lowest L_3 when $f_3 \approx f_2$ (f_3=4100 Hz). As f_3 moved away from 4000 Hz in either direction, the level at which suppression was first observed increased. Complete suppression was observed for the on-frequency case and for low-frequency suppressors, but only within the range of f_3 frequencies from 2667 to 4100 Hz (and perhaps 4333 Hz). For some f_3 frequencies outside this range, the SNR for L_3=85 dB SPL (the highest suppressor level used in the present study) approximates 0 dB, indicating that the response was completely suppressed. However, it is difficult to know from Fig. 4 whether complete suppression occurred for several f_3 frequencies when f_2=4000 Hz because higher suppressor levels could not be tested and, therefore, maximum asymptotic suppression was not evident. For f_3 frequencies at and above 4667 Hz, the results summarized in Fig. 4 indicate that the response was not completely suppressed at the highest L_3. The slope of the decrement function approximated 1 in the on-frequency condition, increased as f_3 decreased below f_2 (with the steepest slope when f_3 was 1 octave below f_2), and decreased as f_3 increased above f_2. These trends are the same as those observed when f_2=500 Hz. The data shown in Figs. 3 and 4 were provided to illustrate general trends in the data and to provide a sense of the variability across subjects, at least as reflected in standard deviations. Decrement-versus-L_3 functions will not be shown for other L_2 levels because the results were similar to those shown in Figs. 3 and 4. Instead, the data for all values of L_2 will be summarized in subsequent figures. Furthermore, our interest is to provide summary descriptions and comparisons of cochlear processing at low and high frequencies in humans. Relevant trends are best reflected in mean data, which will be presented in the figures to follow; however, the variability seen in Figs. 1, 3, and 4 is representative of variability for other L_2 conditions.

Figure 5 plots slope of decrement-versus-L_3 functions as a function of f_3. Each row provides data for a different L_2. Only data for f_2=4000 Hz are shown when L_2=10 dB SL, because the control condition at this L_2 when f_2=500 Hz did not consistently result in a SNR $\geqslant$10 dB. As a result, there was insufficient dynamic range to permit reliable suppression measurements when f_2=500 Hz and L_2=10 dB SL. Within each panel, slopes when f_2=500 Hz are shown as circles, while similar slope estimates when f_2=4000 Hz are shown as triangles. In the left column, a log-frequency scale is used, resulting in separation of the data for the two f_2 frequencies. In the right column, the same data are replotted on a frequency scale in which octaves relative to f_2 are used. In this latter representation, "0" represents the case when $f_2 \approx f_3$, and results in an overlap of the data at the two f_2 frequencies. The impressions of the trends in slope related to f_3, as seen in Figs. 3 and 4, are apparent here. In general, the steepest decrement-versus-L_3 functions occur when f_3 is an octave or more below f_2. There is a transition f_3 region, in which the slope decreases as f_3 moves from just below f_2 to above f_2. The shallowest slopes are observed for the highest suppressor frequencies. Similarities and differences between the

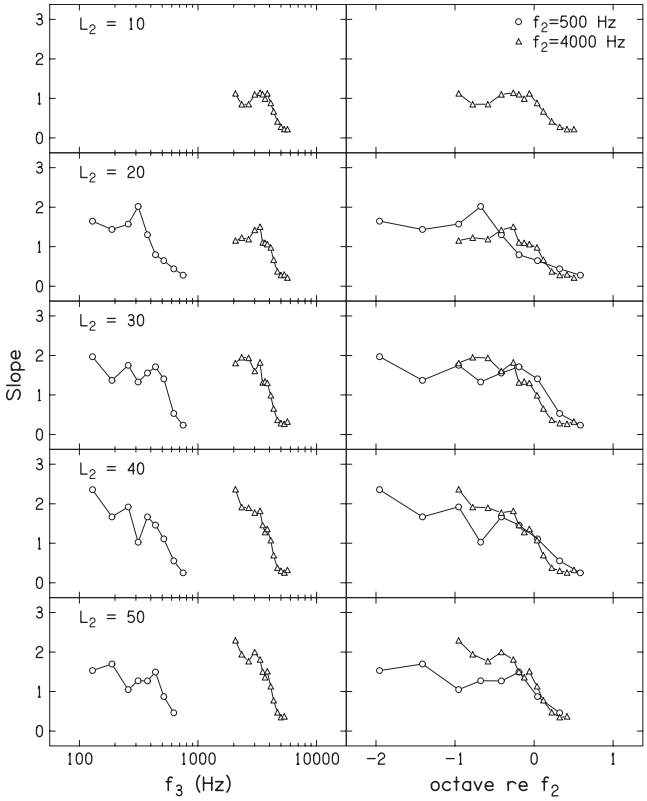

FIG. 5. Mean slopes of the decrement-vs-L_3 functions as a function of f_3 for f_2=500 Hz (circles) and f_2=4000 Hz (triangles). Data are plotted on a log frequency scale in the left column and a relative (octave) frequency scale in the right column.

slopes are emphasized when slope is plotted on a relative scale. For example, it appears that similar slopes are achieved for f_3 frequencies $\geqslant f_2$, whereas there is a tendency at most, but not all, L_2 levels for the slope to be steeper for low-frequency suppressors when f_2=4000 Hz, compared to when f_2=500 Hz.

C. Suppression tuning curves

Figure 6 plots the L_3 needed for 3 dB of suppression as a function of f_3, following the same conventions as those used in Fig. 5. The value of L_3 for 3 dB of suppression represents the D=0 intercept of the linear equations that were fit to the mean decrement-versus-L_3 functions. A decrement of 3 dB was operationally defined as "suppression threshold" for this and other figures to follow. An advantage of using decrements of 3 dB as the criterion for constructing STCs is that it assures that positive SNRs (and, therefore, reliable estimates) existed for every point. Even when f_2 =500 Hz and L_2=20 dB SL (the stimulus condition for which the response had the poorest SNR for the control condition), the SNRs when a 3 dB decrement occurred were typically $\geqslant$7 dB. Higher SNRs were observed at the criterion decrement of 3 dB for all other f_2 and L_2 combinations. Defining STCs with conditions for which the SNR was high reduces the influence of noise level on differences between the results observed at 500 and 4000 Hz, despite the fact that the noise levels were not the same for the two f_2 frequencies.

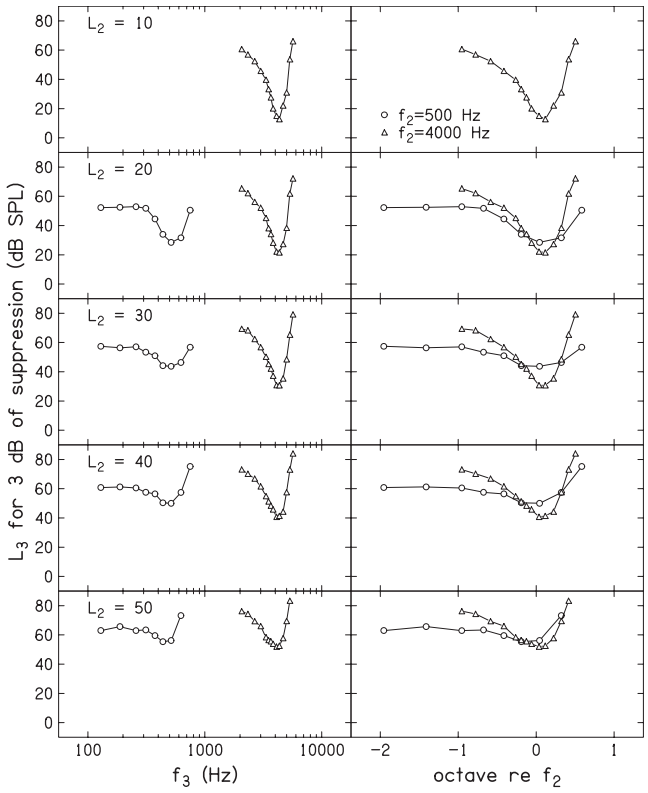

FIG. 6. Mean suppression tuning curves, in which the L_3 for 3 dB of suppression is plotted as a function of f_3, following the conventions used in Fig. 5.

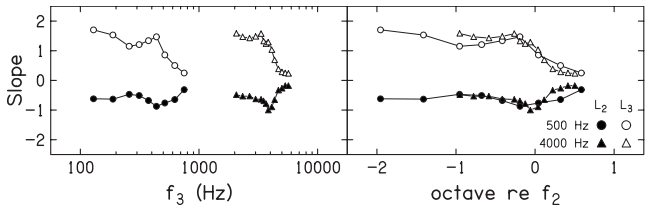

FIG. 7. Slopes of the decrement functions as a function of f_3, based on multiple linear regression in which L_2 and L_3 were included in the regression analysis. Open symbols represent the slopes of the decrement-vs-L_3 functions and closed symbols represent the slope of the decrements vs L_2. Circles represent data when f_2=500 Hz and triangles represent data when f_2=4000 Hz.

There are many examples in the literature of DPOAE STCs when f_2=4000 Hz, and there is nothing unusual about the ones presented in this paper. However, to our knowledge, this is the first time DPOAE STCs have been reported for an f_2=500 Hz. We assume that part of the reason for the lack of data when f_2=500 Hz relates to the difficulty in making reliable measurements at this frequency. This problem is a direct consequence of the higher noise levels around the $2f_1$–f_2 distortion product when f_2=500 Hz, and is why long averaging times were necessary in the present experiment in order to obtain reliable measurements.

The combination of increased averaging times and the criterion at which the DPOAE STCs were constructed resulted in reliable STC measurements for both 500 and 4000 Hz. The STCs at 500 Hz have properties that are similar in several ways to other more direct measures of tuning, such as FTCs. For example, the tuning curves have higher thresholds for suppression for the on-frequency condition, compared to 4000 Hz. This is not unlike the higher thresholds that are observed at CF for single auditory neurons with low-frequency CFs. Some of this effect can be attributed to the fact that the absolute level (in dB SPL) for the probe (L_2) was higher at 500 Hz, compared to 4000 Hz, for equivalent SL. This occurred because the behavioral thresholds which served as the reference for L_2 were, on average, 7.5 dB higher at 500 Hz. There is also less difference between the thresholds at the best frequency, compared to the thresholds on the low-frequency tail, although the more symmetrical pattern around CF that has been observed in the responses from individual auditory neurons is not as evident in the present DPOAE STCs at 500 Hz. This finding was not expected; we have no explanation for why low-frequency tails were evident in our DPOAE STCs, given that they often are not evident in FTCs from individual low-CF auditory neurons in lower animals.

Some of the above-mentioned observations may be more obvious in the right column of Fig. 6, where f_3 is represented in octaves relative to f_2. Notably, there appears to be a range of suppressor frequencies on the low-frequency side for which there is little or no threshold change as f_3 decreases, a pattern that is more evident when f_2=500 Hz. Recall that one concern in relation to some of the previously reported psychophysical estimates of cochlear nonlinearity at low frequencies was that the low-frequency masker was not sufficiently low to be outside of the compressive growth region at the place of the probe frequency. The data shown in both the left and right columns of Fig. 6 indicate that this is less of a concern in the present experiment. In fact, there is virtually no difference between the L_3 for a decrement of 3 dB when f_3=258 Hz (about 1 octave below f_2), compared to when f_3=129 Hz (nearly 2 octaves below f_2). While we are surprised by the unexpected low-frequency tail when f_2=500 Hz, we are confident that low-frequency suppressors 1 octave or more below f_2 have relatively constant thresholds and, therefore, represent the frequency range of interest when f_2=500 Hz. If anything, the results when f_2=4000 Hz suggest that the inclusion of lower f_3 frequencies would have been of value because it is difficult to determine if the lowest f_3 used in the present study was sufficiently on the low-frequency tail of the response, where suppression thresholds might be expected to change slowly or remain relatively constant. Unfortunately, output limitations of our hardware in relation to the levels at which suppression first appears precluded measurements for lower suppressor frequencies when f_2=4000 Hz. The implications of this observation, especially in relation to estimates of cochlear-amplifier gain, will be discussed subsequently.

Up to this point, decrement functions were fit with simple linear regressions (SLR), meaning that each f_3, L_2 combination was fit separately. The coefficients of these regressions are shown as slopes in Fig. 5 and the STCs derived from these fits are shown in Fig. 6. In Fig. 7, we summarize slopes from a multiple linear regression (MLR) in which both L_3 and L_2 were included in the analyses. In Fig. 7, the

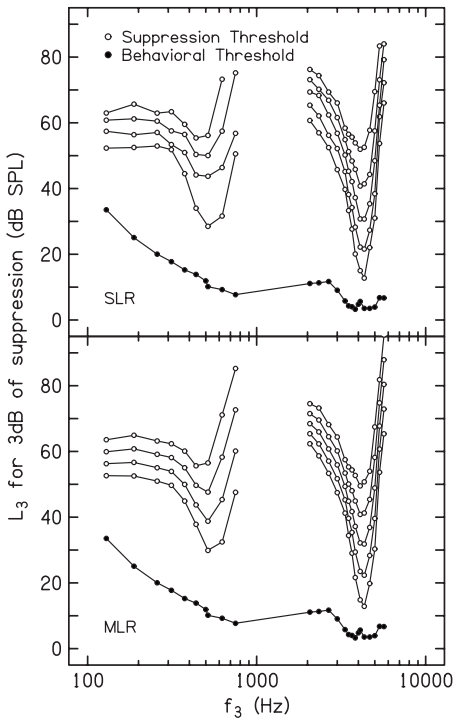

FIG. 8. Mean STCs for 500 and 4000 Hz. Top: STCs constructed using simple linear regressions that were fit to the decrement-vs-L_3 functions. Bottom: STCs constructed using multiple linear regressions that were fit to the decrement-vs-L_3 functions. Within each panel, L_2 increases from the STC with the lowest suppression threshold to the highest. Superimposed in both panels are the mean behavioral thresholds (closed circles) for all the f_2 and f_3 frequencies used in the present study.

open symbols represent slopes of the decrement-versus-L_3 functions as a function of frequency. The closed symbols represent the slopes of the decrement versus L_2. Otherwise, the same conventions used in Fig. 5 are followed in Fig. 7. For both absolute and relative frequencies (left and right panels), the slopes of the L_3 functions are positive and decrease as f_3 increases. In contrast, the slopes of the L_2 functions are negative for all f_3, but are nonmonotonic, achieving a maximum negative slope when $f_3 \approx f_2$, with less negative slopes for both higher and lower f_3 frequencies relative to f_2. The representation of these slopes on a relative frequency scale emphasizes the similarities across frequency. Although variable, the slopes for $f_2=500$ Hz and $f_2=4000$ Hz are superimposed for many suppressor frequencies, especially for low frequencies relative to f_2, suggesting that growth of response to the suppressor is similar at these two frequencies. Even so, there is a tendency for steeper slopes when $f_3 < f_2$ for 4000 Hz, a trend that was also evident in some of the slope estimates from the SLRs, which were shown in Fig. 6. The SLR and MLR accounted for about 98% and 96% of the variance, respectively. Despite this fact, the two models differed significantly. However, the MLR may be preferable in that it required approximately 1/3 of the variables, compared to what were used during SLR. In the interest of completeness, results based on both SLR and MLR will be provided in subsequent figures.

The STCs shown in Fig. 6 are superimposed in the top panel of Fig. 8, with L_2 as the parameter, which increases as the placement of the STC moves up in the figure ($L_2=50$ dB SL shown as the top STC for both f_2 frequencies). The "suppression thresholds" plotted in Fig. 6 and in the STCs shown in the top panel of Fig. 8 represent the $D=0$ intercept of the previously described SLRs that were fit to each mean decrement-versus-L_3 function at each L_2. Thus, the thresholds on the STC at one L_2 were treated as if they were independent from those at other L_2 levels. In the bottom panel of Fig. 8, MLRs, as described earlier, were fit to the decrement functions for each f_3. The MLR forced the shift in suppression threshold with L_2 to be uniform at each f_3. This reduced inconsistencies in the STCs across L_2 levels (but not across f_3), which had the effect of smoothing the STCs. While the STCs derived from decrement functions fit with MLRs are more uniform across L_2, the trends are essentially the same as those seen in the STCs that were obtained when SLRs were fit to the decrement-versus-L_3 functions separately for each L_2. Within both panels of Fig. 8, the closed symbols represent the mean behavioral thresholds for the 23 f_3 frequencies and the two f_2 frequencies. These thresholds confirm that the subjects who participated in this study had normal thresholds for a wide range of frequencies.

The representations shown in Fig. 8 emphasize the differences in changes in thresholds around the "tip" versus changes in threshold on the low-frequency tails of the STCs. For any L_2, threshold differences between the tip and the tail are less when $f_2=500$ Hz. At 4000 Hz, thresholds at the tip move about 10 dB for each 10 dB increase in L_2, as expected. This trend is less evident when $f_2=500$ Hz. For both f_2 frequencies, smaller shifts in L_3 with L_2 are observed for low-frequency suppressors and larger shifts in L_3 with L_2 are seen for high-frequency suppressors relative to f_2. The frequency at which the lowest suppression threshold occurred appears to migrate toward lower frequency as L_2 increases. This latter trend is more evident when $f_2=500$ Hz.

D. Quantitative descriptions of the DPOAE STCs

Figure 9 plots the level of the suppressor (L_3) necessary to produce 3 dB of suppression as a function of L_2. Data for $f_2=500$ and 4000 Hz are shown in the left and right columns, respectively. The top row shows the results that were obtained when the SLRs were used to estimate the suppressor level, whereas the bottom row provides results when MLRs were used to derive the L_3 that caused 3 dB of suppression. In each panel, open symbols represent the results when f_3 was approximately 1 octave lower than f_2 (which is being viewed as the low-frequency condition for which the response presumably is more linear at the f_2 place). Closed symbols represent the results when $f_3 \approx f_2$ (the on-frequency condition for which we assume that the processing is similar and compressive for both f_2 and f_3 at or near the f_2 place). The lines in each panel represent linear fits to the data, with the slopes of the lines provided within each panel adjacent to the set of data to which they apply. For both f_2 frequencies, greater suppressor level was needed when f_3 was 1 octave below f_2, compared to when $f_3 \approx f_2$. The differences between L_3 for low- and on-frequency suppressors were greatest for the lowest L_2, and decreased as L_2 increased. When $f_3 \approx f_2$,

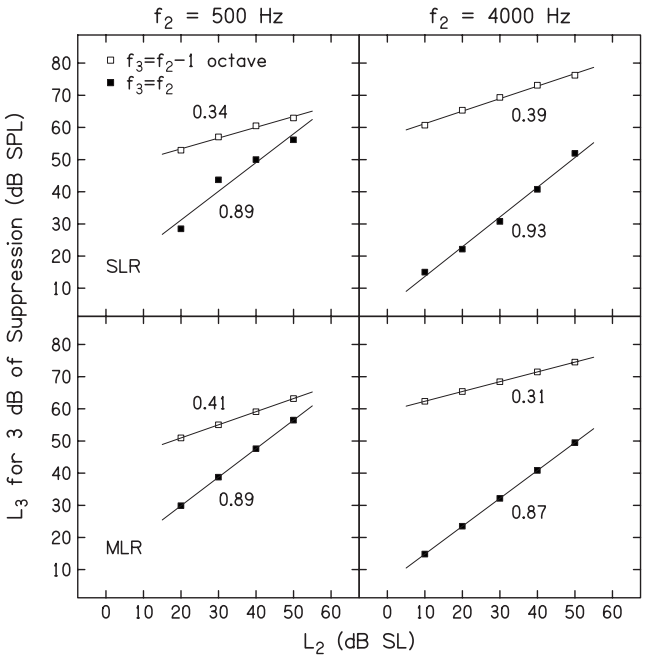

FIG. 9. L_3 for 3 dB of suppression as a function of L_2 (dB SL) for on-frequency (closed squares) and low-frequency (open squares) suppressors. The low-frequency suppressor was approximately 1 octave below f_2. Top and bottom rows show results for simple and multiple linear regressions, respectively. Left and right columns show data for f_2=500 Hz and f_2 =4000 Hz, respectively. The lines represent linear fits to each set of data. Slopes of these lines are provided as insets adjacent to the line to which they apply.

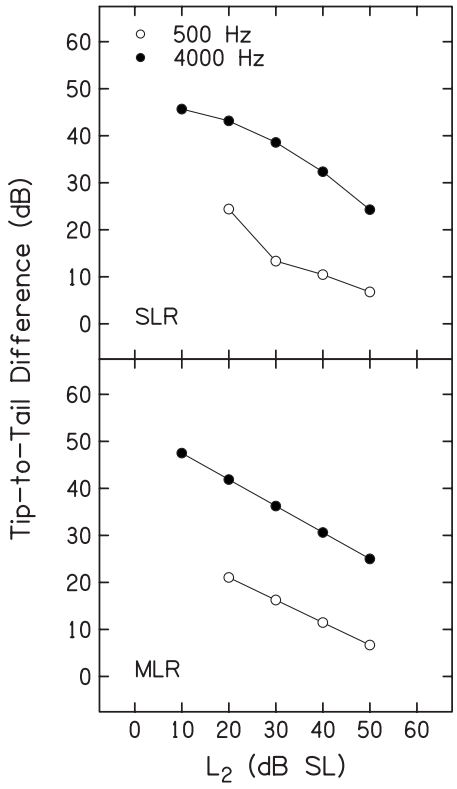

FIG. 10. Tip-to-tail difference (in dB) as a function of L_2 (dB SL) when f_2=500 Hz (open circles) and when f_2=4000 Hz (closed circles). Top and bottom panels show the results for simple and multiple linear regressions, respectively.

the L_3 for 3 dB of suppression increased almost linearly with L_2. At first glance, this may seem surprising, since cochlear responses for best-frequency tones are compressive; however, both f_3 and f_2 are being processed similarly by the compressive nonlinearity, resulting in a linear relationship between L_3 and L_2. An estimate of compression for f_2 can be derived from the slope of the functions when $f_3=f_2-1$ octave on the assumption that the response to this suppressor is linear at or near the f_2 place while the response to f_2 is compressive at the same place. The reciprocal of the slopes for these conditions result in estimates of compression that range from 2.4 (f_2=500 Hz, MLR) to 3.2 (f_2=4000 Hz, MLR).

The data shown in Fig. 9 were converted into tip-to-tail differences by subtracting L_3 when $f_3 \approx f_2$ from L_3 when f_3 was 1 octave below f_2 at each L_2. These tip-to-tail differences are plotted as a function of L_2 in Fig. 10. Results based on SLR and MLR fits are shown in the top and bottom panels, respectively. Within each panel, open and closed symbols are used to represent results for f_2=500 and 4000 Hz, respectively. Tip-to-tail differences decreased as L_2 increased for both f_2 frequencies. However, these differences were 15–25 dB greater when f_2=4000 Hz, depending on L_2. For example, the tip-to-tail differences at 4000 Hz were 49 and 43 dB for L_2 levels of 10 and 20 dB SL (based on analyses in which MLRs were used). In contrast, the tip-to-tail difference at 500 Hz was about 20 dB when L_2=20 dB SL. In fact, the smallest tip-to-tail difference at 4000 Hz (about 22 dB when L_2=50 dB SL) was larger than the largest tip-to-tail difference observed at 500 Hz (about 20 dB when L_2=20 dB SL). As a consequence of the MLR, the function relating tip-to-tail difference to L_2 was a straight line for both f_2 frequencies, as expected. While the functions relating tip-to-tail differences to L_2 are less orderly when the results are based on the SLR, the overall pattern is the same.

Figure 11 provides Q_{ERB} estimates as a function of L_2 for both primary frequencies, following the same conventions that were used in Fig. 10. Q_{ERB} is calculated by dividing the characteristic or best frequency (f_2) by the equivalent rectangular bandwidth (ERB), where ERB is defined as the bandwidth of a rectangular filter with the same best-frequency response that passes the same total power. While sharpness of tuning has frequently been estimated using Q_{10} in the single-unit literature [Q_{10}=characteristic frequency (CF) divided by the bandwidth at 10 dB above the threshold at CF], Q_{ERB} has been used recently to estimate sharpness of tuning for data obtained from humans (e.g., Shera *et al.*, 2002; Gorga *et al.*, 2003). It also has the advantage that it uses data from all points on the STC (appropriately weighted), as opposed to being limited to frequencies close to the tip frequency. Finally, it can be used in cases when a tip region is poorly defined, which was not the case in the present study. For both f_2 frequencies, Q_{ERB} decreased as L_2 increased, more or less smoothly, depending on whether SLR or MLR was used. For both regressions, Q_{ERB} was always larger when f_2=4000 Hz, ranging from about 8 to 4. When f_2=500 Hz, Q_{ERB} ranged from less than 4 to about 2. Thus, this estimate of tuning was greater at 4000 Hz, compared to 500 Hz, and the smallest Q_{ERB} at 4000 Hz (about 4.5 at L_2

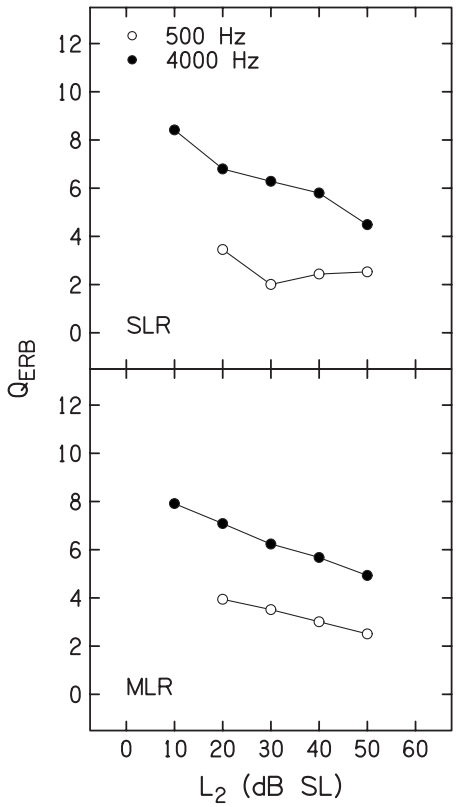

FIG. 11. Q_{ERB} as a function of L_2 (dB SL) following the conventions used in Fig. 10.

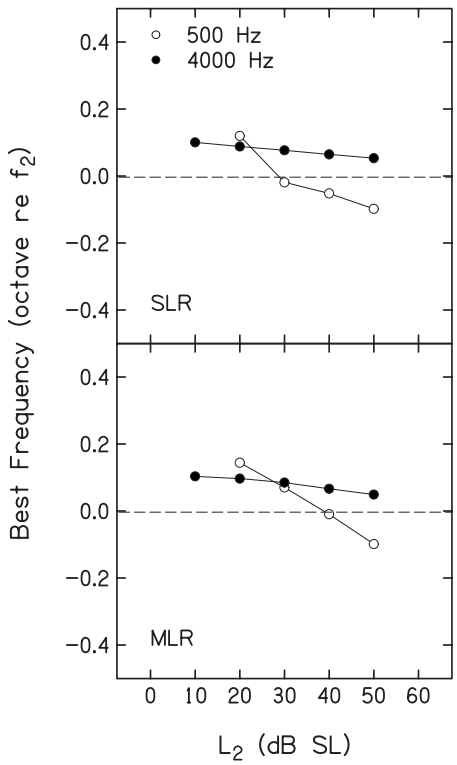

FIG. 12. Best frequency in octaves (re: f_2) as a function of L_2 (dB SL), following the conventions used in Figs. 10 and 11. The dashed line is drawn at 0 octaves relative to f_2 and provides a point of reference.

=50 dB SL) was larger than the largest estimate at 500 Hz (about 4 at L_2=20 dB SL). Larger changes in Q_{ERB} with L_2 were observed when f_2=4000 Hz.

Figure 12 plots the best frequency [(BF), in octaves relative to f_2] as a function of L_2, following the conventions used in Figs. 10 and 11. BF is the frequency for which the suppression threshold occurred at the lowest suppressor level. A cubic spline was used to interpolate to BF. The spline was sampled over a finer mesh based on mean L_3 for 3 dB of suppression and corresponding f_3 frequencies such that the resulting piecewise polynomial function is continuous and smooth between any two adjacent data points. As a result, BF defined from the spline did not necessarily occur at one of the suppressor frequencies used during measurements. The horizontal dashed line drawn at 0 octaves provides a point of reference. Values above this line represent cases in which BF was $>f_2$, while values below represent cases when BF was $<f_2$. Results for SLR and MLR are shown in the top and bottom panels, respectively. For both f_2 frequencies, the best f_3 was slightly higher in frequency than f_2 at low L_2 levels. This is to be expected because the suppressor frequency for the on-frequency condition was chosen intentionally to be slightly higher than f_2. For both f_2 frequencies, BF decreased as L_2 increased, with larger changes (on a relative frequency scale, octaves) at 500 Hz, compared to 4000 Hz. When f_2=4000 Hz, BF decreased as L_2 increased, but always exceeded f_2. In contrast, a larger decrease in BF was observed when f_2=500 Hz, and, at L_2 levels $\geq$40 dB SL, BF was below f_2.

IV. DISCUSSION

A motivating factor for the present measurements was the observation from previous work, in which differences in dynamic range and perhaps cochlear-amplifier gain were observed for 500 and 4000 Hz, but concerns existed that differences in noise floor for these two frequencies might have influenced findings based on DPOAE I/O functions (Gorga *et al.*, 2007). High-level responses were similar at 500 and 4000 Hz, suggesting that there was little or no difference between the two frequencies in the amount of maximum compression (approximately 4:1 in both cases, based on the slopes of the I/O functions). Differences in dynamic range were the result of differences in the low-level portion of the I/O functions. The responses at low levels in many different measurements (e.g., behavioral threshold, thresholds at CF, or low-level portions of a DPOAE I/O function) can be thought of as the result of gain produced by the cochlear amplifier. Thus, the suggestion of a wider dynamic range at 4000 Hz, compared to 500 Hz, in our previous data could be interpreted as an indication of greater cochlear-amplifier gain at the higher frequency. However, we were cautious in the interpretation of those data because the influences of differences in noise level were not completely controlled. Despite long averaging times, it was impossible to reduce the noise to the same low levels at both f_2 frequencies. The effects of noise-floor differences would be manifest at low levels of the I/O function, where the results at the two frequencies differed, affecting how confidently the previous results could be attributed to differences in cochlear processing for low- and high-frequency stimuli.

Like the previous study, measurement-based stopping rules including long averaging times were used in the present experiment in efforts to reduce the noise floor at both frequencies, and, like the previous study, the same noise floors were not achieved at 500 and 4000 Hz. However, unlike the previous study, the influence of differences in noise floor was reduced in the present experiment because the measurements of interest were made under conditions in which the SNR was favorable (although not the same) at both f_2 frequencies. Figure 2 summarized the DPOAE and noise levels for the control conditions at the two frequencies. While the SNR always was greater at 4000 Hz, the SNR was never less than about 12 dB, and often exceeded that value at both 500 and 4000 Hz. STCs were constructed, using 3 dB decrements, meaning that the "suppression threshold" points on the STCs also represent conditions for which the SNR was positive. Thus, these curves presumably are based on reliable measurements where the influence of noise is less, and therefore, the major conclusions of this study, which are based on analyses of the STCs, also are assumed to be relatively unaffected by the noise.

The DPOAE levels measured in the control conditions differed across subjects and between frequencies. However, for a given subject and L_2, the responses in the control conditions remained relatively stable (Tables I and II). This observation provides additional support relative to the reliability of the present measurements. Finally, the conversion of the data into decrements resulted in less variability across subjects for some stimulus conditions (Fig. 1), especially those surrounding the criterion used for constructing STCs. Converting DPOAE levels in the presence of the suppressor into decrements partially took into account differences in the absolute DPOAE levels produced by individual subjects.

The results described in Figs. 3–6 are consistent with previous observations of DPOAE suppression, at least for the case when f_2=4000 Hz (e.g., Abdala, 1998, 2001; Abdala *et al.*, 1996; Gorga *et al.*, 2002a, b, 2003; Kemp and Brown, 1983; Kummer *et al.*, 1995). For example, decrements were observed at the lowest suppressor levels when $f_3 \approx f_2$. Higher suppressor levels were needed for both higher and lower f_3 frequencies. The slopes of the decrement functions (which can be viewed as measures of the response to f_3 at or near the f_2 place) depended on frequency, with the steepest slopes for low frequencies, intermediate slopes for $f_3 \approx f_2$, and the shallowest slopes for $f_3 > f_2$. To our knowledge, similar measurements at 500 Hz have not been reported, and thus, there are no data to which the present results can be directly compared. Even so, the results observed at 500 Hz are at least qualitatively similar to those observed at other, higher f_2 frequencies. Suppression threshold and growth of suppression depended on the relationship between f_3 and f_2 in much the same way at 500 Hz as it did when f_2=4000 Hz (compare decrement functions in Figs. 3 and 4, and the slopes of these functions at both frequencies, which were summarized in Fig. 5). The comparison of slopes for L_2 and L_3 provided in the right panel of Fig. 7 indicates that the rates of growth are nearly identical on a relative suppressor-frequency scale at 500 and 4000 Hz. In total, the results summarized in Tables I and II, Figs. 2–5, and Fig. 7 provide evidence in support of both the validity and reliability of the present measurements.

Results suggesting that there may be differences in cochlear processing at 500 and 4000 Hz are provided in Figs. 6 and 8, where DPOAE STCs are presented for both frequencies. Differences in response properties are highlighted in the summaries of these STCs provided in Figs. 9–12. STCs are broader at 500 Hz, compared to 4000 Hz, which is an expected finding, given the known trends in tuning as a function of frequency, based on other physiological and behavioral measurements. Interestingly, there is more evidence of a low-frequency tail when f_2=500 Hz, with less evidence of the tail at 4000 Hz. As stated earlier, we have no explanation for why low-frequency tails were observed in the present DPOAE STCs at 500 Hz, given previous physiological data from lower animals.

In any event, it is often assumed that the response to a low-frequency tone relative to BF (f_2 in DPOAE suppression studies) is linear if the low-frequency tone is sufficiently low in frequency relative to BF. The fact that suppression thresholds were relatively constant for $f_3 \leqslant 258$ Hz is taken as evidence in support of the view that measurements were made on the linear or, at least, asymptotic low-frequency tail of the response area when f_2=500 Hz. In contrast, we are less convinced that an f_3 was selected that was sufficiently low in frequency relative to 4000 Hz in order to be certain that the response to f_3 is linear (or, at least asymptotic) at or near the f_2 place.

Despite the observation that we may not be in the linear or asymptotic response region with the lowest f_3 used in the present study when f_2=4000 Hz, the differences in threshold between BF and a frequency one octave lower than BF are not the same at 500 and 4000 Hz. There is less threshold difference between on-frequency and low-frequency suppressors, but this cannot be attributed to problems associated with having an insufficiently low, low-frequency suppressor when f_2=500 Hz because at least three suppressor frequencies had about the same thresholds on the tail of the 500 Hz STC. As expected, the slope of the functions relating L_3 to L_2 for on-frequency suppressors approaches 1 (i.e., between 0.87 and 0.93 at both 500 and 4000 Hz; see, for example, the closed symbols in the bottom row of Fig. 10). This is not a surprising outcome, because cochlear processing at or near the f_2 place is nonlinear and compressive for both the signal eliciting the response and the suppressor reducing that response. As a result, the processing of both f_2 and f_3 is similarly nonlinear, resulting in a straight line with a slope approaching 1 when the probe and suppressor are approximately equal in frequency. It is unclear why the slope was not closer to 1. However, for both 500 and 4000 Hz, the "on-frequency" suppressor was slightly higher in frequency than f_2. The observation of slopes less than 1 for $f_2 \approx f_3$ may be a consequence of the fact that the slope of the decrement-versus-L_3 function decreases as f_3 increases above f_2, suggesting that the "growth of response" to f_3 at or near the f_2 place is more gradual, compared to the response to f_2 at or near the same place.

An estimate of compression at f_2 can be obtained by examining the slope of the functions relating L_3 to L_2 when

f_3 is 1 octave below f_2 (open symbols, Fig. 9). Slopes for these conditions provide this estimate on the assumption that the response to f_2 near the f_2 place is compressive, while the response to f_3 at or near the f_2 place is more or less linear. Taking the reciprocal of the slope results in compression ratios that depend on whether the functions were derived from data which were fit with SLR versus MLR. More important, these reciprocals provide estimates of compression that range from about 2.4 to 3.2, and were similar for 500 and 4000 Hz, indicating that the responses were nonlinear at both frequencies. These estimates are less than those typically ascribed to cochlear compression, based on either behavioral data or direct measurements (e.g., Oxenham and Plack, 1997; Oxenham and Bacon, 2003; Robles and Ruggero, 2001; Rosengard *et al.*, 2005). However, the present compression estimates are independent of stimulus level, so they are not directly comparable to estimates based on I/O functions.

In similar fashion, the present estimates of compression also differ from the estimates for maximum compression that were derived from our previous measurements of DPOAE I/O functions (Gorga *et al.*, 2007). While estimates of the dynamic range differed at 500 and 4000 Hz (based on our previous data), the slopes of the functions for high-level inputs were about 0.25 or 0.20 at both frequencies, for a compression ratio of 4:1 or 5:1. In our previous work, we were concerned about the influence of differences in noise levels at the two frequencies. However, those concerns primarily related to measurements for low-level stimuli. Estimates of maximum compression in our previous data were made from high stimulus-level conditions. The influence of noise for high-level inputs is expected to be reduced because the SNR was large at both frequencies, increasing our confidence in the estimates of compression from the previously reported DPOAE I/O functions. One interpretation of the apparent discrepancy between these different estimates of compression is that the slope of the function relating suppression threshold to L_2 is not simply related to the slope of the corresponding I/O function. While both depend upon the existence of a compressive nonlinearity, the transformation between slope of an I/O function and slope of a function relating levels for on- and low-frequency suppressors is not simple.

Mills (1998) used tip-to-tail differences in DPOAE measurements in lower animals as an estimate of cochlear-amplifier gain. Pienkowski and Kunov (2001) and Gorga *et al.* (2002a, b; 2003) applied the same approach to DPOAE suppression data from humans. In general, the estimates of gain from these studies were within the range that would be expected, based on data from lower animals. Maximum observed gain was about 45 dB, and decreased as level (L_2) increased. The results from the present study are similar to the previous findings, but only when f_2=4000 Hz (Fig. 10). While the tip-to-tail difference (the estimate of cochlear-amplifier gain used in this and previous DPOAE studies) decreased as L_2 increased for both f_2 frequencies, smaller estimates of gain were observed at 500 Hz. Recently, Keefe *et al.* (2008) described comparable data based on suppression of stimulus frequency otoacoustic emissions (SFOAE). Tip-to-tail differences based on SFOAE STCs were roughly similar to those based on DPOAE STCs at both 500 and 4000 Hz.

In the present study, the smallest estimate of gain at 4000 Hz (22 dB when L_2=50 dB SL) was greater than the largest estimate of gain at 500 Hz (20 dB when L_2=20 dB SL). At L_2=20 dB SL (the lowest level for which data were available at both f_2 frequencies), the gain at 4000 Hz exceeded the gain at 500 Hz by more than 20 dB, or more than a factor of 10. These results suggest that cochlear-amplifier gain is present both at 500 and at 4000 Hz, but the gain is greater at 4000 Hz. Recall that tip-to-tail differences were based on a comparison of suppression threshold for cases in which $f_3 \approx f_2$ with the results when f_3 was 1 octave below f_2. At 500 Hz, the suppression threshold for the low-frequency f_3 was similar and relatively constant for this and lower frequencies, suggesting that it represented a condition in which the response to f_3 at or near the f_2 place was perhaps linear (see the low-frequency tails of the STCs in Figs. 6 and 8). In contrast, it was less obvious that the suppression threshold for the lowest f_3 at 4000 Hz was on an asymptotic portion of the STC, which might mean that we underestimated the gain at 4000 Hz. The differences in cochlear-amplifier gain between 500 and 4000 Hz, based on tip-to-tail differences, might be even greater if suppression measurements were made at a lower f_3 when f_2=4000 Hz. These gain differences indicate that cochlear processing in humans at these two frequencies is qualitatively similar, but quantitatively different.

The estimate of sharpness of tuning, Q_{ERB}, decreased as L_2 increased for both f_2 frequencies (Fig. 11). No consistent dependence of Q_{ERB} on level was observed in SFOAE STCs (Keefe *et al.*, 2008), but was evident in similar estimates derived from SFOAE latencies (Schairer *et al.*, 2006). These SFOAE data, as well as other Q_{ERB} estimates based on SFOAE latency reported by Shera *et al.* (2002), revealed higher values of Q_{ERB} than those observed in the present study at comparable levels. A possible reason for the smaller Q_{ERB} in the present study is the presence of a second tone in the DPOAE stimulus. Suppression of the cochlear response to either tone is expected to reduce DPOAE level; thus, a wider range of f_3 may be suppressive. In contrast, SFOAEs are elicited by a single tone; thus, the suppressive range of frequencies is expected to be narrower. This stimulus difference could explain why the Q_{ERB} of DPOAE STCs is approximately 20% smaller than the Q_{ERB} of SFOAE STCs (Keefe *et al.*, 2008) or some of the latency-based estimates of SFOAE Q_{ERB} (Schairer *et al.*, 2006), but may be inadequate to explain the apparent discrepancy between our DPOAE Q_{ERB} estimates and other latency-based SFOAE Q_{ERB} estimates (Shera *et al.*, 2002), which are as large as twice the present estimates.

The changes in our Q_{ERB} estimates with level were greater at 4000 Hz, compared to 500 Hz. Part of this difference could relate to the fact that Q_{ERB} was less at 500 Hz, even at the lowest L_2 levels, so there was less "opportunity" for spread in the representation at this frequency with increased level. The analysis summarized in Fig. 11 represents a case in which the results derived from the MLR may have obscured an effect. Specifically, the results based on SLR

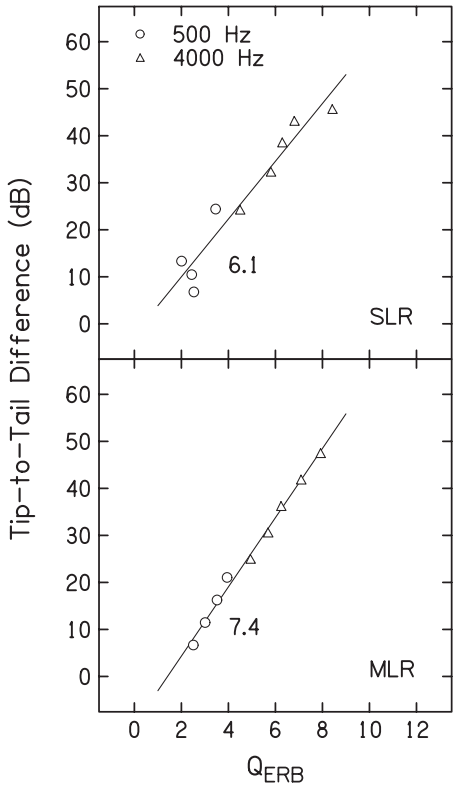

FIG. 13. Tip-to-tail difference as a function of Q_{ERB}, following the convention used in Figs. 10–12. Circles represents data for 500 Hz and triangles represent data for 4000 Hz. For both frequencies, the point with the lowest tip-to-tail difference/Q_{ERB} represents results for the highest L_2 level (50 dB SL at both frequencies) and the points with the largest Q_{ERB}/tip-to-tail difference represent results for the lowest L_2 levels (20 dB SL at 500 Hz and 10 dB SL at 4000 Hz). Lines in each panel (SLR and MLR) represent linear fits to the data.

showed discrete changes in Q_{ERB}, which were smoothed by the MLR. In this case, it is unclear which analysis better describes the changes in Q_{ERB} with level. Having said this, the smallest Q_{ERB} at 4000 Hz (4.5 when L_2=50 dB SL) was greater than the largest Q_{ERB} at 500 Hz (4 when L_2=20 dB SL). Sharper tuning at higher frequencies is the expected outcome, given previous physiological and psychophysical data from both humans and lower animals.

The systematic dependence of both tip-to-tail differences (Fig. 10) and Q_{ERB} (Fig. 11) on L_2 (especially evident in the results based on MLR) suggests a relationship between these two metrics. In Fig. 13, tip-to-tail difference is plotted as a function of Q_{ERB}, following the convention used in previous figures, in that results based on SLR and MLR are shown in the top and bottom panels, respectively. The lines in these two panels represent linear fits to the data, combining the data from both 500 and 4000 Hz to generate the fits. We are unaware of other summaries in which these two variables were plotted against each other. Striking in Fig. 13 is the trade off between sharpness of tuning and cochlear-amplifier gain. As the tuning increases, so does the gain. Although purely speculative, one can imagine a situation in which sharpness of tuning is traded for gain in order to achieve some constant output. Also of interest is the observation that the data at 500 and 4000 Hz appear to fall on the same line. These results lead us to speculate that the nonlinearity at 500 Hz is the same as the nonlinearity at 4000 Hz, with the only difference being that we are operating at different points on the nonlinear function. An expression for "frequency-normalized gain-bandwidth product" (GBW) further emphasizes this point:

$$\mathrm{GBW} = \frac{\text{tip-to-tail}}{Q_{\mathrm{ERB}} - 1}. \tag{2}$$

From SLR and MLR estimates of tip-to-tail and Q_{ERB}, GBW =about 6 or 7 for every L_2 level and for both f_2 frequencies. The invariance of this relationship (across f_2 and L_2) supports the view that the nonlinear mechanism is similar at the 500 and 4000 Hz locations in the cochlea. It may be that different "set points" at these two locations cause the same nonlinear mechanism to operate within different ranges of gains, while consistently maintaining the same GBW at all levels at both locations.

BF decreased as L_2 increased for both f_2 frequencies, although the changes were greater for 500 Hz (Fig. 12). This means that the location of the maximum nonlinear interaction between the primaries whose response was being suppressed shifted toward lower frequencies as level increased. This too is not a surprising observation, as evidence exists to suggest that the maximum representation for a given place occurs at lower frequencies for high levels of stimulation. The differences between frequency in the present study suggest that a greater apical shift occurred when f_2=500 Hz.

In this study, we have not considered how a reflected contribution from the DPOAE place may have affected the present results. It is widely accepted that both a distortion and a reflection source may contribute to the DPOAE measured in the ear canal (e.g., Heitmann *et al.*, 1998; Kalluri and Shera, 2001; Konrad-Martin *et al.*, 2001; Shear and Guinan, 1999; Stover *et al.*, 1996; Talmadge *et al.*, 1999; Zweig and Shera, 1995). No effort was made in this study to eliminate reflection-source contribution. However, it is not apparent how reflection-source contribution could have affected the data we collected or alter our interpretation of the frequency effects observed in this study.

In summary, the present study provides estimates of cochlear-response properties for a high and a low frequency, based on measurements in which efforts were made to account for forward middle-ear transmission, individual differences in optimal primary-level ratios, and the influence of noise. Our results suggest that the responses from the 500 and 4000 Hz regions are similar, in that both show a frequency dependence in the rate at which suppression grows. In fact, the slopes of functions relating decrement to suppressor level are nearly identical at the two frequencies. Estimates of compression also were similar for 500 and 4000 Hz. Although evidence of tuning around the primary frequencies (f_2), and level-dependent changes in cochlear-amplifier gain, tuning and best frequency was present, there were quantitative differences in these measures between the two f_2 frequencies. These differences could not be attributed to differences in noise, which was a concern in our previous efforts to compare cochlear processing for low- and high-frequency stimuli. One of the clearest outcomes in the

present study is evidence to suggest that cochlear-amplifier gain is greater at 4000 Hz, compared to 500 Hz. Assuming that cochlear-amplifier gain is maximal for low-level inputs, the difference in maximum gain was at least 20 dB, if not greater. Even so, it appears that the nonlinearity is similar at 500 and 4000 Hz, and that differences in Q_{ERB} and tip-to-tail differences are the result of the fact that the nonlinear filter operates over different ranges of gain. In total, the results reported in the present study suggest that, in humans, there are both similarities and differences in cochlear processing at the base, compared to the apex, but the differences may represent simply a set-point variation of the same nonlinear mechanism.

ACKNOWLEDGMENTS

This work was supported by the NIH (NIDCD R01 DC002251 and P30 DC004662). We thank Sandy Estee for her assistance in subject recruitment, Sarah Michaels for help constructing some of the figures, and the subjects who made the time commitment that was necessary to complete their participation in the study. We also would like to thank Chris Shera and Andy Oxenham for constructive discussions of these data prior to submission, and two anonymous reviewers who provided helpful suggestions on a previous version of the manuscript.

Abdala, C. (**1998**). "A developmental study of distortion product otoacoustic emission (2fl-f2) suppression in humans," Hear. Res. **21**, 125–138.

Abdala, C. (**2001**). "Maturation of the human cochlear amplifier: Distortion product otoacoustic emission suppression tuning curves recorded at low and high primary levels," J. Acoust. Soc. Am. **110**, 1465–1476.

Abdala, C., Sininger, Y. S., Ekelid, M., and Zeng, F.-G. (**1996**). "Distortion product otoacoustic emission suppression tuning curves in human adults and neonates," Hear. Res. **98**, 38–53.

American National Standards Institute (**1996**). "Specifications for audiometers," ANSI S3.6-1996, New York.

Cooper, N. P., and Rhode, W. S. (**1995**). "Nonlinear mechanics at the apex of the guinea-pig cochlea," Hear. Res. **82**, 225–243.

Cooper, N. P., and Rhode, W. S. (**1997**). "Mechanical responses to two-tone distortion products in the apical and basal turns of the mammalian cochlea," J. Neurophysiol. **78**, 261–270.

Cooper, N. P., and Rhode, W. S. (**1998**). "Apical cochlear mechanics: A review of recent observations," in *Proceedings of the International Symposium on Psychophysical and Physiological Advances in Hearing*, edited by A. R. Palmer, A. Rees, A. Q. Summerfield, and R. Meddis (Whurr, London), pp. 11–18.

Dallos, P., He, D. Z., Lin, X., Sziklai, I., Mehta, S., and Evans, B. N. (**1997**). "Acetylcholine, outer hair cell electromotility, and the cochlear amplifier," J. Neurosci. **17**, 2212–2226.

Dallos, P. J., and Harris, D. M. (**1978**). "Properties of auditory-nerve responses in the absence of outer hair cells," J. Neurophysiol. **41**, 365–383.

Dhar, S., Long, G. R., and Talmadge, C. L. (**2005**). "The effect of stimulus-frequency ratio on distortion product otoacoustic emission components," J. Acoust. Soc. Am. **117**, 3766–3776.

Dorn, P. A., Piskorski, P., Keefe, D. H., Neely, S. T., and Gorga, M. P. (**1998**). "On the existence of an age/threshold/frequency interaction in distortion product otoacoustic emissions," J. Acoust. Soc. Am. **104**, 964–971.

Gaskill, S. A., and Brown, A. M. (**1990**). "The behavior of the acoustic distortion product, $2f_1$–f_2, from the human ear and its relation to auditory sensitivity," J. Acoust. Soc. Am. **88**, 821–839.

Goldstein, J. L. (**1967**). "Auditory nonlinearity," J. Acoust. Soc. Am. **41**, 676–689.

Gorga, M. P., Neely, S. T., Bergman, B. M., Beauchaine, K. L., Kaminski, J. R., Peters, J., and Jesteadt, W. (**1993**). "Otoacoustic emissions in normal and hearing-impaired ears: Distortion product responses," J. Acoust. Soc. Am. **93**, 2050–2060.

Gorga, M. P., Neely, S. T., Dierking, D., Dorn, P. A., Hoover, B. M., and Fitzpatrick, D. (**2003**). "Distortion product otoacoustic emission tuning curves in normal-hearing and hearing-impaired human ears," J. Acoust. Soc. Am. **114**, 263–278.

Gorga, M. P., Neely, S. T., Dorn, P. A., Dierking, D., and Cyr, E. (**2002a**). "Evidence of upward spread of suppression in DPOAE measurements," J. Acoust. Soc. Am. **112**, 2910–2920.

Gorga, M. P., Neely, S. T., Dorn, P. A., and Konrad-Martin, D. (**2002b**). "The use of distortion product otoacoustic emission suppression as an estimate of response growth," J. Acoust. Soc. Am. **111**, 271–284.

Gorga, M. P., Neely, S. T., Dierking, D., Kopun, J., Jolkowski, K., Groenenboom, K., Tan, H., and Stiegemann, B. (**2007**). "Low-frequency and high-frequency cochlear nonlinearity in humans," J. Acoust. Soc. Am. **122**, 1671–1680.

Gorga, M. P., Neely, S. T., Starnes-Ohlrich, B., Hoover, B., Redner, J., and Peters, J. (**1997**). "From laboratory to clinic: A large scale study of distortion product otoacoustic emissions in ears with normal hearing and ears with hearing loss," Ear Hear. **18**, 440–455.

Greenwood, D. D. (**1990**). "A cochlear frequency-position function for several species-29 years later," J. Acoust. Soc. Am. **87**, 2592–2605.

Heitmann, J., Waldmann, B., Schnitzler, H.-U., Plinkert, P. K., and Zenner, H.-P. (**1998**). "Suppression of distortion product otoacoustic emissions (DPOAE) near $2f1$–$f2$ removes DP-gram fine structure: Evidence for a secondary generator," J. Acoust. Soc. Am. **103**, 1527–1531.

Hicks, M. L., and Bacon, S. P. (**1999**). "Psychophysical measures of auditory nonlinearities as a function of frequency in individuals with normal hearing," J. Acoust. Soc. Am. **105**, 285–296.

Hudspeth, A. J. (**1997**). "Mechanical amplification of stimuli by hair cells," Curr. Opin. Neurol. **7**, 480–486.

Johnson, T. A., Neely, S. T., Dierking, D. M., Hoover, B. M., and Gorga, M. P. (**2004**). "An alternate approach to constructing distortion product otoacoustic emission (DPOAE) suppression tuning curves," J. Acoust. Soc. Am. **116**, 3263–3266.

Johnson, T. A., Neely, S. T., Garner, C. A., and Gorga, M. P. (**2006**). "Influence of primary-level and primary-frequency ratios on human distortion product otoacoustic emissions," J. Acoust. Soc. Am. **119**, 418–428.

Kalluri, R., and Shera, C. A. (**2001**). "Distortion-product source unmixing: A test of the two-mechanism model for DPOAE generation," J. Acoust. Soc. Am. **109**, 622–637.

Keefe, D. H. (**2002**). "Spectral shapes of forward and reverse transfer functions between ear canal and cochlea estimated using DPOAE input/output functions," J. Acoust. Soc. Am. **111**, 249–260.

Keefe, D. H., Ellison, J. C., Fitzpatrick, D. F., and Gorga, M. P. (**2008**). "Two-tone suppression of stimulus frequency otoacoustic emissions," J. Acoust. Soc. Am. (in press).

Kemp, D. T. and Brown, A. M. (**1983**). "Suppressibility of the $2f_1$-$2f_2$ stimulated acoustic emissions in gerbil and man," Hear. Res. **13**, 29–37.

Kiang, N. Y.-S., and Maxon, E. C. (**1974**). "Tails of tuning curves of auditory-nerve fibers," J. Acoust. Soc. Am. **55**, 620–630.

Kiang, N. Y.-S., Watanabe, T., Thomas, E. C., and Clark, L. F. (**1965**). *Discharge Patterns of Single Fibers in the Cat's Auditory Nerve*, MIT Research Monograph. No. 35 (MIT, Cambridge, MA).

Konrad-Martin, D., Neely, S. T., Keefe, D. H., Dorn, P. A., and Gorga, M. P. (**2001**). "Sources of distortion product otoacoustic emissions revealed by suppression experiments and inverse fast Fourier transforms in normal ears," J. Acoust. Soc. Am. **109**, 2862–2879.

Kummer, P., Janssen, T., and Arnold, W. (**1995**). "Suppression tuning curves of the $2f_1$-$2f_2$ distortion-product otoacoustic emissions in humans," J. Acoust. Soc. Am. **98**, 197–210.

Kummer, P., Janssen, T., and Arnold, W. (**1998**). "The level and growth behavior of the $2f_1$-f_2 distortion product otoacoustic emission and its relationship to auditory sensitivity in normal hearing and cochlear hearing loss," J. Acoust. Soc. Am. **103**, 3431–3444.

Kummer, P., Janssen, T., Hulin, P., and Arnold, W. (**2000**). "Optimal L_1-L_2 primary tone level separation remains independent of test frequency in humans," Hear. Res. **146**, 47–56.

Levitt, H. (**1971**). "Transformed up-down methods in psychoacoustics," J. Acoust. Soc. Am. **49**, 467–477.

Liberman, M. C. and Dodds, L. W. (**1984**). "Single-unit labeling and chronic cochlear pathology. III. Stereocilia damage and alterations of threshold tuning curves," Hear. Res. **16**, 55–74.

Lopez-Poveda, E. A., Plack, C. J., and Meddis, R. (**2003**). "Cochlear nonlinearity between 500 and 8000 Hz in listeners with normal hearing," J. Acoust. Soc. Am. **113**, 951–960.

Mills, D. M. (**1998**). "Interpretation of distortion product otoacoustic emission measurements. II. Estimating tuning characteristics using three stimulus tones," J. Acoust. Soc. Am. **103**, 507–523.
Neely, S. T., Johnson, T. A., and Gorga, M. P. (**2005**). "Distortion-product otoacoustic emissions with continuously varying stimulus level," J. Acoust. Soc. Am. **117**, 1248–1259.
Neely, S. T., and Kim, D. O. (**1983**). "An active cochlear model showing sharp tuning and high sensitivity," Hear. Res. **9**, 123–130.
Neely, S. T. and Liu, Z. (**1994**). "EMAV: Otoacoustic emission averager," Tech. Memo No. 17 (Boys Town National Research Hospital, Omaha, NE).
Oxenham, A. J., and Bacon, S. P. (**2003**). "Cochlear compression: Perceptual measures and implications for normal and impaired hearing, Ear Hear. **24**, 352–366.
Oxenham, A. J., and Plack, C. J. (**1997**). "A behavioral measure of basilar-membrane nonlinearity in listeners with normal and impaired hearing," J. Acoust. Soc. Am. **101**, 3666–3675.
Pienkowski, M., and Kunov, H. (**2001**). "Suppression of distortion product otoacoustic emissions and hearing thresholds," J. Acoust. Soc. Am. **113**, 1574–1586.
Plack, C. J., and Drga, V. (**2003**). "Psychophysical evidence for auditory compression at low characteristic frequencies," J. Acoust. Soc. Am. **113**, 1574–1586.
Plack, C. J., and O'Hanlon, C. G. (**2003**). "Forward masking additivity and compression at low and high frequencies," J. Assoc. Res. Otolaryngol. **4**, 405–415.
Plack, C. J., and Oxenham, A. J. (**1998**). "Basilar membrane nonlinearity and the growth of forward masking," J. Acoust. Soc. Am. **103**, 1598–1608.
Plomp, R. (**1965**). "Detectability threshold for combination tones," J. Acoust. Soc. Am. **37**, 1110–1123.
Rhode, W. S. (**1971**). "Observations of the vibration of the basilar membrane in the squirrel monkey using the Mossbauer technique," J. Acoust. Soc. Am. **49**, 1218–1231.
Rhode, W. S., and Cooper, N. P. (**1996**). "Nonlinear mechanics in the apical turn of the chinchilla cochlea in vivo," Aud. Neurosci. **3**, 101–121.
Robles, L., and Ruggero, M. A. (**2001**). "Mechanics of the mammalian cochlea," Physiol. Rev. **81**, 1305–1352.
Rosengard, P. S., Oxenham, A. J., and Braida, L. D. (**2005**). "Comparing different estimates of cochlear compression in listeners with a normal and impaired hearing," J. Acoust. Soc. Am. **117**, 3028–3041.
Ruggero, M. A., and Rich, N. C. (**1991**). "Furosemide alters organ of corti mechanics: Evidence for feedback of outer hair cells upon the basilar membrane," J. Neurosci. **11**, 1057–1067.
Schairer, K. S., Ellison, J. C., Fitzpatrick, D., and Keefe, D. H. (**2006**). "Use of stimulus-frequency otoacoustic emission latency and level to investigate cochlear mechanics in human ears," J. Acoust. Soc. Am. **120**, 901–914.
Sewell, W. F. (**1984**). "The effects of furosemide on the endocochlear potential and auditory-nerve fiber tuning curves in cats," Hear. Res. **14**, 305–314.
Shera, C. A., and Guinan, J. J. (**1999**). "Evoked otoacoustic emission arise by two fundamentally different mechanisms: A taxonomy of mammalian OAEs," J. Acoust. Soc. Am. **105**, 782–798.
Shera, C. A., Guinan, J. J., and Oxenham, A. J. (**2002**). "Revised estimates of human cochlear tuning from otoacoustic and behavioral measurements," Proc. Natl. Acad. Sci. U.S.A. **9**, 3318–3323.
Shera, C. A., Guinan, J. J., and Oxenham, A. J. (**2007**). "Otoacoustic estimates of cochlear tuning: Validation in the chinchilla," 30th Midwinter Meeting of the Association for Research in Otolaryngology, Denver, CO.
Siegel, J. H., and Hirohata, E. T. (**1994**). "Sound calibration and distortion product otoacoustic emissions at high frequencies," Hear. Res. **80**, 146–152.
Siegel, J. H. (**2007**). "Calibrating otoacoustic emission probes in *Otoacoustic Emissions: Clinical Applications*," 3rd edition, edited by M. S. Robinette and T. J. Glattke, Thieme Medical, New York, pp. 403–427.
Stover, L. J., Neely, S. T., and Gorga, M. P. (**1996**). "Latency and multiple sources of distortion product otoacoustic emissions," J. Acoust. Soc. Am. **99**, 1016–1024.
Talmadge, C. L., Long, G. R., Tubis, A., and Dhar, S. (**1999**). "Experimental confirmation of the two-source interference model for the fine structure of distortion product otoacoustic emissions," J. Acoust. Soc. Am. **105**, 275–292.
Zinn, C., Maier, H., Zenner, H. P., and Gier, A. W. (**2000**). "Evidence for active, nonlinear, negative feedback in the vibration of the apical region of the in vivo guinea-pig cochlea," Hear. Res. **142**, 159–183.
Zwieg, G., and Shera, C. A. (**1995**). "The origin of periodicity in the spectrum of evoked otoacoustic emissions," J. Acoust. Soc. Am. **98**, 2018–2047.

Cortical sensitivity to periodicity of speech sounds

Santeri Yrttiaho[a)]
Department of Signal Processing and Acoustics, Helsinki University of Technology, P.O. Box 3300, FI-02015 TKK, Finland; Department of Biomedical Engineering and Computational Science, Helsinki University of Technology, P.O. Box 3310, FI-02150 TKK, Finland; and BioMag Laboratory, Hospital District of Helsinki and Uusimaa HUSLAB, Helsinki University Central Hospital, P.O. Box 340, FI-00029 HUS, Finland

Hannu Tiitinen, Patrick J. C. May, and Sakari Leino
Department of Biomedical Engineering and Computational Science, Helsinki University of Technology, P.O. Box 3310, FI-02015 TKK, Finland; and BioMag Laboratory, Hospital District of Helsinki and Uusimaa HUSLAB, Helsinki University Central Hospital, P.O. Box 340, FI-00029 HUS, Finland

Paavo Alku
Department of Signal Processing and Acoustics, Helsinki University of Technology, P.O. Box 3000, FI-02015 TKK, Finland

(Received 27 June 2007; revised 14 January 2008; accepted 6 February 2008)

Previous non-invasive brain research has reported auditory cortical sensitivity to periodicity as reflected by larger and more anterior responses to periodic than to aperiodic vowels. The current study investigated whether there is a lower fundamental frequency (F0) limit for this effect. Auditory evoked fields (AEFs) elicited by natural-sounding 400 ms periodic and aperiodic vowel stimuli were measured with magnetoencephalography. Vowel F0 ranged from normal male speech (113 Hz) to exceptionally low values (9 Hz). Both the auditory N1m and sustained fields were larger in amplitude for periodic than for aperiodic vowels. The AEF sources for periodic vowels were also anterior to those for the aperiodic vowels. Importantly, the AEF amplitudes and locations were unaffected by the F0 decrement of the periodic vowels. However, the N1m latency increased monotonically as F0 was decreased down to 19 Hz, below which this trend broke down. Also, a cascade of transient N1m-like responses was observed in the lowest F0 condition. Thus, the auditory system seems capable of extracting the periodicity even from very low F0 vowels. The behavior of the N1m latency and the emergence of a response cascade at very low F0 values may reflect the lower limit of pitch perception. © *2008 Acoustical Society of America.* [DOI: 10.1121/1.2888489]

PACS number(s): 43.64.Ri, 43.64.Qh, 43.64.Sj [WPS] Pages: 2191–2199

I. INTRODUCTION

In western languages, the majority of speech sounds such as vowels, semivowels and diphthongs are voiced and thus quasi-periodic. Periodicity is an important feature of speech sounds as it enables both phonological and intonational contrasts. Unfortunately, relatively few studies of cortical periodicity detection have employed actual speech stimuli. Instead, synthetic non-speech sounds are favored because their periodicity can easily be manipulated in a controlled way. However, the choice of stimuli can considerably affect the cortical responses to sound periodicity: Irrespective of their periodicity, cortical responses to speech sounds are reported to differ with respect to amplitude and source location from those elicited by non-speech sounds (Hewson-Stoate *et al.*, 2006). Similarly, human voice *per se* elicits stronger activation (Gunji *et al.*, 2003) in the human cortex than do other sound categories and is processed in specialized cortical regions (Belin *et al.*, 2000). Moreover, Whalen *et al.* (2006) presented evidence for a specialized speech system where the earlier cortical treatment of speech is suppressed in favor of a specialized representation formed in the subsequent stages of speech processing. Consequently, the results of human neuroimaging studies using artificial non-speech stimuli cannot be generalized to the processing of speech sounds. Instead, to determine the cerebral mechanisms involved in the processing of voiced speech, it is essential to use realistic speech sound as stimuli. To this end, methods such as semisynthetic speech generation (SSG) (Alku *et al.*, 1999) that yield highly natural, yet fully controllable speech stimuli have become available for the purposes of brain research.

Periodic vowels are produced when air expelled from the lungs makes the vocal folds fluctuate. Consequently, the vocal tract is excited by a quasi-periodic glottal flow waveform resulting in speech pressure signals whose temporal structure consists of repeating periods. The spectra of these sounds are characterized by a comb structure with high-amplitude peaks, or partials, corresponding to integer multiples of the F0. The F0 values of average conversational speech are approximately 200 Hz for female and 125 Hz for male voices. In singing, however, the F0 may reach considerably lower or higher values. In contrast, unvoiced sounds, such as fricatives and whispered vowels, are temporally ape-

[a)]Author to whom correspondence should be addressed. Electronic mail: santeri.yrttiaho@tkk.fi.

riodic and spectrally irregular, that is, they lack the comb structure. Perceptually, most periodic sounds produce a pitch sensation while most aperiodic sounds do not. In addition to the harmonic structure, the spectra of voiced speech sounds are characterized by the overall envelope which gradually decreases towards high frequencies. This envelope comprises local high-energy resonances caused by the vocal tract. These resonances, termed the formants (F1, F2, F3, etc.), determine vowel identity.

The cortical processing of speech involves rapidly changing activity in distinct locations in cortex. Therefore, the study of cortical processing of speech requires both temporally and spatially accurate imaging techniques. Magnetoencephalography (MEG) is a non-invasive technique used to measure the magnetic fields produced by electrical activity in the brain and it combines high temporal acuity with good spatial resolution. Sources of brain activity can be located from multi-channel MEG recordings by mathematical procedures such as equivalent current dipole (ECD) modeling. The most prominent auditory evoked field (AEF), elicited by any audible sound, is the transient N1m response peaking around 100 ms after stimulus presentation (Näätänen and Picton, 1987). The cortical processing of sound features is reflected in the amplitude, latency and source location of the N1m response. Other cortical responses have been studied extensively as well, including the sustained field (SF) which is elicited by prolonged auditory stimulation and reaches its maximum around 400 ms (Hari *et al.*, 1980; Pantev *et al.*, 1994; see also Picton *et al.*, 1978a&b).

Previous MEG studies have reported cortical sensitivity to periodic sounds. For example, larger N1m amplitudes to periodic than to aperiodic stimuli have been reported in studies using non-speech (Gutschalk *et al.*, 2004; Soeta *et al.*, 2005; Lütkenhöner *et al.*, 2006) and artificial speech-like (Hertrich *et al.*, 2000) sounds. Also, an anterior shift of the source location is associated with the AEF elicited by the onset of a periodic vowel after an aperiodic voiceless fricative (Kaukoranta *et al.*, 1987) and by square wave stimulation after aperiodic noise (Mäkelä *et al.*, 1988). Further, when continuous auditory stimulation changes from aperiodic to quasi-periodic iterated ripple noise (IRN), the AEF grows in amplitude and its source shifts in the anterior direction (Krumbholz *et al.*, 2003). However, in a transient stimulation condition, the N1m amplitude enhancement associated with periodicity seems to depend on sound F0: Soeta *et al.* (2005), using 1000 Hz IRN stimuli, reported such an enhancement, whereas Krumbholz *et al.* (2003) found no enhancement when they used IRN stimuli with F0s in the 16–250 range.

Gutschalk *et al.* (2004), separating an anterior and a posterior source of the N1m, showed that only the anterior source was sensitive to auditory periodicity. In contrast, the posterior source was sensitive to the amount of sound energy. Also, the auditory SF responses arise from two separate sources sensitive to the temporal periodicity and sound energy, respectively (Gutschalk *et al.*, 2002; Gutschalk *et al.*, 2004). The periodicity-sensitive AEF source is activated by very different types of stimuli. Specifically, the onset of either monaural (IRN) or binaural (Huggins pitch) periodicity within ongoing noise elicits a periodicity-specific onset response similar to that reported by Krumbholz *et al.* (2003) (Hertrich *et al.*, 2005; Chait *et al.*, 2006). Thus, previous research suggests the existence of a periodicity-sensitive source that makes use of a central and binaural representation of acoustic periodicity. To date, however, the interplay between the neural populations sensitive to pitch and those sensitive to speech sounds has been largely unexplored.

When the F0 of periodic broadband sounds is decreased to sufficiently low values, the perceptual sensation and the underlying neural responses associated with these sounds are substantially affected. In particular, the pitch sensation characteristic to periodic sounds disappears when the F0 is decreased below 19–40 Hz (Ritsma, 1962; Guttman and Julesz, 1963; Krumbholz *et al.*, 2000; Pressnitzer *et al.*, 2001). The cortical responses to periodic broadband sounds, in the corresponding F0 range, have been studied with MEG. For example, Forss *et al.* (1993) examined N1m responses elicited by 40–320 Hz click trains and reported that the N1m amplitude and latency decreased and increased, respectively, as the F0 of the stimuli was decreased. Also, the amplitude of the SF elicited by click trains decreases as the F0 is decreased in the 10–200 Hz range (Gutschalk *et al.*, 2002). Unfortunately, as only non-speech stimuli have been used in these studies, it cannot be established whether the results can be generalized to the processing of periodic speech sounds.

To overcome the validity issues related to the use of non-speech stimuli, recent MEG studies have drawn on the technical advances in speech stimulus generation and investigated human cortical representations of periodicity with realistic speech sounds. Using these advances, Alku *et al.* (2001) and Tiitinen *et al.* (2005) presented subjects with both periodic and aperiodic natural-sounding vowels. The spectral envelope and hence the vowel identity of the periodic and aperiodic vowels were identical but the natural glottal excitation of the periodic vowels was replaced by a noise sequence in the generation of the aperiodic sounds. These studies demonstrated cortical sensitivity to periodicity, as reflected by N1m with larger amplitudes and more anterior response locations to periodic as opposed to aperiodic sounds (Alku *et al.*, 2001; Tiitinen *et al.*, 2005). However, because they only used a single F0 value each, the question of whether cortical sensitivity to periodicity depends on the F0 of speech sounds was left open. Furthermore, while the SF responses have been previously investigated in the contexts of both speech (Eulitz *et al.*, 1995) and periodicity (Gutschalk *et al.*, 2002) separately, the SF dynamics relevant to the combination of speech and periodicity are unknown. Experiments with realistic speech sound stimuli of an extended duration are needed to clarify these issues.

The aim of the current study was to investigate cortical sensitivity to vowel periodicity, as reflected in both N1m and SF amplitude and generator source location, with vowels whose F0 was varied in a controlled manner. In particular, the focus was on the issue of whether there is a lower F0 limit for this cortical sensitivity to periodicity. When the F0 of a periodic complex sound is decreased, the spectral distances between its partials are shortened. Therefore, if there is a critical bandwidth that the spectral distance between the

partials must exceed for the generation of periodicity-specific cortical activity, the cortical sensitivity to periodicity should disappear if the vowel F0 falls below this critical value. Thus, it may be hypothesized that cortical responses evoked by periodic vowels increasingly resemble responses evoked by aperiodic sounds as F0 is decreased. However, in spite of F0 decrements, the periodicity and the harmonic comb structure of periodic vowels, as acoustic stimuli, are preserved. Although the frequency resolving power of the auditory periphery limits the place code representation of the vowel comb structure at low F0 values, the periodicity information is also available in the neural discharge patterns of auditory periphery as shown, for example, by in vivo measurements of cat auditory nerve fibers (Cariani and Delgutte, 1996). Therefore, it is possible that cortical sensitivity to vowel periodicity is maintained although the F0 is decreased notably below the range of normal speech.

The existence of a lower F0 limit for cortical sensitivity to vowel periodicity was determined by using the responses to aperiodic vowels as a baseline. Natural-sounding, fully controlled vowels generated with the SSG method (Alku *et al.*, 1999) were used as stimuli. The F0 of the periodic vowels was decreased in a controlled way from values typical to male speech (113 Hz) to exceptionally low values (9 Hz). Extended vowel durations were used because of long period lengths in the low F0 range. This allowed the investigation of both the N1m and the SF responses elicited by the vowel stimuli.

II. METHODS

A. Subjects

Fourteen subjects (average age 28 years, standard deviation 8.8 years; three females) participated in the study with written informed consent. All subjects reported normal hearing and being right handed. The experiment was approved by the Ethical Committee of Helsinki University Central Hospital. During the experiment, the subjects, instructed not to pay attention to the auditory stimuli, concentrated on watching a silent video. The subjects were also instructed to avoid eye movements and blinks during MEG data acquisition.

B. Stimulus preparation and presentation

The stimuli were created with semisynthetic speech generation (SSG), a method which produces high-quality synthetic vowels from natural glottal excitations in conjunction with artificial vocal tract models (Alku *et al.*, 1999). Using SSG, a glottal excitation pulseform (F0=113 Hz) was first extracted from an utterance produced by a male speaker. Five variants of this periodic excitation waveform, each with different F0, were then created by increasing the lengths of the closed phase durations of the individual glottal pulses. The waveform of the glottal excitation pulseform was similar during the closing phase in all the periodic vowel stimuli of different F0. The closing phase acts as the acoustical main excitation to the vocal tract (Gauffin and Sundberg, 1989; Fant, 1993; Alku *et al.*, 2006). Thus, the characteristics of the synthesized periodic speech sounds during their most energetic time spans were consistent across different F0s. Incremental lengthening of the fundamental period was conducted in order to create excitation waveforms whose F0 decreased in 10% steps on the ERB scale (Glasberg and Moore, 1990). This resulted in glottal sources with the following F0 values: 113 Hz (original glottal excitation), 86, 62, 40, 19, and 9 Hz. In addition to these periodic excitation signals, an aperiodic noise sequence was produced using random numbers with uniform distribution. The power spectrum of this noise sequence was matched to the spectrum of the original periodic glottal pulseform by using low-order filtering computed with linear predictive coding (LPC) (Rabiner and Schafer, 1978).

As the final step of the stimulus synthesis, all six periodic glottal waveforms and the aperiodic sequence were filtered by artificial all-pole vocal tract models mimicking the formant structures of the vowel /a/ and /e/. The vocal tract filters were adjusted to create the following values for the lowest four formant frequencies: 605 Hz (F1), 925 Hz (F2), 2005 Hz (F3), and 3465 Hz (F4) for the vowel /a/ and at 450 Hz (F1), 1960 Hz (F2), 2240 Hz (F3), and 3595 Hz (F4) for the vowel /e/. All the stimuli could be easily identified as the corresponding vowel, that is, either as /a/ or /e/, for all seven excitation waveforms. Figure 1 depicts the time-domain waveforms and the spectra of the vowel /a/ in the case of the periodic stimuli with the highest and lowest F0 and in the case of the aperiodic stimulus.

As the peak-to-average ratio of the vowel waveform amplitude increases with decreasing F0, it is not possible to match the stimuli on both peak and rms waveform amplitudes at the same time. Therefore, instead of matching the stimuli based on the waveform amplitudes, they were matched with respect to the actual acoustic energy, quantified as sound pressure level (SPL), received by the ear. The SPL of the stimuli were measured with a sound level meter using the A frequency weighting and temporal integration so as to approximate the properties of human hearing. Based on these measurements, the stimuli were calibrated to an equal SPL of 75 dB(A).

Stimulus duration was 400 ms, and onsets and offsets were smoothed with a 5 ms Hanning window. The stimuli were created in 22.050 kHz, 16 bit format. They were delivered to the subjects diotically through plastic tubes and earpieces, characterized by a 3 dB pass band from 70 Hz to 4 kHz, with an onset-to-onset interval of 1500 ms. The experiment was run with Presentation® software (Neurobehavioral Systems, Inc.) suitable for real-time delivery of auditory stimuli. Each stimulus was presented in its own sequence and the 14 sequences were presented in pseudorandom order counterbalanced across subjects.

C. MEG data acquisition

Cortical activation elicited by the stimuli was registered with a 306-channel whole-head MEG measurement device (Elekta Neuromag Oy, Finland) in a magnetically shielded room. At the beginning of each stimulus sequence, the head position with respect to the sensor array was determined by using head position indicator coils attached to the subject's scalp, with the locations of the coils with respect to the left

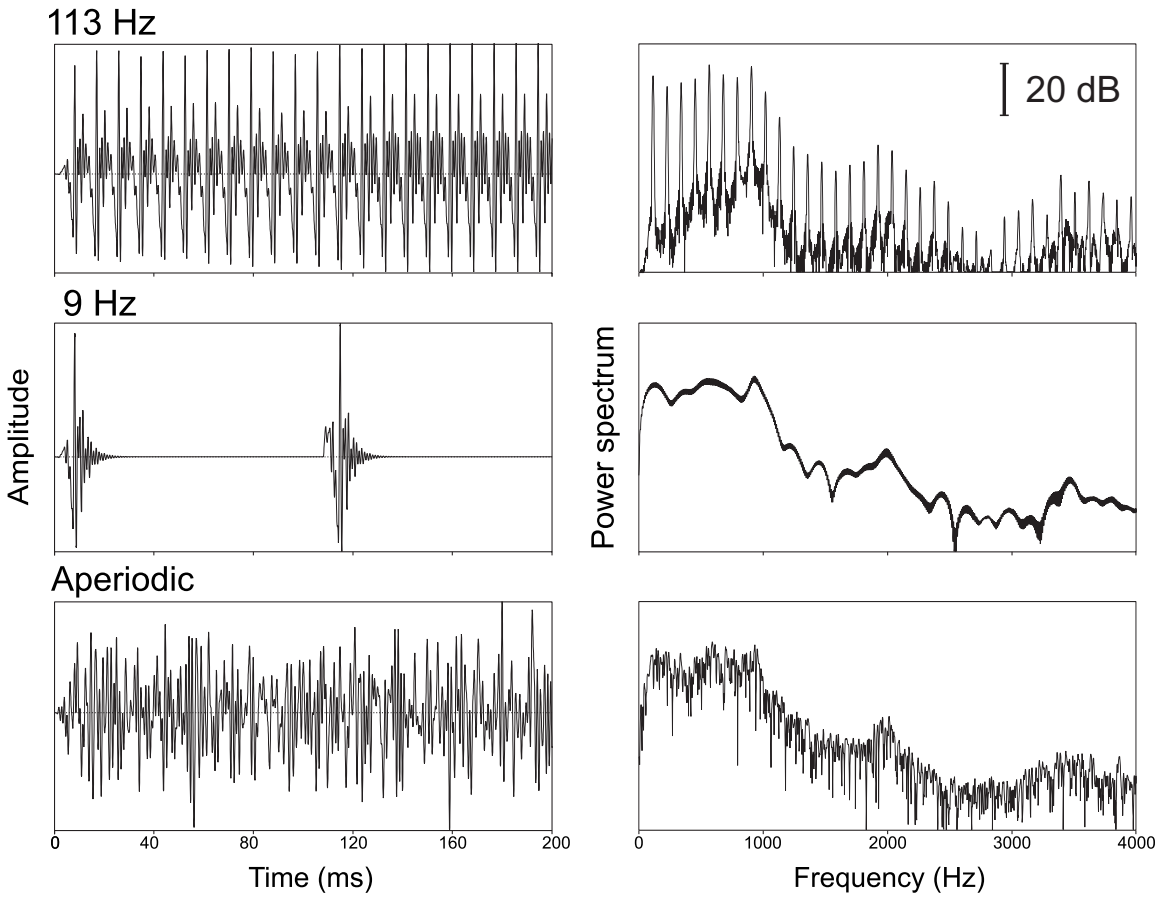

FIG. 1. Examples of the time-domain waveforms and the spectra of the vowel /a/ used in the study. The vowel in the case of periodic glottal excitation with the highest (113 Hz) and lowest (9 Hz) F0 and in the case of aperiodic glottal excitation is shown. A comb structure, characteristic of periodic sounds, is observed in the spectrum of the 113 Hz vowel but becomes very dense for the spectra of the 9 Hz vowel and is lacking in the spectra of the aperiodic vowel. Vowels with F0 between the extreme 113 Hz and 9 Hz values have intermediate period lengths and comb structure densities. The spectral envelope and vowel formant structure are unchanged by the manipulations of vowel periodicity. The first 200 ms of the stimuli are shown in the waveforms; the spectra were calculated from the entire duration of the stimuli.

and right preauricular points and the nasion having been determined prior to the measurement. The data were acquired with a recording bandwidth of 0.1–200 Hz and sampled at 600 Hz. In order to attenuate the cortical activity not time locked to stimulus presentation (e.g., activity related to muscle artifacts, eye movements caused by watching the video) 150 artifact-free evoked responses per stimulus were averaged over a period of 600 ms including a 100 ms prestimulus baseline. Epochs containing artifacts, defined as MEG sensor values exceeding $|3000|$ fT/cm or eye movement potentials exceeding $|150|$ μV, were excluded online.

D. ECD modeling

The amplitudes and generator locations of the N1m and SF responses were investigated with the ECD modeling technique in each hemisphere separately, with the assumption of a single dipole in a spherical volume conductor. Latency analysis was restricted to the transient N1m responses because these (unlike SF responses) have well defined peaks. The MEG waveforms were baseline corrected with respect to the 100 ms prestimulus interval and band-pass filtered at 1–20 Hz prior to ECD analysis. The ECDs were fitted to the maximum amplitude points of the auditory N1m and SF, at 90–150 ms and >340 ms post-stimulus latencies, respectively. Conditions with poor ECD fits were defined as dipoles with goodness-of-fit values <60% or anomalous generator locations. Any poor ECD fits were considered missing values in the statistical analysis stage and led to subject rejection. The average goodness of fit of ECDs was over 85% for the nine subjects that were included in the statistical analyses.

E. Statistical analyses

The means of the ECD model dimensions (amplitude and source location coordinates) obtained from different stimulus conditions were compared with repeated measures analyses of variance (ANOVAs). Mauchley sphericity tests were run in order to test the assumption of sphericity of data, and Huynh-Feldt corrections on the degrees of freedom were made when the assumption of sphericity was violated. The data were analyzed with response×hemisphere×vowel×F0 ANOVAs where "response" comprised response types N1m and SF, "hemisphere" comprised the left and the right hemisphere, "vowel" comprised vowels /a/ and /e/, and the levels of factor "F0" consisted of the six fundamental frequencies and the aperiodic condition. The N1m latencies were analyzed with a hemisphere×vowel×F0 ANOVA. Both the

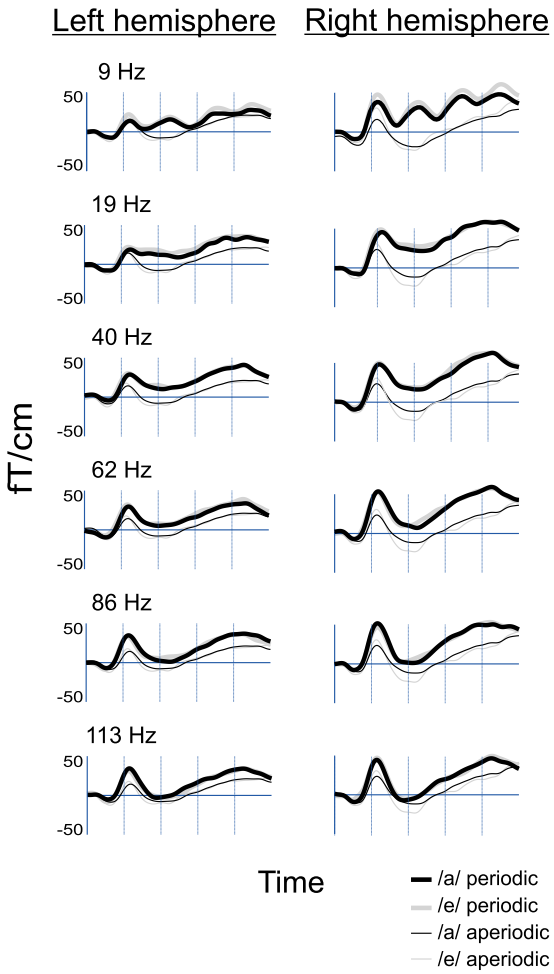

FIG. 2. (Color online) Grand-average response waveforms from the left- and right-hemispheric sensors yielding maximum responses and located directly above the auditory cortices. When the vowel F0 was at and above 19 Hz, a single N1m response was followed by a SF response. When F0 was dropped to 9 Hz, a cascade of transient N1m-like responses became evident. Both the N1m and SF amplitudes are larger for the periodic than for the aperiodic conditions. The time scale, partitioned with vertical lines at 100 ms intervals, ranges from 0 ms to 500 ms relative to the stimulus presentation.

main and the interaction effects of ANOVAs were investigated and all statistically significant effects are reported. Newman-Keuls tests were used as a means of post-hoc analysis for pairwise differences in the data.

RESULTS

Prominent N1m and SF responses were recorded in both hemispheres for both the aperiodic and periodic instances of the vowels /a/ and /e/ and for all F0 values of the periodic vowels. Multiple transient responses were observed in the 9 Hz condition, but not in the other conditions. Figure 2 illustrates grand-average waveforms from MEG sensors with maximum response amplitudes obtained above the left and right auditory cortices. Examples of ECD modeling results from the sensor array of each hemisphere are shown in Fig. 3.

The N1m and SF amplitudes and the N1m latencies are shown in Fig. 4. Both the N1m and SF responses elicited by the periodic vowels were larger in amplitude than those elicited by the aperiodic vowels ($F_{6,48}=6.92$, $p<0.001$). Post-hoc analysis indicated that while the amplitudes in all periodic conditions were larger (23.3–27.3 nAm) than in the aperiodic condition (19.2 nAm), there were no differences in amplitude among the periodic conditions. The effect of F0 differed somewhat between N1m and SF, as indicated by an interaction effect between response type and F0 ($F_{6,48}=3.49$, $p<0.01$). The N1m and SF amplitudes also varied according to vowel ($F_{1,8}=5.51$, $p<0.05$), being larger for /e/ (25.7 nAm) than for /a/ (23.50 nAm). No significant F0 ×vowel interaction was observed.

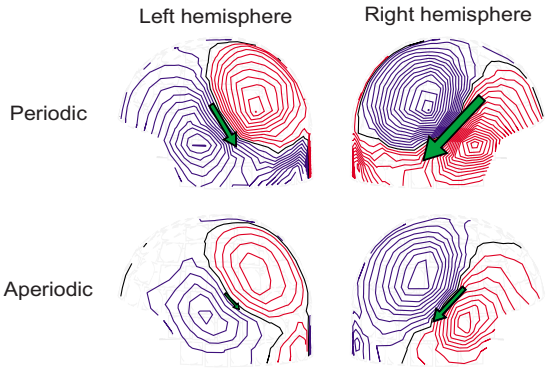

FIG. 3. (Color online) ECDs fitted to the responses elicited by the periodic vowel /a/ (F0=113 Hz) and its aperiodic counterpart. In both hemispheres, the ECD in the case of the periodic vowel is anterior to that fitted in the case of the aperiodic vowel. The magnetic fields are also stronger for the periodic as opposed to the aperiodic condition. The isocontour lines represent the magnetic field distribution measured at the peak latency of the N1m response and indicate the magnetic field entering and exiting the scalp. The isocontour step is 10 fT.

While variations in the F0 of the periodic vowels were not reflected in the amplitude of the cortical responses, they did have an effect on N1m latency ($F_{4.5,36.3}=5.56$, $p<0.001$). A clear monotonically decreasing trend of N1m latency as a function of the F0 was observed in the F0 range of 19–113 Hz, with latency varying from 125 ms (F0 =19 Hz) to 115 ms (F0=113 Hz). The F0 explained on the average 90% of the N1m latency variability. The slopes of linear regression lines, fitted to the data at and above 19 Hz, i.e., excluding the aperiodic and 9 Hz conditions, are −0.08 (/a/) and −0.18 (/e/) in the left hemisphere and −0.08 (/a/) and −0.04 (/e/) in the right hemisphere. The F0×hemisphere interaction was, however, not statistically significant. The N1m latency in the 9 Hz condition (114 ms) was clearly shorter than that predicted by the trend fitted to the other periodic conditions and resembled the latency of the aperiodic condition (112 ms).

The AEF source locations are shown in Fig. 5. Both the N1m and SF responses elicited by the periodic vowels were anterior to those elicited by the aperiodic vowels ($F_{3.4,27.0}=3.35$, $p<0.05$). The responses to periodic and aperiodic vowels were located, on average, 5 and 2 mm, respectively, anterior to the center of the head. No significant differences in ECD location were found among the periodic conditions. The right-hemispheric AEF sources were generated anterior to their left-hemispheric counterparts, being around 9 and 1 mm, respectively, from the center of the head ($F_{1,8}=15.13$, $p<0.01$) in both hemispheres and for both the N1m

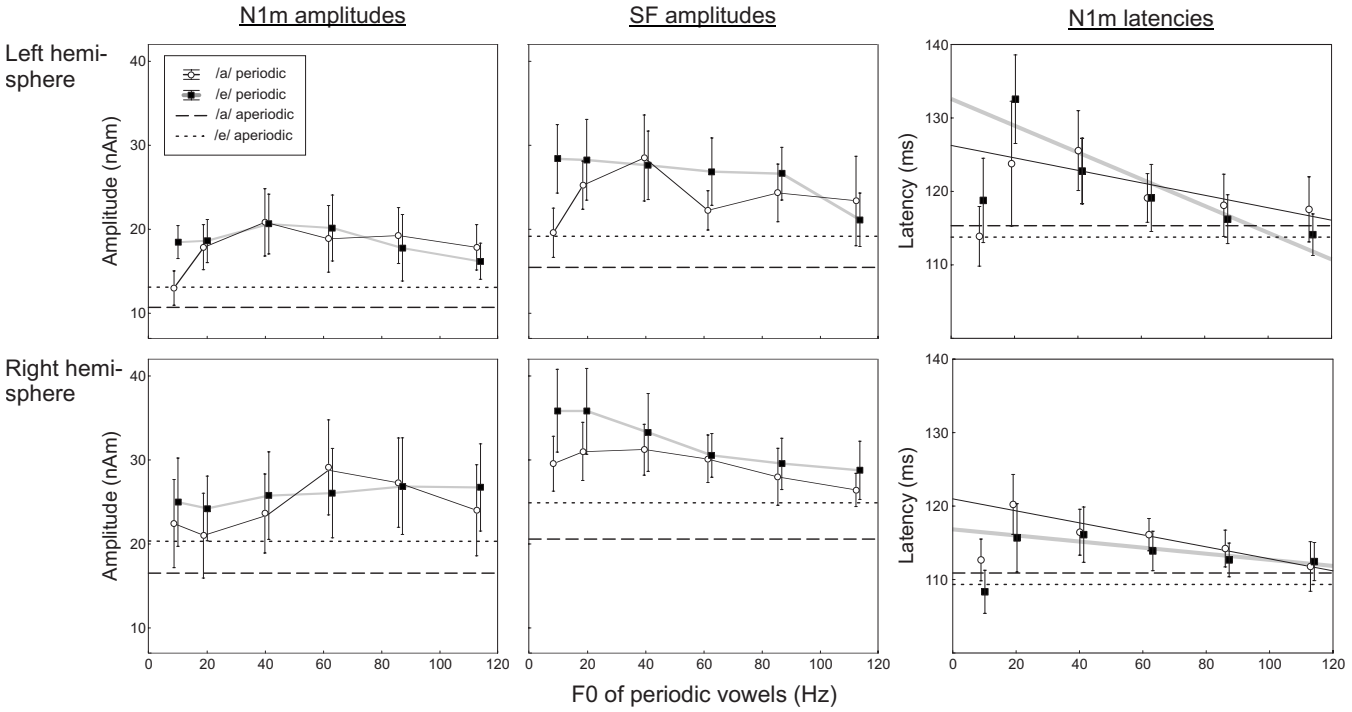

FIG. 4. The mean N1m and SF amplitudes and N1m latencies in both hemispheres. The AEF amplitudes were constantly larger for all periodic conditions relative to the aperiodic condition. The amplitude of both the N1m and SF responses were also larger for the vowel /e/ than for the vowel /a/. The N1m latency decreased as a monotonic function of F0 in the 19–113 Hz range. This monotonic trend, however, broke down for the 9 Hz condition where the latency resembled that obtained from the aperiodic condition. The measurement values for the aperiodic conditions are represented by dashed and dotted lines for the vowels /a/ and /e/, respectively, and those from the periodic conditions are represented by interconnected points. Error bars represent standard error of the mean.

and the SF responses. The N1m responses were located around 54 mm lateral from the head midline and were thus about 2 mm lateral to the SF responses located around 52 mm from the head midline ($F_{1,8}=6.39$, $p<0.05$).

III. DISCUSSION

It has previously been established that auditory cortex is sensitive to the periodicity of speech sounds (Alku *et al.*, 2001; Tiitinen *et al.*, 2005). Here, the importance of the spectral comb structure, inherent in periodic speech sounds, to the elicitation of periodicity-specific responses was examined. Specifically, the aim was to determine whether there exists a limit for vowel comb structure density, manipulated through F0 decrement, beyond which the cortical sensitivity to periodicity disappears. The vowel F0 was decreased between stimulus conditions in equal steps on the ERB scale to very small values that were located below the range of normal speech. An extended stimulus duration of 400 ms was used, enabling the emergence of SF responses which are elicited only by prolonged stimulation. Interestingly, all the periodic vowels, despite the F0 decrements, elicited larger AEF amplitudes than the aperiodic vowels. This enhancement of amplitude was observed for both the N1m and the SF responses. Furthermore, both the N1m and the SF responses elicited by periodic vowels were located anterior to the responses elicited by aperiodic vowels, but no topographic differences according to F0 were found between responses elicited by periodic vowels. These findings extend those of the earlier studies indicating cortical sensitivity to periodicity, each utilizing only a single F0 value for the periodic stimuli (Hertrich *et al.*, 2000; Alku *et al.*, 2001; Tiitinen *et al.*, 2005, Lütkenhöner *et al.*, 2006). Thus, cortical sensitivity to periodicity, as indexed by AEF amplitude and generator source location, is unaffected by the reduction of the spectral distance between sound partials in the vowel comb structure. Instead, the sensitivity to vowel periodicity is maintained down to the lowest F0 values (9 Hz) used in the study.

According to Gutschalk *et al.* (2002 and 2004) the N1m and SF responses each consist of two separate components: an anterior component sensitive to periodicity and a posterior component sensitive to sound energy. These components can be separated with a continuous stimulation paradigm or with a subtraction technique. In the current study, the AEFs were elicited with transient stimulation where the onset of periodicity co-occurs with the sound onset after a silent interval. Therefore, in the AEFs measured here, the activity of the periodicity-sensitive source was likely to be mixed with that from the energy-sensitive source. However, as the stimulus sound pressure level was held constant across all conditions, the differences between the periodic and aperiodic conditions probably indicated differential activation of the periodicity-sensitive components of the AEFs. Thus, the amplitude enhancement and the anterior shift in source location indicate that the periodicity-sensitive component, suggested by Gutschalk *et al.* (2002 and 2004), was activated by all periodic vowels used in the current study.

Among the periodic vowel conditions, the F0 was reflected only in the latency of the N1m. The N1m latency first

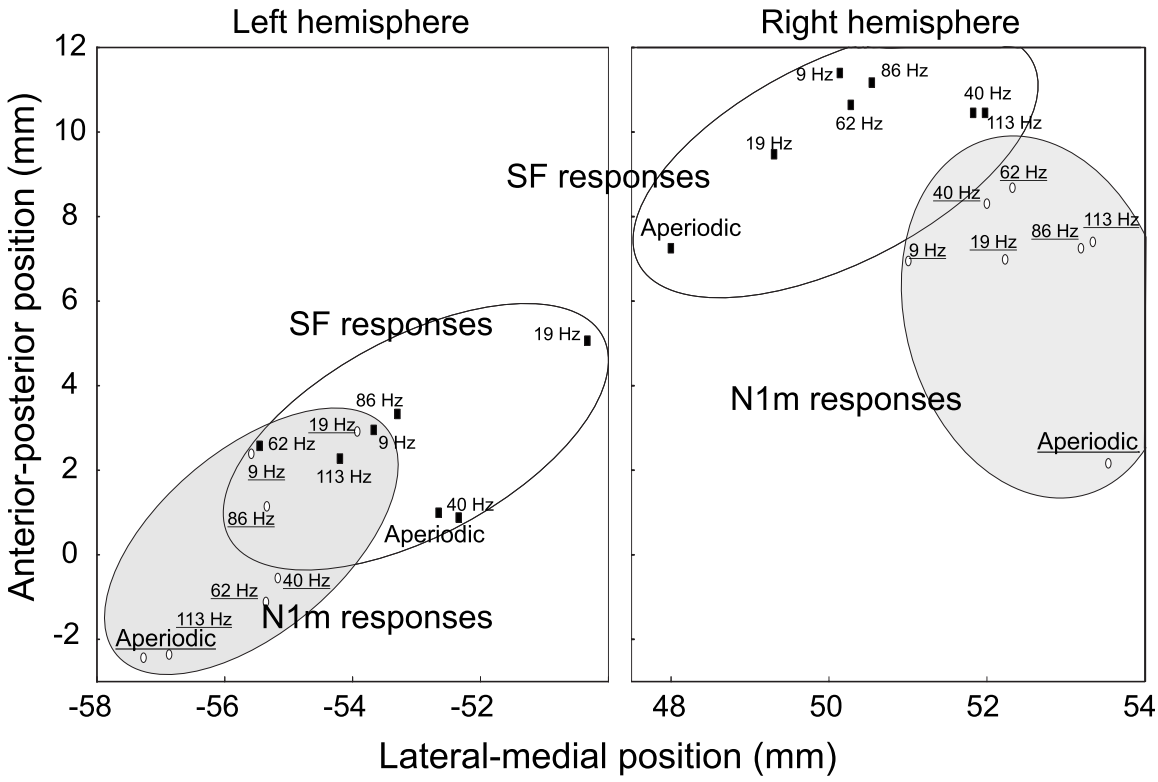

FIG. 5. AEF source locations on the lateral-medial and anterior-posterior axes. The source locations for both the N1m and SF responses were more anterior in the periodic than in the aperiodic conditions. The right-hemispheric responses were generated anterior to the left-hemispheric ones, and the N1m responses originated from locations lateral relative to the SF responses. The periodicity condition is indicated next to the data points. N1m and SF sources are depicted on gray and white backgrounds, respectively.

decreased monotonically as a function of vowel F0 in the range of 19–113 Hz. The increase of N1m latency with decreasing F0 was more moderate than reported by Forss *et al.* (1993) who used click train stimuli with F0 values in the range of 40–320 Hz. They found the N1m latency to be inversely related to the F0. According to Seither-Preisler *et al.* (2006), the decrease of N1m latency as a function of F0 continues from 100 Hz to at least 800 Hz. The F0 range of the vowel stimuli in the current study extended considerably below the F0 range used in the previous studies. Consequently, it turned out that the monotonic trend of N1m latency versus F0 broke down when the F0 was decreased below a limit which is located at or below 19 Hz. This breakdown might be explained in terms of an integration time in the elicitation of N1m responses. As the increasing trend of N1m latency with decreasing vowel F0 continued down to 19 Hz, an integration time explaining the current results would be longer than the 53 ms cycle length of the 19 Hz vowel. This integration window is longer than the one that may be estimated from the results of Onishi and Davis (1968), who found the N1 response to depend on pure tone durations up to 30 ms. This discrepancy might suggest differences in cortical integration of natural speech sounds and simple sinusoids.

Previous MEG studies have shown that the amplitudes of the AEFs elicited by periodic complex sounds decrease as F0 is decreased (Forss *et al.*, 1993; Gutschalk *et al.*, 2002; Krumbholz *et al.*, 2003). In addition, psychophysical results indicate that the pitch perception associated with periodic sounds disappears when the F0 is lowered to around 19 Hz (Guttman and Julesz, 1963), 30 Hz (Krumbholz *et al.*, 2000; Pressnitzer *et al.*, 2001), or 40 Hz (Ritsma, 1962). Thus, the current results, showing persistent cortical sensitivity to periodicity even at very low F0 values, seem to contradict these earlier findings. The discrepancy between the previous and the current MEG results may, however, be explained by the differences in the stimuli (click train vs. vowel) and the range of F0 used (40–320 Hz vs. 9–113 Hz). Nevertheless, the qualitative change in AEFs from one to multiple transient peaks observed in the lowest F0 condition, along with the breakdown in the monotonic trend between F0 and N1m latency, could still be related to traversing the lower limit of pitch perception. Although the origin and the function of the cascade of transient responses to low-frequency vowels are unclear, this cascade may reflect the perception of the low-frequency sound as a series of individual segments corresponding to the repetition cycle rather than as one continuous sound. This interpretation is supported by the reported change in perceived sound quality from pitch to "motorboating" by Guttman and Julesz (1963) or to infrapitch by Warren and Bashford (1981). Their estimates of the lower limit of pitch perception were located at the corresponding F0 range of 19–20 Hz below which multiple transient responses emerged in the current MEG recordings.

The cortical sensitivity to periodic vowels could be linked to a possible reduction of vowel intelligibility of aperiodic vowels relative to periodic ones. However, all the vowels used in the current study could easily be identified in

spite of the manipulations in their periodicity. As two different vowel stimuli were used, it was possible to determine whether there was any interaction of periodicity and vowel identity in the elicitation of the N1m and SF responses. In previous studies of cortical speech processing, different vowel formant settings were reflected in the N1m amplitude (Obleser *et al.*, 2003; Tiitinen *et al.*, 2005) and latency (Tiitinen *et al.*, 2005). A direct comparison between the current and previous studies is, however, difficult because different vowels, or at least different formant values, were used in these previous studies. Nevertheless, the current results demonstrate that in addition to the N1m amplitude, also the SF amplitude was elevated for /e/ in contrast to /a/. As the first two vowel formants are more closely spaced in /a/ than in /e/, the difference of amplitudes in the AEFs elicited by these vowels might be explained by a non-linear response attenuation mechanism, such as lateral inhibition, whose effect depends on the distance between the major spectral peaks of the stimuli. However, further experiments with more vowels of different formant patterns are definitely needed in order to test this explanation. Importantly, no interaction between vowel identity and periodicity was found, suggesting that vowel periodicity is processed independently of vowel identity. Thus, it is unlikely that periodicity-specific cortical responses can be accounted for by differences in vowel intelligibility between periodic and aperiodic conditions.

The current study expanded the design of earlier studies of cortical sensitivity to periodicity by taking a further step to revealing the mechanisms creating this sensitivity. If the mechanism behind the cortical sensitivity to periodicity depends on the sound partials being well separated, the cortical sensitivity to periodicity might be expected to disappear when the distance of the partials is decreased below some critical limit. According to the current results, reducing the spectral distance between sound comb structure partials to very small values does not affect the cortical sensitivity to periodicity as indexed by AEF amplitudes and source locations. The latencies of the N1m, then again, gradually increased as the vowel F0 was decreased until a limit occurring at or below 19 Hz was crossed. This systematic variation of response latency as a function of stimulus F0 may be viewed as reflecting a periodicity extraction process rather than an attenuation in the sensitivity to periodicity. The significance of the emergence of multiple transient responses and the breakdown in the monotonic trend between F0 and N1m latency below 19 Hz is unclear, but may reflect the lower limit of pitch perception. Importantly, no lower limit for cortical sensitivity to periodicity, as indexed by N1m and SF amplitudes and generator source locations, was found. Thus the auditory periodicity detection mechanism seems remarkably efficient in extracting the vowel periodicity even when the F0 is reduced to values far below the range used in normal speech.

ACKNOWLEDGMENT

This study was supported by the Academy of Finland (Project Nos. 111848, -039, -742).

Alku, P., Tiitinen, H., and Näätänen, R. (**1999**). "A method for generating natural-sounding speech stimuli for cognitive brain research," Clin. Neurophysiol. **110**, 1329–1333.

Alku, P., Sivonen, P., Palomäki, K., and Tiitinen, H. (**2001**). "The periodic structure of vowel sounds is reflected in human electromagnetic brain responses," Neurosci. Lett. **298**, 25–28.

Alku, P., Airas, M., Björkner, E., and Sundberg, J. (**2006**). "An amplitude quotient based method to analyze changes in the shape of the glottal pulse in the regulation of vocal intensity," J. Acoust. Soc. Am. **120**, 1052–1062.

Belin, P., Zatorre, R. J., Lafaille, P., Ahad, P., and Pike, B. (**2000**). "Voice-selective areas in human auditory cortex," Nature (London) **403**, 309–312.

Cariani, P. A., and Delgutte, B. (**1996**). "Neural correlates of the pitch of complex tones. I. Pitch and pitch salience," J. Neurophysiol. **76**, 1698–1716.

Chait, M., Poeppel, D., and Simon, J. Z. (**2006**). "Neural response correlates of detection of monaurally and binaurally created pitches in humans," Cereb. Cortex **16**, 835–848.

Eulitz, C., Diesch, E., Pantev, C., Hampson, S., and Elbert, T. (**1995**). "Magnetic and electric brain activity evoked by the processing of tone and vowel stimuli," J. Neurosci. **15**, 2748–2755.

Fant, G. (**1993**). "Some problems in voice source analysis," Speech Commun. **13**, 7–22.

Forss, N., Mäkelä, J. P., McEvoy, L., and Hari, R. (**1993**). "Temporal integration and oscillatory responses of the human auditory cortex revealed by evoked magnetic fields to click trains," Hear. Res. **68**, 89–96.

Gauffin, J., and Sundberg, J. (**1989**). "Spectral correlates of glottal voice source waveform characteristics," J. Speech Hear. Res. **32**, 556–565.

Glasberg, B. R., and Moore, B. C. J. (**1990**). "Derivation of auditory filter shapes from notched-noise data," Hear. Res. **47**, 103–138.

Gunji, A., Koyama, S., Ishii, R., Levy, D., Okamoto, H., Kakigi, R., and Pantev, C. (**2003**). "Magnetoencephalographic study of the cortical activity elicited by human voice," Neurosci. Lett. **348**, 13–16.

Gutschalk, A., Patterson, R. D., Rupp, A., Uppenkamp, S., and Scherg, M. (**2002**). "Sustained magnetic fields reveal separate sites for sound level and temporal regularity in human auditory cortex," Neuroimage **15**, 207–216.

Gutschalk, A., Patterson, R. D., Scherg, M., Uppenkamp, S., and Rupp, A. (**2004**). "Temporal dynamics of pitch in human auditory cortex," Neuroimage **22**, 755–766.

Guttman, N., and Julesz, B. (**1963**). "Lower limits of auditory periodicity analysis," J. Acoust. Soc. Am. **35**, 610.

Hari, R., Aittoniemi, K., Järvinen, M. L., Katila, T., and Varpula, T. (**1980**). "Auditory evoked transient and sustained magnetic fields of the human brain – localization of neural generators," Exp. Brain Res. **40**, 237–240.

Hertrich, I., Mathiak, K., Lutzenberger, W., and Ackermann, H. (**2000**). "Differential impact of periodic and aperiodic speech-like acoustic signals on magnetic M50/M100 fields," NeuroReport **11**, 4017–4020.

Hertrich, I., Mathiak, K., Menning, H., Lutzenberger, W., and Ackermann, H. (**2005**). "MEG responses to rippled noise and Huggins pitch reveal similar cortical representations," NeuroReport **16**, 193–196.

Hewson-Stoate, N., Schönwiesner, M., and Krumbholz, K. (**2006**). "Vowel processing evokes a large sustained response anterior to primary auditory cortex," Eur. J. Neurosci. **24**, 2661–2671.

Kaukoranta, E., Hari, R., and Lounasmaa, O. V. (**1987**). "Responses of the human auditory cortex to vowel onset after fricative consonants," Exp. Brain Res. **69**, 19–23.

Krumbholz, K., Patterson, R. D., and Pressnitzer, D. (**2000**). "The lower limit of pitch as determined by rate discrimination," J. Acoust. Soc. Am. **108**, 1170–1180.

Krumbholz, K., Patterson, R. D., Seither-Preisler, A., Lammertmann, C., and Lütkenhöner, B. (**2003**). "Neuromagnetic evidence for a pitch processing center in Heschl's gyrus," Cereb. Cortex **13**, 765–772.

Lütkenhöner, B., Seither-Preisler, A., and Seither, S. (**2006**). "Piano tones evoke stronger magnetic fields than pure tones or noise, both in musicians and non-musicians," Neuroimage **30**, 927–937.

Mäkelä, J. P., Hari, R., and Leinonen, L. (**1988**). "Magnetic responses of the human auditory-cortex to noise square-wave transitions," Electroencephalogr. Clin. Neurophysiol. **69**, 423–430.

Näätänen, R., and Picton, T. (**1987**). "The N1 wave of the human electric and magnetic response to sound: A review and an analysis of the component structure," Psychophysiology **24**, 375–425.

Obleser, J., Elbert, T., Lahiri, A., and Eulitz, C. (**2003**). "Cortical representation of vowels reflects acoustic dissimilarity determined by formant frequencies," Brain Res. Cognit. Brain Res. **15**, 207–213.

Onishi, S., and Davis, H. (**1968**). "Effects of duration and rise time of tone

bursts on evoked potentials," J. Acoust. Soc. Am. **44**, 582–591.
Pantev, C., Eulitz, C., Elbert, T., and Hoke, M. (**1994**). "The auditory evoked sustained field: Origin and frequency dependence," Electroencephalogr. Clin. Neurophysiol. **90**, 82–90.
Picton, T. W., Woods, D. L., and Proulx, G. B. (**1978a**). "Human auditory sustained potentials: I. The nature of the response," Electroencephalogr. Clin. Neurophysiol. **45**, 186–197.
Picton, T. W., Woods, D. L., and Proulx, G. B. (**1978b**). "Human auditory sustained potentials: II. Stimulus relationships," Electroencephalogr. Clin. Neurophysiol. **45**, 198–210.
Pressnitzer, D., Patterson, R. D., and Krumbholz, K. (**2001**). "The lower limit of melodic pitch," J. Acoust. Soc. Am. **109**, 2074–2084.
Rabiner, L. R., and Schafer, R. W. (**1978**). *Digital Processing of Speech Signals* (Prentice–Hall, Englewood Cliffs, NJ), pp. 396–404.
Ritsma, R. J. (**1962**). "Existence region of the tonal residue. I," J. Acoust. Soc. Am. **34**, 1224–1229.
Seither-Preisler, A., Patterson, R., Krumbholz, K., Seither, S., and Lütkenhöner, B. (**2006**). "Evidence of pitch processing in the N100m component of the auditory evoked field," Hear. Res. **213**, 88–98.
Soeta, Y., Nakagawa, S., and Tonoike, M. (**2005**). "Auditory evoked magnetic fields in relation to iterated rippled noise," Hear. Res. **205**, 256–261.
Tiitinen, H., Mäkelä, A. M., Mäkinen, V., May, P. J. C., and Alku, P. (**2005**). "Disentangling the effects of phonation and articulation: Hemispheric asymmetries in the auditory N1m response of the human brain," BMC Neurosci. **6**, 62–70.
Warren, R. M., and Bashford, Jr., J. A. (**1981**). "Perception of acoustic iterance: Pitch and infrapitch," Percept. Psychophys. **29**, 395–402.
Whalen, D. H., Benson, R. R., Richardson, M., Swainson, B., Clark, V. P., Lai, S., Mencl, W. E., Fulbright, R. K., Constable, R. T., and Liberman, A. M. (**2006**). "Differentiation of speech and nonspeech processing within primary auditory cortex," J. Acoust. Soc. Am. **119**, 575–581.

Temporary hearing loss influences post-stimulus time histogram and single neuron action potential estimates from human compound action potentials

Jeffery T. Lichtenhan[a] and Mark E. Chertoff
Department of Hearing and Speech, University of Kansas Medical Center, Kansas City, Kansas 66103-0001, USA

(Received 23 October 2007; revised 31 January 2008; accepted 1 February 2008)

An analytic compound action potential (CAP) obtained by convolving functional representations of the post-stimulus time histogram summed across auditory nerve neurons $[P(t)]$ and a single neuron action potential $[U(t)]$ was fit to human CAPs. The analytic CAP fit to pre- and postnoise-induced temporary hearing threshold shift (TTS) estimated *in vivo* $P(t)$ and $U(t)$ and the number of neurons contributing to the CAPs (N). The width of $P(t)$ decreased with increasing signal level and was wider at the lowest signal level following noise exposure. $P(t)$ latency decreased with increasing signal level and was shorter at all signal levels following noise exposure. The damping and oscillatory frequency of $U(t)$ increased with signal level. For subjects with large amounts of TTS, $U(t)$ had greater damping than before noise exposure particularly at low signal levels. Additionally, $U(t)$ oscillation was lower in frequency at all click intensities following noise exposure. N increased with signal level and was smaller after noise exposure at the lowest signal level. Collectively these findings indicate that neurons contributing to the CAP during TTS are fewer in number, shorter in latency, and poorer in synchrony than before noise exposure. Moreover, estimates of single neuron action potentials may decay more rapidly and have a lower oscillatory frequency during TTS. © *2008 Acoustical Society of America.* [DOI: 10.1121/1.2885748]

PACS number(s): 43.64.Wn, 43.64.Nf, 43.64.Pg [BLM] Pages: 2200–2212

I. INTRODUCTION

Goldstein and Kiang (1958) proposed a theory that the compound action potential (CAP) is a summation of multiple single neuron action potentials. The summation is described mathematically by the convolution of an action potential from a single auditory nerve neuron with a probability density function representing a neuron's discharge timing and then scaling the convolution by the number of neurons contributing to the CAP. Various investigations of the CAP convolution model since 1958 up to present times have been reviewed elsewhere (Chertoff, 2004) and are not repeated here.

Chertoff (2004) revisited the CAP model by convolving a gamma distribution function representing a summed post-stimulus time histogram $[P(t)]$ from an auditory nerve neuron with a decaying sine wave representing a single-neuron action potential $[U(t)]$ to obtain an analytic CAP. That is,

$$CAP(t) = N\int_{-\infty}^{t} P(\tau)U(t-\tau)d\tau, \tag{1}$$

where

$$P(t) = \left(\frac{t-\alpha}{\beta}\right)^{\gamma-1} e^{-((t+\alpha)/\beta)} \tag{2}$$

and

$$U(t) = e^{-Kt}\sin(\omega t). \tag{3}$$

According to this model t represents time in milliseconds, N is the number of neuronal units contributing to the CAP, and τ is a dummy variable. The width and location of the maximum of $P(t)$ is governed by the value of β, and γ is held constant at a value of 2. $U(t)$ decays by the power of K and $\omega=2\pi F$, where F is frequency in hertz. The solution to Eq. (1) is provided in the Appendix and will be referred to as the "analytic CAP" throughout this manuscript. By fitting this analytic CAP to tone-burst evoked CAPs recorded from the round window of normal hearing gerbils, Chertoff (2004) provided estimates of the *in vivo* $P(t)$ and $U(t)$ and found that the number of neurons contributing to the CAP (N) and the $P(t)$ width (β) increased with signal level while the latency (α) decreased. These findings not surprisingly suggested that with high signal levels, neurons in the basal cochlear region contributed to the CAP for all tone-burst frequencies and at low signal levels CAP neural generators were located at their corresponding characteristic cochlear frequency place. Chertoff (2004) also found that the frequency of $U(t)$ oscillation (F) essentially increased with stimulus frequency and that $U(t)$ damping (K) was greater for 8 kHz tone bursts compared to the other tone-burst stimulus frequencies. This implied that hair cell and/or neu-

[a]Author to whom correspondence may be addressed. Current affiliations: Eaton-Peabody Laboratory of Auditory Physiology, Massachusetts Eye and Ear Infirmary, 243 Charles Street, Boston, Massachusetts 02114 and Department of Otology & Laryngology, Harvard Medical School, Boston, Massachusetts 02115. Electronic mail: jlichtenhan@gmail.com.

ral generators may not everywhere be homogeneous in physiology throughout the cochlear partition.

With the aim of translating the analytic CAP into a clinically useful tool for describing the physiology of the auditory nerve in the presence of hearing loss, we demonstrated that the analytic CAP could be fit to CAPs from gerbils with permanent hearing loss and that noise-induced cochlear pathology could be characterized with the parameters of Eqs. (2) and (3) that describe $P(t)$ and $U(t)$ (Lichtenhan *et al.*, 2005). To continue the development of a clinically useful technique that estimates surviving auditory nerve neurons in hearing impaired ears, in this study we apply the analytic CAP to click-evoked CAPs and examine the influence of temporary noise-induced hearing threshold shift (TTS) on human $P(t)$ and $U(t)$.

II. METHODS

A. Experimental subjects

Thirty-nine normal hearing human subjects were recruited from the greater Kansas City metropolitan area. CAPs could not be recorded on three subjects for some unknown reason and three additional subjects were used to acquire additional pilot data for click-evoked CAPs. The experiment reported here thus includes data from the right ear of 33 subjects: 27 subjects received noise exposure and 6 control subjects received a silent period in place of noise exposure. The median age of our subjects was 26 years, with a semi-interquartile range of three years. The minimum and maximum age of our subjects was 20 and 38 years, respectively. Twenty-nine females and seven males participated in the experiment. The normalcy of subjects' hearing status was evaluated by case history, otoscopy and pure tone audiometry (Grason Stadler GSI 61, Madison, WI), and tympanometry (GSI 33). All subjects had hearing thresholds at 0.25–8 kHz less than 25 dB HL, ear canal volume between 0.9 cm^3–2.0 cm^3, ear drum compliance between 0.30 mmhos and −1.70 mmhos, and middle ear pressure between 50 daPa and −100 daPa (Margolis and Hunter, 1999). Subjects were paid $20.00 for their participation. All experimental procedures were approved by the Human Subjects Committee at KUMC (HSC No. 7881).

B. CAP evoking signal: Generation and delivery

Click-evoked CAPs were produced using a commercially available Bio-logic Traveler Express evoked potentials unit by delivering 100 μs rectangular pulses to a Bio-logic insert earphone. The phase of every other click signal was alternated so that the cochlear microphonic was not recorded. Click signal levels ranged from 125 to 75 dB peak SPL (dB pSPL) decreasing in 10 dB steps and were presented at a rate of 11.1/s.

All stimuli were monitored with an Etymotic Research microphone system (ER-7C). The microphone probe tube was glued (Duro, Super Glue) to the silicone tubing of the tympanic membrane (TM) electrode. The microphone probe tube was attached in a manner so that the front end of the probe tube rested less than 8 mm from the TM to ensure that pressure nulls resulting from interaction between incident and reflected acoustic waves of high frequency portions of our stimulus (i.e., 8–10 kHz) were negligible in the signal monitoring. The microphone signal was routed to a Tektronix oscilloscope (TDS 2014), Richardson, TX, where the level, time wave form, and spectral content were monitored.

C. CAP recording

CAPs were recorded with custom electrodes built according to Ferraro and Durant (2002) that were placed on the TM (noninverting). Teflon™-insulated silver wire was cut to a length of about 2 in. and the ends of the wire were bared. Medical grade silicon tubing was cut to about $1\frac{1}{2}$ in. and placed around the silver wire. The front end of the silver wire was hooked around a small wad of cotton that was soaked in Electrolyte Gel (Nicolet Biomedical) using a 1 cc syringe. The back end (i.e., the nontympanic membrane end) of the wire was attached to a copper microalligator clip that was in turn soldered to the end of an electrode cable. Gold-disk surface electrodes were attached to the low forehead (ground), and ipsilateral ear lobe (inverting).

Electrical signals were bandpass filtered between 100 and 3000 Hz (~12 dB/octave), amplified 200 000 times and digitized at 50 kHz. The artifact rejection was disabled for all recordings. Wave forms were displayed on a 10.24 ms time window yielding a wave form 512 points in length. Electroencephalic activity was monitored online to determine if subjects were physically calm and not producing excessive myogenic electrical artifact. Responses evoked from 125 and 115 dB pSPL were averaged from 1024 presentations; 2048 presentations were used for lower signal levels to improve the signal-to-noise ratio. Wave forms were saved to disk, converted to ASCII format using a Bio-logic program (ep2asci59), transferred to a personal computer suitable for data processing via 5.5 in. floppy disk, and then loaded into MATLAB (The Mathworks) for analysis.

D. Noise exposure

A 115 dB SPL narrow-band noise centered at 2 kHz was used for noise exposure intended to produce TTS. The noise was generated from a Madsen Electronics Clinical Audiometer (OB822), routed to an Optimus Stereo Amplifier (SA-155) and sent to the same Bio-logic headphone that delivered the click stimulus discussed earlier. The probe microphone tubing attached to the TM electrode was used to monitor the noise signal [Fluke Multimeter (8060A)].

The bandwidth of the noise was determined using an insert earphone positioned in a syringe with a 2 cc volume between the earphone and the syringe's rubber stopper. A probe tube from the ER-7C microphone system was placed at the rubber stopper. The microphone signal was sent to a Hewlett Packard Dynamic Signal Analyzer (3561A) and displayed in the frequency domain. The frequencies corresponding to the 3 dB "down points" of the narrow-band noise were 1630 and 2320 Hz.

The 2 kHz center frequency of the noise exposure stimulus was chosen because it is an octave below 4 kHz, which is the primary cochlear region that the click stimulates (Jerger and Mauldin, 1978; Bauch and Olsen, 1986, 1988;

Fowler and Mikami, 1992; Gorga *et al.*, 1985; Shepard *et al.*, 1992; Watson, 1996, 1999) and because Ward, Glorig and Sklar (1959) found a maximum temporary hearing loss occurs an octave above the characteristic spectral content of 100 dB SPL narrow-band noise stimuli. Moreover, it has been shown that narrow-band noise, as opposed to tonal, exposure did not produce as great a TTS, though it affected a wider range of hearing thresholds above the characteristic frequency (CF) of the noise exposure (Ward, 1962; Salvi *et al.*, 1983). In other words, narrow-band noise exposure produces a "flatter" or broader range hearing loss.

E. CAP analysis and curve fitting

CAP wave forms were digitally filtered in MATLAB using a high-pass cut off frequency of 150 Hz to decrease 60 Hz (and the 120 Hz harmonic) artifact. The high-pass filtering also reduced a low-frequency "voltage drift" appearing beyond the second peak of the CAP wave form, which most likely results from components of the auditory brain-stem response. After filtering, the CAP was fit with the analytic CAP using custom written software in TOMLAB (Tomlab Optimization), a constrained nonlinear least-squares fitting routine.

The TOMLAB fitting software allowed us to restrict the range over which analytic CAP parameters could vary, and improved the convergence of the fitting algorithm. The ranges were initially set according to realistic variations of normal, *in vivo* post-stimulus time histograms and single neuron action potentials (Kiang, 1965; Kiang *et al.*, 1976; Wang, 1979; Versnel *et al.*, 1990, 1992a, 1997). The lower boundary for β was set to 0.02 ms based on jitter measures from single neurons (Miller *et al.*, 1999). The upper boundary for parameter β was set to 8.5 ms based on the average maximum cochlear latency for humans of 7.5 ms (Eggermont, 1979) added to the maximum jitter for single neurons (Miller *et al.*, 1999). The lower and upper boundaries for α were defined as 0.6 and 7.5 ms, respectively, based on the minimum latency of high frequency derived band CAPs and maximum human cochlear latency (Eggermont, 1979; Schoonhoven *et al.*, 2001). Because our previous experience showed that N values below 0.01 were not statistically significant, our lower N boundary was defined as 0.01. Our upper N boundary was set to infinity.

The values of $U(t)$ parameters also remained adjustable in the curve fitting process because differences have been found between normal and pathologic single neuron action potentials (Prijs, 1986; Versnel *et al.*, 1992b). The lower boundary of parameter K was defined as 0.5 ms because we found it to improve the fit of the analytic CAP to physiologic CAPs. The upper bound of K was set to 2.0 ms based on a similar $U(t)$ model developed by McMahon and Patuzzi (2002). The lower and upper boundaries of $U(t)$ F were 500 and 2000 Hz; these values were chosen from data obtained by Versnel *et al.* (1992b), who fit separate Gaussian functions to the initial (negative) and second (positive) peak of recorded single neuron action potentials evoked from neurons having varying degrees of thresholds and spontaneous rates.

Parameter starting values and boundaries were provided to the TOMLAB software and the CAP parameters were estimated. Ninety-five percent confidence intervals for each parameter were computed. If a confidence interval included zero, the parameter was deemed insignificant and thus the entire model unuseable. In this case, the boundaries were adjusted and the curve fitting procedure repeated until significance ($p \leqslant 0.05$) for all parameters were obtained. The boundaries rarely had to be adjusted to any marked distance in order to obtain a model entailing all significant CAP parameters.

F. Experimental design

Following an initial hearing screening, subjects reclined in a single walled sound isolated room. Surface electrodes, TM electrode, with associated probe microphone, and insert ear phone were positioned. Prenoise exposure, CAPs were recorded in response to 125 to 75 dB pSPL clicks descending in 10 dB steps. Hearing threshold was subsequently acquired at 4 kHz and the subject was then exposed for 15 min to the narrow-band noise. Following noise exposure, 4 kHz hearing threshold was reexamined and postnoise exposure CAPs were recorded. TTS typically was determined about 30–60 s after cessation of noise exposure. The postnoise CAP recordings commenced about 60 s after the noise exposure ended. The order of postnoise click levels (e.g., 75–125 dB pSPL in 10 dB steps) was alternated between ascending and descending during postexposure CAP recordings for every other subject. Because hearing thresholds were recovering during postnoise recordings, we wanted to ensure that half of our low signal level data was acquired during peak TTS, and that half of our high signal level CAPs were as well recorded during the height of TTS in case there was an unexpected affect of signal direction. Postexposure CAP recordings took less than 30 min. Hearing threshold at 4 kHz was again determined at the conclusion of the experiment. The entire procedure including hearing testing, subject preparation for electrophysiological recording, and experimentation typically required 1.5–2 h.

G. Statistics

1. CAP parameter reliability

The interclass correlation coefficient (ICC) was used to measure the reliability of the curve fitting routine as well as the reliability of the physiologic responses. The ICC statistic was chosen over the Pearson coefficient, another reliability statistic, because a high Pearson correlation can exist even though the means differ between groups/sessions. *t*-tests are commonly used with Pearson correlation measures to determine if the means of independent and dependent variables differ. In contrast, the ICC accounts for both correlation and parameter size with one statistic. For the six control subjects not receiving noise exposure, CAPs were recorded before and after a 15 min silent period instead of the noise exposure and fit with the analytic CAP. ICCs were calculated for all six CAP parameters (β, α, N, K, and F), at each signal level before and after silent the period.

The ICC was defined as

$$\mathrm{ICC} = \frac{MS_B - MS_W}{MS_B + MS_W}, \tag{4}$$

where MS_W is the average squared differences between each score within a session (e.g., average β for presilent period) and the group mean, and MS_B is the average squared differences between each recording condition (e.g., pre- and postsilent period β) mean and the grand mean.

2. CAP parameter growth function analysis

Hierarchical linear modeling [(HLM), Raudenbush and Bryk, 2002] was used to acquire the intercepts and slopes [i.e., π coefficients in Eq. (5)] of $P(t)$ and $U(t)$ parameter-signal-level functions for each subject and to also determine if hearing loss influenced these growth patterns. HLM describes each subject's growth trajectory and is more advantageous than other repeated measures statistics and ordinary least-squares regression because it does not require each subject to have data at each measurement interval, does not require fixed intervals between measures, and is more precise in coefficient estimation (Wu, 1996).

The level 1 HLM model

$$y = \pi_0 + \pi_1(\mathrm{SL}) + \pi_2(\mathrm{SL}^2) + e \tag{5}$$

was fit to each parameter-signal-level function for both pre- and postnoise data from all 33 subjects.[1] In Eq. (5) y is a given CAP parameter from Eq. (A1) (i.e., β, α, N, K, and F), SL is signal level, and e is a random error term. When a given term of Eq. (5) was insignificant, the model was reduced in a backward elimination approach (Mendenhall and Sincich, 2003). Equation (5) described the relationship between signal level and CAP parameters in a regression-like equation. A series of level 2 models,

$$\pi_0 = B_{00} + B_{01}(\mathrm{TTS}) + r_0,$$

$$\pi_1 = B_{10} + B_{11}(\mathrm{TTS}) + r_1,$$

$$\pi_2 = B_{20} + B_{21}(\mathrm{TTS}) + r_2, \tag{6}$$

was fit to each parameter-signal-level function for the 27 subjects receiving noise exposure. In Eq. (6), TTS is the degree of temporary hearing loss at 4 kHz and r_n ($n = 0, 1, 2$) is the random error. Insignificant coefficients of Eq. (6) were also reduced in a backward elimination approach until a model entailing all significant coefficients was found. When multiple significant models were found, chi-square tests were performed on deviance scores of the HLM models to determine the best model. Equation (6) described the influence of hearing loss on the level 1 coefficients. That is, Eq. (6) was used to characterize how the shape of the CAP parameter-signal level functions changed during TTS. A version of Eq. (6) not entailing B_{n1} ($n = 0, 1, 2$) was fit to CAP parameter-signal-level function for each of the 33 subjects before noise exposure. All HLM coefficients were acquired using statistical software HLM 6 by Raudenbush *et al.* (2000).

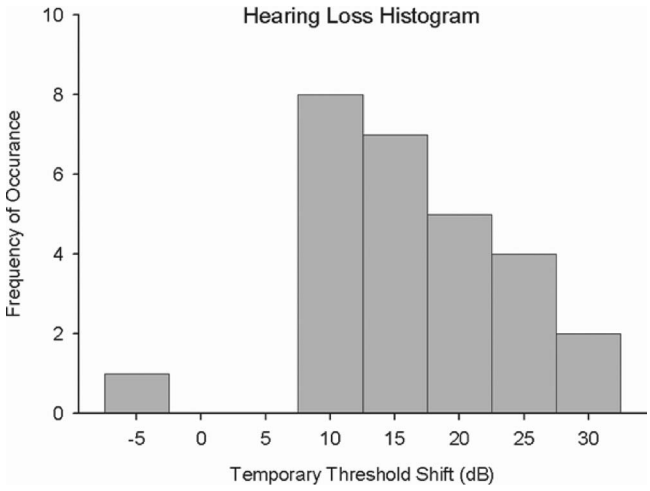

FIG. 1. A histogram indicating the number subjects having a given degree of temporary threshold shift (TTS) measured at the cessation of noise exposure.

When the HLM did not show that the level 1 coefficients for a given CAP parameter varied significantly with hearing loss, paired samples t-tests were used on the pre- and postnoise exposure 75 dB pSPL CAP data from the 27 subjects receiving noise exposure. With the exception of $U(t)$ parameters F, t-tests[2] were performed on 75 dB pSPL CAP parameters because TTS is assumed to alter OHC physiology and it is at low signal levels where OHC feedback to the basilar membrane is responsible for the exceptional sensitivity in normal ears (Ryan and Dallos, 1975).

III. RESULTS

A. Hearing loss

Figure 1 is a histogram illustrating the number of subjects that acquired the various amounts of TTS at 4 kHz. The control subjects who did not receive noise exposure are not included in Fig. 1. The TTS distribution is positively skewed with a median of 15 dB and a semi-interquartile range of 5 dB. Hearing thresholds following noise exposure ranged from a 5 dB improvement to a 30 dB temporary loss. Consistent with typical 5 dB intratest reliability, six control subjects had no TTS, two had a 5 dB improvement, and one had a 5 dB temporary loss of hearing threshold.

Hearing threshold at 4 kHz was measured at the conclusion of the experiment immediately following the postnoise exposure CAP recordings. Time between cessation of noise exposure and the conclusion of the experiment was a positively skewed distribution (not shown) with a median of 20 min and a semi-interquartile range of 1.25 min. The distribution of threshold shifts at the conclusion of the experiment was normally distributed (not shown) with a mean of 6.67 dB (s.d. $\pm$ 5.18 dB).

B. Representative subjects

One subject's CAPs evoked from a 75 dB pSPL stimulus before and after noise exposure are shown in Fig. 2. The gray lines are the CAPs, and the solid black and dotted lines

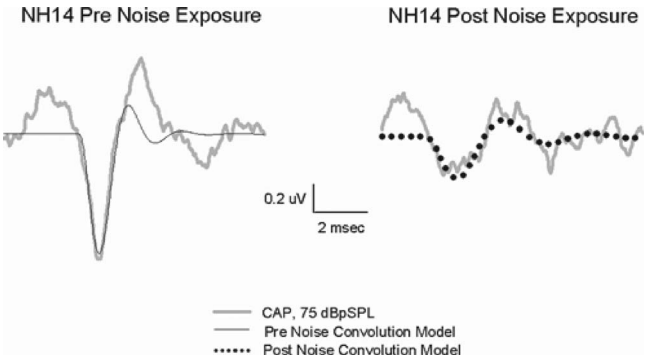

FIG. 2. CAPs evoked from a 75 dB pSPL click stimulus for one subject (NH14) before (left panel) and after (right panel) noise exposure. Gray lines represent the CAPs and the solid and dotted lines represent the analytic CAP.

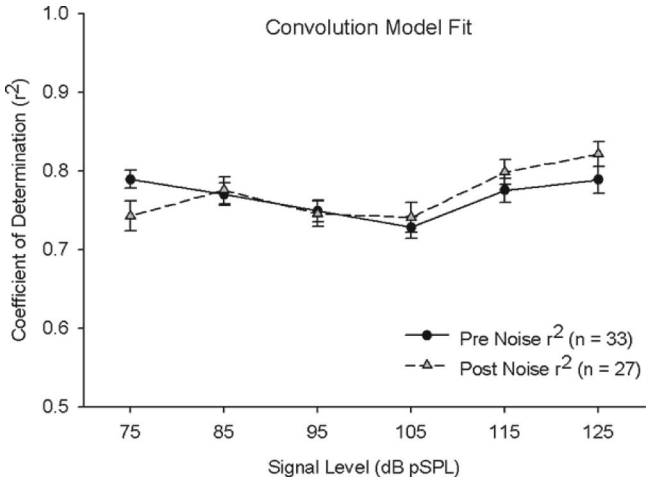

FIG. 4. Average (±1 standard error of mean) Pearson correlations between the analytic CAP and physiologic CAPs as a function of signal level before (solid line) and after (dotted line) noise exposure. Control subjects are not included by postnoise data presented here.

represent the analytic CAP. The $P(t)$ and $U(t)$ estimated from the Fig. 2 CAPs are shown in Fig. 3. In Figs. 2 and 3, the solid and dotted lines correspond to the before and after noise exposure model fits, respectively. Following noise exposure $P(t)$ had a shorter latency from stimulus onset as indicated by the smaller α parameter (cf. two numerical columns in the left panel of Fig. 3). The larger β value following noise exposure indicates that $P(t)$ increased in width and the smaller N following noise exposure indicates a reduction in the number of neurons contributing to the CAP. Following noise exposure $U(t)$ oscillated with a lower frequency and was less damped (i.e., "rang" more) as indicated respectively by parameters F and K.

C. Analytic CAP fit and reliability

Coefficients of determination (r^2) quantifying the goodness of fit between the analytic CAP and the physiologically recorded CAPs were acquired in MATLAB (CORRCOEF). The analytic CAP fit favorably to prenoise, presilence, and postnoise CAPs (Fig. 4). The 33 subjects labeled as "Pre Noise" includes both the 27 noise exposed and 6 control subjects.[3] A subtle difference existed between pre- and postnoise correlations at 75 and 125 dB pSPL though all correlations were still considered adequate.

The ICC calculation for CAP parameters acquired from control subjects' recordings (i.e. pre- and postsilent period) provided reliability estimates of the CAP parameters (Fig. 5). Statistically significant ICCs lie above the solid gray line (0.669) and insignificant values lie below. The significance of a given ICC value was calculated from an F-test similar to that used in analysis of variance (ANOVA),[4] where $F_{\mathrm{ANOVA}}=MS_B/MS_W$ and MS_B and MS_W are the same as in Eq. (4). By rearranging to $MS_B=F_{\mathrm{ANOVA}}MS_W$, and inserting into Eq. (4) yields $\mathrm{ICC}=(F_{\mathrm{ANOVA}}MS_W-MS_W)/(F_{\mathrm{ANOVA}}MS_W+MS_W)$. Using an F_{ANOVA} value corresponding upper 5% of the F_{ANOVA} distribution and 5 degrees of freedom yielded the 0.669 value of the gray line.

As indicated by proximity to the gray line, most of the ICC coefficients were statistically significant, others just below the gray line were close to significance, and others far below the gray line were clearly not significant. We consider

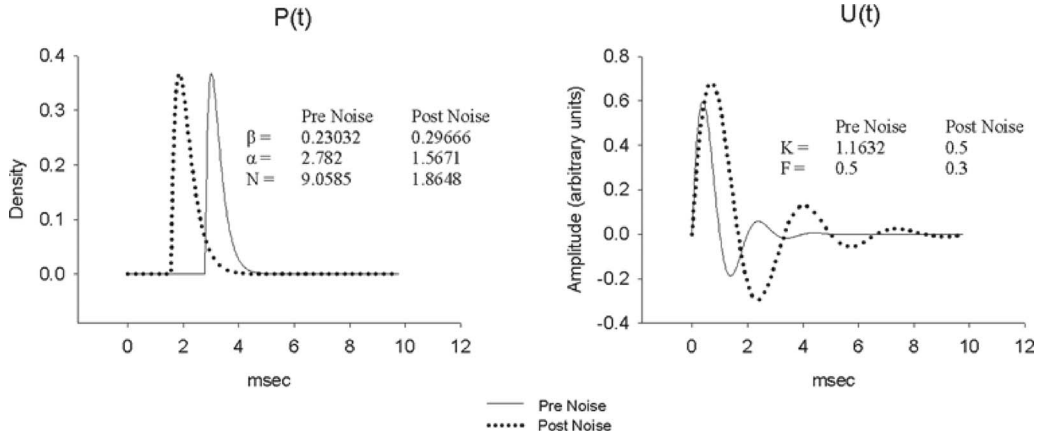

FIG. 3. Post-stimulus time histogram [$P(t)$] (left) and single-neuron action potential [$U(t)$] (right) estimates derived from fitting the analytic CAP [Eq. (A7)] to CAPs of Fig. 2 before (solid line) and after (dotted line) noise exposure. $P(t)$ and $U(t)$ coefficients of Eqs. (2) and (3) are indicated within the respective graphs. Parameter N of Eq. (1) is given in the left panel.

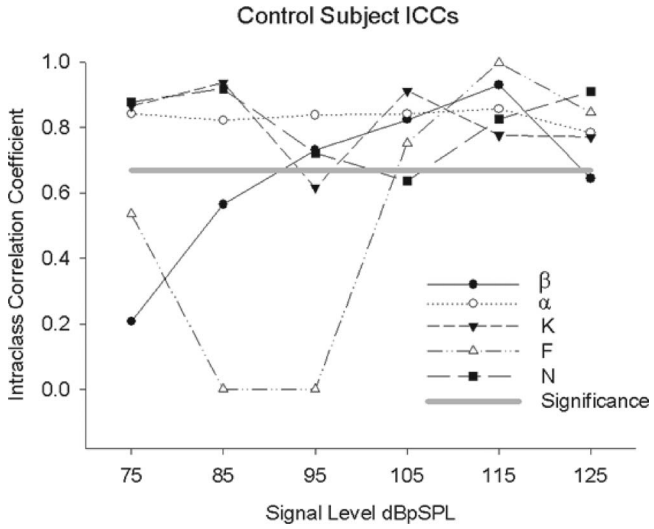

FIG. 5. Interclass correlation coefficients [(ICC), Eq. (4)] for control subject CAP parameters of Eqs. (2) and (3) as a function of signal level acquired before and after a silent period. Given the degrees of freedom, the horizontal gray line indicates a significant ICC.

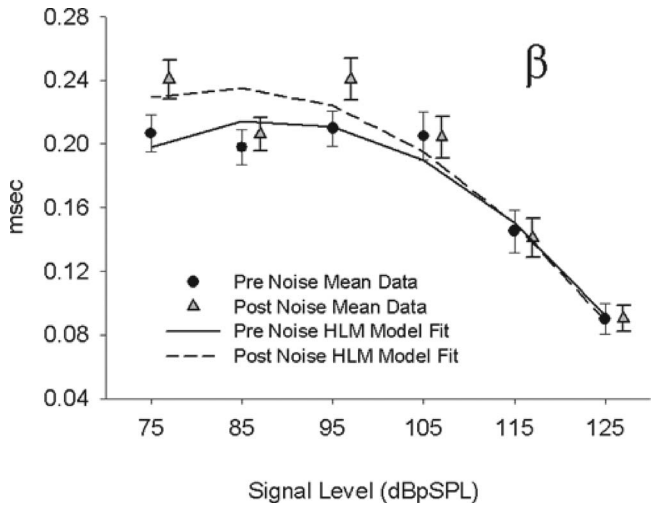

FIG. 6. Poststimulus time histogram [$P(t)$] "width" parameter β of Eq. (2) before (dark circles) and after (gray triangles) noise exposure as a function of signal level. Table I coefficients provided from the hierarchical linear modeling [(HLM), Eqs. (5) and (6)] of the prenoise β were used to construct the solid line. The dashed line represents the results of the postnoise HLM reconstructed from Table II coefficients.

values just below the gray line to be reliable because the significance value (0.669) depends on degrees of freedom (i.e., sample size), which in our situation is low (i.e., $6-1=5$). The zero ICC values for CAP parameter F at 85 and 95 dB pSPL occurred because of limited between and within subject variability. Specifically, when the analytic CAP was fit to control subjects' physiologic CAPs the boundaries governing the range of the parameters was reached. This caused MS_B and MS_W to be zero and the resulting ICC to be zero.

D. *P*(*t*) parameters

The mean and standard error of parameter β for each stimulus level is shown in Fig. 6 both before and after noise exposure. The solid and dotted lines are the HLM models fitted to the respective pre- and postnoise β data, the values of which are listed in Table I and II. The not applicable (NA) initials in Table I are place holders because the TTS level 2 HLM analyses were not performed on prenoise data. Before and after noise exposure β decreased nonlinearly with increases in signal level. The decrease was quadratic in nature, as indicated by the presence of significant B_{20} in both Tables I and II. Following noise exposure, neither the HLM intercept nor slope coefficients varied significantly with degree of hearing loss which is indicated by the zero value for B_{01}, B_{11}, and B_{21} in Table II. However, paired samples t-tests performed between pre- and postnoise β data (control subjects not included in prenoise data) from the lowest signal level indicated a significant difference ($t=-2.210$; $p=0.04$).

Similar to β, α decreased nonlinearly with increasing signal level both before and after noise exposure (top panel Fig. 7). In contrast to β, however, the α-signal-level HLM intercept and linear coefficient varied with degree of hearing loss following noise exposure (significant B_{01} and B_{11} terms in Table II). The intercept decreased as a function of degree of TTS, and is illustrated in the middle panel of Fig. 7, which plots the estimated values of π_0 from the HLM analysis for each subject as a function of TTS. In contrast, the linear coefficient (π_1) increased with TTS (bottom panel of Fig. 7, and Table II) though we chose to not fit a line to π_1 versus TTS because r_1 was not significant.

E. *N* parameter

The CAP parameter N increased nonlinearly with signal level (Fig. 8, left panel). As illustrated by the lack of significant B_{01}, B_{11}, and B_{21} terms in Table II, N did not vary with

TABLE I. Prenoise HLM coefficients

	π_0		π_1		π_2	
	B_{00}	B_{01}	B_{10}	B_{11}	B_{20}	B_{21}
CAP parameter						
β	−0.509 283	NA	0.003 649	NA	−0.000 093	NA
α	10.340 167	NA	−0.137 543	NA	0.000 533	NA
N	193.720 892	NA	−4.297 480	NA	0.024 417	NA
K	3.365 529	NA	−0.045 420	NA	0.000 248	NA
F	0.344 969	NA	0	NA	0.000 041	NA

TABLE II. Postnoise HLM coefficients.

	π_0		π_1		π_2	
	B_{00}	B_{01}	B_{10}	B_{11}	B_{20}	B_{21}
CAP parameter						
β	−0.350 634	0	0.014 054	0	−0.000 084	0
α	11.070 709	−0.030 202	−0.148 307	0.000 203	0.000 576	0
N	201.043 770	0	−4.592 246	0	0.026 745	0
K	0.933 861	0.010 056	0	0	0.000 031	0
F	0.338 681	0	0	0	0.000 036	0

degree of TTS. However, paired samples t-tests performed at 75 dB pSPL indicated a significant decrease in N following noise exposure ($t=3.679$; $p=0.001$).

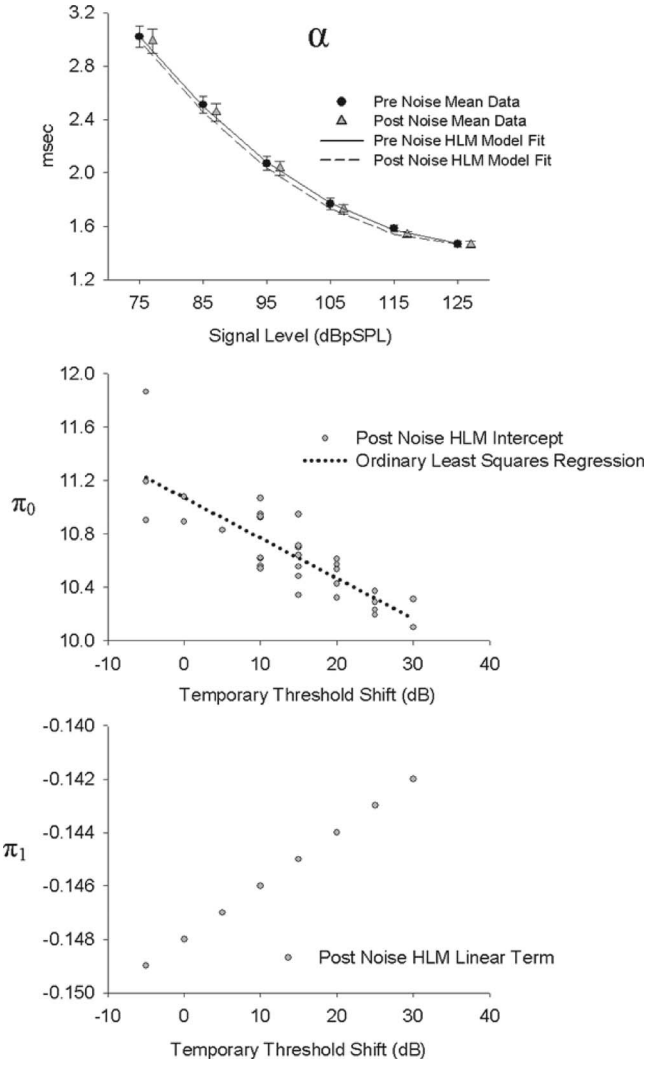

FIG. 7. Top panel illustrates post-stimulus time histogram [$P(t)$] "latency" parameter α of Eq. (2) before (dark circles) and after (gray triangles) noise exposure as a function of signal level. Table I coefficients obtained from HLM [Eqs. (5) and (6)] of prenoise α were used to construct the solid. The dashed line represents HLM coefficients of postnoise α from Table II coefficients. The middle panel shows the variation in the intercept of the α-signal level function with degree of threshold shift (TTS). The dotted line is the solution to Eq. (6) using values from Table II. The lower panel characterizes the behavior of the HLM linear term of the α-signal-level function as degree of TTS. The random error for the linear HLM term was not significant, and thus no scatter appears at the bottom.

F. $U(t)$ parameters

The K parameter, which governs the decay of $U(t)$, increased in a quadratic manner with increasing signal level both before and after noise exposure (top panel, Fig. 9). All K-signal-level HLM terms were significant before noise exposure (Table I), though only the intercept (B_{00}) and quadratic terms (B_{20}) were significant after noise exposure (Table II). Because of the small value of the quadratic term, the postnoise model fit to the data in the top panel of Fig. 9 appears to grow linearly. The significant B_{01} term in Table II indicates that the intercept of the K-signal-level function increased with degree of TTS following noise exposure. In the bottom panel of Fig. 9 are the values of π_0 as a function of degree of TTS estimated from the HLM analysis. The dotted line is the solution to Eq. (6) using coefficients from Table II.

Figure 10 indicates that the frequency of $U(t)$, parameter F, increased nonlinearly with signal level before and after noise exposure. As shown in Tables I and II, only the intercept (B_{00}) and quadratic term (B_{20}) of the HLM models were significant both before and after noise exposure, though neither of the terms were related to degree if TTS. When pre- and postnoise F was collapsed across signal level, however, a paired samples t-tests showed that that frequency of $U(t)$ oscillation was lower during TTS.

IV. DISSCUSSION

A. Temporary hearing loss

The median TTS of 15 dB shown in Fig. 1 is consistent with the extensive literature review by Kryter (1970), who reported a 10–25 dB TTS from noise exposure similar to that used in our study. The mean 6.67 dB (s.d. ± 5.18 dB) threshold shifts at the conclusion of postnoise CAP recordings is essentially consistent with Kryter (1970), who cited reports of hearing thresholds from similar noise exposure that recovered to 5 dB of baseline after 20 min.

The nontonal, high-level, short duration noise exposure probably produced a TTS in our subjects that recovered monotonically. Ward *et al.* (1959) and Hirsh and Ward (1952) reported monotonic TTS recovery from similar noise exposures. The phenomenon commonly referred to as the "two minute bounce"—threshold elevation following the noise cessation, slight recovery near the first postexposure minute followed by maximum TTS around 2 min that then recovers monotonically—was reported by Hirsh and Ward (1952) for low frequency tonal exposure which differs from

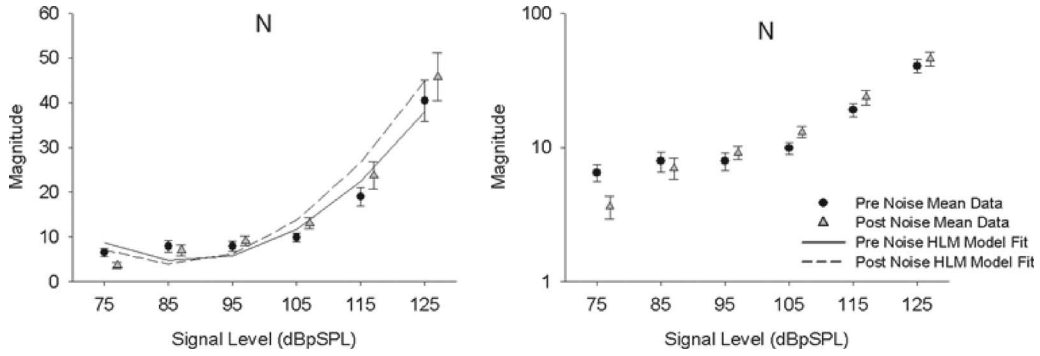

FIG. 8. "Scaling" parameter N from Eq. (1) before (dark circles) and after (gray triangles) noise exposure as a function of signal level (left panel). Results of HLM [Eqs. (5) and (6)] reconstructed from Table I values are represented as the solid line and the postnoise HLM reconstructed from Table II values are represented as the dashed line. In the right panel is the same data as in the left panel, plotted on a log–log axis.

the noise exposure used here. On three separate occasions we measured the time course of one subject's TTS recovery from the noise exposure used in this experiment and indeed did not find a two minute bounce.

B. $P(t)$ parameter β

Parameter β of Eq. (2) estimates the width of the summed *in vivo* probability density function describing the discharge timing of auditory nerve neurons (i.e., summed post-stimulus tine histogram). In other words, β indexes "compound neuronal synchrony." Small β values indicate highly synchronous excitation of a population of neurons, whereas large values suggest less synchrony across neurons. In our study β decreased with increasing signal level suggesting greater synchrony of neuronal discharges at high signal levels. Additional components, however, could contribute to alterations in β with signal level. In their Fig. 10, Antoli-Candela and Kiang (1978) showed that increasing click level evokes post-stimulus time histogram peaks that occur before the tallest peak of single, high frequency nerve post-stimulus time histograms. The duration of the high-level peaks is narrower than the first peak from low-level click stimuli. Since the earliest components of the high-CF post-stimulus time histograms dominate the far-field recorded CAP (Kiang, 1965; Kiang *et al.*, 1976; Antoli-Candela and Kiang, 1978; Wang, 1979; Versnel *et al.*, 1990), these narrow peaks may explain our small β at high signal levels. Similarly, single neuron jitter—the standard deviation of single-neuron spike latency measures from multiple stimulus presentations (Miller *et al.*, 1999)—decreases with increasing electrical stimulus level in a nonlinear fashion akin to our β-signal-level function.

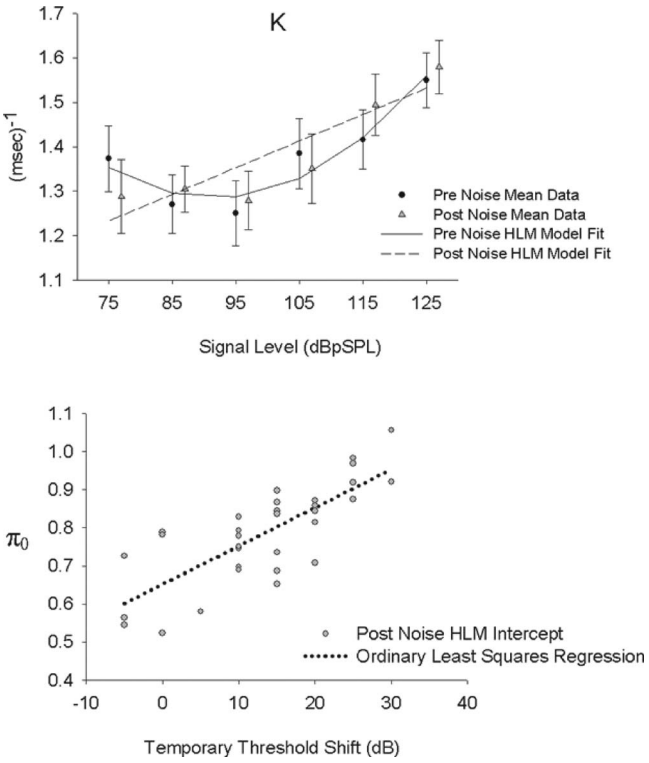

FIG. 9. Single-neuron action potential $[U(t)]$ "decay" parameter K from Eq. (3) before (dark circles) and after (gray triangles) noise exposure as a function of signal level (top panel). The solid line was reconstructed from Table I HLM [Eqs. (5) and (6)] coefficients of prenoise K. Similarly, the dashed line was obtained by solving the HLM Eq. (5) with values given in Table II. The circles in the bottom panel are the intercepts postnoise K-signal level functions—estimated from the HLM—vs TTS. The dotted line is the level 2 HLM function, i.e., Eq. (6).

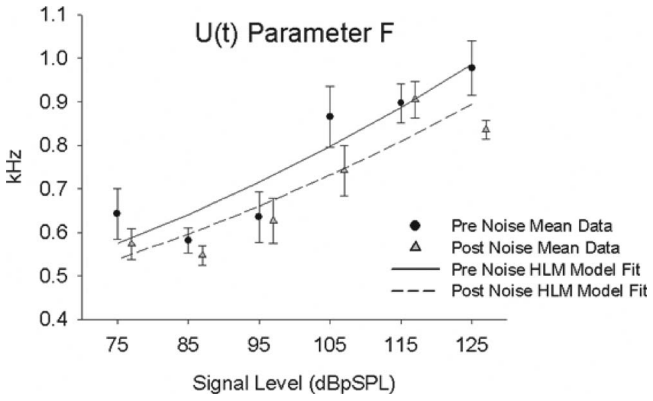

FIG. 10. Single-neuron action potential $[U(t)]$ "frequency" parameter F from Eq. (3) before (dark circles) and after (gray triangles) noise exposure as a function of signal level. The solid line was constructed by solving the HLM Eq. (5) using Table I prenoise HLM coefficients. The dashed line is the postnoise F-signal-level function estimated from the HLM, the coefficients of which are in Table II.

A significant paired samples t-test performed between pre- and postnoise β values evoked from 75 dB pSPL clicks indicates that $P(t)$ was wider during TTS. This conflicts with a report by Versnel *et al.* (1997), who showed narrower single neuron click-evoked post-stimulus time histograms from ears having permanent noise induced threshold shift, and with reports by Salvi *et al.* (1979, 1983) showing no alteration to the post-stimulus time histogram. The discrepancy between our findings and that of Versnel *et al.* and Salvi *et al.* may be explained by the anatomical differences resulting from temporary and permanent hearing loss which may ultimately manifest differently in cochlear physiologic measures. A TTS producing noise exposure leads to bending and separating of stereocilia tips in the third OHC row (Gao *et al.*, 1992) and ultimately to disarticulation with the tectorial membrane (Nordmann *et al.*, 2000). In contrast, noise exposure causing permanent threshold shift can be associated with complete loss of OHCs and buckling of the pillar bodies (Nordmann *et al.*, 2000). Versnel *et al.* (1997) swiftly conjectured that narrow post-stimulus time histograms evoked from ears with permanent hearing loss result from healthy inner hair cell responses during initial deflections of the basilar membrane impulse response. We here elaborate on our interpretation of the short narrative of Versnel *et al.* The initial basilar membrane deflections do not depend on OHC health, though the impulse response wave form illustrates that the basilar membrane vibration transitions into a condition that is dependent on OHC health during later deflections [e.g., Fig. 4, Ruggero and Rich (1991)]. The basilar membrane's impulse response wave form has a low instantaneous frequency during initial deflections and "glides" into a higher vibrational pattern that corresponds to the characteristic frequency place (Shera, 2001a)—a behavior that is independent of signal level and is controlled by the OHCs (Shera, 2001b). Unlike the TTS case in our experiment where OHCs are probably present (Gao *et al.*, 1992) though have altered physiology, absent OHCs in cases of permanent hearing loss would result in a quicker decaying (shorter lasting) basilar membrane impulse response which would thus narrow post-stimulus time histograms to an extent described by Versnel *et al.* (1997).

C. $P(t)$ parameter α

The parameter α from Eq. (2) describes the time delay from stimulus onset to $P(t)$ onset. A linear function fit to the quadratic α-signal-level function of the top panel in Fig. 7 approximates a decrease in α of ~1.5 ms from 125 to 75 dB pSPL. Such estimates in latency shifts are consistent with the nearly −30 μs/dB for the first peak of the human CAP (Durrant and Ferraro, 1999). That is to say, $P(t)$ onset latency varies as a function of signal level decays at about the same rate as the human CAP.

The significant B_{01} and B_{11} in Table II indicate that the intercept and linear term of the α signal level varied with degree of TTS. For individuals with greater amounts of TTS, the α-signal-level function decreased at all signal levels and became more linear. This effect is only minimally noticeable in the top panel of Fig. 7 because individual TTS effects are not noticeable in the mean data. Figure 11 more systematically demonstrates changes in the α-signal-level function for various degrees of TTS. In Fig. 11 the α-signal-level functions were reconstructed from the coefficients of Table II and by varying the independent variable of Eq. (6) (i.e., TTS; 5–30 dB). The large gray arrow emphasizes that a shorter α was acquired during TTS and the amount of shift was related to the degree of TTS. Moreover, comparing the data identified by the star versus cross hairs shows that a greater shift occurred at low intensity levels. Iso-intensity plots in the bottom panel of Fig. 11 acquired from the 75 dB pSPL (stars) and 125 dB pSPL (cross haired circles) extremes of the top panel functions illustrate that α was more at 75 than at 125 dB pSPL.

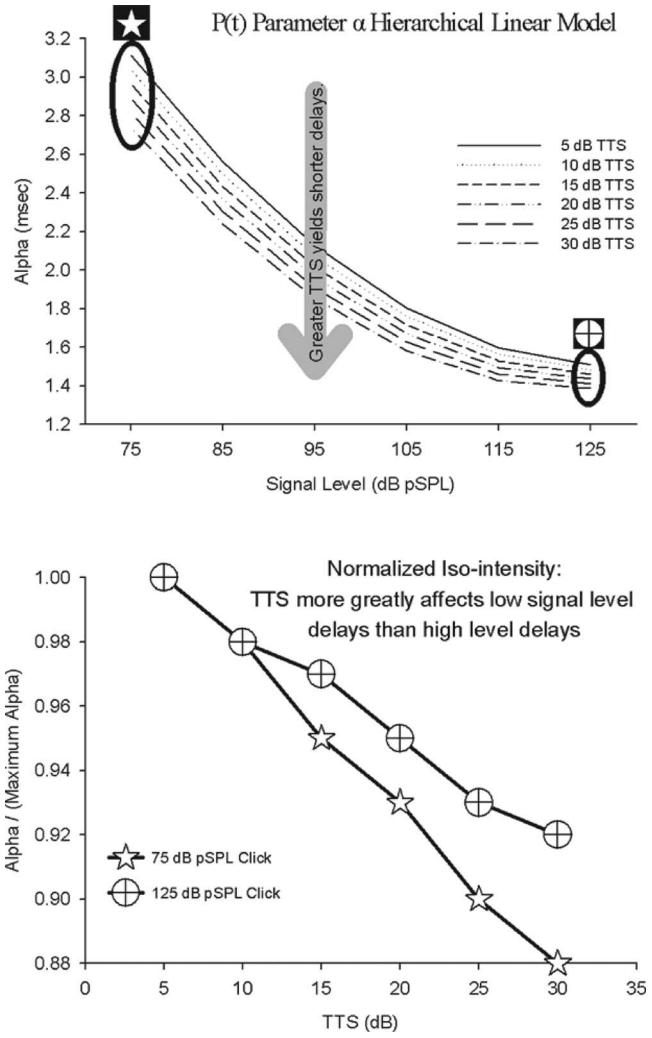

FIG. 11. α-signal-level functions constructed from HLM coefficients of Table II using the TTS level 2 independent variable [Eq. (6)] varying from 5 to 30 dB. Iso-intensity plots for 75 dB pSPL α (stars) and 125 dB pSPL (cross hair circle) derived from data of the top panel are shown in the bottom panel.

Shorter response latency during TTS is consistent with Chertoff *et al.* (1996), who used cochlear microphonic recordings to construct a third-order polynomial describing mechano-electric transduction. During TTS the polynomial coefficients showed a phase lead, or shorter latency, suggesting that responses came from a more basal location. Simi-

larly, CAPs have been shown by Eggermont (1979) to have a shorter latency in hearing impaired subjects as a result of the broadening of cochlear filters following damage. In other words, a reduction in the steepness of the high frequency side of damaged neurons' frequency tuning curves presumably allows responses to stimuli from higher frequencies than CF, thus producing shorter latencies than in the normal case.

Shorter response latency in the presence of outer hair cell damage is not a pervasive finding in the literature, however. High intensity stimuli have been shown to yield normal CAP latencies in animals with permanent outer hair cell damage (Wang and Dallos, 1972; Salvi *et al.*, 1979; Versnel *et al.*, 1997). The disparity between our findings and those reports of normal latency following outer hair cell damage may be because negative damping provided by the outer hair cells is negligible at high signal levels and inner hair cells may respond at high stimulus levels independent of outer hair cell status. Because TTS most likely results from OHC alteration (Gao *et al.*, 1992; Nordmann *et al.*, 2000), it is not surprising that responses from the lower signal levels were more affected by TTS than the higher signal levels as it is at low levels where OHC physiology is influential.

D. Parameter *N*

According to the theoretical CAP model proposed by Goldstein and Kiang (1958), the *N* parameter represents the number of neurons contributing to the CAP. If so, then the nonmonotonic increase in Fig. 8 indicates that the number of neurons contributing to the CAP increased with signal level. This is consistent with the finding that the number of single neuron responses increases with signal level (Kiang, 1965; Versnel *et al.*, 1992a).

The HLM analysis showed that the prenoise *N*-signal-level function had a quadratic coefficient greater than zero, which indicates a nonlinear growth with signal level. Others have reported a similar trend in the growth of CAP amplitude with signal level (e.g., Teas *et al.*, 1962; Portmann *et al.*, 1973; Montandon *et al.*, 1975; Özdamar and Dallos, 1976; Crowley, 1976; Thornton, 1976; Ino, 1976; Versnel *et al.*, 1992a), though others have reported that the CAP amplitude growth function had a negative quadratic term suggesting a compressive growth (e.g., Benitez *et al.*, 1972; Yoshie, 1976; Thornton, 1976; Eggermont *et al.*, 1976; Don and Eggermont, 1978; Salvi *et al.*, 1983). Obvious differences between the various reported growth function could be due to data transformations such as the use of log–log versus linear–log axes. In fact, plotted with log–log axes in the right panel of Fig. 8 *N* appears to grow somewhat compressively at the midsignal levels. Perhaps this subtle indication of compressive growth would be more apparent had we recorded additional data below 75 dB pSPL.

The positive quadratic growth of the *N*-signal-level function could be due to our electrode position. Varying electrode position around the neural generators can affect the profile of the CAP amplitude growth function (Yoshie and Ohahi, 1969), as well as the profile of the single neuron action potential (Kiang *et al.*, 1976; Stegeman *et al.*, 1979). The profile of our *N*-signal-level function could also be related to the frequency content of the click stimulus and the CF for which the TM electrode is most sensitive. Monitoring the ear canal signals (see Sec. II) showed that after passing through the outer ear canal, most of the click energy was around 4 kHz. Four-thousand kilohertz could possibly be below the CF of the cochlear frequency place for which the TM electrode is most sensitive. In a similar off-CF stimulation condition, auditory nerve neurons show a positive quadratic growth function plotted on linear-log axes. Our results could thus reflect the off-CF auditory nerve property that is reviewed by Kiang (1965), Pickles (1988), Ruggero (1992), and Harrison (2001).

Neither the intercept (π_0), linear (π_1), nor quadratic (π_2) coefficients significantly varied with degree of hearing loss. However, paired samples *t*-tests showed that parameter *N* evoked from the lowest signal level was significantly smaller during TTS indicating fewer neurons discharged during TTS. Temporary noise-induced alterations to outer hair cell physiology most likely contributed to the reduction of *N* during TTS. A reduction in negative damping would decrease the low intensity gain provided to the basilar membrane and consequently provide less input to the inner hair cells and associated afferent neurons. The lack of influence of TTS on *N* at higher levels, probably occurred given that outer hair cell feedback is negligible at high stimulus levels (Robles and Ruggero, 2001).

E. *U*(*t*) parameters *K* and *F*

The *K* parameter of Eq. (3) governs the decay of $U(t)$. Small *K* values result in a $U(t)$ profile having less damping while large values of *K* result in a quickly damped $U(t)$. That is to say, small *K* values force the single neuron action potential estimate to "ring" longer than large values of *K*. The top panel of Fig. 9 shows that $U(t)$ had greater damping as signal level increased in both the prenoise and postnoise cases. The large standard error of *K* means seen in the top panel of Fig. 9 is consistent with other reports of large inter- (Kiang *et al.*, 1976; Wang, 1979) and intra- (Prijs, 1986) subject variability in the profiles of the single neuron action potential obtained from spiked triggered averaging. The coefficients from the HLM analysis were significant both before and after noise exposure despite the variability. Moreover, the intercept increased after noise exposure and the increase was proportional to degree of hearing loss indicating less oscillations in $U(t)$ wave forms in subjects with large amounts of TTS. This finding is further illustrated in Fig. 12, where *K*-signal-level functions were reconstructed by using coefficients provided in Table II and by varying the independent variable of Eq. (6) (i.e., TTS; 5–30 dB). The functions shift to larger values of *K* in direct relation to the degree of TTS.

Parameter *F* of Eq. (3) governs the oscillatory frequency of our single neuron action potential estimate. A lower *F* value indicates a slower oscillation of the $U(t)$ wave form for a given unit of time. Figure 10 shows that the $U(t)$ oscillation increased about one octave from 0.5 to 1 kHz over the range of 75–125 dB pSPL. Furthermore, although a change in

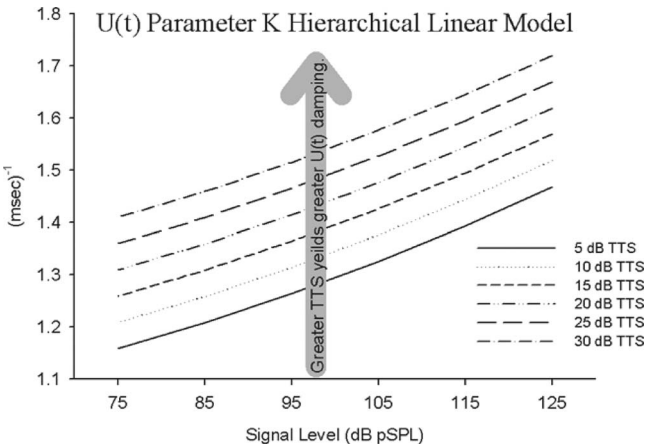

FIG. 12. Parameter *K*-signal-level functions constructed from HLM [Eqs. (5) and (6)] coefficients of Table II using the TTS level 2 independent variable [Eq. (6)] that varied from 5 to 30 dB.

F-signal-level function was not related to degree of TTS, *t*-tests performed on the *F* parameter before and after noise exposure showed that $U(t)$ had a lower frequency of oscillation during TTS.

Despite the assumption of the analytic CAP that the $U(t)$ profile is everywhere constant throughout various characteristic cochlear frequency places (Kiang *et al.*, 1976; Wang, 1979), the situation in damaged cochleae is probably different (Prijs, 1986; Versnel *et al.*, 1992b). Various explanations may account for the changes in $U(t)$ as a result of signal level and TTS. One interpretation could be that the single neuron action potential was altered during TTS due to alterations in neuron physiology, as there is some evidence that the single neuron action potential can change in animals with noise-induced hearing loss (Versnel *et al.*, 1992b). However, there are alternative explanations that need to be examined in future experiments. For example, the $U(t)$ profile may have been altered due to the basal-ward spread of excitation—inherent with increasing signal level—which stimulates neurons residing closer to the TM electrode. Indeed, it has been shown that alterations in the distance from source location to the recording location can change the $U(t)$ profile (Stegeman *et al.*, 1979). Another alternative explanation is that a change in $U(t)$ was due to a limitation of the analytic approach because the chosen $P(t)$ function has only one maximum and can thus not represent post-stimulus time histograms with multiple maxima. The decaying exponential function used for $U(t)$ may have resultantly varied to account for the additional extrema in post-stimulus time histograms.

F. Clinical implications

The ultimate goal of our group's research is to develop clinical tools to identify the locus of lesion(s) and characterize the pathophysiology in ears with sensory-neural hearing loss. Currently available clinical tests are limited in this regard. For example, audiological diagnostics cannot distinguish between hearing loss arising from impairment of the stereocilia, OHC body, stria vascularis, afferent auditory nerve neurons, or impaired K^+ ion current throughout various regions within the cochlear partition. Accurate identification of site of lesion(s) in cases of profound impairment must certainly be known before the promising stem cell or genetic therapies can be applied. Moreover, improved descriptions of pathophysiology of surviving cochlear structures could lead to improved hearing aid and cochlear implant processing algorithms.

Toward our ultimate goal, we have developed a battery of tests that describe cochlear function by using cochlear microphonics (Chertoff *et al.*, 1996, 1997, 2003; Bian and Chertoff, 1998, 2001), summating potentials (Choi *et al.*, 2004), and otoacoustic emissions (Bian *et al.*, 2002, 2004; Krishnan and Chertoff, 1999). Each of these tests has the potential to assist in localizing the site of lesion(s) and in describing pathophysiology in cases of sensory-neural hearing loss. It is in the context of this more comprehensive test battery that we foresee using the analytic CAP. With approaches similar to that reported with the experiments of this manuscript, much of our previous work has aimed at describing the pathophysiology of sensory-neural hearing loss. The aim of our future work is important, as we will relate attributes of this test battery to anatomical lesions verified with histological analyses.

G. Summary and conclusions

Fitting the analytic CAP to physiologic CAPs evoked from human ears provided estimates of the parameters of $P(t)$ and $U(t)$. HLM quantified changes in the CAP parameters as a function of signal level both before and after noise exposure. As click level increased, β decreased indicating a narrowing in the width of $P(t)$. Following noise exposure β was larger for the lowest click levels suggesting a wider $P(t)$ which was related to less synchronous responses. The $P(t)$ latency parameter, α, decreased with increasing signal level and was shorter at all signal levels following noise exposure. Alterations in α values indicated that CAPs were dominated by responses from neurons located more basal-ward as signal level increased and after noise exposure. Parameter *N* increased with signal level and was smaller after noise exposure at the lowest signal level. Postnoise *N* changes imply that responses from fewer neurons were evoked at the lowest click level during TTS. Both the damping and frequency parameters of $U(t)$ increased with signal level. For large amounts of TTS, $U(t)$ from low click levels had greater damping than before noise exposure. Additionally, $U(t)$ oscillation was lower in frequency at all click intensities following noise exposure. The changes in $U(t)$ could be due to alterations in the single-neuron action potential, relative distance from source to electrode, or limitations of the equation used to describe $P(t)$.

ACKNOWLEDGMENTS

We empathetically thank our subjects for participating in this study. Doctor Nelson Y.S. Kiang and Dr. Christopher A. Shera shared in several valuable conversations about this research and commented on various versions of this manuscript. With fantastic attention to detail, Dr. Tiffany A. Johnson edited an earlier report of this research. We thank two anonymous reviewers for their helpful comments. This

research was supported by The University of Kansas Medical Center Biomedical Research Training Program and RO1 DC02117 from the National Institute on Deafness and other Communication Disorders at the National Institutes of Health.

APPENDIX: DERIVATION OF THE ANALYTIC CAP

This derivation of the analytic CAP using functional forms of $P(t)$ and $U(t)$ was initially reported by Chertoff (2004) and is repeated here. The analytic CAP is given as

$$\mathrm{CAP}(t) = N\int_{-\infty}^{t} P(\tau)U(t-\tau)d\tau, \tag{A1}$$

where

$$P(t) = \left(\frac{t-\alpha}{\beta}\right)^{\gamma-1} e^{-((t+\alpha)/\beta)} \tag{A2}$$

and

$$U(t) = e^{-kt}\sin(\omega t). \tag{A3}$$

In the Laplace domain, Eq. (A1) can be expressed as

$$\mathrm{CAP}(s) = NP(s)U(s). \tag{A4}$$

Similarly, $P(t)$ and $U(t)$ are expressed as

$$P(s) = \frac{e^{-s\alpha}(1/\beta)^{\gamma-1}\Gamma(\gamma)}{(s+1/\beta)^{\gamma}} \tag{A5}$$

and

$$U(s) = \frac{\omega}{(s+k)^2+\omega^2}. \tag{A6}$$

Setting $\gamma=2$, substituting Eqs. (A5) and (A6) into Eq. (A4), and converting Eq. (A4) to the time domain via the inverse Laplace transform (MAPLE 7.0), Waterloo, Ontario, Canada, yields

$$\mathrm{CAP}(t) = -\frac{N\beta H(t-\alpha)}{c^2}\{\omega e^{-((t+\alpha)/\beta)}[c(t-\alpha) - 2\beta(\beta k - 1)] + e^{-k(t-\alpha)}[-a\sin(\omega(t-\alpha)) - b\cos(\omega(t-\alpha))]\}, \tag{A7}$$

where

$$a = \beta\omega^2 - (\beta k - 1)^2,$$

$$b = 2\beta\omega(1-\beta k),$$

$$c = \beta^2\omega^2 + (\beta k - 1)^2,$$

$$H = Heaviside.$$

[1]HLM π coefficients of Eq. (5), a mere symbol, should not be confused with the numerical value π of Eq. (3).
[2]The student's t in the name t-tests should not be confused with the time variable t of Eqs. (1)–(3).
[3]The number of subjects in Fig. 4 is indicated by the letter n, not to be confused with CAP parameter N of the analytic CAP.
[4]The letter F in the name F_{ANOVA} should not be confused with the CAP parameter F of Eq. (3).

Antoli-Candela, F. J., and Kiang, N. Y. S. (**1978**). "Unit activity underlying the N1 potential," in *Evoked Electrical Activity in the Auditory Nervous System*, edited by R. F. Naunton and C. Fernandez (Academic, New York), pp. 165–189.
Bauch, C. D., and Olsen, W. O. (**1986**). "The effect of 2000–4000 Hz hearing sensitivity on ABR results," Ear Hear. **7**, 314–317.
Bauch, C. D., and Olsen, W. O. (**1988**). "Auditory brainstem responses as a function of average hearing sensitivity for 2000–4000 Hz," Audiology **27**, 156–163.
Benitez, L. D., Eldredge, D. H., and Templer, J. W. (**1972**). "Temporary threshold shifts in hinchilla: Electrophysiological correlates," J. Acoust. Soc. Am. **52**, 1115–1123.
Bian, L., and Chertoff, M. E. (**1998**). "Differentiation of cochlear pathophysiology in ears damaged by salicylate or pure tone using a nonlinear systems identification technique," J. Acoust. Soc. Am., **104**(4), 2261–2271.
Bian, L., and Chertoff, M. E. (**2001**). "Distinguishing cochlear pathophysiology in 4–aminopyridine and furosmede treated ears using a nonlinear systems identification technique," J. Acoust. Soc. Am., **109**(2), 671–685.
Bian, L., Chertoff, M. E. (**2002**). "Deriving a cochlear transducer function from low-frequency modulation of distortion product otoacoustic emissions," J. Acoust. Soc. Am., **112**(1), 198–210.
Bian L., Linhardt, E. E., and Chertoff, M. E. (**2004**). "Cochlear hysteresis: Observation with low-frequency modulation distortion product otoacoustic emissions," J. Acoust. Soc. Am., **115**(5), 2159–2172
Chertoff, M. E. (**2004**). "Analytic treatment of the compound action potential: Estimating the summed post-stimulus time histogram and unit response," J. Acoust. Soc. Am. **116**, 3022–3030.
Chertoff, M. E., Steele, T. C., Ator, G. A., and Bian, L. (**1996**). "Characterizing cochlear mechano-electric transduction using a nonlinear systems identification procedure," J. Acoust. Soc. Am. **100**, 3741–3753.
Chertoff, M. E., Steele, T., and Bian, L. (**1997**). "Characterizing cochlear mechano-electric transduction in ears damaged with pure tones," J. Acoust. Soc. Am., **102**(1), 441–450.
Chertoff, M. E., Yi, X., and Lichtenhan, J. T. (**2003**). "Influence of hearing sensitivity on mechano-electric transduction," J. Acoust. Soc. Am., **114**(6), 3251–3263.
Choi, C.-H., Chertoff, M. E., Bian, L., and Lerner, D. (**2004**). "Constructing a cochlear transducer function from the summating potential using a low-frequency bias tone," J. Acoust. Soc. Am., **116**(5), 2996–3007
Crowley, D. E. (**1976**). "Animal data as a guide to application of masking in human electrocochleography with particular preference to presbycusis," in *Electrocochleography*, edited by R. Rubin, C. Elberling, and G. Salomon (University Park Press, Baltimore), pp. 277–186.
Don, M., and Eggermont, J. J. (**1978**). "Analysis of the click-evoked brainstem potentials in man using high-pass noise masking," J. Acoust. Soc. Am. **63**, 1084–1092.
Durrant, J. D., and Ferraro, J. A. (**1999**). "Short-latency auditory evoked potentials: Electrocochleography and auditory brainstem response," in *Contemporary Perspectives in Hearing Assessment*, edited by F. E. Musiek and W. F. Rintelmann (Allyn and Bacon, Boston), pp. 197–236.
Eggermont, J. J. (**1979**). "Narrow-band AP latencies in normal and recruiting human ears," J. Acoust. Soc. Am. **65**, 463–470.
Eggermont, J. J., Spoor, A., and Odenthal, D. W. (**1976**). "Frequency specificity of tone-burst electrocochleography," in *Electrocochleography*, edited by R. Rubin, C. Elberling, and G. Salomon (University Park Press, Baltimore), pp. 247–256.
Ferraro, J. A., and Durrant, J. D. (**2002**). *Electrocochleography*, in *Handbook of Clinical Audiology*, 5th ed., edited by J. Katz (Lippincott Williams & Wilkins, Philadelphia), pp. 249–273.
Fowler, C. G., and Mikami, C. M. (**1992**). "Effects of cochlear hearing loss on the ABR latencies to clicks and 1000 Hz tone pips," J. Am. Acad. Audiol **3**, 324–330.
Gao, W. Y., Ding., D. L., Zheng, X. Y., Ruan, F. M., and Liu, Y. J. (**1992**). "A comparison of changes in the stereocilia between temporary and permanent hearing losses in acoustic trauma," Hear. Res. **62**, 27–41.
Goldstein, M. H., and Kiang, N. Y. S. (**1958**). "Synchrony of neural activity in electric responses evoked by transient acoustic stimuli," J. Acoust. Soc. Am. **30**, 107–114.
Gorga, M. P., Worthington, D. W., Reiland, J. K., Beauchaine, K. A., and Goldgar, D. E. (**1985**). "Some comparisons between auditory brain stem response thresholds, latencies, and pure-tone audiogram," Ear Hear. **6**, 105–112.
Harrison, R. V. (**2001**). "The physiology of the cochlear nerve," in *Physiol-*

ogy of the Ear, 2nd ed., edited by A. F. Jahn, and J. Santos-Sacchi (Singular, San Diego), pp. 549–574.
Hirsh, I. J., and Ward, W. D. (**1952**). "Recovery of the auditory threshold after strong acoustic stimuluation," J. Acoust. Soc. Am. **24**, 131–141.
Ino, T. (**1976**). "Comparison of the response threshold between ERA and ECoG," in *Electrocochleography*, edited by R. Rubin, C. Elberling, and G. Salomon (University Park Press, Baltimore), pp. 247–256.
Jerger, J., and Mauldin, L. (**1978**). "Prediction of sensorineural hearing level from the brain stem evoked response," Arch. Otolaryngol., **104**(8), 456–461.
Kiang, N. Y. S. (**1965**). *Discharge Patterns of Single Fibers in the Cat's Auditory Nerve*, MIT Research Monograph No. 35. (MIT, Cambridge, MA).
Kiang, N. Y. S., Moxon, E. C., and Kahn, A. R. (**1976**). "The relationship of gross potentials recorded from the cochlea to single unit activity in the auditory nerve," in *Electrocochleography*, edited by R. Rubin, C. Elberling, and G. Salomon (University Park Press, Baltimore), pp. 95–115.
Krishnan, G., and Chertoff, M. E. (**1999**). "Insights into linear and nonlinear cochlear transduction: Application of a new system-identification procedure on transient-evoked otoacoustic emissions data," J. Acoust. Soc. Am., **105**(2), 770–781.
Kryter, K. D. (**1970**). "Proposed procedures for estimating damage risk to hearing," in *The Effects of Noise on Man* (Academic, New York).
Lichtenhan, J. T., Chertoff, M. E., and Esau, K. S. (**2005**). "Influence of hearing loss on the summed post-stimulus time histogram and unit response obtained from an analytic treatment of the compound action potential," Assoc. Res. Otolaryngol. Abstr. **28**, 78.
Margolis, R. H., and Hunter, L. L. (**1999**). "Tympanometry: Basic principles and clinical applications," in *Contemporary Perspectives in Hearing Assessment*, edited by F. E. Musiek, and W. F. Rintelmann (Allyn and Bacon, Boston), pp. 89–130.
McMahon, C. M., and Patuzzi, R. B. (**2002**). "The origin of the 900 Hz spectral peak in spontaneous and sound-evoked round-window electrical activity," Hear. Res. **173**, 134–142.
Mendenhall, W., and Sincich, T. (**2003**). *A Second Course in Statistics, Regression Analysis*, 6th ed. (Pearson Education, Upper Saddle River, NJ).
Miller, C. A., Abbas, P. J., and Rubinstein, J. T. (**1999**). "An empirically based model of the electrically evoked compound action potential," Hear. Res. **135**, 1–18.
Montandon, P. B., Shepard, N. T., Marr, E. M., Peake, W. T., and Kiang, N. Y. S. (**1975**). "Auditory-nerve potentials from ear canals of patients with otologic problems," Ann. Otol. Rhinol. Laryngol. **84**, 164–173.
Nordmann, A. S., Bohne, B. A., and Harding, G. W. (**2000**). "Histopathological differences between temporary and permanent threshold shift," Hear. Res. **139**, 13–30.
Özdamar, Ö., and Dallos, P. (**1976**). "Input-output functions of cochlear whole-nerve action potentials: Interpretation in terms of one population of neurons," J. Acoust. Soc. Am. **59**, 143–117.
Pickles, J. O. (**1988**). "The auditory nerve," in *An Introduction to the Physiology of Hearing*, edited by J. O. Pickles (Academic, San Diego), pp. 78–111.
Portmann, M., Jean-Marie, A., and Lagourgue, P. (**1973**). "Testing for 'recruitment' by electrocochleography," Ann. Otol. Rhinol. Laryngol. **82**, 33–43.
Prijs, V. F. (**1986**). "Single-unit response at the round window of the guinea pig," Hear. Res. **21**, 127–133.
Raudenbush, S. W., and Bryk, A. S. (**2002**). *Hierarchical Linear Models* (Sage, Thousand Oaks).
Raudenbush, S. W., Bryk, A. S., and Congdon, R. (**2000**). "Hierarchical linear and nonlinear modeling (computer program). HLM6 SSI," Scientific Software International, Lincolnwood, IL.
Robles, L., and Ruggero, M. A. (**2001**). "Mechanics of the mammalian cochlea," Physiol. Rev. **81**, 1305–1352.
Ruggero, M. A. (**1992**). "Physiology and coding of sound in the auditory nerve," in *The Mammalian Auditory Pathway: Neurophysiology*, edited by A. N. Popper and R. R. Fay (Springer, New York), pp. 34–93.
Ruggero, M. A., and Rich, N. C. (**1991**). "Furosemide alters organ of Corti mechanics: Evidence for feedback of outer hair cells upon the basilar membrane," J. Neurosci. **11**, 1057–1067.
Ryan, A., and Dallos, P. (**1975**). "Effects of absence of cochlear outer hair cells on behavioral auditory thresholds," Nature (London) **253**, 44–46.
Salvi, R. J., Hamernik, R. P., and Henderson, D. (**1983**). "Response patterns of auditory nerve fibers during temporary threshold shift," Hear. Res. **10**, 37–67.
Salvi, R. J., Henderson, D., and Hamernik, R. P. (**1979**). "Single auditory nerve fiber and action potential latencies in normal and noise-treated chinchillas," Hear. Res. **1**, 237–251.
Schoonhoven, R., Prijs, V. F., and Schneider, S. (**2001**). "DPOAE group latencies versus electrophysiological measures of cochlear latency in normal human ears," J. Acoust. Soc. Am. **109**, 1503–1512.
Shepard, N. T., Webster, J. C., Baumen, M., and Schuck, P. (**1992**). "Effect of hearing loss of cochlear origin on the auditory brain stem response," Ear Hear. **13**, 173–180.
Shera, C. A. (**2001a**). "Frequency glides in click responses of the basilar membrane and auditory nerve: Their scaling behavior and origin in traveling-wave dispersion," J. Acoust. Soc. Am. **109**, 2023–2034.
Shera, C. A. (**2001b**). "Intensity-invariance of fine time structure in basilar-membrane click responces: Implications for cochlear mechanics," J. Acoust. Soc. Am. **110**, 332–348.
Stegeman, D. F., de Weerd, J. P. C., and Eijkman, E. G. J. (**1979**). "A volume conductor study of compound action potentials of nerves in situ: The forward problem," Biol. Cybern. **33**, 97–111.
Teas, D. C., Eldredge, D. H., and Davis, H. (**1962**). "Cochlear responses to acoustic transients: An interpretation of whole-nerve action potentials," J. Acoust. Soc. Am. **34**, 1438–1459.
Thornton, A. R. D. (**1976**). "Statistical properties of electrocochleographic responses and their use in clinical diagnosis," in *Electrocochleography*, edited by R. Rubin, C. Elberling, and G. Salomon (University Park Press, Baltimore), pp. 257–276.
Versnel, H., Prijs, V. F., and Schoonhoven, R. (**1990**). "Single-fiber responses to clicks in relationship to the compound action potential in the guinea pig," Hear. Res. **46**, 47–160.
Versnel, H., Prijs, V. F., and Schoonhoven, R. (**1997**). "Auditory-nerve fiber responses to clicks in guinea pigs with a damaged cochlea," J. Acoust. Soc. Am. **101**, 993–1009.
Versnel, H., Schoonhoven, R., and Prijs, V. F. (**1992a**). "Single-fiber and whole-nerve responses to clicks as a function of sound intensity in the guinea pig," Hear. Res. **59**, 138–156.
Versnel, H., Schoonhoven, R., and Prijs, V. F. (**1992b**). "Round-window recorded potential of single-fiber discharge (unit response) in normal and noise damaged cochleas," Hear. Res. **59**, 157–170.
Wang, B. (**1979**). "The relation between the compound action potential and unit discharges in the auditory nerve," Doctoral dissertation, Deptartment of Electrical Engineering and Computer Sciences, MIT, Cambridge, MA.
Wang, C., and Dallos, P. (**1972**). "Latency of whole-nerve action potentials: Influence of hair-cell normalcy," J. Acoust. Soc. Am. **52**, 1678–1686.
Ward, W. D. (**1962**). "Damage-risk criteria for line spectra," J. Acoust. Soc. Am. **34**, 1610–1619.
Ward, W. D., Glorig, A., and Sklar, D. L. (**1959**). "Temporary threshold shift from octave-band noise: Applications to damage-risk criteria," J. Acoust. Soc. Am. **31**, 522–528.
Watson, D. R. (**1996**). "The effects of cochlear hearing loss, age and sex on the auditory brainstem response," Audiology **35**, 246–258.
Watson, D. R. (**1999**). "A study of the effect of cochlear loss on the auditory brainstem response (ABR) specificity and false positive rate in retrocochlear assessment," Audiology **38**, 155–164.
Wu, Y.-W. B. (**1996**). "An application of hierarchical linear models to longitudinal studies," Res. Nurs. Health **19**, 75–82.
Yoshie, N. (**1976**). "Electrocochleographic study of Ménière's disease and pontine angle neurinoma," in *Electrocochleography*, edited by R. Rubin, C. Elberling, and G. Salomon (University Park Press, Baltimore), pp. 353–386.
Yoshie, N., and Ohahi, T. (**1969**). "Clinical use of cochlear nerve action potential responses in man for differential diagnosis of hearing losses," Acta Oto-Laryngol., Suppl. **252**, 71–87.

Comodulation detection differences in children and adults

Joseph W. Hall III,[a] Emily Buss, and John H. Grose
Department of Otolaryngology/Head and Neck Surgery, University of North Carolina School of Medicine, Chapel Hill, North Carolina 27599, USA

(Received 1 June 2007; revised 14 November 2007; accepted 8 January 2008)

This study investigated comodulation detection differences (CDD) in children (ages 4.8–10.1 years) and adults. The signal was 30-Hz wide band of noise centered on 2 kHz, and the masker consisted of six 30-Hz wide bands of noise spanning center frequencies from 870 to 4160 Hz. The envelopes of the masking bands were always comodulated, and the envelope of the signal was either comodulated or random with respect to the masker. In some conditions, the maskers were gated on prior to the signal in order to minimize effects related to perceptual fusion of the signal and masker. CDD was computed as the difference between signal detection thresholds in conditions where all bands were comodulated and conditions where the envelope of the signal was random with respect to the envelopes of the maskers. Values of CDD were generally small in children compared to adults. In contrast, masking release related to masker/signal onset asynchrony was comparable across age groups. The small CDDs in children are discussed in terms of sensitivity to comodulation as a perceptual fusion cue and informational masking associated with the detection of a signal in a complex background, an effect that is ameliorated by asynchronous onset.
© *2008 Acoustical Society of America.* [DOI: 10.1121/1.2839006]

PACS number(s): 43.66.Dc, 43.66.Ba [RYL] Pages: 2213–2219

I. INTRODUCTION

The detection of a narrow band of noise in the presence of one or more narrow bands of masking noise is often dependent on the relative fluctuation patterns across the noise bands. Threshold differences between conditions where all bands share the same envelope (comodulated) and conditions where envelope differences exist across bands are termed comodulation detection differences (CDD) (Cohen and Schubert, 1987; McFadden, 1987; Wright, 1990). In the present study, we refer to the case where both the masker and signal bands have the same envelope as an A/A condition, and the case where the signal has a fluctuation pattern independent from the maskers as an A/B condition. The classical CDD effect is that the threshold is lower (better) in the A/B condition than in the A/A condition (e.g., Cohen and Schubert, 1987; McFadden, 1987; Wright, 1990). One interpretation of the relatively poor signal detection in the A/A case is based on sound source segregation (Cohen and Schubert, 1987; McFadden, 1987; Wright, 1990). By this account, the common fluctuation pattern across frequency in the A/A condition perceptually fuses the masker and signal, hindering the detection of the signal as a separate auditory object.

Borrill and Moore (2002) and Moore and Borrill (2002) have pointed out that CDD may not necessarily depend upon processes related to sound source segregation, but instead could hinge upon peripheral auditory processes related to masking/suppression. By this account, the coincidence between the energy peaks of the masker and those of the signal make the masking/suppression of the signal particularly efficient. Performing an experiment in which the masker in the A/A condition had a leading temporal fringe, Moore and Borrill found that their listeners obtained no improvement in signal threshold with this asynchrony. They pointed out that if poor signal detection in the A/A condition were due to perceptual fusion between masker and signal, the powerful sound segregation cue of onset asynchrony should have resulted in a threshold improvement. Their finding of no threshold improvement therefore undermined the perceptual fusion hypothesis and instead provided support for the masking/suppression hypothesis. In a later study by Hall *et al.* (2006), the results from several listeners were consistent with the findings of Moore and Borrill (2002), with A/A thresholds being similar between conditions where signal and masker were gated synchronously and conditions where the masker had a leading fringe. However, Hall *et al.* (2006) found that other listeners, who had relatively high thresholds in the synchronous A/A condition, achieved substantially lower thresholds in the asynchronous A/A condition. They speculated that in these listeners, at least part of the CDD effect was not due to peripheral factors but, instead, was related to perceptual fusion. Further conditions tested by Hall *et al.*, where the masker had spectral uncertainty on a trial by trial basis (e.g., Neff and Callaghan, 1987; Neff and Green, 1987; Neff and Callaghan, 1988; Lutfi, 1990; Leek *et al.*, 1991; Kidd *et al.*, 1994, 2002; Richards *et al.*, 2002; Kidd *et al.*, 2003), were also consistent with an interpretation that perceptual fusion factors contributed to at least part of the CDD effect in some listeners. Nevertheless, results of Hall *et al.* (2006) indicated that the across-frequency difference in fluctuation pattern associated with the A/B conditions was a relatively weak cue for perceptual segregation when contrasted with the cue of onset asynchrony. This is consistent

[a]Author to whom correspondence should be addrdssed. Electronic mail: jwh@med.unc.edu.

with the interpretation of Turgeon *et al.* (2002) that, compared to asynchrony, comodulation is a relatively weak grouping/segregation cue.

The present study examined CDD for fixed-frequency signal/masker stimuli in children and in adults. There are two related reasons that such a developmental approach might be informative. One is that results should provide further insight into the nature of the CDD phenomenon. If the interpretation of Hall *et al.* (2006) is correct that at least part of the CDD in some listeners arises from effects related to perceptual fusion but that the associated cues are relatively weak, then it is likely that, compared to adults, CDD in children should be relatively small. This follows because whereas some children appear to enjoy nearly adult-like release from masking for the relatively strong perceptual segregation cue of signal/masker onset asynchrony (Hall *et al.*, 2005; Leibold and Neff, 2007), there is some evidence that their ability to benefit from less salient cues for masking release can be quite poor in comparison to adults. For example, whereas Hall *et al.* (2005) found that signal/masker onset asynchrony was associated with substantial release from informational masking in both adults and children, the cue of lateralization via interaural intensity difference resulted in a modest masking release for adults and essentially no masking release for children. Thus, if part of CDD in adult listeners is related to the use of a relatively weak cue for sound source grouping/segregation, then relatively small CDD might be expected for children. In addition to providing further insight into the nature of CDD, the present approach should improve our understanding of the development of sound source segregation processes. Specifically, the results should allow examination of the idea that the development of sensitivity to perceptual segregation/grouping cues may be prolonged for cues that appear to be relatively weak in adults.

II. METHODS

A. Listeners

There were nine adult listeners ranging in age from 18 to 51 years. There were fifteen children ranging in age from 4.8 to 10.1 years (with a mean of 8.0 years and standard deviation of 2.0 years). Listeners had thresholds of 20 dB HL (ANSI, 2004) or better between octave frequencies of 0.25 and 8.0 kHz.

B. Stimuli

The signal was a 30-Hz wide band of noise centered on 2 kHz. The masker was a set of 30-Hz-wide noise bands having center frequencies of 0.870, 1.169, 1.540, 2.570, 3.280, and 4.160 kHz. These frequencies were the same as those used in our previous CDD experiment on adult listeners (Hall *et al.*, 2006). Thresholds were obtained for both A/A conditions where both the masking and signal bands were comodulated and A/B conditions where the envelope of the signal was independent with respect to the envelopes of the comodulated masking bands. Each masking band was presented at a level of 48 dB SPL. The stimuli were generated in the spectral domain and were converted to the time domain via inverse fast Fourier transform (FFT). The stimuli were played out of one channel of a real time processor (RP2, TDT) at a rate of 24.4 kHz, routed to a headphone buffer (HB7, TDT), and presented over the left earphone of a pair of Senheisser headphones (HD 265).

TABLE I. Correlations between child age and masked threshold for the A/A condition, A/B condition, and A/A condition with the cue of onset asynchrony. Also shown are correlation between child age and the derived measures of CDD and masking release due to onset asynchrony in the A/A condition. Correlations that were significant ($p < 0.05$, two tailed) are noted by an asterisk.

	Threshold estimates			Derived measures	
	A/A	A/B	A/A Fringe	CDD	Masking release due to onset asynchrony
r	−0.51	−0.58*	−0.59*	0.39	−0.44
p	0.052	0.025	0.026	0.150	0.120

The signal and masking bands were either gated synchronously or were gated such that the masker bands were turned on before the signal band (all bands were gated off together). Gating was accomplished via multiplication with a 50-ms, raised cosine. In the synchronous gating conditions, the signal and masker had a duration of 550 ms, including ramps. In the asynchronous gating conditions, the signal was gated on 200 ms after the masker, and both signal and masker were fully gated off 550 ms later. The interstimulus interval was 400 ms in the synchronous and 200 ms in the asynchronous condition.

C. Procedure

The task used a three-alternative forced-choice procedure with the signal level adjusted in a two-down one-up track estimating the 70.7% correct point on the psychometric function (Levitt, 1971). The signal level was adjusted in steps of 4 dB for the first two reversals and then in steps of 2 dB for the remaining six reversals. Threshold was taken as the average level at the last six reversals. All thresholds were obtained in blocks, by condition, with conditions completed in a random order. Three threshold estimates were obtained in each condition, with a fourth estimate obtained in instances where the first three thresholds varied by more than 3 dB. Listening intervals were marked visually using animation on a video monitor. Over the course of a threshold run, a cartoon picture was revealed, in the form of a jigsaw puzzle, with one piece exposed following each correct response. The cartoon was completely revealed and performed a 2-s animation at the end of the threshold run. All listeners used this method.

III. RESULTS AND DISCUSSION

Data of the children were initially analyzed to determine whether the correlations between age and CDD or between age and the masking release due to onset asynchrony in the A/A condition were significant for the group of children tested here. This was done to determine whether the child data should be separated into subgroups by age for comparisons with adult data. The correlations between age and these derived measures were not statistically significant (see Table

TABLE II. A/A and A/B thresholds (dB SPL) and derived measures of CDD and masking release (dB) due to onset asynchrony. Standard deviations for the mean data are shown in parentheses. The nine adults listeners (A–I) are shown in the top part of the table and the fifteen child listeners (a–o) are shown in the bottom part of the table. Age (years) is shown for children. The entry "NT" indicates incomplete data.

	Fringe absent			Fringe present			Masking release due to onset asynchrony	
	A/A	A/B	CDD	A/A	A/B	CDD_{ASY}	A/A	
A	20.7	15.9	4.8	19.6	14.3	5.3	1.1	
B	34.0	28.7	5.3	18.3	12.2	6.1	15.7	
C	24.0	16.6	7.4	26.8	19.1	7.6	−2.8	
D	26.8	16.7	10.2	29.2	20.8	8.3	−2.3	
E	33.6	18.9	14.7	27.0	16.0	11.0	6.6	
F	46.4	31.3	15.1	27.4	20.4	7.0	19.0	
G	40.8	25.6	15.2	32.6	26.1	6.4	8.3	
H	40.3	25.1	15.3	31.1	22.9	8.2	9.2	
I	44.3	21.4	22.8	26.2	19.2	7.0	18.0	
Mean	34.5	22.3	12.3	26.5	19.0	7.5	8.1	
	(9.2)	(5.7)	(5.9)	(4.7)	(4.3)	(1.7)	(8.3)	
								Age
a	46.9	53.3	−6.4	22.4	17.9	4.5	24.5	6.5
b	65.8	71.4	−5.6	52.5	NT	···	13.3	5.4
c	24.9	29.2	−4.3	29.2	22.4	6.8	−4.3	9.8
d	53.7	56.8	−3.2	27.4	24.1	3.4	26.2	7.9
e	33.6	35.0	−1.4	33.6	29.2	4.4	0.0	6.1
f	32.5	28.9	3.6	28.6	23.1	5.4	3.9	9.3
g	74.3	70.6	3.7	58.9	66.9	−8.3	15.3	5.2
h	31.7	26.5	5.2	28.3	25.4	2.9	3.3	10.0
i	18.0	12.1	5.9	18.7	13.2	5.4	−0.7	9.5
j	29.7	22.7	7.0	NT	26.3	···	···	4.9
k	54.1	46.3	7.9	42.3	32.4	9.8	11.9	9.9
l	56.2	48.0	8.2	50.3	41.7	8.7	5.8	7.2
m	42.5	34.3	8.2	34.6	33.6	1.0	7.9	8.6
n	29.2	19.2	10.0	25.4	23.3	2.1	3.8	9.0
o	36.2	23.0	13.2	29.3	23.8	5.6	6.8	10.1
Mean	41.9	38.5	3.5	34.4	28.8	4.0	8.4	
	(16.0)	(18.3)	(6.1)	(12.0)	(12.9)	(4.4)	(9.0)	

I), indicating that the neither the CDD nor the masking release due to onset asynchrony varied reliably with age in the present sample. Some of the correlations between age and masked thresholds were significant, however, indicating better performance with increasing age (see Table I). The correlation with age was significant for the A/B condition, and approached significance for the A/A condition, using two tailed tests and a criterion probability of 0.05. Table I also shows that the correlation with age was significant for the A/A condition where there was a temporal fringe.

The data of individual listeners are shown in Table II, and Fig. 1 summarizes the mean results for the conditions of this experiment. Inspection of Fig. 1 suggests that the children had higher masked thresholds than adults overall. This was tested with a repeated measures analysis of variance with the within subject factors of comodulation (A/A and A/B) and synchrony and the between subject factor of group. This analysis indicated that the children had significantly poorer thresholds than adults ($F_{1,20}=172$; $p<0.0001$). The analysis also indicated significant effects of comodulation ($F_{1,20}=79$; $p<0.0001$) and synchrony ($F_{1,20}=12.1$; $p=0.002$). The only interaction that was significant was between comodulation and group ($F_{1,20}=14.6$; $p=0.001$). This

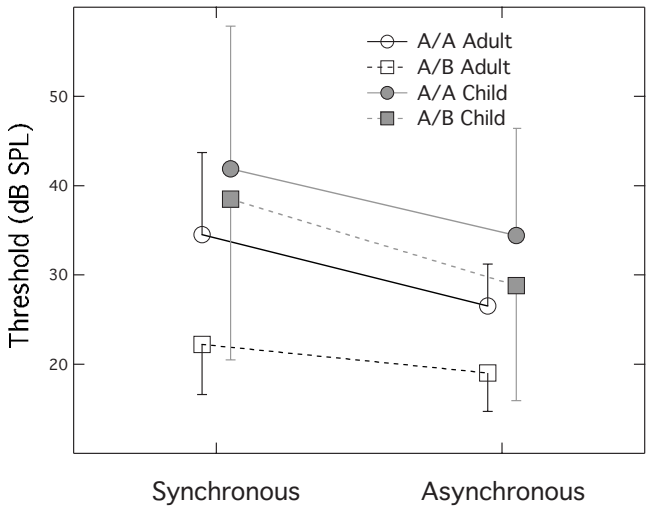

FIG. 1. Mean thresholds (dB SPL) for the synchronous and asynchronous masking conditions, plotted separately for the two masker conditions and observer groups, as indicated in the legend. Error bars show 1 s.d. (only the upper bar is shown for A/A conditions and only the lower bar is shown for A/B conditions for clarity). The data of the adults are depicted by the open symbols and the data of the children are depicted by the closed symbols.

interaction reflects the fact that CDD was larger in adults than children, a finding that is examined more fully in the following sections.

A. CDD and masking release resulting from signal/masker onset asynchrony

Because several aspects of the data of the adults appeared to be related to the magnitude of the CDD, the listeners are ordered alphabetically in Table II in terms of increasing CDD magnitude in order to aid discussion. In agreement with previous investigations of CDD in adults (e.g., McFadden and Wright, 1990; Hall *et al.*, 2006), there was considerable variation in the masked threshold conditions as well as the derived CDDs. In adults, CDD was significant ($t_8=6.8$; $p<0.001$), ranging from 4.8 to 22.8 dB with an average of 12.3 dB; the masking release due to onset asynchrony in the A/A condition was significant ($t_8=2.9$; $p=0.02$), ranging from −2.3 to 19.0 dB with an average of 8.1 dB. In children, the CDD was significant ($t_{14}=2.17$; $p=0.047$), ranging from −6.4 to 13.2 dB with an average of 3.5 dB; the masking release due to onset asynchrony for the A/A stimuli was also significant ($t_{13}=3.5$; $p=0.004$), ranging from −4.3 to 24.5 dB with an average of 8.4 dB. Thus the CDD and the release from masking resulting from onset asynchrony were significant in both adults and children. However, a t-test indicated that the average CDD of 3.5 dB in the children was smaller than the adult average of 12.3 dB ($t_{22}=3.5$; $p=0.002$). The release from masking resulting from onset asynchrony did not differ significantly between adults and children ($t_{21}=0.32$; $p=0.93$). This result suggests that children and adults were, on average, able to use the cue of onset asynchrony with comparable effectiveness.

The difference between the A/A and the A/B thresholds for the case where the masker and signal were gated *asynchronously* was also calculated. We will refer to this as CDD_{ASY} to differentiate it from the more standard CDD where the masker and signal are gated on and off synchronously (see Table II). Whereas the adults showed an average CDD of 12.3 dB, the average CDD_{ASY} was 7.5 dB, a reduction that was statistically significant ($t_8=2.6$; $p=0.03$). The average CDD_{ASY} for the children of 4.0 dB was similar to their average CDD of 3.5 dB, and these values did not differ significantly ($t_{13}=0.053$; $p=0.96$). The CDD_{ASY} for the children was significantly smaller than that for the adults ($t_{20}=3.4$; $p=0.04$).

Although the above-mentioned analyses indicated several statistically significant differences between the results of the children and adults, it is important to note that there were large individual differences such that many children had results that were broadly within the adult range. For example, although the CDD of children was significantly smaller than that of the adults, the CDDs of six of the fifteen children were within 1 s.d. of the adult mean. Similarly, although the masked thresholds were higher in the children than in the adults, there was also considerable overlap between the groups for these thresholds (see Table II).

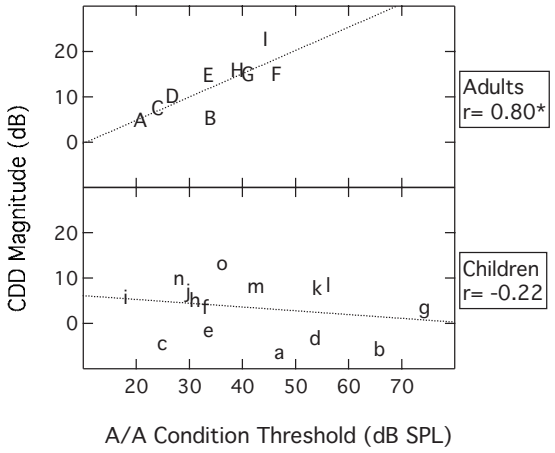

FIG. 2. The magnitude of CDD is plotted against the threshold in the A/A condition. The best-fitting regression line is also plotted. The data of the individual adults and children are plotted in the upper and lower panels, respectively. Correlations that are significant at the 0.05 probability criterion (two-tailed) are identified with an asterisk.

B. CDD and perceptual fusion resulting from comodulation

Several aspects of the results are pertinent to the issue of whether CDD is related to perceptual fusion resulting from comodulation. The top panel of Fig. 2 shows a plot of CDD against the threshold in the A/A condition for the adult listeners. As can be seen in Fig. 2, there was a tendency for the adults with high A/A thresholds also to show relatively high CDDs ($r=0.80$; $p=0.01$). One interpretation of this significant correlation is that a factor contributing to high A/A thresholds in some adult listeners is perceptual fusion of the signal and masker due to comodulation; the threshold improves in the A/B condition because the signal and masker can be segregated when their modulation patterns are independent. Conversely, listeners with relatively low A/A thresholds do not have large effects related to perceptual fusion due to comodulation, and therefore do not show a large benefit when the segregation cue related to independent modulation is available in the A/B condition. Inspection of the bottom panel of Fig. 2 shows that, among children, the relation between CDD and the A/A threshold was not significant ($r=-0.22$; $p=0.44$). Possible reasons for this pattern of results are considered in Sec. IV.

As just discussed, the comparison of thresholds in the A/A condition with the magnitude of CDD may provide an indication of a release from perceptual fusion resulting from comodulation. Release from perceptual fusion can also result when a temporal fringe is introduced in the A/A condition. Figure 3 plots the masking release resulting from onset asynchrony in the A/A stimulus configuration. The top panel indicates a tendency for the adults with high A/A thresholds also to show relatively great making release due to onset asynchrony ($r=0.86$; $p=0.003$). Together, the top panels of Figs. 2 and 3 suggest that adults with high A/A thresholds show improved performance with perceptual segregation cues based upon either across-frequency modulation pattern or onset asynchrony. This interpretation is also consistent with the data trends for CDD and masking release due to

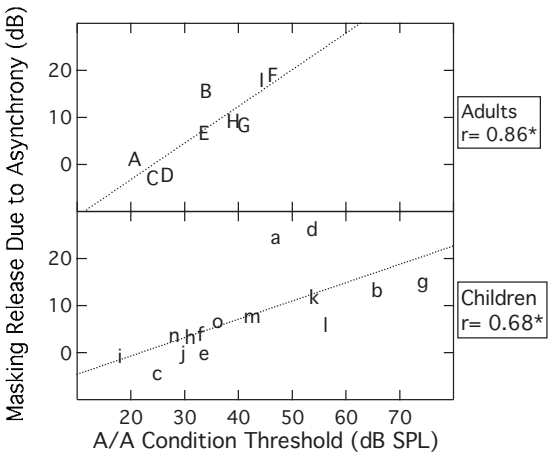

FIG. 3. The magnitude of the masking release resulting from onset asynchrony is plotted against the threshold in the A/A condition. The best-fitting regression line is also plotted. The data of the individual adults and children are plotted in the upper and lower panels, respectively. Correlations that are significant at the 0.05 probability criterion (two-tailed) are identified with an asterisk.

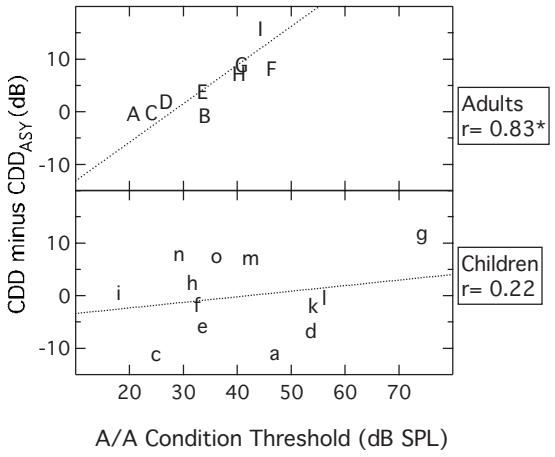

FIG. 4. The difference between CDD and CDD_{ASY} (CDD minus CDD_{ASY}) is plotted against the threshold in the A/A condition. The best-fitting regression line is also plotted. The data of the individual adults and children are plotted in the upper and lower panels, respectively. Correlations that are significant at the 0.05 probability criterion (two-tailed) are identified with an asterisk.

onset asynchrony reported in Hall *et al.* (2006). The bottom panel of Fig. 3 indicates that, among children, there was also a tendency for higher A/A thresholds to be associated with relatively great masking release due to onset asynchrony ($r=0.68$; $p=0.007$). That is, although high thresholds in the A/A masker condition were not associated with larger values of CDD (Fig. 2, bottom), they were associated with greater masking release due to asynchronous onset (Fig. 3, bottom). This suggests that high thresholds in the A/A conditions for children may not be related to fusion due to comodulation, but rather some other nonenergetic masking that can be reduced by onset asynchrony.

Recall that among adults, the CDD_{ASY} was smaller than the CDD. The smaller CDD_{ASY} is consistent with an interpretation that the CDD can result from both energetic masking and masking related to perceptual fusion, and that masking related to perceptual fusion is reduced under conditions of asynchronous gating. By this interpretation, the expectation is that adults showing higher A/A condition threshold values (and therefore relatively large effects related to perceptual fusion due to comodulation) should have a relatively great difference between CDD and CDD_{ASY}. In contrast, if children do not demonstrate a perceptual fusion effect related to comodulation, a strong association between the A/A condition threshold and the difference between CDD and CDD_{ASY} is not expected. Figure 4 supports these expectations: Among the adults (top panel) high A/A condition thresholds were associated with a relatively great difference between CDD and CDD_{ASY} ($r=0.83$; $p=0.006$); among the children, this was not the case ($r=0.22$; $p=0.44$).

IV. GENERAL DISCUSSION

Consistent with the previous study by Hall *et al.* (2006), the results of the present investigation indicated that adults with relatively high A/A thresholds were also likely to have relatively large CDDs. One interpretation of this result involves the idea that CDD (relatively worse performance in the A/A condition than in the A/B condition) can arise from at least two factors: (1) a peripheral/energetic factor wherein comodulated flanking bands provide efficient masking and suppression of a comodulated signal; and (2) a central factor wherein perceptual fusion due to comodulation makes it difficult to separate the signal from the masker. By this interpretation, it is hypothesized that the adults showing the largest CDDs are those for whom the central, perceptual fusion factor has a relatively strong influence. A result that supported this interpretation was that adults with larger CDDs tended also to have higher thresholds in the A/A condition. There were several indications that, on average, children did not show a large CDD component related to perceptual fusion due to common modulation. For example, the CDD in children was relatively small in magnitude (although individual differences were noted), and there was no significant correlation between CDD and the threshold in the A/A condition. Overall, the results of the present study did not provide evidence that the A/A condition thresholds of the children tested were elevated due to perceptual fusion resulting from comodulation. This could occur if children were not very sensitive to comodulation as a perceptual fusion cue. It is possible that sensitivity to this grouping cue has a relatively protracted period of development. A related possibility is that high A/A thresholds in children are dominated by factors other than the comodulation between the signal and masker. For example, children may be more likely than adults to have difficulty honing in on a frequency-specific target in the context of a complex background composed of multiple tones or narrow bands of noise. Consistent with this interpretation, Leibold and Neff (2007) found that children are more likely than adults to show informational masking not only under conditions of masker uncertainty, but also in conditions where a multiple-component maskers are fixed in frequency composition from trial to trial (as was the case in the present study). Such masking in the children of the present study could have overridden weaker effects related to comodulation.

The present CDD results in children are relevant to previous developmental results obtained in a comodulation masking release (CMR) study (Hall *et al.*, 1997). That study indicated that children were able to maintain CMRs similar to those of adults when two unique patterns of comodulation were carried by two separate sets of simultaneously present noise bands. One interpretation of this result was that children were as capable as adults in separating the two sets of noise bands by virtue of their different modulation patterns. This might seem inconsistent with an interpretation that the CDD of children is not influenced by perceptual fusion arising from comodulation. It is possible that this apparent inconsistency is related to stimulus factors. An important feature of the Hall *et al.* (1997) study is that the noise bands were presented continuously throughout a threshold run. This would give a listener extended opportunities to note comodulation among the various noise bands. In the synchronous conditions of the present study, the relatively brief nature of the gated stimuli would have limited the opportunity for the analysis of comodulation, and the common gating among the noise bands could have created a bias for grouping all of the noise components together. It is possible that children are less able to demonstrate grouping/segregation effects related to comodulation under such relatively challenging circumstances.

A finding of the present experiment that does not follow in a straightforward manner from the accounts considered thus far is that the adults showed a larger CDD_{ASY} than the children. It seems reasonable to speculate that the CDD_{ASY} of adults mostly reflects peripheral masking/suppression because masking related to more central auditory grouping cues should be largely overcome by cues related to onset asynchrony. If the CDD_{ASY} is indeed peripherally driven, it is not clear why children would show a smaller CDD_{ASY} than adults. This follows because there is evidence that peripheral auditory processing matures quite rapidly (Olsho, 1985; Abdala and Folsom, 1995). One possible interpretation is that despite a cue of onset asynchrony, a small part of the CDD_{ASY} in adults is driven by a central effect related to grouping by comodulation.

V. CONCLUSIONS

(1) Children showed higher masked detection thresholds than adults, and there was a tendency for masked thresholds to improve with increasing age among the children.
(2) Both adults and children showed a significant CDD. Within the data of the children, there was no significant correlation between age and CDD, and CDD was smaller for children than for adults. The results were consistent with an interpretation that perceptual fusion arising from comodulation plays little or no role in the CDD of child observers. It was speculated that this could derive from poor sensitivity to comodulation as a perceptual fusion cue. Alternatively, a dominant informational masking effect, perhaps related to a difficulty in separating a frequency-specific target from a complex background, could override perceptual fusion effects related to comodulation. Although these interpretations apply to the average data, it was noted that there were large individual differences, with some of the children having CDDs within the adult range.
(3) Both adults and children showed a significant CDD_{ASY}. The CDD_{ASY} was smaller than the CDD for the adults, but not for the children. The CDD_{ASY} was smaller for the children than for the adults. It was suggested that even though the CDD_{ASY} conditions involve onset asynchrony cues that reduce perceptual fusion between the signal and masker, perceptual fusion due to comodulation may nevertheless have a small contribution to the CDD_{ASY} in the adult listeners. Such an effect could account for the finding that the CDD_{ASY} was larger in the adults than in the children.
(4) Both adults and children showed masking release due to onset asynchrony. Among the children, this masking release was not significantly correlated with listener age. The magnitude of this masking release did not differ between adults and children, consistent with earlier findings indicating that the perceptual segregation cue of onset asynchrony shows a relatively early development.

ACKNOWLEDGMENTS

This work was supported by NIH NIDCD Grant No. R01 DC00418. Lori Leibold, Ruth Litovsky, and two anonymous reviewers provided helpful comments on a previous version of this manuscript. Madhu B. Dev and Lisa Whittle assisted in running subjects and supplied technical help.

Abdala, C., and Folsom, R. C. (**1995**). "The development of frequency resolution in humans as revealed by the auditory brain-stem response recorded with notched-noise masking," J. Acoust. Soc. Am. **98**, 921–930.
ANSI (**2004**). "Specification for audiometers," *ANSI S3.6-2004* (American National Standards Institute, New York).
Borrill, S. J., and Moore, B. C. (**2002**). "Evidence that comodulation detection differences depend on within-channel mechanisms," J. Acoust. Soc. Am. **111**, 309–319.
Cohen, M. F., and Schubert, E. D. (**1987**). "The effect of cross-spectrum correlation on the detectability of a noise band," J. Acoust. Soc. Am. **81**, 721–723.
Hall, J. W., Buss, E., and Grose, J. H. (**2005**). "Informational masking release in children and adults," J. Acoust. Soc. Am. **118**, 1605–1613.
Hall, J. W., Buss, E., and Grose, J. H. (**2006**). "Comodulation detection differences for fixed-frequency and roved-frequency maskers," J. Acoust. Soc. Am. **119**, 1021–1028.
Hall, J. W., Grose, J. H., and Dev, M. B. (**1997**). "Auditory development in complex tasks of comodulation masking release," J. Speech Lang. Hear. Res. **40**, 946–954.
Kidd, G., Jr., Arbogast, T. L., Mason, C. R., and Walsh, M. (**2002**). "Informational masking in listeners with sensorineural hearing loss," J. Assoc. Res. Otolaryngol. **3**, 107–119.
Kidd, G., Jr., Mason, C. R., Arbogast, T. L., Brungart, D. S., and Simpson, B. D. (**2003**). "Informational masking caused by contralateral stimulation," J. Acoust. Soc. Am. **113**, 1594–1603.
Kidd, G., Jr., Mason, C. R., Deliwala, P. S., Woods, W. S., and Colburn, H. S. (**1994**). "Reducing informational masking by sound segregation," J. Acoust. Soc. Am. **95**, 3475–3480.
Leek, M. R., Brown, M. E., and Dorman, M. F. (**1991**). "Informational masking and auditory attention," Percept. Psychophys. **50**, 205–214.
Leibold, L. J., and Neff, D. L. (**2007**). "Effects of masker-spectral variability and masker fringes in children and adults," J. Acoust. Soc. Am. **121**, 3666–3676.
Levitt, H. (**1971**). "Transformed up-down methods in psychoacoustics," J. Acoust. Soc. Am. **49**, 467–477.
Lutfi, R. A. (**1990**). "How much masking is informational masking?" J. Acoust. Soc. Am. **88**, 2607–2610.

McFadden, D. (**1987**). "Comodulation detection differences using noise-band signals," J. Acoust. Soc. Am. **81**, 1519–1527.
McFadden, D., and Wright, B. (**1990**). "Temporal decline of masking and comodulation detection differences," J. Acoust. Soc. Am. **88**, 711–724.
Moore, B. C., and Borrill, S. J. (**2002**). "Tests of a within-channel account of comodulation detection differences," J. Acoust. Soc. Am. **112**, 2099–2109.
Neff, D. L., and Callaghan, B. P. (**1987**). "Simultaneous masking by small numbers of sinusoids under conditions of uncertainty," in *Auditory Processing of Complex Sounds*, edited by W. A. Yost and C. S. Watson (Erlbaum, Hillside, NJ), pp. 37–46.
Neff, D. L., and Callaghan, B. P. (**1988**). "Effective properties of multicomponent simultaneous maskers under conditions of uncertainty," J. Acoust. Soc. Am. **83**, 1833–1838.
Neff, D. L., and Green, D. M. (**1987**). "Masking produced by spectral uncertainty with multicomponent maskers," Percept. Psychophys. **41**, 409–415.
Olsho, L. W. (**1985**). "Infant auditory perception: Tonal masking," Infant Behav. Dev. **8**, 371–384.
Richards, V. M., Tang, Z., and Kidd, G. D., Jr. (**2002**). "Informational masking with small set sizes," J. Acoust. Soc. Am. **111**, 1359–1366.
Turgeon, M., Bregman, A. S., and Ahad, P. A. (**2002**). "Rhythmic masking release: Contribution of cues for perceptual organization to the Cross-spectral fusion of concurrent narrow-band noises," J. Acoust. Soc. Am. **111**, 1819–1831.
Wright, B. A. (**1990**). "Comodulation detection differences with multiple signal bands," J. Acoust. Soc. Am. **87**, 293–303.

Perception of suprathreshold amplitude modulation and intensity increments: Weber's law revisited[a)]

Magdalena Wojtczak[b)] and Neal F. Viemeister
Department of Psychology, University of Minnesota, 75 East River Road, Minneapolis, Minnesota 55455

(Received 17 May 2007; revised 3 January 2008; accepted 11 January 2008)

The perceived strength of intensity fluctuations evoked by suprathreshold sinusoidal amplitude modulation (AM) and the perceived size of intensity increments were compared across levels of a wideband noise and a 1-kHz tone. For the 1-kHz tone, the comparisons were made in quiet and in a high-pass noise. The data indicate that suprathreshold modulation depths and intensity increments, perceived as equivalent across levels, follow a pattern resembling Weber's law for noise and the "near miss" to Weber's law for a tone. The effect of a high-pass noise was largely consistent with that observed for AM and increment detection. The data suggest that Weber's law is not a direct consequence of the dependence of internal noise on stimulus level, as suggested by multiplicative internal noise models. Equal loudness ratios and equal loudness differences (computed using loudness for the stationary portions before and after the increment) accounted for the increment-matching data for noise and for the tone, respectively, but neither measure predicted the results for both types of stimuli. Predictions based on log-transformed excitation patterns and predictions using an equal number of intensity just-noticeable differences were in qualitative, but not quantitative, agreement with the data. © *2008 Acoustical Society of America.*
[DOI: 10.1121/1.2839889]

PACS number(s): 43.66.Fe, 43.66.Lj [RYL] Pages: 2220–2236

I. INTRODUCTION

An important general question in psychophysics is whether the phenomena seen using threshold measurements, those based on detection and discrimination, generalize to suprathreshold situations where the stimuli are highly detectable and discriminable. An example, and the focus of this paper, is whether the lawful relationships seen for detecting intensity changes are also seen for changes that are highly detectable. For example, does something analogous to Weber's law hold for intensity changes that are readily perceptible?

There are several reasons such questions are important. Clearly, most real-world listening involves changes that are readily perceived. The amplitude and frequency changes that occur in speech, for example, are orders of magnitude larger than intensity and frequency just-noticeable differences (JNDs). The question is whether or not the effects seen in JND measurements are also applicable to suprathreshold changes. It is possible that the strategies, cues, and processes used by listeners in a threshold task are of little relevance to everyday auditory perception. This raises the question of what "threshold psychophysics" has told us about real listening.

At the theoretical level, threshold psychophysics has provided a wealth of information about normal and impaired hearing. However, the theoretical notions that have been developed based on threshold psychophysics may not be applicable to suprathreshold situations. In addition to the strategy/cue problem mentioned previously, there is the problem of "internal noise." Internal noise is an ill-defined but necessary construct that is invoked in most contemporary models of detection and discrimination (e.g., Green and Swets, 1988; Colburn *et al.*, 2003). It often refers to stochastic limitations that are characteristic of sensory transmission (e.g., Teich and Khanna, 1985) but also may involve notions such as decision noise, memory noise, and nonoptimal processing. Internal noise is necessary because in many, perhaps most, threshold situations performance is not limited by the stochastic properties of the stimuli (e.g., Raab and Goldberg, 1975; Tanner, 1961). In intensity discrimination of pure tones, for example, human performance is far worse than that predicted from the (negligible) variability present in the stimuli: some sort of internal variability seems necessary to account for human performance.

The problem with invoking internal noise is, essentially, that we know very little about it. Measurements of auditory-nerve responses have consistently demonstrated that the variance of the spike count can be approximated by a Poisson process (Young and Barta, 1986; Winter and Palmer, 1991). Estimates of spike count variance at higher stages of the auditory pathway have been very sparse. Limited data from the cochlear nucleus (Palmer and Evans, 1982) and the inferior colliculus (Nelson and Carney, 2007) show no clear dependence of the variance on the mean spike count. It is difficult to measure internal noise psychophysically, although attempts to estimate it have been made (Spiegel and Green, 1981; Jesteadt *et al.*, 2003). Thus, we have an unwanted uncertainty in our theoretical efforts. To return to the example of pure-tone intensity discrimination, it is clear that one can "explain" the JND data, including the fundamental

[a)]Portions of these data were presented at the 135th Meeting of the Acoustical Society of America, 1998. June 20–26, Seattle, WA.
[b)]Electronic-mail: wojtc001@umn.edu

 0001-4966/2008/123(4)/2220/17/$23.00 © 2008 Acoustical Society of America

relationship between the JND and intensity, by postulating arbitrary characteristics of the internal noise (e.g., Allen and Neely, 1997). More generally, if the properties of internal noise are even partly responsible for threshold phenomena, such as Weber's law, then models based on threshold data may not be applicable to suprathreshold processing where the internal noise that limits threshold performance is unlikely to affect perception. In the context of signal detection theory (Green and Swets, 1988), threshold discrimination is limited by internal noise because of the variability it imposes: the distributions of the decision variable overlap. For suprathreshold intensity, changes, the distributions are sufficiently separated and the intensities before and after the change are highly discriminable. An evaluation of a suprathreshold difference (change) between two perceived intensities is therefore affected by the difference between the means of the corresponding distributions, but not by the variability from the internal noise that limits the ability to discriminate them.

The present study is concerned with the perception of suprathreshold intensity/amplitude changes, specifically, those produced by discrete intensity changes and those produced by sinusoidal amplitude modulation (AM). The reason for this emphasis is that such dynamic aspects are crucially important for auditory communication and perception (Plomp, 1970; Drullman, 2005): we need to know whether our understanding of dynamic processing based on threshold psychophysics extends to suprathreshold changes.

There is a wealth of data and theoretical work on intensity discrimination and AM detection (Tanner, 1961; Treisman, 1964; Viemeister, 1983; Viemeister, 1988; Viemeister and Bacon, 1988, Durlach *et al.*, 1986; for a review of studies on AM see Joris *et al.*, 2003). In brief, for broadband sounds of all but short durations, the intensity JND (ΔI) increases proportionally with the intensity (I) of the standard or pedestal: the Weber fraction ($\Delta I/I$) is constant and thus Weber's law describes intensity discrimination thresholds. For band-limited sounds such as pure tones, there are relatively small, but significant, deviations from Weber's law: The Weber fraction decreases as I increases, a phenomenon known as the "near-miss" to Weber's law (McGill and Goldberg, 1968). There is a close counterpart to these results for detection of AM. For broadband carriers, the modulation index at detection threshold (m) is independent of a carrier level for levels above approximately 20 dB SL (Bacon and Viemeister, 1985). As m is a relative measure, like the Weber fraction, this result is analogous to Weber's law. Similarly, for band-limited carriers, m decreases as the carrier level increases and thus this result is analogous to the near-miss. There is a close empirical relationship, but uncertain theoretical relationship, between intensity-increment detection and detection of sinusoidal AM for both broadband and pure-tone continuous pedestals/carriers (Wojtczak and Viemeister, 1999).

In contrast to the extensive data on intensity discrimination and AM detection, there are relatively few data on the perception of suprathreshold intensity/amplitude changes. Fastl (1983) and Terhardt (1968), using magnitude estimation, studied the effects of modulation rate, modulation depth, and carrier level on the "roughness" and "fluctuation strength" of AM. Fluctuation strength appears to reach a maximum at a modulation frequency of 4 Hz and roughness at 70 Hz. Both increase with increasing m, and for a fixed m and modulation frequency, both increase with increasing carrier level. The latter result was observed for pure-tone and for noise carriers. For pure-tone carriers this is qualitatively consistent with the near-miss effects seen for AM detection, i.e., the results suggest that the effective envelope fluctuations are "magnified" at higher carrier levels. For noise carriers, however, the results contradict those based on AM detection: Constant m at detection threshold suggests that fluctuation strength should also be constant, independent of the carrier level. The data to be presented are consistent with the detection results; this issue will be revisited in the discussion in Sec. IV.

In a study related to the aspects of the present study, Moore *et al.* (1996) used a modulation-matching procedure to investigate whether the effective amplitude changes produced by AM are magnified by loudness recruitment. The results, obtained from listeners with a unilateral hearing loss, indicate that for equal perceived fluctuation strength, the modulation depth in the recruiting ear was considerably less than that in the normal ear when the carriers were equally loud. This suggests, in contrast to the results from modulation detection (Bacon and Viemeister, 1985; Zwislocki and Jordan, 1986) and intensity discrimination (Hellman and Hellman, 1990; Schlauch, 1994; Schroder *et al.*, 1994), that suprathreshold perceived fluctuation depths are related to the slope of the loudness function and thus are magnified in the case of recruitment.

Existing loudness models are generally successful at predicting the loudness functions for stationary stimuli (Moore *et al.*, 1997) and for temporally varying stimuli (Zwicker and Fastl, 1999; Glasberg and Moore, 2002). However, none of the existing models have been used to quantify the perceived size of an intensity increment in terms of a change in loudness. There is little doubt that suprathreshold increments in intensity are perceived in terms of an increment in loudness but it is not clear how exactly the perceived loudness increment is "computed." Attempts to relate threshold intensity discrimination to a change in loudness have provided ambiguous results, suggesting that either intensity JNDs do not necessarily correspond to a constant change in loudness or that the method of "computation" of the loudness change (e.g., a loudness ratio versus loudness difference) is stimulus dependent. Hellman and Hellman (2001) demonstrated that Ekman's law (Ekman, 1956, 1959) appears to hold for loudness of 3 sones and above when intensity discrimination thresholds of pulsed tones (Rabinowitz *et al.* 1976) and beat detection thresholds (Riesz, 1928) are considered. The law states that intensity increments and beats are detected when the *ratio* between loudness corresponding to the intensities to be discriminated reaches a constant value (an analog of Weber's law for loudness, a subjective magnitude). For tones presented in quiet and in notched-noise, equal loudness *differences* have been shown to predict intensity discrimination across levels (Parker and Schneider, 1980; Schneider and Parker, 1987). However, the same strat-

egy failed to predict intensity discrimination for tones in broadband noise (Schneider and Parker, 1990), likely due to suppression of the basilar-membrane response to the tone by the noise.

As stated previously, threshold measurements are affected by internal noise (for deterministic stimuli) and/or external noise associated with the stochastic properties of noise stimuli. However, the variability imposed by such noises presumably plays an insignificant role in the perceived magnitude of highly detectable intensity changes: The changes in the stimulus are much larger than those created by the internal noise or those resulting from inherent intensity fluctuations in the noise stimuli. Thus, it is not clear if the findings regarding threshold intensity discrimination hold true for suprathreshold intensity changes.

The present study examines the effects of level on the perception of highly detectable intensity increments and AM. The general approach is to determine the intensity increments and modulation depths that, respectively, produce the same perceived intensity changes and intensity fluctuations when the stimuli are at different levels. The general aim is to describe the perception and processing of suprathreshold intensity changes.

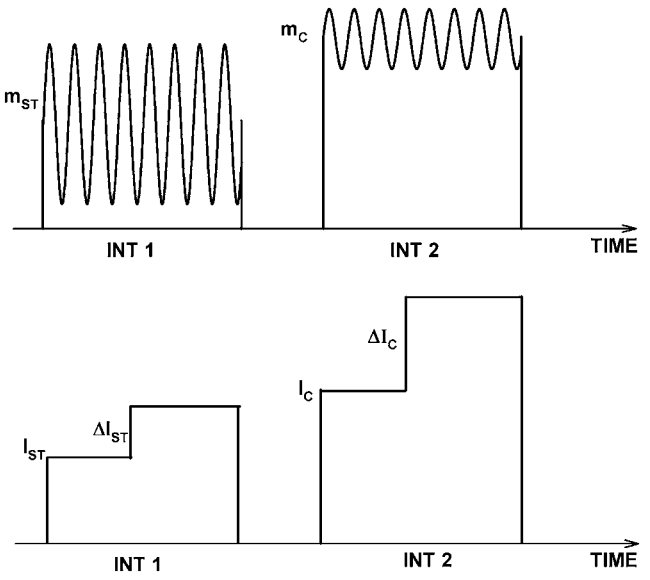

FIG. 1. Examples of envelopes of the stimuli presented in a trial of the modulation-matching (upper panel) and increment-matching tasks. Listeners had to decide which modulation depth, the standard (m_{ST}) or the comparison (m_C), produced stronger perceived fluctuations, or which increment, the standard (ΔI_{ST}) or the comparison (ΔI_C), sounded larger.

II. METHODS

A. Stimuli and procedure

1. Modulation matching

Modulation depths producing perceptually equivalent fluctuations across carrier levels were measured for two types of the carrier: a 1-kHz tone and a Gaussian noise low-pass filtered at 5 kHz. The noise was filtered using an analog filter (Ithaco 4302) with an attenuation rate of 24 dB/oct outside the passband. The carriers were modulated over their entire 500-ms duration by a 16-Hz sinusoid starting at a 0-rad phase. For the tonal carrier, the 500-ms duration included 5-ms raised-cosine ramps. After unsuccessful attempts at using adaptive matching procedures (see Appendix A), a rather complicated roving procedure combined with the two-interval forced-choice (2IFC) technique was used to encourage the listeners to make comparisons between the standard and the comparison intervals within each trial. Examples of the envelopes of the stimuli presented in a trial, consisting of two observation intervals, are shown in the upper panel of Fig. 1. In each trial, a standard and a comparison were presented in a random order. The listeners were instructed to choose the interval, which, according to their subjective judgment, contained stronger intensity fluctuations (terms such as "fluctuations" or "loudness fluctuations" were also used interchangeably to describe the task). The listeners confirmed that they understood the task and they were consistent in their responses, thus no evidence was observed that the instructions were ambiguous. No feedback was provided in this or any subsequent tasks within this study.

Table I lists five conditions (each distinguished by the level of the comparison) in the modulation-matching task, for a 1-kHz carrier. The two numbers used in the name of each condition represent the carrier level of the standard and comparison, respectively. For example, T_60_30 describes a condition where the carrier level of the standard tone (T) was 60 dB SPL and the carrier level of the comparison was 30 dB SPL in every trial within a block. The remaining conditions were: T_60_45, T_60_60, T_60_75, and T_60_90. Thus, for different conditions the carrier level of the comparison was selected from a set of five levels: 30, 45, 60, 75, and 90 dB SPL. In each trial, the modulation depth of the standard was drawn at random from a set of three modulation depths, −6, −8, and −10 dB (in units of 20 log m). As shown by Yost and Sheft (1997), the threshold modulation depth for a 1-kHz carrier gated for 500 ms, presented at a level of 70 dB SPL and modulated by a 16-Hz sinusoid is approximately equal to −28 dB. The three standard modulation depths used in the present study were, therefore, highly detectable (AM detection of the three standard modulation depths would yield an immeasurably large d'). The comparison had a modulation depth drawn at random from a set of eight modulation depths. The exact modulation depths for the comparison were selected for each listener individually, based on pilot sessions. The goal was to use a set of comparison modulation depths for which the proportion of "fluctuations stronger in the comparison" responses would span the range from 0 to 1, approximately. Examples of sets of eight modulation depths for each condition are shown in the fifth column of Table I.

Each standard-comparison pair was presented twice within a block consisting of 48 trials (3 modulation depths of the standard ×8 modulation depths of the comparison ×2) and 25 blocks were run for each condition (i.e., each carrier level of the comparison). The order of conditions was randomized.

For the 1-kHz carrier, the experiment was run with the standard and the comparison presented in quiet in one case and in a background of high-pass noise used to mask the

TABLE I. Conditions in AM matching for a 1-kHz carrier: The standard had a carrier level of 60 dB SPL in each condition and the comparison level changed across conditions from 30 to 90 dB SPL in 15-dB steps. In each trial, the modulation depth of the standard was drawn from the set of the three modulation depths listed in the third column and the modulation depth of the comparison was drawn from the set of the eight depths listed in the fifth column. The sets of comparison depths were different for different listeners and they should be viewed as examples rather than the exact values used for all the listeners (AM depth marked by the asterisk in the fifth column).

	Standard		Comparison*	
Condition	Level	AM depth	Level	AM depth
T_60_30				0
	60	−6	30	−2
		−8		−4
		−10		−6
				−8
				−10
				−12
				−14
T_60_45				−2
	60	−6	45	−4
		−8		−6
		−10		−8
				−10
				−12
				−14
				−16
T_60_60				−3
	60	−6	60	−5
		−8		−7
		−10		−9
				−11
				−13
				−15
				−17
T_60_75				−4
	60	−6	75	−6
		−8		−8
		−10		−10
				−12
				−14
				−16
				−18
T_60_90				−5
	60	−6	90	−7
		−8		−9
		−10		−11
				−13
				−15
				−17
				−19

upper side of the excitation pattern in another case. A high-pass noise has been shown to eliminate the near miss to Weber's law for AM detection by raising thresholds measured at high carrier levels, while having a negligible effect on thresholds at lower levels (Zwicker, 1956; Zwicker, 1970; Wojtczak and Viemeister, 2005). As the noise affected AM detection thresholds, the −10-dB modulation depth produced very small perceived fluctuations, the strength of which was hard to evaluate, for some listeners, in the context of the experiment. Thus, the three standard modulation depths used were −4, −6, and −8 dB. The carrier levels of the standard and comparison tested were the same as those listed in Table I, and the sets of comparison modulation depths were chosen individually in pilot runs. The high-pass noise was generated with a random-noise generator (General Radio 1381) and was presented simultaneously with the standard and the comparison at a spectrum level that was 50 dB below the levels of the respective carriers. It was band-pass filtered with cutoff frequencies at 1.5 and 10 kHz (Kemo VBF/25, 135 dB/Oct). The very steep roll-off and the relatively low level were chosen to prevent or maximally reduce excitation of the 1-kHz place on the basilar membrane by the noise. Even though in precise terms the noise was band-pass, for convenience it will be referred to hereafter as high-pass noise because of its wide bandwidth and high-frequency content (above the frequency of the test tone).

For the noise carrier (N), conditions are listed in Table II. Using the same notation as for the tonal carrier, the first number in the name of each condition indicates the spectrum level of the standard and the second number indicates the spectrum level of the comparison. Thus, in conditions N_20_5, N_20_20, N_20_35, and N_20_50, the standard had a spectrum level of 20 dB SPL (measured at 1 kHz) and the comparison had a spectrum level of 5, 20, 35, and 50 dB SPL, respectively. The order of presentation of different conditions was randomized. Within each condition, the standard could have one of three modulation depths (−4, −6, or −8 dB, in units of $20 \log m$) and the comparison could have one of eight modulation depths (from −2 to −16 dB in 2-dB steps) in a trial. The set of comparison modulation depths was the same for every level of the comparison because pilot runs suggested it always covered a range where proportion of "fluctuations stronger in the comparison" responses extended from just above 0 to the vicinity of 1.

The AM-detection threshold for a 500-ms burst of broadband noise modulated by a 16-Hz sinusoid is about −24 dB, as reported by Viemeister (1979). Therefore, all standard modulation depths used in the present study were highly detectable (AM detection would yield an immeasurably large d').

Except for the high-pass noise that was used to mask spread of excitation, all the stimuli were generated digitally on a NeXT computer using a 16-bit digital/analog converter and a sampling rate of 44.1 kHz. The output was routed through an analog attenuator and presented monaurally via Sony MDR-V6 headphones. The listeners were seated in a sound-insulating booth and provided their responses via computer keyboard.

2. Increment matching

A procedure similar to the one previously described was used to find perceptually equivalent intensity increments across levels, for the same two types of stimuli (a 1-kHz tone

TABLE II. Conditions in AM matching for a noise carrier: The standard had a spectrum level of 20 dB SPL in each condition and the comparison level changed across conditions from 5 to 50 dB SPL in 15-dB steps. In each trial, the modulation depth of the standard was drawn from a set of the three modulation depths listed in the third column and the modulation depth of the comparison was drawn from a set of the eight depths listed in the fifth column. The set of comparison depths was the same in all conditions.

	Standard		Comparison	
Condition	Spectrum level	AM depth	Spectrum level	AM depth
N_20_5				−2
	20	−4	5	−4
		−6		−6
		−8		−8
				−10
				−12
				−14
				−16
N_20_20				−2
	20	−4	20	−4
		−6		−6
		−8		−8
				−10
				−12
				−14
				−16
N_20_35				−2
	20	−4	35	−4
		−6		−6
		−8		−8
				−10
				−12
				−14
				−16
N_20_50				−2
	20	−4	50	−4
		−6		−6
		−8		−8
				−10
				−12
				−14
				−16

and a noise low-pass filtered at 5 kHz). Examples of envelopes of the stimuli presented in a trial are schematically illustrated in the lower panel of Fig. 1.

Each interval of the 2IFC procedure consisted of two 500-ms stimuli whose intensity was incremented halfway through their duration, i.e., a 250-ms increment occupied the second half of the pedestal. The stimuli were separated by a 300-ms silent gap. Listeners were instructed to indicate which increment appeared to be "larger" (terms such as "larger change in intensity" and "larger change in loudness during the stimulus" were also used interchangeably to describe the task). The increments were obtained by an in-phase addition of the appropriately attenuated version of the final 250-ms of the pedestal to itself. The amount of attenuation was chosen to produce the desired increment size. For the 1-kHz tone, the pedestal and its attenuated 250-ms portion added to produce an intensity increment were gated using 5-ms raised-cosine ramps.

TABLE III. Conditions in increment matching for a 1-kHz pedestal: In each condition, two levels of the standard (60 or 63 dB SPL) and two levels of the comparison (either 30 and 45 dB SPL or 75 and 90 dB SPL) were mixed within a block. The middle column shows the set of four standards that were selected at random in each trial. The third column shows the set of 16 comparisons that were also selected at random for each trial. In both cases, the first number represents the level of the pedestal and the second number represents the level of the incremented pedestal. The set of comparison increments was selected individually for each subject in pilot runs and thus, levels of the incremented pedestals (second number) given in the third column (marked by the asterisk) should be viewed as examples and not as the exact levels presented to all the listeners.

Condition	Standards	Comparisons*
T_60/63_30_45		30_35
		30_38
		30_41
		30_44
		30_47
	60_65	30_50
	60_68	30_53
	63_65	30_56
	63_68	
		45_46
		45_48
		45_50
		45_52
		45_54
		45_56
		45_58
		45_60
T_60/63_75_90		75_75.5
		75_76.0
		75_76.5
		75_77.0
	60_65	75_77.5
	60_68	75_78.0
	63_65	75_78.5
	63_68	75_79.0
		90_90.4
		90_90.8
		90_91.2
		90_91.6
		90_92.0
		90_92.4
		90_92.8
		90 93.2

Two levels of the standard and two levels of the comparison were randomly mixed within a block. Table III lists two conditions tested for a 1-kHz pedestal. In condition T_60/63_30/45, the two levels of the comparison mixed within a block were 30 and 45 dB SPL. In condition T_60/63_75/90, the two levels of the comparison mixed within a block were 75 and 90 dB SPL. In both conditions the two levels of the standard were 60 and 63 dB SPL. In each trial, one standard from the middle column and one comparison from the third column were chosen at random.

TABLE IV. Conditions in increment matching for a noise pedestal: Two spectrum levels of the standard (20 or 23 dB SPL) and two spectrum levels of the comparison (5 and 20 dB SPL in one condition and 35 and 50 dB SPL in another condition) were used within a block. The middle column shows the set of the four standards, from which one was selected at random in each trial. The first number represents the level of the pedestal and the second number represents the level of the incremented pedestal. The comparison was drawn from the set of the pedestal-increment combinations listed in the third column, for each condition. The sizes of comparison increments were the same for all conditions $10\log[(\Delta I+I)/I]$ ranged from 1 to 8 dB in 1-dB steps].

Condition	Standards	Comparisons
N_20/23_5_20		5_6
		5_7
		5_8
		5_9
		5_10
	20_24	5_11
	20_25	5_12
	23_24	5_13
	23_25	
		20_21
		20_22
		20_23
		20_24
		20_25
		20_26
		20_27
		20_28
N_20/23_35_50		35_36
		35_37
		35_38
		35_39
	20_24	35_40
	20_25	35_41
	23_24	35_42
	23_25	35_43
		50_51
		50_52
		50_53
		50_54
		50_55
		50_56
		50_57
		50_58

For example, when standard 60_68 and comparison 45_50 were drawn, the standard had a pedestal level of 60 dB SPL and its level was incremented halfway through to the level of 68 dB SPL (an 8-dB increment in units of $10\log[(I+\Delta I)/I]$). The comparison level changed from 45 dB SPL during the pedestal to 50 dB SPL during the increment (a 5-dB increment). The listener decided which stimulus had a larger perceived change in intensity and responded accordingly. After registering the listener's response, the program randomly selected another pair from the sets of the standards and comparisons for the same condition. The eight comparison increments were different for different listeners and were determined based on pilot sessions to produce the proportion of "comparison increment larger" responses that were approximately symmetrically distributed around the 0.5 value (thus, the values in the third column of Table III are only an example). As with the modulation matching, increment matching for the 1-kHz pedestal was performed in quiet and in the presence of a high-pass noise. The high-pass noise had the same bandwidth as in the modulation-matching task, but its spectrum level was −40 dB relative to the level of the pedestal. A higher relative noise level was used because increments in the comparison stimuli were sometimes much larger than the peak-to-carrier decibel difference for the maximum (100%) modulation. The noise needed to be intense enough to make the upper side of the excitation pattern unusable during the increments.

Table IV shows sets of standards and comparisons used for the noise pedestal in two conditions. In condition N_20/23_5/20, two spectrum levels of the comparison used were 5 and 20 dB SPL. In condition N_20/23_35/50, the two spectrum levels of the comparison used were 35 and 50 dB SPL. Two standard levels used in both conditions were 20 and 23 dB SPL. In each trial, the standard was drawn at random from the set shown in the middle column of Table IV and the comparison was drawn from the third column. Each pair of numbers in the middle and the third columns of Table IV indicate the pedestal level and the level after the increment, respectively. The eight comparison increments for the noise pedestals ranged from 1 through 8 dB in 1-dB steps (in units of $10\log[(I+\Delta I)/I]$. This range of increments was chosen because pilot runs showed that it produced the proportion of "comparison increment larger" responses that approximately covered the range from 0 to 1, for at least two of the standard increments.

For both types of pedestals, the 1-kHz tone and the noise, each standard-comparison pair was used once, resulting in 64 trials within one block (4 standards ×16 comparisons). A total of 50 blocks were run for each condition listed in Tables III and IV. The methods for stimulus generation and presentation were the same as in the modulation-matching task.

B. Subjects

A total of six listeners were used in the experiments, one of whom had prior experience in the modulation-matching task. Not every listener provided usable data in all conditions. Data were considered unusable based on the form of the psychometric functions (as will be discussed later). Not all of the listeners were available to complete all the experiments. All listeners had thresholds within 15 dB of the average normal hearing threshold at all audiometric frequencies, as determined by the lab standards obtained by averaging thresholds at these frequencies from a large number of former listeners (mostly undergraduate students) who reported no hearing problems. Listeners were paid an hourly wage for their participation with the exception of listener S1 who is the first author.

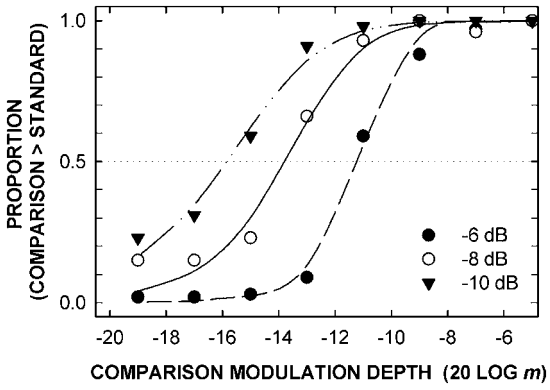

FIG. 2. An example of psychometric functions for a 1-kHz carrier, obtained from modulation matching that used three standard modulation depths, −6, −8, and −10 dB. The carrier level of the standard was 60 dB SPL and the level of the comparison was 90 dB SPL. Data are from listener S1.

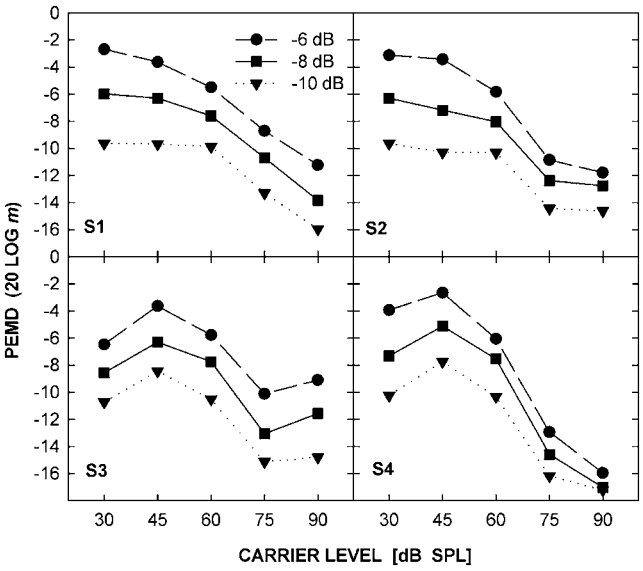

FIG. 3. *PEMDs* for a 1-kHz carrier, plotted as a function of carrier level of the comparison for four listeners. Different symbols and types of connecting lines are for different modulation depths of the standard: −6 dB (circles, dashed line), −8 dB (squares, solid line), and −10 dB (diamonds, dotted line).

III. RESULTS

A. Perceptually equivalent modulation depths (PEMDs)

For each carrier level of the comparison, three psychometric functions were constructed from the modulation-matching data, one for every modulation depth of the standard. Each psychometric function was a plot of the proportion of times the listener evaluated the comparison as having stronger perceived fluctuations than the standard, as a function of the modulation depth of the comparison. Figure 2 shows an example of the three functions obtained from one subject for a 1-kHz tone, where the comparison was presented at 90 dB SPL (condition T_60_90 in Table I).

For a given standard modulation depth, the perceptually equivalent modulation depth (PEMD) of the comparison is defined as the depth yielding the 0.5 proportion of responses that the comparison had stronger fluctuations than the standard. The PEMD was estimated based on a logistic function[1] fitted to the data using a least-squares procedure. As the PEMD is expressed in units of 20 log m, the value of PEMD was constrained to be less than zero while fitting the function.

In the example shown in Fig. 2, the 0.5-point on each psychometric function is shifted toward smaller modulation depths of the comparison relative to the modulation depth of the respective standard. This means that a given modulation depth produces stronger perceived fluctuations in intensity of a 90-dB SPL carrier than in a 60-dB SPL carrier. The psychometric functions are generally distributed over almost the entire range of proportion of "comparison fluctuations stronger" responses between 0 and 1. The functions are ordered along the x-axis according to the magnitude of the standard modulation depth (i.e., the function obtained for the smallest standard modulation depth is to the left of the one for the medium and the largest standard). The fact that the functions do not overlap and that the PEMD increased monotonically with increasing modulation depth of the standard strongly indicates that the listener compared the perceived fluctuation strength between the standard and the comparison intervals rather than making absolute judgments about the fluctuation strength in the comparison.

In general, the psychometric functions were the steepest when the difference between the carrier levels of the standard and comparison was the smallest (15 dB). The functions became shallower as the difference between the levels increased, but the decrease in slope with increasing difference between carrier levels was greater for comparison levels lower than the standard. In all cases, the range of responses was sufficient to reliably estimate the PEMD.

As subjective tasks that require comparisons of perceived magnitudes sometimes produce results that differ substantially across listeners, individual data will be presented when patterns of results vary across listeners and only mean data will be shown when the patterns of results are consistent across listeners. Figure 3 shows estimated PEMDs plotted as a function of the 1-kHz carrier level, for four listeners. Different symbols (and types of connecting lines) correspond to different standard modulation depths.

Since each function shows the PEMD across levels, the three functions plotted in each panel can be thought of as iso-fluctuation-strength curves. For carrier levels below 60 dB SPL, no consistent changes in PEMD with increasing level are apparent in the data. Two listeners, S1 and S2, show a slight decrease in PEMD with increasing carrier level, whereas for S3 and S4, the function is nonmonotonic over the same range of levels. For levels above 60 dB SPL, all four listeners show a relatively sharp decrease in PEMD between 60 and 75 dB SPL. That decrease is followed by an equally sharp decrease in PEMD (S1), no further change (S2), a slight increase (S3), or a more gradual decrease (S4), for levels between 75 and 90 dB SPL.

Figure 4 shows estimated PEMDs for the noise carrier plotted as a function of its spectrum level. No systematic changes in PEMD are apparent although S2 showed a decrease in PEMD with increasing level over a range of spectrum levels between 35 and 50 dB SPL. A t-test was per-

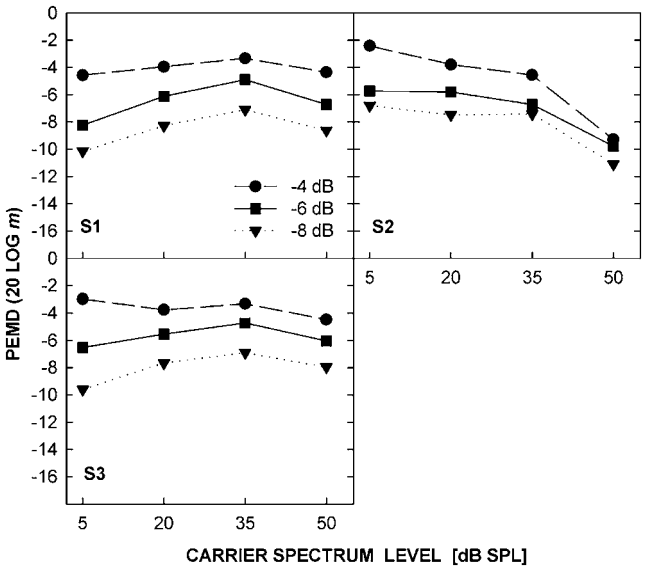

FIG. 4. *PEMDs* for a noise carrier, plotted as a function of carrier level of the comparison for three listeners. Different symbols and types of connecting lines are for different modulation depths of the standard: −4 dB (circles, dashed line), −6 dB (squares, solid line), and −8 dB (diamonds, dotted line).

formed to determine whether or not the slopes of the linear regression functions fitted to each set of data are significantly different from zero, for each listener and each standard modulation depth separately. The test revealed no significant effect of the carrier level on PEMD in all conditions (none of the slopes was significantly different from zero; Howell, 2004).

Thus, the pattern of changes in PEMD depends on the type of carrier, as illustrated by the mean results plotted in Fig. 5, for the 1-kHz tone (left panel) and for noise (right panel). This is not surprising since for tonal carriers, nonlinear spread of excitation is likely to magnify the perceived changes in intensity of the modulated tone at higher levels. For comparison, in the left panel, AM detection thresholds measured for a 1-kHz carrier at different levels are replotted from Wojtczak and Viemeister (1999).

The changes in AM detection threshold across carrier levels for the tone are greater than changes in PEMD over

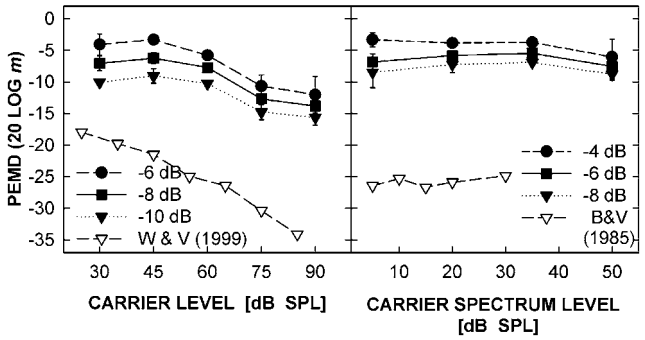

FIG. 5. *PEMDs* averaged across listeners for the 1-kHz carrier (left panel) and the noise carrier (right panel). The error bars represent one standard deviation of the mean. AM detection thresholds are replotted by open triangles from Wojtczak and Viemeister (1999), for a 1-kHz tone (left panel), and from Bacon and Viemeister (1985), for noise (right panel).

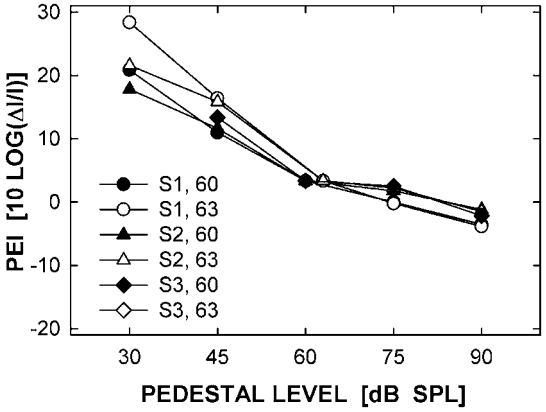

FIG. 6. Individual *PEIs* for a 5-dB increment plotted as a function of the pedestal level of the comparison, for a 1-kHz pedestal. Different types of symbols show data for different listeners. The filled symbols are for the 60-dB SPL pedestal and the open symbols are for the 63-dB SPL pedestal.

the same range of levels (compare the steeper slope of the detection function shown by open triangles with the shallower slopes of the PEMD functions shown by different types of filled symbols, in the left panel). The difference in slopes between the detection function and the PEMD functions in Fig. 5 may in part reflect differences in the stimulus presentation/parameters [a gated carrier modulated at a 16-Hz rate in the present study versus a continuous carrier modulated at a 4-Hz rate, in the study by Wojtczak and Viemeister (1999)]. However, the limited data for pure-tone gated carriers (Zwicker, 1956; Zwicker and Graf, 1987) suggest the level dependence of AM detection is similar to that for continuous carriers and does not differ for the two modulation rates considered. More likely, nonlinear basilar-membrane processing is responsible for the difference between the slopes (as described in detail in the Discussion). The right panel of Fig. 5 shows no change in PEMD across the spectrum level of the noise carrier. This trend is consistent with Weber's law, which holds for AM detection for noise carriers over a comparable range of levels, as shown by the data from Bacon and Viemeister (1985) included for comparison in the right panel (open triangles).[2]

B. Perceptually equivalent increments (PEIs)

Perceptually equivalent increments (PEIs) were estimated from psychometric functions (not presented here) similar to those shown in Fig. 2. For increment matching, the functions showed the proportion of times the listener evaluated the comparison as having a larger intensity increment plotted as a function of the increment in the comparison. As four different standard stimuli were used within each block, four psychometric functions were constructed for every level of the comparison. A logistic function (described in footnote 1) was fitted to the data to estimate the PEI defined as the increment in the comparison yielding the 0.5 proportion of responses that the comparison increment sounded larger than that in the standard. The fitting procedure was performed with a constraint that the PEI expressed in units of $10\log[(\Delta I+I)/I]$ had to be greater than zero.

Figure 6 shows PEIs for a 1-kHz tone plotted as a func-

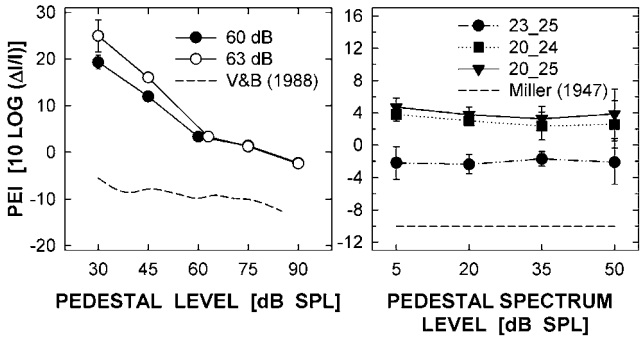

FIG. 7. Mean *PEIs* for a 1-kHz pedestal (left panel) and for a noise pedestal (right panel) averaged across three listeners. The data for the tonal pedestal were obtained for a 5-dB increment in the standard, for two levels of the standard, 60 dB SPL (filled circles) and 63 dB SPL (open circles). The dashed line in the left panel shows increment detection thresholds replotted from Viemeister and Bacon (1988). The data for the noise pedestal (right panel) were obtained for three standards listed in the insert, with the first number representing the spectrum level of the pedestal and the second number representing the spectrum level after the increment. Increment-detection thresholds replotted from Miller (1947) are shown by the dashed line in the right panel. In both panels, error bars represent one standard deviation of the mean.

tion of the pedestal level of the comparison, for three listeners. The PEIs were estimated for only two standard stimuli, the 60-dB pedestal with a 5-dB increment and the 63-dB pedestal with a 5-dB increment (see Appendix B). The functions can be thought of as iso-increment-strength functions.

The PEI (on the y-axis) is expressed in units of $10\log(\Delta I/I)$ to emphasize changes in PEI that would be concealed when using the $10\log[(\Delta I+I)/I]$ units that are more compressive for small intensity increments. The general shape of the function is very similar for all the listeners but there are large intersubject differences between the estimated PEIs at low pedestal levels. For the lowest pedestal level of the comparison (30 dB SPL), the psychometric functions obtained from listener S3 were too shallow to estimate the 0.5-point reliably. Consequently, the data for the lowest level are missing for S3. The PEIs corresponding to a 5-dB increment at comparison levels of 60 and 63 dB SPL were not estimated from the matching data. The points were plotted based on the assumption that equal increments in the same pedestal level must sound equal and thus, the PEI converted to units of $10\log[(\Delta I+I)/I]$ was assigned a value of 5 dB in the two conditions. To evaluate the potential effect of the procedure on the matched increments, one listener ran a set of blocks with the comparison levels of 60 and 63 dB SPL (the same as the standards). The PEIs differed by less than 1 dB from the 5-dB standard increments (data not shown) for both pedestal levels of the standard, proving that the assumption about equal increments for equal pedestal levels is justified. For high pedestal levels of the comparison, there is very little variability in PEI across listeners. The left panel of Fig. 7 shows the PEIs for a 1-kHz tone averaged across listeners for the two pedestal levels of the standard used. Both functions show a decrease in PEI with increasing level that is steeper at levels below 60 dB SPL and shallower at higher levels. This result is generally consistent with the increasing role of spread of excitation as the pedestal level increases. Somewhat surprising is the observation that the greatest rate of change in PEI corresponds to the range of levels over which the PEMD remained approximately constant (cf. left panel in Fig. 5). This apparent inconsistency regarding the role of spread of excitation will be discussed below in more detail. The left panel also shows increment detection thresholds as a function of pedestal level (dashed line), replotted from Viemeister and Bacon (1988). Detection thresholds decrease with increasing pedestal level but the rate of that decrease is slower than for suprathreshold intensity changes, for levels below 60 dB SPL. This result can be explained in terms of greater differences across levels between the spread of excitation produced by the pedestal and a suprathreshold increment compared with that between excitations produced by the pedestal and a level that is just discriminable from the pedestal.[3] Although the qualitative changes in PEI with level are predictable, the size of the effect is striking. The mean data (left panel of Fig. 7) show that a change in level from 60 to 65 dB SPL (a 5-dB increment) sounds perceptually equal to a change in level from 30 to 49 dB SPL (a 19-dB increment). A change in level from 63 to 68 dB SPL (a 5-dB increment) sounds perceptually equal to the change in level from 30 to 55 dB SPL (a 25-dB increment). Thus, the near miss to Weber's law observed for detection of intensity increments for tonal pedestals becomes a "severe departure" from Weber's law for suprathreshold intensity changes.

For the noise pedestal, the PEIs were estimated for three out of the four standard stimuli used in the experiment, a 20-dB pedestal with increments of 4 and 5 dB and a 23-dB pedestal with a 2-dB increment. The right panel of Fig. 7 shows PEIs for noise averaged across three listeners.

A t-test performed separately on each set of data revealed that the slopes of the PEI functions were not significantly different from zero ($p>0.05$). This result is consistent with Weber's law observed for increment-detection threshold, as shown by the dashed line representing the level-independent JND reported by Miller (1947) for broadband noise, expressed in units of $10\log(\Delta I/I)$. Thus, it appears that Weber's law applies to both intensity JNDs and to the perception of suprathreshold intensity increments.

C. Effect of highpass noise on PEMD and PEI functions of level for tones

For tones, AM and increment detection thresholds show level dependence known as the near miss to Weber's law: Thresholds improve with increasing level of the tonal carrier/pedestal due to the nonlinear spread of excitation (Viemeister, 1972; Moore and Raab, 1974; Florentine and Buus, 1981). The level dependence can be eliminated by using a high-pass noise with a cutoff frequency and a level chosen to mask the nonlinear spread of excitation toward regions on the BM that are most sensitive to frequencies above that of the tonal stimulus (e.g., Zwicker, 1956; Plack and Carlyon, 1995). Results presented in the previous sections demonstrate that for a 1-kHz tone, PEMDs and PEIs decrease with increasing stimulus level, although the pattern of the level dependence is different for the two subjective measures. The effect of a high-pass noise on the perception of suprathresh-

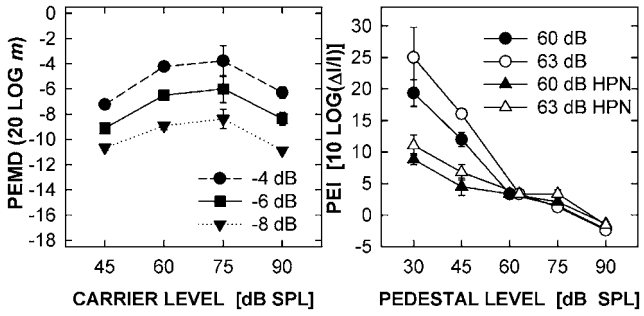

FIG. 8. *PEMDs* (left panel) and *PEIs* (right panel) for a 1-kHz tone in the presence of a high-pass noise. The left panel shows mean data from two listeners, with different symbols representing different standard modulation depths: −4 dB (circles, dashed line), −6 dB (squares, solid line), and −8 dB (triangles, dotted line). The right panel shows mean data for three listeners, with different symbols representing the *PEIs* measured in quiet (circles; replotted from the left panel of Fig. 7) and in high-pass noise (triangles). Filled symbols are for the pedestal level of 60 dB SPL and open symbols are for the level of 63 dB SPL. Error bars represent one standard deviation of the mean.

old fluctuations and intensity increments across levels is illustrated in Fig. 8, which shows the mean PEMDs (left panel) from two listeners (S1 and S2) and the mean PEIs (right panel) from three listeners (S1 and two new listeners who did not participate in the previous experiments).

If the effects of a high-pass noise on the perception of suprathreshold fluctuations and increments were equivalent to those observed for AM and increment detection, the PEMD and PEI should remain constant across levels. The shape of the PEMD function (left panel) differs from that in Fig. 5 (without high-pass noise), but the PEMD remained level dependent. For the 30-dB SPL carrier, the PEMDs (left panel) could not be estimated from the psychometric functions because the functions were very shallow and sometimes nonmonotonic. Consequently, data for only four comparison levels are presented in Fig. 8. Overall, the PEMD varied across carrier levels but the level dependence was nonmonotonic. Multiple t-tests were performed separately on each listener's data. For each carrier level, the estimated *PEMD* was compared to the mean of the PEMDs obtained for the other three carrier levels. These multiple comparisons revealed that for each standard modulation depth, all but one PEMD were significantly different from the mean of the other three at a significance level of 0.05. For S1, the PEMD that was not significantly different from the mean of the other three estimates, for all three standard modulation depths, corresponded to the carrier level of the comparison of 75 dB SPL ($t=2.06$, df=12, $p=0.058$, for the standard modulation depth of −4 dB; $t=2.07$, df=13, $p=0.056$, for the standard of −6 dB; and $t=1.67$, df=11, $p=0.118$, for the standard of −8 dB).[4] All other t-test comparisons yielded $p<0.05$. For S2, the only PEMD that was not significantly different from the mean of the other three corresponded to the carrier level of the comparison of 60 dB SPL ($t=1.72$, df=9, $p=0.124$, for the standard modulation depth of −4 dB, $t=1.31$, df=9, $p=0.226$, for the standard of −6 dB, and $t=0.92$, df=11, $p=0.388$, for the standard of −8 dB). All other t-test comparisons yielded $p<0.05$ indicating significant differences in PEMD across carrier level. Thus, the PEMD function measured in the presence of a high-pass noise differs from that expected based on the effect of a high-pass noise on AM detection (possible reasons for the departure from the expected counterpart to Weber's law in the presence of a high-pass noise will be discussed in Sec. IV.A).

The right panel of Fig. 8 shows average PEIs measured in quiet (circles, replotted from Fig. 5) and the average PEIs measured in three listeners in the presence of a high-pass noise (triangles). The noise substantially reduced the effect of level on the PEI although the slopes of the functions are significantly different from zero (as shown by a t-test of the hypothesis that the slope equals zero, $p<0.05$) for both pedestal levels, likely because the level of the high-pass noise was too low to completely eliminate the use of spread of excitation. The substantial reduction of the slope suggests that subjectively equivalent suprathreshold increments across levels would likely correspond to equal increments in sound level if spread of excitation were made completely unusable.

In summary, the results of matching suprathreshold AM and increments across levels to a large extent reflect the behavior seen in AM and increment detection across levels.

IV. DISCUSSION

The purpose of the study was to examine to what extent lawful relationships observed for detection of amplitude modulation and intensity JNDs generalize to the perception of highly detectable intensity changes and fluctuations. Perceived modulation depths and perceived intensity increments were compared across levels for noise and for a 1-kHz tone. For the tone, additional comparisons were performed in the presence of a high-pass noise that masked upward spread of excitation. Overall, the results appear to mirror threshold data, i.e., for noise, the perceived intensity fluctuation/change does not depend on level, whereas for a pure tone, a given modulation depth and a given change in intensity produces a greater perceived change as the level of the tone increases. Consequently, a counterpart to Weber's law is observed for PEMDs and PEIs for noise, and a counterpart to the near-miss to Weber's law is observed for tones. This is the most important finding of the study as it strongly suggests that the strategies and cues used in AM and increment detection tasks are likely relevant for the perception of suprathreshold intensity changes and that the general laws describing the detection apply to everyday perception of suprathreshold intensity changes.

A. Differences between threshold and suprathreshold perception of intensity fluctuations/changes for tones

Despite the overall qualitative similarities, some differences between the perception of suprathreshold AM and AM detection are worth noting. In the left panel of Fig. 5, the slopes of the PEMD functions (filled symbols) are much shallower than the slope of the threshold function (open triangles). The shallower slope for suprathreshold modulation depths can be explained taking into consideration the presumed shape of the basilar-membrane response function.

Most studies of basilar-membrane compression have found that the growth of response is more linear for levels below 25–30 dB SPL and it becomes compressive above that range of levels (e.g., Nelson *et al.* 2001; Plack *et al.*, 2004). For a 1-kHz tone presented at 30 dB SPL, AM detection threshold is about −20 dB (20 log *m*), as shown by the data in the left panel of Fig. 5 (open triangles) replotted from Wojtczak and Viemeister (1999). The level in the trough for the threshold modulation depth is 29.1 dB SPL. Assuming that the fluctuations in the instantaneous stimulus level fall into a compressive region of the basilar membrane response, the "internal" depth of fluctuations is smaller than that in the stimulus. At 90 dB SPL, excitation produced by the modulated tone spreads into the regions of the basilar-membrane where the response growth is linear. Listeners likely use the upper side of the excitation pattern to detect AM where (due to the linear response growth) the internal modulation depth (in terms of peak-to-through difference in decibels) is similar to that in the stimulus. Assuming a constant output (internal) modulation depth is needed for threshold, the nonlinear processing would predict that a smaller modulation depth is sufficient to detect AM at high carrier levels, as evidenced by the data. For large (suprathreshold) modulation depths used in the modulation-matching experiment, the trough in the modulated waveform may fall into a more linear region of the basilar-membrane response when the carrier level is 30 dB SPL. In fact, for the input level of −4 dB (a value roughly corresponding to the filled circle at 30 dB SPL in Fig. 5), the instantaneous level in the trough is 21.3 dB. Thus, the internal depth of fluctuations may be compressed less (relative to the input) than that for very small modulation depths. Consequently, the difference between the internal depths of fluctuations at 30 vs 90 dB SPL should be smaller for larger modulation depths, resulting in a shallower slope for the PEMD (compared with AM detection) function. It should be noted that the same reasoning could explain the slope differences at higher carrier levels (e.g., between 75 and 90 dB SPL) if it is assumed that the listeners used fluctuations on the upper side of the excitation pattern to detect AM and to perceive suprathreshold AM. Additionally, it has to be assumed that at 75 dB SPL the response at a place on the basilar membrane where the fluctuations are the strongest is still somewhat compressive relative to the response for the 90-dB SPL carrier and that compression increases progressively with increasing level.

Another discrepancy emerges when comparing differences of slopes between threshold and suprathreshold functions, separately for AM and intensity increments. Wojtczak and Viemeister (1999) have demonstrated a close relationship between the modulation depth at AM detection threshold and the change in intensity needed for increment detection. Because the PEI function is much steeper than the function relating threshold intensity increments to the pedestal level, whereas the PEMD function is much shallower than the function relating modulation depth at threshold to the carrier level, the relationship shown by Wojtczak and Viemeister (1999) cannot generalize to suprathreshold intensity changes. The same factor that yields a shallow slope of the PEMD function might be responsible for the steeper suprathreshold PEI function. For intensity increments, the level does not fall below the pedestal level as the increment increases. A steeper slope of the suprathreshold PEI function can be predicted taking into consideration a possibility that the listeners can use spread of excitation into the regions of the basilar membrane where the response grows in a linear manner at high but not at low pedestal levels (see footnote 3).

In the presence of a high-pass noise, the PEMD function is nonmonotonic (left panel in Fig. 8). This contrasts with AM detection in high-pass noise, which exhibits Weber's law. The listeners required smaller modulation depths in a 45-dB SPL comparison to match those in a 60-dB SPL standard. This result suggests that perceived fluctuations for a 60-dB SPL carrier are attenuated in the presence of a high-pass noise relative to those at lower carrier levels. This would be expected if the high-pass noise eliminated the possibility to process fluctuations on the upper side of the excitation pattern on the basilar membrane, where the response growth is more linear than at the 1-kHz place and the listeners were forced to use changes in excitation level where the response growth is compressive. It is possible that the standard fluctuations (around 60 dB SPL) produced smaller internal fluctuations than those in the comparison (around 45 dB SPL), because of stronger compression around 60 dB SPL. Assuming that the perceived strength of fluctuations is directly related to the rate of response growth, less compressive growth would lead to stronger perceived fluctuations and thus a smaller modulation depth at 45 dB SPL would be sufficient to match the perceived standard modulation depth. As anticipated, the high-frequency noise eliminated the decrease in PEMD with increasing level in the range between 60 and 75 dB SPL. As the amount of compression is likely constant over this range of levels, PEMDs were approximately equal. Above that range, the PEMD decreased indicating that the level of the masking noise may have not been sufficiently high to entirely eliminate the use of spread of excitation at the highest level used.

Although some discrepancies, which can be explained in terms of nonlinear basilar-membrane processing, are observed, the results appear to support the idea that the general laws, which describe detection thresholds can be used to describe the perception of highly detectable intensity changes and intensity fluctuations. This is a very important finding because readily perceived rather than threshold intensity changes are used in real-world auditory perception and identification of sounds. Moreover, the finding suggests that the numerous studies describing intensity coding based on threshold psychophysics might be directly relevant for describing the processing of suprathreshold intensity changes.

Apart from these general considerations, the data from matching suprathreshold intensity changes may help make some inferences about more basic characteristics of the auditory system and perhaps other sensory systems for which similar laws apply. Over decades, studies have attempted to develop robust models of a neural mechanism underlying Weber's law that would explain intensity discrimination under various conditions. A concept of internal noise (discussed below) has proven both physiologically plausible and practi-

cally effective in increasing the predictive power of auditory models for detection and discrimination of sound intensity.

B. Internal noise

Almost all contemporary models of detection and discrimination incorporate some form of variability that is intrinsic to the processing. In the language of signal detection theory (Green and Swets, 1988), the decision variable is a random variable, even when the input is deterministic. This variability or internal noise is often ascribed to the characteristics of sensory transmission, for example, to the Poisson-like stochastic properties of auditory nerve discharges (e.g., Siebert, 1968; McGill and Goldberg, 1968; Penner, 1972). In most models of intensity discrimination the internal noise is assumed to increase as the input level increases. This type of internal noise has been dubbed "multiplicative noise" (Eijkman *et al.*, 1966; Green and Swets, 1988). Technically, multiplicative noise refers to the specific situation in which the standard deviation (σ) of the decision variable is proportional to the mean. In the referred studies, the term multiplicative noise is often used to indicate that σ simply increases monotonically with the mean of the decision variable, not necessarily proportionally. This type of internal noise has been used in contrast to additive internal noise, which is independent of the magnitude of the decision variable. The multiplicative-noise models also assume that the neural activity evoked by the stimulus (often integrated over some period of time or/and pooled across a population of neurons) is generally a power function of the stimulus magnitude. Under such assumptions, it can be demonstrated that the multiplicative internal noise would yield Weber's law for intensity discrimination. The sensitivity index for discrimination of two sound intensities, I and $I+\Delta I$ can be expressed as

$$d' = \frac{(I+\Delta I)^n - I^n}{\sigma(I)}, \tag{1}$$

where n is the exponent of the power function that relates stimulus intensity to the internal response and $\sigma(I)$ is the standard deviation characterizing the distribution of the decision variable. Assuming a multiplicative-noise model, $\sigma(I)=kI^n$, where k is a constant. After substituting for $\sigma(I)$, this approach will yield Weber's law, as shown by the following equation, which has been rearranged to solve for the Weber fraction:

$$\frac{\Delta I}{I} = (kd' + 1)^{1/n} - 1. \tag{2}$$

The right side of Eq. (2) has a constant value for a constant d' and thus, it yields an intensity-independent Weber fraction.

Physiological evidence suggests there is a multiplicative component in auditory intensity coding. For example, the variance in spike-counts recorded from auditory nerve fibers increases with discharge rate (Teich and Khanna, 1985; Young and Barta, 1986). The question is whether multiplicative noise plays a determining role in auditory intensity coding and whether it underlies Weber's law, the fundamental law that describes our ability to discriminate intensities at different stimulus levels.

Our results suggest that multiplicative internal noise does not play a major role in intensity discrimination or AM detection. The argument is based on the likely supposition that the internal noise that limits discrimination and detection does not directly affect the perception of the suprathreshold intensity changes used in the present experiments because the variability produced by the noise becomes insignificantly low when compared with changes in the mean internal response produced by the highly detectable AM or intensity increments. Further, the similarity between the PEMD and PEI functions to those for AM detection and intensity discrimination suggests that level-dependent changes in internal noise may not be important in threshold situations. Specifically, the implication is that Weber's law does not result from multiplicative internal noise. An alternative approach that would yield Weber's law for both threshold *and* highly detectable intensity changes is to assume an intensity-independent internal noise combined with a logarithmic transform of the stimulus magnitude (Fechner, 1860; Durlach and Braida, 1969). If the magnitude in question is stimulus intensity, then the sensitivity index characterizing intensity discrimination could be expressed as

$$d' = \frac{\log(I+\Delta I) - \log(I)}{\sigma}, \tag{3}$$

where σ is the standard deviation of the decision variable that does not depend on I. In this case, Eq. (3) can be rearranged to

$$\frac{\Delta I}{I} = 10^{d'\sigma} - 1. \tag{4}$$

For a constant d' that is assumed for threshold, Eq. (4) will yield an intensity-independent Weber fraction. Given the aforementioned physiological evidence, it is possible that the internal noise may have both multiplicative (σ_m) and additive (σ_{add}) components

$$\sigma = \sigma_m + \sigma_{\text{add}}, \tag{5}$$

In that case, Eq. (3) would yield Weber's law if the multiplicative component were negligibly small compared with the additive component. The appeal of this approach is that the log transform would characterize the relationship between the stimulus intensity and the internal response in general and thus would not pose a limiting factor in intensity discrimination. Instead, the predominantly additive internal noise would limit threshold performance but the log transform of stimulus intensity would be responsible for Weber's law observed for threshold intensity discrimination *and* for perception of suprathreshold intensity changes.

C. Loudness

Defining a relationship between the perception of suprathreshold AM and the loudness function is not straightforward, especially for modulation rates that fall into the perceptual category of roughness (Zwicker and Fastl, 1999).

The likely increasing role of forward masking with increasing modulation depth and also with increasing modulation rate makes it impossible to account for the changes in the perceived fluctuation strength or roughness purely in terms of the characteristics of loudness functions for stationary sounds. Because of the possible other factors playing a role in the perception of a 16-Hz AM, the discussion of our results with respect to the loudness function will be limited to intensity increments.

In the increment-matching experiment, listeners were asked to pick the observation interval in which the change in sound intensity appeared larger. As the task was subjective with no "correct" answer, listeners were free to decide what feature of the stimulus they should use as the basis for their judgments about the size of the increment. Based on reports from the listeners, suprathreshold changes in intensity are perceived as changes in loudness. The PEI functions were similar in form across listeners, for a 1-kHz tone and for noise. Thus, the listeners likely used the same strategy to perform the matching task. The shape of the PEI function may provide some cues as to what the strategy and the decision variable were. One possibility is that the listeners used the loudness of the steady-state portions before and after the increment and "computed" the size of the increment using those two end values. Two strategies involving the loudness of the stimulus before the increment (L_1) and the loudness of the incremented portion (L_2) were considered to make predictions about the shape of the PEI functions. The loudness of each steady-state part of the stimulus was computed using a loudness model proposed by Moore *et al.* (1997). One strategy assumes that the listeners perceived intensity increments as equal when the loudness ratio (L_2/L_1) reached the same value for different pedestal levels. This approach is analogous to Ekman's law for loudness JNDs (Ekman, 1956, 1959), except in the current analysis, it was extended to suprathreshold intensity increments. Equal loudness ratios predict that the PEI does not depend on the pedestal level, a result equivalent to that described by Weber's law for intensity discrimination. The predictions based on Ekman's law obtained using the loudness model by Moore *et al.* (1997) account for the PEIs for the noise pedestal very well (see level-independent PEIs the right-hand panel of Fig. 7). The predictions consistent with those obtained using the model by Moore *et al.* (1997; not shown) can also be obtained when Steven's law is used (1957). According to Steven's law, loudness is a power function of stimulus intensity ($L=kI^p$, where k and p are constant values). A loudness ratio for a given suprathreshold intensity increment can be described by $L_2/L_1=k(I+\Delta I)^p/kI^p$. Thus, a constant L_2/L_1 implies a constant $\Delta I/I$ across stimulus levels. Although a constant loudness ratio produces the correct PEI function for noise, it fails to predict the data for the tonal pedestal. Interestingly, Ekman's law generally fails to predict intensity discrimination thresholds across loudness for tones, as demonstrated by Hellman and Hellman (2001).

Another strategy assumed that intensity increments are perceptually equivalent when loudness difference (L_2-L_1) reaches a certain constant value across pedestal levels. This is analogous to a "theory of resolution" based on equal loudness differences, suggested by Parker and Schneider (1980). For the tonal pedestal, the PEI function obtained from the matching task and the predictions assuming constant loudness difference (the left panel in Fig. 9) are in very good agreement, although the predictions slightly underestimate the increment size at most levels. For the noise pedestal, the predictions based on equal loudness differences (with loudness computed using the model by Moore *et al.*, 1997) are compared with the PEI function for the pedestal with a spectrum level of 20 dB SPL and a 4-dB increment. It is clear that for noise, the approach based on equal loudness differences fails to predict the behavioral data (the right panel in Fig. 9). It is worth noting that equal loudness difference cannot predict intensity discrimination for tones in broadband noise (Schneider and Parker, 1990) and would not predict constant intensity JNDs for noise.

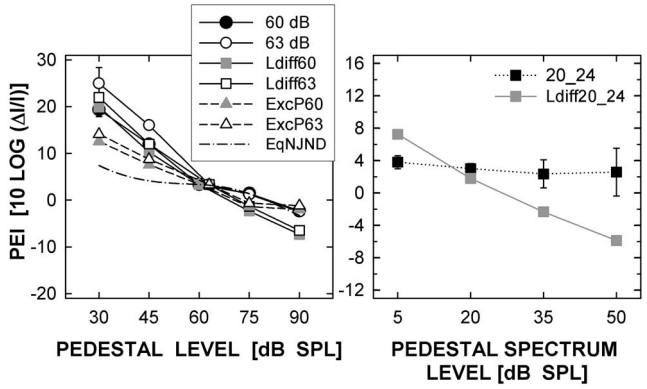

FIG. 9. The left panel shows *PEIs* for a 1-kHz pedestal replotted from the left panel of Fig. 7 (circles) and predictions based on: (i) equal loudness differences (squares); (ii) equal differences between log-transformed excitation patterns integrated over frequency (triangles); and (iii) equal number of JNDs (dashed-dotted line). The filled circles cannot be seen because they overlap with other symbols (they are covered by a gray square at 30 dB SPL, by an open square at 45 dB SPL, and by open circles at 75 and 90 dB SPL). The right panel shows *PEIs* for a noise carrier (replotted from the right panel of Fig. 7 for the 20_24 standard; black squares) and *PEIs* predicted using the assumption of a constant loudness difference (gray squares).

To summarize the previous analyses, equal loudness ratios can account for the data for the noise but not for the tonal pedestal, whereas the opposite is true for equal loudness differences. One implication is that listeners might be using different strategies in the increment-matching task that would depend on the type of the stimulus. More likely, the listeners use the same strategy for both types of stimuli, a strategy that is *not* based on a ratio or difference of loudness of the stationary portions of the stimuli with intensity increments.

Two metrics described below yield predictions that are qualitatively consistent with the PEI function of level for a tone and for noise, but quantitative agreement for the tonal pedestal is quite poor.

D. Constant difference between log-transformed excitation patterns for the pedestal with and without an increment

A metric based on log-transformed excitation patterns was tested for its ability to predict the PEI functions for the

tonal and noise pedestals. For each pedestal level of a 1-kHz tone, the excitation patterns were computed from rounded-exponential filters (Patterson and Moore, 1986), for the pedestal, $E_I(f)$, and the incremented pedestal, $E_{I+\Delta I}(f)$. Differences between the log-transformed excitation patterns were integrated over a frequency range for which the excitation exceeded the threshold excitation level (assumed to be equal to 0 dB). Thus, the metric (D) used can be described as

$$10 \cdot \int_{f_{\mathrm{Inc1}}}^{f_{\mathrm{Inc2}}} [\log(E_{I+\Delta I}(f) - \log(E_I(f)]df = D, \quad (6)$$

where f_{Inc1} and f_{Inc2} denote the frequencies between which the excitation produced by the incremented pedestal was greater than 0 dB. Since for the 1-kHz tone, the range of frequencies stimulated by the pedestal without an increment was smaller than that with the increment, $10\log(E_I(f))$ was set to zero for frequencies between f_{Inc1} and f_{Inc2}, for which its value fell below zero. This is equivalent to assuming, for simplicity, that the excitation level needed for detecting the tone is 0 dB as detection is limited by internal noise at stages above the basilar membrane. Assuming that D needs to be constant for PEIs, first the value of D was computed from Eq. (6) for the 1-kHz standard with a 60-dB SPL pedestal and a 5-dB increment (the same was repeated for a 63-dB SPL pedestal). Subsequently, intensity increments were found for all comparison levels used in the increment-matching task that produced the same value of D. The predicted increments are shown by triangles connected by a dashed line in the left panel of Fig. 9. The increments decrease with increasing pedestal level, consistent with the data, but they underestimate the PEI for the 30-dB pedestal by about 7 dB for the 60-dB SPL pedestal of the standard and by almost 11 dB for the 63-dB SPL pedestal. In addition to the disappointing quantitative agreement, this approach is not physiologically justified as it ignores the band pass filtering due to the outer and middle ear transfer functions. Inclusion of a realistic band pass filter would lead to a value of D that decreases with increasing level for the noise pedestal, because the effective excitation would exhibit spread over a larger area of the basilar-membrane as the noise level increases and more components reach the levels that offset attenuation by the filter.

E. Intensity changes for equal number of JNDs

Lim *et al.* (1977) proposed that different sounds have the same loudness when their levels of presentation correspond to the same proportion of the dynamic ranges for the respective sounds expressed in terms of the number of JNDs. Their approach proved successful in relating intensity discrimination to loudness-matching results (Houtsma *et al.*, 1980). The present study adapted the "proportional JND" hypothesis to increment matching, assuming that for a given stimulus, suprathreshold intensity increments are perceived as equal when their size comprises the same number of intensity JNDs. For noise, the intensity JND does not depend on level over the range of levels tested. This implies that a given suprathreshold intensity increment comprises the same number of intensity JNDs at different pedestal levels. Assuming a constant number of JNDs is perceived as producing the same intensity change at all levels, the predicted PEI will be independent of level leading to a counterpart of Weber's law, which is seen in the data (right panel of Fig. 7). For a tone, the intensity JND decreases with increasing pedestal level. Assuming a constant number of JNDs produces the same perceived intensity change, the PEI should decrease with increasing level, leading to a counterpart of the "near-miss" to Weber's law. The question arises whether or not a constant number of JNDs can account for the sizeable change in PEI across level of the 1-kHz tone in this study. A fourth-order polynomial fit to increment detection thresholds (converted to units of $10\log[(I+\Delta I)/I]$ from the study of Viemeister and Bacon (1988) was first used to determine the number of JNDs in the standard 5-dB increment for the pedestal level of 60 dB SPL. The number of JNDs was computed using the formula provided by Lim *et al.* (1977; footnote 11) using $d'=0.78$ that corresponds to the 70.7% correct responses in a 2IFC task. Next, based on the polynomial fit to the data of Viemeister and Bacon, a size of the intensity increment corresponding to the same number of JNDs was found for every comparison level used in the experiment (through the inverse solution obtained using Mathematica software). The PEIs obtained based on the assumption of an equal number of JNDs are shown by the dashed-dotted line in the left panel of Fig. 9. The results obtained based on an equal number of JNDs predict much lower PEIs for pedestal levels below 60 dB SPL than those measured in the increment-matching task.

In summary, none of the attempted approaches provided a satisfactory account for the data without assuming that the listeners used different decision variables for the noise and tonal stimuli, which seems unrealistic. It is possible that the decisions about the increment size were not based on the loudness of the stationary parts of the stimuli before and after the increment but on some more complicated function describing the transition from the softer to greater loudness during the increment. Additional experiments using pulsed stimuli with differing intensities, for which the listeners cannot hear the transition from softer to louder portion of the stimulus, but have to rely on the stationary loudness, are needed to determine if the dynamic transitional change plays a role in evaluating the size of an increment.

V. CONCLUSIONS

Generally, comparisons of PEMDs and PEIs across level lead to the following observations

(1) For noise carriers, the PEMD does not depend on carrier level. This is consistent with a constant modulation depth needed for AM detection threshold across carrier levels. For tonal carriers, the PEMD decreases slightly (by about 7 dB in units of $20\log m$) with increasing carrier level, with the greatest decrease occurring in the range of levels between 60 and 75 dB SPL. This is consistent with decreasing modulation depth needed for AM detection threshold. The rate of the decrease with in-

creasing level is slower for suprathreshold AM possibly reflecting the role of level-dependent compression on the basilar membrane.

(2) For tonal pedestals, the PEMD varies less across carrier level when a high-pass noise is used to mask the upward spread of excitation.

(3) For noise, the PEI does not depend on the pedestal level revealing a counterpart to Weber's law for suprathreshold intensity increments. For a tone, the PEI decreases with increasing pedestal level. The decrease is much steeper than that observed for threshold intensity increments. Thus, a counterpart to the near-miss to Weber's law is observed for suprathreshold intensity changes, but the level effect is much more sizeable than that seen for intensity-discrimination threshold.

(4) The presence of a high-pass noise greatly reduces the level dependence of the PEI for a tone, implying the involvement of nonlinear spread of excitation when the noise is absent.

(5) The observed counterpart to Weber's law for suprathreshold AM and intensity increments suggests that Weber's law does not reflect changes in the amount of internal noise with stimulus level. Instead, it is consistent with the notion that Weber's law stems from a logarithmic-type transform that relates stimulus intensity to the magnitude of the internal response.

(6) A constant loudness difference and a constant loudness ratio could not account for the functions relating the PEI to the pedestal level, for both the tonal and noise pedestals. This suggests that the listeners might have used different decision variables to determine the size of the increments for the two types of stimuli. Differences between log-transformed excitation patterns integrated across frequency and a model assuming equal JND numbers for PEIs produced predictions that were in qualitative agreement with the data but they severely underestimated the PEIs for levels below 60 dB SPL. It is likely that some transition in loudness that is not related to the stationary loudness before and after the increment in a simple manner was used as a decision variable by the listeners. The nature of that transitional change in loudness remains to be determined.

(7) Overall, the results of the present study indicate that the same strategies and cues are likely used in the perception of suprathreshold intensity changes as those used in increment and AM detection. Thus, findings from threshold psychophysics that use objective procedures to measure just-detectable changes can be, to a large extent, generalized to the perception of more ubiquitous suprathreshold intensity variations.

ACKNOWLEDGMENTS

This study was supported by NIDCD Grant No. DC00683. Two anonymous reviewers provided very helpful comments that improved the earlier version of the manuscript.

APPENDIX A: OBSERVATIONS ON THE USE OF INTERLEAVED ADAPTIVE TRACKING USING ONE STANDARD

Originally, an adaptive matching procedure with two interleaved tracks (Jesteadt, 1980), one upper (3-down, 1-up) and one lower (3-up, 1-down), was first used to estimate the PEMD. This procedure led to some results that failed to fulfill control conditions of symmetry (when comparison B was matched to standard A then comparison A should be matched to standard B, which was not the case) and transitivity (if B was matched to A, and C was matched to B, then A should be matched to C).

Using the Jesteadt procedure, the PEMD was estimated as the mean of two modulation depths, one corresponding to the 79.4% point on the psychometric function and the other corresponding to the 20.6% point. Some listeners showed a large discrepancy between the lower and upper estimates, which suggested very shallow psychometric functions for matching modulation depths at different carrier levels. However, other listeners applied a strategy that led to the lower and upper estimates being very close to one another. That, in turn, suggested very steep psychometric functions, yet the results failed to show symmetry and transitivity. As the standard and the comparison differed in level, it was easy for the listener to identify which stimulus was being manipulated by their responses. Under such circumstances, when comparing fluctuation depths across levels was difficult, it might have been easier for the listeners to "remember" a certain modulation depth of the comparison ("internal PEMD") and perform the matching task without making any comparisons to the "real" standard provided in each trial. In that case the listeners could have made absolute judgments about the modulation depth of the comparison and adjust the modulation depth of the comparison to the internal PEMD. This possibility was informally tested using one listener. To determine how robust matching to an internally stored template is, the standard was unmodulated and the modulation depth of the comparison was adjusted adaptively using the two interleaved tracks, as in the main original experiment. The listener was told to match the comparison modulation depth to the "PEMD" she established on her own during the adaptive tracking. The mean of the six estimates (from six separate runs) had a much smaller standard deviation than the one obtained with the modulated standard, suggesting that it was easier for the listener to provide consistent matches to the memorized modulation depth of the comparison then to compare across the standard and comparison intervals. Moreover, the test was repeated a day later and the subject was instructed to use the same template modulation depth, as she remembered it. Surprisingly, the mean result was within 1 dB (20 log m) of that obtained a day earlier, indicating that listeners may be capable of using a stored internal PEMD over sessions.

The results of matching to the internal template can be very consistent and replicable over days. Moreover, the variability in the data decreases with practice, as training helps establish and fix the template in listener's memory. Therefore, a matching experiment was designed to force the listener to attend to both the standard and the comparison ob-

servation intervals. A fixed-level procedure using a few fixed standards, randomly presented in a block of trials, appears to prevent using an internal template for the PEMD. For each standard, a psychometric function relating the proportion of times a given type of response occurred to the level of the comparison can be constructed. Using this method, the strategy based on an internal template could be easily detected. If the listener ignored the actual standard, the psychometric functions like those presented in Fig. 2, would fall on top of one another.

APPENDIX B: INCOMPLETE PSYCHOMETRIC FUNCTIONS

To cover the range of proportion of "comparison increment larger" responses between 0 and 1 with sufficient density for all the 1-kHz standards shown in the middle column of Table III, a larger (than eight) number of comparison increments would have had to be used within a block. This would have substantially increased the duration of each block. To avoid that, eight comparison increments were selected based on pilot runs. They were chosen to allow for estimating PEIs for the 5-dB increment in 60- and 63-dB SPL pedestals from psychometric functions with data distributed over nearly the entire range of proportion of responses between 0 and 1. By choosing only eight increments we compromised the ability to obtain the whole psychometric function for the two remaining increment sizes, 2 and 8 dB in units of $10\log[(I+\Delta I)/I]$. For these increment sizes, the data (proportion of responses comparison increment larger) concentrated in the range between 0.5 and 1, for the 2-dB increment, and in the range between 0 and 0.5 for the 8-dB increment. Thus, the lack of estimated PEIs for these standards should not be considered as resulting from listeners' inability to perform the task reliably. Instead, they were a result of a compromise that was decided upon when designing the experiment. For the same reason, the PEI could not be estimated for a 1-dB increment in the noise standard with a spectrum level of 23 dB SPL.

[1]The form of the logistic function fitted to the data was the same for modulation and increment matching. The function was defined by $P=1/(1+\exp(b(x_0-x_c)))$, where P denotes the proportion of times the comparison was evaluated as having stronger intensity fluctuations (or a larger intensity increment) than the standard, b characterizes the slope of the logistic function, x_0 is the modulation depth (or an intensity increment) in the comparison corresponding to $P=0.5$, and x_c is the modulation depth of the comparison (or the increment in the comparison). Thus, x_0=PEMD for modulation matching, and x_0=PEI, for increment matching.

[2]Data from Bacon and Viemeister (1985) plotted in the right panel of Fig. 5 represent the mean of AM detection thresholds for listeners S1 and S4 in their study, for a 16-Hz rate at a spectrum level of 30 dB SPL adjusted by the relative shift in threshold observed for lower spectrum levels (plotted in their Fig. 4). The adjustment for a 4-Hz modulation rate was used, as data for a 16-Hz rate were not available. However, the similarity of the relative shifts measured by Bacon and Viemeister (1985) for a 4-Hz rate and at a 70-Hz rate suggests that the adjustments for the 4-Hz rate can be applied without much error to detection of a 16-Hz rate for the purpose of comparison with the suprathreshold data for a 16-Hz rate in this study. The carrier was presented continuously in the study of Bacon and Viemeister and it was gated in this study.

[3]Excitation on the basilar membrane in response to a low-level tone spreads over a small region around the characteristic frequency (CF) equal to the frequency of the tone. As the level of the tone increases, excitation spreads over a larger portion of the basilar membrane, mainly toward places with higher CFs. The response growth is compressive at the CF equal to the stimulus frequency and becomes progressively less compressive at places above that CF. For CFs higher than about an octave above the stimulus frequency, the response becomes linear. This is referred to as nonlinear spread of excitation on the basilar membrane. It seems reasonable to assume that our perception of a change in intensity/level of a 1-kHz tone is directly related to the changes in excitation level at a place where the changes are the greatest. Thus, for a 1-kHz tone presented at 30 dB SPL, a given change in level will be determined by a change in excitation level at or close to CF=1 kHz (because the level is not high enough for the excitation to spread to places where the growth of response is more linear). For the same tone presented at 90 dB SPL, a given change in level will be related to changes in excitation level at places far above CF =1 kHz, where the response growth is linear. Assuming that increment detection thresholds measured at different pedestal levels yield perceptually equivalent increments, the PEI function of level should have a shallower slope for threshold increments than for suprathreshold intensity changes due compressive (at 30 dB SPL) versus linear (at 90 dB SPL) growth of excitation.

[4]The number of the degrees of freedom was determined considering the fact that each PEMD was estimated from a logistic fit to eight data points. Thus, eight samples contributed to the standard error of the PEMD estimate. As the t-test compared each PEMD with the mean of the remaining three PEMDs, the variance of the mean was computed as the sum of variances of each individual PEMD included in that mean. The number of samples contributing to the variance (and the standard deviation) of the mean was then $3\times 8=24$. The number of the degrees of freedom (df) was obtained from the following equation (Devore and Peck, 1997):

$$\mathrm{df}=\frac{(V_1+V_2)^2}{\frac{V_1^2}{n_1-1}+\frac{V_2^2}{n_2-1}},$$

where $V_1=s_1^2/n_1$ and $V_2=s_2^2/n_2$. In the equations, s_1 is the standard deviation of the PEMD that is being compared to the mean of the remaining three PEMDs and s_2 is the standard deviation of that mean. The value of df was truncated to an integer. Correspondingly, $n_1=8$ and $n_2=24$. The differences that based on multiple comparisons were significant remained significant after the Bonferroni correction was applied.

Allen, J. B., and Neely, S. T. (**1997**). "Modeling the relation between the intensity just-noticeable difference and loudness for pure tones and wideband noise," J. Acoust. Soc. Am. **102**, 3628–3646.

Bacon, S. P., and Viemeister, N. F. (**1985**). "Temporal modulation transfer functions in normal-hearing and hearing-impaired listeners," Audiology **24**, 117–134.

Colburn, H. S., Carney, L. H., and Heinz, M. G. (**2003**). "Quantifying the information in the auditory-nerve responses for level discrimination," J. Assoc. Res. Otolaryngol. **4**, 294–311.

Devore, J., and Peck, R. (**1997**). "Small-sample inferences concerning a difference between twp normal population means when samples are independently chosen," *Statistics: The Exploration and Analysis of Data*, 3rd ed. (Duxbury), p. 363.

Drullman, R. (**2005**). "The significance of temporal modulation frequencies for speech intelligibility," in *Listening to Speech: An Auditory Perspective*, edited by S. Greenberg and W. Ainsworth (Lawrence Erlbaum Associates Inc., New Jersey), pp. 39–47.

Durlach, N. I., and Braida, L. D. (**1969**). "Intensity perception. I. Preliminary theory of intensity resolution," J. Acoust. Soc. Am. **46**, 372–383.

Durlach, N. I., Braida, L. D., and Ito, Y. (**1986**). "Towards a model for discrimination of broadband signals," J. Acoust. Soc. Am. **80**, 63–72.

Eijkman, E., Thijssen, J. M., and Vendrik, A. J. H. (**1966**). "Weber's law, power law, and internal noise," J. Acoust. Soc. Am. **40**, 1164–1173.

Ekman, G. (**1956**). "Discriminal sensitivity on the subjective continuum," Acta Psychol. **12**, 233–243.

Ekman, G. (**1959**). "Weber's law and related functions," J. Psychol. **47**, 343–352.

Fastl, H. (**1983**). "Fluctuation strength of modulated tones and broadband noise," in *Hearing—Physiological Bases and Psychophysics*, edited by R. Klinke and R. Hartmann, (Springer, Berlin), pp. 282–286.

Fechner, G. T. (**1860**). *Elemente der Psychophysik*, translated by H. E. Adler, D. H. Howes, and E. G. Boring (Holt, Reinhart, and Winston, New York), Vol. **1**.

Florentine, M., and Buus, S. (**1981**). "An excitation-pattern model for intensity discrimination," J. Acoust. Soc. Am. **70**, 1646–1654.
Glasberg, B. R., and Moore, B. C. J. (**2002**). "A model of loudness applicable to time-varying sounds," J. Audio Eng. Soc. **50**, 331–342.
Green, D. M., and Swets, J. A. (**1988**). *Signal Detection Theory and Psychophysics*, (Peninsula, Los Altos, CA).
Hellman, W. S., and Hellman, R. P. (**1990**). "Intensity discrimination as the driving force for loudness. Application to pure tones in quiet," J. Acoust. Soc. Am. **87**, 1255–1265.
Hellman, W. S., and Hellman, R. P. (**2001**). "Revisiting relations between loudness and intensity discrimination," J. Acoust. Soc. Am. **109**, 2098–2102.
Houtsma, A. J. M., Durlach, N. I., and Braida, L. D. (**1980**). "Intensity perception, XI. Experimental results on the relation of intensity resolution to loudness matching," J. Acoust. Soc. Am. **68**, 807–813.
Howell, D. C. (**2004**). "Hypothesis testing in regression" in *Fundamental Statistics for the Behavioral Sciences*, 5th ed. (Brooks/Cole Inc. Thomson Learning, Belmont, CA), pp. 220–221.
Jesteadt, W. (**1980**). "An adaptive procedure for subjective judgments," Percept. Psychophys. **28**, 85–88.
Jesteadt, W., Nizami, L., and Schairer, K. S. (**2003**). "A measure of internal noise based on sample discrimination," J. Acoust. Soc. Am. **114**, 2146–2157.
Joris, P. X., Schreiner, C. E., and Rees, A. (**2003**). "Neural processing of amplitude-modulated sounds," Physiol. Rev. **84**, 541–577.
Lim, J. S., Rabinowitz, W. M., Braida, L. D., and Durlach, N. I. (**1977**). "Intensity perception VIII. Loudness comparisons between different types of stimuli," J. Acoust. Soc. Am. **62**, 1256–1267.
McGill, W. J., and Goldberg, J. P. (**1968**). "Pure-tone intensity discrimination and energy detection," J. Acoust. Soc. Am. **44**, 576–581.
Miller, G. A. (**1947**). "Sensitivity to changes in the intensity of white noise and its relation to masking and loudness," J. Acoust. Soc. Am. **19**, 609–619.
Moore, B. C. J., Glasberg, B. R., and Bear, T. (**1997**). "A model for the prediction of thresholds, loudness and partial loudness," J. Audio Eng. Soc. **45**, 224–239.
Moore, B. C. J., and Raab, D. H. (**1974**). "Pure-tone intensity discrimination: Some experiments relating to the 'near-miss' to Weber's law," J. Acoust. Soc. Am. **55**, 1049–1054.
Moore, B. C. J., Wojtczak, M., and Vickers, D. A. (**1996**). "Effect of loudness recruitment on the perception of amplitude modulation," J. Acoust. Soc. Am. **100**, 481–489.
Nelson, P. C., and Carney, L. H. (**2007**). "Psychophysically driven studies of responses to amplitude modulation in the inferior colliculus: Comparing single-unit physiology to behavioral performance," in *Hearing — From Sensory Processing to Perception*, edited by B. Kollmeier, G. Klump, V. Hohmann, U. Langemann, M. Mauermann, S. Uppenkamp, and J. Verhey (Springer, Berlin), pp. 133–141.
Nelson, D. A., Schroder, A. C., and Wojtczak, M. (**2001**). "A new procedure for measuring peripheral compression in normal-hearing and hearing-impaired listeners," J. Acoust. Soc. Am. **110**, 2045–2064.
Palmer, A. R., and Evans, E. F. (**1982**). "Intensity coding in the auditory periphery of the cat: Responses of cochlear nerve and cochlear nucleus neurons to signals in the presence of bandstop masking noise," Hear. Res. **7**, 305–323.
Parker, S., and Schneider, B. (**1980**). "Loudness and loudness discrimination," Percept. Psychophys. **28**, 398–406.
Patterson, R. D., and Moore, B. C. J. (**1986**). "Auditory filters and excitation patterns as representations of frequency resolution," in *Frequency Selectivity in Hearing*, edited by B. C. J. Moore (Academic, London).
Penner, M. J. (**1972**). "Neural or energy summation in a Poisson counting model," Percept. Psychophys. **15**, 566–570.
Plack, C. J., and Carlyon, R. P. (**1995**). "Loudness perception and intensity coding," in *Hearing*, edited by B. C. J. Moore (Academic, San Diego), pp. 123–160.
Plack, C. J., Drga, V., and Lopez-Poveda, E. A. (**2004**). "Inferred basilar-membrane response functions for listeners with mild to moderate sensorineural hearing loss," J. Acoust. Soc. Am. **115**, 1684–1695.
Plomp, R. (**1970**). "Timbre as a multidimensional attribute of complex tones," in *Frequency Analysis and Periodicity Detection in Hearing*, edited by R. Plomp, and G. F. Smoorenberg (Sijthoff, Leiden), pp. 376–396.
Raab, D. H., and Goldberg, I. A. (**1975**). "Auditory intensity discrimination with bursts of reproducible noise," J. Acoust. Soc. Am. **57**, 437–447.
Rabinowitz, W. M., Lim, J. S., Braida, L. D., and Durlach, N. I. (**1976**). "Intensity perception, VI. Summary of recent data on deviations from Weber's law for 1000-Hz tone pulses," J. Acoust. Soc. Am. **59**, 1506–1509.
Riesz, R. R. (**1928**). "Differential intensity sensitivity of the ear for pure tones," Phys. Rev. **31**, 867–875.
Schlauch, R. S. (**1994**). "Intensity resolution and loudness in high-pass noise," J. Acoust. Soc. Am. **95**, 2171–2179.
Schneider, B. A., and Parker, S. (**1987**). "Intensity discrimination and loudness for tones in notched noise," Percept. Psychophys. **41**, 253–261.
Schneider, B. A., and Parker, S. (**1990**). "Intensity discrimination and loudness for tones in broadband noise," Percept. Psychophys. **47**, 92–94.
Schroder, A. C., Viemeister, N. F., and Nelson, D. A. (**1994**). "Intensity discrimination in normal-hearing and hearing-impaired listeners," J. Acoust. Soc. Am. **96**, 2683–2693.
Siebert, W. M. (**1968**). "Stimulus transformations in the peripheral auditory system," in *Recognizing Patterns*, edited by, P. S. Kolers and M. Eden (MIT, Cambridge, MA), pp. 104-l33.
Spiegel, M. F., and Green, D. M. (**1981**). "Two procedures for estimating internal noise," J. Acoust. Soc. Am. **70**, 69–73.
Stevens, S. S. (**1957**). "On the psychophysical law," Psychol. Rev. **64**, 153–181.
Tanner, W. P. (**1961**). "Application of the theory of signal detectability to amplitude discrimination," J. Acoust. Soc. Am. **33**, 1233–1244.
Teich, M. C., and Khanna, S. M. (**1985**). "Pulse-number distribution for the neural spike train in the cat's auditory nerve," J. Acoust. Soc. Am. **77**, 1110–1128.
Terhardt, E. (**1968**). "Über akustische Rauhigkeit und Schwankungsstärke (On the acoustic roughness and fluctuation strength)," Acustica **20**, 215–224.
Treisman, M. (**1964**). "Noise and Weber's law: The discrimination of brightness and other dimensions," Psychol. Rev. **71**, 314–330.
Viemeister, N. F. (**1972**). "Intensity discrimination of pulsed sinusoids: The effects of filtered noise," J. Acoust. Soc. Am. **51**, 1265–1269.
Viemeister, N. F. (**1979**). "Temporal modulation transfer functions based upon modulation thresholds," J. Acoust. Soc. Am. **66**, 1364–1380.
Viemeister, N. F. (**1983**). "Auditory intensity discrimination at high frequencies in the presence of noise," Science **221**, 1206–1208.
Viemeister, N. F. (**1988**). "Intensity coding and the dynamic range problem," Hear. Res. **34**, 267–274.
Viemeister, N. F., and Bacon, S. P. (**1988**). "Intensity discrimination, increment detection, and magnitude estimation for 1-kHz tones," J. Acoust. Soc. Am. **84**, 172–178.
Winter, I. M., and Palmer, A. R. (**1991**). "Intensity coding in low-frequency auditory-nervefibers of the guinea pig," J. Acoust. Soc. Am. **90**, 1958–1967.
Wojtczak, M., and Viemeister, N. F. (**1999**). "Intensity discrimination and detection of amplitude modulation," J. Acoust. Soc. Am. **106**, 1917–1924.
Wojtczak, M., and Viemeister, N. F. (**2005**). "Level effects in amplitude modulation tuning," J. Acoust. Soc. Am. **117**, 2535.
Yost, W. A., and Sheft, S. (**1997**). "Temporal modulation transfer functions for tonal stimuli: Gated versus continuous conditions," Aud. Neurosci. **3**, 401–414.
Young, E. D., and Barta, P. E. (**1986**). "Rate responses of auditory nerve fibers to tones in noise near masked threshold," J. Acoust. Soc. Am. **79**, 426–442.
Zwicker, E. (**1956**). "Die Elementaren Grundlagen zur Bestimmung der Informationskapazität des Gehörs (The foundations for determining the information capacity of the auditory system)," Acustica **6**, 365–381.
Zwicker, E. (**1970**). "Masking and psychological excitation as consequences of the ear's frequency analysis," in *Frequency Analysis and Periodicity Detection in Hearing*, edited by R. Plomp and G. F. Smoorenberg, (Sijthoff, Leiden).
Zwicker, E., and Fasti, H. (**1999**). *Psychoacoustics: Facts and Models*, 2nd ed. (Springer, Berlin).
Zwicker, E., and Graf, L. (**1987**). "Modulationsschwellen bei Verdeckung (Modulation thresholds under masking)," Acustica **64**, 148–154.
Zwislocki, J. J., and Jordan, H. N. (**1986**). "On the relations of intensity jnd's to loudness and neural noise," J. Acoust. Soc. Am. **79**, 772–780.

Speech segregation in rooms: Monaural, binaural, and interacting effects of reverberation on target and interferer

Mathieu Lavandier[a] and John F. Culling[b]
School of Psychology, Cardiff University, Tower Building, Park Place, Cardiff, CF10 3AT, United Kingdom

(Received 7 August 2007; revised 16 January 2008; accepted 17 January 2008)

Speech reception thresholds were measured in virtual rooms to investigate the influence of reverberation on speech intelligibility for spatially separated targets and interferers. The measurements were realized under headphones, using target sentences and noise or two-voice interferers. The room simulation allowed variation of the absorption coefficient of the room surfaces independently for target and interferer. The direct-to-reverberant ratio and interaural coherence of sources were also varied independently by considering binaural and diotic listening. The main effect of reverberation on the interferer was binaural and mediated by the coherence, in agreement with binaural unmasking theories. It appeared at lower reverberation levels than the effect of reverberation on the target, which was mainly monaural and associated with the direct-to-reverberant ratio, and could be explained by the loss of amplitude modulation in the reverberant speech signals. This effect was slightly smaller when listening binaurally. Reverberation might also be responsible for a disruption of the mechanism by which the auditory system exploits fundamental frequency differences to segregate competing voices, and a disruption of the "listening in the gaps" associated with speech interferers. These disruptions may explain an interaction observed between the effects of reverberation on the targets and two-voice interferers.
© *2008 Acoustical Society of America.* [DOI: 10.1121/1.2871943]

PACS number(s): 43.66.Pn, 43.66.Dc, 43.55.Hy, 43.71.Gv [RYL] Pages: 2237–2248

I. INTRODUCTION

In order to understand speech in a noisy environment or when many people are talking at the same time, the auditory system has to segregate the target speech from the competing speech or noise. The task becomes even more complicated in rooms, where the auditory system also has to cope with the effects of reverberation. Speech intelligibility against noise or speech interferers decreases when reverberation increases. Lavandier and Culling (2007) showed that the loss of intelligibility could be associated with at least two distinct effects of reverberation.

The reverberation reduced intelligibility by affecting the interfering source. This effect was interpreted as resulting from the decorrelation of the interferer at the two ears. Licklider (1948) showed that speech intelligibility in noise diminishes when the interaural coherence of the noise is reduced, and Robinson and Jeffress (1963) observed a similar effect for tone detection in noise. This effect is predicted by all binaural unmasking theories. For example, the equalization-cancellation (E-C) mechanism of Durlach (1972) predicts that a less correlated masker will be more difficult to equalize at the two ears, and consequently more difficult to cancel, resulting in lower speech intelligibility or poorer tone detection. This effect of reverberation on the interferer depends on the interaural coherence of the interfering source. The interaural coherence of a source evaluates the similarity of the sound waveform it produces at the two ears of the listener. It is calculated by taking the maximum value from the interaural cross-correlation function. The interaural coherence of the interfering source in a room is degraded by the multiple sound reflections reaching the listener, because these reflections are not the same at the two ears (unless the configuration is symmetrical within the room).

The reverberation also directly affected the target. This effect was interpreted as the intrinsic degradation of speech intelligibility in reverberation, occurring even without the interferer. Target intelligibility decreases because of the temporal and spectral distortions resulting from the multiple delayed sound reflections mixing with the direct sound in the room. This effect is related to the direct-to-reverberant (D/R) ratio of the source at the listening position. It can be described by objective measurements such as the useful-to-detrimental ratios (Bradley, 1986; Bradley *et al.*, 1999) or the speech transmission index (STI), which takes into account the reduction of amplitude modulation in the speech signals due to reverberation (Houtgast and Steeneken, 1985). In Lavandier and Culling (2007), the loss of intelligibility due to the effect of reverberation on the target was partially accounted for by STI calculations.

Lavandier and Culling (2007) adopted a parsimonious model to describe their data, hypothesizing that there was no interaction between the two effects described earlier. These two effects are based on different mechanisms (monaural for the target and binaural for the interferer), so there was no reason to suspect that they could interact. However, this remained to be tested. Moreover, discrepancies between STI

[a]Electronic mail: lavandiermn@cardiff.ac.uk.
[b]Electronic mail: cullingj@cardiff.ac.uk.

predictions and speech reception thresholds (SRTs) measured with the target at different levels of reverberation were not explained by this model.

Three new experiments were designed to verify that there was no interaction between the effects of reverberation on target and interferer. They used methods very similar to those of Lavandier and Culling (2007). SRTs (i.e., the level of the target compared to that of the interferer for 50% intelligibility of the target) were measured for spatially separated targets and interferers in a virtual room. The room simulation allowed variation of the absorption coefficient of the room boundaries, thus modifying the D/R ratio and the interaural coherence of sources. A different absorption coefficient was used for target and interferer. This experimental design is not realistic as it implies listening simultaneously to two sources in rooms having different reverberation characteristics, but it offers the advantage of controlling interferer and target reverberation conditions independently, decomposing the influence of reverberation on speech intelligibility. The effects of the room and the head on the sound level of each source at the listener's ears were eliminated by equalizing all stimuli in level, in order to interpret the effect of interaural coherence/direct-to-reverberant ratio unambiguously. Target and interferer were also clearly identified, so that the listener knew which voice to listen to[1].

In Lavandier and Culling (2007), four absorption coefficients were tested for the source with varying reverberation, while a unique absorption coefficient was used for the source with fixed reverberation. In experiments 1 and 3 presented here, four absorption coefficients were used for both sources. They were varied independently for target and interferer across conditions, so that SRTs were measured for the four types of target against the four types of interferer. A potential interaction between the effects of reverberation on target and interferer could then be investigated, by comparing the effect of varying reverberation on the first source at the different levels of reverberation of the second source. Experiment 1 used speech interferers, whereas experiment 3 used noise interferers. Experiment 2 used a subset of the conditions from experiment 1.

As an interaction was observed between the effects of reverberation on the targets and speech interferers, the parsimonious model hypothesized by Lavandier and Culling (2007) had to be refined. Two further experiments investigated more precisely and individually the effects of reverberation on target and interferer. It should be noted that D/R ratio and interaural coherence do not necessarily covary. The example of a symmetrical configuration of the listener and the sound source within a room illustrates this point. Because the configuration is symmetrical, the interaural coherence of the source is 1 even if its D/R ratio is reduced by making the room more reverberant. If the sound reflections are the same at the two ears, they do not affect the interaural coherence. In experiments 4 and 5, the D/R ratio and interaural coherence of sources were then varied independently by considering both binaural and diotic listening conditions. By definition, diotic stimuli had a fixed interaural coherence of 1, whereas the coherence of binaural stimuli was reduced by reverberation. The aim of experiments 4 and 5 was to tease apart the binaural and monaural effects of reverberation, in order to elucidate the mechanism responsible for the observed interaction, and to show that the main effect of reverberation on the target was monaural and associated with the D/R ratio, wheareas the main effect of reverberation on the interferer was binaural and mediated by the coherence.

II. GENERAL METHODS

A. Stimuli

A male voice was used as the target source in each experiment. The corpus of sentences was from the Harvard Sentence List (IEEE, 1969). The anechoic recordings of a male voice digitized at 20 kHz with 16-bit quantization were used as the basis of all stimuli. The sentences have low predictability, and each sentence contains five key words. For instance, one sentence was "the POINT of the STEEL PEN was BENT and TWISTED". Interfering sentences were generated by feminizing the male voice using the Praat PSOLA speech analysis and resynthesis package. The voice was increased in fundamental frequency by a factor of 1.8 (Rendall *et al.*, 2005), and a vocal tract 9% shorter (Fitch and Giedd, 1999) was simulated by shifting the spectral envelope up in frequency (Darwin and Hukin, 2000). The resulting female voice was used to create two-voice interferers. The aim of using a female voice for the interferer was to eliminate some attentional effects encountered in previous experiments using the same voice for target and interferer (Lavandier and Culling, 2007). The difference of voice between target and interferer is a cue that helps the listener to focus his/her attention on the target voice, and this cue has been shown to be very resistant to reverberation (Darwin and Hukin 2000). Noise interferers were also used. They were speech-shaped noises, obtained by filtering Gaussian noises with a finite impulse response (FIR) filter designed to match the long-term excitation pattern (Moore and Glasberg, 1983) of the two-voice interferers.

The virtual rooms used in the experiments were simulated using a ray-tracing method (Allen and Berkley, 1979; Peterson, 1986), implemented in the |WAVE signal processing package (Culling 1996). The absorption coefficients of the room internal surfaces were all set to the same value, and varied together when the reverberation condition was changed. The listener was modeled as two ears with no head between them, using omnidirectional microphones suspended in space at 1.5 m from the floor. The head was not modeled in order to avoid head shadow effects which could complicate the interpretation of the effects associated with interaural coherence. The interferer and target were placed at different positions in the room, also at 1.5 m from the floor. Binaural stimuli were produced by calculating the impulse responses between the source positions and each ear, and convolving the speech samples with these impulse responses.

The convolution by the room impulse response modifies the sound levels of the original stimuli (Bradley *et al.*, 1999). The levels change differently depending on the positions used within the room and the ear considered. To avoid mixing the effects of room-induced changes in sound level and interaural coherence/direct-to-reverberant ratio, all stimuli

were equalized in level after convolution by the room impulse responses. Left and right channels were equalized independently, removing potential interaural level differences.

The D/R energy ratio was calculated at each ear, for every tested source position and absorption coefficient, using the impulse response between the source position and the considered ear. The direct-path and reverberant portions of the impulse response were separated by a time-windowing procedure. This procedure was done by eye and was trivial as our simulated impulse responses were not contaminated by noise. The energy of each portion was computed, and the D/R energy ratio was expressed in decibels.

The interaural coherence of each source at the listening position was also calculated in each experiment. It was computed as the maximum of the absolute value of the crosscorrelation of the waveforms reaching the two ears from the source (Hartmann *et al.*, 2005). These waveforms were filtered between 20 and 1500 Hz prior to calculation, in order to consider only the frequency range for which binaural unmasking is most effective in broadband noise.

B. Procedure

SRTs were measured using a one-up/one-down adaptive threshold method (Plomp and Mimpen, 1979). For each SRT measurement, ten target sentences were presented one after another against the same interferer. For the two-voice interferers, the interfering sentences were displayed on a screen in front of the listeners as they were listening. They were instructed to disregard the female sentences appearing on the screen, and to listen for the male sentence. The target-to-interferer level ratio was initially very low (−32 dB). On the first trial, listeners could either enter a transcript on a computer keyboard, or replay the stimuli. If stimuli were replayed, the target level was increased by 4 dB. Stimuli had to be replayed until the target was loud enough to be judged partially intelligible. Listeners were instructed to attempt a transcript of this first target sentence when they believed that they could hear more than half the words of the sentence. Once the first transcript was entered, the correct transcript was displayed on the computer terminal, with the five key words in capitals. The listener self-marked the number of correct key words. Subsequent target sentences were presented only once, and self-marked in a similar manner. The target level was decreased by 2 dB if the listener correctly identified three or more of the five key words in the previous sentence, and otherwise increased by 2 dB. The SRT for a given condition was taken as the mean target-to-interferer level ratio on the last eight trials.

Each SRT measurement used a different interferer. The session began with two practice runs using unprocessed speech, in order to familiarize listeners with the task. The following runs measured SRTs in each of the N tested conditions in a random order ($N=16$ in experiments 1–3, $N=8$ in experiments 4 and 5). The order of the conditions was rotated for successive listeners, whereas sentence materials remained in the same order. Each target sentence was thus presented to every listener in the same order and, across a group of N listeners, a complete rotation of conditions was achieved. Each experiment therefore used a multiple of N listeners. This procedure also ensured that each condition was presented in each serial position within the experimental session, counterbalancing order effects.

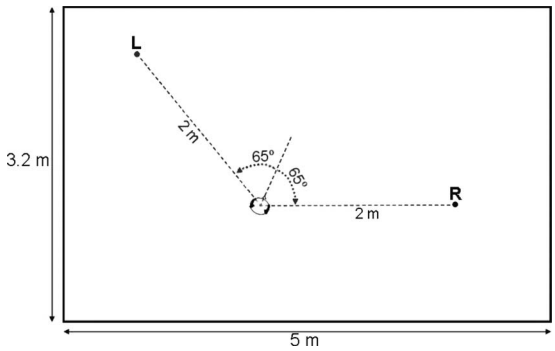

FIG. 1. Virtual room and spatial configuration used in experiments 1–3.

Signals were digitally mixed, D/A converted, and amplified using a 24-bit Edirol UA-20 sound card and an MTR HPA-2 headphone amplifier. They were presented to listeners over Sennheiser HD650 headphones in a single-walled IAC sound-attenuating booth within a sound-treated room. A computer terminal screen was visible outside the booth window. A keyboard was inside the booth to gather the transcripts of listeners.

C. Listeners

Listeners all reported normal hearing and English as their first language. None of them were familiar with the sentences used during the test. Each listener participated in a single session of the first three experiments and/or of the last two experiments. As experiments 4 and 5 used different target sentences from experiments 1 to 3, a listener could participate in a single session from each group of experiments. Listeners were paid for their participation.

III. INTERACTION BETWEEN THE EFFECTS OF REVERBERATION ON TARGET AND INTERFERER

SRTs were measured for a spatially separated interferer and target at fixed positions within the room, but the room absorption coefficient was varied across conditions, independently for target and interferer. The absorption coefficients were chosen so that they led to different values of direct-to-reverberant ratio and interaural coherence at the listener position.

A. Two-voice interferers (experiment 1)

1. Design

Experiment 1 used the same room and listener position as Lavandier and Culling (2007). The room was 5 m long, 3.2 m wide and 2.5 m high (Fig. 1). The listener was modeled as two ears, separated by 18 cm, placed along an axis at 25° to the 5-m wall on either side of a center point located at 1.2 m from the 5-m wall and 2 m from the 3.2-m wall. The source positions R and L were considered. They were situated at 2 m from the center of the ears, at 65° of azimuth on each side of the virtual listener. The interferer was always

TABLE I. Direct-to-reverberant ratio (dB) at the left and right ears for a source at the target (R) and interferer (L) positions, as a function of the room absorption coefficient used in experiments 1–3.

	Target (R)		Interferer (L)	
Absorption coefficient	Left	Right	Left	Right
1	∞	∞	∞	∞
0.7	0.53	0.79	0.39	−0.22
0.5	−3.70	−3.46	−3.80	−4.48
0.2	−10.93	−10.61	−10.76	−11.67

placed at position L, whereas the target was at position R, keeping a constant azimuth separation of 130° between the two competing sources. When computing the impulse responses between the sources and each ear, four absorption coefficients were used for each source: 1, 0.7, 0.5 and 0.2. Table I shows that the direct-to-reverberant ratio at the listening position decreased with the absorption coefficient. In the anechoic room with the absorption coefficient of 1, the direct-to-reverberant ratio was infinite as there was no reverberant field.

Experiment 1 used only two-voice interferers. The reverberation condition was varied across conditions, independently for target and interferer. A session of the experiment consisted of measuring the SRTs for the four types of target against the four types of interferer, resulting in 16 different conditions. One hundred and sixty target sentences and sixteen two-voice interferers were used to test these conditions. The interaural coherence was calculated for the 160 target stimuli at position R and the 16 interferers at position L. Table II presents the mean results for each type of stimulus. As expected, the coherence was 1 in the anechoic room and decreased with increasing reverberation.

For each listener, the SRTs were measured in the 16 tested conditions during a single 70-min session. Thirty-two listeners took part in the experiment.

2. Results

Figure 2 presents the mean SRTs measured in experiment 1. The two panels contain the same data plotted as a function of the absorption coefficients used for the interferer (top panel) or the target (bottom panel). The intelligibility decreased when the reverberation on either source increased. An analysis of variance (ANOVA) confirmed that the main

TABLE II. Mean interaural coherence with standard deviation for targets (in R) and interferers (in L), as a function of the room absorption coefficient used in experiments 1–3.

		Interferer (L)	
Absorption coefficient	Target (R)	Two-voice	Noise
1	1 (0.00)	1 (0.00)	1 (0.00)
0.7	0.86 (0.04)	0.86 (0.03)	0.87 (0.00)
0.5	0.75 (0.06)	0.76 (0.04)	0.77 (0.00)
0.2	0.62 (0.07)	0.63 (0.06)	0.61 (0.01)

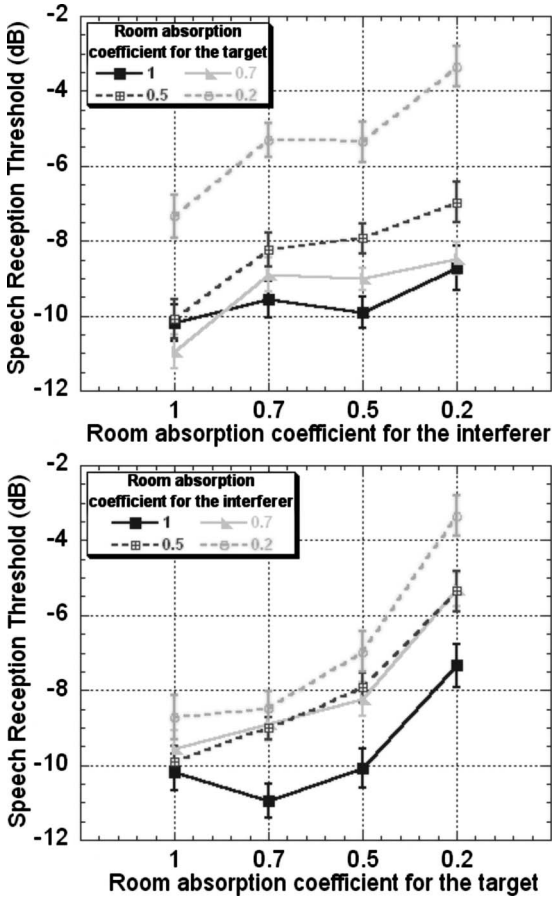

FIG. 2. Mean SRTs with standard errors measured with two-voice interferers in experiment 1, plotted as a function of the absorption coefficient used for the interferer (top) or as a function of the absorption coefficient used for the target (bottom).

effect of the absorption coefficient was significant for both target [$F(3,93)=99.7, p<0.0001$] and interferer [$F(3,93)=31.1, p<0.0001$]. Tukey pairwise comparisons were performed in both cases. For the target, only the absorption coefficients 1 and 0.7 were not significantly different [$q>5$, $p<0.01$ in every other case]. For the interferer, only the coefficients 0.7 and 0.5 were not significantly different [$q>5$, $p<0.01$ in every other case]. The interaction between the effects of the absorption coefficients used for target and interferer was not significant.

3. Discussion

As the absorption coefficient used for the interferer was decreased, reverberation reduced the interferer interaural coherence (Table II). As a result, this interferer produced more masking, in agreement with binaural unmasking theories, leading to higher thresholds. A less coherent interferer is more difficult to cancel using a binaural E-C mechanism, producing less masking release for spatially separated sources. SRTs also increased with decreasing target direct-to-reverberant ratio (Table I), as the absorption coefficient used for the target was decreased. This loss of target intelligibility is in agreement with the intrinsic degradation of speech in-

telligibility in reverberation, occurring even when no interferer is involved, and associated with the loss of amplitude modulation in the speech signal.

As reverberation increased, speech intelligibility suffered first from the effect of reverberation on the interferer, its effect on the target appearing only at higher reverberation levels. When decreasing the absorption coefficient used for the target, SRTs started increasing only when the coefficient reached 0.5, with the main deterioration of intelligibility appearing when the absorption further decreased to 0.2. For the interferer, decreasing the absorption coefficient from 1 to 0.7 had the strongest effect on SRTs. In the most common situation of conversations taking place in moderately reverberant rooms, the loss of intelligibility due to the room might then be due to the detrimental effect of reverberation on the interferer rather than to its effect on the target.

The interaction between the effects of reverberation on target and interferer did not reach significance in experiment 1. However, Fig. 2 shows evidence of interaction, at least when comparing the extreme absorption coefficients 1 and 0.2. Decreasing the absorption coefficient used for the interferer from 1 to 0.2 led to a 1.5-dB SRT increase with the anechoic targets, whereas a 4-dB increase was measured with the most reverberant targets. The interpretation of two independent effects of reverberation described above would not predict such a difference. Experiment 2 was run to test whether this difference was only due to the inherent measurement variability, or if it had not reached significance due to a lack of statistical power.

B. Two-voice interferers (experiment 2)

1. Design

Experiment 2 used a subset of the stimuli from experiment 1, and tested only the conditions involving the extreme absorption coefficients 1 and 0.2. The 16 conditions of experiment 1 were thus reduced to four conditions in experiment 2. These four conditions were tested four times for each listener. A single session of experiment 2 involved 16 SRT measurements and two practice trials, like experiment 1. The same 160 target sentences and 16 interferers were used. Eight listeners took part in a 70-min session of the experiment.

2. Results

Figure 3 presents the mean SRTs measured in experiment 2 as a function of the two absorption coefficients used for interferer and target. SRTs were about 1–1.5 dB lower in experiment 2 compared to experiment 1 (Fig. 2). The observed trends were similar in both experiments, the intelligibility decreasing with increasing reverberation on either source. An ANOVA confirmed that the main effect of the absorption coefficient was significant for both target $[F(1,31)=228.0, p<0.0001]$ and interferer $[F(1,31)=63.2, p<0.0001]$. Decreasing the absorption coefficient used for the interferer from 1 to 0.2 led to a 2-dB SRT increase with the anechoic targets, whereas a 4.5-dB increase was measured with the reverberant targets. The interaction between the effects of the absorption coefficients used for target and interferer was significant $[F(1,31)=17.3, p<0.001]$. A simple-main-effects analysis of this interaction showed that the effect of the absorption coefficient used for each source was significant at both levels of reverberation of the other source $[F(1,31)>12, p<0.0015$ in each case$]$.

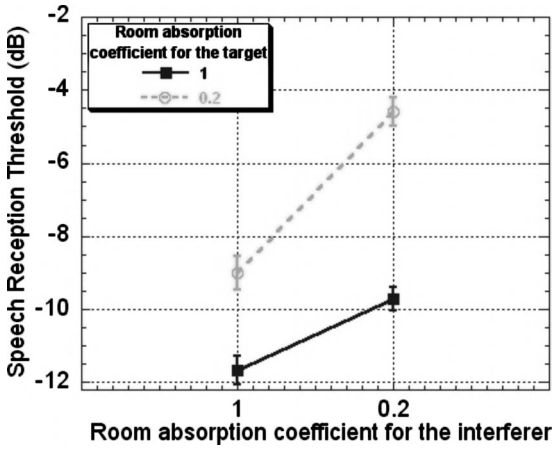

FIG. 3. Mean SRTs with standard errors measured with two-voice interferers in experiment 2, plotted as a function of the absorption coefficient used for the interferer.

3. Discussion

Experiment 2 clarified the results of experiment 1. By remeasuring the SRTs in only a few conditions, the statistical power of our analysis increased. It revealed that the effects of reverberation on the target and two-voice interferers were indeed interacting, and that the parsimonious model adopted by Lavandier and Culling (2007) was not sufficient to fully describe speech segregation in rooms. Mechanisms other than the decorrelation of the interferer and the decrease in D/R ratio of the target need to be taken into account to explain the observed interaction. Figure 2 indicates that these mechanisms became important when extreme reverberation conditions were considered.

Experiment 3 investigated whether these mechanisms were also involved when speech interferers were replaced by noise. If so, the effects of reverberation on target and interferer should interact using noise interferers, as they did using two-voice interferers.

C. Speech-shaped noise interferers (experiment 3)

1. Design

Experiment 3 was similar to experiment 1, but with the two-voice interferers being replaced by noise interferers. They were speech-shaped noises based on the long-term excitation pattern of the 16 two-voice interferers of experiment 1 concatenated. The mean interaural coherences of the 16 noise interferers in the four reverberation conditions are presented in Table II. Thirty-two listeners took part in a 70-min session of the experiment.

2. Results

Figure 4 presents the mean SRTs measured in experiment 3. The two panels contain the same data plotted as a

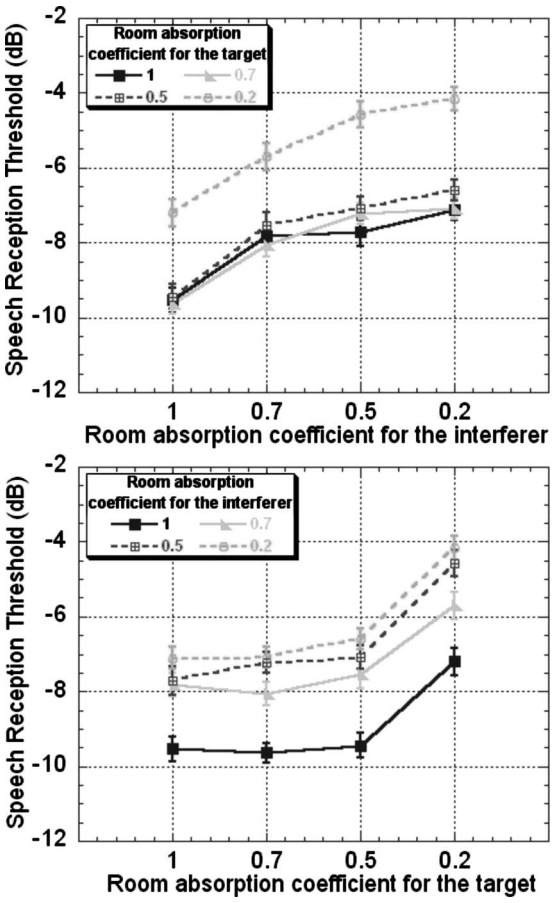

FIG. 4. Mean SRTs with standard errors measured with noise interferers in experiment 3, plotted as a function of the absorption coefficient used for the interferer (top) or as a function of the absorption coefficient used for the target (bottom).

function of the absorption coefficients used for the interferer (top panel) or the target (bottom panel). As with the two-voice interferers of experiment 1 (Fig. 2), the intelligibility decreased when the reverberation of either source increased. An ANOVA confirmed that the main effect of the absorption coefficient was significant for both target [$F(3,93)=85.7$, $p<0.0001$] and interferer [$F(3,93)=76.5$, $p<0.0001$]. Tukey pairwise comparisons were performed in both cases. For the interferer, only the coefficients 0.5 and 0.2 were not significantly different [$q>4.5$, $p<0.01$ in every other case]. For the target, the absorption coefficient 0.2 led to SRTs significantly higher than those measured with the three other coefficients [$q>16$, $p<0.001$ in each case], but the coefficients 1, 0.7 and 0.5 were not significantly different. The effects of the absorption coefficients used for target and interferer did not interact significantly.

3. Discussion

As with the two-voice interferers, speech intelligibility suffered from the effect of reverberation on the noise at lower levels of reverberation than those which affected intelligibility when applied to the target. Decreasing the absorption coefficient used for the target from 1 to 0.7 or 0.5 had no discernible effect on SRTs. The deterioration of intelligibility appeared only when this absorption was further decreased to 0.2. For the interferer, decreasing the absorption coefficient from 1 to 0.7 already resulted in a large increase in SRTs. A further reduction of absorption increased the SRTs only slightly. The coefficients 0.5 and 0.2 did not differ significantly. This outcome is in agreement with the results of Licklider (1948) who showed that, for speech in noise, most of the variation in intelligibility observed as a function of the noise interaural coherence occurred for a noise coherence varying between 1 and 0.75. Table II shows that in experiments 1–3, this coherence range corresponded to an absorption coefficient varying between 1 and 0.5. Decreasing the absorption coefficient below 0.5 still decreased the coherence, but below 0.75, and the influence on intelligibility was then limited.

Whereas the effects of reverberation on target and interferer interacted using two-voice interferers, they did not with noise interferers. Therefore, a parsimonious model involving only the decorrelation of the interferer and the decrease in D/R ratio of the target was sufficient to describe the influence of reverberation in experiment 3. The other mechanisms potentially taking place when speech interferers were involved, responsible for the interaction observed in experiments 1 and 2, would then have to be associated with segregation cues which were available with speech interferers but not noise. Fundamental frequency (F0) differences might have constituted such an additional cue to segregate the male target from the female interfering voices (Brokx and Nooteboom, 1982; Culling and Darwin, 1993). Silent periods or "gaps" in the speech masker could also have allowed the listener to hear "glimpses" of the target (Cooke, 2006; Dusquesnoy, 1983; Festen and Plomp, 1990), whereas this cue was not available with the continuous noise interferers. It should be noted that "listening in the gaps" was probably already limited with two-voice interferers compared to what would have been possible with one-voice interferers (Bronkhorst and Plomp, 1992). These two additional cues available with speech interferers and not noise are known to be disrupted by reverberation, and so could be responsible for the interaction observed in experiments 1 and 2. Culling *et al.* (2003, 1994) showed that reverberation was detrimental to the segregation of nonmonotonous voices by their F0 difference. Bronkhorst and Plomp (1990) showed that listening in the gaps was impaired by reverberation.

The following experiments were designed to investigate more precisely and individually the effects of reverberation on the target (experiment 4) and on the interferer (experiment 5). To separate the effects of reverberation on monaural and binaural processing, the direct-to-reverberant ratio and the interaural coherence were varied independently, by considering both binaural and diotic listening conditions. As in experiments 1 to 3, the coherence of the binaural stimuli was reduced by reverberation, whereas the coherence of the diotic stimuli was by definition fixed to 1 in every condition. In experiments 1 to 3, the D/R ratio and coherence of the sources decreased simultaneously when the room became more reverberant (Tables I and II). In experiments 4 and 5, with the diotic stimuli, the D/R ratio of the sources could be varied without modifying their coherence. In this way, the binaural and monaural effects of reverberation were teased

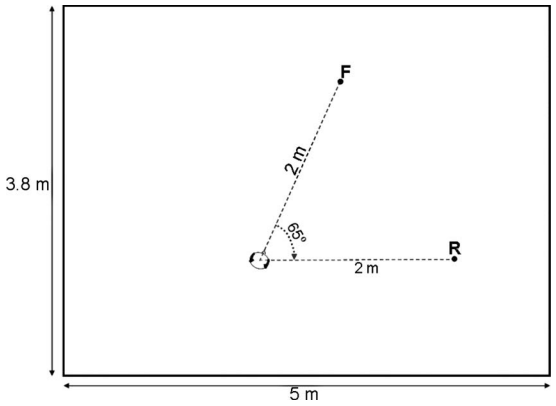

FIG. 5. Virtual room and spatial configuration used in experiments 4 and 5.

apart, in order to reveal the potential mechanisms responsible for the observed interaction in experiments 1 and 2, and to show that the main effect of reverberation on the target was monaural and associated with the D/R ratio, wheareas the main effect of reverberation on the interferer was binaural and mediated by the coherence.

IV. MONAURAL AND BINAURAL EFFECTS OF REVERBERATION ON THE TARGET (EXPERIMENT 4)

In experiment 4, the effect of reverberation on the target was investigated. The listening mode and the reverberation condition of the target were varied, whereas the interferer remained unchanged through the tested conditions.

A. Design

Figure 5 presents the spatial configuration considered in experiment 4. Both binaural and diotic listening modes were tested for the target in this experiment. To avoid any change in azimuth separation between target and interferer across conditions, the azimuth of the target had to remain the same in the binaural and diotic conditions, and thus the target had to be placed in front of the listener. In this spatial configuration, the interaural coherence of the target decreased less with reverberation than when it was on the listener's side. Therefore, experiment 4 used a slightly larger room than experiments 1–3, in order to avoid having the position F too close to the wall and to get a sufficient effect of reverberation on the coherence of the frontal source. The new room had the same length and height as the previous room, but was 3.8 m wide. The listener was still modeled in the same way, and remained with its center point located at 1.2 m from the 5-m wall and 2 m from the 3.8-m wall. The interferer was placed at position R, 65° to the right of the listener, as in experiments 1 to 3, such that the competing sources had a constant azimuth separation of 65°. Both F and R were situated 2 m from the center of the ears.

TABLE III. Direct-to-reverberant ratio (dB) at the left and right ears for a source at positions F and R, as a function of the room absorption coefficient used in experiments 4 and 5.

	Position F		Position R	
Absorption coefficient	Left	Right	Left	Right
1	∞	∞	···	···
0.5	···	···	−3.92	−3.28
0.2	−10.52	−10.50	···	···

When computing the impulse responses between the sources and each ear, different absorption coefficients were used for the two sources. For the interferer at position R, it was fixed to 0.5. This intermediate value was chosen to avoid the interacting effect found for the extreme levels of reverberation in experiment 2. Noise and two-voice interferers were used. For the target at position F, the two absorption coefficients 1 and 0.2 were tested. Table III presents the D/R ratios computed at the listening position as a function of the room absorption coefficient and the source position. The stimuli corresponding to the interferer were always binaural, whereas two listening modes were considered for the target. The target stimuli were either binaural using the impulse responses between the position F and each ear, or diotic using the signal of the right ear (chosen arbitrarily) for both ears. The results of the interaural coherence calculations for each type of stimulus are presented in bold in Table IV. By definition, the interaural coherence of the diotic targets was 1, even in the reverberant condition. Comparing these coherence values with those of Table II, it can be noted that the coherence of a frontal source in the larger room with the absorption coefficient 0.2 was close to the coherence of a source on the side in the smaller room with the higher absorption coefficient 0.5.

By considering the binaural and diotic listening modes and the two reverberation conditions for the target, we were able to decrease the D/R ratio of the target, and simultaneously either decreasing its coherence in the binaural case or keeping this coherence constant at 1 in the diotic case. If the effect of reverberation on the target is mediated by the

TABLE IV. Mean interaural coherence with standard deviation for targets and interferers at positions F or R, as a function of the room absorption coefficient and the listening mode used in experiments 4 (bold) and 5 (italic).

		Interferer	
Absorption coefficient, position and listening mode	Target	Two-voice	Noise
0.5, R, binaural	*0.77 (0.04)*	***0.72*** (***0.03***)	***0.74*** (***0.01***)
1, F, binaural and diotic	***1*** (***0.00***)	*1 (0.00)*	*1 (0.00)*
0.2, F, binaural	***0.77*** (***0.08***)	*0.74 (0.05)*	*0.70 (0.01)*
0.2, F, diotic	***1*** (***0.00***)	*1 (0.00)*	*1 (0.00)*

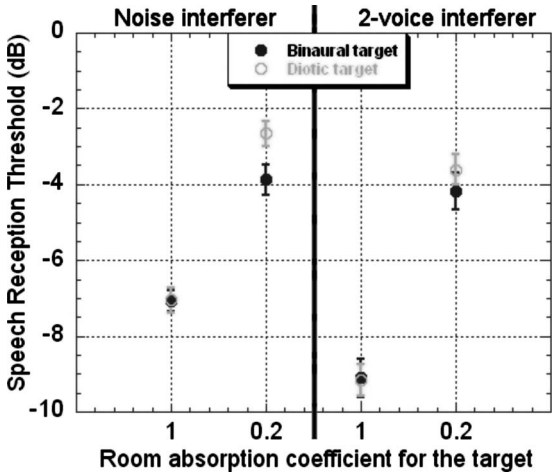

FIG. 6. Mean SRTs with standard errors measured with noise or two-voice interferers in experiment 4, for targets in two reverberation conditions and two listening modes.

D/R ratio and not by the coherence, SRTs in the diotic case should increase with reverberation as in the binaural case.

SRTs were measured in eight conditions corresponding to the two types of interferer (noise and two voice), and the two reverberation conditions (anechoic and reverberant) and two listening modes (binaural and diotic) for the target. Eighty target sentences were used to test these conditions. The sentences were all different from those used in experiments 1–3. Eight interferers of each type were paired with the eight lists of ten target sentences. The noise interferers were based on the long-term excitation pattern of the eight two-voice interferers concatenated. Listeners only heard four interferers of each type, different ones for different listeners, but the order of the conditions was rotated for successive listeners, whereas sentence materials remained in the same order. Across a group of eight listeners, each interferer thus contributed equally to each condition, and any order effect was counterbalanced. Thirty-two listeners took part in a 40-min session of the experiment.

B. Results

Figure 6 presents the mean SRTs measured with noise and two-voice interferers in experiment 4, for the target in the two reverberation conditions and listening modes. For the two types of interferer and the two listening modes, SRTs increased by 3–5 dB when the target was placed in a reverberant room. An ANOVA confirmed that reverberation on the target impaired intelligibility $[F(1,31)=513.7, p<0.0001]$, and also that SRTs were lower with two-voice interferers than with noise $[F(1,31)=31.5, p<0.0001]$. On average, SRTs were higher for the diotic targets than for the binaural ones $[F(1,31)=4.8, p<0.05]$. The interaction between the effects of the listening mode and the reverberation condition of the target was significant $[F(1,31)=4.5, p<0.05]$. A simple-main-effects analysis of this interaction showed that the effect of the listening mode was significant only in the reverberant room $[F(1,31)=9.8, p<0.01]$. The effect of reverberation was significant in both binaural and diotic listening $[F(1,31)>208, p<0.0001$ in each case$]$. The interaction between the effects of the interferer type and the reverberation condition of the target was also significant $[F(1,31)=5.6, p<0.05]$. A simple-main-effects analysis of this interaction showed that the two-voice interferers caused less masking than the noise in the anechoic room $[F(1,31)=9.8, p<0.01]$, but not in the reverberant one. The effect of reverberation was significant for both types of interferer $[F(1,31)>181, p<0.0001$ in each case$]$.

C. Discussion

As in experiments 1–3, the reverberation on the target increased SRTs for binaural listening. However, it was also the case for diotic listening, even if the coherence of the reverberant targets was then 1 as in the anechoic room. The loss of intelligibility in reverberation was therefore primarily a monaural effect related to the target D/R ratio, in agreement with the intrinsic degradation of speech intelligibility in rooms, associated with the loss of amplitude modulation in the reverberant speech signals.

A small but significant binaural advantage was measured in reverberation, indicating that having two ears slightly reduced the deleterious effect of reverberation on the target. This binaural improvement in intelligibility may be associated with the "squelching" effect of binaural hearing on perceived reverberation described by Koenig (1950). It was previously measured by Nábělek and Robinson (1982), at different levels of reverberation, using recordings of a target speech in a room with variable absorption characteristics. The percentage of correct words identified by each listener was evaluated using earphones, binaurally and monaurally (with one earphone disconnected). The binaural scores were in average 5% better than the monaural scores. These measurements involved target speech in quiet, with no interferer in the room. Experiment 4 showed that squelching could also take place in the presence of interferers.

SRTs were lower with two-voice interferers than with noise for the anechoic targets. Therefore, at least one additional segregation cue was available with speech interferers which was not available with noise. Moreover, this cue must have been monaural, as the difference of SRTs between the two-voice and noise interferers was found even in diotic listening. As SRTs were the same for the two-voice interferers and the noise when the target was in the reverberant room, this cue must have been ineffective when reverberation was added to the target.

Fundamental frequency differences between the competing voices may have constituted an additional segregation cue available with the two-voice interferers. Culling *et al.*. (2003, 1994) previously observed a disruption of this cue in reverberation. In those studies, the reverberation was varied simultaneously for target and interferer, but it was hypothesized that the disruption was due to the blurring of the F0 contour of the interferer rather than that of the target, because the segregation mechanism is probably based on the harmonic cancellation of the interferer rather than the harmonic enhancement of the target (de Cheveigné *et al.*, 1995). As the interferer remained unchanged across the tested conditions in experiment 4, if the F0 difference cue was used

and disrupted by reverberation, then it might be relevant to consider also the fundamental frequency of the target.

Listening in the gaps of the speech interferers may also have constituted a segregation strategy which was not available with the continuous noise interferers. These gaps may not have been so useful when the target was reverberant, resulting in an interaction between listening in the gaps and target degradation in reverberation. The deterioration of the target intelligibility would then have been worse when the target was heard through the gaps of the interferer rather than in quiet. It should be noted here that the gaps in the interferer remained the same across the tested conditions, because reverberation was varied for the target but not for the interferer.

Experiment 4 showed that the degradation of intelligibility associated with the loss of amplitude modulation in speech constituted the main effect of reverberation on the target, but that it was not the only mechanism affecting speech segregation in rooms.

V. BINAURAL AND MONAURAL EFFECTS OF REVERBERATION ON THE INTERFERER (EXPERIMENT 5)

In experiment 5, the listening mode and the reverberation condition of the interferer were varied, whereas the target remained unchanged through the tested conditions.

A. Design

Experiment 5 used the same protocol as experiment 4, but replacing the target by the interferer and vice-versa. The same room, listener and source positions were used (Fig. 5), with the same source material for target and interferer, but this time the target was always at position R, whereas the interferer was at position F. The target at position R had a fixed reverberation, with a room absorption coefficient of 0.5. For the interferer at position F, the two absorption coefficients 1 and 0.2 were tested. The target stimuli were always binaural, whereas binaural and diotic listening modes were tested for the interferer. The diotic stimuli used the right channel of the binaural stimuli for both ears. Table III presents the corresponding D/R ratios computed at the listening position and the results of the interaural coherence calculations for each type of stimulus are presented in italic in Table IV.

The coherence of the diotic interferers was always 1, even in the reverberant condition. If the effect of reverberation on the interferer is mediated by its coherence, SRTs should increase with increasing reverberation in the binaural case, but remain constant even when the reverberation is increased in the diotic case.

SRTs were measured for the interferer in eight conditions: two types of stimuli (noise and two-voice), two reverberation conditions (anechoic and reverberant) and two listening modes (binaural and diotic). Thirty-two listeners took part in a 40-min session of the experiment.

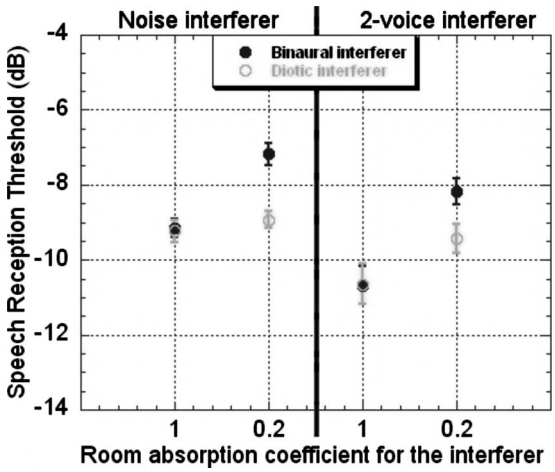

FIG. 7. Mean SRTs with standard errors measured in experiment 5, for noise or two-voice interferers in two reverberation conditions and two listening modes.

B. Results

Figure 7 presents the mean SRTs measured in experiment 5, for noise and two voice interferers in two reverberation conditions and two listening modes. SRTs increased by 2–2.5 dB when the binaural interferers were placed in a reverberant room. The effect of reverberation was very limited for the diotic interferers. An ANOVA confirmed that reverberation on the interferer impaired intelligibility $[F(1,31)=69.0, p<0.0001]$, and also that SRTs were lower with two-voice interferers than with noise $[F(1,31)=21.5, p<0.0001]$. On average, SRTs were lower for the diotic interferers than for the binaural ones $[F(1,31)=10.6, p<0.01]$. The interaction between the effects of the listening mode and the reverberation condition of the interferer was significant $[F(1,31)=10.6, p<0.01]$. A simple-main-effects analysis of this interaction showed that the effect of the listening mode was significant only in the reverberant room $[F(1,31)=20.5, p=0.0001]$. The effect of reverberation was significant in both binaural and diotic listening $[F(1,31)>8.8, p<0.01$ in each case$]$.

C. Discussion

As in experiments 1–3, the reverberation on the interferer increased the SRTs for binaural listening. However, experiment 5 showed that the loss of intelligibility was considerably smaller for diotic interferers. This suggests that adding reverberation to the interferer had a detrimental effect on intelligibility when the interferer coherence was reduced. The effect of reverberation on the interferer was therefore mainly binaural and mediated by interaural coherence. This effect is in agreement with previous binaural unmasking experiments in which reducing the correlation of the interferer at the two ears increased masking (Licklider, 1948; Robinson and Jeffress, 1963).

The decorrelation of the masker constituted the main influence of reverberation on the interferer, but it was not the only one. The effect of reverberation for diotic listening was small but significant. This monaural effect could result from

the reverberation disrupting the segregation cue based on F0 differences between the competing voices. If this cue allows canceling one of the interfering voices by following its F0 contour (de Cheveigné *et al.*, 1995), the disruption could result from the blurring of this contour as reverberation was added to the interferer. Reverberation could also have disrupted the segregation cue based on listening in the gaps of the speech interferers. These interferers could have become more efficient maskers when their potential gaps were filled by the added reverberation, as shown by Bronkhorst and Plomp (1990) when they compared the amount of masking produced by continuous and modulated noises in different reverberation conditions.

The effect of reverberation on the interferer in experiment 5 led to a smaller loss of intelligibility than its effect on the target in experiment 4 (Figs. 6 and 7). However, it should be noted that in these two experiments the source with variable reverberation was placed in front of the listener, and that, in this room, reverberation affects the coherence of a frontal source less than the one of a source on the side, whereas its effect on the D/R ratio mainly depends on the source-listener distance and is rather independent of the azimuth of the source. As a consequence, the decrease of D/R ratio tested for the target in experiment 4 was comparatively larger than the decrease in coherence tested for the interferer in experiment 5.

VI. GENERAL DISCUSSION

The effects measured in experiments 1–5 can be summarized by describing how increasing reverberation sequentially affected speech segregation in the virtual rooms. The increasing reverberation first reduced intelligibility by decorrelating the interferer at the listener's ears, making it a more effective masker as shown by previous binaural unmasking experiments (Licklider, 1948; Robinson and Jeffress, 1963). For example, the equalization-cancellation mechanism (Durlach, 1972) predicts that a less correlated masker should be more difficult to equalize at the two ears, and consequently more difficult to cancel, resulting in lower speech intelligibility. This binaural effect was mediated by the interaural coherence of the interfering source, and affected both the noise and the two-voice interferers. It reduced intelligibility for low levels of reverberation. Further decreases in coherence had less influence, as most of the variation in intelligibility for speech in noise occurs for a noise coherence between 1 and 0.75 (Licklider, 1948). It should be noted that taking into account the influence of the head between the two ears in our simulations might have led to impairments of intelligibility at even lower levels of reverberation. The head would lead to extra interaural decorrelation in asymmetric configurations, particularly for sources to the side (Lindevald and Benade, 1986). This additional decorrelation would make the interferer's coherence drop at even lower levels of reverberation. Because of the floor effect associated with coherence, the maximum intelligibility loss with increasing reverberation should be similar with or without a simulated head.

After decorrelating the interferer, the increasing reverberation distorted the target speech signals (experiments 1–4), as a result of the multiple sound reflections mixing with the direct sound. This monaural effect directly affected the intelligibility of the target for relatively high levels of reverberation. The intelligibility loss was mediated by the direct-to-reverberant ratio of the target at the listening position, and might be described by existing objective measurements (Bradley, 1986; Bradley *et al.*, 1999; Houtgast and Steeneken, 1985). The monaural speech distortions affected the target, but also the two-voice interferers (experiments 1, 2, and 5). Because of these distortions, the fundamental frequency patterns of both target and interferer might have been more difficult to track in reverberation by the auditory system, and thus segregation based on F0 differences could have been disrupted, as noted by Culling *et al.* (2003, 1994). Reverberation might also have filled some silent periods in the two-voice interferers (Bronkhorst and Plomp, 1990). These monaural effects may explain the small but significant additional intelligibility losses measured at the higher levels of reverberation. They might also be responsible for the interaction of the effects of reverberation on the target and two-voice interferers observed in experiments 1 and 2. Because of this interaction, the loss of intelligibility due to the reverberation on one source (target or speech interferer) was larger when the other source was also reverberant rather than anechoic. The D/R ratio of the sources could be relevant to the prediction of these monaural effects. Further investigations are required. For example, it is not clear if the influence of reverberation on the segregation by fundamental frequency difference related to the reverberation of the target, of the interfering voice, or both.

In experiment 4, a small but significant binaural advantage was measured for reverberant targets, with both noise and speech interferers. This advantage might constitute further evidence of a squelching effect (Koenig, 1950; Nábělek and Robinson, 1982). In this effect, having two ears may ameliorate the effect of reverberation on target intelligibility, regardless of the interferer. The monaural D/R ratio of the target would not be sufficient to predict this binaural effect, and the target interaural statistics might have to be considered as well.

In experiment 3, the effects of reverberation on the target and noise interferers did not interact. This is consistent with the interaction observed with speech interferers being associated with the disruption of the fundamental frequency difference cue and/or listening in the gaps. As these two cues did not exist when the interferer was noise, there were no grounds for an interaction. Lavandier and Culling (2007) found discrepancies between SRTs measured with noise and STI calculations. An interaction between the effects of reverberation on target and noise was hypothesized as one of the potential explanations for these discrepancies. Experiment 3 of this study did not support this hypothesis. A second account for the discrepancies between measured SRTs and STI predictions could come from the STI predictions being less reliable below the intelligibility level for which the STI is best calibrated (Steeneken and Houtgast, 1980).

Even though the experiments presented in this paper were realized with a fixed azimuth separation of target and interferer, their results can be generalized to other spatial configurations, as long as target and interferer are not co-located. Spatial unmasking in anechoic situations results partly from head shadow improving the signal-to-noise ratio at the best ear, and partly from binaural interaction associated with the difference in interaural time delays of the competing sources (Bronkhorst and Plomp, 1988). Spatial unmasking depends on the azimuth separation of sources because the head shadow contribution is very dependent on the source azimuths. The binaural interaction contribution proved to be relatively independent of these azimuths as long as the sources are not co-located (Bronkhorst and Plomp, 1988). With increasing reverberation, the head shadow component progressively disappears (Plomp, 1976), and spatial unmasking is reduced to its binaural interaction component. Consequently it becomes independent of the size of the azimuth separation of sources (Beutelmann and Brand, 2006; Plomp, 1976). As our investigations only considered the spatial unmasking associated with binaural interaction, their results should not depend on the magnitude of the tested azimuth separations.

In order to predict speech intelligibility in rooms in the presence of directional noise interferers, the two main effects of interferer coherence and target intrinsic intelligibility should be taken into account, and the parsimonious model hypothesized by Lavandier and Culling (2007) is sufficient. These two effects have been modeled independently. The influence of noise coherence in rooms is implemented in two models based on the equalization-cancellation mechanism (Durlach, 1972). Zurek *et al.* (2004) proposed a model predicting the segregation of a narrow band noise target from a broadband noise interferer, and Beutelmann and Brand (2006) recently developed a model predicting the intelligibility of a near field speech target against a noise interferer. The STI (Houtgast and Steeneken, 1985) or the useful-to-detrimental ratios (Bradley, 1986; Bradley *et al.*, 1999) evaluate the intrinsic degradation of speech by reverberation. Our goal is to implement these two main effects of reverberation in a single model, which should also account for the squelching effect, a binaural mechanism that ameliorates the deleterious influence of reverberation on target speech. Our model also needs to predict the sound levels of target and interferer at the listener's ears. This will allow consideration of the influence of the room on the sound level of each source at the head (Bradley *et al.*, 1999), and the influence of head-shadow (Bronkhorst and Plomp, 1988). This model will require refinements to be able to predict speech segregation against speech interferers in rooms. The two monaural cues based on the F0 differences between competing voices and the gaps in the speech interferers will have to be taken into account, as they are also influenced by reverberation. Even if these cues were limited in the conditions we tested, they could become much more important in other conditions. For example, F0 differences might become predominant for co-located sources, where coherence becomes irrelevant because spatial unmasking is abolished. Listening in the gaps is known to be much larger with one-voice interferers than with the two-voice interferers we used (Bronkhorst and Plomp, 1992). The influence of reverberation on these two cues might become quite large in these situations. If it cannot be assumed that the listener knows who/where to listen to, then additional attentional effects also have to be incorporated in the model (Kidd *et al.*, 2005; Shinn-Cunningham *et al.*, 2005).

VII. CONCLUSION

SRT measurements in virtual rooms showed that reverberation impaired speech intelligibility first by a decorrelation of the interferer at the two ears, and then by a degradation of the intrinsic target intelligibility. The first effect of reverberation is binaural and mediated by the coherence for the interferer. The second is monaural and associated with the direct-to-reverberant ratio for the target. Having two ears reduced to a small extent the detrimental effect of reverberation on the target. Additional effects of reverberation were observed with speech interferers. The sound reflections in rooms might be responsible for a disruption of the mechanism by which the auditory system exploits fundamental frequency differences to segregate competing voices, and a disruption of the listening in the gaps associated with speech interferers. These disruptions might explain an interaction observed between the effects of reverberation on the targets and two-voice interferers, and could be important to model in very reverberant rooms.

ACKNOWLEDGMENTS

This work was supported by the UK EPSRC. The authors are grateful to the associate editor Ruth Litovsky, to Erick Gallun and two anonymous reviewers for their helpful comments on a first version of this paper, and to all listeners who took part in the experiments.

[1]There are some listening situations in which target and interferer dynamically change over time, and other situations in which the listener knows who he/she is listening to, as is the case in many conversations. In our experiments, target and interferer were clearly identified and redirection of attention was not the key issue.

Allen, J. B., and Berkley, D. A. (**1979**). "Image method for efficiently simulating small-room acoustics," J. Acoust. Soc. Am. **65**, 943–950.
Beutelmann, R., and Brand, T. (**2006**). "Prediction of speech intelligibility in spatial noise and reverberation for normal-hearing and hearing-impaired listeners," J. Acoust. Soc. Am. **120**, 331–342.
Bradley, J. S. (**1986**). "Predictors of speech intelligibility in rooms," J. Acoust. Soc. Am. **80**, 837–845.
Bradley, J. S., Reich, R. D., and Norcross, S. G. (**1999**). "On the combined effects of signal-to-noise ratio and room acoustics on speech intelligibility," J. Acoust. Soc. Am. **106**, 1820–1828.
Brokx, J. P. L., and Nooteboom, S. G. (**1982**). "Intonation and the perceptual separation of simultaneous voices," J. Phonetics **10**, 23–36.
Bronkhorst, A. W., and Plomp, R. (**1988**). "The effect of head-induced interaural time and level differences on speech intelligibility in noise," J. Acoust. Soc. Am. **83**, 1508–1516.
Bronkhorst, A. W., and Plomp, R. (**1990**). "A clinical test for the assessment of binaural speech perception in noise," Audiology **29**, 275–285.
Bronkhorst, A. W., and Plomp, R. (**1992**). "Effect of multiple speechlike maskers on binaural speech recognition in normal and impaired hearing," J. Acoust. Soc. Am. **92**, 3132–3139.
Cooke, M. (**2006**). "A glimpsing model of speech perception in noise," J. Acoust. Soc. Am. **119**, 1562–1573.

Culling, J. F. (**1996**). "Signal processing software for teaching and research in psychoacoustics under UNIX and X-windows," Behav. Res. Methods Instrum. Comput. **28**, 376–382.
Culling, J. F., and Darwin, C. J. (**1993**). "Perceptual separation of simultaneous vowels: Within and across-formant grouping by f0," J. Acoust. Soc. Am. **93**, 3454–3467.
Culling, J. F., Hodder, K. I., and Toh, C. Y. (**2003**). "Effects of reverberation on perceptual segregation of competing voices," J. Acoust. Soc. Am. **114**, 2871–2876.
Culling, J. F., Summerfield, Q., and Marshall, D. H. (**1994**). "Effects of simulated reverberation on the use of binaural cues and fundamental-frequency differences for separating concurrent vowels," Speech Commun. **14**, 71–96.
Darwin, C. J., and Hukin, R. W. (**2000**). "Effects of reverberation on spatial, prosodic, and vocal-tract size cues to selective attention," J. Acoust. Soc. Am. **108**, 335–342.
de Cheveigné, A., McAdams, S., Laroche, J., and Rosenberg, M. (**1995**). "Identification of concurrent harmonic and inharmonic vowels: A test of the theory of harmonic cancellation and enhancement," J. Acoust. Soc. Am. **97**, 3736–3748.
Durlach, N. I. (**1972**). "Binaural signal detection: Equalization and cancellation theory," in *Foundations of Modern Auditory Theory*, edited by J. Tobias (Academic, New York), Vol. **II**, pp. 371–462.
Dusquesnoy, A. J. (**1983**). "Effect of a single interfering noise or speech source upon the binaural sentence intelligibility of aged persons," J. Acoust. Soc. Am. **74**, 739–743.
Festen, J. M., and Plomp, R. (**1990**). "Effects of fluctuating noise and interfering speech on the speech-reception threshold for impaired and normal hearing," J. Acoust. Soc. Am. **88**, 1725–1736.
Fitch, W. T., and Giedd, J. (**1999**). "Morphology and development of the human vocal tract: a study using magnetic resonance imaging," J. Acoust. Soc. Am. **106**, 1511–1522.
Hartmann, W. M., Rakerd, B., and Koller, A. (**2005**). "Binaural coherence in rooms," Acta. Acust. Acust. **91**, 451–462.
Houtgast, T., and Steeneken, H. J. M. (**1985**). "A review of the MTF concept in room acoustics and its use for estimating speech intelligibility in auditoria," J. Acoust. Soc. Am. **77**, 1069–1077.
IEEE. (**1969**). "IEEE recommended practice for speech quality measurements," IEEE Trans. Audio Electroacoust. **17**, 227–246.
Kidd, G., Mason, C., Brughera, A., and Hartmann, W. (**2005**). "The role of reverberation in release from masking due to spatial separation of sources for speech identification," Acta. Acust. Acust. **91**, 526–535.
Koenig, W. (**1950**). "Subjective effects in binaural hearing," J. Acoust. Soc. Am. **22**, 61–62.
Lavandier, M., and Culling, J. F. (**2007**). "Speech segregation in rooms: Effects of reverberation on both target and interferer," J. Acoust. Soc. Am. **122**, 1713–1723.
Licklider, J. C. R. (**1948**). "The influence of interaural phase relations upon masking of speech by white noise," J. Acoust. Soc. Am. **20**, 150–159.
Lindevald, I. M., and Benade, A. H. (**1986**). "Two-ear correlation in the statistical sound fields of rooms," J. Acoust. Soc. Am. **80**, 661–664.
Moore, B. C. J., and Glasberg, B. R. (**1983**). "Suggested formulae for calculating auditory-filter bandwidths and excitation patterns," J. Acoust. Soc. Am. **74**, 750–753.
Nábělek, A. K., and Robinson, P. K. (**1982**). "Monaural and binaural speech perception in reverberation for listeners of various ages," J. Acoust. Soc. Am. **71**, 1242–1248.
Peterson, P. M. (**1986**). "Simulating the response of multiple microphones to a single acoustic source in a reverberant room," J. Acoust. Soc. Am. **80**, 1527–1529.
Plomp, R. (**1976**). "Binaural and monaural speech intelligibility of connected discourse in reverberation as a function of azimuth of a single competing sound source (speech or noise)," Acustica **34**, 200–211.
Plomp, R., and Mimpen, A. M. (**1979**). "Improving the reliability of testing the speech-reception threshold for sentences," Audiology **18**, 43–52.
Rendall, D., Kollias, S., Ney, C., and Lloyd, P. (**2005**). "Pitch (F0) and formant profiles of human vowels and vowel-like baboon grunts: the role of vocalizer body size and voice-acoustic allometry," J. Acoust. Soc. Am. **117**, 944–955.
Robinson, D. E., and Jeffress, L. A. (**1963**). "Effect of varying the interaural noise correlation on the detectability of tonal signals," J. Acoust. Soc. Am. **35**, 1947–1952.
Shinn-Cunningham, B., Ihlefeld, A., Satyavarta, and Larson, E. (**2005**). "Bottom-up and top-down influences on spatial unmasking," Acta. Acust. Acust. **91**, 967–979.
Steeneken, H. J. M., and Houtgast, T. (**1980**). "A physical method for measuring speech-transmission quality," J. Acoust. Soc. Am. **67**, 318–326.
Zurek, P. M., Freyman, R. L., and Balakrishnan, U. (**2004**). "Auditory target detection in reverberation," J. Acoust. Soc. Am. **115**, 1609–1620.

Binaural speech unmasking and localization in noise with bilateral cochlear implants using envelope and fine-timing based strategies

Richard van Hoesel[a)]
Cooperative Research Centre for Cochlear Implant and Hearing Aid Innovation, Melbourne, Vic 3002 Australia

Melanie Böhm
Department of Otolaryngology, Medical University of Hannover, 30625 Hannover, Germany

Jörg Pesch
Cochlear GmBH, 3065 Hannover, Germany

Andrew Vandali
Cooperative Research Centre for Cochlear Implant and Hearing Aid Innovation, Melbourne, Vic 3002 Australia

Rolf D. Battmer and Thomas Lenarz
Department of Otolaryngology, Medical University of Hannover, 30625 Hannover, Germany

(Received 26 July 2007; revised 5 December 2007; accepted 24 January 2008)

Four adult bilateral cochlear implant users, with good open-set sentence recognition, were tested with three different sound coding strategies for binaural speech unmasking and their ability to localize 100 and 500 Hz click trains in noise. Two of the strategies tested were envelope-based strategies that are clinically widely used. The third was a research strategy that additionally preserved fine-timing cues at low frequencies. Speech reception thresholds were determined in diotic noise for diotic and interaurally time-delayed speech using direct audio input to a bilateral research processor. Localization in noise was assessed in the free field. Overall results, for both speech and localization tests, were similar with all three strategies. None provided a binaural speech unmasking advantage due to the application of 700 μs interaural time delay to the speech signal, and localization results showed similar response patterns across strategies that were well accounted for by the use of broadband interaural level cues. The data from both experiments combined indicate that, in contrast to normal hearing, timing cues available from natural head-width delays do not offer binaural advantages with present methods of electrical stimulation, even when fine-timing cues are explicitly coded.
© *2008 Acoustical Society of America.* [DOI: 10.1121/1.2875229]

PACS number(s): 43.66.Pn, 43.66.Ts [RYL] Pages: 2249–2263

I. INTRODUCTION

For a listener with normal hearing, the ability to detect a signal in diotic noise is much improved when the signal is delayed in one ear compared to the other (e.g., Hirsch, 1948). Similarly, binaural speech intelligibility in diotic noise improves when speech is imparted with an inter-aural phase delay (IPD) and time-delay (ITD) (Licklider, 1948; Levitt and Rabiner, 1967; Bronkhorst and Plomp, 1988). Often such binaural unmasking advantages are attributed to changes in correlation at the signal frequencies when the signal is added to the noise, or the change in ability to "equalize and cancel" the stimuli at those frequencies (e.g., Colburn and Durlach, 1978; Akeroyd and Summerfield, 2000; Breebart and Kohlrausch, 2001; Culling, 2007). Binaural masking level differences (BMLDs) comparing detection thresholds in diotic broadband noise (N0) for sinusoids that are interaurally out of phase (Sπ), with those that are diotic (S0), show that out-of-phase thresholds are about 10–15 dB lower for low frequencies in the range 200–500 Hz. That difference gradually reduces to just a few dB beyond 1.5 kHz (e.g., Durlach, 1964). Both low- and high-frequency pure-tone BMLDs increase as the bandwidth of the masker decreases (at constant energy), largely as a consequence of the increased difficulty in detecting the signal in narrowband noise when it has the same interaural parameters as the noise. Further studies using high-frequency "transposed tone" stimuli (e.g., van de Par and Kohlrausch, 1997), which are designed such that the available envelope cues after peripheral filtering match the fine-timing cues available from low-frequency sinusoids, have shown that comparable BMLDs can be achieved for 125 Hz stimulation of high- and low-frequency regions of the cochlea. That result supports the suggestion made by Colburn and Equissaud (1976) that fundamental binaural processing is comparable across different regions along the

[a)]Author to whom correspondence should be addressed. Electronic mail: rvanh@bionicear.org

cochlea, at least at rates as low as 125 Hz, and that peripheral processing is responsible for the reduction of cues at higher frequency places.

It has been established for some time now that the use of two cochlear implants, rather than one, offers a robust speech intelligibility advantage in the free field, particularly when speech and noise arrive from different directions (e.g. van Hoesel and Clark, 1999; Gantz *et al.*, 2002; van Hoesel, 2002; Müller *et al.*, 2002; van Hoesel and Tyler, 2003). Although some subjects in some studies have shown a squelch effect, i.e., better performance when using both ears than just the ear with the better signal-to-noise ratio (SNR), the contribution of binaural unmasking to that result has remained speculative. Several confounding factors may play a role in free field studies. For example, asymmetrical performance between the ears may be sufficient to allow the ear with a lower physical SNR to offer better performance than the one benefiting from the head-shadow effect. Improved performance, resulting from the addition of an ear with a lower SNR to the shadowed ear, might in that case be interpreted as evidence of binaural unmasking, but may actually just reflect the listener's ability to attend the better performing ear. Performance may also be better with two ears than one due to redundancy of information and/or because it is the listening condition the bilateral CI user is most familiar with. One aim of the work presented here is to assess more directly whether binaural speech unmasking is available to bilateral implant users by manipulating interaural relations of speech and noise signals, and presenting signals to the direct audio-input connector of a bilateral sound processor. In making that assessment, it is important to keep in mind that the clinical strategies tested ACE (advanced combinational encoder) and CIS (continuous interleaved sampler), preserve only the envelope information in the signal at each ear and discard the low-frequency fine-timing cues that offer important unmasking cues in normal-hearing listeners. For that reason, the PDT strategy ("peak derived timing," van Hoesel, 2002; van Hoesel, 2004), which aims to preserve fine-timing cues at low frequencies, was also included in the present study. Experiment 1 describes binaural speech unmasking results for ACE, CIS and PDT strategies tested in four bilateral cochlear implant (CI) users. Speech reception thresholds (SRTs) were measured in diotic noise for speech that was either diotic (S0N0), or interaurally delayed by 700 μs (S700N0), which corresponds approximately to the maximal ITD delay imparted by the head in free-field listening. Performance was additionally measured for monaural speech and noise presented to the better ear (SmNm), and monaural speech at the better ear in diotic noise (SmN0). Those latter two conditions were included because (unpublished) psychophysical data from the first author's lab had indicated a binaural unmasking effect for low-rate pulse trains in noise, applied to a single electrode in one ear, when a copy of the noise was added contralaterally. The comparison of SmNm and S0N0 data further provides an indication of the diotic (redundancy) benefit in these listeners.

Low-frequency ITD cues in listeners with normal hearing also play a dominant role in sound localization in quiet (Raleigh, 1907; Wightman and Kistler, 1992). In contrast, several studies with bilateral CI users have shown that the broadband ILD (interaural level difference) is the more salient cue when identifying sound-source direction in quiet (van Hoesel *et al.*, 2002; van Hoesel, 2004; Grantham *et al.*, 2007). While that result is perhaps as expected for CI users using clinical strategies that discard fine-timing information, the data from two previous studies with PDT do not preclude the possibility that the same applies with that strategy. In the first of those studies, van Hoesel and Tyler (2003) assessed sound-direction identification abilities using pink noise bursts in quiet. Although at least some of the subjects tested in that study indicated improved performance with PDT compared to the clinical strategy tested, the comparison is confounded by sound-processor hardware differences for the two strategies. In the second study (van Hoesel, 2004), one of two subjects tested with PDT showed better localization of click trains with a repetition rate of 50 Hz than for pink noise bursts comprising faster temporal fluctuations. Using direct input measures, the same subject showed comparable ILD sensitivity when tested with both click trains and pink-noise bursts, but much better ITD sensitivity for the click train. Consequently, improved localization for that subject was hypothesized to be due to the availability of ITD cues in the low-rate click-train but not the noise. However, as localization was also better for the click train than noise when using ACE and CIS strategies, it is not clear that fine timing per se contributed to the PDT result. The present experiment aimed to extend the previous findings by comparing localization performance in four subjects with all three strategies on a common hardware platform, and using click trains with repetition rates of both 100 and 500 Hz. In contrast to previous studies with PDT, localization abilities were tested in the presence of a single interfering noise source rather than in quiet. This was done for several reasons. First, it was considered that everyday situations often are noisy, so an assessment in noise might be more relevant to everyday performance. Further motivation for the inclusion of an interfering noise source was to ensure localization abilities would not be severely under sampled by the relatively large fixed spacing of 30° between adjacent loudspeakers in the available test array (Hartmann *et al.*, 1998). Finally, it was hypothesized that the added difficulty, compared to localizing in quiet, might force listeners to make better use of all available cues, potentially including fine timing in PDT. It was suggested by van Hoesel (2004) that, although localization in quiet for CI users is largely governed by ILD cues, ITDs may play a role when the ILD cues are ambiguous, as is the case in certain spatial regions for bilateral CI users wearing directional ear-level microphones (van Hoesel *et al.*, 2002; van Hoesel, 2004). In the present experiment, additional ambiguity in the total signal-plus-noise ILD was potentially introduced, when signal and noise arrived from different directions, because the level of the signal was roved over a range of six dB but the noise was not. While the main motivation for that rove was to reduce monaural level cues, its inclusion in the task is probably not untypical of everyday requirements where targets of unknown intensity are to be localized in noise that is fairly constant in level. Lorenzi *et al.* (1999) reported frontal horizontal plane localization-in-noise data

for normal-hearing listeners, and suggested that the relative importance of ILD and ITD cues is dependent on noise position. They argued that at low SNRs listeners attend the most reliable cue available, and showed comparable performance was achievable by using ILD or ITD cues when noise was directly ahead, but ILD cues offered better performance than did ITDs when noise was at 90°. To allow for the consideration that CI users might also use different cues for different noise locations, localization tests in experiment 2 in the present paper were conducted for noise fixed at either 0°, or 90°, as separate test conditions.

II. METHODS

A. Strategy descriptions

All three strategies were implemented on a SPEAR3 research sound processor (CRC Hear, Australia), which is capable of bilateral stimulation, and derives audio input from two Cochlear HS-8 behind-the-ear directional microphones, or alternatively from a stereo auxiliary input connector. When using direct input to the SPEAR3, the frequency response of the microphone in free field was approximated by appropriately scaling the gain values of the analysis filters in each strategy. Prior to assigning frequency-to-electrode maps for each strategy with each subject, a psychophysical pitch comparison task was completed to determine average relative offsets of the electrode arrays in the two ears. In the pitch task, three fixed electrodes in the right ear (electrodes 19, 12 and 4, corresponding to apical, mid, and basal locations) were paired with seven electrodes around the same electrode number contralaterally (electrode groups 22-16, 15-9, and 7-1, respectively). Each of the resulting 21 bilateral pairs was presented six times in a single test block. In three of the six presentations, the stimulus in the left ear preceded the right, and in the remaining three the order was reversed. Nominal stimulation levels were 85% of the dynamic range, randomized by up to 10%. The stimulus pulse rate was 1200 pulses per second, and signal duration and inter-stimulus gap were 500 ms. Listeners were to determine whether the left or right ear signal produced a higher pitch. Results for the three places on the right were averaged to provide a single interaural electrode-offset that was used to map all three strategies such that electrodes representing the same (acoustic) frequencies stimulated approximately pitch-matched places along the cochlea in each ear. Both CIS and ACE strategies use only the envelope information, available from each narrowband filter output, to amplitude modulate pulse trains on each associated electrode. The carrier pulse rate is fixed and unrelated to the acoustic signal properties. In (the CIS Strategy Wilson *et al.*, 1991), filter envelope amplitudes are applied to associated electrodes in a round robin fashion. The ACE strategy, which is based on the "SMSP" scheme proposed by McDermott *et al.* (1992), uses a very similar approach except that only a subset of filters containing most of the energy is selected to produce stimulation. The latter approach allows a higher resolution filter bank to be used without increasing overall stimulation rate.

All four participating subjects were regular bilateral users of the ACE strategy, with at least 20 active electrodes (and associated filter bands) in their own clinical processors. Although familiarity with ACE may have biased performance in favor of that strategy, the ACE and PDT implementations used in the present study both employed 19-channel filter banks, with near identical cutoff frequencies. Perceptual adjustment, to the new allocation of frequencies to electrodes, was therefore expected to be similar with those two strategies. In addition to the intended strategy variations and changes in frequency-to-electrode allocation, further small differences between the strategies implemented on the SPEAR3 and the subjects' own clinical processors included minor microphone response variations, and better dynamic range and the absence of an automatic gain control on the SPEAR3. Those parameters will likely have required little adjustment time and, if anything, improved performance in these experiments compared to the clinical processor. Filter bands with ACE and PDT were mapped to the most apical 19 bands available in each subject, while allowing for the insertion offset between ears. The decision to use 19 channels for those strategies was based on the consideration that most Nucleus CI users have at least that many active electrodes (of the 22 nominally available) and allowed for an insertion offset of up to 3 electrodes (2.25 mm) without needing to deactivate some bands in either ear to maintain pitch match. The inclusion of the CIS strategy, which typically employs less filters and electrodes than the ACE approach, was motivated by the concern that the maxima selection process in ACE might result in distorted interaural cues when the spectra at the two ears differ. A 10-channel CIS implementation was chosen in the present study such that the first and last electrodes were identical to those used with ACE/PDT for each ear in each subject, and intervening electrodes were spaced twice as far apart (1.5 mm rather than 0.75 mm). Corresponding bandpass filters with CIS were designed such that audio frequencies were assigned to similar place along the cochlea as in the ACE/PDT implementation, within the constraint that CIS filters were approximately twice as wide and distance between electrodes was doubled. Nominal center frequencies and three dB bandwidths for ACE/PDT and CIS filter banks are shown in Table I. Filter bands are numbered from low to high frequency, and were assigned to electrodes in an apical to basal direction. The center frequencies of the filters in the 10-channel CIS implementation were designed such that the three-dB cutoff frequencies corresponded to the center frequencies of the even numbered filters in the 19-channel ACE/PDT filter bank. That approach was preferable to simply matching CIS center frequencies to those of odd numbered ACE/PDT channels as it better allows for the non-uniform bandwidths of the filters. To ensure that the overall bandwidth of the filter bank remained unchanged across strategies, the low-frequency cutoff for the first CIS filter and high-frequency cutoff for the last CIS filter were matched to those of the ACE/PDT filter bank. As a consequence, differences in center frequencies when comparing CIS and odd-numbered ACE/PDT filters are somewhat larger for those two bands. Because increased familiarity with the finer resolution frequency band representation might bias performance in favor of ACE or PDT, rather than CIS, the results were to be interpreted accordingly. If any benefits were

TABLE I. Center frequencies (Fc) and bandwidths (BW) for both 19-channel (ACE/PDT) and 10-channel (CIS) filter banks used.

ACE/PDT band	Fc (Hz)	BW (Hz)	CIS band	Fc (Hz)	BW (Hz)
1	270	140	1	300	200
2	400	120			
3	535	150	2	543.5	287
4	687.5	155			
5	847.5	165	3	852	330
6	1017.5	175			
7	1192.5	175	4	1194.5	355
8	1372.5	185			
9	1565	200	5	1567	390
10	1762.5	195			
11	1970	220	6	1986	448
12	2210	260			
13	2500	320	7	2532.5	645
14	2855	390			
15	3287.5	475	8	3347.5	985
16	3840	630			
17	4630	950	9	4740	1800
18	5640	1070			
19	6637.5	925	10	6370	1460

found, with CIS compared to ACE, they should be considered as strong evidence of more salient binaural cues with CIS. On the other hand, poorer performance with CIS would not necessarily reflect degraded binaural cues. Both CIS and ACE filter banks were implemented using complex FIR filters acting as Hilbert transforms, which provide envelope information at the output of each band that is only limited in rate by the filter's bandwidth. This potentially allowed a wider range of temporal fluctuations to be coded in CIS than ACE strategy. Both envelope-based strategies activated up to 10 electrodes (selected form 19 for ACE) in each stimulation cycle at 1200 Hz, resulting in total maximal stimulation rate of 12 000 pulses per second (pps).

The PDT strategy implementation used a bank of bandpass Butterworth filters, implemented digitally at the audio sampling rate of 14.4 kHz using infinite impulse response (IIR) filters. While the maximal envelope modulation rate in each band is in this case also limited by the bandwidth of the filter, additional fine-timing cues that are discarded in the complex FIR filter approach were preserved at the full audio sampling rate in the first seven of the 19 filter bands. The outputs in those seven bands, spanning the frequency range from about 200 to 1300 Hz, were subjected to detection of positive peaks in the narrowband signals, and the times of the peaks were represented electrically by applying electrical pulses to corresponding electrodes in a 10 ms buffer. Temporal resolution of the electrical pulses in that buffer was also set to 14.4 kHz, which means peaks in the stimulus waveforms were quantized to about 70 μs intervals. Although that may be somewhat coarse compared to ITD sensitivity in normal hearing with optimal low-frequency signals, it is comparable to, or better than, sensitivity displayed by many CI users (e.g., van Hoesel and Tyler, 2003; Litovsky *et al.*, 2005; van Hoesel, 2007). Because the implant used stimulates on only one electrode at a time, an arbitration scheme was required to resolve competing demands for time slots when combining pulses across multiple channels.[1] For the 12 higher frequency bands that were not subjected to peak picking, envelope cues were explicitly derived by rectifying the IIR filter outputs and low-pass filtering at 400 Hz. Time slots in the 10 ms buffer that were not occupied by pulses from the low-frequency PDT bands (one to seven) were filled with the high-frequency envelope-derived pulses. In that procedure, the first available time slot was filled with information from the filter with the largest envelope level. That filter band was then excluded from subsequent selection for a period of 0.7 ms to allow other filter bands to be represented. That process continued until all available time slots in the buffer had been considered.

Fitting of each strategy for each subject was adjusted prior to the take home period with that strategy. For CIS, ACE, and the high-frequency PDT channels, each electrode's dynamic range was measured at 1200 pps. Threshold levels (T) were set by starting with a soft, but clearly detectable, sound and steadily decreasing stimulation levels until no longer audible. This was repeated three or four times to obtain an average threshold used in the processor. Maximal levels before discomfort (C) were adjusted for the highest level that did not produce an uncomfortable loudness sensation. For lower frequency channels in PDT, T and C levels were determined at the rate corresponding to each associated filter's center frequency. This was based on software simulations of the algorithm during its initial development (van Hoesel, 2002), which showed that the average pulse rate from any PDT channel corresponds well to the filter's center frequency for a wide range of broadband signals. With all three strategies, "live" testing was subsequently used to fine tune stimulation levels to produce a comfortable loudness range in multi-channel operation. If sounds were generally too loud or soft, for example, C levels of all the electrodes were decreased or increased, respectively, by an equal fraction of each electrode's dynamic range. Similarly, T levels were lowered if live background noise levels were objectionable but typical speech levels were comfortable, or increased if speech was unclear, but high level sounds were already sufficiently loud. All three strategies employed monopolar stimulation, with biphasic current pulses that were 25 μs per phase in duration.

B. Subjects and schedules

Participants were tested at the Medical University of Hannover, Germany. They were selected to be moderate-to-good performers, more than 30 and less than 60 years of age, with post-lingual onset of bilateral (severe-to-profound) sensory neural hearing loss, and at least one year experience with bilateral Nucleus 24 devices. All four subjects were well trained on SRT testing with the sentences used in the speech task, as well as free-field localization, as a result of previous participation in similar studies. Although the number of subjects is modest, they are a relatively homogenous group that is particularly well suited to the study, and the requirement for a large subject pool due to substantial inter-subject variability, as is often the case in cochlear implant

studies, is a lesser issue. Each subject was sequentially programmed with the ACE, CIS and PDT speech coding strategies, with the order of strategies randomized across subjects according to an incomplete latin square design. Each subject was initially fitted with the first strategy on the SPEAR3, and then used that on a daily basis for four weeks. After that period, the subject returned for evaluation with that strategy, and was fitted with the next one, at which time the previous strategy was removed from the SPEAR3. This process was repeated for the second and third strategies. Upon completion of the take-home periods and evaluations with all three strategies, the order of strategies was reversed and each one was taken home for a shorter period of two weeks, with a second evaluation at the end of that period. The counterbalanced "ABC-CBA" design was used to reduce learning effect differences among strategies while maintaining a reasonable overall time to complete the experiments (18 weeks). This was a considerable commitment for the subjects as bilateral stimulation at relatively high overall rates required them to replace a single AA battery cell in the SPEAR3 about every 4 h, during each day for four months. To ensure subjects made use only of the strategies on the SPEAR3, they agreed to surrender their clinical devices for the duration of the study.

C. Procedures and materials

Speech perception was tested using the adaptive Oldenburg sentence test (Wagener *et al.*, 1999) using direct audio input to the SPEAR3 processor. In those speech materials, 40 lists comprising 30 sentences each are available. Five-word low-predictability sentences are constructed by selecting from ten different options for each word (i.e., all the sentences are constructed from a restricted pool of 50 words ensuring good homogeneity of the words in the sentences). Continuous noise with the same long-term spectrum as the speech materials was used as a masker. Speech reception thresholds at 50% correct performance (SRT50) were measured using an adaptive procedure (Hagermann and Kinnefors, 1995) for four conditions: monaural speech and noise (SmNm), both presented to the better ear as determined from previous test data; monaural speech at the better ear in diotic noise (SmN0); diotic speech in diotic noise (S0N0); and 700 μs interaurally delayed speech in diotic noise (S700N0). Noise levels were always varied, while the target speech was held fixed at a level equivalent to that which would be obtained using free-field presentation of the same materials at 65 dBA, calibrated by measurement of electrical stimulation levels at the output of the sound processor using custom software and hardware. Each presentation block included 30 sentences. Responses to the last 20 were used to determine the SRT. Four SRTs were measured in total for each combination of strategy and signal-and-noise configuration: two after the first take-home period, and two after the second. The four SRTs were averaged to obtain an overall SRT for each condition, which was used in the statistical analysis.

Sound-direction identification for signals presented in the horizontal plane was assessed in free-field in an anechoic chamber. Target signals comprised click trains that were 300 ms in duration, without ramped onset or offsets. The signals were presented from one of seven loudspeakers spanning the frontal 180° arc with a radius of 1.1 m. Signal presentation level was nominally 65 dB sound pressure level as measured at the position of the listener's head in absentia, and was randomly varied by ± 3 dB to reduce monaural level cues. The repetition rate of the click trains was held fixed at either 100 or 500 Hz in each test block. Clicks presented to the loudspeakers comprised positive monopolar rectangular pulses that were seven samples in duration at 44.1 kHz, resulting in a spectrum that was flat within six dB between 100 Hz and 4 kHz, and rolled off more steeply to a notch at about 6.3 kHz, which was approximately centered on the highest filter band used in all three sound-coding strategies. Interfering noise, spectrally matched to the click trains, was presented at a fixed level of 65 dB (i.e., nominally 0 dB SNR) also measured at the position of the head in absentia. Interfering noise was presented from either the loudspeaker directly ahead, or in an alternative experimental condition, from the one at 90° to the right. The noise used in each presentation was one of 15 possible 1.4 s segments selected from a 3 s sequence. The noise was gated on and off with a rectangular window that started 600 ms before, and finished 500 ms after the target signal. Fifteen repeat presentations of the signal (one for each of the 15 noise samples) were included for each loudspeaker, resulting in 105 presentations in each block with a fixed combination of click rate and noise position. Subjects were informed that interfering noise would arrive from the fixed loudspeaker, and that only the target's direction would vary, and were required to orally indicate which of the seven loudspeakers had produced the target. Prior to each block, subjects were (re-)familiarized with the seven target-plus-noise conditions by playing each one in turn from left to right-most target position. All four subjects were well experienced in the localization task, and had previously participated in studies using the same loudspeaker array. Although listeners were instructed to face the frontal loudspeaker, head movements were not physically restricted or recorded, and feedback was not provided. Informal data collected with normal-hearing listeners under the same conditions showed minimal errors despite the applied target level rove in the fixed level noise.

III. RESULTS AND DATA ANALYSIS

A. Speech in noise

SRT results from each of the four subjects are shown in the four panels in Fig. 1. Within each panel, results from left to right are for SmNm, SmN0, S0N0, and S700N0 conditions. Strategies are indicated using circles for ACE, squares for CIS and triangles for PDT. Note the scale change for subject S2, who showed considerably better performance with ACE and PDT than CIS. In fact, performance with CIS for that subject may have been even poorer than indicated by the SNR because, at high SNRs, the noise level may fall below the threshold of the processor's input dynamic range and not be presented electrically (when there is no speech signal). That nonlinear effect may be the reason why an initial attempt to describe the entire dataset using a two-way

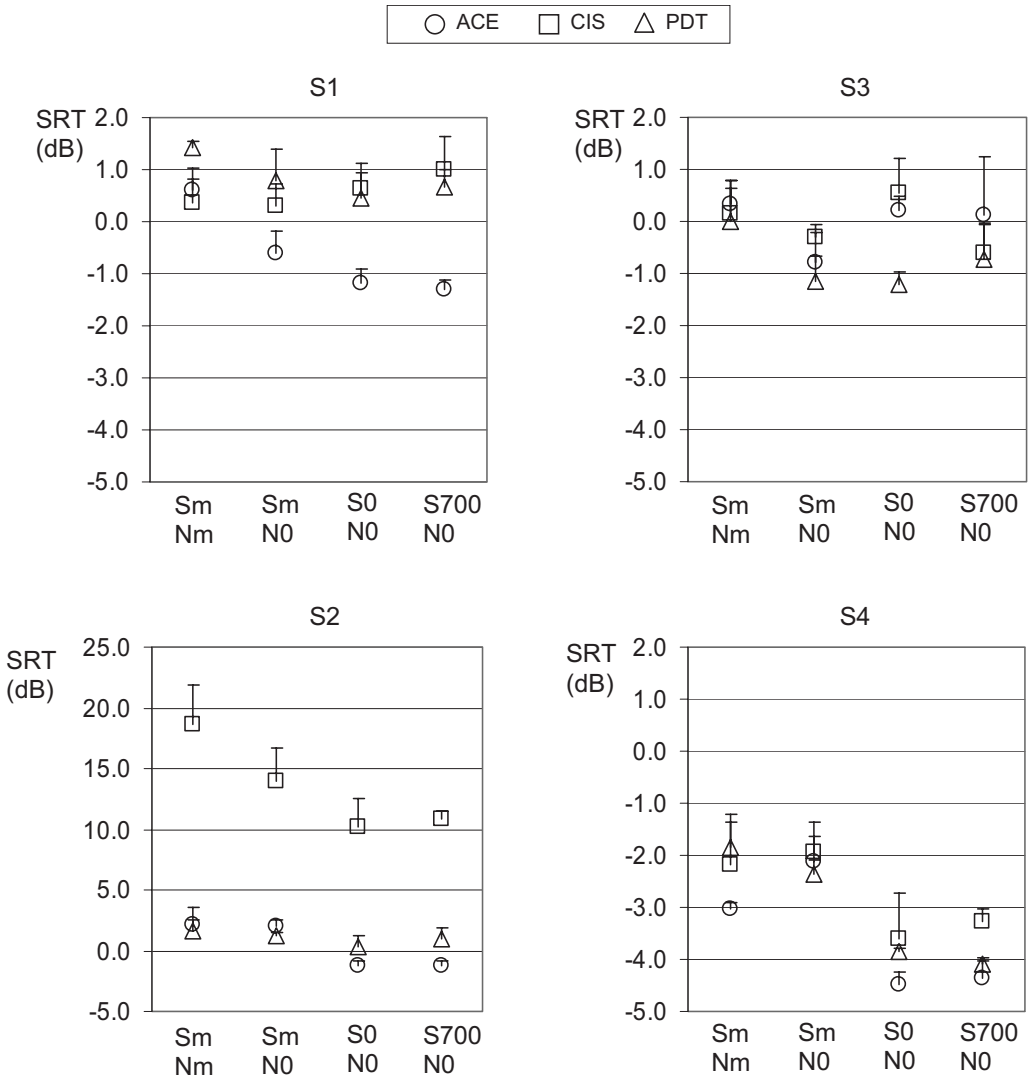

FIG. 1. SRTs for each of the four subjects. Test conditions from left to right in each panel are SmNm, SmN0, S0N0, S700N0. Strategies are indicated by circles for ACE, squares for CIS and triangles for PDT. Note the scale change for subject S2, who required much higher SNRs to obtain 50% when using the CIS strategy. Error bars indicate one standard error (SE) of the mean, based on four SRTs (two per session). For visual clarity only positive halves of the symmetric SE bars are shown.

analysis of variance (ANOVA) resulted in a poor model fit. Two alternative ANOVAs were therefore conducted. In the first of those, the CIS data from just subject S2 were excluded, whereas in the second CIS data from all four subjects were omitted (i.e., only ACE and PDT were compared). In both cases, Strategy and Signal-and-noise-configuration (SN-Config) were included as main factors along with their interaction, and Subject was included as a random factor. Test-order and learning effects were assumed to have been minimized through the use of randomized sequencing across subjects, and averaging of SRTs for each strategy across the two test sessions in the ABC-CBA test protocol. Task learning for all four subjects was further presumed to have been moderated through previous participation in studies employing the same test procedure. Residual task learning was assessed using an ANOVA that incorporated "Session" (first or second test date) as a fixed factor. For the full data set there was no significant effect of Session on SRT (difference less than 0.01 dB, ($F[1,86]=0.00$; $p=0.99$), but when the CIS data for subject S2 were eliminated, a small learning effect was observed (0.5 dB lower SRT for the second session ($F[1,78]=6.07$, $p=0.02$). The ANOVAs described below for data averaged over both sessions were therefore also conducted using data from just the second session, but because the results showed essentially the same conclusions, only the combined session analyses are presented.

When just the CIS data from subject S2 were excluded, the ANOVA showed a significant effect of SN-Config ($F[3,29]=5.1; p=0.006$) but not Strategy ($F[2,29]=2.3, p=0.12$), and no interaction between the two ($F[6,29]=0.73, p=0.57$). Post-hoc analysis using Bonferroni simultaneous tests showed that the significant effect of SN-Config was due to a higher SRT for the SmNm condition than either S0N0 (1.13 dB, $p=0.014$) or S0N700 (1.05 dB, $p=0.027$). Results for S0N0 and S700N0 did not differ significantly (0.09 dB, $p=1.00$), which means binaural unmasking did not result from an ITD of 700 μs applied to the signal in diotic

noise. The SRT for SmN0 condition was slightly lower than SmNm, but the difference was also not significant (0.4 dB, P=1.00). Similar findings resulted when only ACE and PDT data were analyzed from all four subjects: the effect of SN-Config ($F[3,21]=5.7; p=0.005$) was significant, but Strategy ($F[1,21]=1.94, p=0.18$) and the interaction ($F[3,21]=0.36, p=0.78$) were not.

Post-hoc analysis again showed significantly lower means for S0N0 (1.6 dB, P=0.009) and S700N0 (1.4 dB, P=0.027) than SmNm, and no significant difference between the two binaural conditions, S0N0 and S700N0 (0.2 dB, p=1.0). Performance for the SmN0 condition was also not significantly lower than with SmNm (0.56 dB; p=1.00).

In summary, both analyses showed that irrespective of the strategy used, there was a binaural advantage of about 1–1.5 dB when the speech and noise were presented diotically to both ears (S0N0) rather than just to the better ear alone (SmNm), but there was no evidence of further improvements due to binaural unmasking when speech was interaurally delayed by 700 μs while keeping the noise diotic (S700N0). Similarly, there was no indication that binaural information in the SmN0 condition resulted in significantly better performance than for the SmNm condition.

B. Localization in noise

1. Response descriptions

Means and standard deviations of responses to signals presented from each loudspeaker in the localization task are shown for each subject in the lower portion of Fig. 2. Each row describes data from a single subject. The four panels within each row describe the results, from left to right, for noise at N0 with 100 Hz click trains (N0-100 Hz), followed by N0-500, N90-100, and N90-500 Hz. Each panel includes separate results with ACE (circles), CIS (squares), and PDT (triangles). It can be seen that responses were generally similar across all three strategies (as will be discussed in more detail in Sec. III B 2). The upper portion of Fig. 2 summarizes the results by averaging the mean responses, shown in the lower panels, across both subjects and strategies. This was done for each combination of noise position and click rate. The left panel describes results for the N0 noise position at both rates, and the right panel those for N90. The error bars in the upper summary panels indicate ± one standard error of the mean when averaging the mean responses in the lower panels across subjects and strategies.

For noise arriving from the N0 position (left columns), both individual and averaged responses show fairly symmetric patterns around the perfect-performance leading diagonal. Subjects often responded similarly when signals arrived from any of the three loudspeakers on either left, or right sides, resulting in mean-response patterns resembling a step function around the diagonal. Responses for subjects S1 and S3, as well as S4 at 500 Hz, typically ranged between 60 and 90° to the left or right for any of the three speakers on the corresponding side, whereas S2's responses ranged more conservatively between 30 and 60°. Only subject S4, for a rate of 100 Hz, showed an ability to distinguish loudspeakers at 30° (right or left) from more lateral ones on the same side, although was still unable to tell apart signals from the two loudspeakers at 60 and 90°. When the noise was positioned at N90 (right) instead of N0, performance for click trains from the left and right sides was less symmetric. In that case, responses for loudspeakers on the left were very similar to the N0 condition, but signals from the central loudspeaker were more often wrongly perceived as arriving from the left, and signals from the right side were better separated with responses closer to the correct-response diagonal particularly at 30°.

2. Error analyses

Various performance measures were calculated for the localization data. The first consisted of the total root mean square (RMS) error (D-bar: Rakerd and Hartmann, 1986) for all loudspeakers in the array. An ANOVA was applied to that measure using a generalized linear model with main factors: strategy (Strategy), click-train rate (Rate), and noise position (NoisePos), while treating subjects (Subject) as a random factor. Interactions between the main factors were also incorporated. When all data points were included, the effect of Strategy was not found to be significant ($F[2,35]=2.7, p=0.08$), nor were the interactions, but the factors Rate ($F[1,35]=37.8, p<0.001$) and NoisePos ($F[1,35]=9.9, p=0.003$) were. When three outliers (out of 48 data points), from three different subjects and strategies, were excluded, the model fit improved (adjusted r-squared increased from 68 to 81%). In that case, the Strategy effect was significant ($F[2,30]=4.8, p=0.016$), and the significance of the effects of both Rate ($F[1,30]=57.3, p<0.001$) and NoisePos ($F[1,30]=21.7, p<0.001$) increased, whereas the interactions remained non-significant. Figure 3 shows mean RMS errors (D-bar) averaged across the four subjects, with each strategy [ACE (circles), CIS (squares), and PDT (triangles)] for the four combinations of Rate and NoisePos. Error bars show one standard error of the mean, indicating inter-subject differences. It is clear from that figure that the mildly significant Strategy effect is due to slightly poorer performance with CIS compared to the other two strategies. This was confirmed in post-hoc Bonferroni simultaneous tests, which showed that, for the data set excluding the outliers, the CIS RMS error was about 2.3° larger than either ACE or PDT (p=0.05). The same analysis showed that performance with ACE and PDT did not differ significantly. Further comparisons showed that at 500 Hz the overall RMS error was 5.7° larger ($p<0.001$) than at 100 Hz, and that for the N90 noise position it was 3.3° larger ($p<0.001$) than for N0.

Because localization performance in quiet has been shown to vary strongly as a function of loudspeaker position with bilateral CI users (e.g., van Hoesel, 2004), and the total-array RMS error can be biased towards the results for loudspeakers with the largest errors, an additional ANOVA was conducted preserving individual loudspeaker RMS errors. In that case the model fit was improved by averaging the performance at each loudspeaker across subjects, for each combination of Rate and NoisePos. Fixed factors included Loudspeaker, Strategy, Rate and NoisePos. Only two-factor interactions were included in the model, as inclusion of higher order interactions decreased the r-squared value of the

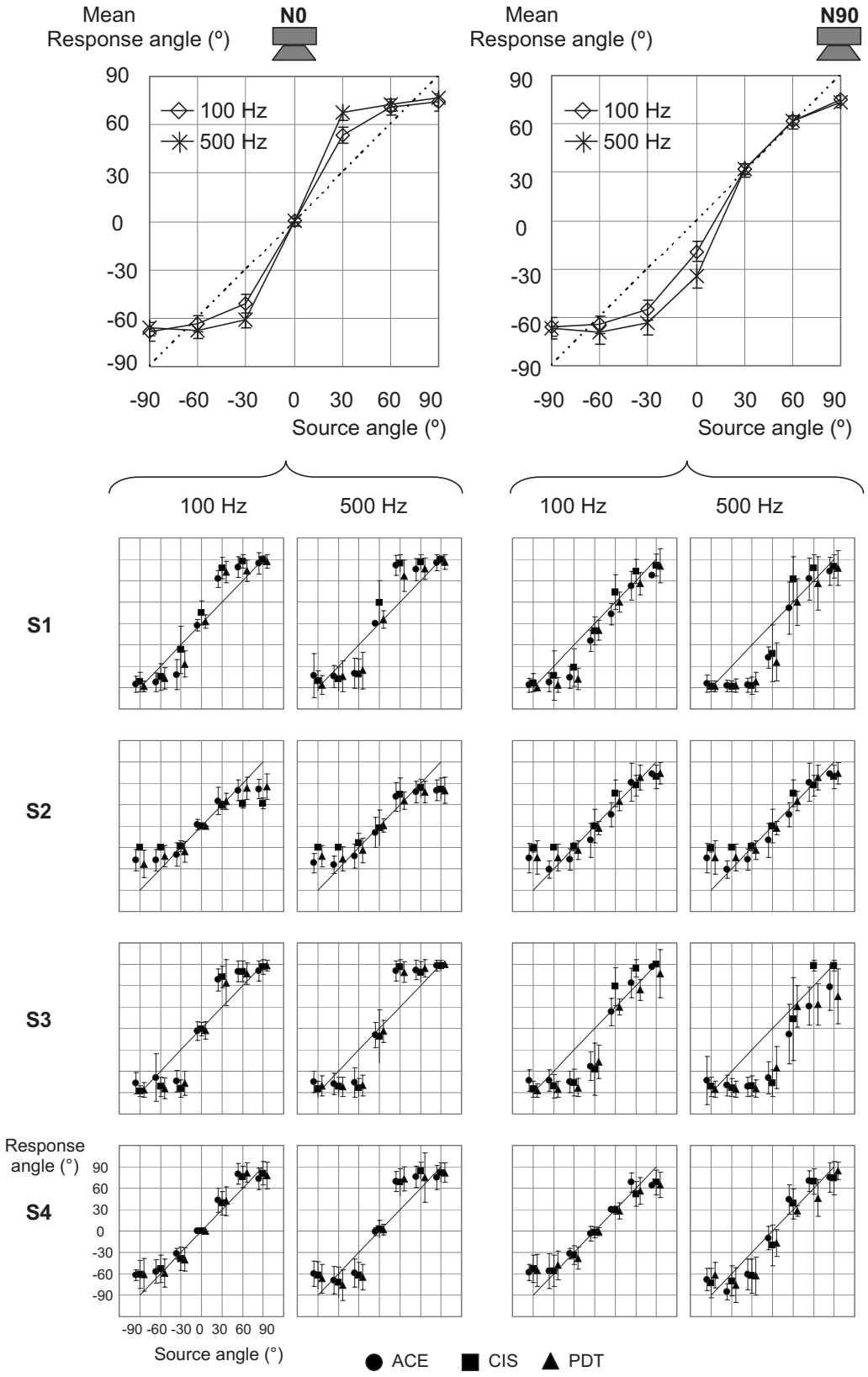

FIG. 2. Lower four rows show localization results for each of the four subjects. Means and standard deviations (± error bars) of responses to signals presented from each loudspeaker are shown for all three strategies: ACE (circles), CIS (squares), and PDT (triangles). The four panels within each row describe, from left to right, results for noise at N0 with 100 and 500 Hz clicks, followed by noise at N90 with 100 and 500 Hz clicks, respectively. The top row summarizes results by averaging the mean responses shown in the lower panels across both subjects and strategies for each combination of noise position and click rate. The left panel describes results at both rates (diamonds 100 Hz, stars 500 Hz) for the N0 noise position, and right panel those for N90. Error bars in the top row indicate ± one standard error of the mean calculated across subjects and strategies.

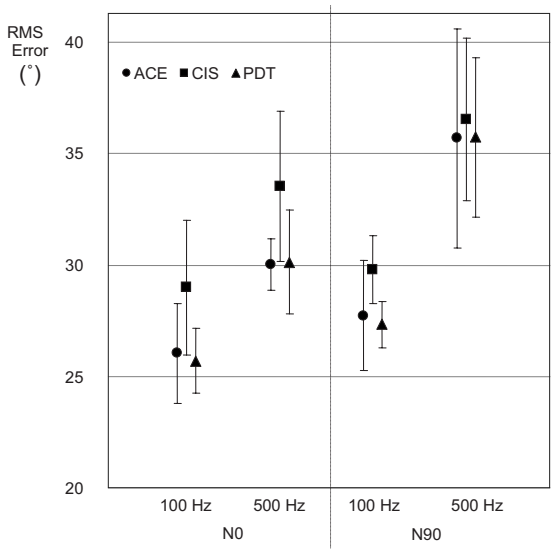

FIG. 3. Total-RMS error across the array (D bar) averaged across the four subjects. RMS errors are shown separately for each combination of Noise position and Rate with each strategy [ACE (circles), CIS (squares), and PDT (triangles)]. Error bars show ± one standard error of the mean, indicating inter-subject differences.

fit. The effect of Strategy was again found to be nonsignificant ($F[2,44]=2.7, p=0.08$), although mean RMS errors were marginally smaller for PDT (26°) than for ACE (27°), or CIS (28°). As in the total-array RMS error analysis, strongly significant effects were seen for Rate ($F[1,44]=68.8, p<0.001$) and NoisePos ($F[1,44]=20.3, p<0.001$). Mean RMS errors at 100 and 500 Hz were 24° and 30°, respectively. Mean RMS errors with the two noise positions were 25° for N0, and 29° for N90. The interaction between Rate and NoisePos was, in contrast to the total-array RMS error analysis, moderately significant in this analysis ($F[1,44]=5.5, p=0.024$), with post-hoc tests indicating an average increase for N90 compared to N0, of only 1.6° ($p=0.8$) at 100 Hz, but 5.1° ($p<0.001$) at 500 Hz. The difference compared to the total-array RMS error analysis is likely due to the strong influence of data from loudspeakers with the largest errors in the total-array RMS measure. As expected, the effect of Loudspeaker was found to be strongly significant ($F[1,44]=20.8, p<0.001$), as were the interactions between Rate and Loudspeaker ($F[6,54]=8.4, p<0.001$), and NoisePos and Loudspeaker ($F[6,44]=24.6, p<0.001$). Post-hoc Bonferroni simultaneous tests examining the Rate-Loudspeaker interaction (combining results for both noise positions) showed significant increases ($p<=0.002$) in RMS error at the higher rate for the three loudspeakers near the middle of the array (RMS errors 9.5 to 13.5° larger at 500 Hz than 100 Hz), but not for more lateral loudspeakers (differences less than 5°, $p=1.0$). Similar tests for the interaction between loudspeaker and noise position (combining across both rates) showed RMS errors that were larger (23°, $p<0.001$) with N90 than N0 for the central loudspeaker, smaller with N90 (10°, $p=0.005$) for the loudspeaker at +30°, and not significantly different for the remaining loudspeakers. Finally, the interaction between Strategy and Loudspeaker was also significant ($F[12,44]=2.8, p=0.006$). Further investigation showed that interaction was due to a different pattern of errors over the three right-most loudspeakers in the N90 condition, with CIS compared to the other two strategies (and particularly PDT).

The arithmetic means of the RMS errors, averaged across both subjects and strategies, are shown for each loudspeaker, and at both rates, in the uppermost left and right panels of Fig. 4, for noise at N0 and N90, respectively. Error bars show ± one standard error of the mean. The middle and bottom rows in Fig. 4 show additional error descriptions. The middle row shows averaged unsigned errors, which describe the arithmetic means, averaged across subjects and strategies, of the magnitudes of the differences between response means shown in the lower panels of Fig. 2 and correct responses. They serve as an indication of average response *bias* at each loudspeaker. The bottom row in Fig. 4 similarly shows the averages of the standard deviations shown by the error bars in the lower panels of Fig. 2. They serve as an indication of the average *variability* of responses at each loudspeaker. Error bars in the middle and bottom row show ± one standard error of the calculated means. It can be seen that the RMS errors, described in the top panels, comprise different contributions from these two sources of error at each loudspeaker. With noise at N0, RMS errors at ±30° were dominated by response bias, whereas for the central loudspeaker response variance played a larger part, and for the remaining loudspeakers both errors contributed. The increased RMS error at the higher rate, found for the central three loudspeakers with N0, is attributable to increased response bias in the case of the two loudspeakers at ±30°and to increased variance in the case of the central loudspeaker. With noise at N90, loudspeakers contralateral to the noise showed similar error distributions to those for the N0 condition. For the central loudspeaker, the RMS error is much larger with N90 than N0 due to much larger response bias as well as increased variance. The decrease in RMS error at 30° for N90, compared to N0, is due to a large decrease in bias, but at 500 Hz is partly offset by increased response variance. For the loudspeaker at 60° the noise bias also decreased with N90 compared to the N0 condition, but the RMS error remained relatively unchanged due to the increase in variance.

Application of ANOVA to the bias and variance error measures at each loudspeaker generally showed similar outcomes to the (individual loudspeaker) RMS analysis. The main exception was that the bias-error ANOVA did not show a significant *overall* dependence on NoisePos, because as discussed, the bias increased at N90 for the central loudspeaker, but decreased for two of the loudspeakers ipsilateral to the noise. As an alternative way to combine the effects of bias and variance into a single error score, the ability to discriminate[2] between signals from adjacent loudspeakers was assessed by transforming individual subject response probabilities to d' values ("d prime," e.g., Macmillan and Creelman, 2005). When assessing individual subject data using this approach, an arbitrary upper limit to bound d' was frequently required for pairs that included the central loudspeaker because it was so well identified. An ANOVA applied to the d' data, limited to maximal values of 3, resulted in similar conclusions as the RMS analyses, with the excep-

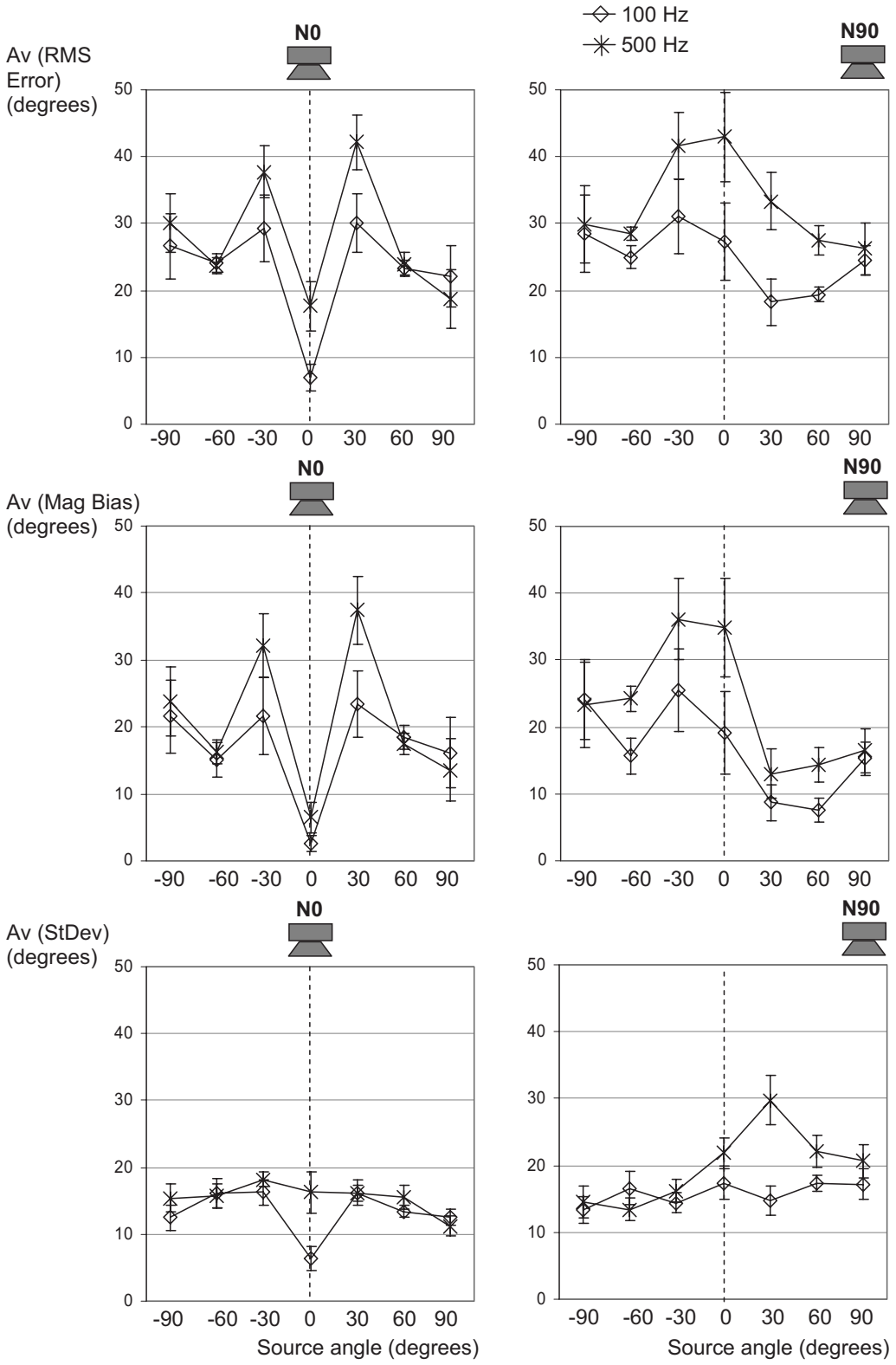

FIG. 4. Individual loudspeaker error plots, averaged across both subjects and strategies. The top row shows RMS errors, the middle row shows deviation from correct response diagonal (bias), and bottom row shows average standard deviation around the mean response. Left panels are for noise at N0, and right panels for N90 noise positions. Data for 100 Hz click trains are shown by open diamonds, and those for 500 Hz by stars. Error bars in all three rows indicate ± one standard error of the mean (calculated across subjects and strategies).

tion that, as in the bias ANOVA, no significant effect of NoisePos was found. The interaction between NoisePos and Loudspeaker was, however, significant ($F[5,37]=14.0, p<0.001$) and post-hoc Bonferroni simultaneous tests examining that interaction were in good agreement with the RMS analysis, showing better discrimination with N90 (than N0) for the loudspeaker pair $(30°,60°)$ ($\Delta d'=0.69, p<0.001$), but worse discrimination for the pair $(-30°,0°)$ ($\Delta d'$

$=0.80, p<0.001$). When subject and strategy data were pooled prior to calculating d' values, the resulting increased overlap in responses for each loudspeaker reduced the need to limit d'. The results from that ANOVA did show a significant effect of NoisePos ($F[1,5]=11.8, p=0.018$), albeit at a more moderate significance level that may be more in keeping with the ANOVA based on the bias error than the RMS data.

To summarize the localization data, several error analyses showed that strategy had little effect on performance, but the use of a higher rate acoustic click-train, and lateral rather than anterior placement of interfering noise resulted in worse overall performance. For the N0 noise position, the use of a higher rate resulted in increased over lateralizing of (signals from) loudspeakers at $\pm 30°$, as well as increased variability for the central loudspeaker. When noise was at N90, the use of the higher rate click train increased the tendency to hear signals from loudspeakers at 0° and −30° as originating too far to the left, and also increased variability in responses to the loudspeaker at +30°. Poorer overall performance, with the noise at N90 compared to N0, resulted mainly from a much larger bias at 0°, which when combined with the increased variance for loudspeakers between 0 and +90°, outweighed the substantial reduction in bias seen at +30° (and to a lesser degree at +60°).

IV. DISCUSSION

A. Speech in noise

The modest diotic benefit reported here, of one to one-and-a-half dB when listening with both ears rather than just the better ear alone, is in good agreement with previous data from CI users tested with the same test materials (van Hoesel *et al.*, 2005). It is also similar to the diotic speech benefit reported for listeners with normal hearing (e.g., Bronkhorst and Plomp, 1988). The absence of binaural speech unmasking in the present study differs from the normal hearing case, which shows at least 5 dB benefit in comparable conditions (Bronkhorst and Plomp, 1988). A similar difference between CI and listeners with normal hearing was noted in an earlier report that described minimal binaural unmasking with 500 Hz tones in noise for two bilateral CI users (van Hoesel, 2004). In contrast to that study as well as the present data, Long *et al.* (2006) reported a large 9 dB envelope-derived unmasking effect for CI users who were required to detect diotic (S0) or phase-inverted ($S\pi$) 125 Hz "transposed-tone" envelopes in diotic narrowband noise centered at 125 Hz. Note that phase inversion at 125 Hz corresponds to an extremely large ITD of 4 ms, which cannot be imparted by natural head-width delays. Although Long *et al.* have also reported a large unmasking effect with a smaller ITD of 600 μs, in that case they did not apply the amplitude compression needed to ensure the signal fell into the electrical dynamic range of the CI users. As a result, only the extreme peaks of the signals will have contributed to auditory percepts, and the 600 μs ITD very likely introduced interaural amplitude cues that would make the task very easy. Unpublished data from two bilateral CI users, tested by the first author of the present paper, indicate that the transposed-tone envelope-derived BMLD is much reduced when the ITD is reduced to approach that available from natural head-width delays and appropriate amplitude compression is incorporated. Those two subjects were required to detect 125 Hz transposed-tone envelopes in the presence of a narrowband (50 Hz) noise modulator envelope centered at 125 Hz. Envelopes were applied to pulse trains at a constant rate of 6000 pps, which was selected to be rather higher than in the study by Long *et al.* (who used 1000 pps carriers) to reduce potential amplitude cues arising from the interaction of envelope and carrier timing. Similar to the results described by Long *et al.*, the two listeners demonstrated 6–9 dB unmasking when comparing detection thresholds for $S\pi$ and S0 in diotic noise. However, when the transposed-tone envelope ITD was reduced from four, to one ms, unmasking decreased to only one or two dB. Given that the ITD in the present speech experiment was even less than that (700 μs), the lack of unmasking altogether is perhaps not surprising based on that consideration alone. In addition, the transposed-tone BMLDs were measured for a low modulation rate of 125 Hz in narrowband noise, whereas temporal fluctuations for speech in noise can be considerably faster and noise bandwidths broader, both of which may reduce unmasking. Effective modulation rates, seen at the nerve, were likely further increased in the speech experiment due to channel interactions when neurons received out-of-phase (envelope) information from multiple nearby electrodes, whereas the transposed-tone data discussed above were for stimulation on a single electrode in each ear. The finding that none of the three strategies in the present study showed evidence of binaural speech unmasking for an ITD of 700 μs implies spatiotemporal distributions of the neural responses offered no advantage over those arising from diotic stimulation (S0N0). That was the case even with PDT, for which fine-timing cues were explicitly coded in low-frequency channels. The combined effects of stimulation rate and channel interaction may largely account for the ineffectiveness of those cues. Previous studies have shown that ITD sensitivity for CI users often decreases for pulse rates beyond a few hundred Hz (e.g., van Hoesel, 2007), whereas in normal-hearing listeners pure-tone sensitivity to ITDs improves from a few hundred to about 1 kHz (e.g., Klumpp and Eady, 1956). In the PDT implementation tested here, only the one or two lowest frequency bands may have produced pulses at rates sufficiently low to preserve sensitivity to timing cues, and as already discussed for modulated signals above, even those bands may have been compromised by out-of-phase stimulation on nearby electrodes, resulting in higher effective rates. The interaction between stimuli on nearby electrodes, and perhaps also the use of relatively coarse fixed filter bands in CI applications, also reduces the independence of cues across frequencies, which may impact adversely on the BMLD. Finally, although it is possible that all four subjects in the present study possessed unusually poor ITD sensitivity, the likelihood of that being so was much reduced by the inclusion of post-lingual deafness in the subject selection criteria (Litovsky *et al.*, 2005). The one subject who showed much reduced performance with CIS compared to ACE or PDT likely did so due to greater familiarity with higher resolution

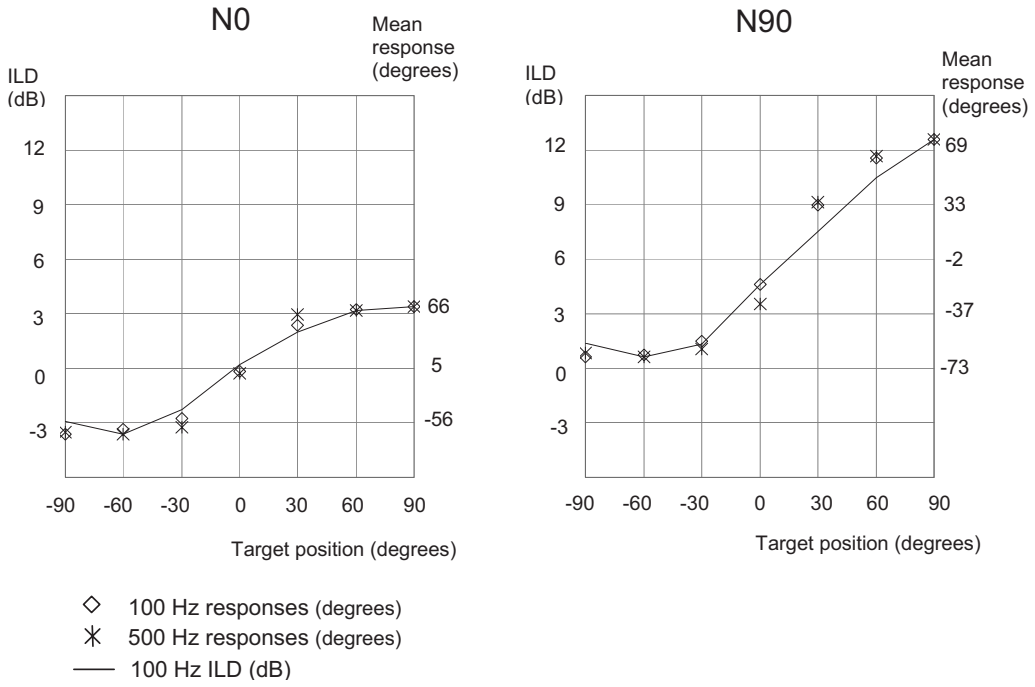

FIG. 5. Solid curves show measured broadband RMS ILD cues (dB, left vertical scale) for the 100 Hz click train presented from each of the seven loudspeakers, with noise at zero dB SNR presented from N0 (left panel), or N90 (right panel). Measurements were made using directional HS-8 headset microphones placed on a KEMAR manikin. Plotted symbols show mean responses (degrees, right vertical scale), averaged across subjects and strategies, and linearly scaled in the figure to span the range of ILDs available for each noise position: open diamonds show responses to 100 Hz click trains, and stars show those to 500 Hz trains.

frequency representation available in ACE and PDT. Although adverse effects of faster temporal fluctuations due to the broader CIS filters could in theory also lead to worse performance with CIS than ACE, it would seem likely that the faster temporal cues available in PDT compared to ACE should in that case similarly reduce performance, which was not the case.

B. Localization in noise

The finding that all three strategies performed similarly in the localization task suggests that the cues used were available equally in all three strategies, and that the added fine-timing information presented in PDT did not improve sound-source location in noise. Although interaural delays in the envelope may in theory have played a role with all three strategies, studies with normal-hearing listeners indicate that the envelope information contributes little to performance when localizing broadband signals in the frontal horizontal plane (e.g., Wightman and Kistler, 1992). As there was also no indication that envelope timing cues were available from the speech experiment, the hypothesis that localization performance (in noise) could be described on the basis of ILD cues alone was examined. Audio recordings were made with the same type of microphone as the subjects had used, mounted on a KEMAR manikin, while playing the 100 Hz click trains from each loudspeaker and with noise at either N0, or N90. Left and right-ear recordings were obtained by placing the same microphone behind either ear in separate recordings. An additional set of recordings was made with a second microphone to verify the results with the first, but as results were very similar, only the data from the first microphone were used in the analysis that follows. Spectral analysis of the recordings showed that the frequency spectrum of the signal plus noise when presented directly in front of the manikin peaked near two kHz and was within six dB of that level between 1000 and 4000 Hz. Broadband ILDs (shown in Fig. 5) were calculated, as were one-third octave ILD cues at 1, 2, and 4 kHz. Pearson correlation coefficients were calculated between subject-averaged mean responses and each of the narrowband and broadband ILD cues. Although all of those showed good correlations, the highest was for broadband ILD, which was able to account for as much as 99% of the variance in the subjects' mean responses. For comparison, correlation of responses with actual loudspeaker positions was 94%, and with monaural mean level cues at the ear with the largest monaural cue[3] was 96%. The use of monaural level cues also would not account well for the near perfect performance observed with the central loudspeaker despite the 6 dB level rove. Note that target-level roving can also affect the interaural level cue with the noise held at a fixed level, but that is not the case for the central loudspeaker when noise is at N0. Of course it is possible that subjects used two concurrent monaural cues and compared those at a higher cognitive level rather than making use of an explicit interaural level cue. While that possibility cannot be precluded, it would be surprising in view of the rapid and seemingly "un-calculating" manner of responding that was observed in these subjects.

Figure 5 shows the measured broadband ILD cues for the 100 Hz click trains, with N0 and N90 noise positions, in the left and right panels, respectively. Within each panel, mean response values (filled symbols) have been plotted

such that range of minimum to maximum ILD cues, shown on the left vertical scale, overlap with the range of response angles shown on the right vertical scale. Pearson correlation coefficients for the noise at N0 indicated that the (100 Hz) broadband ILD cue describes 99.4% and 98.7% of the variance in the subjective responses with 100 and 500 Hz signals, respectively. Similarly, for N90, the broadband ILD describes 99.2% and 98.8% of the variance for signals at 100 and 500 Hz. While the 100 and 500 Hz click trains had a similar overall spectral envelope, the modest decrease in correlation at 500 Hz, compared to 100 Hz, may yet be due to differences in the broadband ILD at the two rates as a consequence of frequency specific level effects due to the different harmonic spacing. Unfortunately, KEMAR recordings were initially only made for 100 Hz click trains, and the same experimental setup was not available at a later date for additional recordings at 500 Hz. As an alternative way to examine at least qualitatively the effect of click rate on the ILD cue, additional KEMAR measurements were made using the same click trains at both 100 and 500 Hz, but without noise, and using a different room and loudspeakers. Those later recordings showed that the broadband ILD was about 1.5 dB larger for the 500 Hz click train for loudspeakers at $\pm 30°$, 0.5 dB larger at $\pm 60°$, and 1.5 dB *smaller* at $\pm 90°$. The net effect was a modest increase in similarity of ILD cues for signals within left or right loudspeaker groups at the higher click rate. As the addition of noise at 0° results in monotonic compression of the ILD cue (in quiet), increased similarity of the cue at the higher rate in quiet will correspond to increased similarity in noise when noise is at N0. Comparison of the rate effect observed in the KEMAR data in quiet, with the subjective responses when noise was added at N0 (Fig. 2), indeed shows mean subjective responses were more similar within either left or right groups of loudspeakers at the higher rate. The dependence of the broadband ILD cue on rate, despite the use of matched overall spectral shape, is therefore at least qualitatively in good agreement with the effect of rate seen in the subjective data, and dependence readily explains why the ILDs measured with 100-Hz click-trains are better correlated with the subjective responses to 100-Hz than 500-Hz click-trains. Although it would be expected that the increased ambiguity in ILD cue at the higher rate should increase the response variance (bottom row in Fig. 4), that result was only observed for loudspeakers ipsilateral to the noise in the N90 condition. That may be explained by the consideration that, for the loudspeaker group contralateral to the noise at N90, as well as for both left and right loudspeaker groups in the N0 condition, total-ILD cue differences among loudspeakers within those groups were difficult to detect even at 100 Hz (<1 dB, Fig. 5) rendering the effect of rate immaterial. The effect on ILD, of roving the signal level but not the noise, will similarly have been inconsequential to the ability to separate loudspeakers within those groups, and appears in fact to have had little effect on performance in general. If the rove had been influential in that regard, the response variance shown in the lowest row in Fig. 4 should have increased with increasing separation between the target and noise (because the total ILD becomes more dependent on the target level), which is clearly not the case for the N90 condition. For the central loudspeaker in the N0 condition, the larger variance at the higher rate is not readily explained by consideration of the *intended* binaural cues available from the signal and noise, as they should have been very close to zero at either rate. One possibility is that inaccuracies in coding the 0-ILD condition were larger at the higher rate due to the sparser harmonic structure, which might lead to greater susceptibility to head movements and loudness mapping function inaccuracies in the processor. It may also be the case that at the lower rate, presentation of both the signal and noise from the central loudspeaker resulted in particularly well fused percept, which might be more diffuse at the higher rate or any condition in which signal and noise were spatially separated. That would be consistent with reports indicating that interaural timing information in CI users degrades as rate increases beyond a few hundred Hz (e.g., van Hoesel, 2007). Note also that the rms error in Fig. 4 for the central loudspeaker, with the 100 Hz signal and noise at N0, was only 10°, which was twice as small as for any other loudspeaker or condition. It may be the case that actual underlying performance for that condition was more prone to being under sampled by the relatively wide loudspeaker spacing of 30°, and that the observed RMS measure overestimated localization abilities in that case.

The strong correlation between responses and noise-position dependent ILD cues indicates that envelope and fine-timing ITD cues in general contributed little to performance. Although the significant interaction between Strategy and Loudspeaker found in the individual loudspeaker ANOVA was of interest with regard to the hypothesis that PDT fine-timing cues might have provided greater benefit for some spatial locations than others, that was not found to be the case: The main contribution to that interaction arose from a different pattern of errors across loudspeakers, with the CIS strategy compared to the other two strategies (and in particular PDT) when signals were presented ipsilateral to the noise in the N90 condition. As seen in Fig. 5, under those conditions the ILD cues were largest and least ambiguous, suggesting differences in ILD coding with wider filters and a reduced number of electrodes in the CIS implementation as a more plausible explanation of the interaction than the addition of fine-timing cues in PDT. It is possible that the reason that ITDs did not contribute to performance is because the noise disrupted the salience of low-frequency ITDs more than it did ILDs. Such is the case at low SNRs for listeners with normal hearing when noise is at 90°, but not when it is at 0° (Lorenzi *et al.*, 1999). In the present CI data, the lack of interaction between strategy and noise position indicates that if the noise did disrupt fine-timing ITDs more than ILDs, it did so for both noise positions, which would be in contrast to normal hearing. Given that previous data with PDT for localization in quiet (van Hoesel and Tyler, 2003; van Hoesel, 2004) also showed little benefit of adding fine-timing cues, a more likely explanation is that the same factors proposed to be responsible for the absence of speech unmasking in experiment one, i.e., rates of stimulation and channel interaction, equally inhibit the salience of fine-timing cues in local-

ization, both in quiet, and perhaps even more so in noise where the potential for undesired interactions is even greater.

A final observation concerns the difference in response patterns across subjects. Subjects S1, S3 and S4 all show mean responses in Fig. 2 that span most of the loudspeaker array irrespective of noise position, despite the large difference in the range of actual ILDs available for the two noise positions. That implies those listeners "scaled" responses to allow for the different noise positions. Presumably they did so by considering the ILD in context of the total anticipated or "learned" ILD range for each test configuration, and/or by comparing the total ILD with that for noise alone, which was available during the short intervals just before and after the signal was gated on. The response patterns for S2 in contrast are narrower for the N0 condition, in agreement with the reduced ILD range compared to that with N90. If it is assumed that this was not due to a different interpretation of the requirements in the task, it seems S2 was less inclined to allow for the effect of the noise on the total ILD. Even if the data from S2 are excluded, some variations remain among the other subjects in this regard. For example, the contralateral shift in mean response for the central loudspeaker, when noise was at N90 rather than N0, was large for S3 at both rates, more moderate for S1 at the high rate, and small for S4 at both rates and S1 at the low rate. Despite such intersubject variations, each subject's response data correlated better with the total ILD than, for example, actual loudspeaker position, irrespective of noise position. It seems likely therefore that the variation in response patterns across subjects shows differences in how the same cue was scaled or interpreted by the subjects, rather than suggesting the use of different cues. It may be a matter of some concern that the *total* signal-plus-noise ILD so strongly governed responses if that means signal and noise were not well separated perceptually, despite differing onset and offset times. That would be an important consideration in complex audition in everyday situations, where the ability to separate "auditory objects" leads to substantial benefits for normal-hearing listeners. Alternatively, it is possible that the underlying *estimated signal-alone* ILD was the cue used to identify the sound source position, rather than the total ILD per se (perhaps with the exception of S2), and that the accuracy of that estimation process was limited by the salience of total ILD. In either case, the total ILD plays a dominant role in determining the ability of implant users to identify sound direction in the presence of interfering noise. Further work in this area will improve our understanding of how to optimize electrical signals for bilateral implant users in more complex everyday listening situations.

V. CONCLUSIONS

- Binaural speech unmasking, resulting from a 700 μs ITD applied to speech in diotic noise, was observed with neither envelope-based ACE nor CIS strategies, nor the fine-timing based PDT strategy.
- Speech test results were generally quite similar for the three strategies, with the exception that one subject showed considerably poorer performance with the 10-channel CIS than the other two 19-channel strategies.
- Diotic benefits (S0N0-SmNm) were on the order of one dB in agreement with previous reports using similar materials (van Hoesel *et al.*, 2005)
- Localization performance in noise was also similar with the three strategies, and was well accounted for by consideration of the total broadband ILD cue, with little indication that ITD cues contributed.
- The degree to which the total signal-plus-noise ILD cue was interpreted in context of the noise position varied somewhat across subjects, with differing extents of normalization of the range of responses for the two noise positions.

The lack of benefit obtained through the addition of low-frequency fine-timing cues in PDT is likely to be the result of several limiting factors. Although the use of fixed filter bands that are relatively coarse in CI applications may limit to some extent the independence of different binaural fine-timing cues across frequencies, of greater concern is the impact of present electrical stimulation methods. The decrease in electrical ITD sensitivity with increasing rate beyond a few hundred Hz (e.g., van Hoesel, 2007) is in contrast to pure-tone ITD sensitivity in normal-hearing listeners, which improves up to about 1 kHz. In the present implementation of PDT, only the lowest few frequency bands may have produced pulse rates that were sufficiently low to convey binaural fine-timing cues. Furthermore, even in those bands fine-timing cues may have been disrupted by current spread from stimuli on nearby electrodes, which may have reduced independence of cues at different locations along the cochlea and increased stimulation rates at the auditory nerve (Jones *et al.*, 2007). Substantially different methods of electrical stimulation, which evoke neural responses that are more similar to those with low frequency acoustic stimuli in normal hearing, appear to be requisite if the fine-timing based benefits available to normal-hearing listeners are to be preserved in bilateral CI applications.

ACKNOWLEDGMENTS

The authors are indebted to the research volunteers who went to considerable efforts in participating in this study, and gratefully acknowledge the helpful comments on an earlier version of the paper made by the anonymous reviewers and section editor. Technical and organizational assistance were kindly provided by Mark Harrison and Bob Cowan, respectively, at CRC HEAR, Melbourne, Australia. Collaboration between researchers in Melbourne and Hannover was further facilitated through Cochlear Ltd. in Australia and Cochlear AG in Europe. This work was jointly sponsored through CRC HEAR in Melbourne, Australia, and MHH Hannover, Germany.

[1]In that arbitration scheme, the four lowest frequency bands always received primary priority, decreasing from low to high frequency. Additional higher frequencies in bands five to seven received secondary priority, again decreasing from low to high frequency, but among those three bands

higher frequency pulses could "dislodge" lower frequency ones if the higher frequency peak was at least twice as large. Dislodged pulses were moved to an adjacent time slot subject to the same arbitration rules. If no free time slot was found within ± two time slots, dislodged pulses were deleted entirely.

[2]Note that in this analysis, we are concerned with how distinct the different signals from the loudspeakers were, without regard to how well responses agree with physical loudspeaker locations.

[3]For N0 monaural cues are similar in each ear, but for the N90 condition they are much more salient at the ear contralateral to the noise.

Akeroyd, M. A., and Summerfield, A. Q. (**2000**). "Integration of monaural and binaural evidence of vowel formants," J. Acoust. Soc. Am. **107**(6), 3394–3406.

Breebart, J., and Kohlrausch, A. (**2001**). "The influence of interaural stimulus uncertainty on binaural signal detection," J. Acoust. Soc. Am., **109**, 331–345.

Bronkhorst, A. W., and Plomp, R. (**1988**). "The effect of head-induced interaural time and level differences on speech intelligibility in noise," J. Acoust. Soc. Am. **83**, 1508–1516.

Colburn, H. S., and Equissaud, P. (**1976**). "An auditory-nerve model for interaural time discrimination of high-frequency complex stimuli," J. Acoust. Soc. Am. **59**, S23.

Colburn, H. S., and Durlach, N. I. (**1978**). "Models of binaural interaction," in *Handbook of Perception* (Academic, New York), Vol. IV, Chap. 11, pp. 467–518.

Culling, J. F. (**2007**). "Evidence specifically favoring the equalization-cancellation theory of binaural unmasking," J. Acoust. Soc. Am., **122**, 2803–2813.

Durlach, N. I. (**1964**). "Note on binaural masking-level differences at high Frequencies," J. Acoust. Soc. Am. **36**, 576–581.

Gantz, B. J., Tyler, R. S., Rubinstein, J. T., Wolaver, A., Lowder, M., Abbas, P., Brown, C., Hughes, M., and Preece, J. P. (**2002**). "Binaural cochlear implants placed during the same operation," Otol. Neurotol. **23**, 169–180.

Grantham, D., Ashmed, D., Ricketts, T., Labadie, R., Haynes, D. (**2007**). "Horizontal-plane localization of noise and speech signals by post-lingually deafened adults fitted with bilateral cochlear implants," Ear Hear., **28**, 524–541.

Hagermann, B., and Kinnefors, C. (**1995**). "Efficient adaptive methods for measuring speech reception threshold in quiet and in noise," Scand. Audiol. **24**, 71–77.

Hartmann, W., Rakerd, B., and Gaalaas, J. (**1998**). "On the source identification method," J. Acoust. Soc. Am. **104**, 3546–3557.

Hirsch, I. J. (**1948**). "The influence of interaural phase on interaural summation and inhibition," J. Acoust. Soc. Am. **20**, 536–544.

Jones, G., Litovsky, R., and van Hoesel, R. (**2007**). "ITD sensitivity in electrical hearing: Effect of channel interactions," *CIAP meeting*, Lake Tahoe, NV.

Klumpp, R. G., and Eady, H. R. (**1956**). "Some measurements of interaural time difference thresholds," J. Acoust. Soc. Am. **28**, 859–860.

Levitt, H., and Rabiner, L. R. (**1967**). "Predicting binaural gain in intelligibility and release from masking for speech," J. Acoust. Soc. Am. **42**, 820–829.

Licklider, J. C. R. (**1948**). "The influence of interaural phase relations upon the masking of speech by white noise," J. Acoust. Soc. Am. **20**, 150–159.

Litovsky, R. Y., Agrawal, S. S., Jones, G. J., Henry, B., and Van Hoesel, R. J. M. (**2005**). "Effect of interaural electrode pairing on binaural sensitivity in bilateral cochlear implant users," *Association for Research in Otolaryngology, midwinter meeting*.

Long, C. J., Carlyon, R. P., Litovsky, R. Y., and Downs, D. H. (**2006**). "Binaural unmasking with bilateral cochlear implants," JARO **7**, 352–360.

Lorenzi, C., Gatehouse, S., and Lever, C. (**1999**). "Sound localization in noise in normal-hearing listeners," J. Acoust. Soc. Am. **105**(3), 1810–1820.

Macmillan, N. A., and Creelman, C. D. (**2005**). *Detection Theory: A User's Guide*, 2nd ed., Lawrence Earlbaum, Mahwah, NJ, ISBN 0-8058-4231.

McDermott, H. J., McKay, C. M., and Vandali, A. E. (**1992**). "A new portable sound processor for the University of Melbourne/Nucleus Limited multielectrode cochlear implant," J. Acoust. Soc. Am. **91**, 3367–3371.

Müller, J., Schön, F., and Helms, J. (**2002**). "Speech understanding in quiet and noise in bilateral users of the MED-EL COMBI 40/40+ Cochlear Implant System," Ear Hear. **23**, 198–206.

Rakerd, B., and Hartmann, W. M. (**1986**). "Localization of sounds in rooms," J. Acoust. Soc. Am. **74**, 1380–1391.

Raleigh, L. (**1907**). "On our perception of sound direction," Philos. Mag. **13**, 214–232.

van de Par, S., and Kohlrausch, A. (**1997**). "A new approach to comparing binaural masking level differences at low and high frequencies," J. Acoust. Soc. Am. **101**, 1671–1680.

van Hoesel, R. J. M., and Clark, G. M. (**1999**). "Speech results with a bilateral multichannel cochlear implant user from spatially separated speech and noise," Aust. J. Audiol. **21**, 23–28.

van Hoesel, R. J. M. (**2002**). "A peak-derived timing stimulation strategy for a multichannel cochlear implant," International Patent No. PCT/AU2002/000660.

van Hoesel, R., Ramsden, R., and O'Driscoll, M. (**2002**). "Sound direction identification interaural time delay discrimination and speech intelligibility advantages in noise for a bilateral cochlear implant user," Ear Hear. **23**, 137–149.

van Hoesel, R., and Tyler, R. (**2003**). "Speech-perception, localization and lateralization with bilateral cochlear implants," J. Acoust. Soc. Am. **113**(3), 1617–1630.

van Hoesel, R. J. M. (**2004**). "Exploring the benefits of bilateral cochlear implants," Audiol. Neuro-Otol. **9**, 234–246.

van Hoesel, R., Bohm, M., Battmer, R. D., Beckschebe, J., and Lenarz, T. (**2005**). "Amplitude-mapping effects on speech intelligibility with unilateral and bilateral cochlear implants," Ear Hear. **26**(4), 381–388.

van Hoesel, R. J. M. (**2007**). "Sensitivity to binaural timing in bilateral cochlear implant users," J. Acoust. Soc. Am. **121**, 2192–2206.

Wagener, K., Brand, T., and Kollmeier, B. (**1999**). "Development and evaluation of a German sentence test Part II: Optimization of the Oldenburg sentence test," Z. Audiol. **38**(2), 44–56.

Wightman, F., and Kistler, D. J. (**1992**). "The dominant role of low-frequency interaural time differences in sound localization," J. Acoust. Soc. Am. **91**, 1648–1661.

Wilson, B., Finley, C., Lawson, D., Wolford, R., Eddington, D., and Rabinowitz, W. (**1991**). "Better speech recognition with cochlear implants," Nature (London) **352**, 236–238.

Effects of in-the-ear microphone directionality on sound direction identification

King Chung[a)]
Lexington Center for the Deaf, Flushing, New York 11370

Arlene C. Neuman[b)] and Michael Higgins[c)]
The Graduate Center, City University of New York, New York, New York 10036

(Received 18 September 2007; revised 25 January 2008; accepted 30 January 2008)

As advanced signal processing algorithms have been proposed to enhance hearing protective device (HPD) performance, it is important to determine how directional microphones might affect the localization ability of users and whether they might cause safety hazards. The effect of in-the-ear microphone directivity was assessed by measuring sound source identification of speech in the horizontal plane. Recordings of speech in quiet and in noise were made with Knowles Electronic Manikin for Acoustic Research wearing bilateral in-the-ear hearing aids with microphones having adjustable directivity (omnidirectional, cardioid, hypercardioid, supercardioid). Signals were generated from 16 locations in a circular array. Sound direction identification performance of eight normal hearing listeners and eight hearing-impaired listeners revealed that directional microphones did not degrade localization performance and actually reduced the front–back and lateral localization errors made when listening through omnidirectional microphones. The summed rms speech level for the signals entering the two ears appear to serve as a cue for making front–back discriminations when using directional microphones in the experimental setting. The results of this study show that the use of matched directional microphones when worn bilaterally do not have a negative effect on the ability to localize speech in the horizontal plane and may thus be useful in HPD design. © *2008 Acoustical Society of America.* [DOI: 10.1121/1.2883744]

PACS number(s): 43.66.Qp, 43.66.Ts, 43.66.Vt, 43.60.Fg [BLM] Pages: 2264–2275

I. INTRODUCTION

The ability to localize sounds serves important practical functions in the areas of speech communication and personal safety. For example, the ability of a listener to identify the location of a person talking to him allows him/her to turn toward the speaker and utilize both auditory and visual cues to enhance communication. Localization ability in high noise environments is also crucial for the safety of the workers (Morata *et al.*, 2001, 2005). The ability to identify the location of sound sources, therefore, has been recognized as an important aspect of hearing instrument performance.

Chung (2007) proposed using advanced signal processing algorithms to enhance the performance of hearing protective devices (HPDs) and conducted a series of experiments to examine the appropriate configurations of adaptive multichannel modulation-based noise reduction and wide dynamic range compression algorithms for HPD applications. Adaptive multichannel modulation-based noise reduction algorithms have been reported in the hearing aid literature to reduce the overall noise level and increase listening comfort without compromising speech recognition ability (Alcantara *et al.*, 2003; Bentler and Chiou, 2006; Boymans *et al.*, 1999; Boymans and Dreschler, 2000; Ricketts and Dhar, 1999; Valente *et al.*, 1998; Ricketts and Hornsby, 2005). Wide dynamic range compression has been reported to enhance the audibility of soft sounds and reduce the level of loud sounds (Villchur, 1973; Jenstad *et al.*, 1999; Kam and Wong, 1999; Laurence *et al.*, 1983; Lippmann *et al.*, 1981; Moore 1987; Moore and Glasberg, 1986; Souza and Turner, 1999; Souza, 2002; Chung *et al.*, 2007). Chung (2007) found that a parallel configuration of noise reduction and compression processing allowed beneficial noise reduction effects while also obtaining benefits of compression with regard to maintaining audibility and comfort.

The directional microphone is another technology that may enhance the performance of HPDs. These microphones, by design, can reduce the level of sounds coming from the sides and back. In situations where the desired signal is in front and noise sources are located at the sides or back, directional microphones can enhance speech recognition performance and improve perceived sound quality for hearing aid and cochlear implant users (Hawkins and Yacullo, 1984; Killion *et al.*, 1998; Ricketts and Dhar, 1999; Kuhnel *et al.*, 2001; Ricketts and Henry, 2002; Bentler *et al.*, 2004; Walden *et al.*, 2004; Amlani *et al.*, 2006; Bentler *et al.*, 2006; Mackenzie and Lutman, 2005; Valente *et al.*, 2006; van Hoesel and Clark, 1995; Wouters *et al.*, 1999; Blamey *et al.*, 2006; Chung *et al.*, 2006; Spriet *et al.*, 2007; van der Beek *et al.*, 2007). It is possible that they can produce similar advantages for HPD users.

[a)]Currently at Department of Speech, Language, and Hearing Sciences, Purdue University, West Lafayette, IN 47907. Electronic mail: kingchung@purdue.edu
[b)]Currently at Department of Otolaryngology, New York University School of Medicine, New York, NY 10016. Electronic mail: arlene.neuman@med.nyu.edu
[c)]Electronic mail: higginsmr@gmail.com

 0001-4966/2008/123(4)/2264/12/$23.00 © 2008 Acoustical Society of America

Both hearing aids and hearing protective devices are reported to degrade sound localization performance (Noble *et al.*, 1990; Abel and Armstrong, 1993; Byrne *et al.*, 1998, Vause and Grantham, 1999; Bolia *et al.*, 2001; Brungart *et al.*, 2004; Simpson *et al.*, 2005, Van den Bogaert *et al.*, 2006). Interaural time and level difference cues are the primary cues used for localization of sound in the horizontal plane (Blauert, 1997). Additional spectral cues used in localization are provided by the pinna and concha. These cues are important for correct front-back identification in the horizontal plane (Weinrich, 1982; Musicant and Butler, 1984) and for localization in the vertical plane (Roffler and Butler, 1968). Pinna and concha cues provide primarily high frequency information (Shaw, 1974). Hearing instruments might disrupt localization cues in several ways: (1) by band-limiting the sound and thus failing to provide high frequency spectral information, (2) by obscuring the pinna and concha resonances caused by covering of the pinna or the alteration of the resonance characteristics, (3) by modifying interaural time differences due to signal processing delays, and (4) by disrupting interaural level differences due to differing amplification/attenuation in the two ears.

In general, the limitations of high frequency information by the frequency response of the hearing instrument and by the earmold coupling are most likely to affect localization in the vertical plane. Errors in the horizontal plane would be primarily front-back confusions (Byrne *et al.*, 1998; Best *et al.*, 2005). The method of coupling hearing instruments to the ear (e.g., supra-aural headphones or putting the microphone above the pinna) also has a negative effect on the availability of outer ear cues. Occlusion of the concha by the hearing aid has been reported to increase front-back localization errors and errors in localizing in the vertical plane (Noble *et al.*, 1990; Byrne *et al.*, 1998). Localization ability in the horizontal plane can be further degraded by altered interaural level and time (phase) differences.

Previous studies have shown that many HPDs degrade users' localization ability and affect the acceptability of HPDs (Noble *et al.*, 1990; Abel and Armstrong, 1993; Vause and Grantham, 1999; Bolia *et al.*, 2001; Brungart *et al.*, 2004; Simpson *et al.*, 2005). A literature search revealed that only a few research studies have examined the effect of directional microphones on hearing aid users' localization performance. Van den Bogaert and colleagues (2006) measured localization performance of hearing-impaired listeners without a hearing aid or wearing bilateral behind-the-ear hearing aids with omnidirectional and adaptive directional microphones. The listeners were asked to identify the location of the sound source for signals emitted from loudspeakers arranged in the frontal horizontal plane (i.e., −90° to +90° clockwise). They found that adaptive directional microphones increased listener's localization errors compared to omnidirectional microphones which in turn were worse than the unaided conditions. These results suggested that adaptive directional microphones should not be applied to HPDs.

Keidser and colleagues (2006) examined the localization ability of hearing aid users wearing behind-the-ear hearing aids with directional microphones. Hearing aid users' localization performance was compared when they were wearing omnidirectional patterns bilaterally, cardioid patterns bilaterally, cardioid in one ear and bipolar in the other, and omnidirectional in one ear and cardioid in the other. The authors found that with hearing aids, the hearing aids, listeners exhibited a larger number of front–back errors than with open ears. Listening with directional microphones having a cardioid pattern reduced front-back confusion errors, but using different (i.e., mismatched) directional microphone patterns in bilateral hearing aids resulted in increased front–back confusion over time.

The goal of the present study was to examine the effects of directional characteristics of in-the-ear (ITE) hearing aid microphones on sound source identification of speech in the horizontal plane. The results of this study would shed light on how directional microphones affect localization of speech in quiet and noisy listening conditions [+10 dB signal-to-noise ratio (SNR)] by listeners with hearing loss and with normal hearing. If directional microphones do not impair sound direction localization, or if they enhance sound direction localization, then they may be beneficial in HPD applications to improve signal detection and communication in noisy environments.

II. METHODS

The effect of headworn microphone directivity was assessed by measuring sound source identification of speech in the horizontal plane using a pseudovirtual technique. Sound direction identification was measured using recordings of speech (in quiet and in noise) made with KEMAR [Knowles Electronic Manikin for Acoustic Research, Burkhard and Sachs, (1975)] wearing bilateral ITE hearing aids with microphones having adjustable directivity. Binaural (stereo) recordings of test materials from microphones placed at KEMAR's eardrum or materials filtered by KEMAR's head-related transfer function (HRTF) are often used in auditory experiments. The technique has been shown to be useful for many applications as the recordings preserve information about interaural time and level difference as a function of azimuth. The major criticism of using this technique for localization testing in the horizontal plane is that individual outer ear resonances affect the filtering of high frequency information used by the listener for accurate front–back identification of sounds. Studies have also reported increased front–back localization errors under headphone stimuli presentations when stimuli are created using nonindividualized versus individualized HRTF (Wightman and Kistler, 1989; Wenzel *et al.*, 1993).

Ideally, all "virtual" localization experiments would be conducted using individualized HRTF. However, we used KEMAR recordings because (1) in-the-ear microphone placement would be typical for hearing aid and HPD applications—in this case the concha is filled and individualized concha and pinna effects on the HRTF would not be available, (2) it was not practical to fabricate a pair of custom in-the-ear hearing instruments with four different microphone directionalities for each listener, and (3) our speech signal did not contain substantial high frequency energy (i.e., "Where am I now?"). As KEMAR's HRTF was identical for

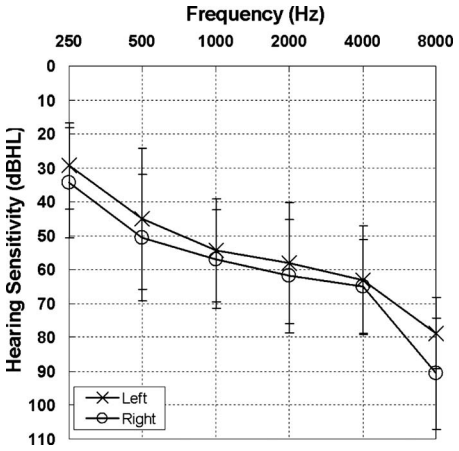

FIG. 1. The average hearing thresholds and standard deviations of listeners with hearing loss.

FIG. 2. (Color online) The left in-the-ear hearing aid with four different microphone directionalities.

the four examined directionalities in this study, the differences in listeners' performance, if any, should reflect the relative effectiveness of the four directionalities for localization tasks.

A. Listeners

Listeners with normal hearing and hearing loss were recruited for this study. The normal hearing listeners ($n=8$) had hearing thresholds better than 25 dB HL at audiometric frequencies 250–8000 Hz in octave intervals and normal middle ear functions as indicated by Type A tympanograms. Listeners ranged in age from 23 to 30 years (mean =26.2 years). All listeners with normal hearing listened to both noise and quiet conditions.

Eight experienced hearing aid users (at least six months hearing aid use bilaterally) with symmetric mild to severe sensorineural hearing loss participated in this study (Fig. 1). Subjects ranged in age between 62 and 80 years (mean =66.0 years). All eight listeners listened to the quiet conditions and six listened to the noise conditions.

B. Hearing aid characteristics

A pair of custom ITE linear hearing aids containing microphones with adjustable directivity was used to record test stimuli (Fig. 2). The directionality of the microphone in the hearing aid could be set to omnidirectional (Omni), cardioid (Card), hypercardioid (Hyper), or supercardioid (Super) by a push-button. Figure 3 shows the polar patterns of Omni, Card, Hyper, and Super when measured in an anechoic chamber in the manufacturer's facility. The frequency responses of all four settings were identical and were designed to compensate for the insertion loss of KEMAR's ear canal resonance. This frequency matching ensured that if there were any differences between the experimental conditions, they were due to the differences in directionality but not the differences in frequency responses.

C. Recording of the testing materials

The loudspeaker array consisted of nine Audax AT080M0 full range single coil loudspeakers with frequency responses ±2 dB between 100 and 10 000 Hz. They were on loudspeaker stands spaced at 22.5° intervals and the center of the diaphragm was a height at the center of KEMAR's pinna. The loudspeaker array was located at the center of a large office ($6.70\times5.80\times2.54$ m) with reverberation time of 400 ms.

The signal presentation system included a personal computer (Computer 1) and an external interface box. The personal computer contained a plug-in DSP board (60 MHz, 32 bit floating point, Texas Instruments TMS320C44) and a SD-16 board with 16 channel analog-to-digital converters and digital-to-analog converters (DAC). The external interface box housed a nine-channel power amplifier that was connected directly to the output of the SD-16 DAC. This amplifier was used to drive the nine loudspeakers used for presenting the stimuli.

1. Quiet conditions

For the recordings of the speech stimuli in quiet, the nine loudspeakers were arranged in the center of a semicircular array (1 m radius). They were placed at Locations 1–9 at 270°, 292.5°, 315°, 337.5°, 0°, 22.5°, 45°, 67.5 °, and 90° azimuths, respectively (Fig. 4). Calibration of the loudspeakers was performed prior to the recording of the testing materials. A composite noise was created to have identical rms level as the phrase "Where am I now?," which was spoken by a male talker in quiet. The level of the noise presented from each loudspeaker was measured using a Type I sound level meter (Bruel & Kjaer 2218) at the center of the loudspeaker array. The gain of the power amplifier was adjusted so that the level of the phrase was measured to be 80 dB SPL from each loudspeaker.

During the recording, the phrase "Where am I now?" was played sequentially from Loudspeakers 1–9 and recorded through KEMAR which was wearing the ITE hearing aids and placed at the center of the array. The output of a pair of ER-11 $\frac{1}{2}$ in. Microphones (Etymotic Research, Elk Grove Village, Illinois) placed in the medial opening of Zwislocki couplers was amplified using ER-11 Amplifiers with the filters set to the flat setting. The outputs of the ER-11 Ampli-

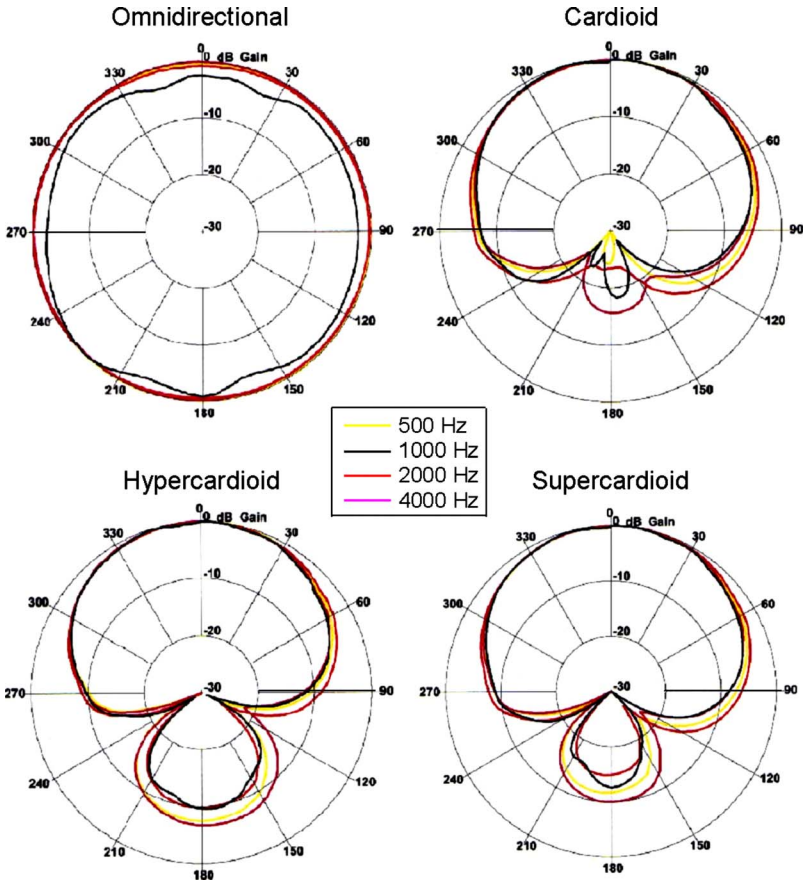

FIG. 3. (Color online) The free-field polar patterns of the omnidirectional and directional microphones at 500, 1000, 2000, and 4000 Hz measured in the anechoic chamber.

fiers were then recorded as stereo wav files (sampling rate =22 050 Hz, 16 bit quantization) in a second computer (Computer 2). The gain of the hearing aids was adjusted so that the left and right channels of the stereo file had the same rms and peak amplitude for speech presented at 0° azimuth.

Once the recordings from Locations 1 to 9 were made, KEMAR was turned 180° with its back to 0°. The phrase "Where am I now?" was presented from Loudspeakers 2 to 8 which were equivalent to presenting from Locations 10 to 16 located at 112.5°, 135°, 157.5°, 180°, 202.5°, 225°, and 247.5° azimuths. A set of recordings was made when the hearing aids were programmed to Omni, Hyper, Super, and Card. The testing tokens were then edited and saved with the appropriate microphone types and loudspeaker location designations.

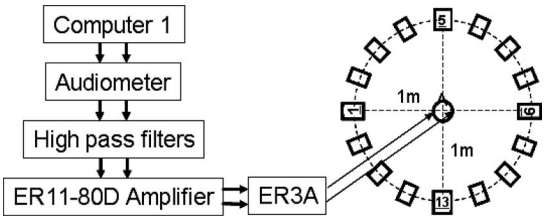

FIG. 4. Instrumentation for testing listeners with normal hearing. The computer delivered the test tokens to an audiometer, two high-pass filters (HPFs), two ER11-80D amplifiers, two ER-3A insert earphones while the listener sat in the center of a loudspeaker array.

2. Noise conditions

For the recordings at signal-to-noise ratios of +10 dB, eight loudspeakers were placed at Locations 1, 3, 5, 7, 9, 11, 13, and 15. The level of a speech spectrum-shaped noise was then measured sequentially from Loudspeakers 1 to 8 using the sound level meter placed at the center of the loudspeaker array. The sound pressure level of individual loudspeakers was measured and adjusted to be 61 dB SPL. A custom program was used to stagger and present the speech spectrum noise to all loudspeakers so that the noise was uncorrelated when presented simultaneously. The overall noise levels was measured to be 70 dB SPL. The level of speech was measured to be 80 dB SPL from each loudspeaker.

During the recording, KEMAR was placed at the center of the loudspeaker array facing Location 5. The custom program presented the noise to all loudspeakers simultaneously and the phrase "Where am I now?" was presented sequentially from Loudspeakers 1 to 8. Then KEMAR was turned 22.5° and the noise and the phrase were presented again. This was equivalent to presenting the phrase at Locations 2, 4, 6, 8, 10, 12, 14, and 16. The same recording procedures were used to record the hearing aid outputs from Omni, Card, Hyper, and Super microphone settings. The recordings were later edited and the test tokens were named with the appropriate microphone types and loudspeaker location designations.

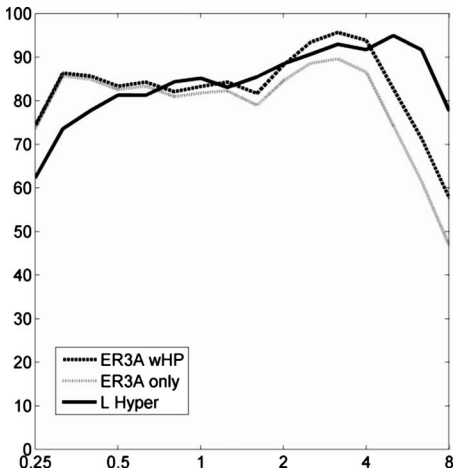

FIG. 5. The frequency response of the left hearing aid with hypercardiod microphone measured in sound field (0° azimuth) at the eardrum location of KEMAR compared with the frequency responses of ER3A insert earphone outputs with and without the high-pass filter (HPF) as measured on KEMAR using the equipment for experimental testing.

D. Sound direction identification test

1. Instrumentation for listeners with normal hearing

A MATLAB testing program was used to present the recorded stimuli and to log listener response. The output of the computer was sent to a GSI Clinical Audiometer (Grason-Stadler Inc., Milford, New Hampshire) which was used to control presentation levels (Fig. 4). The audiometer output was sent to a pair of custom high-pass filters and then to two ER11-80D Amplifiers (Etymotic Research). The high-pass filters were used to compensate for the high frequency roll-off of the insert earphones. Stimuli were presented through ER-3A insert earphones whose frequency response after compensation was matched to yield a frequency response equivalent to that which was present at the eardrum of the Zwislocki coupler during the recording process with the directional microphones. Figure 5 shows the frequency response of the hypercardiod microphone as measured with composite speech noise at KEMAR's eardrum and after playing the same speech noise through the ER3A headphone with and without compensation.

As the interaural time (phase) difference is an important cue for localization, the effect of the high-pass filter and ER 11-80 D Amplifiers on signals was also checked. A stereo file of a 1000 Hz pure tone was presented from a computer to the GSI61 audiometer. The left channel of the audiometer output was presented directly to the left insert earphone and the right channel of the audiometer output was presented to the high-pass filter, ER 11-80 D Amplifier and then the right insert earphone. The outputs of the insert earphones were then picked up by two ER 11 $\frac{1}{2}$ in. microphones placed in the medial opening of the Zwislocki couplers in KEMAR's ears and then recorded in a second computer. The comparison of the left and right channels of the recorded signal indicated that the addition of the high-pass filter and ER 11-80 D did not introduce any delay at the output of the insert earphones. Thus, we inferred that the interaural time (phase) differences of the test stimuli were preserved in the experimental setup.

For calibration of the level of the test stimuli at the ER-3A earphone output, a speech-spectrum shaped calibration noise was created. The rms level of the calibration noise was set equal to the rms level of the speech recorded at 0° azimuth in quiet. This signal was used to adjust the volume unit meter level and the audiometer dial so that the outputs of the ER-3A earphones in a Zwislocki coupler yielded 70 dB SPL on the sound level meter.

2. Test procedure for listeners with normal hearing

Listeners sat in the center of the loudspeaker array in which KEMAR was located during the recording. The 16 loudspeaker locations were numbered, with 9 real loudspeakers arranged in front and 7 dummy loudspeakers/boxes at the back. The rear loudspeakers were visible to the listeners using a mirror placed in the front of the room. The test tokens were presented through insert earphones but the loudspeakers provided visual cues for the listeners.

Before starting the sound direction identification task, a speech-spectrum shaped noise recorded from Loudspeaker 5 was presented binaurally through ER 3A insert earphones and the listeners were asked to identify which loudspeaker the noise was coming from. If the response was other than from Loudspeaker 5, the audiometer attenuator was adjusted so as to achieve a match in levels between the ears. For example, if the sound was perceived as coming from the right (indicating that the signal was louder in the right ear), the level of the right ear was adjusted until the sound moved to the center location. A familiarization task followed prior to each of the test conditions (i.e., recordings in quiet or in noise for a particular microphone type). For example, before testing the quiet condition, the test tokens of Omni, Card, Hyper, and Super were played sequentially from Locations 1 through 16 and the examiner informed the listeners from which loudspeaker it was presented.

During the test, sound direction identification was measured for the four different microphones in random order. The speech level was presented at 70 dB SPL with a rove level of 3 dB. The rove level was used in order to introduce variations in level that were not tied to loudspeaker location. The 3 dB variation was also used in previous hearing research studies (e.g., Keidser *et al.*, 2006). The listeners were instructed to face Loudspeaker 5 at 0° azimuth, to listen for the speech signal, and to call out the number of the loudspeaker from which he/she perceived the sound. The examiner entered the responses to the MATLAB program. Each listener was tested with a total of 1024 presentations (16 loudspeaker locations $\times 4$ microphones $\times 8$ repetitions $\times 2$ listening conditions). Breaks were given every 30 min or at the listener's request. Most listeners finished all the testing in 2 to 3 days. The filenames of the test stimuli and the corresponding responses were then exported in a spreadsheet at the end of the test.

3. Instrumentation for listeners with hearing loss

For testing of this group, the output of the computer was sent through the audiometer and to the hearing aid via direct audio input. Prior to data collection, a pair of two-channel

digital BTE hearing aids were programmed and tested in order to determine the signal level for direct audio input that would yield a hearing aid output equivalent to a 70 dB acoustic signal input. The digital hearing aids were programmed to 1:1 and their frequency responses matched the gain targets recommended by the National Acoustic Laboratory fitting presecription (NAL-R, Byrne and Dillon, 1986) in the 2 cc coupler for the average hearing loss of the hearing-impaired listeners shown in Fig. 1. Each hearing aid was then set up for electroacoustic analysis in Fonix 6500 Hearing Aid Analyzer (Frye Electronics, Inc.). Its output in response to a 70 dB speech-shaped composite noise was displayed and saved on the screen. After that, the composite noise was recorded from the hearing aid analyzer and its level was matched to that of the phrase "Where am I now?" This composite noise was then played through the MATLAB program, the audiometer, and a cable connecting the audiometer and the hearing aid via direct audio input. The hearing aid output was measured in the hearing aid analyzer and the audiometer attenuator was adjusted in 1 dB steps until the hearing aid output was equivalent to the one saved on the screen. This procedure ensured that the input to the hearing aids were equivalent to 70 dB SPL if the stimuli were presented acoustically to the microphone. It also verified that presenting test signals via DAI connections did not alter the frequency responses of the hearing aids compared to acoustic microphone inputs.

Further, as hearing aids with different processing delays were reported to introduce localization errors in bilateral fittings (Frye, 2001), the processing delays of the two digital hearing aids were checked using a Fonix 7000 Hearing Aid Analyzer. The processing delays for the left and right hearing aids were 5.3 and 5.4 ms, indicating that the interaural time differences were preserved using the current experimental setup for listeners with hearing loss.

4. Test procedures for listeners with hearing loss

Prior to sound direction identification tests, listeners with hearing loss were fit with the two-channel digital hearing aids using the NAL-R fitting prescription (Byrne and Dillon, 1986). The two-channel hearing aids were used to provide proper frequency shaping for their hearing loss. Compression was not employed in order to preserve interaural level differences. The hearing aid was coupled to each ear using Comply™ Snap Tips. These are compressible foam tips that attach to a snap tip earpiece that is coupled to the behind-the-ear hearing aid. This type of tip conforms to the shape of the listener's ear canal and alleviates the need for fabricating custom ear molds. The insertion gain of each hearing aid was adjusted to be within 5 dB of the NAL-R target gains from 500 to 4000 Hz using real ear measurements. During data collection, the familiarization and testing procedures were identical to those for testing listeners with normal hearing.

E. Data analysis

1. Interaural time difference

Interaural time differences are important cues for the localization of low frequency sounds. As the phrase "Where am I now?" was mostly comprised of low frequency vowel sounds, the interaural time differences were measured using ADOBE AUDITION 1.0 on the recordings of speech presented from 0°, 90°, 180°, and 270° in the quiet recordings for the four microphone settings. The interaural time differences were defined as the onset of speech between the left and right channels for a test token.

2. Summed rms speech levels

One of the effects of directional microphones was that they reduced the level of sounds originating from the back hemisphere. In order to understand the effects of combined levels on localization performance, the rms levels of the left and right ear microphone outputs for the speech signal experienced by listeners in the quiet conditions were summed by using

$$L_{\text{rms\_Sum}} = 10 \log[\log^{-1}(L_L/10) + \log^{-1}(L_R/10)] \quad (1)$$

where $L_{\text{rms\_Sum}}$=summed rms speech level; L_L and L_R =level of the left and right channel, respectively.

For the noise conditions, the levels of the speech stimuli were calculated using

$$L_S = 10 \log[\log^{-1}(L_{S+N}/10) - \log^{-1}(L_N/10)], \quad (2)$$

where L_S=level of speech; L_{S+N}=level of speech+noise; L_N=level of noise.

Then the summed rms speech levels were calculated using formula (1).

3. Angular error

The angular errors were calculated using two methods. In Method I, the errors were calculated by applying the following logical statements:

$$\begin{aligned} &\text{If} \quad |\text{ResponseL} - \text{TargetL}| \geqslant 9, \\ &\quad \text{Error} = |\text{TargetL} - \text{ReponseL} - 16| \\ &\text{else} \quad \text{Error} = |\text{ResponseL} - \text{TargetL}|, \end{aligned} \quad (3)$$

where ResponseL was the chosen loudspeaker, and TargetL was the presentation loudspeaker.

In other words, if a signal was presented from Loudspeaker 1, but the listener perceived the sound as coming from Loudspeaker 8, the error was calculated to be seven loudspeakers. If the listener chose Loudspeaker 15, the error would be two loudspeakers. This value was converted to angular error by multiplying the loudspeaker difference by 22.5 to convert to degrees. The maximum error possible was eight loudspeakers or 180°.

In Method II, front–back and left–right confusions were eliminated and only lateral confusion were reported. If a signal was presented from Loudspeaker 5 but the listener identified the sound as coming from Loudspeaker 12, the error would be one loudspeaker because of the correction for the front–back confusion. If a signal was presented from Loud-

speaker 1 but the listener perceived the sound as coming from Loudspeaker 8, the corrected error would also equal one loudspeaker. This was because the left–right confusion was discounted. The maximum error possible was four loudspeaker locations or 90°. The following logical statements were used in Method II:

For Loudspeakers 1 through 5:

$$\begin{aligned} &\text{If} \quad 5 \leqslant \text{ResponseL} - \text{TargetL} \leqslant 11, \\ &\quad \text{Error} = |\text{ResponseL} - \text{TargetL} - 8|; \\ &\text{else if} \quad \text{ResponseL} - \text{TargetL} \leqslant 4, \\ &\quad \text{Error} = |\text{ResponseL} - \text{TargetL}|; \\ &\text{else} \quad \text{Error} = |\text{ResponseL} - \text{TargetL} - 16|. \end{aligned} \tag{4}$$

For Loudspeakers 6 though 11:

$$\begin{aligned} &\text{If} \quad 5 \leqslant \text{ResponseL} - \text{TargetL}, \\ &\quad \text{Error} = |\text{ResponseL} - \text{TargetL} - 8|; \\ &\text{else if} \quad \text{ResponseL} - \text{TargetL} \leqslant -5, \\ &\quad \text{Error} = |\text{ResponseL} - \text{TargetL} + 8|; \\ &\text{else} \quad \text{Error} = |\text{ResponseL} - \text{TargetL}|. \end{aligned} \tag{5}$$

For Loudspeakers 12 through 16:

$$\begin{aligned} &\text{If} \quad 5 \leqslant |\text{ResponseL} - \text{TargetL} \leqslant 11, \\ &\quad \text{Error} = |\text{ResponseL} - \text{TargetL} + 8|; \\ &\text{else if} \quad |\text{ResponseL} - \text{TargetL}| \geqslant 12, \\ &\quad \text{Error} = \text{ResponseL} - \text{TargetL} + 16; \\ &\text{else} \quad \text{Error} = |\text{ResponseL} - \text{TargetL}|. \end{aligned} \tag{6}$$

The comparisons of the results obtained from the two calculation methods give us an estimate of front–back, left–right, and lateral localization errors. All statistical analyses were carried out using the average angular errors for individual listeners. Average angular errors, instead of rms errors, were used for easy data interpretation.

III. RESULTS

A. Interaural time differences

The interaural time differences were measured to be 0 ms at 0° and 180° and 0.8 ms at 90° and 270° for all microphone types. These results indicated that there were no microphone dependent changes and the interaural time differences were assumed to be held constant among the microphones at all corresponding loudspeaker locations.

B. Summed rms speech levels

The summed rms speech levels are depicted in Fig. 6 and are similar for quiet and noise conditions. The Omni microphone shows limited level variations among the loudspeaker locations whereas Card, Hyper, and Super have lower levels for the back than for the front loudspeakers. The lowest levels for the three directional settings occur at 180°. The differences between the loudspeakers with maximum and minimum summed rms speech levels were 1.6, 7.7, 7.6, and 8.3 dB for Omni, Card, Hyper, and Super, respectively. For the noise conditions, the differences were 1.5, 7.0, 7.5, and 8.2 dB for the speech stimuli.

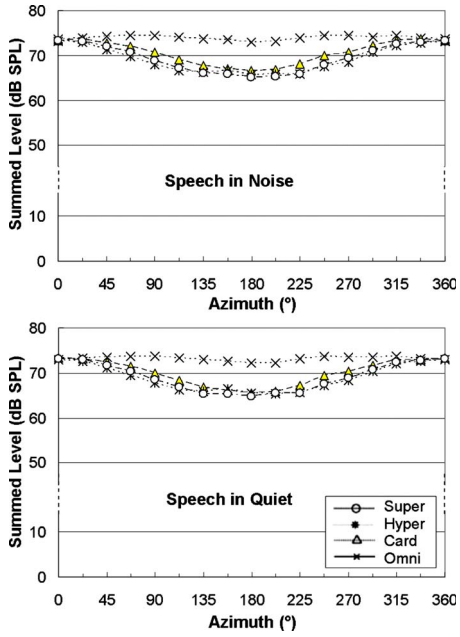

FIG. 6. The summed rms speech levels of left and right microphone outputs for the phrase "Where am I now?"

C. Angular error

Sound direction identification as a function of loudspeaker location and type of microphone in quiet and in noise is plotted in Fig. 7. In these plots, the target (presentation) loudspeaker location appears on the *x* axis and the response (perceived location) appears on the *y* axis. The size of the data points reflects the number of responses for a particular location. In order to allow fair visual comparisons between the quiet and noise conditions, the plots for listeners with hearing loss only included the data for the six listeners who listened to both conditions.

In Fig. 7, points falling on the diagonal represent correct sound direction identification. Points falling elsewhere indicate the locations of incorrect responses. Specifically, the points falling along the axis indicated by Line 1 linking (2, 16) and (8, 10) in the *x* and *y* axes (see Omni) are consistent with front–back confusions for the front loudspeakers. The points falling along Line 2 linking (10, 8) and (16, 2) indicate front–back confusion for the back loudspeakers. In addition, the points along Line 3 linking (10, 16) and (16, 10) and Line 4 linking (1, 9) and (9, 1) indicate left–right confusions for the right and left loudspeakers, respectively.

In order to understand the error patterns of sound direction identification performance as a function of microphone, listening conditions (quiet, noise), and listener group (normal hearing, hearing loss), the average angular error was plotted as a function of loudspeaker location in Figs. 8 and 9. The angular error data are plotted in polar format in order to visualize the locations of the loudspeakers.

A comparison between the plots of the angular errors with and without adjustment for front–back and left–right

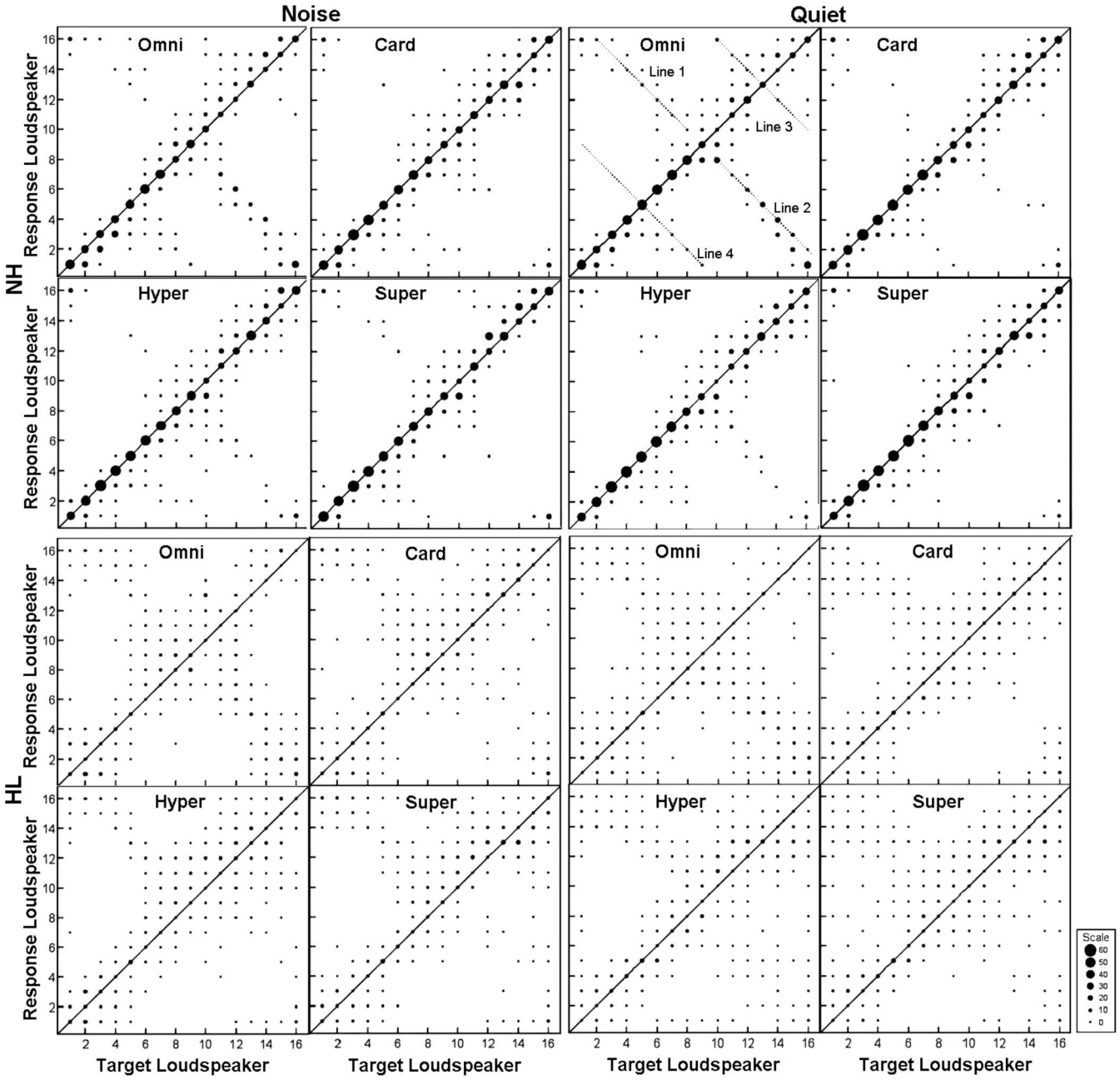

FIG. 7. The sound direction identification patterns of listeners with normal hearing (NH, $n=8$) and hearing loss (HL, $n=6$) for speech recorded via omnidirectional microphone (Omni) and directional microphones with free-field cardioid (Card), hypercardioid (Hyper), and supercardiod (Super) polar patterns.

confusion gives an indication of the prevalence of front–back and left–right confusions. Front-back confusion can be identified as decreases in average errors in the plots with adjustment compared to the ones without adjustment for the loudspeakers located between 315° and 45° or between 135° and 225° clockwise. Similar observations for loudspeakers located between 45° and 135° or between 225° and 315° indicate left–right confusion.

1. Comparisons of front and back loudspeakers

t-tests were used to analyze if there were any statistically significant differences between sound direction identification of speech from the front loudspeakers (i.e., Loudspeakers 2–8) and the back loudspeakers (i.e., Loudspeakers 10–16) for each microphone type. The conditions where the front loudspeakers yielded significantly lower errors than the back loudspeakers are marked with inverted triangles in Fig. 10. Listeners with normal hearing made significantly more errors for the back loudspeakers when listening through Hyper in Noise and to Card, Hyper, and Super in quiet ($p<0.0063$, p adjusted for a total of eight t-tests conducted) whether or not the data were adjusted for front–back and left–right confusions. Figures 8(c), 8(a), 8(d), and 8(b) were also consistent with these results. The comparisons between the front and the back loudspeakers also almost reached statistical significance in quiet ($p=0.0078$ and 0.0085 for data with or without adjustment) and in noise ($p=0.009$ for data without adjustment).

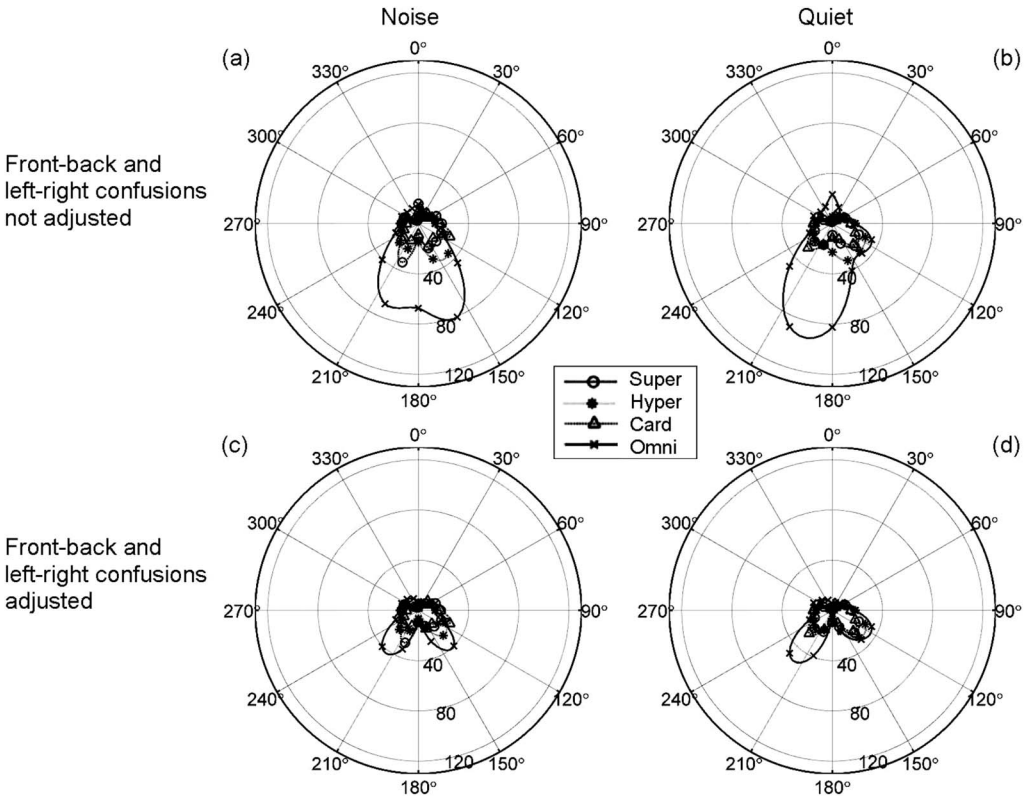

FIG. 8. The average angular error at each loudspeaker location calculated with and without adjustment for front–back and left–right confusions for listeners with normal hearing in quiet and in noise.

For listeners with hearing loss, Omni yielded significantly more errors for the back loudspeakers than for the front loudspeakers in noise when data were not adjusted for front–back and left–right confusions [$p < 0.0063$, Figs. 9(a) and 9(c)]. This difference disappeared when the data were adjusted, suggesting that the errors were mainly due to front–

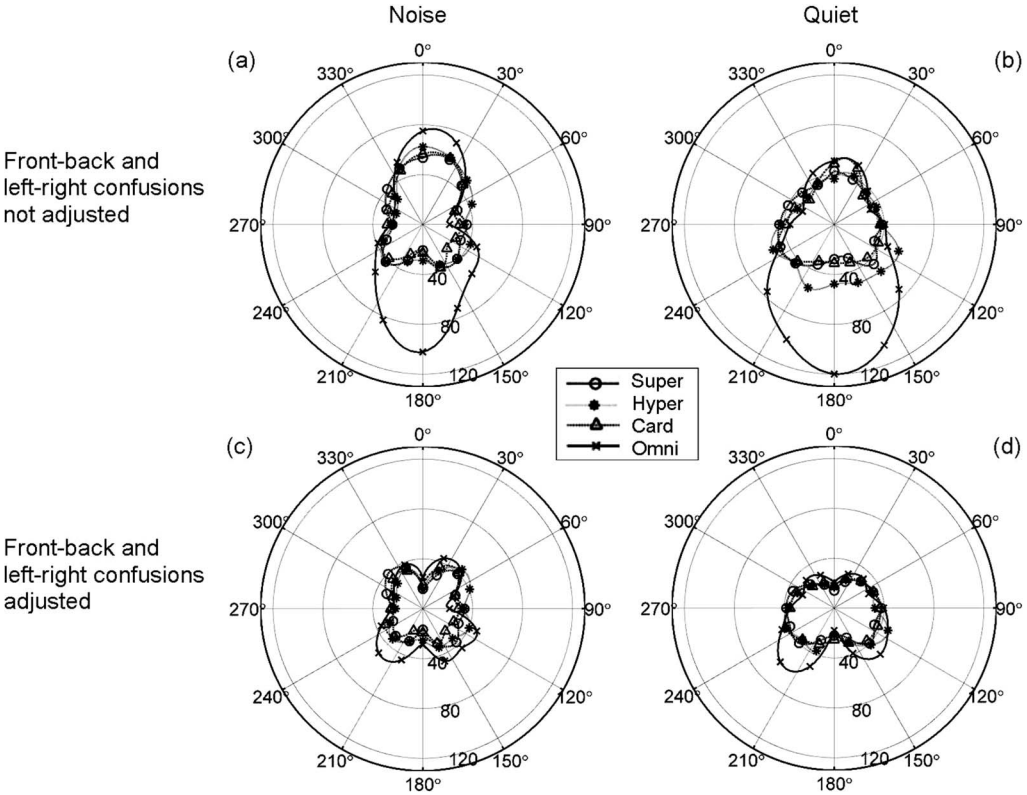

FIG. 9. The average angular error at each loudspeaker location calculated with and without adjustment for front–back and left–right confusions for listeners with hearing loss in quiet and in noise.

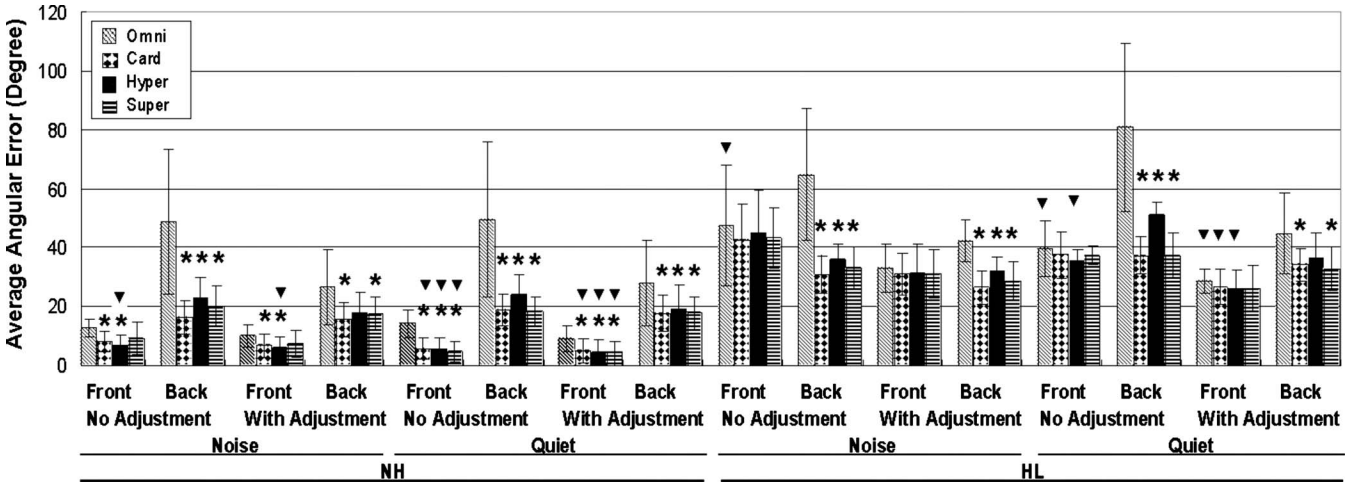

FIG. 10. The unadjusted and adjusted average angular error at front and back loudspeakers for listeners with normal hearing (NH) and hearing loss (HL). The error bars indicate ±1 s.d. (▼) Conditions with significantly lower errors for the front than the back loudspeakers. (*) Conditions with significantly lower errors than Omni ($p<0.0083$).

back confusion. Regardless of whether the front–back and left–right confusions were adjusted, listeners with hearing loss obtained significantly fewer errors for the front than the back loudspeakers when listening to Omni and Hyper in quiet ($p<0.0063$). In addition, Card also resulted in significantly fewer errors for the front than the back loudspeakers in quiet when the front–back and left–right confusions were adjusted [$p<0.0063$, Fig. 9(d)]. These results indicated that listeners with hearing loss were more likely to make front–back and lateral errors for the back loudspeakers when listening to Omni and Hyper and make lateral errors when listening to Card.

2. Comparisons of the microphones

Figure 10 shows the average angular error as a function of front and back loudspeaker locations in noise and in quiet as a function of microphone type. Analyses of variance (ANOVAs) with repeated measure on angular errors yielded a significant Microphone effect [$df=3,6, p<0.05$]. Bonferroni/Dunn post hoc tests revealed directional microphones yielded significantly less errors than the omnidirectional microphone ($p<0.0083$, p adjusted for six tests). These directional microphones are marked with an asterisk in Fig. 10. No significant differences were obtained among the directional microphones for either group of listeners in quiet or in noise.

When performance with the directional microphones was compared to Omni, listeners with normal hearing obtained significantly lower errors for two or all of the directional microphones than Omni for the front and the back loudspeakers in noise and in quiet regardless of whether the front–back and left–right confusion were adjusted ($p<0.0083$). This indicated that they were generally less likely to make localization errors using the directional microphones.

For listeners with hearing loss, ANOVA with repeated measures on angular errors resulted in no significant Microphone effect for the front loudspeakers and significant Microphone effects for the back loudspeakers in quiet and in noise [$df=3,6; p<0.01$] regardless of whether the data were adjusted for front–back and left–right confusions. Bonferroni/Dunn post hoc tests indicated that the average angular errors were significantly higher when listening through Omni than though the directional microphones (except for Hyper adjusted data when speech came from back loudspeakers in quiet). The directional microphones that yielded significantly lower errors are marked with an asterisk in Fig. 10.

IV. DISCUSSION AND SUMMARY

The purpose of this study was to obtain information on the effect of ITE directional microphones on sound direction identification in the horizontal plane with the goal of examining their applications for HPDs. The main finding of this study is that ITE directional microphones improve listeners' ability to identify sound locations in quiet and in noise for listeners with normal hearing and with hearing loss. This confirms the results of Keidser and colleagues (2006), who showed an improvement in localization of sounds from the back with BTE hearing aids having directional microphones with a cardioid pattern. Our finding also extends this notion to hypercardioid and supercardioid microphones. The normal hearing listeners showed better sound localization than the listeners with hearing loss. However, since the listeners with normal hearing were younger than the listeners with hearing loss, it is unclear whether this difference may be attributed to the factor of hearing loss or the factor of age. In order to determine separate contributions of hearing level and age, it would be necessary to test matched groups of young and older adults with normal hearing and with hearing loss. However, these data do provide information relevant to young listeners with normal hearing who might be candidates for using hearing protective devices, as well as older listeners with hearing loss who either use hearing aids with directional microphones or who might be candidates for using hearing protective devices.

Directional microphones introduce a differential level cue between signals arriving from the front and from the back. Our measurement data suggested that the summed rms speech level difference for the left and right ear inputs also appear to contribute to the front–back localization process. As the interaural time difference data showed identical values for all microphone types, it is unlikely a source contributing to the better front–back localization performance for the directional microphones. The data of the summed rms speech level differences, however, showed that Omni had minimal summed rms speech level differences for all loudspeakers (i.e., approximately 1.5 dB) whereas the directional microphones had considerably lower summed levels for the back than the front loudspeakers (i.e., between 6 and 8.3 dB, Fig. 6). In the test situation, both groups of listeners seemed to be able to use the larger summed rms speech level differences to help in deciding whether the sounds were coming from the front or the back in quiet and in noise.

The results of this study are encouraging: Directional microphones did not degrade localization performance and helped listeners with normal hearing improve localization ability in quiet and in noise and for speech originating from the front and back. They also help listeners with hearing loss localize sounds at the back in quiet and in noise. The level difference caused by the directional microphones appeared to yield a usable cue as to whether a sound was coming from the front or the back. It would need to be determined whether such differences in level could be used as cues to localize speech and other warning signals in the real world. Research has shown that in noisy situations, directional microphones can provide benefit for speech signals located in front of the hearing aid user (Valente, 1999; Ricketts, 2000; Chung, 2004). The use of directional microphones might be considered as a method to be used for improving the ability of a person using an HPD to locate the direction of a person speaking with him/her, turning toward that person, and thus improving speech understanding.

Caution must be exerted in the interpretation of the results of this study. Our study tested the effects of microphone types in quiet and in noise at a SNR of +10 dB on the localization of speech using recordings made in a large office. It would be important to carry out further research under conditions more typical of real-world environments. Important factors to consider would include testing in environments with greater reverberation, poorer signal-to-noise ratios, lower speech levels, and dynamic sound sources. An additional factor to consider is the effect of head movement that would occur in real-world listening conditions. Head movement has been shown to be a useful cue in resolving front–back confusions (Wightman and Kistler, 1999).

The results of this and previous studies suggest several implications for HPD design. First, directional microphones with cardioid, hypercardioid, and supercardioid patterns can be used in HPDs to enhance users' localization abilities. Second, bilateral HPDs or hearing aids should utilize the same polar patterns for best localization outcomes because two aids with different polar patterns degrade users' localization ability (Keidser *et al.*, 2006). Third, adaptive directional microphones which may have two different polar patterns for the two ears at any instance were found to negatively affect the localization ability of hearing aid users when their performance were compared with bilateral omnidirectional microphones (Van den Bogaert *et al.*, 2006). This evidence supports the need to use directional microphones with fixed and matched patterns so that users' localization ability would not be compromised. Fourth, as microphone transfer functions may change over time (i.e., microphone drift) and affect the directional microphone performance (Kuk *et al.*, 2000; Matsui and Lemons, 2001), a well-designed automatic microphone matching algorithm would be advisable for HPDs with directional microphones.

In conclusion, the results of this study suggest that directional microphones might be beneficial in HPDs. Further studies to examine the safety and benefits of such an application in real world noisy environments and to identify environments where such application is appropriate and cost-effective are warranted.

ACKNOWLEDGMENTS

This study was funded by Grant No. H133E980010 for the Lexington Center for the Deaf from the National Institute on Disability and Rehabilitation Research (NIDRR) of the United States Department of Education. Opinions expressed herein are those of the grantee and do not necessarily reflect those of the Department of Education. The authors are grateful to Unitron and Oticon for providing the hearing aids for the study. They also want to thank Mark Schmitt, Michael Steele, Gary Chant, and Marcin Wroblewski for technical support and Lance Nelson and Christy Macak for assistance with data collection and measurement.

Abel, S. M., and Armstrong, N. M. (**1993**). "Sound localization with hearing protectors," J. Otolaryngol. **22**, 357–363.

Alcantara, J. L., Moore, B. C., Kuhnel, V., and Launer, S. (**2003**). "Evaluation of the noise reduction system in a commercial digital hearing aid," Int. J. Audiol. **42**, 34–42.

Amlani, A. M., Rakerd, B., and Punch, J. L. (**2006**). "Speech-clarity judgments of hearing-aid-processed speech in noise: Differing polar patterns and acoustic environments," Int. J. Audiol. **45**, 319–330.

Bentler, R., Palmer, C., and Mueller, H. G. (**2006**). "Evaluation of a second-order directional microphone hearing aid. I. Speech perception outcomes," J. Am. Acad. Audiol **17**, 179–189.

Bentler, R. A., and Chiou, L. K. (**2006**). "Digital noise reduction: An overview," Trends Amplif. **10**, 67–81.

Bentler, R. A., Tubbs, J. L., Egge, J. L. M., Flamme, G. A., and Dittberner, A. B. (**2004**). "Evaluation of an adaptive directional system in a DSP hearing aid," Am. J. Audiol. **13**, 73–79.

Best, V., Carlile, S., Jin, C., and van Schaik, A. (**2005**). "The role of high frequencies in speech localization." J. Acoust. Soc. Am. **118**, 353–363.

Blamey, P. J., Fiket, H. J., and Steele, B. R. (**2006**). "Improving speech intelligibility in background noise with an adaptive directional microphone," J. Am. Acad. Audiol **17**, 519–530.

Blauert, J. (**1997**). *Spatial Hearing: The Psychophysics of Human Sound Localization* (MIT, Cambridge, MA).

Bolia, R. S., D'Angelo, W. R., Mishler, P. J., and Morris, L. J. (**2001**). "Effects of hearing protectors on auditory localization in azimuth and elevation," Hum. Factors **43**, 122–128.

Boymans, M., Dreschler, W., Shoneveld, P., and Verschuure, H. (**1999**). "Clinical evaluation in a full-digital in-the-ear hearing instrument," Audiology **38**, 99–108.

Boymans, M., and Dreschler, W. A. (**2000**). "Field trials using a digital hearing and with active noise reduction and dual-microphone directionality," Audiology **39**, 260–268.

Brungart, D. S., Kordik, A. J., and Simpson, B. D. (**2004**). "The effects of

single and double hearing protector on the localization and segregation of spatially-separated speech signals," J. Acoust. Soc. Am. **116**, 1897–1900.
Burkhard, M. D., and Sachs, R. M. (**1975**). "Anthopometric manikin for acoustic research," J. Acoust. Soc. Am. **58**, 214–222.
Byrne, D., and Dillon, H. (**1986**). "The National Acoustic Laboratories (NAL) new procedure for selecting the gain and frequency response of a hearing aid," Ear Hear. **7**, 257–265.
Byrne, D., Sinclair, S., and Noble, W. (**1998**). "Open earmold fittings for improving aided auditory localization for sensorineural hearing losses with good high-frequency hearing," Ear Hear. **19**, 62–71.
Chung, K. (**2004**). "Challenges and recent developments in hearing aids. I. Speech understanding in noise, microphone technologies, and noise reduction algorithms," Trends Amplif. **8**, 83–124.
Chung, K. (**2007**). "Effective compression and noise reduction configurations for hearing protectors," J. Acoust. Soc. Am. **121**, 1090–1101.
Chung, K., Killion, M. C., and Christensen, L. A. (**2007**). "Ranking hearing aid input-output functions for understanding low-, conversational-, and high-level speech in multitalker babble," J. Speech Lang. Hear. Res. **50**, 304–322.
Chung, K., Zeng, F. G., and Acker, K. N. (**2006**). "Effects of directional microphone and adaptive multichannel noise reduction algorithm on cochlear implant performance," J. Acoust. Soc. Am. **120**, 2216–2227.
Frye, G. J. (**2001**). "Testing digital and analog hearing instruments: Processing time delays and phase measurements," Hearing Rev. **8**(10), 34–40.
Hawkins, D. B., and Yacullo, W. S. (**1984**). "Signal-to-noise ratio advantage of binaural hearing aids and directional microphones under different levels of reverberation," J. Speech Hear Disord. **49**, 278–286.
Jenstad, L. M., Seewald, R. C., Cornelisse, L. E., and Shantz, J. (**1999**). "Comparison of linear gain and wide dynamic range compression hearing aid circuits: Aided speech perception measures," Ear Hear. **20**, 117–126.
Kam, A. C., and Wong, L. L. (**1999**). "Comparison of performance with wide dynamic range compression and linear amplification," J. Am. Acad. Audiol **10**, 445–457.
Keidser, G., Rohrseitz, K., Dillon, H., Hamacher, V., Carter, L., Rass, U., and Convery, E. (**2006**). "The effect of multi-channel wide dynamic range compression, noise reduction, and the directional microphone on horizontal localization performance in hearing aid wearers," Int. J. Audiol. **45**, 563–579.
Killion, M. C., Schulien, R., Christensen, L., Fabry, D., Revit, L., Niquette, P., and Chung, K. (**1998**). "Real world performance of an ITE directional microphone," Hear. J. **51**, 24–38.
Kuhnel, V., Margolf-Hackl, S., and Kiessling, J. (**2001**). "Multi-microphone technology for severe-to-profound hearing loss," Scand. Audiol. **52**, 65–68.
Kuk, F., Baekgaard, L., and Ludvigsen, C. (**2000**). "Design considerations in directional microphones," Hear. Res. **7**, 58–63.
Laurence, R. F., Moore, B. C. J., and Glasberg, B. R. (**1983**). "A comparison of behind-the-ear high-fidelity linear hearing aids and two-channel compression aids, in the laboratory and in everyday life," Braz. J. Phys. **17**, 31–48.
Lippmann, R. P., Braida, L. D., and Durlach, N. I. (**1981**). "Study of multichannel amplitude compression and linear amplification for persons with sensorineural hearing loss," J. Acoust. Soc. Am. **69**, 524–534.
Mackenzie, E., and Lutman, M. E. (**2005**). "Speech recognition and comfort using hearing instruments with adaptive directional characteristics in asymmetric listening conditions," Ear Hear. **26**, 669–679.
Matsui, G., and Lemons, T. (**2001**). "A special report on new digital hearing instrument technology," Hear. Res. **8**, 7–31.
Moore, B. C. J. (**1987**). "Design and evaluation of a two-channel compression hearing aid," J. Rehabil. Res. Dev. **24**, 181–192.
Moore, B. C. J., and Glasberg, B. R. (**1986**). "A comparison of two-channel and single-channel compression hearing aids," Audiology **25**, 210–226.
Morata, T. C., Fiorini, A. C., Fischer, F. M., Krieg, E. F., Gozzoli, L., and Colacioppo, S. (**2001**). "Factors affecting the use of hearing protectors in a population of printing workers," Noise Health **4**, 25–32, 38.
Morata, T. C., Themann, C. L., Randolph, R. F., Verbsky, B. L., Byrne, D. C., and Reeves, E. R. (**2005**). "Working in noise with a hearing loss: Perceptions from workers, supervisors, and hearing conservation program managers," Ear Hear. **26**, 529–545.
Musicant, A., and Butler, R. (**1984**). "The influence of pinnae-based spectral cues on sound localization," J. Acoust. Soc. Am. **75**, 1195–1200.
Noble, W., Murray, N., and Waugh, R. (**1990**). "The effect of various hearing protectors on sound localization in horizontal and vertical planes," Am. Ind. Hyg. Assoc. J. **51**, 370–377.
Ricketts, T., Henry, P., and Gnewikow, D. (**2003**). "Full time directional versus user selectable microphone modes in hearing aids," Ear Hear. **24**, 424–439.
Ricketts, T. A. (**2000**). "Directional hearing aids," Trends Amplif. **5**, 139–176.
Ricketts, T. A., and Dhar, S. (**1999**). "Aided benefit across directional and omni-directional hearing aid microphones for behind-the-ear hearing aids," J. Am. Acad. Audiol **10**, 180–189.
Ricketts, T. A., and Henry, P. (**2002**). "Evaulation of an adaptive directional-microphone hearing aid," Int. J. Audiol. **41**, 100–112.
Ricketts, T. A., and Hornsby, B. W. Y. (**2005**). "Sound quality measures for speech in noise through a commercial hearing aid implementing 'Digital Noise Reduction,'" J. Am. Acad. Audiol **16**, 270–277.
Roffler, S. K., and Butler, R. A. (**1968**). "Localization of tonal stimuli in the vertical plane," J. Acoust. Soc. Am. **43**, 1260–1266.
Shaw, E. A. (**1974**). "Transformation of sound pressure level from the free field to the eardrum in the horizontal plane," J. Acoust. Soc. Am. **56**, 1848–1861
Simpson, B. D., Bolia, R. S., McKinley, R. L., and Brungart, D. S. (**2005**). "The impact of hearing protection on sound localization and orienting behavior," Hum. Factors **47**, 188–198.
Souza, P. E. (**2002**). "Effects of compression on speech acoustics, intelligibility, and sound quality," Trends Amplif. **6**, 131–165.
Souza, P. E., and Turner, C. W. (**1999**). "Quantifying the contribution of audibility to recognition of compression-amplified speech," Ear Hear. **20**, 12–20.
Spriet, A., Van Deun, L., Eftaxiadis, K., Laneau, J., Moonen, M., van Dijk, B., van Wieringen, A., and Wouters, J. (**2007**). "Speech understanding in background noise with the two-microphone adaptive beamformer BEAM™ in the Nucleus Freedom™ cochlear implant system," Ear Hear. **28**, 62–72.
Valente, M. (**1999**). "Use of microphone technology to improve user performance in noise," Trends Amplif. **4**, 112–135.
Valente, M., Fabry, D., Potts, L., and Sandlin, R. (**1998**). "Comparing the performance of the Widex Senso digital hearing aid with analog hearing aids," J. Am. Acad. Audiol **9**, 342–360.
Valente, M., Mispagel, K. M., Tchorz, J., and Fabry, D. (**2006**). "Effect of type of noise and loudspeaker array on the performance of omnidirectional and directional microphones," J. Am. Acad. Audiol **17**, 398–412.
Van den Bogaert, T., Klasen, T. J., Van Deun, L., and Wouters, J. (**2006**). "Horizontal localization with bilateral hearing aids: Without is better than with," J. Acoust. Soc. Am. **119**, 515–526.
van der Beek, F. B., Soede, W., and Frijns, J. H. M. (**2007**). "Evaluation of the benefit for cochlear implantees of two assistive directional microphone systems in an artificial diffuse noise situation," Ear Hear. **28**, 99–110.
van Hoesel, R., and Clark, G. M. (**1995**). "Evaluation of a portable two-microphone adaptive beamforming speech processor with cochlear implant patients," J. Acoust. Soc. Am. **97**, 2498–2503.
Vause, N., and Grantham, D. (**1999**). "Effects of earplugs and protective headgear on auditory localization ability in the horizontal plane," Hum. Factors **41**, 282–294.
Villchur, E. (**1973**). "Signal processing to improve speech intelligibility in perceptive deafness," J. Acoust. Soc. Am. **53**, 1646–1657.
Walden, B. E., Surr, R. K., Cord, M. T., and Dyrlund, O. (**2004**). "Predicting hearing aid microphone preference in everyday listening," J. Am. Acad. Audiol **15**, 365–396.
Weinrich, S. (**1982**). "The problem of front-back localization in binaural hearing,," Scand. Audiol. Suppl. **15**, 135–145.
Wenzel, E. M., Arruda, M., Kistler, D. J., and Wightman, F. L. (**1993**). "Localization using nonindividualized hear-related transfer functions," J. Acoust. Soc. Am. **94**, 111–123.
Wightman, F. L., and Kistler, D. J. (**1989**). "Headphone simulation of free-field listening. II. Psychophysical validation," J. Acoust. Soc. Am. **85**, 868–878.
Wightman, F. L., and Kistler, D. J. (**1999**). "Resolution of front-back ambiguity in spatial hearing by listener and source movement," J. Acoust. Soc. Am. **105**, 2841–2853.
Wouters, J., Litiere, L., and van Wieringen, A. (**1999**). "Speech intelligibility in noisy environments with one- and two-microphone hearing aids," Audiology **38**, 91–98.

Pulse-rate discrimination by cochlear-implant and normal-hearing listeners with and without binaural cues

Robert P. Carlyon,[a] Christopher J. Long, and John M. Deeks
MRC Cognition and Brain Sciences Unit, 15 Chaucer Road, Cambridge CB2 7EF, United Kingdom

(Received 25 May 2007; revised 18 January 2008; accepted 21 January 2008)

Experiment 1 measured rate discrimination of electric pulse trains by bilateral cochlear implant (CI) users, for standard rates of 100, 200, and 300 pps. In the diotic condition the pulses were presented simultaneously to the two ears. Consistent with previous results with unilateral stimulation, performance deteriorated at higher standard rates. In the signal interval of each trial in the dichotic condition, the standard rate was presented to the left ear and the (higher) signal rate was presented to the right ear; the non-signal intervals were the same as in the diotic condition. Performance in the dichotic condition was better for some listeners than in the diotic condition for standard rates of 100 and 200 pps, but not at 300 pps. It is concluded that the deterioration in rate discrimination observed for CI users at high rates cannot be alleviated by the introduction of a binaural cue, and is unlikely to be limited solely by central pitch processes. Experiment 2 performed an analogous experiment in which 300-pps acoustic pulse trains were bandpass filtered (3900–5400 Hz) and presented in a noise background to normal-hearing listeners. Unlike the results of experiment 1, performance was superior in the dichotic than in the diotic condition. © *2008 Acoustical Society of America.*
[DOI: 10.1121/1.2874796]

PACS number(s): 43.66.Ts, 43.66.Hg, 43.66.Pn [RLF] Pages: 2276–2286

I. INTRODUCTION

An important finding in the cochlear-implant ("CI") literature concerns a limitation in CI users' sensitivity to changes in the rate of a train of pulses applied to a single channel of their device. At low rates, most listeners can detect rate changes, with average difference limens (DLs) of about 7% (Moore and Carlyon, 2005), and some listeners can make musical judgments, such as the identification of melodies and the production and identification of musical intervals (Pijl and Schwarz, 1995; McDermott and McKay, 1997). However, once the rate exceeds about 300 pps, performance for the majority of CI users deteriorates markedly (Shannon, 1983; Tong and Clark, 1985; Townshend *et al.*, 1987; McKay *et al.*, 2000). The finding has both theoretical and practical implications. In terms of theory, it provides insights into the limitations of pitch perception in the absence of place-of-excitation cues (so-called "purely temporal" pitch perception: Carlyon *et al.*, 2002; Carlyon *et al.*, 2007). In practical terms, a number of authors have suggested novel speech-processing schemes that present temporal fine structure to CI electrodes (Nie *et al.*, 2005; Stickney *et al.*, 2005; Stickney *et al.*, 2007). It seems likely that the success of those schemes will be constrained by the sensitivity of CI users to fast timing differences. The poor rate discrimination above 300 pps strongly suggests that this sensitivity may be limited or absent, and so it seems worthwhile to study the nature of that limitation.

In a previous article (Carlyon and Deeks, 2002), we studied the limitations on rate discrimination in normal-hearing ("NH") listeners, using acoustic pulse trains that had been bandpass filtered so that, in many conditions, harmonics that were resolved by the peripheral auditory filters were removed. A number of other studies have shown that the results obtained with such pulse trains mimic those observed when analogous electric pulse trains are presented to one channel of a CI (McKay and Carlyon, 1999; Carlyon *et al.*, 2002; van Wieringen *et al.*, 2003; Carlyon *et al.*, 2007). Carlyon and Deeks reported a number of findings that shed light on the limitations of temporal pitch perception: (i) Like CI users, NH listeners also showed an "upper limit" for rate discrimination, (ii) that limit increased as the sounds were filtered into higher frequency regions in a way that could not be attributed to the effects of peripheral filtering in the auditory system, (iii) in the highest frequency region tested (7800–10 800 Hz), the limit was 600 pps—substantially higher than that observed for most CI listeners, (iv) for a 600-pps pulse train filtered between 3900 and 5400 Hz, where performance with monotic presentation was at chance, discrimination could be substantially improved by the presentation of another pulse train to the contralateral ear in each interval of a forced-choice trial. The contralateral pulse train was always the same as the lower of the two possible rates presented ipsilaterally, so that the standard (lower-rate) intervals consisted of a diotic pulse train, whereas in the signal interval the stimuli in the two ears differed slightly. This provided a binaural cue, which was the presumed basis of the improvement in performance. This last experiment was inspired by a similar manipulation applied to electric pulse trains having rates between 50 and 200 pps in two CI

[a]Author to whom correspondence should be addressed. Electronic mail: bob.carlyon@mrc-cbu.cam.ac.uk.

 0001-4966/2008/123(4)/2276/11/$23.00 © 2008 Acoustical Society of America

TABLE I. Details of the cochlear implant users who participated in the experiments. The table shows their Patient ID (Pt ID), Date of Birth (DOB) and information for the left ear and then the right ear and finally the Time without Binaural Hearing (in years) and Time with No Hearing (in years). For the left and right ears, we give Etiology, Date of Deafness Onset (in years), Date of Implant Switch on (in years), Electrode used in experiments, and Dynamic range of electrode (dB). The final column shows their performance in a task requiring them to discriminate between a 100-pps pulse train leading by ±234 μs to the left vs. the right ear.

Pt ID	DOB	Etiology (Left)	Date of Deafness Onset (Left)	Date of Implant Switch on (Left)	Electrode Used (Left)	Dynamic Range (Left; dB)	Etiology (Right)	Date of Deafness Onset (Right)	Date of Implant Switch on (Right)	Electrode Used (Right)	Dynamic Range (Right; dB)	Time without Binaural Hearing (Years)	Time with No Hearing (Years)	±234 ms 100-pps ITD (%)
CI 1	1969	Progressive bilat.SNHL/ PVAS	1991	1998	13	19	German Measles	1991	2001	13	17	10	7	70
CI 2	1934	Noise exposure/ idiopathic	1996	2000	13	11	Noise exposure/ idiopathic	1989	2002	13	12	13	4	83
CI 3	1926	Progressive	1994	1997	3	11	Progressive	1994	2002	9	9	8	3	90
CI 4	1947	Progressive/ Crohns	1990	2002	17	15	Progressive/ idiopathic	1991	1999	20	15	11	8	83

listeners by van Hoesel and Clark, (1997). They also observed that, at least at rates below100 pps, the contralateral stimulus improved performance.

Carlyon and Deeks' (2002) observation that rate discrimination of high-rate pulse trains could be improved by introducing a binaural cue led them to conclude that, for NH listeners, the mechanisms underlying the upper limit of rate discrimination included a component that was specific to the pitch mechanism. In particular, they argued that, as performance was no longer at chance when a binaural cue was introduced, some information on the timing of the individual pulses must have been present at the level of the auditory nerve ("AN"). However, as they pointed out, this does not necessarily apply to CI users: the fact that the upper limit of 600 pps observed for NH listeners was higher than the 300 pps observed for most CI listeners suggested that the latter group may have an additional, peripheral limitation to rate discrimination at high rates. Some evidence in support of this interpretation comes from the fact that the discrimination of interaural time differences (ITDs) between equal-rate pulse trains deteriorates with increases in pulse rate (van Hoesel and Tyler, 2003; Majdak *et al.*, 2006; van Hoesel, 2007). The present study therefore measured rate discrimination with and without binaural cues in four bilateral CI users, for pulse rates between 100 and 300 pps. The aim was to determine whether, for pulse rates sufficiently high for monotic or diotic rate discrimination to deteriorate, there was sufficient information at the level of the AN for performance to improve when a binaural cue was added. This first experiment was similar to, but differed in several ways from, a recent study by van Hoesel (2007), which was published during the preparation of this article.[1] A comparison of the methods, results, and conclusions from experiment 1 with those of van Hoesel will be provided in the following sections.

To allow a more direct comparison with the limitations on rate discrimination observed with acoustic stimulation of the normal auditory system, experiment 2 studied rate discrimination in the presence and absence of binaural cues in five NH listeners. That experiment used similar procedures and conditions to experiment 1, and used acoustic pulse trains that had been bandpass filtered to remove resolved harmonics. Experiment 2 differed from most previous acoustic studies in that it compared sensitivity to monaural rate differences with that to a time-varying decorrelation, using stimuli that, we have argued, are directly analogous to those employed with CI users (McKay and Carlyon, 1999; Carlyon *et al.*, 2002; van Wieringen *et al.*, 2003).

II. EXPERIMENT 1: CI USERS

A. Method

1. Listeners

Four bilaterally implanted users of the Nucleus CI 24M cochlear implant took part. They had been without binaural hearing prior to their second CI for between 8 and 13 years (Table I), and were the same listeners as had taken part in the study by Long *et al.* (2006b). The electrode pairs tested in each ear were also the same as used by Long *et al.* They were initially chosen for Long *et al.*'s study using a task that identified electrodes in the two ears that had similar pitches. Listeners then performed a two-interval two-alternative forced-choice task with a pair of pitch-matched electrodes, and in which 100-pps pulse trains were presented first with an ITD of 234 μs leading in one ear, and then the other. If listeners could not reliably identify the location of the second sound relative to the first then a different electrode was chosen in one ear, and the forced-choice task was repeated. Percent-correct scores for the electrode pairs used here and by Long *et al.*, based on a total of 40 trials (60 for listener CI 2), are shown in the final column of Table I.

2. Stimuli

In the diotic[2] condition, synchronized pulse trains (<1 μs resolution) were presented to the two devices using custom software driving the SPEAR3 experimental processor (HearWorks Pty Ltd.). Each pulse was biphasic, had a

duration of 25 μs per phase with an inter-phase gap of 7.4 μs (listener CI 2) or 45 μs (listeners CI 1, CI 3, CI 4), and was presented in monopolar ("MP1+2") mode. The dichotic condition was the same as the diotic condition except that the pulse rate presented to the left ear was the same in all three intervals of each trial. For the two standard intervals the stimuli were the same as for the standard intervals in the diotic condition, and were therefore the same in the two ears. In the signal interval the listener was presented with the standard rate in the left ear and the higher rate in the right ear. This introduced a timing difference between the pulses in each ear, potentially allowing the listener to use binaural mechanisms to perform the task. The standard rate was always 100, 200, 300 pps for listeners CI 2, 3, and 4; listener CI 1 was additionally tested at a standard rate of 400 pps. The interval between stimuli in each trial was 500 ms.

The level of the pulse train in each ear was selected to be close to its "most comfortable level" when presented alone, and to produce a centered image when the two ears were stimulated diotically at a rate of 100 pps. As in the study by van Hoesel (2007), the levels that were presented to each ear did not differ with baseline rate. Also as in van Hoesel's study, listeners reported hearing the diotic stimulus in the center of the head at all rates. The effects of any deviation from a perfectly centered image on performance in the dichotic condition would, as van Hoesel noted, have been reduced by the use of a forced-choice task, and, in addition, by the fact that the signal in the dichotic condition contained ITDs that, at different times throughout the stimulus, passed through the entire range of possible values (see below).

One aspect of the overall design that differed from that used in some previous studies (Carlyon and Deeks, 2002; van Hoesel, 2007) was that the dichotic condition was compared to diotic rather than monotic stimulation. An advantage of the present approach is that it allowed the two conditions to be compared at the same stimulus level per ear *and* at the same overall loudness. In both types of procedure, superior performance in the dichotic condition can unequivocably be attributed to the use of interaural timing cues. However, in our procedure, rate differences were applied only to the right ear in the dichotic condition, so worse sensitivity to rate differences in that condition could be due to poorer sensitivity to rate differences in the right than in the left ear. Therefore, for a subset of conditions where this happened, we remeasured performance in the dichotic and diotic conditions, and at the same time added monotic measurements for each ear separately.

We chose not to rove the level across the intervals in each trial, as has been used in some other studies. Our reasons for not roving level were that (i) loudness changes only gradually with pulse rate between 100 and 300 pps (McKay and McDermott, 1998), and so is unlikely to have provided a salient cue, (ii) a loudness rove can nevertheless degrade performance (Baumann and Nobbe, 2004), either by introducing a salient variation in one stimulus dimension that may interfere with the detection of more subtle discriminations in the percept of interest (Melara and Marks, 1990), or via small influences of level on pitch (Townshend *et al.*, 1987).

TABLE II. (a) The values of Δr used for each standard rate in (a) experiment 1 and (b) experiment 2. The first three columns show the standard rate, Δr expressed as a percentage of that rate, and Δr in pps. The fourth, penultimate, column shows the number of times the pulses in the two ears rotate in and out of phase during the signal. The final column shows the asynchrony between the pulses in the two ears, averaged over the stimulus duration.

Standard rate	Δr (%)	Δr (pps)	Rotations	Mean asynch (ms)
		(a) Experiment 1		
100	2.50	2.50	2	2.50
100	5.00	5.00	4	2.50
100	10.00	10.00	8	2.50
100	20.00	20.00	16	2.50
200	1.25	2.50	2	1.25
200	2.50	5.00	4	1.25
200	5.00	10.00	8	1.25
200	10.00	20.00	16	1.25
200	20.00	40.00	32	1.25
200	35.00	70.00	56	1.25
300	0.83	2.50	2	0.83
300	2.50	7.50	6	0.83
300	10.00	30.00	24	0.83
300	35.00	105.00	84	0.83
		(b) Experiment 2		
300	0.42	1.25	1	0.83
300	0.83	2.50	2	0.83
300	1.25	3.75	3	0.83
300	2.50	7.50	6	0.83
300	5.00	15.00	12	0.83
300	10.00	30.00	24	0.83
300	35.00	105.00	84	0.83

3. Procedure

Each trial had a "3I2AFC" structure, in which two of the stimuli had the same "standard" rate, and where either the second or third stimulus (the "signal") had a higher rate. The listener was instructed to pick the "odd man out," and correct-answer feedback was provided visually after each response.

The method of constant stimuli was used. We chose this method in preference to an adaptive procedure because it requires neither that sensitivity is well above chance at the largest signal-standard differences studied, nor that the underlying psychometric function is monotonic. For each standard rate a psychometric function was measured, incorporating four or five values of Δr, which we define as the difference between standard and signal rates. Those values, expressed both in "raw" pulses per second and as a percentage of the baseline rate, are shown in part (a) of Table II. Figure 1(a) shows a schematic of the pulses in each ear for a signal in the dichotic condition with a baseline rate of 100 pps and $\Delta r = 10$ pps. For clarity, only the first 200 ms of the stimulus is shown. It can be seen that the delay between the nth pulse in one ear and the nth pulse in the other ear increases up to 100 ms ($1/\Delta r$ s), at which point the nth pulse in one ear is synchronous with the $n+1$th in the other. The wide gray line in Fig. 1(b) illustrates this fact: for a Δr of

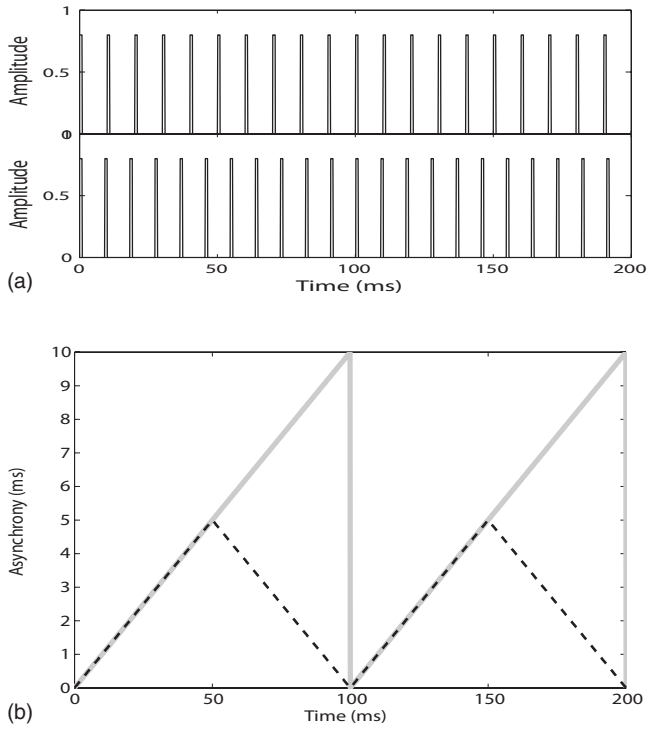

FIG. 1. Part (a) shows a schematic of the pulses in each ear for a signal in the dichotic condition with a baseline rate of 100 pps and $\Delta r = 10$ pps. For clarity, only the first 200 ms of the stimulus is shown. It can be seen that the asynchrony between the nth pulse in each ear increases up to 100 ms ($1/\Delta$r s), at which point the nth pulse in one ear is synchronous with the $n+1$th in the other. The wide gray line in part (b) illustrates this fact: for a Δr of x pps, the ITD between the pulses in the two ears rotates through a whole period once every $1/x$ s, with a sawtooth function. The dotted black line shows the asynchrony between each pulse in one ear and the *nearest* pulse in the other.

x pps, the ITD between the pulses in the two ears rotates through a whole period once every $1/x$ s, with a sawtooth function. The number of times this occurred over the 800-ms duration of our stimuli is shown in the penultimate column of Table II. It can also be seen from Fig. 1(a) that the largest asynchrony between each pulse in one ear and the *nearest* pulse in the other occurs after 50 ms ($0.5/\Delta r$), and is equal to half the period of the baseline rate. This asynchrony is shown by the black dashed line in Fig. 1(b), and its mean value across the entire stimulus is shown in the final column of Table II.

A potentially important feature of the present design, as shown in Table II, was that the ITD between adjacent pulses always rotated through a whole period an integer number of times, so that the pulse trains always started *and* ended in synchrony in the two ears. This meant that performance in the dichotic condition could not have been influenced by timing difference between the last two pulses in each ear, unlike the case in some previous studies (van Hoesel and Clark, 1997; Carlyon and Deeks, 2002; van Hoesel, 2007).

Testing was performed in blocks of 40 trials. Each block was preceded by ten practice trials. For a given standard rate, the procedure started with 40 trials at the largest Δr tested for that rate, in either the diotic or dichotic condition. The same Δr was then tested in the other condition, and the procedure was repeated at successively smaller values of Δr until all such values had been tested. This procedure was then repeated, but with the order of diotic/dichotic conditions at each Δr swapped, so that there were usually a total of 80 trials for each combination of condition and Δr. In some cases—for example, where performance was near chance or ceiling—we omitted some values of Δr from the psychometric function. In addition, when the first 40 trials at the largest Δr tested for a given baseline rate yielded a score of 39 or 40 correct responses, and when performance at the next-lowest Δr was above chance, testing was sometimes stopped after 40 trials. The order in which the standard rates were tested differed across listeners. Listener CI 1 completed the 400-pps rate first, followed by 100, 200, and 300 pps. The order for CI 2 and CI 3 was 100, 200, 300 pps, and that for CI 4 was 200, 100, 300 pps.

III. RESULTS AND DISCUSSION

A. Psychometric functions and estimated DLs

Figure 2 shows psychometric functions for each listener and standard rate, with scores in the diotic and dichotic conditions indicated by circles and triangles, respectively. In the diotic condition, these functions are monotonic, and generally reveal a pattern of decreasing performance with increasing rate. To further examine the effect of baseline rate on performance in the diotic condition, we estimated rate DLs by linear interpolation between the points on each function straddling 70.7% correct; this is the value on which "two-up one-down" adaptive procedures converge (Levitt, 1971). The resulting DLs are shown in Table III, with the case where performance does not reach 70.7% indicated by the asterisk (CI 3, 300 pps). The results show that DLs increase with increasing base rate, in line with the results of numerous studies employing monotic stimulation (Shannon, 1983; Tong and Clark, 1985; Townshend *et al.*, 1987; McKay *et al.*, 2000; van Hoesel, 2007).

In the dichotic condition, two listeners, CI 1 and CI 2, show a clear advantage over diotic stimulation at standard rates of 100 and 200 pps, for all values of Δr at which performance is not at chance or ceiling. However, at 300 pps the dichotic advantage disappears, and, for listener CI 2, turns into a *disadvantage*. The dichotic advantage is also absent for CI 1 at a standard rate of 400 pps (filled symbols), and turns into a disadvantage at $\Delta r = 10\%$ ($p = 0.027$, based on a test of differences between independent proportions[3]). Results from these two listeners therefore indicate that, once the rate is sufficiently high for diotic rate discrimination to deteriorate, no advantage can be gained by adding a binaural cue. A similar finding was also obtained in the three listeners tested by van Hoesel (2007).

The results from listener CI 4 differ slightly from those of the first two listeners. She shows a small dichotic advantage at a 100-pps pulse rate, but only for the two lowest values of Δr, and the difference is significant only at $\Delta r = 5\%$ ($p = 0.002$). As with CI 1 and CI 2, performance in the dichotic condition deteriorates relative to that in the diotic condition as rate increases, here becoming worse than in the diotic condition at 200 as well as at 300 pps. Listener CI 3 shows a dichotic advantage for the lowest Δr at 100 pps (p

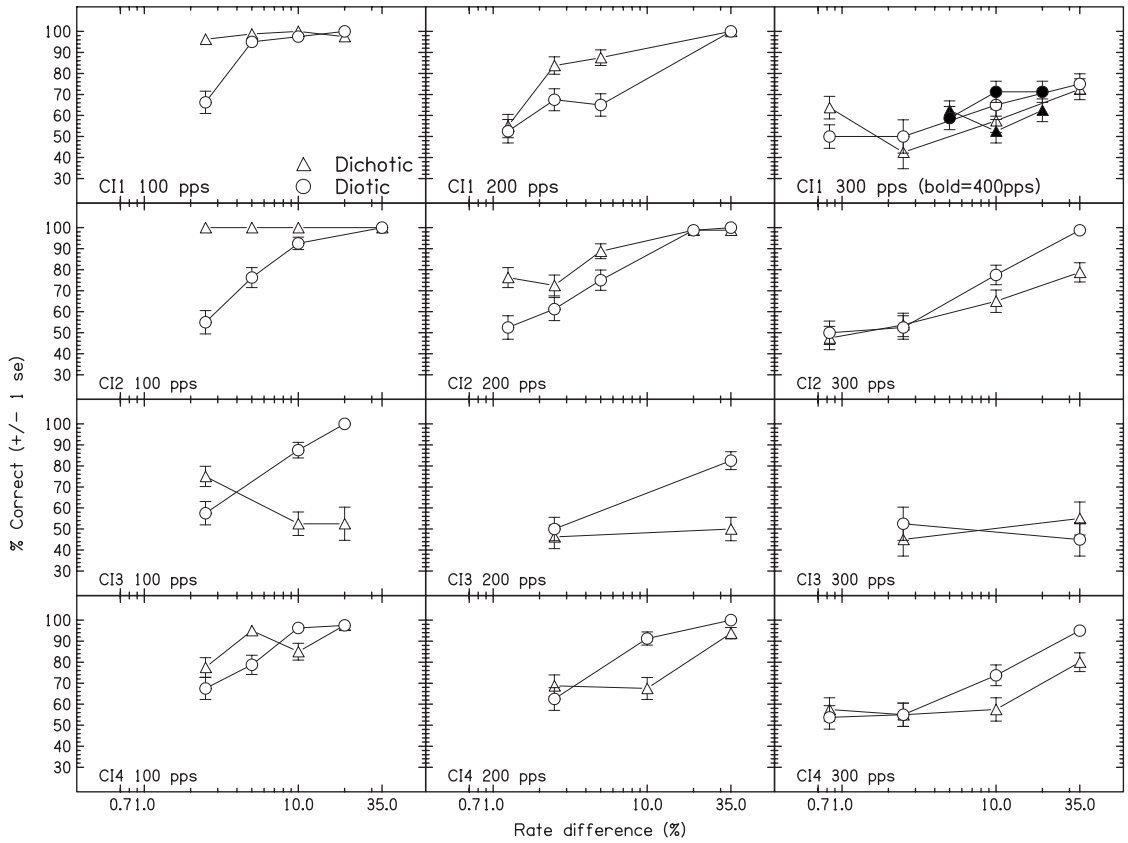

FIG. 2. Psychometric functions describing percent correct as a function of Δr for the four CI users who took part in experiment 1. Each row shows the data for one listener, and each column shows the data for one baseline pulse rate. Performance in the diotic and dichotic conditions is shown by circles and triangles, respectively. Error bars show ± one standard error, estimated from the normal approximation to the binomial distribution. The solid symbols in the top-right panel show performance at a rate of 400 pps for listener CI 1.

=0.019), but performance is worse in the dichotic than in the diotic condition both at higher values of Δr, and at higher standard rates. A striking finding obtained with this listener is that, at a rate of 100 pps, performance in the dichotic condition deteriorates as Δr increases from 2.5 to 10%, a finding which is statistically significant (p=0.003). Other instances of these "reversals" occurred for CI 1 at 300 pps, when Δr was increased from 0.83 to 2.5% (p=0.027), and for CI 4 at 100 pps when Δr was increased from 5 to 10% (p=0.035). A possible explanation comes from the fact that, as Δr increases, so does the number of times the "asynchrony" between pulses in the two ears rotates through one cycle during the stimulus (Table II, penultimate column). It may be that listeners have difficulty in exploiting dichotic cues when the amount of asynchrony between pulses in the two ears is changing rapidly, a finding reminiscent of the results previously obtained in NH listeners by Grantham and Wightman (1978). At the same time, as Δr increases, the "pitch" cue available in the right ear becomes more salient, and so the change in performance with increasing Δr will reflect a trade-off between the ability of the listener to take advantage of this cue, and his/her ability to exploit interaural asynchronies that change quickly over time.

TABLE III. Rate DLs, corresponding to the 70.7% correct, obtained by linear interpolation from the diotic condition of experiment 1. The asterisk indicates the case where performance did not reach 70.7%.

	100 pps	200 pps	300 pps
CI 1	2.9	9.9	24.3
CI 2	4.3	4.2	8.0
CI 3	6.3	17.4	*
CI 4	3.2	4.6	8.8

B. Further investigation of worse performance in dichotic than diotic conditions

In order to investigate that minority of cases where performance was worse in the dichotic than in the diotic condition, a small set of additional measures was obtained from each listener. These measurements were made for a single combination of baseline rate and Δr for each listener, and included estimates of performance for each ear stimulated alone, together with repeats of the measures obtained in the dichotic and diotic conditions. They were obtained between 11 and 20 months after the original psychometric functions were collected.

The results obtained for listener CI 1 at 400 pps and Δr=10% are shown in Table IVa. Performance in the diotic and dichotic conditions had not changed much in the 20 months between tests, although that in the diotic condition had worsened slightly. Combined across the two sets of data, performance was worse in the dichotic than in the diotic condition (p=0.02). One possible reason for this is suggested by the new monotic measures, which showed that perfor-

TABLE IV. Summary of additional measures obtained in experiment 1. In parts a, b, and d, the original data (Fig. 2) are plotted, followed by the new data and finally the two sets averaged. In part c (listener CI 3), the original data are followed by some new measures obtained with the same stimulus levels, followed by some additional measures where the level in the right ear was boosted by 8 CUs.

(a) 400 pps, Δr=10%			
Listener CI 1	July 2005, N=80	March 2007, N=80	Combined N=160
Left		73.75	
Right		58.75	
Dichotic	50.25	55	53.75
Diotic	71.25	61.25	66.25
(b) 300 pps Δr=35%			
Listener CI 2	April 2006, N=80	March 2007, N=80	Combined N=160
Left		85	
Right		95	
Dichotic	78	82.5	80.63
Diotic	90	98.75	94.38
(c) 100 pps, Δr=10%			
Listener CI 3	Dec. 2005, N=80	March, 2007 N=40	March 2007 N=80 R ear boost
Left	100 (N=40)	92.5	
Right	40 (N=40)	52.5	60
Dichotic	52.5	45	97.5
Diotic	87.5	72.5	81.25
(d) 200 pps, Δr=10%			
Listener CI 4	April 2006, N=80	March 2007, N=80	Combined N=160
Left		68.75	
Right		75	
Dichotic	67.5	62.5	65.0
Diotic	91.25	70	80.63

mance was better in the left than in the right ear. The fact that the rate in the left ear was fixed across intervals in the dichotic condition may have led to the poor dichotic performance. In contrast, the same cannot be said for listener CI 2 at a rate of 300 pps and Δr=35% (Table IVb). Although performance remained worse in the dichotic than in the diotic condition, the better monotic performance occurred with right-ear stimulation. If, in the dichotic condition, the listener could have selectively processed the input from the right ear alone, he would have obtained a score of 95%. However, the score of 82.5% in the dichotic condition was significantly worse than this (p=0.01).

The results from the remaining two listeners were less straightforward. When we retested listener CI 3 16 months later, using the same stimuli as before, we replicated the finding that at 100 pps and Δr=10%, performance was worse in the dichotic than in the diotic condition (Table IIIc). However, at this point the listener complained that the stimulus in her right ear was softer than that in her left. When we increased that level by 8 "current units" (approximately 1.4 dB), performance in the dichotic condition improved, and became *better* than that in the diotic condition. We attribute this to a change in the listener's hearing over time, rather than to us initially having set the right-ear level too low, for two reasons. First, an incorrect level setting would not explain why, in the original measures, performance in the dichotic condition was *better* than in the diotic condition for Δr=2.5%, but *worse* when Δr=10% (Fig. 2). Second, using the original levels, listener CI 3 was the best of all at discriminating static ITDs of plus and minus 234 μs, and it seems unlikely that this would have been the case if the relative levels at the two ears was such that the percept was dominated by the input from one ear.

When listener CI 4 was retested after a delay of 11 months at a rate of 200 pps and Δr of 10%, performance in the diotic condition had inexplicably dropped, so that it was no better than in the dichotic condition.

In summary, the results of our additional measures indicate that, monaural rate discrimination was sometimes, but not always, worse in the right than in the left ear. In those cases, this difference could possibly account for the occasional cases of worse performance for the dichotic than for the diotic condition. For those subjects, the difference could also possibly counteract a true dichotic advantage in other conditions. However, this difference occurred only for some subjects, and is unlikely to account for other aspects of the results, such as the nonmonotonic psychometric functions sometimes observed in the dichotic condition.

C. Conclusion

The main conclusion to be drawn from experiment 1 is that there is no evidence that the "upper limit" on rate discrimination can be improved, in CI users, by adding a di-

chotic cue. Hence the limitation does not seem to be specific to tasks requiring listeners to compare the rates of two sequentially presented stimuli. This conclusion, if correct, is at odds with Carlyon and Deeks' (2002) finding that adding a dichotic cue *did* improve NH listeners' rate discrimination of a 600-pps pulse train. To determine whether the discrepancy reflects a difference between NH and CI users, or is instead due to differences between the stimuli used in the two studies, we performed a second experiment employing NH listeners. The method, stimuli, and procedure used in experiment 2 were directly analogous to those used in the 300-pps condition of experiment 1.

IV. EXPERIMENT 2: NH LISTENERS

A. Method

1. Listeners

Five normal-hearing listeners, three of whom were female, took part. Their ages ranged from 19 to 39 years. All had pure tone thresholds in quiet of less than 15 dB hearing level at frequencies of 0.5, 1.0, 2.0 and 4.0 kHz in both ears. They all had previous experience of taking part in psychoacoustic experiments, and were paid for their participation.

2. Stimuli

Acoustic pulse trains were generated in the frequency domain by summing a large number of harmonics in sine phase at a sampling rate of 40 kHz. All pulse trains were 800 ms long inclusive of 10-ms raised cosine onset and offset ramps, and had an overall level of 72.5 dB sound pressure level (SPL). The number of harmonics used to generate each pulse train was always sufficient to "fill" the frequency range from 1500 to 7800 Hz. The pulse trains to be presented to each ear were played out using 16 bit digital-to-analog convertor. (CED1401*plus* laboratory interface), passed through a reconstruction filter, and then bandpass filtered between 3900 and 5400 Hz using lowpass and highpass filters in series (Kemo VBF25.03, attenuation=48 dB/octave). They were then attenuated (TDT PA4) and fed to a headphone amplifier where they were mixed with a continuous diotic pink noise. The pink noise was generated using a custom-built noise generator and had a bandwidth of 20 kHz and a spectrum level at 4 kHz of 27.9 dB SPL. Its purpose was to mask auditory distortion products.

3. Procedure

The method of constant stimuli was used. There was a single standard rate of 300 Hz and eight values of Δr, equal to 0.4167, 0.8333, 1.25, 2.5, 5.0, 10.0, 20.0 and 35% of the standard rate. The rates that were used in this experiment are shown in part (b) of Table II. Standard stimuli were always presented diotically. Depending on the condition type, signal stimuli were also played diotically, or were presented to the right ear with a copy of the standard stimulus played simultaneously to the left ear (dichotic conditions). As in experiment 1, a "3I2AFC" procedure was used, with the signal always occurring in either the second or third interval. The inter-stimulus interval was 500 ms and correct-answer feedback was provided after every trial.

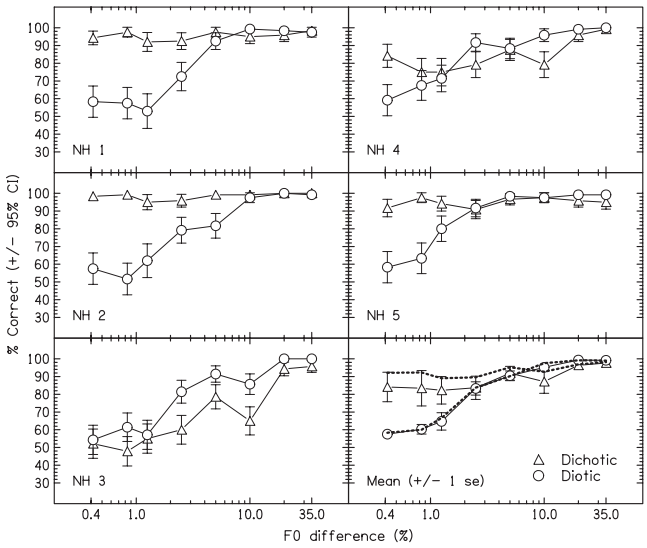

FIG. 3. Psychometric functions describing percent correct as a function of Δr for the five NH listeners who took part in experiment 2. Mean data are shown in the bottom right panel. Performance in the diotic and dichotic conditions is shown by circles and triangles, respectively. Error bars show ± one standard error, which, for the individual listeners' data, were estimated from the normal approximation to the binomial distribution. Dashed lines in bold type show the mean data with listener NH 3 excluded.

In each block of 20 trials the signals had the same value of Δr and the presentation condition (dichotic or diotic) was fixed. Each block was followed by a block with the same Δr but in the other presentation condition. A new value of Δr was then chosen and this procedure was continued until one block had been completed for each Δr and condition. This sequence of blocks was then repeated in reverse order. This whole cycle was continued until between 100 and 140 trials had been completed for every Δr and condition, for each listener. The order in which the different values of Δr were tested was chosen quasi-randomly for each listener.

B. Results

The first five panels of Fig. 3 show psychometric functions for each listener in experiment 2, with the mean data shown in the bottom right-hand panel. Data for the dichotic and diotic conditions are indicated by triangles and circles, respectively. For most listeners there is a clear advantage for the dichotic over the diotic condition, which is greatest at the smaller values of Δr, as revealed by a significant interaction between Δr and condition (two-way repeated-measures analysis of variance, $F(7,28)=10.2$, $p<0.01$, Huynh-Feldt sphericity correction). At larger values of Δr performance in both conditions is close to ceiling.

One listener, NH 3, shows the opposite pattern of results, with slightly superior performance in the diotic than in the dichotic condition. We can think of no reason why NH 3's data differed from that of the others, except to note that listeners do sometimes differ significantly in their ability to use binaural cues (Buss *et al.*, 2007). Further tests, the results

of which are not shown here, failed to show any improvement in the dichotic condition. NH 3 also shows a reversal, reminiscent of that observed occasionally in the CI data, as Δr is increased from 5 to 10% ($p=0.011$). Hints of such reversals, which do not reach statistical significance, are also apparent in two places along NH 4's psychometric function. The mean data with NH 3's results excluded are shown by the dashed lines in the lower-right panel of Fig. 3.

V. DISCUSSION

A. Comparison to previous studies of rate discrimination

The rate discrimination performance reported here for CI users and with diotic presentation is roughly similar to that reported for monotic presentation in a number of studies. Based on a summary of 19 listeners from five studies, Moore and Carlyon (2005) reported average DLs at 100 pps of 7.3%, with a range from 2 to 18% across listeners. The DLs shown in Table III range from 2.9 to 6.3%, and so fall in the better half of the range of scores reported previously. As Moore and Carlyon pointed out, part of the variation in the DLs across studies may have been due to differences in procedure. Our use of an odd-man-out task with feedback would have allowed listeners to use any perceptual difference between the stimuli to perform the task, and this, combined with the absence of a level rove, may have contributed to the generally good performance reported here.

At a rate of 300 pps, Zeng (2002) reported DLs obtained from a three-interval three-alternative forced-choice procedure, with no level rove, that had a mean of 22% and ranged from 12 to 29% across CI listeners. (These DLs were estimated from the functions he fitted to his data.) The DLs for two of our listeners, CI 2 and CI 4, fell below this range, whereas the DL of 21% for CI 1 was close to the mean performance of Zeng's listeners. Performance for CI 3 was below 70.7% correct, even at a Δr of 35%, and so would have been worse than that of any of Zeng's listeners.

The study most similar to that reported here was performed by van Hoesel (2007). Many of the procedural differences, such as the different way of equating stimulus level across conditions, the longer stimulus duration employed here, and our use of a diotic rather than a monotic comparison to the dichotic condition, appear to have made little impact: In both studies the use of a binaural cue helps performance at baseline rates of 100 and 200 pps, but either has no effect or hinders performance at higher rates. One possibly important factor, however, is our decision to constrain the values of Δr such that the asynchrony between pulses in the two ears always rotated through an integer number of cycles (Table II, penultimate column). This had two advantages. First, it discouraged listeners from performing the task based on the last pulse in each ear, and forced them to perform the task based on "ongoing" asynchronies. Second, it meant that the non-monotonic psychometric functions sometimes observed in the dichotic condition could not be caused by an increase in Δr *reducing* the average asynchrony throughout the waveform. It is also worth noting that the functions in the *diotic* condition were always monotonic, which is evidence that the reversals sometimes seen in the dichotic conditions were not simply due to variability in our data.

B. Limitations on performance in rate discrimination and binaural tasks

The experiments reported here studied performance with and without binaural cues, both with electric and with bandpass filtered acoustic pulse trains. Both types of stimulus differ from acoustic pure tones presented to NH listeners in the way that they are represented at the level of the auditory nerve ("AN"). Specifically, neither stimulus produces "place of excitation" cues, neither produces the steep transitions in the phase response of the AN fiber array that have been observed with pure tones (Kim *et al.*, 1979; Kim *et al.*, 1980; van der Heijden and Joris, 2003), and both present low-rate temporal information to AN fibers normally tuned to higher frequencies. In both cases, as the pulse rate increases, performance deteriorates both on monotic rate discrimination tasks and on tasks requiring binaural processing. This subsection briefly reviews the "high rate" deteriorations observed, and considers whether they share a common origin, as has been suggested by a number of authors (van Hoesel and Tyler, 2003; Griffin *et al.*, 2005). It also compares the deterioration observed with NH and CI listeners, and considers the extent to which the latter group suffers from additional limitations on performance.

1. Rate discrimination without temporal cues

One finding already alluded to is that pulse-rate discrimination thresholds increase with increasing pulse rate (Shannon, 1983; Tong and Clark, 1985; Townshend *et al.*, 1987; McKay *et al.*, 2000; Carlyon and Deeks, 2002). A pertinent finding is that the rate above which performance deteriorates markedly is greater (600 pps) for NH listeners than the 300-pps limit normally observed with CI users (Carlyon and Deeks, 2002). It is, however, worth noting that there are some exceptions, consisting of "star" listeners who can perform rate discrimination at higher rates (Townshend *et al.*, 1987; Wilson *et al.*, 1997). Work currently ongoing in our laboratory is investigating such instances of exceptional performance with the aim of controlling for potential confounding cues such as level differences and idiosyncratic changes in place of excitation with increasing rate. To the extent that such factors can be ruled out, the existence of listeners who can perform rate discrimination up to at least 600 pps indicates that although *most* CI users may suffer rate-discrimination limitations over and above that obtained with their NH counterparts, this limitation may not be a necessary feature of electrical stimulation.

2. ITD discrimination

The discrimination of "static" ITDs also deteriorates with increasing pulse rate, in a way that is not observed when the frequency of a pure tone is increased over a similar range. For CI listeners, van Hoesel and Tyler (2003) reported ITD thresholds that ranged between 90 and 250 μs across listeners for a 50-pps pulse train, but which increased markedly as pulse rate was raised to 200 pps. At the next-highest

rate tested, which was 800 pps, no listener could perform the task. More recently, van Hoesel (2007) reported ITD thresholds of between 55 and 220 μs for 100-pps trains, that increased to about 300 μs at 300 pps; at the highest rate tested of 600 pps, two listeners had thresholds of about 400 μs and one could not perform the task. Majdak *et al.* (2006) asked listeners to perform lateralization judgments on pulse trains that were amplitude modulated by a common trapezoidal envelope in the two ears, and measured the effects of ITDs between the pulses in the two ears. Sensitivity to these "fine structure" ITDs differed markedly across CI listeners, but two of them showed some sensitivity at pulse rates as high as 800 pps. This was *higher* than the 600-pps "upper limit" observed when acoustic pulse trains, filtered in a way similar to those used here, were presented to NH listeners. However, it should be borne in mind that, at and above 600 pps, the frequency components of the acoustic pulse train would have been resolved by the peripheral auditory system. As Majdak *et al.* pointed out, this would have reduced the modulation depth of the 600 pps acoustic stimuli at the output of the peripheral auditory filters, possibly limiting performance in the NH group. It is therefore not clear whether the high-rate deterioration observed with CI listeners would be more or less serious than that observed with NH listeners if the effects of peripheral auditory filtering could be ruled out.

3. Interaural decorrelation

The binaural cue introduced by the dichotic conditions used here at high pulse rates can probably best be described as interaural decorrelation; none of our NH listeners reported hearing binaural beats at 300 pps, and instead described the signal interval as differing in the width or diffuseness of the binaural image. Some of our CI listeners did report hearing some movement in the signal interval for low baseline rate (e.g., 100 pps), but, as noted already, performance on this task deteriorated as baseline rate increased from 100 to 300 pps. This deterioration is reminiscent of that observed for ITDs between equal-rate pulse trains (van Hoesel, 2007). One possible reason for both findings is suggested by Hafter *et al.*'s (1983) observation that the improvement in ITD discrimination with increasing duration is smaller at high than at low (acoustic) pulse rates in NH listeners, consistent with ITD judgments being dominated by the first pulse under such conditions (Saberi, 1996; Freyman *et al.*, 1997). Indeed, recent physiological measurements suggest that the sensitivity of cells in the inferior colliculus to ITD differences between electric pulse trains may be dominated by the first pulse in each at high, but not at low, rates (Smith and Delgutte, 2007). Hence it is possible that, for ITD discrimination, performance is poor at high rates because listeners cannot effectively combine information across pulse pairs. For our task, dependence on the first pulse pair would have had an even graver consequence, as this pair was always simultaneous in the two ears. However, an additional possible reason for this finding is that the average asynchrony between the pulses in the two ears decreased from 2.5 ms for a 100 pps train to 0.83 ms at 300 pps (Table II, penultimate column).

Some evidence that the limitations on interaural decorrelation detection at high pulse rates differ from that observed for rate discrimination comes from the study by Carlyon and Deeks (2002). They found, in NH listeners, that the effect of frequency region on performance in rate-discrimination tasks with monotic presentation is different from that observed when binaural cues are available. The highest baseline rate at which listeners could perform a monotic rate discrimination task was greater for pulse trains filtered into a "very high (VHIGH)" frequency band (7800–10 800 Hz) than into a "HIGH" band (3900–5400 Hz). Conversely, when a contralateral standard was added, performance was better in HIGH than in the VHIGH band. This might indicate that the origin of the high-rate limitation is different in the two tasks, but could also be due to generally poorer overall sensitivity of the binaural system for stimuli presented in very high frequency regions (Bernstein and Trahiotis, 1994), which might occur independently of overall rate.

Further evidence on the detection of interaural decorrelation in high frequency stimuli comes from the fact that one can measure a binaural masking level difference (BMLD) using transposed narrowband noises as the masker, to which (prior to transposition) in- or out-of-phase low frequency sinusoids are added (van de Par and Kohlrausch, 1997). We have recently replicated this finding and shown that approximately half of the BMLD disappears when, in the NoSπ condition, the stimuli are processed so that envelope modulations slower than 50 Hz are identical in the two ears (Long *et al.*, 2006a). Hence the BMLD for transposed stimuli appears to be strongly dependent on slow ($<$50 Hz) interaural fluctuations. More striking evidence came from an experiment that used an electrical analog of this technique, in which the low frequency stimuli modulated 1000 pps pulse trains: CI users exhibited a BMLD whose size was similar to that seen for NH listeners using transposed stimuli, but which disappeared *entirely* when the interaural fluctuations slower than 50 Hz were equated between the two ears (Long *et al.*, 2006b). This finding suggests that the reliance of the BMLD on slow interaural fluctuations is even greater for CI listeners than for NH listeners presented with transposed stimuli. It is also consistent with our suggestion that the decreases in performance occasionally observed with increasing Δr in the dichotic condition of experiment 1 may have been due to the increased rate at which interaural differences changed over time.

4. Conclusions

Overall, our results, combined with those of others, are consistent with the following scenario. In NH listeners, as pulse rate increases, there is a drop in sensitivity to rate differences using either binaural or purely monotic cues. There is *some* evidence that this "upper limitation" has a different origin for binaural processing than for monotic rate discrimination; performance at high rates is better in the VHIGH than HIGH region for the monotic task, but the opposite is true when a binaural cue is available (Carlyon and Deeks, 2002). In addition, at high rates, sensitivity can be improved by the addition of a binaural cue. However, for most CI listeners, there is an additional source of limitation. This is reflected in the fact that performance in monotic rate

discrimination tasks usually breaks down above about 300 pps, compared to around 600 pps in NH listeners. This additional factor also appears to limit performance in binaural tasks. The source of the additional limitation is unclear, but could arise at the level of the auditory nerve, where deficits such as cell loss and absence of spontaneous firing rates are known to occur. Another possible explanation is that AN firing to acoustic pulse trains may have been more stochastic than that to electrical stimuli, a factor which could have been enhanced by the addition of background noise in the NH experiments.

It is interesting to note that the above conclusion differs at least slightly from the one reached by van Hoesel (2007). His conclusion that "monotic rate discrimination may be subject to additional limitations that do not affect ITD perception" was based on a comparison between data obtained in a monotic rate discrimination task with those on the detection of "static" ITDs as a function of pulse rate. He converted the latter data into a format that could be compared to the former by subtracting the threshold ITD at each rate from the interpulse interval at that rate, and expressing this value as a percentage of the interpulse interval. When he did so, the slope relating threshold to rate was shallower than in the monotic rate discrimination task. However, it is not clear that this conversion corresponds in any way to a calculation that the auditory system would perform during the task. In addition, he noted that, although performance in the static ITD task may have been helped by subjects attending to the first pulse in each ear—a strategy not possible with rate discrimination—this cannot have accounted entirely for performance at high rates because some subjects' ITD thresholds dropped with increasing duration. It remains possible, though, that if subjects had been prevented from detecting ITD on the first pulse—for example by making the first pulse in each ear simultaneous (e.g., Laback *et al.*, 2007)—ITD thresholds would have grown more steeply with increasing rate (and perhaps as much as did the monotic rate discrimination thresholds). Evidence for this possibility comes from the fact that the improvement with increasing duration was smallest at high pulse rates, suggesting an increased dependence on the first pulse as rate increased.

C. Summary and overall conclusions

(i) Four bilaterally implanted users performed rate discrimination with diotic and dichotic stimulation.

(ii) In the diotic condition, sensitivity deteriorated as the standard rate increased from 100 to 300 pps, consistent with the results of previous studies employing monotic stimulation.

(iii) At a standard rate of 100 pps, performance for two CI listeners was greatly superior in the dichotic than in the diotic condition, due to the presence of a binaural cue in the former case. The remaining two listeners also showed a dichotic advantage, but only for small rate differences.

(iv) As the standard pulse rate increased to 300 pps, performance was never better, and sometimes worse, with dichotic than with diotic stimulation. This is consistent with findings recently obtained in three listeners by van Hoesel (2007), who used slightly different stimuli and methods, and extends that finding to a further four listeners. We conclude that that the deterioration in rate discrimination at high rates, commonly observed for CI users, is not specific to tasks that require sequential rate discrimination.

(v) An acoustic analog of this experiment was performed by presenting filtered acoustic pulse trains to NH listeners, with a standard rate of 300 pps. Unlike the case with CI users, performance was significantly better with dichotic than with diotic stimulation. This suggests that NH listeners are able to take advantage of binaural cues using stimuli that are analogous to the electrical stimuli for which this dichotic advantage breaks down.

[1]Preliminary data from experiment 1 and from the study by van Hoesel (2007) were also presented at the 2003 Conference on Implantable Auditory Prostheses, held at Asilomar, Pacific Grove, California.

[2]Although the levels used in the two ears sometimes differed from each other, we use the term "diotic" to describe this condition. Similar terminology was used by van Hoesel and Clark (1997).

[3]The test is based on estimates of the standard error of the difference between two proportions, which is equal to $\sqrt{(pq[(1/N1)+(1/N2)])}$, where N1 and N2 are the number of trials on which the two proportions are based, and where p is equal to the proportion correct across all trials making up the two proportions, and $q=1-p$. The normal variate z is then given by the difference between the two proportions divided by the standard error (Ferguson, 1989, pp. 173-175). It is used here, without Bonferoni correction, for all comparisons between pairs of scores obtained for a single subject.

Baumann, U., and Nobbe, A. (**2004**). "Pitch ranking with deeply inserted electrode arrays," Ear Hear. **25**, 275–283.

Bernstein, L. R., and Trahiotis, C. (**1994**). "Detection of interaural delay in high-frequency sinusoidally amplitude-modulated tones, two-tone complexes, and bands of noise," J. Acoust. Soc. Am. **95**, 3561–3567.

Buss, E., Hall, J. W., and Grose, J. H. (**2007**). "Individual differences in the masking level difference with a narrowband masker at 500 or 2000 Hz," J. Acoust. Soc. Am. **121**, 411–419.

Carlyon, R. P., and Deeks, J. M. (**2002**). "Limitations on rate discrimination," J. Acoust. Soc. Am. **112**, 1009–1025.

Carlyon, R. P., Mahendran, S., Deeks, J. M., Bleeck, S., Winter, I. M., Axon, P., and Baguley, D. (**2007**). "Behavioral and physiological correlates of temporal pitch perception in electric and acoustic hearing," *Association for Research in Otolaryngology, 30th Annual Midwinter Research Meeting*, Denver, Colorado.

Carlyon, R. P., van Wieringen, A., Long, C. J., Deeks, J. M., and Wouters, J. (**2002**). "Temporal pitch mechanisms in acoustic and electric hearing," J. Acoust. Soc. Am. **112**, 621–633.

Ferguson, G. A. (**1989**). *Statistical Analysis in Psychology and Education*, McGraw–Hill, New York.

Freyman, R. L., Zurek, P. M., Balakrishnan, U., and Chiang, Y.-C. (**1997**). "Onset dominance in lateralization," J. Acoust. Soc. Am. **101**, 1649–1659.

Grantham, D. W., and Wightman, F. L. (**1978**). "Detectability of varying interaural temporal differences," J. Acoust. Soc. Am. **63**, 511–523.

Griffin, S. J., Bernstein, L. R., Ingham, N. J., and McAlpine, D. (**2005**). "Neural sensitivity to interaural envelope delays in the inferior colliculus of the guinea pig," J. Neurophysiol. **93**, 3463–3478.

Hafter, E. F., and Dye, R. H. (**1983**). "Detection of interaural differences of time in trains of high-frequency clicks as a function of interclick interval and number," J. Acoust. Soc. Am. **73**, 644–651.

Kim, D. O., Molnar, C. E., and Matthews, J. W. (**1980**). "Cochlear mechanics: Nonlinear behavior in two-tone responses as reflected in cochlear-nerve-fiber responses and in ear-canal sound pressure," J. Acoust. Soc. Am. **67**, 1704–1721.

Kim, D. O., Siegel, J. H., and Molnar, C. E. (**1979**). "Cochlear nonlinear phenomena in two-tone responses," Scand. Audiol. Suppl. **9**, 63–81.

Laback, B., Majdak, P., and Baumgartner, W.-D. (**2007**). "Lateralization discrimination of interaural time delays in four-pulse sequences in electric and acoustic hearing," J. Acoust. Soc. Am. **121**, 2182–2191.

Levitt, H. (**1971**). "Transformed up-down methods in psychophysics," J.

Acoust. Soc. Am. **49**, 467–477.
Long, C. J., Carlyon, R. P., Litovsky, R., Cooper, H., Rasumov, N., and Downs, D. (**2006a**). "Binaural unmasking by bilateral cochlear implant users," *International Hearing-Aid Conference (IHCON)*, Lake Tahoe, California.
Long, C. J., Carlyon, R. P., Litovsky, R., and Downs, D. (**2006b**). "Binaural unmasking with cochlear implants," J. Assoc. Res. Otolaryngol. **7**, 352–360.
Majdak, P., Laback, B., and Baumgartner, W.-D. (**2006**). "Effects of interaural time differences in fine structure and envelope on lateral discrimination in electric hearing," J. Acoust. Soc. Am. **120**, 2190–2201.
McDermott, H. J., and McKay, C. M. (**1997**). "Musical pitch perception with electrical stimulation of the cochlea," J. Acoust. Soc. Am. **101**, 1622–1631.
McKay, C. M., and Carlyon, R. P. (**1999**). "Dual temporal pitch percepts from acoustic and electric amplitude-modulated pulse trains," J. Acoust. Soc. Am. **105**, 347–357.
McKay, C. M., and McDermott, H. J. (**1998**). "Loudness perception with pulsatile electrical stimulation: The effect of interpulse intervals," J. Acoust. Soc. Am. **104**, 1061–1074.
McKay, C. M., McDermott, H. J., and Carlyon, R. P. (**2000**). "Place and temporal cues in pitch perception: Are they truly independent?," Acoustic Research Letters **1**, 25–30, Online (http://scitation.aip.org/arlo/). Last viewed December 2006.
Melara, R. D., and Marks, L. E. (**1990**). "Interaction among auditory dimensions—Timbre, pitch, and loudness," Percept. Psychophys. **48**, 169–178.
Moore, B. C. J., and Carlyon, R. P. (**2005**). "Perception of pitch by people with cochlear hearing loss and by cochlear implant users," in *Springer Handbook of Auditory Research: Pitch Perception*, edited by C. J. Plack and A. J. Oxenham (Springer-Verlag, Berlin), pp. 234–277.
Nie, K. B., Stickney, G., and Zeng, F. G. (**2005**). "Encoding frequency modulation to improve cochlear implant performance in noise," IEEE Trans. Biomed. Eng. **52**, 64–73.
Pijl, S., and Schwarz, D. W. F. (**1995**). "Melody recognition and musical interval perception by deaf subjects stimulated with electrical pulse trains through single cochlear implant electrodes," J. Acoust. Soc. Am. **98**, 886–895.
Saberi, K. (**1996**). "Observer weighting of interaural delay in filtered impulses," Percept. Psychophys. **58**, 1037–1046.
Shannon, R. V. (**1983**). "Multichannel electrical stimulation of the auditory nerve in man. I. Basic psychophysics," Hear. Res. **11**, 157–189.
Smith, Z. M., and Delgutte, B. (**2007**). "Sensitivity to interaural time differences in the inferior colliculus with bilateral cochlear implants," J. Neurosci. **27**, 6740–6750.
Stickney, G., Nopp, P., Nobbe, A., Schleich, P., and Zierhofer, C. (**2007**). "Improving frequency discrimination in cochlear implant users," *Association for Research in Otolaryngology, 30th Annual Midwinter Research Meeting*, Denver, Colorado.
Stickney, G. S., Nie, K. B., and Zeng, F. G. (**2005**). "Contribution of frequency modulation to speech recognition in noise," J. Acoust. Soc. Am. **118**, 2412–2420.
Tong, Y. C., and Clark, G. M. (**1985**). "Absolute identification of electric pulse rates and electrode positions by cochlear implant listeners," J. Acoust. Soc. Am. **74**, 73–80.
Townshend, B., Cotter, N., Compernolle, D. v., and White, R. L. (**1987**). "Pitch perception by cochlear implant subjects," J. Acoust. Soc. Am. **82**, 106–115.
van de Par, S., and Kohlrausch, A. (**1997**). "A new approach to comparing binaural masking level differences at low and high frequencies," J. Acoust. Soc. Am. **101**, 1671–1680.
van der Heijden, M., and Joris, P. X. (**2003**). "Cochlear phase and amplitude retrieved from the auditory nerve at arbitrary frequencies," J. Neurosci. **23**, 9194–9198.
van Hoesel, R. J. M. (**2007**). "Sensitivity to timing in bilateral cochlear implant users," J. Acoust. Soc. Am. **121**, 2192–2206.
van Hoesel, R. J. M., and Clark, G. M. (**1997**). "Psychophysical studies with two binaural cochlear implant subjects," J. Acoust. Soc. Am. **102**, 495–507.
van Hoesel, R. J. M., and Tyler, R. S., (**2003**). "Speech perception, localization, and lateralization with bilateral cochlear implants," J. Acoust. Soc. Am. **113**, 1617–1630.
van Wieringen, A., Carlyon, R. P., Long, C. J., and Wouters, J. (**2003**). "Pitch of amplitude-modulated irregular-rate stimuli in electric and acoustic hearing," J. Acoust. Soc. Am. **114**, 1516–1528.
Wilson, B., Zerbi, M., Finley, C., Lawson, D., and Honert, C. v. d. (**1997**). "Speech processors for auditory prostheses (Eighth Quarterly Progress Report)." NIH, Project No. N01-DC-5-2103.
Zeng, F.-G. (**2002**). "Temporal pitch in electric hearing," Hear. Res. **174**, 101–106.

A glimpsing account for the benefit of simulated combined acoustic and electric hearing

Ning Li and Philipos C. Loizou[a)]
Department of Electrical Engineering, University of Texas at Dallas, Richardson, Texas 75083-0688

(Received 27 July 2007; revised 29 November 2007; accepted 8 January 2008)

The benefits of combined electric and acoustic stimulation (EAS) in terms of speech recognition in noise are well established; however the underlying factors responsible for this benefit are not clear. The present study tests the hypothesis that having access to acoustic information in the low frequencies makes it easier for listeners to glimpse the target. Normal-hearing listeners were presented with vocoded speech alone (V), low-pass (LP) filtered speech alone, combined vocoded and LP speech (LP+V) and with vocoded stimuli constructed so that the low-frequency envelopes were easier to glimpse. Target speech was mixed with two types of maskers (steady-state noise and competing talker) at −5 to 5 dB signal-to-noise ratios. Results indicated no advantage of LP+V in steady noise, but a significant advantage over V in the competing talker background, an outcome consistent with the notion that it is easier for listeners to glimpse the target in fluctuating maskers. A significant improvement in performance was noted with the modified glimpsed stimuli over the original vocoded stimuli. These findings taken together suggest that a significant factor contributing to the EAS advantage is the enhanced ability to glimpse the target.
© *2008 Acoustical Society of America.* [DOI: 10.1121/1.2839013]

PACS number(s): 43.66.Ts, 43.71.Ky [RYL] Pages: 2287–2294

I. INTRODUCTION

A recent development in cochlear implants is to implant an electrode array only partially into the cochlea so as to preserve the residual acoustic hearing (20–60 dB HL up to 750 Hz and severe to profound hearing loss at 1000 Hz and above) that many patients still have at the low frequencies (von Ilberg *et al.*, 1999; Kiefer *et al.*, 2005; Gantz and Turner, 2003; Gantz *et al.*, 2006). Low frequency information is provided to these patients via a hearing aid and high-frequency (>1000 Hz) speech information is provided via a cochlear implant. Thus, these patients perceive speech via a combined electric and acoustic stimulation (EAS) mode.

The benefit of EAS in terms of better speech recognition in noise has been well documented in the literature and demonstrated by studies involving EAS patients (Kiefer *et al.*, 2005; Gantz and Turner, 2003; Turner *et al.*, 2004; Kong *et al.*, 2005; Gantz *et al.*, 2006) as well as studies involving normal-hearing listeners listening to vocoded speech (Qin and Oxenham, 2006; Dorman *et al.*, 2005; Chang *et al.*, 2006; Kong and Carlyon, 2007). EAS patients fitted with a short-electrode array were shown by Turner *et al.* (2004) to receive a 9 dB advantage in multitalker background when compared to a group of traditional patients who were matched to speech scores in quiet. Kong *et al.* (2005) demonstrated significant improvements (by an average of 8–20 percentage points) on both speech recognition (in competing talker background) and melody recognition tasks for patients with low-frequency (<1000 Hz) residual hearing in the ear contralateral to the cochlear implant. These patients were wearing a hearing aid in one ear and a cochlear implant (CI) in the other. Several studies based on acoustics simulations of cochlear implants were conducted to probe the mechanisms and benefits obtained with simulated EAS conditions (Qin and Oxenham, 2006; Dorman *et al.*, 2005; Kong and Carlyon, 2007; Chang *et al.*, 2006). All studies reported large improvements on speech recognition, particularly in noise. Qin and Oxenham (2006) showed that including acoustic information below 600 Hz improved the speech reception threshold (SRT) by 6 dB in the presence of a competing talker and by 4 dB in the presence of speech-shaped noise compared to the vocoded-only condition. The results from both vocoder simulations and real EAS patients (Kiefer *et al.*, 2005; Kong *et al.*, 2005; Kong and Carlyon, 2007) confirmed a "superadditive" effect with combined acoustic and electric stimulation. That is, performance obtained in the EAS condition exceeded the performance obtained with either the acoustic information alone, electric information alone, or the sum of the two.

While the benefits of EAS are indisputable, the reasons for the large contribution of low-frequency acoustic information to speech intelligibility in noise are less clear. It is worth noting that only F0 and F1 information is present in the low-frequency range (<500 Hz), but the presence of F1 information alone cannot support high levels of speech recognition (Kiefer *et al.*, 2005; Kong *et al.*, 2005), at least in noise. This raises the important question: What is so special about the information in the low frequencies that enables EAS patients to better communicate in noisy environments? Some speculated (Qin and Oxenham, 2006; Turner *et al.*, 2004) that it is the improved access to F0 information that is readily available to the listeners. Voice pitch (F0) has long been thought to be a critical cue in the perceptual segregation of speech in competing-talker listening environments (e.g., Brokx and Nooteboom, 1982). The pitch perception abilities

a)Author to whom correspondence should be addressed. Electronic mail: loizou@utdallas.edu

of cochlear implant listeners are generally poor as evidenced by the poor (chance level) performance of CI users on melody recognition tasks (e.g., Gfeller *et al.*, 2002). Hence, as suggested by Kong *et al.* (2005) it is possible that EAS patients are able to somehow combine (perhaps more effectively) the salient pitch information available in the low-frequencies via acoustic stimulation with the relevantly weak pitch available in the envelope modulations via electric stimulation to enhance speech segregation between the target and the masker.

While the above-noted F0-centric hypotheses are highly plausible and reasonable, the evidence is not overly convincing. Qin and Oxenham (2005) demonstrated that normal-hearing listeners are unable to benefit from F0 differences between competing vowels in a concurrent-vowel paradigm despite the good F0 difference limens (<1 semitone) obtained with 8- and 24-channel vocoder processing. A similar outcome was noted by Stickney *et al.* (2007) with cochlear implant users listening to target and competing sentences with an F0 separation ranging from 0 to 15 semitones. Small improvements were obtained in a subsequent study by Qin and Oxenham (2006) when a five-channel vocoder was supplemented with low-frequency (<600 Hz) information which also included F1 information. It was unclear from that study however, as to whether it was access to improved F0 representation, Fl information, or access to both that contributed to the small improvement in performance with EAS. The improvement was noted primarily over the range of 0–2 semitones, where beating occurs between adjacent harmonics of the two vowels allowing listeners to use spectral cues other than F0 to identify the vowels (Culling and Darwin, 1994). In brief, the evidence from the vocoder simulation studies by Qin and Oxenham (2003, 2005) in support of improved F0 representation as the factor contributing to the EAS advantage was not strong. A recent study by Kong and Carlyon (2007) showed that the F0 information present in the low-frequency acoustic range is neither necessary nor sufficient to obtain an advantage with EAS. Their study showed that the EAS advantage persisted at low signal-to-noise ratio (SNR) levels (5 dB) even when the F0 cues were removed from the low-passed stimulus.[1] Furthermore, the combined EAS advantage disappeared at high SNR levels when F0 cues were preserved but low-frequency phonetic cues were eliminated. This outcome indicated that the low-passed acoustic stimulus contained information other than F0 that is integrated with information in the electrical stimulation to enhance speech recognition in noise. Kong and Carlyon concluded that those cues may include voicing and/or glimpsing information that EAS patients use to segregate the target. No evidence, however, was provided in that study in support of the glimpsing or voicing hypothesis.

The present study examines the hypothesis that a glimpsing mechanism is responsible for the benefit seen with EAS. More specifically, the present study considers and tests the hypothesis that having access to acoustic information in the low frequencies makes it easier for listeners to glimpse the target. We therefore expect that the EAS advantage will be diminished (or eliminated) if the masker signal is steady-state noise, since this masker lacks the waveform dips typically present in competing talker or modulated noise backgrounds. It is well established (e.g., Festen and Plomp, 1990) that listeners are able to exploit the waveform "dips" in fluctuating maskers to glimpse the target, since the SNR is more favorable during those periods. Only a few studies (e.g., Turner *et al.*, 2004) tested EAS subjects with steady-state noise, and those studies reported speech recognition performance in terms of SRT. We cannot infer, however, from a single SRT value how subjects perform as a function of SNR, since the SRT value represents a single point on the psychometric function. To further test the above-mentioned hypothesis, we modified the electric-only stimuli to allow for better glimpsing. This was accomplished using a signal-processing technique (Li and Loizou, 2007) that ensures that the target envelope amplitudes are larger than the masker envelopes in the low-frequency region, thereby rendering this region easier to glimpse. Note that we no longer restrict the definition of glimpsing to the temporal (time) domain wherein "dips" are present in the waveform but rather extend it more generally to time-frequency regions where the local SNR is favorable, i.e., the target is stronger than the masker (Cooke, 2006; Li and Loizou, 2007). If the listeners are able to glimpse the low-frequency envelope information in the modified electric-only stimuli, then we would expect to see an improvement in performance comparable to that attained with the simulated EAS stimuli.

II. EXPERIMENT: EFFECT OF LOW-FREQUENCY GLIMPSING

A. Methods

1. Subjects

Seven normal-hearing listeners participated in this experiment. All subjects were native speakers of American English, and were paid for their participation. Subject's age ranged from 18 to 40 years, with the majority being graduate students at the University of Texas at Dallas.

2. Stimuli

The speech material consisted of sentences taken from the IEEE database (IEEE, 1969). All sentences were produced by a male speaker. The sentences were recorded in a sound-proof booth (Acoustic Systems) in our lab at a 25 kHz sampling rate. Details about the recording setup and copies of the recordings are available in Loizou (2007). Two types of masker were used. The first was continuous (steady-state) noise, which had the same long-term spectrum as the test sentences in the IEEE corpus. The second masker was a competing-talker (female) recorded in our lab. The female talker produced a long sentence taken from the IEEE database. This was done to ensure that the target signal was always shorter (in duration) than the masker.

3. Signal processing

The stimuli were presented in four different processing conditions. The first processing condition was designed to simulate the effects of eight-channel electrical stimulation, and used an eight-channel sinewave-excited vocoder (Loizou *et al.*, 1999). Signals were first processed through a pre-

TABLE I. Filter cutoff (−3 dB) frequencies for the V and LP+V vocoder simulations.

	V		LP+V	
Channel	Low (kHz)	High (kHz)	Low (kHz)	High (kHz)
1	0.080	0.221	Unprocessed (0.080–0.600)	
2	0.221	0.426		
3	0.426	0.724		
4	0.724	1.158	0.724	1.158
5	1.158	1.790	1.158	1.790
6	1.790	2.710	1.790	2.710
7	2.710	4.050	2.710	4.050
8	4.050	6.000	4.050	6.000

emphasis filter (2000 Hz cutoff), with a 3 dB/octave rolloff, and then bandpassed into eight frequency bands between 80 and 6000 Hz using sixth-order Butterworth filters. The Cambridge filter spacing (Glasberg and Moore, 1990) was used to allocate the eight channels in the specified bandwidth. This filter spacing was identical to that used by Qin and Oxenham (2006) and is shown in Table I. The envelope of the signal was extracted by full-wave rectification and low-pass filtering (second-order Butterworth) with a 400 Hz cutoff frequency. Sinusoids were generated with amplitudes equal to the rms energy of the envelopes (computed every 4 ms) and frequencies equal to the center frequencies of the bandpass filters. The sinusoids of each band were finally summed and the level of the synthesized speech segment was adjusted to have the same rms value as the original speech segment.

The second processing condition was designed to simulate the acoustic stimulation alone. Signal was low-pass (LP) filtered to 600 Hz using a sixth-order Butterworth filter. The 600 Hz cutoff was chosen as it closely reflects the situation with EAS patients who have residual hearing up to approximately 500–750 Hz and precipitous hearing loss thereafter (Turner *et al.*, 2004; Kiefer *et al.*, 2005; von Ilberg *et al.*, 1999; Gantz *et al.*, 2006). The third processing condition was designed to simulate combined electric and acoustic stimulation. To simulate the effects of EAS with residual hearing below 600 Hz, we combined the LP stimulus with the upper five channels of the eight-channel vocoder [note that the low-pass cutoff frequency may vary in true EAS patients depending on the electrode array used and the extent (in frequency) of residual hearing in individual users].

The fourth processing condition was designed to assess the effect of low-frequency glimpsing for the electric-only stimuli. The technique is similar to that used in Li and Loizou (2007), although adapted in the present study to operate in the filter-bank (eight channels) domain rather than the Fourier transform domain. As mentioned in Sec. I, the definition of "glimpse" adopted here is similar to that used by Cooke (2006): a time–frequency (T–F) region wherein the speech power is greater than the noise power by a specific threshold value. In our study, we used a threshold of 0 dB, which is the threshold typically used for constructing ideal binary masks (Wang, 2005). The masker signal is first scaled (based on the rms energy of the target) to obtain the desired SNR level. The target and masker signals are independently bandpass filtered as before into eight channels (same frequency spacing), and envelopes are extracted by low-pass filtering (400 Hz cutoff) the rectified waveforms. The masker envelopes in the first three channels (<600 Hz) are appropriately scaled[2] to ensure that the target envelopes are greater or equal (since the SNR threshold is 0 dB) than the masker envelopes. No scaling is done to the masker envelopes if the target envelopes happen to be larger in magnitude than the masker envelopes. Following the scaling of the masker envelopes, the masker envelopes are added to the target envelopes to obtain the modified mixture envelopes of channels 1–3. The mixture envelopes of the five higher frequency channels are obtained by vocoder processing the original mixture signals. Following the scaling of the low-frequency envelopes, the signal is synthesized as before as a sum of eight sine waves with amplitudes set to the envelopes and frequencies set to the center frequencies of the bandpass filters. The scaling done to the masker envelopes of channels 1–3 ensures that the low-frequency envelopes (<600 Hz) are easier to glimpse than the high-frequency envelopes. Note that the modified stimuli do not contain the original target (clean) low-frequency envelopes, but rather the envelopes which are constructed to have positive SNR (i.e., so that the target envelopes are stronger than the masker envelopes). The assumption is that listeners will be able to better glimpse low-frequency envelopes that have positive SNR.

We will be referring to the above-mentioned processing conditions as: vocoded (V), low-passed (LP), combined vocoded and low-passed acoustic (LP+V), and vocoded with low-frequency glimpsing (V+G).

4. Procedure

The experiments were performed in a sound-proof room (Acoustic Systems, Inc.) using a PC connected to a Tucker-Davis system 3. Stimuli were played to the listeners monaurally through Sennheiser HD 250 Linear II circumaural headphones at a comfortable listening level. Prior to the test, each subject listened to vocoded (eight channels) speech to become familiar with the stimuli. The training session lasted for about 15–20 min. During the test, the subjects were asked to write down the words they heard. Subjects participated in a total of 24 conditions (=3 SNR levels ×4 algorithms ×2 maskers). Two lists of sentences (i.e., 20 sentences) were used per condition, and none of the lists were repeated across conditions. Sentences were presented to the listeners in blocks, with 20 sentences/block in each condition. The different conditions were run in random order for each listener.

B. Results

The mean scores for all conditions are shown in Fig. 1. Performance was measured in terms of percent of words identified correctly (all words were scored). The corresponding SRT values (SNR level corresponding to 50% correct), computed by interpolating the scores in Fig. 1, were 2.2, 0.5, and 1.5 dB for the V, V+G, and LP+V stimuli, respectively, in steady-state noise. The computed SRT values in the

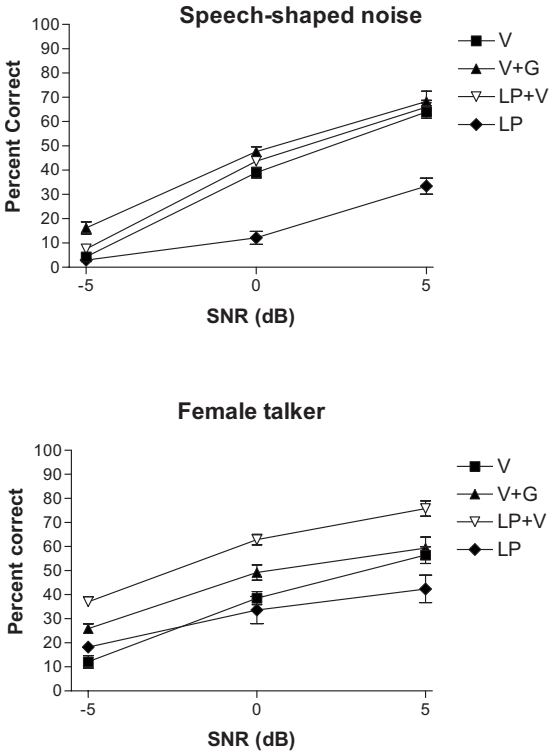

FIG. 1. Mean speech recognition scores as a function of SNR level for two types of background interference. The error bars denote ±1 standard errors of the mean.

female-talker background were 3, 0, and −2.5 dB for the V, V+G, and LP+V stimuli, respectively. The SRT values for the V and LP+V stimuli are similar to those obtained by Qin and Oxenham (2006) with eight channels of stimulation and a low-pass filter of 600 Hz. The SRT values for the V stimuli, for instance, were approximately 3.5 dB for the competing-talker background and 2 dB for steady-state noise (Qin and Oxenham, 2006).

For the conditions in the steady-state noise background, two-way analysis of variance (ANOVA) (with repeated measures) indicated significant effect of SNR ($F[2,12]=426.4$, $p<0.0005$), significant effect of processing condition ($F[3,18]=72.3$, $p<0.0005$), and significant interaction ($F[6,36]=20.4$, $p<0.0005$). Similarly, for the female-talker conditions, two-way ANOVA (with repeated measures) indicated significant effect of SNR ($F[2,12]=205.6$, $p<0.0005$), significant effect of processing condition ($F[3,18]=22.8$, $p<0.0005$), and significant interaction ($F[6,36]=5.4$, $p<0.0005$).

Multiple paired-comparisons (with Bonferroni correction) were run between the scores obtained with LP+V and V stimuli in steady-state noise at the various SNR levels. The comparisons indicated no statistically significant (Bonferroni corrected $p>0.016$, $\alpha=0.05$) differences between the LP+V and V scores at any of the three SNR levels, suggesting no advantage of LP+V in steady-state noise. The scores obtained with the V+G stimuli at −5 dB SNR were significantly higher ($t(6)=3.65, p=0.011$) than those obtained with the LP+V stimuli but did not differ at higher SNR levels.

The pattern in performance differed in the female-talker background. Performance with the LP+V stimuli was significantly higher ($p<0.005$) than performance with the V stimuli at all SNR levels. This outcome is consistent with prior studies (Turner *et al.*, 2004; Kong *et al.*, 2005; Kong and Carlyon, 2007; Qin and Oxenham, 2006). The performance of the V+G stimuli was significantly higher ($p<0.016$) than the performance of the V stimuli at −5 and 0 dB SNR, but not at 5 dB SNR. The performance of the LP+V stimuli was significantly higher ($p<0.016$) than the performance of the V+G stimuli at −5 and 0 dB SNR, and was marginally ($p=0.016$) higher at 5 dB SNR.

The difference in performance between the V and V+G stimuli indicate that listeners are able to receive significant benefit from the glimpsed envelopes in the low frequencies. This suggests that the EAS advantage is partly due to the enhanced ability of listeners to glimpse the target. This ability is diminished when the low-frequency envelope information is provided by the vocoded stimuli (V), but can be enhanced by manipulating the low-frequency envelopes to provide better glimpsing, as done with V+G processing.

III. DISCUSSION AND CONCLUSIONS

The results of the experiments described here indicate that the LP+V stimuli did not provide significant intelligibility advantages over the V stimuli in steady-state noise. This outcome is consistent with the findings by Turner *et al.* (2004) with normal-hearing and cochlear implant listeners. No significant advantages in intelligibility were observed in steady-state noise when speech was processed via an EAS simulation and compared against a sixteen-channel vocoder (i.e., electric-only simulation). Also, the difference in performance in steady-state noise between a group of patients implanted with a traditional 20-electrode array and another group (matched with the first group in terms of consonant scores in quiet) utilizing low-frequency acoustic information (EAS) supplemented with a short-electrode array was very small and nonsignificant. In contrast, the difference in performance between the EAS and electric-only stimuli was striking when speech was presented in the background of two competing talkers. Hence, while the steady-state noise affected the two groups of patients the same way, the use of competing talkers as maskers provided significantly more benefit to the EAS patients. A similar pattern in performance was also observed in the study by Qin and Oxenham (2006) with normal-hearing listeners.

The EAS performance, and benefit, were clearly affected by the type of masker used. The fact that performance in the LP+V condition in steady-state noise background was the same as that in the V condition, but was significantly higher in a competing talker background suggests that low-frequency glimpsing played a critical role. Low-frequency glimpsing allowed the listeners in the present study to hear out the target in the LP+V stimuli corrupted by fluctuating maskers but not the target in the stimuli corrupted by steady-state noise. This is expected given that steady-state noise lacks the temporal envelope "dips" which allow listeners to glimpse the target. Listeners were probably able to glimpse

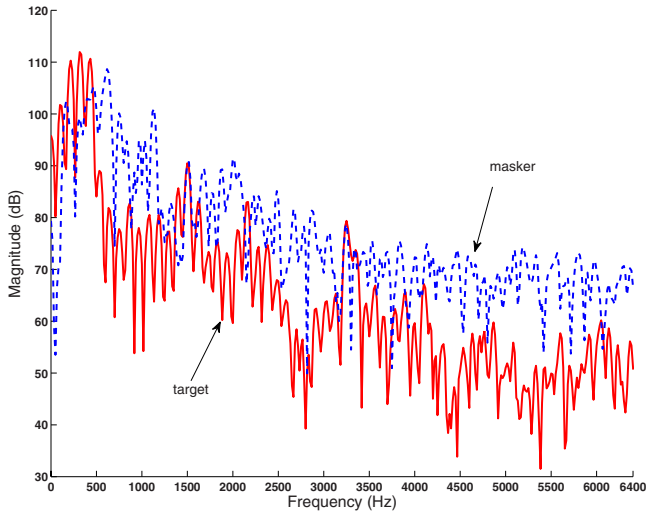

FIG. 2. (Color online) Magnitude spectra of the target and masker signals extracted from a voided segment of an IEEE sentence. The spectra are shown prior to mixing the signals at 0 dB SNR.

the low-frequency envelope information in the V stimuli; however the glimpsed information was not effectively integrated with the high-frequency envelope information. We thus speculate that two factors played a critical role in receiving the EAS benefit when LP information is supplemented with higher-frequency vocoded information: ability to detect glimpses and ability to integrate the glimpsed information (more on this in Sec. III A).

Overall, the present study points to a glimpsing mechanism that contributes to the benefit of EAS in noise and this is discussed next along with the implications in cochlear implants.

A. Glimpsing: Suggested mechanism underlying benefit of EAS

The benefit introduced by glimpsing raises the following question: Which underlying factors or cues present in the low-frequency acoustic stimulus contribute to or facilitate glimpsing? Put differently, what is so special about the low-frequency region in the acoustic stimulus that enables EAS patients to perform better in competing talker backgrounds?

The answer to both questions and key contributing factor is the low-frequency SNR advantage. When speech is corrupted by interferers with low-pass spectral characteristics (e.g., a competing talker), the low-frequency region is masked to a lesser degree compared to the high-frequency region, at least during voiced speech segments (e.g., vowels, semivowels). The LF region is shielded to a certain extent from distortion and noise because of the low-frequency dominance of the long-term speech spectrum, (Assmann and Summerfield, 2004; Loizou, 2007, Chap. 4). The 250–500 Hz region, in particular, contains prominent speech energy with a dominant peak near 500 Hz, a characteristic of the long-term spectrum of speech that is common across 12 different languages (Byrne *et al.*, 1994). Figure 2 shows example spectra of the target and masker signals, prior to mixing them at 0 dB SNR. Note that despite the fact that the long-term rms SNR (measured across the whole sentence) of

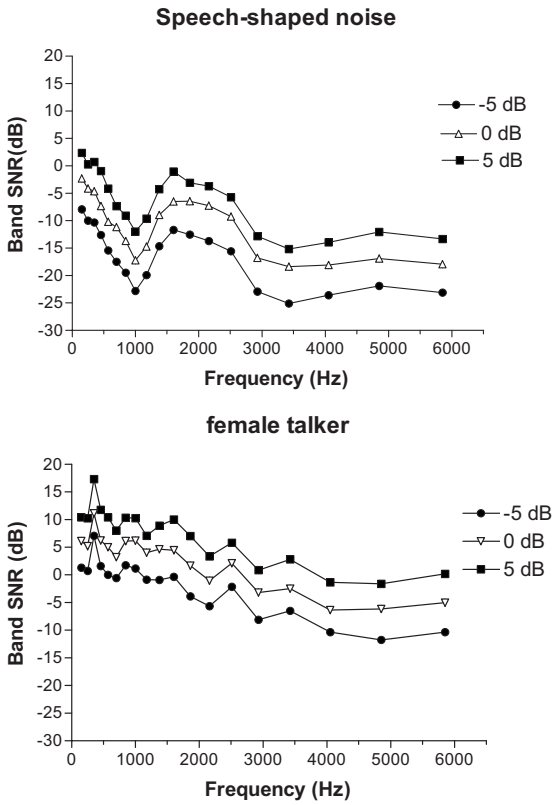

FIG. 3. Average band SNR values of signals embedded in speech-shaped noise (top panel) and female talker (bottom panel) masker at various SNR levels. The average was computed across 20 IEEE sentences (~1 min) and the SNR calculation was restricted only to voiced speech segments.

the stimulus is 0 dB, the target is stronger than the masker in the low frequencies (<500 Hz) but not in the high frequencies. Consequently, it is reasonable to expect that the SNR in the low-frequency region will be, on average, larger than the SNR in the high frequencies, thereby observing a low-frequency SNR advantage. To further assess that, we computed the average spectral SNR (in various bands) of signals embedded in female-talker and speech-shaped noise at various SNR levels. The SNR computation was restricted only to voiced speech segments,[3] where the SNR advantage is to be expected. Figure 3 plots the average band SNR values obtained by filtering the stimuli in 19 bands, spaced according to the critical-band scale (Table I,ANSI, 1997), and computing the SNR in each band. It is clear that the band SNR values in the low frequencies are always larger than the SNR values in the high frequencies, at least for voiced speech segments. The difference between the SNR values in the low frequencies (<600 Hz) and the values at higher frequencies can be as large as 10 dB (see Fig. 3). SNR analysis of the unvoiced segments revealed that the band SNR values of the unvoiced segments were substantially lower than the corresponding SNR values in voiced segments, particularly in the low frequencies (<3 kHz). For instance, in the 0 dB SNR stimuli corrupted by the female masker, the difference was about 15–20 dB in the low frequencies (<3 kHz) and about 1 dB in the high frequencies. Unlike the low-pass nature of the SNR distribution of the voiced segments (Fig. 3), the

SNR distribution of the unvoiced segments was found to be somewhat uniform across all frequencies, and highly variable across sentences.

The low-frequency SNR advantage (Figs. 2 and 3) is critical for several reasons. First, it provides access to a better F0 and F1 representation, and second, it provides a better glimpsing capability as the target will likely be stronger than the masker in the low-frequency region. Speech harmonics falling in the low frequencies will be affected less than the high-frequency harmonics, and listeners will thus have access to reliable F0 cues. Listeners will also have access to reliable F1 information critical for vowel and stop-consonant identification. The study by Parikh and Loizou (2005) demonstrated, via acoustic analysis, that F1 is preserved to a certain degree in noise even at extremely low SNR levels (−5 dB). Based on acoustic analysis of a large vowel database, F1 was identified reliably 60% of the time, whereas F2 was identified only 30% of the time when the vowels were embedded in −5 dB SNR multitalker babble. F1 information is important not only for vowel perception but also for stop-consonant perception as it conveys voicing information. The F1 onset time following the release of prevocalic stops is known, for instance, to be one of the major cues to stop voiced-unvoiced distinction (e.g., Liberman *et al.*, 1958).

Access to a better SNR in the low-frequency region makes it easier for listeners to segregate the target in complex listening situations. Evidence of the advantage introduced by glimpsing the low-frequency region was provided in the study by Li and Loizou (2007). Stimuli were constructed using an ideal $T-F$ masking technique (similar to the V+G technique) that ensures that the target is stronger than the masker in certain $T-F$ regions of the mixture, thereby rendering certain regions easier to glimpse than others. When the glimpses were introduced in the low-frequency band (0–1 kHz) for a fraction (30%) of the utterance duration, small but statistically significant improvements in performance were observed, over that attained by the unprocessed (noisy) stimuli. Considerably larger improvement (about 50 percentage points) was observed when the low-frequency glimpses were available throughout the utterance. A similar outcome was reported by Anzalone *et al.* (2006) who applied, in one condition, the ideal speech energy detector only to the lower frequencies (70–1500 Hz). Significant reductions in SRT were obtained by both normal-hearing and hearing-impaired listeners when the ideal speech detector was applied only to the lower frequencies. The outcome in these studies is consistent with the benefit seen with the V+G stimuli, despite the poor spectral resolution of the stimuli used in the present study.

In summary, the LP+V stimuli contain several phonetic cues that enable listeners to better segregate the target and we contend that the underlying mechanism responsible for the EAS benefit is glimpsing. Glimpsing involves a two-stage process: detection of the target followed by integration of cues contained in the glimpses. The detection process is facilitated by a favorable SNR. Time–frequency regions with positive SNR (i.e., regions wherein the target is stronger than the masker) are easier to detect than regions with negative SNR. As argued earlier and shown in Fig. 3, it is easier to detect the target in the low frequencies than in the high frequencies because the low-frequency region has a more favorable SNR. This suggests a positive correlation between the effective SNR in the low frequencies and the intelligibility scores, at least for the LP+V stimuli which contain intact (nonvocoded) acoustic information in the low frequencies. Figure 4 plots the SNR values computed in the low-frequency region (averaged over the 0–600 Hz frequency range) against the intelligibility scores obtained with the LP+V stimuli in all conditions. The resulting correlation coefficient was high ($r=0.84$, $p=0.034$) consistent with our glimpsing hypothesis. A similar outcome was also found by Cooke (2006) when he computed the correlation between intelligibility scores of VCV consonants and the proportion of the target speech in which the local SNR exceeded 3 dB. The resulting coefficient was 0.95, albeit he considered in his study $T-F$ regions spanning the whole spectrum rather than the low-frequency region.

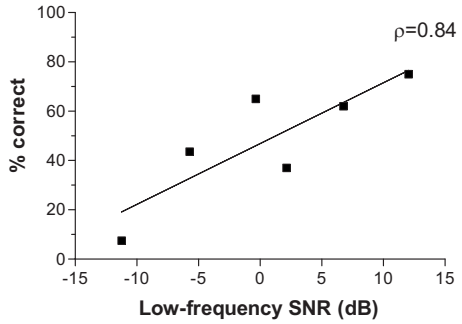

FIG. 4. Scatter plot of low-frequency band SNR values (averaged over the 0–600 Hz range) against intelligibility scores obtained with the LP+V stimuli in the various conditions.

The output of the detection process produces glimpses, which are somehow patched together in the second stage, namely the integration stage. The latter stage involves higher level (central) processing. Multiple cues are likely involved in the integration stage and may include F0 and F1 information, voicing cues, onset cues, and/or other auditory grouping cues (Bregman, 1990). We cannot exclude the possibility that listeners used F0 cues in the present study to segregate the target when the masker was a female talker. There is evidence, however, from another glimpsing study (Li and Loizou, 2007) that F0 cues are not always necessary depending on the task. In the study by Li and Loizou (2007), listeners were able to glimpse successfully the target amidst a background of 20 talkers, suggesting that cues other than F0 may be utilized in the integration process.

The favorable low-frequency SNR was present in both V and LP+V stimuli, yet the LP+V stimuli were recognized more accurately than the V stimuli. We believe that this is because the LP information facilitated better (and perhaps more effective) integration of the glimpses detected in the low (acoustic) frequency regions with the information contained in the high frequency (vocoded) regions. Alternatively, or perhaps equivalently, we can say that the glimpses in the LP stimulus provided information about the target that was missing from the V stimulus. The information (about the target) extracted from the LP stimulus was subsequently in-

tegrated with the V stimulus to yield higher speech recognition scores than those obtained with the V stimulus alone.

The V+G stimuli improved performance of the V stimuli, but did not yield the same level of performance as the LP+V stimuli. We believe that this is because the V+G processing enhanced the ability to detect the target (rendering it easier to glimpse) but the detected (vocoded) glimpses were not integrated as easily and effectively as were the (acoustic) glimpses detected from the LP stimuli. Perhaps the glimpsed envelopes provided some additional bits of information about the target that was missing from the V stimulus, but did not provide all the information available in the LP stimulus. Arguably, it is more difficult to patch together the sparse representation (three channels) of the vocoded target glimpsed in the low frequencies with the envelope information contained in the high-frequency channels. This is akin to the differences in difficulty encountered when putting together two different jigsaw puzzles comprised, of either large or small pieces. It is easier to put together a jigsaw puzzle when the individual pieces are large (and smaller in number) than when the individual pieces are tiny (and larger in number). What constitutes a "useful" glimpse in terms of duration and frequency extent/location remains an open question. Modeling studies by Cooke (2005) showed good agreement with human listener's performance when the glimpses were about 6 equivalent-rectangular-bandwidths (ERBs) wide in frequency.

The glimpsing account provides an explanation for the outcomes in the study by Chang *et al.* (2006). No EAS benefit was observed in that study when high-frequency acoustic information was introduced and combined with low-frequency vocoded information. As shown in Fig. 3, the high-frequency region has on average a nonfavorable SNR (<0 dB), suggesting that it is unlikely that the target will be glimpsed in this region, at least during voiced speech segments. As a result, the detection process will result in fewer (if any) glimpses and the integration process will be ineffective, resulting in no benefit in intelligibility.

B. Implications for cochlear implants

It is important to note that our simulations assumed "ideal" low-frequency residual hearing with normal cochlear function. Some EAS patients may indeed have good residual hearing (<30 dB HL) but others might have moderate-to-severe hearing loss (30–60 dB HL) in the 0–1000 Hz range (Kiefer *et al.*, 2005). In reality, EAS patients will have a low-frequency hearing loss and will be wearing a hearing aid. The acoustic low-pass cutoff frequency may vary (200–1000 Hz) depending on the patient and device used, and the acoustic and electric filter allocations may (or not) overlap in frequency or place. Despite the above-noted differences between the true EAS patients and the present vocoder simulations, studies (Turner *et al.*, 2004; Dorman *et al.*, 2005; Kong *et al.*, 2005) have shown that the outcomes of vocoder simulations have been consistent with those observed with EAS patients. With this caveat in mind, we next discuss some of the implications of our study in cochlear implants.

The obvious implication of the present study is that in order to get traditional implant users (fitted with long electrode arrays) to perform as well as EAS users in noise we need to improve the spectral resolution in the low-frequency region. As argued earlier, this will enhance the integration process and provide better glimpsing of the target. A plausible solution is to place more filters in the low frequencies at the expense of sacrificing resolution in the high frequencies (Mckay and Henshall, 2002; Fourakis *et al.*, 2004; Loizou, 2006). Such an approach was taken by Fourakis *et al.* (2004) and Loizou (2006) and has been found to benefit vowel recognition. The study by Mckay and Henshall (2002) showed that in quiet when more filters were allocated in the low frequencies, the transmission of vowel information improved but the consonant information degraded. When listening in noise, a significant benefit was noted when the low-frequency range (up to 2.6 kHz) was allocated across the nine instead of the five standard electrodes. The latter outcome is consistent with our glimpsing hypothesis, in that having access to a better (finer) spectral representation in the low frequencies will facilitate better glimpse integration. In the context of combined electric and acoustic hearing, it is not clear how many low-frequency channels would be required to achieve the same level of performance as EAS, and further experiments are warranted to investigate that.

The present study demonstrated with the use of the V+G stimuli that there exists an alternative method, other than improving spectral resolution (a challenging task), for improving the ability of listeners to glimpse low-frequency envelope information. Indeed, significant improvements in performance can be obtained with the V+G stimuli. These stimuli enabled listeners to glimpse low-frequency envelope information without having to increase the spectral resolution (note that the V+G and V stimuli had the same spectral resolution, i.e., eight channels). In fact, the performance with the V+G stimuli was significantly higher than the performance of the LP+V stimuli at extremely low SNR levels (−5 dB) in steady-state noise. For both steady-state noise and competing talker backgrounds (−5 dB SNR), performance improved by approximately 10–15 percentage points relative to the performance obtained with the V stimuli, and provided a 2–3 dB reduction in SRT. Construction of the V+G stimuli requires, however, access to the ideal binary mask or equivalently access to the true SNR in each frequency band. Several techniques do exist for estimating the ideal binary mask (e.g., Hu and Wang, 2004; Wang and Brown, 2006) or the (instantaneous) spectral SNR (Hu *et al.*, 2007). One possibility is to use an algorithm to estimate the instantaneous SNR in each channel. By retaining the channel envelopes with positive SNR and discarding the channel envelopes with negative SNR, we can effectively enhance the detection of glimpses, as done with V+G processing. An algorithm for estimating the instantaneous SNR in each channel was presented in Hu *et al.* (2007) and is amenable to real-time implementation. Aside from devising techniques to improve glimpsing of low-frequency envelope information, different techniques can be devised to improve access to voicing information and/or to improve the F1 representation. Such techniques will likely hold promise for improving speech

recognition in noise by CI users who have no residual hearing and therefore no access to low-frequency acoustic information.

ACKNOWLEDGMENTS

This research was supported by Grant No. R01 DC007527 from the National Institute of Deafness and other Communication Disorders, NIH. We would like to thank Dr. Fan-Gang Zeng and two anonymous reviewers for the valuable comments they provided.

[1]It should be pointed out that in some conditions the LP stimuli in the Kong and Carlyon (2007) study were not corrupted by the masker, but the vocoded stimuli were.

[2]The scaling of the masker envelopes of the V+G stimuli increases the global (long-term rms) SNR of the stimulus, but only by a small amount (~0.5 dB).

[3]In our analysis, voiced segments included not only vowels, but also all consonants with vowel-like characteristics (e.g., nasals, semivowels). The onsets following the release of voiced stop consonants (e.g., /b/, /d/) were also included in the analysis.

American National Standards Institute (**1997**). "Methods for calculation of the speech intelligibility index," ANSI S3.5-1997 (American National Standards Institute, New York).

Anzalone, M., Calandruccio, L., Doherty, K., and Carney, L. (**2006**). "Determination of the potential benefit of time-frequency gain manipulation," Ear Hear. **27**, 480–492.

Assmann, P., and Summerfield, Q. (**2004**). "The perception of speech under adverse conditions," in *Speech Processing In The Auditory System*, edited by S. Greenberg, W. Ainsworth, A. Popper, and R. Fay (Springer, New York), pp. 231–308.

Bregman, A. (**1990**). *Auditory Scene Analysis* (MIT, Cambridge, MA).

Brokx, J., and Nooteboom, S. (**1982**). "Intonation and perception of simultaneous voices," J. Phonetics **10**, 23–26.

Byrne, D., Dillon, H., Tran, K., Arlinger, S., Wilbraham, K., Cox, R., Hagerman, B., Hetu, R., Kei, J., Lui, C., Kiessling, J., Kotby, M., Nasser, N., El Kholy, W., Nakanishi, Y., Oyer, H., Powell, R., Stephens, D., Meredith, R., Sirimanna, T., Tavartkiladze, G., Frolenkov, G., Westerman, S., and Ludvigsen, C. (**1994**). "An international comparison of long-term average speech spectra," J. Acoust. Soc. Am. **96**, 2108–2120.

Chang, J., Bai, J., and Zeng, F.-G. (**2006**). "Unintelligible low-frequency sound enhances stimulated cochlear-implant speech recognition in noise," IEEE Trans. Biomed. Eng. **53**, 2598–2601.

Cooke, M. (**2005**). "Making sense of everyday speech: A glimpsing account," in *Speech Separation by Humans and Machines*, edited by P. Divenyi (Kluwer Academic, Dordrecht), pp. 305–314.

Cooke, M. P. (**2006**). "A glimpse model of speech perception in noise," J. Acoust. Soc. Am. **119**, 1562–1573.

Culling, J., and Darwin, C. (**1994**). "Perceptual and computational separation of simultaneous vowels: Cues arising from low-frequency beating," J. Acoust. Soc. Am. **95**, 1559–1569.

Dorman, M., Spahr, A., Loizou, P., Dana, C., and Schmidt, J. (**2005**). "Acoustic simulations of combined eleciric and acoustic hearing (EAS)," Ear Hear. **26**, 371–380.

Festen, J., and Plomp, R. (**1990**). "Effects of fluctuating noise and interfering speech on the speech-reception threshold for impaired and normal hearing," J. Acoust. Soc. Am. **88**, 1725–1736.

Fourakis, M., Hawks, J., Holden, L., Skinner, M., and Holden, T. (**2004**). "Effect of frequency boundary assignment on vowel recognition with the Nucleus 24 ACE speech coding strategy," J. Am. Acad. Audiol **15**, 281–289.

Gantz, B., and Turner, C. (**2003**). "Combining acoustic and electric hearing," Laryngoscope **113**, 1726–1730.

Gantz, B. J., Turner, C., and Gfeller, K. E. (**2006**). "Acoustic plus electric speech processing: Preliminary results of a multicenter clinical trial of the Iowa/Nucleus Hybrid implant," Audiol. Neuro-Otol. **11**, 63–68.

Gfeller, K., Turner, C., Mehr, M., Woodworth, G., Fearn, R., Knutson, J., Witt, S., and Stordahl, J. (**2002**). "Recognition of familiar melodies by adult cochlear implant recipients and normal-hearing adults," Cochlear Implant Int. **3**, 29–53.

Glasberg, B., and Moore, B. (**1990**). "Derivation of auditory filter shapes from notched-noise data," Hear. Res. **47**, 103–138.

Hu, G., and Wang, D. (**2004**). "Monaural speech segregation based on pitch tracking and amplitude modulation," IEEE Trans. Neural Netw. **15**, 1135–1150.

Hu, Y., Loizou, P., Li, N., and Kasturi, K. (**2007**). "Use of a sigmoidal-shaped function for noise attenuation in cochlear implants," J. Acoust. Soc. Am. **122**, EL128–EL134.

IEEE (**1969**). "IEEE recommended practice for speech quality measurements," IEEE Trans. Audio Electroacoust. **17**, 225–246.

Kiefer, J., Pok, M., Adunka, O., Sturzebecher, E., Baumgartner, W., Schmidt, M., Tillein, J., Ye, Q., and Gstoettner, W. (**2005**). "Combined electric and acoustic stimulation of the auditory system: Results of a clinical study," Audiol. Neuro-Otol. **10**, 134–144.

Kong, Y., and Carlyon, R. (**2007**). "Improved speech recognition in noise in simulated binaurally combined acoustic and electric-stimulation," J. Acoust. Soc. Am. **121**, 3717–3727.

Kong, Y., Stickney, G., and Zeng, F.-G. (**2005**). "Speech and melody recognition in binaurally combined acoustic and electric hearing," J. Acoust. Soc. Am. **117**, 1351–1361.

Li, N., and Loizou, P. (**2007**). "Factors influencing glimpsing of speech in noise," J. Acoust. Soc. Am. **122**, 1165–1172.

Liberman, A., Delattre, P., and Cooper, F. (**1958**). "Some rules for the distinction between voiced and voiceless stops in initial position," Lang Speech **1**, 153–167.

Loizou, P. (**2006**). "Speech processing in vocoder-centric cochlear implants," in Cochlear and Brainstem Implants, edited by A. Moller, *Advances in OtoRhino-Laryngol*, Vol. **64** (Basel, Karger), pp. 109–143.

Loizou, P. (**2007**). *Speech Enhancement: Theory and Practice* (CRC Press, Taylor Francis Group, Boca Raton, FL).

Loizou, P., Dorman, M., and Tu, Z. (**1999**). "On the number of channels needed to understand speech," J. Acoust. Soc. Am. **106**, 2097–2103.

Mckay, C., and Henshall, K. (**2002**). "Frequency-to-electrode allocation and speech perception with cochlear implants," J. Acoust. Soc. Am. **111**, 1036–1044.

Parikh, G., and Loizou, P. (**2005**). "The influence of noise on vowel and consonant cues," J. Acoust. Soc. Am. **118**, 3874–3888.

Qin, M., and Oxenham, A. (**2003**). "Effects of simulated cochlear-implant processing on speech reception in fluctuating maskers," J. Acoust. Soc. Am. **114**, 446–454.

Qin, M., and Oxenham, A. (**2005**). "Effects of envelope-vocoder processing on F0 discrimination and concurrent-vowel identification," Ear Hear. **26**, 451–460.

Qin, M., and Oxenham, A. (**2006**). "Effects of introducing unprocessed low-frequency information on the reception of the envelope-vocoder processed speech," J. Acoust. Soc. Am. **119**, 2417–2426.

Stickney, G., Assmann, P., Chang, J., and Zeng, F.-G. (**2007**). "Effects of implant processing and fundamental frequency on the intelligibility of competing sentences," J. Acoust. Soc. Am. **122**, 1069–1078.

Turner, C., Gantz, B., Vidal, C., Behrens, A., and Henry, B. (**2004**). "Speech recognition in noise for cochlear implant listeners: Benefits of acoustic hearing," J. Acoust. Soc. Am. **115**, 1729–1735.

von Ilberg, C., Kiefer, C., Tillein, J., Pfenningdorff, T., Hartman, R., Sturzebecher, E., and Klinke, R. (**1999**). "Electric-acoustic stimulation of the auditory system," ORL **61**, 334–340.

Wang, D. (**2005**). "On ideal binary mask as the computational goal of auditory scene analysis," in *Speech Separation by Humans and Machines*, edited by P. Divenyi (Kluwer Academic, Dordrecht), pp. 181–187.

Wang, D., and Brown, G. (**2006**). *Computational Auditory Scene Analysis* (Wiley, New York).

Effects of upper-frequency boundary and spectral warping on speech intelligibility in electrical stimulation

Matthew J. Goupell,[a] Bernhard Laback, and Piotr Majdak
Acoustics Research Institute, Austrian Academy of Sciences, Wohllebengasse 12-14, A-1040 Vienna, Austria

Wolf-Dieter Baumgartner
ENT-Department, Vienna University Hospital, Währinger Gürtel 18-20, A-1097 Vienna, Austria

(Received 12 February 2007; revised 27 November 2007; accepted 6 December 2007)

Speech understanding was tested for seven listeners using 12-electrode Med-El cochlear implants (CIs) and six normal-hearing listeners using a CI simulation. Eighteen different types of processing were evaluated, which varied the frequency-to-tonotopic place mapping and the upper boundary of the frequency and stimulation range. Spectrally unwarped and warped conditions were included. Unlike previous studies on this topic, the lower boundary of the frequency and stimulation range was fixed while the upper boundary was varied. For the unwarped conditions, only eight to ten channels were needed in both quiet and noise to achieve no significant degradation in speech understanding compared to the normal 12-electrode speech processing. The unwarped conditions were often the best conditions for understanding speech; however, small changes in frequency-to-place mapping (<0.77 octaves for the most basal electrode) yielded no significant degradation in performance from the nearest unwarped condition. A second experiment measured the effect of feedback training for both the unwarped and warped conditions. Improvements were found for the unwarped and frequency-expanded conditions, but not for the compressed condition. These results have implications for new CI processing strategies, such as the inclusion of spectral localization cues. © *2008 Acoustical Society of America.* [DOI: 10.1121/1.2831738]

PACS number(s): 43.66.Ts, 43.71.Ky, 43.72.Dv, 43.72.Lc [AJO] Pages: 2295–2309

I. INTRODUCTION

Large differences are seen in the population of cochlear-implant (CI) listeners for speech understanding, with high-performing CI listeners often being comparable to normal-hearing (NH) listeners using CI simulations in quiet conditions (Friesen *et al.*, 2001). Probable reasons for the large variability in CI performance for understanding speech are a reduced number of functional auditory nerve fibers (dead regions), spread of electrical current fields in the cochlea, and the positioning of the electrodes in relation to the tonotopic place of stimulation, hence the characteristic frequencies of the stimulated auditory nerve fibers. Greenwood's (1990) organ of Corti map has been widely used to relate tonotopic place in a CI to characteristic frequency, although a recent study shows that a spiral ganglion map may be a better model for perimodiolar electrodes (Sridhar *et al.*, 2006). Typically, the most apical electrode is inserted 20–30 mm into the cochlea (Ketten *et al.*, 1998; Gstoettner *et al.*, 1999). According to the Greenwood map, for a 35-mm cochlea, a 30-mm insertion depth corresponds to a 160-Hz center frequency, while a 20-mm insertion depth corresponds to an 1150-Hz center frequency. The lowest frequency electrode often receives frequency information around 300-Hz, yielding a large frequency-to-place mismatch for a 20-mm insertion depth. Even larger mismatches have been reported; Ketten *et al.* showed four patients to have their most apical electrode at a cochlear place tuned to greater than 1.4 kHz.

To address the large variability of speech understanding in CI listeners, different frequency-to-place mappings have been studied to optimize speech understanding in CI listeners with the hope of increasing understanding to a level comparable to NH listeners. A number of studies by Fu and Shannon (1999a, b, c, d) have shown the importance of well-matched frequency-to-place maps for both CI listeners and NH listeners using a CI simulation. Başkent and Shannon showed matched conditions were the best for NH listeners (2003) and CI listeners (2004) when compared to frequency-expanded or frequency-compressed speech. However, frequency-to-place maps need not be perfectly matched. The effect of insertion depth was studied by Dorman *et al.* (1997) with NH simulations. The best performance was seen for a well-matched map, but apical shifts of 0.24 octaves could be tolerated without a significant decrease in speech understanding.

To support the case for unmatched maps, Faulkner *et al.* (2003), from NH simulation data, argued that necessary speech information below 1 kHz is lost if frequencies are matched in the case of shallow insertion depths. Başkent and Shannon (2005) also showed with CI listeners the importance of low-frequency information in a study that held the upper-frequency boundary fixed while varying the lower-frequency boundary. This is one of the few studies that shows an improvement over the matched frequency-to-place condition; for CI listeners with shallower insertions, a mild

[a]Author to whom correspondence should be addressed. Electronic mail: matt.goupell@gmail.com

amount of compression was better than truncating the frequency range to match frequency and tonotopic place.

Despite the variability in the effectiveness of a CI due to the uncertainty of the frequency-to-place map, it turns out that CI listeners can adapt fairly well to frequency mismatches that might be due to shallow insertions or dead regions, hence the successful nature of the field of cochlear implantation as a whole. Most of the previously cited studies on CI speech understanding were acute studies, meaning that there was no long-term training. Rosen *et al.* (1999), Fu *et al.* (2002), McKay and Henshall (2002), and Smith and Faulkner (2006) found that short-term experiments can exaggerate the long-term consequences of spectral shifts.

We studied the frequency-to-place mapping of speech in CI listeners by systematically varying the upper-frequency boundary and range of electrodes at different signal-to-noise ratios (SNRs). We decreased the number of electrodes used from the standard 12 electrodes in the Med-El Combi 40+ or Pulsar implants and we varied the upper-frequency boundary from the standard 8.5 kHz while holding the lower-frequency boundary fixed. Hence, unlike some frequency-to-place mapping studies, which attempt to improve speech understanding scores, we determined the amount of "extra" speech information presented to CI listeners in current strategies and attempted to not appreciably decrease speech scores. Determining the amount of extra speech information presented to CI listeners has implications for new CI processing strategies; namely the inclusion of acoustic information other than speech that is presently neglected.

It is unclear if a compression, expansion, or simple low-pass filtering of the speech information will cause significant changes in speech understanding. Skinner *et al.* (1995) argued that improved vowel discrimination in a group of CI listeners was due to assigning more electrodes to important lower-frequency regions. That is to say it may be possible to increase speech understanding if there is more spectral resolution over the first two formants. A study by McKay and Henshall (2002) tested a similar idea with CI listeners. They tested two frequency-to-place mappings in their study: one that evenly spread ten electrodes over a frequency range of 200–10,000 Hz and one that used nine electrodes for 200–2600 Hz and the last electrode for frequencies 2600–10,000 Hz. They found that assigning more electrodes to lower frequencies helped vowel recognition and sentence recognition, but hurt consonant recognition. Also, a recent study by Başkent and Shannon (2007) showed that there is a greater degradation of speech understanding for low-frequency spectral shifts than high-frequency spectral shifts. Therefore our manipulation of varying only the upper-frequency boundary and upper-stimulation boundary is a practically useful manipulation because it attempts to preserve the spectral information for the low-frequency electrodes.

II. EXPERIMENT 1

A. Methods

1. Stimuli

The Oldenburg Sentence Test (OLSA) (Wagener *et al.*, 1999a, b, c) was used to test speech intelligibility of words under different mapping conditions. The OLSA Test consists of five-word, nonsense sentences. Each sentence is constructed of a name, a verb, a number, an adjective, and an object in that order. Ten different German words comprise a set for each word category. Each word has equal intelligibility. The noise used to mask the sentences has a spectrum that is similar to the spectrum of the speech. The sentences were recorded at a sampling rate of 44.1 kHz.

2. Signal processing

For the electrical stimuli, the sentences were processed using the Continuous Interleaved Sampling (CIS) strategy (Wilson *et al.*, 1991). First, pre-emphasis was applied to the signal using a first-order, high-pass Butterworth filter with a corner frequency at 1200 Hz. Next, the signal was filtered into frequency bands by using fourth-order Butterworth filters. The speech information up to the upper-frequency boundary (determined by M) was mapped to the number of channels (N). The number M is the frequency-boundary index that represents the upper-frequency boundary (f_{upper}) determined by logarithmic spacing of the bands; hence this number enumerates the spectral content of the stimuli. Figure 1 shows how the speech spectrum is subdivided and enumerated by M. Different experimental conditions were created in which the upper-frequency boundary of the speech stimuli was set at either 8500 Hz ($M=12$), 4868 Hz ($M=10$), 2788 Hz ($M=8$), or 1597 Hz ($M=6$). The lower-frequency cutoff was always 300 Hz. For each filter configuration, the stimuli were band-pass filtered into either $N=6$, 8, 10, or 12 contiguous logarithmically-spaced analysis bands, thus creating 16 different filter sets. In conditions that utilized 6, 8, or 10 analysis bands, the filters were respectively mapped to the 6, 8, or 10 most apical electrodes of the CI listeners' implanted arrays. Conditions utilizing 12 analysis bands mapped the filters to the full 12-electrode array. Therefore matched (unwarped) frequency-to-place maps that vary only the stimulation range were tested. Also, unmatched (warped) maps were tested. See Fig. 1 for an illustration of the types of frequency-to-place mappings. Table I shows the center frequency, bandwidth, and shift for each channel for each combination of M and N used in this experiment. The baseline condition, $M=12$ and $N=12$, is labeled $M_{12}N_{12}$ and corresponds to the normal clinical settings of the CI. The other conditions are labeled similarly. Besides the 16 different filter sets, there were two additional conditions, the M_4N_4 case ($f_{\text{upper}}=915$ Hz) and an extended frequency range case to be called $M_{14}N_{12}$. The extended frequency range had $f_{\text{upper}}=16{,}000$ Hz. An illustrative matrix of all the testing conditions can be seen in Fig. 2.[1]

After the signals were filtered into N analysis bands, the Hilbert envelope of each of the bands was calculated and then was compressed by a logarithmic map law. Compression factors, individual electrode threshold levels, and most comfortable levels were set to match the CI listeners' everyday clinical settings. The sentences were presented at a comfortable level, which was chosen by each CI listener.[2]

Like the electrical stimuli, the sentences for the acoustic stimuli for the NH listeners were pre-emphasized. The same procedure was used to select corner frequencies for matched

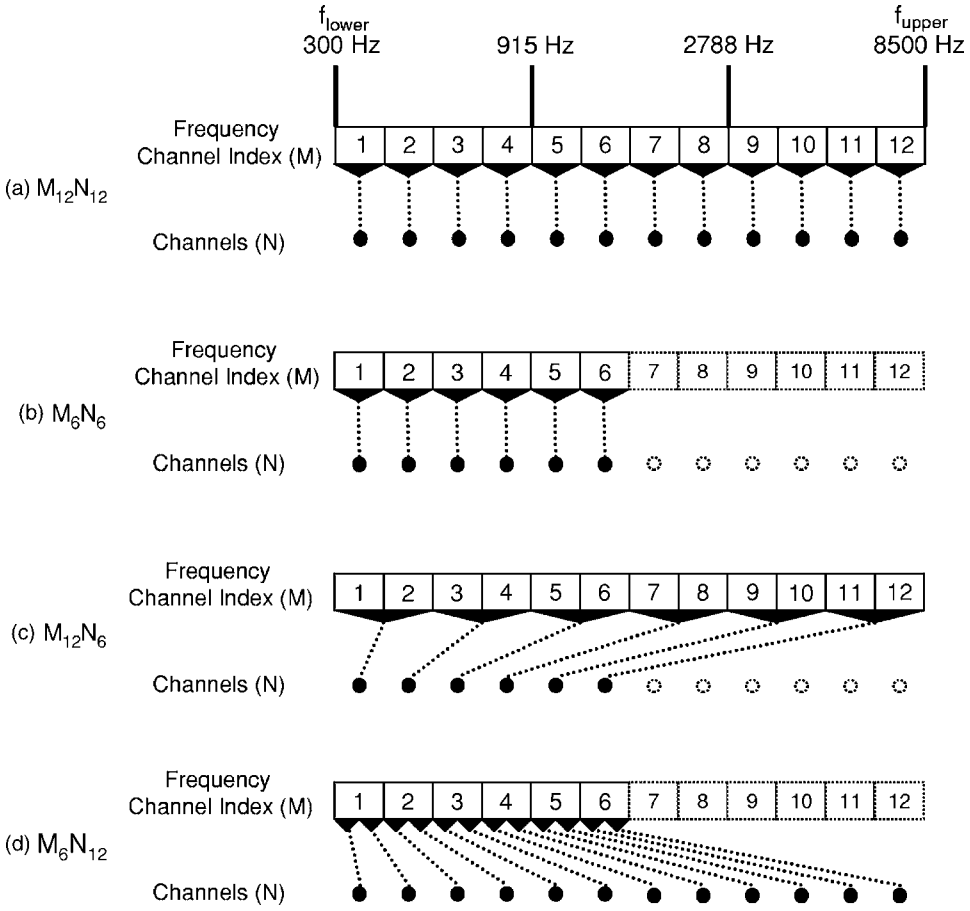

FIG. 1. Different frequency-to-tonotopic place mappings used in this experiment. Panel (a) shows the baseline condition $M_{12}N_{12}$, where frequencies 300–8500 Hz of the speech signal are mapped to 12 channels, essentially the same as the normal clinical mapping. Panel (b) shows the M_6N_6 condition, a matched condition where the spectral content is low-pass filtered, but unwarped from the normal clinical mapping. Panel (c) shows a compression of full spectral content to a limited set of 6 channels. Panel (d) shows an expansion of limited spectral content to a full set of 12 channels.

and unmatched frequency-to-place conditions. The signal was filtered into N bands by fourth-order Butterworth filters and the Hilbert envelope of the bands was calculated. Each speech envelope was multiplied by a narrowband white noise. The noises had a bandwidth and center frequency corresponding to the assumed logarithmic spacing of channels (see Table I, $M_{12}N_{12}$). The N speech-envelope-modulated noise bands were then summed over the bands into an acoustic stimulus. The sampling rate of the vocoded sentences was 44.1 kHz. The acoustic stimuli were normalized to have approximately the same energy. Sentences were presented at approximately 75 dB (A) SPL.[3] Because the noise vocoder introduced random noise to the stimuli, the level of the stimuli was not precisely controlled. The level varied by as much as ± 0.5 dB on a given sentence.

3. Procedure

The task of the listener was to verbally repeat the five words of the OLSA sentences in blocks where the upper-frequency boundary index, M, and number of channels, N, were fixed. No feedback was provided and listeners were encouraged to guess if they were not sure about the correct words, although they were cautioned not to provide the same response for each guess. An experimenter, in the same room as the listener, recorded the number of correct words. At the beginning of each block, ten sentences were presented in quiet so that listeners could adapt to stimulus characteristics that changed from the stimulus processing (e.g., different frequency information or differently warped spectral content). After the initial ten sentences, listeners showed no or insignificant learning over the block. The effects of learning from feedback training over several blocks are explored in experiment 2. Within each block, sentences were presented at four SNRs in random order. The sentences were presented in quiet and at SNR=+10, +5, and 0 dB. Twenty repetitions were presented for each SNR. Thus, including the ten sentence adaptation period, 90 sentences were presented in each block. The subjects had their own randomly generated sentences, meaning that sentences were different from trial to trial and listener to listener. The percent correct (P_c) was calculated from the number of correct words in each five-word sentence from the last 80 sentences. A single block took approximately 15–20 min to complete.

Listeners were procedurally trained without feedback on the $M_{12}N_{12}$ condition until stable performance was achieved and the procedural training period was finished (4–14 blocks). After the $M_{12}N_{12}$ condition was completed, listeners were presented the other 17 conditions in random order. The randomization of condition order also helped minimize any learning effects for the experiment.

4. Listeners and equipment

Seven CI listeners were tested in this experiment and all were native German speakers. The etiologies of the CI listeners are shown in Table II. All were unilaterally implanted, except CI13, who was bilaterally implanted. All seven

TABLE I. Center frequency, bandwidth, and octave shift for each band for each combination of *M* and *N*.

M	N	Channel	1	2	3	4	5	6	7	8	9	10	11	12
12	12	Center (Hz)	348	460	608	804	1062	1403	1854	2449	3236	4276	5651	7467
		BW (Hz)	96	128	168	223	294	388	513	678	896	1184	1565	2067
		Shift (8ve)	…	…	…	…	…	…	…	…	…	…	…	…
10	12	Center (Hz)	339	428	540	681	859	1084	1367	1724	2175	2743	3460	4364
		BW (Hz)	78	99	125	158	198	251	315	399	503	634	799	1009
		Shift (8ve)	0.04	0.11	0.17	0.24	0.31	0.37	0.44	0.51	0.57	0.64	0.71	0.77
8	12	Center (Hz)	331	398	480	578	696	838	1008	1214	1462	1760	2120	2552
		BW (Hz)	61	74	89	107	129	155	186	225	271	326	393	472
		Shift (8ve)	0.07	0.21	0.34	0.48	0.61	0.74	0.88	1.01	1.15	1.28	1.41	1.55
6	12	Center (Hz)	323	371	426	490	563	647	744	856	983	1130	1300	1494
		BW (Hz)	45	51	60	68	78	90	104	119	136	158	181	207
		Shift (8ve)	0.11	0.31	0.51	0.71	0.92	1.12	1.32	1.52	1.72	1.92	2.12	2.32
12	10	Center (Hz)	360	503	702	981	1370	1914	2674	3736	5220	7292		
		BW (Hz)	119	167	232	325	454	634	886	1238	1729	2416		
		Shift (8ve)	−0.05	−0.13	−0.21	−0.29	−0.37	−0.45	−0.53	−0.61	−0.69	−0.77		
10	10	Center (Hz)	348	460	608	804	1062	1403	1854	2449	3236	4276		
		BW (Hz)	96	128	168	223	294	388	513	678	896	1184		
		Shift (8ve)	…	…	…	…	…	…	…	…	…	…		
8	10	Center (Hz)	338	422	528	659	824	1029	1286	1607	2008	2510		
		BW (Hz)	75	94	117	146	183	228	285	357	446	557		
		Shift (8ve)	0.04	0.12	0.20	0.29	0.37	0.45	0.53	0.61	0.69	0.77		
6	10	Center (Hz)	328	387	457	541	639	755	893	1055	1247	1474		
		BW (Hz)	55	64	76	91	106	126	149	176	208	246		
		Shift (8ve)	0.09	0.25	0.41	0.57	0.73	0.89	1.05	1.21	1.38	1.54		
12	8	Center (Hz)	378	574	872	1324	2012	3055	4640	7048				
		BW (Hz)	156	236	359	546	829	1258	1912	2904				
		Shift (8ve)	−0.12	−0.32	−0.52	−0.72	−0.92	−1.12	−1.32	−1.53				
10	8	Center (Hz)	363	514	728	1031	1461	2069	2931	4152				
		BW (Hz)	125	177	251	356	503	714	1010	1432				
		Shift (8ve)	−0.06	−0.16	−0.26	−0.36	−0.46	−0.56	−0.66	−0.76				
8	8	Center (Hz)	348	460	608	804	1062	1403	1854	2449				
		BW (Hz)	96	128	168	223	294	388	513	678				
		Shift (8ve)	…	…	…	…	…	…	…	…				
6	8	Center (Hz)	335	413	509	627	773	952	1174	1447				
		BW (Hz)	70	86	106	130	161	198	245	301				
		Shift (8ve)	0.05	0.16	0.26	0.36	0.46	0.56	0.66	0.76				
12	6	Center (Hz)	412	720	1256	2193	3828	6684						
		BW (Hz)	224	391	682	1191	2080	3632						
		Shift (8ve)	−0.24	−0.65	−1.05	−1.45	−1.85	−2.25						
10	6	Center (Hz)	389	619	985	1566	2492	3964						
		BW (Hz)	177	283	449	714	1137	1808						
		Shift (8ve)	−0.16	−0.43	−0.70	−0.96	−1.23	−1.50						
8	6	Center (Hz)	368	533	773	1121	1625	2356						
		BW (Hz)	135	196	284	411	597	865						
		Shift (8ve)	−0.08	−0.21	−0.35	−0.48	−0.61	−0.75						
6	6	Center (Hz)	348	460	608	804	1062	1403						
		BW (Hz)	96	128	168	223	294	388						
		Shift (8ve)	…	…	…	…	…	…						
4	4	Center (Hz)	348	460	608	804								
		BW (Hz)	96	128	168	223								
		Shift (8ve)	…	…	…	…								
14	12	Center (Hz)	359	500	697	970	1351	1882	2622	3652	5086	7084	9867	13744
		BW (Hz)	118	164	229	318	444	618	861	1199	1670	2326	3240	4513
		Shift (8ve)	−0.04	−0.12	−0.20	−0.27	−0.35	−0.42	−0.50	−0.58	−0.65	−0.73	−0.80	−0.88

listeners used Med-El 12-electrode implants: four CI listeners used the C40+ implant and three CI listeners used the Pulsar implant. In everyday listening, the C40+ users wear the Tempo+processor with the CIS+strategy and the Pulsar users wear the OPUS processor with the FSP strategy. In the experiments, all the listeners were presented with the CIS strategy implemented on a laboratory computer. More details on the Med-EL C40+ can be found in Zierhofer *et al.* (1997).

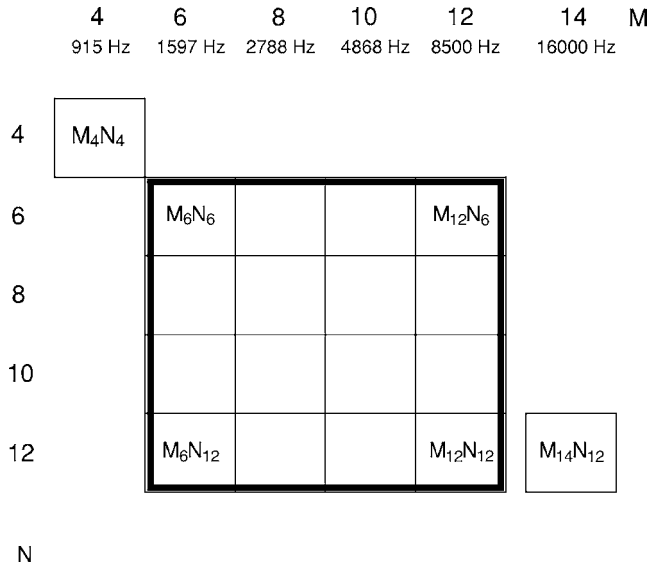

FIG. 2. An illustrative matrix of conditions tested in experiment 1. In total there are 18 different conditions tested, which vary the upper-frequency boundary index (M) or the number of channels (N).

The stimuli were presented via a Research Interface Box, developed at the University of Innsbruck, Austria. For the one bilateral CI user, CI13, the stimuli were presented to the better ear, which was the left. One listener, CI15, had only the 11 most-apical electrodes activated in her clinical setting. In her case, all the conditions with $M=12$ or $N=12$ were replaced by $M=11$ or $N=11$ respectively, but her data is analyzed and plotted as it were the $M=12$ or $N=12$ condition.

Six NH listeners were tested in this experiment. All the listeners were native German speakers except two of the NH listeners. These two listeners were fluent in German and showed no difference in performance compared to the native German speakers. Two NH listeners (NH2, a native German speaker, and NH10, a native English speaker) were the authors of the paper. They had extensive training with the OLSA material for several different processing conditions before data were taken. All six NH listeners had normal hearing according to standard audiometric tests. Since none of the NH listeners had an asymmetric hearing loss, the right ear was used for all of them. They were presented sentences over headphones (Sennheiser HDA200), after amplification from a headphone amplifier (TDT HB6) and passing a programmable attenuator (TDT PA4). The subjects were seated in a double-walled sound booth.

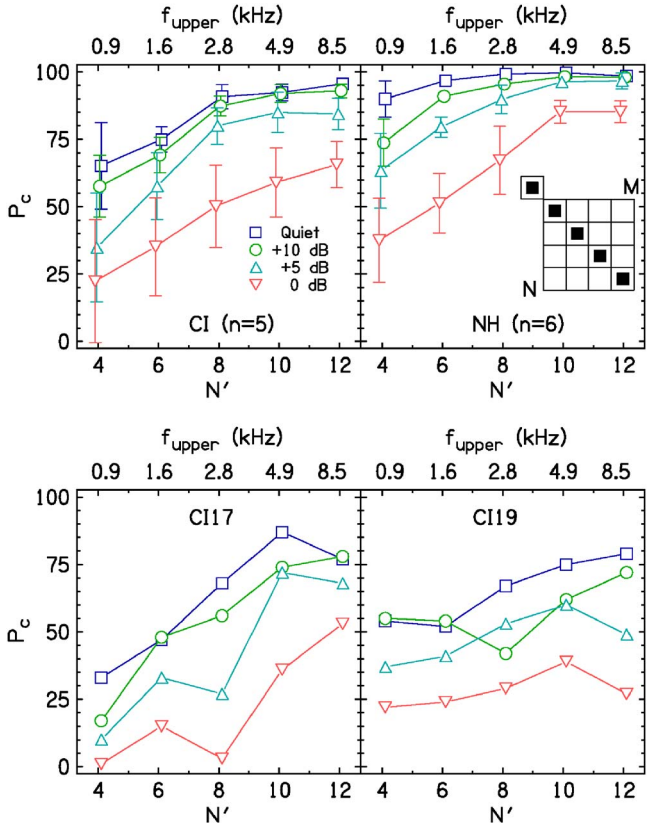

FIG. 3. (Color online) Percent correct scores as a function of matched channels N' ($N=M$) for five high-performance CI listeners (upper-left panel), six NH listeners (upper-right panel), and two low-performance CI listeners (bottom panels). The upper panels have errors bars that are two standard deviations in length.

B. Matched conditions

1. Results

Figure 3 shows the mean P_c scores of the CI and NH listeners for the matched conditions. For these conditions, the upper boundary of the matched stimulation range was varied by changing the number of channels (electrodes for CIs and analysis bands for NHs). The horizontal axis shows the number of matched channels, where $N=M$, and is referred to as N'. The additional horizontal axis at the top shows the corresponding upper-frequency boundary. Note that our definition of "changing the number of channels" does not change the inter-channel distance as the phrase is usually applied in other studies (e.g. Shannon *et al.*, 1995). The CI listeners were split into two groups: a high-

TABLE II. Bibliographic data of the CI listeners.

Subject	Etiology	Age (yr)	Duration of deafness (yr)	Implant use (yr)	Hearing aid use (yr)	Implant type	Insertion depth (mm)
CI13	Progressive	58	1	8	0.5	C40+	?
CI14	Progressive	67	11	6	15	C40+	30.0
CI15	Unknown	73	30	6	30	C40+	30.0
CI16	Progressive	54	8	1	30	Pulsar	21.0
CI17	Morbus Meniere	59	1	1.5	14	Pulsar	32.0
CI18	Progressive	49	11	2	33	Pulsar	30.0
CI19	Progressive	62	14	5	22	C40+	33.0

performance group and a low-performance group. The high-performance CI group (upper-left panel) consists of five CI listeners and each had $P_c > 90\%$ for $M_{12}N_{12}$ in quiet, comparable to the NH listeners (upper-right panel). The low-performance CI group (lower two panels) consists of listeners CI17 and CI19 and had $P_c \approx 75\%$ for $M_{12}N_{12}$ in quiet. The error bars are two standard deviations in overall length.

The performance improved with increasing N' for both the CI and NH listeners for every SNR. The effects of the factors N' and SNR were analyzed by a two-way repeated-measures analysis of variance (RM ANOVA), performed separately for the group of CI listeners ($n=7$) and the group of NH listeners ($n=6$). For all analyses based on ANOVA described in this paper, the P_c scores were transformed using the rationalized arcsine transform proposed by Studebaker (1985) to not violate the homogeneity of variance assumption required for an ANOVA.

For the CI listeners, the main effects were highly significant for N' [$F(4,114)=74.4$; $p<0.0001$] and SNR [$F(3,114)=98.8$; $p<0.0001$], but there was no interaction between the two factors [$F(12,114)=0.57$; $p=0.86$]. For the NH listeners, the main effects were also highly significant for N' [$F(4,95)=129.9$; $p<0.0001$] and SNR [$F(3,95)=214.6$; $p<0.0001$]. In contrast to the CI listeners, there was a highly significant interaction between the two factors [$F(12,95)=4.94$; $p<0.0001$], reflecting the smaller improvement with increasing N' at the higher SNR, which may indicate a ceiling effect.

Helmert contrasts (Chambers and Hastie, 1993) were calculated to determine the level of the factor N' above which no further improvement in performance occurs. Helmert contrasts test the difference of the performance between a given N' and the average performance of all the higher N'. For example, the percent correct for $N'=6$ [$P_c(N'_6)$] can be compared to the average percent correct for $N'=8$, 10, and 12 [$\bar{P}_c(N'_{>6})$]. This method has the advantage of a greater statistical power when compared to adjacent N' comparisons. The contrasts were calculated separately for each SNR.

For all seven CI listeners, increasing N' resulted in a significant improvement of performance up to $N'=8$ in quiet and at the +5-dB SNR [$P_c(N'_6)$ vs $\bar{P}_c(N'_{>6})$: largest $p=0.0001$; $P_c(N'_8)$ vs $\bar{P}_c(N'_{>8})$: smallest $p=0.061$]. At the +10- and 0-dB SNRs, performance improved up to $N'=10$ [$P_c(N'_8)$ vs $\bar{P}_c(N'_{>8})$: largest $p=0.013$; $P_c(N'_{10})$ vs $P_c(N'_{12})$: smallest $p=0.44$]. Said differently, the upper-frequency boundary can be reduced without a significant decrease in performance from 12 to 8 or 10 channels, depending on the SNR. For the five high-performance CI listeners at the three larger SNRs, reducing N' from 12 to 8 resulted in an average decrease in P_c of 4.9%. For the two low-performance CI listeners, the performance either dropped exceptionally quickly (CI17) or slowly (CI19) when the number of channels decreased below ten.

For the NH listeners, increasing N' resulted in a significant improvement of performance up to $N'=8$ in quiet [$P_c(N'_6)$ vs $\bar{P}_c(N'_{>6})$: largest $p=0.004$; $P_c(N'_8)$ vs $\bar{P}_c(N'_{>8})$: smallest $p=0.89$] and up to $N'=10$ for all conditions with noise [$P_c(N'_8)$ vs $\bar{P}_c(N'_{>8})$: largest $p=0.011$; $P_c(N'_{10})$ vs $P_c(N'_{12})$: smallest $p=0.63$].

2. Discussion

Speech understanding of CI listeners was found to improve significantly when the number of matched channels increased up to eight to ten, which corresponds to an upper boundary of the stimulation range of about 2.8 to 4.9 kHz. A different way of interpreting this result is that speech understanding did not decrease substantially when the number of matched channels was reduced to the eight to ten apical-most channels depending on the SNR. All CI listeners showed decreasing performance with decreasing SNR, but the effect of the stimulation range was similar at each SNR. The NH listeners, listening to vocoded speech, showed improvements in performance up to eight channels in quiet and up to ten channels for the conditions with noise. Considering the similar improvements in P_c above N' equal eight for the CI and NH listeners, the "critical" upper boundary of the stimulation range above which the performance saturates was quite similar for the two groups. This comparison is of course based on the assumption that the NH results at higher SNRs were not affected by the ceiling.

Most studies on the effect of the number of channels on speech understanding with CIs involve varying the number of electrodes over a fixed stimulation range. Thus, the CI listeners' results for the matched condition can be compared only with NH results. The NH listeners' performance as a function of N' is roughly in line with predictions of the speech intelligibility index (SII) model (ANSI standard, 1997), using frequency importance functions for either average speech or CID-22 words. We avoided, however, a quantitative comparison with the SII model since an appropriate frequency-importance function seems to be unavailable for the OLSA sentences. Furthermore, the comparison may be complicated by the fact that the SII is based on normal rather than vocoded speech, even though Faulkner *et al.* (2003) have argued that the relative (but not the absolute) values of the SII weights as a function of frequency should not depend on the degree of frequency selectivity. Interestingly, the SII model predictions are not higher than the performance obtained for vocoded speech. This may be surprising, considering that vocoder processing represents spectral smearing, a manipulation well known to hinder speech understanding (Boothroyd *et al.*, 1996; ter Keurs *et al.*, 1992, 1993; Baer and Moore, 1993, 1994). However, differences in the overall intelligibility of the sentence materials should be taken into account. For unprocessed speech at the 0-dB SNR, NH listeners score near 100% in case of the OLSA test (Wagener *et al.*, 1999c) and around 90% in case of the CID-22 test (Studebaker and Sherbecoe, 1991). Thus, the higher intelligibility of the OLSA material may have compensated for potentially detrimental effects of channel vocoder processing. In summary, the effect of varying the upper boundary of the matched stimulation range on speech understanding was found to be quite comparable between our CI listeners and

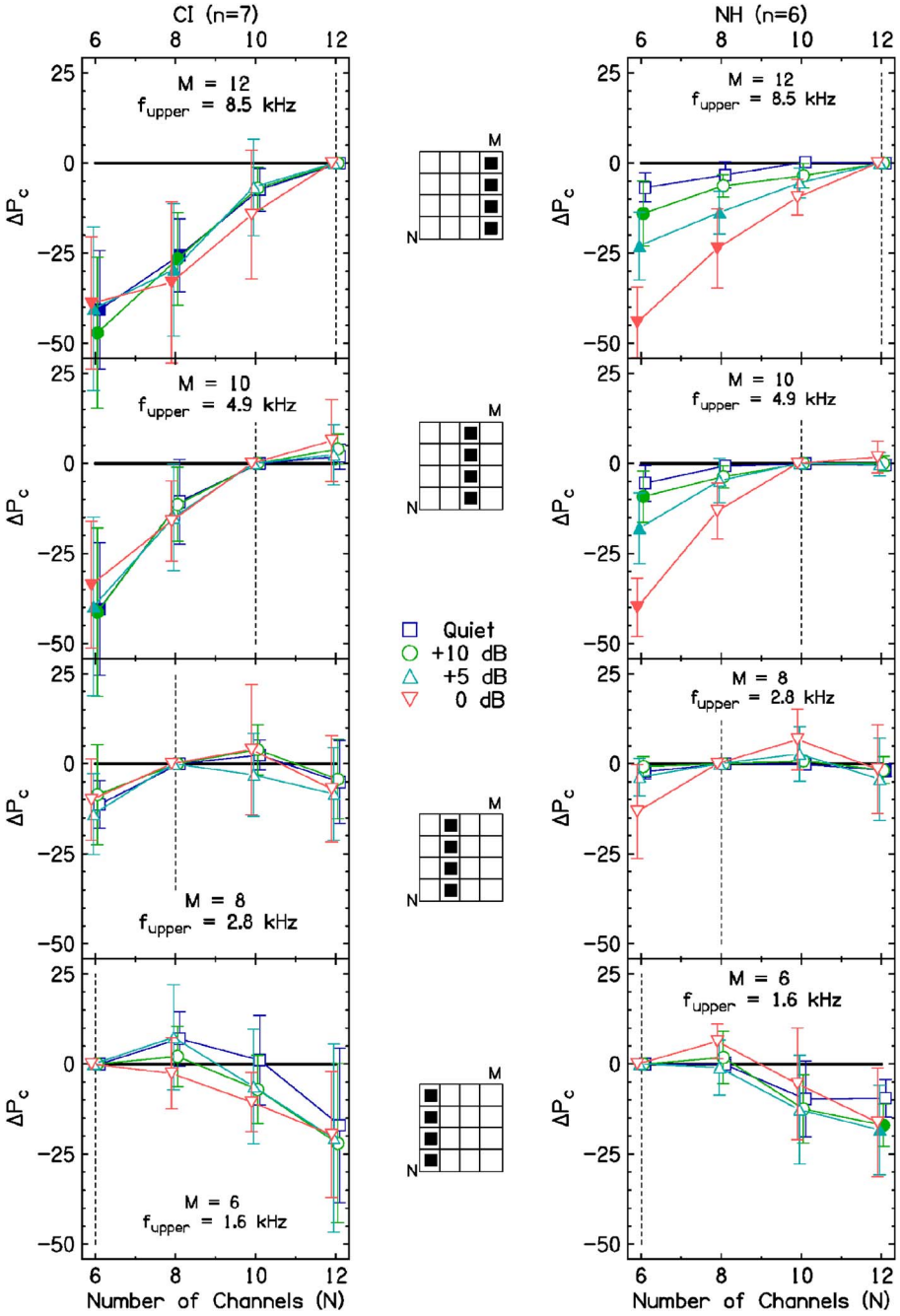

FIG. 4. (Color online) Percent correct scores relative to the matched conditions (shown by the vertical dotted line) vs the number of channels (N) for a fixed upper-frequency boundary and spectral content (M). Open symbols show no significant difference from the matched case. Closed symbols show a significant difference from the matched case ($p<0.05$). The matched case was often the best case. Significant decreases were seen for changes of more than two channels from the matched cases.

our NH listeners listening to an acoustic CI simulation, which is in rough agreement to the SII.

C. Unmatched conditions

1. Results

Figure 4 compares conditions vertically in our matrix of conditions seen in Fig. 2. It shows ΔP_c, the change in P_c from the matched conditions, as a function of number of channels in each panel. Therefore, the matched condition, which is indicated by the dotted vertical line in each panel, has exactly zero ΔP_c and no error bars. The data are plotted as a difference to better identify relative trends and to combine the high-performance and low-performance CI listeners. Note that on this plot the points to the left of the dotted line represent conditions with less channels for a fixed upper-frequency boundary, hence a compressed frequency-to-place map. Points to the right of the dotted line represent conditions with increased frequency resolution, namely with more channels, hence an expanded map. Arcsine-transformed P_c values (not ΔP_c, the points plotted in Fig. 4) were analyzed with a three-way RM ANOVA (factors N, M, and SNR) including Tukey's post-hoc tests. In Fig. 4, open symbols show no significant difference from the matched condition with the post-hoc tests; closed symbols show a significant difference at the 0.05 level.

Figure 4 shows that the matched condition was often the best, although there were several conditions that were not significantly different from the matched condition. Significant decreases from the matched condition occurred only for conditions that were more than plus or minus two channels

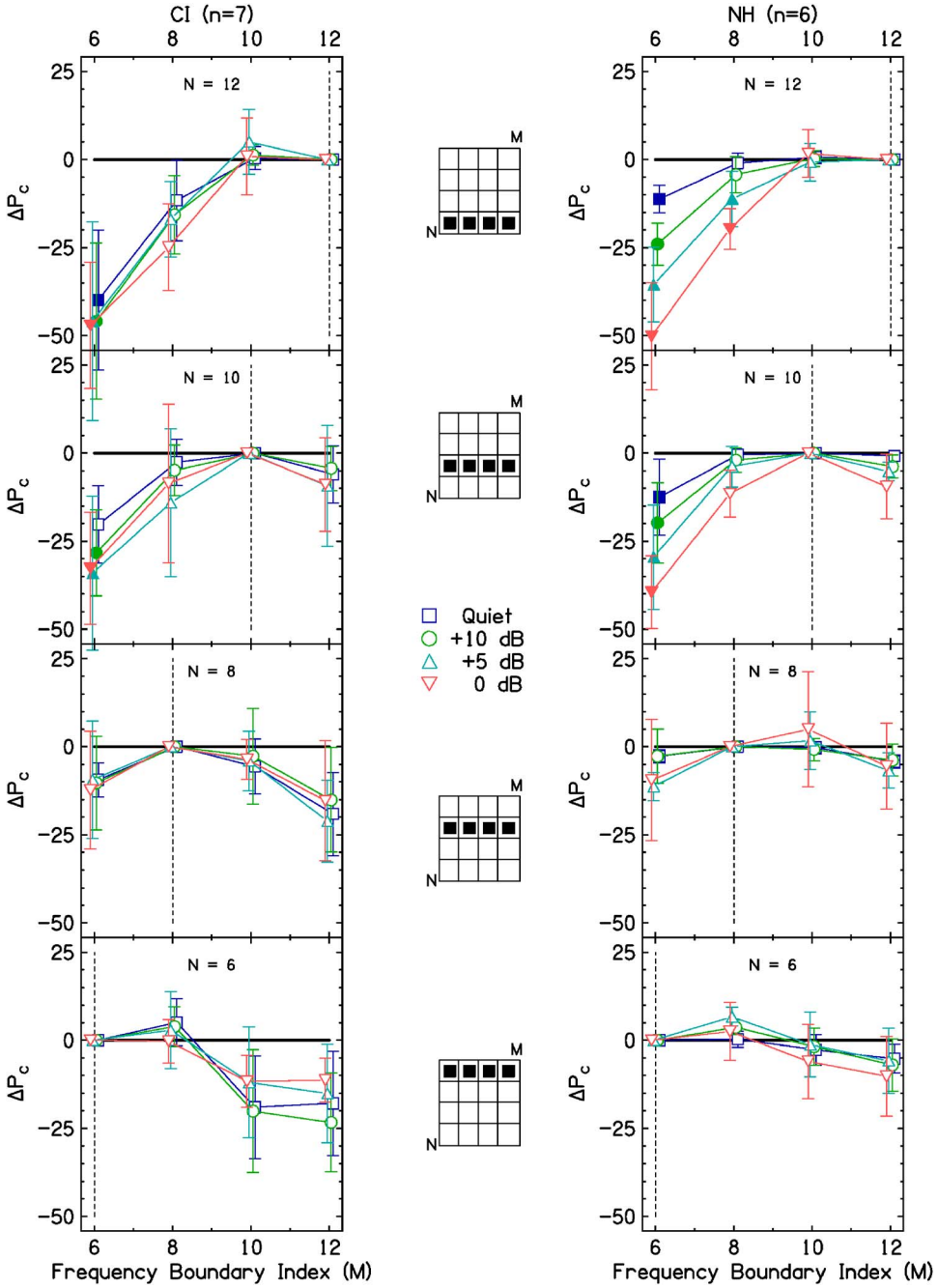

FIG. 5. (Color online) Percent correct scores relative to the matched condition (shown by the vertical dotted line) vs the amount of spectral content (M) for a fixed channel number (N). Open symbols show no significant difference from the matched case. Closed symbols show a significant difference from the matched case. The matched case was often the best case. Significant decreases were seen for changes of more than two frequency boundary indices (M) from the matched cases.

relative to the matched condition. Furthermore, conditions where $M=12$ and 10 had many more significant decreases than $M=8$ and 6.

For $M=12$, there was no significant interaction between N and SNR for the CI listeners in a two-way RM ANOVA [$F(9,96)=0.56$; $p=0.83$]. However, there was a significant interaction for the NH listeners [$F(9,80)=3.59$; $p=0.001$]. Similarly, for $M=10$, there was no significant interaction between N and SNR for the CI listeners [$F(9,96)=0.29$; $p=0.98$] but there was for the NH listeners [$F(9,80)=4.53$; $p<0.0001$]. It could not be determined whether this interaction for the NH listeners was a ceiling effect or a true asymptote. For $M=8$, both CI [$F(9,96)=0.16$; $p=1$] and NH [$F(9,80)=1.49$; $p=0.17$] listeners showed no significant interaction between N and SNR. Similarly, for $M=6$, there was no significant interaction between N and SNR for CI [$F(9,96)=0.43$; $p=0.92$] and NH listeners [$F(9,80)=0.47$; $p=0.83$].

Figure 5 shows ΔP_c as a function of M, comparing conditions horizontally on our matrix of conditions seen in Fig. 2. Note that on this plot the points to the left of the dotted line represent conditions with a decreased frequency range compared to the matched condition (spectral expansion) and points to the right of the dotted line represent conditions with an increased frequency range (spectral compression).

Again, significant decreases from the matched condition occurred only for conditions that were more than plus or minus two M relative to the matched condition. This corresponds to a frequency shift of 0.77 octaves, plus or minus, for the most basal electrode used in presenting the speech

TABLE III. Percent correct differences between the baseline $M_{12}N_{12}$ condition and the other conditions averaged over all four SNRs. The p values were found from Tukey's post-hoc tests from a three-way RM ANOVA. Values not different from the baseline ($p > 0.05$) are marked in bold.

	CI		NH	
Condition	Difference (%)	p	Difference (%)	p
$M_{12}N_{12}$	...	...	...	...
$M_{10}N_{12}$	**1.89**	**1**	**0.50**	**1**
M_8N_{12}	−17.25	<0.0001	−9.04	<0.0001
M_6N_{12}	−44.68	<0.0001	−30.21	<0.0001
$M_{12}N_{10}$	**−8.86**	**0.152**	**−4.54**	**0.052**
$M_{10}N_{10}$	**−1.75**	**1**	**0.29**	**1**
M_8N_{10}	**−9.29**	**0.126**	**−4.17**	**0.299**
M_6N_{10}	−30.61	<0.0001	−25.04	<0.0001
$M_{12}N_8$	−28.71	<0.0001	−11.75	<0.0001
$M_{10}N_8$	−15.00	<0.0001	−5.29	0.034
M_8N_8	−11.04	0.016	−6.67	0.004
M_6N_8	−21.39	<0.0001	−13.21	<0.0001
$M_{12}N_6$	−41.79	<0.0001	−22.00	<0.0001
$M_{10}N_6$	−40.54	<0.0001	−17.87	<0.0001
M_8N_6	−22.00	<0.0001	−11.67	<0.0001
M_6N_6	−24.89	<0.0001	−14.96	<0.0001
M_4N_4	−38.25	<0.0001	−28.50	<0.0001
$M_{14}N_{12}$	−16.00	<0.0001	**0.21**	**1**

information. There was a significant interaction between M and SNR for $N=12$ for the NH listeners [$F(9,80)=3.71$; $p=0.001$] but not for the CI listeners [$F(9,96)=0.56$; $p=0.83$]. No other values of N showed a significant interaction.

To directly compare the baseline condition $M_{12}N_{12}$ to conditions that have $M<12$ and $N<12$ electrodes, and are unmatched ($N \neq M$), differences between the baseline condition and all 18 conditions can be seen in Table III. The difference between $M_{12}N_{12}$ and all other conditions was averaged over all four SNRs. Negative values show an average decrease from the baseline condition. The p values were determined by Tukey's post-hoc comparisons. For both CI and NH listeners, conditions $M_{10}N_{12}$, $M_{12}N_{10}$, $M_{10}N_{10}$, and M_8N_{10} were not different from $M_{12}N_{12}$. An additional condition, $M_{14}N_{12}$, was not different for the NH listeners only and will be discussed in Sec. II D. To summarize Table III, even though several of these conditions showed no significant decrease from the nearest matched condition (e.g., $M_{10}N_8$ is not significantly different than $M_{10}N_{10}$ and M_8N_8 for all SNRs), most of them showed a decrease from the baseline $M_{12}N_{12}$ condition.

Lastly, we observed the interaction of N and M for fixed SNRs. There were highly significant effects for each SNR for the single factors N and M, and also the interactions between N and M (largest $p=0.001$).

2. Discussion

There was considerable agreement in the relative trends of the unmatched conditions between the three groups of listeners (high-performance CIs, low-performance CIs, and NHs). The CI listeners showed most of the trends that were seen for the NH listeners. However, there was one notable difference between the NH and CI listeners for fixed $M=10$ or 12 or fixed $N=10$ or 12. For these conditions, at the larger SNRs, the NH listeners had relatively larger values of ΔP_c than the CI listeners. Either NH listeners were not hindered as much as CI listeners for large spectral shifts and high SNRs, which can be seen in the top two panels of Figs. 4 and 5, or this difference was due to an effect of the ceiling of P_c.

Our results for both the CI and NH groups showed that varying the number of channels (N) by two caused no significant decrease in speech understanding performance compared to the nearest matched condition for a fixed upper-frequency boundary or fixed spectral content. This also held true for applying a gradually increasing spectral shift for a fixed number of channels, either by spectral compression or expansion. However, this was only possible while the upper-frequency boundary was shifted by no more than 0.77 octaves. Note that it was not possible to combine this result with the results from the matched conditions. For example, changing $M_{10}N_{10}$, a condition that showed no difference in the matched analysis to $M_{12}N_{12}$, to $M_{10}N_8$ caused significant decreases in performance compared to $M_{12}N_{12}$. Therefore, there were only three conditions that were not different from the baseline for the unmatched conditions, $M_{12}N_{10}$, $M_{10}N_{12}$, and M_8N_{10}.

The auditory system seemed to be able to fully accommodate small frequency shifts when the task is to understand speech. This result is similar to other experiments on frequency-warped speech material. For example, Başkent and Shannon (2003, 2004) used expansions and compressions where the frequency information at the center electrode was fixed and had a range of shifts from 0.25 octaves to 1 octave for the most apical and basal electrodes. Only the smallest shifts of 0.25 octaves did not significantly decrease sentence recognition scores. Therefore it seems that subjects

TABLE IV. Comparison of the performance in percent correct between the baseline condition ($M_{12}N_{12}$) and the extended frequency range condition ($M_{14}N_{12}$) for all four SNRs. The p values were found by one-way RM ANOVAs.

CI SNR (dB)	$M_{12}N_{12}$		$M_{14}N_{12}$			
	Average	Stand. Dev.	Average	Stand. Dev.	Difference	p
Quiet	90.57	8.79	79.29	13.50	−11.29	0.002
+10	87.86	9.19	72.14	15.14	−15.71	0.004
+5	76.86	15.94	61.86	22.14	−15.00	0.064
0	56.86	16.22	36.43	26.44	−20.43	0.054
NH SNR (dB)	$M_{12}N_{12}$		$M_{14}N_{12}$			
	Average	Stand. Dev.	Average	Stand. Dev.	Difference	p
Quiet	98.50	1.76	98.67	1.03	0.17	0.72
+10	98.00	1.55	97.83	1.17	−0.17	0.41
+5	96.67	3.01	95.17	4.45	−1.50	0.43
0	85.33	4.08	88.33	3.98	3.00	0.19

can tolerate our spectral warping with higher octave shifts of 0.77 octaves because only the high-frequency information was shifted by such a large amount.

Note that there were exceptions for individuals to our spectral warping results. Compared to the matched case, some CI listeners showed significant decreases[4] when a 0.77 octave shift was applied to the spectral information, either by changing the number of electrodes or amount of spectral content via the upper-frequency boundary. However, there were also cases of significantly *increased* speech understanding for deviations from the matched condition. Numerous significant increases were seen for CI18 when the frequency resolution was increased ($N>M$) with an expanded frequency-to-place mapping. In fact, CI18's best speech understanding occurred for $M_{10}N_{12}$, not the matched $M_{12}N_{12}$ condition. On average across the entire population of listeners, $M_{10}N_{12}$ appeared to be a slightly better map than $M_{12}N_{12}$ as shown by the small but insignificant gains seen in Table III.

It was shown that there was a significant interaction between N and M for fixed SNRs. This is contrary to the results of Fu and Shannon (1999a) that showed no interaction between frequency resolution and frequency allocation. It appears that a constant tonotopic shift along the basilar membrane (in mm) is a different manipulation from the spectral warping that we performed. Therefore, unlike Fu and Shannon's, our spectral manipulation appears not to have orthogonal bases.

Figures 4 and 5 show asymmetric decreases in performance when the spectral range or the number of channels was changed. Decreasing the spectral range or number of channels was more detrimental to understanding speech than increasing the spectral range or number of channels, as shown in the number and magnitude of significant decreases from the matched conditions. Said another way, removing information reduced scores more than adding information despite having similar octave shifts. For example, in Fig. 5, the top panels show that decreasing the upper-frequency boundary and removing spectral content from $M=12$ to 6 when $N=12$ decreases P_c by up to 50%, whereas the bottom panels show that adding spectral content from $M=6$ to 12 when $N=6$ decreases P_c by only 25% or less. This is a promising result for the extended frequency range condition, which adds spectral content to include frequencies above 8.5 kHz.

D. Extended frequency range

An additional condition, referred to as the extended frequency range condition ($M_{14}N_{12}$), was included in this experiment. This condition maps the frequencies ranging from $f_{\text{lower}}=300$ Hz[1] to $f_{\text{upper}}=16{,}000$ Hz to the full range of available channels. See Table I for corner frequencies and octave shifts for this condition. It was tested to examine the effects of the inclusion of higher frequencies that contain no important speech cues but are known to be important for sound source localization in the vertical planes for NH listeners. It was hypothesized that listeners would have no degradation in performance due to spectral warping because the most basal electrode was shifted by only −0.88 octaves, close to −0.77 octave shift found to be acceptable from the previous section. The next largest warping tested in this experiment was −1.55 octaves and was found to cause significant decreases in speech understanding.

The results comparing $M_{14}N_{12}$ to $M_{12}N_{12}$ can be seen in Table IV. Significance values were determined from a one-way RM ANOVA for each SNR. For the CI listeners, the performance for $M_{14}N_{12}$ decreased significantly compared to $M_{12}N_{12}$ in quiet (mean decrease of 11.3%) and for the +10-dB SNR (mean decrease of 15.7%). There were decreases of 15.0% and 20.4% for the +5- and 0-dB SNR conditions, respectively, but they were not significant. The reason that these decreases were not significant was the large variance of the average performance for the group of CI listeners in the noisier conditions, which can be seen in the standard deviations in Table IV. For the NH listeners, the performance for $M_{14}N_{12}$ was not significantly different from $M_{12}N_{12}$ for all four SNRs.

The difference between the CI and NH listeners could be due to the ceiling effect that may be affecting the NH listen-

ers, which has been hinted at in the data of the matched and unmatched sections. However, the CI listeners did not show this possible ceiling effect. Therefore, if the speech material were more difficult, the NH listeners might have also shown significant decreases for the extended frequency range condition compared to the baseline. Another reason for this discrepancy between the groups of listeners could be that CI listeners are less resistant to spectral warping than NH listeners as seen in Figs. 4 and 5. All the p values in Table IV were on the verge of significance, implying that a spectral shift of −0.88 octaves was just enough to cause a significant difference. It may be the case that a slightly smaller shift closer to −0.77 octaves would not cause a substantial decrease in this experiment. Thus it may be possible to obtain a condition without a significant decrease in performance if frequencies up to 14.5 kHz, which corresponds to a −0.74 octave shift for the most basal electrode, were used.

III. EXPERIMENT 2

As mentioned in the Introduction, the importance of training with different frequency-to-place maps is well known (Rosen *et al.*, 1999; Fu *et al.*, 2002; Fu *et al.*, 2005). For example, Başkent and Shannon (2006) showed no improvement in speech understanding when maps were altered to reassign information around dead regions in NH simulations. However, in a subsequent study, Smith and Faulkner (2006) showed significant learning with extended training, reducing the problem of holes in hearing and coming to the opposite conclusion as Başkent and Shannon. Furthermore, the results of experiment 1 could have been confounded by the possibility that subjects require more perceptual learning to obtain an asymptote in performance for conditions involving spectral shift than for conditions involving no shift. For example, the matched condition M_6N_6 involves no spectral warping from the clinical setting, whereas the unmatched conditions M_6N_{12} and $M_{12}N_6$ involve large shifts of spectral information for the most basal electrodes. This experiment studied the time course of perceptual learning with three selected conditions from experiment 1, one without spectral warping and two with warping. While previous studies have shown a stronger learning effect for shifted-speech stimuli compared to unshifted stimuli, these results may not be applicable to the unmatched conditions of experiment 1. A major difference is that these studies applied a constant shift across the signal spectrum, whereas we apply a shift that gradually increases with frequency starting at approximately zero shift at the lower frequency end. Thus, there is less shift in the lower spectral region, which is considered to be most important for speech perception. The main goal of the present experiment is to estimate to what extent the relative differences between the results obtained for the unmatched and the matched conditions may change if the subjects are provided with feedback training over several sessions.

A. Methods

Three of the normal-hearing listeners (NH2, NH5, and NH10) that participated in experiment 1 performed this experiment. Three mapping conditions were tested, namely M_6N_6, M_6N_{12}, and $M_{12}N_6$—conditions representative of the matched, expanded, and compressed conditions, respectively (see Table I). The condition without spectral warping was included to separate the adaptation to vocoded speech in general from the adaptation to the spectral warping. While all three conditions may involve vocoded-speech adaptation, only the unmatched conditions involve spectral-warping adaptation.

We trained and tested two different conditions in a single test. We felt this was justified by Dorman and Dahlstrom (2004) who showed listeners probably using two speech maps simultaneously and Hofman *et al.* (1998) who showed that at least two localization maps could be mutually utilized by subjects. First, the M_6N_6 condition was tested with the M_6N_{12} condition. Each subject completed a total of eight experimental sessions. After data were taken for these two conditions, the M_6N_6 condition was tested with the $M_{12}N_6$ condition. Within one session, feedback training and subsequent testing was performed for both signal conditions. The order of matched and unmatched blocks was randomly chosen for each session. Each block consisted of ten sentences in quiet for the initial listener adaptation, followed by 80 sentences (the four SNRs used in experiment 1 presented in random order). The sentences were different from trial to trial, but, in contrast to experiment 1, they were not different from listener to listener. The reason for this was to determine if certain words affect the results of the sentence tests. In the feedback training runs, each sentence was displayed on a computer screen, followed by a gap of 500 ms with subsequent acoustic presentation of the sentence. The subjects initiated each successive trial by pressing a button. All other aspects of the experiment were the same as in experiment 1.

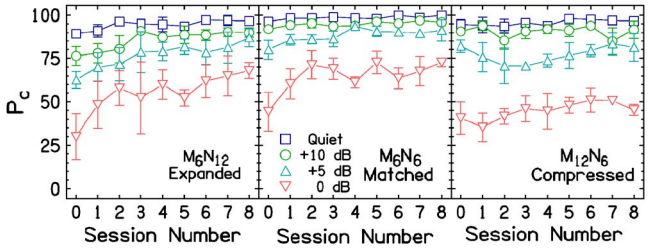

FIG. 6. (Color online) Results from experiment 2 showing percent correct vs session number averaged over three NH listeners. Session 0 contains the baseline data from experiment 1. Sessions 1–8 are from experiment 2.

B. Results

Figure 6 shows the results of experiment 2 averaged over the three listeners. Each plot depicts P_c as a function of session number. The baseline session, labeled as 0, represents the acute data from these three listeners taken in experiment 1. Only eight sessions for the matched M_6N_6 condition (taken from the first test group of M_6N_6 and M_6N_{12}) are shown because learning had saturated after the first eight sessions, which is supported below. Qualitatively, it seems that there was a training effect and more learning seems possible for M_6N_{12} (left panel), the learning seems to have saturated for M_6N_6 (middle panel), and that there was no learning for $M_{12}N_6$ (right panel). To determine the significance of

the learning effect, we compared the acute measurements from experiment 1 and the average of the last three measurements in a two-way RM ANOVA [factors SNR and session (four)]. Two conditions showed significant learning: M_6N_6 ($p<0.0001$) and M_6N_{12} ($p<0.0001$). However, the $M_{12}N_6$ condition did not show significant learning ($p=0.098$). This agrees with the interaction analysis in a three-way RM ANOVA [factors SNR, session (all nine), and condition]. The interaction between conditions M_6N_6 and M_6N_{12}, the conditions with learning, and session number, was insignificant ($p=0.069$). However, the interaction between conditions M_6N_6 and $M_{12}N_6$ and session number was significant ($p=0.011$). The M_6N_6 condition was tested twice, eight sessions with M_6N_{12} and eight sessions with $M_{12}N_6$. The last three sessions of each were compared and the difference between them was insignificant ($p=0.51$). Therefore, learning had truly saturated for M_6N_6 after the first eight sessions.

For the two conditions with learning, the session number where significant learning occurs was determined by Helmert contrasts. For the matched condition, significant learning was seen up to the second session (session 1 vs later: $p=0.002$, session 2 vs later: $p=0.36$). For the expanded condition, significant learning was seen up to the third session (session 2 vs later: $p=0.007$, session 3 vs later: $p=0.17$).

Comparisons between matched and unmatched conditions are most important for this study. First, comparisons between the matched M_6N_6 condition and the unmatched conditions were done. For the acute measurements, there was a significant decrease between the matched condition and each of the compressed and expanded conditions (see, Figs. 4 and 5 or Table III). For the three measurements at the end of the training, there continued to be a significant decrease between the matched and expanded conditions ($p<0.0001$) and between the matched and compressed conditions ($p<0.0001$). This is to be expected between M_6N_6 and $M_{12}N_6$ because the compressed condition showed no significant learning. However, it is noteworthy that the M_6N_{12} condition, although having showed learning, did not improve enough to remove the difference from the M_6N_6 condition.

Second, comparisons between the baseline condition, $M_{12}N_{12}$, and the three conditions tested in experiment 2 were done. Note that all listeners were trained on $M_{12}N_{12}$ until stable performance was achieved. For the three NH listeners used in this experiment, there was always a significant difference between $M_{12}N_{12}$ and the tested conditions in the acute testing. After the training, all three conditions still showed significant decreases from $M_{12}N_{12}$ ($p<0.0001$ for all three comparisons).

As a final note, one difference between experiments 2 and 1 is that experiment 2 used the same sentences for all three listeners. It was found that listeners' P_c values were not significantly correlated over the session number. Therefore, certain words or configurations of words in the OLSA sentences did not significantly affect the outcome of the test.

C. Discussion

After two or three training sessions with feedback, the listeners obtained scores that were only marginally lower (on average across the listeners) than those after eight training sessions with feedback. Qualitatively, the improvement for the M_6N_6 condition appears to have saturated. The $M_{12}N_6$ condition showed no significant improvement. However, the M_6N_{12} condition may still have been improving. We cannot say whether there would be further improvement over months of training as suggested by Fu *et al.* (2002). Nevertheless, we can say that feedback training seems to be very helpful before testing different frequency-to-place mappings (matched and unmatched), even if it is only a couple of sessions. The data of Fu *et al.* (2002) showed that the biggest gains were within the first few days of training, similar to our data. A major difference between these two studies is that the CI listeners in Fu *et al.* used a shifted-spectral map all day long, whereas our NH listeners heard warped sentences for an hour a day. Rosen *et al.* (1999) and Fu *et al.* (2005) also showed the largest improvements within the first few testing sessions for spectrally-shifted material.

There was no evidence that listeners learn differently between the matched M_6N_6 condition and the unmatched M_6N_{12} condition. This is contrary to the studies of Rosen *et al.* (1999) and Fu *et al.* (2005) who found that there was less learning for the matched condition than for the unmatched condition. A major difference between those studies and our study is the type of shift. We held the lower-frequency boundary constant for each listener, which involves less shift at lower frequencies that are more important for speech understanding. Interestingly, the compressed condition, $M_{12}N_6$, was resistant to learning for our listeners. The reason for the difference between the compressed and expanded conditions might be that there is improved resolution of the formants for the expanded condition, which can be adapted to even if the tonotopic place of formant presentation has been altered. However, reducing the resolution of the formants cannot be adapted to when the speech is represented in six channels. Also note that in Table I the octave shifts for the lowest channels are slightly larger for the compressed condition, $M_{12}N_6$, which may have also contributed to the difference in learning.

Even though there was a difference in learning between the compressed condition and the matched and expanded conditions, both of the latter conditions were still significantly lower than the baseline condition. Hence, the results from experiment 2 give insight to adaptation of speech understanding under different matched, expanded, and compressed frequency-to-place maps. Nonetheless, we need to be cautious about these results. First, only three NH listeners were used, no CI listeners. Next, eight sessions was possibly not a sufficient training period for the expanded M_6N_{12} condition; longer testing periods should be attempted in the future. Last, the unmatched conditions chosen for this experiment had the most extreme spectral warpings of those tested in experiment 1. It may be that milder warpings could show changes in the relative differences to the baseline condition, especially conditions with sufficient formant resolution. However, since our goal is to find conditions that are not different from the baseline, this would actually be a positive finding for our study on spectral warping and using different frequency-to-place mappings to implement new CI strategies.

IV. GENERAL DISCUSSION

A. Effects of spectral warpings

The purpose of this study was to test a wide range of spectral mappings and find the effect of varying the upper boundary of the frequency and stimulation range and spectral warpings on speech understanding for CI users, with the hope of gaining insight into the possibility of implementing new processing strategies for CIs. Specifically, we were trying to determine if there is extra speech information currently presented to CI users. The type of spectral warping that we implemented was unique because it kept the lower boundary of the frequency and stimulation range fixed, and introduced an increasing amount of shift towards higher channels. This allowed for testing of both matched frequency-to-place conditions, where speech material was only low-pass filtered, and unmatched conditions.

For the matched conditions, where the spectral content was matched to the place of presentation, it was found that speech understanding in CI listeners saturates at eight to ten electrodes, which does not present frequency information above 2.8 to 4.9 kHz, respectively. There was no significant difference between the twelve and eight or ten channel conditions, depending on the SNR. Care should be taken extrapolating these results to different speech material or different maskers like single- or multi-talker interference. As always, because of the highly individualistic nature of CI users, care should also be taken to derive general conclusions about the entire population.

Combining our results with those obtained by Garnham *et al.* (2002) and by Başkent and Shannon (2005), who used the same type of electrode array and thus the same spacing of electrodes, reveals an interesting observation. Increasing the number of matched channels beyond eight does not improve speech understanding substantially, irrespective if the channels are distributed across a constant stimulation range (Garnham *et al.* 2002), if the lower-frequency boundary of the matched stimulation range is varied (Başkent and Shannon, 2005), or if the higher-frequency boundary of the matched stimulation range is varied (present study). In the study by Garnham *et al.*, this limit appears to be related to the restriction of the number of independent channels as a result of channel interactions (e.g., Shannon, 1983). However, for the Başkent and Shannon study and our experiment, the saturation at eight to ten channels can be understood by a different mechanism. The channel interactions are held constant in both studies. The limit on the number of channels observed in these studies can be explained by the frequency range important for speech perception. This corresponds to approximately 300–5000 Hz, below and above which the SII shows minimal importance of the speech information for NH listeners. In fact, this also explains why there was no difference between the CI and NH listeners for the saturation of speech understanding in quiet and in noise. NH listeners can benefit more than CI listeners from a larger number of channels if they are distributed within the frequency range important to speech perception, particularly at low SNRs (e.g., Dorman *et al.*, 1998).

It was found that it is possible to shift the spectral mapping slightly without decreasing speech understanding. For the 12-electrode Med-El implant, it is possible to change the amount of frequency information by 0.77 octaves for the most basal electrode and have no decrease in speech understanding. This can be done either by varying the upper-frequency boundary and spectral content for a fixed number of electrodes or by changing the number of channels by two for a fixed amount of spectral content. As was mentioned before, only eight to ten channels with frequency content matched to tonotopic place (as assumed by the typical clinical settings) are necessary for no significant decrease in speech understanding. However, it is not possible to then apply a shift of 0.77 octaves to eight matched channels without causing significant decreases from the matched twelve channel condition. In summary, the conditions where speech understanding is not significantly different from the $M_{12}N_{12}$ case are: $M_{10}N_{12}$, $M_{12}N_{10}$, $M_{10}N_{10}$, and M_8N_{10}.

A second experiment was performed to test the adaptation of listeners to matched, expanded, and compressed frequency-to-place maps using feedback training. It was found that listeners' speech understanding improved for the matched and expanded maps, but not for the compressed map. The reason for this may be that the compressed map had insufficient spectral resolution for adequate formant recognition. The expanded map could be adapted to apparently because of the formants could be resolved. This explanation may also be supported by the small but insignificant overall gains seen in Table III for the $M_{10}N_{12}$ condition that also has improved resolution compared to the baseline condition. Similarly, McKay and Henshall (2002) found that after two weeks experience, CI listeners could fully adapt to a "mildly" expanded map, where nine electrodes were assigned to frequencies below 2600 Hz, compared to the normal five electrodes.

A recent study by Başkent and Shannon (2007) studied the effect of combining spectral shift and frequency expansion and compression using noise-vocoded speech with acute measurements. They found a compensatory effect for shifted and compressed maps, hence a relative gain in speech understanding, which may seem contradictory to the poor performance of the compressed condition in experiment 2. The difference between these two studies is that a shift and compression is not the same as a spectral warping where the lower-frequency boundary is fixed. Our lower-frequency boundary always contained frequencies as low as 300 Hz. The stimuli in Başkent and Shannon's study had frequency content as low as 184 Hz for a compressed map, 513 Hz for a matched map, and 1170 for an expanded map. If the low-frequency content was kept fixed and training occurred, then we believe that a compensatory effect may be seen for the expanded maps also.

B. In the context of sound localization

While there are great advances in the area of speech understanding with CIs, there are other areas that are still severely lacking. For example, an area that needs attention is sound localization. For localization in the vertical plane

(front-back and up-down), spectral peaks and notches are needed. These spectral cues are normally introduced by reflections from the pinna, head, and shoulders. The findings of this study are a preliminary step in realizing a CI spatialization strategy, focusing mainly on the possibility of including detectable spectral cues for vertical plane localization. Introducing these cues may have a detrimental effect on speech understanding, especially for the CI listeners with their restricted number of channels. A primary goal in developing a CI spatialization strategy is to have no or very little loss of speech understanding, the main purpose for implantation of a prosthetic hearing device. Any localization strategy that hinders a CI's major reason for existence is not particularly useful. Besides improving the localization abilities of CI users, such a spatialization strategy may someday help speech understanding in noisy situations, an extremely difficult situation for CI users.

The fact that full adaptation to compressed frequency-to-place maps may not be possible is an important fact to consider when designing a CI spatialization strategy. The most important spectral cues used for vertical plane localization occur between 4 and 16 kHz (Hebrank and Wright, 1974; Langendijk and Bronkhorst, 2002). Current processing strategies that use spectral information up to 8.5 or 10 kHz (depending on processor type) would already be able to implement peaks and notches in the lower half of the important spectral region. However, it was seen that CI listeners had significantly lower speech understanding scores, when acutely measured, when the upper-frequency boundary was increased to 16 kHz. A strict interpretation of this result combined with the results from the learning experiment suggests that the mapping of spectral peaks and notches from a straightforward frequency compression may not be the solution to gain access to the localization cues above 10 kHz while preserving adequate speech understanding. This of course is assuming that the lack of learning result for the severely compressed maps applies to the slightly compressed maps, which is probably not the case. Unfortunately, this study did not determine how much spectral compression retains sufficient spectral resolution of the formants to yield sufficient long-term learning of a compressed map. Whether or not a mildly compressed map can be used, a likely solution to implement a CI localization strategy would be to match frequency-to-place up to about eight channels and then apply a novel mapping of higher frequency regions to the remaining channels, depending on the importance of spectral features in these regions. Afterwards, results from this study can be combined with data on the sensitivity of CI listeners to spectral peaks and notches to determine if spectral sound localization cues can be used by CI listeners. Because it is possible for listeners to adapt to new spectral localization cues (Hofman *et al.*, 1998), we believe the auditory system has enough plasticity to make use of a CI localization strategy.

ACKNOWLEDGMENTS

We would like to thank M. Mihocic for running experiments, our listeners who performed a total of 250 h in these experiments, and the Med-El Corp. for providing the equipment for direct electrical stimulation. We would also like to thank the associate editor, Andrew Oxenham, and two anonymous reviewers for improving the quality of this manuscript. This study was funded by the Austrian Science Fund (Project No. P18401-B15) and the Austrian Academy of Sciences.

[1]Two CI listeners, CI16 and CI18, had a lower-frequency boundary of 200 Hz to better match their clinical processor settings. One listener, CI17, had a lower-frequency boundary of 250 Hz. Therefore their center frequencies are shifted downward compared to those found in Table I. For the M_6N_{10} and M_6N_{12} conditions, an unstable filter would be used when the lower-frequency boundary is less than 300 Hz. Therefore, these two conditions had f_{lower}=300 Hz for all 13 listeners, even though this differs from the clinical settings for CI16, CI17, and CI18. The three subjects reported no perceptual abnormality for these two conditions compared to the other conditions in this experiment.

[2]Each CI listener adjusted the stimulus to a comfortable level for each value of *N*. There was no systematic difference in the adjusted level across different *N* values. Therefore, for each listener a common level was used for all *N* values.

[3]For the NH listeners, a preliminary experiment to balance the loudness of the processed sentences was attempted to eliminate possible loudness summation effects from using sentences with different bandwidths. A single sentence was presented processed in two ways: $M_{12}N_{12}$ and M_XN_X where X=4, 6, 8, 10, or 12. For X=8, 10, or 12, the measured loudness difference was at most ±1.5 dB. For X=4 or 6, the measured loudness difference was at most ±3.5 dB. There was a large variability between listeners in the level balancing results, which was probably due to the difficulty of matching the loudness of two sentences with different frequency content. When the loudness balancing results were applied to the sentences in pilot tests, results did not significantly change. In the end, we decided to present the sentences at a nominally equal level of 75 dB (A) SPL.

[4]Significant differences were determined using the binomial model proposed by Thorton and Raffin (1978) and were significant at the 0.05 level. The sample size for one condition in a single block was 100, since 20 sentences consisting of five independent words each were presented.

ANSI (**1997**). ANSI S3.5-1997, "American National Standard Methods for the Calculation of the Speech Intelligibility Index" (American National Standards Institute, New York).

Baer, T., and Moore, B. C. J. (**1993**). "Effects of spectral smearing on the intelligibility of sentences in noise," J. Acoust. Soc. Am. **94**, 1229–1241.

Baer, T., and Moore, B. C. J. (**1994**). "Effects of spectral smearing on the intelligibility of sentences in the presence of interfering speech," J. Acoust. Soc. Am. **95**, 2277–2280.

Başkent, D., and Shannon, R. V. (**2003**). "Speech recognition under conditions of frequency-to-place compression and expansion," J. Acoust. Soc. Am. **113**, 2064–2076.

Başkent, D., and Shannon, R. V. (**2004**). "Frequency-to-place compression and expansion in cochlear-implant listeners," J. Acoust. Soc. Am. **116**, 3130–3140.

Başkent, D., and Shannon, R. V. (**2005**). "Interactions between cochlear implant electrode insertion depth and frequency-to-place mapping," J. Acoust. Soc. Am. **117**, 1405–1416.

Başkent, D., and Shannon, R. V. (**2006**). "Frequency transposition around dead regions simulated with a noiseband vocoder," J. Acoust. Soc. Am. **119**, 1156–1163.

Başkent, D., and Shannon, R. V. (**2007**). "Combined effects of frequency compression-expansion and shift on speech recognition," Ear Hear. **28**, 277–289.

Boothroyd, A., Mulheam, B., Gong, J., and Ostroff, J. (**1996**). "Effects of spectral smearing on phoneme and word recognition," J. Acoust. Soc. Am. **100**, 1807–1818.

Chambers, J., and Hastie, T. J. (**1993**). *Statistical Models* (Chapman and Hall, London).

Dorman, M. F., and Dahlstrom, L. (**2004**). "Speech understanding by cochlear-implant patients with different left- and right-ear electrode arrays," Ear Hear. **25**, 191–194.

Dorman, M. F., Loizou, P. C., and Rainey, D. (**1997**). "Simulating the effect

of cochlear-implant electrode depth on speech understanding," J. Acoust. Soc. Am. **102**, 2993–2996.
Dorman, M. F., Loizou, P. C., Fitzke, J., and Tu, Z. (**1998**). "The recognition of sentences in noise by normal-hearing listeners using simulations of cochlear-implant signal processors with 6–20 channels," J. Acoust. Soc. Am. **104**, 3583–3585.
Faulkner, A., Rosen, S., and Stanton, D. (**2003**). "Simulations of tonotopically mapped speech processors for cochlear implant electrodes varying in insertion depth," J. Acoust. Soc. Am. **113**, 1073–1080.
Friesen, L. M., Shannon, R. V., Başkent, D., and Wang, X. (**2001**). "Speech recognition in noise as a function of the number of spectral channels: Comparison of acoustic hearing and cochlear implants," J. Acoust. Soc. Am. **110**, 1150–1163.
Fu, Q.-J., and Shannon, R. V. (**1999a**). "Recognition of spectrally degraded and frequency-shifted vowels in acoustic and electric hearing," J. Acoust. Soc. Am. **105**, 1889–1900.
Fu, Q.-J., and Shannon, R. V. (**1999b**). "Effects of electrode location and spacing on phoneme recognition with the Nucleus-22 cochlear implant," Ear Hear. **20**, 321–331.
Fu, Q.-J., and Shannon, R. V. (**1999c**). "Effects of electrode configuration and frequency allocation on vowel recognition with the Nucleus-22 cochlear implant," Ear Hear. **20**, 332–344.
Fu, Q.-J., and Shannon, R. V. (**1999d**). "Effect of acoustic dynamic range on phoneme recognition in quiet and noise by cochlear-implant listeners," J. Acoust. Soc. Am. **106**, L65–L70.
Fu, Q.-J., Shannon, R. V., and Galvin, J. J. III (**2002**). "Perceptual learning following changes in the frequency-to-electrode assignment with the Nucleus-22 cochlear implant," J. Acoust. Soc. Am. **112**, 1664–1674.
Fu, Q.-J., Nogaki, G., and Galvin, J. J. III (**2005**). "Auditory training with spectrally shifted speech: Implications for cochlear implant patient auditory rehabilitation," J. Assoc. Res. Otolaryngol. **6**, 180–189.
Garnham, C., O'Driscoll, M., Ramsden, R., and Saeed, S. (**2002**). "Speech understanding in noise with a Med-El COMBI 40+ cochlear implant using reduced channel sets," Ear Hear. **23**, 540–552.
Greenwood, D. D. (**1990**). "A cochlear frequency-position function for several species—29 years later," J. Acoust. Soc. Am. **87**, 2592–2605.
Gstoettner, W., Franz, P., Hamzavi, J., Plenk, H., Baumgartner, W., and Czerny, C. (**1999**). "Intracochlear position of cochlear implant electrodes," Acta Oto-Laryngol. **119**, 229–233.
Hebrank, J., and Wright, D. (**1974**). "Spectral cues used in the localization of sound sources on the median plane," J. Acoust. Soc. Am. **56**, 1829–1834.
Hofman, P. M., Van Riswick, J. G. A., and Van Opstal, A. J. (**1998**). "Relearning sound localization with new ears," Nat. Neurosci. **1**, 417–421.
Ketten, D. R., Vannier, M. W., Skinner, M. W., Gates, G. A., Wang, G., and Neely, J. G. (**1998**). "*In vivo* measures of cochlear length and insertion depth of nucleus cochlear implant electrode arrays," Ann. Otol. Rhinol. Laryngol. **107**, 1–16.
Langendijk, E. H. A., and Bronkhorst, A. W. (**2002**). "Contribution of spectral cues to human sound localization," J. Acoust. Soc. Am. **112**, 1583–1596.
McKay, C. M., and Henshall, K. R. (**2002**). "Frequency-to-electrode allocation and speech perception with cochlear implants," J. Acoust. Soc. Am. **111**, 1036–1044.
Rosen, S., Faulkner, A., and Wilkinson, L. (**1999**). "Adaptation by normal listeners to upward spectral shifts of speech: Implications for cochlear implants," J. Acoust. Soc. Am. **106**, 3629–3636.
Shannon, R. V. (**1983**). "Multichannel electrical stimulation of the auditory nerve in man. II. Channel interaction," Hear. Res. **12**, 1–16.
Shannon, R. V., Zeng, F.-G., Kamath, V., Wygonski, J., and Ekelid, M. (**1995**). "Speech recognition with primarily temporal cues," Science **270**, 303–304.
Skinner, M. W., Fourakis, M. S., and Holden, T. A. (**1995**). "Effect of frequency boundary assignment on speech recognition with the SPEAK speech-coding strategy," Ann. Otol. Rhinol. Laryngol. Suppl. **166**, 307–311.
Smith, M., and Faulkner, A. (**2006**). "Perceptual adaptation by normally hearing listeners to a simulated 'hole' in hearing," J. Acoust. Soc. Am. **120**, 4019–4030.
Sridhar, D., Stakhovskaya, O., and Leake, P. A. (**2006**). "A frequency-position function for the human cochlear spiral ganglion," Audiol. Neuro-Otol. **11**, Suppl 1, 16–20.
Studebaker, G. A. (**1985**). "A 'rationalized' arcsine transform," J. Speech Hear. Res. **28**, 455–462.
Studebaker, G. A., and Sherbecoe, R. L. (**1991**). "Frequency-importance and transfer functions for recorded CID W-22 word lists," J. Speech Hear. Res. **34**, 427–438.
Thornton, A. R., and Raffin, M. J. (**1978**). "Speech-discrimination scores modeled as a binomial variable," J. Speech Hear. Res. **21**, 507–518.
ter Keurs, M., Festen, J. M., and Plomp, R. (**1992**). "Effect of spectral envelope smearing on speech reception. I," J. Acoust. Soc. Am. **91**, 2872–2880.
ter Keurs, M., Festen, J. M., and Plomp, R. (**1993**). "Effect of spectral envelope smearing on speech reception. II," J. Acoust. Soc. Am. **93**, 1547–1552.
Wagener, K., and Brand, T., Kühnel, V., and Kollmeier, B. (**1999a**). "Development and evaluation of a German sentence test I: Design of the Oldenburg sentence test," (in German), Zeitschrift für Audiologie/ Audiological Acoustics **38**, 4–14.
Wagener, K., Brand, T., Kühnel, V., and Kollmeier, B. (**1999b**). "Development and evaluation of a German sentence test II: Optimization of the Oldenburg sentence test," (in German), Zeitschrift für Audiologie/ Audiological Acoustics **38**, 44–56.
Wagener, K., Brand, T., Kühnel, V., and Kollmeier, B. (**1999c**). "Development and evaluation of a German sentence test III: Evaluation of the Oldenburg sentence test," (in German), Zeitschrift für Audiologie/ Audiological Acoustics **38**, 86–95.
Wilson, B. S., Finley, C. C., Lawson, D. T., Wolford, R. D., Eddington, D. K., and Rabinowitz, W. M. (**1991**). "New levels of speech recognition with cochlear implants," Nature (London) **352**, 236–238.
Zierhofer, C. M., Hochmair, I. J., and Hochmair, E. S. (**1997**). "The advanced Combi 40+ cochlear implant," Am. J. Otol. **18**, Suppl, S37–38.

Incorporation of phonetic constraints in acoustic-to-articulatory inversion

Blaise Potard,[a] Yves Laprie,[b] and Slim Ouni[c]
Speech Team, LORIA, UMR 7503, BP 239, 54506 Vandœoeuvre-lès-Nancy Cedex, France

(Received 10 November 2006; revised 31 January 2008; accepted 1 February 2008)

This study investigates the use of constraints upon articulatory parameters in the context of acoustic-to-articulatory inversion. These speaker independent constraints, referred to as phonetic constraints, were derived from standard phonetic knowledge for French vowels and express authorized domains for one or several articulatory parameters. They were experimented on in an existing inversion framework that utilizes Maeda's articulatory model and a hypercubic articulatory-acoustic table. Phonetic constraints give rise to a phonetic score rendering the phonetic consistency of vocal tract shapes recovered by inversion. Inversion has been applied to vowels articulated by a speaker whose corresponding x-ray images are also available. Constraints were evaluated by measuring the distance between vocal tract shapes recovered through inversion to real vocal tract shapes obtained from x-ray images, by investigating the spreading of inverse solutions in terms of place of articulation and constriction degree, and finally by studying the articulatory variability. Results show that these constraints capture interdependencies and synergies between speech articulators and favor vocal tract shapes close to those realized by the human speaker. In addition, this study also provides how acoustic-to-articulatory inversion can be used to explore acoustical and compensatory articulatory properties of an articulatory model.
© *2008 Acoustical Society of America.* [DOI: 10.1121/1.2885747]

PACS number(s): 43.70.Bk, 43.70.Aj, 43.72.Ct [DOS] Pages: 2310–2323

I. INTRODUCTION

Acoustic-to-articulatory inversion remains an open challenge in speech analysis. Although there is a wide range of potential applications, there is as of yet no clear answer to whether or not inversion is possible for all the sounds of speech.[1] However, there do exist numerical simulations that cover both articulatory and acoustical phenomena involved in speech production and which enable the synthesis of acoustical signals close to natural speech. These tools, especially those generating a speech spectrum, are often used to perform inversion. Indeed, most of the existing approaches to acoustic-to-articulatory inversion are analysis-by-synthesis methods.

The key difficulty is that an infinity of vocal tract shapes can produce any given spectrum. In order to reduce the number of inverse solutions, methods of acoustic-to-articulatory inversion incorporate explicit or implicit constraints.

Sorokin,[2] for instance, presents seven possible kinds of constraints: limitations in the contractive force of muscles involved in speech production; anatomy of the vocal tract or equivalently, ranges of articulatory parameters; interdependencies between muscles, i.e., interdependent variations of the articulatory parameters; interdependency between transversal and midsagittal dimensions of the vocal tract; aerodynamic constraints with respect to the kinds of sound produced; level of the acoustical deviation tolerated between analyzed and resynthesized sounds according to style and rate of speech; and last, a constraint concerning the complexity of planning and programming of the articulatory control.

Some of these constraints, those upon articulatory parameters and, to a certain extent, those upon the transversal dimension estimated from the midsagittal profile of the vocal tract, can be incorporated directly in the analyzing model, in the form of an articulatory model. They can rely only on pure geometrical primitives, like those of Coker[3] and Mermelstein.[4] However, despite their flexibility and their ability to copy the natural vocal tract, their control parameters do not capture the natural deformation modes of human vocal tracts.

Therefore, models derived through a factor analysis procedure of x-ray images of a human tract (Maeda[5,6] or Gabioud[7]), or more recently from MRI images,[8] are currently preferred. Building articulatory models from a single speaker could be a strong limitation due to the difficulty of acquiring data for several speakers. However, deformation modes seem to be sufficiently speaker independent to ensure a satisfactory generality to these articulatory models. Indeed, the work of Nix *et al.*,[9] who studied tongue deformation modes for vowels for six speakers (five English speakers and one Icelandic speaker), showed that two cross linguistic factors were sufficient to cover approximately 90% of the articulatory variance, and more important, that they are language independent.

On the other hand, a prior size adjustment (the overall vocal tract length or both mouth and pharynx lengths) should be performed to adapt these articulatory models to a new speaker.[10] The adapted articulatory model imposes geometrical constraints which enable the dimension of the solution space to be reduced, down to often less than ten articulatory

[a]Electronic mail: blaise.potard@loria.fr
[b]Electronic mail: yves.laprie@loria.fr
[c]Electronic mail: slim.ouni@loria.fr

parameters in the model. Even though the benefit of using an articulatory model is obvious, it should be kept in mind that the corresponding constraints may be biased by the geometrical mismatch between the speaker chosen for building the articulatory model and the speaker who uttered speech to be inverted.

Other constraints proposed by Sorokin dealing with contractive forces, interdependencies between articulatory parameters, or the complexity of the articulatory parameters are far too complex to be exploited because there are almost no data available. Indeed, they would require medical investigation technologies that do not exist yet, or that cannot be used easily, e.g., electromyography.

For this reason we investigate the incorporation of constraints upon articulatory parameters derived from standard phonetic knowledge. Their main advantage is to capture speaker independent constraints and a general human expertise about the use of a vocal tract, which both do not exist in an articulatory/acoustical simulation of speech production. This is not the first time the use of phonological or phonetic data is proposed as a constraint for inversion. Boë *et al.*[11] already discussed the use of constraints on the constriction location with respect to vowels. They thus generated 60 000 vocal tract shapes together with their spectra through Maeda's model and the associated acoustical simulation. These shapes were sorted according to the first three formants which enabled the distribution of location and area of the constrictions observed for French vowels to be studied. Strictly speaking, Boë *et al.* did not propose constraints, but describe the constriction characteristics observed for French vowels. Most inversion methods implementing phonetical or phonological constraints (such as those presented by Dusan[12] or Okadome[13]) heavily rely on articulatory data specific to the inverted speaker. Our approach uses purely generic constraints with no prior knowledge over the specific articulation of phonemes by the inverted speaker.

Beside phonetic constraints, our inversion framework[14] also exploits constraints about the dynamics of articulatory parameters. These constraints favor articulatory trajectories which minimize the articulatory effects. Their use is quite general in the domain of acoustic-to-articulatory inversion. Despite their positive effect, i.e., the emergence of smooth articulatory trajectories, they may give rise to very phonetically unrealistic trajectories. This means that regions in the articulatory domain, which are unlikely to be visited by a human speaker, are exploited by error during inversion.

To precisely measure the impact of the phonetic constraints separately, we are only considering the inversion of speech frames independent of the utterance they belong to. Constraints about dynamics are thus not exploited. Furthermore, perturbations due to the adaptation of the articulatory model to the speaker were eliminated through inverting the speaker that was used to build the articulatory model.

In order to obtain a precise assessment of the role of constraints, the acoustical properties of the articulatory model used in this study, i.e., that of Maeda, will be studied through the place and degree of constriction of vowels.

Section II briefly presents the acoustic-to-articulatory method we previously developed. Then Sec. III presents the phonetic constraints and their implementation. As it is important to get a good knowledge of the acoustical behavior of the articulatory model, Sec. IV studies places of articulation and constriction areas of the vocal tract shapes recovered by inversion for French vowels. Then Sec. V describes the derivation of compensatory effects from inversion results for five vowels.

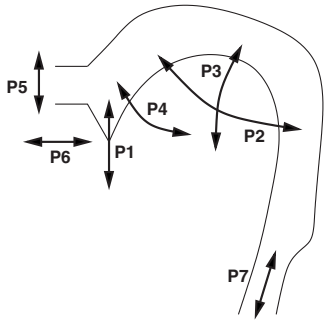

FIG. 1. Parameters of Maeda's articulatory model: P1 (jaw position, vertical movement), P2 (tongue dorsum position that can move roughly horizontally from the front to the back of the mouth cavity), P3 (tongue dorsum shape, i.e., rounded or unrounded), P4 (apex position; this parameter only deforms the apex part of the tongue by moving it up or down), P5 (lip height), P6 (lip protrusion), and P7 (larynx height).

II. PRESENTATION OF THE ACOUSTIC-TO-ARTICULATORY INVERSION FRAMEWORK

A. The articulatory model

Our inversion method[14] relies on Maeda's articulatory model,[6] which describes the vocal tract shape in the form of a weighted sum of seven linear components. Each weight, i.e., each articulatory parameter, is expressed in standard deviation with respect to the corresponding articulatory measures. Each articulatory parameter (see Fig. 1) varies between −3 and +3 to cover most of the possible vocal tract shapes. One component gives the lower jaw position (Jw), three describe the tongue (Tp the tongue position, Ts the tongue shape and Tt the tongue apex), two the lips (Lh the lip opening and Lp the lip protrusion), and the last component Lx correspond to the larynx height. Any vocal tract shape is thus represented in the form of a seven-tuple of articulatory parameters. The linear components were extracted from articulator contours drawn by hand on x-ray images through either a factor analysis method or direct measurement. Since this model was derived from one female speaker's (PB) x-ray images it needs to be adapted to account for a new speaker. A default adaptation consisting in multiplying mouth and pharynx length by a 1.1 factor approximates a default male speaker. Combined with an acoustical simulation,[15] this model can be used to generate artificial speech signals for vowels. The main strength of Maeda's model is to capture the natural deformation modes of the vocal tract shapes through the linear components. However, by construction, i.e., the factor analysis applied to x-ray data, this model cannot capture synergies between components.

Since our objective is to get a precise evaluation of the accuracy of the phonetic constraints, and of the articulatory and acoustical behavior of Maeda's model we chose to invert

vowels of the same female speaker (PB) whose x-ray images were used to create the articulatory model by Maeda. Note that, except in this particular case, no articulatory data of the speaker to be inverted are necessary. The choice of the same speaker was originally intended to eliminate problems related to speaker adaptation, and thus to quantify the efficiency of the phonetic constraints themselves. As the acoustic signal was recorded during shooting of the ten short sentences used to build the articulatory model, these data are very interesting to assess the relevance of the inversion method. Maeda provided the set of articulatory parameters determined for each x-ray frame, along with the audio recording. The acoustic image for each vocal tract shape can be easily computed from these parameters using the articulatory synthesizer and compared to the audio recording. The Appendix describes how the acoustic accuracy of Maeda's model has been improved.

B. Inversion

The articulatory-to-acoustic mapping is represented by an articulatory look-up table, or codebook, which associates vectors of articulatory parameters, i.e., seven-tuples in the case of Maeda's model—corresponding to the seven parameters of the model—with their corresponding three-tuples of the first three formants frequencies (F1, F2, and F3). This codebook thus represents the synthesis facet of the inversion. It is used to recover all the possible seven-tuples of articulatory parameters corresponding to the formant frequencies extracted from a vowel signal at each time frame. One crucial issue is the acoustical and articulatory resolution of such a codebook. The strength of our codebook lies in its quasiuniform acoustic resolution. This property originates in the construction method of the codebook, which evaluates the linearity of the articulatory-to-acoustic mapping at each step. Unlike other methods used to represent the articulatory-to-acoustic mapping, this construction method ensures that no articulatory region compatible with a given three-tuple of formants will be omitted (unless a very strong nonlinearity in the mapping was missed during the exploration used during codebook construction).

Together with specific search algorithms, this codebook enables the recovery of all seven-tuples (with respect to a prior acoustical/articulatory resolution) of articulatory parameters which can generate a given three-tuple of formants.

More details of the inversion method can be found in Ref. 14.

III. INCORPORATION OF PHONETIC CONSTRAINTS FOR VOWELS

Phonetic constraints are derived from standard phonetic knowledge[16] about the articulation of French vowels. This knowledge, and thus the expression of phonetic constraints, is about tongue dorsum position, mouth opening, and lip protrusion. Each constraint is on one vowel, and consequently its relevancy depends on the vowel considered, or in a more general way, on an acoustic region in the formant space. Since the aim of our study is to derive constraints with very little speaker-specific data, the chosen regions are quite large. These constraints return numerical values, decreasing from one, when the constraint is perfectly satisfied, to zero.

TABLE I. Phonetic description of non-nasal French vowels. D stands for "tongue dorsum position," O for "mouth opening," and P for "lip protrusion." See Potard and Laprie (Ref. 19) for more details.

Vowel	Tongue dorsum	Mouth opening	Lip protrusion
i	D6	O1	P1
e	D6	O2	P1
ɛ	D6	O3	P1
a	D7	O4	P1
y	D6	O1	P4
ø	D6	O2	P3
œ	D6	O3	P2
u	D8	O1	P4
o	D8	O2	P3
ɔ	D8	O3	P2

It should be noted that phonetic constraints are not intended to guide inversion toward very precise vowel templates a speaker would use to "jump" from one template to another but to delimit a phonetically relevant subdomain of the articulatory domain. The union of the articulatory regions corresponding to a level of satisfaction of one is thus an approximation of the phonetically relevant articulatory domain.

Table I summarizes the phonetic description for the ten non-nasal French vowels derived from phonetic knowledge.[16,17] This description designed within the context of labial coarticulation modeling[18] has already been used in our preliminary work about phonetic constraints.[19] D stands for "tongue dorsum position," O for "mouth opening," and P for "lip protrusion." The coding is straightforward: The higher the number, the higher the value associated with the given constraint. For example, a constraint O1 means that the mouth has a small opening and a value of O4 means a very big opening. These data are average values of the way native French speakers articulate vowels, and thus may be different from the way a particular speaker articulates French sounds. Note that for the main place of articulation of vowels, corresponding to D in the case of vowels, the range of possible values is a subdomain of the values acceptable for consonants. The full domain of articulation places ranges from 1 for /p,b,m/ to 9 for /ʁ, ɹ/ in French: 1 for labial, 2 for dental, 3 for alveo-dental, 4 for alveolar, 5 for post-alveolar, 6 for palatal, 7 for post-palatal, 8 for velar, 9 for uvular places of articulation. This scale samples the vocal tract roughly linearly.

A. Translation of phonetic constraints in the articulatory model

In most articulatory models, translating simple phonetic features into parameters of the model can be quite complex. In our case, we use Maeda's model, in which the parameters are easily interpretable from a phonetic point of view. Consequently, expressing the phonetic constraints in terms of Maeda's articulatory parameters is straightforward: Lip protrusion and tongue dorsum position are already parameters of

TABLE II. Actual target values for each phonetic constraint. The first column contains the respective values of D6, D7, D8, the second one O1, O2, O3, O4, and finally the third one P1, P2, P3, P4.

Tongue dorsum	Mouth opening	Lip protrusion
−1.5	−2.0	−1.0
0.0	−1.0	−0.5
1.5	0.0	0.5
	0.5	1.5

the model, and the mouth opening is a linear combination of two parameters (jaw position, and intrinsic lip opening).

Actually, the mouth opening constraint also uses the tongue position in order to take into account compensatory effects described by Maeda:[6] He observed that for nonrounded vowels (/i/, /a/, /e/), the tongue position and the jaw opening had similar effects on the acoustic image, and therefore were mutually compensating. He also observed that this compensatory effect was indeed used by his test subjects. Furthermore, it appeared that the direction of compensation did not depend on the vowel pronounced: There was a linear correlation

$$\mathrm{Tp} + \alpha \mathrm{Jw} = \mathrm{Constant},$$

where Tp is the tongue position, Jw the jaw position, and α a linearity coefficient that is the same for both /a/ and /i/. The other vowels were not studied because there were not enough occurrences of them in the x-ray database. Maeda observed this compensation in both his subjects (but the coefficients of correlation were of course different). The α coefficient we use in this study was the one Maeda found experimentally on x-ray data for his speaker PB (the same as in our study), which was approximately equal to 0.66. This compensatory effect allowed Maeda to explain most of the articulatory variability for /a/ and /i/.

The mouth opening is thus given by

$$\mathrm{O} = \min(\mathrm{Tp} + \alpha \mathrm{Jw}, \mathrm{Lh})$$

where Lh is the lip aperture.

Tongue dorsum position is simply given by

$$\mathrm{D} = \mathrm{Tp}$$

and tongue protrusion by

$$\mathrm{P} = \mathrm{Lp}.$$

Maeda's articulatory parameters can vary between −3 and +3 units. The actual constraint values corresponding to each target were adjusted using a visual representation of the articulatory model in order to obtain correct canonical shapes. Table II presents the target values for each constraint.

B. Acoustic space partitioning

For a given acoustic vector, the set of phonetic constraints to apply has to be determined. This consists in attaching the acoustic vector to a phoneme. That could be done manually, but in order to obtain a fully automatic process, we need to define, for each phoneme, an acoustic domain where the corresponding phonetic constraints are considered to be valid.

Since we are currently using the first three formant frequencies as input for acoustic-to-articulatory inversion, the acoustic domains are regions in a three-dimensional space. We tested different models for the partitioning of the acoustic space: (a) Voronoi diagram around the vowels and (b) Voronoi diagram weighted by the standard deviation of each formant frequencies (cf. Fig. 2). Voronoi diagrams can be seen as a nearest-neighbor partitioning: A particular vector of the acoustic space is attached to the point which is the closest with regards to a certain metric. In the first case (a), the metric is simply the Euclidean distance. In the second case (b), the distance takes into account the standard deviations on formant frequencies for each phoneme. The second gives slightly better results in phoneme discrimination and is therefore the only one displayed here. Generic vowels centers and standard deviations depend on the speaker's gender and are specific to the French language; they were obtained from Lonchamp.[20] More information on Voronoi diagrams can be found in, e.g., Aurenhammer.[21]

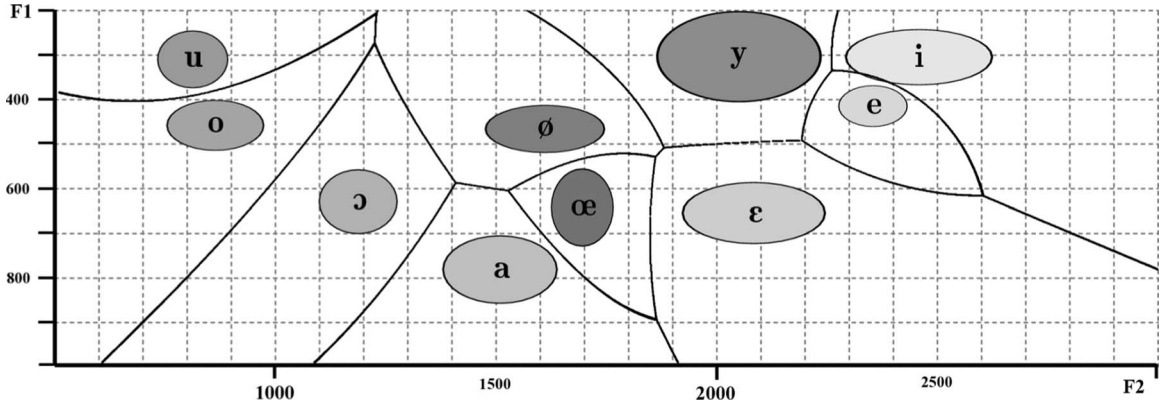

FIG. 2. Partition of the acoustic space using a weighted Voronoi diagram of the vowels center, projected in the F1/F2 space. The weights are the standard deviations of each formant frequency.

C. Phonetic scoring

Now that we have partitioned the acoustic space, we still have to explain how a phonetic score can be associated to each inverse solution. Basically, a given acoustic vector is attached to an "ideal articulatory domain," as defined by the constraints in Table I, corresponding to the region of the acoustic space it belongs to. Then each inverse solution V corresponding to this three-tuple can be given a "phonetic score" according to the distance of the articulatory vector to the "ideal domain." A simple way to do that would be by computing the norm of the vector defined by V and its orthogonal projection onto the domain. Actually, we compute a score relative to each type of constraint: tongue dorsum, mouth opening, and lip protrusion.

The computation of the score depends on two values: the target value of the considered constraint $\theta(v,t)$, where v is the vowel and t is the type of constraint, and a margin $\sigma(v,t)$, which defines a validity interval $I(v,t)=[\theta(v,t)-\sigma(v,t);\theta(v,t)+\sigma(v,t)]$. If the value of the constraint for V is within $I(v,t)$, then it gets a perfect score of 1 for that type of constraint. Otherwise, it gets a positive score less than 1 which exponentially decreases according to the distance to $I(v,t)$. The value of $I(v,t)$ depends on the vowel and the type of constraint considered, and is tuned to take into account the phonetic importance of a particular constraint for the phoneme considered. This tuning process can be done, for the two "visual" phonetic constraints (i.e. mouth opening and lip protrusion), using statistical analysis on visual data from ten French speaker, similar to Robert *et al.*[18] For the last constraint (tongue dorsum position), the only possibility is by studying a corpus of x-ray or MRI images. In our case, $\sigma(v,t)$ varies between 0.1 and 0.6 depending on the vowel and the type of constraint considered. The overall phonetic score is simply a linear combination of the three types of constraints, normalized to get scores within the interval [0; 1] (1 being the best score), all constraints getting equal weights.

D. Constraint specificity

Each constraint applies for a specific vowel, or equivalently to a specific region in the formant space, which thus has to be found beforehand. Even if these regions do not need to be known very precisely there is a risk of mismatching constraints, i.e., applying a constraint dedicated to a given vowel to invert acoustic parameters corresponding to a very different vowel from an articulatory point of view.

Imagine that we attempt to invert acoustical occurrences of the vowel /i/ and to apply constraints corresponding to /a/. Consider the distribution of the places of articulation and the satisfaction level of the inverse solutions for the formants of /a/ [Fig. 4(b)]. The front place of articulation, near 13 cm, intersects the region corresponding to inverse solutions of /i/ [Fig. 6(b)]. However, as can be seen from Fig. 4(b), this articulatory region gets very poor satisfaction levels (i.e., rendered by light gray levels). The fact that all the inverse solutions would get a very poor satisfaction level enables the mismatch of constraints to be easily diagnosed.

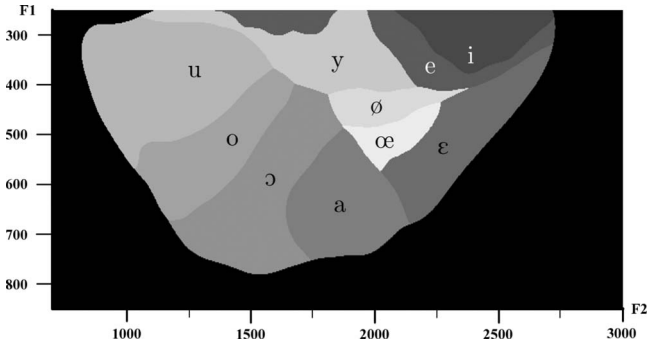

FIG. 3. Constraint used as a function of the input formants represented in the F1–F2 plane.

Based on this observation we evaluated a strategy for triggering constraints which does not require the prior vowel identification. Indeed, if the articulatory domains and constraints are correctly defined, the relevant constraint, i.e., the one to use, is the one which yields the highest average phonetic score over all inverted VT shapes from one three-tuple of formants. We thus carried out an experiment consisting in inverting three-tuples of formants covering the vocalic space of our subject. Figure 3 represents the set of constraints (i.e., the vowel) which returns the highest number of articulatory vectors with a perfect score as a function of the input formants. The first three formants have been used but results are presented in the F1–F2 plane for sake of clarity. It appears there is a strong coherence between the set of constraints giving the highest number of perfect vectors and the acoustical region considered, in particular the general topology of the vocalic triangle is conserved, though some minor discrepancies can be observed. Comparing Fig. 3 to Fig. 2 shows that the regions that maximize the number of perfect articulatory vectors tend to have a higher F2 frequency for open vowels compared to the acoustic domains of the corresponding phonemes in the generic acoustical map (Fig. 2). Additionally, the area for the /y/ appears to be too wide, and appears too small for the /ø/.

However, since we are interested in the impact of each constraint independently we kept the phoneme identification layer to control the application of phonetic constraints in the experiments presented in the following.

IV. RECOVERY OF THE PLACE OF ARTICULATION OF FRENCH VOWELS

A. Inversion experiments

Boë *et al.*[11] used Maeda's articulatory model to study the place of articulation for French vowels. However, their work still did not provide a complete set of solutions, since instead of using an inversion method, they used a limited number of random articulatory configurations. Indeed, it should be noted that the 60 000 articulatory configurations used by Boë *et al.* correspond approximately to the choice of only four values for each of the articulatory parameters. The codebook used in our study was obtained using an improved version of Ouni's hypercube codebook construction method, and contained approximately 60 000 hypercubes, each describing a

TABLE III. A set of French vowels from speaker PB and their phonetic context, first three formants (Hz), number of inverse solutions synthesized, and average error (Hz) between formants measured and those obtained by inversion.

Vowels	Context	F1	F2	F3	No.	ΔF1	ΔF2	ΔF3
a	t**a**bac	749	1701	2785	103 578	19.1	25.0	24.4
e	t**e**s habits	458	2341	3070	208 502	10.7	27.8	35.8
i	roussi**e**s	349	2305	3345	52 799	15.8	19.4	54.1
u	b**ou**gies	367	1050	2495	5 147	22.6	49.8	10.7
y	d**u** guet	341	1956	2523	21 748	11.1	60.3	27.4

first-order approximation of the local articulatory-to-acoustic relation, allowing for codebook inversion with an acoustic precision of 1 bark. During the construction process, about 30 million articulatory vectors were sampled, compared to 300 000 for Boë.

Besides the classical way of describing the vocal tract by specifying the position of articulators, it is possible to calculate representative geometrical measures. In fact, Stevens and House[22] and Fant[23] pointed out that the most important characteristics of vowels from an acoustic phonetic point of view are the position of the main constriction between the tongue and the vocal tract wall and the degree of constriction (cross-sectional area) at that position.

Inversion experiments were conducted using cineradiographic data from a French female speaker, PB. Vowels presented in this paper come from continuous speech, more precisely small sentences recorded together with cineradiographic data. The corresponding acoustic signal recorded at the same time as the x-ray acquisition was of poor quality, but still useable. Formants were extracted from a spectrum computed by the "true envelope" algorithm,[24] which is an iterative cepstral smoothing procedure that takes into account only spectral peaks, i.e., mainly harmonics. All the vowels have been listened to, to ensure that the vowels are perceptually correct. Formants F2 and F3 of /u/ were particularly difficult to extract because the energy of this vowel is weak which means this vowel was dominated by the noise of the x-ray machine. The occurrence retained corresponds to a stronger /u/ and a slightly less intense noise.

For each vowel, the possible vocal tract shapes were recovered by applying the inversion procedure to its formant frequencies. To check the accuracy of the inversion results, we resynthesized spectra, evaluated formants, and compared them against formants measured in original vowels. We pruned all inversion results that had acoustic images too distant from the target frequencies: We imposed an acoustical precision of 30 Hz to F1, 50 Hz to F2, and 75 Hz to F3. Table III presents the five inverted vowels with their first three formant frequencies, the number of inverse solutions, and the average error of the acoustic images of resynthesized solutions (before pruning).

In this vowel study, we present the results according to two parameters: cross-sectional area of the main constriction (A_c, cm^2), also called degree of constriction, and the position of the main constriction in the vocal tract (X_c, cm), also called place of articulation, counted from the larynx. These parameters are obtained by retrieving the vocal tract section where the cross-sectional area is minimal. We do not consider the constriction formed at the lower part of the pharynx (close to the larynx at 2 cm from the glottis) or the constriction formed at the lips. As mentioned earlier, the constriction considered is the lingual one: formed by the tongue and outer vocal tract wall (mostly motionless).

For each vowel, the results are presented in two different forms: constriction area according to the position of the main constriction [Figs. 4(b), 5(b), 6(b), 7(b), and 8(b)], and midsagittal slices of characteristic vocal tract shapes recovered [Figs. 4(a), 5(a), 6(a), 7(a), and 8(a)]. The position of the main constriction varies between 0 cm (glottis) and 16 cm (lips). In order to keep constriction areas consistent with the production of vowels, we eliminated shapes which present a constriction area of less than 0.2 cm^2. We did not eliminate any other solutions from diagrams of Figs. 4(b), 5(b), 6(b), 7(b), and 8(b). However, in order to save space, they are presented with the values of the phonetic constraints (rendered by gray levels) defined in Sec. III. In addition, two or three characteristic vocal tract slices of PB from the book of Bothorel *et al.*[25] are given for each of these places of articulation in order to get an idea of the vocal tract shape [Figs. 4(c), 5(c), 6(c), 7(c), and 8(c)].

Finally, the average geometric distance of inverse solutions to the actual vocal tract shape that produced the sound was computed, in function of the phonetic score of the shapes. The results of this experiment are presented for /a/ and /i/ in Figs. 9(a) and 9(b). The geometrical distance was measured by projecting the vocal tract shapes on Maeda's grid, and by computing the square difference with the projection of the reference VT shape. In other words, if we denote as $P_{0,j}$ the coordinates of the projections of the reference VT shape on Maeda's grid, and $P_{i,j}$ the coordinates of the projections of a given VT shape on the grid, we compute a geometric distance using

$$d(0,i) = \sqrt{\frac{\sum_{j=1}^{N} |P_{i,j} - P_{0,j}|^2}{N}},$$

in which N is the total number of points on Maeda's grid. Figures 9(a) and 9(b) are obtained by plotting this average error for all VT shapes with a phonetic score within a very small window (0.001) from a given value.

B. Analysis of results

The first observation is about the number of vocal tract shapes recovered. The inversion procedure, and especially the exploration of the null space (see Ref. 14), roughly samples the articulatory space in a uniform fashion. This

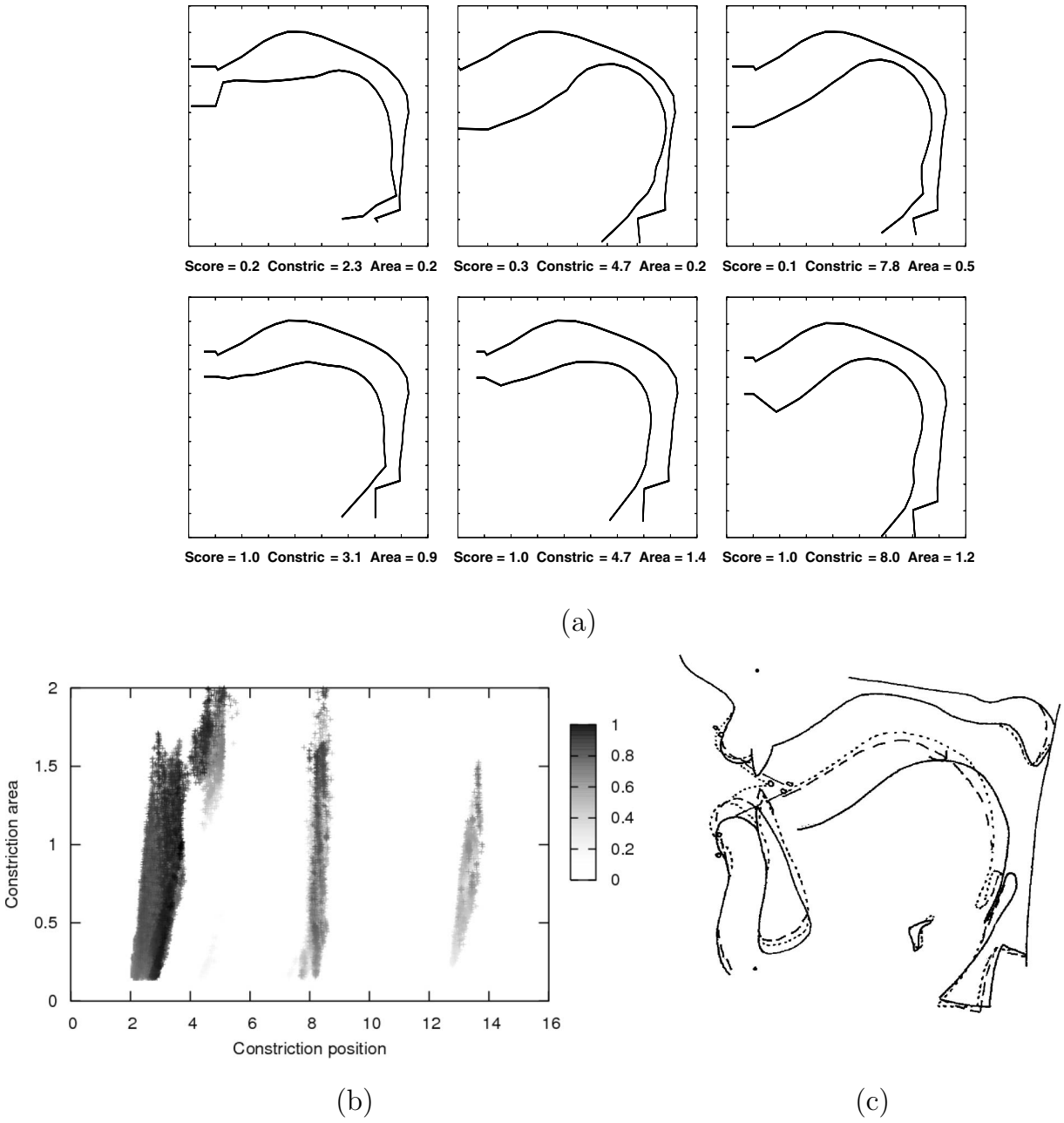

FIG. 4. (a) Midsagittal slices of the vocal tract for /a/. For each slice the phonetic score, the maximum constriction place (Constric) with respect to the glottis, and the area in square centimeters is given. (b) Inversion results for vowel /a/ represented in a constriction position/constriction area plan. The position of the maximum constriction is in centimeters with respect to the glottis, the constriction area is in square centimeters. The shade of a point indicates its phonetic score (darker is better). (c) X-ray midsagittal slices for /a/: /aba/ (solid line), /maʃ/ (dashed line), /vwal/ (dotted line).

means that the number of solutions is tightly connected to the extent of the articulatory region corresponding to vowels. If there was no mismatch between the analyzing model and the human vocal tract, these figures would directly represent the degree of precision required to articulate a vowel. In our case, despite the favorable situation, i.e., the analyzing model was derived from images of the speaker being inverted, and the attention we paid to the adaptation of the analyzing model, there is some model mismatch. However, formants values in Table III clearly show that the articulation of vowels /i, y, u/ and especially /u/ requires more articulatory precision than /e/ and /a/. The small number of solutions for /u/ is probably due to the difficulty of the model to mimic the natural articulation. This problem is not specific to Maeda's model since /u/ is always more difficult to mimic than other vowels with the available articulatory synthesizers (like ASY[26] or TractSyn[27] for instance). Another explanation could be related to the construction of the articulatory model itself. Indeed, the number of solutions for /a/ is approximately half that of /e/ although one would rather expect a larger number of solutions for /a/ because of its well-known articulatory variability. It is likely that the factor analysis[6] applied to vocal tract shape contours penalizes vowels located at the extremities of the articulatory domains /a, i, u/ and to a lesser extent /y/ because they are farther from the average vocal tract shape.

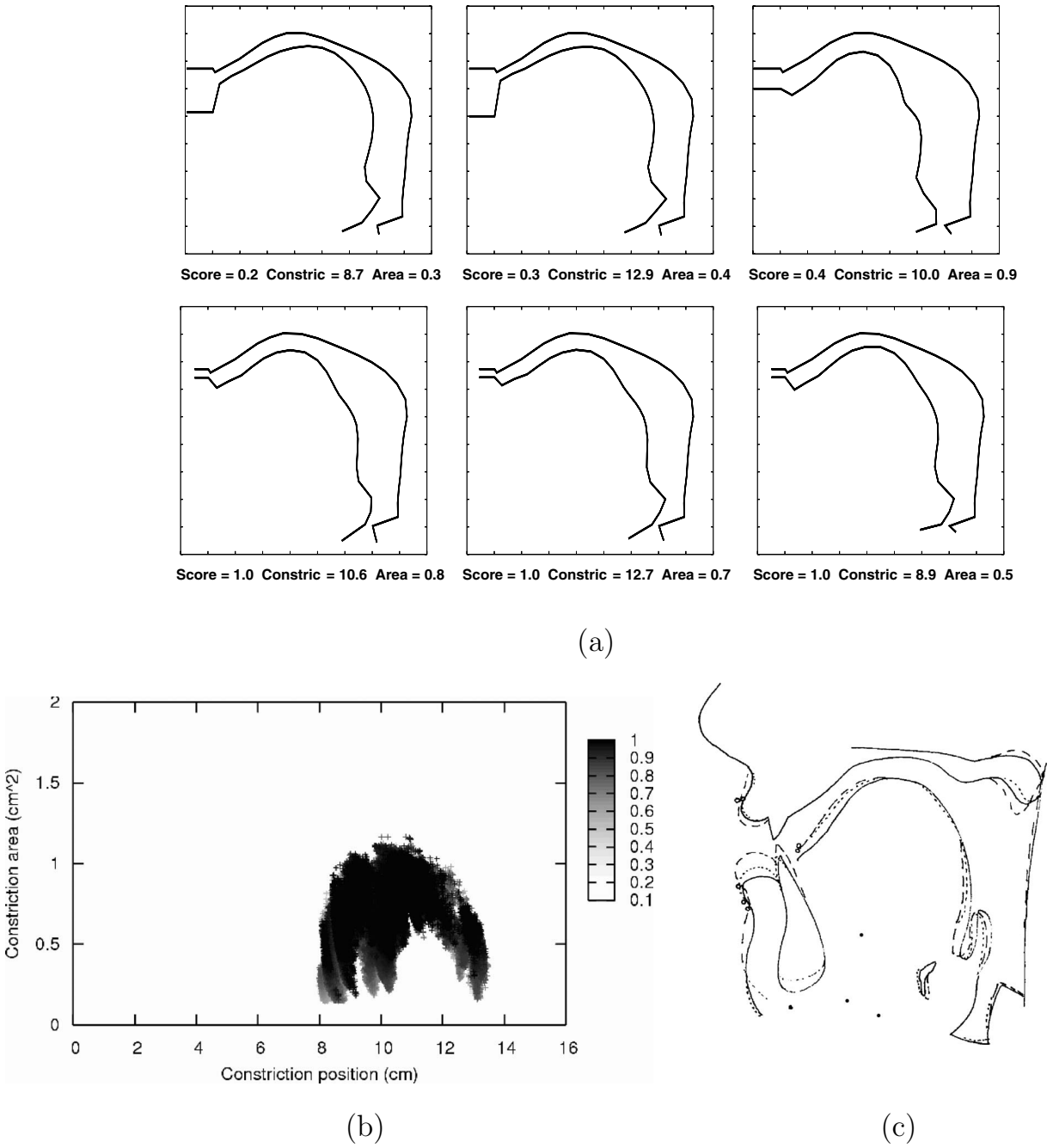

FIG. 5. (a) Midsagittal slices of the vocal tract for /e/. For each slice the phonetic score, the maximum constriction place (Constric) with respect to the glottis, and the area in square centimeters is given. (b) Inversion results for vowel /e/ represented in a constriction position/constriction area plan. The position of the maximum constriction is in centimeters with respect to the glottis, the constriction area is in square centimeters. The shade of a point indicates its phonetic score (darker is better). (c) X-ray midsagittal slices for /e/: /dyge/ (solid line), /debu/ (dashed line), /tebo/ (dotted line).

Examining Figs. 4(b), 5(b), 6(b), 7(b), and 8(b), we observe some key properties of the places of articulation. First, the discretization of the vocal tract, and consequently of the area function, gives rise to discrete points of articulation [which often correspond to the roughly vertical lines in Figs. 4(b), 5(b), 6(b), 7(b), and 8(b)]. However, despite this local spreading, places of articulation are organized in a small number of compact regions, always less than three. In some cases, these regions merge together as the area of the constriction increases. This is particularly visible in the case of /e/.

Second, the computation of the articulation place given by the point where the area function is minimal depends on both the motionless vocal tract wall and the tongue. Some places of articulation which seems different, especially for /a/, actually correspond to very similar vocal tract shapes. The three distinct areas of articulation of /a/ all correspond to the pharyngeal part of the vocal tract as exhibited by the midsagittal slices.

Third, the results are in good agreement with the data of Wood[28] for both the places of articulation and the constriction area. The constriction area of /e/ is on average greater

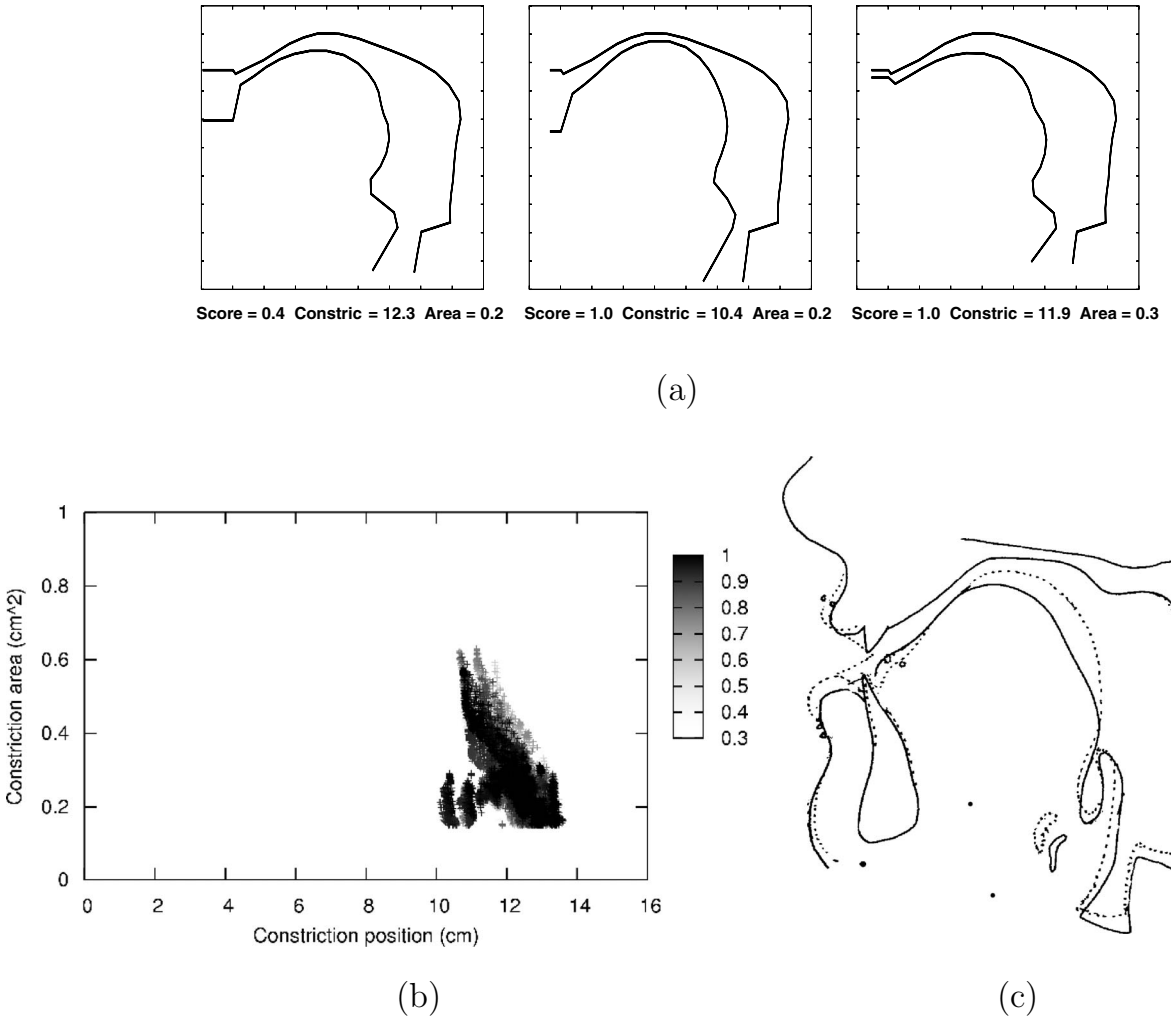

FIG. 6. (a) Midsagittal slices of the vocal tract for /i/. For each slice the phonetic score, the maximum constriction place (Constric) with respect to the glottis, and the area in square centimeters is given. (b) Inversion results for vowel /i/ represented in a constriction position/constriction area plan. The position of the maximum constriction is in centimeters with respect to the glottis, the constriction area is in square centimeters. The shade of a point indicates its phonetic score (darker is better). (c) X-ray midsagittal slices for /i/: /abi/ (solid line), /lwipɑ̃/ (dotted line).

than that of /i/ as shown by the vocal tract configurations presented by Wood. Wood's data also confirm that the place of articulation of /a/ can be spread over a large part of the pharynx.

Fourth, phonetically relevant and unrealistic vocal tract shapes share common places of articulation. This comes from the fact that the acoustical properties of vowels put very strong constraints onto the places of articulation. Consequently, unrealistic vocal tract shapes cannot be eliminated from the knowledge of their places of articulation.

Examining Figs. 4(a), 5(a), 6(a), 7(a), and 8(a), i.e., examples of vocal tract shapes recovered with inversion, and comparing them to the original x-ray midsagittal slices [Figs. 4(c), 5(c), 6(c), 7(c), and 8(c)] obtained by Bothorel *et al.*[25] provides a finer analysis of the vocal tract shapes.

The places of articulation correspond with phonetic knowledge and the results provided by two-tube vocal tract models of vowels proposed by Fant.[23] Despite this good agreement with the two-tube approximation, it turns out that there exists a large articulatory variability allowed by the articulatory model, as shown by the midsagittal slices of Figs. 4(a), 5(a), 6(a), 7(a), and 8(a). Only some of this variability corresponds to realistic vocal tract shapes. For each of the vowels studied, the first midsagittal slices shown are the least realistic according to the phonetic constraints presented earlier. One example of good and bad slices is given for three places of articulation of /a/ (i.e., roughly 3, 4.7, and 8 cm from the glottis). It has been shown that the least realistic slices correspond to extreme positions of the articulators. The upper left slice of Fig. 4(a), for instance, presents a wide lip opening together with a small jaw opening, and a very low position of the tongue which gives a strong constriction close to the glottis. Clearly, this vocal tract shape cannot be realized by a human speaker, or at least it is very unlikely.

In the case of /e/, the three least realistic vocal tract shapes, Fig. 5(a) (upper row), present a fairly high protrusion. Besides, the first two examples present a high lip opening together with the tongue in a high position, which seems difficult to realize for a human speaker.

Similarly, the worst vocal tract shapes of /i/ and /u/ both correspond to very unlikely configurations. For /y/, the worst

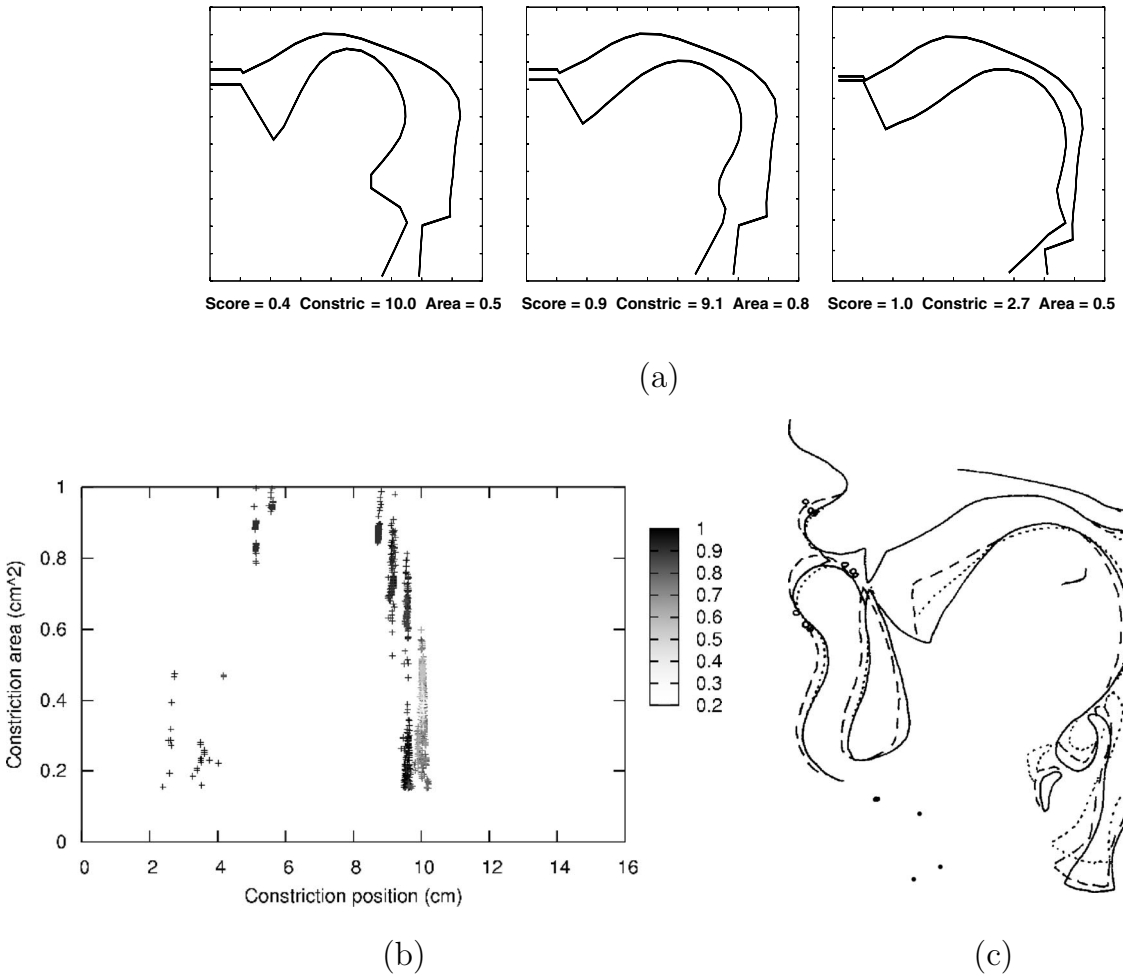

FIG. 7. (a) Midsagittal slices of the vocal tract for /u/. For each slice the phonetic score, the maximum constriction place (Constric) with respect to the glottis, and the area in square centimeters is given. (b) Inversion results for vowel /u/ represented in a constriction position/constriction area plan. The position of the maximum constriction is in centimeters with respect to the glottis, the constriction area is in square centimeters. The shade of a point indicates its phonetic score (darker is better). (c) X-ray midsagittal slices for /u/: /iku/ (solid line), /ʃu/ (dashed line), /ʁusi/ (dotted line).

configurations correspond to a very small protrusion and lip opening together with a low position of the apex and a compact shape of the tongue.

Two places of articulation exist for /u/. The second one [represented by the third midsagittal slice of Fig. 7(a)] is located in the lower part of the pharynx. However, Fig. 10, which gives the area function, shows that the entire pharynx actually corresponds to a narrow tube. As it can be noted the number of vocal tract shapes giving this place of articulation is substantially smaller than for the first place of articulation. This means that this kind of vocal tract shape cannot be reached as easily as the first one from an articulatory point of view.

Vocal tract shapes recovered correspond very well with original x-ray midsagittal slices. This is all the more important since the acoustical simulation is unable to copy original formant data with a high precision as mentioned before. Despite this acoustical mismatch the inversion procedure was able to capture speaker specificities as shown by the inversion of the vowel /i/. As shown in Figs. 6(a) and 6(c), the second vocal tract shape recovered for /i/ has a lip opening value substantially larger than expected. However, it turns out that this female speaker sometimes realizes /i/ with a fairly large lip opening [as shown by the dotted contour in Fig. 6(c)], compared to other speakers of the study of Bothorel *et al.* (not displayed here). Therefore, even if the second midsagittal slice presents a slightly larger value of lip opening than that observed in the x-ray contour, it is consistent with the articulation of the subject PB.

Finally, we observe in Figs. 9(a) and 9(b) that, generally speaking, the average geometric error between inverse solutions and the real vocal tract shape decreases as the phonetic score increases. The effect is particularly clear for /i/, as the average geometrical error goes from 0.7 down to 0.2 cm. The effect is, however, weaker for /a/: The average distance goes from 0.47 cm for a score of 0, to 0.32 cm for scores close to 1. The same tendency is observed for all inverted vowels, with the strongest contrasts being observed for vowels with localized places of articulation, such as /i/, and the weakest for vowels with very wide places of articulation, such as /a/. The residual distance is thus all the greater since the place of articulation is spread over a large interval of

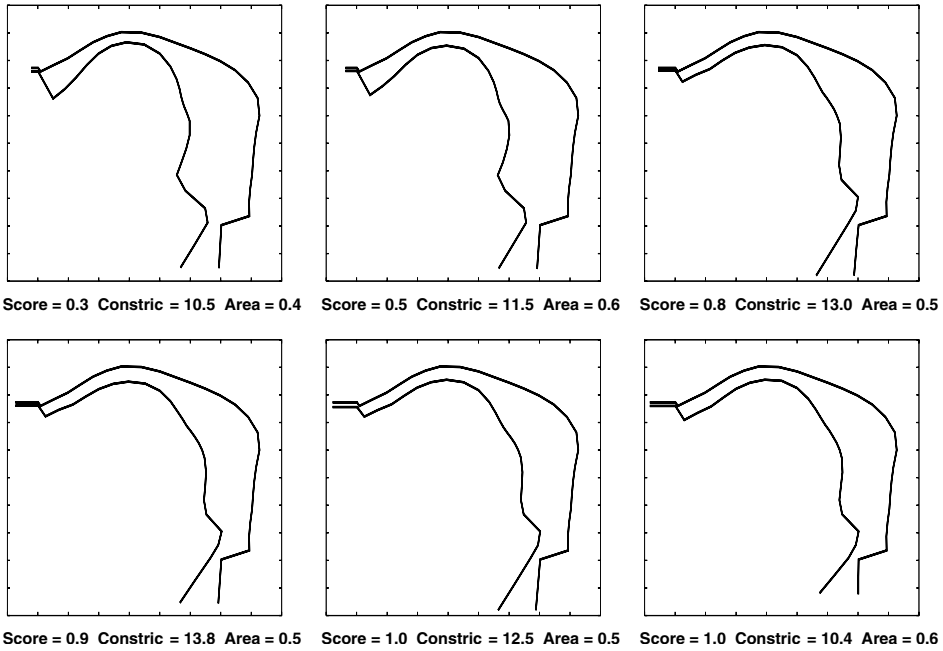

(a)

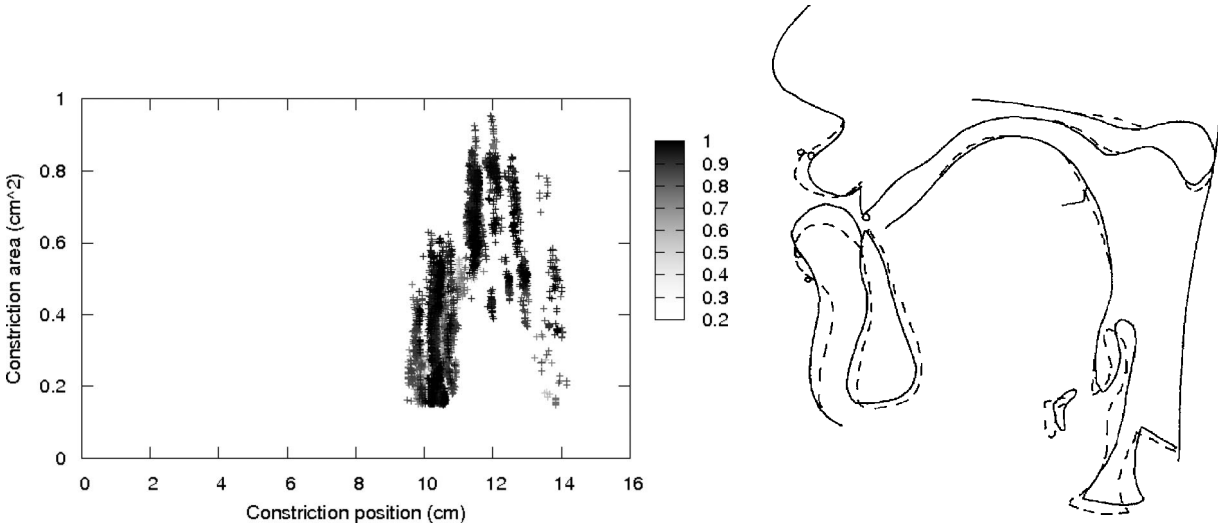

(b) (c)

FIG. 8. (a) Midsagittal slices of the vocal tract for /y/. For each slice the phonetic score, the maximum constriction place (Constric) with respect to the glottis, and the area in square centimeters is given. (b) Inversion results for vowel /y/ represented in a constriction position/constriction area plan. The position of the maximum constriction is in centimeters with respect to the glottis, the constriction area is in square centimeters. The shade of a point indicates its phonetic score (darker is better). (c) X-ray midsagittal slices for /y/: /igy/ (solid line), /yn/ (dashed line).

vocal tract as /a/. This distance corresponds to a good phonetic realism and directly depends on the severity of phonetic constraints.

These experiments show that the phonetic constraints proposed penalize unrealistic vocal tract shapes. They also help clarify the respective roles of the articulatory model and phonetic constraints with respect to the process of inversion. The articulatory model essentially provides constraints about the geometrical location of the constriction in the vocal tract. On the other hand, the phonetic constraints focus on the interdependencies between articulators.

V. DERIVATION OF COMPENSATORY ARTICULATORY EFFECTS THROUGH INVERSION

The above-presented experiments about the place of articulation of five vowels for a female speaker proved that there exist only a limited number of articulation places. However, the number of inverse solutions is large and information provided by these experiments only concern one point of the vocal tract shape. It is thus interesting to provide an additional point of view by investigating the shape variability, in other words the compensatory articulatory effects, for each of the vowels studied.

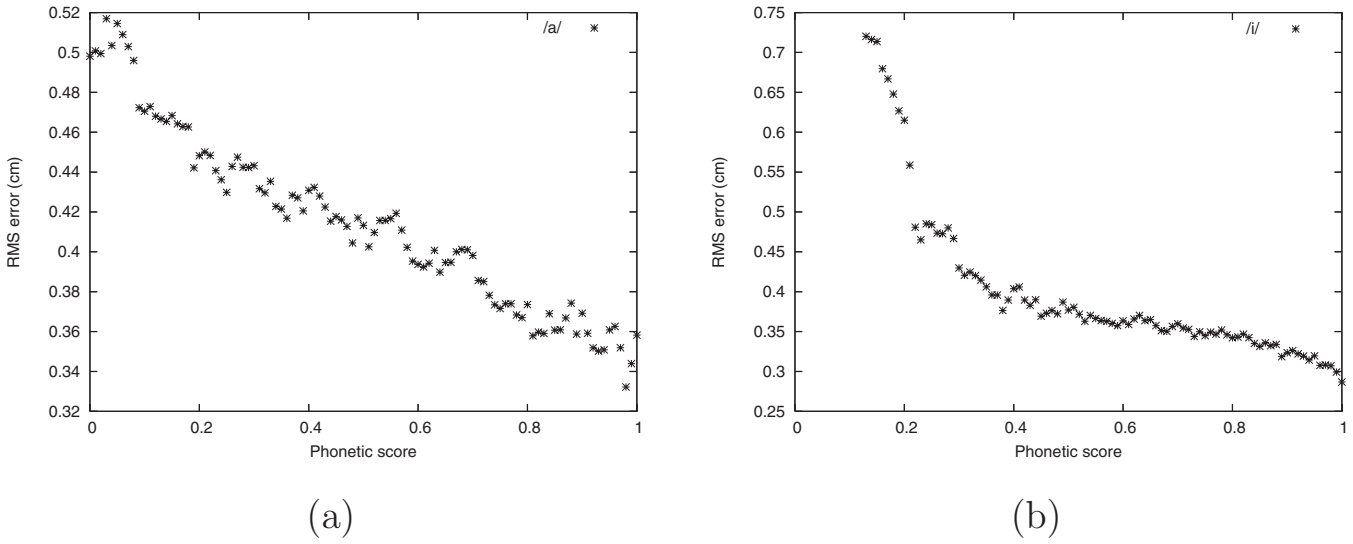

FIG. 9. Average rms distance (in centimeters) from the real VT shape in function of the phonetic score for inversion solutions of /a/ and /i/.

For that purpose, principal component analysis (PCA) was applied to all the shapes recovered for a given vowel and presenting a sufficient phonetic score. Compared to the notion of "articulatory fiber" introduced by Atal *et al.*[29] this approach gives a global overview of all the shapes corresponding to a vowel. The eigenvectors provided by PCA describe the spreading of vocal tract shapes, and consequently vocal tract deformations that keep formants unchanged. We tested two levels of constraint satisfaction: 0.2 and 0.9. The first score (0.2) allows very unrealistic shapes to be eliminated and the second (0.9) only allows shapes in full agreement with phonetic constraints to be kept.

We found out that eigenvectors are quite close for both scores (although eigenvalues differ). This is probably due to the fact that good and poor vocal tract shapes according to the phonetic measure share the same places of articulation.

The results are given in Fig. 11 for the first level of satisfaction (phonetic score greater than 0.2). For clarity's sake, only the first two components are presented. Table IV gives the amount of variance explained by the first two eigenvectors. As can be seen in Table IV, a greater phonetic constraint generally increases the contribution of the first two coefficients, sometimes dramatically (for example, the first coefficient of /a/).

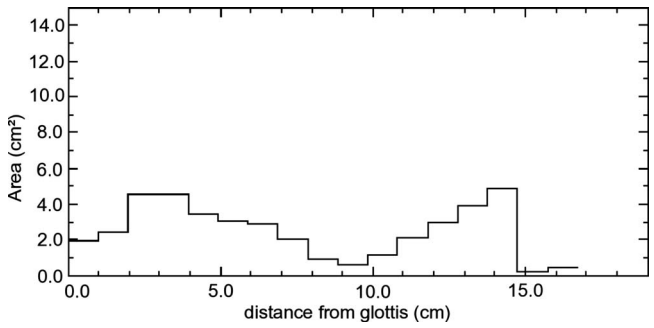

FIG. 10. Area function for /u/ with a pharyngeal constriction.

It clearly appears that the first deformations keeping formants unchanged for the vowels studied explain the spreading of places of articulation as shown in Figs. 4–8 (bottom left).

The first deformation of /a/ corresponds to narrowing the pharynx region and thus to changing the place of articulation among one of the three constriction regions, or from one of these regions to another. It should be noted that this deformation is somewhat surprising because one would rather expect the compensatory effect of simultaneous tongue and jaw movements (lowering the jaw while moving the tongue back preserves the acoustics). Actually, this first deformation occurs in a very small acoustical region (less than 25 Hz on each formant) compared to the allowable acoustical region for /a/, and it corresponds more to a deformation that keeps the overall geometrical shape of the vocal tract unchanged rather than to a true articulatory compensatory effect. The second deformation of /a/ plays only a marginal role considering the small amount of variance it explains (0.06 for the shapes with a phonetic score above 0.9), and is essentially a movement of the tongue tip.

Unlike deformations of /a/ those of /e/ have comparable weights. They correspond to a slight change of the constriction location. The first one also exhibits deformations larger at lips than at other regions of the vocal tract. Both of them involve deformations in the larynx region which compensate for deformations at lips. It should be noted that the involvement of the larynx also occurs for /i/, /y/, and /u/.

Deformation modes of /i/ show that the degree of freedom on lip aperture and protrusion is larger (related to the allowable domain for each articulatory parameter) than that of other articulators.

The first deformation of /u/ corresponds to the change of the constriction location from the palatal region to the pharynx region. The small number of inverse solutions in the pharynx region explains that this first deformation actually focuses more on the palato-velar region than between the

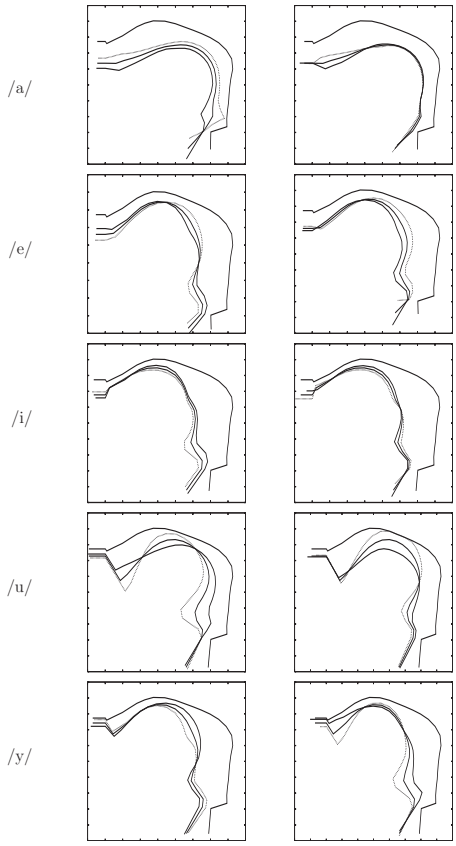

FIG. 11. First two deformation modes keeping formant frequencies unchanged for /a,e,i,u,y/. For each phoneme, the left figure is the first deformation mode, the right figure is the second deformation mode. The bold solid contour corresponds to the average vocal tract shape for the vowel studied. The thin and dotted contours correspond, respectively, to +3 and −3 standard deviation units.

palato-velar and pharynx regions. The second mode of deformation clearly shows a wide variability on the degree of constriction.

Finally, the two modes of deformation of /y/ show that the location of the constriction remains quasiconstant; the first allowable deformation is mainly on the aperture while the second is on the volume of the front and back cavities without changing either the overall shape or ratio between the two cavities.

VI. CONCLUDING REMARKS

It turns out that the results obtained for a speaker, when x-ray images and speech signal were simultaneously available, are in very good agreement with x-ray contours even if this kind of evaluation can be carried out in very few cases, i.e., for the few speakers for whom simultaneous x-ray and acoustic data exist. However, the mismatch between the analyzing model and the vocal tract of the speaker involved in the experiment prevents a very precise acoustical inversion to be carried out. This suggests that incorporation of additional constraints, for instance upon the position of visible articulators, should be accompanied by the reduction of the acoustical precision imposed for inversion.

TABLE IV. Variances of the first two components obtained through PCA, applied to the vowel samples with phonetic scores greater than 0.2 and 0.9, respectively.

Score	>0.2		>0.9	
Vowel	Coef. 1	Coef. 2	Coef. 1	Coef. 2
a	0.33	0.25	0.84	0.06
e	0.30	0.23	0.42	0.30
i	0.39	0.24	0.53	0.19
u	0.67	0.17	0.59	0.25
y	0.41	0.27	0.57	0.23

This work clearly shows the importance of phonetic constraints and their relation with the articulatory model. The articulatory model provides constraints in the form of deformation modes allowed to represent a vocal tract shape. However, the articulatory model does not control the synergy between deformation modes since they are independent by construction. This explains why very phonetically unrealistic shapes can be recovered during inversion. Phonetic constraints capture the synergies between articulators linked to physiological properties which cannot be observed directly easily because it requires somewhat invading medical acquisition techniques like electromyography, or which cannot be modeled reliably due to the limited amount of articulatory data available.

In the current work the constraints were designed for each French vowel and used independently from each other. However, it is imaginable, and this will be investigated in a future work, to develop a complete phonetic model that would integrate all the constraints in a single "phonetic model." Indeed, as shown in Sec. III D prior phoneme identification is not necessary to apply constraints and they can be applied simultaneously because the most relevant constraints will provide the highest phonetic scores. This "phonetic model" thus would complement the articulatory model. A key point is that this phonetic model would be very general because it is derived from speaker independent knowledge.

The phonetic constraints are designed to delimit phonetically relevant articulatory domains. One could object that the domains are attached to French since we used French templates. However, any language providing vowel templates corresponding to a good articulatory coverage can be used. French offers a reasonably good articulatory coverage except maybe for close central vowels which do not exist in French. We also could have added vowel references of other languages. However, we think that the gain would be small.

Even though it is not the central object of this paper, it clearly appears that acoustic-to-articulatory inversion offers a very efficient means to investigate the acoustical and articulatory properties of an articulatory model. It is especially interesting to determine which compensatory effects are available. It should be noted that the compensatory effects studied here only correspond to a precise three-tuple of formant frequencies. This means that the compensatory effects measured in this way are underevaluated compared to what they are when considering the entire acoustic domain allowed for a vowel. The corollary is that there is a large amount of variability in the planning of articulatory gestures by speakers.

ACKNOWLEDGMENTS

The authors acknowledge the financial support of the Future and Emerging Technologies (FET) programme within the Sixth Framework Programme for Research of the European Commission, under FET-Open Contract No. 021324. We would like to thank Shinji Maeda for his very helpful feedback and for making his model and data available. We also thank the three anonymous reviewers for their helpful comments.

APPENDIX: IMPROVING THE ACOUSTIC ACCURACY OF MAEDA'S MODEL

Even though the overall formant trajectories resynthesized from articulatory parameters provided by Maeda for subject PB were quite similar to those extracted from speech uttered by PB, we observed a non-negligible deviation between original and resynthesized formants. Actually, the geometrical precision of the model depended on two scale factors that have been set arbitrarily because the calibration of the x-ray machine was not known precisely. The first parameter is the conversion coefficient from a specific coordinate system—used when digitalizing the x-ray films—to centimeters, and the other is a multiplication coefficient on the area function obtained. The adjustment of these two factors was not possible in 1979 when the model was constructed because it would have required too much computation time. Therefore, we sampled ranges of reasonable values for these two factors to find better values. It turned out that the ad-hoc area increase set to 40% in the original model to increase the acoustical agreement with original acoustical data can be removed provided that the scaling factor is set to 196 (instead of 187). The overall frequency error thus decreases from 114 to 54 Hz for formants F1 and F2. The residual acoustical errors probably originate in the calculation of the area function from the midsagittal slice, which exploits $\alpha-\beta$ coefficients proposed by Heinz and Stevens,[30] wherein the area at section i A_i is derived from the midsagittal measurement d_i through

$$A_i = \alpha_i d_i^{\beta_i}.$$

The α_i and β_i coefficients depend on the vocal tract zone considered. In our case, $1.8 \leqslant \alpha_i \leqslant 2.6$ and $1.2 \leqslant \beta_i \leqslant 1.5$.

[1]J. Schroeter and M. M. Sondhi, "Techniques for estimating vocal-tract shapes from the speech signal," IEEE Trans. Speech Audio Process. **2**, 133–150 (1994).
[2]V. Sorokin, A. Leonov, and A. Trushkin, "Estimation of stability and accuracy of inverse problem solution for the vocal tract," Speech Commun. **30**, 55–74 (2000).
[3]C. H. Coker, "A model of articulary dynamics and control," Proc. IEEE **64**, 452–460 (1976).
[4]P. Mermelstein, "Articulatory model for the study of speech production," J. Acoust. Soc. Am. **53**, 1070–1082 (1973).
[5]S. Maeda, "Un modèle articulatoire de la langue avec des composantes linéaires (an articulatory model of the tongue with linear components)," in *Actes 10èmes Journées d'Etude sur la Parole* (International Speech Communication Association, Grenoble, France, 1979), pp. 152–162.
[6]S. Maeda, "Compensatory articulation during speech: Evidence from the analysis and synthesis of vocal-tract shapes using an articulatory model," in *Speech Production and Speech Modelling*, edited by W. J. Hardcastle and A. Marschal (Kluwer Academic, Dordrecht, 1990).
[7]B. Gabioud, "Articulatory models in speech synthesis," in *Fundamentals of Speech Synthesis and Speech Recognition*, edited by E. Keller (Wiley, West Sussex, UK, 1994), Chap. 10.
[8]O. Engwall, "Modelling of the vocal tract in three dimensions," in Proceedings of EUROSPEECH, Budapest, 1999, pp. 113–116.
[9]D. Nix, G. Papcun, J. Hogden, and I. Zlokarnik, "An investigation of locus equations as a source of relational invariance for stop place categorization," J. Acoust. Soc. Am. **90**, 1309–1325 (1991).
[10]A. Galván-Rodrigez, "Études dans le cadre de l'inversion acoustico-articulatoire: Amélioration d'un modèle articulatoire, normalisation du locuteur et récupération du lieu de constriction des occlusives (Studies in the context of acoustic-to-articulatory inversion: Improvement of an articulatory model, speaker normalization and determination of the constriction places of plosives)," Thèse de l'Institut National Polytechnique de Grenoble, Grenoble, France, 1997.
[11]L.-J. Boë, P. Perrier, and G. Bailly, "The geometric vocal tract variables controlled for vowel production: Proposals for constraining acoustic-to-articulatory inversion," J. Phonetics **20**, 27–38 (1992).
[12]S. Dusan, "Statistical estimation of articulatory trajectories from the speech signal using dynamical and phonological constraints," Ph.D. thesis, Waterloo University, Electrical and Computer Engineering, Waterloo, Ontario, Canada, 2000.
[13]T. Okadome, S. Suzuki, and M. Honda, "Recovery of articulatory movements from acoustics with phonemic information," in Proceedings of The Fifth Seminar on Speech Production: Models and Data, Kloster Seeon, Germany, 2000.
[14]S. Ouni and Y. Laprie, "Modeling the articulatory space using a hypercube codebook for acoustic-to-articulatory inversion," J. Acoust. Soc. Am. **118**, 444–460 (2005).
[15]S. Maeda, "A digital simulation of the vocal tract system," Speech Commun. **1**, 199–229 (1982).
[16]A. Marchal, *Les sons et la parole (Sounds and Speech)* (Guérin, Montréal, 1980).
[17]P. Ladefoged, *A Course in Phonetics*, 5th ed. (Thomson/Wadsworth, Boston, MA, 2006).
[18]V. Robert, B. Wrobel-Dautcourt, Y. Laprie, and A. Bonneau, "Strategies of labial coarticulation," in Interspeech, Lisboa, 2005.
[19]B. Potard and Y. Laprie, "Using phonetic constraints in acoustic-to-aticulatory inversion," in Interspeech, Lisboa, 2005, pp. 3217–3220.
[20]F. Lonchamp, "Les sons du Français—Analyse acoustique descriptive," Cours de Phonétique, Institut de Phonétique, Université de Nancy II, Nancy, France, 1984.
[21]F. Aurenhammer and R. Klein, "Voronoi diagrams," in *Handbook of Computational Geometry*, edited by J. Sack and J. Urrutia (Elsevier, Amsterdam, 1999).
[22]K. N. Stevens and A. S. House, "Development of a quantitative description of vowel articulation," J. Acoust. Soc. Am. **27**, 484–493 (1955).
[23]G. Fant, *Acoustic Theory of Speech Production* (Mouton & Co., The Hague, 1960).
[24]P. Halle, "Techniques cepstrales améliorées pour l'extraction d'enveloppe spectrale et la détection du pitch (improved cepstral techniques for spectral envelope extraction and pitch detection)," in Actes du Séminaire Traitement du Signal de Parole, Paris, 1983, pp. 83–93.
[25]A. Bothorel, P. Simon, F. Wioland, and J.-P. Zerling, *Cinéradiographies des voyelles et consonnes du Français (Cineradiographies of vowels and consonants in French)* (Travaux de l'institut de Phonétique de Strasbourg, Strasbourg, France, 1986).
[26]P. Rubin, T. Baer, and P. Mermelstein, "An articulatory synthesizer for perceptual research," J. Acoust. Soc. Am. **70**, 321–328 (1981).
[27]P. Birkholz and D. Jackèl, "A three-dimensional model of the vocal tract for speech synthesis," in 15th International Congress of Phonetic Sciences—ICPhS'2003, Barcelona, Spain, 2003, pp. 2597–2600.
[28]S. Wood, "A radiographic analysis of constriction locations for vowels," J. Phonetics **7**, 25–43 (1979).
[29]B. S. Atal, J. J. Chang, M. V. Mathews, and J. W. Tukey, "Inversion of articulatory-to-acoustic transformation in the vocal tract by a computer-sorting technique," J. Acoust. Soc. Am. **63**, 1535–1555 (1978).
[30]J. M. Heinz and K. N. Stevens, "On the relations between lateral cineradiographs, area functions and acoustic spectra of speech," in Proceedings of the Fifth International Congress on Acoustics, Stuttgart, Germany, 1965, p. A44.

Spatiotemporal classification of vocal fold dynamics by a multimass model comprising time-dependent parameters

Tobias Wurzbacher,[a] Michael Döllinger, and Raphael Schwarz
Department of Phoniatrics and Pediatric Audiology, University Hospital Erlangen, Medical School, Erlangen, Germany

Ulrich Hoppe
Department of Audiology, University Hospital Erlangen, Medical School, Erlangen, Germany

Ulrich Eysholdt and Jörg Lohscheller
Department of Phoniatrics and Pediatric Audiology, University Hospital Erlangen, Medical School, Erlangen, Germany

(Received 19 April 2007; revised 20 December 2007; accepted 21 December 2007)

A model-based approach is proposed to objectively measure and classify vocal fold vibrations by left–right asymmetries along the anterior–posterior direction, especially in the case of nonstationary phonation. For this purpose, vocal fold dynamics are recorded in real time with a digital high-speed camera during phonation of sustained vowels as well as pitch raises. The dynamics of a multimass model with time-dependent parameters are matched to vocal fold vibrations extracted at dorsal, medial, and ventral positions by an automatic optimization procedure. The block-based optimization accounts for nonstationary vibrations and compares the vocal fold and model dynamics by wavelet coefficients. The optimization is verified with synthetically generated data sets and is applied to 40 clinical high-speed recordings comprising normal and pathological voice subjects. The resulting model parameters allow an intuitive visual assessment of vocal fold instabilities within an asymmetry diagram and are applicable to an objective quantification of asymmetries.
© *2008 Acoustical Society of America.* [DOI: 10.1121/1.2835435]

PACS number(s): 43.70.Bk, 43.70.Gr, 43.70.Dn, 43.72.Ar [AL] Pages: 2324–2334

I. INTRODUCTION

The objective quantification of hoarseness plays a central role in medical voice assessment. Hoarseness arises from phonatory air loss and/or irregular vocal fold vibrations.[1] The former can be detected and measured by acoustical analysis[2–6] while the latter is investigated by laryngeal endoscopic techniques.[7–10] Since acoustic signals provide only symptomatic information about the laryngeal pathology,[1] a diagnosis by means of acoustic parameters alone is ambiguous.[11] Therefore, it is necessary to include vocal fold vibration characteristics in the process of diagnosis.

Vocal fold instabilities occur especially in dysphonic voices and are induced either by pathological changes of the mechanical properties or by dysfunction of the neural control.[12] Among laryngoscopic methods stroboscopy is technically restricted to observing steady state vibrations. In contrast, high-speed (HS) recording systems allow for a correct interpretation of aperiodic, irregular, and nonstationary vocal fold vibrations.[1,7,13] Hence, HS imaging techniques are adequate for real-time observations of healthy and pathological vocal fold vibrations during voice production.

In clinical routine, HS recordings are typically performed for sustained vowels of constant pitch and loudness. However, such stationary phonation paradigms can only detect the vibration irregularities that become apparent at the specific pitch and intensity level.[14] Other pitch and loudness combinations remain untested and the extent of the voice disorder may not be revealed. Nonstationary phonation paradigms may overcome this drawback.[15] They originate from changing muscle activities and incorporate dynamical vibration transitions and thus scan a continuous phonation range within a single HS examination. For example, a pitch and/or a loudness increase are nonstationary paradigms for HS recordings,[15,16] which may complement or confirm the findings attained in stationary phonation.[14]

The analysis of HS recordings provides the basis for objective and quantitative measures of vocal fold vibrations.[1,17,18] For this purpose, the glottis is segmented and the movements of the vocal fold edges are tracked over time by image processing algorithms.[19–21] Within the literature, methods are proposed that assess perturbations in the glottal area wave form or different ratios between the open and closed duration time of the glottis.[22,23] Other approaches extend the analysis by left–right (LR) asymmetry measures of amplitude and phase shifts in the medial part of the vocal folds.[17,24] A further approach in quantifying vocal fold vibrations is to automatically adapt the dynamics of a biomechanical two-mass model (2MM) to the extracted vocal fold vibrations.[25,26] The adapted model parameters quantitatively assess LR asymmetry of the underlying vocal fold vibrations. Further refinements in the 2MM adaptation process enabled a model-based classification in the case of unilateral vocal fold paralysis.[27] Recently, we extended the parameters of the 2MM approach to be time-variant in order to also simulate

[a]Electronic mail: twurz@web.de

 0001-4966/2008/123(4)/2324/11/$23.00 © 2008 Acoustical Society of America

vocal fold vibrations of nonstationary phonation paradigms.[14] The dynamics of the time-dependent 2MM were adapted to the observed nonstationary vocal fold vibrations of normal and dysphonic voices. Based on the calculated time-variant model parameters both groups were separated from each other. Further on, a 2MM with time-dependent parameters and an additional coupling to a vocal tract was fitted to a realistic oral airflow for an utterance.[28]

Asymmetries in vocal fold vibrations are not restricted to LR asymmetries and may also be found in other vibration modes.[29] Especially longitudinal asymmetries along a vocal fold side, which literature denotes anterior–posterior (AP) modes, are observable in HS recordings.[1,30] The vibration behavior at the dorsal, medial, and ventral vocal fold regions contributes information for characterizing the vibration pattern. For a model-based analysis of longitudinal vibration asymmetries the 2MM is not suited, since the complete vocal fold length is represented by only a single mass and thus does not allow for an independent oscillation in AP direction. Within the literature a finite-element model of the vocal folds was used to study and simulate AP biphonation.[31] Wong *et al.*[32] proposed a lumped-element model (hereafter called the WO91 model) that is a hybrid of the 2MM[33–36] and the longitudinal string model proposed by Titze.[37] In the WO91 model the 2MM is divided in the AP direction and thus enables the simulation of longitudinal vibration asymmetries.

Based on the WO91 model, we proposed a multimass model with constant parameters for quantifying stationary vocal fold vibrations of the dorsal, medial, and ventral regions.[38] Here, this approach is extended and generalized to a time-dependent multimass model (TMM). The TMM dynamics are synchronously fitted to healthy and pathological vocal fold vibrations extracted at dorsal, medial, and ventral positions by optimizing the time-dependent model parameters. The parameters serve as an objective measure for quantitatively assessing LR as well as AP asymmetries of vocal fold vibrations. The optimization procedure is initially verified with synthetically generated vocal fold vibrations and then applied to 40 HS recordings. The results show that a separation of normal and pathological vocal fold vibrations can be made by the optimized TMM parameters.

II. METHODS

A. Clinical data

Real-time recordings of vocal fold vibrations were performed with a digital HS camera (HS ENDOCAM 5560, 256×256 pixels spatial and $f_s=4000$ Hz temporal resolution, grayscale) that was coupled to a rigid endoscope (90° optic, 9 mm diameter). A more detailed overview on the general recording situation is found within Refs. 1, 7, and 27. Two different phonation paradigms on the vowel /a/ were used for the HS recordings:

(1) SSP—sustained stationary phonation: phonation at a comfortable, constant pitch and intensity.
(2) MPR—monotonous pitch raise: phonation from a low pitch to an arbitrary higher one.

TABLE I. Subject overview for the endoscopic HS recordings.

Subject	Voice diagnosis	Gender	Age	Paradigm
1–10	Normal	Three male Seven female	19.9 ± 1.5	SSP
11–20	Dysphonic (Six organic, four functional)	Two male Eight female	43.8 ± 13.7	SSP
21–30	Normal	Four male Six female	19.1 ± 1.6	MPR
21–30	Dysphonic (Seven organic, three functional)	Two male Eight female	44.8 ± 14.4	MPR

In this study, 40 subjects participated in the HS examination. The subject group consisted of four groups as given in Table I. There were 20 subjects for each phonation paradigm, in which ten normal voice subjects were opposed to ten pathological voices. The age between the normal and dysphonic voice groups was not matched. Although aging effects may play a role in voice assessment, the effects of the diagnosed disorders were dominant compared to aging.[39]

The vocal fold dynamics were extracted from the HS recordings by tracking the movements of specific vocal fold edge points in the segmented video.[21] The analyzed parts of the HS sections were chosen to contain no voicing onsets and to provide a view onto the glottal plane not hidden by the supraglottal laryngeal anatomy. Figure 1(a) shows the nth frame of a segmented HS recording. The glottal axis is the connection line between the anterior $\mathbf{ac}=ac(x,y)$ and posterior **pc** commissures, which defines the glottal length. In the following, variables in bold letters represent two-dimensional vectors in the xy plane. The points $\mathbf{g}_j[n]$, for $j=1,\ldots,3$, are located at 25%, 50%, and 75% of the glottal length and represent the dorsal, medial, and ventral third of the vocal folds. Six vocal fold edge points $\mathbf{p}_i$ were computed by the intersection of the segmented contour and three trajectory lines (Fig. 1), which pass through $\mathbf{g}_j$ and are perpendicular to the glottal axis. In terms of these points, the vocal fold trajectories are defined as

$$c_i[n] := \xi\cdot\|\mathbf{p}_i[n]-\mathbf{g}_j[n]\|_2 \tag{1}$$

with $i=1,\ldots,3$ for the right and $i=4,\ldots,6$ for the left vocal fold and $j\equiv\mathrm{mod}(i,-3)+3$. The factor ξ, defined as $\xi=+1$ for the left-hand side and $\xi=-1$ for the right-hand side, is used in order to get different signs for the left and the right deflections. Here, $\|\cdot\|_2$ denotes the Euclidean norm. The trajectories $c_i[n]$ were scaled from pixel to metrical units by assuming a 1 cm length of the vibrating portion of the vocal folds within the images, being in the same order of magnitude as values given previously in the literature.[25,34–43] Scaling with another vocal fold length as reference scale yields increased or decreased deflections of the trajectories. Existing asymmetries are evenly scaled. Hence, scaling without knowing the correct factor does not restrict asymmetry detection. Figure 1(b) depicts trajectory sections of 30 ms, which correspond to $N=120$ frames, for a normal voice. The curves $c_i[n]$ are regular over time, and no LR asymmetries emerge. However, there are differences between the dorsal and medial-ventral vibration behavior: Glottal closure occurs for the trajectories in the medial and ventral region as indi-

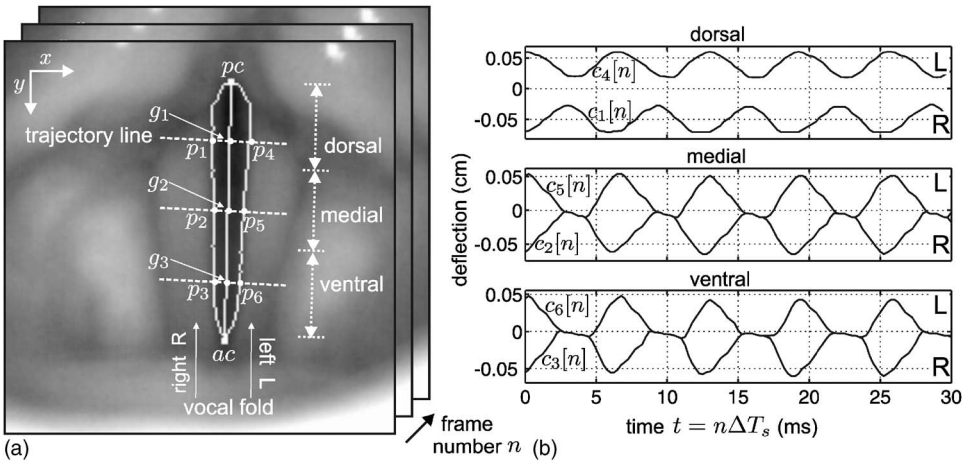

FIG. 1. (a) A single frame of an endoscopic HS recording of the larynx. The vocal fold edges are segmented and the glottal axis connects the anterior **ac** and posterior **pc** commissures. The points $\mathbf{p}_i$ and $\mathbf{g}_j$ mark vocal fold edges and positions on the glottal axis in the dorsal, medial, and ventral regions of the vocal folds. (b) Corresponding trajectories $c_i[n]$ of the points $\mathbf{p}_i$.

cated by the contact of opposing trajectories, whereas the dorsal trajectories show a closure insufficiency.

B. Time-dependent multimass model: TMM

A model-based approach is proposed for the analysis and interpretation of the extracted trajectories $c_i[n]$. The suggested TMM is an adjusted and extended version of the WO91 model.[32] Figures 2(a) and 2(b) provide a top and frontal sketch of the TMM with time-dependent parameters. It is a two-dimensional model allowing oscillations in the lateral and longitudinal direction and no vertical movements appear. The mass elements are denoted as $m_{i,s}(t)$, with $i=1,\ldots,3$ for the right and $i=4,\ldots,6$ for the left-hand side. The lower and upper masses are identified by $s=1$ and $s=2$, respectively. Different forces act on the mass element $m_{i,s}(t)$, which are described in detail for constant TMM parameters:[38]

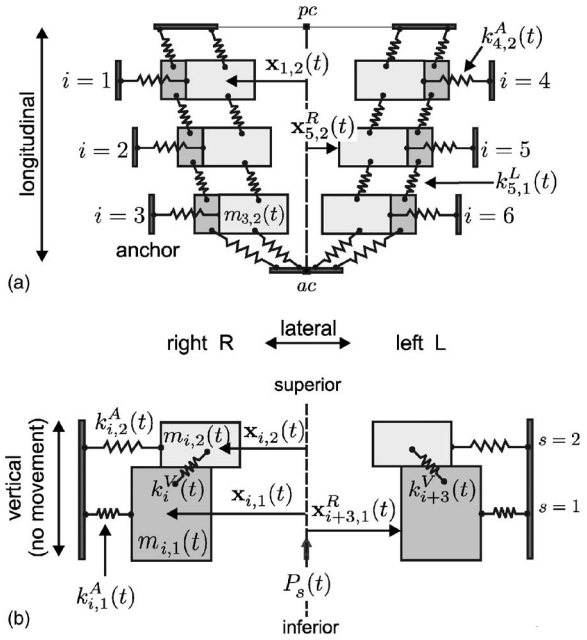

FIG. 2. Sketch of the TMM in (a) endoscopic/top view and (b) frontal view. The lower and upper masses are colored in dark and light gray. The spring elements are drawn in while damping elements are not shown to keep clarity of the drawing.

(1) The driving force $\mathbf{F}^D_{i,s}$ is determined by the subglottal pressure $P_L(t)$, the ratio between the upper and lower area formed by the mass elements $m_{i,s}(t)$, and the Bernoulli flow.
(2) The vertical coupling force $\mathbf{F}^V_{i,s}$ results from the connection of the lower and upper masses by a spring $k^V_i(t)$. Due to the restriction of having no vertical movements, $\mathbf{F}^D_{i,s}$ is split up in components projected into the lateral and longitudinal direction.
(3) The anchor force $\mathbf{F}^A_{i,s}$ acts due to the anchor springs $k^A_{i,s}(t)$ and dampers $r^A_{i,s}(t)$.
(4) The force $\mathbf{F}^L_{i,s}$ describes the longitudinal coupling of the TMM elements by stiffnesses $k^L_{i,s}(t)$ and dampers $r^L_{i,s}(t)$. At the ventral end, the left and right model sides are fixed together at an anchor that represents the anterior commissure (Fig. 1). In contrast, each side of the dorsal endings is coupled to its own fixed position associated with the nonvibrating region of the vocal folds at the transition to the arytenoid cartilages.
(5) During collision additional spring elements $k^C_{i,s}(t)$ result in a restoring force $\mathbf{F}^C_{i,s}$ in the direction to the anchor.

The deflections of the masses are denoted as $\mathbf{x}_{i,s}(t)$ and the associated rest positions as $\mathbf{x}^R_{i,s}(t)$, which are also time dependent due to possible changes of abduction–adduction of the vocal folds during nonstationary phonation paradigms.[14,28] Different glottal shapes can be reproduced by variation of $\mathbf{x}^R_{i,s}(t)$, i.e., typical configurations seen in HS recordings, as for example parallel, "v"-like or oval shapes. The time derivatives $\dot{\mathbf{x}}_{i,s}(t)$ and $\ddot{\mathbf{x}}_{i,s}(t)$ indicate velocity and acceleration of the mass $m_{i,s}(t)$. Since $m_{i,s}(t)$ is time dependent, the more general form of Newton's second law with a term for $\dot{m}_{i,s}(t)$ must be used in the equation of motion:[14,44]

$$m_{i,s}\ddot{\mathbf{x}}_{i,s} = -\dot{m}_{i,s}\dot{\mathbf{x}}_{i,s} + \mathbf{F}^A_{i,s} + \mathbf{F}^V_{i,s} + \mathbf{F}^L_{i,s} + \mathbf{F}^C_{i,s} + \mathbf{F}^D_{i,s}. \quad (2)$$

Equation (2) is numerically integrated to obtain the deflections $\mathbf{x}_{i,s}(t)$ with a fourth-order Runge-Kutta and a step size of 0.25 ms. In order to compare the TMM dynamics with the trajectories obtained from the HS recordings, model trajectories $c_i^M[n]$ are calculated as the minimal lateral distance of the upper/lower mass pair toward the glottal axis. Hence, only the current inner vocal fold mass contributes to the model trajectories $c_i^M[n]$. The trajectories of the TMM and associated parameters are denoted by superscript M. The main differences of the TMM to the WO91 model are:

(1) WO91 has constant model parameters and therefore does not allow the simulation of vocal fold vibrations of nonstationary phonation paradigms.
(2) Besides the movements in the lateral direction, the mass elements $m_{i,s}(t)$ in the TMM are also allowed to move in the longitudinal direction, which experimental studies have shown to exist even though they are small compared to the lateral displacements.[45,46]
(3) The TMM uses a more generalized form of collision detection. Instead of defining the event of collision as crossing the glottal axis, collision is detected as a mass contacts one of the opposite mass–spring elements. This is especially important in the case of LR asymmetries in pathological voices.

C. Automatic parameter optimization

The TMM has a large number of degrees of freedom due to the independent masses, springs, and dampers. In order to reduce the dimensionality (63 parameters) some of the TMM parameters are coupled by introducing a set of optimization parameters. The TMM parameters are initialized to start optimization in an oscillation region that is close to the observed characteristics.[25]

1. Initialization and optimization of parameters

Initially, the TMM parameter values are based on the constant standard parameters of Ishizaka *et al.*[33] However, these masses and stiffnesses of one model side are additionally allocated equally among the three oscillating 2MM elements. Further, the initial rest positions $\mathbf{x}^R_{i,1}$ of the lower model plane are estimated from the extracted trajectories $c_i[n]$ as

$$\mathbf{x}^R_{i,1} = \frac{1}{2N}\sum_{n=1}^{N} c_i[n]. \quad (3)$$

Here, the mean is reduced by a factor of 2, to prevent an overestimation of $\mathbf{x}^R_{i,1}$ according to collision between the left and the right vocal fold side. The initial rest positions of the upper plane are shifted by 10^{-3} cm toward the glottal axis to start with a convergent glottal profile.[40]

The time dependency of the TMM parameters are expressed in terms of the standard parameters[33] (labeled with a tilde) by introducing the following Q factors:

$$k^{\eta}_{i,s}(t) = \tilde{k}^{\eta}_{i,s} Q_i(t), \quad \eta \in \{A,V,L,C\},$$

$$m_{i,s}(t) = \tilde{m}_{i,s}/Q_i(t),$$

$$P_L(t) = \tilde{P}_L Q_p(t), \quad \mathbf{x}^R_{i,s}(t) = \mathbf{x}^R_{i,s} \cdot Q_r(t), \quad (4)$$

for the elements $i=1,\ldots,6$. With $t=n\Delta T_s$, where $n=1,\ldots,N$ denotes the number of frames, a set

$$S[n] := \{Q_1[n], \ldots, Q_6[n], Q_p[n], Q_r[n]\}, \quad (5)$$

of eight time-dependent optimization parameters is used to adjust the TMM dynamics and gives a concise description of vocal fold vibrations.

The initialization of Q_i is based on the mass–spring oscillator equation[25] and the oscillation frequency f_i of the trajectories $c_i[n]$ within the first four periods:

$$Q_i = 2\pi f_i \sqrt{\frac{\tilde{m}_{i,s}}{\tilde{k}_{i,s}}}. \quad (6)$$

The initial factor Q_p, which mainly effects the oscillation amplitude, is determined by varying Q_p from 0.5 to 4. The value that results in the smallest amplitude difference between $c_i[n]$ and $c_i^M[n]$ within the first four periods is the initial Q_p. The optimization parameter Q_r is set to one, since the rest positions are already initialized according to Eq. (3).

2. Objective function

The objective function Γ measures the error between $c_i[n]$ and the adapted trajectories $c_i^M[n]$. For a compact signal representation, a discrete wavelet transform (DWT) using Coifman wavelets of order two is applied to each trajectory.[47,48] Wavelet analysis decomposes a given signal, e.g., the trajectories $c_i[n]$, into a set of coefficients: the approximation coefficients $a_{Z,i}[\nu]$ containing the low-frequency signal components and the corresponding detail coefficients $d_{l,i}[\nu]$ $(l=1,\ldots,Z)$ representing the high-frequency components. The maximum decomposition level $Z=\lceil \mathrm{ld}(N/11) \rceil$ is given by the upper bound of the base-2 logarithm of the ratio signal length N to the number of wavelet filter coefficients. The DWT is applied to the trajectories $c_i[n]$ and $c_i^M[n]$.

After decomposition the coefficients are thresholded to obtain only the dominant components which form the trajectories and to achieve a smoothing. The coefficient values that contribute more than 5% to the energy E_i of all coefficients

$$E_i := \sum_{\nu} a_{Z,i}[\nu]^2 + \sum_{l}\sum_{\nu} d_{l,i}[\nu]^2 \quad (7)$$

are kept, while the others are set to zero. With

$$\Delta a_i := \sum_{\nu} (a_{Z,i}[\nu] - a^M_{Z,i}[\nu])^2,$$

$$\Delta d_i := \sum_{l}\sum_{\nu} (d_{l,i}[\nu] - d^M_{l,i}[\nu])^2, \quad (8)$$

the objective function is defined as

$$\Gamma := \frac{\Sigma_i \Delta a_i + \Delta d_i}{\Sigma_i E_i}. \quad (9)$$

The smaller the value of Γ the better is the match between the trajectories $c_i[n]$ and $c_i^M[n]$.

3. Optimization

The aim is to minimize Γ by variation of the optimization parameters in $S[n]$ [Eq. (4)], so that $c_i^M[n]$ is best fitted to $c_i[n]$. The time dependency of the model requires in principal an optimization of each sample for all of the eight optimization factors in the set $S[n]$, which is computationally highly expensive. However, the complexity can be reduced since the change in vocal fold vibrations and the corresponding time constants for muscle contraction ($\approx$30 ms) and mechanical delays ($\approx$20 ms)[49,50] are continuous functions and are slow relative to the numerical integration step size. Hence, not every time sample in the set $S[n]$ needs to be optimized.[14]

The trajectories $c_i[n]$ are divided into $b=1,\ldots,B$ blocks, each with four oscillation periods. The number of samples in the block trajectories $c_i[n]_b$ ranges from $n=1,\ldots,N_b$. The blocks overlap by 50% in order to assure smoothness and continuity of the optimization parameters. The model dynamics $c_i^M[n]_b$ are adapted to $c_i[n]_b$ of the first block and then subsequently to the following blocks by minimizing the objective function Γ_b with Powell's direction set method[51] for each block. Powell's optimization algorithm starts from an initial point with the unit vectors as the search direction. It finds the minimum of Γ_b along the given directions, moves to the minimum found, and takes the moving direction as new search direction.[52] The following listing passes through the individual steps of the minimization process:

Step (1) DWT of $c_i[n]_b$.

Step (2) Initialize the first and last sample of the optimization parameters $S[n]_b$ associated with the current block b: $S[1]_b=S[N_b]_b=S[N_{b-1}/2]_{b-1}$. Due to the 50% overlap the samples are depicted at $N_{b-1}/2$.

Step (3) Do a line minimization with Powell's method for all eight optimization factors in $S[N_b]_b$.

(a) Construct the time samples between $n=2,\ldots,N_b-1$ by linear interpolation: $S[n]_b=S[1]_b+\{S[N_b]_b-S[1]_b\}/N_b-1(n-1)$.
(b) Scale the TMM parameters according to Eq. (4) with $S[n]_b$ and computation of the new model trajectories $c_i^M[n]_b$.
(c) DWT of $c_i^M[n]_b$.
(d) Compute Γ_b.
(e) Evaluate termination condition: If local minimum is sufficient (2) $|\Gamma_{\text{best}}-\Gamma_b|\leqslant 0.01(|\Gamma_{\text{best}}|+|\Gamma_b|)$,[52] go to *Step* (1) for $b=b+1$, i.e., process the next block. Here, Γ_{best} denotes the best objective function value found so far. Otherwise, continue *Step*(3) with updated search directions.

4. Validation

The reliability and the capability of the optimization in finding correct parameters are evaluated for two test situations.

First, the TMM optimization is applied to synthetically generated data: 40 parameter sets $S^\star[n]$ are taken as predefined values and the TMM trajectories synthesized from them are used as data from which the TMM parameters are to be estimated. The optimized parameters $S[n]$ are compared to the predefined parameters $S^\star[n]$ by the relative error

$$\varepsilon_{\text{rel}}[n]=\frac{|S^\star[n]-S[n]|}{S^\star[n]}. \tag{10}$$

A second test verifies that the time-dependent parameters derived from HS recordings are independent of the starting frame of the analysis. Valid parameters are characterized by similar time courses within identical time sections of the HS recording. To evaluate this, the TMM is adapted four times (cases A, B, C, and D) to nonstationary trajectories of a MPR with a duration time of 384 ms. For each optimization the starting point is delayed by 100 ms ($t_A=0$ ms, $t_B=100$ ms, $t_C=200$ ms, $t_D=300$ ms) and the resulting four parameter sets are graphically compared.

D. Classification criterion

A scalar measure of asymmetry in the TMM parameters is introduced. The factors $Q_i[n]$ $(i=1,\ldots,6)$ comprise information about LR and AP asymmetry. The absolute value of the distance to the symmetry line

$$d_j^{\text{sym}}[n]:=\left|1-\frac{Q_{j+3}[n]}{Q_j[n]}\right| \tag{11}$$

for the three positions dorsal $(j=1)$, medial $(j=2)$, and ventral $(j=3)$ is averaged over time to define a LR symmetry ratio

$$R_j=\frac{1}{N}\sum_{n=1}^{N} d_j^{\text{sym}}[n]. \tag{12}$$

Hence, the combination of

$$\bar{R}=\frac{1}{3}\sum_{j=1}^{3} R_j, \tag{13}$$

which measures the total average of LR asymmetry, and

$$\sigma_R=\frac{1}{2}\sum_{j=1}^{3}(R_j-\bar{R})^2, \tag{14}$$

which describes the variance of the LR asymmetry in the AP direction, results in the rating

$$\Psi:=\bar{R}+\sqrt{\sigma_R}. \tag{15}$$

Neither $Q_p[n]$ nor $Q_r[n]$ capture asymmetry information, and thus they are omitted in the calculation of Ψ. Vocal fold vibrations can be classified according to the rating Ψ: The larger Ψ the larger the asymmetries. A decision tree classification on the data set using the random tree classification is applied to automatically find a Ψ boundary that separates normal from dysphonic voices for the given subjects.[53,54]

III. RESULTS

First, the validation results of the TMM optimization are presented. Second, examples of observed vocal fold dynamics are given and the adapted TMM trajectories are compared. Finally, the interpretation and classification of vocal fold vibrations are demonstrated with the model-based asymmetry measure Ψ.

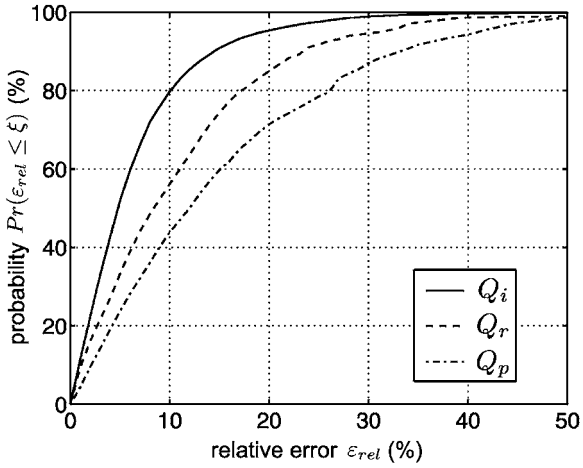

FIG. 3. The probability of getting the predefined parameter set $S^{\star}[n]$ for a given relative error $\varepsilon_{\mathrm{rel}}$ acceptance level. The curve for Q_i, on which the rating Ψ is based on, is calculated with the highest accuracy.

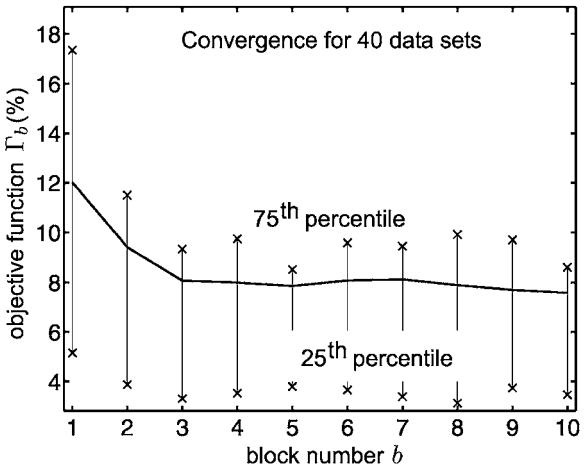

FIG. 5. Objective function Γ_b as a function of the block number b averaged over 40 synthetic data sets. The match of the first four-period block is less accurate than for the following blocks.

A. Validation

The relative error $\varepsilon_{\mathrm{rel}}$ of Eq. (10) for the 40 synthetic data sets amounts to $6.6\% \pm 6.6\%$, $11.0\% \pm 10.5\%$, and $15.1\% \pm 12.4\%$ for $Q_i[n]$, $Q_r[n]$, and $Q_p[n]$ an average. Figure 3 displays the probability $\Pr(\varepsilon_{\mathrm{rel}} \leqslant \xi)$ that $\varepsilon_{\mathrm{rel}}$ is lower or equal a given boundary ξ. For a boundary of $\varepsilon_{\mathrm{rel}}=20\%$ the optimization parameters $Q_i[n]$, $Q_r[n]$, and $Q_p[n]$ are calculated with a probability of 95.3%, 85.0%, and 71.4%. The error between the synthetic and the adapted trajectories amounts $\Gamma=4.6$ in the average.

Figure 4 illustrates the four optimized parameter sets $S[n]$ for different starting times (t_{A}, t_{B}, t_{C}, and t_{D}) of a MPR phonation. The time courses of the optimization parameters $Q_i[n]$, $Q_p[n]$, and $Q_r[n]$ are displayed. The six factors $Q_i[n]$ are split into the dorsal ($i=\{1,4\}$), medial ($i=\{2,5\}$), and ventral ($i=\{3,6\}$) positions to facilitate visual inspection. During the time course the optimized parameters converge to the same solution. Minor differences, if any, occur only at the beginning for each case, since here the optimization has to find a parameter combination that minimizes Γ_b starting from the roughly estimated initial values. Therefore, Γ_b has increased values for the first four-period block and decreases in the following blocks. This is illustrated in Fig. 5, where the convergence as a function of the block number is evaluated for the 40 data sets.

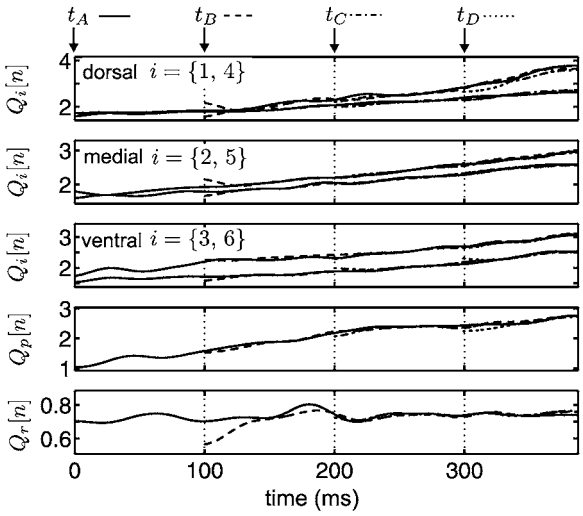

FIG. 4. Optimization verification with four different starting times (t_{A},t_{B},t_{C},t_{D}). The optimized parameters for each case converge to the same solution.

B. Application to vocal fold vibrations

The subjects managed phonating the instructed paradigm, either SSP or MPR, during the HS recordings. Especially, the dysphonic voice group performed the MPR just as well as the normal voice group. They phonated in a comfortable way within their scope of ability in terms of frequency stability/range, intensity level, and duration. Table II summarizes duration and frequency range for the normal and pathological voice group as well as for the paradigms SSP and MPR.

Exemplarily, Fig. 6 displays the adaptation result $c_i^M[n]$ (dashed) to $c_i[n]$ (solid) for four subjects—one from each of the groups in Table I. Only a short time section of the trajectories is depicted, since the match between the trajectories would be graphically not distinguishable if the entire duration time was plotted. The objective function Γ amounts are 12.6, 3.6, 7.2, and 8.1 for the presented subjects s9, s16, s26, and s38. Hence, it is in the same order of magnitude as Γ for the adaptation to synthetic data. A closer look reveals that it is also in the order of magnitude as the errors induced by the limited HS camera resolution and the quantization errors dur-

TABLE II. Overview of duration and frequency range (highest–lowest) averaged for the subject groups (SSP—sustained stationary phonation; MPR—monotonous pitch raise).

Paradigm	Feature	Normal	Dysphonic
SSP	Duration (ms)	283.5 ± 82.0	96.1 ± 20.0
	Frequency range (Hz)	9.7 ± 5.5	5.5 ± 3.3
MPR	Duration (ms)	376.7 ± 116.6	321.3 ± 112.2
	Frequency range (Hz)	106.1 ± 53.2	92.5 ± 65.6

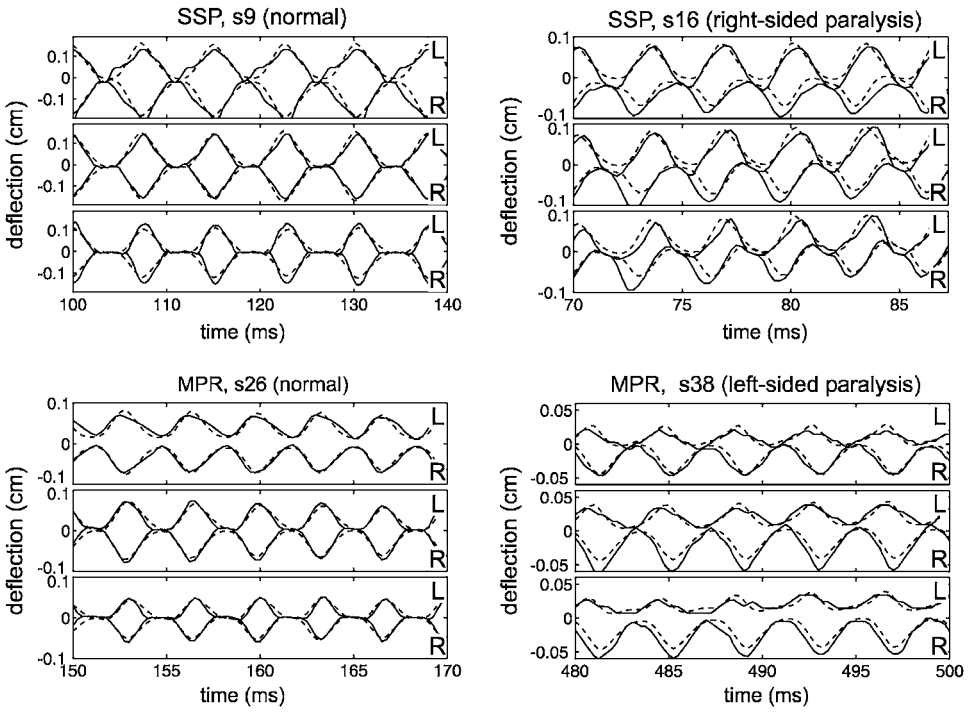

FIG. 6. Match of trajectories $c_i^M[n]$ (dashed lines) to $c_i[n]$ (solid lines) for a short section of phonation. Exemplarily, four different cases are depicted—one from each group in Table I.

ing image segmentation and tracking of the vocal fold edges.[14,21] In general, there is a match in amplitude, frequency, and phase shift between the adapted and given trajectories. In particular, the TMM dynamics fit the symmetric oscillation pattern of subject s9. The TMM reproduces the phase shifts between the left and right sides of subject s16 as well as the dorsal closure insufficiency of subject s26. The TMM dynamics are fitted to the phase shifts and the amplitude asymmetries as well as the ventral closure insufficiency of subject s38.

The adapted TMM dynamics lead to a set $S[n]$ of optimized model parameters. As seen in Eq. (12), the parameters $Q_i[n]$ of $S[n]$ comprise information of LR and AP asymmetries of vocal fold vibrations. These asymmetries are exemplarily visualized in Fig. 7 for the subjects from Fig. 6 (s9, s16, s26, and s38). Within this plane LR symmetry is located along the bisecting line. Perfect AP symmetry exists if the curves for the dorsal, medial, and ventral regions are identical. The curves for subject s9 are typical for a normal voice performing a SSP. They concentrate to a point near the bisecting line. In the case of a pathological voice subject (s16) performing a SSP, the curves exhibit a LR asymmetry. There is variation in the left-sided parameters (~2.5 to ~3.5), whereas the right-sided parameters do not vary that much (~2 to ~2.25). This subject s16 suffers from a right-sided unilateral recurrent laryngeal nerve paralysis and the associated paths can be interpreted as follows: The paralyzed side contributes only in a passive manner to the oscillation. This is reflected by the small variations of the parameters. In contrast, the healthy side tries to actively compensate for the insufficient oscillation and therefore larger variations of the corresponding parameters occur. For a normal voice performing a MPR (s26), the curves are distributed along the bisecting line. The curves of subject s38 (pathological voice, MPR phonation) cover a wide range in the upper half of the asymmetry plane. The different profiles of the dorsal, medial, and ventral curves indicate additional AP asymmetries. Subject s38 has a left-sided unilateral recurrent laryngeal nerve paralysis, which is opposite to subject s16. Accordingly, the left-sided parameters vary less than the right-sided ones.

Besides the visual inspection of the curves in the asymmetry plane, asymmetries can be measured by determining the fraction of the curves that lie within a given distance to the bisecting line. This distance d_j^{sym} is evaluated in Eqs. (11) and (12) and constitutes the abscissa in Fig. 8. The associated ordinate is called symmetry fraction—100% of this measure

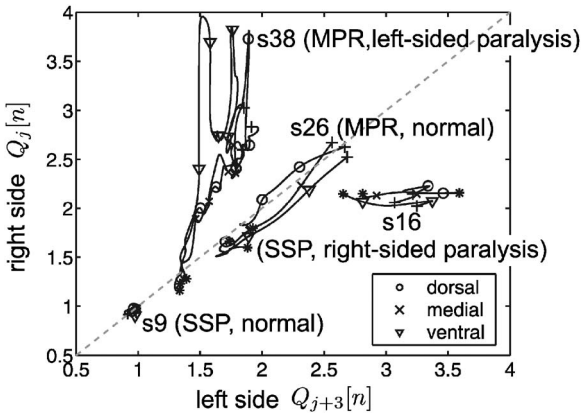

FIG. 7. Asymmetry diagram: LR asymmetry plane of the optimization parameters $Q_{j+3}[n]$ and $Q_j[n]$ for the subjects of Fig. 6. Each subject is represented by a path in the asymmetry plane for the dorsal, medial, and ventral regions. The bisecting line (dashed gray) denotes perfect LR symmetry. AP asymmetries are identified among a subject's three paths. (∗) marks the beginning and (+) the ending of each curve.

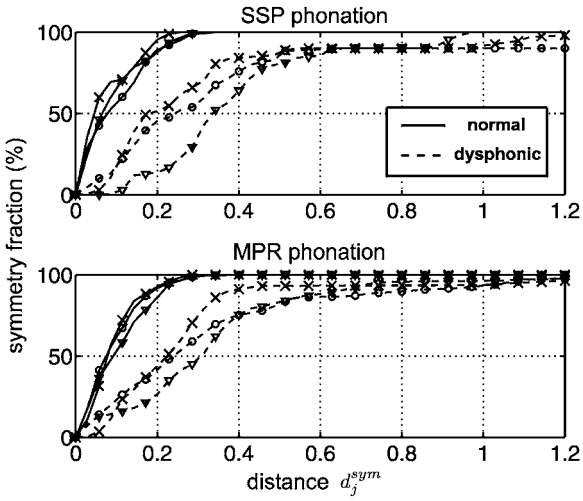

FIG. 8. The graphs display the fraction of symmetry averaged for the normal (solid) and pathological (dashed) voices within a given distance d_j^{sym} to the bisecting line. (○) Dorsal, (×) medial, and (∇) ventral.

means that the curves entirely lie within the specified distance region. Figure 8 displays the symmetry fraction for the dorsal, medial, and ventral parts averaged over the groups of normal (solid lines) and pathological voices (dashed lines) for each phonation paradigm. For the normal voices the gradient of the symmetry fraction is approximately two times higher than for the pathological voices. Hence, in the case of normal voices the symmetry fraction amounts $90.6\% \pm 4.2\%$ (mean and standard deviation for the dorsal, medial, and ventral curves) at a distance of 0.2 and is only $36.8\% \pm 20.3\%$ in the case of pathological voices for the SSP paradigm at this distance. The corresponding values of the MPR paradigm are $90.1\% \pm 3.7\%$ and $37.4\% \pm 9.4\%$. In the average SSP paradigm, a symmetry fraction of more than 80% implies a distance of 0.17 for the normal voice group and 0.46 for the dysphonic voice group. The distances for the MPR paradigm are 0.17 and 0.4, respectively. For the investigated subjects, the curves for pathological voices are farther away from the symmetry line by a factor of ≈ 2.5 and scatter more within the asymmetry diagram than the curves of normal voices.

C. Classification

Figure 9 depicts the rating Ψ for the normal and pathological voice subjects for the SSP and MPR phonations. The two Ψ summands $\bar{R}$ and $\sqrt{\sigma_R}$ are identified by light and dark gray color. The contribution of LR asymmetry $\bar{R}$ outweighs the contribution of the AP asymmetry measure $\sqrt{\sigma_R}$. All the Ψ values for pathological voices are greater than those for normal voices for each phonation paradigm. As revealed by a Wilcoxon rank sum test (nonparametric, non-normal distributed population), the healthy and the pathological subjects represented by the Ψ values differ highly significant ($p < 0.001$). Thus, the rating Ψ provides a way to separate the vocal fold vibrations into normal and pathological groups. A tree-based classification yields boundaries of $\Psi = 0.25$ and $\Psi = 0.22$ for the SSP and MPR phonations. All normal voice

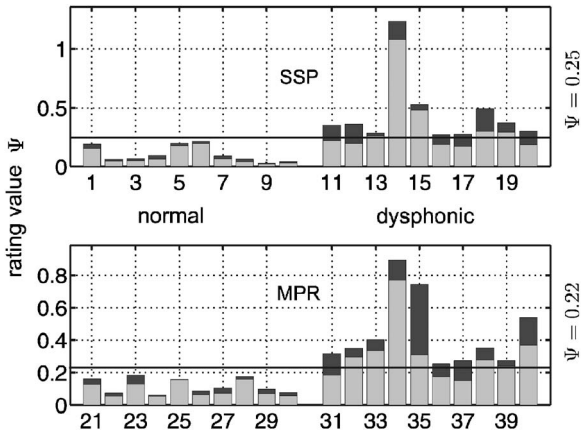

FIG. 9. Rating value Ψ for the 40 subjects. The two summands of Ψ are coded in light ($\bar{R}$) and dark ($\sqrt{\sigma}$) gray. The horizontal lines at $\Psi = 0.25$ for SSP and $\Psi = 0.22$ for MPR are the determined boundaries of a decision tree algorithm to separate normal from pathological vocal fold vibrations.

subjects are less than these boundaries and a correct grouping for the given subjects is achieved.

IV. DISCUSSION

Laryngoscopic HS recording techniques provide the basis for real-time recordings of even nonstationary and aperiodic vocal fold vibrations. Appropriate analysis and interpretation methods are needed for the objective and quantitative evaluation of the recorded vocal fold dynamics. Within this work a model-based approach is proposed for classifying normal and pathological vocal fold vibrations by means of LR and AP asymmetry measures.

The TMM dynamics are synchronously fitted to the vocal fold dynamics at dorsal, medial, and ventral positions. The time dependency of the model parameters also enables an adaptation to nonstationary vibrations. Compared to prior work,[14] the error between the vocal fold and model trajectories is measured by a subset of wavelet coefficients, which contain the dominant oscillation characteristics. In smoothing the objective function, this stabilizes the optimization and helps it converge in a reasonable number of iterations. The model dynamics are controlled by the optimization parameters $Q_i[n]$, $Q_p[n]$, and $Q_r[n]$. These parameters are used as control parameters in two-mass model approaches as well.[28] The optimized model parameters describe the time-varying characteristic of LR and AP asymmetries in a condensed form.

Clinical voice measurement is mostly directed toward the evaluation of the ability to sustain vowels.[55] Indeed, this clinical paradigm evaluates the principal functionality. However, it neglects dynamical transitions found in fluent speech. These can be systematically investigated by the MPR paradigm. As seen in the asymmetry diagram (Fig. 7), the MPR paradigm checks the symmetry of vocal fold vibrations for a wider phonation range in a single HS examination. Thus, it may help in a more complete diagnosis of the extent of a voice disorder.

The verification of the optimization algorithm demonstrates that the calculated parameters are independent of the starting time (Fig. 4). The adaptation to synthetic data sets

with predefined parameters reveals that the optimization parameters are reproduced with different accuracies: $Q_i[n]$, from which the asymmetry rating Ψ is derived, is calculated with the highest accuracy. A lower accuracy is obtained for the optimization factors $Q_r[n]$ and $Q_p[n]$. Since these two factors are not involved in calculating the rating Ψ, their relative inaccuracy does not negatively affect the reliability of Ψ. It is noted that an increased subglottal pressure can induce chaotic and asymmetric vibration even for symmetric vocal fold configurations as revealed in biomechanical model simulations.[36] However, chaotic vocal fold vibrations are rare within laryngological examinations[56] and thus, for a start, we do not go into a detailed model-based classification of chaotic vibrations.

The calculated asymmetry measures are derived from the extracted vocal fold trajectories. The trajectories in turn could be affected by the endoscopic recording situation. For example, the endoscope could have an angle to the vocal fold plane yielding asymmetries between the left and right side deflections. Further, there could be vertical laryngeal movements due to position changes of the cartilaginous framework.[57] Such vertical movements are accompanied by a tilt of the vocal fold plane resulting in a different recording resolution for the dorsal, medial, and ventral parts. Assuming a tilt of 8° by a distance of 7 cm between the endoscope and the vocal fold plane[41,57] and a 1 cm vocal fold length yields a difference of 1.3% between the dorsal and the ventral deflections for the used HS camera system. This is much smaller than segmentation errors of image processing[21] that are of the order of 10% and thus negligible.

A direct physiological interpretation of the TMM parameters is not given because of our limited ability to assign model elements to anatomical structures.[40] A finite-element method (FEM) model[58,59] of vocal fold vibration may indeed provide a more realistic representation concerning the physiological completeness. With a FEM approach AP asymmetry mechanisms[31] as well as vertical dynamics, which exist in vocal fold vibrations as shown in experimental studies,[60,61] can be simulated in principle. However, the detailed and layered structure of FEM models involve a larger number of mass nodes than the TMM and so would have prohibitively increased computational costs for the dynamic optimization. In contrast, this is possible for the TMM approach, although the implementation still has to be optimized for clinical use in order to reduce the adaptation time. It currently takes 30–45 min for typical MPR trajectories of 400 ms on a standard PC (Pentium IV, 3 GHz). For the future, the TMM-based classification method will be validated on a larger subject group. Especially, it will be investigated whether the paths in the asymmetry diagram for different kinds of voice disorders trace out different patterns and therefore lead to a clustering of dysphonias. Further developments will extend the TMM to additionally simulate the vertical vocal fold movements,[62,63] which can be extracted from endoscopic recordings by laser triangulation.[42] In addition, such laser calibration methods can be used to calibrate the endoscopic HS recordings for the purpose of extracting metrical scaled dimensions and dynamics of the vocal folds.[41,43] In doing so, the arbitrary scaling of the trajectories from pixel to metrical units could be avoided.

In all, the optimized TMM parameters capture a compact description of vocal fold vibration characteristics, and thus facilitate the analysis and interpretation of vocal fold dynamics and allow for a classification into normal and pathological voice groups. The parameters estimate the degree of laryngeal asymmetry and provide a quantitative measure of voice disorders that could serve as a diagnostic tool for the planning and control of surgical and nonsurgical voice therapies.

V. CONCLUSION

By means of a model-based approach high-speed recorded vocal fold vibrations are objectively and quantitatively assessed. Fitting the dynamics of a multimass model to the vocal fold dynamics delivers optimized model parameters which measure left–right and anterior–posterior asymmetries. The graphical representation of the time-dependent parameters gives an intuitive view of the actual degree of asymmetry. A rating value derived from the parameters provides a classification into normal and pathological vocal fold vibrations.

ACKNOWLEDGMENT

This work was supported by Grant No. DFG HO 2177/3 from the Deutsche Forschungsgemeinschaft (DFG).

Nomenclature

$a_{Z,i}[n]$ = wavelet approximation coefficients
$\mathbf{ac}, \mathbf{pc}$ = anterior and posterior commmisure
b = block number
B = total number of blocks
$c_i[n]$ = vocal fold trajectory
$d_j^{\mathrm{sym}}[n]$ = distance to symmetry line
$d_{l,i}$ = wavelet detail coefficients
$\varepsilon_{\mathrm{rel}}$ = relative error
E_i = energy of wavelet coefficients
f_i = vibration frequency
f_s = sampling frequency
$\mathbf{F}_{i,s}^{\eta}$ = force η on mass $m_{i,s}$
$\mathbf{F}_{i,s}^{D}$ = driving force on mass $m_{i,s}$
$\mathbf{g}_j$ = specific points on the glottal axis
Γ = objective function
i = TMM mass number
η = Anchor, vertical, longitudinal, or collision case
j = index for specific points on the glottal axis
$k_{i,s}^{A}, k_{i,s}^{C}, k_{i,s}^{V}$ = TMM anchor, collision, and vertical spring
$k_{i,s}^{L}$ = TMM longitudinal spring between mass $m_{i,s}$ and $m_{i+1,s}$
l = wavelet decomposition level
$m_{i,s}$ = TMM mass element
$\overset{M}{\cdot}$ = TMM trajectories and corresponding variables

$\tilde{\cdot}$ = standard model parameters of the literature
n = discrete time index
ν = wavelet index
$N, (N_b)$ = total number of frames/samples (in block b)
$\mathbf{p}_i$ = specific points on the vocal fold edges
P_L = subglottal pressure
Q_i, Q_p, Q_r = optimization factors for TMM elements
$r^A_{i,s}, r^L_{i,s}$ = TMM anchor and longitudinal damping elements
R_j = left–right asymmetry ratios
$\bar{R}$ = total average of left–right asymmetry
s = TMM plane number
σ_R = variance of left–right asymmetry in anterior–posterior direction
S = set of optimization parameters
t = time
Δt = sampling period
x, y = image coordinates
$\mathbf{x}_{i,s}$ = TMM position of mass $m_{i,s}$
$\mathbf{x}^R_{i,s}$ = TMM rest position of mass $m_{i,s}$
ξ = ± 1 factor for the left and the right vocal fold side
Ψ = rating of asymmetry
Z = number of wavelet decomposition levels

[1]U. Eysholdt, F. Rosanowski, and U. Hoppe, "Irregular vocal fold vibrations caused by different types of laryngeal asymmetry," Eur. Arch. Otorhinolaryngol. **260**, 412–417 (2003).
[2]D. Michaelis, M. Fröhlich, and H. W. Strube, "Selection and combination of acoustic features for the description of pathologic voices," J. Acoust. Soc. Am. **103**, 1628–1639 (1998).
[3]E. Yumoto, W. J. Gould, and T. Baer, "Harmonics-to-noise ratio as an index of the degree of hoarseness," J. Acoust. Soc. Am. **71**, 1544–1550 (1982).
[4]H. Kasuya, S. Ogawa, K. Mashima, and S. Ebihara, "Normalized noise energy as an acoustic measure to evaluate pathologic voice," J. Acoust. Soc. Am. **80**, 1329–1334 (1988).
[5]S. Hadjitodorov and P. Mitav, "A computer system for acoustic analysis of pathological voices and laryngeal diseases screening," Med. Eng. Phys. **24**, 419–429 (2002).
[6]J. I. Godino-Llorente and P. Gomez-Vilda, "Automatic detection of voice impairments by means of short-term cepstral parameters and neural network based detectors," IEEE Trans. Biomed. Eng. **51**, 380–384 (2004).
[7]T. Wittenberg, M. Moser, M. Tigges, and U. Eysholdt, "Recording, processing, and analysis of digital high-speed sequences in glottography," Mach. Vision Appl. **8**, 399–404 (1995).
[8]Q. Qiu and H. K. Schutte, "A new generation videokymography for routine clinical vocal fold examination," Laryngoscope **116**, 1824–1828 (2006).
[9]S. Hertegård, H. Larsson, and T. Wittenberg, "High-speed imaging applications and development," Logoped. Phoniatr. Vocol. **28**, 133–139 (2003).
[10]J. Wendler, "Stroboscopy," J. Voice **6**, 149–154 (1992).
[11]S. Niimi and M. Miyaji, "Vocal fold vibration and voice quality," Folia Phoniatr Logop **52**, 32–38 (2000).
[12]R. Titze, *Principles of Voice Production* (Prentice-Hall, Englewood Cliffs, NJ, 1994).
[13]P. Mergell, I. R. Titze, and H. Herzel, "Irregular vocal-fold vibration—High-speed observation and modeling," J. Acoust. Soc. Am. **108**, 2996–3002 (2000).
[14]T. Wurzbacher, R. Schwarz, M. Döllinger, U. Hoppe, U. Eysholdt, and J. Lohscheller, "Model-based classification of nonstationary vocal fold vibrations," J. Acoust. Soc. Am. **120**, 1012–1027 (2006).
[15]O. Rasp, J. Lohscheller, M. Döllinger, U. Eysholdt, and U. Hoppe, "The pitch raise paradigm: A new task for real-time endoscopy of non-stationary phonation," Folia Phoniatr Logop **58**, 175–185 (2006).
[16]U. Hoppe, F. Rosanowski, M. Döllinger, J. Lohscheller, and U. Eysholdt, "Visualization of the laryngeal motorics during a glissando," J. Voice **17**, 370–376 (2003).
[17]U. Eysholdt, M. Tigges, T. Wittenberg, and U. Pröschel, "Direct evaluation of high-speed recordings of vocal fold vibrations," Folia Phoniatr Logop **48**, 163–170 (1996).
[18]D. Maurer, M. Hess, and M. Gross, "High-speed imaging of vocal fold vibrations and larynx movements within vocalizations of different vowels," Ann. Otol. Rhinol. Laryngol. **105**, 975–981 (1996).
[19]A. K. Saadah, N. P. Galatsanos, D. Bless, and C. A. Ramos, "Deformation analysis of the vocal folds from videostroboscopic image sequences of the larynx," J. Acoust. Soc. Am. **103**, 3627–3641 (1998).
[20]Y. Yan, X. Chen, and D. Bless, "Automatic tracing of vocal-fold motion from high-speed digital images," IEEE Trans. Biomed. Eng. **53**, 1394–1400 (2006).
[21]J. Lohscheller, H. Toy, F. Rosanowski, U. Eysholdt, and M. Döllinger, "Clinically evaluated procedure for the reconstruction of vocal fold vibrations from endoscopic digital high-speed videos," Med. Image Anal. **11**, 400–413 (2007).
[22]Y. Yan, K. Ahmad, M. Kunduk, and D. Bless, "Analysis of vocal-fold vibrations from high-speed laryngeal images using a Hilbert transform-based methodology," J. Voice **19**, 161–175 (2005).
[23]Q. Qiu, H. K. Schutte, L. Gu, and Q. Yu, "An automatic method to quantify the vibration properties of human vocal folds via videokymography," Folia Phoniatr Logop **55**, 128–136 (2003).
[24]J. G. Švec and H. K. Schutte, "Videokymography: High-speed line scanning of vocal fold vibration," J. Voice **10**, 201–205 (1996).
[25]M. Döllinger, U. Hoppe, F. Hettlich, J. Lohscheller, S. Schuberth, and U. Eysholdt, "Vibration parameter extraction from endoscopic image series of the vocal folds," IEEE Trans. Biomed. Eng. **49**, 773–781 (2002).
[26]M. Döllinger, T. Braunschweig, J. Lohscheller, U. Eysholdt, and U. Hoppe, "Normal voice production: Computation of driving parameters from endoscopic digital high speed images," Methods Inf. Med. **42**, 271–276 (2003).
[27]R. Schwarz, U. Hoppe, M. Schuster, T. Wurzbacher, U. Eysholdt, and J. Lohscheller, "Classification of unilateral vocal fold paralysis by endoscopic digital high-speed recordings and inversion of a biomechanical model," IEEE Trans. Biomed. Eng. **53**, 1099–1108 (2006).
[28]J. C. Lucero and L. L. Koenig, "Simulations of temporal patterns of oral airflow in men and women using a two-mass model of the vocal folds under dynamic control," J. Acoust. Soc. Am. **117**, 1362–1372 (2005).
[29]D. A. Berry, H. Herzel, I. R. Titze, and K. Krischer, "Interpretation of biomechanical simulations of normal and chaotic vocal fold vibrations with empirical eigenfunctions," J. Acoust. Soc. Am. **95**, 3595–3604 (1994).
[30]J. Neubauer, P. Mergell, U. Eysholdt, and H. Herzel, "Spatio-temporal analysis of irregular vocal fold oscillations: Biphonation due to desynchronization of spatial modes," J. Acoust. Soc. Am. **110**, 3179–3192 (2001).
[31]C. Tao and J. J. Jiang, "Anterior-posterior biphonation in a finite element model of vocal fold vibration," J. Acoust. Soc. Am. **120**, 1570–1577 (2006).
[32]D. Wong, M. Ito, N. B. Cox, and I. R. Titze, "Observation of perturbations in a lumped-element model of the vocal folds with application to some pathological cases," J. Acoust. Soc. Am. **89**, 383–394 (1991).
[33]K. Ishizaka and J. L. Flanagan, "Synthesis of voiced sounds from a two-mass model of the vocal cords," Bell Syst. Tech. J. **51**, 1233–1268 (1972).
[34]J. C. Lucero, "Dynamics of the two-mass model of the vocal folds: Equilibria, bifurcations, and oscillation region," J. Acoust. Soc. Am. **94**, 3104–3111 (1993).
[35]I. Steinecke and H. Herzel, "Bifurcations in an asymmetric vocal fold model," J. Acoust. Soc. Am. **97**, 1571–1578 (1995).
[36]J. J. Jiang, Y. Zhang, and J. Stern, "Modeling of chaotic vibrations in symmetric vocal folds," J. Acoust. Soc. Am. **110**, 2120–2128 (2001).
[37]I. R. Titze, "The human vocal cords: A mathematical model. I," Phonetica **28**, 129–170 (1973).
[38]R. Schwarz, "Model-based quantification of pathological voice production," Ph.D. thesis, ISBN: 978-3-8322-6322-5, Shaker (2007).
[39]R. J. Sinard, "The aging voice: How to differentiate disease from normal changes," Geriatrics **53**, 76–79 (1998).
[40]B. H. Story and I. R. Titze, "Voice simulation with a body-cover model of the vocal folds," J. Acoust. Soc. Am. **97**, 1249–1260 (1995).
[41]S. Schuberth, U. Hoppe, M. Döllinger, J. Lohscheller, and U. Eysholdt, "High-precision measurement of the vocal fold length and vibratory amplitude," Laryngoscope **112**, 1043–1049 (2002).
[42]H. Larsson and S. Hertegård, "Calibration of high-speed imaging by laser triangulation," Logoped. Phoniatr. Vocol. **29**, 154–161 (2004).

[43]M. Schuster, J. Lohscheller, P. Kummer, U. Eysholdt, and U. Hoppe, "Laser projection in high-speed glottography for high-precision measurements of laryngeal dimensions and dynamics," Eur. Arch. Otorhinolaryngol. **262**, 477–481 (2005).
[44]H. B. Nudelman and B. D. Hoyt, "Comments on 'Two-mass models of the vocal cords for natural sounding voice synthesis'," J. Acoust. Soc. Am. **85**, 2220–2221 (1989).
[45]M. Döllinger, N. Tayama, and D. A. Berry, "Empirical eigenfunctions and medial surface dynamics of a human vocal fold," Methods Inf. Med. **44**, 384–391 (2005).
[46]M. Döllinger and D. A. Berry, "Computation of the three-dimensional medial surface dynamics of the vocal folds," J. Biomech. **39**, 369–374 (2006).
[47]C. S. Burrus, R. A. Gopinath, and H. Guo, *Introduction to Wavelets and Wavelet Transforms—A Primer* (Prentice Hall, Upper Saddle River, NJ, 1998).
[48]S. Mallat, *A Wavelet Tour of Signal Processing* (Elsevier, San Diego, 1999).
[49]A. B. Perlman and F. Alipour-Haghighi, "Comparative study of the physiological properties of the vocalis and cricothyroid muscles," Acta Oto-Laryngol. **105**, 372–378 (1988).
[50]I. R. Titze, B. Story, M. Smith, and R. Long, "A reflex resonance model of vocal vibrato," J. Acoust. Soc. Am. **111**, 2272–2282 (2002).
[51]R. P. Brent, *Algorithms for Minimization without Derivatives* (Prentice-Hall, Englewood, Cliffs, NJ, 1973).
[52]W. H. Press, S. A. Teukolsky, W. T. Vetterling, and B. P. Flannery, *Numerical Recipes in C: The Art of Scientific Computing*, 2nd ed. (Cambridge University Press, Cambridge, 1994).
[53]I. Mierswa, M. Wurst, R. Klinkenberg, M. Schulz, and T. Euler, "YALE: Rapid prototyping for complex data mining tasks," in *Proceedings of the International Conference on Knowledge Discovery and Data Mining* (ACM Press, New York, 2006).
[54]D. Hand, H. Mannila, and P. Smyth, *Principles of Data Mining, Adaptive Computation and Machine Learning* (MIT, Cambridge, 2001).
[55]D. Z. Huang, F. D. Minifie, H. Kasuya, and S. X. Lin, "Measures of vocal function during changes in vocal effort level," J. Voice **9**, 429–438 (1995).
[56]J. Schoentgen and R. D. Guchteneere, "Predictable and random components of jitter," Speech Commun. **21**, 255–272 (1997).
[57]K. Honda, H. Hirai, S. Masaki, and Y. Shimada, "Role of vertical larynx movement and cervical lordosis in f0 control," Lang Speech **42**, 401–411 (1999).
[58]F. Alipour-Haghighi, D. A. Berry, and I. R. Titze, "A finite-element model of vocal fold vibration," J. Acoust. Soc. Am. **108**, 3003–3012 (2000).
[59]H. E. Gunter, "A mechanical model of vocal-fold collision with high spatial and temporal resolution," J. Acoust. Soc. Am. **113**, 994–1000 (2003).
[60]M. Döllinger, D. A. Berry, and G. S. Berke, "A quantitative study of the medical surface dynamics of an in vivo canine vocal fold during phonation," Laryngoscope **115**, 1646–1654 (2005).
[61]M. Döllinger, D. A. Berry, and G. S. Berke, "Medial surface dynamics of an in vivo canine vocal fold during phonation," J. Acoust. Soc. Am. **117**, 3174–3183 (2005).
[62]T. Koizumi, S. Taniguchi, and S. Hiromitsu, "Two-mass models of the vocal cords for natural sounding voice synthesis," J. Acoust. Soc. Am. **82**, 1179–1192 (1987).
[63]M. Döllinger and D. A. Berry, "Visualization and quantification of the medial surface dynamics of an excised human vocal fold during phonation," J. Voice **20**, 401–413 (2006).

A three-dimensional articulatory model of the velum and nasopharyngeal wall based on MRI and CT data

Antoine Serrurier and Pierre Badin[a)]
GIPSA-lab, UMR 5216 CNRS-INPG-UJF-Université Stendhal, Département Parole and Cognition/ICP, 46 avenue Félix Viallet, 38031 Grenoble Cedex 01, France

(Received 1 June 2007; revised 21 January 2008; accepted 23 January 2008)

An original three-dimensional (3D) linear articulatory model of the velum and nasopharyngeal wall has been developed from magnetic resonance imaging (MRI) and computed tomography images of a French subject sustaining a set of 46 articulations, covering his articulatory repertoire. The velum and nasopharyngeal wall are represented by generic surface triangular meshes fitted to the 3D contours extracted from MRI for each articulation. Two *degrees of freedom* were uncovered by principal component analysis: first, VL accounts for 83% of the velum variance, corresponding to an oblique vertical movement seemingly related to the *levator veli palatini* muscle; second, VS explains another 6% of the velum variance, controlling a mostly horizontal movement possibly related to the sphincter action of the *superior pharyngeal constrictor*. The nasopharyngeal wall is also controlled by VL for 47% of its variance. Electromagnetic articulographic data recorded on the velum fitted these parameters exactly, and may serve to recover dynamic velum 3D shapes. The main oral and nasopharyngeal area functions controlled by the articulatory model, complemented by the area functions derived from the complex geometry of each nasal passage extracted from coronal MRIs, were fed to an acoustic model and gave promising results about the influence of velum movements on the spectral characteristics of nasals. © *2008 Acoustical Society of America.*
[DOI: 10.1121/1.2875111]

PACS number(s): 43.70.Bk, 43.70.Jt, 43.70.Aj [CHS] Pages: 2335–2355

I. INTRODUCTION

According to Crystal (1997), "*nasality* is a term used in the phonetic classification of speech sounds on the basis of manner of articulation: it refers to sounds produced while the soft palate [or velum] is lowered to allow an audible escape of air through the nose." Understanding the production of nasal sounds therefore requires a good knowledge of the variable shape of the velopharyngeal port that connects the rigid nasal tract to the vocal tract, and that is delimited by the velum and the nasopharyngeal wall. A large number of studies have been devoted to the production of nasality (see, e.g., Ferguson, Hyman, and Ohala, 1975 or Huffman and Krakow, 1993).

A first gross estimation of the nasal tract geometry was proposed by House and Stevens (1956) from anatomical considerations. The first systematic anatomical measures of the nasal tract that we know of were performed by Bjuggren and Fant (1964), who traced cross-sectional contours from slices cut from a plastic mold of the nasal passages of a cadaver. The cross-sectional contours and nasal passage areas that they proposed have served as a standard reference for many decades, and have been used for acoustical simulations. The first, and as far as we know the only, sets of transversal images of the velopharyngeal port obtained by x-ray tomography were recorded by Björk (1961) for ten subjects uttering sustained articulations. Associating these images with sagittal x-ray tomography images of the same subjects, he found a linear relation between the nasal tract transverse coupling area and the velum/pharyngeal wall sagittal distance in the midsagittal plane for distances greater than 0.2 cm. The magnetic resonance imaging (MRI) technique is still considered to be the only imaging technique that is safe for the subject and that delivers comprehensive three-dimensional (3D) data. It has thus been largely used for determining the geometry of the vocal tract in speech (see, e.g., Baer, Gore, Gracco, and Nye, 1991, Story, Titze, and Hoffman, 1996; Engwall and Badin, 1999; Badin, Bailly, Revéret, Baciu, Segebarth, and Savariaux, 2002) and has allowed new measurements on live subjects and permitted researchers to obtain more accurate area functions of the nasal tract. In 1992, Matsumura and Sugiura (1992) published the first cross-sectional profiles of nasal passages from MRI images. Area functions derived from these measurements were thus proposed by Matsumura, Niikawa, Shimizu, Hashimoto, and Morita (1994) two years later. At the same time, Dang, Honda, and Suzuki (1994) led a similar study which proposed new area functions and compared their results with those obtained by Bjuggren and Fant (1964). They highlighted in particular the importance of mucosa in the nasal passages. Demolin, Lecuit, Metens, Nazarian, and Soquet (1998) subsequently performed a unique 3D study of velopharyngeal port opening from MR images recorded on four subjects pronouncing French nasal vowels and their oral counterparts; more details on the cross-sectional contours and areas of velopharyngeal port were then provided by Demolin, Delvaux, Metens, and Soquet (2003). Delvaux, Metens and Soquet (2002) studied the position and shape of the velum and the associated coordination of other articula-

[a)]Author to whom correspondence should be addressed. Electronic mail: pierre.badin@gipsa-lab.inpg.fr

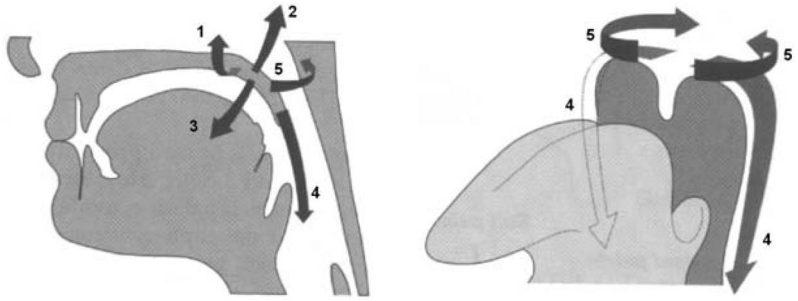

a) Sagittal view b) Oblique anterior view

FIG. 1. Midsagittal view (a) and oblique anterior view (b) of vocal tract and schematic directions of action of the principal muscles involved in the velum and velopharyngeal port movements (from Kent, 1997); 1: Tensor veli palatini; 2: Levator veli palatini; 3: Palatoglossus; 4: Palatopharyngeus; 5: Pharyngeal superior constrictor.

tors such as tongue movements used by French speaking subjects in the production of French nasal vowels. Interestingly, they noted a possible contact between the velum and the tongue for low velar positions.

Physiologically, the velopharyngeal port is organized in a complex way. A network of muscles linking the surrounding organs, i.e., the velum, the lateral and posterior pharyngeal walls and the tongue, controls the velopharyngeal port's opening/closing mechanism. The velum, the principal organ involved in the mechanism, is known to be controlled mainly by five muscles (see Fig. 1). Its major muscle, the *levator veli palatini*, stretches symmetrically from the medial region of the velum to the right and left Eustachian tubes. The two other muscles of the velum are the *tensor veli palatini*, stretching laterally and symmetrically from the medial region of the velum to the base of the cranium and passing through a tendon acting as a pulley to ensure a lateral tensing of the velum, and the *uvulae muscle* (not visible in Fig. 1), located entirely in the uvula—an appendix of the velum in the midsagittal region (see, for example, Fig. 2 for various uvula positions), which is believed to have only a small impact on the velopharyngeal mechanism in speech. In addition, the

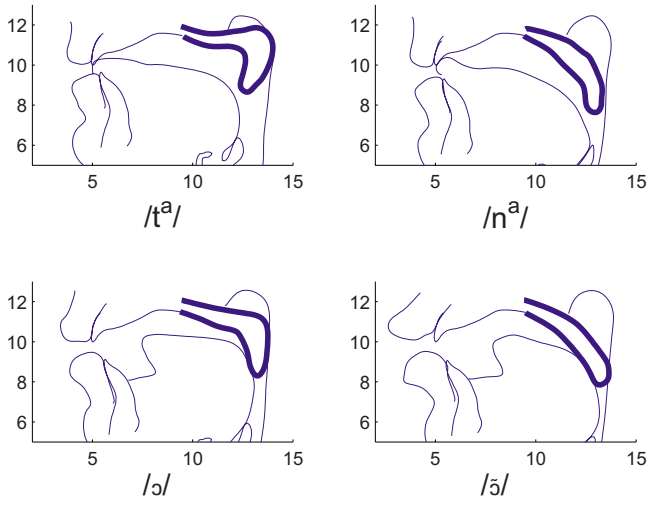

FIG. 2. (Color online) Midsagittal contours of the vocal tract for oral and nasal stop consonants /t^a/ and /n^a/ (top) and for oral and nasal vowels /ɔ/ and $\tilde{ɔ}$ (bottom). The thicker lines represent the velum contours.

velum is connected with its two neighboring organs: first with the tongue, through the *palatoglossus* muscle, with origin in the medial lower part of the velum and linking the lateral basis of the tongue along the borders of the oral cavity, known as the *anterior faucial pillars*; second with the pharyngeal walls, through the *palatopharyngeus* muscle, with its main origin in the medial upper part of the velum and linking the pharyngeal walls by forming the two *posterior faucial pillars* on both sides of the oral cavity (see, for example, Kent, 1997, for more detailed description of these muscles). The pharyngeal walls are principally active through the *superior, middle and inferior constrictor* muscles that surround the tract. The muscular structure of this region, in particular the interspersion between muscles from the velum, the pharyngeal walls, and the tongue, leads to a sphincter-like behavior (Amelot, Crevier-Buchman, and Maeda, 2003). Note that the contraction of the fibers of the *palatopharyngeus* muscle with those of the *pterygopharyngeal* portion of the superior constrictor leads to a prominence of the posterior wall called *Passavant's pad* (Zemlin, 1968), which contributes also to the sphincter effect. This effect may be speaker dependent, and at least four velopharyngeal closure patterns, depending on the anatomy of the speaker, have been reported (see, for example, Kent, 1997, and Amelot *et al.*, 2003, from fiberscopic data). The active or passive role played by each muscle involved in the closure mechanism during speech has led to various interpretations (see, for example Dickson and Dickson (1972); Bell-Berti (1976); Kollia, Gracco, and Harris (1995) and Wrench, 1999), although "the *levator (veli)palatini* muscle is widely accepted as the muscle primarily responsible for closing the velopharyngeal port by exerting an upward and backward pull on the velum" (Bell-Berti, 1993).

Due to the complex organization of the velopharyngeal port, the relative difficulty collecting geometric information in this region of the vocal tract, and consequently of measuring velopharyngeal movements, only a few articulatory models deal with nasals. House and Stevens (1956) proposed a basic model of nasal tract to oral tract coupling where the coupling seems to be implemented simply through a linear interpolation of the area function from the first velopharyngeal cross-sectional area to the first nasal tract area considered as fixed; they used this model for acoustical simulations

and perceptual studies of nasality. Fant (1960) investigated the influence of nasal area coupling in terms of acoustics by modeling the area function of the velopharyngeal port by a single tube. Maeda (1982) and Fant (1985) used a model similar to that of House and Stevens (1956), augmented with sinus cavities, in order to assess the contribution of these sinuses to the overall acoustic characteristics of nasals. Mermelstein (1973) proposed a crude geometric midsagittal model of velum shape and assumed the velar opening area to be proportional to the square of the distance between the current uvula position and the position attained when the velopharyngeal port is closed. This model has been used in particular by Teixeira, Vaz, Moutinho, and Coimbra (2001) for perceptual tests of synthesized Portuguese nasals (Teixeira, Moutinho, and Coimbra, 2003).

The development of more realistic models of speech production—and particularly of nasals—calls for more detailed 3D articulatory models of the velopharyngeal port and of the nasal cavities. Indeed, the accurate area functions of the complex nasal passages and velopharyngeal port that are needed to feed acoustical models, and thus to generate speech, cannot be obtained with simple models: for some nasal articulations, e.g., the French back nasal vowels, as highlighted by Demolin *et al.* (2003), the uvula can be in contact with both the back of the tongue and the pharyngeal wall in the midsagittal region (see Fig. 2), leading to a midsagittal occlusion, though the channels on each side of this occlusion remain open. Such articulations thus require a 3D description. More or less successful ad hoc transformations from midsagittal shape to area function have been proposed for the oral tract (see, e.g., Sundberg, Johansson, Wilbr, and Ytterbergh, 1987; Beautemps, Badin, and Bailly, 2001); but the only model proposed for the velopharyngeal port (Mermelstein, 1973) cannot deal with a midsagittal occlusion. It thus appears that a 3D model in which appropriate information is provided about the transverse structure of the vocal and nasal tracts is clearly needed.

This present study is intended to result in a nasal tract that complements the 3D linear articulatory models previously built in our laboratory (Beautemps *et al.*, 2001; Badin *et al.*, 2002) in the framework of the development of talking heads (Badin, Bailly, Elisei, and Odisio, 2003). Specifically, we attempted to reconstruct 3D nasal cavities, velum and nasopharyngeal wall shapes from MRI images from one subject uttering a corpus of sustained French articulations, and to develop a corresponding 3D linear articulatory model. This *organ-based* approach, as opposed to the *tract* approach that cannot take into account the complex geometry of the various speech articulators, aims in particular to explore the articulatory degrees of freedom of the articulators, following the approach of Badin *et al.* (2002) to modeling of the tongue and lips, based on the same French subject and the same corpus.

The following sections present the various articulatory data acquired on the subject, their analysis in terms of uncorrelated linear articulatory degrees of freedom, and the associated linear articulatory models. A preliminary acoustical evaluation of this articulatory model is also presented. This study constitutes an extension of the 3D articulatory modeling of nasals initiated in Serrurier and Badin (2005a) and Serrurier and Badin (2005b).

II. ARTICULATORY DATA

A. Subject and speech material

Designing a corpus and recording appropriate data obviously constitutes the first important stage of a data-based approach to articulatory modeling. As the principle underlying linear modeling is that any articulation should be decomposable into a weighted sum of basic shapes, that constitutes a minimal basis for the space of articulations, the corpus should constitute a representative sampling for this space. One way to achieve this is to include in the corpus all articulations that the subject can produce in his language. The corpus thus consisted of: the 10 French oral vowels [a ɛ e i y u o ø ɔ œ], the four French nasal vowels [ɑ̃ ɛ̃ œ̃ ɔ̃], the artificially sustained consonants [p t k f s ʃ m n ʁ l] produced in three symmetric contexts [a i u], and, finally, a "rest" position and a "prephonatory" position. These last two are produced without sound, lips open, nasal tract connected to the oral tract, jaw open, in a neutral position for the rest articulation and in a position ready to phonate for the prephonatory articulation. Altogether, there are 46 target articulations. This limited corpus proved to be sufficient for developing midsagittal articulatory models with nearly the same accuracy as corpora 40 times larger (Beautemps *et al.*, 2001). This corpus will be referred to as the *main corpus*.

As the present study constitutes the first attempt to elaborate a 3D articulatory model from MRI data, only one subject was considered: we chose the male French speaker already involved in the development of a midsagittal articulatory model based on a cineradio-film (Beautemps *et al.*, 2001), and of 3D models of tongue, lips, and face based on MRI and video data (Badin *et al.*, 2002). He was about 1.65 m tall and 43 years old at the time of recording the main corpus.

B. Data

As highlighted in the introduction, one of the most efficient and accessible methods of collecting 3D sets of vocal tract shapes, and considered to be safe for the subjects, is magnetic resonance imaging. Following Badin *et al.* (2002), the present study is based on 3D sets of MR images collected for each articulation of the main corpus, i.e., 46 stacks of sagittal images, from which 3D shapes of the soft organs are extracted. However, due to the difficulty of distinguishing air from bones in MRI, a set of computed tomography (CT) scans of the subject at rest was also recorded to serve as a reference and to help interpret the MR images.

Other data were also collected on the same subject for specific purposes. The geometry of the nasal passages being very complex and air passages sometimes very narrow, a set of coronal images considered to be perpendicular to the direction of the nasal tract has been recorded in order to optimize air/tissue detection. In order to complement the MRI

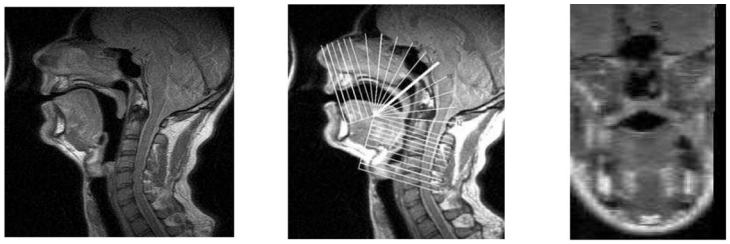

a) Sagittal – Original image – [i] b) Re-slicing grid – [a] c) Reconstructed transverse image – [a]

FIG. 3. Examples of MR images for [i] and [a] articulations (a and b) and (c) of a transverse image for [a] reconstructed along the thick white line in (b).

static shapes with dynamic data, electromagnetic midsagittal articulatory (EMA) data have also been recorded.

1. Sagittal MRI

Stacks of sagittal MR images were recorded using the 1 Tesla MRI scanner Philips GyroScan *T*10-NT available at the Grenoble University Hospital. The subject was instructed to sustain the articulation throughout the whole acquisition time, approximately 35 s for each of the 46 articulations. The consonants were produced in three different symmetrical vocal contexts [VCV], V belonging to [a i u]. A set of 25 sagittal images with a size of 25×25 cm, a thickness of 0.36 cm, and an inter-slice center to center distance of 0.4 cm was obtained for each articulation. The image resolution is 0.0977 cm/pixel, approximated to 0.1 cm/pixel in the rest of the article, the images size being 256×256 pixels. From these images it was possible to make the distinction between soft tissues and air, and to discriminate the soft tissues, but not to clearly distinguish the bones. They have thus been used to collect the 3D shapes of soft organs, but the CT scans were required to identify the bony structures. Note that the subject was in a supine position, which may alter somehow the natural shape of articulators (cf. Tiede, Masaki, and Vatikiotis-Bateson, 2000, and Kitamura, Takemoto, Honda, Shimada, Fujimoto, Syakudo, Masaki, Kuroda, Oku-uchi, and Senda, 2005). Examples of midsagittal images for the vowels [i] and [a] are shown in Figs. 3(a) and 3(b).

2. CT images

A stack of 149 axial images with a size of 512×512 pixels, a resolution of 0.05 cm/pixel, and an inter-slice space of 0.13 cm, spanning from the neck to the top of the head, was recorded by means of a Philips Mx8000 scanner for the subject at rest (see one example image in Fig. 4(a)). These images allow us to distinguish bones, soft tissues and air, but do not allow for the identification of different soft tissues. They have been used to locate bony structures and to determine accurately their shapes for reference (see Sec. II C 2).

3. Coronal MRI

A stack of 32 coronal images with a size of 256×256 pixels, a resolution of 0.1 cm/pixel, and an inter-slice space of 0.4 cm, spanning from the atlas bone to the tip of the nose, was recorded for the subject at rest (see Fig. 5(a)) to optimize detection of the nasal cavities.

4. EMA

Dynamic data were collected through an electromagnetic midsagittal articulograph (Rossato, Badin, and Bouaouni, 2003). One of the coils of the articulograph was attached to the velum about halfway between the hard palate-velum junction and the tip of the uvula, so as to provide a robust estimation of velum movements (see Fig. 13(a)). The corpus consisted of all the combinations of nonsense words [VCV], V being one of the 14 French oral or nasal vowels and C one of the 16 French consonants [b d g p t k v z ʒ f s ʃ m n ʁ l].

C. Preprocessing of images

1. Re-slicing of the original image stacks

Due to the complexity of the contours of the various organs, the relatively low resolution of the images, and the need for an accurate reconstruction of the organs, extraction of the contours was performed manually, plane by plane. This is a rather reliable process, except for regions where the surface of the structure is tangent to the plane, and thus difficult to trace and not very accurate. For instance, while the

a) Axial – original image b) Reconstructed coronal image c) Reconstructed sagittal image

FIG. 4. Example of original (a) and reconstructed (b and c) CT images.

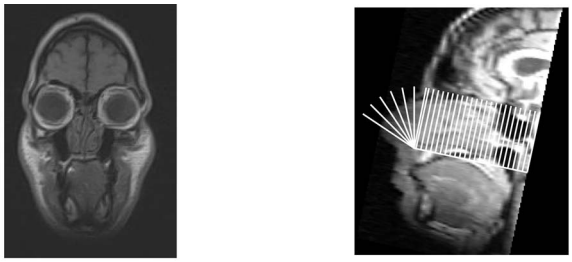

a) Example of original coronal MR image b) Semipolar grid of nasal tract sampling

FIG. 5. Original coronal MRI located between the atlas bone and the beginning of the nose (a), and semipolar grid showing the location of the original and reconstructed images (b).

pharyngeal wall is easy to trace in the midsagittal plane, the sidewalls of the pharynx are nearly tangent to the off-midline sagittal planes. This is why we have supplemented the original stacks of images used for the articulatory model with a single orientation (*axial* for CT images and *sagittal* for MR images) by extra sets of images reconstructed by intersection of the initial stack with planes having a more useful orientation, i.e., being more perpendicular to the organ surface.

The CT images have thus been resliced/interpolated in two stacks of 512 coronal images and 512 sagittal images, leading altogether to three stacks of perpendicular CT images with a high resolution of 0.05 cm/pixel in the three orientations (see Fig. 4).

For the sagittal MR images, the initial sagittal stack was resliced in images perpendicular to the vocal tract, considering that they will be used to extract organ shapes delimiting the vocal tract (e.g., velum, tongue, etc.). They were thus re-sliced in 27 planes orthogonal to the midsagittal plane and intersecting it along a semipolar grid, as illustrated in Fig. 3(b). Each new image was given a resolution of 0.1 cm/pixel. Finally, we disposed of two redundant orthogonal stacks of MR images for each articulation.

In the same way, sagittal MR images have been re-sliced in the nostril region along a polar grid, as shown on Fig. 5, in order to follow the nearly 90° bend of the nasal passages near the nostrils, and thus to maintain the images perpendicular to the nasal tract and therefore optimally adapted to border tract detection. Eight new images of arbitrary size 256×256 pixels, which have the same 0.1 cm/pixel resolution as the original images, have thus been created.

The original coronal images, being already perpendicular to the tract between the cavum and the beginning of the nostrils, were used as is.

2. Extraction of bony structures and alignment of the image stacks on a common reference

Regarding the data processing, a contour drawn on a specific image (such as the solid line on Fig. 9(a) which represents the velum) can be expressed in three different types of units: (1) two-dimensional (2D) coordinates in the image plane of the contour in a continuous pixel unit (i.e., subpixel resolution), referred to as *2D pixels*; (2) 2D coordinates in the image plane in cm, which can be transformed into continuous pixel units (and vice versa) by using the image pixel resolution parameter, referred to as *2D cm*; and (3) 3D coordinates in cm, which can be transformed into *2D cm* and vice versa using the knowledge of the image plane 3D location, referred to as *3D cm*. The following process refers to these various coordinates depending on the requirements.

As the subject's head may have moved between the recordings of the various articulations, it was necessary to align the image stacks of each articulation on a common reference framework, before attempting to determine the shape of the soft structures.

Fixed bony structures such as the cranium, hard palate, and various paranasal sinuses (maxillary, sphenoidal and frontal sinuses) that can be seen—at least partially—on each image, were used as landmarks. The set of 3D triangular meshes of the surface outlines of these structures was made from the stack of CT images where bones appear clearly, and were then used as a common reference.

This process was implemented in the following way. Manual segmentation of each organ outline was done plane by plane, in one of the three CT stacks, or a combination of them, depending on the shape and orientation of the organ, in such a way as to maximize the accuracy of complex organs (e.g., the maxillary sinuses were manually segmented in the coronal stack while the sphenoid sinus was segmented in the sagittal one). The planar contours are edited as 2D splines controlled by a limited number of points; for example, Figs. 9(a) and 9(b) illustrate (with a solid line) the contour of the velum manually segmented from MR images of articulation $[l^a]$. The whole set of 2D planar contours, whose coordinates are originally in 2D pixels, were then expressed in 2D cm and expanded into 3D cm to form a set of 3D planar contours representing the specific organ (see Fig. 9(c) for the set of 3D planar contours of the velum for the configuration $[l^a]$). These 3D points have been then processed through a 3D meshing software (Fabri, 2007) to form a 3D surface mesh based on triangles (see further Fig. 10 for the velum and pharyngeal wall).

The alignment of each stack of images on the common framework defined by the fixed bony structures is performed in three steps. First, the rigid fixed bony structures (hard palate, nasal passages, paranasal sinuses, etc.) are chosen as an arbitrary common reference. An absolute 3D reference coordinate system, attached to the skull of the subject, is arbitrarily defined as follows: (1) the x axis is oriented from anterior to posterior in the midsagittal plane and approxi-

mately in the occlusal plane, the y axis from left to right, and the z axis from feet to head; (2) the lower edge of the upper incisors in the midsagittal plane is considered as the origin of the coordinate system. Second, the stacks of CT images are manually aligned with this reference as a rigid body; thus, the associated transformation gives the position of the three stacks of CT images in the common reference coordinate system. This transformation corresponds to the six degrees of freedom of a rigid body and is thus defined by six parameters: three parameters for the 3D rotation and three parameters for the 3D translation; it will be referred to as a (3D) *rototranslation*. Finally, as the subject may have slightly changed position between two MRI stacks recordings, each stack was aligned with the common reference by using the appropriate 3D rototranslation. This rototranslation was determined by aligning specific rigid structures (hard palate and paranasal sinuses), extracted from CT images, with each stack of the MR images. This alignment is a semiautomatic process: (1) anchor points of the rigid structures are manually marked with care on some of the MR images of the stack, (2) the associated 3D rototranslation is determined by a simple minimization of the added distance between these 3D points (originally 2D planar points expressed in 2D pixels, then expressed in 2D cm and finally expanded in 3D cm) and the corresponding nearest points on the 3D rigid structures. A similar approach was proposed by Takemoto, Kitamura, Nishimoto, and Honda (2004), the main difference being that their minimization error was the value of the volume overlap between the reference to align and the target data.

The same alignment procedure was also applied to the jaw for each articulation, in order to determine its relative position in relation to the fixed rigid structures: by combining these relative 3D rototranslations and the absolute one corresponding to the given stack, the positions of these two structures are known in the common reference to each articulation.

Note that this procedure provides the geometric transformation between the 3D reference coordinate system, in which contours and meshes are expressed in 3D cm, and the stacks of images, in which contours are expressed in 2D pixels. This transformation can obviously be considered in both direct and reverse directions, the two sets of coordinates being thus equivalent. Note, however, that in order to maximize the accuracy of the contours detection, we decided to draw contours (in 2D pixels) on original images whenever they existed, and to use this geometric transformation to produce planar contours in 3D cm in the reference coordinate system, rather than applying the transformation to an image and drawing contours in 3D cm on this transformed image that is necessarily more noisy.

D. Nasal passages: 3D geometry and area function

1. Contours extraction

The nasal passage contours were manually segmented on the 24 coronal MR images and the eight resliced images defined by the grid visible in Fig. 5(b). The corresponding set of contours for the nasal tract is illustrated in Fig. 6. Three different regions can be considered in the nasal tract: (1) the cavum, which is the cavity located above the velum and behind the septum wall of the nasal passages (its cross-sectional contours are visible on the slices numbered from −1.2 to 0 cm in Fig. 6), (2) the choanae, which form the middle region of the nasal tract from the cavum to the nostrils (their cross-sectional contours are visible on the slices numbered from 0.4 to 6.4 cm in Fig. 6), and (3) the nostrils, which are the outlet of the nasal tract (their cross-sectional contours are visible on the slices numbered from 6.8 to 9.2 cm in Fig. 6).

The complex shape of the nasal passages, particularly in the middle region, combined with the relatively low resolution of the images (0.1 cm/pixel) makes it difficult to trace the nasal passage contours. In order to improve the accuracy of detection, the contours of the nasal passages were extracted from the CT images in the same way along the same grid, and were superimposed on the MR images. This provided a useful help for the determination of nasal passages, as soft tissues/air boundaries are better defined in CT images. We noticed, however, that the areas extracted from the CT images were about twice as large as those extracted from the MR images (cf. Fig. 7). This may be ascribed to the fact that nasal mucosa have low tissue densities and thus may not be visible on CT images. Figure 7 illustrates the resulting cross-sectional areas extracted from CT and MR images.

These results are in overall agreement with the observations made by Dang *et al.* (1994) and complement their study of four subjects. Note that the volume of the cavum is highly dependent on the position of the velum, which is very low in our case (see Fig. 5(b)); a low velum position results in large cross-sectional areas, as can be seen in Fig. 7 for slices located on the back of the septum, i.e., having negative abscissa. Note also the asymmetry between the left and right passages and the irregularities between two consecutive sections. These characteristics are related to the rather intricate shape of the nasal passages which are made up of many thin and interlaced partitions (see Fig. 6 that illustrates the nasal passage contours). Each nasal passage constricts mildly at a point located between the choanae and the nostrils. This constriction of about 1 cm^2 is located around 7 cm from the separation point of the nasal tract into choanae and 2.4 cm from the nostrils' outlet (at $x=6.6$ cm). The size of this constriction has often been discussed in the literature: it varies from 0.23 cm^2 for House and Stevens (1956) to about 2 cm^2 for Bjuggren and Fant (1964); Feng and Castelli (1996) estimated it to range between 0.5 and 1 cm^2 and fixed it at 0.6 cm^2 for their acoustic simulations; based on measurements from MR images, Dang *et al.* (1994) showed constrictions of about 1 cm^2, and Matsumura *et al.* (1994) between 0.5 and 1 cm^2. Ultimately, the significant difference between areas extracted from CT and MR images emphasizes the importance of mucosa in the nasal passages.

2. Area function determination

Oral and nasal tracts can be approximated in speech by a succession along a horizontal line of cylindrical tubes whose lengths and cross-sectional areas represent more or less finely the real tract; the area function provides this cross-sectional area as a function of the abscissa along the midline

FIG. 6. (Color online) Cross sectional contours of the nasal tract along the grid lines shown on the bottom right subplot: cavum (from −1.2 to 0 cm), left and right choanae (from 0.4 to 6.4 cm) and left and right nostrils (from 6.8 to 9.2 cm).

of the tract. An area function for the nasal passages has been computed from the cross-sectional contours extracted along the grid, assuming that the cavities are geometrically sampled in each image plane. The elementary tubes making up the area function are then assumed to be located between two adjacent sections and are determined as follows.

Each section area is calculated from the contours in each image plane: areas corresponding respectively to multiple *outer* contours (i.e., for which tissues are outside and air inside) are accumulated (see, e.g., the two contours defining the left nasal passage on slice 3.6 cm in Fig. 6), and conversely areas corresponding to *inner* contours (i.e., for which tissues are inside and air outside) are subtracted (see, e.g., the two contours defining the interior limitations of the tract on slice 0 cm in Fig. 6). The center of the tract in this section is calculated as the average of the center of gravity of each contour, weighted by the corresponding area, counted as positive for outer contours and negative for inner contours.

A multiplicative correction factor is applied to the area in order to compensate the bias introduced by the fact that the vocal tract is usually not intersected by a plane that is exactly orthogonal to its midline. This oblique section actually increases the section area by a factor which is the cosine of the angle between the ideal plane that would be orthogo-

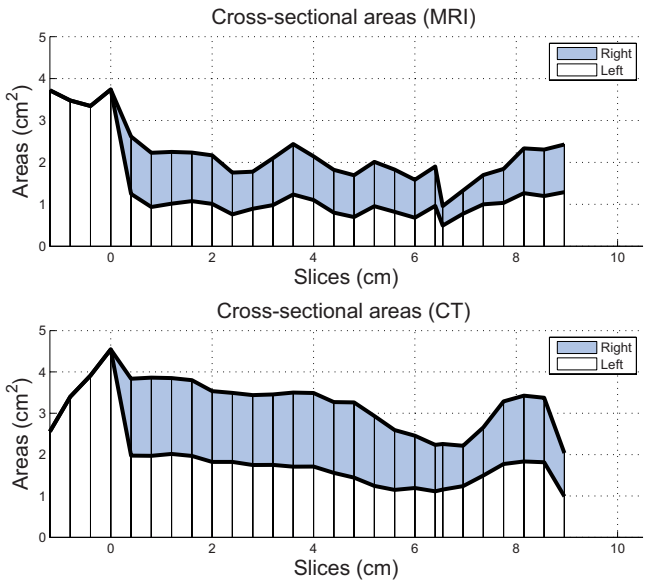

FIG. 7. (Color online) Cross-sectional areas of the nasal tract extracted from MR (top) and CT (bottom) images: cavum, left and right passages areas. The x axis represents the distance in cm from the cavum to the nostrils. The origin is arbitrarily chosen as the first image plane where nasal tract splits into two choanae separated in the midsagittal plane by the septum wall; the gap between each point is fixed to 0.4 cm, which is exactly the distance between two consecutive images in the back and middle part, and an extrapolation of this distance to the front part.

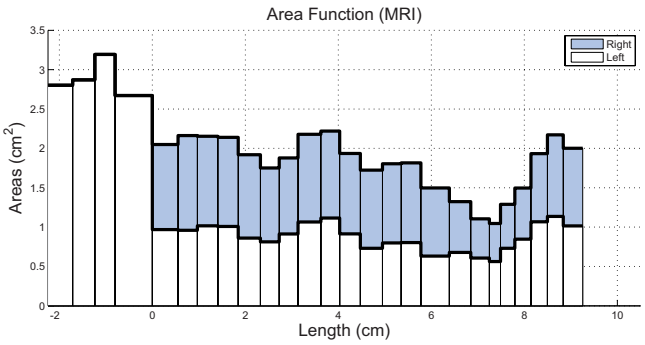

FIG. 8. (Color online) Area function of the nasal tract: each tube is represented by a length on the x axis and an area on the y axis.

nal to the midline and the actual cutting plane. The correction factor is thus computed as the cosine of the angle between (1) the 3D vector normal to the *actual* cutting plane of the tract and (2) the 3D vector normal to the *ideal* cutting plane of the tract. The tract midline is approximated locally by a circle passing through the center of gravity of the cross-sectional contour actually computed and those of its two neighboring sections, and thus the 3D vector normal to the *ideal* cutting plane is the tangent to this circle in the section considered.

The area of the tube is finally computed as the mean of the corrected areas of the two adjacent sections.

The length of the tube is computed as the distance between the 3D coordinates of the centers of the tract in each of the two sections.

3. Nasal passage area functions

The area functions of the nasal passages derived from the MR contours are illustrated in Fig. 8. Each elementary tube is represented by a line whose length is plotted on the x axis and whose area is plotted on the y axis. We observe a length of about 9.2 cm for the nasal passages, from the beginning of the septum (at $x=0$ cm) to the final outlet from the nostrils, and a constriction of about 0.6 cm long and 1 cm^2 large at 1.7 cm from the outlet of the nostrils (at $x=6.9-7.5$ cm).

In comparison, the length of the nasal passages proposed by House and Stevens (1956) is around 8.5 cm long and the area decreases from 5.9 to 0.23 cm^2 at the nostrils, which is considered as the constriction. If the cross-sectional contours proposed by Bjuggren and Fant (1964) seem similar to our data extracted from the MR images and the length of 7–8 cm for nasal passages appears slightly smaller, their areas seem largely overestimated, from more than 7 cm^2 in the middle part to around 2 cm^2 for the nostrils, which constitutes the constriction. Dang *et al.* (1994) highlighted the importance of the mucosa in the nasal passages by comparing the nasal contours of the same subject in a normal condition and in a condition where the nasal mucosa had been spread with a vaso-constrictor substance, and concluded that Bjuggren and Fant overestimated the areas due to a retraction of mucosa on the cadaver. This assumption is confirmed in this study, where cross-sectional areas extracted from CT images appear overestimated, likely due to the low density mucosa not visible on these images. The areas reported by Matsumura *et al.* (1994) appear significantly lower than those of Bjuggren and Fant (1964) (less than 3 cm^2 for the middle and front part) and the constriction appears between 0.8 and 2.8 cm from the tip of the nose, depending on the subject. Finally, as discussed above, our results correspond globally with those reported by Dang *et al.* (1994).

E. Determination of the soft structures

The shapes of the soft structures, i.e., the velum and the nasopharyngeal wall, were determined for each articulation in much the same way as the rigid structures, using both original sagittal MR image stacks and associated sets of reconstructed images. In addition, the 3D rigid structures meshes, properly aligned with the MR image stacks as described above, were then intersected by the planes corresponding to the MR images, leading to 3D planar contours in centimeters, easily expressed in 2D pixel planar contours, and superimposed on the MR images in order to provide some useful anchor points for the interpretation of the images and for the tracing of the soft structure contours (see dashed lines in Figs. 9(a) and 9(b)). Figure 9 illustrates the segmentation of the velum in both MRI stacks for the consonant [l^a]. In addition to the bony structures, previously manually segmented soft structures other than the velum are also superimposed on the images to help the detection of the velum, and to maintain coherence in tracing the various organs (see the tongue contours previously segmented in dash-dotted lines in Figs. 9(a) and 9(b)). The definition of the outline of a soft organ is of prime importance for the 3D shape extraction process. Air/tissue boundaries are obvious borders and are generally easy to detect on MRI (see, e.g., Fig. 9(a) where the velum contour appears clearly). As our primary goal is modeling the vocal tract boundaries, the borders of organs that are never in contact with air are not very important but may, however, play an important role in the elastic deformation of the organ under consideration (as discussed later in this section). Contour tracing in these regions has thus been performed according to the principle of coherence: the border choice aims to ensure coherence across configurations, as well as anatomic likelihood. This difficulty arises particularly for the superior part of the velum in lateral regions on both sides of the velopharyngeal tract (see Fig. 9(b)). Indeed, the velum shape was designed as a closed surface (except at the connection with the hard palate) and consequently the planar contours must be closed as well. The back and lateral pharyngeal wall outlines of the velopharyngeal port are on the contrary designed as a single open surface from the uvula level to the beginning of the cavum. Contours have therefore been traced in such a way as to stick on the velum contours in lateral regions in order to ensure closure of the tract. The set of all 2D planar contours traced in this way, initially expressed in 2D pixels, then in 2D cm, expanded into 3D cm and finally aligned with the common reference by using the 3D rototranslation of the corresponding images stack (see Sec. II C 2), forms a 3D description of the given soft organ (see, e.g., Fig. 9(c)).

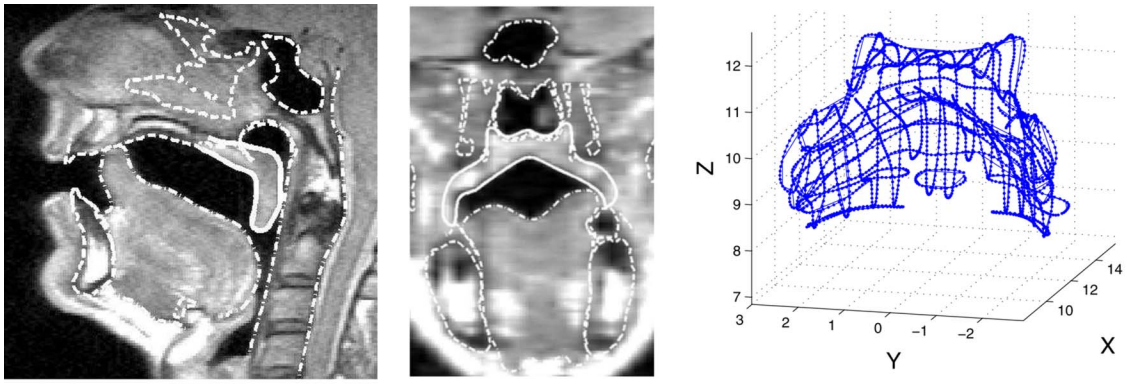

a) Segmentation in a sagittal plane

b) Segmentation in a transverse plane

c) Set of all 2D planar contours

FIG. 9. (Color online) Example of manual segmentation (a and b), and of 3D representation (c) of the velum for a [l^a] articulation. In a and b, the dashed lines correspond to bony structures superimposed on the images while dash-dotted lines correspond to soft structures other than the velum edited. The solid line corresponds to the manually edited velar contour.

As linear analysis methods such as principal component analysis or multiple linear regressions require each observation to bear on the same number of variables, it was necessary to ensure a common geometric representation of each soft organ for all the articulations in the corpus. A unique generic 3D surface mesh, made of triangles, was thus defined for each organ. These generic meshes were then fitted by elastic deformation to each of the 3D shapes of the corpus, providing a 3D representation of each organ surface with the same 3D vertices. The generic meshes were derived from the set of 3D planar contours of the [$\tilde{a}$] articulation by means of a 3D meshing software (Fabri, 2007). This articulation presents the advantage of a minimal contact between the velum and the surrounding structures, and thus is the most efficient way to extract the full 3D surfaces. Furthermore, the generic meshes (shown in Fig. 10) were slightly smoothed with the help of the *SmoothMesh* software (Huber, 2007) in order to reduce the noise introduced by the meshing procedure and the discrepancies due to the general problem of sampling 3D surfaces by a relatively small number of planar contours. The fit to each 3D shape extracted was computed by means of the matching software *TestRigid* developed at the TIMC laboratory in Grenoble (Couteau, Payan and Lavallée, 2000), and based on the elastic deformation of the generic meshes to the target configuration (see example of such a target in Fig. 9(c)). In order to ensure convergence of the matching algorithm, the deformation from generic source meshes to target configurations was supervised. About ten intermediate targets were obtained by linear interpolation from the planar contours which were achieved by intersections of the source mesh with planes of the target contours to the target contours themselves. The matching procedure was then applied in stages by introducing these targets one after the other. This method avoids unrealistic deformations that may occur when fitting the source mesh to too disjoint a target. The deformations of the soft organs obtained in such a way are believed to be close to the real deformations, i.e., the vertices of the mesh can be considered as flesh points and their relative positions coherent across configurations. This reconstruction process finally provides a set of soft organ surfaces described in terms of triangular meshes having the same number of vertices for all the articulations of the corpus and expressed in a common reference coordinate system. For all these articulations, each of the 46 closed velum surfaces is com-

a) Anterior view of the velum

b) ¾ posterior view of the velum

c) ¾ posterior sagittal view of the left-half pharyngeal wall

FIG. 10. (Color online) Three-dimensional generic meshes of the velum (a and b) and of the back pharyngeal wall (c) reconstructed for the [$\tilde{a}$] articulation.

posed of 5239 vertices and each of the 46 pharyngeal wall surfaces from the uvula level to the beginning of the cavum is composed of 2110 vertices. This matching process has resulted in a root mean square (RMS) reconstruction error between the fitted mesh and the target points over the 46 configurations of 0.06 cm for the velum and of 0.04 cm for the pharyngeal wall.

These sets of 3D data form the basis of the articulatory modeling of the subject speech organs, as will be described in the next sections.

III. 3D LINEAR ARTICULATORY MODELS OF VELOPHARYNGEAL PORT

A. Principles of articulatory modeling

As emphasized by Kelso, Saltzman, and Tuller (1986), the speech organs are made of a large number of neuromuscular components that offer a potentially large dimensionality and which must be functionally coupled in order to produce relatively simple gestures. Thus, following the approach used by Beautemps *et al.* (2001) and Badin *et al.* (2002), we consider that these simple gestures for a given organ can be represented in terms of *independent degrees of freedom* defined as the specific displacements and deformations of the organ which are linearly uncorrelated with the other degrees of freedom of this organ over the considered set of tasks. These degrees of freedom can be determined by observing the correlations between the various parameters that constitute the accurate geometrical description of the articulators' shapes and positions, and retaining only independent parameters. These correlations stem from a series of implicit or explicit constraints: physical continuity of the articulators, biomechanical constraints, and the nature of the task in relation to the control.

The movements of a speech organ can be modeled at two levels: a *physical* level, which deals with the displacements and deformations of the organ as *biomechanical* responses to muscle actions, and a *functional* level, which deals with the geometrical representation of the displacements and deformations of the organ. Linear articulatory modeling aims to determine the functional degrees of freedom of the organs and their associated control parameters. The correlations between the various movements observed on the articulator over the set of considered tasks are exploited to reduce the number of degrees of freedom and to determine the associated components. However, this approach is carefully used with the biomechanical likelihood constraint: the components must correspond to plausible movements in terms of biomechanics and must not result from a pure control strategy of the subject.

The linearity of the model means that the shape of an articulator for a given articulation is expressed as a linear combination of the components of the model, weighted by the set of control parameters corresponding to the articulation. In other words, assuming that the shape of an articulator is defined by the set of the coordinates of all its points means that varying a single input value corresponding to a specific component, while keeping all others constant, leads to a displacement of each point of the articulator along a straight line.

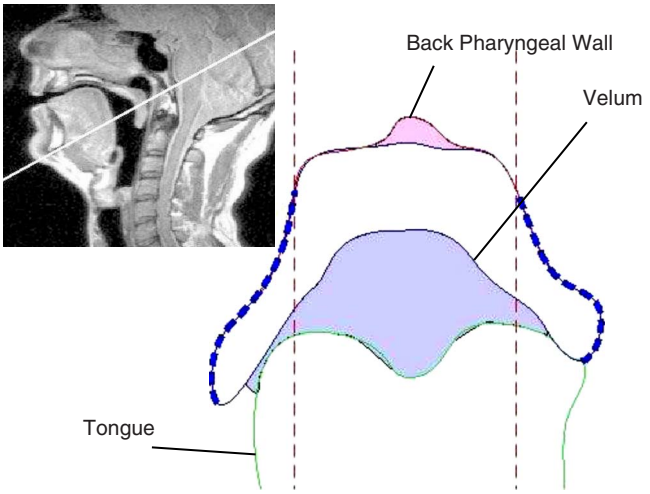

FIG. 11. (Color online) Cross-sectional contours of the velum, the pharyngeal wall and the tongue in the transverse plane shown on the MRI in the upper left corner for an [i] articulation. Oral and nasal cross-sectional areas are marked by a slightly dark color. The vertical dashed lines show the lateral limits of the analysis region of the velum at 1.5 cm on both sides of the midsagittal plane; the dashed contours of the velum beyond these vertical lines are considered to be irrelevant for the study.

Before describing the articulatory model based on this approach of the velopharyngeal port, i.e., of the velum and nasopharyngeal walls, we define the selection of the data used for the analysis and assess the contribution of head tilt to the movement of these articulators.

B. Selection of data for analysis

As explained above, the planar contours of the organs have also been traced in regions that do not bring information about the 3D shape of the vocal tract. The main objective of this study is to model the boundaries of soft organs that contribute to the 3D vocal tract shape: the organs' contours in these regions were thus considered irrelevant for the model and not included in the analysis.

According to combined criteria of anatomic likelihood and coherence across articulations, some regions of the velum considered as irrelevant for the model have, however, been traced, as illustrated in Fig. 11 by dashed lines. In order to simplify the choice of relevant regions, we applied a conservative approach and restricted the analysis to a region no further than 1.5 cm on both sides from the midsagittal plane (cf. Fig. 11). As will be explained in Sec. III E, the model was based on the analysis of this central part of the velum composed of 2812 vertices. In addition, the external regions will be shown to be very well correlated with the central region, which is in the end not surprising, considering the fact that the muscular fibers of the velum stretch continuously from the center to the more external regions.

C. Head tilt influence

Considering that the subject's head may have moved during the recording session, the stacks of images have been

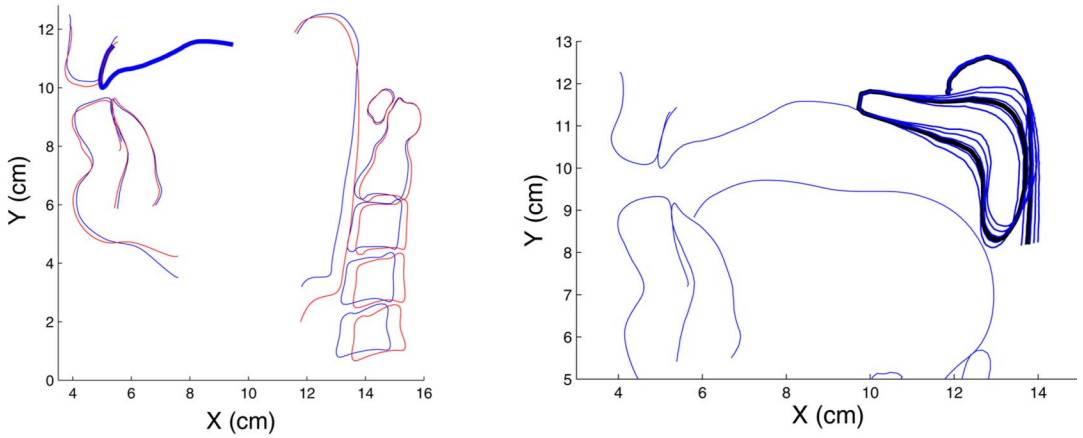

a) Superposition of contours in a sagittal image for [i] and [t^a] articulations

b) Nomogram of HT parameter for [a] articulation

FIG. 12. (Color online) Influence of the head tilt on organ shapes. Superimposition of contours in the sagittal image plane closest to the midsagittal one for the articulations of the 3D corpus corresponding to extreme tilts [i] and [t^a] (a). (b) Trace in the midsagittal plane for an [a] articulation of the 3D nomogram of the velum and pharyngeal wall for the HT parameter between the two extreme tilts of the data, −1.5 and 2.5.

aligned with a common reference system attached to the cranium (see Sec. II C 2). However, a change of head tilt, that produces rotation of the head within a sagittal plane, as for example when the chin and nose rotate down closer to the chest, introduces a variation of the vocal tract shape suggested by Kitamura *et al.* (2005) which is not taken into consideration in this alignment. Such a head movement may increase the variability of the data without being related to a precise degree of freedom of the articulators and is therefore considered to be a global articulatory degree of freedom of the head that is not specifically related to speech production. Therefore, it appears necessary, before modeling speech articulators independently, to remove the variability related to this degree of freedom from the data: the global component associated with the tilt is computed on the whole vocal tract and its contribution removed from each organ's data. Anatomically, a tilt change that affects the pitch of the head corresponds to a rotation of the cranium structure in a sagittal plane around the cervical vertebrae apex to which it is attached through various ligaments. As the cranium structure is aligned with a fixed coordinate system in the current study, a change of head tilt creates a rotation of the spine in the reference system and an associated deformation of the vocal tract in the pharyngeal region and of the midsagittal trace of the posterior longitudinal ligament. The most posterior line in Fig. 9(a) illustrates the midsagittal trace of posterior longitudinal ligament, attached to cervical vertebrae. The deformation of this latter trace—also obviously related to the cervical vertebrae position—can thus be considered as a good marker of the head tilt variation, though the posterior pharyngeal wall would be a more convenient marker. Therefore, the relationships between vocal tract posterior pharyngeal wall and posterior longitudinal ligament have been investigated using a set of midsagittal MRI recorded for three typical positions of the head (normal, forward and backward tilt), for the same subject on a subset of 38 phonemes of the main corpus. The recording conditions were similar to those of the sagittal MRI recordings presented in Sec. II B 1. The velum, the posterior longitudinal ligament and the back pharyngeal wall were manually segmented, from glottis to cavum, on the images of this set, and aligned with the cranium in the midsagittal plane. As could be expected, it was found that the first Principal Component Analysis (PCA) component of the pharyngeal wall coordinates is strongly correlated with the first PCA component extracted from the posterior longitudinal ligament, for a corpus including large tilt movements (correlation of 0.99), as well as for a corpus where there are only small movements, corresponding to our data (correlation of 0.83). The first PCA pharyngeal wall component was thus considered to be a good head tilt predictor, as illustrated on Fig. 12(a). Finally, we verified that the horizontal coordinate of the back pharyngeal wall in the midsagittal plane at the height of the uvula, the lower limit of our analysis data, was correlated with this first pharyngeal wall component; it was used as a tilt predictor, and referred to as *Head Tilt* (HT) parameter.

The contribution of this parameter to the explanation of the total variance of the data has been computed by means of linear regression of the central part of the velum and of the pharyngeal wall on this parameter. It was found that 17% of the accumulated variance of the 2812×3 variables of the velum and 31% of the 2110×3 variables accumulated variance of the pharyngeal wall were explained by the HT parameter. The effect of this parameter in the midsagittal plane is demonstrated on Fig. 12(b). The nasopharyngeal wall movement appears to be coherent with a pure head tilt movement: it moves along in a horizontal direction, maximally in the lower region and remains fixed in the upper region. The velum movement corresponds to a simultaneous motion along horizontal and vertical axis which suggests a correlation with the principal movement measured through the EMA coil (cf. Fig. 13(a)). Indeed, since the shape of the vocal and nasal tracts changes under an independent action of the head tilt, the subject may introduce a compensatory action to correct for the tilt influence and thus attain the phonetic target. The fairly constant midsagittal distance be-

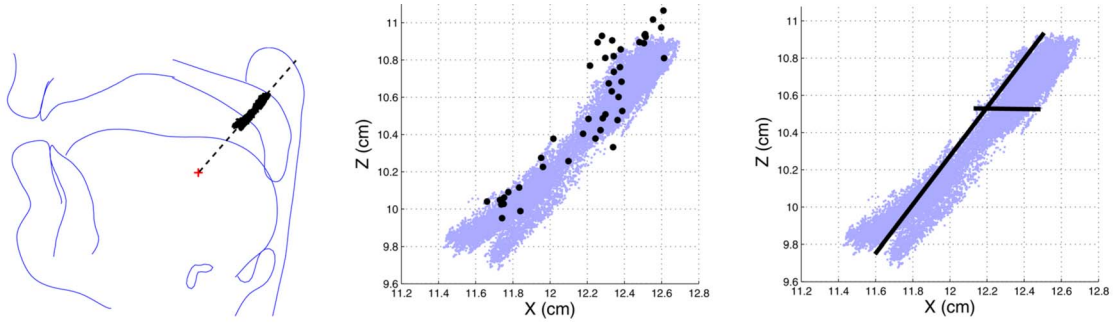

a) Midsagittal space covered by the EMA coil for the EMA corpus

b) Superimposition of MRI data positions on EMA data

c) Superimposition of nomograms of VL (oblique line) and VS (horizontal line) on EMA data

FIG. 13. (Color online) Midsagittal space covered by the velum EMA coil for the corpus of VCV sequences (a); superimposition on these EMA data of the *X-Z* coordinates of the *pseudo-EMA vertex* of the velum mesh: for the 46 configurations of the main corpus (b), for a movement associated with VL (oblique line on c) and to VS (horizontal line on c).

tween the velum and the back pharyngeal wall suggests an active compensation by the subject, logically related to the principal movement of the velum.

The following models are built from 46 velum and pharyngeal wall meshes for which the linear contribution of the HT parameter has been removed from the raw data.

D. Articulatory degrees of freedom of a fleshpoint on the velum

Before exploring the various articulatory degrees of freedom of the velum and back pharyngeal wall 3D surfaces, it is worth analyzing the articulatory degrees of freedom of the EMA velum coil presented in Sec. II B 4. Figure 13 displays the whole midsagittal space covered by the coil for the corpus of VCV sequences produced by the subject. This figure clearly reveals two main displacement directions: one dominant direction along an oblique axis over a range of about 1.6 cm, and a secondary direction along the horizontal axis over a range of about 0.35 cm. This observation suggests two articulatory degrees of freedom for a fleshpoint in this region of the velum located halfway between hard palate and uvula.

E. 3D linear articulatory model of the velum and of the nasopharyngeal wall

In order to determine the number and nature of the articulatory degrees of freedom of the velum, principal component analysis (PCA) was applied to the 2812×3 vertex coordinates that represent the surface of the central part of the velum over the 46 articulations corrected for tilt variations. The first PCA parameter VL explains 83% of the accumulated variance of all the central velum points while the associated RMS reconstruction error is 0.08 cm. This parameter can then be used to predict the entire velum surface based on a linear regression of the whole set of velum points on this parameter. In other words, the external regions of the velum can be predicted from the central region by means of this first PCA parameter with a very slight increase of global RMS reconstruction error of less than 0.01 cm. The effect of VL on the whole velum is illustrated on Figs. 14(a) and 14(b) by the shape associated with the two extreme values of VL found in the data and on two planes by the re-sliced contours for a regular succession of VL values between these two extremes (Fig. 14(c)). The main movement associated with VL is a movement in an oblique direction similar to that observed in the EMA data. Considering its orientation and its prime importance for speech (Bell-Berti, 1993), the *levator veli palatini* muscle can be thought to be much involved in this movement; this control parameter is thus referred to as *Velum Levator*. Moreover, the deformation of the velum in the midsagittal plane (Fig. 14(c) left) as it is raised from a low flat position to a high horizontal position broken at a right angle in its middle suggests a mechanism attached to the middle of the velum and pulling at about 45° degrees, the rest of the velum following this movement passively. This deformation could be ascribed to the *levator veli palatini* contraction.

The second velum PCA parameter, VS, explains 6% of the total variance of the central points of the velum. The accumulated variance explained by the two parameters VL and VS attains 89% while the accumulated RMS reconstruction error lowers to 0.06 cm. This second parameter, whose effects on the whole velum are displayed on Fig. 15, is related to a horizontal displacement coupled with a vertical elongation of the velum, which complements the velopharyngeal port closure by a front to back movement and may significantly modify the velopharyngeal port constriction (see Sec. IV B).

The third PCA parameter explains less than 3% of the full variance and corresponds to a slight movement in the left-right direction that has no coherent explanation and can be considered to be an inaccurate parameter. It was thus not retained for the model.

It has been shown in the literature (Amelot *et al.*, 2003) that the velopharyngeal port closure is controlled by a combination of velum pulling and superior constrictor sphincter action. A strong correlation between pharyngeal wall and velum could thus be expected for our data. It was first shown by linear regression applied to the 2110×3 variables of the

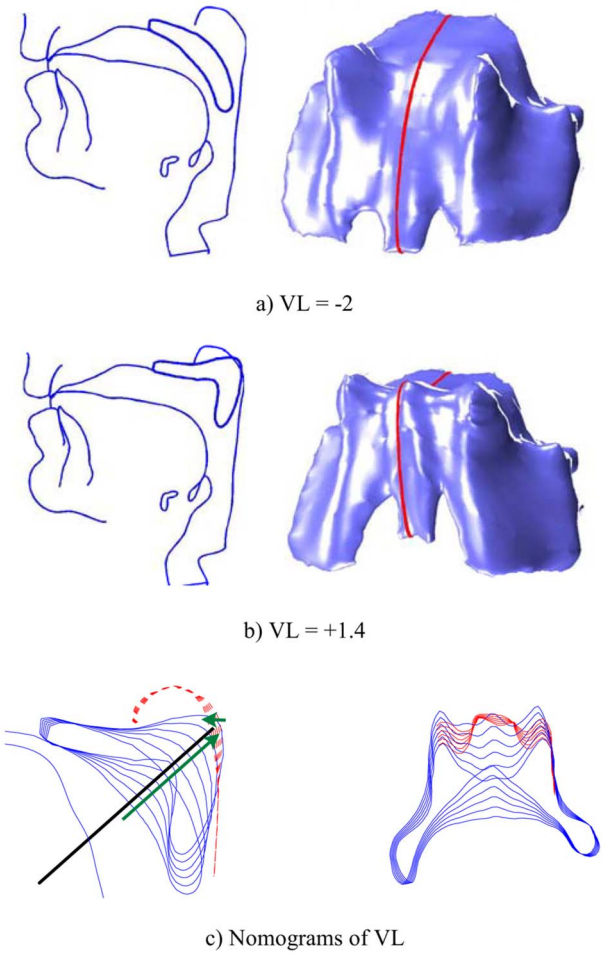

FIG. 14. (Color online) Posterior views of velum model 3D meshes (a and b right) and corresponding midsagittal contours (a and b left) for two extreme values of parameter VL (−2 in a and +1.4 in b); regular nomograms between these two values for the velum and the pharyngeal wall (c) displayed in the midsagittal plane (c left) and in the transverse plane (c right) indicated by the transverse solid line on the left graph (in the same way as in Fig. 11).

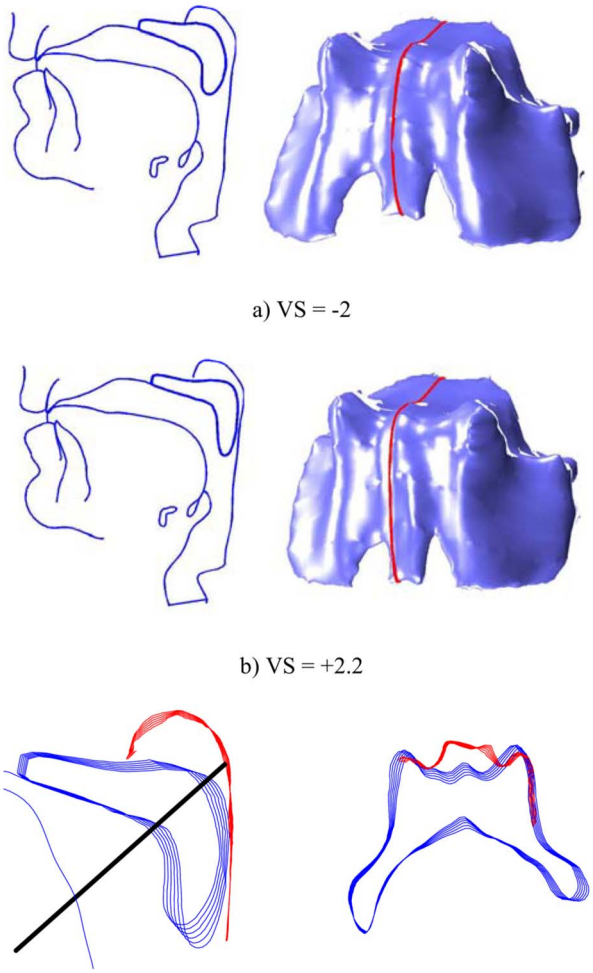

FIG. 15. (Color online) Posterior views of velum model 3D meshes (a and b right) and corresponding midsagittal contours (a and b left) for two extreme values of parameter VS (−2 in a and +2.2 in b); regular nomograms between these two values for the velum and the pharyngeal wall (c) displayed in the midsagittal plane (c left) and in the transverse plane (c right) indicated by the transverse solid line on the left graph (in the same way as in Fig. 11).

pharyngeal wall over the main corpus, that the VL parameter explains 47% of the total pharyngeal wall variance and allows a reconstruction with an RMS error of 0.07 cm. The validity of the contribution of this parameter to the pharyngeal wall variance explanation was further confirmed by a PCA applied to the pharyngeal wall: the first PCA parameter, which explains 50% of the total pharyngeal wall variance, is correlated with VL with a coefficient of 0.96. This confirms the strong relation between velum and pharyngeal wall and justifies a combined velum/pharyngeal wall model—i.e., a velopharyngeal port model—controlled by the VL parameter. The effect of VL on the pharyngeal wall can be seen in Fig. 14(c). The associated deformation in the midsagittal plane occurs in the upper region, along the main direction of velum deformation, but in an antagonist way, i.e., in the backward direction when the velum lowers and in the forward direction when the velum pulls up, so as to complement the velopharyngeal port closure. This movement corresponds to a variation of thickness of the Passavant's Pad, related to the contraction of the *palatopharyngeus* muscle and of the *pterygopharyngeal* portion of the *superior pharyngeal constrictor*, and participates in a global sphincter behavior of the velopharyngeal port.

The parameter VS explains only 5% of the full variance and the associated deformation of the pharyngeal wall does not seem to correspond to a meaningful movement, as visible in Fig. 15(c). This parameter was thus not retained in the pharyngeal wall model. Note that the global variance of pharyngeal wall is about four times smaller than that of the velum surface; this means that 5% of the variance of the pharyngeal wall corresponds—in terms of movement—to much less than 6% of the velum surface variance.

Finally, note that for a number of articulations, the velum, and especially the uvula, is in contact with the tongue dorsum: the velum seems thus to undergo a mechanical deformation, pushed backward by the tongue more than if no contact was established (see, for example, Fig. 2 for [ɔ̃]). This is due to the fact that the tongue dorsum may be stronger than the uvula. In order to assess the possible effects of this contact, a model similar to the previous one was devel-

oped from the 28 of the 46 configurations of the main corpus that were free of velum/tongue contact. To complement this contactless model, the region of the velum in contact with the tongue was geometrically shifted in order to simulate the tongue push. This type of modeling did not bring significant improvement in terms of variance explanation and RMS error reconstruction and was thus not considered any further.

F. Consistency between MRI and EMA measurements

In order to establish more precisely the relation between the 3D velum model and the EMA velum coil coordinates, which represent the displacement of a real flesh point of the velum, the specific vertex of the velum mesh that could be considered as the flesh point on which the coil is attached was determined, according to the following method. (1) Each of the 46 articulations of the MRI corpus were linked with one or more occurrences of the same articulation in the EMA corpus; (2) for each occurrence, the velum vertices were sorted according to their distance from the corresponding EMA velum coil location; (3) the general rank of a given vertex was then defined as the maximum of its distance rank in each occurrence, that corresponds to the maximal distance over all the occurrences; (4) the *pseudo-EMA vertex* was finally chosen as the vertex with the smallest global rank, which ensures that it has the smallest of the maximal distances over the occurrences.

Figure 13(b) displays, on top of the midsagittal space covered by the EMA velum coil, the *pseudo-EMA vertex* position for the 46 shapes of the velum mesh constituting analysis data. The accurate correspondence between *pseudo-EMA vertex* and the real EMA velum coil confirms the consistency between the two sets of data.

Due to the linear nature of the velum model, each control parameter drives the displacement of each vertex along straight lines. Figure 13(c) displays such lines for the *pseudo-EMA vertex* as a function of VL and of VS in the midsagittal plane on top of the midsagittal space covered by the EMA velum coil. This confirms the excellent correspondence between the movements of the real EMA coil and of the *pseudo-EMA vertex* reconstructed from the MRI images, and thus the validity of our approach.

Finally, note that despite a relatively small gain in the amount of variance that is explained, VS appears as a coherent complementary degree of freedom to the velum: (1) it reduces the RMS reconstruction error by 25%, (2) it may modify the velopharyngeal constriction in a meaningful way, and (3) it helps the *pseudo-EMA vertex* trajectories to cover the 2D space of the real EMA data in a coherent way.

G. Recovery of 3D velum shape from midsagittal measurements

In the general context of speech production research, the relation between a 3D shape of an organ and its midsagittal contours constitutes an interesting issue. Badin *et al.* (2002) have shown that the 3D shapes could be predicted for the most part from midsagittal contours for the tongue, the face and the lips. Thus, it may be interesting to infer the time trajectories of the 3D velum and pharyngeal wall from midsagittal measurements such as EMA velum coil recordings. Therefore we assessed the possibility of recovering the 3D geometry of the velopharyngeal port from the position of the velum EMA coil in the *X-Z* plane by means of the model. We attempted to estimate the values of the two parameters VL and VS from the position in the *X-Z* plane of the *pseudo-EMA vertex* on the velum mesh for each of the articulations of the main corpus. As the coordinates of this point in the *X-Z* plane are linearly related to VL and VS by the velum model, the determination of these two parameters is straightforward. Note that the reconstruction error for this point is null, but may be non-optimal for the other vertices. A global RMS reconstruction error of 0.08 cm was finally observed over the full corpus of the 46 configurations for the model driven by VL estimated from the *pseudo-EMA vertex*; the error was down to 0.07 cm for the model driven by combined VL and VS. These results seem to be acceptable in comparison with the model RMS reconstruction errors of 0.08 and 0.06 cm for VL and VL plus VS, respectively. Moreover, the real VL values and their estimation from the *pseudo-EMA vertex* are correlated with a coefficient of 0.98; similarly, a correlation of 0.95 was found for VS. These results confirm the possibility of predicting the global 3D shape of the velopharyngeal port from midsagittal data and from a single point such as an EMA coil record in particular.

IV. ARTICULATORY MODELING AND AREA FUNCTIONS

The new articulatory model represents important knowledge about the articulatory behavior of the subject's velum and nasopharyngeal wall. However, since an aim of speech production modeling is to predict the speech signal, it is very important to be able to derive area functions from the 3D shape of the oral and nasal tracts in order to be able to characterize the resulting acoustics.

A. Oral and velopharyngeal area function determination

At this level, a complete articulatory model of the oral tract of the subject is not yet available. Thus, in order to assess the acoustic influence of the velum movements, the complete area functions of the oral and nasal tracts for various values of parameters VL and VS were needed. We have thus manually traced oral tract cross-sectional contours on all the transverse images defined by the semipolar grid illustrated in Fig. 3(b) for the three point vowels [a i u]. Note that the superimposition on the images of the bony structure contours, including the teeth as illustrated in Fig. 9(a), allows more accurate and reliable vocal tract contours to be drawn. For a given articulation and given values of VL and VS, the velum and pharyngeal wall have then been intersected with transverse planes in the velum region (see top left of Fig. 16), with an angle of 8° between two adjacent planes. As visible in Fig. 11, the nasal tract in such planes is delimited by the velum and nasopharyngeal wall contours, while the oral tract is delimited by the velum and tongue contours. Thus, the tongue contours have been manually traced in the

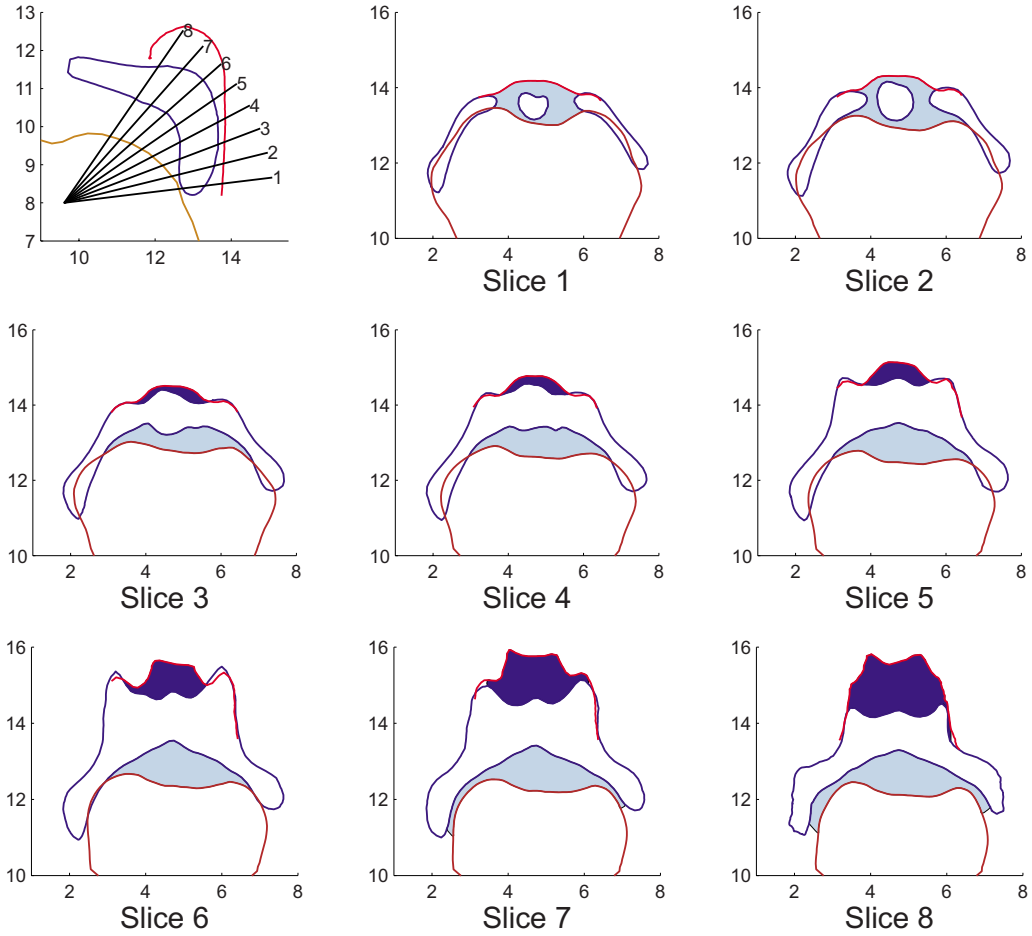

FIG. 16. (Color online) Display of cross sections of oral and nasal tracts for VL=0.3, VS=0, and for the tongue shape of [a] along the eight planes in the velum region shown by the midsagittal grid on the top left of the figure. Oral cross-sectional areas are displayed in clear and nasal tract areas in dark. The velum intersections in grids 1 and 2 correspond to isolated flesh areas inside the oral tract.

corresponding intersecting planes for [a, i, u]. Then, the oral and nasal tracts' cross-sectional contours in these planes have been automatically detected. This detection assumes necessarily that the contours are closed. Therefore, organs separated by less than 0.03 cm were considered to be in contact, which ensured that the associated tract contours were closed. This was particularly needed in regions where the tongue and velum were in contact. Note that in planes near the horizontal ones, the intersection with the velum—in fact the uvula—can be limited to a closed contour isolated inside the oral tract (see slices 1 and 2 of Fig. 16). In this case, the cross-sectional area of the inner contour must be subtracted from that of the outer contour, to take into account the reduction of tract area due to the presence of the uvula. Figure 16 displays the cross-sectional organ outlines and corresponding oral and nasal cross-sectional areas in the velum region for VL and VS equal respectively to 0.3 and 0 and for the tongue shape of [a].

Oral and nasal area functions have then been computed from the cross-sectional contours following the process described in Sec. II D 2. The first cross section with a distinct nasal tract (e.g., grid 3 in Fig. 16) is considered as the beginning of the nasal tract, and thus connected to the nasal passages described in Sec. II D 1 through the cavum. The eight oral tract cross sections corresponding to the velum region are integrated into the whole set of the vowel cross sections already traced, in order to obtain complete oral area functions from the glottis to the lips. Note that the outlet tube at the lips has been lengthened by 1.1 cm to take into account the labial horn, i.e., the region of lips ahead of the lip corner where the cross-sectional vocal tract outline is not a closed contour any longer (Badin, Motoki, Miki, Ritterhaus, and Lallouache, 1994). The next two sections describe the influence of the velum position on oral and nasal area functions.

B. Influence of velum movement on the velopharyngeal area function

Figure 17 displays nomograms of the velopharyngeal area function for variations of VL and VS corresponding to those of Figs. 14 and 15. As expected, variations of VL (Fig. 17(a)) induce important area function variations: the volume of the velopharyngeal tract from beginning of its separation from oral tract to the point of separation into two nasal passages varies from 9.70 cm^3 for a velum maximally open to 4.25 cm^3 at occlusion. The velopharyngeal port constriction is located close to its lower end. When the velopharyngeal port closes, the velum pulls up, while the uvula, the lower end of the velopharyngeal tract, and the constriction location

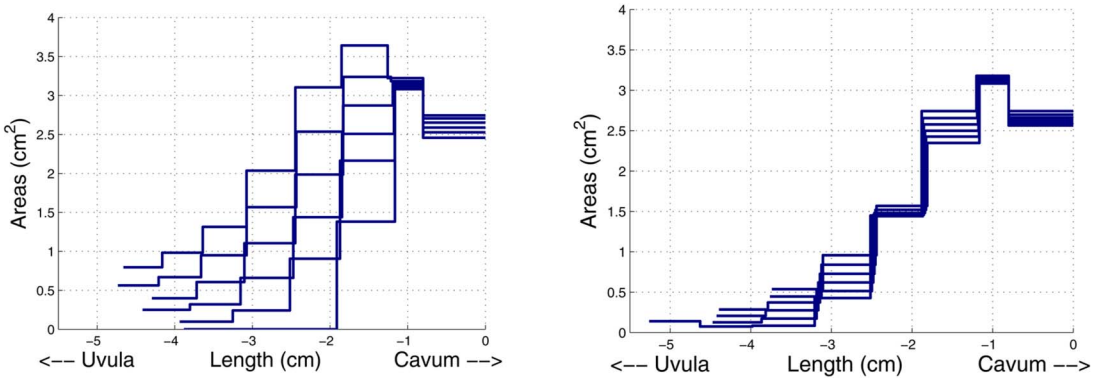

FIG. 17. (Color online) Variations of velopharyngeal port area function as a function of VL (a) and VS (b) parameters. The origin of the abscissa along the tract is arbitrarily chosen as the point where the nasal tract splits into two choanae on each side of the septum wall. Each tube is represented by a length on the x axis and an area on the y axis.

move upwards. The constriction area varies from 0.8 cm^2 for a velum maximally open to 0 at occlusion, while its location, considered as the midpoint of the constriction tube, moves upwards simultaneously over a range of 0.9 cm. These observations are consistent with those of Demolin *et al.* (2003) who found for a velum maximally lowered a maximum of the constriction area ranging from 0.66 to 1.93 cm^2, depending on the subject. Moreover, they found that the cross-sectional area increases towards the cavum, as we observe in our data (see Fig. 17). The second parameter VS (Fig. 17(b)) induces smaller variations of the area function, but the relative variations of the constriction area might be large, up to a factor of 3. Contrary to the VL effects, the constriction area reduction controlled by VS is accompanied by a downward movement of the constriction location: while the constriction area decreases from 0.3 to 0.1 cm^2, its location moves about 0.2 cm towards the glottis.

C. Relation between velopharyngeal area function, velum height, and midsagittal distance

The present 3D articulatory model is very detailed, and thus rather complex to use. As access to 3D data and models is not commonly granted, we have derived from our data a simplified model that delivers directly the velopharyngeal area function as a function of velum height.

Velum height can be defined as the distance of a midsagittal velum point about halfway between the hard palate-velum junction and the tip of the uvula along an oblique line. In the present study, the oblique line obtained by linear regression on the 46 *pseudo-EMA vertex* of the data (Fig. 13(b)) is oriented at about 50° from an horizontal plane; velum height (referred to as *VelHei*) is thus defined as the distance along this line of the *pseudo-EMA vertex* projection from an arbitrary reference point (cf. the cross in Fig. 13(a)). The velopharyngeal port area function represents the velopharyngeal tract from the beginning of the nasal tract to the point where it splits into the two choanae. Considering that the tube number may change across articulations, the area function is resampled for each articulation into 11 tubes of identical length. The cross-sectional area of each of the 11 tubes is calculated so that the volume enclosed in it is equal to the total volume enclosed between the same boundaries along the midline in the original tract. The 11 cross-sectional areas and the common length of the tubes of the velopharyngeal area function are then linearly controlled by the *VelHei* parameter, the corresponding coefficients being determined by linear regression analysis over the set of 46 area functions.

As expected, a significant amount of the variance of the 11 tubes of the velopharyngeal port area function is explained by this parameter (87%). The constriction, which constitutes a critical parameter from the acoustic point of view, displayed an area RMS reconstruction error of 0.14 cm^2 and a position error of 0.41 cm. These errors are very close to those obtained when the articulatory model is controlled by only the VL parameter as in Sec. III G (area error of 0.16 cm^2 and position error of 0.38 cm). The variations of the constriction area and position as a function of *VelHei* are illustrated in Fig. 18. The linear modeling implies moreover that for each tube, area and length vary linearly with *VelHei*. Note that the step-like behavior of the constriction location can be ascribed to changes of the constriction tube index when the velum moves; increasing the number of tubes would reduce the step size without altering the general behavior. The velopharyngeal port area function is thus fairly well predictable directly from the midsagittal measurement of a single EMA point without resorting to an articulatory model.

A complementary approach was used by Björk (1961): based on sagittal and transverse x-ray tomograms taken from ten subjects, he established a linear relation between the minimal velum/pharyngeal wall midsagittal distance and the transverse constriction area for distances greater than 0.2 cm.

We applied the same approach with the articulatory model. A set of midsagittal contours was obtained from the 3D velum and pharyngeal wall meshes for VL varying between the extreme values found from the data. Figure 19 displays the relation between the minimal velum/pharyngeal wall midsagittal distance and the constriction area. This relation is not perfectly linear, but close to Björk's results.

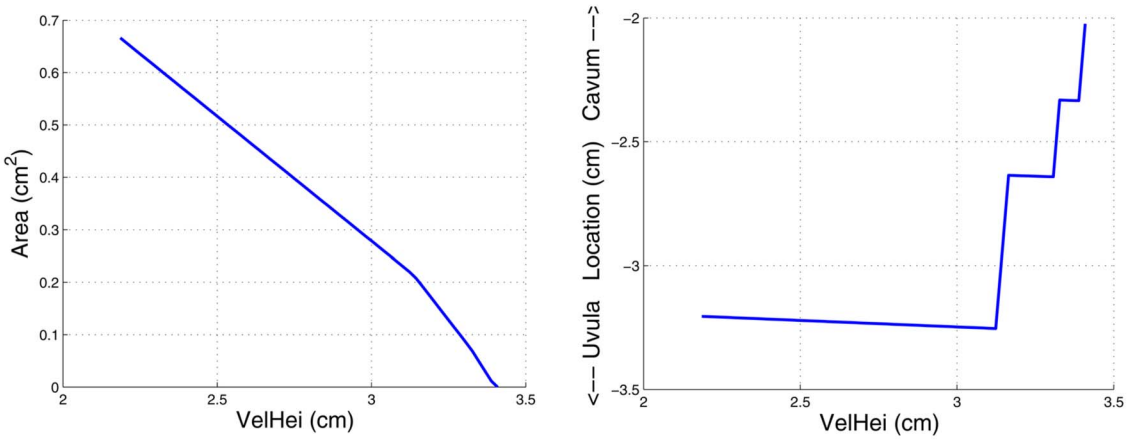

a) Constriction area b) Constriction location

FIG. 18. (Color online) Variations of the area (a) and location (b) of the velopharyngeal port constriction as a function of Velum Height (*VelHei*). The origin of the tract is arbitrarily chosen as the point where the nasal tract splits into two choanae on each side of the septum wall.

Note that the sagittal distance is null for small values of the constriction area, which is explained by a full midsagittal contact between velum and pharyngeal wall while the channels on both sides remain open.

D. Influence of velum movement on the oral area function

An important question in the articulatory-acoustic study of nasals lies in the co-variation of the oral and nasal areas when the velum moves. Some researchers have assumed that the velum acts as a trap door (Fujimura and Lindqvist, 1971), while others have considered that the oral area decreases as much as the nasal area increases when the velum lowers, the total of both areas remaining constant (Maeda, 1982; Feng and Castelli, 1996). Feng and Kotenkoff (2006) have moreover suggested that the decrease of oral tract constriction area induced by the velum lowering may play an important role in nasalization. This present model allows studying this phenomenon.

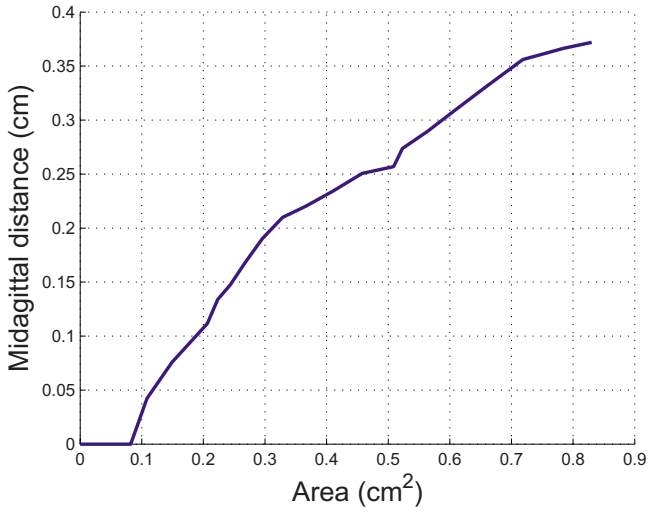

FIG. 19. (Color online) Variations of the velopharyngeal port midsagittal constriction distance as a function of the constriction area for VL varying linearly between the maximal values found in the data.

The influence of velum movements on the oral area function is illustrated by Fig. 20, which displays nomograms of the oral area function for the articulation [a] for VL and VS variations corresponding to those of Figs. 14 and 15. Note that the complete tract is considered fixed and that the area variations are only due to velum position variations as function of VL and VS. We observe, for this articulation, an important variation of the oral area function, from 0.2 to 3 cm^2 for the tube with maximal variation range between the two extreme positions of the velum corresponding to VL in the corpus, and from 1.4 to 2.3 cm^2 for the positions corresponding to VS. Important variations were observed for [i] and [u] as well, with areas varying from 5.1 to 8.5 cm^2 for [i] and from 0 to 2.9 cm^2 for [u] as a function of VL, and from 6.5 to 8 cm^2 for [i] and from 2.4 to 3.6 cm^2 for [u] as a function of VS.

In addition, we have characterized the co-variation of the areas of both tracts when the velum moves. Considering the relatively small variation of the oral area function with VS, we only investigated the effects of VL. As an illustration, Fig. 21 displays the variations of the oral and nasal areas of the first tube of the area functions at the location of the nasal tract branching for the three oral articulations [a], [i] and [u]. We observe that the oral area clearly increases faster than the nasal area decreases when the velum rises. The same behavior was found for the other tubes downstream, i.e., towards the lips or nostrils, though this asymmetric effect becomes less prominent.

V. INFLUENCE OF VELUM MOVEMENTS ON THE ACOUSTIC VOWEL SPACE

Nasalization is envisaged by Feng and Castelli (1996) as a trend from a pure oral articulation—from glottis to lips—to a pure nasopharyngeal target—from glottis to nostrils. These two extreme articulations correspond to single tracts without any other parallel tract (we do not consider in this study any of the various paranasal sinuses). The present model allows simulating the variations of the vocal tract induced by the velum alone, for transitions from a pure oral articulation to a

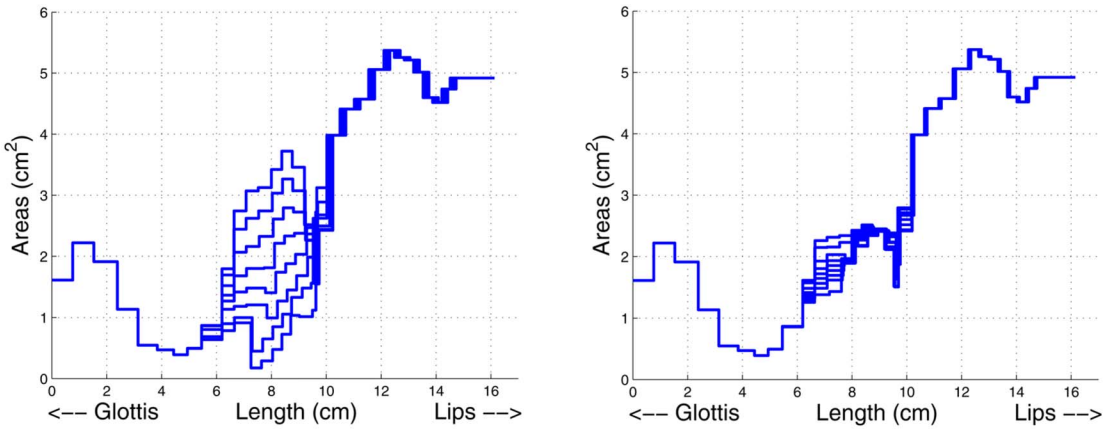

FIG. 20. (Color online) Variations of oral tract area function as a function of VL (a) and VS (b) parameters around the fixed articulation of [a]. The origin of the abscissa along the tract is arbitrarily chosen as glottal exit. Each tube is represented by a length on the x axis and an area on the y axis.

pure nasopharyngeal articulation, without influence of the coarticulatory movements usually observed on other organs, such as the tongue, in natural productions. The area functions of both tracts were determined according to the process described above. Using an acoustic model fed by these area functions, it is thus possible to investigate the influence of the velum movements on the acoustic transfer functions of the tracts between glottis and lips/nostrils. In the present study, we used a standard frequency domain electrical line analog model of acoustic plane wave propagation based on Badin and Fant (1984), and on Fant (1985) for the coupling of the nasal tract in parallel to the oral one. One may define at least three acoustic transfer functions: (1) the *oral transfer function*, i.e., the ratio between the acoustic velocity at the lips over the acoustic velocity at the glottis; (2) the *nasopharyngeal transfer function*, i.e., the ratio between the acoustic velocity at the nostrils over the acoustic velocity at the glottis; (3) the *total transfer function*, i.e., the sum of both, assuming as a first approximation that the sound radiated at some distance from the mouth and nostrils is just the sum of both contributions. The connection of a tract in parallel with the other tract both changes the poles of the transfer function of the tract considered and introduces zeros as well (see, e.g., Fant, 1985). Figure 22 displays, for example, the evolution of the *total* transfer function induced by variations of VL from a pure oral tract to a pure nasopharyngeal tract for a fixed articulation [a]. The two extreme *total* transfer functions, displayed in bold, correspond to the two articulatory targets, and contain only poles, while intermediate transfer functions contain poles and zeros due to the presence of parallel tracts.

We observe in the 500–1500 Hz frequency band that a bound pole-zero pair evolves from the first formant toward the second formant. Our simulations showed that the F1-F2

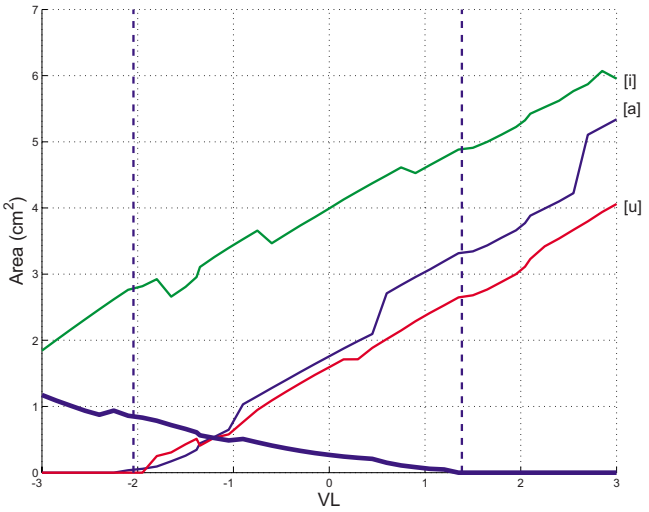

FIG. 21. (Color online) Oral (rising lines) and nasal (falling line) areas of the first tube of the area functions at the location of the nasal tract branching as a function of VL for the three articulations [a], [i] and [u]. The vertical dashed lines mark the minimal and maximal VL values found in the data.

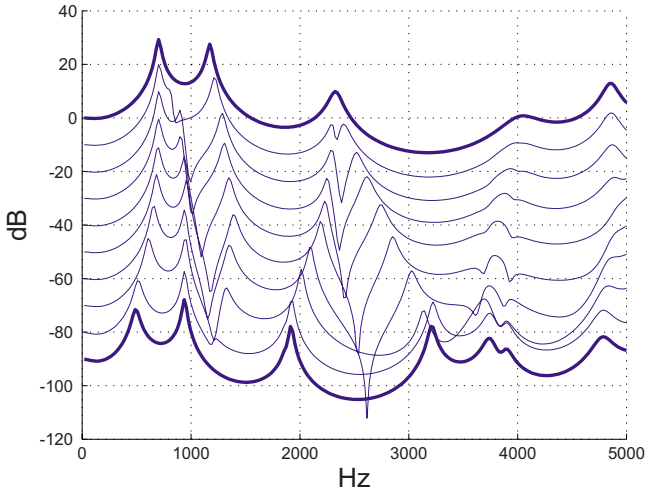

FIG. 22. (Color online) Nomograms of the *total* transfer function of the vocal tract obtained by varying VL from a pure oral tract (VL=1.4, upper bold line) to a pure nasopharyngeal tract (VL=−2.6, lower bold line) for a fixed articulation [a]. Each curve is arbitrarily separated from its neighbors by 10 dB for better reading. The two extreme transfer functions in bold correspond to oral tract (top) and nasopharyngeal tract (bottom) and contain only poles without zeros.

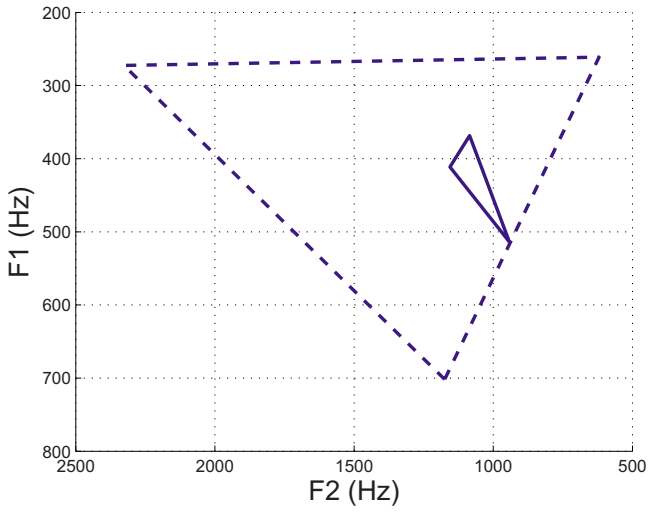

FIG. 23. (Color online) Representation in the acoustic F1-F2 vowel space of the pure oral articulations (high velum) for [a i u] (dashed lines) and of the corresponding pure nasopharyngeal articulations (low velum, solid lines).

formants associated with the pure nasopharyngeal tract for [a] are both lower than those associated with the pure [a] oral tract. Similar simulations for [i] and [u] led us to plot the vocalic triangle based on the three point vowels [a i u] for the two extreme positions of the velum (Fig. 23). The dashed triangle corresponds to the velum maximally high (pure oral tract) while the solid one corresponds to the velum maximally low (pure nasopharyngeal tract). We observe for the nasopharyngeal target a reduction of the vocalic space in a zone close to 450–1000 Hz, globally consistent with the simulations of Feng and Castelli (1996).

VI. SUMMARY AND PERSPECTIVES

A. Summary

This study has resulted in an original set of three-dimensional geometric data and in an original three-dimensional model of the velopharyngeal port, i.e., of the velum and of the nasopharyngeal wall. More precisely, sets of CT and MRI images have been collected from a French subject who sustained a set of 46 articulations covering the range of sounds that he can produce. Generic triangular surface meshes have been derived for the velum and the nasopharyngeal wall; their shapes, fitted by elastic deformation to each of the articulations, constitute accurate and consistent 3D geometric representations of these organs, with a constant number of vertices; they establish a unique reference collection of accurate 3D articulatory data. Moreover, each point of the generic meshes can be assumed to be a flesh point whose variations over the corpus represent the variability of a real flesh point. In addition, 3D shapes of rigid structures such as the nasal passages, the various paranasal sinuses, the hard palate, the jaw, etc. have been extracted from CT and MRI images of the subject. These data complement the various data already collected on the same French subject (cf. Beautemps *et al.*, 2001; Badin *et al.*, 2002; and Badin and Serrurier, 2006) and constitute a rich and accurate basis for further developments in articulatory and acoustic modeling of nasals and more generally of all articulations.

The second series of valuable results is the determination of the degrees of freedom of the velum and of the nasopharyngeal wall, and the associated 3D linear articulatory models. The first component extracted by PCA from the data was a head tilt movement in a sagittal plane; as it was not related to speech its contribution was removed from data. It was nevertheless hypothesized that this general head movement could induce an active compensation of the velum shape by the subject. A PCA applied to the velum data corrected for head tilt uncovered two main degrees of freedom: the first—dominant—component, that accounts for 83% of the velum coordinates' variance, corresponds to an oblique vertical movement clearly related to the pulling action that could be expected from the *levator veli palatini* muscle; the second component, that explains another 6% of the variance and controls smaller movements, represents a mostly horizontal movement that corresponds rather well to the more sphincter-like action plausible for the *superior pharyngeal constrictor*. It was also shown that the nasopharyngeal wall, though its variance is four times smaller than that of the velum, is very much correlated to the first parameter which was found to be able to account for 47% of its variance.

As a means to further assess the validity of the data and of the model, the midsagittal coordinates of a flesh point on the lower face of the velum were collected by means of an EMA system for the same subject uttering a comprehensive set of VCV sequences. It was found that the midsagittal space covered by this point is very similar to the midsagittal space covered by the particular point of the 3D velum generic mesh considered to be the same flesh point.

The velopharyngeal port model is thus efficiently controlled by these two articulatory parameters. Note that the RMS reconstruction error of the organs is less than one millimeter, which is consistent with results obtained on the tongue (cf. Badin *et al.*, 2002, and Badin and Serrurier, 2006).

Area functions could be derived from these 3D geometric representations. The precise 3D geometry of the nasal passages and the corresponding area functions constitute a new set of data consistent with the few investigations found in the literature and confirms in particular a constriction of about 1 cm^2 large and 0.6 cm long located 1.7 cm before nostrils outlet. The nasal coupling area was found to raise up to 0.8 cm^2 while the corresponding constriction location may move over a range of about 1 cm. In addition, a simplified model of velopharyngeal port area function controlled directly by the velum height was derived. The strong influence of the velum movement on the oral tract area function has been confirmed. Finally, acoustic simulations based on the model gave results similar to that of Feng and Castelli (1996), i.e., a reduction of the F1-F2 acoustic vowel space when going from pure oral vowels to the corresponding pure nasopharyngeal tract in the 450–1000 Hz zone, sometimes referred to as the *nasal gap*.

B. Perspectives

A part of the complex geometry of the nasal passages remained unexploited in the present study. The shape of the various sinuses should be integrated into the area functions of the nasal passages, and their influence on the acoustics should be further assessed. More generally, the formants determined from the articulatory model should be compared to those measured on the subject for the same articulations in order to validate the model at the acoustic level. In particular, separate mouth-nose acoustic recordings performed on the same subject by Feng and Kotenkoff (2006) will reveal very useful information. It is also likely that the complex shape of the nasal passages should be used to elaborate more realistic acoustic models, including more realistic losses.

In order to be fully operational for the study of nasality, the new model of velopharyngeal port presented should be integrated into a complete articulatory model, including especially the tongue (cf. Badin and Serrurier, 2006). This would allow accurate control of the complete 3D geometry of the oral and nasal tracts, to obtain corresponding area functions from the glottis to the lips and the nostrils, and finally to determine the resulting acoustic characteristics in terms of formants or speech sounds. This complete model also opens the possibility to characterize the importance of tongue backing for French nasal vowels as discussed by Maeda (1993), Delvaux *et al.* (2002), or Feng and Kotenkoff (2006). The complete model would also allow the determination of the covariation between oral and nasal coupling areas related to velum movements usually assumed to be linear in the literature (see, e.g., Maeda, 1982, or Feng and Castelli, 1996).

The use of this articulatory model makes it possible to study the influence of sole velum movements on the vocal tract without the coarticulatory movements usually made by other organs during normal velum transitions in natural speech. More precisely, in the continuity of the work led by Feng and Castelli (1996) and Feng and Kotenkoff (2006), it will be useful to perform simulations to assess the acoustic consequences of the velum movement separately on the velopharyngeal constriction, oral constriction and nasal coupling place in the oral tract, in order to contribute to the characterization of the acoustic cues of nasality.

The model, in relation with the dynamic articulatory midsagittal trajectories of fleshpoints on the velum and the tongue provided by the EMA device, will allow the *articulatory copy synthesis* of VCV sequences through the recovery of the complete 3D geometry of the vocal tract. The control of the various articulators for dynamic speech could thus be investigated. In particular, assuming that the principal parameter of the velopharyngeal port, e.g. VL, allows the control of the constriction from closure to maximal aperture, it would be interesting to evaluate the possibility of controlling the velum with only the VL parameter, which would reduce the complexity of articulatory control.

Finally, the articulatory synthesizer available would be useful to study the perception of nasality. In particular, the study of the interaction between nasalization and height in vowel perception led by Macmillan, Kingston, Thorburn, Walsh Dickey, and Bartels (1999) using a formant synthesizer could be replicated with more ecological stimuli, i.e., stimuli that could really be produced by a human subject.

ACKNOWLEDGMENTS

We would like to thank Christoph Segebarth, Jean-François Lebas, and Monica Baciu for the main corpus sagittal MR images acquisition at the Radiology Department of the University Hospital, Grenoble, France, and Kiyoshi Honda, Shinobu Masaki, Sayoko Takano, Yasuhiro Shimada, and Ichiro Fujimoto for coronal MRI and head tilt MRI acquisition at ATR, Kyoto, Japan. The EMA data have been recorded at ICP, Grenoble, France, thanks to the help of Alain Arnal, Christophe Savariaux, and Solange Rossato. We are grateful to Jacques Lebeau and Franz Chouly for their valuable discussions and bibliographic advice about anatomy. We acknowledge the help of the GMCAO team at TIMC for the use of the elastic matching software *TestRigid* (Yohan Payan, Maxime Bérar), Daniel Huber for the smoothing software *SmoothMesh* (VMR Lab at Carnegie Mellon University, USA) and Andreas Fabri (Geometrica Research Group at INRIA, France) for the 3D meshing software. We are also grateful to David Pritchard for the English corrections. Finally, we would like to thank three anonymous reviewers and the associate editor of the journal, Christine Shadle, for their pertinent comments on the first and second versions of the manuscript, and for their very detailed and helpful editorial help.

Amelot, A., Crevier-Buchman, L., and Maeda, S. (**2003**). "Observations of the velopharyngeal closure mechanism in horizontal and lateral directions from fiberscopic data," In *Proceedings of the 15th International Congress of Phonetic Sciences*, edited by M.-J. Solé, D. Recasens, and J. Romero, Barcelona, Spain, pp. 3021–3024.

Badin, P., Bailly, G., Elisei, F., and Odisio, M. (**2003**). "Virtual Talking Heads and Audiovisual Articulatory Synthesis (Invited talk at the symposium "Articulatory synthesis. Advances and prospects")." In *Proceedings of the 15th International Congress of Phonetic Sciences*, M.-J. Solé, D. Recasens, and J. Romero, editors, Barcelona, Spain, Vol. **1**, pp. 193–197.

Badin, P., Bailly, G., Revéret, L., Baciu, M., Segebarth, C., and Savariaux, C. (**2002**). "Three-dimensional articulatory modeling of tongue, lips and face, based on MRI and video images," J. Phonetics **30**(3), 533–553.

Badin, P., and Fant, G. (**1984**). "Notes on vocal tract computation," Speech Transmission Laboratory-Quarterly Progress Status Report-Stockholm, **25**, 53–108.

Badin, P., Motoki, K., Miki, N., Ritterhaus, D., and Lallouache, T. M. (**1994**). "Some geometric and acoustic properties of the lip horn," J. Acoust. Soc. Jpn. (E) **15**(4), 243–253.

Badin, P., and Serrurier, A. (**2006**). "Three-dimensional modeling of speech organs: Articulatory data and models," In *Transactions on Technical Committee of Psychological and Physiological Acoustics*, The Acoustic Society of Japan, Kanazawa, Japan, Vol. **36**(5), H-2006-77, pp. 421–426.

Baer, T., Gore, J. C., Gracco, L. C., and Nye, P. W. (**1991**). "Analysis of vocal tract shape and dimensions using magnetic resonance imaging: Vowels," J. Acoust. Soc. Am. **90**(2, Pt. 1), 799–828.

Beautemps, D., Badin, P., and Bailly, G. (**2001**). "Linear degrees of freedom in speech production: Analysis of cineradio- and labio-film data and articulatory-acoustic modeling," J. Acoust. Soc. Am. **109**(5), 2165–2180.

Bell-Berti, F. (**1976**). "An electromyographic study of velopharyngeal function in speech," J. Speech Hear. Res. **19**, 225–240.

Bell-Berti, F. (**1993**). "Understanding velic motor control: Studies of segmental context," In *Phonetics and Phonology, Nasals, Nasalization, and the Velum*, edited by M. K. Huffman and R. A. Krakow, (Academic, New York), pp. 63–85.

Björk, L. (**1961**). *Velopharyngeal Function in Connected Speech. Studies Using Tomography and Cineradiography Synchronized with Speech Spec-*

trography (Appelbergs Bocktryckeri AB, Stockholm, Sweden).
Bjuggren, G., and Fant, G. (**1964**). "The nasal cavity structures," STL-QPSR **5**(4), 5–7.
Couteau, B., Payan, Y., and Lavallée, S. (**2000**). "The mesh-matching algorithm: An automatic 3D mesh generator for finite element structures," J. Biomech. **33**, 1005–1009.
Crystal, D. (**1997**). *A Dictionary of Linguistics and Phonetics* (Blackwell, MA).
Dang, J., Honda, K., and Suzuki, H. (**1994**). "Morphological and acoustical analysis of the nasal and the paranasal cavities," J. Acoust. Soc. Am. **96**, 2088–2100.
Delvaux, V., Metens, T., and Soquet, A. (**2002**). "French nasal vowels: Acoustic and articulatory properties," In *Proceedings of the 7th International Conference on Spoken Language Processing*, Denver, Vol. **1**, pp. 53–56.
Demolin, D., Delvaux, V., Metens, T., and Soquet, A. (**2003**). "Determination of velum opening for French nasal vowels by magnetic resonance imaging," J. Voice **17**(4), 454–467.
Demolin, D., Lecuit, V., Metens, T., Nazarian, B., and Soquet, A. (**1998**). "Magnetic resonance measurements of the velum port opening," In *Proceedings of the 5th International Conference on Spoken Language Processing*, edited by R. H. Mannell and J. Robert-Ribes, Sydney, Australia, Australian Speech Science and Technology Association Inc., Vol. **2**, pp. 425–428.
Dickson, D. R., and Dickson, W. M. (**1972**). "Velopharyngeal anatomy," J. Speech Hear. Res. **15**, 372–381.
Engwall, O., and Badin, P. (**1999**). "Collecting and analyzing two- and three-dimensional MRI data for Swedish," Tal Musik Hörsel - Quarterly Progress Status Report - Stockholm, **40**(3–4), 11–38.
Fabri, A. 3D meshing software (http://cgal.inria.fr/Reconstruction, link available **May 29, 2007**).
Fant, G. (**1960**). *Acoustic Theory of Speech Production* (Mouton, The Hague).
Fant, G. (**1985**). "The vocal tract in your pocket calculator," STL-QPSR **26**(2–3), 1–19.
Feng, G., and Castelli, E. (**1996**). "Some acoustic features of nasal and nasalized vowels: A target for vowel nasalization," J. Acoust. Soc. Am. **99**(6), 3694–3706.
Feng, G., and Kotenkoff, C. (**2006**). "New considerations for vowel nasalization based on separate mouth-nose recording," In *Proceedings of Interspeech'06*, Pittsburgh, pp. 2242–2245.
Ferguson, C. A., Hyman, L. M., and Ohala, J. J. (Editors), (**1975**). *Nasalfest: Papers from a symposium on nasals and nasalization*, Stanford, CA.
Fujimura, O., and Lindqvist, J. (**1971**). "Sweep-Tone measurements of vocal-tract characteristics," J. Acoust. Soc. Am. **49**, 541–558.
House, A. S., and Stevens, K. N. (**1956**). "Analog studies of the nasalization of vowels," J. Speech Hear Disord. **21**, 218–232.
Huber, D., The SmoothMesh software (http://www.cs.cmu.edu/~vmr/software/meshtoolbox/downloads.html, link available at **May 29th, 2007**).
Huffman, M. K., and Krakow, R. A. (**1993**). *Phonetics and Phonology. Nasals, Nasalization, and the Velum* (Academic Press, New York), Vol. **5**.
Kelso, J. A. S., Saltzman, E. L., and Tuller, B. (**1986**). "The dynamical theory of speech production: Data and theory," J. Phonetics **14**, 29–60.
Kent, R. D. (**1997**). *The Speech Sciences* (Singular, Stockholm, Sweden).
Kitamura, T., Takemoto, H., Honda, K., Shimada, Y., Fujimoto, I., Syakudo, Y., Masaki, S., Kuroda, K., Oku-uchi, N., and Senda, M. (**2005**). "Difference in vocal tract shape between upright and supine postures: Observation by an open-type MRI scanner," Acoust. Sci. & Tech. **5**, 465–468.
Kollia, H. B., Gracco, V. L., and Harris, K. S. (**1995**). "Articulatory organization of mandibular, labial, and velar movements during speech," J. Acoust. Soc. Am. **98**(3), 1313–1324.
Macmillan, N. A., Kingston, J., Thorburn, R., Walsh Dickey, L., and Bartels, C. (**1999**). "Integrality of nasalization and F_1. II. Basic sensitivity and phonetic labeling measure distinct sensory and decision-rule interactions," J. Acoust. Soc. Am. **106**(5), 2913–2932.
Maeda, S. (**1982**). "The role of the sinus cavities in the production of nasal vowels," In *Proceedings of the IEEE International Conference on Acoustics, Speech and Signal Processing*, Paris, France, pp. 911–914.
Maeda, S. (**1993**). "Acoustics of vowel nasalization and articulatory shifts in French nasal vowels," In *Phonetics and Phonology. Nasals, nasalization and the velum* (Academic, New York), pp. 147–167.
Matsumura, M., Niikawa, T., Shimizu, K., Hashimoto, Y., and Morita, T. (**1994**). "Measurement of 3D shapes of vocal tract, dental crown and nasal cavity using MRI: Vowels and fricatives," In *Proceedings of the 3rd International Conference on Spoken Language Processing*, Yokohama, Japan, Vol. **2**, pp. 619–622.
Matsumura, M., and Sugiura, A. (**1992**). "Modeling of 3-dimensional vocal tract shapes obtained by magnetic resonance imaging for speech synthesis," In *Proceedings of the 2nd International Conference on Spoken Language Processing*, Banff, Canada, pp. 425–428.
Mermelstein, P. (**1973**). "Articulatory model for study of speech production," J. Acoust. Soc. Am. **53**, 1070–1082.
Rossato, S., Badin, P., and Bouaouni, F. (**2003**). "Velar movements in French: An articulatory and acoustical analysis of coarticulation," In *Proceedings of the 15th International Congress of Phonetic Sciences*, edited by M.-J. Solé, D. Recasens, and J. Romero, Barcelona, Spain, pp. 3141–3144.
Serrurier, A., and Badin, P. (**2005a**). "A three-dimensional linear articulatory model of velum based on MRI data," In *Interspeech'2005 - Eurospeech - 9th European Conference on Speech Communication and Technology*, Lisbon, Portugal, pp. 2161–2164.
Serrurier, A., and Badin, P. (**2005b**). "Towards a 3D articulatory model of velum based on MRI and CT images," ZAS Papers in Linguistics, Speech production and perception: Experimental analyses and models, edited by Susanne Fuchs, Pascal Perrier and Bernd Pompino-Marschall, Vol. 40, pp. 195–211.
Story, B. H., Titze, I. R., and Hoffman, E. A. (**1996**). "Vocal tract area functions from Magnetic Resonance Imaging," J. Acoust. Soc. Am. **100**(1), 537–554.
Sundberg, J., Johansson, C., Wilbr, H., and Ytterbergh, C. (**1987**). "From sagittal distance to area. A study of transverse, vocal tract cross-sectional area," Phonetica **44**, 76–90.
Takemoto, H., Kitamura, T., Nishimoto, H., and Honda, K. (**2004**). "A method of teeth superimposition on MRI data for accurate measurement of vocal tract shape and dimensions," Acoust. Sci. & Tech. **25**, 468–474.
Teixeira, A., Moutinho, L. C., and Coimbra, R. L. (**2003**). "Production, acoustic and perceptual studies on European Portuguese nasal vowels height," In *Proceedings of the 15th International Congress of Phonetic Sciences*, edited by M.-J. Solé, D. Recasens, and J. Romero, Barcelona, Spain, pp. 3033–3036.
Teixeira, A., Vaz, F., Moutinho, L., and Coimbra, R. L. (**2001**). "Articulory Synthesis of Portuguese," In *III Encontro do Forum International de Investigadores Portugueses* (Institut EETA, Aveiro, Portugal).
Tiede, M. K., Masaki, S., and Vatikiotis-Bateson, E. (**2000**). "Contrasts in speech articulation observed in sitting and supine conditions," In *Proceedings of the 5th Seminar on Speech Production: Models and Data & CREST Workshop on Models of Speech Production: Motor Planning and Articulatory Modelling*, Kloster Seeon, Germany, pp. 25–28.
Wrench, A. A. (**1999**). "An investigation of sagittal velar movement and its correlation with lip, tongue and jaw movement," In *Proceedings of the 14th International Congress of Phonetic Sciences* edited by J. J. Ohala, Y. Hasegawa, M. Ohala, D. Granville, and A. C. Bailey, San Francisco, pp. 2259–2262.
Zemlin, W. R. (**1968**). *Speech and Hearing Science-Anatomy and Physiology* (Prentice-Hall, NJ).

Seeing pitch: Visual information for lexical tones of Mandarin-Chinese

Trevor H. Chen and Dominic W. Massaro[a)]
University of California, Santa Cruz, Santa Cruz, California 95064

(Received 26 September 2006; revised 14 November 2007; accepted 7 January 2008)

Mandarin perceivers were tested in visual lexical-tone identification before and after learning. Baseline performance was only slightly above chance, although there appeared to be some visual information in the speakers' neck and head movements. When participants were taught to use this visible information in two experiments, visual tone identification improved significantly. There appears to be a relationship between the production of lexical tones and the visible movements of the neck, head, and mouth, and this information can be effectively used after a short training session. © *2008 Acoustical Society of America.* [DOI: 10.1121/1.2839004]

PACS number(s): 43.71.An, 43.71.Es, 43.71.Gv, 43.71.Bp [DOS] Pages: 2356–2366

I. INTRODUCTION

A developing principle is that humans perceive by using multiple sources of information (Massaro, 1998). In the case of face-to-face speech, we use (at least) audition and vision to perceive what is spoken. Dozens of empirical studies and theoretical analyses indicate that perceivers combine or integrate audible and visible speech (e.g., Massaro, 1998; Massaro *et al.*, 2001). For example, when hearing the sound of an auditory /ba/ and seeing the mouth movement of a visual /ga/, perceivers usually perceive /da/, /∂a/, or /va/ (Massaro, 1998; McGurk and MacDonald, 1976). Although there might be interlanguage differences in the degree of visual influence for different segments (e.g., Hayashi and Sekiyama, 1998; Sekiyama, 1997; Sekiyama and Tohkura, 1991, 1993), there is strong evidence for the principle that speakers of different languages integrate auditory and visual speech in a similar manner (e.g., Chen and Massaro, 2004; Massaro *et al.*, 1995, 1993).

Research on audiovisual speech perception has paid more attention to segmental information and less attention to lexical-tone information. In what seems to be the first study on the audiovisual perception of lexical tones, native identification of the six Cantonese tones was tested with auditory (sound), visual (face), and bimodal (both) stimuli (Burnham *et al.*, 2000). Performance averaged about 20% correct across certain visual-only conditions, which were statistically significant above the chance level of (1/6 Cantonese tones) 16.67% (Burnham *et al.*, 2000). In a same-different discrimination study on Cantonese tones, native Thai and Australian-English speakers also performed significantly better than chance under visual-only conditions (Burnham *et al.*, 2001).

In a study on the identification of Mandarin tones (Mixdorff *et al.*, 2005b), native Mandarin speakers identified tones with sound alone as well as sound plus the video (watching the lower part of a speaker's face). Under clear auditory conditions, the addition of the video did not significantly improve performance. However, under some noise-masked conditions, the addition of video did significantly improve tone-identification performance relative to that of sound alone (but the effect was fairly small). The same patterns of results were also found in the native tone-identification of Vietnamese (Mixdorff *et al.*, 2006) and Thai (Mixdorff *et al.*, 2005a) as well as in the non-native discrimination of Cantonese tones by Thai speakers (Burnham *et al.*, 2001).

In another study (Burnham *et al.*, 2006), head motion was found to be informative for the perception of Cantonese tones. This interesting result fits well with the finding that head motion is also related to intonation (Yehia *et al.*, 2002). Others studies explored visual information for various supra-segmental prosodic (intonation, stress, etc.) features and found that head and eye-brow movements can be perceptually informative (e.g., Munhall *et al.*, 2004; Srinivasan and Massaro, 2003; Yehia *et al.*, 2002).

On the other hand, there may be additional visual information for lexical tones, but perhaps the perceivers did not use it because they were not fully aware of where to look and what to look for. Mandarin-Chinese presents an interesting case because the physical-acoustical properties of its lexical tones are well studied and well known (e.g., Chen, 1999; Connell *et al.*, 1983; Garding *et al.*, 1986; Jongman *et al.*, 2005). This tone-rich language may provide additional insights about the production of lexical tones and possible relationships with visible speech movements. There are four lexical tones in Mandarin, commonly referred to as tones 1, 2, 3, and 4. Based on the fundamental frequency (F0) patterns, tone 1 has been described as high level (5-5), tone 2 midrising (or mid-high-rising; 3-5), tone 3 mid-falling-rising (or low-dipping or low-falling-rising; 2-1-4), and tone 4 high-falling (5-1) (Chao, 1968; Lee-Schoenfeld, 2002). Mandarin tones also tend to differ on other dimensions such as vowel duration and amplitude. For example, vowel duration tends to be longest for tone 3 and shortest for tone 4; amplitude tends to be lowest for tone 3 and highest for tone 4 (Tseng, 1981).

[a)]Electronic mail: massaro@fuzzy.ucsc.edu

 0001-4966/2008/123(4)/2356/11/$23.00 © 2008 Acoustical Society of America

A. Perception of Mandarin tones

Mandarin tone judgments are influenced by multiple sources of information: F0 pattern (both height and contour), vowel duration, and amplitude (Tseng *et al.*, 1986). F0 pattern appears to be the most influential information, with F0 height and F0 contour about equally effective. These cues are independently evaluated and optimally integrated for tone perception (Massaro *et al.*, 1985).

Although there is agreement that F0 pattern (perceived as voice pitch) is the most important/dominant phonetic cue for Mandarin tones, there are other acoustic dimensions that can be perceptually informative. Duration is systematically different depending on the tone. In isolation, phrase-final position, or citation form, tone 3 tends to be longer than tone 2, which tends to be longer than tones 1 and 4 (Blicher *et al.*, 1990; Chao, 1968). This duration difference is acoustically salient: Longer durations of auditorily presented /bi/, /ba/, and /bu/ elicited more tone 3 (and fewer tone 2) identifications for both native Mandarin and English speakers (Blicher *et al.*, 1990).

Another informative acoustic dimension is amplitude. Whalen and Xu (1992) manipulated natural speech (/ba/ and /yi/) by eliminating F0 but retaining amplitude contours. Tones 2, 3, and 4 were acoustically distinguishable on the basis of amplitude (and not duration) alone. They also found a positive correlation between F0 and amplitude (Whalen and Xu, 1992). Moreover, even in the presence of the F0 pattern, duration and amplitude can each be used as functional cues for tone judgments (Tseng *et al.*, 1986). Finally, vowel quality (i.e., the type of the vowel) did not systematically influence tone identification (Tseng *et al.*, 1986; Massaro *et al.*, 1983).

B. The current study

Given the previous findings on the auditory perception of Mandarin lexical tones, one can speculate on the possible visible dynamics in producing these different tones. Duration differences might be seen from the speaker even if the sound is not available. For example, visible speech rate has been shown to influence the perception of voice onset time of initial consonants (Green and Miller, 1985). Also, it may be possible that loudness or intensity can be reflected by the degree of hyperarticulation or exaggeration of mouth movements (Kim and Davis, 2001) or simply perceived effort (Rosenblum and Fowler, 1991). It is also conceivable that speakers may somehow express lexical tone information in terms of some visible paralinguistic cues, whether consciously or unconsciously.

The goals of the current study are to determine: (1) a baseline accuracy of Mandarin lexical-tone identification from visual-only information; 2) if there are systematic visible changes from lexical tone production and the nature of this information; and 3) whether Mandarin speakers can be taught to use this information to significantly improve visual identification performance.

In addition, it is also interesting to examine performance for each of the four tones. For example, tones 2 and 3 tend to be the most acoustically confusable pair (Blicher *et al.*, 1990), and it will be interesting to see if this is also the case visually. Finally, we ask the question whether it is easier to recognize one's own visible speech more accurately than the speech of others. Previously, one study found no overall significant differences in speech-reading performance (of numbers in French) comparing watching one's own face with watching the faces of others (Schwartz and Savariaux, 2001). The present study will assess whether this is also the case for Mandarin lexical tones.

II. EXPERIMENT 1: TRAINING VISUAL SPEECH PERCEPTION

There may be additional visual information for lexical tones, but perceivers may not have taken full advantage of this information because they were not fully aware of where to look and what to look for. If we learn about the nature of this information, it may be possible to teach the participants to use it. Experiment 1 was a within-subjects design involving three different sessions. The strategy was to measure visual tone identification before and after training on potential visual information.

A. Method

1. Participants

Eight Chinese participants were recruited from the University of California, Santa Cruz (UCSC). They are all native speakers of Mandarin. Four of them are from Mainland China: Two females (one was 26 years old, and the other chose not to reveal her age but appeared to be in her 30's) who had been in the United States for about 3.5 and 1.75 years, and two males (ages 31 and 29) who had been in the United States for about 1.5 and 3 years. The other four participants are from Taiwan: Two females (ages 19 for both) who had been in the United States for about 4 and 9 years, and two males (ages 25 and 21; one of them was the senior author) who had been in the United States for about 12 and 8 years. The ages when exposure to English began were 10 and 12 for the females from Mainland China (FC), 13 and 12 for the males from Mainland China (MC), 13 and 7 for the females from Taiwan (FT), and 12 and 14 for the males from Taiwan (MT). They were paid at the rate of $10/h for their participation.

2. Stimuli

We made sets of audio/video recordings from four speakers (one female from Mainland China, FC; one male from Mainland China, MC; one female from Taiwan, FT; and one male from Taiwan, MT) pronouncing 40 (10 syllables $\times 4$ tones) Mandarin-Chinese characters or words (chosen from Liu and Samuel, 2004), which are shown in Appendix A. These four speakers also served as participants for this experiment. The words were all familiar to the participants. Speakers from Mainland China read abbreviated (simplified) words, and speakers from Taiwan read traditional words. The words to be read were displayed as slides (Microsoft POWERPOINT™) on a standard computer screen. The words were read both in isolation and following a neutral context phrase in separate blocks of 40 trials. The trials were randomized in

four different versions—two versions for characters in isolation (i.e., citation form) and two versions for characters in a neutral sentential context (i.e., "the next word is"). The speakers were recorded pronouncing all words in the four versions of randomization.

3. Design

The experiment took place on three days: 1, 2, and 3. Day 1 was the recording session: The four speakers were told that the experimental purpose was to understand "how people say words," and their task was to do their best to pronounce the characters or words "clearly and distinctively." After day 1 was completed, eight participants (including the original four speakers) were later contacted to schedule for day 2.

On day 2, they participated in a tone-identification task: They were told to watch the video (with no sound available) and choose (circle) what character or word was said for each trial. There were four versions of randomization [2 conditions (context or citation) $\times 2$ versions for each], and 16 blocks (4 speakers $\times 4$ versions) were arranged from pseudo-randomization (randomization but making sure that no speakers of the same gender appeared in consecutive blocks). Appendix B shows an example of one of the response sheets used for the tone-identification task. The total number of trials was 640 (16 blocks $\times 40$ words each) for each of the participants in each session. There were approximately 5 s between the word presentations on isolation trials and 7 s on context trials. The video was displayed on a JVC color video monitor (TM-131 SU) screen, which was approximately 11.25 in. in width and 8.5 in. in height. The faces averaged approximately 4.75 in. in width and 5.7 in. in height.

A few days after day 2, all of the participants were contacted to schedule for another day (day 3). On day 3, this time they were taught to use a specific strategy for tone identification, and they completed the tone-identification task again. Afterwards, they completed an optional questionnaire.

4. Procedure

The participants were not told about their subsequent participation. On day 1, they were not told that they would participate for day 2; on day 2, they were not told that they would participate for day 3. There were at least 14 days between day 1 and day 2, and there were at least 6 days between day 2 and day 3. All instructions and interactions with the experimenter (MT) were spoken in Mandarin. One MT (senior author) served as his own experimenter. This person was one of the participants, and he had not anticipated his subsequent participation for day 2 (although he expected a subsequent participation for day 3).

5. Day 1: Recording

After day 1 was completed for one speaker (MT), the recording was visually examined for possible sources of visual information. The first author observed that some visible information for Mandarin lexical tones seemed to be available from the activity around the lower parts of the neck and from head movements. Its visual-perceptual clarity surprised both a native and a non-native Mandarin speaker. The judgments about the sources of information were made and agreed on by the experimenter and another researcher. It appeared that there were the least (or minimal) neck movement for tone-1 words, some movements for tone-2 words, most movements for tone-3 words, and some (brief) movements for tone-4 words. Figure 1 illustrates the visible information for each of the four Mandarin tones. The bulge on the side of the neck changes across the four tones. Tone 1 has minimal movement, tones 2 and 4 have some movement, and tone 3 has the biggest bulge. Although the speakers were not told about this, an effort was made to indirectly persuade two participants during the recordings to replace or put back hair and/or clothing because they covered parts of the neck.

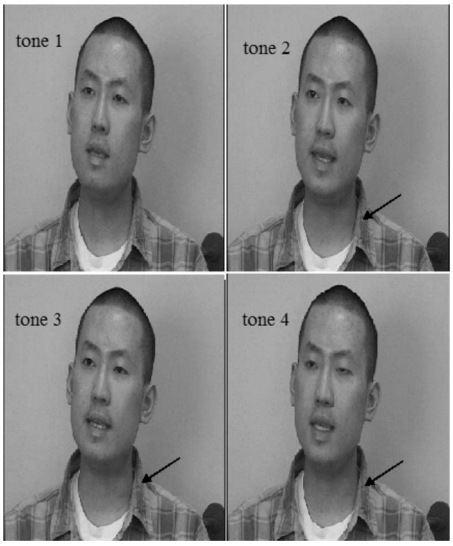

FIG. 1. Pictorial illustration of visible information for Mandarin tones at the lower parts of the neck. The bulge on the side of the neck changes across the four tones. Tone 1 has minimal movement, tones 2 and 4 have some movement, and tone 3 has the biggest bulge.

One speaker's (FC) hair was covering the left and right sides of her lower neck, while another speaker's (MC) shirt was buttoned-up and the collar covered parts of his lower neck. Indirect efforts trying to uncover all areas of their neck were unsuccessful. However, examination of the video, after all recording sessions were complete, revealed that all speakers showed some visible information. In particular, FC appeared to drop/dip her head/chin on tone-3 words (despite her hair covering her neck); MC's glottis and a part of his uncovered neck appeared to display activity patterns consistent with those hypothesized from MT; and for FT, her neck also appeared to display activity patterns consistent with MC and MT, at the same time her head/chin movements seemed consistent with speaker FC. These observed visible patterns are summarized in Table I, and this table was used in an information sheet to inform participants about the strategy for day 3. (It is possible that the lexical tones differed in duration, which could be seen visually. These possible durational cues were also mentioned on day 3.)

6. Day 2: Identification

For day 2, participants were not given the information sheet and not told about any strategy; they were only in-

TABLE I. Summary sheet used to inform participants about the visible-information strategy (Experiments 1 and 2).

	Tone 1	Tone 2	Tone 3	Tone 4
Pitch (frequency)	High-level	Mid-rising	Mid-falling-rising	High-falling
Loudness (amplitude/ intensity)	In-between	In-between	Quiet	Loudest
Duration (Time)	Short	Long	Longest	Shortest
	Tone 1	Tone 2	Tone 3	Tone 4
Neck	No (least) activity	Some activity	Most activity	Some (brief) activity
Chin			Females drop head/chin	
Mouth				

structed to watch the speaker and choose (circle) what character or word was spoken in each trial. Participants used response sheets in the forms similar to that shown in Appendix B, except those from Mainland China saw abbreviated (simplified) characters and those from Taiwan saw traditional characters (Appendix B shows traditional characters). The experimental sessions were approximately 2 h long, with 10 min breaks after approximately every 15 min.

7. Day 3: Training and identification

For day 3, participants were informed about the acoustic-physical characteristics of Mandarin tones and how these dimensions may relate to visible activities of the neck, head, and mouth movements. Participants were allowed to take the summary information sheet (Table I) into the subject-testing room during the experiment. They were instructed to pay attention to mouth, head/chin movements, and especially activities of the neck. Although there were no special written descriptions for the mouth on the summary information sheet, it was specifically pointed out that duration (time) differences may be reflected from the mouth. During the strategy-training time, they were shown a short VHS tape (for no more than about 15 min) that included samples of representative trials (in order to illustrate the strategy), and they were also given roughly 10–20 practice trials with feedback (to help learn this strategy). The whole training time lasted for no more than about 45 min for each participant. After this training time, participants completed the tone-identification task again.

B. Results

The results from the identification task were pooled over versions of randomization because an initial analysis showed no significant differences between them. The independent variables were day (two levels: day 2 and day 3), v-gender (two levels: gender of the speakers in the video, not gender of the perceiver), context (two levels: with or without), and lexical tone (four levels). The dependent variables were accuracy of tone-identification performance and *d* prime (d').

Figure 2 shows the accuracy of tone-identification performance plotted as a function of each of the four tones on

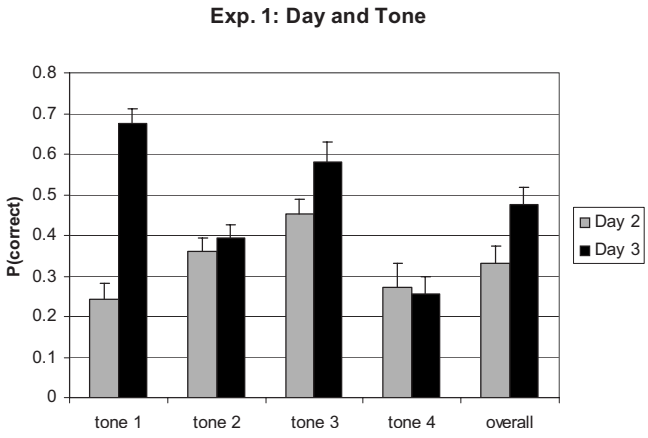

FIG. 2. Experiment 1: Tone-identification performance, plotted as the probability of correct responses (*Y* axis), for overall and each of the four tones on day 2 and day 3.

day 2 and day 3, as well as overall across the four tones. Analysis of variance revealed that performance on day 3 (mean=0.48) was significantly higher than day 2 (mean =0.33), $F(1,7)=68.79$, $p<0.001$. In follow-up t-tests, both day-2 and day-3 mean performances were significantly greater than the chance level of 0.25 [day-2: $t(127)=5.16$, $p<0.001$; day-3: $t(127)=11.49$, $p<0.001$]. Also, performance was generally better when the speaker of the video was a female than when the speaker was a male, $F(1,7)=20.06$, $p<0.01$. It is conceivable that, because the two females in the videotape tended to moved their head/chin in a dipping fashion (consistent with the tone-3 frequency pattern) while pronouncing tone-3 words, this extra information would have helped increase performance over the two male speakers whose head movements, if any, were not as salient. The significant interaction between tone and v-gender [$F(3,21)=22.79$, $p<0.001$] indicated that the female-speaker advantage was most pronounced for tone-3 words.

There was a significant main effect for tone [$F(3,21)=11.77$, $p<0.001$] and a significant interaction between day and tone, $F(3,21)=12.54$, $p<0.001$. Consistent with our hypotheses, tone-1 and tone-3 words improved more than tone-2 and tone-4 words. We computed the 95% confidence intervals (CI) around the means of each of the tones for both days; this allows comparisons to the chance value of 0.25. Within a given experiment, if a CI is completely above 0.25, its mean is significantly higher than this chance value. On day 2, tone 1 was not significantly different from chance, but on day 3 it became significantly above the chance level. The tone-1 performance was the lowest among the four tones on day 2 but highest among the tones on day 3. For tones 2 and 3, their CI's were above the chance level on both days, although tone 3 performance improved much more relative to that of tone 2. Improvement on these tones did not appear to come at the detriment of other tones. On both days, tone-2 performance was slightly higher than chance, and tone-4 performance was not significantly different from chance.

The main effect of context was not significant, $F(1,7)=0.94$, $p=0.37$. The only other significant interaction was between v-gender and context [$F(1,7)=22.10$, $p<0.01$], with the female-speaker advantage more pronounced under

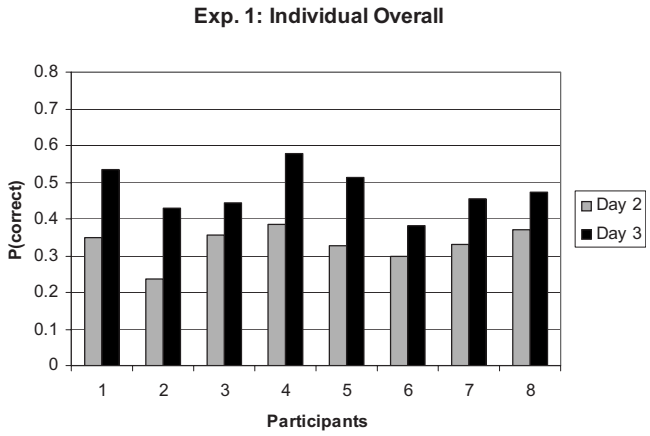

FIG. 3. Experiment 1: Individual performances, plotted as the probability of correct responses (Y axis), for the tone-identification task on day 2 and day 3.

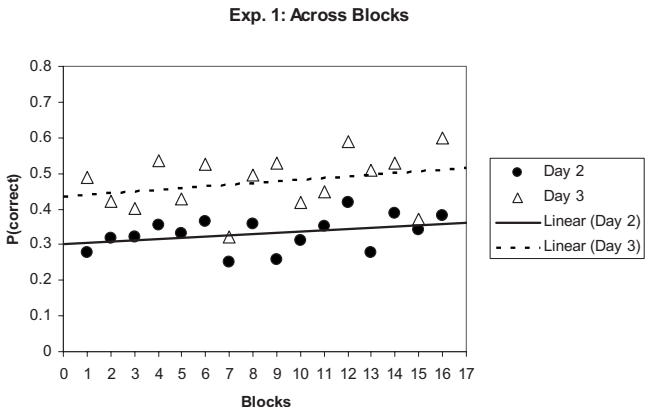

FIG. 5. Experiment 1: The overall tone-identification performance across blocks.

the no-context condition. Figure 3 plots the accuracy performance of all the individual participants for the tone-identification task on day 2 and day 3. As can been in Fig. 3, every individual improved from day 2 to day 3.

In another analysis of variance, day (two levels) and syllable (ten levels) were included as independent variables. This analysis revealed significant effects for day [$F(1,7)=68.79$, $p<0.001$] and syllable [$F(9,63)=3.71$, $p<0.01$]. There was no significant interaction between day and syllable [$F(9,63)=1.13$, $p=0.35$]. Figure 4 plots the tone-identification accuracy performance for the syllables on day 2 and day 3. As can be seen in Fig. 4, the day-3 training advantage was reflected for all of the syllables.

Given the seemingly dramatic improvement on visual tone identification after training, an important question is whether the day-3 advantage was mainly due to simply experience in the identification task. Obviously, participants had practice on day 2, and one might argue that improvement could be due to previous exposure, learning, and/or memory. To test whether this practice was a major factor, we analyzed the results across trial blocks on days 2 and 3. Figure 5 plots the overall performance across blocks on day 2 and day 3, which shows no learning within a given day. Linear regression analyses showed that the slopes of the best fit lines were not significantly above zero for either day 2 (slope=0.004, $p=0.17$) or day 3 (slope=0.005, $p=0.27$), suggesting that experience in the task was not a significant factor.

We calculated d-prime (d') values as a measure of identification performance independent of any decision bias. We computed hit and false alarm (FA) rates for each participant, for each tone, and for each day. A given participant's tone-1 hit rate, for example, is the probability of correctly identifying that tone (i.e., the number of correct tone-1 responses divided by the number of tone-1 trials). A given participant's FA rate for tone 1, for example, is the probability of mistakenly responding tone 1 to stimulus tones 2, 3, and 4 (i.e., the number of incorrect tone-1 responses divided by the total number of trials of tones 2, 3, and 4). The d' is an index of how well the participant distinguishes one lexical tone from the others. The bigger the d' value, the better the participant is at recognizing the tone.

Figure 6 plots the d' values for overall and the four tones on days 2 and 3. We carried out an analysis of variance on d' values. The independent variables were tone (four levels) and day (two levels). This analysis revealed significant effects for day [$F(1,7)=60.55$, $p<0.001$], tone [$F(3,21)=105.29$, $p<0.001$] and their interaction [$F(3,21)=17.50$, $p<0.001$]. The d' values for day 3 were higher than those

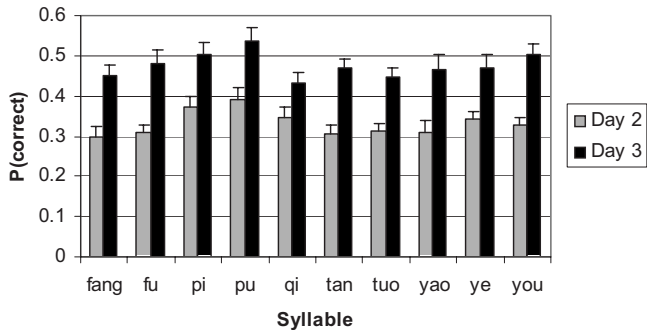

FIG. 4. Experiment 1: Tone-identification performance, plotted as the probability of correct responses (Y axis), for each of the syllables on day 2 and day 3.

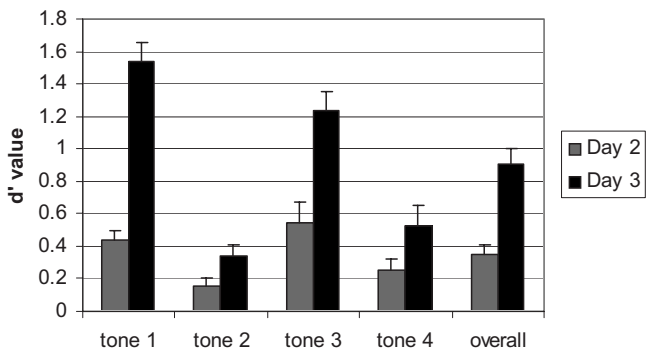

FIG. 6. Experiment 1: The d' values for overall and each of the four tones on day 2 and day 3.

for day 2 (both were significantly greater than zero), and this was the case for all four tones, with the biggest increase at tones 1 and 3. This suggests that the improvement was unlikely due to guessing or item biases—participants were better at identifying all four of the target tones on day 3 than on day 2.

Finally, an analysis of variance compared the accuracy performance from watching one's own face and that from watching another's face. Four of the eight participants watched both their own faces and other's faces, so only data from these participants were used in this analysis. There was no significant difference in performance between watching one's own face (mean=0.467) and watching another's face (mean=0.396), $F(1,3)=1.62$, $p=0.29$. There was also no interaction between face (own or another) and day, $F(1,3)=0.12$, $p=0.75$.

C. Discussion

Our results suggest that (1) untrained native-Mandarin visual tone identification is close to but statistically significantly above chance, and (2) when participants are taught a specific identification strategy (i.e., using mouth, head/chin movements, and especially activities of the neck), their tone-identification performance improves significantly to a level well above chance. Specifically, tone-1 and tone-3 words improved more than tone-2 and tone-4 words. Identification was better when the speakers were female (particularly for tone 3), probably because they tended to dip their head more prominently when speaking tone-3 words.

Our baseline results without training are consistent with the findings of Burnham *et al.* (2000) in that their Cantonese observers also performed just slightly above chance. Also consistent with the study by Schwartz and Savariaux (2001), we found no significant difference in performance between watching one's own face and watching others' faces.

Overall, the accuracy of tone-identification performance improved from about 33% before training to about 48% after training. Half of the participants in this experiment recorded the test stimuli, and this could have given them some advantage. The recording experience might have rendered them somewhat "special." However, separate analyses indicated that these participants' performance and response patterns were very similar to the rest of the participants, as the significant effects of day and v-gender and their significant interaction were observed even when the participants were divided into these two groups. In both groups, the improvement was greatest for tones 1 and 3. Nevertheless, a next step was taken to determine if the findings could be replicated.

Furthermore, it is still logically possible that the advantage after training was due to experience in the task. Experiment 2 compares the positive effect of instructions without prior experience in the task. In addition, we eliminated neck information for another group of participants in order to determine to what extent it contributed to performance of untrained participants.

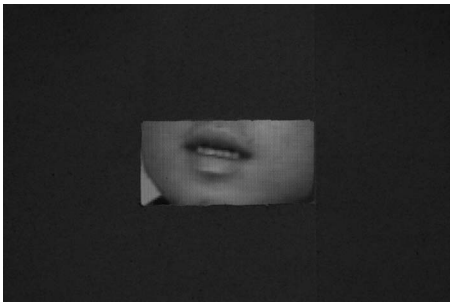

FIG. 7. Experiment 2: A picture showing the TV screen in the box condition.

III. EXPERIMENT 2: REPLICATION AND EXTENSION

Experiment 2 was a 1 day, mixed-subjects design. Participants completed the tone-identification task under one of three conditions: regular (normal), strategy (special instruction), or partially obstructed (only seeing the mouth). If the instruction group performed higher than the regular group, this would provide strong evidence in favor of the potential effectiveness of the visual information.

A. Method

A total of 24 Chinese participants were recruited from UCSC. They are all native speakers of Mandarin. Their ages ranged from 19 to 33 years old. Of the 21 participants who revealed their age (2 chose not to reveal their age but appeared to be in their 20's, and 1 hinted that she was in her early 40'), the average age was 24.3. Of those who chose to answer the question, participants on average had been in the United States for 5.2 years, and English exposure began around the average age of 10.7. They were either paid a $15 gift certificate (for the UCSC Bay-Tree Bookstore) or given course credits for their 2 h participation.

There were eight participants under each of the three conditions: normal, box, and strategy. The same set of stimuli from the previous experiment was used, and participants completed the same tone-identification task: They were told to watch the speaker (with no sound available) and choose (circle) what character or word was said for each trial. Under the normal condition, participants simply watched the video screen and performed the task. Under the box condition, participants could only see the mouth region of the speakers—a piece of cardboard covered the screen except for a cut-out rectangle hole (8 cm width $\times$ 4 cm height) in its approximate center, showing the middle of the screen. Figure 7 shows a picture of the screen in the box condition. Under the strategy condition, participants were taught and instructed to use our specific strategy in the same manner as the last day of Experiment 1. The rest of the procedure is the same as the previous experiment. All instructions and interactions were spoken in Mandarin.

B. Results and discussion

We carried out analysis of variance and pairwise comparisons. The independent variables were group (between-subjects, three levels: box, normal, strategy), v-gender (two

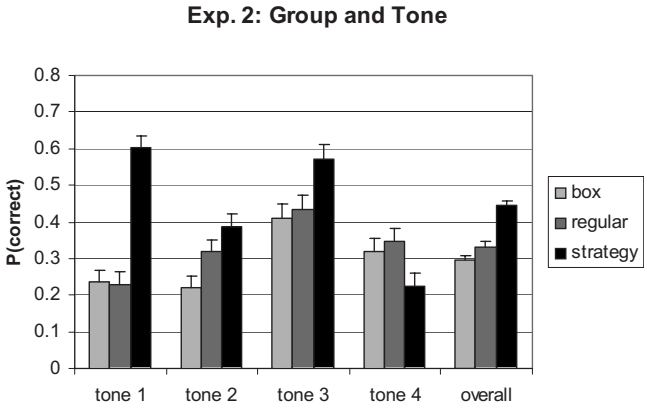

FIG. 8. Experiment 2: Tone-identification performance, plotted as the probability of correct responses (Y axis), for overall and each of the four tones for the three groups.

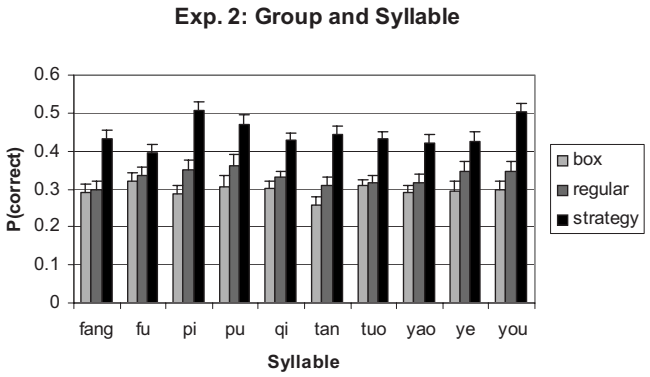

FIG. 9. Experiment 2: Tone-identification performance, plotted as the probability of correct responses (Y axis), for each of the syllables of the three groups.

levels: gender of the speakers in the video, not gender of the perceiver), context (two levels: with or without), and lexical tone (four levels).

Figure 8 shows each of the tone's overall identification performance for all three groups. There was a significant overall difference among the three groups, $F(2,21)=37.60$, $p<0.001$. Specifically, group 3 (strategy, mean=0.45) scored significantly higher than both group 2 (normal, mean=0.33) and group 1 (box, mean=0.30). The difference between groups 1 and 2 was not quite significant [$F(1,14)=3.97$, $p=0.07$], so it remains an open question whether neck information is used by naïve untrained observers. There was a significant main effect for tone [$F(3,63)=13.08$, $p<0.001$], and there was a significant interaction between group and tone [$F(6,63)=8.91$, $p<0.001$]. We obtained CI around the means for each tone and for each group. For group 1 (box), only tone 3 was significantly higher than chance. For group 2 (normal), tones 3 and 4 were significantly higher than chance. For group 3 (strategy), tones 1, 2, and 3 were significantly higher than chance. Improvement on these tones did not appear to come at the detriment of other tones. Performance was the highest for group 3 on all of the tones (with the biggest differences at tones 1 and 3) except tone 4. There was no significant difference between the three conditions (box, normal, strategy) in terms of tone-4 performance.

Performance was again generally better when the speaker in the video was a female than when the speaker was a male, $F(1,21)=23.97$, $p<0.001$. The interaction between v-gender and tone was again significant [$F(3,63)=31.42$, $p<0.001$], with the video-female advantage most pronounced for tone 3. There was no significant main effect for sentential context [$F(1,21)=0.49$, $p=0.49$], and no significant interaction between tone and context, [$F(3,63)=1.06$, $p=0.38$]. The only other significant interaction was between v-gender and context [$F(1,21)=8.64$, $p<0.01$], with the female-speaker advantage again being more pronounced under the no-context condition.

In another analysis of variance on tone-identification performance, group (three levels) and syllable (ten levels) were included as independent variables. This analysis revealed significant effects for group [$F(2,21)=37.60$, $p<0.001$] and syllable [$F(9,189)=2.56$, $p<0.01$]. There was only a marginally significant interaction between group and syllable, $F(18,189)=1.62$, $p=0.06$. Figure 9 shows the tone-identification accuracy for the syllables of the three groups. As can be seen in Fig. 9, group 3 (strategy) had the highest tone-identification accuracy for all of the syllables.

We computed the d' values for all participants, for each tone and each group. An analysis of variance on the d' values with the independent variables tone (four levels) and group (between-subjects, three levels) revealed significant effects for group [$F(2,21)=34.15$, $p<0.001$], tone [$F(3,63)=84.65$, $p<0.001$], and their interaction [$F(6,63)=24.73$, $p<0.001$]. Pairwise comparisons showed that the d' values for group 3 (strategy) were higher than those for group 2 [$F(1,14)=36.74$, $p<0.001$] and group 1 [$F(1,14)=60.20$, $p<0.001$], while the difference between groups 2 and 1 was not significant [$F(1,14)=3.77$, $p<0.07$].

Figure 10 plots the d' values for each of the four tones of the three groups and also averaged across the four tones. As can be seen from Fig. 10, the d' values from group 3 were the highest for all four tones, and the differences were the most pronounced at tones 1 and 3. Specifically, as neck movement for tone 1 was minimal or nonexistent compared to the other three tones, it seemed to be the most visually distinctive tone. Tones 2, 3, and 4 were more visually con-

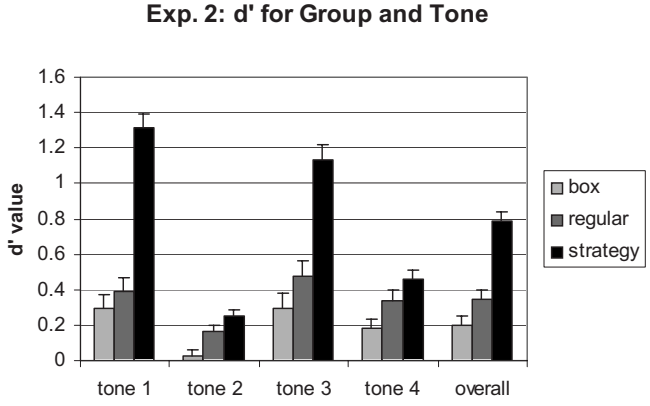

FIG. 10. Experiment 2: The d' values for overall and each of the four tones of the three groups.

fusable because they all had some neck movements. Neck movements for tone 3 tended to be more pronounced than those for tones 2 and 4, and neck movements for tone 4 tended to be slightly shorter than (and differ in timing from) tone 2. Some speakers (especially females in our video) spoke tone-3 words with a dipping head/chin movement, thus providing an extra source of visual information, which presumably helped improve tone-3 performance. Tones 2 and 4 were relatively harder to visually distinguish from each other, with the difference in onset and timing being the only reliable information observed.

Although the current study found that training improves visual tone identification, an argument might be that this training was only effective for some of the current particular speakers in our video. To explore this important question, we examined whether performance improvement occurred for each of the individual speakers. The tone-identification improvement was significant for all four speakers in both experiments 1 and 2. For both experiments, we conducted separate analyses of variance for each of the four speakers. In experiment 1, comparing performance on day 2 and day 3, identification accuracy significantly improved for each of the four speakers: Mainland-China female $[F(1,7)=16.78,\ p<0.01]$, Mainland-China male $[F(1,7)=7.63,\ p<0.05]$, Taiwan female $[F(1,7)=50.40,\ p<0.001]$, and Taiwan male $[F(1,7)=65.81,\ p<0.01]$. For all four speakers, day 3 performance was significantly greater than that of day 2 as well as greater than the chance level. Moreover, in experiment 2, comparing performance among groups 1 (box), 2 (regular), and 3 (instruction), identification accuracy also significantly improved for each of the four speakers: Mainland-China female $[F(2,21)=6.04,\ p<0.01]$, Mainland-China male $[F(2,21)=9.45,\ p<0.01]$, Taiwan female $[F(2,21)=30.77,\ p<0.001]$, and Taiwan male $[F(2,21)=37.99,\ p<0.001]$. For all four speakers, performance in group 3 was greater than that of groups 1 and 2 as well as greater than the chance level.

Another argument might be that the training may only be effective for the particular stimuli used under the particular condition. This may be true, because the current speakers were asked to speak "clearly and distinctively." It is not clear whether these potential sources of visual information can be effective in the everyday real world outside of the laboratory. Nevertheless, the current findings are unexpected and may serve as a first step raising the possibility of ecological and functional visual tonal information in the real world. Future research can test more speakers under various conditions or environments.

In both experiments 1 and 2, performance on the tone-identification task was better when the participants followed a specific strategy of using neck and head/chin movements. In addition, performance was generally higher when the speaker was female, especially for tone 3. However, perhaps it is important to emphasize that the interactions between tone and v-speaker likely arose from the specific behavioral patterns of the individuals in our video, rather than from their gender per se. For example, the two female speakers in our video tended to dip their head/chin while pronouncing tone-3 words, whereas the males did not.

Mandarin tones also differ in duration, and it is possible that duration differences might be visible. We measured the duration (in seconds) of the spoken words in citation (using both the spectrogram and the wave forms), and indeed the general pattern of duration differences between tones was replicated. Overall, tone-3 words (mean=0.647 s) were longer than tone-2 words (mean=0.623 s), which were longer than tone-1 (mean=0.593 s) and tone-4 (mean =0.483 s) words. An analysis of variance was carried out on stimulus duration, with the independent variables of syllable, tone, and version. The only significant results were the main effects for tone $[F(3,9)=6.39, p<0.05]$ and syllable $[F(9,27)=9.59, p<0.01]$. None of the interactions was significant. Pairwise comparisons showed that tones 1, 2, and 3 were all significantly longer in duration than tone 4, but there were no significant differences among tones 1, 2, and 3. Although the tones did not differ much in duration, it is still possible that duration information contributed to performance.

IV. GENERAL DISCUSSION

We found that naïve participants only recognize Mandarin visual tones slightly above chance, and this finding is consistent with previous research on Cantonese tones (e.g., Burnham *et al.*, 2000). In addition, the present study found that there is more visual information for Mandarin tones than anticipated. With instruction, participants appeared to be able to use the speakers' neck activities and head/chin movements to identify tone. Previous research found that head movements are related to the perception of intonation (e.g., Yehia *et al.*, 2002; Srinivasan and Massaro, 2003) and Cantonese tones (Burnham *et al.*, 2006), and it is likely that this can also be the case for other lexical tones (e.g., Mandarin tone 3), at least when speaking clearly and distinctively.

It is possible that this finding represents only one case of a general phenomenon. Singers' neck and head movements may also reflect musical changes in pitch, intensity, and/or duration. Other examples may be observed from talking (stress) and yelling. For the neck, it is possible that its visible activity may be most pronounced with changes in frequency (though different parts of the neck may be visible for high or low frequencies).

Initially, the neck seemed to be an unexpected source of visual information. Although the speech production of pitch changes is typically described in terms the vocal fold's vibration caused by subglottal pressure and laryngeal musculature/tension (Ladefoged, 2001; Lass, 1976; Lehiste, 1970; Lieberman, 1967; Mullin *et al.*, 2003), whether there is any activity visible on the neck surface is virtually never discussed or even mentioned. However, the current study's finding is not that surprising in hindsight. At high frequency, the glottis tends to rise (this can be felt by putting fingers on the glottis); at low frequency, the muscles at the lower part of the neck tend to bulge outward (this can be felt by putting fingers on the lower neck). Our tentative speculation is that some muscles around the neck move (or move along with) the glottis, and the movement is visible, but which specific muscles are involved in lexical-tone production remain to be

identified. The current study at least revealed that some of their activities could be seen on the neck surface.

We believe that the improvement in visual tone-identification performance in the current study was mainly due to training the participants to use movements of the head and neck. Although extensive training with prolonged feedback usually improved performance (e.g., Gesi *et al.*, 1992; Massaro *et al.*, 1993; Massaro and Light, 2004; Wang *et al.*, 1999), these long-term training sessions spanned across days to weeks. In our current study, the one-time training was mostly verbal instruction and show-and-tell, and there were only a few practice trials in which feedback was given. The instruction, show-and-tell, plus practice trials lasted no longer than about 45 min. In experiment 1, there was a sudden change in the patterns of responses after training relative to before training. While we do not deny that feedback helps, it is likely that telling participants where to look and what to look for was sufficient to enable the participants to identify the tones.

In our study, we showed that performance significantly improved when participants were taught a specific visual-information strategy. This one-time training was mostly instruction and show-and-tell with feedback; participants were only given about 10–20 practice trials before the test session but no feedback during the test session. Teaching this strategy improved performance both within subjects (experiment 1) and between subjects (experiment 2). It is true that we only compared training versus no training, and we did not carry out an "incorrect training" group. However, Burnham *et al.* (2000) found that feedback (feedback versus no feedback as a between-subjects factor, total $N=48$) did not improve native-Cantonese visual-tone identification performance. Their interpretation was that, "the hypothesis that feedback would enhance performance was not upheld" (Burnham *et al.*, 2000, p. 90). Similarly, our subjects did not improve across blocks of testing (see Fig. 5). The failure to find that feedback improves visible tone identification contrasts sharply with the learning that occurs when speechreading segmental differences such as place and manner of articulation (Gesi *et al.*, 1992; Massaro *et al.*, 1993). These studies together show that, without the appropriate strategy of where to look and what information to use, subjects do not learn tone identification with feedback, although they can learn to speechread visible properties of speech articulation such as manner and place of articulation.

To provide an idea about the effectiveness of the visual information, consider a study that provided auditory training to American listeners in the identification of Mandarin tones (Wang *et al.*, 1999). The training was eight sessions over 2 weeks, and there was an overall improvement around 21% (there was probably no significant ceiling effect, as only one out of the eight participants scored 100% on the posttest). Our visual training was one session of no more than 45 min, and there was an overall improvement in the following identification task of around 13%. The relative improvements for the most visually distinctive tones (tone 1 increased about 40% and tone 3 about 13%) in native visual identification were actually comparable to improvements in trained non-native auditory identification (tone 1 increased about 15% and tone 3 about 18%).

Future research can evaluate the extent to which visual training generalizes to new speakers and words, as Wang *et al.* (1999) had done for auditory training. Other future research can examine the possible presence, nature, and usefulness of neck and/or head movements for other languages. These patterns can be compared to the Mandarin visual tonal information to determine if there is any consistent pattern across languages among high/mid/low level tones, tones with a rising/falling/changing contour, tone at specific pitch ranges, etc.

Potential applications/implications. Learning a tonal language like Mandarin by hard-of-hearing individuals may be facilitated by having the speaker pronouncing distinctively as well as teaching the visual information. Massaro and Light (2004) trained seven students with hearing loss to discriminate minimal pairs of words bimodally (auditorily and visually). The students were also trained to produce various speech segments by using visual information about how the inside oral articulators work during speech production. The articulators were displayed from different vantage points so that the subtleties of articulation could be optimally visualized. The speech was also slowed down to emphasize and elongate the target phonemes, allowing for clearer understanding of how the target segment is produced in isolation or with other segments. Intelligibility ratings of the posttest productions were significantly higher than pretest productions, indicating significant learning. An analogous training regimen could be instantiated for the perception and production of lexical tone.

Visual tonal information may also help individuals learn tones in a new language. Massaro and Light (2003) investigated the effectiveness of Baldi (a synthetic talking head) for teaching non-native phonetic contrasts, by comparing instruction illustrating the internal articulatory processes of the oral cavity versus instruction providing just the normal view of the tutor's face. Eleven Japanese speakers of English as a second language were bimodally trained under both instruction methods to identify and produce the American English /r/ and /l/ in a within-subject design. Both the perception and production of words by the Japanese trainees generally improved from one day of training to the next. The first language speakers of a non-tonal language like English have difficulty perceiving lexical tones at the initial stages of learning, and extra visual information may improve not just tonal perception but also tonal production, as relevant head and neck movements may help the learner more easily increase awareness and monitor their own speech production processes.

Visual information adds to the richness of our multisensory experience, and we envision this line of inquiry to have the potential of training tone perception and production, pro-

moting prosodic/pitch awareness in speech/music, and adding realism and usefulness to synthetic talking heads.

V. CONCLUSION

When unexpected findings occur in science, they may help refine theories or even create paradigms. For example, the discovery of the existence and influence of visible segmental speech helped to inspire a field of research in audiovisual speech and related technology. In an analogous way, it is possible that the realization in the existence and nature of visible tonal information may eventually help further refine theories of speech perception and production. Starting with the original studies by researchers such as Burnham (Burnham *et al.*, 2000; 2001) and Mixdorff (Mixdorff *et al.*, 2005a; b, 2006), there is gradually accumulating evidence suggesting that visual information can be useful in the identification (and discrimination) of lexical tones. We encourage further research on the relationship between changes in acoustic-physical dimensions (frequency, amplitude, and duration) and visible movements of the neck, head, and mouth (for audiovisual integration of prosody, see Srinivasan and Massaro, 2003). It would be interesting to determine if extended training can improve the performance even more. Other possible future research may examine tone production and visual perception of other tonal languages, and how visual and auditory information for tones are integrated.

Tone languages are estimated to be spoken by over half of the world's population (Connell, 2000; Ladefoged, 2001), and more than 60 million Chinese are deaf (Jiang *et al.*, 1999). Mandarin (and comparative) psycholinguistics can be a useful tool to study perception, cognition, and memory. Psycholinguistic theories and findings based on just one language may be limited in the same manner as anthropological theories and findings based on just one culture. We hope this direction of inquiry will contribute to speech science and technology, while simultaneously expanding our understanding of the mind, as well as increasing our appreciation of a language rooted in a culture still thriving after more than 5000 years.

ACKNOWLEDGMENTS

The research and writing of this paper was supported in part by grants from the National Science Foundation (NSF CHALLENGE Grant No. CDA-9726363 and NSF Grant No. BCS-9905176), a grant from the Public Health Service (Grant No. PHS R01 DC00236), cooperative grants from the Intel Corporation and the University of California Digital Media Program (D97-04), the Eugene Cota-Robles Fellowship from the University of California, Santa Cruz, and the Federico and Rena Perlino Scholarship Award. The authors thank editors and reviewers for their valuable time and comments and Michael M. Cohen for providing expert technical assistance.

APPENDIX A: THE 40 MANDARIN WORDS (SELECTED FROM LIU AND SAMUEL, 2004) USED AS STIMULI.

Pinyin/Bpmf	IPA Transcription	Tone 1	Tone 2	Tone 3	Tone 4
Fang/ㄈㄤ	faŋ	方/方	房/房	访/訪	放/放
Fu/ㄈㄨ	fu:	夫/夫	服/服	府/府	富/富
Pi/ㄆㄧ	$p^{h}i$:	批/批	皮/皮	匹/匹	僻/僻
Pu/ㄆㄨ	$p^{h}u$:	扑/扑	菩/菩	谱/譜	瀑/瀑
Qi/ㄑㄧ	$tɕ^{h}i$:	妻/妻	骑/騎	起/起	气/氣
Tan/ㄊㄢ	t^{h}an	贪/貪	谈/談	坦/坦	探/探
Tuo/ㄊㄨㄛ	$t^{hw}ɔ$:	脱/脫	驼/駝	妥/妥	唾/唾
Yao/ㄧㄠ	jɑu	妖/妖	摇/搖	咬/咬	耀/耀
Ye/ㄧㄝ	jɛ:	噎/噎	爷/爺	也/也	夜/夜
You/ㄧㄡ	jeu	优/优	游/游	有/有	又/又

The 40 Mandarin characters or words used as stimuli in the study (selected from Liu & Samuel, manuscript). Participants from Mainland China read abbreviated (simplified) forms (left), and participants from Taiwan read traditional forms (right). The words were spoken under two conditions: Neutral (a character or word by itself) or the context of "下一个/個字是___" (i.e., "the next word is___").

APPENDIX B: AN EXAMPLE OF A RESPONSE SHEET (TRADITIONAL CHARACTERS). PARTICIPANTS FROM MAINLAND CHINA SAW SIMPLIFIED WORDS, AND PARTICIPANTS FROM TAIWAN SAW TRADITIONAL WORDS.

1	噎	爺	也	夜	21	脫	駝	妥	唾
2	方	房	訪	放	22	扑	菩	譜	瀑
3	妻	騎	起	氣	23	优	游	有	又
4	批	皮	匹	僻	24	貪	談	坦	探
5	妖	搖	咬	耀	25	方	房	訪	放
6	批	皮	匹	僻	26	貪	談	坦	探
7	脫	駝	妥	唾	27	脫	駝	妥	唾
8	夫	服	府	富	28	优	游	有	又
9	噎	爺	也	夜	29	批	皮	匹	僻
10	妻	騎	起	氣	30	貪	談	坦	探
11	噎	爺	也	夜	31	扑	菩	譜	瀑
12	夫	服	府	富	32	妖	搖	咬	耀
13	妻	騎	起	氣	33	脫	駝	妥	唾
14	扑	菩	譜	瀑	34	方	房	訪	放
15	夫	服	府	富	35	批	皮	匹	僻
16	貪	談	坦	探	36	噎	爺	也	夜
17	妻	騎	起	氣	37	优	游	有	又
18	优	游	有	又	38	妖	搖	咬	耀
19	夫	服	府	富	39	扑	菩	譜	瀑
20	妖	搖	咬	耀	40	方	房	訪	放

Blicher, D. L., Diehl, R. L., and Cohen, L. B. (**1990**). "Effects of syllable duration on the perception of the Mandarin tone 2/tone 3 distinction: Evidence of auditory enhancement," J. Phonetics **18**, 37–49.

Burnham, D., Ciocca, V., Lauw, C., Lau, S., and Stokes, S. (**2000**). "Perception of visual information for Cantonese tones," in *Proceedings of the Eighth Australian International Conference on Speech Science and Technology*, edited by M. Barlow and P. Rose (Australian Speech Science and Technology Association, Canberra) pp. 86–91.

Burnham, D., Lau, S., Tam, H., and Schoknecht, C. (**2001**). "Visual discrimination of Cantonese tone by tonal but non-Cantonese speakers, and by non-tonal language speakers," Proceedings of the International Conference on Auditory-Visual Speech Processing, edited by D. Massaro, J. Light, and K. Geraci (Aalborg, Denmark, September 7–9, 2001), pp. 155–160.

Burnham, D., Reynolds, J., Vatikiotis-Bateson, E., Yehia, H., Ciocca, V., Morris, R. H., Hill, H., Vignali, G., Bollwerk, S., Tam, H., and Jones, C. (**2006**). "The perception and production of phones and tones: The role of rigid and non-rigid face and head motion," in *Proceedings of the Seventh International Seminar on Speech Production*, edited by H. Yehia, D. Demolin, and R. Laboissiere (Ubatuba, Sao Paolo, Brazil), pp. 185–192.

Chao, Y. R. (**1968**). *A Grammar of Spoken Chinese* (University of California Press, Berkeley).

Chen, J.-Y. (**1999**). "The representation and processing of tone in Mandarin Chinese: Evidence from slips of the tongue," Appl. Psycholinguist. **20**, 289–301.

Chen, T. H., and Massaro, D. W. (**2004**). "Mandarin speech perception by ear and eye follows a universal principle," Percept. Psychophys. **66**, 820–836.

Connell, B. (**2000**). "The perception of lexical tone in Mambila," Lang Speech **43**, 163–182.

Connell, B. A., Hogan, J. T., and Rozsypal, A. J. (**1983**). "Experimental evidence of interaction between tone and intonation in Mandarin Chinese," J. Phonetics **11**, 337–351.

Garding, E., Kratochvil, P., Svantesson, J.-O., and Zhang, J. (**1986**). "Tone 4 and tone 3 discrimination in modern standard Chinese," Lang Speech **29**, 281–293.

Gesi, A. T., Massaro, D. W., and Cohen, M. M. (**1992**). "Discovery and expository methods in teaching visual consonants and word identification," J. Speech Hear. Res. **35**, 1180–1188.

Green, K. P., and Miller, J. L. (**1985**). "On the role of visual rate information in phonetic perception," Percept. Psychophys. **38**, 269–276.

Hayashi, Y., and Sekiyama, K. (**1998**). "Native-foreign language effect in the McGurk effect: A test with Chinese and Japanese," Proceedings of Auditory-Visual Speech Processing 1998 International Conference, Terrigal-Sydney, Australia, 4–7 December, pp. 61–66.

Jiang, X., Wang, Y., and Zhang, F. (**1999**). "Visual speech analysis and synthesis with application to Mandarin speech training," Virtual reality software and technology (VRST **1999**), pp. 111–115.

Jongman, A., Wang, Y., Moore, C. B., and Sereno, J. A. (**2005**). "Perception and production of Mandarin Chinese tones," http://www.ku.edu/~kuppl/sereno/Handbookjong%20in%20press.pdf.

Kim, J., and Davis, C. (**2001**). "Visible speech cues and auditory detection of spoken sentences: An effect of degree of correlation between acoustic and visual properties," Proceedings of the International Conference on Auditory-Visual Speech Processing, edited by D. Massaro, J. Light, and K. Geraci (Aalborg, Denmark, September 7–9, 2001), pp. 127–131.

Ladefoged, P. (**2001**). *A Course in Phonetics*, 4th ed. (Thompson, Learning, Boston).

Lass, N. J. (**1976**). *Contemporary Issues in Experimental Phonetics* (Academic, New York).

Lee-Schoenfeld, V. (**2002**). "Third tone prominence," http://people.ucsc.edu/~vls/Papers/T3_Prominence.pdf.

Lehiste, I. (**1970**). *Suprasegmentals* (MIT, Cambridge, MA).

Lieberman, P. (**1967**). *Intonation, Perception, and Language* (MIT, Cambridge, MA).

Liu, S., and Samuel, A. G. (**2004**). "Perception of Mandarin lexical tones when F0 information is neutralized," Lang Speech **47**, 109–138.

Massaro, D. W. (**1998**). *Perceiving Talking Faces: From Speech Perception to a Behavioral Principle* (MIT, Cambridge, MA).

Massaro, D. W., Cohen, M. M., Campbell, C. S., and Rodriguez, T. (**2001**). "Bayes factor of model selection validates FLMP," Psychonomic Bull. Rev. **8**, 1–17.

Massaro, D. W., Cohen, M. M., and Gesi, A. T. (**1993**). "Long-term training, transfer, and retention in learning to lipread," Percept. Psychophys. **53**, 549–562.

Massaro, D. W., Cohen, M. M., and Smeele, P. M. T. (**1995**). "Cross-linguistic comparisons in the integration of visual and auditory speech," Mem. Cognit. **23**, 113–131.

Massaro, D. W., Cohen, M. M., and Tseng, C. Y. (**1985**). "The evaluation and integration of pitch height and pitch contour in lexical tone perception in Mandarin Chinese," J. Chin. Linguist. **13**, 267–289.

Massaro, D. W., and Light, J. (**2003**). "Read my tongue movements: Bimodal learning to perceive and produce non-native speech /r/ and /l/," Proceedings of Eurospeech (Interspeech), Eight European Conference on Speech Communication and Technology, Geneva, Switzerland.

Massaro, D. W., and Light, J. (**2004**). "Improving the vocabulary of children with hearing loss," Volta Rev. **104**, 141–174.

Massaro, D. W., Tseng, C. Y., and Cohen, M. M. (**1983**). "Vowel and lexical tone perception in Mandarin Chinese: Psycholinguistic and psychoacoustic contributions," J. Quant. Linguist. **19**, 76–102.

Massaro, D. W., Tsuzaki, M., Cohen, M. M., Gesi, A., and Heredia, R. (**1993**). "Bimodal speech perception: An examination across languages," J. Phonetics **21**, 445–478.

McGurk, H., and MacDonald, J. (**1976**). "Hearing lips and seeing voices," Nature **264**, 746–748.

Mixdorff, H., Charnvivit, P., and Burnham, D. (**2005a**). "Auditory-visual perception of syllabic tones in Thai," Proceedings of Auditory-Visual Speech Processing Workshop 2005, edited by E. Vatikiotis-Babeson (British Columbia, Canada, July 24–27, 2005) pp. 3–8.

Mixdorff, H., Hu, Y., and Burnham, D. (**2005b**). "Visual cues in Mandarin tone perception," Proceedings of Eurospeech 2005 (InterSpeech-2005), Lisbon, Portugal, pp. 405–408.

Mixdorff, H., Luong, M. C., Nguyen, D. T., and Burnham, D. (**2006**). "Syllabic tone perception in Vietnamese," Proceedings of International Symposium on Tonal Aspects of Languages 2006, La Rochelle, France, pp. 137–142.

Mullin, W. J., Gerace, W. J., Mestre, J. P., and Velleman, S. L. (**2003**). *Fundamentals of Sound with Applications to Speech and Hearing* (Pearson Education, Boston, MA).

Munhall, K. G., Jones, J. A., Callan, D. E., Kuratate, T., and Vatikiotis-Bateson, E. (**2004**). "Visual prosody and speech intelligibility: Head movement improves auditory speech perception," Psychol. Sci. **15**, 133–137.

Rosenblum, L. D., and Fowler, C. A. (**1991**). "Audiovisual investigation of the loudness-effort effect for speech and nonspeech events," J. Exp. Psychol. Hum. Percept. Perform. **17**, 976–985.

Schwartz, J.-L., and Savariaux, C. (**2001**). "Is it easier to lipread one's own speech gestures than those of somebody else? It seems not!," Proceedings of the International Conference on Auditory-Visual Speech Processing, pp. 18–23.

Sekiyama, K. (**1997**). "Cultural and linguistic factors in audiovisual speech processing: The McGurk effect in Chinese subjects," Percept. Psychophys. **59**, 73–80.

Sekiyama, K., and Tohkura, Y. (**1991**). "McGurk effect in non-English listeners: Few visual effects for Japanese subjects hearing Japanese syllables of high auditory intelligibility," J. Acoust. Soc. Am. **90**, 1797–1805.

Sekiyama, K., and Tohkura, Y. (**1993**). "Inter-language differences in the influence of visual cues in speech perception," J. Phonetics **21**, 427–444.

Srinivasan, R. J., and Massaro, D. W. (**2003**). "Perceiving prosody from the face and voice: Distinguishing statements from echoic questions in English," Lang Speech **46**, 1–22.

Tseng, C. (**1981**). "An acoustic phonetic study on tones in Mandarin Chinese," Ph.D. dissertation, Brown University, Providence, RI.

Tseng, C. Y., Massaro, D. W., and Cohen, M. M. (**1986**). "Lexical tone perception in Mandarin Chinese: Evaluation and integration of acoustic features," in *Linguistics, Psychology, and the Chinese Language*, edited by H. S. R. Kao and R. Hoosain (Centre of Asian Studies, University of Hong Kong), pp. 91–104.

Wang, Y., Spence, M., Jongman, A., and Sereno, J. (**1999**). "Training American listeners to perceive Mandarin tones," J. Acoust. Soc. Am. **106**, 3649–3658.

Whalen, D. H., and Xu, Y. (**1992**). "Information for Mandarin tones in the amplitude contour and in brief segments," Phonetica **49**, 25–47.

Yehia, H. C., Kuratate, T., and Vatikiotis-Bateson, E. (**2002**). "Linking facial animation, head motion and speech acoustics," J. Phonetics **30**, 555–568.

Spectral weighting strategies for hearing-impaired listeners measured using a correlational method

Lauren Calandruccio[a] and Karen A. Doherty
Department of Communication Sciences and Disorders, Institute for Sensory Research, Syracuse University, Syracuse, New York 13244

(Received 13 July 2007; revised 13 January 2008; accepted 4 February 2008)

Spectral weighting strategies using a correlational method [R. A. Lutfi, J. Acoust. Soc. Am. **97**, 1333–1334 (1995); V. M. Richards and S. Zhu, J. Acoust. Soc. Am. **95**, 423–424 (1994)] were measured in ten listeners with sensorineural-hearing loss on a sentence recognition task. Sentences and a spectrally matched noise were filtered into five separate adjacent spectral bands and presented to listeners at various signal-to-noise ratios (SNRs). Five point-biserial correlations were computed between the listeners' response (correct or incorrect) on the task and the SNR in each band. The stronger the correlation between performance and SNR, the greater that given band was *weighted* by the listener. Listeners were tested with and without hearing aids on. All listeners were experienced hearing aid users. Results indicated that the highest spectral band (~2800–11 000 Hz) received the greatest weight in both listening conditions. However, the weight on the highest spectral band was less when listeners performed the task with their hearing aids on in comparison to when listening without hearing aids. No direct relationship was observed between the listeners' weights and the sensation level within a given band. © *2008 Acoustical Society of America.*
[DOI: 10.1121/1.2887857]

PACS number(s): 43.71.Es, 43.66.Ts, 43.71.Ky [PEI] Pages: 2367–2378

I. INTRODUCTION

The relationship between audibility and speech recognition has been studied for more than half a century (French and Steinberg, 1947; ANSI, 1997). The most frequently used method to predict speech intelligibility based on audibility is the articulation index (Fletcher and Galt, 1950; ANSI, 1969), which was revised in the late 1990s and renamed the Speech Intelligibility Index [(SII); ANSI, 1997)]. The SII includes correction factors that account for the upward spread of masking and high presentation levels of speech. In addition to frequency-importance functions (FIF) for nonsense syllables, the SII also includes FIF data for words and sentences, which are more representative of every day speech. Data reported in the SII indicate that normal-hearing listeners weight spectral information differently depending on the type of speech stimuli they are attending to. Specifically, normal-hearing listeners tend to weight higher frequency information in sentences (Bell *et al.*, 1992) less than higher frequency information in nonsense syllables. However, it is not clear how listeners with hearing loss weight spectral information compared to normal-hearing listeners. This study examines how hearing-impaired listeners weight spectral information in sentences.

Recently, Calandruccio and Doherty (2007) reported how listeners with normal hearing weight spectral information in sentences using a correlational method (Richards and Zhu, 1994; Lutfi, 1995). They found that normal-hearing listeners weight lower frequency information greater than higher-frequency information in sentences when compared to nonsense syllables (see Fig. 9, Calandruccio and Doherty, 2007). However, spectral weights have been shown to depend on hearing status (e.g., Doherty and Lutfi, 1996, 1999; Mehr *et al.*, 2001; Pittman and Stelmachowicz, 2000). For example, in 2001, Mehr *et al.* compared the weighting strategies for normal-hearing listeners to those of cochlear implant users. A subset of the Nonsense Syllable Test (Resnick *et al.*, 1975) was used to determine how both groups of listeners weighted the spectral information in the speech stimuli across six spectral bands. Results indicated that normal-hearing listeners weighted the six spectral bands approximately equally, however the cochlear implant users weighted the six bands unequally. Pittman and Stelmachowicz (2000) also provided evidence that normal-hearing listeners weight spectral information differently than hearing-impaired listeners. They examined how these two groups of listeners weighted three segmental features (i.e., vowel, transition, and fricative) of voiceless fricative vowel–consonant pairs. Results indicated that for the vowel–consonant pair /uθ/ normal-hearing children and adults weighted the segmental features unequally. In contrast, the hearing-impaired children and adults weighted the information equally across the three segments.

Doherty and Lutfi (1996, 1999) also measured weighting strategies for both normal-hearing and hearing-impaired listeners on a synthetic and an analytic level-discrimination nonspeech task. Their results indicated that listeners with hearing loss used different weighting strategies than listeners with hearing loss to perform the discrimination tasks. Leibold *et al.*, (2006) replicated the Doherty and Lutfi (1996) study to determine if presentation level and/or sensation level, instead of hearing loss, could account for the differ-

[a]Current affiliation: The Roxelyn and Richard Pepper Department of Communication Sciences and Disorders, Northwestern University, Evanston, IL 60208. Electronic mail: l-calandruccio@northwestern.edu

TABLE I. Hearing thresholds in dB HL for ten listeners.

Listener	Ear	0.25	0.50	0.75	1.0	1.5	2.0	3.0	4.0	6.0	8.0	(kHz)
HI1	R	25	30	35	45	50	45	45	60	85	85	(dB HL)
	L	30	30	30	50	40	50	55	65	80	75	
HI2	R	35	35	40	45	50	55	55	55	65	65	
	L	45	45	45	50	50	50	55	65	65	65	
HI3	R	40	40	45	45	55	45	55	60	65	65	
	L	50	45	45	45	60	50	65	65	70	70	
HI4	R	60	45	45	50	60	65	60	70	70	75	
	L	50	45	45	50	60	65	65	70	80	85	
HI5	R	15	40	55	60	60	60	65	60	70	75	
	L	25	40	55	65	75	70	70	70	75	75	
HI6	R	35	30	35	40	50	60	70	70	65	70	
	L	35	25	30	35	60	60	60	70	75	75	
HI7	R	10	15	25	30	35	45	50	55	70	65	
	L	10	15	30	35	45	45	60	55	70	60	
HI8	R	40	50	40	50	50	50	50	55	80	80	
	L	35	60	50	60	55	55	55	60	70	75	
HI9	R	40	40	45	45	40	45	45	50	55	55	
	L	45	35	35	35	40	40	50	45	55	65	
HI10	R	45	45	45	50	50	50	45	50	50	60	
	L	55	50	55	50	55	55	50	45	60	55	

ences in weighting strategies between the two groups of listeners. After equating both presentation level and sensation level, Leibold *et al.* suggested that the difference in weights observed between normal-hearing and hearing-impaired listeners was due to overall presentation level and not sensation level.

It remains unclear how hearing-impaired listeners weight spectral information in sentences and how sensation level could affect listeners' weights. Although the correlational method has been well established in measuring reliable weighting strategies for different types of speech stimuli and psychophysical tasks for listeners with normal hearing (Doherty and Turner, 1996; Stellmack *et al.*, 1997; Willihnganz *et al.*, 1997; Turner *et al.*, 1998; Lentz and Leek, 2002; Apoux and Bacon, 2004; Calandruccio and Doherty, 2007), there are limited data on spectral weights for listeners with hearing loss. Those data that are reported for listeners with hearing loss all have used a limited set of nonsense syllable stimuli (Kordas, 1999; Mehr *et al.*, 2001; Pittman and Stelmachowicz, 2000). The purpose of the present study was twofold: (1) to determine spectral-weighting strategies for sentences for listeners with hearing loss, and (2) to assess the effect of hearing aids on hearing-impaired listeners' spectral weighting strategies for sentences. These data will provide a greater understanding of *how* hearing-impaired listeners use spectral information to perceive sentences.

II. METHODS: EXPERIMENT I, WITHOUT HEARING AIDS

A. Subjects

Spectral-weighting strategies for sentences using the correlational method were obtained for ten native American-English speaking listeners (five female, five male; age 56–77 years, mean age 69.5 years) with symmetrical (within 10 dB) sensorineural-hearing loss (air conduction and bone conduction thresholds within 10 dB at 500, 1000, 2000, and 4000 Hz). Audiometric thresholds were recorded using a GSI-16 (Grason-Stadler; Madison, WI) audiometer using standard audiometric procedures (ANSI, 2004) at octave and interoctave frequencies between 250–8000 and 500–8000 Hz, respectively, and are shown in Table I. Loudness discomfort levels (LDL) were measured binaurally at 750, 1500, and 3000 Hz (Bentler and Nelson, 2001) and for conversational speech using monitored-live voice. Overall presentation levels of the sentence stimuli used throughout testing were selected based on each listener's dynamic range of hearing and were presented approximately in the center of their dynamic range. The presentation levels of the sentences were fixed, and the noise varied around the level of the speech. Stimuli were never presented above a listener's LDL.

B. Stimuli

The speech stimuli used for all intelligibility testing were the Harvard/IEEE sentence lists [IEEE, 1969; recorded by Galvin and Fu, 2003 (16 bit, 22 kHz sampling rate)] spoken by a female speaker. The Harvard/IEEE sentence lists contain 72 lists of 10 sentences (720 sentences in total) with five key words in each sentence. The noise stimuli were generated in MATLAB (MathWorks, Natick, MA) and consisted of a noise (16 bit, 22 kHz sampling rate) spectrally matched to the long-term average speech spectrum (LTASS) of the Harvard/IEEE sentences. Specifically, this was created by applying white noise to a FIR filter with a magnitude response equal to the LTASS of the 720 sentences. Therefore, the average spectrum of the speech and the noise were almost identical.

Stimulus generation. The stimulus generation is identical to that described in detail in Calandruccio and Doherty (2007). Briefly, the sentences and noise were filtered into five approximately equal intelligible frequency bands generated

TABLE II. Cutoff frequencies for five spectral bands.

Band No.	Low hertz Cut-off	High hertz Cut-off
1	111	561
2	562	1 113
3	1114	1 788
4	1789	2 806
5	2807	11 000

in MATLAB using rectangular FIR filters of length 4096 (see Table II for cutoff frequencies). The passband gain was 0 dB, and the stop-band gain was −120 dB for all five filters. The rolloff of the filter skirts ranged between 180 and 18 000 dB/octave. To the best of our knowledge there are no FIF data reported for the Harvard/IEEE sentences and the only FIFs reported for sentence stimuli are for the Connected Speech test (Cox *et al.*, 1987; Sherbecoe and Studebaker, 2002) and the Speech Perception in Noise (SPIN) (Kalikow *et al.*, 1977; Bell *et al.*, 1992) test. Previous experiments in our laboratory indicated that basing the cut-off frequencies on either of these FIFs did not change the relative shape of a listeners' weighting strategy. FIF data reported for the SPIN test sentences were most easily divided into five equal bands with the least amount of variability. Therefore, the bandwidths for these experiments were based on previously reported 1/3 octave band frequency-importance functions for sentences from the SPIN test (Bell *et al.*, 1992; ANSI, 1997) and were divided so that each band contained approximately equal intelligibility. In other words, if presented in isolation all five bands should theoretically contribute equal information to the sentence recognition task. A PC and Tucker-Davis Technologies (Alachua, FL) DSP board were used to combine the respective filtered sentences and noises on each trial at various signal-to-noise ratios (SNRs) randomly chosen from a specified 13 dB SNR range. The same 13 dB SNR range was used for all five bands. The five noisy speech bands were then recombined to create a noisy sentence (see Fig. 1).

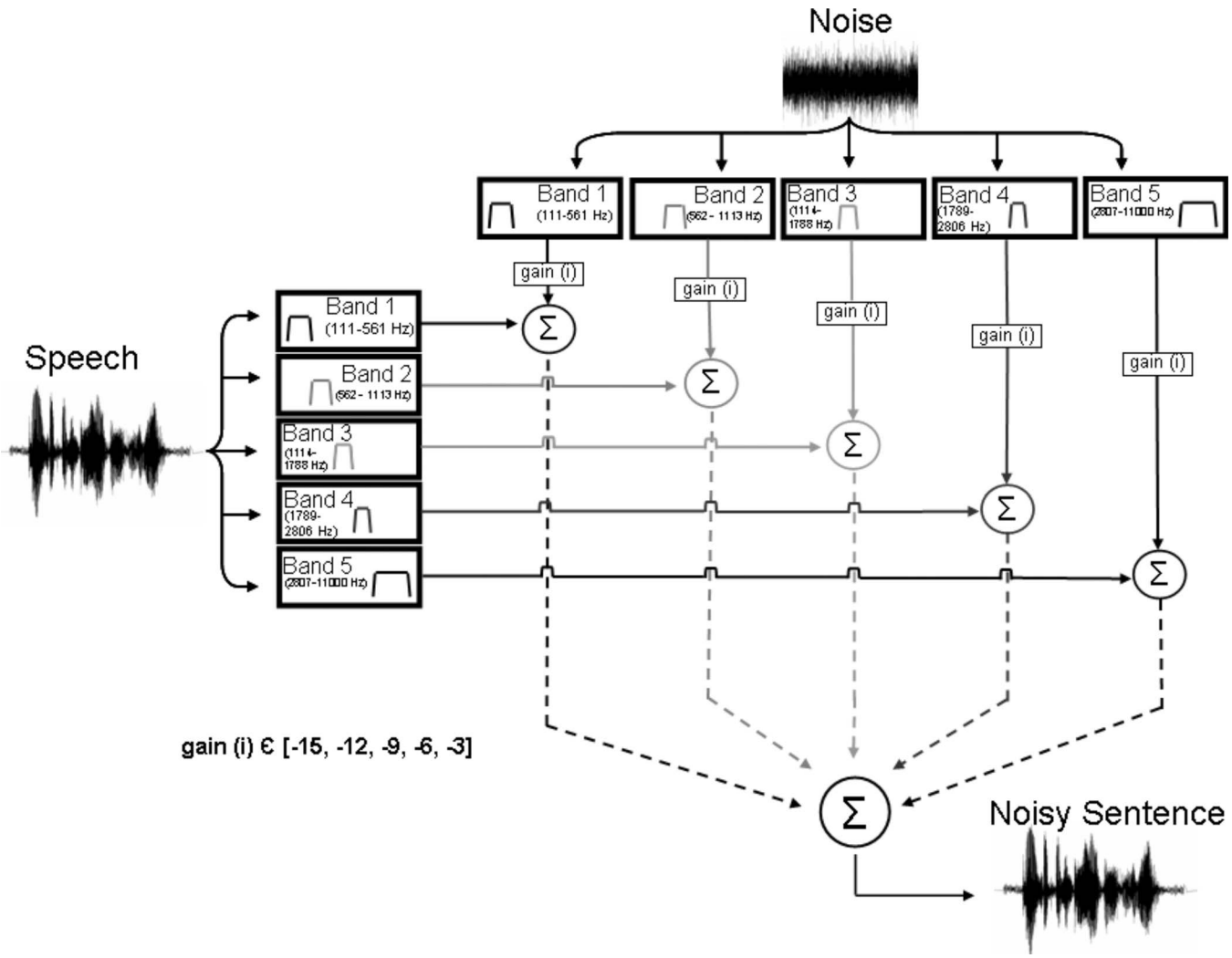

FIG. 1. Schematic illustration of stimulus generation. On each trial the sentence and the spectrally matched noise are filtered into five bandpass filters. The filtered speech and noise are combined at various SNRs chosen from a specified range of SNRs dependent upon the listeners' overall performance score completed during pilot testing (e.g., gain (i) $\varepsilon[-15,-12,-4,-6,-3]$). The same SNR range is used for all five bands. Once all five bands of the speech and noise have been combined, the five passbands are recombined to result in one noisy sentence.

TABLE III. Normalized point-biserial correlations for ten listeners with hearing loss (Experiment I). Boldfaced numbers indicate point-biserial correlations that are significantly different from zero (α=0.05) in a one tailed test. SNR midpoints and overall-percent correct scores are also shown.

Subject	Midpoint	Overall PC	Band 1	Band 2	Band 3	Band 4	Band 5
HI1	2	83.9	0.019	**0.316**	**0.160**	−0.027	**0.478**
HI2	4	80.2	**0.203**	**0.094**	0.072	−0.075	**0.557**
HI3	4	74.7	**0.126**	**0.203**	**0.178**	0.033	**0.460**
HI4	4	81.0	0.053	**0.258**	**0.105**	**0.117**	**0.467**
HI5	4	84.1	0.091	**0.127**	**0.208**	0.066	**0.507**
HI6	3	82.2	**0.215**	**0.197**	0.093	0.009	**0.485**
HI7	−2	77.3	**0.197**	**0.282**	0.033	**0.148**	**0.340**
HI8	3	69.8	**0.212**	**0.226**	−0.010	0.045	**0.507**
HI9	2	77.1	0.063	**0.254**	**0.127**	**0.137**	**0.419**
HI10	2	66.7	0.085	**0.147**	**0.173**	0.063	**0.533**

C. Procedure

Prior to any experimental testing listeners completed the Short Portable Mental Status Questionnaire (Pfeiffer, 1975). Each listener was required to score 100% on the questionnaire to continue participation in the experiments.

Listeners were then seated in a sound-treated double-walled sound booth 1 m in front of a custom-made speaker with a flat-frequency response through 10 000 Hz and were asked to repeat back the sentence they heard. The signal level was controlled by a Crown D-75 amplifier and was adjusted so that the long-term average rms of the stimulus was kept above listeners' audiometric thresholds through 4000 Hz, but did not exceed their LDLs. This was not possible for one listener, and those data are not included. Speech stimuli were presented approximately in the center of each listener's dynamic range (within $\pm$10 dB of center). This was true for all listeners except HI7. The presentation level for HI7 was 15 dB below center and still audible through 6000 Hz. As a result, the range in signal-presentation levels was between 92.0 and 99.8 dB SPL (mean-presentation level=95.9 dB SPL) across listeners.

An examiner outside of the booth scored each listener's verbal responses online. Listeners' responses were also digitally recorded using an Olympus© WS-100 Digital Voice Recorder and were later scored offline to minimize scoring error. Responses that were difficult to hear for the first examiner were noted and reevaluated posttesting by a second examiner using the listeners' digitally recorded responses. On average, 3% of each listener's responses were rescored. To ensure tester reliability, the entire data set for three listeners also was rescored using the digital voice recordings. When a difference in scoring was found, both examiners listened to the recording and a score was agreed upon. This happened in less than 1% of the total trials scored.

Pilot testing was conducted on each listener to determine the specific SNR values needed for a listener's overall intelligibility score to be between 60% and 80% correct on the sentence recognition task. Specifically, 30 sentences were presented to the listener. The initial SNR range was determined based on listeners' audiometric thresholds. The listeners' responses to these sentences were scored. If the listeners' performance was too high, the SNR range was made more difficult; if performance was too poor, the SNR range was made easier. The SNR range was always 13 dB, which included 5 SNR values with a 3 dB resolution. The midpoint of the SNR range was adjusted for each listener based on each listener's overall recognition score during pilot testing and was the same for all five bands. For example, for one listener the SNRs for all five bands included [−4, −1,2,5,8], with a midpoint of 2 dB, which resulted in a 77.1% score; whereas for another listener the SNRs for all five bands included [−2,1,4,7,10], with a midpoint of 4 dB, which resulted in a 74.4% score. Once the SNR midpoint was determined, spectral-weighting strategies were computed based on a total of 600 sentences (600 sentences $\times$5 key words=3000 key words) randomly presented to each listener. Testing was completed in two 2 h listening sessions.

D. Analysis

A data file for each subject was updated on each trial with the sentence played, the SNR for each of the five bands and the listener's scores for the five key words in each sentence (correct=1, incorrect=0). Weighting strategies were calculated using a point-biserial correlation between a listener's responses (1=correct, 0=correct) and the SNR within a given spectral band in each trial. That is, if a listener (consistently) performed well when the SNR was favorable in band 2 and poorly when the SNR was poor, then the correlation, or the weight of band 2 would be high. For each listener, point-biserial correlations were computed for each of the five spectral bands. The five correlations were normalized to sum to one for ease of comparing weighting strategies across listeners. Normalization was conducted by summing the absolute value of all five spectral bands' correlations and dividing the correlation for each band into the total sum of the five bands' correlations. A plot of the normalized correlations is referred to as a "relative" weighting strategy.

III. RESULTS: EXPERIMENT I, WITHOUT HEARING AIDS

Normalized point-biserial correlation coefficients for the five spectral bands are shown in Table III along with the SNR midpoints that were used for testing. SNR midpoints

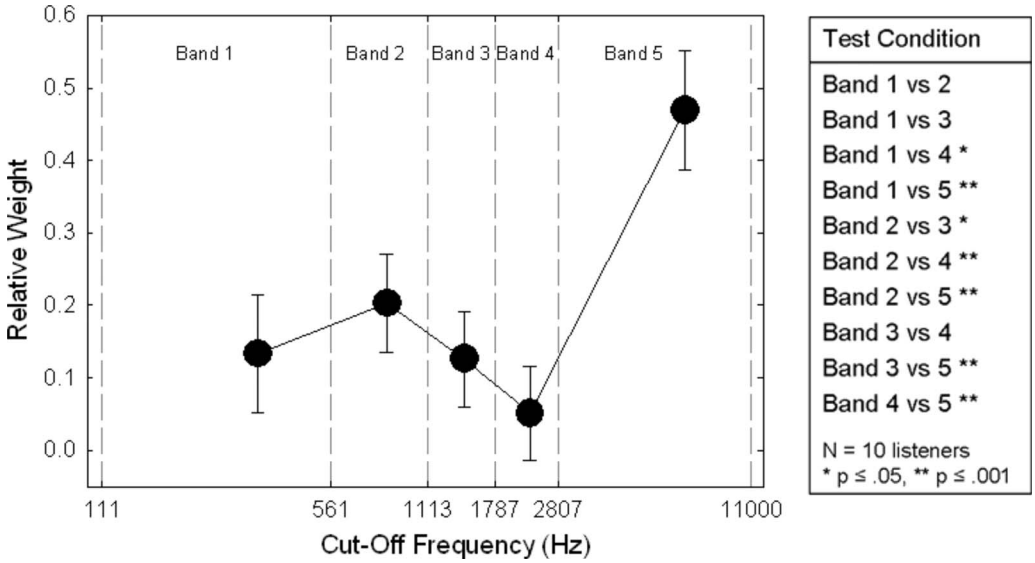

FIG. 2. Average normalized-weighting strategies for sentences for ten listeners with hearing loss. Data points represent average normalized correlation coefficients for each of the five spectral bands for Experiment I. Error bars represent one standard deviation from the mean. The cutoff frequencies used for each of the spectral bands are designated by the dashed-vertical lines. Statistical comparisons between the weights on each band are depicted in the table shown to the right.

varied from −2 to 4 dB, generating performance scores between 66.7% and 84.1% correct. Seventy-two percent of the raw correlations were significantly different from zero ($\alpha = 0.05$) in a one tailed test. Averaged normalized weighting strategies for sentence stimuli are shown in Fig. 2. Regression analyses, testing the equality of the regression coefficients with a dichotomous variable (Chiswick and Chiswick, 1975), indicated that the weight on band 5 was significantly greater than the weight on all other bands (p values <0.0001). The weight on band 2 was significantly greater than the weight on bands 3 and 4 (p values, 0.0033 and <0.0001, respectively), but not significantly different from band 1 (p value=0.258). A statistical comparison of the weights obtained between pairs of spectral bands is reported in the table to the right of Fig. 2.

Two listeners were tested twice several months apart to determine if their weighting strategies were consistent across time. One listener (HI3) was tested with 3 months between test sessions, while the other listener (HI11) was tested with 6 months between test sessions. The weighting strategies and overall percent correct scores were similar across test sessions for both listeners. Also, to determine the stability of weighting strategies across *test days*, weighting strategies were computed for all listeners based only on the sentences presented on one specific day. On average, listeners completed 325 of the 600 sentences in the first session and completed the remaining sentences in the second test session. The two test sessions were never more than 1 week apart. Regression analyses indicated no significant differences between the listeners' weights on any of the five spectral bands across the two test days (p values ranging from 0.2832 to 0.9102).

The spectral weighting strategies for listeners with hearing loss presented in the current study were compared to those reported for normal-hearing listeners reported in an earlier study (Calandruccio and Doherty, 2007). Regression analyses indicated that normal-hearing listeners weighted the spectral information within bands 2 and 4 (562–1113 and 1789–2806 Hz, respectively) greater (p values=0.0005, <0.0001) than listeners with hearing loss, but weighted band 5 (2807–11 000 Hz) less (p value <0.0001). No significant differences in weights were observed for bands 1 and 3 across the two groups of listeners (p values=0.1671, 0.8319).

IV. METHODS: EXPERIMENT II, WITH HEARING AIDS

A. Subjects

The same ten listeners who participated in Experiment I also participated in Experiment II. These listeners were all experienced (at least 6 months) bilateral hearing aid users. Eight of the ten listeners wore digital WDRC hearing aids, and the remaining two listeners wore programmable analog WDRC hearing aids.

B. Stimuli

The stimuli were the same Harvard/IEEE sentences as those used in Experiment I. Also, the generation of the stimuli was identical to that of Experiment I. Sentences were presented to the listeners while wearing hearing aids at a fixed level of 75 dB SPL. An illustration of the average presentation level of the speech for both experimental conditions with respect to the average audiometric thresholds of the ten listeners is shown in Fig. 3.

C. Procedure

A period of 6 months passed between experimental test sessions (with and without hearing aids). Listeners were fit binaurally with digital behind-the-ear Starkey Destiny 1200© hearing aids. The hearing aids were programmed for each listener using NOAH™, a commonly used hearing aid

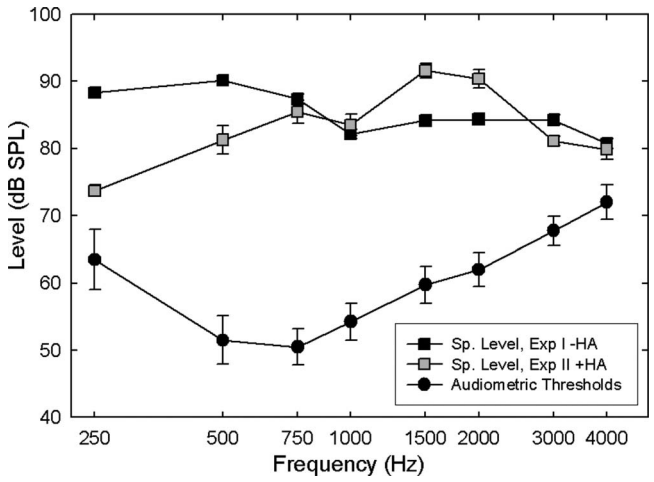

FIG. 3. Average presentation levels for the speech stimuli for Experiment I and Experiment II. Average audiometric thresholds for ten listeners with hearing loss. Error bars represent one standard error from the mean. (The noise used is not illustrated here. All listeners had the same 13 dB wide range of SNRs; the midpoint of those SNRs changed however, based on listeners performance.)

fitting software system. Gain was prescribed using the NAL-R [National Acoustics Laboratories, Australia (Byrne and Dillon, 1986)] fitting algorithm. To eliminate confounding effects of compression across trials, hearing aids were set in a linear mode (compression ratio=1.0). All circuit features and directional characteristics were either turned off or disabled. Hearing aids were coupled to the listeners' ears via custom made Lucite™, full-shell earmolds with a select-a-vent pinhole vent. An electroacoustic evaluation of the hearing aids was performed before each test session for every listener using an AudioScan Verifit (VF-1) system. All hearing aids met the ANSI (1996) standards. Real-ear insertion gain targets for each subject were within ±10 dB from the prescribed NAL-R targets at 250–6000 Hz (Humes *et al.*, 2004). Prescriptive NAL-R targets, insertion gains, and deviations from the targets for each listener are shown in Table IV.

Pilot testing was performed to determine the appropriate SNR needed to obtain overall-percent correct score between 60% and 80% correct while wearing hearing aids. After the appropriate SNR range was determined the same experimental procedure and analyses that were used in Experiment I were employed in Experiment II. That is, weighting strate-

TABLE IV. NAL-R prescriptive targets and insertion gain values for ten listeners. Target gains are represented by (T). Insertion gain values are represented by (IG). Deviations from the target gains (IG-T) are represented by (D).

Listener		0.25	0.50	0.75	1.0	1.5	2.0	3.0	4.0	6.0 (kHz)
HI1	(T)	0	7	15	21	21	19	18	23	30
	(IG)	5	4	15	23	24	28	18	17	25
	(D)	5	−3	0	2	3	9	0	−6	−5
HI2	(T)	1	10	16	22	23	23	22	22	25
	(IG)	1	3	19	26	24	27	14	15	18
	(D)	0	−7	3	4	1	4	−8	−7	−7
HI3	(T)	2	11	17	21	21	18	22	23	25
	(IG)	2	10	20	18	30	22	18	23	19
	(D)	0	−1	3	−3	9	4	−4	0	−6
HI4	(T)	10	14	20	25	28	27	27	28	28
	(IG)	4	6	14	22	22	27	18	19	19
	(D)	−6	−8	−6	−3	−6	0	−9	−9	−9
HI5	(T)	0	12	22	28	28	26	26	26	29
	(IG)	6	19	24	22	29	27	16	19	25
	(D)	6	7	2	−6	1	1	−10	−7	−4
HI6	(T)	0	8	14	20	23	24	25	26	25
	(IG)	4	5	12	12	22	21	15	17	27
	(D)	4	−3	−2	−8	−1	−3	−10	−9	2
HI7	(T)	0	1	8	15	18	17	18	20	24
	(IG)	1	3	7	13	28	26	14	15	19
	(D)	1	2	−1	−2	10	9	−4	−5	−5
HI8	(T)	3	15	20	24	24	22	22	23	30
	(IG)	5	18	23	25	31	32	14	15	29
	(D)	2	3	3	1	7	10	−8	−8	−1
HI9	(T)	2	11	17	21	21	19	19	20	22
	(IG)	8	18	18	23	28	19	17	29	29
	(D)	6	7	1	2	7	0	−2	9	7
HI10	(T)	4	13	19	24	24	22	21	21	21
	(IG)	5	15	19	18	25	20	14	15	21
	(D)	1	2	0	−6	1	−2	−7	−6	0
Average	(T)	2.2	10.2	16.8	22.1	123.1	21.7	22	23.2	25.9
	(IG)	4.1	10.1	17.1	20.2	26.3	24.9	15.8	18.4	23.1
	(D)	1.9	−0.1	0.3	−1.9	3.2	3.2	−6.2	−4.8	−2.8

TABLE V. Estimated sensation levels (dB SL) for bands 1–5 for ten listeners with hearing loss for both experimental conditions.

	Exp I band 1		Exp II band 1		Exp I band 2		Exp II band 2		Exp I band 3	Exp II band 3	Exp I band 4	Exp II band 4	Exp I band 5		Exp II band 5	
Listener	0.25	0.50	0.25	0.50	0.75	1.0	0.75	1.0	1.5	1.5	2.0	2.0	3.0	4.0	3.0	4.0 (kHz)
HI1	37.4	47.7	23.1	31.7	44.4	30.7	39.4	34.0	27.7	31.7	31.4	39.4	28.8	9.8	27.1	7.1
HI2	26.9	42.2	8.4	26.0	38.9	30.2	38.4	36.4	27.2	31.4	20.9	28.7	18.3	14.3	12.5	9.5
HI3	21.4	36.7	4.7	27.4	33.4	29.7	34.1	29.0	21.7	33.0	30.4	33.4	17.8	8.8	17.3	13.1
HI4	5.4	35.7	−4.3	18.7	37.4	28.7	28.1	28.0	20.7	20.0	14.4	18.4	16.8	2.8	12.1	0.5
HI5	47.4	37.7	33.7	36.7	24.4	15.7	28.7	18.4	17.7	27.4	16.4	24.1	8.8	9.8	4.8	9.1
HI6	26.9	47.2	11.1	32.7	43.9	35.2	36.4	27.4	27.2	29.7	15.9	17.7	3.3	0.7	2.9	1.5
HI7	47.4	57.7	33.4	45.7	49.4	40.7	41.1	38.4	37.7	50.7	26.4	37.7	18.8	9.8	17.7	8.5
HI8	19.4	24.7	7.1	25.4	36.4	22.7	42.7	30.7	24.7	39.0	23.4	38.4	20.8	11.8	17.5	9.5
HI9	18.4	33.7	12.4	35.7	30.4	26.7	32.4	33.7	33.7	45.7	27.4	30.1	24.8	15.8	26.1	28.8
HI10	17.4	32.7	2.4	27.7	34.4	25.7	33.1	24.0	27.7	32.4	26.4	26.1	28.8	19.8	22.8	14.8

gies were based on a total of 600 sentences (3000 total key words). Overall-presentation levels were recorded with each listener's right hearing aid connected to a digital Bruel and Kjaer sound level meter with a 1/3 octave filter via a 2 cc coupler. Levels were measured using a speech-shaped noise generated in MATLAB that had an average magnitude equal to the speech signals used in these experiments. The right hearing aid alone was used to simplify the calculations; however, since listeners had symmetrical hearing losses either hearing aid could have been used. A 2 cc coupler to free-field conversion was used to account for coupler differences (Bentler and Pavlovic, 1989). Overall-presentation levels ranged between 87.2 and 97.0 dB SPL (average presentation level =93.9 dB SPL) for the ten listeners.

D. Comparison of sensation levels

One goal of this paper was to assess the effect of hearing aids on a listener's spectral-weighting strategies. To do so, it was necessary to determine differences in sensation levels (SLs) between the listening conditions in Experiment I and Experiment II. SLs were *estimated* for each listener for the five spectral bands. These estimated SLs were never used to compare the SL across bands, rather they were simply used to compare SLs within each spectral band across experimental conditions.

A Bruel and Kjaer sound-level meter with 20 1/3 octave bands between 125 and 10 000 Hz was used to measure the level of the speech. The 1/3 octave band measurements that fell within the bandwidth of one of the five spectral bands and approximately corresponded to one of the audiometric test frequencies were selected to estimate the SL within a given band. These 1/3 octave bands were centered at 250 and 500 Hz for band 1, 750 and 1000 Hz for band 2, 1500 Hz for band 3, 2000 Hz for band 4, and 3000 and 4000 Hz for band 5. Bands 1, 2, and 5 have two corresponding 1/3 octave bands and bands 3 and 4 only have one because the bandwidths of the five spectral bands were different. It was assumed that the reference equivalent threshold SPL for 1/3 octave band noise was equal to audiometric pure-tone thresholds in listeners with hearing loss (Cox and McDaniel, 1986). Since this method was not able to provide exact measurements of the total sensation level within each band, these estimates were only used to compare across experimental conditions and *not* across bands. Speech presentation levels were compared to listeners' audiometric thresholds at approximately the same frequencies. To account for natural resonances of the ear, average adult real-ear unaided gain (REUG) values were incorporated into all SL calculations (Dillon, 2001). Specifically, dB SL was determined using the following equation: $\text{dB SL}_{(-\text{HA})} = (\text{Speech presentation level}_{\text{freq}(x)} + \text{REUG}_{\text{freq}(x)}) - \text{HTL}_{\text{SPL}}$, where REUG is the real ear unaided gain, and HTL is the hearing threshold in dB SPL, see Table V.

SLs were estimated for the listening condition in Experiment II using the same technique as the one described for computing SLs for the listening condition in Experiment I, except the real-ear aided-gain (REAG) values recorded using the AudioScan Verifit at the same test frequencies (i.e., 250, 500, 750, 1000, 1500, 2000, 3000, and 4000 Hz) were added to the SL values. Thus, $\text{dB SL}_{(+\text{HA})} = (\text{Speech presentation level}_{\text{freq}(x)} + \text{REAG}_{\text{freq}(x)}) - \text{HTL}_{\text{SPL}}$; see (Table V).

V. RESULTS: EXPERIMENT II, WITH HEARING AIDS

Normalized point-biserial correlation coefficients for five spectral bands are shown in Table VI along with the SNR midpoints used for testing and the overall percent correct scores. Overall percent correct scores ranged between 61.5% and 80.5%. Average normalized weights are shown in Fig. 4. Eighty percent of the weights were significantly different from zero (α=0.05). Regression analyses, testing the equality of the regression coefficients with a dichotomous variable, indicated that while wearing hearing aids, listeners placed the greatest weight (p values ranging from 0.0008–$<$0.0001) on the spectral information within band 5 (2807–11 000 Hz). Also, the weight placed on band 2 (562–1113 Hz) was significantly greater than the weight placed on bands 1, 3, and 4 (p values ranging from 0.0409–$<$0.0001). Bands 1, 3, and 4 were not weighted significantly different from each other (p values ranging from 0.1569 to 0.8329).

TABLE VI. Normalized point-biserial correlations for five spectral bands while wearing hearing aids (Experiment II). Boldfaced numbers indicate point-biserial correlations that were significantly different from zero (α =0.05) in a one-tailed test. SNR midpoints and overall-percent correct scores are also shown.

Subject	Midpoint	Overall PC	Band 1	Band 2	Band 3	Band 4	Band 5
HI1	−2	70.1	**0.152**	**0.306**	**0.187**	0.044	**0.312**
HI2	2	69.7	0.058	**0.252**	**0.205**	**0.091**	**0.393**
HI3	2	72.4	0.086	**0.219**	**0.246**	0.082	**0.366**
HI4	4	80.2	0.032	**0.212**	**0.247**	0.083	**0.425**
HI5	1	80.5	**0.252**	**0.241**	**0.097**	−0.038	**0.372**
HI6	0	75.0	**0.224**	**0.205**	**0.158**	0.037	**0.376**
HI7	−3	74.9	**0.237**	**0.212**	0.057	**0.242**	**0.252**
HI8	3	67.2	**0.239**	**0.181**	**0.111**	**0.096**	**0.373**
HI9	1	61.5	0.067	**0.338**	0.048	**0.193**	**0.353**
HI10	1	65.7	0.002	0.333	0.064	**0.101**	**0.499**

Average weighting strategies for the ten listeners were compared across Experiments I and II (Fig. 5) and to average weighting strategy data for normal-hearing listeners (Calandruccio and Doherty, 2007). Regression analyses testing the equality of the regression coefficients indicated that there were no significant differences in weights obtained for bands 1–4 between Experiments I and II (p values ranging from 0.1850 to 0.8271). However, the weight on band 5 for Experiment I (without hearing aids) was significantly greater than the weight on band 5 for Experiment II [with hearing aids (p value=0.0018)]. Normal-hearing listeners placed significantly greater weight on band 4 1789–2806 Hz (p value=0.0244)] in comparison to hearing-impaired listeners while wearing hearing aids, however, no significant differences in weights were observed for bands 1, 2, 3, and 5 (p values ranging from 0.0692 to 0.9518).

A comparison of SLs between Experiments I and II is shown in Fig. 6. Although the weight on band 5 was significantly different between experimental conditions, a one-way analysis of variance indicated the SLs were only significantly different in bands 1, 3, and 4 (p values ranging from 0.0244 to 0.0443), and not in bands 2 and 5 (p values =0.4222, 0.9657).

VI. DISCUSSION

Spectral-weighting strategies for sentences were obtained for ten hearing-impaired listeners. Listeners were tested in two experimental conditions. In the first condition (Experiment I) listeners were presented noisy speech via a loudspeaker in a sound field. An amplifier was used to provide the appropriate gain to amplify the noisy speech. In the second condition (Experiment II) listeners were fit with linear hearing aids. Again, listeners were presented noisy speech via a loudspeaker in a sound field, however, the hearing aids the listeners wore provided the appropriate gain to amplify the speech. Listeners with hearing loss, whether they were fit with hearing aids or not, always weighted the highest frequency band, band 5 (2807–11 000 Hz), the greatest. However, the weight on band 5 was significantly greater

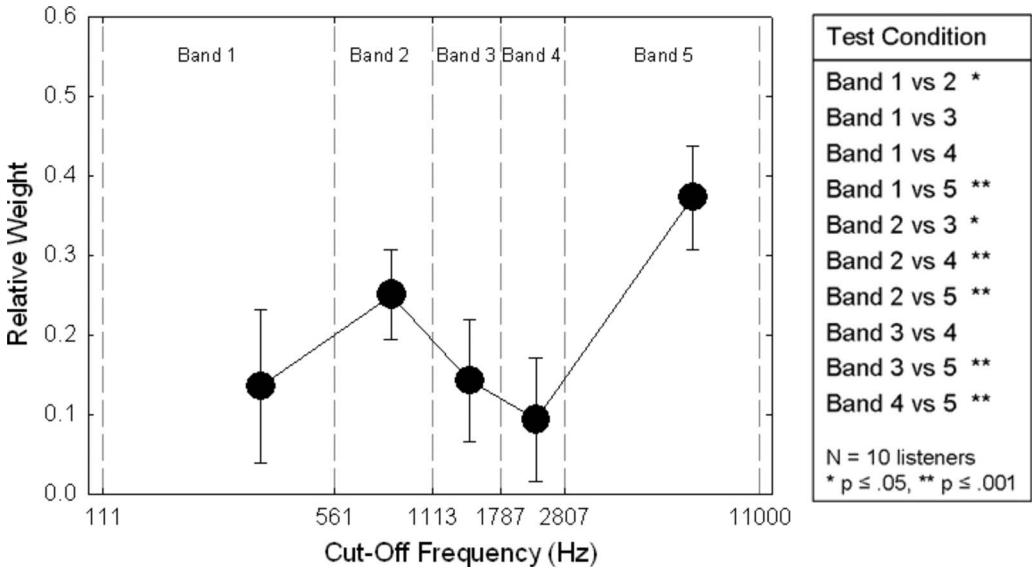

FIG. 4. Average normalized weighting strategies for sentences while wearing hearing aids. Data points represent the average normalized correlation coefficients for each of the five spectral bands for Experiment II. Statistical comparisons between the weights on each band are depicted in the table shown to the right.

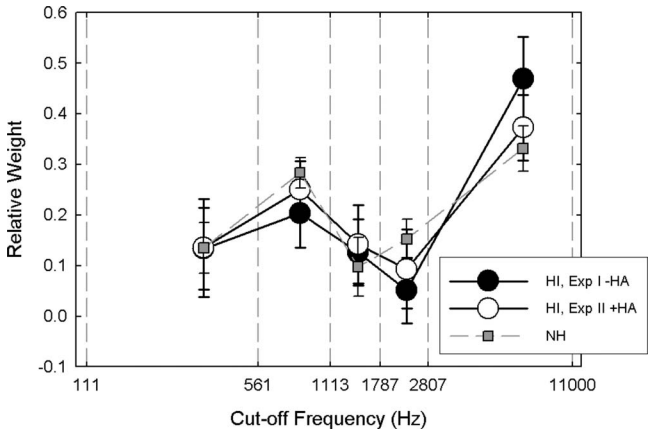

FIG. 5. Mean normalized weighting strategies from Experiments I (closed circles) and II (open circles). Error bars represent one standard deviation from the mean. Normal-hearing data taken from Calandruccio and Doherty (2007).

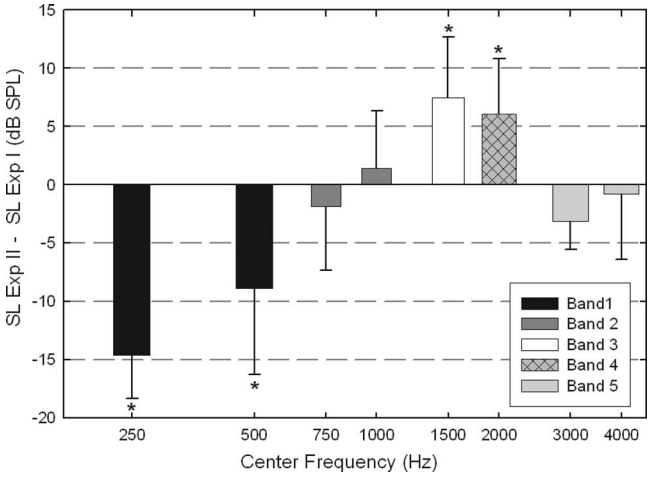

FIG. 6. Sensation level differences for the five bands for Experiments I and II. One-third octave bands centered at 250 and 500 Hz, 750 and 1000 Hz, 1500, 2000, 3000, and 4000 Hz, represent bands 1–5, respectively. An asterisk indicates a significant difference (α=0.05) between the aided and unaided condition within bands.

when listeners were not wearing hearing aids than the weight on band 5 while they were wearing hearing aids.

The tasks in this study required data collection over several days. One concern was that a listener's weighting strategy may change over time. Kordas (1999) measured spectral weighting strategies for nonsense syllables every 2 weeks over a 6 week period and reported that listeners' weighting strategies changed across test sessions. In the present study, it was critical for listeners' strategies to remain stable across test sessions for two reasons. First, none of the listeners were able to complete all 600 sentence trials in one test session. Therefore, listeners required two 2 h test sessions to complete one experimental condition, which were always completed within 1 week. Second, to make comparisons between the two experimental conditions, it was imperative to ensure that weighting strategies were not changing over time. Two listeners (HI3 and HI11) were tested across longer periods of time. Both listeners' weighting strategies remained consistent with a 3 month (HI3) and 6 month (HI11) time gap between test sessions.

A confounding factor of conducting sentence recognition tasks is the limited number of sentences. There are 720 Harvard/IEEE sentences. However, 600 trials were completed for each experimental condition. Therefore, listeners were presented the same 600 sentences during both experimental procedures. To reduce the potential of listeners learning the sentences, a time period of 6 months always passed between experiments. Two listeners (HI4 and HI8) were tested using the same SNR range in both experimental conditions, yet their recognition scores hardly changed (see Tables III and IV). Thus, it is unlikely that these listeners remembered the sentences they heard during the first experiment. Recall that the sentences presented to the listeners are very noisy, and often listeners do not hear all five key words in each sentence. Therefore, due to the time interval between experimental sessions and the noise within the sentences, it appears that listeners did not learn the sentences they heard.

Sensation levels were estimated for each band in Experiments I and II. These measurements were considered an "estimate" because the entire rms of each speech spectral band was not computed in these measurements. Instead it was based on the energy of specific frequencies within each band. This method was adequate to determine if differences in the SL *between* the experimental conditions accounted for the listeners' weighting strategies. The SL in three of the bands (1, 3, and 4) was significantly different between the two conditions, but the SL in the other two bands, 2 and 5, did not differ significantly across the two experimental conditions. Given that band 5 was the only band weighted significantly different between the two conditions it suggests the SL between the two conditions did not account for differences in the weighting strategies. In fact, the SL in band 5 was small for both listening conditions. In Experiment I the stimuli were unshaped and were presented below the listeners' LDLs, thus the SL in the high frequency region, in which listeners thresholds were most severe, was limited. In Experiment II SL was limited in the high frequencies due to limitations in providing high-frequency gains via the hearing aids as well as the small amount of prescribed gain at those frequencies. Similar results were reported by Leibold *et al.* (2006) on a level-discrimination task. Low- and high-pass noise maskers were used to manipulate the SLs across frequencies. They showed that listeners' weighting strategies were affected primarily by overall presentation level, not sensation level.

Overall presentation level was the main difference between the data presented here and the data reported for normal-hearing listeners (Calandruccio and Doherty, 2007). The differences in presentation levels need to be given great consideration when comparing the data between normal-hearing and hearing-impaired listeners (see Fig. 5). Kortekaas *et al.* (2003), Leibold *et al.* (2006), and Lentz (2007) all report increases in spectral weights for high frequencies with increases in presentation level. All of these data were reported for normal-hearing listeners for nonspeech auditory tasks. However, similar results, in which higher frequency

information received greater weight as presentation level increased for speech recognition tasks, have also been reported (Calandruccio, 2007).

The two major qualitative differences observed between the weighting strategies obtained for listeners with hearing loss and normal-hearing listeners occurred in bands 2 and 5. Based on the cutoff frequencies of the bandpass filters, band 2 contains a great amount of formant frequency information; whereas band 5 contains consonant cues, such as place of articulation. Previous research has shown that hearing-impaired listeners use formant information and place of articulation information differently than normal-hearing listeners (e.g., Turner and Brus, 2001; Dorman *et al.*, 1985; Hedrick *et al.*, 1995). Hedrick *et al.* (1995) reported that some hearing-impaired listeners are not able to make use of formant transition cues. These results are in agreement with the data reported in Fig. 5, where the hearing-impaired listeners (when not fit with hearing aids) weight band 2 less than normal-hearing listeners. Perhaps, since listeners with hearing loss do not use this information "like" normal-hearing listeners (i.e., they use different strategies, combine acoustic cues differently), their weighting strategies are less effective and thus may account for the poorer speech recognition scores obtained by the listeners with hearing loss. It is interesting that in Experiment II hearing aids appeared to permit the hearing-impaired listeners to use spectral information in sentences more similarly to normal-hearing listeners. In fact, the only difference between the weighting strategies used by normal-hearing listeners compared to the results in Experiment II is that normal-hearing listeners weighted band 4 significantly greater than hearing-impaired listeners. Further research is needed to evaluate whether differences in weighting strategies for speech between normal-hearing and hearing-impaired listeners are due to hearing status, presentation level, or hearing aid use.

In this study listeners were fit binaurally with linear hearing aids. It is possible that if listeners wore compression hearing aids their weighting strategies may have changed as a result of low audibility speech. For example, certain spectral features that may be audible to the listener with linear hearing aids may become louder once compression circuitry is used. This might allow the listeners to improve their recognition scores, or take advantage of different spectral cues. However, since SL did not appear to account for differences in listeners' weighting strategies it is difficult to speculate these results. Further research is needed to determine how compression, and other hearing aid features (e.g., attack and release times, noise reduction algorithms, etc.) would affect the listeners' weighting strategies.

The data from Experiments I and II lend support to the idea that listeners with hearing loss (if the speech is made audible to the listeners either through hearing aids or via an external amplifier) are able to make use of high frequency information to perform a sentence recognition task when listening in noise. Hornsby and Ricketts (2003, 2006) investigated the effect of low- and high-frequency spectral information on listeners' sentence-recognition performance in noise. All listeners, regardless of hearing loss configuration, benefited from the addition of high- and low-frequency information. Plyler and Fleck (2006) also examined the effects of high-frequency audibility on listeners with various degrees of symmetrical high-frequency hearing loss when listening through a commercially available hearing aid. Having the additional high-frequency amplification did not benefit listeners in quiet. However, listeners' speech recognition scores were significantly better when high-frequency amplification was provided to the listeners when tested in *noise*. The data reported here, based on the results of Experiments I and II, add additional proof to the growing body of research that implies that high frequencies cannot be discarded for hearing-impaired listeners when performing sentence recognition tasks. The previously reported data that are in agreement with this argument (Hornsby and Ricketts, 2003, 2006; Turner and Henry, 2002; Plyler and Fleck, 2006) all tested listeners in a fixed SNR condition. Therefore, it is hard to determine whether or not different levels of noise would have affected listeners' scores in these previous experiments in a more adverse or in a more favorable manner.

In the current study, five different SNRs were used across trials and across spectral bands. Thus, conclusions can be inferred about different noise levels and how they affect specific spectral information. For example, when listening at more favorable SNRs, listeners are able to use high frequency information (band 5) more than the lower frequency information presented by the other four spectral bands. That is, average performance at the listeners' most favorable SNR was approximately 80% correct for bands 1–4. However, average performance for band 5 was approximately 90% correct. This being said, when high frequency information is competing with very difficult SNRs, listeners with hearing loss may be more susceptible to masking in the high frequencies (band 5) in comparison to the other four spectral bands. Average performance at the most difficult SNR was approximately 62% correct while performance for the other four bands ranged between 70% and 75% correct with the same level of SNR difficulty. Pilot psychometric function data that were also collected in our lab using broader SNR ranges (up to 25 dB wide) indicated that the range of noise that was used to degrade the speech stimulus in these experiments was adequate for all five bands.

It is difficult to explain the differences observed between the weighting strategies in Experiments I and II. However, it should be noted that weights for these two listening conditions were significantly different only in band 5, where significantly less weight for band 5 was observed while the listeners performed the task with hearing aids.

Interestingly, the greater weight on band 5 for Experiment I did not relate to a decrease in weight on any one specific band, but rather was evenly distributed across bands 2, 3, and 4. Throughout these experiments listeners' raw correlations were normalized to sum to one, which has been referred to as a listener's relative weighting strategy. Therefore, in the unaided condition, the high weight on band 5 is relatively much higher than the other four bands compared to the aided condition. The high weight on band 5 may be

excessive in that listeners do not weight the spectral information in the other bands enough, which could have a negative impact on the listeners' overall performance scores.

VII. CONCLUSIONS

Hearing-impaired listeners weight high frequency information (2807–11 000 Hz) relatively the greatest when performing a sentence recognition task. However, it is unclear if the use of this information is beneficial to the listeners' performance. Unfortunately, the bandwidth of band 5 in these experiments is quite broad and therefore, it is impossible to determine if the entire band or just portions of the band were important for sentence recognition. Further studies are needed to (1) examine spectral-weighting strategies using narrower bands to obtain finer spectral resolution (especially in the high frequencies), and (2) to identify the most efficient weighting strategy to perform sentence recognition tasks.

ACKNOWLEDGMENTS

This work was supported in part by the ASHFoundation Student Audiology Research Grant awarded to L.C. and the Jerome R. and Arlene L. Gerber Fund. The authors would like to thank Dr. Brent Edwards and Dr. Tim Trine at Starkey Corporation for providing the hearing aids used for testing. These data have also been published by L.C. as part of her requirement for her dissertation at Syracuse University. Many thanks to Dr. Laurel Carney, Dr. Kathy Vander Werff, and especially Dr. Larry Humes for helpful comments while writing this manuscript. Comments from three anonymous reviewers and Dr. Paul Iverson, the associate editor, have tremendously strengthened this manuscript.

American National Standards Institute (ANSI 53.5). (**1969**). "American National Standards methods for the calculation of the articulation index," New York.

American National Standards Institute (ANSI). (**1996**). "American National Standard specifications for audiometers," ANSI S3.6-1996, New York.

American National Standards Institute (ANSI). (**1997**). "American National Standard methods for the calculation of the speech intelligibility index," ANSI S3.5-1997. New York.

American National Standards Institute (ANSI). (**2004**). "American National Standard specifications for audiometers," ANSI S3.6-2004, New York.

Apoux, F., and Bacon, S. P. (**2004**). "Relative importance of temporal information in various frequency regions for consonant identification in quiet and in noise," J. Acoust. Soc. Am. **116**, 1671–1680.

Bell, T. S., Dirks, D. D., and Trine, T. D. (**1992**). "Frequency-importance functions for words in high- and low-context sentences," J. Speech Hear. Res. **35**, 950–959.

Bentler, R. A., and Nelson, J. A. (**2001**). "Effect of spectral shaping and content on loudness discomfort," J. Am. Acad. Audiol **12**, 462–470.

Bentler, R. A., and Pavlovic, C. V. (**1989**). "Transfer functions and correction factors used in hearing aid evaluation and research," Ear Hear. **10**, 58–63.

Byrne, D., and Dillon, H. (**1986**). "The National Acoustic Laboratories' (NAL) new procedure for selecting the gain and frequency response of a hearing aid," Ear Hear. **7**, 257–265.

Calandruccio, L. (**2007**). "Spectral weighting strategies for sentences measured by a correlational method," Doctoral dissertation, Syracuse University, Syracuse, NY.

Calandruccio, L., and Doherty, K. (**2007**). "Spectral weighting strategies for sentences measured by a correlational method," J. Acoust. Soc. Am. **121**, 3827–3836.

Chiswick, B. R., and Chiswick, S. J. (**1975**). *Statistics and Econometrics—A Problem Solving Text* (University Park Press, London).

Cox, R. M., Alexander, G. C., and Gilmore, C. (**1987**). "Development of the Connected Speech Test (CST)," Ear Hear. **8**, 119S–126S.

Cox, R. M., and McDaniel, D. M. (**1986**). "Reference equivalent threshold levels for pure tones and 1/3-oct noise bands: Insert earphone and TDH-49 earphone," J. Acoust. Soc. Am. **79**, 443–446.

Dillon, H. (**2001**). *Hearing Aids* (Thieme, New York).

Doherty, K. A., and Lutfi, R. A. (**1996**). "Spectral weights for overall level discrimination in listeners with sensorineural hearing loss," J. Acoust. Soc. Am. **99**, 1053–1058.

Doherty, K. A., and Lutfi, R. A. (**1999**). "Level discrimination of single tones in a multitone complex by normal-hearing and hearing-impaired listeners," J. Acoust. Soc. Am. **105**, 1831–1840.

Doherty, K. A., and Turner, C. W. (**1996**). "Use of a correlational method to estimate a listener's weighting function for speech," J. Acoust. Soc. Am. **100**, 3769–3773.

Dorman, M. F., Lindholm, J. M., and Hannley, M. T. (**1985**). "Influence of the first formant on the recognition of voiced stop consonants by hearing-impaired listeners," J. Speech Hear. Res. **28**, 377–380.

Fletcher, H., and Galt, R. H. (**1950**). "The perception of speech and its relation to telephony," J. Acoust. Soc. Am. **22**, 89–150.

French, N. R., and Steinberg, J. C. (**1947**). "Factors governing the intelligibility of speech sounds," J. Acoust. Soc. Am. **19**, 90–119.

Galvin, J. J. III, and Fu, Q. J. (**2003**). "IEEE Subcommittee on Subjective Measurements (1969)," Recorded at House Ear Institute, Los Angeles, CA.

Hedrick, M. S., Schulte, L., and Jesteadt, W. (**1995**). "Effect of relative and overall amplitude on perception of voiceless stop consonants by listeners with normal and impaired hearing," J. Acoust. Soc. Am. **98**, 1292–1303.

Hornsby, B. W., and Ricketts, T. A. (**2006**). "The effects of hearing loss on the contribution of high- and low-frequency speech information to speech understanding. II. Sloping hearing loss," J. Acoust. Soc. Am. **119**, 1752–1763.

Hornsby, B. W. Y., and Ricketts, T. A. (**2003**). "The effects of hearing loss on the contribution of high- and low-frequency speech information to speech understanding," J. Acoust. Soc. Am. **113**, 1706–1717.

Humes, L. E., Humes, L. E., and Wilson, D. L. (**2004**). "A comparison of single-channel linear amplification and two-channel wide-dynamic range compression amplification by means of an independent-group design," American Journal of Audiology **13**, 39–53.

IEEE Subcommittee on Subjective Measurements (**1969**). "IEEE recommended practices for speech quality measurements," IEEE Trans. Audio Electroacoust. **17**, 227–246.

Kalikow, D., Stevens, K., and Elliott, L. (**1977**). "Development of a test of speech intelligibility in noise using sentence materials with controlled word predictability," J. Acoust. Soc. Am. **61**, 1337–1351.

Kordas, T. (**1999**). "The relationship between hearing aid benefit and the use of spectral information in speech," Masters thesis, Syracuse University, Syracuse, NY.

Kortekaas, R., Buus, S., and Florentine, M. (**2003**). "Perceptual weights in auditory level discrimination," J. Acoust. Soc. Am. **113**, 3306–3322.

Leibold, L., Tan, H., and Jesteadt, W. (**2006**). "Spectral weights for level discrimination in quiet and in noise," Association for Research in Otolaryngology, Mid-Winter Meeting, Baltimore, MD.

Lentz, J. J. (**2007**). "Variation in spectral-shape discrimination weighting functions at different stimulus levels and signal strengths," J. Acoust. Soc. Am. **122**, 1702–1712.

Lentz, J. J., and Leek, M. R. (**2002**). "Decision strategies of hearing-impaired listeners in spectral shape discrimination," J. Acoust. Soc. Am. **111**, 1389–1398.

Lutfi, R. A. (**1995**). "Correlation coefficients and correlation ratios as estimates of observer weights in multiple-observation tasks," J. Acoust. Soc. Am. **97**, 1333–1334.

Mehr, M. A., Turner, C. W., and Parkinson, A. (**2001**). "Channel weights for speech recognition in cochlear implant users," J. Acoust. Soc. Am. **109**, 359–366.

Pfeiffer, E. (**1975**). "A short portable mental status questionnaire for the assessment of organic brain deficit in elderly patients," J. Am. Geriatr. Soc. **23**, 433–441.

Pittman, A. L., and Stelmachowicz, P. G. (**2000**). "Perception of voiceless fricatives by normal-hearing and hearing-impaired children and adults," J. Speech Lang. Hear. Res. **43**, 1389–1401.

Plyler, P. N., and Fleck, E. L. (**2006**). "The effects of high-frequency amplification on the objective and subjective performance of hearing instrument users with varying degrees of high-frequency hearing loss," J. Speech Lang. Hear. Res. **49**, 616–627.

Resnick, S., Dubno, J. R., Hoffnung, S., and Levitt, H. (**1975**). "Phoneme errors on a nonsense syllable test," J. Acoust. Soc. Am. **58**, 114.
Richards, V. M., and Zhu, S. (**1994**). "Relative estimates of combination weights, decision criteria, and internal noise based on correlational coefficients," J. Acoust. Soc. Am. **95**, 423–424.
Sherbecoe, G. A., and Studebaker, R. L. (**2002**). "Audibility-Index functions for the connected speech test," Ear Hear. **23**, 385–398.
Stellmack, M. A., Willihnganz, M. S., Wightman, F. L., and Lutfi, R. A. (**1997**). "Spectral weights in level discrimination by preschool children," J. Acoust. Soc. Am. **101**, 2811–2821.
Turner, C. W., and Brus, S. L. (**2001**). "Providing low- and mid-frequency speech information to listeners with sensorineural hearing loss," J. Acoust. Soc. Am. **109**, 2999–3006.
Turner, C. W., and Henry, B. A. (**2002**). "Benefits of amplification for speech recognition in background noise," J. Acoust. Soc. Am. **112**, 1675–1680.
Turner, C. W., Kwon, B. J., Tanaka, C., Knapp, J., and Doherty, K. A. (**1998**). "Frequency-weighting functions for broadband speech as estimated by a correlational method," J. Acoust. Soc. Am. **104**, 1580–1585.
Willihnganz, M. S., Stellmack, M. A., and Lutfi, R. A. (**1997**). "Spectral weights in level discrimination by preschool children," J. Acoust. Soc. Am. **101**, 2803–2810.

Using blind source separation techniques to improve speech recognition in bilateral cochlear implant patients

Kostas Kokkinakis and Philipos C. Loizou[a)]
Department of Electrical Engineering, The University of Texas at Dallas, Richardson, Texas 75080, USA

(Received 22 February 2007; revised 11 January 2008; accepted 11 January 2008)

Bilateral cochlear implants seek to restore the advantages of binaural hearing by improving access to binaural cues. Bilateral implant users are currently fitted with two processors, one in each ear, operating independent of one another. In this work, a different approach to bilateral processing is explored based on blind source separation (BSS) by utilizing two implants driven by a single processor. Sentences corrupted by interfering speech or speech-shaped noise are presented to bilateral cochlear implant users at 0 dB signal-to-noise ratio in order to evaluate the performance of the proposed BSS method. Subjects are tested in both anechoic and reverberant settings, wherein the target and masker signals are spatially separated. Results indicate substantial improvements in performance in both anechoic and reverberant settings over the subjects' daily strategies for both masker conditions and at various locations of the masker. It is speculated that such improvements are due to the fact that the proposed BSS algorithm capitalizes on the variations of interaural level differences and interaural time delays present in the mixtures of the signals received by the two microphones, and exploits that information to spatially separate the target from the masker signals. © *2008 Acoustical Society of America.* [DOI: 10.1121/1.2839887]

PACS number(s): 43.66.Pn, 43.72.Kb, 43.72.Qr [DOS] Pages: 2379–2390

I. INTRODUCTION

Much progress has been made over the last three decades in the development of new speech coding strategies for cochlear implants (CIs) (Loizou, 1998). Although CI recipients perform well in quiet listening conditions, several clinical studies have provided evidence that their ability to correctly identify speech degrades sharply in the presence of background noise and other interfering sounds, when compared against that of normal-hearing listeners (Qin and Oxenham, 2003; Stickney *et al.*, 2004). Poor performance in noise can be generally attributed to the significantly reduced spectral resolution provided by current implant devices.

To improve speech intelligibility in noisy conditions, a number of single microphone noise reduction techniques have been proposed over the years (Hochberg *et al.*, 1992; Weiss, 1993; Müller-Deile *et al.*, 1995). Several pre-processing noise reduction strategies have been applied to cochlear implants, but most of these algorithms were implemented on first-generation cochlear implant processors, which were based on feature extraction strategies (e.g., see Loizou, 2006). A few pre-processing algorithms were also evaluated using the latest implant processors. Yang and Fu (2005) investigated the performance of a spectral-subtractive algorithm using subjects wearing the Nucleus22®, Med −El®, and Clarion® devices. Significant benefits in sentence recognition were observed for all subjects with the spectral-subtractive algorithm, particularly for speech embedded in speech-shaped noise. Loizou *et al.* (2005) evaluated a subspace noise reduction algorithm that was based on the idea that the noisy speech vector can be projected onto "signal" and "noise" subspaces. Results indicated that the subspace algorithm produced significant improvements in sentence recognition scores compared to the subjects' daily strategies, at least in continuous (stationary) noise.

In short, the previous pre-processing methods attempt to boost the overall speech quality and speech intelligibility by "denoising" the received signal before feeding it to CI listeners. Overall, tests with CI patients have demonstrated some relative improvement in speech recognition. To further improve on open-set speech recognition amidst noise, van Hoesel and Clark (1995) considered a two-microphone noise reduction technique, based on adaptive beamforming, by employing a generalized sidelobe canceller structure originally proposed by Griffiths and Jim (1982), in which a single directional microphone is mounted behind each implanted ear. Their results showed some improvement for all four CI patients tested, however, the effectiveness of the method is limited to only zero-to-moderate reverberation settings (e.g., see Greenberg and Zurek, 1992).

Hamacher *et al.* (1997) assessed the performance of two adaptive beamforming algorithms in different everyday-life noise conditions. The benefit of the two algorithms was evaluated in terms of the dB reduction in speech reception threshold. The mean benefit obtained using the beamforming algorithms for four CI users (wearing the Nucleus22® device) varied between 6.1 dB for meeting-room conditions to 1.1 dB for cafeteria noise conditions. A number of studies focusing on speech perception in noise with bilateral cochlear implants, have indicated a substantial and consistent increase with regard to word recognition performance tasks with bilateral electric stimulation when compared to monaural listening conditions (e.g., see van Hoesel and Clark, 1997; Lawson *et al.*, 1998; Müller *et al.*, 2002; Tyler *et al.*, 2002; van Hoesel and Tyler, 2003; Tyler *et al.*, 2003). Posi-

a)Author to whom correspondence should be addressed. Electronic mail: loizou@utdallas.edu.

tive findings, in terms of improvement on localization and speech reception, with bilaterally implanted adults and children, have been documented in both quiet and noisy settings. In the Tyler *et al.* (2002) study, a positive outcome was observed for eight out of ten subjects tested. Much of the benefit documented was due to the "head-shadow" effect (Shaw, 1974), which amounts to the advantage gained by placing a second ear with a better signal-to-noise ratio contralateral to the competing noise source. The true "binaural advantage" or "squelch" effect has been found to be considerably smaller (1–2 dB) than the head-shadow effect.

In this contribution, we aim to exploit the presence of two microphones using an adaptive multichannel processing technique other than beamforming. In the multisensor array configuration investigated in this work, speech is assumed to be collected simultaneously over several (two or more) spatially distributed sensors, possibly the microphones located in each of the two (one per ear) behind-the-ear (BTE) processors worn by the bilateral cochlear implant subjects. The main objective is to recover and perceptually enhance the waveform of the desired (target) source signal from a set of composite (or mixed) signals. This paper is organized as follows. The next section offers a general introduction to the topic of blind source separation (BSS) for linear convolutive speech mixtures and a mathematical description of the model and separation algorithm used throughout the paper. Section III investigates the performance of the BSS algorithm in anechoic settings (Experiment 1). Section IV further evaluates the performance of the BSS algorithm in the challenging scenario of reverberant enclosures (Experiment 2).

II. BLIND SOURCE SEPARATION: BACKGROUND

BSS and independent component analysis (ICA), which is the most effective and most widely used technique to perform BSS (Comon, 1994), were first introduced in the early 1990s. Both methods quickly emerged as areas of intense research activity showing huge potential for numerous practical applications. By definition, BSS deals with the task of "blindly" recovering a set of unknown original signals, the so-called *sources* from their observed *mixtures*, based on little to no prior knowledge about the source characteristics or the mixing structure itself. The lack of any *a priori* knowledge regarding the origin of the linearly mixed observations can be compensated well by the statistically strong yet physically plausible[1] assumption of statistical independence amongst all sources (Comon, 1994; Hyvärinen *et al.*, 2001; Stone, 2004).

Proceeding blindly exhibits a number of advantages, with the most important one being that assumptions regarding the room configuration and the source-to-sensor geometry are relaxed (by being only implicitly used) in the separation process (Parra, 2000). The simplest approximation of this type of problem where the mixing coefficients are assumed to be just scaling factors (memoryless channel) has been extensively studied in the literature with the earliest of approaches tracing back to the pioneering work of Cardoso (1989); Jutten and Hérault (1991) and also Comon (1994). Still, this hypothesis of *instantaneous* (static) mixing is unrealistic for signal propagation inside a natural (or typical) acoustic environment. In reverberant enclosures, each microphone captures the weighted sum of multiple time-delayed versions of the sources instead, which in fact is the convolution of each signal with the acoustic transfer function of the room itself. Accordingly, the task of BSS then becomes equivalent to estimating the unknown room transfer functions (or their inverse) by relying only on combining information obtained from the observed *convolutive* mixtures captured in each input channel of the microphone array.

Over the years, a number of techniques have been developed to address the problem of separating convolutive mixtures (e.g., see Haykin, 2000; Hyvärinen *et al.*, 2001). In time, the BSS framework has blossomed into a new discipline that has widely benefited the fields of signal processing and neural computation. Recently, some potential advantages stemming from the use of spatial separation schemes to improve speech intelligibility in hearing aid applications have been discussed by Zhao *et al.* (2002). The *adaptive decorrelation filtering* approach of Yen and Zhao (1999) was investigated in a "dinner-table" scenario, whereby the target speech is corrupted by a number of speech jammers, as well as noise. Experiments with eight normal-hearing and three hearing-impaired subjects produced an increase in speech reception, albeit the proposed method was somewhat limited to cases where the hearing and microphones were placed closer to the target sources than to the competing speakers.

A. Mathematical model

Focusing on the realistic dynamic scenario of signal propagation inside a typically reverberant acoustic environment, we are normally confronted with a set of m observed signals denoted here by vector $\mathbf{x}(t)=[x_1(t),\ldots,x_m(t)]^T$, which are considered to be *convolutive* mixtures of a set of n unknown, yet statistically independent (at each time instant) source signals $\mathbf{s}(t)=[s_1(t),\ldots,s_n(t)]^T$. In this paradigm, the transformation imposed on the sound sources can be essentially seen as being equivalent to linear convolution. As such, the proposed convolutive structure can take into account basic binaural cues used by the auditory system. In the model, these cues can be incorporated in the form of interaural time delays (ITDs) expressed as the delay or lag operator, and also interaural level differences (ILDs) modeled by the variation of the amplitude coefficients of the *finite impulse response* (FIR) filters.

Consider the system shown in Fig. 1. In the context of convolutive BSS, the signal $x_i(t)$ observed at the output of the ith sensor, after being transformed in the z-domain can be written as

$$X_i(z)=\sum_{j=1}^{n} H_{ij}(z)S_j(z), \quad i=1,2,\ldots,m, \tag{1}$$

where in our case $m=2$ and $n=2$. Note also that here $H_{ij}(z)$ represents the z-transform of the room transfer function or as otherwise referred to, the *acoustic impulse response* (AIR)[2] observed between the jth sound source and the ith microphone (or sensor). The AIR is given by

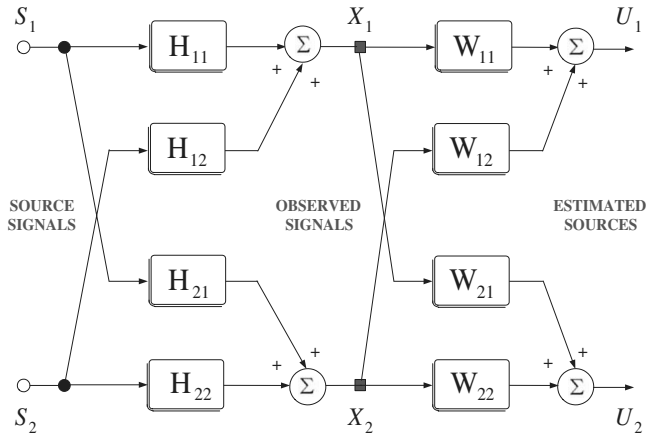

FIG. 1. Cascaded mixing and unmixing MBD system configuration in the two-source two-sensor convolutive mixing scenario.

$$H_{ij}(z) = \sum_{k=0}^{\ell-1} h_{ij}(k) z^{-k} \tag{2}$$

where k denotes the discrete-time index, z^{-k} is the time-shift (unit-delay) operator and finally ℓ defines the order of the FIR filters used to model the room acoustic (or channel transmission) effects. In the most general sense, the goal of BSS is to produce a set of n signals denoted by vector $\mathbf{u}(t) = [u_1(t), \ldots, u_n(t)]^T$, namely the source estimates, which when recovered would essentially correspond to the reconstructed waveforms of the original and otherwise unknown source signals, such that

$$U_j(z) = \sum_{i=1}^{m} W_{ji}(z) X_i(z), \quad j = 1,2, \ldots, n. \tag{3}$$

In practice, $W_{ji}(z)$ defines the z-transform of the unmixing or separating transfer function between the ith sensor and the jth source estimate written as

$$W_{ji}(z) = \sum_{k=0}^{\ell-1} w_{ji}(k) z^{-k}. \tag{4}$$

The cascaded mixing and unmixing system in the case of a two-source two-sensor configuration is shown in Fig. 1. Normally, to use BSS one must presume that the number of microphones is greater than or equal to the number of observed signals, such that $m \geqslant n$. In addition, it is often assumed that the unknown mixing system of Eq. (1) can be modeled by using a matrix of FIR filter polynomials. In theory, AIR estimates need to be several thousands of coefficients long, especially when sampled at a sufficiently high sampling rate. However, considering relatively short reverberation times[3] and assuming adequately long filters, virtually any source-to-sensor configuration can be adequately modeled by using an FIR filter.[4] From a practical standpoint, such a task can be facilitated by resorting to the FIR matrix algebra proposed by Lambert (1996) and Lambert and Bell (1997). Based on this formalism, both mixing and unmixing systems may be ultimately expressed as FIR polynomial matrices, denoted here as $\underline{\mathbf{H}}(z)^{(i \times j \times k)}$ and $\underline{\mathbf{W}}(z)^{(j \times i \times k)}$ having complex-valued FIR polynomials as elements, which in turn are given by Eqs. (2) and (4). Note also that in this case $i = [1,2,\ldots,m]$, $j = [1,2,\ldots,n]$, and $k = [0,1,\ldots,\ell-1]$, are the indices corresponding to the observations, sources, and to each filter coefficient, respectively.

B. Algorithm

Since its inception, the entropy maximization algorithm or INFOMAX (see Bell and Sejnowski, 1995) fairly quickly catalyzed a significant surge of interest in using information theory to perform ICA. The potential of entropy (or information) maximization in the framework of BSS for convolutive speech mixtures was explored shortly after by Lambert and Bell (1997) and also Lee *et al.* (1997). In short, it was shown that an efficient way of updating the separating FIR polynomial matrix $\underline{\mathbf{W}}$ with respect to its entropy gradient is to use the *natural gradient algorithm* (NGA) first devised by Amari *et al.* (1996). In this paper, we opt to use a more efficient implementation of the same algorithm. This employs a two-step optimization strategy. The first step is to use the NGA method to learn the unmixing filters shown in Eq. (4) with independently and identically distributed or temporally independent (white) observations of the sound sources written as

$$\epsilon_i(z) = \sum_{i=1}^{m} A_i(z) X_i(z), \quad i = 1,2, \ldots, m, \tag{5}$$

namely the outputs of the linear prediction (LP) analysis FIR polynomial matrix $\underline{\mathbf{A}}(z)$ such that:

$$\underline{\mathbf{A}}(z) = \mathrm{diag}[A_1(z), \ldots, A_m(z)] \tag{6}$$

with its elements subsequently given by

$$A_i(z) = 1 - \sum_{k=1}^{p} \alpha_i(k) z^{-k}, \tag{7}$$

where each vector $[\alpha_i(k)]$ represents the LP coefficients and is defined for $1 \leqslant k \leqslant p$, as well as for every $i = 1,2,\ldots,m$. Following this, the second step is to apply the estimated unmixing filters to the initial streams of source observations in order to restore the signals back to their original form (e.g., see Kokkinakis and Nandi, 2004). This alternative "spatial-only" technique proposed for the separation of temporally correlated speech sources by modifying the popular NGA update rule is depicted in Fig. 2. By processing the observed mixtures in such manner, we avoid whitening[5] the speech sources as we are successfully differentiating between the actual speech production system, namely the vocal tract and the influence of the acoustic path on the signals at hand. Ultimately, the filtering indeterminacies normally associated with existing BSS techniques are completely alleviated, and the source signals are recovered with their spectral information intact, by resorting to the following update rule (Kokkinakis and Nandi, 2004, 2006):

$$\underline{\mathbf{W}}_{k+1} = \underline{\mathbf{W}}_k + \lambda [\underline{\mathbf{I}} - \mathrm{FFT}(\varphi(\mathbf{u})) \mathbf{u}^H] \underline{\mathbf{W}}_k \tag{8}$$

operating solely on the spatially and temporally independent outputs, written as

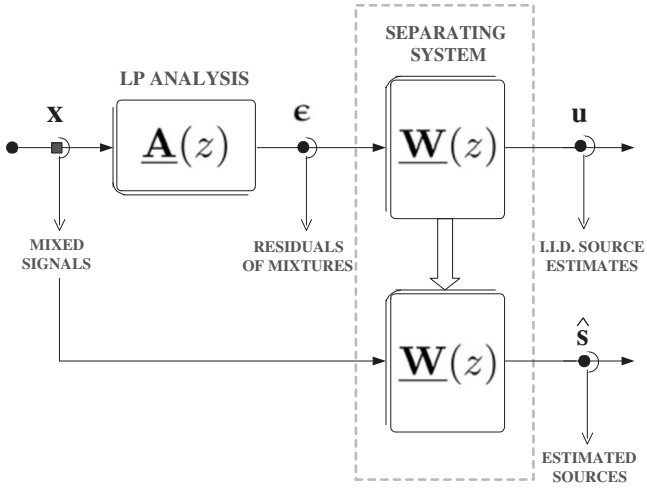

FIG. 2. Schematic diagram of the alternative BSS system configuration, whereby the observations are first decorrelated through the LP analysis stage yielding a set of temporally independent signals, which are then used to adapt the spatial separation FIR filters.

$$\mathbf{u}(z) = \underline{\mathbf{W}}(z)\boldsymbol{\epsilon}(z), \tag{9}$$

where $(\cdot)^H$ is the Hermitian operator, λ denotes the step-size (or learning rate), $\underline{\mathbf{I}}$ defines the FIR identity matrix, FFT$[\cdot]$ denotes the elementwise fast Fourier transform operation, and finally, vector $\varphi(\mathbf{u})=[\varphi_1(u_1),\ldots,\varphi_n(u_n)]^T$ represents the nonlinear monotonic activation (or score) functions. Note that here these functions operate solely in the time domain and can be further expressed as

$$\varphi_i(u_i) = -\frac{d}{du_i}\log p_{u_i}(u_i) \tag{10}$$

with the term $p_{u_i}(u_i)$ denoting the (unknown) probability density function of each source estimate u_i. Optimal score activation functions used in the BSS update can be derived by resorting to a fixed family of densities or, alternatively, they can be learned adaptively (e.g., see Kokkinakis and Nandi, 2005).

C. Implementation

When using BSS, it is often necessary to employ many different FIR filters, and in realistic scenarios should contain thousands of filter coefficients. Conventional adaptive filtering techniques choose to operate solely in the time domain, in which case the filter updates are carried out on a sample-by-sample basis. In such cases, the complexity of the algorithm can become prohibitive. Instead, to reduce excessive computational requirements and potentially achieve considerable savings in complexity, we can make use of a frame-based—or as otherwise known block-based implementation—by relying on the efficient use of the fast Fourier transform (FFT). Such efficient block-wise operations are based on the presumption that parameters remain invariant over a block of data, for example over a predetermined length of time. Block-based implementations demonstrate substantial savings, which in some cases have been reported to be up to 10× faster, when compared against conventional sample-by-sample iterative procedures (Shynk, 1992). In our implementation, all transforms have been assumed to be of length $2L$, where L denotes the chosen block size. The overlap between successive frames (or blocks) of data has been set to 50% in all cases.

III. EXPERIMENT 1. SPEECH RECOGNITION BY BILATERAL COCHLEAR IMPLANT SUBJECTS IN ANECHOIC SETTINGS

A. Methods

1. Subjects

A total of five postlingually deafened adults were recruited for testing. The participants of the study, three females and two males, were all bilateral implant patients fitted with the Nucleus24® multichannel implant device manufactured by Cochlear®. Their ages ranged from 36 to 67 years old ($M=61$) and they were all native speakers of American English. Special provisions were made to acquire subjects having a minimum of at least 2 years of experience with their bilateral device. Biographical data for the subjects tested is given in Table I.

2. Stimuli

The speech stimuli used in this study, were sentences from the IEEE database IEEE (1969), which consists of a total of 72 phonetically balanced lists of 10 sentences each. Each sentence is composed of approximately 7 to 12 words, with 5 key words identified for the purposes of scoring. Every sentence in the IEEE speech corpus that was produced by a male talker was designated as the target speech. In order to simulate the speech interferer or competing voice in this experiment, a female talker uttering the sentence "*Tea served from the brown jag is tasty*" (also taken from the IEEE database) was chosen as the female masker (or non-target). Speech-shaped noise generated by approximating the average long term spectrum of the speech to that of an adult male taken from the IEEE corpus, was also selected to act as the second type of noise masker. This is an effective masker of speech. Twenty sentences (2 lists) were used for each condi-

TABLE I. Cochlear implant patient description and history.

	S1	S2	S3	S4	S5
Age	61	58	36	65	67
Gender	M	F	F	M	F
Etiology of impairment	Noise	Rubella	Unknown	Congenital	Hereditary
Years of implant experience (L/R)	5/5	4/4	4/3	3/4	6/6
Years of deafness	15	8	15	12	22

tion. Different sets of sentences were used for each condition.

B. Signal processing

The test sentences were originally recorded with a sampling frequency of 25 kHz, but were later downsampled to 16 kHz to reduce overall computational time during the processing of the stimuli. In addition, each sentence was scaled to the same root-mean-square value, which corresponded to approximately 65 dB. The sound level of each masker was also adjusted relative to the fixed level of the target speech, yielding a target-to-masker ratio (TMR) equal to 0 dB. Both target and masker speech had the same onset, and, where deemed necessary, the masker signals were edited to have equal duration to the target speech tokens.

A set of free-field-to-eardrum (or anechoic) head-related transfer functions (HRTFs) measured in an acoustic manikin (Head Acoustics®, HMS II.3) as described in the AUDIS catalog (see Blauert *et al.*, 1998), were used to simulate different spatial locations of the speech target and the masker signals. HRTFs provide a measure of the acoustic transfer function between a point in space and the eardrum of the listener, and also include the high-frequency shadowing component due to the presence of the head and the torso. The length of the HRTFs was 256 sample points, amounting to a relatively short delay of 16 ms and no reverberation. To generate the multisensor composite (or mixed) signals observed at the pair of microphones, the target and masker stimuli for each position were *convolved* with the set of HRTFs for the left- and right-hand ear, respectively. For this experiment, the target speech source was assumed to be placed directly in front of the subject at 0° azimuth at the realistic conversational distance of 1 m. To generate stimuli in various spatial configurations, we set the azimuth angles of the masker positions to 0°, 30°, 45°, 60°, and 90°. In all cases, the vertical position of the sources was adjusted to 0° elevation.

The BSS algorithm, described in Sec. II B, was implemented to run in an adaptive off-line mode with a multipass processing scheme. Thus, the estimation of the unmixing filters was performed iteratively over a block of data and the estimates obtained in the last iteration were then used to perform source separation for the same data block. By observing Eq. (8) we note that the separating system is characterized by the following two parameters: (1) The length of the separating filters composing the unmixing FIR polynomial matrix denoted by $\underline{\mathbf{W}}$ and (2) parameter λ that controls the adaptive step size (or learning rate). Theoretically, the BSS system can remove more interference with longer FIR filters, albeit at the cost of more computation and longer adaptation time. Here, in order to achieve the best separation quality possible, we chose the size of the unmixing filters to be twice the size of the HRTFs previously used to generate the target-masker signal mixtures. The BSS algorithm was run with 512 sample point adaptive FIR filters and a fixed large step size of $\lambda=0.01$ maximized up to the stability margin to ensure fast adaptation time and algorithm convergence. In addition, the algorithm was allowed to execute 20 passes through the data. This corresponds to a total of 60 s training time as the average sentence duration is 3 s. Each set of the mixtures was processed individually in order to extract the speech target estimates. Upon algorithm convergence, all the recovered (or enhanced) target speech segments were saved locally in the lab computer.

1. Procedure

All subjects were wearing the Cochlear Esprit™ 3G BTE processor with two directional microphone elements (Knowles EL-7189). During their visit, however, all subjects were temporarily fitted with the new SPEAR3® wearable research processor. SPEAR3® has the ability to independently drive two implant devices and was developed by the Cooperative Research Center (CRC) for Cochlear Implant and Hearing Aid Innovation, Melbourne, Australia, in collaboration with HearWorks®. Before the scheduled visit, we used the Seed–Speak® GUI application to adjust the amplitudes for both threshold (T) and comfortable loudness levels (C) previously established for each electrode and subsequently program the processor separately for each patient. In addition, all participants used the device programmed with the advanced combination encoder (ACE) speech coding strategy (e.g., see Vandali *et al.*, 2000) with the stimulation rates set to the values used in their daily processor. The volume of the speech processor (values between 0 and 9) was also adjusted to a comfortable loudness.

To evaluate recognition in anechoic conditions, the following conditions were used for each masker type and masker azimuth angle: (1) binaural unprocessed and presented bilaterally and (2) BSS-processed and presented diotically. Hence, in total there were 20 different conditions (2 maskers × 5 angles × 2 algorithms) using a total of 40 sentence lists. In the binaural unprocessed case, the two simulated sensor observations captured from one microphone were fed to one ear and similarly the composite signals observed in the other microphone, were presented to the other ear via the auxiliary input jack of the SPEAR3® processor. In the processed case, the BSS-enhanced signal was presented diotically to the bilateral users via the auxiliary input jack of the SPEAR3® processor. Prior to testing, all subjects were given a short practice session, in order to gain familiarity with the experiment. Separate practice sessions were used for single talker and noise maskers. No score was calculated for these practice sets. During the testing, the participants typed their response using the computer keyboard and were encouraged to guess if unsure. Feedback was provided during the practice session but not during the experimental sessions. The listeners participated in two separate experimental sessions with duration of 2–3 h each, that included several breaks. The list number presentation order was randomized across different participants, in order to counterbalance possible order effects in the test, such as learning or fatigue effects. After each test session was completed, the responses of each individual were collected, stored and scored off-line by the percentage of the keywords correctly identified.

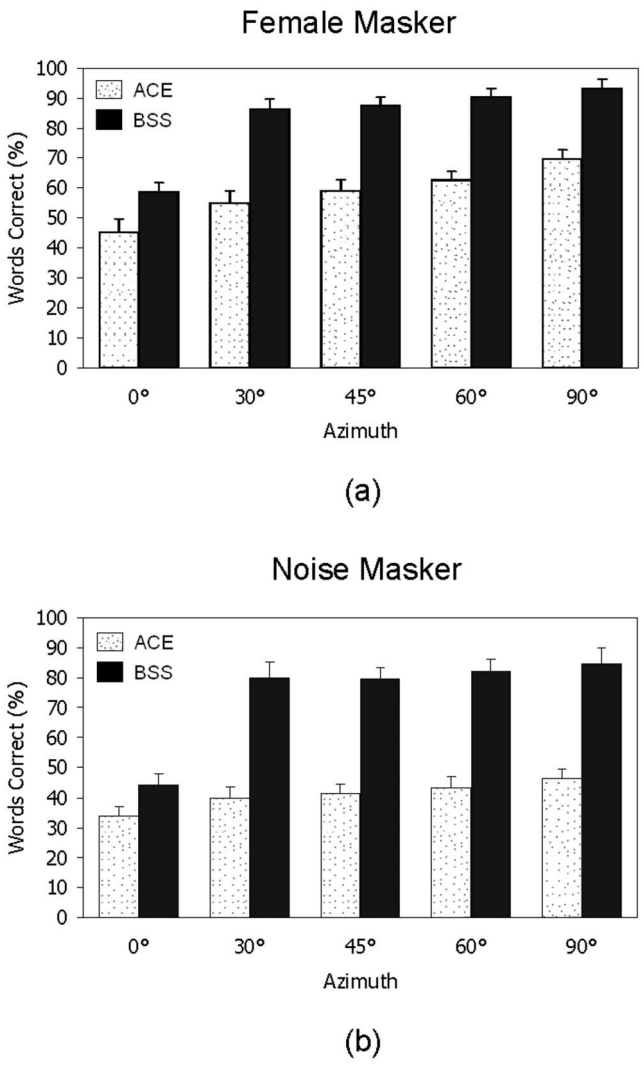

FIG. 3. Mean percent word recognition scores for five Nucleus 24® implant users on IEEE sentences embedded in female speech (top) and speech-shaped noise (bottom), both at TMR=0 dB. Scores for sentences processed only through the default processor ACE strategy are shown in white, and scores for sentences processed first through the BSS algorithm and then the ACE strategy are in black. Error bars indicate standard deviations.

C. Results and discussion

The mean scores on speech recognition obtained with and without BSS are shown in Fig. 3 for the female masker (top) and the noise masker (bottom).

1. Statistical analysis and comparisons

Two-way analysis of variance (ANOVA) (with repeated measures) was performed separately for each masker condition to assess significant effects of the processing algorithm and spatial configuration. ANOVA performed on the female masker data, indicated a significant effect $[F(1,4)=1615.02, p<0.0005)$ of processing with the BSS algorithm, a significant effect $[F(4,16)=419.2, p<0.0005]$ of the spatial configuration of the masker, and a significant interaction $[F(4,16)=34.4, p<0.0005]$. ANOVA performed on the noise masker data, also indicated a significant effect $[F(1,4)=1311.5, p<0.0005]$ of processing with the BSS algorithm, a significant effect $[F(4,16)=206.3, p<0.0005]$ of the spatial configuration of the masker, and a significant interaction $[F(4,16)=127.7, p<0.0005]$. Post-hoc comparisons using Fisher's LSD between the scores obtained with the BSS algorithm and the subject's daily processor indicated that the BSS algorithm yielded significantly $(p<0.005)$ higher scores in all azimuth conditions and for both maskers. Interestingly, the BSS scores obtained at 0° azimuth were also significantly higher $(p<0.005)$ than the scores obtained with the subject's daily processor in both masker conditions. There is no theoretical explanation for this outcome, and hence we can make no claims that BSS is able to segregate co-located sources. This outcome may be instead attributed to small variations in intelligibility among individual IEEE sentence lists and the absence of counterbalancing on those sentence lists.[6] These small variations in intelligibility might explain the differences in scores at 0° azimuth, but do not in general account for the comparatively larger differences in scores for other spatial configurations.

As shown in Figs. 3(a) and 3(b), the scores obtained with the unprocessed sentences were higher in the 90° condition, where the masker and target signals were spatially separated, than in the 0° condition, in which case the masker and target signals originated from the same location. This suggests that the bilateral-implant subjects were able to benefit from spatial release of masking, an observation that is consistent with previous studies (e.g., van Hoesel and Tyler, 2003; Stickney *et al.*, 2004; Tyler *et al.*, 2002, 2003). That release, however, seemed to be largely dependent on the separation between the masker and target signals, as expected. According to Fig. 3, we can conclude that as long as the separation between the target and masker signals is at least 30° or more, the BSS algorithm can produce large improvements in intelligibility. In the noise masker condition for instance, word recognition scores improved from roughly 40% correct with unprocessed sentences to 80% correct with BSS-processed sentences. Large improvements in performance were obtained with the BSS algorithm for both maskers (female and noise). Spatially separating the target speech from its respective maskers by filtering the composite signals through a set of FIR unmixing filters results in a compelling release from masking. From a theoretical standpoint, the fact that BSS performs equally well in settings of both informational and energetic masking and for all configurations is to be anticipated, as the algorithm utilizes no prior knowledge with regard to the original signals or their underlying mixing structure.

2. Effect of different training strategies on speech recognition performance

Given that the BSS algorithm requires no previous information on the specifics of the acoustical setup, some amount of training is essential in order to achieve a considerable amount of masker suppression. In the present experiment, a total of 60 s was required to achieve the level of performance shown in Fig. 3. Logically, this raises the question of the amount of training required for the BSS algorithm to produce a reasonable separation performance and further to achieve similar word recognition scores as the ones previously obtained in Fig. 3. To thoroughly investigate the ef-

fect of training on speech recognition for bilateral users, the BSS algorithm was re-applied to enhance the male target embedded in female speech and speech-shaped noise, synthesized binaurally with HRTFs. The same subjects were used and an identical procedure to the one described in Sec. III A was followed.

The main difference here is that training was not carried out individually for every single speech token as before. Instead, filters were adapted just for a randomly selected set of signals. The algorithm was executed with identical parameters as before. After convergence to a separating solution, the unmixing filters were saved, and then without any further modification used to enhance the remaining sentences. Note that in fact, we employed the *same* set of estimated filters to enhance signals embedded either in female speech or noise. The rationale behind this approach is that BSS should ideally remain truly "blind" to the original sources, and hence performance should not suffer. Based on this strategy, only a limited number of filters, namely one set for every spatial position of the maskers is required. This results in considerable savings in processing time. To further assess to what degree training affects separation quality the algorithm is allowed only 2, 3, and 5 passes (or iterations) through the data, which in effect correspond to 5, 10, and 15 s of total training time.

The results obtained for different training times are given in Fig. 4 for two spatial configurations (30° and 90°). The data obtained in Fig. 3 with 60 s of training are also included for comparative purposes. Nonlinear regression analysis was run to determine the minimum amount of training time required to achieve high levels of performance. Good fits, with correlation coefficients ranging from 0.67 to 0.77 ($p<0.05$), were determined with a log-shaped function in all conditions. The asymptote in performance was achieved with 15 s of training. Performance obtained with 15 s of training was not significantly ($p=0.05$) different to the performance obtained after a total of 60 s of training in all conditions. From Fig. 4 we can draw the following conclusions. First, as expected from theory, by increasing the adaptation time and hence the available signal length, the separation performance improves. This is reflected by the high recognition scores obtained when a total of 60 s (20 passes) of training is performed. Second, the BSS algorithm requires no more than a few seconds of data (5–10 s) in order to converge to a solution yielding an audibly distinguishable performance. Such observation can be confirmed by the plots in both Figs. 4(a) and 4(b), showing relatively high word recognition scores for the 10 s case, for both types of maskers and for both the 30° and 90° azimuths.

IV. EXPERIMENT 2. SPEECH RECOGNITION BY BILATERAL COCHLEAR IMPLANT SUBJECTS IN REVERBERANT ENVIRONMENTS

The previous experiment focused on assessing the performance of the BSS algorithm in anechoic environments. In the current experiment, we assess the performance of the BSS algorithm in more challenging (and more realistic) conditions, where reverberation is present.

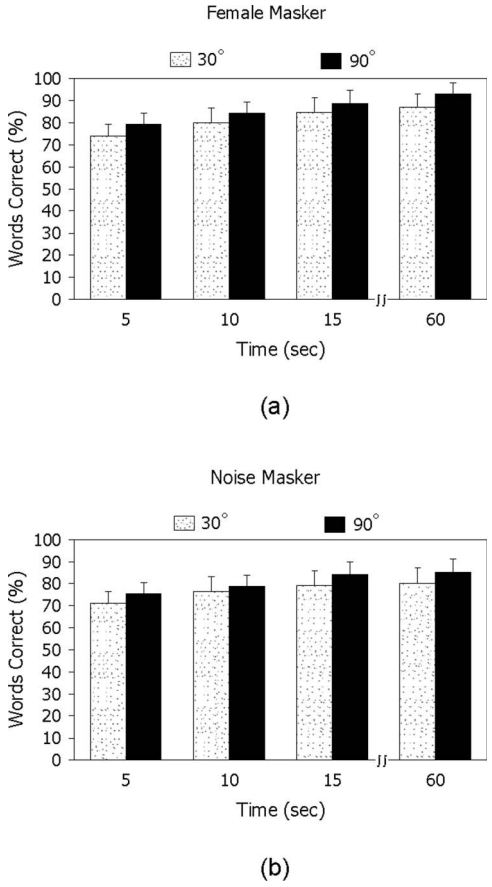

FIG. 4. Mean percent word recognition scores plotted against training time for five Nucleus 24® implant users on IEEE sentences embedded in female speech (top) and speech-shaped noise (bottom) at TMR=0 dB. Scores for sentences processed first through the BSS algorithm and then the default ACE strategy for a masker placed at 30° dB are in white. Scores for sentences processed first through the BSS algorithm and then the default ACE processor strategy for a masker placed at 90° dB are in black. Error bars indicate standard deviations.

A. Methods

1. Subjects

The same five postlingually deafened bilateral implantees tested in Experiment 1, were asked back to participate as subjects in this experiment.

2. Stimuli

The test material for the target and masker sentences was again selected from the IEEE corpus IEEE (1969) used in Experiment 1. None of the sentences previously used as the target speech (or masker) was reused in an effort to avoid potential learning effects.

3. Signal processing

To investigate the potential of BSS on speech intelligibility inside challenging reverberant environments, the target and masker stimulus for each position are convolved with a set of binaural room impulse responses (BRIRs) (Shinn-Cunningham *et al.*, 2005). Before filtering the signals with the impulse responses, the level of each individual acoustic interference was adjusted relative to the fixed level of the target speech to reach a TMR=0 dB. The BRIRs were mea-

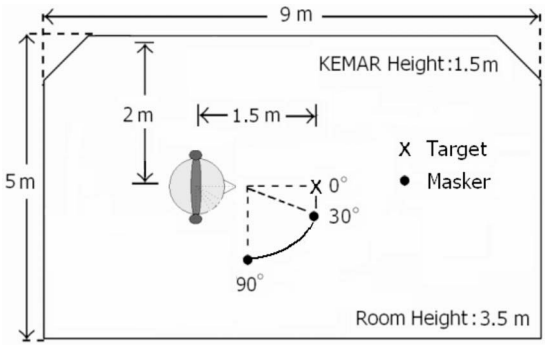

FIG. 5. Schematic diagram depicting the layout of the reverberant room and location of the KEMAR manikin where the BRIRs were measured.

sured in a small rectangular classroom with dimensions 5 $\times 9 \times 3.5$ m and a total volume of $V=157.5$ m^3 using the Knowles Electronic Manikin for Auditory Research (KEMAR), positioned at 1.5 m above the floor and at ear level as described in the study by Shinn-Cunningham *et al.* (2005). In contrast to the relatively smooth free-field anechoic HRTFs used in Experiment 1, these BRIRs exhibit *rapid* variations with frequency in both phase and magnitude and are in general, fairly difficult to invert even with FIR filters that employ a very large number of coefficients. Yet, only when resorting to such BRIRs we are capable of achieving a truly realistic binaural synthesis, and thus simulate a sound source at the desired location in space by filtering the audio stream with the left- and right-ear impulse responses corresponding to a specific sound location in the room. To reduce extraneous noise artifacts in their original measurements, Shinn-Cunningham *et al.* (2005) used Butterworth filters to bandpass filter the raw binaural responses in the 0.1–20 kHz range. These BRIRs were then multiplied by a 500 ms time window using a 50 ms cosine-squared fall time to produce the final BRIRs.

Before performing any filtering on the speech tokens, we downsampled the impulse responses to 16 kHz from their original 44.1 kHz recorded sampling rate. After convolving the signals with the pre-measured left- and right-ear responses obtained from the KEMAR, the target sound source was placed directly at the front of the listener in virtual space at 0° azimuth. Following the same procedure, the target speech was positioned at either a distance of 0.90 or 1.50 m away from the KEMAR dummy head. The female and noise maskers were placed at an angle of incidence of either 30° or 90°, and also at either a distance of 0.90 or 1.50 m away from the KEMAR. A total of 16 (2 distances $\times$ 2 angles $\times$ 2 maskers $\times$ 2 algorithms) different conditions were considered in this experiment using a total of 320 sentences. Figure 5 provides a schematic representation of the aforementioned configurations, as well as the location of the KEMAR manikin inside the classroom where the actual measurements took place in the Shinn-Cunningham *et al.* (2005) experiment.

The broadband reverberation time of the room was calculated from the pre-measured impulse responses by resorting to the Schroeder integration procedure (Schroeder, 1965). This technique first estimates the energy decay curve and

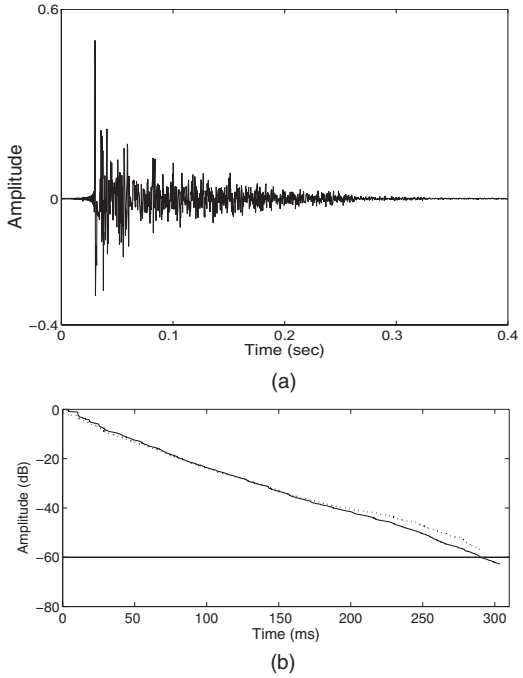

FIG. 6. (Top) Center-target to left-ear impulse response recorded inside the classroom shown in Fig. 5. The reverberation time T_{60} of this enclosure ranges from 150 to 300 ms depending on the source-to-sensor distance. (Bottom) Energy decay curves of the left-ear (solid line) and right-ear (dash line) impulse responses at 30°. The time taken for the amplitude to drop by 60 dB (thick line) below the original sound energy level is equal to 300 ms.

ultimately reveals the length of time required for the sound pressure to decrease by 60 dB. We choose, as an example, the topology where the source-to-sensor distance was equal to 1.50 m and the masker was placed at a 30° angle to the right of the target signal. As Fig. 6(b) reveals, for this particular enclosure, reverberation time is equal to around $T_{60}=300$ ms. In general, a rapidly decaying impulse response corresponds to a short reverberation time, whereas longer reverberation times are usually associated with impulse responses having much heavier tails. The first peak corresponds to the sound coming directly from the source, whereas the exponentially decaying tails, caused by successive absorption of sound energy by the walls, account for the later reflection paths in the enclosure. Figure 6(a) depicts one of the acoustic impulse responses used for the stimulus synthesis, measured inside the rectangular classroom when the KEMAR was placed 1.50 m away from the target speech (see Fig. 5).

To generate a set of shorter (and less reverberant) binaural impulse responses, an exponential regression to the decay curve was calculated from the original 0.90 m impulse responses obtained in the Shinn-Cunningham *et al.* (2005) KEMAR experiment. These responses were then faded in a natural manner by applying an exponentially decaying time window that was flat for up to around 100 ms and had a cosine-squared fall time from 100 to 300 ms. This reshaping ensured that most reverberant energy was removed from the original set of the impulse responses, hence yielding a shorter reverberation time, which was adjusted to be approximately $T_{60}=150$ ms. Also computed were the averaged direct-to-reverberant ratios (DRRs) for the $(0°, 30°)$ and

(0°,90°) configurations in both the 0.90 and 1.50 m settings. DRR is simply defined as the log energy ratio of the direct and reverberant portions of an impulse response and essentially measures how much of the energy arriving is due to the direct (source) sound and how much is due to late arriving echoes (e.g., see Zahorik, 2002). In general, the DRR will change depending on the source-to-listener distance. As perceived reverberation increases the DRR decreases, since the energy in the latter part of the impulse response will increase relative to that in the direct wave front. When the KEMAR is placed at 0.90 m away from the speech source, $DRR_{90}=0.21$ dB, whereas for the 1.50 m setting, the estimated DRR_{150} is equal to −4.87 dB.

The main goal of the present experiment was not only to suppress the masker in order to allow the bilateral subject to better focus on the target speech, but also to remove the corrupting acoustic properties of the room and yield a nearly anechoic (or clean) target source. In this context, convolutive BSS is also usually referred to as multichannel blind deconvolution (MBD) (e.g., see Haykin, 2000; Haykin and Chen, 2005; Kokkinakis and Nandi, 2006; Lambert, 1996). Clearly, if a source is successfully canceled, the output is then statistically independent from the masker or interfering sound source. To do so and enhance the target speech, we applied the BSS algorithm to the binaural convolutive mixtures. The setting chosen for the unmixing filters was 4,096 sample points, which correspond to an overall delay of 256 ms at the sampling rate of 16 kHz. Such filter size should be adequate to invert the acoustic properties of the room in the moderately reverberant 0.90 m setting with $DRR_{90}=0.21$ dB and $T_{60}=150$ ms. However, note that the length of the impulse response in the 1.50 m distance condition with $DRR_{150}=-4.87$ dB and $T_{60}=300$ ms is somewhat longer than the length of the unmixing filters. Due to this, we anticipate that some degradation on the perceived speech due to reverberation will remain. As before, the BSS algorithm was executed in an adaptive off-line mode based on a multipass processing scheme with the learning rate equal to $\lambda=0.001$ to ensure prompt algorithm convergence. The training time in this case was set to approximately 30 s.

4. Procedure

The experimental procedure was identical to the one followed previously. The enhanced speech target signal processed by our BSS method, was presented identically to both implants (diotically), whereas the unprocessed speech signals were presented binaurally to the subjects. Overall, there were 16 different conditions that involved a total of 32 sentence lists (2 lists per condition). The invited subjects completed the data collection process over a period of 4–5 h with regular breaks provided as needed. Performance was scored separately for each subject as the percentage of words that were correctly identified in each condition.

B. Results

The mean subject scores obtained with the BSS method in reverberant conditions are shown in Figs. 7 and 8.

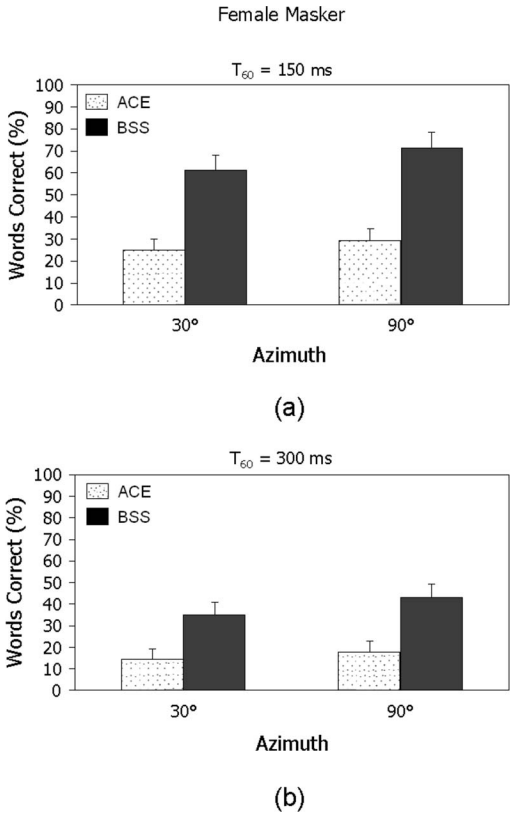

FIG. 7. Mean percent word recognition scores for five Nucleus 24® implant users on IEEE sentences embedded in female speech at TMR=0 dB. Top graph corresponds to a source-to-sensor-distance of 0.90 m and $T_{60}=150$ ms, and bottom graph to 1.50 m and $T_{60}=300$ ms. Scores for sentences processed only through the default processor ACE strategy are shown in white, and scores for sentences processed first through the BSS algorithm and then the ACE strategy are in black. Error bars indicate standard deviations.

1. Speech recognition performance in 150 ms reverberation

Figures 7(a) and 8(a) show the mean word recognition score values for the female talker and noise maskers, respectively, in moderate reverberant conditions. The target speech was placed at 0° azimuth and the female and noise interferers were located at 30° and 90° both at a distance of 0.90 m away from the listener. For the female masker conditions, two-way ANOVA (with repeated measures) indicated a significant effect $[F(1,4)=164.02, p<0.0005]$ of processing with the BSS algorithm, a significant effect $[F(1,4)=106.3, p<0.0005]$ of the chosen spatial configuration for the maskers, and a significant interaction $[F(1,4)=53.15, p=0.002]$. Paired samples t-tests showed that the scores obtained with BSS were significantly ($p<0.0005$) higher than the scores obtained with the daily implant processor (unprocessed signals) in both the 30° and 90° masker positions. For the noise masker conditions, two-way ANOVA (with repeated measures) indicated a significant effect $[F(1,4)=461.95, p<0.0005]$ of processing with the BSS algorithm, a significant effect $[F(1,4)=111.455, p<0.0005]$ of the spatial configuration, and a nonsignificant interaction $[F(1,4)=2.27, p=0.206]$. Based on this analysis, we can reason that the scores obtained with BSS were substantially better than the scores obtained with the subjects' daily processors alone for both masker configurations.

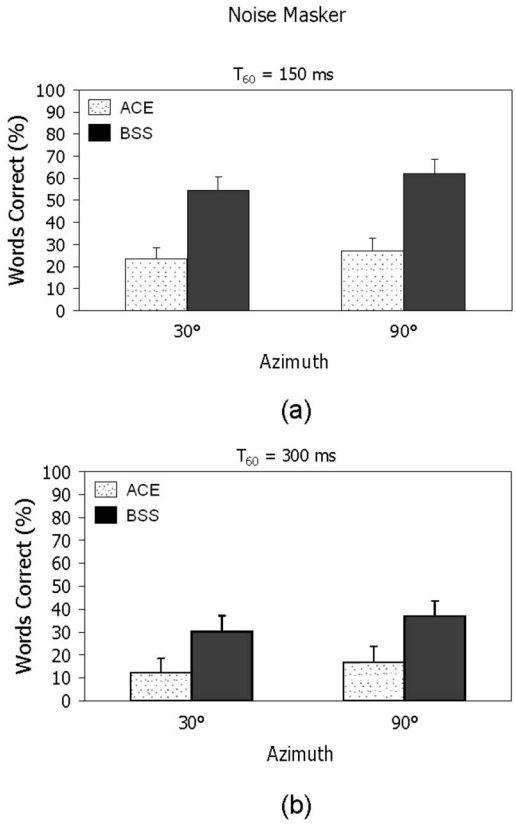

FIG. 8. Mean percent word recognition scores for five Nucleus 24® implant users on IEEE sentences embedded in speech-shaped noise at TMR=0 dB. (Top) Corresponds to a source-to-sensor distance of 0.90 m and T_{60} =150 ms and (bottom) corresponds to 1.50 m and T_{60}=300 ms. Scores for sentences processed only through the default processor ACE strategy are shown in white, and scores for sentences processed first through the BSS algorithm and then the ACE strategy are in black. Error bars indicate standard deviations.

In the unprocessed conditions, both the single talker and noise maskers degraded speech intelligibility significantly. Compared to the anechoic condition, performance decreased in the female masker condition from nearly 60% correct as shown in Fig. 3, to nearly 30%. A similar degradation in performance was also observed in the noise masker conditions. The performance obtained at 90° was not significantly ($p>0.05$) better than the performance observed at 30° for either masker. This points to the conclusion that the performance of the BSS algorithm was not affected by the spatial configuration. Equally large improvements in intelligibility were noted in both angles and for both maskers. On average, the subjects' scores were 2×better (and in some cases 3 ×better) when the mixtures were passed through the proposed BSS algorithm.

2. Speech recognition performance in 300 ms reverberation

Figures 7(b) and 8(b) show the mean word recognition scores for the female and noise maskers, respectively, in highly reverberant conditions. In this setup, the target speech was placed at 0° azimuth and the female talker and noise interferers were located at 30° and 90° both at a distance of 1.50 m away from the listener. The reverberation time as measured from the binaural impulse responses, was equal to around 300 ms [see Fig. 6(b)]. Two-way ANOVA (with repeated measures) in the female masker conditions, indicated a significant effect [$F(1,4)=545.5, p<0.0005$] of the BSS processing algorithm, a significant effect [$F(1,4)=27.7, p=0.006$] of the designated spatial configuration, and a nonsignificant interaction [$F(1,4)=19.4, p=0.012$]. Similar results were obtained for the noise masker. ANOVA showed a significant effect [$F(1,4)=60.1, p=0.001$] of processing with the BSS algorithm, a significant effect [$F(1,4)=97.6, p=0.001$] of the spatial configuration, and a nonsignificant interaction [$F(1,4)=2.17, p=0.214$]. Paired samples t-tests confirmed that the scores obtained after enhancing the target signals with BSS, were significantly ($p<0.0005$) higher than the scores obtained with the daily processor in both the 30° and 90°masker positions and for both maskers.

Speech intelligibility in the unprocessed conditions was reduced considerably as the reverberation time increased from 150 to 300 ms. Mean scores dropped to 17% correct in the female masker condition for 90° azimuth and to 15% correct in the noise masker condition (same angle). Equally low were the scores observed at the 30° configuration, where subjects scored 14% and 12% for speech signals embedded in speech-shaped noise. Performance improved significantly for the stimuli processed with the BSS algorithm in both masker conditions. Word recognition scores in the 90° position were found to be equal to 43% and 36% for the female and noise maskers, respectively. Equal improvements were noted in the 30° masker position. Overall, the above data demonstrate that the BSS method can yield substantial benefits in speech intelligibility even in reverberant listening conditions.

C. Discussion

Comparing the outcomes of Experiments 1 and 2, we observe that the bilateral cochlear-implant subjects' abilities to communicate in reverberant conditions is severely compromised. This was found to be true in both the female masker [$F(2,8)=344.1, p<0.005$] and steady-noise masker [$F(2,8)=78.4, p<0.005$] conditions. As shown in Figs. 7 and 8, the subject's ability to benefit from spatial release of masking is reduced substantially within reverberant settings. This is consistent with studies involving normal-hearing and hearing-impaired subjects (Culling *et al.*, 2003; Nabelek *et al.*, 1989; Nabelek and Picket, 1994; Freyman and Zurek, 2002; Shinn-Cunningham and Kopco, 2002). Culling *et al.* (2003) carried out experiments with normal-hearing subjects within a virtual room with controlled reverberation, and concluded that reverberation can abolish a listeners ability to exploit differences in spatial location, and hence to receive benefit from release of masking. Reverberation has been shown to blur temporal and spectral cues, to flatten formant transitions, reduce amplitude modulations associated with the fundamental frequency (F_0), and increase low-frequency energy which in turn results in greater masking of higher frequencies (e.g., see Bistafa and Bradley, 2000). In effect, reverberation can severely degrade consonant perception by smoothing out the envelope modulations that carry informa-

tion about the abrupt onsets and offsets of consonants (Nabelek *et al.*, 1989). In the context of cochlear implants, Poissant *et al.* (2006) were the first to demonstrate, using acoustic simulations, that the aforementioned temporal smearing effects can become even more detrimental when listening through only a limited number of spectral channels that are usually available to implant subjects.

Beamforming techniques are known to work well in anechoic settings, but their performance degrades in reverberant conditions (Hamacher *et al.*, 1997; van Hoesel and Clark, 1995). In the study by van Hoesel and Clark (1995), beamforming attenuated (spatially separated) noise by 20 dB in anechoic settings, but only by 3 dB in highly reverberant settings. Additionally, beamformers are more prone to target signal cancellation, when longer adaptation filters are used (e.g., see Greenberg and Zurek, 1992). In contrast, the proposed BSS method seems to be robust in both anechoic and reverberant conditions. No comparisons were provided in the present study between the beamforming and BSS algorithms, as the main scope of this paper is to provide a proof of concept and establish the potential of BSS as an efficient pre-processing technique that can be used in bilateral cochlear implant devices. Nevertheless, further experiments are warranted comparing the performance of beamforming and BSS algorithms using the same filter parameters and data.

The proposed BSS method operates by gaining access to a single processor driving two implants. Such a processor, the SPEAR3®, is currently made available from CRC for research purposes. As illustrated in Fig. 1, the signals acquired by the two microphones (placed in each of the two ears) are fed as input to the BSS algorithm running on a single processor. The main advantage in using this paradigm (single processor driving two implants) is that it provides access to intact binaural cues present in the incoming signals (left and right). As the BSS algorithm is formulated using a convolutive setup, we can take advantage of binaural cues, such as ITDs (expressed as filter delays) and ILDs (variations in the filters coefficients). Consequently, the ITD and ILD information is implicitly modeled and exploited by the BSS algorithm. It should be noted that the BSS technique described here, can also be easily applied to a unilateral implant configuration, as long as the speech processor is furnished with two microphones. An example of such speech processor is the Nucleus Freedom™ implant system currently being marketed by Cochlear®. The present study focused on the potential of BSS in providing benefits in intelligibility for bilateral implant subjects in anechoic and reverberant conditions. Further work will assess whether the BSS-processed signals (presented diotically) diminish the bilateral subject's ability to localize sounds.

V. CONCLUSIONS

The present study assessed the performance of BSS, which has been largely unexplored in the context of bilateral cochlear implants. Evaluation of the proposed BSS algorithm with five bilateral cochlear implant users indicated significant benefits in intelligibility in both anechoic and reverberant conditions. The documented improvement in intelligibility was consistent for the two types of maskers tested and was quite substantial particularly in the 90° and 30° spatial configurations.

In our opinion, the established BSS framework is a crucial contribution to the future development of novel speech processing strategies for bilateral cochlear implants. Further work is needed to reduce the computational load involved with long adaptation filters, which can become increasingly heavy within reverberant conditions. One possibility, currently under investigation, is to apply the BSS algorithm to speech processed in subbands (e.g., see Kokkinakis and Loizou, 2007). This is similar to the subband processing schemes widely applied to several commercially available coding strategies to date.

ACKNOWLEDGMENTS

This work was in part supported by Grant No. R01-DC07527 from the National Institute on Deafness and Other Communication Disorders (NIDCD) of the National Institutes of Health (NIH). The authors would like to thank the bilateral cochlear implant patients for their time and dedication during their participation in this study.

[1]BSS exploits the fact that two (or more) signals, such as speech emitted from different physical sources (e.g., two different talkers) are mutually *statistically independent* (Comon, 1994). Put simply, two or more speech signals are said to be independent of each other, if and only if the amplitude of one signal provides no information with respect to the amplitude of the other, at any given time.

[2]This is a somewhat confusing term, as an AIR can only describe a point-to-point transfer function and it therefore insufficient to characterize a room as a whole (Kinsler *et al.*, 2000).

[3]The reverberation time (T_{60}) is defined as the interval in which the reverberating sound energy, due to decaying reflections, reaches one millionth of its initial value. In other words, it is the time it takes for the reverberation level to drop by 60 dB below the original sound energy present in the room at a given instant, as shown in Fig. 6(b).

[4]The advantage using such an approximation lies in the fact that FIR filters are inherently stable (Orfanidis, 1996).

[5]In the signal processing literature, the "whitening" effect is defined as the unwanted flattening in the estimated signal power spectrum, essentially causing energy at higher frequencies to increase at the expense of energy in lower frequency bands (e.g., see Kokkinakis and Nandi, 2006). In general, whitening is responsible for generating audibly meaningless signal estimates with impaired listening quality and so far has been a major deterrent towards the use of BSS techniques on speech enhancement applications. Here, we manage to completely avoid whitening by managing to cancel (or deconvolve) the slowly time-varying effects of the reverberant room, while preventing temporal smearing on the recovered source estimates, by essentially preserving the rapidly time-varying responses due to the vocal tract.

[6]The IEEE sentence lists were not counterbalanced among subjects in the present study (only the conditions were counterbalanced to avoid order effects), due to the small number of subjects available. Nevertheless, we believe that by using two lists (20 sentences) per condition rather than one (10 sentences) we minimize the variability in scores between individual IEEE lists.

Amari, S.-I., Cichocki, A., and Yang, H. H. (**1996**). *A New Learning Algorithm for Blind Signal Separation*, Advances in Neural Information Processing Systems, Vol. **8** (MIT, Cambridge), pp. 757–763.

Bell, A. J., and Sejnowski, T. J. (**1995**). "An information maximization approach to blind separation and blind deconvolution," Neural Comput. **7**, 1129–1159.

Bistafa, S. R., and Bradley, J. S. (**2000**). "Reverberation time and maximum background-noise level for classrooms from a comparative study of speech intelligibility metrics," J. Acoust. Soc. Am. **107**, 861–875.

Blauert, J., Brueggen, M., Bronkhorst, A. W., Drullman, R., Reynaud, G., Pellieux, L., Krebber, W., and Sottek, R. (**1998**). "The AUDIS catalog of human HRTFs," J. Acoust. Soc. Am. **103**, 3082.

Cardoso, J.-F. (**1989**). "Source separation using higher-order moment," in *Proceedings of the IEEE International Conference on Acoustics, Speech and Signal Processing*, Glasgow, Scotland, pp. 2109–2112.

Comon, P. (**1994**). "Independent component analysis: A new concept?," Signal Process. **36**, 287–314.

Culling, J. F., Hodder, K. I., and Toh, C.-Y. (**2003**). "Effects of reverberation on perceptual segregation of competing voices," J. Acoust. Soc. Am. **114**, 2871–2876.

Freyman, R. L., and Zurek, P. M. (**2002**). "Effects of room reverberation on spatial release from masking," J. Acoust. Soc. Am. **111**, 2421.

Greenberg, Z. E., and Zurek, P. M. (**1992**). "Evaluation of an adaptive beamforming method for hearing aids," J. Acoust. Soc. Am. **91**, 1662–1676.

Griffiths, L. J., and Jim, C. W. (**1982**). "An alternative approach to linearly constrained adaptive beamforming," IEEE Trans. Antennas Propag. **AP-30**, 27–34.

Hamacher, V., Doering, W., Mauer, G., Fleischmann, H., and Hennecke, J. (**1997**). "Evaluation of noise reduction systems for cochlear implant users in different acoustic environments," Am. J. Otol. **18**, S46–S49.

Haykin, S. (**2000**). *Blind Source Separation, Unsupervised Adaptive Filtering*, Vol. **1** (Wiley, New York).

Haykin, S., and Chen, Z. (**2005**). "The cocktail party problem," Neural Comput. **17**, 1875–1902.

Hochberg, I., Boothroyd, A., Weiss, M., and Hellman, S. (**1992**). "Effects of noise and noise suppression on speech perception for cochlear implant users," Ear Hear. **13**, 263–271.

Hyvärinen, A., Karhunen, J., and Oja, E. (**2001**). *Independent Component Analysis* (Wiley, New York).

IEEE (**1969**). "IEEE recommended practice speech quality measurements," IEEE Trans. Audio Electroacoust. **AU-17**, 225–246.

Jutten, C., and Hérault, J. (**1991**). "Blind separation of sources. I An adaptive algorithm based on neuromimetic architecture," Signal Process. **24**, 1–10.

Kinsler, L. E., Frey, A. R., Coppens, A. B., and Sanders, J. V. (**2000**). *Fundamentals of Acoustics*, 4th edition (Wiley, Chichester, UK).

Kokkinakis, K., and Loizou, P. C. (**2007**). "Subband-based blind signal processing for source separation in convolutive mixtures of speech," in *Proceedings of the IEEE International Conference on Acoustics, Speech and Signal Processing*, Honolulu, HI, pp. 917–920.

Kokkinakis, K., and Nandi, A. K. (**2004**). "Optimal blind separation of convolutive audio mixtures without temporal constraints," in *Proceedings of the IEEE International Conference on Acoustics, Speech and Signal Processing*, Montréal, Canada, pp. 217–220.

Kokkinakis, K., and Nandi, A. K. (**2005**). "Exponent parameter estimation for generalized Gaussian probability density functions with application to speech modeling," Signal Process. **85**, 1852–1858.

Kokkinakis, K., and Nandi, A. K. (**2006**). "Multichannel blind deconvolution for source separation in convolutive mixtures of speech," IEEE Trans. Speech Audio Process. **14**, 200–213.

Lambert, R. H. (**1996**). "Multichannel blind deconvolution: FIR matrix algebra and separation of multi-path mixtures," Ph.D. thesis, University of Southern California, Los Angeles.

Lambert, R. H., and Bell, A. J. (**1997**). "Blind separation of multiple speakers in a multipath environment," in *Proceedings of the IEEE International Conference on Acoustics, Speech and Signal Processing*, Munich, Germany, pp. 423–426.

Lawson, D. T., Wilson, B. S., Zerbi, M., van den Honert, C., Finley, C. C., Farmer, J. C., Jr., McElveen, J. J., Jr., and Roush, P. A. (**1998**). "Bilateral cochlear implants controlled by a single speech processor," Am. J. Otol. **19**, 758–761.

Lee, T.-W., Bell, A. J., and Orglmeister, R. (**1997**). "Blind source separation of real world signals," in *Proceedings of the IEEE International Conference on Neural Networks*, Houston, TX, pp. 2129–2135.

Loizou, P. C. (**1998**). "Mimicking the human ear," IEEE Signal Process. Mag. **15**, 101–130.

Loizou, P. C. (**2006**). "Speech processing in vocoder-centric cochlear implants," in *Cochlear and Brainstem Implants*, edited by A. Moller (Karger Basel, Switzerland), Vol. 64, pp. 109–143.

Loizou, P. C., Lobo, A., and Hu, Y. (**2005**). "Subspace algorithms for noise reduction in cochlear implants," J. Acoust. Soc. Am. **118**, 2791–2793.

Müller, J., Schon, F., and Helms, J. (**2002**). "Speech understanding in quiet and noise in bilateral users of the MED-EL COMBI 40/40+ cochlear implant system," Ear Hear. **23**, 198–206.

Müller-Deile, J., Schmidt, B. J., and Rudert, H. (**1995**). "Effects of noise on speech discrimination in cochlear implant patients," Ann. Otol. Rhinol. Laryngol. Suppl. **166**, 303–306.

Nabelek, A. K., Letowski, T. R., and Tucker, F. M. (**1989**). "Reverberant overlap- and self-masking in consonant identification," J. Acoust. Soc. Am. **86**, 1259–1265.

Nabelek, A. K., and Picket, J. (**1994**). "Monaural and binaural speech perception through hearing aids under noise and reverberation with normal and hearing-impaired listeners," J. Speech Hear. Res. **17**, 724–739.

Orfanidis, S. (**1996**). *Introduction to Signal Processing*. (Prentice Hall, Englewood Cliffs, NJ).

Parra, L. (**2000**). "Realistic application of acoustic blind source separation," J. Acoust. Soc. Am. **108**, 2628.

Poissant, S. F., Whitmal, N. A., III, and Freyman, R. L. (**2006**). "Effects of reverberation and masking on speech intelligibility in cochlear implant simulations," J. Acoust. Soc. Am. **119**, 1606–1615.

Qin, M. K., and Oxenham, A. J. (**2003**). "Effects of simulated cochlear-implant processing on speech reception in fluctuating maskers," J. Acoust. Soc. Am. **114**, 446–454.

Schroeder, M. R. (**1965**). "New method for measuring the reverberation time," J. Acoust. Soc. Am. **37**, 409–412.

Shaw, E. A. G. (**1974**). "Transformation of sound pressure level from free field to the eardrum in the horizontal plane," J. Acoust. Soc. Am. **56**, 1848–1861.

Shinn-Cunningham, B. G., and Kopco, N. (**2002**). "Effects of reverberation on spatial auditory performance and spatial auditory cues," J. Acoust. Soc. Am. **111**, 2440.

Shinn-Cunningham, B. G., Kopco, N., and Martin, T. J. (**2005**). "Localizing nearby sound sources in a classroom: Binaural room impulse responses," J. Acoust. Soc. Am. **117**, 3100–3115.

Shynk, J. J. (**1992**). "Frequency-domain and multirate adaptive filtering," IEEE Signal Process. Mag. **9**, 14–37.

Stickney, G. S., Zeng, F.-G., Litovsky, R., and Assmann, P. F. (**2004**). "Cochlear implant speech recognition with speech maskers," J. Acoust. Soc. Am. **116**, 1081–1091.

Stone, J. V. (**2004**). *Independent Component Analysis: A Tutorial Introduction* (MIT, Cambridge, MA).

Tyler, R. S., Dunn, C. C., Witt, S., and Preece, J. P. (**2003**). "Update on bilateral cochlear implantation," Curr. Opin. Otolaryngol. Head Neck Surg. **11**, 388–393.

Tyler, R. S., Gantz, B. J., Rubinstein, J. T., Wilson, B. S., Parkinson, A. J., Wolaver, A., Preece, J. P., Witt, S., and Lowder, M. W. (**2002**). "Three-month results with bilateral cochlear implants," Ear Hear. **23**, 80S–89S.

van Hoesel, R. J. M., and Clark, G. M. (**1995**). "Evaluation of a portable two-microphone adaptive beam-forming speech processor with cochlear implant patients," J. Acoust. Soc. Am. **97**, 2498–2503.

van Hoesel, R. J. M., and Clark, G. M. (**1997**). "Psychophysical studies with two binaural cochlear implant subjects," J. Acoust. Soc. Am. **102**, 495–507.

van Hoesel, R. J. M., and Tyler, R. S. (**2003**). "Speech perception, localization, and lateralization with binaural cochlear implants," J. Acoust. Soc. Am. **113**, 1617–1630.

Vandali, A. E., Whitford, L. A., Plant, K. L., and Clark, G. M. (**2000**). "Speech perception as a function of electrical stimulation rate: Using the Nucleus 24 cochlear implant system," Ear Hear. **21**, 608–624.

Weiss, M. (**1993**). "Effects of noise and noise reduction processing on the operation of the Nucleus 22 cochlear implant processor," J. Rehabil. Res. Dev. **30**, 117–128.

Yang, L.-P., and Fu, Q.-J. (**2005**). "Spectral subtraction-based speech enhancement for cochlear implant patients in background noise," J. Acoust. Soc. Am. **117**, 1001–1004.

Yen, K.-C., and Zhao, Y. (**1999**). "Adaptive co-channel speech separation and recognition," IEEE Trans. Speech Audio Process. **7**, 138–151.

Zahorik, P. (**2002**). "Direct-to-reverberant energy ratio sensitivity," J. Acoust. Soc. Am. **112**, 2110–2117.

Zhao, Y., Yen, K.-C., Soli, S., Gao, S., and Vermiglio, A. (**2002**). "On application of adaptive decorrelation filtering to assistive listening," J. Acoust. Soc. Am. **111**, 1077–1085.

Measurement of vocal-tract influence during saxophone performance

Gary P. Scavone,[a] Antoine Lefebvre, and Andrey R. da Silva
Computational Acoustic Modeling Laboratory, Centre for Interdisciplinary Research in Music Media and Technology, Music Technology, Schulich School of Music, McGill University, Montreal, Québec, Canada H3A 1E3

(Received 5 July 2007; revised 11 January 2008; accepted 13 January 2008)

This paper presents experimental results that quantify the range of influence of vocal tract manipulations used in saxophone performance. The experiments utilized a measurement system that provides a relative comparison of the upstream windway and downstream air column impedances under normal playing conditions, allowing researchers and players to investigate the effect of vocal-tract manipulations in real time. Playing experiments explored vocal-tract influence over the full range of the saxophone, as well as when performing special effects such as pitch bending, multiphonics, and "bugling." The results show that, under certain conditions, players can create an upstream windway resonance that is strong enough to override the downstream system in controlling reed vibrations. This can occur when the downstream air column provides only weak support of a given note or effect, especially for notes with fundamental frequencies an octave below the air column cutoff frequency and higher. Vocal-tract influence is clearly demonstrated when pitch bending notes high in the traditional range of the alto saxophone and when playing in the saxophone's extended register. Subtle timbre variations via tongue position changes are possible for most notes in the saxophone's traditional range and can affect spectral content from at least 800–2000 Hz. © *2008 Acoustical Society of America.* [DOI: 10.1121/1.2839900]

PACS number(s): 43.75.Ef, 43.75.Pq, 43.75.St, 43.75.Yy [NFH] Pages: 2391–2400

I. INTRODUCTION

Since the late 1970s, there has been significant interest in understanding the role and influence of a player's vocal tract in wind instrument performance. Acousticians generally agree that, in order for such influence to exist in reed-valve instruments, the player's upstream windway must exhibit input impedance maxima of similar or greater magnitude than those of the downstream air column.[1] Most musicians concur that they can influence sound via vocal-tract manipulations, though there is less consensus in terms of the extent of such influence or the specifics of how this is done.[2] A number of previous studies have been reported but attempts to demonstrate and/or quantify vocal-tract influence have not been conclusive. These analyses have been complicated by the fact that measurement of the upstream windway configuration and impedance are difficult under performance conditions.

It is the aim of this study to provide experimental results that substantiate the discussion on the role of vocal tract manipulations in wind instrument performance. The results are obtained using a measurement system that allows the analysis of vocal tract influence in real time during performance.

Most previous acoustical studies of vocal-tract influence have focused on the measurement of the input impedance of players' upstream windways while they simulate or mimic oral cavity shapes used in playing conditions.[1,3–6] These measurements have then been compared with the input impedance of the downstream instrument air column to show instances where the vocal tract might be able to influence the reed vibrations. The majority of these investigations are in agreement with regard to the existence of an adjustable upstream wind-way resonance in the range of 500–1500 Hz, which corresponds to the second vocal-tract resonance.[3–6] On the other hand, musicians do not appear to manipulate the first vocal-tract resonance, which is typically below about 300 Hz.[6] In Ref. 6, players reported using a fairly stable vocal-tract shape for most normal playing conditions, with upstream manipulations taking place mainly in the altissimo register and for special effects. A brief review of previous studies and a discussion of their limitations is provided by Fritz and Wolfe.[6]

Numerical investigations have also been reported that couple an upstream windway model to a complete wind instrument system.[7–10] Simplified, single-resonance models of a player's windway have been shown to reproduce bugling, pitchbend, multiphonics, and glissando characteristics in clarinet and saxophone models, effects generally associated with vocal-tract influence.[8,9]

Many performers have used x-ray fluoroscopic or endoscopic approaches to analyze the vocal tract shapes and manipulations used while playing their instruments.[2,11–15] These studies have reported some general trends in vocal-tract configurations for different registers, produced mainly by variations of the tongue position, but have not well addressed the underlying acoustic principles involved.

A fundamental limitation of previous acoustical investigations is related to the fact that the measurements were not conducted in real time. Subjects were required to mime and

[a]Electronic mail: gary@music.mcgill.ca.

hold a particular vocal-tract setting for up to 10 s, a task that is likely difficult and uncomfortable for the player. Despite the results of Fritz and Wolfe[6] that indicate players' have consistent "muscle" (or procedural) memory, it is not clear that subjects can accurately reproduce the exact vocal-tract configurations of interest in this study without playing the instrument because auditory, and perhaps vibrotactile, feedback is important in fine-tuning and maintaining an oral cavity configuration. Further, these methods only provide data for the held setting, without indicating the time-varying characteristics of vocal-tract manipulations. This last issue remains for a recently reported approach that allows the upstream impedance to be measured while the instrument is played.[16]

This paper addresses the previously mentioned limitations by providing a running analysis of vocal-tract influence over time (not solely at discrete moments in time). This is achieved using a measurement system embedded in an E♭ alto saxophone that allows a relative comparison of the upstream windway and downstream air column impedances under normal playing conditions. The same approach could also be applied to clarinets, though we chose to concentrate on saxophones given our own playing experience with them.

This paper is organized as follows: Section II describes the measurement approach, including the system and procedures used to evaluate vocal-tract influence. Section III presents the measured data for playing tasks involving traditional and extended registers, pitch bend, bugling, multiphonics, and timbre variation. Finally, Sec. IV concludes with an analysis of the results in the context of saxophone performance practice.

II. MEASUREMENT APPROACH

Measurements made for this study were based on continuity of volume flow at the reed junction,

$$U_u = U_d = \frac{P_u}{Z_u} = \frac{P_d}{Z_d} \Rightarrow \frac{Z_u}{Z_d} = \frac{P_u}{P_d}, \tag{1}$$

where u and d subscripts represent upstream and downstream quantities, respectively. This expression is attributed first to Elliot and Bowsher[17] in the context of brass instrument modeling. This implies that a *relative* measure of the upstream and downstream impedances can be obtained from the entrance pressures in the player's mouth and the instrument mouthpiece, which is sufficient to indicate when vocal-tract influence is being exerted. That is, it is assumed that the upstream system can be influential when values of Z_u are close to or greater than those of Z_d and this can be determined from their ratio without knowing the distinct value of each. Because measurements of the mouth and mouthpiece pressures can be acquired *while* the instrument is being played, this approach allows the player to interact normally with the instrument. Further, as modern computers can calculate and display the pressure spectra in real time, players and researchers can instantly see how vocal tract changes directly affect the upstream impedance.

In this context, the reed is assumed to be primarily controlled by the pressure difference across it and thus, a measurement of these two pressures can provide a good indication of how the reed oscillations are influenced by the two systems on either side of it. While it may not be possible to use this approach to reconstruct or calculate an upstream impedance characteristic from measurements of Z_d, P_d, and P_u (as attempted by Wilson[5]), it is valid to indicate instances of upstream influence. This argument ignores the possible effect of hydrodynamic forces on the behavior of the reed due to unsteady flow.[18–20]

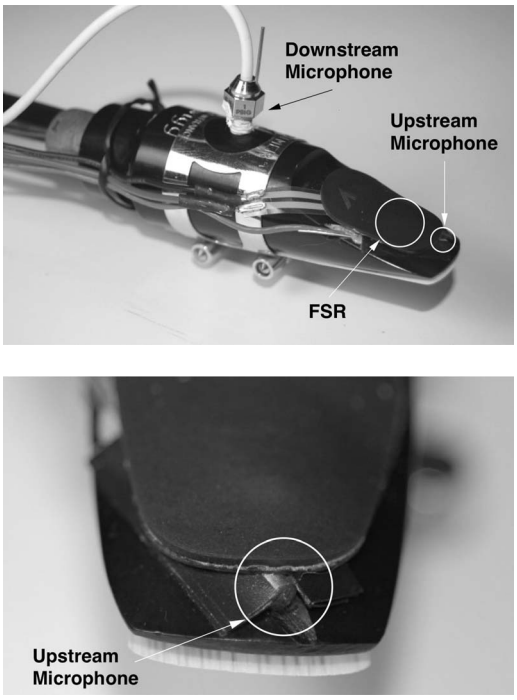

FIG. 1. Saxophone mouthpiece system.

A. Measurement system

The measurement approach used in this study requires the simultaneous acquisition of the "input" pressures on the upstream and downstream sides of the instrument reed under normal playing conditions. Therefore, it was necessary to find a nonintrusive method for measuring pressures in the instrument mouthpiece and the player's mouth near the reed tip. Such measurements are complicated by the fact that the sound pressure levels (SPL) in a saxophone mouthpiece under playing conditions can reach 160 dB or more[21] and that the dimensions of the alto saxophone mouthpiece require relatively small microphones to allow normal playing conditions and to avoid interference with the normal reed/mouthpiece interaction.

After tests with a prototype system,[22] a special saxophone mouthpiece was developed as shown in Fig. 1. An Endevco 8510B-1 pressure transducer was threaded through the top of the mouthpiece 55 mm from the mouthpiece tip to obtain internal pressure values. For pressure measurements inside the player's mouth, a groove was carved in the top of the saxophone mouthpiece for an Endevco 8507C-1 miniature pressure transducer of 2.34 mm diameter such that the transducer tip was positioned 3 mm behind the front edge of

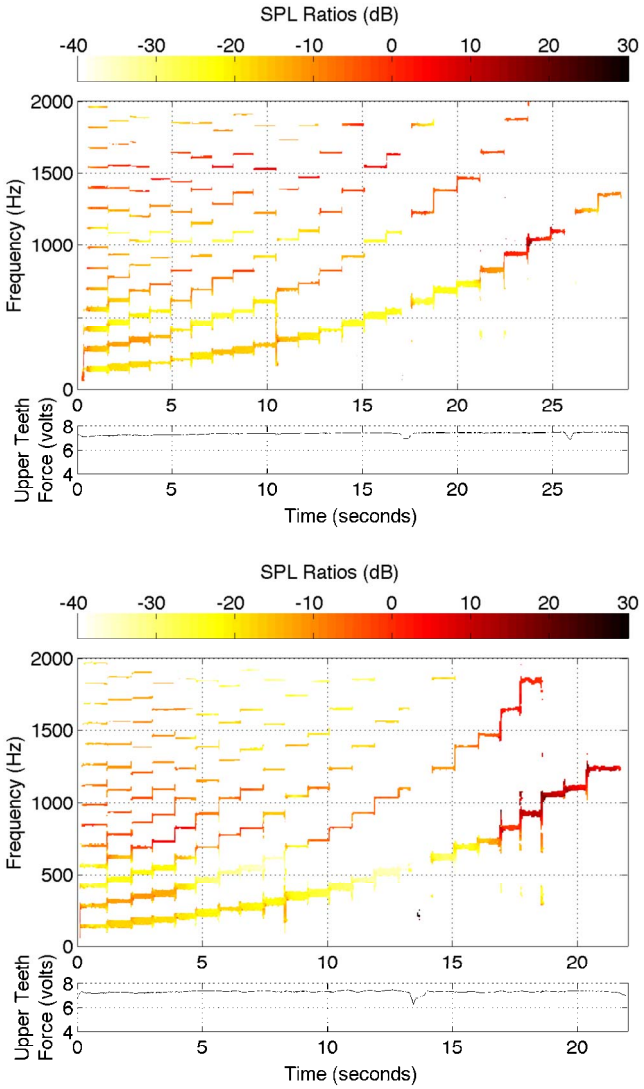

FIG. 2. (Color online) Spectrograms of the SPL ratio between the mouthpiece and the mouth pressures when playing a scale (Subjects A and D, from top to bottom).

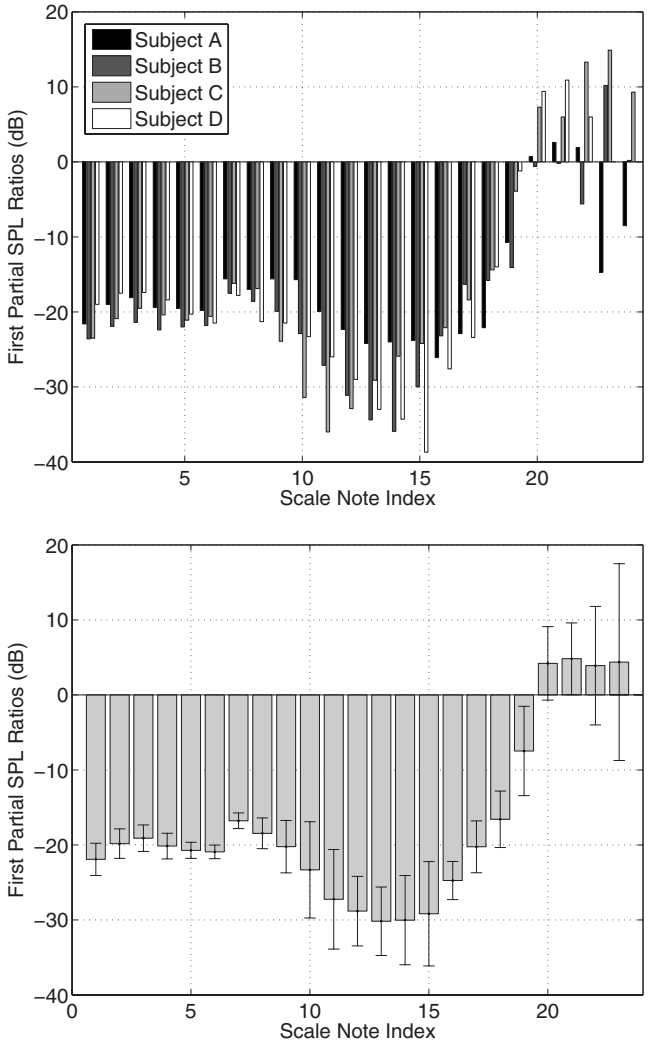

FIG. 3. Average SPL ratios for first partials of scale: individual by subject (top) and for all subjects (bottom).

the mouthpiece. This position is well within the mouth given that the player's teeth typically rest anywhere from about 13 to 20 mm from the mouthpiece tip. Both Endevco transducers are rated for maximum SPLs between 170 and 180 dB and were found to be unaffected by moisture.

Ideally, both microphones would be located at the front edge of the mouthpiece (inside and outside), which represents the input to both the downstream and upstream air columns. Wilson[5] experimented with two mouthpiece transducer locations on a clarinet and selected the more distant position (39 mm) because of noise due to unsteady flow nearer the reed tip. The results from a digital waveguide simulation using a cylinder-cone model[23] suggest that the signal recorded by the 8510B-1 transducer at a distance of 55 mm from the tip differs from the downstream input impedance peak values by less than 2 dB for frequencies up to 1500 Hz and less than 3.7 dB for frequencies up to 2000 Hz. Thus, the microphone positioning does not represent a limitation, considering that the frequency range analyzed in this study does not exceed 2000 Hz and that we are mainly interested in the use of a vocal-tract resonance that runs from about 500 to 1500 Hz.

The pressure transducers were connected to an Endevco 136 differential voltage amplifier and the signals from there were routed to a National Instruments (NI) PCI-4472 dynamic signal acquisition board. The acquisition card sample rate was set to 12 000 Hz. An NI LABVIEW interface was designed to allow real-time display of the spectra of the two pressure signals. The Endevco transducers were calibrated relative to one another prior to the experiment, as described in the Appendix.

To help distinguish between vocal tract and embouchure changes, a small circular (12.7 mm diameter) force sensing resistor (FSR) made by Interlink Electronics was placed under the cushion on the top of the saxophone mouthpiece to obtain a relative measure of the upper teeth force (see Fig. 1). The time-varying sensor voltages were input to the signal acquisition board for storage and to provide a running display of "embouchure movement" in the LABVIEW interface. Although this setup provided no data on movements of the lower lip, normal embouchure adjustments involve a simul-

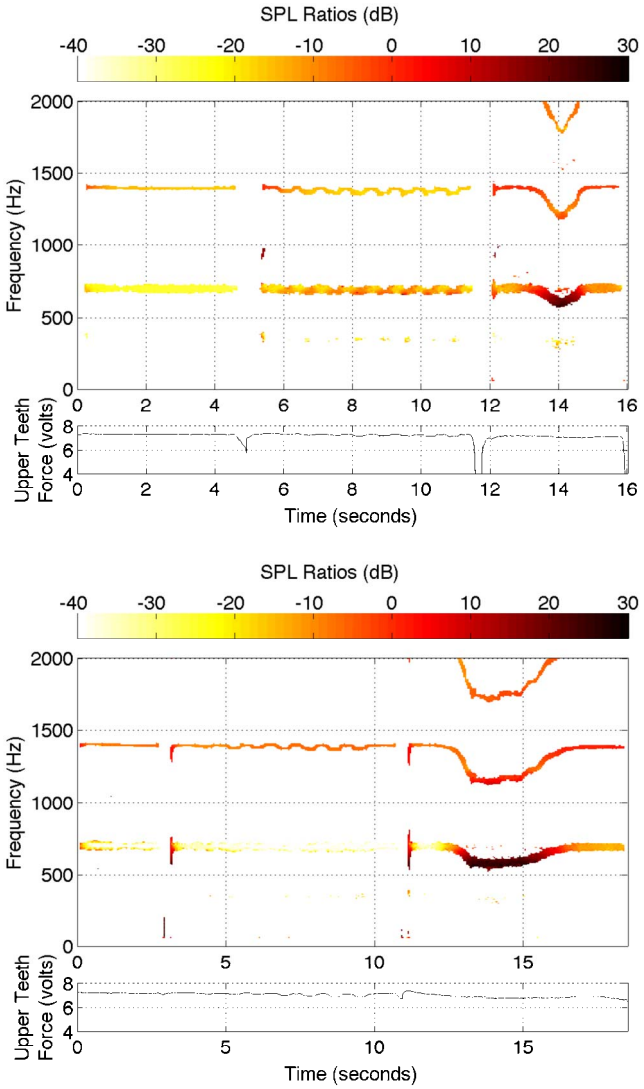

FIG. 4. (Color online) Spectrograms of the SPL ratio between the mouthpiece and the mouth pressures when playing a written D6 without vibrato, with a slow lip vibrato, and bending via vocal tract manipulations (Subjects B and D, from top to bottom).

taneous variation of both the upper teeth and lower lip. The primary purpose of this sensor was to provide players with visual feedback to help them focus on maintaining a fixed embouchure setting, rather than acquiring an absolute measure of lip or teeth force.

Playing tests were conducted in an IAC (Industrial Acoustics Company) double-walled sound isolation booth to minimize external sound interference. In addition to the mouthpiece described previously, a single Vandoren #3 (medium hardness) reed and Selmer Super Action Series II alto saxophone (serial number 438024) were used for the entire experiment.

B. Player tests

Upstream influence was evaluated using the measurement system through a series of playing tests with a group of four professional saxophonists. Subject C was the first author of this paper. The subjects filled out a questionnaire about their saxophone background and experience and were given

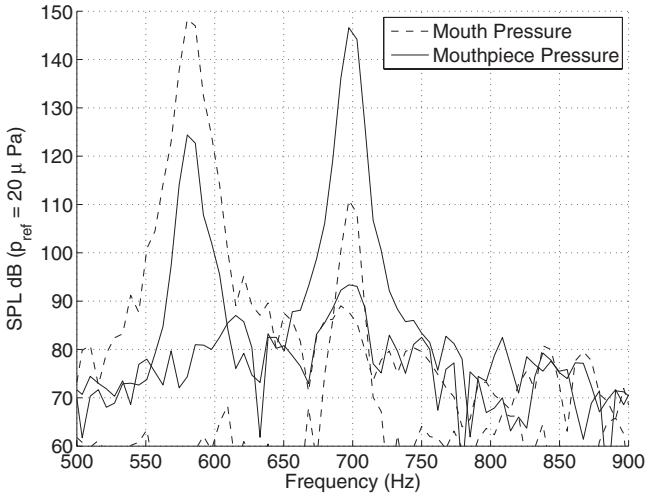

FIG. 5. Overlaid snapshots of the pitch bend spectra on an alto saxophone at the starting frequency (700 Hz) and at the lowest frequency trajectory (580 Hz) for Subject D.

about 5 min to become accustomed to the mouthpiece and saxophone setup. They were allowed to practice the requested tasks before the recording began. After the subjects were comfortable with all the tasks, data storage was initiated and each task was performed in sequential order. When subjects had difficulty with a given task, they were allowed to repeat it. A large real-time display of the FSR reading was provided and the subjects were told to avoid making embouchure changes while performing the tasks.

III. RESULTS

To examine variations of upstream influence over time, many of the results in the subsequent sections are displayed via spectrograms of the ratio of the SPL in decibels (or power spectral densities) of the mouth and mouthpiece pressures. To reduce artifacts arising from the ratio calculation, spectral bins containing no significant energy in both the upstream and downstream power spectra were masked. The measured upper teeth force is also plotted to indicate the relative steadiness of a player's embouchure setting.

A. Traditional and extended registers

The traditional range of a saxophone is from written B♭3–F♯6, which on an alto saxophone corresponds to the frequency range 138.6–880 Hz. Advanced players can play a further octave or more using cross-fingerings, a range referred to as the "altissimo" or extended register. In order to evaluate general player trends over the full range of the instrument, each subject was asked to play an ascending legato written B♭ (D♭ concert pitch) scale from the lowest note on the instrument to the highest note that could comfortably be held (which was typically near a written C7 in the extended register), playing each note for about 0.5 s.

Representative spectrograms of the SPL ratios of upstream and downstream pressures for this task are shown in Fig. 2, as played by Subjects A and D. Breaks in the measured upper teeth force indicate instances where subjects stopped to breath. SPL averages computed at the fundamen-

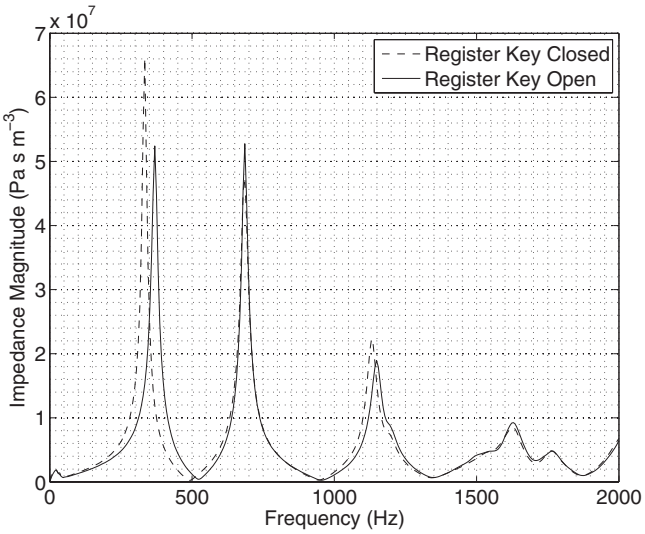

FIG. 6. Input impedance of the alto saxophone for the D6 fingering.

tal frequencies for each scale note are shown in Fig. 3 for each subject and averaged across all subjects. For most notes in the traditional range, the SPL ratios at the fundamental frequencies are below −20 dB. In other words, pressures in the mouthpiece for these notes are typically 10 times greater than those in the players' mouths. Based on the assumptions outlined in Sec. II, this indicates a similar ratio of input impedance peak levels at the fundamental playing frequencies on either side of the reed and thus minimal upstream influence for notes in this range. These ratios display a local minima centered at the thirteenth note of the scale (466 Hz), which may be related to the fact that notes in this range are relatively easy to play. The standard deviation of the SPL ratios are shown by the error bars in the lower plot of Fig. 3.

A fairly abrupt change in SPL ratios is evident when subjects prepare to enter the extended register, a result that was also reported by Fritz and Wolfe.[6] Scale note index 19 in Fig. 3 is the highest note (written F6) in the scale that falls within the traditional register. An alternate fingering exists for F6 on the saxophone that has a playing behavior more like extended register notes (it is based on the use of a third air column partial), though the fingering used by subjects in this study was not specified or recorded. Averaged SPL ratios across all subjects for the extended register notes are between 3 and 5 dB, though the standard deviation is significant. In particular, Subjects A and B show large variations in SPL ratios from note to note in this range, whereas the results for Subjects C and D are more consistent. It should be noted that the task called for a legato scale, or slurring from note to note. Future studies could investigate potential variations of SPL ratios in the extended register when the notes are attacked individually, with or without breaks between each.

It has been suggested by Wilson[5] that performers might tune upstream resonances with higher harmonics of a played note. There are some instances in Fig. 2 (and the data for the other subjects) where the ratios for upper partials of notes are near 0 dB, typically in the range 600–1600 Hz, though this varies significantly among the subjects. However, no systematic note-to-note tuning with an upper harmonic was found. It is unlikely that upstream tuning would help stabilize a note unless the fundamental is weak and only one or two higher partials exist below the cutoff frequency of the instrument. That said, variations of upper partial ratios could affect the timbre of the instrument and this is investigated further in Sec. III E.

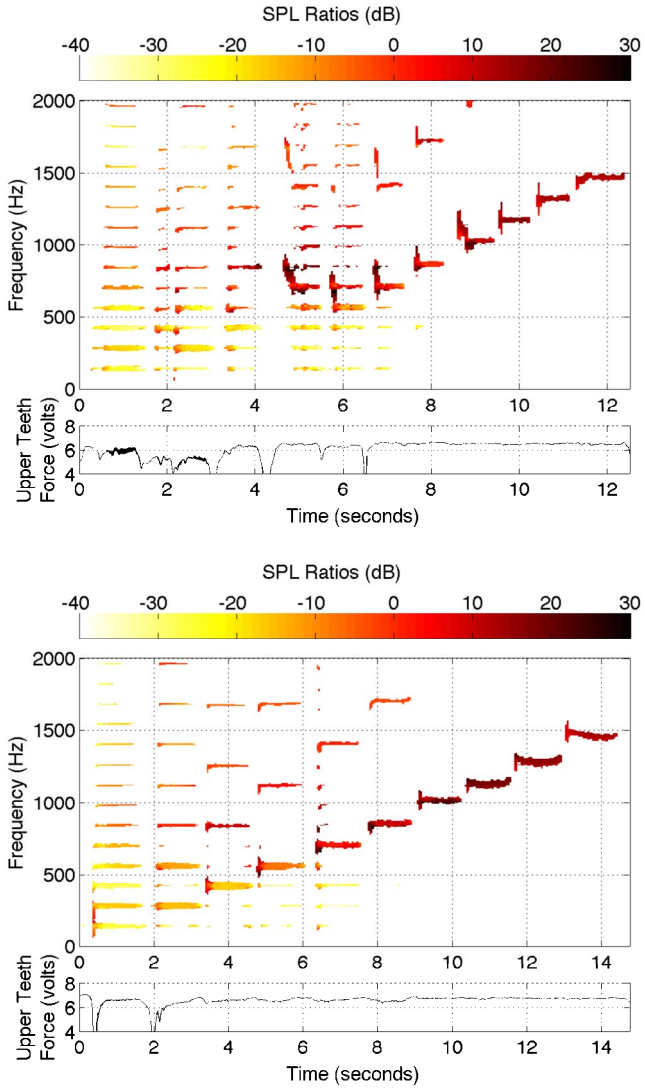

FIG. 7. (Color online) Spectrograms of the SPL ratio between the mouth and mouth piece pressures when performing the bugling task (Subjects B and C, from top to bottom).

B. Pitch pending

Saxophonists make frequent use of pitch bends in their playing, especially in jazz contexts. There are several ways such frequency modifications can be achieved, including lip pressure and tonehole key height changes, as well as vocal tract manipulations. Lip pressure variations, which are used to produce vibrato, affect the average reed tip opening and can yield maximum frequency modulations of about half a semitone. The use of vocal tract manipulations for pitch bend can achieve downward frequency shifts of a musical third or more. Significant upward frequency shifts using lip pressure

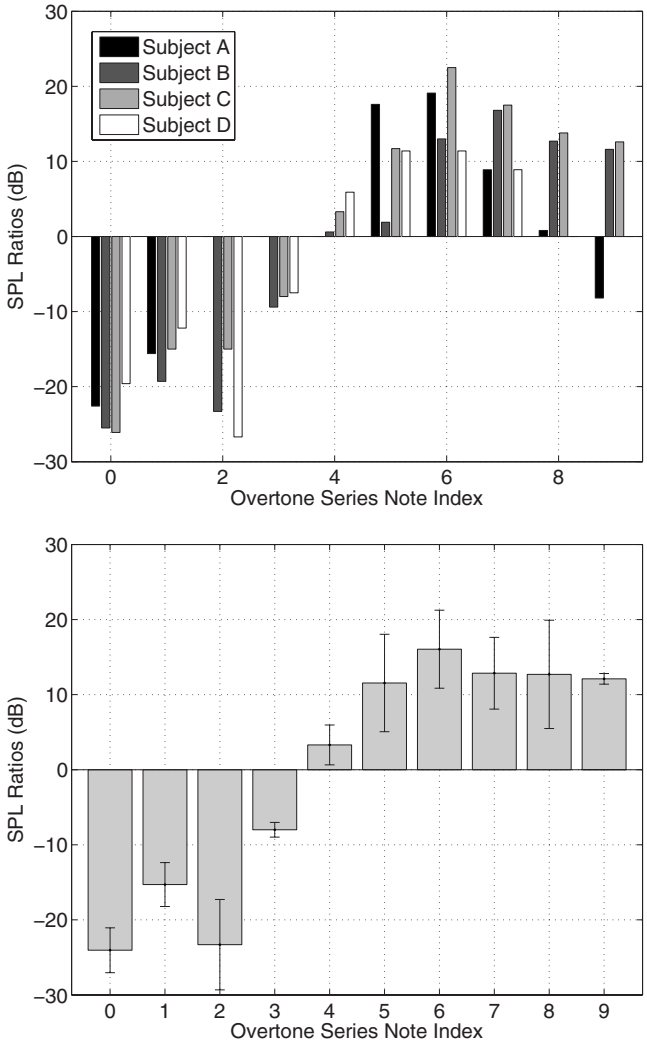

FIG. 8. Average SPL ratios at each overtone series frequency: individual by subject (top) and for all subjects (bottom).

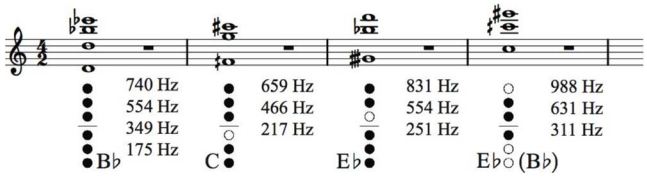

FIG. 9. (Color online) Fingerings and approximate sounding notes (written and frequencies) for four requested multiphonics.

or the vocal tract are not possible. On an alto saxophone, bends produced via vocal-tract manipulations are easiest when starting on notes above concert E♭5. Bends that start above a concert C5 tend to have a lower limit around the C5 frequency (523 Hz). In other words, the fingered note controls the starting (and highest) frequency of the bend range but the minimum frequency is generally always between 500 and 600 Hz.

Pitch bending has previously been investigated with respect to vocal tract influence.[5,6] In the present study, subjects were asked to finger a written high D6 (698 Hz) with the first palm key and to play the note normally, without vibrato, for about 3 s. They were then asked to play the note with a slow vibrato (about 1 Hz), modulating the pitch up and down as much as possible *using lip pressure only*. Finally, subjects were instructed to perform, *without varying their lip pressure*, a slow downward pitch bend to the lowest note they could comfortably maintain, hold that note for about 1 s, and then bend the note back to the starting D pitch.

Figure 4 shows representative spectrograms of the SPL ratios of upstream and downstream pressures for Subjects B and D when performing the requested tasks. The average SPL ratio at the fundamental frequency, across all subjects, when played normally without vibrato was −25 dB, with a standard deviation of 9.3. Subjects B, C, and D demonstrated a consistent vibrato frequency range, using lip pressure variations only, of about 677–700 Hz (or 54 cents down and about 5 cents up). Subject A's range for the same task was 655–690 Hz, but his SPL fundamental ratios were as high as 3.4 dB at the vibrato frequency dips, indicating that he used some vocal-tract manipulation as well. For the pitch bend performed without lip pressure variation, the lower frequency limits of the four subjects were 583, 597, 558, and 570 Hz, respectively, with corresponding fundamental frequency SPL ratios of 29.1, 22.7, 30.7, and 25.1 dB. The subjects averaged a frequency drop of 330 cents with a SPL ratio of 26.9 and a standard deviation of 3.7. Snapshots of the upstream and downstream spectra at the starting frequency and lowest frequency trajectory of the pitch bend task for Subject D are overlaid in Fig. 5. At the starting frequency of about 700 Hz, the upstream and downstream SPLs differ by about −35 dB, while at the bottom of the bend, they differ by about 25 dB.

The input impedance of the alto saxophone used for this study with a D6 fingering is shown in Fig. 6, from which it is clear that the instrument has no strong resonance between 400 and 650 Hz. This measurement was obtained using a two-microphone transfer function technique.[24,25] Given the fixed fingering and relatively constant lip pressure used by the subjects, as well as the fact that lip pressure variations alone can only produce bends of about 54 cents, the pitch bends of 300 cents and more can only be the result of vocal-tract manipulation. The high SPL ratio during the bend indicates that a significantly stronger resonance exists in the players' mouths during the pitch bend than in the downstream air column. The implication is that performers can create a resonance in the upstream windway in the range 700–550 Hz (for this task) that is strong enough to override the downstream air column and assume control of the reed vibrations.

The upstream resonance frequency is mainly controlled via tongue position variations. The pitch bend is only possible for notes higher in the traditional range, where the air column resonance structure is relatively weak. We speculate that the lower frequency limit on the pitch bend is related to the vocal-tract physiology and players' control of the second upstream resonance within an approximate range of about 520–1500 Hz, which is close to that reported by Benade.[3] This is corroborated by the fact that a similar lower frequency limit is found when pitch bending on both soprano and tenor saxophones. Informal tests on a B♭ clarinet indi-

cate a greater variance in the lower pitch bend range with different fingerings, though the overall range still falls within the limits mentioned earlier.

C. "Bugling"

Bugling involves the articulation of the notes of an overtone series while maintaining a fixed low note fingering. Beginning students can normally produce the first and second overtones, sometimes inadvertently while trying to play the fundamental. It typically takes many years of practice to develop the flexibility that allows one to cleanly attack the higher overtones. In this task, subjects were asked to finger a written B♭3 (all holes closed) and to play an overtone series, attacking each note individually.

Representative spectrograms of the SPL ratios for the bugling exercise are shown in Fig. 7, as played by Subjects B and C. Individual subject averages, as well as averages across all subjects, computed at the fundamental frequencies of each overtone are shown in Fig. 8. Subject D did not play overtones 8–9 and Subject A was unable to play overtones 2–4 and 9. Vocal tract influence is not clearly evident until the third overtone, where downstream instrument resonances begin to weaken. In general, it is difficult to play the third overtone without some vocal tract manipulation and it appears that a ratio of about −7 dB is sufficient to allow this to happen. It also may be possible that, when playing the third overtone, players reinforce the 1130 Hz component with an upstream resonance rather than the component at 563 Hz, which falls at the lower end of the adjustable upstream resonance range. Averaging across Subjects B, C, and D, the SPL ratio of the 1130 Hz component when playing the fundamental of the overtone series is −8.7 dB. The ratio at this same frequency when playing the third overtone is 4.8 dB.

D. Multiphonics

Multiphonics involve oscillations of the reed based on two inharmonic downstream air column resonance frequencies and their intermodulation components.[26] Two relatively easy and two more difficult multiphonics were chosen for analysis with respect to potential vocal-tract influence. The four multiphonic fingerings and their approximate sounding notes are illustrated in Fig. 9.

Figure 10 shows the SPL ratios for four different multiphonics, as played by Subjects B and D. The sounds produced by the two subjects differed significantly. From the plots, there are more spectral components evident in the sounds of Subject D. We expect that a player can influence the sound quality of a multiphonic by aligning an upstream resonance with one or more components. For example, both subjects appear to reinforce a group of partials in the range 875–1075 Hz for the last multiphonic. SPL ratio levels for Subject D were, across all tasks, generally higher than those of Subject B. This suggests that Subject D makes use of stronger upstream resonances, which likely explains both the higher ratios for this task, as well as the greater spectral density of the multiphonic sounds.

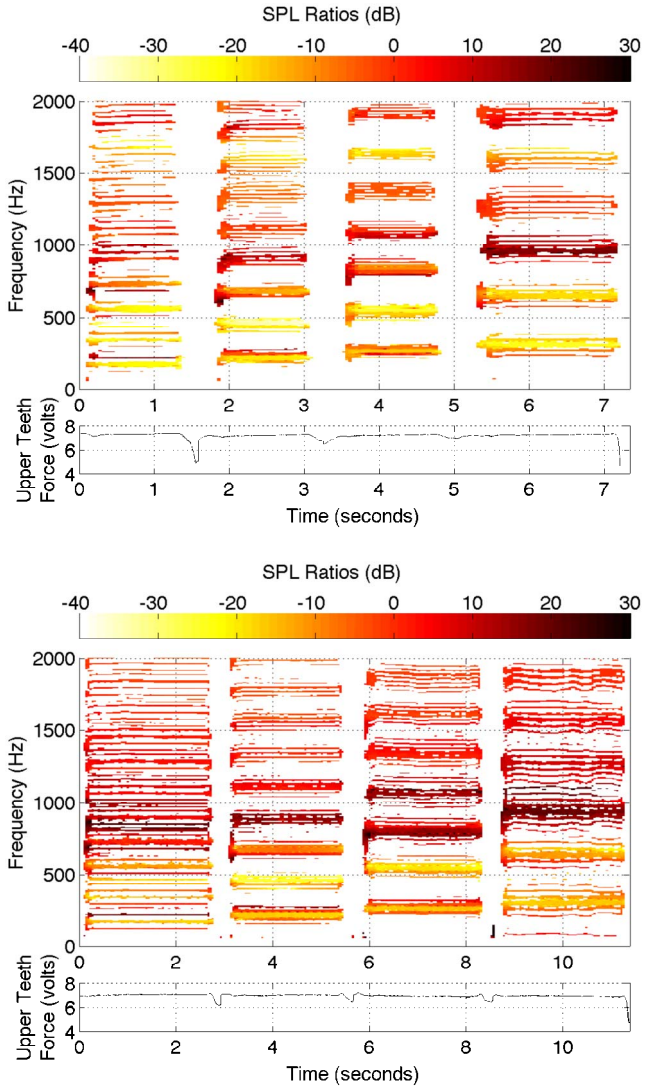

FIG. 10. (Color online) Spectrograms of the SPL ratio between the mouth and mouthpiece pressures when playing four multiphonics (Subjects B and D, from top to bottom).

E. Timbre variations

In a questionnaire, all subjects indicated that they thought they could influence the sound of the saxophone via vocal-tract variations. They reported using upstream influence to control and adjust tone color (timbre), pitch, and extended register notes. To investigate timbre variations via vocal-tract manipulation, subjects were asked to play a steady written F4 (207.7 Hz) and to move their tongue periodically toward and away from the reed while maintaining a constant embouchure setting.

Figure 11 shows spectrograms of the SPL ratios resulting from this task, as played by Subjects A and C. Partials four and higher show clear variations in SPL ratios with tongue motion. Snapshots of the mouth and mouthpiece spectra for Subject C are shown in Fig. 12 at times of 4 and 5 seconds. Although both the upstream and downstream spectra varied with tongue position, the upstream changes were most significant. For example, the downstream SPL of the fourth partial only changes by +3 dB between the two

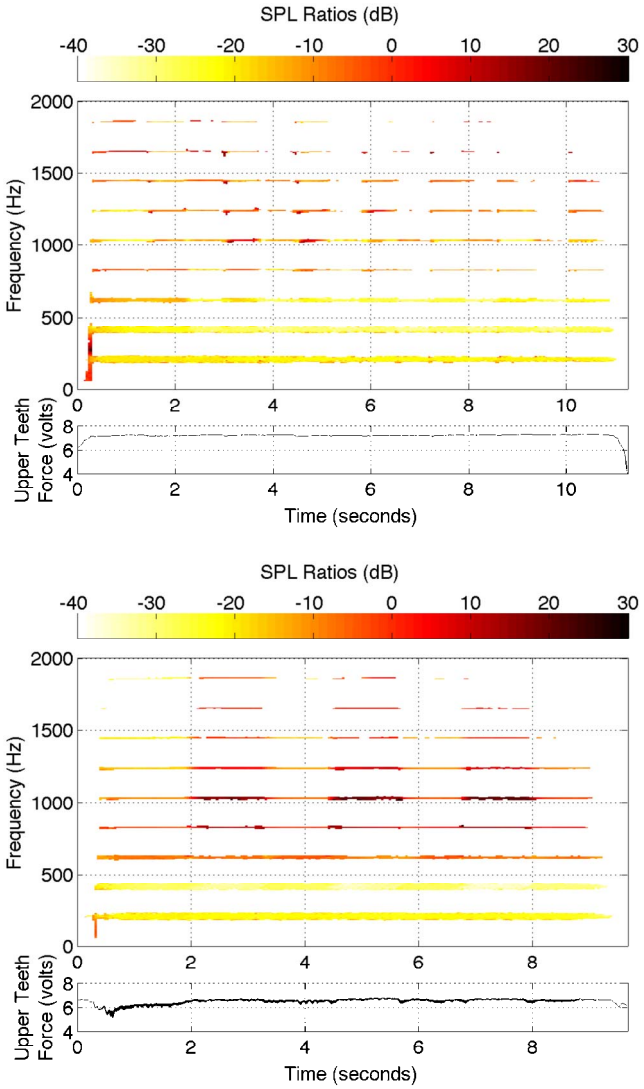

FIG. 11. (Color online) Spectrograms of the SPL ratio between the mouth and mouthypiece pressures when varying tongue position while holding an F3 (Subjects A and C, from top to bottom).

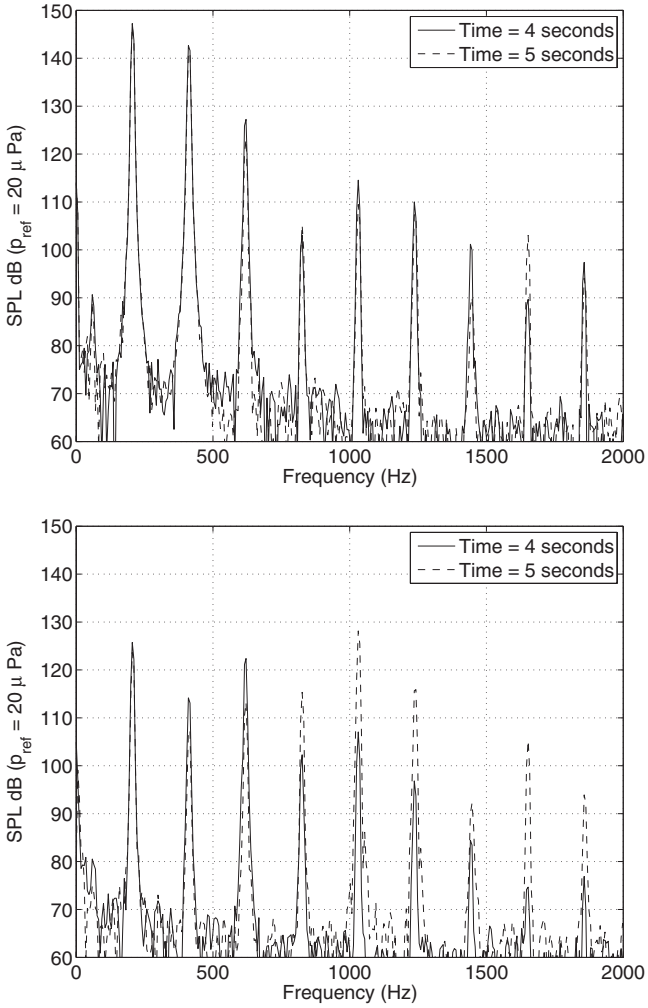

FIG. 12. Snapshots of the mouthpiece (top) and mouth (bottom) spectra for the tongue variation task at times of 4 and 5 s as played by Subject C.

times, whereas the upstream SPL increases by +13 dB. For this partial and subject, the SPL ratio goes from an average of −0.7 to 9.9 dB, or a difference of 10.6 dB between the two tongue positions. The change of downstream and upstream SPL for two tongue position extremes is collated for partials 1–9 and Subjects A-C in Fig. 13. Subject D's results showed no clear variation of SPL ratios over time and it is likely this person did not properly understand the requested task. In general, tongue movements toward the reed tended to boost upstream frequency components from about 800 Hz to at least 2000 Hz. Note that these spectral changes occur simultaneously over a wide frequency range and thus are likely the result of a more wide bandwidth upstream resonance. Below 800 Hz, the effect of the tongue position movement varied significantly among the subjects. It is not possible to say whether these variations were the result of differences in physiology or tongue positions.

IV. DISCUSSION

Results of the tongue movement task indicate that vocal-tract manipulations can be used throughout the playing range of the saxophone to produce subtle timbre variations involving frequency components from at least 800–2000 Hz. These timbre variations simultaneously affect partials over a wide frequency range, which implies the use of a relatively wide bandwidth upstream resonance. The pitch bend, extended register, and bugling tasks, however, indicate that vocal-tract influence significant enough to override downstream air column control of reed vibrations is only possible when the downstream system provides weak support of a given note. This is normally the case for notes with fundamental frequencies an octave below the downstream air column cutoff frequency (around 1500 Hz for the alto saxophone[27]) and higher. Thus, significant vocal-tract influence can be exerted for notes near the top of the alto saxophone's conventional range and on into the extended (or altissimo) register. This type of influence makes use of a narrow upstream resonance that the player manipulates to control the fundamental vibrating frequency of the reed.

Various special fingerings are used when playing notes in the saxophone's extended register but these provide only weak downstream support of a note. When students unaccustomed with altissimo register playing try these fingerings, they produce a weak tone lower in the traditional range of

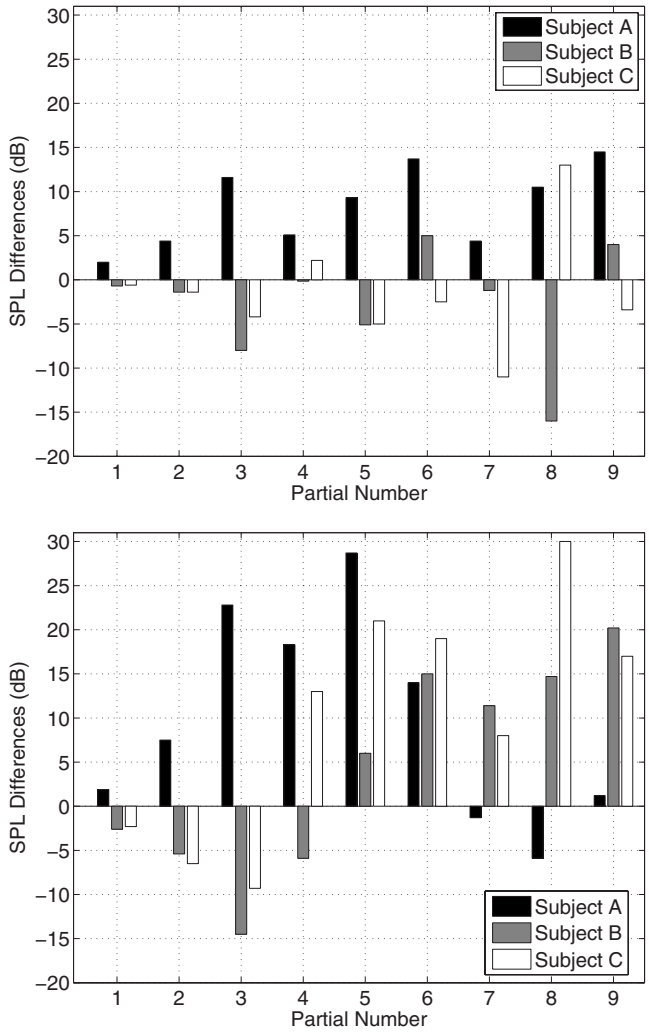

FIG. 13. SPL changes in mouthpiece (top) and mouth (bottom) between two tongue position extremes for partials 1–9 of held F3 (Subjects A, B, and C).

the instrument. From the discussion above, this implies the need for vocal-tract influence when playing in the extended register. There were a few instances when the SPL ratios for Subjects A and B fell below 0 dB while playing in this range (see Figs. 3 and 8). This might happen because a given fingering produced a relatively strong downstream resonance at the fundamental playing frequency or it is possible these subjects made embouchure adjustments that were not detected by the FSR on the top of the mouthpiece. The subjects were instructed to avoid making embouchure changes for all tasks in this study. However, it is common for performers to move their lower lip forward, away from the reed tip, in preparation for playing in the saxophone's altissimo register. The authors assume this reduces the reed damping, with a corresponding increase in the reed resonance frequency, and that this may help to maintain normal operation of the reed in its "stiffness controlled" region. As well, extended register playing is generally easier with stiffer reeds. Notes near the top of the extended register, with fundamentals in the range 1400–2000 Hz, may be beyond the range of a high-Q second vocal-tract resonance. It is not clear whether players stabilize these extreme high notes, which are difficult to produce consistently even for professionals, with a vocal-tract resonance and/or by manipulating the reed resonance frequency.

One of the clearest examples of the use of vocal-tract influence involves pitch bending, with downward frequency modulations 5–6 times greater than that possible via lip pressure variations alone. Pitch bends are not possible for notes lower than about a concert C5 (523 Hz), at the lower extreme of the main adjustable upstream resonance and where several downstream air column resonances can help stabilize a note.

The results of this study are less conclusive with respect to the production of multiphonics. Performers who are unable to play in the extended register of the saxophone normally also have trouble producing the more difficult multiphonics. This would imply the use of an upstream resonance to support one or more intermodulation components. A future study should compare successful and unsuccessful multiphonic attempts for a fixed fingerings in an effort to verify this behavior. There were considerable differences in the sound and quality of the multiphonics produced by the subjects of this study and this is likely related to variations in the upstream system.

Finally, there is a common misconception among some scientists and players that vocal-tract influence is exerted on a nearly continuous basis while playing a single-reed instrument in its *traditional range*.[5,13] For example, an early study by Clinch *et al.*[13] concluded "that vocal tract resonant frequencies must match the frequency of the required notes in clarinet and saxophone performance." Likewise, Wilson[5] claims that for most tones in analyzed melodic phrases, "the performer's airways were tuned to the first harmonic or to the second harmonic, or there was a resonance aligned with both the first and second harmonics." A related conclusion is made by Thompson[28] with respect to variations of the reed resonance. These suggestions have no basis in performance practice. Although it is true that effects such as pitch slides common to jazz playing may involve some level of vocal-tract influence, most professional musicians use and advocate a relatively fixed vocal-tract shape during normal playing. This behavior is corroborated by Fritz and Wolfe.[6] It seems likely that players vary their embouchure and perhaps their vocal-tract shape gradually when moving from low to high register notes, but this should be understood to vary with register and not on a note-by-note basis (until one gets to the altissimo register). The results of this study indicate that vocal-tract influence for "normal" playing within the traditional range of the alto saxophone is primarily limited to timbre modification because most of these notes are well supported by the downstream air column.

A website and video demonstrating the measurement system described in this paper is available online.[29]

ACKNOWLEDGMENTS

The authors thank the anonymous reviewers for their insightful comments and suggestions. They also acknowledge the support of the Natural Sciences and Engineering Research Council of Canada, the Canadian Foundation for

Innovation, and the Centre for Interdisciplinary Research in Music Media and Technology at McGill University. The doctoral research of the second and third authors is supported by the Fonds Québécois de la Recherche sur la Nature et les Technologies and CAPES (Funding Council of the Brazilian Ministry of Education), respectively. Finally, we would like to thank Bertrand Scherrer for his help in developing the first prototype of the National Instruments LABVIEW measurement system.

APPENDIX: TRANSDUCER CALIBRATION

A JBL 2426H compression driver was connected to a steel cylindrical pipe of 150 mm length and 25.4 mm diameter. The calibration is valid up to the cutoff frequency of the first higher order mode, which is $f_c = 1.84c/(2\pi a) \approx 8$ kHz for a radius $a = 12.7$ mm and a speed of sound $c = 347$ m/s.[30] At the far end of this pipe, the two transducers were fit through a cap such that they extended a few millimeters beyond the cap surface. A 60-s noise sequence was played through the system and power spectral densities were determined using a modified averaged periodogram of 1024 data points and 50% overlap (Hanning windows) at a sampling rate of 48 kHz. In order to match fast Fourier transform bins used in the LABVIEW interface and the subsequent data analysis, the calibration data was downsampled to 12 kHz. The power spectral densities were computed with the `pwelch` and `cpsd` functions in MATLAB. The transfer function relating the gain and phase differences between the microphones was obtained as:[31]

$$\hat{H}_{12} = \frac{\hat{S}_{22} - \hat{S}_{11} + \sqrt{(\hat{S}_{11} - \hat{S}_{22})^2 + 4|\hat{S}_{12}|^2}}{2\hat{S}_{21}},$$

where

$$\hat{S}_{11} = \texttt{PWELCH(P1,HANNING(N),N/2,N,FS)},$$

$$\hat{S}_{22} = \texttt{PWELCH(P2,HANNING(N),N/2,N,FS)},$$

$$\hat{S}_{12} = \texttt{CPSD(P1,P2,HANNING(N),N/2,N,FS)},$$

and

$$\hat{S}_{21} = \texttt{CPSD(P2,P1,HANNING(N),N/2,N,FS)}.$$

A similar calibration technique was previously reported by Seybert and Ross.[24]

[1] J. Backus, "The effect of the player's vocal tract on woodwind instrument tone," J. Acoust. Soc. Am. **78**, 17–20 (1985).
[2] M. Watkins, "The saxophonist's vocal tract. 1," Saxophone Symp. **27**, 51–78 (2002).
[3] A. H. Benade, "Air column, reed, and player's windway interaction in musical instruments," in *Vocal Fold Physiology, Biomechanics, Acoustics, and Phonatory Control*, edited by I. R. Titze and R. C. Scherer (Denver Center for the Performing Arts, Denver, CO, 1985), Chap. 35, pp. 425–452.
[4] P. L. Hoekje, "Intercomponent energy exchange and upstream/downstream symmetry in nonlinear self-sustained oscillations of reed instruments," Ph.D. thesis, Case Western Reserve University, Cleveland, OH, 1986.
[5] T. D. Wilson, "The measured upstream impedance for clarinet performance and its role in sound production," Ph.D. thesis, University of Washington, Seattle, WA, 1996.
[6] C. Fritz and J. Wolfe, "How do clarinet players adjust the resonances of their vocal tracts for different playing effects?," J. Acoust. Soc. Am. **118**, 3306–3315 (2005).
[7] S. D. Sommerfeldt and W. J. Strong, "Simulation of a player-clarinet system," J. Acoust. Soc. Am. **83**, 1908–1918 (1988).
[8] R. Johnston, P. G. Clinch, and G. J. Troup, "The role of the vocal tract resonance in clarinet playing," Acoust. Aust. **14**, 67–69 (1986).
[9] G. P. Scavone, "Modeling vocal-tract influence in reed wind instruments," in *Proceedings of the 2003 Stockholm Musical Acoustics Conference*, Stockholm, Sweden, pp. 291–294.
[10] P. Guillemain, "Some roles of the vocal tract in clarinet breath attacks: Natural sounds analysis and model-based synthesis," J. Acoust. Soc. Am. **121**, 2396–2406 (2007).
[11] R. L. Wheeler, "Tongue registration and articulation for single and double reed instruments," Natl. Assoc. College Wind Percussion Instruct. J. **22**, 3–12 (1973).
[12] W. E. J. Carr, "A videofluorographic investigation of tongue and throat positions in playing flute, oboe, clarinet, bassoon, and saxophone," Ph.D. thesis, University of Southern California, Los Angeles, CA, 1978.
[13] P. G. Clinch, G. J. Troup, and L. Harris, "The importance of vocal tract resonance in clarinet and saxophone performance: A preliminary account," Acustica **50**, 280–284 (1982).
[14] J. T. Peters, "An exploratory study of laryngeal movements during performance on alto saxophone," Master's thesis, North Texas State University, Denton, TX, 1984.
[15] M. Patnode, "A fiber-optic study comparing perceived and actual tongue positions of saxophonists successfully producing tones in the altissimo register," Ph.D. thesis, Arizona State University, 1999.
[16] J.-M. Chen, J. Smith, and J. Wolfe, "Vocal tract interactions in saxophone performance," in *Proceedings of the International Symposium on Musical Acoustics*, Barcelona, Spain, 2007.
[17] S. Elliott and J. Bowsher, "Regeneration in brass wind instruments," J. Sound Vib. **83**, 181–217 (1982).
[18] A. R. da Silva, G. P. Scavone, and M. van Walstijn, "Numerical simulations of fluid-structure interactions in single-reed mouthpieces," J. Acoust. Soc. Am. **122**, 1798–1809 (2007).
[19] J. van Zon, A. Hirschberg, J. Gilbert, and A. Wijnands, "Flow through the reed channel of a single reed instrument," J. Phys. (Paris), Colloq. **54**, C2 821–824 (1990).
[20] A. Hirschberg, R. W. A. van de Laar, J. P. Marrou-Maurières, A. P. J. Wijnands, H. J. Dane, S. G. Kruijswijk, and A. J. M. Houtsma, "A quasi-stationary model of air flow in the reed channel of single-reed woodwind instruments," Acustica **70**, 146–154 (1990).
[21] X. Boutillon and V. Gibiat, "Evaluation of the acoustical stiffness of saxophone reeds under playing conditions by using the reactive power approach," J. Acoust. Soc. Am. **100**, 1178–1889 (1996).
[22] G. P. Scavone, "Real-time measurement/viewing of vocal-tract influence during wind instrument performance (A)," J. Acoust. Soc. Am. **119**, 3382 (2006).
[23] G. P. Scavone, "Time-domain synthesis of conical bore instrument sounds," in *Proceedings of the 2002 International Computer Music Conference*, Göteborg, Sweden, pp. 9–15.
[24] A. Seybert and D. Ross, "Experimental determination of acoustic properties using a two-microphone random excitation technique," J. Acoust. Soc. Am. **61**, 1362–1370 (1977).
[25] A. Lefebvre, G. P. Scavone, J. Abel, and A. Buckiewicz-Smith, "A comparison of impedance measurements using one and two microphones," in *Proceedings of the International Symposium on Musical Acoustics*, Barcelona, Spain, 2007.
[26] J. Backus, "Multiphonic tones in the woodwind instrument," J. Acoust. Soc. Am. **63**, 591–599 (1978).
[27] A. H. Benade and S. J. Lutgen, "The saxophone spectrum," J. Acoust. Soc. Am. **83**, 1900–1907 (1988).
[28] S. C. Thompson, "The effect of the reed resonance on woodwind tone production," J. Acoust. Soc. Am. **66**, 1299–1307 (1979).
[29] G. P. Scavone, http://www.music.mcgill.ca/~gary/vti/, 2007 (last viewed 11 January 2008).
[30] N. H. Fletcher and T. D. Rossing, *The Physics of Musical Instruments* (Springer, New York, 1991).
[31] J. H. P. R. White and M. H. Tan, "Analysis of the maximum likelihood, total least squares and principal component approaches for frequency response function estimation," J. Sound Vib. **290**, 676–689 (2006).

Numerical simulation of a piano soundboard under downbearing

Adrien Mamou-Mani,[a] Joël Frelat, and Charles Besnainou
Institut Jean Le Rond d'Alembert, UPMC/CNRS, Paris, Ile de France, 75005, France

(Received 30 October 2007; revised 27 December 2007; accepted 2 January 2008)

A finite element model of a piano soundboard is used to study the effect of the strings tension (downbearing) on its vibration, considering the ribs, the bridges and the crown. The downbearing is modeled with the prestress theory. Prestress calculation with linear and nonlinear models including geometric rigidity are compared in terms of the modal frequencies. The effects of the downbearing in modal frequencies and mobility are investigated and the importance of the crown on these results is evaluated. A simple phenomenological law is exhibited, which characterizes the evolution of eigenfrequencies with downbearing, including the initial crown.
© *2008 Acoustical Society of America.* [DOI: 10.1121/1.2836787]

PACS number(s): 43.75.Mn [NHF] Pages: 2401–2406

I. INTRODUCTION

In 1940, Bilhuber and Johnson[1] tackled the question of the importance of the downbearing of the soundboards in the piano sound quality. They observed notable differences in the energy of vibration related to the downbearing level, but they did not come to a conclusion about changes in perceivable timbre due to downbearing. From that work, measurements have dealt with the soundboards' properties,[2–8] for different kinds of pianos, including a one-design prototype.[2] Moore and Zietlow[3] are the only ones who make a comparison in modal shapes for an upright piano without and with strings. They observed large changes in the first modal shapes and frequencies with the strings application. Wogram[4] and Conklin[5] showed that the soundboard mobility on the bridges depends on the strings tension in terms of frequencies and quality factor.

Some authors have proposed models of piano soundboards. Wogram felt the possible use of the finite element analysis to simulate the making process. Giordano[9] showed that a simple model made of an orthotropic plate and ribs is sufficient to simulate the global properties. Berthaut *et al.*[6] chose a precise finite element model, and confirmed the performance of this method thanks to a comparison with an experimental modal analysis. But even if the downbearing was considered as one of the most important techniques for piano making, its influence has never been modeled. This paper proposes one modeling of the downbearing by using a prestress approach, including the crown amplitude.

If one considers the vibration, the prestress theory consists of attributing a geometric energy due to an external loading. The total rigidity is the sum between the classical elastic rigidity and the geometric one. Finite element softwares are able to express this total rigidity. Considering small deformation due to the wood characteristics and with the hypothesis of an elastic and linear material, the nonlinearity may come only from the change in geometry during the loading. Two approaches to include prestresses have to be decided:

- the linearized one.[10] The geometric energy is simplified as a linear expression of the loading parameter. This approximation reduces the time of calculus but is limited by the amplitude of displacement.
- the geometrically nonlinear one,[11] including the hypothesis of static large displacements and small deformations of the structure. The geometric rigidity is calculated by an iterative method. The updating at each step of displacement requires much more time for calculus but is necessary if the shape of the system is greatly modified by the loading process.

This paper proposes to find the best way to model the effect of the downbearing on the soundboard properties. This model is made of a soundboard with ribs and bridges coming from a real one. The downbearing is introduced by an induced geometric rigidity. An emphasis is given to the influence of the initial crown on downbearing effects.

II. FINITE ELEMENT MODEL

The finite element model is based on the soundboard of a 1.80 m IBACH piano in Fig. 1. It is made of the plate, 15 ribs and two bridges. The model considers precisely the geometry of the plate and the ribs, the position of the ribs and the bridges. Implemented with CAST3M software,[12] the mesh has 3742 nods and triangle elements with a kinematic of Kirchhoff plates, modeling the whole soundboard. The material properties have been found in the literature,[6] and are presented in Table I.

The thickness is here considered as a 8 mm constant, and the shape of the bass bridge is simplified as a simple plate. The formulation of the discretized eigenvalue problem is

$$\mathbf{Kq} = \omega^2 \mathbf{Mq}, \tag{1}$$

where $\mathbf{K}$ is the elastic rigidity, $\mathbf{q}$ a eigenvector of a mode, ω the associated modal pulsation and $\mathbf{M}$ the mass matrix of the actual system. Adding a simply supported boundary condi-

[a]Author to whom correspondence should be addressed. Electronic mail: mamou-mani@lmm.jussieu.fr

FIG. 1. (Color online) Photographs of the piano soundboard.

tion in Eq. (1), we find the modal shapes presented in Fig. 2. The effects of simple boundary conditions in the first eigenfrequencies of the soundboard are presented in Table II.

These results are the classical flexuring modes, close to the literature ones. However, Suzuki[7] found an extra mode with a geometry close to the second mode but a little larger. He explains this mode by the presence of the rim in the experiment, and calls it the "rim mode." But the model of the present paper does not consider the rim and this mode is not observed. The other modes are close to his results. Table II gives the influence of the boundary conditions on the modal frequencies. Further in this paper, we use a simply supported boundary condition, to simply model the rim possible displacement and the diminution of thickness of the spruce plate close to the rim.

A. Crown modeling

The initial crown of the soundboard is also implemented into the finite element model. The making process to obtain crown depends on the maker and consists of gluing the ribs and using the humidity.[13] Because of the too large complexity of these processes, the crown is only modeled as a geometric change, excluding the induced prestress field resulting from the process.

The crown is incurred by solving a harmonic scalar problem of the soundboard on the mesh with a constant source in the whole domain and Dirichlet boundary conditions. We then get the altitude at each point of the plate through a smooth function of the coordinates with a zero value on the boundary. The crown level is characterized by the altitude of the top of the crown, named b and expressed as a multiple of the thickness. A modal calculus gives the evolution of the frequencies and the modal shapes with b. Figure 3 shows an increase of all frequencies for values above about $b>1$. A cross between the first two modes is observed for $b=5$ due to the geometric changes.

B. Downbearing modeling

The downbearing is modeled as a vertical force per unit length between 0 and 5000 N/m applied on the two bridges, perpendicular to the soundboard. The value of 5000 N/m is approximately the double of the maximum force used in pi-

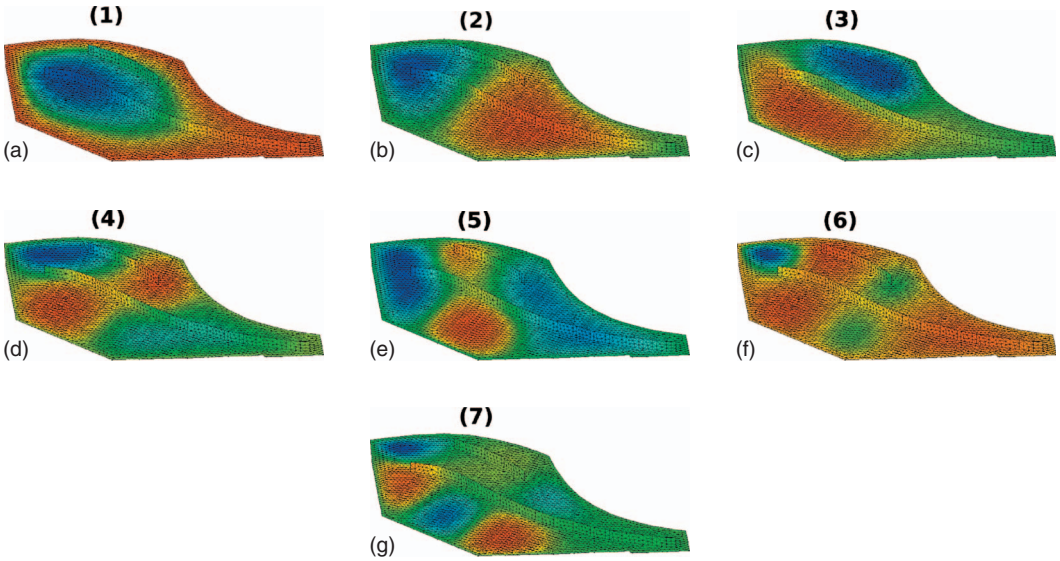

FIG. 2. Shapes of the first seven modes of the piano soundboard with fixed boundaries.

TABLE I. Mechanical properties of a spruced soundboard (see Ref. 6).

ρ	E_x	E_y	ν_{xy}	G_{xy}
392 kg m^{-3}	11.5 GPa	0.47 GPa	0.005	0.5 GPa

ano making.[5] The loading parameter is finally the maximum displacement of the soundboard induced by the load, denoted λ.

C. Linearized or geometrically nonlinear model?

The downbearing is modeled using the prestress theory. The Hamilton principle for a soundboard subjected to an initial stress σ_0 (due to the downbearing on the two bridges here) is (see Ref. 10)

$$\delta\int_{t_1}^{t_2}(T^* - V_{\text{int}}^* - V_g - V_{\text{ext}}^*)dt = 0, \tag{2}$$

$$\delta u_i^*(t_1) = \delta u_i^*(t_2) = 0, \tag{3}$$

where

$$T^* = \int_{\Gamma^*}\rho^* \dot{u}_i^* \dot{u}_i^* dV \text{ the kinetic energy}, \tag{4}$$

$$V_{\text{int}}^* = \int_{\Gamma^*} C_{ijkl}\left(\frac{1}{2}\varepsilon_{ij}^{*(1)}\varepsilon_{kl}^{*(1)}\right)dV \text{ the linear strain energy}, \tag{5}$$

$$V_g = \int_{\Gamma^*}\sigma_{ij}^0\varepsilon_{ij}^{*(2)}dV \textbf{ the geometric strain energy due to the downbearing}, \tag{6}$$

$$V_{\text{ext}}^* \text{ the potential of the external dynamical loading}, \tag{7}$$

$$u_i^* \text{ the displacement during the interval of time } [t_1, t_2], \tag{8}$$

where Γ^* is the prestressed soundboard, σ_{ij}^0 is the initial stress field due to downbearing, ρ^* is the density $\varepsilon_{ij}^{*(1)} = 1/2\left(\partial u_{i/}^*\partial x_j + \partial u_{j/}^*\partial x_i\right)$ and $\varepsilon_{ij}^{*(2)} = 1/2\left(\partial u_{m/}^*\partial x_i\, \partial u_{m/}^*\partial x_j\right)$ are, respectively, the linear part and the quadratic part of the strain field, C_{ijkl} is the elasticity tensor.

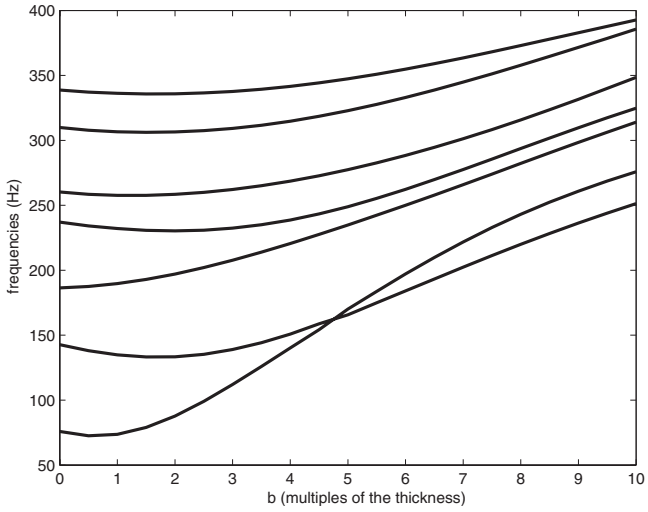

FIG. 3. Evolution of frequencies with crowning without downbearing.

Using a finite element method, the discretized Hamilton principle is

$$\delta\int_{t_1}^{t_2}\left(\frac{1}{2}\dot{\mathbf{q}}^T\mathbf{M}\dot{\mathbf{q}} - \frac{1}{2}\mathbf{q}^T\mathbf{K}\mathbf{q} - \frac{1}{2}\mathbf{q}^T\mathbf{K_g}\mathbf{q} + \mathbf{q}^T\mathbf{g}\right)dt = 0, \tag{9}$$

where $\mathbf{M}$ is the mass matrix, $\mathbf{K}$ is the stiffness matrix $\mathbf{K_g}$ is **the geometric stiffness matrix**, $\mathbf{g}$ is the dynamical load vector and $\mathbf{q}$ are the generalized coordinates of the problem.

The discretized equations of the motion are

$$(\mathbf{K} + \mathbf{K_g})\mathbf{q} + \mathbf{M}\ddot{\mathbf{q}} = \mathbf{g}(t) \tag{10}$$

and the discretized eigenvalue problem

$$(\mathbf{K} + \mathbf{K_g})\mathbf{q} = \omega^2\mathbf{M}\mathbf{q}, \tag{11}$$

where ω is the eigenpulsations of the structure.

The shape of the soundboard Γ^*, the natural rigidity $\mathbf{K}$, the mass $\mathbf{M}$ and the geometric rigidity due to downbearing $\mathbf{K_g}$ may be calculated using two approaches: a linearized one, usually used in engineering, and a nonlinear one which considers static large displacements. The first one consists to suppose that the static displacements are small and the geometric rigidity is then proportional to the loading parameter λ:

$$\mathbf{K_g} = \lambda\mathbf{K_g^*} \tag{12}$$

where $\mathbf{K_g^*}$ is the geometric rigidity obtained under a unitary load. Equation (11) becomes

TABLE II. Frequencies of the first seven modes of the piano soundboard for different boundary conditions.

Mode	Clamped (Hz)	Fixed (Hz)	Free (Hz)
1	93.7	75.9	34.0
2	169	143	52.4
3	216	186	81.8
4	273	237	89.8
5	299	260	119
6	356	310	123
7	383	339	147

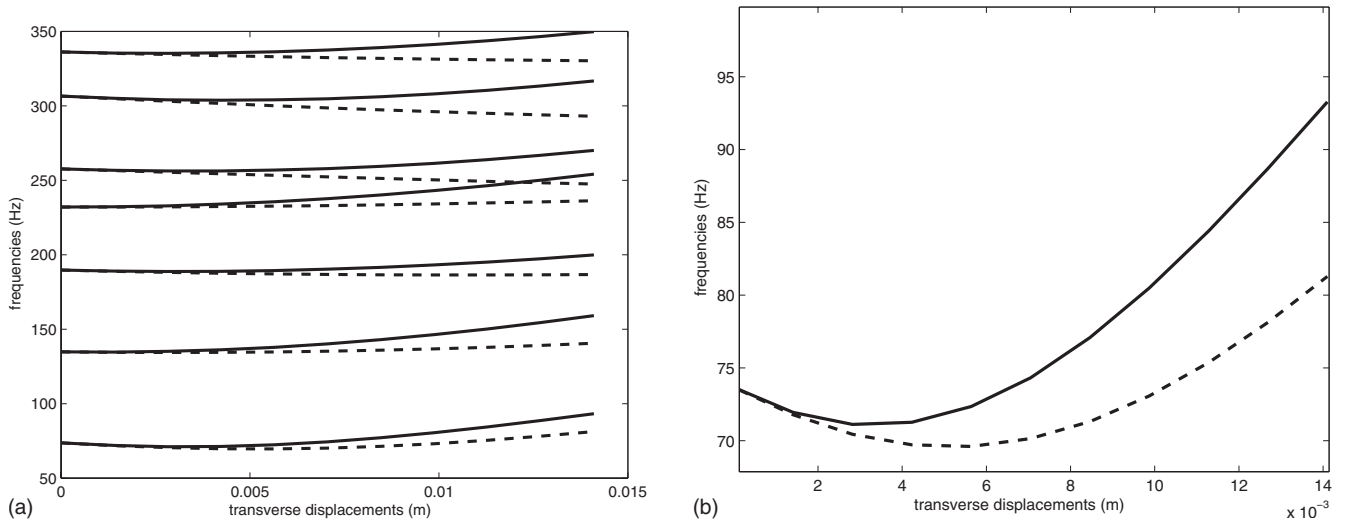

FIG. 4. Evolution of eigenfrequencies with the transverse loading for an initial crown $b=1$ with linearized (dashed) and nonlinear prestresses approaches (non-dashed) (left) and a zoom on the first frequency (right).

$$(\mathbf{K}+\lambda\mathbf{K}_{\mathbf{g}}^{*})\mathbf{q}=\omega^{2}\mathbf{M}\mathbf{q} \tag{13}$$

This approximation drives to fast calculus, because only one calculus of $\mathbf{K}_{\mathbf{g}}^{*}$ is needed. But it gives erroneous results when the displacements are large enough.

In the case of large displacements, an iterative method with an updated geometric rigidity $\mathbf{K}_{\mathbf{g}}$ and shape of the soundboard Γ^{*} at each step of calculus are necessary. The Newton–Raphson method has to be used.

Figure 4 shows the evolution of the first seven eigenfrequencies with these two methods, for the example where $b=1$ (top of the crown=8 mm). Significant differences occur, particularly when the displacements become about the thickness of the plate (8 mm), that is large displacements. The initial crown has also effects on these differences in frequency (see Fig. 5). When $b=2$ (top of the crown=16 mm), 25% of differences occurs for $\lambda=10$ mm (1.125 times the thickness). The linearized prestress model seems to be unacceptable in this case and a complete nonlinear one is then chosen.

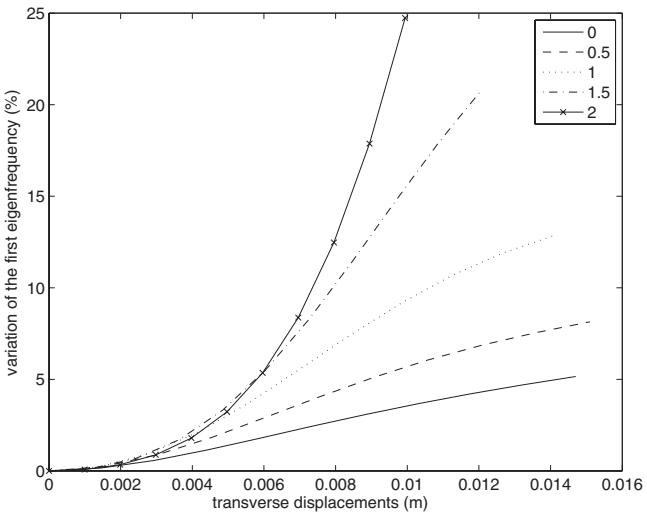

FIG. 5. Effect of the initial crown (value of $b=0,0.5,1,1.5,2$) on the relative differences between linearized and nonlinear prestresses approaches for the first eigenfrequency $((f_{\text{nonlinear}}-f_{\text{linear}})/f_{\text{nonlinear}})$.

III. EFFECT OF DOWNBEARING ON MODAL FREQUENCIES

As known experimentally, the modal frequencies are noticeably modified by the down-bearing. In the case of an initially flat soundboard, the eigenfrequencies are only increasing with downbearing. These results are presented in Fig. 6 and are in a good qualitative concordance with the experimental measurements. But when $b=1$, a new situation is observed numerically (see Fig. 4). The first frequency primary decreases then increases for the transverse displacement λ about 3.5 mm (about half of the thickness). The first decreasing of frequency comes from the global compression introduced by the downbearing. In this case, the effects of downbearing are in opposition with the initial crown. When $b>1$ (Fig. 6), the first frequency only decreases, the upper range of downbearing 5000 N/m is not sufficient to induce a global traction and then an increase of the eigenfrequencies. These results are more or less identical for all modal frequencies, but with different variations.

We tried to fit the evolution of the frequency as a polynomial function of the loading parameter. Calculations have shown the second degree function of Eq. (14) is sufficient to obtain an excellent fit as one can see in Table III.

$$\left(\frac{\omega}{\omega_0}\right)^2=k_0+k_1\frac{\lambda}{e}+k_2\left(\frac{\lambda}{e}\right)^2, \tag{14}$$

where ω is the eigenpulsation, ω_0 the eigenpulsation without downbearing λ, and e the thickness of the plate.

The values of the interpolating coefficients for different crowns are presented Table III. This function models very well the relation between the square of the pulsation ω^2 and λ, for all values of b. The value of k_0 has to be equal to 1

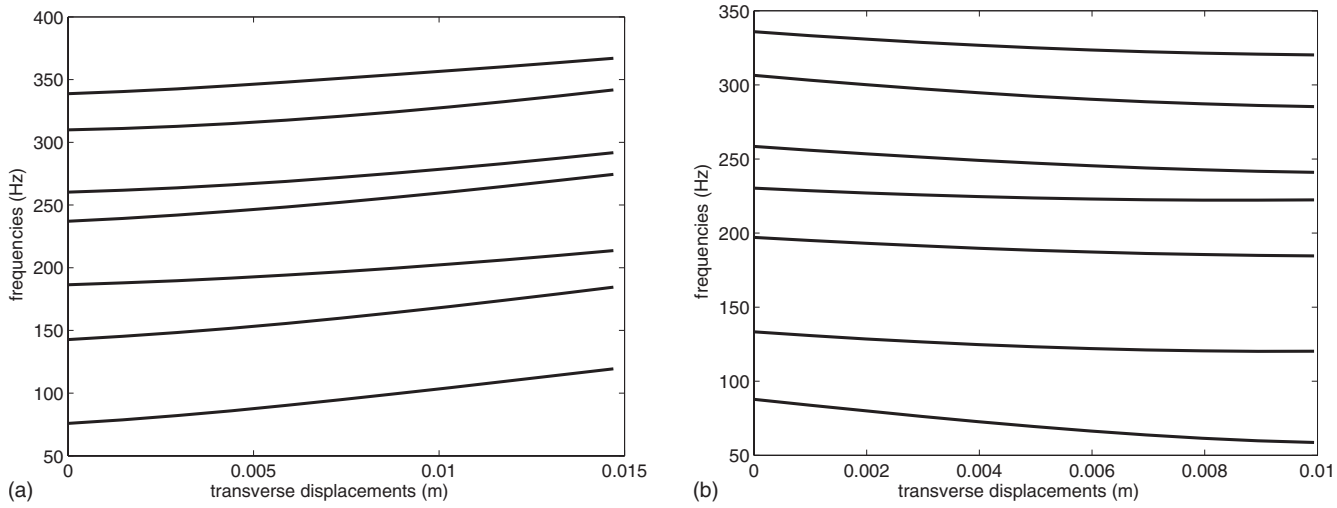

FIG. 6. Effects of downbearing on a flat soundboard (left) and the case $b=2$ (right), using a geometric nonlinearity calculus.

because it gives the relation $\omega=\omega_0$ without downbearing ($\lambda=0$). The values of k_1 give the initial slope. The sign of k_1 seems to be independent of the eigenmode and is negative for $b\neq 0$ (due to the opposition between downbearing and crown). The quadratic term k_2 is never negligible relatively to k_1, which characterizes the importance of taking into account the large displacements in the model. It is important to note that the crown b affects these values. That means the downbearing effects are very dependent of the initial crown.

A. Effects on mobility

1. The question of dissipation

The question of losses has not been considered in the previous calculus. But the losses largely characterize the soundboard, which acts as a strings vibration filter. There are many sources of losses in the soundboard because of the material, the radiation and the assembling with rim, ribs, bridges and finally strings. Suzuki[7] expressed these losses as modal damping factor and found a value of 0.064 for the first mode and about 0.02 for the others.

2. Examples of mobility

The experimental values of the damping (see H. Suzuki[7]) are introduced in complement the finite element results. The transverse mobility of the bridge Y is easy to express as $Y=v/F$ where v is the vertical velocity and F is the vertical applied force. The mobility for the middle of the treble bridge is presented Fig. 7.

TABLE III. Coefficients of the interpolating quadratic functions for $b=0$, $b=1$, and $b=2$.

Mode	k_2	k_1	k_0	Error max
1	0.212	0.421	0.992	$8.00.10^{-3}$
2	0.0980	0.1871	0.999	$2.10.10^{-3}$
3	0.0497	0.0796	1.00	$4.43.10^{-4}$
4	0.0458	0.102	1.00	$9.04.10^{-4}$
5	0.0425	0.0625	1.00	$1.10.10^{-3}$
6	0.0435	0.0388	1.00	$1.00.10^{-3}$
7	0.0156	0.0675	0.998	$2.00.10^{-3}$
Mode	k_2	k_1	k_0	Error max
1	0.365	−0.293	0.994	$8.10.10^{-3}$
2	0.150	−0.0410	1.00	$2.86.10^{-4}$
3	0.0627	−0.0476	1.00	$5.47.10^{-4}$
4	0.0658	−0.00260	1.00	$3.30.10^{-4}$
5	0.0616	−0.0525	1.00	$1.87.10^{-4}$
6	0.0586	−0.0647	1.00	$4.16.10^{-4}$
7	0.0432	−0.0287	1.00	$3.65.10^{-4}$
Mode	k_2	k_1	k_0	Error max
1	0.254	−0.766	1.00	$2.90.10^{-3}$
2	0.136	−0.320	1.00	$1.07.10^{-4}$
3	0.0640	−0.179	1.00	$1.73.10^{-4}$
4	0.0594	−0.128	1.00	$2.04.10^{-4}$
5	0.0519	−0.171	1.00	$7.78.10^{-4}$
6	0.0606	−0.183	1.00	$5.37.10^{-4}$
7	0.0461	−0.1304	1.00	$4.80.10^{-5}$

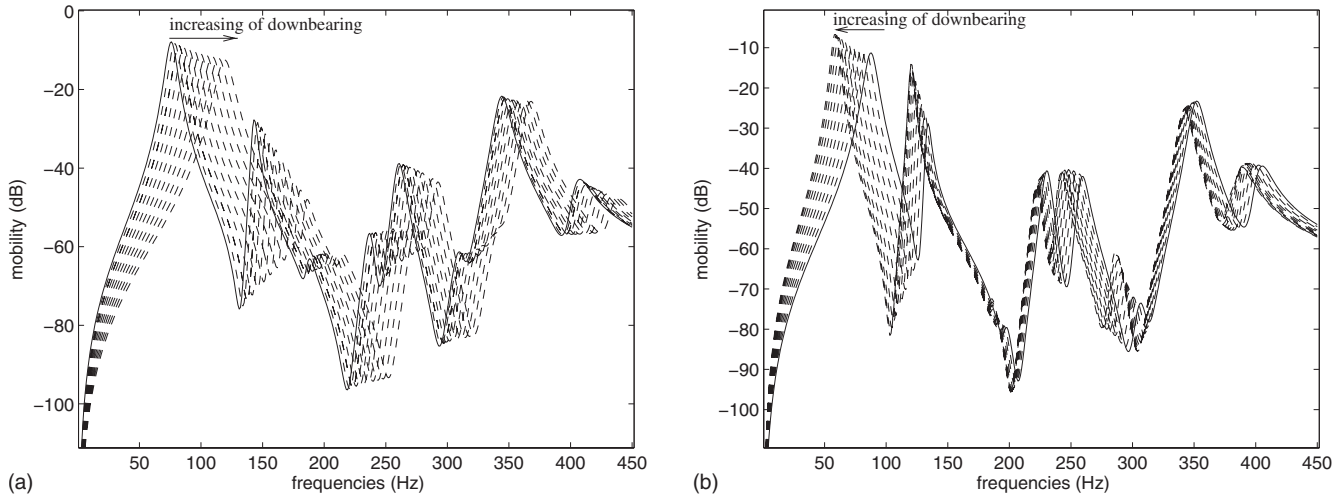

FIG. 7. Mobility on the middle of the treble bridge for $b=0$ (left) and $b=2$ (right).

The general shape of the mobility is similar to the results of the experimental literature in the range of [0,450 Hz] (see, for example, H. Suzuki[7]). One can see the noticeable effects of the downbearing when $b=0$, as it has been shown experimentally by Wogram.[4] The modifications of frequencies have been explained in a previous section.

The amplitude of the pics of mobility are also modified by downbearing, due to the slight changes in the modal shapes. When $b=2$, the mobility differs from the previous case, and the tendancies are inverted.

IV. CONCLUSION

This numerical work describes the changes in the soundboard vibrations due to the downbearing. To be correctly modeled, the downbearing must be calculated with a geometric nonlinear approach with prestresses (including the hypothesis of large displacements), because a linear model gives erroneous modal behavior in the range of the making process. Frequencies and modal shapes are affected by this part of piano makers know-how.

The experimental increase of eigenfrequencies is numerically obtained for an initially flat soundboard. However, the initial crown modifies largely these effects, introducing an initial decrease of eigenfrequencies, and has to be considered for future experiments.

This work is part of a research about consequences of making processes on the quality of musical instruments. Even if this paper is focused on the mechanical effects of the downbearing, the objective is to link these effects to changes in perceivable timbre. An interesting way to create this link is to include the results of this paper into some synthesis of piano sounds.

ACKNOWLEDGMENTS

The authors want to thank R. Bresson and F. Conti, students of the Ecole Nationale des Ponts et Chaussées, for their contributions in the finite element mesh.

[1]H. Bilhuber and C. A. Johnson, "The influence of the soundboard on the piano tone quality," J. Acoust. Soc. Am. **11**, 311–320 (1940).
[2]I. Nakamura, "The vibrational characteristics of a piano soundboard," *Proceedings of the 11th ICA*, Paris **4**, 385–388 (1983).
[3]T. R. Moore and S. A. Zietlow, "Interferometric studies of a piano soundboard," J. Acoust. Soc. Am. **119**, 1783–1793 (2006).
[4]K. Wogram, "The string and the soundboard," *Five lectures on the Acoustics of the Piano*, Royal Swedish Academy of Music, Stockholm, edited by Anders Askenfelt (1990).
[5]H. A. Conklin, "Design and tone in the mechanoacoustic piano: Part II. Piano structure," J. Acoust. Soc. Am. **100**, 695–707 (1996).
[6]J. Berthaut, M. Ichchou, and L. Jezequel, "Piano soundboard: Structural behavior, numerical and experimental study in the modal range," Appl. Opt. **64**, 1113–1136 (2003).
[7]H. Suzuki, "Vibration and sound radiation of a piano soundboard," J. Acoust. Soc. Am. **80**, 1573–1582 (1986).
[8]N. Giordano, "Mechanical impedance of a piano soundboard," J. Acoust. Soc. Am. **103**, 2128–2133 (1998).
[9]N. Giordano, "Simple model of a piano soundboard," J. Acoust. Soc. Am. **102**, 1159–1168 (1997).
[10]M. Géradin and D. Rixen, *Mechanical Vibrations. Theory and Application to Structural Dynamics* (Wiley, New York, 1994).
[11]J. N. Reddy, *An Introduction to Nonlinear Finite Element Analysis* (Oxford University Press, Oxford, 2004).
[12]Cast3M (version 2006): finite element software, http://www-cast3m.cea.fr(last viewed October 30, 2007).
[13]K. Fenner, "La table d'harmonie: Construction neuve et réparation (The soundboard: New building and restoration)," *Europiano*, **38**, No. 1 (1998).

Negative dispersion in bone: The role of interference in measurements of the apparent phase velocity of two temporally overlapping signals

Adam Q. Bauer, Karen R. Marutyan, Mark R. Holland, and James G. Miller[a)]
Department of Physics, Washington University in Saint Louis, Saint Louis, Missouri 63130, USA

(Received 5 October 2007; revised 7 January 2008; accepted 13 January 2008)

In this study the attenuation coefficient and dispersion (frequency dependence of phase velocity) are measured using a phase sensitive (piezoelectric) receiver in a phantom in which two temporally overlapping signals are detected, analogous to the fast and slow waves typically found in measurements of cancellous bone. The phantom consisted of a flat and parallel Plexiglas™ plate into which a step discontinuity was milled. The phase velocity and attenuation coefficient of the plate were measured using both broadband and narrowband data and were calculated using standard magnitude and phase spectroscopy techniques. The observed frequency dependence of the phase velocity and attenuation coefficient exhibit significant changes in their frequency dependences as the interrogating ultrasonic field is translated across the step discontinuity of the plate. Negative dispersion is observed at specific spatial locations of the plate at which the attenuation coefficient rises linearly with frequency, a behavior analogous to that of bone measurements reported in the literature. For all sites investigated, broadband and narrowband data (3–7 MHz) demonstrate excellent consistency. Evidence suggests that the interference between the two signals simultaneously reaching the phase sensitive piezoelectric receiver is responsible for this negative dispersion. © *2008 Acoustical Society of America.* [DOI: 10.1121/1.2839893]

PACS number(s): 43.80.Ev, 43.80.Jz, 43.80.Qf, 43.80.Vj [FD] Pages: 2407–2414

I. INTRODUCTION

A number of studies have addressed the anomalous negative dispersion (decreasing phase velocity with increasing frequency) widely observed in ultrasonic studies of bone *in vitro*[1–5] and *in vivo*.[6] In those studies, for the sites that display negative dispersion, the bone specimens investigated typically exhibit an attenuation coefficient that rises approximately linearly with frequency. A positive dispersion might be expected in these cases based on consideration of the causality-induced Kramers–Kronig relations.[7–9]

In previous work we proposed an alternative explanation of the observed negative dispersion and presented the results of numerical simulations demonstrating that negative dispersion can result from the interference of two propagating modes, each of which exhibits a positive dispersion, consistent with the Kramers–Kronig predictions.[10,11] The goal of the present study is to demonstrate this negative dispersion experimentally using the simplest example of a phantom that is capable of producing two such interfering waves.

Most ultrasonic experimental data are acquired using phase sensitive piezoelectric devices. Effects associated with phase cancellation at a piezoelectric detector on ultrasonic measurements have consistently been investigated over the past fifty years.[12–21] Artifacts resulting from phase aberrations can manifest themselves as acoustic speckle in *B*-mode images,[22] or as gross overestimations of the (apparent) attenuation coefficient.[12,14,23] In a previous paper,[21] we addressed the issue of phase cancellation at a phase sensitive piezoelectric receiving aperture and its effect on the validity of measurements made with an experimental setup sensitive to phase cancellation errors. Other authors have addressed these issues in bone, and have demonstrated the artifacts inherent in phase sensitive measurements.[20,24,25]

II. METHODS

A. Sample preparation

The phantom used in this investigation was constructed from a single sheet of polymethyl methacrylate (Plexiglas™) initially machined into a flat and parallel plate 2 in. (50.8 mm) long, 1 in. (25.4 mm) wide, and 0.5 in. (12.7 mm) thick. The resulting plate then had a small step discontinuity of 0.3 mm milled into one of its surfaces, as seen in Fig. 1. This step size was chosen so that phase cancellation artifacts would occur at approximately the midbandwidth frequency of the insonifying ultrasonic field, which for our experiment was approximately 5 MHz. Additional details can be found in Bauer *et al.*[21]

B. Equipment and experimental setup

Through-transmission measurements were performed in a water tank ($T=21.50\pm0.02$ °C) using separate transmitting and receiving 5 MHz center frequency, 0.25 in. diam-

a)Electronic Mail: james.g.miller@wustl.edu.

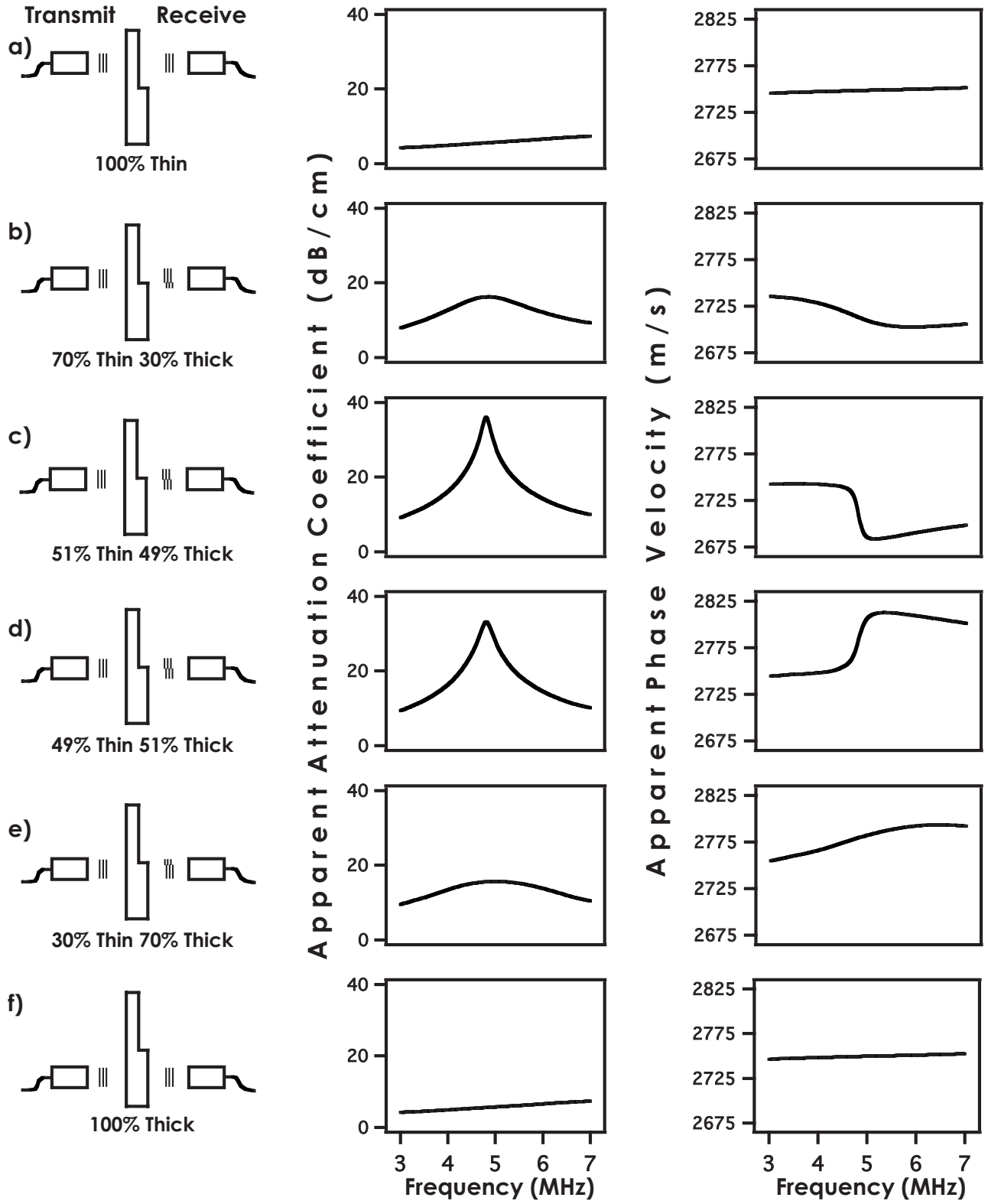

FIG. 1. Measured attenuation coefficient (second column) and phase velocity (third column) as a function of insonification location. Panels (a) and (f) show the measured ultrasonic properties for the thin and thick regions, respectively. Panels (b)–(e) show the measured apparent ultrasonic properties as the interrogating field traverses the step from the thin side to the thick side. The percentages shown serve as a qualitative description of the amount of the thin and thick side of the plate interrogated by the ultrasonic field.

eter, single element, unfocused, immersion transducers (Panametrics V310; Waltham, MA). The propagation path between the transmitting and receiving transducers was 3 in.

Broadband measurements were collected by exciting the transmitting transducer with a broadband radio frequency (rf) pulse from a pulser/receiver (Panametrics 5800, Waltham, MA) in through-transmission mode. The output of the receiving transducer was fed into the 50 Ω input of an 8-bit digitizing oscilloscope (Tektronix 5052b, Beaverton, OR). The resulting time-domain broadband signals were digitized

at a 2.5 GS/s digitization rate (400 ps/pt) and temporally averaged 256 times.

Narrowband measurements were performed using a pulse/function generator (Hewlett-Packard HP8116A; Palo Alto, CA) to create a sinusoidal tone burst at selected frequencies from 3 to 7 MHz in steps of 500 kHz. The sinusoidal tone bursts were used to drive the transmitting transducer and the output from the receiving transducer was fed into the 50 Ω input of the Tektronix 5052b oscilloscope. The received time-domain narrowband signals were digitized at a rate of 1.25 GS/s (800 ps/pt) and averaged 256 times. The number of cycles in each tone burst was varied so that each frequency component exhibited the same absolute bandwidth. The length of the tone burst was chosen to be sufficiently long (4 μs) to minimize correlation errors associated with the transients occurring at the beginning and end of each tone burst.

The phase velocity and attenuation properties of the plastic were measured by utilizing a substitution method.[26] Systematic measurements of different locations of the stepped plastic plate were achieved by motion control (Aerotech Unidex 511; Pittsburgh, PA). Values for the phase velocity and attenuation of the Plexiglas plate uncomplicated with details of the stepped region were obtained by averaging the results 25 individual sites for the thin and thick regions. The stepped region of the plate was investigated by translating the region of insonification in increments of 0.050 mm (0.002 in.) from the thin region of the stepped plastic plate to the thick region, as seen in Fig. 1. One hundred and fifty one (151) sites were insonified across the step, from the thin side of the plate to the thick side of the plate. (Only selected regions are displayed in Fig. 1 for illustrative purposes.)

C. Data

1. Broadband analysis

The data collected were analyzed using a phase spectroscopy broadband ultrasonic technique described elsewhere.[21] The frequency resolution of the acquired signals was enhanced by zero padding the digitized time-domain wave forms prior to data reduction in order to achieve an interpolated frequency spacing of $\Delta\omega/2\pi=25$ kHz between successive data points. The frequency dependent phase velocity, $c(\omega)$, of the sample was calculated by comparing the difference in the phase spectra, $\Delta\varphi$, of the sample trace to that of the reference trace,

$$c(\omega) = c_w\left[\frac{\omega d}{\omega d + c_w\Delta\varphi(\omega)}\right], \tag{1}$$

where c_w is the known speed of sound in the water[27] and d is the effective sample thickness. The effective sample thickness in the region of the step was calculated by linearly interpolating the sample thickness from the thin side, d_{thin}, of the plate to the thick side

$$d = d_{\text{thin}} + \frac{m}{n}\Delta x, \tag{2}$$

where $m=1,2,3,\ldots,151$, Δx is the thickness of the step, and $n=151$, the number of locations investigated across the step.

The amplitude attenuation coefficient of the sample (dB/cm) is determined from a log-spectral subtraction technique,[28]

$$\alpha(\omega) = \frac{20\log(|\tilde{U}_w(\omega)|) - 20\log(|\tilde{U}_s(\omega)|) + 10\log(T_{ws}^I T_{sw}^I)}{d}, \tag{3}$$

where $|\tilde{U}_w(\omega)|$ and $|\tilde{U}_s(\omega)|$ are the magnitudes of the Fourier transforms of the water and sample path signals, and T_{ws}^I and T_{sw}^I are the intensity transmission coefficients of the water–sample and sample–water interfaces, respectively.

D. Narrowband analysis

The received sample path and reference path narrowband signals were gated with a 10 μs rectangular window. The narrowband phase velocity measurements of the stepped plastic plate were calculated with a time-domain rf correlation technique using a positive-peak criterion. The narrowband attenuation coefficient calculations were performed using Eq. (3) applied to each individual frequency component transmitted in the total bandwidth.

III. RESULTS

The first column of Fig. 1 illustrates the experimental procedure outlined in Sec. II A. As shown, the six horizontal panels of Fig. 1 encompass the measured apparent ultrasonic properties of the stepped plastic plate as the ultrasonic field produced by the transmitting and receiving transducers moves from the thin side of the plate, across the step, to the thick side of the plate. The thin and thick percentages indicated at the bottom of each panel are intended to give the reader a qualitative measure of how much of the thick and thin portions of the plate are interrogated by the ultrasonic field, and are not meant as a quantitative description of the behavior of the ultrasonic field at this location. The second and third columns of Fig. 1 show the measured attenuation coefficient and measured phase velocity as a function of location along the stepped plastic plate.

Figure 1(a) shows the measured attenuation and phase velocity for investigation of the thin, flat, and parallel portion of the plate. Figures 1(b)–1(e) show the behavior of the measured attenuation coefficient and phase velocity as the stepped region of the plate is moved through the ultrasonic field from the thin side to the thick side. Figure 1(b) shows the measured properties for the ultrasonic field that traverses approximately 70% of the thin part of the plate and approximately 30% of the thick part. Figures 1(c) and 1(d) show the measured attenuation and phase velocity as the incident ultrasonic field is approximately "cut in half" by the step, though more of the thin side of the plate is present in Fig. 1(c) (51% thin 49% thick), whereas more of the thick side is present in the detected ultrasonic field in Fig. 1(d) (49% thin 51% thick). Pictured in Fig. 1(e) are the measured ultrasonic properties of the phase sensitively detected field where ap-

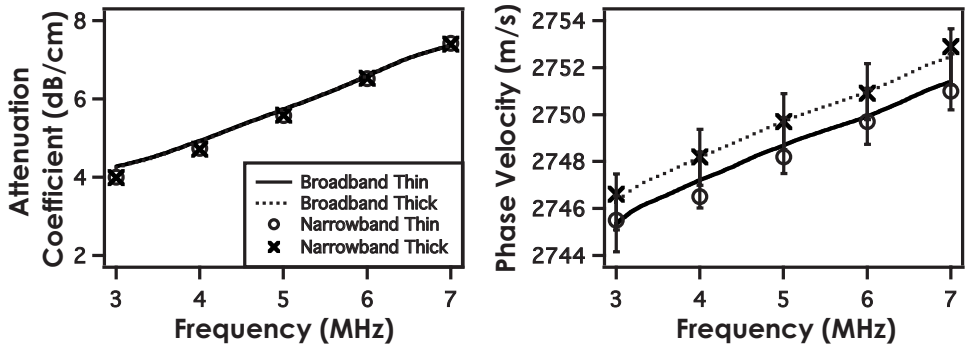

FIG. 2. Broadband and narrowband phase velocity and attenuation coefficient measurements of the thin and thick sides of the stepped plastic plate.

proximately 30% of the field passes through the thin portion of the plate and 70% of the field passes through the thick portion of the plate. In Fig. 1(f), the measured attenuation coefficient and phase velocity for the investigation of the thick, flat, and parallel side of the plate are presented.

Figure 2 shows the comparison of broadband and narrowband measurements made on the 100% thin and 100% thick sides of the stepped plastic plate. As shown, the attenuation and phase velocity properties of both regions agree within the experimental uncertainty for both broadband and narrowband measurements. Error bars for the attenuation coefficient data are too small to be seen on this plot, and are not shown. The errors bars shown in the phase velocity plot are two standard deviations from the mean of the broadband measurements made by averaging the results of 25 sites. The phase velocity data of the 100% thin and 100% thick regions do not statistically differ. The broadband and narrowband measurements within the stepped region of the plate are compared in Fig. 3. The broadband and narrowband data were collected from the same spatial locations along the stepped plastic plate, and represent the same locations illustrated in Fig. 1.

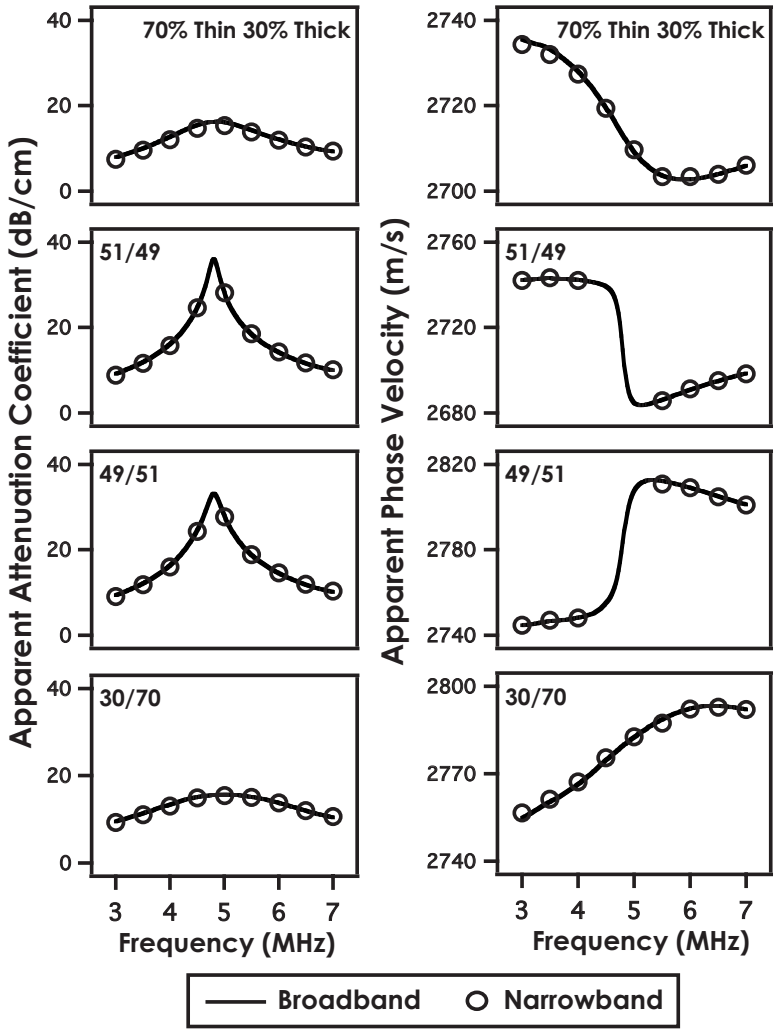

FIG. 3. Broadband and narrowband phase velocity and attenuation measurements of the stepped region of the plate as a function of insonification location. The rows correspond to panels (b)–(e) of Fig. 1.

IV. DISCUSSION

For the flat and parallel regions of the plate, an attenuation coefficient that rises approximately linearly with frequency, as well as an approximately logarithmically increasing phase velocity was observed, and is shown in Figs. 1(a), 1(e), and 2. The behavior of the ultrasonic field as it passes through the flat and parallel (thick and thin) regions of the plate remains relatively undisturbed when compared with that of the field emerging from the stepped region of the plate. After compensation for the sample thickness, the attenuation coefficient and phase velocity of the thin and thick regions of the plate are nearly identical as shown in Fig. 2. However, a comparison of the ultrasonic properties in Figs. 1(b) and 1(e) with those of Figs. 1(a) and 1(f), indicate that even a modest amount of the step discontinuity introduced to the system results in dramatic changes in measurements of ultrasonic properties obtained with a phase sensitive piezoelectric receiver. The data presented in Figs. 1(c) and 1(d) serve as extreme examples of how a phase aberrating medium affects the apparent properties of a sample when they are detected by a phase sensitive aperture.

A. Attenuation coefficient

The trend in the frequency dependence of the attenuation coefficient in Figs. 1(a)–1(f) can be explained by considering the phase fronts of the incident ultrasonic field as they pass through the step. When the two transducers are transmitting and receiving a broadband pulse through the flat and parallel sides of the plate, the frequencies contained in the pulse (with a −6 dB bandwidth of 3–7 MHz) are attenuated in a uniform way, commensurate with the native attenuation properties of the sample. Because these surfaces are nominally flat and parallel, the planes of constant phase entering the sample remain constant as they emerge from the plastic plate. If, instead, the ultrasonic field begins to traverse the stepped region of the plate, the phase fronts of the field passing through the thin portion of the plate will be out of phase with those passing though the thick portion of the plate by an amount, $\Delta\varphi=(k_w-k_s)\Delta x$, where k_w and k_s are the wave numbers of the water and sample, respectively, and Δx is the step thickness. This step thickness was chosen so that (approximately) the 5 MHz component of the incident ultrasonic field, when emerging from the stepped region of the plate, would be nominally cancelled upon detection with a phase sensitive aperture.[21] Because the phase of the wave fronts passing through the thicker part of the plate are advanced by an odd multiple of π radians relative to the phase fronts emerging from the thinner region, the charge distribution induced on the receiving piezoelectric transducer, when summed across the receiver, nominally cancels the 5 MHz component of the incident field. The frequency components above and below 5 MHz are progressively less and less out of phase with each other. The apparent attenuation coefficient therefore reaches a maximum near 5 MHz and decreases slowly on either side of this frequency to that of the native attenuation coefficient of the sample.

B. Phase velocity

As the transmitted field progresses from the thin region of the plate to the thick region of the plate, the behavior of the apparent phase velocity appears to be more complicated than that of the apparent attenuation coefficient. The apparent phase velocity starts as an approximately logarithmically increasing function of frequency [Fig. 1(a)], but begins to deform as a result of the step's influence on the transmitted ultrasonic field. As the insonifying field further progresses towards the step [Fig. 1(b)], this deformation increases and the apparent phase velocity goes through its maximum in dispersion with a specific curvature [Fig. 1(c)]. As the field continues towards the thick side of the plate, the sign of the curvature of the apparent phase velocity changes [Fig. 1(d)]—the data are reflected about a horizontal axis—and then the apparent phase velocity gradually returns to its logarithmic dependence on frequency, the native dispersion of the sample [Fig. 1(f)].

This trend can be accounted for by writing the ultrasonic field incident on the stepped plastic plate as two signals: one signal, Ψ_{Thin}, describing the portion of the field traversing the thin region of the plate, and another signal, Ψ_{Thick}, that describes the portion of the field traveling through the thick region of the plate. The ultrasonic field, Ψ, is then a superposition of these two signals:

$$\Psi = \Psi_{\text{Thin}} + \Psi_{\text{Thick}}. \tag{4}$$

This superimposed signal will be referred to as a mixed signal. The role each signal plays in the detected ultrasonic field, and ultimately the phase velocity, becomes apparent by writing Ψ_{Thin} and Ψ_{Thick} as a complex phasor in polar (magnitude and phase) form,

$$\tilde{\Psi}(x=L,\omega) = |\tilde{\Psi}_{\text{Thin}}(\omega)|e^{i\varphi_{\text{Thin}}} + |\tilde{\Psi}_{\text{Thick}}(\omega)|e^{i\varphi_{\text{Thick}}}, \tag{5}$$

where $|\tilde{\Psi}_{\text{Thin}}(\omega)|$ and $|\tilde{\Psi}_{\text{Thick}}(\omega)|$ are the complex magnitudes of the thin and thick signals, and φ_{Thin} and φ_{Thick} are the phases of the thin and thick signals, respectively.

After some algebraic manipulation, the overall phase of the mixed signal can be written in terms of its real and imaginary parts as

$$\varphi_{\text{Mixed}}(\omega) = a\tan\left[\frac{|\tilde{\Psi}_{\text{Thin}}(\omega)|\sin(\varphi_{\text{Thin}}(\omega)) + |\tilde{\Psi}_{\text{Thick}}(\omega)|\sin(\varphi_{\text{Thick}}(\omega))}{|\tilde{\Psi}_{\text{Thin}}(\omega)|\cos(\varphi_{\text{Thin}}(\omega)) + |\tilde{\Psi}_{\text{Thick}}(\omega)|\cos(\varphi_{\text{Thick}}(\omega))}\right] + 2\pi m, \tag{6}$$

where the factor of $2\pi m$ comes from the ambiguity resulting from a four quadrant inverse tangent operation.[29] The phases of the thin and thick signals are themselves also ambiguous to an integer multiple of 2π. As noted in Trousil, *et al.*,[29] an improper choice of m results in dramatic changes in the apparent dispersion, so it is often possible to infer the proper choice of m based on some a priori knowledge about the system under investigation.

It is clear from Eq. (6) that the phase of the overall mixed signal is a function of the magnitudes and phases of the individual thin and thick signals. In the limit that the transmitting and receiving transducers are only interrogating the thin region, the detected ultrasonic field is only a function of the magnitude and phase of the thin signal, and similarly for the thick signal. The interesting behavior arises as a result of the superposition, or interference, of these two signals as the magnitude of one signal dominates that of the other in their relative contributions to the mixed signal. The reflection in the curvature of the measured apparent phase velocity occurs because the phasor of the mixed signal at 5 MHz undergoes an abrupt 180° rotation in the complex phase plane as the ultrasonic field traverses from the thin side of the plate to the thick side [Figs. 1(c) and 1(d)]. As the field approaches the step discontinuity, the mixed signal becomes composed approximately of equal parts thin and thick signal, with a slightly greater contribution from the thin signal [Fig. 1(c)]. As the beam crosses the step, the mixed signal suddenly receives a greater contribution from the thick signal [Fig. 1(d)]. The 5 MHz phasor of the mixed signal therefore immediately rotates 180° in the complex phase plane as the second signal becomes more dominant. Because the thin and thick signals are nominally π radians out of phase at 5 MHz, higher frequencies contained within the experimental bandwidth have rotated almost completely around the complex phase plane, thus almost moving from one phase sheet (e.g., the phase sheet of the lower frequencies) to the next (the phase sheet of the higher frequencies). In the context of the phase sheet offset discussed in Trousil *et al.*,[29] the frequencies from ~5 to 7 MHz have a phase sheet offset of $+1/2$ in Fig. 1(c) and $-1/2$ in Fig. 1(d) relative to the frequencies from 3 to 5 MHz.

The results of Fig. 1 indicate that given two measurements of the phase velocity in this stepped plastic plate, one could measure two different phase velocity values. For instance, in Figs. 1(c) and 1(d), at 6 MHz, one could measure a phase velocity of 2690 m/s while insonifying one site, whereas another measurement taken 100 μm away would yield a result of 2809 m/s. This apparent inconsistency is due to the standard method used to measure the phase velocity of a sample supporting two temporally overlapping signals with broadband spectroscopic techniques on data collected with phase sensitive devices.

If the two waves were of finite extent, and were able to be temporally gated from one another, then this apparent inconsistency could be resolved. By isolating the two signals from one another (e.g., by using a gate applied in the time domain), the native ultrasonic properties underlying each wave could be determined. However, when a single rf signal is detected, regardless of the constituent waves or modes superposed to create it, one is left with little choice but to use traditional phase spectroscopy (i.e., treating the received signal as a single signal).

C. Narrowband

Because of the initially puzzling behavior of the broadband phase velocity data, narrowband measurements were carried out over the same spatial locations as the broadband measurements. As a check on the consistency of the broadband measurements, Figs. 2 and 3 demonstrate the marked agreement between the broadband and narrowband data over the flat and parallel sides of the plate, as well as over the stepped portion, respectively. For all narrowband frequency components used to interrogate the sample, a positive peak correlation method was used to determine the appropriate time shift between the sample path and water path rf signals. The 4.5 and 5 MHz components of the 51% thin 49% thick and 49% thin 51% thick narrowband data are not shown in Fig. 3. For these four points the positive peak correlation criterion gave results consistent with a phase sheet offset of 2π.[29] That is, if the next nearest peak in the correlation wave was chosen as the appropriate time shift, these four data points would lie directly on top of the broadband data, in line with the other narrowband data points. Even without these four points, the narrowband results agree quite well with the broadband data collected over this phantom.

D. Negative dispersion

The results of measuring selected locations across the phantom used in this study (over a slightly different bandwidth than that of Figs. 1–3) are shown in Fig. 4. The bandwidth of 2.25 to 4.5 MHz was chosen to illustrate a specific behavior that is characteristic of many measurements on bone. Over this bandwidth, spanning a factor of 2 in frequency, the data exhibit many apparent attenuation coefficients, all of which increase approximately linearly with frequency. Yet over this same bandwidth, at exactly the same sites, an apparent phase velocity is measured that appears to decrease with increasing frequency (i.e., to exhibit negative dispersion.)

The slope of the attenuation coefficient plotted as a function of frequency is often used to characterize biological materials. Researchers who investigate bone refer to this parameter as normalized broadband ultrasound attenuation, or nBUA. Fig. 4 clearly shows that one can measure many different apparent slopes of attenuation, or nBUA, for which one finds an apparently negative dispersion even though the material itself exhibits a positive dispersion as shown in Fig. 2. (For clarity, only a few locations from the total observed on the plate displaying negative dispersion are shown in Fig. 4.)

In Waters and Hoffmeister,[3] rf data from trabecular bone samples exhibiting three different mass densities are shown (low, medium, and high). It was observed that even for low-density specimens, for which a seemingly undistorted rf is obtained, one could still measure negative dispersion. In Fig. 5 of the present manuscript, three different time-domain ultrasonic signals (typical of data collected for this study) are

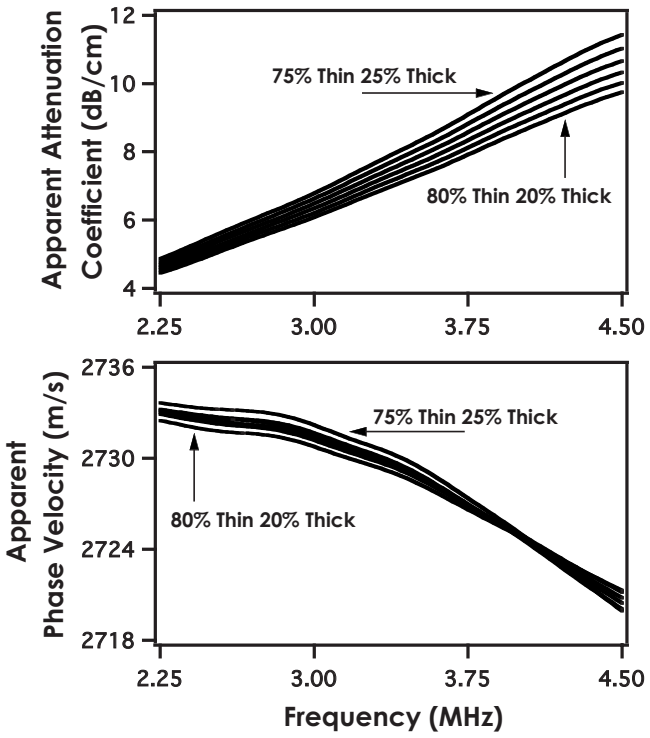

FIG. 4. Broadband measurements of regions of the stepped plastic plate exhibiting a linearly increasing attenuation coefficient and negative dispersion for the selected bandwidth.

shown. The left-most panel shows an rf signal acquired from the 100% thin side of the plate. To the right are two different rf signals acquired as one insonifies locations closer and closer to the step, 80% thin 20% thick and 51% thin 49% thick, respectively. Even when a modest amount of the step is interrogated by the ultrasonic field, and then when the observed rf signal appears to be relatively undistorted, one still measures a linearly increasing attenuation coefficient with an apparently negative dispersion. Hence the presence of only a small amplitude of a second signal (in bone, for example, a fast wave mode in a signal dominated by a slow wave mode, or visa versa) could account for the presence of negative dispersion observed in many measurements of bone.[1–6] This hypothesis is the basis for a model introduced by our laboratory that might account for the measurements of (anomalous) negative dispersion observed in studies of cancellous bone.[11] More sophisticated models, such as the stratified model[30–32] or extensions of the porous media model of Biot,[33–35] will be necessary to account for the detailed behavior of bone. But such models are likely to include the simultaneous existence of multiple modes of propagation, which is the fundamental feature of the unsophisticated phantom employed in the present experiment to demonstrate the underlying physics resulting in apparent negative dispersion.

E. Limitations of the present study

The ultrasonic frequencies used to investigate the phantom described in this study are substantially higher than those typically used in the quantitative ultrasonic study of bone. However, the range of frequencies (3–7 MHz) represents a fractional bandwidth similar to that employed in many studies of bone (300–700 kHz).

The sample used in the present study was not capable of propagating fast and slow modes, nor did it exhibit the ultrasonic attenuation and speed of sound of cancellous bone. The purpose of this study was to address the frequency dependence of an apparent attenuation coefficient and an apparent phase velocity of a sample that mimicked the anomalous properties of those often reported for cancellous bone: a linearly increasing attenuation coefficient and a negatively decreasing phase velocity. The sample with which we chose to pursue this goal was designed to be the simplest possible type of phantom that could propagate two temporally overlapping signals. The goal was to illustrate the fact that when one detects two overlapping signals, analogous to the superimposed fast and slow modes common to studies of cancellous bone, it is possible for traditional phase spectroscopy to yield negative dispersion.

We suggest that for some signals transmitted through cancellous bone, one often cannot distinguish whether there are, in fact, two superimposed signals. For low and medium density cancellous bone,[3] the acquired signal through the bone can be a single rf signal that appears relatively undistorted, yet this signal might be comprised of two modes. The potential misinterpretations of this undistorted signal are the focus of this manuscript.

The mechanism described in this manuscript may not be the sole explanation for the observation of negative dispersion. Scattering and mode conversion within the stratified microarchitecture of the trabeculae presumably result in complex signals that may contribute to other sources of negative dispersion. Although the totality of possible sources of the causal inconsistency between a linearly increasing attenuation coefficient and a simultaneously decreasing with frequency phase velocity remains unclear, evidence in this

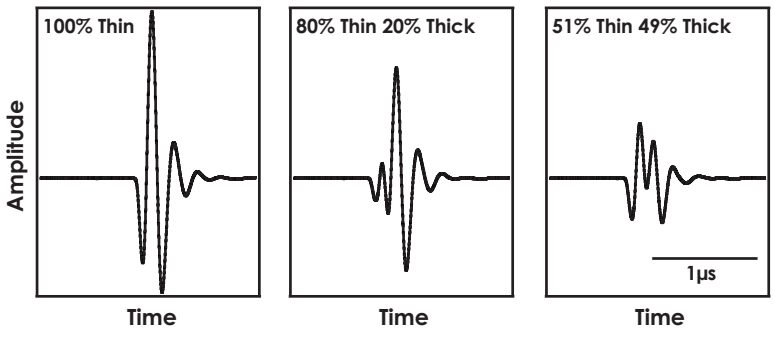

FIG. 5. Representative time-domain rf signals for the 100% thin, 80% thin 20% thick, and 51% thin 49% thick locations measured along a stepped plastic plate illustrating progressively more overlap in the received signals.

study suggests that the anomalous dispersion observed in ultrasonic studies of cancellous bone can arise from an interference between two waves, such as the fast and slow waves predicted by Biot theory.

V. SUMMARY

Broadband and narrowband measurements were made on two overlapping signals arising from propagation through a simple phantom. The phase sensitively measured broadband phase velocity and attenuation coefficient were observed to undergo drastic changes in frequency dependence as a function of location on the sample. Despite this behavior, narrowband measurements agreed very well with broadband data taken at the same spatial locations. Further, it was possible to measure negative dispersion at sites exhibiting a linearly increasing attenuation coefficient, in contrast to what might be expected based on the nearly local form of the once-subtracted Kramers–Kronig equations.

ACKNOWLEDGMENTS

This study was supported, in part, by NSF Grant No. CBET-071783 Scholar in Residence at the FDA and by NIH Grant No. R37 HL40302.

[1]P. Droin, G. Berger, and P. Laugier, "Velocity dispersion of acoustic waves in cancellous bone," IEEE Trans. Ultrason. Ferroelectr. Freq. Control **45**, 581–592 (1998).
[2]P. H. F. Nichoison, G. Luwet, C. M. Langton, J. Dequeker, and G. VanderPerre, "A comparison to time domain and frequency domain approaches to ultrasonic velocity measurement in trabecular bone," Phys. Med. Biol. **41**, 2421–2435 (1996).
[3]K. R. Waters and B. K. Hoffmeister, "Kramers-Kronig analysis of attenuation and dispersion in trabecular bone," J. Acoust. Soc. Am. **118**, 3912–3920 (2005).
[4]K. A. Wear, "Measurements of phase velocity and group velocity in human calcaneus," Ultrasound Med. Biol. **26**, 641–646 (2000).
[5]R. Strelitzki and J. A. Evans, "On the measurement of the velocity of ultrasound in the os calcis using short pulses," Eur. J. Ultrasound **4**, 205–213 (1996).
[6]K. A. Wear, "Group velocity, phase velocity and dispersion in human calcaneus *in vivo*," J. Acoust. Soc. Am. **121**, 2431–2437 (2007).
[7]M. O'Donnell, E. T. Jaynes, and J. G. Miller, "Kramers-Kronig relationship between ultrasonic attenuation and phase velocity," J. Acoust. Soc. Am. **69**, 696–701 (1981).
[8]K. R. Waters, M. S. Hughes, J. Mobley, G. H. Brandenburger, and J. G. Miller, "On the applicability of Kramers-Kronig relations for ultrasonic attenuation obeying a frequency power law," J. Acoust. Soc. Am. **108**, 556–563 (2000).
[9]K. R. Waters, J. Mobley, and J. G. Miller, "Causality-imposed (Kramers-Kronig) relationships between attenuation and dispersion," IEEE Trans. Ultrason. Ferroelectr. Freq. Control **52**, 822–833 (2005).
[10]K. R. Marutyan, G. L. Bretthorst, and J. G. Miller, "Bayesian estimation of the underlying bone properties from mixed fast and slow mode ultrasonic signals," J. Acoust. Soc. Am. **121**, EL8–15 (2007).
[11]K. R. Marutyan, M. R. Holland, and J. G. Miller, "Anomalous negative dispersion in bone can result from the interference of fast and slow waves," J. Acoust. Soc. Am. **120**, EL55–61 (2006).
[12]L. J. Busse and J. G. Miller, "Detection of spatially nonuniform ultrasonic radiation with phase sensitive (piezoelectric) and phase insensitive (acoustoelectric) receivers," J. Acoust. Soc. Am. **70**, 1377–1386 (1981).
[13]L. J. Busse and J. G. Miller, "A comparison of finite aperture phase sensitive and phase insensitive detection in the near field of inhomogeneous material," Proc.-IEEE Ultrason. Symp. **2**, 617–626 (1981).
[14]L. J. Busse, J. G. Miller, D. E. Yuhas, J. W. Mimbs, A. N. Weiss, and B. E. Sobel, "Phase cancellation effects: A source of attenuation artifact eliminated by a CdS acoustoelectric receiver," Ultrasound Med. Biol. **3**, 1519–1535 (1977).
[15]P. H. Johnston and J. G. Miller, "Phase-insensitive detection for measurement of backscattered ultrasound," IEEE Trans. Ultrason. Ferroelectr. Freq. Control **33**, 713–721 (1986).
[16]H. Seki, A. Granato, and R. Truell, "Diffraction effects in the ultrasonic field of a piston source and their importance in the accurate measurement of attenuation," J. Acoust. Soc. Am. **28**, 230–238 (1956).
[17]R. Truell, C. Elbaum, and B. B. Chick, *Ultrasonic Methods in Solid State Physics* (Academic, New York, 1969), pp. 107–108.
[18]R. Truell and W. Oates, "Effect of lack of parallelism of sample faces on the measurement of ultrasonic attenuation," J. Acoust. Soc. Am. **35**, 1382–1386 (1963).
[19]O. T. von Ramm, F. L. Thurstone, and J. Kisslo, "Cardiovascular diagnosis with real time ultrasound imaging," in *Acoustical Holography*, edited by N. Booth (Plenum, New York, 1975), Vol. **6**, pp. 91–102.
[20]K. A. Wear, "The effect of phase cancellation on estimates of calcaneal broadband ultrasound attenuation *in vivo*," IEEE Trans. Ultrason. Ferroelectr. Freq. Control **54**, 1352–1359 (2007).
[21]A. Q. Bauer, K. R. Marutyan, M. R. Holland, and J. G. Miller, "Is the Kramers-Kronig relationship between ultrasonic attenuation and dispersion maintained in the presence of apparent losses due to phase cancellation?," J. Acoust. Soc. Am. **122**, 222–228 (2007).
[22]C. B. Burckhardt, "Speckle in ultrasound B-mode scans," IEEE Trans. Sonics Ultrason. **25**, 1–6 (1978).
[23]L. J. Busse and J. G. Miller, "Response characteristics of finite aperture, phase insensitive ultrasonic receive based upon the acoustoelectric eftect," J. Acoust. Soc. Am. **70**, 1370–1376 (1981).
[24]G. W. Petley, P. A. Robins, and J. D. Aindow, "Broadband ultrasonic attenuation: Are current measurement techniques inherently inaccurate?," Br. J. Radiol. **168**, 1212–1214 (1995).
[25]R. Strelitizki, S. C. Metcalfe, P. H. F. Nicholson, J. A. Evans, and V. Paech, "On the ultrasonic attenuation and its frequency dependence in the os calcis assessed with a multielement receiver," Ultrasound Med. Biol. **25**, 133–141 (1999).
[26]J. Mobley, C. S. Hall, J. N. Marsh, M. S. Hughes, K. R. Waters, G. H. Brandenburger, and J. G. Miller, "Measurements and predictions of the phase velocity and attenuation coefficient in suspensions of elastic microspheres," J. Acoust. Soc. Am. **106**, 652–659 (1999).
[27]L. E. Kinsler, A. R. Frey, A. B. Coppens, and J. V. Sanders, *Fundamentals of Acoustics*, 4th ed. (Wiley, New York, 2000), pp. 179–184.
[28]S. L. Baldwin, K. R. Marutyan, M. Yang, K. D. Wallace, M. R. Holland, and J. G. Miller, "Measurements of the anisotropy of ultrasonic attenuation in freshly excised myocardium," J. Acoust. Soc. Am. **119**, 3130–3139 (2006).
[29]R. L. Trousil, K. R. Waters, and J. G. Miller, "Experimental validation of the use of Kramers-Kronig relations to eliminate the phase sheet ambiguity in broadband phase spectroscopy," J. Acoust. Soc. Am. **109**, 2236–2244 (2001).
[30]E. R. Hughes, T. G. Leighton, G. W. Petley, and P. R. White, "Ultrasonic propagation in cancellous bone: A new stratified model," Ultrasound Med. Biol. **25**, 811–821 (1999).
[31]M. Schoenberg, "Wave propagation in alternating solid and fluid layers," Wave Motion **6**, 303–321 (1984).
[32]K. A. Wear, "A stratified model to predict dispersion in trabecular bone," IEEE Trans. Ultrason. Ferroelectr. Freq. Control **48**, 1079–1083 (2001).
[33]M. A. Biot, "Theory of propagation of elastic waves in a fluid-saturated porous solid. I. Low frequency range," J. Acoust. Soc. Am. **28**, 168–178 (1956).
[34]M. K. Biot, "Theory of propagation of elastic waves in a fluid-saturated porous solid. II. Higher frequency range," J. Acoust. Soc. Am. **28**, 179–191 (1956).
[35]H. Roh, K. I. Lee, and S. W. Yoon, "Acoustic characteristics of a non-rigid porous medium with circular cylindrical pores," J. Korean Phys. Soc. **43**, 55–65 (2003).

Application of Biot's theory to ultrasonic characterization of human cancellous bones: Determination of structural, material, and mechanical properties

Michal Pakula,[a] Frederic Padilla, and Pascal Laugier
Laboratoire d'Imagerie Parametrique, Universite Paris 6, 15 rue de l'Ecole de Medicine, 75006 Paris, France

Mariusz Kaczmarek
Institute of Environmental Mechanics and Applied Computer Science, Kazimierz Wielki University in Bydgoszcz, ul. Chodkiewicza 30, 85-064 Bydgoszcz, Poland

(Received 21 September 2007; revised 7 January 2008; accepted 8 January 2008)

This paper is devoted to the experimental determination of distinctive macroscopic structural (porosity, tortuosity, and permeability) and mechanical (Biot–Willis elastic constants) properties of human trabecular bones. Then, the obtained data may serve as input parameters for modeling wave propagation in cancellous bones using Biot's theory. The goal of the study was to obtain experimentally those characteristics for statistically representative group of human bones (35 specimens) obtained from a single skeletal site (proximal femur). The structural parameters were determined using techniques devoted to the characterization of porous materials: electrical spectroscopy, water permeametry, and microcomputer tomography. The macroscopic mechanical properties, Biot–Willis elastic constants, were derived based on the theoretical consideration of Biot's theory, micromechanical statistical models, and experimental results of ultrasonic studies for unsaturated cancellous bones. Our results concerning structural parameters are consistent with the data presented by the other authors, while macroscopic mechanical properties measured within our studies are situated between the other published data. The discrepancies are mainly attributed to different mechanical properties of the skeleton frame, due to strong structural anisotropy varying from site to site. The results enlighten the difficulty to use Biot's theory for modeling wave propagation in cancellous bone, implying necessity of individual evaluation of input parameters.
© *2008 Acoustical Society of America.* [DOI: 10.1121/1.2839016]

PACS number(s): 43.80.Ev, 43.80.Qf, 43.80.Cs, 43.20.Jr [KA] Pages: 2415–2423

I. INTRODUCTION

Quantitative ultrasound has received significant attention during the last decade, for its potential to noninvasive assessment of bone quality, in particular in the context of osteoporosis (Williams, 1992; Williams *et al.*, 1996; Hosokawa and Otani, 1997, 1998; Haire and Langton, 1999; Hughes *et al.*, 1999, 2003, 2006; Laugier *et al.*, 1997; Padilla and Laugier, 2000; Kaczmarek *et al.*, 2002, 2005; Lee *et al.*, 2003; Fellah *et al.*, 2004; Sebaa *et al.*, 2006; Wear *et al.*, 2005; Wear, 2007). Compared to reference x-ray absorptiometry techniques, which measure the amount of bone mineral content, ultrasound is sensitive not only to bone mass but also to structural and material properties of the propagation medium. Therefore, it should allow an advanced assessment of bone strength. Despite the relatively large number of multidisciplinary approaches reported so far, the potential of ultrasound techniques is not fully exploited yet because of misunderstanding of basic physical mechanisms implied in the interaction between the ultrasound and bone structure. Therefore, currently one of the important issues is to develop a comprehensive theoretical model, which will be helpful in solving the inverse problem, i.e., in extracting bone structural and mechanical properties from ultrasonic measurements. Modeling propagation of ultrasound in trabecular bone (also termed cancellous or spongious bone) is difficult because of the complexity of the medium. Trabecular bone at the macroscopic level is a two-phase, anisotropic material composed of solid rod-like or plate-like skeleton filled *in vivo* with viscous fluid-like marrow (Baron, 1999). Considering ultrasonic wave propagation in trabecular bone, both the mechanical properties as well as the structure strongly influence wave parameters such as attenuation and velocity. As theoretical basis for modeling elastic wave propagation in cancellous bone, mostly two-phase theory of dynamics of fluid-saturated porous materials proposed by Biot (1956a,b)and extended by Johnson *et al.* (1994a,b) has been used (Williams, 1992; Williams *et al.*, 1996; Haire and Langton, 1999; Hosokawa and Otani, 1998, 1997; Padilla and Laugier, 2000; Kaczmarek *et al.*, 2002, 2005; Lee *et al.*, 2003; Fellah *et al.*, 2004; Wear *et al.*, 2005; Sebaa *et al.*, 2006). However, currently no consensus has been reached among the researchers working in the field about the relevance of Biot's theory for modeling of wave propagation. A reasonable agreement between Biot's theory and experiments has consistently been obtained when the phase velocity was

[a]Permanent address: Institute of Environmental Mechanics and Applied Comp. Science, Kazimierz Wielki University in Bydgoszcz, 85-064 Bydgoszcz, Poland. Electronic mail: michalp@ukw.edu.pl

considered (Williams, 1992; Williams *et al.*, 1996; Hosokawa and Otani, 1997, 1998; Padilla and Laugier, 2000; Wear *et al.*, 2005; Wear, 2007). However, in the case of attenuation, significant discrepancies were observed between predictions reported by different authors (Williams *et al.*, 1996; Kaczmarek *et al.*, 2002, 2005; Lee *et al.*, 2003; Fellah *et al.*, 2004). One of the reasons for the discrepancy between predictions obtained by different laboratories comes from the difficulties in measurements of many input parameters, with high accuracy, required by the model. While these parameters vary from one specimen to another, usually generic (constant) values are used in the model. These parameters are three macroscopic pore structure parameters (porosity, permeability, and tortuosity), mechanical properties of the solid frame, as well as physical and mechanical properties of the solid, the fluid phase.

Measurements of porosity of human and bovine cancellous bone has been reported by many authors. Usually porosity is calculated from three-dimensional (3D) microcomputed tomography (μCT) (Salome *et al.*, 1999) or measured using Archimede's principle by weighting dry and fully saturated bone specimens (Williams *et al.*, 1996; Hosokawa and Otani, 1997, 1998; Wear *et al.*, 2005). The values of porosity for human cancellous bones vary from 55% to 95%, depending on the anatomical site and bone status.

Permeability is the physical property that measures the ability of a fluid to filter through a porous medium. The published values of permeability for human cancellous bones range over three orders of magnitude and depend strongly on porosity and anatomical site (Arramon and Naumann, 2001; Grimm and Williams, 1997; Nauman *et al.*, 1999). Arramon and Naumann (2001) reported permeability values for both human and animal cancellous bones. They concluded that generally animal bones are more permeable than human bones, mainly because of their higher porosity. For human femoral bone with a porosity ranging from 60% to 95%, the permeability was found to vary from 5×10^{-6} to 1×10^{-4} cm^2, respectively. Grimm and Williams (1997) published the results of permeability measurements in human calcaneal trabecular bone using linseedoil as the flowing medium. Their results ranged from 0.1 to 1.1×10^{-6} cm^2 (for porosity values between 78% to 93%) and correlated strongly with porosity ($r^2=0.91$). Nauman *et al.* (1999), compared the permeability of human vertebral and femoral bone specimens measured for two different flow directions (longitudinal and transverse). They reported that permeability is strongly influenced by both: (i) relative orientation between flow direction and the principal orientation of trabecular network ($p<0.0001$) and (ii) anatomic site ($p<0.0001$). For vertebral specimens, permeability for longitudinal and transverse directions were found to be 8×10^{-5} and 3.6×10^{-5} cm^2, while for femoral specimens the values for those two directions were 10^{-6} and 2.8×10^{-6} cm^2, respectively.

Only a few papers report tortuosity values for human cancellous bones. Tortuosity values of human calcaneus obtained by Williams *et al.* (1996) using the electrical spectroscopy method were found between 1.6 and 2.3 for porosities ranging from 58% to 82%. Wear *et al.* (2005) following Williams (1992) and Hosokawa and Otani (1997, 1998) calculated the tortuosity from the relation $tortuosity=1-s(1-1/porosity)$, where the structural parameter s was assumed to be 0.25. He calculated tortuosity values between 1.01 and 1.16 for narrow porosity range of 86%–97% (Wear *et al.*, 2005). Fellah *et al.* (2004) and Sebaa *et al.* (2006) have measured the tortuosity of three unsaturated human cancellous bone samples (porosities of 83%, 77%, 88%) using a wave reflectometry method. Their results (tortuosity values of 1.05, 1.01, and 1.02) are generally lower than that obtained by the other authors using electrical spectroscopy method. Finally, Attenborough *et al.* (2005) measured tortuosity as a function of structural anisotropy and porosity for "original" and "inverse" air-filled stereolithographical bone replicas using audio-frequency pulses. Their results obtained for three perpendicular directions of original replica of femoral head bone (having porosity about 74%) range from 1.274 to 1.694. They confirmed anisotropy in the tortuosity and that the value of tortuosity decreases as porosity increases.

Macroscopic elastic coefficients of the saturated porous frame, usually denoted as P, Q, and R [see Eq. (7)], introduced by Biot and Willis (1957), are related to the bulk and shear moduli of the solid skeleton (N,K_b) as well as to the intrinsic bulk compression moduli of the solid (K_s) and fluid phases (K_f). To the authors' knowledge, no study focused on the determination of the Biot–Willis elastic coefficients for human cancellous bones has been reported. However, each time Biot's theory is applied for modeling wave propagation in cancellous bone, these coefficients need to be calculated or estimated. Usually, intrinsic physical and mechanical properties of each phase are assumed (extracted from literature), or, when it is possible, measured by means of modern experimental techniques like atomic force microscopy (Hengsberger *et al.*, 2001), nanoidentation method (Zysset *et al.*, 1999), or acoustical microscopy (Turner *et al.*, 1999; Litniewski, 2005). Once the intrinsic material properties are known, micromechanical models (e.g., Biot and Willis, 1957; Bourbie *et al.*, 1987; Roberts and Garboczi, 2002a,b) can be applied in order to calculate values for bulk and shear modulus of the solid frame (Kaczmarek *et al.*, 2005). The intrinsic properties of marrow or water commonly filling the pore space are taken from the literature (Hosokawa and Otani, 1997, 1998; Kaczmarek *et al.*, 2002, 2005; Fellah *et al.*, 2004; Wear *et al.*, 2005).

The absence of comprehensive study reporting measurements, for the same set of bone specimens, mechanical, and structural properties required by the Biot model motivated the present work. Our study aims at providing an experimental determination of these parameters for a statistically representative group of cancellous bone specimens, collected from the same anatomical site. Therefore, within the present paper combined experimental and theoretical approaches are used to measure the material, structural, and elastic parameters for the set of 35 human trabecular bone samples obtained from proximal femur. The results are compared with the values reported in the literature. In a subsequent paper, these individual parameters will be used to predict phase velocity and attenuation according to the macroscopic two-

phase Biot's model. The relevance of the theory will be evaluated by comparison of the model predictions and experimental data obtained from ultrasonic studies.

II. BONE SPECIMENS AND EXPERIMENTAL SETUP

A. Bone specimens

Twenty-eight human right femur specimens were dissected from fresh cadavers (9 women, mean age of 78 ± 11 years, age range 55–91; and 21 men, mean age of 71 ± 10 years, age range 45–86). Ethical approval for collection of samples was granted by the Human Ethics Committee of the Institute of Anatomy at the University René Descartes (Paris, France). The tissue donors or their legal guardians provided informed written consent to provide their tissues for investigation, in accord with legal clauses stated in the French Code of Public Health (Code de la Sant Publique Français). None of the donors underwent femoral prosthesis surgery. The skeletal status of the donors was undocumented. The specimens were stored at −20 °C after dissection. The bone specimens were prepared in several steps. The femoral head and the diaphysis were first removed leaving the proximal part of the femur (neck and trochanter). Slices of trabecular bone with parallel faces and 10 mm thickness were cut from the proximal femur, in the plane defined by the cephalo-caudal and medio-lateral directions using a circular saw under continuous irrigation. The samples thickness was measured using an electronic caliper. Finally, cylindrical cores were machined in the prepared specimens (typically 10 mm in height and 8 mm in diameter), leading to a total of 35 cores specimens. The specimens were defatted using a dichloromethane ($C_2H_2C_{12}$) solution (immersion for two or three days) and water jet. They were stored in air at room temperature after marrow removal.

B. Measurements of porosity

Porosity was measured from 3D reconstructions of the trabecular structures obtained after scanning the specimens with high resolution synchrotron radiation (SR) μCT at the European Synchrotron Radiation Facility (ESRF, Grenoble, France). SR μCT allows 3D reconstruction of volumes with an isotropic spatial resolution of 10 μm. The detailed description of the experimental device has been reported elsewhere (Salome *et al.*, 1999). Starting with 3D data sets reconstructed from projections of the bone samples, a global threshold was applied to separate bone from background, leading to 3D binary data sets from which the bone volume fraction (bone volume/total volume, BV/TV=1 porosity) could be extracted. Because the reconstructed 3D data sets provide complete information on the bone volume, no model assumption is required to obtain the porosity (Nuzzo *et al.*, 2002). Porosity is denoted f_v in what follows.

C. Measurement of skeleton material density

The mass of the specimens (m_S) was measured precisely using a high precision (Δm_s=0.1 mg) balance (TB-224 Denver Instruments GmBH, Göttingen, Germany). Then, the density of solid phase (ρ_s) constituting the skeleton of the porous material was derived as the ratio of the mass over the bone volume BV:

$$\rho_s = m_s/\mathrm{BV}. \tag{1}$$

D. Permeability measurements

Permeability measurements have been performed for water saturated bone samples. Because of the high porosity and relatively high permeability of cancellous bone, the falling head method was applied using custom-made digital system for falling time measurement. Satisfying the condition for laminar flow through the bone samples [Reynolds number=1 (Arramon and Naumann (2001)], intrinsic permeability k was determined based on Darcy's law of fluid flow through porous media accordingly to the following formula:

$$k = \frac{\eta}{\rho_f g}\frac{a^2}{A^2}\frac{L}{t_{i+1}-t_i}\ln\left(\frac{h_i}{h_{i+1}}\right). \tag{2}$$

In Eq. (2), L denotes sample thickness, η is the dynamic viscosity, ρ_f is the fluid density, g is acceleration due to gravity, t_i is the time corresponding to the hydraulic head height h_i, A and a are cross-sectional area of the sample and the measuring tube, respectively. In order to improve the accuracy of the method, a four points time control system (instead of standard two points) was used. Permeability was calculated as an average value of six measurements: two series of three measurements with intermediate repositioning between the two series.

E. Tortuosity measurements

Tortuosity was determined using an electrical spectroscopy method (Lukowski *et al.*, 2000). The experimental setup for conductivity measurements includes: the chamber made from transparent PVC, system of two electrodes made from stainless steel, and the RLC electrical bridge (HIOKI 3532 LCR HiTester, HIOKI E.E. Corporation, Nagano, Japan). Prior to the experiments, cancellous bone specimens were saturated under vacuum with isotonic physiological liquid (0.15 mol/L of NaCl). It is worth noticing that the determination of the formation factor and then tortuosity (α_T) using conductometric method on porous samples filled with conducting liquid is possible in the case when the volume conductance dominates over the surface conductance (Brown, 1980; Lukowski *et al.*, 2000). Given that, the tortuosity was determined from the consecutive measurements of the conductivity of the electrolyte (λ_E) and the bone specimen filled with electrolyte (λ_B) (Brown, 1980; Lukowski *et al.*, 2000). The tortuosity is given by the relation (Brown, 1980; Lukowski *et al.*, 2000):

$$\alpha_T = f_v\frac{\lambda_E}{\lambda_B}. \tag{3}$$

F. Estimation of shear and bulk modulus of solid skeleton from ultrasonic measurements

The shear (N) and bulk (K_b) moduli of the solid frame can be derived based on the knowledge of the speed of sound of the longitudinal (V_L) and shear waves (V_{SH}) propagating in dry bone, the density of the solid skeleton (ρ_s), and the porosity (f_v). Assuming that the frame is isotropic and is composed by homogeneous material the relationships proposed by Bourbie *et al.* (1987) and Cieszko *et al.* (2000) allows one to calculate these moduli:

$$N = V_{SH}^2(1-f_v)\rho_s, \quad K_b = (1-f_v)\rho_s\left(V_L^2 - \tfrac{4}{3}V_{SH}^2\right), \tag{4}$$

The longitudinal wave velocity of the skeleton frame was estimated by transmission measurements through the unsaturated bone specimens. A pair of longitudinal contact ultrasonic transducers of center frequency 0.5 MHz (Panametrics V101-RB, Waltham, MA) was excited by a high voltage pulser-receiver (Panametrics 5058PR) and the signal was acquired by Digital Storage Oscilloscope (DSO-28200, Link Instruments Inc., Fairfield NJ). A shear wave couplant (SWC Panametrics, Waltham, MA) was used between the probes and the specimens. The transducer frequency of 0.5 MHz was selected in order to ensure propagation of bulk wave in the bone samples and to avoid propagation of a bar mode that appears at lower frequencies. Typical diameter of the specimens was 8 mm (see Sec. II A) therefore for 0.5 MHz frequency measured wavelengths range approximately from 3 to 5 mm. Given that, one can conclude that the lateral dimensions of our specimens are not significantly smaller than the wavelengths and necessary condition for propagation of bulk wave is fulfilled (Achenbach, 1980; Nicholson and Strelitzki, 1999). For each specimen the transmission time of flight was evaluated automatically as the first sample after the uniform threshold set as 5% of maximum amplitude of the transmitted pulse. The speed of sound was then derived as the ratio between the thickness of the specimens, measured by digital caliper (Mitutoyo Corp., Japan) having 0.01 mm precision, and the time of flight. Tests were made to measure the propagation of a shear wave through the dry specimens, but it was observed that two kinds of waves (longitudinal and shear) were generated simultaneously by the shear wave transducer with comparable amplitudes. As a result, in most cases it was not possible to distinguish the pulse associated with the shear wave from the signal associated with the longitudinal wave. Therefore, it was decided to derive the shear wave velocity of the skeleton frame, assuming bone to be isotropic and using the following relationship (Achenbach, 1980):

$$V_{SH} = V_L\sqrt{\frac{1-2\nu_b}{2(1-\nu_b)}}, \tag{5}$$

where ν_b is the Poisson ratio of the skeleton frame. Kaczmarek *et al.* (2005) showed that for cancellous bones ν_b can be related to the porosity and Poisson ratio of bone tissue (ν_s) according to the equation proposed by Roberts and Garboczi (2002a):

$$\nu_b = \nu_s + \frac{f_v(0.233-\nu_s)}{0.886}, \tag{6}$$

where ν_s was assumed to be 0.3, an average value of the measured Poisson ratio in cortical bone (Shahar *et al.*, 2007). Equation (6) was proposed by Roberts and Garboczi (2002a,b), who have calculated the relationship between mechanical properties of the porous materials at the microscopic and macroscopic levels, based on various statistical 3D random models of microstructure. From this study, the so-called Gaussian open-cell model was chosen, because the structure described by this model is very similar to the structure observed in cancellous bones (Gibson, 1985).

G. Derivation of the Biot–Willis elastic constants

The shear (N) and bulk (K_b) moduli of the skeleton frame were obtained, based on the results from ultrasonic measurements of our unsaturated bone specimens. Assuming then mechanical properties of the fluid (K_f=2.25 GPa for water) and solid phase [K_s=10.8 GPa for bone tissue—Sebaa *et al.* (2006)] and knowing the porosity f_v from the measurements, it was possible to derive the so-called macroscopic Biot–Willis elastic constants (P,Q,R) for water-saturated cancellous bone. Following Biot and Willis (1957) these constants can be defined as

$$P = \frac{(1-f_v)(1-f_v-K_b/K_s)K_s + f_vK_bK_s/K_f}{1-f_v-K_b/K_s+f_vK_s/K_f},$$

$$Q = \frac{f_v(1-f_v-K_b/K_s)K_s}{1-f_v-K_b/K_s+f_vK_s/K_f}, \tag{7}$$

$$R = \frac{f_v^2K_s}{1-f_v-K_b/K_s+f_vK_s/K_f}.$$

III. RESULTS AND DISCUSSION

Porosity measured by SR μCT within our studies ranges from 67% to 96% (mean value $\pm$ s.d.: $88\pm6\%$). These values are in the range of published values for cancellous bone at other skeletal sites (Chaffai *et al.*, 2000; Lundeen *et al.*, 2000; Chappard *et al.*, 2006; Khosla *et al.*, 2006).

Density of the solid phase (ρ_s) was found to be in the range 1.04–1.88 g/cm^3 (mean value 1.46 ± 0.06 g/cm^3). The results are consistent with those obtained by Morgan *et al.* (2003) and Keaveny and Hayes (1993), who reported values ranging from 1.76 to 2.41 g/cm^3 and from 1.6 to 2.2 g/cm^3, respectively. It is worth noticing that for a few samples the obtained density was low (around 1.1 g/cm^3). Because no information about the pathological status of the donors is available, it is difficult to interpret these low values of material density.

Figure 1 shows intrinsic permeability as a function of porosity. Both quantities are significantly correlated (Spearman rank correlation coefficient rs=0.66, p=0.002). Such behavior is in agreement with results found in the literature both for saturated porous materials following the Kozeny–Carman relation (Carman, 1956) as well as for cancellous

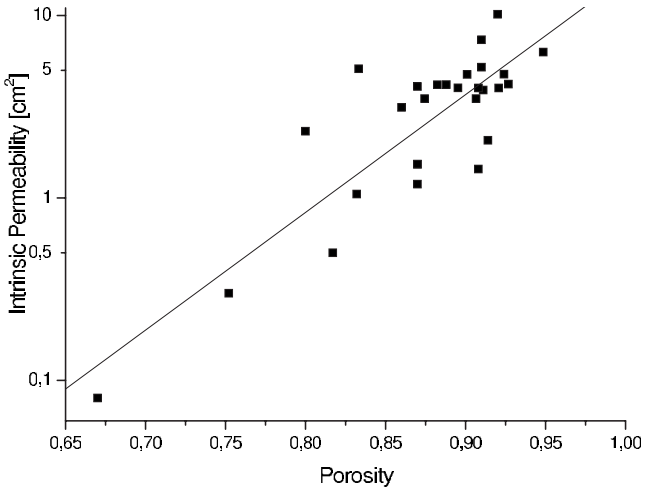

FIG. 1. Intrinsic permeability ($\times 10^{-6}$) measured using falling head method vs porosity.

bones (Arramon and Naumann, 2001; Grimm and Williams, 1997). Values of permeability, ranging from 0.08 to 10.15 $\times 10^{-6}$ cm^2, are of the same order of magnitude as those measured by other authors for human trabecular bone (Arramon and Naumann, 2001). It is worth noticing, as also observed by Arramon and Naumann (2001) for cancellous bones, that permeability can vary at fixed porosity even one order of magnitude (in our studies from 1 to 10×10^{-6} cm^2 around 90% porosity, see Fig. 1). It suggests that permeability is related not only to porosity itself but also to void shapes, and orientation of the trabeculae, which can be included in the so-called specific surface function (Arramon and Naumann, 2001).

Tortuosity as a function of porosity is displayed in Fig. 2. Most of the measured values are concentrated around 1.5 and ranges from 1.1 to 2.8. The absolute errors were calculated using error propagation method. The error values do not exceed 10%. Tortuosity is a decreasing function of porosity, like for the other porous materials (Salem and Chilingarian, 2000). These values of tortuosity are in agreement with the values obtained by Williams *et al.* (1996), who used

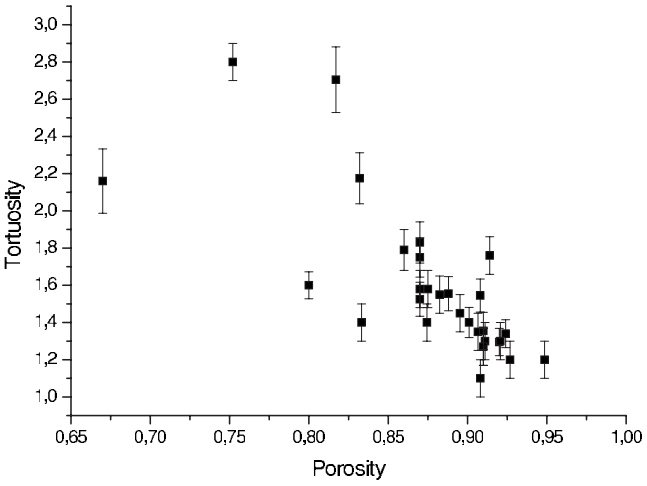

FIG. 2. Tortuosity measured by electrical spectroscopy vs porosity.

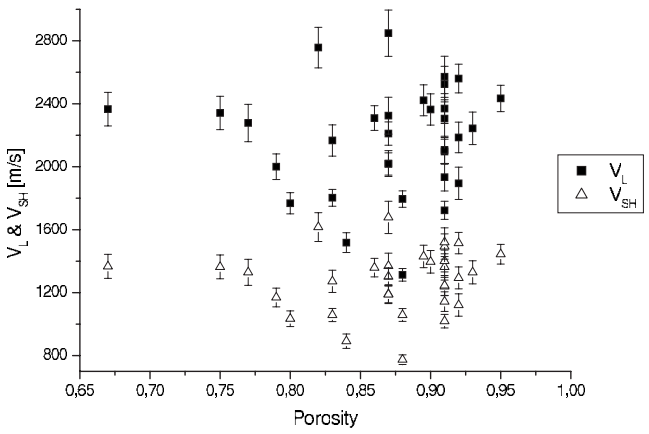

FIG. 3. Sound velocity of longitudinal V_L and shear V_{SH} waves vs porosity. Ultrasonic studies were performed for dry cancellous bones.

the same experimental method on human calcaneus specimens. In comparison with the results obtained by Wear *et al.* (2005), Fellah *et al.* (2004), and Sebaa *et al.* (2006) our values are higher. This apparent discrepancy may be attributed to several reasons, including difference in investigated anatomical sites and differences in measurement methods.

Figure 3 displays values of speeds of sound of longitudinal wave (V_L) and the estimated [based on Eqs. (5) and (6)] values of shear wave velocities (V_{SH}) as a function of porosity. The velocity values range from 1313 to 2848 m/s (V_L) and from 774 to 1678 m/s (V_{SH}). No correlation was observed between V_L or V_{SH} and porosity. To the knowledge of the authors there are no data for the longitudinal and shear wave velocities obtained for completely dry human cancellous bones. However, ultrasonic experiments using similar experimental technique were done by Vastel *et al.* (2007) for moist human cancellous bones obtained from the center of femoral head. The values they measured for velocity of longitudinal wave, obtained using low frequency (60 kHz) and high frequency (2 MHz) transducers, are of the same order of magnitude as in our studies. However, detailed comparison with present studies is not possible because of the different frequencies used (in our studies 500 kHz) and different bone status (in our case bones were completely dry).

Figures 4–6 show the calculated [based on Eq. (7)] values of the Biot–Willis elastic moduli P, Q, and R as a function of porosity. P presented in Fig. 4 is found in the range 0.5–3.5 GPa and correlates to porosity (r^2=0.77). The absolute measurement errors [calculated based on Eq. (7) using error propagation method] are low (mean error value =0.05 GPa). The absolute measurement errors of Q (Fig. 5) were found to be the same as for P, but the relative errors were higher than for P because of smaller absolute values of Q, which were varying in the interval 0.08–0.38 GPa. Q was also strongly correlated with porosity (r^2=0.81). Finally, a very high correlation was found between R (range: 1.1–2.1 GPa) and the porosity (r^2=0.99). In addition, for comparison, Figs. 4–6 present the values of the P, Q, R moduli obtained by other authors. Table I summarizes the values assigned in different studies to all input parameters that are required for the calculation of Biot–Willis elastic

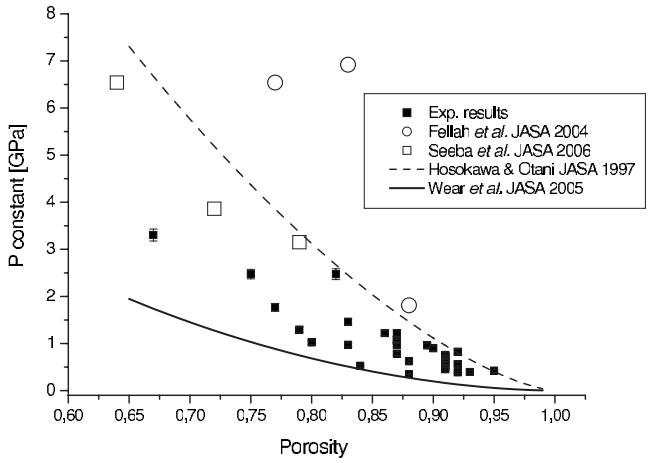

FIG. 4. *P* elastic constant vs porosity. Our experimental results (closed squares) are compared with the data obtained by the other authors, Hosokawa and Otani (1997), Wear *et al.* (2005), Fellah *et al.* (2004), Sebaa *et al.* (2006).

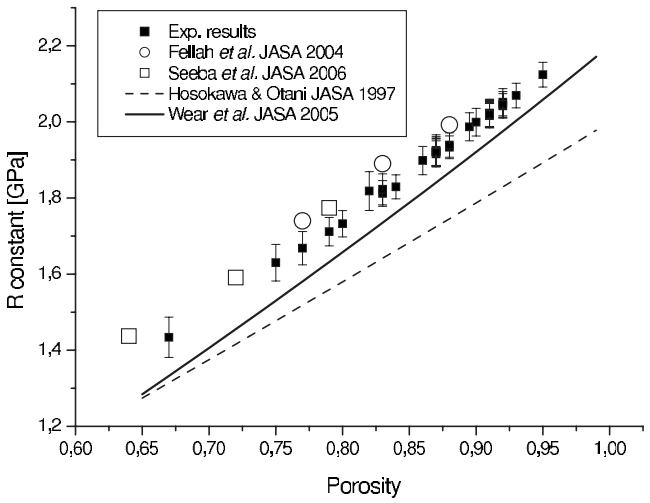

FIG. 6. *R* elastic constant vs porosity. Our experimental results (closed squares) are compared with the data obtained by the other authors, Hosokawa and Otani (1997), Wear *et al.* (2005), Fellah *et al.* (2004), Sebaa *et al.* (2006).

moduli [based on Eq. (7)]. These parameters were chosen for specimens having porosity 79% from bovine (Hosokawa and Otani, 1997) and human (Fellah *et al.*, 2004; Wear *et al.*, 2005; Sebaa *et al.*, 2006) cancellous bone specimens. These values are compared with the data obtained within our study (presented in the last column of Table I), for one typical specimen having the same porosity as the specimens investigated by the other authors.

When the *P* parameter is considered (Fig. 4), it is worth noticing that the results obtained following the input parameters used by Fellah *et al.* (2004), Sebaa *et al.* (2006), or Hosokawa and Otani (1997), are higher than our experimental values, while the results obtained following Wear *et al.* (2005) are lower than our data. Focusing on the studies performed for human bones and considering that in Eq. (7) five parameters—two phase-specific (K_f, K_s) and three macroscopic (f_v, K_b, N)—define the Biot–Willis elastic constants, one can conclude that source of discrepancy between results presented by the different authors comes from different values of K_b, N, and K_s, because the porosity f_v of the specimens and the bulk modulus of fluid phase K_f in all studies are almost the same. The values of K_s for human femoral neck reported by Sebaa *et al.* (2006) and in the present paper are the same (10.8 GPa). Therefore the main source of discrepancy for *P* between our results and the data reported by Sebaa *et al.* (2006) has to be found in the values of bulk and shear moduli of the porous frame (our values are lower than these in Seeba's study). Sebaa *et al.* (2006) observed propagation of two longitudinal waves in their specimens which were characterized by tortuosity almost equal to 1. It implies that average orientation of trabecular network was mostly parallel to the direction of wave propagation (Hosokawa and Otani, 1998; Hughes *et al.*, 1999, 2006; Padilla and Laugier, 2000; Kaczmarek *et al.*, 2002, 2005; Fellah *et al.*, 2004; Sebaa *et al.*, 2006). In our study, tortuosity varied from 1.1 to 2.8 and the propagation of two longitudinal waves was observed only in a few samples (data not shown). This suggests that the orientation of trabecular network is perpendicular to the wave propagation. Given that, it is likely that discrepancies in bulk and shear moduli of the porous frame, leading to different values of *P*, result from differences in anisotropic structural properties of the specimens. It is also worth noticing lower values of *P* derived based on the data taken from Wear *et al.* (2005) for calcaneal bone specimens. One of the hypotheses of the discrepancy are lower values of the mechanical properties of the calcaneus (K_s, K_b, and N see Table I) chosen by Wear *et al.* (2005) compared to our values. However, there is not consensus among researchers working in the field if comparison of the mechanical properties from different anatomic sites is reasonable.

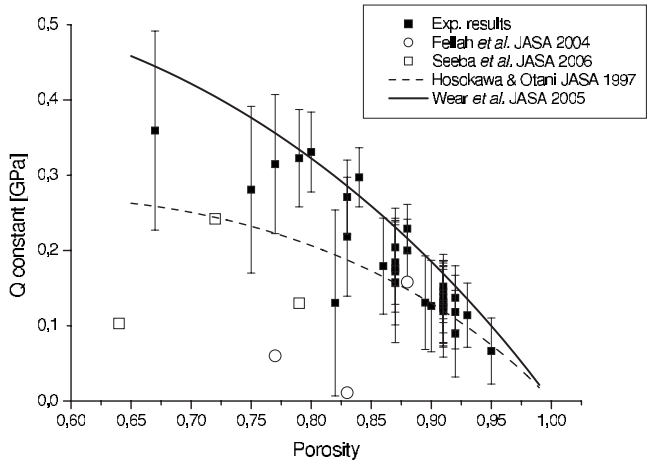

FIG. 5. *Q* elastic constant vs porosity. Our experimental results (closed squares) are compared with the data obtained by the other authors, Hosokawa and Otani (1997), Wear *et al.* (2005), Fellah *et al.* (2004), Sebaa *et al.* (2006).

In contrast to the results obtained for *P*, the values for *Q* measured by Fellah *et al.* (2004) and Sebaa *et al.* (2006) are lower than our experimental data, while the values obtained following Wear are higher (see Fig. 5). Again, the source of the discrepancy between the different studies comes from the different values of (K_s, K_b, and N) used in the calculation of

TABLE I. Input parameters for calculations of P,Q,R elastic moduli. In the case of Fellah *et al.* (2004) and Sebaa *et al.* (2006), data for the sample M2 were chosen. All modulus are in GPa. Opt: Value obtained using optimization; m: Marrow; w: Water; b.f.: Bovine femur; h.f.: Human femur; h.c.: Human calcaneus.

Parameter		Hosokawa and Otani, 1997 b.f.	Fellah *et al.*, 2004 h.f.	Wear *et al.*, 2005 h.c.	Sebaa *et al.*, 2006 h.f.	Our studies h.f.
Fluid density g/cm^3	ρ_f	$0.93^{(m)}$	$1^{(w)}$	$1^{(w)}$	$1^{(w)}$	$1^{(w)}$
Fluid viscosity g/(cm s)	η	$15^{(m)}$	$0.01^{(w)}$	$0.01^{(w)}$	$0.01^{(w)}$	$0.01^{(w)}$
Bulk modulus of fluid	K_f	$2^{(m)}$	$2.28^{(w)}$	$2.2^{(w)}$	$2.28^{(w)}$	$2.28^{(w)}$
Density of solid phase g/cm^3	ρ_s	1.96	1.96	1.8	1.99	1.8
Young modulus of solid phase	E_s	22	⋯	8.3	13	13
Poisson ratio of solid phase	ν_s	0.32	⋯	0.3	0.3	0.3
Bulk modulus of solid phase	K_s	20.37[a]	20	6.9[a]	10.8[a]	10.8[a]
Porosity	f_v	0.79	0.77	0.79	0.79	0.79
Exponent	n	$1.46^{(Opt)}$	⋯	$1.75^{(Opt)}$	⋯	⋯
Young Modulus of trabecular frame	E_b	2.25[b]	⋯	0.54[b]	$2.47^{(Opt)}$	⋯
Poisson ratio of trabecular frame	ν_b	0.32	⋯	0.23	$0.25^{(Opt)}$	0.24
Bulk modulus of solid frame	K_b	2.08[c]	4	0.33[c]	1.64[c]	0.67
Shear modulus of solid frame	N	0.85[d]	1.7	0.22[d]	0.99[d]	0.42

[a]Calculated using the formula $K_s=E_s/(3(1-2\nu_s))$.
[b]Calculated using the formula $E_b=E_s(1-f_v)^n$.
[c]Calculated using the formula $K_b=E_b/(3(1-2\nu_b))$.
[d]Calculated using the formula $N=E_b/(2(1+\nu_b))$.

Q. The best agreement between our results and those reported by different authors is obtained for R (see Fig. 6), because this modulus is mainly associated with the properties of fluid phase (water or marrow), which, for a porosity of 80%, dominates over the solid phase (Cieszko *et al.*, 2000).

IV. SUMMARY AND CONCLUSIONS

The present study was focused on the experimental evaluation of macroscopic structural (porosity, permeability, and tortuosity) and macroscopic elastic properties of human cancellous bone specimens treated as homogeneous saturated porous material. The structural parameters were measured using standard methods dedicated to the study of porous materials: electrical spectroscopy (tortuosity) and water permeametry (intrinsic permeability). Macroscopic elastic constants, introduced by Biot–Willis, were calculated using the data derived from ultrasonic measurements of unsaturated specimens. The values of the measured structural parameters were found to be in agreement with previous published values. Interestingly, our results showing a substantial variability of the permeability (approximately one order of magnitude) for fixed porosity suggest that permeability is not only sensitive to porosity, but also probably to microstructure. For the macroscopic Biot–Willis elastic moduli (P, Q, R), our data were situated between the results obtained by the other authors, the discrepancies are attributed to differences in values of macroscopic mechanical properties of the skeleton frame, due to strong structural anisotropy varying from site to site. These results enlighten the difficulty to use Biot's model in such kind of specimens with a tremendous variability in structure. As a consequence, because of the lack of comprehensive knowledge of the elastic, structural, and material properties of cancellous bone, it seems unavoidable to carefully and individually measure these properties before using them in the Biot's model.

The present study therefore presents three major strengths: (i) the first one is to provide almost complete characterization of the parameters that play a role in the Biot's model. Previous investigations were the subject of many complementary studies, performed on bovine or human specimens taken from different anatomical sites. (ii) The second one is the statistically representative number of studied specimens, which cover, in comparison with previous studies, a relatively large range of porosities (67%–95%), and which were well localized in the proximal femur (neck and great trochanter). (iii) Finally it is worth noticing that, to the knowledge of the author, there is lack in the literature of experimental data concerning such statistically representative data of macroscopic Biot's elastic coefficients for human cancellous bones.

The results stress the wide variability found for some parameters even when they are measured within a single skeletal (proximal femur) site for a single specimens (human). For example, the permeability was found to vary by a factor of 100, the tortuosity and the Biot–Willis moduli by a factor of approximately 3. Therefore, the individual determination of macroscopic mechanical and structural properties for each tested cancellous bone specimen seems mandatory for an accurate prediction of both static and dynamical processes. Such theoretical predictions of ultrasonic wave dispersion and attenuation will be the subject of further work.

ACKNOWLEDGMENT

The studies were performed within the Marie Curie Intra European Fellowship project: QUSOB 038731 *Ultrasonic Assessment of Osteoporosis in Cancellous Bone* funded under EU's Sixth Framework Programme.

Achenbach, J. D. (**1980**). *Wave Propagation in Elastic Solids* (North Holland, Amsterdam).

Arramon, Y. P., and Naumann, E. A. (**2001**). "Intrinsic permeability of cancellous bone," in *Bone Mechanics Handbook*, edited by S. C. Cowin (CRC Press, Boca Raton, FL), pp. 25.1–25.17.

Attenborough, K., Shin, H.-C., Qin, Q., Fagan, M. J., and Langton, C. M. (**2005**). "Measurements of tortuosity in stereo-lithographical bone replicas using audio-frequency pulses," J. Acoust. Soc. Am. **118**, 2779–2782.

Baron, R. (**1999**). *Anatomy and Ultrastructure of Bone* (Lippincott Williams & Wilkins, Philadelphia).

Biot, M. A. (**1956a**). "Theory of propagation of elastic waves in a fluid-satured porous solid. I. Low-frequency range," J. Acoust. Soc. Am. **28**, 168–178.

Biot, M. A. (**1956b**). "Theory of propagation of elastic waves in a fluid-satured porous solid. II. Higher frequency range," J. Acoust. Soc. Am. **28**, 179–191.

Biot, M. A., and Willis, D. G. (**1957**). "The elastic coefficients of the theory of consolidation," J. Appl. Mech. **24**, 594–601.

Bourbie, T., Coussy, O., and Zinszler, B. (**1987**). *Acoustics of Porous Media* (Gulf Publishing, Houston).

Brown, R. J. S. (**1980**). "Connection between formation factor for electrical resistivity and fluid-solid coupling factor in Biot's equations for acoustic waves in fluid filled with porous media," Geophysics **45**, 1269–1275.

Carman, P. C. (**1956**). *Flow of Gases Through Porous Media* (Butterworths Scientific, London).

Chaffai, S., Padilla, F., Berger, G., and Laugier, P. (**2000**). "In vitro measurement of the frequency-dependent attenuation in cancellous bone between 0.2 and 2 mHz," J. Acoust. Soc. Am. **108**, 1281–1289.

Chappard, C., Basillais, A., Benhamou, L., Bonassie, A., Brunet-Imbault, B., Bonnet, N., and Peyrin, F. (**2006**). "Comparison of synchrotron radiation and conventional x-ray microcomputed tomography for assessing trabecular bone microarchitecture of human femoral heads," Med. Phys. **33**, 3568–3577.

Cieszko, M., Kaczmarek, M., and Kubik, J. (**2000**). *Dynamics of Saturated Porous Materials* (in Polish), Biblioteka Mechaniki Stosowanej. Seria A. Monografie (IPPT PAN, Warsaw).

Fellah, Z. E., Chapelon, J. Y., Berger, S., Lauriks, W., and Depollier, C. (**2004**). "Ultrasonic wave propagation in human cancellous bone: Application of Biot theory," J. Acoust. Soc. Am. **116**, 61–73.

Gibson, L. J. (**1985**). "The mechanical behaviour of cancellous bone," J. Biomech. **18**, 317–328.

Grimm, M. J., and Williams, J. L. (**1997**). "Measurements of permeability in human calcaneal trabecular bone," J. Biomech. **30**, 743–745.

Haire, T. J., and Langton, C. M. (**1999**). "Biot theory: A review of its application to ultrasound propagation through cancellous bone," Bone (N.Y.) **24**, 291–295.

Hengsberger, S., Kulik, A., and Zysset, P. (**2001**). "A combined atomic force microscopy and nanoindentation technique to investigate the elastic properties of bone structural units," Eur. Cells Mater **1**, 12–7.

Hosokawa, A., and Otani, T. (**1997**). "Ultrasonic wave propagation in bovine cancellous bone," J. Acoust. Soc. Am. **101**, 558–562.

Hosokawa, A., and Otani, T. (**1998**). "Acoustic anisotropy in bovine cancellous bone," J. Acoust. Soc. Am. **103**, 2718–2722.

Hughes, E. R., Leighton, T. G., Petley, G. W., and White, P. R. (**1999**). "Ultrasonic propagation in cancellous bone: A new stratified model," Ultrasound Med. Biol. **25**, 811–821.

Hughes, E. R., Leighton, T. G., Petley, G. W., and White, P. R. (**2006**). "Investigation of an anisotropic tortuosity in a biot model of ultrasonic propagation in cancellous bone," J. Acoust. Soc. Am. **121**, 568–574.

Hughes, E. R., Leighton, T. G., Petley, G. W., White, P. R., and Chivers, R. C. (**2003**). "Estimation of critical and viscous frequencies for Biot theory in cancellous bone, Ultrasonics **41**, 365–368.

Johnson, D. L., Plona, T. J., and Kojima, H. (**1994a**). "Probing porous-media with 1st and 2nd sound. II. Acoustic properties of water-saturated porous-media," J. Appl. Phys. **76**, 115–125.

Johnson, D. L., Plona, T. J., and Kojima, H. (**1994b**). "Probing porous media with first and second sound. I. Dynamic permeability," J. Appl. Phys. **76**, 104–114.

Kaczmarek, M., Kubik, J., and Pakula, M. (**2002**). "Short ultrasonic waves in cancellous bone," Ultrasonics **40**, 95–100.

Kaczmarek, M., Kubik, J., and Pakula, M. (**2005**). "Wave propagation in saturated high porosity materials," in *Poromechanics III - Biot Centennial (1905–2005)*, edited by A.-D. C. . F.-J. U. Y. N. Abousleiman (Balkema, London).

Keaveny, T. M., and Hayes, W. C. (**1993**). "A 20-year perspective on the mechanical properties of trabecular bone," J. Biomech. Eng. **115**, 534–542.

Khosla, S., Riggs, B. L., Atkinson, E. J., Oberg, A. L., McDaniel, L. J., Holets, M., Peterson, J. M., and Melton, L. J. (**2006**). "Effects of sex and age on bone microstructure at the ultradistal radius: A population-based noninvasive in vivo assessment," J. Bone Miner. Res. **21**, 124–131.

Laugier, P., Droin, P., Laval-Jeantet, A. M., and Berger, G. (**1997**). "In vitro assessment of the relationship between acoustic properties and bone mass density of the calcaneus by comparison of ultrasound parametric imaging and quantitative computed tomography," Bone (N.Y.) **20**, 157–165.

Lee, K. I., Roh, H. S., and Yoon, S. W. (**2003**). "Acoustic wave propagation in bovine cancellous bone: Application of the modified Biot-Attenborough model," J. Acoust. Soc. Am. **114**, 2284–2293.

Litniewski, J. (**2005**). "Determination of the elasticity coefficient for a single trabecula of a cancellous bone: Scanning acoustic microscopy approach," Ultrasound Med. Biol. **31**, 1361–1366.

Lukowski, J., Kaczmarek, M., and Kubik, J. (**2000**). "Anisotropic properties of trabecular bone. Conductometric and ultrasonic studies," Acta Bioeng. Biomech. **2**, 17–28.

Lundeen, G. A., Vajda, E. G., and Bloebaum, R. D. (**2000**). "Age-related cancellous bone loss in the proximal femur of caucasian females," Osteoporosis Int. **11**, 505–511.

Morgan, E. F., Bayraktar, H. H., and Keaveny, T. M. (**2003**). "Trabecular bone modulus-density relationships depend on anatomic site," J. Biomech. **36**, 897–904.

Nauman, E. A., Fong, K. E., and Keaveny, T. M. (**1999**). "Dependence of intertrabecular permeability on flow direction and anatomic site," Ann. Biomed. Eng. **27**, 517–524.

Nicholson, P. H. F., and Strelitzki, R. (**1999**). "On prediction of Young's modulus in calcaneal cancellous bone by ultrasonic bulk and bar velocity measurements," Clin. Rheumatol. **18**, 10–16.

Nuzzo, S., Lafage-Proust, M. H., Martin-Badosa, E., Boivin, G., Thomas, T., Alexandre, C., and Peyrin, F. (**2002**). "Synchrotron radiation microtomography allows the analysis of three-dimensional microarchitecture and degree of mineralization of human iliac crest biopsy specimens: effects of etidronate treatment," J. Bone Miner. Res. **17**, 1372–1382.

Padilla, F., and Laugier, P. (**2000**). "Phase and group velocities of fast and slow compressional waves in trabecular bone," J. Acoust. Soc. Am. **108**, 1949–1952.

Roberts, A. P., and Garboczi, E. J. (**2002a**). "Computation of the linear elastic properties of random porous materials with a wide variety of microstructure," Proc. R. Soc. London, Ser. A **458**, 1033–1054.

Roberts, A. P., and Garboczi, E. J. (**2002b**). "Elastic properties of model random three-dimensional open-cell solids," J. Mech. Phys. Solids **50**, 33–55.

Salem, H. S., and Chilingarian, G. V. (**2000**). "Influence of porosity and direction of flow on tortuosity in unconsolidated porous media," Energy Sources **22**, 207–213.

Salome, M., Peyrin, F., Cloetens, P., Odet, C., Laval-Jeantet, A. M., Baruchel, J., and Spanne, P. (**1999**). "A synchrotron radiation microtomography system for the analysis of trabecular bone samples," Med. Phys. **26**, 2194–2194.

Sebaa, N., Fellah, Z. E. A., Fellah, M., Ogam, E., Wirgin, A., Mitri, F. G., Depollier, C., and Lauriks, W. (**2006**). "Ultrasonic characterization of human cancellous bone using the biot theory: Inverse problem," J. Acoust. Soc. Am. **120**, 1816–1824.

Shahar, R., Zaslansky, P., Barak, M., Friesem, A. A., Currey, J. D., and Weiner, S. (**2007**). "Anisotropic poisson's ratio and compression modulus of cortical bone determined by speckle interferometry," J. Biomech. **40**, 252–264.

Turner, C. H., Rho, J., Takano, Y., Tsui, T. Y., and Pharr, G. M. (**1999**). "The elastic properties of trabecular and cortical bone tissues are similar: Results from two microscopic measurement techniques," J. Biomech. **32**, 437–441.

Vastel, L., Masse, C., Crozier, E., Padilla, F., Laugier, P., Mitton, D., Bar-

donnet, R., and Courpied, J. P. (**2007**). "Effects of gamma irradiation on mechanical properties of defatted trabecular bone allografts assessed by speed-of-sound measurement," Cell Tissue Bank **8**, 205–210.
Wear, K. A. (**2007**). "Group velocity, phase velocity, and dispersion in human calcaneus in vivo," J. Acoust. Soc. Am. **121**, 2431–2437.
Wear, K. A., Laib, A., Stuber, A. P., and Reynolds, J. C. (**2005**). "Comparison of measurements of phase velocity in human calcaneus to Biot theory," J. Acoust. Soc. Am. **117**, 3319–3324.
Williams, J. L., Grimm, M. J., Foster, K. B., Wehrli, F. W., and Chung, H.-W. (**1996**). "Prediction of frequency and pore size dependent attenuation of ultrasound in trabecular bone using Biot's theory," in *Mechanics of Poroelastic Media*, edited by A. P. S. Salvadurai (Kluwer Academic Publishers, Dordrecht, The Netherlands), pp. 263–274.
Williams, J. L. (**1992**). "Ultrasonic wave propagation in cancellous and cortical bone: Prediction of some experimental results by Biot's theory," J. Acoust. Soc. Am. **91**, 1106–1112.
Zysset, P. K., Guo, X. E., Hoffler, C. E., Moore, K. E., and Goldstein, S. A. (**1999**). "Elastic modulus and hardness of cortical and trabecular bone lamellae measured by nanoindentation in the human femur," J. Biomech. **32**, 1005–1012.

Automated species recognition of antbirds in a Mexican rainforest using hidden Markov models

Vlad M. Trifa,[a] Alexander N. G. Kirschel,[b] and Charles E. Taylor[c]
Department of Ecology and Evolutionary Biology, University of California Los Angeles, 621 Charles Young Drive South, Los Angeles, California, 90095

Edgar E. Vallejo[d]
Department of Computer Science, ITESM-CEM, Carretera Lago de Guadalupe km. 3.5, Col. Margarita Maza de Juárez, Atizapán de Zaragoza, 52926, Estado de México, México

(Received 21 February 2007; revised 8 January 2008; accepted 9 January 2008)

Behavioral and ecological studies would benefit from the ability to automatically identify species from acoustic recordings. The work presented in this article explores the ability of hidden Markov models to distinguish songs from five species of antbirds that share the same territory in a rainforest environment in Mexico. When only clean recordings were used, species recognition was nearly perfect, 99.5%. With noisy recordings, performance was lower but generally exceeding 90%. Besides the quality of the recordings, performance has been found to be heavily influenced by a multitude of factors, such as the size of the training set, the feature extraction method used, and number of states in the Markov model. In general, training with noisier data also improved recognition in test recordings, because of an increased ability to generalize. Considerations for improving performance, including beamforming with sensor arrays and design of preprocessing methods particularly suited for bird songs, are discussed. Combining sensor network technology with effective event detection and species identification algorithms will enable observation of species interactions at a spatial and temporal resolution that is simply impossible with current tools. Analysis of animal behavior through real-time tracking of individuals and recording of large amounts of data with embedded devices in remote locations is thus a realistic goal.
© *2008 Acoustical Society of America.* [DOI: 10.1121/1.2839017]

PACS number(s): 43.80.Ka, 43.72.Ne, 43.60.Lq [JAS] Pages: 2424–2431

I. INTRODUCTION

Bird songs play an important role in species-specific communication, primarily for mate attraction and territory defense (Catchpole and Slater, 1995). Species identification based on acoustic communication is particularly important in rainforest environments because of the limited visibility caused by dense vegetation. Within such environments there is a need to efficiently distinguish between species' songs in order to understand how species interact. While there is no substitute for the experienced human observer, automated monitoring, using sensor networks, is increasingly recognized for its unobtrusiveness, constant alertness, and extended presence for localization and situational awareness (Sczewczyk *et al.*, 2004). The required software methods to automatically analyze bird vocalization from using *embedded networked sensors* have only very recently become available. This study focuses on a class of methods called *hidden Markov models* to automate recognition of birds in a Mexican rainforest.

Species recognition based on objective analysis of vocalization has been applied to a wide variety of animals, including whales (Scheifele *et al.*, 2005), marmots (Blumstein and Munos, 2005), grasshoppers (Chesmore, 2004), and birds (Fagerlund, 2004). Previous studies have used a variety of methods for species recognition. At the simplest level, that of filtering for species or individual identification, several approaches have been explored. These approaches include: multivariate statistical analysis of song properties (Clark *et al.*, 1987; McIlraith and Card, 1997), cross correlations of spectra (Clark *et al.*, 1987), artificial neural networks with or without backpropagation (Ashiya and Nakagawa, 1993; McIlraith and Card, 1997), dynamic time warping (Anderson *et al.*, 1996; Kogan and Margoliash, 1998), Kohonen self-organizing maps (Somervuo, 2000), and sinusoidal modeling of syllables (Härmä, 2003).

Some researchers have attempted to describe and separate species' song according to temporal and spectral features of the acoustic signal. Typically, from the large number of features that can be extracted from bird songs, a small percentage is generally sufficient for correct classification. However, these distinguishing features are not invariant, but rather change from population to population, based on community structure (Nelson, 1989). Other variants of feature analysis include metrics to quantify song similarity (Tchernichovski *et al.*, 2000), linear discriminant functions (Fager-

[a]Current address: Institute for Pervasive Computing, ETH Zurich, Haldeneggsteig 4, 8092 Zurich, Switzerland. Electronic mail: vlad.trifa@ieee.org
[b]Electronic mail: kirschel@ucla.edu
[c]Electronic mail: taylor@biology.ucla.edu
[d]Electronic mail: vallejo@itesm.mx

lund and Härmä, 2004), and data mining (Vilches *et al.*, 2006) to identify rules for maximum discriminative power.

In the last decade, most of these efforts have benefited from progress in the field of automated speech recognition, in particular with hidden Markov models (HMMs) (Kogan and Margoliash, 1998; Kwan *et al.*, 2004; Wilde and Menon, 2003). These methods are usually more efficient than knowledge-based recognition methods, especially when used in noisy environments. This method is commonly used in automated speech recognition and is generally known to be effective for modeling time-series data (Rabiner, 1989). Vilches *et al.* (2006) presents a comparison between HMMs and Bayes classifiers where the features used had been identified by data mining for the ability to discriminate among three species of antbirds. They found that both methods performed very well, over 90% of correct classification. Data mining is a more statistically optimal method for classification, but the drawback is that it requires extensive data preparation. Most previous work used laboratory recordings, which simplifies the analysis as it increases signal-to-noise ratio (SNR), minimizing any background noise interference. In principal, HMMs have the advantage of not requiring expert human intervention for preprocessing (feature extraction) and thus can run in real-time [in Vilches *et al.* (2006), features were extracted manually], while still exhibiting comparable performance to data mining methods.

The study reported here employs HMMs to distinguish among the songs of antbirds from a tropical rainforest in Southern Mexico. The goal is to provide a standard, yet efficient, method of bird species classification that can be easily implemented, customized, and run in real-time using off-the-shelf hardware and software. In contrast with most previous work, whole songs rather than individual syllables were used in the classification. In addition, the role of several parameters of the HMM analysis was investigated, particularly the quality of data used for training and for testing, and the minimal number of samples required to train the models while ensuring sufficiently good recognition.

II. METHODS

A. Data collection and filtering

Bird songs were recorded at the Estacion Chajul in the Reserva de la Biosfera Monte Azules, in Chiapas, Mexico (approximately 16°6′44″ N and 90°56′27″ W), during June 2005 and February 2006. Recordings were made using a Sennheiser ME67/K6 directional microphone and a Marantz PMD670 digital recorder directly onto Compact Flash cards at a sample rate of 44.1 kHz and a resolution of 16 bits per sample. Recordings were collected at various distances from subjects, resulting in a high variation in SNR to replicate conditions of recordings that would be collected from remote recording devices. Full recordings were processed with a high-pass filter to remove noise in the low frequencies with the filtering function implemented within RAVEN (high-pass filter with cutoff frequency 400 Hz). Afterward, single songs were manually extracted and classified in order to provide the set of songs used for the training of the models (typical length of each song: between 2 and 3.6 s, depending on the species). Each song was initially assigned a value (A–E) to reflect the quality of the recording based on subjective estimation of its SNR, where highest quality songs were assigned an A and the poorest quality ones were assigned an E. Songs rated A, B, or C are considered as high quality, while D or E are considered too noisy. Training samples (TS) refers to the number of random samples (grades A–E) used to train the network; clean training samples (CTS) refers to only clean recordings (grades A–C) used for training. Every individual antbird song was extracted from the recordings using the RAVEN 1.3 program (Charif *et al.*, 2006), and then used for the HMM analysis as a training or test song. Such a subjective measure of the recording quality was chosen—as opposed to a quantitative SNR estimated (e.g., ratio of peak power versus noise power)—because there is interest to see how such a system could perform mainly with songs that human experimenters can discern, while discarding the ones that would be too weak to be recognized by human observers (as it is difficult to obtain any meta information about the caller, e.g., the location, species, and other individual characteristics). The real-time detection and extraction of full songs in noisy environments is not addressed in this article, therefore interested readers are invited to consult Ali *et al.* (2007) for details about how this procedure would be implemented.

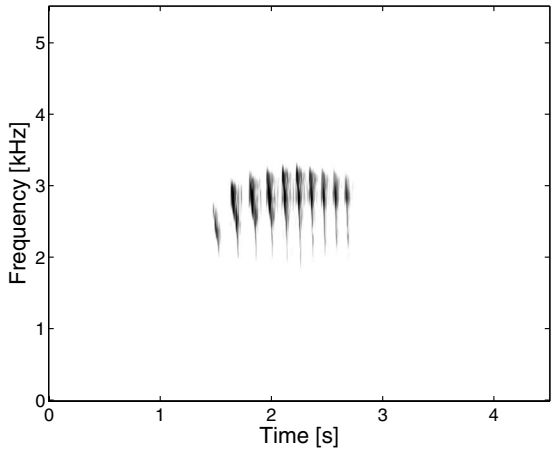

FIG. 1. Spectrograms of songs of species used in this study: Dusky Antbird (DAB) (*Cercomacra tyrannina*).

Five antbird species were included in the analysis. These are the typical antbirds (Thamnophilidae): Great Antshrike (GAS) (*Taraba major*), Barred Antshrike (BAS) (*Thamnophilus doliatus*), Dusky Antbird (DAB) (*Cercomacra tyrannina*), Dot-winged Antwren (DWAW) (*Microrhopias quixensis*), and the ground antbird (Formicariidae) Mexican Antthrush (MAT) (*Formicarius analis*). Spectrograms of the songs of these species are illustrated in Figs. 1–5.

B. Hidden Markov models

A HMM is a statistical tool that can model a discrete-time dynamical system described by a Markov process with unknown parameters. In the context discussed here a bird song can be considered as a sequence of observations produced by such a dynamical system. A simple representation

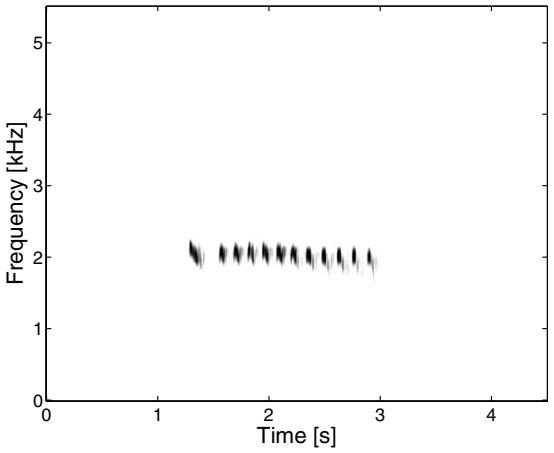

FIG. 2. Spectrogram of song from Mexican Antthrush (MAT) (*Formicarius analis*).

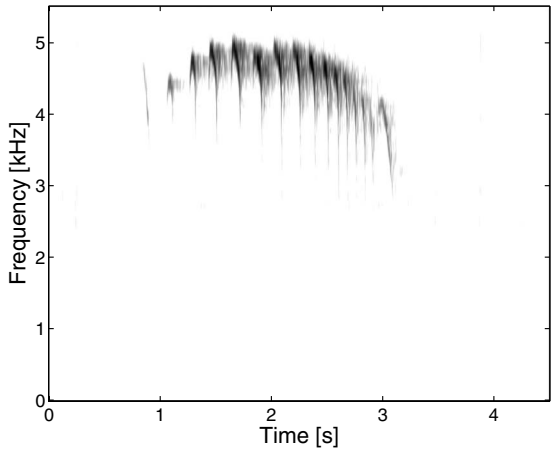

FIG. 4. Spectrogram of song from Dot-winged Antwren (DWAW) (*Microrhopias quixensis*).

where each state of this Markov process corresponds to an observable event is too restrictive to be applied to real world problems, because of the difficulty in relating the states with observable events. Accordingly, the model is extended to allow each observation to be modeled as a probabilistic function of the state. In this paradigm, the sequence of observations will not tell anything about the state sequence that generated them, because the sequence of states that produced the observation is not visible. For each bird species, a different HMM is used to model the temporal progression of the acoustic features of its species, and recognition can be done by inferring from observed data which HMM is the most likely one to produce the given sequence of observations. The challenge becomes to estimate the parameters of the HMM from sample observations (*training observation*), and then use the estimated parameters to infer the probability that a dynamical system produced a given observed sequence, so as to find the most probable sequence of unobservable states that produced the observed sequence (this sequence can be used as a classification method).

Opposed to pattern matching, the concept of knowledge-based methods requires one to analyze the signal in order to quantify a set of features at regularly spaced discrete time steps, and then compare songs based upon this information. For example, a vector of features is extracted from a signal at discrete time step (each of these vectors will be called an *observation*), and these vectors will result in a time series. Afterwards, an HMM for each class to recognize (here each class refers to a different bird species) is used to model the temporal evolution of the features of its class, and recognition is done by looking at which HMM is the most likely to produce a given sequence of observations. The ability to model such time series with subtle temporal structure makes HMMs an interesting alternative to pattern-matching methods, as HMMs are very efficient for modeling patterns of varying length.

Experimental evidence has shown that the human ear does not resolve frequencies linearly across the audio spectrum, and empirical evidence suggests that designing a front-end to operate in a similar manner typically yields better recognition performance than a simple Fourier transform. The principle of this approach, called *mel-frequency cepstral coefficients* (MFCC), is similar in principle to a Fourier transform, but the frequency bands in the MFCC filters are equally spaced in mel frequency, a linear-log function of frequency which explains the sensitivity of human pitch percep-

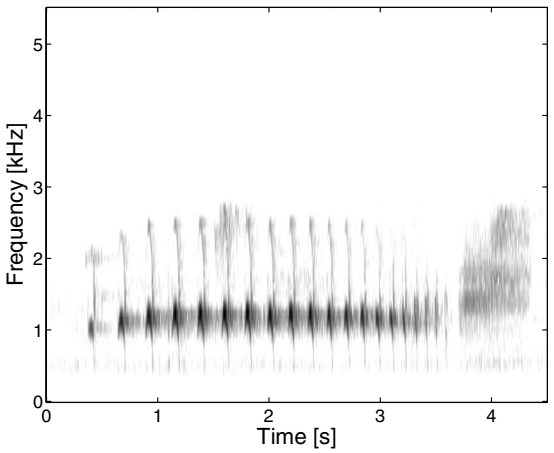

FIG. 3. Spectrogram of song from Great Antshrike (GAS) (*Taraba major*).

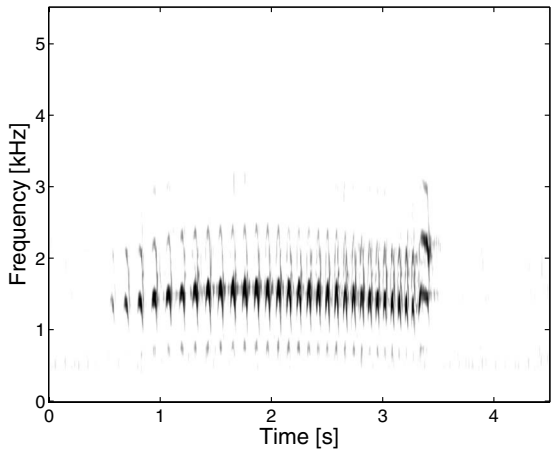

FIG. 5. Spectrogram of song from Barred Antshrike (BAS) (*Thamnophilus doliatus*).

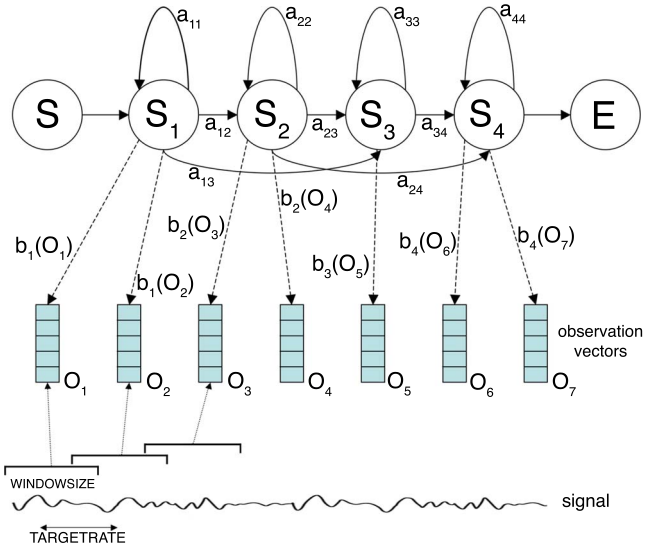

FIG. 6. (Color online) Illustration of the HMM theory. From the original acoustic signal, observation vectors (O_i) are extracted from blocks of duration WINDOWSIZE ms. The interval between two observations is TARGETRATE ms. The transition probability from state i to state j is a_{ij}, and the probability of observing a vector k while in the state i, is denoted by $b_i(O_k)$. Illustration inspired from Young *et al.* (2002).

tion. Such a filter bank can be implemented by taking the magnitude of the Fourier transformation for a window of data, and then multiplying the resulting magnitudes coefficients using triangular filters for different frequency bands. Thus, each band will contain a weighted sum representing the spectral magnitude in the corresponding particular channel.

An alternative method to generate the observation vectors from a signal is to use *linear predictive coding* (LPC), which is commonly used in communication systems. Usually, there exists a correlation between the samples in a segment of acoustic data, and the idea behind LPC is to encode an acoustic segment as a set of coefficients in a given equation that allows one to predict the value of all samples in the segment according to the preceding samples ones. The coefficients are then chosen so that they minimize the error between the actual values of the samples and the values predicted by the equation.

1. HMMs theory

Formally, a HMM is a five-tuple $(\mathbf{\Omega}_X, \mathbf{\Omega}_O, \boldsymbol{A}, \boldsymbol{B}, \boldsymbol{\pi})$, where $\mathbf{\Omega}_X = [S_1 \ldots S_N]$ is a finite set of N distinct states, while $\mathbf{\Omega}_O = [v_1 \ldots v_k]$ is the set of possible observation symbols (the alphabet of observation), where $\boldsymbol{\lambda} = (\boldsymbol{A}, \boldsymbol{B}, \boldsymbol{\pi})$ denotes the parameters of the hidden Markov chain, with $\boldsymbol{A}_{N\times N}$ the transition probabilities matrix, $\boldsymbol{B}_{N\times k}$ the probabilities of observing each symbol for each state, and $\boldsymbol{\pi}_{1\times N}$ the distribution of the initial state (see illustration Fig. 6).

The state of the system can change at discrete time steps, and the next state is defined by the matrix of transition probabilities A. The state of the system at time t is denoted q_t. The Markov chain assumption states the probability of passing from state S_i into state j at time t depends only on the current state only and not on the previous state changes, that is

$$P(q_t = S_j | q_{t-1} = S_i, q_{t-2} = S_k, \ldots) = P(q_t = S_j | q_{t-1} = S_i) = a_{ij}. \quad (1)$$

Also, this probability is considered as being independent of the time, and a_{ij} is called the state transition (from state i to state j) coefficient (A is the matrix composed of a_{ij} for all i, j), having the following properties:

$$0 \leqslant a_{ij} \leqslant 1, \quad \sum_{j=1}^{N} a_{ij} = 1. \quad (2)$$

The probability of observing a particular multidimensional configuration is modeled using Gaussian mixture models, as follows

$$b_j(O_t) = \sum_{m=1}^{M} c_{\mathrm{dim}} N(O_t; \mu_{\mathrm{dim}}, \Sigma_{\mathrm{dim}}), \quad (3)$$

where M is the number of mixtures, c_{dim} is the weight of mixture m, $N(O_t; \mu_{\mathrm{dim}}, \Sigma_{jm})$ is a Gaussian density with mean vector $\mu_{1\times P}$ and covariance matrix $\Sigma_{P\times P}$, both of same dimension as the observation vector O_t, that is P.

In practice the parameters of HMMs are unknown and have to be estimated from data during the training phase. The choices made for these parameters are determinant for performance of the model, and thus should reflect as reliably as possibly the data to be modeled.

2. The three problems of HMMs

There are three major problems to solve when using HMMs for real-world applications. The reader is invited to consult Rabiner and Juang (1993) and Rabiner (1989) for detailed explanations about mathematical description of HMMs and solutions used for each of these problems, which are presented here only for general understanding:

a. Problem 1. Given an observation sequence $\boldsymbol{O} = O_1 \ldots O_T$ and a model $\boldsymbol{\lambda} = (\boldsymbol{A}, \boldsymbol{B}, \boldsymbol{\pi})$, how to estimate the probability $P(\boldsymbol{O}|\boldsymbol{\lambda})$ that the sequence $\boldsymbol{O}$ has been produced by the model $\boldsymbol{\lambda}$? In other terms, how to score each model according to how well it matches the observation?

A straightforward solution to this problem is simply to enumerate every possible sequence of length T and compute their probability to be observed (assuming statistical independence between observations), that is

$$P(\boldsymbol{O}|\boldsymbol{Q}, \boldsymbol{\lambda}) = \prod_{t=1}^{T} P(O_t | q_t, \boldsymbol{\lambda}) = b_{q_1}(O_1) \ldots b_{q_T}(O_T). \quad (4)$$

The probability of the observation is simply a sum of this joint probability over all possible sequences of length T,

TABLE I. Average recognition performance (% of correctly classified songs) for five species of antbirds using the method MFCC_0_A_D, thus the size of the observation vector is 39. Numbers in parentheses are the standard deviation of the results over 50 trials. TS refers to the number of random samples that were to train the network (grades A–E); CTS refers to the number of clean recordings (grades A–C only). All results refer to tests against the remaining grade A–E songs.

Species	Total songs	10 TS	20 TS	50 TS	100 TS	10 CTS	50 CTS
Barred Antshrike (BAS)	360	95.2 (3.2)	96.23 (2.1)	97.7 (0.9)	97.8 (0.9)	95.3	98.4
Dusky Antbird (DAB)	1333	93.1 (3.4)	95.05 (1.83)	96.2 (1.0)	96.5 (1.0)	85.9	95.2
Dot-winged Antwren (DWAW)	237	96.3 (1.7)	96.3 (1.45)	96.8 (1.0)	97.1 (1.7)	99.5	99.5
Great Antshrike (GAS)	525	91.0 (3.6)	92.58 (2.22)	93.3 (2.3)	94.2 (1.7)	81.4	90.5
Mexican Antthrush (MAT)	913	92.5 (4.1)	93.99 (2.59)	96.3 (1.3)	96.8 (1.2)	91.3	95.6
Overall performance (%)		93.04 (1.65)	94.59 (1.04)	95.97 (0.63)	96.38 (0.51)	88.56	95.19

$$P(\boldsymbol{O}|\boldsymbol{\lambda}) = \sum_{\boldsymbol{Q}} P(\boldsymbol{O}|\boldsymbol{Q},\boldsymbol{\lambda}) \cdot P(\boldsymbol{Q}|\boldsymbol{\lambda}) = \sum_{q_1 \cdots q_T} \pi_{q_1} b_{q_1}(O_1) a_{q_1 q_2} b_{q_2}(O_2) \ldots a_{q_{T-1} q_T} b_{q_T}(O_T). \quad (5)$$

However, using Eq. (5) to compute $P(\boldsymbol{O}|\boldsymbol{\lambda})$ is not feasible in practice, as the computational complexity of this procedure is far too big to be useful, so much more efficient methods to compute this value have been proposed.

b. Problem 2. Given an observation $\boldsymbol{O}$ and a model $\boldsymbol{\lambda}$, how to choose the "correct" state sequence $\boldsymbol{Q}=q_1 \ldots q_T$ that best explains the observation $\boldsymbol{O}$? Here, the problem is to attempt to discover the hidden part of the model.

c. Problem 3. How to adjust the model parameters $\boldsymbol{\lambda}$ in order to maximize $P(\boldsymbol{O}|\boldsymbol{\lambda})$? This is a crucial aspect of HMMs as it is the training procedure, i.e., adapt the parameters of $\boldsymbol{\lambda}$ to fit optimally each of the samples of the training data set.

C. Hidden Markov model toolkit (HTK)

As described in Young *et al.* (2002), HTK is a package of libraries and tools written with the C programming language that provides sophisticated facilities for designing, training, and testing of HMMs, as well as analyzing the results. HTK has been chosen in this project as it is one of the most common and flexible implementation of HMMs and has been successfully applied in many automatic speech recognition applications. Also, the source code is freely available, thus HTK could be compiled and run on customized embedded computers.

D. Model parameters

The experiments presented used two standard feature extraction methods proposed by HTK, MFCC, and LPC were used. Observations are extracted from a segment of the signal of length WINDOWSIZE, and a segment is extracted every TARGETRATE.

To improve the recognition performance, one can add to the coefficients generated using MFCC or LPC, other information extracted from the signals, and some of these terms were also investigated here. These were: the logarithm of the signal energy (_E), the first-order regression coefficients (the rate of change) of the basic static parameters (the LPC/MFCC coefficients) between two consecutive time frames, (delta coefficients _D), and second-order regression coefficients (the second time derivative, acceleration _A), and the zeroth-order cepstral coefficient (_0). The other parameters are set to HTK default values (the filterbank has 26 channels and 12 MFCC coefficients are output, LPC order is 12).

Practical use of HMMs is still an art, as much as it is a science. One of the difficulties in using HMMs is that the procedure requires parameters for which there is no algorithm to obtain an optimal value based on the data at hand. From pilot studies, the following settings were found to best represent the data: WINDOWSIZE=25 ms and TARGETRATE =15 ms. If the songs differ greatly in length across species, then increasing the state length (increase the TARGETRATE parameter, so a state is responsible for a longer segment of the song) should be considered. The resulting state transition probabilities will be more different across models, resulting in less ambiguous recognition. The number of states was set to 5, based on the simplicity of antbird songs. More complex songs would be expected to require models with a higher number of states.

E. Experimental design

The number of songs recorded for each species varied from 237 for Dot-winged Antwrens to 1333 for Dusky Antbird (see Table I). The files were selected so as to contain very different amounts of background noise and highly variable song lengths, thus providing a realistic environment for testing the system. Unless otherwise noted, features were extracted using the method MFCC_0_A_D. Several HMMs design issues were investigated:

1. Number of training samples

HMMs were trained with 10, 20, 50, and 100 samples (TS) to test the relative performance of training set size. In each case, 50 recognition trials were performed. For each test there was a random repartition of the song samples into training and testing sets, with no overlap between the two.

2. Quality of training and testing samples

The effects of sample quality were investigated by using one set of 50 songs with high quality recordings. First, HMM performance was measured with these clean training samples (CTS), 10 samples for training and 40 for testing. In a second set of experiments, HMM performance was measured again, but this time using 10 and 50 CTS for training, and all the remaining A–E quality songs for testing.

3. Feature extraction methods

The performance of two different song feature extraction methods, MFCC and LPC, was investigated in order to determine which one was best for each species. Optional MFCC features included: Energy (E), Delta coefficients (D), Acceleration (A), and zeroth order (0).

4. Frequency range and number of states

The role of frequency range was addressed in a final series of experiments. In one set of experiments, features were extracted over the entire frequency range of the recording, while in another set features were extracted only in the frequency range [800–4000] Hz. The experiment was run 50 times using the method MFCC_E_D_A, with WINDOWSIZE =25 ms and TARGETRATE=15 ms, with 50 TS and the remaining samples for testing. The set of tests was repeated, this time varying the number of states in the Markov model, from 5 to 15 states.

III. RESULTS

In this section a brief summary of the obtained results is presented to illustrate several aspects of HTK for bird species recognition.

A. Number and quality of training samples

The percentage of calls correctly identified to species was almost perfect (99.5% overall recognition) when only clean recordings (grades A–C) were used for both training and testing, and only one song out of 200 test samples was misidentified even though only 10 samples per species have been used to train the models. Performance decreased slightly when the testing set included calls of all grades A–E, though recognition was still typically quite high, as seen in Fig. 7 and Table I. For both training sets, performance increased when more training samples were used, though not linearly. Looking first at the TS training sets, recognition was most successful with 100 training files (96.38% overall recognition), but was still high (93.04% overall) with just 10 training files per species. It appears that the standard deviation of performance decreased when more training sets were used, probably because more training samples captured a better approximation of the background noise. The results are substantially the same for all species, but different feature extraction methods are more appropriate for some species and less for others, suggesting that antbirds might use different features to convey information, though many more testing samples would be required to statistically test this idea.

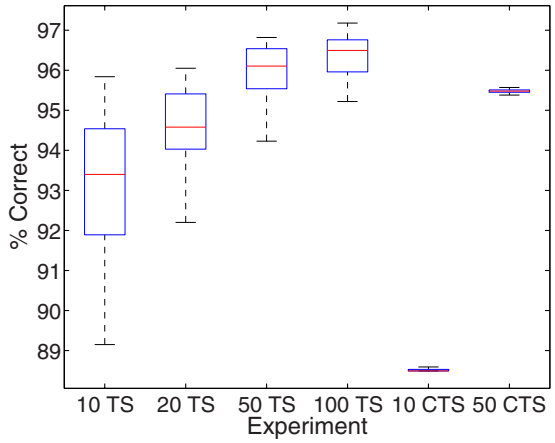

FIG. 7. (Color online) Recognition performance averaged across all species, with variable numbers of training samples. The box has lines at the lower quartile, median, and upper quartile values. The lines extending from each end of the box show the extent of the rest of the data.

Concerning the CTS training set, the overall performance was slightly lower when a large training set (50 songs per species) was used, but poorest overall (89%) with a small (10 CTS) training set. This suggests that recognition performance is highly related with the amount of background noise in the set used for training, and that data with various amounts and nature of noise during training permitted better generalization, and subsequently had better performance when tested in real environments. The standard deviation of performance in these cases is quite small because the same training data were used in every test, and a high proportion of the test songs were used in all tests, resulting in only a few independent tests.

B. Feature extraction, frequency range, and number of states

The different MFCC feature extraction methods did not differ appreciably in performance, though LPC was substantially poorer for all species (see Table II).

Given that noise affects the recognition performance, as seen in the difference between the TS and CTS trials, band-limiting is often useful to reject unwanted frequencies or avoid allocating filters to frequency regions in which there is no useful signal energy. This limitation is actually used by the MFCC method, where the frequency bands are distrib-

TABLE II. Effects of varying parameters in HTK for species recognition. The models were trained using 10 CTS. The characters after the underscore are optional features for HMM recognition: E stands for energy, D stands for delta coefficients, 0 for zeroth-order coefficients, and A stands for acceleration (the reader is invited to refer to the text for more information about the optional features).

Species	Total songs	MFCC	MFCC_E	MFCC_E_D	MFCC_0_A_D	MFCC_E_D_A	LPC
Barred Antshrike (BAS)	360	96.20	95.31	95.61	95.30	97.94	47.53
Dusky Antbird (DAB)	1333	92.76	88.12	93.68	85.84	87.98	45.28
Dot-winged Antwren (DWAW)	237	96.33	95.87	100.00	99.54	97.26	35.79
Great Antshrike (GAS)	525	80.04	74.69	82.41	81.23	77.47	28.25
Mexican Antthrush (MAT)	913	90.49	92.18	90.17	91.28	91.72	38.37
Overall performance (%)		90.78	88.42	91.60	88.50	89.03	40.37

uted only across a restricted range, instead of whole frequencies between 0 Hz up to the Nyquist frequency. As expected, the performance of the system is significantly superior when the frequency range is bounded according to the spectrum of the bird under consideration; the reason is that the noise located outside this frequency range is not taken into account by the HMMs. An average performance of 88.4% was observed when the frequency range was unrestricted, and 95.5% when the frequency was limited to the range [800–4000] Hz.

Overall performance decreased when the number of states was varied between 5 and 15 states. When 20 TS are used, performance dropped from 94.6% to 82.5%, when using six states instead of five. Adding more than 15 states degraded the performance strongly. One explanation would be that the addition of more states degrades performance because it increases the number of parameters to be estimated, thereby increasing the number of training samples that are required to obtain good generalization properties.

IV. DISCUSSION

The results presented earlier suggest that hidden Markov models are an effective method for discriminating bird species using vocalizations recorded in the field. Correct classification was superior to 95% in several experiments reported here, with 50 training samples used to discriminate between the songs of five antbird species in the tropical rainforest. When only songs with a high SNR (which is still low in comparison with laboratory recordings due to considerable ambient noise present in rainforest) were used for training and testing, only one song out of 200 was misidentified. This indicates the potential of using these methods to differentiate signals, even where noise is prevalent.

Because bird songs are modeled as a time series when using HMMs—unlike with pattern-matching methods, the length of the songs can vary without significantly affecting the recognition performance. In a Markov chain, every single observation is assumed to be statistically independent from the previous ones. Even if this is rarely the case with real signals such as bird songs or human speech, the performance was observed to be reasonably high.

Performance could be improved by developing methods to increase SNR. Recent progress in acoustic source localization using in microphone arrays allows one to implement beamforming algorithms that can enhance the quality of a signal coming from a particular direction. Approximate maximum likelihood methods that can localize antbird songs quite accurately have been developed, and experiments where beamforming is used to efficiently separate the songs of two distinct sources recorded simultaneously are presented in Chen *et al.* (2006).

HMM methods have been developed largely for understanding human speech. As a result, the most widely used software packages, such as HTK, are optimized for that application, rather than for bird songs. One example of this was observed in the experiments reported here, where LPC feature extraction performed poorly compared to MFCC. Kogan and Margoliash (1998) pointed out that LPC is appropriate to model quasilinear signals such as human voice. Such linear parametrizations do not have the ability to efficiently represent sharp transitions and other nonlinearities commonly present in bird songs. Nelson (1989) demonstrated that the dominant frequency of a call is one of the most efficient acoustic cues used by animals to convey individual information. In contrast to linear prediction coefficients, it is more likely for a bird brain to process and extract frequency information from a signal. It is possible then, that HMM models that are optimized for bird vocalizations might lead to an improved performance, for example by using specific feature extraction methods based on information gathered with data mining methods.

The methods described here were kept consistent across the five species, despite differences in signal structure. One might increase performance by introducing separate bandpass filters for every training and test signal for each species. One might also increase performance by introducing specific feature analyses that aid in species recognition from data mining methods (e.g., Vilches *et al.*, 2006). However, to run such a method in real time, it would be necessary to run the tests sequentially for one species at a time, and this for every species. In practice, the computational demands would certainly become overwhelming as the number of considered species increases.

HMMs do have certain limitations. Special care must be taken when preparing and choosing the training samples in order to obtain a high generalization ability. Performance was comparable when using 50 and 100 training samples with five antbird species, but many more samples would be required for discriminating between signals that are more similar, and particularly between songs of different individuals of the same species. Nonetheless, this method has been successfully used to identify different individuals of acorn woodpeckers.

Detecting each species occurring within a community appears to be an achievable goal. The focus in this article has been on classification. An automated species recognition system would also require event detection from streaming data with a classification system. Event detection algorithms have been developed recently using energy and entropy as the identifying criterion, e.g., (Ali *et al.*, 2007; Trifa, 2006, 2007), with varying success rates. Detected events are then sent to HTK for classification and species presence, and performance of this fully automated procedure using raw field recordings lasting several hours can be ascertained.

Combining sensor network technology with effective event detection and species identification algorithms can allow for observation of species interactions at a finer spatial and temporal scale than previously possible. Analysis of animal behavior through unattended real-time tracking of individuals and recording of large amounts of data with remote devices has become a realistic goal.

ACKNOWLEDGMENTS

This research was supported by the National Science Foundation under Award No. 0410438. The authors would like to thank Edward Stabler, Yuan Yao, Yoosook Lee, Ying

Lin, and Ansgar Koene for their help and valuable comments on this paper. We also thank Martin Cody for his help with the field collections, Robert Walsh for his able assistance with the recordings, and the people of Estacion Chajul for their hospitality while we were collecting the data.

Ali, A. M., Yao, K., Collier, T. C., Taylor, C. E., Blumstein, D. T., and Girod, L. (**2007**). "An empirical study of collaborative acoustic source localization," in *Proceedings of the Sixth International Conference on Information Processing in Sensor Networks*, Cambridge, MA (ACM, New York), pp. 41–50.

Anderson, S. E., Dave, A. S., and Margoliash, D. (**1996**). "Template-based automatic recognition of birdsong syllables from continuous recordings," J. Acoust. Soc. Am. **100**, 1209–1219.

Ashiya, T., and Nakagawa, M. (**1993**). "A proposal of a recognition system for the species of birds receiving bird calls—An application of recognition systems for environmental sound," IEICE Trans. Fundamentals **E76-A**, 1858–1860.

Blumstein, D. T., and Munos, O. (**2005**). "Individual, age and sex specific information is contained in yellow-bellied marmot alarm calls," Anim. Behav. **69**, 353–361.

Catchpole, C. K., and Slater, P. J. B. (**1995**). *Bird Song: Biological Themes and Variations* (Cambridge University Press, New York).

Charif, R. A., Clark, C. W., and Fristrup, K. M. (**2006**). "Raven 1.3 user's manual," Technical Report, Cornell Laboratory of Ornithology, Ithaca, NY.

Chen, C., Ali, A., Wang, H., Asgari, S., Park, H., Hudson, R., Yao, K., and Taylor, C. E. (**2006**). "Design and testing of robust acoustic arrays for localization and beamforming," in *IEEE Proceedings of the Sixth International Conference on Information Processing in Sensor Networks*, Cambridge, MA.

Chesmore, D. (**2004**). "Automated bioacoustic identification of species," An. Acad. Bras. Cienc. **76**, 435–440.

Clark, C., Marler, P., and Beeman, K. (**1987**). "Quantitative analysis of animal vocal phonology: An application to swamp sparrow sound," Ethology **76**, 101–115.

Fagerlund, S. (**2004**). "Automatic recognition of bird species by their sounds," Master's thesis, Helsinki University of Technology, Helsinki, Finland.

Fagerlund, S., and Härmä, A. (**2004**). "Parametrization of inharmonic bird sounds for automatic recognition," in 13th European Signal Processing Conference, Antalya, Turkey, September 4–8, 2005.

Härmä, A. (**2003**). "Automatic identification of bird species based on sinusoidal modeling of syllables," in IEEE International Conference on Acoustics, Speech, Signal Processing (ICASSP 2003), April 6–10, Hong Kong, China.

Kogan, J. A., and Margoliash, D. (**1998**). "Automated recognition of bird song elements from continuous recordings using dynamic time warping and hidden Markov models: A comparative study," J. Acoust. Soc. Am. **103**, 2185–2196.

Kwan, C., Mei, G., Zhao, X., Ren, Z., Xu, R., Stanford, V., Rochet, C., Aube, J., and Ho, K. (**2004**). "Bird classification algorithms: Theory and experiemental results," in Acoustic, Speech, and Signal Processing, 2004 Proceedings, IEEE International Conference, Montreal, Canada, May 2004.

McIlraith, A. L., and Card, H. C. (**1997**). "Birdsong recognition using backpropagation and multivariate statistics," IEEE Trans. Signal Process. **45**, 2740–2748.

Nelson, D. A. (**1989**). "The importance of invariant and distinctive features in species recognition of bird song," Condor **91**, 120–130.

Rabiner, L. E. (**1989**). "A tutorial on hidden Markov models and selected applications in speech recognition," in Proc. IEEE **77**, 257-286.

Rabiner, L. E., and Juang, B.-H. (**1993**). *Fundamentals of Speech Recognition* (Prentice Hall, Englewood Cliffs, NJ).

Scheifele, P. M., Andrew, S., Cooper, R. A., Darre, M., Musiek, F. E., and Max, L. (**2005**). "Indication of a Lombard vocal response in the St. Lawrence River beluga," J. Acoust. Soc. Am. **117**, 1486–1492.

Sczewczyk, R. E., Osterweil, J., Pllastre, M., Hamilton, M., Mainwaring, A., and Estrin, D. (**2004**). "Habitat monitoring with sensor networks," Commun. ACM **47**, 34–40.

Somervuo, P. (**2000**). "Self-organizing maps for signal and symbol sequences," Ph.D. thesis, Helsinki University of Technology, Helsinki, Finland.

Tchernichovski, O., Nottebohm, F., Ho, C. E., Pesaran, B., and Mitra, P. P. (**2000**). "A procedure for an automated measurement of song similarity," Anim. Behav. **59**, 1167–1176.

Trifa, V. (**2006**). "A framework for bird songs detection, recognition and localization using acoustic sensor networks," Master's thesis, University of California Los Angeles and École Polytechnique Fédérale de Lausanne.

Trifa, V., Girod, L., Collier, T., Blumstein, D., and Taylor, C. (**2007**). "Automated wildlife monitoring using self-configuring sensor networks deployed in natural habitats," in *Proceedings of the International Symposium on Artificial Life and Robotics (AROB 12th 2007)*, Beppu, Japan.

Vilches, E., Escobar, I. A., Vallejo, E. E., and Taylor, C. E. (**2006**). "Data mining applied to acoustic bird species recognition," in 18th International Conference on Pattern Recognition (ICPR 2006), 20–24 August, Hong Kong, China.

Wilde, M., and Menon, V. (**2003**). "Bird call recognition using hidden Markov models," Technical Report, EECS Department, Tulane University.

Young, S., Kershaw, D., Odell, J., Ollason, D., Valtchev, V., and Woodland, P. (**2002**). "HTK Book 3.2.1," Cambridge University Engineering Department.

Erratum: "Impact of ocean variability on coherent underwater acoustic communications during the Kaual experiment (KauaiEx)" [J. Acoust. Soc. Am. 123 (2), 856–865 (2008)]

Aijun Song and Mohsen Badiey
College of Marine and Earth Studies, University of Delaware, 114 Robinson Hall, Newark, Delaware 19716

H. C. Song and William S. Hodgkiss
Marine Physical Laboratory, Scripps Institution of Oceanography, La Jolla, California 92093-0238

Michael B. Porter and the KauaiEx Group
Heat, Light, & Sound Research Inc., 3366 North Torrey Pines Court, Suite 310, La Jolla, California 92037

(Received 6 September 2007; revised 15 November 2007; accepted 24 November 2007)
[DOI: 10.1121/1.2897041]

PACS number(s): 43.60.Dh, 43.60.Gk, 43.60.Fg, 43.60.Mn, 43.10.Vx

There is a publisher's error in the title of this paper. The word "Kauai" is spelled incorrectly. The correct title is "Impact of ocean variability on coherent underwater acoustic communications during the Kauai experiment (KauaiEx)".

 0001-4966/2008/123(4)/2432/1/$23.00 © 2008 Acoustical Society of America

Erratum: “Phoneme representation and classification in primary auditory cortex” [J. Acoust. Soc. Am. 123 (2), 899–909 (2008)]

Nima Mesgarani, Stephen V. David, Jonathan B. Fritz, and Shihab A. Shamma
Electrical and Computer Engineering & Institute for Systems Research, University of Maryland, College Park, Maryland 20742

(Received 5 June 2007; revised 15 October 2007; accepted 30 October 2007)
[DOI: 10.1121/1.2907536]

PACS number(s): 43.64.Sj, 43.71.Qr, 43.10.Vx

There is a publisher’s error in Figure 2 of this paper. The errors are: 1) the text in the box to the right of Section B.I is incorrect, and 2) the title panel B.II should be “Scale-Rate” and not “Rate-Scale”.

The online version of the article has been corrected and the correct Figure 2 and its caption are printed below.

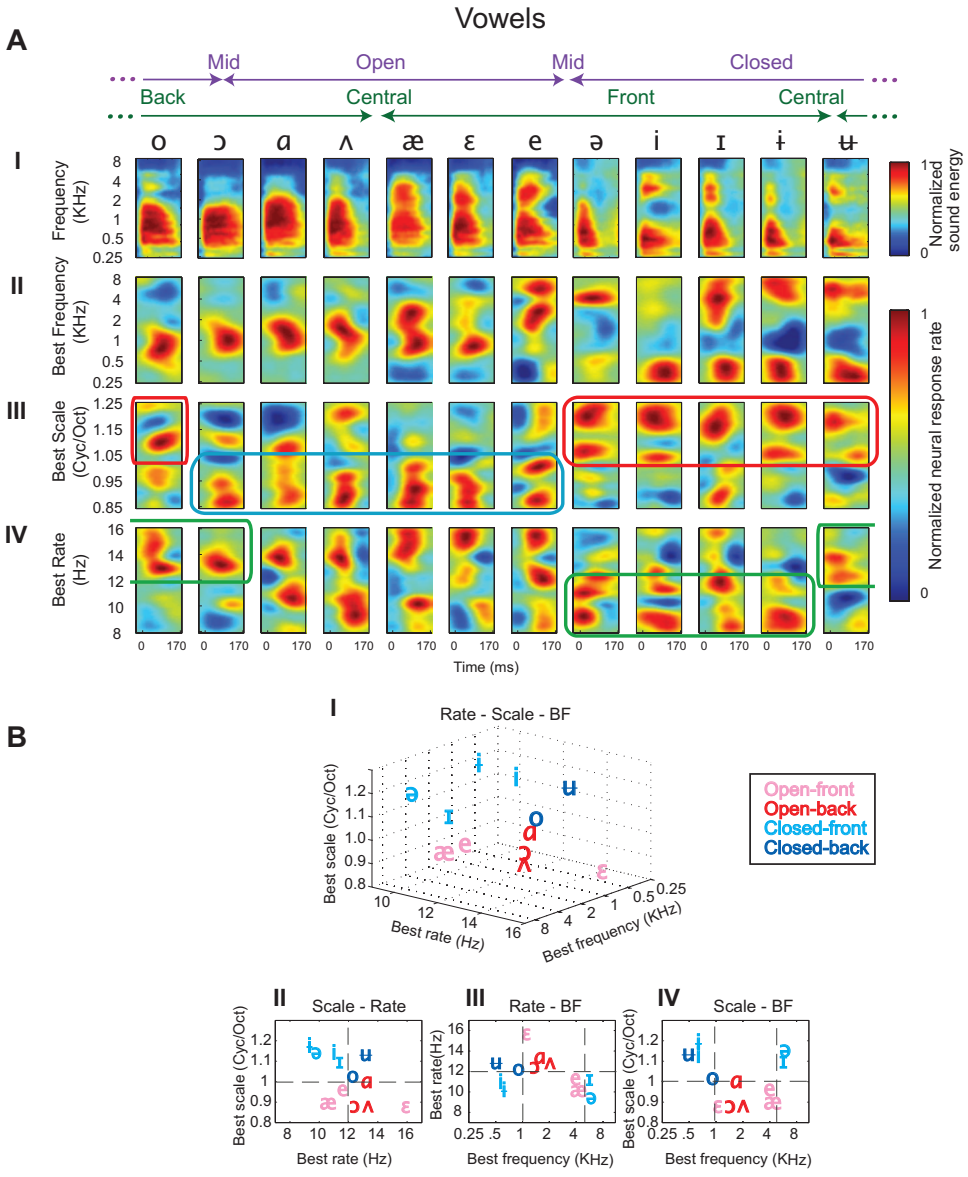

FIG. 2. Population response to vowels. (A) I. Average auditory spectrogram of 12 vowels organized approximately according to their open-closed and front-back articulatory features. The arrows at top indicate the *degree* of these features, with arrow “tips” representing minima (mid or central) and midpoints representing maxima. For example /ʌ/ is maximally open, but is neutral (central) on the front/back axis. Note also that the axes are presumed to loop around the page from right to left (dashed ends joining) creating a circular representation (II, III, IV): Average PSTH responses of 90 neurons to each vowel. Within each heat map, each row indicates the average response of a single neuron to the corresponding phoneme. Red regions indicate strong responses, and blue regions indicate weak responses. The average PSTH responses are sorted by neurons’ best frequency (II), best scale (III) and best rate (IV) to emphasize the role of that parameter in the encoding of each vowel. (Details of the analysis and generation of these plots are given in Sec. II). (B) I. Each vowel is plotted at the centroid frequency, rate and scale of its average neuronal population response. The centroid values are calculated from the average PSTH responses sorted by the corresponding parameter (2A). “Open” vowels are shown in red, “Closed” vowels in blue, “Front” vowels with *light* font and “Back” vowels with *dark*. To visualize the contribution of each tuning property to vowel discrimination, the location of each vowel is also shown collapsed in 2–D plots of (II) scale-rate, (III) rate-BF and (IV) scale-BF. All other details of the analysis and generation of these plots are given in Sec. II (Experimental Procedures).

 0001-4966/2008/123(4)/2433/1/$23.00 © 2008 Acoustical Society of America